

SPRINGER
REFERENCE

Yashwant R. Mahajan
Roy Johnson
Editors

Handbook of Advanced Ceramics and Composites

Defense, Security, Aerospace
and Energy Applications

 Springer

Handbook of Advanced Ceramics and Composites

Yashwant R. Mahajan • Roy Johnson
Editors

Handbook of Advanced Ceramics and Composites

Defense, Security, Aerospace and
Energy Applications

With 723 Figures and 155 Tables

 Springer

Editors

Yashwant R. Mahajan
International Advanced Research Centre
for Powder Metallurgy and New
Materials (ARCI)
Balapur, Hyderabad, India

Roy Johnson
International Advanced Research Centre for
Powder Metallurgy and New Materials (ARCI)
Balapur, Hyderabad, India

ISBN 978-3-030-16346-4 ISBN 978-3-030-16347-1 (eBook)
ISBN 978-3-030-16348-8 (print and electronic bundle)
<https://doi.org/10.1007/978-3-030-16347-1>

© Springer Nature Switzerland AG 2020

This work is subject to copyright. All rights are reserved by the Publisher, whether the whole or part of the material is concerned, specifically the rights of translation, reprinting, reuse of illustrations, recitation, broadcasting, reproduction on microfilms or in any other physical way, and transmission or information storage and retrieval, electronic adaptation, computer software, or by similar or dissimilar methodology now known or hereafter developed.

The use of general descriptive names, registered names, trademarks, service marks, etc. in this publication does not imply, even in the absence of a specific statement, that such names are exempt from the relevant protective laws and regulations and therefore free for general use.

The publisher, the authors, and the editors are safe to assume that the advice and information in this book are believed to be true and accurate at the date of publication. Neither the publisher nor the authors or the editors give a warranty, expressed or implied, with respect to the material contained herein or for any errors or omissions that may have been made. The publisher remains neutral with regard to jurisdictional claims in published maps and institutional affiliations.

This Springer imprint is published by the registered company Springer Nature Switzerland AG.
The registered company address is: Gewerbestrasse 11, 6330 Cham, Switzerland

Preface

Advanced ceramics and composites containing ceramics either in the form of matrix or reinforcement (e.g., monolithic ceramics, CMCs, MMCs, PMCs, hybrid composites, porous ceramics, etc.) have recently emerged as high-performance functional and structural materials. They find applications in strategic areas such as defense, aerospace, security, and energy. The editors believe that this book is comprehensive and unique with a wide range of coverage on relevant and emerging topics. Excellent reviews on various topics have been contributed by leading researchers from India and abroad. The primary motivation for compiling this book is to bring out a coherent portrayal of the wide span of up-to-date status of advanced materials from leading research groups working in the sectors of defense, security, aerospace, and sustainable and nuclear energy. The topics have been judiciously selected by the editors on the basis of their vast experience in the relevant fields. Contributors were advised to design their manuscripts on recent technological advances particularly addressing the challenges and innovations, which conveys the vital information to arrive at the research directions for the benefit of the users of the book.

The book is structured into eight parts which involve ceramic materials for defense applications, ceramic materials for ballistic armor applications, transparent and optical ceramics for defense and aerospace, advanced ceramics and CMCs for nuclear applications, ceramics CMCs and PMCs for aeronautics and space applications, intermediate and very high temperature ceramics materials, materials for sustainable energy applications, and ceramics coatings and their critical applications.

We have made an attempt that the book is a blend of underlying technology development in various paradigms. We do hope that this book will immensely benefit experts in their specific fields ranging from defense to security to aerospace and energy who wish to have an overview of the related disciplines, as the book provides extensive coverage of the broad spectrum of relevant subjects.

The editors are indebted to numerous individuals and institutions in India and abroad in many ways.

We are extremely thankful to the authors for sparing their valuable time to contribute to this book. We are especially thankful to the Section Editors for their dedicated efforts in critically reviewing the manuscripts pertaining to their domains of expertise.

One of the editors (YRM) is particularly grateful to Ms. Anita Lekhwani, Executive Editor, Springer Nature, who initiated this book project and for her encouragement and suggestions given from time to time.

The editors profusely thank Ms. Shruti Datt, Associate Editor, Springer Nature, and Ms. Sonal Nagpal, Consultant, Springer Nature, for meticulously managing the overall activities of the project and interfacing with the authors at various stages of this endeavor.

Last but not least, our special thanks go to Ms. Raasika Dhandapani, Project Manager, SPi Global, for copyediting, typesetting, verifying necessary permissions, etc., during the production of manuscripts.

August 2020
Hyderabad, India

Yashwant R. Mahajan
Roy Johnson

Contents

Volume 1

Part I Ceramic Materials for Defense Applications	1
1 Manifestations of Nanomaterials in Development of Advanced Sensors for Defense Applications	3
Rohini Kitture and Sangeeta Kale	
2 Nanocrystalline PNS-PZT-Based Energy Harvester for Strategic Applications	35
H. H. Kumar, C. M. Lonkar, and Balasubramanian Kandasubramanian	
3 2D-Nanolayered Tungsten and Molybdenum Disulfides: Structure, Properties, Synthesis, and Processing for Strategic Applications	75
Harish Kumar Adigilli, A. K. Pandey, and Joydip Joardar	
4 Nanoporous Aerogels for Defense and Aerospace Applications ...	121
Neha Hebalkar, Keerthi Sanghamitra Kollipara, Yamini Ananthan, and Murali Krishna Sudha	
5 Microwave Materials for Defense and Aerospace Applications ...	165
J. Varghese, N. Joseph, H. Jantunen, S. K. Behera, H. T. Kim, and M. T. Sebastian	
6 Development of PLZT Electroceramics with Ultrahigh Piezoelectric Properties by a Novel Material Engineering Approach	215
A. R. James and Ajeet Kumar	
7 Slip-Cast Fused Silica Radomes for Hypervelocity Vehicles: Advantages, Challenges, and Fabrication Techniques	251
Ibram Ganesh and Yashwant Ramchandra Mahajan	

8 Patent Trends in Additive Manufacturing of Ceramic Materials	319
Priya Anish Mathews, Swati Koonisetty, Sanjay Bhardwaj, Papiya Biswas, Roy Johnson, and G. Padmanabham	
Part II Ceramic Materials for Ballistic Armor Applications	355
9 Ceramic Composite Armour for Ballistic Protection	357
P. Rama Subba Reddy, S. Geasin Savio, and Vemuri Madhu	
10 Multilayered Ceramic-Composites for Armour Applications	403
Kiran Akella	
11 Transparent Ceramics for Ballistic Armor Applications	435
Senthil Kumar Rajendran, Papiya Biswas, Roy Johnson, and Yashwant Ramchandra Mahajan	
Part III Transparent and Optical Ceramics for Defense and Aerospace	459
12 Transparent and Machinable Glass-Ceramics	461
Himadri Sekhar Maiti	
13 Processing of Infrared Transparent Magnesium Aluminate Spinel	495
Papiya Biswas, Roy Johnson, Yashwant Ramchandra Mahajan, and G. Padmanabham	
14 Zinc Sulfide Ceramics for Infrared Optics	533
Roy Johnson, Papiya Biswas, Pandu Ramavath, and Yashwant Ramchandra Mahajan	
15 Advances in Nano-finishing of Optical Glasses and Glass Ceramics	569
Mahender Kumar Gupta, I. Abdul Rasheed, and M. Buchi Suresh	
16 Electric Field/Current-Assisted Sintering of Optical Ceramics ...	601
Hidehiro Yoshida	
Part IV Advanced Ceramics and CMCs for Nuclear Applications	639
17 Advanced SiC-SiC Composites for Nuclear Application	641
Tetsuji Noda	
18 Advanced Ceramic Fuels for Sodium-Cooled Fast Reactors	667
Baldev Raj, P. R. Vasudeva Rao, P. Puthiyavinayagam, and K. Ananthasivan	

19	Boron-Based Ceramics and Composites for Nuclear and Space Applications: Synthesis and Consolidation	703
	Tammana S. R. C. Murthy, J. K. Sonber, K. Sairam, Sanjib Majumdar, and Vivekanand Kain	
20	Novel Inorganic Compound Based Sensors for Their Application in Nuclear Energy Programs	739
	V. Jayaraman and T. Gnanasekaran	
21	Processing of Barium Zinc Tantalate (BZT) Microwave Dielectric Ceramics for RF Window Application in Fusion Reactor	793
	Swathi Manivannan and Dibakar Das	

Volume 2

Part V	Ceramics, CMCs, and PMCs for Aeronautics and Space Applications	829
22	SiC-Based Composites Through Liquid Infiltration Routes	831
	Suresh Kumar, Ashok Ranjan, L. M. Manocha, and N. Eswara Prasad	
23	Carbon Fiber Reinforced Silicon Carbide Ceramic Matrix Composites	877
	Andi Udayakumar, M. Rizvan Basha, Sarabjit Singh, Sweety Kumari, and V. V. Bhanu Prasad	
24	Development of Polycarbosilane (PCS) Polymer and PCS-Derived SiC Fibers and Their Composites	913
	Rakesh Kumar Gupta, Raghvesh Mishra, Suresh Kumar, Ashok Ranjan, L. M. Manocha, and N. Eswara Prasad	
25	Development of Carbon Nanotube-Reinforced Ceramic Matrix Nanocomposites for Advanced Structural Applications ...	929
	Luv Gurnani and Amartya Mukhopadhyay	
26	Polymer-Derived Ceramics and Their Space Applications	975
	S. Packirisamy, K. J. Sreejith, Deepa Devapal, and B. Swaminathan	
27	PZT and Lead-Free Piezo Ceramics for Aerospace and Energy Applications	1081
	P. K. Panda and B. Sahoo	
28	Processing of Ceramic Foams for Thermal Protection	1105
	Sujith Vijayan, Praveen Wilson, and Kuttan Prabhakaran	
29	Silicon Carbide-Based Lightweight Mirror Blanks for Space Optics Applications	1135
	Dulal Chandra Jana and Bhaskar Prasad Saha	

Part VI Intermediate and Very High Temperature Ceramic	1165
30 Silicides and Silicide Matrix Composites for High-Temperature Structural Applications	1167
R. Mitra	
31 High-Temperature Environmental Degradation Behavior of Ultrahigh-Temperature Ceramic Composites	1221
R. Mitra, M. Mallik, and Sunil Kashyap	
Part VII Materials for Sustainable Energy Applications	1257
32 Hybrid Supercapacitor-Battery Energy Storage	1259
Mainul Akhtar and S. B. Majumder	
33 Recent Developments in Electrode Materials for Lithium-Ion Batteries for Energy Storage Application	1297
Moodakare B. Sahana and Raghavan Gopalan	
34 Nano-configured Opto-electric Ceramic Systems for Photo-electrochemical Hydrogen Energy	1335
Pramod H. Borse	
Part VIII Ceramic Coatings and Their Processes for Critical Applications	1369
35 New-Generation Ceramic Coatings for High-Temperature Applications by Liquid Feedstock Plasma Spraying	1371
S. Joshi, N. Markocsan, P. Nylén, and G. Sivakumar	
36 Multifunctional Sol-Gel Nanocomposite Coatings for Aerospace, Energy, and Strategic Applications: Challenges and Perspectives	1413
R. Subasri and K. R. C. Soma Raju	
37 Materials Aspects of Thermal Barrier Coatings	1443
Ashutosh S. Gandhi	
38 Processing of Ceramic and Cermet Composite Coatings for Strategic and Aerospace Applications	1465
L. Rama Krishna, P. Suresh Babu, Manish Tak, D. Srinivasa Rao, G. Padmanabham, and G. Sundararajan	
Index	1527

About the Editors



Dr. Yashwant R. Mahajan is presently working as a Technical Advisor at International Advanced Research Centre for Powder Metallurgy and New Materials (ARCI), Hyderabad, India. He obtained his Ph.D. degree in Physical Metallurgy in 1978 from Polytechnic Institute of Brooklyn, New York. Dr. Mahajan carried out his postdoctoral research in the areas of titanium base alloys, powder metallurgy, and high temperature dispersion strengthened aluminum base alloys at the Air Force Materials Laboratory, Wright Patterson Air Force Base, Ohio, for 4 years. He has worked in various capacities, namely, Scientist/Joint Director at the Defence Metallurgical Research Laboratory, ARCI, and Defence Research and Development Laboratory, Hyderabad, India, and Hindustan Aeronautics Ltd., Bangalore, India. Dr. Mahajan made major contributions in the areas of MMCs, advanced ceramics, and CMCs. Under his leadership, a number of ceramic-based technologies were developed and transferred to the industry. He has published more than 130 technical papers in peer-reviewed journals and conference proceedings and holds 13 patents (including 2 US). Dr. Mahajan is a recipient of NRC Associateship of National Academy of Sciences, USA, the best metallurgist of the year award (IIM), MRSI Medal, MRSI-IISC superconductivity award, and VASVIK Medal. He is a professional member of ASM International, TMS, MRS-USA, SPIE-USA, Institute of Materials-UK, American Ceramic Society, MRSI, and IIM.

Dr. Mahajan had initiated and successfully implemented a number of programs concerning selection and application of advanced materials for defense applications, which

includes Development of Infrared Domes and Windows Based on Transparent Ceramics, SiAlON Radomes for Hypersonic Missile Applications, Ultra-High Temperature Materials for the Airframe and Scramjet Engine of Hypersonic Technology Demonstrator Vehicle, Reaction Bonded Silicon Carbide Thrust Bearings for Naval Application, and Silicon Carbide Based Mirror Substrates for Satellite Application.



Dr. Roy Johnson is currently Scientist “G” and Associate Director of International Advanced Research Centre for Powder Metallurgy and New Materials (ARCI), Department of Science and Technology, Government of India, Hyderabad. Dr. Johnson was awarded the Ph.D. degree in Chemistry from Nagpur University for the research carried out at National Environmental Engineering Research Institute, Nagpur. He joined ARCI in 1994 and worked in various capacities and led several research projects in the area of advanced ceramics, transparent ceramics, cellular ceramics, chemical vapor deposition, and isostatic shaping. In addition to the basic research, he was successful in realizing various technologies leading to commercialization of products in the strategic and civilian sectors for potential applications. Ceramic honeycomb-based energy efficient heaters and anti-mine boots, which are the first of its kind, and infrared transparent windows and domes are some of the successful technology development programs led by him. Several focused R&D initiatives conceptualized by him in the past few years have resulted in the establishment of unique facilities and a team of scientists with leading expertise in ceramic processing and shaping in the country. Currently, in the capacity of Associate Director, ARCI, he provides leadership to three major centers of excellence, namely, ceramic processing, non-oxide ceramics, and sol-gel based nano-composite coatings.

Dr. Johnson has 100 research publications in reputed journals, 11 Indian patents to his credit, and co-authored one book and two book chapters. He is a recognized research supervisor and guided 6 students for their PhD degree. Dr. Johnson is a frequent reviewer for several international journals. He is a Fellow of Indian Institute of Ceramics and Institution of Chemists and also a member of several Indian and international professional

bodies. Dr. Johnson was the theme leader for advanced ceramics session during Indo-German Frontiers of Engineering Symposium 2014. He is also the recipient of many awards including MRSI Medal 2012 (Materials Research Society), ARCI Technology award 2012, and Pandit Madan Mohan Malaviyaji award (Indian Ceramic Society – 2011).

About the Section Editors



Himadri Sekhar Maiti
Department of Ceramic Technology
Government College of Engineering and
Ceramic Technology
Kolkata, West Bengal, India



L. M. Manocha
Defence Materials and Stores Research
and Development Establishment
DRDO, Kanpur, India

**L. Rama Krishna**

International Advanced Research
Centre for Powder Metallurgy and
New Materials (ARCI)
Balapur, Hyderabad, India

**Vemuri Madhu**

Defence Metallurgical Research Laboratory
Defence Research and Development Organization
Hyderabad, Telangana, India

**Pramod H. Borse**

International Advanced Research Centre
for Powder Metallurgy and New Materials (ARCI)
Balapur, Hyderabad, India

**Rahul Mitra**

Department of Metallurgical and Materials Engineering
Indian Institute of Technology Kharagpur
Kharagpur, West Bengal, India



Roy Johnson

International Advanced Research Centre
for Powder Metallurgy and New Materials, (ARCI)
Balapur, Hyderabad, India



Tetsuji Noda

National Institute for Materials Science
Tsukuba, Japan

Contributors

Harish Kumar Adigilli International Advanced Research Centre for Powder Metallurgy and New Materials (ARCI), Balapur, Hyderabad, India

Department of Metallurgical and Materials Engineering, National Institute of Technology, Warangal, India

Kiran Akella Research and Development Establishment (Engineers), Defence Research and Development Organisation, Pune, India

Mainul Akhtar Materials Science Centre, Indian Institute of Technology, Kharagpur, India

Yamini Ananthan International Advanced Research Centre for Powder Metallurgy and New Materials, Balapur, Hyderabad, India

K. Ananthasivan Indira Gandhi Centre for Atomic Research [IGCAR], Kalpakkam, India

Priya Anish Mathews International Advanced Research Centre for Powder Metallurgy and New Materials (ARCI), Hyderabad, India

P. Suresh Babu International Advanced Research Centre for Powder Metallurgy and New Materials, Balapur, Hyderabad, India

M. Rizvan Basha Materials Science Division, CSIR-National Aerospace Laboratories, Bengaluru, India

S. K. Behera Department of Electronics and Communication Engineering, NIT Rourkela, Rourkela, India

Sanjay Bhardwaj International Advanced Research Centre for Powder Metallurgy and New Materials (ARCI), Hyderabad, India

Papiya Biswas Center for Ceramic Processing, International Advanced Research Centre for Powder Metallurgy and New Materials (ARCI), Hyderabad, Telangana, India

Pramod H. Borse Center for Nanomaterials, International advanced research center for Powder Metallurgy and New Materials, (ARCI), Hyderabad, India

Dibakar Das School of Engineering Sciences and Technology (SEST), University of Hyderabad, Hyderabad, India

Deepa Devapal Ceramic Matrix Products Division, Analytical Spectroscopy and Ceramics Group, PCM Entity, Vikram Sarabhai Space Centre, Indian Space Research Organization, Thiruvananthapuram, India

Ashutosh S. Gandhi Metallurgical Engineering and Materials Science, Indian Institute of Technology Bombay, Mumbai, India

Ibram Ganesh Centre of Excellence for Ceramic Processing, International Advanced Research Centre for Powder Metallurgy and New Materials (ARCI), Hyderabad, Telangana, India

T. Gnanasekaran Materials Chemistry Division, Materials Chemistry and Metal Fuel Cycle Group, Indira Gandhi Centre for Atomic Research, Kalpakkam, India

Raghavan Gopalan Centre for Automotive Energy Materials, International Advanced Research Centre for Powder Metallurgy and New Materials, IITM Research Park, Chennai, India

Mahender Kumar Gupta Research Centre Imarat, Hyderabad, India

Rakesh Kumar Gupta Defence Materials and Stores Research and Development Establishment, Kanpur, India

Luv Gurnani High Temperature and Energy Materials Laboratory, Department of Metallurgical Engineering and Materials Science, IIT Bombay, Powai, Mumbai, India

Neha Hebalkar International Advanced Research Centre for Powder Metallurgy and New Materials, Balapur, Hyderabad, India

A. R. James Ceramics and Composites Group, Defence Metallurgical Research Laboratory, Hyderabad, India

Dulal Chandra Jana Centre for Non-Oxide Ceramics, International Advanced Research Centre for Powder Metallurgy and New Materials (ARCI), Hyderabad, India

H. Jantunen Microelectronics Research Unit, University of Oulu, Oulu, Finland

V. Jayaraman Materials Chemistry Division, Materials Chemistry and Metal Fuel Cycle Group, Indira Gandhi Centre for Atomic Research, Kalpakkam, India

Joydip Joardar International Advanced Research Centre for Powder Metallurgy and New Materials (ARCI), Balapur, Hyderabad, India

Roy Johnson International Advanced Research Centre for Powder Metallurgy and New Materials (ARCI), Balapur, Hyderabad, India

N. Joseph Microelectronics Research Unit, University of Oulu, Oulu, Finland

S. Joshi University West, Trollhättan, Sweden

Vivekanand Kain Materials Processing and Corrosion Engineering Division/
Department of Atomic Energy, Materials Group, Bhabha Atomic Research Centre,
Mumbai, India

Homi Bhabha National Institute, Mumbai, India

Sangeeta Kale Department of Applied Physics, Defence Institute of Advanced
Technology (Deemed University), Girinagar, Pune, India

Balasubramanian Kandasubramanian Department of Metallurgical and Mate-
rials Engineering, Defence Institute of Advanced Technology (Deemed University),
Pune, India

Sunil Kashyap Department of Metallurgical and Materials Engineering, Indian
Institute of Technology Kharagpur, Kharagpur, West Bengal, India

H. T. Kim Korean Institute for Ceramic Engineering and Technology, Jinju-si,
South Korea

Rohini Kitture Department of Applied Physics, Defence Institute of Advanced
Technology (Deemed University), Girinagar, Pune, India

SpringerNature Technology and Publishing Solutions, Magarpatta City, Pune, India

Keerthi Sanghamitra Kollipara International Advanced Research Centre for
Powder Metallurgy and New Materials, Balapur, Hyderabad, India

Swati Koonisetty International Advanced Research Centre for Powder Metallurgy
and New Materials (ARCI), Hyderabad, India

L. Rama Krishna International Advanced Research Centre for Powder Metallurgy
and New Materials (ARCI), Balapur, Hyderabad, India

Ajeet Kumar Ceramics and Composites Group, Defence Metallurgical Research
Laboratory, Hyderabad, India

H. H. Kumar Armament Research and Development Establishment, Pune, India

Suresh Kumar Defence Materials and Stores Research and Development Estab-
lishment, DRDO, Kanpur, India

Sweety Kumari Ceramics and Composites, Defence Metallurgical Research Lab-
oratory, Hyderabad, India

C. M. Lonkar Armament Research and Development Establishment, Pune, India

Vemuri Madhu Defence Metallurgical Research Laboratory, Defence Research
and Development Organization, Hyderabad, Telangana, India

Yashwant Ramchandra Mahajan International Advanced Research Centre for
Powder Metallurgy and New Materials (ARCI), Balapur, Hyderabad, India

Himadri Sekhar Maiti Department of Ceramic Technology, Government College of Engineering and Ceramic Technology, Kolkata, West Bengal, India

Sanjib Majumdar Materials Processing and Corrosion Engineering Division/Department of Atomic Energy, Materials Group, Bhabha Atomic Research Centre, Mumbai, India

Homi Bhabha National Institute, Mumbai, India

S. B. Majumder Materials Science Centre, Indian Institute of Technology, Kharagpur, India

M. Mallik Department of Metallurgical and Materials Engineering, National Institute of Technology Durgapur, Durgapur, West Bengal, India

Swathi Manivannan School of Engineering Sciences and Technology (SEST), University of Hyderabad, Hyderabad, India

L. M. Manocha Defence Materials and Stores Research and Development Establishment, DRDO, Kanpur, India

N. Markocsan University West, Trollhättan, Sweden

Raghvesh Mishra Defence Materials and Stores Research and Development Establishment, Kanpur, India

R. Mitra Department of Metallurgical and Materials Engineering, Indian Institute of Technology Kharagpur, Kharagpur, West Bengal, India

Amartya Mukhopadhyay High Temperature and Energy Materials Laboratory, Department of Metallurgical Engineering and Materials Science, IIT Bombay, Powai, Mumbai, India

Tammana S. R. C. Murthy Materials Processing and Corrosion Engineering Division/Department of Atomic Energy, Materials Group, Bhabha Atomic Research Centre, Mumbai, India

Homi Bhabha National Institute, Mumbai, India

Tetsuji Noda National Institute for Materials Science, Tsukuba, Japan

P. Nylén University West, Trollhättan, Sweden

S. Packirisamy Ceramic Matrix Products Division, Analytical Spectroscopy and Ceramics Group, PCM Entity, Vikram Sarabhai Space Centre, Indian Space Research Organization, Thiruvananthapuram, India

Advanced Polymeric Materials Research Laboratory, Department of Chemistry and Biochemistry, School of Basic Sciences and Research, Sharda University, Greater Noida, India

Gadhe Padmanabham International Advanced Research Centre for Powder Metallurgy and New Materials (ARCI), Hyderabad, India

P. K. Panda Materials Science Division, CSIR-National Aerospace Laboratories, Bangalore, India

A. K. Pandey Department of Metallurgical and Materials Engineering, National Institute of Technology, Warangal, India

Kuttan Prabhakaran Department of Chemistry, The Indian Institute of Space Science and Technology (IIST), Thiruvananthapuram, Kerala, India

N. Eswara Prasad Defence Materials and Stores Research and Development Establishment, DRDO, Kanpur, India

V. V. Bhanu Prasad Ceramics and Composites, Defence Metallurgical Research Laboratory, Hyderabad, India

P. Puthiyavinayagam Indira Gandhi Centre for Atomic Research [IGCAR], Kalpakkam, India

Baldev Raj National Institute of Advanced Studies (NIAS), Bengaluru, India

Senthil Kumar Rajendran International Advanced Research Centre for Powder Metallurgy and New Materials (ARCI), Hyderabad, India

K. R. C. Soma Raju Centre for Sol-Gel Coatings, International Advanced Research Centre for Powder Metallurgy and New Materials (ARCI), Hyderabad, India

Pandu Ramavath Center for Ceramic Processing, International Advanced Research Centre for Powder Metallurgy and New Materials (ARCI), Hyderabad, Telangana, India

Ashok Ranjan Defence Materials and Stores Research and Development Establishment, DRDO, Kanpur, India

D. Srinivasa Rao International Advanced Research Centre for Powder Metallurgy and New Materials, Balapur, Hyderabad, India

I. A. Rasheed Research Centre Imarat, Hyderabad, India

P. Rama Subba Reddy Defence Metallurgical Research Laboratory, Defence Research and Development Organization, Hyderabad, Telangana, India

Bhaskar Prasad Saha Centre for Non-Oxide Ceramics, International Advanced Research Centre for Powder Metallurgy and New Materials (ARCI), Hyderabad, India

Moodakare B. Sahana Centre for Automotive Energy Materials, International Advanced Research Centre for Powder Metallurgy and New Materials, IITM Research Park, Chennai, India

B. Sahoo Materials Science Division, CSIR-National Aerospace Laboratories, Bangalore, India

K. Sairam Materials Processing and Corrosion Engineering Division/Department of Atomic Energy, Materials Group, Bhabha Atomic Research Centre, Mumbai, India

Homi Bhabha National Institute, Mumbai, India

S. Geasin Savio Defence Metallurgical Research Laboratory, Defence Research and Development Organization, Hyderabad, Telangana, India

M. T. Sebastian Korean Institute for Ceramic Engineering and Technology, Jinju-si, South Korea

Sarabjit Singh Ceramics and Composites, Defence Metallurgical Research Laboratory, Hyderabad, India

G. Sivakumar International Advanced Research Centre for Powder Metallurgy and New Materials (ARCI), Hyderabad, India

J. K. Sonber Materials Processing and Corrosion Engineering Division/Department of Atomic Energy, Materials Group, Bhabha Atomic Research Centre, Mumbai, India

K. J. Sreejith Ceramic Matrix Products Division, Analytical Spectroscopy and Ceramics Group, PCM Entity, Vikram Sarabhai Space Centre, Indian Space Research Organization, Thiruvananthapuram, India

R. Subasri Centre for Sol-Gel Coatings, International Advanced Research Centre for Powder Metallurgy and New Materials (ARCI), Hyderabad, India

Murali Krishna Sudha International Advanced Research Centre for Powder Metallurgy and New Materials, Balapur, Hyderabad, India

G. Sundararajan International Advanced Research Centre for Powder Metallurgy and New Materials, Balapur, Hyderabad, India

M. Buchi Suresh International Advanced Research Centre for Powder Metallurgy and New Materials, Hyderabad, India

B. Swaminathan Ceramic Matrix Products Division, Analytical Spectroscopy and Ceramics Group, PCM Entity, Vikram Sarabhai Space Centre, Indian Space Research Organization, Thiruvananthapuram, India

Morgan Advanced Materials, Murugappa Mogan Thermal Ceramics Ltd., Ranipet, Vellore District, Tamil Nadu, India

Manish Tak International Advanced Research Centre for Powder Metallurgy and New Materials, Balapur, Hyderabad, India

Andi Udayakumar Materials Science Division, CSIR-National Aerospace Laboratories, Bengaluru, India

J. Varghese Microelectronics Research Unit, University of Oulu, Oulu, Finland

P. R. Vasudeva Rao Homi Bhabha National Institute (HBNI), Mumbai, India

Sujith Vijayan Department of Chemistry, The Indian Institute of Space Science and Technology (IIST), Thiruvananthapuram, Kerala, India

Praveen Wilson Department of Chemistry, The Indian Institute of Space Science and Technology (IIST), Thiruvananthapuram, Kerala, India

Hidehiro Yoshida Department of Materials Science, School of Engineering, The University of Tokyo, Tokyo, Japan

Part I

Ceramic Materials for Defense Applications



Manifestations of Nanomaterials in Development of Advanced Sensors for Defense Applications

Rohini Kitture and Sangeeta Kale

Contents

Introduction to the Advanced Sensors	4
The Strategic Requirements of Advanced Sensors in Defense	7
Research Overview in Sensor Development	9
Low-Frequency Detections	9
High-Frequency Detections	13
Extremely Low (ppm/ ppb) Concentration Detections for CBW Diagnostics	17
Low Electric and Magnetic Field Detections	25
Challenges in Current Technologies and the Route Ahead	27
Conclusion	28
References	28

Abstract

In recent times, the global science and technology is dominated by research in the nanotechnology domain, especially to explore novel materials with exotic properties, which are attributed to their nano-size regimes. Typically explored examples are metals (gold, silver, copper, etc.), organic and inorganic materials (metal

R. Kitture

Department of Applied Physics, Defence Institute of Advanced Technology (Deemed University),
Girinagar, Pune, India

SpringerNature Technology and Publishing Solutions, Magarpatta City, Pune, India

e-mail: kitture.rohini@gmail.com; rohini.kitture@springernature.com

S. Kale (✉)

Department of Applied Physics, Defence Institute of Advanced Technology (Deemed University),
Girinagar, Pune, India

e-mail: sangeetakale2004@gmail.com

oxides, polymers), carbon (graphene, CNTs, etc.), and so on, typically, in their pure and composites forms. The polymers are playing a vital role in this domain, to make the polymer-based nanocomposites, which are used for different applications in textiles, pharmaceutical, chemical, instrumentation, aerospace, aeronautical, and mechanical domains of engineering. However, one particular domain, which has sought the maximum attention of these nanomaterials, is the sensors. Sensors are an integral part of any instrumentation, mechanical assembly, automobile engineering, heavy engineering, and drug delivery vehicles or in national surveillance gadgets or in any electromagnetic application unit, such as antennas and communication electronics. A need for smart, miniaturized, extremely sensitive, selective, and accurate sensor is always on anvil.

This chapter starts with a brief outline on the progress of science and technology, particularly in the domain of sensors, for low-field and low-frequency (electric and magnetic fields and ultra-low-frequency signals) detections and chemical-biological hazardous environment detections. Various approaches for sensing, used in the authors' laboratory, would be elaborated, namely, the radio-frequency sensing approach, optical fiber approach, metamaterial approach, and conventional resistive approach. The relationships of the obtained properties would be associated with the physics and chemistry at nano-level and their energy dynamics for sensing a particular physical parameter. The chapter will be closely related to defense applications, such as chemical and biological warfare (CBW) diagnostics and hazardous environmental detections, and electromagnetic shielding applications, along with low-frequency detections for sonar technology.

Keywords

Nanomaterials · Nanocomposites · Electromagnetic shielding · Sensors · Optical fibers

Introduction to the Advanced Sensors

Since the introduction of man-made thermostats in the early 1880s, sensors have been widely used by mankind. In general, a device that measures and converts the physical phenomenon (temperature, displacement, force, composition, field, etc.) to produce proportional output signal in various readable form (electrical, mechanical, magnetic, optical, etc.) can be called as sensor. This is sometimes confused with transducers, which, in general, are known to convert one form of energy into the other. Sensors respond to the exposure of the specific physical phenomenon or the changes in the phenomenon to give a measurable equivalent. With the recent advances in science and technology, most of the sensors are integrated with electronic circuits to record and communicate the detailed reading of the measurands [1]. As described in [1], while a sensor device produces/converts output signal due to external stimuli, the integration of this device with assorted signal processing

hardware (analog or digital) and communication system can form a complete sensor system.

Sensors can be classified in various ways. One of the simplest classifications is active and passive sensors; the former requires external power input/signal, whereas the latter does not require such external signal. The other classification is based on the type of detection, viz., chemical, electrical, etc., or on the conversion phenomenon in the sensor, like electrochemical, thermoelectric, etc. Based on the way of contact between the sensor and the measurand/analyte, sensors can be classified as contact sensors (strain gauges, conventional thermometers, etc.) and non-contact sensors (e.g., infrared sensors, optical sensors, magnetic sensors, etc.). Depending upon the measurands, sensors can be broadly classified [2] as follows (Fig. 1).

Sensors are one domain of technology which has been around for decades now, because of their applications not only in the industrial sector but also in areas such as biomedicine, healthcare, entertainment, fitness, and so on. As the industrial process industry has improved from simple, semiautomatic machines to complicated, completely automatic, intelligent, and adaptive control systems, sensors have seen a tremendous improvement from simple passive transducers to miniaturized smart sensors. A simple pressure transducer has been now converted into smart sensor which helps to operate an automated conveyer belt system. Concepts of automation, robotics, and artificial intelligence have increased the scope of sensors from an individual component (device) to an array of devices working together and remotely (wirelessly), controlled by a software (or hardware). Wireless sensor networks find huge applications in this new technological era, wherein not only the sensors have been extremely high-end but so are the networks which connect them and coordinate them to do a certain activity following a pre-defined flowchart. Huge heavy engineering machinery, automobile sector, manufacturing industries, chemical industries, pharmaceutical industries, entertainment electronics, textile industries, cosmetic industries, energy sectors, all require extremely well-equipped machinery, which have to use large number of sensors. These not only have to be accurate, highly sensitive, and repeatable; but they also have to be cheaper and miniaturized.

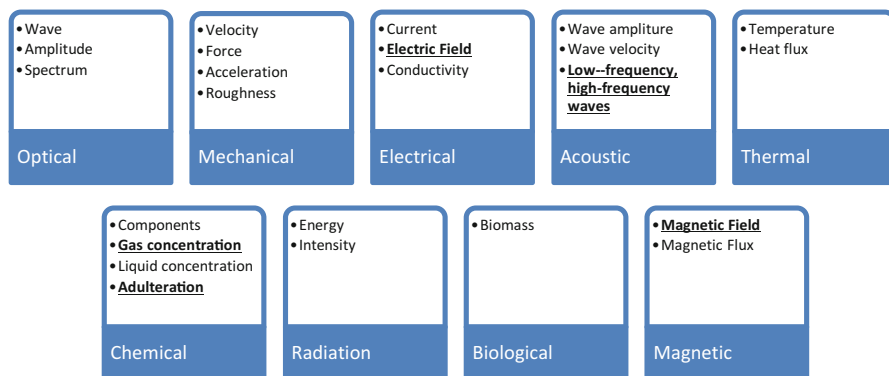


Fig. 1 Sensor classification scheme based on the type of measurand [2]

Sensors have seen a progress from primitive resistive-type operating processes to improved and smart sensing.

Many factors have been instrumental in boosting the phenomenal growth of sensors technology. First is the need, second is the invention of new materials, and third is the improvement of support electronics. The first point, which is the “need,” is quite normal and is responsible for growth of any technological domain. As any industry is established and a product is launched in the market, the competition and the demand always keep the technologists on their toes and ensure that the product is better, more efficient, and also affordable. This enforces the manufacturing industries to develop high-end instrumentation, and therefore the sensors, which are embedded in these machineries, also gets upgraded with time. Secondly, the materials science continues to make its progress with a fast pace, inventing new materials, with advanced property space. The past six to seven decades have seen phenomenal growth in materials science, right from simple metals and insulators to semiconductors to exotic materials like superconductors, perovskite systems, manganites, and optoelectronic materials (to name a few). Due to the evolution of different materials, in different forms (such as alloys, compounds, composites, and so on), the sensors domain has also widened to give better materials for similar kind of sensing. Embedded electronics, robotics, high-end interfacing tools, and software-driven machineries have been responsible to offer extremely good interfacing facilities to the sensors. This is the third reason for improvement in sensor technology, i.e., “advanced electronics.” A simple coaxial cable interface of the sensor has been upgraded to the optical interface, wherein a small sensor signal is conditioned and made appropriate to drive huge motors and turbines with extremely fine precision, via a sophisticated computer interface. The electronic interfacing circuitries have become faster, and hence the sensing also has to be done with better speed and with minimal errors. Repeatability, sensitivity, accuracy, recovery, and everything have improved in the past few decades. Though there is a huge domain of sensor instrumentation which has improved the sensor technology, in this chapter, we will mostly cover the materials aspect, which has fundamentally changed the quality of sensing.

As is said, any technological advances come to the defense sector first, and then it is taken up in the civilian market. Defense technologies are always much advanced as compared to any consumer market technologies, merely because they are related to the security of any country. Therefore, it is always said that any technology is developed in the defense laboratories first, before it comes to civilian markets and subsequently followed by industrial production. Surveillance systems, arms and armament manufacturing, explosive manufacturing, healthcare sector, small-to-big missile launchers, tank technologies, air vehicles, guided missiles, robotics, and everything require the technology and industrial setups which will have hundreds of sensors embedded to do a scheduled job. Hence, sensors find huge applications in defense technologies.

Miniaturization and adaptive technologies have been the mother of any progress and research. As the industrial demands increased, the types of materials used for sensing also became multifaceted. Optoelectronic materials, electrochromic materials, photovoltaic materials, luminescent materials, fluorescent materials, magneto-optic materials, spintronic materials, magneto-resistive materials, and so on were discovered and applied in various sensor applications. Fundamental materials

properties were explored and used to yield precise sensing. Either the properties were of the original materials found in nature, or the materials were engineered to give a desired property. Natural materials include quartz, silica, iron, nickel, copper, aluminum, and so on, which show property manipulation when subjected to specific stimuli (pressure, temperature, voltage, movement, etc.). Specially synthesized materials include manganites, diluted magnetic semiconductors, and superconductors, which are artificially made using materials processing techniques. There is one more category of materials, which has caught the attention of researchers in recent times, and these are “metamaterials.” These are artificially engineered materials in their entirety, and their configurational arrangement is responsible for the properties they exhibit, rather than the type of atomic/molecular structure they possess (materials themselves).

As mentioned above, sensors are of various types. They measure one of multiple physical/chemical parameters right from displacement, motion, direction, pressure, stress, strain, temperature, speed, light intensity, frequency, electric/magnetic field, concentration and nature of chemical species, etc. A sensor can be realized, by measuring the temporary changes in the basic/intrinsic properties of the material, in the form of electrical parameter. The intrinsic properties of the materials, which tinker the sensor operation, include their atomic arrangements, stoichiometry, phase transition, energy gap, luminescence, phosphorescence, molecular vibrational frequencies, atomic disorders, lattice matching (or mismatching), and so forth. As these properties change, when a stimulus is applied to them, it is said that the material has “responded” to the sensing parameter. The “response” is exhibited in the form of change in resistance of the sensing material, or the voltage generated (or altered) or changes in current flow, or modification in the frequency (if the material is frequency selective), quenching (or enhancing), luminescence (or phosphorescence), and so on. These are calibrated in the form of their sensing action, per unit change in the parameter which has to be sensed. Potentiometric sensors, impedance sensors, frequency sensors, piezoelectric sensors, and luminescent sensors are a few examples, which have been developed and used in sensor electronics market.

In this chapter, we focus on such novel materials which have been invented and developed to yield high-end sensors. We discuss the property space of these materials and unleash their potential in the upcoming sensor technology. We limit the discussion to defense applications, in terms of their requirements, and look into the future scope and challenges envisaged.

The Strategic Requirements of Advanced Sensors in Defense

Security of any country and military personnel increasingly rely on intelligent sensor technology for surveillance and electronic intelligence. Millions of people enter into a country through various routes and passages to either to earn their living or otherwise. Similarly, there is a constant danger against known and unknown enemies at the border of any country, and therefore, a strong base of Army, Navy, and Air Force is made ready and well equipped to guard these borders. As the terrorists become more and more powerful and well equipped with advanced instrumentation,

the country's security forces should also be equipped with equivalent (if not superior) surveillance instrumentation and combat equipments. Sharp and very focused weapons, long-range missiles and weaponry, smart surveillance sensors, and extremely competent human force are required, along with very good communication equipments. Similarly, technology to handle the security of the men in uniform is also of utmost importance. Smart bandages, camouflage technique for tents and uniforms, drug delivery systems, tissue engineering, and communication tools are required to ensure the safety and security of the people who are actually at the war front or who are doing constant surveillance at the borders of country, be it air, water, or land [3]. It is the prime job of defense sector of any country to guard their country and fellow countrymen against the people and technologies which enter their country or intend to create damage in a country and have illegitimate status and intentions. Along with the manpower (people in uniform), it is extremely important to equip them with advanced instrumentation, so that they can combat the enemy and also protect themselves. All the scientific and technological communities strive hard to make significant strides in technology, particularly in the vital areas of intelligence and surveillance.

“Being successful in detecting and classifying harmful threats helps ensure our physical well-being. The main and most challenging task is to detect and classify dangerous chemicals, materials, explosives, and people that may be threatening. The challenge is not only to correctly detect threats from a safe distance and ahead of time, but to do so very quickly in order to limit the impact.” It is through the application of today's advanced radars, sensors, cameras, and software that this very real challenge should be met, Partynski suggests [3], rather than by building fences or walls. Defense technologies, which apply to critical infrastructure, airports, seaports, land borders, ports of entry, and inland waterway and coastal borders, gather critical information to ensure that the defense technologies are aptly used, whenever required and wherever needed. These are the areas where high-end sensors are required, which should be implanted, monitored, and acted upon. Technology solutions are needed that will reduce operator workload and enable one person to manage many surveillance systems efficiently and effectively. It is at this juncture that smart sensors enter. Smart sensors are the goal for our future deployments of intelligence and surveillance systems. Automated systems that detect, track, and classify threats without radar experts, or even people continuously staring at camera video, will allow any country to deploy a nationwide system which would be secure, having low false alarms, and attract armed-forces attention only when action is needed.

In addition to providing critical information on potential threats, intelligence and surveillance systems to ensure a safety cover for people in uniform (and also civilians) are also necessary. Having such technologies broadly deployed will help find people in trouble by locating them with advanced radars, sensors, cameras, and software or via their cell phones or radios. Smart sensors would allow us to determine if activities are not normal and warrant someone to take a closer look and possibly assist. Man-wearable sensor-embedded uniforms (or suits) are on anvil, which would help persons of interest identify themselves, when they are in panic.

A quick response mechanism can be then built, when such an alarm is raised by any individual or a group of people. Video capture and display equipments, graphics capabilities, and global positioning systems are additional features required over a conventional smart sensing material, which will do a job with high precision to stimulate an action plan. Man-wearable 2D/3D graphics and video-intensive deployed unmanned aerial vehicle/unmanned ground vehicle (UAV/UGV) control, mission planning, biometric, computer-assisted maintenance, and command, control, communications, computer, intelligence, and surveillance are few applications envisaged in recent times. Various defense laboratories in India are tirelessly working to develop such sensors and surveillance equipments. Many of these laboratories are involved in developing small and big arms, guided missiles, propellant systems, UAVs, radar technologies, and tanks and submarines.

All these technologies have evolved (or are evolving) and developed over and above the basic building block of a sensor, and that is the “material.” No sensor, with whatever advanced electronics and computing capability, can be realized without the basic ingredient, “the material used for sensing.” In the coming paragraphs, let us go through the progress profile of various fascinating materials, on which many research laboratories are working to envisage advanced sensors.

Research Overview in Sensor Development

Low-Frequency Detections

Low acoustic frequency signals, especially those under the water (refer to Fig. 2), have been of immense interest and research for several decades, typically for defense applications. In an acoustic transducer, the mechanical energy of sound waves gets converted into electric energy (as in hydrophones, microphones, etc.), or electric

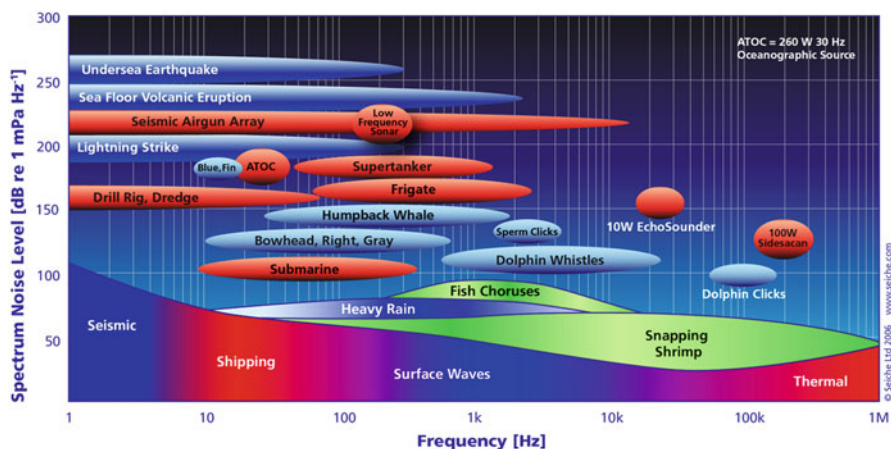


Fig. 2 Underwater frequency spectrum and the categorization of various frequency ranges

energy gets converted into sound waves (as in transmitters, loudspeakers, etc.). Piezoelectric materials, having the ability to generate an electrical charge in response to a mechanical stress and vice versa, have been favored for acoustic transducers. For example, piezoelectric ceramics, single crystals, composites, and polymers have been widely used for over a century in underwater acoustic transducers. The first use of piezoelectric material in underwater acoustic applications was reported in 1917 by a French physicist Paul Langevin, wherein quartz was used as the piezoelectric material in developing an underwater acoustic transducer useful in submarines detection. Since then, there has been extensive research in the field [4, 5].

Low-frequency sonar waves which traverse under the water for submarine surveillance are extremely difficult to detect. This is due to the large impedance offered by the water medium and also due to the noise generated due to other water bodies. Ocean surface waves, internal gravity waves, temperature, salinity, and scattering also have a major impact on the recorded signals. Similarly, for Naval applications, magnetic de-gaussing is also another issue. This is required to nullify the magnetic field accumulated on the ship due to the travelling in the sea for longer durations of time. Magnetic field measurements are required to estimate the life (age) of the ship on the sea. Various passive as well as active surveillance and security systems have been employed to detect such low-frequency signals, typically for aquatic life monitoring, sonar signal detections, undersea earthquake/volcano detection, and submarine detection. Due to poor signal-to-noise ratio, unstable shape and amplitude, and short-duration nature of the signals, this domain of sensor development has proved to be rather challenging.

Though there would be many approaches for underwater surveillance, hydrophone is one of the best option, which has its own limitations on low-frequency detections. Optical fiber-based approach is recently envisaged and is very good, especially from the defense applications perspective. Owing to the low electric losses and high coupling coefficient, lead zirconate titanate (PZT) ceramics were one of the favorite piezoelectric materials widely used for sonar application. Wherever electronic sensors fail due to the electronic interference effects of neighboring circuitry (and vice versa, also), the optical fiber technology offers good promise [6, 7]. Moreover the optical fiber technology has several other advantages over the conventional PZT-based technology, namely, the electrically passive nature of the hydrophones and lighter and more reliable sensor network which is less prone to water-induced failures, besides their high sensitivity, big dynamic range, and wide bandwidth [8–11]. In this context, few efforts have been made in the recent past. Optical fiber-related acoustic pressure-sensing schemes have been reported using a single-mode fiber (SMF) microphone [12], SMF laser-based hydrophone [13, 14], and fiber Bragg grating hydrophone array [15]. However, the sensitivity is an issue for most such cases. As compared with conventional SMF, the phase sensitivity is significantly improved with speciality fibers such as photonic crystal fibers (PCFs), hollow-core photonic bandgap fiber (HC-PBF), and hi-bi polarization-maintaining photonic crystal fiber (HiBi PM-PCF). Due to significant variations in Young's modulus because of the air columns running along the fiber length of HC-PBF or PCFs, these systems prove to be good sensors for axial strain applied acoustic

pressure parameter sensing. Recently, little effort has been put into developing the -PCF-based acousto-optic devices including hollow-core PCF [16–18], solid-core PCF [19, 20], dual-core PCF [21], twin-core PCF [22], and highly birefringent PCFs [23, 24]. Pang and Jin [17] have demonstrated a Michelson interferometer-based system using a 5.7 m fiber to sense the frequencies in a wide range (40–3000 Hz) at 1550 nm, with phase shift as the function of pressure. Yang et al. [16] have used the similar interferometric technique using an etched and then polymer-coated fiber to yield high sensitivity. A Sagnac interferometer has been used by a group [18] to detect the pressures (0–4000 psi) using a wavelength shift as the conversion parameter. However, the challenge of a miniaturized system for typical sonar frequency (especially, low acoustic frequencies between 5 and 200 Hz) detection and that too with a good sensitivity is always on the anvil. While the efforts have been few, the system is either quite large (in terms of length of fiber), or is fragile (etched fiber, for instance), or has limited sensitivity. Mostly, with the noise in such low-frequency underwater signals, the issue is more challenging, which could probably be addressed by a sensor with good sensitivity and dual-scale (both in terms of power and wavelength change) detection.

In this context, in recent times, various sensors have been demonstrated. A Mach-Zehnder interferometric hydrophone is demonstrated in [25] using polarization-maintaining photonic crystal fiber (PM-PCF). This fiber is spliced between two SMFs, operated at 1550 nm source. The experimental scheme is based on dual parameter detection for a change in frequency, i.e., both intensity modulation and wavelength shift. The measured data have been compared with the standard hydrophone, and it was found that the PM-PCF sensor shows better response. Figure 3 shows the configuration, and Fig. 4 shows the response of the interferometer so formed. A fusion loss of 0.3 dB was found while splicing the sensor fiber (PM-PCF) between two SMFs. This configuration formed the sensor bed. A broadband laser source of 1550 nm was used, and an Optical Spectrum Analyzer (OSA) was used, both as the source and detector. This sensor bed was passed through a tank filled with water, and the acoustic frequency (5–200 Hz) was passed. The data was compared with the reference hydrophone (GRAS, 10CS) data, which was also placed at a fixed distance from the acoustic source. When the acoustic frequencies were transmitted through the water, the corresponding interference spectrum was recorded at the detector. This was an in-line type of Mach-Zehnder interferometer, having the same physical lengths in both the reference arm and the sensing arm, but having different optical path lengths due to the different effective indices of core (n_{core}) and clad (n_{clad}). Figure 4a shows the comparison data of the power shift (change in power received at the OSA detector, in dBm) as a function of frequency. However, it was seen that the SMF and MMF spliced sensor showed negligible power shift, as compared to the PM-PCF sensor, which showed a shift from 0.8 to 2.32 dBm. The raw data is shown in Fig. 4b. As shown in the inset of Fig. 4a, the change in power was accompanied by shift in wavelength of the signal as well. The wavelength shifted from 50 to 392.8 pm, with the change in acoustic frequency from 5 to 200 Hz. The sensitivity of the sensor was found to be 3.15×10^{-3} dBm/Pa (in terms of power) and 5.12×10^{-4} nm/Pa (in terms of wavelength).

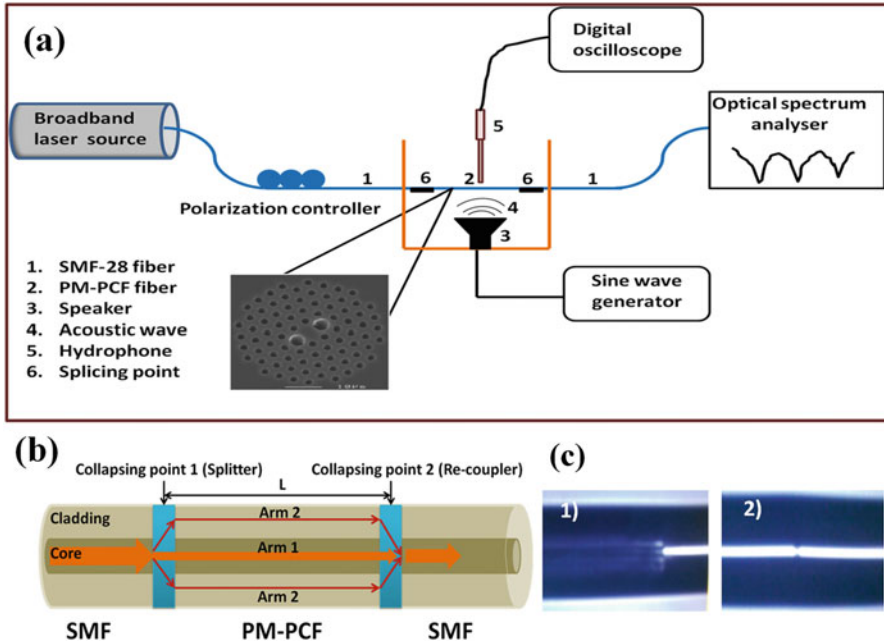
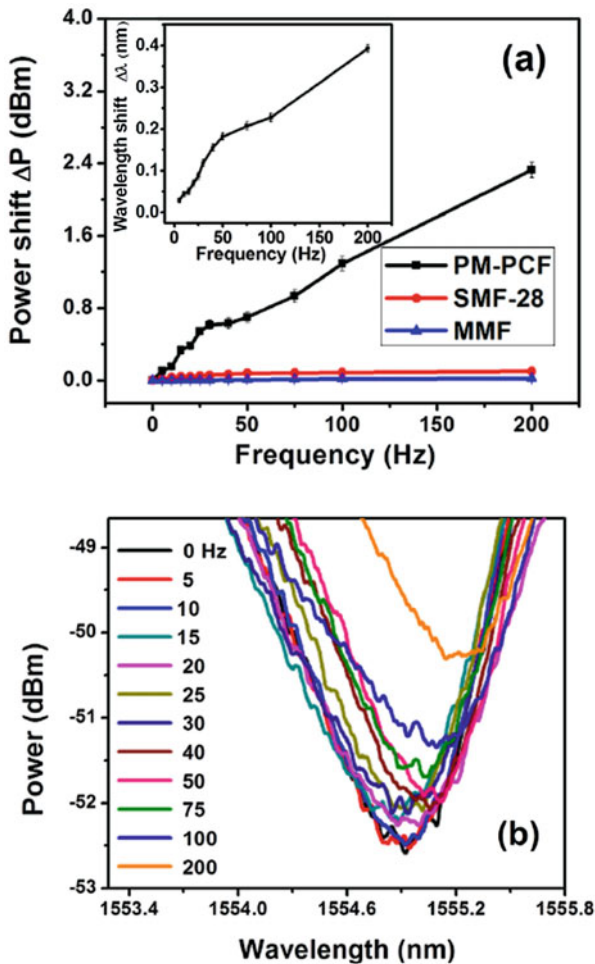


Fig. 3 (a) The experimental setup for the proposed low acoustic frequency detection sensor. (b) The schematic of Mach-Zehnder interferometer and (c) The microscopic image at the interface of the SMF and PM-PCF spliced region

The results are mainly understood through the strain-optic effect. Further, the changes in Young's modulus of PM-PCF fiber due to the higher axial strain imparted by the acoustic pressure were seen to be responsible to the cause. Using the theory of beam bending, the "core modes" and "surface modes" interaction is envisaged and is attributed to the energy transfer between the two fundamental air core modes, which is possible only through the silica wall. When the pressure is exerted onto the PM-PCF fiber, the thickness of the silica cladding region is reduced, and refractive index increases. For higher air-filling ratios, refractive index is larger. Also, as the acoustic pressure is induced on this fiber, the difference between the fast and slow axes ($n_x - n_y$) changes, owing to the phase change in the propagation waves, which further changes the birefringence value, contributing to the sensing phenomenon.

Use of optical fiber approach for low-frequency detections, hence, is a very accurate, reliable, and repeatable sensor option; the same can be explored for structural health monitoring where the complex structures such as bridges and towers and other building structures could be deployed with these sensors. These could be used to evaluate the vibrational effects on the structures and could be monitored 24×7 for their health (in terms of wear and tear, cracks, fatigue, and so on).

Fig. 4 (a) A comparison of power shift for SMF, MMF, and PM-PCF sensors as a function of acoustic frequency. The inset shows acoustic frequency as a function of wavelength shift for PM-PCF. The raw data for PM-PCF are shown in (b)



High-Frequency Detections

These types of sensors are typically related to radar applications. Though it may be slightly debatable if radar-absorbing materials form the part of the discussion on sensors, or not, it is still discussed in this chapter because the material does show property, which is sensitive to the frequency of the incident radiations. Therefore, these are high-frequency detections, when the user is at radar end, and high-frequency absorbers, when the user is at the flight end. In applications with the frame of reference as the “flight,” it is necessary for the flight to remain “hidden” from the radar waves of the enemy radar transmitter, so that the entire aircraft is not identified in the enemy’s air zone. These types of applications are mostly called electromagnetic shielding (EMS). The higher the shielding is, the better is our security in enemy’s air territory. Exactly opposite is our requirement of defense

when we are at the radar end. The visibility of every other air flight and moving objects entering in the radar cross section has to be identified. Therefore, when the radar signal (usually in the X band of 8–12 GHz) is sent by the radar station, if it comes back and is detected, indicates that the object has reflected the signal back and therefore there is a flight in the cross section. The time required by the signal to come back to the radar station decides the distance of the object from the radar surveillance station.

There are many efforts to this effect. One simple way for the aircraft to reduce the electromagnetic detection is to have reflectors on the aircraft body, which would reflect the radiations out of the radar cross section. This is a good option, and fairly good engineering has to be done for the chassis of the aircraft; however still 100% stealth is not guaranteed. The second option is to have the aircraft completely behave as a transparent object to the entire radiation frequency range and the radiations completely pass through, thereby no reflection and hence the stealth application. This is of course extremely difficult and requires a domain of metamaterials for converting this hypothesis into reality. The third way is to completely absorb the electromagnetic radiations which are incident upon them. Therefore, there would be no reflection, and hence radar station would not detect the aircraft. It is at this level that the high-frequency sensing and absorbing materials come into vogue.

Traditionally various ceramic materials have been used along with polymeric systems such as PVA, PVDF as absorbers. Such materials work on the concept of skin depth, and the radiations penetrate inside the material and get absorbed there. The thickness of such materials is hence required to be quite large (few mm to cm), and hence the technology gives rise to extremely bulky sheets for electromagnetic absorption. With the advent of nanotechnology, materials of different forms and their composites have shown good promise with lightweight and high EMS properties. Carbon-based nanomaterials, along with magnetic nanoparticles, can form a composite with a polymer to give polymer nanocomposites which are seen to show extremely good EMS. Not only the coatings are thin, but they also have good mechanical strength. Such materials find applications in radar EMS and also for other EMS applications which are related to data protection and electromagnetic shielding of devices and high-security enclosures. The materials have to be carefully chosen so as to give the effect in a particular frequency range.

The electromagnetic absorption is a function of two primary parameters, namely, the electrical permittivity and magnetic permeability. The material used as Electromagnetic (e-m) absorber has to have a fine combination of these two properties. While electrical permittivity is responsible for the e-m radiations to be absorbed through the conductivity within the absorbing matrix, the magnetic permeability contributes via the hysteresis loss. The basic idea of the EMS material is to help the e-m energy to get dissipated within the material matrix itself, so that none of the energy is reflected/transmitted. Extremely interesting models have emerged in the recent times, especially with the advent of nanocomposites. Conventionally, iron oxide, nickel oxide, and such other magnetic materials have been used to manipulate the magnetic permeability. Ceramic materials (e.g., alumina) and also polymeric systems (e.g., PVDF) have been used conventionally as the basic material. However,

recently, polymer nanocomposites have been used wherein the concept of percolation threshold dominates the EMS phenomenon. Here, a small (and optimized) quantity of nanomaterial is added in the conventional polymeric matrix, and the material shows good conducting properties which manipulate the electrical permittivity parameter. Optimal doping is sufficient to make the entire polymer matrix convert into a good EMS material. The thicknesses have become much lesser (from centimeters to millimeters), and the frequency response has become much wider. Carbon-based nanomaterials have been at the forefront in this sense. PVA, PVDF, and PTFE are the standard polymers which have been explored in this context. Additional additives such as iron oxide and nickel have been added to improve the shielding efficiency.

Therefore, the future of EMI shielding is ongoing to finally develop lightweight and strong absorption coefficient materials. To attain substantial shielding properties, materials should have suitable dielectric permittivity and losses [26–29]. Higher dielectric loss and latitudinal increase of permittivity lead to better absorption coefficient and EM reflection properties, respectively. In the past, numerous studies have been done on materials such as ceramics and polymers. Traditional ceramics (BaTiO_3 and PbTiO_3) possess high dielectric constant, but their processing routes, brittleness, and low dielectric strength restricted their usage [30–32]. On the other hand, polymers having numerous merits like easy processing, flexibility, high dielectric breakdown strength, but their low dielectric constant restricted the application. At present, polymer nanocomposites showed continuous attention due to their synergetic effect of polymer matrix and ceramic fillers and thus having superior properties than individual [33–35]. Earlier work has been done on polymers such as poly(vinylidene fluoride) (PVDF) and their copolymers [36] by embedding various nano-fillers such as barium titanate (BaTiO_3) [37], silver [38], and calcium copper titanate enhancing the dielectric and EMI shielding properties. However, the potential application is still confined due to huge dielectric difference between the polymer and filler, causing limited enhancement. The dielectric and shielding properties of the composites depend upon physical properties, interfacial interactions, connectivity among the fillers within the polymeric matrix, and intrinsic conductivity of the fillers [28, 29, 38]. Thus, there is a need to embed semiconducting fillers having special morphology in the polymer matrix in order to achieve suitable dielectric properties (dielectric loss and conductivity) for EMI shielding applications.

Several efforts have been done on the authors laboratory, with varied materials and their composites [29, 39, 40]. Various materials like ZnO, PVA, PVDF, graphene, CNTs, graphene oxides, Fe_3O_4 , and porous graphene have been used to study the EMS properties of such materials. Properties such as dielectric constants, magnetic permeability, percolation threshold, flexibility, thickness, and mechanical strength of these materials have been studied for various types of material composites. Few efforts are summarized below.

Aepuru et al. [39] have demonstrated zinc oxide in polymer composite form, along with poly(vinylidene fluoride) (PVDF) to make nanocomposite thin film. They have observed significant improvement in dielectric properties and electromagnetic absorption with the ZnO fillers. The key results are reproduced in Fig. 5. Negative

Fig. 5 EMI shielding effectiveness (dB) versus frequency plots of PVDF, PVDF-RZnO (50 wt%) nanocomposite film, and PVDF-CZnO (50 wt%) nanocomposite film with varying average thickness (a) 105 μm , (b) 210 μm , and (c) 315 μm

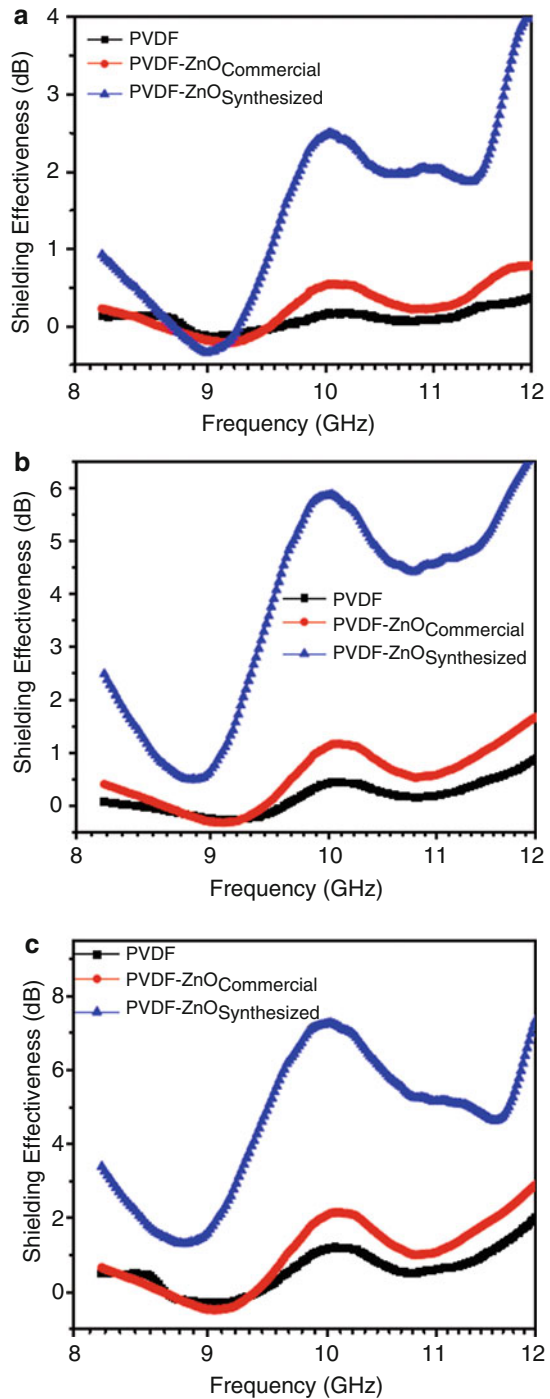
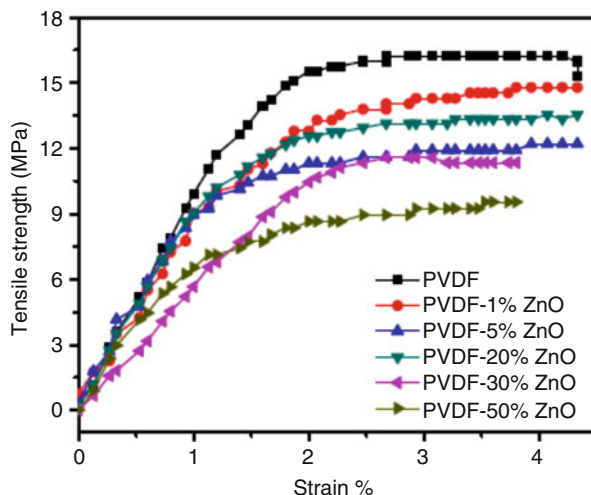


Fig. 6 Stress-strength curves for PVDF and PVDF-RZnO nanocomposites under uniaxial tension



permittivity phenomenon has been envisaged, and the results have been projected for generating lighter shielding materials, which can be used on aircraft bodies or any radar applications. Their results also predict good mechanical properties of the composite film, which is also of utmost important for aerospace applications (refer Fig. 6).

Extremely Low (ppm/ ppb) Concentration Detections for CBW Diagnostics

One of the most important applications of sensors from the point of defense perspective is for chemical and biosensing purposes. These are supposed to be miniaturized smart sensors which would detect toxic gases/liquids/moieties in highly sensitive surveillance zones. Typically for defense applications, such type of chemical and biological moieties is extremely challenging to sense, either in their vaporized form or the liquid or in their powder forms. Challenge is mainly the concentration of the hazardous moieties. The detection, if is done in the ml concentrations, can be of less use because the hazard is probably done. However, sensing extremely low concentrations (preferably ppm or ppb) of such toxic moieties is extremely useful and important. Various sensitive zones in the defense estates require this type of sensor deployment. Similarly, chemical and biological warfare (CBW) diagnostics is a requirement of any country. Therefore, these types of sensors are quite at the forefront.

Biological materials have been sensed using electrical parameters in the past decades using both conventional electrochemical and microelectrodes methods. Due to recently prevalent micromachining techniques, surface plasmon resonance (SPR) is another parameter which is used to sense bio-entities [41, 42]. Few other methods are fluorescence [43, 44], electromechanical transduction [45, 46], use of

nanomaterials [47, 48], and other electrochemical tools [49, 50]. Quartz crystal microbalance [51] and resonance-based cantilevers [52, 53] are also being explored for biosensing in recent times. Though these methods are quite accurate in nature, major limitation is of the nature of process itself. These are mainly laboratory setups and require a bigger infrastructure for detection. A point-of-care type of detection is not possible with these methods [54]. Even the preparation of sample requires good and lengthy chemical procedures, which are good theoretically and also at lab scale, but are cumbersome, if used at hospital level or near the patient bed or at the hazard-stricken site. Therefore a lookout for low-cost, on-site sensing device such as disposable biosensors [55, 56] is always there. Frequency-based biosensors have received more attention recently, because of their simplicity and being easy to detect, despite being less accurate along with lesser sensitivity compared to other sensing techniques. Microcalorimeter falls under this category and is used to develop a biosensor which has a simple detection scheme [57, 58]; however, its fabrication is rather complicated. Conventional sensors also pose standard issues of selectivity, recovery, and detection temperatures. In this context, metamaterial-based sensors are newly emerging, because of the extraordinary properties, in terms of both frequency values used for detection and the accuracy with which they demonstrate sensing. Metamaterials are an offshoot of the recently explored unconventional sensing procedures using nanostructured materials, which are being explored due to their ability to “see,” “manipulate,” and “arrange” micromolecules, creating a path for making nanostructured artificial patterns in the submicron regime.

Metamaterials [59] are artificially engineered electromagnetic materials that are in the form of arrays of structures, made of metals or any other material with their periodicity less than the wavelength of incident electromagnetic (EM) radiation [60, 61]. These have been explored for sensing in recent times and have shown extremely good promise. They can be used in both resonant and nonresonant composite right left-handed (CRLH-based) metamaterial types, and various types of sensing parameters have been studied such as displacement [62, 63], rotation [64], dielectric characterization [65, 66], strain sensing [67, 68], mass flow sensor, differential sensor, temperature sensor, level sensor [69, 70], and so on. The main property of such sensors is that they have extremely small size (much less than wavelength/2) and large Q factor, thereby showing high sensitivity to the parameter which is to be sensed. Various applications have already been realized such as sensing of solid dielectrics [71], liquids [72], hybrid fuels, hazardous chemicals [66, 73, 74], gas [75, 76], and biomolecules [77, 78]. Therefore, this new category of sensors is here to stay for the coming few decades and needs further evaluation to replace existing sensors. In this context the authors' group has put in various efforts on sensing of high explosive materials, hybrid fuels, and hazardous gaseous moieties using the metamaterial-inspired ring resonator approach [79–81].

Studies on three different high-energy materials, namely, 2-bromo-2-nitropropane-1,3-diol (BNP), bis(1,3-diazidoprop-2-yl)malonate (AM), and bis(1,3-di-azidopropyl)glutarate (AG), have been documented in one of our studies. A complementary split-ring resonator has been fabricated at resonant frequency of 4.48 GHz using copper on FR4 substrate. The volume of liquids was varied from 0.5

to 3 mL. Prominent and explicit shifts in the transmission resonant frequency and amplitude were seen as a signature of each energetic material. Simulation results concur with the observations. An extremely sensitive, ultrafast, and recoverable sensor is hence described in this work. Figure 7 shows the three different liquid moieties, which form the base of propellant molecules. As can be seen, they have similar structures, and therefore, to discriminate (and, hence, sense) them using a chemical approach is very difficult. Figure 8 shows the experimental setup used for the metamaterial-inspired CSRR structure sensing. It merely comprises of the CSRR

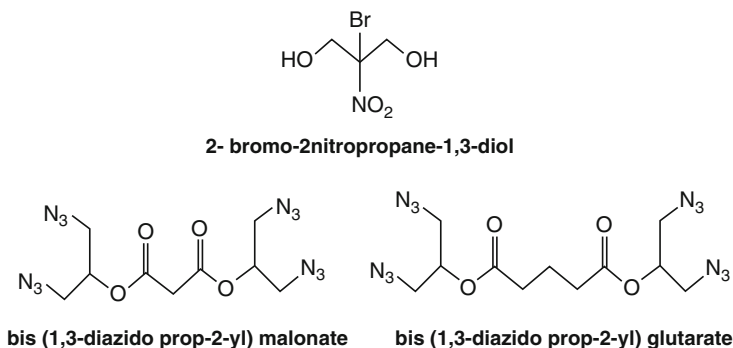


Fig. 7 Chemical structures of the high-energy materials

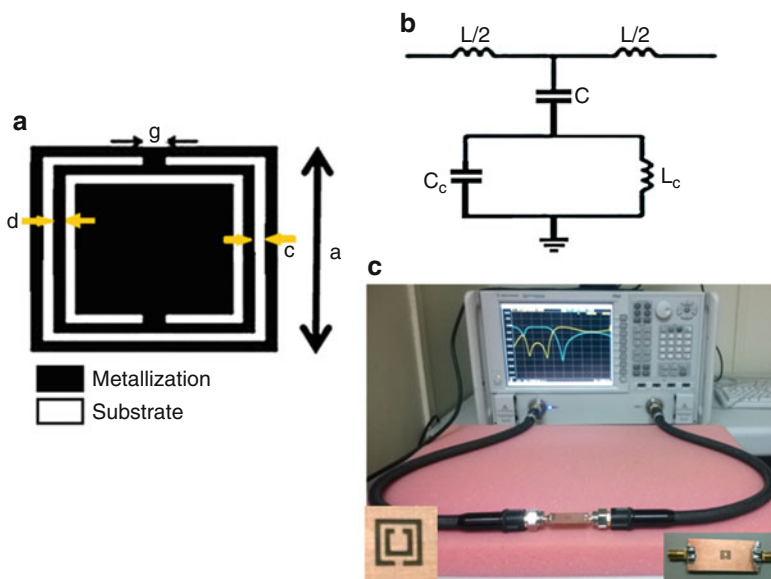


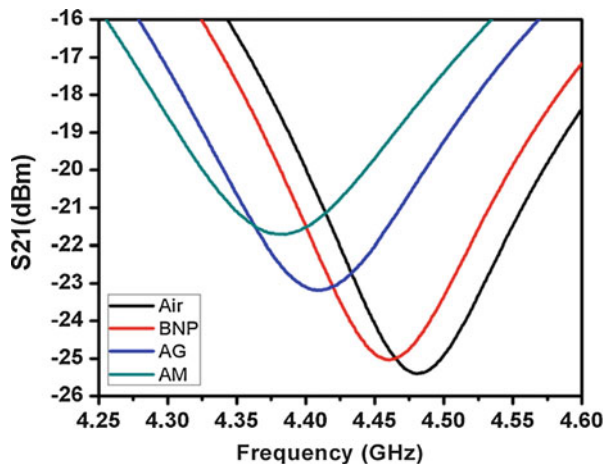
Fig. 8 (a) The design of complementary split-ring resonator (CSRR) along with the dimensions; (b) The equivalent circuit of CSRR; (c) The experimental setup. The inset shows enlarged view of CSRR-based microstrip (bottom right) and enlarged view of CSRR (bottom left)

structure, which works as the ground of the sensor, and there is a microstrip line for carrying the signal. The signal is an RF signal which is sent from a vector network analyzer, and the detector in the same VNA collects the response. The CSRR works as a ground which cuts the electromagnetic lines of the propagating waveform in the transverse direction, giving rise to a dip in the resonant frequency. Figure 9 shows this response for various different hazardous propellant moieties, which show unique and different values. Since their resonant frequencies are very unique, their signatures with this metamaterial-inspired CSRR structures are also unique.

This kind of sensor which can be used for various sensing environments includes flex-fuel sensing, fuel adulteration, and also other biosensing. One can also functionalize the sensor bed with a nanomaterial which is exclusively sensitive to few moieties, to make them extremely sensitive and selective. For example, with gold nanoparticles functionalization, the metamaterial sensor could work as a selective hydrogen sulfide gas sensor. This is because gold has special affinity toward sulfur. Hence the sensor will respond to H_2S with high selectivity and highest frequency shift, as compared to any other gaseous moieties such as oxygen or hydrogen or CO. This is a newly upcoming strategy which has been employed to improve the metamaterial-inspired SRR/CSRRs for selective, fast, and highly sensitive sensing.

Another approach in sensing is related to an optical fiber approach. Optical fibers, as are known, have tremendous advantages as compared to conventional sensors, owing to their response via photon, and not via electrons. Less e-m interference and hence high noise immunity are their main advantage. Optical fibers could be used in various interferometric modes (such as Fabry-Perot, Mach-Zehnder, and so on), along with nanomaterial manipulations, to envisage the sensing. To associate a nanomaterial with optical fiber, various techniques are used, such as mirror coating (fiber-end coated with a nanomaterials) or clad manipulation (in which a section of clad region is etched out and nanomaterial is deposited there) or simple fiber manipulations (subjecting it to stress, strain, and torsions – typically for structural

Fig. 9 The measured S21 response of CSRR loaded microstrip for free space and the three high-energy materials



health monitoring/sensing). A speciality fiber such as photonic crystal fibers can also be used, and the holes in the fiber could be filled up with a nanomaterial to envisage sensing of weak fields (electric/magnetic).

In one of our efforts to sense H_2S gas [82], nanomaterial-modified optical fiber sensor was studied for sensing at room temperature for very low concentrations from 1 to 5 ppm. ZnO nanoparticles were embedded into polymethyl methacrylate (PMMA) matrix and coated on the mirror tip of the single-mode fiber in the Fabry-Perot interferometric configuration to a 1550 nm laser source. The sensor response was found to be 1950 p.m. for 5 ppm gas. The detailed study of response of the sensor modified with nanocomposite (and their individual counterparts) suggested that the swelling property of PMMA offers enhanced gas adsorption opportunity and optical transparency of the ZnO nanoparticles exhibit sensing. A real-time sensor, operating at room temperature, is hence projected. This work paves a new avenue for sensing via manipulation of refractive index of the materials, thereby inducing change in the optical fiber response, in terms of the shift in the interference pattern, both in terms of wavelength and signal power, when subjected to the sensing environment. Figure 10 shows the experimental setup of the optical fiber-based sensing, and Fig. 11 shows the results of the sensor so formed and its comparison with the optical sensing data of individual counterparts, namely, PMMA and ZnO.

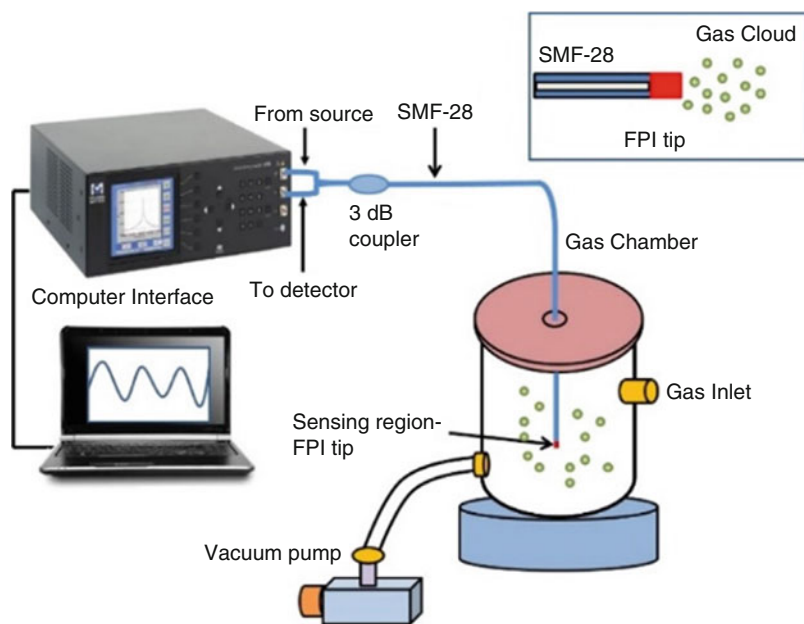
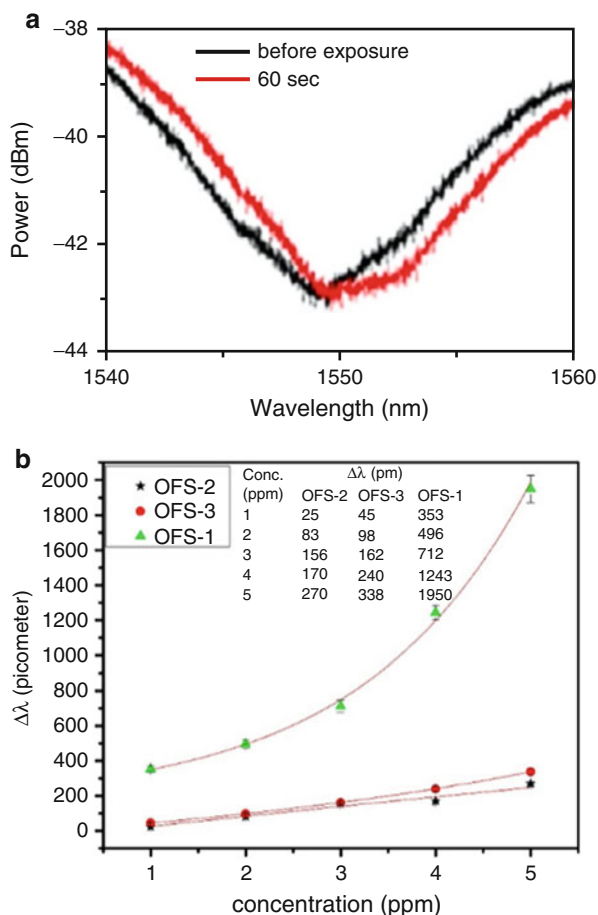


Fig. 10 Simplified presentation of FPI-OFS setup. Inset represents the FPI tip, which works sensing tip

Fig. 11 (a) The spectral response of the ZnO-PMMA composite before and after exposure to H₂S gas for 60 s; (b) Effect of H₂S concentration on sensitivity of OFS-1 for 60 s. Inset represents numerical values of peak shift with concentration for OFS-1, OFS-2, and OFS-3



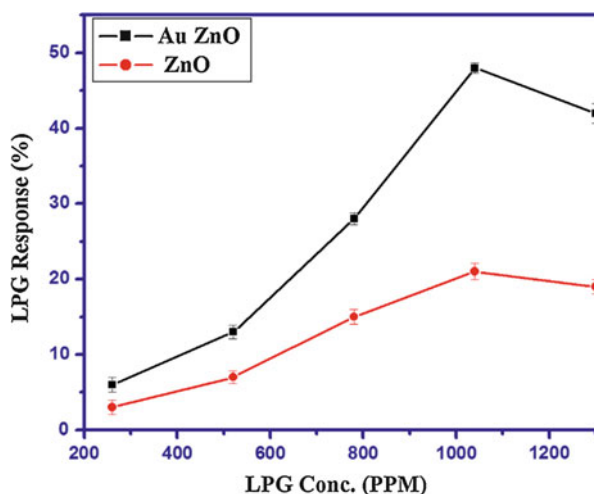
Owing to the electron configuration of the analyte, it is clear that H₂S will interact easily with the PMMA matrix, followed by negligible interaction between PMMA and O₂ (mostly only physisorption). This is because the polar molecule H₂S readily gives electron to PMMA (hence inducing substantial swelling), which is further given to the entrapped ZnO. This modifies the electrical and optical properties of ZnO, which induces the change in the effective refractive index of the material.

There are other approaches such as resistive sensors, in which the resistance of the sensor bed changes with their exposure to various gases. Mainly they work in oxidative or reducing environment, and the sensor changes its resistance depending upon the ambience of the subjected environment. The typical nanostructured metal oxide materials, which have been used for gas sensing applications, are TiO₂ [83], SnO₂ [84], ZnO [85], CdO [86], and WO₃ [87]. There are an umpteen number of papers in this context [88–108], and mainly the interactions are of oxidative/

reducing types, which change the resistance of the sample when they are subjected to the sensing environment. Several parameters are taken into account for evaluation of a sensor, namely, sensitivity, response and recovery time, detection limit, stability, selectivity, etc. Due to their excellent merits over the other sensors, zinc oxide nanostructures have been one of the most favored materials for various sensing applications. For example, Kumar et al. have reviewed various ZnO nanostructures, their synthesis techniques, and various parameters like sensitivity and response time for NO₂ gas [109]. Their study shows that the response time of as low as 9 s can be achieved with the help of nanorods, while in case of nanoparticles, it goes to 6 s, and the recovery time is ~17 s. Another review by A. Wei et al. covers recent developments in ZnO sensors, wherein they note that the ZnO films have lowest detection limit of 60 ppb for NH₃ and sensitivity of ~32,000% for ZnO nanowires for CO gas sensing [110]. It can be deduced that the response time, recovery time, sensitivity, and stability of the sensors are dependent on many factors including morphology, the substrate-analyte chemistry, surface area of the ZnO nanostructure, concentration of the gas, oxygen vacancies, operating temperature, etc.

Though much work has been done in this domain, this approach suffers the issues of selectivity [109–113]. In this context, a novel approach has been taken up in recent times, which is of doping the metal oxides with rare elements and noble metals such as gold, silver, platinum, and palladium. U.T. Nakate et al. [114] have reported the improved LPG sensing using gold (Au)-sensitized ZnO nanorod film. The ZnO nanorods were grown on glass substrate, and the response to LPG gas was studied both in only ZnO film and Au-sensitized ZnO at different temperatures. Similar studies were done by the same group, varying the gas (LPG) concentration as well. The transient gas response and recovery times for sensor were explained under the light of chemical sensitization and/or electronic sensitization. Figure 12 shows the response of the sensor to the gaseous environment.

Fig. 12 Response curves of the ZnO thin film at 623 K upon exposure of various concentration of LPG



In the electronic mechanism, the action with target gas molecules takes place on the surface of the additives along with metal oxide surface. These additives change their charge state, which results in a variation of the surface barrier height and as a result change in conductance of the metallic oxide. Au additive as an active catalyst creates more active sites that are believed to be crucial for the enhanced in sensitivity. Surface defects modulated by the chemical and electrical effects of Au also improve the sensing ability. Au (or any such noble metal) serves as specific adsorption sites to dissolve oxygen molecules and adsorb target gas molecules [115, 116]. The addition of Au increases adsorption and enhances dissociation of chemisorbed air oxygen molecules into oxygen ion species O_2^- [117]. A phenomenon called “spillover effect” [118, 119] comes into play in the Au-sensitized ZnO nanorods. Oxygen diffuse increases and capture free electrons from the conduction band of ZnO to create more oxygen ion species as compared to pure ZnO. This more number of oxygen ion species reacts with more number of LPG (refer to Fig. 13). The band diagram used to explain this sensing is shown typically in Fig. 13.

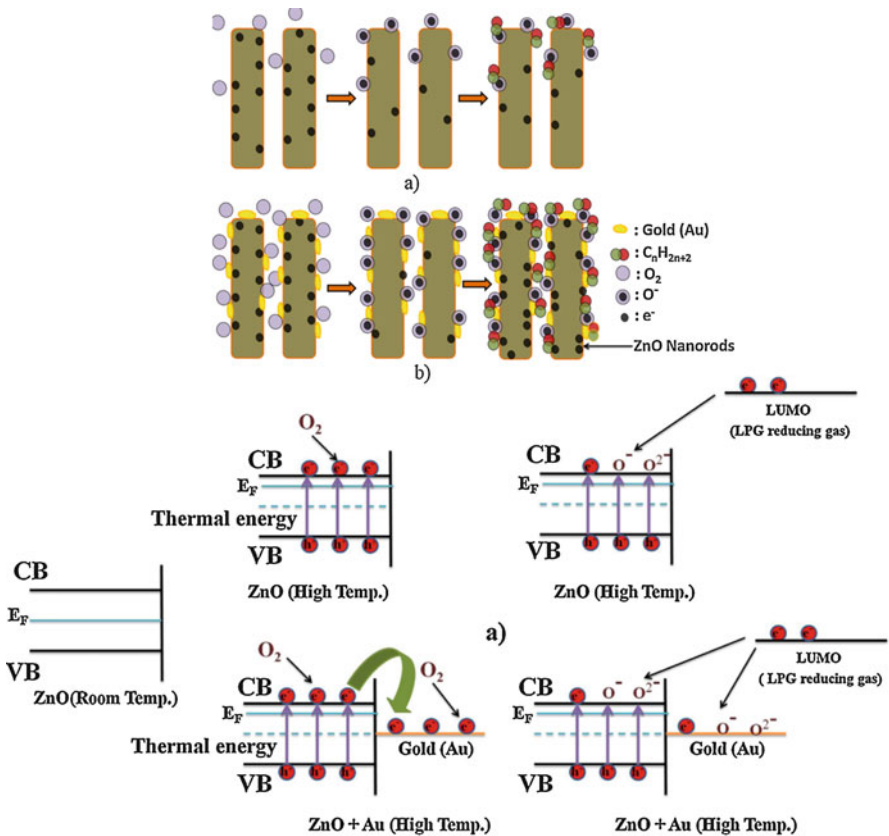


Fig. 13 The cartoon of the process and the schematic band diagram: (a) pure ZnO nanorods; (b) ZnO nanorods sensitized with Au

Low Electric and Magnetic Field Detections

As has been mentioned briefly above, low-field detections are one field which has its requirement right from the automotive industries to the shipping industries, to electronic industries, and to mining applications. Though there has been immense research done and various sensors being realized in the form of weak electric and magnetic field detections, the requirement of miniaturized and highly sensitive sensors is always there. Moreover, with the advent of micro-/nanoelectronics, extremely low values of such fields are required to be detected. Many efforts have been done in this regard, such as use of Hall probes, SQUID magnetometry, and so on. However, a new approach is also been studied, which is via using of optical fibers and manipulating their mirror end by a nanomaterial which is sensitive to magnetic fields and then studying its magneto-optic response using a specific interferometric technique as has been discussed in the section above. The second method is via using a photonic crystal fiber and filling their holes with magneto fluids and observing the response to applied fields (electric/magnetic). The results are indeed interesting and promising too.

Thakur et al. [120] have published their work on development of a magnetic field sensor having advantages of both photonic crystal fiber and opto-fluidics, combining them on a single platform by infiltrating small amount of Fe_3O_4 magneto-opto-fluid/nanofluid in cladding holes of polarization-maintaining photonic crystal fiber. It has been demonstrated that magnetic field of few mT can be easily and very well detected with higher sensitivity of 242 pm/mT. The change in the birefringence values has been correlated to the response of nanofluid to applied field. The advantages of polarization-maintaining photonic crystal fiber (PM-PCF) and Fe_3O_4 magnetic nanofluid have been exploited using simple birefringent interferometric technique to fabricate the magnetic sensor. Figure 14 shows their experimental setup used and SEM image of PM-PCF fiber. The sensor works on the principle of birefringent interferometer and consisted of a piece of PM-PCF connected between two in-line fiber polarizers. An optical sensing analyzer with an inbuilt broadband source (1510–1590 nm) has been used to measure the fringe pattern obtained in the transmission spectrum. Magnetic field was varied from 0 to 80 mT. Figure 15 shows the response of the sensor to the applied magnetic fields.

Higher magnetic field sensitivity of 242 pm/mT for 0.6 mg/ml concentration of Fe_3O_4 is reported in this work. Response of iron oxide nanofluid to applied magnetic fields may be related to their anisotropic microstructure and alignments in the form of chain-like structures in the fiber microchannels [121, 122]. Such works have been reported independently by few other research groups, as well. Hence these kinds of sensors could be categorized as those wherein the sensor fabrication technique is easy and simple.

This work will lead to design of a miniaturized PCF-based magnetic field sensor, utilizing very small quantity of magnetic nanofluid. Similar efforts are documented using cobalt nanoparticles [123].

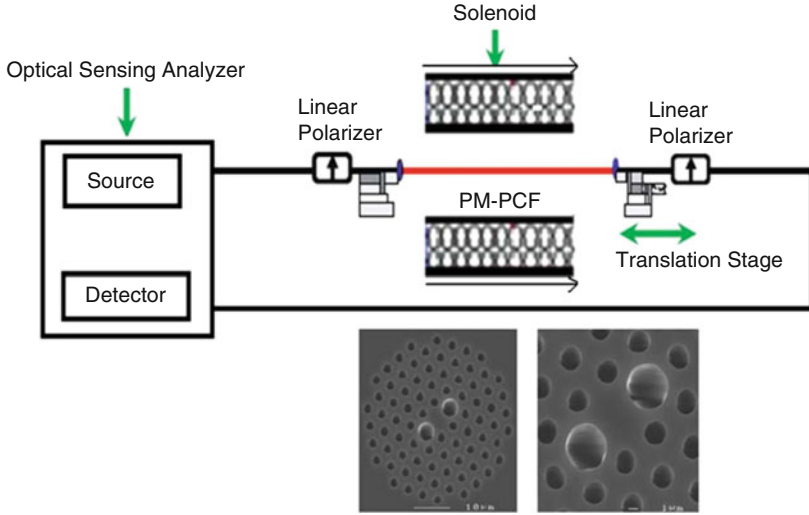


Fig. 14 Experimental setup and SEM image of PM-PCF

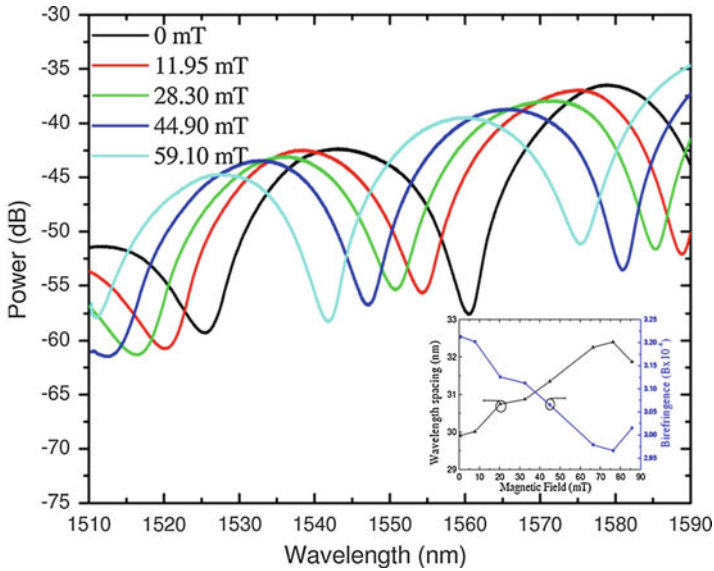


Fig. 15 (Color online) Fringe pattern of PM-PCF filled with 0.6 mg/ml concentrated Fe_3O_4 nanofluid at different magnetic fields. Inset shows wavelength spacing and birefringence versus magnetic field

Challenges in Current Technologies and the Route Ahead

The key building blocks of information security are confidentiality, integrity, and availability. Confidentiality refers to the idea that only authorized users have correct access to assets (in this case means the data transmitted over a wireless network). Sensor-based intelligence gathering has some advantages over more traditional forms (of intelligence gathering), specifically in the areas of ease of deployment, camouflage, and redundancy. Sensors are small footprint in terms of size and weight, and therefore many can be deployed at once as part of reconnaissance, prior to an engagement. Also, their small size means that sensors can be disguised easily for a range of environments. Further, sensors can overlap which provides redundancy, if one or more are rendered inoperative. This dependency on sensors comes at a cost, however. Potok et al. [124] point out that in such systems, information must be transmitted securely under often suboptimal network conditions; otherwise their value is severely negated.

As is said, it is practically impossible to construct a truly secure information system. Communications are secure if transmitted messages can be neither affected nor understood by an adversary, likewise, information operations are secure if information cannot be damaged, destroyed, or acquired by an adversary. They go on to define software challenges for a future combat system including (but not limited to) network security and accessibility, fault tolerance, and information analysis and summary of large data streams from the network. Further, Shostack and Stewart [125] claim that most software is insecure. This could be because, as Wysopal et al. [126] have observed, security requirements are often omitted from requirements specifications altogether. This has been noted as being particularly problematic in other safety-critical domains such as automotive control software as well [127]. In terms of the problem domain (military operations), wireless sensors of various types can be distributed on ground before a battle while being connected to autonomous software agents in a multi-agent system to give an on-field tactical advantage, provided that the communications between the sensors cannot be subverted. A public key infrastructure is an obvious solution to the integrity problem; however, issues of secure storage for the private key and over-the-air transmission of either public or private keys will still prove problematic. The issue of key management is perhaps further complicated by the ever-decreasing cost of the hardware required to conduct a brute-force attack. For example, a multi-TeraFLOP GPGPU cluster can be purchased for as little as AUD\$10,000. Another area of concern is whether the agents themselves can be subverted. As noted above, while truly secure software is almost impossible to create, it may be that security-oriented software development methods that place security requirements at the forefront of all stages of the development lifecycle will reduce or eliminate vulnerabilities in this area.

Conclusion

In conclusion, a literature survey of different kinds of sensors for various applications pertaining to defense sector is done. The main domains cover the chemical and biological warfare diagnostics, radar electromagnetic shielding applications, low- and high-field electric/magnetic field sensing, and low-frequency (SONAR) sensing. Various approaches to envisage these sensors are discussed, such as optical fiber approach, metamaterial-inspired antenna approach, nanomaterials resistive-sensor approach, and polymer nanocomposite films approach for electromagnetic absorption/reflectance/transmission. These are all new and upcoming techniques used to combat eavesdropping using miniaturized sensing elements. The miniaturization is achieved via use of nanomaterials which provide more sensing area in lesser volumes and metamaterial approaches, which shrink the antenna sizes to sizes lesser than $\lambda/2$. Though there is a long way to go to develop these sensors using a non-silicon fabrication approach, this is sure to take up the commercial market in coming years. Sensors development is going to be one of the most promising and impending technologies, which would connect to various IOT devices to make them smarter, smaller, sensitive, selective, and faster.

References

1. National Research Council (U.S.). Committee on New Sensor Technologies: Materials and Applications (1995) Expanding the vision of sensor materials. National Academy Press, Washington, DC
2. White RM (1987) A sensor classification scheme. *IEEE Trans Ultrason Ferroelectr Freq Control* 34(2):124–126
3. Howard Courtney E, Smart sensors – Military & Aerospace Electronics Available <https://www.militaryaerospace.com/communications/article/16706952/smart-sensors>
4. Li H, Deng ZD, Carlson TJ (2012) Piezoelectric materials used in underwater acoustic transducers. *Sens Lett* 10(3–4):679–697
5. Liu J-C, Cheng Y-T, Ho S-Y, Hung H-S, Chang S-H (2017) Fabrication and characterization of high-sensitivity underwater acoustic multimedia communication devices with thick composite PZT films. *J Sensors* 2017:1–7
6. Cranch GA, Nash PJ, Kirkendall CK (2003) Large-scale remotely interrogated arrays of fiber-optic interferometric sensors for underwater acoustic applications. *IEEE Sensors J* 3(1):19–30
7. Digonnet MJF, Vakoc BJ, Hodgson CW, Kino GS (2004) Acoustic fiber sensor arrays. *Proc SPIE Second European Workshop on Optical Fibre Sensors* 5502:39
8. Giallorenzi T et al (1982) Optical fiber sensor technology. *IEEE J Quantum Electron* 18(4):626–665
9. Digonnet MJF, Vakoc BJ, Hodgson CW, Kino GS (2004) Acoustic fiber sensor arrays, Conference Paper In: Second European workshop on optical fibre sensors. International Society for Optics and Photonics 5502:39–51. <https://doi.org/10.1117/12.566514>
10. Nash P (1996) Review of interferometric optical fibre hydrophone technology. *Sonar Navig IEE Proc – Radar* 143(3):204
11. Wang Z, Hu Y, Meng Z, Ni M, Luo H (2008) A fiber-optic hydrophone with an acoustic filter. *Proc SPIE* 6830:683011

12. Wooler JPF, Crickmore RI (2007) Fiber-optic microphones for battlefield acoustics. *Appl Opt* 46(13):2486
13. Hocker GB (1979) Fiber-optic sensing of pressure and temperature. *Appl Opt* 18(9):1445
14. Hughes R, Jarzynski J (1980) Static pressure sensitivity amplification in interferometric fiber-optic hydrophones. *Appl Opt* 19(1):98
15. Beverini N et al (2010) Fiber laser hydrophone for underwater acoustic surveillance and marine mammals monitoring. *Proc SPIE* 7994:79941D
16. Yang F et al (2013) Enhancement of acoustic sensitivity of hollow-core photonic bandgap fibers. *Opt Express* 21(13):15514
17. Pang M, Jin W (2009) Detection of acoustic pressure with hollow-core photonic bandgap fiber. *Opt Express* 17(13):11088
18. Sadeghi J, Latifi H, Santos JL, Chenari Z, Ziaee F (2014) Behavior of a hollow core photonic crystal fiber under high radial pressure for downhole application. *Appl Phys Lett* 104(7):071910
19. Qiu M, Zhang H, Liu B, Dong H, Yang C, Miao Y (2013) Acoustic birefringence suppression in a fiber acoustic grating employing solid-core photonic crystal fiber with hexagonal air-hole array cladding. *Opt Eng* 52(3):035008
20. Jewart CM, Quintero SM, Braga AMB, Chen KP (2010) Design of a highly-birefringent microstructured photonic crystal fiber for pressure monitoring. *Opt Express* 18(25):25657
21. Chen D, Hu G, Chen L (2011) Dual-core photonic crystal fiber for hydrostatic pressure sensing. *IEEE Photon Technol Lett* 23(24):1851–1853
22. Liu Z, Tse M-LV, Wu C, Chen D, Lu C, Tam H-Y (2012) Intermodal coupling of supermodes in a twin-core photonic crystal fiber and its application as a pressure sensor. *Opt Express* 20(19):21749
23. Fu HY et al (2010) High pressure sensor based on photonic crystal fiber for downhole application. *Appl Opt* 49(14):2639
24. Fávero FC et al (2010) Hydrostatic pressure sensing with high birefringence photonic crystal fibers. *Sensors* 10(11):9698–9711
25. Pawar D, Rao C, Choubey R, Kale S (2016) Mach-Zehnder interferometric photonic crystal fiber for low acoustic frequency detections. *Appl Phys Lett* 108(4). <https://doi.org/10.1063/1.4940983>
26. Kong L, Yin X, Ye F, Li Q, Zhang L, Cheng L (2013) Electromagnetic wave absorption properties of ZnO-based materials modified with ZnAl₂O₄ Nanograins. *J Phys Chem C* 117(5):2135–2146
27. Dang Z-M, Yuan J-K, Zha J-W, Zhou T, Li S-T, Hu G-H (2012) Fundamentals, processes and applications of high-permittivity polymer–matrix composites. *Prog Mater Sci* 57(4):660–723
28. Li N et al (2006) Electromagnetic interference (EMI) shielding of single-walled carbon nanotube epoxy composites. *Nano Lett* 6(6):1141–1145
29. Rao BVB, Yadav P, Aepuru R, Panda HS, Ogale S, Kale SN (2015) Single-layer graphene-assembled 3D porous carbon composites with PVA and Fe₃O₄ nano-fillers: an interface-mediated superior dielectric and EMI shielding performance. *Phys Chem Chem Phys* 17(28):18353–18363
30. Gregorio R, Cestari M, Bernardino FE (1996) Dielectric behaviour of thin films of β-PVDF/PZT and β-PVDF/BaTiO₃ composites. *J Mater Sci* 31(11):2925–2930
31. Suresh MB, Yeh T-H, Yu C-C, Chou C-C (2009) Dielectric and ferroelectric properties of Polyvinylidene fluoride (PVDF)-Pb_{0.52}Zr_{0.48}TiO₃ (PZT) nano composite films. *Ferroelectrics* 381(1):80–86
32. Zhang Q, Jiang S, Yang T (2012) Pyroelectric, dielectric, and piezoelectric properties of MnO₂-doped (Na_{0.82}K_{0.18})_{0.5}Bi_{0.5}TiO₃ lead-free ceramics. *J Electroceram* 29(1):8–11
33. Venkatragavaraj E, Satish B, Vinod PR, Vijaya MS (2001) Piezoelectric properties of ferroelectric PZT-polymer composites. *J Phys D Appl Phys* 34(4):487
34. Choi YJ, Yoo M-J, Kang H-W, Lee H-G, Han SH, Nahm S (2013) Dielectric and piezoelectric properties of ceramic-polymer composites with 0–3 connectivity type. *J Electroceram* 30(1–2):30–35

35. Vacche SD, Oliveira F, Leterrier Y, Michaud V, Damjanovic D, Manson J-AE (2012) The effect of processing conditions on the morphology, thermomechanical, dielectric, and piezoelectric properties of P(VDF-TrFE)/BaTiO₃ composites. *J Mater Sci* 47(11):4763–4774
36. Date M, Fukuda E, Wendorff JH (1989) Nonlinear piezoelectricity in oriented films of PVDF and its copolymers. *IEEE Trans Electr Insul* 24(3):457–460
37. Channal CV, Jog JP (2008) Dielectric relaxations in PVDF/BaTiO₃ nanocomposites. *Express Polym Lett* 2:294–301
38. Joseph N, Singh SK, Sirugudu RK, Murthy VRK, Ananthakumar S, Sebastian MT (2013) Effect of silver incorporation into PVDF-barium titanate composites for EMI shielding applications. *Mater Res Bull* 48(4):1681–1687
39. Aepuru R, Bhaskara Rao BV, Kale SN, Panda HS (2015) Unique negative permittivity of the pseudo conducting radial zinc oxide-poly(vinylidene fluoride) nanocomposite film: enhanced dielectric and electromagnetic interference shielding properties. *Mater Chem Phys* 167:61–69
40. Bhaskara Rao BV, Kale N, Kothavale BS, Kale SN (2016) Fabrication and evaluation of thin layer PVDF composites using MWCNT reinforcement: Mechanical, electrical and enhanced electromagnetic interference shielding properties. *AIP Adv* 6(6):065107
41. Wang C et al (2013) Multichannel scan surface plasmon resonance biochip with stationary optics and baseline updating capability. *J Biomed Opt* 18(11):115002
42. Oh BK, Lee W, Kim YK, Lee WH, Choi JW (2004) Surface plasmon resonance immunosensor using self-assembled protein G for the detection of Salmonella paratyphi. *J Biotechnol* 111(1):1–8
43. Pickup JC, Hussain F, Evans ND, Rolinski OJ, Birch DJ (2005) Fluorescence-based glucose sensors. *Biosens Bioelectron* 20(12):2555–2565
44. Viveros L, Paliwal S, McCrae D, Wild J, Simonian A (2006) A fluorescence-based biosensor for the detection of organophosphate pesticides and chemical warfare agents. *Sensors Actuators B Chem* 115(1):150–157
45. Fritz J et al (2000) Translating biomolecular recognition into nanomechanics. *Science* 288(5464):316–318
46. Lee H-J, Lee H-S, Yoo K-H, Yook J-G (2010) DNA sensing using split-ring resonator alone at microwave regime. *J Appl Phys* 108(1):014908
47. Guan WJ, Li Y, Chen YQ, Zhang XB, Hu GQ (2005) Glucose biosensor based on multi-wall carbon nanotubes and screen printed carbon electrodes. *Biosens Bioelectron* 21(3):508–512
48. Alivisatos P (2004) The use of nanocrystals in biological detection. *Nat Biotechnol* 22(1):47–52
49. Murphy L (2006) Biosensors and bioelectrochemistry. *Curr Opin Chem Biol* 10(2):177–184
50. Wang J (2006) Electrochemical biosensors: towards point-of-care cancer diagnostics. *Biosens Bioelectron* 21(10):1887–1892
51. Janshoff A, Galla H-J, Steinem C (2000) Piezoelectric mass-sensing devices as biosensors – an alternative to optical biosensors? *Angew Chem Int Ed* 39(22):4004–4032
52. Daniels JS, Pourmand N (2007) Label-free impedance biosensors: opportunities and challenges. *Electroanalysis* 19(12):1239–1257
53. Ziegler C (2004) Nanotechnologies for the biosciences. *Anal Bioanal Chem* 379(7):903–903
54. Singh A, Kaushik A, Kumar R, Nair M, Bhansali S (2014) Electrochemical sensing of cortisol: a recent update. *Appl Biochem Biotechnol* 174(3):1115–1126
55. Abayomi LA, Terry LA, White SF, Warner PJ (2006) Development of a disposable pyruvate biosensor to determine pungency in onions (*Allium cepa* L.). *Biosens Bioelectron* 21(11):2176–2179
56. Muhammad-Tahir Z, Alcolija EC (2004) A disposable biosensor for pathogen detection in fresh produce samples. *Biosyst Eng* 2(88):145–151
57. Winter W, Höhne GWH (2003) Chip-calorimeter for small samples. *Thermochim Acta* 403(1):43–53
58. Sun J, Huang M, Yang J-J, Li T-H, Lan Y-Z (2011) A microring resonator based negative permeability metamaterial sensor. *Sensors* 11(8):8060–8071

59. Bhansali S, Vasudev A (2012) *Mems for biomedical applications*. Woodhead Publishing Series in Biomaterials. Elsevier Science. ISBN 978-0-85709-627-2
60. Chen T, Li S, Sun H (2012) Metamaterials application in sensing. *Sensors* 12(3):2742–2765
61. Pendry JB (2000) Negative refraction makes a perfect lens. *Phys Rev Lett* 85(18):3966–3969
62. Horestani AK, Fumeaux C, Al-Sarawi SF, Abbott D (2013) Displacement sensor based on diamond-shaped tapered split ring resonator. *IEEE Sensors J* 13(4):1153–1160
63. Naqui J, Durán-Sindreu M, Martín F (2011) Novel sensors based on the symmetry properties of split ring resonators (SRRs). *Sensors* 11(8):7545–7553
64. Horestani AK, Abbott D, Fumeaux C (2013) Rotation sensor based on horn-shaped split ring resonator. *IEEE Sensors J* 13(8):3014–3015
65. Withayachumnankul W, Jaruwongrungrsee K, Tuantranont A, Fumeaux C, Abbott D (2013) Metamaterial-based microfluidic sensor for dielectric characterization. *Sensors Actuators A Phys* 189:233–237
66. Rawat V, Dhobale S, Kale SN (2014) Ultra-fast selective sensing of ethanol and petrol using microwave-range metamaterial complementary split-ring resonators. *J Appl Phys* 116(16):164106
67. Melik R, Unal E, Perkgoz NK, Puttlitz C, Demir HV (2010) Metamaterial-based wireless RF-MEMS strain sensors. *Conference Proceedings In: 2010 IEEE SENSORS*. IEEE pp 2173–2176. <https://doi.org/10.1109/ICSENS.2010.5690582>
68. Li J et al (2013) Flexible terahertz metamaterials for dual-axis strain sensing. *Opt Lett* 38(12):2104–2106
69. Schueler M, Mandel C, Puentes M, Jakoby R (2012) Metamaterial inspired microwave sensors. *IEEE Microw Mag* 13(2):57–68
70. Schüller M, Mandel C, Puentes M, Jakoby R (2011) Capacitive level monitoring of layered fillings in vessels using composite right/left-handed transmission lines. *Conference Proceedings In: 2011 IEEE MTT-S International Microwave Symposium*. IEEE pp 1–1. <https://doi.org/10.1109/MWSYM.2011.5973159>
71. Boybay MS, Ramahi OM (2007) Double negative metamaterials for subsurface detection. *Conference Proceedings In: 29th annual international conference of the IEEE engineering in medicine and biology society*. IEEE pp 3485–3488. <https://doi.org/10.1109/IEMBS.2007.4353081>
72. Ebrahimi A, Withayachumnankul W, Al-Sarawi S, Abbott D (2014) High-sensitivity metamaterial-inspired sensor for microfluidic dielectric characterization. *IEEE Sensors J* 14(5):1345–1351
73. Rawat V, Kitture R, Kumari D, Rajesh H, Banerjee S, Kale SN (2016) Hazardous materials sensing: an electrical metamaterial approach. *J Magn Magn Mater* 415:77–81
74. Rawat V, Nadkarni V, Kale SN, Hingane S, Wani S, Rajguru C (2015) Calibration and optimization of a metamaterial sensor for hybrid fuel detection. *Conference Proceedings In: 2nd international symposium on physics and technology of sensors (ISPTS)*. IEEE pp 257–259. <https://doi.org/10.1109/ISPTS.2015.7220124>
75. Zarifi MH, Farsinezhad S, Abdolrazzagh M, Daneshmand M, Shankar K (2016) Selective microwave sensors exploiting the interaction of analytes with trap states in TiO₂ nanotube arrays. *Nanoscale* 8(14):7466–7473
76. Kaushik A, Kumar R, Arya SK, Nair M, Malhotra BD, Bhansali S (2015) Organic–inorganic hybrid nanocomposite-based gas sensors for environmental monitoring. *Chem Rev* 115(11):4571–4606
77. Lee H-J et al (2012) A planar split-ring resonator-based microwave biosensor for label-free detection of biomolecules. *Sensors Actuators B Chem* 169:26–31
78. Clark AW, Glidle A, Cumming DRS, Cooper JM (2009) Plasmonic split-ring resonators as dichroic nanophotonic DNA biosensors. *J Am Chem Soc* 131(48):17615–17619
79. RoyChoudhury S, Rawat V, Jalal AH, Kale SN, Bhansali S (2016) Recent advances in metamaterial split-ring-resonator circuits as biosensors and therapeutic agents. *Biosens Bioelectron* 86:595–608

80. Rawat V, Nadkarni V, Kale SN (2016) High sensitive electrical metamaterial sensor for fuel adulteration detection. *Def Sci J* 66(4):421–424
81. Rawat V, Kitture R, Kumari D, Rajesh H, Banerjee S, Kale SN (2016) Hazardous materials sensing: an electrical metamaterial approach. *J Magn Mater* 415:77–81
82. Kitture R, Pawar D, Rao CN, Choubey RK, Kale SN (2017) Nanocomposite modified optical fiber: a room temperature, selective H₂S gas sensor: studies using ZnO-PMMA. *J Alloys Compd* 695:2091–2096
83. Singh AK, Patil SB, Nakate UT, Gurav KV (2013) Effect of Pd and Au sensitization of bath deposited flowerlike TiO₂ thin films on CO sensing and photocatalytic properties. *J Chem.* [Online]. Available: <https://www.hindawi.com/journals/jchem/2013/370578/>. Accessed 17 Nov 2018
84. Trung DD et al (2014) Effective decoration of Pd nanoparticles on the surface of SnO₂ nanowires for enhancement of CO gas-sensing performance. *J Hazard Mater* 265:124–132
85. Guo J, Zhang J, Zhu M, Ju D, Xu H, Cao B (2014) High-performance gas sensor based on ZnO nanowires functionalized by Au nanoparticles. *Sensors Actuators B Chem* 199:339–345
86. Chandrasekaran G, Sundararaj A, Therese HA, Jeganathan K (2015) Ni-catalysed WO₃ nanostructures grown by electron beam rapid thermal annealing for NO₂ gas sensing. *J Nanopart Res* 17(7):292
87. Yamazoe N, Sakai G, Shimanoe K (2003) Oxide semiconductor gas sensors. *Catal Surv Jpn* 7(1):63–75
88. Xu J, Pan Q, Shun Y, Tian Z (2000) Grain size control and gas sensing properties of ZnO gas sensor. *Sensors Actuators B Chem* 66(1):277–279
89. Feng P, Wan Q, Wang TH (2005) Contact-controlled sensing properties of flowerlike ZnO nanostructures. *Appl Phys Lett* 87(21):213111
90. Wan Q et al (2004) Fabrication and ethanol sensing characteristics of ZnO nanowire gas sensors. *Appl Phys Lett* 84(18):3654–3656
91. Comini E, Faglia G, Sberveglieri G, Pan Z, Wang ZL (2002) Stable and highly sensitive gas sensors based on semiconducting oxide nanobelts. *Appl Phys Lett* 81(10):1869–1871
92. Huang J, Wan Q (2009) Gas sensors based on semiconducting metal oxide one-dimensional nanostructures. *Sensors* 9(12):9903–9924
93. Choi KJ, Jang HW (2010) One-dimensional oxide nanostructures as gas-sensing materials: review and issues. *Sensors* 10(4):4083–4099
94. Park GC, Hwang SM, Lim JH, Joo J (2014) Growth behavior and electrical performance of Ga-doped ZnO nanorod/p-Si heterojunction diodes prepared using a hydrothermal method. *Nanoscale* 6(3):1840–1847
95. Oh E et al (2009) High-performance NO₂ gas sensor based on ZnO nanorod grown by ultrasonic irradiation. *Sensors Actuators B Chem* 141(1):239–243
96. Rashid J, Barakat MA, Salah N, Habib SS (2015) ZnO-nanoparticles thin films synthesized by RF sputtering for photocatalytic degradation of 2-chlorophenol in synthetic wastewater. *J Ind Eng Chem* 23:134–139
97. Adolph D, Tingberg T, Ive T (2015) Growth of ZnO(0001) on GaN(0001)/4H-SiC buffer layers by plasma-assisted hybrid molecular beam epitaxy. *J Cryst Growth* 426:129–134
98. Krunk M, Dedova T, Oja Açıık I (2006) Spray pyrolysis deposition of zinc oxide nanostructured layers. *Thin Solid Films* 515(3):1157–1160
99. Dedova T et al Chemical spray deposition of zinc oxide nanostructured layers from zinc acetate solutions. *Phys Status Solidi A* 205(10):2355–2359
100. Ilican S, Caglar M (2007) The effect of deposition parameters on the physical properties of Cd_xZn_{1-x}S films deposited by spray pyrolysis method. *J Optoelectr Adv Mater* 09(5): 1414–1417. <https://doi.org/10.1007/s10853-012-6362-x>
101. Zou AL et al (2016) Ethanol sensing with Au-modified ZnO microwires. *Sensors Actuators B Chem* 227:65–72

102. Kaneti YV et al (2015) Experimental and theoretical studies on noble metal decorated tin oxide flower-like nanorods with high ethanol sensing performance. *Sensors Actuators B Chem* 219:83–93
103. Kim S, Park S, Park S, Lee C (2015) Acetone sensing of Au and Pd-decorated WO₃ nanorod sensors. *Sensors Actuators B Chem* 209:180–185
104. Wang Y et al (2014) Room-temperature hydrogen sensor based on grain-boundary controlled Pt decorated In₂O₃ nanocubes. *Sensors Actuators B Chem* 201:351–359
105. Van Tong P, Hoa ND, Van Duy N, Le DTT, Van Hieu N (2016) Enhancement of gas-sensing characteristics of hydrothermally synthesized WO₃ nanorods by surface decoration with Pd nanoparticles. *Sensors Actuators B Chem* 223:453–460
106. Jin W, Yan S, Chen W, Yang S, Zhao C, Dai Y (2014) Preparation and gas sensing property of Ag-supported vanadium oxide nanotubes. *Funct Mater Lett* 07(03):1450031
107. Şennik E, Alev O, Öztürk ZZ (2016) The effect of Pd on the H₂ and VOC sensing properties of TiO₂ nanorods. *Sensors Actuators B Chem* 229:692–700
108. Salunkhe RR, Dhawale DS, Patil UM, Lokhande CD (2009) Improved response of CdO nanorods towards liquefied petroleum gas (LPG): effect of Pd sensitization. *Sensors Actuators B Chem* 136(1):39–44
109. Kumar R, Al-Dossary O, Kumar G, Umar A (2015) Zinc oxide nanostructures for NO₂ gas-sensor applications: a review. *Nano-Micro Lett* 7(2):97–120
110. Wei A, Pan L, Huang W (2011) Recent progress in the ZnO nanostructure-based sensors. *Mater Sci Eng B* 176(18):1409–1421
111. Dey (2018) Semiconductor metal oxide gas sensors: a review. *Mater Sci Eng B* 229:206–217. <https://doi.org/10.1016/J.MSEB.2017.12.036>
112. Mirzaei A, Kim SS, Kim HW (2018) Resistance-based H₂S gas sensors using metal oxide nanostructures: a review of recent advances. *J Hazard Mater* 357:314–331
113. Zhu L, Zeng W (2017) Room-temperature gas sensing of ZnO-based gas sensor: a review. *Sensors Actuators A Phys* 267:242–261
114. Nakate UT, Bulakhe RN, Lokhande CD, Kale SN (2016) Au sensitized ZnO nanorods for enhanced liquefied petroleum gas sensing properties. *Appl Surf Sci* 371:224–230
115. Min BK, Friend CM (2007) Heterogeneous gold-based catalysis for green chemistry: low-temperature CO oxidation and propene oxidation. *Chem Rev* 107(6):2709–2724
116. Daniel M-C, Astruc D (2004) Gold nanoparticles: assembly, supramolecular chemistry, quantum-size-related properties, and applications toward biology, catalysis, and nanotechnology. *Chem Rev* 104(1):293–346
117. Hongstith N, Wongrat E, Kerdcharoen T, Choopun S (2010) Sensor response formula for sensor based on ZnO nanostructures. *Sensors Actuators B Chem* 144(1):67–72
118. Kung MC, Davis RJ, Kung HH (2007) Understanding au-catalyzed low-temperature CO oxidation. *J Phys Chem C* 111(32):11767–11775
119. Xiang Q et al (2010) Au nanoparticle modified WO₃ nanorods with their enhanced properties for photocatalysis and gas sensing. *J Phys Chem C* 114(5):2049–2055
120. Thakur HV, Nalawade SM, Gupta S, Kitture R, Kale SN (2011) Photonic crystal fiber injected with Fe₃O₄ nanofluid for magnetic field detection. *Appl Phys Lett* 99(16):161101
121. Tackett R, Sudakar C, Naik R, Lawes G, Rablau C, Vaishnava PP (2008) Magnetic and optical response of tuning the magnetocrystalline anisotropy in Fe₃O₄ nanoparticle ferrofluids by co doping. *J Magn Magn Mater* 320(21):2755–2759
122. Kruse T, Krauthäuser H-G, Spanoudaki A, Pelster R (2003) Agglomeration and chain formation in ferrofluids: two-dimensional x-ray scattering. *Phys Rev B* 67(9):094206
123. Gupta S, Nalawade SM, Hatamie S, Thakur HV, Kale SN (2011) Sensitive, weak magnetic field sensor based on cobalt nanoparticles deposited in micro-tunnels of PM-PCF optical fiber. *AIP Conf Proc* 1391(1):437–439
124. Potok T, Phillips L, Pollock R, Loebel A, Sheldon F (2003) Suitability of agent-based systems for command and control in fault-tolerant, safety-critical responsive decision networks. In: ISCA PDCS, pp 1283–1290

125. Shostack A, Stewart A (2008) *The new school of information security*, 1st edn. Addison-Wesley Professional, Upper Saddle River
126. Wysopal C, Nelson L, Dustin E, Zovi DD (2006) *The art of software security testing: identifying software security flaws* (Symantec Press). Pearson Education. ISBN: 0321304861
127. Koscher K et al (2010) Experimental security analysis of a modern automobile. Conference Proceedings In: 2010 IEEE symposium on security and privacy. IEEE pp 447–462. <https://doi.org/10.1109/SP.2010.34>



Nanocrystalline PNS-PZT-Based Energy Harvester for Strategic Applications

2

H. H. Kumar, C. M. Lonkar, and
Balasubramanian Kandasubramanian

Contents

Introduction	36
Synthesis of Compositions	40
Synthesis of Precursor NiSb_2O_6 and TG-DT Analysis	40
Synthesis of <i>nano</i> -La-PNS-PZT Composition by MA and Characterization	43
Progressive Phase Formation During MA and XRD Studies	44
Effect of MA on Particle Morphology and HRTEM Studies	46
Processing of La-PNS-PZT Powder	47
Binder Addition and Granulation	47
Forming	48
Sintering	48
Lapping	48
Microstructural Analysis: SEM Studies	49
Electroding	49
Poling	49
Characterization	50
Effect of Mechanical Activation and Reactive Sintering	51
Effect of Mechanical Activation	52
Effect of Reactive Sintering Temperature	55
Comparison of Properties: Micrometer and Nanometer Particle Size	61
Demonstration of Power Harvesting for Strategic Application	61
Concept of Power Harvesting	61
Power Harvesting Module	64
Conclusions	67
References	69

H. H. Kumar · C. M. Lonkar
Armament Research and Development Establishment, Pune, India

B. Kandasubramanian (✉)
Department of Metallurgical and Materials Engineering, Defence Institute of Advanced Technology
(Deemed University), Pune, India
e-mail: balask@diat.ac.in; meetkbs@gmail.com

Abstract

Today is an era of low-power devices mainly dependent on battery source for energy which needs to be replaced when gets exhausted for its power or ends its life. Usually, devices are embedded in structure or employed at remote places; hence, obtaining them for their replacement can become a very expensive task or even may not be feasible in some of the cases. Batteries of such devices could be replaced by “PZT-based power harvesting unit” since they are excellent electro-mechanical energy converting devices. This necessitates formulating and processing the PZT composition so as to achieve properties suitable for power harvesting in order to generate optimum electrical output. Here, nanostructured $\text{Pb}_{0.98}\text{La}_{0.02}(\text{Ni}_{1/3}\text{Sb}_{2/3})_{0.05}[(\text{Zr}_{0.52}\text{Ti}_{0.48})_{0.995}]_{0.95}\text{O}_3$ composition, suitable for power harvesting applications, was synthesized by columbite precursor method followed by mechanical activation (MA) from 5 h to 40 h of dry oxide powders using high-energy ball mill, thereby circumventing the calcination stage. Nanometer particle size and its morphology were confirmed by transmission electron microscopy (TEM). X-ray diffractometer (XRD) was used to probe for progressive perovskite phase formations and transformations during MA as well as reactive sintering. Effect of MA and reactive sintering (1170–1320 °C) on microstructure was analyzed using scanning electron microscopy (SEM). Electromechanical properties of samples were evaluated and systematically correlated with crystallographic and microstructural effects. Processing parameters were optimized to obtain superior piezoelectric properties for power harvesting applications. Compact microstructure, composition at morphotropic phase boundary, optimum tetragonality, and crystallinity obtained for the samples for 10 h mechanical activation and sintered at 1220 °C resulted in best possible piezoelectric charge coefficient, d_{33} (449×10^{-12} C/N); piezoelectric voltage coefficient, g_{33} (32×10^{-3} m.V/N); and figure of merit for power harvesting, FoM_{PH} ($14,400 \times 10^{-15}$ m-V.C/N²). Further, power harvesting module was developed, and electrical output in response to simulated random vibrations of aerospace vehicles was measured in frequency band of 20–2000 Hz which explored the suitability of this composition for power harvesting applications for aerospace vehicle.

Keywords

Power harvesting · Piezoelectric · PNS-PZT · Mechanical activation · Nano-PZT

Introduction

Nowadays, scientists and technologists have focused their attention on miniaturization of electronic devices due to which power requirement of electronic systems has drastically reduced. Although they require low power, these systems entirely depend upon batteries for their operation. Device is required to be retrieved for battery replacement, when it gets exhausted for its power. Retrieval of devices may be

expensive or even may be impossible in some of the cases when those are remotely placed or even may be embedded in structure. Other important issues with the batteries are recurring cost, potential leakage, shelf life, environmentally conscious disposal, downtime due to unexpected battery failure, etc. “Pb(ZrTi)O₃ (PZT) based power harvesting module” can be solution to the problem since it can harvest mechanical energy by converting ambient mechanical energy which is in the form of vibrations and movements available on large scale in the nature. This requires (i) tailoring of PZT composition to obtain properties suitable for power harvesting application, (ii) further designing of power harvesting module to tune with type of input available in the environment of application, and (iii) storing and utilization of the electrical energy.

Electromagnetic induction [1], electrostatic generation [2], dielectric elastomers [3], and piezoelectric materials [4] are discussed in the literature, as energy conversion mechanisms. Piezoelectric materials are best suited for transduction into electrical energy when input source is in the form of mechanical energy like movements, vibrations, pressure, etc.

In the past couple of decades, it is seen that innumerable research articles are published related to design of efficient power harvesting devices, improving efficiency of electronic circuits, implantable and wearable electronic devices, MEMS-based harvesting devices, wireless sensors, and many power harvesting techniques vis-a-vis piezoelectric materials. But very less work has been reported on the development of newer piezoelectric materials, scavenging power from vibrations of aerospace vehicles in high-g environment. Several review articles are available on progress related to energy harvesting devices and applications based on piezoelectric materials [5, 6].

Presently, piezoelectric devices are in the forefront for powering electronic devices at low-power range, μW to mW level, portable and wearable devices, wireless sensors, health monitoring devices, etc. [7].

Solid solutions of lead zirconate titanate (PZT) were discovered by Jaffe et al. in 1952. These compositions show superior piezoelectric properties (compared to barium titanate) at their morphotropic phase boundary (MPB) [8]. This invention opened the possibility of achieving intended properties by tailoring composition with the help of dopants [9].

The development of piezoelectric ceramics with superior properties for certain application falls under two types:

- Piezoelectric compositions with new phase diagrams
- Tailoring of microstructure of existing compositions

According to literature, the second approach has yielded superior electromechanical properties [10].

PZT-type piezo materials and their variants are commonly deployed for vibration-based power harvesting applications. Due to constraint on lead-based materials in many countries, researchers have started working on lead-free piezoceramic materials. Na_{0.5}Bi_{0.5}TiO₃-BaTiO₃ (NBT-BT) is the most researched lead-free piezoelectric composition. The properties of this composition and its variants have inferior

temperature stability compared to PZT-based materials. Also, the electromechanical properties like piezoelectric coefficients and coupling coefficients of many lead-free compositions could not touch the superior properties of PZT compositions [11].

$\text{Pb}(\text{Ni}_{1/3}\text{Sb}_{2/3})\text{O}_3\text{-PbZrTiO}_3$, (PNS-PZT), is a solid solution of complex perovskite-type $\text{Pb}(\text{B}'_{1/3}\text{B}''_{2/3})\text{O}_3\text{-P}(\text{B})\text{O}_3$. Some of the researchers have studied this composition in the vicinity of MPB which is 0.12 PNS -0.40 PZ -0.48 PT with various additives to investigate the effect on sintering temperature [12] and properties like bulk density, k_p , Q_m , K_3^T , and $\tan \delta$ were reported [13].

Zahi et al. investigated the composition for the properties, viz., dielectric constant (K_3^T), coupling factor (k_p), and curie temperature (T_c) [14]. The composition 0.10 PNS -0.46 PZ -0.44 PT having presence of F_T and F_R showed optimum $K_3^T = 3100$ and $k_p = 0.69$. For 10 mol % of PNS, when Zr/Ti ratio was decreased from 46/44 to 41/49, curie temperature showed rising trend from 250 °C to 305 °C [14].

Irena Jankowska-Sumara et al. studied elastic compliance s^{11} , coupling coefficient k_{31} , charge coefficient d_{31} , Q_m , elastic constant, and phase transition behavior as a function of compositional variations [15].

Lonkar et al. reported suitability of La-doped $\text{Pb}(\text{Ni}_{1/3}\text{Sb}_{2/3})\text{O}_3\text{-PbZrTiO}_3$ (La-PNS-PZT) composition for powder harvesting and sensor applications. They also compared the voltage output of this material with commercially available PZT-5A and found that La-PNS-PZT generates 2.5 times higher voltage and power compared to PZT-5A [16].

The brittle nature of bulk PZT ceramics does not provide feasibility of incorporating them in wearable and flexible electronic devices. By incorporating PZT material in flexible polymers, the devices can be extended to newer applications for power harvesting. Piezo-polymer composites, ferroelectrets can deliver better output power compared to bulk devices under similar conditions of application of strain energy [17–19].

Polyvinylidene fluoride (PVF₂) is a popular piezoelectric polymer that generates electric voltage and power on application of stress. Newnham et al. synthesized various piezopolymer composites and introduced various connectivities (0-0, 0-1, 0-2, 0-3, 1-1, 1-2, 1-3, 2-2, 2-3, and 3-3) for getting superior piezoelectric properties [18]. These composites demonstrate functional properties of both the bulk PZT and flexible polymer and achieve desired effect [20].

Harvesting of energy from respiration, rainfall, footsteps, wind, etc. has been demonstrated. Some researchers have used powder of lead-free piezoelectric materials in polymers and reported their findings [21].

The very first power harvesting prototype unit was reported by Harbauer et al. in year 1984 [22]. A PVDF power harvesting unit was devised by them and fitted onto ribs of a dog and was able to get 18 V and 17 μW from this device in response to mechanical vibrations due to respiration [22]. Power generation due to impact during walking was demonstrated by Kymissis et. al. (1998) [91]. They fitted multilayer of PVDF transducer inside the sole and THUNDER actuator inside the heel of the shoe. Flexible harvester generated 1.1 mW during bending of foot, and THUNDER actuator produced 1.8 mW power during walking.

Various geometries of piezoceramics which can be deployed for vibration-based power harvesting are as follows:

- Bulk devices, like cantilever, cymbal, and stack
- Thin films, which can be deployed in the form of microelectromechanical systems
- Nanocrystalline materials which can be used along with flexible polymers

The power delivered by a harvester depends on applied force, acceleration, vibration frequency, electrical and mechanical impedance matching, mass of the device, ambient conditions, structural design, and piezoelectric material used [5].

A piezoelectric power harvesting device in the form of cantilever produces large output voltage in response to applied strain. A piezoelectric body, a shim, and proof mass are the constituent elements of cantilever harvester. It operates in 31 mode of piezoelectric response. Using suitable design tools (COMSOL, ANSYS, etc.), it is possible to devise a harvester which can deliver large output voltage due to larger deformation [5]. Kim et al. worked on piezoceramic power harvester based on thick-film unimorph cantilever and could generate 17.3 mW electrical power and 2.08 mW/cm³ power density at 20 Hz for 4 g acceleration [23].

Choi et al. used Pb[(Zn_{0.4}Ni_{0.6})_{1/3}Nb_{2/3}]O₃ (PZNN) composition for cantilever power harvester and were able to achieve 231 mW/cm³ power density at frequency of 84 Hz and acceleration 1 g, from this composition [24]. Song et al. manufactured cantilever power harvester using 0.7PMN-0.3PT single crystal and compared it with PZT-based cantilever [25]. The former harvester delivered 1070 μW electrical power at 89 Hz under 0.53 g which was much large compared to PZT cantilever. The comparison of unimorph cantilevers made out of PMN-PZT and commercially available PZT materials by Karami et al. revealed that maximum output is produced by single-crystal cantilever which was 226 W/g² at 819 Hz [26]. Cymbal is type V flex tensional transducer usually used for low-power ultrasonic applications. It consists of a piezo disc sandwiched between two concave metal caps which perform the function of force amplifier. Palosaari et al. used cymbal design and demonstrated that a power harvesting module delivers electrical power of 660 μW at 1.19 Hz with 24.8 N force and the power densities of 0.31 mW/cm³ [27].

Power harvesting module consists of piezoelectric component, electronic circuit, and storage capacitor. For optimum power transfer from piezoelectric device to storage device, electronic circuit needs to be designed with high efficiency. This circuit consists of a rectifier, a DC-DC converter, and complex impedance matching circuit [4, 28]. The power requirement of microelectronic devices is usually few μW. For powering these microcircuits, piezoelectric power harvesting devices can be introduced inside the circuit using MEMS technology [4, 29]. MEMS-based piezo harvester using cantilever design can produce few tens of microwatt which is just sufficient power to run microelectronic circuits [30].

Uchino and co-workers have recently presented comprehensive review of vibration-based energy harvesting. He has systematically discussed the stages and the approach to increase the output of power harvesting modules [31].

Aerospace vehicles, like, satellite launch vehicles or missiles, generate random vibrations during their motion. These space vehicles are subjected to vibration environment during their useful life [32]. There is not much literature available on power spectrum density, nor on utilization of this mechanical energy. This vibration energy remains unutilized which can be converted into useful electrical energy by making use of piezoceramic components, stored and fed to microcircuits of launch vehicles [6]. Steven R. Anton et al. proposed the possibility of power harvesting from random vibrations and solar energy in unmanned aerial vehicle(UAV) [6]. The experimental work was performed on remotely controlled (RC) glider aircraft. Vibrations of wings and the mechanical energy of body of moving aircraft were tapped by means of two numbers of piezoceramic power harvesting modules fitted under the wings and a cantilever piezo power harvester fitted on the fuselage for harvesting energy. Solar energy was collected by means of photovoltaic panels which were placed on the top of the wings. UAV solar power harvesting device was able to charge 170 mAh battery to 14% of the total capacity, whereas piezo harvester charged EH300 4.6 mJ internal capacitor to 70% of the total capacity. This power is sufficient for working of microelectronics of UAV. They also proposed that piezo power harvesting can deliver power during nighttime and cloudy weather [6].

Present study relates synthesis of $\text{Pb}_{0.98}\text{La}_{0.02}(\text{Ni}_{1/3}\text{Sb}_{2/3})_{0.05}[(\text{Zr}_{0.52}\text{Ti}_{0.48})_{0.995}]_{0.95}\text{O}_3$ composition, with particle size in nanoregime (*nano*-La-PNS-PZT), comprising the properties suitable for power harvesting applications. Mechanical activation method was adopted for synthesis, and compositions were characterized for various piezoelectric properties, correlated with structure and further evaluated for power harvestability for simulated random vibrations of aerospace vehicles.

Synthesis of Compositions

Composition $\text{Pb}_{0.98}\text{La}_{0.02}(\text{NiSb})_{0.05}[(\text{Zr}_{0.52}\text{Ti}_{0.48})_{0.995}]_{0.95}\text{O}_3$ was processed as per process chart given at Fig. 1. Desired *nano*La-PNS-PZT ceramic composition was synthesized in two steps to evade the formation of unwanted pyrochlore phase, $\text{Pb}_2\text{Sb}_2\text{O}_7$. In the first stage, NiSb_2O_6 (NS), a columbite precursor, was obtained and *nano*-La-PNS-PZT composition in latter stage through process known as “mechanical activation” for 5–40 h. Activated powders were characterized for progressive phase formation and particle morphology studies.

Synthesis of Precursor NiSb_2O_6 and TG-DT Analysis

NS was obtained by reacting NiO and Sb_2O_5 according to the following reaction 1 by process of calcination.



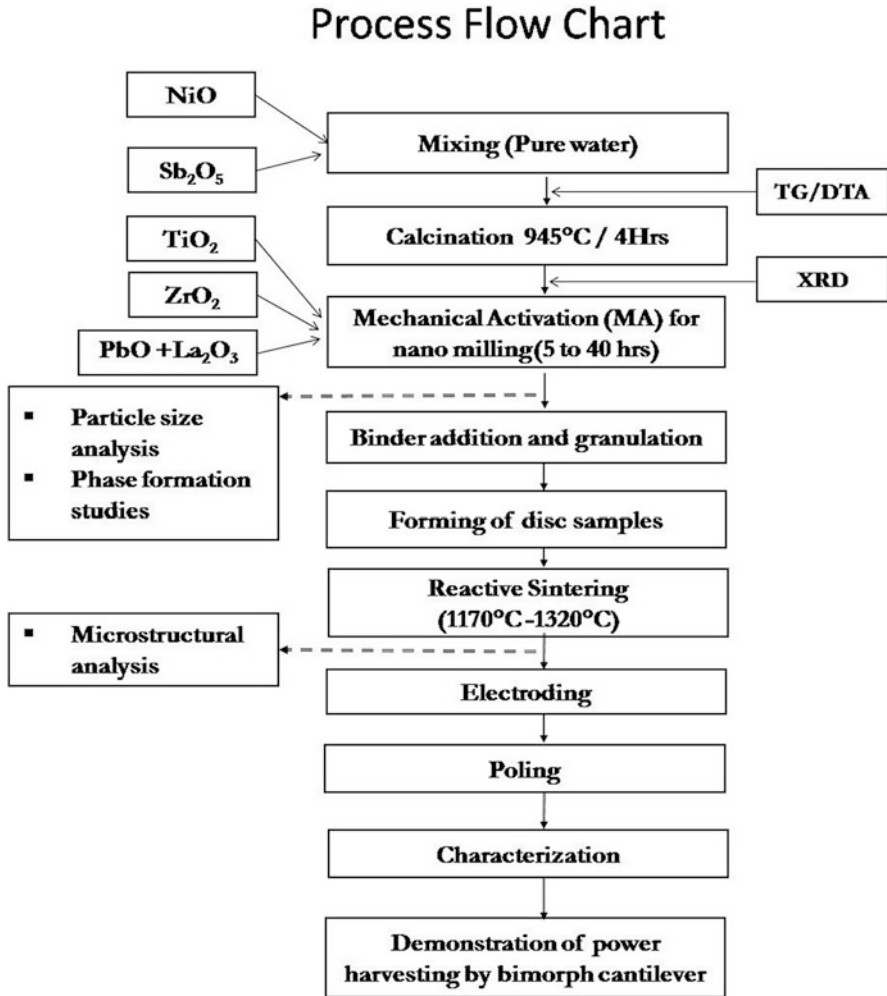


Fig. 1 Process flow chart for synthesis and characterization of *nano-La-PNS-PZT* composition and device

However, it was essential to estimate calcination temperature profile so that entire amounts of raw materials get converted into pure NS according to Eq. 1. It was achieved by subjecting the mixture of milled raw materials powders to thermogravimetric analysis and differential thermal analysis (TGA-DTA), simultaneously. Thermogravimetric analysis (TGA) records the changes in weight of the powder sample as a function of temperature. The technique is also useful to identify the temperature of absorption or evolution of gases from a sample consisting of a condensed phase. Differential thermal analysis (DTA) is graph of change in temperature of test sample recorded continuously as function of temperature or time [33].

Stoichiometric proportions of powders as per Eq. 1 were mixed and milled together for 24 h in jar, consisting of zirconia balls as grinding media and pure water as medium. Dried powder was subjected to TG- DTA using analyzer Mettler Toledo 851e, and change in weight of a sample with temperature over a period of time was recorded.

Powder sample was analyzed from room temperature to 1100 °C @ 5 °C/min, and plots recorded are shown in Fig. 2. Powders were calcined at the temperatures indicated by peaks in TG-DTA curves and further investigated for the phase formations at corresponding temperatures by analyzing XRD (Bruker AXS, GmbH, Model – D8 Advance) patterns shown in the Fig. 3.

Up to 350 °C, broad exothermic peak was observed in DT curve which is accompanied by a slight weight loss as observed in TG curve which relates to loss of water [34]. Water molecules which are adsorbed on the surface of the particle get evaporated at comparatively lower temperatures, while the molecules, which are entrapped between the particles, during milling, require larger temperatures [34]. Without any loss in weight, a drastic reduction in temperature was observed between 380 °C and 400 °C. This corresponds to melting of Sb_2O_5 . Between 690 °C and 740 °C, small exothermic peak which is followed by larger endothermic peak was observed which does not correspond to formation of NS as indicated by XRD pattern, shown in the Fig. 3. Comparing XRD pattern for mixture with individual patterns for raw material powders, peaks are observed to be shifted to lower side at 740 °C, indicating rise in unit cell dimensions. The peak may correspond to formation of metastable state before formation [35] of NS. An endothermic peak

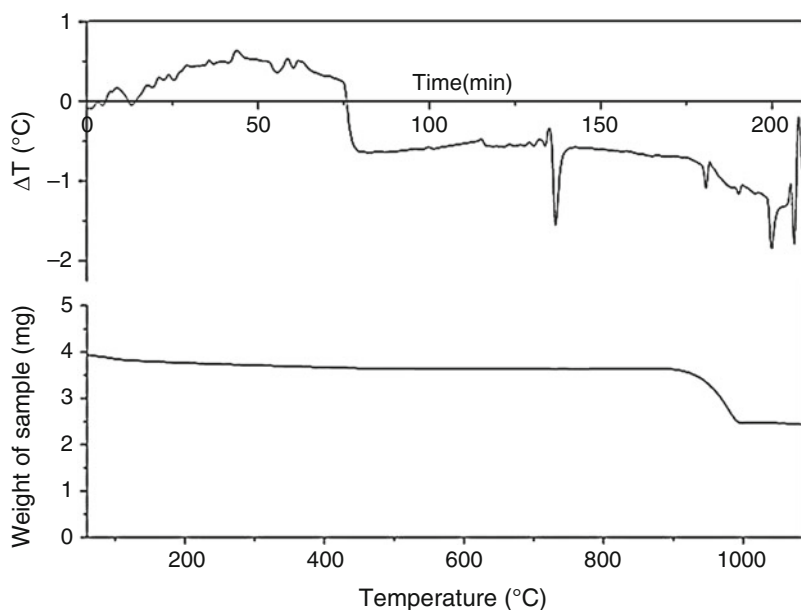


Fig. 2 TG-DTA plots for NiSb_2O_6

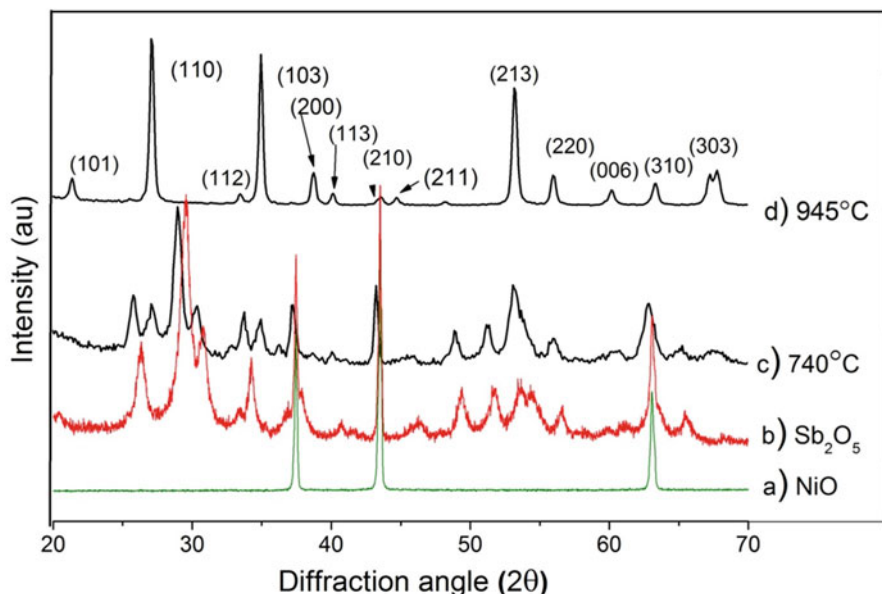
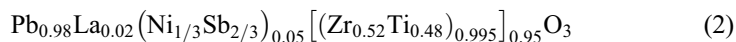


Fig. 3 XRD pattern for (a)NiO, (b)Sb₂O₅ (c)NS calcined at 740 °C, and (d) NS calcined at 945 °C

observed at 945 °C corresponds to formation temperature of NS as indicated by XRD pattern and confirmed by ICDD data for NS. NS was found to take tetragonal symmetry. No other phases were detected since all the peaks matched with the standard ICDD data [36] representing tetragonal crystal symmetry.

Synthesis of *nano*-La-PNS-PZT Composition by MA and Characterization

Stoichiometric formula of the composition under study is represented by Eq. 2:



Further, properties of desired *nano*-La-PNS-PZT composition were compared with La-PNS-PZT composition having particle size in μm range obtained by solid-state route which is described in Table 3.

Composition as per stoichiometric formula 2 was prepared by considering mol% of NS prepared in first stage, mixed with the remaining raw material oxide powders. However, to compensate the lead loss, which takes place at 886 °C [37], 0.5 mol% of PbO was taken in excess.

Mechanical activation (MA) was carried out for 5 h, 10 h, 20 h, 30 h, and 40 h. Progressive phase formation of raw material powders to desired composition through MA was studied by X-ray diffraction (XRD) technique, whereas particle

morphology was studied by high-resolution transmission electron microscopy (HRTEM), (FEI, model TECNAI G²).

MA is a solid-state powder processing route in which repeated welding, fracturing, and re-welding of powder particles take place, thereby performing solid-state reaction, in a high-energy ball mill [38]. High-energy ball mill (Retsch GmbH, model PM 400, Germany) was used for carrying out solid-state reaction among the raw material powders as well as to reduce particle size of the phase formed composition in nanometer regime. This mill has four milling jars lined with tungsten carbide material and contains grinding media in the form of balls of tungsten carbide. Ball to powder ratio was set to 13:1, while rotations were set to 300 rpm.

Mechanical activation process employs high-energy ball milling (HEBM) in which raw material powders are milled intimately. Due to combined effect of mechanical energy and temperature in the HEBM [39], particles are fused together and ruptured continuously [40]. This initiates the chemical reaction among raw material powders and reduction in particle size to nanometer regime, simultaneously, thereby skipping the “calcination” step of conventional mixed oxide route [41]. Nanomaterials attracted researchers since they created possibility of improving the properties due to variation in crystallite size [39].

Effect of activation duration on crystal structure and microstructure was investigated. Further, disc samples were prepared out of these activated powders and sintered between 1170 °C and 1320 °C for 30 min in lead-rich atmosphere and evaluated for crystal structure, microstructure, and piezoelectric properties. An appropriate activation duration was identified which would result in superior piezoelectric properties for power harvesting application. Piezoelectric properties and structures developed in progressive phase formations were correlated.

Progressive Phase Formation During MA and XRD Studies

X-ray diffraction (XRD) technique is an indispensable tool for determination of crystal structure, estimation of various lattice parameters, and quantification of phases [42]. Knowledge of the crystal structure is essential since it has greater influence on the properties of material [43]. Diffraction leads to intense peaks by those crystallographic planes which satisfy the Bragg's condition $2d \sin \theta = n\lambda$. Intensity Vs 2θ pattern gives information of size and shape of the unit cell by the relative 2θ positions, while atomic positions, within the unit cell by the relative intensities of the diffraction peaks [42, 44]. XRD patterns are unique to each material [42].

Progressive phase formation of raw materials into desired compound by means of MA was investigated from XRD technique. This technique was also used to investigate the effect of reactive sintering temperature on crystal structure. XRD patterns were recorded for position 2θ from 20° to 60° using X-ray diffractometer with copper K_{α1} radiation having wavelength of 1.54 Å. XRD data was recorded at room temperature for step-scan mode with step size 0.02 and about 0.1 s per step. Refinement and analysis of XRD pattern and measurements of unit cell parameter were carried out using TOPAS [45].

Multiplot X-ray diffraction pattern for scanning angle 2θ from 20° to 60° for samples of activated powders for 5–40 h indicating progressive transition of raw materials into desired nanostructured compound consisting of perovskite phase is shown in Fig. 4.

Five hour of milled powder show presence of mixture of starting raw powders along with formation of PbTiO_3 in cubic phase [46] on smaller scale and show presence of PbTiO_3 in tetragonal phase [47] and PbZrO_3 [48] on larger scale indicating that powder particles have acquired necessary kinetic energy in milling to initiate the solid-state reaction [40]. In addition, the presence of perovskite phase was also noticed [49]. For 10 h activation, rise in the peak intensity by representing perovskite planes [50, 51] and reduction in peaks for starting components were observed. Transformation of PbTiO_3 from cubic phase to tetragonal was revealed from related change in peak intensities [47].

The said transformation of PbTiO_3 from paraelectric (cubic) to ferroelectric (tetragonal) for 10 h activation may be due to improved crystallization which exceeds the critical crystallite size as observed by Hsiang et al., in case of BaTiO_3 [52]. Individual peaks for NS and La_2O_3 disappeared for 10 h activation time signifying their occupancy in perovskite crystal lattice. Though it is not very

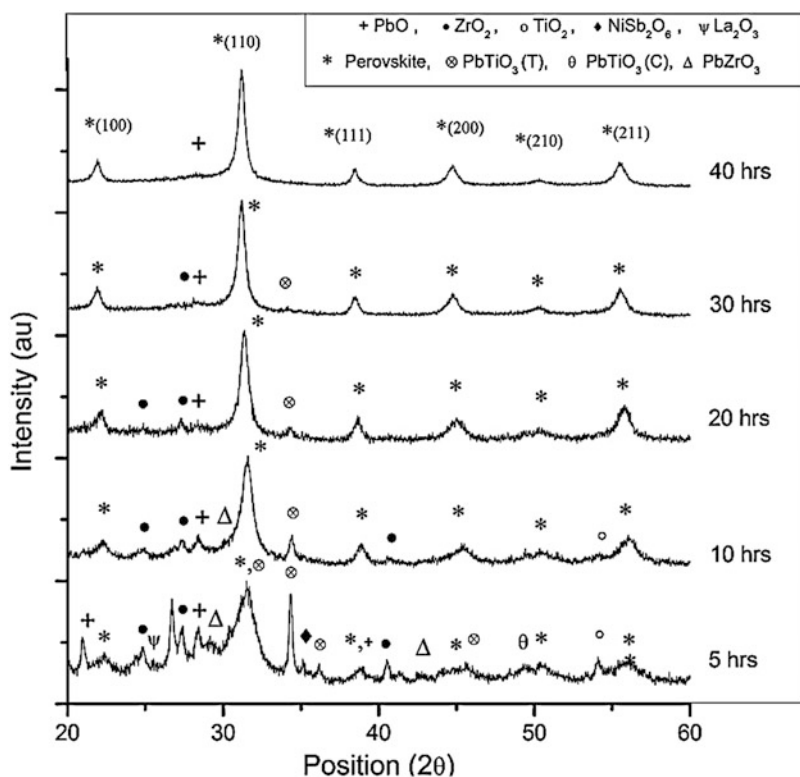


Fig. 4 XRD patterns: progressive phase formation by mechanical activation

prominent, splitting of peak intensity at (200) plane signifies the simultaneous presence of ferroelectric tetragonal (F_T) and ferroelectric rhombohedral (F_R) phases [53]. PbZrO_3 and PbTiO_3 , peaks for raw materials still exist, indicating the evidence of unreacted raw materials. Increasing the activation duration to 20 and 30 h, these peaks reduced significantly demonstrating the advancement in formation of La-PNS-PZT in perovskite phase by solid-state reaction by mechanical activation. Peak widths are also reduced, specifying the increased crystallinity. Entire quantity of starting materials is transformed into desired La-PNS-PZT composition for 40 h activation time, as evident from peaks representing single perovskite phase. However, presence of PbO in trivial extent is as expected since it is taken in excess amount to compensate the loss in succeeding sintering process. Furthermore, compositions synthesized by this route were found to be free from pyrochlore phase ($\text{Pb}_2\text{Sb}_2\text{O}_7$) as the associated peaks for (2) plane at 30° , (440) plane at 49° , and (622) plane at 58° were absent in the XRD pattern [36].

Effect of MA on Particle Morphology and HRTEM Studies

HRTEM is a technique that provides a reliable estimation of particle size, shape, and their arrangement which make up the specimen as well as their relationship to each other on the scale of atomic diameters [54]. In this imaging technique, a beam of electrons is passed through a thin specimen. The formed image is magnified and directed toward fluorescent screen. Images with superior magnification and resolution are obtained with HRTEM. This technique is employed especially when particle size is in nanometer range.

It is required to prepare a sample for HRTEM analysis. A very small quantity of powder sample was added in ethyl alcohol in a vial and subjected to ultrasonication for 45 min. Drop of sample was taken on graphite-coated copper grit [55] and dried under UV lamp. Particle imaging was carried out using HRTEM, with electron beam accelerated at 200 kV. The particle morphology shown in Fig. 5 depicts the effect of mechanical activation for 5–40 h duration as recorded by HRTEM. In all the cases, distinct particles accompanied by few tight aggregates were seen, as they usually observed [56]. Wider size distribution (up to 50 nm) of spherical particles was pragmatic, suggesting insufficient milling and mixing in case of 5 h activation. Fine and spherical-shaped several distinct particles were present for 10 h activation.

Furthering the activation to 20 h, few irregular-shaped particles were detected without size reduction. On further increasing the activation duration, several particles with slight increase in size were noticed. Such particle morphology and trend are apparent, since mechanical activation is process in which continuous fracturing and rejoining of particles take place. The average particle size was 32 nm, 21 nm, 21 nm, 24 nm, and 25 nm, respectively, for 5–40 h activation.

Suryanarayana et al. reported the risk of contamination at higher milling time [40]. Analyzing for the contaminations of tungsten carbide from XRD was difficult because of merger of peaks. Hence, samples were investigated by EDS which show presence of tungsten carbide traces for 30 h activation (0.22 atomic %) which further augmented at 40 h activation (0.29 atomic %).

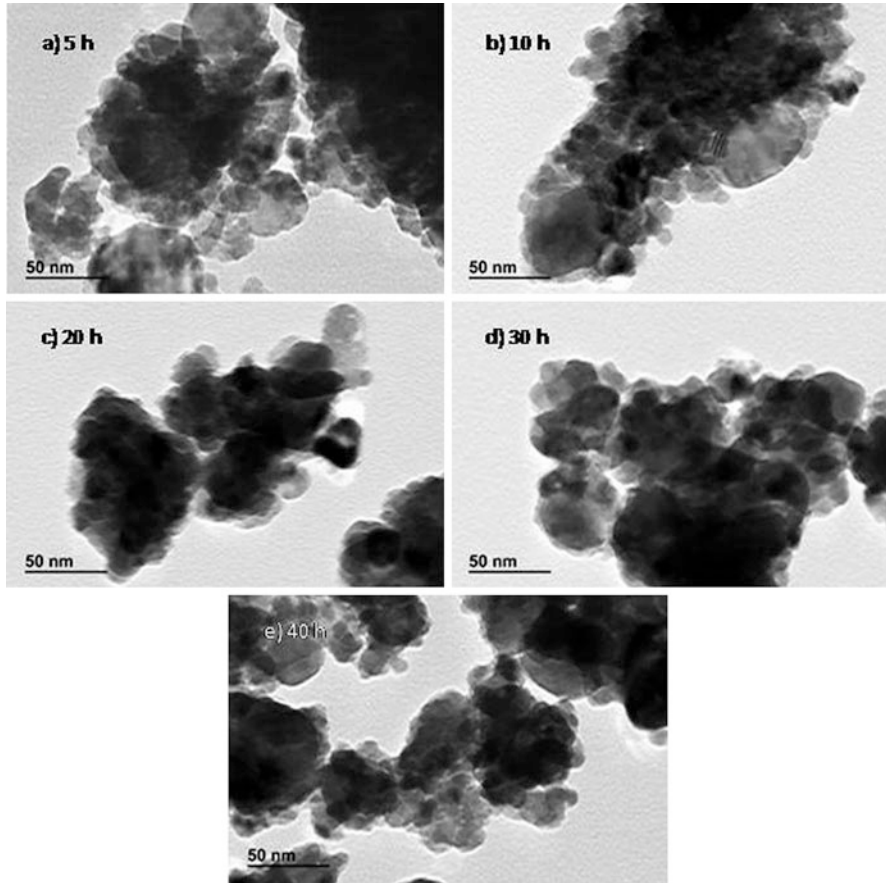


Fig. 5 HRTEM images: effect of activation duration on particle size (a) 5 h, (b)10 h, (c)20 h, (d)30 h, and (e)40 h

Processing of La-PNS-PZT Powder

Mechanically activated powder was processed as per Fig. 1.

Binder Addition and Granulation

Mechanically activated powder contains agglomerates and hence do not flow freely as required for the process of forming. Free flow material powder is obtained by granulating binder-added powders [57]. Polyvinyl alcohol at 10% V/W of powder was added, intimately mixed, and passed through sieve of mesh size 250 μm to obtain free flow granules of desired size.

Forming

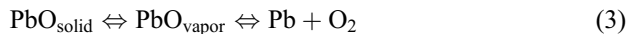
Using double-acting die punch machine (Make-GMT) granulated powder was compacted to form discs of $\phi 11.5$ mm and thickness of 1.5 mm keeping the green density to 4.8 ± 0.05 g/cc which is about 60% of theoretical density of PZT. Subsequently, samples were subjected to 650 °C temperature for binder removal.

Sintering

Sintering is a process of strengthening/densification where gradual conversion of material, without melting, from a state of agglomeration of particles to a denser material through firing takes place. In this process, densification takes place by reduction of surface area or removal of pores from powder compacts [58]. A larger number of preliminary point contacts, smaller pores, and uniform pore distribution lead to high density in sintered compact. During sintering, pores are removed, grain and grain boundaries are formed leading to permanent shape, better physical [59] and electromechanical characteristics in the sample. Sintering has greater influence on final properties; hence, determination of appropriate sintering parameters is essential.

Whenever chemical reaction takes place along with densification, it is termed as reactive sintering [60]. Sintering temperature and time play important role since they decide the grain size and thus controls the electromechanical properties on larger scale [61, 62].

Volatilization of lead occurs at 886 °C which is well below the sintering temperatures of PZT, leading to distraction in the stoichiometry and thus affecting the properties of the sintered component [37]. To avoid or to compensate the lead loss, components are sintered in lead-rich environment. Equation 3 indicates the vaporization and recondensation for PbO vapor till equilibrium is attained [63].



Hence, to obtain the superior properties, it is essential to sinter the component at appropriate sintering parameters which would lead to denser microstructure with uniform average grain size and narrow grain size distribution [64].

Components formed from mechanically activated powder from 5 to 40 h were reactively sintered between 1170 °C and 1320 °C for 30 min. In all, six samples from every composition were sintered, and averages of the properties were reported.

Lapping

The aim of lapping is to remove variations in flatness like camber and waviness developed during sintering and to maintain the plan-o-parallelism of surfaces to be electroded. Process involves moving of a sample against flat tool in the presence of

fine abrasive powder and water. Here, lapping of samples is carried out using fused alumina powder in lapping machine, Make-GMT, to achieve the thickness to 1.2 mm.

Microstructural Analysis: SEM Studies

Scanning electron microscopy (SEM) is a powerful tool for study of topographical features; surface morphology like grain morphology, grain size, and grain size distribution [65]; and various defects [66] like intergranular and the intragranular pores which influence the properties of the sintered sample, largely [37]. In this technique, a beam of electrons is raster scanned over a test sample which produces backscattered electrons, secondary electrons, and fluorescence as a result of interaction of electron beam and sample. Secondary electron provides microstructural information [67].

Samples were polished by polishing machine (Valco Industries) using levigated alumina paste of grade III (0.024 μm), grade II (0.017 μm), and further grade I (0.014 μm). Using the fact that grain boundaries have high energy compared to grains, they can be etched using appropriate etchant. Preparation of etchant is critical since it is expected to react only with grain boundaries, to reveal them, without affecting the grain. Five millilitre of concentrated HCl and two drops of HF, both, added in 95 ml of pure water were used to prepare etchant. Polished and etched samples were analyzed using field emission scanning electron microscope (ZEISS, Germany). Averaged grain size was evaluated by linear intercept method at different places on micrograph.

Electroding

Electrodes provide electrical connections for capturing electrical output and also to pole the sample to introduce piezoelectric effect in it. Metals like silver, gold, nickel, platinum, etc. are the choices for electrode material, while, depending upon geometry of sample and electrode, choices for methods like manual, vacuum, screen printing, etc. are available. Silver electrode paste was applied to the samples by screen printing method and cured at 600 °C for 10 min to form electrodes on parallel surfaces.

Poling

Until now, component does not exhibit piezoelectric effect, owing to random alignment of ferroelectric domains within the grain giving zero net polarization to material. It is necessary to align all the domains in one particular direction in order to incorporate piezoelectric properties in it. This is achieved by a process known as poling in which sufficiently strong DC electric field (few kV/mm) is applied between the electrodes of sample. Since air has dielectric strength below 1 kV/mm, generally,

poling is carried out in oil baths to avoid dielectric breakdown [8]. For ease of poling, it is carried out in heated oil bath.

Poling was performed by applying DC field of 3.0 kV/mm for 30 min at 100 °C in heated silicon oil bath. Although domains are locked during poling, forced alignment of domains generates strain in the material, and domains try to regain their pre-poling position leading to aging of properties on logarithmic scale. Therefore, samples were allowed to age for 10 days and then characterized.

Characterization

Apart from structural properties, samples were characterized for dielectric and piezoelectric properties for disc samples using the following characterization tools:

- Piezoelectric charge coefficient (d_{33}): Measured at 100 Hz using d_{33} Berlincourt meter (CPDT 3330).
- Variable frequency LCR meter (HiTester, model-3532, Hioki, Japan) was used to measure:
 - Impedance (Z_m)
 - Resonance frequency (f_r)
 - Antiresonance frequency (f_a)
 - $\tan \delta$ and capacitance(C) at 1 kHz

The following properties were calculated using standard equations:

- Densities were measured from weight and physical dimensions.
- The following Eqs. 4, 5, 6, 7, and 8 were used to evaluate, ϵ_r , g , $FoM_{PH}k_p$ and Q_m , respectively.

$$\epsilon_r = \frac{Ct}{\epsilon_0 A} \quad (4)$$

where ϵ_r is relative dielectric constant, a unitless quantity.

C = capacitance (F)

ϵ_0 = permittivity of the free space (8.854×10^{-12} F/m)

A = area of electrode (m^2)

t = thickness separating electrodes (m)

$$g = \frac{d}{\epsilon_0 \epsilon_r} = \frac{d}{\epsilon} \quad (5)$$

$$FoM_{PH} = d \times g \quad (6)$$

$$k_p = \sqrt{2.51 \frac{f_a - f_r}{f_r}} \quad (7)$$

where, f_r = resonance frequency(Hz), f_a = antiresonance frequency (Hz)

$$Q_m = \frac{1}{2\pi Z_m C f_r} \frac{f_a^2}{(f_a^2 - f_r^2)} \quad (8)$$

- Phase transition studies were carried out using broadband dielectric analyzer (Novocontrol, GmbH Model-Novatherm Quatro).
- **Evaluation of power harvestability:** Electrical power was evaluated for disc samples and for “bimorph cantilever power harvesting module,” in response to simulated conditions of random vibrations of aerospace vehicle in frequency band ranging from 20 Hz to 2000 Hz at related PSD values reported in the literature [32].
 - **Power harvestability of disc samples:** Components obtained from powders activated for 10 h were mounted on the fixture made up of stainless steel, and further the fixture was mounted on vibration bench (Saraswati Dynamics, India) by means of steel bolts. Components were free to vibrate in vertical direction with bench, and there were no other applied stresses. Input random vibrations were applied and controlled using vibration controller (VR9500, Vibration Research Corporation, US) at predetermined PSD values in the corresponding frequency band as reported by Manoj et al. [32]. Voltage generated by samples was recorded at various PSD values and further correlated to piezoelectric properties for power harvesting applications.
 - **Power harvestability of bimorph cantilever harvester:** In order to demonstrate enhanced power harvestability, “bimorph cantilever power harvesting module” was fabricated and evaluated under identical conditions mentioned above.

Effect of Mechanical Activation and Reactive Sintering

Effect of mechanical activation (MA) and reactive sintering was studied, and appropriate parameters were identified in order to achieve superior properties for power harvesting, viz.:

- Piezoelectric charge coefficient (d_{33})
- Piezoelectric voltage coefficient (g_{33})
- Figure of merit for power harvesting (FoM_{PH})
- Coupling coefficient (k_p)

Disc samples were prepared out of MA-5 to MA-40 powders and processed as per process chart 1.1 and sintered at 1220 °C temperatures.

Effect of Mechanical Activation

Here, we discuss effect of MA on crystal structure, microstructure, and piezoelectric properties.

Effect of MA on Crystal Structure

Figure 6 depicts the X-ray diffraction pattern recorded from 20° to 60° for sintered samples which were prepared from mechanically activated powders. The peaks indicated by planes (100), (110), (111), (200), (210), and (211) are for single perovskite phase [50, 51], and there is no evidence of pyrochlore, $\text{Pb}_2\text{Sb}_2\text{O}_7$ [51, 68]. XRD pattern does not show peaks of raw materials, as the unreacted oxides were fully converted into single perovskite phase during reactive sintering. Simultaneous presence of ferroelectric tetragonal (F_T) and ferroelectric rhombohedral (F_R) phases is evidenced by splitting in the peak intensity of plane corresponding to (h00), (h10), and (h11) indicating composition close to MPB [53]. The unit cell parameter is found to reduce as the peak corresponding to (002) has moved toward higher position.

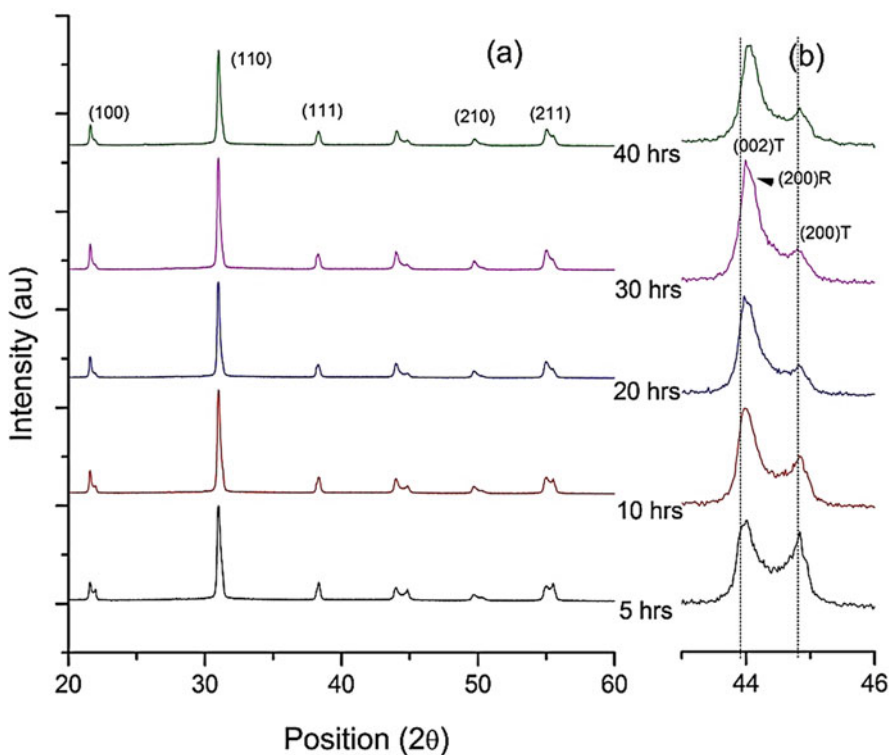


Fig. 6 XRD patterns: effect of mechanical activation on crystal structure

Table 1 Tetragonal unit cell parameters and phase content

MA duration(h)	a(°A)	c(°A)	c/a	V(°A) ³	F _T (%)	F _R (%)
5	4.0432	4.1173	1.0183	67.31	46.6	53.4
10	4.0418	4.1157	1.0183	67.24	51.8	48.2
20	4.0443	4.1154	1.0175	67.32	48.7	51.3
30	4.0433	4.1133	1.0173	67.25	47.3	52.7
40	4.0399	4.1110	1.0175	67.10	49.0	51.0

The unit cell volume and c/a ratio are found to decrease with increase in the activation duration. The composition approaches MPB of PZT for 10 h activation duration, and on further increasing the activation duration, it deviates from MPB. On analyzing the XRD pattern of sintered samples and those for mechanically activated powder, it is observed that there is increase in chemical reactivity due to thermal energy leading to completion of solid-state reaction. The reduction in the peak width indicates increase in crystallinity. Lattice parameters and volume fractions of F_T and F_R phases obtained from Rietveld analysis are given in Table 1.

Effect of MA on Microstructure

Figure 7 shows FESEM images for components which are reactively sintered at 1220 °C for various mechanical activation durations. Linear intercept method was used to measure average grain size. On increasing the activation duration from 5 h to 10 h, the average grain size was reduced. It slightly increases for activation duration of 30 h and reduces drastically for 40 h. For 5 h activation duration, large number of polygonal grains having wide distribution (up to 12 μm) were noticed along with large number of pores. This indicates that powder requires further milling (Fig. 7a). These results are in conformity with TEM results, where the distribution of particle size is wider for this milling duration. For 10 h milling duration, there is large change in morphology (Fig. 7b). The microstructure is seen to be compact, grain size is uniform, and the grain size distribution is narrow. The hexagonal grains with straight edges are observed, specifying that the grain growth is complete [57].

The numbers of pores are found to be very less. Hence, 10 h milling duration has resulted into superior mixing and milling. On further increasing the milling duration to 20 h, the grain size does not change. The grain morphology changes to some extent as some grains loose the hexagonal geometry due to which the compactness decreases (Fig. 7c). On further increasing the activation duration to 30 h, many grains become oval. The grain morphology completely changes at 40 h activation duration. Though the microstructure appears dense, the size and shape of the grains become assorted. While HRTEM results indicate that the powder particle size gets reduced by increasing the activation duration, it is seen that enhanced sinterability improves the grain size due to reactive sintering process. Sintering enhances reduction in free surface energy which was increased due to reduction in particle size [69].

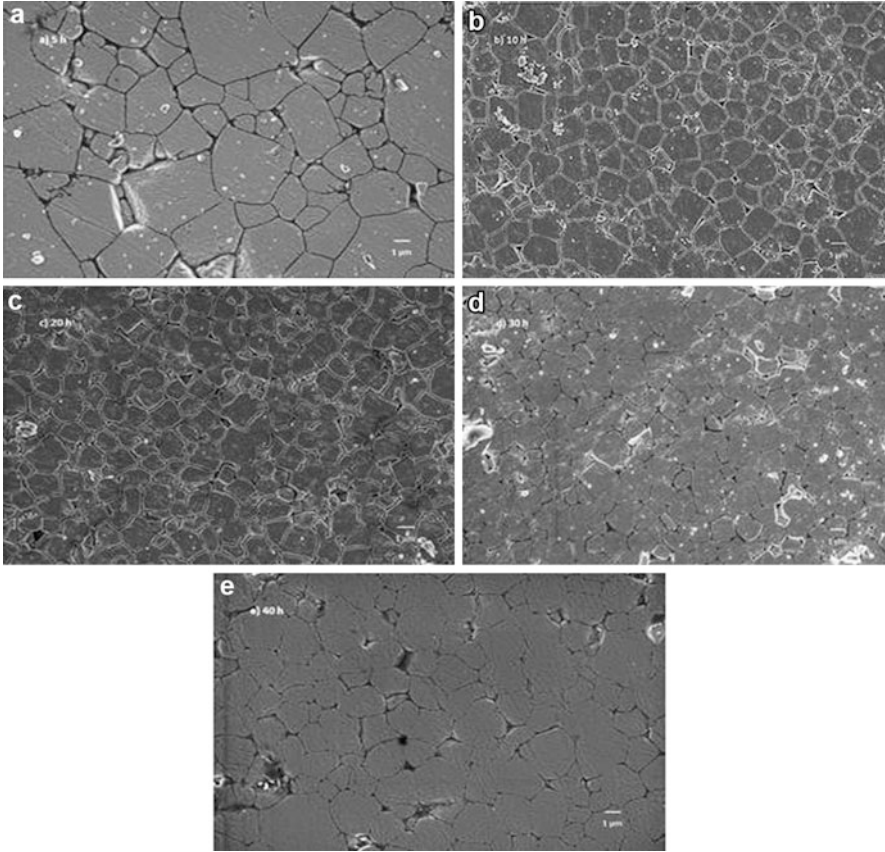


Fig. 7 FESEM images: effect of activation duration, (a) 5 h, (b) 10 h, (c) 20 h, (d) 30 h, and (e) 40 h on microstructure

Effect of MA on Electromechanical Properties

Q_m and k_p

Figure 8 shows the effect of mechanical activation duration on mechanical quality factor (Q_m) and electromechanical coupling coefficient (k_p). Q_m is the power handling capacity, while k_p is the electromechanical energy transduction efficiency of the piezoelectric material. Initially, up to 10 h of milling duration, Q_m reduces, while k_p increases. Increase in domain wall mobility [8, 70] is responsible for enhanced polarizability attributing to decrease in Q_m and hence increase in k_p values [8, 50]. When activation duration is further increased, the Q_m augments and k_p reduces. This shows that the material becomes electrically harder [50] with activation duration [60].

Figure 9 shows the effect of mechanical activation on power harvesting parameters, viz., piezoelectric charge coefficient (d_{33}), piezoelectric voltage coefficient (g_{33}), and figure of merit for power harvesting (FoM_{PH}). Values of d_{33} for 10 h of

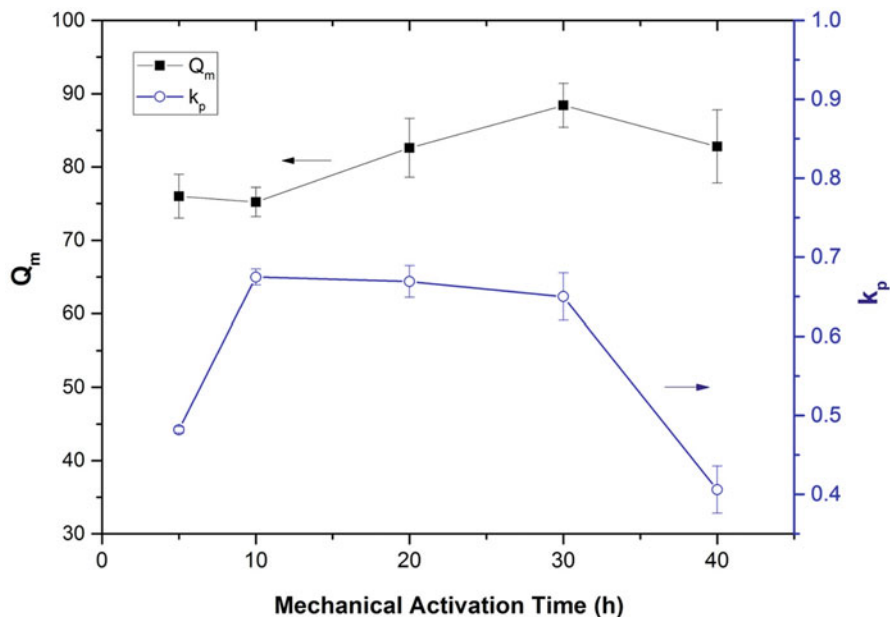


Fig. 8 Effect of MA on Q_m and k_p

milling (449 pC/N) and 20 h of milling (457 pC/N) are very close to each other and are better due to enhanced polarizability and denser microstructure [63] with best possible grain size achieved for these milling durations [71]. d_{33} decreases to 229 pC/N for 40 h activation duration [16, 50, 72].

Effect of Reactive Sintering Temperature

Effect of Reactive Sintering Temperature on Crystal Structure

Figure 10 shows X-ray diffraction patterns for Bragg's angle 2θ from 20° to 60° for partially phase formed mechanically activated powder (MA-10), reactively sintered samples (1170–1320 °C), and slowly scanned ($42\text{--}48^\circ$) XRD patterns for (200) planes. Table 2 shows phase analysis and lattice parameters as computed using Rietveld analysis. For 10 h activation, the diffraction pattern shows presence of perovskite phase in addition to traces of starting powders PbO [73], ZrO_2 [74], and TiO_2 [75] and transition compounds $PbTiO_3$ [47] and $PbZrO_3$ [48]. Peaks corresponding to La_2O_3 and $NiSb_2O_6$ are absent as the solid-state reaction took place due to acquisition of kinetic energy by the particles during mechanical activation. This indicates that powder particles acquire requisite kinetic energy which initiated the solid-state reaction. At this stage, perovskite phase is formed along with transitional compounds during 10 h mechanical activation. Existence of ferroelectric tetragonal (F_T) and ferroelectric rhombohedral (F_R) phases is indicated

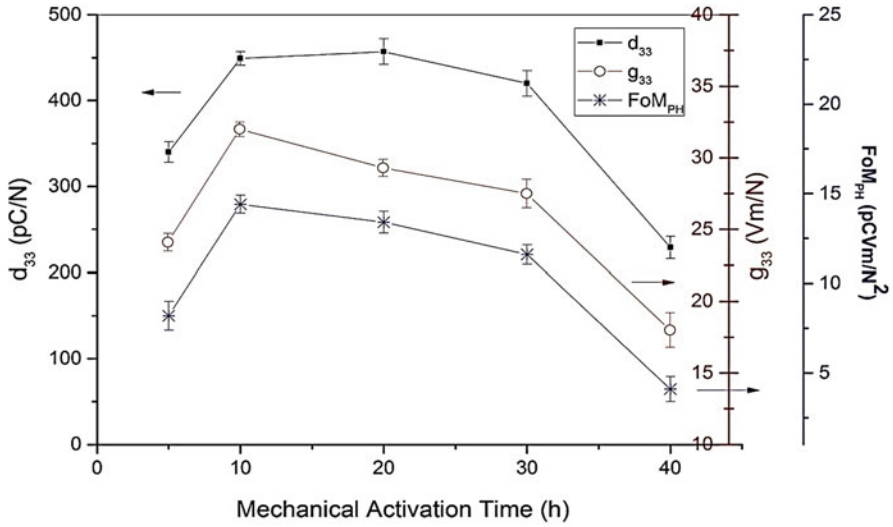


Fig. 9 Effect of MA on d_{33} , g_{33} , and FoM_{ph}

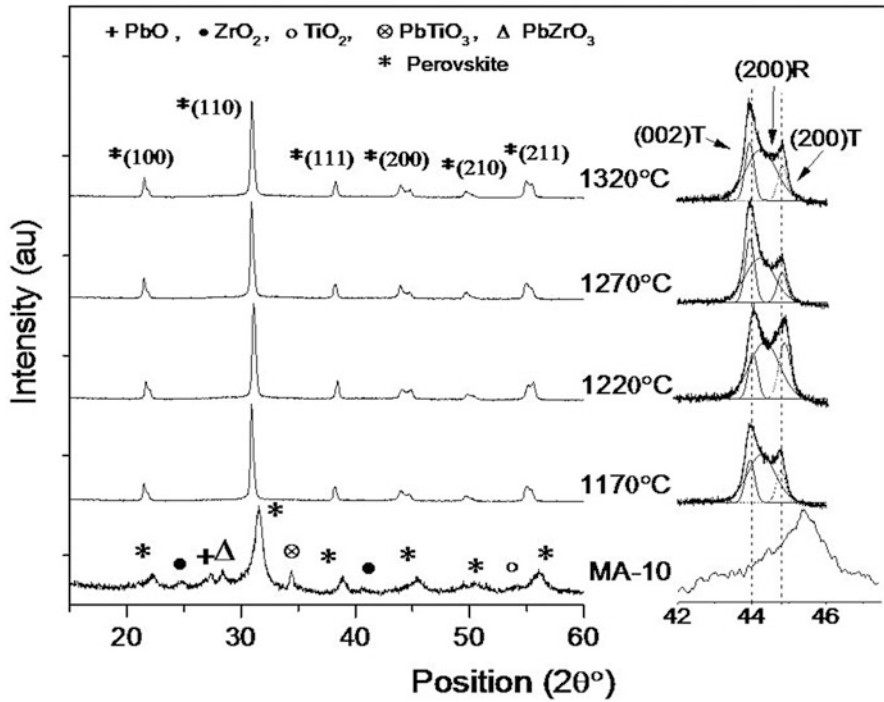


Fig. 10 XRD patterns: effect of reactive sintering on crystal structure

Table 2 Effect of reactive sintering temperature on lattice parameters and phase content

RS Temp ^{°C}	a(°Å)	c(°Å)	c/a	F _T (%)	F _R (%)
1170	4.0444	4.1167	1.0178	33.6	66.4
1220	4.0373	4.1112	1.0183	51.8	48.2
1270	4.0425	4.1169	1.0184	41.2	58.8
1320	4.0401	4.1165	1.0189	35.3	64.7

by splitting of peak intensity at (200) plane [53]. This splitting is not predominant. Also, peaks corresponding to raw material powders and peaks corresponding to transitional compounds are present, which indicate that the reactive sintering is essential for the formation of perovskite phase [76]. The broad peaks indicate the nanocrystalline nature of the composition.

Peaks corresponding to (100), (110), (111), (200), (210), and (211) planes indicate presence of perovskite phase without pyrochlore phase for all reactively sintered samples. The transitional compounds like PbTiO₃ and PbZrO₃ change to requisite perovskite phase by reactive sintering process carried out at 1170 °C. These peaks are seen to move toward lower angle indicating increase in lattice parameters. Table 2 shows Rietveld data for phases F_T and F_R, and lattice parameters analyzed from deconvoluted peaks. The improved splitting of peaks (002)T and (200)T and their shifting to higher position imply decrease in lattice parameters and increase in c/a ratio. This was confirmed from Rietveld analysis as shown in Table 2. The composition was seen to move little away from MPB for the samples sintered at 1270 °C. For this temperature, there was increase in easy axis domain as indicated by increase in peak intensity of (002)T plane. Also, reduction in hard axis domain was indicated by reduction in peak intensity of (200)T plane, without affecting the c/a ratio. The composition was seen to move away from MPB for samples sintered at 1320 °C temperature. The c/a ratio did not change much. It is seen that for the samples sintered at 1220 °C, the composition was close to MPB of PZT.

Effect of Reactive Sintering Temperature on Microstructure

Figure 11 shows microstructure of MA-10 samples for various reactive sintering temperatures as recorded by FESEM. It is seen that, as the temperature increases, the grain size increases. For 1170 °C (Fig. 11a), the grains showed varied geometry and are less densely packed which shows necessity of further sintering so as to get compact and dense microstructure. The grain morphology changes at 1220 °C. Majority of grain become hexagonal with straight edges which are indicated by white lines in Fig. 11b. This shows that the grain growth is complete [57] indicating compact microstructure. At 1270 °C, the polygonal grains grow randomly forming pores at triple grain point. On increasing the sintering temperature to 1320 °C, the morphology of grains changes drastically. Large grain growth was observed. The increase in sintering temperature, increases the grain size, indicate improved sinterability. Hence, 1220 °C is the proper sintering temperature where uniform, best possible grain growth is observed along with dense microstructure.

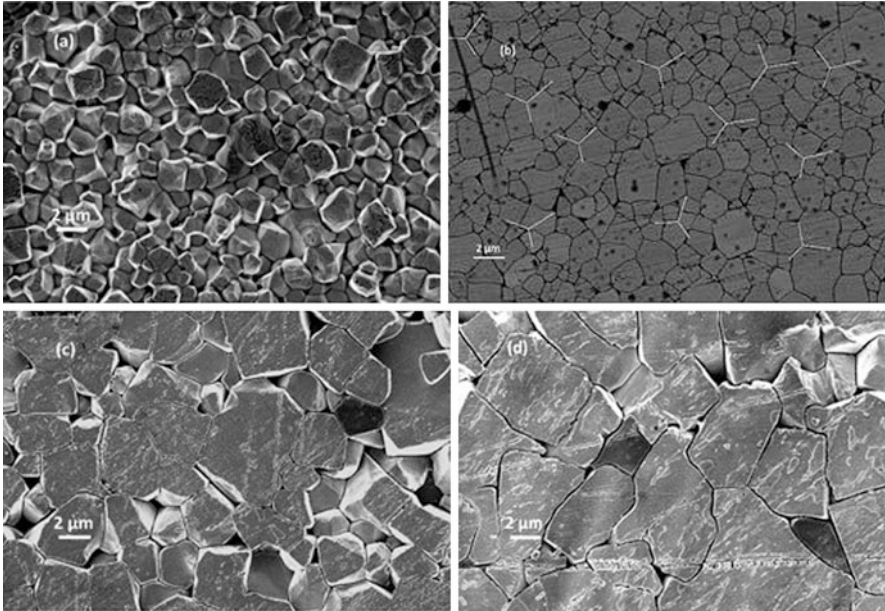


Fig. 11 FESEM images: effect of reactive sintering temperature on microstructure of MA-10 samples for (a) 1170 °C, (b) 1220 °C, (c) 1270 °C, (d) 1320 °C

Effect of Reactive Sintering Temperature on Electromechanical Properties

Q_m and k_p

The variation of mechanical quality factor (Q_m) and electromechanical coupling coefficient (k_p) with change in reactive sintering temperature is depicted in Fig. 12. Polarizability was superior and almost same for 1220 °C and 1270 °C indicated by k_p values.

d_{33} , g_{33} and $FoMPH$

The variation of piezoelectric properties for power harvesting, viz., piezoelectric charge coefficient (d_{33}), piezoelectric voltage coefficient (g_{33}), and figure of merit for power harvesting ($FoMPH$) with change in reactive sintering temperature, is shown in Fig. 13. As the sintering temperature increases from 1170 °C to 1220 °C, the d_{33} increases from 281 pC/N to 449 pC/N. This is due to increase in polarizability [77, 78]. On further increasing the temperature to 1270 °C, the d_{33} (454 pC/N) does not increase substantially. These better values are attributed to compositions being closed to MPB [8, 79], shown by XRD analysis. As explained earlier, there are 6 domain states of F_T and 8 domain states of F_R , totaling to 14 states, being available at MPB, for the dipoles to get aligned during poling process which assist to enhance the piezoelectric properties of the materials [80].

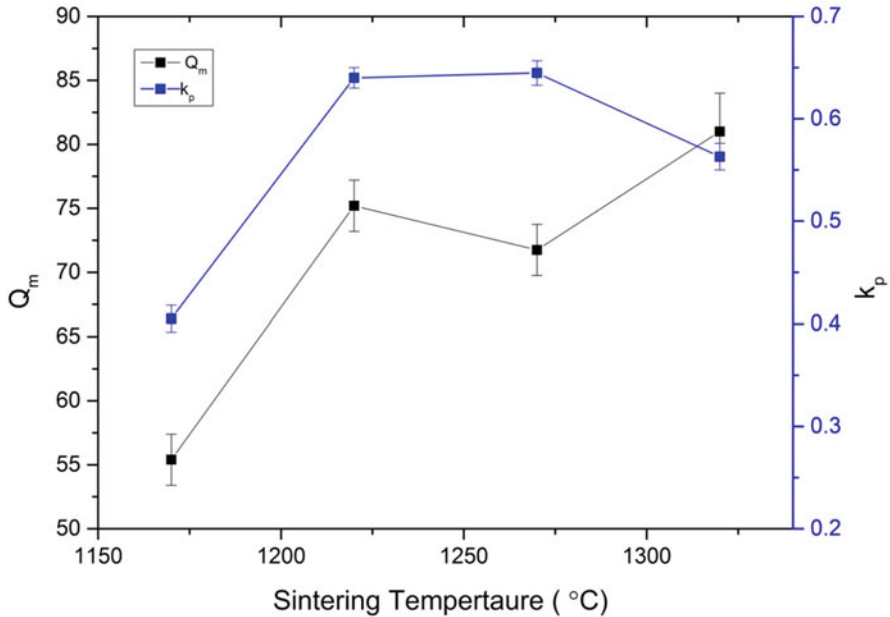


Fig. 12 Effect of reactive sintering temperature on Q_m and k_p

Also, SEM images for these compositions have shown compact microstructure [51], and optimal grain size [71, 81, 82] adds to enhancement of polarization per unit volume, d_{33} [16]. It is observed that d_{33} decreases (323pC/N) on increasing the sintering temperature to 1320 °C. This is because of the composition moving away from MPB and distorted microstructure. For 1220 °C, the power harvesting parameters, viz., g_{33} ($32 \times 10^{-3} \text{m.V/N}$) and FoM_{PH} ($14,400 \times 10^{-15} \text{m.V.C/N}^2$), were optimal, compared to other temperatures. Hence, it is seen that 1220 °C is suitable reactive sintering temperature for getting superior properties for power harvesting applications [58, 83, 84].

Curie Temperature and Phase Transition Behavior

The change in permittivity with temperature for samples sintered at 1220 °C for different frequencies is shown in Fig. 14.

Permittivity steadily increases in ferroelectric area of the curve. After the steep rise at Curie point ($T_c = 286 \text{ °C}$), it decreases paraelectric part of the curve. The increase in permittivity with temperature is due to distortion in oxygen octahedra and increased polarizability [85]. During transition from ferroelectric (F_T and F_R) phase to paraelectric cubic phase (Pc), the spontaneous dipoles disappear, and permittivity reduces. The phase change at high frequencies looks defused. Since the Curie temperature does not change with frequency, the material is normal ferroelectric and not relaxor ferroelectric [65, 86]. It is also observed that, as the frequency increases, the permittivity falls, implying dielectric relaxation. Due to inertia of ions, the polarization does not follow the

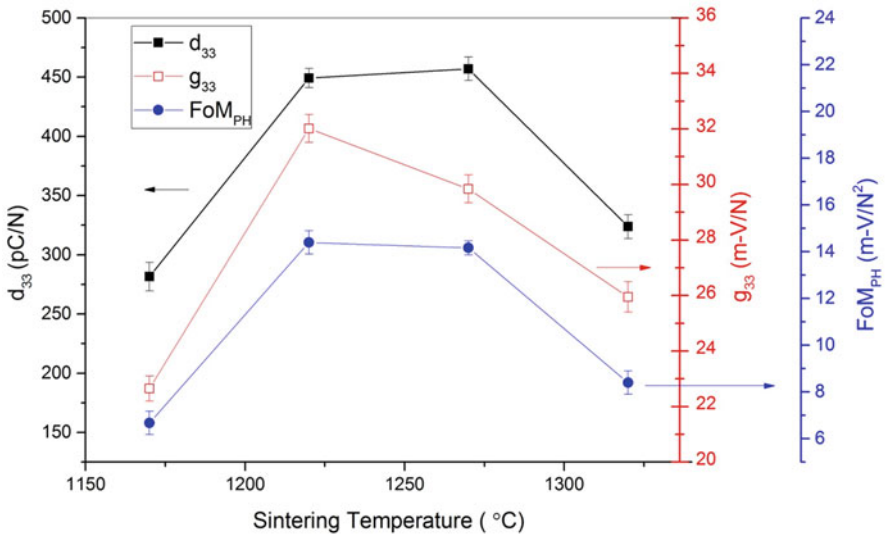


Fig. 13 Effect of reactive sintering on d_{33} , g_{33} , and FoM_{PH}

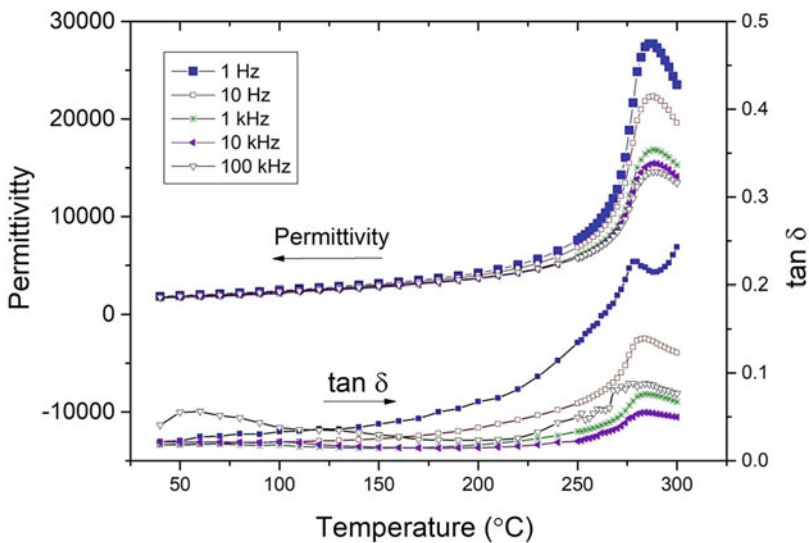


Fig. 14 Phase transition behavior

increasing frequency; hence, the permittivity reduces with increase in frequency [15, 86]. Doping La^{3+} for Pb^{2+} (A site) and Sb^{5+} and Ni^{2+} for Zr^{4+} , Ti^{4+} (B site) is responsible for substitutional disorder which produces several local Curie points. The phase transition does not occur at a point. The phase transition thus occurs at many nearby temperatures leading to broadening of transition temperature called diffused phase transition [45, 65].

Table 3 Effect of particle size on piezoelectric properties of La-PNS-PZT composition [87]

Property	Micro ($\sim 1.2 \mu\text{m}$)	Nano ($\sim 25 \text{ nm}$)
$d_{33} \times 10^{-12}(\text{C/N})$	428	449
$g_{33} \times 10^{-3}(\text{m.V/N})$	32.4	32
$\text{FoM}_{PH} \times 10^{-15}(\text{m.V.C/N}^2)$	13,500	14,400

Reorientation of domains generates domain wall friction. $\tan \delta$ is used to measure dissipation or losses due to friction. It increases with temperature. At 1 Hz, as the temperature rises, the domains get aligned to pre-poling condition. The viscosity drops, the losses due to friction of rotating dipoles are decreased, the $\tan \delta$ decreases at Curie point specifying that the reorientation of domains is complete [86], $\tan \delta$ has maximum value at Curie point for rest of the frequencies.

Comparison of Properties: Micrometer and Nanometer Particle Size

Table 3 shows comparison of piezoelectric properties for micro and nanometer particle size of La-PNS-PZT composition.

Demonstration of Power Harvesting for Strategic Application

The aerospace vehicle during its flight experienced vibrations right from launching till completion of the journey. These vibrations are random in nature and predominant in the frequency range of 20 to 2000 Hz [88]. Although undesirable, generated random vibrations by aerospace vehicles contain mechanical energy which further can be transduced into electrical energy by means of piezoelectric ceramics, accumulated and further can be used to power the low-power electronic circuitry in the missile, like MEMS devices, low-power sensors, etc.

Electromechanical properties of *nano*-La-PNS-PZT, obtained by reactively sintering MA-10 powder disc samples at 1220 °C, indicated the usefulness for power harvesting applications. Kumar and co-authors have reported power harvestability of the disc samples ($\varnothing 10 \text{ mm} \times 1.0 \text{ mm}$ thick), which were evaluated in response to simulated random aerospace vehicle vibrations reported [32]. Further, “bimorph cantilever power harvesting module” was developed, and its harvestability was evaluated under identical conditions and compared with that of disc.

Concept of Power Harvesting

In broad sense, power harvesting is capturing ambient energy in the form of movements, stress, vibrations, etc. and its conversion into useful electrical energy and its storage and application. As far as power harvesting application is concerned, direct piezoelectric effect is taken into account. From electromechanical properties

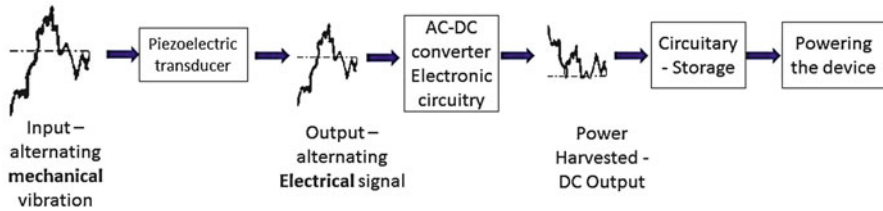


Fig. 15 Process of power harvesting from random mechanical vibrations

point of view, power harvestability of piezoceramics is governed mainly by FoM_{PH} , d_{33} and g_{33} [5, 58, 72, 85, 89, 90], which are superior for this composition processed at appropriate processing parameters derived in the study.

Piezoelectric effect is anisotropic, i.e., direction-dependent, and hence compressive force generates voltage with opposite polarity to that of tensile force. Figure 15 depicts the transduction of mechanical vibrations to electrical output by piezoelectric transducer and further its conversion into DC, storage, and utilization. Furthermore, maximum electrical power and thus energy can be acquired when impedance of the piezo element matches with load. Impedance, in general, is responsible for the opposition to the flow of current through a circuit when an alternating voltage is applied. Impedance matching is the process of adjusting the impedance of the source and load to achieve maximum power transduction [7, 91].

Evaluation of Power Harvestability

Measurement of electrical output of the disc samples using vibration bench (Saraswati Dynamics, India) is shown in Fig. 17. It shows the test samples mounted on the stainless steel fixture, and further the fixture is bolted on vibration bench.

Components were permitted to vibrate only in “Z” direction (vertical) with bench, and no other stresses were applied. Input mechanical excitation, in the form of random vibrations, was applied and controlled by vibration controller (VR9500 of Vibration Research Corporation, US) at various PSD values in the corresponding frequency band (Table 4), computed from data reported by earlier researchers as shown in Fig. 16 [32]. Voltage output for test samples was measured across 1–7 k Ω load resistance and recorded by oscilloscope. The analysis of time domain data is carried out by converting it in the frequency domain which was further correlated to piezoelectric properties suitable for harvesting the power.

Electrical Output from MA-10 Discs

Figure 18 shows the voltage output for disc samples. As shown, superior electrical output (3 mv) was obtained for MA-10 samples at 1 k Ω which was attributed to matching of load resistance [7, 91, 92]. The output was superior over entire range of frequency and PSD values.

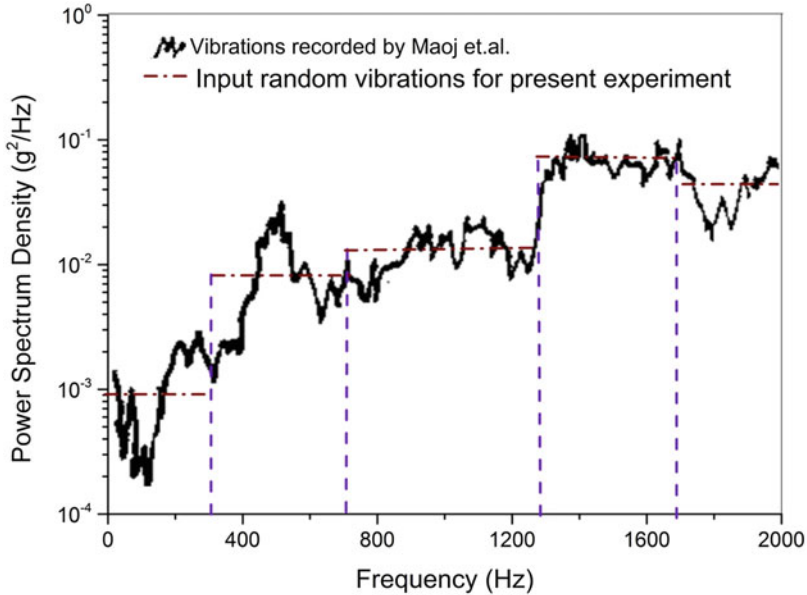
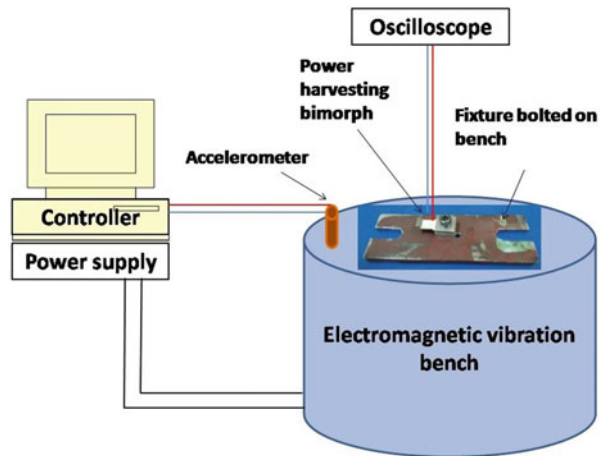


Fig. 16 Random vibration profile of aerospace vehicle

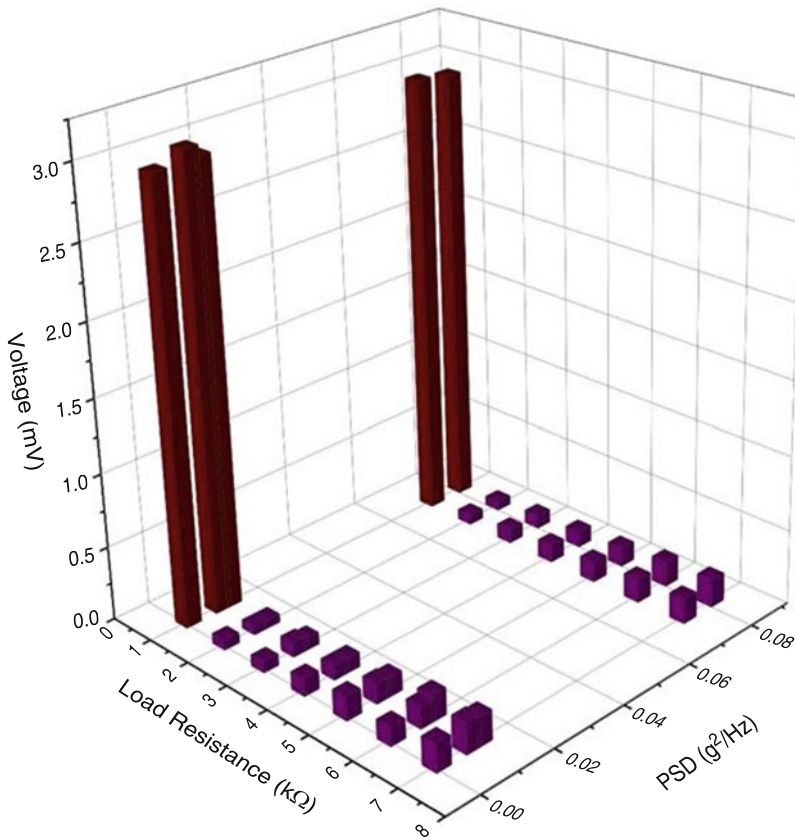
Fig. 17 Random vibration setup



In order to generate more power, it is suggested to use piezoceramic components in the form of transducer device. Several forms of devices like conventional cymbal, bridge cymbal, unimorph, bimorph, moonie, THUNDER, etc. are available. However, selection of type and design of transducer device for harvesting the power in particular environment depend upon the type of mechanical input offered to harvest the power.

Table 4 Parameters for input random vibrations

Sl. No.	Frequency band (Hz)	PSD (g^2/Hz)
1	30–300	0.001
2	300–700	0.009
3	700–1200	0.012
4	1200–1700	0.082
5	1700–2000	0.073

**Fig. 18** Electrical output at various PSD values

Power Harvesting Module

To obtain greater electrical output in response to vibrations, bimorph cantilever design is preferred [5].

Construction of Bimorph

A thin metal shim is sandwiched between piezo wafers by means of adhesive. One end of the cantilever is fixed to support, and proof mass is attached to free end. Figure 19 shows construction of bimorph, and details of components are given in Table 5.

Actual photograph of birmorph module and harvester assembly are shown in Fig. 20.

Harvester assembly shown in Fig. 20(b) was mounted on vibration bench (Fig. 17). Random vibrations of PSD values were applied to the harvester in the related frequency band as per Table 4. Voltage output was recorded by 16 channel oscilloscope (Yokogava, Model- DL750P) across load resistance of 100–7000 Ω . Output power was calculated from Eq. 9.

$$P_{\max} = \frac{V_{\max}^2}{R} \quad (9)$$

where:

P_{\max} = maximum power associated with positive pulse (W)

V_{\max} = maximum voltage associated with positive pulse(V)

R = resistance(Ω)

Voltage and thus power generated for various PSD values, in related frequency band across various load resistance, are shown in Figs. 21 and 22, respectively. Voltage was seen to increase with PSD values and load resistance values as observed from Fig. 21.

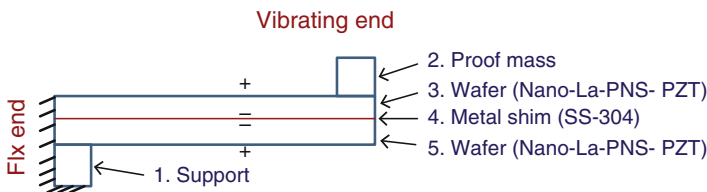


Fig. 19 Bimorph construction

Table 5 Structural details of power harvesting bimorph module

Sl. No.	Component	Material	Dimensions (WxDxT) (mm)
1.	Support	SS304	20 × 20 × 6
2.	Proof/seismic mass	SS304	2.8 × 9.8 × 3
3.	Piezo wafer	nano-La-PNS-PZT	15 × 9.8 × 0.4
4.	Metal shim	SS304	15 × 9.8 × 0.1
5.	Piezo wafer	nano-La-PNS-PZT	15 × 9.8 × 0.4

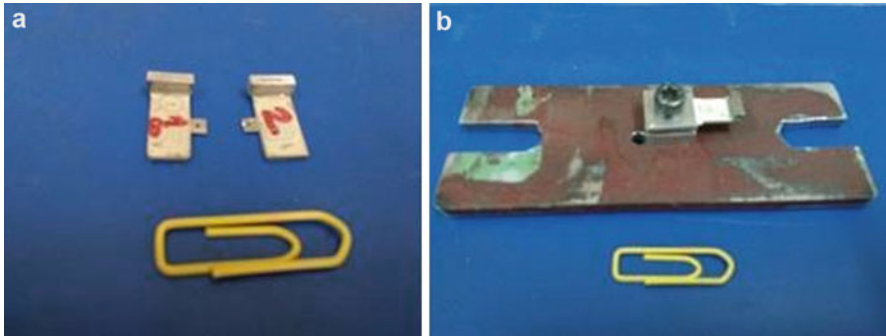


Fig. 20 (a) Bimorph module. (b) Harvester assembly

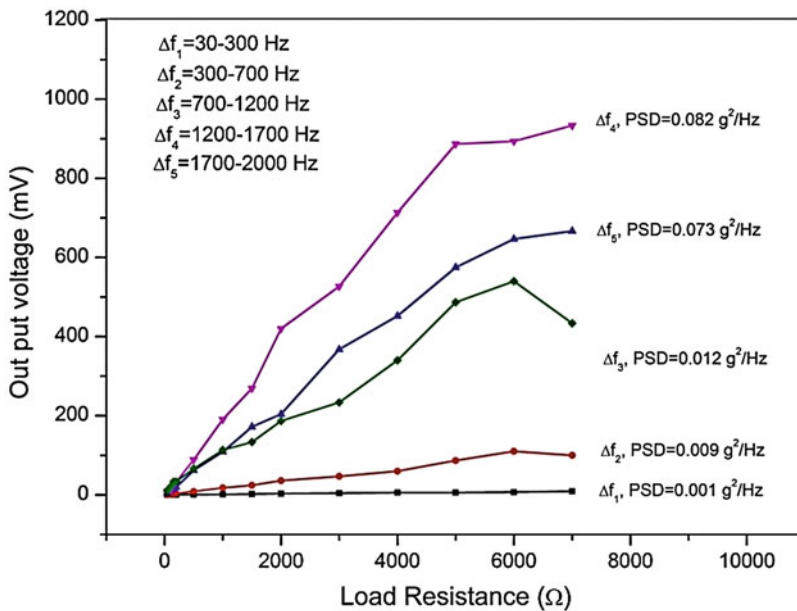


Fig. 21 Voltage generated by harvester in response to random vibrations

Power was observed to increase linearly with PSD values, and load resistance values up to 5000 Ω (Fig. 22). Five thousand ohm can be considered as matching load resistance since maximum power was generated for it. Maximum voltage, 933 mV, was obtained at PSD value of 0.082 g^2/Hz across matching load resistance of 5000 Ω which is remarkably superior compared to output from disc (3 mV) fabricated from the same powder (MA-10).

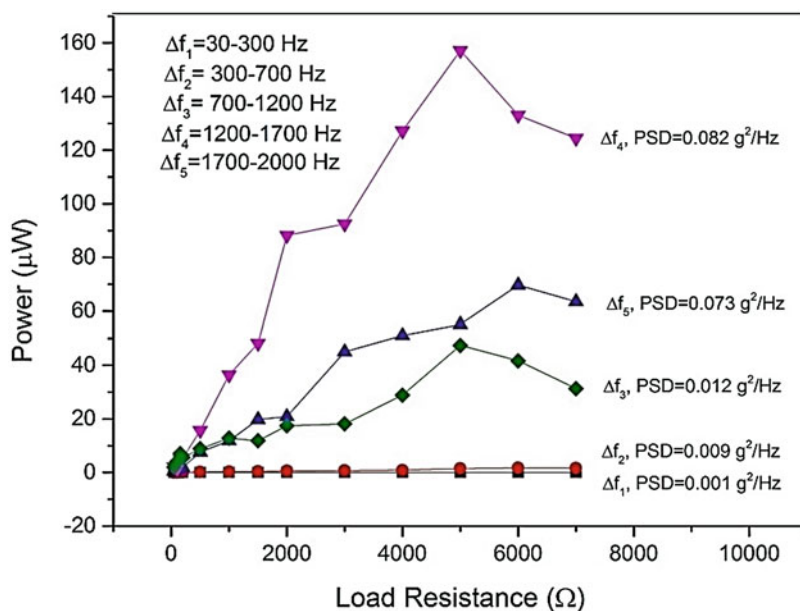


Fig. 22 Power harvested by harvester in response to random vibrations

Conclusions

The present work describes the synthesis and characterization of *nano*-La-PNS-PZT composition, having stoichiometric formula $Pb_{0.98}La_{0.02}(NiSb)_{0.05}[(Zr_{0.52}Ti_{0.48})_{0.995}O_{0.95}]O_3$, suitable for power harvesting in “Strategic Applications.” To avoid the formation of $Pb_2Sb_2O_7$, an undesired pyrochlore phase, desired composition was synthesized in two stages. In the initial stage, columbite precursor $NiSb_2O_6$ (NS) was obtained by calcining milled and mixed oxide powders of Ni and Sb at the temperature $945^\circ C$, determined from TG-DT Analysis. *nano*-La-PNS-PZT compositions in later stage by “Mechanical Activation” for 5–40 h duration (designated as MA-5 to MA-40) and investigated by XRD technique for understanding of progressive transformation of raw material powders into desired *nano*-La-PNS-PZT composition. Particle morphology was studied from HRTEM analysis. It was concluded from these studies that:

- Large quantum of starting powders were transformed into preferred perovskite phase for 10 h activation which, although further completed at 40 h, shows presence of contamination of tungsten carbide.
- Presence of intermediary compounds like $PbZrO_3$ and $PbTiO_3$ at lower activation duration was observed indicating need for reactive sintering for obtaining contamination-free desired compound.
- The average particle size was obtained in nanometer range.

Powders were converted into pellets and reactively sintered at 1220 °C for 30 min and evaluated for crystal structure, microstructure, and piezoelectric properties. An appropriate MA duration was identified in order to achieve properties suitable for power harvesting application. Results and analysis show:

- XRD pattern of reactively sintered samples which were prepared, from powders activated for various durations, show conversion of entire powders into single perovskite phase with coexistence of F_T and F_R phases associated with improved crystallinity during reactive sintering.
- Grain size and size distribution were uniform and fine for samples sintered at 1220 °C and prepared out of powder activated for 10 h activation.
- MA-10 resulted in superior values of piezoelectric charge coefficient, d_{33} (449×10^{-12} C/N), piezoelectric voltage coefficient, g_{33} (32×10^{-3} m.V/N), and figure of merit for power harvesting, FoM_{PH} ($14,400 \times 10^{-15}$ m.V.C/N²).

In the next step, MA-10 samples were “reactively sintered” between 1170 °C and 1320 °C and evaluated for crystal structure, microstructure, piezoelectric properties, and phase transition behavior. An appropriate sintering temperature was identified in order to achieve properties suitable for power harvesting application. From results and analysis, it is revealed that:

- XRD pattern shows formation of single homogeneous perovskite phase with coexistence of F_T and F_R phases associated with improved crystallinity during entire range of reactive sintering temperature.
- Grain size increased with sintering temperature.
- Samples sintered at 1220 °C had (i) compact and uniform microstructure and (ii) composition close to morphotropic phase boundary of PZT with optimum tetragonality.
- Phase transition studies showed the normal ferroelectric behavior with Curie point 286 °C.
- Thousand two hundred and twenty degree celsius (1220 °C) can be concluded to be appropriate reactive sintering temperature for composition, mechanically activated for 10 h that resulted in superior values of piezoelectric charge coefficient, d_{33} (449×10^{-12} C/N); piezoelectric voltage coefficient, g_{33} (32×10^{-3} m.V/N); and figure of merit for power harvesting, FoM_{PH} ($14,400 \times 10^{-15}$ m.V.C/N²), which is attributed to composition at MPB, better crystallinity, tetragonality, and compact and uniform microstructure indicating suitability for power harvesting applications. These samples were further used for estimation of power harvestability in response to random vibrations.

Further, power harvestability of MA-10 disc samples sintered at 1220 °C was evaluated in response to simulated random vibrations of aerospace vehicle between 20 Hz and 2000 Hz. Electrical output of 3 mv was obtained across 1 k Ω for 0.082 g²/Hz between 1200 and 1700 Hz frequency band.

Cantilever-based bimorph power harvesting module from MA-10 was fabricated and evaluated for power harvestability under identical conditions to that of disc samples across load resistance of 100–7000 Ω . It was concluded from the results that:

- Power was observed to increase linearly with PSD values and load resistance values up to 5000 Ω .
- Five thousand ohm can be considered as matching load resistance since maximum power was.
- Generated across this resistance.
- Maximum voltage, 933 mV, was obtained at PSD value of 0.082 g^2/Hz across matching load resistance of 5000 Ω which is remarkably superior compared to output from disc (3 mV) fabricated from the same powder (MA-10).

References

1. Glynne-Jones P, Tudor MJ, Beeby SP, White NM (2004) An electromagnetic, vibration-powered generator for intelligent sensor systems. *Sensors Actuators A Phys* 110:344–349. <https://doi.org/10.1016/j.sna.2003.09.045>
2. Mitcheson PD, Yeatman EM, Rao GK, Holmes AS, Green TC (2008) Energy harvesting from human and machine motion for wireless electronic devices. *Proc IEEE* 96:1457–1486
3. Kornbluh RD, Pelrine R, Pei Q, Heydt R, Stanford S, Oh S, Eckerle J (2002) Electroelastomers: applications of dielectric elastomer transducers for actuation, generation, and smart structures. In: McGowan A-MR (ed) SPIE's 9th annual international symposium on smart structures and materials. San Diego, pp 254–270
4. Roundy S, Wright PK (2004) A piezoelectric vibration based generator for wireless electronics. *Smart Mater Struct* 13:1131–1142. <https://doi.org/10.1088/0964-1726/13/5/018>
5. Kang M-G, Jung W-S, Kang C-Y, Yoon S-J (2016) Recent progress on PZT based piezoelectric energy harvesting technologies. *Actuators* 5:1–5. <https://doi.org/10.3390/act5010005>
6. Anton SR, Sodano HA (2007) A review of power harvesting using piezoelectric materials (2003–2006). *Smart Mater Struct* 16:R1–R21. <https://doi.org/10.1088/0964-1726/16/3/R01>
7. Beeby SP, Tudor MJ, White NM (2006) Energy harvesting vibration sources for microsystems applications. *Meas Sci Technol* 17:R175–R195. <https://doi.org/10.1088/0957-0233/17/12/R01>
8. Jaffe B, Cook W, Jaffe H (1971) *Piezoelectric ceramics*, 1st edn. Academic, London
9. Uchino K (2010) *Advanced piezoelectric materials*, 1st edn. Woodhead Publishing Limited, Cambridge, UK
10. Yan Y, Cho KH, Maurya D, Kumar A, Kalinin S, Khachatryan A, Priya S (2013) Giant energy density in [001]-textured $\text{Pb}(\text{Mg}_{1/3}\text{Nb}_{2/3})\text{O}_3\text{-PbZrO}_3\text{-PbTiO}_3$ piezoelectric ceramics. *Appl Phys Lett* 102. <https://doi.org/10.1063/1.4789854>
11. Maurya D, Kumar A, Petkov V, Mahaney JE, Katiyar RS, Priya S (2014) Local structure and piezoelectric instability in lead-free $(1 - X)\text{BaTiO}_3\text{-xA}(\text{Cu}_{1/3}\text{Nb}_{2/3})\text{O}_3$ (A = Sr, Ca, Ba) solid solutions. *RSC Adv* 4:1283–1292. <https://doi.org/10.1039/c3ra44886j>
12. Wang MC, Huang MS, Wu NC (2001) Effects of $30\text{B}_2\text{O}_3\text{-}25\text{Bi}_2\text{O}_3\text{-}45\text{CdO}$ glass addition on the sintering of $12\text{Pb}(\text{Ni}_{1/3}\text{Sb}_{2/3})\text{O}_3\text{-}40\text{PbZrO}_3\text{-}48\text{PbTiO}_3$ piezoelectric ceramics. *J Eur Ceram Soc* 21:695–701. [https://doi.org/10.1016/S0955-2219\(00\)00272-7](https://doi.org/10.1016/S0955-2219(00)00272-7)
13. Yu CS, Hsieh HL (2005) Piezoelectric properties of $\text{Pb}(\text{Ni}_{1/3}\text{Sb}_{2/3})\text{O}_3\text{-PbTiO}_3\text{-PbZrO}_3$ ceramics modified with MnO_2 additive. *J Eur Ceram Soc* 25:2425–2427. <https://doi.org/10.1016/j.jeurceramsoc.2005.03.075>

14. Zahi S, Bouaziz R, Abdessalem N, Boutarfaia A (2003) Dielectric and piezoelectric properties of $\text{PbZrO}_3\text{-PbTiO}_3\text{-Pb}(\text{Ni}_{1/3}, \text{Sb}_{2/3})\text{O}_3$ ferroelectric ceramic system. *Ceram Int* 29:35–39. [https://doi.org/10.1016/S0272-8842\(02\)00086-X](https://doi.org/10.1016/S0272-8842(02)00086-X)
15. Jankowska-Sumara I (2010) Phase transitions in $\text{Pb}[(\text{Ni}_{1/3}\text{Sb}_{2/3})_x\text{TiyZrz}]\text{O}_3$ solid solution ceramics studied by piezoelectric measurements. *J Electroceram* 25:168–173. <https://doi.org/10.1007/s10832-010-9611-x>
16. Lonkar CM, Kharat DK, Kumar HH, Prasad S, Balasubramanian K (2013) Effect of sintering time on dielectric and piezoelectric properties of lanthanum doped $\text{Pb}(\text{Ni}_{1/3}\text{Sb}_{2/3})\text{-PbZrTiO}_3$ ferroelectric ceramics. *Def Sci J* 63:418–422. <https://doi.org/10.14429/dsj.63.4866>
17. Chang J, Dommer M, Chang C, Lin L (2012) Piezoelectric nanofibers for energy scavenging applications. *Nano Energy* 1:356–371. <https://doi.org/10.1016/j.nanoen.2012.02.003>
18. Newnham RE, Zhang J, Meyer R (2002) Cymbal transducers: a review. In: ISAF 2000. Proceedings of the 2000 12th IEEE international symposium on applications of ferroelectrics. IEEE, Honolulu, Hawaii, USA, pp 29–32
19. Qi Y, Jafferis NT, Lyons K, Lee CM, Ahmad H, McAlpine MC (2010) Piezoelectric ribbons printed onto rubber for flexible energy conversion. *Nano Lett* 10:524–528. <https://doi.org/10.1021/nl903377u>
20. Ramadan KS, Sameoto D, Evoy S (2014) A review of piezoelectric polymers as functional materials for electromechanical transducers. *Smart Mater Struct* 23:033001. <https://doi.org/10.1088/0964-1726/23/3/033001>
21. Jeong CK, Il PK, Ryu J, Hwang GT, Lee KJ (2014) Large-area and flexible lead-free nanocomposite generator using alkaline niobate particles and metal nanorod filler. *Adv Funct Mater* 24:2620–2629. <https://doi.org/10.1002/adfm.201303484>
22. Harbauer G, Stein L (1984) Implantable physiological power supply with PVDF film. *Ferroelectrics* 60:277–282. <https://doi.org/10.1080/00150198408017528>
23. Kim KB, Il KC, Jeong YH, Lee YJ, Cho JH, Paik JH, Nahm S (2013) Performance of unimorph cantilever generator using Cr/Nb doped $\text{Pb}(\text{Zr}_{0.54}\text{Ti}_{0.46})\text{O}_3$ thick film for energy harvesting device applications. *J Eur Ceram Soc* 33:305–311. <https://doi.org/10.1016/j.jeurceramsoc.2012.09.001>
24. Choi CH, Seo IT, Song D, Jang MS, Kim BY, Nahm S, Sung TH, Song HC (2013) Relation between piezoelectric properties of ceramics and output power density of energy harvester. *J Eur Ceram Soc* 33:1343–1347. <https://doi.org/10.1016/j.jeurceramsoc.2012.12.011>
25. Song HC, Kang CY, Yoon SJ, Jeong DY (2012) Engineered domain configuration and piezoelectric energy harvesting in $0.7\text{Pb}(\text{Mg}_{1/3}\text{Nb}_{2/3})\text{O}_{3-0.3}\text{PbTiO}_3$ single crystals. *Met Mater Int* 18:499–503. <https://doi.org/10.1007/s12540-012-3018-y>
26. Karami MA, Bilgen O, Inman DJ, Friswell MI (2011) Experimental and analytical parametric study of single-crystal unimorph beams for vibration energy harvesting. *IEEE Trans Ultrason Ferroelectr Freq Control* 58:1508–1520. <https://doi.org/10.1109/TUFFC.2011.1969>
27. Palosaari J, Leinonen M, Hannu J, Juuti J, Jantunen H (2012) Energy harvesting with a cymbal type piezoelectric transducer from low frequency compression. *J Electroceram* 28:214–219. <https://doi.org/10.1007/s10832-012-9713-8>
28. Kong N, Ha DS, Erturk A, Inman DJ (2010) Resistive impedance matching circuit for piezoelectric energy harvesting. *J Intell Mater Syst Struct* 21:1293–1302. <https://doi.org/10.1177/1045389X09357971>
29. Shen D, Park JH, Ajitsaria J, Choe SY, Wickle HC, Kim DJ (2008) The design, fabrication and evaluation of a MEMS PZT cantilever with an integrated Si proof mass for vibration energy harvesting. *J Micromech Microeng* 18:055017. <https://doi.org/10.1088/0960-1317/18/5/055017>
30. Deng L, Wen Z, Zhao X, Yuan C, Luo G, Mo J (2014) High voltage output MEMS vibration energy harvester in $\text{Sd}_{\{31\}}\text{S}$ mode with PZT thin film. *J Microelectromech Syst* 23:855–861. <https://doi.org/10.1109/JMEMS.2013.2296034>
31. Uchino K (2018) Piezoelectric energy harvesting systems—essentials to successful developments. *Energy Technol* 6:829–848. <https://doi.org/10.1002/ente.201700785>

32. Kumar M, Rao TN, Jagadisan K, Jayathirtha Rao K (2002) Tailoring of vibration test specifications for a flight vehicle. *Def Sci J* 52:41–46. <https://doi.org/10.14429/dsj.52.2147>
33. Vold MJ (1949) Differential thermal analysis. *Anal Chem* 21:683–688. <https://doi.org/10.1021/ac60030a011>
34. Guo L, Lyashchenko A, Dong XL (2002) Synthesis of zirconium-rich PZT ceramics by hydroxide coprecipitation under hot-press. *Mater Lett* 56:849–855. [https://doi.org/10.1016/S0167-577X\(02\)00626-2](https://doi.org/10.1016/S0167-577X(02)00626-2)
35. James AR, Subrahmanyam J (2006) Processing and structure-property relation of fine-grained PLZT ceramics derived from mechanochemical synthesis. *J Mater Sci Mater Electron* 17:529–535. <https://doi.org/10.1007/s10854-006-8236-y>
36. International Centre for Diffraction Data ICDD-0110
37. Ryu J, Choi JJ, Kim HE (2001) Effect of heating rate on the sintering behavior and the piezoelectric properties of lead zirconate titanate ceramics. *J Am Ceram Soc* 84:902–904. <https://doi.org/10.1111/j.1151-2916.2001.tb00766.x>
38. Intrater J (2007) Mechanical alloying and milling, C. Suryanarayana. *Mater Manuf Process* 22:790–791. <https://doi.org/10.1080/10426910701416344>
39. Miclea C, Tanasoiu C, Gheorghiu A, Miclea CF, Tanasoiu V (2004) Synthesis and piezoelectric properties of nanocrystalline PZT-based ceramics prepared by high energy ball milling process. *J Mater Sci* 39:5431–5434. <https://doi.org/10.1023/B:JMSSC.0000039260.82430.f9>
40. Suryanarayana C, Ivanov E, Boldyrev V (2001) The science and technology of mechanical alloying. *Mater Sci Eng A* 304–306:151–158. [https://doi.org/10.1016/S0921-5093\(00\)01465-9](https://doi.org/10.1016/S0921-5093(00)01465-9)
41. Lee SE, Xue JM, Wan DM, Wang J (1999) Effects of mechanical activation on the sintering and dielectric properties of oxide-derived PZT. *Acta Mater* 47:2633–2639. [https://doi.org/10.1016/S1359-6454\(99\)00141-X](https://doi.org/10.1016/S1359-6454(99)00141-X)
42. Cullity BD (1978) *Elements of X-ray diffraction*, 1st edn. Addison-Wesley Publishing, Reading
43. Tasaka S, Miyata S (1985) Effects of crystal structure on piezoelectric and ferroelectric properties of copoly(vinylidene fluoride-tetrafluoroethylene). *J Appl Phys* 57:906–910. <https://doi.org/10.1063/1.334691>
44. Evans C, Brundle R, Wilson S (1992) *Encyclopedia of materials characterization*. Butterworth-Heinemann, Greenwich
45. Yadav KL, Choudhary RNP (1994) Structural and electrical properties of PZT (La, Na) ceramics. *Mater Lett* 19:61–64. [https://doi.org/10.1016/0167-577X\(94\)90106-6](https://doi.org/10.1016/0167-577X(94)90106-6)
46. International Centre for Diffraction Data ICDD-00-026-0142
47. International Centre for Diffraction Data ICDD-01-070-4258
48. International Centre for Diffraction Data ICDD-01-070-4844
49. International Centre for Diffraction Data ICDD-00-056-0762
50. Lonkar CM, Kharat DK, Kumar HH, Prasad S, Balasubramanian K (2013) Effect of La on piezoelectric properties of $\text{Pb}(\text{Ni}_{1/3}\text{Sb}_{2/3})\text{O}_3\text{-Pb}(\text{ZrTi})\text{O}_3$ ferroelectric ceramics. *J Mater Sci Mater Electron* 24:411–417. <https://doi.org/10.1007/s10854-012-0765-y>
51. Wang M, Huang M, Wong T, Science NW-J of materials, 2002 U (2002) Sintering and piezoelectric properties of $\text{Pb}(\text{Ni}_{1/3}\text{Sb}_{2/3})\text{O}_3\text{-PbZrO}_3\text{-PbTiO}_3$ ceramics. *J Mater Sci* 37:663–668. <https://doi.org/10.1023/A:1013746414023>
52. Hsiang HI, Yen FS (1996) Effect of crystallite size on the ferroelectric domain growth of ultrafine BaTiO_3 powders. *J Am Ceram Soc* 79:1053–1060. <https://doi.org/10.1111/j.1151-2916.1996.tb08547.x>
53. Tipakontitkul R, Ananta S (2004) A modified two-stage mixed oxide synthetic route to lead zirconate titanate powders. *Mater Lett* 58:449–454. [https://doi.org/10.1016/S0167-577X\(03\)00523-8](https://doi.org/10.1016/S0167-577X(03)00523-8)
54. Williams DB, Carter CB, Williams DB, Carter CB (2013) Inelastic scattering and beam damage. In: *Transmission electron microscopy*. Springer US, Boston, pp 49–65
55. Sarney WL (2004) Sample preparation procedure for TEM imaging of semiconductor materials. Army Research Laboratory, Adelphi

56. Kong LB, Tan O (2000) Preparation and characterization of $\text{Pb}(\text{Zr}_{0.52}\text{Ti}_{0.48})\text{O}_3$ ceramics from high-energy ball milling powders. *Materials Letters*, 42:232–239
57. Reed J (1995) *Principles of ceramics processing*, 2nd edn. Wiley, New York
58. Moulson AJ, Herbert JM (2008) *Electroceramics: materials, properties, applications*. John Wiley and Sons Ltd., NJ, USA
59. Sinha AK (1998) *Powder metallurgy*, 2nd edn. Dhanpat Rai Publications, Delhi
60. Kumar HH, Lonkar CM, Balasubramanian K (2017) Structure-property correlation and harvesting power from vibrations of aerospace vehicles by nanocrystalline $\text{La-Pb}(\text{Ni}_{1/3}\text{Sb}_{2/3})\text{-PbZrTiO}_3$ ferroelectric ceramics synthesized by mechanical activation. *J Am Ceram Soc* 100:215–223. <https://doi.org/10.1111/jace.14557>
61. He Z, Ma J (2003) Constitutive modeling of the densification of PZT ceramics. *J Phys Chem Solids* 64:177–183. [https://doi.org/10.1016/S0022-3697\(02\)00170-1](https://doi.org/10.1016/S0022-3697(02)00170-1)
62. Carter C, Norton M (2007) *Ceramic materials: science and engineering*. Springer Science +Business Media, New York
63. Wang M-C, Huang M-S, Wong T-S, Wu N-C (2002) Sintering and piezoelectric properties of $\text{Pb}(\text{Ni}_{1/3}\text{Sb}_{2/3})\text{O}_3\text{-PbZrO}_3\text{-PbTiO}_3$ ceramics. *J Mater Sci* 37:663–668. <https://doi.org/10.1023/A:1013746414023>
64. Naceur H, Megriche A, El Maaoui M (2014) Effect of sintering temperature on microstructure and electrical properties of $\text{Sr}_{1-x}(\text{Na}_{0.5}\text{Bi}_{0.5})_x\text{Bi}_2\text{Nb}_2\text{O}_9$ solid solutions. *J Adv Ceram* 3:17–30. <https://doi.org/10.1007/s40145-014-0089-x>
65. Goel P, Yadav KL, James AR (2004) Double doping effect on the structural and dielectric properties of PZT ceramics. *J Phys D Appl Phys* 37:3174–3179. <https://doi.org/10.1088/0022-3727/37/22/019>
66. Han W, Jiao H, Fox D (2018) Scanning electron microscopy. In: *Springer tracts in modern physics*. Wiley, Hoboken, pp 35–68
67. Smith GC (2014) Concise encyclopedia of materials characterization. *Int Mater Rev* 39:48–48. <https://doi.org/10.1179/imr.1994.39.1.48>
68. International Centre for Diffraction Data ICDD-00-74-1354
69. Uchino K (2003) Piezoelectric ceramics. In: *Handbook of advanced ceramics*, 2nd edn. Elsevier, London, pp 107–159
70. Govindan A, Sharma A, Pandey AK, Gaur SK (2011) Piezoelectric and pyroelectric properties of lead lanthanum zirconate titanate (PLZT) ceramics prepared by sol gel derived nano powders. *Indian J Phys* 85:1829–1832. <https://doi.org/10.1007/s12648-011-0187-3>
71. Kungl H, Hoffmann MJ (2010) Effects of sintering temperature on microstructure and high field strain of niobium-strontium doped morphotropic lead zirconate titanate. *J Appl Phys* 107:054111. (1–12). <https://doi.org/10.1063/1.3294648>
72. Kim HW, Priya S, Uchino K, Newnham RE (2005) Piezoelectric energy harvesting under high pre-stressed cyclic vibrations. *J Electroceram* 15:27–34. <https://doi.org/10.1007/s10832-005-0897-z>
73. International Centre for Diffraction Data ICDD-03-065-0399
74. International Centre for Diffraction Data ICDD-01-074-1200
75. International Centre for Diffraction Data ICDD-01-074-9521
76. Kumar HH, Lonkar CM, Balasubramanian K (2016) Harvesting power through random vibrations of aerospace vehicles from nanostructured $\text{La-Pb}(\text{Ni}_{1/3}\text{Sb}_{2/3})\text{-PbZrTiO}_3$ Ferroelectric Ceramics. *Def Sci J* 66:353. <https://doi.org/10.14429/dsj.66.10208>
77. Wang M-C, Huang M-S, Wu N-C (2002) Low-temperature sintering of $12\text{Pb}(\text{Ni}_{1/3}\text{Sb}_{2/3})\text{O}_3\text{-40PbZrO}_3\text{-48PbTiO}_3$ with V_2O_5 and excess PbO additives. *J Eur Ceram Soc* 22:697–705. [https://doi.org/10.1016/s0955-2219\(01\)00374-0](https://doi.org/10.1016/s0955-2219(01)00374-0)
78. Wang P, Zakeeruddin SM, Exnar I, Grätzel M (2002) High efficiency dye-sensitized nanocrystalline solar cells based on ionic liquid polymer gel electrolyte. *Chem Commun* 8:2972–2973. <https://doi.org/10.1039/b209322g>
79. Haertling GH (1999) Ferroelectric ceramics: history and technology. *J Am Ceram Soc* 82:797–818. <https://doi.org/10.1111/j.1151-2916.1999.tb01840.x>

80. Shaji Karapuzha A, Kunnamkuzhakkal James N, van der Zwaag S, Groen WA (2016) On the use of non-MPB lead zirconium titanate (PZT) granules for piezoelectric ceramic–polymer sensorial composites. *J Mater Sci Mater Electron* 27:9683–9689. <https://doi.org/10.1007/s10854-016-5029-9>
81. Chen M, Yao X, Zhang L (2002) Grain size dependence of dielectric and field-induced strain properties of chemical prepared (Pb, La)(Zr, Sn, Ti)O₃ antiferroelectric ceramics. *Ceram Int* 28:201–207. [https://doi.org/10.1016/S0272-8842\(01\)00078-5](https://doi.org/10.1016/S0272-8842(01)00078-5)
82. Lu PW, Xue WR, Huebner W (2002) A study of the sintering mechanism of PZT-based piezoceramics. In: Proceedings of 1994 IEEE international symposium on applications of ferroelectrics. IEEE, Pennsylvania, USA, pp 122–125
83. Kumar HH, Lonkar CM, Balasubramanian K (2017) Structure–property correlation and harvesting power from vibrations of aerospace vehicles by Nanocrystalline La–Pb(Ni_{1/3}Sb_{2/3})–PbZrTiO₃ ferroelectric ceramics synthesized by mechanical activation. *J Am Ceram Soc* 100:215–223. <https://doi.org/10.1111/jace.14557>
84. Maurya D, Yan Y, Priya S (2015) Piezoelectric materials for energy harvesting. *Adv Mater Clean Energy*:143–178. <https://doi.org/10.1201/b18287>
85. Kim JS, Jang MS, Kim IW, Lee KS (2006) Niobium doping effects and ferroelectric relaxor behavior of bismuth lanthanum titanate. *J Electroceram* 17:129–133. <https://doi.org/10.1007/s10832-006-5410-9>
86. Rai R, Sharma S (2004) Structural and dielectric properties of (La, Bi) modified PZT ceramics. *Solid State Commun* 129:305–309. <https://doi.org/10.1016/j.ssc.2003.10.020>
87. Kumar HH, Lonkar CM, Balasubramanian K (2016) Phase formation studies, investigation of piezoelectric properties and dielectric response of pyrochlore-free La–Pb(Ni_{1/3}Sb_{2/3})–PbZrTiO₃ ceramics. *Mater Focus* 4:464–470. <https://doi.org/10.1166/mat.2015.1283>
88. Prasad GD, Narayan KL, Manoj K, Subramanyam BV (2015) Random vibration analysis of aerospace vehicle structure load set step. *IPASJ Int J Mech Eng* 3:1–6
89. Lonkar CM, Kharat DK, Prasad S, Kandasubramanian B (2015) Synthesis, characterization, and development of PZT-based composition for power harvesting and sensors application. *Handb Nanoceramic Nanocomposite Coatings Mater*:551–577. <https://doi.org/10.1016/B978-0-12-799947-0.00025-0>
90. Priya S, Taneja R, Myers R, Islam R (2008) Piezoelectric energy harvesting using bulk transducers. *Piezoelectric Acoust Mater Transducer Appl*:373–388. https://doi.org/10.1007/978-0-387-76540-2_18
91. Kymissis J, Kendall C, Paradiso J, Gershenfeld N (1998) Parasitic power harvesting in shoes. In: Digest of papers. Second international symposium on wearable computers. IEEE Comput. Soc, Washington, DC, USA, pp 132–139
92. Umeda M, Nakamura K, Ueha S (1997) Energy storage characteristics of a piezo-generator using impact induced vibration. *Jpn J Appl Phys* 36:3146–3151. <https://doi.org/10.1143/JJAP.36.3146>



2D-Nanolayered Tungsten and Molybdenum Disulfides: Structure, Properties, Synthesis, and Processing for Strategic Applications

Harish Kumar Adigilli, A. K. Pandey, and Joydip Joardar

Contents

Introduction	78
Structural Aspects	80
Crystal Structure	80
Electronic Structure	81
Microstructure	82
Properties	83
Phase Stability – 2H and 1T	84
Mechanical Behavior	85
Tribological Properties	86
Oxidation Behavior	87
Thermoelectric Behavior	87
Piezoelectricity	88
Optical Properties	88
Magnetic Properties	89
Superconductivity	90

H. K. Adigilli

International Advanced Research Centre for Powder Metallurgy and New Materials (ARCI),
Balapur, Hyderabad, India

Department of Metallurgical and Materials Engineering, National Institute of Technology,
Warangal, India

A. K. Pandey

Department of Metallurgical and Materials Engineering, National Institute of Technology,
Warangal, India

J. Joardar (✉)

International Advanced Research Centre for Powder Metallurgy and New Materials (ARCI),
Balapur, Hyderabad, India

e-mail: joydip@arci.res.in

Synthesis Methods	91
Top-Down Methods	92
Bottom-Up Methods	94
Emerging Applications	97
Electronic Devices	97
Optoelectronic Devices	97
Memory Devices	102
Sensors	102
Catalysis and Energy Storage	105
Lubrication	106
Environmental	110
Biomedical	112
Concluding Remarks	113
References	113

Abstract

In the past one-decade, nanostructured two-dimensional (2D) version of tungsten and molybdenum disulfides have found major attention after the emergence of graphene and its unique properties in 2004. It is now well established that the 2D-nanolayered MoS₂ and WS₂ can have a stable structure in the form of multilayered nanosheets (NS) or inorganic graphene (IG) if it has monolayer or few (less than ten) layers. Such 2D structured MoS₂ and WS₂ have shown spectacular properties primarily due to changes in the electronic structure caused by the lattice strain induced on such nanostructuring. The enormous prospect of these materials has triggered major efforts in the development of various top-down and bottom-up synthesis routes as well as post-synthesis processing for potential applications. In the present article, the evolution of these materials and various aspects of their properties and emerging strategic applications have been reviewed critically.

Keywords

2D-materials · WS₂ · MoS₂ · Nanosheets · Nanolayered · Inorganic graphene

Abbreviation:

2D	Two-dimensional
3D	Three-dimensional
AB	Acetylene black
AFM	Atomic force microscope
ALD	Atomic layer deposition
CCB	Conductive carbon black
CMC	Carboxymethyl cellulose
CNT	Carbon nanotube
CoF	Coefficient of friction
CVD	Chemical vapor deposition

DCB	Dichlorobenzene
DCP	Dichloropentane
DEC	Diethyl carbonate
DFT	Density functional theory
DI	Deionized
DLC	Diamond-like carbon
DMC	Dimethyl carbonate
DMF	Dimethylformamide
EC	Ethylene carbonate
ECEX	Electrochemical exfoliation
EDLT	Electric double-layer transistor
FEC	Fluoroethylene carbonate
FE-SEM	Field emission scanning electron microscope
FETs	Field-effect transistor(s)
GBs	Grain boundaries
Gr or GR	Graphene
h-BN	Hexagonal boron nitride
HCNC	Hollow carbon nanocage
HDR	Hydrodesulfurization
HER	Hydrogen evolution reaction
HSP	Hansen's solubility parameter
IF/IFs	Inorganic fullerene(s)
IG	Inorganic graphene
INT	Inorganic nanotubular
IPA	Isopropyl alcohol
IR	Infrared
ITO	Indium tin oxide
LED	Light-emitting diode
LP	Liquid paraffin
LPCVD	Low-pressure chemical vapor deposition
MFC	Mass flow controller
MOCVD	Metal-organic chemical vapor deposition
MoDDP	Molybdenum dialkyldithiophosphate
NBR	Nitrile butadiene rubber
NMP	N-methyl-2-pyrrolidone
NS/NSs	Nanosheet(s)
NT	Nitrotoluene
NVP	N-vinylpyrrolidone
OAm	Oleylamine
PAO	Polyalphaolefin
PC	Polycarbonate
PEG	Polyethylene glycol
PEN	Polyethylene naphthalate
PET	Polyethylene terephthalate
PTFE	Polytetrafluoroethylene

PVA	Polyvinyl alcohol
PVD	Physical vapor deposition
PVDF	Polyvinylidene fluoride or polyvinylidene difluoride
RF	Radio frequency
rGO	Reduced graphene oxide
SCI	Science citation index
STEM	Scanning transmission electron microscope
s-TMD	Semiconducting TMD
SWCNT	Single-walled carbon nanotube
TDC	Thin dense chrome
TEA	Triethylamine
TEM	Transmission electron microscope
THF	Tetrahydrofuran
TMDs or TMDCs	Transition metal di-chalcogenides
TMI	Tandem molecular intercalation
TMS	Transition metal sulfide

Introduction

Production of two-dimensional (2D) MoS₂ dates back to 1960s with the successful mechanical exfoliation of bulk MoS₂ [1, 2]. It is intriguing to note that such experiments were carried out long before the successful extraction of 2D-form of carbon, i.e., graphene in 2004, by a seemingly similar mechanical exfoliation technique [3]. Both, MoS₂ and WS₂ in 2D form were also extracted by Lithium ion exfoliation of bulk MoS₂ and WS₂, respectively, in 1980s [4–7]. However, interest on two-dimensional (2D) inorganic materials picked up exponentially only in the past decade ever since carbon-graphene made its mark in 2004 with the pioneering efforts of the Russian physicists, Andre Geim and Konstantin Novoselov at the University of Manchester in UK [3]. Their work on graphene fetched them the Nobel Prize in 2010, as by then it became clear that the 2D-graphene has unique properties and capabilities.

Molybdenum disulfide (MoS₂) and Tungsten disulfide (WS₂) are the most widely studied candidates among a large number of 2D-inorganic materials, which includes the transition metal dichalcogenides (TMDs) of the form of MX₂ (M = Mo, W, Sn, Ti, Cr, Co, Fe, Ni, etc. and X = S, Se, Te) and also the MAXene phases. Studies in 1980s and 1990s have shown enhancement in their properties on nanostructuring. Notable among these studies have been on inorganic fullerene (IF) like layered spherical and inorganic nanotubular (INT) structures [8–10]. WS₂ and MoS₂ have received a fresh relook at their structure and properties alongside carbon graphene as these are now known to have a stable or metastable 2D nanostructure in the form of nanosheets (NS) and/or inorganic grapheme (IG) like if it has monolayer or few (less than ten) layered structure. Both WS₂ and MoS₂ in NS and IG form have shown a wide range of properties hitherto unknown in any given material, prompting major research initiatives world over in the recent years. Figure 1a shows the number of

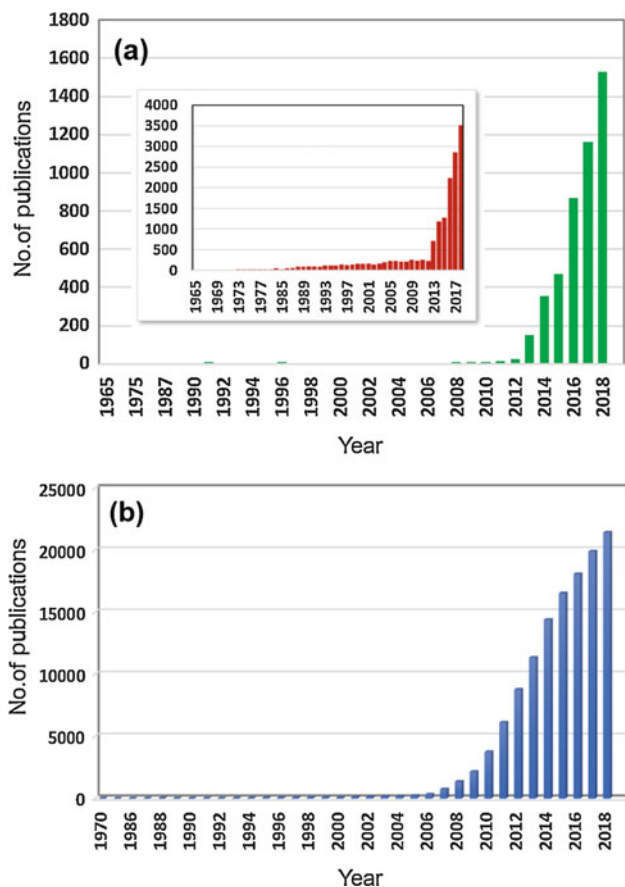


Fig. 1 Publications in SCI journals from Scopus search between 1965 and 2018. (a) 2D form of WS₂ and MoS₂. Inset shows publications in all form of WS₂ and MoS₂. (b) Graphene

SCI journal publications exclusively on 2D-WS₂ and 2D-MoS₂ in the past few decades. Such figure for all versions of WS₂ and MoS₂ is shown as inset of Fig. 1a. For comparison, publications on graphene are also shown in Fig. 1b. Even though in terms of the number of journal publications, 2D form of WS₂ and MoS₂ lags far behind carbon graphene, its rapid emergence is quite evident from the exponential growth beyond 2005.

It is now well established that the alteration of properties on nanostructuring has its roots in their crystal structure, microstructure, and electronic structure. These are significantly influenced by lattice strain induced by nanostructuring or introduction of dopants or vacancies. In spite of a significant volume of work in this area in recent years, there remain many more issues that need fundamental as well as applied research initiatives. Current understanding on the unique structure and properties has revealed their huge potential in the development of next generation technologies.

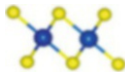
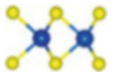
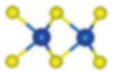
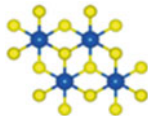
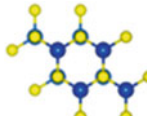
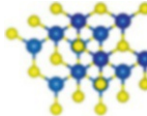
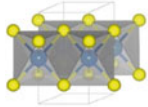
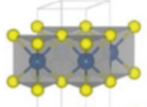
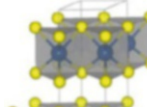
This article reviews some of the key aspects on 2D-MoS₂ and WS₂, viz., structure, properties, synthesis methods, and some of their potential strategic applications in the areas of electronic, optoelectronic, and magnetic devices, sensors, environmental and biomedical sectors.

Structural Aspects

Crystal Structure

Crystal structure holds the key to various properties and performance of any material. Table 1 shows the crystal structures of different polymorphic forms of WS₂ and MoS₂ viz. 1T, 2H, and 3R. Both Mo and W- disulfides are known to have a stable 2H structure in which W or Mo atoms have a trigonal prismatic arrangement (hexagonal symmetry) with sublayers of S atoms on either side. Atoms within this S-M-S layer (M = Mo or W) are held together by strong covalent bonds while two such layers are stacked one above the other in a unit cell, which are held together by

Table 1 Typical 1T, 2H, and 3R-MX₂ atomic structures with M = W or Mo (●: M, ●: S) indicating difference in the stacking sequence. (Adapted with permission from [11] ©2015 American Chemical Society and from [12] ©2015 Royal Society of Chemistry)

Structural information	1T	2H	3R
Crystal structure			
Side view			
Top view			
Unit cell	1 S-M-S layer per unit cell 	2 S-M-S layer per unit cell 	3 S-M-S layer per unit cell 
Space group	<i>P-3m1</i>	<i>P6₃/mmc</i>	<i>R3m</i>
M coordination	Octahedral	Trigonal prismatic	Trigonal prismatic
Stacking sequence	AbC	BaB AbA	BcB CaC AbA

weak van der Waal bonds giving it the freedom to slide even under low shear stress. This imparts excellent lubricating property in the material. Depending on the synthesis mode or conditions, 1T structure is also possible in these disulfides. As evident from Table 1, the 1T structure appears to involve a shift in the position of S atoms in one of the sublayers while the metal atoms have a tetragonal symmetry with octahedral coordination. The 1T structure consists of only one S-M-S layer per unit cell. Occasionally, WS_2 and MoS_2 are also known to exhibit metastable 3R type polymorphic structure (Table 1). The 3R structure is characterized by rhombohedral symmetry of the metal atoms in the S-M-S layer with three such layers per crystallographic unit cell. The stable crystal structure of 2D- WS_2 and MoS_2 is predominantly 2H type for thicker version of nanosheet structure (>10 layers), while thinning down of the 2D structure may lead to more of the metastable 1T fraction depending on the synthesis/deposition parameters.

Electronic Structure

The electronic band structure of WS_2 and MoS_2 shows considerable change with the crystal structure and with the number of layers in the 2D form due to substantial changes in their orbital projected density of states. Fig. 2a and b show the band structure of 2H- WS_2 for monolayer when compared to bulk WS_2 . It is evident that the band gap changes with the thickness of the WS_2 crystal so that the otherwise indirect band gap material (0.88 eV) turns into a direct band gap material with band gap of 1.94 eV in the monolayer form [13]. The trigonal 1T polymorph, on the other hand, shows a band structure with no gap in-between the valence and conduction band (Fig. 2c). Consequently, the 1T structure shows metallic character [14]. Recent

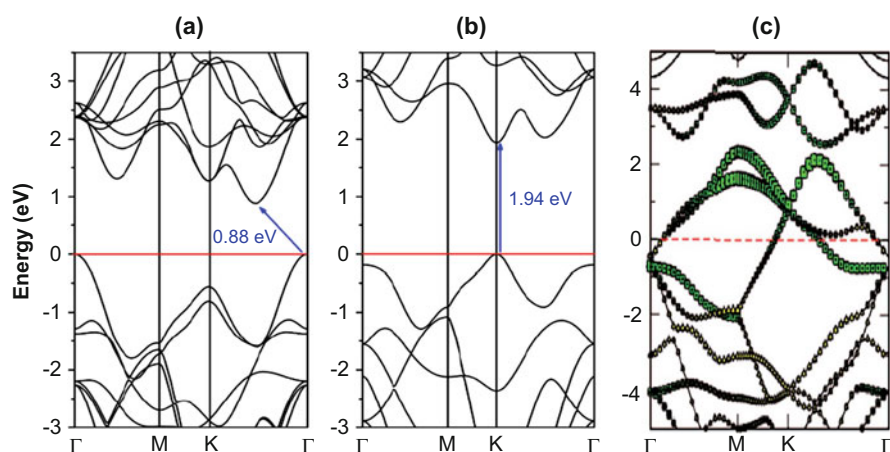


Fig. 2 Electronic structure of (a) bulk 2H- WS_2 ; (b) WS_2 monolayer. (Adapted with permission from [13] ©2013 Springer Nature); (c) 1T- WS_2 . (Adapted with permission from [14] ©2018 John Wiley and Sons)

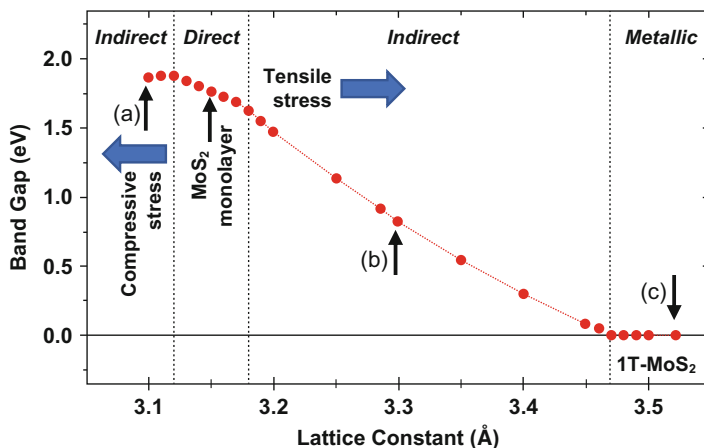


Fig. 3 Change in the band gap energy with change in lattice constant in MoS₂ monolayer under biaxial strain. Band gap of MoS₂ monolayer increases to 1.73 eV at (a) under 1.9% compressive stress, decreases to 0.89 eV at (b) and 0 eV at (c) under a tensile stress of 4% and 11%, respectively. (Adapted with permission from [15] ©2012 American Physical Society)

studies show that the band gap type and energy in these materials can change under applied tensile or compressive strain [15] for example, MoS₂ monolayer shows a lattice contraction under compressive strain with a simultaneous increase in the band gap energy and a concomitant transition from direct to indirect band gap (Fig. 3). Under tensile strain, it shows an increase in the lattice parameter, with lowering of band gap energy and a transition to indirect band gap while in case of very higher strain; the band gap disappears with the transition to 1T polymorphic form (Fig. 3). The observed change in the band gap value with the reduction in the grain dimension is related to quantum confinement effect as the dimension approaches Bohr exciton radius of the material [16]. In recent years, WS₂/MoS₂ heterostructures have also shown interesting electronic properties as its band gap disappear under suitable electric field [17]. Thus, nanostructuring and/or thinning of the layered structure or introduction of lattice strain or generation of WS₂/MoS₂ heterostructures provide an effective option of band gap engineering and opening up new possibilities for new generation technologies. Some of these have been reviewed in subsequent section of this article.

Microstructure

The 2D-WS₂ and MoS₂ are known to crystallize in different type of microstructures (Fig. 4) depending on the synthesis technique or deposition parameters. A stable monolayer structure is possible to extract from bulk WS₂ or MoS₂ using various exfoliation techniques and/or may be synthesized in as-deposited form on a given substrate by bottom-up approach as well (Fig. 4a). Figure 4b shows a typical

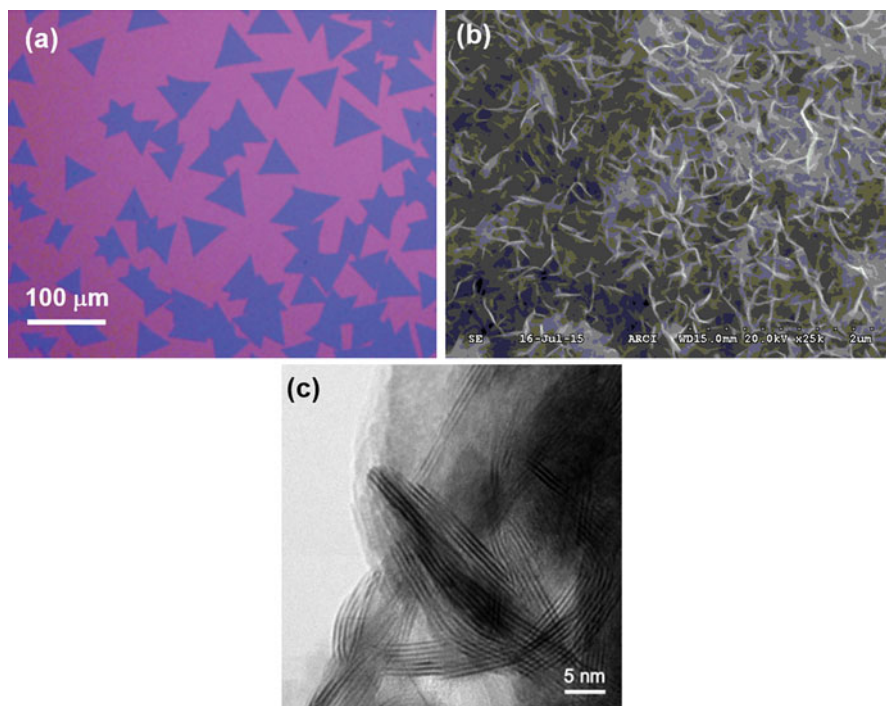


Fig. 4 (a) Optical image of MoS₂ monolayer. (Adapted with permission from [18] ©2013 Nature Publishing Group). (b) FE-SEM image of WS₂ nanosheets produced by ARCI, India [19]. (c) High-resolution TEM image of the cross section of 2D-MoS₂ nanosheets [20]

2D-WS₂ microstructure with a crumpled multilayered nanosheet structure obtained by gas-solid reaction synthesis [19]. The number of layers in such nanosheet structure may be altered by the synthesis parameters. Figure 4c shows the cross section of such nanosheets containing about 8–10 layers, which can be termed as inorganic graphene (IG) like structure. Such microstructure leads to very high surface area in these types of materials.

Properties

It is evident from the preceding section that the 2D-WS₂ and MoS₂ have unique microstructure and electronic structure when compared to their bulk forms. Such structural features lead to a tuneable band gap, high surface area, as well as quantum confinement effects. All these are expected to cause significant variation in their properties. Some of the key properties of the 2D-WS₂ and MoS₂ are discussed in this section.

Phase Stability – 2H and 1T

Among the 2H and 1T structure of WS_2 and MoS_2 , 2H is the most stable form. The 1T structure is usually metastable, which can, however, be stabilized by adopting various techniques. As for example, DFT-based theoretical studies indicate that covalent functionalization can easily stabilize the 1T structure with slight increase in the band gap between 0 to 1 eV [21]. As shown by Ouyang et al., using DFT calculations [22], 2H to 1T structural transition is thermodynamically easier for a sandwiched heterostructure like MoS_2/Si , MoS_2/Ge , or MoS_2/Sn when compared to a free-standing MoS_2 particle. Such structural transition can also be attained with small strain induced by small deformation as already shown in previous section (Fig. 3). The critical change in the lattice parameters and biaxial strain to trigger 2H to 1T transition for free standing MoS_2 were found to be $\Delta a/a_0 > 0.2$, $\Delta b/b_0 > 0.2$, and biaxial strain of 15%. These values reduced to 0.13, 0.15, and 0.06, respectively, for MoS_2/Si heterostructure and further dropped to 0.05, 0.06, and 0.03, respectively, for a $\text{Si}/\text{MoS}_2/\text{Si}$ sandwiched heterostructure. TEM studies as well as DFT calculations have shown the role of anion (sulfur) vacancies, as induced by electron beam irradiation in TEM, on the 2H to 1T transition in MoS_2 [18]. It may be noted that a vacancy formation is expected to induce strain in the lattice. The obtained 1T structure reverts back spontaneously when exposed to air due to localization of electrons caused by re-adsorption and filling up of the vacant sulfur sites. Recent studies have shown that exfoliation by organolithium intercalation of bulk WS_2 and MoS_2 can easily lead to 1T form of WS_2/MoS_2 [6, 7, 23], as the 1T structure gets stabilized by accepting electrons donated by Lithium during the intercalation process. Recently, a highly stable monolayer with 1T- WS_2 grown alongside a 2H- WS_2 monolayer in butterfly shape with a sharp interface (Fig. 5) has

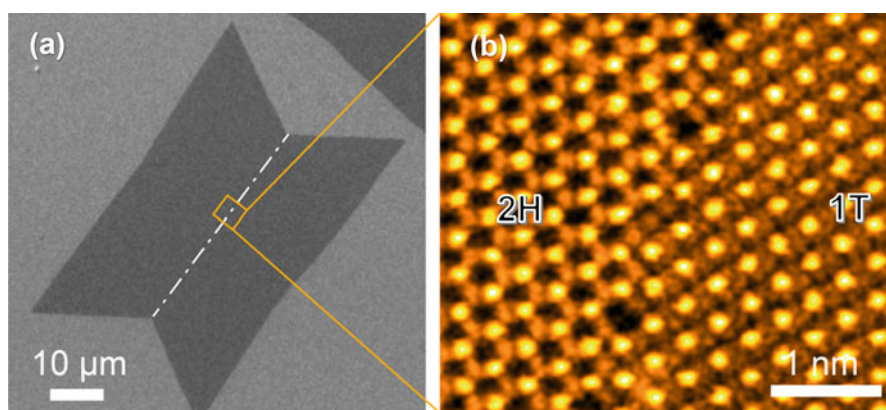


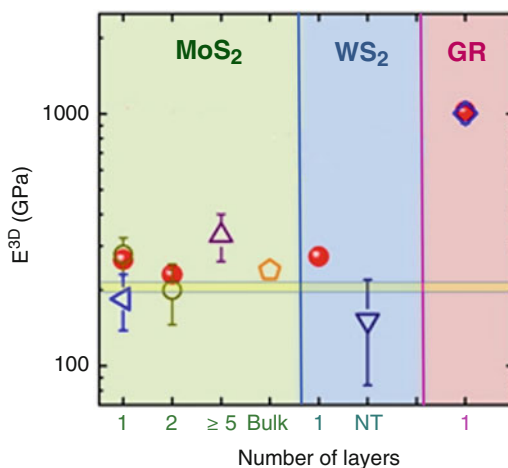
Fig. 5 (a) Monolayers of 2H and 1T WS_2 butterfly grown by low pressure CVD. (b) Annular dark field image in STEM showing sharp interface of the 2H and 1T- WS_2 monolayers. (Adapted with permission from [24] ©2018 American Chemical Society)

been generated on a sapphire substrate by low pressure CVD in presence of catalysts like iron oxide or indium oxide and some alkali halide like sodium chloride [24].

Mechanical Behavior

The monolayer and few layered versions of MoS_2 and WS_2 have been extensively investigated by various groups for their mechanical properties. It is worthwhile mentioning that some variations in the reported data have been observed depending on the extraction or synthesis technique. As for example, the average in plane breaking strength and Young's modulus of the mechanically exfoliated MoS_2 monolayer, as estimated by AFM, were found to be around 15 ± 3 N/m and about 270 GPa, respectively, [25] while Liu et al. [26] have measured the elastic moduli of CVD grown WS_2 and MoS_2 monolayers using AFM and have reported Young's modulus values between 200 and 300 GPa. Figure 6 compares the experimentally determined values of Young's modulus of graphene, MoS_2 , and WS_2 as reported by several groups. Liu et al. [20] have also shown that the 2D- MoS_2 -graphene heterostructures have significantly higher elastic constant when compared to even pristine graphene. It may be noted that the Young's modulus (E) and in plane breaking strength of pure graphene obtained through mechanical exfoliation have been reported to be around 1000 GPa and 42 N/m, respectively, via indentation technique using AFM [27]. The Young's modulus of MoS_2 nanosheets with 5–10 layers has been reported to be around 330 GPa, which is higher than that in many other 2D materials such as h-BN (250 GPa), graphene oxide (200 GPa), and carbon nanosheets (1 nm thick) (10–50 GPa) [28]. The 2D- WS_2 and MoS_2 -based polymer matrix composites have also shown enhanced mechanical properties when compared to their fullerene and nanotube forms due to their higher mechanical stiffness and strength [29].

Fig. 6 Young's moduli of 2D- MoS_2 , 2D- WS_2 , and graphene and their variation with respect to number of layers. Each symbol corresponds to values reported by a specific research group. Approximate range of Young's modulus in bulk steel is indicated with yellow band for comparison. (Adapted with permission from [26] ©2014 American Chemical Society)



Tribological Properties

Weakly held layered structure of WS_2 and MoS_2 promotes the sliding of the adjacent layers (triatomic layers) one over the other upon application of the shear forces. It is the reason behind the self-lubricating nature of both the sulfides [30]. Ultra-low coefficient of friction (CoF) values could be attained in MoS_2 - and WS_2 -based lubricants due to weak bonding of the interlayers, independent of organic/inorganic sorbates to activate the lubrication. The lubrication performance of these sulfides under vacuum condition is further enhanced due to the absence of humidity/oxidizing conditions, making them highly suitable for the space and vacuum applications. The 2D nanosheets of WS_2 and MoS_2 were reported to have superior tribological properties than that of their IF (inorganic fullerene) version as well as bulk structures. The ultra-low friction, high load bearing capability, and reduced wear of the lubricating oils containing WS_2 and MoS_2 nanosheets as additives are due to the effective penetration of 2D sheets into the crevices and pits, which prevents the moving parts from direct contact as schematically shown in Fig. 7. Studies based on frictional force microscopy investigations on the mechanically exfoliated few and monolayers of MoS_2 , graphene, and h-BN revealed an increase in the frictional forces of these layered materials (only when freely suspended or weakly adhered to a substrate) with a decrease in the number of layers (Table 2). This phenomenon has been ascribed to the puckering effect between the AFM tip and the 2D layer, which originates from the thickness dependent flexural rigidity. However, such effect was found to be absent in case of monolayers, which were adhered strongly to the substrate [31].

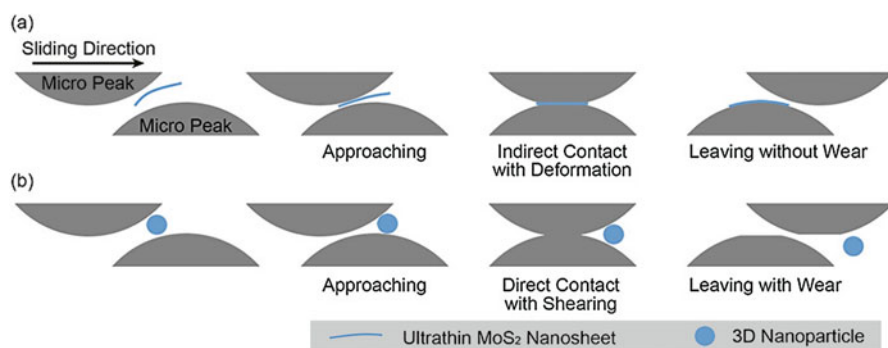


Fig. 7 Schematic of the lubrication mechanism of 2D- MoS_2 sheets (a) and 3D nanoparticles (b). (Reproduced with permission from [32] ©2015 Nature)

Table 2 Normalized friction values (i.e., friction force divided by the friction force in monolayer) of graphene and MoS_2 with the different number of layers) [31]

Material	Bulk	3-layers	Monolayer
Graphene	~0.45	~0.8	1
MoS_2	~0.3–0.4	~0.8	1

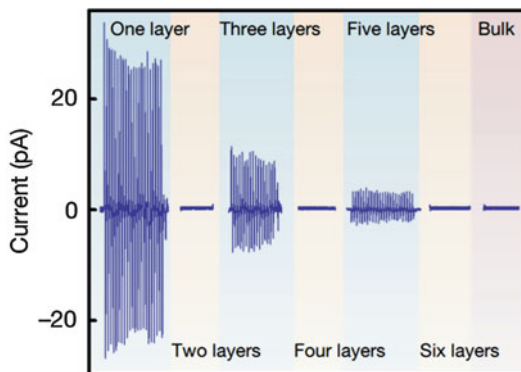
Oxidation Behavior

Bulk WS_2 and MoS_2 are oxidation resistant up to 485°C and 430°C , respectively, in air depending on the size and experimental conditions [33] whereas nanosheets (5–15 nm) get oxidized at lower temperatures due to increased surface area to volume ratios. Nanosheets of WS_2 get oxidized by 350°C while MoS_2 get oxidized between 200°C and 250°C [34]. Studies on monolayers of WS_2 and MoS_2 , on the other hand, reported gradual oxidation even at room temperature when exposed to ambient environment for several months [35]. Presence of humidity, and structural defects (grain boundaries, stacking faults, and sulfur vacancies) lead to accelerated rate of oxidation reaction. Recent works have shown the possibility to restrict such oxidation when these are grown by CVD on graphene. The enhanced oxidation resistance in the presence of graphene substrate is believed to be caused by the absence of defects in the as deposited WS_2 monolayer and the screening of the local surface electric field by the graphene substrate [36]. It is worth mentioning that even though oxidation could be detrimental to the applications in optoelectronics or microelectronics, selective or controlled oxidation of these 2D materials may lead to lateral heterostructures, e.g., $\text{WS}_2/\text{WO}_3\cdot\text{H}_2\text{O}$, which shows significantly enhanced photocatalytic properties [37].

Thermoelectric Behavior

Efficiency of the thermoelectric materials is characterized by a figure-of-merit denoted as $ZT (=S^2\sigma T/k)$ where S = Seebeck coefficient; σ = electrical conductivity; T = Temperature in kelvin; k = thermal conductance contribution both from the electrons and phonons, i.e., $k = (k_e + k_{ph})$. The ZT value of most of the practical thermoelectric materials is close to one. Therefore, for a given temperature, increasing the power factor ($S^2\sigma$) and decreasing the k is expected to enhance the efficiency of the thermoelectric materials. In semiconducting materials, it is possible to decrease k_{ph} , which has major contribution in the thermal conductance without much alteration in the electrical conductivity [38, 39]. The CVD grown MoS_2 monolayers with the Seebeck coefficient values of around 30 mV/K were reported by Wu et al. [31]. These values are more than 100 times higher than that of graphene [40]. Recently, the thermoelectric properties of hydrothermally synthesized 1T- WS_2 nanosheets (~10 nm thick) have been reported to have a similar Seebeck coefficient of 30 mV/K. Such high value has been attributed to an increased electrical conductivity and lower thermal conductivity of the 1T phase. Interestingly, the 2H- WS_2 nanosheets exhibit poor thermoelectric performance due to low electrical conductivity when compared to 1T- WS_2 [41]. It has been proposed that a layered MoS_2/WS_2 heterostructures may show higher ZT values when compared to the individual compounds due to their reduced lattice or phonon thermal conductivity (k_p), which results from the reduction in the phonon transmission at the interface of WS_2/MoS_2 [42].

Fig. 8 Evaluation of piezoelectric current with respect to number of layers. (Adapted with permission from [45] © 2014 Springer Nature)



Piezoelectricity

Non-centrosymmetric or absence of inversion centered atomic structure is an essential prerequisite for the materials to exhibit piezoelectricity [43]. Although, bulk crystals of MoS₂ and WS₂ do not exhibit piezoelectric behavior, the monolayers of MoS₂ were reported to exhibit piezoelectric effect [44, 45]. This behavior has been attributed to the broken inversion symmetry in such atomically thin structures. The influence of the number of layers in the 2D structure on its piezoelectric response is shown in Fig. 8. A marked difference in the piezoelectric response to odd and even number of layers is evident from the figure, which is caused by destruction and reconstruction of the inversion symmetry. The Piezoelectric coefficient (e_{11}) of MoS₂ monolayer has been found to be around $2.9 \times 10^{-10} \text{ cm}^{-1}$ and produced a power density of 2 mW/m^2 . Such figures reflect about 5.08% efficiency of mechanical-electrical energy conversion when strained to 0.53% [44, 45].

Optical Properties

Optical behavior of 2D- WS₂ and MoS₂ has demonstrated many interesting possibilities. Since these TMDCs show direct bandgap in monolayer form, they are expected to absorb photons having higher energy than the bandgap, leading to various altered optical properties, e.g., photoluminescence and photoconductivity. Figure 9 shows the relative photoluminescence peak intensity in a PL spectrum with number of layers in WS₂.

Studies by density functional theory have shown that the optical properties of lateral type MoS₂/WS₂ heterostructures may be optimized under uniaxial tensile strain, which brings about change in the optical bandgap E_g and conduction band minimum offset ΔE_c [47]. As for example, a mere 4% uniaxial tensile strain induces a significant increase in the power conversion efficiency by ~35% for a lateral WS₂/MoS₂ heterostructure-based optoelectronic device, which can be used for solar energy harvesting (Fig. 10).

Fig. 9 Change in relative PL peak intensity with number of layers in WS_2 nanosheet. Inset shows the relative change in the peak shape of the spectra for monolayer and bilayer. (Adapted with permission from [46] © 2013 Nature)

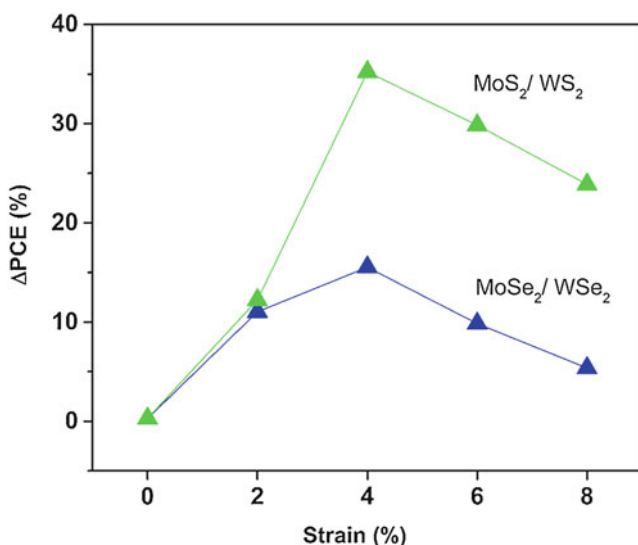
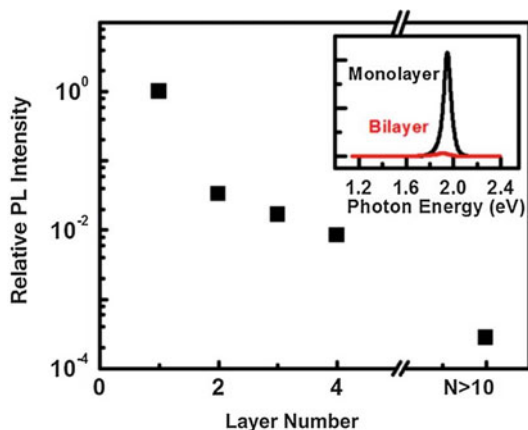


Fig. 10 Change in the power conversion efficiency of MoS_2/WS_2 heterostructures compared with $\text{MoSe}_2/\text{WSe}_2$ heterostructures and pure MoS_2 and WS_2 . (Adapted with permission from [47] ©2017 IOPSCIENCE)

Magnetic Properties

The pure and bulk structures of MoS_2 and WS_2 are known to be diamagnetic. However, in monolayer or 2D-form, these materials are reported to show ferromagnetic behavior. Such alteration in the magnetic behavior is believed to originate at the edges of the 2D structured material terminating in a zigzag manner where the magnetic moments exist in the Mo or W clusters due to the presence of partially filled 4d or 5d orbital, respectively [48, 49]. Ferromagnetism in 2D sheets of $\text{WS}_2/$

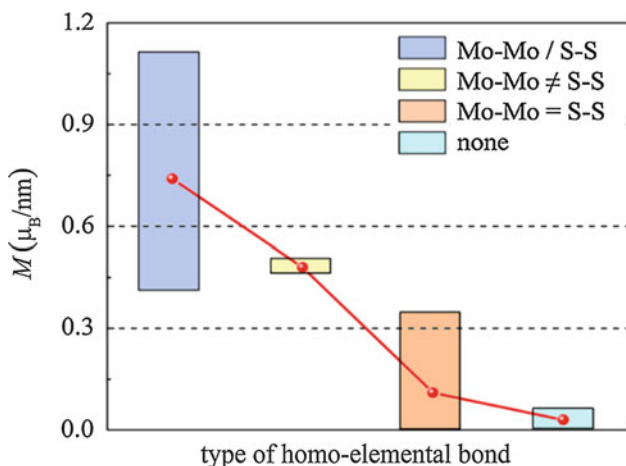


Fig. 11 First principle calculations showing the effect of type of the homo-elemental bonds at the GBs on the magnetic moment. (Adapted with permission from [51] ©2017 American Chemical Society)

MoS₂ may be tuned by controlling various parameters, viz., type and quantity of dopants, defects (vacancies, grain boundaries, and antisites), and lattice strain [50]. First principle calculations by Gao et al. have shown that the magnetic properties of defective MoS₂ monolayers are related to the number and type of the homo-elemental bonds at the grain boundaries (GB). As shown in Fig. 11, if GBs have a single type of either Mo–Mo bonds or S–S bonds and an unequal number of homo-elemental bonds (Mo–Mo \neq S–S), the material is ferromagnetic and has intrinsic magnetic moments between 0.38 and 1.1 μ_B/nm . Whereas, if the GBs have equal number of or with no homo-elemental bonds, the material is either anti-ferromagnetic or nonmagnetic [51]. In yet another interesting theoretical study, it has been found that Co substitution in Mo atomic sites of MoS₂ can produce a stable magnetic moment, which has its origin in the p-d hybridization (involving d orbital of Co, nearest neighbor Mo atoms and p orbitals of nearest neighbor S atoms). Higher value of the magnetic moment of about 3 μ_B may be attained at a lower doping concentration of Co (4–6.5 at %) as at higher concentration level Co atoms tend to form clusters [52].

Superconductivity

2D-Superconductors are expected to play a major role in the development of new generation electronic devices. In this regard, 2D-WS₂ and MoS₂ provide a promising option as their monolayer form can exhibit metallic character, which can turn superconducting at lower temperature. Superconductivity with T_c of 7.3 K has been reported in alkali metal intercalated MoS₂ while electrically tunable T_c between 0 to 11 K has been observed in multilayer MoS₂ by electrostatic electron doping [53, 54].

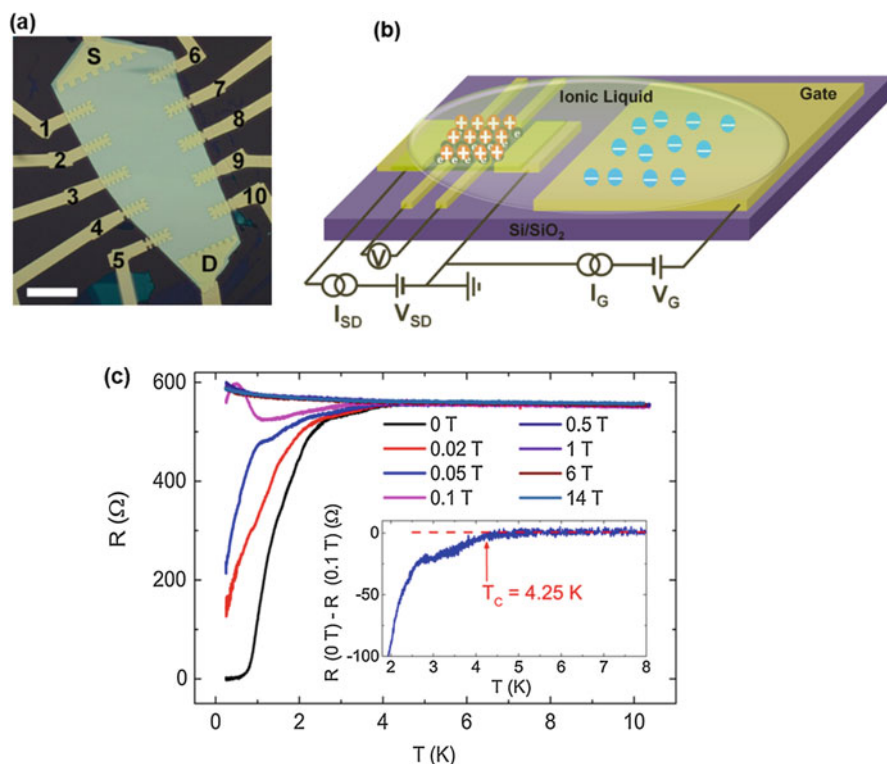


Fig. 12 (a) Optical image of FET device made with 2D-WS₂ (thickness = 20 nm) with ten contacts. (b) Schematic showing the setup of the ionic liquid-gated FET device. (c) Variation of R₂ as a function of temperature at different applied magnetic field. Inset shows the precisely estimated T_c. (Adapted with permission from [55] ©2015 American Chemical Society)

Jo et al. [55] have shown a gate-induced superconductivity below a T_c of about 4 K in exfoliated WS₂-based field effect transistors (FETs) (Fig. 12). Similarly, superconductivity in WS₂ monolayer with a critical temperature of 3.15 K has been induced by electron doping of WS₂ single layer in an electric double layer transistor (EDLT) device [56]. Theoretical studies indicate the possibility of higher T_c in 2D-MoS₂ and WS₂. As for example, in Calcium intercalated bilayers of MoS₂ and WS₂, theoretically estimated T_c can be as high as 13.3 and 9.3 K, respectively [57].

Synthesis Methods

As mentioned at the beginning of this article, early reports on extraction of 2D-MoS₂ date back to 1960s by mechanical exfoliation while Li-intercalation was used for generating 2D structured MoS₂ and WS₂ in the 1980s. However, the yield and

efficiency of such synthesis route remained quite poor. With the renewed interest on 2D-MoS₂ and WS₂ in recent years, there has been a growing impetus on the development of new and improved methods for better yield and quality. Large volume of work has been reported so far on the synthesis of 2D structured MoS₂ and WS₂ with several review articles published elsewhere [58–60]. Usually, the choice of the synthesis technique depends on the end use. As for example, many of the electronic applications require mono or few-layer deposition while catalytic, lubricating, and composite applications would prefer these phases in powder state and bulk quantity. The various top-down and bottom-up methods for the synthesis of 2D- MoS₂ and WS₂ are briefly explained in this section.

Top-Down Methods

Mechanical Exfoliation

The first mechanical exfoliation of MoS₂ was reported in 1966 [2]. Mechanical exfoliation involves the peeling off weakly held (similar to 2H-Graphite) layers of MoS₂ or WS₂ from their bulk lumps using adhesive tape. Repeating this process on the freshly peeled area results in obtaining a few layers' thick sheets to single layers. The obtained layer(s) is transferred to desired substrate for further processing or desired application. The major limitations of the mechanical exfoliation method have been its inapplicability to bulk production and lack of control over the number of layers in the product.

Chemical Exfoliation

This technique is also called as liquid/solvent exfoliation. In this method, suitable chemical solvents with the aid of sonication are employed to obtain 2D structures of MoS₂ and WS₂ ranging from ultrathin to monolayers. There are two types of chemical exfoliation viz. direct exfoliation and Lithium-intercalation. **In direct exfoliation**, bulk MoS₂ or WS₂ powder is dissolved in a proper solvent and the solution is subjected to ultrasonication. N-vinyl-Pyrrolidone (NVP), N-methyl-2-pyrrolidone (NMP), and N, N-dimethylformamide (DMF) are most commonly used solvents. Vibration and cavitation forces generated during the ultrasonication process disintegrate the bulk crystals into ultrathin to individual layers. Later these exfoliated layers are separated using centrifugation. In order to disperse the 2D structures in the solvent, use of specific solvent or blend of solvents is carefully selected on the basis of certain range of Hansen's solubility parameter (HSP), which takes into account the dispersion, polar, and H-bonding constituent of cohesive energy density. Coleman et al. [61] suggested that minimizing the enthalpy of mixing per unit volume denoted by ($\Delta\bar{H}_{Mix}$) leads to the effective dispersion and exfoliation. Minimization of ($\Delta\bar{H}_{Mix}$) is achieved by selecting the solvents and solutes whose dispersion, polar, and H- bonding parameters match closely. This method is capable of producing appreciable quantities of few or monolayers. However, the main disadvantages are longer sonication periods, fracturing of the sheets (rendering the product unsuitable for electronic applications), and disposal of

the used solvents. Recently, pretreatment of the bulk powders in liquid nitrogen before sonication has shown to produce the quantum dots in MoS₂, WS₂, Graphite, and others structures [62] and safe solvents such as mixtures of water-propanol or water-ethanol were also identified to improve the reaction kinetics and production yield.

The second type of liquid exfoliation method is Li-intercalation-assisted exfoliation. This technique was first reported by Joensen et al., in 1986. Here the bulk MoS₂ or WS₂ powder is intercalated with Li-ions by soaking them in the solution of n-butyl lithium and hexane for 2–3 days under inert and dry conditions. Under such conditions, Li-ion enters the interlayer spacing of the layered sulfides and interacts with the metal sulfide and forms Li_xMS₂. Later, Li_xMS₂ compound is immersed in water-sonicating bath where H₂ gas evolved due to the interaction of Li with H₂O, helps in exfoliating the layers. This technique has additional benefit of producing metallic 1T-phases of WS₂ and MoS₂. Longer soaking periods (above 72 h) and poor control over the Li-ion interactions with bulk crystals are the major drawbacks of this approach. However, the modified form of this method known as Electrochemical Exfoliation (ECEX) has been developed to overcome the issues encountered in conventional Li-intercalation method [63]. ECEX is a relatively fast and controlled exfoliation technique for single layer 2D-TMDs. It involves electrochemical lithiation of the bulk TMD and subsequent sonication of the Li-intercalated TMD in water or ethanol for exfoliation. Figure 13 shows a typical flow diagram of the process. The bulk TMD is used as the cathode in the electrochemical cell with Li-foil anode and LiPF₆ electrolyte bath. The lithiation process is controlled by applied current, which ensures a significantly enhanced process when compared to the conventional lithiation technique. Metallic 1T phase developed via this route has been shown to exhibit excellent catalytic activity in Hydrogen Evolution Reaction (HER) [64].

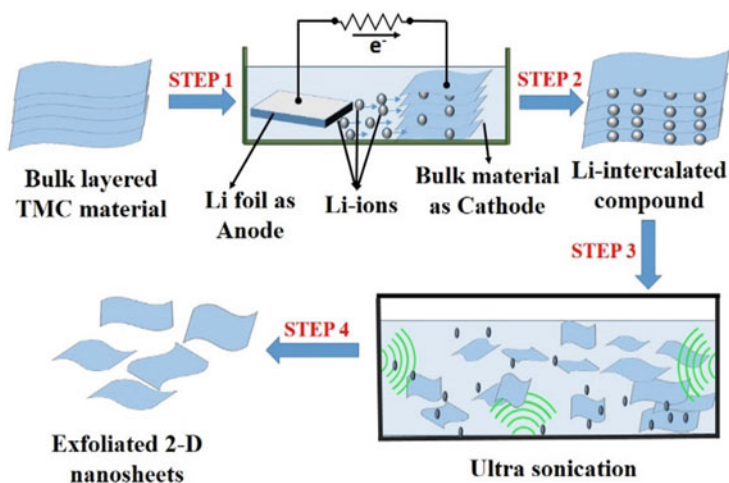


Fig. 13 Schematic of exfoliation method involving electrochemical lithiation

A recent innovation to the exfoliation method is the TMI technique developed by Jeong et al. [65]. The method is a single step process carried out at room temperature, which leads to monolayer form of TMDs without any sonication. Two Lewis base molecules are used in this method, as for example, a short initiator molecule like propylamine and a long primary initiator molecule like hexylamine in dimethyl sulfoxide. The short initiator molecule intercalates and expands the TMD layers to facilitate subsequent intercalation by the long primary initiator molecule, which leads to further expansion of the TMD layers and spontaneous exfoliation into monolayers.

Laser Thinning and Chemical Etching

Unlike exfoliation techniques, these methods produce 2D structures by sublimation of top layers through laser heating in an inert atmosphere. These are destructive techniques and not suitable for bulk scale applications.

Bottom-Up Methods

Vapor Deposition Techniques

It involves production of MoS_2 or WS_2 phases in the vapor state and their subsequent deposition on the selected substrates through vapor transport phenomenon. Vapor deposition methods are of two types, namely, Physical Vapor Deposition (PVD) and Chemical Vapor Deposition (CVD).

PVD involves a sputtering process in which the target material, i.e., either MoS_2 or WS_2 is placed as cathode and positively charged ions are accelerated onto the target so that MoS_2 or WS_2 targets are sublimed upon the impact of the ions. The target material should be of high purity to avoid the contamination. The vapors are subsequently condensed onto the substrate which is maintained at lower temperature and located in the proximity of the target. Whole process is performed under low pressure. The schematic of a typical sputtering process is shown in the Fig. 14a. The nonsputtering methods were developed recently to deposit the monolayers of MoS_2 where MoS_2 powder is evaporated by heating at around 900°C under pressures of around 20 mTorr. The vapors are transported by carrier gas onto the SiO_2/Si substrates maintained at the temperature of around 600°C [66].

CVD process involves chemical reaction(s) between the precursors (oxides, chloride, carbonyl, sulfur, H_2S etc.) to produce the product (MoS_2 or WS_2) phase in vapor form, which is subsequently deposited on the selected substrates [67–69]. CVD is one of the most widely used routes for the synthesis of large area mono- and multilayered 2D-TMDs. Various starting materials are possible for appropriate control of the product grade and yield. Figure 14b shows a schematic of metal-organic CVD (MOCVD) approach for mono and multilayered WS_2 and MoS_2 formation starting with transition metal carbonyl precursors under hydrogen. The growth of the 2D structure is controlled by the hydrogen flow rate, as evident from the microstructure of the product (Fig. 14c–e).

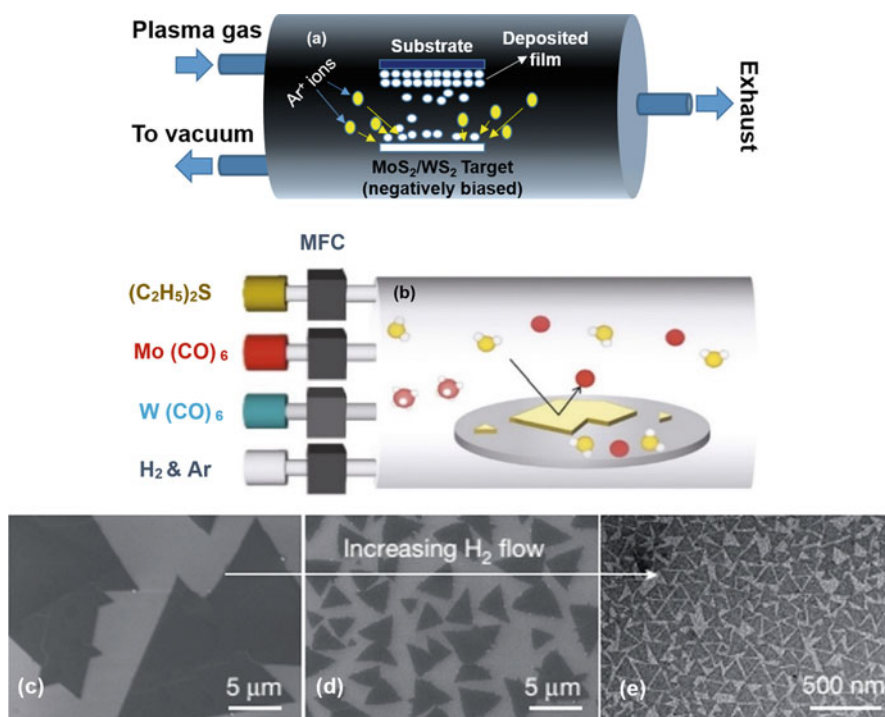


Fig. 14 (a) Schematic of PVD process. (b) Schematic of MOCVD process where flow of ingredients is controlled with mass flow controller (MFC). (c, d, e) Influence of hydrogen flow rate in (b) on the microstructure of the TMD monolayer. (Adapted with permission from [68]©2015 Nature Publishing Group)

Sulfurization of Metal or Metal Oxides

It is an alternative method, which has been used in recent years for the development of monolayer TMDs like MoS_2 or WS_2 directly from the transition metal oxide precursor using a setup shown schematically in Fig. 15 [70]. In this process, metal or metal oxide films get deposited on the selected substrates using thermal evaporation, e-beam evaporation, sputtering, and atomic layer deposition (ALD) techniques. The oxide is subsequently sulfurized either with sulfur or H_2S in the presence of H_2 , Ar, N_2 , or a mixture of these gases. Employing the more reactive gases such as H_2 or H_2S has been found to improve the reaction kinetics and shifting the reaction temperatures to lower value. The thickness of the sulfide films obtained in this route depends on the thickness of the starting metal/metal oxide.

Mechanically activated methods involving temperature or temperature-pressure-controlled reactor systems have been developed by many groups. Several of these efforts have reported large-scale synthesis of 2D-TMDs like WS_2 and MoS_2 nanosheets from mechanically activated nanostructured precursors of transition metal oxides. The setup for the processing reactor in this case is somewhat similar to that used in LPCVD. However, instead of WO_3 deposited on silica substrate,

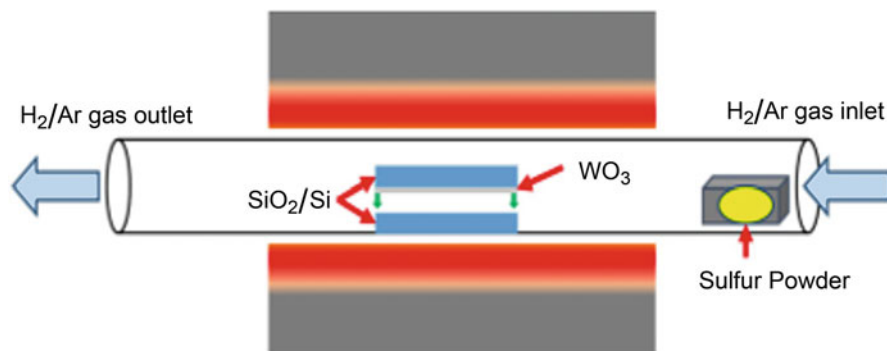


Fig. 15 LPCVD setup for the synthesis of 2D-TMD monolayer like WS₂. (Reproduced with permission from [70] ©2015 Nature). A modified version of the reactor can be used for processing of mechanically activated powder precursors to generate 2D-TMD nanosheet powders

mechanically activated nanostructured oxide powders are used as the precursor. A simple scalable method has been established recently for the synthesis of 2D-TMD nanosheets like MoS₂ and WS₂, in large scale and reproducible quality, using a modified form of such reactor under controlled pressure, temperature, and atmosphere [71].

Hydrothermal

Hydrothermal routes for the synthesis of 2D-TMDs involve the precipitation of product from the liquid medium under controlled pressure and temperatures. Ammonium molybdate, Sodium molybdate, ammonium tungstate, etc. are used for metal precursors whereas dibenzyl disulfide, thiourea are used as sulfur precursors. All the precursors are homogeneously mixed in deionized water with or without the presence of catalyst followed by heating in autoclave at the required temperatures (150–220 °C) and time period (few hours). Finally, the product powders are washed and dried. Synthesis of nanosheets (~10 nm) and quantum dots (3.7 nm) morphologies and 2H and 1T structures of MoS₂ and WS₂ have been successfully synthesized via this route by several groups [41, 72–74].

Thermolysis

A new technique, viz., thermolysis has come up recently for the synthesis of 2D-TMDs. This method involves thermal decomposition of ammonium tetrathiomolybdate ((NH₄)₂MoS₄) or ammonium tetrathiotungstate ((NH₄)₂WS₄), which leads to the formation of MoS₂ or WS₂ phase, respectively. Liu et al. [75] have reported the synthesis of MoS₂ trilayers on SiO₂/Si substrates by a two-step procedure involving thermal decomposition of (NH₄)₂MoS₄ at 120–500 °C in N₂ or H₂ or Ar/S, Ar/H₂ flow and post annealing at 1000 °C (to improve the crystallinity). Annealing under H₂ was found to reduce the decomposition reaction temperature [75]. A chronological summary of all the above synthesis routes is given in Table 3.

Emerging Applications

The enhanced properties of 2D-WS₂ and MoS₂ have huge potential for applications in the major industrial sectors such as automobile, energy, manufacturing, electronics, aerospace, and medicine. Some of the key potential applications have been identified from the recent progress in the area and are introduced in this section. It is envisaged that some of these would eventually make a major mark in the development of next-generation technologies in various areas of strategic importance.

Electronic Devices

2D-MoS₂ and WS₂ have been highly promising as a replacement for silicon in digital electronic devices, which usually require a high current on-off ratio (typically between 10⁴ and 10⁷) coupled with a bandgap of above 400 meV and reasonable field effect mobility. Figure 16a shows a general comparison between semiconducting 2D-TMD nanosheets, graphene, and other semiconducting materials for the large-area flexible electronics [51]. It is evident that the 2D-TMD nanosheets, which are a subset of semiconducting transition metal chalcogenides (s-TMDC), are much better placed when compared to graphene and other semiconducting materials. Figure 16b shows a schematic of a typical 2D-MoS₂ monolayer-based transistor with HfO₂ gate insulator [52] with an extremely high value of current on-off ratio (10⁸) and current mobility of 200 cm² V⁻¹ s⁻¹.

Optoelectronic Devices

Direct bandgap semiconductors are efficient for optoelectronic devices as they can readily absorb or emit light. Direct bandgap semiconducting nature of mono layered 2D-MoS₂ and WS₂ (bandgap energies of 1.88 and 2.1 eV, respectively) with tunable carrier mobility, I_{on}/I_{off} ratios, and viable synthesis routes made them attractive for various optoelectronic applications such as photodetectors, LEDs, lasers, and flexible displays [101, 102]. Materials having high stretchability, i.e., high elastic strain limits (along with high charge mobility) are suitable for the flexible displays. Figure 17a shows the maximum elastic strain limits of various materials. Semiconducting TMD (s-TMD) monolayers possess strain limits close to graphene. Figure 17b shows the schematic of WS₂ monolayer buried gate FET fabricated on flexible PEN (Polyethylene naphthalate) and Fig. 17c shows a flexible FET arrays with WS₂ monolayers on PEN substrate. The device exhibits mobility and ON/OFF ratios of 0.99 cm² V⁻¹S⁻¹ and 6 × 10⁵, respectively, without any degradation even after 100 bending cycles (Fig. 17d).

Optoelectronic properties of 2D-MoS₂ and WS₂ have novel bioelectronic applications too. For example, human eye inspired MoS₂-Graphene (Gr) (4 nm and 2 nm, respectively)-based soft optoelectronic curved image sensor arrays have been reported recently as an effective intraocular retinal prosthesis for patients suffering

Table 3 List of various synthesis methods for 2D WS₂ and MoS₂ along with few notable reports

Synthesis method	Year	Primary precursor(s)	Technique/solvent/electrolyte/atmosphere/growth condition	Morphology/structure	Ref.
Top-down approaches					
Mechanical exfoliation	1963, 1966	Naturally available MoS ₂ crystal (Molybdenite)	Cleavage/stripping using scotch tape.	<10 nm thickness sheets	[1, 2]
	2012	Bulk MoS ₂ crystal	Peeling off using poly dimethylsiloxane stamp	5–10 layer thick	[28]
	2013, 2012	2H-WS ₂ /MoS ₂	Sandpaper and polymers (PTFE, PET, PC) for rubbing and smoothing medium; PET or PC substrate	50–5 nm thick few layered nanosheets	[76, 77]
	2017	Bulk WS ₂	Deposited on quartz wafer using scotch tape	Mono or few layered	[78]
	2015	Bulk 2H-WS ₂ /MoS ₂	Water, ultrasonication	Atomically thin platelets	[79]
Chemical exfoliation	2017	Bulk 2H-WS ₂ /MoS ₂	Liquid N ₂ , IPA-water mixture, ultrasonication	2D quantum dots	[62]
	1986, 1988, 1996, 2011	Bulk 2H-WS ₂ /MoS ₂	N-butyl lithium in hexane; water, ultrasonication	1 T-MoS ₂ , monolayers, few layers (5 nm)	[4, 5, 23, 80]
Li-intercalation	2014	Bulk 2H-MoS ₂ /WS ₂	N-butyl lithium in hexane, ammonium chloride, water, ultrasonication	MoS ₂ /WS ₂ nanosheets (2 nm thick) or their hybrids	[81]
Electrochemical Li-intercalation	2018	Bulk 2H-WS ₂	N-butyl lithium in hexane, sodium chlorate/water solution, ultra-sonication	1–2 layered WS ₂ nanosheets	[82]
	2011	2H-WS ₂ /MoS ₂	1 M LiPF ₆ in the mixture of dimethyl carbonate (DMC) and ethylene carbonate (EC) as an electrolyte, Li-foil as an anode; Bulk WS ₂ or MoS ₂	Mono-layered MoS ₂ and WS ₂	[63]

				as a cathode, exfoliation in water/ethanol (with the aid of ultrasonication)		
	2017	Bulk MoS ₂ pellet or natural MoS ₂ crystal		MoS ₂ (as a working electrode), electrolyte (1 M LiClO ₄ in the mixture of dimethyl carbonate and ethylene carbonate, exfoliation in deionized and deoxygenated water)	1 T-MoS ₂ nanosheets (3 layers)	[64]
Laser thinning	2012	Mechanically exfoliated natural MoS ₂ flakes (1–20 layers thick) supported on Si/SiO ₂ substrate		Green laser ($\lambda = 532$ nm); 10 mW power,	MoS ₂ monolayer	[83]
	2017	CVD grown few layered WS ₂ film		Laser ($\lambda = 514$ nm); under ambient environment	WS ₂ monolayer	[84]
	2018	MoS ₂ bulk flake (60 nm) on Si/SiO ₂ substrate		Green laser ($\lambda = 532$ nm)	Few-layer MoS ₂ (2.5 nm)	[85]
Chemical/plasma/thermal etching	2013	Mechanically exfoliated MoS ₂ nanosheets on Si/SiO ₂		Thermal annealing in air at 330 °C for 1 h	MoS ₂ monolayer	[86]
	2013	Multilayered MoS ₂ supported on Si/SiO ₂ by mechanical exfoliation.		Ar plasma irradiation at room temperature	MoS ₂ monolayer	[87]
Bottom-up approaches						
PVD	2007	Tungsten		Reactive magnetron sputtering, dc at 13.56 MHz and RF at 27.12 MHz Ar-H ₂ S gas, substrate temperature 200–620 °C, chamber pressure 1×10^{-4} Pa	70–110 nm thick WS _{2-x} films on Si/SiO ₂ substrate	[88]
	2013	MoS ₂ powder		Evaporation of MoS ₂ under low pressures (20 Torr), Ar flow, furnace heating zone at 900 °C, Substrate at 650 °C, 15 min reaction time.	MoS ₂ monolayer on Si/SiO ₂ substrate	[66]
	2016	Bulk WS ₂		RF magnetron sputtering, 2×10^{-7} torr, substrate temperature 350 °C	310 nm thin films	[89]
	2017	MoS ₂		RF magnetron sputtering, deposition chamber pressure 10^{-6} m bar	200 nm MoS ₂ films on Si substrate	[90]

(continued)

Table 3 (continued)

Synthesis method	Year	Primary precursor(s)	Technique/solvent/electrolyte/atmosphere/growth condition	Morphology/structure	Ref.
CVD	2015	W(CO) ₆ (heating at 60 °C) + S (170 °C)	He flow, 600 °C (on graphene substrate) (5–20 min)	3–4 layers	[91]
	2017	WS ₂ + NaCl (4:1) to produce WCl _x + S (heating at 950 °C)	5%Ar + 95% H ₂ , 700–750 °C, 3–5 torr	Monolayers and few layers on SiO ₂ /Si	[92]
Sulfurization of metal or metal oxides	2012	WO ₃ /MoO ₃ , Toluene, S	H ₂ , H ₂ + N ₂ , Temperature and Pressure controlled	WS ₂ and MoS ₂ nanosheet powder (5–10 nm)	[71]
	2017	WO ₃ , S	Ar flow, 750–950 °C (on SiO ₂ /Si substrate), 1 atm	Monolayers	[93]
	2017	WO ₃ (980–1000 °C), S (heating at 200 °C)	Ar flow, 800–860 °C (on SiO ₂ /Si substrate)	Triangular monolayers	[94]
	2018	S (heating at 110 °C), WO ₃ (heating at 920–940 °C)	Argon flow, 980 °C (on SiO ₂ /Si substrate), 0.16 Torr	monolayers	[95]
Hydrothermal	2018	WO ₃ , S	Ar flow, 1050 °C (on Al ₂ O ₃ substrate), 10 mbar	Monolayers	[96]
	2013	WCl ₆ , thioacetamide (C ₂ H ₅ NS)	Autoclave, 265 °C, 24 h	Nanosheets (1–5 nm)	[97]
	2016	(NH ₄) ₂ WS ₄ , water	Autoclave, 180 °C, 10 h	Nanosheets	[98]
	2017	WCl ₆ , C ₂ H ₅ NS, de-ionized (DI) water	Autoclave, 220 °C, 24 h	2 nm thick nanosheets	[99]
	2018	(NH ₄) ₆ H ₂ W ₁₂ O ₄₀ ·xH ₂ O (ammonium tungsten oxide hydrate), thiourea, oxalic acid	Autoclave, 220 °C, 48 h	1 T-WS ₂ nanosheets	[41]
Thermal decomposition	2011	(NH ₄) ₂ MoS ₄ or (NH ₄) ₂ WS ₄ + Oleylamine	360 °C, 30–90 min reaction/heating time under continuous stirring	Oleylamine coated single or few layered nanosheets	[75, 100]

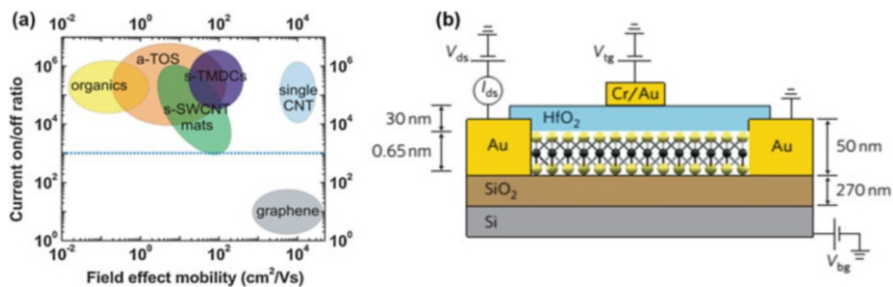


Fig. 16 (a) Current on-off ratio and field effect mobility of several semiconducting materials. (Reproduced with permission from [51] ©2014 American Chemical Society). (b) Schematic of a 2D-MoS₂ monolayer (thickness of 0.65 nm)-based field-effect transistor. (Reproduced with permission from [52] ©2011 Nature Publishing Group)

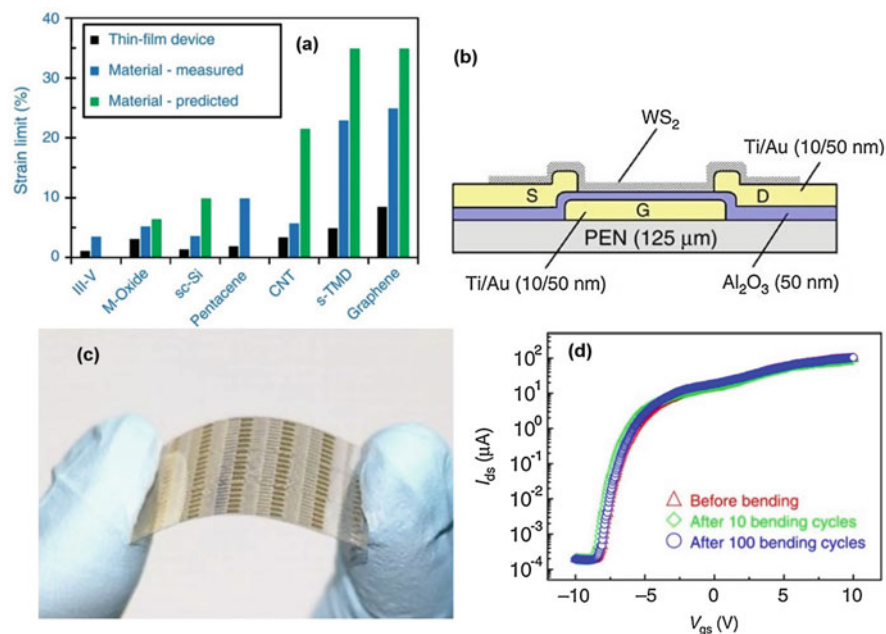


Fig. 17 (a) Maximum elastic strain limits of the various candidate materials used for thin-film transistors. (Reproduced with permission from [101] ©2014 Springer Nature); (b) Cross-sectional schematic of WS₂ buried gate FET. (c) Photo of the flexible FET arrays made up of WS₂ monolayers on PEN substrate. (d) Device logarithmic transfer features with respect to bending cycles showing no degradation in the performance even after 100 cycles. (Reproduced with permission from [102] ©2015 Nature)

from retinal degeneration disease such as macular degeneration retinitis pigmentosa. Owing to nanoscale size, soft nature, high photo-response coefficient, and good elastic strain limits, 2D-MoS₂/Gr sensors show greater advantages than that of conventional retinal implants [103]. Figure 18 shows the schematic of the human eye, sensor array, and associated components. As shown in the Fig. 18e, the photoresponsivity of the MoS₂/Gr phototransistor is 2–3 times higher than that of Si-based photodetector due to higher photo-absorption of 2D-MoS₂. In vivo tests on rats with the implanted soft optoelectronic device showed good biocompatibility.

Memory Devices

The monolayers of WS₂ and MoS₂ have shown promising performance as next generation memory devices material. As for example, 2D-MoS₂-graphene oxide-based nanosheets comprising of MoS₂-graphene oxide layer sandwiched between Aluminum and ITO (indium tin oxide coating on glass substrate) have been successfully tried as a memory device requiring extremely low energy [104]. Figure 19a shows the writing-reading-erasing cycle based on the application of voltage and current density in the memory device. In a recent work, Zhang et al., have shown an exceptionally high memory window of about 20 V in a tunable dual gate charge trap device based on a few layers of MoS₂, generated by mechanical exfoliation, and atomic-layer-deposited Al₂O₃-HfO₂-Al₂O₃ gate structure as shown in Fig. 19b and c.

Sensors

Ultrahigh sensitivity of the 2D-MoS₂ and WS₂ structures to radiation, vibrations, and various chemicals coupled with excellent electronic properties promise the fabrication of cheap, compact, low-power, highly efficient and advanced nanoscale sensing devices for various strategic applications such as visible and IR detectors, vibration sensors, stealth coatings, gas detectors, and actuators. Field effect phototransistors based on 2D-MoS₂ nanosheets of 10–20 nm thickness were reported to display an ultrahigh photoresponsivity of around 10⁵ AW⁻¹ in the visible light spectrum (at $\lambda = 454$ nm) with the minimum detection ability of 17 picowatts. Moreover, the device was also reported to respond to near infrared light signals between 980 and 1550 nm with a maximum photoresponsivity of 2.3 AW⁻¹ at $\lambda = 980$ nm owing to bolometric effect [106].

Recently, WS₂ nanosheets incorporated melamine-formaldehyde and hydrophobic silica sponges have shown extremely high sensitivity towards minute level of vibrations in water and ground. Such ultrahigh sensitivity along with its hydrophobicity and high flexibility makes it an excellent candidate for amphibious vibration sensor [107].

Sensing and identifying harmful gases in industries, polluted areas, and in chemical warfare is an important issue. Large surface area to volume ratios and sensitivity to different chemical vapors make mono- or few-layered 2D-TMDs as a

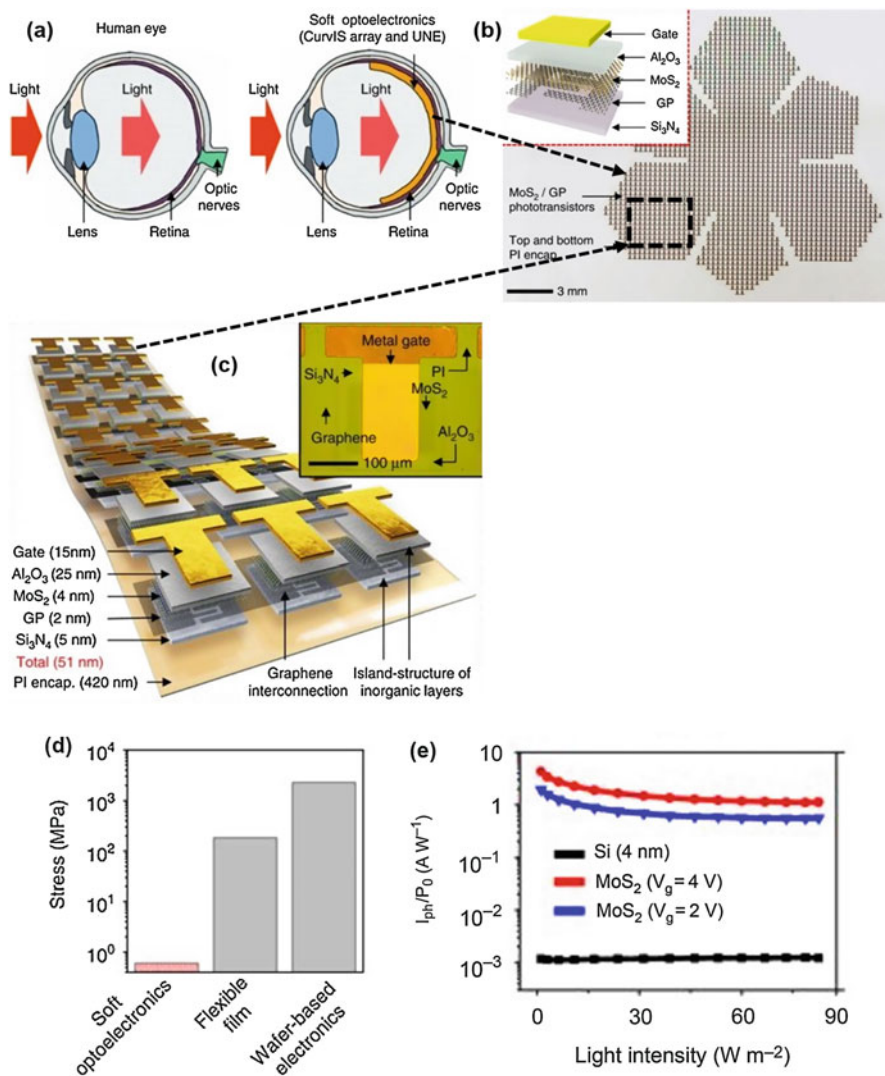


Fig. 18 (a) Schematic ocular structure of human eye. (b) Human eye-inspired truncated icosahedron MoS₂/Gr phototransistor array. (c) Exaggerated schematic of highlighted portion of (b) along with an inset of single phototransistor. (d) Comparison of stress induced by three different implanted devices. (e) Photoresponsivity of MoS₂/Gr single phototransistor compared to Si photodetector where the thickness of Si and MoS₂ are same. (Adapted with permission from [103] ©2017 Nature)

highly attractive material for low cost and highly efficient chemoresistive gas sensors. 2D-WS₂ or MoS₂-based gas sensors are being studied for detecting gases such as NO₂, NH₃, CO, CO₂, H₂S, etc. [108–110]. It has been observed that these sensors respond better to donor-type analytes such as

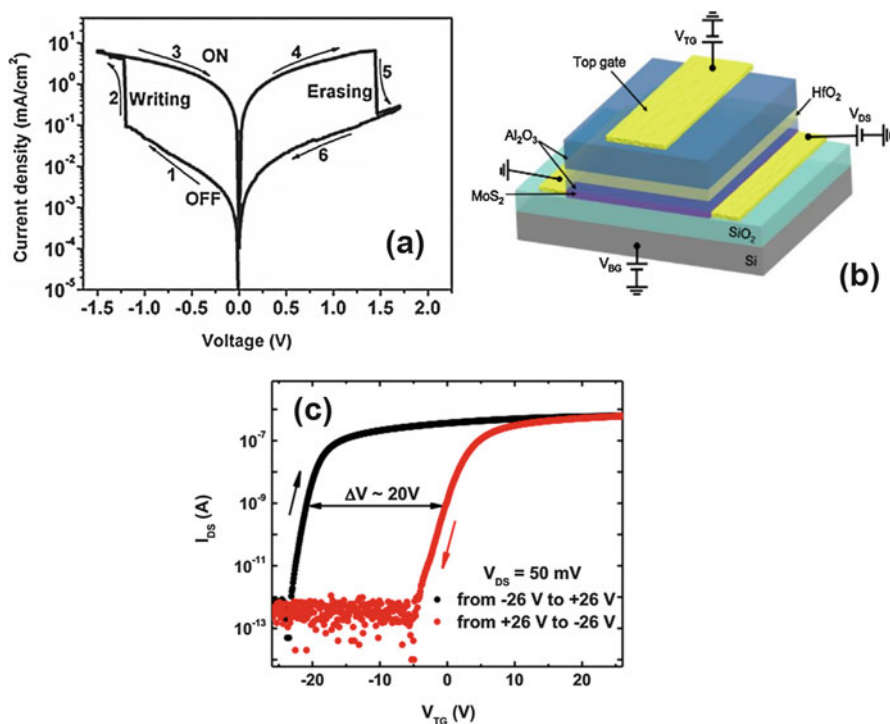


Fig. 19 (a) Al/2D-MoS₂/graphene/ITO-based memory device showing writing-reading-erasing cycle with application of voltage and current density. (Adapted with permission from [104] ©2012 John Wiley and Sons). (b) Schematic of Al₂O₃/HfO₂/Al₂O₃/2D-MoS₂/SiO₂ gate stack structure. (c) Memory window of 20V shown by gate structure shown in (b). (Adapted with permission from [105] ©2015 American Chemical Society)

triethylamine (TEA) (a V-series nerve gas agent's decomposition product), acetone, etc. when compared to graphene- and CNT-based sensors. Figure 20a shows relative performance of MoS₂ monolayer and CNT-based sensors for different analytes. Maximizing the edge site density (which has high reactivity due to low gas adsorption energy) through surface functionalization, defect control, and making heterostructures or composites showed further enhanced sensitivity and recovery rate in these materials [111, 112]. Figure 20b shows excellent response of WS₂ nanoplate confined Co, N doped hollow carbon nanocage-based gas sensor even for very low concentration of the analytes.

2D-MoS₂/graphene composites are also being studied for microwave absorption because of their good dielectric loss and thermal conductivity. Reflection loss of around -10 dB has been reported in full Ku band (12.2–18 GHz) with the sample thickness of around 2.6–3.0 mm and at 30 wt.% of MoS₂/graphene content in paraffin wax [113]. These coatings have applications in stealth technology.

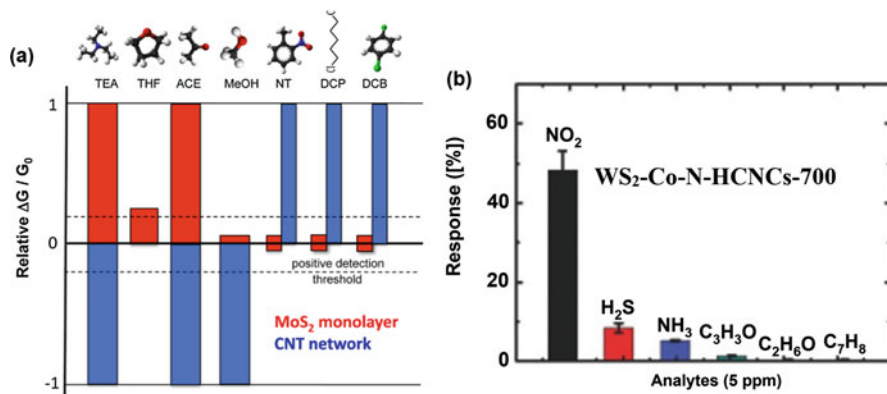


Fig. 20 (a) Comparison between MoS_2 and CNT network-based sensor responses to different analytes. The analytes mentioned on top are (left to right) triethylamine (TEA), tetrahydrofuran (THF), acetone, methanol, nitrotoluene (NT), 1,5-dichloropentane (DCP), and 1,4-dichlorobenzene (DCB). (Reproduced with permission from [112] ©2013 American Chemical Society). (b) Response of WS_2 nanoplates (2–3 layers) confined Co, N-doped hollow carbon nanocage ($\text{WS}_2\text{-Co-N-HCNC}$)-based gas sensor exposed to various analytes at 5-ppm concentration. (Adapted with permission from [111] ©2018 John Wiley and Sons)

Catalysis and Energy Storage

2D-MoS_2 and WS_2 have enhanced catalytic activity when compared to their bulk forms. Mono- or few-layered structures of WS_2 or MoS_2 or their heterostructures and composites are being studied largely for hydrogen evolution reactions (HER) and hydrodesulfurization reactions (HDR). These materials have attracted major attention as constituent of electrodes in Li-ion batteries and supercapacitors. It has been demonstrated that such enhanced performance is primarily due to the changes in their electronic structure and the presence of highly active sites at the edges.

Hydrogen Evolution Reaction (HER) Catalyst

Recent studies revealed that 1T metallic phases of either WS_2 or MoS_2 have superior electrocatalytic and photocatalytic activity for HER when compared to their semiconducting 2D–2H phases and in fact, their performance was reported to be close to Pt [64, 114–117]. Voiry et al. have shown that the tensile strain induced in the 1T structure of the exfoliated WS_2 leads to improved catalytic performance in HER as it helps in reducing the free energy of atomic hydrogen adsorption and thereby facilitating hydrogen binding [118]. Such catalytic behavior of 2D- WS_2 and MoS_2 materials is highly promising and expected to turn the process an economically viable route for H_2 fuel production. Table 4 shows a selected list of notable reports on the use of 2D- WS_2 and MoS_2 in HER.

Li-ion Batteries

2D-MoS₂ and WS₂ have shown tremendous potential as an electrode material for Li-ion battery as well as supercapacitors. As for example, WS₂ nanosheet-based electrodes have shown a stable reversible capacity of 539 mAhg⁻¹ (after 60 cycles) at a current density of 0.2 Ag⁻¹ [123]. 2D-TMD and graphene composites have shown enhanced performance with significantly improved reversible specific capacity. A typical example is 2D-MoS₂-graphene composite, which has shown a specific capacity of 1290 mAhg⁻¹ at a current density of 100 mAg⁻¹ (Fig. 21) [124]. A list of notable reports on the performance of 2D-WS₂ and MoS₂ as electrode material for Li-ion battery is presented in Table 5.

Supercapacitors

Recently, ternary composites of 2D structured MoS₂/WS₂/Graphene oxide-based supercapacitors have displayed high specific capacitance (365 Fg⁻¹ at 1 Ag⁻¹) with excellent cyclic stability when compared to individual rGO-MoS₂ or rGO-WS₂ composites [135]. Supercapacitor electrodes based on 1T metallic phases of 2D-MoS₂ and WS₂ monolayers have shown an improved performance when compared to 2D-2H semiconducting structures, which has been attributed to their high hydrophilicity, higher electrical conductivity (10⁷ times), and the ability to intercalate the ionic species dynamically [64, 136, 137]. According to Ejigu et al., the device fabricated from 1T MoS₂ exhibited the specific capacitance of 102 Fg⁻¹ at 10 mv/s in 6 M KOH (aq) which is nearly 17 times higher than that of its semiconducting 2D-2H phase, and around 5.7 times higher than pristine graphene. Increasing the conductivity of 1T phases by adding graphene further enhanced the device performance to about 147 Fg⁻¹ at 10 mV/s in 6 M KOH (aq), i.e., around 44% higher capacitance with an excellent retention of capacitance by over 90% even after 5000 cycles. Volumetric energy vs. power densities data given by Ragone plots is shown in the Fig. 22, which indicates the performance of devices, prepared from different materials in comparison to the above 1T-MoS₂/graphene composites. The performance reports of various major studies on 2D-MoS₂/WS₂-based supercapacitor electrodes are given in the Table 6.

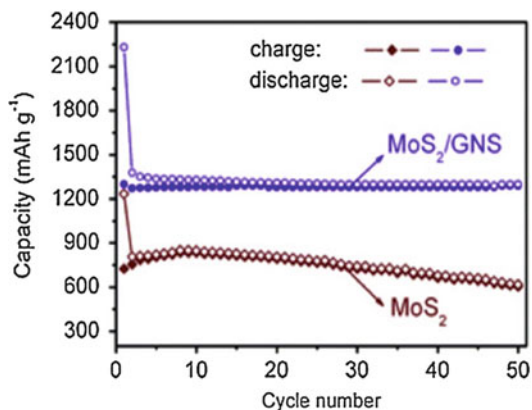
Lubrication

The 2D-TMD nanosheets like MoS₂ and WS₂ have significantly enhanced lubrication properties because of their inherent layer structures and ability to enter into the microscopic pits and crevices. They have many uses like solid lubricants coatings, composites, and additives to oil or grease-based lubricants under high load when compared to other variants like micron grade and IF. For example, Fig. 23a and b shows the performance of MoS₂ nanosheets, as an additive (1 wt.%) dispersed in liquid paraffin (LP) base oil, compared to other forms like IF-MoS₂, micron size MoS₂, and molybdenum dialkyldithiophosphate (MoDDP) lubricant additives under highest load with no seizure. Similarly, antifriction and antiwear performance of base

Table 4 Performance of 2D-WS₂ and MoS₂ as Co-catalyst in photocatalytic HER

2D-TMS	Synthesis route of 2D-TMS	Size/thickness/number of layers	Composite composition	Reagent composition	Light source	H ₂ generation (mmol g ⁻¹ h ⁻¹)	Ref.
2D-WS ₂	Colloidal synthesis	Monolayers	TiO ₂ -wt.% 1 T-WS ₂	Water+ Methanol (3:1)	Visible light (300 W Xe λ ≥ 400 nm)	2.57	[115]
	Hydrothermal	2 nm	CdS-10 wt.% (WS ₂ -MoS ₂)	Water+ Lactic acid (4:1)	Simulated sun light (150 W Xe)	209.79	[99]
	Li- intercalation	1-2 layers of 2H-WS ₂	CdS- 8 wt.% WS ₂	20 Vol.% Lactic acid solution	Visible light (300 W Xe λ > 420 nm)	11.41 17.73 (simulated sunlight)	[82]
	Exfoliation by sonication	3-4 nm	ZnS- 0.5 wt.% WS ₂	0.1 M Na ₂ S+ 0.1 M Na ₂ SO ₃	300 W Xe lamp	0.30	[119]
2D-MoS ₂	Hydrothermal	Nanosheets (~5 nm)	TiO ₂ -50 wt.% MoS ₂	0.35 M Na ₂ S+ 0.25 M Na ₂ SO ₃	300 W Xe lamp λ (280 nm- 700 nm)	1.6	[120]
	Hydrothermal	2D	CdS- 1.15 wt.% (MoS ₂ -graphene)	1 M Na ₂ SO ₄ (Aq. sol.)	Visible light (350 W Xe λ > 420 nm)	2.19	[98]
	Hydrothermal + Sonication	Nanosheets	CdS- 9 wt.% MoS ₂	20 Vol. % lactic acid (Aq. Sol.)	Visible light (300 W Xe λ > 400 nm)	95.7	[121]
	Hydrothermal	Nanosheets	CdS- wt.% B-doped MoS ₂	20 Vol. % lactic acid (Aq. Sol.)	Simulated solar light	196	[122]
	Li-Intercalation + Sonication	Nanosheets	CdS-10 wt.% 1 T-MoS ₂	10 Vol. % lactic acid (Aq. Sol.)	Visible light (300 W Xe λ > 420 nm)	39.7	[114]

Fig. 21 Specific capacity of 2D-MoS₂-graphene composite electrode when compared to 2D-MoS₂ electrode in Li-ion battery. (Reproduced with permission from [124] ©2011 Royal Society of Chemistry)



oils such as Polyalpha olefin (PAO), 500 SN are also shown to be greatly improved when they are formulated with 2D-WS₂ additives (1–2 wt.%) [144, 145]. Moreover, metal and polymer matrix composites reinforced with 2D-MoS₂ and WS₂ structures at lower weight fractions have shown strengthening of these structures along with reduced friction and wear [29, 146, 147]. Such enhancements in the structural, tribological properties are expected to greatly improve the efficiency of automobiles by reducing the friction, fuel consumption, and material loss. Possible exploitation of the 2D-WS₂ or MoS₂ as lube oil additives and self-lubricating composites/coatings for the defense applications like submarines, ships, tanks, artillery, fighter jets, satellites, rovers, antennas of radar, and telescopes have attracted major attention.

2D-MoS₂ nanosheets reinforced nitrile butadiene rubber (NBR) composites showed reduction in the friction and vibrational noise of water lubricated rubber stern tube bearings in boundary and mixed lubrication conditions. This has shown improved lifetime and concealing ability of underwater vehicles [176]. However, the thermal stability of MoS₂ which may get severely affected under humid conditions was not discussed in this report [148]. MoS₂ and WS₂ are the effective lubricants for the space and vacuum applications where lubricants like oils/grease and graphite are ineffective (graphite requires adsorbed moisture to lubricate which is not possible in vacuum). Coatings or composites based on nano-MoS₂ and WS₂ such as MoS₂-Ti (MoST), WC/DLC/WS₂ were reported to be good candidate for the aerospace applications [149, 150]. Aerosol MoS₂ coatings backed with diamond like carbon (DLC) and thin dense chrome (TDC) were reported to be good candidates for reducing the friction, enhancing the load carrying capability and endurance life of rifle barrels [151].

In the above reports related to aerospace and artillery applications, sizes of MoS₂ and WS₂ have not been mentioned (probably micron grade powders might be used as 2D forms of TMS were not in wide spread use at that time); however, 2D-MoS₂/WS₂ and their composites which have superior load carrying capacity and friction and wear reduction properties than that of IF and micron structures are expected to perform better and promising for the modern weapons [32, 145, 152, 153].

Table 5 Performance of 2D-WS₂ and MoS₂ as Li-ion battery electrode

2D-TMS	Synthesis route	Electrode composition	Electrolyte composition	Specific capacity (mAh/g)	Reversible cycle stability	Ref.
2D-WS ₂	Hydrothermal	WS ₂ -nanosheets/graphene + acetylene black (AB) + Polyvinylidene fluoride (PVDF) (70:20:10 by weight)	1 M LiPF ₆ in ethylene carbonate (EC)/dimethyl carbonate(DMC)/diethyl carbonate (DEC) (1:1:1 by volume)	766 (at 0.1 mA g ⁻¹)	100 cycles (at 0.1 mA g ⁻¹)	[125]
	Hydrothermal	WS ₂ @SWCNT foam	1 M LiPF ₆ in EC + DEC mixture (1:1 by volume)	1050 (at 0.1 Ag ⁻¹)	1000 cycles (at 1 Ag ⁻¹)	[126]
	Hydrothermal	Nano-honeycomb WS ₂ (80%) + 10% PVDF+ 10% conductive carbon black (CCB)	1 M LiPF ₆ + (EC+ DMC) in 1:1 by volume, 3% fluoroethylene carbonate (FEC)	953.1 (at 0.1 Ag ⁻¹)	350 cycles (at 1 Ag ⁻¹)	[127]
	Hydrothermal	N-doped graphene-WS ₂ on graphene sheets + CCB + PVDF (80:10:10 by weight) in NMP	1.0 M LiPF ₆ in (EC + DMC) (1:1 by volume)	1309.4 (at 0.1 Ag ⁻¹)	320 cycles (at 1 Ag ⁻¹)	[128]
2D-MoS ₂	Solvothermal	N doped- C@MoS ₂ nanobox + CCB + PVDF (70:20:10 by weight)	1 M LiPF ₆ + (EC + DMC) (1:1 by volume)	1000 (at 0.4 Ag ⁻¹)	200 cycles (at 0.4 Ag ⁻¹)	[129]
	Hydrothermal	TiO ₂ @MoS ₂ + CCB + PVDF (80:10:10 by weight) in NMP	1 mol LiPF ₆ + (EC+ DMC) (1:1 by volume)	971 (at 0.1 Ag ⁻¹)	200 cycles (at 0.1 Ag ⁻¹)	[130]
	Hydrothermal	MoS ₂ /m-C + CCB + PVDF (80:10:10 by weight)	1 M LiPF ₆ in EC+ DMC mixture (1:1 by volume)	1113 (at 0.4 Ag ⁻¹)	200 cycles (at 0.4 Ag ⁻¹)	[131]
	Hydrothermal	MoS ₂ /Graphene+ AB + PVDF (70:15:15 by weight) in NMP	1 M LiPF ₆ + (EC+ DMC) + Ethyl methyl carbonate (1:1:1 by volume)	1077 (at 0.1 mA g ⁻¹)	400 cycles (at 1 mA g ⁻¹).	[132]
	Hydrothermal process	(SnS -MoS ₂ -C) + CMC+ AB (70:15:15 by weight)	1 M LiPF ₆ + (EC + DMC) (1:1 by volume)	989.7 (at 0.2 Ag ⁻¹)	700 cycles (at 2 Ag ⁻¹)	[133]
	Polymerization and sulfidation/ carbonation process	MoS ₂ @C nanospheres + CCB + PVDF (8:1:1 by weight) in NMP solvent.	1 M LiPF ₆ + (EC + DMC) (1:1 by volume)	1119 (at 0.1 Ag ⁻¹)	100 cycles (at 2 Ag ⁻¹)	[134]

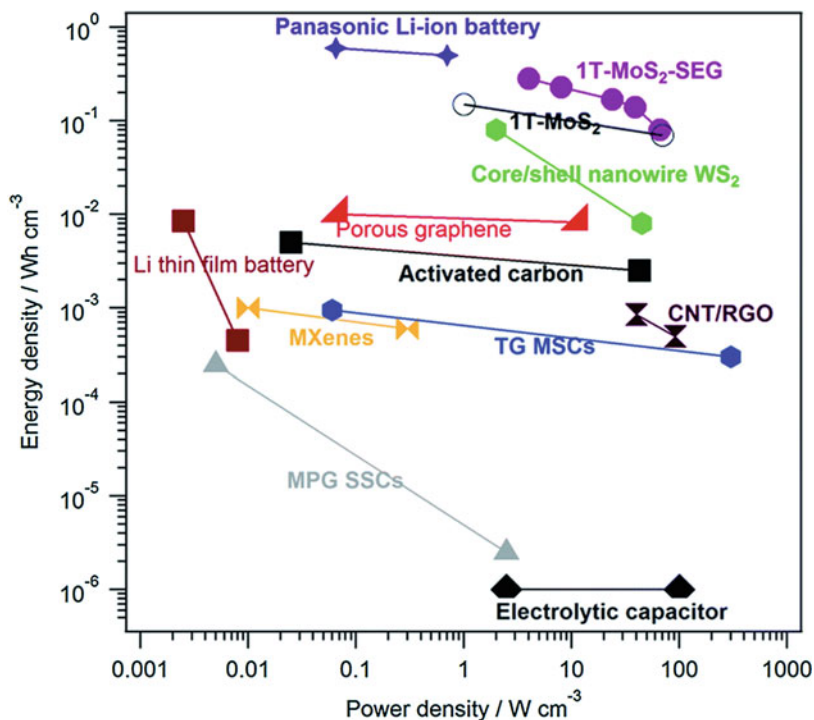


Fig. 22 Ragone plot showing the energy versus power densities variation trend of the various best performance materials in comparison to 1T-MoS₂ and graphene composites [64] ©2013 Royal Society of Chemistry

Environmental

2D forms of WS₂ and MoS₂ have shown promising performance in water purification and desalination processes. Based on molecular dynamics simulations, Heiranian et al. have predicted that MoS₂ monolayers with nanopores (pore areas 20–60 (Å)² obtained via defect engineering or electron beam irradiation) could be highly effective in rejection of more than 80% of ions during desalination of ~1 M of salt water (Fig. 24a). Pores terminated with only Mo atoms showed higher flux due to the special arrangement of hydrophobic edges and hydrophilic center in the pore region [154]. The water permeation rate in 2D-MoS₂ has been found to be 2–5 orders of magnitude higher than all commercially available membrane materials as shown in Fig. 24b. Hirunpinyopas et al. studied the desalination and nanofiltration performance of functionalized MoS₂ nanolayers (1–5 layers thick, exfoliated in PVA and water mixture) supported on PVDF membrane having a pore size of around 100 nm. It was reported that 5 μm thick laminar membranes of MoS₂ rejected nearly 99% of the ions from the salt water along with the higher water flux [155].

Table 6 Performance of 2D-WS₂ and MoS₂ as supercapacitors electrode

	Synthesis route of TMS	Size/thickness/ number of TMS layers	Electrode composition	Specific capacitance (Fg ⁻¹)	Electrolyte	Capacitance retention w.r.t. no of cycles	Ref.
2D-TMS	Hydrothermal	2D sheets (1–5 nm)	RGO- WS ₂ nanosheets	350 (at 0.5 Ag ⁻¹) (at 2 mV/s)	1 M Na ₂ SO ₄ (Aq. sol)	100% after 1000 cycles (at 3 Ag ⁻¹)	[97]
2D-WS ₂	Molten salt process	2D sheets	RGO - WS ₂ nanosheets	1285 (at 2 Ag ⁻¹)	1 M KOH + 0.5 M KCl (Aq. sol)	98.6% after 5000 cycles (at 2 Ag ⁻¹)	[138]
2D-MoS ₂	Electrochemical lithiation followed by water treatment	1 T 2D-MoS ₂ Majority-3 layer thick	Graphene- 1 T MoS ₂ (1:1)	147 (560 F/cm ³) (at 10 mV/s) 120 (458 F/cm ³) (at 100 mV/s)	6 M KOH (Aq. sol)	96% after 5000 cycles	[64]
	Hydrothermal	Nanosheets	Core-shell type mesoporous hollow carbon spheres-MoS ₂ composite	613 (at 1 Ag ⁻¹) 358 (at 10 Ag ⁻¹)	1 M Na ₂ SO ₄	90.3% after 2000 cycles	[139]
	Hydrothermal	Nanosheets 2.5 nm	MoS ₂ nanosheets on carbon fabric	103.5 mF/cm ² (at 3 mA/cm ²)	1 M LiOH (Aq. sol)	83.7 mF/cm ² (81%) after 15,000 cycles (at 3 mA/cm ²)	[140]
	Hydrothermal	Nanosheets	1 T&2H MoS ₂ nanosheets on rGO	752 (at 1 Ag ⁻¹) 282.3 (at 50 Ag ⁻¹)	1 M H ₂ SO ₄	80.4% after 50,000 cycles (at 50 Ag ⁻¹)	[141]
	Supramolecular self-assembly	Nanosheets 20 nm	Carbon nanoparticles (5 wt. %)/MoS ₂	394 (at 5 mV/s) 303 (at 1 Ag ⁻¹) 250 (at 200 mV/s)	1 M Na ₂ SO ₄ (Aq. sol)	(~61% after 2000 cycles (at 40 mV/s)	[142]
Only Carbon-based	Liquid-liquid interfacial precipitation	2D mesoporous micro belts	2D mesoporous micro belts on glassy carbon electrode	360 (at 5 mV/s) 290 (at 1 Ag ⁻¹)	1 M H ₂ SO ₄ (Aq. sol)	(49% after 10,000 cycles (at 10 Ag ⁻¹)	[143]

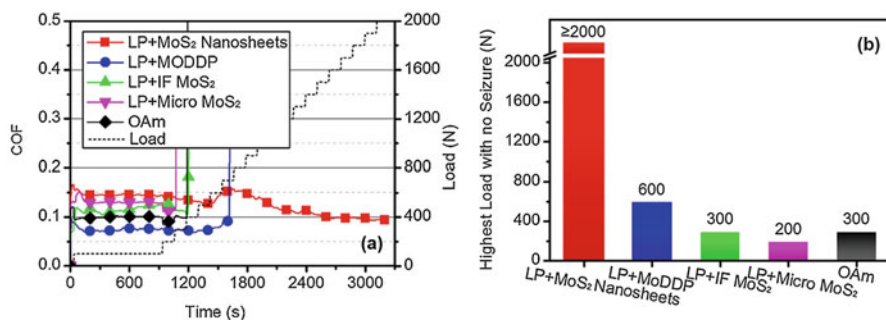


Fig. 23 (a) Coefficient of friction (COF) observed during friction tests using LP with various additives. For comparison, oleylamine (OAm) was also tested as it was used to modify the nanosheet surface for better dispersion in the base oil. (b) Performance of various lubricants under load without seizure. (Reproduced with permission from [32] ©2015 Nature)

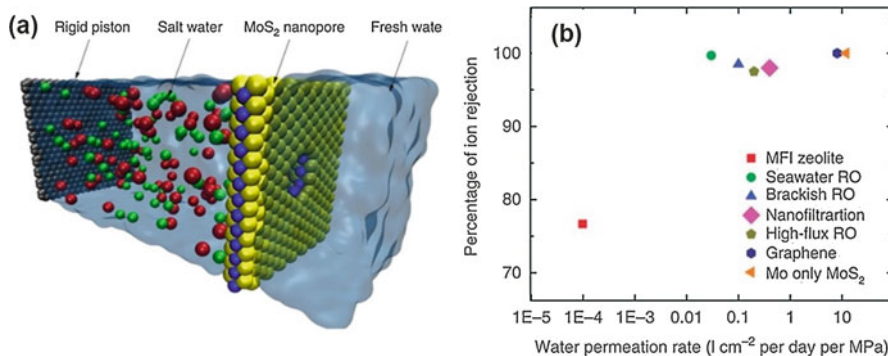


Fig. 24 (a) Schematic of desalination by MoS₂ monolayer. (b) Performances of MoS₂ when compared to various commercially available membranes in terms of their ion rejection percentage and water permeability rate (l/cm²/day/MPa). (Reproduced with permission from [154] ©2015 Nature)

Biomedical

Major breakthroughs have been reported on application of 2D-WS₂ in the treatment of critical diseases. As for example, clinical trials with 2D-WS₂ nanosheets have shown that it can cross the blood-brain barrier and can effectively inhibit the amyloid- β peptide aggregation through its van der Waals and electrostatic interactions, which is the most crucial step in the Alzheimer disease treatment [156]. Liu et al. [157] have shown excellent performance of a PEG-2D-MoS₂ hybrid composite in drug delivery of chemotherapy drugs like doxorubicin and ethyl-hydroxycamptothecin (SN38) paving way for a highly effective photothermal therapy of cancer.

2D form of WS_2 and MoS_2 has also shown promises as a biocompatible material for the development of biodevices. Parlak et al. [158] have developed a 2D bioreactor with nanoparticle of gold and 2D- WS_2 nanosheet, which has shown excellent electrocatalytic activity providing a means to control bioelectrocatalytic reactions at the interface.

Concluding Remarks

Various aspects of 2D- WS_2 and MoS_2 have been reviewed in this article to highlight the major synthesis routes currently available and their versatile properties, which are likely to get translated into a wide range of applications in strategically important areas like aerospace, defense, automotive, manufacturing, and environmental and biomedical sectors. It is envisaged that the various techniques in the bandgap engineering and the emerging heterostructures in these materials will have a profound role in further advancement leading to the development of new generation technologies in near future.

References

1. Frindt RF, Yoffe AD, Bowden FP (1963) Physical properties of layer structures: optical properties and photoconductivity of thin crystals of molybdenum disulphide. *Proc R Soc Lond A Math Phys Sci* 273:69–83
2. Frindt RF (1966) Single crystals of MoS_2 several molecular layers thick. *J Appl Phys* 37:1928–1929
3. Novoselov KS, Geim AK, Morozov SV, Jiang D, Zhang Y, Dubonos SV, Grigorieva IV, Firsov AA (2004) Electric field effect in atomically thin carbon films. *Science* 306:666–669
4. Joensen P, Frindt RF, Morrison SR (1986) Single-layer MoS_2 . *Mater Res Bull* 21:457–461
5. Miremadi BK, Morrison SR (1988) The intercalation and exfoliation of tungsten disulfide. *J Appl Phys* 63:4970–4974
6. Py MA, Haering RR (1983) Structural destabilization induced by lithium intercalation in MoS_2 and related compounds. *Can J Phys* 61:76–84
7. Mulhern PJ (1989) Lithium intercalation in crystalline $LixMoS_2$. *Can J Phys* 67:1049–1052
8. Tenne R, Margulis L, Genut M, Hodes G (1992) Polyhedral and cylindrical structures of tungsten disulphide. *Nature* 360:444–446
9. Tenne R (2006) Inorganic nanotubes and fullerene-like nanoparticles. *J Mater Res* 21:2726–2743
10. Feldman Y, Frey GL, Homyonfer M, Lyakhovitskaya V, Margulis L, Cohen H (1996) Bulk synthesis of inorganic fullerene-like MS_2 ($M = Mo, W$) from the respective trioxides and the reaction mechanism. *J Am Chem Soc* 118:5362–5367
11. Heine T (2015) Transition metal chalcogenides: ultrathin inorganic materials with tunable electronic properties. *Acc Chem Res* 48:65–72
12. Kuc A, Heine T (2015) The electronic structure calculations of two-dimensional transition-metal dichalcogenides in the presence of external electric and magnetic fields. *Chem Soc Rev* 44:2603–2614
13. Terrones H, López-Urías F, Terrones M (2013) Novel hetero-layered materials with tunable direct band gaps by sandwiching different metal disulfides and diselenides. *Sci Rep* 3:1549 (1–7)

14. Radhakrishnan S, Das D, Deng L, Sudeep PM, Colas G, de los Reyes CA, Yazdi S, Chu CW, Marti AA, Tiwary CS, Filletter T, Singh AK, Ajayan PM (2018) An insight into the phase transformation of WS₂ upon fluorination. *Adv Mater* 30:1803366 (1–10)
15. Yun WS, Han SW, Hong SC, Kim IG, Lee JD (2012) Thickness and strain effects on electronic structures of transition metal dichalcogenides: 2H-MX₂ semiconductors (M=Mo, W; X=S, Se, Te). *Phys Rev B* 85:033305 (1–5)
16. Scholes GD, Rumbles G (2006) Excitons in nanoscale systems. *Nat Mater* 5:683–696
17. Li W, Wang T, Dai X, Wang X, Zhai C, Ma Y, Chang S, Tang Y (2017) Electric field modulation of the band structure in MoS₂/WS₂ van der waals heterostructure. *Solid State Commun* 250:9–13
18. van der Zande AM, Huang PY, Chenet DA, Berkelbach TC, You Y, Lee G-H, Heinz TF, Reichman DR, Muller DA, Hone JC (2013) Grains and grain boundaries in highly crystalline monolayer molybdenum disulphide. *Nat Mater* 12:554–561
19. Harish Kumar A, Pandey AK, Joardar J (unpublished work)
20. Sylvester MS, Hebalkar NY, Joardar J (unpublished work)
21. Tang Q, Jiang D-E (2015) Stabilization and band-gap tuning of the 1T-MoS₂ monolayer by covalent functionalization. *Chem Mater* 27:3743–3748
22. Ouyang B, Xiong S, Yang Z, Jing Y, Wang Y (2017) MoS₂ heterostructure with tunable phase stability: strain induced interlayer covalent bond formation. *Nanoscale* 9:8126–8132
23. Eda G, Yamaguchi H, Voiry D, Fujita T, Chen M, Chhowalla M (2011) Photoluminescence from chemically exfoliated MoS₂. *Nano Lett* 11:5111–5116
24. Lin Y-C, Yeh C-H, Lin H-C, Siao M-D, Liu Z, Nakajima H, Okazaki T, Chou M-Y, Suenaga K, Chiu P-W (2018) Stable 1T Tungsten disulfide monolayer and its junctions: growth and atomic structures. *ACS Nano* 12:12080–12088
25. Bertolazzi S, Brivio J, Kis A (2011) Stretching and breaking of ultrathin MoS₂. *ACS Nano* 5:9703–9709
26. Liu K, Yan Q, Chen M, Fan W, Sun Y, Suh J, Fu D, Lee S, Zhou J, Tongay S, Ji J, Neaton JB, Wu J (2014) Elastic properties of chemical-vapor-deposited monolayer MoS₂, WS₂, and their bilayer heterostructures. *Nano Lett* 14:5097–5103
27. Lee C, Wei X, Kysar JW, Hone J (2008) Measurement of the elastic properties and intrinsic strength of monolayer graphene. *Science* 321:385–388
28. Castellanos-Gomez A, Poot M, Steele GA, van der Zant HSJ, Agraït N, Rubio-Bollinger G (2012) Elastic properties of freely suspended MoS₂ nanosheets. *Adv Mater* 24:772–775
29. Eksik O, Gao J, Shojae SA, Thomas A, Chow P, Bartolucci SF, Lucca DA, Koratkar N (2014) Epoxy nanocomposites with two-dimensional transition metal dichalcogenide additives. *ACS Nano* 8:5282–5289
30. Allam IM (1991) Solid lubricants for applications at elevated temperatures. *J Mater Sci* 26:3977–3984
31. Lee C, Li Q, Kalb W, Liu X-Z, Berger H, Carpick RW, Hone J (2010) Frictional characteristics of atomically thin sheets. *Science* 328:76–80
32. Chen Z, Liu XW, Liu YH, Gonsel S, Luo JB (2015) Ultrathin MoS₂ nanosheets with superior extreme pressure property as boundary lubricants. *Sci Rep* 5:12869 (1–7)
33. Lavik MT, Medved TM, Moore GD (1968) Oxidation characteristics of MoS₂ and other solid lubricants. *ASLE Trans* 11:44–55
34. Adigilli HK, Padya B, Venkatesh L, Chakravadhanula VSK, Pandey AK, Joardar J (2019) Oxidation of 2D-WS₂ nanosheets for generation of 2D-WS₂/WO₃ heterostructure and 2D and nanospherical WO₃ *Phys. Chem Chem Phys* 21:25139–25147
35. Gao J, Li B, Tan J, Chow P, Lu T-M, Koratkar N (2016) Aging of transition metal dichalcogenide monolayers. *ACS Nano* 10:2628–2635
36. Kang K, Godin K, Kim YD, Fu S, Cha W, Hone J, Yang E-H (2017) Graphene-assisted antioxidation of tungsten disulfide monolayers: Substrate and electric-field effect. *Adv Mater* 29:1603898 (1–8)

37. Pengshang Z, Qun X, Hongxiang L, Yun W, Bo Y, Yunchun Z, Jiafu C, Jianan Z, Kaixi W (2015) Fabrication of two-dimensional lateral heterostructures of $WS_2/WO_3 \cdot H_2O$ through selective oxidation of monolayer WS_2 . *Angew Chem Int Ed* 54:15226–15230
38. Shakouri A (2011) Recent developments in semiconductor thermoelectric physics and materials. *Annu Rev Mater Res* 41:399–431
39. Jin Z, Liao Q, Fang H, Liu Z, Liu W, Ding Z, Luo T, Yang N (2015) A revisit to high thermoelectric performance of single-layer MoS_2 . *Sci Rep* 5:18342 (1–7)
40. Wu J, Schmidt H, Amara KK, Xu X, Eda G, Özyilmaz B (2014) Large thermoelectricity via variable range hopping in chemical vapor deposition grown single-layer MoS_2 . *Nano Lett* 14:2730–2734
41. Mingxing P, Jin C, Xiao W, Yao C, Heng Z, Chaolong L, Haofei S, Min-Kyu J (2018) Hydrothermal synthesis of stable metallic 1T phase WS_2 nanosheets for thermoelectric application. *Nanotechnology* 29:025705 (1–8)
42. Zhang Z, Xie Y, Peng Q, Chen Y (2016) A theoretical prediction of super high-performance thermoelectric materials based on MoS_2/WS_2 hybrid nanoribbons. *Sci Rep* 6:21639 (1–8)
43. Duerloo K-AN, Ong MT, Reed EJ (2012) Intrinsic piezoelectricity in two-dimensional materials. *J Phys Chem Lett* 3:2871–2876
44. Zhu H, Wang Y, Xiao J, Liu M, Xiong S, Wong ZJ, Ye Z, Ye Y, Yin X, Zhang X (2014) Observation of piezoelectricity in free-standing monolayer MoS_2 . *Nat Nanotechnol* 10:151–155
45. Wu W, Wang L, Li Y, Zhang F, Lin L, Niu S, Chenet D, Zhang X, Hao Y, Heinz TF, Hone J, Wang ZL (2014) Piezoelectricity of single-atomic-layer MoS_2 for energy conversion and piezotronics. *Nature* 514:470–474
46. Zeng H, Liu G-B, Dai J, Yan Y, Zhu B, He R, Xie L, Xu S, Chen X, Yao W, Cui X (2013) Optical signature of symmetry variations and spin-valley coupling in atomically thin tungsten dichalcogenides. *Sci Rep* 3:1608 (1–5)
47. Lee J, Huang J, Sumpter BG, Yoon M (2017) Strain-engineered optoelectronic properties of 2D transition metal dichalcogenide lateral heterostructures. *2D Mater* 4:021016 (1–8)
48. Tongay S, Varnoosfaderani SS, Appleton BR, Wu J, Hebard AF (2012) Magnetic properties of MoS_2 : Existence of ferromagnetism. *Appl Phys Lett* 101:123105 (1–4)
49. Zhang J, Soon JM, Loh KP, Yin J, Ding J, Sullivan MB, Wu P (2007) Magnetic molybdenum disulfide nanosheet films. *Nano Lett* 7:2370–2376
50. Salami N, Shokri AA, Elahi SM (2016) Tunable electronic and magnetic properties of a MoS_2 monolayer with vacancies under elastic planar strain: ab-initio study. *Phys E* 77:138–143
51. Gao N, Guo Y, Zhou S, Bai Y, Zhao J (2017) Structures and magnetic properties of MoS_2 grain boundaries with antisite defects. *J Phys Chem C* 121:12261–12269
52. Wang Y, Li S, Yi J (2016) Electronic and magnetic properties of Co doped MoS_2 monolayer. *Sci Rep* 6:24153 (1–9)
53. Ye JT, Zhang YJ, Akashi R, Bahramy MS, Arita R, Iwasa Y (2012) Superconducting dome in a gate-tuned band insulator. *Science* 338:1193–1196
54. Zhang R, Tsai IL, Chapman J, Khestanova E, Waters J, Grigorieva IV (2016) Superconductivity in potassium-doped metallic polymorphs of MoS_2 . *Nano Lett* 16:629–636
55. Jo S, Costanzo D, Berger H, Morpurgo AF (2015) Electrostatically induced superconductivity at the surface of WS_2 . *Nano Lett* 15:1197–1202
56. Zheliuk O, Lu J, Yang J, Ye J (2017) Monolayer superconductivity in WS_2 . *Phys Status Solidi Rapid Res Lett* 11:1700245 (1–3)
57. Szczyński R, Durajski AP, Jarosik MW (2017) Strong-coupling superconductivity induced by calcium intercalation in bilayer transition-metal dichalcogenides. *Front Phys* 13:137401 (1–7)
58. Brent JR, Savjani N, O'Brien P (2017) Synthetic approaches to two-dimensional transition metal dichalcogenide nanosheets. *Prog Mater Sci* 89:411–478
59. Chhowalla M, Shin HS, Eda G, Li L-J, Loh KP, Zhang H (2013) The chemistry of two-dimensional layered transition metal dichalcogenide nanosheets. *Nat Chem* 5:263–275

60. Lv R, Terrones H, Elías AL, Perea-López N, Gutiérrez HR, Cruz-Silva E, Rajukumar LP, Dresselhaus MS, Terrones M (2015) Two-dimensional transition metal dichalcogenides: clusters, ribbons, sheets and more. *Nano Today* 10:559–592
61. Coleman JN, Mustafa L, Arlene O, Bergin SD, King PJ, Khan U (2011) Two-dimensional nanosheets produced by liquid exfoliation of layered. *Mater Sci* 331:568–571
62. Wang Y, Liu Y, Zhang J, Wu J, Xu H, Wen X, Zhang X, Tiwary CS, Yang W, Vajtai R, Zhang Y, Chopra N, Odeh IN, Wu Y, Ajayan PM (2017) Cryo-mediated exfoliation and fracturing of layered materials into 2D quantum dots. *Sci Adv* 3:e1701500 (1–7)
63. Zeng ZY, Yin ZY, Huang X, Li H, He QY, Lu G (2011) Single-layer semiconducting nanosheets: high-yield preparation and device fabrication. *Angew Chem Int Ed* 50:11093–11097
64. Ejigu A, Kinloch IA, Prestat E, Dryfe RAW (2017) A simple electrochemical route to metallic phase trilayer MoS₂: evaluation as electrocatalysts and supercapacitors. *J Mater Chem A* 5:11316–11330
65. Jeong S, Yoo D, Ahn M, Miró P, Heine T, Cheon J (2015) Tandem intercalation strategy for single-layer nanosheets as an effective alternative to conventional exfoliation processes. *Nat Commun* 6:5763 (1–7)
66. Wu S, Huang C, Aivazian G, Ross JS, Cobden DH, Xu X (2013) Vapor-solid growth of high optical quality MoS₂ monolayers with near-unity valley polarization. *ACS Nano* 7:2768–2772
67. Yi-Hsien L, Xin-Quan Z, Wenjing Z, Mu-Tung C, Cheng-Te L, Kai-Di C, Ya-Chu Y, Tse-Wei WJ, Chia-Seng C, Lain-Jong L, Tsung-Wu L (2012) Synthesis of large-area MoS₂ atomic layers with chemical vapor deposition. *Adv Mater* 24:2320–2325
68. Kang K, Xie S, Huang L, Han Y, Huang PY, Mak KF, Kim C-J, Muller D, Park J (2015) High-mobility three-atom-thick semiconducting films with wafer-scale homogeneity. *Nature* 520:656–660
69. Park J, Lee W, Choi T, Hwang S-H, Myoung JM, Jung J-H, Kim S-H, Kim H (2015) Layer-modulated synthesis of uniform tungsten disulfide nanosheet using gas-phase precursors. *Nanoscale* 7:1308–1313
70. Kang KN, Godin K, Yang E-H (2015) The growth scale and kinetics of WS₂ monolayers under varying H₂ concentration. *Sci Rep* 5:13205 (1–9)
71. Joardar J, Sylvester MS (2012) A method for the synthesis of WS₂ nanosheets. *Indian Patent* 320209
72. Ren X, Pang L, Zhang Y, Ren X, Fan H, Liu S (2015) One-step hydrothermal synthesis of monolayer MoS₂ quantum dots for highly efficient electrocatalytic hydrogen evolution. *J Mater Chem A* 3:10693–10697
73. Wang D, Pan Z, Wu Z, Wang Z, Liu Z (2014) Hydrothermal synthesis of MoS₂ nanoflowers as highly efficient hydrogen evolution reaction catalysts. *J Power Sources* 264:229–234
74. Lu X, Lin Y, Dong H, Dai W, Chen X, Qu X, Zhang X (2017) One-step hydrothermal fabrication of three-dimensional MoS₂ nanoflower using polypyrrole as template for efficient hydrogen evolution reaction. *Sci Rep* 7:42309 (1–8)
75. Liu K-K, Zhang W, Lee Y-H, Lin Y-C, Chang M-T, Su C-Y, Chang C-S, Li H, Shi Y, Zhang H, Lai C-S, Li L-J (2012) Growth of large-area and highly crystalline MoS₂ thin layers on insulating substrates. *Nano Lett* 12:1538–1544
76. Yu Y, Jiang S, Zhou W, Miao X, Zeng Y, Zhang G, Liu S (2013) Room temperature rubbing for few-layer two-dimensional thin flakes directly on flexible polymer substrates. *Sci Rep* 3:2697 (1–8)
77. Yu Y, Jiang S, Zhang G, Zhou W, Miao X, Zeng Y, Wang J, He J, Zhang L (2012) Universal ultrafast sandpaper assisting rubbing method for room temperature fabrication of two-dimensional nanosheets directly on flexible polymer substrate. *Appl Phys Lett* 101:073113 (1–4)
78. Liu J, Lo TW, Sun J, Yip CT, Lam CH, Lei DY (2017) A comprehensive comparison study on the vibrational and optical properties of CVD-grown and mechanically exfoliated few-layered WS₂. *J Mater Chem C* 5:11239–11245
79. Kim J, Kwon S, Cho D-H, Kang B, Kwon H, Kim Y, Park SO, Jung GY, Shin E, Kim W-G, Lee H, Ryu GH, Choi M, Kim TH, Oh J, Park S, Kwak SK, Yoon SW, Byun D, Lee Z, Lee C

- (2015) Direct exfoliation and dispersion of two-dimensional materials in pure water via temperature control. *Nat Commun* 6:8294 (1–9)
80. Yang D, Frindt RF (1996) Li-intercalation and exfoliation of WS₂. *J Phys Chem Solids* 57:1113–1116
81. Anto Jeffery A, Nethravathi C, Rajamathi M (2014) Two-dimensional nanosheets and layered hybrids of MoS₂ and WS₂ through exfoliation of ammoniated MS₂ (M = Mo,W). *J Phys Chem C* 118:1386–1396
82. Xu D, Xu P, Zhu Y, Peng W, Li Y, Zhang G, Zhang F, Mallouk TE, Fan X (2018) High yield exfoliation of WS₂ crystals into 1–2 layer semiconducting nanosheets and efficient photocatalytic hydrogen evolution from WS₂/CdS nanorod composites. *ACS Appl Mater Interfaces* 10:2810–2818
83. Castellanos-Gomez A, Barkelid M, Goossens AM, Calado VE, van der Zant HSI, Steele GA (2012) Laser-thinning of MoS₂: on demand generation of a single-layer semiconductor. *Nano Lett* 12:3187–3192
84. Park J, Kim MS, Cha E, Kim J, Choi W (2017) Synthesis of uniform single layer WS₂ for tunable photoluminescence. *Sci Rep* 7:16121 (1–8)
85. Gong L, Zhang Q, Wang L, Wu J, Han C, Lei B, Chen W, Eda G, Goh KEJ, Sow CH (2018) Emergence of photoluminescence on bulk MoS₂ by laser thinning and gold particle decoration. *Nano Res* 11:4574–4586
86. Wu J, Li H, Yin Z, Li H, Liu J, Cao X, Zhang Q, Zhang H (2013) Layer thinning and etching of mechanically exfoliated MoS₂ nanosheets by thermal annealing in air. *Small* 9:3314–3319
87. Liu Y, Nan H, Wu X, Pan W, Wang W, Bai J, Zhao W, Sun L, Wang X, Ni Z (2013) Layer-by-layer thinning of MoS₂ by plasma. *ACS Nano* 7:4202–4209
88. Weiß V, Seeger S, Ellmer K, Mientus R (2007) Reactive magnetron sputtering of tungsten disulfide (WS_{2-x}) films: Influence of deposition parameters on texture, microstructure, and stoichiometry. *J Appl Phys* 101:103502 (1–9)
89. Koçak Y, Akaltun Y, Emre G (2016) Magnetron sputtered WS₂; optical and structural analysis. *J Phys Conf Ser* 707:012028 (1–6)
90. Serpini E, Rota A, Ballestrazzi A, Marchetto D, Gualtieri E, Valeri S (2017) The role of humidity and oxygen on MoS₂ thin films deposited by RF PVD magnetron sputtering. *Surf Coat Technol* 319:345–352
91. Bianco GV, Losurdo M, Giangregorio MM, Sacchetti A, Prete P, Lovergine N, Capezzuto P, Bruno G (2015) Direct epitaxial CVD synthesis of tungsten disulfide on epitaxial and CVD graphene. *RSC Adv* 5:98700–98708
92. Modtland BJ, Navarro-Moratalla E, Ji X, Baldo M, Kong J (2017) Monolayer tungsten disulfide (WS₂) via chlorine-driven chemical vapor transport. *Small* 13:1701232 (1–7)
93. Liu P, Luo T, Xing J, Xu H, Hao H, Liu H, Dong J (2017) Large-area WS₂ film with big single domains grown by chemical vapor deposition. *Nanoscale Res Lett* 12:558 (1–10)
94. Li C, Yamaguchi Y, Kaneko T, Kato T (2017) Large single-domain growth of monolayer WS₂ by rapid-cooling chemical vapor deposition. *Appl Phys Express* 10:075201
95. Lan C, Zhou Z, Zhou Z, Li C, Shu L, Shen L, Li D, Dong R, Yip S, Ho JC (2018) Wafer-scale synthesis of monolayer WS₂ for high-performance flexible photodetectors by enhanced chemical vapor deposition. *Nano Res* 11:3371–3384
96. Lan F, Yang R, Xu Y, Qian S, Zhang S, Cheng H, Zhang Y (2018) Synthesis of large-scale single-crystalline monolayer WS₂ using a semi-sealed method. *Nanomaterials* 8:100 (1–7)
97. Ratha S, Rout CS (2013) Supercapacitor electrodes based on layered tungsten disulfide-reduced graphene oxide hybrids synthesized by a facile hydrothermal method. *ACS Appl Mater Interfaces* 5:11427–11433
98. Xiang Q, Cheng F, Lang D (2016) Hierarchical layered WS₂/graphene-modified CdS nanorods for efficient photocatalytic hydrogen evolution. *ChemSusChem* 9:996–1002
99. Reddy DA, Park H, Ma R, Kumar DP, Lim M, Kim TK (2017) Heterostructured WS₂-MoS₂ ultrathin nanosheets integrated on CdS nanorods to promote charge separation and migration and improve solar-driven photocatalytic hydrogen evolution. *ChemSusChem* 10:1563–1570

100. Altavilla C, Sarno M, Ciambelli P (2011) A novel wet chemistry approach for the synthesis of hybrid 2D free-floating single or multilayer nanosheets of $MS_2@oleylamine$ ($M = Mo, W$). *Chem Mater* 23:3879–3885
101. Akinwande D, Petrone N, Hone J (2014) Two-dimensional flexible nanoelectronics. *Nat Commun* 5:5678 (1–12)
102. Gao Y, Liu Z, Sun D-M, Huang L, Ma L-P, Yin L-C, Ma T, Zhang Z, Ma X-L, Peng L-M, Cheng H-M, Ren W (2015) Large-area synthesis of high-quality and uniform monolayer WS_2 on reusable Au foils. *Nat Commun* 6:8569 (1–10)
103. Choi C, Choi MK, Liu S, Kim MS, Park OK, Im C, Kim J, Qin X, Lee GJ, Cho KW, Kim M, Joh E, Lee J, Son D, Kwon S-H, Jeon NL, Song YM, Lu N, Kim D-H (2017) Human eye-inspired soft optoelectronic device using high-density MoS_2 -graphene curved image sensor array. *Nat Commun* 8:1664 (1–11)
104. Yin Z, Zeng Z, Liu J, He Q, Chen P, Zhang H (2013) Memory devices using a mixture of MoS_2 and graphene oxide as the active layer. *Small* 9:727–731
105. Zhang E, Wang W, Zhang C, Jin Y, Zhu G, Sun Q, Zhang DW, Zhou P, Xiu F (2015) Tunable charge-trap memory based on few-layer MoS_2 . *ACS Nano* 9:612–619
106. Jing-Yuan W, Tea CY, Shunpu L, Tong Z, Junzhan W, Kumar SP, Daping C (2018) Broadband MoS_2 field-effect phototransistors: Ultrasensitive visible-light photoresponse and negative infrared photoresponse. *Adv Mater* 30:1705880 (1–7)
107. Ruixin X, Kaili Z, Xiangyang X, Minghui H, Fachuang L, Bin S (2018) Superhydrophobic WS_2 -nanosheet-wrapped sponges for underwater detection of tiny vibration. *Adv Sci* 5:1700655 (1–10)
108. Ko KY, Song J-G, Kim Y, Choi T, Shin S, Lee CW, Lee K, Koo J, Lee H, Kim J, Lee T, Park J, Kim H (2016) Improvement of gas-sensing performance of large-area tungsten disulfide nanosheets by surface functionalization. *ACS Nano* 10:9287–9296
109. Cho B, Hahm MG, Choi M, Yoon J, Kim AR, Lee Y-J, Park S-G, Kwon J-D, Kim CS, Song M, Jeong Y, Nam K-S, Lee S, Yoo TJ, Kang CG, Lee BH, Ko HC, Ajayan PM, Kim D-H (2015) Charge-transfer-based gas sensing using atomic-layer MoS_2 . *Sci Rep* 5:8052 (1–6)
110. Yu N, Wang L, Li M, Sun X, Hou T, Li Y (2015) Molybdenum disulfide as a highly efficient adsorbent for non-polar gases. *Phys Chem Chem Phys* 17:11700–11704
111. Won-Tae K, Jun-Hwe C, Ji-Won J, Seon-Jin C, Ji-Soo J, Dong-Ha K, Il-Doo K (2018) Few-layered WS_2 nanoplates confined in Co, N-doped hollow carbon nanocages: Abundant WS_2 edges for highly sensitive gas sensors. *Adv Funct Mater* 28:1802575 (1–11)
112. Perkins FK, Friedman AL, Cobas E, Campbell PM, Jernigan GG, Jonker BT (2013) Chemical vapor sensing with monolayer MoS_2 . *Nano Lett* 13:668–673
113. Wang X, Zhang W, Ji X, Zhang B, Yu M, Zhang W, Liu J (2016) 2D MoS_2 /graphene composites with excellent full Ku band microwave absorption. *RSC Adv* 6:106187–106193
114. Du P, Zhu Y, Zhang J, Xu D, Peng W, Zhang G, Zhang F, Fan X (2016) Metallic 1T phase MoS_2 nanosheets as a highly efficient co-catalyst for the photocatalytic hydrogen evolution of CdS nanorods. *RSC Adv* 6:74394–74399
115. Mahler B, Hoepfner V, Liao K, Ozin GA (2014) Colloidal synthesis of 1T- WS_2 and 2H- WS_2 nanosheets: applications for photocatalytic hydrogen evolution. *J Am Chem Soc* 136:14121–14127
116. Yi J, She X, Song Y, Mao M, Xia K, Xu Y, Mo Z, Wu J, Xu H, Li H (2018) Solvothermal synthesis of metallic 1T- WS_2 : a supporting co-catalyst on carbon nitride nanosheets toward photocatalytic hydrogen evolution. *Chem Eng J* 335:282–289
117. He Q, Wang L, Yin K, Luo S (2018) Vertically aligned ultrathin 1T- WS_2 nanosheets enhanced the electrocatalytic hydrogen evolution. *Nanoscale Res Lett* 13:167 (1–9)
118. Voiry D, Yamaguchi H, Li J, Silva R, Alves DCB, Fujita T, Chen M, Asefa T, Shenoy VB, Eda G, Chhowalla M (2013) Enhanced catalytic activity in strained chemically exfoliated WS_2 nanosheets for hydrogen evolution. *Nat Mater* 12:850–855
119. Zhong Y, Shao Y, Huang B, Hao X, Wu Y (2017) Combining ZnS with WS_2 nanosheets to fabricate a broad-spectrum composite photocatalyst for hydrogen evolution. *New J Chem* 41:12451–12458

120. Zhou W, Yin Z, Du Y, Huang X, Zeng Z, Fan Z, Liu H, Wang J, Zhang H (2013) Synthesis of few-layer MoS₂ nanosheet-coated TiO₂ nanobelt heterostructures for enhanced photocatalytic activities. *Small* 9:140–147
121. He J, Chen L, Wang F, Liu Y, Chen P, Au C-T, Yin S-F (2016) CdS nanowires decorated with ultrathin MoS₂ nanosheets as an efficient photocatalyst for hydrogen evolution. *ChemSusChem* 9:624–630
122. Kumar DP, Song MI, Hong S, Kim EH, Gopannagari M, Reddy DA, Kim TK (2017) Optimization of active sites of MoS₂ nanosheets using nonmetal doping and exfoliation into few layers on CdS nanorods for enhanced photocatalytic hydrogen production. *ACS Sustain Chem Eng* 5:7651–7658
123. Yang W, Wang J, Si C, Peng Z, Frenzel J, Eggeler G, Zhang Z (2015) [001] preferentially-oriented 2D tungsten disulfide nanosheets as anode materials for superior lithium storage. *J Mater Chem A* 3:17811–17819
124. Chang K, Chen W (2011) In situ synthesis of MoS₂/graphene nanosheet composites with extraordinarily high electrochemical performance for lithium ion batteries. *Chem Commun* 47:4252–4254
125. Huang G, Liu H, Wang S, Yang X, Liu B, Chen H, Xu M (2015) Hierarchical architecture of WS₂ nanosheets on graphene frameworks with enhanced electrochemical properties for lithium storage and hydrogen evolution. *J Mater Chem A* 3:24128–24138
126. Ren J, Wang Z, Yang F, Ren R-P, Lv Y-K (2018) Freestanding 3D single-wall carbon nanotubes/WS₂ nanosheets as ultra-long-life anodes for rechargeable lithium ion batteries. *Electrochim Acta* 267:133–140
127. Song Y, Liao J, Chen C, Yang J, Chen J, Gong F, Wang S, Xu Z, Wu M (2019) Controllable morphologies and electrochemical performances of self-assembled nano-honeycomb WS₂ anodes modified by graphene doping for lithium and sodium ion batteries. *Carbon* 142:697–706
128. Li T, Guo R, Luo Y, Li F, Liu Z, Meng L, Yang Z, Luo H, Wan Y (2018) Innovative N-doped graphene-coated WS₂ nanosheets on graphene hollow spheres anode with double-sided protective structure for Li-Ion storage. *Electrochim Acta* 290:128–141
129. Yu X-Y, Hu H, Wang Y, Chen H, Lou XW (2015) Ultrathin MoS₂ nanosheets supported on N-doped carbon nanoboxes with enhanced lithium storage and electrocatalytic properties. *Angew Chem Int Ed* 54:7395–7398
130. Guo B, Yu K, Fu H, Hua Q, Qi R, Li H, Song H, Guo S, Zhu Z (2015) Firework-shaped TiO₂ microspheres embedded with few-layer MoS₂ as an anode material for excellent performance lithium-ion batteries. *J Mater Chem A* 3:6392–6401
131. Jiang H, Ren D, Wang H, Hu Y, Guo S, Yuan H, Hu P, Zhang L, Li C (2015) 2D monolayer MoS₂-carbon interoverlapped superstructure: engineering ideal atomic interface for lithium ion storage. *Adv Mater* 27:3687–3695
132. Teng Y, Zhao H, Zhang Z, Li Z, Xia Q, Zhang Y, Zhao L, Du X, Du Z, Lv P, Świerczek K (2016) MoS₂ nanosheets vertically grown on graphene sheets for lithium-ion battery anodes. *ACS Nano* 10:8526–8535
133. Pan Q, Zheng F, Wu Y, Ou X, Yang C, Xiong X, Liu M (2018) MoS₂-covered SnS nanosheets as anode material for lithium-ion batteries with high capacity and long cycle life. *J Mater Chem A* 6:592–598
134. Wang J-G, Liu H, Zhou R, Liu X, Wei B (2019) Onion-like nanospheres organized by carbon encapsulated few-layer MoS₂ nanosheets with enhanced lithium storage performance. *J Power Sources* 413:327–333
135. Tsung-Wu L, Thangarasu S, Ai-Yin W, Ting-Yu C, Jeng-Yu L, Li-Dong S (2018) Ternary composite nanosheets with MoS₂/WS₂/graphene heterostructures as high-performance cathode materials for supercapacitors. *ChemElectroChem* 5:1024–1031
136. Acerce M, Voiry D, Chhowalla M (2015) Metallic 1T phase MoS₂ nanosheets as supercapacitor electrode materials. *Nat Nanotechnol* 10:313–318
137. Khalil A, Liu Q, He Q, Xiang T, Liu D, Wang C, Fang Q, Song L (2016) Metallic 1T-WS₂ nanoribbons as highly conductive electrodes for supercapacitors. *RSC Adv* 6:48788–48791

138. Tu C-C, Lin L-Y, Xiao B-C, Chen Y-S (2016) Highly efficient supercapacitor electrode with two-dimensional tungsten disulfide and reduced graphene oxide hybrid nanosheets. *J Power Sources* 320:78–85
139. Zheng L, Xing T, Ouyang Y, Wang Y, Wang X (2019) Core-shell structured MoS₂@mesoporous hollow carbon spheres nanocomposite for supercapacitors applications with enhanced capacitance and energy density. *Electrochim Acta* 298:630–639
140. Yin H, Liu Y, Yu N, Qu H-Q, Liu Z, Jiang R, Li C, Zhu M-Q (2018) Graphene-like MoS₂ nanosheets on carbon fabrics as high-performance binder-free electrodes for supercapacitors and Li-ion batteries. *ACS Omega* 3:17466–17473
141. Chao J, Yang L, Liu J, Hu R, Zhu M (2018) Oxygen-incorporated and polyaniline-intercalated 1T/2H hybrid MoS₂ nanosheets arrayed on reduced graphene oxide for high-performance supercapacitors. *J Phys Chem C* 122:8128–8136
142. Gao A, Zeng D, Liu Q, Yi F, Shu D, Cheng H, Zhou X, Li S, Zhang F (2019) Molecular self-assembly assisted synthesis of carbon nanoparticle-anchored MoS₂ nanosheets for high-performance supercapacitors. *Electrochim Acta* 295:187–194
143. Tang Q, Bairi P, Shrestha RG, Hill JP, Ariga K, Zeng H, Ji Q, Shrestha LK (2017) Quasi 2D mesoporous carbon microbelts derived from fullerene crystals as an electrode material for electrochemical supercapacitors. *ACS Appl Mater Interfaces* 9:44458–44465
144. Jiang Z, Zhang Y, Yang G, Yang K, Zhang S, Yu L, Zhang P (2016) Tribological properties of oleylamine-modified ultrathin WS₂ nanosheets as the additive in polyalpha olefin over a wide temperature range. *Tribol Lett* 61:24 (1–14)
145. Zhang X, Xu H, Wang J, Ye X, Lei W, Xue M, Tang H, Li C (2016) Synthesis of ultrathin WS₂ nanosheets and their tribological properties as lubricant additives. *Nanoscale Res Lett* 11:442 (1–9)
146. Madeshwaran SR, Jayaganthan R, Velmurugan R, Gupta NK, Manzhirav AV (2018) Mechanical and thermal properties of MoS₂ reinforced epoxy nanocomposites. *J Phys Conf Ser* 991:012054 (1–6)
147. Wozniak J, Kostecki M, Cygan T, Buczek M, Olszyna A (2017) Self-lubricating aluminium matrix composites reinforced with 2D crystals. *Compos Part B* 111:1–9
148. Dong C, Yuan C, Wang L, Liu W, Bai X, Yan X (2016) Tribological properties of water-lubricated rubber materials after modification by MoS₂ nanoparticles. *Sci Rep* 6:35023 (1–12)
149. Voevodin AA, O'Neill JP, Zabinski JS (1999) Nanocomposite tribological coatings for aerospace applications. *Surf Coat Technol* 116–119:36–45
150. Renevier NM, Fox VC, Teer DG, Hampshire J (2000) Coating characteristics and tribological properties of sputter-deposited MoS₂/metal composite coatings deposited by closed field unbalanced magnetron sputter ion plating. *Surf Coat Technol* 127:24–37
151. Trivedi HK, Massey MM, Bhattacharya RS, Strahl GA, Collum D (2001) Next generation lubrication system for weapons. *Tribol Lett* 10:229–235
152. Chen Z, Liu Y, Gunsel S, Luo J (2018) Mechanism of antiwear property under high pressure of synthetic oil-soluble ultrathin MoS₂ sheets as lubricant additives. *Langmuir* 34:1635–1644
153. Zheng D, Wu Y-P, Li Z-Y, Cai Z-B (2017) Tribological properties of WS₂/graphene nanocomposites as lubricating oil additives. *RSC Adv* 7:14060–14068
154. Heiranian M, Farimani AB, Aluru NR (2015) Water desalination with a single-layer MoS₂ nanopore. *Nat Commun* 6:8616 (1–6)
155. Hirunpinyopas W, Prestat E, Worrall SD, Haigh SJ, Dryfe RAW, Bissett MA (2017) Desalination and nanofiltration through functionalized laminar MoS₂ membranes. *ACS Nano* 11:11082–11090
156. Li M, Zhao A, Dong K, Li W, Ren J, Qu X (2015) Chemically exfoliated WS₂ nanosheets efficiently inhibit amyloid β -peptide aggregation and can be used for photothermal treatment of Alzheimer's disease. *Nano Res* 8:3216–3227
157. Liu T, Wang C, Gu X, Gong H, Cheng L, Shi X, Feng L, Sun B, Liu Z (2014) Drug delivery with PEGylated MoS₂ nano-sheets for combined photothermal and chemotherapy of cancer. *Adv Mater* 26:3433–3440
158. Onur P, Preethi S, Ingemar L, Anthony PFT, Ashutosh T (2014) Two dimensional gold-tungsten disulphide bio-interface for high-throughput electrocatalytic nano-bioreactors. *Adv Mater Interfaces* 1:1400136 (1–5)



Nanoporous Aerogels for Defense and Aerospace Applications

4

Neha Hebalkar, Keerthi Sanghamitra Kollipara, Yamini Ananthan, and Murali Krishna Sudha

Contents

Introduction	124
General Preparation Methods of Aerogels	125
Types of Aerogels and Their Properties	125
Silica Aerogels	125
Metal Oxide Aerogels	132
Metallic Aerogels	134
Core-Shell Aerogels	134
Organic Aerogels	135
Carbon Aerogels	137
Various Aerogel Forms: Monoliths, Granules, and Composites	139
Applications	142
Aerogels as Energy Absorbers	142
Aerogels for Thermal Insulation	143
Aerogels for Storage	148
Aerogels as Adsorbent and Purifier for Toxic Gases	148
Aerogels for Environmental Remediation	149
Applications Based on Optical Properties	150
Sensors	151
Self-Cleaning Surfaces	152
Microelectromechanical Systems (MEMS)	152
Infrasound Detection	152
Energy Storage Devices	153
Artificial Muscles for Robots	153

N. Hebalkar (✉) · K. S. Kollipara · Y. Ananthan · M. K. Sudha
International Advanced Research Centre for Powder Metallurgy and New Materials, Balapur,
Hyderabad, India
e-mail: neha@arci.res.in; kerthi.sangham@gmail.com; yaminiananthan@gmail.com;
muralik431@gmail.com

Aerogels as Mirror Substrates	154
Aerogels as Dielectric Materials	154
Aerogels as Radar Antennas	154
Summary	155
References	155

Abstract

The choice of materials in strategic applications is a challenge due to very stringent requirements in size, weight, and power constraints. Most of these materials are specifically designed and developed to obtain unique properties and hence belong to special class of materials. “Aerogel” is one of such unique materials possessing extraordinary properties together. The ultralightweight and highly nanoporous nature give rise to excellent insulation for heat, sound, and electricity. It is possible to tailor-make them for desired chemical composition; physical forms such as monolith, powder, granules, sheets, etc.; surface chemistry to make them hydrophilic or hydrophobic; and so on. Aerogels can also serve as a host matrix for other materials to make lightweight and functional composites. Such flexibility in aerogel manufacturing can give customized solutions to many tactical requirements in the strategic field.

To name a few applications, aerogel-based materials serve as thermal insulation in lightweight protective clothing and footwear for extreme temperatures, shelters for military personnel in the field, military and aerospace vehicles, protection for electronic equipment, tank engine, etc. It can serve as acoustic insulation along with the heat insulation. Aerogel composites can be specially made for stealth and sensor applications. The potential usage of this extraordinary material is limited by our imagination.

This chapter introduces the aerogel material and describes its general methods of preparation, properties, and applications. Further, it illustrates the known and possible applications in defense and aerospace areas.

Keywords

Aerogel · Nanoporous · Silica · Composite · Sol-gel · Lightweight · Thermal insulation · Energy absorption · Aerospace · Military

Abbreviations

AMCC	Aerogel mesh contamination collector
APXS	Alpha particle X-ray spectrometer
BET	Brunauer, Emmett, and Teller method
C	Catalyst
CAD	Computer-aided drafting
CMOS	Complementary metal oxide semiconductor
CNC	Cellulose nanocrystal
CNF/GO	Cellulose nanofibril/graphene oxide

CNT	Carbon nanotubes
CS	Orthochlorobenzalmalononitrile
DMMP	Dimethyl methylphosphonate
DSSC	Dye-sensitized solar cells
DTMS	Dodecyltrimethoxysilane
EMI	Electromagnetic interference
EMId	Electromagnetic induction
EMU	Extravehicular mobility unit
FBB	Fire blocking blanket
FLIR	Forward-looking infrared
FTO	Fluorine-doped tin oxide
GA	Graphene aerogel
GCNTA	Graphene-CNT aerogel
IR	Infrared
MANPADS	Man-portable air-defense system
MEMS	Microelectromechanical systems
MLI	Multilayer insulation
MTES	Methyltriethoxysilane
MTMS	Methyltrimethoxysilane
NASA	National Aeronautics and Space Administration
ORR	Oxygen reduction reaction
PAN	Polyacrylonitrile
PCM	Phase change material
PCNTA	Polymer/CNT aerogel
PDA	Polydiacetylene
PEMFC	Proton exchange membrane fuel cell
PGA	Polymer-graphene aerogel
PU	Polyurethane
PVNNRA	Platinum-free porous vanadium nitride nanoribbon aerogels
RF	Resorcinol-formaldehyde
rGO/BP	Reduced graphene oxide/black phosphorus
RHU	Radioisotope heater units
RTV	Room temperature vulcanizing
SCD	Supercritical drying
SEM	Scanning electron microscope
STEP	Satellite test of the equivalence principle
STS	Space Transportation System
SWIR	Shortwave infrared
TEM	Transmission electron microscope
TEOS	Tetraethoxysilane
TMG	Thermal meteoroid garment
TMOS	Tetramethyl orthosilicate
TPS	Thermal protection system
UV	Ultraviolet

Introduction

Aerogels are man-made, ultralightweight, highly porous materials which have found a place in the Guinness World Records for its lightweight. These are derived from gels where the liquid in the gel is replaced by air. The resultant product is like solid foam with more than 95% porosity. The pore size in aerogels is in the nanometer range. These can be made in a variety of chemical compositions such as oxides, mixed oxides, polymeric, carbon, metals, semiconductors, and their composites. Due to the common factor of high porosity, all of them are the best thermal and acoustic insulators. Carbon and metallic aerogels can possess the best electrical conductivity accompanied with the best thermal insulation property. However, the oxide aerogels are best insulators of heat, sound, and electricity altogether. Very large surface area and pore volume due to nanoporosity are other unique characteristics of aerogels. Hence aerogels are a unique class of materials possessing a combination of exceptional properties together in one single material. These properties in aerogels can be integrated with specific designs to make use of them in several defense and strategic applications.

Intelligent and functional materials play a crucial role in defense systems which is becoming more advanced and complex day by day. The environments in these systems are extreme and hostile. The accuracy, sensitivity, robustness, performance guaranty, the convenience of use, etc. are the key requirements of the defense systems to reduce risks and damages for our soldiers and ultimately conquering over the threats to the nation's safety. Similar to defense systems, needs in strategic projects such as space missions, atomic energy, renewable energy, power generation, environmental protection, and so on are also very critical. In all these domains, the new technologies need the support of novel and advanced materials which will make the systems improved in performance, lowering the maintenance and cost.

The soldiers face extreme weather condition such as severe cold, storm at high-altitude places, and also extremely hot deserts. The clothing, shelters, and food supply requirements are too different in both these situations. For instance, the clothing and footwear for soldiers in severe cold conditions are desired to be extra lightweight and warm. Several layers of foam, wool materials make it thick and heavy. Every effort to reduce the weight and thickness will help the soldier to increase the efficiency and performance in their duties. The uniforms of the soldiers in the desert have pockets to keep cool packs to maintain the comfortable body temperature. If the cool packs are insulated thermally, the time for its replacement will prolong, and comfort can be maintained for a longer time. In both types of clothing, superior, ultralightweight thermal insulation materials are desired. Similar is the requirement in the shelters where the thermal insulating materials used to protect against extreme temperature should have the capability of either trapping the heat in the shelter or reflecting the heat away in cold and hot conditions, respectively. Such thermal insulating materials also are required to preserve food, medicines, and fuel and protect equipment, heat insulation in automobiles, ships, and aircraft, arresting heat emission to hide from infrared (IR) cameras and radars and many more like these for better performance.

To add on, the supply of electricity in remote areas of war field is another important and difficult aspect to manage. New age batteries, fuel cells, and super capacitors can come to rescue to increase the longevity of the power requirements in the battlefield.

The space vehicles, missiles, satellites, etc. also need extra lightweight thermal protection systems (TPS) which can withstand the rapid temperature rise, aerodynamic friction, and vibrations. A space researcher would like to capture the cosmic dust to study the universe and a suitable capturing device where such high-velocity particles can be trapped is required. Highly flexible, lightweight but still mechanically strong materials are a special class of materials which has a role to play in the aerospace industry.

Aerogels are the class of material which can serve in all the domains mentioned above but not limited to the list. This book chapter will give an overview of various types of aerogels, its preparation processes, properties, and their unique place in defense and strategic applications.

General Preparation Methods of Aerogels

A common approach for the synthesis of aerogels is sol-gel reaction to produce the gel which is followed by drying of the formed gel in such a way that the original 3D network of solid particles in the gel does not collapse or shrink. Sol-gel reaction involves the hydrolysis of the precursor molecules and then condensation of hydrolyzed molecules which happens three-dimensionally. The sol-gel chemistry is well known for decades, and more details can be learned from the popular book [1]. Figure 1 depicts the synthesis process to form an aerogel from sol and gel. The following subsections will elaborate the specific precursors and processes respective to the type of aerogels. In general, a metal alkoxide is used as a precursor for oxide aerogels, which undergoes hydrolysis and condensation reactions to bond into a network forming a gel.

This gel contains a 3D network of primary nanoparticles where the solvent used in the reaction is trapped in it. In the next step, this liquid is removed by any of the special techniques like supercritical drying (SCD), subcritical drying or freeze-drying. Each of these techniques has its own advantages and limitations. More details can be found in the vastly available literature [2]. The most effective and popular method of drying aerogel is SCD where the aerogel product has minimal shrinkage and highest porosity with respect to its gel.

Types of Aerogels and Their Properties

Silica Aerogels

Among all the aerogels, silica aerogels are the most studied and successfully commercialized, especially for thermal insulation applications. This is an amazing material popularly known as “solid smoke,” “frozen smoke,” and “blue air.” The

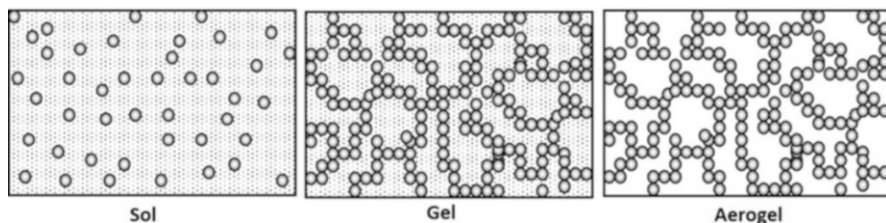


Fig. 1 Schematic representation of aerogel formation

beauty complements extraordinary properties of silica aerogel. This ultralow density and transparent synthetic substance is the best insulator of heat, sound, and electricity. Figure 2 shows the picture of silica aerogel, made in the author's lab.

The sol-gel technique is the commonly used method for making silica gels as described in section “[General Preparation Methods of Aerogels](#).” The sol-gel reactions are catalyzed either by bases or acids or by both in two steps. Various kinds of silica precursors are used for synthesizing silica aerogels [3, 4]. Tetraethoxysilane (TEOS) is the most common precursor used among all. The chemical reaction of the sol-gel process is described in Fig. 3.

The obtained alcogel (gel filled with alcohol) is then dried using either of the drying techniques mentioned in section “[General Preparation Methods of Aerogels](#)” to obtain mesoporous silica aerogel.

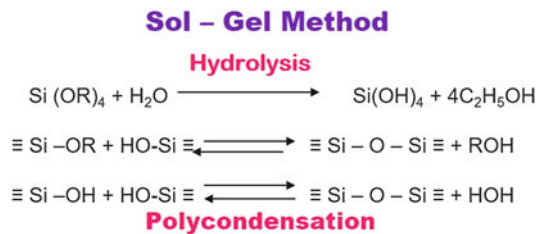
Apart from TEOS and Tetramethyl orthosilicate (TMOS), tetrafunctional silicon alkoxide precursors which give rigid aerogels, silica aerogels can be formed from trifunctional silicon alkoxide precursors such as methyltrimethoxysilane (MTMS), methyltriethoxysilane (MTES), etc., also to form flexible as well as superhydrophobic silica aerogels [5, 6]. Two or more silica precursors can be used for synthesizing silica aerogel. This method of synthesis is called co-precursor method [7]. Organic precursors are used to modify silica gel. Generally, polyisocyanates, epoxides, polystyrene, and polyimides are used as cross-linkers in silica gel to form silica X-aerogel [8]. The polymer is impregnated into the gel and then allowed to cross-link with the surface silanol groups (—Si—OH) of the gel network to obtain polymer cross-linked silica gels. Also, colloidal or noncolloidal solid particles of interest, e.g., colloidal platinum (Pt), colloidal gold (Au), carbon black, fullerene, zeolite crystallites, titania particles, etc., are incorporated into the about-to-gel silica sol to obtain doped aerogels [9]. The colloidal particles can be immobilized in the silica aerogel for obtaining the desired property. Organic precursors such as bridged polysilsesquioxanes, carbon nanotubes, biopolymers, etc. are also used with inorganic silica precursors giving rise to a new class of hybrid aerogels [10–12].

Sol-gel route of synthesizing silica aerogels involves playing with different synthesis parameters at the molecular level that allows controlling porosity which is the key property to find applications in many fields. All the synthesis parameters, like type and concentration of solvent, precursor, and catalyst(s), concentration of water, pH of the medium, temperature, aging conditions, method of drying, etc., play an important role in producing mesoporous silica aerogel of a particular density, pore

Fig. 2 Transparent silica aerogel made in the author's laboratory



Fig. 3 Chemical reactions involved in the sol-gel process to make silica gel



size distribution, and surface functional groups with hydrophilic or hydrophobic nature [1, 13, 14]. Figure 4a shows the scanning electron microscope (SEM) image of silica aerogel made in the author's laboratory by using TEOS as precursor and ammonia as a catalyst, showing fine porous network. Figure 4b is a transmission electron microscope (TEM) image showing pore wall made up of necking of primary silica particles in a typical mesoporous silica aerogel. Figure 4c shows a typical isotherm generated in Brunauer, Emmett, and Teller (BET) method where surface area and porosity are measured by nitrogen adsorption technique. Figure 4d shows cumulative pore volume versus pore size of silica aerogel. A comparison of the densities of commonly known materials is shown in Table 1.

Silica aerogel can be tailored for multiple compositions and functional groups. This is the lightest solid material with huge porosity (98%) [15] and high surface area (1200 m²/g). Hence silica aerogels are used as filters, hydrogen fuel storage, waste containment, catalysts, and catalyst supports and in desiccation as absorbing media, sensors, ion exchange, targets for inertial confinement as a fusion, as a drug delivery system, and X-ray lasers [16].

In porous materials like aerogels, heat transfer happens through three basic modes, conduction, convection, and radiation. The nanoporous structure of silica aerogels plays a significant role in reducing all three modes of heat transfer.

The gaseous heat conduction is caused by the collision of gas molecules. It is reported that convection is negligible for porous materials with pore diameters less

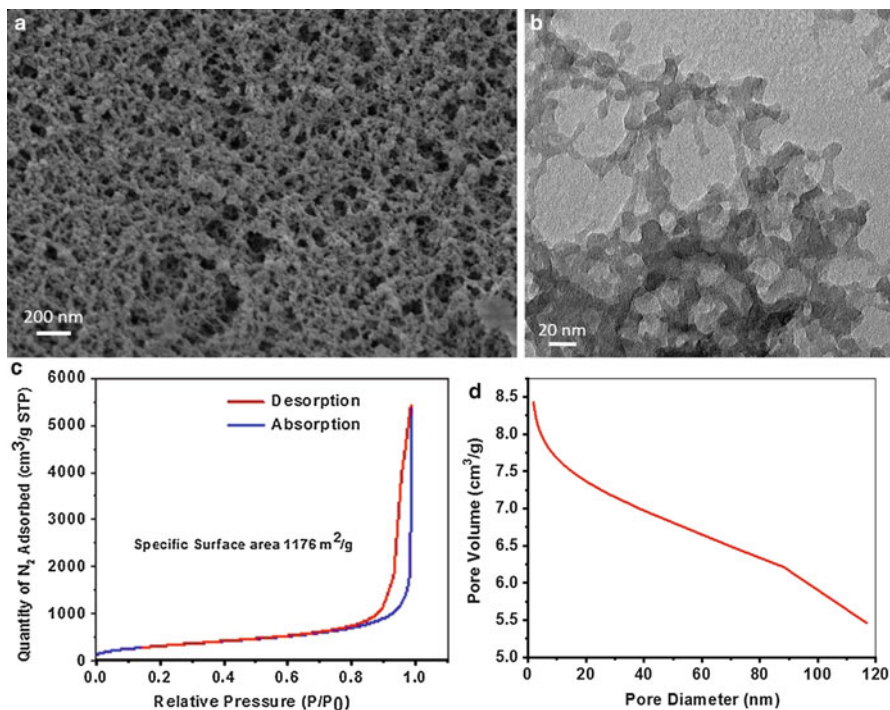


Fig. 4 (a) SEM image of TEOS-based silica aerogel showing porous morphology; (b) TEM image showing network of silica particles to form porous structure; (c) BET isotherm of mesoporous silica aerogel of high surface area; (d) Cumulative pore volume versus pore size of silica aerogel

Table 1 Comparison of densities of common materials

Material	Density (g/cm^3)
Iron	7.87
Diamond	3.5
Graphite	2.3
C60	1.7
Paper	0.7
Charcoal	0.57
Glass	2.4
Aerogel	0.003 to 0.3
Air	0.0013

than 4 nm [17]. The mean pore diameters of silica aerogels range between 20 and 40 nm [18], while the mean free path length of air under standard temperature and pressure is about 70 nm. The diameter of aerogel pores is less than or equal to the mean free path of air which helps in restricting the movement of air in pores and greatly reduces the gaseous heat conduction. The type of gas present in the aerogel

pores also has significant effect on thermal loss coefficient [19]. Conductive heat transfer happens through the vibration of molecules and atoms and through movement of free electrons. In a porous medium, both solid phase and gas phase contribute for conductive heat transfer.

Solid heat conduction mainly depends on SiO_2 network, i.e., on the lattice vibration around their equilibrium positions. Hence, the solid conduction increases with increase in density. Thus silica aerogels show low thermal conductivity compared to other porous silica-based materials [19].

Any material above zero degree Kelvin emits radiation. Any material when exposed to such radiation either absorbs, reflects, or scatters it. Silica aerogels show appreciable absorption of IR radiation of wavelengths 7–30 μm [19]. At ambient temperatures, silica aerogels attenuate radiative flux. But at high temperatures, silica aerogel is almost transparent to radiation of wavelengths between 3 and 5 μm which leads to the rapid rise of radiative heat transfer [20]. IR-opacifying agents are incorporated into silica aerogel to suppress the radiative heat transfer at high temperature [21, 22].

Also, all three modes of heat transfers interact with each other inside silica aerogel to give a coupling effect as shown in Fig. 5. However, when compared to conventional materials, heat transfer contributed by all three modes is greatly reduced, and so silica aerogels exhibit lowest thermal conductivity.

A comparison of silica aerogel with other insulating materials is given in Table 2.

Recent advances in silica aerogels by incorporating various IR opacifiers have led them to be best thermally insulating material coupled with lightweight and transparency. This enables them to be used as thermal insulation for buildings, skylights, exterior glazing, fabric-based roofing membranes, insulation for space vehicles, portable coolers, automobiles, pipes, fire resistant textile, cryogenic insulation, casting molds, etc. [16].

Silica aerogels are not only thermally super insulating materials but also exhibit unusual acoustic property. They are made up of interconnected tiny particles and are prone to compression easily (low Young's modulus of 10^6 – 10^7 N/m^2). This combination of elastic and mechanically soft structure makes silica aerogel an acoustic insulation material. The speed of longitudinal sound waves is measured to be 100–300 m/s for aerogel with densities ranging 70–300 g/l [23]. The sound is carried by the delicate SiO_2 structure. The speed of the sound in silica aerogel can be brought down to 20 m/s by reducing the density. Hence, silica aerogels can be used for isolating sound at high temperatures and acoustic impedance matching for transducers and as range finders [16].

Silica aerogel is inherently fragile in nature. It has very low compressive and tensile strength and elastic modulus. These parameters mostly depend on aerogel density and network connectivity. By aging the gel in the precursor solution, the network can be chemically stiffened, especially, the necks between the particles. Despite their brittle characteristic, the easily compressible nature of silica aerogels is advantageous for kinetic energy absorbing applications. However, a lot of research was carried out to improve the mechanical strength of the silica aerogel. Many polymers have been used to cross-link with the silica network to improve the

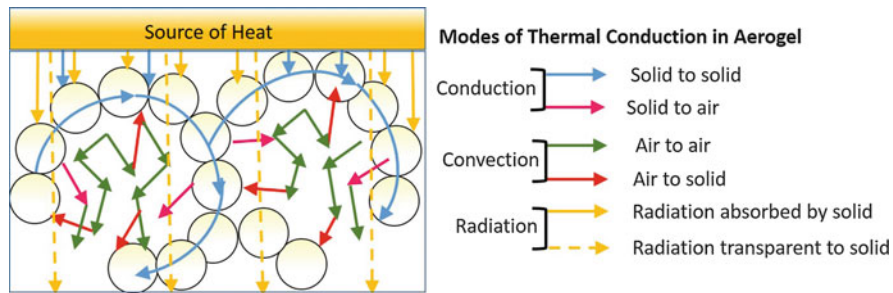


Fig. 5 Schematic representation of coupled heat transfer in silica aerogel

Table 2 Comparison of thermal conductivity and operating temperature range of silica aerogel with other insulating materials

Insulation material	Thermal conductivity at 25 °C (W/mK)	Application temperature range (°C)
Glass fiber mat	0.035	−200 to 500
Cellular glass	0.048	−200 to 400
Polyurethane	0.036	−40 to 105
Calcium silicate	0.065	Up to 650
Mineral fiber	0.037	Up to 650
Expanded perlite	0.076	Up to 650
Polystyrene	0.037	−40 to 80
Ceramic fiber	0.08	Up to 1260
Silica aerogel pure	0.01	−200 to 800
Cellulose	0.035	Subzero–100
Vacuum insulation panels	0.003	Subzero–ambient
Gas (air, argon, krypton)-filled panels	0.0361–0.0867	Subzero–ambient
Phase change materials	0.103–1.6	50 to 150
Fiber-reinforced aerogel sheets	0.013	−200 to 800

interface bonding strength. The load-strain curves of a flexural bending test of poly (hexamethylene diisocyanate)-cross-linked silica aerogel with a 100-fold increase in mechanical strength are shown in Fig. 6 [24].

With improved mechanical strength, silica aerogels could be used as lightweight composite structures, optical sensors, aircraft structural components, heat shields for spacecraft re-entry, membranes for fuel cells, run flat tires, armors, etc. [16].

Silica aerogels are almost transparent to visible light. When illuminated, silica aerogel displays bluish color against a dark background, and the transmitted light is yellowish. Silica aerogels show very high light and solar transmittances. Figure 7 shows the solar transmittance against wavelength [25]. Figure 8 shows the photographs of silica aerogel in different colors when viewed in different optical conditions. Their refractive index values are between 1.0 and 1.05, which is very low for a

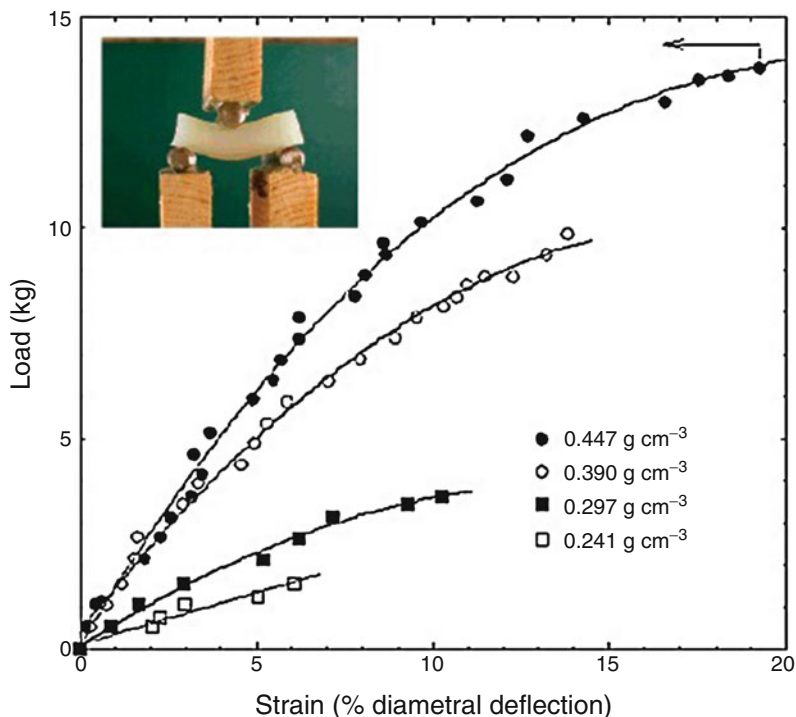


Fig. 6 Load versus strain curves of four composites of different densities. The curve with black filled circular dots corresponds to the monolithic aerogel with a density of 0.447 g/cm^3 . The inset shows bending of this aerogel under 14.4 kg load. (Reproduced from Ref. [26])

solid material. This combination of properties makes silica aerogel suitable for Cherenkov detector application, lightweight optics, light guides, and special effect optics [16].

Different optical phenomena have been investigated by studying silica aerogels in combination with other materials. There are many attempts to embed semiconductor nanoparticles like ZnS, CdS, and ZnO in the silica aerogel matrix. ZnS nanoparticles in silica aerogel matrix were made and its structure was studied [26]. Zinc oxide nanocrystals in silica aerogel matrix were formed by SCD, and its strong green-yellow photoluminescence was undisturbed [27].

Apart from the widely studied silica aerogel and carbon-based aerogels, synthesis of many metal-based aerogels has been pursued by different groups across the world. Innumerable variety of aerogels made up of metals, metal oxides, metal chalcogenide (also called chalcogels), their combinations with other aerogel forms and various nanoparticles, are being the point of interest for the scientific community for specifically targeted applications. Comprehensive reviews of these aerogels are available [28–30].

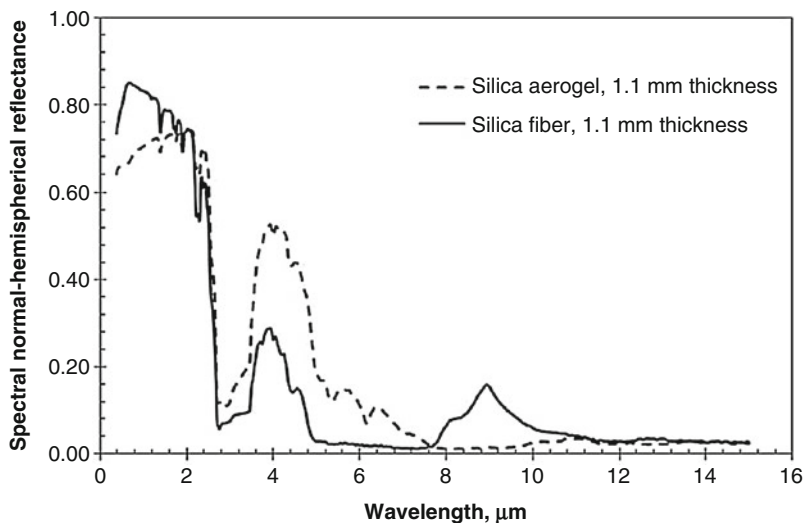


Fig. 7 A typical optical absorbance and scattering coefficient of a typical silica aerogel in UV-Vis-mid IR wavelength range. (Reproduced from Ref. [27])

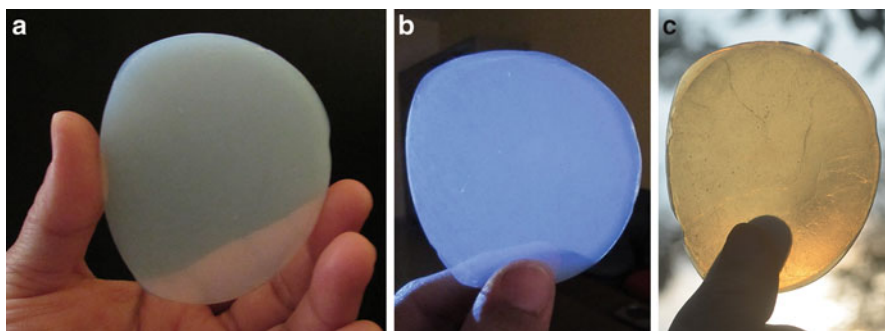
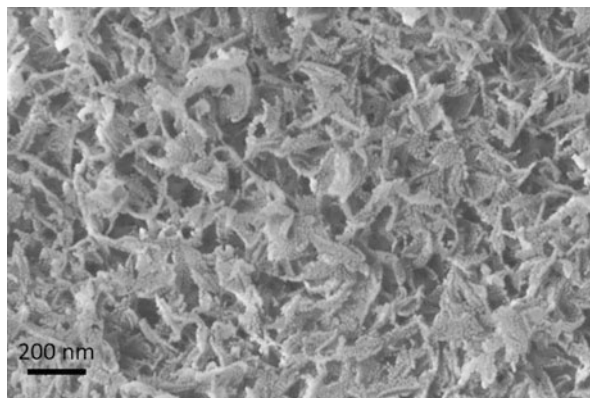


Fig. 8 Various colors of silica aerogel when viewed in (a) normal ambient daylight, (b) against darkness, and (c) in bright light

Metal Oxide Aerogels

There are a wide variety of metal oxide aerogels that are investigated and optimized for specific properties and applications. Alumina, titania, vanadia, zirconia, and zinc oxide are few of them that are studied in detail. Alumina aerogels were first formed by Bulent E Yoldas in 1975 using alkoxide precursors [31]. Gash and group used epoxide approach with aluminum salt precursors [32]. Figure 9 shows SEM image of alumina aerogel prepared in author's lab, using aluminum nitrate as a precursor and propylene oxide as gelation agent. The aerogels have a network of leaflike structures, with surface area $898 \text{ m}^2/\text{g}$. These properties give rise to interesting applications as

Fig. 9 SEM image of alumina aerogel prepared in author's lab



catalysts and catalyst support [33, 34], for the removal of mustard gas [35], etc. They are also a possible replacement to silica aerogel for cometary particle capture [36] and all thermal insulation applications.

Titania is a well-known photocatalyst, and it is an acknowledged fact that in aerogel form, their photocatalytic efficiency will increase. Numerous studies have been carried out for the formation of titania aerogels using different precursors via alkoxide sol-gel method [37]. Titanium dioxide aerogels with different dopants such as niobium, thallium, and vanadium have been studied for use in proton exchange membrane fuel cell (PEMFC) as a catalyst support. The electronic properties of the TiO_2 produced are significantly affected by the dopant used [38]. They can be used for photocatalytic degradation of pollutants [39], photoelectrochemical cell [40], as porous electron collectors in dye-sensitized solar cell [41], etc.

Vanadium oxide aerogel is an interesting metal oxide aerogel with unique energy and sensing applications. It is used as a cathode material in Li-ion batteries. Its high porosity and surface area can host many ions apart from Li^+ . Graphene-decorated vanadium oxide aerogel with nanowire structures has been reported to have a large interlayer spacing of 11.3 Å [42]. Also the porosity in the aerogel network helps in providing shorter diffusion paths and open framework, thereby enabling them to achieve very high specific capacities of 325, 250, and 150 mAh/g at C/10, 1 C, and 7 C, respectively [43]. V_2O_5 aerogel mixed with TiO_2 aerogel can also be used for catalytic activity like reduction of nitrous oxide by ammonia [44].

BaTiO_3 aerogels were studied as they have superior piezo-, pyro-, and ferroelectric properties. These aerogels were formed by bottom-up approach wherein, first, the nanoparticles of desired dimensions were formed and then a 3D network was created by forming a suspended stable sol of the nanoparticles in ethanol initially and later destabilizing them with water. All the electrically conductive aerogels have suitable applications in electrocatalysis, battery, solar, and fuel cell materials. Niobia aerogels can also be prepared using niobium ethoxide as a precursor [45]. Ruthenium Oxide (RuO_2) is a well-known material for electrochemical applications. An alternative for the solid RuO_2 can be derived by doping RuO_2 in titania aerogel. The

electrochemical properties of solid RuO_2 and RuO_2 -doped TiO_2 aerogels were similar owing to the availability of nanoscale domains of RuO_x [46].

Urania aerogels were prepared by sol-gel polymerization using hydrated uranyl nitrate as precursor and propylene oxide as a gelling initiator. The average particle size was found to be 5–20 nm with a surface area $236 \text{ m}^2/\text{g}$ and pore diameter of 2–20 nm [47]. Possible applications using urania aerogel could be as a catalyst and also as nuclear fuel. Similarly, thoria aerogel can also be synthesized using thorium nitrate [48].

Mixed metal oxide aerogels are useful when the required application needs a combination of properties from different materials. For example, iron oxide is the material of choice for the transformation of methanol to dimethyl ether. When it is formed in combination with titania aerogel, its catalytic activity increases as the transition metal oxide helps to transfer the oxygen ions from external surface to its inner lattice structure. The resultant iron oxide-titania aerogel catalyst, having a surface area $105 \text{ m}^2/\text{g}$, showed promising results for methanol oxidation [49].

Metallic Aerogels

Platinum is the most efficient cathode material for PEMFC. There have been numerous studies to improve the efficiency of the catalyst to meet the economic standards for commercialization. The combination of Pt_xPd_y aerogel in comparison with pure Pt and pure Pd materials was studied, and it was found that the former was more efficient and durable when compared to the pure forms [50]. Obtaining metallic aerogels is not possible by direct molecular route, and hence alternate routes are being employed. One such is the additional step of thermal treatment in reducing atmospheres. Metallic gold aerogels were made using amyloid fibers as templates that are best suited for pressure sensors were obtained [51]. Gold-copper aerogels have been developed for use as a catalyst utilizing freeze-drying methodology using HAuCl_4 and CuCl_2 as precursors. The resultant aerogel with atomic ratio 1:1 named as $\text{Au}_{52}\text{Cu}_{48}$ proved to be a better catalyst for use in fuel cell stacks when compared to commercially available Pt/C catalyst [52].

Core-Shell Aerogels

Metallic core-shell aerogels have been made in a two-step synthesis. Pd-M (M = Au, Cu, Co, and Ni) aerogel was first synthesized by spontaneous gelation method and then coated with a monolayer of copper by underpotential deposition. Later the copper shell was replaced by galvanically exchanging with platinum. The Pd_x -Au alloyed aerogels had a 3D structure consisting of nanowires of diameter 4.5 nm with specific surface area varying from 83 to $105 \text{ m}^2/\text{g}$ [53].

Organic Aerogels

First organic aerogel was made by Pekala and his group in the 1980s via polycondensation of resorcinol (R) with formaldehyde (F) through a gelation mechanism similar to the sol-gel processing and then drying supercritically [54]. A variety of organic aerogels are prepared using various phenols, aldehydes, other polymers, and their combinations such as resorcinol-furfural, cresol-formaldehyde, phenolic novolak-furfural, novolak-methylethylketone, novolak-hexamethylenetetramine, phenolic resoles-methylolated melamine, phenol-formaldehyde, phenol-furfural, polyurethane (PU), polyvinyl chloride-based precursor [55], and cellulose. RF-based aerogels are most studied among them.

Resorcinol ($C_6H_4(OH)_2$) and formaldehyde (CH_2O) are reacted in presence of sodium carbonate (Na_2CO_3) (which acts as catalyst (C)) and distilled water (H_2O) to make resorcinol-formaldehyde (RF) gel. The R:F ratio, R:C ratio, and the total concentration of (R + F + C) in the solution are varied to tailor the porosity in RF aerogel. The gelation is carried out at 85 °C, and formed gel is subjected to solvent exchange followed by drying through different drying processes, i.e., SCD [56], freeze-drying [57], microwave drying [58], ambient drying [59], and vacuum drying [60] to form the RF aerogel.

Another kind of organic aerogels, which are eco-friendly and biocompatible, are cellulose aerogels. Cellulose can be extracted from a wide range of different sources, which mainly include plants and plant-based materials such as rice straw, cannabis, cotton, wood, potato tubers, bagasse, and even from bacteria [61]. Cellulose aerogel has an added advantage because cellulose is inexhaustible. Syntheses from renewable source are simple because of the presence of active hydroxyl groups, and chemical modifications can be easily done. The cellulose gel can be made by agglomeration of polymers or by a phase separation process when coagulate regenerator is used and can be regenerated in four steps: cellulose dissolution, cellulose regeneration, solvent exchange, and SCD or vacuum freeze-drying [62].

Pure cellulose nanocrystal (CNC) synthesis by freeze-drying shows minimal shrinkage and damage. This type of aerogel is suitable to fabricate 3D-printed structures which are currently a revolution in manufacturing sector. Customized and complicated structures can be made easily with this process, but the cartridge used for printing varies according to the application. CNC-based aerogel cartridges can be used in tissue scaffold templates, drug delivery, packaging, etc., due to their inherent sustainability, biocompatibility, and biodegradability [63]. The important steps of Direct Ink Write (DIW) 3D printing are shown in Fig. 10 [64].

Other organic aerogels studied are derived from PU [65], polyurea [66], polyamide [67], and polyimide [68]. National Aeronautics and Space Administration (NASA) has developed a low density, highly flexible, durable polyimide-based aerogel with surface area up to 600 m^2/g , compressive strength as high as 225 MPa and thermal stability up to 300 °C, which can be potentially used for several aerospace applications [69].

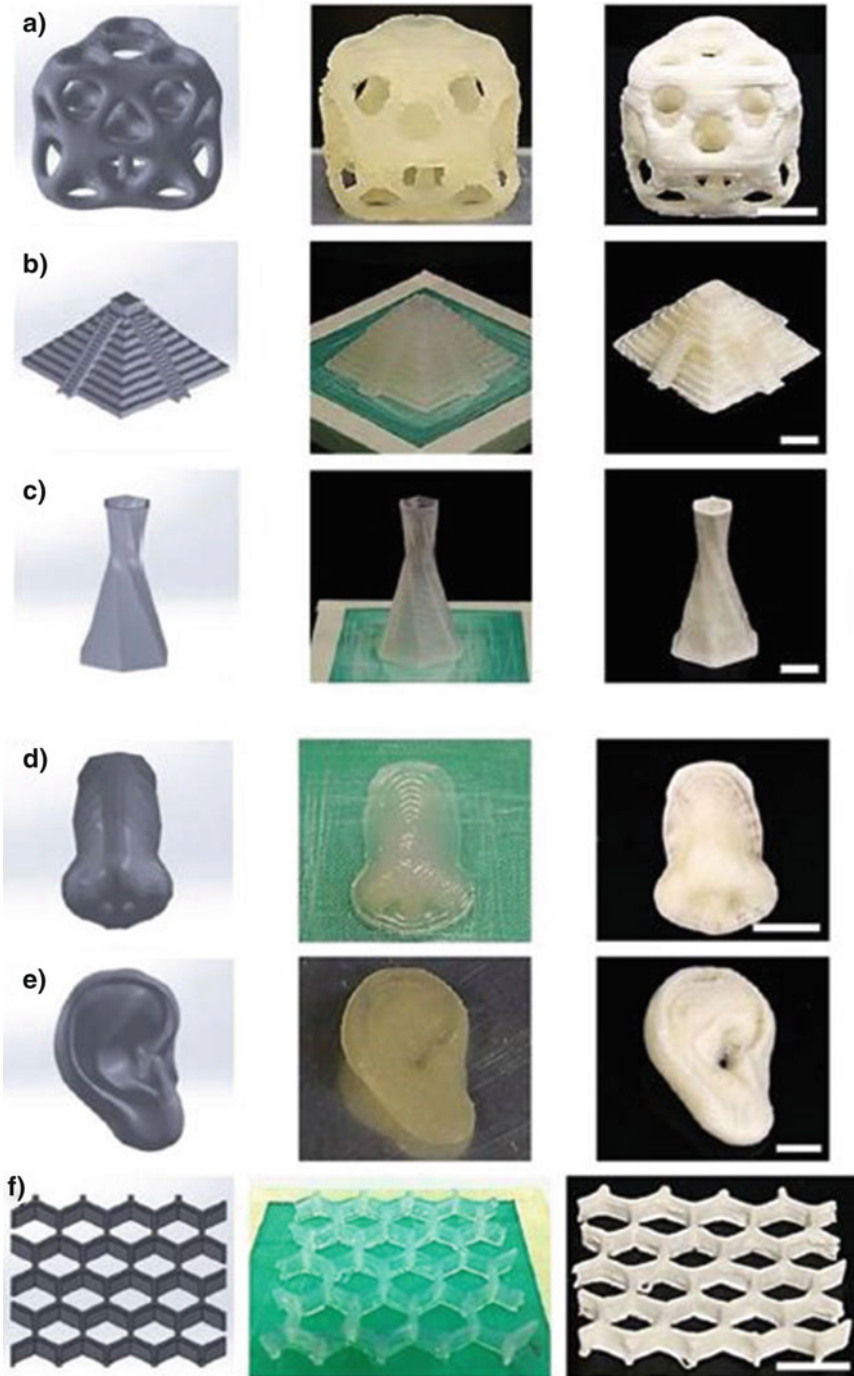


Fig. 10 (continued)

X-aerogels was synthesized by cross-linking (X-process) of polymers with silica aerogel (X-silica) and vanadia aerogel (X-vanadia). These are extremely strong among the all classes of aerogels [70]. These can overcome the problem of fragility issue which happened at the space exploration of NASA's Stardust program and Mars rover. The lignin aerogel was synthesized [71], using cellulose as an adhesion agent, and this aerogel is having low thermal conductivity (0.128 W/(m.K)) and high sound absorption property. Here, both cellulose and lignin are first and second highly abundant renewable biopolymers.

Carbon Aerogels

There are mainly three types of carbon aerogels. First type is obtained from the pyrolysis of organic aerogels. Normally in this process, the organic aerogel is heated in the presence of inert (i.e., argon or nitrogen) atmosphere to remove hydrogen and oxygen contents. Mostly, resorcinol-formaldehyde aerogels are generally used for making carbon aerogels. The final properties of aerogel are dependent on the pyrolysis temperature [72]. Graphene aerogel (GA) and carbon nanotube (CNT) aerogels are second type of carbon aerogels. To fabricate these aerogels, the graphene or CNTs are used as precursors, and the properties of aerogel depend on the synthesis and assembling conditions. The surface-functionalized CNTs and graphene are suspended in the solvents by adding dispersant agents to create strong and permanent chemical bonding between CNTs. This interaction facilitates gelation by formation of a multi-walled carbon nanotube (MWCNT) percolation network [73]. Once the gel is formed, it is dried by suitable method. The third type of carbon aerogels are composites of polymer-GA aerogel (PGA), polymer/CNT aerogel (PCNTA), and graphene-CNT aerogel (GCNTA). The gel preparation of these composites is done by combining their individual gel making processes. For instance, PGA gel is made by mixing graphene suspension with RF sol allowing it to gel and further drying in supercritical condition. To make a gel of PCNTA, the CNT sol is added to RF sol while it is forming a gel. The gel to make GCNTA is prepared by hydrothermal synthesis where the suspension of graphene and CNT mixture were treated with or without reducing agent [74].

The electrical property mainly depends on the type of carbon aerogel, the size of a primary building block in the aerogel network, the morphology of porous structure, and the specific surface area. The highest reported specific surface area for carbon aerogel made from RF in aqueous solution is 3200 m²/g [75]. This is a key property required to use carbon aerogel as an electrode material in supercapacitor which does



Fig. 10 Direct Ink Write (DIW) 3D-printed (a) octet cube, (b) pyramid, (c) hexagonally twisting vase, (d) nose model, (e) ear model, and (f) honeycomb from 20 wt% CNC gel and 500 μm nozzle tip. The first column is CAD model, the second column is photos of DIW 3D-printed gel structures, and third column is resultant structures after freeze-drying. Displayed scale bars are 1 cm. (Reproduced from Ref. [75])

not participate in redox reactions at the applied voltage, and the material possesses charge capacity of 386 mAh/g due to charge double layer formation [76].

Having the porosity in nanometer size range, the carbon aerogels also exhibit good thermal insulation property. During the pyrolysis where polymeric aerogels are turned into carbon aerogels, the temperature of pyrolysis decides the balance between the thermal and electrical conductivity. The higher the pyrolysis temperature, the more is the electrical conductivity and the lesser the thermal conductivity and vice versa. The thermal conductivity of the carbon aerogel is always little higher than the oxide aerogels due to the shrinkage and agglomeration of the carbon particles [77]. Carbon aerogel can withstand till 2500 °C in N₂ or inert atmosphere [78]. Carbon aerogel is a promising material for thermally insulating space shuttles and nuclear reactors.

The first-ever made graphene has very high thermal conductivity (2500–5300 W/(m.K)). Few research groups calculated the graphene conductivity by adding defects and dopants and found that the graphene conductivity can be reduced to 3.19 W/(m.K) [79]. N-doped graphene hydrogel synthesized by hydrothermal method followed by SCD showed the lowest thermal conductivity of 0.023 W/(m.K) [80].

3D-printed GA is stronger than steel at 0.2% weight of steel, and this is the world's least dense (0.5 mg/cm³) 3D-printed material [81]. This technique facilitates to fabricate gel in any complex shape and size. These types of materials are very much useful to make advanced space suits, electronics, batteries, and supercapacitors. Figure 11 [82] shows the Guinness World Records holding graphene aerogel of cubic inch volume for its lightweight (density of 0.16 g/cm³) which could stand on a blade of grass. X-aerogels (carbon-silica aerogel and carbon-vanadia aerogel) are the strongest aerogels among all types of aerogels. These aerogels are prepared by cross-linking carbon with silica aerogel and carbon with vanadia aerogel

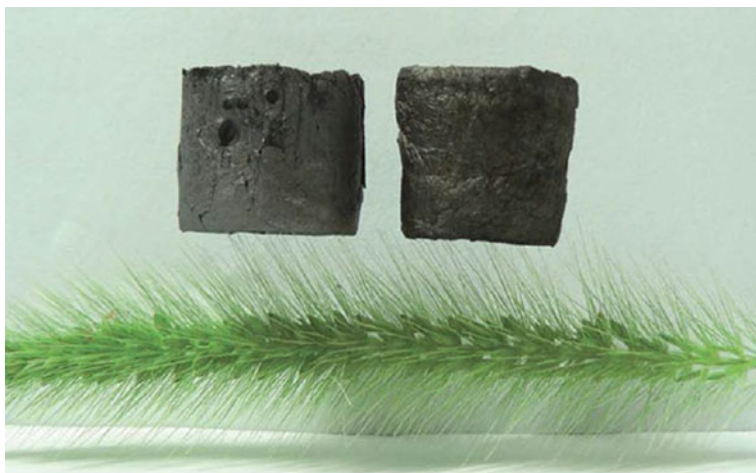


Fig. 11 Ultralightweight GA balanced on a blade of grass. (Reproduced from Ref. [96])

[70]. The X-aerogels can be cut into required shape and size of the material without losing their properties to integrate with the circuit [83].

Various Aerogel Forms: Monoliths, Granules, and Composites

Monolithic aerogels are the purest form of aerogels that are in bulk structure. The intrinsic properties of any aerogel are basically mentioned for its monolithic form. All the best possible properties are possible to achieve only in the monolithic form of aerogel. For example, the thermal insulation property of silica aerogel is maximum for the monolithic form than any other form. Ideally, monoliths can be made in any shape and size, e.g., tiles, disks, sheets, etc. The gel takes the shape of the mold used for its casting. The restriction on the size of the aerogel is only due to the size of the apparatus available. In spite of this, making crack-free, flawless aerogel is extremely difficult and time-consuming due to the fact that the delicate gel has to be handled with extreme care to avoid any cracks, and solvent exchange schedules are very lengthy to completely replace gel liquid with pure solvent and longer drying procedures. This slow process yields monolithic forms with 10–20% shrinkage in volume w.r.t. initial mold [36]. Due to the fragile nature, precise and critical shapes of monolithic aerogels are not realizable without any wastage during production and usage. In order for aerogels to remain in monolithic forms, various methodologies can be adopted for the strengthening of its network like cross-linking with polymers, the addition of precursors during solvent exchange process, etc. [84]. Hence, usage of monolithic aerogels is restricted to some special applications. In the field of high energy physics, they are used as Cherenkov radiators [85]. The monolithic, transparent nature of aerogel which is made for this purpose with a refractive index ranging from 1.02 to 1.20 helps in filling up the gap between liquid and gas. The drying of the gel was done by ambient drying method through a pinhole. This slow-drying process helped in achieving the density and the refractive index required for the application. Monolithic forms help in accommodating fast moving foreign objects into its network, thereby finding usage in capturing cometary particles from space.

To utilize the advantageous properties of this extraordinary material, these are made in other easy-to-use forms such as granules and composites with fiber reinforcements. Granules of aerogel are made to compensate the monolithic form where the brittleness of monolithic aerogel hinders the usage for various applications. Granules are smaller bead-like structures ranging less than 1 cm in diameter and are easy to handle. Their properties are closer to the parent monoliths under compaction. Due to the ease in synthesizing and usage of the granulate forms of aerogel, they are made by different methodologies for numerous applications. Aerogel granules can be conveniently used in many ways such as filling the gaps around the article to be insulated, as an additive, e.g., to paints or building materials, sandwiching between the layers of fabric or sheets. Granules can be prepared by powdering the monoliths, by normal sol-gel process using a surfactant and drying under ambient conditions, by spray drying the sol [86], or by using a polymer foam as a template for the granule [87]. Silica aerogel granules are available commercially

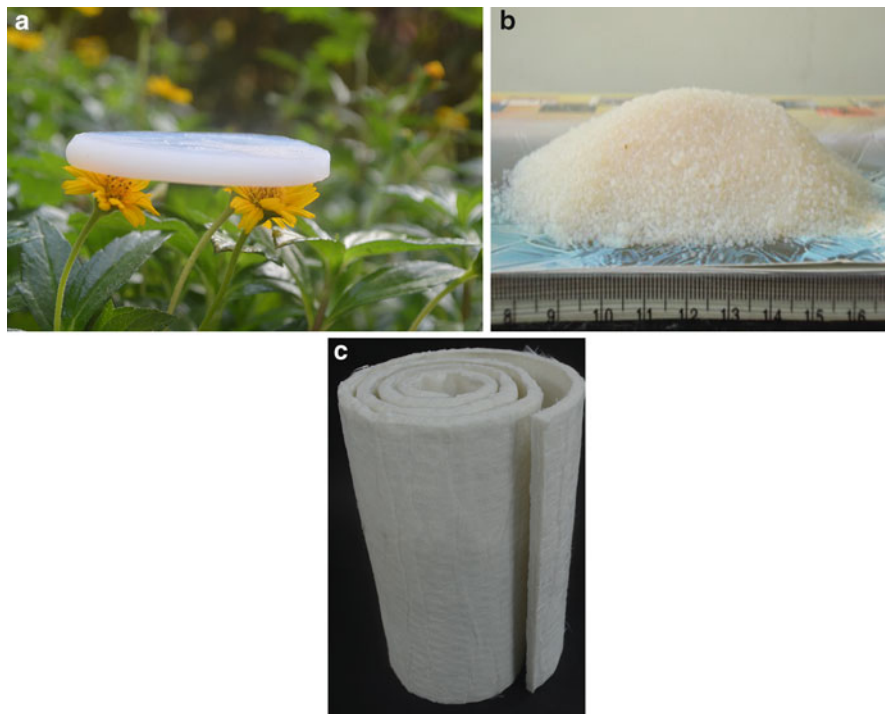


Fig. 12 (a) Monolithic, (b) granular, and (c) fiber-reinforced flexible sheet composite of silica aerogel made in author's laboratory

also and are used as a substitute where monolithic aerogels cannot be used. They are used in window glazing, in paints for coating as thermal insulation, as fillers, in sandwich form between two polymer layers, etc.

The need for composites basically arises for the sake of getting mechanical strength and flexibility in aerogel structure. Reinforcement of inorganic or organic fibers like aramid, Nomex, glass fibers, carbon fibers, and epoxy fibers in aerogel structure can make the aerogel composite in flexible sheet form, which can be easily used for wrapping around the objects [88]. Generally, the fibers in the form of a mat, either woven or non-woven, are used as a substrate to infiltrate the gel-forming precursor. The gel is formed within the pores of the fiber mat to make a gel-sheet which is then dried by a suitable method to make aerogel sheet [89–91]. Opacifiers like TiO_2 and carbon black are also used to form composites that give additional functionality. The aerogel content in such composite sheets can be tailored by choosing the density of the base fiber mat.

Silica aerogel composite filled with fibers is the predominantly in-use aerogel composite for various applications ranging from thermal insulation, acoustic impedance, etc. Several products are commercially available. The author's group has

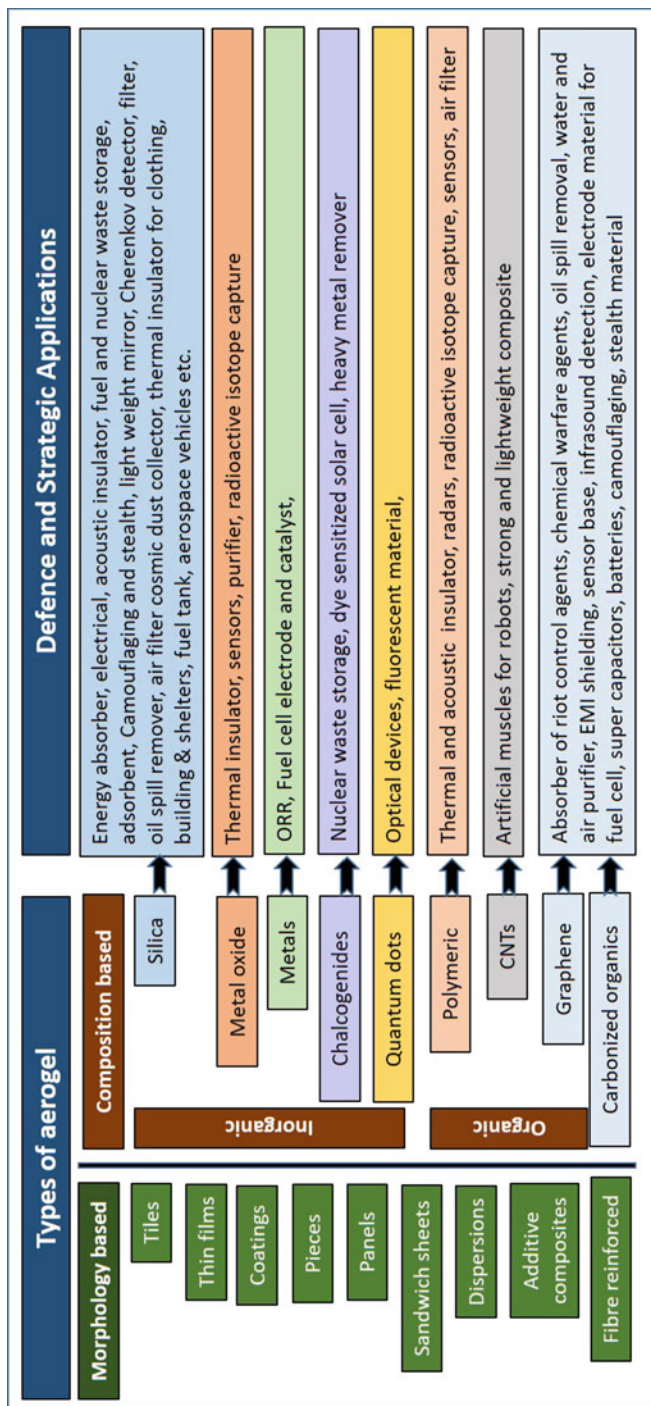


Fig. 13 Various types of aerogels and their application range

developed silica aerogel fiber mat composites with density as low as 0.2 g/cm^3 and BET surface area of $\sim 500 \text{ m}^2/\text{g}$.

Rational properties like the electromagnetic absorption of aerogels can be used by making composites of suitable combination. Magnetic ferrite nanoparticles grown on a strong CNTs network can give rise to a robust and lightweight material for use in aviation, aerospace, and smart electronics. The CNT network acts as the template for the in situ growth of iron oxide nanoparticles, while the nanoparticles themselves act as cross-linkers for the CNTs. Flexible magnetic nanopaper could be formed from the above by compaction [92].

Chalcogenes are known to have high affinity to heavy metals, radioactive materials, and iodine. On a research scale, the test is usually made with small quantities in powder or granular form. On the field, a more mechanically robust material is required, and hence making hybrids with polyacrylonitrile (PAN) fibers makes them more durable to use as a sorbent. Different composites were synthesized by varying the mass % ratio of PAN versus tin sulfide (SnS). PAN with SnS 50% showed maximum mechanical durability and maximum iodine capture [93].

Among all aerogels, silica aerogel products in the above various forms are available in the global market for several applications [94]. Some forms developed in the author's lab are shown in Fig. 12.

As seen from the discussions above, aerogel is a class of material, possessing extraordinary properties together, and has flexibility in the synthesis to have large choice of composition and physical forms. As a result, aerogels are the most promising materials in specialized applications. Fig. 13 gives classification of aerogels based on physical forms and composition and their broad range of applications in the field of strategic and defense domain. The following section illustrates these applications in detail.

Applications

Functionalities like ultralightweight, capacity to absorb kinetic energy, huge surface area and pore volume, excellent thermal and acoustic insulation, tunable electrical and optical properties, and flexibility in tailoring chemical compositions and physical forms lead to consider "aerogel" as a class of materials to solve many complex and stringent problems for the need of defense and strategic sector. The following section illustrates some of the important applications.

Aerogels as Energy Absorbers

The most notable application of aerogel as an energy absorber is to capture extra-terrestrial material, e.g., the cosmic dust from the tail of a comet. Silica aerogels were first sent on Space Transportation System (STS-47) in September 1992. This is owing firstly to its poor load-bearing capacity so that they get shattered easily when a hypervelocity particle hits, thereby slowing the particle and capturing them intact.

Secondly, it does not constitute inorganic contaminants and cosmochemical elements of much importance. The aerogel captured at least four large hypervelocity particles during this preliminary mission without any damage to the aerogel during launch and re-entry. Stardust mission launched from the Kennedy Space Center in 1999 was the most successful aerogel-related mission that unveiled many scientific discoveries. The function of the mission was to carry a tennis racket-shaped metal frame collector consisting of silica aerogel blocks of different volumes which would meet with Comet 81P/Wild 2 to capture interstellar dust and coma samples around the nucleus of the comet to be brought on earth for laboratory analysis [95]. Silica aerogel remains to be the ideal material for hypervelocity particle capture.

Yet another application of aerogel as energy absorber can be realized in the mitigation of blasts and explosions. Regardless of the cause, explosions generate shock waves, intense heat, and gas, with pressure much greater than ambient pressure. Thermal tolerance and mechanical strength in combination with low density and low acoustic velocity make aerogel structures most suitable for this purpose [96]. In order to protect people, vehicles and other process facilities, barriers, or armors are typically used. Mechanically strong silica aerogels could be incorporated into the armor to protect military personnel which reduces the weight of the armor and covers more areas of the body. Polymer cross-linked silica aerogel plate was used along with existing constituents of the armor. A 0.308 Winchester bullet fired with a velocity of 906.8 m/s didn't penetrate through the armor plate. The armor plate containing aerogel shows 120% less back face deflection than baseline armor plate showing the superiority of aerogel in energy absorption [97].

In day-to-day life, one of the safety gears that are commonly used is helmets. Expanded polystyrene and expanded polypropylene are being used as impact absorbers in helmets. These materials show good kinetic behavior in the direction of the motion of head during an impact, but the stored energy is returned to the deforming agent, i.e., head. Silica aerogel composites can be used as a shock absorbing material in this application. They not only store and release the kinetic energy but also eliminate the bounce back effect on the head [98].

Aerogel and its various forms can be contained in envelopes such as body paddings for sports, police, and military, knee padding for gardeners and workers, muzzle pads for dogs, padding for dog handlers, saddle pads for horses, etc., for energy absorption [99].

Aerogels for Thermal Insulation

It is already established in the previous pages of the chapter that one of the earliest applications of aerogels was to serve as thermal insulators. As part of the Pathfinder mission in 1997, silica aerogel was first used as an insulator on the Mars Sojourner rover to protect the primary battery pack of alpha particle X-ray spectrometer (APXS) from extremely low temperatures. Room temperature vulcanizing (RTV) based components have been used on Mars Pathfinder. RTV-655, even though

majorly used, has limitations due to its high density (1.2–1.45 g/cm³) and tendency to attract dust particles because of electrostatic charging [100]. A polymer-reinforced (cross-linked) silica aerogel with metal oxide pigment was developed with better strength, hydrophobicity, optical property, and decreased density as a substitute for RTV-655 [101]. In 2003, the aerogel was used to insulate additional parts like radioisotope heater units (RHU) in Mars Exploration Rovers Opportunity and Spirit owing to its efficiency. Silica aerogels have proved to sustain relatively large temperature fluctuation and harsh environments [102].

Space missions require cryopumping, i.e., storage of water, liquefied air, ice, and dense air for use at space which should be maintained at cryogenic temperatures. An insulation which is hydrophobic, breathable, durable, and lightweight is required to maintain these fluids at cryogenic temperatures as liquid hydrogen and liquid oxygen are to be maintained at $-253\text{ }^{\circ}\text{C}$ and $-183\text{ }^{\circ}\text{C}$, respectively, mainly during lift-off and reentry into the earth's atmosphere where sudden changes in temperature and pressure are experienced. Silica aerogel in the form of blankets and beads had been lab tested as cryogenic insulation at NASA Kennedy Space Center and proved to be the best suitable material [103, 104].

The most recent subject under scientific proposals in the field of aerospace is manned mission to Mars. It has been proposed that the mission should last for a long time for about 3 years, for which human factor must be taken seriously into account to overcome sociopsychological problems that generally occur in isolated and confined environments. For this, a big comfortable and human-friendly habitat has been designed. Silica aerogel composite has been chosen for thermal insulation in this habitat structure like windows, floors, and walls [105].

Solid rocket motor casing consists of a solid propellant grain, designed to undergo combustion, thereby giving the thrust for rocket motor propulsion. During the burning of propellant, high temperature generates, which could damage the rocket motor casing. An elastomer-based insulation is being used to protect rocket motor casing from high temperature. Hydrophobic silica aerogel particles are incorporated in the elastomer-based polymer to increase tear strength and elasticity of insulation [106].

Silica aerogel-based thermal protection system (TPS) developed at author's lab was studied for its use in launch vehicles on coupon level. A high silica cloth laminated silica aerogel sheet was fixed on the metal surfaces using high-temperature adhesives. This was evaluated for thermal protection performance up to $850\text{ }^{\circ}\text{C}$ by rapid heating in a duration of 100 s where the back wall temperature was observed to be $90\text{ }^{\circ}\text{C}$ with 5 mm thick TPS. The TPS along with its adhesion to the metal surface successfully passed the vibration tests where it was subjected to the vibration frequency range of 10–2000 Hz with the high acceleration for 150 s.

When it comes to military applications, silica aerogel composites can be used as Fire Blocking Blanket (FBB) for stored ammunition. Storing of munitions in open area invites various external threats which can lead to their detonation. Particularly, pallets of ammunition stored in close proximity to each other is a much vulnerable situation as the detonation of one stack will promote detonation of another making a chain reaction destroying the entire ammunition depot. Therefore, protective FBB is

required not only to prevent propagation of fire but also to prevent penetration of low-velocity projectiles and hot fragments. Silica aerogel blanket shows better results than other conventional materials such as silica mat, refractory ceramic fibers, ceramic paper, and ceramic blankets [107, 108].

Transportable shelters are a must for the military to facilitate comfort and operational effectiveness where ever on earth. Various materials are being used to extend their operational life and for maintaining temperature and humidity required for equipment and personnel [109]. Silica aerogel-based blankets are being used for insulating the shelter both from extreme cold and hot environments to mitigate energy loss [110].

Recirculating air purifiers are required in military depots to deactivate chemical and biological contaminants. Chemical agents need to be deactivated by oxidation, and biological agents are to be deactivated by exposing them to high temperatures (250–400 °C). Therefore, thermocatalytic air purifiers are developed for this purpose. Silica aerogel-based high-temperature insulating panels are being used for thermally insulating these air purifiers and proved to be highly efficient. Conventional insulation requires 15 cm thick insulation, whereas 1.5 cm thick silica aerogel vacuum insulation panels are sufficient to achieve the same result [111].

The use of night vision goggles is a crucial strategic application in battlefields. Silica aerogel helps in thermal isolation of pyroelectric imaging element to achieve the maximum thermal and temporal resolution. Its thin film is deposited to provide thermal isolation between the oxidized silicon substrate and pyroelectric magnetic element. This technique helped to increase the signal-to-noise ratio by 43% rendered by commercially available night vision goggles [112].

A study had been carried out on thermal jacket for military canteen water bottles 718 to store ice slurry for armed forces personnel. Maintaining the body temperature is important for armed forces personnel to keep themselves safe from heat injuries. It is a known fact that ingesting ice slurries is a better way to cool the body core temperature than drinking cold water. While vacuum flasks are effective at maintaining the temperature of ice slurry for longer period, their cost and weight became an issue for practical use. To overcome these issues, a sandwich made of nylon, cellulose aerogel, and neoprene was made to form flexible thermal insulation jacket at just 20% total cost of vacuum flasks with comparable thermal insulation [113].

Whether it is to keep air conditioning systems cold, or for cleaning night vision devices and weapons or for welding and torch operations, the army requires compressed industrial gases to support every unit. Transportation and handling of compressed gases are very risky as the pressure inside the cylinder increases when exposed to heat. This pressure needs to be released to the environment to avoid rupture of the cylinder. In some cases, the releasing of pressure is not ideal as the gas can catch fire or it might be toxic to inhale. Silica aerogel insulation can be used for shipping hazardous materials such as compressed gas cylinders to provide flame and thermal protection [114].

Many defense applications require not only temperature protection but also mechanical strength where compressive forces exist, e.g. aeroengine insulation

applications. In this case, two or more materials are required to maintain the desired conditions which add extra costs and weight. Silica aerogel in blanket form is not always useful, especially when irregular shapes are involved. A sprayable silica aerogel insulation, having a blend of silica aerogel agglomerates and ceramic particles, could be used. The ceramic particles with low melting point soften and provide necessary adhesive capability to achieve mechanically robust thermal insulated coating [115].

Aerogel has been studied for applications such as its suitability for space suits, for firefighter and cold water diver garments, etc. Its suitability to protect the feet from extreme temperatures has also been worked on.

Aerogels can be incorporated on fabrics after they are formed externally or can be incorporated as layers in between fabrics or can be used as a non-woven fabric-aerogel composite depending upon its suitability. Silica aerogel that is organically modified for hydrophobic nature with anatase titanium dioxide particles coated on cotton fabrics showed to have self-cleaning property [116].

Space suits of astronauts require materials with precise specifications to ensure safety in extreme temperature and pressure conditions and in the harsh dust. The extravehicular mobility unit (EMU) consists of different classes of layers.

The inner layers maintain the pressure of the suit. The remaining layers form the thermal meteoroid garment (TMG) which provides micrometeoroid and thermal protection. The present TMG is limited to hard vacuum medium as on moon and low orbit where radiative heat transfer is dominant, and the multilayer insulation (MLI) in TMG is inefficient in atmospheres like on Mars, due to the presence of interstitial gases. MLI should possess a thermal conductivity of 5 mW/m.K for effective thermal insulation. Aerogels are the only materials which could come close to this requirement with 7.5 mW/m.K thermal conductivity. They are the best suitable insulation material for future space suits [117].

Aerogel incorporated liners were used for studying the thermal insulation performance in fabrics for divers. It helped divers stay underwater for 43% greater duration when compared to commercial insulation. Apart from providing an average of 3 °C higher temperature for the body, it also helped the divers to have warmer feet and hands (approximately 4 °C and 5 °C higher temperature for finger and toe, respectively, than commercial suits). Also, they were durable when laundered and required to be air dried instead of machine drying [118].

For the ease of applicability and to have superior thermal comfort, aerogel powders were mixed with eicosane – a phase change material (PCM) which usually changes phase at 80 °C. The eicosane remains stable inside the microparticle powder of aerogel and does not drip even at temperatures higher than 120 °C. This property wherein the surface morphology of aerogel powders helps to keep the PCM intact without dripping and where the PCM helps to make a composite easy to coat on fabrics opens new windows in terms of thermal insulation fabrics [119]. Organic PCMs are known to fuel the ignition when in direct contact with flame, and, hence, material like aerogel helps to safeguard the life of the firefighters by reducing the risks of catching fire. The addition of aerogel as an extra coating to

the existing firefighting garment with PCM has found to increase the mean ignition temperature (temperature at which the garment catches fire) from 3.3 to 5.5 s. It also helped in decreasing the overall weight of the garment and reduced the spreading of the flame [120]. Recent studies showed that when used as reinforcement material and/or batting in thermal liner for moisture barrier of firefighting clothing, aerogel as non-woven batting can provide eight times more thermal resistance than existing commercial reinforcement material and existing thermal batting material. When used as a thermal liner, the heat resistance increased by five times than existing thermal liner and thrice when compared to the combined performance of existing thermal liner and moisture barrier. This increases the escape time for the firefighter from the direct flame situation from 5 s (for existing solutions) to 1 min.

For those who work in extremely cold environments, the footwear and clothing used have to give additional functionality of thermal protection against the freezing temperature. Currently the conventional materials used include natural material like wool and fur or the commercially available products like Thinsulate™ (3 M), Primaloft (PrimaLoft, Inc.), Heatseeker™ (The North Face), Opti-Warm™ (Merrell), etc.. In recent days, both aerogel and PCM have joined the foray and have proven to be an efficient alternative.

Silica aerogel incorporated in the PU foams of the footwear helped to increase the cell density and better cell dispersion. Incorporation of silica aerogel into the PU foams as a composite helped to maintain the flexibility of the PU foam, and still, there was no dustiness of the aerogel powder. The compressive strength and shock attenuation capacity of the foam increased with increase in aerogel content. When used in cold environment, the thermal conductivity of the footwear decreased by 45% for a total of 15 wt% aerogel loading. This improved insulation is attributed to the fact that the gas phase and solid phase of the foam are now constricted with the nanocellular structure of aerogel [121].

Studies are being done to understand how to efficiently arrange the aerogel composites and PCMs in different ways to ensure optimum performance in terms of low thermal conductivity, structure withstanding capability even after 30,000 cycles of flexing, breathability, minimum thickness, etc. Thus, it can be concluded that laminated aerogel composite consisting of Pyrogel 2250 in its thinnest form, arranged with upper and lower lining materials, gave waterproof breathable footwear and insulation. It is to be noted that this CLO value is suitable enough to give protection against extreme cold of around -25°C [122].

Silica aerogel being thermal, electrical, and acoustic insulator makes it best suitable for architectural insulation. This insulation is not only useful for new construction but also refurbishment of existing buildings. Various forms of silica aerogel are being used for different needs of architectural insulation such as transparent silica aerogel for glazing systems [123], silica aerogel concrete or plaster [124], and silica aerogel panels and blankets for walls and ground insulation [125, 126].

Using various forms of silica aerogel insulation for architectures reduces energy consumption and saves space and cost.

Aerogels for Storage

A significant use of silica aerogel is to act as cryogenic fluid container. To test the equivalence principle, which is the heart of the Einstein's theory of gravitation, general relativity, satellite test of the equivalence principle (STEP) was proposed to launch in 2004. STEP payload consists of accelerometers based on superconducting technology mounted in a superfluid helium dewar. Liquid helium at cryogenic temperatures (1.8 K) is required in the satellite to sustain stability of test masses and detectors from solar pressure, air drag, and magnetic field. Suppressing of helium tides due to the gradient in earth's field is critical in this mission as such tides produce gravitational disturbances on test masses. Silica aerogels, being open cell structured and highly porous, have been identified as suitable container for liquid helium storage. An assembly of geometrically shaped silica aerogel pieces put in required shape and are filled with liquid helium not only could successfully prevent bulk flow of helium to occur but also could withstand launch vibration environment [127, 128]. Although STEP mission couldn't be launched, this technology was successfully applied on Gravity Probe B mission.

Nuclear waste disposal has been a major challenge for scientists. The nuclear fuel remains highly radioactive for thousands of years even after it was being used for power generation and of no further use for commercial reactors. An approach for disposal of nuclear waste is to confine the nuclear waste in chemically durable, thermally and mechanically stable material. Silica aerogel, functionalized silica aerogels like silver-functionalized silica aerogel, and silica aerogel composites like silver-loaded aluminosilicate, silsesquioxane-imine aerogel, etc. can be used as a host matrix for the confinement of different nuclear waste such as actinides, radioiodine, etc. [129–131].

Out of the various chalcogenide-based aerogels studied [132], PtGe₂S₅ aerogels were found to have the best capture efficiency of 98% for technetium-99 and 99.4% for uranium 238, both of which are again radioactive wastes. Apart from chalcogenide-based aerogel, composites like iron-polyaniline-GA ternary composite were also used to study the removal of uranium ions from radioactive wastewater from nuclear energy processing. This composite showed an efficiency of removing 350.47 mg of U (VI) per gram of the composite [133].

Aerogels as Adsorbent and Purifier for Toxic Gases

Riot control agent such as CS which is orthochlorobenzalmalononitrile, a white to yellow crystalline powder used for temporarily incapacitating the unmasked personnel with immediate effect, is used to control the violent crowd. Exposure to low concentrations of agent CS may itself cause extreme burning of eyes and induces tears, difficulty in breathing, chest tightness, runny nose, and dizziness. When a small concentration of silica aerogel blends with CS, it produces required respiratory effects. The silica aerogel not only reduces agglomeration but increases the flowing capacity of CS [134].

Hierarchical porous GA is capable of adsorption of chemical warfare agent dimethyl methylphosphonate (DMMP) [135]. Polydiacetylene (PDA) embedded within an aerogel acts like artificial nose because it exhibits the rapid color/fluorescence when it interacts with the volatile organic compounds [136].

Aerogels for Environmental Remediation

Space-based microelectronic and high-performance optical components and military systems of high-density integrated circuits are prone to degradation due to contamination. To address this problem, contamination collector devices are generally used. Silica aerogel could be used as a contamination collector. An aerogel mesh contamination collector (AMCC) to collect and contain molecular and particulate contaminants was developed which is suitable for spacecraft environment [137].

There has been a worldwide concern to control accidental releases of oil and organic liquids in water bodies during transportation and storage as it causes long-term effects on the ecosystem. Oil may spill on water because of leakage from tanks, drilling rigs, and wells. Oil spills harm aquatic life. Fishes, birds, mammals, and reptiles, which consume the oil, suffer serious health problems, and furred animals exposed to the oil have their mobility and body temperatures affected. Normally there are a lot of methods to separate oil from water. Aerogels can be used to separate oil by mechanical sorption method. In this method, the oil sticks to the material by sorption (i.e., adsorption or absorption). A sorbent material that is hydrophobic but oleophilic is the prime requirement along with retention, recovery of the oil from sorbent, and reusability of sorbent. Superhydrophobic silica aerogels could absorb oils by nearly 15 times its own weight [138]. Different classes of aerogels have different absorption capacity of oils, e.g. graphene/cysteamine aerogel can absorb 251 times of its own weight and MTMS/dodecyltrimethoxysilane (DTMS)-based aerogels that can absorb 8–13.5 times [139]. Carbon nanofiber aerogels and cellular graphene aerogel can absorb 139 times and 226 times of its weight, respectively [140].

Aerogels helps in water purification also. The sensors used in environmental remediation for the removal of mercury ions from water streams can be fabricated using MoS_2 aerogel which is doped with graphene sheets and has gold and iron oxide nanoparticles embedded in them. These composites shows a very high sensitivity to Hg^+ ions and help colorimetrically to detect and remove by absorbing a maximum of 1527 mg/g [141]. An electrically regenerated electrosorption process known as carbon aerogel capacitive deionization has been developed for continuously removing ionic impurities from aqueous streams [142]. 3D regenerated cellulose/graphene oxide composite aerogel [143] and Bi_2MoO_6 /reduced graphene oxide (rGO) aerogel composite [144] are capable of high adsorption of methylene blue. Cellulose nanofibril/graphene oxide (CNF/GO) hybrid aerogel is capable of adsorbing 21 kinds of antibiotics from water [145]. Poly(amidoamine)-grafted CNF aerogels can effectively remove Cr(VI) [146], GAs decorated with FeOOH can effectively adsorb arsenic [147], and three-dimensional barium-sulfate-

impregnated reduced graphene oxide aerogel can adsorb strontium from aqueous solutions [148]. Iron-polyaniline-GA composite effectively adsorbs radioactive U (VI) from the wastewater [149]. Green-synthesized carbon nanotube-graphene hybrid aerogels can effectively remove organic dyes and heavy metal ions (Pb^{2+} , Hg^{2+} , Ag^{2+} , Cu^{2+}) and deionize the light metal salts [150].

Not only in water purification, aerogels could also be used for blood purification. Heavy metal lead (Pb) is toxic and can damage almost every organ in the human body and particularly the brain. A microelectromechanical system (MEMS) with inner walls coated with carbon aerogel helps in absorbing Pb from the blood [151]. This device can filter 62.55 L blood per week.

Applications Based on Optical Properties

In 1974, aerogel was put to its first scientific application as Cherenkov radiation detector [152]. The use of aerogel as a radiator has significantly simplified the Cherenkov counter construction in particle physics experiments [153]. Aerogels could bring down the indices of refraction to a very low value of 1.02 which otherwise could be obtained only with gases at cryogenic temperatures or with pressurized gases. Ultralow refractive indices coupled with less weight and ability to make large volume counters make aerogels best suitable for Cherenkov radiation detection. Later in 1982, monolithic highly transparent tiles of silica aerogel were mass produced to equip TASSO Cherenkov detector [154].

IR cameras are generally used to find the targets of enemies. All objects such as human body, aircrafts, tanks, etc. emit heat as IR radiation. The emissivity mainly depends on the temperature of the objects. Stealth materials are used to mask this emission to hide from the IR cameras which can detect these objects even in the darkness of the night. These materials applied to the objects to be hidden can strongly absorb IR radiation of short, mid, and long wavelength making that object completely invisible to the IR cameras. The technologies such as forward-looking infrared (FLIR) imaging and shortwave infrared (SWIR) sensing make the detection of the invisible spectrum better. The thermally insulating materials such as aerogels show the remarkable capability to stop heat propagation in all three modes, namely, conduction, convection, and radiation.

A strategy may be adapted to give a false signal to the IR camera by creating false emissions to divert the enemy's attention. Combustible materials impregnated in aerogels can produce IR radiation which can last for a long duration [155]. The impregnated material such as metal powders, organometallic compounds, and phosphorous reacts exothermically in the air to produce heat and IR radiation which can last for 15 min or more.

In nature, we find various biological mechanisms in animals such as chameleons to match the body color with surroundings by tuning the visible light reflectivity. This inspires to make artificial materials or surfaces to match the visual appearance with the surroundings, and this technique is known as camouflage. The most difficult is thermal or radar camouflaging as it is difficult to have a tunable IR absorptivity or

reflectivity or emissivity in a single material without changing the temperature. The inclusion of aerogel in the form of a coating, lamination, layering, or as an additive to the camouflaging system has shown improved masking of heat emissions and radar suppression [156].

Man-portable air-defense system (MANPADS) is a very significant threat to all aircrafts as they are relatively easy to use, highly portable, lethal, and proliferated. The IR radiation generated by exhaust plume and hot metal components could be a susceptible guide for an enemy weapon. However, the atmosphere significantly absorbs the IR signature of the exhaust plume at long ranges. To suppress the IR signature of the hot metal components, aerogel IR shield could be used. Using aerogels as IR-suppressing device, very little weight is added to the aircraft, and also the IR signature of the aircraft is very low beyond 5000 feet which otherwise is significant till 15,000 feet [157].

Electromagnetic interference (EMI) waves which are considered to be environmental pollution are emitted from most of the electronic devices like televisions, mobile, antennas, and mobiles. From the past few years, the metal plates and metal sheets are being used as protective layers from the EMIs. Still, these protective materials are having disadvantage like heavy, corrosive, and poor processability. As metals reflect the EMIs rather than absorb; hence use of these materials is prevented in some main applications like in military and aircraft. To overcome from this problem, researchers should move to another material; therefore, a continuous search is going on to develop novel materials associated with excellent absorption features with the purpose to reduce EMI in circuits, chips, and radiation controllers. Aerogels are excellent EMI absorbers with less weight and flexible nature. Hence they find practical applications in various fields like aircraft, aerospace, automobiles, and portable electronics and wearable devices. Porosity, pore diameter, and specific surface area are the key factors for the EMI shielding. For this purpose, GA was synthesized from graphene oxide by customized sol-gel polymerization chemistry [158]. The synthesized carbon aerogel is having 516 m²/g density and 2.5 nm sized particles. This gel is effectively shielded by the microwaves with 20.0 dB of reflection loss at 0.2 g in the frequency range of 12.4–18.0 GHz. Another study has reported the synthesis by reduced graphene oxide/black phosphorus (rGO/BP) composite aerogel through dialysis and freeze-drying. The composite rGO/BP showing reflection loss value of 46.9 dB with a thickness of 2.53 mm was obtained, and a wide absorption band of 6.1 GHz (reflection loss <10 dB) was achieved [159].

Sensors

Humidity sensor based on gold aerogel was made to identify human breath and to monitor health conditions. These sensors are wearable and can form a part of the mask to monitor real-time health conditions of the wearer [160]. These hybrid poly-N-isopropyl acrylamide and gold nanoparticle aerogels have high sensitivity to relative humidity and can differentiate between fast breath, normal breath, and different whistle patterns. WS₂ aerogels have been used to identify NO₂

gases [161]. PDA-embedded alumina aerogel can help to identify the concentration of the volatile organic compounds colorimetrically and can be used for air purification [162].

Self-Cleaning Surfaces

Superhydrophobic surfaces are very difficult to wet and hence become self-cleaning surfaces. These hydrophobic coatings are used in textiles, paints, coatings, and marine vessels. By coating low surface energy materials on rough surfaces, the hydrophobicity can increase. There are a variety of methods to measure hydrophobicity of aerogels, but droplet contact angle method is simple and easy to test the result. If the contact angle is between 0° and 90° , surface is considered as hydrophilic; if the angle lies between 90° and 150° , the surface is considered to be hydrophobic; and if the angle lies between 150° and 180° , the surface is considered to be superhydrophobic. GA can be used to make hydrophobic surfaces, and when functionalized with 1H,1H,2H,2H-perfluorodecyl-trichlorosilane (FDTS), they become superhydrophobic. This is because FDTS/hexane reacts with the hydroxyl groups of GA finally leaving C-F₂ and C-F₃ groups to reduce the surface energy of the aerogel, thereby creating a superhydrophobic surface [163].

Microelectromechanical Systems (MEMS)

MEMS are nanoscale technology-based devices with moving parts. Amidst different types of MEMS-based sensors, a capacitive-based CMOS-MEMS humidity sensor was made with resorcinol-formaldehyde (RF) aerogel [164]. These sensors are successfully implemented by Taiwan Semiconductor Manufacturing Company 0.18 μm 1P6M CMOS standard process. They have sensitivity measurement of 0.595% of relative humidity. These sensors are widely used in automotive, biomedical, industrial products and domestic appliances. Recently they are installed in mobile phones to act as personal weather stations.

Infrasound Detection

Infrasound is an inaudible frequency range less than 20 Hz. These frequencies can be detected by the electromagnetic induction (EMId). EMId is a mechanism which converts the energy from mechanical to electrical or electrical to mechanical. Carbon nanotube aerogel sheet which is coated with a thin layer of aluminum has been developed, which responds to infrasound waves and vibrates [165]. By converting this vibrational energy to electrical energy by EMId, the device can detect infrared sounds. The same material can also work as a mechanical actuator by applying current in the range of millivolts.

Energy Storage Devices

There is a strong need to develop clean and renewable energy sources to displace our current dependence on nonrenewable energy sources such as oil, natural gas, and uranium. Such challenges can be overcome by alternative energy sources like solar cells, supercapacitors, batteries, and fuel cells. These device electrodes can be made from different kinds of materials including carbon, organic, and polymer based aerogels. The structure and surface functional groups play an important role in the electrochemical behavior of carbon aerogels [166]. PU wrapped on MXene-graphene composite aerogel electrode material has excellent self-healing ability. This type of electrodes is used to fabricate lifelong electronic devices [167]. Also, electrode materials with stretching capacity of 200% elongation have been prepared and can be used in aerospace, smart robots, and wearable devices [168]. 3D printing of GA electrodes has given rise to integrated energy storage devices [169].

The next choice in the alternate energy sources are fuel cells. They can greatly reduce the pollution of air from volatile organic compounds, sulfur, and nitrogen oxides. The basic working principle of the fuel cell is converting the fuel energy to electrical energy by mixing of hydrogen with air in the absence of combustion. For this, evolution of oxygen at the cathode material is important. Again, these cathode materials can be made by hybrid aerogels. The flowerlike V_3S_4 homogeneously grown on the three-dimensional porous GA is an efficient catalyst for oxygen reduction reaction (ORR) [170]. Also, a study of N-doped carbon-based aerogels prepared by salt-templating method which includes nonvolatile ionic liquids as precursors mentioned that carbon possess favorably high electrocatalytic performance in ORR and not found for similar materials made by other pathways [171].

Fuel cells can be used in the military as energy sources for aerial vehicles, undersea vehicles, light-duty trucks, and wearable power systems because fuel cells are compact, lightweight, and low maintenance and have zero lubricants.

Harvesting solar energy can help to generate instant electricity on the field and fulfill the local energy needs. Platinum-free porous vanadium nitride nanoribbon aerogel (PVNNRA) was prepared for use in dye-sensitized solar cells (DSSC). When compared to silicon-based solar cells, DSSC offers low production cost and better efficiency. The counter electrode prepared by spray coating the PVNNRA dispersion on to fluorine-doped tin oxide glass (FTO) showed a conversion efficiency of 7.05% which is comparable to Pt electrodes. These aerogels produced by the low-cost hydrothermal method are best alternatives to the high-cost Pt electrodes [172].

Artificial Muscles for Robots

Electrically activated artificial muscles are used to generate force and move objects. The range of applications of artificial muscles extends to different fields such as robotics, prosthetics, orthotics, and human-assistive devices.

CNT aerogel-based artificial muscles were formed that can elongate 10 times more than natural muscles, at rates 1000 times higher than a natural muscle. Its operating temperature is from $-196\text{ }^{\circ}\text{C}$ to $1538\text{ }^{\circ}\text{C}$ [173].

Aerogels as Mirror Substrates

Silica aerogel could be used as optical substrate material. A study of the suitability of silica aerogel as an ultralight substrate for reflective coatings was done. To yield an ultralightweight mirror, the aerogel surface has to be polished and smoothed, and then a diamond lapping film is to be coated using Freon spray and dry nitrogen. This process increases the transmissive properties. An aerogel mirror substrate which is six times less dense than conventional ultralow expansion glass substrate was fabricated, which could have a substantial impact on the STS weight which in turn reduces the launch and on-orbit costs [174]. Much more research needs to be carried for fabricating realistic optic for use in space missions.

Aerogels as Dielectric Materials

Dielectric materials can store electrical energy/charge and their electrical conductivity is low. Molecules present in dielectric materials align themselves when exposed to external charge by accumulating positive and negative charges on either side of the material. Air, distilled water, ceramic, glass, mica, plastics, and oxides of various metals are good examples of dielectric materials. Normally dielectric materials are used in capacitors to reduce the size of the capacitors and to insulate the semiconductor transistors from each other. Polyimide composites with low dielectric constant of 2.4 and hydrophobic nature can be used in the field of microelectronics which is currently a booming field owing to the demand for miniaturization and weight reduction [175].

Aerogels as Radar Antennas

In a typical aircraft with complex structural integration, one can find 15–100 radar antennas. With advance in the aerospace industry, lightweight antennas with wider bandwidth and higher gain are required.

Aerogels are dielectric materials having a linear relationship of density with dielectric constant. The value measured for silica aerogel films was 1.1 for the 0.1 g/cm^3 dense sample [176]. The lowest dielectric constant measured was 1.008 for silica aerogels with density 0.008 g/cm^3 . However, absorption of moisture and the low mechanical strength limit their use in antenna applications. Polyimide aerogels that are hydrophobic developed by NASA proved its feasibility to be used as patch antennas [177].

Another organic aerogel with polybutylene succinate incorporated in it was used for the radio-frequency and microwave filter application. This material is biodegradable and has a dielectric constant of 4.5. This biocompatible material is used for wideband and ultra-wideband antennas covering a bandwidth of 9.4 (2.3–11.7) GHz with stop bands from 5.5 to 5.8 GHz and 7.0 to 8.3 GHz [178].

Summary

The “aerogel” class of material is uniquely placed in the defense, aerospace, energy and strategic applications due to its diverse combination of properties in a single material. The unique combination of the properties such as ultralow density, high surface area, thermal and electrical conductivity, etc. are originated from the highly nano porous nature. The chemistry and the processes used in making aerogels are very much flexible to tailor-make the compositions and various physical forms. It is easy to achieve control over the extent of porosity and pore size distribution. Aerogels also serve as best host materials to other compounds or materials to produce advanced functional materials. In general, the stringent property requirements and severe application conditions limit the choice of materials in highly specialized areas. Aerogel class of materials can extraordinarily perform well in a variety of domains such as thermal insulation, energy absorber, stealth, and camouflaging.

References

1. Brinker CJ, Scherer GW (2013) Sol-gel science: the physics and chemistry of sol-gel processing. Academic, London
2. Pierre AC, Pajonk GM (2002) Chemistry of aerogels and their applications. *Chem Rev* 102(11):4243–4266
3. Feng Q, Chen K, Ma D, Lin H, Liu Z, Qin S, Luo Y (2018) Synthesis of high specific surface area silica aerogel from rice husk ash via ambient pressure drying. *Colloids Surf A Physicochem Eng Asp* 539:399–406
4. Wagh PB, Begag R, Pajonk GM, Rao AV, Haranath D (1999) Comparison of some physical properties of silica aerogel monoliths synthesized by different precursors. *Mater Chem Phys* 57(3):214–218
5. Nadargi DY, Rao AV (2009) Methyltriethoxysilane: new precursor for synthesizing silica aerogels. *J Alloys Compd* 467(1–2):397–404
6. Nadargi DY, Lathe SS, Hirashima H, Rao AV (2009) Studies on rheological properties of methyltriethoxysilane (MTES) based flexible superhydrophobic silica aerogels. *Microporous Mesoporous Mater* 117(3):617–626
7. Li Z, Cheng X, He S, Huang D, Bi H, Yang H (2014) Preparation of ambient pressure dried MTMS/TEOS co-precursor silica aerogel by adjusting NH₄OH concentration. *Mater Lett* 129:12–15
8. Zhang G, Dass A, Rawashdeh AMM, Thomas J, Council JA, Sotiriou-Leventis C, McCorkle L (2004) Isocyanate-crosslinked silica aerogel monoliths: preparation and characterization. *J Non-Cryst Solids* 350:152–116

9. Morris CA, Anderson ML, Stroud RM, Merzbacher CI, Rolison DR (1999) Silica sol as a nanogluue: flexible synthesis of composite aerogels. *Science* 284(5414):622–624
10. Piñero M, del Mar Mesa-Díaz M, de los Santos D, Reyes-Peces MV, Díaz-Fraile JA, de la Rosa-Fox N, Morales-Florez V (2018) Reinforced silica-carbon nanotube monolithic aerogels synthesised by rapid controlled gelation. *J Sol-Gel Sci Technol* 86(2):391–399
11. Loy DA, Shea KJ (1995) Bridged polysilsesquioxanes. Highly porous hybrid organic-inorganic materials. *Chem Rev* 95(5):1431–1442
12. Maleki H, Montes S, Hayati-Roodbari N, Putz F, Huesing N (2018) Compressible, thermally insulating, and fire retardant aerogels through self-assembling silk fibroin biopolymers inside a silica structure an approach towards 3D printing of aerogels. *ACS Appl Mater Interfaces* 10(26):22718–22730
13. Hench LL, West JK (1990) The sol-gel process. *Chem Rev* 90(1):33–72
14. Pope EJ, Mackenzie JD (1986) Sol-gel processing of silica: II. The role of the catalyst. *J Non-Cryst Solids* 87(1–2):185–198
15. Tillotson TM, Hrubesh LW (1992) Transparent ultralow-density silica aerogels prepared by a two-step sol-gel process. *J Non-Cryst Solids* 145:44–50
16. Hrubesh LW (1998) Aerogel applications. *J Non-Cryst Solids* 225:335–342
17. Hrubesh LW, Pekala RW (1994) Thermal properties of organic and inorganic aerogels. *J Mater Res* 9(3):731–738
18. Pierre AC, Rigacci A (2011) SiO₂ aerogels. In: *Aerogels handbook*. Springer, New York, pp 21–45
19. Fricke J (1988) Aerogels – highly tenuous solids with fascinating properties. *J Non-Cryst Solids* 100(1–3):169–173
20. Bi C, Tang GH (2013) Effective thermal conductivity of the solid backbone of aerogel. *Int J Heat Mass Transf* 64:452–456
21. Wang J, Kuhn J, Lu X (1995) Monolithic silica aerogel insulation doped with TiO₂ powder and ceramic fibers. *J Non-Cryst Solids* 186:296–300
22. Wang XD, Sun D, Duan YY, Hu ZJ (2013) Radiative characteristics of opacifier-loaded silica aerogel composites. *J Non-Cryst Solids* 375:31–39
23. Gronauer M, Kadur A, Fricke J (1986) Mechanical and acoustic properties of silica aerogel. In: *Aerogels*. Springer, Berlin/Heidelberg, pp 167–173
24. Leventis N, Sotiriou-Leventis C, Zhang G, Rawashdeh AMM (2002) Nanoengineering strong silica aerogels. *Nano Lett* 2(9):957–960
25. Fu T, Tang J, Chen K, Zhang F (2015) Visible, near-infrared and infrared optical properties of silica aerogels. *Infrared Phys Technol* 71:121–126
26. Tan M, Cai W, Zhang L (1997) Optical absorption of ZnS nanocrystals inside pores of silica. *Appl Phys Lett* 71:3697–3699. <https://doi.org/10.1063/1.120485>
27. Lorenz C, Emmerling A, Fricke J et al (1998) Aerogels containing strongly photoluminescing zinc oxide nanocrystals. *J Non-Cryst Solids* 238:1–5
28. Rechberger F, Niederberger M (2017) Synthesis of aerogels: from molecular routes to 3-dimensional nanoparticle assembly. *Nanoscale Horizons* 2:6–30. <https://doi.org/10.1039/c6nh00077k>
29. Bryce CT, Stephen AS, Luther EP (2010) Nanoporous metal foams. *Angew Chem Int Ed* 49:4544–4565. <https://doi.org/10.1002/anie.200902994>
30. Ziegler C, Wolf A, Liu W et al (2017) Modern inorganic aerogels. *Angew Chem Int Ed* 56:13200–13221. <https://doi.org/10.1002/anie.201611552>
31. Yoldas BE (1975) Alumina gels that form porous transparent Al₂O₃. *J Mater Sci* 10:1856–1860. <https://doi.org/10.1007/BF00754473>
32. Gash AE, Tillotson TM, Satcher JH et al (2001) New sol-gel synthetic route to transition and main-group metal oxide aerogels using inorganic salt precursors. *J Non-Cryst Solids* 285:22–28. [https://doi.org/10.1016/S0022-3093\(01\)00427-6](https://doi.org/10.1016/S0022-3093(01)00427-6)
33. Osaki T, Mori T (2009) Characterization of nickel-alumina aerogels with high thermal stability. *J Non-Cryst Solids* 355:1590–1596. <https://doi.org/10.1016/j.noncrsol.2009.06.006>

34. Courthéoux L, Popa F, Gautron E, Rossignol S, Kappenstein C (2004) Platinum supported on doped alumina catalysts for propulsion applications. Xerogels versus aerogels. *J Non-Cryst Solids* 350:113–119. <https://doi.org/10.1016/j.jnoncrysol.2004.06.051>
35. Bakardjieva S, Ma M, Stengl V, Subrt J (2004) Aerogel nanoscale magnesium oxides as a destructive sorbent for toxic chemical agents. *Cent Eur J Chem* 2:16–33
36. Jones SM (2010) Non-silica aerogels as hypervelocity particle capture materials. *Meteorit Planet Sci* 45:93–100. <https://doi.org/10.1111/j.1945-5100.2009.01007.x>
37. Schneider M, Baiker A (1997) Titania Based Aerogels 35:339–365
38. Beauger C, Testut L, Berthon-Fabry S et al (2016) Doped TiO₂ aerogels as alternative catalyst supports for proton exchange membrane fuel cells: a comparative study of Nb, V and Ta dopants. *Microporous Mesoporous Mater* 232:109–118. <https://doi.org/10.1016/j.micromeso.2016.06.003>
39. Kibombo HS, Weber AS, Wu C et al (2013) Effectively dispersed europium oxide dopants in TiO₂ aerogel supports for enhanced photocatalytic pollutant degradation. *J Photochem Photobiol A Chem* 269:49–58. <https://doi.org/10.1016/j.jphotochem.2013.07.006>
40. Wang C-T, Huang H-H (2008) Photo-chargeable titanium/vanadium oxide composites. *J Non-Cryst Solids* 354:3336–3342. <https://doi.org/10.1016/j.jnoncrysol.2008.02.005>
41. Guo W, Wu L, Chen Z et al (2011) Highly efficient dye-sensitized solar cells based on nitrogen-doped titania with excellent stability. *J Photochem Photobiol A Chem* 219:180–187. <https://doi.org/10.1016/j.jphotochem.2011.01.004>
42. An Q, Li Y, Deog Yoo H et al (2015) Graphene decorated vanadium oxide nanowire aerogel for long-cycle-life magnesium battery cathodes. *Nano Energy* 18:265–272. <https://doi.org/10.1016/j.nanoen.2015.10.029>
43. Moretti A, Maroni F, Osada I, Nobili F (2015) V₂O₅ aerogel as a versatile cathode material for lithium and sodium batteries. *ChemElectroChem* 2(4):529–537. <https://doi.org/10.1002/celec.201402394>
44. Reiche MA, Ortelli E, Baiker A (1999) Vanadia grafted on TiO₂-SiO₂, TiO₂ and SiO₂ aerogels: structural properties and catalytic behaviour in selective reduction of NO by NH₃. *Appl Catal B Environ* 23:187–203. [https://doi.org/10.1016/S0926-3373\(99\)00076-4](https://doi.org/10.1016/S0926-3373(99)00076-4)
45. Brodsky CJ, Ko EI (1996) Effects of preparative and supercritical drying parameters on the physical properties of niobia aerogels. *Langmuir* 12(25):6164–6166
46. Long JW, Swider KE, Merzbacher CI, Rolison DR (1999) Voltammetric characterization of ruthenium oxide-based aerogels and other RuO₂ solids: the nature of capacitance in nanostructured materials. *Langmuir* 15:780–785. <https://doi.org/10.1021/la980785a>
47. Reibold RA, Poco JF, Baumann TF et al (2003) Synthesis and characterization of a low-density urania (UO₃) aerogel. *J Non-Cryst Solids* 319:241–246. [https://doi.org/10.1016/S0022-3093\(03\)00012-7](https://doi.org/10.1016/S0022-3093(03)00012-7)
48. Reibold RA, Poco JF, Baumann TF et al (2004) Synthesis and characterization of a nanocrystalline thoria aerogel. *J Non-Cryst Solids* 341:35–39. <https://doi.org/10.1016/j.jnoncrysol.2004.05.008>
49. Wang C, Ro S (2007) Nanoparticle iron – titanium oxide aerogels. *Mater Chem Phys* 101:41–48. <https://doi.org/10.1016/j.matchemphys.2006.02.010>
50. Liu W, Rodriguez P, Borchardt L et al (2013) Bimetallic aerogels: high-performance electrocatalysts for the oxygen reduction reaction. *Angew Chem Int Ed* 52:9849–9852. <https://doi.org/10.1002/anie.201303109>
51. Nyström G, Fernández-Ronco MP, Bolisetty S et al (2016) Amyloid templated gold aerogels. *Adv Mater* 28:472–478. <https://doi.org/10.1002/adma.201503465>
52. Wang J, Chen F, Jin Y, Johnston RL (2018) Gold–copper aerogels with intriguing surface electronic modulation as highly active and stable electrocatalysts for oxygen reduction and borohydride oxidation. *ChemSusChem* 11:1354–1364. <https://doi.org/10.1002/cssc.201800052>
53. Cai B, Hübner R, Sasaki K et al (2018) Core–shell structuring of pure metallic aerogels towards highly efficient platinum utilization for the oxygen reduction reaction. *Angew Chem Int Ed* 57:2963–2966. <https://doi.org/10.1002/anie.201710997>

54. Pekala RW (1989) Organic aerogels from the polycondensation of resorcinol with formaldehyde. *J Mater Sci* 24(9):3221–3227
55. Yamashita J, Ojima T, Shioya M, Hatori H, Yamada Y (2003) Organic and carbon aerogels derived from poly (vinyl chloride). *Carbon* 41(2):285–294
56. Şahin İ, Özbakır Y, İnönü Z, Ulker Z, Erkey C (2017) Kinetics of supercritical drying of gels. *Gels* 4(1):3
57. Anoshkin IV, Campion J, Lyubchenko DV, Oberhammer J (2018) Freeze-dried carbon nanotube aerogels for high frequency absorber applications. *ACS Appl Mater Interfaces* 10(23):19806–19811
58. Durães L, Matias T, Patrício R, Portugal A (2013) Silica based aerogel like materials obtained by quick microwave drying. *Mater Werkst* 44(5):380–385
59. Zhu L, Wang Y, Cui S, Yang F, Nie Z, Li Q, Wei Q (2018) Preparation of silica aerogels by ambient pressure drying without causing equipment corrosion. *Molecules* 23(8):1935
60. Chen D, Gao H, Jin Z, Wang J, Dong W, Huang X, Wang G (2018) Vacuum-dried synthesis of low-density hydrophobic monolithic bridged silsesquioxane aerogels for oil/water separation: effects of acid catalyst and its excellent flexibility. *ACS Appl Nano Mater* 1(2):933–939
61. Foresti ML, Vázquez A, Boury B (2017) Applications of bacterial cellulose as precursor of carbon and composites with metal oxide, metal sulfide and metal nanoparticles: a review of recent advances. *Carbohydr Polym* 157:447–467
62. Long LY, Weng YX, Wang YZ (2018) Cellulose aerogels: synthesis, applications, and prospects. *Polymers* 10(6):623
63. Sannino A, Demitri C, Madaghiale M (2009) Biodegradable cellulose-based hydrogels: design and applications. *Materials* 2(2):353–373
64. Li VCF, Dunn CK, Zhang Z, Deng Y, Qi HJ (2017) Direct Ink Write (DIW) 3D printed cellulose nanocrystal aerogel structures. *Sci Rep* 7(1):8018
65. Rigacci A, Marechal JC, Repoux M, Moreno M, Achard P (2004) Preparation of polyurethane-based aerogels and xerogels for thermal superinsulation. *J Non-Cryst Solids* 350:372–378
66. Lee JK, Gould GL, Rhine W (2009) Polyurea based aerogel for a high performance thermal insulation material. *J Sol-Gel Sci Technol* 49(2):209–220
67. Williams JC, Nguyen BN, McCorkle L, Scheiman D, Griffin JS, Steiner SA III, Meador MB (2017) Highly porous, rigid-rod polyamide aerogels with superior mechanical properties and unusually high thermal conductivity. *ACS Appl Mater Interfaces* 9(2):1801–1809
68. Guo H, Meador MAB, McCorkle L, Quade DJ, Guo J, Hamilton B, Cakmak M, Sprowl G (2011) Polyimide aerogels cross-linked through amine functionalized polyoligomeric silsesquioxane. *ACS Appl Mater Interfaces* 3(2):546–552
69. Meador MAB, Gyo H (2015) Porous cross-linked polyimide network. US Patent US9109088B2, 18 Aug 2015
70. Leventis N, Sotiriou-Leventis C, Dharani L, Winiarz J, Xing Y, Peng Z, Blum F, Bertino M (2014) Advanced polymer systems for defence applications: power generation, protection and sensing. <https://apps.dtic.mil/docs/citations/ADA614979>. Accessed 11 July 2019
71. Wang C, Xiong Y, Fan B, Yao Q, Wang H, Jin C, Sun Q (2016) Cellulose as an adhesion agent for the synthesis of lignin aerogel with strong mechanical performance, Sound-absorption and thermal Insulation. *Sci Rep* 6:32383
72. Bakierska M, Chojnacka A, Świętosławski M, Natkański P, Gajewska M, Rutkowska M, Molenda M (2017) Multifunctional carbon aerogels derived by sol–gel process of natural polysaccharides of different botanical origin. *Materials* 10(11):1336
73. Zou J, Liu J, Karakoti AS, Kumar A, Joung D, Li Q, Khondaker SI, Seal S, Zhai L (2010) Ultralight multiwalled carbon nanotube aerogel. *ACS Nano* 4(12):7293–7302
74. Wan W, Zhang R, Li W, Liu H, Lin Y, Li L, Zhou Y (2016) Graphene–carbon nanotube aerogel as an ultra-light, compressible and recyclable highly efficient absorbent for oil and dyes. *Environ Sci Nano* 3(1):107–113
75. Kabbour H, Baumann TF, Satcher JH, Saulnier A, Ahn CC (2006) Toward new candidates for hydrogen storage: high-surface-area carbon aerogels. *Chem Mater* 18(26):6085–6087

76. Wang L, Schütz C, Salazar-Alvarez G, Titirici MM (2014) Carbon aerogels from bacterial nanocellulose as anodes for lithium ion batteries. *RSC Adv* 4(34):17549–17554
77. Wu X, Zhong Y, Kong Y, Shao G, Cui S, Wang L, Jiao J, Shen X (2015) Preparation and characterization of C/Al₂O₃ composite aerogel with high compressive strength and low thermal conductivity. *J Porous Mater* 22(5):1235–1243
78. Moreno-Castilla C, Maldonado-Hódar FJ (2005) Carbon aerogels for catalysis applications: an overview. *Carbon* 43(3):455–465
79. Zhong Y, Zhou M, Huang F, Lin T, Wan D (2013) Effect of graphene aerogel on thermal behavior of phase change materials for thermal management. *Sol Energy Mater Sol Cells* 113:195–200
80. Yue C, Feng J, Feng J, Jiang Y (2016) Low-thermal-conductivity nitrogen-doped graphene aerogels for thermal insulation. *RSC Adv* 6(12):9396–9401
81. Zhang Q, Zhang F, Medarametla SP, Li H, Zhou C, Lin D (2016) 3D printing of graphene aerogels. *Small* 12(13):1702–1708
82. Li J, Li J, Meng H, Xie S, Zhang B, Li L, Ma H, Zhang J, Yu M (2014) Ultra-light, compressible and fire-resistant graphene aerogel as a highly efficient and recyclable absorbent for organic liquids. *J Mater Chem A* 2:2934–2941
83. Kim CH, Zhao D, Lee G, Liu J (2016) Strong, machinable carbon aerogels for high performance supercapacitors. *Adv Funct Mater* 26(27):4976–4983
84. Randall JP, Meador MAB, Jana SC (2011) Tailoring mechanical properties of aerogels for aerospace applications. *ACS Appl Mater Interfaces* 3:613–626. <https://doi.org/10.1021/am200007n>
85. Tabata M, Adachi I, Kawai H (2012) Recent progress in silica aerogel Cherenkov radiator. *Phys Procedia* 37:642–649. <https://doi.org/10.1016/j.phpro.2012.02.410>
86. He S, Li Z, Shi X et al (2015) Rapid synthesis of sodium silicate based hydrophobic silica aerogel granules with large surface area. *Adv Powder Technol* 26:537–541. <https://doi.org/10.1016/j.apt.2015.01.002>
87. Hebalkar N (2017) Improved method for producing carbon containing silica aerogel granules. Indian Patent IN290370, 7 Dec 2017
88. Śłosarczyk A (2017) Recent advances in research on the synthetic fiber based silica aerogel nanocomposites. *Nanomaterials* 7:44. <https://doi.org/10.3390/nano7020044>
89. Ramamurthi S, Ramamurthi M (1994) Aerogel matrix composite, US patent 5306555, 26 April 1994
90. Stepanian CJ, George G, Redouna B (2003) Aerogel composite with fibrous batting US Patent 7078359 B2, 18 July 2006
91. Frank D, Zimmermann A (1998) Aerogel composites, process for producing the same and their use US Patent US5789075A, 4 Aug 1998
92. Jia X, Wang J, Zhu X, Wang T, Yang F, Dong W, Wang G, Yang H, Wei F (2017) Synthesis of lightweight and flexible composite aerogel of mesoporous iron oxide threaded by carbon nanotubes for microwave absorption. *J Alloys Compd* 697:138–145
93. Riley BJ, Pierce AD, Chun J, Matyáš J, Lepry WC, Garn TG, Law JD, Kanatzidis MG (2014) Polyacrylonitrile-chalcogel hybrid sorbents for radioiodine capture. *Environ Sci Technol* 48:5832–5839
94. Ananthan Y, Sanghamitra KK, Hebalkar N (2017) Silica aerogels for energy conservation and saving. In: Raj B, Van de Voorde MH, Mahajan YR (eds) *Nanotechnology for energy sustainability*, vol 2. Wiley, Weinheim, pp 937–966
95. Brownlee D, Tsou P, Aléon J, Alexander CMD, Araki T, Bajt S, Baratta GA, Bastien R, Bland P, Bleuet P, Borg J (2006) Comet 81P/Wild 2 under a microscope. *Science* 314(5806):1711–1716
96. Gettle GL (2013) Blast effect mitigating assembly using aerogels. US Patent 8,590,437
97. Staggs SE (2009) Penetration resistance of polymer crosslinked aerogel armor subjected to projectile impact. Doctoral dissertation, Oklahoma State University
98. Clavell RC (2004) Inner cushions for helmets. US Patent 6,704,943

99. Sereboff JL (2015) Energy absorbing composition and impact and sound absorbing applications thereof. US Patent 8,987,367.B171
100. Sabri F, Werhner T, Hoskins J, Schuerger AC, Hobbs AM, Barreto JA, Britt D, Duran RA (2008) Thin film surface treatments for lowering dust adhesion on Mars rover calibration targets. *Adv Space Res* 41(1):118–128
101. Sabri F, Leventis N, Hoskins J, Schuerger AC, Sinden-Redding M, Britt D, Duran RA (2011) Spectroscopic evaluation of polyurea crosslinked aerogels, as a substitute for RTV-based chromatic calibration targets for spacecraft. *Adv Space Res* 47(3):419–427
102. Schenker P, Sword L, Ganino G, Bickler D, Hickey G, Brown D, Baumgartner E, Matthies L, Wilcox B, Balch T, Aghazarian H, Garrett M (1997) Lightweight rovers for Mars science exploration and sample return. In: *Proceedings of SPIE XVI Intelligent Robots and Computer Vision Conference* 3208:24–36. <https://doi.org/10.1117/12.290300>
103. Fesmire JE, Augustynowicz SD, Rouanets S (2002) Aerogel beads as cryogenic thermal insulation system. In: *AIP conference proceedings*, vol 613, no 1, AIP, pp 1541–1548, May 2002
104. Fesmire JE (2006) Aerogel insulation systems for space launch applications. *Cryogenics* 46(2–3):111–117
105. Kozicki J, Kozicka J (2011) Human friendly architectural design for a small Martian base. *Adv Space Res* 48(12):1997–2004
106. Harvey AR, Ellertson JW (2003) Rocket motor insulation containing hydrophobic particles. US Patent 6,606,852
107. Frame BJ, Hansen JG (2004) Fire blocking blanket for protection of stored ammunition. In *thirty-first department of defense explosives safety seminar proceedings*, San Antonio, August 2004
108. Hansen JGR, Frame BJ (2008) Flame penetration and burn testing of fire blanket materials. *Fire Mater Int J* 32(8):457–483
109. Riemer NM, Johnson D, Kohn B, Matheson S, Williams C, Gillespie B (2006) Designing transportable collectively protective shelters for thermal efficiency. Air Armament Center Eglin (AFB) FL
110. Biszko L (2011) Net Zero Plus JCTD results: evaluation of energy saving technologies for expeditionary shelters. Army Natick soldier research development and engineering center, Natick
111. Powell MR, Hong SH, Paulsen S (2006) Recirculating thermocatalytic air purifier for collective protection. Mesosystems Technology Inc, Kennewick
112. Ruffner JA, Clem PG, Tuttle BA, Brinker CJ, Sriram CS, Bullington JA (1998) Uncooled thin film infrared imaging device with aerogel thermal isolation: deposition and planarization techniques. *Thin Solid Films* 332(1–2):356–361
113. Duong HM, Xie ZC, Wei KH, Nian NG, Tan K, Lim HJ (2017) Thermal jacket design using cellulose aerogels for heat insulation application of water bottles. *Fluids* 2(64). <https://doi.org/10.3390/fluids204006>
114. Logan RS, Frazier JF (2012) Container for transporting compressed gas cylinders, US Patent 8,210,388
115. Bheekhun N, Talib A, Rahim A, Hassan MR (2018) Tailoring aerogel for thermal spray applications in aero-engines: a screening study. *Adv Mater Sci Eng* 2018:1
116. Xu B, Ding J, Feng L, Ding Y, Ge F, Cai Z (2015) Self-cleaning cotton fabrics via combination of photocatalytic TiO₂ and superhydrophobic SiO₂. *Surf Coat Technol* 262:70–76
117. Tang HH, Orndoff ES, Trevino LA (2006) Thermal performance of space suit elements with aerogel insulation for moon and Mars exploration (No. 2006-01-2235). SAE Technical Paper
118. Nuckols ML, Hyde DE, Wood-putnam JL et al (2009) Design and evaluation of cold water diving garments using super-insulating aerogel fabrics. *Proc Am Acad Underw Sci 28th Symp* 7:237–244
119. Shaïd A, Wang L, Islam S et al (2016) Preparation of aerogel-eicosane microparticles for thermoregulatory coating on textile. *Appl Therm Eng* 107:602–611. <https://doi.org/10.1016/j.applthermaleng.2016.06.187>

120. Shaid A, Wang L, Fergusson SM, Padhye R (2018) Effect of aerogel incorporation in PCM-containing thermal liner of firefighting garment. *Cloth Text Res J* 1–14. <https://doi.org/10.1177/0887302X18755464>
121. Yang G, Liu X, Lipik V (2018) Evaluation of silica aerogel-reinforced polyurethane foams for footwear applications. *J Mater Sci* 53(13):9463–9472
122. Zrim PK, Mekjavic IB, Rijavec T (2016) Properties of laminated silica aerogel fibrous matting composites for footwear applications. *Text Res J* 86(10):1063–1073. <https://doi.org/10.1177/0040517515591781>
123. Jensen KI, Schultz JM, Kristiansen FH (2004) Development of windows based on highly insulating aerogel glazings. *J Non-Cryst Solids* 350:351–357
124. Buratti C, Moretti E, Belloni E (2016) Aerogel plasters for building energy efficiency. In: *Nano and biotech based materials for energy building efficiency*. Springer, Cham, pp 17–40
125. Nocentini K, Achard P, Biwolé P (2018) Hygro-thermal properties of silica aerogel blankets dried using microwave heating for building thermal insulation. *Energy Buildings* 158:14–22
126. Martinez RG, Goiti E, Reichenauer G, Zhao S, Koebel M, Barrio A (2016) Thermal assessment of ambient pressure dried silica aerogel composite boards at laboratory and field scale. *Energy Buildings* 128:111–118
127. Worden PW, STEP Team (2007) STEP payload development. *Adv Space Res* 39(2):259–267
128. Wang S, Torii R, Vitale S (2001) Silica aerogel vibration testing. *Class Quantum Gravit* 18(13):2551
129. Matyáš J, Canfield N, Sulaiman S, Zumhoff M (2016) Silica-based waste form for immobilization of iodine from reprocessing plant off-gas streams. *J Nucl Mater* 476:255–261
130. Coleman SJ, Coronado PR, Maxwell RS, Reynolds JG (2003) Granulated activated carbon modified with hydrophobic silica aerogel-potential composite materials for the removal of uranium from aqueous solutions. *Environ Sci Technol* 37(10):2286–2290
131. Aravind PR, Shajesh P, Mukundan P, Pillai PK, Warriar KGK (2008) Non-supercritically dried silica-silica composite aerogel and its possible application for confining simulated nuclear wastes. *J Sol-Gel Sci Technol* 46(2):146–151
132. Subrahmanyam KS, Sarma D, Malliakas CD, Polychronopoulou K, Riley BJ, Pierce DA, Chun J, Kanatzidis MG (2015) Chalcogenide aerogels as sorbents for radioactive iodine. *Chem Mater* 27:2619–2626. <https://doi.org/10.1021/acs.chemmater.5b00413>
133. Chen L, Feng S, Zhao D, Chen S, Li F, Chen C (2017) Efficient sorption and reduction of U(VI) on zero-valent iron-polyaniline-graphene aerogel ternary composite. *J Colloid Interface Sci* 490:197–206
134. Lentz RE, Adams DC, Norton J, Russell KB (1983) Civil disturbance countermeasures – chemical (No. ARCSL-SP-83020). Army armament research and development command aberdeen proving ground md chemical systems lab
135. Han Q, Yang L, Liang Q, Ding M (2017) Three-dimensional hierarchical porous graphene aerogel for efficient adsorption and preconcentration of chemical warfare agents. *Carbon* 122:556–563
136. Dolai S, Bhunia SK, Beglaryan SS, Kolusheva S, Zeiri L, Jelinek R (2017) Colorimetric polydiacetylene-aerogel detector for volatile organic compounds (VOCs). *ACS Appl Mater Interfaces* 9(3):2891–2898
137. Hotaling SP (1993) The aerogel mesh contamination collector (In-House report No. RL-TR-93-148). Rome lab, Airforce material Command
138. Rao AV, Hegde ND, Hirashima H (2007) Absorption and desorption of organic liquids in elastic superhydrophobic silica aerogels. *J Colloid Interface Sci* 305(1):124–132
139. Wang J, Wang H (2018) Facile synthesis of flexible mesoporous aerogel with superhydrophobicity for efficient removal of layered and emulsified oil from water. *J Colloid Interface Sci* 530:372–382
140. Wu ZY, Li C, Liang HW, Zhang YN, Wang X, Chen JF, Yu SH (2014) Carbon nanofiber aerogels for emergent cleanup of oil spillage and chemical leakage under harsh conditions. *Sci Rep* 4:4079

141. Zhi L, Zuo W, Chen F, Wang B (2016) 3D MoS₂ Composition Aerogels as Chemosensors and Adsorbents for Colorimetric Detection and High-Capacity Adsorption of Hg²⁺. *ACS Sustain Chem Eng* 4:3398–3408. <https://doi.org/10.1021/acssuschemeng.6b00409>
142. Farmer JC, Richardson JH, Fix DV, Thomson SL, May SC (1996) Desalination with carbon aerogel electrodes (No. UCRL-ID-125298-REV-1). Bechtel National Inc, San Francisco
143. Ren F, Li Z, Tan WZ, Liu XH, Sun ZF, Ren PG, Yan DX (2018) Facile preparation of 3D regenerated cellulose/graphene oxide composite aerogel with high-efficiency adsorption towards methylene blue. *J Colloid Interface Sci* 532:58–67
144. Liu X, Wang J, Dong Y, Li H, Xia Y, Wang H (2018) One-step synthesis of Bi₂MoO₆/reduced graphene oxide aerogel composite with enhanced adsorption and photocatalytic degradation performance for methylene blue. *Mater Sci Semicond Process* 88:214–223
145. Yao Q, Fan B, Xiong Y, Jin C, Sun Q, Sheng C (2017) 3D assembly based on 2D structure of cellulose nanofibril/graphene oxide hybrid aerogel for adsorptive removal of antibiotics in water. *Sci Rep* 7:45914
146. Zhao J, Zhang X, He X, Xiao M, Zhang W, Lu C (2015) A super biosorbent from dendrimer poly(amidoamine) – grafted cellulose nanofibril aerogels for effective removal of Cr(VI). *J Mater Chem A* 3:14703
147. Andjelkovic I, Tran DN, Kabiri S, Azari S, Markovic M, Losic D (2015) Graphene aerogels decorated with α -FeOOH nanoparticles for efficient adsorption of arsenic from contaminated waters. *ACS Appl Mater Interfaces* 7(18):9758–9766
148. Jang J, Lee DS (2018) Three-dimensional barium-sulfate-impregnated reduced graphene oxide aerogel for removal of strontium from aqueous solutions. *J Nucl Mater* 504:206–214
149. Chen L, Feng S, Zhao D et al (2017) Efficient sorption and reduction of U(VI) on zero-valent iron-polyaniline- graphene aerogel ternary composite. *J Colloid Interface Sci* 490:197–206. <https://doi.org/10.1016/j.jcis.2016.11.050>
150. Sui Z, Meng Q, Zhang X, Ma R, Cao B (2012) Green synthesis of carbon nanotube–graphene hybrid aerogels and their use as versatile agents for water purification. *J Mater Chem* 22(18):8767–8771
151. Kumar DK, Ganesan AV, Swaminathan S, Sharma NN, Mittal RK (2013) A novel MEMS device for selective surface adsorption of lead (II) ions from blood using carbon aerogel. In ASME 2013 international mechanical engineering congress and exposition (pp V015T16A009–V015T16A009). American Society of Mechanical Engineers, November 2013
152. Cantin M, Casse M, Koch L, Jouan R, Mestreau P, Roussel D, Bonnin F, Moutel J, Teichner SJ (1974) Silica aerogels used as Cherenkov radiators. *Nucl Inst Methods* 118(1):177–182
153. Blyth D, Alarcon R, Begag R, Holmes J, Stryker J (2018) Performance of new silica aerogels in a threshold Cherenkov counter. arXiv preprint arXiv:1801.04047
154. Poelz G, Riethmüller R (1982) Preparation of silica aerogel for Cherenkov counters. *Nucl Instrum Methods Phys Res* 195(3):491–503
155. Merzbacher C, Limpapis K, Brenstein R, Rolinson D, Homrighaus Z, Berry A (2001) Long duration infrared-emitting material. US Patent WO2001/016258, 8 Mar 2001
156. Cincotti KD, Kracker TJ (2012) Visual camouflage with thermal and RADAR suppression and methods of making the same. US Patent 8340358 B2, 25 Dec 2012
157. Truett III LF (2001/2002) An insight into aerogels-past present and future, joint technical coordinating group on aircraft survivability, Arlington
158. Singh S, Tripathi P, Bhatnagar A, Patel CRP, Singh AP, Dhawan SK, Bipin KG, Srivastava ON (2015) A highly porous, light weight 3D sponge like graphene aerogel for electromagnetic interference shielding applications. *RSC Adv* 5(129):107083–107087. <https://doi.org/10.1039/c5ra19273k>
159. Hao C, Wang B, Wen F, Mu C, Xiang J, Li L, Liu Z (2018) Superior microwave absorption properties of ultralight reduced graphene oxide/black phosphorus aerogel. *Nanotechnology* 29(23):235604
160. Ali I, Chen L, Huang Y, Song L, Lu X, Liu B, Zhang L, Zhang J, Hou L, Chen T (2018) Humidity-responsive gold aerogel for real-time monitoring of human breath. *Langmuir* 34:4908–4913

161. Yan W, Harley-trochimczyk A, Long H, Chan L, Pham T, Hu M (2017) Conductometric gas sensing behavior of WS₂ aerogel. *FlatChem* 5:1–8
162. Gao B, Yuan G, Ren L (2018) Polydiacetylene-functionalized alumina aerogels as visually observable sensing materials for detecting VOCs concentration. *J Mater Sci* 53(9):6698–6706
163. Lin Y, Ehlert GJ, Bukowsky C, Sodano HA (2011) Superhydrophobic functionalized graphene aerogels. *ACS Appl Mater Interfaces* 3(7):2200–2203
164. Chung VP, Yip MC, Fang W (2015) Resorcinol–formaldehyde aerogels for cmos-mems capacitive humidity sensor. *Sensors Actuators B Chem* 214:181–188
165. Kang TJ, Kim T, Jang EY, Im H, Lepro-Chavez X, Ovalle-Robles R, Oh J, Kozlov ME, Baughman RH, Lee HH, Kim YH (2014) Nanotube aerogel sheet flutter for actuation, power generation, and infrasound detection. *Sci Rep* 4:6105
166. Hebalkar N, Arabale G, Sainkar SR, Pradhan SD, Mulla IS, Vijayamohan K, Ayyub P, Kulkarni SK (2005) Study of correlation of structural and surface properties with electrochemical behaviour in carbon aerogels. *J Mater Sci* 40(14):3777–3782
167. Yue Y, Liu N, Ma Y, Wang S, Liu W, Luo C, Zhang H, Cheng F, Rao J, Hu X, Gao Y, Su J (2018) Highly self-healable 3D microsupercapacitor with MXene–graphene composite aerogel. *ACS Nano* 12(5):4224–4232
168. Guo F, Jiang Y, Xu Z, Xiao Y, Fang B, Liu Y, Gao W, Zaho P, Wang H, Gao C (2018) Highly stretchable carbon aerogels. *Nat Commun* 9(1):881
169. Zhu C, Liu T, Qian F, Han TYJ, Duoss EB, Kuntz JD, Spadaccini CM, Worsley MA, Li Y (2016) Supercapacitors based on three-dimensional hierarchical graphene aerogels with periodic macropores. *Nano Lett* 16(6):3448–3456
170. Xu Z, Zhang Y, Wang Y, Zhan L (2018) Flower-like nanostructured V₃S₄ grown on three-dimensional porous graphene aerogel for efficient oxygen reduction reaction. *Appl Surf Sci* 450:348–355
171. Elumeeva K, Fechler N, Fellingner TP, Antonietti M (2014) Metal-free ionic liquid-derived electrocatalyst for high-performance oxygen reduction in acidic and alkaline electrolytes. *Mater Horiz* 1(6):588–594
172. Wang G, Hou S, Yan C, Lin Y, Liu S (2017) Three-dimensional porous vanadium nitride nanoribbon aerogels as Pt-free counter electrode for high-performance dye-sensitized solar cells. *Chem Eng J* 322:611–617
173. Aliev AE, Oh J, Kozlov ME, Kuznetsov AA, Fang S, Fonseca AF, Ovalle R, Zhang M (2009) Giant-stroke, superelastic carbon nanotube aerogel muscles. *Science* 323(5921):1575–1578
174. Hotaling SP (1993) Ultra-low density aerogel mirror substrates (No. RL-TR-93-42). Rome Laboratory, Rome
175. Kim J, Kwon J, Kim M, Do J, Lee D, Han H (2016) Low-dielectric-constant polyimide aerogel composite films with low water uptake. *Polym J* 48(7):829–834
176. Lee BI, Chou K (1996) Processing effect on structural changes of high acid-catalysed silica gel. *J Mater Sci* 31(5):1367–1373
177. Meador MAB, Wright S, Sandberg A, Nguyen BN, Keuls FWV, Mueller CH, Rodríguez-Solis R, Miranda FA (2012) Low dielectric polyimide aerogels as substrates for lightweight patch antennas. *ACS Appl Mater Interfaces* 4(11):6346–6353
178. Ullah MH, Mahadi WNL, Latef TA (2015) Aerogel poly (butylene succinate) biomaterial substrate for RF and microwave applications. *Sci Rep* 5:12868



Microwave Materials for Defense and Aerospace Applications

5

J. Varghese, N. Joseph, H. Jantunen, S. K. Behera, H. T. Kim, and M. T. Sebastian

Contents

Introduction	167
Dielectric Resonators	168
Ceramic Substrates/Packages and Inks for Military and Aerospace Applications	172
HTCC and LTCC Substrate/Packages	173
Ultralow Temperature Co-Fired Ceramic Packages	177
Dielectric Inks/Paints	178
Polymer-Ceramic Composites for Microwave Substrate Applications	179
Rubber-Ceramic Composites for Flexible and Stretchable Applications	185
Radomes	187
Ceramic-Based Radomes	189
Polymer-Based Radome Materials	190
EMI Shielding Materials for Military and Aerospace Applications	191
EMI Shielding Mechanism	192
EMI Shielding Materials	192
Applications of Microwave Materials	197
Antennas	197
Dielectric Resonator Filters	204
Dielectric Resonator Oscillators	205
Conclusion	205
References	206

J. Varghese (✉) · N. Joseph · H. Jantunen
Microelectronics Research Unit, University of Oulu, Oulu, Finland
e-mail: jobin.var@gmail.com; ninajoseph11@gmail.com; heli.jantunen@oulu.fi

S. K. Behera
Department of Electronics and Communication Engineering, NIT Rourkela, Rourkela, India
e-mail: skbehera@nitrkl.ac.in

H. T. Kim · M. T. Sebastian
Korean Institute for Ceramic Engineering and Technology, Jinju-si, South Korea
e-mail: hytek@kicet.re.kr; mailadils@yahoo.com

Abstract

Microwave materials are fundamental building blocks for defense and aerospace applications, which have been used as dielectric resonators, radomes, multilayer packages, electromagnetic shield, and so on. These materials and devices made of them should survive in harsh environmental conditions, and hence the availability of suitable materials is limited. Microwave materials are used for signal propagation as well as shielding unwanted signals in military and aerospace applications depending on their properties. The essential material characteristics required for signal propagation applications are very low relative permittivity, low dielectric loss, low-temperature variation of relative permittivity/resonant frequency, and low coefficient of thermal expansion. The materials used for these applications are in the form of substrates, foams, inks, bulk resonators, high-temperature co-fired ceramics (HTCC), low-temperature co-fired ceramics (LTCC), printed circuit boards (PCBs), etc. The materials should absorb or reflect microwaves for electromagnetic interference (EMI) shielding applications. The present chapter gives an overview of microwave material requirements, properties, and their applications in antennas, filters, and oscillators in the military and aerospace sector.

Keywords

Microwave materials · HTCC · LTCC · ULTCC · EMI Shielding · Composites · Rubber-Ceramics · PCBs · Dielectric Resonators · Microstrip antenna · Dielectric Resonator Antenna · Bandwidth · Metamaterials · Oscillator · Filter · Reflection Coefficient Gain · Beamwidth

Abbreviations

5G	Fifth generation
AESA	Active electronically steered antennas
BoPET	Biaxially oriented poly-ethylene terephthalate
BSE	Bore sight errors
CTE	Coefficients of thermal expansion
DR	Dielectric resonator
DRA	Dielectric resonator antenna
DRO	Dielectric resonator oscillator
EBG	Electromagnetic bandgap
ECM	Electronic countermeasures
EMI	Electromagnetic interference
EMP	Electromagnetic pulse
ESD	Electrostatic discharge
GPS	Global positioning systems
HARP	Halpern anti-radiation paint
HPSN	Hot-pressed silicon nitride

HTCC	High-temperature co-fired ceramics
HTPAHs	Heat-treated polyaromatic hydrocarbons
ICs	Integrated circuits
IoT	Internet of Things
IT	Information technology
ITS	Intelligent transport system
LTCC	Low-temperature co-fired ceramics
MCM	Multi-chip module
MCMB	Mesocarbon microbead
MICs	Microwave integrated circuits
MLC	Multilayer capacitor
MMICs	Monolithic microwave integrated circuits
MP	Melting point
MWCNT	Multiwall carbon nanotube
NRI	Negative refractive index
PCB	Printed circuit board
POE	Polyolefin elastomer
PPCP	Polypropylene random copolymer
PTFE	Polytetrafluoroeten
RBSN	Reaction-bonded silicon nitride
RF	Radio-frequency
RFI	Radio-frequency interference
RFID	Radio-frequency identification
SCFS	Slip-cast fused silica
SiP	System in package
SOP	System on package
TC	Thermal conductivity
UWB	Ultra-wideband
Wi-Fi	Wireless fidelity
WiMAX	Worldwide interoperability for microwave access
WLAN	Wireless local area network

Introduction

Microwave dielectric materials designed for wireless communication have been a booming area of growth. Microwave materials are fundamental building blocks for military and aerospace applications, which have been used as dielectric resonators, radomes, substrates, inks, multilayer packages, electromagnetic shield, etc. However, the stringent conditions and property requirements for the military and aerospace applications limit the availability of suitable materials. These materials and devices made of them should survive in harsh environmental conditions. Microwave materials can be used for signal propagation as well as shielding unwanted signals in defense and aerospace application depending on their properties. The properties which control the

material requirements for the signal propagation applications are very low relative permittivity to increase the signal speed; low dielectric loss to improve the selectivity as well as speed of the device; a low-temperature variation of relative permittivity/resonant frequency for the reliable operation; and low coefficient of thermal expansion to prevent failure during the harsh environmental conditions. The materials used for these applications are in the form of bulk resonators; microwave substrates such as HTCC, LTCC, PCBs; etc. There is a growing demand for miniaturized and lightweight antennas with the reduction in the device size, platform, and budgets. The military and aerospace applications include different types of antennas such as microstrip antennas, dielectric resonator antennas, textile antenna, etc. Microwave materials, especially with dielectric constants of 2.2, 3.2, and 4.4, are used for the design of microwave filters as well as fractal antennas, ultra-wideband (UWB) antennas, reconfigurable microstrip antennas, etc. These antennas are suitable for modern communication systems (viz., Wi-Fi, WiMAX, Bluetooth, etc.). The microwave/millimeter-wave shielding materials are being used for EMI reduction, antenna pattern shaping, radar cross section and stealth technology. Presently, the demand for these EMI materials is increasing because of the growing number of warfare gadgets and space vehicles. Most of these applications used classified frequency ranges with integrated multiple antennas which need absorber materials to maintain the peak performance by reducing interference from nearby objects such as metal structures and other surrounded electronics. Electronic devices operating at high frequencies emit high-frequency noise which will cause resonance at specific frequencies when put inside the enclosure and hence hinder the device performance. Materials that are lossy (conductive/dielectric/magnetic loss) at these frequencies can attenuate the incoming electromagnetic interference. The present chapter gives an overview of microwave material requirements, properties, and their applications in antennas, filters, or oscillators in the defense and aerospace sector.

Dielectric Resonators

A dielectric resonator is an electromagnetic device that exhibits resonance for a short range of frequencies. It is similar to that of a cylindrical metallic waveguide except that the boundary is defined by a substantial change in permittivity rather than by a conductor. Dielectric resonator (DR) is an unmetalled piece of the dielectric puck, which functions as a resonant cavity using reflections at the dielectric-air interface. The critical properties required for a dielectric resonator are low dielectric loss tangent (high-quality factor Q ; $Q \sim 1/\tan \delta$), suitable relative permittivity (ϵ_r) (high permittivity for miniaturization and low permittivity for mm wave frequency communication and high-speed signal transmission), and near-zero temperature coefficient of resonant frequency (τ_f). A dielectric resonator that satisfies all these three properties simultaneously is difficult to realize in a particular material. In the early microwave systems, bulk metallic cavities were used as resonators but were huge in size and not integrable with microwave integrated circuits (MICs). Although the stripline resonator is small and integrable in MIC, it has a poor quality factor with a poor temperature stability resulting in the instability of the circuit. Hence, the

importance of DRs, are due to easy integration in MICs with low loss and thermally stable frequency. DRs are important components for the manufacture of filters, oscillators, and antennas. They offer a size-reducing design alternative to bulky waveguide filters and low-cost alternatives for electronic oscillator frequency-selective limiter and antennas. The device performance is closely related to material properties. In addition to cost and size, other advantages that dielectric resonators possess over conventional metal cavity resonators are lower weight, material availability, and ease of manufacturing.

Richtmeyer theoretically predicted that a piece of dielectric with regular geometry and high ϵ_r can confine electromagnetic energy within itself but still be prone to energy loss due to radiation [1]. It was found that through the total multiple internal reflections, a piece of the high ϵ_r dielectric can confine microwave energy at a few discrete frequencies, provided the energy is fed in the appropriate direction. If the transverse dimensions of the sample are comparable to the wavelength of the microwave, then certain field distributions or modes will satisfy Maxwell's equations and boundary conditions. The reflection coefficient approaches unity as ϵ_r approaches infinity. In the microwave frequency range, free space wavelength is in centimeters, and hence the wavelength inside the dielectric will be in millimeters only when the value of ϵ_r is in the range 20–100. To get resonance, dimensions of the dielectric must be of the same order (in millimeters). Still larger ϵ_r gives higher confinement of energy, reduced radiation loss, and better miniaturization. However, high ϵ_r will result in higher dielectric losses because of inherent material properties. The size of a DR is considerably smaller than the size of an empty resonant cavity operating at the same frequency, provided the relative permittivity (ϵ_r) of the material is substantially higher than unity. Higher ϵ_r shrinks overall circuit/device size proportional to $1/(\epsilon_r)^{1/2}$. For example, a circuit is compressed by a factor of six when a high Q ceramic with $\epsilon_r = 36$ is substituted for a high Q air cavity $\epsilon_r = 1$. The shape of a DR is usually a solid cylinder but can also be tubular, spherical, and parallelepiped. A commonly used resonant mode of a cylindrical DR is $TE_{01\delta}$.

At the resonant frequency, electromagnetic fields inside a resonator store energy equally in electric and magnetic fields. When ϵ_r is about 40, more than 95% of the stored electrical energy and over 60% stored magnetic energy are located within the dielectric cylinder. The remaining energy is distributed in the air around the resonator, decaying rapidly with distance away from the resonator boundary. This is of great advantage since it enables one to couple microwave power easily to the DR by matching the field pattern of the coupling elements to that of the DR. The DR can be incorporated into a microwave network by exciting it with, e.g., microstrip transmission lines. The distance between the resonator and the microstrip conductor determines the amount of coupling. To prevent losses due to radiation, the entire device is usually enclosed in a metallic shielding box. High Q minimizes circuit insertion losses and can be used as a highly selective circuit. Besides, high Q suppresses the electrical noise in oscillator devices. When exposed to free space, a DR can also radiate microwave energy when it is fed suitably and can be used as efficient radiators, called dielectric resonator antennas (DRA).

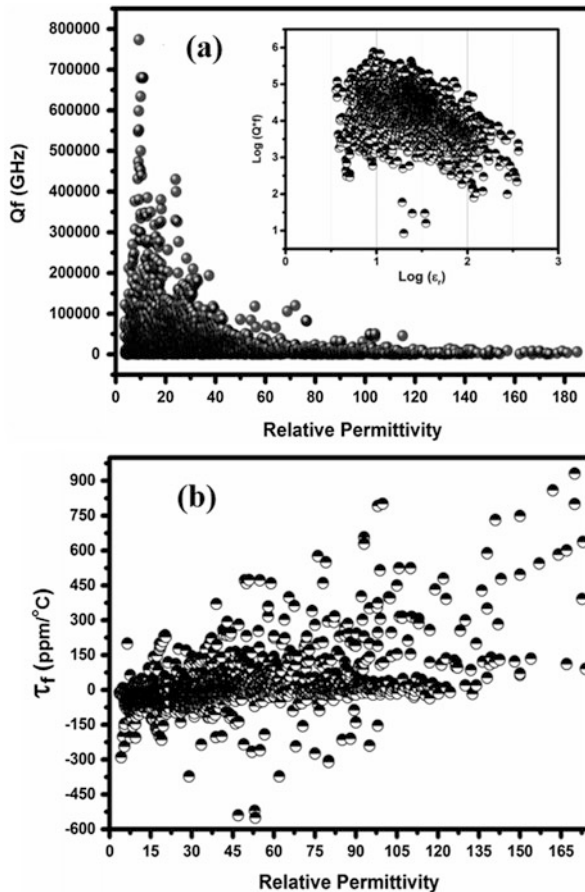
The term dielectric resonator (DR) first appeared in 1939 when Richtmeyer showed that suitably shaped dielectric blocks could function as a microwave resonator; however, it took more than 20 years to generate further interest in DRs and to verify Richtmeyer's prediction experimentally. In the early 1960s, Okaya and Barash rediscovered DRs while working on rutile single crystals [2]. They measured the permittivity and Q of single crystals rutile at room temperature and down to 50 K in the microwave frequency range. In the early 1960s, Cohen and his co-workers performed extensive theoretical and experimental work on DRs [3]. Rutile ceramics that had an anisotropic permittivity of about 100 were used for their experiments, but rutile (TiO_2) has unfortunately, ($+450 \text{ ppm}/^\circ\text{C}$) resonant frequency stability that prevented its commercial exploitation. The first microwave filter using TiO_2 ceramics was reported by Cohen in 1968, but it was not useful for applications because of its high ϵ_r and frequency instability with temperature. A real breakthrough in dielectric resonator ceramic technology occurred in the early 1970s when the first temperature-stable low-loss barium tetra titanate (BaTi_4O_9) ceramic was developed by Masse et al. [4]. Later, barium nano-titanate ($\text{Ba}_2\text{Ti}_9\text{O}_{20}$) with the improved performance was reported by Bell Laboratories. The next breakthrough came from Japan when Murata Manufacturing Company produced $(\text{Zr},\text{Sn})\text{TiO}_4$ ceramics [5]. They offered adjustable compositions so that temperature coefficients could be varied between $+10$ and $-10 \text{ ppm}/^\circ\text{C}$. Later, in 1975, Wakino et al. realized the miniaturization of the DR-based filters and oscillators [6]. Since then extensive theoretical and experimental work and development of several DR materials has occurred [7]. This early work resulted in the actual use of DRs as microwave components. Commercial production of DRs started in the early 1980s. About 4000 low-loss ceramic dielectrics are reported in the literature [8]. However, only a limited number of dielectric ceramic materials are useful for applications in the electronic industry. Especially ceramics with low permittivity are feasible for millimeter-wave communications and as substrates for microwave integrated circuits. The most common application area for the ceramics with medium permittivity in the range 25–50 is satellite communication and cell phone base stations. High- ϵ_r materials are used in mobile phones where miniaturization of components is very important. For millimeter-wave applications, temperature-stable, low-permittivity, and high- Q (low-loss) substrates are required for high-speed signal transmission with minimum attenuation. Table 1 gives a list of useful resonator materials for possible applications in space and defense. It may be noted that there are several factors such as porosity, grain boundaries, grain size, crystal defects, micro cracks, etc. that may affect the dielectric properties. For an ideal material, the main reason for the loss is due to the interaction of the microwaves with the phonons. One can tailor the properties of a particular material to some extent by suitable doping, substitution, additives, or mixture formation. The quality factor (Q) decreases with increasing frequency as shown in Fig. 1a, but the Qf remains nearly constant. However, smaller samples inherently contain less defects and shows higher Qf factor. The Qf decreases as temperature increases due to increase in lattice vibration. In general, the materials having high relative permittivity show a positive τ_f as

Table 1 Shows some of the important DR materials useful for applications in space and defense [8].

Material	Sintering temp	ϵ_r	Qf GHz	τ_f
Fused silica		3.7	122,100	–
SiO ₂	1650	3.8	80,400	–16
(Cordierite) Mg ₂ Al ₄ Si ₅ O ₁₈ + 7 wt.% Yb ₂ O ₃	1420	4.9	112,500	
Li ₂ MgSiO ₄ + 1 wt% LBS	925	5.5	114,300	
Willemite (Zn ₂ SiO ₄)	1340	6.6	219,000	–61
Mg ₂ SiO ₄ Fosterite	1450	6.8	270,000	–67
MgAl ₂ O ₄	1650	8.5	10,500	–63
Zn ₂ SiO ₄ + 11 wt% TiO ₂	1200	9.1	150,800	–1
Al ₂ O ₃	1550	10.1	680,000	–60
Mg ₄ Ta ₂ O ₉	1250	12.0	347,000	–65
0.895Al ₂ O ₃ –0.105TiO ₂	1350	12.5	340,000	2
0.83ZnAl ₁₂ O ₄ –0.17TiO ₂	1410	12.6	100,200	0
MgTiO ₃	1350	16.1	289,400	–54
0.94(Mg _{0.95} Zn _{0.05}) ₂ TiO ₄ –0.06SrTiO ₃	1270	18.0	125,600	0
0.77(0.5ZnAl ₂ O ₄ –0.5TiO ₂)–0.23MgTiO ₃	1390	18.7	190,000	–2
0.96 mg(Zr _{0.05} Ti _{0.95})O ₃ –0.04SrTiO ₃		20.8	257,000	0
Ba(Mg _{1/3} Ta _{1/3})O ₃	1650	25.0	430,000	0
Ba(Zn _{1/3} Ta _{2/3})O ₃		28.0	168,000	1
Ba(Zn _{1/3} Ta _{2/3})O ₃ + 1 wt% V ₂ O ₃	1600	28.4	236,000	0
0.7Ba(Co _{1/3} Nb _{2/3})O ₃ –0.3Ba(Zn _{1/3} Nb _{2/3})O ₃	1400	34.5	97,000	0
Ba ₂ Ti ₉ O ₂₀		37.0	57,000	0
.95Ba(Zn _{1/3} Nb _{2/3})O ₃ –0.05Ba(Ga _{1/2} Ta _{1/2})O ₃		38.0	102,900	19
Zn _{0.95} Co _{0.05} Ta ₂ O ₆		38.5	112,000	11
(Zr _{0.8} Sn _{0.2})TiO ₄		40.0	53,000	0
0.4LaAlO ₃ –0.6SrTiO ₃	1680	42.1	83,000	8
Bi ₁₂ SiO ₂₀	800	43.0	86,800	–10
0.7CaTiO ₃ –0.3NdAlO ₃	1450	45.0	44,000	0
0.4ZnNb ₂ O ₆ –0.6TiO ₂	1125	46.2	48,000	–1
0.66CaTiO ₃ –0.34(La _{0.5} Nd _{0.5})GaO ₃	1540	49.0	43,000	0
0.48Nd(Zn _{1/2} Ti _{1/2})O ₃ –0.52SrTiO ₃	1350	54.2	84,000	0
CaTi _{0.7} (Al _{1/2} Nb _{1/2}) _{0.3} O ₃	1450	65.4	19,300	–2
Ba _(2-x) Sm _(4 + 2/3x) Ti ₉ O ₂₈ (x = 0.2)	1370	74.8	10,900	2
Ba _{6-3x} Sm _{8 + 2x} Ti ₁₈ O ₅₄	1300	91.0	11,000	3
TiO ₂ + 0.05 Mol% Fe ₂ O ₃	1500	102.0	50,100	400
Sr ₃ Ce ₂ Ti ₆ O ₁₉ (Sr _{1-3x/2} Ce _x TiO ₃ x = 0.333)	1350	123.0	10,000	392

shown in Fig. 1b. The resonant frequency of the sample depends on the relative permittivity and dimensions. The higher the permittivity, the smaller the resonant frequency and higher dimensions give smaller resonant frequency. Hence, for very high-frequency applications such as mm-wave applications, materials with lower permittivity and smaller dimensions are required.

Fig. 1 Plot of (a) Q_f and (b) τ_f versus permittivity



Ceramic Substrates/Packages and Inks for Military and Aerospace Applications

The military and aerospace sector is one of the fastest-growing industries in the world. The rapid growth in military and aerospace telecommunication applications requires precise device performance, which is one of the extremely important factors as compared to the general telecommunication applications. Most of the military and aerospace equipment are working in the most hostile areas of the earth and in challenging environments such as battlefields, on land, under water, and in air. Most of these specific applications are in the microwave/millimeter-wave frequency ranges. Hence, high-quality ceramic substrate/packages with good thermal and mechanical stability along with excellent microwave/millimeter-wave dielectric properties are commonly required for these applications. IBM first utilized a multi-chip module (MCM) in its high-end system 370 in the early 1980s. Later on, 50 mm

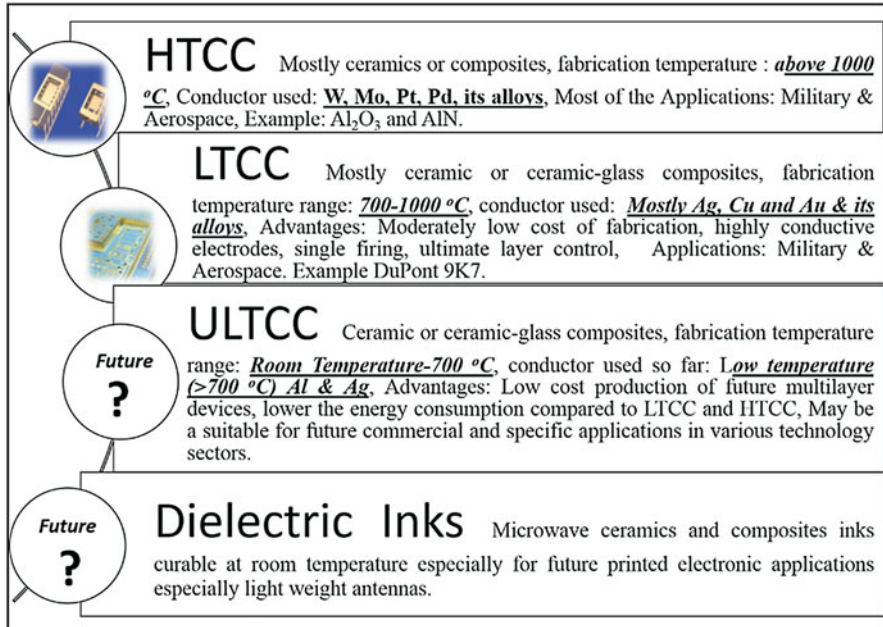


Fig. 2 Past, present, and future trends of ceramic processing technology

square, nine-chip MCM replaced 700 of the previous generation module. Multilayer capacitor (MLC) products are still made today in the same way as the original RCA products of the 1950s and 1960s [9–11]. From a historical perspective, guided electromagnetic wave propagation in dielectric media received much attention in the early days of microwave research.

Later, the technological growth demanded high-temperature co-fired ceramics (HTCC), low-temperature co-fired ceramics (LTCC), ultralow temperature ceramics (ULTCC), and very recently inks/paints [7, 12]. Among these ceramic processing technologies, HTCC and LTCC substrate or packages are the key products of air traffic, defense, and space applications. However, ULTCC and ceramic inks are in the growing stage of research for these application areas. In this section, we discuss the commercially useful and suitable HTCC, LTCC, and ULTCC substrates/packages and dielectric inks for military and aerospace applications such as active electronically steered antennas (AESA) with hundreds or even thousands of T/R modules operating in different platforms and systems [13, 14]. Figure 2 shows the past, present, and future trends of ceramic processing based on the ceramic technology growth.

HTCC and LTCC Substrate/Packages

The HTCC (fabrication temperature above 1000 °C)/LTCC (fabrication temperature ranges 700–1000 °C) materials used as microwave substrates or packages in

microelectronic devices especially in the harsh environments should fulfil diverse requirements like low dielectric loss, low relative permittivity, good temperature stability, high thermal conductivity, and low coefficient of thermal expansion [7, 12]. Low relative permittivity minimizes capacitive coupling as well as signal delay, and low dielectric loss tangent reduces signal attenuation along with better device performance [15]. The most common electrode materials used for co-firing the HTCC and LTCC are W (MP: 3410 °C), Mo (MP: 2610 °C), Pt (MP: 1769 °C), Pd (MP: 1552 °C), Cu (MP: 1083 °C), Au (MP: 1063 °C), and Ag (MP: 961 °C) and their alloys due to the desired electrical conductivity, fabrication temperature, and integration compatibility or reactivity with HTCC/LTCC materials [7]. The dielectric materials as HTCC/LTCC substrates or packages contribute essential control over a wide range of electrical and microelectronic device applications utilized in high-temperature environment.

Most commonly used HTCC substrate and packaging material is Al_2O_3 due to its low-cost superior thermal, mechanical, and electrical properties. The alumina substrate and packages have been extensively used in microelectronic packages for decades especially in the military and aerospace sector. Military and aerospace systems utilize the current transceiver manufacturing approach and are based on ceramic packages (either HTCC or LTCC) [7, 12, 16]. This can be achieved by fulfilling the following conditions such as (a) meeting the high performance specifications of the applications, (b) scalability in terms of circuit density and power density characteristics, (c) compatibility with low-volume military and aerospace assembly facilities, and (d) compatibility with existing infrastructures [17]. There are large numbers of materials reported in the literatures for HTCC and LTCC applications [7, 17]. However, in the last two decades, Al_2O_3 -based HTCC substrate/packages are mostly employed in the military and aerospace sector especially for microwave telecommunications. The raw material of HTCC alumina for these specific applications is different from general-purpose HTCC alumina, and more importantly, there is no glass additive in this alumina material for co-firing processes [17]. Chen et al. reported that a high-temperature co-fired ceramic (HTCC) alumina material improved dielectric performance at high temperatures as compared with the 96% alumina substrate suggesting its potential use for high-temperature packaging applications. Moreover, they demonstrated a prototype 32-I/O (input/output) HTCC alumina package with platinum conductor for 500 °C low-power silicon carbide (SiC)-integrated circuits, and such devices are currently under development for aerospace applications [18]. These hard ceramics have plethora of applications in military, aerospace, medical devices, and telecommunications. Hard ceramic substrates and package are widely used for multi-chip module (MCM) and monolithic microwave integrated circuits (MMICs) used in high-temperature environment [19, 20]. Recently, Varghese et al. reported natural zircon (ZrSiO_4)-based HTCC substrate which has good and comparable thermal, mechanical, and dielectric properties as that of commercial Al_2O_3 HTCC substrates. Figure 3 shows the (a) photograph of ZrSiO_4 sand, (b) cast green tape of processed ZrSiO_4 , inset shows the microstructure of green cast tape, and (c) sintered ZrSiO_4 HTCC substrate, inset shows the microstructure of sintered substrate at 1600 °C [21, 22]. The detailed thermal, mechanical, and dielectric properties are shown in Table 2 [23–27]. More recently Roshni et al. reported

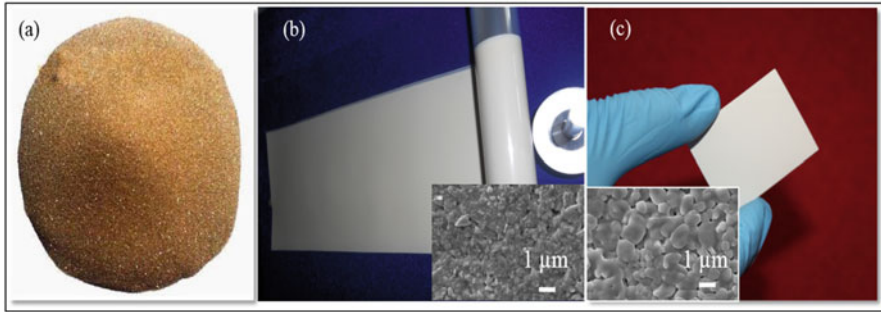


Fig. 3 (a) photograph of $ZrSiO_4$ sand, (b) cast green tape of processed $ZrSiO_4$, inset shows the microstructure of green cast tape, and (c) sintered $ZrSiO_4$ HTCC substrate, inset shows the microstructure of sintered substrate at 1600 °C. (Source: Adapted from [12])

Table 2 Commercial and suitable reported HTCC/LTCC substrates or packages for military and aerospace applications [7, 23–27]

Substrates or packages (electrodes)	Microwave dielectric properties (>5 GHz)		Thermal properties		Mechanical properties	
	ϵ_r	$\tan\delta$ (10^{-4})	TC $Wm^{-1} K^{-1}$	CTE (ppm/°C)	Hardness (Moh's)	FS (MPa)
Al_2O_3 96% (W, Mo, CuW)	9.5–9.9	1–4	25–35	6–8	9.0	450–650
$ZrSiO_4$ (Pt)	9.2	3	15	–2.5	6.5–7.5	150–200
AlN (W)	8.6	170	200–230	4.2–5.8	7.0	300–450
$0.83ZnAl_2O_4-0.17TiO_2$	9.6	8	31.3	6.59	7–8	–
DuPont 9 K7	7.1	10	4.6	4.4	5–6	230
DuPont 951	7.8	100	3.3	5.8	5–6	320
Ferro A6M	5.7	20	2	7	6	170
Kyocera GL330	7.7	5	4.3	8.2	9	400
Kyocera GL570	5.7	7	3.4	2.8	6.5	200
NTK NOC	5.9	6	3	5.2	6.5	250
NTK GM-1	6.5	20	2	3.5	6.5	250
$Li_2ZnTi_3O_8-1wt.\%$ LMZBS	21.3	7	5.8	11.97	–	–
$Bi_4(SiO_4)_3$	13.3	7	2.82	7.9	–	–
LiMgPO ₄	6.4	2	7.1	10.5		

yet another alternative HTCC substrate based on zinc aluminate-titania with better thermal conductivity than alumina [28]. Table 2 also represents the common and suitable HTCC/LTCC package properties for military and aerospace applications. HTCC substrates such as aluminum nitride (AlN) and beryllium oxide (BeO) are also used in some specific applications due to their high thermal conducting (TC) properties such as

$TC > 200 \text{ Wm}^{-1} \text{ K}^{-1}$ and $TC > 100 \text{ Wm}^{-1} \text{ K}^{-1}$ [28]. Kaneko et al. reported a comparative study of various HTCC substrates such as AlN, ceramic-glass, and alumina with different electrodes such as Ti(0.008mil)/Cu(0.08mil)/Ni(0.04mil)/Au(0.08mil) [29]. In the MW studies, AlN-based HTCC multichip module (MCM) shows good electrical performance and high reliability due to good thermal management, matching CTE, and the hermeticity with extremely simplified structure suitable for mass production [29]. For many envisioned applications such as military and aerospace, operational durability is a critical factor. There are also several reports on SiC-based HTCC JFET ICs which exhibits prolonged ($>10,000$ h) durability, stability, and reliability near 500°C similar to Al_2O_3 and AlN [30, 31]. The HTCC are mainly used for Quad Flat No-lead (QFN) package. These packages from Barry Industries have low-loss broadband transitions with a superior performance over frequency of about 40 GHz. Important benefits of HTCC constructions against the LTCC ones are enhanced mechanical strength and higher thermal conductivity [32].

In comparison with HTCC, LTCC substrates are the present generation low-cost multilayer technology with fabrication temperature in the range of $700\text{--}1000^\circ\text{C}$. In this technology, highly conductive Ag, Cu, and Au electrodes are widely used for co-firing purpose. In addition to this, ceramic-glass and glass-free LTCC substrates are also reported to have wide range of applications especially in the military and aerospace telecommunications. From manufacturing aspects, the system-in-package (SiP) integration solution offers the best balance between cost and performance to satisfy the demands of these different applications. So far, the state-of-the-art demonstrators have been accomplished in LTCC substrates. On the other hand, millimeter-wave antennas and arrays with wideband and high integration are receiving increasing demand in aerospace and military applications.

The LTCC technology is a good option for integration at mm-wave because of lightweight, low profile, compactness, easy integration, and excellent high-frequency performance. Moreover, most of these applications required high routing density, low dielectric losses, cost-effective interconnects, and packaging solutions. LTCC technology combines these characteristics, making it as a well-suited System On Package (SOP) and densely populated multichip modules (MCM). Commonly used commercial LTCC for high-frequency (up to 100 GHz and beyond) applications are DuPont 9 k7. It has permittivity of 7.1 and dielectric loss of 0.001 reported at 10 GHz. Moreover, 9 k7 has X, Y shrinkage of 9.1% and Z shrinkage of 11.8% along with flexural strength of 230 MPa, thermal conductivity of 4.6 W/mK , coefficient of thermal expansion (CTE) of $4.4 \text{ ppm}^\circ\text{C}$, and surface roughness of $0.52 \mu\text{m}$ [33, 34]. Another low permittivity LTCC tape from Ferro Corporation, A6M (material unknown, firing temperature $450\text{--}850^\circ\text{C}$) has permittivity of 5.9 and dielectric loss of 0.002 at (1–100 GHz), along with X, Y shrinkage of 15.4% and Z shrinkage of 28%. It has CTE of $7 \text{ ppm}^\circ\text{C}$, thermal conductivity of 2 W/m.K , flexural strength of 170 MPa, and surface roughness of $0.9 \mu\text{m}$ [25]. Recently Varghese et al. reported that indialite/cordierite- Bi_2O_3 LTCC with relative permittivity of 6 and dielectric loss of 0.0001 when fired at 900°C is a potential candidate for applications [21]. This composite has less than 20% X, Y and Z shrinkages and are shown in Fig. 4.

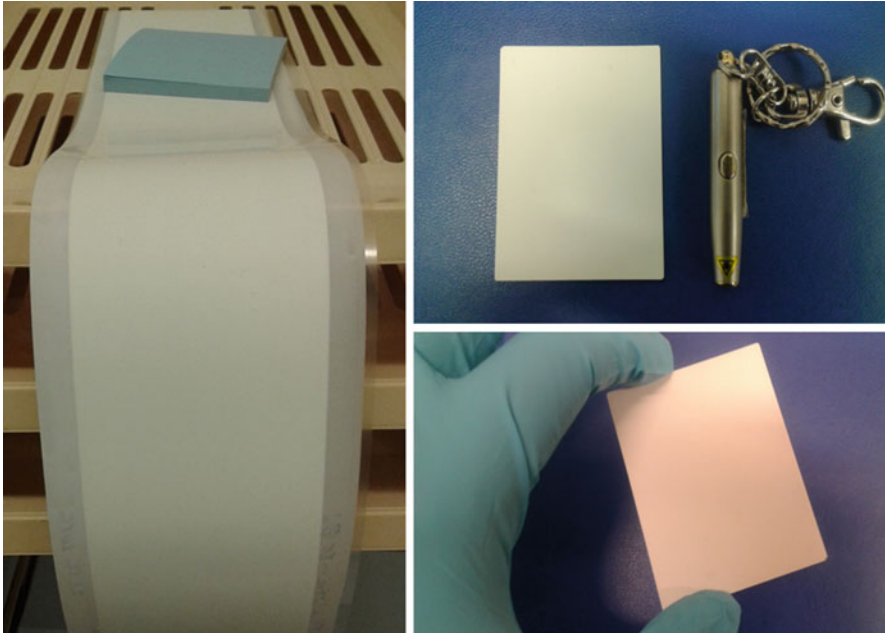


Fig. 4 Low permittivity and low dielectric loss LTCC system based on indialite-Bi₂O₃. (Adapted from [21])

Ultralow Temperature Co-Fired Ceramic Packages

Ultralow temperature co-fired ceramic (ULTCC) technology is a new promising ceramic technology based on the concept of HTCC and LTCC. The ULTCC research is in the rudimental stage for applications in the commercial as well as military and aerospace sectors. It brings down the fabrication temperature below 700 °C and mostly co-firable with Al or Ag or its alloys. Recent review by Sebastian et al. forecasted the materials research strategy for future ULTCC-based devices [7].

Based on the review, there are few materials, which are suitable for the military and aerospace applications such as substrates for antennas and other packaging and embedded devices such as capacitors and resistors [7]. Table 3 presents a few ULTCC materials which may be suitable for future military- and aerospace-based substrate and packaging solutions based on their dielectric properties at microwave frequency [35] ranges. It is clear from Table 3 that only a very few materials are reported to have highest Qf which are suitable for high-frequency applications especially military and aerospace sectors. The temperature coefficient of resonant frequency is also one of the key requirement for these applications. Still more research such as co-firability and thermal and mechanical properties needs to be done for ULTCC to reach real applications to meet the stringent requirements of military and aerospace sectors.

Table 3 List of possible materials for future ULTCC substrate/package applications [35–39]

Materials (ULTCC)	Sintering temperature	Microwave dielectric properties at > 5 GHz		Electrode compactability
		ϵ_r	Qf	
$\text{Li}_2\text{Ca}_2\text{Mo}_3\text{O}_{12}$	630	8.5	108,000	Not for Ag and Al
CaV_2O_6	675	10.2	123,000	Not studied
Li_2CeO_3	690	11.2	100,000	Yes for Al
$\text{Ba}_{16}\text{V}_{18}\text{O}_{61}$	620	9.7	80,100	Yes for Ag
$\text{Sr}_{16}\text{V}_{18}\text{O}_{61}$	660	9.8	75,600	Yes for Ag
$\text{Ca}_{16}\text{V}_{18}\text{O}_{61}$	680	11.1	79,100	Yes for Ag
$\text{Li}_2\text{Zn}_2\text{Mo}_3\text{O}_{12}$	630	11.1	70,000	Yes for Ag, Al
$\text{Zn}_2\text{Te}_3\text{O}_8$	610	14.2	70,100	
Li_2WO_4	640	5.5	62,000	Not for Ag, yes for Al
MgTe_2O_5	700	10.5	61,000	Not studied
$\text{Sm}_2\text{Mo}_4\text{O}_{15}$	690	10.7	63,500	Yes for Ag
$\text{Nd}_4\text{Mo}_4\text{O}_{15}$	700	11.1	61,500	Yes for Ag
$\text{Zn}_2\text{Te}_3\text{O}_8 + 10 \text{ wt}\%$ TiTe_3O_8	600	16.5	65,400	Yes for Al
CuMoO_4	650	7.9	53,000	Yes for Al
$\text{CuMoO}_4\text{--Ag}_2\text{O}_3$	500	8.3	32,000	Yes for Al
$\text{TiO}_2\text{--GO17}$	400	15.5	3300	Yes for Ag

Dielectric Inks/Paints

Microwave dielectric ink research has been getting increasing interest in the recent years for focusing the low-density applications like printed electronics. The ultimate goal of this research is to develop highly efficient lightweight portable devices, which may have good demand in the military and aerospace sectors in the near future. The research in this area is expanding to explore the low permittivity and low dielectric loss dielectric ink even at room temperature. Varghese et al. reported the first room temperature curable dielectric SiO_2 ink printed on commercial BoPET film with relative permittivity of 2.4–2.3 and dielectric loss of 0.003–0.006 in the frequency range of 8–18 GHz [7]. The ZrSiO_4 ink deposited on BoPET shows relative permittivity of 3.4–3.3 and dielectric loss of 0.003–0.004 in the X and Ku band frequency ranges [7]. Table 4 gives the microwave dielectric properties of room temperature curable as well as sintered dielectric ink which may find applications in military and aerospace especially printed dielectric antennas. The dielectric ink research is still in the rudimental stage for processing as well as device level testing.

Table 4 Room temperature curable dielectric ink suitable for microwave applications [40–45]

Dielectric inks	Microwave dielectric properties at >5 GHz	
	ϵ_r	$\tan\delta$
SiO ₂ on BoPET	2.4–2.3	0.003–0.006
ZrSiO ₄ on BoPET	3.4–3.3	0.003–0.004
Al ₂ O ₃ on BoPET	2.9	0.004
Bi ₂ MoO ₂ on Al ₂ O ₃ substrate	35	0.001
Boron nitride on BoPET	1.9	0.01
Nano Bi ₄ (SiO ₄) ₃ on BoPET	4.2	0.01

Polymer-Ceramic Composites for Microwave Substrate Applications

Polymer-ceramic composites, especially type 0–3, are a potential group of materials suitable for functional packages, which combine the electrical properties of ceramics and the mechanical flexibility, chemical stability, and processing features of polymers. The important characteristics required for microwave substrates for packaging technology are high-frequency compatibility, low dielectric losses, moderate dielectric constant, low coefficient of thermal expansion, high thermal conductivity, low-temperature variation of relative permittivity, low or no moisture absorption, and high dimensional stability. The dielectric loss tangent of base dielectric substrates are not so critical while designing circuits below 1 GHz. Hence, comparatively low dielectric loss tangent PCB materials made from epoxy/woven fabric composites are often used as base substrates. However, as the operational frequencies exceed 1 GHz, the dissipative signal loss in the substrate becomes more significant, and the $\tan\delta$ parameter of the substrate cannot be ignored. The ϵ_r value of the substrate material also has a profound influence on signal propagation, as the speed of the signal passing through the dielectric medium is inversely proportional to the square root of ϵ_r . Thus, the choice of the substrate material becomes very important at the designing stage of a microwave circuit for various electronic devices used in defense, space, and information technology (IT). Presently, the microwave component industry uses several substrate materials comprising hard and soft substrates. The ceramic substrates have the advantage of withstanding the localized heat caused during the wire-bonding process. In general, the hard ceramic substrates are highly isotropic with high operating temperature along with high thermal conductivity (k), low CTE, low or high permittivity and low dielectric loss. However, they exhibit brittleness, difficulty in machining, and a relatively high cost of chemically and thermally compatible conducting layer. The polymers have a low dielectric constant and low loss tangent but a high CTE, high-temperature variation of relative permittivity ϵ_r , very low thermal conductivity, and good mechanical properties. Hence, by using the composite approach, one can get reasonably good properties

for practical applications in microelectronics. The soft polymer-ceramic substrates made out of both thermoset plastic and thermoplastic materials generally have good machinability, better shock resistance, a low-cost conduction/metallization layer, tailor-made properties, and useful electrical properties.

It is well known that connectivity between the phases in the composite materials is very important in achieving the desired properties. The interspatial relationships in a multiphase material, the connectivity, control the mechanical and electrical properties and thermal fluxes between the phases. The ceramic filler particle size, shape, interfacial properties, percolation level, and porosity play a crucial role on the properties of the composite [7, 46]. Polymer matrix composites can be classified into two categories depending on the nature of the matrix used, i.e., thermoset or thermoplastic. Thermoplastic materials have a melt temperature associated with them, whereas dimensional behavior of thermosets is characterized by its glass transition temperature (T_g). Among them, thermoset matrix composites are most preferred for low-end applications, whereas thermoplastic composites are the material of choice for high-end microwave circuit applications. The main advantages of thermoplastic matrix composites compared with thermoset matrix composites are an unlimited shelf life and does not require curing, reprocess ability, chemical inertness, lower moisture absorption, higher service temperature, and high environmental tolerance. However, the processing difficulties and relatively high viscosity are some drawbacks of thermoplastic materials. Most common base substrate used for microwave circuit fabrication is the epoxy/glass substrate (FR-4) having a relative permittivity of 4.4 with loss tangent of 0.05 at 800 MHz. FR-4 is fabricated through hot pressing of woven fabric/brominated epoxy composites [47]. However, the use of FR-4 substrates at high frequencies (>1 GHz) is restricted due to their higher loss tangent [48]. Several materials based on thermosetting polymer matrix are available for high-frequency applications [7, 49]. One of the most common PCBs for high-frequency application is filled poly(1,2-butadiene) composites [50]. These composites exhibit a low porosity content even at a filler loading of 60 vol.%. Poly(1,2-butadiene)-based substrates have dielectric constants of 3.27, 4.5, 6, 9.2, and 9.8 with a loss tangent <0.0025 at 10 GHz and are commercially available. Table 5 shows the properties of some of the poly(1,2-butadiene)-based high-frequency substrate materials (TMM of Rogers corporation) that are commercially available. Laminates based on thermoset polymers need only ordinary processing techniques but suffer from a high moisture absorption content and low tensile strength. Long-term exposure of these thermoset matrix substrates to a highly oxidative environment may lead to change in the dielectric properties of hydrocarbons and hence the substrates. It is difficult to use this class of materials in an extreme chemical environment [51].

Thermoplastic materials compared to the thermoset ones have higher chemical inertness and service temperature. Various thermoplastics having with low dielectric losses are used as the matrix in flexible microwave substrates. The research on polymer composites was mainly focused on thermoplastic polymers like polyimide, polydimethylsiloxane, polystyrene, polyethylene, benzocyclobutene, polymethyl methacrylate, metallocene cyclic olefin, polyphenylene sulfide, polyolefin elastomer

Table 5 Ceramic-filled polymer composites [7, 46]

Polymer	Filler	V_f	ϵ_r	$\tan\delta$
PTFE	CeO ₂	0.6	5.0	0.0064
PTFE	SiO ₂	60 wt%	2.9	0.0024
PTFE	ZnAl ₂ O ₄ -TiO ₂	0.6	4.8	0.008
PTFE	SrTiO ₃	63 wt%	13.1	0.0055
PTFE	TiO ₂	0.67	10.2	0.022
PTFE	2MgO-2Al ₂ O ₃ -5SiO ₂	60 wt%	3.2	0.0034
PTFE	Bi ₂ O ₃ -ZnO-Nb ₂ O ₅	0.6	12.5	0.001
PTFE	Al ₂ O ₃	0.66	4.3	0.0021
PTFE	MgO	0.56	3.3	0.015
PTFE	CaTiO ₃		11.8	0.0036
PTFE	BaNdSmTi ₄ O ₁₂	67 wt%	8.0	0.009
PTFE	Sr ₂ Ce ₂ Ti ₅ O ₁₆	0.4	7.7	0.08
PTFE	MgTiO ₃	50 wt%	4.3	0.0009
PTFE	CaTiO ₃	0.4	13	0.001
PTFE	TiO ₂ /SiO ₂	5 wt% / 50 wt%	2.8	0.00075
PTFE	Sr ₂ ZnSi ₂ O ₇	0.5	4.4	0.003
PTFE	BaWO ₄	74 wt%	4.3	0.004
PTFE	BMT	67 wt %	6.7	0.0018
PTFE	TeO ₂	0.6	5.4	0.006
PTFE	Sm ₂ Si ₂ O ₇	0.4	3.9	0.0054
PTFE	AlN	0.5	4.2	0.006
PTFE	Mg ₂ SiO ₄	0.5	3.2	0.009
Polyethylene	Sm ₂ Si ₂ O ₇	0.4	4.8	0.0055
Polyethylene	Ca([Li _{1/3} Nb _{2/3}] _{0.8} Ti _{0.2})O ₃	0.4	7.7	0.004
Polyethylene	Li ₂ MgSiO ₄	0.4	3.5	0.0032
Polyethylene	Sr ₉ Ce ₂ Ti ₁₂ O ₃₆	0.4	12.1	0.004
Polystyrene	Li ₂ MgSiO ₄	0.4	3.8	0.012
Polystyrene	Sm ₂ Si ₂ O ₇	0.4	4.34	0.0101
Polystyrene	Sr ₂ Ce ₂ Ti ₅ O ₁₅	0.5	13.6	0.0004
Polystyrene	Ca([Li _{1/3} Nb _{2/3}] _{0.8} Ti _{0.2})O ₃	0.4	7.4	0.003
Polystyrene	Mg ₂ SiO ₄	0.5	4.0	0.006
HDPE	Sr ₂ Ce ₂ Ti ₅ O ₁₅	0.4	11.0	0.006
HDPE	Ca ₄ La ₆ (SiO ₄) ₄ (PO ₄) ₂ O ₂	0.4	5.1	0.0023
HDPE	CeO ₂	0.4	11.0	0.006
HDPE	Mg _{0.95} Ca _{0.05} TiO ₃	0.5	7.32	0.001
HDPE	Li ₂ MgSiO ₄	0.4	3.54	0.0032
HDPE	Sm ₂ Si ₂ O ₇	0.5	5.3	0.009
HDPE	ZrSiO ₄	0.4	4.8	0.0018
POE	SrTiO ₃	0.4	11.0	0.010
POE	SrTiO ₃ -NiZn ferrite		5.4	0.0018
PEEK	TiO ₂	25 wt%	4.9	0.0087

(continued)

Table 5 (continued)

Polymer	Filler	V_f	ϵ_r	$\tan\delta$
PEEK	SrTiO ₃	27 wt%	5.2	0.003
Poly(methyl methacrylate)	Ba _{0.6} Sr _{0.4} TiO ₃	0.416	1212	0.026
Metallocene cyclic olefin copolymer	Soda lime borosilicate	0.36	1.92	0.0009
Cyclo-olefin polymer	MgO	0.3	3.8	0.0005
COC	BST	0.25	6.0	0.0023
Polyphenylene sulfide (PPS)	BST	0.7	13.5	0.0025
PPS	Mica/SrTiO ₃	0.38	6.4	0.0052
PPS	Mica/SrTiO ₃	14	6.4	0.0053
Polyimide	BaTiO ₃	0.1	35.0	0.0082
LCP	–	–	3.0	0.002
DGEBA	Mg ₂ SiO ₄	0.4	3.8	0.014
Epoxy	Sr ₉ Ce ₂ Ti ₁₂ O ₃₆	0.4	14.1	0.022
Epoxy	PMN-PT/BaTiO ₃ (3:1)	0.7	89.0	0.017
Epoxy	BaTiO ₃	0.6	45.0	0.035
Epoxy	BaTiO ₃	0.45	13.1	0.025
Epoxy	PMN-PT-BaTiO ₃	0.7	110.0	0.016
Epoxy	Ca(Li,Nb,Ti)O ₃	0.3	8.0	0.009
Epoxy	Ca(Li, Nb,Ti)O ₃ -Ag	0.26 Ag	72.3	0.065
Epoxy	(Ba _{0.9} Sr _{0.1})(Ti _{0.9} Zr _{0.1})O ₃	70 wt%	25.2	0.035
Polypropylene	Zn ₂ SiO ₄	0.335	2.9	0.00018
Polypropylene	MgAl ₂ O ₄	0.2	3.0	0.00017
RT duroid 6010 LM	PTFE – ceramic	–	10.2	0.0018
RT duroid 5870	PTFE – glass microfibers	–	2.3	0.0023
RT duroid 6002		–	2.9	0.0012
RO 4533			3.3	0.0020
RO 4534			3.4	0.0022
RO 4535			3.5	0.0032
RO 4350			3.4	0.004
FR4	Fiberglass-reinforced epoxy		4.2	0.020
TFG			3.2	0.003
TPG30			2.8	0.0027
TLG-29, TLG-30, TLG-32, TLG-33, TLG-34, TLG-35			2.8–3.5	0.0024–0.0029
TLT	PTFE-fiberglass fabric		2.5	0.0006
TLP	PTFE-fiberglass fabric		2.1	0.0009
TLC			2.7–3.20	0.0030
TLE			2.9–3.00	0.0028
RF-35			3.5	0.0028
RF-35P			3.5	0.0035
TSM-30			2.9	0.0012

(continued)

Table 5 (continued)

Polymer	Filler	V_f	ϵ_r	$\tan\delta$
TLY	PTFE woven glass		2.1–2.4	0.0009
TLX	PTFE woven glass		2.4–2.6	0.0019
Taclamplus			2.1	0.0004
RF-60A			6.1	0.0038
RF-41,RF-43,RF-45			4.1–4.5	0.0033–0.0038
TRF -41,TRF-43,TRF-45	PTFE woven glass reinforced		4.1–4.5	0.0035
RF-30			3.0	0.0014
HyRelex			2.6	0.0020
Cr-10			10.0	0.0035
Arlon 25FR and 25 N			3.3	0.0025
FASTRISE 27			2.7	0.0020
TSM29			2.9	0.0014
CLTE			2.9–3.0	0.0012–0.0023
TC350			3.5	0.0020
TC600			6.1	0.0020
AD255A,AD260, AD300A,AD320A, AD350A,AD410A, AD430A			2.5–4.3	0.0015–0.0035
AD1000A			10.2	0.0023
AD600			6.0	0.003
AR1000			9.8	0.003
25 N			3.3	0.0025
25FR			3.5	0.0035
DiClad 880-PIM			2.1	0.0009
IsoClad 917			2.1	0.0013
CuClad 250 GT			2.4	0.001
Nelco N4000–13			3.7	0.008
Nelco 4000–13 SI			3.4	0.008
Nelco 400013SI			3.3	0.007
TMM3 ^a			3.2	0.002
TMM4 ^a			4.5	0.002
TMM6 ^a			6.0	0.0022
TMM10 ^a			9.2	0.0023
TMM10i ^a			9.8	0.002

^aTMM is the registered trademark of poly (1, 2-butadiene)-based substrates by M/s. Rogers Corporation, USA

(POE), polypropylene, and polyurethane copolymers. In these composites, the polymers are commonly reinforced with glass or ceramic. PTFE is also the most preferred host matrix due to its excellent dielectric properties such as low permittivity and extremely low loss tangent, and it is very stable in a wide frequency range.

The properties of PTFE such as chemical inertness, low moisture absorption, high service temperatures, etc. are also important for many microwave applications. All the reported polymer-ceramic composites show an increase in loss tangent with increasing frequency. Recently Krupka et al. found that polypropylene-silicon composites show a decrease in loss tangent with increasing frequency and propose it as a useful composite for 5G and IoT which operate at very high frequencies [52]. Table 5 gives a list of polymer-ceramic composites useful for practical applications like electronic packages for device encapsulation protecting them from an adverse environment and increasing their long-term reliability. The electrical characteristics of microelectronic devices, such as signal attenuation, propagation velocity, and cross talk, are influenced by the dielectric properties of the packaging materials. An important role of the packaging materials is to ensure the electrical insulation of the silicon chip and circuit pins. A low conductivity is needed to avoid leakage current, a low ϵ_r to minimize the capacitive coupling effects, and a low loss factor to reduce signal loss.

The 0–3 type polymer-ceramic composites offer an opportunity to manufacture materials combining the electrical and mechanical properties of both polymers and ceramics. A composite with three-dimensionally connected polymer phase loaded with isolated ceramic particles (0–3 connectivity) finds extensive applications in microelectronic industry. One of the biggest advantages is the possibility of adjusting the electrical, thermal, and mechanical properties continuously as a function of ceramic loading, enabling unique freedom to component designers. The relative permittivity and thermal conductivity increase with ceramic loading, whereas the CTE decreases. The loss tangent in general increases with ceramic loading. The dielectric properties are mainly dependent on the polymer matrix until the level of the percolation limit. Usually the filler addition is limited to about 50–60 volume fraction. Preparation of composites with a larger volume fraction of filler (more than 50–60) is difficult, and the amount of porosity increases.

The polymer-ceramic composites facilitate the fabrication of inexpensive and very complex three-dimensional (3D) structures. This offers a tremendous application potential in 3D antennas. The relative permittivity of polymer-ceramic composites cannot increase to a very high value, even at maximum filler loading [53] since the 0–3 type composite follows an exponential relationship between relative permittivity of the composite and the volume fraction of the filler. At low volume fractions, the filler particles are randomly distributed in the polymer matrix with poor connectivity between the ceramic particles. At higher volume fractions or near the percolation threshold, the ceramic filler particles are connected, and hence the relative permittivity shows an abrupt increase. However, it is difficult to mix large amounts of ceramic fillers in the polymer matrix. It was found that the use of a coupling agent, such as silane treatment to modify the surface of the filler powders, although slightly improves the relative permittivity and mechanical properties, it degrades the microwave dielectric loss factor. The silane treatment is found to lower the porosity. The volume fraction of the ceramic that can be incorporated into the polymer depends on the density, powder particle size, and shape or morphology of the ceramic powder. When the powder particle size is very small, they have a high surface area, and only a small volume fraction can be incorporated.

Rubber-Ceramic Composites for Flexible and Stretchable Applications

Recently electronic systems that can cover large areas on flexible substrates have received increasing attention because they enable wide range of applications such as flexible displays, electronic textiles, sensory skins, active antennas, etc. [54]. Devices based on this new technology are stretchable, twistable, and deformable into curvilinear shapes, thereby enabling applications that would be impossible to achieve by using the hard and rigid substrates [55]. Flexible electronics, an emerging field in electronic industry, enables a wide range of applications including capacitors for energy storage, antennas for wireless communication, electronic packaging, and electromagnetic interference (EMI) shielding. They can be folded and unfolded and fitted into non-planar forms for packaging or storage [46, 56]. The flexible substrates have many potential applications ranging from neural prosthetics in the medical field to microwave devices in electronics, which provides the advantage of three-dimensional designs of conformal structures [57, 58]. Conventional polymers filled with ceramic are rigid and cannot be bend or stretched. Stretchability means that the circuits should have the capacity to absorb large levels of strain without degradation in their electronic properties. In this context, the elastomer-ceramic composites can be used for stretchable and bendable electronic applications.

The requirements of a material to be used as a flexible dielectric are good mechanical flexibility, high thermal conductivity, low coefficient of thermal expansion, optimum permittivity (low ϵ_r for fast signal speed and high ϵ_r for miniaturization), good process ability, low dielectric loss, and low cost [46]. It is very difficult to identify a single material, which possess all these properties simultaneously. Butyl and silicone rubbers have low dielectric loss with good mechanical flexibility and stretchability, but they have low relative permittivity, low TC, and high CTE. By integrating the flexibility, stretchability, and low processing temperature of butyl and silicone rubbers with the high relative permittivity, low loss, and low CTE of ceramics [59], a composite may be formed, which can deliver improved performance. Composite electro ceramics introduce not only new functionalities but also an extremely wide range of properties that can be seamlessly adjusted in addition to a significant flexibility in fabrication. The relative permittivity of butyl rubber and silicone rubber can be tailored over a wide range by reinforcing with low-loss ceramics having different range of relative permittivity and volume fraction of the fillers in the rubber matrix [60].

In the pure form, silicone and butyl elastomers are thermoset polymer; once cross-linked they cannot be brought back to the former shape. Silicone and butyl rubber molecules exist above their glass transition temperature, and hence considerable segmental motions are possible. The glass transition temperature of silicone elastomer is about -127°C and that of butyl rubber is about -63°C . The long polymer chains will cross-link during curing, and the process is known as vulcanization. Dicumyl peroxide is used for the vulcanization of silicone rubber and sulfur for butyl rubber. The elastomer exhibits large elongation from which they recover rapidly on the removal of the applied stress.

Recently Sebastian and co-workers reported [7, 59] the microwave dielectric properties of silicone and butyl rubbers filled with several ceramics of varying dielectric constants. The composites were prepared by hot pressing at 200 °C by applying a pressure of 2 MPa. The volume fraction of the ceramic that can be incorporated into the butyl rubber depends on the density, powder particle size, and shape or morphology of the ceramic powder. The addition of ceramic fillers in silicone and butyl rubbers gradually increased the relative permittivity. The increase in the relative permittivity depends on the amount of ceramic filler, its relative permittivity, and the frequency of measurement. As the relative permittivity of the fillers is higher than that of the elastomers, the ϵ_r of the composites show an increasing trend with filler content. The microwave dielectric and physical properties of rubber-ceramic composites with the highest volume fraction with homogeneous dispersion of fillers are given in Tables 6 and 7. The loss tangent of the composite depends on the loss factor of the filler ceramics and is relatively small for alumina, silica, etc. since they are low-loss ceramics. The loss tangent increases considerably for BaTiO₃ since it is a lossy ferroelectric material. The composites are found to be flexible, bendable, and stretchable. The microwave dielectric and thermal properties are improved with ceramic loading. The composite preparation is difficult for ceramic loading higher than 40 vol.%. It is found that one can get only a relative permittivity of about 14 even with maximum loading with high-permittivity ceramics. The thermal conductivity increases, and coefficient of thermal expansion decreases with increase in filler content. The water absorption increases with increase in ceramic loading. The composites are found to have good dielectric properties and flexibility and are suitable for antenna fabrication and capacitive applications. One of the most attractive features of these particulate composites is that their electrical and physical properties can be varied over a wide range by choosing the appropriate volume fraction of the fillers in the rubber matrix.

Table 6 Microwave dielectric, thermal, and physical properties of silicone rubber-ceramic composites (5 GHz) [7]

Material	Average powder particle size μm	V_f of filler	ϵ_r	$\tan \delta$	CTE (ppm/°C)	TC ($\text{Wm}^{-1} \text{K}^{-1}$)	Water absorption vol %
SiO ₂	0.5	0.5	3.3	0.008	116	0.5	0.10
Al ₂ O ₃	2 0.0	0.4	5.7	0.009	114	1.6	0.34
AlN	1.3	0.4	4.7	0.017	138	1.0	0.10
Ba(Zn _{1/3} Ta _{2/3})O ₃	0.7	0.2	6.5	0.009	149	0.9	0.11
Ba(Mg _{1/3} Ta _{2/3})O ₃	0.5	0.2	5.1	0.011	152	0.4	0.11
BaTiO ₃	0.9	0.2	13.3	0.043	188	0.4	0.11
SrTiO ₃	0.8	0.3	14.2	0.011	142	1.0	0.08
Li ₂ ZnTi ₃ O ₈	0.7	0.3	7.4	0.009	144	0.8	0.11
Ca _{0.61} Nd _{0.26} TiO ₃	0.9	0.4	11.9	0.011	156	0.5	0.07

Table 7 Microwave dielectric, thermal, and physical properties of butyl rubber-ceramic composites (5 GHz) [7, 59]

Filler	Powder particle size	V_f	ϵ_r	$\tan\delta$	CTE	Water absorption (vol %)	TC W/mK
SiO ₂	<1 μm	0.4	3.1	0.004	80	0.09	0.5
Al ₂ O ₃	~1 μm	0.4	4.7	0.002	55	0.08	0.5
Ba(Zn _{1/3} Ta _{2/3})O ₃	<1 μm	0.3	5.8	0.002	86	0.05	0.3
Sr ₂ Ce ₂ Ti ₅ O ₁₆	~5 μm	0.4	11.0	0.001	30	0.07	0.4
TiO ₂	~2 μm	0.4	12.5	0.002	108	0.08	0.7
SrTiO ₃	~5 μm	0.4	13.2	0.002	26	0.08	0.5
Ba _{0.7} Sr _{0.3} TiO ₃	<5 μm	0.3	13.1	0.009	29	0.06	0.4
BaTiO ₃	~1 μm	0.3	12.7	0.020	33	0.12	0.4

Radomes

A radome (radar dome) is a protective cover for the delicate antenna mounted on air vehicles, (airplanes, missiles, etc.) from severe surrounding environments such as the effects of humidity, high or low temperature, bird strike, insects, UV damage, wind, rain, or dust. Radomes are composed of panels that form a spherical shell to protect the enclosed antenna. The radomes equipped in supersonic or hypersonic aircraft may encounter high levels of mechanical and thermal loadings [61, 62]. For example, if the aircraft is flying at a velocity of more than 5 Mach, then radome has to withstand a high temperature of more than 1400 °C [63]. More importantly, the radome must not interfere with the utility of the antenna, which is responsible for communication, detection, or imaging [64]. A radome contains dielectric materials and sometimes paints layers. The important characteristics required for a radome material are:

- (i) The electromagnetic radiation should pass with the minimum transmission loss, and it depends on the materials dielectric constant and loss tangent.
- (ii) The material should be capable of being fabricated into a suitable structure, and this requires good knowledge of the material mechanical properties such as density, strength, and durability and should have the life lasting that of the vehicle in operation.
- (iii) The material should withstand the thermal conditions, for which good knowledge of the material thermal conductivity, emissivity, thermal shock, and behavior with temperature change is improved.
- (iv) The material should withstand the environmental and contamination conditions without any degradation.

The high tensile strength and fracture toughness together with a low CTE prevent stress failures and suppress the formation and propagation of cracks resulting from erosive environment. A stable dielectric constant, with temperature, reduces bore

sight errors (BSE) caused by aerodynamic heating, and a low dielectric constant permits enhanced fabrication tolerance in wall thickness. The materials with good mechanical and thermal properties generally have higher dielectric constant. Hence, an optimal design for radome wall structures are needed for high temperature broad band applications. The radars are designed in the high frequency or microwave domain, and hence the thickness of the radome produces wavelength multiples which modifies the antenna patterns. Hence, the process of radar design should consider not only the radome structure but also the protective layers over it. A non-optimized radome can lead to several problems such as gain loss, bore sight errors (BSE), etc. degrading the radar range, ghost effects, artifact detections, or angular error detection. Thus, the importance of design and optimization of the radome layers for good transparency towards the antenna with minimum spurious reflections. Safety, security, and reliability are important features of communication, telemetry, and radar systems.

The EM wave undergoes two basic mechanisms of reflection and transmission when incident normally on a foreign medium which are governed by the following equations:

$$R = (Z_2 - Z_1)/(Z_2 + Z_1) \quad (1)$$

$$T = 2Z_2/(Z_2 + Z_1) \quad (2)$$

where

R = reflection coefficient

T = transmission coefficient

Z_i = complex impedance of *i*th medium, which is given by:

$$Z = [j \omega \mu / (\sigma + j \omega \epsilon_r)]_{1/2} \quad (3)$$

where

Z = complex impedance of the medium

ω = angular velocity of the wave

μ = magnetic permeability of the material

σ = electrical conductivity of the material

The materials required for the fabrication of radomes should be transparent to microwave in either a narrow- or a broadband of the EM spectrum. Equation (2) indicates the necessary condition for perfect transmission across a material (i.e., T = 1) and to ensure an impedance matching of the material with that of free space ($Z_2 = Z_1$). This actually eliminates any reflection loss from the surface. The dielectric constant ϵ_r and the magnetic permeability μ (both real and imaginary part of each) of the material should be as low as possible to reduce the loss of microwave energy through the radome. In general, the radomes are made of non-magnetic materials, and so the importance is to reduce ϵ' and ϵ'' of the materials and design them to be as close as possible to those of the free space ($\epsilon_0 = 1 + j_0$). It may be noted that the radome performances are often also sensitive to the thickness of the

material. The radomes used in supersonic, in hypersonic, and for the reentry-type vehicles experience high skin temperatures. Hence, the materials should have, in addition to low dielectric constant and loss tangent, high glass transition temperature and good thermal and oxidation stability. Based on these requirements, the materials that qualify as candidates for different grades of airborne radomes can be broadly classified as ceramic based and polymer based.

The ideal radome material must be electrically very transparent to electromagnetic energy (a minimum power is lost on passing through the material) and should retain its physical integrity structurally throughout the entire flight trajectory under conditions of aerodynamic loads, thermal stresses, environmental conditions, and with long life with that of vehicle. The ideal radome material electrically is one which behaves as free space over all wavelengths. However, no such ideal material exists which will give the structural and physical protection to the vehicle. Hence finding a suitable material is difficult and is a compromise between electrical, thermal, and mechanical properties and physical requirements. There are a quite good number of low-loss materials satisfying radome requirements with varying dielectric constant, strength, working temperature range, etc. For example, a low dielectric constant may be considered for a wide frequency band application, whereas a high dielectric constant may be useful for a relative narrow frequency band with minimum aberration requirement. A high-density material such as alumina may be useful at high temperature. Lighter materials are available in resin-glass sandwich or solid laminate composites for the lower temperatures and ceramic-type materials for the higher temperatures.

Ceramic-Based Radomes

The materials based on ceramics become critical for radome applications that have to withstand high temperatures ($\leq 400^\circ\text{C}$) as in the cases of most supersonic/hypersonic missiles and spacecrafts. Each of these ceramic materials and their composites has their own advantages and disadvantages with respect to their dielectric properties, mechanical strength, thermal properties, and fabrication ease. The slip-cast fused silica (SCFS) stands out to be one of the best for high velocity applications (even up to Mach 8) for their favorable combinations of different properties like dielectric constant and loss, cost, CTE, etc. Most of the missile radomes are made of Pyroceram and slip-cast fused silica (SCFS). Other ceramics that have received attention or are being considered for advanced applications are Rayceram, nitroxyceram, reaction-bonded silicon nitride (RBSN), hot-pressed silicon nitride (HPSN), and celsian. Pyroceram 9606 and Rayceram8 are cordierites based and are composed of magnesia, silica, and alumina. Nitroxyceram contains silicon nitride, boron nitride, silica, and celsian barium oxide, alumina, and silica. RBSN and HPSN are made almost from silicon nitride along with small amounts of sintering additives. Slip-cast fused silica has excellent electrical performance and satisfactory mechanical performance but may erode considerably in a rain field. Nitroxyceram is promising, but it requires a difficult and expensive manufacturing process. The

Table 8 List of important radome applications

	ϵ_r	Loss tangent	Density gm/cm ³	Melting point	Hardness Mohs
Alumina	9.6	0.0001	3.7	2015	9
Fused silica	3.7	0.0002	1.7	1680	6
Pyroceram	5.6	0.0003	2.6	1350	–
Cordierite	6.2	0.0002	2.5	1435	7
Boron nitride	4.5	0.0004	2.0	2730	2
Silicon nitride	7.9	0.004	3.2	1900	7–9

Table 9 Dielectric properties of polymers

Material	ϵ_r	Loss tangent
Epoxy	3.4–4.0	0.02
Polyester	2.8	0.003
Polyimide	3.0	0.004
Cyanate ester	3.3	0.007
Polycarbonate	2.8–3.4	0.001
PTFE	2.1	0.0001
Polypropylene	2.2	0.0003
Polystyrene	2.5	0.0003

dielectric properties of some commonly used alumina, fused silica, cordierite, boron nitride, silicon nitride, Pyroceram ceramic-glass of Corning, etc. are given in Table 8. There are a large number of ceramics with excellent microwave dielectric properties (low dielectric constant and loss tangents). However, no investigation was reported for possible use as radomes. The reader is referred to the reference [7] for a list of low-loss dielectric materials.

Polymer-Based Radome Materials

Some of the important polymers used for making radomes are given in Table 9. Quartz with $\epsilon_r = 3.8$ and loss tangent 0.0002 and D-glass with $\epsilon_r = 4.0$ and loss factor 0.0026 are usually used as reinforcement in the polymers. One can tailor the dielectric, thermal, and mechanical properties by selecting appropriate ceramic filler materials and their volume fractions in the polymer matrix.

Radomes for millimeter-wave applications were earlier made of pure thermoplastic polymer which nowadays are replaced with more advanced thermoplastics having superior resistances to rain erosion, moisture absorption, and impact loads. The thermoset resins are most commonly used for civilian and defense radomes, mainly owing to their easier processability, improved mechanical properties, and significantly lower coefficients of thermal expansion (CTE). It may be noted that some of the thermoset epoxy-based composites even withstand temperatures up to about 350 °C. Epoxy-based composites are extensively used for the aerospace industry. However, the relatively higher dipole activity and the presence of hydrogen

bonding result in a higher $\tan \delta$ for epoxies. Moreover, the dielectric constant and loss tangent of these materials tend to increase further with increase in temperature. However, the epoxies or the polyesters are best to operate up to a temperature of 150 °C, which is often a major limitation for many applications. The thermoset polyimides, PTFE, and cyanate esters can withstand temperatures close to 300 °C. It must be noted that the final dielectric behaviors of the composites will depend on the amount and dielectric properties of the matrix resins and the reinforcements. Thus, both the polymer and the reinforced filler are important in determining the overall performance of the radomes. Polyurethane foams as dielectric materials are extensively used in the construction of radomes. Polyurethanes are commonly used as a composite material in land-based, space frame radomes. This is a cost-efficient solution enabling self-supporting radome panels that are hydrophobic and antimicrobial. Furthermore, two- and three-layer sandwich panels for desired thermal insulation can be formed. Polyurethanes are also used as composite materials in aircraft and as protective structures on leading edges of aircraft radomes to protect from erosion damage while ensuring proper signal from the aircraft antenna. Polyurethanes are especially useful in aerospace applications where functional, lightweight materials are imperative. There are several low ϵ_r and low-loss polymer-ceramic and rubber ceramic composites reported in the literature and may be useful for radome applications [7].

EMI Shielding Materials for Military and Aerospace Applications

Digital transformation is happening in aerospace and defense applications, platforms, and environments due to the increase of portable electronics devices and embedded electronic systems. They contribute a significant rise in RF emissions that could cause interference, data corruption, or mal functioning of devices. Aircraft, combat vehicles, ships, communication equipment, safety equipment, missile systems, and launchers – all platforms and vehicles, components, and systems need EMI/RFI shielding to operate functionally. Electronic warfare is a key component of battle space where electromagnetic emissions are used to interrupt or disrupt military equipment [65, 66]. For aerospace and defense applications, the requirements for EMI shielding will be more stringent as the shielding structure and material should also withstand potential high power EM attacks such as electromagnetic pulse (EMP) and electrostatic discharge (ESD), which can result in electrical short or dielectric breakdown [67, 68]. Germany developed a carbonyl iron powder loaded rubber sheet of thickness 0.3 inches and resonant frequency at 3 GHz named “Wesch” as a radar camouflage for submarines during World War II [69]. During this period, the USA developed materials known as “HARP” (Halpern Anti-Radiation Paint). MX-410, its airborne version, consists of base dielectric with high permittivity of 150 due to loading with highly oriented disk-shaped aluminum flakes suspended in a rubber matrix and carbon black. This material offered a 15–20 dB reduction in reflectivity in the X band [70, 71]. Shielding results of 20–35 dB may be sufficient to protect the interference resulted from low-power

consumer electronics but is not enough to meet EMI shielding requirements for defense and aerospace applications. Shielding of 50 dB and above is required for defense and aerospace applications [66, 72].

Effective EMI shielding is obtained with low surface resistance and high conductivity. There is an increase in the number and complexity of electronic equipment and the threat of electronic countermeasures (ECM), ranging from radar jamming and deception to a devastating electromagnetic pulse (EMP) attack. These aspects result in the need for greater protection from electromagnetic interference (EMI) and radio-frequency interference (RFI), which pose challenge to aerospace and defense engineers today and could have disastrous effects on safety and mission critical systems. Loss of a safety or mission critical system means somebody could die, a piece of equipment could be destroyed, or that the mission may failed. Hence, the demand for efficient shielding materials that are resilient to extreme environmental conditions, lightweight, and optically transparent while providing military-compliant shielding performance is on rise due to much more electromagnetic radiation in the air in comparison with a decade ago [65, 66].

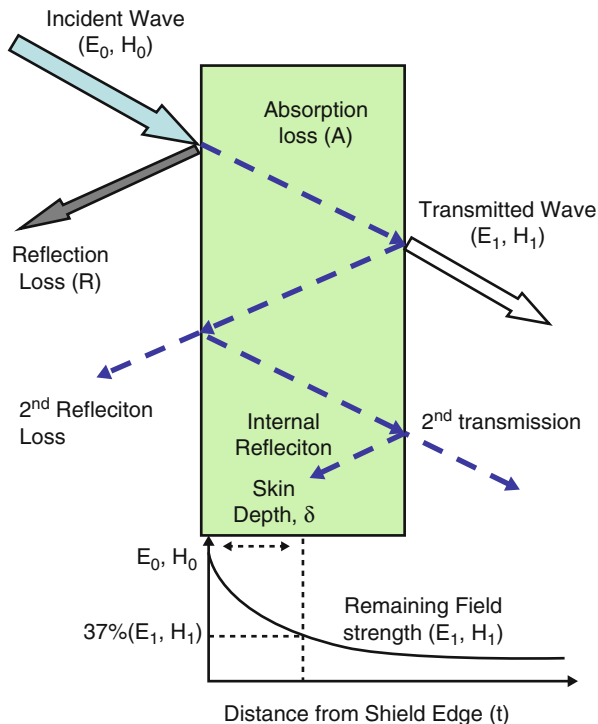
EMI Shielding Mechanism

Shielding of electromagnetic radiation is done by three mechanisms, viz., reflection, absorption, and multiple reflections. Reflection mechanism occurs in highly electrically conductive structures, such as metals, and relies on mobile charge carriers. Electric and/or magnetic dipoles in the shielding material can contribute to significant absorption of the waves. Attenuation by absorption depends on shield thickness, σ_r and μ_r . With increasing frequency, absorption increases, while reflection tends to decrease. Figure 5 shows the schematic representation of EMI shielding mechanism. Another mechanism is the multiple reflections that occur at surfaces or interfaces within the shield. This mechanism depends on the geometry of the materials, as it requires the presence of large surface areas or interfaces within the shield [72, 73].

EMI Shielding Materials

Metallic shielding products have been in use for several years in the endless applications owing to the high attenuation it offers. Broadband absorbers have been made from solid metallic particles or dielectric-filled metallic dispersed in a matrix. Iron oxide, powdered iron, powdered aluminum and copper, silver, steel, evaporated metal or nickel chromium alloy, and metal wires are some of the conductive materials commonly used for high shielding applications [73, 74]. Table 10 gives a list of some of the reported metal-based EMI shielding materials. These materials are selected based on the measured high frequency and thickness less than 2 mm especially suitable for military and aerospace applications. Advanced composite materials are trying to replace metals in a wide range of applications mainly in aerospace due to its attractive properties like lightweight,

Fig. 5 Schematic representation of EMI shielding mechanism



high stiffness, dimensional stability, and chemical/temperature resistance. One of the major obstacles is that these composite materials do not provide the shielding levels close to that of metals and is a major challenge in aircraft designs [73, 74, 104, 105]. Currently considerable interest is paid on the development of effective EMI shields based on carbon composites as an alternative to the metal-based shields in areas of aerospace, defense, automobiles, and next-generation flexible electronics owing to its unique properties of good electrical and thermal conductivity, as well as low density [72, 73]. Two-dimensional metal carbides and nitrides known as MXenes that combine metallic conductivity and hydrophilic surfaces are possible candidates owing to its good shielding properties with minimum thickness. Shahzad et al. reported $Ti_3C_2T_x$ film of 45 μm thick with EMI shielding effectiveness (EMI SE) of about 92 dB, which is highest among all synthetic materials of comparable thickness [106].

Recently, a promising EMI shielding material for the defense and aircraft industries is developed by Chaudhary et al. based on multiwall carbon nanotube (MWCNT)-mesocarbon microbead (MCMB) composite paper which has high conductivity and is lightweight and easily foldable by simple, efficient, and cost-effective strategy (Fig. 6). It is reported as the first efficient EMI shielding material in the X-band frequency region having low density of 0.26 g/cm^3 and absorption-dominated shielding effectiveness of 31 and 56 dB at 0.15–0.6 mm thickness,

Table 10 Some of the reported materials having thickness less than 2 mm with good EMI SE in the high-frequency region

SL No	Material	EMI SE dB	Frequency GHz	Ref
1.	Cu deposited polymer substrate	50–60	2–18	[75]
2.	Nanocrystalline Cu on Heat-treated polyaromatic hydrocarbons (HTPAHs)	58.7	12.4–18	[76]
3.	Poly(vinyl chloride)/graphite/nickel Nanoconducting composites	45–60	1–12	[77]
4.	Polyvinyl chloride reinforced graphite/copper nanoparticles	22–70	1–20	[78]
5.	Ti ₃ C ₂ T _x films	90	8–12	[79]
6.	Ti ₃ C ₂ T _x -SA composites	50–60	8–12	[80]
7.	MWCNT-mesocarbon microbead composite paper	56	8–12	[81]
8.	Polyvinylidene fluoride-graphite flake composite	55–57	8–18	[82]
9.	10 wt% CNT/UHMWPE nanocomposite	50	8–12	[83]
10.	Graphene foam/5 wt% CNT/PDMS composite	70–80	8–12	[84]
11.	Graphene oxide-cellulose aerogel	50–58	8–12	[85]
12.	ABS copolymer (Cycolac Ex39)/15 wt% MWCNT	50	8.2	[85]
13.	Thermally reduced graphene oxide	80.8	12.4–18	[86]
14.	PEEK/10 wt% expanded graphite	57.9	10	[87]
15.	Polyaniline/5 wt% graphene	51–52	2–12	[88]
16.	5.7% multiwalled carbon nanotubes/polydimethylsiloxane composites (MWNT/PDMS)	70–80	8.2–12.4	[89]
17.	Poly(vinylidene fluoride) (PVDF) and multiwall carbon nanotubes (15 wt% MWCNTs) with three-dimensional (3D) networks	50–70	8–12	[90]
18.	Polyimide/graphene composite foams	51	8–12	[91]
19.	Exfoliated graphite	130		[92, 93]
20.	Acrylonitrile butadiene rubber/4 wt% graphene nanocomposites	40–75	1–12	[94]
21.	Multilayer graphene anchored TiO ₂ in PPY matrix	53	12.4–18	[95]
22.	4.6 vol% multiwall carbon nanotubes (MWCNTs) within polypropylene random copolymer (PPCP)	45–50	12.4–18	[96]
23.	Graphite-nanoferrite-fly ash composites	40–98	8.2–12.4	[97]
24.	Graphene paper	60	8–12	[98]
25.	Mesocarbon microsphere (MCMS) composite with Fe ₃ O ₄ particles	76		[99]
26.	Carbon foam with SiC nanowires	79	8.2	[100]
27.	Polypyrrole	49	12–18	[101]
28.	Polyaniline nanofiber	74	8.2–18	[102]
29.	Polyaniline nanofiber-2.3 wt.% of graphite flakes	87	8.2–18	[43]
30.	5 wt.% Fe ₃ O ₄ in 10 wt.% PAN/DMF	65–68	8.2–12.4	[103]

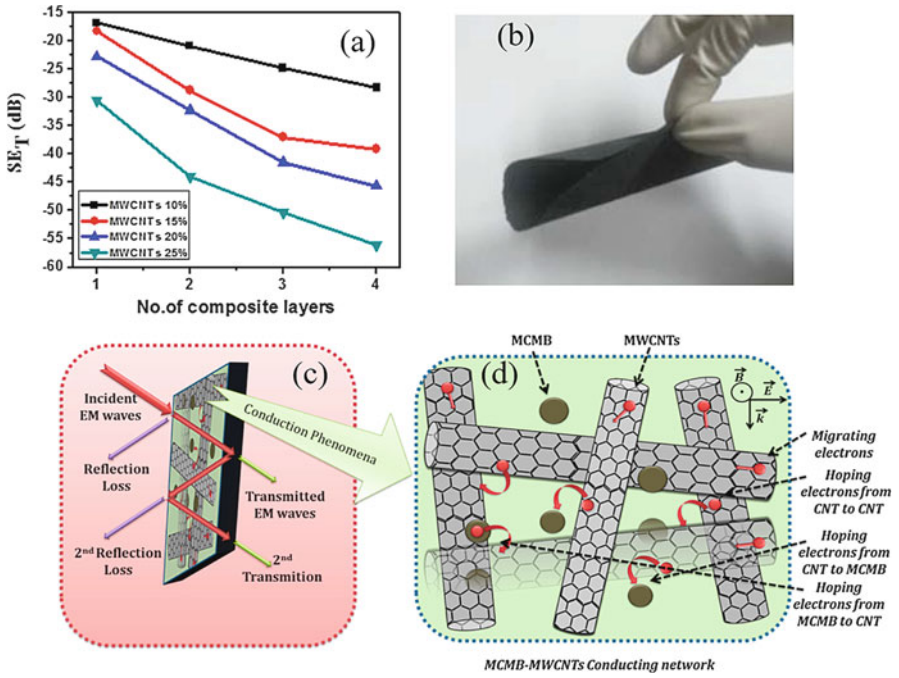


Fig. 6 (a) EMI shielding efficiency, (b) photograph, and (c, d) mechanism of MWCNT-MCMB composite paper. (Accessed from [81])

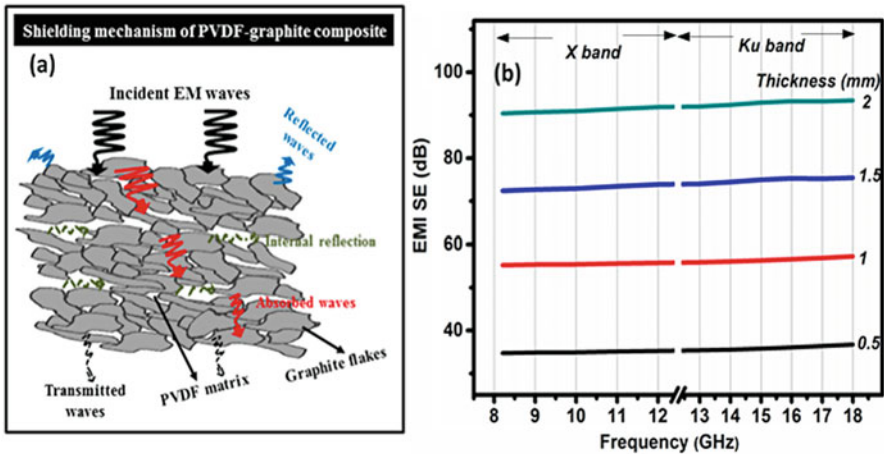


Fig. 7 Mechanism and EMI shielding efficiency of PVDF-70 vol% graphite composite. (Accessed from [82])

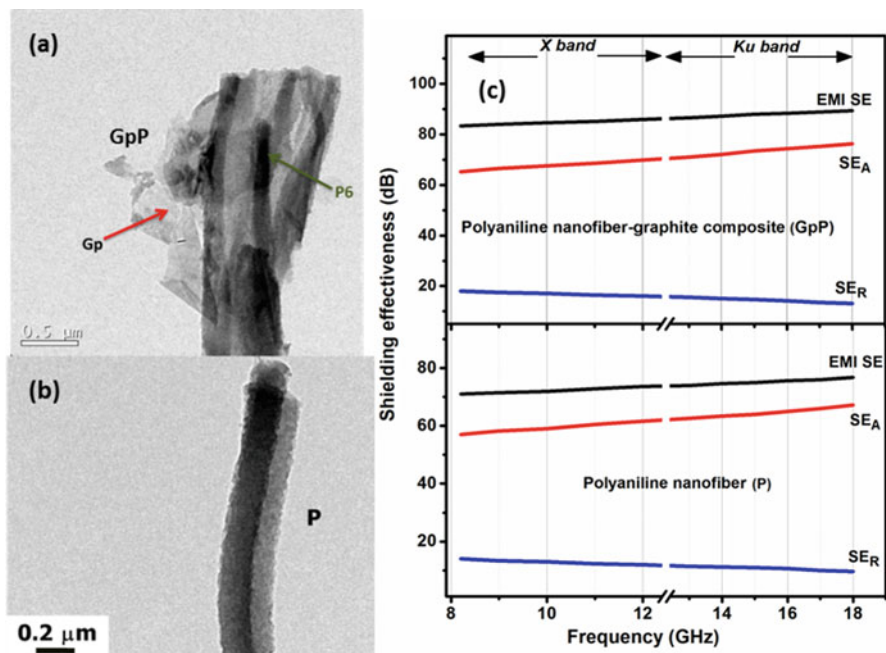


Fig. 8 TEM images and EMI shielding efficiency of polyaniline nanofiber and its graphite composite. (Accessed from [102, 107])

respectively [81]. Joseph et al. reported polyvinylidene fluoride-graphite flake (Fig. 7) composite of thickness 1 mm prepared by simple mixing and hot pressing method exhibits EMI SE of 55–57 dB in the 8.4–18 GHz frequency range [82]. Table 10 gives basic information on the research on the carbon-based high EMI shielding materials, which can be found useful for military and aerospace applications.

Another possible candidate to get good shielding materials is conducting polymers whose conductivity arises by the phonon-assisted hopping between randomly distributed localized states [43, 102]. The conducting polymers do not have great physical properties and are mostly used as composite of other materials such as latex, fibers, or polymer blends. The permittivity and permeability of conducting polymers can be controlled by synthetic means and hence are attractive electrical materials [43, 80, 102]. Figure 8 represents the microstructure and shielding properties of polyaniline nanofiber and its graphite composite. Electric-magnetic materials offer best potential candidates for thin broadband absorption but exhibit attenuation not enough for military and aerospace applications [108, 109]. The dielectrics are usually mixed with metal or carbon particles to get the desired shielding for these applications. Magnetic materials are limited to carbonyl iron and ferrites, which are prone to poor corrosion resistance [110]. It is more convenient to

use the EMI material as a paint, but not much attention was paid on this option [111]. Further research is needed in this area to make them useful for military and aerospace applications.

Applications of Microwave Materials

Dielectric resonators using high-permittivity materials were initially developed for microwave circuits, such as filters and oscillators [112]. Later, Mcallister and Long [113] proposed the use of dielectric resonator as an antenna element. In recent years extensive work has been reported on dielectric resonator antenna (DRA) [114, 115]. Over the last two decades, two classes of antennas, i.e., the microstrip antenna and the DRA, have been extensively researched for modern wireless applications. Being low-loss (high Q) antennas, the microstrip antennas possess narrow bandwidth.

Antennas

Microstrip Antennas

Microstrip antennas, the most widely used types of antennas in the microwave frequency range, are often used in the millimeter-wave frequency range as well [116]. Below about 1 GHz, the size of a microstrip antenna is however usually too large for practical applications, and thus other types of antennas like wire antennas dominate. Also called patch antennas, microstrip patch antennas consist of a metallic patch of metal that is on top of a grounded dielectric substrate. The metallic patch may be of various shapes, with rectangular and circular being the most common. Microstrip antennas are suitable for space and missile applications due to their low profile, small size, lightweight, affordability, durability, and ease of fabrication and installation. They are structurally reliable due to their mechanical robustness withstanding also shock and vibration. In addition, they are conformable to a curved surface and feasible with the MMIC design, are versatile in terms of antenna parameters, and can be easily designed to produce linear or circular polarization with high gain. A typical substrate thickness is about $0.02 \lambda_0$. Commercially available RT duroid, FR-4, Rogers, DuPont, Taconic, etc. substrates are commonly used for fabricating microstrip patch antennas. The DuPont 951 and 9 K7 LTCC are useful for applications in harsh adverse environments. The DuPont LTCC Green Tape™ 951 material system is designed for general applications up to 35 GHz. Green Tape™ 9 K7 is useful for high-frequency applications up to 100 GHz. A list of possible low-loss soft and hard dielectric materials with varying dielectric properties useful for microstrip antenna fabrication are given in Tables 1, 2, 3, 5, 6, and 7.

The dielectric constant has an impact on the dimension of microstrip conductors fabricated on the substrate material. Additionally, the dimensions are determined by the size of the fractional wavelengths (such as quarter wavelengths) of the signal frequencies to be carried by those circuit conductors. Thus, the dimensions decrease with the increasing frequencies. The dielectric constant also affects the dimensions

of microstrip conductors, shrinking their dimensions with increasing dielectric constant. Microstrip patch antenna is usually fabricated on substrates with a relative permittivity from 2.2 to 12. The higher the permittivity of dielectric material, the smaller the size of the antenna, but it achieves also lower efficiency and narrower bandwidth. This can play a role in the fabrication of a circuit and its conductor widths at higher frequencies. A lower dielectric constant is preferred at millimeter-wave frequencies, to avoid degradation of antenna properties. At higher frequencies, the use of thin samples results in finer conductor line widths for a controlled impedance line, such as the 50-Ohm lines commonly used in microwave circuits. Although thin dielectric materials may be attractive for making low-profile, lightweight PCBs, a thin microwave PCB with a high dielectric constant can result in extremely fine microstrip circuit dimensions. Also, the most compact microstrip antenna designs have decreased antenna gain due to the antenna size reduction. A high-permittivity substrate is used to fabricate compact microstrip patch antenna to overcome this disadvantage and obtain an enhanced antenna gain. If a substrate with a high permittivity is used for an antenna, achievable gain is 10 dBi with a smaller radiating patch. Conductor and dielectric losses become also more severe for thinner substrates. In addition, the surface wave losses become more acute for thicker substrate. Although the performance of microstrip antenna mainly depends on its structure and dimensions, the substrate material also has a significant role in performance such as reflection coefficient (S_{11}), bandwidth, etc. Thus, the microstrip antenna is usually narrowband, with typical bandwidths of a few percent. The patch antennas also tend to have lower radiation efficiency than some other types, with efficiencies typically between 70% and 90%. Anyway, they are widely used in mobile communications, satellite communications, direct broadcast service, remote sensing, biomedical radiators, and military systems such as missile, rockets, aircraft, etc. In addition, for spacecrafts and missiles applications, the ceramic antennas are more preferred than the ones based on polymer composites since environment is often harsh with large temperature variations. A large number of papers on antenna design and applications using different materials of varying dielectric constants are available in open literature, and the reader is referred to these books for details [117–120].

Ultra-wide band (UWB) technology has extremely wide operating bandwidth but has very low emission level which limits the wireless connection range to a few meters. Hence, the UWB radiotechnology is more likely to be applied in consumer electronics such as handset/laptop-centric and home networks which require short range but high data-rate wireless solutions. UWB systems will coexist with other traditional communication systems in the same frequency band by using low power levels. Recently considerable amount of interest has been paid on the possibility of developing antennas that employ fractal geometry in their design. Fractals can be used to miniaturize patch elements as well as wire elements. Recently, new forms of fractal antennas (combination of fractal geometry) are proposed for miniaturization, WLAN, and UWB applications.

Dielectric Resonator Antenna

To confine radiation and maintain a high-quality factor important for filter and oscillator applications, the ceramic dielectric resonators are often enclosed inside metal cavities. However by removing the metallic shield and suitable feeding to excite appropriate mode, the resonators could become efficient radiators being thus feasible for antenna applications as proposed by McAllister and Long [112]. The reader is referred to the recent reviews related to these dielectric resonator antennas (DRA) [115, 121, 122]. The DRA is constructed from dielectric resonator, substrate, and ground with different excited feeding techniques. DRA consists of dielectric materials as its radiating patch also called as DR on one side of the substrate and has a ground plane (metal) on the other side. DRA is a resonant antenna, fabricated from low-loss microwave dielectric material. There is no inherent conductor or surface wave loss in dielectric resonators which leads to high radiation efficiency. In case of DRA, various modes are excited to produce a broadside or omnidirectional radiation pattern for different coverage requirements. Simple coupling schemes can be used for DRA to most of the transmission lines used in microwave and millimeter-wave frequencies. Experimental and theoretical studies are extensively done on DRA with different shapes or geometries. The dimensions of the DRA (D) are related to the free space resonant wavelength (λ_0) by the approximate relation $D \propto \lambda_0 \epsilon_r^{-0.5}$ and by choosing a high ϵ_r ; the size of the DRA can be significantly reduced at the expense of bandwidth. The operating bandwidth can be varied for a wide frequency range by suitably selecting the resonator parameters, and a bandwidth of 140% has been reported [123]. The lowest frequency of DRA reported is 55 MHz [124] and the highest 94 GHz [125]. DRAs with dimensions ranging from a few millimeters with ϵ_r in the range of 6–100 have been reported [115, 121, 122]. The use of a wide range of dielectric permittivity values allows the designer to have control over size and bandwidth, i.e., wide bandwidth is achievable using low permittivity, and compact size is achievable with high permittivity. Very thin (<4 mm) structures are needed especially when integrated to portable terminals. Ceramic dielectric materials are widely used for GPS patch antennas leading to high performance and miniaturization. Ceramic antennas have also been proposed for multipurpose targets like machine-to-machine communication [126]. The DRAs are characterized by low phase noise, compact size, frequency stability with temperature, ease of integration with other hybrid MIC circuitries, simple construction, and the ability to withstand harsh environments. It has some interesting characteristics like lightweight, high permittivity, wide impedance bandwidth, low production cost, and ease of excitation.

The impedance bandwidth is a function of the dielectric constant and dimensions of the sample. Higher dielectric constant facilitates size reduction, whereas lower dielectric constant increases the bandwidth. In the millimeter-wave frequency range, the DRA are smaller size than the conventional antennas by a factor of square root of the dielectric constant of the material (ϵ_r). The DRA has also high radiation efficiency (>95%) because of the absence of losses due to conductor or surface wave, increased bandwidth, low cost, and compatibility to planar antenna feeding

techniques. The DRA has wider impedance bandwidth as compared to microstrip antenna. A bandwidth of 10% can be achieved for a dielectric constant of ten or less for a rectangular DRA. It must be also noted that the microstrip antenna radiates through two narrow edges of the patch, while the DRA radiates through its entire surface except the grounded portion. Surface waves are also absent in the DRA in contrast to the microstrip antenna thus improving the efficiency and reducing distortions in the radiation pattern. The DRA can have different shapes such as conical, tetrahedral, hexagonal, pyramidal, elliptical, and stair-stepped shapes or hybrid antenna designs using dielectric resonator antennas in combination with microstrip patches, monopoles, or slots. Extensive work has been reported on designing dielectric resonator antennas for applications like WiMAX, WLAN applications, UWB applications, RFID, and all dielectric wireless receivers. The size of antenna can be reduced by increasing the relative permittivity of the material making it viable for low-frequency operations. However excessive miniaturization may degrade the efficiency and BW of antenna. The radiation efficiency of a dielectric resonator antenna is not significantly affected by its dielectric constant, and a wide range of values can be used. However, the bandwidth of the DRA is inversely related to the dielectric constant and may limit the choice of values for a given application. An antenna with high gain must be larger in size with low Q-factor and therefore will have a higher BW. As the size of the antenna decreases, the effective aperture size is reduced, lowering directivity. A high-permittivity DRA can be used as a small and low-profile antenna. The DRAs made from high dielectric constant materials have a single resonant frequency with a well-defined internal field structure and hence do not have the bandwidth required for modern communication systems. Several designs such as mono DRA, poly DRAs, hybrid DRAs, annular ring DRA, parasitic DRA, etc. have been reported to achieve bandwidth enhancements for DRAs [125]. Recently, Antenova Ltd., UK, has developed a pair of lightweight, flexible antennas with better than 75% efficiency which can provide radio links to navigation satellites, as well as in wireless connectivity bands such as Bluetooth and Wi-Fi, for IoT and M2M applications. The properties of several DRA geometries with different permittivity and feeding are given in Tables 11 and 12.

Metamaterial-Based Antennas

The recent growth in telecommunication increased the demand for small and versatile antennas for multifunctional systems such as cell phones, handheld portable wireless devices for Internet connection, short- and long-range communication devices, radio-frequency identification (RFID), etc. Similarly small equipment and devices used for data transmission and navigation (GPS systems) require small antennas with omnidirectional radiation patterns. For reducing antenna size and volume, traditional miniaturization methods such as shorting pins, meandering, and dielectric loading [132] are adopted. This often results in low radiation efficiency, narrow bandwidth, and undesired radiation patterns. Therefore, in recent years, a strong interest has been generated on using periodic structures (metamaterials) to lower antenna profile as a method to optimize or enhance antenna performance. Metamaterials are typically constructed from periodic arrangements of

Table 11 Mono DRA designs [122, 127–131]

S. N	DRA geometry	Relative permittivity (ϵ_r)	Feed mechanism	~BW %
1	Flipped staired pyramid	12	Slot	62
2	Strip-fed rectangular	9.8	Conducting strip	43
3	Inverted L shaped	9.2	Probe	38
4	Cylindrical DRA	12	Probe	30
5	Half hemispherical	10	Probe	35
6	Cylindrical cup	10.2	L-shaped probe	32
7	Two-step stair shaped	12	Slot square cross section	54
8	Rectangular with an offset well	20	Slot	18
9	U shaped	9.8	Elliptical patch	72
10	Rectangular with a tunnel	20	Slot	20
11	H shaped	9.8	Trapezoidal patch	62
12	L shaped	9.8	Conformal inverted trapezoidal patch	71
13	Rectangular high aspect ratio (5.2:1)	25	Microstrip line	16
14	Rectangular with a moat	20	Slot	35
15	Cylindrical	10	Conformal metallic strip connected to SMA probe	66
16	Rectangular placed on a concave ground plane	9.8	Probe	55
17	Embedded multi-segment rectangular	9.8	Vertical feeding strip	50
18	Trapezoidal	10	Probe	55
19	Cylindrical	10.2	Dual coaxial probe	68
20	Bowtie	9.8	Probe	49
21	Cylindrical	10.5	Narrow slot in a rectangular waveguide	20
22	Circular disk	10.5	Waveguide probe	50
23	Rectangular on a conductor backed CPW	48	Coplanar	8
24	Rectangular	48	L strip	17
25	Elliptical	48	T strip	14
26	Seven element log periodic	2.1,6,9.8,10,10.2	Microstrip line	92
27	Capacitive coupled log periodic	2.1	Microstrip series feed	65.2
28	Nine element log periodic	12	Microstrip line	95

conventional materials to exhibit electromagnetic properties not found in any of their bulk individual constituents. An early boost to this research was the initial experimental verifications of electromagnetic bandgap structures (EBGs) and negative refractive index media (NRI or equivalently $\epsilon < 0$ and $\mu < 0$ media). Printed circuit realizations of metamaterials led to smaller radio-frequency (RF) devices such as

Table 12 Monopole UWB DRA geometries and properties [123, 132–141]

S. N.	Geometry	ϵ_r	Operating frequency GHz	BW
1	Annular ring DRA centrally excited by $\lambda/4$ monopole	10	6.0–18.0	3:1
2	Eye-shaped monopole DRA excited by coaxial probe connected to SMA connector	10	3.0–20.0	6:1
3	Annular DRR excited by T-shaped monopole	10	4.5–16.0	3.5:1 (112%)
4	Pawn-shaped DRR excited by $\lambda/4$ monopole	10	5.5–22.0	4:1
5	Inverted truncated annular conical DRA excited by monopole	9.8	3.4–5.0	–
6	Conical DRR excited by $\lambda/4$ monopole	10	5.7–23	4:1
7	Hemispherical DRR excited by $\lambda/4$ monopole	10	5.7–23	4:1
8	Stepped radius annular DRR excited by $\lambda/4$ monopole	10	3.0–10.3	110%
9	Mushroom-shaped DRR with three materials	4, 5, 7	4–25	137%
10	Mushroom-shaped DRR	2.1	3–4	137%
11	Annular DRR loaded monopole	10	5–20	100%
12	Inverted conical DRR-loaded monopole + skirt-shaped ground plane	10	4–15	111%
13	Annular DRR loaded t-shaped monopole	10	Probe	112%
14	Pawn-shaped DRR loaded monopole	10	Probe	122%
15	Conical and hemispherical DRA-loaded monopole	10	Probe	126%
16	Stacked conical DRR	10	Probe	138%
17	Stacked annular DRR	2.2	Probe	140%

phase shifters, couplers, and antennas. Introduction of metamaterials into the antenna system can provide exciting challenges for antenna engineers to meet the need for an increasing demand for military and space systems [141].

Low-Temperature Co-fired Ceramics Antennas

The recent advances in aerospace technologies demand new ways to package electronics for high temperature and harsh environments, the low-temperature co-fired ceramic (LTCC). LTCC is a multilayer design and packaging system that can embed passive components and thermal management structures within a substrate. LTCC packaging techniques uses stacked layers of a ceramic dielectric material to create printed circuit boards with embedded passives (such as thick-film resistors and capacitors), embedded heat sinks, and hermetic sealing using Kovar-TM lids. The low loss and relatively high dielectric constant of the LTCC materials make them desirable for high-frequency applications and are discussed in section “HTCC and LTCC Substrate/Packages.” Low-temperature co-fired ceramics (LTCC) have become an attractive technology for miniaturization of portable electronic devices and have been used for packaging integrated circuits (ICs) and applied

to actuators, sensors, and integrated microsystems with relatively low cost and high productivity. The LTCC-based multilayer technology has an extensive range of applications in areas such as telecommunications, automotive, aeronautics, radio-frequency (RF) modules (mobile phone, Bluetooth (2.4 GHz), Home RF, IEEE 802.11), microwave modules, optoelectronic modules, global positioning systems (GPS, 1.6 GHz), broadband access connection systems (5.8–40 GHz), and medical, military, and sensors packaging [142].

Antennas have been designed at different frequencies using the LTCC technology [143] approach ranging from 1 to 270 GHz. LTCC antenna in IEEE 802.15.3c band shows a vast area of applications. For example, LTCC Ferro A6M materials are used for ($\epsilon_r = 5.9$, $\tan\delta = 0.002$) the above band. In some designs the microstrip line antenna is using a silver conductor on the top surface of the LTCC substrate having a ground plane for antenna on the bottom surface. The permittivity of the substrate used is $\epsilon_r = 7.8$ and $\tan\delta = 0.002$. For multiple-frequency GSM band of 900/1800 MHz (lowest known frequency), LTCC technology is also implemented. Here LTCC tapes with dielectric constant and loss tangent value ($\epsilon_r = 7.8$, $\tan\delta = 0.0047$), respectively, are used to integrate the monopole helix antenna. LTCC technology is also used in electronically steerable antennas. Steerable antennas are the antennas that can change or steer its beam to the desired direction at a particular angle. This beamforming technique can be used for transmission and reception.

LTCC-based antenna is also designed with broadband and high gain at 60 GHz band, which is the internationally allocated band for communication. This antenna is designed with a substrate RNE5M ($\epsilon_r = 6$, $\tan\delta = 0.0035$). Nowadays LTCC-based ultra-wideband antenna [144] is also gaining interest among researchers. In this regard, LTCC substrate (type GL-550) with a dielectric constant of 5.7 ($\tan\delta = 0.0006$) is considered for designing UWB antenna to reduce the size of frontend modules in wireless transceivers. The future broadband wireless communication systems will have the need for more bandwidth in order to satisfy the increasing demands to achieve higher data rates. In this sense, the millimeter-wave frequency band will play a key role in fifth-generation (5G) wireless cellular networks. Here LTCC-based dielectric flat lens antennas and switched-beam arrays are very much effective for future 5G millimeter-wave communication systems. In order to design the LTCC lens prototypes dielectric material, DuPont 9 k7 ($\epsilon_r = 7.1$, $\tan\delta = 0.0009$) is used. With this design there can be scanning of high-gain radiation in both azimuth and ($\epsilon_r = 7.1$, $\tan\delta = 0.0009$) elevation planes, necessary for supporting high data transmission (>1.5 Gbps) as it is recommended in the IEEE 802.15.3c standard [142, 145]. It also helps in avoiding the requirement of high number of RF switches to perform such 2D radiation pattern configuration.

LTCC-based antennas can be designed to best suit modern-day miniaturized communication devices operating almost anywhere in the frequency spectrum, and the performance of the antenna can be improved by using different permittivity materials. Hence, it is a better choice for future wireless communication applications and an even more viable option compared with other traditionally used integration technologies. The DuPont 9 k7 material has been shown to perform well up to 100 GHz. The LTCC in general has a lower thermal expansion coefficient and higher

flexural strength, varying relative permittivity and low loss tangent and good thermal conductivity than polymer-based composites. LTCC-based circuits have an extensive range of applications in areas such as telecommunications, automotive, aeronautics, radio-frequency (RF) modules (mobile phone, Bluetooth, Home RF, IEEE 802.11), microwave modules, optoelectronic modules, and medical, military, and sensors packaging.

Dielectric Resonator Filters

High-performance DR filters are widely used in wireless and satellite communication systems due to their superior characteristics, such as high unloaded Q, excellent temperature stability, and smaller size compared to their air-filled counterpart [146–149]. Temperature-stable high-Q dielectric materials with a wide range of dielectric constants from 4 to 100 are available [6, 7]. Two types of dielectric-loaded resonator filters are commonly used:

- (a) Dual-mode filter, operating in HE_{11} mode, providing low loss, smaller volume, and elliptic function realizations. Here only half the number of physical cavities is needed.
- (b) Single-mode filter with all resonators operating in $TE_{01\delta}$ mode, providing low loss, flexible layout structure, and better spurious-free performance.

The drawback of the dielectric-loaded resonator filters is their inferior spurious characteristics, especially in the dual-mode configuration. By mixing the $TE_{01\delta}$ and HE_{11} modes in filter realization with proper cavity design, the spurious performance of the DR filter can be improved while maintaining the advantages of elliptic function filters. The dual-mode filter can halve the number of physical resonator cavities, therefore significantly reducing the weight and volume of the unit. It has been widely used in satellite communication systems. TE_{01} single-mode filters offer the advantages of design simplicity and flexibility in layout options over HE_{11} dual-mode filters, while dual-mode filters have significant advantages in the mass and volume of the products. Mixing the TE_{01} and HE_{11} modes, dielectric-loaded resonator filters achieve the advantages of dual mode HE_{11} DR filters and the excellent spurious performances of the TE_{01} mode ring resonator filters [148].

In recent works the designing of balanced/balun filters with differentially feeding method to DR is accomplished [147]. Similarly, triple-mode dielectric resonator is machined from a single piece of Trans-Tech 3500 series ceramic dielectric material with a dielectric constant of 35. This triple-band dielectric filter offers high Q and is miniature in size in comparison to previously reported multiband filter designs. This also allows independent control of each coupling matrix parameters [146]. The design of a high-efficiency filter-integrated class-F power amplifier (PA) in which high-Q-factor dielectric resonator (DR) filter is employed as the output matching network of the class-F PA shows excellent performance. It employs the dielectric material with $\epsilon_r = 38$, $\tan\delta = 0.0002$, respectively, for designing the filter [149].

Dielectric Resonator Oscillators

Oscillators producing energy at microwave frequencies are an essential component in most microwave communication systems, such as communication links, radar, frequency synthesizers, and so on. The dielectric resonator when coupled with two or three terminal active devices provides a vehicle for producing high-quality fixed frequency or narrowband tunable oscillators. A dielectric resonator (DR) can be used to form the stabilizing element in an oscillator. The dielectric resonator oscillators (DRO) are known as one of the most suitable devices for generating low-cost microwave signals. Dielectric resonator oscillators (DROs) are characterized by the following properties: high-frequency stability, high efficiency, and low manufacturing cost [150]. They also can be made to provide good temperature stability. The key elements to be optimized with respect to oscillator performance are output power, start-up stability, phase noise, DC-RF efficiency, tuning range, sensitivity to DR placement, and frequency pushing/pulling. In order for microwave oscillation to begin, a means to overcome the resistive losses in the circuit has to be provided. These losses include undesired stray and parasitic resistances and also the load into which the oscillator must operate (usually 50Ω). To do this the concept of negative resistance is introduced. If the amount of negative resistance exactly cancels the sum of the positive resistances, then the circuit will have a resonant or oscillation frequency where the inductive reactance is equal to the capacitive reactance. This condition is known as the steady-state oscillation condition. In order for oscillation to build up, an excess of negative resistance is required. Then, any small perturbation in the circuit, such as electrical noise, will kick-start a resonance. As oscillation builds the amount of negative resistance decreases until the steady-state condition is met. A negative resistor can be formed from an unstable active device with suitable feedback applied. Dielectric resonators can be used in both negative resistance (reflection) and feedback-type oscillators. The property of being easily coupled to a microstrip line is another reason to use dielectric resonators on integrated circuits.

The DRO design provides many types of active devices. For example, GaAs technology is considered as one of the most suitable transistor for microwave applications because of its frequency stability against temperature variation and its low noise characteristic. On the other hand, GaAs MESFET [151] is able to offer better performance than GaAs FET. As the dielectric resonator, Trans-Tech 8300 series dielectric resonator ($\epsilon_r = 35.5$) is used. The unloaded quality factor of this resonator can be up to 15,000. The design of Ka-band monolithic differential launcher for mode excitation integrated with the cylindrical DR ($\epsilon_r = 30.51$) monolithic differential DRO using SiGe technology shows excellent performance [152].

Conclusion

Microwave dielectric materials play a key role in global society, with a wide range of applications straddling terrestrial and satellite communications although the first real devices were reported only 50 years ago. The recent progress in the IoT, microwave

telecommunications, satellite broadcasting, and intelligent transport systems (ITSs) has resulted in an increasing demand for low-loss dielectric materials and EMI shielding materials. Low-loss dielectric materials are extensively used in wireless communication systems as well as in several electronic devices. There are a large number of materials reported in the literature, and ideal materials should be judiciously selected depending on the applications. The fast progress in microwave materials is mainly due to the demands critical for defense and aerospace applications being in the forefront of the research. These demands include, e.g., low permittivity with high Qf values for resonators and antennas, much higher EMI shielding performance, and good stability of the dielectric properties in harsh and hostile environments not so severe in the common wireless communication. The emerging microwave materials in the forms of inks, composites, and foams are expected to form solutions also in the future. Conformable, bendable, or stretchable shielding, resonating, or radiating devices are on the way, but further research is needed especially for defense and aerospace applications where the high-frequency performance is less negotiable than in the other areas.

References

1. Richtmeyer R (1939) Dielectric resonators. *J Appl Phys* 15:391–398
2. Okaya A (1960) The rutile microwave resonator. *T Proc IRE* 48:1921–1921
3. Cohen S (1968) Microwave band pass filters containing high Q dielectric resonators. *IEEE Trans Microw Theory Tech MTT-16*:1628–1629
4. Masse DJ, Purcel RA, Ready DW, Maguire EA, Hartwig C (1971) A new low loss high K temperature compensated dielectric for microwave applications. *Proc IEEE* 59:1628–1629
5. Wakino K, Nishikawa T, Tamura S, Ishikawa Y (1975) Microwave bandpass filters containing dielectric resonators with improved temperature stability and spurious response. *IEEE-MTT-S Int Microw Symp Dig, Palo Alton, CA*, 63–65
6. Sebastian MT (2008) Dielectric materials for wireless communication. Elsevier, Amsterdam
7. Sebastian MT, Ubic R, Jantunen H (2017) Microwave materials and applications. Two Volume sets John Wiley & Sons Inc., West Sussex
8. Sebastian MT, Ubic R, Jantunen H (2015) Low-loss dielectric ceramic materials and their properties. *Int Mater Rev* 60(7):392–412
9. Jain T (2013) Technology advancement in wireless communications. *Int J Sci Technol Res* 2 (8):2277–8616
10. Seraphim DP, Feinberg I (1981) Electronic packaging evolution in IBM. *IBM J Res Dev Res Dev* 25:617–618
11. Tummula PK (1996) Microelectronic packaging handbook. Springer, New York
12. Varghese J (2016) Zircon based hard. LAP LAMBERT Academic Publisher, Soft Microwave Substrates and Devices
13. Ralf R, Patrick S, Martin O (2014) SMTR[®] module – evolution towards Airborne Applications. International Radar Conference-2014, <https://doi.org/10.1109/RADAR.2014.7060400>
14. Schuh H (2009) X-band T/R-module front-end based on GaN MMICs. *Intern J Microw Wirel Technol* 1:387–394
15. Yu H, Liu J, Zhang W, Zhang S (2015) Ultra-low sintering temperature ceramics for LTCC applications: a review. *J Mater Sci Mater Electron [Internet]*:1–10. Springer. Available from: <http://link.springer.com/10.1007/s10854-015-3282-y>
16. Jin Y, Wang Z, Chen J (2010) Introduction to microsystem packaging technology. CRC Press, Boca Raton

17. Chen L-Y, HiTEC, HiTEN, & CICMT (2014), Vol. 2014, No. HITEC, pp. Dielectr. Perform. a High Purity HTCC Alumina High Temp. – a comparison study with other polycrystalline alumina,” Additional Conferences Device Packaging HiTEC, HiTEN, & CICMT; January 2014, p 000271–7
18. Chen L-Y, Neudeck PG, Hunter G (2016) Electrical Performance of a High Temperature 32-I/O HTCC Alumina Package. 21000 Brookpark Road Cleveland, Ohio 44135 2 NASA Glenn Research Center, 21000 Brookpark Road, Cleveland, Ohio 44135
19. Blackwell E, Raton B (2000) The electronic packaging handbook. Press CRC, Boca Raton
20. Harper C (2000) Electronic packaging and interconnection handbook, 3rd edn. McGraw-Hill, New York
21. Varghese J, Vahera T, Ohsato H, Iwata M, Jantunen H (2017) Novel low-temperature sintering ceramic substrate based on indialite/cordierite glass ceramics. *Jap J Appl Phys* 56:10PE01
22. Varghese J, Joseph T, Sebastian MT (2011) ZrSiO₄ ceramics for microwave integrated circuit applications. *Mater Lett* 65(7):1092–1094
23. Pullanchiyodan A, Surendran KP (2016) Formulation of Sol–Gel derived bismuth silicate dielectric ink for flexible electronics applications. *Ind Eng Chem Res*:7108–7115. Available from: <http://pubs.acs.org/doi/abs/10.1021/acs.iecr.6b00871>
24. Arun S, Sebastian MT, Surendran KP (2017) Li₂ZnTi₃O₈ based high κ LTCC tapes for improved thermal management in hybrid circuit applications. *Ceram Int* 43(7):5509–5516
25. Ferro Corporation (2015) Low temperature co – fired ceramic systems A6M/A6M – E high frequency LTCC tape system [Internet]. Tech. data sheet LTCC. 2015. pp 1–2. Available from: <http://www.ferro.com/Our+Products/ColorsGlass/Electronic/Electronic-Materials/docs/A6M-E LTCC Tape System.pdf>
26. Dupont. LTCC [Internet]. Datasheet (2017) (cited 1 Jan 2017). Available from: http://www.dupont.com/content/dam/dupont/products-and-services/electronic-and-electrical-materials/documents/prodlib/GreenTape_Design_Layout_Guidelines.pdf
27. Thomas D, Abhilash P, Sebastian MT (2013) Casting and characterization of LiMgPO₄ glass free LTCC tape for microwave applications. *J Eur Ceram Soc* 33(1):87–93
28. Roshni SB, Sebastian MT, Surendran KP (2017) Can zinc aluminate-titania composite be an alternative for alumina as microelectronic substrate? *Sci Rep*[Internet] 7:40839. Nature Publishing Group; Available from: <http://www.nature.com/articles/srep40839>
29. Kaneko T, Watanabe H, Akaishi M, Wada K (1999) AlN HTCC super miniaturized millimeter wave transceiver MCMs, the novel structure for the high reliability, the high performance and the mass productivity. *IEEE MIT-S Dig* 2:449–452. (0–7803–5135–5/99/\$10.00 0 1999 IEEE)
30. Cressler JD, Mantooth HA (2013) Extreme environment electronics. Chapters 1–5. CRC Press, Boca Raton\Florida, pp 1–47
31. Spry DJ, Neudeck PG, Chen L, Lukco D, Chang CW, Beheim GM, Krasowski MJ, Prokop N (2016) Processing and characterization of thousand-hour 500 °C durable 4H-SiC JFET integrated circuits. In: Proceedings of the 2016 IMAPs international conference on high temperature electronics (HiTEC 2016). International Albuquerque, New Mexico
32. Catalog Smt (2017) HTCC QFN Packages to 40 GHz [Internet]. 2017 [cited 1 Jan 2017]. p 1. Available from: https://smtnet.com/company/index.cfm?fuseaction=view_company&company_id=47300&component=catalog&catalog_id=19408
33. Dupont (2009) DuPont™ Green Tape™ 951 Technical Datasheet. 2009;3
34. Sebastian MT, Jantunen H (2008) Low loss dielectric materials for LTCC applications: a review. *Int Mater Rev* 53:57–90
35. Sebastian MT, Wang H, Jantunen H (2016) Low temperature co-fired ceramics with ultra-low sintering temperature: a review. *Curr Opin Solid State Mater Sci* 20:151–170
36. Suresh EK, Prasad K, Arun NS, Ratheesh R (2016) Synthesis and microwave dielectric properties of A₁₆V₁₈O₆₁ (a = Ba, Sr and ca) ceramics for LTCC applications. *J Electron Mater* 45(6):2996–3002
37. Varghese J, Ramachandran P, Sobocinski M, Vahera T, Jantunen H (2019) ULTCC glass composites based on rutile and anatase with co-firing at 400 °C for high frequency applications. *ACS Sustain Chem Eng* 7(4):4274–4283

38. Joseph N, Varghese J, Teirikangas M, Sebastian MT, Jantunen H (2018) Ultra-low sintering temperature ceramic composites of CuMoO₄ through Ag₂O addition for microwave applications. *Compos Part B* 141:214–220
39. Joseph N, Varghese J, Teirikangas M, Sebastian MT, Jantunen H (2016) Glass-free CuMoO₄ ceramic with excellent dielectric and thermal properties for ultralow temperature co-fired ceramic applications. *ACS Sustain Chem Eng* 4(10):5632–5639
40. Varghese J, Surendran KP, Sebastian MT (2014) Room temperature curable silica ink. *RSC Adv* 4(88):47701–47707
41. Varghese J, Teirikangas M, Puustinen J, Jantunen H, Sebastian MT (2015) Room temperature curable zirconium silicate dielectric ink for electronic applications. *J Mater Chem C* 3(35): 9240–9246
42. Joseph AM, Nagendra B, Bhoje Gowd E, Surendran KP (2016a) Screen-printable electronic ink of ultrathin boron nitride Nanosheets. *ACS Omega* 1(6):1220–1228
43. Joseph N, Sebastian MT (2016) A facile formulation and excellent electromagnetic absorption of room temperature curable polyaniline nanofiber based inks. *J Mater Chem C* 4:999–1008
44. Liu W, Wang H, Zhou D, Li K (2010) Dielectric properties of low-firing Bi₂Mo₂O₉ thick films screen printed on Al foils and alumina substrates. *J Am Ceram Soc* 93(8):2202–2206
45. Pullanchiyodan A, Surendran KP (2016) Formulation of sol–gel derived bismuth silicate dielectric ink for flexible electronics applications. *J Eur Ceram Soc* 36(8):1939–1944
46. Sebastian MT, Jantunen H (2010a) Polymer-ceramic composites of 0-3 connectivity for circuits in electronics: a review. *Int J Appl Ceram Technol* 7(4):415–434
47. Wall L (1972) Fluoropolymers. Wiley, New York
48. Willis OR (2008) Characterizing fluoropolymeric materials for microelectronics and MEMS packaging. ProQuest Information and Learning Company, USA
49. Bur A (1985) Dielectric properties of polymers at microwave frequencies: a review. *Polymer (Guildf)* 26:963–977
50. Allen F, Robert L, Michael E (1996) Ceramic filled composite polymeric electrical substrate materials exhibiting high dielectric constant and low thermal coefficient of dielectric constant
51. Allen FHIII (1994) Fluoropolymeric electrical substrate material exhibiting low thermal coefficient of dielectric constant, US Patent No. 5358775
52. Sebastian MT, Krupka J, Arun S, Kim CH, Kim HT (2018) Polypropylene-high resistivity silicon composite for high frequency applications. *Mater Lett* (232):92–94
53. Popielarz R, Chiang C (2007) Polymer composites with dielectric constant comparable to that of barium titanate ceramics. *Mater Sci Eng B* 139:48–54
54. Sun Y, Rogers J (2007) Inorganic semiconductors for flexible electronics. *Adv Mater* 19:1897–1916
55. Rogers J, Huang Y (2009) A curvy, stretchy future for electronics. *Proc Natl Acad Sci* 106:10875–10876
56. Seol Y, Noh H, Lee S (2008) Mechanically flexible low-leakage multilayer gate dielectrics for flexible organic thin film transistor. *Appl Phys Lett* 93:013305–1–013305–3
57. Gubbels F, Jaeger R, Gleria M (2007) Silicones in industrial applications. In: Jaeger R, Gleria M (eds) *Inorganic polymers*. Nova Science Publishers, New York, pp 61–162
58. Yang S, Jiang K (2012) Elastomer Application in Microsystem and Microfluidics. In: Boczkowska A (ed) *Advanced elastomers – technology, properties and applications*. InTech. Open Science mind, Rijeka, pp 203–222
59. Sebastian MT, Chameswary J (2016) Flexible and stretchable electronic composites, springer series on polymer and composite materials. In: Ponnamma D (ed) *Poly(Isobutylene-co-Isoprene) compos flex electron appl*. Springer International Publishing, Switzerland, pp 335–365
60. Sebastian MT, Ananthalarum S, Subodh G, Juuti J, Teirikangas M, Jantunen H (2012) Composite electroceramics. In: Nicolais L, Borzacchiello A (eds) *Wiley encyclopedia of composites*, 2nd edn. Wiley, Inc., Boston

61. Amin A, Sierakowski R (1990) Effect of thermomechanical coupling on the response of elastic solids. *AIAA J* 28(7):1319–1322
62. Dasgupta S (2015) Polymer matrix composites for electromagnetic applications in aircraft structures. *J Indian Inst Sci* 95:75–296
63. Chen F, Shen Q, Zhang L (2010) Electromagnetic optimal design and preparation of broadband ceramic radome material with graded porous structure. *Prog Electromagn Res* 105:445–461
64. Hong T, Song M-Z, Liu Y (2011) RF directional modulation technique using a switched antenna array for communication and direction-finding applications. *Prog Electromagn Res* 120:195–213
65. Military aerospace (2011) Shielding-against-electromagnetic-and-rf-interference-for-safety-and-mission-success [Internet]. *Technol. Focus*. 2017 [cited 20 Jul 2011]. Available from: <http://www.militaryaerospace.com/articles/print/volume-28/issue-7/technology-focus/shielding-against-electromagnetic-and-rf-interference-for-safety-and-mission-success.html>
66. Chauhan S, Abraham M, Choudhary V (2016) Superior EMI shielding performance of thermally stable carbon nanofiber/poly(ether-ketone) composites in 26.5–40 GHz frequency range. *J Mater Sci* 51:9705–9715
67. Pascucci N. (2016) EMI shielding caulk delivers superior performance in military radar systems, [internet]. Available from: www.parker.com/chomerics
68. Wen B, Cao M, Lu M, Cao W, Long H, Wang X et al (2014) Reduced graphene oxides light weight and high efficiency electromagnetic interference shielding at elevated temperatures. *Adv Mater* 26:3484–3489
69. Saville P (2005) Review of Radar Absorbing Materials. *RDC Atl. TM* 2005-003
70. Halpern O (1960) Method and means for minimizing reflection of high frequency radio waves, US Patent No. 2923934
71. Halpern O, Johnson MHJ, Wright RW (1960) Isotropic absorbing layers, US Patent No. 2951247
72. Joseph N, Singh S, Sirugudu R, Murthy V, Ananthakumar S, Sebastian MT (2013) Effect of silver incorporation into PVDF-barium titanate composites for EMI shielding applications. *Mater Res Bull* 48:1681–1687
73. Chauhan S, Abrahamand M, Choudhary V (2016) Electromagnetic shielding and mechanical properties of thermally stable poly (ether ketone) multiwalled carbon nanotube composites prepared using twin screw extruder equipped with novel fractional mixing elements. *RSC Adv* 6(2016):113781–113790
74. Klemperer C, Maharaj D (2009) Composite electromagnetic interference shielding materials for aerospace applications. *Compos Struct* 91:467–472
75. Byeon J, Kim J-W (2011) Aerosol based fabrication of a Cu/polymer and its application for electromagnetic interference shielding. *Thin Solid Films* 520:1048–1052
76. Kumar A, Singh A, Kumari S, Dutta P, Dhawan S, Dhar A (2014) Polyaromatic-hydrocarbon-based carbon copper composites for the suppression of electromagnetic pollution. *J Mater Chem A* 2:16632
77. Al-Ghamdi AA, El-Tantawy F, Aal N, El-Mossalamy E, Mahmoud W (2009) Stability of new electrostatic discharge protection and electromagnetic wave shielding effectiveness from poly(vinyl chloride)/graphite/nickel nanoconducting composites. *Polym Degrad Stab* 94:980–986
78. Al-Ghamdi A, El-Tantawy F (2010) New electromagnetic wave shielding effectiveness at microwave frequency of polyvinyl chloride reinforced graphite/copper nanoparticles. *Compos Part A* 41:1693–1701
79. Shahzad F, Alhabeb M, Hatter C, Anasori B, Hong SM, Koo C et al (2016) Electromagnetic interference shielding with 2D transition metal carbides (MXenes). *Science* 353:1137–1140
80. Skotheim TA, Elsenbaumer R, Reynolds JR (1998) *Handbook of conducting polymers*. Marcel Dekker, New York

81. Chaudhary A, Kumari S, Kumar R, Teotia S, Singh B, Singh A et al (2016) Lightweight and easily foldable MCMC-MWCNTs composite paper with exceptional electromagnetic interference shielding. *ACS Appl Mater Interfaces* 8:10600–10608
82. Joseph N, Varghese J, Sebastian MT (2017a) Graphite reinforced polyvinylidene fluoride composites an efficient and sustainable solution for electromagnetic pollution. *Compos Part B Eng* 123:271–278
83. Al-Saleh M (2015) Influence of conductive network structure on the EMI shielding and electrical percolation of carbon nanotube/polymer nanocomposites. *Synth Met* 205:78–84
84. Sun X, Liu X, Shen X, Wu Y, Wang Z, Kim J-K (2016) Graphene foam/carbon nanotube/poly (dimethyl siloxane) composites for exceptional microwave shielding. *Compos Part A* 85:199–206
85. Al-Saleh M, Saadeh W, Sundararaj U (2013) EMI shielding effectiveness of carbon based nanostructured polymeric materials: a comparative study. *Carbon NY* 60:146–156
86. Kumar R, Dhawan S, Singh H, Kaur A (2016) Charge transport mechanism of thermally reduced graphene oxide and their fabrication for high performance shield against electromagnetic pollution. *Mater Chem Phys* 180:413–421
87. Goyal R (2013) Cost-efficient high performance polyetheretherketone/expanded graphite nanocomposites with high conductivity for EMI shielding application. *Mater Chem Phys* 142:195–198
88. Modak P, Kondawar S, Nandanwar D (2015) Synthesis and characterization of conducting polyaniline/graphene nanocomposites for electromagnetic interference shielding. *Procedia Mater Sci* 10:588–594
89. Theilmann P, Yun D-J, Asbeck P, Park S-H (2013) Superior electromagnetic interference shielding and dielectric properties of carbon nanotube composites through the use of high aspect ratio CNTs and three-roll milling. *Org Electron* 14:1531–1537
90. Wang H, Zheng K, Zhang X, Ding X, Zhang Z, Bao C et al (2016) 3D network porous polymeric composites with outstanding electromagnetic interference shielding. *Compos Sci Technol* 125:22–29
91. Li Y, Shen B, Pei X, Zhang Y, Yi D, Zhai W et al (2016) Ultrathin carbon foams for effective electromagnetic interference shielding. *Carbon NY* 100:375–385
92. Luo X, Chugh R, Biller BC, Hoi Y, Chung D (2002) Electronic applications of flexible graphite. *J Electron Mater* 31(5):535–544
93. Luo X, Chung D (1996) Electromagnetic interference shielding reaching 130 dB using flexible graphite. *Carbon NY* 34:1293–1299
94. Al-Ghamdi A, Al-Ghamdi A, Al-Turki Y, Yakuphanoglu F, El-Tantawy F (2016) Electromagnetic shielding properties of graphene/acrylonitrile butadiene rubber nanocomposites for portable and flexible electronic devices. *Compos Part B* 88:212–219
95. Gupta A, Varshney S, Goyal A, Sambyal P, Gupta B, Dhawan S (2015) Enhanced electromagnetic shielding behavior of multilayer graphene anchored luminescent TiO₂ in PPY matrix. *Mater Lett* 158:167–169
96. Verma P, Saini P, Malik R, Choudhary V (2015) Excellent electromagnetic interference shielding and mechanical properties of high loading carbon nanotubes/polymer composites designed using melt recirculation equipped twin-screw extruder. *Carbon NY* 89:308–317
97. Mishra M, Singh A, Dhawan S (2013) Expanded graphite–nanoferrite–fly ash composites for shielding of electromagnetic pollution. *J Alloys Compd* 557:244–251
98. Zhang L, Alvarez N, Zhang M, Haase M, Malik R, Mast D et al (2015) Preparation and characterization of graphene paper for electromagnetic interference shielding. *Carbon NY* 82:353–359
99. Dhawan R, Kumari S, Kumar R, Dhawan S, Dhakate S (2015) Mesocarbon microsphere composites with Fe₃O₄ nanoparticles for outstanding electromagnetic interference shielding effectiveness. *RSC Adv* 5:43279
100. Farhan S, Wang R, Li K (2016) Electromagnetic interference shielding effectiveness of carbon foam containing in situ grown silicon carbide nanowires. *Ceram Int* 42:11330–11340

101. Kaur A (2012) Ishpal, Dhawan S. tuning of EMI shielding properties of polypyrrole nanoparticles with surfactant concentration. *Synth Met* 162:1471–1477
102. Joseph N, Varghese J, Sebastian MT (2015) Self-assembled polyaniline nanofibers with enhanced electromagnetic shielding properties. *RSC Adv* 5:20459–20466
103. Bayat M, Yang H, Ko F, Michelson D, Mei A (2014) Electromagnetic interference shielding effectiveness of hybrid multifunctional Fe₃O₄/carbon nanofiber composite. *Polymer (Guildf)* 55:936–943
104. Cabrera C, Miranda F (2015) *Advanced nanomaterials for aerospace applications*. CRC press, Taylor and Francis group
105. Joseph N, Janardhanan C, Sebastian MT (2014) Electromagnetic interference shielding properties of butyl rubber-single walled carbon nanotube composites. *Compos Sci Technol* 1:139–144
106. Tong X (2009) *Advanced materials and design for electromagnetic interference shielding*. CRC Press, Taylor and Francis group, New York
107. Joseph N, Varghese J, Sebastian MT (2016) A facile formulation and excellent electromagnetic absorption of room temperature curable polyaniline nanofiber based inks. *J Mater Chem C* 4:999–1008
108. Joseph N, Varghese J, Sebastian MT (2017b) In situ polymerized polyaniline nanofiber-based functional cotton and nylon fabrics as millimeter-wave absorbers. *Nat Polym* 49:391–399
109. Zhou P, Chen J, Liu M, Jiang P, Li B, Hou X-M (2017) Microwave absorption properties of SiC@SiO₂@Fe₃O₄ hybrids in the 2–18 GHz range. *Int J Miner Metall Mater* 24:804–813
110. Kong L, Li Z, Liu L, Huang R, Abshinova M, Yang Z et al (2013) Recent progress in some composite materials and structures for specific, electromagnetic applications. *Int Mater Rev* 58:203
111. Folgueras L, Alves M, Rezende M (2010) Microwave absorbing paints and sheets based on carbonyl iron and polyaniline: measurement and simulation of their properties. *J Aerosp Technol Manag* 1:63–70
112. Kajfez D, Guillon P (1986) *Dielectric resonators*. Artech House, Norwood
113. Mcallister M, Long S (1983) Rectangular dielectric resonator antenna. *IEEE Electron Lett* 19:218–219
114. Luk K, Leung K (2002) *Dielectric resonator antennas*. Electronic & electrical engineering research studies series. Research Studies Press, Taunton
115. Petosa A (2007) *Dielectric resonator antenna handbook*. Artech House, Boston
116. Garg R, Bhartia P, Bahl I, Ittipiboon A (2000) *Microstrip antenna design hand book*. Artech house Inc., Norwood
117. Garg R (2001) *Microstrip antenna design handbook*. Artech house Inc., Norwood
118. Imbriale W (ed) (2006) *Spaceborne antennas for planetary exploration*. Wiley, Hoboken
119. Kumar G, Ray K (2003) *Broadband microstrip antennas*. Artech House, Boston
120. Pozar D, Schaub D (eds) (1995) *Microstrip antennas: the analysis and design of microstrip antennas and arrays*. Institute of Electrical and Electronics Engineers, New York
121. Petoso A, Ittipiboon A (2010) Dielectric resonator antennas. A historical review and the current state of the art. *IEEE Antennas Propag Mag* 52:91–116
122. Soren D, Ghatak R, Mishra R, Poddar D (2014) Dielectric resonator antennas: designs and advances. *Progr Electromag Res B* 60:195–213
123. Ozzaim C (2014) Monopole antenna loaded by stacked annular ring dielectric resonators for ultrawide bandwidth. *Microw Opt Technol Lett* 56:2395–2398
124. Kingley S, OKeefe S (1999) Beam steering and monopulse processing of probe fed dielectric resonator antenna. *Proc Rada Sonar Navig* 3:121–125
125. Svedin J, Huss L, Karlen D, Enoksson P, Rusu C (2007) A micromachined 94 GHz dielectric resonator antenna for focal plane array applications. In: *IEEE international microwave symposium, Honolulu, -IEEE MTT-S*, pp 1375–1378
126. Liflander J (2010) Ceramic chip antennas vs. PCB trace antennas: a comparison. MPDIGEST [Internet]. 2010; Available from: Feature article, White paper, www.pulseelectronics.com/download/3721/g041/pdf

127. Bijumon P, Menon S, Lethakumari B, Sebastian MT, Mohanan P (2006) Broad band elliptical dielectric resonator antennas excited with geometry modified microstrip lines. *Microw Opt Technol Lett* 48:65–67
128. Kumari R, Behera S (2014) Investigation on log periodic dielectric resonator antenna array for Ku band applications electromagnetics. *Electromagnetics* 34(1):19–33. Taylor Francis
129. Kumari R, Behera S (2013b) Nine element frequency independent dielectric resonator array for X- band applications. *Microw Opt Technol Lett* 55(2):400–403
130. Menon S, Lethakumary B, Bijumon P, Sebastian M, Mohanan P (2005) L-strip fed wide band rectangular dielectric resonator antenna. *Microw Opt Technol Lett* 45:227–228
131. Suma M, Menon S, Bijumon P, Sebastian M, Mohanan P (2005) Rectangular dielectric resonator antenna on a conductor -backed co-planar waveguide. *Microw Opt Technol Lett* 45(2):154–156
132. Caloz C, Itoh T (2006) *Electromagnetic metamaterials: transmission line theory and microwave applications*. Piscataway, Wiley
133. Ganguly D, Guha D, George S, Kumar C, Sebastian M, Antar Y (2017) New design approach for hybrid monopole antenna to achieve increased ultra-wide bandwidth. *IEEE Antennas Propag Mag* 11:139–144
134. Ghosh S, Chakrabarty A (2008) Ultrawide band performance of dielectric loaded T-shaped monopole transmit and receive antenna/EMI sensor. *IEEE Antennas Wirel Propag Lett* 7:358–361
135. Guha D, Gupta B, Antar Y (2012) Hybrid monopole-DRAs using hemispherical/conical-shaped dielectric ring resonators: improved ultrawide band designs. *IEEE Trans Antennas Propag* 60:393–398
136. Guha D, Gupta B, Antar Y (2009) New pawn-shaped dielectric ring resonator loaded hybrid monopole antenna for improved ultrawide bandwidth. *IEEE Antennas Wirel Propag Lett* 8:1178–1181
137. Guha D, Antar Y, Ittipiboon A, Petosa A, Lee D (2006) Improved design guidelines for the ultra wideband monopole-dielectric resonator antenna. *IEEE Antennas Wirel Propag Lett* 5:373–377
138. Jazi M, Denidni T (2008) A new hybrid skirt monopole dielectric resonator antenna. In: *Proceedings of the IEEE antennas propagation society international symposium*, pp 1–4
139. Kumari R, Behera S (2013c) Mushroom shaped dielectric resonator antenna for WiMAX applications. *Microw Opt Technol Lett* 55:1360–1365
140. Ozzaim C, Ustuner S, Tarim N (2013) Stacked conical ring dielectric resonator antenna excited by a monopole for improved ultrawide bandwidth. *IEEE Trans Antennas Propag* 61:1435–1438
141. Sheeja K, Behera S, Sahu P (2012) Bandwidth improvement of a zeroth order resonant antenna for WiMax applications. *Int J RF Microw Comput Eng* 22(4):569–574
142. Ullah U, Ain M, Mahyuddin N, Othman M, Ahmad Z, Abdullah M et al (2015) Antenna in LTCC technologies: a review and the current state of the art. *IEEE Antennas Propag Mag* 57:241–260
143. Kim D, Kang D, Shin M, Jung H, Lim J (2016) Design of a low temperature co-fired ceramic (LTCC) based antenna with broadband and high gain at 60 GHz bands. In: *IEEE international conference on consumer electronics Asia. ICCE-Asia*, pp 1–3
144. Abbosh A, Bialkowski M, Jacob M, Mazierska J (2005) Investigations into an LTCC based ultra-wide band antenna. In: *Asia-Pacific microwave conference (APMC)*, p 4
145. Imbert M (2017) Assessment of LTCC based dielectric flat lens antennas and switched beam arrays for future 5G millimeter – wave communication systems. *IEEE Trans Antennas Propag* 65:6453–6473
146. Li J, Zhan Y, Qin W, Wu Y, Chen J-X (2017) Differential dielectric resonator filters. *IEEE Trans Compon Packag Manuf Technol* 7:637–645
147. Qin W, Chen J-X (2017) Balanced/balun filters based on dielectric resonators. In: *IEEE global symposium on millimeter-waves*
148. Wang ZK (2007) Dielectric resonators and filters. *IEEE Microw Mag* 8:115–127

149. Zhu L, Mansour R, Yu M (2017) Triple-band dielectric resonator bandpass filters. In: IEEE MTT-S international microwave symposium. pp 745–747
150. Webster J (1999) Dielectric resonator oscillators. In: Wiley encyclopedia of electrical and electronics engineering. Wiley, Chichester
151. Ugurlu S (2011) Dielectric resonator oscillator design and realization at 4.25 GHz. In: International conference 2011, p II-205-II-208
152. Hamed K, Freundorfer A, Antar Y (2007) A monolithic differential coupling mechanism for dielectric resonators excitation in conductive silicon substrates. IEEE Microw Wirel Components Lett 17:25–27



Development of PLZT Electroceramics with Ultrahigh Piezoelectric Properties by a Novel Material Engineering Approach

6

A. R. James and Ajeet Kumar

Contents

Introduction	216
Novel Techniques for Material Processing	221
High-Energy Mechanochemical Ball Milling (Mechanical Activation)	221
Cold Isostatic Pressing (CIP)	221
Poling of the PLZT Ceramics	222
Phase Analysis and Microstructural Characterization	222
Dielectric Property Studies and Nature of Phase Transitions	225
Ferroelectric Polarization vs. Electric Field Hysteresis Loops	228
Poling Study for Ultrahigh Piezoelectric Properties	229
Effect of Poling Parameters on the Piezoelectric and Dielectric Properties of PLZT 8/60/40 Ceramics	230
Aging in Piezoelectric and Dielectric Properties of PLZT 8/60/40 Ceramics	234
Piezoelectric Strain vs. Electric Field Hysteresis Loops	236
Temperature-Dependent Ferroelectric and Electromechanical Properties for the Confirmation of Nature of the Phase Transitions	238
Temperature-Dependent <i>P-E</i> Hysteresis Loops	238
Temperature-Dependent Electromechanical Coupling Factor of PLZT Ceramics	241
Applications of PLZT Ceramics in the Defense Sector	242
Energy Harvesting Applications	242
Ring and Stack Actuators	243
Nondestructive Test (NDT)	244
Conclusions	245
References	246

A. R. James (✉) · A. Kumar
Ceramics and Composites Group, Defence Metallurgical Research Laboratory (DMRL),
Hyderabad, India
e-mail: james@dmrl.drdo.in; jkajeet@yahoo.co.in

Abstract

Lead lanthanum zirconium titanate (PLZT) ceramics belong to the family of materials known as smart materials, which can be used as sensors and actuators; however, the high dielectric, ferroelectric (P_r), and piezoelectric (d_{33} and g_{33}) properties decide the end applications. The d_{33} is related to charge generation or electric field-induced strain in the materials. On the other hand, g_{33} and k_p are related to the voltage generation and conversion of mechanical stress to the electric charge, respectively. High values of d_{33} , g_{33} , and k_p are good for energy harvesting applications; however, the high-strain materials are more useful for actuators. The remanent polarization (P_r) and coercive field (E_c) are taken into cognizance for memory and energy density applications. High dielectric constant materials can be used for charge storage applications. $(\text{Pb}_{0.92}\text{La}_{0.08})(\text{Zr}_{0.60}\text{Ti}_{0.40})\text{O}_3$ (PLZT 8/60/40) ceramics are known to show all of the above electrical properties. Further improvement of these properties is possible by modified processing approaches. In this study, it was found that a combination of mechanical activation (high-energy milling or HEM) with a cold isostatic process (CIP) not only reduces the processing temperatures and time but also circumvents the need to add any excess PbO in the starting materials. At the same time, the high density of ceramics was not compromised. No binder was added in this process, thereby avoiding the contamination risk involved and also the possibility of reduced density. Apart from the above two processes, yet another process that was used to improve the electrical properties output was a scientific study of the electrical poling process. The optimized poling results in the significant enhancement of electrical properties, which successfully increased piezoelectric properties multiple times. The PLZT 8/60/40 ceramics were effectively poled at fields less than the coercive field ($<0.5E_c$), which could be very advantageous especially in the case of ceramics having poor resistivity. Such PLZT ceramics are used for different types of defense applications.

Keywords

PLZT ceramics · Mechanical activation · Cold isostatic pressing · Poling conditions · Defense applications

Introduction

Piezoelectric ceramics can be made much more sensitive to electrical or mechanical input than naturally available piezoelectrics such as quartz and tourmaline. The composition, shape, and dimensions of such ceramics can be tailored to meet the requirements of a specific purpose. In spite of their toxic nature, lead-based ceramics like lead zirconate titanate (PZT) are still being widely used in different applications such as sensors, actuators, buzzers, transducers, and nano-positioners due to the commercial non-availability of lead-free materials [1–5]. Since at present it is

difficult to replace lead-based materials, the immediate thrust is to minimize the lead that comes out into the atmosphere as much as possible. Substitution of Pb by off-valent donors (A-site Pb^{2+} replaced by X^{3+} or B-site Zr^{4+} replaced by Y^{5+}) in PZT system not only enhances the electrical properties but is also a route to reduce the lead content. These off-valent modified materials also are known as soft electroceramics [6, 7]. Based on the above description, many researchers have tried to prepare PZT ceramics, which are doped or substituted with different modifiers. However, the highest electrical properties for PZT ceramics were achieved by a modification, in which Pb^{2+} is substituted by La^{3+} due to its comparable ionic size, such materials are usually known as PLZT ceramics [6, 8]. La-modified PZT ceramics possess higher dielectric and piezoelectric properties compared to the original PZT system because of the donor effect. While replacing divalent Pb^{2+} ions, trivalent La^{3+} ions generate vacancies at the A-site of the perovskite ABO_3 structure to neutralize the system. These vacancies counteract the natural p-type conductivity of the PZT ceramics, which results in the increase in electrical resistivity of the modified PZT materials. These donors also help to enhance domain reorientation, which results in the softening of PZT domain wall motion as well as easy reorientation of dipoles during poling. The electronic properties of La-substituted PZTs are greatly enhanced as compared to the basic PZT system. The general formula of PLZT is given by $(\text{Pb}_{1-x}\text{La}_x)(\text{Zr}_{1-y}\text{Ti}_y)\text{O}_3$, and a ratio of La/Zr/Ti determines whether PLZT ceramics show ferroelectric (FE), antiferroelectric (AFE), and relaxor ferroelectric (RFE) behavior. Depending upon the specific requirements for different applications of piezoelectric ceramics, various compositions of the Pb/La ratios may be chosen. The electrical properties of different La-modified PZT compositions are listed in Table 1.

Like other electroceramics, an optimum piezoelectric activity in PZT solid solutions was found at the MPB, which separates the rhombohedral ($R3c$) phase and tetragonal ($P4mm$) phase [6]. The MPB of electroceramics has been the subject of intense scientific studies to understand its behavior. The solid solution of $\text{Pb}(\text{Zr}_x\text{Ti}_{1-x})\text{O}_3$ (PZT) displays a complex phase diagram, which shows a high-symmetry, primitive cubic structure at high temperatures. At low temperatures a variety of cation shifts, octahedral tilts, and deformations occur leading to different structures. At room temperature PbZrO_3 ($\text{Ti} = 0\%$) shows the lower-symmetry, antiferroelectric, orthorhombic (A_O) structure [21]. With increasing Ti content (0% to 100%), two ferroelectric, rhombohedral phases, FR_{LT} and FR_{HT} , are observed up to $x = 0.48$ where there is a transition to a ferroelectric tetragonal phase, F_T , continuing to the end PbTiO_3 ($\text{Zr} = 0\%$) [22]. The high-resolution synchrotron XRD data of PZT ceramics shows the existence of monoclinic phase with space group Cm at the MPB [23–26]. The monoclinic phase fraction depends on the average composition and temperature of the ceramics [27]. The monoclinic Cm phase relieves the stress in PZT ceramics, which was generated due to the interaction between $R3m$ and $P4mm$ phases at MPB [28]. The discovery of a stable monoclinic phase at the MPB provides a new perspective to view the rhombohedral to tetragonal phase transformation for the PZT system [24]. The polar axis of this monoclinic phase is in the (110) plane along a direction between the tetragonal and rhombohedral polar axes [24]. After investigation of several compositions at the MPB,

Table 1 Electrical properties of La-substituted PZT ceramics (K = dielectric constant at 1 kHz, RT)

S. No.	Compositions	P_r ($\mu\text{C}/\text{cm}^2$)	E_c (kV/cm)	d_{33} (pC/N)	k_p (%)	K	T_c ($^\circ\text{C}$)	Refs.
1	(Pb _{0.92} La _{0.08}) (Zr _{0.60} Ti _{0.40}) _{0.98} O ₃	21.90	6.65	569	–	3413	156	[9]
2	(Pb _{0.95} La _{0.05}) (Zr _{0.60} Ti _{0.40})O ₃	7.00	6.51	–	–	–	250	[10]
	(Pb _{0.91} La _{0.09}) (Zr _{0.60} Ti _{0.40})O ₃	6.20	5.29	–	–	–	116	
	(Pb _{0.88} La _{0.12}) (Zr _{0.60} Ti _{0.40})O ₃	2.89	1.00	–	–	–	55	
3	(Pb _{0.98} La _{0.02}) (Zr _{0.535} Ti _{0.465}) _{0.995} O ₃	–	–	415	49	1030	371	[11]
4	(Pb _{0.98} La _{0.02}) (Zr _{0.54} Ti _{0.46})O ₃	45	11.1	–	–	–	–	[12]
5	Pb _{0.91} La _{0.09} (Zr _{0.4} Ti _{0.6}) O ₃	36.6	21.1	–	–	2500	–	[13]
6	(Pb _{0.99} La _{0.01}) (Zr _{0.52} Ti _{0.48}) _{1-x/4} O ₃	–	–	–	48	1334	–	[14]
7	(Pb _{0.94} La _{0.06}) (Zr _{0.65} Ti _{0.35})O ₃	16.0	2.95	–	–	3000	180	[15]
8	(Pb _{0.92} La _{0.08}) (Zr _{0.60} Ti _{0.40}) _{0.98} O ₃	–	–	520	29	5700	163	[16]
9	(Pb _{0.97} La _{0.03}) (Zr _{0.53} Ti _{0.47})O ₃	–	–	458	–	1880	–	[17]
10	(Pb _{0.97} La _{0.03}) (Zr _{0.60} Ti _{0.40})O ₃	58.1	7.10	208	42.1	1210	320	[18]
	(Pb _{0.93} La _{0.07}) (Zr _{0.60} Ti _{0.40})O ₃	49.2	6.92	450	52.0	1875	221	
	(Pb _{0.92} La _{0.08}) (Zr _{0.60} Ti _{0.40})O ₃	43.6	6.67	387	52.0	2511	188	
	(Pb _{0.92} La _{0.08}) (Zr _{0.60} Ti _{0.40})O ₃	–	–	–	–	–	–	
11	(Pb _{0.92} La _{0.08}) (Zr _{0.60} Ti _{0.40})O ₃	20.5	9.98	–	–	2785	145	[19]
12	(Pb _{0.924} La _{0.076}) (Zr _{0.70} Ti _{0.30})O ₃	26.41	7.76	410	–	–	96.4	[20]

Guo et al. [29] have shown a modified PZT phase diagram as shown in Fig. 1a. From previous studies, a second phase boundary has been theoretically predicted to exist between the zirconium-rich region and a region containing lead atoms observed by Zhang et al. [30] The studies revealed that the region containing lead is composed of two types of structures. In one structure, the lead atoms have a lot of space to be affected by external mechanical stress, but in the other structure, the lead atoms do not have nearly as much space to move. This first type of structure is strongly preferable for maximizing the piezoelectric response in PZT. The two possible monoclinic phases are denoted by M_A and M_B , where the atomic displacements lie within $\{110\}$ mirror planes. The M_A monoclinic phase has cation displacements

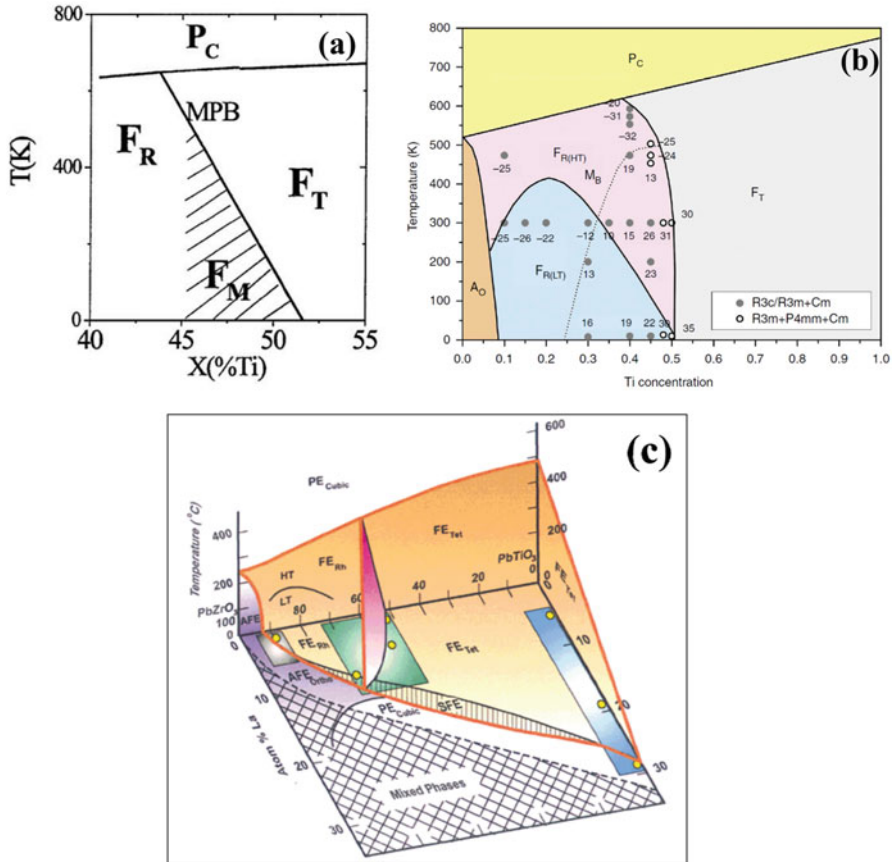


Fig. 1 (a) Schematic of the PZT phase diagram at MPB showing the monoclinic region. (Reprinted figure, Copyright (2019) by the Phys. Rev. Lett.) [29], (b) the new phase diagram for PZT. The crossover between M_A and M_B region is separated by a dashed line. The phase regions, which are shown in Fig. 1(b), are cubic (P_C), orthorhombic (A_O), tetragonal (F_T), and rhombohedral ($F_{R(LT)}$ and $F_{R(HT)}$). (Reprinted figure, Copyright (2019) by the Nature Communications) [30]. (c) The phase diagram of the $(Pb_yLa_{1-y})(Zr_xTi_{1-x})O_3$ (PLZT) solid solution system. (Reprinted figure, Copyright (2019) by the Journal of American ceramic society) [7]

between the R and T positions, whereas the M_B monoclinic phase can be found between R and O regions. Figure 1b shows the newly proposed phase diagram of PZT ceramics. La substitution into PZT ceramics also modifies the MPB, and the influence of La doping on the MPB of PZT ceramics was studied and reported by many researchers [10, 16, 31–38]. As per the phase diagram, PLZT 8/60/40 compositions lie close to the MPB and were selected for further studies [7]. Figure 1c shows the PLZT phase diagram, which shows the reduction in the transition temperature (T_c) with increasing La substitution, due to the decrease in ferroelectric phase stability in favor of the paraelectric and antiferroelectric phases, as indicated

by the red line. The cross-hatched area represents a region of diffuse and metastable relaxor phases, which can be brought to the ferroelectric phase by application of an electric field. The solubility of La in the PZT lattice is related to the amount of PT as indicated by the dashed line adjacent to the mixed-phase region in Fig. 1c.

Since most of the Pb loss occurs at the processing stage, suitable care in the form of materials engineering approach will go a long way in alleviating the same and also serves the dual purpose of reducing the toxic effect of Pb on the environment. This study is an endeavor along those lines. This can be possible if (1) no excess lead is added to the starting materials and (2) ceramics should be prepared at reduced processing temperatures. However, the density and other electrical properties of the ceramics should not be compromised. Processing of lead-based ceramics at relatively low temperatures can be made possible by using the high-energy mechanical milling technique, which is the most suitable technique as suggested by Kong et al. [39, 40]. The properties of electroceramics are also greatly affected by milling conditions. The addition of La to PZT, use of HEM resulting in fine powders with a consequent reduction in processing temperatures, etc. all contribute to the reduction in environmental pollution by 15–25% compared to conventional PZT ceramics processing. Ferroelectric ceramics with a narrow particle size distribution results in the lowering of processing temperatures. Mechanical milling is superior to the conventional solid-state reaction and the wet chemistry-based ones to get nanosized and homogeneous ferroelectric powders. The most significant characteristic of this technique is that the formation of the desired compounds is due to the reactions of low-cost oxide precursors which are activated by mechanical energy, instead of the heat energy (conventional solid-state reaction process). High density (>95% of theoretical density) and uniform grain size are required to get the maximum electrical performance of ferroelectric ceramics. This problem is addressed by a combinatorial approach of high-energy milling and cold isostatic pressing as per previous reports [41–44].

The ferroelectric domains are randomly reoriented and do not show any piezoelectric property, as the bulk ferroelectric ceramics are cooled after sintering. The piezoelectric property can be induced in the ferroelectric ceramic by a method called “poling.” In this process, a direct current (dc) electric field with strength larger than the coercive field strength is applied to the ferroelectric ceramic at a high temperature. On the application of an external dc field, the spontaneous polarization within each grain gets oriented toward the direction of the applied field. This leads to net polarization in the direction of poling. The piezoelectric response of the ceramics highly depends on the poling conditions. Thus the optimization of poling conditions is also very important. The PLZT ceramics, which are poled at optimum poling parameters, show enhanced piezoelectric properties. Usually, the PZT and PLZT ceramics show the piezoelectric charge coefficient (d_{33}) in the range of 400–500 pC/N which is considered to be high as mentioned in previous reports (Table 1). However, the improved processing approach shows the enhancement in the d_{33} , (more than 700 pC/N), which is termed as ultrahigh piezoelectric coefficient. The value of d_{33} above 800 pC/N is termed as giant piezoelectricity [45]. These materials with high piezoelectric activity are good for device fabrication.

Novel Techniques for Material Processing

PLZT ceramics were prepared via the high-energy mechanochemical (HEM) ball milling and cold isostatic pressing (CIP) method.

High-Energy Mechanochemical Ball Milling (Mechanical Activation)

Commercially available raw oxides of PbO (99.9%), La₂O₃ (99.9%), ZrO₂ (99%), and TiO₂ (99.9%) (Sigma-Aldrich, USA) were weighed as per stoichiometric formula and HEM ball milled for 5 hours by using a Fritsch Pulverisette 5 planetary milling system in an air atmosphere at room temperature. Milling was done using an agate and zirconia vials (250 ml), zirconia balls (YTZ of Tosoh, Japan, dia~3 mm, 250 gms), and distilled water with milling speed of 150 rpm. These are the optimized milling conditions to synthesize the PLZT ceramics [46].

It is reported and found that the mechanical activation techniques reduce the particle sizes and result in enhanced electrical properties. The term milling is referred to as the breaking down of relatively coarse materials to the ultimate fineness. The principal aim of the milling process is to reduce the primary particle size (to increase the reactivity of fine-scale particles) and agglomerate size (ideally to primary particle size) and to achieve the desired particle size distribution [47, 48]. Planetary ball mills are widely used as high-energy ball mills for producing nanometer-scale powders of ferroelectric materials. The milling balls collide with each other as well as with the walls of the milling vial. Planetary ball mills show high performance for grinding and pulverization of the ceramic powders. A combination of impact and frictional forces between the balls and vial is responsible for size reduction of particles and at the same time for the micro-strains produced in them [49]. If a milling medium like water is used, it is presumed that the energy of milling comes down on account of the viscosity of the liquid, but at the same time, this has the advantage that the liquid ensures that the powders are constantly in contact with the balls, thereby ensuring better milling efficiency. If dry conditions are used, there is a possibility that the powders might settle down at the bottom of the vial, whereas the balls only impact each other or the walls, without serving the purpose of milling the powders [50]. Milling enhances both mixing and size reduction and provides for an intimate interface in each collision, momentarily.

Cold Isostatic Pressing (CIP)

Before sintering of electroceramics, green bodies should possess a certain minimum density, which can be achieved by various techniques such as wet pressing, dry pressing, slip casting, cold isostatic pressing, and extrusion. The choice of the method depends on the type of ceramic powder, desired shape, particle size distribution, and state of agglomeration. In this study, the PLZT calcined powders were filled in a rubber mold and cold isostatically pressed (Ciped) in the form of a cylindrical rod at a pressure of 3 kbar (300 MPa). Figure 2 shows the schematic

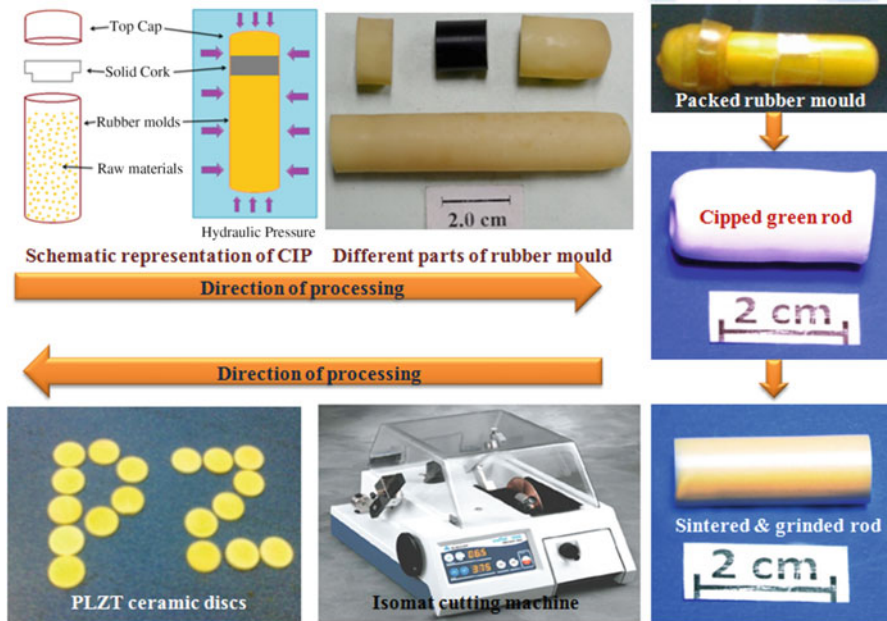


Fig. 2 Schematic representation of the PLZT ceramics processing

representation of the PLZT processing which includes CIP process, rubber mould setup used for CIP, obtained green PLZT rod, sintered and ground PLZT rod, and PLZT ceramics disks. The ceramic disks were obtained by using isomet cutting machine. Sintering was typically carried out at 1200 °C for about 4 h.

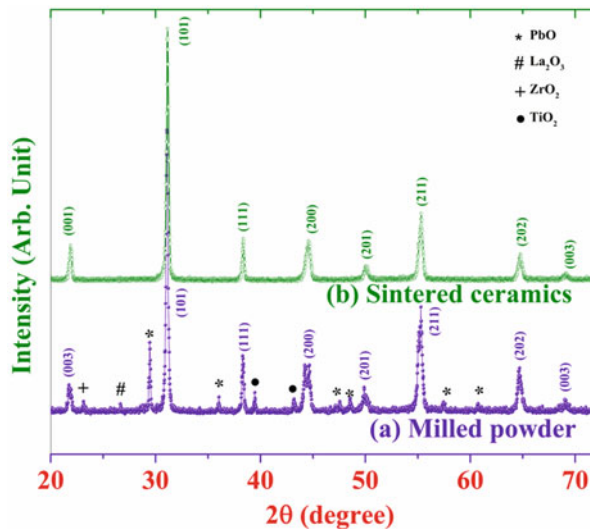
Poling of the PLZT Ceramics

The sample geometries for measurement of the material's electrical properties were in conformity with the IEEE standards [51]. High-temperature conductive silver paste was applied to both surfaces of the disks as electrodes and then fired at 500 °C for 15 min for proper curing. Poling study was done by immersing the samples in silicone oil (Dow Corning 704) [44]. The d_{33} was determined using a d_{33} meter (SENSOR SS01 Piezo-d Meter, Canada). The detailed poling study for PLZT ceramics is given in section “[Poling Study for Ultra-high Piezoelectric Properties](#).” The details regarding processing can be found in the patent by A.R. James and J. Subrahmanyam [52].

Phase Analysis and Microstructural Characterization

The XRD patterns were obtained for both as-milled powders and sintered compacts of La-substituted PZT ceramics. Figure 3a shows the XRD patterns of the as-milled powders of PLZT 8/60/40 ceramics, which indicate the presence of some peaks

Fig. 3 XRD patterns for the PLZT 8/60/40 (a) milled powders and (b) sintered ceramics



related to the perovskite phase. High-energy ball milling provides enough energy to refine the size of the starting powders to nanometer range at the initial stage of milling. The impact generated during mechanochemical milling is high enough to break down the particles of the PLZT powder to nanometer sizes. The refined milled powders become more and more reactive due to the decrease in their surface to volume ratio, resulting in very fine-scale size and highly reactive nano-powders. This leads to partial chemical reaction, thus giving rise to partial perovskite phase during milling itself as can be seen in the Fig. 3a. Milled powders of PLZT 8/60/40 composition shows almost complete perovskite phase transformation with few extra unmatched peaks which correspond to the unreacted raw materials. All the peaks of unreacted raw oxides were matched by using their respective JCPDS cards.

Figure 3b shows the XRD pattern for the sintered compact of PLZT 8/60/40 ceramics. After the heat treatment, the disappearance of these extra peaks shows that the reaction between the unreacted raw oxides took place and a complete phase transformation into the desired perovskite PLZT phase is observed. The above results and phase formation are confirmed by comparing with the JCPDS (53–0698) file. The broadening of X-ray diffraction peaks was used for the calculation of average crystallite size. As we know, the crystallite size is a measure of the size of coherently diffracting regions/domains of a material and is inversely proportional to the peak width or FWHM. Similarly, the lattice strain is also proportional to the peak width or FWHM. As the width of the diffraction peak increases, the crystallite size decreases. Optimal lanthanum substitution at the A-site of the PZT ceramics results in lattice relaxation which leads to a decrease in lattice strain. All the aforementioned reasons are sufficient for the binding of crystallites in clusters leading to an increase in their size. Hence, lower lattice strain indicates larger crystallites or in other words increased coherently diffracting regions/domains. The average crystallite size (P) was calculated by using the Scherrer equation [53, 54]. PLZT 8/60/40 ceramics show a maximum crystallite size of ~30 nm.

The particle size of milled powders can be measured by many methods; however, the following techniques (1) Scanning electron microscopy (SEM) (2) Transmission electron microscopy (TEM) and (3) Small angle x-ray scattering (SAXS) were used in this study. Figure 4a, b shows the SEM and TEM images of milled powders of PLZT ceramics, respectively. Figure 4a indicates the agglomeration of milled powders due to the highly reactive nature of the fine size of the PLZT particles. The reduction in particle size results in an increase in the surface to volume ratio making the particles highly reactive and causing an agglomeration between the particles. Due to the agglomeration of milled powder, the resolution of the SEM is not sufficient to see the particles; hence a TEM was used to examine the microstructure of the material. The TEM image (Fig. 4b) of milled powders shows that the shape of the PLZT 8/60/40 particles deviated from sphericity with a nonuniform particle size distribution in the range of 15–40 nm. Agglomeration is also evident from the TEM image. The sol-gel process results in spherical particles, whereas mechanochemical processing (MCP) has elongated/flaky particles on account of the high impaction and forces reactivity and mechanical deformation of the same [16, 55].

Figure 4c shows the SAXS graph for the PLZT 8/60/40 milled powders. In SAXS technique, the small-angle scattered data can be approximated by a Gaussian curve, which can be used to characterize the structure of the materials with large interplanar

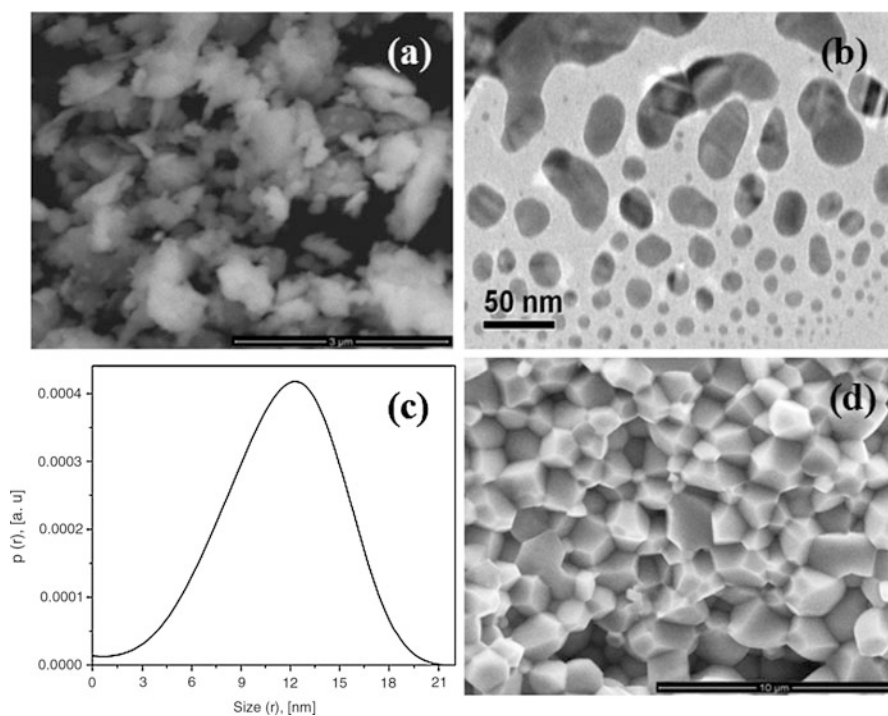


Fig. 4 (a) SEM image, (b) TEM image, (c) SAXS graph of PLZT milled powders, and (d) SEM image of fractured surface of sintered PLZT ceramics

spacing and also to measure the size and shape of the particles. The x-axis shows the particle size, and any tilt in the distribution shows a deviation from sphericity. For the PLZT 8/60/40 ceramics, the particle size was found to be ~ 21 nm, and particle shape is deviating from sphericity. The particle size measured from TEM and SAXS shows a good agreement with the particle size data obtained from the Scherrer formula.

SEM was also used for the microstructural and morphological studies of sintered PLZT ceramics. The base composition of PZT shows larger grains (~ 9 μm) compared to La-substituted ones with a less dense microstructure [38]. The grain shape for the PZT system was also not uniform which is detrimental to the electrical properties. When lead is substituted by lanthanum at the A-site of PZT, a sharp decrease in grain size was observed. SEM images of the fractured surface of sintered PLZT 8/60/40 ceramics indicate a very dense structure with a uniform grain size (Fig. 4d). The average grain size for PLZT 8/60/40 ceramics was found to be ~ 1.35 μm . Clear and visible grain boundaries, uniformity in grain sizes, and lack of porosity in the PLZT materials may be the reasons for the good properties exhibited. It was deemed that minute chemical inhomogeneities on the A- and B-sites of the perovskite and formation of secondary phases on a very small scale at the grain boundaries prevented the growth of grains [37].

Dielectric Property Studies and Nature of Phase Transitions

PLZT 8/60/40 ceramics show the highest dielectric constant of ~ 2335 measured at room temperature and 1 kHz. The value of dielectric constant for PLZT 8/60/40 ceramics is ~ 6 times more than PZT ceramics and comparatively same as PMN-PT [56]. The marked increase can be attributed to the improvement in the microstructure (density, grain size, and uniformity in grain size) along with intrinsic factors like the grains behaving more like strain-free crystals. The dielectric constant of ferroelectric ceramics usually increases with increasing density. PLZT sintered ceramics with very fine grain sizes (nanometer) and large grain sizes (micrometer) showed lower dielectric constant [57]. In the case of very fine grains, the magnitude of the dielectric constant gradually decreased probably due to the diminished mobility of the domain walls. At optimum conditions, not only ceramics have fewer defects and vacancies, but also the unclamped dipoles inside the grains are free to respond to the oscillating electric field with minimum restrictions yielding a higher dielectric constant with a lower value of the dielectric loss. The dielectric loss for PLZT 8/60/40 ceramics was found to be less. Generally, for electroceramics, dielectric loss increases as a function of temperature and frequency. This phenomenon is attributed to the polarization relaxation mechanism of the ceramics. Usually, dielectrics with higher dielectric constant, which have more polarizing mechanisms, show higher dielectric loss than materials with lower dielectric constant. The increase in the dielectric loss as a function of temperature is attributed to the increase in conduction current of the electroceramics. The dielectric losses, in dielectric materials, occur due to rotations and internal friction of dipolar molecules. The energy loss in the molecular transfer from one position to another is also one of the main reasons for dielectric losses.

According to the phase transition behavior, the ferroelectric ceramics can be categorized into three groups, ferroelectrics with (1) normal phase transition with sharp dielectric peak at T_c , (2) diffuse type of phase transition with broad dielectric peak at dielectric maxima temperature (T_m), and (3) relaxor phase transition with broad dielectric peak at frequency-dependent dielectric maxima temperature. Apart from that normal ferroelectrics show square P - E hysteresis loops and zero saturation polarization (P_s) at T_c ; however, relaxor ferroelectrics (RFE) show slim P - E hysteresis loops with some value of P_s above T_m [58]. The origin in relaxor properties is believed to be the presence of polar-nano-regions or nano-clusters compared to macro domains of normal ferroelectrics. Different theories and explanations have been given by many researchers to understand the relaxor behavior. Burns et al. suggested the nucleation of polar-nano-regions at Burns temperature ($T_B > T_m$), which is close to the temperature at which Curie-Weiss law starts to deviate from normal behavior [59–61]. These polar-nano-regions also freeze at a low temperature similar to the dipolar glasses [62, 63]. Cross et al. suggested that chemical heterogeneity due to B-site modification creates a small range of favorable directions (Local polar regions) separated by the low energy barrier. The size of polar-nano-regions is restricted by the low energy and does not extend to a larger size as in normal ferroelectrics [64, 65]. These small regions were considered to be identical, independent, and nano-size ideal superparaelectric clusters by Bell et al. [66]. However, Glazounov et al. [67] give the idea about the size distribution of polar-nano-regions with the different local transition temperatures. This size distribution is considered as exponential by Lu et al. [68]. The model proposed by Cheng et al. gives information about the freezing of polar clusters ($T < T_m$) and production rate and the concentration of polar-nano-regions ($T > T_m$) [69–71].

PZT ceramics show a normal phase transition with a narrow dielectric peak at T_c [72, 73]. However, some other lead-based systems such as modified PZT (PLZT x/65/35) [74] and PMN-based systems show the relaxor-type phase transition [45]. The dielectric studies for the PLZT 8/60/40 ceramics as a function of temperature at different frequencies (1 to 100 kHz) were carried out to understand the nature of the ferroelectric phase transition, shown in Fig. 5a, b. The broadened peak in the dielectric constant vs. temperature curve rather than a sharp and narrow peak (as in normal ferroelectrics) around T_c is one of the most important characteristics of a disordered perovskite structure with a diffuse phase transition. Substitution of La on the A-site of the PZT system modifies the MPB [75], which results in the deviation from the normal phase transition to diffuse-type phase transition (DPT). Improved electrical properties were observed for the PLZT ceramics which show the broadened dielectric peak at the transition temperature. This peak broadening in PLZT ceramics is believed to be due to compositional fluctuations and/or substitutional disordering in the arrangement of cations in one or more crystallographic sites of the structure, which leads to microscopic or nanoscopic heterogeneity in the compounds, with different local Curie points [76–78]. These compositional fluctuations occur when Pb^{+2} , Zr^{+4} , and Ti^{+4} are replaced by La^{+3} . The changes are ascribed to the lead vacancies (donor dopants such as W^{6+} , Nb^{5+} , La^{3+} , Th^{4+} , Ta^{5+} , B^{3+} , and Sb^{5+} which cause Pb vacancies by substituting a higher valence ion for Pb^{2+}) and the

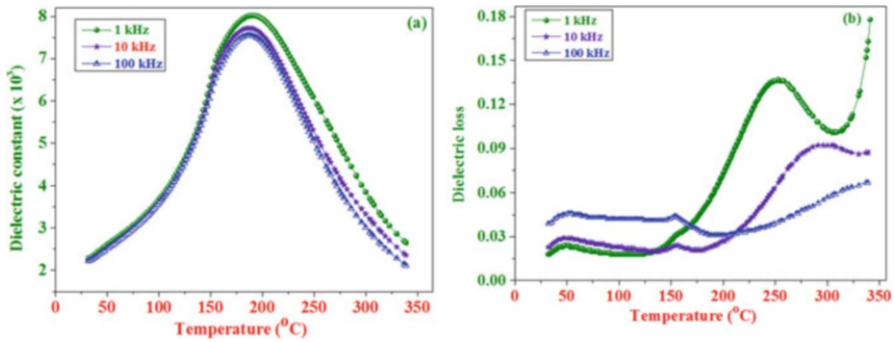


Fig. 5 (a) Dielectric constant and (b) dielectric loss vs. temperature curves from 1 to 100 kHz for PLZT ceramics

resulting increase in domain wall mobility [79]. La modification affects the nature of the ferroelectric phase transition of PZT and deviates toward a diffuse-type phase transition (DPT). The effect of La substitution in the A-site of PZT ceramics is discussed and has already been reported [56, 80].

The broad peak in dielectric constant vs. temperature curve for PLZT 8/60/40 ceramics shows a deviation from the normal phase transitions. The degree of deviation from the Curie-Weiss law is denoted by the parameter ΔT_m ($\Delta T_m = T_{cw} - T_m$). T_{cw} denotes the temperature from which permittivity starts to deviate from the Curie-Weiss law, and T_m represents the corresponding temperature of the maximum dielectric constant. The degree of diffuseness (γ) in the dielectric peak of PLZT ceramics can be calculated by the slope of the linear curve fit $\ln(1/\varepsilon - 1/\varepsilon_{\max})$ vs. $\ln(T - T_m)$. $\gamma = 1$ stands for the normal Curie-Weiss behavior with a sharp phase transition, while $\gamma = 2$ represents the complete relaxor-type phase transition [57, 81]. The value of γ lying in between 1 and 2 indicates the diffuse nature of the phase transition. Figure 6a shows the reciprocal of dielectric constant as a function of temperature measured at 1 kHz. The linear fitting of the reciprocal of dielectric constant shows the dielectric maxima temperature, and the intercept of linear fitting on the temperature axis does not coincide. This is a clear indication of deviation from the normal to DPT or relaxor-type phase transition. The ΔT_m and T_{cw} parameters were calculated by using this graph. Figure 6b shows the plots between the $\ln(1/\varepsilon - 1/\varepsilon_{\max})$ and $\ln(T - T_m)$ for PLZT 8/60/40 ceramics at 1 kHz. A linear relationship was observed, and the slope of the fitted $\ln(1/\varepsilon - 1/\varepsilon_{\max})$ vs. $\ln(T - T_m)$ curve was used to determine the value of γ , which was found to be 1.93, (< 2) at 1 kHz. The value of γ ($1 < \gamma < 2$) and the large value of ΔT_{diff} at the measured frequency confirm the deviation of the phase transition from the Curie-Weiss-type phase transition to DPT phase transition and the high degree of disorderliness in the material.

The electroceramics, which show a broad dielectric peak at their transition temperature, revealed high-temperature piezoelectric activity, well above the dielectric maxima. The diffuse phase transition occurs in a temperature range called as the Curie range, above which ceramics do not show any ferroelectricity. The existence of polarization,

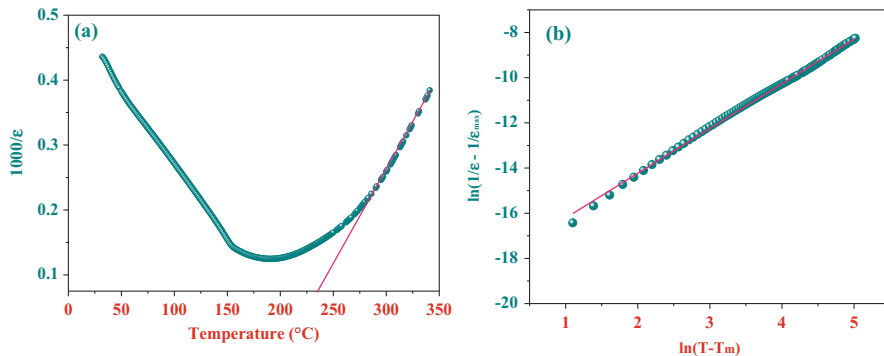


Fig. 6 (a) Reciprocal of the dielectric constant w.r.t. temperature and (b) fitting with empirical Curie-Weiss law for the PLZT 8/60/40 ceramics at 1 kHz

after dielectric maxima temperature for the materials showing DPT and relaxor phase transition, can be explained on the basis of the existence of polar regions. The relaxor behavior in ferroelectrics is believed to be the consequence of the presence of dynamic polar-nano-regions which are ever more active and are of fine scale in the vicinity of T_m in a classical relaxor system. With an increase in temperature, the direction of a net polarization (P_s) fluctuates or becomes very dynamic.

The dielectric study suggests that the PLZT ceramics can be used for high-temperature applications, multilayer ceramic capacitors (MLCC), and energy storage applications.

Ferroelectric Polarization vs. Electric Field Hysteresis Loops

Ferroelectric polarization vs. electric field (P - E) hysteresis loops are the source of important key information, which are required for the understanding of ferroelectric materials. These studies reveal the true nature of the materials and help to confirm the ferroelectric behavior in PLZT ceramics. The P - E hysteresis loops of ferroelectrics are one of the most important electrical characteristics due to their similarity with the magnetization versus magnetic field loops of ferromagnetics. As we know, the P_r of a ferroelectric material is related to the polarization value after removal of an applied electric field. The necessary electric field required to bring the P_r to zero is called as E_c and can be evaluated from the saturated P - E hysteresis loops. For an ideal ferroelectric system, the observed P - E hysteresis loops should show symmetry in their shape. The positive and negative value of the P_r and E_c should be equal ($E_c = -E_c$ and $P_r = -P_r$). In reality, the shape of the ferroelectric hysteresis loops is affected by many factors such as material composition, preparation conditions, thickness of the samples, mechanical

stresses, presence of charged defects, measurement conditions, and thermal treatment. The high leakage currents in ceramics can affect the shape of the hysteresis loop, especially at high voltages and low frequencies. It is known that the poling electric field is related to the coercive field of the ferroelectrics and can be evaluated from the P - E and current vs. electric field (I - E) curves. When an electric field is applied to a ferroelectric, along with the polarization, it also shows the current response. This current response consists of different types of current signals and is equal to the total current generated from the ferroelectrics. Damjanovic et al. [82] suggested that the total current consists of two parts. The first part is mainly due to the fast linear response of the dielectric, and the second part is due to polarization switching. The effect of different current responses, rather than polarization switching current, is visible in the low field region, but when the domain starts switching after crossing a threshold field, the domain switching current becomes more prominent. The occurrence of a peak in the current signal before reaching the maximum electric field indicates domain switching in ferroelectrics. The electric field, which is corresponding to the domain switching current peak in I - E loops, is identified as the coercive field.

Figure 7 shows the saturated P - E and I - E loops for PLZT 8/60/40 un-poled ceramics, which were used for the identification of the E_c value (is almost the same ~ 12 kV/cm). The value of remanent polarization is found to be larger than previously reported values for the same composition [32, 83]. For soft PLZT ceramics, the shape of the hysteresis loop (Fig. 7) shows a high squareness and is well saturated. These also indicate good homogeneity and uniformity of grain size. The high value of P_r reported in the present study could possibly be attributed to any or all of the following: uniform distribution of grain size in the samples, uniform distribution of composition, low defect density, etc. [84, 85]. Ferroelectric materials always contain electrical and elastic defects and imperfections that can affect the movement and switching of domain walls and polarization within individual grains. Domain wall movement can be restricted by defects and imperfections. The reason for higher P_r and strain value for the PLZT 8/60/40 ferroelectric material obtained could be due to fewer defects and imperfections in the crystallites [82].

The high remanent polarization is good for memory applications.

Poling Study for Ultrahigh Piezoelectric Properties

The d_{33} , electromechanical coupling factor (k_p), dielectric constant (K), and loss (D) properties of the piezoelectric ceramics are greatly influenced by the following poling conditions: (1) poling electric field, (2) poling time, and (3) poling temperature. Therefore to get the highest electrical properties for PLZT 8/60/40 ceramics, the aforesaid poling conditions should be optimized carefully.

Effect of Poling Parameters on the Piezoelectric and Dielectric Properties of PLZT 8/60/40 Ceramics

Figure 8 shows the change in piezoelectric coefficients and dielectric constant of PLZT 8/60/40 ceramics as a function of poling field, confirming the influence of poling field on the aforesaid properties. The electric field, which was used for the poling process, causes the switching and reorientation of domains in ferroelectrics and makes them piezoelectrically active. The value of d_{33} , k_p , and K increases rapidly with the poling electric field over the range of ~ 0.8 to ~ 5 kV/cm, which is less than half of the coercive field. However, when the poling electric field exceeds ~ 5 kV/cm, no significant change was observed in piezoelectric parameters. The rapid increase in d_{33} and k_p may be attributed to the switching of 180° domains at lower poling electric fields due to their easier switching than non- 180° domains. Generally, poling of piezoelectric materials is done by applying an electric field higher than their coercive fields. However, in this study, the values of K , d_{33} , and k_p parameters show that PLZT 8/60/40 ceramics can be poled at ~ 5 kV/cm ($< 0.5 E_c$), which is contrary to common practice of poling. The poling of ferroelectrics at significantly reduced poling voltages is very advantageous especially if the samples have high conductivity, which is a common problem at high temperatures. Moreover, the induced high piezoelectricity of PLZT ceramics was not compromised in any way as a consequence of lowering the poling field. Figure 9a–c represents the schematic orientations of domains for un-poled, poled ($\sim 0.5 E_c$), and excess poled ($\sim 3 E_c$) PLZT ceramics, respectively. Figure 9a shows the randomly oriented domains in

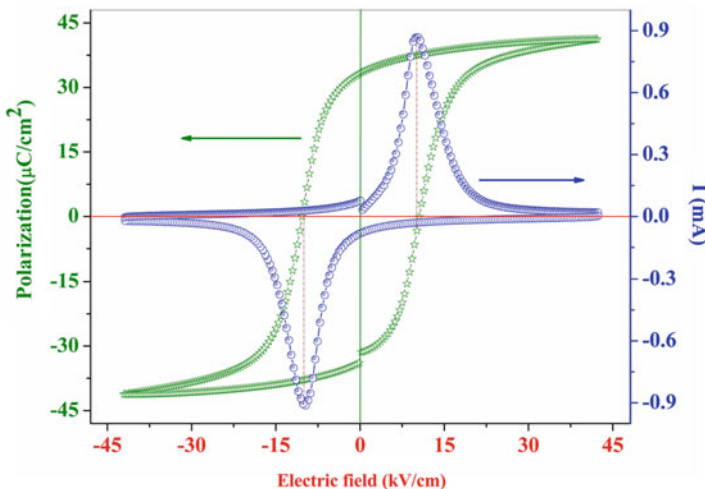


Fig. 7 Polarization vs. electric field (P - E) and current vs. electric field (I - E) curves for the PLZT 8/60/40 un-poled ceramic sample at 1 Hz. A dotted line shows the electric field value at domain switching current peak that matches with polarization reversal field. (Reprinted figure, Copyright (2015) by the Eur. Phys. J. B) [16]

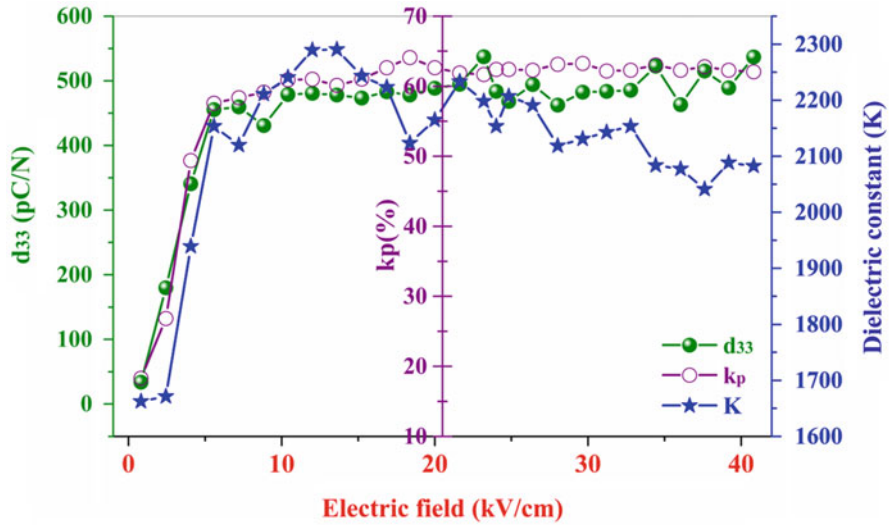


Fig. 8 Variation in piezoelectric charge coefficient (d_{33}), electromechanical coupling factor (k_p), and dielectric constant (K) as a function of poling electric field

un-poled PLZT ceramics at $E = 0$. When an electric field is applied to the un-poled ceramics, domains begin to align in the direction of applied electric field. After crossing the threshold electric field, most of the domains suddenly switch into the direction of the applied electric field (Fig. 9b) that can be seen in Fig. 8 (~ 5 kV/cm, $\sim 0.5 E_c$). After domain switching, the piezoelectric properties do not show much change with an increase in the electric field ($0.5 E_c \leq E \leq 3E_c$), when the remaining domains get aligned (Fig. 9c) [44].

Figure 10 shows the change in d_{33} , k_p , and K as a function of poling time. The other poling conditions were kept constant. The d_{33} , k_p , and K show the same trend as in the case of poling field and time. The increase in the parameters with an increase in poling time is due to the switching of 180° domains. This is because the switching of 180° domains is easier than non- 180° domains. When the ceramics are poled for more than 30 min, the electrical properties were found to diminish. Likewise, prolonged poling may result in the unleashing of leakage current that is responsible for lowering of piezo properties. The PLZT 8/60/40 composition is close to the morphotropic phase boundary. The latter provides 14 possible domain-orientation states in perovskite-structured ferroelectrics from a crystallographic perspective. These 14 states are a combination of 6 states in tetragonal and 8 states in rhombohedral phases, which contain a number of 180° and non- 180° domains. The 180° domain reversal is easier than the non- 180° domain switching. The 180° domain reversal requires minimal structural strains or electric field; however, the switching of non- 180° domains is associated with the larger deformation or higher electric field. In the presence of an external electric field, both 180° and non- 180° domains try to align in the electric field direction [86]. Many domains cannot

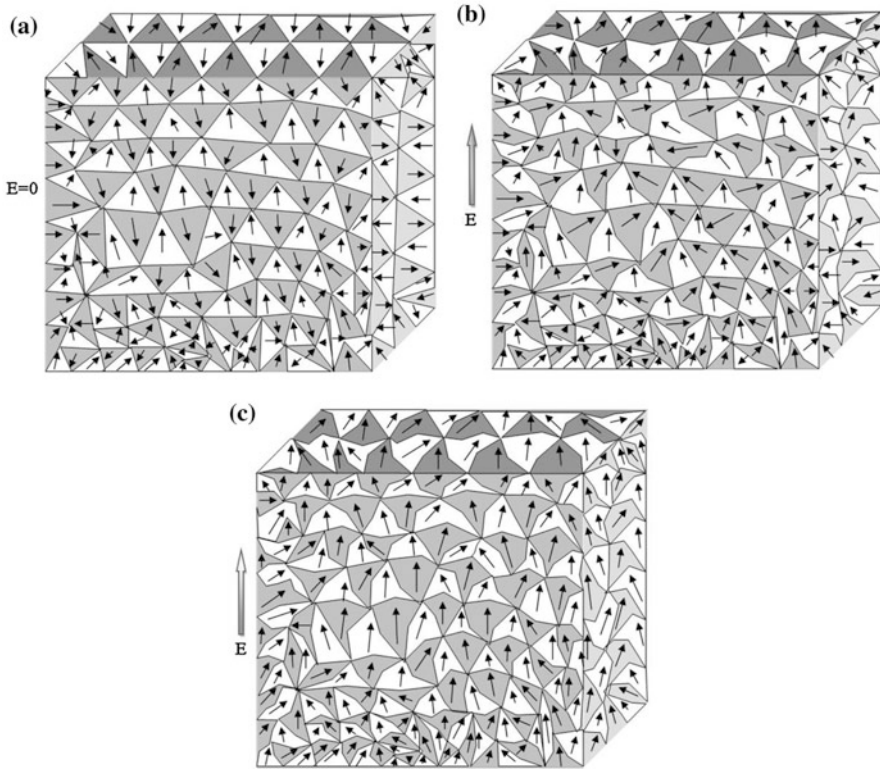


Fig. 9 Schematic representation of orientations of domains for (a) un-poled, (b) poled ($\sim 0.5 E_c$), and (c) excess poled ($\sim 3 E_c$) PLZT ceramics, respectively. (Reprinted figure, Copyright (2015) by the Journal of Material Science: Material in Electronics) [44]

reorient due to their complex set of internal stresses and electric fields in grains [82]. During the poling process, the spontaneous strain of piezoelectric materials is affected only by non- 180° domains. The switching of 180° domains does not contribute to the strain; thereby the switching of 180° domains is easier than non- 180° domains. The dipoles in ferroelectrics possess minimum potential energy only when they are aligned in the direction of the electric field. The average dipole moment contribution per dipole (P^l) within the range 0° – 180° is given by [87]:

$$P^l = p \coth\left(\frac{pE}{kT}\right) - \frac{kT}{pE} \quad (1)$$

where p = dipole moment, E = applied electric field, k = Boltzmann's constant, and T = ceramic temperature.

Equation (1) explains the effect of the poling electric field on the piezoelectric properties of PLZT 8/60/40 ceramics. When the applied electric field is very high at low temperature, the maximum number of dipoles aligns along the direction of the

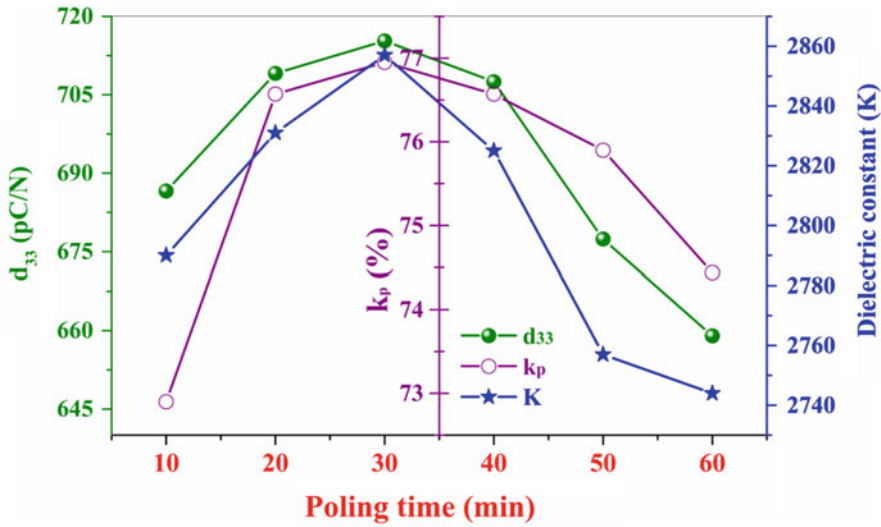


Fig. 10 Variation in piezoelectric charge coefficient (d_{33}), electromechanical coupling factor (k_p), and dielectric constant (K) as a function of poling time

electric field. Not only the high applied electric field but also the application of this field for a longer duration (poling time) results in the generation of free electrons. The number of these free electrons increases with increase in poling electric field and poling duration. The generated electrons get accelerated and collide with other atoms and release more charge carriers, which results in increased conduction in PLZT ceramics. The accumulated energy leads to an increase in temperature of the piezoelectric ceramics, which results in the fall in piezoelectric properties and finally thermal breakdown. Due to the quantum tunnelling effect, free electrons of piezoceramics may move from the valance band to the conduction band, which speeds up the electron impact ionization in a high field and an increase in electric leakage current [88, 89]. Thereafter this results in the decline of poling-dependent electrical properties and eventually electrical as well as a physical breakdown of the ceramics. This may be due to vacancy defects, pores, and other physical flaws in the ceramics. These flaws and defects can move easily at high electric fields compared with the coercive field of PLZT ceramics and result in an increase in electrical conductivity.

To study the effect of poling temperature on piezoelectric properties, PLZT ceramics were poled at different poling temperatures, a fixed poling field ($\sim 0.5E_c$), and a fixed poling time. Figure 11 shows the change in d_{33} , k_p , and K as a function of poling temperature for PLZT 8/60/40 ceramics. At first, d_{33} , k_p , and K increase as a function of poling temperature and attain their highest value in the temperature range of 75–125 °C. Usually, high poling temperature enhances domain motion. An increase in poling temperature facilitates switching of domains, which results in an increase in electrical properties. However, when the poling temperature of PLZT

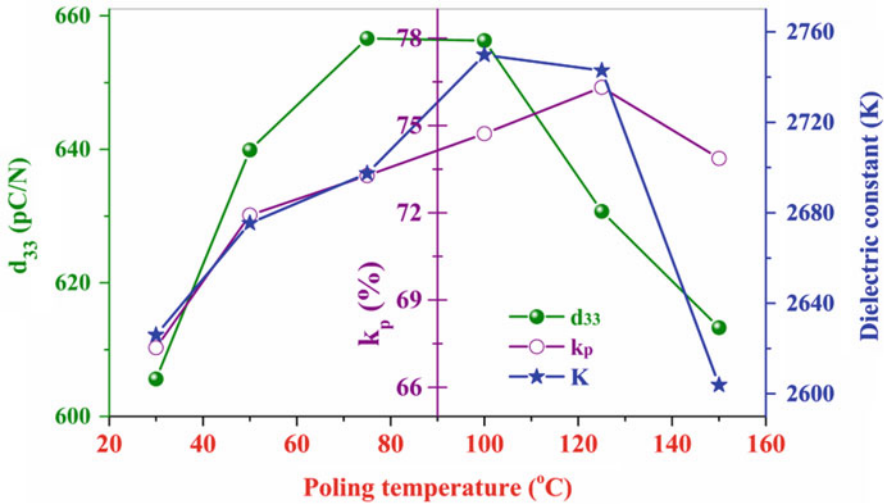


Fig. 11 Variation in piezoelectric charge coefficient (d_{33}), electromechanical coupling factor (k_p), and dielectric constant (K) as a function of poling temperature

ceramics exceeds the temperature, at which the ceramics show their highest values, the piezoelectric properties start decreasing. At sufficiently high temperatures, the increase in leakage current is the main reason for the remarkable decrease in the said parameters.

Figures 8, 10, and 11 show the change in dielectric constant of PLZT 8/60/40 ceramics poled at the various poling electric fields, poling times, and poling temperatures, respectively. The dielectric constant of PLZT ceramics increases rapidly as a function of poling parameters and reaches its maximum value at optimum poling conditions, the same as in the case of piezoelectric parameters. The increase in dielectric constant for poled ceramics can be correlated with an increase in lattice constant as suggested by Du et al. [90]. According to his report, the diffraction peaks of ceramics after poling shift toward the lower 2θ angles, which indicate an increase in lattice constant of the ceramics after poling. In this study, the poled PLZT 8/60/40 ceramics show high dielectric constant, when compared with un-poled ceramic samples. A total increase of ~31% was found for the poled PLZT ceramics. However, if this optimal poling field exceeds a certain threshold value, the dielectric constant reduces. Once the poling process is completed, the crystallites are clamped yielding a lower value of dielectric constant compared with the peak value as a clamped crystal would be less polarizable. Optimized poling parameters are given in Table 2.

Aging in Piezoelectric and Dielectric Properties of PLZT 8/60/40 Ceramics

This study suggests that the use of low poling electric field also can give high piezoelectric properties for PLZT ceramics, which is contrary to the previous reports.

Table 2 Structural, dielectric, ferroelectric, and piezoelectric parameters for PLZT 8/60/40 5 h milled ceramics

Parameters	Values
Crystallite size from XRD	30 nm
Particle size from TEM	15–40 nm
Particle size from SAXS	21 nm
Dielectric constant	2335
Loss	0.43
T_c	201 °C
γ	1.93
ΔT_{diff}	33 °C
T_{cw}	286 °C
ΔT_m	96 °C
Remanent polarization (P_r)	34 $\mu\text{C}/\text{cm}^2$
Coercive field (E_c)	12 kV/cm
Optimum poling field (E_p)	~5 kV/cm
Optimum poling temperature	~100 °C
Optimum poling time	30 min
Change in K (After poling)	31%
Piezoelectric charge coefficient (d_{33})	715 pC/N
Piezoelectric voltage coefficient (g_{33})	28.03×10^{-3} (Vm/N)
Electromechanical coupling coefficient (k_p)	77%
Strain	0.22% at 60 kV/cm

These reports suggest the use of a high electric field due to the stability issue for lower field poled ceramics. However, low electric field poled ceramics show almost the same properties as in the case of high electric field poled ceramics. If the ceramics are subjected to higher electric fields, the probability of electrical breakdown is more compared with low field poling. The piezoelectric properties of the PLZT ceramics are also affected by the high leakage current at high poling fields. To support our findings and experimental results, the aging factor can be considered here as reliable evidence.

To study the aging phenomenon in PLZT ceramics, two sets of ceramic samples were poled at different poling field and the poling temperature while keeping the poling time constant. The first set of PLZT ceramic samples was poled at an electric field of $0.6E_c$, and the second set of ceramic samples was poled at $3E_c$. Figure 12a–c shows the effect of aging on the piezoelectric, electromechanical, and dielectric properties of PLZT 8/60/40 ceramics, poled at $0.6E_c$ and $3E_c$ respectively. The time for the aging study taken here is ~300 days, and the values of all the parameters were measured at random intervals. The change (%) in the values show the decrease from the values just after the poling. A previous study reveals that ceramics dimensions also affect the electrical properties [44]. Therefore, certain changes in the properties of both sets of ceramics arise due to slight variation in their dimensions. The measured value of electrical parameters of PLZT ceramics also depends on measurement conditions such as temperature, humidity, instrumental errors, etc., which

are responsible for some fluctuations in the measured values of d_{33} , k_p , and K . Figure 12a–c shows the relative change in d_{33} , k_p , and K for PLZT 8/60/40 ceramics, which were poled at $0.6E_c$ and $3E_c$. The d_{33} and k_p for $0.6E_c$ poled ceramics are relatively more stable than $3E_c$ poled ceramics. However, the dielectric constant for both sets of ceramic samples shows an almost similar rate of change even after ~300 days.

Piezoelectric Strain vs. Electric Field Hysteresis Loops

The measurement of an electric field-induced unipolar and bipolar ferroelectric strain vs. electric field (S - E) hysteresis curves is also very important because these curves give an idea about piezoelectric properties of piezoelectric ceramics. When an electric field is applied to the ceramic sample, in addition to the polarization, the strain is also developed due to the converse piezoelectric effect of the lattice, switching, and movements of domain walls. Apart from P - E hysteresis loops, the

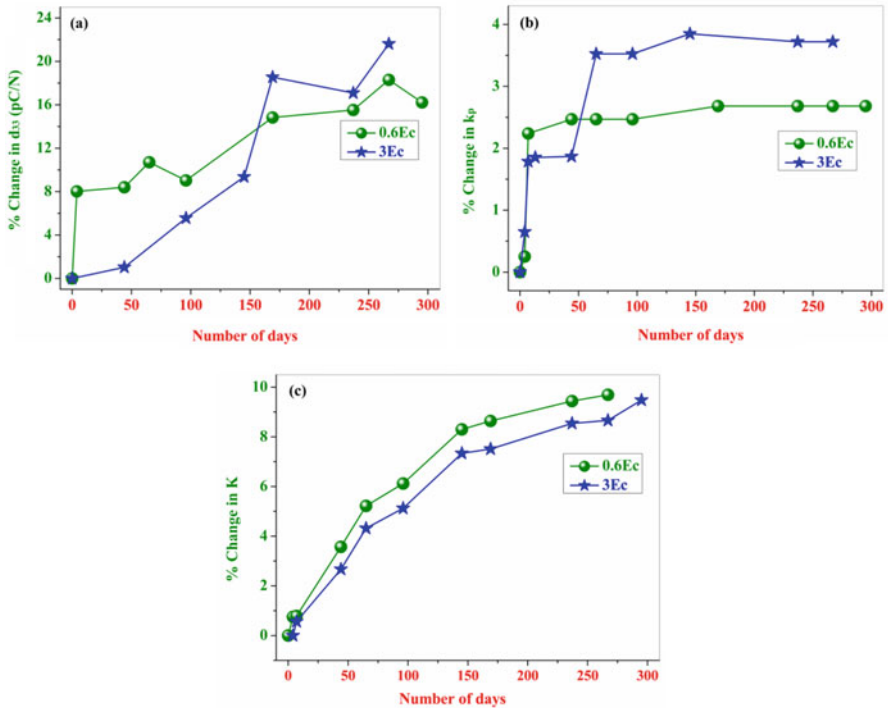


Fig. 12 Change (% decrease) in (a) d_{33} , (b) k_p , and (c) dielectric constant for PLZT 8/60/40 ceramics poled at $0.6E_c$ and $3E_c$, respectively

ferroelectrics also show strain-electric field hysteresis loops. An application of electric field results in the creation of a large strain linked to the piezoelectric effect. The S - E hysteresis loops were used for the calculation of piezoelectric charge coefficients (d_{33}). The strain hysteresis loops can be measured in the unipolar or bipolar direction. The bipolar strain-electric field hysteresis loop which resembles the shape of a butterfly occurs due to the converse piezoelectric effect of the lattice as well as switching and movement of domain walls (Fig. 13). The bipolar S - E hysteresis curve was measured for un-poled PLZT 8/60/40 ceramics. For unipolar S - E curves, large hysteresis is mainly due to the extrinsic contribution by domain switching. The hard ferroelectrics show asymmetric “butterfly” bipolar S - E curves and linear, hysteresis-free unipolar S - E curves.

In the presence of a low dc field, the S - E curves obey a linear relationship, corresponding to the piezoelectric effect. The switching of ferroelastic domain walls is believed to be due to the large hysteresis in bipolar S - E curves and the large negative strain in ferroelectrics [82]. The equation of state relating the electric and elastic variables can be written for the converse piezoelectric effect as [6]:

$$S = s^E T + d E \quad (2)$$

where S = strain, s = material compliance, T = stress, d = piezoelectric coefficient, and E = applied electric field.

Electric field-induced unipolar strain curves of PLZT 8/60/40 ceramics were recorded at room temperature as shown in Fig. 14. The unipolar strain increased with increase in the applied electric field. Ceramic samples usually contain a number of non-180° domains. In addition to the pure piezoelectric response, the movement and switching of non-180° walls involve a significant change in dimensions of the sample, resulting in an increase in strain in the ceramics. The average d_{33} was calculated from

Fig. 13 Bipolar S - E hysteresis loop for un-poled PLZT 8/60/40 ceramics at 1 Hz

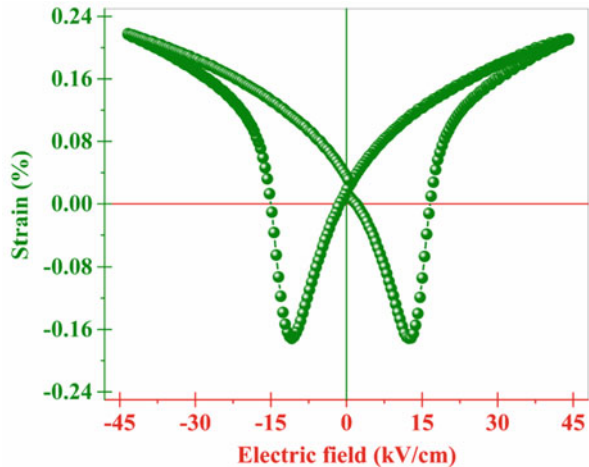
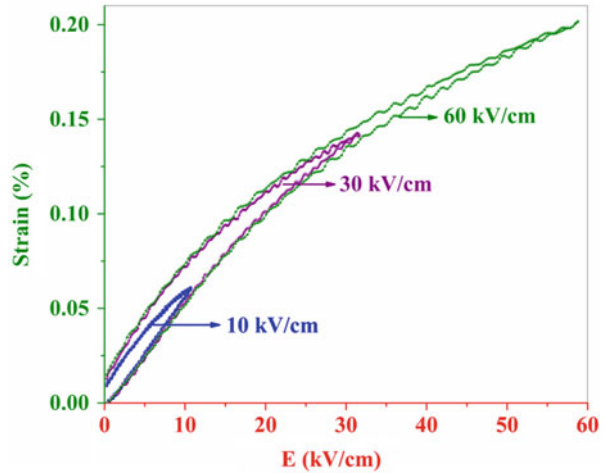


Fig. 14 Unipolar S - E hysteresis loop for poled PLZT 8/60/40 ceramics at 1 Hz frequency



unipolar measurements, which can be defined as the slope of the displacement vs. electric field hysteresis loop. The unipolar strain of 0.22% was found for PLZT ceramics with minimal strain hysteresis loss of 3%. Figure 15 shows the calculated d_{33} value from the slope of S - E hysteresis loops and normalized strain coefficient (S_{\max}/E_{\max}) as a function of applied electric fields for PLZT 8/60/40 electroceramics.

The high piezo strain suggests that PLZT 8/60/40 ceramics are useful for actuator applications.

Temperature-Dependent Ferroelectric and Electromechanical Properties for the Confirmation of Nature of the Phase Transitions

The dielectric measurements of PLZT 8/60/40 ceramics suggest that the La modification in PZT ceramics results in a deviation of nature of the ferroelectric phase transition from a normal to the diffuse-type phase transition (DPT). To support this study, the polarization vs. electric field hysteresis loop of PLZT ceramics was measured in the temperature range of 30–170 °C. Apart from that, the electromechanical coupling factor was also measured as a function of temperature (up to 210 °C). Temperature-dependent ferroelectric and electromechanical studies are useful for the better understanding of ferroelectric phase transitions in PLZT electroceramics.

Temperature-Dependent P - E Hysteresis Loops

Figure 16 shows the temperature-dependent P - E hysteresis loops for the PLZT ceramics from 30°C to 170°C. The effect of temperature on the hysteresis

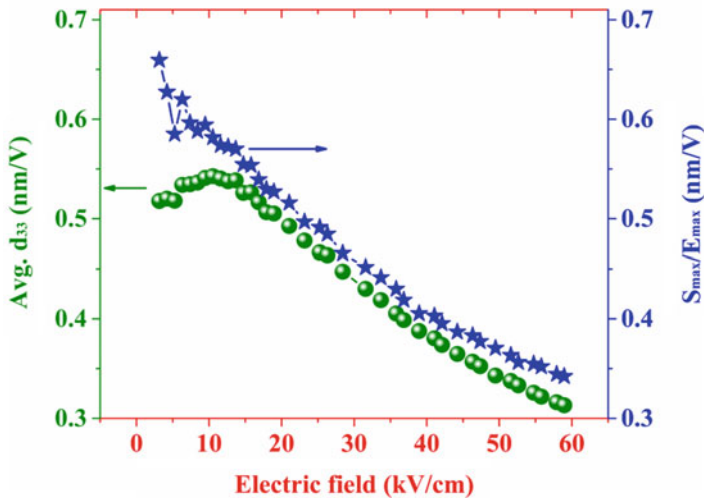


Fig. 15 The change in average d_{33} calculated from the slope of unipolar S - E curve and S_{\max}/E_{\max} as a function of applied electric field

behavior of P - E loops of PLZT ceramics was studied in detail. Well-saturated P - E hysteresis loops confirm the ferroelectric nature of PLZT ceramics. Figure 16 shows that the shape of the P - E hysteresis loop changes with increasing temperature. With further increase in temperature, the P - E loops of PLZT ceramics become slimmer which is the same as in the case of the P - E loops for dielectric materials [91]. For ferroelectric materials the values of maximum polarization (P_{\max}), P_r , and E_c decrease with an increase in temperature. At T_c , the polarization is zero for a normal ferroelectric and non-zero for ferroelectrics, which show relaxor or DPT-type phase transitions. The presence of ferroelectricity at temperatures, close to T_c , can also be noted from Fig. 16 and inset of Fig. 16, in which the P_r is non-zero near to T_c . In section “Dielectric Property Studies and Nature of Phase Transitions,” the dielectric properties of the PLZT ceramics were discussed in detail, and it was found that the PLZT 8/60/40 ceramics show deviation from the normal-type phase transition. Such ceramics possess polar regions. In the case of relaxor ceramics, the size of these polar regions is in nanometers called as polar-nano-regions (PNRs); however, ceramics with DPT-type phase transitions have polar regions larger than PNRs. The persistence of ferroelectricity at this temperature may be due to the existence of polar regions.

Figure 16 shows the P - E hysteresis loop for a PLZT 8/60/40 ceramics, measured at high temperature (170°C). The temperature-dependent ferroelectric measurements were performed by immersing the PLZT ceramics in silicone oil. The oil breaks down at temperatures beyond 170°C . This condition limits the

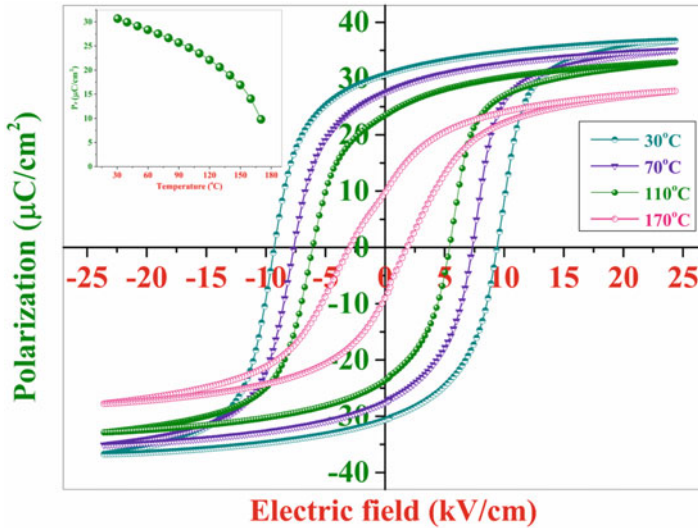


Fig. 16 Polarization vs. electric field hysteresis loops for PLZT 8/60/40 electroceramics, measured at different temperatures. Inset shows the change in remanent polarization as a function of temperature

measurement of P - E loops within the temperature range of 30–170 °C, which is less than the transition temperature of the PLZT 8/60/40 ceramics. However, the high P_r ($\sim 10 \mu\text{C}/\text{cm}^2$) of PLZT ceramics at 170 °C shows the possibility of non-zero remanent polarization with low coercive field value even beyond the transition temperature. The coercive field value was also found to be very less at high temperatures. The non-zero remnant polarization, which is a necessary condition for the existence of ferroelectricity and coercive field above the dielectric maxima temperature, confirms the DPT-type phase transition for PLZT 8/60/40 ceramics.

The inset of Fig. 16 shows the change in P_r as a function of temperature for the PLZT 8/60/40 electroceramics. With the application of an electric field, dipoles begin to align in the direction of the applied field. Such an orientation is opposed by the thermal agitation which tends to randomize the dipoles. By using Boltzmann's statistics, Langevin calculated the average dipole moment contribution per dipole (P^l) within the range 0° – 180° as shown by Eq. 1 [87]. Equation 1 shows two possibilities: (i) high electric field and low temperature, indicating maximum alignment of the dipoles along the direction of the electric field, and (ii) when the temperature of ceramics increases, the total polarization of the ceramics starts decreasing on account of the domains inside the ceramics grains getting randomly oriented with increasing temperature. At a certain temperature known as the Curie or transition temperature (T_c), the polarization disappears. The crystal does not exhibit ferroelectricity above the Curie temperature.

Temperature-Dependent Electromechanical Coupling Factor of PLZT Ceramics

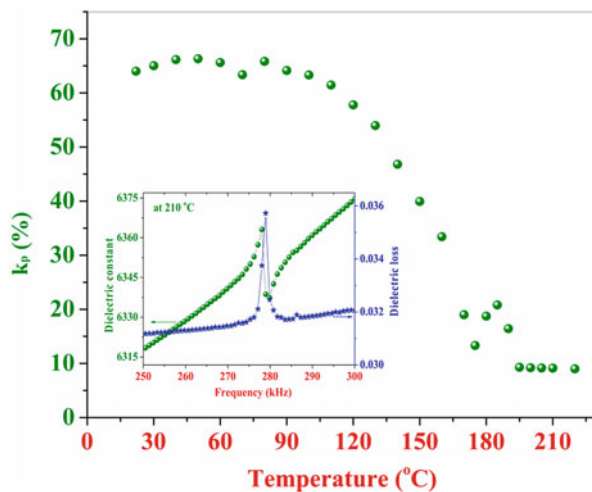
Figure 17 shows the change in k_p of poled PLZT 8/60/40 ceramics as a function of temperature. This measurement was performed from room temperature to 210 °C. Electromechanical coupling coefficients can be calculated by using the resonant and antiresonant frequencies. The planar coupling factor (k_p) was calculated by using the equation:

$$k_p = \sqrt{\frac{2.51(f_a - f_r)}{f_r}} \quad (3)$$

where f_r is the resonant frequency and f_a is the antiresonant frequency.

In Fig. 17, PLZT ceramics show a coupling factor of ~10% even beyond the dielectric maxima temperature. The inset of the figure shows the existence of a resonance phenomenon at 210 °C with resonance and antiresonance frequencies, which gives the non-zero k_p value above the dielectric maxima temperature. The broad phase transition studies revealed that piezoelectric activity could be observed at temperatures well above the dielectric maxima. The diffuse transition occurs in a temperature range called as the Curie range. At temperatures well above the Curie range, ceramics do not show any ferroelectricity [76]. The existence of polarization in relaxor materials after T_m can be explained on the basis of the existence of polar regions. The relaxor behavior in ferroelectric ceramics is believed to be the consequence of the presence of dynamic polar-nano-regions which are ever more active and are of fine scale in the vicinity of T_m in a classical relaxor system. The direction of a net polarization (P_s) fluctuates or becomes very dynamic with temperature.

Fig. 17 Electromechanical coupling factor (k_p) vs. temperature graph for poled PLZT 8/60/40 ceramics. The inset shows the existence of resonance and antiresonance peaks at 210 °C ($>T_m$)



The short-range interactions between the polar regions control the fluctuations of P_s , leading to its freezing at a characteristic temperature far below the T_m [92]. In this study also, it can be concluded that the non-zero k_p value in Fig. 17, above dielectric maxima temperature, is due to the existence of polar-nano-regions. The existence of polar-nano-regions is responsible for the resonance phenomenon. This study suggests that the PLZT ceramics are suitable for the high-temperature sensing applications.

Applications of PLZT Ceramics in the Defense Sector

As discussed in the introduction section, lead-based ceramics find their applications in sensors, actuators, nano-positioners, etc. Bulk piezoelectric actuators are the candidate of choice for applications that include high force, low to high frequency, and low power and are widely used in sonar, fuel injection systems, precise positioning systems, adaptive optics systems, and active damping control. However, the use of PLZT ceramics is not limited to the above mentioned applications. PLZT ceramics are widely used not only in general applications but also in the defense sector. The PLZT ceramics-based developed device or applications at DMRL will be discussed in this section.

Energy Harvesting Applications

Motion and vibration are the most versatile and ubiquitous ambient energy source available. During recent years, energy harvesting from vibration and motion sources has attracted much interest, particularly as power sources. The mechanical to electrical energy transformation is most efficiently done by piezoelectric materials. Electromechanical coupling factors (k_p , k_{33} , and k_{31}) are an indicator of the effectiveness with which a piezoelectric material converts input mechanical energy to the output electrical energy or converts input electrical energy to output mechanical energy. High “ k ” is usually desirable for efficient energy conversion. Bulk piezoceramics are used in piezoelectric flooring at railway stations or bus stands, tennis racquets, running tracks, dancing floors, etc. However, inserting piezo in the shoe is the most tried and efficient way to harvest the energy from piezoelectric ceramics. The PLZT 8/60/40 ceramics were used for the energy harvesting purpose due to its superior properties when compared to PZT-5H (PZT-5H is a commercially piezoelectric powder from American Piezo Ceramics (APC,USA). The list of all desirable properties is given in Table 2.

In this energy harvesting work, PLZT ceramic disks were fitted in the heels of shoes. The energy was generated while walking and stored in a battery. This harvested energy can be used for powering electronic circuits and devices. The generated voltages depend on the weight of the person and vary with applied pressure. The working model was developed and demonstrated. A patent for this energy harvesting device has been filed by authors [93, 94]. Figure 18a shows the

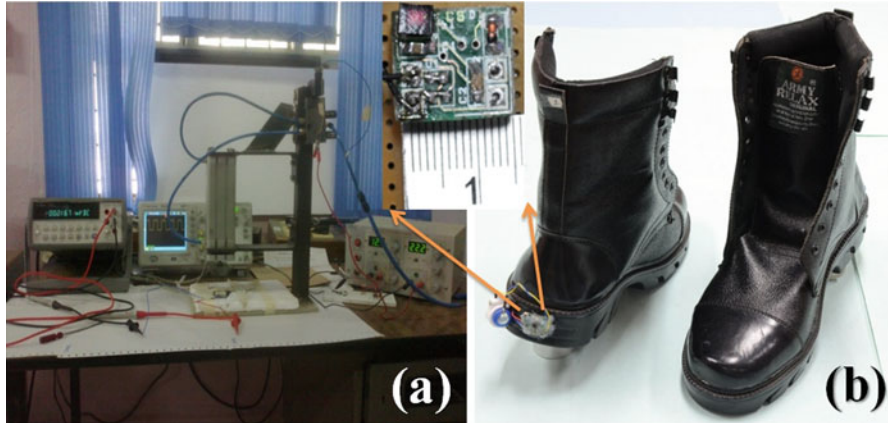


Fig. 18 (a) Setup for testing the PLZT ceramics for energy harvesting purpose (b) final product

setup to mimic the walk of a human. In this setup, a pneumatic system is controlled by a timer, and the piezoelectric sample is hit 15–25 time per minute. The generated charge is measured and stored in a battery. Figure 18b shows the actual pictures of the shoe with an electronic circuit with the battery. PLZT ceramics are inserted inside the heel (not visible). One of the main challenges faced with such a contraption is that there is a huge impedance mismatch that occurs due to the fact that the ceramics have a resonant frequency around 250 kHz, whereas such devices are driven at frequencies far below this; hence the entire energy or charge generated by them cannot be used to charge batteries that they are connected to.

Ring and Stack Actuators

Piezoelectric actuators provide large displacement and large force actuation necessary to achieve high-performance switches using low actuation voltages. Multilayer structures show high generative force, electromechanical coupling, and energy density properties. Usually, commercial multilayer actuators (designed for pseudo-static and pulsed displacement) have been used for optical modulations (optical interferometers and deformable mirrors), fluid control, printer heads, and vibration suppression and active damping [95]. These multilayer actuators also can be used in high-power piezoelectric devices [96–100]; however this application is limited by the high losses at large electric field. To overcome this problem, Yao et al. [95] developed stacked multilayer actuators with 3 mm diameter and hollow structure (Ring shaped) from hard PZT ceramics. In DMRL also two types of actuators were developed. Figure 19a, b shows the stack or multilayer and ring actuators, respectively.

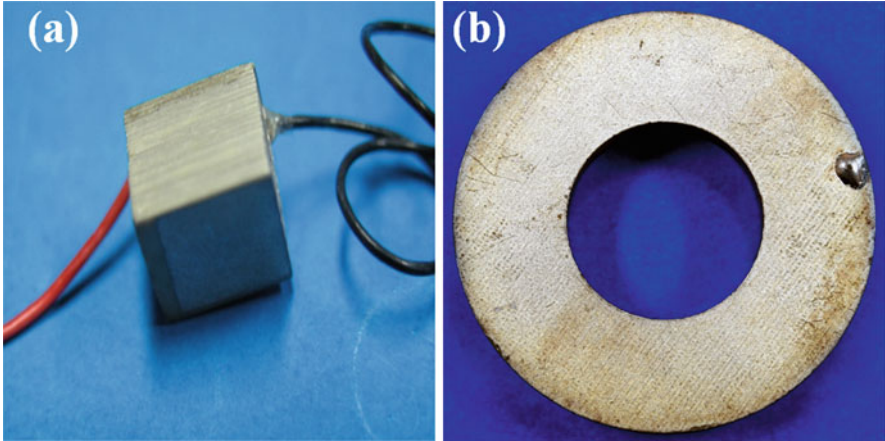


Fig. 19 (a) Stack or multilayer and (b) ring actuator from PLZT ceramics

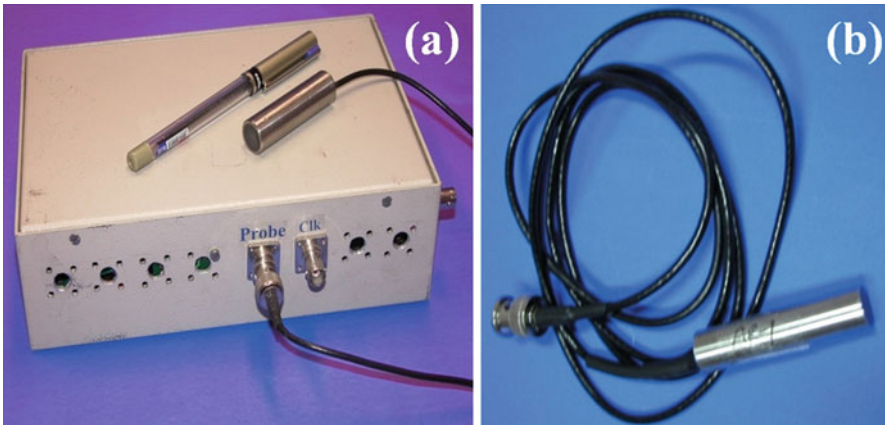


Fig. 20 (a) The signal generator and (b) NDT probe developed from PLZT ceramics

Nondestructive Test (NDT)

Nondestructive testing is a testing and analysis technique used in science and industry to evaluate the properties of a material, component, or system. NDT plays an important role in assuring that structural and mechanical components perform their function in a safe, reliable, and cost-effective manner. Some of the NDT techniques are visual and optical testing, radiography, ultrasonic testing, magnetic particle testing, and penetrant testing. PLZT-based ultrasonic NDT probes were

developed in DMRL along with a transmitter and receiver circuit (in collaboration with M/s Vivace Sonics, Hyderabad) and are shown in Fig. 20a, b. These were found to exhibit excellent receiver characteristics.

Conclusions

PLZT ceramics were prepared by a novel synthesis technique. It was found that a combination of mechanical activation (high-energy mechanochemical ball milling) with the cold isostatic process could not only reduce processing temperatures and time but also circumvent the need to add excess PbO in the starting materials. It is also important to highlight the fact that no excess PbO was added in the starting compositions due to the fine-scale particles resulting from high-energy milling. Apart from that no binder was added in this process and avoided the contamination risk involved. To prevent the lead loss particularly at high temperatures, a small crucible with lead zirconate powders with 10 wt% excess PbO was placed with CIPed rod in a double-crucible configuration. At the same time, this could be done without compromising the high density of such ceramics due to this process (Due to CIP). The microstructural and morphological studies confirm the formation of the partial perovskite phase, which proves that partial chemical reaction took place at the milling stage itself. The average particle size of milled powders, relative density, and grain size of sintered compacts were found to be ~ 30 nm, 97.23%, and ~ 1.45 μm , respectively. PLZT 8/60/40 ceramics show the dielectric constant ~ 2350 , which is again the highest, reported for the said system. The diffused phase transition of PLZT was discussed based on temperature-dependent (i) dielectric, (ii) resonance, and (iii) ferroelectric studies. The existence of resonance phenomenon and high value of P_r near the dielectric maximum temperature are the evidence for the deviation from normal phase transition to diffuse-type phase transition ($I < \gamma < 2$). The PLZT 8/60/40 ceramics show the highest P_r of ~ 34 $\mu\text{C}/\text{cm}^2$, domain switching current $I_{\text{max}} \sim 2.06$ mA, and high shape symmetry with low $E_c \sim 12$ kV/cm, which is suitable for memory applications. The highest piezoelectric charge coefficient ~ 715 pC/N and electromechanical coupling factor $\sim 75\%$ are suitable for energy harvesting applications. The PLZT 8/60/40 system shows the highest unipolar strain $\sim 0.22\%$ with minimal loss ($< 3\%$), which is desirable for actuator applications. A detailed poling study was carried out, which shows that PLZT ceramics can be poled at ~ 5 kV/cm compare to the regular practice of 20–30 kV/cm (below coercive field), which could be very advantageous if the process has to be scaled up to industrial levels. Also, it greatly simplifies the problem if the samples have poor resistivity. The work, which is reported here, not only overcomes lead volatility issues but also successfully increased the ferroelectric and piezoelectric properties multiple times which is very desirable feature for different applications.

Acknowledgments Authors would like to thank DRDO for the financial support and express their gratitude to the DG NSM Dr. S.V. Kamat and Director, DMRL, for their interest in this work.

References

1. Hagiwara M, Noguchi H, Hoshina T et al (2013) Growth and characterization of $\text{Ca}_2\text{Al}_2\text{SiO}_7$ piezoelectric single crystals for high-temperature sensor applications. *Jpn J Appl Phys* 52(9S1):09KD03
2. Dittmer R, Webber KG, Aulbach E, Jo W, Tan X, Rödel J (2013) Optimal working regime of lead-zirconate-titanate for actuation applications. *Sensors Actuators A Phys* 189:187–194
3. Priya S (2007) Advances in energy harvesting using low profile piezoelectric transducers. *J Electroceram* 19(1):167–184
4. Koduri R, Lopez M (2008) Influence of Mn on dielectric and piezoelectric properties of A-site and B-site modified PLZT nano-ceramics for sensor and actuator applications. *J Mater Sci Mater Electron* 19(7):669–675
5. Fousek J (1991) Ferroelectricity: remarks on historical aspects and present trends. *Ferroelectrics* 113(1):3–20
6. Jaffe B, Cook WR (1971) *Piezoelectric ceramics*. Academic, London/New York
7. Haertling GH (1991) Ferroelectric ceramics: history and technology. *J Am Ceram Soc* 82(4):797–818
8. Jaffe H, Berlincourt DA (1965) Piezoelectric transducer materials. *Proc IEEE* 53(10):1372–1386
9. Shannigrahi SR, Tay FEH, Yao K, Choudhary RNP (2004) Effect of rare earth (La, Nd, Sm, Eu, Gd, Dy, Er and Yb) ion substitutions on the microstructural and electrical properties of sol-gel grown PZT ceramics. *J Eur Ceram Soc* 24(1):163–170
10. Shannigrahi SR, Choudhary RNP (2000) Structural and dielectric properties of sol-gel derived PLZT (x/60/40). *J Electroceram* 5(3):201–209
11. Garg A, Agrawal D (2001) Effect of rare earth (Er, Gd, Eu, Nd and La) and bismuth additives on the mechanical and piezoelectric properties of lead zirconate titanate ceramics. *Mater Sci Eng B* 86(2):134–143
12. Laurent M, Schreiner U, Langjahr P, Glazounov A, Hoffmann M (2001) Microstructural and electrical characterization of La-doped PZT ceramics prepared by a precursor route. *J Eur Ceram Soc* 21(10–11):1495–1498
13. Zhang Y, Ding AL, Qiu PS et al (2003) Effect of La content on characterization of PLZT ceramics. *Mater Sci Eng B* 99(1–3):360–362
14. Pdungsap L, Udomkan N, Boonyuen S, Winotai P (2005) Optimized conditions for fabrication of La-dopant in PZT ceramics. *Sensors Actuators A Phys* 122(2):250–256
15. Singh S, Thakur OP, Prakash C (2005) Synthesis, structural and electrical properties of lanthanum-modified Lead-zirconate-titanate system. *Def Sci J* 55(3):349–356
16. Dutta S, Choudhary RNP, Sinha PK (2007) Structural, dielectric and piezoelectric properties of aluminium doped PLZT ceramics prepared by sol-gel route. *J Alloys Compd* 430(1–2):344–349
17. Praveenkumar B, Kumar HH, Kharat DK, Murty BS (2008) Investigation and characterization of La-doped PZT nanocrystalline ceramic prepared by mechanical activation route. *Mater Chem Phys* 112(1):31–34
18. Thakur OP, Prakash C (2010) Structural, dielectric and piezoelectric properties of PLZT (x/60/40) ceramics. *Integr Ferroelectr* 122(1):100–107
19. García-Zaldívar O, Peláiz-Barranco A, Guerra JDS, Mendoza ME, Calderón-Piñar F, Hall DA (2011) Influence of the A and B vacancies on the dielectric and structural properties of the PLZT 8/60/40 ferroelectric ceramic system. *Phys B Condens Matter* 406(8):1622–1626
20. Zhang N, Feng Y, Xu Z (2011) Effects of lanthanum modification on electrical and dielectric properties of $\text{Pb}(\text{Zr}_{0.70}\text{Ti}_{0.30})\text{O}_3$ ceramics. *Mater Lett* 65(11):1611–1614
21. Corker DL, Glazer AM, Dec J, Roleder K, Whatmore RW (1997) A re-investigation of the crystal structure of the perovskite PbZrO_3 by X-ray and neutron diffraction. *Acta Crystallogr Sect B Struct Sci* 53(1):135–142

22. Glazer AM, Mabud SA (1978) Powder profile refinement of lead zirconate titanate at several temperatures. II. Pure PbTiO_3 . *Acta Crystallogr Sect B Struct Crystallogr Cryst Chem* 34(4): 1065–1070
23. Singh AK, Pandey D, Yoon S, Baik S, Shin N (2007) High-resolution synchrotron x-ray diffraction study of Zr-rich compositions of $\text{Pb}(\text{Zr}_x\text{Ti}_{1-x})\text{O}_3$ ($0.525 \leq x \leq 0.60$): evidence for the absence of the rhombohedral phase. *Appl Phys Lett* 91(19):192904
24. Noheda B, Cox DE, Shirane G, Gonzalo JA, Cross LE, Park SE (1999) A monoclinic ferroelectric phase in the $\text{Pb}(\text{Zr}_x\text{Ti}_{1-x})\text{O}_3$ solid solution. *Appl Phys Lett* 74(14):2059–2061
25. Noheda B, Gonzalo JA, Cross LE et al (2000) Tetragonal-to-monoclinic phase transition in a ferroelectric perovskite: the structure of $\text{PbZr}_{0.52}\text{Ti}_{0.48}\text{O}_3$. *Phys Rev B* 61(13):8687–8695
26. Noheda B, Cox DE, Shirane G, Guo R, Jones B, Cross LE (2000) Stability of the monoclinic phase in the ferroelectric perovskite $\text{PbZr}_{1-x}\text{Ti}_x\text{O}_3$. *Phys Rev B* 63(1):014103
27. Frantti J, Ivanov S, Eriksson S et al (2000) Phase transitions of $\text{PbZr}_{1-x}\text{Ti}_x\text{O}_3$ ceramics. *Phys Rev B* 66(6):064108
28. Topolov VY, Turik AV (2001) A new monoclinic phase and features of stress relief in $\text{PbZr}_{1-x}\text{Ti}_x\text{O}_3$ solid solutions. *J Phys Condens Matter* 13(33):L771–L775
29. Guo R, Cross LE, Park SE, Noheda B, Cox DE, Shirane G (2000) Origin of the high piezoelectric response in $\text{PbZr}_{1-x}\text{Ti}_x\text{O}_3$. *Phys Rev Lett* 84(23):5423–5426
30. Zhang N, Yokota H, Glazer AM et al (2014) The missing boundary in the phase diagram of $\text{PbZr}_{1-x}\text{Ti}_x\text{O}_3$. *Nat Commun* 5(1):5231
31. Hinterstein M, Schoenau KA, Kling J et al (2010) Influence of lanthanum doping on the morphotropic phase boundary of lead zirconate titanate. *J Appl Phys* 108(2):024110
32. Guerra JDS, García JE, Ochoa DA, Pelaíz-Barranco A, García-Zaldívar O, Calderón-Piñar F (2012) Interrelationship between phase transition characteristics and piezoelectric response in lead lanthanum zirconate titanate relaxor ceramics. *J Mater Sci* 47(15):5715–5720
33. Craciun F, Cordero F, Ciuchi IV, Mitoseriu L, Galassi C (2015) Refining the phase diagram of $\text{Pb}_{1-x}\text{La}_x(\text{Zr}_{0.9}\text{Ti}_{0.1})_{1-x/4}\text{O}_3$ ceramics by structural, dielectric, and anelastic spectroscopy investigations. *J Appl Phys* 117(18):184103
34. Guerra JDS, Silva AC, Mcintosh R, Hoque MM, Guo R, Bhalla AS (2015) Investigation of the physical properties of PLZT ferroelectric ceramics—effect of the lanthanum content. *Integr Ferroelectr* 166(1):158–167
35. Falcão EA, Eiras JA, Garcia D, Santos IA, Medina AN, Baesso ML, Catunda T, GuO R, Bhalla AS (2015) Effects of lanthanum content on the thermo-optical properties of $(\text{Pb},\text{La})(\text{Zr},\text{Ti})\text{O}_3$. *Ferroelectrics* 494(1):33–42
36. Somwan S, Funsueb N, Limpichaipanit A, Ngamjarurojana A (2016) Influence of low external magnetic field on electric field induced strain behavior of 9/70/30, 9/65/35 and 9/60/40 PLZT ceramics. *Ceram Int* 42(11):13223–13231
37. Kumar A, Raju KCJ, James AR (2018) Micro-structural, dielectric, ferroelectric and piezoelectric properties of mechanically processed $(\text{Pb}_{1-x}\text{La}_x)(\text{Zr}_{0.60}\text{Ti}_{0.40})\text{O}_3$ ceramics. *J Mater Sci Mater Electron* 29(16):13483–13494
38. Kumar A, Prasad VVB, Raju KCJ, Sarkar R, Ghosal P, James AR (2016) Effect of lanthanum substitution on the structural, dielectric, ferroelectric and piezoelectric properties of mechanically activated PZT electroceramics. *Def Sci J* 66(4):360
39. Kong L, Zhu W, Tan O (2000) Preparation and characterization of $\text{Pb}(\text{Zr}_{0.52}\text{Ti}_{0.48})\text{O}_3$ ceramics from high-energy ball milling powders. *Mater Lett* 42(4):232–239
40. Kong L, Ma J, Zhu W, Tan O (2001) Preparation and characterization of PLZT ceramics using high-energy ball milling. *J Alloys Compd* 322(1–2):290–297
41. Kumar TS, Kumar A, James AR, Pamu D (2011) Enhanced microwave dielectric properties of MgTiO_3 ceramics prepared by mechanochemical method. *J Aust Ceram Soc* 47(2):44–49
42. Mahesh MLV, Prasad VVB, James AR (2016) A comparison of different powder compaction processes adopted for synthesis of lead-free piezoelectric ceramics. *Eur Phys J B* 89(4):108

43. Kumar A, Prasad VVB, James Raju KC, James AR (2014) Ultra high strain properties of lanthanum substituted PZT electro-ceramics prepared via mechanical activation. *J Alloys Compd* 599:53–59
44. Kumar A, Prasad VVB, James Raju KC, James AR (2015) Poling electric field dependent domain switching and piezoelectric properties of mechanically activated $(\text{Pb}_{0.92}\text{La}_{0.08})(\text{Zr}_{0.60}\text{Ti}_{0.40})\text{O}_3$ ceramics. *J Mater Sci Mater Electron* 26(6):3757–3765
45. Baek S-H, Rzchowski MS, Aksyuk VA (2012) Giant piezoelectricity in PMN-PT thin films: beyond PZT. *MRS Bull* 37(11):1022–1029
46. Kumar A (2016) Structure-property correlations in ultra high strain PLZT ceramics prepared via high energy mechanical milling. Ph.D. thesis, University of Hyderabad
47. El-Eskandarany MS (2001) Mechanical alloying for fabrication of advanced engineering materials. William Andrew Publishing/Noyes, New York
48. Suryanarayana C (2001) Mechanical alloying and milling. *Prog Mater Sci* 46(1–2):1–184
49. Nath AK, Jiten C, Singh KC (2010) Influence of ball milling parameters on the particle size of barium titanate nanocrystalline powders. *Phys B Condens Matter* 405(1):430–434
50. James AR, Thakur OP (2012) Recent trends in the synthesis of ferroelectric ceramics. In: Bharadwaja SSN, Dorey RA (eds) Dielectric and ferroelectric reviews. Research Signpost, Trivandrum, pp 33–54
51. IEEE (1987) IEEE standard on piezoelectricity standards committee of the IEEE ultrasonics, ferroelectrics, and frequency control society. IEEE Standards Board American National Standards Institute
52. James AR, Subrahmanyam J (2012) A process for the synthesis of lead lanthanum zirconium titanate ceramics Patent 262329
53. Cullity BD (1978) Elements of X-ray diffraction, 2nd edn. Addison-Wesley, Reading
54. Klug HP, Alexander LE (1974) X-ray diffraction procedures for polycrystalline and amorphous materials, 2nd edn. Wiley, New York
55. Roy S, James AR, Bysakh S, Subrahmanyam J (2007) Metals, materials and processes. *Met Mater Process* 19(1/4):143–152
56. Kumar A, James Raju KC, James AR (2017) Diffuse phase transition in mechanically activated $(\text{Pb}_{1-x}\text{La}_x)(\text{Zr}_{0.60}\text{Ti}_{0.40})\text{O}_3$ electro-ceramics. *J Mater Sci Mater Electron* 28(18):13928–13936
57. Viehland D, Wuttig M, Cross LE (1991) The glassy behavior of relaxor ferroelectrics. *Ferroelectrics* 120(1):71–77
58. Samara GA (2003) The relaxational properties of compositionally disordered ABO_3 perovskites. *J Phys Condens Matter* 15(9):R367–R411
59. Burns G, Dacol FH (1983) The observation of glassy polarization behavior in crystalline ferroelectric materials. *Ferroelectrics* 52(1):103–113
60. Burns G, Dacol FH (1983) Crystalline ferroelectrics with glassy polarization behavior. *Phys Rev B* 28(5):2527–2530
61. Burns G, Dacol FH (1983) Glassy polarization behavior in ferroelectric compounds $\text{Pb}(\text{Mg}_{13}\text{Nb}_{23})\text{O}_3$ and $\text{Pb}(\text{Zn}_{13}\text{Nb}_{23})\text{O}_3$. *Solid State Commun* 48(10):853–856
62. Viehland D, Jang SJ, Cross LE, Wuttig M (1990) Freezing of the polarization fluctuations in lead magnesium niobate relaxors. *J Appl Phys* 68(6):2916–2921
63. Viehland D, Li JF, Jang SJ, Cross LE, Wuttig M (1991) Dipolar-glass model for lead magnesium niobate. *Phys Rev B* 43(10):8316–8320
64. Cross LE (1987) Relaxor ferroelectrics. *Ferroelectrics* 76(1):241–267
65. Cross LE (1994) Relaxor ferroelectrics: an overview. *Ferroelectrics* 151(1):305–320
66. Bell AJ (1993) Calculations of dielectric properties from the superparaelectric model of relaxors. *J Phys Condens Matter* 5(46):8773–8792
67. Glazounov AE, Bell AJ, Tagantsev AK (1995) Relaxors as superparaelectrics with distributions of the local transition temperature. *J Phys Condens Matter* 7(21):4145–4168
68. Lu ZG, Calvarin G (1995) Frequency dependence of the complex dielectric permittivity of ferroelectric relaxors. *Phys Rev B* 51(5):2694–2702

69. Cheng Z, Zhang L, Yao X (1996) Investigation of glassy behavior of lead magnesium niobate relaxors. *J Appl Phys* 79(11):8615–8619
70. Cheng Z-Y, Katiyar RS, Yao X, Guo A (1997) Dielectric behavior of lead magnesium niobate relaxors. *Phys Rev B* 55(13):8165–8174
71. Cheng Z-Y, Katiyar RS, Yao X, Bhalla AS (1998) Temperature dependence of the dielectric constant of relaxor ferroelectrics. *Phys Rev B* 57(14):8166–8177
72. Prabu M, Shameem Banu IB, Gobalakrishnan S, Chavali M (2013) Electrical and ferroelectric properties of undoped and La-doped PZT (52/48) electroceramics synthesized by sol-gel method. *J Alloys Compd* 551:200–207
73. Parashar SKS, Parashar K (2010) Nanoscale effects on structural and giant dielectric of PZT synthesized by high energy ball mill. *Integr Ferroelectr* 121(1):106–112
74. da Silva PS, Venet M, Florêncio O (2015) Influence of diffuse phase transition on the anelastic behavior of Nb-doped $\text{Pb}(\text{Zr}_{0.53}\text{Ti}_{0.47})\text{O}_3$ ceramics. *J Alloys Compd* 647:784–789
75. Zhu WZ, Kholkin A, Mantas PQ, Baptista JL (2001) Effect of lanthanum-doping on the dielectric and piezoelectric properties of PZN-based MPB composition. *J Mater Sci* 36(17):4089–4098
76. Lines ME, Glass AM (2001) Principles and applications of ferroelectrics and related materials. Clarendon Press, Oxford
77. Goel P, Yadav KL, James AR (2004) Double doping effect on the structural and dielectric properties of PZT ceramics. *J Phys D Appl Phys* 37(22):3174–3179
78. Yadav K, Choudhary R (1995) Dielectric and piezoelectric properties of modified PZT ceramics. *Bull Pure Appl Sci D* 14:23
79. Fu S-L, Cheng S-Y, Wei C-C (1986) Effects of doping pairs on the preparation and dielectricity of PLZT ceramics. *Ferroelectrics* 67(1):93–102
80. Kumar A, Prasad VVB, James Raju KCJ, James AR (2016) Lanthanum induced diffuse phase transition in high energy mechanochemically processed and poled PLZT 8/60/40 ceramics. *J Alloys Compd* 654:95–102
81. Uchino K, Nomura S (1982) Critical exponents of the dielectric constants in diffused-phase-transition crystals. *Ferroelectrics* 44(1):55–61
82. Damjanovic D (1998) Ferroelectric, dielectric and piezoelectric properties of ferroelectric thin films and ceramics. *Rep Prog Phys* 61(9):1267–1324
83. James AR, Kumar R, PremKumar M et al (2010) Chemical synthesis, structural, thermo-physical and electrical property characterization of PLZT ceramics. *J Alloys Compd* 496(1–2):624–627
84. James AR, Kumar A, Prasad VVB et al (2018) Tunability, ferroelectric and leakage studies on pulsed laser ablated $(\text{Pb}_{0.92}\text{La}_{0.08})(\text{Zr}_{0.60}\text{Ti}_{0.40})\text{O}_3$ thin films. *Mater Chem Phys* 211:295–301
85. James AR, Subrahmanyam J, Yadav KL (2006) Structural and electrical properties of nanocrystalline PLZT ceramics synthesized via mechanochemical processing. *J Phys D Appl Phys* 39(10):2259–2263
86. Su S, Zuo R, Lu S, Xu Z, Wang X, Li L (2011) Poling dependence and stability of piezoelectric properties of $\text{Ba}(\text{Zr}_{0.2}\text{Ti}_{0.8})\text{O}_3\text{-(Ba}_{0.7}\text{Ca}_{0.3})\text{TiO}_3$ ceramics with huge piezoelectric coefficients. *Curr Appl Phys* 11(3):S120–S123
87. Wahab MA (2013) Solid state physics structure and properties of materials. Narosa Publishing House, New Delhi
88. Zhang L, Sun Q, Ma W, Zhang Y, Liu H (2012) The effect of poling condition on the piezoelectric properties of 0.3PNN-0.7PZT ceramics in the vicinity of MPB. *J Mater Sci Mater Electron* 23(3):688–691
89. Kamel TM, Kools FXNM, de With G (2007) Poling of soft piezoceramic PZT. *J Eur Ceram Soc* 27(6):2471–2479
90. Du H, Tang F, Luo F, Zhou W, Qu S, Pei Z (2007) Effect of poling condition on piezoelectric properties of $(\text{K}_{0.5}\text{Na}_{0.5})\text{NbO}_3\text{-LiNbO}_3$ lead-free piezoelectric ceramics. *Mater Sci Eng B* 137(1–3):175–179
91. Yan H, Inam F, Viola G et al (2011) The contribution of electrical conductivity, dielectric permittivity and domain switching in ferroelectric hysteresis loops. *J Adv Dielectr* 1:107–118

92. Bootchanont A, Triamnak N, Rujirawat S et al (2014) Local structure and evolution of relaxor behavior in $\text{BaTiO}_3\text{-Bi}(\text{Zn}_{0.5}\text{Ti}_{0.5})\text{O}_3$ ceramics. *Ceram Int* 40(9):14555–14562
93. James AR (2012) An improved piezoelectric power generator system. Patent 2222/DEL/2012
94. James AR (2012) Low load, low frequency piezo-electric power generator. Patent 658/DEL/2012
95. Yao K, Uchino K, Xu Y, Shuxiang D, Leong CL (2000) Compact piezoelectric stacked actuators for high power applications. *IEEE Trans Ultrason Ferroelectr Freq Control* 47(4): 819–825
96. Uchino K, Kato K, Tohda M (1988) Ultrasonic linear motors using a multilayered piezoelectric actuator. *Ferroelectrics* 87(1):331–334
97. Saigoh H, Kawasaki M, Maruko N, Kanayama K (1995) Multilayer piezoelectric motor using the first longitudinal and the second bending vibrations. *Jpn J Appl Phys* 34(5B):2760–2764
98. Funakubo T, Tsubata T, Taniguchi Y, Kumei K, Fujimura T, Abe C (1995) Ultrasonic linear motor using multilayer piezoelectric actuators. *Jpn J Appl Phys* 34(5B):2756–2759
99. Vries JWC de Jedeloo P, Porath R (1996) 10th IEEE international symposium on applications of ferroelectrics ISAF'96. In: Co-fired piezoelectric multilayer transformers, pp 173–176
100. Inoue T, Yamamoto M, Kawashima S, Hirose S (1998) Third order longitudinal mode piezoelectric ceramic transformer for high voltage power inverter. *IEICE Trans Commun* E81-C(7):1128–1135



Slip-Cast Fused Silica Radomes for Hypervelocity Vehicles: Advantages, Challenges, and Fabrication Techniques

7

Ibram Ganesh and Yashwant Ramchandra Mahajan

Contents

Introduction: The Strategic Necessity and the History of Radomes Development	252
Bore-Sight Error and Desired Shape of a Radome for Hypervelocity Vehicles	258
Derivation of Tangent Ogive Radome Shape Using Mathematical Equations	262
Glass and Fiber Reinforced Plastics for Radome Applications	266
Ceramic Materials of Choice for Hyper-velocity Radome Applications	267
Alumina	271
Cordierite Based-Glass (Sitall)	273
Slip-Cast Fused-Silica	274
Silicon Nitride and β -SiAlON	277
Beryllium Oxide and Boron Nitride	277
Comparison of Slip-Cast Fused-Silica Characteristics with Other Radome Ceramics	278
The Raw Material Resources of Fused Silica and its Characteristics	287
Fused Silica Radomes: The General Methods of Fabrication	290
Slip-Casting of Fused-Silica Radomes	290
Characteristics of Precursor Powders, Slips, and Plaster Molds	293
Effect of Pressure Casting on the Formation of Wall Thickness	295
Electrophoretic Deposition Process	297
Gelcasting of Fused Silica Radomes	299
Hydrolysis-Induced Aqueous Gelcasting of Fused Silica Radomes	299
Surface Passivation to Seal Porous Structure of Fused Silica Radomes	300
Fused-Silica Ceramic Composites with Other Materials	301

I. Ganesh (✉)

Centre of Excellence for Ceramic Processing, International Advanced Research Centre for Powder Metallurgy and New Materials (ARCI), Hyderabad, Telangana, India
e-mail: ibramganesh@arci.res.in

Y. R. Mahajan

International Advanced Research Centre for Powder Metallurgy and New Materials (ARCI),
Balapur, Hyderabad, India
e-mail: mahajanyrm@gmail.com

© Springer Nature Switzerland AG 2020

251

Y. R. Mahajan, R. Johnson (eds.), *Handbook of Advanced Ceramics and Composites*,
https://doi.org/10.1007/978-3-030-16347-1_55

Fused Silica-Boron Nitride-Silicon Nitride Composites (Nitroxyceram)	302
Concluding Remarks and Future Perspectives	309
References	312

Abstract

Today, the development of ceramic radome materials for hyper velocity ($>$ Mach 5) missiles is a top research priority for several countries for the purposes of both surveillance and combat. The ceramic materials with low and stable dielectric properties against frequency and temperature variation among others are especially important. The radome property requirement for missiles launched from surface-to-air, air-to-surface, and air-to-air differs considerably. Moisture absorbing materials despite having desired dielectric and thermal properties are not suitable for radome applications as the dielectric constant of water is significantly high (80.4). So far no single material has been identified to meet all the requirements of a high-speed radome application. The advantages and disadvantages associated with various ceramic radome materials have been presented and discussed in this chapter together with the information about the radome design with respect to the wall thickness vs. radar frequency (RF) signals, bore-sight error, and the importance as well as generation principle of ogive shaped radome. Among various materials investigated so far, the slip-cast fused silica (SCFS) has been identified to be superior for hypervelocity radome applications. Furthermore, SCFS radomes can be fabricated with near-net shape using aqueous colloidal suspensions. However, SCFS radomes suffer from poor mechanical strength and from low rain and abrasion resistance properties apart from having considerably high internal porosity (up to 18%). Various methods employed so far to improve the properties of SCFS radomes required for hyper-velocity applications have been reviewed in this chapter while citing all the important references. Among the various fused-silica composites, the Nitroxyceram ($\text{SiO}_2\text{-BN-Si}_3\text{N}_4$ composite) exhibits the best combination of properties required for radome applications, and it can be consolidated and densified by following conventional powder processing techniques prevalent at industry.

Keywords

Radome · Ogive shape · Bore-sight error · Reinforced plastics · Slip-cast fused-silica · Sital · Activated-sintering · Slip-casting · Electrophoresis · Nitroxyceram · Surface passivation

Introduction: The Strategic Necessity and the History of Radomes Development

The scientific and technical progress made during the nineteenth century and at the beginning of the twentieth century has been found to be responsible not only for the steep improvements in the living standards of the people but also for the development of several military armaments as well [1–7]. Particularly, the progress made in the aviation technology has been found to be responsible not only for easy travelling

from any country to any country spread across the globe but also for the development of aircrafts required for both surveillance and combat. However, the maximum attainable flight speeds and altitudes of early aircraft were considerably low, and the vehicles involved in war conflicts were vulnerable to ground-based weapons (i.e., rifles and machine guns) [1–7]. The subsequent developments in aviation technology ensured the modern aircraft with higher speeds, altitudes, and greater maneuverability required for military conflicts. The today's modern aircraft and the antiaircraft missile complexes (AMC) can be equipped with cannons and machine guns required for air combats and ground use [1]. Today's surveillance systems have also reached the capability to detect any kind of approaching airborne targets while creating an excellent air-defense system. During the middle of the last century, jet airplanes have been inducted into the military arsenal with a travelling speed of about 800–900 km/h (i.e., 245–260 meters/second, whereas the sound speed in air – 340 meters/second – is referred to as Mach 1), which are less vulnerable to conventional antiaircraft weapons as the time periods available for the pilots to react and use the on-board cannons and machine guns will be considerably short [1–7]. Three types of missiles, namely, (i) air-to-air, (ii) air-to-surface, and (iii) surface-to-air, have been developed. The air-to-air missiles are launched from airplanes to target the objects in flight, whereas the air-to-surface missiles are launched from airplanes to target the objects on both ground and water. The surface-to-air missiles are launched from stationary as well as mobile platforms and containers to target missiles and airplanes coming from long distances. An analysis of the tactical and technical characteristics (TTCs) of airplanes and potential missile carriers and the radar-guided missiles listed in Tables 1 and 2 indicate that the capabilities, speeds, and achievable ranges of several military arsenal developed so far are almost comparable [1–7]. Furthermore, today's state-of-the-art on precision-guidance systems also allows missiles to hit any target very accurately regardless of the weather conditions and the location of the launch pad. However, with the everyday increasing developments in the propulsion chemistry, the velocity capabilities of missiles are being pushed beyond the hypersonic speed ($> \text{Mach } 5$), which in turn demand to realize the corresponding systems to detect and destroy the enemy's airborne objects as quickly as possible in the air [1–7]. A missile is not only required to receive the signals from the radar (radio detection and ranging) placed on the ground but also should send signals from its antenna to detect the approaching target in the air to destroy the target successfully. A radar system uses ultra-high-frequency (UHF) or microwave part of the radio frequency waves and is used to detect the position and the movement of objects in the air. The performance characteristics, maximum attainable altitudes, and aerodynamic heating loads of interceptor aircraft fairing accessories and missiles is mainly dictated by the functional efficiency of the materials used for their construction. A paraboloidal antenna (or a dish) called as a radar frequency (RF) seeker is mounted in the missile's nose, and it is a vital part of the signal receiving system to achieve high precision and accuracy while hitting the target (Fig. 1a) [1]. In supersonic/hypersonic, air-to-air, and surface-to-air missiles, the RF seeker is affixed in the nose of a missile. To protect that antenna from the aerodynamic loads that are generated during missile flight through the atmosphere, it needs to be housed in an enclosure called radome or

Table 1 Tactical-technical characteristics of airplanes and potential missile carriers (adopted from reference [1])

Country	Model of airplane	Type of airplane	Characteristics of the airplane					Length, m	
			Maximum speed, m/h, at the altitude		Range (km)	takeoff run	landing run		
			>10 km	<3 km					
Russia	MiG-23ML	Tactical fighter	2500	1350	—	500	750		
	MiG-29-9B	The same	2400	1500	680	240	600		
	MiG-31	Fighter-interceptor	3000	1500	2200	1200	800		
USA	SU-30	The same	2450	1300	250	550	670		
	F-111	Multipurpose attack plane	2650	1470	2400	—	—		
	F-16	Multipurpose fighter	2140	1470	925	—	—		
	F-22A	The same	2335	—	1285	—	—		
	Phantom	The same	2300	1460	1270	—	—		
France	Mirage 1	Multipurpose fighter-bomber	2350	1470	900	—	—		
	Mirage 2000	Fighter-bomber	2330	100	1480	—	—		
	Rafale	Multipurpose fighter	2100	1390	1000	300	400		
England	Harrier	—	—	1200	500	—	—		
	Hawk-2000	Ground attack plane	—	1020	1200	—	—		
China	J-7	Fighter	2150	—	1300	900	800		
	J-8	The same	2330	—	1000	670	1000		
Israel	KFIRS-7	Multipurpose fighter	2440	1370	1185	—	—		
	Fiat E-91	Reconnaissance-attack fighter	2025	1130	600	—	—		
Sweden	Viggen	Fighter-bomber	2125	1470	>1000	—	—		
	Gripen	Multipurpose fighter	2550	1470	—	—	—		
+ England	Tornado	Multipurpose airplane	2300	1480	1900	—	—		
	+ Italy	Jaguar	1700	1320	1400	—	—		

Table 2 Tactical-technical characteristics of radar-guided missiles (a–c) (adopted from reference [1])

(a) Air-to-air missiles										
Indices	Russia			USA			England	France		
	Kh-15	Kh-22	Kh-58	AGM-129 A	Shrike	Harm	Alarm	Armat		
Flight speed (m/sec)	1800	100	1300	250	1000	820	800	830		
Range of fire (km)	<300	<550	<120	<300	<50	<80	<70	<150		
Type of carrier	Tu-95MS,	Tu-22 K,	Su-17 MZ,	B-52,	F-4,	Air force,	Tornado	Jaguar,		
	Tu-22MZ,	Tu-95 K-22,	Su-17 MU,	B-1,	F-105,	Navy		Mirage,		
	Tu-160,	Tu-22 M2,	Su-24,	B-2	A-6			Rafale		
	Su-27 K,	Tu-22MZ	Su-24 M							
	Su-27IV		MiG-25BM							
(b) Air-to-surface missile										
Indices	Russia			USA (“sparrow”)				England	France	Italy
	RVV-AE	R-27 R	R-33 R	AAM-N-2	AIM-7E	AIM-7F	AIM-7 M	Skyflash	Matra-super	Askand-7A
Flight speed (m/sec)	1450	1250	1250	700	1000	1120	1120	1450	750	1100
Range of fire (km)	100	<130	<80	8.0	25	70	100	50	18	50
Type of carrier	Su-27, MiG-29	MiG-29 K, MiG-29 M, Su-27, Su-27 K	MiG-23 M, MiG-23MR, MiG-23MLD	F-4, F-8, F-14	F-8, F-14, F-111	F-4, F-8, F-14, F-111	F-4, F-8, F-14, F-111	F-4, Tornado	Mirage, F-104, Starfire	F-104-S
(c) Surface-to-air missile										
Indices	Russia					U.S.				
	AMC S-300 V	AMC S-300 PMU	AMC S-300 PMU 1	AMC BUK	AMC ShTIL	Patriot ground rocket				
Flight speed (m/sec)	1700	2100	2400	1230	1230	1600				
Maximum range (km)	400	90	400	–	–	60				
Target altitude range (m)	25–30,000	25–25,000	10–25,000	15–25,000	15–25,000	60–24,000				
Target-speed range (m/sec)	≤3000	≤2255	≤6450	≤1200	≤1200	≤1800				
Mobility	Self-propelled	Self-propelled	Self-propelled	Selp-propelled	Ship-based	Transportable (by vehicle)				

radar dome (Fig. 1b) [1]. Thus, a radome is one of the most important parts of the modern radar-guided missile systems, which is also employed on high performance hypersonic airplanes, satellites, etc. [8–10]. In fact, among the various fairing accessories of a missile and aircraft, the radome occupies a highly important place.

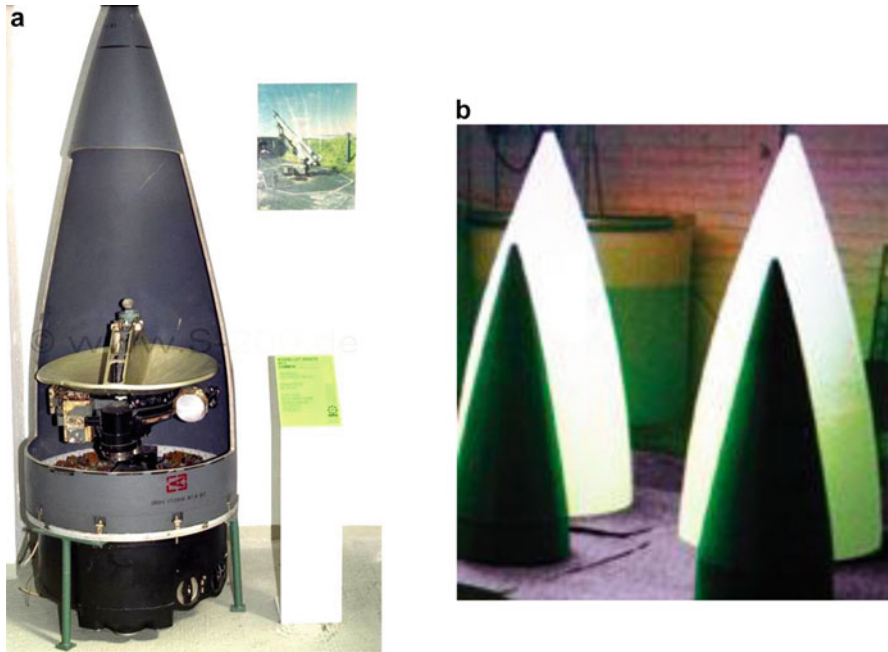


Fig. 1 A digital photograph of (a) a cut-radome component showing the housing of antenna in it, and (b) commercial sintered silica radomes (white colored ones) (adopted from reference [111–114])

In view of these, the material used for radome construction is of highly demanding on the account of the extreme environment that arises during missile travelling through the atmosphere and it has to withstand the severe aerodynamic heating; high mechanical stresses; erosion due to wind, rain, and dust to successfully hit the intended target. Therefore, the radome construction material should have an optimum combination of mechanical, thermal, and dielectric properties to ensure the highest level of performance of a missile. Furthermore, as the speed of the missile increases, the difficulty in the design and development of radome also increases as the obstruction to the radar tracking signals in the RF also increases [1]. In fact, the radome decides the precision with which the missile is guided to meet the target while withstanding the main thermal and mechanical loads generated during maneuvers [1–7]. A high-speed missile with higher maneuverability, higher target range, and all-weather withstanding capabilities needs a radome constructed out of the right kind of material.

The prerequisite conditions that a radome material must possess are summarized in Table 3. Furthermore, a radome should electrically behave as a free space over all wavelengths and be shaped in such a way that it is structurally stable and generates a minimum drag during high-speed missile flight with lots of aerodynamic loads. Thus, the ideal radome material shall be electrically highly transparent to electromagnetic signals such that a minimum power is lost in passing through the material,

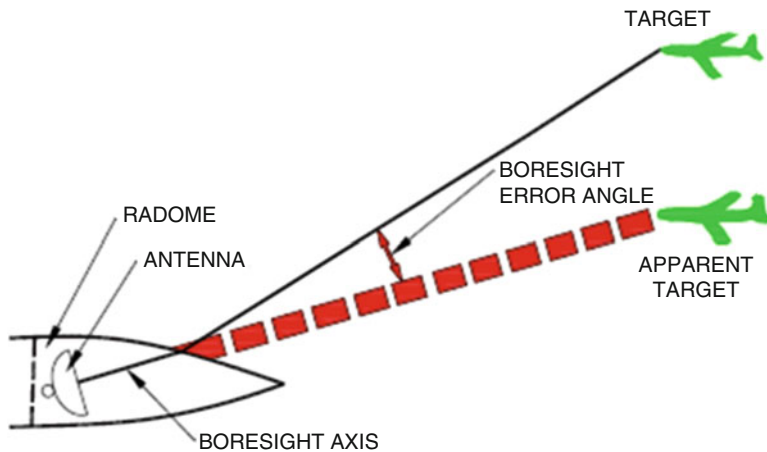
Table 3 The prerequisite properties of a material to be used for radome fabrication for missile applications (adopted from reference [1–7])

Property	Purpose
Dielectric constant (ϵ)	A stable and low dielectric permittivity vs. temperature and frequency is necessary to allow the radar energy to pass with minimum dissipative and reflective losses and to minimize the “bore-sight error (BSE)
Loss tangent ($\tan \delta$)	A low $\tan \delta$, which arises due to signal absorption by the radome wall, and to be kept at a minimum up to high temperatures for high microwave transmission without much loss of the signals
Mechanical strength	High tensile and flexural strength at ambient and high temperatures (1500–2000 °C for hyper velocity vehicles)
Elastic modulus and stiffness	High elastic modulus and stiffness are required to keep the thin wall radomes from buckling
Thermal shock resistance	A high thermal shock resistance to withstand high aerodynamic loads
Weather capability	High rain erosion and particle (dust) impact resistance
Irradiation resistance	To keep the structure intact during flight of the missile
Thermal conductivity	Low thermal conductivity is required to keep the inside antenna at low temperatures
Temperature withstanding capability	A high temperature withstanding capability is required to keep the shape of the radome intact during flight
Specific gravity	A low specific gravity is preferred
Chemical stability	A high chemical stability is required
Moisture absorbing capability	A high resistance against moisture absorption is required
Fracture toughness	A high fracture toughness is necessary
Fabrication ability	An easy and simple fabrication ability is necessary
Cost	A low cost is advantageous
Coefficient of thermal expansion (CTE)	A low CTE is necessary to prevent stress failures and to preclude the formation and propagation of cracks resulting from rain and dust impact (erosion environment)

and structurally must retain its physical integrity throughout the entire flight trajectory while withstanding aerodynamic loads, thermal stresses, and environmental effects [11]. No such ideal material is identified as of now that provides all the necessary structural and physical protection to the hypersonic vehicles. Hence, the selection of a material is a compromise, and it should have properties that will reasonably satisfy electrical, mechanical, and physical requirements [11]. Normally, a low dielectric constant material is chosen for a wide frequency band application, whereas a relatively high dielectric constant material is chosen for a narrow frequency band with minimum aberration requirement. In most cases, the dielectric constant should be less than 10, with not more than 10% variation in the value over the anticipated temperature range seen by a missile radome during its flight, and the value for the loss tangent should be less than 0.01 [5]. However, these requirements might be tightened for actual service conditions.

Bore-Sight Error and Desired Shape of a Radome for Hypervelocity Vehicles

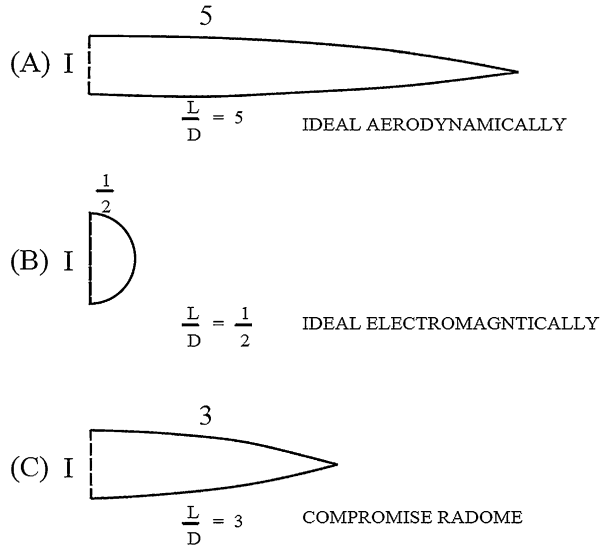
The bore-sight error (BSE) sets in as the RF beam emitted from radar, while propagating through the dielectric radome wall, gets attenuated, experiences electrical phase shift, and undergoes internal reflection and refraction. Thus, the refracted beam upon received by the scanning dish of antenna results in an angular displacement of target from its true position with respect to the antenna dish. The angle of displacement between the missile seeker dish and the target is called the BSE angle of the radome (Fig. 2) [6, 7, 12–14]. Another important parameter affecting the electrical performance of the radome is the bore-sight error (BSE) slope (BSES), which is defined as the rate of change of BSE with seeker antenna scan angle. BSES can adversely impact the performance of a missile by restricting its maneuverability and speed. All these parameters make the radome design a quite complex process. An hemispherical radome shape is too blunt and generates too much drag. To minimize it, an aerodynamically streamlined radome with high fineness ratio (L/D) of the length (L) of a nose cone compared with its base diameter (D) is considered. An aerodynamicist prefers a long pointed shape for the nose of the missile (Fig. 3). However, such a geometric shape would severely degrade the electrical performance characteristics of enclosed seeker antenna. Whereas the hemispherical shape of the radome is highly advantageous from the point of view of the electrical performance since such a shape would yield a much lower BSE. In view of these conflicting requirements, a balance between the aerodynamic and electrical characteristics is normally utilized. Furthermore, to achieve the highest transmission of the radar signals, the use of very thin (equivalent to $\approx \lambda/10$) radome wall is an ideal



GEOMETRY OF BORESIGHT ERROR ANGLE

Fig. 2 Angle displacement is called radome's bore sight error angle. The angle is usually less than 1 degree. Effect is similar to looking at fish in water (adopted from reference [6, 7, 12–14])

Fig. 3 Ideal shapes for electromagnetic and aerodynamic requirements are almost opposite. Compromise shape is shown in (C) (adopted from reference [6, 7, 12–14])



approach [15]. However, such radome will have low strength, and be more prone to rain erosion during flight, and might get damaged during handling. For maximizing the design efficiency, the radome wall thickness should desirably be one half of the wavelength (or an integer multiple of one half wavelength) in the dielectric medium of the radar [14]. Weight of the material is also important and less weight provide long range. This consideration would limit the radome length even if no other consideration is present, as the radome becomes longer it also becomes heavier. Eventually, the range decreases due to increasing weight balances the increment due to decreasing drag, and at this point, the radome length gives maximum flight range. Since the radome forms the contour of the missile nose, it is subjected to structural loading from the pressures of the air. This loading is of two types: a compression along the radome length due to the drag force and a bending load, which occurs when the missile nose is inclined at an angle to the flight direction. Because of radome geometry, the maximum bending moment occurs at the point where the radome joins the missile.

Different shapes considered for radomes construction are given in Fig. 4 [14–16]. Below Mach 0.8, the nose pressure drag is essentially zero for all shapes, and the pressure drag increases dramatically in the transonic region and beyond, where the effect of nose shape on drag becomes highly significant. The factors influencing the pressure drag are the general shape of the nose cone, its fineness ratio, and its bluntness ratio. At supersonic speeds, the fineness ratio has very significant effect on nose cone wave drag. Fineness ratio of 5 is critical as the fineness ratio increases, and the wetted area and the skin friction components of drag increase. Most commercially made tangent ogive nose cones are blunt for a bluntness ratio of about 0.1 [14, 17].

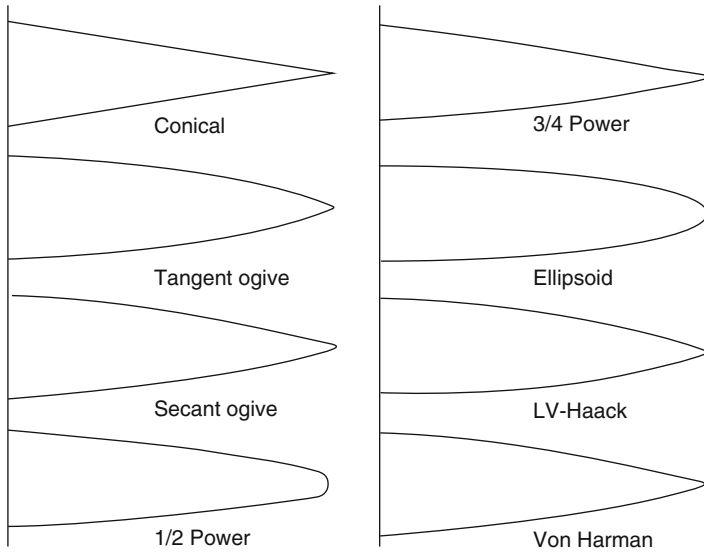
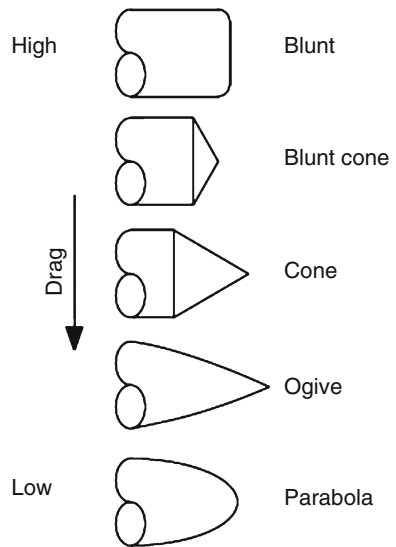


Fig. 4 Different types of radome nose shapes (adopted from reference [13])

Fig. 5 Performance of drag on various nose shapes (adopted from reference [13])



Comparison of drag for different nose shapes of radomes is shown in Fig. 5 [15]. The radome dielectric constant varies with the aerodynamic heating which causes the change in target's apparent location and the BSE variation [6]. The change in BSE limits the ability of the missile guidance system, and the change in BSE slope is a function of the change in BSE angle. The BSE slope should be kept below 0.010 to

0.020 degree per degree of look angle (i.e., 1–2%) to eliminate the need for guidance compensation [6]. For optimum performance of a high speed airborne vehicle, the tangent of ogive shaped radome has been found to be optimum [18]. The BSE shift gets influenced by factors such as antenna location and design, radome shape, axial temperature gradients, whose control facilitates the accurate estimation of BSE shift. For every radome material, a separate assessment has to be made to find out the BSE shift [6]. The radome wall thickness decreases with the rain erosion which also alters the BSE. The resultant radome wall change needs to be compensated by making changes in the radar transmission frequency considered for evaluating the BSE shift

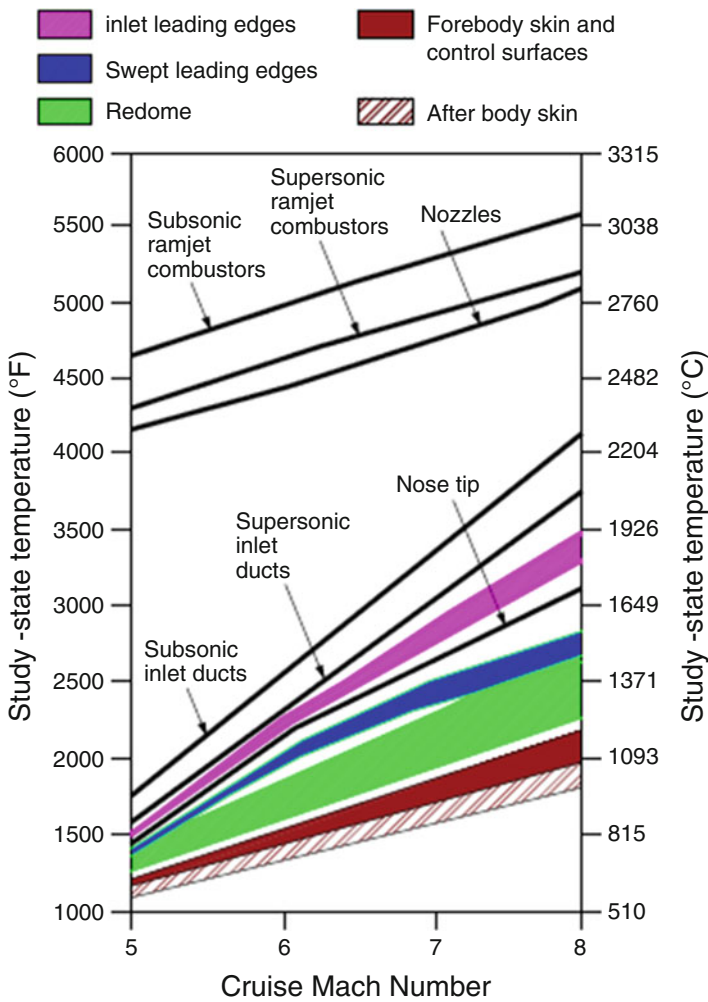


Fig. 6 Typical maximum temperatures at 80,000 feet altitude as a function of cruise Mach number for critical components (adopted from reference [7]).

theoretically. The maximum speeds of future tactical missiles are expected to move from the supersonic (between Mach 1 and 5) to the hypersonic (Mach >5) regime [7]. Figure 6 shows the maximum temperatures that are seen by major components of missiles cruising at Mach 5 to 8 at 80,000 feet [7]. The radome, body, and swept leading edge temperatures apply to both rocket and air-breathing missiles, whereas the remaining temperatures are for air-breathing propulsion components.

Derivation of Tangent Ogive Radome Shape Using Mathematical Equations

Figure 7 defines the key parameters needed to describe mathematically a tangent ogive shaped radome. Any point on the outside surface must satisfy the Eq. (1), which applies for fineness ratio of 0.5 or larger [14, 19]. If the x -axis corresponds to the radome axis, then the radome shape is a surface of revolution formed by revolving a tangent ogive curve about the x -axis. The cross sections through this three-dimensional shape are circular in the y - z plane with the radome radius given by Eq. (2). From Fig. 7, it can be clearly seen that Eqs. (3 and 4) are true. By simultaneous solution of Eqs. (3 and 4), the expressions shown in Eqs. (5 and 6) can be obtained for the two unknowns in terms of the radome length (L) and diameter (D). By substituting Eqs. (5 and 6) into Eq. (1), one can obtain the formula of the tangent ogive shape in terms of known constants L_0 and D_0 [14, 19].

$$(r_p + B)^2 + x_p^2 = R^2 \quad (1)$$

$$r_p = \sqrt{(z_p^2 + y_p^2)} \quad (2)$$

$$R^2 = L_0^2 + B^2 \quad (3)$$

$$\frac{D_0}{2} = R - B \quad (4)$$

$$B = \frac{(4L_0^2 - D_0^2)}{4D_0} \quad (5)$$

$$R = \frac{(4L_0^2 + D_0^2)}{4D_0} \quad (6)$$

Figure 8a shows the tangent of ogive shaped radome with dimensions of 460.8 mm length, 192 mm base diameter, and 4.572 mm wall thickness generated using Eq. (1) and a digital photo of fused silica radome consolidated by following an “*hydrolysis induced aqueous gelcasting (GCHAS)*” route with the same dimensions is shown in Fig. 8b [9, 10, 20, 21].

Fig. 7 Tangent ogive radome geometry (adopted from reference [19, 27])

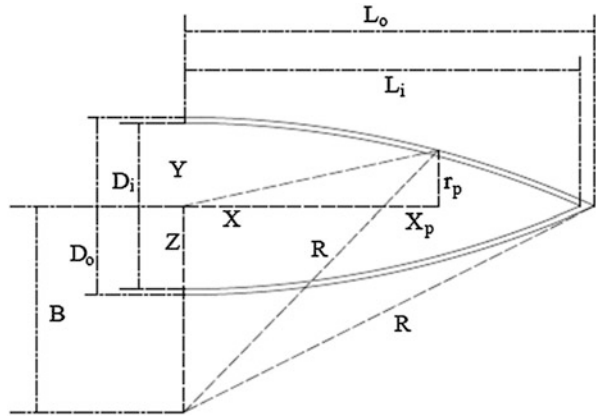
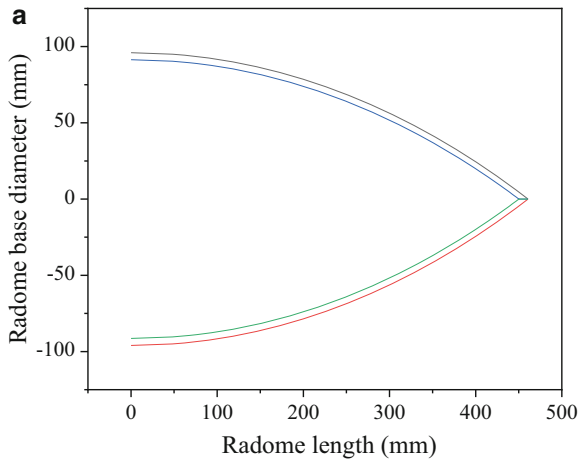


Fig. 8 (a) Tangent ogive radome shape with dimensions of 460.8 mm length, and 192 mm base diameter and a wall thickness of 4.572 mm generated using the diagram given in Fig. 7, and **(b)** a fused silica radome shape produced with same dimensions at ARCI, Hyderabad, by following an “hydrolysis induced aqueous gelcasting (GCHAS)” route developed at ARCI, Hyderabad (adopted from reference [10, 20, 31, 76, 115–117])



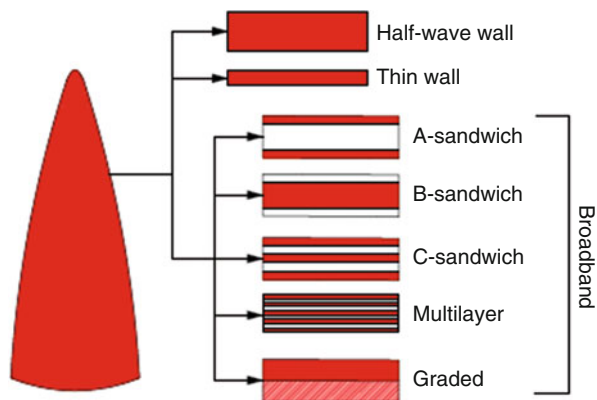
Based on the wall thickness, radomes are normally divided into thin-walled or half-wave radomes and single or multilayer (two-layer or three-layer) radomes [1, 14, 19]. Conventionally, the radome is designed to be a single wall structure in which wall thickness is equivalent to a thickness $\frac{1}{2}$ of the wavelength desired. However, this structure has a very narrow bandwidth and lacks adequate strength when the wavelength is <2 cm. As shown in Fig. 9, the multilayer broadband designs, designated by A-, B-, and C-sandwich structures, have been proposed to solve this problem [22]. The radome wall structure greatly determines the use of the defined frequencies and/or broadband (1–18 GHz) wave transmission, and half-wave wall structure is used for the defined frequency application [14, 15, 19]. The most commonly used and reported broadband radome wall structure consists of A-sandwich, C-sandwich, and multilayer. However, these structures are not suitable for high-temperature environment due to the big mismatch of the thermal properties of each layer, which may restrain their application in the high-speed missile radome [15]. The structure is designed to be composed of an odd multiple layers with no central matching layers at the design frequency. Investigations show that the multilayer structures exhibit multiband transmission property [23, 24]. To relieve the thermal stresses between the layers, functionally graded materials have been employed, and were used for ultrahigh temperature applications [14, 19, 25].

To optimize electrical transmission, the wall thickness of a single layered ceramic radome is always tailored to an even multiples of half-the radar wavelength in the material according to Eq. (7), where d is the half-wave wall thickness, λ is the free space radar wavelength, ϵ is the dielectric constant, and ϕ is the angle between the radar beam and a vector normal to the radome wall [6, 14, 19].

$$d = \lambda/2(\epsilon - \sin^2\phi)^{1/2} \quad (7)$$

Figure 10 shows the monolithic half-wave radome wall thickness of various radome materials vs. four different bands of radar signals (X, Ku, K, and Ka bands) [6, 14, 19]. It can be seen that, in general, the radome wall thickness depends

Fig. 9 Schematic diagram of radome wall structure (adopted from reference [13–15, 19])



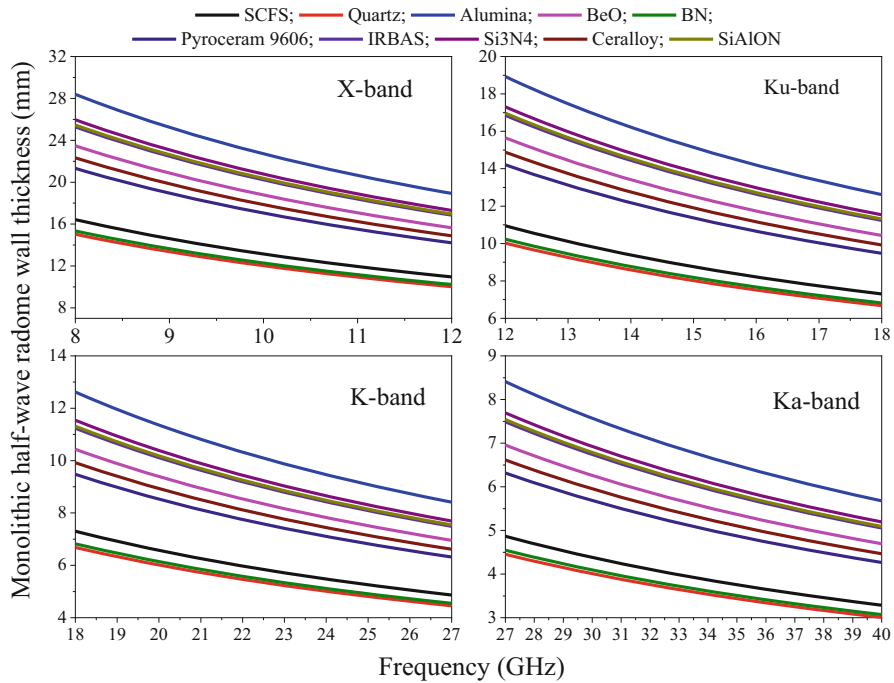


Fig. 10 Monolithic half-wave radome wall thickness of various radome construction materials used on various types of missiles vs. radio-frequency of radar signals (adopted from reference [6])

on dielectric constant of the material. Low dielectric constant material permits higher wall thickness of radome fabricated which has implication on mechanical strength of radome. For X- and Ku-band frequencies, irrespective of the dielectric constant, the half-wave wall thickness of all the materials is higher than 5 mm, which is manageable to fabricate radome structure with up to one meter long height, and half-a-meter long base diameter. When wall thickness is less than 5 mm, then the walls of certain low strength radome materials will crumble down with their own weight. Furthermore, the thin wall thickness radomes are not only difficult to be machined with close tolerances but also difficult to fabricate. For low dielectric constant materials such as, fused silica ($\epsilon = 3.4$), quartz ($\epsilon = 2.9$), boron nitride ($\epsilon = 3.01$), etc., for K- and Ka-band frequencies, the wall thickness is less than 4 mm. For this reason, X-band radomes are usually designed with half-wave wall thickness, whereas radomes designed to transmit at Ka-band generally require full-wave or 3/2-wave walls to maintain their structural integrity [6, 14, 19]. As rising radome temperatures increase the material dielectric constant, the electrical thickness of the radome wall will also increase. The electrical thickness of the walls of radomes for direction finding or direction controlling radar instruments is performed by measuring the phase shift of microwave energy propagating through the radome wall at pre-determined incidence angle and relative polarization, between relatively strong

signal transmitting and receiving points. In effect, these changes shift the center-band transmission frequency of the radome downward, thereby detuning the antenna. It should be pointed out in principle that the radome shape, as related to impact angle, can be designed to reduce the rain erosion damage to any material [5, 14, 19].

Glass and Fiber Reinforced Plastics for Radome Applications

The electrical properties of fiber-reinforced plastics (FRPs) listed in Table 4 are relatively good up to the temperatures indicated [3, 26–28]. The most widely employed resins for RF radome fabrication are polyester, epoxy, phenolic, and silicone. Epoxies are generally superior for speeds less than Mach 2 at sea level where the maximum reachable temperature is about 205 °C. Silicone resins yield good performance when electrical properties are of prime importance and temperatures are about 290 °C. Other resins include polyurethane (low temperature capability, used on commercial aircraft), silicones (good elevated temperature properties but low strength), phenyl silanes (similar to silicones, used on F-14, USA), Teflon (noncharring ablator), and polybutadiene (a newly developed high temperature resin, manufactured by Firestone, USA). The low cost phenolic resins exhibit superior-mechanical strength, high-resistance to a large range of environmental degradations, and high-temperature withstanding capability. These FRP-based radomes can be easily attached to the main missile body by using conventional means of attachments such as, threading, adhesives bonding, clamp rings, latches, bolts, rivets, screws, etc. However, the care must be taken when the glass-based FRP radomes are attached to the missile main body to overcome the “weak links” inherent in them such as, low bearing strength, low interlaminar tension, and interlaminar shear [7]. In order to improve the rain-erosion resistance of FRP radomes employed for Mach 3 to 5 applications, two ablator coatings, Avcoat 8029 and Duroid 5650 M, were employed [7]. As on today, none of the multitude of FRP resin systems has been found to be suitable for radomes travel at a speed of Mach 3 to 3.5. However, this class of materials is experiencing steady development for uses up to this range

Table 4 Candidate radome materials for high performance aircraft and missiles (adopted from reference [3])

Material	Decomposition or melt temp. (°C)	Thermal shock resistance	Rain erosion resistance	Weight	Ease of fabrication	Relative cost
Glass reinforced polyester	120–150	Good	Poor	Low	Good	Low
Glass reinforced epoxy	150–205	Good	Poor	Low	Good	Low
Glass reinforced polyimide	315	Good	Poor	Low	Good	Low
Glass reinforced polybenzimidazole	315	Good	Poor	Low	Good	Low

Mach numbers; polybutadiene resin and PRD-49 are the newest additions and are becoming available in commercial quantities.

Radomes that travel at a speed of Mach 3 are typically made of polymer matrix composites, such as, glass fiber/epoxy, quartz fiber/bismaleimide, quartz fiber/cyanate ester, glass fiber/polyimide, alumina-boria-silica fibers/polybenzimidazole, etc. [3, 26–28]. When radomes are used at high speeds (Mach 3 to Mach 5), their physical and mechanical properties have to be considered to withstand temperatures in the range of 500–800 °C and for tougher environmental conditions [29]. For intermediate (i.e., medium) speed missiles that travel at a speed of up to 4 to 5 Mach, ceramic matrix composites, such as quartz fiber/polysiloxane, quartz fiber/poly-silazane, oxide/oxide composites including alumina-boria-silica fibers/aluminum silicate, are considered. The glass reinforced polyesters, epoxies, and silicones are normally employed for the fabrication of aircraft fairings. The radomes made of quartz glass reinforced polyimide withstood temperatures up to 540 °C and were employed for USA B-1 aircraft that travels at Mach 3 speed [3, 16]. The strength of this glass reinforced polyimide can be tailored by increasing the wall thickness to certain extent but is mainly influenced by its thermal properties [3]. The important glass fibers are E-glass (most common), S-glass (slightly higher temperature capability than E-glass), fused quartz (highest temperature capability and most expensive), and PRD-49 (a high temperature organic fiber related to nylon and manufactured by DuPont) [3]. As a class, the glass fiber reinforced plastics are usually preferred over ceramics for radome applications where mission requirements are mild enough for them to be operated successfully. They do not suffer from the brittleness of ceramics and are lightweight, relatively easy to fabricate, and relatively low in cost [3, 16].

Ceramic Materials of Choice for Hyper-velocity Radome Applications

For high speed missile applications (Mach 6 to 8), only ceramics such as silica (SiO_2) (fused silica [8]), alumina (Al_2O_3), magnesia (MgO), beryllia (BeO), boron nitride (BN), reaction-bonded silicon nitride (RBSN), hot-pressed silicon nitride (HPSN), silicon aluminum oxynitride ($\beta\text{-SiAlON}$), cordierite ($2\text{MgO}\cdot 2\text{Al}_2\text{O}_3\cdot 5\text{SiO}_2$) based glasses (Pyroceram-9606, Pyroceram-9608, AS-418, AS-370, which are known as Sital glasses in Russia), a composite of barium aluminum silicate (termed as Celsian), a composite of silicon nitride, boron nitride and silica ($\text{Si}_3\text{N}_4\text{-BN-SiO}_2$) (termed as Nitroxyceram), etc., can be the candidate materials of choice (Tables 5 and 6). Figure 11a–c shows some examples of modern missile complexes equipped with radomes made of slip-cast fused-silica (SCFS) and Sital radomes produced in Russia [1, 2]. Ceramic materials own higher temperature capabilities than FRPs and are high resistance to rain erosion at supersonic velocities. However, most of these ceramics are susceptible to thermal shock. Also, in comparison to metal, ceramic materials' brittleness and relatively low coefficient of thermal expansion (CTE) demand to take a special care while attaching these ceramic radomes to missiles

Table 5 Comparative properties of ceramic radome materials (adopted from reference [2, 6, 7, 11–15, 18, 26, 28, 34, 59, 60, 87, 100–105]¹⁸)

Material & trade name	SCFS	Alumina	Pyroceram 9606	IRBAS	3 M™ Si ₃ N ₄ 147-31 N	Ceralloy 147-01 EXP	SiAlON
Manufacturer name	Ceradyne CTM	–	Corning, Inc.	Lockheed Martin	CTM	CTM	RMSC and ORNL
Composition	SiO ₂	SA (99%)	Cordierite	In-situ reinforced BAS with Si ₃ N ₄	Sinter RBSN	RBSN	β-Si ₃ Al ₂ O ₂ N ₆
Density (g/cm ³)	2.0	3.9	2.6	3.18	3.21	1.8–2.5	3.02
Elastic modulus (GPa)	37	380	121	280	310	50–200	230
Flexural strength (MPa)	43	270	240	550	800	180	260
CTE (10 ⁻⁶ /°C)	0.7	8.1	4.7	3.2	2.9	3.1	4.1
Thermal conductivity (W/m.K)	0.8	34.59	3.3	20	25	6	16
Dielectric constant (ε) at 10 GHz	3.3	9.6	5.5	7.6	8	4–6	7–7.7
Loss tangent (tan δ)	0.003	0.0001	0.0005	0.002	0.002	0.002–0.005	0.001
Thermal shock resistance	Excellent	Poor	Good	Very good	Very good	Fair	Very good
Maximum use temperature (°C)	1538	1925	1349	1538	1538	1538	1300

Water absorption capacity (%)	5	0	0	0	0	0	20	0
Rain and dust erosion resistance	Poor	Excellent	Good	Very good	Very good	Very good	Very good	Very good
Ease of manufacture	Very good	Fair	Good	Fair	Fair	Fair	Fair	Fair
Max. operating speed (Mach)	8	3-4	5-6	6-7	6-7	6-7	6-7	6
Missile system carrying ^b	(I)	(II)	(III)	(IV)	-	(V)	(VI)	(VI)

^aRMSC: Raytheon missile systems company-formerly Hughes missile systems company; SCFS: slip cast fused silica (SiO₂); SA: sintered alumina (Al₂O₃); ORNL: Oak ridge national laboratory; CTM: Ceradyne thermo materials, a subsidiary of 3 M; RBSN: reaction bonded silicon nitride (Si₃N₄); BAS: barium aluminum silicate; CTE: coefficient of thermal expansion; GC-MAS-225: glass ceramics – magnesium aluminosilicate (2MgO·2Al₂O₃·5SiO₂; cordierite)
^b(I): Aegis, Arrow Patriot, Standard Missile (SM), AA-13 “Arrow” (Vympel R-37) air-to-air missile, S 400; (II): Sparrow III air-to-air missile Mach 3; (III): Falcon, Hawk, Phoenix, Sidewinder, Sparrow AIM-7F, Svenska, Tartar, Terrier, Typhon, Standard missile for surface to air, antiaircraft operation; (IV): PAC-3 (Patriot Advanced Missile System); (V): PAC-3 Patriot Advanced Missile System was under development by Ceradyne, Inc.; (VI): Prototype of AMRAAM-AIM-120C air-to-air missile



Fig. 11. Examples of modern missile complexes and missiles equipped with antenna housings made of radio-transparent materials: (a) anti-aircraft missile complex (AMC) S-300; (b) launch of quartz-radome-equipped 48H63 missiles from AMC S-300 BUK; (c) launch of sitall-radome-equipped 9 M317 missiles from AMC BUK (adopted from reference [1]).

main bodies [7]. Each of these ceramics has its own limitations and advantages with respect to dielectric properties, thermal shock resistance, and strength properties. For high-speed missiles that travel at the speed of Mach 5–12, where the surface of the radome wall see a temperature of about 2000 °C, and the aerodynamic mechanical loads increase up to 10 Tonnes. For these reasons, the most important requirement of the radome material must be undoubtedly the refractoriness. The major differences of mostly employed quartz, Sitall, and alumina radome materials are given in Tables 5 and 6 [6]. The six performance criteria to be employed while choosing a material for radome applications are given in Table 7 [6]. The rating system chosen is poor to excellent. When all the ratings of a material are above good, it will certainly perform well as a radome in all adverse conditions, and when any of the ratings are below good, it does not perform to the required extent in adverse conditions. Furthermore, for radome materials that possesses all ratings above good, for them the theoretical estimation of BSE is relatively easy [6]. The Johns Hopkins University and the Advanced Physical Laboratory (APL), Maryland, USA, developed a method to predict the environmental flight performance boundaries for ceramic radome materials. The relevant parameters were combined into a unified radome limitations (URLIM) computer program that can predict the flight limits of radome

Table 6 Selected properties of beryllium oxide (beryllia), silica (clear glass fused silica and fused quartz), boron nitride, and Sitall glasses suitable for radome applications (adopted from reference [5])

Radome material	Beryllia (BeO)	Silica (SiO ₂)	Boron nitride (BN)	Sitall
Chemical composition	High purity	Fused quartz	IPBN	Cordierite
Major phase (%)	>99	99.8	99.9	2MgO-2Al ₂ O ₃ -5SiO ₂
Density (g/cm ³)	2.85–2.95	1.68	1.25	2.45
Theoretical density (%)	95–98	76	55	98
Water absorption capacity (%)	0	24	0	0
Flexural strength (10 ³ psi)	35	4.8	14	18
Young's modulus (10 ⁶ psi)	50	2.5 ^a	1.75	17
Thermal conductivity (Btu/ft-hr-°F)	120	2.4	16	~2
Coefficient of thermal expansion (×10 ⁻⁶ in/in/°F)	4.6	0.3	2.1	1.45
Specific heat (cal/g-°C)	0.26	0.246	0.29	0.19
Poison's ratio	0.34	Unknown	0.23	0.27
Dielectric constant at 8–10 GHz	6.6	2.9	3.01	4.8
Loss tangent at 8–10 GHz	0.0005	0.01 max.	0.0006	0.002

^aCalculated

materials on the basis of electrical degradation, surface melting, thermal stress, and mechanical load [30]. For ceramic radome materials, the thermal shock resistance and the capability to withstand the cyclic thermal loading are the important properties to be tested for the desired radome performance. If any ceramic material wall prevents transmission of heat from outer side to inside very well, that can be considered as the best material for radome applications as far as thermal properties are concerned. Sometimes, alumina is preferred for radome applications as it satisfies a high temperature requirement, but a lighter material can satisfy a low temperature operation with consequent weight advantage. A stable dielectric constant, which is a temperature-dependent property, reduces BSE caused by aerodynamic heating and allows relaxed manufacturing tolerances of wall thickness.

Alumina

Alumina (Al₂O₃) has a clear advantage in terms of refractoriness (melting point 2072 °C) but it has a low resistance to thermal shock and possesses a high dielectric constant. The temperature at which alumina structure changes is 2050 °C, while it is 1200–1350 °C for Sitall and no higher than 1300 °C for ceramics based on SiO₂. However, owing to its excellent rain erosion resistance and high refractoriness [31], Al₂O₃ was employed to construct radomes employed for Sparrow III air-to-air missile that travels at a speed of up to about Mach 4–4.5. However, above Mach

Table 7 Advantages and disadvantages of popularly employed commercial radomes (adopted from reference [6, 106]^a)

Performance criteria	SCFS	Celsian	Pyroceram 9606	Rayceram 8	Nitroxyceram	RBSN	HPSN
Maximum temperature	Good	Fair	Fair	Fair	Good	Good	Very good
Thermal shock resistance	Excellent	Fair	Good	Good	Very good	Fair	Very good
Maneuvering capability	Fair	Good	Good	Good	Good	Good	Excellent
Radar transmission	Excellent	Very good	Good	Good	Very good	Good	Good
Rain and dust erosion	Fair	Fair	Good	Good	Very good	Very good	Very good
Ease of manufacture	Very good	N/A	Very good	Good	Fair	Fair	Fair

^aSCFS: slip-cast fused silica (SiO₂); Celsian: barium aluminum silicate; Pyroceram and Rayceram: 2MgO.2Al₂O₃.5SiO₂; cordierite ceramics; Nitroxyceram: silicon nitride, boron nitride and silica composite (Si₃N₄-BN-SiO₂); RBSN: reaction bonded silicon nitride (Si₃N₄); HPSN: hot-pressed Si₃N₄

4.5, Al_2O_3 cannot withstand the thermal shock resulting from aerodynamic heating [1, 2]. Thus, alumina radome can be employed on missiles that travel at a speed of above Mach 2 but below Mach 5 [12]. Alumina with purity higher than 97% can withstand temperatures up to 1760 °C. Lucalox, which is 99.9% pure, is the best grade of alumina. By adding <0.5 wt% magnesium oxide as an additive to Lucalox, the growth of grains can be prevented and a high density material can be achieved [32]. Its dielectric constant at X-band frequency is about 9.6. The high sintering temperature, the significant contraction of the preform during sintering, warping, and deformation, difficulty in machining due to high strength and stiffness, low resistance to thermal shock, and high dielectric constant are some of the drawbacks that have limited the use of alumina in radome applications that travel at speeds > Mach 5.

Cordierite Based-Glass (Sitall)

The main attractive properties of Sitall ceramics include the absence of porosity, exceptional long-term resistance to the effects of seawater, dust, and high concentrations of moisture, and high rain erosion resistance, which make them very attractive as radome materials for missiles launched from sea- and aerodrome-bases [1, 2]. Whereas the limitations of Sitall ceramics are low melting point, moderate thermal shock resistance, lack of strength, and the increase of dielectric loss with temperature above 600 °C. Until now, all attempts to resolve these problems have met with limited success [29]. Sitall ceramics (refer Table 6) were initially developed and deployed by Russia, NATO member countries and USA to make radomes for ground-to-air and for air-to-air missile applications operating at speeds of Mach 4–7. They were also employed on the US Navy's Standard Missiles for surface-to-air antiaircraft operation. They were also the leading candidates for the US Army's Sam-D missiles, but were eventually discarded in favor of slip-cast fused-silica (SCFS) radomes because of thermal shock considerations and the fact that these are manufactured by following a proprietary expensive and complex process [1–3]. The pyroceram, one of the Sitall glasses, is a nonporous crystalline glass material with a density of 2.4–2.62 g/cm³, the mechanical strength, and the dielectric constant of pyroceram do not change almost up to 700 °C, and its loss tangent at temperatures above 750 °C is 0.02. In comparison to Al_2O_3 , pyroceram is more stable against temperature variations at higher temperatures and they better disperse and dissipate the heat. During flight at an altitude of 30 km and speed of Mach 5, the surface of pyroceram reaches ~700 °C. Under similar conditions, Al_2O_3 heats up to 980 °C. The higher moisture resistance and the lower density of pyroceram glasses in comparison to Al_2O_3 have led to their use as radomes [16]. Pyroceram 9606 is a magnesium-aluminum silicatebased cordierite ($2\text{MgO}\cdot 2\text{Al}_2\text{O}_3\cdot 5\text{SiO}_2$) with high thermal shock resistance and resistance against corrosion and abrasion. This material is also more resistant against corrosion than SCFS; however dielectrically, it is not stable against temperature variations and cannot be used at speeds higher than Mach 5. Hallse et al. [33] have shown that Pyroceram 9603 enjoys a better thermal performance but a higher loss tangent.

Slip-Cast Fused-Silica

Since 1956, the majority of the structural work with slip-cast fused-silica (SCFS), which is also called as the re-bonded fused silica or fused quartz glass (particularly by Russians), was directed toward its application as a material of choice for radome applications for flight velocities above Mach 5 as it possesses a low specific gravity, high residual porosity (up to 18%), low dielectric constant (3.06–3.32 from 25 to 1000 °C), low loss tangent $\tan \delta$ (0.00053–0.0065) up to 800 °C, high thermal shock resistance (it does not break even after subjecting it to >20 thermal cycles between 25 °C and 1000 °C), high radiation resistance, low thermal conductivity (0.8 W/m.K), low coefficient of thermal expansion (CTE) ($0.54\text{--}0.7 \times 10^{-6} \text{ }^\circ\text{C}^{-1}$) between RT and 800 °C, high electrical resistance, good high temperature capability, low mass ablation rate when exposed to oxyacetylene flame (0.0025 mm/s at 2500 °C) and however, a low mechanical strength (37–65 MPa) (refer Tables 5 and 6) [6, 11, 34]. The major information on SCFS ceramics was published by Russians [1, 2] and by the Georgia-institute of Technology, Atlanta, GA, in a series of project reports available in open literature [4, 5]. SCFS exhibits two excellent features: its resistance to thermal shock, and its radar transmission qualities. In fact, SCFS possesses one of the lowest dielectric constant of all the materials under consideration for radome applications, thus has less stringent radome wall thickness tolerances. These qualities derived from a stable dielectric constant and extremely low CTE. The high degree of porosity present in the fused silica ceramic structure is in favor of the thermal and dielectric properties but causes an insufficient mechanical strength and high degree of water absorption, which are also responsible for low rain erosion and particle impact resistance. The SCFS radomes were employed successfully on US Patriot and Standard missiles. The SCFS, like Pyroceram 9606, has a large technology base and a proven application history [4, 5]. The mechanical strength limitation can usually be overcome by using thicker radome walls without compromising radar transmission properties; however, the tensile and flexural strength of SCFS have been considered to be too low for radome applications [5]. Nevertheless, these strength levels have been found to be sufficient for aero-mechanical loads associated with hypersonic missile flight [9, 10], whereas for most other radome materials, the high strength is required to survive the thermal shock associated with such flight environments [5]. It has been found that the low CTE of SCFS causes to develop low thermal stresses in the walls of SCFS radomes during temperature gradient across the wall thickness that occurs during flight in the atmosphere, and thus really requires a lesser strength to withstand the thermal stresses generated during the flight. Furthermore, the strength of SCFS radome increases with the increase of exposure temperature up to about 1093 °C and becomes stronger upon exposure to higher temperatures [5]. The melt limit for SCFS has been found to be about 1704 °C, the temperature at which radar transmission begins to deteriorate as the material softens. The room temperature design tensile strength of SCFS has been considered to be ~28 MPa [6]. This strength is sufficient for applied mechanical stress, and its low thermal expansion prevents thermal stresses from becoming a problem. The problem of water absorption may be overcome by sealing the surface with coating of organic or ceramic materials, fiber-reinforced composites,

dense-porous layered structures, microstructure-controlled fused silica ceramics, and by frequency selective surface (FSS) layers [5, 8]. Fused silica is also used for fabricating crucibles for metallurgy and polysilicon industry, thermal resistance ceramics in the aircraft industry, and high-temperature microwave-transparent materials. SCFS was widely employed in Russia in the production of radomes for different classes of high-speed missiles that travel at speeds of 5–10 Mach [1, 2]. Both in Russia and NATO member countries, the main materials used for aerial fairings of high-speed aircraft controlled by radar guidance are also SCFS, and heat-resistant devitrified-glass materials (Sitall glasses) [2].

Although the terms fused quartz and fused silica are used interchangeably, the optical and thermal properties of fused silica glass are superior to those of fused quartz [35]. One can say that the fused silica is a relatively high purity version of quartz glass. The unusually low CTE of SCFS is responsible for its excellent thermal shock resistance in comparison to those normally exhibited by other ceramic materials employed for fabricating radomes for high-speed missiles [4, 5, 36]. Fused silica also exhibits (i) an optical transparency from infrared to ultraviolet radiation, (ii) high chemical stability, (iii) high resistance on exposure to radiation and neutron flux, and (iv) dielectric property stability over a wide range of frequencies and temperatures [1, 2, 4, 5, 37, 38]. The lowest value of a dielectric permittivity (i.e., the ability of a substance to hold an electrical charge) of a material is of very important to ensure low distortion of antenna waves while travelling through its radome walls and also to simplify the machining operations and tolerance of wall thickness. Thus, the lower dielectric properties ($\epsilon = 3.3\text{--}3.5$) of SCFS makes its wall-thickness tolerance is less demanding (0.1 mm), whereas it is about 0.01 mm and 0.001 mm, respectively, for radomes made of Sitall (with $\epsilon = 6\text{--}8$) and alumina (with $\epsilon = 9\text{--}10$) (refer Table 5) [1]. Owing to its peculiar thermal and chemical properties, and excellent structural and functional characteristics, the SCFS products and engineered components, such as crucibles employed in metallurgy and polysilicon industry, thermal resistance ceramics employed in the aircraft industry, and high-temperature microwave-transparent ceramics, show exceptionally longevity of over hundreds and thousands of years [1, 2, 4, 5, 37, 38]. Fused silica also exhibits high resistance to corrosion attack by acids, alkalis, molten metals, and gases and to the radiation damage. In fact, among different forms of silica, the fused silica is the one employed mostly in many important applications including high intensity lamps, and laboratory ware, which normally exposed to rapid temperature changes. It is also employed to fabricate dimensionally highly stable components such as telescope mirrors, precision optical products. [5]. Nontransparent fused silica is employed for applications in ferrous and nonferrous metallurgies, and glass, ceramic, and chemical industries, whereas the transparent one is employed for illumination engineering, electronics, electrical engineering, in the preparation of pure chemicals, etc. Transparent fused silica is also employed for the fabrication of special optical instruments intended for operation over a wide range of temperature, and a wide optical wavelength region, and in fiber-optical systems, etc. [2].

The mechanical (flexural) strength (~ 28 MPa) of fused silica is insufficient to meet the requirements of advanced re-entry vehicles, especially hypersonic

spacecraft [34]. The open porosity of fused silica articles and ceramics consolidated by following aqueous colloidal processing route is in the range of 5–20%, which significantly limits the scope of its applications [39]. The associated moisture absorption behavior of fused silica adversely affects the transmission capabilities of radar frequency (RF) waves. Upon exposure to ambient moisture, the electrical properties of fused silica ceramics diminish very severely [13]. The loss tangent of these ceramics increases substantially, even with the presence of minor humidity in the samples (higher than 0.3%). Under real conditions, it is impossible to use bare fused silica radomes for any of the existing missile applications without a special cover on it [1, 2, 40, 41]. The low erosion resistance of porous fused silica ceramics is also mainly responsible for the quick damage of radome structure upon the action of rain during its flight. Also, its high wear rate and formation of layering under high temperature conditions also worsens its radio engineering characteristics as well. Owing to the moisture absorbing characteristics, the porous fused silica radomes with uncovered surface are not employed for missiles that are launched from ship and aviation bases, although it is the mostly employed radome for several other tactical missile applications [1, 2, 4, 5, 13, 37]. Fused silica radomes experience high temperatures and high shears when travel at a speed of above Mach 5, which can cause deformation of the radome structure due to plastic flow, and these conditions can also cause a stripping away of the surface layers [4].

Efforts were made to improve the strength of fused-silica by reinforcing it with certain hard ceramic dispersoids and fibers [42, 43]. Attempts were also made to provide hydrophobic and dense ceramic/polymer surface coatings to prevent moisture/water from intrusion within the interior of radome wall as well as to reduce the rain and dust erosion. Recently, Miao et al. [8] reviewed the processing, strengthening, and water-proof coating methods, and ways to improve the transmission of microwaves of fused silica ceramics, and their composites for radome applications. They have suggested to realize the composites of fused silica with dense layers-porous core structure, a continuous fiber reinforcement, a multilayered structure, FSS layers/meta-materials, etc., in order to achieve higher mechanical strength and higher RF transmission efficiency [9, 10].

Fused silica ceramics with varying porosities were consolidated by colloidal processing routes and then sintered. Special purpose fused silica ceramics were also fabricated with [2] (i) an increased radiating capacity (TSM 983 material, with chromium oxide addition); (ii) a low sintering temperature (TSM 107 material, with boron nitride addition); (iii) a controlled dielectric constant (TSM 109 material, with TiO_2 addition); and (iv) an increased resistance to thermal failure (TSM 108 and OTM 353 materials, with Si_3N_4 and SiC addition). Most of the efforts in this area have been directed at developing technologies that would enable fabrication of components from fused silica with free of shrinkage, buckling, and other kinds of deformation. These features, in turn, would enable minimizing the tolerance for fine mechanical finish and save labor cost for large-scale production. A detailed study of the sintering mechanism revealed that

heating at temperatures not exceeding 950–1000 °C caused no critical deformation for fused silica ceramics, and the needed properties for high performance in that temperature range could be attained via chemical activation of the contact bonds between fused silica glass particles [1, 2].

Silicon Nitride and β -SiAlON

The need for having high-temperature materials for radomes has attracted researchers' attention to silicon nitride (Si_3N_4), an high-temperature material, with excellent mechanical and thermal properties [12]. Si_3N_4 is one of the most promising inorganic radome materials combining wave permeability, good high temperature strength, heat insulation, and corrosion resistance together with a good thermal shock resistance, and it is a hotspot in the radome research field for its excellent comprehensive performance. Si_3N_4 in comparison with fused silica and Sital glasses enjoys superior properties, and it can also be used at speeds higher than Mach 7 [13]. Reaction sintered silicon nitride (RSSN), hot-pressed silicon nitride (HPSN), and silicon aluminum oxynitride (SiAlON) offer good thermal shock resistance in aerodynamic heating, much better rain erosion resistance and higher strength than SCFS, hence, considered for radomes construction that travel at Mach 6 range [3]. However, Si_3N_4 needs complex fabrication techniques and it possesses relatively higher dielectric constant. Using the slip casting technique for the Si_3N_4 ceramics, a dielectric constant in the range of 3.7–4 and a strength in the range of 63.9–143 MPa, respectively, have been achieved for the samples sintered at temperature range of 1300–1600 °C, and at the frequency range of 12–18 GHz, which are suitable values for radome applications [13].

Beryllium Oxide and Boron Nitride

Beryllium oxide (BeO) has excellent rain erosion resistance and good thermal shock resistance although it was never used for an operational radome, primarily because of the toxic nature of its finely divided powders and costs involved in the machining of its components. It has been used for high power transmission windows. Boron nitride (BN), both hot pressed and isotropic pyrolytic one, have excellent thermal shock resistance but poor rain erosion resistance. Owing to these properties, BN has not been seriously considered for radome applications because radomes of BN cannot be fabricated in large shapes, and even if a fabrication technology is developed, its cost would probably be prohibitive [3, 4, 44–49]. However, BeO and BN both are good candidates for small windows operating at Mach 8 or higher [44–49].

Comparison of Slip-Cast Fused-Silica Characteristics with Other Radome Ceramics

Figure 12 shows the change in the dielectric constant as a function of temperature for a number of candidate radome materials at X-band frequency [5]. The dielectric permittivity of SCFS, Pyroceram 9606, and alumina in the temperature range of 25–500 °C are 1%, 2.7%, and 4.8%, respectively, whereas in the range of 25–1000 °C, they are about 3%, 6.2%, and 18%, respectively [1]. The change in the ϵ value of SCFS up to 1200 °C is only about 4%, and this value does not increase above 4.1% even when it melts at temperatures in the range of 1800–2000 °C [40, 41, 50–54]. The low thermal conductivity of SCFS keeps high temperatures limits within a thickness of about 0.5 mm from outer surface when it is subjected to unilateral heating and due to which its electronic properties do not vary much upon exposure to high temperatures.

Figure 13 shows a plot of loss tangent vs. temperature for the candidate radome materials [5]. The radome material should possess the lowest possible dielectric loss tangent. In fact, it has been reported that in order to achieve high power transmission efficiency in a radome material, the loss tangent value should be less than 0.01 [18]. Among various materials available, SCFS and alumina show the lowest and

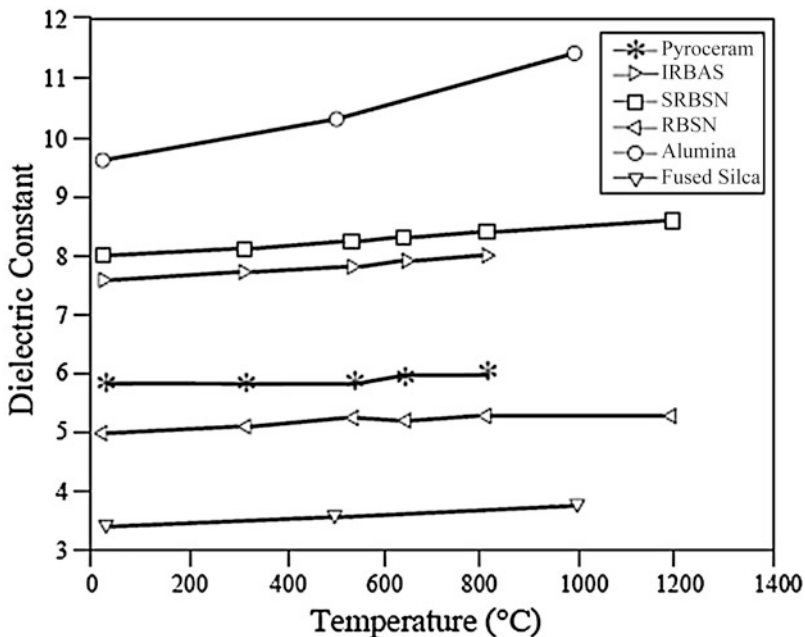


Fig. 12 Dielectric constant as a function of temperature for Pyroceram 9606, IRBAS, SRBSN, RBSN, alumina and slip cast fused silica; (IRBAS- In-situ reinforced boro-aluminate silicate, SRBSN- Sintered reaction bonded silicon nitride, RBSN- Reaction bonded silicon nitride) (adopted from reference [5])

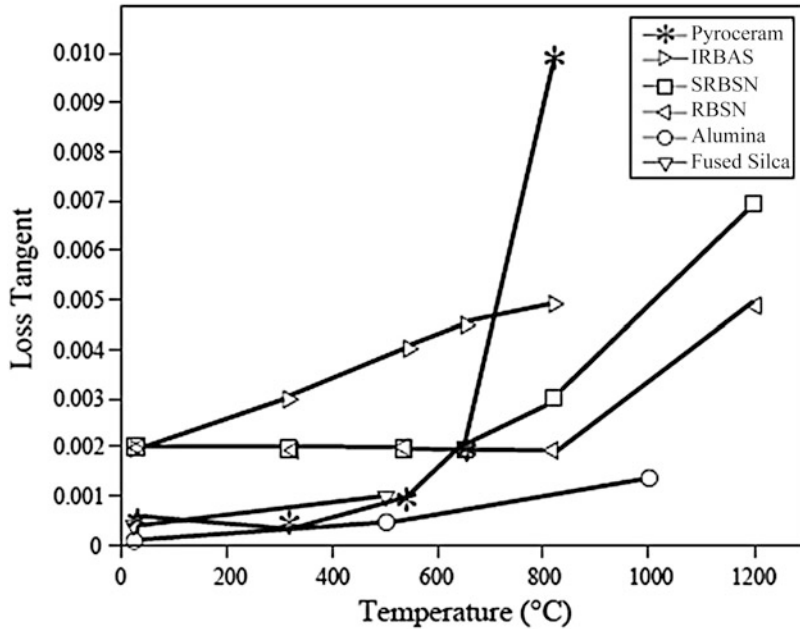
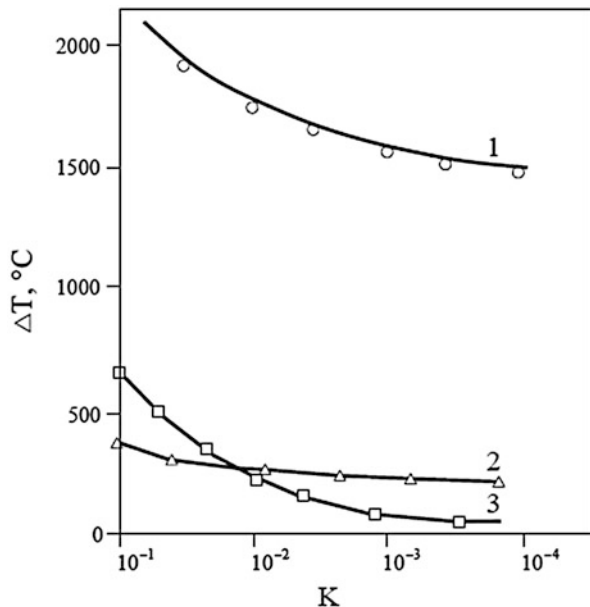


Fig. 13 Loss tangent as a function of temperature for Pyroceram 9606, IRBAS, SRBSN, RBSN, alumina and slip cast fused silica; (IRBAS- In-situ reinforced boro-aluminate silicate, SRBSN- Sintered reaction bonded silicon nitride, RBSN- Reaction bonded silicon nitride) (adopted from reference [5])

most stable loss tangent (Fig. 13). The SCFS and several other ceramic radome materials possess an acceptable value of less than 0.01 at temperatures up to 1371 °C [5].

The relatively low weight of SCFS for a half-wave radome wall for operation at X-band (8–12 GHz) frequency is compared with other ceramic radome materials (refer Table 5) [5, 55, 56]. In fact, among various ceramic radome candidate materials investigated so far, fused silica is the second lightest material after BN. The weight of a particular radome used in a missile depends on the shape of the radome which in turn depends on its dielectric constant and on the electrical and aerodynamic loads withstanding requirements. The relatively low dielectric constant of SCFS allows using radomes with thicker-walls. Furthermore, these thicker walls do not create the weight problem as the specific gravity and bulk density of SCFS are quite low when compared with other ceramic radome materials usually employed. The low thermal conductivity of silica also does not allow heat to transfer to the inner wall of the radome to a great extent; hence, the antenna is protected from being exposed to high temperatures. The low thermal expansion of SCFS gives a unique thermal shock resistance [5]. The thermal shock-properties of SCFS are well known, and the ability of SCFS to withstand thermal shock is one of the most attractive advantages for radome applications. Figure 14 shows how the thermal shock (i.e., temperature gradient ΔT)

Fig. 14 Resistance of inorganic radio-transparent materials to thermal shock ΔT : 1) quartz ceramic (adopted from reference [28]); 2) Pyroceram 9606 (siall cordierite) (adopted from reference [14]); 3) quartz based on Al_2O_3 (adopted from reference [18]); $K = ad/2$, where d -is the thickness of the wall of the product and a -is heat-transfer coefficient (adopted from reference [1])



depends on the quantity $K = ad/2$ for SCFS [28], Pyroceram 9606 [14], and Al_2O_3 [18], where d - is the thickness of the wall of the radome and a - is the heat-transfer coefficient [1]. When a spacecraft enters the dense layers of atmosphere, its thermal loads (K) reach values up to between 10^{-1} and 10^{-4} . As can be seen from Fig. 14, such thermal loads are experienced by Pyroceram 9606 and alumina at temperatures below 500 °C, whereas for SCFS, it is about 1500 °C; hence, SCFS possesses very-high thermal shock resistance [1]. This advantage of SCFS can be attributed to its low CTE.

As missile speeds increase, improvements are also needed in ablation and rain erosion resistance while retaining the other desirable physical and electrical attributes of a radome material [5]. The rain erosion property of SCFS is kept in the category of poor (Table 7), whereas Al_2O_3 and BeO are placed in good category, and cordierite glass ceramic (Pyroceram 9606) and slip-cast cordierite are adjusted as fair category [5]. It is known that SCFS exhibits improved rain erosion resistance at high temperatures as its sintering and density (i.e., bonding among particles) increases. The impact damage mechanism in SCFS produced by lead pellets from a 12-gauge shotgun exhibited considerable change between room temperature and 1649 °C [5]. When SCFS and dense fused silica glass were evaluated at Mach 3, it was found that the erosion resistance of the dense material was superior to that of slip-cast one. However, when these materials were tested at Mach 5, it was found that the dense material failed catastrophically, whereas the slip-cast material merely increased rain erosion rate over that of Mach 3 environment [5]. Surprisingly, the dense strong materials such as slip-cast cordierite also failed catastrophically at Mach 5 when the tip area was not protected. This reversal in merit suggests that

strong dome materials may show relatively poor rain erosion resistance at hypersonic velocities. Nevertheless, the rain erosion and ablation resistance of SCFS radomes for high-speed ($> \text{Mach } 5$) applications needs to be improved [5]. For improving rain erosion and ablation resistance, it is important not to degrade the dielectric, thermal shock, and thermal conductivity properties of the SCFS. One method of accomplishing this effect is by the addition of small quantities of very refractory and very hard materials, which will not react chemically with silica. It has been shown by Kingery and others that the addition of small quantities of material to a major phase has very little effect on properties such as thermal conductivity and dielectric constant of that major phase [4]. However, small additions of refractory material could make the silica more viscous and less likely to flow under high temperatures and high shears. It could also prevent the propagation of surface cracks in silica caused by high velocity impact with rain or other materials [4].

It can be seen from Fig. 15a that the coefficient of linear thermal expansion (CLTE) of SCFS is appreciably below in comparison to those exhibited by

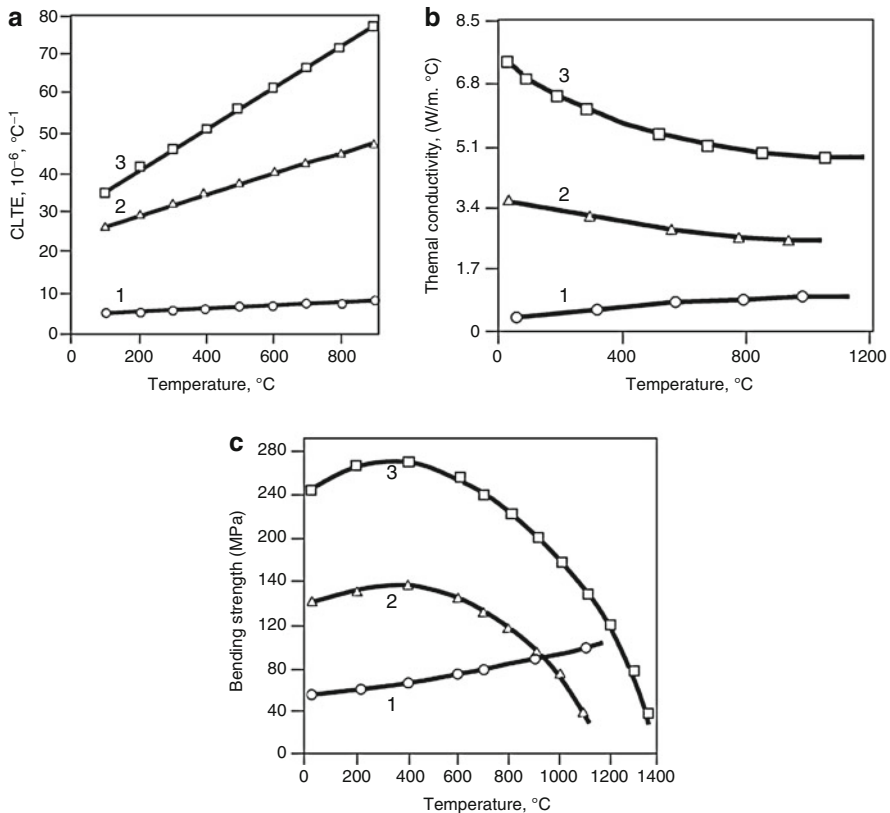
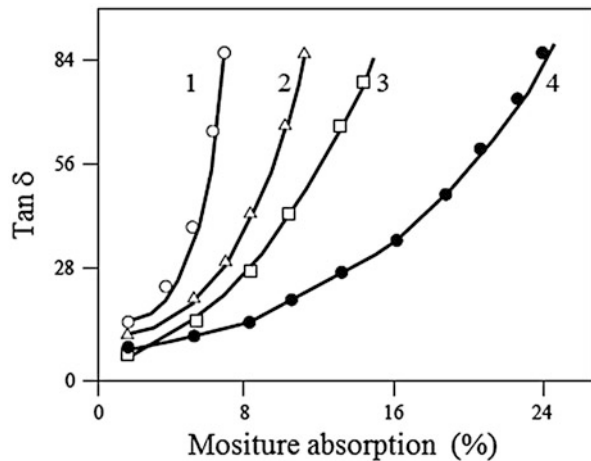


Fig. 15 Temperature dependence of the CLTE (a), thermal conductivity λ (b), and ultimate flexural strength σ_{bnd} of (1) quartz ceramic; (2) Pyroceram 9606 (sitalt cordierite); (3) quartz doped Al_2O_3 (adopted from reference [1])

Pyroceram 9606 and quartz silica doped Al_2O_3 [1]. This low CLTE of SCFS is attributed primarily to its stress relaxation that takes place when it is heated to adequate temperature of about 900°C , and this stress relaxation aspect of SCFS is influenced by its starting raw material and the shape and structure of its finished product [1]. In fact, the SCFS shows the lowest thermal conductivity among all the inorganic dielectric materials investigated so far. Figure 15b shows the temperature dependence of thermal conductivity for SCFS with a porosity of 8–10%, Pyroceram 9606, and a nonporous quartz silica doped Al_2O_3 [1]. It can be seen that in comparison to other two materials SCFS shows the lowest thermal conductivity up to the temperature of 1000°C . The thermal calculations performed while designing the half-wave wall thickness for surface-to-air missiles that travel at a speed of Mach 6–12 indicated that the radomes made of SCFS provide adequate protection to the antenna placed inside of the radome against the aerodynamic heat loads generated [1]. Nevertheless, SCFS exhibits the lower elastic strength in comparison to those exhibited by Pyroceram 9606 and the quartz-doped Al_2O_3 [1, 9, 10]. It is surprising to see that the strengths of SCFS, Pyroceram 9606, and the quartz-doped Al_2O_3 become equal at a temperature of about 1200°C (Fig. 15c) [1]. The increase noted in the strength of SCFS with an increase in temperature can be attributed to the stress relaxation that takes place with the occurrence of plastic deformation.

The SCFS radomes with 8–10% porosity and covered with a pore blocking surface coating were successfully employed on S-300 and Patriot missiles developed by Russia and USA, respectively [1]. It is very important to note that without employing any surface coating on SCFS radomes, they cannot be utilized for any of the existing missiles. Even with the surface coating, the SCFS radomes cannot be employed for missiles that are launched from sea-bases and from the un-covered mobile launch pads as its porosity absorb considerable amount of moisture from the surroundings, hence, cannot meet the required electrical performance as moisture's dielectric constant value is considerably high ($\epsilon =$ about 80.4). Even the 0.3% moisture absorption can cause the considerable changes in the dielectric characteristics of SCFS radome. Figure 16

Fig. 16 Dependence of $\tan \delta$ for a quartz ceramic on moisture absorption capacity (W) and porosity (%): 1) 6.8; 2) 11.5; 3) 16.3; 4) 18.7 (adopted from reference [1])

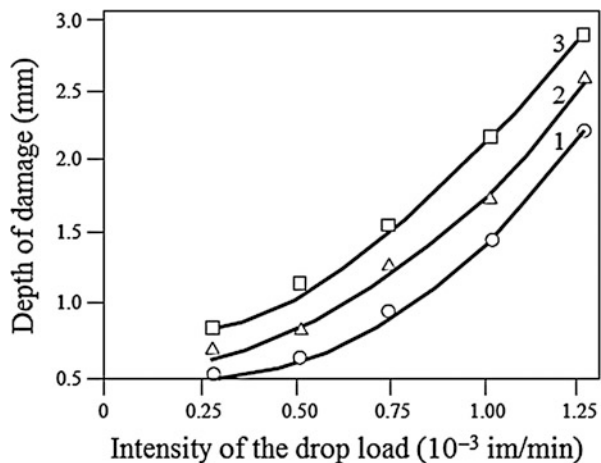


shows the variation of $\tan \delta$ of SCFS with varying porosity from 6.8% to 18.7% [1, 57, 58]. It can be seen that irrespective of the amount of porosity and moisture absorption capacity of SCFS, its $\tan \delta$ value increases very sharply from about 0.001 to about 84. The SCFS radome wall will be damaged up to about 3 mm depth when it is impacted with a drop load (Fig. 17) as dust and rain erosion resistance properties are very poor [1, 57, 58]. For the missiles launched from sea-base, the Sital glasses (e.g., Pyroceram 9606) and alumina radomes are employed by USA, and the ship-based and airfield missiles in Russia are equipped with mostly Sital based radomes only.

Figure 18 presents the surface temperature histories determined at an axial distance of 2.5 cm from the tip of seven radome materials commonly employed for high-speed missile applications [6]. Usually, during aerodynamic heating, the radome materials see up to 65% to 80% of their intended maximum temperatures. However, with 20% margin temperature, these radome materials can pass the thermally stressful missile trajectory. As can be seen from Fig. 18 although all the radome materials see almost the same temperature during flight, the material with lowest thermal conductivity protects antenna placed in the radome very well, and for such materials change to be recorded in BSE slope is also minimum [6]. The aerodynamic heating causes compressive stresses on outer surface of the radome wall and the tensile stresses on the inner surface of the radome. Figure 19 reveals the thermal stress histories for several radome materials in terms of the percentage maximum design tensile strength at an axial distance of 2.5 cm from the tip [6]. Usually the highest stress is experienced by the radome wall during the boost phase of the flight as there will be the maximum through-wall temperature gradient.

The tensile strength of the radome materials usually decreases with the increasing temperature. At the time of maximum stress, however, the average through-wall temperatures have not raised enough to lower the material strength significantly (Fig. 20). The thermal-stress performance of several X-band radome materials was computed for a thermally severe trajectory (Fig. 20) [7]. It can be seen that SCFS,

Fig. 17 Dependence of the depth of the damage l to a quartz ceramic with a porosity of 8.5% on the intensity of the drop load N for different impact velocities, m/s; (1) 120; (2) 150; (3) 180 (adopted from reference [1])



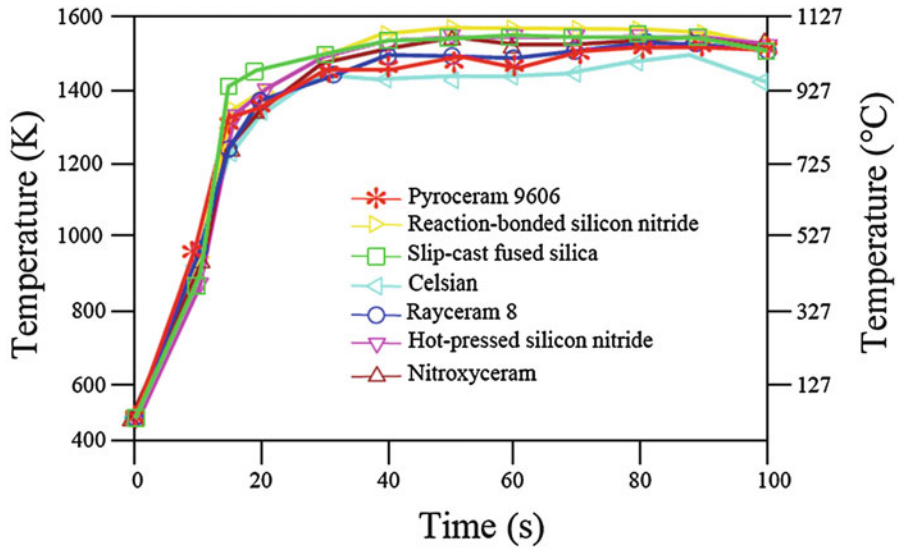


Fig. 18 Surface temperature histories for seven radome materials at an axial distance of 2.5 cm from the tip (adopted from reference [6])

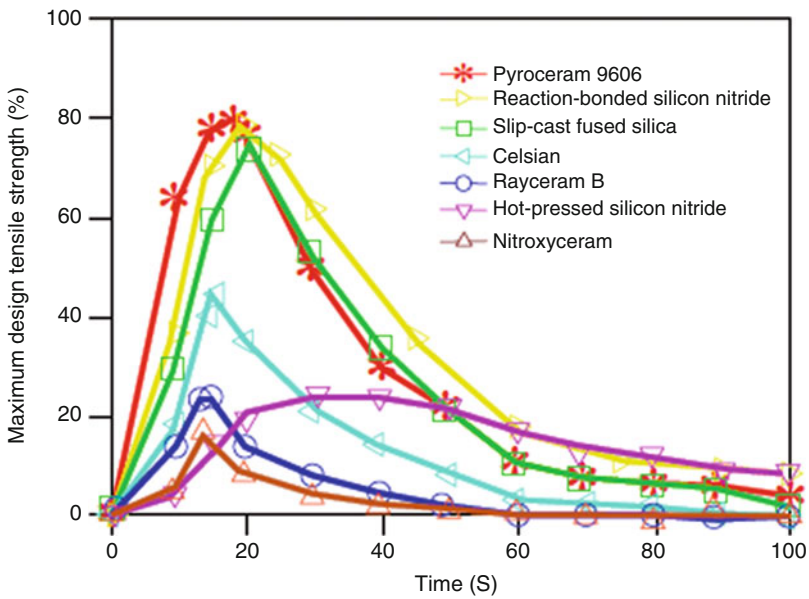


Fig. 19 Thermal stress histories for seven radome materials as a percentage of maximum design tensile strength (adopted from reference [6])

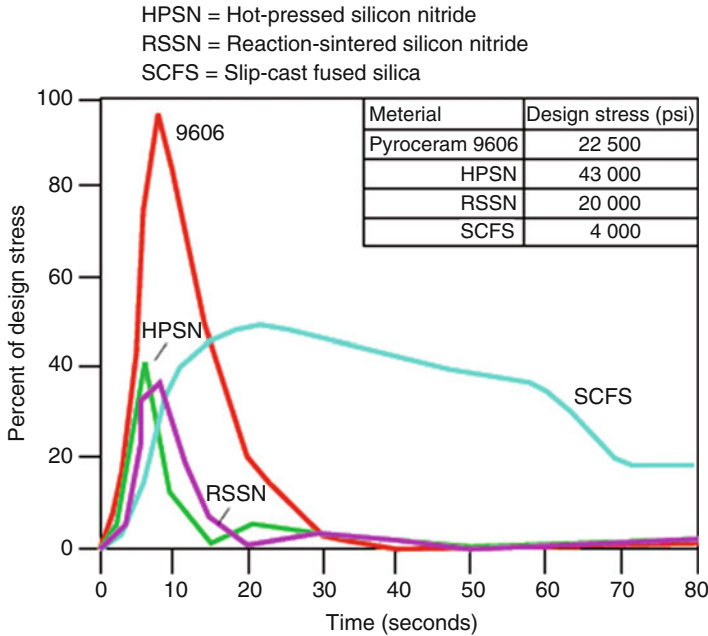


Fig. 20 Thermal stress performance of several radome materials (adopted from reference [7])

Nitroxyceram, and HPSN clearly have superior thermal stress performance, with 18% to 25% of their thermal stress limits reached. RBSN reaches 43% of its stress limit and thus demonstrates good thermal stress performance. Thermal stresses in the remaining materials reach 74% to 80% of the material strength limit. For Celsian, the 20% margin of safety will be eroded when the tensile strength values are adjusted downward to account for size effects (relating measurements on small coupons to a full-size radome). Thus, Celsian currently has a marginal thermal shock capability [6]. The results indicate that Pyroceram 9606 experiences thermal stresses very near its design allowable stress, while the other materials demonstrate a comfortable margin. To explore further the capabilities of the SCFS, two experimental programs were carried out in which Standard Missile-size radomes were subjected to flow conditions simulating a hypersonic environment.

The URLIM software is usually employed to calculate the change occurs in BSE slope to judge the electrical performance of any radome material [6]. It is required that a missile interceptor withstand a nuclear blast [1, 2, 37]. In the theoretical predictions, in order to test whether a particular radome material will survive or not the heat loads generated from a nuclear blast at which thermal stresses are in peak, while evaluating the temperatures that are seen by each of the radome materials the aerodynamic heating was also included to the radiative heat flux and found that many materials either reached or exceeded their intended peak temperature limits, and caused a melt layer to form on their outer surfaces. Furthermore, the electrical performance and radome structural integrity of these radome materials at these tested aerodynamic loads are not known [1, 2, 37].

For all the radome materials mentioned in Figs. 18 and 19, at the nominal flow conditions of Mach 2.8, at 2200 °C temperature and 200 psi pressure, a free jet test was performed [7]. These combined conditions are equivalent to those prevalent at Mach 8 flight speed and an altitude of 86,000 feet. The fused silica X-band radome withstood a 35 second test under these conditions including 10 seconds at 15° angle of attack [7]. However, the low strength and low CTE of SCFS at high-temperatures of hypersonic flight make it difficult to attach its radome to the missile body.

As far as the fabrication of radome shapes are concerned, the high- Al_2O_3 radomes are fabricated by following hot-slip casting of a slurry containing up to 10 wt.% organic binder, which releases hazardous gases during further processing operations, whereas the Sital radomes are fabricated by centrifugal forming of the hot-melt at high-temperatures [1, 2]. The sintering of large size Al_2O_3 radomes at 1650 °C requires normally the gas-fired furnaces. In the case of SCFS, the radome shapes are fabricated by slip-casting of aqueous slurries in gypsum molds, followed by drying, and firing at 1240–1270 °C in electric furnaces. The low-hardness of sintered SCFS radomes makes the machine processes easier to the desired tolerance levels. Furthermore, the overall linear shrinkage associated with the fabrication of SCFS radome from casting to firing is only about 1.5%, whereas for Al_2O_3 radomes, it is about 10%. The low shrinkage also allows fabrication of large-size near-net shape radomes with minimum strain and distortion. The other available near-net shape forming methods including gel casting, pressure casting, cold iso-static pressing (CIP), etc., can also be employed to fabricate SCFS radomes [1, 2]. Low shrinkage characteristics of SCFS helps in the requirement of minimum machining operations.

It is also desirable that the radome wall thickness should be one-half of the wavelength of the RF radiation to achieve high transmission efficiency. The silica being a low dielectric material allows the use of thicker wall radomes in comparison with other ceramic radome materials [1, 2, 4, 5, 13]. The thicker wall radomes are less prone to damage while handling and to travel through rain impacts. Furthermore, in silica, the requirement of machining tolerances with respect to the radome wall thickness is much higher as compared with other radome materials. For example, for silica, the machining tolerances required is of the order of 0.1 mm, whereas in case of pyroceram 9606 and alumina, they are about 0.01 and 0.001, respectively [59].

Although the fused-silica shows the lowest strength among the various radome materials, unlike others its strength increases with increasing exposed temperature. This increase has been attributed to the stress relaxation phenomenon associated with development of plastic deformation occurring in silica ceramic at high temperatures [60]. With long time exposure to temperatures of about 900 °C, onset of sintering takes place and is associated with further strengthening effect. Beyond 1100 °C, devitrification occurs with the formation of cristobalite, which is accompanied by reduction in strength [59]. However, with short term heating as it occurs in the case of missile travel, the strength is maintained even at considerably higher temperatures. The temperature range at which the SCFS radome can be operated for short times is further extended to 2000 °C [59].

The above discussed properties of ceramic radome materials suggest that the SCFS has certain advantages over other ceramic materials and it can be fabricated by

following quite inexpensive consolidation technique at low-stringent conditions, whereas other materials need very expensive consolidation techniques as well as expensive and cumbersome machining operations. Hence, it is desirable to realize the SCFS radomes suitable for hypervelocity ($> \text{Mach } 5$) missile applications. In the following sections, the fabrication methods of SCFS are presented and discussed.

The Raw Material Resources of Fused Silica and its Characteristics

Silicon dioxide (silica, SiO_2) exists in three crystalline forms each having two-different phases of low and high temperatures (i.e., α - & β -quartz, α - & β -tridymite, and α - & β -cristobalite) [4, 5, 36]. These crystalline forms are transformed from α -phase state to β -phase when they are exposed to high temperature treatments. This transformation is associated with a sudden volume change (known as inversion) that causes the material to be very sensitive to a thermal shock. The vitrified (i.e., noncrystalline or amorphous) form of silica known as fused silica, fused quartz glass (mainly by Russian scientists), or fused quartz, exhibits no inversion property and is the least dense one among the various forms of silica (Fig. 21) [36]. In 1956, SCFS was termed as re-bonded fused silica at Georgia Institute of Technology, Atlanta [4, 5]. Although the terms fused quartz and fused silica are used interchangeably, the one with superior optical and thermal properties are termed as fused silica in comparison with fused quartz [35]. One can say that the fused silica is a relatively high purity version of quartz glass. Fused silica exhibits (i) an optical transparency from infrared to ultraviolet radiation, (ii) high chemical stability, (iii) high resistance on exposure to radiation and neutron flux, and (iv) the most important dielectric property stability required for radome applications over a wide range of frequencies and temperatures [1, 2, 4, 5, 37, 38]. However, fused silica begins to convert to cristobalite at high temperatures at about 871°C and continue till its melting temperature. However, the cristobalite phase formation is influenced by many factors including the starting grade of SiO_2 , impurities, exposed temperature and holding time, and the atmosphere present during heating [5]. The α -cristobalite is stable from $<204^\circ\text{C}$ to 260°C , and above 260°C it gets transformed into β -cristobalite phase. As mentioned above, this phase transformation from α - to β - is accompanied with a huge volume change and is known as inversion process [5]. Hence, if cristobalite is present in excess amounts in fused silica ceramics, the inversion process that takes upon exposure to temperature will weaken or completely destroy the radome structure of SCFS [5]. Furthermore, fused silica's low strength and fracture toughness makes it vulnerable to rain and dust erosion. In fact, fused silica does not exhibit a true melting point in a sense that it does not show a sudden rapid decrease in its viscosity [1, 2, 4, 5, 37]. The generally quoted melting temperature normally defined as softening point of glasses and corresponds to a viscosity of $10^{7.6}$ poise (1 Poise = 1000 cP; 1 cP = 1 mPa) for fused silica is about 1704°C . Above this temperature its viscosity continues to decrease slowly and will be still greater than 10^4 poise at 2482°C [4]. For certain high temperature applications where low-shear is involved, fused silica can be employed at temperatures much above its stated melting point.

Fig. 21 Specific volume of different forms of silica (adopted from reference [36])

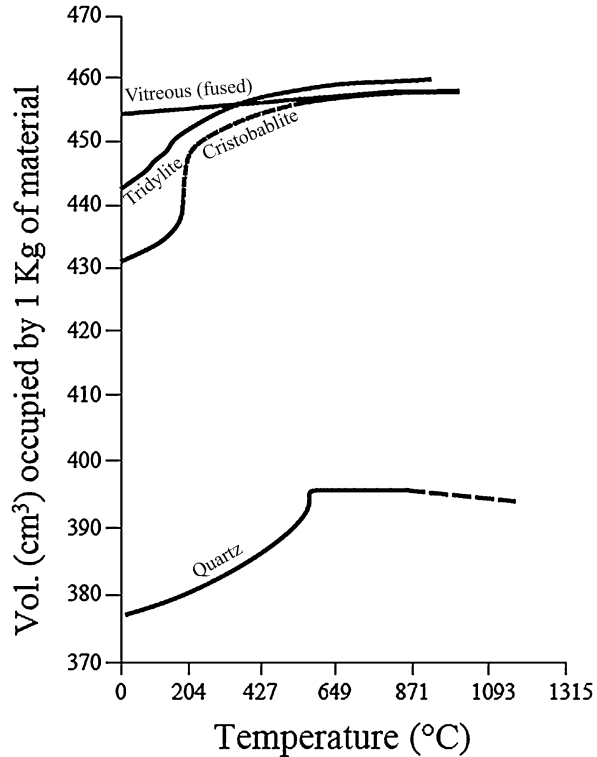


Figure 22 shows the viscosity of fused silica with respect to temperatures from 760 °C to 2426 °C [5]. The softening point of a glass (ASTM C338) is defined as the temperature at which the elongation of a uniform fiber with a diameter of 0.55 to 0.75 mm and length of 23.5 mm takes place at a rate of 1 mm per minute when the top 1 cm length of the fiber is heated at a rate of 5 °C per min. The processing of fused silica into any shape requires its viscosity to be below 10^4 poise, and as can be seen from Fig. 22 this viscosity value for fused silica attains only at the temperature of about 2482 °C.

Fused silica is produced by the flame or arc fusion melting of quartz sand or any crystalline forms of silica. If a very high purity grade fused silica is needed, high purity quartz crystals or synthetic SiO_2 are to be melted. In fact, the fused silica is a high temperature working material as it differs from traditional glasses in containing no other ingredients, which are typically added to lower the melt temperature of the a particular glass material. The raw material resources of fused silica are (i) natural quartz sands high in silica (99.6 wt.% at least), (ii) quartz crystals or veined quartz (with impurities not in excess of 0.01 wt.%), and (iii) rock crystal, with impurities not higher than 0.00001 wt.%. These are virtually inexhaustible but need to be beneficiated to the required purity levels [37]. Various beneficiation technologies are available for the production of optical, illumination engineering, and electronic

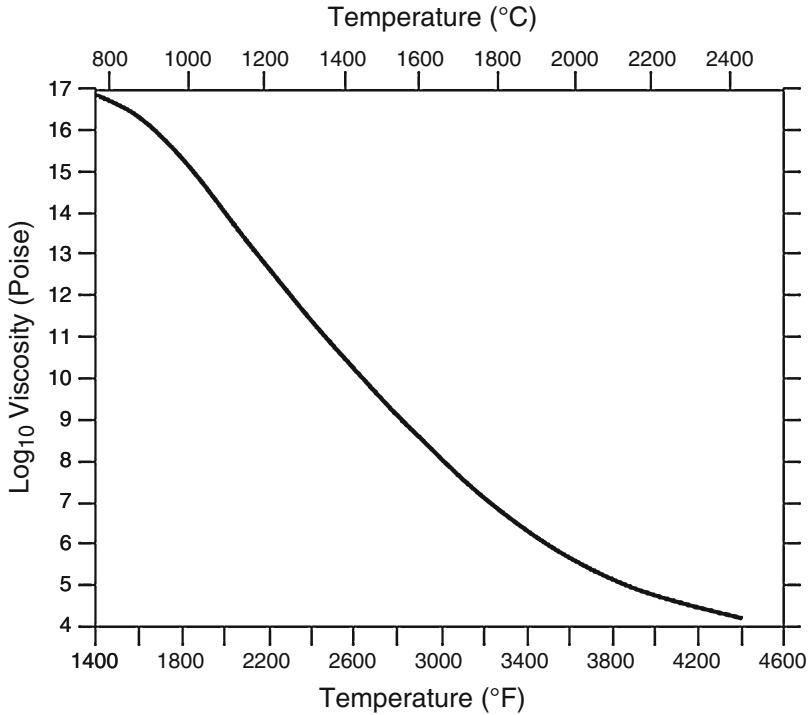


Fig. 22 Viscosity of fused silica as a function of temperature (adopted from reference [5])

grade glasses of fused silica [1, 2, 4, 5, 37, 38]. However, the origin of raw materials, the recovery technology, transportation, and processing are the factors that affect the quality of a commercial fused silica product.

Another major advantage of fused silica is its component making process is well suited for industrial practice. The beneficiated quartz materials are normally processed at temperatures of up to 2000 °C in resistor heating, induction heating, arc melting, or gas and flame melting furnaces to produce fused silica. The corrosion attack of molten silica on refractory materials has been a major obstacle that limits the wide-spread usage of fused silica products. At present, graphite and molybdenum are employed as refractory materials to produce fused silica. In fact, the manufacturing of fused silica does not need very expensive equipment and machinery. The highest purity fused silica is prepared by vapor-phase synthesis, and fused silica is divided into three different grades; (i) nontransparent glass, (ii) transparent glass for illumination engineering application, and (iii) optically transparent fused silica glass over a wide spectral range. Nontransparent fused silica glass is prepared from quartz sand with an impurity content of 0.1 wt.% (i.e., 1000 ppm), whose annual output is many thousand tons, whereas the annual output of transparent quartz glass amounts to only several hundreds of tons [1, 2, 4, 5, 37]. The annual output of optical quality fused silica glass is some tens of tons only. Quartz glass of different grades and its

wastes are used as the starting material for the production of several general-purpose glass ceramics [37]. The semi-finished fused silica disks can be machined to obtain any desired shape and are fabricated typically in batch-type furnaces, whereas the tubes, rods, plates of different size and other shapes of fused silica are fabricated using continuously operated furnaces. Several large-size fused silica components are fabricated by following the spin-casting of molten fused silica, whereas the large-size fused silica radome shapes are fabricated by following aqueous colloidal consolidation techniques [1, 2, 4, 5, 37].

Fused Silica Radomes: The General Methods of Fabrication

The fabrication of fused silica radomes does not require the use of costly or energy-intensive equipment. However, the conventional ceramic forming methods such as dry-powder pressing in a die uni-axially, extrusion, hot-pressing, etc., cannot be employed for the fabrication of fused silica radomes as they are large and thin-walled shells of semi-spherical or parabolic shape [8]. The main methods employed for making the fused silica radomes are slip casting [61], gelcasting [62, 63], hydrolysis induced aqueous gelcasting (GCHAS) [9, 10], and cold iso-static pressing (CIP) [41, 64]. The shapes formed in these techniques can be managed to have porosity in the range of 0 to 90%. The processing details, major advantages, and disadvantages associated with each of these fabrication techniques have been briefly presented and discussed in the following sections.

Slip-Casting of Fused-Silica Radomes

The low shrinkage (about 1.5%) occurs during the drying and sintering operations of SCFS radome is an advantage. The slip casting of aqueous colloidal suspensions in Plaster of Paris (POP) molds followed by drying and sintering is simple and low-cost method and allows the fabrication of thin-walled radomes and other intricate shapes such as complex-shaped large-size aerial fairings with close tolerances [36, 39, 61]. Otherwise, fabrication of these radomes would be prohibitively expensive when the conventional molten silica forming techniques are used. The final dimensions of SCFS components are easily obtained by machining with diamond grinding operation. Detailed studies into the physical chemistry of grinding, molding, and sintering made it possible to optimize the process parameters such as granular composition, moisture content, viscosity, slip pH, and the conditions for shaping and drying and sintering of SCFS radomes with tailored properties are presented in [4, 5]. The technological process of SCFS ceramics with a porosity of 7–12% involves (i) “wet” grinding of quartz-glass waste to obtain suspensions with the required technological properties, (ii) stabilization of suspensions to improve their casting properties, (iii) formation of cast by pouring the suspension in porous moulds, (iv) sintering of the preforms at 1220–1260 °C, and (v) machine-finishing to the required dimensions [41]. Some of the physical properties of SCFS is

considerably different from the conventional molten-cast fused-silica (MCFS), while some properties, such as thermal expansion, specific heat, are unchanged. The thermal conductivity of molten fused silica, SCFS, and foamed fused silica slip as a function of mean specimen temperature is shown in Fig. 23 [36]. The resistivity of SCFS is also quite stable in comparison to the MCFS (Fig. 24) [36]. The relative softness of the SCFS also increases the speed of machining operation [1, 2]. Fused silica is unique among slip casting materials as it is associated with a small amount of drying and shrinkage percentage. If other materials do show similar shrinkage patterns, much better advantage could be taken of slip casting as a fabrication technique.

The general slip-casting route followed at Tekhnologiya Research and Production Enterprise, Obninsk, a Russian research institute, is schematically shown in Fig. 25 [4, 5, 13, 36]. The main factors controlled during the fabrication of radomes by slip-casting process are: density, medium pH, granular composition of suspensions, molding conditions, and calcination regime [13]. The major advantage of these materials is that they allow one to mold components of irregular shape with holes, depressions, or protrusions as well. For technologies based on the use of fused silica, the rheological properties of suspensions are of minor importance but the most important ones are the amount of binder present in the suspension, the molding pressure, and the cooling and sintering temperatures. The green preforms are molded in perforated molds by squeezing out water under pressure. The preforms are calcined at 1060–1460 °C. The porosity of components is controlled by varying the fiber size, the concentration of the solid phase in the casting mixture, the molding pressure, and the calcination temperature. These materials are used for thermal protection of space vehicles, various power units, and test stands.

The main conditions required for preparing high-strength thin-walled fused silica radomes are high purity and high density (86–90% of theoretical value) of the precursor starting raw material with approximate characteristics shown in Table 8. Optimum properties of aqueous suspensions employed for fabricating SCFS radomes are: density, 1.87–1.92 g/cm³; viscosity; 20–40 sec; pH, 4.0–7.0; granular

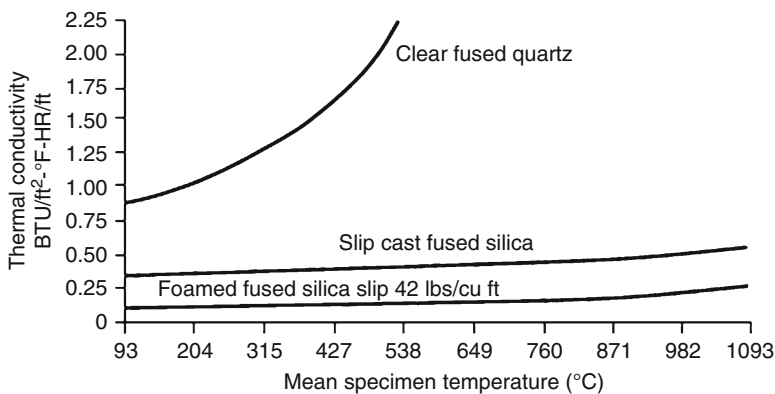


Fig. 23 The thermal conductivity of clear fused silica, slip-cast (re-bonded) fused silica, and foamed fused silica slip as a function of mean specimen temperature (adopted from reference [36])

Fig. 24 Resistivity of clear fused silica and slip-cast fused silica (SCFS) as a function of temperature (adopted from reference [36])

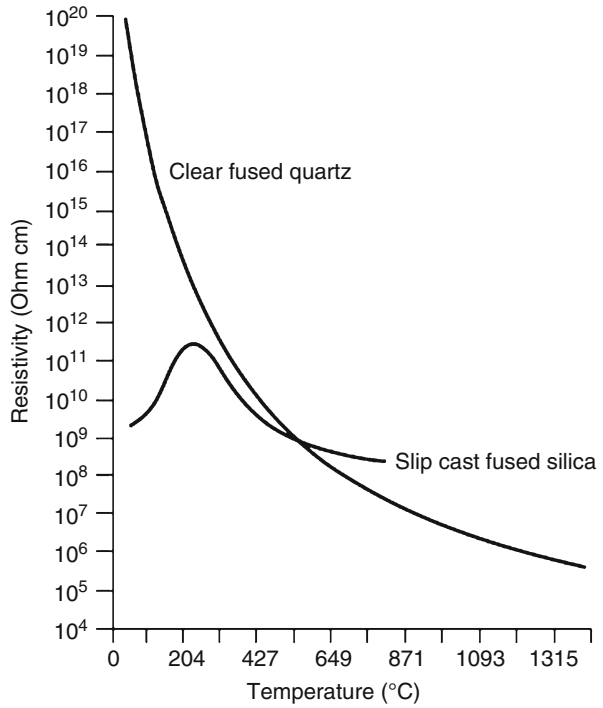


Fig. 25 Pressure slip-casting set-up employed for making slip-casting fused silica (SCFS) radomes (adopted from reference [4, 5, 13, 36])

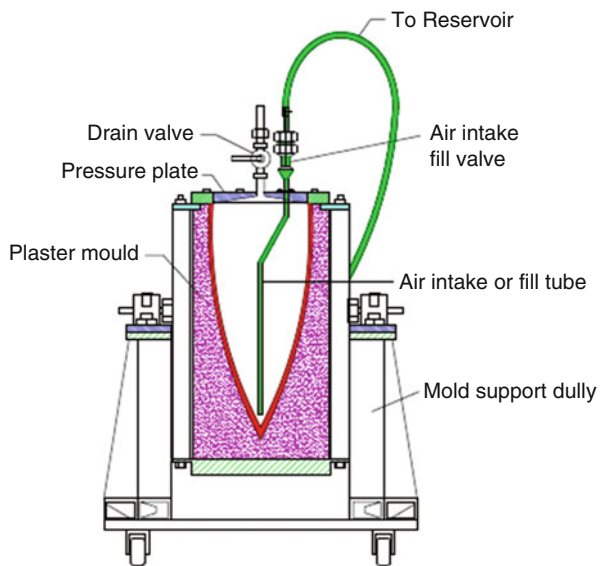


Table 8 Typical spectroscopic analysis of fused silica grains used for slip-casting of radome shapes (adopted from reference [4, 5])

Oxide	Technical grade (%)	High-purity (%)
SiO ₂ (by difference)	99.78	99.97
Al ₂ O ₃	0.140	0.018
Fe ₂ O ₃	0.001	0.0015
CaO	0.030	0.0025
MgO	0.022	0.0002
TiO ₂	0.021	0.0008
Na ₂ O	0.002	0.0015
Li ₂ O	0.002	0.0012
K ₂ O	0.002	0.001

composition: particles $\leq 5 \mu\text{m}$, 20–30%; 63 to 500 μm , 4–8%; 5 to 63 μm , and the rest are as given in Table 9. Green preforms are normally calcined in furnaces fitted with silicon carbide (SiC) heaters that allow high heating and cooling rates (300–500 °C/h) at a sintering temperature of 1200–1260 °C (Table 10). The high-rate regimes provide sintering with a linear shrinkage of $\leq 2\%$, without formation of a cristobalite crystalline phase in the ceramic, which is a necessary condition for preparation of high-strength thin-walled radomes. Pore-free vacuum-dense ceramic is normally prepared by short-term (15–30 min) sintering in a vacuum furnace at 1300–1350 °C. Perhaps, a better alternative for pore-less ceramic is the process in which 0.5–1.5 wt.% boron-containing additives are introduced into the aqueous fused silica slip. The powdered additives boron nitride (BN) and silicon tetraboride (SiB₄) can activate the sintering to obtain pore-free SCFS ceramics at sintering temperatures of 1240 °C (BN) and 1200 °C (SiB₄) [4, 5]. The properties of un-doped SCFS ceramics sintered by following the reaction conditions given in Table 10 are summarized in Table 11 [41].

Characteristics of Precursor Powders, Slips, and Plaster Molds

Typical spectroscopic analysis of fused silica grains used for preparing SCFS radomes is given in Table 8 [4, 5]. The typical characteristics of slips normally employed for fabricating SCFS radomes are given in Table 9 [41]. The slip casting processing parameters employed for fabricating SCFS radomes and information about the plaster mold and its advantages and limitations and how to improve the service life of the plaster mold have been described elsewhere [65, 66]. The setting time of a gypsum paste formed out of water (W) and gypsum (G) at a ratio of 100:100 is only about 8–10 min. In this short span of time, it is difficult to mix the paste with the desired homogeneity but its homogeneity can be improved with the aid of certain materials such as rosin-turpentine solutions, borax, zinc or copper sulfate, potassium alum [65, 66]. It has also been reported that different plasters produce varying degrees of surface devitrification in SCFS. However, it was also

Table 9 Typical properties of precursor slips and cast preforms of slip-cast fused silica (SCFS) radomes (adopted from reference [41])

Parameter	Parameter value	
	Slip	Cast preform
Density (g/cm^3)	1.87–1.90	1.93–1.96
Moisture content (%)	14–17	12–15
Viscosity ($^\circ\text{E}$)	4.0–7.5	–
pH	4.0–7.5	–
Particle mean diameter (%)		
Up to 5 μm	20–30	20–30
63–500 μm	5–10	5–10
Porosity (%)	–	12.0–14.5

Table 10 Sintering regime parameters typically employed in the production of slip-cast fused silica (SCFS) radomes (adopted from reference [41])

Parameter	Parameter value
Onset in-furnace temperature ($^\circ\text{C}$)	25–100
Average heating rate (T_{AV}) ($^\circ\text{C}/\text{h}$)	15–300
Cooling	Inertial (in-furnace)
Maximum sintering temperature ($^\circ\text{C}$)	1230–1280
Holding time at maximum temperature (h)	2.0–2.5
Holding time at intermediate temperature (h)	
130	3.0–5.0
900	1.0
970	1.0
1070	1.0
1100	1.0
Total operational regime time (h)	36.0–42.0

Table 11 The properties of un-doped slip-cast fused silica (SCFS) ceramics sintered according to schedule given in Table 10 (adopted from reference [41])

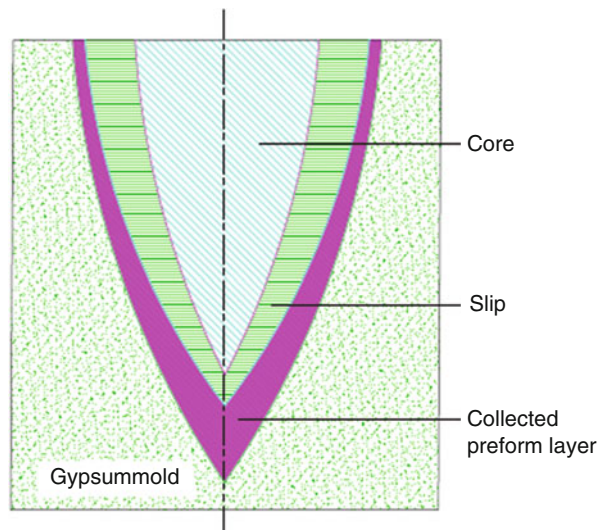
Property	Property value
Apparent bulk density (g/cm^3)	1.96–2.05
Open porosity (%)	7–11
Static bending strength at 20 $^\circ\text{C}$ (MPa)	35–65
CTE (20–900 $^\circ\text{C}$) ($^\circ\text{C}^{-1}$)	Not higher than 0.54×10^{-6}
Heat conductivity (50–500 $^\circ\text{C}$) (W/m.K)	0.6–1.4
Compressive strength at 20 $^\circ\text{C}$ (MPa)	100–300
Impact toughness (kJ/m^2)	0.8–1.5
Elastic modulus (MPa)	$(0.27–0.55) \times 10^5$
Dielectric constant at 20 $^\circ\text{C}$ & 10^{10} Hz	3.36–3.53
Dielectric loss tangent at 20 $^\circ\text{C}$ & 10^{10} Hz	Not higher than 0.004

noted that these differences in surface devitrification seemed to have no effect on bulk devitrification or sintering behavior. For this reason, any commercially available pottery plaster can be used. Inert materials such as porous ceramics and resin bonded grain exhibit promise in high volume production areas such as sanitary and dinnerware production [4, 5]. They are also suitable for use in radome fabrication, but introduce additional design problems such as mold shrinkage during curing and sintering. Their use can only be recommended in cases where the longer mold life is required to offset the greatly increased mold manufacturing cost. A mold release agent, such as graphite, ammonium alginate, sodium alginate, can be employed as a thin film between the mold and the fused silica casting. This film aids in removing the cast piece from the porous mold relatively easily. Sodium alginate should be avoided since alkalis increase devitrification rates greatly [4, 5]. As a general rule mold releasing agents should be avoided, they tend to produce uneven, rough surfaces. When used they should be held to as small a thickness as possible. A lot of modifications employed to slip-casting process to improve its efficiency have been presented in [4, 5].

Effect of Pressure Casting on the Formation of Wall Thickness

The thickness gradient (Fig. 26) normally observed along the length of radome wall thickness can be reduced by applying the pressure during slip-casting process. The thickness of the wall increases with the time of the slip left in the mold. When sufficient thickness is built up, the excess slip is drained out by vacuum or gravity leaving a dense but somewhat leathery shape in the mold. The rate of wall build-up

Fig. 26 Fundamental layout of molding large complex-profile ceramic preform with slip-casting in a gypsum mold (adopted from reference [118])



follows a parabolic filtration equation as given in (Eq. 8), where W is the wall thickness in inches, and θ is the casting time in minutes [4, 5].

$$W = 0.048(\theta - 0.27)^{\frac{1}{2}} - 0.0207 \tag{8}$$

This expression has proved satisfactory for estimating casting times at the atmospheric pressure. Long casting times should be avoided due to problems such as settling of the slip in the mold. As an alternative, the slip may be pressurized to reduce casting times drastically. In this latter case, Eq.8 changes to Eq. 9, where P is gas pressure in *psi*. This latter expression (Eq. 9) can be used to estimate casting times [4, 5].

$$W = 0.012(\theta P)^{\frac{1}{2}} - 0.47 \tag{9}$$

Figure 27 shows the data for both the expressions (Eqs. 8 and 9) graphically. In either case, casting at atmospheric or at increased pressure, the time for a given wall thickness may be estimated from a trial casting by the relationship given as Eq. 10, where W_1 is the wall thickness at time θ_1 ; and W_2 is the wall thickness at time θ_2 [4, 5].

$$\frac{W_1^2}{W_2^2} = \frac{\theta_1}{\theta_2} \tag{10}$$

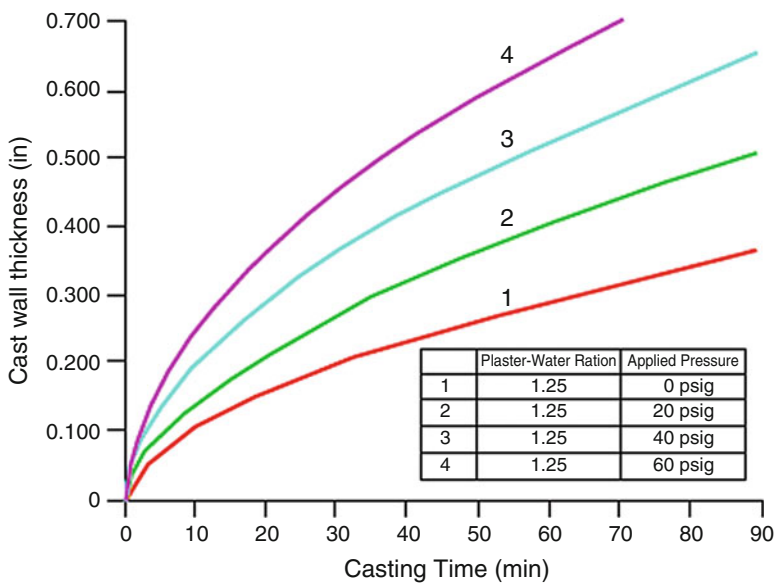


Fig. 27 Relation between cast wall thickness and time, for fused silica slip pressure cast at 0, 20, 40, and 60 psig applied pressure (adopted from reference [36])

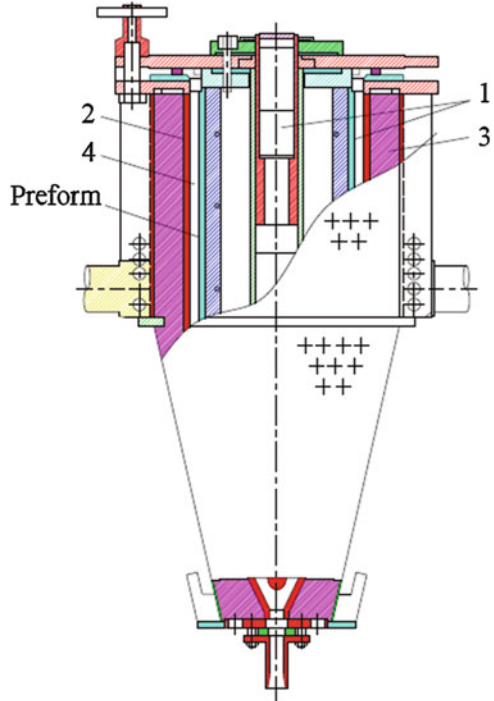
In this way, casting times necessary to produce a given wall thickness may be readily determined. These curves are generally accurate to within $\pm 10\%$ for slips with $7\ \mu\text{m}$ mean particle diameters. Coarser slips will cast more rapidly while finer grinds will cast more slowly. Since the coarse fractions of most fused silica slips settle to some extent, it is advisable to use pressure casting to hold casting times to a reasonably short periods of up to 6 h. From Eq. (9), it can be seen that a wall of 0.97 inches for C-band frequency can be reached in 6 h at 20 psi pressure [4, 5]. X-band and higher frequency radomes could be cast in correspondingly shorter time periods.

Electrophoretic Deposition Process

Electrophoresis has been identified to be a promising route for shaping complex-shaped large-size ceramic articles from inorganic slips while overcoming the limitations associated with conventional slip-casting route [67–69]. The principle of electrophoretic shaping of ceramic products is quite simple. The particles that are suspended in a slip start moving under the action of an electric field (generated by applying voltage to the electrodes of mold equipment) towards the electrode that bears an opposite charge to become deposited on it; thereby, a body for the preform is built [68]. Positive or negative charge can be applied to the shaping electrode (depending on the surface charge of the particle); usually, the shaping electrode serves as an anode considering that the particles typically carry a negative charge. The cathodic processes are of minor importance for electrophoretic deposition, whereas the processes that occur on the anode merit more attention. In fact, electric current passing through the aqueous slip causes water electrolysis, which is manifested in the release of oxygen at the anode and hydrogen at the cathode. The released oxygen may behave in two ways. First, it is capable of reacting with the material of anode during the process of the preform buildup and thus becomes bound to it [68]. Second, the oxygen can form a protective oxide film layer which will prevent further oxidation of the anode material. If the released oxygen is unable to further react with the anode material, it will accumulate at the anode surface. Situations may arise where oxygen is unable to escape through the contact clearance between the anode surface and preform surface, which will finally break the deposited material and escape, or causes the formation of pits, blisters, or blow-holes [68]. Therefore, the choice of a proper material for the shaping electrode (anode) has become an issue of a major concern. Design and fabrication of the counter electrode for mold equipment intended for electrophoretic shaping of large-sized complex-profiled preforms likewise has been a challenging problem [67].

A mold equipment for fabricating radomes with the dimensions of 250 mm base diameter, 650 mm height and 17 mm wall thickness has been designed and fabricated, whose schematic diagram is given in Fig. 28 [68]. The main components of this device are: shaping electrode (core) 1, brass electrode 2 embedded in the mold body 3, and fore-electrode plaster layer 4 reinforced with a cloth. The principle of operation is as follows. Slip is poured in the space between the plaster mold and the core; voltage is applied for shaping electrode 1 and electrode 3 embedded to a depth

Fig. 28 A mold equipment for electrophoretic shaping of large sized, thick-walled, complex-profiled preforms (preform dimensions: base diameter = 250 mm, height (h) = 650 mm, wall thickness (δ) = 17 mm): (1) shaping electrode; (2) electrode; (3) plaster mold; (4) fore-electrode layer (adopted from reference [68])



of 1–5 mm from the profile-forming surface. Material is deposited on the core (anode); water is driven towards the mold to moisten the fore-electrode layer 4 (reinforced with a cloth, for example, a gauze bandage), which improves conductivity and electrophoretic shaping parameters. Under these conditions, water is diverted completely, and preforms with a smooth surface are obtained. The dried and hardened surface of the electrode is obtained upon grinding to the required size and shape. The advantages of this engineering mold are: large-sized cores of any size and profile can be prepared; smooth surface of the core that allows easy extraction of the core from the body of the shaped preform; the core can be easily prepared under laboratory conditions; and small consumption of the material. By utilizing this electrode, large-sized ceramic products of complex shape with a smooth inner surface can be prepared successfully by following the electrophoretic deposition route. The use of a reinforced fore-electrode layer made it possible to extend the service life of the mold to ten shaping cycles, whereas in all previous techniques, the service life did not exceed two shaping cycles [68]. Furthermore, in the mold equipment thus designed, the electrode, being embedded in the mold, does not come in direct contact with the preform shaped and thus allows a less strict tolerance on size, profile, and metal used. Thus, it is shown that the electrophoretic deposition method can be used for fabricating large-sized, thick-walled, complex-profiled ceramic preforms from aqueous fused silica slips; preforms prepared by this

technology can have a more uniform density than those prepared by conventional slip-casting technologies. Furthermore, preforms can be shaped using finely dispersed slips. Materials have been chosen and electrodes have been designed for the fabrication of large-sized complex-shaped SCFS products, whose details are thoroughly described elsewhere [68].

Gelcasting of Fused Silica Radomes

Segregation always occurs during the time-consuming slip-casting process, resulting in density variations, and degrades the properties of the material especially for big and complicate shapes [9, 20, 70–76]. Gelcasting is a process for molding powder materials with the help of an initiator, catalyst, and organic monomers to obtain strong green bodies with the help of in situ polymerization of organic monomers in the green body formed. The green body is characterized with a three-dimensional network, which holds the particles together, eliminating the tendency of the migration or segregation of particles. By using gelcasting process, green bodies in various profiles have been produced with high green strength, and such green bodies can be cut, ground and machined without the risk of breakage [9, 20, 70–76]. In a study, Yichen et al. [70] employed the conventional aqueous gelcasting process to consolidate traditional fused silica ceramics. In another study, Wang et al. [62] have employed gelcasting process to consolidate the large square crucibles of fused silica with dimensions of $720 \times 720 \times 420$ mm and with a wall thickness of about 14 mm to be employed for polycrystalline silicon melting, as well as to consolidate fused silica radomes up to 500 mm in diameter and 1000 mm in height with a wall thickness of 10 to 12 mm and sintered with excellent homogeneity. A large size fused silica crucible was also consolidated by following the aqueous gelcasting route [63]. The green compacts with solids of 80 wt.% were obtained when the addition ratio of dispersant to fused silica quartz powders was 0.3 wt.%, the ratio of quartz powders in D_{50} of 1.9 μm and 7.6 μm was adjusted to 3:7, the addition ratio of acrylamide to quartz powders was 1.0 wt. %, and the ratio of acrylamide to coupling agent was 16:1. The bending strength of the sintered fused silica products was found to be 76.0 MPa with the bulk density of 1.94 g/cm^3 . Fused quartz crucible prepared under these conditions was 800 mm in length, 800 mm in width, and 400 mm in height.

Hydrolysis-Induced Aqueous Gelcasting of Fused Silica Radomes

Recently, Ganesh et al. [10, 31] have developed a modified aqueous gelcasting process, called the *Hydrolysis Induced Aqueous Gelcasting (GCHAS)*, for consolidating all alumina (minimum 1–5 wt.%) containing ceramic powders including β -SiAlON, alumina, AlON, ZTA, etc., into defect free radome shapes. By following the same technique, fused silica radomes with a tangent ogive shape of 460.8 mm length, 192 mm base diameter, and a wall thickness of 4.572 mm have been successfully fabricated as shown in Fig. 29 [10, 31].

Fig. 29 The green dried tangent ogive shaped fused silica radome with a base diameter of 192 mm, a length of 460.8 mm length and a wall thickness of 4.572 mm consolidated by following hydrolysis induced aqueous gelcasting (GCHAS) route with the help of bare AlN powder equivalent to 5 wt.% Al₂O₃ introduced into 50 vol.% fused silica slurry (adopted from reference [10, 31])



Surface Passivation to Seal Porous Structure of Fused Silica Radomes

Irrespective of the consolidation method employed to form fused silica green body from its powder, the pressure-less sintering is carried out to form the sintered body as hot-isostatic pressing is too expensive. As mentioned above, fused silica cannot be sintered to acquire full density as over-temperature or overtime sintering causes the crystallization of the fused silica glass into cristobalite [8]. The unavoidable micropores mean that the surface of the sintered and machined body should be treated by surface pore-filling material and by water-proofing coatings. This treatment can also increase the mechanical strength of the SCFS radome to certain extent. The surface pores can be filled with inorganic fillers such as fused silica particles, nano-sized silica sols [8, 77], CVD Si₃N₄ coating [18], preceramic polymers, or polymer precursors. The filled surface can be further modified with a dense coating of organic components such as fluoro-resin, silicon-resin, and polyphenylene sulfide (PPS), which may also contain some ceramic fillers [78]. At Georgia Institute of Technology, Atlanta, GA, several methods of sealing of SCFS radomes have been tried as

described in [36]. Among them, only two methods appeared practical at that time, which are surface melting, and Teflon coating. By using an arc-plasma jet or oxygen acetylene torch, it is possible to flame seal the surface of SCFS. This process is referred to as flame glazing. After flame glazing, the fused surface is annealed by holding at 1177 °C for 15 min., followed by cooling at 4 °C per min to 1340 °C, and then removing it from the glazing furnace. A Teflon coating is being considered for use as a simpler and more economical method of sealing. DuPont's PTFE resin with clear finish 852–201 is sprayed on to the surface of the radome to achieve a thickness of approximately 0.001-inch. After drying, it is heated to 400 °C. At this temperature the Teflon melts and produces a continuous coating. Teflon is a noncharring, low-temperature ablator with a dielectric constant of 3. Therefore, it is expected that no radome electrical performance difficulties will arise since the thin coating would be completely ablated away almost immediately in any hyper-thermal environment. In a study by Hu [79], SCFS with a SiO₂ content of ≥99.7%, bulk density of 1.90–1.95 g/cm³, porosity of 10–13%, and a flexural strength of 50–60 MPa was subjected to a surface densification at a high-temperature flame of 2500 °C to 3000 °C, which was generated using a mixture of hydrogen-oxygen gases. When the SCFS ceramic was surface treated at this temperature for about 15 seconds, the flexural strength was increased from 55 MPa to 72.71 MPa, and the thickness of the dense surface layer generated was about only 1.2 mm with a porosity of <0.5%.

Fused-Silica Ceramic Composites with Other Materials

Although the SCFS radomes surface pores can be blocked by applying the thin coatings of various materials, which also improves the strength of the radome to certain extent, it was advised to improve the strength of the SCFS radome itself. For this purpose, fused silica ceramic composites have been developed and investigated. When the high-purity fused silica short fibers were introduced into the SCFS radome walls, an improvement of strength up to 15% was noted [8]. In another study, the continuous silica fibers were employed to reinforce SCFS and measured the bending strength of the resultant composite as 70 MPa, and its tensile strength as 39 GPa [8, 80]. Yet in another study, a fused silica fiber cloth was employed as reinforcement to strengthen the fused silica bodies. For this purpose, the fused silica cloth was impregnated with polysiloxane that resulted in the formation of SiO_{2f}/SiO₂ composite [81]. To realize the fiber reinforced fused silica bodies, the polymer infiltration and pyrolysis (PIP) process has been considered as the best process [8]. It was also found that by improving the bulk density of the SCFS bodies, the strength properties can be improved to certain extent. The higher density of SCFS bodies can be accomplished by employing three methods, viz. (i) infiltration of SiO₂ sol into the sintered SCFS body followed by heat treatment, (ii) with the aid of sintering aids, and (iii) by utilizing the varied particle size of SCFS powder, whereas the finer particles are filled into the pores formed in packing pores of larger-size powder particles. In another method of improving the strength of SCFS radomes, a glassy SiO₂ coated was given by following the CVD method [8].

The various methods and additives utilized so far for enhancing the strength of the fused silica ceramics are summarized in Table 12. The fused-silica composites produced so far are nano-sized silica-silica [70], silica fibers (SiO_2f) reinforced-silica [8, 82], 3D $\text{SiO}_2\text{f-SiO}_2$ [80, 83], 2.5D braided silica fibers reinforced nitride (SFRN) [84], silicon nitride (Si_3N_4)-doped silica [85], air-oxidized silica and Si_3N_4 [86], zirconia (ZrO_2) doped silica [34], alumina doped silica [87], $\beta\text{-Si}_4\text{Al}_2\text{O}_2\text{N}_6$ -silica [10, 88, 89], and BN-silica [44–48, 90] as listed in Table 12 [1, 2, 4, 5, 36, 61]. Various dopants were also added to confer different properties to fused silica ceramics consolidated by several techniques [1, 2]. In many of these fused silica composites, the secondary material does not dissolve in the SCFS matrix but is retained as a discrete phase. A general conclusion is that although the information about impact resistance, ablation resistance, rain-erosion resistance, and the resistance to moisture absorption is not available, the strength and porosity properties exhibited by these composites suggest that the consolidation of radome shapes by following simple colloidal processing route is very attractive for pure SCFS [1, 2]. A closer look into Table 12 reveals that only BN (0.5 wt.%)–silica composites have exhibited the lowest dielectric constant ($\epsilon = 3.8$) at a porosity of $<2.5\%$ with a flexural strength of 186 MPa [45].

Fused Silica-Boron Nitride-Silicon Nitride Composites (Nitroxyceram)

For application as electromagnetic wave transparent windows, h-BN and Si_3N_4 have proven to be relatively good reinforcement materials, since they both have relatively low dielectric constant (~ 5) and low loss tangent ($\sim 10^{-4}$) at room temperature. Many researchers have suggested using the fibrous Si_3N_4 matrix saturated with SiO_2 and BN, which is a composite termed as Nitroxyceram ($\text{Si}_3\text{N}_4\text{-BN-SiO}_2$) [1]. These substances (SiO_2 and BN) have a lower dielectric constant relative to Si_3N_4 . Also, investigations have shown that the preforms obtained after the heat treatment contain a large number of pores (12–20%). With regard to dielectric properties, Nitroxyceram is as good as fused silica, and it is similar to pyroceram from the perspective of resistance against abrasion [1]. To improve the mechanical properties of porous Si_3N_4 ceramics with a low dielectric constant, the sandwich structure can be designed so that the internal layer has a higher thermal expansion coefficient, and a lower dielectric constant than Si_3N_4 . BN is a good material for this purpose. Due to the weak sintering ability of BN, using a mixture of (BN + Si_3N_4) is better than pure BN. Many researchers have recently worked on the warm sintering of laminar ceramics of $\text{Si}_3\text{N}_4/\text{Si}_3\text{N}_4 + \text{BN}$ and obtained porous ceramics with dielectric constants in the range of 2.93–5.89 [91]. This Nitroxyceram composition with acceptable dielectric constant and mechanical strength can be sintered without the need of high-pressures (>1 atm.) after consolidation by following the slip casting, gel casting, etc., techniques into large size radome shapes close to the final design [46, 80, 92–99]. However, high-temperature oxidation of BN and Si_3N_4 is also inevitable, which will deteriorate the mechanical and dielectric properties along with the ablation resistance of the fused silica matrix, especially for BN-reinforced fused silica ceramics.

Table 12 Properties of fused silica ceramics and composites consolidated by following various routes and densified under different sintering conditions

Dopant added to fused silica	Consolidation technique	Sintering temp. (°C) (time, h)	Bulk density (g/cm ³)	Relative density (%)	Dielectric Constant (ϵ) at 10–31 GHz	Fracture toughness (MPa.m ^{1/2}) (± 0.25)	Flexural Strength (MPa) (± 5)	Porosity (%)	Ref.
Fused silica (100 wt.%)	Slip-casting	1210–1250 (2.5 h)	1.94–2.05	>88	3.3–3.5	0.8–1.5	35–65	7–11	[2]
Fused silica (100 wt.%)	Slip-casting	1300–1350 (2.5 h)	2.19–2.20	>88	3.8	–	≥ 50	≤ 0.1	
BN/SiB ₄ (0.5–1.0 wt.%)	Slip-casting	1250 (2.5)	2.00–2.20	>88	3.5–3.8	1.3–2.0	60–85	0.5	[90]
Fused silica (100 wt.%)	Slip casting	1250 (4 h)	1.83	>80	2.99	–	29.50	16.83	[8]
Fused silica (100 wt.%)	Gelcasting	1250 (4 h)	1.80	>80	3.05	–	47.38	18.18	
Pure fused silica radome	Gelcasting	1200 (2 h), LPG kiln	1.96	>90	–	–	65.2	<10	[62]
Silica gel coating	Dip-coating of porous body	Water proof coating at 550 (4 h)	–	<85	2.65	–	–	–	[107]
Nano-SiO ₂ (1 wt.%)	Gelcasting	1300 (10 min)	2.1	–	–	–	40	~ 10	[70]
(SiO ₂) _n /SiO ₂ composites (47 wt.% yarn)	Silicon-infiltration-sintering	450 (2 h)	1.71	Shown both brittle and ductile fracture behavior	–	–	62	–	[108]
SiO ₂ /SiO ₂	PIP into oven fiber	800	–	–	3.16–3.29	–	–	–	[8]
SiO ₂ /SiO ₂	Liquid phase infiltration	800	1.71	–	3.0	–	–	–	[82]
2.5D SiO ₂ /SiO ₂	Sol-gel and infiltration	900	1.65	–	3.40	–	80.86	–	[109]
3D SiO ₂ /SiO ₂	PIP into oven fiber	800	1.65	–	–	–	75	–	[80]

(continued)

Si ₃ N ₄ -2Al ₂ O ₃ -4Y ₂ O ₃ (100 wt.%)	Gelcasting of porous Si ₃ N ₄ and vacuum infiltration of SiO ₂	1750 (0.5 h) & 1000 (1 h)	1.62	–	2.65	1.05	92.6	49.3	[85]
Si ₃ N ₄ -2Al ₂ O ₃ -4Y ₂ O ₃ (74 wt.%)			2.18	–	3.61	1.70	148.1	22.0	
Si ₃ N ₄ (56 wt.%)	Dry-powder pressing and open-air atmospheric sintering	1200 (4 h)	–	<65	3.1	–	47.4	42.6	[86]
Si ₃ N ₄ (55 wt.%)		1300 (4 h)	–	<70	4.3	–	71.1	30.0	
Si ₃ N ₄ (63 wt.%)		1400 (4 h)	–	<65	4.5	–	64.2	35.0	
Si ₃ N ₄ (68 wt.%)		1500 (4 h)	–	<66	4.1	–	57.1	33.7	
Si ₃ N ₄ (55 wt.%)		1300 (0.5 h)	–	<60	3.5	–	45.6	42.1	
Si ₃ N ₄ (56 wt.%)		1300 (2 h)	–	<80	4.6	–	136.9	19.4	
Si ₃ N ₄ (54 wt.%)	1300 (8 h)	–	<83	4.5	–	112.8	16.2	[34]	
ZrO ₂ -3Y ₂ O ₃ (0 wt.%)	Gelcasting and pressureless sintering	1250 (4 h)	2.03	–	–	–	70.9	6.2	
ZrO ₂ -3Y ₂ O ₃ (0 wt.%)		1275 (4 h)	2.15	–	–	–	74.2	1.1	
ZrO ₂ -3Y ₂ O ₃ (5 wt.%)		1275 (4 h)	2.20	–	–	–	90.1	0.7	
ZrO ₂ -3Y ₂ O ₃ (10 wt.%)		1275 (4 h)	2.26	–	–	4.63	–	1.4	
ZrO ₂ -3Y ₂ O ₃ (15 wt.%)		1275 (4 h)	2.32	–	–	–	87.4	1.5	
ZrO ₂ -3Y ₂ O ₃ (20 wt.%)		1275 (4 h)	2.38	–	–	–	88.9	4.0	
ZrO ₂ -3Y ₂ O ₃ (10 wt.%)		1250 (4 h)	2.08	–	–	–	75.9	11.8	
ZrO ₂ -3Y ₂ O ₃ (10 wt.%)		1300 (4 h)	2.31	–	–	–	91.1	0.38	

(continued)

Table 12 (continued)

Dopant added to fused silica	Consolidation technique	Sintering temp. (°C) (time, h)	Bulk density (g/cm ³)	Relative density (%)	Dielectric Constant (ϵ) at 10–31 GHz	Fracture toughness (MPa.m ^{1/2}) (± 0.25)	Flexural Strength (MPa) (± 5)	Porosity (%)	Ref.
Al ₂ O ₃ (0 wt.%)	Gelcasting and pressureless sintering	1200 (4 h)	1.68	–	3.34	–	32.9	22.9	[87]
Al ₂ O ₃ (0 wt.%)		1225 (4 h)	1.84	–	3.44	–	67.0	15.5	
Al ₂ O ₃ (0 wt.%)		1250 (4 h)	2.03	–	3.71	–	70.9	6.2	
Al ₂ O ₃ (0.25 wt.%)		1250 (4 h)	1.83	–	3.75	–	80.6	17.0	
Al ₂ O ₃ (0.50 wt.%)		1250 (4 h)	1.84	–	3.54	–	79.9	17.0	
Al ₂ O ₃ (0.75 wt.%)		1250 (4 h)	1.84	–	3.73	–	78.7	16.8	
Al ₂ O ₃ (1.0 wt.%)		1250 (4 h)	1.82	–	3.68	–	77.0	17.9	
Al ₂ O ₃ (0.5 wt.%)		1275 (4 h)	1.89	–	4.41	–	69.9	14.8	
Al ₂ O ₃ (0.5 wt.%)		1300 (4 h)	2.01	–	3.97	–	67.7	9.3	
β -Si ₄ Al ₂ O ₂ N ₆ (84 wt.%) + Y ₂ O ₃ (7 wt.%)	Gelcasting	1675 (4 h)	3.13	>95	5.896	3.42	199	3.31	[88]
β -Si ₄ Al ₂ O ₂ N ₆ (60 wt.%) + Al ₂ O ₃ (1 wt.%)	Extrusion and sintering of β -Si ₄ Al ₂ O ₂ N ₆ precursors, and GCHAS of fused silica- β -Si ₄ Al ₂ O ₂ N ₆ powder mixture	1750 (3 h)	2.72	>95	6.313	3.33	100	0.5	[10, 89]
β -Si ₄ Al ₂ O ₂ N ₆ (60 wt.%) + Al ₂ O ₃ (2 wt.%)			2.73	>95	6.155	3.35	110	0.48	
β -Si ₄ Al ₂ O ₂ N ₆ (60 wt.%) + Al ₂ O ₃ (3 wt.%)			2.78	>95	6.154	3.41	114	0.41	
β -Si ₄ Al ₂ O ₂ N ₆ (60 wt.%) + Al ₂ O ₃ (4 wt.%)			2.82	>95	5.900	4.06	128	0.39	

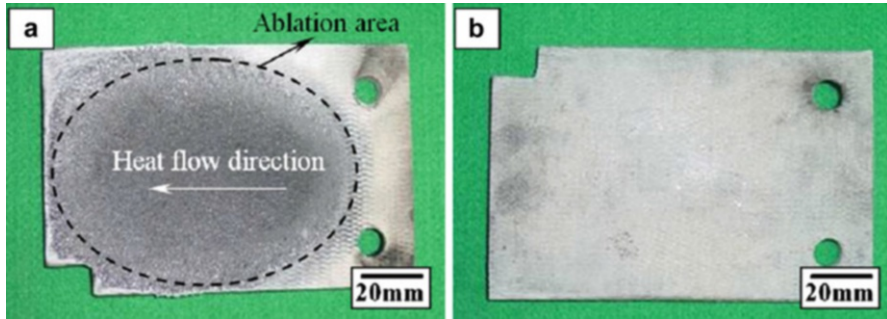


Fig. 30 The front and back side of the 3D $\text{SiO}_{2f}/\text{Si}_3\text{N}_4\text{-BN}$ composite slab subjected to ablation test at 1925°C using kerosene–oxygen ablation tester (Model YA-6804, Beijing Material Machining and Testing Center, China) with the sample dimension size $170\text{ mm} \times 120\text{ mm} \times 18\text{ mm}$ and ablation time was 12 s (adopted from reference [83])

In a study, the 3D $\text{SiO}_{2f}/\text{Si}_3\text{N}_4\text{-BN}$ composites were prepared with three infiltration-cure-pyrolysis cycles using hybrid preceramic precursor polyborosilazane (PBSZ) [83]. The polymer infiltration and pyrolysis (PIP) process is a fast route to fabricate dense 3D $\text{SiO}_{2f}/\text{Si}_3\text{N}_4\text{-BN}$ composites using PBSZ due to its good wettability with quartz fibers and high ceramic yield. This 3D $\text{SiO}_{2f}/\text{Si}_3\text{N}_4\text{-BN}$ nitride composite exhibited a low ablation recession rate of 0.038 mm/s during kerosene–liquid oxygen ablation tests after exposing to a near constant heat flux of 8 MW/m^2 with a temperature of about 1925°C from a nozzle distance of 110 mm at interangle between the impinging heat flux and the specimen plane was 30° [83]. Figure 30a shows that the ablation area is shaped like a pear and the specimen is in good condition (Fig. 30b) except for some mass loss in the middle of the slab after the ultra-high temperature load, exhibiting an average mass loss of 0.77 g/s [83]. No cracks and no residue were found on the ablation surface. The ablation process can be described as follows. Quartz fibers melted and swept off along the heat flux direction, leaving the matrix directly exposed to the heat flux which resulted in matrix erosion. Ablation test showed that the 3D $\text{SiO}_{2f}/\text{Si}_3\text{N}_4\text{-BN}$ composites have excellent ablation and shock damage resistance with a low surface recession rate of 0.038 mm/s . The flexural strength of the ablated specimen was 96.5 MPa , which is 8.79% lower than that of the as-received specimen. SEM microstructures revealed that there was a reaction at the fiber/matrix interface during ablation testing (Fig. 31) [83]. Almost no effects of the ultra-high temperature load on the strength were noted. Fiber pull-out and de-bonding mechanisms contributes to the high mechanical properties.

Concluding Remarks and Future Perspectives

As discussed in this review, the development of aerospace technology is responsible for the stimulated research focusing to develop ceramic radome materials with combined properties of high thermal stability, low heat conductivity, and constancy

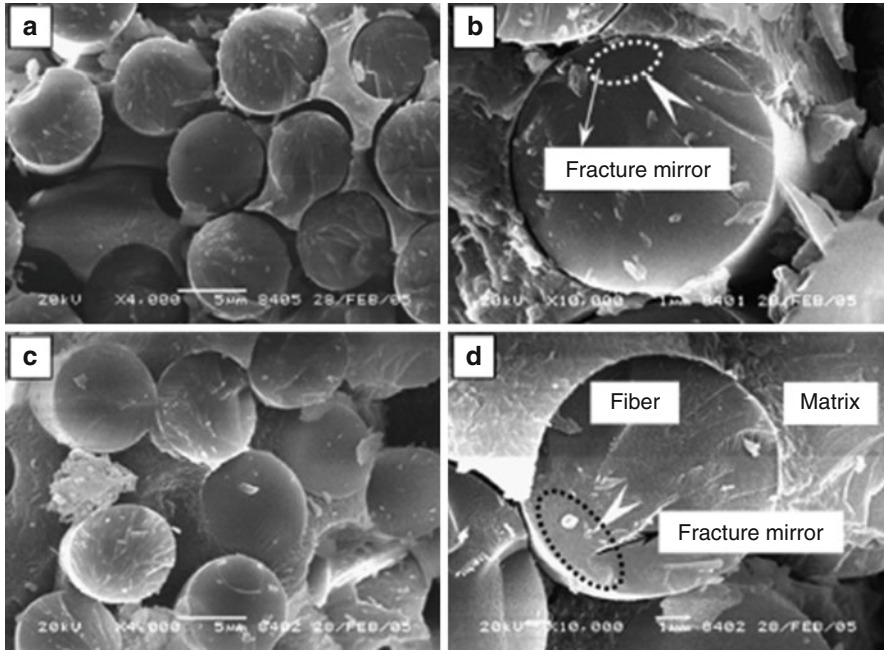


Fig. 31 SEM micrographs of the fracture surface of 3D $\text{SiO}_2/\text{Si}_3\text{N}_4\text{--BN}$ composites (specimen A is as received and specimen B is the one subjected to ablation test) before and after subjecting to the ablation test followed by 3-point bend test (adopted from reference [83])

of low-dielectric properties over a wide range of temperatures and frequencies suitable for hypersonic radome applications. Furthermore, these materials also need to be resistant to optical, high frequency, and ionizing radiation and be operable in vacuum and in oxidizing and reducing media. All these requirements are offered only by a few ceramic materials. A close scrutiny of the information indicates that (i) the fiber reinforced plastics (FRP) based radomes are suitable for vehicles that travel only up to Mach 3 speed, (ii) cordierite-based Sital glass is suitable for radomes that travel at about Mach 5, (iii) SCFS is the strong candidate for fabricating radomes for missiles that travel at Mach 5 but exhibits low strength, high-porosity, and poor rain erosion resistance, hence, are needed to be surface passivated with coatings to seal the surface porous structure, (iv) beryllium oxide and the boron nitrides are not suitable for radomes because of fabrication difficulties and high-cost; however, they are useable for, dielectric windows, and (v) isotropic pyrolytic boron nitride (BN) can be used up to Mach 9 to 10, which needs to be consolidated by following an hot-isostatic pressing (HIP) route to achieve the desired densification; hence; fabrication of radome shapes is quite expensive for BN. However, majority of radomes employed today on vehicles launched from sea-base are based on Sital glass such as pyroceram 9609, barium aluminum silicate, cordierite and those launched from air-to-surface and air-to-air are SCFS.

As far as radome shape designing is concerned, the blunt shape is ideal for smooth transmission of radar frequency (RF) signals without any loss or aberration, and the sharp radome shape is ideal from the point of view of aerodynamic loads withstanding capability. Hence, there should be a compromise between these two extremes. The best radome shape identified for these high-speed radomes has been the ogive shape, which is also suitable for minimizing the bore-site error (BSE) generated during maneuverability of the missile.

The radome wall constructions include half wavelength wall, thin wall, sandwich wall, and multilayer wall. The half wavelength wall possesses performances meeting the normal radome applications, but it has relatively narrow bandwidth of about 5%. The thin wall radome requires a thickness less than 5% of wavelength of the operating frequency in order to obtain satisfactory transmission capability. So it finds limited aircraft applications above X-band, since the wall would be too thin to have enough mechanical strength. Multilayer or sandwich radome wall which offers a high strength-to-weight ratio satisfies the need for increased operating bandwidth. The hypervelocity radomes that usually transmit X- and Ku-band frequency signals are needed to be fabricated according to the half-wavelength wall thickness. The wall thickness of the radome increases with the increase of dielectric constant of the material. Majority of the ceramics as discussed in this review such as, fused silica, Sital glass (e.g., pyroceram 9606, etc.), alumina, silicon nitride (RBSN and HPSN), β -SiAlON, barium aluminum silicate (BAS), and Nitroxyceram can have a half-wavelength wall thickness of >6 mm at X- and Ku-band frequency (8–18 GHz). With this thickness, majority of these ceramic materials can be fabricated into dense radome shapes of any usual size by following the well-established inexpensive aqueous colloidal processing routes such as slip-casting, gelcasting, electrophoretic slip-deposition.

Among the various ceramic materials discussed in this review, SCFS has been identified to be an ideal material for fabricating radomes that are to be travelled at speed of $>$ Mach 6 owing to its several important combination of properties desired by the high-speed missile applications. Apart from this, the SCFS also owns most abundantly available inexpensive raw materials in all the countries and it can be consolidated quite easily into a desired near-net shape by following very inexpensive and simple aqueous colloidal slip-casting route. The simple aqueous slip-casting and modified electrophoretic slip-deposition routes have been identified to be the routes to be followed for the commercial large-scale industrial production of actual-size SCFS radomes at affordable costs. The only problems of SCFS radomes are their poor mechanical strength (~ 28 MPa) and high structural (7–18%) porosity, due to which SCFS radomes exhibit poor resistance to rain and abrasion impact, and also absorb considerable amounts of moisture, which hamper their dielectric properties very severely while they are in the actual usage for radome applications. Furthermore, due to very poor packing of particles achieved in this slip-casting route, the consolidated body do not attain full density when the crystallization of fused-silica into cristobalite phase is restricted, which damages radome body during its usage due to the prevalent inversion process. However, this problem can be solved by using very small amounts (<1 wt.%) of boron-based sintering aids, such as, BN or SiB₄,

which facilitates attaining very high density and low porosity without losing important dielectric properties during the sintering process. Nevertheless, without applying the surface passivation coatings, it is not possible to use SCFS radomes on any of the existing radome applications as it absorbs the moisture from the atmosphere, which damages the dielectric properties very severely. In fact, the surface passivation and reinforcement with various fibers are not only required to arrest the moisture absorbing capability of SCFS but also to improve the mechanical strength to some extent. Interestingly, the SCFS exhibit a very peculiar property of having increased high-temperature mechanical strength in comparison to the one measured at room temperature. This is attributed to the improved sintering of SCFS upon exposure to elevated temperatures that enhances the densification, hence, the strength of the material. In view of these reasons, the surface passivated and reinforced SCFS radomes consolidated by following inexpensive aqueous slip-casting route can be employed for all the hypervelocity ($>Mach\ 6$) radome applications that are not launched from sea-base.

Among net-shape consolidation techniques, such as slip-casting, gelcasting, hydrolysis induced aqueous-gelcasting, electrophoretic slip-cast deposition, cold iso-static pressing (CIP), the aqueous slip-casting and electrophoretic slip-cast deposition processes have been found to be inexpensive and suitable for consolidating SCFS radomes. Among these later two methods, the electrophoretic slip-cast deposition has been found to be best by Russian scientists for the commercial large-scale industrial production of actual-size radomes suitable for several missile applications. As explained in this chapter, the fused-silica slips should be prepared by using required proportions of different average particle size and by using suitable dispersing agents. These slips should not be stored in metal containers before casting into the plaster molds. The drying and sintering regimes are also of very important to have defect free high-yield acceptable radomes with desired mechanical strength and sintered properties such as high bulk density and low porosity.

References

1. Suzdal'tsev EI (2015) Radio-transparent ceramics: yesterday, today, tomorrow. *Refract Ind Ceram* 55:377–390
2. Suzdal'tsev EI (2002) Radio transparent, heat-resistant materials for the 21st century. *Refract Ind Ceram* 43:103–110
3. Joy EB, Huddleston G K, Bassett UL, Gorton CW, Bomar Jr SH (1974) Analysis and evaluation of radome materials and configurations for advanced RF seekers, Final Report Projects E-21-628 & A-1535, Contract No. DAAHO1–73-C-0796, Prepared for RF guidance technology branch, Advanced Sensors Directorate Research, Development, Engineerings and Missile Systems Laboratory, U.S. Army missile command, redstone arsenal, Alabama by Goergia Institute of Technology, Georgia
4. Welsh EA, Byers SA, Harris, JN. An investigation of fused silica composites for improvement of ablation and rain erosion resistance, and an alternate method for manufacture of fused silica radomes, Final Technical Report – Project A-1381, prepared for U.S. Army Missile Command Redstone Arsenal, Alabama, 35809; Engineering Experiment Section, Georgia Institute of Technology, Atlanta, 30332; 23 April 1973. Contract DAAHO1–72-C-0400

5. Harris JN, Welsh EA (1973) Fused silica design manual-I. Georgia Institute of Technology, Atlanta, 30332; p 151
6. Kouroupis JB (1992) Flight capabilities of high-speed-missile radome materials. J Hopkins APL Tech Dig 13:386–392
7. Caywood CW, Rivello MR, Weckesser LB (1983) Tactical Missile Structures and Matreials Technology 4
8. Miao X, Qu Y, Ghezze F, Fang X, Yue Y, Zhao Z, Liu R (2014) Fused silica ceramics and composites for radome applications. Adv Mater Res (Durnten-Zurich, Switz.) 900:123–129:128
9. Ganesh I (2017) Novel composites of β -SiAlON and radome manufacturing technology developed at ARCI, Hyderabad, for hypervelocity vehicles. Bull Mater Sci 40(4):719–735
10. Ganesh I, Sundararajan G (2010) Hydrolysis-induced aqueous gelcasting of beta-SiAlON-SiO₂ ceramic composites: the effect of AlN additive. J Am Ceram Soc 93:3180–3189
11. Cary RH. Avionic Radome Materials, DTIC Report, Accession No. ADA007956; Oct. 1974; <http://www.dtic.mil/dtic/tr/fulltext/u2/a007956.pdf> (17th March 2020)
12. Crone GAE, Rudge AW, Taylor GN (1981) Design and performance of airborne radomes: a review, IEE proceedings F – communications. Radar Signal Process 128:451–464
13. Heydari MS, Ghezavati J, Abbasgholipour M, Alasti BM (2017) Various types of ceramics used in radome: a review. Sci Iran Trans B. Mech Eng 24:1136–1147
14. Kozakoff DJ (2010) Analysis of radome-enclosed antennas, 2 edn. Artech House Inc., Norwood
15. Kandi KK, Thallapalli N, Chilakalapalli SPR (2015) Development of silicon nitride-based ceramic radomes - a review. Int J Appl Ceram Technol 12:909–920
16. Suzdal'tsev EI, Kharitonov DV, Anashkina AA (2010) Analysis of existing radioparent refractory materials, composites and technology for creating high-speed rocket radomes. Part 1. Analysis of the level of property indices and limiting possibilities of radioparent inorganic refractory materials. Refract Ind Ceram 51:202–205
17. Crowell Sr GA (1996) The descriptive geometry of nose cones. <http://www.myweb.cableone.net/ejcrowell/NCEQN2.doc> (17th March 2020)
18. Leggett H, Chatsworth U. Ceramic broadband radome. US Patent No 4358772, 30 Apr 1980
19. Renuka A, Borkar VG (2005) Computer-aided analysis for tangent ogive airborne radome using physical optics method. In: 2005 Asia-Pacific Microwave Conference Proceedings, 4:1–4
20. Ganesh I (2012) Hydrolysis-induced aqueous gelcasting: the latest concept for net-shape consolidation of ceramics-a review. Mater Manuf Proc 27:233–241
21. Ganesh I (2011) Aqueous slip casting of MgAl₂O₄ spinel powder. Bull Mater Sci 34:327–335
22. Lin S, Ye F, Ma J, Ding J, Yang C, Dong S (2016) Fabrication of multilayer electronic magnetic window material by Si₂N₂O decomposition. Mater Design 97:51–55
23. Chen F, Shen Q, Zhang L (2010) Electromagnetic optimal design and preparation of broadband ceramic radome material with graded porous structure. Prog Electromagn Res 105:445–461
24. Ziolkowski FP. Lightweight, multiband, high angle sandwich radome structure for millimeter wave frequencies. US Patent No 9,099,782 B2, 4 Aug 2015
25. Mortensen A, Suresh S (1995) Functionally graded metals and metal-ceramic composites. Part 1. Processing. Int Mater Rev 40:239–265
26. Romashin AG, Rusin MY, Borodai FY (2004) Structural ceramic and fibrous materials based on quartz glass. Refract Ind Ceram 45:387–391
27. Borkar VG, Renuka A, Ghosh A, Kapoor AK (2001) Simulation method identifies multipath tracking errors - a mathematical model determines how multipath reflections cause errors in tracking radars 40
28. Waldrop III JC, Driemeyer DE, Riegel LS, Lawton SA. Thermal barrier coated radio-frequency radomes. US Patent 2014/0299712 A1; 9 Oct 2014
29. Barta J, Manela M, Fischer R (1985) Si₃N₄ and Si₂N₂O for high performance radomes. Mater Sci Eng 71:265–272

30. Frazer RK. A unified radome limitations computer program (URLCP). Proceed 12th symp on Electromagnetic Windows, 12–14 June 1974
31. Ganesh I, Sundararajan G, Olhero SM, Torres PMC, Ferreira JMF (2010) A novel colloidal processing route to alumina ceramics. *Ceram Int* 36:1357–1364
32. Pavlov V (1966) Radome materials. ONTI VIAM (All-Union Institute for Aircraft Materials) 101–5
33. Hallse RL, Rizley JH 1965 Fused silica as an aerospace material. Symposium on Newer Structural Materials for Aerospace Vehicles, ASTM International
34. Wan W, Feng Y, Yang J, Bu W, Qiu T (2016) Microstructure, mechanical and high-temperature dielectric properties of zirconia-reinforced fused silica ceramics. *Ceram Int* 42:6436–6443
35. Reynolds S. Quartz vs. fused silica: what's the difference?. <https://www.swiftglass.com/blog/quartz-vs-fused-silica-whats-the-difference/> (17 March 2020)
36. Walton JD, Poulos NE (1964) Slip-cast fused silica. Technical Documentary Report No. MI-TDR-64-195; AF Materials Laboratory, Research and Technology Division, Air Force Systems Command, Wright-Patterson Air Force Base, Ohio Georgia Institute of Technology, Engineering Experiment Station, Atlanta
37. Suzdal'tsev EI, Lesnikov AK (2005) Amorphous silicon dioxide: preparation techniques and applications. *Refract Ind Ceram* 46:189–192
38. Fleming JD. Fused silica manual – materials for high temperature nuclear engineering applications. Project B-153, Prepared for U. S. Atomic Energy Commission Oak Ridge Operations Office Oak Ridge, Tennessee, Contract No. AT-(40-1)-2483, Engineering Experiment Station, Georgia Institute of Technology, Atlanta, 1959–64;1
39. Borodai FY (2017) Method of producing high density quartz ceramics and articles thereof. AOO "NPP "Tekhnologiya" im. A. G. Romashina", Russia, 1–8
40. Suzdal'tsev EI (1986) Investigating the "aging" process in quartz ceramics. *Refractories* 27:33–38
41. Suzdal'tsev EI (2003) The sintering process of quartz ceramics. *Refract Ind Ceram* 44:236–241
42. Liu HK, Majidi AP (1992) The effect of particle addition in the manufacture of ceramic matrix composites by sol-gel process. *Ceram Eng Sci Proc* 13:642–649
43. Liu HK, Majidi AP (1998) Effect of particle additions on drying stresses and the green density of sol-gel-processed three-dimensional ceramic-matrix composites. *J Am Ceram Soc* 81:1824–1828
44. Du M, Bi JQ, Wang WL, Sun XL, Long NN (2011) Microstructure and properties of SiO₂ matrix reinforced by BN nanotubes and nanoparticles. *J Alloy Comp* 509:996–10002
45. Li Q, Yang Z, Miao Y, Liang B, Cai D, Wang S, Duan X, Jia D, Zhou Y (2017) Effect of the BN content on the thermal shock resistance and properties of BN/SiO₂ composites fabricated from mechanically alloyed SiBON powders. *RSC Adv* 7:48994–49003
46. Wen G, Wu GL, Lei TQ, Zhou Y, Guo ZX (2000) Co-enhanced SiO₂-BN ceramics for high-temperature dielectric applications. *J Eur Ceram Soc* 20:1923–1928
47. Jia D, Zhou L, Yang Z, Duan X, Zhou Y (2011) Effect of preforming process and starting fused SiO₂ particle size on microstructure and mechanical properties of pressurelessly sintered BNp/SiO₂ ceramic composites. *J Am Ceram Soc* 94:3552–3560
48. Wang J, Wen GW, Meng QC (2005) Preparation of BN/SiO₂ ceramics by PIP method. *J Central South Univ Tech* 12:31–34
49. Sun G, Bi J, Wang W, Zhang J (2018) Enhancing mechanical properties of fused silica composites by introducing well-dispersed boron nitride nanosheets. *Ceram Int* 44:5002–5009
50. Suzdal'tsev EI (2005) Fabrication of high-density quartz ceramics: research and practical aspects. Part 3. Sintering of quartz ceramics. *Refract Ind Ceram* 46:384–390
51. Suzdal'tsev EI (2005) Fabrication of high-density quartz ceramics: research and practical aspects. Part 2. Shaping methods. *Refract Ind Ceram* 46:371–379
52. Suzdal'tsev EI (2005) Fabrication of high-density quartz ceramics: research and practical aspects. Part 4. Properties of mixed quartz glass slips and preforms prepared by casting into porous molds. *Refract Ind Ceram* 46:391–395

53. Suzdal'tsev EI (1982) Rules for shaping quartz ceramic blanks by freezing from water suspensions. *Refractories* 23:200–202
54. Borodai FY, Suzdal'tsev EI (1975) The influence of the technological parameters on the properties of quartz ceramic. *Refractories* 16:648–651
55. Gutierrez-Mora F, Goretta KC, Singh D, Roubort JL, Sambasivan S, Steiner KA, Adabie J, Rangan KK (2006) High-temperature deformation of amorphous AlPO_4 -based nanocomposites. *J Eur Ceram Soc* 26:1179–1183
56. Wang Y, Liu J (2009) Aluminum phosphate-mullite composites for high-temperature radome applications. *Int J Appl Ceram Technol* 6:190–194
57. Suzdal'tsev EI, Semizorov YP (1978) Effect of processing factors on the erosion resistance of quartz ceramics. *Aviats Promst* 6:75–76
58. Solomin NV, Borodai FY, Komissarova NY (1968) Dielectric properties of quartz ceramics. *Elektron Tekh Ser* 14:25–31
59. Suzdal'tsev EI, Kharitonov DV, Anashkina AA (2010) Analysis of existing radioparent refractory materials, composites and technology for creating high-speed rocket radomes. Part 3. Manufacturing technology for glass ceramic radomes, problems and future improvement. *Refract Ind Ceram* 51:289–294
60. Podobeda LG, Romashin AG, Borodai FY (1974) High temperature structural radioparent ceramic. *Heat-Resistant Inorganic Materials (In Russian)* ONTO NITS, Moscow
61. Andi UK, Selvaraj SK (2011) Method for manufacturing high-density slip-cast fused silica body. CSIR, India:1–8
62. Wang S, Cui W, Yang X, Yuan X (2007) Forming of large thin walled fused silica shapes by gelcasting. *Key Eng Mater* 336–338:1005–1008
63. Sun CG, Niu JY, Li HJ, Luoan Q, Yu HJ, Zhang FF (2012) Gelcasting of fused quartz crucible with large scale. *Key Eng Mater* 512–515:399–402
64. Hao HS, Cui WL, Fu P, Xu LH, Wang SH, Gong L, Song T, Dong F (2007) The comparison of shaping technique of fused silica ceramic. *Bull Chinese Ceram Soc* 5:1036–1039
65. Suzdal'tsev EI, Kharitonov DV, Dmitriev AV, Kamenskaya TP (2006) Improving mold sets for large-sized components prepared from aqueous slips. Part 2. Intensified technology for preforms slip-cast into porous molds. *Refract Ind Ceram* 47:158–164
66. Suzdal'tsev EI, Kharitonov DV, Dmitriev AV, Kamenskaya TP (2006) Improving mold sets for large-sized components prepared from aqueous slips. Part 1. Working material for the mold set. *Refract Ind Ceram* 47:116–120
67. Tabellion J, Clasen R (2004) Electrophoretic deposition from aqueous suspensions for near-shape manufacturing of advanced ceramics and glasses – applications. *J Mater Sci* 39:803–811
68. Suzdal'tsev EI, Kharitonov DV (2004) Development of a mold equipment for electrophoretic shaping of ceramic products. *Refract Ind Ceram* 45:58–63
69. Borodai FY, Platonov VV, Volkov MA (2011) Molding of conical ceramic articles from aqueous slurry. *Refract Ind Ceram* 51:447–451
70. Hu Y, Wang Z, Lu J (2008) Study on the gel casting of fused silica glass. *J Non-Cryst Solids* 354:1285–1289
71. Janney MA, Ren W, Kirby GH, Nunn SD, Viswanathan S (1998) Gelcast tooling: net shape casting and green machining. *Mater Manuf Process* 13:389–403
72. Janney MA, Walls CA, Kupp DM, Kirby KW (2004) Gelcasting SiAlON radomes. *Am Ceram Soc Bull* 83:9201–9206
73. Kirby KW, Jankiewicz A, Kupp D, Walls C, Janney MA (2001) Gelcasting of ceramic radomes in the $\text{Si}_3\text{N}_4\text{-Al}_2\text{O}_3\text{-AlN-SiO}_2$ system. *Mater Technol (Poulton-le-Fylde, U. K.)* 16:187–190
74. Omatete OO, Janney MA, Nunn SD (1997) Gelcasting: from laboratory development toward industrial production. *J Eur Ceram Soc* 17:407–413
75. Omatete O, Janney MA, Strehlow RA (1991) Gelcasting – a new ceramic forming process. *Am Ceram Soc Bull* 70:164–169

76. Ganesh I (2009) Near-net shape beta-Si₄Al₂O₂N₆ parts by hydrolysis induced aqueous gelcasting process. *Inter J App Ceram Soc* 6(1):89–101
77. Cheng CB, Heng CB, Wang CH, Wang HS, Liao R, Wei QH, Zhai P, Zhou CL, Liu FT (2012) Research progress of ceramic radome inorganic coating. *Bull Chinese Ceram Soc* 31:116–119
78. Wei M, Teng X, Zhao X, Cheng Z, Li G (2005) Study on enhanced coating of quartz radome. *Bull Chinese Ceram Soc* 4:3–5
79. Hu W (2015) Surface densification of silica ceramic. *Key Eng Mater* 633:69–72
80. Chen H, Zhang LM, Jia GY, Luo WH, Yu S (2003) The preparation and characterization of 3D-silica fiber reinforced silica composites. *Key Eng Mater* 249:159–162
81. Purinton DL, Semff LR. Broadband composite structure fabricated from inorganic polymer matrix reinforced with glass or ceramic woven cloth. US Patent 6,037,023, 14 Mar 2000
82. Wang CH, Wei QH, Wang HS, Li L, Luan Q, Liao R (2012) Dielectric properties of silica fiber reinforced silica composites. *Key Eng Mater* 512–515:547–550
83. Jiang YG, Zhang CR, Cao F, Wang SQ, Hu HF, Cao YB (2008) Effects of thermal load on mechanical properties and microstructures of 3D SiO₂/Si₃N₄–BN composites using polyborosilazane. *Mater Sci Eng A* 487:597–600
84. Jiang YG, Zhang CR, Cao F, Wang SQ, Li B (2008) Ablation performance and surface texture of the nitride composites reinforced by the braided silica fibers. *Key Eng Mater* 368–372:980–982
85. Zou C, Zhang C, Li B, Cao F, Wang S (2012) Improved properties and microstructure of porous silicon nitride/silicon oxide composites prepared by sol–gel route. *Mater Sci Eng A* 556:648–652
86. Ding S, Zeng YP, Jiang D (2007) Oxidation bonding of porous silicon nitride ceramics with high strength and low dielectric constant. *Mater Lett* 61:2277–2280
87. Wan W, Yang J, Feng Y, Bu W, Qiu T (2016) Effect of trace alumina on mechanical, dielectric, and ablation properties of fused silica ceramics. *J Alloys Comp* 675:64–72
88. Ganesh I, Thiyagarajan N, Jana DC, Mahajan YR, Sundararajan G (2008) Influence of chemical composition and Y₂O₃ on sinterability, dielectric constant, and CTE of β-SiAlON. *J Am Ceram Soc* 91(1):115–120
89. Ganesh I, Sundararajan G (2011) Novel route to beta-SiAlON-SiO₂ ceramic composites. *Adv Appl Ceram* 110:87–94
90. Suzdal'tsev EI (2006) Fabrication of high-density quartz ceramics: research and practical aspects. Part 6. A comprehensive study of the properties of BN-modified densely sintered ceramics. *Refract Ind Ceram* 47:101–109
91. Zuo KH, Zeng YP, Jiang D (2012) The mechanical and dielectric properties of Si₃N₄-based sandwich ceramics. *Mater Design* 35:770–773
92. Chen Z, Zhang L, Cheng L, Xu Y (2005) Properties and microstructure of Nextel 720/SiC composites. *Ceram Int* 31:573–575
93. Funayama O, Tashiro Y, Kamo A, Okumura M, Isoda T (1994) Conversion mechanism of perhydropolysilazane into silicon nitride-based ceramics. *J Mater Sci* 29:4883–4888
94. Liu HK, Huang CC (2001) Impact response and mechanical behavior of 3-D ceramic matrix composites. *J Eur Ceram Soc* 21:251–261
95. Manocha LM, Panchal CN, Manocha S (2002) Silica/silica composites through electrophoretic infiltration. *Ceram Eng Sci Proc* 23:655–661
96. Qi GJ, Zhang CR, Hu HF (2006) Continuous silica fiber reinforced silica composites densified by polymer-derived silicon nitride: mechanical properties and microstructures. *J Non-Cryst Solids* 352:3794–3798
97. Qiu J, Cao X, Tian C, Zhang J (2005) Ablation property of ceramics/carbon fibers/resin novel super-hybrid composite. *J Mater Sci Technol (Shenyang, China)* 21:92–94
98. Sawyer LC, Jamieson M, Brikowski D, Haider MI, Chen RT (1987) Strength, structure, and fracture properties of ceramic fibers produced from polymeric precursors: I. base-line studies. *J Am Ceram Soc* 70:798–810

99. Su K, Remsen EE, Zank GA, Sneddon LG (1993) Synthesis, characterization, and ceramic conversion reactions of borazine-modified hydridopolysilazanes: new polymeric precursors to silicon nitride carbide boride (SiNCB) ceramic composites. *Chem Mater* 5:547–556
100. Brochure from Ceradyne Inc. and Bruce Lockhart, Ceradyne Thermo Materials; <https://www.linkedin.com/in/bruce-lockhart-a0613447> (17th March 2020)
101. Faber KT, Shanti NO (2012) Gelcasting of ceramic bodies. In: Bansal NP, Boccaccini AR (eds) *Ceramics and composites processing methods*. Wiley, pp 199–234,
102. Janney MA, Kupp DM, Kirby KW, Walls CA (2003) Gelcasting Sialon radomes. *Ceram Trans* 142:253–260
103. Li YS, Bu JL, Li RC (2004) Preparation and research on high temperature performance of composition of SiAlON-bonded SiC. *Hebei Ligong Xueyuan Xuebao* 26(4):50–53
104. Wan W, Luo J, Yang J, Feng Y, Ouyang Y, Chen D, Qiu T (2018) High-temperature ablation properties of nano zirconia reinforced fused silica ceramics. *Ceram Int* 44:7273–7275
105. Jia DC, Zhou Y, Lei TC (2003) Ambient and elevated temperature mechanical properties of hot-pressed fused silica matrix composite. *J Euro Ceram Soc* 23:801–808
106. Inna GT, Curtis AM, Deborah AH, Anh HL. Electromagnetic window. US Patent 5,573,986, 12 Nov 1996
107. Niu SX, Yang T, Liu SQ (2016) Preparation of waterproof silica gel coatings on porous silica ceramic substrates. *Key Eng Mater* 680:327–330
108. Li B, Zhu J, Chen Z, Jiang Y, Hu F (2013) Flexural properties and fracture mechanism of three-dimensional and four-directional braided $(\text{SiO}_2)_f/\text{SiO}_2$ composites. *Asian J Chem* 25:7221–7224
109. Han SA, Jiang KH, Tang JW (2009) Studies on preparation and property of 2.5D $\text{SiO}_2f/\text{SiO}_2$ composites. *Adv Mater Res* 79–82:1767–1770
110. Guo JK, Ning JW, Pan YB (2003) Fabrication and properties of carbon nanotube/ SiO_2 composites. *Key Eng Mater* 249:1–4
111. <https://www.scimagojr.com/journalsearch.php?q=145541&tip=sid&clean=0>. (2004) Boeing to build Arrow components, *Jane's Missiles and Rockets*; (17th March 2020)
112. Anon (2009) Ceradyne to manufacture combat helmets. *Am Ceram Soc Bull* 88:5
113. Anon (2005) Ceradyne opens new manufacturing facility. *Am Ceram Soc Bull* 84:12
114. Anon (2001) Global news: Ceradyne expansion. *Am Ceram Soc Bull* 80:11–12
115. Ganesh I, Reddy GJ, Sundararajan G, Olhero SM, Torres PMC, Ferreira JMF (2011) Hydrolysis-induced aqueous gelcasting of magnesium aluminate spinel. *Inter J Appl Ceram Tech* 8:873–884
116. Ganesh I (2011) Fabrication of near net shape magnesium aluminate (MgAl_2O_4) spinel components via aqueous processing. *Adv Appl Ceram* 110:496–511
117. Ganesh I, Olhero SM, Torres PMC, Alves FJ, Ferreira JMF (2009) Hydrolysis-induced aqueous gelcasting for near-net shape forming of ZTA ceramic composites. *J Euro Ceram Soc* 29:1393–1401
118. Suzdal'tsev EI, Kharitonov DV, Anashkina AA (2011) Analysis of existing radioparent refractory materials, composites and technology for creating high-speed rocket radomes. Part 4. Ceramic technology for producing glass ceramic radomes. Advantages and disadvantages. Prospects for modernization. *Refract Ind Ceram* 51:349–357



Patent Trends in Additive Manufacturing of Ceramic Materials

8

Priya Anish Mathews, Swati Koonisetty, Sanjay Bhardwaj,
Papiya Biswas, Roy Johnson, and G. Padmanabham

Contents

Introduction	320
Additive Manufacturing	320
Broad Classification of AM Process	321
Patenting Scenario of Additive Manufacturing of Ceramics	324
Part A: Overview of Patenting Trends in AM of Ceramics	325
Part B: Overview of Focus Fields	331
Part C: AM of Ceramics and Composites for Strategic and Aerospace Applications	345
Conclusion	347
References	347

Abstract

Ceramics due to their good mechanical, thermal, and chemical properties are one of the sought-after engineering materials. These materials cater to wide range of applications, such as household pottery, advanced ceramics and other components for strategic sector. Owing to their unique properties such as high structural

P. Anish Mathews (✉) · S. Koonisetty · S. Bhardwaj · G. Padmanabham
International Advanced Research Centre for Powder Metallurgy and New Materials (ARCI),
Hyderabad, India
e-mail: priya@arci.res.in; swati.arci@gmail.com; sanjay@arci.res.in; gp@arci.res.in

P. Biswas
Center for Ceramic Processing, International Advanced Research Centre for Powder Metallurgy
and New Materials (ARCI), Hyderabad, Telangana, India
e-mail: papiya@arci.res.in

R. Johnson
International Advanced Research Centre for Powder Metallurgy and New Materials, (ARCI),
Balapur, Hyderabad, India
e-mail: royjohnson@arci.res.in

stability, resistance to corrosion, compatibility with other printing materials, and high strength, ceramics are considered as a promising material for additive manufacturing for development of various parts; components related to medical and dental implants; aircraft components; architectural, aesthetic, or decorative purposes; mechanical and metallurgical applications; etc. This chapter attempts to review the current state-of-the-art and latest trends in the field of additive manufacturing of ceramics through patents, with a special focus on ceramic materials for aerospace and strategic applications. Recent advancements and progress in the field of additive manufacturing of ceramics and methods thereof from a patent viewpoint have been presented in terms of patent landscapes, themes, and trends generated using important parameters such as patenting timelines, priority applications, key players, etc. From the patent landscaping and review, it is noted that additive manufacturing of ceramics has progressed remarkably in Asia when compared to other regions of the world. Three-dimensional printing of ceramic materials has been widely accepted by the healthcare sector especially dentistry and orthopedics, and 3D printing is also making its mark in aerospace industry. Innovations in ceramic-based composite materials suitable for additive manufacturing are on the rise owing to their adaptability, suitability, and mechanical properties for high-end applications.

Keywords

Ceramics · Additive manufacturing · 3D printing · Three-dimensional printing · Patenting trend · Patent landscaping · 3D printing of ceramics · Composites

Introduction

Additive Manufacturing

Additive manufacturing (AM) is also synonymously known as three-dimensional printing, 3DP, 3D printing, rapid prototyping (RP), rapid manufacturing, solid free forming (SFF), generative manufacturing (GM), layer manufacturing (LM), layer-by-layer fabrication, additive fabrication, etc. [1–3]. AM is a fast-developing branch of manufacturing technology that has accelerated the manufacturing processes in various aspects, with respect to time, ease of processing, cost of manufacture, dimensional accuracy of the product, design flexibility, etc. [3, 4]. AM technology has been continuously evolving, and its adaptation to a wide range of materials has given rise to development of various layer-by-layer manufacturing techniques, thereby widening the scope of domestic as well as commercial applications. As each of the AM processes has its own strengths and limitations, there has been a continuous and progressive development world over to eliminate the shortcomings and to make the process into a more attractive and viable manufacturing technique.

The basic principle of three-dimensional printing is well documented and involves generation of 3D model with the help of computer-aided design (CAD)

followed by conversion of 3D model to a Standard Tessellation Language (STL) format. The converted STL file is then used to develop 3D structures in layer-by-layer fashion by the printing machine [1, 5]. Components with complex and near net shapes can be manufactured by this process. Different types of materials require different types of AM processes, and therefore based on the material and final characteristics of the fabricated objects, various printing techniques, equipment, and methods have emerged to suit different applications.

Broad Classification of AM Process

As AM process is a new and evolving manufacturing technique when compared to traditional manufacturing routes, one comes across various synonymously named techniques and classifications across literature. The classification presented in Fig. 1 is broadly based on ASTM classification for AM processes for the convenience of the reader [6].

The choice of AM process broadly depends on the type of material used for fabrication and the desired product properties such as shape, finish, structure, etc. Three-dimensional products through AM process can be formed for almost all types of raw materials (also popularly referred to as build materials, printing materials, inks, or feedstock) such as metals, plastic polymers, ceramics, composites, clay, cement, etc. [7–9].

Ceramics are one of the most interesting materials owing to its ancient roots as well as its suitability to advanced applications. The limitation posed by traditional methods in manufacturing of geometrically intricate-shaped ceramic components with the desired compositions has paved the way for the introduction of advanced manufacturing techniques such as AM for development of ceramic-based components. This advanced manufacturing technology has extended the scope of application of ceramic-based materials not only in the traditional ceramic industry (e.g., household utilities, artware, architecture, decorative) but also in the development of components suitable for high-performance applications (e.g., aerospace) and components suitable for healthcare applications (dental implant, bone implants, surgical tools, etc.) [8–10]. AM process minimizes the overall weight of the products especially those that require joining different parts to develop a single intricately designed component, thus indirectly reducing the effort and cost involved in manufacturing the final product, which in contrast to traditional manufacturing methods which would require numerous pre-trials, specific molds, and more raw materials, thereby increasing the time required to manufacture the components. The three-dimensional additive fabrication technology of ceramics has made a good progress in the recent times, and a variety of processes for three-dimensional manufacturing of ceramics are now available. As mentioned above, 3D-printed ceramic components can be developed by various routes based on the final requirement.

Typically, for a material extrusion-based AM process, specific binder materials are prepared and compounded with the ceramic materials and converted into a filament or paste suitable for extruding. In order to get the finer dimensional accuracy, the green body in certain cases may undergo edge trimming before the

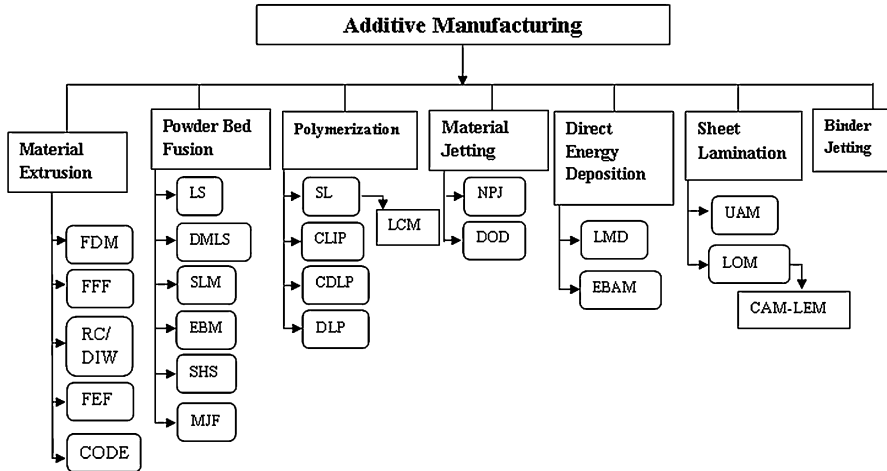


Fig. 1 AM technology classification. Abbreviations: *FDM* fused deposition modeling, *FFF* fused filament fabrication, *RC* robocasting, *DIW* direct ink writing, *FEF* freeze-form extrusion fabrication, *CODE* ceramic on-demand extrusion, *LS* laser sintering, *DMLS* direct metal laser sintering, *SLM* selective laser melting, *EBM* electron beam melting, *SHS* selective heat sintering, *MJF* multi-jet fusion, *SL* stereo-lithography, *LCM* lithography-based ceramic manufacturing, *CLIP* continuous liquid interphase printing, *CDLP* continuous direct light processing, *DLP* digital light processing, *NPJ* nanoparticle jetting, *DOD* drop-on-demand ink jetting, *LMD* laser metal deposition, *EBAM* electron beam additive manufacturing, *UAM* ultrasonic additive manufacturing, *LOM* laminated object manufacturing, *CAM-LEM* computer-aided manufacturing of laminated engineering materials

binder is removed by suitable heat treatment procedures [11, 12]. Additionally, sintering helps in densification of the part or component. As represented in Fig. 1, FDM, FFF, DIW, FEF, and CODE are extrusion-based printing techniques. Fused deposition printing of ceramics includes printing of ceramic parts or components by extruding a paste or a filament of the printing material made up of binder and ceramic powder through a hot extrusion nozzle [9]. FDM is a trademark of Stratasys Inc. FFF by RepRap is largely based on FDM process and is popularly used for fabricating components at a smaller scale wherein the filament of printing material is continuously passed into a heated nozzle such that it melts and extrudes which is then deposited on to a printing platform in the desired form [13, 14]. In robocasting process, the feedstock of the print material is in the form of a slurry typically made up of water, ceramic particles, and other additives. This process employs robotics for deposition and development of 3D parts. RC is reported to have been first developed by Sandia National Laboratories, USA, and is synonymously known as DIW, direct-write assembly, and microrobotic deposition [15–17]. FEF process involves layer-by-layer development using slurries as in the case of robocasting. However, the printing is carried out under freezing temperatures. This helps in the solidification of the water content in the slurry there by minimizing the binder requirement [18, 19]. In certain cases, after the development of the ceramic build part or green body

by extrusion process, the green body is kept under freezing conditions followed by heat treatment for binder removal and sintering to obtain the end product [20]. In ceramic on-demand extrusion (CODE), the extrusion of the build material is carried out in ambient temperatures, and the layer-by-layer deposition of the build part takes place by surrounding it by an oil medium in order to avoid evaporation of water content from the layers during buildup followed by treating with IR radiation. This process is adopted till the entire part is fabricated [21, 22]. Based broadly on the above mentioned techniques, some of the other versions suitable for three-dimensional printing of ceramics based on extrusion mechanism are extrusion free forming (EFF) [23, 24], fused deposition of ceramics (FDC) [25, 26], multiphase jet solidification (MJS) [27, 28], and fused feedstock deposition (FFD) [29].

In the powder bed fusion process, three-dimensional components are fabricated by employing a radiation source such as laser, electron beam, or other heat sources to melt or fuse the powder particles together. Different types of powder bed fusion-based process are available to the end user based on the source of melting. The popular techniques available for ceramic materials are selective laser sintering (SLS) [30], multi-jet fusion (MJF) [31, 32], and direct laser microfusion (DLM) [33]. In laser sintering process often referred to as SLS process, a solid component is fabricated in a layer-by-layer fashion by directing a laser at predefined points such that ceramic powder particles are sintered at a desired location. MJF process was launched during the end of 2014, and advanced versions were commercially available during 2016–2017 [31, 34]. According to reports, these printers are expected to reduce the cost of manufacturing the product by half [34]. In this process, in addition to the heat source, a fusing agent and detailing agent are used on the build material during deposition in order to get the high-quality finished part [31, 32, 35]. Selective laser melting (SLM) process involves melting of the material particles during layer deposition using laser source. Direct laser microfusion (DLM) is suitable for ceramic materials and is based on SLM. This process does not require a post-heat treatment step and is especially suitable for bioceramics such as hydroxyapatite, etc. [33, 36].

Jetting or material jetting technology involves the release of droplets of photosensitive printing materials through nozzles present in the print head. As in the case of any 3D manufacturing technique, here too deposition takes place in layer-wise fashion onto a platform where the build layers are cured under ultraviolet light. Nanoparticle jetting [37, 38] based on jetting technology is suitable for metals as well as ceramic materials. Cartridges containing nanoparticles of ceramic printing material as well as soluble support materials are loaded into the system. Thin layer of nanoparticles of different sizes and shapes dispersed in a liquid as well as support material is deposited in a manner such that it facilitates the formation of dense structures [37, 38].

In certain non-extrusion-based techniques such as binder jetting, the 3D printers have mechanisms/arrangements to feed both the ceramic powder and the binder material onto the platform in a layered fashion such that the simultaneous binder distribution on the ceramic layer in a repetitive manner aids in better adhesion between the build material and the binder. After layer-by-layer printing, the green body of the component is subjected to post-printing operations such as sintering or glazing to strengthen the printed component [39]. Some of the AM machines based

on this printing process suitable for ceramic-based materials are phenol direct binding (PDB) [40, 41], 3D printers (S-Max, S-MAX+) [42], CerPrint [43], and Ceramo One [44, 45].

Three-dimensional printing by polymerization or vat polymerization typically involves a tank (known as vat) containing the liquid photopolymer material (build material). Curing sources such as lasers, ultraviolet light, digital light, liquid crystal display, etc. are focused on particular areas of the liquid build material layer to cure it, and then the next layers are formed in a similar manner till the part is fabricated. In case of ceramic materials, the particles of ceramic materials are loaded into the photopolymer material. Some of the polymerization-based AM process are stereolithography (SL), lithography-based ceramic manufacturing, continuous liquid inter-phase printing (CLIP), continuous direct light processing (CDLP), and digital light processing (DLP). AM machines based on the above mentioned processes suitable for ceramic material are fast ceramic production (FCP) [46], CeraFab 7500 and the CeraFab 8500 systems based on LCM [47], Admaflex 130 3D ceramic printer based on DLP technology [48], MOVINGLight – ProMaker V series – industrial ceramic 3D printers based on DLP [49], and large area maskless photopolymerization (LAMP) [50].

Ceramic 3D printing can also be achieved by laminated object manufacturing process. Here, sheets of build materials are fused together by application of adhesive, heat, and pressure and cut into a desired shape with the help of a laser/blade/knife [51].

Patenting Scenario of Additive Manufacturing of Ceramics

Although AM has been around for about 30 years, it garnered public attention and gained momentum only in the recent past (i.e., 10–11 years) owing to factors such as increased availability of domestic printers and technological advancements witnessed in terms of software, equipment, materials, etc. [9, 52]. The patents (granted, published applications, utility models –published and granted) during the momentum period, i.e., past 11 years, addressed innovations or inventions primarily related to the following four fields (hereinafter referred to as focus fields): (1) ceramic materials for 3D printing, (2) applications of 3D-printed ceramics, (3) apparatus/equipment for 3D printing of ceramic materials, and (4) process for 3D printing of ceramics.

This chapter presents the progress made by AM especially for ceramic materials and the recent advancements that have taken place in the field from a patent viewpoint. One important factor that helps in assessing a particular technology is through patents, as patent literature contains rich technical and bibliographic information. Patinformatics generated through such information helps in understanding the growth and significance of a technology effectively [53, 54]. Resulting insights in turn help the organizations, companies, and academia to make key decisions. The overall growth trends of AM of ceramics during the past 11 years (about 950 published applications) have been discussed in this chapter. It may be noted

that the review of latest patents is based on the machine translation version for the non-English patents. The patent data source, graphs, and figures presented in this chapter are based on PatSeer Pro™.

Part A: Overview of Patenting Trends in AM of Ceramics

Patenting Trends: Year-Wise

The number of inventions (one patent per family) in 3D printing of ceramics during the initial years has been slow and gradual; however, a sudden and rapid growth in this field is evident from the patent filing trend observed during the years 2015–2017 as depicted in Fig. 2. This peak is a positive indication of the enhanced research interest in the field of 3D printing of ceramics. The publication trend as depicted in Fig. 3 also follows a similar trend as the patent filing trend in Fig. 2.

The number of patent applications during year 2018 is expected to be much higher than 80, as most of the applications filed during 2018 will be available in the public domain after the publication of patent applications which is usually 18 months from the date of filing.

The publication trend of the applications including publication of granted patents is depicted in Fig. 3. The number of patents published is highest in year 2017. A progressive trend of patent publications is observed during period 2015–2017. From application and publication trends, it is clear that AM of ceramics has seen remarkable growth during the second half of the period.

AM in itself has turned into a very vast subject of study with newer techniques, methodologies, materials, and equipment being developed around the world at a rapid pace. Patent classification codes are an interesting and logical way to find the subject matter of such developments. It may be noted that a single patent can be

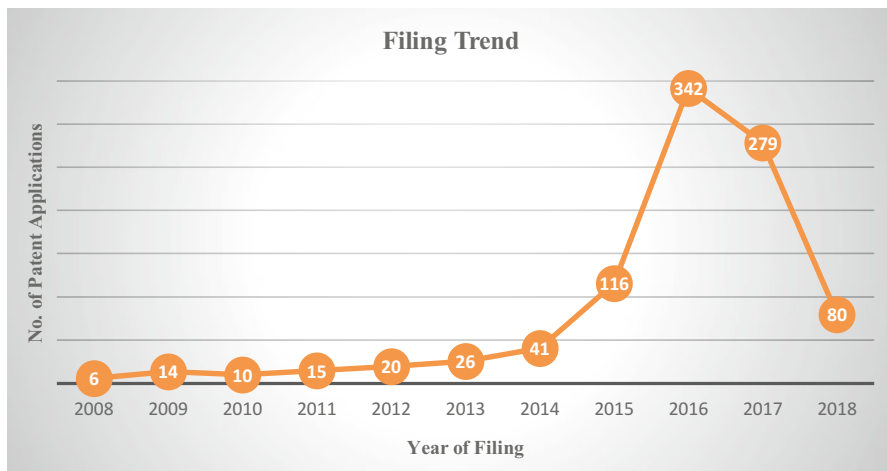


Fig. 2 Patent application filing trend



Fig. 3 Publication trend

Table 1 Top international patent classification codes

IPC codes	Definitions	No. of patent records
B 33Y	Additive manufacturing	515
C04B	Lime; magnesia; slag; cements; compositions thereof	343
B28B	Shaping clay or other ceramic compositions, slag, or mixtures containing cementitious material	231
B29C	Shaping or joining of plastics; shaping of substances in a plastic state, in general; aftertreatment of the shaped products	212
B22F	Working metallic powder; manufacture of articles from metallic powder; making metallic powder	151
A61L	Methods or apparatus for sterilizing materials or objects in general; disinfection, sterilization, or deodorization of air; chemical aspects of bandages, dressings, absorbent pads, or surgical articles; materials for bandages, dressings, absorbent pads, or surgical articles	91
C08K	Use of inorganic or non-macromolecular organic substances as compounding ingredients	52
C08L	Compositions of macromolecular compounds	49
A61C	Dentistry; apparatus or methods for oral or dental hygiene	44
C03B	Manufacture or shaping of glass or of mineral or slag wool; supplementary processes in the manufacture or shaping of glass or of mineral or slag wool	36

classified under more than one classification code. It can be seen from Table 1 that the highest number of patents is placed under the International Patent Classification (IPC) main class B33Y followed by C04B, B28B, B29C, B22F, A61L, C08K, C08L, A61C, and C03B.

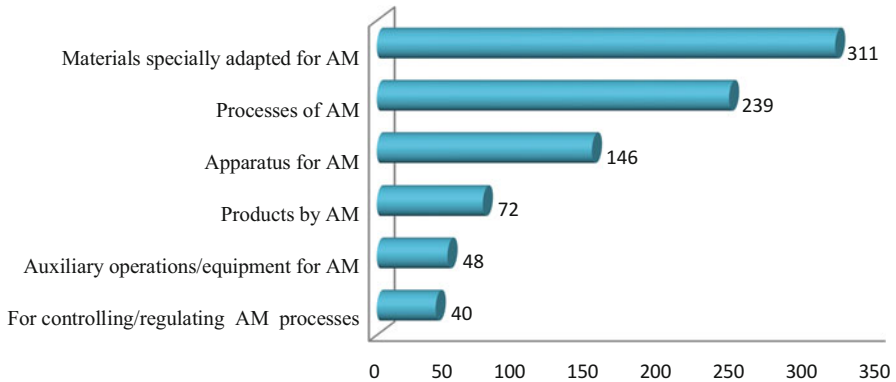


Fig. 4 Distribution of areas across IPC code B33Y

B33Y is a broader topic covering patents with a primary focus on AM. The top subclasses under this category include B33Y50/02 (for controlling/regulating AM processes), B33Y40/00 (auxiliary operations/equipment for AM), B33Y80/00 (products by AM), B33Y30/00 (apparatus for AM), B33Y10/00, and B33Y70/00 with 40, 48, 72, 146, 239, and 311 patent records, respectively.

From Fig. 4 it can be stated that under IPC B33Y, the material especially suited for AM is the most researched topic with 311 patent records. Research progress into AM based-process, apparatus, and products made specifically by AM is not too far behind.

IPC code C04B as shown in Table 1 is related to materials, and the leading topics of research under this main class are (a) forming and processing of powders for manufacturing ceramic components and (b) materials based on aluminum oxide, silicon carbide, zirconium oxides, hafnium oxides, silicon nitride, silica, etc. Classification codes B28B, B29C, and C03B comprise patents related to shaping of clay, ceramics, glass, etc. A61L and A61C are related to the healthcare sector (dentals, surgical, sterilizers, etc.), and it can be seen that AM ceramic-based process and products account to about at least 100 patent records. This shows that healthcare sector is one of the leading industries where AM of ceramics has gained momentum.

Patenting Trend: Country-/Organization-Wise

Distribution of patent records across top applicants is represented in Fig. 5. A patent applicant may be an individual or a firm. Universities from China seem to have contributed a great deal toward the growth of AM of ceramics as can be seen from applicant statistics. The University of Guangdong Technology has filed the largest number of patent applications with about 13% share followed by the Huazhong University of Science and Technology with 10%, Xi'an Jiaotong University with 9%, and University of Jinan and Central South University with 6% each. The Huazhong University of Science and Technology and Xi'an Jiaotong University were reported to be among the first universities in China to have conducted focused research and development activities in additive manufacturing [55].

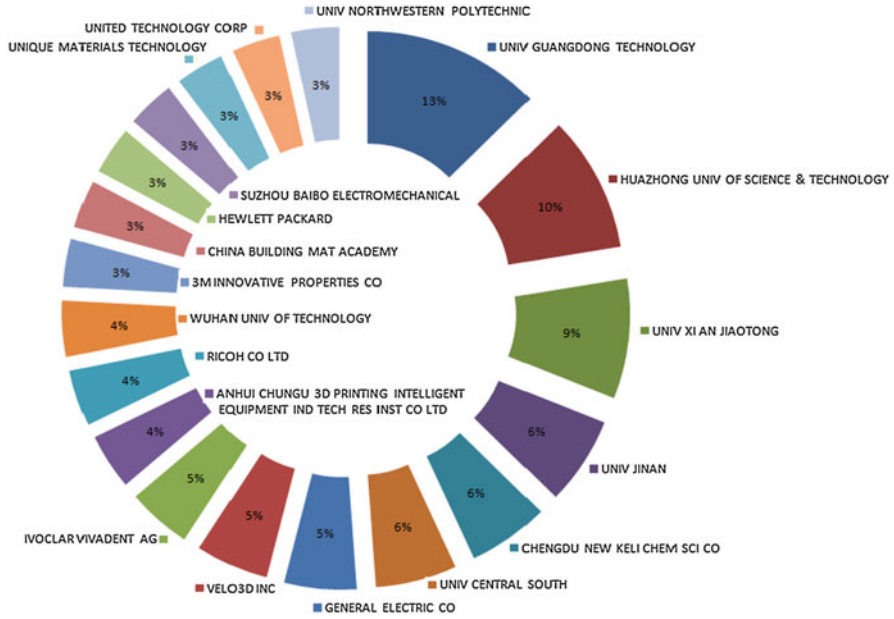


Fig. 5 Top applicants in the field of 3D printing of ceramics

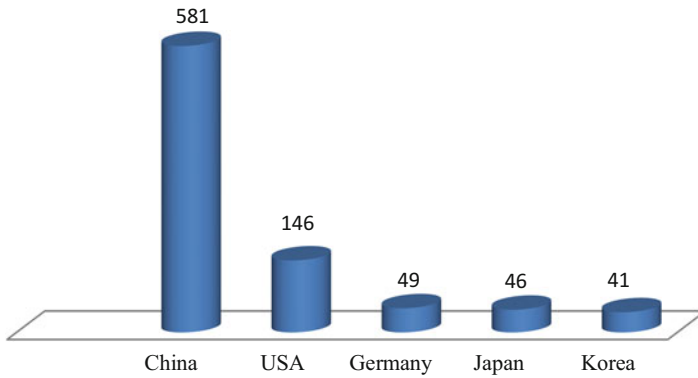


Fig. 6 Applicant country

The applicant country (Fig. 6) indicates the country from where the applicant belongs. The applicant country as an analytical indicator can be used to assess the innovative potential of a country. The assignee or applicant country statistics as seen in Fig. 6 shows a very strong presence of China-based innovations in the AM of ceramics. This trend may also be indicative of the demand and market for 3D

manufacturing equipment and products in China. Potential technology planning or road mapping, broader technology ecosystem, and skilled manpower also go a long way in choosing a country for protection of an invention. It has been reported in literature that China targets to reach 3 billion US\$ market size in AM by year 2020 [56, 57]. The extensive patenting activity as seen above can be considered as steps taken by China toward achieving that objective.

Country of priority indicates the preference the patent applicant gives to a particular country for protecting their invention and in most cases is the country of the applicant. Distribution of these patents based on the region of priority showed that 71% of the patents had their priority in Asia with China being the major contributor; 16% from Americas (i.e., North and South American continents), the USA being the major contributor; and 13% from Europe, Germany being one of the significant contributors followed by France. Distribution of patents across the region is depicted in Fig. 7a. The distribution of patents based on the country of priority is depicted in Fig. 7b, and it can be seen that 566 patents filed have China as country of priority followed by the USA with 146, Japan with 42, South Korea with 41, Germany with 37, and Taiwan with 23 patents, respectively. It may be noted that in Fig. 7b, 46 patent applications have their priority in Europe which represents the patent applications filed with the European Patent Office.

From the bibliographic patent distribution, an important aspect that can be noticed is the dominant role played by China in the field of AM of ceramics. Consistent efforts made by China to record a positive growth trend toward becoming a global leader are evident. This positive trend could be the result of various initiatives taken by the Government of China in promoting generative manufacturing by involving various entities such as educational institutions, firms, and organizations [58]. The active participation and contribution by such entities are evident from Fig. 5.

Some of the initiatives taken by the Government of China to encourage research activity in the area of AM technologies for different applications are “Made in China 2025,” “National 3D Printing Industry Development Promotion Plan (2015–2016),” etc. [59, 60]. The two major verticals that China is focused on promoting three-dimensional printing are aerospace and biomedical applications [55, 59–61]. All these above-discussed factors on patent distribution derived from patent statistics as

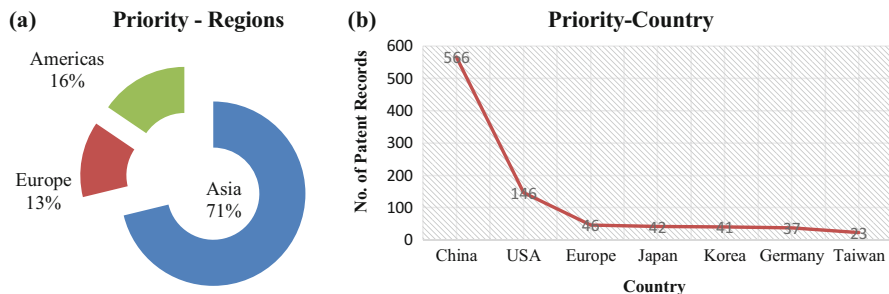


Fig. 7 (a) Priority distribution region-wise and (b) top priority countries for patent applications

well as from literature indicate the rapid and deep penetration of China in the field of additive manufacturing.

Patenting Trend: Focus Field-Wise

There has been a keen interest by researchers worldwide both from academia and industry toward adopting AM as an advanced manufacturing technique to find suitable solutions through development of novel, unique, advanced ceramic materials, processing routes and apparatus that cater to diverse requirements. As indicated in the introduction of this chapter, bibliographic data present in patent documents is a very important aspect of patinformatics that help commercial players in drawing business intelligence for developing business strategies, key decision-making, and road mapping. However, theme-based approach for understanding technical disclosure present in the patent document plays a very crucial role in drawing useful insight about a technology domain, and it complements the business intelligence developed through bibliographic patinformatics. Therefore, the patent distribution across four themes called focus fields is presented in Fig. 8.

Out of the patent records published during the AM's momentum period, 421 of the records focused on development of various types of printing material compositions and their preparation, 345 records dealt with development of various processes and methodologies of AM of ceramics, and 189 records were on application development using AM of ceramics. These applications include products and components used by healthcare sector, dentistry, engineering, decorative, aesthetic purposes, etc. One hundred fifty-five records focused on inventions and/or innovations pertaining to equipment used for 3D printing to achieve various objectives including enhancing the ease of operation, simpler process, product quality, functionality, less wastage of materials, etc. About one-third of these records focused on the development of auxiliary or supporting devices, structures, materials, etc. for 3D printing.

Information on the common patents or shared records among the focus fields can be known through the landscape network map of the focus fields. For this

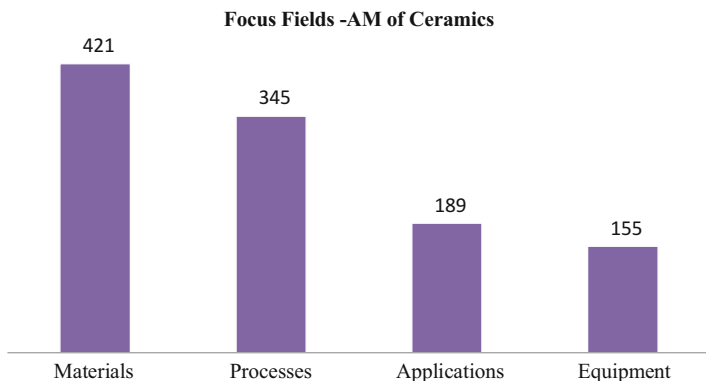


Fig. 8 Distribution of patents according to themes (focus fields)

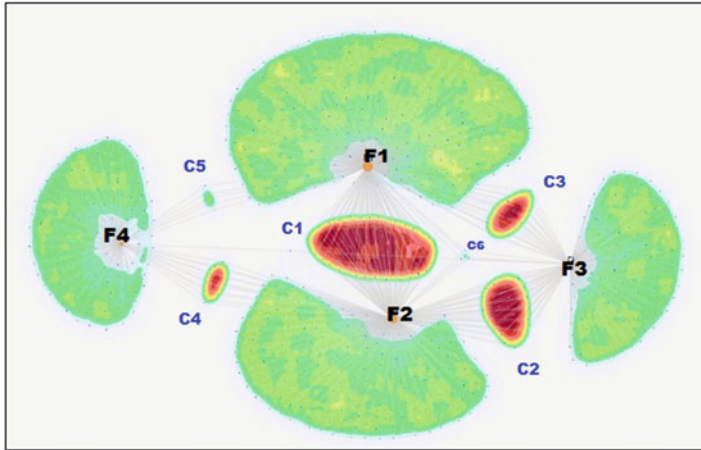


Fig. 9 A landscape representation of focus fields

purpose, a landscape representation of the patents across the major four focus fields is presented in Fig. 9.

Islands F1, F2, F3, and F4 represent the focus fields – *ceramic materials for 3D printing*, *process for 3D printing of ceramics*, *applications of 3D-printed ceramics*, and *apparatus/equipment for 3D printing of ceramic materials*, respectively. Clusters C1, C2, C3, C4, C5, and C6 represent the common patents between various focus fields. The larger cluster C1 has patent records shared between F1 and F2 indicating that most number of common patents are related to the process for developing 3D material compositions. C2 represents the share of patent records between F2 and F3, C3 represents the sharing of patent records between F1 and F3, and the smallest cluster C6 represents the common patent records between F1, F2, and F3. C4 is the cluster of patents shared between F4 and F2 and C5 is the cluster shared between F1 and F4.

Part B: Overview of Focus Fields

F1: Ceramic Materials for 3D Printing

Nearly 45% of patents on 3D printing of ceramic focused on the development of specific ceramic-based materials and compositions of build materials for enhancing the product strength, quality, performance, finish, etc. The patent records under this particular focus field can be broadly classified under oxide ceramics, non-oxide ceramics, glass materials, and ceramic composites. Constant innovations were being made in composition of build materials for different AM processes/techniques for achieving the desired properties and improving quality in the end product. Research into ceramic-based composite materials were on the rise due to their suitability for high-performance applications owing to their excellent mechanical properties. Table 2 represents the different types of materials on which research was conducted to enhance their suitability in 3D printing.

Table 2 Ceramic materials in 3D printing

Material	Type	Advantages	
Traditional ceramics	Clay, phyllosilicates, kaolin, montmorillonite, porcelain	Environment-friendly Plasticity Smooth discharge of the material Good dimensional precision Low cost Low molding temperature Simple formulation	
Advanced ceramics	Oxides		
	Copper oxide, aluminum oxide, zirconium oxide, silicon oxide/silica, hafnium dioxide, yttrium oxide, cerium oxide, magnesium oxide, calcium oxide, lanthanum oxide, aluminosilicate, germanium dioxide, sodium silicate, titanium oxide	Oxidation resistance Cost-effective High heat conductive Improved casting quality Good uniformity of printing particles Good translucency Corrosion resistance High mechanical load bearing Good porosity	
	Non-oxides		
	Carbides	Calcium carbonate, sodium carbonate, silicon carbide, tantalum carbide, tungsten carbide, silicon carbide, chromium carbide, niobium carbide, vanadium carbide, chromium carbide, zirconium carbide, hafnium carbide	Improved strength Heat stability Good compactness Maintained density Corrosion resistance
	Nitrides	Silicon nitride, aluminum nitride, boron nitride	High-temperature resistance Environment-friendly
Borides	Titanium diboride, zirconium diboride, hafnium diboride	Improved toughness	
Sulfate	Gypsum (CaSO ₄ .2H ₂ O), barium sulfate, calcium sulfate	Environment-friendly	

(continued)

Table 2 (continued)

Material	Type	Advantages
		Crack resistance Excellent surface glossiness Biocompatible Nontoxic
Cement	Quartz sand-fly ash and other additives, slag-based geopolymer cement, rock-based geopolymer cement, and fly ash-based geopolymer cement	High tensility Improved toughness High ductility High strength
Composites	<p>Polymer-ceramic based: <i>Polymeric materials</i> –polyoxymethylene (POM), polyolefins, polypropylene or polyethylene, polyurethanes (PU), polyamides (PA), polyethers (PETH), polycarbonates (PC), polyesters (PES) <i>Ceramic</i> – Silicon oxide, calcium oxide, aluminum oxide, zinc carbide, magnesium carbonate, aluminum silicate, calcium silicate, magnesium silicate, magnesium carbonate or sodium carbonate, barium sulfate, mica, zeolite, montmorillonite, kaolinite</p> <p>Inorganic-ceramic based: Combination of clay powder, oxide powder, nitride powder, or carbide powder</p> <p>Metal-ceramic based: Ni-Al₂O₃, Fe-Al₂O₃, niobium-nitride</p> <p>Biomaterial-ceramic/bioceramic based: Hydroxyapatite-metal oxide/hydroxyapatite (tricalcium phosphate)</p> <p>Oxide and non-oxide ceramic based: (<i>zirconia, alumina, silica</i>) – (silicon nitrides, boron nitride, carbon, porcelain)</p> <p>Glass-ceramic based: (boron glass powder-zinc oxide, lithium oxide)</p> <p>Carbon-ceramic based: (silicon oxide-carbon)</p>	Improved strength Cost-effective Good biocompatibility (bioceramics) Good stability Low shrinkage material Improved fluidity High molding precision Improved physical properties Environment-friendly Uniformity/homogeneous morphology Good bonding strength Good adhesion To produce dense objects High heat stability Thermal shock resistance Good air permeability High rigidity Improved heat conduction High insulation properties Low material shrinkage Less expansion Biocompatibility

(continued)

Table 2 (continued)

Material	Type	Advantages
		High melting point
Glass	Lithium silicate glass, fused silica, synthetic silica, alumina silicate, amorphous silica, glass ceramic, soda glass, lithium borosilicate glass, barium glass, strontium glass, zinc glass	Good optical appearance Improved mechanical properties Increased tensile strength Cost effective High processing efficiency Wear resistance

A Brief on Latest Patents in Focus Field 1

Over the years, 3D printing technology was adapted not just to traditional ceramics but also to advanced ceramics and composite materials. The summary of latest developments (i.e., patents filed during 2018) from a patent perspective is presented below.

During the past year too, inventions related to development of various ceramic compositions related to specific printing techniques or particular applications such as bioceramics, etc. were observed. Traditional ceramic material preparation for 3D printing involving preparation of ceramic slurry containing porcelain clay and lithium-based powder for 3D printing of ceramic parts having high plasticity and reduced cracks was reported [62]. Purple sand mud material comprising plastic clay, silicon oxide, iron oxide, titania, alumina, calcium oxide, etc. in different proportions for improved dimensional accuracy due to reduction in defects due to shrinkage, deformation, and cracking [63] and preparation of clay material for 3D printing of objects of different shapes by a cost-effective production process having advantages of smooth discharge, liquidity, and homogeneity [64] were also observed.

Development of oxide-based ceramic printing materials for enhancing the performance was reported by many researchers during the past year. Zhang Yue et al. invented alumina and water-based ceramic slurry material that can (a) overcome the disadvantages of excess fluidity with sufficient solid content, (b) facilitate smooth extrusion, and (c) produce crack proof parts [65]. Wang et al. disclosed the ceramic printing material which is mainly composed of alumina and photosensitive resin that helps in avoiding deformation due to shrinkage of printing material [66].

Composite material made up of oxide or non-oxide materials for improved structural properties, print quality, and reduction in air holes was developed. Zeng Tao et al. disclosed preparation of SiCw/SiC/SiC ceramic matrix composite material that could lead to enhanced compactness and toughness by overcoming the problems of porosity and brittleness in printed part [67]. Duan Tao invented a ceramic composite composition for 3D printing comprising silicon carbide-tantalum carbide

and polymer. The composition imparts enhanced mechanical properties and high wear resistance to the printed object. Zhang Dongyun et al. prepared composite material consisting of aluminum alloy matrix powder and silicon carbide particles. The material has uniform distribution with improved strength of the build part [68]. Qin Hai Jun disclosed a ceramic composite material including oxides such as aluminum oxide, zirconium oxide, zinc oxide with polypropylene, and other additives for AM in order to achieve even grain dispersion and good print quality [69]. Wu Shang Hua et al. prepared a silicon nitride-based ceramic composite printing material containing ingredients such as photosensitive resin and dispersing agents to obtain good-quality printed objects with reduced air holes [70].

Composite materials are also well-known for their functional properties such as high temperature and oxidation resistance, good mechanical properties, and high stability. MA Qingsong et al. formulated a 3D printing material which is made up of silicon carbide-reinforced alumina-zirconia composite material with high functional properties [71]. Shen Chunxia et al. invented alumina, molybdenum disulfide, and eutectic powder (mixture of calcium fluoride and lanthanum fluoride) ceramic composite material that provided high-temperature workability [72]. Guo Weiming et al. proposed titanium diboride-based ceramic material which is prepared using titanium and boron carbide that are ball milled in tungsten carbide medium. The ball milling results in boron carbide coated with titanium that can be printed by selective laser melting in an inert atmosphere to obtain the desired complex-shaped ceramic parts with improved toughness that find application in aerospace sector [73].

Some of the ceramic printing materials were developed to suit particular printing techniques so as to achieve better products in terms of improved surface finish, mechanical properties, etc. Reese Riley et al. invented a composite material suitable for fused filament fabrication wherein the material is made up of a nano-filler, a polymer mixture, and one or more fibers such as a glass fiber [74]. Duan Tao describes the preparation method of ceramic composite material that includes silicon carbide-tantalum carbide, polycarbonate resin, copolymer, carbon fiber, wax, anti-oxidant, and rare-earth-doped strontium aluminate fluorescent powder. This composition is suitable for printing objects through 3D stereo deposition [75]. Ali Emamjomeh et al. prepared a composite build material that includes polymeric material, reinforcing materials such mica, talc, or glass. This composite material is suitable for 3D printing using piezo printing systems or thermal inkjet printing systems, MJF, thermal inkjet (TIJ) printing, and drop-on-demand digital patterning [76]. Alumina- and silicon carbide-based ceramic printing slurry suitable for use in direct ink writing or stereolithography was developed by Wang Xiaofeng et al. [77]. Cheng Laifei et al. developed a SiC ceramic whisker composite suitable for printing complex shapes by stereolithography process [78]. Huang Mingyang et al. disclosed gypsum-based composite material suitable for extrusion-based 3D printing process which is environment-friendly and exhibits excellent extrusion performance, mechanical properties, water impermeability, and crack resistance [79].

Ceramic-metal composites were also researched in the recent past. Cao Sainan et al. disclosed a nanoceramic-based composite material wherein TiC, TiB, and Al₂O₃ were added to metal-based matrix in a definite proportion to achieve good

mechanical bonding, compact structure, high density, and enhanced mechanical properties [80]. Metal-glass-based composites were particularly used to achieve better toughness in the build part. Hofmann Douglas C demonstrated the preparation and printing of metallic glass composite materials showing improved properties in terms of strength and toughness by incorporation of iron-based metallic composition [81]. Demuth Benjamin A et al. introduced a bulk metallic glass composite material for AM. The bulk metallic glass composition includes Zr-Cu-Al and additional metallic composition of Ti or Zr alloyed with one or more elements from V, Nb, Ta, Mo, or Fe. The parts formed exhibit improved mechanical performance [82]. Zhu Mo developed composite material for colored 3D printing. The composite printing material includes ceramic filler like metal carbonates/silicates, polymer, water-absorbing polymer resin, toughener, and coupling agent. The printing material has low melting point and high density and can print multicolored components [83]. Hofmann Douglas C disclosed a method for preparing metallic glass matrix to improve strength and toughness and to inhibit crack propagation [84].

Bioceramic-based printing material also garnered extensive attention in recent times due to compatibility, toughness, and long life provided to the 3D-printed parts. Zhang Xunren et al. disclosed bioceramic material made of oxide ceramics and glass to produce artificial bone and bone joints [85]. Materials imparting antibacterial property were developed by Zhou Wuyi et al. wherein the composite material (silicon rubber, zirconia, zinc oxide, and additive such as hydroxyl apatite) was suitable for forming dental pulp cavity. This material also contains a high molecular polymer, blocking agent, antibacterial agent, diffusion oil, modifier, and other additives [86]. Another 3D printing material with low shrinkage and antibacterial property was reported by Yang Fanwen et al. This composite was based on zinc oxide and silicon carbide [87]. Yan Chunze et al. disclosed a method of preparing composite material composed of polyetheretherketone/nano-hydroxyapatite suitable for implants [88].

Other inventions reported during this period were on the development of SiCO-based photosensitive ceramic material for forming 3D-printed parts of high precision and performance [89]; ceramic matrix print material coated with an organic adhesive and low melting point metals for anti-cracking [90]; ceramic-based support material comprising calcium carbonate, sodium carbonate, sodium aluminate, and their combination with a polymeric matrix [91]; and composition for an inkjet dopant with thermoplastic polymer and ceramic particles [92].

Focus Field F2: Process/Methods for Ceramic 3DP

Apart from development of equipment, components, and materials for 3D printing, a very crucial aspect is the process and methodology employed in 3D printers in order to achieve the desired results. Both of these are important aspects that determine the characteristics of the final printed object. Patents dealing with process and methodology can be broadly classified into *equipment-based* and *application-based* records. One hundred seventy-six records were found to be equipment based and 169 on application based. Industry segments to which they cater are shown in Fig. 10, and it was found that 242 records dealt with manufacturing of various components that included not only engineering components but also other industrial components (that

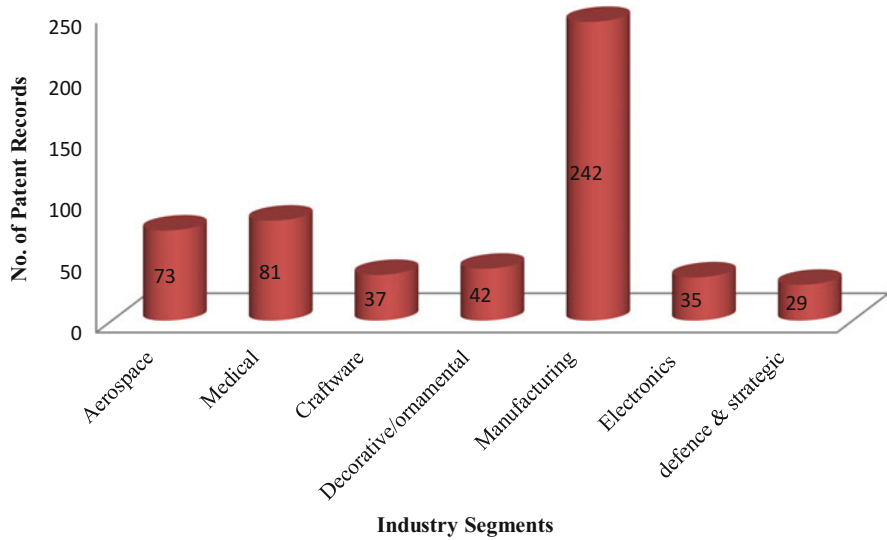


Fig. 10 Process and methods developed to cater to various industries

did not have a specific mention in the patent document). The next leading industrial segment in this focus field is the medical industry with 81 records closely followed by the aerospace industry (73 records). Novel processes in decorative purposes and architectural purposes are not far behind with 42 and 37 records, respectively. It is interesting to note that 3D printing technology has made inroads into the electronics and defense sectors as well.

A Brief on Latest Patents in Focus Field 2

Various methods and processes of three-dimensional printing developed during the past year (2018) are presented in this section. Extrusion-based printing method is popularly used to form complex-shaped parts having good mechanical advantages. Demuth Benjamin A et al. developed a filament extrusion-based method where a ceramic printing material and a polymeric support material are extruded through an extruder that is subjected to elevated temperatures to strengthen the build structure. The support structure and binder material are later removed by using suitable solvents and other means, respectively. The support structure provides necessary firmness required to form a better finished 3D ceramic object having improved stability [82]. The process of preparing gypsum-based composite material and printing by extrusion-based 3D printing technology has been reported. These printed structures exhibit enhanced mechanical property and crack resistance and are leak-proof [79]. Another invention based on extrusion-based 3D printing process using ceramic slurry was reported to be cost-effective production process having easy control over printing parameters and capability to produce complicated structures [65]. Su Jianqiang developed a process to fabricate metal-ceramic objects by FDM which provided better finished products and is cost-effective [93], and Hikmet Rifat

invented a process for fabrication of 3D objects by FDM process that involved printing build (matrix) material and fiber materials through nozzles in controlled fashion. This process enables production of large-sized complex-shaped objects for aesthetic and functional applications [94]. Benzur Ofer et al. disclosed a method of developing 3D object by combining AM process such as FDM and a molding process to form a ceramic or metallic product [95]. Mark Gregory Thomas disclosed a process of printing ceramic/metal body by extrusion-based 3D printing technology to form dense ceramic structures [96]. Wang Xiaofeng et al. introduced a process of fabricating porous structures by direct ink writing method. This process enables control of morphology such as pore diameter, pore volume, and porosity of the material being printed [97].

Powder bed fusion is another important technique in 3D printing. Ali Emamjomeh et al. disclosed a powder bed printing process to build a part with composite material having enhanced physical properties, and this process enables printing of non-spherical materials [76]. Gao Xuesong et al. proposed the method of forming ceramic coating on substrate using SLS and magnetron sputtering to develop high strength and wear resistance to the substrate [98]. The process for printing flexible 3D ceramic objects by SLS was disclosed where the protruding phenomenon of printing objects from printing bed could be eliminated [99]. A number of patents using selective sintering or melting process for silicon carbide and silicon nitride material have been reported. Tang Kaiyuan et al. disclosed a process for printing of SiC material by selective laser sintering to develop a combustion chamber. The process is able to produce high-density ceramic objects [100]. SLS process for development of SiC-based 3D object having high strength and wear resistance was reported by Zhang Zhihui et al. [101]. Wu Shanghua et al. disclosed the process of preparing silicon nitride-based ceramic material by SLS to form dense 3D objects. The method includes dispersion of printing material and solidification by photosensitive resin followed by degreasing of ceramic green-printed object [102]. Guo Weiming et al. introduced a SLM-based printing process to fabricate titanium diboride-based multiphase ceramic 3D-printed parts. The process enables production of toughened objects [73]. Highly dense 3D components made of composite material were produced using SLM process [68]. Developments in SLS and SLM processes for forming defect-free objects have been observed during this period [90, 103]. Use of image sensors that enable to monitor the printing process so as to make the component defect-free has been reported by Jurg Marten et al. [103]. Rudisill Stephen G et al. invented a process of 3D printing which employs MJF. The printing material is dispersed on a build platform, wherein the fusing material is deposited over printing material selectively and is exposed to electromagnetic radiation that causes the fusion of build material and fusing material. The process is repeated to form complete 3D structure. This process allows the use of multiple fusing agents, at different deposition points as per the required strength of the 3D structure that is being formed [104]. One or more printing processes were combined to develop better and desired products. Stasiak James William described a method of forming 3D objects by combination of powder bed

fusion-type printing and inkjet printing processes to achieve high-density objects [92].

Photopolymerization-based process of 3D printing of composite material has been reported by Lin Pierre et al. which provides controlled photopolymerization by controlling the photoinhibition using light of a particular wavelength that inhibits curing of photoactive resin [105]. Guo Qiuquan et al. also reported the preparation of a nanocomposite and its printing by ultralow-temperature 3D printing. The method of printing is based on photo curing. The printed object exhibits good mechanical strength [106]. Certain printing processes that provide plurality of properties or functionality in a printed object were disclosed, for example, manufacturing of 3D object having varying degrees of strength within the printed object. The method involves certain steps by which different portions of the printed object are exposed to irradiation for different time periods to provide varying degrees of strength to the printed object [107]. The process for development of high-performance 3D printing SiC-based components by stereolithography was disclosed by Cheng Laifei et al. These SiC-based 3D parts are suitable for high-performance application in aerospace sector, and the process provides for high precision and efficiency [78].

Application-based process, i.e., methods or process of 3D printing suited for development of components used in certain application, was also seen. A process of selective laser sintering which enables the reuse of the build materials for fabrication of dental parts [108] and a cost-effective double-extrusion-based 3D printing method process to print bioceramic for medical applications were introduced [109]. It was observed that AM was also used for fabrication of civil structures. Ma Guowei et al. proposed an extrusion-based 3D printing process wherein the printed concrete structure is cured by water or high-temperature steam-based process to obtain a highly toughened structure. This process is automated and is cost-effective [110]. Ye Niancui disclosed a simple and highly efficient process and moving mechanism for 3D printing of clay materials [111]. Zhu Fei et al. developed a process to manufacture ceramic honeycomb carrier for automobiles by selective laser sintering. The process consists of 3D modeling of honeycomb carrier, printing of ceramic, drying, and immersing in high-temperature binder which is later removed from the printed object. The method provides for an object with improved mechanical strength [112].

Progress was also made in the field of electronics – Yang Gongshou et al. disclosed an extrusion-based printing method to build components for the power and electronic industry that requires high efficiency and heat dissipation. The method involves printing of multilayers of ceramic material of predefined thickness on a copper substrate. Later circuit layers made up of metal or metal alloys are again printed onto these ceramic multilayers, which are then printed with thin layers of ceramic material [113]. Li Kefeng et al. developed a laser sintering-based AM process for fabricating protective cover plate for application in electronics. This process is reported to decrease sintering, thereby reducing the printing processing time [114]. Another simple and time-saving printing process for printing of ceramic-metal-printed components with dissolvable support structures has also been reported [115].

Focus Field F3: Applications of 3D Printing of Ceramics

As discussed in the previous sections of this chapter, 3D printing technology due to its unique advantages such as ease of forming complex-shaped ceramic parts and components, advanced printing techniques, cost-effectiveness, rapid production, reduction in material wastage, etc. is progressing at a rapid pace toward replacing traditional manufacturing technologies. Some of the industries where 3D printing has gained tremendous momentum in the recent times are the medical industry (bioactive ceramic scaffolds/stents, artificial joints, bone grafting, tissue engineering), dental restoration (implants, artificial tooth, crowns), engineering manufacturing industry especially with respect to mechanical and metallurgical fields, aerospace industry, etc. In this focus field, the focus was on the patent records that specifically dealt with the development of specific application (component/product, etc.) using ceramic materials employing 3D printing technology. Out of the 189 patents in this category, it was interesting to note that about 63% of the records belonged to the medical field (118 patents), 15% catered to the manufacture of engineering components from mechanical and metallurgical fields (29 patents), and about 7% belonged to the field of aesthetics and architecture (13 patents). Figure 11 clearly depicts the distribution of patent records across this focus field, and it is very evident that 3D

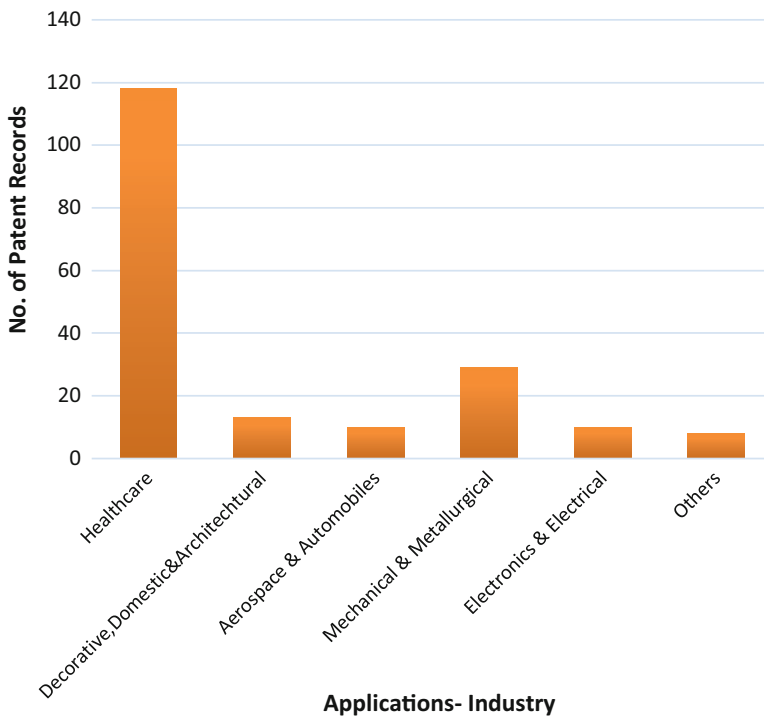
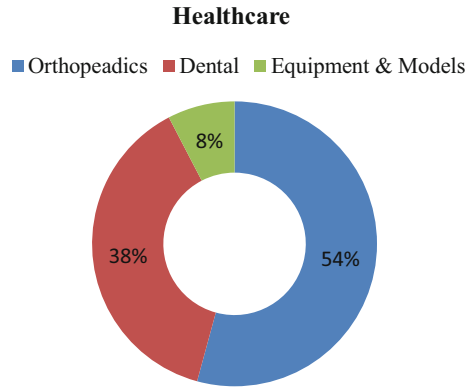


Fig. 11 Component development for specific applications

Fig. 12 Distribution of patents across the healthcare segment



printing using ceramic materials has made remarkable inroads into the healthcare industry.

Sixty-three percent of medical-related patent records were on orthopedic, dental, and medical equipment and model-based applications. The distribution across these patents across the healthcare segments is depicted in Fig. 12, and it is clear that the orthopedic sector has been very receptive to adopting 3D printing of ceramics as more than half of the research and development in the medical field using additive manufacture has been toward development of orthopedic applications. The primary focus was on tissue engineering involving bone restoration, regeneration, and repair through scaffolds, stent implants, bionic cartilage and bones, etc. Intervertebral fusion cages, vertebral scaffold implants for spine treatment and artificial eye tibia, etc. are other important developments where additive manufacture has come in handy. Application of 3D printing of ceramics in dentistry is ranked second with 38% of contribution. Orthodontic applications for dental restoration purpose – dental implants, artificial tooth, dentures, and dental crowns – are being some of areas of development. Bioceramics such as zirconia, calcium phosphate, and titania happen to be one of the most popular materials used for dental restoration by additive manufacturing.

3D-printed human anatomy (skeletons) and models for ear surgery and dental treatment are being used for medical training and other purposes. Instruments used in dentistry have also been developed by AM approach. Such developments account for about 8% of the inventions in this field.

A Brief on Latest Patents in Focus Field 3

The versatility of 3D printing to cater a gamut of applications ranging from domestic to advanced applications has made penetration of this technology possible in all industries. The review of patents filed during the past year (2018) referring to the applications of 3D printing using ceramics reveals that the research and development activities were largely concentrated on medical applications especially in dental and orthopedic fields.

MA Jianfeng et al. disclosed preparation of zirconia-based dental implants [108], and Yoo Hag Dong developed an artificial tooth using ceramic material resulting in increased productivity and reduction in cost [116]. 3D printing is now a promising technology in the orthopedic area. A cost-effective intervertebral fusion cage made up of ceramic composite material having good biocompatibility and mechanical properties [109, 117], an artificial vertebral body implant having high accuracy and long-term stability [118], bioceramic-based scaffolds with good surface density, and improved mechanical properties for application in tissue engineering are a few developments that were made using AM last year [119]. Zhang Xunren et al. reported artificial bone manufacturing using oxide-based composite materials by 3D printing. The printed artificial bone exhibited improved toughness [85]. Mommaerts Maurice Yves disclosed preparation of bone prosthesis preserving the functionality of the original bone [120]. Zhihua et al. disclosed the printing of bone tissue bracket made up of hydroxyapatite having good biocompatibility, improved strength, and uniformity of printing material composition [121]. The 3D-printed ceramic models are also used as the teaching aids for effective learning; Wang Kai et al. proposed a cost-effective ceramic alumina bone model preparation. The obtained bone model can be used as a teaching aid [122].

Focus Field 4: Apparatus/Equipment for 3DP of Ceramics

Innovations in equipment also are a very important factor that contributes to the progress in three-dimensional manufacturing. In the past few years, researchers have devised various ways to improve the equipment functionality, size, features, productivity, quality of the product, etc. One hundred fifty-five records under this focus field primarily deal with the inventions related to equipment including auxiliary devices such as supporting structures and mechanisms, etc. that are associated with 3D printing of ceramics. While some inventions addressed improving the efficiency of spraying, improving the rate of curing, etc., some others directed their research toward printing colored ceramics, extrusion restricting mechanisms, and extruding/printing specific type of ceramic materials such as clay, plasters, etc.

Advanced version of 3D printers are being developed for improving the efficiency of the printers; widening the scope of materials that can be used as build materials, thereby enhancing the gamut of applications, reducing robustness, and making printer structures more user-friendly; and improving precision, thereby having defect-free products, enhancing mechanical stability, reducing wastage of material, etc. Development of support mechanisms contribute to about one-third of the records under this category. The support devices invented for 3D printing include improved working platforms, product display platforms, powder discharging units, nozzles, special frames for printing articles of medical relevance, printer heads, stirring and grinding devices, waste recyclers, etc. Some of the recent innovations in 3D printers for ceramics are represented in Fig. 13.

A Brief on Latest Patents in Focus Field 4

Various developments were made in recent times in order to bring advancements and improvements in traditionally existing 3D printing equipment. The innovations in

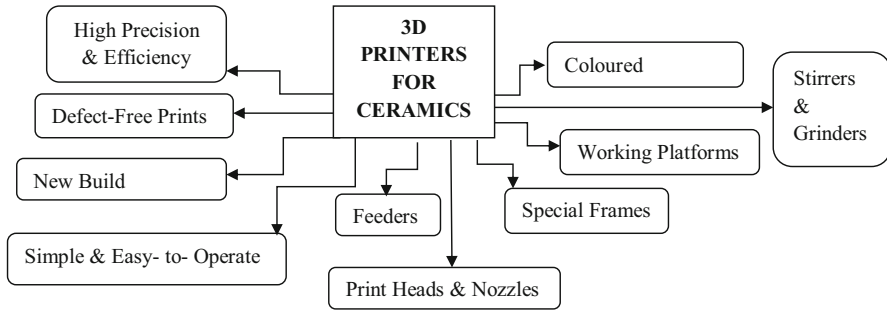


Fig. 13 Recent innovations in 3D printers for ceramics

the last 1 year (2018) were toward providing ease of operation and better product, minimizing printing errors, and enhancing efficiency and development of additional accessories to improve printing equipment.

Sterna Erik et al. designed an extrusion element which can move in relation to print bed to build article. The exerted force on print bed by extrusion element is detected by a sensor that is passed to the control system which then records the position of either print bed or extrusion element that helps to print the pre-designed CAD model of an article. The invention enhances the control over the printing process and helps in detecting the errors in extrusion by monitoring the extrusion element movement with respect to force sensed by sensors [123].

Chen Yan et al. invented a device to form ceramic components used for piezoelectric applications. The device contains energy converter and transducer arrays, printing device, movable platform, laser source, lens, and automated control system. The device is efficient and can produce high-density ceramic components [124]. Hikmet et al. described an extruder which enables the printer to extrude the required quantity and dimensions of the filament material. The printer is applicable for printing ceramic objects [125].

Additional accessories integrated to the printing equipment play an important role in printing processes; Wang Yuqin developed an adjusting means to manipulate the position of printing platform for fused deposition modeling. The equipment provides high-precision printing and reduction in cost [126]. Wang Hui et al. proposed a printing aid assembly having an arm for printing, a nozzle that is equipped to a feeding device and system for adjusting such as lifting, and a moving printing arm. The proposed machine provides ease of operation and has a simple structure [127]. Li Junmei et al. provided an equipment design for clay 3D printing equipment which administers convenient, controlled, and uniform feeding of printing material [128]. Luo Xiaolong et al. designed a 3D workbench/printer table model for 3D printer which can be moved in specific directions. The model overcomes the disadvantage of discontinuous printing and helps in improving the printing efficiency [129]. Zhou Liquan developed a 3D printing external frame for printing complex parts. This external printing frame

constitutes left, right, lower, and upper frame plates. The printing frame has a stable structure and is convenient to print complex parts [130]. Shim Patrick Yongshig invented a movable flexible substrate to move in upward direction so as to enable the flow of photo-curable resin between the substrate and inner bottom surface of the resin-containing container. The process and mechanism improve the speed of the printing process [131].

The feeders are the material input system which also affects the printing process and print quality. Chen Jingsong et al. disclosed a feeder which is an assembly of printing material storage tank, air cylinder, and piston, conveying system and control valves. The printer has a simple structure, enables high-precision printing, and is easy to operate [132]. Zhao Zhanyong et al. developed a feeding device that has an extrusion mechanism, has a cooling mechanism which increases the rate of cooling, and prevents the printing equipment from the damages caused due to high-temperature buildup [133].

Singov Sergey developed a 3D printer that includes a frame, a printing material storage tank, dispensers for printing material and support material powders, actuating assembly, and control assembly. The printing material and support material powders are dispensed in the pattern as designed in 3D model, and the binder binds the dispensed powders. The printer is inexpensive, requires low maintenance, and is less complex [134].

Ma Xiangnuan invented a multi-tasking screw extrusion-type 3D printer that is equipped with a screw-based motor, a hopper and barrel which are connected to each other, and an adapter. The printer also includes a die which is connected to an adapter. The printer is capable of printing melted material by extrusion-based process [135–137]. Franke, Carsten et al. disclosed a method and apparatus of printing adhesives on substrate by photopolymerization process. The equipment contains an actinic radiation transparent component through which the radiation passes and solidifies the adhesive layer on the desired material. The equipment is able to deliver defined amount of adhesive that solidifies with radiation [138].

A 3D printing head having a plasma cleaning mechanism for removal of pollutants during the printing process by surface treatment so as to achieve the printed matter with improved strength was developed [139]. Lin Xiaoli developed a nozzle device for 3D printer; the device consists of a frame with a platform that is provided with printing plate which is connected to a lifting means. The developed method and device are able to print parts rapidly and more accurately [140].

Printing machines were specifically designed to provide aesthetic features to the product by enabling development of the desired pattern on the built products. Cho Teruji et al. invented a 3D gravure printing machine to print 3D colored patterns on flat surfaces such as glass. The machine comprises a cylindrical blanket roll, a moving system, and an ink transfer system which contains ink transfer squeezing means. The printing could be performed in a single cycle with improved printing speed and efficiency [141].

Part C: AM of Ceramics and Composites for Strategic and Aerospace Applications

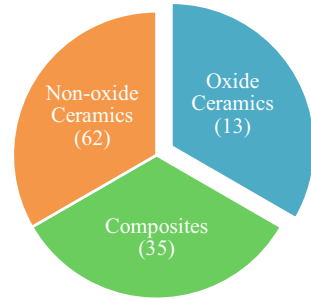
Due to high penetration of the technology in all fields of science and engineering, there has been a great demand for advanced manufacturing technologies in various industrial sectors. AM is one of the most suitable methods to manufacture the desired tangible patterns with enhanced precision as this technology offers design flexibility and fabrication solutions to manufacture critical multifunctional components within short time frames which otherwise would require multiple steps, tools, and mechanisms for manufacture.

In the recent years, AM has become extremely popular in the medical industry and has made a significant mark as an important manufacturing technique for fabrication of implants used in orthopedics and dentistry. However, now the industries dealing with critical and high-performance applications such as aerospace, space craft, military, and defense are also considering AM for providing design solutions for fabrication of critical components. It has been reported that Boeing has adopted AM technology to manufacture components for their flight and space programs on a large scale with thousands of parts already being manufactured and used by Boeing in their aircrafts [142, 143] and recently, Boeing in collaboration with Thermwood Corporation, USA, fabricated single large components using large-scale additive manufacturing technique for aircraft applications [144, 145]. Airbus has also started using components made by 3D printing in their aircrafts [146, 147]. Thus, it is clear that aerospace-based original equipment manufacturers (OEMs) have begun adopting generative manufacturing technologies for development of components for their aerospace programs.

Three-dimensional printing of advanced ceramic materials has witnessed a continuous progress in research and development activities and has made significant strides owing to their cutting-edge performance in extreme conditions. Part C of this chapter deals with patents on 3D printing of ceramics for aerospace and strategic applications filed during AM's momentum period. It was found that 105 patent records addressed innovations in the aerospace and strategic sector, and the majority of patents were on the development of ceramic printing materials, method of preparing ceramic printing material, and/or the fabrication of specific components.

Innovations on ceramic materials were largely focused toward enhancement of quality, properties of existing materials, and inventing novel materials in response to technical challenges posed during development of various applications. Based on the requirement, a variety of ceramic materials such as carbides, nitrides, oxides, borides, and ceramic-based composite materials [148] are available to the end user for three-dimensional printing. Patent distribution of ceramic materials (Fig. 14) is as follows: non-oxide ceramics (62 patents), ceramic-based composite materials (35 patents), oxide ceramics (13 patents), and a small section of patent records which were on the use of glass-based materials for making optical components suitable for aerospace and strategic applications using 3D printing technology.

Fig. 14 Distribution of patent records across different types of ceramic materials



In some cases, a single patent record mentions more than one ceramic or composite material, and hence, an overlap of patent records across oxide, non-oxide, and composite ceramic materials is possible. Among ceramic materials, non-oxide ceramics and composite materials seem to be preferred over oxide ceramics for aerospace and strategic applications. The most commonly used non-oxide ceramic materials were silicon carbide, silicon nitride, tungsten carbide, aluminosilicate, and quartz. The non-oxide ceramic materials like silicon carbide, tungsten carbide, and silicon nitride are known for the production of high-performance structural components. Silicon carbide is a lightweight material well-known for its excellent hardness, thermal conductivity, and low thermal expansion and resistance to acid and alkali which makes this material highly suitable for aerospace and strategic applications [149]. Silicon nitride is popularly used for strategic components as it exhibits resistance to high-temperature oxidation and thermal shock and has very low density [150, 151]. Tungsten carbide is also a desired material for production of wear-resistant parts used for high-performance applications in combination with other ceramic or metallic materials [152, 153]. Ceramic-based composite materials are made from ceramic materials and other materials such as reinforcing fibers, metals, alloys, and other ceramics wherein the resultant product material has different properties (desired properties) compared to individual materials [68, 80]. Carbon fibers and whiskers, carbon nanotubes, graphene, tungsten, niobium, molybdenum, vanadium, etc. were used to develop ceramic-based composite materials. Oxide-based ceramic materials mentioned in the patents were mostly alumina, silica, and zirconia, and these could have been the preferred choice for making built parts as they are known to exhibit high strength and excellent wear resistance suitable for strategic applications [154]. Thus, it is evident that progressive work is being carried out worldwide in the area of ceramic material either to obtain the required performance parameters or to provide cost-effective and environment-friendly [155–163] options for industrial manufacture.

About 45% of patents (including patent records having an overlap with materials) focused on the manufacturing of specific high-performance structural and functional parts for aerospace and strategic applications. Such parts built using AM include machine components such as flow control parts, pumps, bearings, bolts, valves, valve components, centrifuge components, and disk stacks and/or fluid handling components such as combustion chamber, ceramic capacitors, marine propeller, grin

lenses in aeroplanes, nozzles, nuclear fuel pellets, stator vane, ceramic filter, pressure vessels, missile head, turbine blades, and other turbine components.

The 3D printing methods used for fabrication of aerospace components using ceramic materials are SLS, stereolithography, extrusion-based 3D printing, DMLS, FDM, photo-polymerization, inkjet printing, LENS, RC, electron beam freeform fabrication, EBM, SHS, LOM, SLA, DLP, DOD, FEF, and direct material deposition.

Conclusion

Additive manufacturing technology has entered into the forefront in manufacturing technologies. It has the potential to revolutionize the manufacturing industry as the innovation and development in this sector are so rapid that traditional manufacturing routes may soon fade away and become a thing of the past. This generative manufacturing process has set a new scale for ceramic research and development in manufacturing components of highly complex geometries. Asian continent is leading in three-dimensional printing of ceramics with China being the key player. From the review of patents in the 2018, it was found that innovations were driven toward development of novel ceramic-based composite materials to suit various applications; development of processes and methodologies intended to improve productivity, efficiency, and product quality; and manufacture of 3D printers and support structures that are simple, cost-effective, and reliable. 3D printing has witnessed acceptance in almost all fields; the largest penetration has been in the healthcare sector from a patent viewpoint. Three-dimensional manufacturing of ceramics and composites is gradually gaining momentum in the aerospace and strategic sectors. Materials such as non-oxide ceramics and composites and laser based additive manufacturing techniques seem to be the preferred choice in the aerospace and strategic sectors.

References

1. Travitzky N, Bonet A, Dermeik B, Tobias F, Filbert-Demut I, Schlier L, Schlordt T, Greil P (2014) Additive manufacturing of ceramic based materials. *Adv Eng Mater* 16(6):729–754
2. Ruiz-Morales JC, Tarancón A, Canales-Vázquez J, Méndez-Ramos J, Hernández-Afonso L, Acosta-Mora P, Marín Rueda JR, Fernández-González R (2017) Three dimensional printing of components and functional devices for energy and environmental applications. *Energy Environ Sci* 10:846–859
3. Andrea Z, Colombo P, Gomes CM, Günster J (2015) Additive manufacturing of ceramics: issues, potentialities and opportunities. *J Am Ceram Soc* 98(7):1983–2001
4. Pandian A, Cameron B (2016) A review of recent trends and challenges in 3D printing. In: *Proceedings of the 2016 ASEE north central section conference, USA*
5. Tania RT (2017) 3D printing technology: the surface of future fashion. *Int J Comput Appl* 157(5):48–51

6. Standard terminology for additive manufacturing technologies. Designation: F2792-12a. ASTM International. <http://web.mit.edu/2.810/www/files/readings/AdditiveManufacturingTerminology.pdf>
7. Gonzalez-Gutierrez J, Cano S, Schuschnigg S, Kukla C, Sapkota J, Holzer C (2018) Additive manufacturing of metallic and ceramic components by the material extrusion of highly-filled polymers: a review and future perspectives. *Materials (Basel)* 11(5):840
8. Jimenez M, Romero L, Dominguez IA, Espinosa MM, Domínguez M (2019) Additive manufacturing technologies: an overview about 3D printing methods and future prospects. *Complexity* 2019:9656938
9. Lu B, Li D, Tian X (2015) Development trends in additive manufacturing and 3D printing. *Engineering* 1(1):85–89
10. Wang L, Alexander CA (2016) Additive manufacturing and big data. *Int J Math Eng Manag Sci* 1(3):107–121
11. Chen Z, Li Z, Li J, Liu C, Lao C, Fu Y, Liu C, Li Y, Wang P, He Y (2019) 3D printing of ceramics: a review. *J Eur Ceram Soc* 39:661–687
12. Faesa M, Valkenaers H, Vogelera F, Vleugelsb J, Ferrarisa E (2015) Extrusion-based 3D printing of ceramic components. *Proc CIRP* 28:76–81
13. Nötzel D, Eickhoff R, Hanemann T (2018) Fused filament fabrication of small ceramic components. *Materials (Basel)* 11(8):1463
https://reprap.org/wiki/Fused_filament_fabrication
15. Revelo CF, Colorado HA (2018) 3D printing of kaolinite clay ceramics using the direct ink writing (DIW) technique. *Ceram Int* 44(5):5673–5682
16. <https://www.euroceram.org/en/technologies/material-extrusion/robocasting-direct-ink-writing.html>
17. Materials Research Society (1999) Materials Research Society Symposium Proceeding, vol 542 © 1999. <https://doi.org/10.1557/PROC-542-133>. <https://www.cambridge.org/core/terms>
18. Leu MC, Deuser BK, Tang L, Landers RG, Gregory Hilmas GE, Watts JL (2012) Freeze-form extrusion fabrication of functionally graded materials. *CIRP Ann* 61(1):223–226
19. Huang T, Mason MS, Hilmas GE, Leu MC (2006) Freeze-form extrusion fabrication of ceramic parts. *Virtual Phys Prototy* 1(2):93–100
20. Ming CL, Tang L, Deuser B, Landers RG, Hilmas GE, Zhang S, Watts J (2011) Freeze-form extrusion fabrication of composite structures. <http://sffsymposium.engr.utexas.edu/Manuscripts/2011/2011-09-Leu.pdf>
21. Li W, Armani A, Mcmillen D, Leu MC, Hilmas GE, Watts J (2017) Fabricating ceramic components with water dissolvable support structures by the ceramic on-demand extrusion process. *CIRP Ann* 66(1):225–228
22. Ghazanfari A, Li W, Leu MC, Hilmas GE. A novel extrusion-based additive manufacturing process for ceramic parts. In: *Solid Freeform Fabrication 2016: proceedings of the 26th annual international solid freeform fabrication symposium – an additive manufacturing conference*
23. Vaidyanathan R, Lombardi JL, Walish J, Kasichainula S, Calvert P, Cooper K (2000) Extrusion freeform fabrication of functional ceramic prototypes. In: *Ceramic engineering and science proceedings*, vol 16, pp 121–128
24. Hilmas GE, Lombardi J, Hoffman R (1996) Advances in the fabrication of functional graded materials using extrusion freeform fabrication. In: *Proceedings of the 4th international symposium on functionally graded materials*, Japan, pp 319–324
25. Agarwal MK, Weeren RV, Bandyopadhyay A, Whalen PJ, Safari A, Danforth SC (1996) Fused deposition of ceramics and metals: an overview. <https://sffsymposium.engr.utexas.edu/Manuscripts/1996/1996-47-Agarwala.pdf>
26. Agarwal MK, Bandyopadhyay A, Weeren RV, Langrana NA, Safari A, Danforth SC, Jamalabad VR, Whalen PJ, Donaldson R, Pollinger J (1996) Fused deposition of ceramics (FDC) for structural silicon nitride components. <https://sffsymposium.engr.utexas.edu/Manuscripts/1996/1996-40-Agarwala.pdf>

27. Greul M, Pintat T, Greulich M (1995) Multiphase jet solidification (MJS). A rapid prototyping process for functional metallic and ceramic parts. In: European conference on advanced PM materials. Proceedings, Birmingham, vol 1, pp 590–596
28. http://www.wtec.org/loyola/rp/p1_ifam.htm
29. <https://www.aniwaa.com/product/3d-printers/3d-figo-ffd-150h/>
30. <https://www.3dsystems.com/selective-laser-sintering>
31. <https://www.engineering.com/3DPrinting/3DPrintingArticles/ArticleID/15982/HP-Releases-New-MJF-3D-Printer-Sets-Sights-on-Metal.aspx>
32. <https://www.3dhubs.com/knowledge-base/hp-mjf-vs-sls-3d-printing-technology-comparison>
33. <https://www.3dprintingmedia.network/additive-manufacturing/am-technologies/what-is-direct-laser-microfusion/>
34. <https://www.computerworld.com/article/3071035/hp-begins-selling-its-jet-fusion-3d-printer-says-its-50-cheaper-10x-faster-than-others.html>
35. <https://www8.hp.com/us/en/printers/3d-printers/products/multi-jet-technology.html>
36. <https://www.osseomatrix.com/technology/?lang=en>
37. <https://xjet3d.com/>
38. <https://all3dp.com/4/xjet-opens-worlds-largest-center-metals-ceramics-israel/>
39. Zocca A, Lima P, Günster J (2017) LSD-based 3D printing of alumina ceramic. *J Ceram Sci Technol* 8(1):141–148
40. <https://www.3ders.org/articles/20141125-voxeljet-announces-new-phenolic-direct-binding-3d-printing-method-at-euromold.html>
41. <https://www.3dprintingmedia.network/additive-manufacturing/am-technologies/what-is-phenol-direct-binding/>
42. <https://www.exone.com/>
43. <https://www.wzr.cc/en/cerprint/>
44. <http://kwambio.com/#/>
45. <https://www.3dnatives.com/en/ceramo-one-3d-printer-kwambio-050120184/>
46. <https://www.3dprintingmedia.network/additive-manufacturing/am-technologies/what-is-fast-ceramics-production/>
47. <http://www.lithoz.com/en/our-products/am-systems>
48. <https://admateceurope.com/>
49. <https://www.prodways.com/en/technologie/industrial-ceramic-3d-printer/>
50. <http://www.ddmsys.com/technologies>
51. Zhong H, Yao X, Zhu Y, Zhang J, Jiang D, Chen J, Chen Z, Liu X, Huang Z (2015) Preparation of SiC ceramics by laminated object manufacturing and pressureless sintering. *J Ceram Sci Technol* 6(2):133–140
52. <https://www.cmtc.com/blog/additive-manufacturing-past-present-and-future>
53. Anish Mathews P, Bhardwaj S, Padmanabham G, Rao DS (2016) Patent trends of detonation spray coating technology. *Recent Pat Mech Eng* 9(1):9–19
54. Mathews PA, Kalanidhi SRC, Bhardwaj S, Subasri R (2013) Sol-gel functional coatings for solar thermal applications: a review of recent patent literature. *Recent Pat Mater Sci* 6(3):195–213
55. <https://3dprintingindustry.com/news/china-action-plan-3d-printing-3-billion-2020-126119/>
56. <https://constructionclimatechallenge.com/2018/05/29/output-chinas-3d-printing-industry-will-reach-3-billion-2020/>
57. Eric A (2013) Additive manufacturing in China: aviation and aerospace applications (part-2). Study of Innovation and Technology in China, pp 1–4
58. <http://global.chinadaily.com.cn/a/201903/01/WS5c78e642a3106c65c34ec375.html>
59. <https://www.forbes.com/sites/ralphjennings/2018/02/01/china-lays-groundwork-for-asian-world-lead-in-3d-printing/#c3cbf977f54e>
60. Xiaodong X, Yang L (2015) A glance at the recent additive manufacturing research and development in China. In: Proceeding of the Solid Freedom Fabrication (SFF) symposium, Austin, pp 1612–1634
61. http://namic.sg/wp-content/uploads/2018/04/global-additive-manufacturing-market_1.pdf

62. Xianwei Z, Zhang HE, Chunwei W, Zexiong Z, Enhui W, Yiqing C (2018) Hectorite modified 3D printing ceramic clay and preparation method thereof. Chinese Patent application 108840662A
63. Aili Z, Longsheng C, Huimin S, Youjun M, Shangquan Y, Kun W, Xiang G (2018) Purple sand mud material suitable for LMD method 3D printing and preparation method and application. Chinese Patent application no. 108793951A
64. Cong L, Jialin L, Jiemei G, Honghao G, Yuming H (2018) Formula of ceramic 3D printing mud. Chinese Patent application no. 108484110A
65. Yue Z, Lina D, Liangliang Y, Feng B (2018) Water-based ceramic slurry for free extruding and molding as well as preparation method and application thereof. Chinese Patent application no. 108191409A
66. Tao W, Yong W (2018) 3D (three dimensional) printing molded cation light-curing type aluminum oxide ceramic slurry composition. Chinese Patent application no. 108191410A
67. Tao Z, Kun Z, Yikai Z (2018) Preparation method of SiC_W/SiC/SiC ceramic-based composite material. Chinese Patent application no. 108264353A
68. Dongyun Z, Yan Z, Weidong W (2018) Silicon carbide particle reinforced aluminum-based composite material forming method based on selective laser melting technology. Chinese Patent application no. 108480625A
69. Haijun Q (2018) Preparation method for ceramic composites for 3D printing. Chinese Patent application 108726977A
70. Wu S, Huang R, Wu H, Jiang Q, Li Y (2018) Silicon nitride ceramic and preparation method thereof. Chinese Patent application 108675798A
71. Qingsong M, Kuanhong Z (2018) Three-dimensional silicon carbide fiber reinforced aluminum oxide-zirconium oxide composite material and preparation method thereof. Chinese Patent application no. 108033803A
72. Chunxia S, Wenxin W, Jing C (2018) Self-lubrication ceramic material and preparation method thereof. Chinese Patent application no. 108555294A
73. Weiming G, Lixiang W, Wenbin N, Zhiwei C, Huatai L, Shanghua W (2018) Titanium diboride-based multiphase ceramic and preparation method and application thereof. Chinese Patent application no. 108610052A
74. Riley R, Hemant B (2018) Method to manufacture polymer composite materials with nano-fillers for use in additive manufacturing to improve material properties. US Patent application no. 2018327552A1
75. Tao D (2018) High molecular ceramic composite 3D (three dimensional) printing fluorescent material and preparation method thereof. Chinese Patent application no. 108795011A
76. Ali E, Erica MF, Alexey SK (2018) Composite particulate build materials. Indian Patent application no. 201847024065A
77. Xiaofeng W, Kai Y (2018) Preparation method of 3D (three-dimensional) printing ceramic slurry. Chinese Patent application no. 108069704A
78. Laifei C, Xinyuan L, Fang Y, Shangwu F, Shuyin Y, Yongsheng L, Litong Z (2018) Ceramic material SiC whisker suitable for stereolithography, and preparation method thereof. Chinese Patent application no. 108395249A
79. Mingyang H, Xiangpeng C, Lecheng L (2018) Gypsum-based composite binding material for extruded 3D printing and preparation method thereof. Chinese Patent application no. 108383465A
80. Sainan C, Hai G, Jianchun Y, Jie J, Bin L, Jie Z, Guoqing W, Tiancheng H, Jinjin L (2018) Multiphase nano ceramic particle hybrid reinforced nickel-based alloy composite material and laser forming method thereof. Chinese Patent application no. 108728695A
81. Hofmann DC (2018) High toughness metallic glass-based composites for additive manufacturing. WIPO Patent application no. 2018223117A2
82. Demuth BA, Pawloski AR (2018) Ceramic support structure. US Patent application no. 2018339426A1
83. Zhu M (2018) Dyeable water absorbent polymer resin 3D printing material. Chinese Patent application no. 108034236A

84. Hofmann DC (2018) High toughness metallic glass-based composites for additive manufacturing. US Patent application no. 2018345366A1
85. Xunren Z, Yedong L (2018) Artificial bone joint made of thermoplastic carbon fiber resin composite material. Chinese Patent application no. 108815573A
86. Wuyi Z, Jianliang N, Huaxiong C, Siqi C, Xianming D, Meiling W, Wenliang G (2018) Dental pulp cavity gum 3D printing composite material preparation method and application thereof. Chinese Patent application no. 108676348A
87. Fanwen Y, Chengguang L, Jiahao S, Weiqi T, Jianting L, Meixi C, Mengmeng X, Xiumei T, Xiaoming C, Jixiang Z (2018) Low-shrinkage 3D printing material, and preparation method and application thereof. Chinese Patent application no. 108659476A
88. Chunze Y, Yusheng S, Yi F, Yunsong S, Teng P, Yan W, Qingsong W, Jie L (2018) Peek/Nano-Ha composites for SLS and preparation methods thereof. US Patent application no. 2018155496A1
89. Li W, Zhiqiang Y, Bingheng L, Wanqing D (2018) Preparation method of ceramic precursor resin, 3D printing method and 3D printer. Chinese Patent application no. 108705775A
90. Shanghua W, Yanhui L, Lian L, Minglang W (2018) Powder for selective laser sintering (SLS)/selective laser melting (SLM) as well as preparation method and application thereof. Chinese Patent application no.108752014A
91. Benjamin DA, Pawloski AR (2018) Ceramic support structure. US Patent application no. 2018339426A1
92. William SJ (2018) 3-dimensional printing. Indian Patent application no. 201847026122A
93. Jianqiang S (2018) Printing method adopting fused deposition modeling for metal three-dimensional printer. Chinese Patent application no. 108746626A
94. Rifat H (2018) Method for 3D printing a 3D item. WIPO Patent application no. 2018189062A1
95. Benzur O, Peled H (2018) Molding method and apparatus, particularly applicable to metal and/or ceramics. WIPO Patent application no. 2018203331A1
96. Thomas MG (2018) Supports for sintering additively manufactured parts. US Patent application no. 2018162061A1
97. Xiaofeng W, Kai Y (2018) Method for preparing hierarchical porous material with direct ink writing technology. Chinese Patent application no. 108298965A
98. Xuesong G, Shuang L, Meng X, Tao Z (2018) Composite ceramic coating preparation method based on electromagnetic deposition and selective laser sintering technology. Chinese Patent application no. 108754445A
99. Benyamin B, Tasso L, Rueben M, Rick LA (2018) Skillful three-dimensional printing. US Patent application no. 2018161875A1
100. Kaiyuan T (2018) Preparation method of 3D printing SiC core material and high-density glass carbon packaging combustion chamber. Chinese Patent application no. 108709198A
101. Zihui Z, Hujun W, Pengyu L, Zhenning L, Yunhong L, Xiujuan L, Zhichao M, Jie Z, Qiang L, Long Z, Zhenglei Y, Luquan R (2018) Building method of friction surface of ceramic layer of porous structure. Chinese Patent application no. 108383529A
102. Shanghua W, Rongji H, Haidong W, Qiangguo J, Yehua L (2018) Silicon nitride ceramic and preparation method thereof. Chinese Patent application no. 108675798A
103. Jurg M, Molotnikov A (2018) Method and system for quality assurance and control of additive manufacturing process. WIPO Patent application no. 2018204981A1
104. Rudisill SG, Kasperchik V, Kabalnov AS, Woodruff SR, Sabo TM, Jake W, Lebron H, Verzwylt V, Schramm MT, Shepherd MA (2018) Three-dimensional (3d) printing. US Patent 2018333914A1
105. Pierre L, Jonathan P, Arian A, Brian A (2018) Viscous film three-dimensional printing systems and methods. US Patent application no. 2018333913A1
106. Qiuquan G, Zixiang W, Jun Y (2018) Photosensitive resin compound material for ultralow-temperature resistant 3D printing and preparation thereof. Chinese Patent application no. 108546393A

107. Daniel C, Blasius BT, Benyamin B, Erel M, Joseph MR, Rick LA (2018) Skillful three-dimensional printing. US Patent application no. 2018318928A1
108. Jianfeng M, Ruibin Z, Yi Y, Tingting L (2018) Method for preparing zirconia toughened alumina dental infiltrated ceramic. Chinese Patent application no. 108726998A
109. Jing Z, Kunxue D, Yuyu Y (2018) Interbody fusion device based on 3D printing and preparation method of device. Chinese Patent application no. 108670505A
110. Guowei M, Li W, Zhijian L (2018) Method for toughening 3D printed concrete structure through high-ductility cement-based material. Chinese Patent application no. 108590187A
111. Niancui Y (2018) Three-dimensional movement mechanism for 3D printing of argil. Chinese Patent application no. 108568887A
112. Fei Z, Huiyan X (2018) Method for producing honeycomb ceramic carrier for 3D printing car. Chinese Patent application no. 108724428A
113. Gongshou Y, Xiaoping Z, Chengming L, Jian C, Lyujun N, Wang Q, Guoyi Z (2018) 3D printing method for ceramic substrate multilayer circuit. Chinese Patent application no. 108834319A
114. Kefeng L, Weidong Z, Ren X, Wei W (2018) Protective cover plate and preparation method and application thereof. Chinese Patent application no. 108640530A
115. Hildreth O, Nassar A, Simpson TW (2018) Fabricating metal or ceramic components using 3D printing with dissolvable supports of a different material. Israel Patent application no. 261144D0
116. Dong YH (2018) Plastic device of the teeth and method thereof. Korean Patent application no. 101835539B1
117. Jing Z, Kunxue D, Yuyu Y (2018) Personalized 3D printing interbody fusion cage and preparation method thereof. Chinese Patent application no. 108606860A
118. Feng L, Yunlong S, Zhiliang S, Xiaolong L, Zhong F, Wei W, Yong L, Guangwu L, Yong Z (2018) Personalized artificial vertebral body implant based on additive manufacturing and design method thereof. Chinese Patent application no. 108670504A
119. Tingting Y, Huachao G, Pan L, Xiaosu Q, Qinghua C (2018) Calcium phosphate-silicon dioxide porous scaffold and preparation method thereof. Chinese Patent application no. 108478860A
120. Mommaerts MY (2018) Bone prostheses. WIPO Patent application no. 2018172982A1
121. Zhihua L, Yudong M, Weina W (2018) Hydroxyapatite-based bone tissue engineering bracket and powder 3D printing method thereof. Chinese Patent application no. 107998455A
122. Kai W, Changhao P, Lizhi Y, Zhong W, Wanzhong W, Yan G (2018) Temporal bone model for surgery training and forming method thereof. Chinese Patent application no. 107993547A
123. Sterna E, Svanberg J, Gatenholm E, Martinez H (2018) 3D printer and a method for 3D printing of a construct. US Patent application no. 2018345563A
124. Yan C, Jian C, Xuanrong J (2018) Piezoelectric ceramic and preparation method thereof as well as 3D printing piezoelectric ceramic device. Chinese Patent application no. 108752010A
125. Rifat H, Jacobus VO (2018) FDM printer and method with force feedback for printing non-uniform filaments. WIPO Patent application no. 2018219698A1
126. Yuqin W (2018) 3D printer for glass. Chinese Patent application no. 108821547A
127. Hui W, Haoxi M, Hongtao X (2018) Ceramic 3D printer. Chinese Patent application no. 108789772A
128. Junmei L, Zifan H, Ouyang L, Mengfei D, Ming H (2018) Colored clay 3D printer and feeder thereof. Chinese Patent application no. 208034948U
129. Xiaolong L, Jian G (2018) 3D printer workbench facilitating piece taking. Chinese Patent application no. 108656548A
130. Liquan Z (2018) Medical 3D printing frame. Chinese Patent application no. 108724719A
131. Yongshig SP (2018) Apparatus for enhancing speed of 3d printer. Korean Patent application no. 20180019628A
132. Jingsong C, Long C, Jian G, Dazhi H (2018) Novel ceramic forming device based on 3D printing technology. Chinese Patent application no. 108297244A

133. Zhanyong Z, Wenjie Z, Peikang B, Zhonghua L, Xiaofeng L, Yu W, Bin L, Yuxin L, Jianhong W (2018) Metal amorphous 3D printing conveying device. Chinese Patent application no. 108465816A
134. Sergey S (2018) 3D printer. US Patent application no. 2018169956A1
135. Xiangnuan M (2018) Screw extruding type 3D printer. Chinese Patent application no. 108466423A
136. Xiangnuan M (2018) Multipurpose screw rod extrusion type 3D printer. Chinese Patent application no. 108372657A
137. Xiangnuan M (2018) Extrusion type three-dimensional (3D) printer. Chinese Patent application no. 108312501A
138. Carsten F, Smith KL, Behnke JR, Smithson RLW, Crestik LD, Benson OJ, Huffman AJ (2018) Continuous additive manufacturing apparatus. India Patent application no. 201847024124
139. Nantong Wote Optoelectronics Tech Co Ltd (2018) 3D printing spray head with plasma processing device, and 3D printing machine. Chinese Patent application no. 108839337A
140. Xiaoli L, Chen Y (2018) Sprayer device of 3D printer. Chinese Patent application no. 107901410A
141. Teruji C, Hidetsura C, Shuichi S (2018) Multi color gravure offset printing device and method. Korean Patent application no. 20180021052A
142. <https://www.boeing.com/features/innovation-quarterly/nov2017/feature-thought-leadership-3d-printing.page>
143. <https://additivemanufacturing.com/2018/10/10/boeing-and-thermwood-partnership-to-demonstrate-new-3d-printing-technology/>
144. <https://www.compositesworld.com/news/afri-boeing-thermwood-partner-to-develop-low-cost-autoclave-capable-tooling>
145. <https://www.aero-mag.com/boeing-and-thermwood-corp-form-am-partnership/>
146. <https://www.metal-am.com/airbus-helicopters-begins-large-scale-metal-additive-manufacturing-of-a350-components/>
147. <https://3dprintingindustry.com/news/airbus-helicopters-commences-production-of-large-3d-printed-parts-for-a350-aircraft-140309/>
148. Steyer TE (2013) Shaping the future of ceramics for aerospace applications. *Int J Appl Ceram Technol* 10(3):389–394
149. Gerhardt R (2011) Properties and applications of silicon carbide. InTech, Rijeka
150. Huizhi L, Peizhi Z, Chong C, Yingzi W, Chongjuan X (2017) 3D laser sintering printing technology for silicon nitride nano powder the preparation of. Chinese Patent application no. 104788102B
151. Hagen K (2010) Silicon nitride for high-temperature applications. *J Am Ceram Soc* 93(6): 1501–1522
152. Schwanekamp T, Reuber M (2016) Additive manufacturing of application optimized tungsten carbide precision tools. In: Proceedings of 6th international conference on additive technologies, Nurnberg, Germany, pp 100–114
153. Eckart U, Andre B, Robert B (2018) Manufacturing of carbide tools by selective laser melting. *Proc Manuf* 2018:765–773
154. Zhixiang C, Linghui R, Sheng Y, Fei X, Hongting W, Zhilong S (2018) Print ceramic material's novel laser 3D printer. Chinese Patent application no. 207206676U
155. Masoudi M (2017) Catalytic converters having non-linear flow channels. US Patent application no. 2017175609A1
156. Yue W, Hongchao S, Gaojian X, Deng B, Jiang Y, Tingyu L, Haifeng Y (2017) 3D printing aluminum oxide covered composite material and preparation method thereof. Chinese Patent application no. 106623897A
157. Folgar LN, Folgar Christian E (2018) Direct writing for additive manufacturing systems. US Patent application no. 9981314B2
158. Zhi LH, Zhi ZP, Chong C, Wang YZ, Takashi XJ (2017) 3D laser sintering printing technology for silicon nitride nano powder the preparation of. Chinese Patent application no. 104788102B

159. Chong C, Jinhuan H, Huizhi L, Peizhi Z (2016) Preparation method of laser sintering 3D printing rapid prototyping silicon nitride powder material. Chinese Patent application no. 104744049B
160. Stoyanov P, Prichard P (2016) Methods of making sintered articles. US Patent application no. 2016375493A1
161. Zhongliang L, Dichen L, Feng L, Jiwei C, Bingheng L (2014) Preparation method of SiCf/SiC ceramic matrix composite turbine blades. Chinese Patent application no. 103113123B
162. Li H Z, Lu Y, Ha Q (2018) This invention claims a method for 3d laser sintering printing forming barium titanate ceramic powder body prepared. Chinese Patent application no. 106316388B
163. Schloffer M (2017) Method for producing a rotor blade for a fluid flow engine. Germany Patent application no. 102016203785

Part II

Ceramic Materials for Ballistic Armor Applications



Ceramic Composite Armour for Ballistic Protection

9

P. Rama Subba Reddy, S. Geasin Savio, and Vemuri Madhu

Contents

Introduction	359
Materials and Manufacturing Methods	361
Ceramic Materials	361
Processing of Ceramic Materials	364
Polymer Composites	366
Fabrication of Armour-Grade Composite Laminates	373
Penetration Mechanisms	375
Penetration in Ceramics	375
Penetration in Composite Laminates	377
Ballistic Test Methodologies	380
Threat Levels and Standards	382
Depth of Penetration Test	383
Semi-Infinite Backing Test Method	388
Residual Velocity Test Method	389
Ballistic Limit Test	390
Protective Areal Density Method	393
Ceramic Composite Armour Modules	394
Fabrication of Armour Modules	395
Ballistic Performance Evaluation of Modules	397
Conclusion	398
References	399

P. R. S. Reddy · S. G. Savio · V. Madhu (✉)
Defence Metallurgical Research Laboratory, Defence Research and Development Organization,
Hyderabad, Telangana, India
e-mail: rsreddy@dmrl.drdo.in; geasin@dmrl.drdo.in; madhu.vemuri@dmrl.drdo.in

Abstract

Survivability of the combat system depends on three key parameters such as mobility, protection, and firepower. Armour materials are used to provide protection to the combat systems against various threats with a minimal weight penalty. Low Dense ceramics and polymer composite materials are explored by various researchers to design lightweight armours for personnel and vehicular armour applications. Ceramics such as high purity alumina, silicon carbide, and boron carbide are used in combination with some composite laminates. Advanced fiber-reinforced laminates such as glass, aramid, and high-modulus polyethylene are used as stand-alone as well as a backing to ceramic armours both in add-on and structural composite armour applications. The present chapter describes the various types of ceramic and composite laminates used to design lightweight armours, and their processing methods. It has also covered ballistic test standards, penetration mechanisms, and the way forward for future armour materials.

Keywords

Ceramics · Composite laminates · Light weight ceramic composite armour · Ballistic impact

Acronyms and Abbreviations

AD	Areal density
AEP	Allied Engineering Publication
Al ₂ O ₃	alumina
AK	Avtomat Kalashnikova
AP	Armour piercing
ARL	Army Research Laboratory
B ₄ C	Boron carbide
BFS	Back face signature
CE	Chemical energy
CP	Complete penetration
DEF	Differential efficiency factor
DOP	Depth of penetration
EFP	Explosively formed projectile
EN	European Nation
E-glass	Electrical grade glass
FXR	Flash X-ray
FSP	Fragment simulating projectile
GSM	Grams per square meter
GOST	Gosudarstvennyy standart (state standard)
HAP	Hard armour panel
HCP	Hexagonal close-packed

HESH	High-explosive squash head
HMPE	High-modulus polyethylene
HPPE	High-performance polyethylene
IS	Indian Standards
KE	Kinetic energy
ILSS	Interlaminar shear strength
MIL	Military standard
NATO	North Atlantic Treaty Organization
NBE	Normalized ballistic efficiency
NDEF	Normalized differential efficiency
NIJ	National Institute of Justice
PAD	Protective areal density
PE	Polyethylene
PMC	Polymer matrix composite
PP	Polypropylene
PP	Partial penetration
PVB	Polyvinyl butyral
RBAO	Reaction-bonded aluminum oxide
RBBC	Reaction-bonded boron carbide
RBSiC	Reaction-bonded silicon carbide
RBSN	Reaction-bonded silicon nitride
RHA	Rolled homogenous armour
SAP	Soft armour panel
SiC	Silicon carbide
SHS	Self-propagating high-temperature synthesis
SIS	Styrene-isoprene-styrene
S-glass	Structural grade glass
TiB ₂	Titanium diboride
UHMWPE	Ultrahigh-molecular-weight polyethylene
UD	Unidirectional
VARTM	Vacuum-assisted resin transfer mold
VPAM	Association of test laboratories for attack resistance materials and constructions
WC	Tungsten carbide
WHA	Tungsten heavy alloy
ZTC	Zirconia-toughened ceramic
ZTA	Zirconia-toughened alumina

Introduction

The present battlefield conditions demand combat systems of lightweight, high-fire power, and quick deployment capabilities. Therefore, demand for lightweight armour for ballistic protection is growing steadily. Steel popularly known as rolled

homogenous armour (RHA) has been the traditional armour for a long time. However, steel alone can no longer give lightweight armour solutions as it requires higher thickness, may be up to hundreds of millimeters to provide protection against the latest threats which has led to the increase of total weight of the combat vehicle. This constraint has directed the armour research fraternity to investigate different types of advanced materials which have got high specific strength and modulus. Different types of armour solutions based on materials and their configurations have been proposed by various researchers which have resulted into a significant reduction of armour weight. During World War II, laminated composites were recognized as superior materials over steel for armour applications especially against bullets fired from hand guns and rifles. During Korean War, polymer materials such as nylon fabric plies were successfully used as chest armour to decrease the number of chest wounds with reduced severity.

However, composite laminates alone cannot provide entire lightweight armour solutions for all the threats. Though they have got high specific properties, they are inferior in terms of hardness and compressive strength which are essential to defeat Armour piercing (AP) projectiles. Therefore, the combination of hard ceramics and polymer composite laminates was found to be a promising approach. Dense ceramics were introduced as armour material in the early 1970s; the advantages of ceramics are their high compressive strength, hardness, and low density. High hardness ceramics blunt the incoming projectile thereby, losing the projectile impact energy. The ductile backing laminate absorbs the remaining impact energy by arresting the broken fragments of ceramic and projectiles. Laminated structure can transfer the impact stress effectively in transverse and longitudinal direction due to the presence of long-fiber reinforcements. Figure 1 gives reduction in armour weight over a period of time against 7.62 mm mild steel and armour-piercing (AP) rifle bullets due to the advancement of materials.

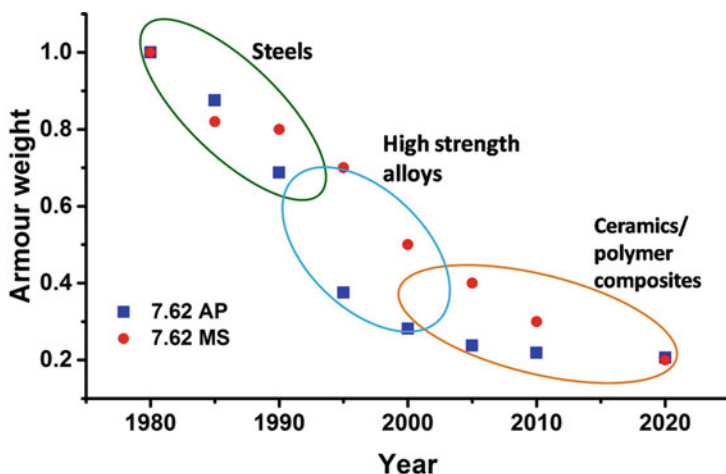


Fig. 1 Reduction in armour weight against 7.62 mm projectiles

Materials and Manufacturing Methods

Different types of ceramics including oxide and non-oxide types and composite laminates are being used for armour applications. The selection of ceramic for armour application is primarily based on density, compressive strength, flexural strength, and hardness. In the case of composite laminates, it is based on density, strength, strain to failure, and modulus. Figure 2 shows broad classification of ceramic and composite materials for making ceramic composite armour. The brief details of various ceramics, composite laminates, and their fabrication methods are discussed below.

Ceramic Materials

Alumina

Alumina is the first and extensively used oxide ceramic material till date due to its ready availability, relatively low cost, and ease to manufacture. The stable phase of alumina is called corundum or $\alpha\text{-Al}_2\text{O}_3$ with hexagonal crystal structure. Bauxite is the primary source of alumina and the aluminum hydroxides, and these are separated through Bayer process which is further calcined to get alumina [1]. The prepared alumina will have polycrystallinity with density of 3.9 g/cc. It is projected that the theoretical strength of alumina is 58 GPa; however, the strength of any brittle material is limited by flaws present in the material that are generated during the manufacturing. Hence, sintered polycrystalline alumina properties will be much lower than their theoretical values. Dense alumina can be made either by melting, hot pressing, or

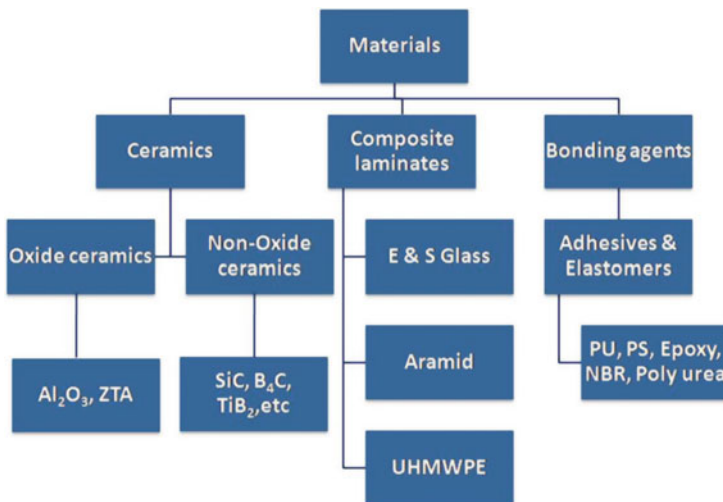


Fig. 2 Classification of materials for ceramic composite armour

sintering. Melting and hot pressing processes are not industrially friendly due to the requirement of very high temperature ($>2000\text{ }^{\circ}\text{C}$) which can lead to higher production cost. Therefore, polycrystalline alumina for armour applications is generally processed by dry pressing or slip casting method followed by pressure less sintering.

Even though alumina has got many attractive properties, it suffers from problems like low fracture toughness and tendency to form abnormal grain growth during sintering. These are detrimental for its performance in ballistic applications. Hence, in order to strengthen and toughen the alumina through controlled grain growth, various methods such as adding dopants (like Ca, Mg), inclusion of secondary phase (like ZrO_2 , SiC), etc. were explored [2]. In the last two decades, zirconia has emerged as an important material for toughening of ceramic materials. Ceramics toughened with zirconia are called as zirconia-toughened ceramics (ZTCs). Similarly, in case of alumina-zirconia composite system too, a small addition of ZrO_2 into alumina matrix significantly increases material strength and toughness, which is called zirconia-toughened alumina (ZTA). In order to increase strength and fracture toughness of ZTA, either tetragonal phase or monoclinic phase zirconia or both types of particles are added into alumina. Enhancement of toughness is controlled by stress-induced transformation toughening in case of addition of tetragonal phase and by microcrack toughening mechanism for monoclinic phase [3].

Silicon Carbide

The second-generation ceramic which is being used as lightweight ceramic armour compared to alumina for many vehicular applications is silicon carbide (SiC). This material has got lower density and better mechanical properties as compared to alumina. It can give higher ballistic mass efficiency. Therefore, SiC has been used in many armour systems for defeating more tenacious threats. Silicon carbide is commercially manufactured by a process called Acheson process in which a mixture of silica and coke is electrically heated at a temperature of $2600\text{ }^{\circ}\text{C}$. It is a covalently bonded material and the ionicity of SiC bonds estimated by Pauling to be approximately 12% [4]. The long-range structure of SiC is complex and often formed by one-dimensional stacking difference which is called polytypism. There are more than 75 polytypes that have been identified for SiC. Although many polytypes are known for SiC, the cubic 3C polytype, designated as β -SiC, and rhombohedral or hexagonal polytypes, designated as α -SiC, are the most important ones [5]. In order to bring down the cost of the SiC and improving its multihit protection, reaction-bonded silicon carbide (RBSiC) is used for making SiC tiles. The advantages of RBSiC is its affordability, reasonably good ballistic performance, and ease to produce near net-shaped components without utilization of sophisticated machining requirements. The reaction bonding process of SiC consists of infiltration of silicon in liquid or vapor form into the SiC + carbon preform. After the completion of reaction bonding process, i.e., after consumption of all the carbon, a resultant product of porous SiC (in case of vapor infiltration) or dense Si/SiC (in case of liquid infiltration) is obtained.

Boron Carbide

Boron carbide is the third hardest material next to diamond and cubic boron nitride. It was discovered in the year 1858 and first prepared by Joly in the year 1883. The composition of boron carbide is assigned between $B_{4.3}C$ and $B_{10.4}C$, but the commercial composition is close to B_4C . The structure of B_4C may be described as a cubic primitive lattice elongated in the direction of the body diagonal with 12-atom icosahedra located at all vertices of the rhombohedra lattice (R3m space group) and the 3-atom linear chains that link the icosahedra along the (111) rhombohedral axis. Boron carbide powder is produced on a commercial scale by carbothermic reduction of hydroboric acid or boron oxide with graphite, petroleum coke, starch, etc. at 1500–2500 °C using electrical resistance or arc furnace. Even though B_4C has got excellent properties like high hardness and low density, it suffers from the reduction of shear strength at high pressures due to shock-induced amorphization [6]. This limits the use of B_4C to protect against large caliber ammunition where impact velocity will be more than a km per second. The density of B_4C varies with respect to carbon content present. The stoichiometric B_4C has density of 2.52 g/cc, and for $B_{10.4}C$, it is 2.46 g/cc. Since the hot-pressed B_4C is more expensive and difficult to produce complex-shaped components, reaction-bonded boron carbide (RBBC) was explored as an alternative material for ballistic application. The RBBC-based ceramic tiles have shown good ballistic performance with reasonable cost and used in body armour applications in many countries. The final properties of RBBC composite are governed by processing conditions, microstructure, and composition of phases present in it. The fabrication details of RBBC composite can be found in the literature [7, 8].

Titanium Diboride

Titanium diboride (TiB_2) is another potential ceramic for armour applications due to their high strength and hardness notwithstanding its higher density compared to other ceramics. There are many methods to produce TiB_2 powder, but the inexpensive process to produce the powder is by the carbothermal reduction of TiO_2 by B_4C and C. Nanocrystalline TiB_2 powder has been produced by using self-propagating high-temperature synthesis (SHS) and by solvothermal reaction of metallic sodium with amorphous B and $TiCl_4$ [9, 10]. TiB_2 is a stable intermetallic compound, and its crystal structure is hexagonal close-packed (HCP), P6/mmm space group, with lattice parameters $a = b = 3.029 \text{ \AA}$, $c = 3.229 \text{ \AA}$, in which the layers of B atoms form two-dimensional (2D) graphite-like rings that alternate with the Ti layers. The excellent properties of TiB_2 like high hardness, elastic modulus, and chemical resistance are attributed to its inherent crystal structure and atomic bonding. TiB_2 is not a line compound but exists over a narrow stoichiometry range between 28.5 and 30 weight percent of B. Densification of TiB_2 is very difficult due to its low self-diffusion coefficient, extremely high melting point, and high vapor pressure, which are due to the presence of strong covalent bonding. Hence, sintering of this material to its near theoretical density without applying pressure, at a temperature of greater

Table 1 Some properties of ceramic materials

Property	Al ₂ O ₃	ZTA	SiC	RBSiC	B ₄ C	RBBC	TiB ₂
Density, g/cc	3.90	4.10	3.21	3.10	2.52	2.58	4.52
Bend strength, MPa	310–370	400–500	300–400	300–350	350–410	319–415	500–750
Modulus, GPa	300–370	360–400	410–480	300–400	400–460	300–350	560–560
Hardness, GPa	14–15	16–16.5	24–27	18–20	30–32	20–22	26–28
Fracture toughness, MPa√m	3.5–4.5	6.0–8.0	2.5–4.5	5.0–6.0	2.5–3.5	5.5–7.9	6.8–7.5
Cost comparison	1	3.7	5.3	2.0	8	4.6	10

than 2000 °C, and long sintering durations are essential. Therefore, in order to improve densification of TiB₂, sintering additives and external pressure are often used. Hot pressing is used for full densification of TiB₂; other techniques like reactive processing and spark plasma sintering are also used for densification of this material. Table 1 shows properties of different ceramic armour materials [11].

Processing of Ceramic Materials

The ceramic components are fabricated from its powder by shaping it into any required shape and then densified into a solid body by a process called sintering. There are many shaping methods which are used to produce ceramic compacts which all can be grouped into three categories such as powder compaction, casting, and plastic forming. The powder compaction method is nothing but pressing of a free flowing powder. Casting is the process in which the ceramic powder particles are suspended in a liquid to form slurry, and the slurry is poured out into a porous mold to remove the liquid so that the desirable shape is formed. Plastic forming is the process in which the ceramic powder is mixed with a large volume fraction of a liquid to produce a mass that is deformable (plastic) under pressure. For ceramic materials other than clay, generally, an organic binder is used in place of water or in addition to the water. Some important processing methods relevant to fabrication of armour- grade ceramic products, like die pressing, pressure-less sintering, reaction bonding, and hot pressing, are briefly discussed here.

Pressing

Pressing is the most widely used method for shaping ceramic components, since this process produces relatively complex parts with close dimensional tolerances with high productivity [12]. There are two types of powder pressing operations which are

routinely used in ceramic forming such as die pressing (pressing in a rigid die) and isostatic pressing (pressing in a rubber mold). Pressing requires ceramic powders with good flow characteristics and homogenous die filling in order to get uniform densities in a reproducible way. Ceramic powder particles with spherical shape and diameter more than 50 μm have good flow capability. Hence, ceramic powders in the form of granules are generally used for pressing. The die pressing process is carried out by pressing of ceramic powder in a rigid die through the application of uniaxial compression pressure. This type of powder consolidation method is generally called as die pressing or otherwise as cold pressing. The die pressing is usually done with or without the binder and lubricant. Hence, the die pressing method is also called as dry (with no or very less binder) or damp (with more binder) pressing depending on the amount of binder/lubricant content. This process is a good method for fabrication of components like discs and tiles even with screws or holes parallel to the compaction axis with high production rates. Hence, it is used for fabrication of simple shapes. In die pressing, green body dimensions will be kept within precise tolerances in order to achieve near net shape of the component and to reduce machining costs. Die pressing is generally done with steel dies and sometimes with more wear-resistant dies made up of tungsten carbide liners.

Sintering

Sintering is the heat treatment process in which a powder material already formed into the required shape is converted into a useful solid. The porous ceramic solid is densified during the sintering process. Sintering is generally done at a temperature in the range between approximately at 50% and 80% of the powder melting temperature [13]. If the sintering is carried out without simultaneous application of any external pressure to the body, it is called as pressure-less sintering. Generally, the sintering processes are divided into several categories such as solid-state sintering, liquid-state sintering, viscous sintering, and vitrification. The sintering phenomena in polycrystalline materials are more complex. In these materials, the sintering mechanism is through joining together of the powder particles by atomic diffusion in the solid state. This mechanism is called solid-state sintering. However, many times it is very difficult to attain the required density or microstructure using solid-state sintering for many ceramic materials, or sometimes the required sintering temperature may be too high. Therefore, in such situations, some additives are added to the ceramic powder so that a small amount of liquid phase is formed between the particles and grains during the sintering process, and this sintering process is called as liquid-phase sintering. Another type of sintering process that occurs in amorphous materials such as glasses is called viscous sintering, in which matter transport occurs predominantly by viscous flow.

Pressure Sintering

Many times it is difficult to densify ceramic bodies through pressure-less sintering route. In such situations, the externally applied pressure to the body, either in solid-state or liquid-phase sintering process, provides a driving force for densification. This method of application of pressure during heating is called as pressure-assisted sintering or pressure

sintering. The well-known examples for pressure sintering processes are hot pressing and hot isostatic pressing. Hot pressing has many advantages while comparing with sintering process. The main advantages of hot-pressing method over pressure-less sintering processes is that even with a less critical material preparation, highest-quality products can be fabricated. In case of pressure-less sintering, a high degree of material uniformity is required to produce products with the same quality. Another advantage of this process is that in some cases, the densification can be obtained at a lower temperature so that extensive grain growth is prevented; as a result, higher mechanical properties can be achieved. All the densification mechanisms discussed previously for sintering process are applicable for hot pressing also. Hot pressing can be applied to several covalently bonded ceramic materials such as boron carbide, silicon carbide, and silicon nitride to get nearly theoretical density. However, the disadvantage with hot-pressing techniques is difficulty in application of this method to larger shapes, and also the time required for heating the mold and sample is very high, which makes the method slow and expensive.

Reaction Bonding

Generally, the term reaction bonding is used to describe the fabrication routes where a porous solid preform reacts with a gas or a liquid to produce the desired chemical compound and bonding between the grains. This process is also known by different names such as self-bonding, reaction sintering, and melt infiltration. The reaction-bonded ceramics are being used in armour applications due to their cost-effectiveness and have got advantage of forming complex-shaped components. This process also has advantage of reduced processing temperatures and times compared with conventional processing, and the shrinkage produced in this process is very low so that near-net shaped processing can be achieved. The ceramic materials fabricated using the reaction-bonded method are reaction-bonded aluminum oxide (RBAO), reaction-bonded boron carbide (RBBC), reaction-bonded silicon carbide (RBSC), and reaction-bonded silicon nitride (RBSN).

Polymer Composites

Composite is a multiphase material made up of a continuous phase called matrix and discontinuous phase called reinforcement. Matrix surrounds and holds together; the other phase called dispersed phase or reinforcement phase acts as main load bearing one. Composites generally exhibit significant proportion of properties of both the constituent phases. The properties of the composite are mainly governed by the following aspects:

- Type of matrix and reinforcement.
- Relative amounts of matrix and reinforcement phase.
- Geometry of the reinforcement.
- Uniform dispersion/spread of the reinforcement phase in the matrix.
- Interfacial bond strength.

Composite made using polymer as a matrix is called as polymer matrix composite (PMC). In the present chapter, discussion will be restricted to continuous fiber-reinforced polymer composites known as laminated composites which are suitable for armour applications. The most widely used reinforcement form in these composites is fiber tows. These typically consist of thousands of fine filaments arranged in a single bundle. A fiber tow in woven or non-woven forms is used as reinforcement in the matrix.

Composites for Armour Applications

Composite laminates are used in either add-on armour or stand-alone armour applications. As the name itself explains add-on, the armour is placed over an existing structure. In later case, armour will be independent of the structure. In a few areas, composites are also used as structural armour as well; in that case, the armour should perform functional roles such as absorbing impact energy and load-bearing capabilities also as part of the structural requirements. The main difference between structural-grade composite and armour-grade composite laminate is the amount of matrix. Generally, armour-grade laminates will have low volume fraction of matrix (not more than 35%) against 45% vol. in structural-grade composites. The use of composite laminates in the field of armour has progressed significantly. For instance, today's lightweight body armour technology to provide protection against mild steel and lead-core rifle bullets is totally based on laminates. There are various research programs going on all over the world to develop lightweight ceramic composite armour for various combat systems [14]. To provide protection against splinters, composite laminates are more effective than monolithic materials due to the presence of layered structure in the former. The most widely used application is spall liner which is fitted inside the vehicle to protect the crew from splinters in the event of main armour is defeated.

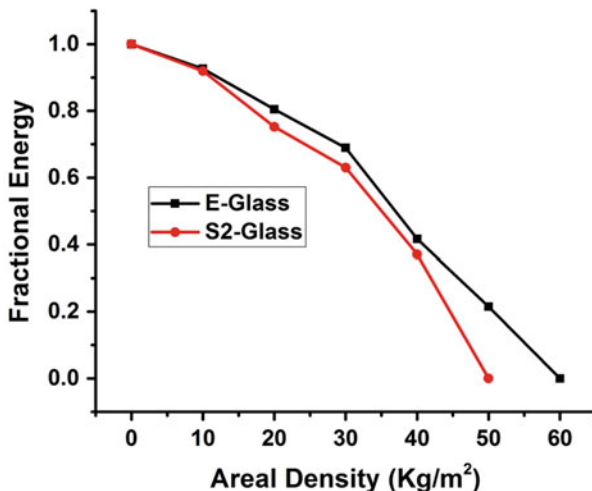
Reinforcements

The main role of reinforcement in the laminate is to absorb bullet impact energy either by undergoing elastic plastic deformation or fracture and arrest the perforation of the projectile. Mainly, three types of fibers are used for armour applications. These are glass, aramid, and ultrahigh molecular weight polyethylene (UHMWPE). Armour made of these advanced fibers could provide adequate protection against soft bullets such as lead, mild steel, and fragments. However, to provide protection against armour-piercing rifle bullets, composites are needed to be combined with hard ceramics such as Al_2O_3 , B_4C , SiC , etc. Brief details of different types of fibers used as reinforcement for making armour-grade laminates are discussed below.

Glass Fibers

Initial scientific and engineering understanding of composites was based on studies of glass fiber-reinforced composites. The reason for widespread use of glass fibers in composites, both in the past and present, is due to their competitive price, availability, and ease of processing. Furthermore, the advent of highly efficient silane-coupling coatings on fibers, which are very compatible with phenolics, polyester,

Fig. 3 Comparison of energy absorption of E-glass and S-glass fiber-based laminates



or epoxy matrices, has provided strong and much-needed boost in load transfer and environmental durability for the finished product. Though there are many grades of glass fibers available commercially, only E and S type of glass fibers are chosen for armour applications. The difference between E- and S-glass fiber is their chemical composition and strength [15]. The fibers are produced through melt-spinning technique using palladium spinneret at a temperature higher than 1372 °C. The major raw materials for glass fibers are silica, limestone, and soda ash. The glass fiber has isotropic properties due to its amorphous structure. Ductility of the fiber increases with the reduction of fiber diameter. The typical diameter of continuous filament would be about 15–20 μm. Glass fibers mainly in the form of woven roving fabric are used for fabricating laminates. Studies have been reported that S-glass fiber-based laminates show 20% higher ballistic performance compared to E-glass fiber-based laminates against lead and mild steel projectiles [16]. Figure 3 shows comparison of energy absorption for E-glass and S-glass fiber-based laminates against mild steel rifle bullets. The reason for higher performance of S-glass is due to their superior mechanical properties as compared to E-glass fiber.

Aramid Fibers

Aramid is a generic term for aromatic polyamide fibrous materials. Its chemical name is poly paraphenylene terephthalamide and derived from aromatic acids and amines. The polymer is invented by DuPont chemist Stephanie Kwolek in the year 1965. The polymer is synthesized through condensation polymerization method in solution polymerization technique using 1, 4 phenylene diamine and terephthaloyl chloride as monomers as shown in Fig. 4. Solvent solution of N-methyl pyrrolidone and calcium chloride is used as medium. The prepared polymer is poly paraphenylene terephthalamide liquid crystalline polymer with hydrochloric acid as by-product. The definition of liquid crystalline polymer is “capable of forming

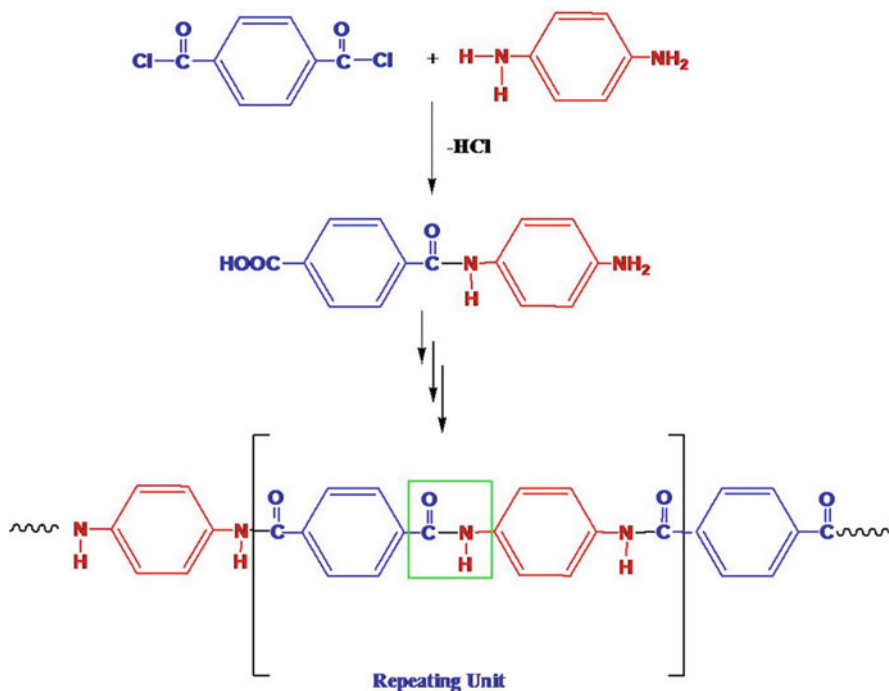
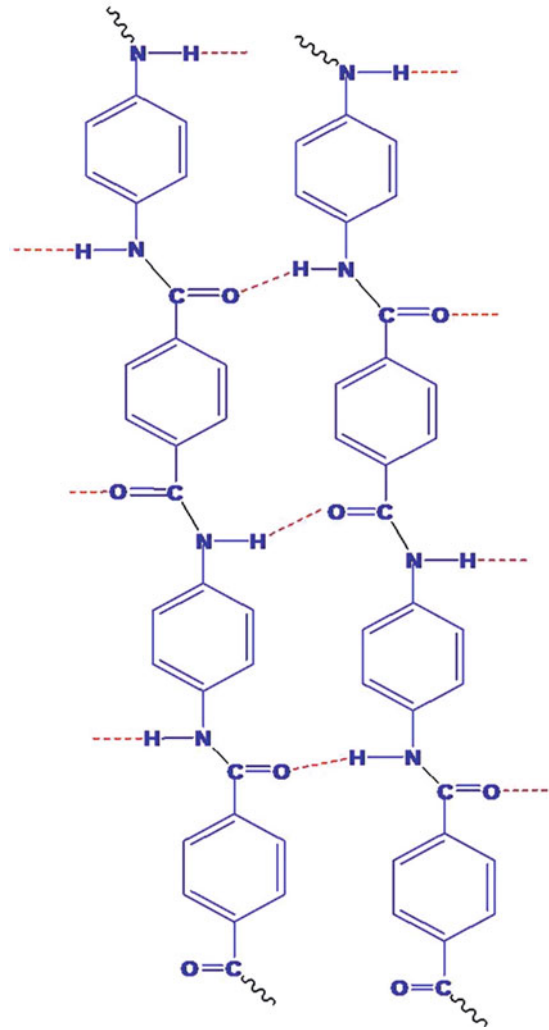


Fig. 4 Preparation of poly paraphenylene terephthalamide polymer

regions of highly ordered structure while in the liquid phase.” Aramid has unique property, i.e., though it is technically called as thermoplastic polymer, rather than melting when heated, it undergoes decomposition before reaching its projected melting temperature. Hence, the fiber is produced through dry-jet wet spinning method spun from a liquid crystalline solution prepared in sulfuric acid solvent. The viscosity of polymer solution increases initially and then reduces due to the alignment of polymer molecules in solution which is called as nematic state. This solution is further pumped through a small orifice, where more and more alignment of polymer molecules takes place. The molecules in aramid chains are said to be ordered in long parallel with radial orientation of benzene ring that gives symmetric rigid rodlike structure and strong hydrogen bonds between the chains [17]. Figure 5 shows molecular structure of aramid fibers. During the fiber spinning and drawing, further orientation of crystals takes place, and thus, the fiber has got high tenacity, modulus, and thermal resistance than aliphatic polyamides. The greater degree of benzene ring conjugation and more linear structure of para linkages are primarily responsible for the increased strength. The high strength combined with modulus considerably higher than S-glass gave rise to early applications in combat vehicles and personal protective systems. The fiber is claimed to be three times stronger than nylon which was used for personnel armour prior to the advent of this fiber and is four times stronger than steel. The weaving of fiber is possible while maintaining the flexibility

Fig. 5 Molecular structure of para-aramid fibers



and drapability due to its finesses. The fibers are converted into fabric both in unidirectional and woven fabric forms to suite personnel and vehicular armour applications. However, in recent times, the use of aramid fiber for lightweight personnel armour applications has come down due to the development of new high specific strength fibers. Currently, aramid fiber is used mainly in helmet and vehicle armour applications. Commercially, two brands, namely, Kevlar[®] and Twaron[®], are available.

Ultra-high Molecular Weight Polyethylene Fibers

The development of ultra-high molecular weight polyethylene (UHMWPE) which is also known as high-performance polyethylene (HPPE) or high-modulus

polyethylene (HMPE) has changed the perception of armour designers. Chemically, the polymer is similar to the commercially available polyethylene. However, HPPE has linear long chains with molecular weight in the range of 4–7 million amu [18]. The polymer is produced by Ziegler-Natta polymerization method. It is very tough and having highest impact strength due to the presence of long chains which can transfer load more effectively by stretching intermolecular interactions [19]. The fiber is said to be ten times stronger than steel. As the polymer cannot be dissolved in any solvent at room temperature due to its high molecular weight, the fibers are produced through the process called gel spin. Prior to gel spinning, sol gel is prepared by soaking the polymer in decalin solvent at high temperature. The polymer concentration in the solution may vary from 5% to 25%. During the sol-gel process, the long polymer chains uncoil and form a network called gel. In the next stage, these uncoiled molecules (in the form of sol-gel) are drawn as fiber through the spinning process called gel spinning. During spinning, very high draw ratio is maintained to get the maximum number of molecules aligned along the fiber axis. The produced fiber will have crystallinity of about 85% or more with molecular orientation of more than 90%. The typical diameter of fibers is about 15–20 μm . Commercially two brands of HPPE fibers are available, viz., Dyneema[®] and Spectra[®], manufactured by M/s. DSM, the Netherlands, and M/s. Honeywell, USA, respectively. The fiber is converted into unidirectional (UD) preregs by using either styrene-isoprene-styrene (SIS) or polyurethane matrix. These preregs are ready to be used for making soft armour panel (SAP) and hard armour panel (HAP) for personnel and vehicular armour applications. Table 2 summarizes the mechanical properties of different advanced fibers used in armour applications.

The advantages of UHMWPE preregs are there is no shelf life issue and environmentally friendliness as no volatiles evolved during the laminate fabrication. The laminate is designed to undergo deformation in the shape of cone upon impact of high-velocity bullet; thereby it can delay the failure of fiber and increase the contact duration between the projectile and fibers. This behavior is possible due to the presence of weak van der Waals forces between the long polymer molecules which support for easy sliding of long chains and also the presence of elastomeric matrix in the laminate which allows the fiber to undergo stretching to their maximum limit. These merits in addition to their high specific strength have put HMPE fiber on top of the table for armour applications.

Table 2 Some properties of high-performance fibers

Property	E-glass	S2-glass [®]	Aramid Kevlar KM2 [®]	UHMWPE Dyneema SK-99 [®]
Density	2.54	2.46	1.44	0.97
Tensile strength	3.1–3.5	4.3–4.6	3.6–4.2	3.8–4.1
Tensile modulus	72–78	88–91	84–90	150–155
Elongation at break	3.9–4.2	5.5–5.7	4.3–4.8	3.0–4.0

Fiber to Fabric Form

It is essential to convert the fibers into fabric forms before using them for making laminates. Fiber orientation (how the individual strands are positioned) determines the mechanical strength of the composite laminate and the fiber direction in which the strength will be the greatest. Both non-woven and woven fabric forms are used for armour applications. Figure 6 shows different weave patterns of fabrics commonly used for making armour-grade laminates. Non-woven fabric also called as unidirectional (UD) fabric has maximum composite strength and modulus in the direction of the fiber axis. In this case, the fibers do not undergo any crimping or interlocking. Hence, the laminate tends to show more deflection or deformation upon impact of projectile; as a result, more energy absorption is observed. Present body armour components both SAP and HAP are made using UD fabrics only, since they can provide high-energy absorption per unit weight. On the other hand, woven fabrics are made by weaving the yarn with the help of looms. Generally, two types of weaves are used for armour applications, i.e., plain weave and basket weave [20]. The yarn in length direction is called warp, and other direction yarn is called weft or fill. The mechanical properties in any direction are proportional to the amount of fiber by the volume oriented in that direction. The fabric is specified with its weight in grams per square meter (GSM), type of weave, and count. The woven fabrics will have crimp effect and thus restrict the movement of fibers during ballistic penetration. Woven fabric-based laminates are more stiff compared to UD fabric-based laminates; therefore, deformation of the laminate during ballistic impact is relatively less. Therefore, these fabrics are used to make laminates for helmet and vehicle armour applications. However, the merits and demerits of both woven fabric and non-woven fabrics for armour applications are still debatable.

Matrix

The main roles of matrix in armour-grade composites are:

- To keep the fibers together.
- Distribute the impact load uniformly across the layers.
- To protect the reinforcement layers from environmental and mechanical degradation.
- To support fiber layers for undergoing progressive delamination during impact.

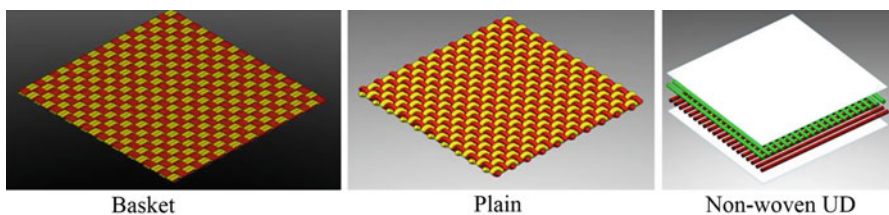


Fig. 6 Different types of weave patterns commonly used for armour applications

Two types of polymer matrices, namely, thermoset and thermoplastic, are used for making laminates. Polymers which undergo irreversible cross-linking reaction and become rigid plastics during the curing process are referred to as thermosets. Examples for thermoset matrixes are epoxy, phenolic, vinyl ester, etc. Phenolic modified with rubber such as polyvinyl butyral (PVB) is the first accepted matrix for making armour-grade laminates as per MIL-L-62474B standard. Comparative study has been carried out on modified phenolic and epoxy matrix using glass fiber as common reinforcement and reported that modified phenolic shows better ballistic performance than the epoxy matrix against small arms ammunition [21]. Major advantages of thermoset matrix are that they have got good wettability with reinforcements due to their low viscosity, presence of functional groups, ease of fabrication and its relatively low cost. The fabricated laminates show excellent environmental stability, moisture resistance, fire retardancy, and durability. However, thermoset resins have got certain limitations such as limited storage life of prepregs, environmental issues, unable to recycle, and importantly low strain to failure which limits the deformation of laminates under high-impact loads generated by high-velocity projectiles. These properties limit their usage for certain specialized applications. On the other hand, polymers which do not undergo any chemical reaction during the curing process and undergo only reversible physical changes through melting by the application of heat and pressure are called thermoplastic polymer matrix. Polypropylenes (PP), polyethylene (PE), and styrene-isoprene-styrene (SIS) are examples of thermoplastic polymers. In the case of UHMWPE fibers, thermoplastic matrix such as styrene-isoprene-styrene (SIS) and polyurethane elastomer are used [22]. As thermoplastic matrix does not form any chemical bond with the reinforcements, the laminates are generally less stiff compared to thermoset matrix-based laminates and undergo large deformation during the ballistic impact. The advantages of thermoplastic materials are their unlimited storage life, shorter fabrication time, and environmental friendliness. The thermoplastics have low service temperature; however, this is not very critical factor for armour applications.

Fabrication of Armour-Grade Composite Laminates

Laminate fabrication process also plays an important role on ballistic performance of armour besides their material properties. Commonly used fabrication methods for making composite laminates are hot compression molding, vacuum-assisted resin transfer mold (VARTM), and autoclave molding process. The type of fabrication process to be followed is depending on application, cost, and production numbers. Out of these three methods, hot compression molding is the widely used technique due to its low cost and high productivity. Since the armour composite will have lower resin content, the application of high amount of pressure during laminate fabrication gives excellent consolidation and supports for higher energy absorption especially in the case of HPPE laminates. Figure 7 shows photograph of laminating hydraulic press and schematic drawing of mold. In the case of thermoset laminate, the fabrication process is slightly different. Figure 8 shows various steps involved

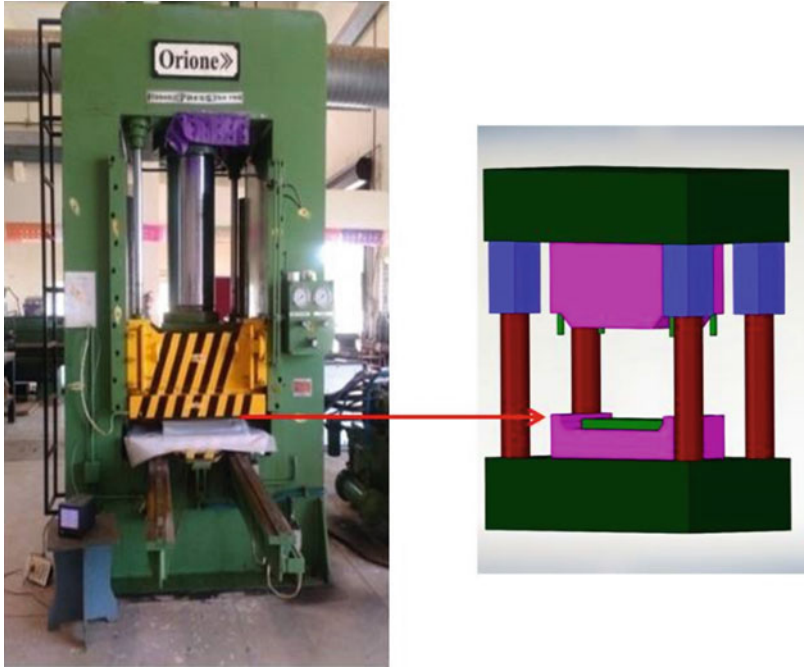


Fig. 7 Photograph of laminating hydraulic press and schematic drawing of mold

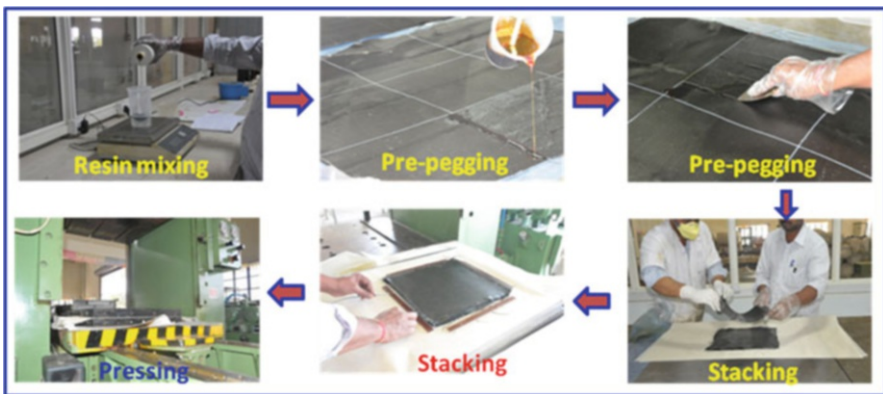


Fig. 8 Sequence of various steps followed during laminate fabrication process

during the fabrication of composite laminate. Essentially, the process involves application of resin on fabrics followed by curing the stack of resin-coated fabric layers under heat and pressure. Cure parameters such as pressure, temperature, and holding time depend on type of resin, size of the laminate, and its thickness. Coating of resin on dry fabric layers is carried out either manually or through automatic process, and the resin-coated fabrics are called prepreps. Generally, fiber volume

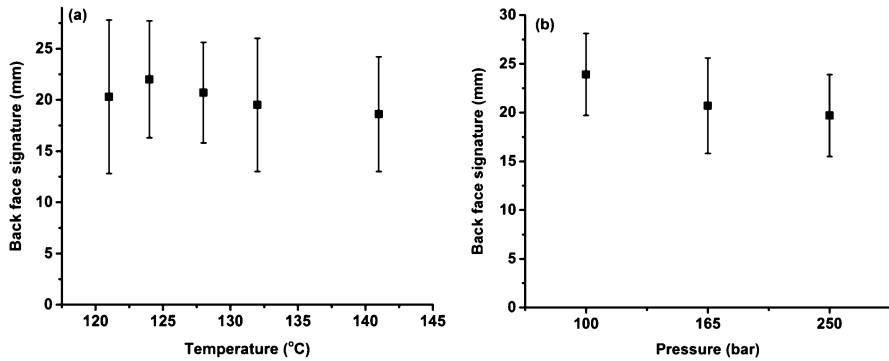


Fig. 9 Effect of temperature and pressure on body armour back face signature

fraction in the final cured laminate will be maintained in the range of 0.62 ± 0.02 . Studies have been carried out on the effect of pressure and temperature on ballistic performance of HMPE laminates and found that increasing the pressure from 165 bars to 250 bars has resulted in reduction of back face signature (bulge) which is very critical for body armour applications. Figure 9 shows change in back face signature of laminate pressed under different pressure conditions. However, increasing the processing temperature beyond 135°C was found to be detrimental to the ballistic performance as it degrades the HMPE fiber properties.

Autoclave process is used for making complex-shaped armour components which cannot be made by any other fabrication techniques. In autoclave process, pressure, vacuum, and temperature are applied simultaneously on the component. Hence, the quality of the laminate will be better, but production cost is very high as compared to other techniques. The typical pressure applied during autoclave process is in the range of 10–15 bars which is very low when compared to compression molding technique. In spite of low pressure, the fabricated laminate will have good quality due to the presence of vacuum environment inside the component. Another process is VARTM which is generally used for making larger size armour components. The advantage of this process is that there is no size limitation. However, curing has to be carried out at room temperature only. Therefore, resin system should be selected suitably, and final cured laminate will have lower glass transition temperature than the resin cured at higher temperature. The process is more suitable for making structural armour components for vehicles.

Penetration Mechanisms

Penetration in Ceramics

Failure behavior of ceramic materials on projectile impact has been of the interest for many researchers for better understanding and also development of new materials. Despite of the great efforts by many researchers, even today a complete

understanding about the failure mechanisms and quantitative prediction of ceramic performance is still lacking. However, over the years, a fairly good qualitative understanding on the ceramic failure process upon projectile impact has been generated. The complexities involved in quantitative prediction of ballistic performance are that it is not only an intrinsic material property, but it also depends on the geometry and boundary conditions of both the target and the projectile material. An important contribution to armour science was from Hauver et.al, who discovered that the projectile can be completely defeated at the ceramic surface itself without penetrating into it, which is called as “interface defeat” [23]. Following Hauver, the studies of Lundberg et.al are very fundamental for the understanding of projectile defeat and ceramic failure by “dwell” and “interface defeat” [24]. The erosion and radial flow of high-velocity projectile at the ceramic surface with no significant penetration are called “dwell.” Moreover, the duration of dwell can vary from fraction of projectile interaction time to complete defeat of the projectile. The duration of “dwell” is continued till the complete erosion of the projectile at the target surface; it is termed as “interface defeat” [25]. The work of Shockey et.al has given considerable insight into the failure mechanisms of ceramic materials; they studied ceramic materials such as Al_2O_3 , SiC, B_4C , and TiB_2 and observed a similar cracking pattern but different numbers and sizes of cracks on all ceramic materials [26, 27]. They found that there was no damage below the threshold projectile velocity, and the velocity is increased to form cone cracks, radial cracks, lateral cracks, and median vent cracks. As the projectile velocity is further increased, more and longer ring cracks were formed similar to the quasi-static Hertzian ring cracks, with the innermost cone to grow first.

Sherman et.al studied the failure of thin ceramic tiles using quasi-static and dynamic projectile impact and found that the projectile impact on ceramic tiles produced both types of damages such as quasi-static damage and dynamic damage caused by stress waves [28]. The quasi-static damage is characterized by large fragments, and dynamic damage is characterized by small fragments. They also found that the major failure modes are through the formation of tensile radial cracks at the rear side, shear-dominated cone cracks initiated from contact zone, and fragmentation of cone crack envelope under compressive stresses.

Several penetration studies on confined thick ceramic tiles by long rod projectiles have shown that the resistance to projectile penetration on a ceramic target is governed by two processes such as comminution followed by granular flow behavior of the pulverized ceramic fragments [29–31]. The flow motion of the ceramic particle around the projectile also erodes the length of the projectile which further dissipates energy. Therefore, understanding of the mechanism of comminution and flow behavior of comminuted ceramic is important to predict the rate and extent of penetration. The projectile penetration process on a confined ceramic target by a long rod is shown in Fig. 10. The ballistic impact studies on ceramic targets have shown the crushing of a small quantity of the ceramic within about two penetrator radii in front of the advancing penetrator, and the highly comminuted ceramic at the leading edge of the penetrator is often called as “Mescall zone” [32–34]. The penetrator can only penetrate into a confined ceramic target by moving out the failed ceramic

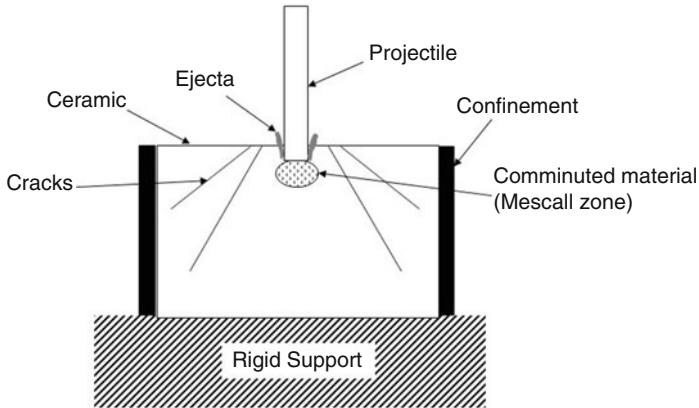


Fig. 10 Projectile penetration in confined thick ceramic tile

material at the front edge of the penetrator initially in the lateral direction and then in the direction opposite to the penetration, so that a tunnel with diameter larger than the projectile is produced. It has also been found that the resistance to comminution is a significant factor that governs the ballistic performance of a ceramic material [35]. Hence, the penetration resistance in ceramic targets is governed by the shear strength of both the intact and comminuted material. Shear failure in ceramics can be accommodated either by plastic deformation, wing-crack formation, or combination of both. Therefore, ceramic materials' ability to accommodate the shear failure by microplasticity decreases the potential for (macro) brittle failure of the material. In summary, for better ceramic armour performance, cone and lateral crack formation should be resisted, more dilatant (bulking) fragment beds should be formed by opening up of wing cracks, comminution time should be prolonged so that it creates more difficulty to introduce Mescall zone, and the flow resistance of the fragments should be increased through fragment geometries which can give more resistance to the flow.

Penetration in Composite Laminates

The penetration mechanism in laminates is totally different. During ballistic impact, if the projectile travels through the thickness of the target plate and breaches the rear surface of the target, it is referred to as perforated or complete penetration (CP); otherwise, it is considered as partial penetration (PP). Ballistic performance of a composite laminate depends on many aspects such as type of laminate, its thickness, type of projectile, strike velocity, angle of impact, etc. Failure behavior of composite laminate at entry and exit side of projectile is different. This is more predominant when the thickness of laminate is twice the projectile caliber. At the entry stage, compression and shear cutting of fibers are predominant, whereas at back side of the laminate, the failure is mainly by fiber stretching, displacement of fibers, and

delamination [36]. Many of the researchers observed that ballistic limit is a function of laminate thickness. Figure 11 shows change in energy absorption and failure mode with increase of laminate thickness. The energy absorption of laminate increased nonlinearly with increase of thickness; this is due to change of laminate failure modes.

In the case of thin targets (<10 mm this case), delamination is not a major failure mechanism since there is not much interaction time available between the target and projectile, but it is predominant in thick composite laminates. Due to this reason, higher thickness laminates show higher energy absorption. Figure 12 shows change in laminate failure mode with increase of thickness.

Since the laminates show different failure modes across the thickness, it is an ideal choice to use hybrid concept by using combination of fibers along the projectile path which can amplify different energy absorption mechanisms. Figure 13 shows

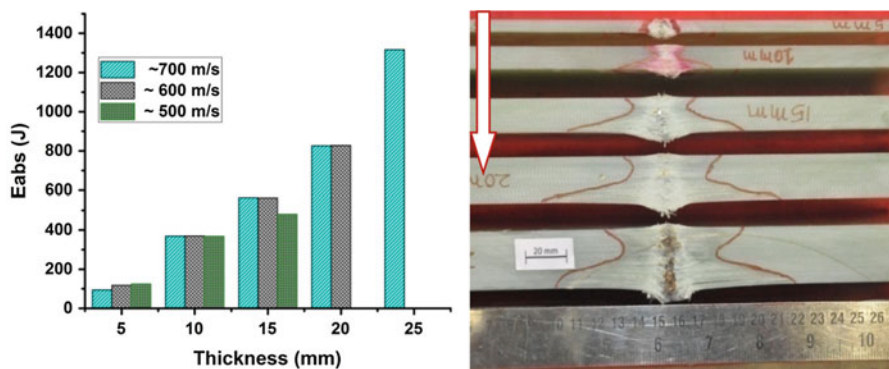


Fig. 11 Change in energy absorption and failure mode with change of thickness in E-glass/epoxy against AK-47 Projectile Refs. [24, 41]

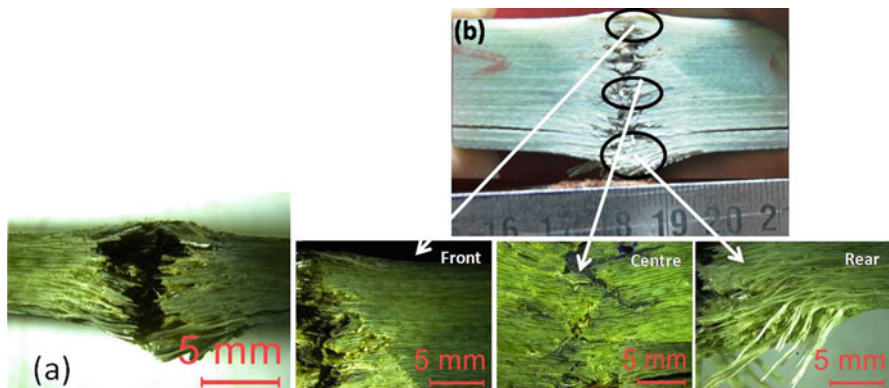


Fig. 12 Stereo images of post-impacted E-glass/epoxy composite laminates (a) 5 mm and (b) 25 mm thick

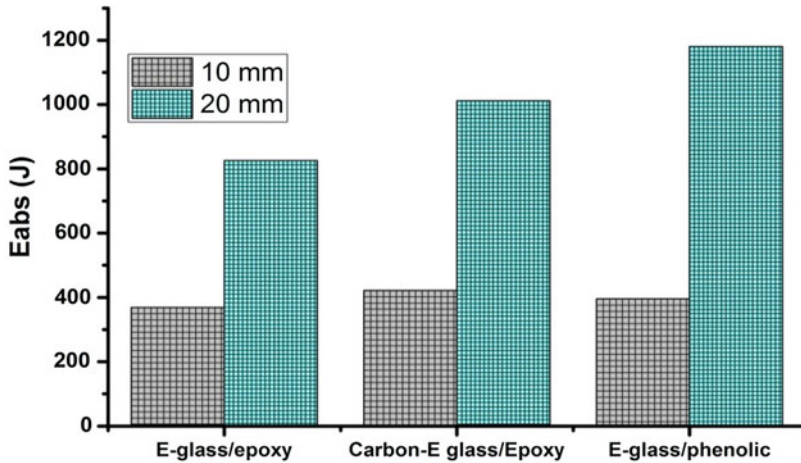


Fig. 13 Comparison of energy absorption among different composite laminates

comparison in energy absorption for different composite laminates having combination of fibers and matrices against AK-47 mild steel projectile. At lower thickness (10 mm), energy absorption between the laminates was found to be similar, whereas at higher thickness, the energy absorption was varied from 780 to 1200 J with the change in type of fibrous reinforcements and matrix.

Though the fiber is the main responsible constituent for energy absorption of composite laminate, matrix has also a significant role to play. Generally, in armour-grade composites, the amount of matrix is very low. The influence of laminate properties like interlaminar shear strength (ILSS) and resin content on ballistic behavior of composite laminate has been studied and reported by many authors. It is said that the ballistic performance increases with the decrease of laminate shear strength. For example, Dyneema laminate which has lower ILSS shows higher ballistic performance than carbon/epoxy laminate [37]. Modification of matrix and its effect on mechanical and ballistic impact properties of glass composites laminate has been studied and found that the addition of reactive liquid rubbers to polyester matrix leads to decrease in damage area and increase in residual strength and fracture toughness of the composite [38]. During the penetration process, significant amount of energy is absorbed by interfacial sliding between matrix and fiber during delamination and fracture of composites. The type of matrix used and matrix/fiber interface in the composite laminate decides ease of interfacial sliding. Figure 14 shows high-speed video images of 25-mm-thick glass laminates made of two different matrices impacted against AK-47 projectile. Phenolic matrix which has moderate bond strength with fiber has supported for more delamination and stretching than epoxy matrix. Due to this, the damage area also varies; Fig. 15 shows C-scan analysis of impacted laminates having varying amount of delamination generated under ballistic impact. The difference in damage area is due to the presence of different matrices and their interfacial properties.

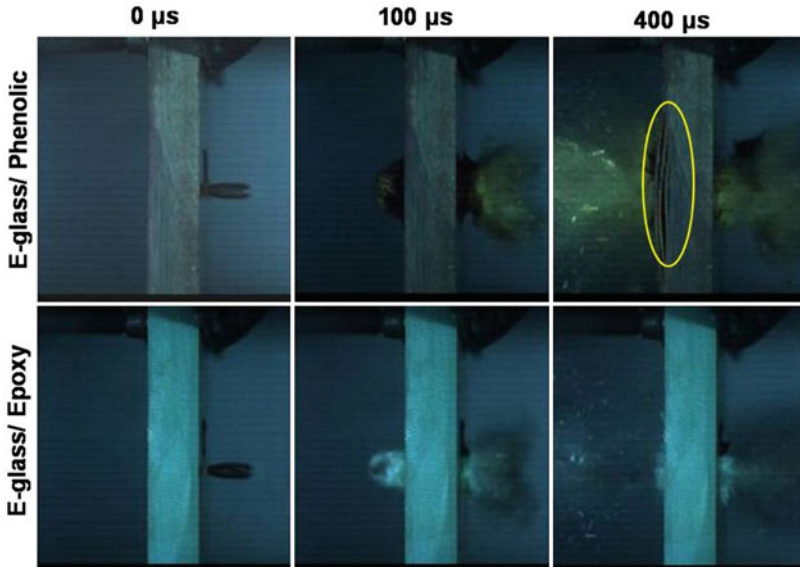


Fig. 14 High-speed video images of 25-mm-thick composite laminate

Ballistic Test Methodologies

In general, armour designer looks for protective solutions with a lesser weight penalty against any given threat. However, assessing armour performance with its absolute weight is not a good idea since the weight increases with increase in armouring area. Therefore, the weight of the armour system per unit area otherwise simply called its areal density (AD) is generally used to measure the performance of any armour system. The unit of AD is kg/m^2 .

$$\text{Areal density (AD)} = \text{Weight of the armour system}/\text{area of the protection} \quad (1)$$

But, if it is required to compare the ballistic performance of any two armour systems, the standard way is to compare the ballistic performance of the armour with that of RHA steel. The mass efficiency (E_m) is a dimensionless quantity used for comparing the ballistic performance of any armour system defined as below [1].

$$E_m (\text{Armour}) = \text{AD}_{(\text{RHA})}/\text{AD}_{(\text{Armour})} \quad (2)$$

In order to design any new armour, the selection of suitable materials is done either based on the existing ballistic test data available with the designer, literature data or combination. This ballistic test data is generated from various types of tests conducted on a laboratory scale. Techniques pertaining to testing of ceramics and composites can be broadly categorized into three groups, namely phenomenological, armour material

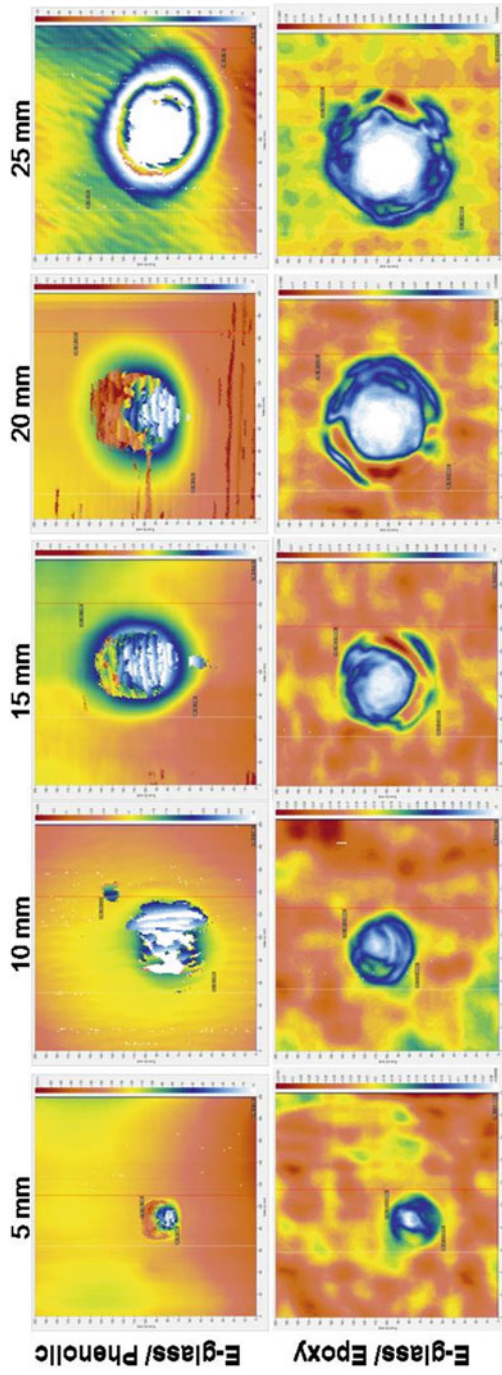


Fig. 15 C-scan images of post-impacted composite laminates Ref. [21]

characterization and armour design oriented [39]. Out of these, the armour material characterization techniques such as depth of penetration (DOP), semi-infinite penetration, residual velocity, design-oriented tests like ballistic limit test (V_{50}), and protective areal density test (PAD) are discussed here.

Threat Levels and Standards

Ballistic evaluation of armour is essential to approve any design. Test methodology to be adopted for accepting the armour design has to be decided mutually by the designer and the user. Depending on the application, various types of ammunition and standards are being used worldwide for proofing armour products. Threats are divided into two types that are kinetic energy (KE)- and chemical energy (CE)-based threats. The broad classification of different threats is shown in Fig. 16.

Kinetic energy threats are further divided into two types, namely, deformable and non-deformable. Bullets made of lead or mild steel material are called deformable or soft bullets. Examples are small arm ammunition such as 9 mm SMC, AK-47, SLR, etc. In the case of non-deformable bullets which are also called as armour piercing (AP), the bullet material is made from either hard steel, tungsten carbide (WC), or tungsten heavy alloy (WHA). For deformable bullet, the best armour is polymer composite material, and 100% lightweight protection can be achieved with PMC alone. In the case of hard core bullets, PMCs alone cannot provide 100% lightweight protection. High hardness ceramics backed by composite material are considered to be the best choice of material. For WHA projectiles, a combination of steel, composite, and ceramic is considered to be an ideal approach. Depending on armour application, the ammunition is categorized into different groups in various test standards for carrying proofing of armour

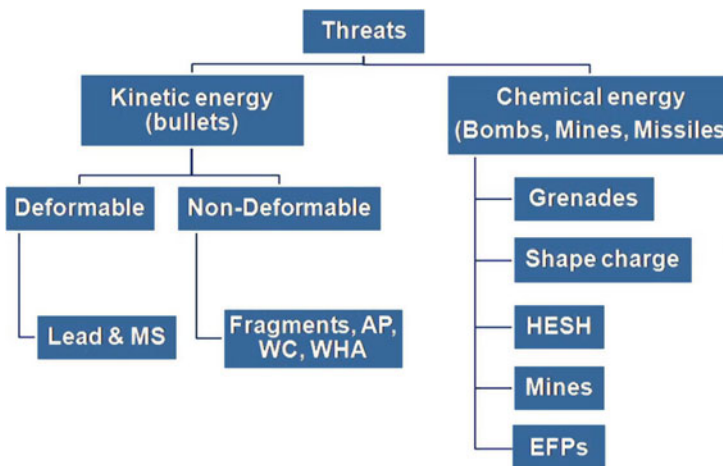


Fig. 16 Classification of threats

Table 3 Various armour testing standards and their applications

S. no	Standard	Country	Application
1	NIJ Standard 0101.06 (2008)	USA	Bullet proof jacket
2	IS 17051-2018	India	Bullet proof jacket
3	GOST 34282-2017	Russia	armour protection of cars
4	VPAM PM-2007	Germany	Ballistic materials
5	EN1063:1999/ EN 1522:1999	European	Glasses, windows, doors, ballistic materials, etc.
6	STANAG 4569 (AEP-55, Vol.1, 2005)	NATO	Logistic and light combat vehicles
7	CDA-99, 2005	India	Steel armour plates

products. For personnel armour applications, test standards such as Indian standard IS 17051:2018, National Institute of Justice (NIJ) 0108.01, and European nation (EN) 1522/1523 are referred for the evaluation of armour products [40]. In the case of vehicle armour testing, Russian GOST R50963-96, CDA-99, North Atlantic Treaty Organization (NATO) standard STANAG 4569, and AEP-Vol-1 are followed [41, 42]. GOST R50963-96 has total six levels covering 9 mm to 7.62X54 R AP projectiles. GOST and CDA-99 standards are suitable for steel armour materials. STANAG 4569 has six levels covering from 5.56X45 to 30X173 APDS projectiles. This standard is being widely adopted by many users for evaluation of light combat vehicle or armoured personnel carrier made of steel, ceramic composite, and transparent materials. Table 3 gives brief details of various standards used for armour testing.

Depth of Penetration Test

In the mid-1980s, an attempt to standardize an experimental method to rank ceramics for armour applications led to the development of this technique [43, 44]. Since then, the depth of penetration (DOP) test has been widely used for many years for ranking the protective value of ceramic materials. This test is essentially a simple and straightforward method which can give definitive results. In practice, however, a significant number of factors must be taken into account to achieve reliable and comparable results, because this is an indirect ballistic test method in which the ballistic efficiency of ceramic material is evaluated using the residual DOP obtained in a ductile (metallic) backing material. The DOP test configuration is shown in Fig. 17.

In DOP test configuration, the backing material thickness is chosen as large (semi- infinite) as possible, so that the projectile penetration in the backing is not influenced by the backing thickness. In this test configuration, the ballistic performance is measured using the ballistic data on reference DOP (projectile penetration in the backing material) and the residual DOP (projectile penetration in the backing material after penetrating ceramic tile). The ballistic efficiency of

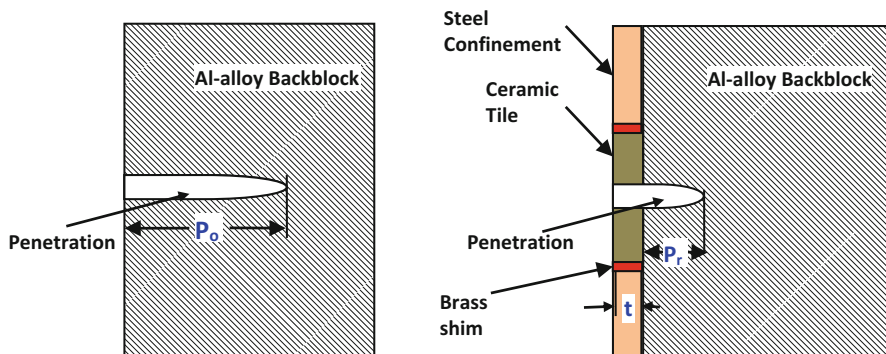


Fig. 17 Schematic diagram for the depth of penetration (DOP) test. (i) Reference depth of penetration (P_o) in the backing material. (ii) Residual depth of penetration (P_r) in the backing

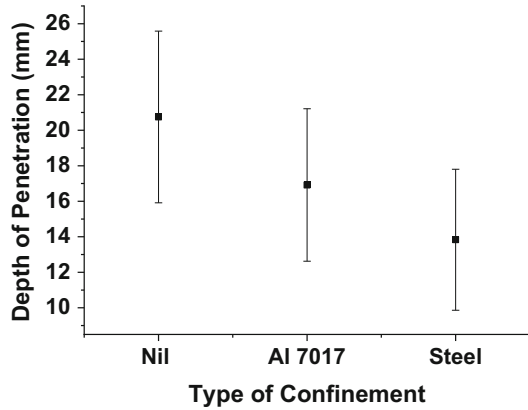
ceramic materials tested with DOP configuration is measured using differential efficiency factor (DEF) as given by Rosenberg et.al during the late 1980s. The formula is given below:

$$\text{Differential efficiency factor (DEF)} = \frac{\rho_b \times (P_o - P_r)}{(\rho_c \times t)} \quad (3)$$

where ρ_c is the density of the ceramic material, ρ_b is the density of the backing material, P_o is the reference depth of penetration in the backing material, P_r is the residual depth of penetration in the backing material, and t is the thickness of the ceramic tile.

Steel confinement is often used around the ceramic tile in order to mimic the effects of a laterally infinite ceramic target. The confinement is used to minimize the reflection of impact-induced stress wave from the periphery of the ceramic tile and to maintain impact-induced pressure. The steel confinement is tight fitted with the ceramic tile by inserting a fully annealed brass shim in between the steel confinement and the ceramic. This shim has similar acoustic impedance to that of steel, but being soft will conform to any small irregularities in the mating surface between the steel and the ceramic, providing an excellent acoustic interface. Any small pre-compression of the ceramic has a negligible effect upon the intrinsic ceramic performance as the small amount of pressure that can be applied is negligible compared to the 5–20 GPa required to increase significantly the failure strength of the material [45]. In order to prevent the tile size from influencing the DOP result, ceramic tile size should be kept at least 30 times the projectile diameter for relatively low projectile velocities and at least 15 times for impact velocity above 1600 m/s. Therefore, if the available ceramic tile is smaller in size, it should be confined in a steel frame to mimic a larger tile. The important factors which can affect the ballistic performance of ceramic materials in DOP test are briefly discussed below with experimental results.

Fig. 18 Effect of radial confinement on the residual DOP of B_4C ceramic



Effect of Radial Confinement

It is well known that the confinement has a positive effect on the ballistic performance of ceramic materials. Moreover, the type of the confinement material also has an effect on the ballistic performance. The effect of different radial confinements on boron carbide tile is shown in Fig. 18.

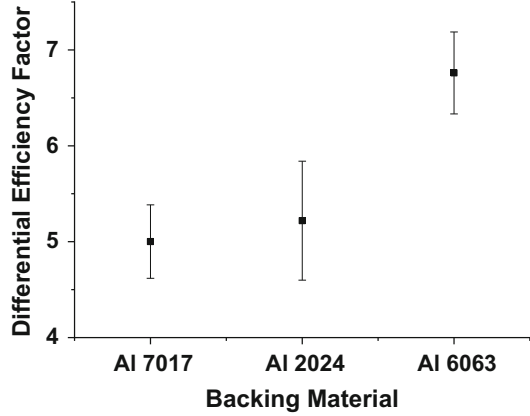
It is found that B_4C tile without confinement produced more residual DOP followed by Al7017 alloy and steel confinement produced least residual DOP. This decrease in residual DOP of B_4C tile radially confined in steel compared to aluminum alloy or no radial confinement is due to higher acoustic impedance and high strength of steel.

Effect of Backing Material

Even though the DOP test is a simple and easy method for ballistic evaluation of ceramic materials, it suffers from a major disadvantage of producing inconsistency in ballistic results due to variation in backing material properties. Therefore, often the reported ballistic efficiency of identical ceramic materials is found to differ considerably. Another problem in dealing with DOP test data is that often the ballistic efficiency of ceramic material is not evaluated using a single type of backing material. Instead it is evaluated with different types of backing materials which makes the comparison of ballistic efficiency among different ceramic materials very difficult. In DOP test, both reference and residual depth of penetration (DOP) increase with decrease in strength of the backing material. Moreover, the residual DOP also increases (nearly) proportional with reference DOP. Hence, the calculated DEF is found to increase with decrease in strength of the backing material, even if calculated for identical ceramic tiles, as shown in Fig. 19.

In order to overcome this disadvantage, a normalization procedure was suggested by Savio et.al, which eliminates the influence of backing material properties on the calculated ballistic efficiency [46, 47]. The newly defined normalised differential efficiency factor (NDEF) is defined as below:

Fig. 19 The differential efficiency factor (DEF) of B₄C with respect to different backing material



$$\text{Normalized differential efficiency factor (NDEF)} = \frac{(P_0^* - P_r^*) \times \rho_b}{t \times \rho_c} = \frac{(100 - P_r^*)}{t} \times \frac{\rho_b}{\rho_c} \tag{4}$$

where normalized residual

$$\text{DOP } (P_r^*) = \left(\frac{P_r}{P_0} \right) \times 100 \tag{5}$$

and normalized reference

$$\text{DOP } (P_0^*) = \left(\frac{P_0}{P_0} \right) \times 100 = 100 \tag{6}$$

In Eq. (4), the term $\frac{(100 - P_r^*)}{t}$ is called normalized thickness efficiency factor (NTEF), and the ratio $\frac{\rho_b}{\rho_c}$ can be called as density efficiency (DE) of the tested ceramic material in comparison with the backing material.

Since the penetration produced in the target material is not influenced by the target density in Eq. (4), the backing material density (ρ_b) can be assumed to be unity. Therefore, another modified ballistic efficiency, called normalized ballistic efficiency (NBE), is also defined as below.

$$\text{Normalized ballistic efficiency (NBE)} = \frac{(100 - P_r^*)}{t} \times \frac{1}{\rho_c} = \frac{(100 - P_r^*)}{t \times \rho_c} \tag{7}$$

The effect of above normalization is best described in Fig. 20. It can be found from the figure that both NDEF and NBE have produced different values but almost the same ballistic efficiency trend for different backing materials for B₄C tiles.

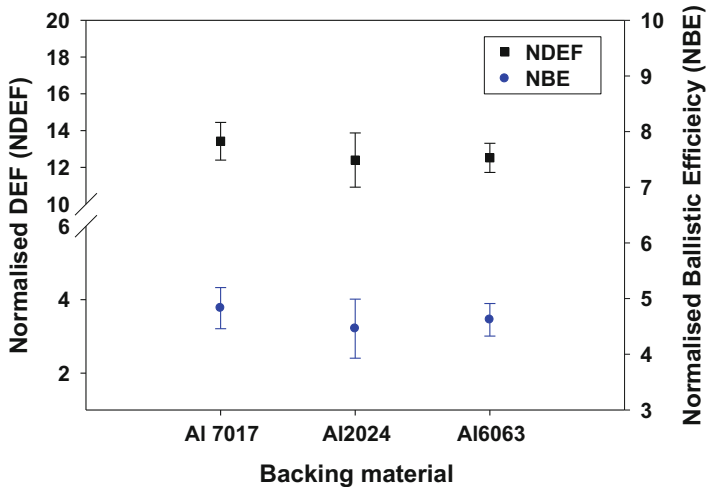


Fig. 20 The NDEF and NBE of B₄C tiles with respect to different backing materials

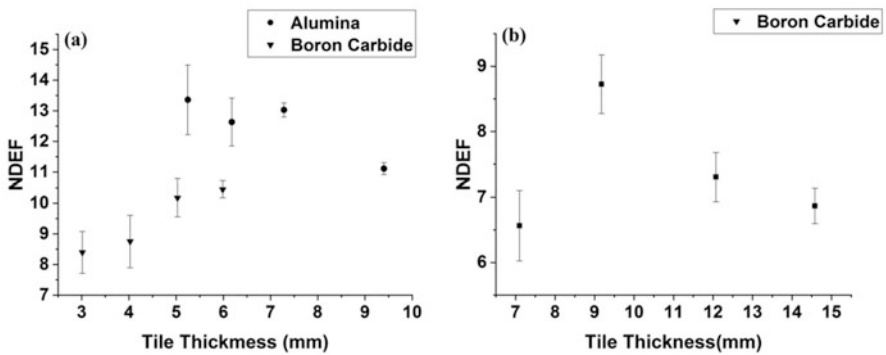


Fig. 21 Effect of tile thickness on the ballistic performance of different ceramic tiles (a) against 7.62 mm AP, (b) 12.7 mm AP projectiles

Effect of Tile Thickness

The performance of ceramic is not linear with respect to its thickness increase. Initially, ceramic efficiency increases with increase of ceramic thickness, and after reaching a saturation point, there is no improvement in the performance with further increase of thickness. Effect of tile thickness on NDEF for two ammunitions such as 7.62 mm AP and 12.7 mm AP has been shown in Fig. 21. It is observed that there exists some optimum tile thickness, for each type of ammunition, which produces maximum ballistic efficiency, and all other tile thickness (both lower and higher thickness) than optimum thickness invariably produces lower efficiency. Also it is found that the optimum tile thickness changes with respect to the type of ammunition and type of ceramic materials.

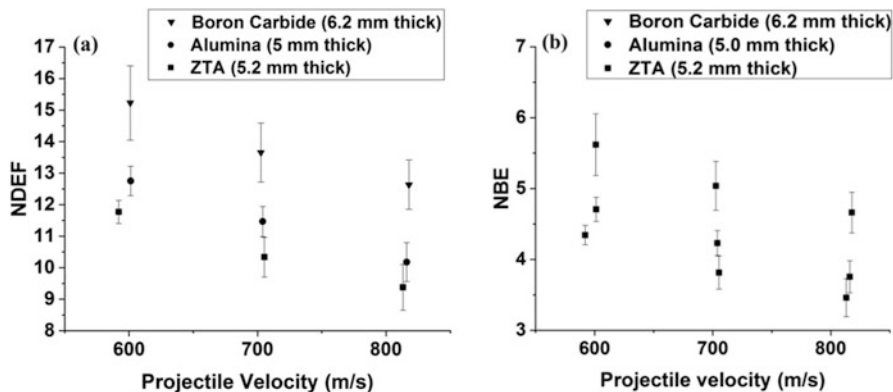


Fig. 22 Effect of projectile velocity on (a) NBE (b) NBE for different ceramic materials against 7.62 mm AP

Effect of Projectile Velocity

Projectile penetration efficiency in ceramic materials increases as the projectile velocity increases [48, 49]. Therefore, ballistic efficiency of ceramic materials is expected to decrease with increase in projectile velocity. Figure 22 shows change in ballistic efficiency of different ceramic materials with increase of projectile velocity.

Semi-Infinite Backing Test Method

In metallic targets, performing the semi-infinite penetration test is simple. In the case of ceramic targets, it is difficult to test due to their inherent brittleness and the material shatters during projectile penetration. Hence, metallic confinements are often used while performing semi-infinite penetration test on ceramic materials. The semi-infinite penetration experiments with ceramic materials are performed in reverse ballistic mode with the confined ceramic target launched at the desired velocity and impacted against a stationary tungsten long rod penetrator [50–53]. Details of experimental setup for carrying out reverse ballistic test are available [54]. The advantages of reverse ballistic experiments are many such as due to small-scale targets; it is easy to view the penetration depth as a function of interaction inside the target using flash X-rays. This data is useful for calculating penetration velocity and erosion of rod. Ballistic tests can be carried out with unconventional projectile geometries such as segmented projectiles [55]. But the major drawback in reverse ballistic experiments is since the ceramic target size is small (which is mainly controlled by the size of the gas gun), the corresponding projectile size should also be reduced accordingly, and hence, the issue of scaling becomes very important.

Semi-infinite penetration experiments can also be performed in forward ballistic mode, in which the projectile is launched to impact a stationary ceramic target. The

advantage of forward ballistic test is that it offers the possibilities of studying the realistic target configuration, and the test can be carried out using the service gun and ammunition or by using gas gun system. Since the target size will be larger compared to reverse ballistic test target, it is difficult to use X-rays for studying the penetration mechanisms inside the target. The semi-infinite penetration experiments are generally used to study the transition velocity of the projectile from interface defeat to penetration in ceramic materials. The data obtained from the tests can also be used to calculate penetration velocity and prediction of hydrodynamic on the behavior of ceramics and projectile during penetration. Further, comparison of semi-infinite penetration experimental results with hydrodynamic equation has also shown that when projectile velocity is sufficiently high, the linear equation can be reduced to hydrodynamic equation, i.e., $U = b_h V$, where $b_h = 1 / \left(1 + \sqrt{\frac{\rho_t}{\rho_p}} \right)$, and here the linear relationship between U and V is found within 7% of the hydrodynamic curve for high-impact velocities above 6 km/s [56, 57].

Residual Velocity Test Method

Residual velocity test is used for comparison of ballistic performance of various armour materials. In this test, projectile velocity is measured before and after the target. Velocity difference and projectile mass are used for calculating the change in projectile kinetic energy which is equal to the target energy absorption. Figure 23 shows schematic view of residual velocity test method. The tests can be carried out using either powder guns or gas guns with a suitable type of projectiles. This method is more suitable for lower thickness and soft target materials like composites, etc. However, for brittle targets like ceramics, it is difficult to measure residual velocity of projectile due to the generation of heavy splinters. Hence, this method is generally used for testing composite laminates and fabric layers. The advantage of the test is thin targets can be used and no backing material is required. Therefore, the complete penetration process can be viewed by deploying high-speed video or flash X-ray (FXR) systems. Figure 24 shows images of failure of target and

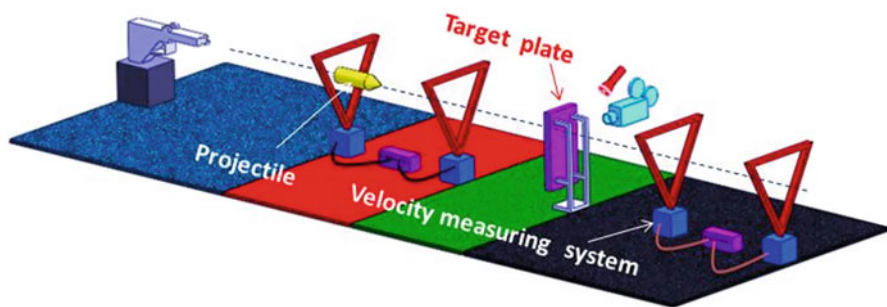


Fig. 23 Schematic experimental test setup for residual velocity testing

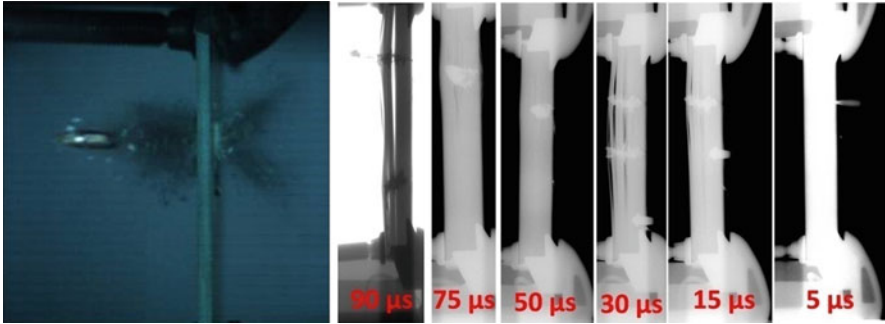


Fig. 24 Penetration behavior of laminate and projectile captured through high-speed video and FXR systems

projectile during the penetration captured by using flash X-ray and high-speed video systems.

Strike and residual velocities of the projectile can be measured by using suitable velocity measuring equipment placed before and after the target plates. Energy absorption of the armour material is calculated based on projectile strike and residual velocities using the given formula.

$$E_{\text{abs}} = \frac{1}{2}m(V_i^2 - V_r^2) \quad (8)$$

where.

m : Mass of the projectile

V_i : Initial velocity

V_r : Residual velocity

Ballistic Limit Test

Ballistic limit tests are design-oriented test methods used in applications. Generally, these tests demand large number of experiments to produce statistically meaningful results [39]. The ballistic testing is carried out by varying any one of two principal variables such as projectile velocity or the thickness/areal density of the target. In the first approach, the projectile velocity is varied while keeping the thickness/areal density as constant, and this test method is called as V_{50} test or the ballistic limit test. Crouch [58] in his recent book has given an excellent description about this test method. As per the military standard, the term ballistic limit is defined as the highest velocity at which a particular projectile consistently fails to penetrate the armour or the lowest velocity at which it penetrates the armour, at a specified angle of obliquity.

The underlying principle behind the ballistic limit testing is that for the given armour system, there will be mixed results (penetration/partial penetration) for a fairly narrow velocity band. The mixed result region is represented in a schematic probability curve for defeat of the armour as a function of projectile velocity as shown in Fig. 25. In Fig. 25, the velocity below which all projectiles are stopped by the armour is called V_0 , and the velocity above which all the projectiles are penetrated is called as V_{100} , and also an in-between velocity, called V_{50} , can be defined as 50% of the projectiles would be stopped and 50% of the projectiles would be perforated through the target. As per Zukas [59], any velocity in the mixed region can be used as the ballistic limit velocity, such as V_{10} , V_{90} , or V_{50} , but the advantage of V_{50} limit velocity is that the slope of the curve is greatest at V_{50} so that it can be located with greater precision. Therefore, as already described, in V_{50} ballistic test method, the target (armour) design (thickness, areal density, etc.) is fixed, but the impact velocity of the projectile is varied, so that the 50% protection velocity (i.e., there is a 0.5 probability that the target will be completely penetrated), otherwise called V_{50} , is often determined. Moreover, for design considerations, the velocity of zero penetration probability, V_0 , is also determined so that the armour can always be designed for a velocity (V_D) which is well below V_0 . In armour design, the safety margin (Δ) is defined as the velocity difference between the two quantities, V_0 and V_D , and finally the selected degree of safety margin (Δ) will depend upon the tradeoff between the required level of confidence and the desirability of achieving lightweight solution.

The reader can also refer to the US military standard “MIL-STD-662F, V_{50} ballistic test method” in which the V_{50} determination procedure has been elaborately described [60]. This standard is derived using Brucceton test method. The standard defines the procedure to be followed to establish the ballistic limit of armour materials in terms of precise velocity of impact which will produce 50% penetration.

Fig. 25 Schematic probability curve for defeat of the armour as a function of projectile velocity

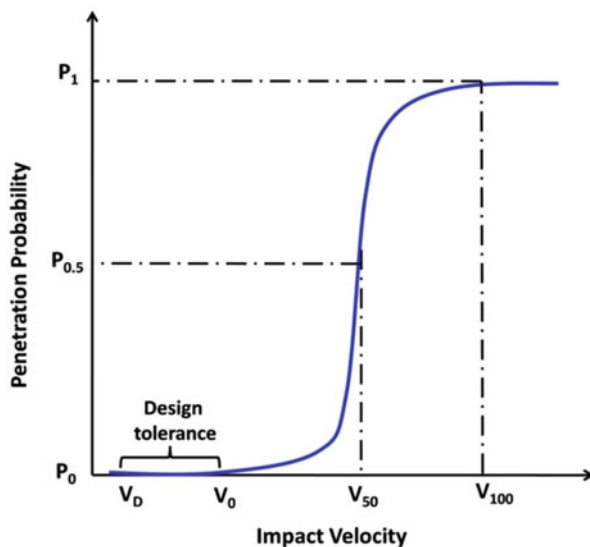


Table 4 Acceptable velocity limits for different pairs of shots

S. no.	Number of pairs	Acceptable velocity limit (m/s)
1	2	18
2	3	27
3	4	30
4	5	38

Fig. 26 Different caliber ammunition and fragment simulating projectiles

The impact velocity of the projectile is varied by increasing or decreasing the charge mass to get an equal number of partial penetrations and complete penetrations. The average of these velocities is said to be V_{50} value of that particular sample. The difference between the highest partial penetration velocity and lowest complete penetration velocity should be within the specified limits, and this limit varies with number of pairs. Table 4 shows acceptable velocity span for different pairs of shots. During ballistic limit determination, it is essential to follow strictly the velocity limits; otherwise, the test becomes invalid.

V_{50} ballistic limit test can be carried out using service ammunitions and or fragment simulating projectiles (FSPs). There are three different calibres of FSPs namely 0.22", 0.30", and 0.50" (Fig. 26) are used. Commercial armour material suppliers will specify their product V_{50} values against FSPs.

The caliber of FSP is chosen based on material thickness and its mechanical properties. MIL specifications of armour materials specify FSP V_{50} value for different thickness. The advantage of these data is that there is no confidential information disclosed and not related to any particular applications. Table 5 shows V_{50} ballistic limit of different materials according to MIL specifications [61–63].

Table 5 V_{50} ballistic limit of different armour materials against 0.30 FSP

Material	MIL STD	Areal density, kg/m ²	Ballistic limit, m/s
UHMWPE	MIL32398	4.9–5.0	≥623
Glass/phenolic	MIL-DTL-64154B	12.0–12.5	≥656
Aramid/phenolic	MIL-DTL-62474F Class C&D	25.0–25.5	≥793

Protective Areal Density Method

Generally, the requirement of any new armour is defined in terms of the threat projectile and its impact velocity. Therefore, the goal of any armour designer is to find out the lightest weight armour system by minimizing the areal density. This objective can be achieved by performing ballistic experiments in which only the parameter of interest is measured at a time by keeping all other variables as constant. It is known that in case of ceramic armour systems, the finite thickness of the backing does influence the ballistic performance of the ceramic material. Therefore, in ceramic armour design, it is essential to optimize the backing thickness also. Moreover, when the ceramic material is evaluated as “components” in a system, the most unambiguous method by which ballistic performance can be measured is through determining whether the target is partially penetrated or completely penetrated by the projectile. Therefore, in the second approach of ballistic testing, the impact velocity of the test projectile is fixed, and the AD of the target components (ceramic/backing) is varied. This test method is generally called as the protective areal density (PAD) test which was developed at Army Research Laboratory (ARL) for evaluation of materials, components, and armour systems in order to overcome the inadequacy of the existing ballistic testing techniques. In this test method, the test projectile characteristics such as projectile type, impact velocity, obliquity, and yaw are fixed. In essence, the PAD test involves determination of target AD (i.e., $PAD_{(pp = 0.5)}$), which provides 50% protection against a particular projectile with a specified impact velocity. Detailed description on this test method can be found in the papers of Adams and Savio et.al [64, 65]. The design and analysis of PAD test have been illustrated in Fig. 27. The PAD test can be performed in two possible ways such as along (i) constant backing areal density test line or (ii) constant ceramic areal density test line. But generally, the PAD tests are conducted along constant ceramic areal density test line, by varying backing areal density while keeping the ceramic areal density constant, since varying of backing thickness is a relatively easy task. In PAD test, ballistic test data on complete penetration/partial penetration is generated as a function of armour thickness or areal density for the armour system being studied. This binary data of complete penetration/partial penetration from PAD test can be statistically analyzed using probit, logistic (logit), or complementary log-log methods. NIJ standard 0101.06 has prescribed logistic regression method for the analysis of

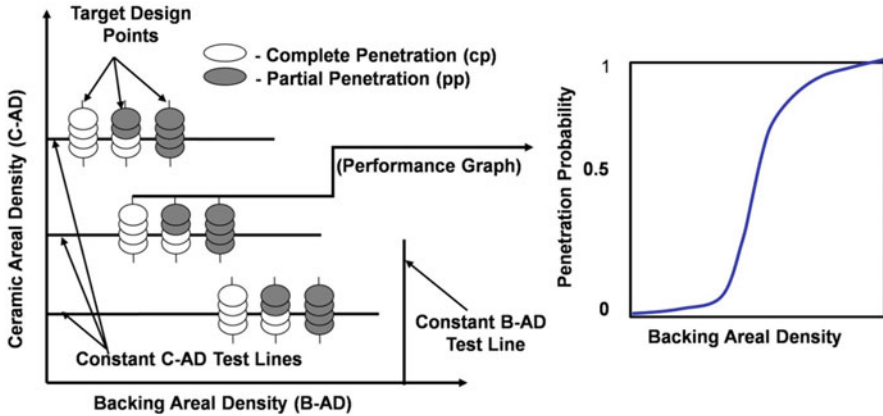


Fig. 27 Design and analysis of experiments in PAD test configuration

ballistic limit test data for body armour [66]. From the statistical analysis of binary ballistic data, the protective areal density, $PAD_{(pp = 0.5)}$, of the armour can be estimated along with its lower and upper bounds of confidence interval which is very much useful in the design of armour. Therefore, similar to the armour design criteria followed in V_{50} ballistic limit testing, in PAD test too, the zero penetration probability, i.e., $PAD_{(pp = 1.0)}$, can be determined so that the new armour can be designed for protective areal density (PAD)_D which is well above $PAD_{(pp = 1.0)}$.

Ceramic Composite Armour Modules

The use of ceramics and polymer composites for armour systems is well known because of their lightweight yet provides similar ballistic performance compared to RHA material. Figure 28 shows typical mass requirements of RHA and ceramic composite armour to defeat 12.7 mm AP(I) projectile. Ceramics are distinguished by their high hardness, compressive strength, and very rigid structure. Different types of ceramics are developed and established on the commercial scale. Among all the ceramics available for armour applications, Al_2O_3 is the oldest and cheapest one and has been explored by many researchers for various threats. If weight is not very critical issue, then Al_2O_3 is the appropriate choice of ceramic material. Till today, most of the countries in the world use Al_2O_3 for manufacturing vehicle armour. The next alternative material for vehicle armour is SiC which can give weight saving due to its lower density and higher hardness. For personnel applications, B_4C is used due to its lowest density among the ceramics with highest hardness. However, cost of the armour also increases with the decrease of weight due to their high processing and machining cost. Hence, B_4C is restricted to specific applications like BPJ, helicopter armour where weight saving of few hundred grams is also significant reduction.

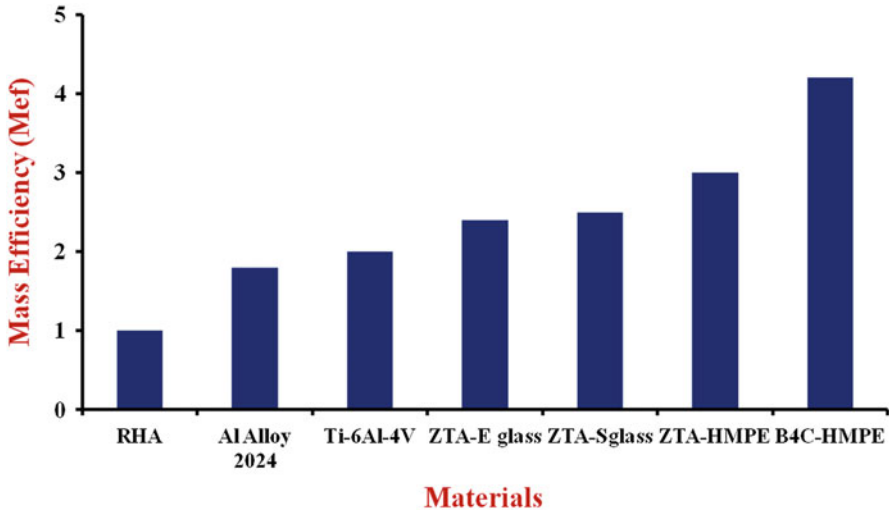


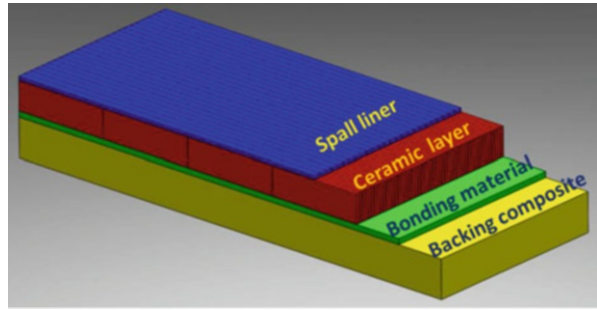
Fig. 28 Mass efficiency comparison for different armour materials against 12.7 mm AP (I)

Fabrication of Armour Modules

Sometimes good armour shows inferior ballistic performance due to defect fabrication method followed. Especially these types of problems are more common in ceramic polymer composite armour modules. Hence, it is very important to use an appropriate fabrication technique while fabricating the armour modules. Ceramic composite armour consists of various layers made of different materials. Figure 29 shows typical cross section of ceramic composite armour. Each of these layers has very important role to play, and armour fabricator has to integrate these layers carefully to get the best ballistic performance.

The role of frontal ceramic layer is to withstand the shock of an incoming projectile and shatter it. In the process, ceramic also gets shattered due to brittleness. It is common to provide a polymer composite or metal backing behind the ceramic to support and withstand the deformation of the ceramic as it is impacted. Since ceramics are brittle and undergo cracking easily due to impact load and shock, it is difficult to get multihit protection with larger size ceramic plates or monolithic armour. This problem can be avoided by using smaller size and different-shaped ceramics. Researchers have developed various shapes of ceramics such as pellets, stars, hexagonal, circular, and square thanks to the improvement in ceramic processing methods. The performance of armour is synergy of materials and mechanics. Hence, one should use proper shape of ceramic which can amplify the projectile defeat mechanisms. As discussed previously, to get multihit capability as per STANAG standards, it is essential for the armour to withstand against close inter-shot distances against AP threats. To achieve this, each ceramic body has to behave independently, and propagation of the impact shock waves needs to be minimized or completely arrested to control the collateral damage of surrounding ceramics thereby

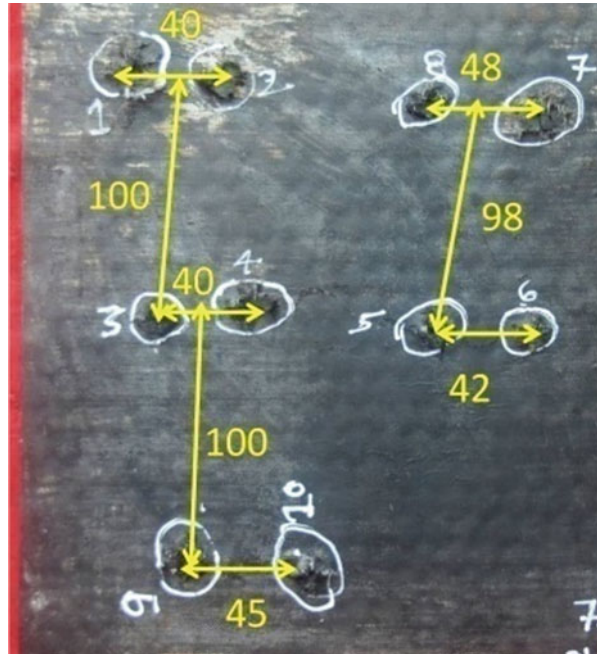
Fig. 29 Cross-sectional view of typical ceramic composite armour



enabling it to withstand the next impact successfully. Keeping in view of the above requirements, it is crucial to select a suitable matrix material which can fulfil the following requirements while housing the ceramic segments. The matrix material should behave like a viscous fluid locally at high strain rates; thereby, it can isolate the adjacent ceramic components from the impact shock by attenuating the stress waves and vibrations coming from the backing plate. It should also absorb the shock waves and accommodate fractured ceramic pellets to avoid the lateral displacement. Figure 30 shows ballistic impact damage in ceramic armour subjected to multiple impacts.

Another important requirement of the matrix material is that it should withstand the weather conditions as seen by the combat system. Hence, each of these individual layers is prepared separately before integrating them. Mainly, three techniques are used for the fabrication of ceramic composite armour panels which are similar to composite processing techniques such as hot compression, autoclave, and VARTM process. Depending on the type of material and application, one of the above processing methods is used. In the hot press method, both pressure and temperature are used to fabricate armour panels. Ceramic bodies either in tile form or other shapes like pellets, etc. are embedded in a polymer matrix, and this process is called fabrication of ceramic armour panel. It is carried out using hot press with polymer elastomeric such as rubber, polysulfide, polyurethane, etc. The reason for choosing polymer elastomer is that they can be stretched up to 3–5 times of their original dimensions. Furthermore, after removal of the stress, these materials return rapidly to almost their initial size with no induced damage. Rubber matrix is preferred than other elastomers due to their availability, cost, and ease of processing. The second important component in ceramic composite armour is backing composite which allows the ceramic to perform at its best level. Polymer composites made of glass, aramid, or HMPE-based composites are the ideal choice of material to use as backing composites. These are bonded to ceramic layers with proper adhesives, and finally, spall liner is provided on top. However, the thickness of ceramic and composite layers is decided based on the threat level and application. Autoclave process is more suitable when bonding of backing plate to curved ceramic panels because pressure is applied uniformly on the entire area of armour panels. The process

Fig. 30 Ceramic armour panel tested as per STANAG 4569 standard (Distance between the shots in mm)



involves application of pressure, temperature, and vacuum simultaneously which ensures perfect and void-free bonding. However, autoclave process is the most expensive as it required sophisticated machinery compared to other fabrication methods.

Ballistic Performance Evaluation of Modules

Defeat mechanism in ceramic composite armour is different than what is seen in RHA. Upon impact of AP projectile on ceramic layer, the hard strike surface causes fragmentation of projectile tip, thereby increasing projectile ceramic contact area. Simultaneously, ceramic tile also undergoes cracking by formation of radial and conical cracks. Figure 31 shows schematic view of AP projectile interaction with ceramic composite armour and radiography image of post-impacted ceramic tile with radial cracks. The residual energy of the broken projectile and ceramic fragments is absorbed in the form of plastic or elastic deformation of backing composite layers.

Ballistic testing of ceramic armour is evaluated according to NIJ standard for personnel protection where the ceramic armour panel has to withstand single shot of 7.62X54 AP M2 projectiles on a 250X300 mm size panel. The back face signature (BFS) or bulge is very important, and it should not be more than 44 mm. For vehicle armour applications, EN 1063 or STANAG 4569 standard is used. These standards have covered a wide range of ammunition. The important points to be followed while testing ceramic armour is shot-to-shot distance, between the pair of shots,

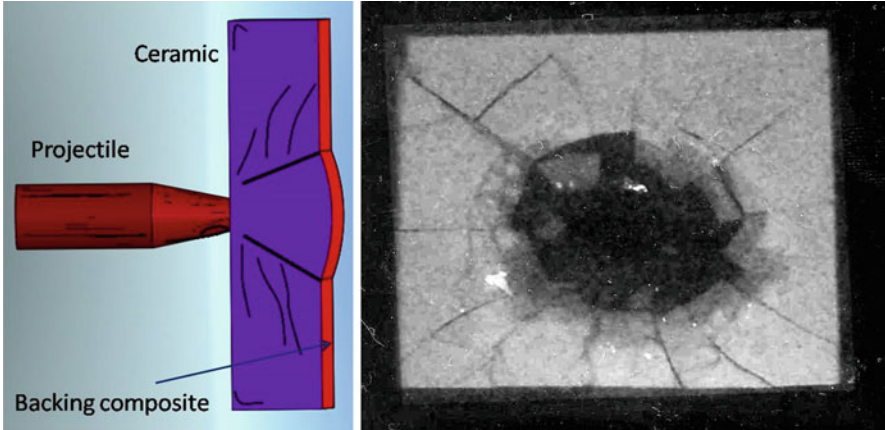


Fig. 31 Schematic view of AP projectile interaction with ceramic composite armour and radiography image of ceramic

Dimension definition	Value	Size (mm)	
		L 1-L3	L4
Distance between shots pairs(#1 & #2, #3 & #4)	N	25	50
Distance from midpoint of shots #1 & #2 to #3	L	100	200
Maximum tolerance on shot impact position	T	-0/+20	-0/+50
EZ (Min. dist. to component target edge/boundary)	E	25	50

The diagram to the right of the table shows a layout of four shot impact points labeled #1, #2, #3, and #4. Dimension N is the distance between pairs (#1, #2) and (#3, #4). Dimension L is the distance from the midpoint of the first pair to the second pair. Dimension T is the tolerance on the impact position. Dimension E is the distance from the impact points to the edge of the target.

Fig. 32 Details of inter shot distances for different threat levels

distance from the edge, and number of pairs. These distances vary depending on threat level. Figure 32 shows inter-shot distances and pattern of shots for evaluating multihit capability of armour for different protection levels as per STANAG 4569 test standard. The shots have to be fired in pairs while maintaining the specified distance between the pairs and within the pair of shots. It is usually 25 mm to 100 mm for rifle bullets and 50 mm to 200 mm for high-caliber 14.5 mm AP bullets and more than 300 mm for canon ammunition.

Conclusion

This chapter explains the various types of materials being used for making lightweight ceramic composite armours. The manufacturing methods of materials and armour modules are discussed including their advantages and disadvantages. Various penetration mechanisms involved during the ballistic impact on ceramic and composite laminates are described. The details of threats and standards followed across the globe for evaluating armour materials and modules are

presented briefly. However, the continuous improvement in armament technology and today's fragmented battlefield conditions has created a scope for the development of lighter armour solutions. Therefore, there is a need to study and establish the production of various advanced ceramic materials such as AlN, AlON, cubic boron nitride, and nano ceramics which are currently at nascent stage. The same is true in the case of advanced polymer fibers too, where higher modulus, high strength with higher elongation to failure fiber have to be explored to get the best armour designs. There is a need to carry out research on advanced fibers based on nanotechnology to get higher ballistic figure of merit. Currently, nano material is used only in the matrix for making composite through which it is difficult to get any significant improvement in armour performance. Similarly, there is also a need to focus on developing smaller grain size and defect-free ceramics having high fracture toughness along with high hardness in the order of 25–30 GPa. Finally, the performance of armour is decided based on its ballistic efficiency, weight, and cost. Hence, the cost and fabricability of materials at large scale are also important factors to consider while developing the new armour systems.

References

1. Weimer AW (ed) (1997) Carbide, nitride and boride materials synthesis and processing. Chapman & Hall, London
2. Liu G, Xie Z, Wu Y (2010) Effectively inhibiting abnormal grain growth of alumina in ZTA with low-content fine-sized ZrO₂ inclusions introduced by Infiltration and In Situ Precipitation. *J Am Ceram Soc* 93(12):4001–4004
3. Hannink RHJ, Kelly PM, Muddle BC (2000) Transformation toughening in zirconia-containing ceramics. *J Am Ceram Soc* 83(3):461–487
4. Somiya S, Inomata Y (eds) (1991) Silicon carbide ceramics 1- fundamental and solid reaction. Elsevier Science Publishers Ltd, London
5. Biswas K (2009) Solid state sintering of SiC ceramics. *Mater Sci Forum* 624:71–89
6. Chen M, McCauley JW, Hemker KJ (2003) Shock induced localized amorphization in boron carbide. *Science* 299:1563–1566
7. Karandikar PG, Wong S, Evans G, Aghajanian MK (2010) Microstructural development and phase changes in reaction bonded boron carbide, *Advances in ceramic armour VI. Ceramic Sci Eng Proc* 31(5):251–259
8. Hayun S, Weizmann A, Dariel MP, Frage N (2010) Microstructural evolution during the infiltration of boron carbide with molten silicon. *J Eur Ceram Soc* 30:1007–1014
9. Mishra SK, Pathak LC (2009) Self-propagating high-temperature synthesis (SHS) of advanced high-temperature ceramics. *Key Eng Mater* 395:15–38
10. Gu Y, Qian Y, Chen L, Zhou F (2003) A mild solvothermal route to nanocrystalline titanium diboride. *J Alloy Comp* 352:325–327
11. Janardhana Reddy J, Saivardan N, Bhanu Prasad VV. Indigenous development of Titanium diboride and other ceramics for armour applications. DMRL Technical report No. DRDO-DMRL-CCG-085-2015
12. Boch P, Niepce J-C (2007) Ceramic materials processes, properties and applications. ISTE Ltd, London
13. Rahaman MN (2007) Sintering of ceramics. CRC Press, Taylor & Francis Group, Boca Raton
14. <http://www.np-aerospace.co.uk>. Accessed on 28 Apr 2019
15. Fredrick TW, James CW, Hong L (2001) ASM hand book, vol 21, Chapter: Constituent of materials; Glass fibers, pp 27–34

16. Reddy PRS, Rao VVVSS, Reddy CJR, Mogulanna K, Ramanjaneyulu K, Madhu V, Gogia AK. Studies on energy absorption of glass composite laminates subjected to ballistic impact of soft projectiles. DMRL Technical report No. DRDO-DMRL-038-2013
17. Karl KC (2001) ASM hand Book: Chapter: Constituent of materials, Aramid fibers, 21, pp 41–45
18. Bhat TB, Madhu V (2017) Composite armour materials and modules. DRDO, DESIDOC Publications, New Delhi
19. Donald VR, Dominick VR (2004) Reinforced plastics hand book, 3rd ed, Elsevier advanced technologies, UK, p 56
20. Cheeseman BA, Bogetti TA (2003) Ballistic impact into fabric and compliant composite laminates. *Compos Struct* 61:161–173
21. Rama Subba P, Reddy T, Sreekantha Reddy I, Srikanth V, Madhu KVR (2016) Effect of viscoelastic behaviour of glass laminate on energy absorption subjected to high velocity impact. *Mater Des* 98:272–279
22. Bhatnagar A (2016) Light weight ballistic composites: military and Law enforcement applications. 2nd ed, Woodhead publishing composite science and engineering, UK, pp 217–227
23. Hauver GE, Rapacki EJ Jr, Netherwood PH, Benck RF (2005) Interface Defeat of Long-Rod Projectiles by Ceramic Armour, ARL-TR-3590
24. Lundberg P, Renstrom R, Lundberg B (2000) Impact of metallic projectiles on ceramic targets: transition between interface defeat and penetration. *Int J Impact Eng* 24:259
25. Behner T, Heine A, Wickert M (2016) Dwell and penetration of tungsten heavy alloy long-rod penetrators impacting unconfined finite-thickness silicon carbide ceramic targets. *Int J Impact Eng* 95:54–60
26. Shockey DA, Marchand AH, Skaggs SR, Cort GE, Burkett MW, Parker R (1990) Failure phenomenology of confined ceramic targets and impacting rods. *Int J Impact Eng* 9(3):263–275
27. Shockey DA, Simons JW, Curran DR (2010) The damage mechanism route to better armour materials. *Int J Appl Ceram Technol* 7(5):566–573
28. Sherman D, Brandon DG (1997) The ballistic failure mechanisms and sequence in semi-infinite supported alumina tiles. *J Mater Res* 12(5):1335
29. McGinn JT, Klopp RW, Shockey DA (1995) Deformation and comminution of shock loaded α -Al₂O₃ in the Mescall Zone of Ceramic Armour. In: Grant NJ, Armstrong RW, Ottooni MA, Baker TN, Ishizaki K (eds) Material research society symposium proceedings, vol 362. Materials Research Society, Pittsburgh, pp 61–66
30. Weinong W, Chen AMR, Song B, Nie X (2007) Dynamic fracture of ceramics in armour applications. *J Am Ceram Soc* 90(4):1005–1018
31. LaSalvia JC, McCauley JW (2010) Inelastic deformation mechanisms and damage in structural ceramics subjected to high-velocity impact. *Int J Appl Ceram Technol* 7(5):595–605
32. James B. Direct evidence for ceramic comminution ahead of a penetrator, 17th international symposium on ballistics, Midrand, South Africa, 23–27 March 1998
33. LaSalvia JC, Horwath EJ, Rapacki EJ, Shih CJ, Meyers MA (2001) Microstructural and micromechanical aspects of ceramic/long-rod projectile interactions: dwell/penetration transitions. In: Staudhammer KP, Murr LE, Meyers MA (eds) Fundamental issues and applications of shock-wave and high-strain-rate phenomena. Elsevier Science, Oxford, UK, pp 437–446
34. Lankford J (2004) The role of dynamic material properties in the performance of ceramic armour. *Int J Appl Ceram Technol* 1(3):205–210
35. Stepp D (2001) Damage mitigation in ceramics: historical developments and future direction in army research. In: McCauley JM, Rajendran AM, Gooch WA Jr, Bless SJ, Wax S, Crowson A, Logan KV, Normandia M (eds) Ceramic transactions, vol 134, Ceramic armour materials by design. American Ceramic Society, Westerville, pp 421–439
36. Rama Subba P, Reddy T, Sreekantha Reddy V, Madhu AK, Gogia KVR (2015) Behaviour of E-glass composite laminates under ballistic impact. *Mater Des* 84:79–86
37. Karthikeyan K, Russell BP, Fleck NA, Wadley HNG, Deshpande VS (2013) The effect of shear strength on the ballistic response of laminated composite plates subjected to steel projectiles. *Eur J Mech A/Solids* 42:35–53

38. Barcikowski M (2013) Effect of resin modification on the impact strength of glass- polyester composites. *Polimery* 56:nr6
39. Normandia MJ, Gooch WA (2002) An overview of ballistic testing methods of ceramic materials, ceramic armour materials by design. *Ceram Trans* 134:113–138
40. EN1522/23, Windows, doors, shutters and blinds – Bullet resistance – Test method
41. GOST R 50963, Armour protection of special cars. General technical requirements, 1 Jan 2009
42. NATO AEP-55 STANAG 4569 – Protection levels for Occupants of Logistic and Light Armoured Vehicles
43. Bless SJ, Rosenberg Z, Yoon B (1987) Hypervelocity penetration of ceramics. *Int J Impact Eng* 5:165–171
44. Rosenberg Z, Bless SJ, Yeshurn Y, Okajima K (1988) A new definition of ballistic efficiency of brittle materials based on the use of thick backing plates. *Impact Loading Dyn Behav Mater* 1:491–498
45. James B (2002) Depth of penetration testing, ceramic armour materials by design. *Ceram Trans* 134:165–172
46. Savio SG, Madhu V (2017) Effect of tile thickness and projectile velocity on the ballistic performance of boron carbide against 12.7mm AP. *Procedia Eng* 173:286–292
47. Savio SG, Madhu V (2018) Ballistic performance evaluation of ceramic tiles with respect to projectile velocity against hard steel projectile using DOP test. *Int J Impact Eng* 113:161–167
48. Normandia MJ (2004) Impact response and analysis of several silicon carbides. *Int J Appl Ceram Technol* 1(3):226–234
49. Orphal DL, Franzen RR, Charters AC, Menna TL, Piekutowski AJ (1997) Penetration of confined Boron carbide targets by tungsten long rods at impact velocities from 1.5 to 5km/s. *Int J Impact Eng* 19(1):15–29
50. Subramanian R, Bless SJ (1995) Penetration of semi-infinite AD995 alumina targets by tungsten long rod penetrators from 1.5 to 3.5 km/s. *Int J Impact Eng* 17:807–816
51. Orphal DL, Franzen RR, Piekutowski AJ, Forrestal MJ (1996) Penetration of confined aluminum nitride targets by tungsten long rods at 1.5–4.5 km/s. *Int J Impact Eng* 18 (4):355–368
52. Orphal DL, Franzen RR (1997) Penetration of confined silicon carbide targets by tungsten long rods at impact velocities from 1.5 to 4.6 km/s. *Int J Impact Eng* 19(1):1–13
53. Orphal DL, Franzen RR, Charters AC, Menna TL, Piekutowski AJ (1997) Penetration of confined boron carbide targets by tungsten long rods at impact velocities from 1.5 to 5.0 km/s. *Int J Impact Eng* 19:15
54. Anderson CE Jr, Behner T, Holmquist TJ, Orphal DL (2011) Penetration response of silicon carbide as a function of impact velocity. *Int J Impact Eng* 38:892–899
55. Orphal DL (2002) Long rod penetration of ceramics, Ceramic armour materials by design. *Ceram Trans* 134:151–164
56. Orphal DL, Anderson CE Jr (2006) The dependence of penetration velocity on impact velocity. *Int J Impact Eng* 33:546–554
57. Behner T, Orphal DL, Hohler V, Anderson CE Jr, Mason RL, Templeton DW (2006) Hypervelocity penetration of gold rods into SiC-N for impact velocities from 2.0 to 6.2 km/s. *Int J Impact Eng* 33:68
58. Crouch IG, Eu B (2016) Ballistic testing methodologies. In: Crouch IG (ed) *The science of armour materials*. Elsevier, San Diego
59. Zukas JA (1982) Penetration and perforation. In: Zukas JA, Nicholas T, Swift HF, Greszczuk LB, Curran DR (eds) *Impact dynamics*. Wiley, New York
60. V₅₀ Ballistic test for armour, MIL-STD-662F, 1997
61. MIL-DTL-32398, Detail specification: Laminate: cross-plyed ultra-high molecular weight polyethylene (UHMWPE) unidirectionally reinforced plastic armour (09-jun-2013)
62. MIL-DTL-62474E, Detail specification: Laminate: aramid-fabric-reinforced, plastic (12 Jul 2007)
63. MIL-DTL-64154B (W/Amendment-1), Detail Specification: Laminate: Fiberglass-Fabric-Reinforced, Phenolic (19-Jan-2012)

-
64. Adams MA (2002) Theory and experimental test methods for evaluating ceramic armour components, ceramic armour materials by design. *Ceram Trans* 134:139–150
 65. Savio SG, Madhu V (2018) Methodology to measure the protective areal density of ceramic tiles against projectile impact. *Def Sci J* 68(1):76–82
 66. Ballistic Resistance of Body Armour, NIJ Standards – 0101.06, U.S. Department of Justice, July 2008



Multilayered Ceramic-Composites for Armour Applications

10

Kiran Akella

Contents

Introduction	405
Ceramic-Composite Armour	405
Integral Armour	406
Manufacturing Processes	407
Mechanics of Ballistic Impact Penetration	407
Ballistic Impact Phenomenon	407
Mechanics of Wave Propagation	408
Penetration, Perforation, and Ballistic Limit	408
Depth of Penetration (DOP)	409
Energy-Dissipating Mechanisms	409
Parameters Affecting Penetration Resistance	412
Effects of Projectile Parameters	412
Material Choices	413
Ceramics	413
Composites	415
Ceramic-Composite Combinations	420
Design Issues	421
Relative Thickness of Components	421
Ceramic Tile Configuration	423
Confinement and Wrapping	425
Approaches for Improving Energy Dissipation	425
Layered Ceramics	426
Nanofillers in Composites	427
Residual Strength	428
Multiple Hit Resistance	429
Summary and Future Directions	430
References	431

K. Akella (✉)

Research and Development Establishment (Engineers), Defence Research and Development Organisation, Pune, India

e-mail: kiranakella@gmail.com

Abstract

In this chapter, configurations of ceramic-composite armour for resisting ballistic impact shall be introduced. Mechanics of impact shall be explained. Penetration, perforation, and various energy-absorbing mechanisms shall be enlisted. Relative contributions of multiple parameters to penetration resistance such as material properties and geometric configurations shall be discussed. A range of materials can be used for armour. Effect of the choice of material on aspects such as armour weight and thickness shall be included. Key issues of concern while designing ceramic-composite armour such as relative thicknesses of constituents, shape of ceramic tiles, and their sizes shall be discussed. A few probable approaches for improving energy absorption during impact and post-impact residual strength such as use of layered ceramics, embedding nanofillers, and improving toughness of the composite matrix shall be presented. Aspects of multi-hit resistance in ceramic-composite armour and key challenges encountered by armour designers to achieve multi-hit capability shall be discussed. In closure, shortcomings in currently used ceramic-composite armour design and envisioned future trends for improving its performance shall be highlighted.

Keywords

Ballistic impact · Penetration · Perforation · Materials · Design parameters · Performance aspects · Trends

List of Abbreviations

AP	Armour piercing
CAI	Compression after impact
CFRP	Carbon fiber-reinforced polymer
CNF	Carbon nanofibers
CP	Complete penetration
DOP	Depth of penetration
FRP	Fiber-reinforced polymer
GFRP	Glass fiber-reinforced polymer
HMPE	High modulus polyethylene
ILSS	Inter-laminar shear strength
L/D	Length-to-diameter
MWCNT	Multi-walled carbon nanotubes
NIJ	National Institute of Justice
PAN	Polyacrylonitrile
PBI	Polybenzimidazole
PBO	Polyphenylenebenzobisoxazole
PMC	Polymer matrix composites
RFI	Resin film infusion
RHA	Rolled homogeneous armour

UD	Unidirectional
UHMWPE	Ultrahigh molecular weight polyethylene
VARTM	Vacuum-assisted resin transfer molding

Introduction

Early armour was made using steel. It was efficient for energy absorption but heavy. Therefore, multiple alternatives were explored by researchers to reduce weight. Stronger, tougher steels and other iron-based alloys were developed. Light metals such as aluminum and titanium alloys were explored.

Subsequently, ceramics were introduced to replace a part of the metal layer. Ceramics with lower density, higher compressive strength, and greater hardness than steel along with reduced armour weight. The next major shift in armour materials occurred when metals were replaced with FRP composites. Ceramics were sandwiched between fiber-reinforced polymer (FRP) composite layers. Hard ceramics shattered the projectiles, and remaining energy was absorbed by composites. Weight of armour reduced substantially due to the low density of composites. Ceramic-composite armour is today the lightest commercially available alternative to metal armour. Typical weights of armour are listed in Table 1.

There are other forms of armour using only FRP composites or dry fabrics without ceramics. They are popularly known as soft armour. This armour is the lightest solution for lower threats such as handgun bullets. The performance of soft armour is highlighted in section “[Performance Comparison](#).” However, as the energy of the threat increases, ceramic-composite armour is the lightest alternative. For even higher threats such as projectiles that main battle tanks face, there is no alternative to metal or metal-ceramic armour. In this chapter, further discussion is restricted only to ceramic-composite armour. For the composites part, the discussion is restricted to the most widely used composites – polymer matrix composites (PMC) or FRP.

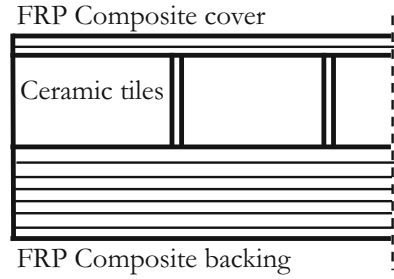
Ceramic-Composite Armour

Multilayered ceramic-composite armour consists of minimum three macro-layers. The outermost macro-layer first facing the projectile is FRP composite cover. The second macro-layer is the ceramics. The third or innermost layer is FRP composites

Table 1 Areal densities of different types of armour [1]

Armour type	Areal density (kg/m ²)
Steel	283
Aluminum	267
Titanium	220
Ceramic-aluminum	195
Ceramic-composite	98

Fig. 1 Cross section of ceramic-composite armour



backing. A schematic illustration of the cross section of ceramic-composite armour is included in Fig. 1.

The first layer holds the ceramics layer in place and also confines it. The ceramic layer is the primary ballistic impact energy-absorbing layer. It deforms and shatters the projectile absorbing majority of its energy. The third layer is the secondary energy-absorbing layer. The third layer also holds the ceramics in place during the ballistic impact event. A weak third layer will cause premature damage and prevent the ceramic layer from absorbing energy to its complete potential.

If the structural area requiring armour protection is large or it involves complex shapes, the ceramic layer is made using an assembly of smaller tiles. Armour is generally configured such that the projectile almost stops within the ceramic layer and does not penetrate much into the backing composites layer. This choice is made since the resistance to penetration of FRP composites is much lower than that of ceramics.

Integral Armour

Ceramic-composites armour for vehicles and other large structures can be used predominantly in two forms – add-on armour and integral armour. Add-on armour solution is used when an existing structure is to be protected. An integral armour is used when the entire metallic primary structure can be replaced with a composite structure. As the name suggests, in integral armour, the armour and structure are integrated together. The backing FRP composites layer of armour performs dual role – secondary ballistic energy absorption and primary structural load bearing. The FRP composites backing layer is better utilized in integral armour and therefore is more efficient and lightweight. The parasitic masses in add-on armour are avoided.

Though integral armour brings additional challenges in design and repair due to the dual role of the backing layer, future lightweight armoured vehicles could be made using composite-ceramic integral armour due to their high efficiency, lower thickness, and weight. However, integral armour restricts the choice of backing materials as they have to be made based both on structural and ballistic requirements.

Ceramic-composite armour can be further made multifunctional by adding additional layers for stealth, fire protection, and any other functionality such as electromagnetic interference protection. Often in integral armour, an elastomeric layer is added between the ceramics and the FRP composites backing layer to act as a

compliant member between stiff ceramics and flexible FRP composites. For improved damage mitigation, researchers have also attempted introducing additional layers in between such as metal foams.

Manufacturing Processes

Multiple layers of armour can be integrated using different processes. Individual layers can be made separately and adhesively bonded. The entire stack can be pressed under high temperature using the compression molding process. Large composite structures with integrated armour can be made monocoque without additional bonding using vacuum-assisted resin transfer molding (VARTM), resin film infusion (RFI) processes, and their variants. In some studies reported [2, 3], VARTM process has been adapted for manufacturing ceramic-composite armour. These processes are suitable for cost-effective manufacturing of large thick structures. Other known composites manufacturing processes [4] can also be adapted to make composite structures with embedded ceramics.

Bonding of ceramics to FRP composites and maintaining integrity during routine structural, handling loads and severe ballistic impact loads pose a challenge due to the low bond strength between ceramics and adhesives. Special purpose toughened adhesives are often used. Other methods include mechanical features such as incorporating ceramic beads in front of ceramic tiles or wrapping of individual ceramic tiles with fabric are adopted to address this issue.

Mechanics of Ballistic Impact Penetration

Ballistic Impact Phenomenon

The phenomena of two or more bodies colliding is defined as impact. A special case of impact is ballistic impact, wherein the velocity of impacting bodies is often large enough to cause severe material damage. An object – a target – is impacted by another object, a projectile. The target is typically stationary or moving at much lower velocity than the projectile. Also, the target generally has a much larger mass than the projectile. The projectile inevitably damages the target and also gets damaged in the process. A description of different types of impact and the range of strain rates is specified in Zukas [5]. The range of impact velocities varies from less than 50 m/s to more than 12,000 m/s. Correspondingly, the rate of application of strain varies from 10 to 100 million.

Ballistic impact is a local phenomenon. The response of the target is dependent on the performance of a small zone in the vicinity of impact. The material properties and local configuration have to play a key role in absorbing the energy of the projectile. Unlike other dynamic phenomena such as low velocity impact and blast, in ballistic impact, the boundary and configuration of the larger structure that forms the target have little influence on performance.

Mechanics of Wave Propagation

Waves are generated during ballistic impact at the point of impact and propagate in all directions. These waves are longitudinal or shear depending on the direction of propagation of waves and motion of particles. Based on the stress generated, these waves can be classified as compressive, tensile, and shear waves.

Interfaces are present in ceramic-composite armour due to various features in its configuration. Interfaces along the thickness are due to the presence of layers of different materials. In-plane interfaces occur due to the finite extent of ceramic tiles or plates. The presence of interfaces results in transmission and reflection of waves. The amount of reflection depends on the impedance ratio of the materials adjacent to the interface. This is typically the boundary between two adjacent ceramic tiles or armour panels. At every such interface, wave propagation is altered. This affects the stresses experienced by different parts of armour and thereby its damage and performance.

Understanding wave propagation is vital for design of armour. Typical ceramic-composite armour is made using a ceramic layer facing the projectile. The ceramic layer is backed by a FRP composite layer. Compression waves are generated on impact in the ceramic layer. A part of these waves get reflected back as tensile waves at the ceramic-composite interface along the thickness direction. The remaining part gets transmitted into the composite layer. The ratio of impedance of the two layers defines the amount of stress reflected and transmitted. The level of transmitted stress defines the damage that can occur in FRP composite.

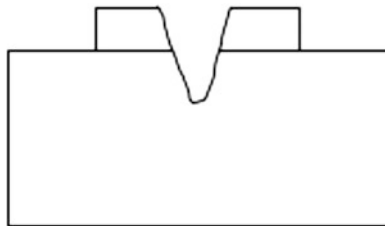
Ceramics are weak in tension. The amount of compressive stress waves reflected as tensile stress waves initiate tensile damage in ceramics. Due to this tensile damage, the penetrating projectile encounters damaged material and not intact material. As a result, depth of penetration increases. Thus, the location and nature of the ceramic-composite interface play a major role in armour performance. Similar reflections occur at the in-plane faces at the edges of ceramic tiles. Therefore, the size of tile also influences armour performance.

The overall extent to which the shear waves travels in the plane of armour is determined by the extent of cone formation. Schematic illustrations of the effects of wave propagation and corresponding damage mechanisms are explained in section “[Energy-Dissipating Mechanisms](#).”

Penetration, Perforation, and Ballistic Limit

If the projectile partially damages the target and forms a crater, it is called penetration. If the projectile completely penetrates the target and exits from the other side, it is called perforation. The difference between kinetic energy of the projectile before impact and after exit is the energy absorbed. When the projectile is just stopped by the target or it just exits with near zero velocity, the corresponding striking velocity is called the ballistic limit of the target-projectile combination. It is also defined as the lowest striking velocity of the projectile that will result in complete penetration [6]. Due to

Fig. 2 Schematic illustration of a sample after DOP test



variability in material properties and projectile striking, ballistic limit is also defined as the velocity at which the bullet is expected to penetrate the armor half of the time. This velocity is denoted as V_{50} . However, determination of V_{50} requires a large number of tests to be performed.

Depth of Penetration (DOP)

Similar to ballistic limit, another important parameter to compare the relative performance of materials is the DOP test. In this test, the material to be evaluated is placed on relatively thick backing material. Rolled homogeneous armour (RHA) is commercially available and a widely used armour steel and hence often used as the witness backing plate. Other reasons for choosing RHA are its easy availability, well-determined material behavior at high strain rates, its ductility, and availability of models to predict penetration.

The depth of penetration in the witness backing plate is compared for different materials for a given projectile and striking velocity. Thereby, performance of different materials can be quantitatively evaluated. A typical DOP sample is illustrated in Fig. 2.

The performance of ceramics can be studied using a DOP test. In this test, a ceramic-metal target is impacted by a projectile. The penetration of the projectile in the sample is studied. The performance advantage due to the ceramics can be compared by the reduction in DOP due to replacement of the metallic layer with ceramics.

Different specimen configurations have been used in the test. In one such configuration, a ceramic tile is adhesively bonded to a solid metallic block, and the combined sample is subjected to impact (Fig. 2). In another configuration, the ceramic tile can be placed inside the cavity in a metallic block. A metallic cover can also be placed above the ceramic tile. In the former configuration, ceramic tile is unconfined, while the effect of confinement is also included in the latter. The bonding is used to keep the tile in place, and it has no major role in penetration resistance.

Energy-Dissipating Mechanisms

Various energy-absorbing mechanisms dissipate the energy of the projectile [7]. A part of this energy is absorbed by damage and deformation of the projectile itself. The remaining part is absorbed by the damage and deformation of armour. The

energy-absorbing mechanisms in armour can be divided in two categories – energy absorbed by ceramics and energy absorbed by composites backing plate.

Immediately after the impact event, ceramic material around the vicinity of the projectile is under compression. If the stress exceeds limit, compressive failure and fracture of ceramic would occur. As compression occurs, ceramic layer is in tension along the radial direction. If the tensile stress exceeds the limit, ring cracks and radial cracks are formed due to tensile failure. As ceramics are weaker in tension than compression, the ring and radial cracks always occur in tension. Also, shear stresses are generated around the periphery of the projectile.

Failure is initiated as micro-cracks which coalesce to form macro-cracks. As a result ceramic granules are formed. This process is called pulverization or comminution. These micro-cracks exist due to the presence of prior defects or pores.

Fractured ceramic formed in this process also offers resistance to penetration. This resistance is substantial if the ceramic is effectively confined. If the ceramic is unconfined, the fractured ceramic granules will fly and offer almost no resistance.

Compression waves generated are reflected as tensile waves at the interface between ceramic and composite layer. If the tensile stresses exceed limit, failure initiates at the ceramic-composite interface and proceeds toward the projectile. This entire process causes a cone-shaped failure zone in the ceramic layer in the vicinity of impact.

As the penetration progresses, compression occurs in composite backing layer. Shear stresses are also generated. The composite backing layer forms a cone or a bulge resulting in tension in the composite yarns. If the compression, shear, or tension exceeds limit, corresponding failure occurs. When matrix stresses or strains exceed limit, matrix cracking occurs.

In this process, layers of composite may separate causing delamination. The compression waves generated in composites are reflected from their outer face as tensile waves. If the tension so generated exceeds its limit, delamination occurs. Hence, delamination initiates in the outermost layer and progresses in the inner layers.

Some of the damage mechanisms in the ceramic layer are schematically illustrated in Figs. 3 and 4. Through-the-thickness damage is illustrated in Fig. 3 and in-plane failure damage such as the ring cracks and radial cracks are in Fig. 4. The overall energy dissipation mechanisms in the ceramics are listed below:

1. Compression damage of ceramics below the projectile
2. Ring crack and radial cracks due tensile damage
3. Shear plugging
4. Pulverization
5. Friction and heat generation
6. Resistance of fractured ceramic material

A schematic illustration of damage mechanisms in the backing composites is included in Fig. 5. The overall energy dissipation mechanisms in the backing composites are listed below:

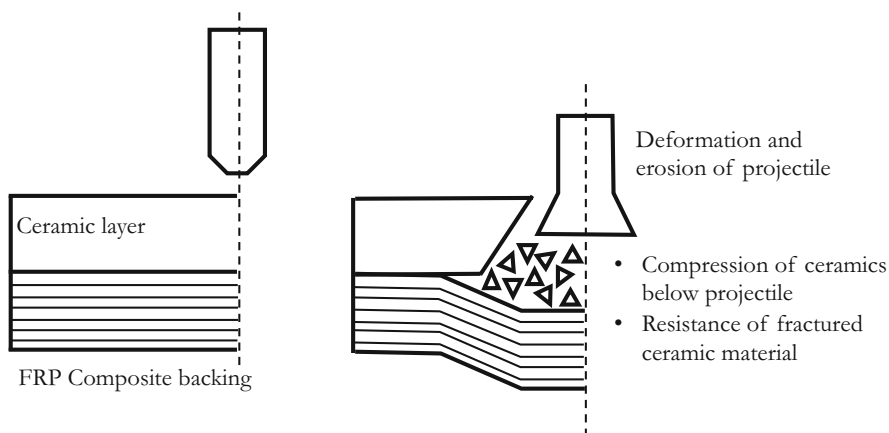
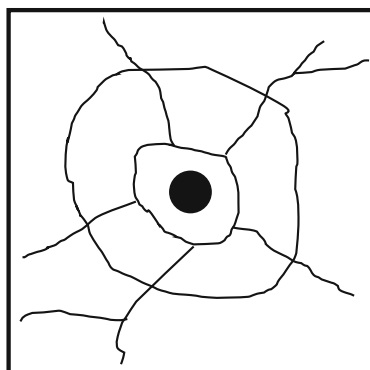


Fig. 3 Through-the-thickness damage of ceramic layer

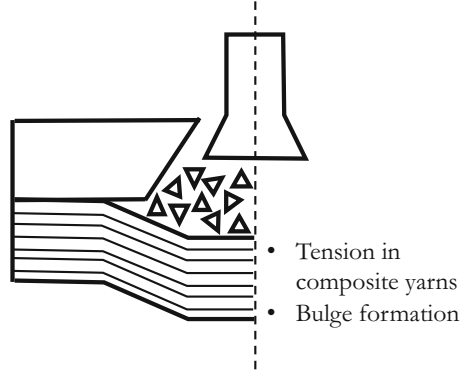
Fig. 4 Radial cracks and ring cracks in ceramic layer



1. Compression damage of composites below the projectile
2. Tension in the yarns
3. Shear plugging
4. Delamination and matrix cracking
5. Bulge formation of the back face
6. Friction and heat generation

The relative contribution of each of these mechanisms to armour performance is not widely known. In one of such attempts made [7], ceramic layer was reported to absorb nearly 50% energy of impacting projectile. Another 35% energy is absorbed by the damage in the projectile during penetration such as its deformation and erosion. The remaining 15% energy is absorbed by the backing material.

Fig. 5 Damage mechanisms in FRP composite layer



Parameters Affecting Penetration Resistance

Multiple parameters affect ballistic impact penetration and damage characteristics of armour. The parameters can be categorized as the nature of the projectile, choice of material systems, and geometric configuration of armour. Effects of the projectile parameters are discussed in the following subsection. Effects of material choices, geometric configurations, and other armour design parameters on ballistic performance are discussed in the subsequent sections.

Effects of Projectile Parameters

The material of the projectile – soft or hard – effects penetration. It also depends on mass, velocity, and shape of the bullet. Other characteristics of the projectile material such as its toughness affect the penetration characteristics.

Bullets can be classified as handgun bullets, fragment-simulating projectiles, small arms bullets, and hard armour-piercing kinetic energy bullets [8]. Typically, bullets have a soft core (lead, soft steel. etc.) or a hard core (hard steel). The bullets are covered with a jacket often made of soft copper for durability of the gun barrel against wear. The jacket also protects the core material.

Handgun bullets are heavy with large diameter but travel with low velocities. On the other hand, rifle bullets have smaller diameter and are lighter but travel with higher velocity. As a result, the latter is more lethal.

In one study [9], areal densities of armour that can be achieved for protection against different bullets are listed. The reported data is presented in Table 2. As the threat level increases, muzzle diameter, projectile mass, and muzzle velocity increase. Therefore, depending on the threat to armour, areal density varies between 15 and 190 kg/m². For higher threats, armour weight can increase further.

Bullets have aerodynamic shape to reduce drag. The shape of the projectile tip influences the projectile deceleration characteristics to a certain extent [10, 11]. This

Table 2 Areal densities of armour for protection against different bullets [9]

Threat	Areal density (kg/m ²)
5.56 × 45 NATO, 7.62 × 51 NATO	15–27
7.62 × 39 AK47, 7.62 × 54R Dragunov LPS	
7.62 × 39 API AK47, 5.56 × 45 AP	25–35
7.62 × 51 AP (P80/PPI), 300 Winch, 868S	
7.62 × 54 API Dragunov, 0.3006 AP M2s	
7.62 × 51 FFV Bofors (WC)	50–55
12.7 AP, 14.5 API B32	75
20 mm, 25 mm APDS 60° incidence	110
25 mm APDS 45° incidence	190

influence is limited for hard-faced targets with ceramic front plate. However, for softer targets, its influence is higher. For 3–6.5 mm thick carbon fiber-reinforced polymer (CFRP) laminates, the maximum influence of projectile tip shape on ballistic limit was found to be 16% [12]. When thin two-layered targets made of Spectra-1000(R)TM were used, projectiles with flat and hemispherical tips showed 33% higher delamination than those with conical and ogival tips [13]. When single-layer TwaronTM targets were used [14], conical projectiles displayed lower ballistic limit of 56 m/s, while hemispherical projectiles displayed higher ballistic limit of 159 m/s.

These studies lead us to two conclusions – (a) less energy is absorbed by sharper projectiles and (b) the influence of projectile tip shape reduces with thickness [15]. These inferences are however applicable to composite targets and not to ceramic-composite targets with hard face. The effect of projectile tip shape further reduces for ceramic-composite armour.

The length-to-diameter (L/D) ratio of projectiles effects penetration and perforation characteristics. Projectiles with longer length and smaller diameter (greater L/D ratio) penetrate more than shorter projectiles of the same mass. Hence, ballistic limit reduces with increasing L/D ratio. In one such study on metallic targets [5], 13% reduction in ballistic limit was reported when the projectile L/D ratio increases from 5 to 10.

Material Choices

The two primary materials that constitute ceramic-composite armour are ceramics and composites. The effect of choice of these materials on armour weight, thickness, and performance is briefly discussed in this section.

Ceramics

Commercially available ceramics that are widely used for armour applications are alumina (Al₂O₃), aluminum nitride (AlN), boron carbide (B₄C), silicon carbide (SiC), titanium diboride (TiB₂), and tungsten carbide (WC).

With RHA as the benchmark, ceramics can be classified on the basis of density. Those with density greater than RHA are called high-density ceramics (WC). If the density is less than RHA, they are called low-density ceramics (Al_2O_3 , AlN , B_4C , SiC).

Typical sample configuration for a DOP test used to evaluate and compare ceramics is schematically illustrated in Fig. 6. DOP in a ceramic-metal target is compared with a RHA target. The difference in DOP and the reduction in weight due to replacement of metal with ceramics are used. Using the experimental data, volume gain V_g due to ceramics is obtained using

$$V_g = \frac{P_{RHA} - P_{res}}{T_{cer}}$$

Using this equation the reduction in DOP due to the presence of ceramics can be obtained. If ceramic layer has same performance as RHA, then $P_{RHA} = P_{res} + T_{cer}$. Volume gain V_g is then 1. Reciprocal of V_g shall be the relative thickness t_{rel} of ceramics normalized with RHA:

$$t_{rel} = \frac{1}{V_g}$$

Mass gain M_g due to ceramics over RHA can be obtained from the volume gain against using

$$M_g = V_g \frac{\rho_{RHA}}{\rho_{cer}}$$

where ρ_{RHA} and ρ_{cer} are the densities of RHA and ceramic layer. Correspondingly, relative mass reduction ρ_{rel} due to the presence of ceramics can be estimated using

$$\rho_{rel} = \frac{1}{M_g}$$

Mass gain and volume gain of different ceramics were compared and reported in [16, 17]. The reported results are listed in Tables 3 and 4.

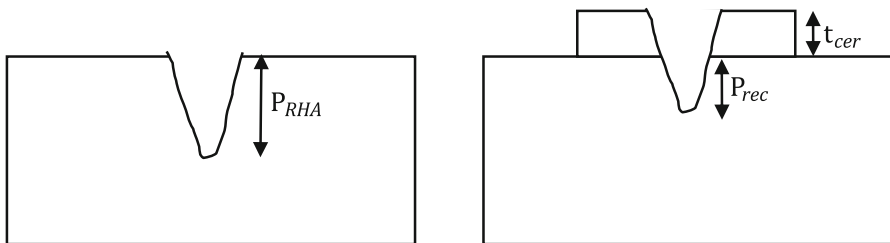


Fig. 6 Test specimen for DOP tests to compare ceramics

Table 3 Comparison of performance of various ceramics based on DOP [16]

Ceramic	Density	V_g	t_{rel}	M_g	ρ_{rel}
RHA	7810	1	1	1	1
Al ₂ O ₃	3680	1.01	0.99	2.14	0.47
B ₄ C	2500	1	1	3.13	0.32
SiC	3200	1.25	0.8	3.05	0.33
TiB ₂	4400	1.67	0.6	2.96	0.34

Table 4 Comparison of performance of various ceramics based on DOP [17]

Ceramic	Density	V_g	t_{rel}	M_g	ρ_{rel}
RHA	7810	1	1	1	1
Al ₂ O ₃ – sintered 95%	3680	0.7	1.43	1.67	0.6
Al ₂ O ₃ – sintered 98%	3780	0.78	1.29	1.67	0.6
Novel Al ₂ O ₃ – sintered	3690	0.88	1.14	2	0.5
AlN – hot-pressed	3270	1	1	2.5	0.4
B ₄ C – hot-pressed	2520	0.78	1.29	2.5	0.4
SiC – hot-pressed	3230	1	1	2.5	0.4
Reaction-bonded SiC	3210	0.88	1.14	3.33	0.3
TiB ₂ – hot-pressed	4520	1.75	0.57	3.33	0.3

A maximum of 70% mass reduction over RHA was reported using SiC. Long-rod kinetic energy projectiles were used by the authors with mass of 105 g and velocity between 1550 and 1800 m/s. In another study, 30 and 40 mm diameter armour-piercing fin-stabilized discarding sabot projectiles were used.

Mass reduction using B₄C and TiB₂ is also of similar order. However, the lowest thickness for matching performance is of TiB₂. All other ceramics have thickness almost similar or more than RHA. So, if best armour performance is desired at minimum thickness and lowest weight, TiB₂ is the material of choice. However, TiB₂ is known to be an expensive material. If cost is governing factor, then B₄C and SiC are equally attractive alternatives but require higher thickness. An approximate cost comparison of ceramics is presented in Table 5 using the data in [17]. Cost of all ceramics is listed relative to the cost of the most expensive ceramic TiB₂. TiB₂ is 100 times expensive than RHA. SiC is 70% of TiB₂ cost. Alumina is the cheapest ceramic. AlN and B₄C lie in between.

Composites

FRP composites consist of two main components – reinforcement and matrix. Reinforcement for armour is made of long or continuous fibers. Fibers are used by armour manufacturers in the form of a fabric. Different layers of the fabric are stacked to achieve the desired armour thickness held together by a matrix. The matrix can be applied externally to dry fabric or, the fabric could be pre-impregnated

Table 5 Relative cost of ceramics [17]

Ceramic	Density	Relative cost
RHA	7810	0.01
Al ₂ O ₃ – sintered 95%	3680	0.02
Al ₂ O ₃ – sintered 98%	3780	0.03
Novel Al ₂ O ₃ – sintered	3690	0.05
AlN – hot-pressed	3270	0.35
B ₄ C – hot-pressed	2520	0.7
SiC – hot-pressed	3230	0.35
Reaction-bonded SiC	3210	0.08
TiB ₂ – hot-pressed	4520	1

(prepregs) by the matrix. Thus, choice of composite backing material for armour involves three sub-choices – fibers, fabric architecture, and matrix.

Fibers

High-performance fibers used for armour can be classified in four categories [18] as follows:

1. Classical: Glass, carbon
2. Rigid chain aromatic: Nylon 6, nylon 66, nomex, para-aramids – Kevlar, Twaron, Technora
3. Thermoplastic: Liquid crystal fiber , Vectran; high modulus polyethylene (HMPE), Spectra, Dyneema, Tekmilon
4. High temperature: Polybenzimidazole (PBI), polyphenylenebenzobisoxazole (PBO) – Zylon

Glass fibers are one of the most popular and cost-effective high-performance fibers. Three types of glass fibers are known – Eglass, Rglass, and Sglass. Carbon fibers are the next most popular high-performance fibers. They are rarely used for armour applications due to their brittleness. Types of carbon fibers are based on the base material used – polyacrylonitrile-based (PAN) and pitch-based. Graphite fibers are also a superior form of carbon fibers. Properties of some of the fibers are included in Table 6.

Spectra fibers are the lightest and have moderate stiffness and high strength. The heaviest fibers are Eglass but have low stiffness, high strength, and highest elongation. They are also cost-effective. Kevlar fibers have moderate weight but have low stiffness and high strength. Carbon has moderate density, high stiffness, and high strength. But carbon fibers are most brittle due their lowest elongation. Zylon fibers have moderate density but have high stiffness and very high strength. However, these PBI/PBO fibers are known to be substantially expensive.

Of all these fibers, glass, aramids, and high-modulus polyethylene (HMPE) are widely used. Glass is popular for its low cost, whereas aramids and HMPE are popular for their lower weight and better performance. HMPE is the lightest of all

Table 6 Properties of fibers

Fiber	Density (kg/m ³)	Modulus (GPa)	Tensile strength (MPa)	Elongation (%)	Source
Eglass	2540	72	3448	4	[4]
Carbon T300	1760	231	3750	1.4	[4]
Nylon-66	1140	5	1006	18.2	[19]
Kevlar-29	1440	67	2794	3.5	[19]
Kevlar-129	1440	96	3429	3.3	[19]
Kevlar-KM2	1440	64	3429	4.3	[19]
Spectra-900	970	79	2610	3.6	[19]
Spectra-1000	970	113	3250	2.9	[19]
Spectra-2000	970	124	3510	2.9	[19]
Zylon-AS	1540	180	5800	3.5	[19]
Zylon-HM	1560	270	5800	2.5	[19]

and therefore often preferred when low weights are of primary importance. Typical areal densities of Spectra Shield™ plates for threat levels as per National Institute of Justice (NIJ), USA [20], are listed in Table 7 based on [21, 22]. As the threat level increases, armour weight increases from 2 to 41 kg/m². This study reports that Spectra plates are 30% lighter than ceramic-composite armour up to NIJ level 3 [20]. For NIJ level 4 and beyond, ceramic face plates are required. Hence, the areal density for threat level 4 shown in Table 7 depends on ceramic face plate.

Fabrics

Fabrics can be classified as woven and non-woven. Non-woven fabrics are held together by a web and/or bonded. Woven fabrics are made by interweaving the yarns. Based on architecture, fabrics can be classified into two-dimensional (2D) and three-dimensional (3D) configurations. Based on weaving pattern, fabrics can be divided into unidirectional (UD), plain, twill, and satin weaves.

Basket weave is similar to plain weave but a group of two yarns interlaced instead of a single yarn. Twill weave is similar to basket weave, but only one yarn is woven over a pair of two yarns. In 2 × 2 twill, single yarn is woven under two yarns. Accordingly in 4 × 4 twill, four yarns are bridged. Basket weave and twill weave are more drapable in complex shapes and avoid fiber buckling.

Satin weave can be classified based on the number of harnesses [19]. For example, in 4-harness satin, a yarn is woven over every fourth yarn. Similarly, there can be 5-harness or 8-harness satin weaves.

The interweaving is highest in plain weave, lower in twill weave, and lowest in satin weave. Due to interweaving, fibers crimp and therefore the efficiency of fibers reduce. As a result, mechanical properties and ballistic performance degrade. Highest crimping occurs in plain weave fabrics. Fabrics with finer yarns (fewer filaments per yarn) but densely woven (more yarns per area) performed better [19].

Weave patterns affect the ballistic performance. In one such study [23], satin weave laminates showed 9–19% improved performance over plain weave. The

Table 7 Areal densities of Spectra plates for different threats [21, 22]

NIJ threat	Bullet	Areal density (kg/m ²) [21]	Areal density (kg/m ²) [22]
IIA	9 mm FMJ RN, .40 S&W FMJ	2	3–4
II	9 mm FMJ RN, .357 Magnum JSP	4	4–5
IIIA	.357 SIJ FMJ RN, .44 Magnum SJHP	5	5–7
III	7.62 mm NATO FMJ	19	17–32
IV	.30 caliber M2 AP	32–41	32–37

results are tabulated in Table 8. Thickness-corrected ballistic limit was obtained assuming its linear variation with thickness.

In 3D fabrics, through-the-thickness reinforcement is also woven. 3D fabric can be made by braiding or weaving. Out-of-plane reinforcement improves out-of-plane damage tolerance. But it degrades in-plane properties. Certain studies have shown much localized damage than 2D. However, reduction in the effectiveness in absorption of the projectile kinetic energy was also observed [19].

The benefit of 3D weaving on ballistic limit was studied [24]. The performance of 2D plain weave Eglass-epoxy was compared with 3D woven Eglass-epoxy samples of same thickness. Ballistic limit of 3D-woven composites was 260.4 m/s and 2D-composites was 244.2 m/s.

In 2D laminates, a fiber volume fraction of 50% was achieved. Whereas in 3D, only 45% could be achieved. Due to 3D weaving, they observed a reduction of fiber direction Young's modulus from 16 to 12 GPa. But out-of-plane modulus increased from 8 to 11 GPa. Thus with 3D weaving, ballistic limit and out-of-plane properties improve, but in-plane properties degrade.

Another way of introducing through-the-thickness reinforcement is by stitching a stack of 2D fabric layers. Such stitching might also be done to hold the fabrics together during manufacturing. The effect of stitching on ballistic performance was quantified and reported in [23]. The results are tabulated in Table 10. They reveal that stitching reduces ballistic limit and thereby degrades performance. The data is presented in Table 9.

Matrix

Polymers are the most widely used matrix materials. Polymers can be classified as thermosets or thermoplastics [4, 19, 21]. Thermosets cannot be melted with increase in temperature but are generally strong and durable. Popular thermosets are epoxies, polyesters, phenolics, and vinyl esters. Often two or more components are mixed together. These components cross-link at room temperature or under pressure at high temperature. Most thermosets cannot sustain beyond 150 °C.

Thermoplastics soften and melt as temperature rises and harden again as temperature reduces. They are more versatile as they can be melted and repaired. Popular thermoplastics are polyimide (PI), polysulphone (PS), polyetheretherketone (PEEK), polyethylene (PE), and polyphenylene sulfide (PPS). Thermoplastics

Table 8 Effect of weave pattern on ballistic limit

Layers	Weave	Thickness	Ballistic limit (m/s) [23]	Ballistic limit thickness corrected	Improvement
7	Plain	2.8	61	61	1
7	Satin	3.5	86	69	1.13
17	Plain	5.7	102	102	1
17	Satin	8	171	121	1.19
37	Plain	13.8	232	232	1
37	Satin	14.3	262	252	1.09

Table 9 Effect of 3D weaving on Eglass-epoxy performance [24]

Property	2D plain weave	3D woven
Laminate thickness (mm)	12	12
Fiber volume fraction	0.5	0.45
Density (kg/m^3)	1850	1700
In-plane Young's modulus (GPa)	16	12
Out-of-plane Young's modulus (GPa)	8	11
Shear plugging strength (MPa)	120	142
Dynamic strain energy release rate G_{IIcd} (J/m^3)	1000	2000
Ballistic limit velocity (m/s)	244.2	260.4

require high temperatures for processing and sustain temperatures in the range of 300 °C. Properties of some popular matrix materials are included in Table 11 where T_g denotes glass transition temperature.

Performance Comparison

There are few studies comparing the performance of different composites. In one such study [26], the performance of glass-epoxy laminates was compared with the performance of carbon-epoxy laminates of the same thickness. Ballistic limit velocity (V_{50}) of carbon-epoxy laminates was 17% lower than that of glass-epoxy laminates. Due to the brittle nature of carbon fibers, they generally underperform in comparison with glass when subjected to impact.

In another study [22], the areal density required for protection against two threats using two different composite materials – aramid-phenolics and Spectra – are compared (see Table 12). For both the threats, Spectra is about 40% lighter than aramid.

One more inference can be drawn from the data presented in Table 12. It can be noted that areal density of steel increases as the threat level increases. However, areal density of soft armour increases far more than steel. While areal density of steel increases by a factor of 1.4, areal density of soft armour increases by 3.7. Therefore, beyond a certain threat, weight benefits of fabrics reduce. For lower threats, soft armour is substantially lighter – 20% of steel. But for higher threats, fabric weight is

Table 10 Effect of through-the-thickness stitching on ballistic limit

Stitching type	Layers	Weave	Ballistic limit (m/s) [23]
Unstitched	7	Plain	61
Stitched at a grid of 12.7 mm	7	Plain	61
Stitched at a grid of 25.4 mm	7	Plain	50
Unstitched	17	Plain	102
Stitched at a grid of 12.7 mm	17	Plain	97
Stitched at a grid of 25.4 mm	17	Plain	88
Unstitched	7	Satin	86
Stitched at a grid of 12.7 mm	7	Satin	66
Stitched at a grid of 25.4 mm	7	Satin	43
Unstitched	17	Satin	171
Stitched at a grid of 12.7 mm	17	Satin	113
Stitched at a grid of 25.4 mm	17	Satin	94

Table 11 Properties of some popular matrix materials [4, 25]

Polymer	Density (KG/M ³)	Modulus (GPa)	Tensile strength (MPa)	Elongation (%)	Tg (°C)
Epoxy – low modulus	1163	2.2	55	8.1	177
Epoxy – intermediate modulus low strength	1273	3.4	48	1.4	216
Epoxy – intermediate modulus high strength	1218	3.4	103	2	216
Epoxy – high modulus	1246	5.2	138	2	216
PI	1218	3.4	103	2	371
PEEK	1310	1.1	70.3–103	30–150	143
LDPE	925	0.172–0.282	8.3–31.4	100–650	–110
HDPE	959	1.08	22.1–31	10–1200	–90
UHMWPE	940	0.69	38.6–48.3	320–525	–

about 50% of steel. Thus, the weight benefit reduces from one-fifth to half. As the threat increases further, fabrics are not attractive. Ceramics are required and therefore ceramic-composite combinations are the lightest solutions for higher threats.

Ceramic-Composite Combinations

The choice of ceramics and FRP composites is the primary aspect of armour design. In previous sections, the performance of independent materials was separately presented. In this section, the relative performance of combinations is presented. In one such study [9], the performance of a few armour combinations is compared. Bullet $7.62 \times 54R$ Dragunov LPS was used. The reported results are listed in Table 13.

With lighter materials, armour weight can be reduced by more than 2.5 times below RHA. However, the cost of armour increases more than ten times as the

Table 12 Areal densities of different soft armour (kg/m^2) [22]

Armour material	Areal density 9 mm FMJ	Areal density AK-47
Steel	24.4	34.9
Woven aramid/phenolics	7.9	29.4
Spectra Shield TM	4.8	18.4

Table 13 Ceramic-composite combinations against $7.62 \times 54\text{R}$ Dragunov [9]

Armour (ceramic + backing)	Areal density (kg/m^2)	Relative mass	Relative cost
RHA	73	1	1
Al_2O_3 + S2 glass	47	0.65	2.5
SiC + Kevlar-29	41	0.56	6.5
B_4C + Kevlar	32	0.43	11.2

weight reduces. Using even lighter backing materials such as UHMWPE and tougher ceramics such as TiB_2 , weight and thickness of armour can be further reduced at an even higher cost.

Design Issues

Design of ceramic-composite armour involves multiple configurational choices. Thickness of the two primary components and their optimal ratio is the first choice to be made. To protect large structures and provide multi-hit resistance, a single ceramic plate cannot cover the entire area. It has to be constructed using an arrangement of finite tiles. Hence, size of ceramic tiles and their shape is to be decided. There are other aspects involved in design such as ceramic-composite bond, wrapping, confinement, and use of response modification layers between ceramics and composites. Effects of these design choices on performance are briefly explained in this section.

Relative Thickness of Components

Ballistic limit improves almost linearly with increase in composite thickness. The variation of ballistic limit with thickness [23] is presented in Table 14. The same data plotted in Fig. 7 highlights the linear increase of ballistic limit in FRP composites with thickness.

Ceramic-composite armour designers always faced the question whether ceramic or composite thickness be increased to defeat a threat. Certain experiments provide vital insights [27] as listed in Table 15. Projectile of mass 46.8 g and 0.5 in. caliber was used in these experiments, and alumina ceramics are used.

For a fixed areal density, thick ceramics and thin GFRP improve the performance. Energy absorbed by 6 + 5 mm sample is more than 4 + 8 mm sample. Similarly, energy

absorbed by 9 + 5 mm sample is much more than 6 + 10 mm sample. Therefore thicker ceramics with thinner backing is more efficient given a fixed areal density.

Experiments in this study [27] can be used to draw some more inferences. Keeping GFRP thickness constant, energy absorbed by armour increases with ceramic thickness. This variation is plotted in Fig. 8. Similarly, keeping ceramic thickness constant, it was observed that energy absorbed increases with GFRP thickness. This variation is plotted in Fig. 9. Comparing Figs. 8 and 9, we can observe that the curve is significantly flatter for GFRP than ceramic thickness. Once again, we can observe that armour performance can be improved more by increasing ceramic thickness and keeping the composite backing minimum.

Predictions using models in the same study [27] showed that ceramic-composite thickness ratio of 1.8 is optimal (lowest areal density). However, the curve is very flat near the optimum, and hence thickness ratios in a wide range around this value do not affect the performance.

Studies were also performed to obtain optimal ratio ceramic-metal armour. In one such study [17], alumina-aluminum armour systems were evaluated against 7.62 AP rounds. An optimal ceramic thickness/metal thickness ratio of 1.5–2 was experimentally deduced. It was also observed that the optimal ratio depends on impact velocity and impact angle. An approximation was obtained by fitting experimental data on an empirical equation:

$$\frac{t_c}{t_m} = \frac{V}{60000} \times (90 - \alpha)$$

where t_c is the ceramic thickness, t_m the metal thickness, V the velocity and α the angle of impact. For normal impact ($\alpha = 0$) and impact velocity (V) of 1000 m/s, a ratio of 1.5 is obtained using this equation.

Table 14 Effect of thickness on ballistic limit

Thickness	Weave	Stitch pattern	Ballistic limit (m/s) [23]
2.8	Plain	Unstitched	61
5.7	Plain	Unstitched	102
13.8	Plain	Unstitched	232
3.5	Satin	Unstitched	86
8	Satin	Unstitched	171
14.3	Satin	Unstitched	262
2.8	Plain	Stitched at 12.7 mm grid	61
5.7	Plain	Stitched at 12.7 mm grid	97
3.5	Satin	Stitched at 12.7 mm grid	66
8	Satin	Stitched at 12.7 mm grid	113
2.8	Plain	Stitched at 25.4 mm grid	50
5.7	Plain	Stitched at 25.4 mm grid	88
3.5	Satin	Stitched at 25.4 mm grid	43
8	Satin	Stitched at 25.4 mm grid	94

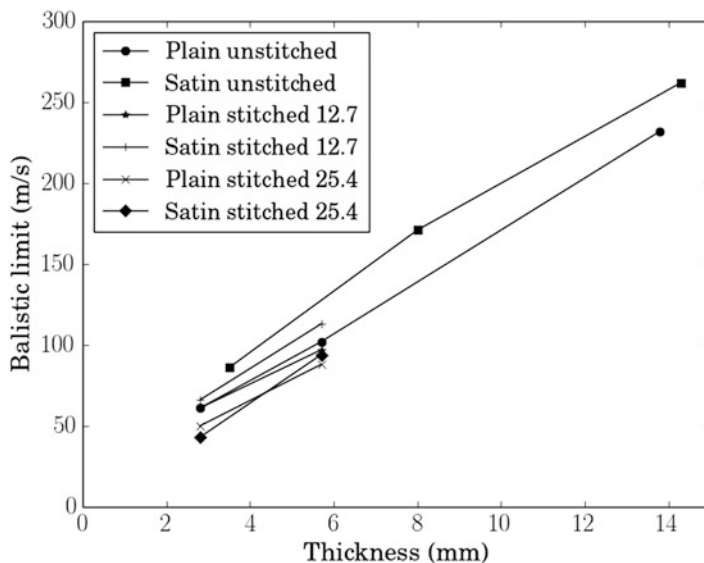


Fig. 7 Effect of thickness of ballistic limit

Table 15 Component thickness effect on armour performance [27]

Ceramic thickness (mm)	GFRP thickness (mm)	Areal density (kg/m ³)	Impact velocity (m/s)	Residual velocity (m/s)	Energy absorbed (J)
4	8	32	882.3	826.3	2239
6	5	32	880.7	800.5	3155
6	10	43	878.1	760.6	4506
9	5	43	898.2	693.9	7611

Ceramic Tile Configuration

Ceramic tile shape was classified [9] as flat tiles or shaped tiles. Flat tiles can be square, hexagonal, or any other shape. Square and hexagonal are most popularly used. Hexagonal tiles have no right-angled corners and might perform better than square. Square tiles are easy to make and assemble. However, they might be weak at the corners. However, details quantifying the comparison of performance are not available. Using flat tiles, armour can be made with one monolithic ceramic layer (thick tiles) or layered ceramics (thin tiles).

Tiles with shapes such as balls, pellets, and cylinders have also been used for armour. Such shapes were found to sustain multi-hit. However, weight and cost improvement due to the choice of such shapes is not yet quantified [9].

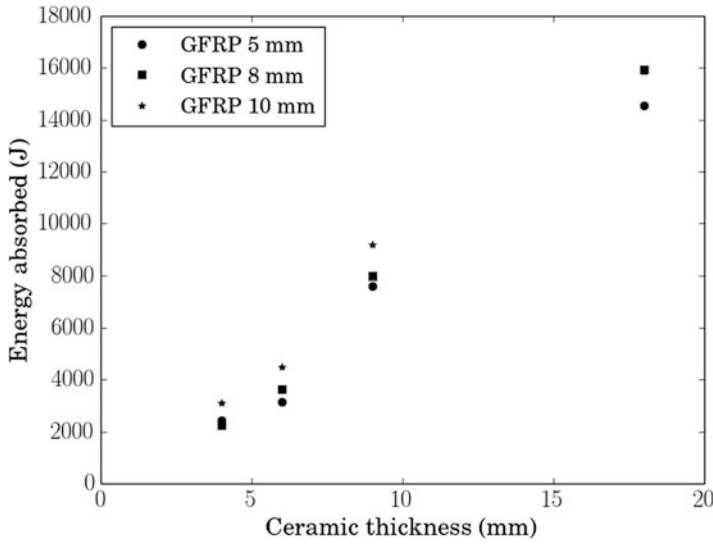


Fig. 8 Effect of ceramic thickness on energy absorbed

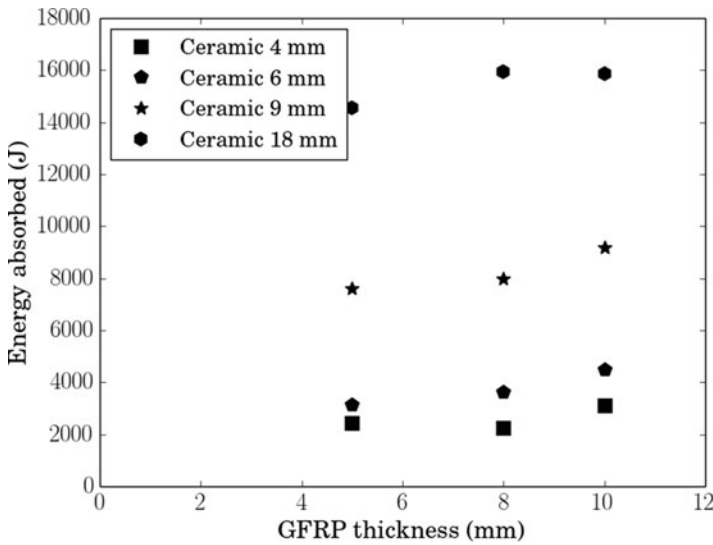
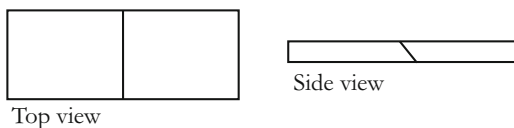


Fig. 9 Effect of GFRP thickness on energy absorbed

Ceramic tile size also influences armour performance. Larger ceramic tiles improve energy absorption. Smaller tiles improve multi-hit capability, but damage is localized and hence has lesser energy absorption. However, quantified data could not be found on the effects of these parameters.

Fig. 10 Tile edge profile for minimum degradation



In another study, the effect of tile edge geometry was studied [17]. Different tile edge profiles and inclined edges instead of vertical tiles edges were evaluated. Tiles with 45° of inclined edges were found to perform best with minimum degradation at the edges. Typical edge profile is illustrated in Fig. 10.

Confinement and Wrapping

Individual ceramic tiles are backed by composites and subjected to impact fracture early during the impact event. The fractured ceramic easily moves out of the impact zone and offers no resistance during penetration. However, if the ceramics are held in place and the movement of the fractured ceramic is restricted, projectile penetration is resisted and armour performance improves. Attempts were made to quantify this effect [16]. As the lateral dimension of the tile increased, the residual penetration reduced. The additional intact material in larger tiles confines the material in the vicinity of impact. Similar effect was observed by laterally confining the tile. Quantitative data is presented in Table 16.

Wrapping ceramic tiles with a membrane improves armour performance [28]. Wrapped ceramics show more penetration resistance than unwrapped ceramics. However, no clear effect of thickness of the wrapping material was observed on performance. Thicker wrapping did not always translate into improved resistance to penetration. There was also no clear correlation between different wrapping materials and performance. Wrapping of alumina tiles with one layer of Eglass showed the best performance at the lowest weight penalty. Some data on wrapping is presented in Table 17. Targets were subjected to impact by 10.6 g projectiles at a velocity of 900 m/s. The lowest residual velocity can be observed when the ceramic tile is wrapped with Eglass. More than 24% lower residual velocity can be observed just by wrapping the ceramic tile. Substantial benefit can hence be achieved by such a small design feature.

Approaches for Improving Energy Dissipation

Various approaches can be adopted to improve the ballistic energy absorption during impact. The improvement in energy absorption due to certain approaches has been quantified. Some of the possible approaches are described below. Works done on some of these approaches are presented in the subsequent subsections:

Table 16 Effect of confinement [16]

Armour material	Residual penetration (mm)
Unconfined glass with 100 mm tile	100
Unconfined glass with 310 mm tile	85
Confined glass with 100 mm tile	85
Unconfined alumina with 100 mm tile	70
Unconfined alumina with 270 mm tile	50
Confined alumina with 100 mm tile	50

Table 17 Effect of wrapping [28]

Wrapping material	Residual velocity (m/s)
Unconfined	677
Glass fiber tape	555
Ti – 0.127 mm	605
Ti – 0.254 mm	599
Ti – 0.508 mm	616
Carbon – 1 layer	633
Carbon – 3 layers	539
Eglass – 1 layer	560
Eglass – 3 layers	525

1. Tougher ceramics – making ceramics tougher and cheaper by modifying the manufacturing process, reinforcing with nanofillers, multi-ceramic composites, or any other such methods.
2. Layered ceramics – using layers instead of one thick monolithic ceramics block.
3. Tougher resin systems – using tougher resins to improve energy absorption and post-impact residual strength, lower damage area especially delamination, and improve multi-hit capability.
4. Nanofillers in composites – embedding nanofillers in composites to improve their mechanical and impact properties.
5. Ceramic-coated fabrics – coating ceramics on fabrics to improve their resistance to penetration.
6. Hybrid composites – using multiple fabrics and matrix in the same stack to achieve better performance at lower cost.

Layered Ceramics

Instead of monolithic ceramics, it is interesting to evaluate whether use of layers can improve ballistic performance. A thin layer of polymer adhesive can be used to bond the ceramic layers. Other methods to keep the layers together can also be explored.

However, the ability of layered ceramics to improve resistance to penetration when subjected to ballistic impact is not clearly established. Certain researchers [29] have reported continuous degradation in penetration resistance as the number of layers increase from 1 to 6. In another study [30], it was observed that three layers performed better than monolithic, but six layers were inferior. It was also noted that presence of layers delayed the rise of stress and reduced the peak stress [31].

Thus, the utility of layered ceramics is not established. It has been seen that more layers degrade performance. However, improved attenuation of the stress wave is also reported.

DOP increases when layers are used [32]. However, with increasing layers, damage area reduces consistently. As a result, multi-hit capability and post-impact residual strength improve. The second hit can be closer to the first hit when layered ceramics are used instead of monolithic ceramics. Simulations predicted that DOP in layered ceramics depends on the strength of interface between the layers [33]. DOP is reduced at higher interface strength. Layered ceramics can match the performance of monolithic ceramics with higher interface strength.

Though more studies are required in this area, layered ceramics seem promising. Thinner ceramics could be easier to manufacture than thick monolithic ceramics. Ceramics, due to their brittle nature, are flaw dependent. Chances of flaws reduce as ceramic thickness reduces, thereby improving its performance.

Nanofillers in Composites

Embedding nanofillers in composites can improve their performance. Many researchers have studied performance improvement of FRP composites by embedding nanofillers such as polymer nanofibers, nanosilica, multi-walled carbon nanotubes (MWCNTs), carbon nanofibers (CNFs), nanoclay, and many others.

Multiple approaches can be adopted to embed nanofillers in FRP composites. Nanofibers at certain grams per square meter (gsm) can be interleaved on dry fabrics by using deposition methods such as electrospinning. They can be dispersed in the polymer matrix. They can also be grown on the fabric or attached directly to it. Many such methods have been reported.

Reasonable amounts of enhancement of certain properties have been reported by numerous researchers. Property-wise enhancement observed by some researchers is tabulated below. A few studies on the effect of nanofillers on compressive strength are presented in Table 18. Similarly, few studies on inter-laminar shear strength (ILSS) and residual compressive strength after impact (CAI) are presented in Tables 19 and 20.

Effect of nanofillers on the performance of FRP composites subjected to ballistic impact was also studied by multiple researchers. Conflicting results were reported by different researchers. Multiple studies showed minimal increase in performance, whereas certain studies showed reasonable increase.

Residual Strength

The structural strength of armour after ballistic impact is its residual strength. It defines the ability of armour to take routine structural loads after impact. Such a capability is necessary when the ceramic-composite configuration performs the role of both structure and armour. Such armour is commonly known as composite integral armour or composite structural armour. Composite armour can truly replace metallic armour if this dual role can be performed by the same configuration. Composite armour is generally known to have lower residual strength than metallic armour. Negligible documentation is available in open literature quantifying its residual strength and comparing with metallic armour.

The extent of damage after impact governs the residual strength. Any improvement in choice of materials, interfaces, or armour design that reduces the damage area improves the residual strength. Smaller ceramic tiles reduce the extent of damage. Similarly, tougher polymer matrix in composite backing reduces the extent of delamination. Though, delamination has little contribution to energy absorption during penetration, post-impact strength of the backing material depends on its extent.

Use of certain layers between ceramics and composites which reduce the transmitted stress to the backing material can also reduce the extent of damage. Many strategies can be adopted. However, quantified data on the effect of such design improvements on residual strength is not documented.

In the future, more research is therefore required on this aspect. It can lead to an efficient armour design with residual strength matching metallic armour.

Table 18 Effect of nanofillers on compressive strength

Description of nanofilled composite	Maximum increase in performance (%)	Source
0.4 gsm electrospun nanofibers directly deposited on UD Eglass fabric and subsequently laminated with epoxy using RFI process	30	[34]
0.2% by weight nanosilica dispersed in epoxy laminated with UD Eglass fabric using RFI process	29	[35]
0.2% by weight nanosilica dispersed in epoxy laminated with UD carbon fabric using RFI process	35	[35]
0.2% by weight MWCNTs dispersed in epoxy laminated with UD Eglass fabric using RFI process	24	[36]
0.5% by weight CNFs dispersed in epoxy laminated with UD Eglass fabric using RFI process	40	[37]
5% by weight nanoclay dispersed in epoxy laminated with UD Eglass fabric using RFI process	15	[38]
5% by weight nanoclay dispersed in epoxy laminated with UD carbon fabric using RFI process	21	[38]

Table 19 Effect of nanofillers on ILSS

Description of nanofilled composite	Maximum increase in performance (%)	Source
0.4 gsm electrospun nanofibers directly deposited on UD Eglass fabric and subsequently laminated with epoxy using RFI process	17	[34]
0.4% by weight nanosilica dispersed in epoxy laminated with UD Eglass fabric using RFI process	4	[35]
0.8% by weight nanosilica dispersed in epoxy laminated with UD carbon fabric using RFI process	0	[35]
0.5% by weight CNFs dispersed in epoxy laminated with UD Eglass fabric using RFI process	33	[37]

Table 20 Effect of nanofillers on CAI

Description of nanofilled composite	Maximum increase in performance (%)	Source
0.4 gsm electrospun nanofibers directly deposited on UD Eglass fabric and subsequently laminated with epoxy using RFI process	19	[34]

Multiple Hit Resistance

Multiple hit resistance is the capability of armour to sustain multiple impacts. Due to the threats faced by protection structures and ambush scenarios observed during combat, this capability is of primary importance. Certain standards [39] have been evolved to evaluate the multi-hit performance of armour. Such standards specify a shot pattern and the distance between the centers of individual shots. Performance of an armour design is determined based on visual observations of the tested sample. Complete penetration (CP) is considered as failure.

Ceramic-composite armour is generally known to have inferior multi-hit capabilities than metallic armour. Negligible documentation is available in open literature on the parameters for achieving multiple hit resistance efficiently using ceramic-composite armour. Various aspects of armour design govern the multi-hit performance such as extent of damage after a hit, size of the ceramic tile, nature of interfaces between ceramics tiles, shape of the ceramic tiles, confinement of ceramics, strength of bonding materials, and fracture toughness of ceramics. Other parameters such as extent of damage and delamination in the backing structure also affect the multi-hit performance. However, quantified data on each of the parameters and its effect on performance are not documented.

Multi-hit performance of an armour can be quantified by the minimum distance between the first impact and the second impact. Armour that can prevent CP of the second hit closest to the first hit has the best multi-hit performance. Restricting the extent of damage and keeping it local improve multi-hit capability. This conflicts with the overall requirement of impact energy absorption. A larger area of damage

results in greater energy absorption. Hence, armour design such that maximum energy is absorbed, keeping the damage localized, is challenging.

Armour is often made using finite size ceramic tiles. Due to the brittle failure characteristics of armour, the tile subjected to impact is shattered and offers no resistance to the second hit. As a result of these fracture characteristics of ceramics, a single tile may never sustain multiple hits unless ceramic toughness is substantially improved.

Waves originating from the point of impact reach the tile edge and get transmitted into adjacent tiles. By leaving a small gap between adjacent tiles, damage can be restricted only to the impacted tile. The second bullet can then impact the adjacent tile, just one tile length away. Smaller tiles therefore allow closer second hit and improve multi-hit capability.

However, the presence of gaps between adjacent tiles introduces weak zones. Resistance to penetration in the zone near the gaps is much lower than the resistance to penetration at the center of tiles. A way of reducing weak zones is by minimizing the gap. The number of weak zones can also be reduced by increasing tile size thereby improving multi-hit performance.

This requirement conflicts with the requirement of smaller tiles. Smaller tiles with gaps between adjacent tiles improve multi-hit performance by restricting damage to one tile and allow closer second hit. However, these gaps introduce vulnerable zones. Reduction of vulnerable zones required larger tiles.

This problem of multi-hit armour design exists and requires unique alternative approaches. There is no widely accepted solution and the problem is still open. Various attempts have been made with partial success. However, every such attempt degrades other aspects of armour performance, such as its areal density. Some such alternatives are listed below:

1. Development of tougher ceramics such as bioinspired or nacre-inspired systems which do not shatter on impact like conventional ceramics
2. Changing the shape of the top and bottom flat faces of ceramic tile to dome-shaped so that the bullets are deflected
3. Improving the resistance to penetration at tile gaps by chamfering the tile edges
4. Using multiple layers of ceramics instead of a single monolithic tile in a brick and mortar architecture

In the future, more research can lead to alternative design eliminating the drawbacks of existing designs. Such armour can be substantially lighter than metal but still matching its multi-hit performance.

Summary and Future Directions

Ceramic-composite armour is the lightest alternative to metal armour especially at higher threats. An improved form of this armour is integral armour where armour and structure are integrated together as a single multifunctional unit. Integral armour

ensures optimal utilization of the components and avoids parasitic masses is thereby lighter than add-on armour.

Ballistic impact phenomenon is local and dependent on wave propagation characteristics. Features in armour design effect wave propagation. Various energy-dissipating mechanisms absorb the energy of the projectile. Ceramic layer absorbs approximately 50% of the energy. Thirty-five percentage of energy is absorbed by deformation of the projectile, and the remaining 15% is absorbed by the backing material.

Various parameters affect the penetration resistance of armour. Material choices, design configuration, and projectile parameters are some of them. Multiple design choices have to be made for design of armour such as relative thickness of its constituents, ceramic tile shape, size, confinement, and wrapping. Multiple approaches can be adopted to further improve its energy absorption such as layered ceramics and nanofillers.

A key challenge in the future is to further reduce the weight and thickness of armour. It will involve development of better basic materials and manufacturing processes such as tougher ceramics or more damage-mitigating composites. Alternative approaches such as bioinspired ceramics, functionally graded materials, and extensive use of nanomaterials can also be explored.

Light armour today is expensive, and any study for cost reduction has great importance. Another key challenge is improving the residual strength and multi-hit capability of armour. Sustaining many more hits and that too at close vicinity to each other without degrading its functionality is an area where lot of work is required. New and innovative concepts have to be evolved in all these aspects. Though a lot of work has already been done, there is an even greater potential in the future.

References

1. Fink BK (2000) Performance metrics for composite integral armour. *Journal of Thermoplastic Composite Materials* 13:417–431
2. Mohan A, Harshe R, Akella K (2005) Fabrication of composites integral armour. In: Proceedings of the fourth ISAMPE national conference on composites (INCCOM-4). Amrita School of Engineering and Karunya Institute of Technology and Sciences, Coimbatore
3. Mahdi S, Gama BA, Yarlagadda S, Gillespie JW Jr (2003) Effect of manufacturing process on the interfacial properties and structural performance of multi-functional composite structures. *Composites Part A* 34:635–647
4. Gibson RF (1994) Principles of composite material mechanics. CRC Press. www.crcpress.com
5. Zukas J, Nicholas T, Swift HF, Greszczuk LB, Curran DR (1982) Impact dynamics. Wiley, New York; Chichester
6. Abrate S (1998) Impact on composite structures. Cambridge: Cambridge University Press. <https://doi.org/10.1017/CBO9780511574504>
7. Naik NK, Kumar S, Ratnaveer D, Joshi M, Akella K (2012) An energy-based model for ballistic impact analysis of ceramic-composite armours. *International Journal of Damage Mechanics* 22:145–187
8. Bhatnagar A (2006) Bullets, fragments and bullet deformation. In: *Lightweight ballistic composites*. Woodhead Publishing Limited

9. Salame JM, Quefelec B (2006) Ceramic faced molded armour. In: *Lightweight ballistic composites*. Woodhead Publishing Limited
10. Shahkarami A, Cepus E, Vaziri R, Poursartip A (2006) Material responses to ballistic impact. In: *Lightweight ballistic composites*. Woodhead Publishing Limited
11. Wen HM (2000) Predicting the penetration and perforation of frp laminates struck normally by projectiles with different nose shapes. *Composite Structures* 49:321–329
12. Ulven C, Vaidya UK, Hosur MV (2003) Effect of projectile shape during ballistic perforation of vartm carbon/epoxy composite panels. *Composite Structures* 61:143–150
13. Tan VBC, Khoo KJL (2005) Perforation of flexible laminates by projectiles of different geometry. *International Journal of Impact Engineering* 31:793–810
14. Tan VBC, Lim CT, Cheong CH (2003) Perforation of high-strength fabric by projectiles of different geometry. *International Journal of Impact Engineering* 28:207–222
15. Montgomery TG, Grady PL, Tomasino C (1982) The effects of projectile geometry on the performance of ballistic fabrics. *Textile Research Journal* 52:44–2450
16. Ernst H-J, Volker W, Wolf T (2001) Armour ceramics under high-velocity impact of a medium caliber long-rod penetrator. In: *Ceramic armor materials by design: proceedings of the Ceramic Armor Materials by Design Symposium held at the Pac Rim IV International Conference on Advanced Ceramics and Glass, November 4–8, 2001 in Wailea, Maui, Hawaii*. Westerville, Ohio, American Ceramic Society.
17. James B (2001) Practical issues in ceramic armour design. In: *Ceramic armor materials by design: proceedings of the Ceramic armor materials by design Symposium held at the Pac Rim IV International Conference on Advanced Ceramics and Glass, November 4–8, 2001 in Wailea, Maui, Hawaii*. Westerville, Ohio, American Ceramic Society.
18. Tam T, Bhatnagar A (2006) High performance ballistic fibers. In: *Lightweight ballistic composites*. Woodhead Publishing Limited
19. Song JW (2006) Fabrics and composites for ballistic protection of personnel. In: *Lightweight ballistic composites*. Woodhead Publishing Limited
20. National Institute of Justice Standard (2008) Ballistic resistance of body armour – NIJ-0101.06 www.ojp.usdoj.gov/nij
21. Hannibal A, Weir B (2006) Ballistic material processing. In: *Lightweight ballistic composites*. Woodhead Publishing Limited
22. Bhatnagar A, Lang D (2006) Military and law enforcement applications of lightweight ballistic composites. In: *Lightweight ballistic composites*. Woodhead Publishing Limited
23. Hosur MV, Vaidya UK, Ulven C, Jeelani S (2004) Performance of stitched/unstitched woven carbon/epoxy composites under high velocity impact loading. *Composite Structures* 64:455–466
24. Udatha P, Sesha Kumar CV, Nair NS, Naik NK (2012) High velocity impact performance of three-dimensional woven composites. *The Journal of Strain Analysis for Engineering Design* 47:419–431
25. Callister WD Jr (2003) *Materials science and engineering – an introduction*. Wiley
26. Pandya KS, Pothnis JR, Ravikumar G, Naik NK (2013) Ballistic impact behaviour of hybrid composites. *Materials and Design* 44:128–135
27. Hetherington JG, Rajagopalan BP (1991) An investigation into the energy absorbed during ballistic perforation of composite armours. *International Journal of Impact Engineering* 11:33–40
28. Nemat-Nasser S, Sarva S, Isaacs JB, Lischer DW (2001) Novel ideas in multi-functional ceramic armour design. In: *Ceramic armor materials by design: proceedings of the Ceramic Armor Materials by Design Symposium held at the Pac Rim IV International Conference on Advanced Ceramics and Glass, November 4–8, 2001 in Wailea, Maui, Hawaii*. Westerville, Ohio, American Ceramic Society.
29. Holmquist TJ, Templeton DW, Bishnoi KD (2001) Constitutive modeling of aluminum nitride for large strain, high strain-rate, and high pressure applications. *International Journal of Impact Engineering* 25:211–231

30. Yadav S, Ravichandran G (2003) Penetration resistance of laminated ceramic/polymer structures. *International Journal of Impact Engineering* 28:557–574
31. Tasdemirci A, Hall IW (2009) Development of novel multilayer materials for impact applications: a combined numerical and experimental approach. *Materials and Design* 30:1533–1541
32. Akella K (2015) Studies for design of layered ceramic armour inspired by seashells. PhD thesis, Indian Institute of Science
33. Akella K (2017) Studies for improved damage tolerance of ceramics against ballistic impact using layers. *Procedia Engineering* 173:244–250
34. Anand A, Kumar N, Harshe R, Joshi M (2017) Glass/epoxy structural composites with interleaved nylon 6/6 nanofibers. *Journal of Composite Materials* 51:3291–3298
35. Panse P, Anand A, Murkute V, Ecka A, Harshe R, Joshi M (2016) Mechanical properties of hybrid structural composites reinforced with nanosilica. *Polymer Composites* 37:1216–1222
36. Anand A, Harshe R, Joshi M (2013) Resin film infusion: towards structural composites with nanofillers. *Journal of Applied Polymer Science* 129:1618–1624
37. Anand A, Harshe R, Joshi M (2013) On the processing and properties of carbon nanofibers reinforced hybrid structural composites. *Journal of Composite Materials* 47:2937–2943
38. Anand A, Joshi M (2015) Structural composites hybridised with nanofillers: an overview. *Journal of the Indian Institute of Science* 95:233–247
39. AEP-55 Volume 1 (Edition 1). Procedures for evaluating the protection level of armoured vehicles. NATO, 2011



Transparent Ceramics for Ballistic Armor Applications

11

Rajendran Senthil Kumar, Papiya Biswas, Roy Johnson, and
Yashwant Ramchandra Mahajan

Contents

Introduction	436
Requisites of Transparency for Armor Applications	436
Requisites of Mechanical Properties for Armor Applications	439
Typical Armor Assembly	441
Traditional and Advanced Ceramic Armors	442
Traditional (Soda-Lime Glass Based) Transparent Armor and Limitations	442
Emerging Transparent Ceramic Materials	443
Conclusions	454
References	455

Abstract

Ceramic materials that are transparent to visible light with excellent mechanical properties are emerging as suitable candidate materials for ballistic armor applications. Various advanced materials such as single crystal sapphire, spinel, and aluminum oxynitride have been developed to withstand the penetration of the projectile during impact. The armors produced from these materials exhibit outstanding

R. Senthil Kumar

International Advanced Research Centre for Powder Metallurgy and New Materials (ARCI),
Hyderabad, India
e-mail: senthil@arci.res.in

P. Biswas

Center for Ceramic Processing, International Advanced Research Centre for Powder Metallurgy
and New Materials (ARCI), Hyderabad, Telangana, India
e-mail: papiya@arci.res.in

R. Johnson · Y. R. Mahajan (✉)

International Advanced Research Centre for Powder Metallurgy and New Materials, (ARCI),
Balapur, Hyderabad, India
e-mail: royjohnson@arci.res.in; mahajanyrm@gmail.com

ballistic performance compared to the conventional soda-lime glass and glass-ceramics due to their remarkable hardness in combination with other superior mechanical properties. This chapter presents an overview of various transparent ceramic materials that have been explored hitherto for the armor applications along with various processing fundamentals required to produce these materials. This chapter also reviews the fabrication and comparative evaluation of conventional and advanced transparent armor materials for ballistic applications.

Keywords

Transparent ceramics · Ballistic armor · Glass · Sapphire · Magnesium aluminate spinel · Aluminium oxynitride

Introduction

Transparent armor is a functionally tailored system of transparent materials designed to provide protection from blast or ballistic threats. Field performance of the transparent armor is not only determined by the structural integrity but also the high degree of in-line transmission from visible to infrared region in the extreme environments in which it is intended to operate. This unique class of materials deployed in a wide spectrum of applications, ranging from wind shields and side windows in military ground vehicles, VIP armored cars, noncombat riot face shields/visors, explosive disposal equipment, missile domes, and night vision goggles [1–5]. Applications are also extended to civilian sectors such as infrared temperature sensors, components of optical fibers, laser host materials, encapsulation for high pressure arc lamps, scintillation counters for computed topography scanners, alternative to quartz and sapphire in semiconductors, for scratch resistant surfaces, watch glasses, and in synthetic opals and rubies [6–11]. Few of the applications of transparent ceramic armor in commercial use for actual systems are shown in Fig. 1.

Requisites of Transparency for Armor Applications

Unlike opaque armor, transparency is one of the most essential requirements for transparent armor application in addition to the mechanical property requirements [12, 13]. Transparency is a function of negligible interaction with electromagnetic radiation of interest. Transparency being an intrinsic property of the material, it is dictated by the atomic structure as well as the crystal structure of the material.

Transparent ceramics for armor applications are generally used in the visible region of the electromagnetic radiation. When the photons in the incident beam of the light fall on a transparent material, the total transmission depends on the lattice vibrations or excitation of electrons between energy levels. The absorption of incident radiation is affected by lattice vibration or by the excitation of electrons between energy bands. It is well known that excitation followed by absorption takes

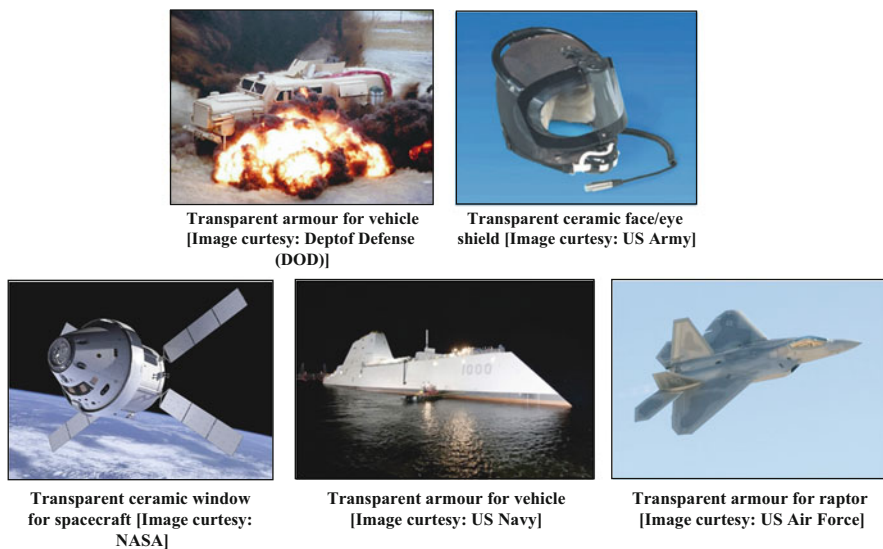


Fig. 1 Commercial applications of transparent ceramic armor for destroyer

place only if the photon energy is greater than that of the band gap as per the equation “ $h\gamma = hc/\lambda$,” where h is Plank’s constant = 4.13×10^{-15} eV, γ is frequency of incident light, λ is wave length of incident light. Hence, the prerequisite for absorption to take place can be regarded as $hc/\lambda > \text{Energy gap}$. A band gap energy greater than 3.1 eV results in the total absence of absorption and the crystal structure will be transparent if no other type of scattering encounters with the crystal structure. The solid will be opaque if the band energy is less than 1.8 eV and translucent if it falls between the above mentioned ranges. So, ceramics with band gap greater than 3.1 eV can be ideal candidates for transparent armor applications in the visible range [14].

Reflection is another way of interaction when light travels from one medium to another. Scattering of light takes place at the interface between the medium due to difference in refractive index (n). The reflectivity which is the ratio of intensities of incident and reflected beams gives a measure of reflection at the surface. When light is transmitted from air or vacuum into the solid, then the reflectivity is given by $R = (n_s - 1)^2 / (n_s + 1)^2$, Where n_s is the refractive index of solid. Refractive index of air or vacuum is taken as one. From the above equation, we can see that for higher refractive index of solid, the reflectivity will be higher. So, reflection losses on the surface of solid have to be minimized to make high transparent ceramics. A thin layer of antireflection coating is generally applied to cater this issue.

However, the extent of achieving the theoretical transparency of a given material is dependent on the microstructure and the defects that can be originated from processing. Krell et al. described the effect of residual porosity as a function of achieved transparency in case of alumina [15]. Residual porosity need to be

decreased preferably to zero or $<0.05\%$ to obtain high transmission values [15]. This can be attributed to the large difference between refractive indices of the air-filled pore and the material cause the scattering of the electromagnetic radiation to a larger extent. Materials with cubic crystals are more adaptable for transparent ceramic applications due to isotropic refractive index in all crystallographic axes. Grain coarsening in case of materials with cubic crystallography improves the transparency through reducing the overall grain boundary fraction which acts as the scatter points. However, materials with noncubic crystallography exhibit anisotropy along different axes. This results in birefringence scattering as the light passes from one randomly oriented grain to another in case of polycrystalline transparent ceramics. Further, transparency exhibited by the materials is also a strong function of distortion free surface with high durability.

Birefringent crystals provide another source of scattering in the case of crystal structure with lower symmetry than the cubic crystallography [16]. However, the birefringent effect does not exhibit if the light is parallel to the axis of symmetry of the crystal. According to Beer-Lambert rule, intensity of transmitted light is given by $I = I_0 (1 - R)^2 \exp(-\mu x)$, where I_0 is intensity of incident beam, R is reflectivity of the material, μ is absorption coefficient, and x is thickness of sintered body. From the above equation, we can see that the intensity of transmitted beam depends on reflectivity of the material, absorption coefficient, and thickness of sintered body. Hence, the key factors under consideration to achieve the transparency in ceramics are to control all the factors mentioned above which reduces transmittance by scattering of the light. A schematic of source of scatter points is shown in Fig. 2.

Though the transparency can be qualitatively perceived through simple observations, a more systematic approach is the in-line transmission measurements. Optical devices such as common spectrophotometers with measurement aperture in the range of $3-5^\circ$ generally measures scattered and unscattered light which can lead to wrong conclusions. In order to exclude the scattered intensity, it is important to measure the real in line transmission through the measurement aperture close to zero. Philips-NGK has published their investigations and recommend the use of an

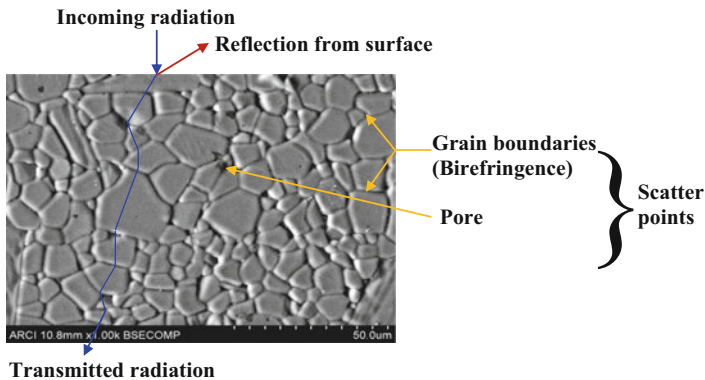


Fig. 2 Source of scatter points due to processing defects (Schematic)

aperture of about 0.5° to obtain real inline transmission RIT values [17]. Unlike single crystals, diffuse scattering occurs in polycrystalline ceramics through microstructural components such as pores or second phases with different refractive indices. Additionally, in noncubic crystals, birefringent splitting of the beams occurs at grain boundaries and hence it is possible to minimize the scattering loss in the submicron ranges. Depending on the Mie theory, considering the difference in ratio of refractive index polarisation occurs perpendicular and parallel to c – axis. RIT can be correlated to the grain size and thickness of the sample through the following equation:

$$RIT = T_{th} \exp \left\{ -3\pi^2 \frac{\Delta n^2 r d}{n^2 \lambda^2} \right\} \quad (1)$$

where r is the radius, d is the thickness, λ the wavelength, and n is the refractive index. Further the theoretical limit of the transmission could be defined by the equation

$$T_{th} = (1 - R_2) = \frac{2n}{n^2 + 1} \quad (2)$$

It is clear from the equation (1) that RIT is function of λ and r and also d .

Requisites of Mechanical Properties for Armor Applications

Basic mechanical properties requirement for the armor can be generalized for opaque as well as transparent armor. Hardness is the dominant property that determines the ballistic performance of ceramic armor. It is considered that ceramic with high hardness will resist the penetration of the projectile by deforming, fragmentation, and deflection. Additionally, the ceramic will also blunt and causes the projectile to erode on impact. The studies have shown that the vickers hardness of the ceramics cannot be exclusively correlated with their ballistic performance. A correlation between hardness and toughness for ballistic performance has been proposed. While hardness determines the ballistic performance potential of a material, the toughness is important in achieving the same. Hence, the resistance in fracture (also known as fracture toughness) is also considered as an important property to achieving the ballistic performance. It is desirable that to obtain the optimum ballistic efficiency, a balance between the hardness and fracture toughness become critical [18].

Ballistic performance shall be correlated with the strength of the material under tensile, compressive, shear, and bending modes, rather than a single strength value [19]. Fracture strength of ceramics is very sensitive to size, shape, and surface finish of a given material [20]. Tensile or flexure in ceramics often initiates at the surface unless volume distributed flaws are larger than the surface flaws. When the tensile stress reaches the material tensile strength, the material will fail. Crack pattern

caused by static load is different from the high-speed projectile impact. The wing cracks generally developed during the projectile impact due to localized tensile region assumes the importance of tensile strength in ballistic performance. Since, the tensile cracks are originated from the sliding motion of the preexisting defects, coefficient of friction also contribute towards ballistic efficiency.

Compressive strength of the ceramic is mainly controlled by the processing defects which in turn play a major role in resistance offered by the ceramic for the penetration of the projectile under impact. Origin of the crack leading to failure occurs generally from the tip of the preexisting flaws propagating in the direction of compression. A higher compressive strength is expected to perform better under the impact. The projectile on impact is fractured, deformed, or deflected based on the compressive strength of the ceramic. Though not very significant, the compressive strength of ceramic material can aid in the defeat of projectile on impact. Shear strength has also been linked to ballistic performance. During the impact, a large level of dislocation densities is generated in the confined compression zone directly underneath the projectile core and tensile region in the surrounding area of the projectile. A higher shear strength is advantageous in defeating the projectile. Shear strength being a volume effect, thickness of ceramic should be sufficient enough to the projectile dimensions.

Impact of the high-velocity projectile is a dynamic phenomenon which comprises of events such as penetration, wave propagation, cracking into fragments, ejection of fragments, and erosion of projectiles followed by the projectile capture in the back plate. In view of the impact of the projectile to a small region of ceramic, higher stiffness resist large deflection. The bulk and shear modulus of the material play a major role in achieving the ballistic resistance. Young modulus (E) can be calculated as follows where C_L is longitudinal wave velocity, C_s is shear wave velocity, ν is Poisson's ratio, Z is acoustic impedance, and ρ is density.

$$Z = \rho \sqrt{\frac{E(1 - \nu)}{\rho(1 + \nu)(1 - 2\nu)}} \quad (3)$$

$$C_L = \sqrt{\frac{E(1 - \nu)}{\rho(1 + \nu)(1 - 2\nu)}} \quad (4)$$

$$C_s = \sqrt{\frac{E}{2\rho(1 + \nu)}} \quad (5)$$

The stress wave propagation impedance in a material is the product of material density and the wave propagation speed, and decreasing the transmission of blast wave magnitude transmitted through the ceramic is important for the superior ballistic performance. During the high-velocity projectile impact, ceramics experience the high transient pressures and are shocked under uniaxial dynamic loading and exceed the yield stress of the ceramic (Hugoniot Elastic Limit). Shocking above

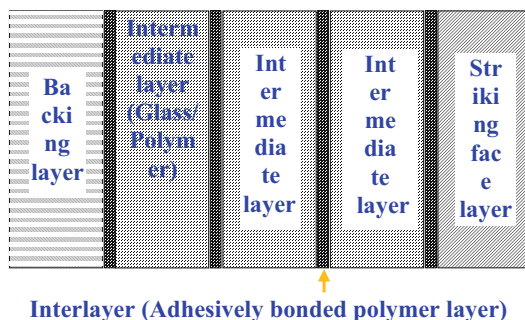
the Hugoniot Elastic Limit is reported to result in significant loss of shear strength lowering the ballistic performance. Further, the internal stresses due to wave reflection exceed the tensile strength of the material spalling occur which is a dynamic failure process leading to internal rupture or cavitation.

Typical Armor Assembly

A typical transparent armor system consists of multi-laminated elements as shown in Fig. 3. It is evident that it is not only the striking face but also the overall ceramic armor system design that plays a key role in realizing the ballistic performance [21]. As per schematic representation shown in Fig. 3, this system has the first layer of striking face material consists of glass, glass-ceramic, or transparent ceramic which possess the ability to deform or erode the projectile. The intermediate region typically comprises layers of glass or glass ceramics, devitrified glass-based lithium aluminum silicate or polymers such as PMMA (poly methyl methacrylate), PU (Poly urethane), or polymers backed by PC (poly carbonate). Additionally, thin layer of polyurethane or polyvinyl butyral (PVB) is also provided between the glass/glass or glass/polymer laminate to mitigate the stresses arising from the thermal expansion mismatches.

Though each functional layer has a role to play, the ballistic performance is a strong function of the front mounted striking layer. According to hierarchical ranking approach, attempts have been made to distinguish the upper level (dwell phase) and lower level (penetration phase) that influences the ballistic performance [22]. During the dwell phase, the nominal velocity of projectile is almost zero at the ceramic front phase and a penetration phase, during which the projectile passes through fragmented ceramic. In case of interface defeat, the projectile is stopped at the striking surface, from the point of view of projectile defeat, prolonging of dwell time of the projectile during the dwell phase to enhance the tip blunting is highly desirable. Dynamic stiffness and high rate inelastic deformation resistance behavior are the two influencing parameters during dwell phase which are significantly enhanced by finer grain sizes of projectile facing layer [23]. During

Fig. 3 Transparent ceramic armor system (schematic)



penetration phase, erosion/plastic deformation of the projectile is controlled by the interaction of the debris of the striking face materials [24]. Harder the fragments of the striking face, efficient wear-out of the projectile will occur. The thickness of the front layer generally used as minimum as possible as the transparency reduces with increasing thickness and the higher cost involved in comparison to conventional armor materials [23]. Good resistance to environmental factors such as thermal gradients and ultra-violet radiation as well as low-velocity impact damage resistance due to stones and pebbles are also desirable characteristics [23].

Intermediate and backing layers separated by the polymer interlayers, which provide additional resistance to penetration and also to stop crack propagation from hard face to polymer [25]. The inter layers are generally bonded by adhesives which primarily mitigate the stresses related to thermal expansion mismatch. The final layer is usually polycarbonate that serves as to contain the projectile as well as armor spall. These layers also should have high optical transparency in the visible as well as infrared wavelength regions. High shock absorption capability, high bending stiffness, and restricted crack propagation to enhance the multi hit performance as well as good environmental resistance are other desirable properties. Engineering the striking face material, order of tiles, thickness of the piles, interlayer hardness, interlayer thickness, and number of tiles provides the opportunity to design armor systems with desirable levels of protection. In case of transparent armor for ground level occupant protection, the capability for high ballistic resistance to cater the multi-hit blasts, lower areal density to reduce the payloads, low wear properties, scratch resistance, etc. are desirable.

Traditional and Advanced Ceramic Armors

Traditional (Soda-Lime Glass Based) Transparent Armor and Limitations

Soda-lime glass (SLG) is widely available on a commercial scale. SLG is commercially manufactured by float glass process [26]. Float glass process is flexible in processing simple and complex shapes in large sizes with near-net shapes at a lower cost compared to single crystal and other polycrystalline ceramics. PPG industries are the leading manufacturer of SLG under the trade name Starphire. A typical comparison of glass, single crystal, and polycrystalline transparent materials with respect to process, optical and mechanical properties as described by Krell et al. [27] is shown in Table 1.

Traditionally used transparent armor system consists of laminates of soda-lime glasses bonded to polymeric inter-layers using strong adhesives. Conventional soda-lime glass laminates scale up in thickness to provide necessary protection against the threats. Higher thickness in combination with the density of 2.52 g/cc not only increases the higher armor pay loads but also significant reduction of usable crew space [28]. Additionally, thicker sections also result in optical distortions,

Table 1 Comparison of glass, single crystal, and polycrystalline transparent ceramics [27]

Attributes	Glass	Single crystal	Polycrystalline transparent ceramics
Process	Inexpensive Excellent shape formation	Very expensive Simple shapes	Medium costs Complex shaping
Transparency	Very high	Very high	Isotropic (macroscopic scale) Good transparency
Strength Hardness	Poor	Good	Frequently better than single crystals

haze, and glare due to increased layers of the laminate leading to poor clarity limiting visibility [29]. Under harsh service conditions, armor system with traditional soda lime glass which is the striking face can be eroded by the wind blowing sand or dust storms common in the desert areas due to comparatively poor mechanical properties as is evident from Table 2. The transparent armor during service should be able to withstand mechanically induced vibrations, shocks, high g-loads, and stresses arising due to thermal expansion mismatch resulting from temperature extremes (for example, Rajasthan deserts in India has a wide temperature variation from -2°C in winter to as high as 48°C in summer). Traditional glass-based armor exhibit less tolerance in such extreme weather conditions due to low thermal shock resistance resulting from high thermal expansion in combination with poor strength values as is evident from Table 2.

A typical visible transmission plot of soda lime glass is shown in Fig. 4. It is evident from the figure that the transmission properties of traditional glass-based armor are limited only in the visible range [30]. This is a major limitation in view of gaining importance of the requirement of transmission properties in the multispectral ranges from visible extending up to mid-wave infrared range (MWIR, $3\text{--}5\ \mu\text{m}$) for their compatibility to night vision devices (NAD) [31].

Emerging Transparent Ceramic Materials

Transparent ceramic materials such as corundum (as polycrystalline submicron alumina and single crystal sapphire (Al_2O_3)), aluminum oxynitride (AlON), and spinel (MgAl_2O_4) in combination with advanced polymers result in high performance armor systems. Table 2 provides an overview of various emerging transparent armor ceramics such as single crystalline sapphire, polycrystalline magnesium aluminate spinel, and aluminum oxynitride along with soda lime glass. Table 2 also depicts the manufacturer or developer of the product; manufacturing process; status of commercialization; cost; mechanical, physico-chemical, and optical properties, and advantages with respect to the applications of the emerging materials.

Table 2 Transparent ceramics: a comparison of the mechanical, physicochemical, and transmission properties [13, 21, 25, 28, 32–36]

Property	Soda-lime glass	Sapphire (single crystal alumina)	Magnesium aluminate spinel (MgAl ₂ O ₄)	Magnesium aluminate spinel (MgAl ₂ O ₄)	Magnesium aluminate spinel (MgAl ₂ O ₄)	Aluminum oxynitride (<i>γ</i> -AlON)
Manufacturer/ Developer	PPG Industries, Inc.	Saint-Gobain Crystals	Surnet Corp.	Amorline Corp. (Spinel technology acquired from Technology Assessment & Transfer, Inc.)	Materials and Electrochemical Research (MER) Corp. (Technology was developed at Naval Research Lab. And licensed to MER Corp.)	Surnet Corp.
Product Name	Starfire	Saphikon® EFG® Sapphire	NA	NA	–	NA
Density (g/cc)	2.5	3.97	3.58	3.58	3.58	3.69
Areal density (kg/mm²)	130	77	64	64	64	63
Grain Size (μm)	Amorphous	Single crystal	25–150 (bimodal)	100–200	70–120	200–300
Knoop Hardness (kg/mm²)	470	1900 to C-axis 2200 ⊥ to C-axis	1450–1650	1350	1600	1800
Elastic Modulus (GPa)	73.1	435 to C-axis	276	277	277	320
Figure of merit (M) = E/H/ρ	1.4	22.9	12.2	13.0	12.6	15.9
Flexural Strength (MPa)	41	1035 to C-axis 760 ⊥ to C-axis	170	185–250	300	300–700
Compressive Strength (GPa)	325	Approx. 2.0	3.02–3.40 (quasi-static at 2×10^{-4})	–	–	2.67

Fracture Toughness (MPa·m ^{1/2})	0.9	4.54 (0001) direction	1.5	1.5–2.0	1.7	2.0
CTE (10 ⁻⁶ K ⁻¹)	9.28	8.8 to C-axis 7.9 ⊥ to C-axis	6.97	6.09	6.34	5.65
Typical Transparency in Visible Range (%)	89–91%	75–82%	75–80%	86–87%	80–87%	82–85%
Typical Transmission Wavelength Range (μm)	0.335–2.5	0.25–6.0	0.25–6.50	0.25–6.50	0.30–5.50	0.22–6.0
Typical Haze (in the visible range)	~0.6	~1	<10	<10	<10	<2
Typical Clarity (in the visible range)	–	–	>95	>95	>95	>98
Manufacturing Process	Float glass process	Continuous single crystal growing process involving very high temperatures for long durations; difficult to machine due to its very high hardness	Conventional ceramic processing involving moderate temperatures and short times (<1day); easier machining due to its lower hardness than sapphire and AION	Hot pressing followed by hot isostatic pressing route is preferred cost effective approach for producing large windows; easier machining due to its lower hardness than sapphire and AION	Ready to mix nano-mixture+ low pressure NNS green forming by Freeze forging + HIP/HIP + edge bonding; easier machining due to its lower hardness than sapphire and AION	Conventional ceramic processing using expensive proprietary powders, which involves very high temperatures for long durations; demanding precision machining requirements due to its high hardness

(continued)

Table 2 (continued)

Property	Soda-lime glass	Sapphire (single crystal alumina)	Magnesium aluminate spinel ($MgAl_2O_4$)	Magnesium aluminate spinel ($MgAl_2O_4$)	Magnesium aluminate spinel ($MgAl_2O_4$)	Aluminum oxynitride (γ -AlON)
Status of Commercialization	Widely available on a commercial scale	Commercialized by Saint Gobain Crystals	Established technology and capable of producing 18×3.5 in. size windows	Commercially producing $16.25'' \times 16.25''$ size spinel blanks and curved plates of 16×16 in. size	The product line includes domes of 2'' to 10'' diameter, windows (up to 800 in. ² , and 1.5'' thick), and 3-D shape parts	Acquired AlON technology from Raytheon Electronic Systems and Sumet has been manufacturing 15×27 -in. ALON windows on a regular basis. Available in limited quantities
Cost	The lowest cost material produced by relatively low cost float glass process	Sapphire is prohibitively expensive (much higher than AlON and spinel) due to the high cost and long times involved in single crystal growing process	The projected production cost of bulletproof transparent spinel is 10 and 5 times lower than sapphire and AlON, respectively	The projected production cost of bulletproof transparent spinel is 10 and 5 times lower than sapphire and AlON, respectively	The projected production cost of bulletproof transparent spinel is 10 and 5 times lower than sapphire and AlON, respectively	3–5 times more expensive than traditional transparent glass armor as it uses expensive proprietary powders and it involves very high temperatures for long durations

<p>Advantages</p>	<p>Low cost solution as it obviates the need for expensive machining processes These materials can be produced in large size sheets with curved shapes Excellent optical homogeneity with high transparency in visible range</p>	<p>>50% weight and thickness reduction as compared to glass armor at the same ballistic performance Enhanced night vision transmittance High hardness and abrasion resistance</p>	<p>Better optical transmittance in MWIR range than either sapphire or AION 50–60% weight savings and thickness reductions in comparison with conventional glass armor Easier processing route due to its amenability to densify at lower sintering temperatures for shorter durations than AION</p>	<p>Better optical transmittance in MWIR range than either sapphire or AION 50–60% weight savings and thickness reductions in comparison with conventional glass armor Easier processing route due to its amenability to densify at lower sintering temperatures for shorter durations than AION</p>	<p>Better optical transmittance in MWIR range than either sapphire or AION 50–60% weight savings and thickness reductions in comparison with conventional glass armor Easier processing route due to its amenability to densify at lower sintering temperatures for shorter durations than AION An innovative adhesive free edge bonding technology developed by MER is capable of producing defect-free, high strength spinel windows for armor applications with sizes as large as 30" × 30" × 0.5" in a cost effective manner</p>	<p>AION outperforms glass-based armor with 60% weight reduction and <50% thickness The ballistic performance of AION is 10–20% better than spinel and sapphire, respectively. It also shows 150% superior ballistic performance as compared to glass-based armor. It is capable of defending against various multi-hit threats such as 30 calAPM2 and 50 calAPM2 rounds. Demonstrates excellent performance against IED threats Exhibit superior transmittance, which is well suited for night vision devices (NVD) as well</p>
--------------------------	--	--	---	---	---	--

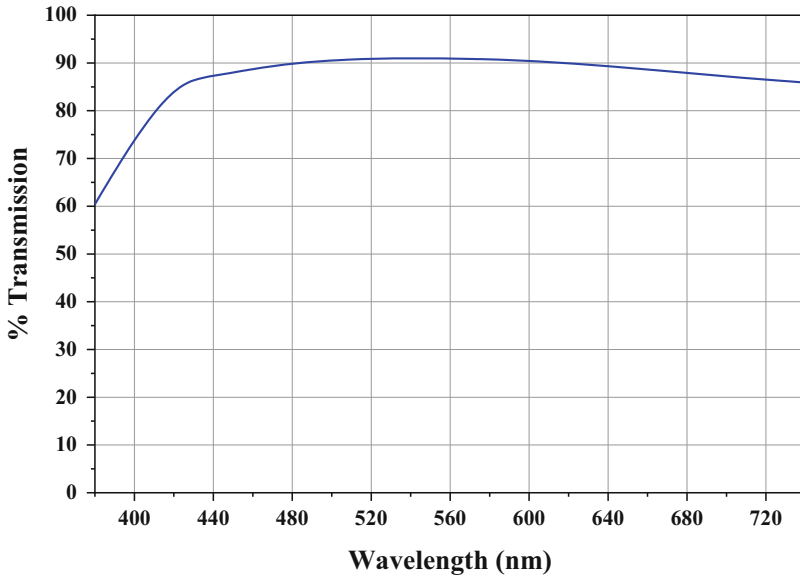


Fig 4 A typical transmission plot of soda-lime glass

Glass Ceramics Armor Systems

Among glass ceramics, lithium zinc silicate is one of the candidate materials that is used for armor applications. Glass ceramics are generally prepared by melting of the ingredients and followed by recrystallization through heat treatment of bulk glass. Basically, due to the crystallization that occurs in the material, the material becomes stronger, tougher, as well as stiffer than the original glass formulation suited for striker face in an armor system. However, there is a loss of transparency in the visible range when crystallization occurs. Not only the glass formulations but also the heat treatment schedule provides the flexibility in engineering the mechanical properties of the glass ceramics. As discussed, in case of soda-lime glass, glass ceramic is also used in combination with the backing plate. Horsfall et al. [37] reported the heat treatment effect on mechanical and ballistic properties of lithium zinc silicate glass ceramics and compared it with 95% alumina sample. Typical mechanical properties with respect to the heat treatment are shown in Fig. 5. The study has also been carried out under dynamic condition, and ballistic limit velocity and depth of penetration (DoP) against the high velocity projectile are estimated. It was proposed that due to the low hardness of 915 HV of lithium zinc silicate glass against 1500 HV in case of alumina limits the application of glass ceramics to soft core rounds; however, it is comparable or even better than alumina occasionally with similar areal densities. Though the study reported improvement with the configuration of striking face such as corrugation in case of 7.62 AP, the performance was quite poor compared to alumina.

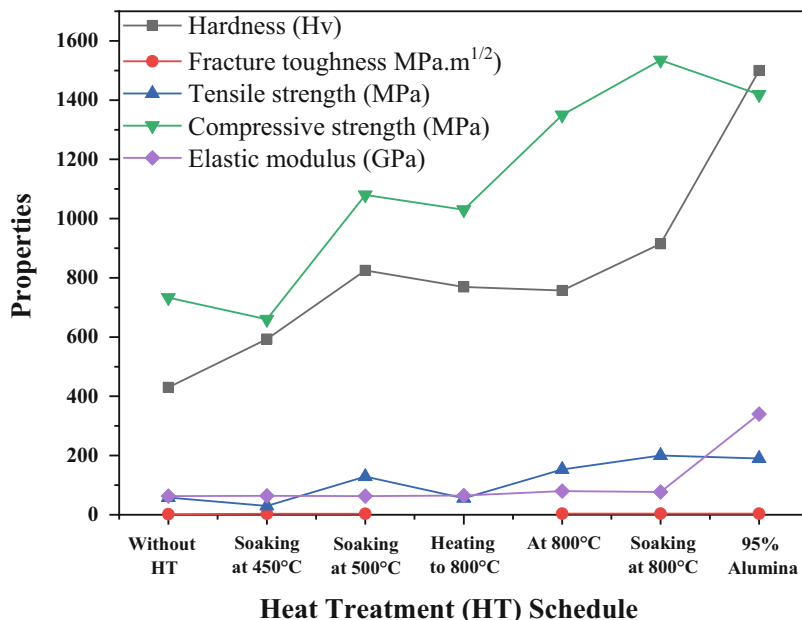


Fig. 5 Mechanical properties of lithium zinc silicate with respect to heat treatment schedule

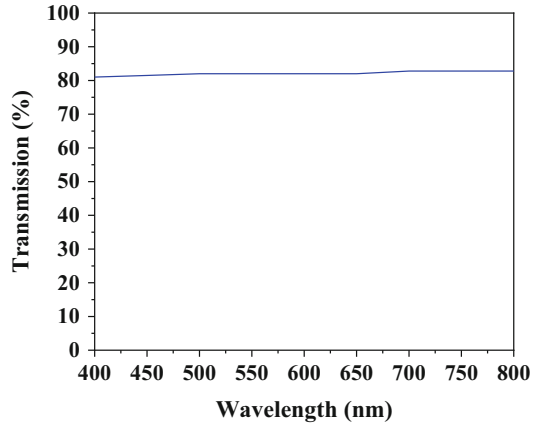
Sapphire (Single Crystal Alumina) Transparent Polycrystalline Armor

Sapphire is a single crystal having the chemical formula of Al_2O_3 commonly known as corundum [38]. Among the transparent ceramics, sapphire is the most demanding candidate material for transparent armor and other applications because of its ballistic performance in combination with superior optical and mechanical properties as is evident from Table 2. As a strike plate, material use of sapphire is reported to cut the weight and thickness close to about 50% of classical glass and also resists abrasion and scratches in extremely harsh environments. It is reported a reduction in areal density by around 58% and 65% can be obtained during multi-hit threats of level 2 and 3, respectively against classical glass armor.

Further, sapphire also offers the multispectral transmission aiding night vision capabilities. However, the cost of post process machining is one of the limitations in addition to the complex shaping. M/s. Saint Gobain Crystal is the major manufacturer of sapphire with the trade name of Saphikon[®]. Sapphire is industrially prepared by continuous single crystal growing process involving at elevated temperature for longer durations. M/s. Saint Gobain also developed Edge-defined Film-fed Growth (EFG) process for the sapphire in the sizes of greater than 300 mm width and 775 mm in length [39].

Typical crystal growing techniques in addition to above are Stockbarger-Bridgman, Czochralski, Vernouil, Directional Solidification, and Heat Exchanger methods [40]. These methods provide the flexibility to produce crystals of different orientations, sizes,

Fig. 6 A typical transmission plot of sapphire window (5 mm thick)



and optical qualities. Large single crystals preparation by Stockbarger-Bridgman involves placing of the seed of the single crystal in a vessel filled with powder according to the chemistry which in turn subjected to high temperature melting in a furnace. Upon slow withdrawal of the vessel from the hot zone, liquid solidifies on the surface of the seed forming large single crystal. Czochralski crystal growth method involves dipping and rotating of single crystal seed out of the molten material leading to the formation of cylindrical mass. The crystal is further pulled at a slow rate. In heat exchanger method, the oxide of aluminum is melted in a crucible with a sapphire seed placed in a high temperature furnace. A typical transmission plot of sapphire in the visible range is shown in Fig. 6.

Aluminum Oxynitride (AlON) Transparent Polycrystalline Armor

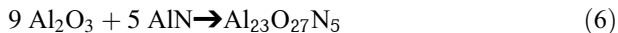
Aluminum oxynitride (AlON) is an emerging polycrystalline transparent armor material. It is a unique compound in the Al_2O_3 -AlN system and according to the phase diagram constituting with 75 mol% Al_2O_3 and 25 mol% AlN. There are 13 different AlON phases depending upon their crystallographic structure. AlON can be synthesized mainly by three methods. Simultaneous reduction of nitridation of Al_2O_3 is the most common method employed for making AlON. Combustion reaction and gas phase reaction are other methods, which are also employed.

Aluminum Oxynitride (AlON) is an emerging transparent ceramic material exhibits transparency from UV to the MWIR wavelength regions with excellent mechanical properties. AlON by virtue of its cubic crystallography shows isotropic optical characteristics with the in-line transmissions up to 86% in the wavelength region between 0.22 and 6 μm [41]. Owing to its outstanding optical and mechanical characteristics, AlON attracts attention in transparent bullet proof armor for helicopters and aircrafts, transparent armor for ground vehicles, domes for IR-guided missile systems, and IR sensors [42, 43].

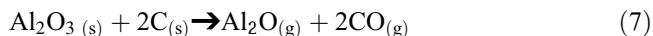
AlON is synthesized mainly following two routes such as carbothermal nitridation and solid-state reactions between α - Al_2O_3 and AlN for the synthesis of

γ – AION. Although both these procedures were generally chosen, synthesis through carbothermal nitridation involves stringent synthesis procedures to maintain the molecular ratio between Al_2O_3 and carbon molecules, where part of the Al_2O_3 reacts with carbon to form AlN as an intermediate compound which will further reacts with the remaining Al_2O_3 at high temperatures to form γ – AION. This procedure often resulted in AION powder with carbon contamination [44, 45]. Therefore, most of the studies reported solid-state reaction between Al_2O_3 and AlN for synthesizing γ – AION due to various factors such as process simplicity, commercial availability of ultra-high pure Al_2O_3 and AlN raw materials, and formation of phase pure γ – AION with minimum contaminations.

Synthesis of γ – AION through this solid-state reaction followed two different directions of processing procedures such as single-stage processing and double-stage processing. In a single-stage process, the starting Al_2O_3 and AlN powders were mixed, shaped, and sintered for densification. The γ – AION phase forms at temperature between 1700 °C and 1800 °C from the following reaction followed by densification at temperatures above 1900 °C.



Though researchers have successfully produced dense γ – AION, optical transparency was not achieved in their dense AION samples. Report states that α – Al_2O_3 volatilize by several orders of magnitude and form Al_2O and CO gases under reduced atmospheres at AION phase formation temperatures (1800 °C) as per the following reactions [40].



Since the single stage processing involves simultaneous phase formation and densification, the gases formed during the phase formation temperatures occlude in the inter and intra granular sites as pores indicated by arrows within the dense AION microstructures as shown in Fig. 7a [46]. As per the Mie theory and experimental studies conducted by Peelan et al., these pores act as scattering points and reduce the light transmission drastically [47]. Krell et al. states that even 0.1% of porosity in the microstructure is sufficient to drastically reduce the light transmission from 80% to less than 40% [48]. As discussed in the previous section, 100% intrinsic light transmission is obtained from pore-free sintered body.

Therefore, γ – AION for the transparent armor applications in specific has been produced through two stage process involving synthesis of AION powder in the first stage followed by shaping and sintering in the second stage. In this route, the volatile gases such as Al_2O and CO have the scope to escape during the first stage of powder synthesis. The single-phase powder is further milled with appropriate sintering aids and binders followed by shaping to produce AION green articles. Cold isostatic pressing was the major route followed for shaping and other processes such as hydrolysis-assisted solidification; aqueous slip casting, gel casting were also utilized for forming AION green bodies [49–51]. The shaped components were made fully

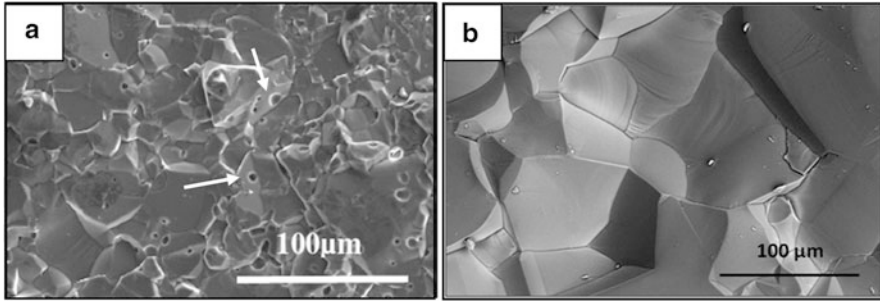


Fig. 7 Microstructures of AION produced through (a) single stage with pores, (b) two stages without pores. (Image Curtsey Ref. [46, 50])

dense and transparent through pressureless sintering and hot isostatic pressing procedures. The resultant sintered body through two stage processing exhibit pore-free microstructures as shown in Fig. 7b and display high in-line light transmission of up to 86% in the visible to IR wavelength regions. Figure 8a shows a typical AION transparent sample produced at International Advanced Research Centre, India, through aqueous colloidal-forming technique and Fig. 8b shows its optical transmission plot [50].

AION armors exhibit improved ballistics performance over conventional glass armors where they stood firm and optically clear after the shot with 0.50 caliber armor-piercing bullets. The 0.5 caliber bullet pierced at least 3 in. through the conventional glass armor before it stops whereas, the AION armor stopped the bullet in half the distance. On the above, it also stayed firm in the multi hit trials with 0.30 caliber rounds which is generally used in anti-aircraft weapons. All these performances were conducted on the AION armors having half the thickness (1.6") of the conventional glass armor [52].

The technology of producing transparent AION was initially developed by Raytheon and was later transferred to Surmet Corporation for commercial production. Surmet Corporation is producing AION in the trade name of ALON[®] Optical Ceramic with wide range of shapes from simple flat tiles to complex ogives and domes. Currently, Surmet Corporation is producing AION monoliths as large as 18 × 35 in. and windows with engineered invisible seams of sizes up to 24 × 27 in. [43]. AION exhibit equivalent ballistic performances with half of the weight and thickness compared to the glass – polymer laminate armors and displayed multi-hit performances.

Magnesium Aluminate Spinel Armor

Magnesium aluminate ($MgAl_2O_4$) spinel is an emerging transparent ceramic in view of the superior mechanical and ballistic properties and also demonstrates significant weight reduction that can be achieved in comparison to the soda-lime glass and glass ceramics. There are three major manufacturers of transparent magnesium aluminate spinel armor ceramics, namely, Surmet Corporation, ArmorLine

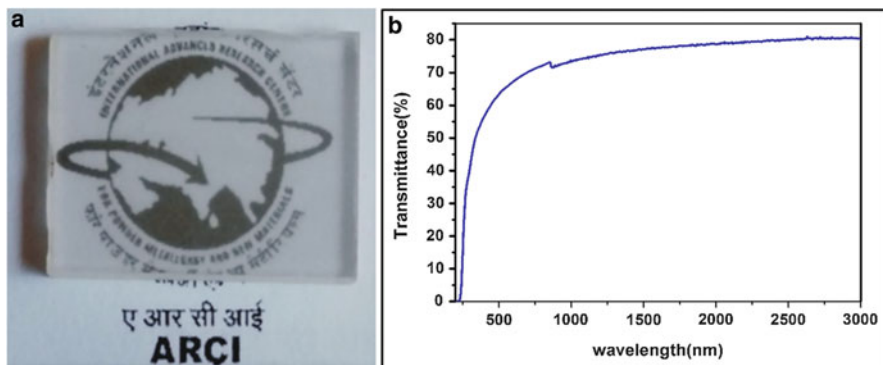


Fig. 8 (a) 2 mm thick polished transparent AlON, (b) A typical transmission plot for 2 mm thick AlON. (Image Courtesy Ref. [50])

Corporation Materials, and Electrochemical Research Corporation. Typical properties of the product are also depicted in Table 1.

According to the phase diagram [53], 71.8% Al_2O_3 and 28.2% MgO by weight forms the stoichiometry and melts congruently at 2105 °C [54, 55]. Spinel powder can be synthesized by several processes [56–62]; however, it is still a challenge to produce powder with properties that can lead to transparency while post processing. There are only a few global suppliers (Baikowski, Nanocerox and Taimci Chemicals) for the commercial scale spinel powder [63] which can be used for the armor production.

Spinel armor can be shaped using different shaping techniques such as slip casting, uni-axial pressing, cold isostatic pressing, hot pressing, hot isostatic pressing, and spark plasma sintering. Krell et al. [58] attempted the slip casting of spinel powder in aqueous medium and further sintered and HIPed at 1360 °C to achieve hardness of 14.6 GPa and 85% real in-line transmission. This study also compared transparent spinel ceramics with submicron alumina ceramics which is the hardest of all transparent ceramics, and it was found that the ballistic performance is reported to be at par [58].

Biswas et al. [64] studied the fabrication of transparent magnesium aluminate spinel with honeycomb structure and rectangular blanks based on methyl cellulose gel casting process. Samples were sintered at 1700 °C followed by HIPing at 1800 °C and 195 MPa pressure. The samples were characterized for density, hardness, flexural strength, and visible transmission (400–800 nm). The samples achieved density of 3.58 g/cc, hardness of 13 GPa, flexural strength of 188 MPa, and 67–80% transmission. This process demonstrated the fabrication of spinel blanks suitable for armor applications. A typical transparent spinel blank along with transmission plot is shown in Fig. 9.

Room temperature uniaxial and isostatic compaction, and high temperature uniaxial and isostatic compaction are the processes widely practiced individually or in combination for the fabrication of transparent magnesium aluminate spinel

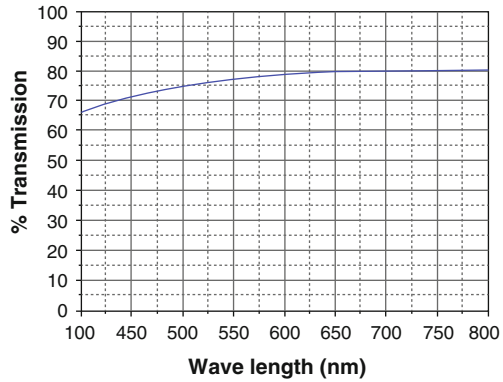
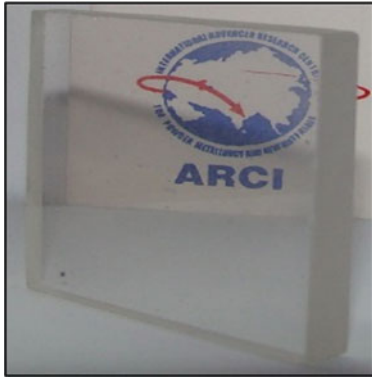


Fig. 9 A typical transparent spinel blank

ceramics especially for armor applications [65, 66]. In case of uniaxial and isostatic compaction, the parts are pressureless sintered to achieve minimum of 96% of TD to ensure closure of open pores before undertaking isostatic compaction at hot condition which will ensure close to 100% TD which is essential for exhibiting transparency and ballistic properties simultaneously.

The typical properties of the spinel transparent armor ceramics obtained from three manufacturers are discussed in the Table 2. The products manufactured by the three manufacturers show similar densities with identical hardness. Elastic modulus was also at par; however, flexural strength is varied from 170 to 300 MPa which can be attributed to the processing methodologies employed as discussed in Table 2. Optical properties such as transmission, haze, etc. are also found in the similar ranges.

Conclusions

An overview on characteristics of various transparent ceramic materials including conventional soda-lime glass, glass ceramics, and advanced emerging materials such as AlON and Spinel have been presented. Conventional transparent armor systems exhibit outstanding optical transmission. However, due to the lower mechanical properties, they were built in large thickness to withstand the advanced high-velocity projectiles. Advanced transparent ceramic materials, however, due to their excellent combinations of optical transparency and extreme hardness values, withstand in harsh environments and show improved ballistic performances even at very low thickness compared to the traditional armor systems. AlON and MgAl₂O₄ spinel demonstrated for protection against advanced threats and also multi-hit capabilities, emerging as leading futuristic transparent armor materials.

References

1. Harris DC (2009) Materials for infrared windows and domes: properties and performance, SPIE, Press monograph, PM70. SPIE-The International Society for Optical Engineering, Bellingham
2. Patel PJ (2000) Transparent ceramics for armor and EM window applications. In: Proceedings of SPIE, inorganic optical materials II, vol. 4102, p 1, International Symposium on Optical Science and Technology, San Diego, CA, United States
3. Stefanik T (2007) Nanocomposite optical ceramics for infrared widows and domes. Proc SPIE 6545
4. Klementa R (2008) Transparent armor materials. J Eur Ceram Soc 28:1091
5. Lundin L (2005) Air force testing new transparent armor, air force research laboratory public affairs, <https://www.af.mil/News/Article-Display/Article/133073/air-force-testing-new-transparent-armor/>
6. Kasim HA, Susumu N, Sadao A (1994) Optical constants of sapphire ($\alpha\text{-Al}_2\text{O}_3$) single crystals. J Appl Phys 76:8032–8036
7. Na-Phattalunga S, Limpijunnong S, T-Thienpraserte J, Yu J (2018) Magnetic states and intervalence charge transfer of Ti and Fe defects in Al_2O_3 : the origin of the blue in sapphire. Acta Mater 143:248–256
8. Grobosch M, Schmidt C, Naber WJM, van der Wiel WG, Knupfer M (2010) A photoemission study of interfaces between organic semiconductors and Co as well as $\text{Al}_2\text{O}_3/\text{Co}$ contacts. Synth Met 160:238–243
9. Dobrovinskaya ER, Litvinov LA, Pischik V (2009) Sapphire: material, manufacturing, applications. Springer, Berlin
10. Khattak CP, Shetty R, Schwerdtfeger CR, Ullal S (2016) World's largest sapphire for many applications. J Cryst Growth 452:44–48
11. Harris DC (2004) A century of sapphire crystal growth. In: Proceedings of 10th DoD electromagnetic windows symposium, Norfolk, pp 1–17
12. Binar T, Svare J, Vyroubal P, Kazda T, Rolec S, Dvorak A (2018) The comparison of numerical simulation of projectile interaction with transparent armor glass for buildings and vehicles. Eng Fail Anal 92:121–139
13. Straßburger E (2009) Ballistic testing of transparent armor ceramics. J Eur Ceram Soc 29:267–273
14. Johnson R, Biswas P, Ramavath P, Kumar RS, Padmanabham G (2012) Transparent polycrystalline ceramics: an overview. Trans Indian Ceram Soc 71:73–85
15. Krell A, Hutzler T, Klimke J (2009) Transmission physics and consequences for materials selection, manufacturing, and applications. J Eur Ceram Soc 29:207–221
16. Apetz R, Van Bruggen MPB (2003) Transparent alumina: a light scattering model. J Am Ceram Soc 86:480–486
17. Yamamoto H, Mitsuoko T, Iio S Translucent polycrystalline ceramic and method for making same. Europe Patent application EP 1 053 983 A2, IPK7 C04B35/115, 22 Nov 2000
18. Fakolujo O, Merati A, Bielawski M, Bolduc M, Nganbe M (2016) Role of microstructural features in toughness improvement of zirconia toughened alumina. J Miner Mater Charact Eng 4:87–102
19. Kaufmann C, Cronin D, Worswick M, Pageau G, Beth A (2003) Influence of material properties on the ballistic performance of ceramics for personal body armor. Shock Vib 10:51–58
20. Franco A, Roberts SG, Warren PD (1997) fracture toughness, surface flaw sizes and flaw densities in Al_2O_3 . Acta Mater 45:1009–1015
21. Benitez T, Gomez SY, Novaes de Oliveira AP, Travitzky N, Hotza D (2017) Transparent ceramic and glass-ceramic materials for armor applications. Ceram Int 43:13031–13046
22. Krell A, Strassburger E (2014) Order of influences on the ballistic resistance of armor ceramics and single crystals. Mater Sci Eng A 597:422–430

23. Krell A, Strassburger E, Hutzler T, Klimke J (2013) Single and polycrystalline transparent ceramic armor with different crystal structure. *J Am Ceram Soc* 96:2718–2721
24. Krell A, Strassburger E (2012) Discrimination of basic influences on the ballistic strength of opaque and transparent ceramics. *Ceram Eng Sci Proc* 33:161–176
25. Grujicic M, Bell WC, Pandurangan B (2012) Design and material selection guidelines and strategies for transparent armor systems. *Mater Des* 34:808–819
26. Talladay TG, Templeton DW (2014) Glass armor—an overview. *Int J Appl Glas Sci* 5:331–333
27. Barnak R, Franks LP, Holm D (2008) Transparent armor cost benefit study. In: *Proceedings of the structures and materials intelligence seminar*. McLean. pp 1–2
28. Grujicic M, Pandurangan B, Coutris N, Cheeseman BA, Fountzoulas C, Patel P, Strassburger E (2008) A ballistic material model for starphire[®], a soda-lime transparent-armor glass. *Mater Sci Eng A* 491:397–411
29. Swab JJ, Lasalvia JC, Gilde GA, Patel PJ, Motyka MJ (1999) Transparent armor ceramics: AION and spinel. In: *23rd annual conference on composites, advanced ceramics, materials and structures: b: ceramic engineering science proceedings, vol. 20*. pp 79–84, Cocoa Beach, Florida
30. Sheikh MZ, Wang Z, Suo T, Lia Y, Ahmeda S, Dar UA (2018) Effect of polymeric interlayer on wave propagation in transparent soda-lime glass. *Proc Struct Integr* 13:2120–2125
31. Walley SM (2010) Historical review of high strain rate and shock properties of ceramics relevant to their application in armour. *Adv Appl Ceram* 109:446–466. 2010
32. Grujicic M, Pandurangan B, Bell WC, Coutris N, Cheeseman BA, Fountzoulas C, Patel P, Templeton DW, Bishnoi KD (2009) An improved mechanical material model for ballistic soda-lime glass. *J Mater Eng Perform* 18:1012–1028
33. Salem JA (2013) Transparent armor ceramics as spacecraft windows. *J Am Ceram Soc* 96:281–289
34. Krell A, Hutzler T, Klimke J (2005) Physics and technology of transparent ceramic armor: sintered Al₂O₃ vs cubic materials. In: *Nanomaterials technology for military vehicle structural applications, RTO-MP-AVT-122*. pp 14-1–14-10, Paper 14. Neuilly-sur-Seine, France: RTO, <http://www.rto.nato.int/abstracts.asp>.
35. Ramisetty M, Sastri S, Kashalikar U, Goldman LM, Nag N (2013) Transparent polycrystalline cubic spinels protect and defend. *Am Ceram Soc Bull* 92:20–25
36. Goldman LM, Twedt R, Balasubramanian S (2011) ALON optical ceramic transparencies for window, dome, and transparent armor applications. *Proc SPIE* 8016:77
37. Horsfall I (2001) Glass ceramic armor system for light armor applications. In: *Proceedings of 19th international symposium on ballistics, Interlaken, Switzerland*
38. Hanev EJ, Subhash G (2013) Damage mechanisms perspective on superior ballistic performance of Spinel over Sapphire. *Exp Mech* 53(1):31–46
39. Shockey DA, Simons JW, Curran DR (2010) The damage mechanism route to better armor materials. *Int J Appl Ceram Technol* 7(5):566–573
40. Krell A, Strassburger E (2014) Order of influences on the ballistic resistance of armor ceramics and single crystals. *Mater Sci Eng A* 597:422–430
41. Wahl JM, Hartnett TM, Goldman LM, Twedt R, Warner C (2005) Recent advances in AION optical ceramic, Window and Dome Technologies and Materials IX. *Proc SPIE* 5786:71–82
42. Goldman LM, Twedt R, Balasubramanian S, Sastri S (2011) ALON optical ceramic transparencies for window, dome, and transparent armor applications, Window and Dome Technologies and Materials XII. *Proc SPIE* 8016:1–14
43. <http://www.surmet.com/technology/alon-optical-ceramics/>. Reference dated 31 Dec 2018
44. Xie X, Wang Y, Qi J, Wang S, Feng Z, Hou G, Liu W, Zhang W, Xu Q, Lu T (2016) Ethanol-water-derived sucrose-coated-Al₂O₃ for sub-micrometer AION powder synthesis. *J Am Ceram Soc* 99(8):2601–2606
45. Corbin ND (1989) Aluminum oxynitride spinel: a review. *J Eur Ceram Soc* 5:143–154

46. Senthil Kumar R, Rajeswari K, Praveen B, Hareesh US, Johnson R (2010) Processing of aluminum oxynitride through aqueous colloidal forming techniques. *J Am Ceram Soc* 93(2):429–435
47. Peelen JGJ, Metselaar R (1974) Light scattering by pores in polycrystalline materials: transmission properties of alumina. *J Appl Phys* 45:216–220
48. Krell A, Hutzler T, Klimke J (2006) NATO-OTAN – nano materials technology for military vehicle applications. 14-1–14-10. <http://www.dtic.mil/get-tr-doc/pdf?AD=ADA469603>
49. Miller L, Kalpan WD (2008) Water-based method for processing of aluminium oxynitride (AlON). *Int J Appl Ceram Technol* 5(6):641–648
50. Senthil Kumar R, Johnson R (2016) Aqueous slip casting of transparent aluminium oxynitride. *J Am Ceram Soc* 99(10):3220–3225
51. Wang J, Zhang F, Chen F, Zhang H, Tian R, Dong M, Liu J, Zhang Z, Zhang J, Wang S (2014) Fabrication of aluminum oxynitride (c-AlON) transparent ceramics with modified gel casting. *J Am Ceram Soc* 97(5):1353–1355
52. Parker A (2011) Aluminum oxynitride armor production and modeling of next generation transparent armor for the global war on terror, thesis report, Brigham Young University, Physics and Astronomy
53. Ganesh I (2013) A review on magnesium aluminate ($MgAl_2O_4$) spinel: synthesis, processing and applications. *Int Mater Rev* 58:63–112
54. Muan A, Osborn EF (1965) Phase equilibria among oxides in steel making. Addison-Wesley, Reading
55. Meir S, Kalabukhov S, Froumin N, Dariel MP, Frage N (2009) Synthesis and densification of transparent magnesium aluminate spinel by SPS processing. *J Am Ceram Soc* 92:358–364
56. Ganesh I, Sundararajan G, Ferreira JMF (2011) Aqueous slip casting and hydrolysis assisted solidification of $MgAl_2O_4$ spinel. *Adv Appl Ceram* 110:63–69
57. Shafeiey A, Enayati MH, Al-Haji A (2017) The effect of slip casting parameters on the green density of $MgAl_2O_4$ spinel. *Ceram Int* 43:6069–6074
58. Krell A, Klimke J, Hutzler T (2009) Advanced spinel and sub- μm Al_2O_3 for transparent armor applications. *J Eur Ceram Soc* 29:275–281
59. Zhang P, Liu P, Sun Y, Wang J, Wang Z, Wang S, Zhang J (2015) Aqueous gelcasting of the transparent $MgAl_2O_4$ spinel ceramics. *J Alloys Compd* 646:833–836
60. Krell A, Hutzler T, Klimke J, Potthoff A (2010) Fine-grained transparent spinel windows by the processing of different nanopowders. *J Am Ceram Soc* 93:2656–2666
61. Gajdowski A, Böhmler J, Lorgouilloux Y, Lemonnier S, d’Astorg S, Barraud E, Leriche A (2017) Influence of post-HIP temperature on microstructural and optical properties of pure $MgAl_2O_4$ spinel: from opaque to transparent ceramics. *J Eur Ceram Soc* 37:5347–5351
62. Shimada M, Endo T, Saito T, Sato T (1996) Fabrication of transparent spinel polycrystalline materials. *Mater Lett* 28:413–415
63. Krell A, Hutzler T, Klimke J (2014) Defect strategies for an improved optical quality of transparent ceramics. *Opt Mater* 38:61–74
64. Biswas P, Rajeswari K, Ramavath P, Johnson R, Maiti HS (2013) Fabrication of transparent spinel honeycomb structures by methyl cellulose based thermal gelation processing. *J Am Ceram Soc* 96:3042–3045
65. Biswas P, Ramavath P, Kumbhar CS, Patil DS, Chongdar TK, Gokhale NM, Johnson R, Mohan MK (2017) Effect of room and high temperature compaction on optical and mechanical properties of HIPed transparent spinel ceramics. *Adv Eng Mater* 19:1700111-1–1700111-7
66. Ramavath P, Biswas P, Rajeswari K, Suresh MB, Johnson R, Padmanabham G, Kumbhar CS, Chongdar TK, Gokhale NM (2014) Optical and mechanical properties of compaction and slip cast processed transparent polycrystalline spinel ceramics. *Ceram Int* 40:5575–5581

Part III

**Transparent and Optical Ceramics for Defense
and Aerospace**



Transparent and Machinable Glass-Ceramics

12

Himadri Sekhar Maiti

Contents

Introduction	463
Metastability and Crystallization of Glasses	464
Glassy State and Glass Transition	464
Crystallization of Glass and Formation of Glass-Ceramics	465
Basic Concepts of Nucleation and Growth Phenomenon	467
Kinetics of Crystallization	470
Important Glass-Ceramic Systems: Their Properties and Applications	473
Transparent Glass-Ceramics	477
Theories of Light Scattering	478
Anomalous Scattering	480
Transparent Glass-Ceramics Systems	481
Machinable Glass-Ceramics	485
Machinable Glass-Ceramics with Alkaline Phlogopite Phase	485
Important Properties and Applications of MACOR [®]	487
Machinable Glass-Ceramics Other Than MACOR [®]	488
Alternative Method of Preparation	490
Conclusions	490
References	491

Abstract

“Glass-ceramics” are glasses with controlled crystallization having certain extraordinary properties and therefore unique applications. Since their accidental discovery in the early 1950s of the last century, extensive research and development have been carried out leading to commercialization of several products for both consumer and

H. S. Maiti (✉)

Department of Ceramic Technology, Government College of Engineering and Ceramic Technology, Kolkata, West Bengal, India

e-mail: hsmaiti2009@gmail.com

© Springer Nature Switzerland AG 2020

Y. R. Mahajan, R. Johnson (eds.), *Handbook of Advanced Ceramics and Composites*,
https://doi.org/10.1007/978-3-030-16347-1_13

461

strategic sectors. Glass structure being thermodynamically metastable is prone to get converted to a stable crystallized structure through a diffusion-controlled nucleation a growth mechanism. Crystallization is normally facilitated by adding a nucleating agent, the refractory oxides which do not normally dissolve in the glassy matrix. Microstructurally, glass-ceramic materials invariably contain some residual glassy phase together with one or more crystalline phases.

Glass-ceramics possess a wide range of unusual properties; they are much tougher than conventional glasses with a wide range of thermal expansion coefficient and unlike crystalline ceramics do not contain any porosity. It is easier to seal them with metallic counter parts and therefore used extensively in different kind of seals.

Glass-ceramic materials become transparent to visible light if the dispersed crystallites are much smaller than the wavelength of visible light or the difference between the refractive index of the crystallites and that of glassy matrix is very small. There are several aluminosilicate-based glass-ceramic systems in which these conditions are satisfied and therefore can be referred as “transparent glass-ceramics.” The crystal phases are solid solutions of β -quartz, β -spodumene, spinel, mullite, cordierite, etc. One of the most widely used transparent glass-ceramic products is known as Zerodur[®] made by Schott AG, Germany. It possesses extremely low coefficient of thermal expansion, which is very close to zero or slightly negative in certain temperature ranges. Its transparency is quite good in the range 400–2,300 nm. “Zerodur” is extensively used for lightweight mirror blanks used in large astronomical telescopes and satellites. Their size ranges from a few centimeters to more than 8 m. The most recent application of transparent glass-ceramics is, however, in the area of lighting systems based on white LEDs for which the glass-ceramics are used as the dispersion medium for the phosphors replacing commonly used organic silicone.

Certain varieties of glass-ceramics particularly containing mica crystals are fairly soft, giving rise to their machinable property. Different manufacturers market them with their trade names. The most common is the MACOR[®] developed and marketed by Corning Glass Works and is used extensively in different technologies; DICOR[®] on the other hand is primarily used to make dental crown. MACOR[®] contains around 55% fluorophlogopite mica ($\text{KMg}_3\text{AlSi}_3\text{O}_{10}\text{F}_2$) and 45% borosilicate glass. Complex shapes can be machined with precision dimensional tolerance, thermally stable up to a temperature of 1000 °C. They possess very good electrical as well as thermally insulating property. Combined with zero porosity, they are excellent materials for fabrication of vacuum feedthroughs. In addition, there are several other applications in electronics, aerospace, defense, and nuclear technologies. They also find extensive use in microwave tube industry.

Keywords

Glass-ceramics · Glass transition · Crystallization · Nucleation and growth · Light scattering · Transparent glass-ceramics · Zero thermal expansion · Machinable glass-ceramics · White LED

List of Abbreviations

CTE	Coefficient of thermal expansion
LAS	Lithium aluminosilicate
LS	Lithium silicate
MAS	Magnesium-aluminosilicate
RE	Rare earth
SA	Saturable absorber
WLEDs	White light-emitting diodes

Introduction

“Glass-ceramics” are a specific group of in situ formed “composites” in which crystalline ceramic phase(s) are dispersed in a glassy matrix. As glasses are thermodynamically metastable, they tend to get stabilized by in situ formation of selective crystalline phases, depending on the base composition of the glass, for which thermal activation is required. The crystals may be of different size ranges (nanometer to micrometer) depending on the base glass composition and the heat treatment conditions. Nucleation of the crystalline phase is often facilitated by a nucleating agent, normally refractory oxides, e.g., TiO_2 , ZrO_2 , CeO_2 , etc., added to the parent glass composition.

This unique group of materials was discovered under a serendipitous situation in the early 1950s of the last century by S. D. Stookey at Corning Glass Works, USA, later renamed as Corning Inc., while experimenting with lithium silicate-based photosensitive glasses containing silver and ceria [1, 2]. Since then extensive research and developmental work have been carried out by a large group of researchers and several companies throughout the globe leading to commercialization of a large number of products for both consumer and strategic applications. By the early 1960s, Corning had developed and commercialized three very important glass-ceramic compositions: lithium silicate (LS)-based composition with code no. 8603, magnesium aluminosilicate (MAS) composition with code no. 9606, and the code no. 9608 based on the lithium aluminosilicate (LAS) system. An excellent account of chronological development over the next 50 years has been published a few years back by G. H. Beal [3], a co-worker of Donald Stookey. Very recently a special volume of MRS bulletin [4] has been published comprising of a set of eight updated review articles covering many interesting properties and applications, e.g., transparent, strong and tough, ferroelectric, ionically conducting, bioactive glass-ceramics, etc.

Importance of glass-ceramics lies in the fact that one gets the advantages of glass and ceramics in the same material. A few of the attractive features of the glass-ceramics are:

1. Like any other glass, fabrication to different shapes is relatively simple as it is done before the precipitation of the dispersed phase.

2. Mechanical strength and toughness are greatly enhanced compared to the base glass.
3. Like any other composite material, most of the properties like thermal expansion, thermal and electrical conductivity, and different mechanical properties can be tailored to expand their application potentiality.
4. Unlike most of the ceramics, they are nonporous and therefore conveniently used as “feedthroughs” in vacuum systems.
5. Possibility of tailoring the thermal expansion coefficient has made them a useful material for glass-metal seals and also as “zero expansion” material for different applications.
6. Glass like transparency/translucency can be maintained by controlling the size of the ceramic phase below the wavelength of light.
7. Unlike both glass and ceramics, they can be made relatively soft so as to be machined by conventional metal forming tools (diamond tools are not necessary as in case of most ceramics).
8. Through suitable adjustment of the chemical composition and heat treatment conditions, the material can be made transparent to microwave radiation and at the same time sufficiently strong and abrasion resistant and also can be fabricated into complex shapes to make it suitable for use as radomes for missiles and other aerospace vehicles.

In addition to understanding the mechanism of crystallization, scattering of light by a glass matrix dispersed with fine crystals and the structure-property relationship of different varieties of glass-ceramics, this chapter particularly focuses on the composition and the properties of two specific types, namely, (i) transparent and (ii) machinable glass-ceramics and their applications in both civilian and strategic sectors.

Metastability and Crystallization of Glasses

Glassy State and Glass Transition

From the consideration of the physical properties such as viscosity, density, mechanical strength, etc., glasses behave as a solid, but structurally they resemble more like a liquid with the absence of long-range order of the constituent ions, and therefore thermodynamically they possess a metastable state. Conventionally glasses are prepared by cooling a glass-forming melt at a sufficiently rapid rate, so that the formation of the stable crystalline phase (with long-range periodic arrangement of the ions) gets suppressed and the resulting material with a solid-like consistency is termed as “glass.” This transition from the supercooled liquid to either the glassy state or the crystalline phase is best represented with the help of a plot of different

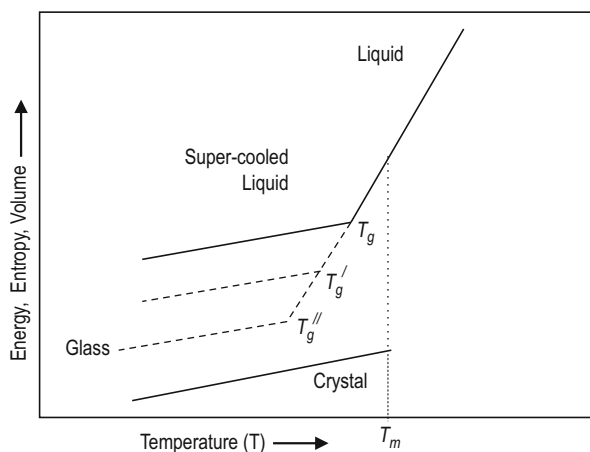
parameters such as internal energy, entropy, or specific volume of the system as functions of temperature schematically presented in Fig. 1. It may be noted that the liquid melt, when cooled very slowly maintaining the thermodynamic equilibrium condition, transforms to a crystalline phase at the thermodynamic freezing point of the melt (denoted by T_m) with a sudden change of the abovementioned parameters. However, if the cooling rate is fast enough, the supercooled liquid transforms to a glassy state with an inflection point at a temperature known as “glass transition temperature” represented by T_g , where there is a change in slope of the plot. Incidentally the slope of the plot below T_g is nearly the same as that of the crystalline phase, which indicates that the glass, for all practical purposes, behave as a solid but without any crystalline order.

Unlike the melting point of a crystalline solid or freezing point of the corresponding liquid, the “glass transition temperature” is not a fixed temperature, but changes slightly with the rate of cooling of the glass melt of any particular chemical composition. With increasing rate of cooling, the extent of supercooling increases and the transition temperature decreases ($T_g'' < T_g' < T_g$) as shown in Fig. 1, in which T_m represents the thermodynamic freezing point of the glass melt to a crystalline solid of the same composition.

Crystallization of Glass and Formation of Glass-Ceramics

The metastable glassy phase is prone to transform to a stable crystalline phase particularly on thermal activation (heating) but not necessarily through a single-step process. More often than not, it goes through one or more metastable crystalline phases depending on the complexity of the chemical composition of the parent glass and the nature of the phase diagram. For obvious reasons, the free energy of the

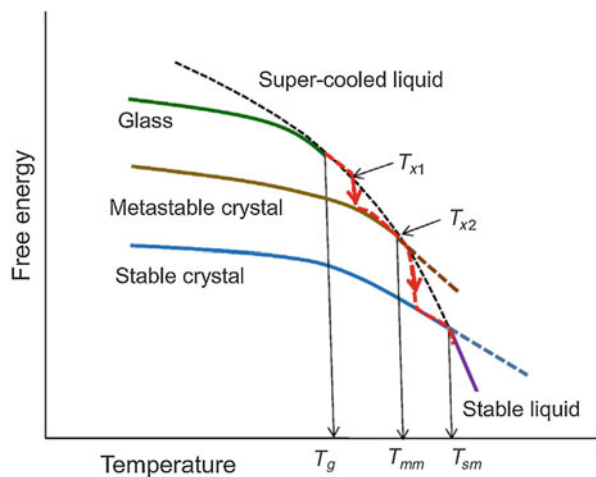
Fig. 1 Schematic illustration of glass transition temperature (T_g) in comparison to the thermodynamic freezing temperature of the glass melt or the melting point of the stable crystalline solid of the same composition



glass melt or in other words the supercooled liquid is the highest as shown schematically in Fig. 2, that of the solidified glass is slightly lower, that of the metastable crystalline phase is still lower, and that of the fully crystalline phase possesses the lowest free energy compared to all the above states. In this figure, the dotted lines indicate the notional free energies of the different thermodynamically unstable states of the glass-forming system, whereas the solid lines represent the free energies of either the metastable (glass or metastable crystal) or the stable (fully crystalline) state of the system. The points of intersection of the free energy curve representing the liquid phase with those of the other three phases (glass, metastable crystal, and stable crystal) are the three characteristic temperatures of the glass-forming system. They are designated as T_g , the glass transition temperature; T_{mm} , the melting point of the metastable crystalline phase; and T_m , the melting point of the stable crystalline phase. T_{x1} and T_{x2} are the crystallization temperatures of the metastable crystalline and stable crystalline phases, respectively. It may be noted in Fig. 2 that the temperatures T_{x1} and T_{x2} are slightly higher than the temperatures T_g and T_{mm} , respectively, due to the slower kinetics of the entire range of transformation.

In practice, these temperatures are the crystallization temperatures of the glass. When heated to these temperatures, there is partial crystallization of the glass, and the product is referred to as “glass-ceramics” in which there are crystals dispersed in a glassy matrix. Theoretically, all glasses, being metastable, are prone to crystallization at a suitable temperature if held for a sufficiently long time which, however, may not be always realizable in practice. Only the glasses with sufficient instability, based on their chemical composition, can be converted to “glass-ceramics.” This process of crystallization follows the conventional “nucleation and growth” mechanism of phase transformation, which is diffusion controlled and therefore temperature and time dependent. The higher is the temperature, the greater is the rate of

Fig. 2 Schematic illustration of the temperature-dependent free energies of different phases, e.g., glass, metastable crystal, stable crystal, supercooled liquid, and the stable liquid. (Reproduced from Ref. [5] with permission from the publisher)



transformation/crystallization, and with increasing time, there is enhancement in the overall volume fraction of the crystalline phase with the growth of the individual crystallites.

Basic Concepts of Nucleation and Growth Phenomenon

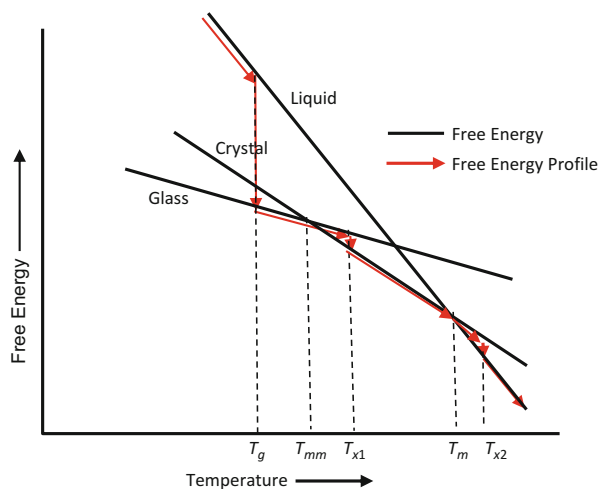
As mentioned above, crystallization of glass takes place following “nucleation and growth” mechanism of phase transformation. The primary driving force for crystallization is the lower free energy of the crystalline phase compared to that of the glassy phase. However, this lowering of free energy is offset by surface energy terms arising from the new interfaces created between the original glassy matrix and the crystalline phase, which gets nucleated within the glassy phase either homogeneously or heterogeneously. The variation of free energies of the different phases as a function temperature is presented schematically in Fig. 3.

The glass is stable up to a temperature of T_{mm} beyond which the crystals are more stable, and above the temperature of T_m , only the liquid phase of nominal glass composition is stable as it has the lowest free energy of all the possible phases. In practice, crystallization does not take place exactly at T_{mm} but at a slightly higher temperature of T_{x1} . The difference between these two temperatures ($\Delta T = T_{x1} - T_{mm}$) is the superheating required to compensate for the surface energy term.

Homogenous Nucleation

The overall change of Gibbs free energy (ΔG) for the system during the crystallization process particularly through homogenous nucleation at a specific temperature may be expressed as:

Fig. 3 Schematic variation (assumed to be straight lines) of free energies of different phases in crystallization of glass, as a function of temperature. The red lines show the profile of the free energy change in practice



$$\Delta G = -\frac{4}{3}\pi r^3 \Delta G_v + 4\pi r^2 \gamma_{cg} \quad (1)$$

In this equation, the first term on the right of the equality sign is the difference of free energy between the glassy phase and the corresponding crystalline phase at a specific temperature. This term is negative as the crystalline phase has a lower free energy than that of the glassy phase. ΔG_v is the free energy change per unit volume, and r is the radius of the nucleus of the crystalline phase, which has just formed within the matrix of the glassy phase. The second term arises from the additional surface energy resulting from the interfacial energy γ_{cg} per unit surface area of the nucleus. The assumption is that a spherical nucleus of the crystalline phase has just initiated within the glassy matrix due to a superheating of ΔT , which is essential to compensate the additional surface energy term. Figure 4 represents the plot of Eq. (1), i.e., ΔG against r at a particular temperature.

As the two energy terms oppose each other, the resulting free energy initially increases, goes through a peak, and finally becomes negative. The diagram provides an important concept of critical radius of the nucleus (r^*) corresponding to the maximum of the free energy curve. At lower values of radius (r), the curve has a positive slope, indicating that the free energy increases with increasing value of “ r .” No spontaneous growth of the nucleus is possible under this situation. So, any nucleus, if formed due to temperature fluctuation at the local level, will be dissolved back within the glassy matrix. Such small-sized unstable nuclei having radius smaller than “ r^* ” are referred to as “embryos.” Only the nuclei having sizes larger than “ r^* ” are expected to grow larger and larger. The exact value of “ r^* ” depends on the value of ΔT , the superheating. The higher the value, or in other words, the higher the temperature of heat treatment, the smaller the size of the critical nucleus (r^*); therefore the process of crystal growth becomes easier and faster. From Eq. (1), one can derive the value of “ r^* ” as follows:

Fig. 4 Variation (schematic) of the overall free energy change of the glass system as a function of the radius (r) of the nucleus of the crystalline phase when the heat treatment is carried out at a temperature above T_{mm} mentioned in Fig. 3

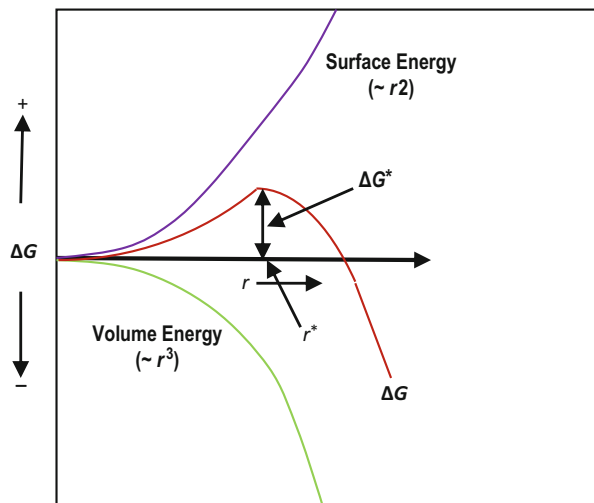
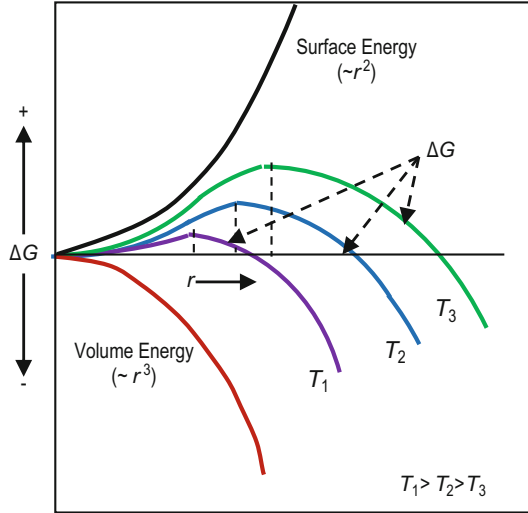


Fig. 5 Schematic variation of ΔG with r at different temperatures of heat treatment (Adapted from Ref. 7)



$$r^* = \frac{2\gamma_{cg}}{\Delta G_v} \tag{2}$$

And the corresponding free energy change (ΔG^*) may be expressed as

$$\Delta G^* = \frac{16\pi\gamma_{cg}^3}{3\Delta G_v^2} \tag{3}$$

As ΔG_v is proportional to ΔT , the superheating, r^* is inversely proportional to ΔT .

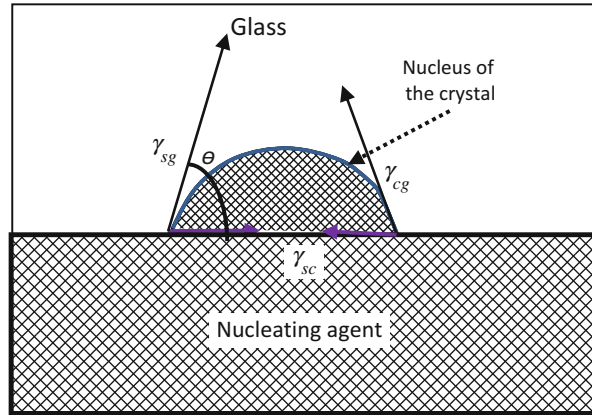
The position of the ΔG versus r curve changes with the heat treatment temperature as shown in Fig. 5 [7]. In this figure, $T_1 > T_2 > T_3$. The “ r ” value of the point of intersection with the zero energy line decreases with increasing temperature. The values of “ r^* ” as well as “ ΔG^* ” decrease with temperature, i.e., with increasing superheating (ΔT); thereby crystallization kinetics becomes faster and faster.

Heterogeneous Nucleation

There are two different situations for nucleation to take place: (i) homogenous and (ii) heterogeneous. The discussion in the previous section refers to homogenous nucleation for which there is no preferred site for the initiation of the process. It may take place at any point throughout the volume of the transforming phase on a random manner. On the other hand, heterogeneous nucleation takes place on certain preferred sites usually on the surface of a foreign particle particularly for a solid-to-solid transformation as in the case of crystallization of glass or the surface of the container in case of a liquid-to-solid transformation, e.g., freezing of a liquid melt. The situation of the heterogeneous nucleation is represented in Fig. 6.

Compared to homogenous nucleation involving only one surface energy term γ_{sl} , in heterogeneous nucleation, there are three surface energy terms, which are γ_{sl} , γ_{lc} ,

Fig. 6 Schematic representation of heterogeneous nucleation on the surface of a nucleating agent. (Adapted from Ref. [6])



and γ_{sc} . These are the surface energies of the surfaces between the transforming and the transformed phases, nucleating surface and that of the transforming phase, and nucleating surface and that of the transformed phase, respectively. By considering the Gibbs free energy change for heterogeneous nucleation similar to Eq. (1), it can be shown that

$$r_{\text{het}}^* = \frac{2\gamma_{cg}}{\Delta G_v} \quad (4)$$

which is same as that corresponding to homogenous nucleation and

$$\Delta G_{\text{het}}^* = S(\theta) \cdot \Delta G_{\text{hom}}^* \quad (5)$$

This shows a multiplication factor of $S(\theta)$ to ΔG_{hom}^*

Where $S(\theta) = \frac{(2 + \cos \theta)(1 - \cos \theta)^2}{4}$ and θ is the contact angle between the heterogeneous nucleating surface and that of the transforming phase as indicated in Fig. 6.

The activation energies (ΔG^*) for homogenous and heterogeneous nucleation processes are compared schematically in Fig. 7. It clearly indicates that the energy required for heterogeneous nucleation is much smaller than that of homogenous nucleation even though the critical nucleus size (r^*) for both the processes is nearly identical.

Kinetics of Crystallization

The overall crystallization process consists of two independent but overlapping steps, i.e., “nucleation” and “growth.” In order to understand the rate of crystallization, one can look at the rates of nucleation and growth independently. The rate of nucleation represented by \dot{N} is exponentially related to two terms: Q_d , the activation energy for solid-state diffusion, and ΔG^* , the free energy change at r^* , the radius of the critical nucleus.

$$\dot{N} \sim \exp\left(-\frac{Q_d}{kT}\right) \exp\left(-\frac{\Delta G^*}{kT}\right) \tag{6}$$

In this equation, Q_d is relatively independent of temperature, but ΔG^* has a strong temperature dependence, and therefore the plot of nucleation rate as a function of temperature gives rise to a bell-shaped curve as shown in Fig. 8 (red curve). More or less in a similar manner, one can derive an expression for the growth rate, which when plotted against temperature also gives rise to a bell-shaped curve (blue curve in Fig. 8) with a peak at a higher temperature compared to that of the nucleation rate. The overall rate of crystallization is the product of nucleation and growth rates represented by the green curve in the same figure. The important point to note from this figure is that the rate of crystallization reaches its peak at an optimum temperature of heat treatment. Microstructure of the crystallized glass strongly depends on

Fig. 7 Comparison of the activation energies of homogenous and heterogeneous nucleation processes. (Adapted from Ref. [6])

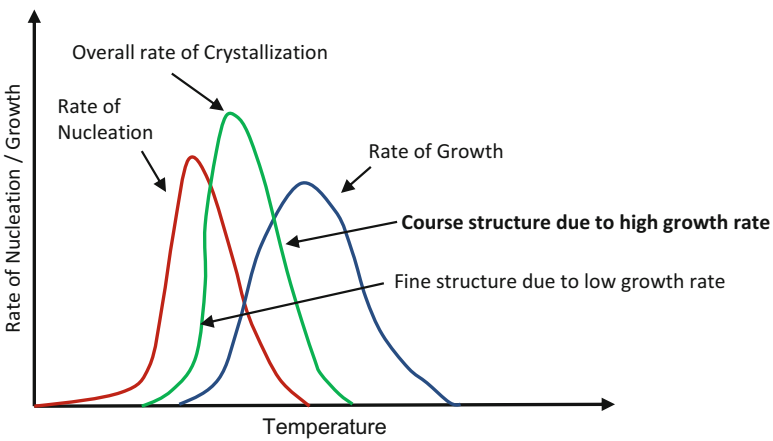
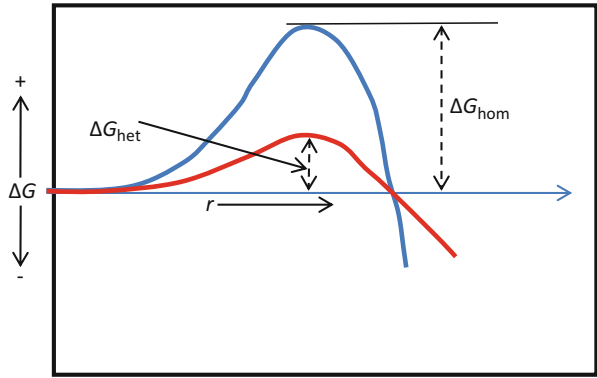


Fig. 8 Schematic variation of (i) rate of nucleation, (ii) rate of growth, and (iii) overall rate of crystallization as a function of temperature above the glass transition temperature (T_g)

the heat treatment conditions, in particular the heating schedule and the holding time at different temperatures.

In particular, the nucleation rates, both analytical and graphical representations, for homogenous and heterogeneous nucleation processes are compared in Fig. 9. As expected heterogeneous nucleation process requires a much less superheating. Consequently the overall crystallization process becomes easier and faster. Nucleating agents used in different glass systems are those which have very low solubility in the molten glass and remain as finely distributed particles even after cooling. The surfaces of these particles act as the nucleation sites for heterogeneous nucleation process. The examples of a few nucleating agents are ZrO_2 , TiO_2 , Cr_2O_3 , Fe_2O_3 , and P_2O_5 (particularly for silicate glasses).

Microstructure of the crystallized glass strongly depends on the heat treatment conditions, in particular the heating schedule and the holding time at different temperatures. For crystallization, the annealed glass shapes need to be heated beyond the temperature T_{mm} (Fig. 3), typically in two steps, first for nucleation and then for crystal growth. For a finer structure (say for generation of nano-size crystals), a large number of nuclei need to be generated before they are allowed to grow. Holding at a higher temperature for a longer time frame would allow the crystals to grow exaggeratedly making the glass-ceramics more brittle than the virgin glass. For any kind of glass-ceramics, the exact temperature and time of heat treatment have to be determined experimentally. The chemical composition of the crystals(s) depends on the nominal composition of the virgin glass and the associated phase diagram. A typical heat treatment schedule for glass and glass-ceramics is presented in Fig. 10, in which the initial downward changes of temperature in multiple steps reflect the melting, forming, and annealing processes. After inspection the temperature is once again raised in two steps, the first one is low temperature step corresponding to nucleation of the crystalline phase and the second one is a slightly higher temperature step to allow further growth of the nuclei. One can optimize these temperatures and time to develop the required properties in the glass-ceramic

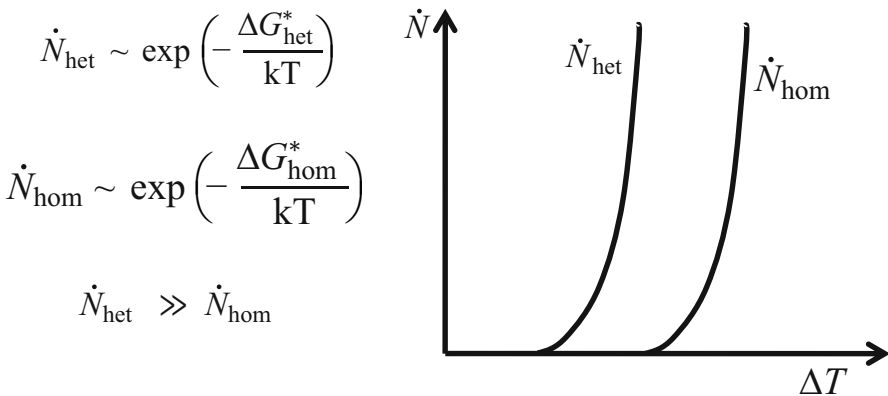
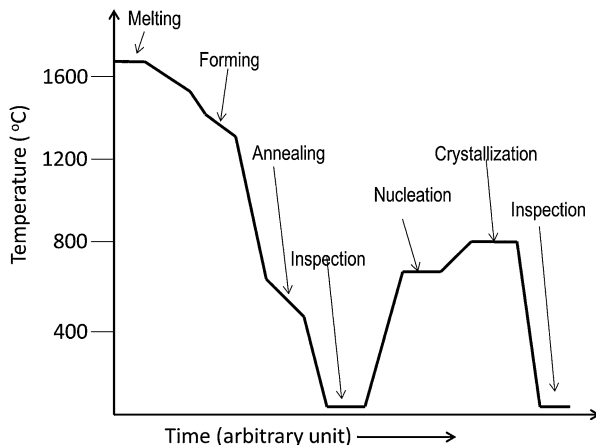


Fig. 9 Comparison for homogenous and heterogeneous nucleation rates. (Adapted from Ref. [6])

Fig. 10 A typical heat treatment schedule of a glass-ceramics starting from melting of the raw materials till the inspection of the final product. (Adapted from Ref. [8])



product. However, the basic chemical composition of the virgin glass and the intrinsic properties of the precipitated crystals are always important determining factors.

Important Glass-Ceramic Systems: Their Properties and Applications

Researchers have studied a large variety of glass-ceramic systems, which are described in details in a book by Holland and Beall [9]. A few of the important systems, studied extensively or commercially exploited, are listed in Table 1 together with the respective crystalline phase(s) and their important properties and applications.

It is well known that glass-ceramic materials possess certain unique combination of properties, which can be obtained by selection of right chemical composition of the original glass followed by selection of appropriate processing conditions. The useful combinations may be grouped as follows:

1. Ease of fabrication into intricate shapes but with no porosity (unlike normal ceramics).
2. High temperature stability with a wide range of coefficient of thermal expansion (CTE), in certain cases zero or slightly negative value.
3. High strength with temperature stability and translucency to different electromagnetic radiations.
4. Chemical stability together with biocompatibility and bioactivity leading to their use as dental implant.
5. High strength, toughness, and electrical insulation with machinability.
6. A wide range of dielectric constant together with low dielectric loss and machinability leads to their use as electronic components.

Table 1 A few important glass-ceramic systems investigated/commercialized. (Compiled based on information available in Ref. [9])

Glass system	Approximate composition (wt%)	Major crystalline phase	Trade name if any	Important property/application	Remarks if any
Lithium alumina silicate (LAS)	80SiO ₂ , 4Al ₂ O ₃ , 10.5Li ₂ O, 5.5K ₂ O, 0.02CeO ₂ , 0.04AgCl	Lithium disilicate (2SiO ₂ ·Li ₂ O)	Photoceram [®] by Corning, USA	Photosensitive	First ever glass-ceramics discovered by Stookey
	72.5SiO ₂ , 22.5Al ₂ O ₃ , 5Li ₂ O	-do-	Cercor [®] by Corning, USA	Used in gas turbines	
	74SiO ₂ , 13Li ₂ O, 4Al ₂ O ₃ , 3K ₂ O, 1B ₂ O ₃ , 3P ₂ O ₅ , 2ZnO	-do-		Sealant for SOFC	-
Lithium alumina silicate (LAS) with other additives	69SiO ₂ , 3Li ₂ O, 19Al ₂ O ₃ , 2MgO, 1ZnO, 2ZrO ₂ , 3TiO ₂ , 1As ₂ O ₃	β-Quartz solid solution	Vision [®] by Corning, USA	Transparent, very low thermal expansion	Developed in the 1990s
	55.5SiO ₂ , 4Li ₂ O, 25.5Al ₂ O ₃ , 1MgO, 1(Na ₂ O + K ₂ O), 1.5ZnO, 2ZrO ₂ , 2TiO ₂ , 7P ₂ O ₅ , 0.5As ₂ O ₃	-do-	Zerodur [®] by Schott AG, Germany	-do-	Developed in the 1970s
	65SiO ₂ , 4Li ₂ O, 23Al ₂ O ₃ , 0.5MgO, 1(Na ₂ O + K ₂ O), 1.5ZnO, 3ZrO ₂ , 2TiO ₂ , 0.5P ₂ O ₅ , 0.5As ₂ O ₃	-do-	Narumi [®] by Nippon Electric, Japan	-do-	-
	64SiO ₂ , 3.5Li ₂ O, 21.5Al ₂ O ₃ , 1(Na ₂ O + K ₂ O), 1.5ZnO, 2.5BaO, 1.5ZrO ₂ , 2.5TiO ₂ , 1Sb ₂ O ₃ , 0.5MnO ₂	-do-	Ceran [®] by Schott AG, Germany	Translucent, very low thermal expansion Used in Cook tops	
	70SiO ₂ , 3Li ₂ O, 19Al ₂ O ₃ , 2.5MgO, 0.5(Na ₂ O + K ₂ O), 4.5TiO ₂ , 0.5As ₂ O ₃	β-Spodumene solid solution	ComingWare [®] by Corning, USA	Low CTE, used in cookware	

Multicomponent system	43SiO_2 , $30\text{Al}_2\text{O}_3$, $14\text{Na}_2\text{O}$, 5.5BaO , 6.5TiO_2 , $1\text{As}_2\text{O}_3$	$\text{BaAl}_2\text{Si}_2\text{O}_8$, $\text{NaAlSi}_3\text{O}_8$, and TiO_2	Corning 9609 [®] / Centura [®] by Corning, USA	Tableware	
Magnesium aluminosilicate	56SiO_2 , $20\text{Al}_2\text{O}_3$, 15MgO , 9TiO_2	$\text{Mg}_2\text{Al}_4\text{Si}_5\text{O}_{18}$ (Cordierite) & TiO_2	Corning 9606 [®] by Corning, USA	High strength, high fracture toughness, low CTE	One of the first glass-ceramics developed by Corning and used in radomes
Fluorosilicates	47SiO_2 , $16\text{Al}_2\text{O}_3$, 14MgO , $8\text{B}_2\text{O}_3$, $9\text{K}_2\text{O}$, 6F	$\text{K}_{1-x}\text{Mg}_3\text{Al}_{1-x}\text{Si}_3\text{O}_{10}\text{F}_2$ (flat crystals)	MACOR [®] by Corning, USA	Machinable glass-ceramics	
	$56-64\text{SiO}_2$, $0-2\text{Al}_2\text{O}_3$, $15-20\text{MgO}$, $12-18\text{K}_2\text{O}$, $4-9\text{F}$, $0-5\text{ZrO}_2$	$\text{K}_{1-x}\text{Mg}_{2.5+x}\text{Si}_4\text{O}_{10}\text{F}_2$ ($x < 0.2$) (flat crystals)	DICOR [®] by Corning/Dentsply	Machinable with translucency	

In general, they have enhanced mechanical strength (compared to glass), high hardness, and fracture toughness even though certain varieties are relatively soft so as to be machined by conventional metal cutting tools. They also possess a range of optical properties – translucent to fully opaque, enhanced temperature resistance, a wide range of coefficient of thermal expansion, and a spectrum of electrical properties – insulating to semiconducting, varied dielectric properties, and so on. Useful mechanical properties, e.g., flexural strength and fracture toughness of different groups of materials, when plotted against each other, a nice sectorial distribution occurs for the different groups as shown in Fig. 11. It clearly indicates that the glass-ceramics as a group are stronger and tougher than most of the common glasses but are slightly less strong and less tough than the engineering ceramics like alumina and zirconia. Therefore glass-ceramics materials, in general, are quite useful for many engineering applications where very high strength and toughness are not essential. It is interesting to note that “mica” group of materials are positioned between the glasses and the glass-ceramics. In fact the flexural strength as well as the fracture toughness of this group are lower than most of the glass-ceramics. This fact has been exploited for designing the “machinable glass-ceramics” which can be machine to intricate shapes using conventional metal cutting tools.

Another quite interesting property of glass-ceramics is the very wide range of coefficient of thermal expansion (CTE) depending on the basic chemical composition of the glassy matrix and the dispersed crystalline phase. The value can be as low as “zero” or slightly negative, particularly for a very important commercial glass-ceramics with the registered trade name “Zerodur[®],” developed and marketed by

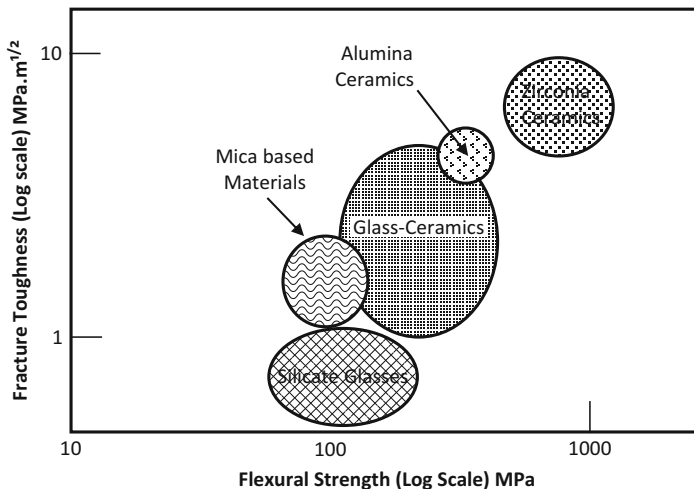


Fig. 11 Comparison of mechanical properties of various groups of materials: glass, mica, glass-ceramics, and engineering ceramics like alumina and zirconia. (Based on data presented in Ref. [10])

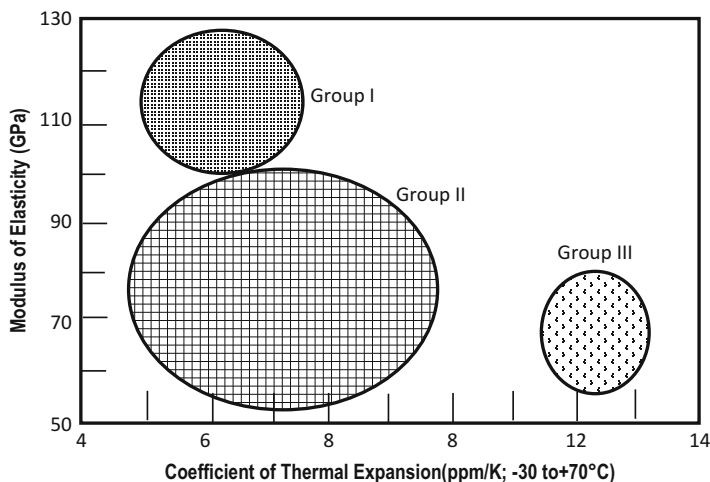


Fig. 12 Modulus of elasticity plotted against coefficient of thermal expansion (CTE) for most of the known glass-ceramic materials. Interestingly they can be broadly classified under three groups as shown. $-30\text{ }^{\circ}\text{C}$ to $+70\text{ }^{\circ}\text{C}$ indicates the temperature range of measurement. (Based on data presented in Ref. [11])

Schott AG of Germany. This is a translucent material extensively used as blanks for telescope and space mirrors. On the other hand, the CTE of certain glass-ceramics can be as high as 12–14 ppm/K which is close to that of certain metallic alloys, making them useful for glass-to-metal seals, feedthrough, etc. In general the complete range of glass-ceramic materials can be classified under three distinct groups as shown in Fig. 12. Group I materials are having high modulus of elasticity (Young’s modulus) but low CTE. Group III materials, which are relatively small in number, on the other hand, possess low modulus of elasticity but very high CTE. Most of the glass-ceramics, however, are categorized under Group II possessing properties in between the two extreme groups as shown in the figure.

Having discussed the definition and general principle of preparation of glass-ceramics, combination of their important properties, and examples of a few common glass-ceramic systems, an attempt is now made to go into the details of two most important types, namely, “transparent” and “machinable” glass-ceramics.

Transparent Glass-Ceramics

Unlike polycrystalline ceramics, glasses are transparent due to their uniform ionic distribution (chemical homogeneity) and absence of scattering centers such as grain boundaries. However, glass-ceramics, by definition, are constituted of a glassy matrix dispersed with fine crystalline particles and therefore give rise to considerable opacity. Only under special circumstance they can be made transparent or translucent

particularly by controlling the size and refractive index of the dispersed crystalline phase. One of the very first papers on transparent glass-ceramics was published way back in 1969 by Beall and Duke [12] who reviewed the different theories of scattering of light, which are summarized below.

Theories of Light Scattering

There are several mechanisms by which electromagnetic radiation gets attenuated/absorbed when it interacts with a medium: (i) enhancement in atomic/molecular vibration resulting in heat evolution, (ii) transition of outer cell electrons from the ground state to excited state, and (iii) absorption and simultaneous re-emission by the ions/atoms particularly present on the surfaces of the inhomogeneities (dispersed particle or grain boundaries), the last one being referred to as “scattering.” This phenomenon of scattering by small particles was first investigated by Lord in the year 1871 [13] and is referred to as “Rayleigh scattering.” Considering the incidence of a linearly polarized monochromatic radiation on a heterogeneous medium, he quantified the “scattering cross section (σ_s)” as follows:

$$\sigma_s = \frac{8}{3\pi} \left(\frac{2\pi}{\lambda} \right)^4 |\beta|^2 \quad (7)$$

in which λ is the wavelength of the incident radiation and β is the polarizability of the medium. Based on an assumption of uniform distribution of spherical particles, $|\beta|^2$ can be expressed as:

$$|\beta|^2 = \alpha^6 \left| \frac{M^2 - 1}{M^2 + 2} \right|^2 \quad (8)$$

where α is the radius of the dispersed particles and M is the ratio of the refractive index of the particle to that of the matrix.

The angular intensity of the scattered radiation $I(\theta)$ can be expressed as a function of θ and the scattering angle as follows:

$$I(\theta) = \left(\frac{1 + \cos^2\theta}{r^2} \right) \frac{8\pi^4}{\lambda^4} \alpha^6 \left| \frac{M^2 - 1}{M^2 + 2} \right|^2 I_0 \quad (9)$$

where r is the distance between the scattering center and the point, where the scattering intensity is being measured, and I_0 is the intensity of the incident radiation. This equation indicates that the scattering intensity is proportional to 6th power of the radius of the second-phase particle (α) and inversely proportional to the 4th power of the wavelength (λ). Thus the two most important conditions of transparency are (i) $\alpha \ll \lambda$, i.e., the particle size must be much smaller than the wavelength of the incident radiation, and (ii) $M \cong 1$, i.e., the refractive indices of the matrix and the

dispersed phase should be as close as possible. Irrespective of these two conditions, the overall absorption by the material must be as low as possible.

Rayleigh's scattering theory is particularly applicable for very small (i.e., smaller than the wavelength of the radiation) particles. A more generalized theory has been later proposed by Mie [14], which is better suited when the particle sizes are about the same or larger than that of the wavelength of the radiation. The distinction between the two theories has been discussed in an article by Hahn [15] in which he clearly demonstrated the difference in the absolute values of differential scattering cross section for different sizes of the particles (Fig. 13), e.g., 17 nm, 170 nm, and 1700 nm (1.7 μm). For 17 nm particle, the scattering cross section is nearly independent of scattering angle, a distinctive characteristic of Rayleigh scattering. However, if the particle size increases by an order of magnitude (to 170 nm), the scattering cross section still remains monotonic but decreases by three orders of magnitude. On further increase of the particle size to 1700 nm, the scattering cross section shows a periodic pattern, a distinctive feature of Mie scattering. In addition, the order of magnitude of the scattering cross section is largely different. Note the multiplier of 10^6 for the 17 nm particle compared to a multiplier of 10^{-3} for 1.7 μm particles. Therefore the scattering cross section increases by nearly ten orders of magnitude by decreasing the particle size by only two orders of magnitude.

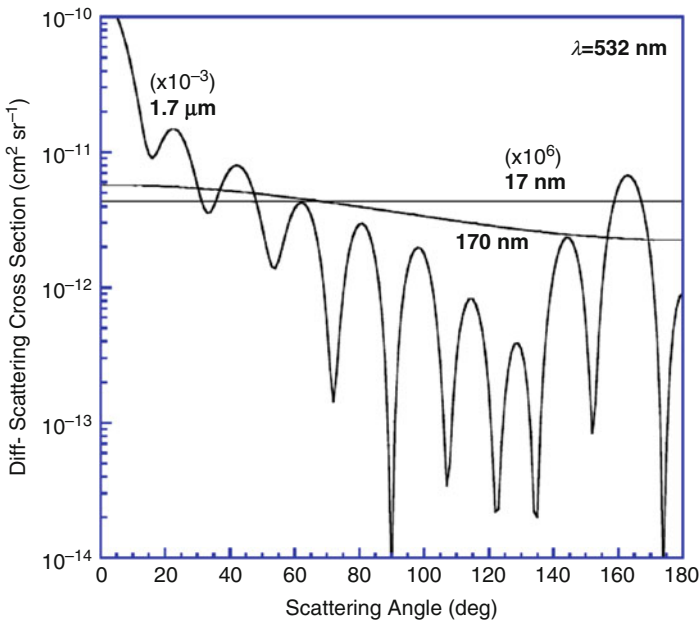


Fig. 13 Plots of differential scattering cross section against scattering angle for particles of different sizes (17–1700 nm) showing the nature and extent of scattering for different particle size ranges. (Ref. [15]; open source)

Anomalous Scattering

Scattering leads to loss of transmission of light and therefore loss of transparency or in other words development of turbidity (inverse of transparency). It may be seen from Eq. (9) that the turbidity, $I(\theta)/I_0$, is proportional to λ^{-4} . This is particularly true if the predominant mechanism of scattering is “Rayleigh scattering.” However, based on their own experimental results and analysis of the data published by others, a group of Russian scientists under the leadership of Alexander Zhilin [16–19] have claimed that this relationship is not always true. Instead, they have proposed a more generalized dependence of λ^p , where p can vary from ≤ 4 to a much larger value of ~ 9 . This means that the turbidity can be much less (or transparency may be much higher) than that predicted by Rayleigh’s scattering theory discussed above. This observation has been termed as “anomalous scattering” by these scientists.

With the experimental study on the system $\text{Na}_2\text{O-Nb}_2\text{O}_5\text{-SiO}_2$ [16] for which the crystalline phase is NaNbO_3 , it has been shown that the exponent $p \approx 9$ at the initial stage of crystallization (0–1 h) goes through a minimum value of $p \approx 4.5$ at an intermediate stage (2–12 h) and finally stabilizes at $p \approx 6.5$ (12–24 h with 25–30 volume fraction of the crystalline phase) particularly for the wavelength (λ) range 400–600 nm and the heat treatment is carried out at 680 °C. Consequently the transmittance is 10–20 times larger than that could be calculated based on Rayleigh’s scattering theory. A part of the experimental data is presented in Fig. 14. This

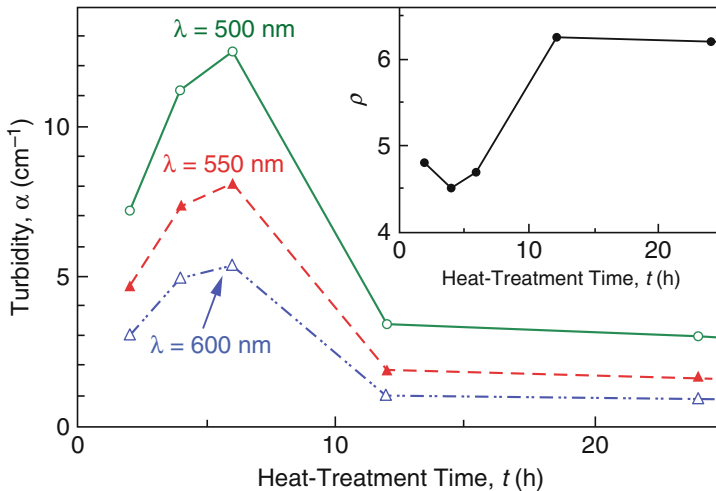


Fig. 14 Variation of turbidity (absorption coefficient α) at three different wavelengths λ (500, 550, and 600 nm) as function of heat treatment time (t) in hour during crystallization of $\text{Na}_2\text{O-Nb}_2\text{O}_5\text{-SiO}_2$ glass. The inset shows the variation of the exponent p with the heat treatment time. At the early stage of crystal growth ($t \leq 6$ h), the value of p varies in the range 4.5–4.8, which is close to the ideal Rayleigh value of 4, the characteristics of very small isolated scatterers, i.e., nanocrystals. However, at $t > 6$ h the value of p is around 6.2 characterizing an anomalous scattering. (Reproduced with permission from Ref. [18])

anomaly has been explained by considering the interference of the scattered beams due to short-range ordering of the precipitated crystalline phase. The greater is the dispersion in the scattering properties of the crystalline phase in a glass-ceramics, the lower is the interference and the higher is overall scattering effect and consequently a lower transmittance. Such an interference effect has been exploited to develop glass-ceramics for laser components and standards of whiteness with high diffuse reflectance by the same group of researchers [18].

Transparent Glass-Ceramics Systems

Transparent glass-ceramics are based on many different systems, and their applications are also of a wide range. While most them are based on oxide systems, chalcogenide [20, 21] and oxyfluoride [22, 23] systems have also been investigated in recent years and used for a number of interesting applications. Oxide systems in particular have been developed since long and marketed by several glass companies across the globe for a variety of uses. A few of the important ones are already listed in Table 1.

Zero Expansion Transparent Glass-Ceramics

One of the most challenging applications in the history of glass-ceramic development is the mirror blanks for telescopes (both earth and space based) and satellites requiring combination of properties, e.g., transparency, near-zero CTE (less than that of fused silica), good mechanical strength, good machinability, achieving high surface finish, etc. The glass-ceramics developed by Schott AG., Germany, under the trade name Zerodur[®], has been the most widely used material for these purposes [24]. Typical composition of Zerodur[®] is indicated in Table 1 for which the primary crystalline phase is β -quartz solid solution. The CTE of the material is controlled primarily by the disordered nanocrystalline phase, whose CTE is very close to zero or slightly negative. The CTE value of the bulk material is controlled precisely by adjustment of the chemical composition and the heat treatment schedule. Typical heat treatment schedule, thermal expansion behavior, and the transmission spectra are presented in Figs. 15, 16, and 17, respectively. The size requirements are from a few centimeters to several meters, which pose a tremendous technological challenge. In addition to low thermal expansion, transparency, and machinability, the material also possesses extremely low helium gas diffusivity, which has led to its another unique application as the housing of laser gyroscope, a modern navigation system for aircrafts, missiles, satellites, and other space vehicles.

Transparent glass-ceramics with low CTE have also been developed by different companies for household applications, e.g., cook tops and tablewares. Examples are Vision[®] by Corning Inc., USA; Keraglas[®] by EuroKera (Corning and St. Gobain, France); Ceran[®] and Robax[®] by Schott AG, Germany; and also Neoceram[™] by Nippon Electric Glass, Japan. Materials with similar properties have also been developed by other companies. These are Vision[®] by Corning, USA, and Narumi[®] by Nippon Electric, Japan. However, their use is not as widespread as that of Zerodur[®].

Fig. 15 Typical heat treatment schedule for Zerodur® glass-ceramics. (Reproduced with permission of the publisher of Ref. [24])

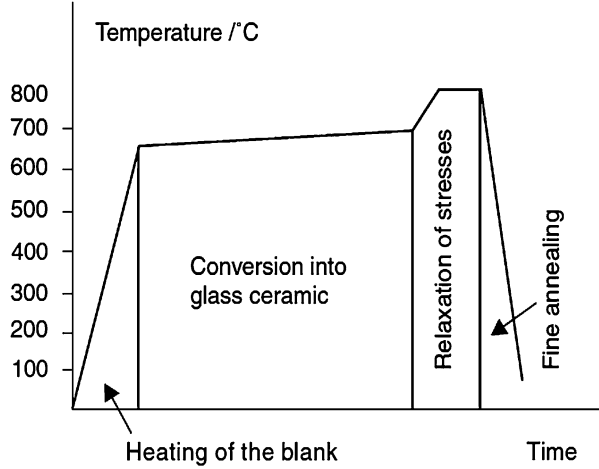


Fig. 16 Relative length change of Zerodur® glass-ceramics as function of temperature in the range 0–900 K. (Reproduced with permission of the publisher of Ref. [24])

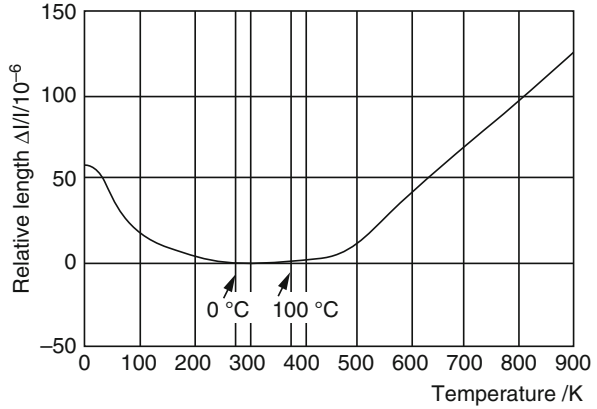
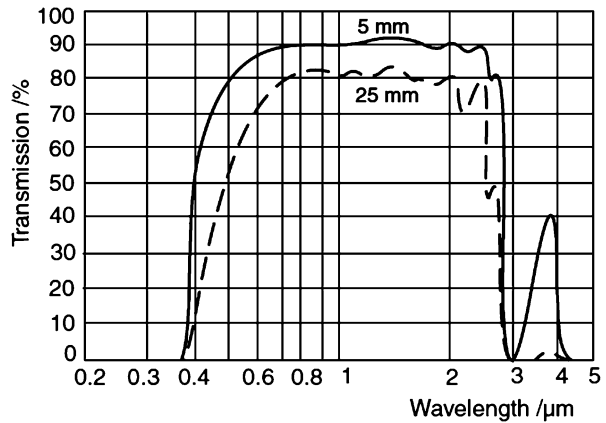


Fig. 17 Transmission spectra of Zerodur® glass-ceramics for two different specimen thicknesses. (Reproduced with permission of the publisher of Ref. [24])



Transparent Glass-Ceramics for Photonic Applications

This subject is relatively new, but several reviews have already been published in recent times [18, 25, 26] indicating the importance and fast-growing nature of the research area. Salient points from these reviews are presented here.

Rare earth (RE) ions play a very important role in photonics; it may be used as a lasing ion for the solid-state laser devices, amplification of laser intensity in optical communication, up-conversion of radiation frequency, and preparation of luminescent materials and phosphors of different kinds, to name a few; different systems of transparent glass-ceramics have been used as the host of RE ions. In addition to the conventional oxide systems, e.g., LAS, MAS, and ZAS, silicon oxyfluoride glass-ceramics have been investigated quite extensively as the host. Quite early in 1975, a glass-ceramic material containing glass-forming oxides like SiO_2 , GeO_2 , and P_2O_5 with addition of PbF_2 and a RE oxide was reported as a phosphor material showing a luminescent efficiency two times that of $\text{LaF}_3:\text{Yb}:\text{Er}$, one of the common phosphors of that time [27]. Since then many different glass-ceramic systems have been investigated; a few of them are presented in Table 2.

Transparent glass-ceramics with different RE ions have also been investigated in the different other systems like germanate-oxyfluoride, e.g., $\text{GeO}_2\text{-PbO-PbF}_2\text{-TmF}_3$ containing ~ 16 nm $\beta\text{-PbF}_2:\text{Tm}^{3+}$ crystals, Yb-doped $\text{PbF}_2\text{-GeO}_2\text{-Al}_2\text{O}_3\text{-Tm}_2\text{O}_3$, telluride-oxyfluoride like $\text{TeO}_2\text{-ZnO-ZnCl}_2$, purely fluoride systems like $\text{ZrF}_4\text{-LaF}_3\text{-ErF}_3\text{-GaF}_3\text{-LaF}_3$, and lithium-borate-oxide-based systems like $\text{Li}_2\text{B}_4\text{O}_7\text{-Bi}_2\text{WO}_6$ and $\text{Li}_2\text{B}_4\text{O}_7\text{-SrO-Bi}_2\text{O}_3\text{-Nb}_2\text{O}_5$.

In recent times Er lasers with emission wavelengths in the range 1.5–1.7 μm have gained considerable importance as “eye safe” laser, because the wavelength is safe for human eye. However, its application requires nanosecond pulses with significantly high peak power. This is accomplished through passive Q-switching, which requires insertion of a saturable absorber (SA) in to the laser cavity [18]. Co^{2+} -doped MgAl_2O_4 single crystal with an emission wavelength of ~ 1.54 μm has been recognized as the best material as SA. In an attempt to replace the costly single crystal, researchers have now been successful to develop Co^{2+} -doped transparent glass-ceramics in the $\text{ZnO-Al}_2\text{O}_3\text{-SiO}_2$ (ZAS) system for which the crystalline phase is ZnAl_2O_4 , which is structurally identical to MgAl_2O_4 . It has also been possible to develop transparent glass-ceramics containing nanocrystals of Co^{2+} -doped MgAl_2O_4 in the glass system $\text{MgO-Al}_2\text{O}_3\text{-SiO}_2$ (MAS).

Table 2 Composition of some transparent oxyfluoride glass-ceramic system investigated by different researchers. (Adapted from Ref. [25])

Sl. no.	Host oxide glass system	Base glass composition (mol%)	Crystalline phase
1.	$\text{SiO}_2\text{-Al}_2\text{O}_3$	$30\text{SiO}_2\text{-}15\text{AlO}_{1.5}\text{-}24\text{PbF}_2\text{-}20\text{CdF}_2\text{-}10\text{YbF}_3\text{-}1\text{ErF}_3$	$\text{Pb}_x\text{Cd}_{2-x}\text{F}_2$
2.	$\text{SiO}_2\text{-Al}_2\text{O}_3$	$30\text{SiO}_2\text{-}15\text{AlO}_{1.5}\text{-}17\text{PbF}_2\text{-}29\text{CdF}_2\text{-}4\text{YF}_3\text{-}5\text{ZnF}_2$	$(\text{Cd,PbZnY})\text{F}_{2.3}$
3.	$\text{SiO}_2\text{-Al}_2\text{O}_3\text{-Na}_2\text{O}$	$48.5\text{SiO}_2\text{-}25.1\text{AlO}_{1.5}\text{-}13.1\text{LaF}_3\text{-}2.5\text{AlF}_3\text{-}10.7\text{Na}_2\text{O}\text{-}0.1\text{ErF}_3$	$\text{LaF}_3\text{-}0.1\text{ErF}_3$
4.	SiO_2	$50\text{SiO}_2\text{-}50\text{PbF}_2\text{-}4/5\text{ErF}_3$	$\beta\text{-PbF}_2\text{:Er}^{3+}$

Transparent glass-ceramics also act as good hosts for RE-based luminescent and phosphor materials even though β -quartz solid solution, the primary crystalline phase in LAS, one of the most common glass-ceramic systems, is not that suitable for this purpose as this phase does not accept significant amount of RE ions in its structure. An alternate approach has therefore been adopted to adjust the base composition of the glass in such a way that RE titanates, niobates, or titanate-zirconates are precipitated as the primary crystalline phases [28–32]. For this, the LAS or MAS systems are nucleated with TiO_2 and ZrO_2 with the addition of RE ions; in most cases a compound like $\text{RE}_2(\text{Zr,Ti})_2\text{O}_7$ having a defect fluorite structure gets precipitated, which, on further heating, gets transformed initially to a disordered and then to a ordered pyrochlore-type phase. The transparent glass-ceramics loaded with either Er^{3+} or Yb^{3+} ions give rise to nearly ten times enhancement of up-conversion efficiency at ~ 650 nm, [30] which is important for phosphors and solid-state lighting applications.

Extensive research work is currently underway for the use of transparent glass-ceramics as the phosphors for white light-emitting diodes (WLEDs) [26]. This is a very important area of research from the commercial point of view as WLEDs are the most energy-efficient devices for general as well as specialized lighting systems replacing the incandescent and conventional fluorescent lamps. There are two primary approaches to get white light from GaN-based chip LEDs: (1) first is multi-LED chip route, in which light from three monochromatic chips, red, blue, and green (RBG), is mixed in right proportion to get the white light and (2) second is a phosphor-based conversion route in which GaN-based blue or UV LED chip is coated with either yellow or multi-chromatic phosphors to produce the white light. Major constituent of the yellow phosphor is $\text{Y}_3\text{Al}_5\text{O}_{12}:\text{Ce}^{3+}$ or in short Ce:YAG. A transparent polymeric base in the form of low temperature curable silicone is used as an adhesive as well as the carrier for the powdery Ce:YAG. The polymer is used extensively due to its low cost and ease of fabrication. However, one of the most important disadvantages of this carrier is its degradation with time and consequently the loss of lumens as well as change of color of the light source. In contrast, transparent glass-ceramics is highly stable even though relatively costly. Extensive research is therefore in progress to make this group of materials technologically and commercially acceptable.

Primary phosphors remaining same (Ce:YAG) attempts have been made to incorporate and disperse the nano-/microparticles of the phosphor in a matrix of transparent glass-ceramics. In 2005, Fujita and Tanabe first reported the successful fabrication of Ce:YAG-based glass-ceramic phosphor [33, 34]. The primary glass was based on $\text{SiO}_2\text{-Al}_2\text{O}_3\text{-Y}_2\text{O}_3\text{-Ce}_2\text{O}_3$ system. Several other host glass systems have also been tried, for example, $\text{SiO}_2\text{-Na}_2\text{O-Al}_2\text{O}_3\text{-CaO}$ [35], $\text{TeO}_2\text{-B}_2\text{O}_3\text{-Sb}_2\text{O}_3\text{-ZnO-Na}_2\text{O-La}_2\text{O}_3\text{-BaO}$ [36], etc. There are, however, several challenges/problems to be solved as the maximum quantum efficiency reached so far is only 30% primarily due to difficulty in incorporating all the Ce^{3+} ions into YAG crystals during crystallization of the glass systems. In addition, the YAG crystals get contaminated by the other ions present in the glass. It is expected that further research would provide necessary clues to take care of these issues.

Machinable Glass-Ceramics

Glasses are known to be hard and brittle, and therefore machining of glass is nearly impossible except cutting and grinding by diamond impregnated tools. Glass-ceramics, by definition, are a nano-/micro-composite material and can be designed to develop a wide range of properties depending on the individual properties of the nano-/microcrystals and the glassy matrix. In general glass-ceramics are stronger and tougher than the parent glass, and consequently they also require the same diamond impregnated tools for their cutting and grinding; machining in a lathe machine is nearly impossible. However, in case the crystalline phase is softer than the parent glass, one can have the resulting glass-ceramics to be softer, and there is a possibility of their machining/fabrication in a lathe machine using conventional metal cutting tools. Such materials are termed as “machinable glass-ceramics” and have found a wide range of technological applications and usefulness in industry.

In order to develop such a material, the target has been incorporation of a soft phase within a glassy matrix by choosing the appropriate chemical composition and heat treatment condition. G. H. Beall and his co-workers [37–41] at Corning Glass Works, USA, at the instance of NASA, were successful in designing and developing such glass-ceramics based on fluorosilicate system with a general formula $\text{SiO}_2\text{-(R}^{3+}\text{)}_2\text{O}_3\text{-MgO-(R}^{2+}\text{)O-(R}^+\text{)}_2\text{O-F}$, which is the general formula of different forms of fluorine-containing mica in which R represents different types of cations such as Al^{3+} , B^{3+} , Ca^{2+} , K^+ , Na^+ , H^+ , etc. Structurally, they have a layered structure with a weak van der Waals bond between the layers and therefore an easy cleaving between these layers. An overview of the developmental activity particularly by the Corning group on different types of mica-containing glass-ceramics has been presented in their book by Holland and Beall [9]. Important points are discussed in the following sections.

Machinable Glass-Ceramics with Alkaline Phlogopite Phase

Mica is a multicomponent system with a structural formula $\text{X}_{0.5-1}\text{Y}_{2-3}\text{Z}_4\text{O}_{10}(\text{OH, F})_2$, in which X is the alkali or large alkaline earth ions, Y is the small alkaline earth ions or aluminum in octahedral coordination, and Z represents the sum of Al^{3+} and Si^{4+} ions in the tetrahedral building blocks and also oxygen, hydroxyl, and/or fluoride ions. The very first machinable glass-ceramics developed by Beall [37] contained the mica crystals of alkaline phlogopite mica (also referred to as fluorophlogopite with general formula $\text{K}_{1-x}\text{Mg}_3(\text{Al}_{1-x}\text{Si}_{3+x}\text{O}_{10})\text{F}_2$, where $x = 0-0.5$). The process of crystallizing this phase was quite a challenging one as it required a several intermediate steps. The details are as follows:

- (i) They started with a base glass composition of 30–50 SiO_2 , 3–20 B_2O_3 , 10–20 Al_2O_3 , 4–12 K_2O , 15–25 MgO , and 4–10 F (all in wt%). The glass formation as well as crystallization potentials of this composition could not be predicted based on the simple ternary system MAS because the system is

completely changed and expanded by the addition of several other oxides. By looking at the microstructure of the glass, signs of liquid-liquid phase separation was evident in the form of spherical droplets of 0.5 μm in size composed of an F-rich potassium alumino borosilicate glass. This was a blessing in disguise as this phase-separated glass has been useful for the initiation of the crystallization process. No other nucleating agent was necessary. In fact it was later analyzed that the phase-separated glass contained MgF_2 which is isostructural with the rutile form of TiO_2 [40].

- (ii) Although the nucleation is initiated by the phase-separated glass droplets, it does not lead directly to the formation of the mica phase. Instead, an intermediate phase in the form of chondrodite having an approximate formula of $2\text{Mg}_{2-x}(\text{Al},\text{B})_{2x}\text{Si}_{1-x}\text{O}_4 \cdot \text{MgF}_2$ gets formed at the surface of the phase-separated glass.
- (iii) In the third stage, at an approximate temperature of 750 $^\circ\text{C}$, formation of another phase, namely, norbergite ($\text{Mg}_2\text{SiO}_4 \cdot \text{MgF}_2$), takes place. This happens through a solid-state reaction between the droplet-shaped phase-separated glass and chondrodite, which forms in the second stage. During this process both the glass and the chondrodite phase get completely dissolved. Finally the phlogopite mica phase is formed at a temperature above 850 $^\circ\text{C}$ at expense of the norbergite together with the formation of a secondary phase in the name of magnesium fluoroborate [$\text{Mg}_3(\text{BO})_3\text{F}_3$]. The final heat treatment temperature is however 950 $^\circ\text{C}$ in order to optimize the properties. Structural studies have indicated that there exists a structural similarity between the (100) plane of norbergite and the (002) plane of phlogopite. The deviation of lattice parameter is within 5%, suitable for epitaxial interaction. So there is no difficulty in the heterogeneous growth of the latter on the surface of the former.
- (iv) Minimum amount of the mica phase required for demonstration of the machinability is around 33% by volume. However, the optimum property is obtained if the volume is 55–65%.

Based on the development of Beall and co-workers, Corning Incorporated, USA (previously known as Corning Glass Works), has been manufacturing the phlogopite mica-containing machinable glass-ceramics under the trade name MACOR[®] since the mid-1970s of the last century, and it is having a very good demand in the market even today. Exact composition of this material together with those of the few others marketed by other companies is listed in Table 3.

Even after the commercialization of MACOR[®], the research interest on the material has not died down. There have been a large number of research publications and dissertation by several researchers in different countries on various aspects of this wonder material [42–47]. Typical microstructures of a MACOR-type material are presented in Fig. 18, in which presence of elongated platelets of the mica phase (fluorophlogopite) is evident. EDAX analysis confirms the chemical composition [47].

Table 3 Composition and crystal phases of commercial machinable glass-ceramics. (Adapted from Ref. [9])

Oxides (wt%)	MACOR [®] (Corning)	DICOR [®] (Corning/Dentsply)	BIOVERIT [®] II (Vitron)
SiO ₂	47.2	56–64	48.9
B ₂ O ₃	8.5	–	–
Al ₂ O ₃	16.7	0–2	27.3
MgO	14.5	15–20	11.7
Na ₂ O	–	–	3.2
K ₂ O	9.5	12–18	5.2
F	6.3	4–9	3.7
ZrO ₂	–	0–5	
CeO ₂	–	0.05	
Crystal phase	K _{1-x} Mg ₃ Al _{1-x} Si _{3+x} O ₁₀ F ₂ (flat crystals)	K _{1-x} Mg _{2.5+x/2} Si ₄ O ₁₀ F ₂ (x < 0.2) (flat crystals)	(Na _{0.18} K _{0.82})(Mg _{2.24} Al _{0.61})(Si _{0.278} Al _{1.22})O _{10.1} F _{1.90} (curved crystals) ^a

^aCurved crystals have been observed only in a glass-ceramic system. No such phase has been observed under natural condition

Important Properties and Applications of MACOR[®]

MACOR[®] is one of the most widely used machinable glass-ceramics. It is being manufactured and marketed not only by Corning Incorporated, USA, the original inventor of the product, but several other companies across the globe with license from the inventor primarily because it possesses many useful properties which are difficult to be matched by any other available material. Important properties are (i) zero porosity and non-shrinking, (ii) high dielectric strength, (iii) high electrical resistivity, (iv) withstands high temperatures up to 1000 °C, (v) tight tolerance capability, and (vi) easily and economically machined into complex shapes and precision parts. A few of the quantified properties are presented in Table 4.

The excellent machinability property of MACOR[®] arises from its fracture mechanics. Firstly, the mica crystals are easily cleaved under the externally applied stress, and secondly the cracks are propagated along the crystal-glass interface without any micro-cracking of the glassy phase [48]. Different machining aspects of the material were earlier studied by Grossman [49]. Possibility of using ultrasonically vibrating tool has also been investigated [50]. Examples of a few intricate shapes fabricated from MACOR[®] are presented in the brochures of different manufacturers [51, 52].

Major applications include (i) vacuum feedthroughs; (ii) hermetic seals; (iii) insulators and supports for vacuum environment; (iv) spacers, headers, and windows for microwave tube devices; (v) sample holders for microscopes; (vi) aerospace components; (vii) welding nozzles; (viii) fixtures; (ix) substrates for electronic devices; and (x) components for medical instruments. It is said that there are ~200 components of MACOR[®] used in a space shuttle [51].

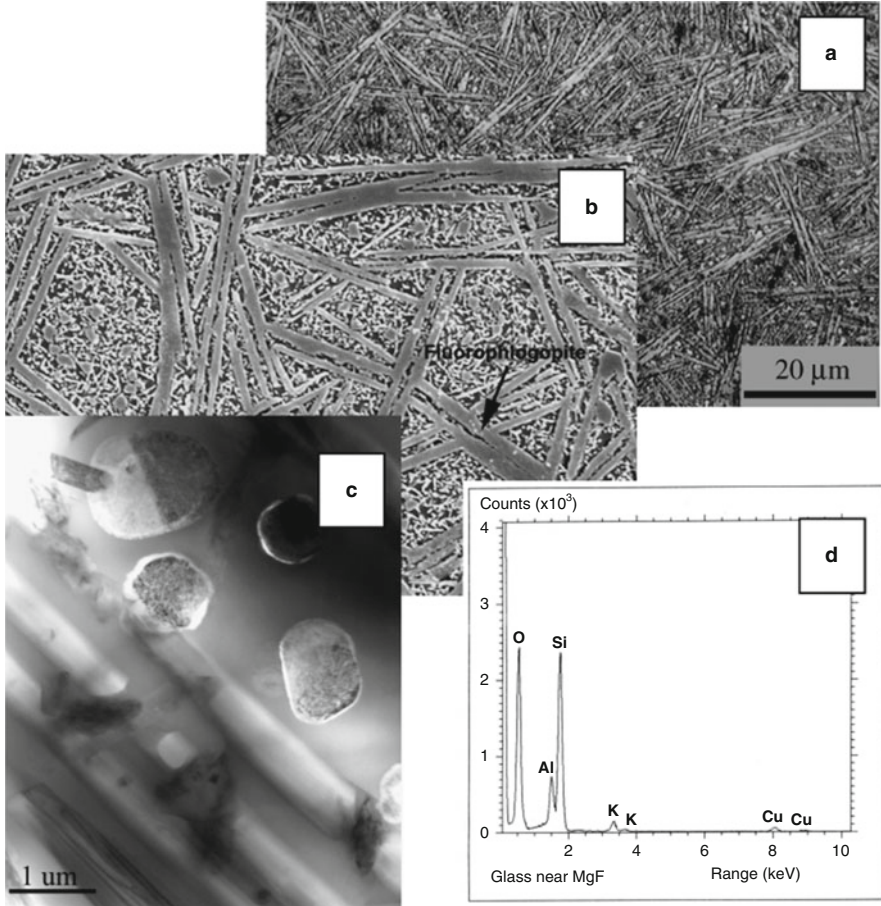


Fig. 18 Typical microstructures of a MACOR-type glass-ceramics. (a) Reflected light, (b) secondary electron imaging scanning electron microscopy, (c) bright-field transmission electron microscopy (BF TEM), and (d) energy dispersive spectroscopy of glass in TEM. (Reproduced with permission from the publisher of Ref. [47])

Machinable Glass-Ceramics Other Than MACOR[®]

Glass-ceramics based on tetrasilic mica were developed from a relatively simple system such as $\text{SiO}_2\text{-K}_2\text{O-MgO-F}$ by Grossman in [41]. The primary crystalline phase was of the type $\text{KMg}_{2.5}\text{Si}_{10}\text{O}_{10}\text{F}_2$. The crystals developed in this system were smaller in sizes together with a smaller aspect ratio giving rise to translucency of the material. The developed phase is known as “tetrasilic mica,” which is not available in nature but grows within a glassy matrix under appropriate heat treatment conditions. Based on the development of Grossman [41] and by Beall [53], Corning and Dentsply jointly commercialized the product under the trade name DICOR[®], a

Table 4 Typical quantified properties of MACOR[®]. (Based on data presented in Ref. [52])

Sl. no.	Property	Value	Sl. no.	Property	Value
1.	Density (g/cm ³)	2.52	10.	Continuous operating temperature (°C)	800
2.	Porosity (%)	0.00	11.	Knoop hardness (100 g)	250
3.	Compressive strength (Gpa)	345	12.	Coefficient of thermal expansion ($\times 10^{-7}/^{\circ}\text{C}$ in range 25–300 °C)	93
4.	Flexural strength (Gpa)	94			
5.	Modulus of elasticity (Gpa)	67	13.	Dielectric strength (KV/mm)	40
6.	Shear modulus (Gpa)	25.5	14.	Dielectric constant at 1 KHz	6.03
7.	Fracture toughness (Mpa m ^{0.5})	1.53	15.	Dielectric loss tangent (25 °C) ($\times 10^{-3}$ at 1 KHz)	4.7
8.	Poisson's ratio	0.29	16.	Volume resistivity (ohm-cm) at 50% RH	>10 ¹⁶
9.	Max operating temp (°C)	1000	17.	Thermal conductivity (25 °C) W/m°C	1.46

typical composition for which is presented in Table 3. In comparison to MACOR[®], this composition contains 0–5% ZrO₂ as the nucleating agent. Crystallization of the glass starts at around 650 °C and continues up to 950 °C. At still higher temperature of around 980 °C, enstatite (MgSiO₃) gets precipitated as a secondary phase. This glass-ceramics has certain favorable properties compared to MACOR[®], e.g., high mechanical strength, high electrical resistance and dielectric constant, low loss tangent, and excellent chemical durability together with translucency, which have made the product suitable for dental implants.

Machinable glass-ceramics have also been developed with non-alkaline phlogopite phases, replacing alkali metal ion by alkaline earth metal ions. Examples of these phases are:

- (i) Ca-phlogopite (Ca_{0.5}Mg₃AlSi₃O₁₀F₂)
- (ii) Sr-phlogopite (Sr_{0.5}Mg₃AlSi₃O₁₀F₂)
- (iii) Ba-phlogopite (Ba_{0.5}Mg₃AlSi₃O₁₀F₂)
- (iv) Mixed ion Sr-Ba or Ca-Ba, phlogopites are also possible

The parent glass compositions used for crystallization of these phases are as follows: SiO₂, 35–40%; Al₂O₃, 10–15%; and MgO, 20–30% (all in wt%). Alkaline earth oxides could be 0–20% BaO or 0–25% SrO or 0–6% CaO. Phase evolution process in these glasses is slightly different than that takes place in MACOR[®] containing alkali metals. Initial phase separation also takes place in these systems, after that the course changes. Mica phases are directly formed within a temperature of 650 °C. Initially very small crystals of the order of 50 nm appears, which grow significantly in the temperature range 700–800 °C. Final heat treatment can be made

at 1100 °C where the phases except Ca-phlogopite are stable. The latter has a tendency to decompose at this temperature. So far as the properties of these glass-ceramics are concerned, the dielectric properties are better than that of MACOR[®] due to elimination of the alkali ions.

The third product listed in Table 3, namely, BIOVERIT[®] II, was developed by Vogel and Höland [54] and Höland et al. [55, 56] when they discovered an unusual crystalline phase in the form of a curved phlogopite, for which there is no analogy in nature. The origin of this curved morphology was later explained by investigated by Höche et al. [57]. Typical composition of the product and the crystalline phase is presented in Table 3.

Alternative Method of Preparation

In recent years attempts have been made to prepare the machinable glass-ceramics not by the conventional glass melting-crystallization route but through powder metallurgy/sintering route. In one case [58] machinable fluoroamphibole glass-ceramics have been fabricated by sintering commercially available powders of fluoromica whose chemical composition is close to that of stoichiometric fluorophlogopite with recycled window glass powder at a temperature of 860–1000 °C. Fluoroamphibole crystals were formed through the interaction of the fluoromica and the glass powder. Machinability has been demonstrated but the material was not fully dense (pore free). A more recent publication [59] reports on the preparation of a mica/nepheline glass-ceramics by melting followed by sintering at a relatively low temperature. Initially a glass containing SiO₂-CaO-B₂O₃-MgO-Na₂O-ZnO was melted at around 1000 °C and ground. The powder glass was mixed with crystalline powder of fluorophlogopite mica and once again melted at around 1300 °C to synthesize the final glass frit which was subsequently sintered at a relatively low temperature of 800–900 °C. In some of the compositions, the nepheline phase gets separated before the mica phase during cooling of the glass melt. The authors have claimed good mechanical strength (97.42 ± 10.2 MPa) but with a residual porosity of around 10%.

Conclusions

Glass-ceramics discovered accidentally more than 60 years back have developed into a strong area of research and development. A large variety of technologically important materials have been developed and commercialized primarily by two major glass companies of the world, namely, Corning Incorporated, USA, and Schott AG, Germany. The materials as a group possess a wide range of unique properties and are relatively easy to fabricate. Unlike advanced ceramic materials, they are pore-free and sufficiently strong and tough, many a times transparent/translucent and occasionally machinable to make them suitable for several engineering and advanced technology applications. Scientific basis of glass crystallization and the

principle of their application in different technologies are very well understood. In this chapter attention has been particularly paid to two major varieties of the material, namely, transparent glass-ceramics and machinable glass-ceramics. For the development of the former, advantage has been taken of the theories of light scattering by a fine-particle-dispersed medium like glass-ceramics. Both the varieties of glass-ceramics have found their inroads in strategic as well as civilian sectors and attained huge commercial success. While the German firm has the monopoly over the transparent glass-ceramics, the US company has attained the uniqueness in the area of machinable glass-ceramics. Currently a significant attention is being paid to rare earth ion containing transparent glass-ceramics for up-conversion and as a possible replacement of organic silicone for the manufacture of white LEDs.

References

1. Stookey SD (1953) Chemical machining of photosensitive glass. *Ind Eng Chem* 45:115–118
2. Stookey SD (1954) Photosensitivelyopacifiable glass. US Patent 2,684,911
3. Beall GH (2014) Milestones in glass-ceramics: a personal perspective, *Int J Appl Glas Sci* 1–11. <https://doi.org/10.1111/ijag.12063>
4. Davis MJ, Zanutto ED (eds) (2017) *Glass-Ceramics*, *Mater Res Soc Bull* 42(3):195–238
5. Komatsu T (2015) Design and control of crystallization in oxide glasses. *J Non-Cryst Solids* 428:156–175
6. Zhigilei L. Web based lecture notes on MSE 3050, phase diagrams and kinetics, University of Virginia. <https://gradebuddy.com/doc/3018173/lecture-notes>
7. Jiang Z-H, Zhang Q-Y (2014) The structure of glass: a phase equilibrium diagram approach. *Prog Mater Sci* 61:144–215
8. Götz H, Kosmas I, Naß P et al (2005) Development and production of glass ceramic cooktop panels. In: Bach H, Krause D (eds) *Low thermal expansion glass ceramics*, 2nd edn. Springer, Berlin, pp 81–103
9. Höland W, Beall GH (2012) *Glass ceramic technology*. Copyright by The American Ceramic Society, published by John Wiley & Sons Inc. Hoboken, New Jersey, USA
10. Fu Q, Beall GH, Smith CM (2017) Nature-inspired design of strong, tough glass-ceramics, *Mater Res Soc Bull* 42(3):220–225
11. Davis MJ, Zanutto ED (2017) Glass-ceramics and realization of the unobtainable: property combinations that push the envelope. *MRS Bull* 42(3):195–199
12. Beall GH, Duke DA (1969) Transparent glass-ceramics. *J Mater Sci* 4:340–352
13. Rayleigh L (1871) *Philos Mag* 4XLI:274, 447 and (1899) XLVII:375 quoted in Ref. 12
14. Mie G (1908) *Ann Phys* 25:377 quoted in Ref. 12
15. Hahn D (2009) Light scattering theory. Open access. <http://plaza.ufl.edu/dwhahn/Rayleigh%20and%20Mie%20Light%20Scattering.pdf>
16. Shepilov M, Dymshits O, Golubkov V, Zhilin A (2008) Anomalously low light scattering in the $\text{Na}_2\text{O-Nb}_2\text{O}_5\text{-SiO}_2$ glass-ceramics. *Adv Mater Res* 39–40:273–276
17. Alekseeva IP, Dymshits OS, Zhilin AA et al (2014) Anomalies in light scattering by glass-ceramics of the zinc aluminum silicate system, caused by low nickel oxide doping. *J Opt Technol* 81(12):729–734
18. Dymshits O, Shepilov M, Zhilin A (2017) Transparent glass-ceramics for optical applications. *MRS Bull* 42(3):200–205
19. Shepilov MP, Dymshits OS, Zhilin AA (2018) Light scattering in glass-ceramics: revision of the concept. *J Opt Soc Am B* 35(7):1717–1724
20. Calvez L (2014) *Transparent chalcogenide glass-ceramics*. Woodhead Publishing Limited, pp 310–343

21. Lin C, Rüssel C, Dai S (2018) Chalcogenide glass-ceramics: functional design and crystallization mechanism. *Prog Mater Sci* 93:1–44
22. Dejneka MJ (1998) Transparent oxyfluoride glass ceramics. *MRS Bull* 22:57–62
23. Fedorov PP, Luginina AA, Popov AI (2015) Transparent oxyfluoride glass ceramics. *J Fluor Chem* 172:22–50
24. Bach H, Krause D (2005) *Low thermal expansion glass ceramics*, 2nd edn. Springer, Berlin, pp 121–235
25. Gonçalves MC, Santos LF, Almeida RM (2002) Rare-earth-doped transparent glass ceramics. *C R Chim* 5:845–854
26. Chen D, Xiang W, Liang X et al (2015) Advances in transparent glass–ceramic phosphors for white light-emitting diodes—a review. *J Eur Ceram Soc* 35:859–869
27. Auzel F, Pecile D, Morin D (1975) Rare earth doped vitroceraamics: new, efficient, blue and green emitting materials for infrared up-conversion. *J Electrochem Soc* 122(1):101–107
28. Dymshits O, Zhilin A, Alekseeva I, Skoptsov N, Malyarevich A, Yumashev K (2012) Synthesis and spectro-luminescence properties of lithium aluminosilicate glass–ceramics containing $\text{Er}_x\text{Yb}_{2-x}\text{Ti}_2\text{O}_7$ nanocrystals. *J Opt Mater Technol* 79:45–57
29. Loiko PA, Dymshits OS, Alekseeva IP, Zhilin AA, Tsenter MY, Vilejshnikova EV, Bogdanov KV, Mateos X, Yumashev KV (2016) Transparent glass–ceramics with $(\text{Eu}^{3+}, \text{Yb}^{3+})\text{:YbNbO}_4$ nanocrystals: crystallization, structure, optical spectroscopy and cooperative upconversion. *J Lumin* 179:64–73
30. Dymshits OS, Loiko PA, Skoptsov NA, Malyarevich AM, Yumashev KV, Zhilin AA, Alekseeva IP, Tsenter MY, Bogdanov K (2015) Structure and upconversion luminescence of transparent glass-ceramics containing $(\text{Er}, \text{Yb})_2(\text{Ti}, \text{Zr})_2\text{O}_7$ nanocrystals. *J Non-Cryst Solids* 409:54–62
31. Dymshits OS, Alekseeva IP, Zhilin AA, Tsenter MY, Loiko PA, Skoptsov NA, Malyarevich AM, Yumashev KV, Mateos X, Baranov AV (2015) Structural characteristics and spectral properties of novel transparent lithium aluminosilicate glass-ceramics containing $(\text{Er}, \text{Yb})\text{NbO}_4$ nanocrystals. *J Lumin* 160:337–345
32. Alekseeva I, Dymshits O, Tsenter M, Vasilevskaya A, Zapalova S, Zhilin A Volokitina A, Loiko P, Bogdanov K, Baranov A (2017) Glass-ceramics with $\text{Ho}^{3+}\text{:YbNbO}_4$ nano-crystals: nucleation, structure and special properties. In: *Conference proceedings on physics, chemistry and application of nanostructures*, Nanyang Technological University, pp 373–376
33. Fujita S, Yoshihara S, Sakamoto A, Yamamoto S, Tanabe S (2005) YAG glass–ceramic phosphor for white LED (I): background and development. *Proc SPIE* 5941:594111
34. Tanabe S, Fujita S, Yoshihara S, Sakamoto A, Yamamoto S (2005) YAG glass–ceramic phosphor for white LED (II): luminescence characteristics. *Proc SPIE* 5941:594112–594117
35. Chen LY, Cheng WC, Tsai CC, Huang YC, Lin YS, Cheng WH (2014) High performance glass phosphor for white-light-emitting diodes via reduction of Si-Ce^{3+} : YAG inter-diffusion. *Opt Mater Express* 4:121–128
36. Zhang R, Lin H, Yu YL, Chen DQ, Xu J, Wang YS (2014) A new-generation color converter for high-power white LED: transparent Ce^{3+} :YAG phosphor-in-glass. *Laser Photonics Rev* 8:158–164
37. Beall GH (1971) Structure, properties, and nucleation of glass – ceramics. In: Hench LL, Freiman SW (eds) *Advances in nucleation and crystallization in glasses*. Special publication no. 5. The American Ceramic Society, Columbus, pp 251–261
38. Beall GH (1983) Alkali metal, calcium fluorosilicate glass – ceramic article. US Patent 4,386,162
39. Chyung CK, Beall GH, Grossman DG (1971) Microstructures and mechanical properties of mica glass-ceramics. In: Thomas G (ed) *Electron microscopy and structure of materials*. University of California Press, Los Angeles, pp 1167–1194
40. Chyung CK, Beall GH, Grossman DG (1974) Fluorophlogopite mica glass-ceramics. In: *Tenth international congress on glass*, vol 14. The Ceramic Society of Japan, pp 33–40

41. Grossman DG (1972) Machinable glass-ceramics based on tetrasilicic mica. *J Am Ceram Soc* 55(9):446–449
42. Arshad SE, James PF, Lee WE (2002) ‘Microstructural characterization of commercial glass ceramics’, Proceedings of the XIX international congress on glass, Edinburgh, July 16, 2001. *Glass Technol* 43C:185–190
43. Arshad SE (2005) Comparing crystal evolution in model and commercial glass-ceramics systems. PhD thesis, University of Sheffield, Sheffield
44. Baik DS, No KS, Chun JS, Yoon YJ (1995) Mechanical properties of mica glass-ceramic. *J Am Ceram Soc* 78(5):1217–1222
45. Baik DS, No KS, Chun JS, Cho HY (1997) Effect of the aspect ratio of mica crystals and crystallinity on the micro-hardness and machinability of mica glass-ceramics. *J Mater Process Technol* 67:50–54
46. Mukherjee DP, Molla AR, Das SK (2016) The influence of MgF_2 content on the characteristic improvement of machinable glass ceramics. *J Non-Cryst Solids* 433:51–59
47. Lee WE, Arshad SE, James PF (2007) Importance of crystallization hierarchies in microstructural evolution of silicate glass-ceramics. *J Am Ceram Soc* 90(3):727–737
48. Cai H, Stevens Kalceff MA, Hooks B, Lawn BR (1994) Cyclic fatigue of a mica – containing glass – ceramic at Hertzian contacts. *J Mater Res* 9(10):762–769
49. Grossman DG (1977) Machining of machinable glass-ceramics. *Vacuum* 28(2):55–61
50. Weber H, Herberger J, Pilz R, Karl TH (1984) Turning of machinable glass-ceramics with an ultrasonically vibrated tool. *Ann CIRP* 33(1):85–87
51. Corning brochure. <https://www.corning.com/in/en/innovation/the-glass-age/glass-a-clear-solution/glass-ceramics.html>
52. pgo brochure. <https://www.pgo-online.com/intl/macor-machinable-glass-ceramic.html>
53. Beall GH (1992) Design and properties of glass-ceramics. *Annu Rev Mater Sci* 22:91–119
54. Vogel W, Holand W (1987) The development of bioglass ceramics for medical application. *Angew Chem Int Ed Engl* 26:527–544
55. Höland W, Vogel W, Mortier WJ, Duvigneaud PH, Naessens G, Plumet E (1983) A new type of phlogopite crystal in machinable glass ceramics. *Glass Technol* 24:318–322
56. Höland W, Naumann K, Vogel W, Gummel J (1983) Maschinell bearbeitbare bioaktive Glaskeramik. *Wiss Z Uni Jena Mat Nat Wiss Reihe* 32:571–580
57. Höche T, Habelitz S, Khodos II (1998) Origin of unusual fluorophlogopite morphology in mica glass-ceramics of the system SiO_2 - Al_2O_3 - MgO - K_2O - Na_2O - F_2 . *J Cryst Growth* 192:185–119
58. Zhang W-y, Gao H, Li B-y, Jiao Q-b (2006) A novel route for fabrication of machinable fluoramphibole glass-ceramics. *Scr Metall* 55:275–278
59. Wei W, Yong L, Yanni T et al (2017) A mica/nepheline glass-ceramics prepared by melting and powder metallurgy at low temperatures. *Mater Today Commun* 11:87–93



Processing of infrared Transparent Magnesium Aluminate Spinel: An Overview

13

Papiya Biswas, Roy Johnson, Yashwant Ramchandra Mahajan, and G. Padmanabham

Contents

Introduction	496
Spinel Crystallography	498
Spinel Phase Diagram	498
Spinel Powder Production	499
Spinel Powder for Transparent Ceramic Applications: Commercial Sources	502
Shaping and Densification of Spinel Parts	503
Methods to Develop Transparent Spinel Samples	509
Slip Casting of Spinel Powder	509
Densification of Spinel by Spark Plasma Sintering	514
Flash Sintering of Magnesium Aluminate Spinel Ceramics	518
Characterization of Transparent Specimens Processed through Different Routes	523
Conclusions	525
References	526

P. Biswas

Center for Ceramic Processing, International Advanced Research Centre for Powder Metallurgy and New Materials (ARCI), Hyderabad, Telangana, India
e-mail: papiya@arci.res.in

R. Johnson (✉) · Y. R. Mahajan

International Advanced Research Centre for Powder Metallurgy and New Materials, (ARCI), Balapur, Hyderabad, India
e-mail: royjohnson@arci.res.in; mahajanyrm@gmail.com

G. Padmanabham

International Advanced Research Centre for Powder Metallurgy and New Materials (ARCI), Hyderabad, India
e-mail: director@arci.res.in

Abstract

Transparent magnesium aluminate (MgAl_2O_4) spinel is a material of special interest due to its superb optical properties coupled with excellent mechanical properties. MgAl_2O_4 exhibit cubic crystal structure if processed under optimum conditions, effect of thickness on transparency can be minimized allowing fabrication of complex geometries for harsh environment. Further, broadband transparency from $0.4\ \mu\text{m}$ to $6.0\ \mu\text{m}$ is an added advantage in most of the applications. Transparent windows for armor and high Mach number missile domes are a few of the emerging applications in the strategic sector. Spinel is also used as the high-energy laser windows, as high-temperature furnace monitoring windows, and also as a part for nuclear fusion reactor power core insulations. In view of the significant scientific and technological importance, spinel is regarded as one of the futuristic transparent polycrystalline ceramics. Though spinel offers flexibility in processing through powder metallurgy route, the mechanical and optical properties are a strong function of starting powder properties and also dictated by the processing route and parameters. This chapter presents an overview on transparent spinel processing along with the comparative evaluation of various processing techniques.

Keywords

Transparent ceramics · Magnesium aluminate spinel · Slip casting · Spark plasma sintering · Flash sintering

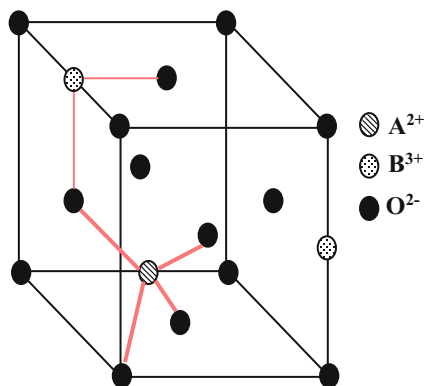
Introduction

Magnesium aluminate (MgAl_2O_4) spinel is an emerging material not only due to its excellent optical properties coupled with superior mechanical properties [1, 2] but also relatively low production cost. The major attributes that outperform the other transparent ceramics are broadband transparency from $0.4\ \mu\text{m}$ to $6.0\ \mu\text{m}$ and the flexibility in processing through powder metallurgy route. Further, having a cubic crystalline structure, no thickness limitation exists for engineering various complex geometries for harsh environment. Major applications include transparent armored window, high-energy laser windows, high Mach number missile domes, and high-temperature furnace monitoring windows [3–7]. It is also proposed for biomedical applications like visible orthodontic bracket [8]. Further, spinel is gaining interest as a potential material in the nuclear fusion reactor power core insulation due to its good resistance in radiation-induced swelling and strength degradation during irradiation [9]. It is well known that the spinel is an attractive refractory replacement for chrome-based refractories containing hexavalent chrome, in cement rotary kilns and steel ladles, which create both environmental and health hazards [10]. Spinel is also explored as an environmental barrier coating material for the blades and vanes in the hot section components for gas turbines [11]. The typical properties of polycrystalline spinel ceramics are shown in Table 1 [12–17].

Table 1 Typical properties of polycrystalline spinel ceramics [12–17]

Physicochemical properties		Crystal structure		Melting point			
Chemistry	Density	Crystal structure		Melting point			
MgAl ₂ O ₄	3.58 g/cc	Cubic		2105 °C			
Mechanical properties							
Elastic modulus	Poisson's ratio	Bulk modulus	Shear modulus	Flexural strength	Compressive strength	Toughness (K_{1c})	Vickers hardness
277 GPa	0.26	192 GPa	110 GPa	250 MPa	2.69 GPa	1.9 MPa. m ^{1/2}	1300–1350 kg/mm ²
Thermal properties							
Specific heat	Coefficient of thermal expansion						
0.28 cal/g.K (at 25 °C)	0.79 × 10 ⁻⁶ / K (at 25–1000 °C)						
Optical properties							
Dielectric constant	Dielectric loss	Range of transmission		Refractive index at 3 μm	Theoretical transmission at 3 μm		
8.2	0.00025	0.2–6 μm		1.66	87%		

Fig. 1 Magnesium aluminate spinel (MgAl_2O_4): unit cell structure



Spinel Crystallography

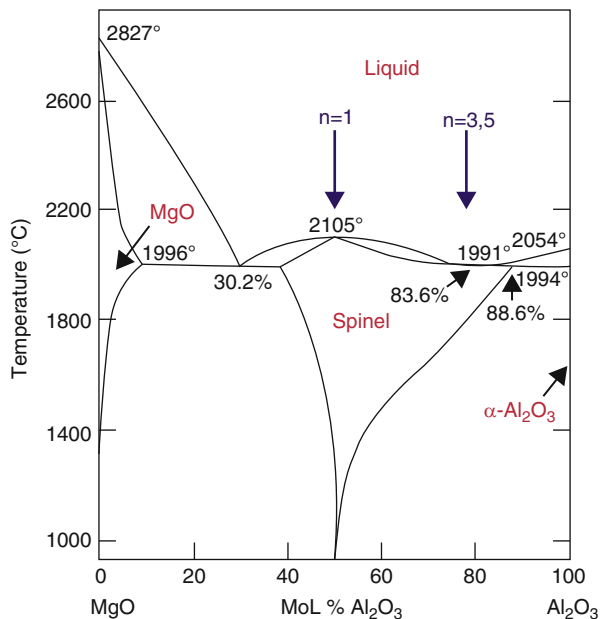
The spinel structure is named after the mineral spinel (MgAl_2O_4), and the general formula is AB_2O_4 , where A and B are divalent and trivalent cations, respectively [18]. Spinel structure is two types – normal and inverse. In normal spinel, a unit cell contains 8 FCC oxygen sublattices in a cubic array with 32 oxygen ions, 16 octahedral cations, and 8 tetrahedral cations. Oxygen anions form the ABCABC-packed face-centered cubic sublattice, where A^{2+} and B^{3+} cations occupy tetrahedral and octahedral void in the FCC crystal lattice, respectively. Fifty percent of the octahedral sites and 12.5% of tetrahedral sites are filled in spinel crystal structure. A few examples of normal spinel are MgAl_2O_4 , ZnAl_2O_4 , and MnAl_2O_4 . In inverse spinel, octahedral sites are occupied by A^{2+} and half of B^{3+} cations, and remaining B^{3+} cations fill tetrahedral sites. A few examples of inverse spinel are Fe_3O_4 , NiFe_2O_4 , and CoFe_2O_4 . Schematic of magnesium aluminate spinel unit cell structure is shown in Fig. 1.

Spinel Phase Diagram

The phase diagram of $\text{MgO}-\text{Al}_2\text{O}_3$ is shown as Fig. 2 [19]. According to the phase diagram, 71.8% Al_2O_3 and 28.2% MgO by weight form the stoichiometry and melt congruently at 2105 °C [20, 21]. The presence of precursor oxide other than the spinel stoichiometry can result in reducing the melting point of the composition.

Spinel can be classified in two groups such as magnesia-rich spinel which contains excess MgO and alumina-rich spinel which contain excess Al_2O_3 which form either side of the stoichiometry corresponding to the ratio of 71.8% Al_2O_3 and 28.2% MgO (Fig. 2) [22]. Due to the spinel phase region, at high temperatures up to 1900 °C, a spinel phase containing 90% Al_2O_3 can be produced and maintained by rapid cooling. At lower temperatures, e.g., 1600 °C during steel production, this high alumina content in alumina-rich spinel becomes unstable, and a mixture of spinel and free corundum (Al_2O_3) is formed. Alumina-rich spinel phase remains stable at temperatures around 1600 °C. Towards MgO end, the solid solution formation of the spinel phase is much less, so that magnesia-rich spinel on purpose contains traces of periclase (MgO).

Fig. 2 MgO-Al₂O₃ phase diagram [19]



Spinel Powder Production

In order to produce fully dense transparent spinel, the powder properties become very crucial especially chemical purity. Commercial production of spinel powder is currently carried out in large quantities through solid-state reaction of alumina and magnesia at elevated temperature depending on the initial particle size of the starting precursor oxides. In case of micron-sized precursor oxide powders, spinel is obtained generally at high temperature exhibiting a very wide distribution of particle size which necessitates milling operation before further processing. Additionally, over the recent years, various wet chemical powder synthesis techniques such as combustion synthesis [23], hydroxide coprecipitation [24, 25], flame spray pyrolysis [26], sol-gel synthesis of metal alkoxides or inorganic salts [27–29], freeze-drying [30] and modified Pechini process [31] have been developed and successfully used for the production of pure spinel powders. Since the powder produced through the wet chemical process offers inherent high degree of chemical homogeneity at the atomic level, these processes result in better control of stoichiometry in comparison to the solid-state method. However, these wet chemical processes require challenging engineering solutions and close monitoring of the parameters in order to avoid the agglomeration which affects the further processing of the powder to a larger extent.

Magnesium aluminate spinel powder for transparent ceramic application was synthesized through flame spray pyrolysis by Goldstein et al. [32] and evaluated the suitability of the process and powder properties to achieve the desired transparency values. The powder with surface area of 50 m²/g and average particle size of <100 nm was synthesized as studied by TEM micrographs. The powder was

subjected to shaping by cold isostatic pressing (CIP) followed by pressureless sintering and hot isostatic pressing (HIP) approach to fabricate transparent ceramic parts. The powder exhibited excellent sinterability with a density of 99.9% of TD while sintering; however, HIPing was essential to achieve the transparency. HIPing conditions applied were 1700 °C, 200 MPa pressure, and 3 h of soaking.

In another study, Suarez et al. [33] have synthesized spinel powder by reverse chemical coprecipitation route using a series of precursors such as $\text{Mg}(\text{NO}_3)_2 \cdot 9\text{H}_2\text{O}$, $\text{Al}(\text{NO}_3)_3 \cdot 6\text{H}_2\text{O}$, and $\text{MgCl}_2 \cdot 6\text{H}_2\text{O}$, $\text{AlCl}_3 \cdot 6\text{H}_2\text{O}$, respectively. The powder synthesized by this route resulted in the single-phase crystalline powder at temperature as low as 800 °C with submicron particle size. This powder on spark plasma sintering has resulted in 83% transmission at MWIR (3–5 μm) range. This study revealed that a careful control of synthesis and processing and sintering conditions will result in close to theoretical transmission.

Balabanov et al. [34] prepared sol-gel-derived magnesium aluminate nanopowder and evaluated for suitability for transparent spinel. In this study metallic Mg and Al of greater than 99% purity and isopropyl alcohol were used as starting materials. Mg and Al metals were subjected to melting at 600 °C in argon in the ratio of 32:68% by weight, respectively. The powder thus obtained was also subjected to doping by LiF. Average particle size of as synthesized spinel powder in undoped condition was 30 nm which was increased to 700–1000 nm upon doping. The doped spinel with LiF has exhibited an in-line optical transmission of 83.7% in the visible region on 1 mm thick sample.

In a study carried out by Reimanis et al. [35], an attempt was made to synthesize spinel powder to fabricate transparent spinel parts in three-step, single-pot process. Synthesis starts with hydrolysis of aluminum sec-butoxide ($\text{Al}(\text{CH}_2\text{CH}(\text{O})\text{CH}_2\text{CH}_3)_3$) to produce boehmite sol and ultrahigh purity $\text{Mg}(\text{acac})_2$. Stoichiometric reaction mixture was stirred and spray-dried to obtain the white powder with high surface area of 200 m^2/g . This spray-dried powder was calcined and subjected to hot press experiments at 1550 °C for 2 h with a pre-load of 3.5 MPa prior to heating. The study revealed that microstructure and transparency are a strong function of the purity level of spinel powder. It was suggested that impurity in the ppm range alters the relative grain boundary to surface energy resulting in the modification of pore evolution and removal mechanism. The study could demonstrate a transmission of >80% in the visible range with ultrahigh pure starting precursor compared to a maximum of 40% transmission with relatively impure starting precursors.

Cook et al. [36] have demonstrated the synthesis of magnesium aluminate spinel powder reaction between organo-Mg compounds and boehmite powder with surface modification. It was reported that this powder production technique permits close control on particle size and its distribution as well as the purity and stoichiometry. This can be attributed to the mechanism involved in the formation of boehmite gel as a result of hydrolysis of aluminum alkoxide followed by surface modification of boehmite particles using carboxylic acid. The surface-modified boehmite nanoparticles can be metal exchanged with magnesium acetylacetonate at room temperature which forms the precursor and transform into magnesium aluminate spinel powder on calcination. Hot pressing of this powder resulted in transparent spinel; however, exhibited black spots originated from the presence of impurity.

Sutorik et al. [37] have attempted the production of magnesium aluminate spinel powder for transparent ceramic applications using the reaction between $\text{Mg}(\text{OH})_2$ with 99.99% purity, γ -alumina, and AlOOH . Investigations reported the transmission of $84 \pm 1\%$ at 550 nm for the mix based on 99.99% pure $\text{Mg}(\text{OH})_2$ and γ -alumina. However, the other mixes have exhibited lesser transmission values indicating the sample inconsistency. However, mechanical properties of all mixes found to be identical indicating that presence of impurity is critical.

Nam et al. [38] synthesized magnesium aluminate spinel powder with controlled morphology through coprecipitation technique employing carbonate precipitation. The morphology of the powder was controlled into rod, cone, and spherical shapes by varying the concentration of aluminum ions and growth rate. Investigation has shown the powder with spherical morphology resulted in the lower calcination temperature in comparison to other synthesized morphologies which can be attributed to the higher packing densities. The powders were subjected to SPS sintering which has exhibited to 200 nm grain sizes in combination with total forward transmission (TFT) value of 63.75% at 550 nm.

Ewais et al. [39] studied the optical properties of magnesium aluminate spinel synthesized from industrial waste. The author has employed a coprecipitation method using industrial waste of magnesium and aluminum. The optical properties of spinel powder revealed a strong dependence of reflectance on calcination temperature. However, transmission values were not reported in this study.

Magnesium aluminate spinel powder with varying chemical compositions ($\text{MgO} \cdot n\text{Al}_2\text{O}_3$, where $n = 1.0, 1.5, \text{ and } 2.0$) was synthesized by Dericioglu et al. [40] using commercially available MgO and Al_2O_3 powder mix following standard conventional solid-state processing routes. The study indicated relatively poor optical transparency for the spinel ceramics with $n = 1.0$ due to the significant light scattering; however, Al-rich composition has exhibited higher degree of transparency. Further, a fracture toughness of $2.02 \text{ MPa}\cdot\text{m}^{1/2}$ was also exhibited for the spinel with $n = 2.0$.

Waetzig et al. [41] also studied the effect of chemical composition on the optical properties and hardness. The study investigated the transmission and hardness of Al-rich spinel ceramics for the composition ranging from $\text{MgO} \cdot n\text{Al}_2\text{O}_3$ where $1 \leq n \leq 2.5$. The powder was prepared by reaction sintering in air followed by HIPing. Single-phase spinel could be obtained for the compositions $n \leq 1.5$ with excess alumina which gets dissolved in the composition. However, beyond $n > 1.5$ resulted in the biphasic compositions with residual alumina. It was reported that the excess alumina in the residual form during the sintering stage could be incorporated in the spinel lattice as a result of HIPing leading to high in-line transmission close to theoretical. It was also observed that $\text{MgO} \cdot n\text{Al}_2\text{O}_3$ sample with $n < 2.5$ resulted in the larger grains exhibiting the hardness of 13 GPa and no improvement could be observed in the hardness values on increasing the alumina content beyond $n = 2.5$.

Shahbazi et al. [42] explored the synthesis of magnesium aluminate spinel from the elementary oxides of magnesium and aluminum by solid-state reaction. The study used precursor oxides with average particle size of 90 nm and purity of 99.99%. The formulation was prepared according to the stoichiometric ratio with

addition of sintering aid of 0.8 wt% LiF. The formulation was calcined at 1300 °C to ensure the spinel formation. The study has also concentrated on the extensive characterization of the spinel powder. It was proposed that LiF melts at 850 °C and remains as a liquid phase and stays between alumina and magnesia particles and reduces activation energy and promotes diffusion process resulting in spinel formation at lower temperature. Thus produced powder could be gel casted and sintered to achieve >99.5% density at relatively lower temperature.

The effect of LiF doping in magnesium aluminate spinel stoichiometry as a sintering aid has been studied by Sutorik et al. [43]. This leads to transparency in the alumina-rich spinel with composition $\text{MgO} \cdot 1.5\text{Al}_2\text{O}_3$. Commercially available high purity $\text{Mg}(\text{OH})_2$ and γ -alumina were thoroughly mixed into a homogeneous aqueous slurry which was dried and calcined to eliminate all the organic impurities. The composition was doped with LiF in the range of 0.2 to 0.75 wt% by using an aqueous mixture to ensure a homogeneous distribution of LiF within the powder mass. Hot pressing of these compositions was carried out under the vacuum at 1600 °C and 220 MPa pressure for 5 h. The authors investigated the effect of LiF doping on lattice parameters, density, and transmission. Doping of LiF has exhibited sintered density of 3.584, 3.587, and 3.580 g/cc and transmission of $83.3 \pm 0.9\%$, $60 \pm 4.7\%$, and $29.3 \pm 2.0\%$ at 550 nm for 0.25, 0.5, and 0.75 wt% LiF, respectively. The study clearly revealed the effect of doping with LiF play a significant role in achieving the transparency to the desired level.

Meir et al. [44] also carried out similar studies to determine the effect of LiF doping on transmission, and 1 wt% LiF was added into the mixture of MgO and Al_2O_3 . The study reported the addition of LiF promotes the formation of spinel that starts with 900 °C which almost resulted in the completion at 1100 °C. The study reported LiF addition wets the spinel on its melting which enhances the densification and also aids the removal of residual carbon. The fully dense spinel exhibited to achieve close to theoretical transmission value after HIPing.

Spinel Powder for Transparent Ceramic Applications: Commercial Sources

Several techniques have been developed for synthesizing ceramic powders [45–50] with improved physico-chemical properties; however, it is still a challenge to produce powder with properties that are increasingly in demand for high-performance ceramics. Unlike opaque high-performance ceramics, for transparent ceramics, the powder properties become very critical to achieve a combination of desired mechanical and optical characteristics [51, 52]. Powder synthesis methods should allow stringent control of composition, particle size, and its distribution and surface area. Traces of secondary phases, inhomogeneity originating from hard agglomerates while processing, can bring down the transparency to a significant level. Reimanis et al. [35] reported the effect of impurities on the optical transmission of spinel ceramics as discussed in the earlier chapter. The presence of impurity ions >500 ppm leads to poor optical quality because of higher haze and foggy appearance and, hence, light

scattering. Because of the inherent chemistry, processing, and stoichiometry-related issues associated with magnesium aluminate (MgAl_2O_4) spinel, there are only a few global suppliers for the commercial high purity grade powder. The major suppliers along with techno-commercial ranking are listed in Table 2 (Krell et al. [51]).

It is evident from Table 2 that spinel powder of grade S30CR from M/s. Baikowski, France, has obvious advantages on the commercial aspects, and also the powder properties are almost at par with other suppliers. In addition to the procurement of commercial powder, in-house synthesis of powder has also been attempted targeting the benchmark specifications of commercially available powder (S30CR) procured from M/s. Baikowski, France.

Shaping and Densification of Spinel Parts

Ceramic materials are generally shaped through various processes which are mainly classified into two categories, namely, wet processing and dry processing. Slip casting, gel casting, injection molding, and extrusion are some of the forming processes based on the viscous plastic processing; however, uniaxial pressing and cold isostatic pressing are the dry processes followed. The green ceramic parts formed through these processes are exposed to sintering temperature which results in the densification and fabrication of final components with desired properties. In recent times the advanced single-step processings such as spark plasma sintering, flash sintering, and hot pressing are gaining interest; however, there are limitations with respect to shape, size, etc. Hot isostatic pressing is generally employed as post sintering pressure-assisted process with simultaneous application of temperature and pressure to achieve or enhance the transparency. An overview of the processes which are relevant to magnesium aluminate spinel processing is given below.

Shaping through wet chemical processing is adaptable especially for transparent ceramics as it permits high level of homogeneity. However, because of the basic nature of the spinel powder particle surface, surface modification is essential and part of the study during aqueous slip or gel casting process. Only a few studies are reported on slip cast shaping method for magnesium aluminate spinel powder.

Olhero et al. [53] developed a process for surface passivation of spinel powder. In this process, magnesium aluminate spinel powder synthesized by the author was added to the ethanol to achieve suspension of 30 vol%, and the formulation was transferred to a round bottom flask and refluxed. A solution of aluminum dihydrogen phosphate [$\text{Al}(\text{H}_2\text{PO}_4)_3$] digested with orthophosphoric acid was mixed with 50 ml of ethanol and added to the spinel suspension. The refluxing was continued at 80 °C for 24 h under nitrogen flow of 100 ml/min while stirring the formulation continuously. The refluxed mass was filtered and washed to obtain surface-modified spinel powder. In another study, Ganesh et al. [54] modified the spinel powder surface under identical process discussed above and subjected the slurry to conventional slip casting process. The study reported a green density of 45% of theoretical density (TD) which is enhanced to 95% of TD upon sintering. Shafeiey et al. [55] attempted the fabrication of magnesium aluminate spinel ceramics through slip casting route.

Table 2 Commercially available spinel powder: Techno-commercial ranking as reported by Krell et al. [51]

Manufacturer and grade	Synthesis technique	Purity	BET surface area	Equivalent ^a particle size (from BET)	Cost ^b relative to α -alumina with 150 nm particle size and purity 99.995%
Nanocerox (USA)	Flame spray pyrolysis	~99.995% (Fe: ~20 ppm)	29–34 m ² /g	~53 nm	~3000%
Baikowski Chimie (France), S30CR	Thermal decomposition of alum salts	~99.995% (Fe: ~10 ppm)	28–31 m ² /g	~57 nm	~150%
Taimei Chemicals (Japan), TSP-20	Thermal decomposition of ammonium carbonates	~99.995% (Fe: ~1–6 ppm)	13–15 m ² /g	~120 nm	~300%

^aEquivalent spherical particle size D_{BET} calculated from specific surface area S by $D_{\text{BET}} = 6/(S \cdot \rho)$ assuming a density, $\rho = 3.58 \text{ g/cm}^3$

^bCosts for laboratory batches (5–20 kg)

The slurry was prepared with the particle size of 90 to 500 nm using ammonium polyacrylate – Dolapix – as dispersant. The formulation was milled for several hours and finally achieved a solid loading of 65 wt%. Slip casting of this slurry has resulted in the cast sample with green density of 67% TD. However, sintered density was not reported. Effect of the mold chemistry was studied by Kim et al. [56]. The slurry was prepared by conventional method and was cast in the porous alumina and gypsum molds. Casting in gypsum mold resulted in infiltration of Ca (~500 ppm) in green compact which has significant effect on microstructure evolution. Krell et al. [57] attempted the slip casting of magnesium aluminate spinel powder in aqueous medium and cast into shapes. The sample was further sintered and HIPed at 1360 °C to achieve hardness of 14.6 GPa and 85% real in-line transmission.

In addition to slip casting, researchers also investigated gel casting due to its inherent high green strength property which permits green machining. The process of polymerization of monomer which in turn forms the organic skeletons provides the matrix for the particle consolidation. Zhang et al. [58] have studied aqueous gel casting process for fabricating transparent spinel sample. In this study, commercially available spinel powder was used as starting material. A water-soluble copolymer consisting of isobutylene and maleic anhydride (PIBM) was used as both dispersant and gelling agent. Green density of gel cast sample was 63.5%. The organics were burn out at 800 °C for 2 h followed by vacuum sintering at 1650 °C for 6 h, and HIPing at 1650 °C and 200 MPa for 4 h. Thus obtained sample exhibited 85.3% of in-line transmittance at 1100 nm wavelength. Shahbazi et al. [42] also investigated gel casting for the fabrication of magnesium aluminate spinel sample and reported a green density of 62% of TD and green strength of 11.6 MPa for gel cast sample.

Room temperature uniaxial and isostatic compaction and high-temperature uniaxial and isostatic compaction are the processes widely practiced individually or in combination for the fabrication of transparent magnesium aluminate spinel ceramics for various applications. In case of uniaxial and isostatic compaction, the parts are pressureless sintered to achieve 96% of TD to ensure closure of open pores before undertaking isostatic compaction at hot condition.

Tokariev et al. [59] employed uniaxial pressing for nano-sized magnesium aluminate spinel powder after spray granulation using polyvinyl alcohol as a binder. The granules were pressed into a square of 100 × 100 mm, which were subjected to debinding at 700 °C and sintering at 1550 °C followed by HIPing at 1650 °C and 200 MPa for 2 h. Thus produced spinel sample has exhibited transmission of 82% at 350–850 nm. The authors [60] have also compared the mechanical properties of spinel samples fabricated with different particle size powders and hot pressing parameters. It was reported that Young's modulus of 270 GPa, hardness of 13–17 GPa, fracture toughness of 1.8 MPa.m^{1/2}, and ring-on-ring fracture strength of 169 MPa for spinel sample was fabricated with 70 nm powder. A study by Krell et al. [61], on the particle size and surface area of spinel powder produced by flame spray pyrolysis, has reported a maximum transmission of 83% in the range of 300–800 nm. Spinel powder was cold isostatically pressed (CIP) at 350 MPa followed by sintering at 1600 °C and HIPed at 1750 °C. Gajdowski et al. [62]

uniaxially compacted the spinel powder of 490 nm particle size followed by CIP at 300 MPa. Green samples were vacuum sintered at 1500 °C for 2 h and HIPed under argon atmosphere at 190 MPa and 1800 °C, which has reported to have close to theoretical transmission at 850 nm wavelength.

Cold isostatic pressing (CIP) is essentially carried out to improve the density of uniaxially pressed sample or directly the powder packed in polymer bag. Tsukuma et al. [63] CIPed B₂O₃ incorporated magnesium aluminate spinel powder at 200 MPa. Further, the green samples were vacuum sintered at 1450 °C and HIPed at 1300 °C to achieve transmission of 80% at 550 nm. Shimada et al. [64] attempted the fabrication of transparent magnesium aluminate spinel by reactive sintering of alumina and magnesia or spinel and alumina to form the solid solution. Powder was CIPed at 400 MPa followed by sintering at 1550 °C and further HIPed at 1800 °C which resulted in high transmission property at 1–5 μm wavelength, fracture strength of 250 MPa, and fracture toughness of 2.8 MPa.m^{1/2}. Bratton et al. [65] in their paper have studied the effect of CaO doping on magnesium aluminate spinel densification through the formation of liquid. Sintered sample has achieved a density of 99% TD with poor transmission of 67–78% in the visible region depending on the CaO doping. Krell et al. [66] studied single crystal and polycrystalline spinel for the mechanical properties, especially the hardness. A maximum hardness of 14 GPa is achieved for the polycrystalline spinel with grain size <1 μm.

The major manufacturer of transparent magnesium aluminate spinel generally follows the process of hot pressing (HP) of powder followed by HIP. Esposito et al. [67] reported production of highly transparent cost-effective magnesium aluminate spinel for optical applications. Stoichiometric MgO-Al₂O₃ powder mixes along with ultrapure LiF as a sintering additive is employed in this study. The author undertook thermodynamic studies to understand the mechanism affecting the optical properties especially in carbonaceous environment. A transparency of 70–78% in the visible range has been obtained for HP spinel sample. The study revealed the production of transparent spinel under the moderate pressure of 40 MPa and 1600 °C and interactions between carbonaceous material and molten LiF, and the formation of LiAlO₂ is also evaluated. The study confirmed that high pressure up to 200 MPa under isostatic condition is essential to achieve the transparency.

Villalobos et al. [68] have studied the effect of LiF as sintering aid on degradation of magnesium aluminum spinel while hot pressing. It is reported that spinel particles to be etched by LiF while hot pressing in current study resulted in Mg-rich regions leading to opaque pocket in the transparent matrix. LiF is reported to be necessary to densify spinel to achieve transparency. It is proposed that, adequate time shall be provided to homogeneously distribute the sintering aids without allowing to react with aluminium in spinel matrix in order to avoid the formation of opaque spots.

Gilde et al. [69] have evaluated parameters related to HP and HIP to achieve optical transparency in spinel. The study correlated the size of scattering points with wavelength of light. It was observed that higher HIPing temperature and pressure resulted in decreasing of the optical extinction values. The results indicated that HIP at 1550 °C exhibited better transparency in mid-infrared (IR) region; however, visible transparency required HIPing at high temperature. Li et al. [1] have evaluated

transparent spinel fabrication through combined vacuum sintering, hot pressing, and sintering in H_2 atmosphere and HIPing. Out of the various methods tried for forming transparent spinel, optical property of sample sintered at $1500\text{ }^\circ\text{C}$ followed by HIPing at $1800\text{ }^\circ\text{C}$ was found to be close to the single crystal.

Esposito et al. [70] have evaluated the effect of precursor oxides of magnesia and alumina with different particle sizes, and results were compared with magnesium aluminate spinel powder. Hot pressing parameters were varied with respect to heating rate, keeping the peak temperature constant. The study revealed HP as viable technique for the production of spinel component with transmission of 70% in visible range and 80% in near IR range. Prominent densification occurred by the reactive sintering of stoichiometric mixture of magnesia and alumina with 1% LiF as sintering aid. The starting powder purity and initial particle size have found to have a significant effect on microstructure, however, not on final transmittance. It was also suggested that formation of MgF_2 liquid phase among the reaction constituent during intermittent soaking at $1220\text{ }^\circ\text{C}$ is also critical in achieving the transparency. A transmission of $>70\%$ was achieved in the visible range.

Goldstein et al. [71] have evaluated the effect of LiF and its concentration in the fabrication of magnesium aluminate spinel during HP. The current study has varied LiF concentrations from 0.5 to 1 wt%. A unique mechanism of closure of pore below $1350\text{ }^\circ\text{C}$ with LiF is suggested to avoid inclusion of carbon which in turn enhances the transparency of HP samples. It was observed that the transparent spinel could be achieved at temperature of $1650\text{ }^\circ\text{C}$ and less than 50 MPa pressure with a transmission value of 84% for optimized LiF concentration.

Spark plasma sintering (SPS) is an emerging technique and gaining importance because of its inherent capability to sinter the material with less time and lower peak temperature in combination with retaining fine grain size.

Morita et al. [72] have studied the sintering of magnesium aluminate spinel using SPS with spinel powder filled in a graphite die and covered with graphite foil to prevent the contact between graphite die and powder. The study revealed that the final product is affected by carbon contamination mainly from two sources, namely, CO_3 residue as a part of the powder synthesis and also from graphite die and foil. Pre-calcination of spinel powder for decomposition of CO_3 to CO_2 can limit the carbon source for contamination. However, carbon resulting from graphite die could not eliminate totally through several heating rate experiments. This resulted in discoloration of the sintered spinel limiting transmission value. Current study reported a transmission of $>70\%$ at $2\text{ }\mu\text{m}$ wavelength for SPS sample.

Bernard-Granger et al. [73] have studied the influence of carbon contamination on optical property of SPS magnesium aluminate spinel. The study revealed that carbon contamination is the major issue with SPS processing mainly resulting from graphite die and other parts. The SPS samples exhibited dark brown color due to the finely dispersed carbon particles in the spinel matrix. TEM study carried out by author indicated that foreign particles composed of carbon correspond to graphite. Such graphite particles have large influence on optical property due to interaction with incoming radiation with foreign particles. The study also proposed that carbon contamination arises from CO_2 containing residual atmosphere during SPS

processing. Diffusion of CO_2 in pre-sintering stage which in turn transform to CO/C during pore closure or pore pinching in the final stage of sintering may precipitate as the foreign particles in the matrix. The paper reported a maximum transmission of 68% at 2 μm wavelength against 84%, the theoretical value.

Morita et al. [74] in another study have investigated the discoloration-related issue of SPS-densified magnesium aluminate spinel powder and effect of pre- and post annealing on optical property. In this study pre-annealed powder and also as-received powder without annealing were employed in SPS processing. It was observed that due to inherent CO_3 present in the powder, densified sample fabricated out of as-received powder has led to discoloration which necessitates post SPS annealing and loss of transparency. The SPS sample fabricated with as-received powder has exhibited a maximum transmission of ~42% at 0.55 μm and 75% at 2 μm wavelength after post annealing at 1100 °C. SPS sample densified with pre-annealed powder has shown less discoloration in comparison to as-received powder sample. The sample exhibited a better transparency in comparison to sample fabricated with as-received powder as mentioned above, which is ~58% at 0.55 μm and 82% at 2 μm wavelength after post annealing at 1100 °C.

Morita et al. [2] have also studied the effect of heating rate on the transmission of SPS-densified magnesium aluminate spinel sample. It was observed that heating rate plays a very significant role since a higher heating rate beyond 10 °C/min results in exaggerated grain growth and entrapment of pores within microstructure. The study was carried out at a heating rate of 2, 5, 10, 50, and 100 °C/min. It was reported that heating rate of 100 °C/min resulted in opaque sample. Heating rate more than 10 °C/min has resulted in low transparency. However, maximum transmission is exhibited by the sample processed with heating rate lower than 10 °C/min. The authors in another study [75] have investigated the effect of SPS temperature on the optical property of transparent magnesium aluminate spinel. It was reported that SPS temperature >1300 °C exhibited rapid grain growth which resulted in coalescence of residual pores and precipitation of second phase. These act as scattering points and degrade the transmission of spinel.

Morita et al. [76] studied the effect of loading with respect to the temperature of SPS processing and its effect on the transparency of magnesium aluminate spinel. Load was applied systematically at 25, 1000, 1100, 1200, 1250, and 1300 °C keeping the peak temperature and load constant. It was observed that transmission value has increased with increase in the temperature at which load applied. A maximum transmission of ~74% at 2 μm wavelength was reported for loading temperature of 1300 °C.

Kim et al. [77] investigated the preheating of magnesium aluminate spinel powder in context of carbon contamination suggesting that the graphite die and foil are responsible for contamination in SPS process. It was also pointed out that external source significantly contributes in discoloration and brings down the transmission though preheating has improved the transmission. Sokol et al. [78] have studied the effect of pressure on SPS processing of magnesium aluminate spinel. Study has used commercially available spinel powder, and SPS was carried out at

1200 °C with varying pressures of 150–400 MPa. The study reported an increase in grain size from 108 to 171 nm for applied pressure of 150–400 MPa. The maximum transparency was observed for SPS sample sintered at 300–400 MPa pressure.

Bonnefont et al. [79] have studied the effect of powder properties on optical property of SPS-processed magnesium aluminate spinel. The author has synthesized three different spinel powders denoted as S30CR, S30XCR, and SA30XCR with surface areas of 31, 21, and 28 m²/g and particle size (d_{50}) of 1.12, 0.32, and 1.92 μm, respectively. All powders were subjected to SPS densification under identical conditions. Rather than powder particle size and surface area, formation of agglomerates is detrimental. It can be attributed to poor densification resulting in formation of pores which are scattering points. Out of three powders, S30CR powder has higher surface area of 31 m²/g and is more effective in transmission property which is very near to theoretical value. This study clearly indicates the role of powder properties on achieving final transparency in spinel.

Methods to Develop Transparent Spinel Samples

Slip Casting of Spinel Powder

Preparation of Spinel Slurry with Higher Solid Loading

For fabrication of transparent sample, it is essential to achieve sintered density >96% of TD prior to HIP. Sintered density depends on green density which is controlled by maximum solid loading of slurry. Therefore, to increase the initial green density, an attempt has been made to increase solid loading of slurry. Hydrolysis of spinel powder due to the surface charges resulting from the association of surface AlOH and MgOH groups has been well known. This basic nature of spinel affects significantly the stability and solid loading of the slurry. In the chemical process, surface treatment of powder using an ethanol solution of H₃PO₄ and Al (H₂PO₄)₃ [53] is well known; however, the process being cumbersome, a simple calcination process is employed to prevent the hydrolysis. Though compaction can achieve higher green density, it cannot provide homogeneity throughout the sample which is a prime requisite for fabrication of transparent sample, and also complex shape cannot be made by uniaxial compaction. Surface passivation, i.e., a minimum temperature of 1360 °C, is essential to achieve a solid loading of >65 wt% leading to >50% of the TD. Surface passivation temperature below 1360 °C has only negligible effect up to 1160 °C. Further increase beyond 1360 °C has been found to be negligible on green density; hence, surface passivation is carried out at a temperature of 1360 °C. In order to evaluate the slurry stability prepared through with and without surface passivated powders, two independent techniques were used. Rheological behavior of slurry with respect to time and quasi-elastic neutron scattering (QENS) measurements at identical interval of time were carried out, which in turn provide information on the hydrolysis of spinel due to its basic nature. Plots showing the viscosity and elastic friction with respect to time are shown in Fig. 3a, b.

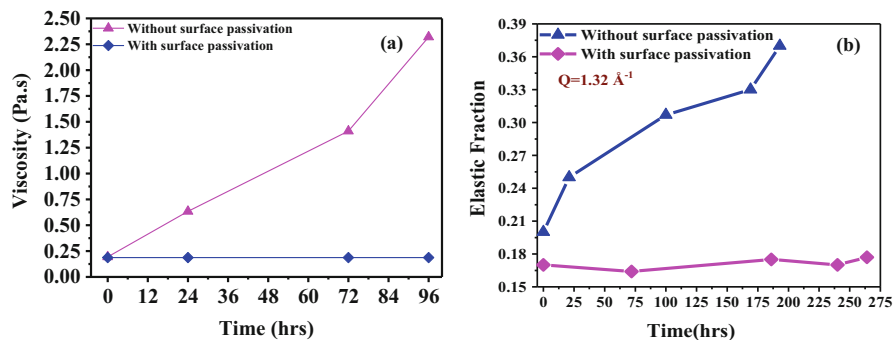
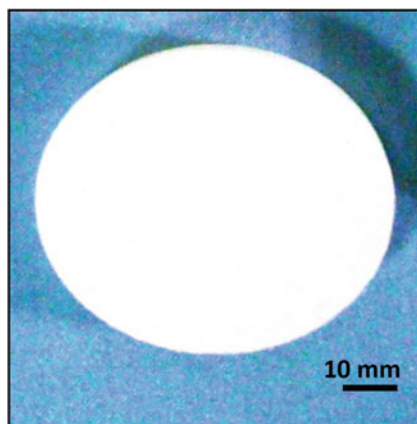


Fig. 3 Plot of (a) viscosity with respect to time and (b) elastic fraction with respect to time of spinel slurries [80]

Fig. 4 Cast and dried spinel disc



A significant increase in slurry stability with surface passivated powder due to absence of hydrolysis is clearly seen from this figure.

Slurry with high solid loading is slip cast into a cylindrical shape and subjected to drying in humidity oven to avoid drying cracks; the green density of the sample was found to be 1.89 g/cm^3 (52% of TD). A typical slip-casted sample is shown in Fig. 4.

Densification of Slip Cast Spinel Samples

Sintering Kinetics Studies

Activation energy of sintering and sintering mechanism are very important criteria to predict the kinetics of material transport and microstructural evolution. In order to evaluate the activation energy of sintering, spinel pellets were made by slip casting with 10 mm diameter and 5 mm thickness dimensions and were subjected to dilatometric measurements. Sintering was carried out by using a single pushrod dilatometer (Model No. 402C, Netzsch, Germany), and data was recorded from

room temperature to 1650 °C at a heating rate of 5, 10, and 20 °C/min. The plot of dilatometric shrinkage with respect to temperature and time of slip cast samples has been shown in Fig. 5 for the constant heating rates of 5, 10, and 20 °C/min. All samples exhibited almost a similar shrinkage pattern with an onset of shrinkage at temperatures around 1100 °C and extending to 1650 °C with the highest shrinkage observed for the heating rate of 5 °C/min as is evident from the close to plateau behavior.

The entire dilatometer data for three different heating rates have been plotted as shown in Fig. 6a. The absolute value of shrinkage in percentage was taken as ordinate with respect to temperature. It is evident from the figure that there was no shrinkage up to 1100 °C, and above this temperature the significant shrinkage was observed. Figure 6b shows the entire shrinkage region of slip-casted spinel samples. The data of the shrinkage region (1150–1650 °C) has been considered for MSC construction. Arrhenius plot of spinel is shown in Fig. 7, and the activation energy of the sintering is found to be 384 kJ/mol which is in good agreement with earlier studies corresponding to densification by grain boundary diffusion [81–83].

Fig. 5 Linear shrinkage of the slip cast spinel specimens during sintering at heating rates of 5, 10, and 20 °C/min

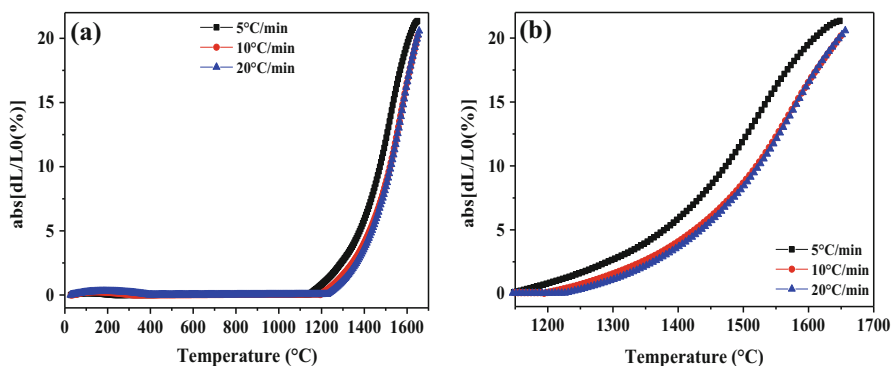
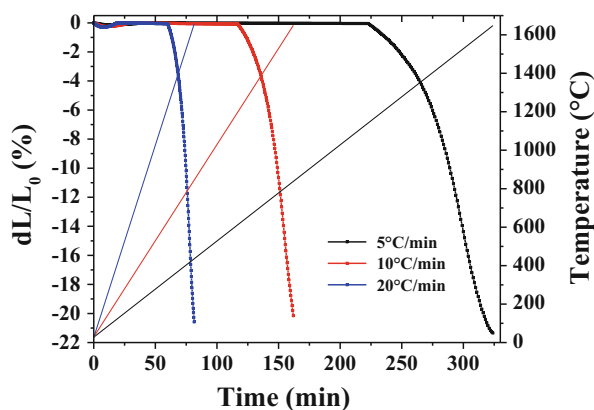


Fig. 6 Shrinkage versus temperature plots of (a) entire dilatometric data and (b) shrinkage region

Fig. 7 Arrhenius plot of spinel

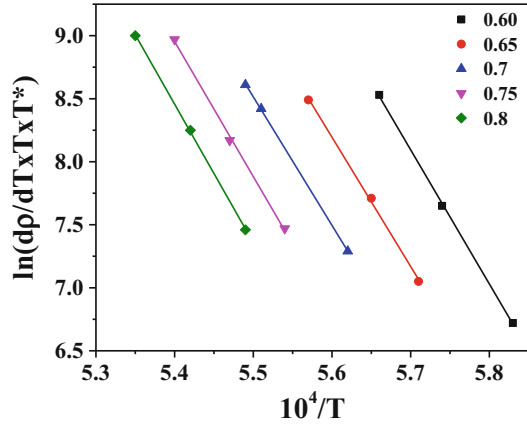
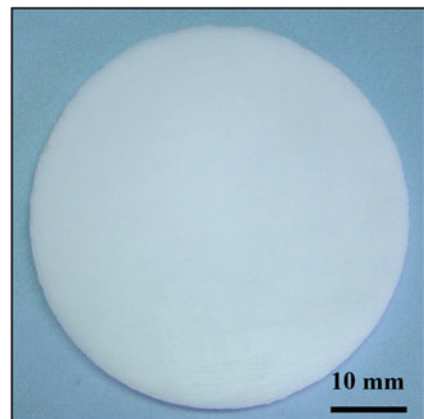


Fig. 8 Image of sintered spinel disc



Based on the dilatometric plots and several sintering experiments at our laboratory, the dried samples were sintered at 1650 °C and the photograph of a sintered samples are shown in Fig. 8.

Hot Isostatic Pressing of Sintered Slip Cast Spinel Samples

Hot isostatic pressing (HIP) is a process in which the job is simultaneously subjected to high temperatures and isostatic pressures simultaneously close to plastic deformation regime of the material to achieve isotropic properties. Though the primary objective of HIP technology was to achieve near net shaping with pore-free sintered parts, applications of this technology are growing rapidly in the area of metals and ceramics. A typical layout of HIP is shown in Fig. 9. HIP system generally consists of a pressure vessel which is one of the major components, and design considerations should allow the maximum stresses for better service life owing to the enormous accumulated energy and the cyclic operations. Furnace consists of a heater which

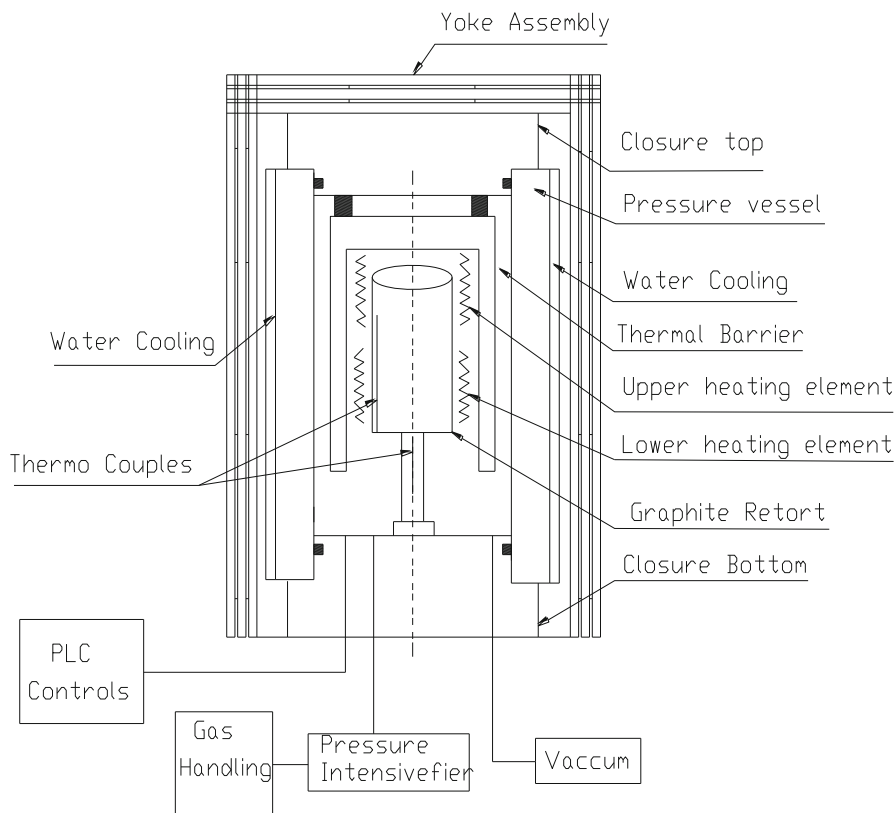


Fig. 9 A schematic of hot isostatic pressing

produces the required temperature and a thermal barrier which protects the pressure vessel from internal high temperature. The furnace elements mainly depend on the peak temperature (Kanthal A-1 ($<1200\text{ }^{\circ}\text{C}$), molybdenum ($<1600\text{ }^{\circ}\text{C}$), and graphite ($<2200\text{ }^{\circ}\text{C}$)) and atmosphere of use. Temperature measurement in HIP equipment is usually done by using the commercially available thermocouples, and tungsten-rhenium thermocouples are used for high-temperature measurements. Due to its inertness, argon is the most popular pressure transmitting medium for HIP though nitrogen and helium gases are also employed. During HIP cycle, the gas expands and causes a rise in pressure; however, multistage gas pressure intensifiers are also essential (depending upon the hot zone dimensions) part of HIP to increase the gas pressure. Auxiliary vacuum systems, cooling system, loading and unloading systems also form part of the HIP system. A programmable logic controller (PLC) generally forms the heart of the control system which integrates all the components and functions. Many densification mechanisms are operative during HIPing in addition to the lattice diffusion, grain boundary diffusion, plastic deformation, and creep becomes significant under applied pressure.

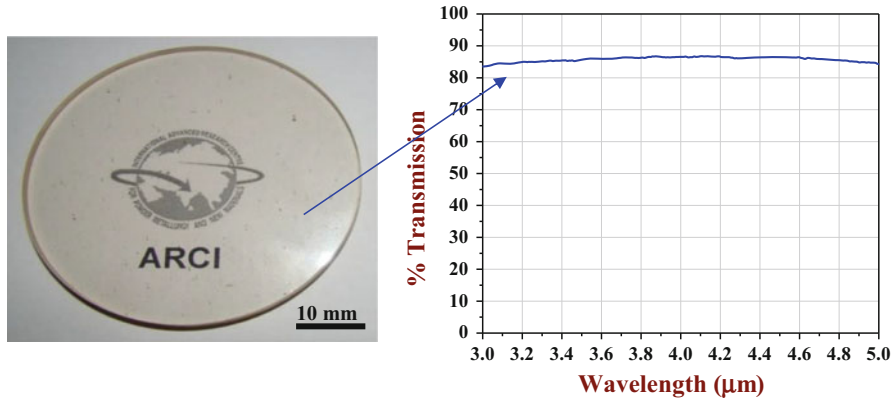


Fig. 10 HIPed spinel sample along with transmission pattern

The mechanism that predominates during HIPing operation depends on several parameters such as powder size, geometry, and interface properties and also processing parameters such as pressure, temperature, and time. Selection of threshold pressure is a strong function of particle size, and applied pressure is more significant in the initial and intermediate stages of sintering as it aids in particle rearrangement, plastic deformation, and particle sliding and pore shrinkage. Based on the geometry of the pore, the densification process can split into two steps. In stage I the pores are interconnected, and the powder particle share small area of contact with their neighbors. In stage II on exposure to pressure, at temperature $0.5\text{--}0.7 T_m$ (melting point), it results in pore separation from the grain boundaries leading to the suppression of diffusive mechanisms. Grain boundary motion is generally a strong function of intrinsic drag on the grain boundaries, drag caused by the solute and boundary pinning of pores or particle. At this stage, boundary pinning by pores becomes less effective, and the grain growth becomes prominent. Several HIP cycles are employed with respect to the temperature and pressure and also with respect to the nature of the jobs. A HIP furnace procured from American Isostatic Press, USA, with graphite heating elements has been used for HIPing of sintered spinel samples. The pressure is increased to a desirable level followed by the increase of temperature; a simultaneous increase in temperature and pressure is employed for the HIPing of spinel sample to reduce the cycle time.

For HIPing sintered spinel samples (depicted in Fig. 8) were visually inspected for the presence of any cracks and were further HIPed at a temperature of $1800\text{ }^\circ\text{C}$ and pressure of 195 MPa in argon atmosphere for a soaking period of 5 h based on the earlier studies. Hot isostatically pressed transparent spinel sample is shown in Fig. 10 along with the transmission curve.

Densification of Spinel by Spark Plasma Sintering

Spark plasma sintering (SPS), also known as field-assisted sintering technique (FAST) or pulsed electric current sintering (PECS), is a densification technique which utilizes

uniaxial force and pulsed (on-off) direct current (DC) under low atmospheric pressure to perform faster densification of the powder [84–86]. The *on-off* DC pulse energizing method generates: (1) spark plasma, (2) spark impact pressure, (3) rapid Joule heating and cooling, and (4) an electrical field diffusion effect [86].

Recently, SPS technique has attained the importance for fabrication of transparent polycrystalline ceramic samples as it has significant advantages over conventional techniques and other advanced techniques such as hot isostatic pressing and hot pressing. Frange et al. [87] and Morita et al. [88] have reported a light transmission of spinel fabricated by SPS process in various heating rates, and transmission has increased with decreasing heating rate, and also high heating rate can entrap branching porosity. Jiang et al. [89], Meir et al. [44], and Morita et al. [88] reported that discoloration due to graphite contamination is usual phenomenon in SPS processing specially for transparent spinel. Though high density (>99.9% TD) was achieved by SPS, discoloration lowers the transmission significantly. This discoloration was often due to the carbon contamination and oxygen vacancies generated during SPS process [73, 77, 90, 91]. In addition to the graphite dies, Morita et al. [74] also explained that commercial spinel powder which was used in this study contains carbonate and chlorine as impurity. During SPS process carbon originating from carbonate continue to exist along the grain boundary, which causes discoloration and also possible source of light scattering. Hence, in earlier SPS studies, an essential step of oxidation of carbon is followed to remove the carbon that contaminates transparent spinel. Generally, carbon particles get included throughout the bulk sample from the die, fixtures, and graphite parts. It was proposed that post annealing can effectively remove carbon particles, which has already been reported in several articles [73, 74, 92]. However, as the carbon inclusion was significant in comparison to conventional process, oxidation of carbon particles in air with SPS sample will be difficult. As post-annealing oxidation being an exothermic reaction, nonuniform thermal profile was generated within the sample, which leads to inhomogeneity and significantly affects transmission of the sample. Hence, the main issues in SPS spinel samples have been the following: (i) as the SPS involves direct powder processing, the inclusion of carbon particles was probable throughout the sample; (ii) being non-equilibrium technique, faster processing included carbon particles through the bulk; and (iii) during exothermic oxidation temperature generated most probably more than the SPS process temperature leading to hot spots [74, 92].

Authors have focused to evolve a solution for the inherent graphite contamination and hence discoloration of the transparent spinel sample by SPS processing. The SPS which was used in the present investigation (Dr. Sinter 1050, Japan) has been shown in Fig. 11. Schematic diagram of SPS process along with graphite die has been shown in Fig. 12. During SPS processing in the present study, 5 gm of surface-modified (process described in previous section) spinel powder was filled directly into conductive graphite die cavity (as shown in Fig. 13a) of 15 mm diameter which covered with graphite foil of 500 μm thickness. Similar experiments were also carried out by eliminating the graphite foil and replacing the same with the platinum foil. In this case, 5 gm powder from the same batch was filled into same graphite die cavity which covered with 100 μm -thick platinum foil (as shown in Fig. 13b). These



Fig. 11 Photograph of spark plasma sintering unit

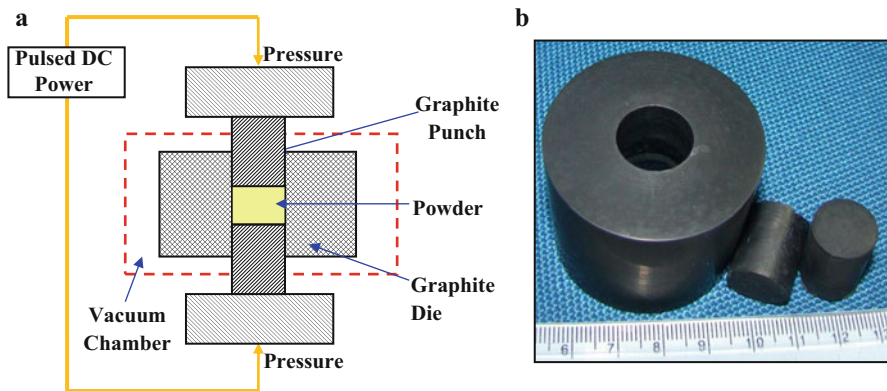


Fig. 12 (a) Schematic diagram of SPS process and (b) SPS graphite die

foils were used to avoid direct contact between the powder compact and the graphite die parts. SPS was carried out under identical conditions of 1300 °C and uniaxial pressure of 70 MPa with a heating rate of 100 °C/min. After sintering SPS samples were taken out from the die. In case of platinum foil-processed sample, sample was subjected to ultrasonication in isopropyl alcohol medium for 15–20 min for safe removal of platinum foil to reuse. In case of graphite-processed sample, sample is ground to remove the foil. Sample processed with graphite foil has shown discoloration due to carbon contamination which basically requires annealing in air.

Photographs of polished SPS spinel specimens processed with platinum and graphite foils without post SPS annealing have been shown in Fig. 14a, b, respectively. Photograph of graphite die punches along with platinum foil and sample before and after ultrasonication has been depicted in Fig. 15a, b, respectively. It is clear from Fig. 14 that use of platinum foil has notably eliminated graphite

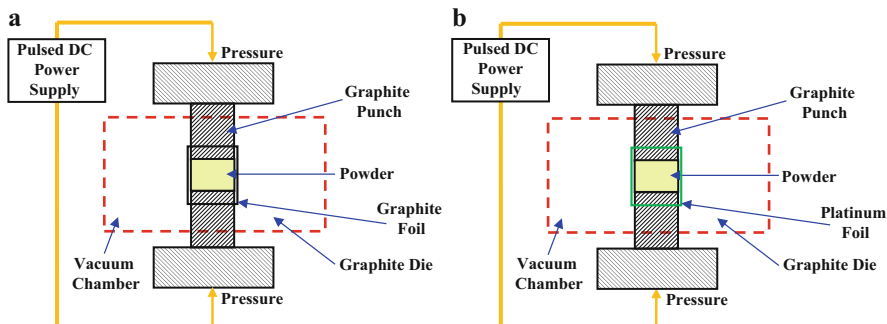


Fig. 13 Schematic diagram of SPS process with (a) graphite foil and (b) platinum foil

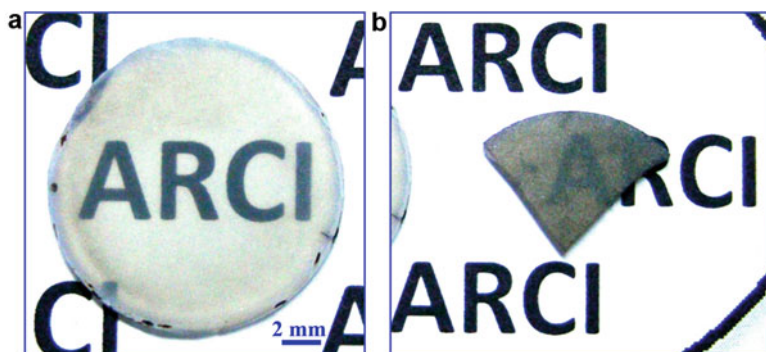


Fig. 14 Digital images of SPS spinel samples as processed using (a) platinum foil and (b) graphite foil [93]

contamination and observed no discoloration that takes place in presence of graphite foil and punches which usually employed while SPS processing. Additionally, higher thermal conductivity of chemically inert platinum foil also plays a significant role during densification by SPS process. Though considerable efforts have been made by varying the SPS conditions in the presence of graphite foil, they were cumbersome or have resulted in limited successes and also essentially require post SPS annealing in air to remove graphite contamination. Moreover, annealing of graphite-contaminated spinel samples in air through in situ oxidation of carbon results in hot spot formation due to exothermic nature of the oxidation reaction leaving opaque spots in the sample. These inhomogeneities act as scatter points, which often result in reduction of transmission values and sample become opaque (Fig. 16).

IR transmission spectrum of platinum foil-processed SPS spinel (3 mm thick) is shown in Fig. 17. It is clear from the figure that this sample has achieved transmission of 84–85% which is close to the theoretical value and demonstrating the homogeneity throughout the spinel sample. In the case of graphite-processed

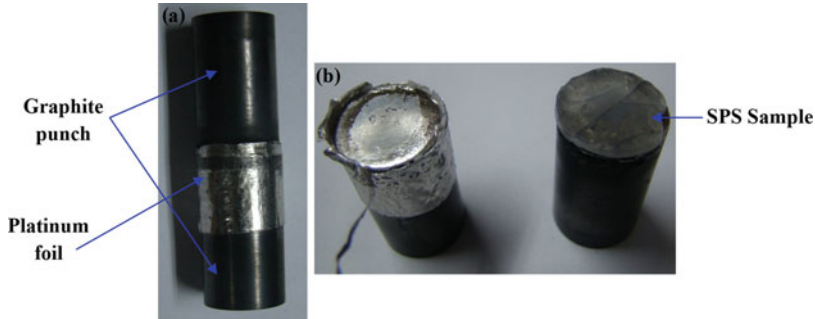


Fig. 15 Graphite punches along with sample after SPS (a) before ultrasonication and (b) after ultrasonication

Fig. 16 Photograph of SPS sample processed with graphite foil after annealing

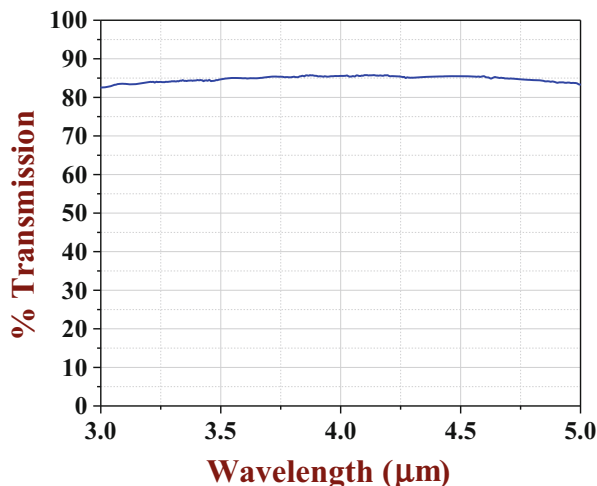


sample, transmission could not be measured due to the graphite contamination (as shown in Fig. 14), and after post-annealing spinel, sample exhibited poor transmission in comparison to platinum-processed sample (as shown in Fig. 17) as essential requirement to achieve theoretical transmission is the absence of any kind of inhomogeneity even residual porosity to eliminate diffuse scattering.

Flash Sintering of Magnesium Aluminate Spinel Ceramics

Flash sintering is an energy-efficient sintering technique under DC which involves electrical Joule heating and allows very rapid densification, i.e., almost immediately (typically <5 second) [94–96]. This has attracted immense attention as an innovative sintering technique compared to conventional sintering techniques. The flash sintering has been demonstrated in various ceramics, and nearly full density has been achieved at relatively low furnace temperature for very short time [97–103]. This not only results in significant retardation of grain growth but also

Fig. 17 Transmission curves of sample processed using platinum foil [93]



substantial economic benefits. Unlike SPS technique, flash sintering takes place under pressureless condition within a short span of time with relatively comparable temperature. In this study, flash sintering was employed to consolidate MgAl_2O_4 ceramic from surface-modified spinel powder. Though various methodologies for the sintering of spinel have been investigated including SPS, flash sintering of MgAl_2O_4 spinel has not been reported so far. Hence, in the present study, an attempt has been made and demonstrated that MgAl_2O_4 spinel ceramics under DC field at 1000 V/cm can trigger flash sintering resulting in dense polycrystalline sample with theoretical density.

Ionic conductivity of spinel is mainly exhibited beyond 400 °C, and electrical conductivity values depend on spinel composition, temperature, and microstructure [104]. In spinel main charge carriers for conductivity are magnesium cations (Mg^{2+}) or vacancies (V''_{Mg} in Kroger-Vink notation), and oxygen partial pressure does not influence significantly [82, 105, 106]. However, in case of sintering of spinel, rate-controlling mechanism is oxygen anion diffusion through vacancies, as oxygen anion diffusion coefficient is significantly lower than aluminum and magnesium cations. MgAl_2O_4 stoichiometry (expressed by n in $\text{MgO}.n\text{Al}_2\text{O}_3$) mostly varies during sintering due to MgO vaporization particularly at surfaces and grain boundaries. Oxygen vacancies (V''_{O}) are the principal charge-compensating defects; therefore, electrical compensation occurs by the anion vacancy in Mg-depleted spinel. Al-rich spinel shows higher oxygen diffusion than stoichiometric spinel, and densification is improved by oxygen anion vacancies generation which is associated with Mg evaporation [82].

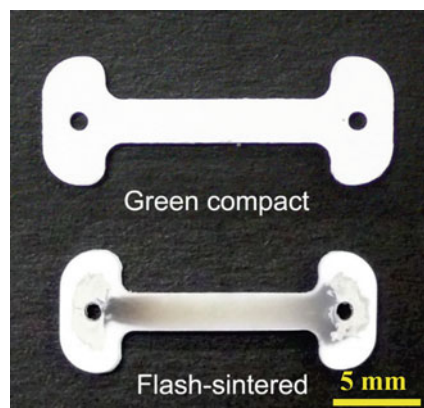
Surface-modified spinel powder was mixed with polyvinyl alcohol in water and dried at 90 °C in oven and further ground to press the powder for compaction. This powder was uniaxially pressed in a dog bone-shaped die with a green density of 45% of the theoretical density. The green specimen shown in Fig. 18 was 20 mm long with 1.4 mm thickness and gauge width of 3.3 mm. A schematic sketch of flash

sintering setup is shown in Fig. 19, and it shows that the specimen suspended at center of the furnace in air through two platinum wires which was attached to the handles of the specimen. A constant DC voltage ranging from 300 to 1000 V/cm was applied to the specimen by a high-voltage power supply (HAR-3P100; Matsusada Precision, Shiga, Japan). As the flash sintering expertise and facility was not available with ARCI and, further, Dr. Yoshida's team has expertise in carrying out flash sintering of ceramics, we have approached National Institute for Materials Science (NIMS), Japan, to carry out flash sintering of spinel. The current limit at the power supply was set to 60 mA. The furnace temperature was raised up to 1410 °C using a heating rate of 10 °C/min in air. The power supply was switched to current control once current reached the limit value. The furnace and voltage supply were turned off for 60 s after flash event. A CCD camera had recorded the sample dimensions through a quartz window which is located in front of the furnace. Specimen temperature was also concurrently measured by a pyrometer (IR-CAS; Chino, Tokyo, Japan) through another quartz window placed behind the furnace.

The densification curves for the MgAl_2O_4 spinel specimens measured for different applied DC field values as a function of furnace temperature have been shown in Fig. 20. Spinel specimen at 0 V/cm which is comparable to conventional sintering has exhibited a relative density of 68.6% of TD at 1410 °C, and there was no significant increase in relative densities at the fields from 300 to 750 V/cm as these fields have not exhibited significant effect on the densification behavior of the spinel specimen. At 1000 V/cm, FAST was followed by flash sintering, which was characterized by almost vertical slopes of the shrinkage curves; the densification was accelerated at temperatures greater than 1200 °C and the density of 97.9% of TD achieved at 1410 °C. The temperature for the onset of the flash was 1408 °C at 1000 V/cm. The flash sintering can reduce the furnace temperature required for full densification of the spinel. Photographs of the flash-sintered spinel specimen at 1000 V/cm are shown in Fig. 18.

Qin et al. [108] have shown that flash-sintered TZP specimen has identical grain sizes throughout the gauge section. Hence, grain size gradient within the gauge

Fig. 18 Photograph of dog bone-shaped green sample and sintered sample after flash sintering [107]



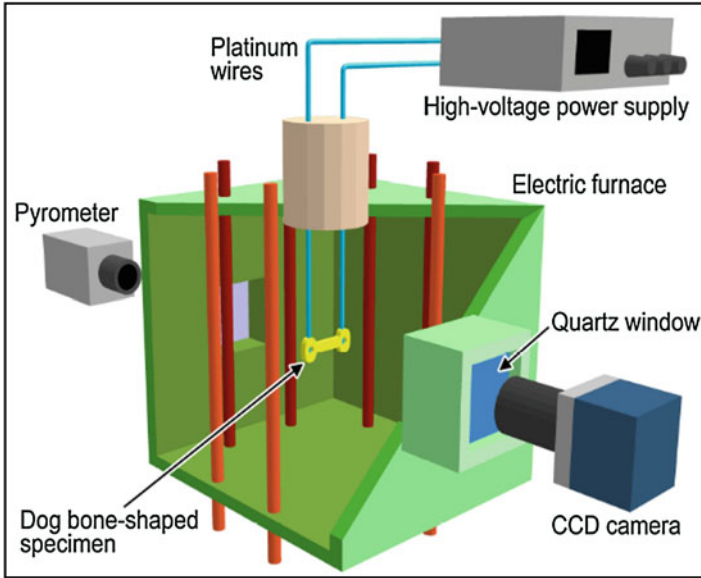
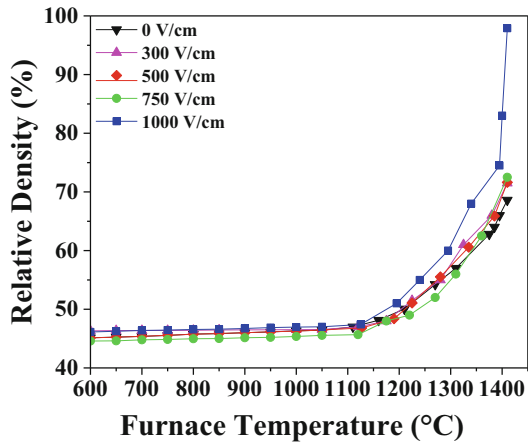


Fig. 19 A schematic sketch of flash sintering setup

Fig. 20 Relative density of spinel specimens flash sintered with different DC fields with respect to furnace temperature [107]



section of flash-sintered specimen can be due to other mechanisms except temperature gradient. As mentioned earlier, densification and grain growth in $MgAl_2O_4$ spinel specimen were accelerated by generation of oxygen vacancies due to Mg evaporation and Mg vacancies, the main charge carriers. Therefore, in the FAST regime, dominant conduction mechanism is migration of Mg^{2+} and V''_{Mg} to the negative and positive electrodes, respectively, and electrical neutrality at the gauge

portion of Mg-depleted spinel could be maintained by oxygen vacancies where V''_{Mg} concentration was high and V''_{Mg} and V''_{O} gradient could be produced throughout the gauge section between two electrodes. During flash sintering, diffusional mass transport was enhanced by the Joule heating in MgAl_2O_4 spinel sample.

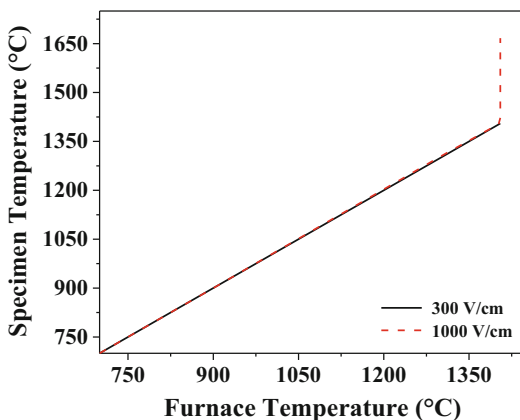
MgAl_2O_4 specimens were subjected to the fields of 300 and 1000 V/cm, and the specimen temperature was measured as a function of furnace temperature using a pyrometer. A plot of measured sample temperature with respect to the furnace temperature has been shown in Fig. 21. It has been observed that the furnace temperature and sample temperature were same at 300 V/cm; however, temperature increased at 1000 V/cm beyond 1405 °C. A rapid increase to 1667 °C was observed at furnace temperature of 1410 °C. The larger variation in temperature with respect to furnace temperature can be attributed to the joule heating. Electrical conductivity (σ) during flash sintering experiments under the electric fields was calculated by the following equation:

$$\sigma = \frac{IL}{VA} \quad (1)$$

where σ is electrical conductivity, I is current, V is applied voltage, L is length of the gauge section, and A is cross-sectional area of the gauge section.

Further, a part of the flash-sintered spinel sample (having locations 3–5) was HIPed at 1800 °C under argon pressure of 195 MPa for soaking period of 5 h. This HIPed sample exhibited 100% of TD and a transmission of 81% at 3–5 μm wavelength length region as depicted in Fig. 22 and an image of HIPed sample (sample for the measurement was not as per the standard due to limitation of sample dimension associated with flash sintering).

Fig. 21 Specimen temperatures measured by a pyrometer under the fields of 300 and 1000 V/cm as a function of the furnace temperature [107]



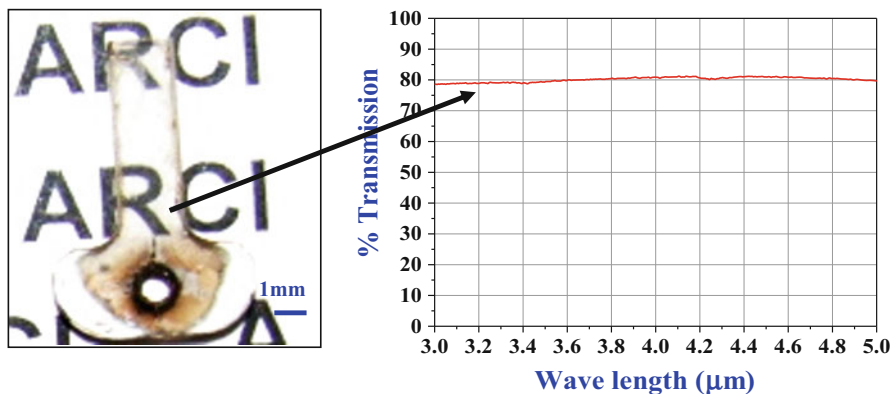


Fig. 22 Transmission plot of flash-sintered spinel sample after HIPing along with transparent spinel sample

Characterization of Transparent Specimens Processed through Different Routes

All the specimens processed through different routes are designated as S-SHIP for spinel-sinter + HIP, S-SPS for spinel-spark plasma, S-FS for spinel-flash sintering, and S-FHIP for spinel-flash sintering + HIP. All the samples produced by above techniques have been characterized for physico-chemical properties (XRD phase analysis, density), mechanical properties (flexural strength, Vickers hardness), and optical properties (visible, mid-wave infrared (MWIR)).

Density of all the S-SHIP, S-SPS, S-FS, and S-FHIP was measured by Archimedes' principle following ASTM 792. Phase analysis of all the samples was carried out by X-ray diffraction technique employing Cu K α using D8 Advanced system (Bruker, Germany). The samples were also ceramographically polished and thermally etched, and microstructure of etched samples was characterized by scanning electron microscope (Hitachi 2400, Japan). Mechanical characterizations such as Vickers hardness (LECO, St. Joseph, MI) at 10 kgf and the flexural strength were measured by using three-point bend samples with dimensions of 45 × 4 × 3 mm using universal testing machine (4483, Instron, UK) following ASTM C-1161-02C. The flexural strength (σ_f) under three-point bend loading is calculated as

$$\sigma_f = \frac{3}{2} \left(\frac{P_f \times L}{bd^2} \right) \quad (2)$$

where P_f is the maximum load at failure, L is the span length (40 mm), b is the width of specimen, and d is the thickness of the specimen.

Comparison of Characterization Results

It is evident from Table 3 that both S-SHIP and S-SPS samples have exhibited a density of 3.58 g/cm^3 ; however the density of S-FS sample was relatively low showing 3.51 g/cm^3 which on HIPing (S-FHIP) resulted in the theoretical value of 3.58 g/cm^3 . Microstructures of the S-SHIP, S-SPS, and S-FHIP are shown in Fig. 23a–c. S-SHIP samples have shown more uniform microstructure with average grain size of $40 \text{ }\mu\text{m}$. SPS-processed samples have shown finer grain size of $0.5 \text{ }\mu\text{m}$ (average) as is evident from the microstructure when compared to $40 \text{ }\mu\text{m}$ observed with S-SHIP samples. This can be attributed to the unique spark plasma sintering mechanism operative during densification as reported by earlier researchers in combination with low sintering temperatures and along with the application of pressures. S-FHIP samples have shown uniform microstructure with average grain size of $11 \text{ }\mu\text{m}$ due to the additional HIPing process involved.

Vickers hardness of S-SHIP, S-SPS, and S-FHIP were found to be 1275–1295, 1460–1500, and 1331–1359 Kg/mm^2 , respectively. Flexural strength of S-SHIP is found to be 180–190 MPa. Flexure strength of S-SPS, S-FS, and S-FHIP could not be measured due to limitation in sample size.

It is evident from Table 3 that both the samples exhibited similar hardness values ($1460\text{--}1510 \text{ kg/mm}^2$) which are significantly higher in comparison to reported values ($1300\text{--}1350 \text{ kg/mm}^2$) of our earlier studies of samples processed through slip casting followed by PLS and HIPing. Figure 23 has shown the microstructure of SPS sample processed with platinum foil. Hardness values were also complemented by the microstructure. The enhanced hardness of SPS-processed samples was

Table 3 A comparison of properties of S-SHIP, S-SPS, S-FS, and S-FHIP

Sr. no.	Property	Slip casting + PLS + HIP (S-SHIP)	Spark plasma sintering (S-SPS)	Flash sintering (S-FS)	Flash sintering + HIP (S-FHIP)
1	Density (g/cm^3)	3.58	3.58	3.51	3.58
2	Average grain size (μm)	47	0.5	5	11
3	Vickers hardness at 10 kgf (kg/mm^2)	1275–1295	1460–1500	1280–1300	1330–1360
4	3-point bending strength (MPa)	180–190	Could not measure due to limitation in sample size (standard $45 \times 4 \times 3 \text{ mm}$)		
5	Transmission (%) ($3\text{--}5 \text{ }\mu\text{m}$)	82–86	81–85	Opaque	80–81
6	Transmission (%) ($0.4\text{--}0.8 \text{ }\mu\text{m}$)	80–85	Could not measure due to limitation in sample size (standard $25 \times 25 \text{ mm}$)		

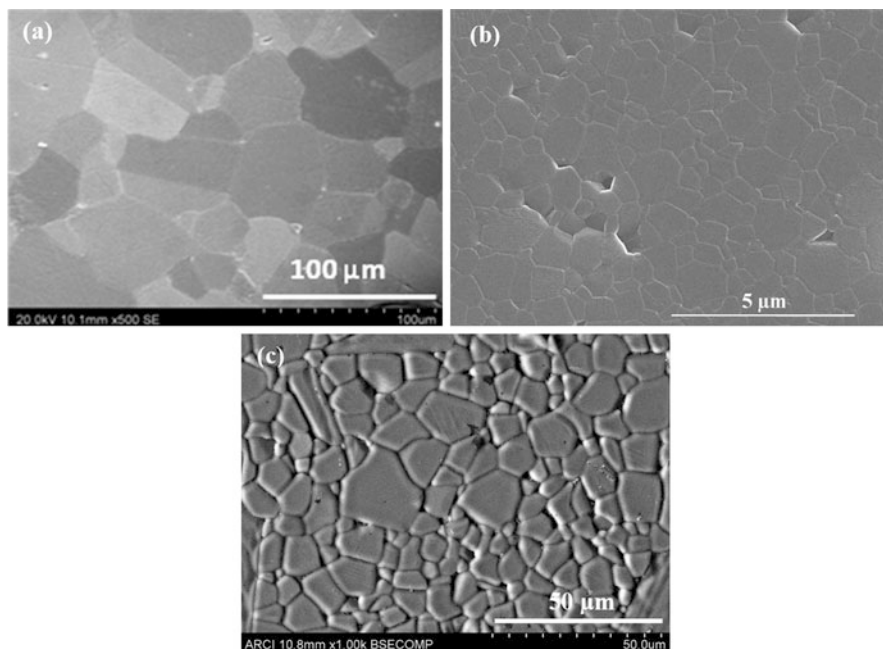


Fig. 23 Microstructure of (a) S-SHIP, (b) S-SPS, and (c) S-FHIP [92, 109]

obviously due to the finer grain size of $0.5 \mu\text{m}$ (average) as is evident from the microstructure. Marginally low hardness values resulted in case of flash sintering can also be attributed with the grain sizes observed.

Transmission measurements carried out for S-SHIP, S-SPS, and S-FHIP are presented in Figs. 9, 16, and 21, respectively. It is well known that in case of materials with cubic crystallography, distribution of grain sizes and microstructural changes arising out of the processing routes have minimal effect on transmission. Hence, spinel ceramics being cubic and optically isotropic, negligible effect on transmission properties is expected due to microstructural changes.

Conclusions

Magnesium aluminate ceramics are processed through different routes of sinter + HIP, spark plasma sintering, and flash sintering using S30CR commercial grade powder successfully. physico-chemical, mechanical, and optical properties of transparent magnesium aluminate spinel which are processed using different techniques are comparatively evaluated and presented in Table 3.

A thermal passivation process for the powder without altering the chemistry is found to be very effective in achieving the high solid loading slurry with high stability as revealed by quasi-elastic neutron scattering technique and viscosity

measurements. Transparent spinel ceramics with the density of 3.58 g/cm^3 , transmission of 86% close to theoretical in 3–5 μm region, and mechanical properties (flexural strength, 190 MPa, and Vickers hardness – 1295 kg/mm^2) on par with literature values were successfully fabricated through defect-free slip casting process followed by pressureless sintering and hot isostatic pressing. The samples exhibited transparency close to theoretical value of 82–86% in the 3–5 μm region.

Encapsulation of magnesium aluminate spinel powder in platinum foil and spark plasma sintering (SPS) of the same to theoretical transparency without decolorization and decarbonization is discussed in the current chapter. The sample also exhibited a marginally higher density and hardness in comparison to conventional SPS-processed samples and transmission value of 81–85% in the 3–5 μm region was achieved.

Flash sintering was applied to densify magnesium aluminate spinel, and a density value close to 99% theoretical density was achieved at a DC field of 1000 V/cm and at a temperature of 1410 °C. Flash-sintered sample was hot isostatically pressed at a temperature and pressure of 1800 °C and 195 MPa, respectively, and achieved transparency of 80–81% in the 3–5 μm region.

References

1. Li F-H, Li J-B, Lin H, Huang C-X, Lei M-Y, Du H-B (2010) Development of transparent MgAl_2O_4 spinel ceramics. *Key Eng Mater* 434–435:649–652
2. Morita K, Kim BN, Hiraga K, Yoshida H (2008) Fabrication of transparent MgAl_2O_4 spinel polycrystal by spark plasma sintering processing. *Scripta Mater* 58:1114–1117
3. Ramisetty M, Sastri S, Kashalikar U, Goldman LM, Nag N (2013) Transparent polycrystalline cubic spinels: protect and defend. *Am Ceram Soc Bull* 92:20–25
4. Chen F, Doty FP, Houk RJT, Loutfy RO, Volz HM, Yang P Characterizations of a hot-pressed polycrystalline spinel: Ce Scintillator. *J Am Ceram Soc* 93(2010):2399–2402
5. Harris DC (1999) *Materials for Infrared Windows and Domes: Properties and Performance*, SPIE, PM70.
6. Grujicic M, Bell WC, Pandurangan B (2012) Design and material selection guidelines and strategies for transparent armor systems. *Mater Des* 34:808–819
7. Bausa LE, Vergara I, Garcia-Solé J, Strek W, Deren PJ (1990) Laser-excited luminescence in Ti-doped MgAl_2O_4 spinel. *J Appl Phys* 68:736–740
8. Krishnan M, Brijesh T, Arora V, Biswas P, Rajeswai K, Suresh MB, Johnson R (2014) Transparent magnesium aluminate spinel: a prospective biomaterial for esthetic orthodontic brackets. *J Mater Sci: Mater Med* 25:2591–2599
9. Sharafat S, Ghoniem NM, Cooke PIH, Martin RC, Najmabadi F, Schultz KR, Wong CPC (1993) Materials analysis of the TITAN-I reversed-field-pinch fusion power core. *Fusion Eng Des* 23:99–113
10. Maschio RD, Fabbri B, Fiori C (1988) Industrial application of refractories containing magnesium aluminate spinel. *Inds Ceram* 8:121–126.
11. Mathur S (2002) NATO ASI, vol 91. Kluwer, Dordrecht
12. Kingery WD, Bowen HK, Uhlmann DR (1976) *Introduction to ceramics*. Wiley, New York, pp 656–667
13. Ramavath P, Biswas P, Rajeswari K, Suresh MB, Johnson R, Padmanabham G, Kumbhar CS, Chongdar TK, Gokhale NM (2014) Optical and mechanical properties of compaction and slip cast processed transparent polycrystalline spinel ceramics. *Ceram Int* 40:5575–5581
14. Harris DC (2005) History of development of polycrystalline optical spinel in U.S. *Proc SPIE* 5786:1–22

15. Mroz T, Goldman LM, Gledhill AD, Li D, Padture NP (2012) Nanostructured, infrared-transparent magnesium aluminate spinel with superior mechanical properties. *Int J Appl Ceram Technol* 9:83–90
16. Biswas P, Ramavath P, Kumbhar CS, Patil DS, Chongdar TK, Gokhale NM, Johnson R, Mohan MK (2017) Effect of room and high temperature compaction on optical and mechanical properties of HIPed transparent spinel ceramics. *Adv Eng Mater* 19:1700111-1–1700111-7
17. Liu J, Lv X, Li J, Jiang L (2016) Pressureless sintered magnesium aluminate spinel with enhanced mechanical properties obtained by the two-step sintering method. *J Alloys Compd* 680:133–138
18. Meir S (2008) Fabrication of transparent magnesium aluminate spinel by the spark plasma sintering technique. Ben-Gurion University of the Negev
19. Ganesh I (2013) A review on magnesium aluminate ($MgAl_2O_4$) spinel: synthesis, processing and applications. *Int Mater Rev* 58:63–112
20. Muan A, Osborn EF (1965) Phase equilibrium among oxides in steel making. Addison-Wesley, Reading
21. Hallstedt B (1992) Thermodynamic assessment of the system $MgO-Al_2O_3$. *J Am Ceram Soc* 75:1497–1507
22. Schmidtmeier D, Büchel G, Buhr A (2009) Magnesium aluminate spinel raw materials for high performance refractories for steel ladles. *Ceram Mater* 61:223–227
23. Bhaduri S, Bhaduri SB, Prisbrey KA (1999) Auto ignition synthesis of nanocrystalline $MgAl_2O_4$ and related nanocomposites. *J Mater Res* 14:3571–3580
24. Hokazono S, Manako K, Kato A (1992) The sintering behavior of spinel powders produced by a homogeneous precipitation technique. *British Ceram Trans* 91:77–79
25. Bratton RJ (1969) Coprecipitates yielding $MgAl_2O_4$ spinel powders. *Ceram Bull* 48:759–762
26. Bickmore CR, Waldner KF, Treadwell DR, Laine RM (1996) Ultrafine spinel powders by flame spray pyrolysis of a magnesium aluminum double alkoxide. *J Am Ceram Soc* 79:1419–1423
27. Yamaguchi O, Omaki H, Shimizu K (1975) Formation of spinel hydroxides prepared by alkoxy-method. *J Jpn Soc Powder Metall* 22:202–204
28. Pasquier J-F, Komarneni S, Roy R (1991) Synthesis of $MgAl_2O_4$ spinel: seeding effects on formation temperature. *J Mater Sci* 26:3797–3802
29. Varnier O, Hovnanian N, Larbot A, Bergez P, Cot L, Charpin J (1994) Sol-gel synthesis of magnesium aluminum spinel from a heterometallic alkoxide. *Mater Res Bull* 29:479–488
30. Wang CT, Lin LS, Yang SJ (1992) Preparation of $MgAl_2O_4$ spinel powders via freeze-drying of alkoxide precursors. *J Am Ceram Soc* 75:2240–2243
31. Adak AK, Saha SK, Pramanik P (1997) Synthesis and characterization of $MgAl_2O_4$ spinel by PVA evaporation technique. *J Mater Sci Lett* 16:234–235
32. Goldstein A, Goldenberg A, Yeshurun Y, Hefez M (2008) Transparent $MgAl_2O_4$ spinel from a powder prepared by flame spray pyrolysis. *J Am Ceram Soc* 91:4141–4144
33. Suarez M, Rocha V, Fernandez A, Menendez JL, Torrecillas R (2014) Synthesis and processing of spinel powders for transparent ceramics. *Ceram Int* 40:4065–4069
34. Balabanov SS, Yavetskiy RP, Belyaev AV, Gavrishchuk EM, Drobotenko VV, Evdokimov II, Novikova AV, Palashov OV, Permin DA, Pimenov VG (2015) Fabrication of transparent $MgAl_2O_4$ ceramics by hot-pressing of sol-gel-derived nanopowders. *Ceram Int* 41:13366–13371
35. Reimanis IE, Kleebe HJ, Cook RL, DiGiovanni A (2004) Transparent spinel fabricated from novel powders: synthesis, microstructure and optical properties. In: Proceedings of defense security symposium
36. Cook R, Kochis M, Reimanis I, Kleebe H-J (2005) A new powder production route for transparent spinel windows: powder synthesis and window properties. In: Proceedings of defense security symposium, SPIE 5786
37. Sutorik AC, Gilde G, Swab JJ, Cooper C, Gamble R, Shanholtz E (2012) The production of transparent $MgAl_2O_4$ ceramic using calcined powder mixtures of $Mg(OH)_2$ and $\gamma-Al_2O_3$ or $AlOOH$. *Int J Appl Ceram Technol* 9:575–587

38. Nam S, Lee M, Kim B-N, Lee Y, Kang S (2017) Morphology controlled co-precipitation method for nano structured transparent MgAl_2O_4 . *Ceram Int* 43:15352–15359
39. Ewais EMM, Besisa DHA, El-Amir AAM, El-Sheikh SM, Rayan DE (2015) Optical properties of nanocrystalline magnesium aluminate spinel synthesized from industrial wastes. *J Alloys Compd* 649:159–166
40. Dericioglu AF, Boccaccini AR, Dlouhy I, Kagawa Y (2005) Effect of chemical composition on the optical properties and fracture toughness of transparent magnesium aluminate spinel ceramics. *Mater Trans* 46:996–1003
41. Waetzig K, Krell A (2016) The effect of composition on the optical properties and hardness of transparent Al-rich $\text{MgO-nAl}_2\text{O}_3$ spinel ceramics. *J Am Ceram Soc* 99:946–953
42. Shahbazi H, Shokrollahi H, Alhaji A (2017) Optimizing the gel-casting parameters in synthesis of MgAl_2O_4 spinel. *J Alloys Compd* 712:732–741
43. Sutorik AC, Gilde G, Cooper C, Wright J, Hilton C (2012) The effect of varied amounts of LiF sintering aid on the transparency of alumina rich spinel ceramic with the composition $\text{MgO-1.5 Al}_2\text{O}_3$. *J Am Ceram Soc* 95:1807–1810
44. Meir S, Kalabukhov S, Froumin N, Dariel MP, Frage N (2009) Synthesis and densification of transparent magnesium aluminate spinel by SPS processing. *J Am Ceram Soc* 92:358–364
45. El-Amir AAM, Ewais EMM, Abdel-Aziem AR, Ahmed A, El-Anadouli BEH (2016) Nano-alumina powders/ceramics derived from aluminum foil waste at low temperature for various industrial applications. *J Environ Manag* 183:121–125
46. Mohan SK, Sarkar R (2016) Effect of in situ generated nascent magnesia and alumina from nitrateprecursor on reaction sintered magnesium aluminate spinel. *Mater Des* 110:145–156
47. Liu Q, Jiang N, Li J, Sun K, Pan Y, Guo J (2016) Highly transparent AlON ceramics sintered from powder synthesized by carbothermal reduction nitridation. *Ceram Int* 42:8290–8295
48. Jabbarzare S, Abdellahi M, Ghayour H, Chami A, Hejazian S (2016) Mechanochemically assisted synthesis of yttrium ferrite ceramic and its visible light photocatalytic and magnetic properties. *J Alloys Compd* 688:1125–1130
49. Kracker M, Thieme C, Häbler J, Rüssel C (2016) Sol–gel powder synthesis and preparation of ceramics with high- and low-temperature polymorphs of $\text{Ba}_x\text{Sr}_{1-x}\text{Zn}_2\text{Si}_2\text{O}_7$ ($x = 1$ and 0.5): a novel approach to obtain zero thermal expansion. *J Eur Ceram Soc* 36:2097–2107
50. Zhang W, Lu TC, Wei N, Shi YL, Ma BY, Luo H, Zhang ZB, Deng J, Guan ZG, Zhang HR, Li CN, Niu RH (2015) Co-precipitation synthesis and vacuum sintering of Nd:YAG powders for transparent ceramics. *Mater Res Bull* 70:365–372
51. Krell A, Hutzler T, Klimke J (2014) Defect strategies for an improved optical quality of transparent ceramics. *Opt Mater* 38:61–74
52. Kong LB, Huang Y, Que W, Zhang T, Li S, Zhang J, Dong Z, Tang D (2015) *Transparent ceramics*. Springer International Publisher. Topics in mining, Metallurgical and materials engineering, Series Editor: Carlos P. Bergmann
53. Olhero SM, Ganesh I, Torres PMC, Ferreira JMF (2008) Surface passivation of MgAl_2O_4 spinel powder by chemisorbing H_3PO_4 for easy aqueous processing. *Langmuir* 24:9525–9530
54. Ganesh I, Sundararajan G, Ferreira JMF (2011) Aqueous slip casting and hydrolysis assisted solidification of MgAl_2O_4 spinel. *Adv Appl Ceram* 110:63–69
55. Shafeiey A, Enayati MH, Al-Haji A (2017) The effect of slip casting parameters on the green density of MgAl_2O_4 spinel. *Ceram Int* 43:6069–6074
56. Kim J-M, Kim H-N, Park Y-J, Ko J-W, Lee J-W, Kim H-D (2016) Microstructure and optical properties of transparent MgAl_2O_4 prepared by Ca-infiltrated slip-casting and sinter-HIP process. *J Eur Ceram Soc* 36:2027–2034
57. Krell A, Klimke J, Hutzler T (2009) Advanced spinel and sub- μm Al_2O_3 for transparent armour applications. *J Eur Ceram Soc* 29:275–281
58. Zhang P, Liu P, Sun Y, Wang J, Wang Z, Wang S, Zhang J (2015) Aqueous gelcasting of the transparent MgAl_2O_4 spinel ceramics. *J Alloys Compd* 646:833–836
59. Tokariev O, Gestel TV, Bram M, Malzbender J (2013) Strength enhancement of transparent spinel ceramics. *Mater Lett* 107:364–366

60. Tokariev O, Schnetter L, Beck T, Malzbender J (2013) Grain size effect on the mechanical properties of transparent spinel ceramics. *J Eur Ceram Soc* 33:749–757
61. Krell A, Hutzler T, Klimke J, Pothhoff A (2010) Fine-grained transparent spinel windows by the processing of different nanopowders. *J Am Ceram Soc* 93:2656–2666
62. Gajdowski C, Böhmler J, Lorgouilloux Y, Lemonnier S, d’Astorg S, Barraud E, Leriche A (2017) Influence of post-HIP temperature on microstructural and optical properties of pure $MgAl_2O_4$ spinel: from opaque to transparent ceramics. *J Eur Ceram Soc* 37:5347–5351
63. Tsukuma K (2006) Transparent $MgAl_2O_4$ spinel ceramics produced by HIP post-sintering. *J Ceram Soc Jpn* 114:802–806
64. Shimada M, Endo T, Saito T, Sato T (1996) Fabrication of transparent spinel polycrystalline materials. *Mater Lett* 28:413–415
65. Bratton RJ (1974) Translucent sintered $MgAl_2O_4$. *J Am Ceram Soc* 57:283–286
66. Krell A, Bales A (2011) Grain size-dependent hardness of transparent magnesium aluminate spinel. *Int J Appl Ceram Technol* 8:1108–1114
67. Esposito L, Piancastelli A, Miceli P, Martelli S (2015) A thermodynamic approach to obtaining transparent spinel ($MgAl_2O_4$) by hot pressing. *J Eur Ceram Soc* 35:651–661
68. Villalobos GR, Sanghera JS, Agarwal ID (2005) Degradation of magnesium aluminum spinel by lithium fluoride sintering aid. *J Am Ceram Soc* 88:1321–1322
69. Gilde G, Patel P, Patterson P (2005) Evaluation of hot pressing and hot isostatic pressing parameters on the optical properties of spinel. *J Am Ceram Soc* 88:2747–2751
70. Esposito L, Piancastelli A, Martelli S (2013) Production and characterization of transparent $MgAl_2O_4$ prepared by hot pressing. *J Eur Ceram Soc* 33:737–747
71. Goldstein A, Raethel J, Katz M, Berlin M, Galun E (2016) Transparent $MgAl_2O_4/LiF$ ceramics by hot-pressing: host–additive interaction mechanisms issue revisited. *J Eur Ceram Soc* 36:1731–1742
72. Morita K, Kim B-N, Yoshida H, Hiraga K, Sakka Y (2015) Influence of spark plasma sintering (SPS) conditions on transmission of $MgAl_2O_4$ spinel. *J Am Ceram Soc* 98:378–385
73. Bernard-Granger G, Benameur N, Guizard C, Nygren M (2009) Influence of graphite contamination on the optical properties of transparent spinel obtained by spark plasma sintering. *Scripta Mater* 60:164–167
74. Morita K, Kim B-N, Yoshida H, Hiraga K, Sakka Y (2016) Influence of pre- and post-annealing on discoloration of $MgAl_2O_4$ spinel fabricated by spark-plasma-sintering (SPS). *J Eur Ceram Soc* 36:2961–2968
75. Morita K, Kim B-N, Yoshida H, Hiraga K (2009) Spark plasma sintering condition optimization for producing transparent $MgAl_2O_4$ spinel polycrystal. *J Am Ceram Soc* 92:1208–1216
76. Morita K, Kim B-N, Yoshida H, Zhang H, Hiraga K, Sakka Y (2012) Effect of loading schedule on densification of $MgAl_2O_4$ spinel during spark plasma sintering (SPS) processing. *J Eur Ceram Soc* 32:2303–2309
77. Kim B-N, Morita K, Lim J-H, Hiraga K, Yoshida H (2010) Effects of preheating of powder before spark plasma sintering of transparent $MgAl_2O_4$ spinel. *J Am Ceram Soc* 93:2158–2160
78. Sokol M, Kalabukhov S, Dariel MP, Frage N (2014) High-pressure spark plasma sintering (SPS) of transparent polycrystalline magnesium aluminate spinel (PMAS). *J Eur Ceram Soc* 34:4305–4310
79. Bonnefont G (2012) Fine-grained transparent $MgAl_2O_4$ spinel obtained by spark plasma sintering of commercially available nanopowders. *Ceram Int* 38:131–140
80. Rajeswari K, Biswas P, Johnson R, Prabhudesai S, Sharma VK, Mitra S, Mukhopadhyay R (2014) Effect of surface passivation in spinel slurry towards hydrolysis: neutron scattering and rheological studies. *J Dispers Sci Technol* 35:1442–1448
81. Rozenburg K, Reimanis IE (2008) Sintering kinetics of $MgAl_2O_4$ spinel doped with LiF. *J Am Ceram Soc* 91:444–450
82. Reddy KPR, Cooper AR (1981) Oxygen diffusion in magnesium aluminate spinel. *J Am Ceram Soc* 64:368–371

83. Frost HJ, Ashby MF (1982) Olivines and spinels: Mg_2SiO_4 and $MgAl_2O_4$ (Chapter 15). Deformation-mechanism maps, the plasticity and creep of metals and ceramics. PhD thesis, Pergamon Press, Oxford, UK
84. Suárez M, Fernández A, Menéndez JL, Torrecillas R, Kessel HU, Henicke J, Kirchner R, Kessel T (2013) Challenges and opportunities for spark plasma sintering: a key technology for a new generation of materials. In: Ertug B (ed) Sintering applications. ISBN 978-953-51-0974-7
85. Chen XJ, Khor KA, Yu LG (2003) Preparation yttria-stabilized zirconia electrolyte by spark-plasma sintering. *Mater Sci Eng A* 341:43–46
86. Shen Z, Johnsson M, Zhao Z, Nygren M (2002) Spark plasma sintering of alumina. *J Am Ceram Soc* 85:1921–9023
87. Frage N, Cohen S, Meir S, Kalabukhov S, Darie MP (2007) Spark plasma sintering (SPS) of transparent magnesium-aluminate spinel. *J Mater Sci* 42:3273–3275
88. Morita K, Kim BN, Hiraga K, Yoshida H (2008) Fabrication of transparent $MgAl_2O_4$ spinel polycrystals by spark plasma sintering processing. *Scripta Mater* 58:1114–1117
89. Jiang DT, Hulbert DM, Anselmi-Tamburini U, Ng T, Land D, Mukherjee AM (2008) Optically transparent polycrystalline Al_2O_3 produced by spark plasma sintering. *J Am Ceram Soc* 91:151–154
90. Morita K, Kim BN, Yoshida H, Higara K, Sakka Y (2015) Influence of spark-plasma-sintering (SPS) conditions on transmission of $MgAl_2O_4$ spinel. *J Am Ceram Soc* 98:378–385
91. Morita K, Kim BN, Yoshida H, Higara K, Sakka Y (2015) Spectroscopic study of the discoloration of transparent $MgAl_2O_4$ spinel fabricated by spark-plasma sintering (SPS) processing. *Acta Mater* 84:9–19
92. Anselmi-Tamburini U, Woolman JN, Munir ZA (2007) Transparent nanometric cubic and tetragonal zirconia obtained by high-pressure pulsed electric current sintering. *Adv Funct Mater* 17:3267–3273
93. Biswas P, Chakravarty D, Suresh MB, Johnson R, Mohan MK (2016) Fabrication of graphite contamination free polycrystalline transparent $MgAl_2O_4$ spinel by spark plasma sintering using platinum foil. *Ceram Int* 42:17920–17923
94. Cologna M, Rashkova B, Raj R (2010) Flash sintering of nanograin zirconia in <5 s at 850°C . *J Am Ceram Soc* 93:3556–3559
95. Todd RI, Zapata-Solvas E, Bonilla RS, Sneddon T, Wilshaw PR (2015) Electrical characteristics of flash sintering: thermal runaway of joule heating. *J Eur Ceram Soc* 35:1865–1877
96. Raj R, Cologna M, Francis JSC (2011) Influence of externally imposed and internally generated electrical fields on grain growth, diffusional creep, sintering and related phenomena in ceramics. *J Am Ceram Soc* 94:1941–1965
97. Dancer CEJ (2016) Flash sintering of ceramic materials. *Mater Res Express* 3:102001–102026
98. Prette ALG, Cologna M, Sglavo VM, Raj R (2011) Flash-sintering of Co_2MnO_4 spinel for solid oxide fuel cell applications. *J Power Sources* 196:2061–2065
99. Yang D, Raj R, Conrad H (2010) Enhanced sintering rate of zirconia (3Y-TZP) through the effect of a weak DC electric field on grain growth. *J Am Ceram Soc* 93:2935–2937
100. Cologna M, Francis JSC, Raj R (2011) Field assisted and flash sintering of alumina and its relationship to conductivity and MgO-doping. *J Eur Ceram Soc* 31:2827–2837
101. Yu M, Grasso S, Mckinnon R, Saunders T, Reece MJ (2017) Review of flash sintering: materials, mechanisms and modeling. *Adv Appl Ceram* 116:24–60
102. Yoshida H, Sakka Y, Yamamoto T, Lebrun JM, Raj R (2014) Densification behaviour and microstructural development in undoped yttria prepared by flash-sintering. *J Eur Ceram Soc* 34:991–1000
103. Jha SK, Raj R (2014) The effect of electric field on sintering and electrical conductivity of titania. *J Am Ceram Soc* 97:527–534
104. Martinelli JR, Sonder E, Weeks RA, Zuhr RA (1986) Mobility of cations in magnesium aluminate spinel. *Phys Rev B* 33:5698–5701

105. Bates JL, Garnier JE (1981) Electrical conductivity of MgAl_2O_4 and $\text{Y}_3\text{Al}_5\text{O}_{12}$. *J Am Ceram Soc* 64:C138–C141
106. Sonder E (1983) Ionic transference numbers and electrical conduction in MgAl_2O_4 spinel. *J Am Ceram Soc* 66:50–53
107. Yoshida H, Biswas P, Johnson R, Mohan MK (2017) Flash-sintering of magnesium aluminate spinel (MgAl_2O_4) ceramics. *J Am Ceram Soc* 100:554–562
108. Qin W, Majidi H, Yun J, van Benthem K (2016) Electrode effects on microstructure formation during FLASH sintering of yttrium-stabilized zirconia. *J Am Ceram Soc* 99:2253–2259
109. Biswas P, Rajeswari K, Ramavath P, Johnson R, Maiti HS (2013) Fabrication of transparent spinel honeycomb structures by methyl cellulose based thermal gelation processing. *J Am Ceram Soc* 96:3042–3045



Roy Johnson, Papiya Biswas, Pandu Ramavath, and
Yashwant Ramchandra Mahajan

Contents

Introduction	535
Processing of Zinc Sulfide	539
Processing of Zinc Sulphide by CVD (CVD-ZS)	539
Heat Treatment of CVD-ZnS (CVDHT-ZS)	543
Hot Isostatic Pressing of CVD-ZnS (CVDHIP-ZS)	545
Hot Isostatic Pressing of ZnS Powder (PHIP-ZS)	545
Characterization of the ZnS Specimens (CVD-ZS, CVDHIP-ZS, CVDHT-ZS, and PHIP-ZS)	547
Density Measurement	547
X-Ray Diffraction	548
Microstructural Analysis	549
Mechanical Properties	550
Transmission Measurements	558
Anti-reflection Coating [16, 70]	559
Erosion Protection Coatings [16, 71–73]	562
Conclusions	562
References	564

Abstract

Zinc sulfide (ZnS) is a well-known wide gap semiconductor ceramic that finds application in infrared (IR) optics, electroluminescent devices, flat panel displays, and photocatalysis. This chapter presents an overview of ZnS

R. Johnson (✉) · Y. R. Mahajan

International Advanced Research Centre for Powder Metallurgy and New Materials (ARCI),
Balapur, Hyderabad, India

e-mail: royjohnson@arci.res.in; mahajanyrm@gmail.com

P. Biswas · P. Ramavath

Center for Ceramic Processing, International Advanced Research Centre for Powder Metallurgy
and New Materials (ARCI), Hyderabad, Telangana, India

e-mail: papiya@arci.res.in; pandu@arci.res.in

ceramic as a candidate material for focusing on IR optics. Monolithic ZnS fabrication by various processes such as chemical vapor deposition (CVD) and hot isostatic pressing (HIP) of high purity ZnS powders and also post-CVD thermal treatments under pressure and pressure-less conditions to enhance the transmission of desired wavelength ranges are attempted. Physico-chemical, thermal, mechanical, and optical properties of CVD, post-thermal CVD-processed, and powder-processed ZnS specimens are reported. The results were correlated with the type of process employed in addition to process parameters. The thermodynamic feasibility of the CVD reaction based on zinc and hydrogen sulfide was evaluated and deposition conditions along with flow parameters are elucidated. Physico-chemical and optical properties indicated the superiority of CVD processing in achieving optical quality ZnS. Single-step consolidation of ZnS powder under HIP conditions resulted in relatively low density along with the presence of minor quantities of hexagonal wurtzite phase, leading to relatively low transmission values. Unlike post-CVD thermal treatment under pressure-less conditions, the HIP eliminates not only zinc hydride but also the healing of residual micro-porosity, extending transmission to the mid-wave infrared and visible ranges. Microstructure of ZnS is significantly influenced by process conditions, which in turn dictate the mechanical properties.

Keywords

Zinc sulphide · Infrared optics · Chemical vapour deposition · Hot isosttic pressing · Optical property

List of Abbreviations

AR coating	Anti-reflection coating
CTE	Coefficient of thermal expansion
CVD	Chemical vapor deposition
CVD-ZS	Chemical vapor deposited zinc sulfide
CVD HIP-ZS	Chemical vapor deposited and hot isostatic pressed zinc sulfide
CVD HT-ZS	Chemical vapor deposited and heat-treated zinc sulfide
FTIR	Fourier transform infrared spectroscopy
HIP	Hot isostatic pressing
HP	Hot pressing
LEFM	Linear elastic fracture mechanism
LWIR	Long wave infrared
MWIR	Med wave infrared
PHIP-ZS	Powder hot isostatic pressed zinc sulfide
SEM	Scanning electron microscopy
SENB	Single edge notch beam
Zn-H	Zinc hydride

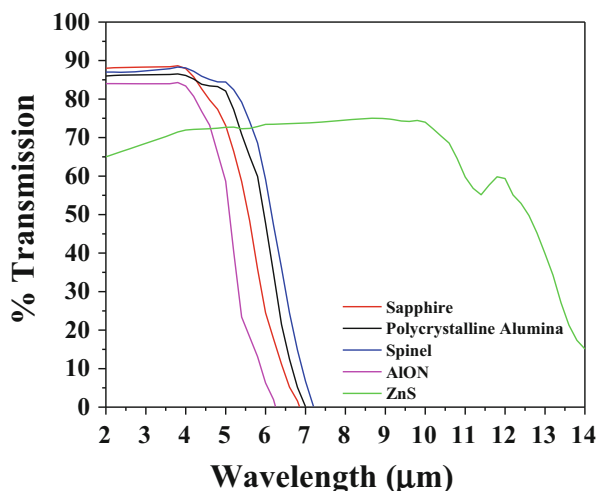
Introduction

Transparent ceramics exhibit a unique combination of optical and mechanical properties that make an interesting new class of material, having significant potential for application in various areas. Transparent ceramics currently being explored are single crystal sapphire (Al_2O_3), polycrystalline submicron alumina (Al_2O_3), magnesium aluminate spinel (MgAl_2O_4), aluminum oxynitride (AlON), zinc sulfide (ZnS), zinc selenide (ZnSe), and yttria (Y_2O_3). Typical transmission curves and the optical properties of the currently used transparent ceramic samples are shown in Fig. 1 and Table 1, respectively. It is well known that for optical applications, the primary requirement is the higher transmission for a broad and multispectral range. ZnS is regarded as the candidate material for the fabrication of infrared (IR) optics as the ZnS intrinsically exhibit very high multispectral transparency from visible through mid-wave infrared (MWIR) to long wave infrared (LWIR) spectral band of 0.4-14 micron.

Sphalerite is the well-known naturally occurring mineral of zinc sulfide (ZnS) usually associated with several impurities, such as cadmium and manganese [2, 3]. Pure ZnS, by virtue of its unique combination of mechanical and transmission properties has recently gained interest as a transparent ceramic for diverse applications [4–9]. Commercial applications of ZnS vary from prism, beam splitter, lenses, windows, high-energy lasers, radiation detectors for non-destructive testing and medical imaging [10–12]. ZnS is also a candidate coating material for retroreflective security applications, highway signs, and anti-reflective and solar coatings [13, 14]. In the strategic sector, ZnS is widely used as the thermal imaging domes and windows of IR-seeking missiles owing to their transmission of wider wavelength ranges in combination with moderate durability in harsh environments [15–17].

Information on the processing of ZnS is limited in the literature. The evaluation of ZnS as an infrared material has been recently reported by Harris [24] and McCloy [25]. Hot pressing of ZnS powder for fabrication of ZnS optics was

Fig. 1 Typical transmission curves of currently used transparent ceramics [1]



introduced by Kodak in 1950s. Chemical vapor deposition (CVD) ZnS was first produced in 1970s by Raytheon. Further, owing to emerging optoelectronic applications, significant work has been carried out by UK, former Soviet Union and Russia, Israel, and most recently in Asian countries such as Japan [26], China [27], and India [22].

Yashina [28] studied the processing of ZnS by CVD for IR optics. ZnS crystal prepared by melt growth in an inert atmosphere and at elevated pressure has exhibited large grains with poor mechanical properties in comparison with CVD ZnS. In addition to poor mechanical properties, the presence of impurities and imperfections reduces transmission properties of melt-grown ZnS. Another way of producing large ZnS is reported to be by the sublimation of ZnS fine particles followed by vapor condensation on the substrate material. The limitations of this process are the temperature gradient, which in turn shows deviation in its chemistry and heterogeneities. Shibata [34] has reported hot pressing (50–60 MPa and 950 °C) of ZnS powder with a particle size of 1–2 μm and achieved 70% transmission in a sample of 2 mm in thickness. In comparison with all the above processes, CVD offers better optical homogeneities with high density and minimum impurity content. The major limitation of the process is the toxicity of the gases employed, along with a very low deposition rate extending the fabrication time. A comparison of the processes is depicted in Table 2.

ZnS, although known to process starting from a high purity ZnS powder through hot isostatic pressing (HIP) at elevated temperature and pressure, recently CVD has

Table 1 Typical properties of transparent ceramics used currently [18–23]

Property	Sapphire	Submicron alumina	Spinel	Aluminum oxynitride	Zinc sulfide	Zinc selenide	Yttria
Range of transmission (μm)	0.2–5.5	0.2–5.5	0.2–6	0.2–5.5	0.4–12	0.6–18	0.25–8.5
Refractive index at 3 μm	1.71	1.71	1.66	1.73	2.25	2.43	1.87
Theoretical transmission (%) at 3 μm	86.5	86.5	87.4	85.7	70.4	65.2	81.6

Table 2 Processes for the fabrication of ZnS

Process	Temperature (°C)	Pressure (Pa)	Deposition rate ($\mu\text{m}/\text{h}$)	Transmission at 10 μm	References
Chemical vapor deposition	630–800	$<10^4$	50–100	72	[29–31]
Sublimation	>1000	1–10	100–1,000	≤ 70	[32, 33]
Hot pressing	900–1000	10^7 – 10^8	$>1,000$	>70	[34]
Melt growth	>1830	10^6 – 10^7	–	58	[35–37]

gained interest because of the inherent advantages of full densification along with homogeneous properties, which are the pre-requisite for achieving theoretical transmission values [38–40]. In the CVD process, volatile precursors react in the vapor phase and deposit on the heated substrate under optimal CVD operating parameters. CVD mainly operates according to chemical engineering principles and combines several other scientific disciplines that dictate the deposit properties. Although the optical properties of ZnS are outstanding, due to moderate mechanical properties, optical applications generally use ≥ 4 mm thickness, requiring a relatively high deposition rate [41, 42]. The key process parameters are temperature, pressure, flow velocities and reactant concentrations. In addition, the uniformity of the deposits is also a function of reactor geometry, substrate configurations, surface specificity and rate of deposition [43].

During CVD ZnS, the deposition is generally carried out in a hot wall reactor and the precursors of zinc vapor and hydrogen sulfide are injected with carrier gas such as argon or nitrogen. The reaction is sensitive to kinetics, thermodynamics, and transport phenomena, which are rather complex. The primary measure of the optical quality of ZnS is the visible color and scatter. Bredikhin et al. [44] studied the loss of transmission in polycrystalline CVD ZnS. The studies indicated that light scattering by faceted submicron inclusion with a refractive index of 1 (pores) makes a significant contribution toward optical losses. Additionally, when polarized light passes linearly through ZnS bulk, this results in de-polarization and an increase in the de-polarization ratio reduces the transmittance and optical losses occur. McCloy et al. [45] discussed the anisotropy in structural and optical properties of CVD ZnS. Because of the inherent complexity of CVD processing, the structure of bulk deposition may vary from nodules, cross-section banding, columnar structure with exaggerated grain growth and occasionally nano-scaled twinning. The origin of these defects plays a key role in optimizing CVD processing parameters to achieve optical quality ZnS.

It was assumed that ZnS is formed in the gas phase and then diffuses and deposits on the substrate during the CVD process [46]. From an optical point of view, this is undesirable and the heterogeneous reaction and low growth rate are preferable to producing more homogeneous cubic crystallography [47]. Choice of substrate material also plays a major role in obtaining ZnS with a defect-free structure. Alumina, fused silica, and molybdenum were investigated by earlier studies as substrates; however, they are found to be very reactive and result in limited reusability. Graphite substrates are found to be the most suitable and commonly used today on commercial basis [48]. Configuration of the substrate is also reported to be important as per the release of the deposit of concern, as revealed by the study by Goela et al. [49]. The mandrel reusability and precision are important for the replication of ZnS domes by CVD process. ZnS parts with 2-inch thickness were reported by a replication using a substrate with a surface finish of 20–180 Å RMS. Further, replication was also demonstrated with alumina and silica formulations. Reusability is a function of integrity of the release of coating, in addition to recoating methodologies employed with durable materials.

Generally, ZnS deposition temperatures of hot wall substrate are reported to range from 300 °C to 1,200 °C, with a reactor pressure of 40 torr [51]. Earlier studies indicated that a larger grain size generally occurs at high temperatures [52]. Another important

factor that plays a major role is the stoichiometry of ZnS shifting towards zinc-rich or sulfur-rich formulation, which is a function of the flow inputs of the reactants and their molar ratio [17]. During CVD, grains grow with a columnar structure as the grains parallel to the substrate surface grow more rapidly [53, 54]. Additionally, the $\text{Zn}_{(g)} + \text{H}_2\text{S}_{(g)} = \text{ZnS}_{(s)} + \text{H}_2_{(g)}$ -based CVD process results in undesired zinc hydride (Zn-H) phase as a by-product with occasional residual porosity. Hence, CVD-ZnS exhibits considerable scatter, especially in the visible region of the spectral band. Zn-H is reportedly removed by post-thermal treatment. Drezner et al. [5] correlated the microstructure, chemistry, and optical properties of ZnS specimens prepared using the CVD technique. Inherent Zn-H bond at 6 μm is a by-product due to the reaction between Zn and H_2 , the concentration of which is reported to have a significant effect on deposition temperature. An increase in the concentration of the Zn-H bond is reported with a decrease in temperature of the deposition.

Post-CVD annealing treatments of ZnS in various atmospheres, such as argon, vacuum, hydrogen, sulfur including air, have been used in experiments [55]. Annealing treatments are expected to remove the yellowish tinge that is a characteristic of CVD ZnS, along with homogenization expanding the window of transmission in the broadband IR and visible region. Studies have shown the best annealing temperature at around 500 °C for 125 h in a sulfur atmosphere, which yielded the maximum transmission values. One of the critical issues to be addressed in designing the heat treatment schedule is the cubic to hexagonal transformation that is sensitive to the temperature. The rate of transformation can be determined by X-ray diffraction studies based on the peak intensity. Application of HIP to CVD ZnS is reported to increase the visible and infrared region transmission, which can be obtained as in the case of single-crystal ZnS. Dynamic recrystallization, as indicated by extensive twinning, is proposed to be the mechanism operative for ZnS CVD HIP in addition to a high-temperature creep process, such as dislocation creep (slip and climb), Nabarro–Herring creep, and Coble creep [56]. However, HIP is reported to cause grain growth and phase transformation to wurtzite, which is undesirable for the mechanical and optical properties respectively [57]. Shchurov et al. [58] evaluated the properties of hot isostatically pressed CVD ZnS with respect to elastic and optical properties. HIP is reported to increase the Young's modulus in combination with transmission properties. Non-equilibrium boundaries with dangling bonds responsible for the formation of bond charges are significantly decreased on HIP through secondary recrystallization with the formation of thin equilibrium grain boundaries. Karaksina et al. [59] analyzed the recrystallization behavior under HIP conditions by varying argon pressure from 89 to 200 MPa and temperatures of 810–1,100 °C. The mechanism of the recrystallization process is mainly diffusion within the temperature range of 810–985 °C, whereas a combination of diffusion assisted by plastic deformation occurs at an elevated temperature range of 985–1,100 °C.

Hot pressing and HIP of ZnS powder have also been reported for optical fabrication of polycrystalline ZnS ceramics [60–63]. Hot pressing of ZnS below its transformation temperature produces ZnS with no hexagonal phase. However, dynamic crystallization and twinning was evident in earlier studies, which is

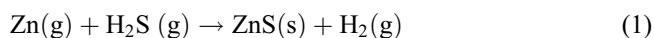
attributed to the flow stresses associated with the temperature and pressure at the peak temperature. This was also observed in the case of CVD ZnS under HIP conditions as discussed above. ZnS can also be attempted by vacuum encapsulation and direct powder HIP, which will eliminate long hours of CVD run in the hazardous environment of H₂S [61]. The physical and chemical properties of the powder, especially the chemical purity, play a very critical role in achieving transparency.

In the current chapter, preparation of self-standing ZnS by chemical vapor deposition (CVD) and direct powder consolidation by HIP are discussed. Additionally, attempts to improve the transmission through post-CVD thermal treatment such as annealing under pressure-less conditions in addition to simultaneous application of pressure and elevated temperature through HIP are also described. All the ZnS samples produced by the above techniques have been characterized for physico-chemical properties (X-ray diffraction [XRD] phase analysis, density), thermal property (coefficient of thermal expansion), mechanical properties (flexural strength, Knoop hardness, fracture toughness, fracture release rate, R-curve behavior, compressive strength), and optical properties (visible, MWIR, and LWIR). The results were further analyzed and comparatively evaluated and correlated with respect to the processing methodology followed and processing parameters with respect to the processing techniques. It was observed that although CVD based on the reaction between zinc and hydrogen sulfide results in relatively dense ZnS parts, the specimens exhibited a yellowish tinge and opacity in the visible range, requiring post-thermal treatment to extend the transmission range in the visible region and also to enhance the transmission in the MWIR and LWIR regions. Elimination of the Zn-H band (which is occluded in the bulk ZnS, the by-product formed by the CVD reaction) in combination with the residual porosity can be achieved by simultaneous application of temperature and pressure through HIP. This chapter also describes an outline of the optical polishing and anti-reflection coating on ZnS samples with dimensions of 25 × 25 × 4 mm. The authors' hands-on experience in the above field is discussed in the following sections.

Processing of Zinc Sulfide

Processing of Zinc Sulphide by CVD (CVD-ZS)

Monolithic ZnS samples were prepared by the CVD reaction (designated as CVD-ZS) between zinc vapor and hydrogen sulfide gas in the temperature range of 650–750 °C and reactor pressures of 50–100 mbar according to Reaction-1 [46, 50]. Formation of bulk CVD ZnS deposit depends upon the feasibility of the CVD reaction employed.



For CVD ZnS, the deposition was determined based on the calculated Gibbs free energy ΔG . In the reaction, (g) and (s) refer to gas and solid reactants. For the CVD

reaction to occur, first of all the reaction should be thermodynamically feasible, i.e., if the free energy change (ΔG) of the reaction is negative. To calculate ΔG of reaction (ΔG_r) it is necessary to know the thermodynamic properties of each component, specifically their ΔG . The relationship can be expressed by the following Eq. 2 [38, 46]:

$$\Delta G_r^{\circ} = \sum \Delta G^{\circ} \text{products} - \sum \Delta G^{\circ} \text{reactants} \quad (2)$$

The free energy of formation is not a fixed value, but varies as a function of several parameters, including the type of reactants, the molar ratio of the reactants, the process temperature, and the process pressure. The relationship is represented by Eq. 3 [46]:

$$\Delta G_r = \Delta G^{\circ} + RT \ln Q \quad (3)$$

By definition, ΔG_r at equilibrium is zero; thus, $\Delta G = -RT \ln Q$:

$$\Delta G = 82.1T - 5.9T \ln T - 0.62 \times 10^{-3} T^2 - 76,400 \text{ cal/mol} \quad (4)$$

Based on the available thermo-chemical data, ΔG of the reaction was estimated as per Eq. 4 and the ΔG of the reaction is found to be -37.3 kcal/mol at a temperature of around 680 °C [61]. An acceptable quality of bulk CVD materials at a temperature of 650 – 750 °C can be produced under the temperature regime in which ΔG of the reaction is negative and is within the range of -35 to -45 kcal/mol. It is well known that as a rule of thumb, good quality CVD deposits can be produced when ΔG is negative and further when its magnitude is around -30 kcal/mol. If the temperature is below the 630 °C, deposition rate as low as 50 micron/hr following the Arrhenius equation, the cost of the process will become exorbitant owing to excessive deposition time when a self-standing optical monolith is to be fabricated [46]. On the other hand, with very high deposition rates, the deposits will have inherent microstructural defects in addition to microcracks, which can be attributed to the bowing of the deposits from the substrates. A schematic of the hot wall CVD reactor and the process, along with the deposition sequence, is shown in Fig. 2. It is evident from the Fig. 2 that initially vaporized precursors are transported to the CVD reactor and reactive chemical species are generated from the precursors reacting on the hot substrate, forming ZnS.

Precursor Transport Phenomena

Rather than the velocity of the gas flow, the flow pattern is also a key factor in achieving the desired bulk properties in the mass controlled regime desired to form monolithic self-standing ceramics. The flow pattern due to natural convection can be characterized by the Rayleigh number (R_a) [46]:

$$R_a = \frac{\alpha g C_p d^3 \Delta T Q^2}{\eta K} \quad (5)$$

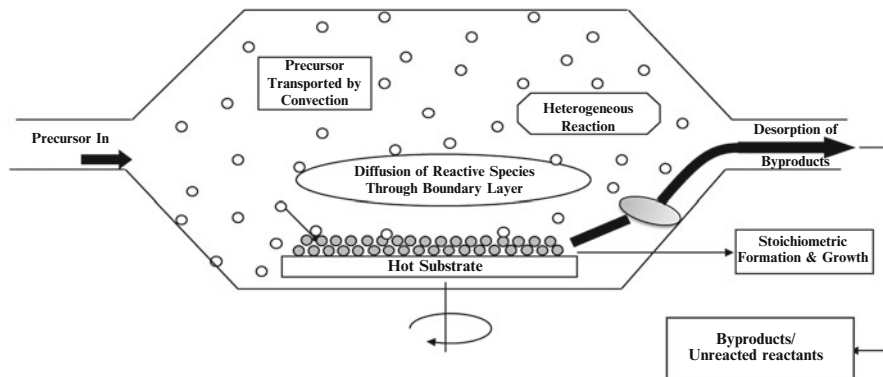


Fig. 2 Chemical vapor deposition (CVD) process steps and deposition sequence (schematic illustration)

where,

α : Thermal expansion coefficient ($= 1/T$ for an ideal gas) ($7.1 \times 10^{-6}/^{\circ}\text{C}$)

g : Acceleration due to gravity

C_p : Specific heat at constant pressure

Q : Density

d : Characteristic distance

ΔT : Temperature difference between the hot and cold regions

K : Thermal conductivity

η : Viscosity

Critical parameters that affect the vapor precursor transport are reactor temperature and distribution within the reactor, reactor pressure, reactor geometry, flow velocities, and properties of the gases. As the gaseous reactants are injected into the reaction chamber through the orifice located in the injector, flow velocity along the axis is expected to be high and as the distance from the orifice increases, the flow pattern decays. As it enters into the rotating boundaries of the substrate, turbulence is generated, which results in intermixing, generating a recirculating flow. Flow rates of carrier gas and revolutions per minute of the substrate play a major role in maintaining the velocities and hence the flow patterns. The flow velocities of the gaseous reactants along with argon carrier gas are kept within the range of 1.54×10^{-6} m/s for the CVD Reaction-1, in the present study. Further, the Rayleigh number (R_a) is estimated to be within the range of 10^6 , confirming the laminar flow [46].

As depicted in the schematic (Fig. 2) the chemical species are transferred to the substrate surface to form the deposit through the boundary layer. The by-products are further flown out of the reactor. The CVD reaction was carried out at a temperature of 600–700 °C at a pressure of 50–100 mbar, with a molar ratio of Zn:H₂S 1:1.2 and a deposition rate of 70–120 μm . These conditions are optimized based on several trials carried out at our laboratory [46].

Selection of Substrate

It is important to select the substrate material with similar thermal expansion behavior to avoid mismatch after deposition between the deposit and the substrate, as cooling results in the cracking of the ZnS deposit. The thermal expansion plots dL/L_0 (%) with respect to the temperature of ZnS, along with graphite substrate measured at our laboratory, are shown in Fig. 3. The matching of the CTE of graphite with ZnS can be attributed to the orientation of the anisotropic crystallography of c-axis while processing. An engineering drawing of substrate fabricated for the deposition of ZnS, along with the holder and fixtures, is shown in Fig. 4.

Deposited material has shown nodular growth on the surface and spherical features in the order of a few microns in diameter (as shown in Fig. 5). This may

Fig. 3 Dilatometric curve of graphite and ZnS

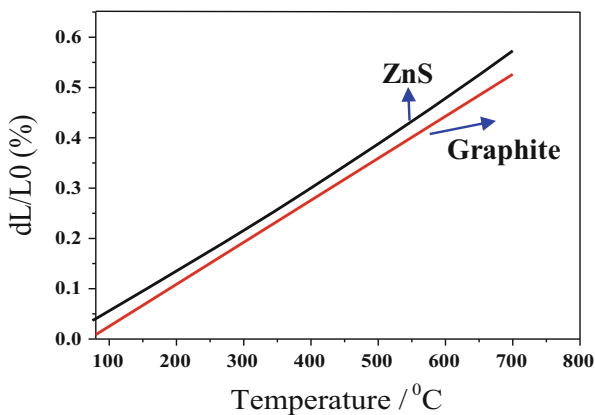


Fig. 4 Engineering drawing of graphite substrate holder

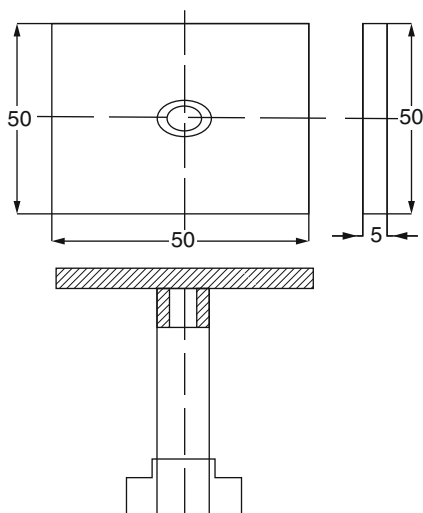
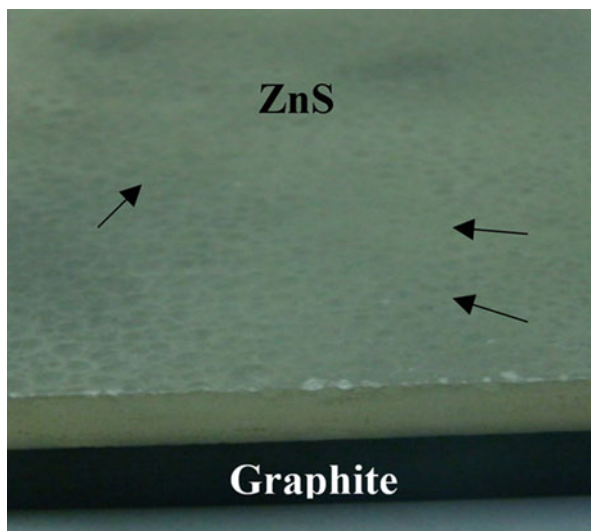


Fig. 5 Deposited ZnS on graphite substrate [46]



be due to the heterogeneous nucleation sites, as the growth still proceeds, whereas cooling at slow rates leads to preferential build-up on the surface that is not stable. Further, reactant concentration gradients may also result in such protrusions. Earlier studies also reported that long duration of CVD can result in deposition morphology, such as alligator skins, globules [53], and pebbles [64]. Typical grinding steps involve rough grinding using silicon carbide grits of 120 μm in size for the removal of uneven surfaces and surface defects such as protrusions. This is followed by smooth grinding with a series of alumina slurry up to 3 μm . The fine finished surface is further subjected to optical polishing with high-purity alumina slurry of 1 μm .

A typical ZnS sample produced by the above CVD conditions and further ground and optically polished is shown in Fig. 6, along with the IR transmission pattern. It is evident from Fig. 6 that the CVD-deposited zinc sulfide has an inherent zinc hydride (Zn-H) band, which is produced as the results of a by-product of the CVD Reaction-1. This not only reduces the transmission within the range of 7–10 μm but also exhibits an absorption peak at 6.2 μm . The average transmission is greater than 70% in the 7–10- μm region and was lowered to around 60% in the lower regions of 3–6 μm . The presence of Zn-H, the by-product due to the CVD reaction between Zn and H_2 , has shown a strong absorption band at 6.2 μm for CVD-ZS. The presence of Zn-H limits the broadband transmission within the range 3–10 μm , which essentially requires post-CVD thermal treatment to enhance the transmission capability within the range specified above.

Heat Treatment of CVD-ZnS (CVDHT-ZS)

In an attempt to eliminate the Zn-H absorption peak and improve the transmission, the CVD-ZS samples were heat treated at 950 $^{\circ}\text{C}$ in an argon atmosphere for a

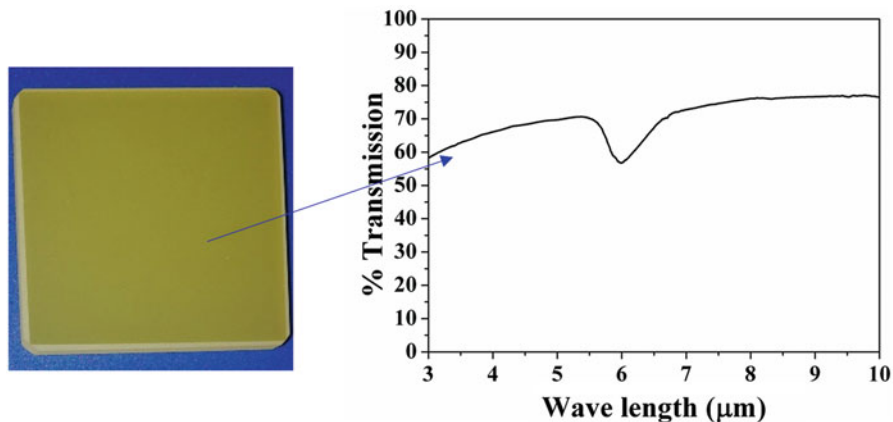
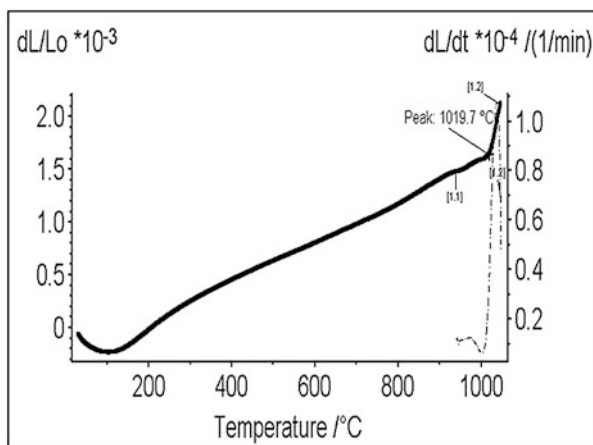


Fig. 6 A typical image of CVD-ZS, along with the infrared (IR) transmission plot [22, 46, 50]

Fig. 7 Dilatometric plot of ZnS [46]



soaking period of 1 h. The temperature of 950 °C was selected based on the dilatometric study, which indicated that a sudden change in the slope of the dilatometric curve was observed at 1,020 °C, corresponding to the crystallographic transformation of sphalerite to wurtzite. XRD was recorded for the sample after exposure to 1,020 °C and was confirmed to be wurtzite. A typical dilatometric curve demonstrating transformation is shown in Fig. 7.

A typical sample of ZnS after heat treatment along with the transmission plot is shown in Fig. 8. Post-CVD thermal treatment under pressure-less conditions have eliminated the absorption band at 6.2 μm and the chemical vapor deposition heat-treated zinc sulfide (CVDHT-ZS) sample was translucent. However, IR transmission

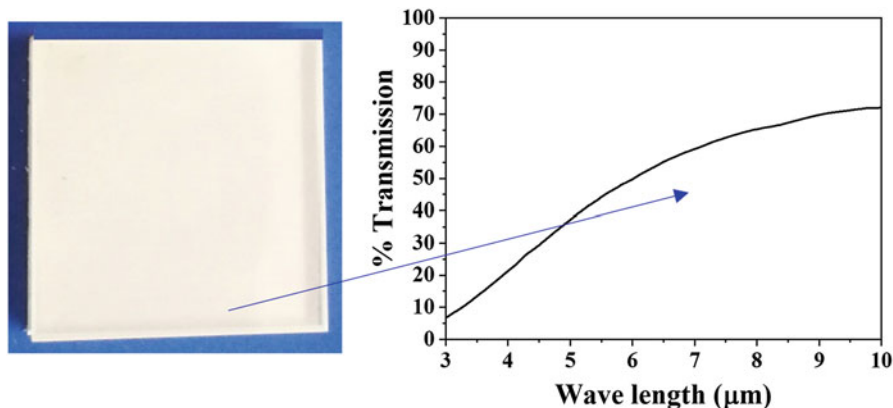


Fig. 8 A typical image of chemical vapor deposition heat-treated zinc sulfide along with IR transmission plot [22]

was reduced drastically in the region of 3–6 μm , whereas only a marginal reduction was observed in the 7–10 μm region. The reason for the scattering observed at the 3–6 μm region for the CVDHT-ZS sample is the micro-porosity generated because of the elimination of Zn-H.

Hot Isostatic Pressing of CVD-ZnS (CVDHIP-ZS)

Based on the observations in the presence of the micro-porosity of the CVDHT-ZS samples, which was also confirmed by the microstructural studies in the following section (see Fig. 14), heat treatment under pressure using HIP was attempted. An optimized HIP cycle used in the current study based on several experiments is shown in Fig. 9. HIP of CVD-ZS samples were carried out at a temperature of 950 $^{\circ}\text{C}$ and a pressure of 135 MPa, for a soaking period of 4 h. A typical CVDHIP-ZS sample after HIP is shown in Fig. 10, along with the transmission pattern. It is evident from the Fourier-transform infrared spectroscopy (FTIR) pattern that the CVDHIP-ZS sample showed a clear improvement in transmission in the 3–10 μm region and is uniformly $>70\%$. This can be attributed to the simultaneous application of temperature and pressure through HIP, resulting in removal of residual microporosity.

Hot Isostatic Pressing of ZnS Powder (PHIP-ZS)

Morphology and XRD pattern of ZnS powder (99.99% pure; Emerk, Germany) are depicted in Fig. 11a, b and is used in the current study. It is evident from Fig. 11b that the powder shows a pure sphalerite phase with irregular morphology (Fig. 11a) and mostly fine (average particle size $<1 \mu\text{m}$) powder agglomerates. Powder was encapsulated under vacuum in an HIP capsule fabricated out of a

Fig. 9 Optimized hot isostatic pressing (HIP) schedule

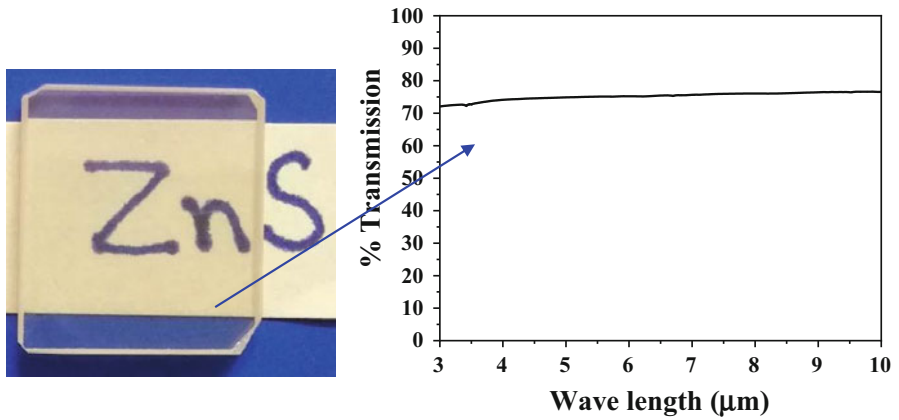
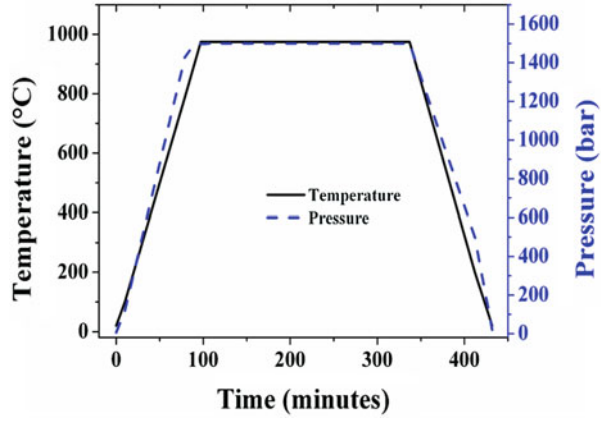


Fig. 10 A typical image of CVDHIP-ZS along with IR transmission plot [22]

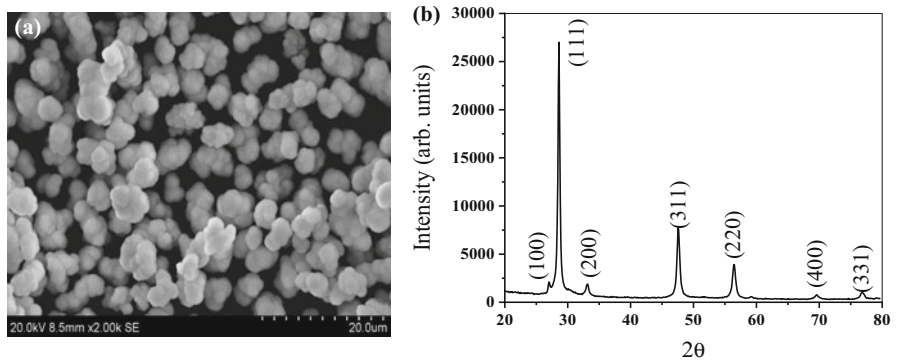


Fig. 11 (a) Morphology and (b) X-ray diffraction pattern of ZnS powder [62]

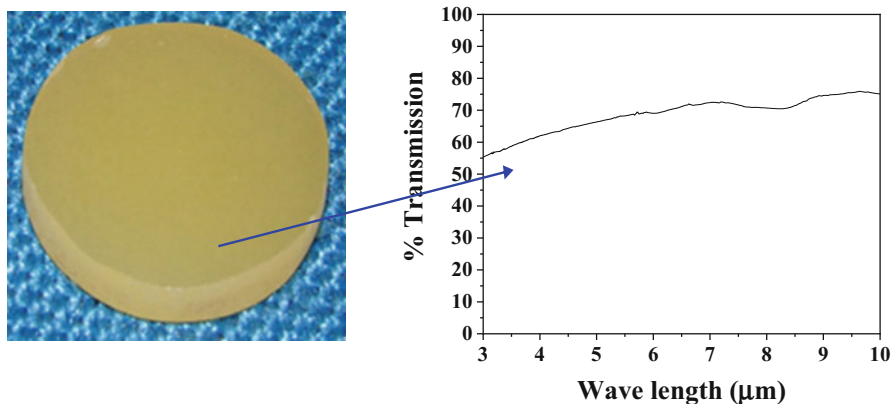


Fig. 12 A typical image of CVDHIP-ZS, along with the IR transmission plot [62]

0.5-mm-thick SS304 sheet, degassed at 400 °C in a dynamic vacuum of 5×10^{-6} torr and sealed. HIP capsule material of SS304 was selected based on the inertness with ZnS and the machinability in addition to weldability. The capsule under vacuum was subjected to HIP (designated as Processing of Powder Hot Isostatic Pressing ZnS (PHIP-ZS)) under standardized parameters identical to CVD-ZS and the HIP schedule is depicted in Fig. 9. A typical ZnS sample produced by the powder HIP process is shown in Fig. 12 along with the transmission pattern.

Characterization of the ZnS Specimens (CVD-ZS, CVDHIP-ZS, CVDHT-ZS, and PHIP-ZS)

Density Measurement

Density of all the specimens of CVD-ZS, CVDHIP-ZS, CVDHT-ZS, and PHIP-ZS were measured by the Archimedes' principle following ASTM 792. CVDHIP-ZS samples have exhibited the highest density of 4.0860 g/cm³ close to theoretical values in comparison with 4.0850 g/cc for CVD-ZS and 4.0831 g/cm³ observed for CVDHT-ZS samples. This can be attributed to the high-temperature recrystallization that occurs under pressure in combination with the homogenization of the structure of the material by elimination of disordered structures and non-equilibrium boundaries generated by the CVD process. Further, the elimination of residual porosity generated because of the removal of Zn-H during HIP also results in a marginal increase in density values. However, in the case of the PHIP-ZS sample, on direct powder consolidation by HIP, it showed a relatively lower density value of 4.079 g/cc.

X-Ray Diffraction

Phase analysis of all the samples was carried out by an XRD technique employing Cu K α using D8 Advanced (Bruker, Germany) system. Further, the transverse I ratio calculated based on the X-ray data recorded for parallel and perpendicular to the coating direction using the equation $I_{(111)}/(I_{(111)} + I_{(220)})$, where $I_{(111)}$ and $I_{(220)}$ are the net area of the peaks corresponding to reflections from (111) and (220) planes for CVD-ZS, CVDHIP-ZS, CVDHT-ZS, and PHIP-ZS XRD patterns of CVD-ZS, CVDHIP-ZS, CVDHT-ZS, and PHIP-ZS samples, are shown in Fig. 13a–d. Unlike the specimens undergoing post-treatment after CVD, CVD-ZS samples are found to be more isotropic. Except for XRD recorded on PHIP-ZS, which has shown evidence of (100) reflection at 2 theta (26.93°) corresponding to a hexagonal wurtzite phase in traces, all other XRD patterns have shown phase pure sphalerite. Anisotropy is evident from the XRD patterns of CVDHIP-ZS and CVDHT-ZS samples as all the diffraction peaks disappeared or minimized except for the (111) diffraction peaks, where an increase in intensity was observed. Further, the transverse I ratio obtained from the X-ray diffraction pattern, which is a measure of the extent of anisotropy, is also in good agreement with the observed anisotropy. The transverse I ratio is found to be 0.6489 for CVD-ZS, in comparison with 0.9172 and 0.9434 for CVDHIP-ZS and CVDHT-ZS samples, respectively. XRD studies also confirmed that the loss of isotropy is imparted by exposure to temperature rather than pressure.

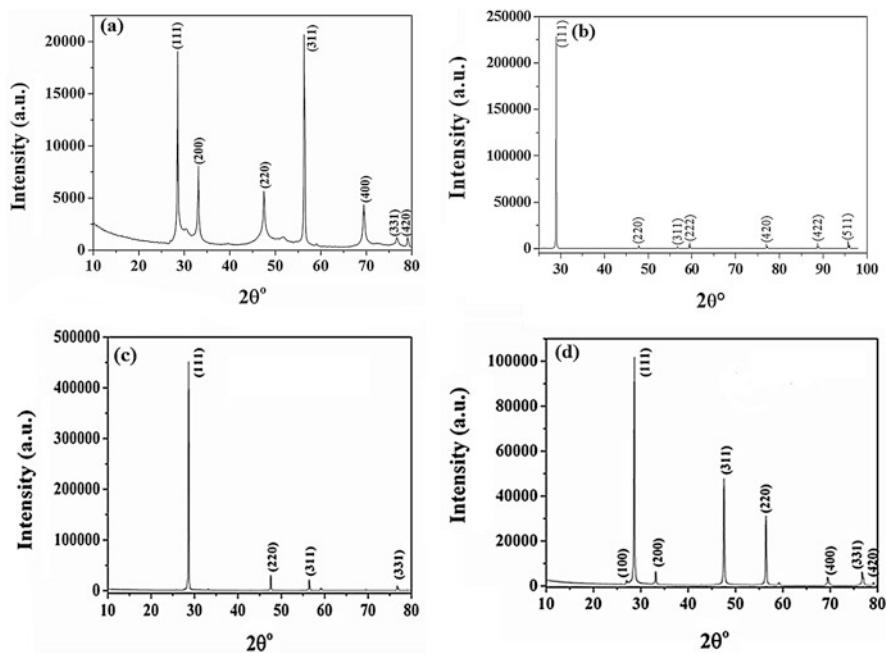


Fig. 13 XRD pattern of (a) CVD-ZS, (b) CVDHIP-ZS, (c) CVDHT-ZS, and (d) PHIP-ZS [22, 62]

The transverse I ratios of the surface (perpendicular to the direction of coating) and cross-section (parallel to the direction of coating) for CVD-ZS, CVDHIP-ZS, and CVDHT-ZS samples were also estimated. CVD-ZS surface showed a transverse I ratio of 0.6489 in comparison with 0.3724 for CVD-ZS cross-section indicating preferred orientation of crystals perpendicular to the direction of coating. Further, a similar trend is seen for CVDHIP-ZS and CVDHT-ZS samples as well. Transverse I ratio value of 0.9172 and 0.9434 for CVDHIP-ZS surface and CVDHT-ZS surface in comparison with the values of 0.56621 and 0.5574 for CVDHIP-ZS cross section and CVDHT-ZS cross section respectively indicated a highly preferred orientation perpendicular to the direction of coating. A higher transverse I ratio difference of 0.3509 and 0.3860 for CVDHIP-ZS and CVDHT-ZS samples compared with 0.2765 for CVD-ZS sample shows more preferential orientation.

Microstructural Analysis

The samples were also ceramographically polished. CVD-ZS samples were chemically etched; however, all other samples were subjected to thermal etching at 900 °C. The microstructure of the etched samples were characterized by scanning electron microscopy (Hitachi 2400, Japan). Microstructure of the CVD-ZS, CVDHIP-ZS, CVDHT-ZS, and PHIP-ZS samples are compared in Fig. 14a–d. A linear array of columnar grain with lamellar types of structures within the grain oriented parallel to the coating direction is evident from the CVD-ZS microstructures. Average grain size of the CVD-ZS is found to be 5–10 μm. It is clear from Fig. 14b, c that post-thermal treatments resulted in a substantial increase in the grain sizes, with larger grains within the range 50–100 μm with twin fractions and recrystallization also resulting in the disappearance of conventional grain boundaries and lamellar structures inherently present in CVD-ZS. PHIP-ZS samples have shown grain size of 60–100 μm, as is evident from Fig. 14d, which is similar to CVDHIP-ZS, although there is a strong dependence on the size of the initial starting powder used for HIP, as reported by Reddy and Rao [65]. Densification and microstructure development under simultaneous application of temperature and pressure during HIP operate through plastic deformation. Hot isostatic process proceeds through particle rearrangements in the initial stages; however, the pressure reaches the yield strength of ZnS particles effecting isotropic plastic deformation and densification accordingly. ZnS, when subjected to a temperature of at least half the melting point, undergoes macroscopic deformation, as revealed by (111) orientation (Fig. 13b) due to a translational slip occurring along the cleavage planes. Curvature-driven grain boundary diffusion becomes more active at higher temperatures and the grain growth rate supersedes the densification rate, resulting in grain growth. The trace of hexagonal phase present in a few samples can also be explained by the plastic deformation (strain), which promotes phase transformation.

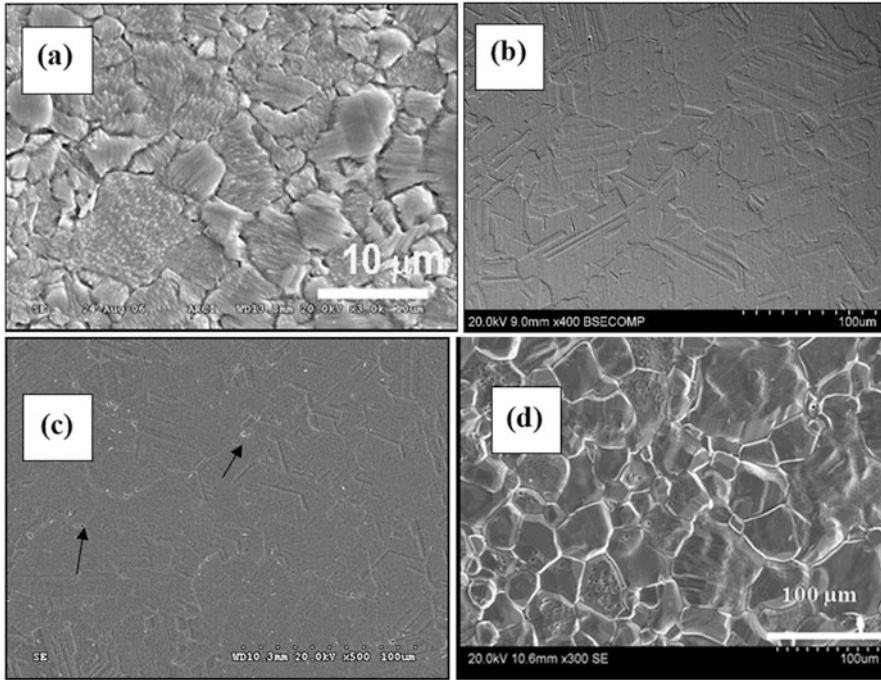


Fig. 14 XRD pattern of (a) CVD-ZS, (b) CVDHIP-ZS, (c) CVDHT-ZS, and (d) PHIP-ZS [22, 62]

Mechanical Properties

Knoop Hardness, Flexural Strength, and Compression Strength

Mechanical characterizations such as Knoop hardness (Leco, St. Joseph, MI) at 200 gf and the flexural strength were measured by using three-point bend samples of the dimensions $45 \times 4 \times 3$ mm using a universal testing machine (4483; Instron, UK) following ASTM C-1161-02C.

$$\sigma_f = \frac{3}{2} \left(\frac{P_f \times L}{bd^2} \right) \quad (6)$$

where, P_f is the maximum load at failure, L is the span length (40 mm), b is the width of the specimen and d is the thickness of the specimen. There have been considerable changes in the mechanical behavior of the samples on HIP. Knoop hardness of CVD-ZS, CVDHIP-ZS, CVDHT-ZS, and PHIP-ZS is 210, 180, 172, and 178 kg/mm^2 (average of five samples). Flexural strength of CVD-ZS, CVDHIP-ZS, and CVDHT-ZS are found to be 79, 50, and 45 MPa (average of five samples). Flexural strength of PHIP-ZS could not be measured owing to limitations in sample size. Decreases in Knoop hardness and flexural strength were observed as a result of

HIP, which can be attributed to the ~ 10 times increase in grain sizes in the case of CVDHIP-ZS and PHIP-ZS samples.

Compression strength of the samples are measured by using samples of dimensions $5 \times 5 \times 5$ mm, employing a universal testing machine (4483; Instron, UK) following the ram rate 0.5 mm/min. Further, the compression strength is estimated by the load/area.

Samples of CVD-ZS, CVDHT-ZS, and CVDHIP-ZS were subjected to quasi-static compression tests using Instron 4483 at a ram rate of 0.5 mm/min. A sample size of $6 \times 6 \times 6$ mm was used for the testing. Typical engineering stress–strain curves obtained from CVD-ZS, CVDHT-ZS, and CVDHIP-ZS are shown in Fig. 15. Although a minimum of six specimens were tested in each case, for the sake of clarity, only one stress–strain curve for each condition is shown in Fig. 19. It is evident that the nature of stress–strain curves of CVD-ZS, CVDHT-ZS, and CVDHIP-ZS is almost the same within a narrow range of experimental variation for each set of specimens. The material in all three processed conditions showed significant elastic deformation prior to the small non-linear deformation behavior. The CVDHIP-ZS material exhibited a peak

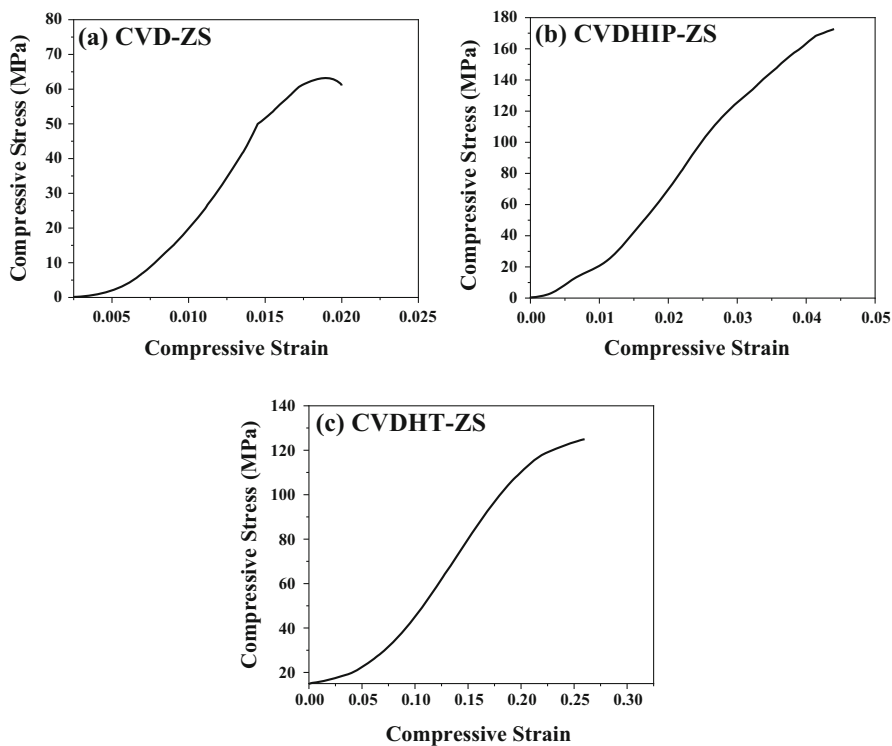


Fig. 15 Compressive stress–strain curves of (a) CVD-ZS, (b) CVDHIP-ZS, and (c) CVDHT-ZS [66]

compressive strength before fracture (165 ± 6 MPa), which is 235% higher than the corresponding compressive strength of the CVD-ZS material (70 ± 4 MPa). The CVDHT-ZS has exhibited a peak compressive strength before fracture (138 ± 8 MPa), which is 197% higher than the corresponding compressive strength of the CVD-ZS samples and 81% lower than that of the CVDHIP-ZS specimen. The lower strength of CVDHT-ZS samples in comparison with CVDHIP-ZS samples can be attributed to the fine distribution of residual pores formed because of the decomposition of Zn-H during thermal treatment, as is evident from the microstructure in Fig. 14. CVD, being a non-equilibrium process, results in unique grain boundaries, and pebble-like and lamellar structures (Fig. 14) initiate microcracks under compression where the fracture initiated needs to relocate to the neighboring grains for further crack extension. This leads to the 100% increase in compressive strength observed in CVDHIP-ZS samples, which can be attributed to the high degree of microstructural homogeneity that is evident from the absence of lamellar structures observed with CVD-ZS sample.

Fracture Toughness, Fracture Resistance, and Fracture Energy Release Rate

To estimate the fracture release rate (J_c), dimensions of different notches according to ASTM E-399 (0.3–0.55) times the width of the single-edge notch beam (SENB) specimens were cut at the midpoint. Plane strain fracture toughness, K_{Ic} , was estimated by ASTM C-1421-99 for the notch length of 0.45–0.55 times the width. The flexural strength (σ_f) under three-point bend loading is also calculated.

The procedure outlined by Prasad et al. [67] was used for evaluating the fracture resistance of ZnS material employing K_{Ic} and for estimation of the total fracture energy release rate, J_c . As described above, the fracture resistance of the present material was evaluated on specimens with notches of different initial lengths, introduced using a 0.15-mm-thick diamond wafer blade. To ensure that notches are straight across the cutting plane, a specially designed jig was fabricated and used. The notches thus introduced were found to have a finite root radius, ρ typically of the order of 100 μm . The ρ values were determined by optical profilometer and the crack lengths were found to be within the range of 0.3–0.55 times the specimen width. Among these, only specimens with crack lengths within the range specified by the ASTM standard E-399 [68] (0.45–0.55) times the width of the specimen were considered for the determination of K_{Ic} values. Tests were conducted using an Instron 4483 with computer-controlled software. A ram rate of 0.5 mm/min was used during the test. Samples were loaded using a self-articulating point bend fixture with a span length of 40 mm. Further, K_{IQ} values were estimated using Eq. 7.

$$K_{IQ} = \frac{P_Q S}{BW^{3/2}} f\left(\frac{a}{W}\right) \quad (7)$$

where

$$f\left(\frac{a}{W}\right) = 3\left(\frac{a}{W}\right) \left[\frac{1.99 - \left(\frac{a}{W}\right) \left(1 - \frac{a}{W}\right) \times \left(2.15 - 3.93 \frac{a}{W} + 2.7 \frac{a^2}{W^2}\right)}{2 \left(1 + 2\left(\frac{a}{W}\right)\right) \times \left(1 - \frac{a}{W}\right)^{3/2}} \right] \quad (8)$$

P_Q or P_{\max} is the load corresponding to an unstable fracture (the determination of values is specified in ASTM standard C-1421-99), S is the span of the three-point bend loading specimen, B is the thickness, W is the width, and a is the crack length. The other specimens with larger crack lengths were essentially used to determine the values of the total fracture energy release rate (J_c) [69]. The load-displacement curves thus obtained were analyzed to calculate the fracture resistance.

Plane Strain Fracture Toughness (K_{Ic})

Plane strain fracture toughness studies were limited to CVD-ZS and CVDHIP-ZS samples. Variation of load with respect to displacement of the notched specimens is obtained from the three-point bend loading curves and further evaluated for plane strain fracture toughness, K_{Ic} . The details of the specimen dimensions, notch length values used, and the conditioned fracture toughness (K_{IQ}) values are given in Table 3.

The load-displacement curves in Fig. 16 clearly indicate that all the specimens failed without a noticeable stable crack extension and thus the P_{\max} values corresponded to failure. Use of P_{\max} values in Eq. 7 yielded the K_{IQ} values, which provided the characteristic material fracture toughness K_{Ic} . However, these K_{Ic} values are notch root radius-specific. Although specimens with varied a/W ratio were tested, data corresponding to specimens with a/W values in the range of 0.45–0.55, as specified by ASTM standard E-399/ASTM standard C-1421-99, were only used to derive K_{Ic} values. The values of K_{\max} and K_Q derived from these tests are also listed in Table 3. The data in Table 3 clearly indicate that the

Table 3 Fracture toughness data of ZnS material under CVD and CVD + HIP conditions

Material and specimens ID	B (mm)	W (mm)	a (mm)	a/W	f(a/W)	$P_Q = P_{\max}$ (N)	$K_{IQ} = K_{\max}$ (MPa \sqrt{m})
CVD-ZS							
1	3.04	4.15	1.2	0.30	1.89	20.45	1.18
2	2.96	4.02	1.6	0.40	2.01	14.86	1.18
3	3.05	3.86	2.1	0.54	2.42	8.25	1.03 ^a
CVDHIP-ZS							
1	3.05	4.05	1.2	0.30	1.89	13.01	0.75
2	3.07	4.05	1.6	0.47	1.47	9.73	0.90 ^a
3	3.06	3.99	2.1	0.53	2.35	7.99	0.91 ^a

^aValid plane strain fracture toughness (K_{Ic})

a/W values considered for the calculation of the Valid plane strain fracture toughness (K_{Ic})

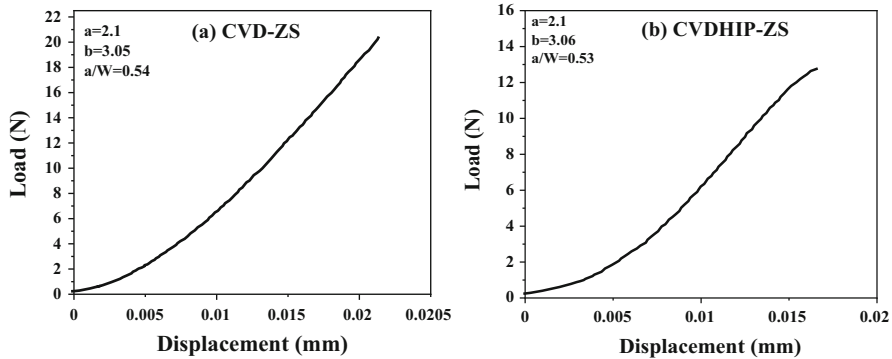


Fig. 16 Typical load-displacement plot of (a) CVD-ZS and (b) CVDHIP-ZS conditions [69]

material exhibits valid K_{\max}/K_Q values (<1.1) for all values of a/W within the range 0.45–0.55. In view of these observations, the K_{IQ} values derived from specimens with a/W of 0.54 in the case of CVD-ZS and 0.47 and 0.53 in the case of CVDHIP-ZS are only considered to yield valid K_{Ic} . The K_{Ic} values thus determined were found to be higher in the CVD condition ($1.03 \text{ MPa}\sqrt{\text{m}}$) compared with that in CVDHIP-ZS condition ($0.91 \text{ MPa}\sqrt{\text{m}}$). The data in test values of conditional fracture toughness (K_{IQ}) were found to decrease moderately with increase in the crack length. This is due to the change in mode of fracture with increased crack length. At higher crack lengths, the fracture mode gradually changed to predominantly shear, whereas the same at lower crack lengths ($a < 0.55 W$) is predominantly tensile. This is true for both CVD-ZS and CVDHIP-ZS conditions, as is evident from the fractographs (described in later sections). As all the specimens with lower a/W values (<0.55) failed under predominantly tensile fracture, the values thus determined in this section provide meaningful and true K_{Ic} values, which are only root radius-dependent.

Total Fracture Energy Release Rate (J_c)

The load-displacement curves obtained from the three-point bend specimen with varied crack length employed for the evaluation of the total fracture energy release rate (J_c) are presented in Fig. 17a, b. Crack length values, along with their normalized a/W values (crack length “a” normalized with the specimen width “W”), used for the determination of J_c values of the CVD-ZS material (indicated as 1, 2, and 3 in Fig. 17a, b) are given in Table 3. Although six samples with different a/W values were tested in the case of both CVD-ZS and CVDHIP-ZS samples, for the sake of clarity, only one of the three load-displacement plots for each case are included in Fig. 16.

The total fracture energy release rate (J_c) is obtained using the procedure outlined in ASTM Standard E-399 and [68] as:

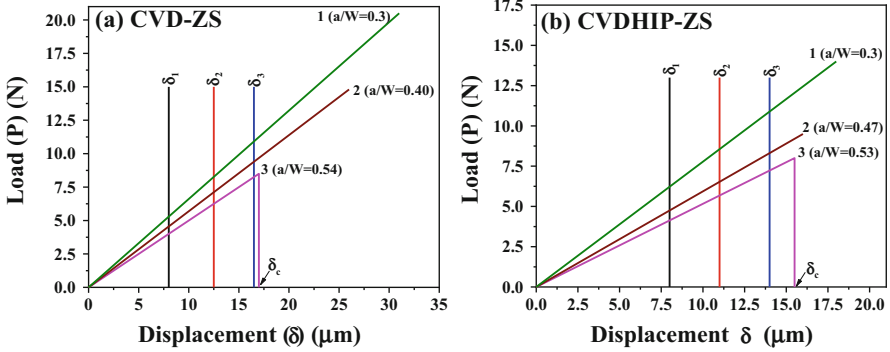


Fig. 17 Load-displacement curves obtained from a notched specimen of (a) CVD-ZS and (b) CVDHIP-ZS [69]

$$J_c = \{-(\Delta E_{fr}/\Delta a)\}/B \quad (9)$$

where $\Delta E_{fr}/\Delta a$ is the slope of the linear regression curve fit between the fracture strain energy (E_{fr}), which is the area under the load-displacement curve, and the crack length (a). The value of fracture energy (E_{fr}) varies with the chosen value of displacement (δ). Three different displacement values, namely δ_1 , δ_2 , and δ_3 , were chosen to evaluate J_c , and corresponded to different regions of crack extension, such as elastic region, crack initiation and crack propagation. However, as stated earlier, the present material in both CVD and CVD + HIP conditions exhibited little or no noticeable stable crack extension. The three displacement values were selected in such a way that the first two displacements (δ_1 and δ_2) essentially encompassed the elastic region, whereas the third displacement, δ_3 , encompassing all the major fracture events corresponding to failure, provided the highest value of fracture strain energy for the specimens with largest crack length and maximum possible displacement.

The fracture energy (E_{fr}) value thus obtained is plotted as a function of crack length, as in Fig. 18a, b for CVD and CVDHIP-ZS materials respectively. The basic load-displacement data in Fig. 16 are used to calculate the fracture energy, E_{fr} , for the three different displacement values of δ . In both the ZnS materials, the higher values of displacements yielded higher fracture strain energy (E_{fr}). The slopes of the fracture energy (E_{fr}) versus crack length (a), i.e., $(\Delta E_{fr}/\Delta a)$, when normalized with specimen thickness (B), yielded the values of J_c as per Eq. 9. The value of J_c varied significantly with the chosen value of displacement, δ . The total fracture energy release rate (J_c) increased progressively with an increase in the displacement, as higher displacements included more and more fracture events that enhanced the ultimate fracture resistance of engineering materials. Normally, a displacement value corresponding to the average displacement at peak loads of the specimens tested with different initial crack lengths is chosen as critical displacement (δ_c) for

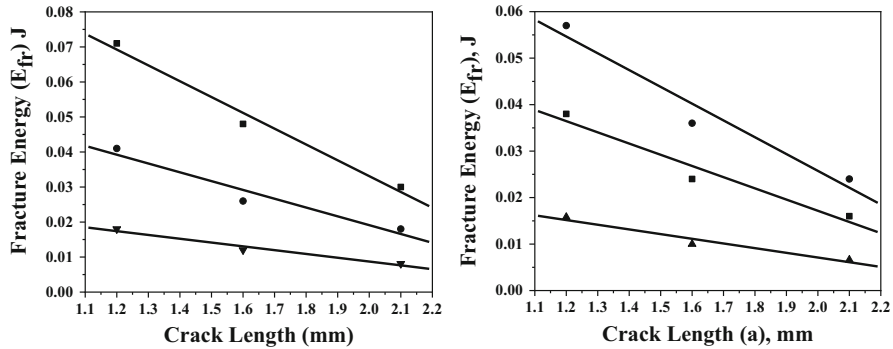


Fig. 18 Variation of fracture energy (E_{fr}) with crack length for (a) CVD-ZS and (b) CVDHIP-ZS conditions [69]

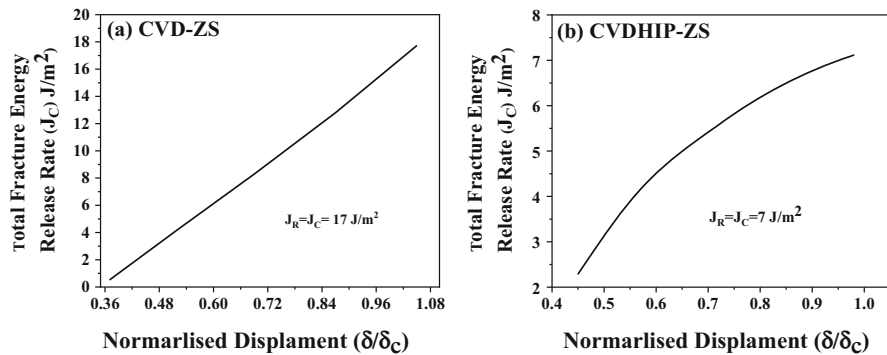


Fig. 19 R-curve of (a) CVD-ZS and (b) CVDHIP-ZS [69]

normalizing any selected displacement values, δ . Such a procedure provides a material characteristic J_c -based R-curve, irrespective of the changes in the dimensions of fracture-resistant specimens and their specific crack lengths. Critical displacement (δ_c) values of 18 μm for CVD-ZS and 15 μm for CVDHIP-ZS material are found to be appropriate in the present case, as the two materials showed no drop in load values after attaining peaks, which correspond to maximum displacement that any specimen displays before fracture. The variation of total fracture energy release rate (J_c) as a function of normalized displacement (δ/δ_c) is shown in Fig. 19a, b for two types of ZnS materials. The data in Fig. 19 clearly exhibit an increase in the total fracture energy release rate, J_c , with the normalized displacement (δ/δ_c), and is an indication of constantly rising R-curve behavior. The highest value of J_R is quantified to be the characteristic critical value, as it is termed J_c , the total fracture energy release rate.

R-Curve

R-curves provide significant insight into the scope of material development [67]. Rising R-curves are desirable as the materials that exhibit such behavior provide ample scope for stable crack extension, as well as predominant toughening possibilities. Moreover, toughening mechanisms, including crack blunting and crack arrest, can also be obtained. The R-curves determined in the present study are high rising without any saturation. The ZnS material in the CVD condition exhibits higher J_c (17 J/m^2), with no saturation there, by exhibiting a totally linear elastic fracture mechanism (LEFM) based controlled fracture. On the other hand, the post-processing of HIP showed a lower J_c (7 J/m^2), with slight evidence of saturation.

Fractography

Figure 20a, b shows the scanning electron microscopy fractographs obtained from the three-point flexural strength specimens for the CVD-ZS and CVDHIP-ZS conditions respectively. Several fractographs of different magnifications are obtained in each of the two process conditions; however, only one representative fractograph for each condition is shown. A mixed fracture comprising a low degree of ductile microdimples (marked as A in fractographs) and a transgranular shear fracture is evident on the fractographs. Further, a predominant extent of a low-energy quasi-cleavage faceted fracture (marked B in the fractographs) is also seen. In the case of CVD-ZS (Fig. 20a), the size of the quasi-cleavage facets is much finer because of the inherently finer grains of the CVD-ZS material. Crack extension proceeds under these conditions with more cleavage planes, where the fracture front initiated needs to relocate additional facets in the neighboring grains. Such a process needs higher fracture energy compared with the situation in which the cleavage facets have to encounter a smaller number of grain/crystallite boundaries. In addition, the more the energy required for the fracture process, the more the material would withstand fracture until higher stresses and higher stress intensity factors, such as K_{IQ} or K_{Ic} , are reached. Such high fracture stresses facilitate the formation of a greater number of microdimples and a greater extent of transgranular shear

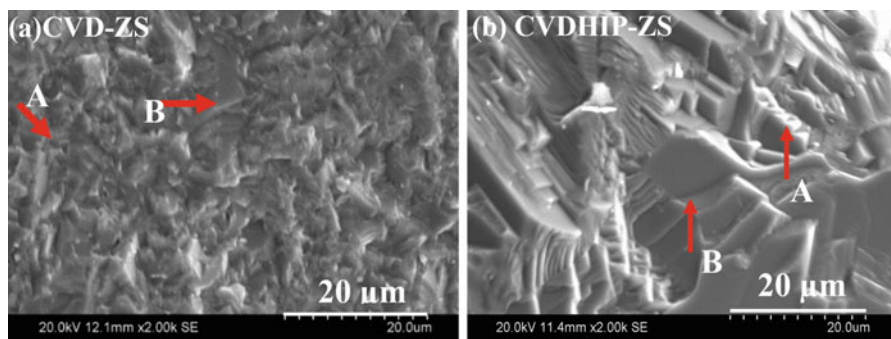


Fig. 20 Scanning electron microscopy fractographs obtained from the fracture toughness-tested specimen: (a) CVD-ZS and (b) CVDHIP-ZS [69]

fracture. Hence, with increasing grain/crystallite size, the facets are much coarser and the extent of the microdimples and transgranular shear is much smaller (Fig. 20b); thus, resulting in much lower flexural strength and fracture energy values K_{I_Q} or K_{I_c} or J_c or $J_R - \Delta a$.

Transmission Measurements

Infrared transmission measurements carried out for CVD-ZS, CVDHIP-ZS, CVDHT-ZS, and PHIP-ZS samples have already been discussed in the section on ZnS processing. It is well known that in the case of materials with cubic crystallography, distribution of grain sizes and microstructural changes arising out of the processing routes have a minimal effect on transmission. Hence, ZnS ceramics being cubic and optically isotropic, a negligible effect on transmission properties is expected owing to microstructural changes. However, it is evident that post-CVD thermal treatment under pressure-assisted conditions eliminates the absorption band at 6.2 μm and in combination with other processing defects results in improved transmission. Being cubic, it is expected to have a minimal effect of thickness on the transmission values, provided that no second phase responsible for absorption and pores to scatter the radiation are present in these specimens. A typical transmission plot recorded for CVD-processed ZnS samples with 3-, 4-, and 5-mm thickness is shown in Fig. 21. It is evident that the effect of thickness is minimal, as expected, because of the absence of impurities or other heterogeneities, indicating that CVD processing parameters in the current study is within the optimal window.

The visible transmission pattern of CVDHIP-ZS provided in Fig. 22 indicates increased transmission in the visible region to around 68%. The transmission in the visible region was found to be less than 1% in the case of CVD-ZS and CVDHT-ZS

Fig. 21 Infrared transmission of CVD-ZS samples with 3-, 4-, and 5-mm thickness [46]

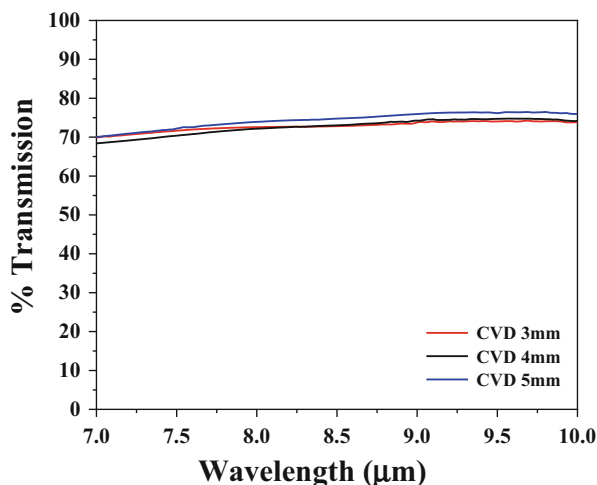
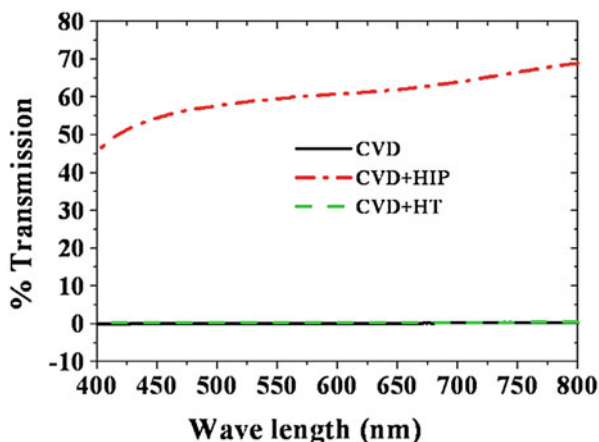


Fig. 22 Visible transmission of (a) CVD-ZS, (b) CVDHIP-ZS, and (c) CVDHT-ZS [22]



samples. Although the grain growth and homogenization to the sphalerite cubic phase was observed with CVDHT-ZS samples, residual microporosity is a major cause of scatter and low transmission values.

Anti-reflection Coating [16, 70]

Theoretical transmission of ZnS is limited to 75% in the 7–10- μm regions. It is understood that when electromagnetic radiation interacts with material, it undergoes many phenomena, such as reflection, refraction, absorption due to heterogeneity, and finally gets transmitted through the other side of the sintered body [16]. It is evident from the figure that in the current study, ZnS exhibited almost theoretical transmission, indicating negligible absorption or scattering resulting from secondary phase inclusions and rough surfaces and pores etc. The observed loss of transmission due to reflection can be minimized by anti-reflection coatings.

The principle of operation of quarter-wave regarding anti-reflection coating application is pictorially represented in Fig. 23. The plane polarized light whose electric field is considered to oscillate in the plane of this page. The refractive index bulk material to be subjected to anti-reflection coating is represented as n_2 , the anti-reflection coating as n_1 and atmospheric air as n_0 . If the wavelength of the light traveling from air where n_0 is equal to 1 is λ_0 , as it passes through the anti-reflection coating the wavelength can be regarded as λ_0/n_1 . In Fig. 23 curve I represents the electric field of the incident light and when light strikes the first surface of the anti-reflection coating, part of it is reflected, i.e., V, and part of it passes through the anti-reflection coating (II). As the light wave proceeds and hits the bulk material, part of II is reflected (III) and transmitted. Light wave, IV, is reflected back from the anti-reflection coating. The two exiting waves, i.e., V and IV from the anti-reflection coating and bulk, can be considered as equal in magnitude and opposite in sign, nullifying the reflection.

Fig. 23 Interaction of the electromagnetic wave with anti-reflection coating and bulk material [16]

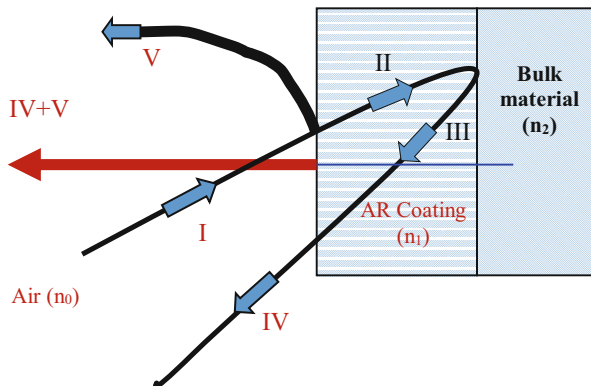


Table 4 Potential anti-reflection coating materials for ZnS

Sr. number	Material	Infrared refractive index	Useful wavelength ranges Micron (μm)
1	Barium fluoride	1.40	<0.2–14
2	Silica	1.44	0.2–4.5
3	Thorium fluoride	1.50	0.23–12

The reflectance from the outer surface, i.e., from the air to the anti-reflection coating, and from the inner surface, i.e., the anti-reflection coating to the bulk material, can be estimated using Eqs. 10 and 11, respectively.

$$\text{Reflectance from outer side} = R = \left(\frac{n_1 - n_0}{n_1 + n_0} \right)^2 \tag{10}$$

$$\text{Reflectance from inner side} = R = \left(\frac{n_2 - n_1}{n_2 + n_1} \right)^2 \tag{11}$$

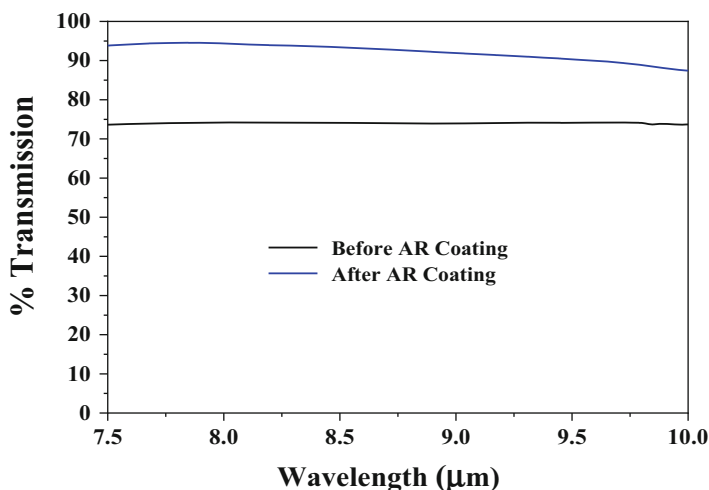
On achieving the two reflectances equal to each other permits solving the refractive index of the anti-reflection coating (n_1) using the Eq. 12. On achieving a 180° phase difference between the two reflected waves, the thickness of the anti-reflection coating should be one-quarter of the wavelength in the coating (as shown in Eq. 13). When these two conditions are met, the reflection of the light of the wavelength λ_0 will be nearly zero. Accordingly, the refractive index of the anti-reflection coating for ZnS is estimated to be close to 1.48. Table 4 lists some of the candidate anti-reflection coating materials of ZnS.

$$n_1 = \sqrt{n_0 n_2} \tag{12}$$

$$\text{Thickness of coating} = \frac{1}{4} \lambda_0 \sqrt{n_1} \tag{13}$$

Table 5 Required thickness of anti-reflection coating materials [16]

Sr. number	Material	Anti-reflection coating thickness
1	Barium fluoride	1.517
2	Silica	1.475
3	Thorium fluoride	1.416

**Fig. 24** Infrared transmission pattern of CVD-ZS sample before and after anti-reflection coating

Refractive index of AR coating for ZnS : $(1) \times (2.2)^{1/2} = 1.48$

As mentioned above, the thickness of the coating can also be estimated based on the wavelength of interest. The anti-reflection coating thickness of all the materials, such as barium fluoride, silica and thorium fluoride is calculated for the range of 7–10 μm with center point 8.5 μm and depicted in Table 5.

A typical plot showing the effect of anti-reflection coating is shown in Fig. 24.

Studies on Coating Durability

Anti-reflection coated samples are subjected to an abrasion resistance test by rubbing the coated specimens with a 1/4-inch thick eraser for 50 strokes with a minimum force of 1.0 lb and adhesion by pressing a 1/2-inch-wide cellophane tape firmly against the coated surface so as to cover the stained area, and then quickly removing it at an angle normal to the coated surface. The coatings are also subjected to humidity by exposing coated samples in an oven at 50 °C and to 95% relative humidity in a humidity oven for 24 h, salt solubility by immersing the coated sample in 5% salt water for 24 h and cleanability

by exposing them for 10 min each to trichloroethylene, acetone, and ethanol. Retention or negligible loss of transmission under these conditions is considered to establish the performance and durability of the anti-reflection coating.

Erosion Protection Coatings [16, 71–73]

The relatively low hardness of ZnS components limits its use in harsh environments subjected to particle and rain erosion. The studies are reported that an engineered protective coating can reduce the damage without affecting the transparency in the desired spectral region. A thin layer of high modulus material coating can offer protection against impact damage to the brittle ZnS substrate. On impact due to the high modulus of the coating, it results in less stress to the ZnS substrates. The protection is directly proportional to the modulus in addition to the thickness of the coating. An erosion-resistant coating of boron phosphide (BP) has been demonstrated on ZnS in Glasgow, UK, as one of the choices of materials because it has the best erosion-resistant properties. BP is a crystalline compound with boron and phosphorous in the atomic ratio of 1:1. Additionally, gallium phosphide (GaP) has also been used as an erosion-resistant coating material with lower absorption than BP; hence, a composite structure of a thin layer of BP on top of a thicker layer of GaP is preferred. Diamond-like carbon and germanium carbide coatings are also reported to provide excellent scratch protection.

Conclusions

An overview of the processing of self-standing zinc sulfide monoliths is presented, along with authors' hands on experience of CVD and post-CVD processing of ZnS ceramics. Additionally, direct powder consolidation through HIP to achieve transparent ZnS is also discussed. The chapter also outlines various physico-chemical, mechanical, and optical characterization procedures and properties of processed ZnS under various conditions. Also discussions are attempted to engineer the transmission properties within the desired wavelength ranges and to enhance the transmission by pressure-less and pressure-assisted heat treatments with respect to the applications envisaged.

Feasibility of the CVD reaction can be accessed through free energy calculations as illustrated. As in the case of Reaction-1, ΔG of -37.3 kcal/mol at 680°C confirms the thermodynamic feasibility of the CVD processing of ZnS and a Rayleigh number (R_a) within the order of 10^6 corresponds to a laminar flow favoring CVD deposition. Graphite substrate with CTE close ($7-8 \times 10^{-6}$ /C) to ZnS provides crack-free ZnS deposition in combination with the easy release of ZnS deposits through machining. Physico-chemical and optical properties indicate the superiority of CVD processing in achieving optical quality ZnS IR transparent ceramics of $7-10 \mu\text{m}$.

Pressure-less heat treatment in an argon atmosphere of chemical vapor deposited ZnS samples resulted in removal of zinc hydride, as demonstrated by the FTIR

pattern; however, the optical transmission properties are found to be poor. The residual porosity generated as a result of zinc hydride removal remains as not healed and acts as scatter points. Hot isostatic pressing of CVD-ZS eliminates the yellowish tinge in addition to zinc hydride in combination with the healing of residual microporosity owing to the simultaneous application of temperature and pressure below the transformation temperature of 1,020 °C. HIP not only extends the transmission to the MWIR and visible region but also enhances the transmission in the LWIR region. Powder HIP facilitates the single-step consolidation of ZnS powder under HIP conditions; however, the presence of minor quantities of hexagonal wurtzite phase is evident from XRD studies. The presence of hexagonal phase along with relatively low densities of powder HIP samples can be correlated with the lower transmission values.

Physico-chemical, thermal, mechanical, and optical properties of CVD-ZS, CVDHT-ZS, CVDHIP-ZS, and PHIP-ZS are discussed. CVD-ZS samples have shown phase pure sphalerite; however, heat treatment under pressure-less and HIP conditions impart a preferred crystallographic orientation along the (111) plane, as evident from the XRD transverse I ratio calculations. All the samples, CVD-ZS, CVDHT-ZS, CVDHIP-ZS, and PHIP-ZS, have shown density within a comparable range close to theoretical values; however, the transmission properties are very sensitive to the presence of residual porosity. CVDHIP-ZS samples exhibit the highest density of 4.0860 g/cm³, in comparison with 4.0850 g/cm³ for CVD-ZS and 4.0831 g/cm³ observed for CVDHT-ZS samples. In the case of the PHIP-ZS sample, on direct powder consolidation by HIP, it has shown a relatively lower density value of 4.079 g/cm³.

The microstructure of the CVD-ZS sample reveals a linear array of columnar grain structure oriented parallel to the direction of coating with maximum grain size distribution within the range of 5–10 μm. In addition, it is also observed that there are lamellar types of structures within the grain with elongated layers along the grain boundaries. HIP and heat treatment under pressure-less conditions result in grain growth induced on the material, leading to a substantial increase in the grain sizes. In the case of HIP, larger grains within the range of 50–100 μm with increased twin fractions are observed. Further, ZnS recrystallization also results in the disappearance of conventional grain boundaries and lamellar structures from the microstructures in the cases of both HIP and heat treatment. The microstructure of CVDHT-ZS samples exhibits a fine distribution of residual pores and can be attributed to the decomposition of Zn-H during thermal treatment. Grain sizes of CVD-ZS samples are similar for CVDHIP-ZS and PHIP-ZS samples owing to the prominent mechanisms operative under HIP. Powder HIP of the prominent operative mechanism for densification is by plastic deformation, as revealed by (111) orientation emerging because of translational slip along the cleavage planes.

Knoop hardness of CVD-ZS, CVDHIP-ZS, CVDHT-ZS, and PHIP-ZS is 210, 180, 172, and 178 kg/mm² and the flexural strength of CVD-ZS, CVDHIP-ZS, and CVDHT-ZS are found to be 79, 50, and 45 MPa (average of five samples). A decrease in Knoop hardness and flexural strength is observed as a result of HIP, which can be attributed to the grain sizes, as described by the Hall–Petch relation.

The peak compressive and flexural strength values are explained on the basis of variation in the microstructure and distribution of defects such as micropores and microcracks. R-curves of both CVD-ZS and CVDHIP-ZS materials exhibit rising behavior that is a variation of J_c with δ/δ_c and no signs of saturation were observed. The fractographs of both CVD-ZS and CVDHIP-ZS materials have shown a mixed mode of fracture, with features of transgranular shear fracture with a predominant extent of low-energy quasi-cleavage fracture. The cleavage facet size and its extent are significantly higher in the case of CVDHIP-ZS material compared with the CVD condition.

Samples of CVD-ZS, CVDHIP-ZS, CVDHT-ZS, and PHIP-ZS have shown IR transmission values 70%, 72%, 60%, and 65%, respectively. Further, ZnS samples of 3-, 4-, and 5-mm thickness have shown negligible variation in transmission values owing to the inherent cubic crystallography, which exhibits a minimal effect on thickness. CVDHIP samples also show transmission in the visible region. Anti-reflection coating demonstrates an increase in transmission from 74% to 94% at 7.5- μm wavelength in the case of CVD samples.

References

1. Johnson R, Biswas P, Ramavath P, Kumar RS, Padmanabham G (2012) Transparent polycrystalline ceramics: an overview. *Trans Indian Ceram Soc* 71:73–85
2. Arrzurr M (1981) Investigation of phase transition of natural ZnS minerals by high resolution electron microscopy: reply. *Am Mineral* 66:1006–1012
3. Adachi S (1999) Cubic zinc sulphide (β -ZnS), optical constants of crystalline and amorphous semiconductors. Springer, Boston, pp 445–458
4. McCloy JS, Bliss M, Miller B, Wang Z, Stave S (2015) Scintillation and luminescence in transparent colorless single and polycrystalline bulk ceramic ZnS. *J Luminescence* 157:416–423
5. Drezner Y, Berger S, Hefetz M (2001) A correlation between microstructure composition and optical transparency of CVD-ZnS. *Mater. Sci. Eng.* B87:59–65
6. Lee K-T, Choi B-H, Woo J-U, Kang J-S, Paik J-H, Chu B-U, Nahm S (2018) Microstructural and optical properties of the ZnS ceramics sintered by vacuum hot-pressing using hydrothermally synthesized ZnS powders. *J Eur Ceram Soc* 38:4237–4244
7. McCloy JS, Korenstein R, Zelinski B (2009) Effects of temperature, pressure, and metal promoter on the recrystallized structure and optical transmission of chemical vapor deposited zinc sulfide. *J Am Ceram Soc* 92(8):1725–1731
8. Chlique C, Delaizir G, Merdignac-Conanec O, Roucau C, Dollé P, Rozier M, Bouquet V, Zhang XH (2011) A comparative study of ZnS powders sintering by hot uniaxial pressing (HUP) and spark plasma sintering (SPS). *Opt Mater* 33:706–712
9. Li Y, Liu Y, Fedorov VV, Mirov SB, Wu Y (2016) Hot-pressed chromium doped zinc sulfide infrared transparent ceramics. *Scripta Mater* 125:15–18
10. Vasilyev S, Moskalev I, Mirov M, Smolski V, Mirov S, Gapontsev V (2017) Ultrafast middle-IR lasers and amplifiers based on polycrystalline Cr:ZnS and Cr:ZnSe. *Opt Mater Express* 7:2636–2650
11. Fang XS, Bando Y, Liao MY, Gautam UK, Zhi CY, Dierre B, Liu BD, Zhai TY, Sekiguchi T, Koide Y, Golberg D (2009) Single-crystalline ZnS nanobelts as ultraviolet-light sensors. *Adv Mater* 21:2034–2039

12. Bujnakova Z, Dukova E, Kello M, Mojzis J, Balaz M, Balaz P, Shpotyuk O (2017) Mechanochemistry of chitosan-coated zinc sulfide (ZnS) nanocrystals for bio-imaging applications. *Nanoscale Res Lett* 12:32
13. Firsov KN, Gavrishchuk EM, Ikonnikov VB, Kazantsev SY, Kononov IG, Rodin SA, Savin DV, Timofeeva NA (2016) High-energy room-temperature Fe²⁺:ZnS laser. *Laser Phys Lett* 13:015001–015008
14. Salih AT, Najim AA, Muhi MAH, Gbashi KR (2017) Single-material multilayer ZnS as anti-reflective coating for solar cell applications. *Opt Commun* 388:84–89
15. Singh SS, Pratap S, Prasad J, Kumar R, Murari A (2001) Effect of grain size on the transmission of zinc sulphide windows in the 8–12 micron range of infrared, *Ind. J Eng Mater Sci* 8:18–21
16. Harris DC (1999) *Materials for infrared windows and domes: properties and performance*. SPIE Press
17. Ghosh A, Upadhyaya AS (2009) Broad band antireflection coating on zinc sulphide simultaneously effective in SWIR, MWIR and LWIR regions. *Infrared Phys Tech* 52:109–112
18. Krell A, Strassburger E, Hutzler T, Klimke J (2013) Single and polycrystalline transparent ceramic armor with different crystal structure. *J Am Ceram Soc* 96:2718–2721
19. Krell A, Klimke J, Hutzler T (2009) Advanced spinel and sub- μm Al₂O₃ for transparent armour applications. *J Eur Ceram Soc* 29:275–281
20. Corbin ND (1987) Aluminium oxinitride spinel (AlON): a review. U.S. Army Technology Laboratory
21. Harris DC (2005) History of development of polycrystalline optical spinel in U.S. *Proc SPIE* 5786:1–22
22. Biswas P, Kumar RS, Ramavath P, Mahendar V, Rao GVN, Hareesh US, Johnson R (2010) Effect of post CVD thermal treatments on crystallographic orientation, microstructure, mechanical and transmission properties of ZnS ceramics. *J Alloys Compd* 496:273–277
23. Hogan P, Stefanik T, Willingham C, Gentilman R (2004) Transparent yttria for IR windows and domes – past and present. In: 10th DoD electromagnetic windows symposium, Norfolk, 19 May 2004
24. Harris DC (2007) History of the development of hot-pressed and chemical-vapour-deposited zinc sulphide and zinc selenide in the United States. *Proc SPIE* 6545
25. McCloy J (2007) International development of chemical, vapour deposited zinc sulphide. *Proc SPIE* 6545:654503-1–654503-12
26. Sato T, Furukawa, Kashi H (1986) CVD-ZnS IR dome. *J Jpn Soc Infra Sci Technol* 11:44–49
27. Han Y (1995) On development of high grade ZnS bulk materials for mid and far infrared in China. *J Northwestern Polytech Ins* 13:158–159
28. Yashina EV (2003) Preparation and properties of polycrystalline ZnS for IR applications. *Inorg Mater* 39:663–668
29. Donadio RN, Connolly JF, Taylor RL (1981) New advances in chemical vapor deposited (CVD) infrared transmitting materials. *Proc SPIE–Int Soc Opt Eng* 297:65–69
30. Goela JS (2001) Low stress, water clear zinc sulphide. US Patent 6,221,482
31. Braudeau PH, Keller G, Torre JP (1986) CVD of IR transmitting ZnS. *J Phys Colloq* 47:1-193–1-196
32. Mochizuki K (1985) Vapor growth and polarity on ZnS crystals. *J Cryst Growth* 71:459–462
33. Hartmann H (1962) Growth of ZnS single crystals from the vapor phase. *Phys Status Solidi* 2:585–589
34. Shibata K (2000) Optical component, zinc sulfide sintered compact, and fabricating method thereof. US Patent 6,111,689
35. Kozelsky MJ (1967) Growth of ZnS single crystals from the melt. *J Cryst Growth* 1:293–296
36. Green LC, Reynolds DC, Cryzac SJ, Baker WM (1958) Melt grown ZnS single crystal. *J Chem Phys* 29:1375–1377
37. Kuznetsov VA (1964) Melt-grown zinc sulfide crystals. *Rost Krist* 29:144–147
38. Goela J, Taylor RL (1988) Monolithic material fabrication by chemical vapor deposition. *J Mater Sci* 23:4331–4339

39. Sharifi Y, E. Achenie L (2007) Using density functional theory to postulate a mechanism for zinc sulfide formation in a CVD reactor. *J. Crystal Growth* 307:440–447
40. diBenedetto BA, Pappis J, Capriulo AJ (1973) Chemical vapor deposition of multispectral windows. AFAL-TR-73-252
41. Lewis KL et al (1984) The mechanical properties of CVD-grown zinc sulphide and their dependence on the conditions of growth. *Proc Electrochem Soc PV84-6:530–545*
42. Savage JA, Lewis KL, Pitt AM, Whitehouse RHL (1984) The role of a CVD research reactor in studies of the growth and physical properties of ZnS infrared optical material. *Proc SPIE* 0505:47–51
43. Gavrishchuk EM, Yashina EV (1994) The growth mechanism of zinc sulfide from the gas phase. *Vysokochistye Veshchestva* 328:36–39
44. Bredikhin VI, Garishchuk EM, Ikonnikov VB, Karaksina EV, Ketkova LA, Kuznetsov SP, Mal'shakova OA (2009) Optical losses in polycrystalline CVD ZnS. *Inorg Mater* 45:235–241
45. McCloy J, Fest E, Korenstein R, Poisl WH (2011) Anisotropy in structural and optical properties of chemical vapor deposited ZnS. *Proc SPIE* 8016:80160I-1–80160I-11
46. Biswas P, Ramavath P, Johnson R, Ravi KV (2016) Fabrication of IR transparent ZnS plate by chemical vapour deposition. *Ind J Chem Technol* 23:400–404
47. Yu H (2000) The study of the relationship between inside defects and optical properties of CVD ZnS. *Proc SPIE* 4231:224–230
48. Goela JS (1999) Fabrication of conformal ZnS domes by chemical vapor deposition. *SPIE* 3705:227–236
49. Goela JS, Askinazi J, Robinson B (2001) Mandrel reusability in precision replication of ZnS conformal domes. *Proc SPIE* 4375:114–127
50. Zhenyi F, Yichao C, Yongliang H, Yaoyuan Y, Yanping D, Zewu Y, Hongchang T, Hongtao X, Heming W (2002) CVD growth of bulk polycrystalline ZnS and its optical properties. *J Crystal Growth* 237–239:1707–1710
51. Devyatykh GG, Gavrishchuk EM, Yashina EV (1996) Effect of deposition conditions on the microstructure of CVD ZnS. *Inorg Mater* 32:589–591
52. Devyatykh GG, Gavrishchuk EM, Fatenkov AN, Yashina EV (1995) Effect of CVD conditions on the porosity of zinc sulphide. *Inorg Mater* 31:936–938
53. Campbell A, Hayman C (1988) Manufacturing aspects of zinc sulphide. *Proc SPIE* 0915:79–83
54. Sato T, Furukawa, Kashi H (1986) CVD-ZnS IR domes. *J Jpn Soc Infrared Sci Tech* 11:44–49
55. Zscheckel T, Wisniewski W, Gebhardt A, Russel C (2014) Recrystallization of CVD-ZnS during thermal treatment. *Opt Mater Express* 5:1885–1894
56. Wilkinson DS, Ashby MF (1975) Pressure sintering by power law creep. *Acta Metall* 23:1277–1285
57. Willingham CB, Pappis J (1990) Polycrystalline zinc sulphide and zinc selenide articles having improved optical quality. US patent 4,944,900
58. Shchurov AF, Gavrishchuk EM, Ikonnikov VB, Yashina EV, Syseov AN, Shevarenkov DN (2004) Effect of hot isostatic pressing on the elastic and optical properties of polycrystalline CVD ZNS. *Inorg Mater* 40:336–339
59. Karaksina EV, Ikonnikov VB, Gavrishchuk EM (2007) Recrystallization behavior of ZnS during hot isostatic pressing. *Inorg Mater* 43:452–454
60. Aknic M, Celikkaya A (1989) Synthesis and hot pressing of ZnS powder. *Proc SPIE* 1112:60–67
61. Ramavath P, Biswas P, Johnson R, Reddy GJ, Laxminarayana P (2014) Hot isostatic pressing of ZnS powder and CVD zinc sulphide ceramics and comparative evaluation of physico-chemical, microstructural and transmission properties. *Trans Ind Ceram Soc* 73:299–302
62. Xue LA, Raj R (1991) Effect of hot pressing temperature on the optical transmission of zinc sulphide. *Appl Phys Lett* 58:441–443
63. Zwaag SVD, Field JE (1982) Liquid jet impact damage on zinc sulphide. *J Mater Sci* 17:2625–2636

64. Ramavath P, Biswas P, Senthil Kumar R, Mahendar V, Rao GVN, Hareesh US, Johnson R (2011) Effect of sphalerite to wurtzite crystallographic transformation on microstructure, optical and mechanical properties of zinc sulphide ceramics. *Ceram Int* 37:1039–1046
65. Reddy GJ, Rao ESB (1995) The infrared transmission performance of hot isostatically pressed zinc sulphide. *Int J Powder Metall* 31:265–269
66. Ramavath P, Ravi N, Hareesh US, Johnson R, Eswara Prasad N (2010) Compressive and flexural strength properties of ZnS optical ceramics. *Trans Ind Ins Metals* 63:847–852
67. Prasad NE, Kumari S, Kamat SV, Vijayakumar M, Malakondaiah G (2004) Fracture behaviour of 2D-waved silica-silica continuous fibre-reinforced, ceramic-matrix composites (CFCCs). *Eng Fract Mech* 71:2589–2605
68. ASTM Standard E-399 (1997) Standard test method for plane strain fracture toughness of metallic materials. Annual book of ASTM standards vol.03.01. American Society for Testing and Materials, West Conshohocken, pp 408–438
69. Ramavath P, Mahender V, Hareesh US, Johnson R, Kumari S, Prasad NE (2011) Fracture behavior of chemical vapour deposited and hot isostatically pressed zinc sulphide. *Mater Sci Eng A* 528:5030–5035
70. Joseph S, Kassous E, Yadlovker D, Levi A, Marcovich O, Shinman A, Zipin H (2013) Challenges of developing hemispherical ZnS domes coated with a durable anti-reflection coating. *Proc SPIE* 8708:870800-1–870800-11
71. Korenstein R, Goldman L, Hallock R Diamond coated ZnS for improved erosion resistance. *SPIE* 3060:181–195
72. Mackowski JM, Cimma B, Pignard R (1992) Rain erosion behavior of germanium carbide (GeC) films grown on ZnS substrates. *SPIE* 1760:201–209
73. Hu C, Zheng W, Tian H, Xn L, Jiang Q (2006) Effects of the chemical bonding on the optical and mechanical properties for germanium carbide films used as antireflection and protection coating of ZnS windows. *J Phys Condensed Matter* 18:4231–4241



Advances in Nano-finishing of Optical Glasses and Glass Ceramics

15

Mahender Kumar Gupta, I. Abdul Rasheed, and M. Buchi Suresh

Contents

Introduction	570
Introduction to Glass and Glass Ceramics	571
Glass and Its Importance	571
Glass Ceramics and Its Importance	571
Low Expansion Glasses and Glass Ceramics and Its Importance	572
Various Polishing and Nano-finishing Techniques	572
Ductile Grinding	573
Fresh-Feed Polishing	573
Chemical Polishing	574
Bowl-Feed Polishing (Float Polishing)	575
Elastic Emission Machining (EEM)	576
Magnetorheological Finishing (MRF)	577
Laser Polishing	585
Ion Beam Polishing	586
Abrasive Slurry Jet (ASJ) Micro-machining	587
Plasma-Assisted Etching (PAE)	588
Characterization Techniques	589
Test Plate Technique	589
Stylus Profiler Technique	591
Atomic Force Microscope (AFM)	591
Scanning Electron Microscope (SEM)	591
White Light Interferometry	592
Phase Shift Interferometry (PSI)	593
Coherence Correlation Interferometry (CCI)	593

M. K. Gupta (✉) · I. A. Rasheed
Research Centre Imarat, Hyderabad, India
e-mail: mkg19662002@yahoo.co.in; ab_rasheed81@yahoo.com

M. B. Suresh
International Advanced Research Centre for Powder Metallurgy and New Materials, Hyderabad,
India
e-mail: suresh@arci.res.in

Case Study for Polishing/Finishing Techniques Used for Achieving the Nano-finished Optics Using Glass and Glass Ceramic Material	594
Float Polishing Using Pitch Lap	595
Summary	597
References	598

Abstract

Optical glass and glass ceramic components with angstrom-level surface roughness and nanometer-level dimensional accuracy are in potential demand for sophisticated optical fabrication. In recent years, aspherical and free-form surfaces are gaining prominence for high performance applications. Moreover, the new optical materials and fabrication process which exhibit superior mechanical properties are being developed to meet the stringent requirements and harsh environment. Fabrication of complex-shaped high optical finish components becomes a significant challenge as conventional finishing techniques are unable to machine aspherical or free-form surfaces precisely. This situation demands few highly advanced and precise finishing processes which ensure stress-free surfaces. Mostly, the optical components are fabricated by shaping or pre-finishing methods followed by final finishing processes. Final finishing processes include more deterministic and flexible polishing techniques that can achieve desired surface finish, figure accuracy and surface integrity to make it suitable for shorter wavelength applications. In this chapter, basic principle, mechanism of various material removal processes, and precision polishing techniques such as magnetorheological fluid-based finishing were discussed and are compared with the convention polishing techniques.

Keywords

Glass ceramics · Optical components · Surface roughness · Material removal · Polishing · Magnetorheological finishing

Introduction

The surface quality of glass and glass ceramics is one of the important parameters that affects the functionality of the final product. Most of the products essentially require nanolevel surface finish. The processes of nano finishing have flexible finishing tools, which can be employed for such type of work pieces. This chapter provides a comprehensive review of nano-finishing processes and their applications.

Traditional polishing processes cannot finish complex-shaped work pieces, 3D components, etc. Therefore, there is a requirement of finishing processes with characteristics such as deterministic, in-process externally controllable forces acting on the work pieces, capable of surface finishing complex-shaped components and also providing surface finish superior to the traditional finishing processes. Selection

of suitable machining conditions plays an important role in the control of surface and/or subsurface defects [1].

Traditionally for generating flat or spherical nano-finished optical surfaces, freely movable abrasive as well as brittle mode grinding techniques are being adopted. These are also termed as self-correcting processes, where two initially imperfect surfaces get into contact with slurries, pitch pad, and tool surface, so that an area averaging mechanism occurs resulting in low surface roughness value of the order of 0.5 nm rms. These processes have an advantage in removing stresses and subsurface cracks, which are easily generated in brittle materials like glass and glass ceramics [2, 3]. This chapter includes the following:

Introduction to Glass and Glass Ceramics

Glass and Its Importance

Glass is a form of supercooled state of silicon dioxide and various other ingredients like calcium and other certain alkalies. It is a supercooled state containing an amorphous and noncrystalline structures. Optical glasses are high-quality glasses compared to window glasses, which are formulated specifically with required characteristics that affect the transmission of light. The quality standards have a number of criteria, like highly transparent over the visible spectrum, optically homogeneous, and inclusion-, strain-, and stress-free with defined optical constants, which have a small dependency over temperature. It should have high mechanical strength for easy handling of optical components during processing and assembling and also with high resistance to chemicals. There are special-purpose glasses like laser glass, color filter glass, and technical sheet glass, which are specially formulated for the use in optical systems. Laser glasses are used in optically pumped high-power lasers, and the laser rods that are made from these materials emit light in the near-infrared region of the spectrum at about 1.06 μm . They are also used as disk amplifiers in large laser fusion experiments and also used as a source element in number of commercially available laser systems. Color filter glasses are used in optical systems, as they have specific spectral transmittance characteristics within the range of optical spectrum.

Glass Ceramics and Its Importance

Glass ceramics are also known as vitrocerams, pyrocerams, vitrocerâmicos, vitroceramiques, and sittals. They are processed by controlled crystallization of certain glasses, induced by nucleating agents. Glass ceramics always contain one or more embedded crystalline phases along with a residual glassy phase. The crystallinity in the glass ceramics varies most frequently between 30% to 70%. Controlled ceramization yields an array of materials with interesting combination of properties which are inherently free from porosity. The first commercially viable

glass ceramic was developed by US aerospace industry in the late 1950s as radomes. It was used to protect the radar equipment in the nose cones of aircraft and rockets. Glass ceramics used in the above applications must exhibit a combination of properties to withstand critical conditions like rain erosion, atmospheric reentry, homogeneity, low dielectric constant, low coefficient of thermal expansion (CTE), low dielectric loss, high mechanical strength, and high abrasion resistance. No glass or polycrystalline material or single crystal can simultaneously meet all the required specifications.

Low Expansion Glasses and Glass Ceramics and Its Importance

Optical materials like fused quartz, fused silica, and crystal quartz and low expansion materials such as Pyrex, Cer-Vit, Sital, and Zerodur have special properties like semitransparent and nonporous glass ceramics, which help in the grinding and polishing process very easily and also maintain the structure over a wide range of operating temperatures. They are also chemically stable and mechanically strong. Fused quartz and fused silica belong to a very hard and transparent materials with excellent optical clarity. The raw material contains 100% pure silicon dioxide (SiO_2), with crystalline structure, which is fused at high temperature to form amorphous or vitreous material.

Another important material is Zerodur, which is a semitransparent, nonporous glass ceramic having an extremely low coefficient of thermal expansion of $0.00 \pm 0.02 \times 10^{-6}/\text{K}$ between 0°C and 50°C . Unique characteristic of this material is its exceptional good homogeneity and good transparency in the range 400 to 2300 nanometers. This material is preferred for lightweight honeycomb mirror mounts for satellite mirrors, manufacturing of precision optics, high-quality mirror substrates for large-size astronomical telescopes, X-ray telescopes, optical elements for comet probes, ring laser gyroscopes, and optical standards for precision measurement technology [4–6].

Various Polishing and Nano-finishing Techniques

Optical elements of glass and glass ceramics, utilized in sophisticated instruments like laser-based optical rotation sensors, gradiometers, and accelerometers, instruments of photolithography in ultraviolet regions, and high-power laser-based equipment, should have:

- Shape integrity and accuracy to ensure better imaging performance
- Ultrasmooth to nano-finished surfaces to avoid scattering
- Minimum subsurface damage to avoid deterioration in the performance

Hence, a number of fabrication techniques have been evolved based on the requirement, and it also depends on the characteristics of the optical component.

To generate the required surface on brittle material, two steps are generally followed, namely, rough shaping mode and finishing mode. The rough shaping mode is characterized by high material removal rate leaving a rough surface finish with a highly stressed layer of subsurface damage approximately from 1 to 10 micron depth in loose abrasive grinding process. In finishing mode, the roughness and the subsurface damage generated during grinding process has to be removed using fine grit abrasives or by using polishing powders whose average particle size varies from micron to nanometer levels with different polishing techniques which has been evolved during the late nineteenth and twentieth centuries [7, 8].

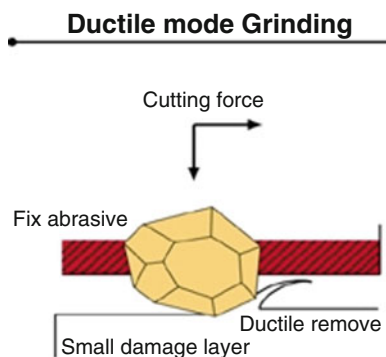
Ductile Grinding

In this process, the material removal is being accomplished by plastic flow and not by brittle fracture. It also depends on Young's modulus and rigidity modulus of the material and machining depth [9]. To achieve a perfect ductile grinding finish, single-point diamond turning (SPDT) concept can be utilized instead of loose abrasive grinding. This ductile grinding helps in achieving higher material removal, i.e., 30 $\mu\text{m/hr.}$, than fresh-feed polishing. Major disadvantage of this process is that it leaves a highly stressed surface. In order to achieve the machining depths of nanometer scale, a high infeed resolution is necessary [10]. The surface roughness achieved by this technique is approximately 2–3 nm rms in BK7 material. Figure 1 shows the schematic of ductile grinding process.

Fresh-Feed Polishing

It is a chemico-mechanical process, which reduces the roughness, stress, and subsurface cracks formed during the previous ground surface. It causes a minimum subsurface damage, using pitch-flow effects and in-process correction of the generated shape. A small amount of wear occurs during the process, and the fundamental

Fig. 1 Schematic of ductile grinding process. (Courtesy: <http://www.kinik.com.tw/en-us/Products/ReclaimedWafer.html>)



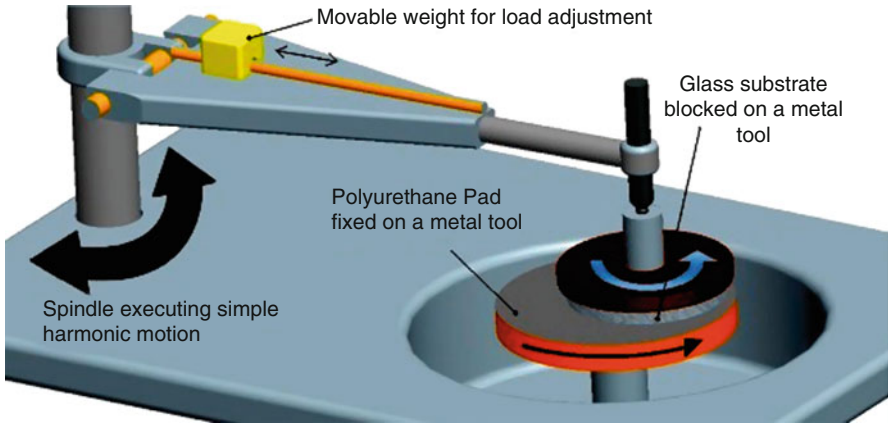
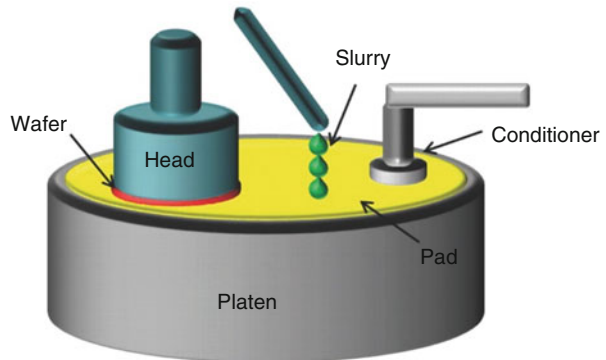


Fig. 2 Schematic of fresh-feed polishing process. (Courtesy: www.iopscience.iop.org, obtained from Ref. [12])

Fig. 3 Schematic of chemo-mechanical polishing process. (Courtesy: www.jss.ecsdl.org)



variables involved are more in this type of polishing technique [11]. The surface roughness achieved in BK7 glass material is about 0.5 nm rms. The schematic of fresh-feed polishing process is shown in Fig. 2 [12].

Chemical Polishing

chemico-mechanical polishing (CMP) is a planarization technique that includes a combination of chemical and mechanical processes, which is mainly used in the semiconductor manufacturing industries. In CMP, the reaction takes place between the abrasive-based polishing fluid and the work piece, and the abrasive removes the reaction products of the surface of the work piece by mechanical action [13]. Figure 3 shows the schematic of CMP planarization process.

It is an acid and base reaction, in which the material will be removed using reagents like hydrofluoric acid, sulfuric acid, nitric acid, and glycerine. Later the components will be subjected to base solution wherein sodium hydroxide solution is used in general. Due to this chemical etching process, a kind of polished surface gets generated with a low level of surface roughness, and a high accuracy in shape associated with marginal amount of subsurface damages can be produced. The disadvantage of this technique is that the chemicals stick onto the surface and were removed later [14]. Hence, this reaction is highly sensitive to inhomogeneous material, and the surface roughness obtained by chemical bowl-feed polishing technique is 0.5 nm rms for silicon samples.

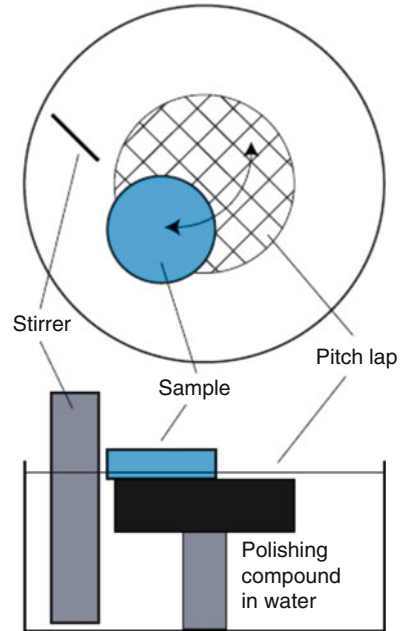
Bowl-Feed Polishing (Float Polishing)

Bowl-feed polishing is also referred to as super-polishing. Similar to the conventional polishing techniques, in the bowl-feed polishing technique, the sample oscillates with 28 number of strokes per minute over the rotating pitch lap. The basic difference between bowl-feed polishing and traditional (fresh-feed) polishing is the use of a bowl with a suspension of aqueous polishing material, rotating with the same speed as the pitch lap [15]. Because of the centrifugal and gravitational forces acting simultaneously, the particles of the polishing material in the suspension move toward the perimeter and to the bottom of the bowl. This is confirmed by the fact that the polishing material sinks visibly to the bottom within an hour in the rotation bowl if no obstacles are encountered. Figure 4 shows the top and side views of the bowl-feed polishing [16].

The bowl-feed polishing starts with a stirrer in the bowl and provides a fairly homogeneous distribution of the polishing material in the bowl. Then, a continuous deposition of new polishing material occurs on the pitch lap, because the suspension flows over its edges. The stirrer is removed after a good contact between the rotating pitch lap, and the surface of the work piece is obtained. At this stage, the suspended particles start sinking, and the quantity of polishing material falling on the pitch lap gradually decreases until pure water flows over the lap [16]. Since the polishing particles are broken and pushed into the pitch during polishing, the surface of the pitch lap tends to become smoother in nature. Subsequently, the smooth lap surface enormously reduces the surface roughness of the polishing material [17].

The sample along with the lap are located in the bowl and submerged in a fluid containing the polishing material in powder form. The sample and the lap rotates in the same direction and with the same speed. It generates a super smooth surface and a damage-free surface. Initially, there is a mechanical contact between the lap and sample, but later they are separated only by a layer of water. The disadvantage of this technique is to achieve high shape accuracy and to maintain a temperature control over the whole surface of the sample [18]. Using this technique, the surface roughness of 0.2 nm rms has been achieved on the flat surface of quartz and 0.13 nm rms on flat surface of BK7.

Fig. 4 Top and side views of the bowl-feed polishing. (Adopted from Ref. [16])



Elastic Emission Machining (EEM)

Elastic emission machining (EEM) is a precise surface finishing technique that uses the reaction between the surfaces of the work piece and finer powder particles. It is one of the ultraprecision machining methods used to fabricate shapes with an accuracy of 0.1 nm [19]. When the powder particle surface and the surface of the work piece come into contact with each other and during the process, the material is being removed from the surfaces, and there is a notable probability that the atoms on one surface will stick and move onto the other. EEM has already been applied to obtain a surface finish of the high-quality X-ray mirror optical surfaces and single-crystal Si(001) surfaces. The schematic of elastic emission machining process is shown in Fig. 5.

In this technique, a polyurethane sphere is made to float on the liquid layer containing the abrasive particles. While polishing, the diameter of the polyurethane sphere exceeds the applied abrasive particle size, and material removal will be activated chemically which occurs on an atomic scale. The work piece and rotating tool are all taken in a pool of slurry. The tool is made of polyurethane rubber, which is a soft material. EEM method makes use of the hydrodynamic effect to create a lubrication film between the surface of the work piece and the rotating tool. The article size should be much smaller than the thickness of the film. The abrasive particles are carried into a region between the rotating tool and the work surface by a drag force of the moving fluid. Because of the contacts between the particles and the

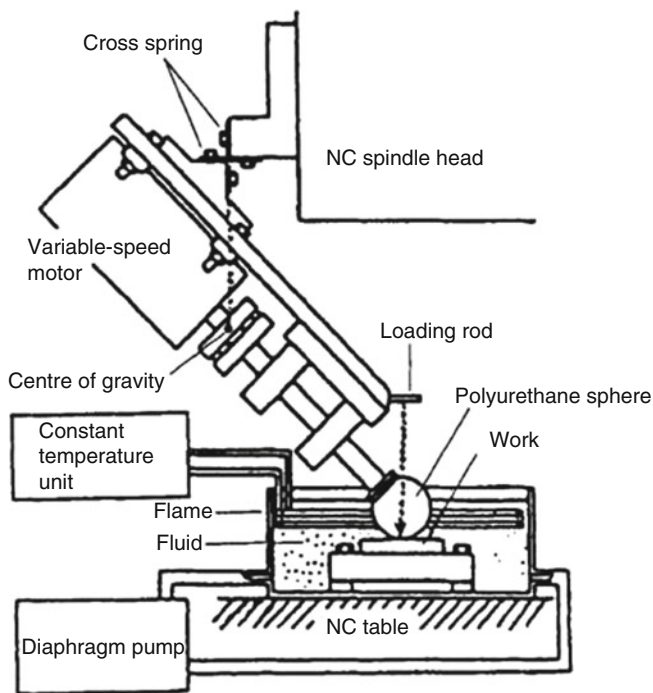


Fig. 5 Schematic diagram of the EEM process. (Adopted from Ref. [20])

work surface, machining occurs on an atomic scale. Till now, no super-polished samples have been generated whose surface roughness is less than 0.5 nm rms. The elastic behavior and wear rate of the applied polyurethane sphere systematically have to be investigated for obtaining super smooth surface finish on glass surface. Elastic emission polishing technique has been applied to silicon sample to polish to the surface roughness of <math><0.5\text{ nm}</math> using ZrO_2 as a polishing abrasive material [20].

Magnetorheological Finishing (MRF)

Traditional methods of finishing high precision lenses, optical glasses, optical ceramics, and glass ceramics are very expensive and labor-intensive. To overcome the difficulty in manufacturing high precision lenses, the Center for Optics Manufacturing (COM) in Rochester, New York, has developed a unique technology to automate the optical lens finishing process known as magnetorheological finishing (MRF) jointly with A.V. Luikov Heat and Mass Transfer Institute (AVLHMTI), Belarus [21–25].

Figure 6 shows the position of a convex or flat or concave work piece above a reference surface in the magnetorheological finishing process. A magnetorheological fluid material deposited on the rotating wheel is built into a form of a ribbon in the

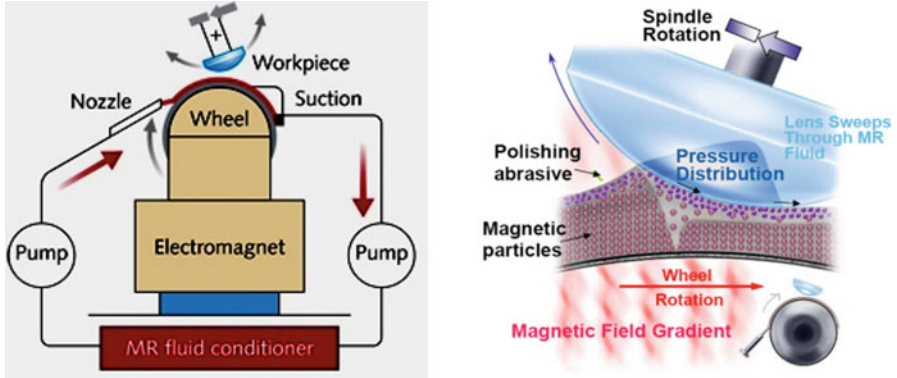


Fig. 6 Schematic of magnetorheological finishing process. (Adopted from Ref [21])

presence of magnetic field, and a finishing area is created by stiffened region. When the lens rotates on a spindle at a constant speed about its radius of curvature through the stiffened finishing zone, it results in surface smoothing, and additionally removal of subsurface damage and figure correction are also accomplished. Converging gap between the work piece and carrier surface created a shear stress, which is mainly responsible for material removal. The zone of contact is restricted to a spot, which conforms perfectly to the local topography of the part [26].

The magnetorheological fluid, which mainly consists of carbonyl iron (CI), abrasive particles, carrier fluids, and additives, governs the material removal in MRF. Magnetic fluid containing magnetically sensitive particles is mixed with polishing material (abrasive), namely, cerium oxide. It is stiffened with an external magnetic field and is used for local polishing and shaping. These magnetically sensitive particles under the influence of magnetic field and rotating wheel provide high shear stress to the floating abrasive particles on the polishing fluid. This causes the friction between abrasives and surface of the work piece, which needs to be polished [27].

The selection of the carrier fluid is based on the choice of the temperature ranges in which the MR fluid can be applied. Even though silicone oil is the most frequently used carrier fluid, hydrocarbon oil has an advantage due to its lower viscosity, suitability for high shear rate use, and better lubrication property. Additionally, a hydrocarbon oil-based magnetorheological fluid material has lower viscosity in the absence of magnetic field, which is about 0.6 times less than that of silicone oil-based fluid. On the other hand, aqueous-based MR fluid can minimize the wastage and allows the particles to be easily recycled from the fluid material (Fig. 7).

The strength of the MR fluid is restricted by the magnetic saturation of the magnetic particles. Due to remnant magnetization of the particles, undesired particle aggregation arises in concentrated MR fluids. As a result, the formation of stiff sediments, which are very difficult to re-disperse, occurred. In order to minimize the aggregation of the particles and their settling, different procedures have been proposed: (a) adding thixotropic agents such as carbon fibers and silica nanoparticles,

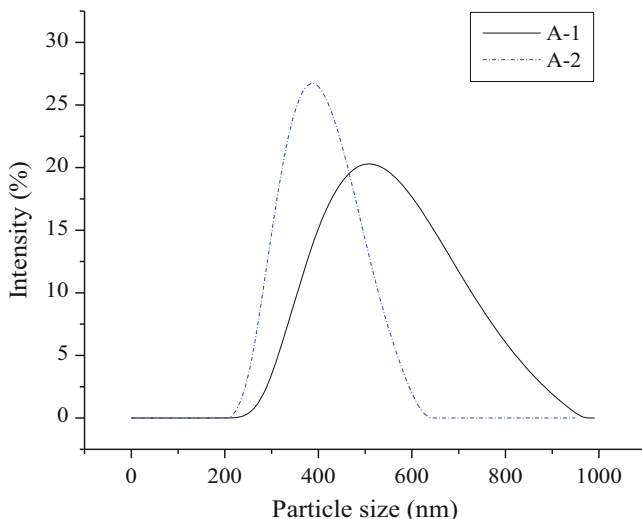


Fig. 7 Particle size distribution of abrasives A-1 and A-2 (Ref. [28])

(b) adding surfactants such as oleic/stearic acid, (c) adding magnetic nanoparticles, (d) using visco-plastic media as a continuous phase, and (e) using water-in-oil emulsions as carrier liquids. Glycerol and surfactants are used in aqueous-based fluid as stabilizers. Alkali also helps to improve the stability and resistance to rust. This technique is also termed as sub-aperture polishing, and the surface finish that has been achieved is 1 nm rms on glass surface [21]. The kinetic property of the fluid has made the tool to wear out less and less occurrence of debris during the process.

Recently, a study has been done, and it was found that, in the process of material removal during finishing, the rheology of fluid plays an important role [28]. The rheology of MRF can get affected due to several reasons like temperature, concentration of magnetic particles and abrasive particles, concentration of additives, and type of carrier fluid used to prepare MR fluid. It is observed that particle size distribution of abrasive particles affects the rheological behavior of MR polishing fluid [29]. It was also observed that the fluid containing abrasives having narrow particle size distribution was found to be inducing higher shear stress and higher viscosity, whereas the fluid which contained broad particle size distribution was found to impart considerably lower shear rate and lower viscosity at room temperature. In addition to this, it is also observed that the fluid with broad particle size distribution of abrasive (A-1) showed near to Newtonian fluid behavior, whereas the fluid containing narrow particle size distribution (A-2) showed pseudoplastic behavior (Fig. 7).

In one of the case studies given here, two magnetorheological polishing fluids MRPF-1 and MRPF-2 were prepared. The composition of these fluids includes magnetite as magnetic particles (77 wt%) and ceria as nonmagnetic abrasive particles (10 wt%) and silicone oil (13 wt%) as carrier fluid. MRPF-1 contains A-1 as

abrasive particles, whereas MRPF-2 contains A-2 as abrasive particles. Particle characterization data is given in Table 1. Two MR polishing fluids were prepared having abrasives with different particle size distribution but almost similar average particle size. The magnetic particles (magnetite) used are same in both the fluids. Particle size distribution of abrasive A-1 is broad corresponding to higher polydispersity index, whereas A-2 depicts narrow particle size distribution corresponding to lower polydispersity index. The rheological studies on the above mentioned MR fluids were carried out using MCR 51, Anton Paar rheometer, and parallel plate configuration measurement system.

The particle size distribution depicts a Gaussian-type distribution curve. The abrasives A-1 and A-2 are found to have nearly same average particle size of around 600 nm. The particle size distribution of abrasive A-1 is broad having 133.30 nm distribution width and 0.0528 as polydispersity index. The particle size distribution of abrasive A-2 is found to be narrow corresponding to 71.58 nm distribution width and 0.0136 as polydispersity index.

Phase identification and crystal structure of abrasives were studied using Bruker D8 Advanced diffractometer by using monochromatic Cu-K α radiation ($\lambda = 1.5405 \text{ \AA}$). X-Ray diffraction pattern of both abrasives A-1 and A-2 is shown in Fig. 8. XRD pattern of A-1 and A-2 matches with JCPDS 96-154-1461 and

Table 1 Viscosity and shear stress data at minimum and maximum shear rate (Ref. [28])

Abrasive	Viscosity (shear rate 65.8 s^{-1}) (Pa.s)		Viscosity (shear rate 1250 s^{-1}) (Pa.s)		Shear stress (shear rate 65.8 s^{-1}) (Pa)		Shear stress (shear rate 1250 s^{-1}) (Pa)	
	25 °C	40 °C	25 °C	40 °C	25 °C	40 °C	25 °C	40 °C
A-1	4.02	1.11	2.16	0.87	264	72.9	2700	1090
A-2	10	1.79	2.42	1.05	659	118	3020	1310

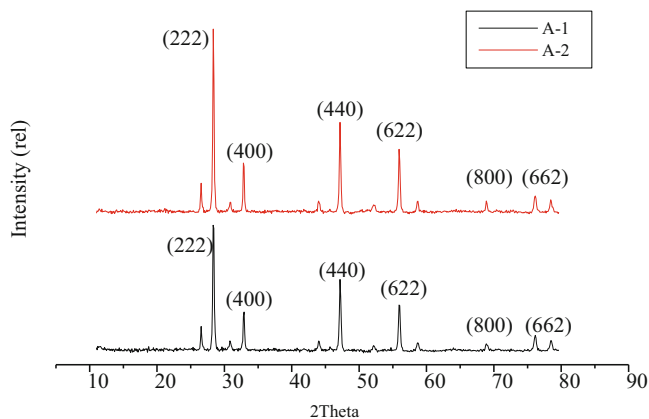


Fig. 8 XRD pattern of abrasives (Ref. [28])

JCPDS 96-434-3153, respectively. The prominent peaks at $2\theta = 28.37^\circ$, 32.81° , 47.16° , and 55.87° correspond to cubic phase of cerium dioxide (CeO_2). In both the abrasives, i.e., A-1 and A-2, crystal phase is found to be same having cell parameter $a = 5.448$ and 10.893 \AA , respectively. The crystallite size of A-1 is found to be 7.176 \AA and of A-2 is found to be 7.170 \AA .

EDS analysis was carried out to reveal the elemental composition of the abrasives A-1 and A-2 as shown in Fig. 9. Analysis confirmed that cerium and oxygen were present in A-1 and A-2 fluids.

Figure 10a, b depicts the morphology of abrasives A-1 and A-2, which are used in MRPF-1 and MRPF-2 polishing fluids, respectively. Sample preparation for SEM analysis was done by dispersing small quantity of abrasive powder on conductive carbon tape, which is further sputtered with gold to get an electrical conductivity on the surface. It can be seen from the images that the particles have spherical morphology in both the abrasive powders. This indicates that the morphological characteristics of both the abrasive powders are similar to each other.

Figure 11 shows the rheological behavior of MR polishing fluids in the absence of magnetic field at room temperature. Results obtained from rotational shear measurements depict that both fluids, i.e., MRPF-1 and MRPF-2, show shear thinning

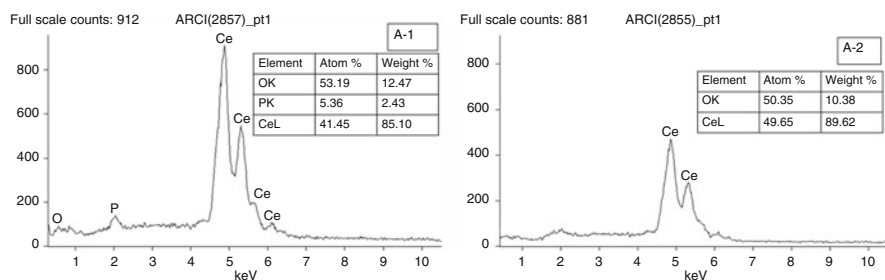


Fig. 9 EDS spectra of abrasives A-1 and A-2 (Ref. [28])

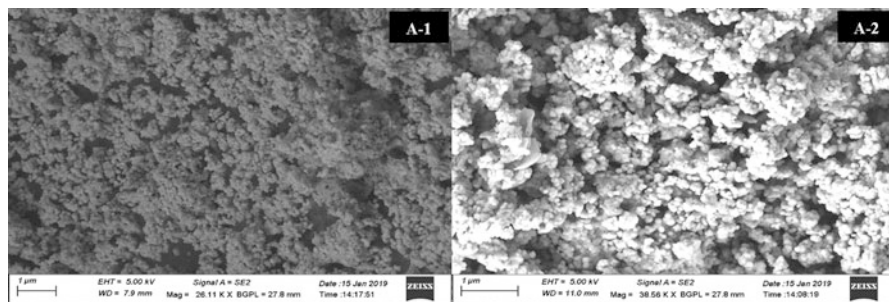


Fig. 10 (a) SEM microstructure of abrasive A-1, (b) SEM microstructure of abrasive A-2 (Ref. [28])

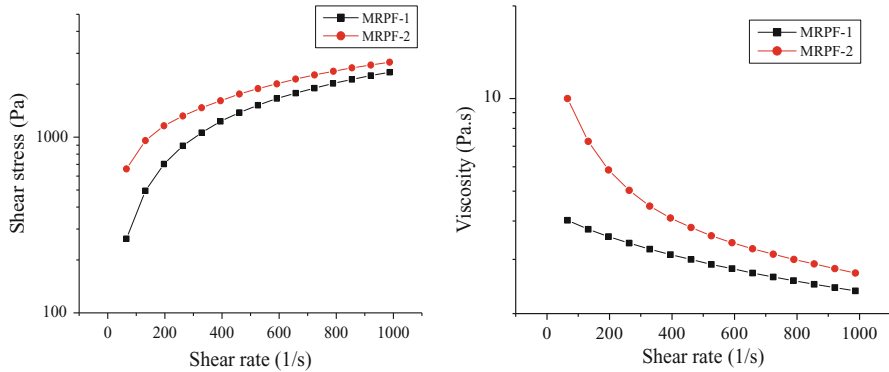


Fig. 11 Rheological behavior of MR polishing fluids in absence of magnetic field at 25 °C (Ref. [28])

behavior. Rheology of the particle systems can be influenced by the size distribution of the dispersed particles present in it [19]. Hence, in order to study the influence of particle size distribution of nonmagnetic abrasive particles, off-state rheology measurements were carried out. Rheological study was carried out by application of shear rate from 1000 S-1. Shear rate vs shear stress graph shows that MRPF-1 follows non-Newtonian fluid-like pseudoplastic behavior, whereas MRPF-2 follows Bingham plastic behavior. MRPF-1 is composed of abrasive A-1, which has broad particle size distribution; hence the shear stress observed is lower as compared to shear stress observed in case of MRPF-2 which suggests significantly higher shear stress values due to presence of abrasive A-2 corresponding to narrow particle size distribution. Although XRD results have confirmed both A-1 and A-2 abrasives in cubic ceria phase, EDS results give additional information about the presence of phosphorous element in A-1 which may be an impurity. This presence of phosphorous in A-1 could be probably one of the reasons for its decreased off-state shear stress behavior and viscosity.

Rheological behavior of MR polishing fluids in the absence of magnetic field at 40 °C is shown in Fig. 12. While performing MR finishing on a work piece, there is a chance of increase in temperature in the work piece as well as in the fluid. Moreover, seasonal temperature variation can also induce increase in temperature in the fluid. Hence, a rheology study was carried out at slightly higher temperature (40°C) to study the effect of temperature. It was observed that at 40°C there was significant decrease in shear stress as well as viscosity of both the fluids, i.e., MRPF-1 and MRPF-2. The initial shear stress was decreased by 2.7 times and 6 times for A-1 and A-2, respectively, whereas the initial viscosity was decreased by 3.63 times and 5.55 times for A-1 and A-2 abrasives, respectively.

Figure 13 shows the rheological behavior of MR polishing fluids in presence of magnetic field at room temperature (25°C). The above graph portrays magnetorheological study of MRPF-1 and MRPF-2. The rheology of fluids in absence and in presence of magnetic field shows similar trends. As observed earlier, the viscosity of MRPF-2 is higher than MRPF-1. This concludes that the particle size distribution of

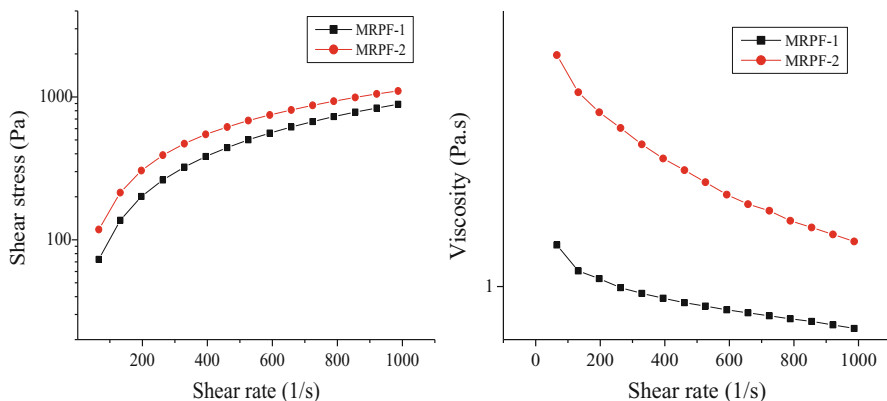
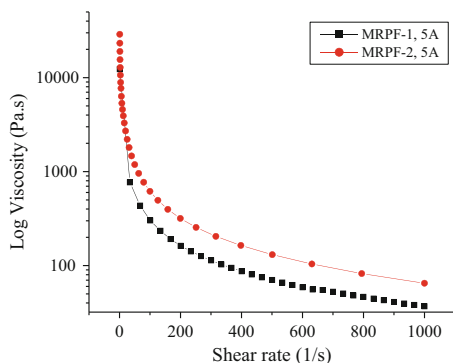


Fig. 12 Rheological behavior of MR polishing fluids in absence of magnetic field at 40 °C (Ref. [28])

Fig. 13 Rheological behavior of MR polishing fluids in presence of magnetic field at 25 °C (Ref. [28])



abrasive particles affects the rheology in presence of magnetic field as well. In the presence of magnetic field, the magnitude of viscosity is significantly higher as compared to viscosity in the absence of magnetic field. Viscosity variation with shear stress at different shear rates is given in Table 1.

Mechanism of MR Finishing

Magnetorheological (MR) polishing fluid is composed of magnetic particles, abrasive particles, carrier fluid, and additives in the form of a suspended liquid. When this fluid is placed in the magnetic field, the apparent viscosity and yield stress of the MR polishing fluid increase by several orders of magnitude. This leads to stiffening of the fluid. This transition from fluid to stiff nature is reversible and very rapid. When the fluid is under the influence of magnetic field, the abrasives float on the surface of fluid and come in contact with the surface of polishing glass ceramic work piece. This leads to material removal from the surface of work piece, hence resulting in high precision polishing. The rate of material removal during polishing in MRF is

controlled by regulating and tuning the applied magnetic field. In Zhang et al.'s study of MRF polishing, the surface roughness was measured by an atomic force microscopy before and after polishing as shown in Fig. 14.

From Fig. 14, it can be observed that the mean roughness (Ra) of the surface decreases from 1.239 to 0.684 nm and RMS (Rq) decreases from 1.857 to 1.074 nm. Since the material removal in MR polishing was on a microscale level, it is easy to eliminate the residual subsurface damage effectively. MRF has high efficiency and can reach nanoscale surface finishing quality as compared to conventional polishing methods. The microphotograph of glass ceramic surface is shown in Fig. 15.

Figures 14 and 15 show many protuberances on the finished surface, which indicate crystalline grains of glass ceramic. There is an even distribution of

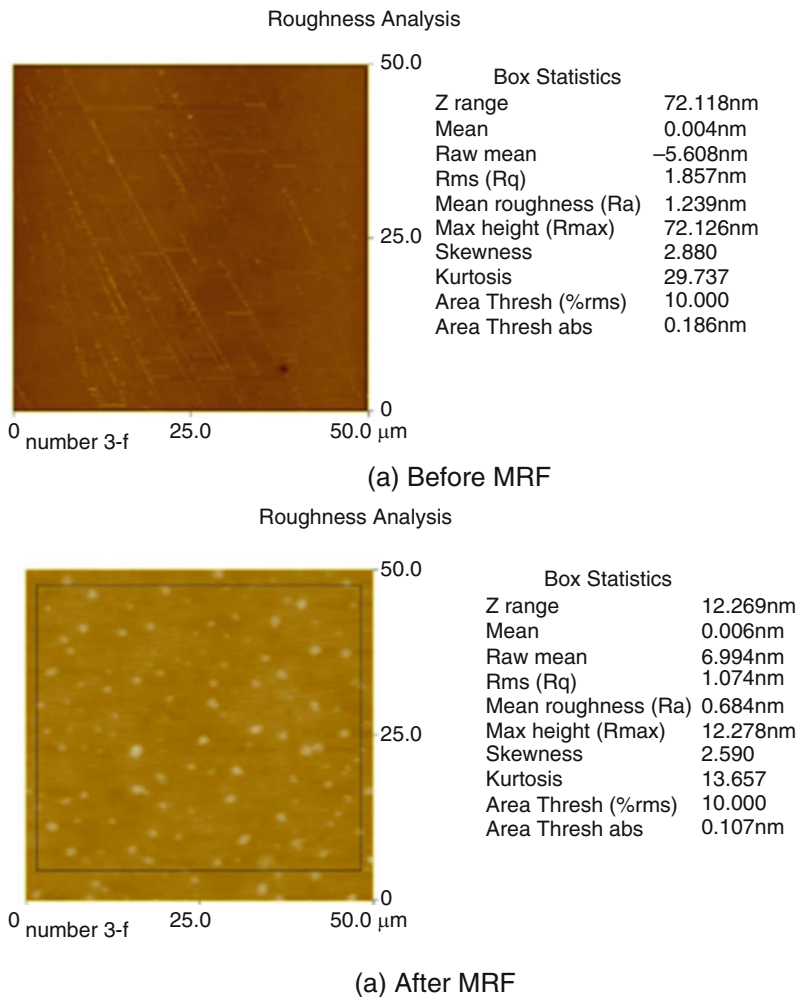


Fig. 14 AFM images of glass ceramic samples (a) before MRF and (b) after MRF

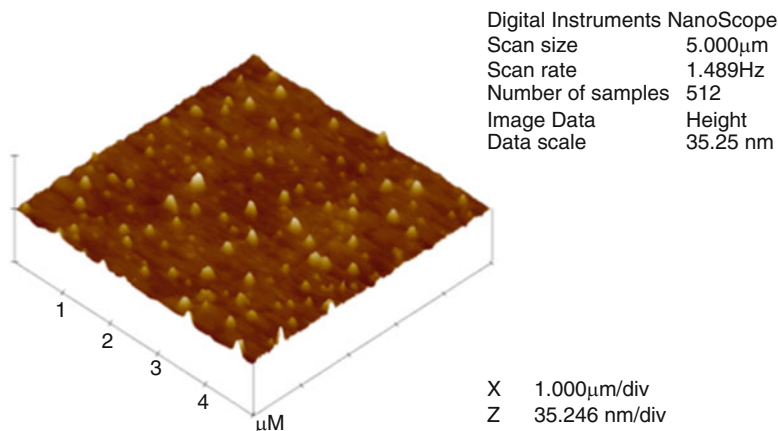


Fig. 15 AFM surface picture of glass ceramic after MRF

crystalline grains on the surface of glass ceramic, which is nothing but fundamental composition of glass ceramics. Glass phase and crystalline phase are the two phases present in glass ceramic. Crystalline phase of glass ceramic has a polycrystalline structure. Due to the higher hardness of crystalline grains than the glassy phase, glassy phase can be easily removed from the surface of the work piece during finishing. The surface seems uneven due to residual crystalline grains [30].

Laser Polishing

A laser beam (CO_2 laser) or a flame is utilized in this process, and the glass sample is heated approximately to its transformation point. This technique involves two effects: fast heating of the surface, i.e., the surface melts slightly, and it gets heated up sufficiently to a temperature so that any subsurface damage of the previous rough shaping mode can be rectified. Hence, in this process a large amount of energy acts for a very short duration of time onto the material, resulting in thermal stress on the surface. There are some chances of adverse effects due to chemical reactions between the glass and environment, diffusion of gases, separation of glass, and increased corrosion. Research has already been conducted on laser polishing of fused silica since 1982. Using defocused continuous wave CO_2 laser radiation and a meandering scanning strategy, an initial roughness of $\text{rms} = 0.33 \text{ nm}$ could be reduced to $\text{RMS} 0.27 \text{ nm}$. Due to a fast movement of the defocused laser beam ($d_s > 6 \text{ mm}$), a homogenous temperature distribution in the quasi-line on the surface was achieved. The first laser polishing method with pulsed CO_2 laser radiation for industrial usage by fabricating micro optics was a starting point [31].

With laser polishing, the polishing time can be considerably reduced, and the wear of hard tooling is avoided. For laser polishing, a very thin surface layer of the glass is heated up below its evaporation temperature due to the interaction of glass

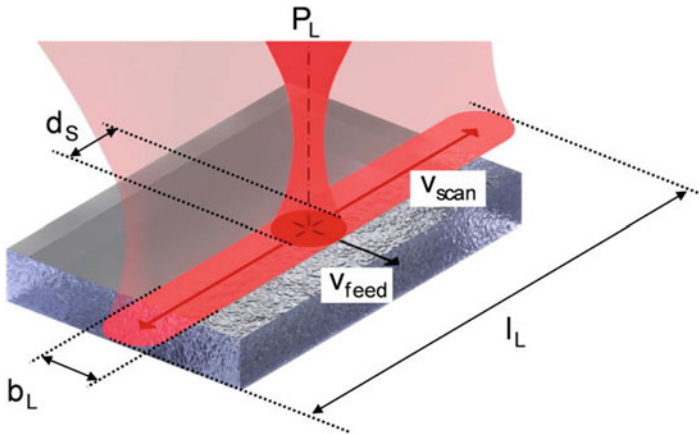


Fig. 16 Procedural principle of laser polishing glass material. (P_L , laser power; v_{feed} , feed speed; v_{scan} , scan speed; b_L , l_L , width, length of the quasi-line; and d_s , laser beam diameter) (Adopted from Ref. [32])

material and laser radiation. With an increase in temperature, the reduction in the viscosity in the surface layer leads to the reduction in the surface roughness due to the surface tension effect. In this method, a surface roughness of the order of 1 nm rms was achieved on BK7 glass material. Figure 16 shows the schematic of laser polishing technique [32].

Ion Beam Polishing

The optical surfaces are exposed to ion beam, and the material removal is done by sputtering technique. The sputtering rate depends upon the angle of incident beam and the local normal to the surface. The main characteristic of this technique is that an initial coating has to be deposited onto the surface, which has to be polished. The film is exposed to the ion beam, and the material is sputtered uniformly until the film is totally removed. This results into a uniformly smooth surface. It is also termed as sputtering erosion of the surface by atom-by-atom material removal process [33]. In this technique, there is no mechanical contact between the work piece and the polisher and if a focused ion beam is used then the finishing of various shapes such as aspheric shaping is also possible. Figuring of 5 μm flat ceramic surface to 2 nm rms roughness can be maintained by this technique. The schematic of ion beam polishing technique is shown in Fig. 17.

The drawback of this technique is that vacuum is needed, implantation of ions occurs into the material, sputtering itself is an erosion reaction, and chemical reaction may occur between the ions and atoms of the surface and is very sensitive to the existing subsurface damages [34].

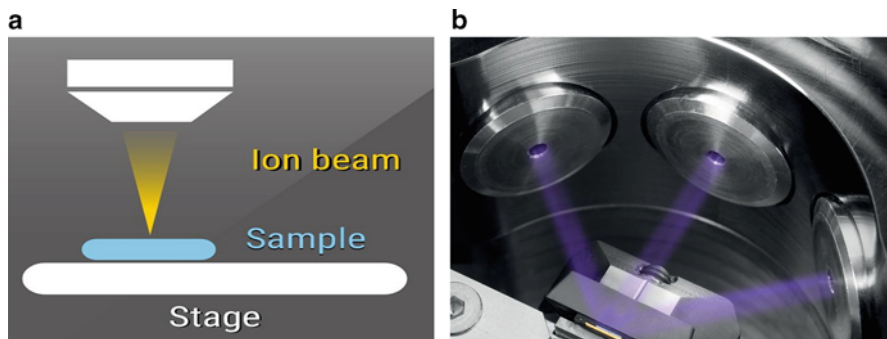
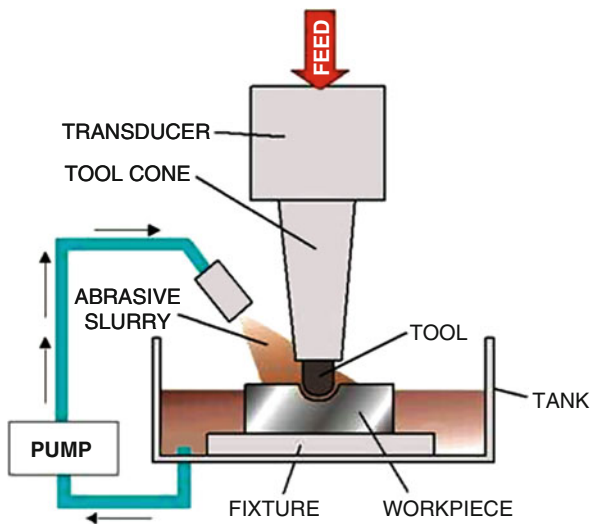


Fig. 17 (a) Schematic of ion beam polishing (courtesy: www.istgroup.com) and (b) experimental facility of ion beam polishing. (Courtesy: leica-microsystems.com)

Fig. 18 Schematic of abrasive slurry jet micromachining process. (Courtesy: <https://mechanicalstudents.com>)



Abrasive Slurry Jet (ASJ) Micro-machining

Figure 18 shows the schematic of abrasive slurry jet micromachining process. In abrasive slurry jet micromachining (ASJM), pressurized water is used to accelerate the suspended abrasive particles such as garnet or aluminum oxide (Al_2O_3) [35]. For the same jet dimension and flow speed, slurry jets have a much lower divergence angle than air jets, allowing for the micromachining of smaller features without the use of patterned masks. High-pressure ASJM uses a slurry at a pressure of 70 MPa to cut micro-slots into metals and composite materials. In the study on the mechanism of micro-hole formation in glass with ASJM, it was concluded that ductile erosion mechanism is mainly dominated [36]. Also, it was shown that increasing the pressure and erosion time increased the hole depth, with an insignificant effect on

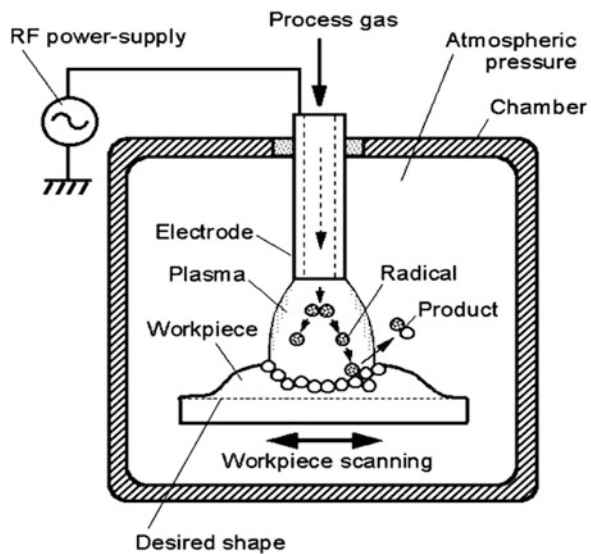
the hole diameter. In addition, the machined channels suffer from severe waviness due to the mechanical vibration of the set-up in this technique, whereas slurry jets have a more uniform distribution of impacting velocities across the jet, thereby leading to more uniform machining, much flatter bottoms, and steeper side walls without the use of erosion-resistant masks.

Slurry with high viscosity containing polymer abrasives is guided through a nozzle with a high pressure greater than 50 bar which is used laterally onto the glass surface. As the polymer molecules whose sizes range from 10 to 200 μm hit the surface laterally, the surface roughness also gets changed with respect to the high-pressure polymer abrasive. The requirement of high stream pressure and high viscosity slurry are the main disadvantage of this technique. Till now no data has been projected after polishing the glass sample with abrasive slurry jet machining process.

Plasma-Assisted Etching (PAE)

Plasma-assisted etching is an essential part of the microstructuring process in fabrication of integrated semiconductor circuits and micro-mechanic devices. Thereby structures down to the submicron range are etched. Such etch processes must show a high degree of anisotropy and a high selectivity with respect to the etch mask and the substrate [37]. These demands can be satisfied by a chemical etch reaction which is induced by impinging energetic particles such as ions, electrons, or photons as shown in Fig. 19.

Fig. 19 Schematic of plasma-assisted etching process. (Courtesy: www.iopscience.iop.org)



In this process, a small, confined plasma tool is moved over the surface of the glass material, and later shaping and polishing of the sample can be done locally. It is a noncontact method. Here the tool dimension and construction of the same are quite complicated. These two factors play a major role in finishing of curved optical surfaces [38]. The roughness value of 1 nm RMS on a flat silicate glass sample has been achieved by this process.

Characterization Techniques

A critical optical surface has to be tested during the fabrication process and should be precise in dimensions while measuring. This helps in verification of the quality of optical surface whether it has been achieved or not. Earlier, test plate mechanism was utilized for verifying the flatness or sphericity measurement of optical surface during fabrication process. Nowadays, versatile shop interferometers are being used to measure the surface figure, surface distortion, surface topography, and radius of curvature for spherical optics. Sophisticated autocollimators, in conjunction with computer technology, have been developed to measure small angular deviations in terms of arcsec accuracies and also help in the measurement of parallelism of plane-parallel surfaces. The qualitative determination of surface roughness measurements is also possible with advanced technology using phase shifting interferometry technique, coherence correlation interferometry technique, and polarized light in the advanced interferometry to analyze the subsurface damages that occurred during fabrication.

Test Plate Technique

It is the simplest and common method of testing the flatness or sphericity of optically polished surfaces. The concept of Fizeau fringes or Newton's rings has been adopted since earlier years of the nineteenth century. Fraunhofer was the first person to test the optically polished surface using test plate method. This technique is also termed as contact interferometry, where the optically polished surface and the test plate are in close contact. The affinity of the work piece with respect to the master test plate can be determined based on the formation of fringes. This helps in correcting the flatness or sphericity of the job during fabrication process in order to achieve the desired close and regular surface fit.

Newton's rings or Fizeau fringes represent a special case of interference where localized air film is trapped between two closely fitted transparent surfaces as shown in Fig. 20. This condition exists when test plates are used on matching optically polished surfaces. When the light is monochromatic depending on the wavelength and the thickness of the layer, it is either extinguished or reinforced. This results in the formation of characteristic alternate light and dark bands when the thin layer is wedge shaped.

Another way of describing is when one of the rays travels a slightly shorter path than the other, resulting in a phase difference between the two. If the phase difference resulting from the optical path difference (OPD) is exactly equal to the wavelength of

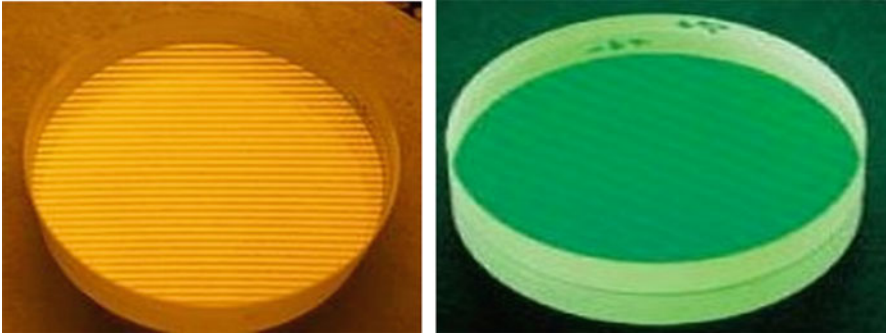


Fig. 20 Newton rings/Fringes formation at the contact of work piece and test plate

Fig. 21 Formation of color fringes in the work piece
<http://scitation.aip.org/content/aip/proceeding/aipcp/1728?ver=pdfcov>



the monochromatic light source, then constructive interference occurs, and a bright fringe is seen. If the optical path difference is a half wave, then destructive interference occurs with the formation of a dark fringe (Fig. 21).

Testplating with white light illumination results in color fringes. The thickness of the air film between the surfaces increases from violet to red corresponding to the increase in wavelength. This provides the optician to measure the surface with high (convex) or low (concave) surface match, and to select the blue fringes from the multicolored bands or rings as reference. The optical path difference (OPD) or $\lambda/2$ of blue fringe is about $0.25 \mu\text{m}$. Convex or concave conditions are also indicated by the way the fringes will move when the test plate is wedged slightly relative to the test surface.

When the fringe order or fringe is counted, it should always result in a whole number or integer, but that is not true in real cases. There will be always a partial fringe in every test plate match. These partial fringes cannot be counted with any degree of accuracy, and they are usually ignored. But, for very critical test plate matches, these partial fringes can introduce significant errors. Modern phase interferometers with sophisticated fringe analysis technique can account for these partial

fringes, and the measurement is much more precise than the test plate technique. Therefore, the use of test plate is restricted to shop floor analysis or in-process check, while the interferometers are used for final inspection and QC clearance.

Stylus Profiler Technique

In this method, especially stylus profiler, and optical methods such as scanning tunnelling microscopes (STM) and atomic force microscopes (AFM), contact mechanism is utilized.

Atomic Force Microscope (AFM)

It is ideal for measuring features with very small lateral dimension; tip sizes are typically 10 nm or smaller. It is limited by the maximum dimensions that can be measured typically 90 microns in x and y directions and 10 microns in z direction as shown in Fig. 22. Measurement time and speed are ten times greater than interferometry.

Scanning Electron Microscope (SEM)

This is traditionally being used for submicron analysis; however it does have some limitations. It can give very good lateral resolution, but it is not capable of analyzing in true z direction. Normally samples in Z-dimensions have been measured by sectioning them, and because of this, measuring of steps is a problem. Any sample that is to be measured has to be conducting in nature, and

Fig. 22 Schematic of atomic force microscope. (Courtesy: www.vu.nl)

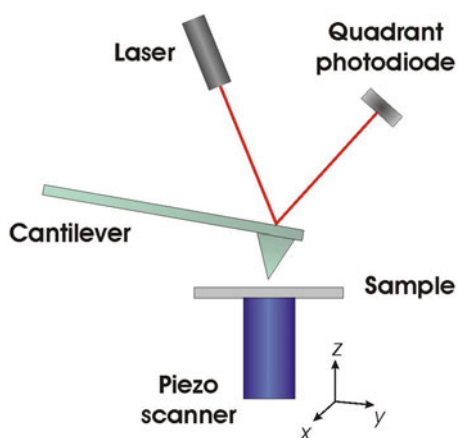
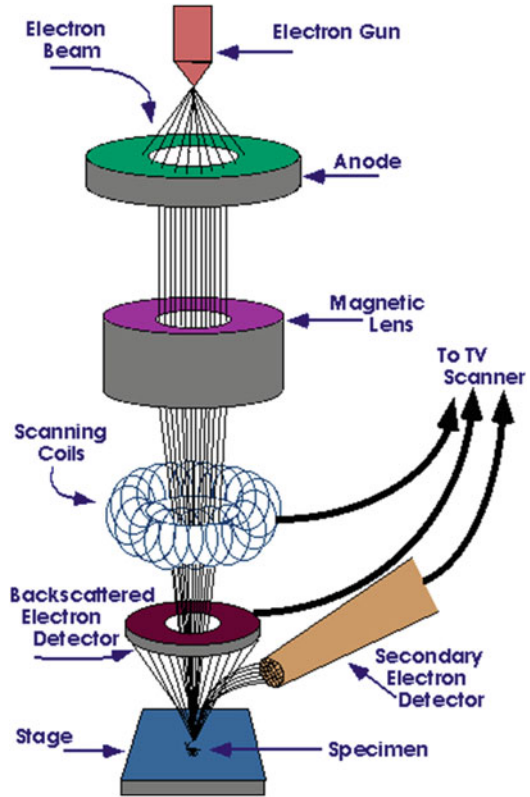


Fig. 23 Schematic of scanning electron microscopy. (Courtesy: www.purdue.edu)



if it's an insulator, they are normally to be coated with a metal thin film. Sample preparation can be complicated and time-consuming issue. The schematic of the scanning electron microscopy is shown in Fig. 23.

White Light Interferometry

For precise components where the specifications are of the order of angstrom level, above mentioned kind of surface topography measurement techniques is not suitable. The most accurate technique for assessing surface topography is noncontact method, which includes optical methods, especially methods of interference. There have been rapid developments in interferometry in the last two decades, as a result of the new possibilities for digital recording and analysis of interference images. The fastest growing interference methods include:

- Phase shift interferometry (PSI)
- Coherence correlation interferometry (CCI)

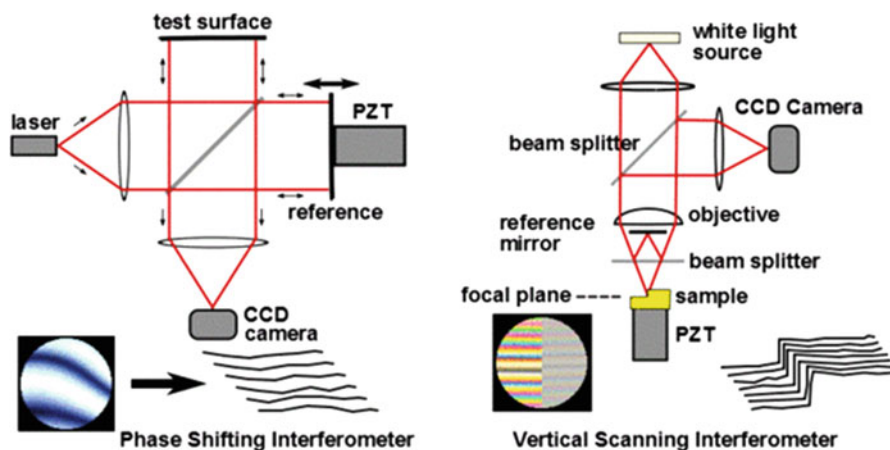


Fig. 24 Schematic of phase shifting interferometer and vertical scanning interferometer. (Courtesy: www.en.wikipedia.org)

Phase Shift Interferometry (PSI)

It is a well-established technique for surface characterization which relies on digitization of interference data during controlled phase shift. It provides a complete three-dimensional image with typical height measurement with a repeatability of less than 1 nm independent of field size. It consists of analysis of light phase distribution on the measured surface and accurately measures the height of surface irregularities. The measuring range is relatively small. Tracking and analyzing the degree of temporal coherence of interfering waves offer the possibility to measure the irregularities in the height of the surface over a greater range. It utilizes narrow-band width filtered light. The objective lens does not move, and it has a single focus point. It processes the intensity signal to calculate the surface heights. Schematic of phase shifting interferometer and vertical scanning interferometer is shown in Fig. 24.

Coherence Correlation Interferometry (CCI)

CCI is an ideal technique for quick measurement of surface roughness or step heights up to 400 nm with high accuracy and repeatability. Large steps can be measured by combining different measurements together. Lateral dimensions range from 0.5 microns up to 7 mm in a single measurement. It is based on the cross-coherence of two low-coherence light rays, where an object light ray is being reflected from the object while the reference light ray is reflected from reference mirror. A high-contrast interference pattern arises, if the optical path length in the object arm is equal to the optical path length in the reference arm.

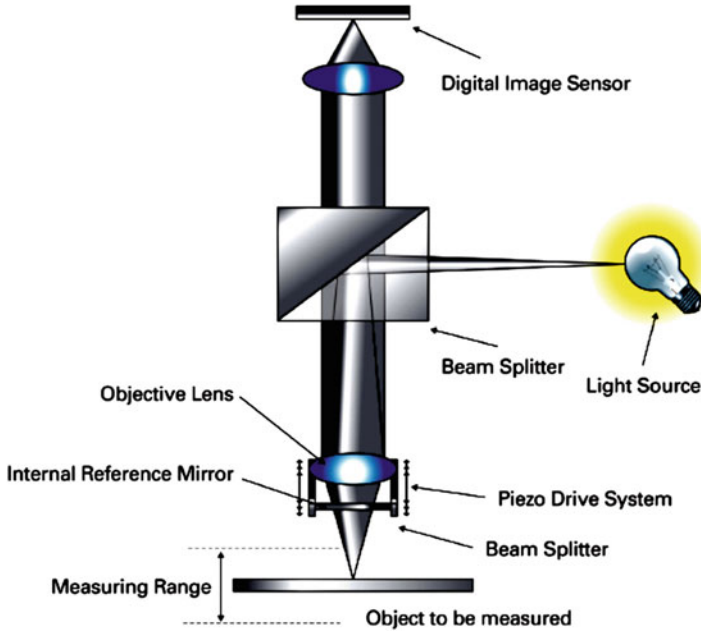


Fig. 25 Schematic of coherence correlate interferometer. (Courtesy: www.npl.co.uk)

Features of CCI

Schematic of coherence correlate interferometer is shown in Fig. 25. It is provided with features of wide measuring range and high resolution, a large measurement area on the object, short time for data acquisition and measurement, and exceptional versatility for measuring objects made from different materials. This also helps in the analysis of polymer materials, measurement of surface topography of the precision machined parts and elements, measurement of smooth and super smooth optical elements such as micro lenses and diffractive optics.

Case Study for Polishing/Finishing Techniques Used for Achieving the Nano-finished Optics Using Glass and Glass Ceramic Material

Optics are made not only of amorphous materials such as optical glasses and fused quartz, but are also made for low expansion glass ceramic materials like Cer-Vit and Zerodur, ultralow expansion quartz, and single-crystal materials such as sapphire. Super smooth surfaces can be obtained on most of these materials by special polishing techniques like bowl-feed polishing. In bowl-feed technique, the surface to be polished is immersed inside the slurry. The abrasives that were used get embedded inside the lap, and the slurry tends to become in a form of a pure water. Hence the surface produced by this technique has no fine scratches. For sapphire kind of materials, polishing is done very slowly either by bowl-feed

or by conventional fresh-feed techniques in which a small amount of water-abrasive mixture is used and it is polished to dryness.

Similarly, other polishing techniques have been studied for special applications such as substrates for microelectronic circuits. For Mn-Zn ferrite single crystal, a noncontact float polishing technique has been successfully utilized. In all the cases, the objective is to reduce the damaged layer on the surface that was usually produced by conventional polishing. In a case study, various glass materials like fused quartz, Zerodur, Corning glass ceramic, Cer-Vit, ULE quartz, and sapphire were used and obtained an approximately 2.4 Å rms roughness value. In their experiments conducted, a tin lap with its slurry-retaining bowl mounted to the spindle was utilized. The disadvantage of the system is that the grooves cannot be recut or surface-cut the top of the lands, and while shutting down and while starting the machine, the parts occasionally touch the lap producing two sets of circular scuff marks onto the lap.

Float Polishing Using Pitch Lap

For processing of highly precise components, the basic conventional polishing technique is used. As a result, the average roughness measured by Veeco 3D profiler as shown in Fig. 26 (phase shift interferometer) is 7 Å.

Fig. 26 3D profiler



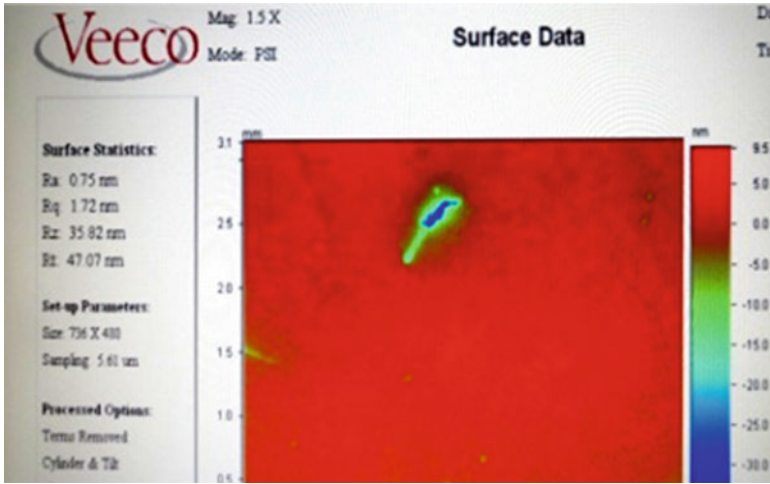


Fig. 27 Surface roughness measurement (before polishing) (<http://scitation.aip.org/content/aip/proceeding/aipcp/1728?ver=pdfcov>)

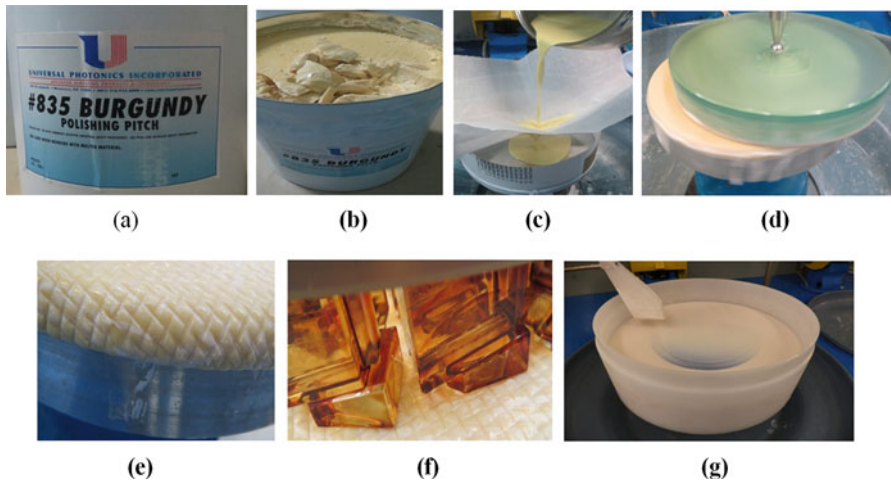


Fig. 28 (a–g) Polishing material used and the processing steps involved in preparing polishing slurry (<http://scitation.aip.org/content/aip/proceeding/aipcp/1728?ver=pdfcov>)

The concept of tin lap was applied by replacing the tin lap with the 835 Burgundy polishing pitch. The polishing pitch was prepared with the burgundy, melting it and pouring it onto aluminum plate. It was precisely matched, and a mesh-like pattern was impregnated onto the pitch. The polishing pitch was maintained at room temperature

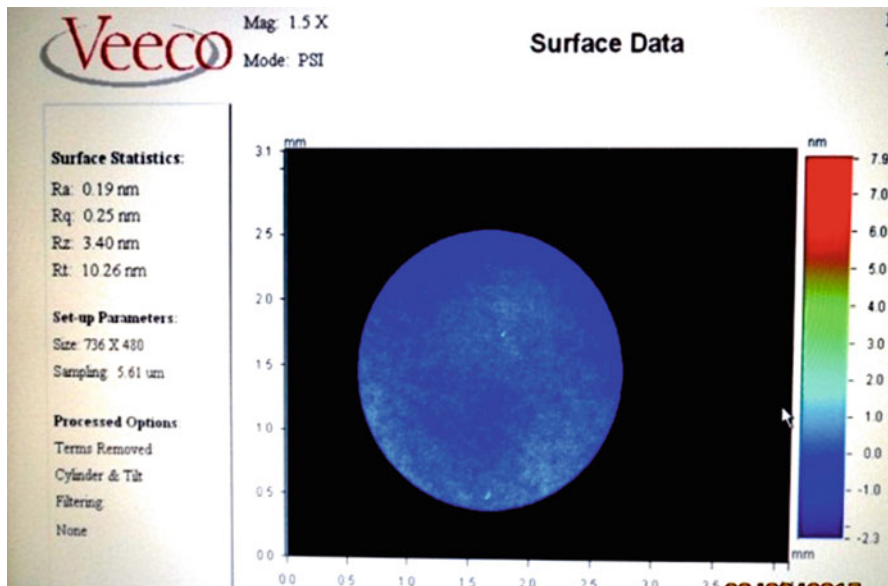


Fig. 29 Surface roughness measurement (after polishing)

and the relative humidity is 60%. The rotation speed of the spindles was approximately between 6 and 12 rpm, and the substrate was fused quartz (Fig. 27).

The substrate was polished with nano-ceria polishing slurry in float polishing technique for 8 h continuously inside the float polishing drum as shown in Fig. 28 (a–g). After processing the substrate was analyzed for its roughness value in Veeco 3D profiler and was found to be approximately 2 Å, which was better than the result obtained using tin lap.

The optical components such as mirror/prism, which has been polished using the conventional polishing technique, resulted in the average surface roughness value as 7 Å. With the modified float polishing technique, the surface roughness was measured as 2 Å as shown in Fig. 29. Thus, nano-finishing on glass/glass ceramics has been obtained by adopting a float polishing technique, and it was characterized by noncontact measuring technique by Veeco 3D optical profiler).

Summary

This chapter briefly discussed few novel polishing techniques for the fabrication of optical materials. Magnetorheological finishing is a novel polishing technique for deterministic subsurface damage correction.

References

1. Church EL, Jenkinson HA, Zavada JM (1979) Relationship between surface scattering and micro-topographic features. *Opt Eng* 18:125–136
2. Hank H (1993) Karow, fabrication methods for precision optics. A Wiley Interscience Publications, New York
3. Fahnle OW, Van Brug H (1999) novel approaches to generate aspherical optical surfaces, part of SPIE conference on optical manufacturing and testing III Denver, July 1999
4. Yamauchi K, Yamamura K, Mimura H, Sano Y, Saito A, Souvorov A, Yabashi M, Tamasaku K, Ishikawa T, Mori Y (2002) Nearly diffraction-limited line focusing of a hard X-ray beam with an elliptically figured mirror. *J Synchrotron Radiat* 9:313–316
5. Mimura H, Yamauchi K, Yamamura K, Kubota A, Matsuyama S, Sano Y, Ueno K, Endo K, Nishino Y, Tamasaku K, Yabashi M, Ishikawa T, Mori Y (2004) Image quality improvement in a hard X-ray projection microscope using total reflection mirror optics. *J Synchrotron Radiat* 11:343–346
6. Mimura H, Takei Y, Kume T, Takeo Y, Motoyama H, Egawa S, Matsuzawa Y, Yamaguchi G, Senba Y, Kishimoto H, Ohashi H (2018) Fabrication of a precise ellipsoidal Mirror for soft X-ray Nanofocusing. *Rev Sci Instrum* 89:093104
7. Yumoto H, Mimura H, Matsuyama S, Hara H (2005) Fabrication of elliptically figured mirror for focusing hard X-rays to size less than 50nm. *Rev Sci Instrum* 76:063708
8. Matsuyama S, Mimura H, Yumoto H (2005) Diffraction-limited two-dimensional hard X-ray focusing at the 100nm level using a kirkpatrick-baez mirror arrangement. *Rev Sci Instrum* 76:083114
9. Bifano TG, Dow TA, Scattergood RO (1991) Ductile-regime grinding: a novel technology for machining brittle materials. *Trans ASME* 113:184–189
10. Kim J-D, Nam S-R (1996) A piezoelectric driven micro-positioning system for the ductile-mode grinding of brittle materials. *J Mater Process Tech* 16:309–319
11. Allen SD, Braunstein M, Guiliano C, Wang V (1974) Laser induced damage in optical materials: NBS special publication 414:66–75
12. Bennet JM, King RJ (1970) Effect of polishing technique on the roughness and residual surface film on fused quartz optical flats. *Appl Opt* 9(1):236–238
13. Xu W (2019) Yanyao Cheng, min Zhong, effects of process parameters on chemical-mechanical interactions during sapphire polishing. *Microelectron Eng* 216:111029
14. Mao M, Chen W, Liu J, Hu Z, Qin C (2020) Chemical mechanism of chemical-mechanical polishing of tungsten cobalt cemented carbide inserts. *Int J Refract Met Hard Mater* 88:105179
15. Dietz RW, Bennet ZL (1966) Bowl feed technique for producing supersmooth optical surface. *Appl Opt* 5:881–882
16. Van Wingerden J, Frankena HJ, Van der Zwam BA (1992) Production and measurement of super polished surfaces. *Opt Eng* 31(5):1086–1092
17. Dietz RW, Bennett JM (1966) Bowl feed technique for producing Supersmooth optical surfaces. *Appl Opt* 5:881
18. Soares SF, Baselt DR, Black JP, Jungling KC, Stowell WK (1994) Float-polishing process and analysis of float polished quartz. *Appl Opt* 33(1):89–95
19. Hirata T, Takei Y, Mimura H (2014) Machining property in smoothing of steeply curved surfaces by elastic emission machining. *Proc CIRP* 13:198–202
20. Mori Y, Yamauchi Y, Yamamura K (2001) Development of plasma chemical vaporization machining and elastic emission machining systems for coherent x-ray optics. *Proc SPIE* 4501:30
21. Kordonski WI, Golini D (1998) Magnetorheological suspension-based high precision finishing technology (MRF). *J Intell Mater Syst Struct* 9(8):650–654
22. Kordonski WI, Golini D (1999) Fundamentals of magnetorheological fluid utilization in high precision finishing. *J Intell Mater Syst Struct* 10(9):683–689

23. Kordonski WI, Golini D (1999) Progress update in magnetorheological finishing. *Int J Mod Phys B* 13:2205–2212
24. Kordonski WI, Jacobs S (1996) Magnetorheological finishing. *Int J Mod Phys B* 10:2837–2848
25. Kordonski WI (2014) Magnetorheological Fluid-Based High Precision Finishing Technology, Chapter 11. In: Wereley NM (ed) *Magnetorheology: Advances and Applications*. RSC Smart Materials, Cambridge, pp 261–277
26. Liu J, Li X, Zhang Y, Dong T, Ye M, Wang C (2020) Predicting the material removal rate in surface magnetorheological finishing based on synergistic effect of pressure and shear stress. *Appl Surf Sci* 504:144492
27. Nie M, Cao J, Li J, Maohui F (2019) Magnet arrangements in a magnetic field generator for magnetorheological finishing. *Int J Mech Sci* 161-162:105018
28. Dhongade SH, Suresh MB, Shanker V, Rao YS (2019) Impact of particle size distribution of non-magnetic abrasive particles on rheology of magneto-rheological polishing fluids. In: *International conference advances in chemical sciences and technology*
29. Luckham PF, Ukeje MA (1999) Effect of Particle Size Distribution on the Rheology of Dispersed Systems. *J Colloid Interface Sci* 356:347–356
30. Zhang FH, Kang GW, Qiu ZJ, Dong S (2004) Magnetorheological finishing of glass ceramic. *Key Eng Mater* 257-258:511–514
31. Xiao YM, Bass M (1983) Thermal stress limitations to laser fire polishing of glasses. *Appl Opt* 22:2933–2936
32. Weingarten C, Schmickler A, Willenborg E, Wissenbach K (2017) Laser polishing and laser shape correction of optical glass. *J Laser Appl* 29:011702
33. Carter G, Nobes MJ, Katardjiev IV (1993) The theory of ion beam polishing and machining. *Vacuum* 44:303–309
34. Gruner D, Faldt J, Jansson R, Shen Z (2011) Argon ion beam polishing: a preparation technique for evaluating the interface of asseointegrated implants with high resolution. *Int J Oral Maxillofac Implants* 26:547–552
35. Haghbin N, Zadeh FA, Spelt JK, Papini M (2016) High pressure abrasive slurry jet micro machining using slurry entrainment. *Int J Adv Manuf Technol* 84:1031–1043
36. Nouraei H, Wodoslawsky A, Papini M, Spelt JK (2013) Characteristics of abrasive slurry jet micro machining: A comparison with abrasive air jet micromachining. *J Mater Process Technol* 213:1711–1724
37. Mader H (1990) Plasma-assisted etching. *Micro Syst Technol* 90:357–365
38. Coburn JW (1998) Mechanisms in plasma-assisted etching. *Phys Scr* 23:1–7



Electric Field/Current-Assisted Sintering of Optical Ceramics

16

Hidehiro Yoshida

Contents

Introduction	603
Role of Microstructure on Optical Properties	604
Operating Principle of SPS	606
Basic Apparatus of SPS	606
Mechanisms of Densification by SPS	608
Historical Background of SPS	610
Materials of Transparent Ceramics	611
Al ₂ O ₃	611
Y ₂ O ₃	615
ZrO ₂	617
MgO	620
MgAl ₂ O ₄	622
Y ₃ Al ₅ O ₁₂ (YAG)	624
Hydroxyapatite	625
AlON	626
AlN	627
Zinc Sulfide (ZnS)	628
New Technologies of ECAS/SPS	629
Multistep SPS	630
Water-Assisted SPS Process	631
Flash Sintering	632
Concluding Remarks	634
References	635

H. Yoshida (✉)

Department of Materials Science, School of Engineering, The University of Tokyo, Tokyo, Japan
e-mail: hyoshida@material.t.u-tokyo.ac.jp

© Springer Nature Switzerland AG 2020

Y. R. Mahajan, R. Johnson (eds.), *Handbook of Advanced Ceramics and Composites*,
https://doi.org/10.1007/978-3-030-16347-1_19

601

Abstract

This chapter aims to provide an updated and comprehensive description of the development of electric field/current-assisted sintering (ECAS) technique for the production of dense, structural/functional ceramics, particularly transparent polycrystalline ceramics. ECAS is gaining interest in recent decades due to the accelerated consolidation compared to conventional, pressureless sintering and pressure-assisted sintering (such as hot-pressing). In particular, spark plasma sintering (SPS) or pulsed electric current-assisted sintering (PECS), in which pulsed direct current is applied to directly heat up material under compressive stress, has been extensively studied as an extremely powerful tool. This process is capable of producing nanoceramics and transparent ceramics in a relatively short sintering time and low sintering temperature, being promoted for practical use. The short sintering time and low sintering temperature are in fact desirable for attaining high transparency and excellent mechanical properties for polycrystalline materials.

ECAS process is still drastically improving with new findings and technologies being actively reported. For instance, flash sintering, where densification occurs almost immediately (typically <5 s) under strong electric field, has been developed in recent decade and has been attracting extensive attention as an innovative sintering technique. In this chapter, the earlier experimental works on SPS methods and characteristic properties of the produced transparent materials are summarized, and recent attempts for elucidation of the underlying mechanisms responsible for the SPS are briefly introduced.

Keywords

Electric current · Electric field · Electric current-assisted sintering · Spark plasma sintering · Oxide ceramics · Densification · Grain size · Mechanical strength

Abbreviations

3Y-TZP	3 mol% yttria-stabilized tetragonal zirconia polycrystal
DC	Direct current
ECAS	Electric field/current-assisted sintering technique
EELS	Electron energy loss spectrometry
HA	Hydroxyapatite, $\text{Ca}_{10}(\text{PO}_4)_6(\text{OH})_2$
HIP	Hot isostatic pressing
HP	Hot pressing
IR	Infrared
PECS	Pulsed electric current-assisted sintering
SPS	Spark plasma sintering
TEOS	Tetraethyl orthosilicate
YAG	Yttrium aluminum garnet, $\text{Y}_3\text{Al}_5\text{O}_{12}$
YSZ	Y_2O_3 -stabilized ZrO_2

Introduction

Common optically transparent materials, such as glasses and polymers, have been widely used in industrial applications and daily life. However, these materials have relatively poor mechanical strengths and sometimes insufficient chemical and physical stabilities. Also, they usually possess relatively low melting temperatures and low resistance against corrosive atmosphere, so that they cannot be used for applications at high temperatures or other harsh environment. Ceramic materials therefore emerge as a powerful candidate for transparent materials used in high temperature and/or corrosive environments. Single crystals of ceramics, such as sapphire (Al_2O_3) and YAG ($\text{Y}_3\text{Al}_5\text{O}_{12}$), are essentially optically transparent and have been actually in practical use for various industrial applications. However, growth of single crystals requires very high temperature and long processing time, leading to expensive products and components. Hence, transparent polycrystalline ceramics are of practical importance in the field of optical applications. The advantage of polycrystals is that they can be larger in dimensions and can be produced at lower temperatures, comparing to single crystals. In addition, functionalization of ceramic body by doping or manufacturing functionally graded materials can be more easily prepared for polycrystalline ceramics than single crystals. In contrast to single crystals, polycrystalline ceramics are in general opaque, because of the presence of light-scattering sources as mentioned later. In order to attain optical transparency in polycrystalline ceramics, it is necessary to eliminate residual pores and other defects from sintered body, because the presence of such defects drastically deteriorates optical quality.

A number of efforts have been made to eliminate residual defects from sintered bodies by various synthesis methods so far. Improving sinterability is essential to minimize defects (residual pores in sintered body), leading to optical transparent ceramics, so that researchers have optimized sintering conditions from raw powder synthesis to consolidation methods. As for sintering processes, pressure-assisted techniques such as hot-pressing (HP) and hot isostatic pressing (HIP) are widely employed to improve the quality of sintered materials and to fabricate transparent ceramic bodies. HIP synthesis, in fact, is an effective technique to produce transparent bulk ceramic body.

Among pressure-assisted sintering, spark plasma sintering (SPS), also known as electric field/current-assisted sintering technique (ECAS) or pulsed electric current-assisted sintering (PECS) method, has attracted considerable attention as a short-time and low-temperature synthesis method for production of transparent ceramics. SPS is a solid compressive and pulsed electric-current-energizing sintering method. In recent decades, owing to the remarkable development of SPS machines and techniques, a considerable number of studies were performed to produce high-performance ceramics by ECAS/SPS. SPS is also capable of producing highly dense and nanostructured sintered compacts, even in case of ceramics with poor sinterability. Recently, SPS has proved to be a powerful method to manufacture transparent polycrystalline ceramics. In addition, power consumption of the SPS synthesis is about one-third to one fifth of that of traditional techniques, including normal pressureless sintering, HP, and HIP [1, 2].

SPS takes advantage of both high applied currents and mechanical pressure to deliver significantly higher densification rates than conventional pressureless sintering or HP [1]. In fact, several advantages over conventional sintering techniques are provided by SPS for fabricating transparent ceramics. In addition, new technologies regarding ECAS processes are still being reported actively, to promote low-temperature and short-time consolidation of powder compacts. Also, mechanisms underlying ECAS and SPS are being enthusiastically investigated. This chapter aims to briefly summarize ECAS and SPS techniques and to cover transparent oxide ceramic materials produced by SPS. Also, several new attempts of ECAS to enhance full densification of ceramic materials are introduced.

Role of Microstructure on Optical Properties

It has been widely accepted that the microstructure of polycrystalline ceramics plays a key role in their optical properties. It is beneficial to briefly summarize important microstructural features which determine optical transparency for visible and near-infrared (IR) wavelength in polycrystalline ceramic materials. Owing to wide bandgap of common ceramic materials, ceramic single crystal is essentially transparent for visible and IR wavelength. However, polycrystalline ceramics are generally opaque, due to the presence of various light-scattering factors.

The critical factors which determine optical transparency in ceramics are refractive index of crystals (i.e., isotropy of crystal structures), grain boundaries and interfaces, and porosity of polycrystalline body. For attainment of optical transparency in polycrystalline ceramics, isotropic, high symmetry of the crystals, i.e., similar refractive index in all directions, is preferable. Cubic symmetry is therefore an ideal crystalline structure for transparency. But, the dominant microstructural feature that sensitively influences transparency is porosity. Residual pores in sintered ceramic bodies degrade transparency of the materials due to scattering of light at the pores. The refractive index significantly different between material and pore, resulting in reflection and refraction of light [2, 3].

It has been widely accepted that the in-line transmission should increase with the increasing grain size, because the increased number of grain boundaries gains light-scattering source. In fact, optical scattering decreases with the increasing grain size and with decreasing the number of the grain boundaries in fully densified Al_2O_3 polycrystals with the grain size beyond 20 μm , the size of which is much larger than the wavelength of visible light [4]. However, recent investigations have revealed that the contribution of grain boundaries to scattering is rather small in oxide polycrystals with submicron grain sizes [5–8]. Hayashi et al. examined transmission optical properties of HIPed Al_2O_3 polycrystals with the average grain size in a range of 0.82–1.43 μm [5] and confirmed that the transmission monotonically increases with the decreasing average grain size.

Important microstructural features and their interaction with visible/IR radiation light are schematically described in Fig. 1 [2, 3]. Figure 1a illustrates polycrystalline ceramics with micrometer-sized grains and pores. In materials with pore sizes in the

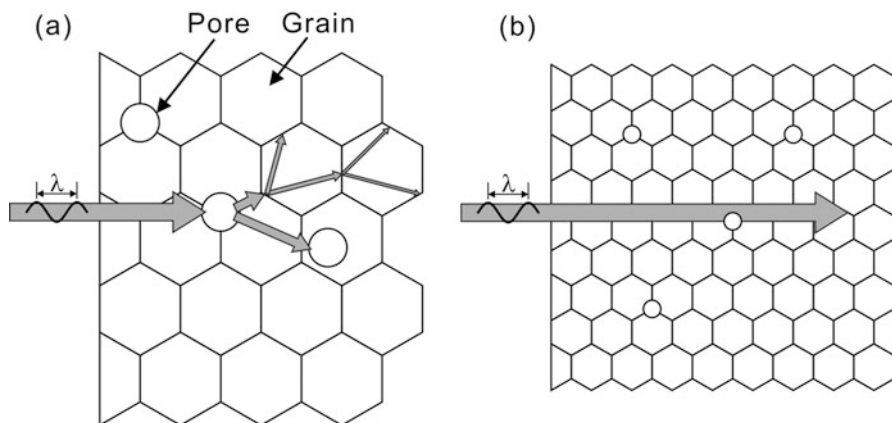


Fig. 1 Microstructure of polycrystalline ceramics and light transmission through the ceramics. (a) Polycrystalline ceramics with micrometer-sized grains and pores and (b) nanometer-sized grains

micrometer range (i.e., dimensions comparable to the wavelength of the light λ), pores significantly scatter light. In order to achieve high transparency in ceramics with micrometer-sized pores, the porosity must be reduced to much less than 0.1%. As mentioned above, when the pore sizes decrease to the nanometer range, their interaction with visible light becomes minimal, and the optical transparency increases. In addition, grain boundary is another scattering source because of anisotropic refractive indices of grains; light is refracted at each grain boundary since each grain in a random polycrystalline ceramic represents a discontinuity in refractive index. Taking these light-scattering sources into account, conventional transparent ceramics are developed by eliminating residual pores and by increasing grain sizes (i.e., decreasing number of grain boundaries). Compression sintering, such as HIP, is often employed to attain fully densified and large grain-sized microstructure; compressive stress effectively facilitates breaking agglomerated grains and eliminating residual intergranular pores.

Recent development on SPS methods allows fabrication of fully densified ceramic body consisting of ultrafine (submicron-sized) grains, in comparison to HP and HIP methods. In SPS, material temperature is raised by pulsed direct current (DC) applied through graphite die and punches, not by heating from outside die. The almost direct heating of material in SPS may allow densification at lower temperature in shorter holding time, compared with HP and HIP. As shown later, the characteristics of SPS contribute to enhance densification and to reduce grain sizes of sintered body. Hence, the strategy to attain the transparency of ceramics has been changed to full densification of nanocrystallized ceramics. Figure 1b illustrates an anisotropic material with grain sizes in nanocrystalline range. By reducing the grain size lower than the wave length of visible light, light is not scattered at grain boundaries [2, 3]. Furthermore, refinement of grain size is also advantageous to

improve mechanical strength of polycrystalline material. Production of transparent ceramics by means of SPS technique will be beneficial for industrial application in comparison to traditional HP or HIP processing.

Operating Principle of SPS

Basic Apparatus of SPS

A schematic of the typical apparatus of SPS is shown in Fig. 2a, together with an illustration of HP setup (Fig. 2b). In HP, the process of diffusion and/or plastic flow of powder compact is promoted by both heating from outside die and compressive stress; these two factors contribute to promote sintering densification. Due to the usage of graphite die in HP, the sintering is usually conducted in vacuum or inert gas (but thanks to the atmosphere, tungsten mesh heating elements can be used in the chamber).

ECAS/SPS machine also consists of a mechanical loading system, as well as HP, but the loading jigs act at the same time as electrodes, placed in a chamber under vacuum. The sintering of SPS is carried out in vacuum by using a graphite die, and compressive stress is applied to graphite punches, as well as conventional HP. But, the material is heated up by means of pulsed DC current, supplied by a patented power generator, applied through electrodes at the top and bottom of the graphite punches [9–11]. Owing to the high electrical conductivity of the materials used for dies and punches, low voltage is applied to the whole setup including material, die, and punches, to yield high current, leading to efficient Joule heating of the material.

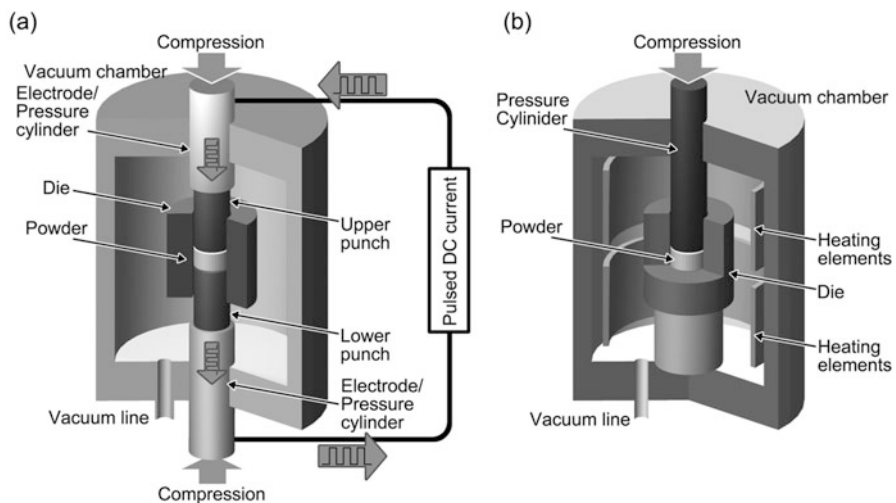


Fig. 2 A schematic of (a) typical apparatus of spark plasma sintering (SPS) machine and (b) hot-pressing (HP) setup

The typical voltage applied to the whole setup in SPS is usually in a range of 4–20 V. The average value of current is in a range of 500 A to 40 kA, depending on sintering conditions and electric conductivity of the material.

Because only die and punches are heated in SPS, heating rates can be in SPS as high as several hundred degrees over a minute. Standard cooling rates up to 150 °C/min are usually employed; additional active cooling under gas flow enables to reach quenching rates of 400 °C/min. As a result, heating rate typically used is 20–200 °C/min, and much faster heating rate up to 1000 °C/min can be employed. Even in the case of electrically non-conductive raw powder, heat is quickly transferred to the material inside the die, owing to high thermal conductivity of the die and punches. SPS therefore enables to significantly reduce the total duration of the process and energy costs. Maximum temperature achieved by using standard graphite tools lies beyond 2000 °C. The pulsed DC current is automatically controlled to attain target temperature. The pulse and pause durations for SPS operation is typically in the order of a few milliseconds.

In the operation of ECAS/SPS, the control of temperature of die or punches during SPS, with heating rates of several hundreds of °C/min, is an important and critical matter; the SPS temperature must be monitored with high responsivity to control heating schedule. Main requirements for a reliable temperature measurement are a short reaction time and a high reproducibility. The temperature is usually measured by an optical pyrometer focused onto the surface of the die or the punches or by a thermocouple placed inside the die.

Attempts to measure the temperature of the material inside the die during SPS have been carried out so far. For instance, Misawa and co-workers measured the temperature of ZnO specimen as well as the internal current of the powder compact inside a graphite die during SPS process by using Pt electrodes and magnetic probe (coil), as schematically shown in Fig. 3 [12]. In the case of ZnO specimen, decrease of electric resistance was detected during sintering process. The initial current that

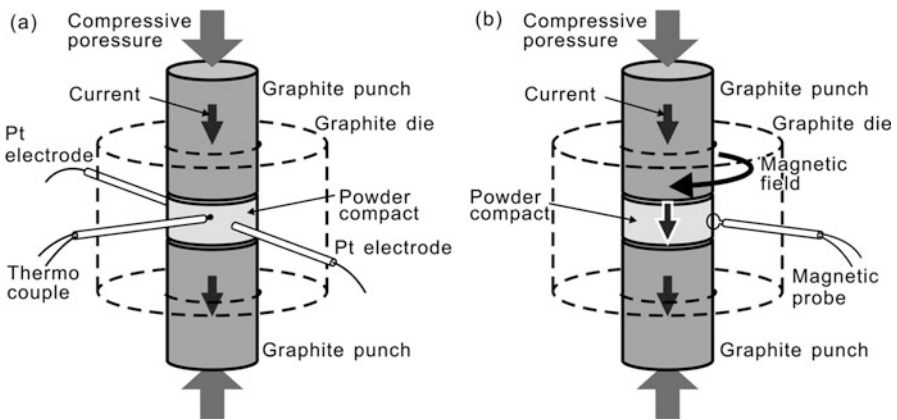


Fig. 3 Schematic of (a) temperature, electric resistance, and (b) magnetic field measurement system inside a graphite die during SPS processing [7]

flowed through the ZnO powder compact was several hundred amperes, and the ratio of the internal current through the specimen to the total current increased with the progress of densification. However, it is still technically difficult to directly measure the materials' temperature during SPS synthesis. Probably we need theoretical approach, such as finite element modeling (FEM), to estimate the material temperature. In particular, FEM is an important tool to predict the distribution of temperature, current, electrical potential, and stress that emerged during SPS process at the micro-, meso-, and macroscopic scales. FEM analysis has been widely employed for elucidation and controlling of specimen temperature and stress distribution developed in SPS operation. Detailed overview of calculation works is given by Orru et al. [13].

At the same time, the simultaneous application of a uniaxial mechanical pressure enhances densification as well as HP and HIP. The compressive stress is typically in a range of 20–100 MPa, but ultrahigh pressure of several hundred MPa–1 GPa can also be employed (for ultrahigh-pressure SPS, we need to use some special dies). Recently, pressure or displacement becomes another important controlling parameter for SPS operation.

Advantages of SPS are fast sintering process, suppressed grain growth, and single step compaction and sintering processes. However, SPS method has some disadvantages, particularly only simple symmetrical shapes and limited sizes being allowed in SPS synthesis. The drawbacks in SPS have always been pointed out as well as in HP, but at least enlarged dimensions of the sintered bodies have been gradually attained in recent years.

Mechanisms of Densification by SPS

SPS technique has a significant advantage over HP and HIP, because it can complete the powder consolidation within a short time duration [14]. SPS has a potential to densify nanosized powders without significant grain coarsening which is unavoidable during the conventional densification routes. The densification process in SPS is generally divided into three stages [15]. The first stage is characterized by the packing of raw particles, the second stage is a diffusional process including the neck formation and grain sliding, and the final stage is the removal of closed pores mainly through grain boundaries.

It was expected that electrical discharge plasma takes place between powder particles, resulting in localized and momentary heating of the particle surfaces [9]; self-heat generation by the electric discharge plasma between particles at an early stage of on-off DC pulse application would act on promoting sintering. In addition, it has been speculated that the surfaces of the particles are purified and activated due to the electric discharge plasma on the particle surfaces; the purified surface layers of the particles could melt and fuse to each other forming necks between the particles [10]. However, the occurrence of the discharge has been questioned in recent years.

It is widely accepted that electric field can accelerate densification of ceramics, while the primary purpose of imposed electric field/current in SPS is usually supposed to provide the required amount of resistive heating. For instance, DC electrical fields of approximately 20 V/cm lower the sintering temperature of 3 mol% yttria-stabilized tetragonal zirconia polycrystal (3Y-TZP) from 1400 °C to 1300 °C [16]. However, the origin of the electric field on the enhancement of mass transport is still unclear. In the case of SPS, the applied voltages are usually rather low, lower than the required value to trigger electromigration. Recently, it has been reported that electric field/current can involve formation of anion vacancies in ceramics [17]; electron energy loss spectrometry (EELS) analysis suggested that Y₂O₃ polycrystal consolidated by SPS exhibited reduced state in comparison to Y₂O₃ sintered in air and in vacuum. Highly reduced state in other oxide ceramics densified under strong electric field or current have also been revealed by EELS analysis, as mentioned later. The role of DC field and/or current is still an open question, but it would seem that field/current can trigger the formation of ionic defects and consequently facilitate diffusional mass transport, leading to acceleration of densification of ceramic materials.

Besides these electric field/current effects, the densification behavior in SPS can be quantitatively analyzed based on high-temperature mass transport rate equation. In the early stage of sintering, the temperature of the punches and die is raised prior to the heating of the compacted powder, due to low electric conductivity of the raw powders [18]. The temperature of the compact is gradually increased by the heating of the die and punches, and then the electric current through the compacted powder accordingly increases, resulting in Joule heating of the material [18]. An applied pressure strongly affects the initial packing and densification in the second and third stages. A high pressure is constantly applied in common SPS process. Heating rate is another important sintering parameter for densification in the second and third stages; high heating rate is supposed to be one of the strong advantages of SPS synthesis over HP and HIP. In SPS, specimen temperature can be raised in relatively short time, resulting in suppression of grain growth during the heating process of sintering.

Here, we take a look at an example of phenomenological analysis of the densification process in SPS [19]. Mass transport during sintering with or without an external load can be regarded as analogous to that occurring in high-temperature creep. The steady-state creep strain, ϵ , can be described by a general constitutive relationship where the creep rate is a minimum and remains at an almost constant value:

$$\frac{d\epsilon}{dt} = \dot{\epsilon} = A \frac{\phi \mu b}{kT} \left(\frac{b}{G}\right)^p \left(\frac{\sigma}{\mu}\right)^n \quad (1)$$

where $\dot{\epsilon}$ is the creep rate, t the time, A a constant, ϕ the diffusion coefficient, μ the shear modulus, b the Burgers vector, k the Boltzmann's constant, T the absolute temperature, G the grain size, σ the macroscopic applied stress, and p and n the grain size and stress exponents, respectively. The HP kinetics can be written in a simplified

version by dropping the negligible small thermodynamic driving forces. The densification rate is then given by

$$\frac{1}{D} \frac{dD}{dt} = \frac{B\Phi\mu_{\text{eff}}b}{kT} \left(\frac{b}{G}\right)^p \left(\frac{\sigma_{\text{eff}}}{\mu_{\text{eff}}}\right)^n \quad (2)$$

where D is the instantaneous relative density, B a constant, σ_{eff} the instantaneous effective stress acting on the powder compact, and μ_{eff} the instantaneous shear modulus of the powder compact. Taking into account the porosity dependence of the material's physical properties, Eq. (2) can be modified as

$$\frac{1}{\mu_{\text{eff}}} \frac{1}{D} \frac{dD}{dt} = K \frac{\exp(-Q_d/RT)}{T} \left(\frac{b}{G}\right)^p \left(\frac{\sigma_{\text{eff}}}{\mu_{\text{eff}}}\right)^n \quad (3)$$

Here $K = Bb\Phi_0/k$ is a constant (with Φ_0 the pre-exponential term of the diffusion coefficient) and Q_d the apparent activation energy for the mechanism which rate-controls densification. From Eq. (3), the parameters of p , n , and Q_d are experimentally determined, enabling the identification of the rate-controlling mechanisms of densification of the powder compact during SPS. For example, for diffusion-controlled densification, the strain rate is proportional to the effective stress ($n = 1$). Because densification process is a thermally activated process, densification is also characterized by the activation energy of the rate-controlling mechanism (grain-boundary diffusion, etc.). When the pressure in SPS increases up to several hundreds of MPa, powder agglomerates may break. The particle rearrangement at low temperature increases packing and reduces pore size, allowing homogeneous subsequent densification and limited grain growth. When temperature increases, additional densification mechanisms may occur, including plastic deformation or power-law creep (i.e., n typically takes more than 3). According to the above analysis [19], the rate-controlling mechanisms of the densification of tetragonal zirconia polycrystal (TZP) powders during SPS have been determined. When the applied macroscopic compaction stress is low and/or the temperature is low, a pure diffusion mechanism is responsible for the densification. At intermediate macroscopic compaction stresses and/or medium temperatures, a stress exponent of 2, associated with an apparent activation energy of 450 kJ/mol, has been determined; in this case, densification proceeds by grain-boundary sliding accommodated by diffusional mechanism controlled by the interface reaction. For high temperatures and/or high stresses, the stress exponent in a range of 3–5 suggested that densification proceeds by a dislocation-climb-controlled mechanism.

Historical Background of SPS

Historical background of SPS has been comprehensively described by Grasso et al. [20]. In short, direct origin of SPS machines in use today is “spark sintering” apparatus based on pulsed current, invented by Inoue in the early 1960s. However,

the commercialization did not come to a large success. After Inoue's patents expired in the late 1980s, Japanese companies (including Sumitomo Coal Mining Co., Ltd.) started the industrial production of "spark plasma sintering" machines. Since then, the practicality and reproducibility of SPS machines have been drastically improved, and the academic research as well as the industrial application has accordingly increased. Nowadays, more than ten companies from China, Korea, the USA, Germany, and Japan commercially produce ECAS/SPS apparatus.

Because SPS method features rapid and quick heating, homogeneous sintering of large components is a major issue from the beginning of the invention. In particular, in the material with a diameter of >100 mm, nonuniformity of stress and heating due to the thermal conductivity and particle rearrangement during SPS process poses significant problem for rapid and uniform sintering. However, recent technical progress and enlargement of SPS machines enable the manufacturing of large-size sintered Al_2O_3 bodies with a diameter of 300 mm [21]. Another recent SPS development is process automation. Five types of semi- or fully automated SPS manufacturing systems have been developed: multihead, batch, tunnel, rotary, and shuttle systems. Each type of apparatus is applied to specific condition of industrial application and product according to size and configuration, demanded characteristic production cycle time, production cost, and economics.

Materials of Transparent Ceramics

Efforts aimed at attaining transparency of polycrystalline ceramics focus on the parameters of density (or porosity) and grain size. As noted in section "[Role of Microstructure on Optical Properties](#),". As described above pores and grain boundaries are light-scattering origins, but as has been shown, porosity plays a more determining role [7, 22]. Here several transparent oxide and non-oxide ceramics manufactured by SPS are briefly summarized, focusing on the critical factor(s) to determine transparency of polycrystalline ceramic body.

Al_2O_3

$\alpha\text{-Al}_2\text{O}_3$, known as corundum, is a thermodynamically stable material with high strength, hardness, and corrosion resistance. Translucent or transparent polycrystalline Al_2O_3 has been used as light-transmitting component exposed at high temperatures and in corrosive environments, e.g., in high-pressure sodium lamps. Conventional translucent Al_2O_3 polycrystal is characterized by a very low porosity ($<0.1\%$) and a relatively large grain size (>10 μm) [7]. However, several studies reported that sub-micron grain size is rather advantageous for improving the light transmittance of alumina (Fig. 4). For attaining transparency in fine-grained alumina ceramics, a full density or an extremely low porosity is a mandatory requirement. Since residual pores have a significant negative effect on light transmission, for transparent alumina, porosity should generally be reduced to less than 0.05%

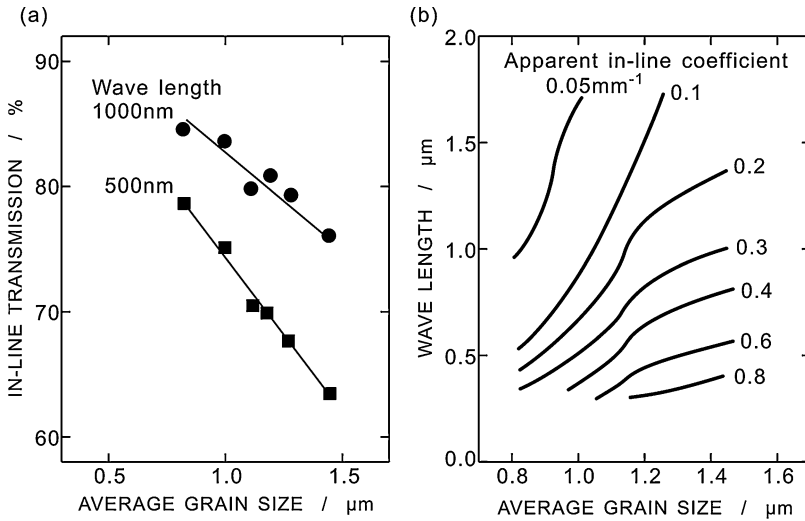


Fig. 4 (a) In-line transmission of fully densified Al_2O_3 polycrystals prepared by HIP as a function of the average grain size for wavelength of the incident light of 500 and 1000 nm. (b) Relationship between wavelength of the incident light and the average grain size for different apparent in-line coefficients in the fully densified Al_2O_3 polycrystals prepared by HIP [5]

[23]. Low porosity also allows good mechanical properties such as strength, wear resistance, and hardness. Traditional transparent Al_2O_3 ceramics were prepared by sintering in reducing atmosphere such as a mixture of nitrogen and hydrogen gases at temperatures of generally above 1700 °C [24, 25]. The high sintering temperature caused extensive grain growth, which in turn seriously degraded mechanical strength and hardness of the materials.

Transparent Al_2O_3 with fine-grain sizes can be also produced by using SPS technique [26–30]. For example, a fully densified (i.e., with the relative density of almost 100%) Al_2O_3 with a grain size of around 0.5 μm was obtained at 1200 °C by SPS [27]. During SPS of the alumina ceramics, the heating rate was usually set to a very high value (>100 °C/min), and the holding time at sintering temperature was set to be short (3–10 min); it has been believed that the short heating time at low temperatures can significantly suppress the grain growth during heating process, resulting in rapid densification by easy grain-boundary sliding and enhanced diffusion mass transport due to small powder particles under applied mechanical pressure.

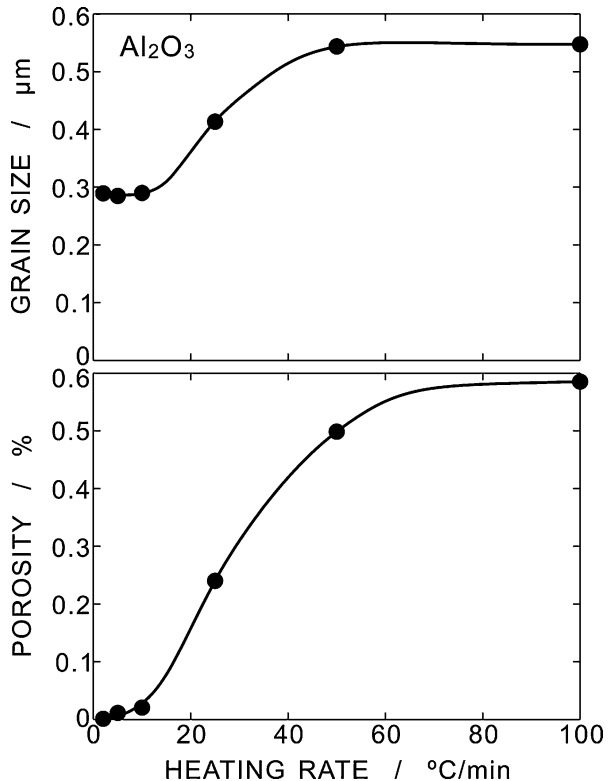
However, in the last decade, it has been pointed out that low heating rate is rather effective to improve transparency of Al_2O_3 polycrystals prepared by SPS. Kim et al. found that grain size as well as porosity can be effectively reduced by retarding heating rate during SPS, leading to higher transparency of Al_2O_3 polycrystals [27], though rapid heating rate is recognized as one of the advantages of SPS. They examined the microstructure and optical transparency in SPSed Al_2O_3 at a heating rate in the range of 2–100 °C/min. Figure 5 shows the grain size and porosity values of the sintered Al_2O_3 at the sintering temperature of 1150 °C for 20 min under the

compressive stress of 80 MPa. For the alumina sintered at 1150 °C for 20 min, the grain size was smaller at lower heating rates. The porosity was 0.59% at a heating rate of 100 °C/min and decreased to 0.02% at 10 °C/min and 0.002% at 2 °C/min. The heating-rate dependence of the porosity in Fig. 5 is quite similar to that of the grain size. Low heating rates resulted in small grain size and high density in the alumina polycrystals prepared by the SPS. Such an effect of the heating rate on the transparency has appeared not only in Al₂O₃ but also in MgAl₂O₄ and Y₂O₃, as described hereafter. Kim et al. assumed that an electric field and/or current may increase the concentration of vacancies in Al₂O₃ during SPS [29]. In fact, unusual rapid grain growth can be observed in Al₂O₃ sintered by rapid heating rate SPS [28]. A large DC current for heating could trigger the defect formation, resulting in small inter-/intragranular pores and reduced optical transparency in Al₂O₃ [29].

The theoretical in-line transmission was calculated by Apetz and Bruggen [7], on the basis of Rayleigh-Gans-Debye theory. When light scattering occurs only at grain boundaries (zero porosity), the theoretical in-line transmission T is represented as

$$T = (1 - R_s) \exp\left(-\frac{3\pi^2 G \Delta n^2 t}{2\lambda^2}\right) \quad (4)$$

Fig. 5 The grain size and porosity values of the SPSed Al₂O₃ under different heating rates at the sintering temperature of 1150 °C for 20 min under the compressive stress of 80 MPa [28]



where R_s is the total surface reflection losses, G is the grain size, Δn is the refractive index difference ($=0.0053$), t is the sample thickness, and λ is the wavelength of the incident light. Calculating Eq. (4) with $d = 0.27 \mu\text{m}$, $t = 0.88 \text{ mm}$, and $\lambda = 640 \text{ nm}$, we obtain an in-line transmission of 68%. The in-line transmission in the Al_2O_3 bodies SPSed at different heating rates as a function of wavelength is shown in Fig. 6 [28]. Figure 6 also shows the theoretical prediction of Eq. (4) for zero porosity. The alumina changed gradually the appearance from opaque to transparent with decreasing heating rate. The transmission increases with the decreasing heating rate. The transmission-wavelength curves approach the value of heretical value (86%) with the increasing wavelength, whereas it decreases rapidly with the decreasing wavelength, particularly in the ultraviolet region ($\lambda < 400 \text{ nm}$). Although the in-line transmission (46%) lower than the theoretical value is mainly due to the residual porosity, it is comparable to the transmission of 40–57% obtained by using HIP for the alumina doped with 0.03 wt% MgO [23]. As a result, during SPS of alumina, low heating rates resulted in fine-grain size, low porosity, and high transparency: for sintering at $1150 \text{ }^\circ\text{C}$ for 20 min, a grain size of $0.29 \mu\text{m}$, a porosity of 0.002%, and an in-line transmission of 46% were obtained at a heating rate of $2 \text{ }^\circ\text{C}/\text{min}$. The fine microstructure at low heating rates can be explained by using the assumption of low defect concentration and the low porosity (high density) by the accelerated grain-boundary diffusion owing to a large grain-boundary area. The authors concluded that slow heating also homogenized the powder during SPS, which should contribute to result in the fine microstructure and high density. The same tendency that lowers heating rate results in lower porosity and finer-grain size is also observed in Y_2O_3 and MgAl_2O_4 , as depicted later.

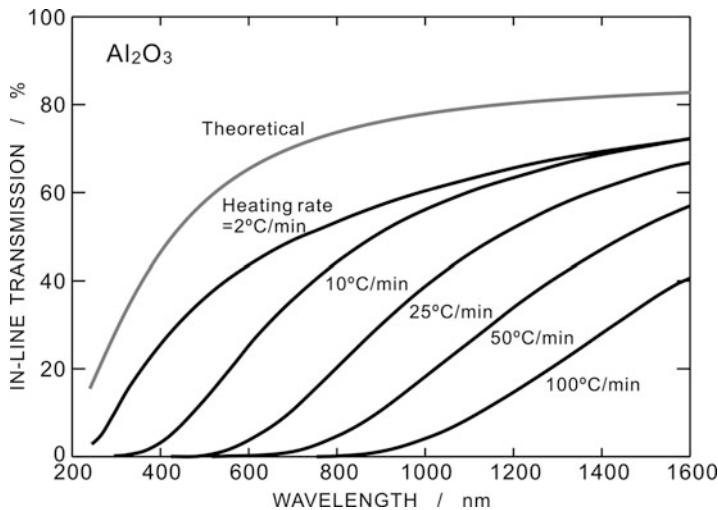


Fig. 6 The in-line transmission in the Al_2O_3 bodies SPSed at different heating rates as a function of wavelength [28]. The theoretical prediction of Eq. (4) for pore-free Al_2O_3 polycrystal is also depicted for comparison [23]

Recently, transparent, rare-earth-doped Al_2O_3 polycrystal for photoluminescent application has been successfully produced by SPS [31]. Tb^{3+} ions up to a concentration of 0.5 at% were incorporated into a dense alumina matrix by SPS at 1200 °C for 10–30 min, and a transmittance of about 75% at an incident light wavelength of 800 nm was obtained. The relative densities and average grain sizes in the SPSed materials were more than 99% and around 200–400 nm, respectively. These doped Al_2O_3 displayed photoluminescent peaks centered at 485 and 543 nm, which were characteristic of Tb^{3+} emission. This result shows great potential of SPS for manufacturing of alumina-based light-producing devices, such as high-powered lasers.

Y_2O_3

Y_2O_3 has excellent physical and chemical properties, such as a high melting point (2430 °C) and broad range of transparency (200–8000 nm). Y_2O_3 has a cubic crystal with group of Ia3. In addition, Y_2O_3 exhibits thermal conductivity of 13.6 W/mK at room temperature, thermal expansion coefficient of 8.7×10^{-6} 1/K, and refractive index of 1.93 (at 532 nm). These properties make Y_2O_3 a promising optical material. Y_2O_3 possesses a higher thermal conductivity and a lower thermal expansion coefficient than the widely used $\text{Y}_3\text{Al}_5\text{O}_{12}$ (YAG); the physical properties are critical for thermal management as laser powers continue to increase and generate heat during operation [32]. Furthermore, Y_2O_3 exhibits excellent resistance against fluorite plasma, which is generally used for etching of silicon wafer as semiconductor devices. The plasma-proof property of Y_2O_3 is in fact remarkably superior than Al_2O_3 , sapphire, and YAG. Other potential applications of Y_2O_3 include infrared domes, nozzles, refractories, components of semiconductor devices, and efficient NIR-visible up-converters [33–35]. Due to its optical characteristics, Y_2O_3 has been mainly developed in transparent body for optical application.

Y_2O_3 is, however, difficult to sinter among oxide ceramics. It is also difficult to grow single crystals of Y_2O_3 to a large size due to its high melting point. Therefore, polycrystalline Y_2O_3 ceramics with a high optical transparency have been developed by pressureless sintering in a vacuum or hydrogen atmosphere at high temperature (typically >1600 °C) [36, 37], by HP sintering [38, 39] and by HIP process [40–42]. The first translucent Y_2O_3 ceramic was fabricated by pressureless sintering in hydrogen atmosphere at very high temperature of beyond 2000 °C, doped with 10 wt% of thorium oxide (ThO_2) particles as second crystalline phase [38].

HP and HIP are also effective techniques to produce transparent Y_2O_3 . Hou et al. [43] fabricated transparent Y_2O_3 ceramics by using HP at 1800 °C for 20 h. Another example was reported by Podowitz et al. [44] by using HP at a maximum pressure of 40 MPa and a maximum temperature of 1580 °C. Optical transparency could be optimized through a stepwise application of pressure.

Several research groups have also attempted to produce transparent Y_2O_3 by SPS method. For instance, An et al. [45] reported the synthesis of transparent Y_2O_3

ceramics by using SPS at moderate temperature and pressure profiles. The samples sintered at 1300 °C and annealed at 1050 °C had a transmittance of 81.7% at wavelength of 2000 nm. Here, it is noteworthy that Y_2O_3 can be densified by low-temperature SPS at a sintering temperature of about or less than 1000 °C: translucent Y_2O_3 material can be synthesized from a commercial Y_2O_3 powder by the low-temperature SPS synthesis at 1050 °C for 1 h, exhibiting the in-line transmittance in a range of 6–46% in the wavelength range of 400–800 nm [17, 46]. In comparison with HP at the same sintering temperature and pressure, SPS was significantly effective to improve sinterability of Y_2O_3 .

The effectiveness of SPS must result from the role of electric field/current and is probably related to the reduced state of Y_2O_3 under the application of pulsed field/current. As mentioned above, EELS analysis suggested that Y_2O_3 polycrystal consolidated by SPS exhibited reduced state in comparison to Y_2O_3 sintered in air and in vacuum. The pulsed DC field and/or current must induce excess anion vacancies and must accelerate diffusional mass transport and densification of Y_2O_3 materials. In fact, grain growth behavior in Y_2O_3 during SPS also indicated accelerated grain-boundary mobility under the pulsed DC field/current: according to the grain growth experiment in Y_2O_3 during isothermal SPS, grain-boundary mobility is highly enhanced by SPS in comparison with pressureless sintering of Y_2O_3 . The grain-boundary mobility at 950 °C during SPS was comparable to the previously reported data for Y_2O_3 by pressureless annealing at around 1500 °C in air [17]. This result suggested that diffusion of yttrium cation in Y_2O_3 is highly accelerated by SPS process. It is possible that an electric field applied during SPS enhances some defect reactions that involve an electron emission. The SPS may activate the formation of oxygen vacancies and interstitial yttrium cations and consequently accelerate mass transport in Y_2O_3 , leading to enhanced densification in low-temperature SPS.

Also, heating-rate dependence of the translucency of SPSed body has been investigated in Y_2O_3 , and it has been found that low heating rate (2 °C/min) was preferable to produce high transmittance of the SPSed body, as well as SPSed Al_2O_3 described above. Furthermore, by employing high pressure, transparent Y_2O_3 body can be obtained even by low-temperature SPS. For example, transparent Y_2O_3 ceramics could be prepared at 1050 °C for 1 h with a heating rate of 10 °C/min under a uniaxial pressure of 300 MPa [47]. The obtained samples possessed nanometric grains (around 400 nm) and high density (>99.95%). Figure 7 shows in-line transmittance of Y_2O_3 densified by the low-temperature and high-pressure SPS under the uniaxial compressive stresses of 200 and 300 MPa, respectively. In-line transmittance of 68% at 700 nm and comparable performances of single-crystal yttria in the near-infrared wavelength region were attained in the Y_2O_3 body by the high-pressure SPS processing.

Recently, it has been reported that an addition of sintering aids can effectively improve the sinterability of Y_2O_3 during SPS process. Yoshida and co-workers investigate densification behavior and optical transparency of 1 mol% Zn^{2+} -doped Y_2O_3 consolidated by the SPS technique, by varying the most relevant process parameters, i.e., heating schedule, sintering temperature, holding time at the sintering temperature, and loading stress [48]. Transparent, Zn^{2+} -doped Y_2O_3

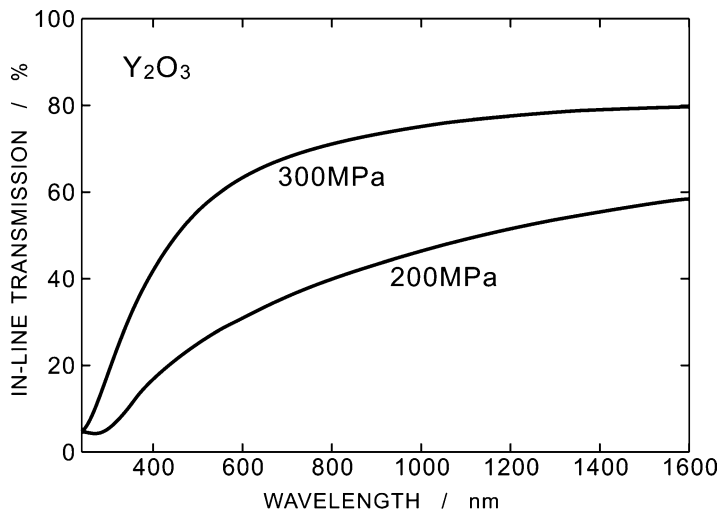


Fig. 7 The in-line transmittance of Y_2O_3 densified by the low-temperature and high-pressure SPS at $1050\text{ }^\circ\text{C}$ for 1 h with a heating rate of $10\text{ }^\circ\text{C}/\text{min}$ under a uniaxial pressure of 200 or 300 MPa [47]

polycrystals were successfully produced at the heating rate of $2\text{ }^\circ\text{C}/\text{min}$, sintering temperature of $890\text{ }^\circ\text{C}$, holding time of 30 min, and loading stress of 150 or 170 MPa. The grain size of the SPSed Zn- Y_2O_3 was about 200 nm, and the highest transmittance in the Zn^{2+} - Y_2O_3 bodies at a wavelength of longer than 600 nm was comparable to those in the undoped SPSed Y_2O_3 in the literature. The Zn^{2+} -doping effectively reduced the sintering temperature for fully densified Y_2O_3 by SPS; according to the literature, undoped Y_2O_3 was fully densified by SPS at $1050\text{ }^\circ\text{C}$ and 200 MPa or $1300\text{ }^\circ\text{C}$ and 100 MPa. High-resolution transmission electron microscopy analysis revealed that Zn^{2+} cations segregated in the vicinity of the grain boundaries. The grain-boundary segregation of Zn cations contributed to the reduction of the sintering temperature required for attainment of transparency in the Y_2O_3 by SPS.

ZrO₂

Zirconia ceramics have been used for various engineering applications since Garvie et al. [49] discovered phase transformation toughening in partially stabilized ZrO₂ (PSZ). The stable phases at high temperatures, i.e., tetragonal and cubic phases, can be stabilized by dopants that induce oxygen vacancies and/or are oversized with respect to Zr cations. Dopants of CaO, MgO, Y_2O_3 , and CeO₂ are generally known as stabilizers of the tetragonal phase, and among them, Y_2O_3 is most extensively used as the stabilizer of zirconia ceramics in engineering applications. Y_2O_3 -stabilized tetragonal ZrO₂ polycrystal (Y-TZP) with excellent mechanical properties has been the most extensively commercialized for use in optical fiber connectors

(ferrules), grinding media, precision parts, and dental applications. In addition, Y_2O_3 -stabilized cubic ZrO_2 (c-YSZ) has been investigated as a candidate for a solid-electrolyte material in fuel cells because of its high oxygen anion conductivity. These properties strongly depend on the microstructures and phase stability in Y_2O_3 -stabilized ZrO_2 (YSZ) [50]. For instance, excellent mechanical strength and toughness in Y-TZP are explained in terms of transformation toughening, in which crack propagation is inhibited by stress-induced, martensitic tetragonal-to-monoclinic (t-m) phase transformation; the t-m phase transformation yields the expansion of unit cell volume of approximately 4%.

Significant attention has been paid to the fabrication of optically transparent polycrystalline c-YSZ [51–53]. One of the motivations for the studies stood on the development of c-YSZ as a multifunctional ceramic with the combination of optical transparency (high refractive index of 2.2), excellent thermal properties, and high ionic conductivity. Since fully densified c-YSZ polycrystal is difficult to produce due to its rapid grain growth, polycrystalline c-YSZ is usually prepared at high temperatures using HIP [52–54] for high density and good transparency. For instance, transparent c-YSZ ceramics were made from cubic-stabilized ZrO_2 powder by sintering under vacuum at 1650 °C for 3 h, followed by HIP treatment at 1750 °C for 1 h at a pressure of 196 MPa [54]. Post-thermal annealing at 1000 °C was conducted to decolorize the as-sintered samples. The optical properties of these zirconia ceramics were comparable to those of their single-crystal counterparts. Owing to high sintering temperatures, however, the resultant materials typically have large grain sizes. The reduction of grain boundaries is preferable for optical transparency, but the coarsened grain size deteriorates the mechanical properties, which are also important requirements for optical applications.

In contrast with HIP and other common sintering methods, SPS enables fabrication of transparent c-YSZ ceramics with fine-grain sizes. For example, SPS was performed on a commercial 8 mol% Y_2O_3 -stabilized cubic ZrO_2 powders at the sintering temperature of 1200 °C, heating rate of 200 °C/min, and pressure of 141 MPa, and transparent c-YSZ with the grain size of 55 nm was successfully obtained [55]. The SPSed samples became increasingly deep red in color with the increasing holding time. Darkening of the nanostructured c-YSZ was probably attributed to excess oxygen anion vacancies caused by the highly reducing environment of hot graphite.

Another example is the use of high-pressure SPS for production of transparent c- ZrO_2 from a commercial raw powder [56, 57]. A nanosized cubic ZrO_2 -8 mol% Y_2O_3 powder was consolidated by using SPS at 1000 °C under a pressure of 600 MPa, resulting in the final grain size of around 50 nm and the transmittance in the near-infrared region (1-mm-thick samples) of higher than 60% [56]. Taking into account the reflective losses of the end surfaces, the maximum allowable transmittance for the SPSed c-YSZ was between 70% and 80% of the theoretical value. In the c-YSZ specimens, the residual porosity was about 0.01, and the pore size was less than 20 nm, which was too small to produce significant scattering. It is suggested that the observed light absorption in the SPSed c-YSZ was related to the presence of large amounts of color centers, generated by the reducing environment in the SPS

processing. In another case, commercial 8 mol% Y_2O_3 - ZrO_2 powders were consolidated by employing SPS with the optimum conditions of the sintering temperature, pressure, heating rate, and soaking time of 1100 °C, 400 MPa, 10 °C/min, and 10 min, respectively [57]. The as-sintered zirconia exhibits a yellowish-brown appearance, which is a typical phenomenon in oxide ceramics produced by SPS. This discoloration is related to the formation of oxygen anion vacancies. In fact, annealing in oxidizing environment at 700 °C for 100 h can reduce oxygen vacancies through diffusing oxygen back into c-YSZ. Typical in-line transmittance spectrum of the post-SPS annealed c-YSZ is shown in Fig. 8. TEM observation revealed that the SPSed c- ZrO_2 exhibited uniform, very fine, and equiaxed microstructure with the average grain size of 30 nm.

In contrast to c-YSZ, it is difficult to improve transparency in tetragonal ZrO_2 ceramics even by SPS techniques. SPS processing is actually effective to suppress grain growth during sintering, so that fully densified TZP ceramics with grain sizes of 50–55 nm have been obtained by using SPS [55]. However, dense tetragonal ZrO_2 ceramics were less transparent than fully densified c-YSZ, though the TZP and c-YSZ materials have the same density and grain size. For instance, translucent tetragonal ZrO_2 doped with 3 mol% Y_2O_3 ceramics was produced by SPS processing from nanosized raw powders [56]. The typical SPS conditions were at 1000 °C for 5 min under a pressure of 800 MPa. The tetragonal ZrO_2 ceramics had an average grain size of about 50 nm. The transmittance with 1 mm thickness was >50% in the near-infrared region but was less than 20% in visible light region for the tetragonal ZrO_2 ceramics. The samples had a yellowish-brown color, which

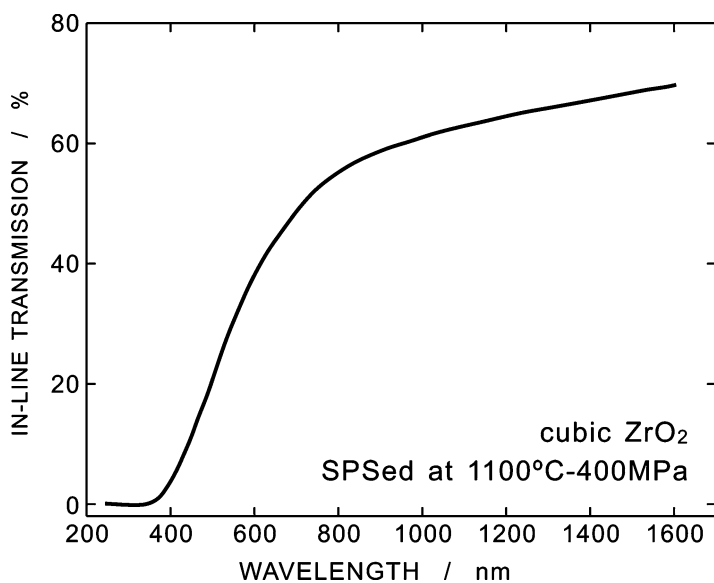


Fig. 8 Typical in-line transmittance spectrum of 8 mol% Y_2O_3 -stabilized cubic ZrO_2 SPS at 1100 °C and 400 MPa followed by annealing in oxidizing environment at 700 °C [57]

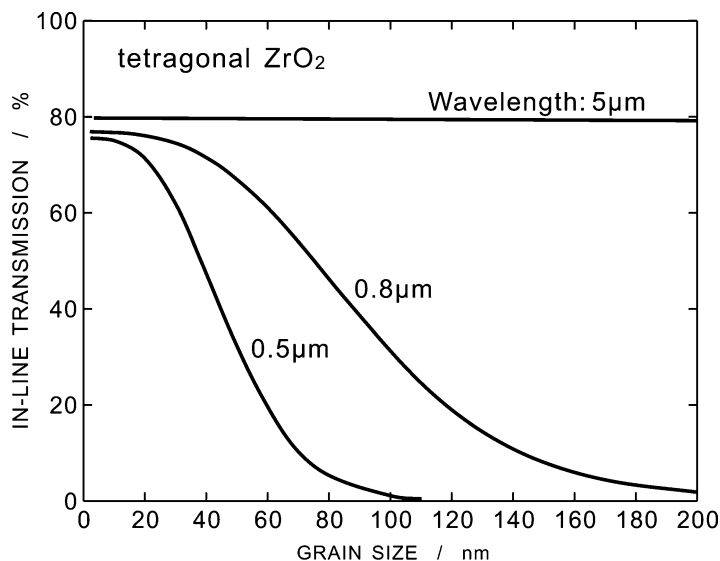


Fig. 9 Predicted in-line transmission of fully dense sintered tetragonal ZrO_2 (thickness 1 mm) without absorption calculated for a grain size <200 nm using Mie theory for mean birefringence in range 0.03–0.04 for visible light and 0.035 for IR wavelength [58]

was attributed to the presence of color centers. It was confirmed that optical birefringence was the main factor that limited the transparency of pore-free, tetragonal ZrO_2 ceramics. Klimke and co-worker predicted the conditions to obtain transparent tetragonal ZrO_2 ceramics by comparing the experimental data for sintered nanopowder with scattering calculations [58]. Figure 9 shows predicted in-line transmission data of fully dense sintered tetragonal ZrO_2 (thickness 1 mm) without absorption calculated for a grain size <200 nm using Mie theory for mean birefringence in range 0.03–0.04 for visible light and 0.035 for IR wavelength [58]. According to their calculation, in-line transmission of about 50% at visible light and 1 mm thickness is expected at a mean grain size <40 nm. In order to obtain a better quality with transmission of 70%, for instance, grain size of less than 20 nm is required according to the calculation. In addition, the influence of grain size becomes insensitive in the IR region; at an IR wavelength of 5 μm , there should not be any scattering caused by birefringence for grain sizes <200 nm.

MgO

MgO shows a high melting point of 2850 $^{\circ}\text{C}$ and low density of 3.58 g cm^{-3} , though vapor pressure of MgO is relatively high in comparison to other oxides such as

Al_2O_3 and ZrO_2 . MgO has an isotropic cubic crystal structure, which is desirable for attainment of transparency. Polycrystalline infrared-transparent MgO is a potential substitute for sapphire IR windows and protectors for sensors.

Dense MgO ceramics have been produced by the traditional sintering method, such as pressureless sintering and vacuum sintering [59–61]. Chen et al. fabricated translucent MgO ceramics by sintering at 1400 °C for 2 h under ambient atmosphere from the MgO powders synthesized via a wet precipitation process, and the average grain size of the ceramics was about 6 μm [60]. Suzuki et al. reported that transparent MgO ceramics with an average grain size of about 10 μm were prepared by sintering the powders at 1600 °C for 3 h in an oxygen atmosphere with the existence of chloride ion [61]. The conventional techniques for the fabrication of dense MgO ceramics require high sintering temperature (typically >1400 °C), which leads to coarsened grains in sintered body. The preparation of MgO ceramics using HP or HIP method was also previously studied [62–65]. Itatani et al. reported that translucent MgO ceramics with a relative density of 99.7% and grain size of about 0.8 μm was obtained by HP at a temperature of 1100 °C for 30 min [65]. In addition, HIPing of pressureless sintered MgO body at 1500–1600 °C produced transparent MgO ceramics with the average grain size in a range of 100–200 μm [65]. Addition of LiF is a common technique to prepare transparent MgO by vacuum HP of MgO [66, 67]. The addition of LiF as sintering aid could reduce the sintering temperature of MgO transparent ceramics [68, 69]. It has been acknowledged that densification of MgO with LiF was enhanced due to the formation of a liquid phase [70].

The SPS process was also used for fast densification of the MgO ceramics, yielding a high density and fine-grain sizes. For example, densification of nanocrystalline MgO powders by SPS was examined at SPS temperature between 700 °C and 825 °C under applied pressures of 100 and 150 MPa [71]. As a result, fully densified transparent nanocrystalline MgO with a 52 nm average grain size was fabricated by the SPS at 800 °C and 150 MPa for 5 min. In-line transmissions of 40% and 60% were attained compared to MgO single crystal, for the yellow and red wavelengths, respectively. Tran et al. reported a fully dense Ca-doped MgO ceramics with a transmittance of about 90% in the IR range and a final grain size of 25–70 nm, prepared by SPS at 650–800 °C under a uniaxial pressure of 300–500 MPa [72]. Liu et al. reported that undoped MgO ceramics with a relative density of 99.1% and an average grain size of 50 nm were obtained at 1347 °C with the utilization of an ultrahigh heating rate (>1700 °C/min) and high pressure (up to 170 MPa) by the combustion reaction plus quick pressing method [73]. In another case, Jiang and co-workers investigated the effect of LiF addition on SPS of MgO [74]. In their experiments, transparent MgO ceramics doped with 1 wt% LiF were successfully obtained by SPS at 900 °C with the heating rate of 100 °C/min under the pressure of 30 MPa, and the corresponding grain size was about 0.7 μm . The transmittance of the transparent MgO ceramics (1.5 mm thick) was above 85% in the range of 3–5 μm . The recent studies have proved that SPS processing is beneficial in the production of transparent and fine-grained MgO ceramics.

MgAl₂O₄

Magnesium aluminate (MgAl₂O₄) spinel is a synthetic material with cubic crystal structure and excellent thermal, mechanical, and optical properties [75]. High optical transmission for visible and IR wavelength range in MgAl₂O₄, in particular, is attractive for various optical applications. These properties made MgAl₂O₄ an indispensable material for optically transparent windows, domes, and armors and for certain refractory applications. The spinel does not exhibit birefringent scattering at its grain boundaries owing to the symmetric cubic crystal structure and, hence, can exhibit an excellent transparency even in the polycrystals. For engineering applications, because the shape forming by powder processes is an economical route rather than the machining from single crystals, the development of a simple powder processing method is desirable.

However, spinel powder is difficult to sinter, and the fabrication of full-dense and transparent spinel polycrystals involves high costs through conventional routes such as pressureless sintering. The volume expansion (about 8%) associated with MgAl₂O₄ phase formation from alumina and magnesia does not allow obtaining dense MgAl₂O₄ bodies in a single-stage reaction sintering process [75]. Thus, in most of the earlier studies, dense polycrystalline spinel has been obtained through high-temperature conventional sintering (typically >1500 °C) [76, 77], HP [78–80], and HIP [81–84]. Sintering aids such as LiF [85], CaO [86], and B₂O₃ [87] have also been used for consolidation of spinel powder. Densification using sintering aids and/or high sintering temperatures, however, often causes grain coarsening, and this may degrade the mechanical properties. In the viewpoint of engineering application, fine-grained materials are desirable due to their high mechanical strength. SPS has been therefore employed [88, 89] for production of transparent MgAl₂O₄ bodies.

In SPS processing of MgAl₂O₄ spinel ceramics, significant heating-rate dependence of the transparency of sintered bodies were pointed out, as well as in the case of Al₂O₃. For instance, according to the report by Morita et al. [89], high transmission was attained by reducing residual porosity and pore size, which were achieved by the application of low-heating rate. At high heating rates, many closed pores were formed due to the high densification rate during the heating process and remained as large pores at the grain junctions. The heating-rate dependence on in-line transmission in the SPSed MgAl₂O₄ spinel ceramics sintered at 1300 °C for 20 min under the pressure of 80 MPa is shown in Figure 10. The plots of transmission clearly show that the heating rate influences the transmission, particularly in the visible-wavelength range. For sintering at 1300 °C, the transparency increases with the decreasing heating rate.

It is generally accepted that mechanical properties such as flexure strength and hardness of polycrystalline materials are gained by the reduction of their grain sizes. The improved mechanical strength is often depicted by Hall-Petch law; the strength of material is proportional to the inverse of square root of grain size. The strength-grain size relationship has been reported not only in metallic but also ceramic materials so far. Figure 11 shows Vickers hardness as function of square root of grain size for SPSed MgAl₂O₄ spinel materials [90]. The SPSed MgAl₂O₄ spinel

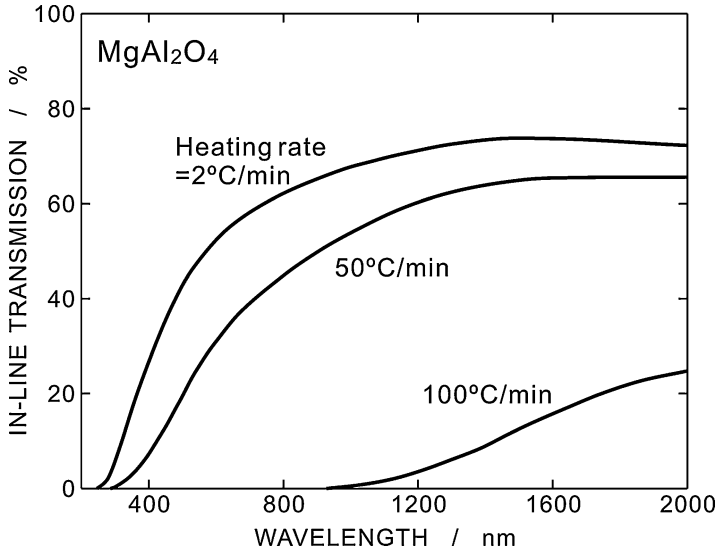


Fig. 10 Heating-rate-dependent in-line transmission in MgAl_2O_4 spinel plotted as a function of wavelength [89]

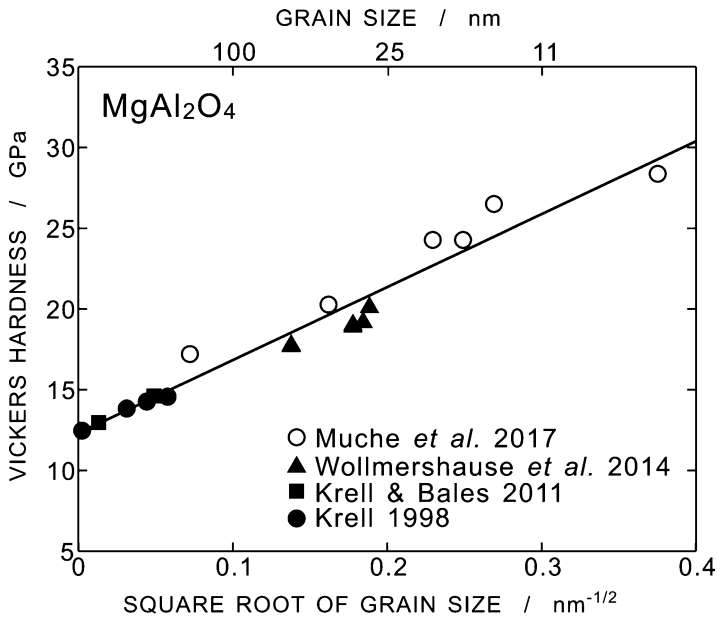


Fig. 11 Vickers hardness as function of square root of grain size for the SPSed MgAl_2O_4 spinel ceramics [90]. Literature data [88–90] for spinel ceramics at different grain sizes are plotted as a comparison. The straight line represents the trend line for linear response of Hall-Petch relationship in terms of inverse of the square root of the grain size

materials were prepared at 720–870 °C for 4–5 min under 1.4–2.0 GPa. Literature data for MgAl_2O_4 spinel at different grain sizes are plotted as a comparison. Nanocrystalline MgAl_2O_4 spinel has limited reports with grain sizes lower than 100 nm, and no studies have been reported in the literature for grain sizes below 20 nm. The straight line represents the trend line for linear response of Hall-Petch relationship in terms of the inverse of square root of grain size. As a result, no correlation of Hall-Petch relation is observed down to the smallest tested size. As shown in Fig. 11, the refinement of grain size is beneficial for the improvement of mechanical properties as well as transparency of optical ceramic materials.

It is noteworthy that the origin of discoloration observed in fully densified, SPSed MgAl_2O_4 has been revealed by spectroscopic techniques. Discoloration after SPS synthesis is often seen in various ceramics, and the discoloration has been regarded as a major source of limited light transmission. Recently, Morita et al. extensively investigated the origin of the discoloration in SPSed MgAl_2O_4 spinel by Raman spectroscopy, Fourier transform infrared (FT-IR) spectroscopy, and transmission electron microscopy [91]. According to their analysis, the discoloration is explained by the combination of carbon contamination and lattice defects (color centers), which are introduced in the spinel matrix depending on the SPS conditions. For low heating rates of 10 °C/min, trace carbonate CO_3 preexisting in the starting raw powder remained as glassy carbon, irrespective of the sintering temperature. For a high heating rate of 50 °C/min, additional carbon contamination occurred by evaporating the carbon phases from the carbon papers and graphite dies during the heating process and showed a tendency to be enhanced by the increasing heating rate. The color center (F^+ -center) may be generated by the formation of oxygen vacancies. Since the rate of sintering, namely, the deformation rate, increased with the increasing heating rate, the concentration of the dislocation-related color centers may increase with the heating rate, but may decrease with the increasing sintering temperature due to the reduction of the oxygen anion vacancies.

For the spinel, the contamination was sensitive to the SPS conditions, such as the heating rate and loading schedules, but less sensitive to the sintering temperature. This suggested that the carbon contamination was caused by evaporation of CO gas from the carbon paper/dies. At the high heating rates, the carbon evaporation is enhanced due to the rapid heating, and then the evaporated CO gases are encapsulated into the closed pores during the heating process and remain in the matrix. The carbon contamination can be suppressed by a high-temperature loading even at the high heating rate [92].

$\text{Y}_3\text{Al}_5\text{O}_{12}$ (YAG)

Yttrium aluminum garnet $\text{Y}_3\text{Al}_5\text{O}_{12}$ (YAG) is one of the three stable phases in Y_2O_3 - Al_2O_3 system. YAG has a cubic crystal structure [93] and therefore shows isotropic optical properties. Owing to its high thermal stability and homogenous optical properties, transparent YAG ceramics are applied to an excellent host material for fluorescence application and high-power solid-state lasers [94]. Nd and Er cations

are typical dopants of YAG for laser application. Ce-doped YAG (Ce:YAG) is used as phosphor in cathode ray tubes and white light-emitting diodes and as scintillator.

It is well-known that excellent transparent, Nd-doped YAG ceramics can be produced by solid-state reaction sintering in vacuum at 1750 °C for 10 h with the addition of tetraethyl orthosilicate (TEOS) [94]. One of the procedures that has been put forward for the manufacture of a polycrystalline laser material is a multistage process of high-temperature vacuum sintering followed by HIP in the 1450–1550 °C range for 5 h under 200 MPa argon, yielding high optical quality transparent YAG with a grain size of 1–2 μm [95].

Transparent, undoped YAG ceramics have been fabricated by various technologies, including vacuum sintering, HP, and HIP. Zych and Brecher [96] derived YAG transparent ceramics from the mixture of Y₂O₃ and Al₂O₃ by using HP at 1750 °C for 4 h under a pressure of about 300 atm. SPS was also applied to fabricate transparent YAG ceramics [97–99]. One example of SPS conditions for manufacturing transparent YAG was the sintering temperature of 1400 °C and duration time of 3 min using nanocrystalline YAG powders as starting material. In this case, fully dense and transparent polycrystalline cubic YAG ceramics with micrometer-grain sizes were obtained. In another case, transparent YAG was produced by SPS from nanocrystalline YAG powder dispersed by ultrasonication: heating rate, sintering temperature, duration time, and applied stress employed were 8 °C/min, 1325 °C, 15 min, and 74 MPa, respectively. As a result, fine-grained (330 nm), transparent YAG ceramics was obtained with the transmittance of 66% at the wavelength of 600 nm [99]. Moreover, transparent YAG doped with 0.25 wt% of LiF was also produced by SPS at 1300 °C for 2 h under a pressure of 80 MPa [98]. The addition of LiF promoted transparency of YAG body but increased grain growth during SPS.

Hydroxyapatite

Hydroxyapatite (Ca₁₀(PO₄)₆(OH)₂: HA) is a major component of human bone. A range of HA-based biomaterials have been developed for biomedical applications [100, 101]. Several studies have shown that transparent HA ceramics enable direct observations of living cells on HA substrates to determine the interactions between HA and cell/tissue [102–104]. Transparent HA materials have been fabricated using a range of sintering methods, such as HIP [105–107], microwave sintering [108], and SPS [109, 110]. For instance, a transparent HA material, which exhibited an in-line transmittance of 30–73% over the wavelength range of 400–700 nm with a very fine-grain size of less than 200 nm, was fabricated by SPS at 1000 °C from nanoparticle raw powders [110].

It should be noted that the transparent, fine-grained hydroxyapatite prepared by SPS exhibited superplastic deformation. Superplasticity is a characteristic of polycrystalline material, which exhibits large elongation to failure in tensile manner. High-strength, structural ceramics is in general very brittle, with limited plastic deformability. But if the grain size is reduced to typically less than 1 μm, then even structural ceramics can show superplastic deformation. SPSed hydroxyapatite

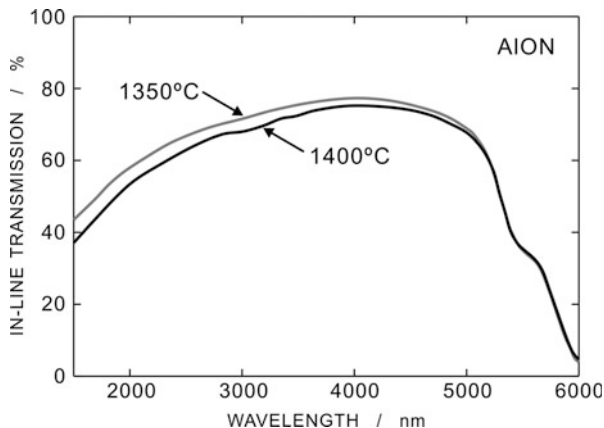
is the same situation such that fully densified and nanostructured body was obtained owing to the SPS process. The superplasticity can be applicable for near-net shape forming and joining of structural materials, and hence a number of studies were performed to improve superplasticity, i.e., increasing tensile ductility, reducing superplastic temperature, and accelerating deformation rate, in structural ceramics such as TZP. The superplastic flow behavior of transparent, nanocrystalline HA specimen prepared by SPS at 1000 °C was examined at temperatures ranging from 950 °C to 1050 °C [111], and the HA specimens exhibited superplasticity under the test conditions examined. An elongation of 270% was obtained even at 950 °C and an initial strain rate of $1.0 \times 10^{-3} \text{ s}^{-1}$. A maximum elongation of 486% (nominal strain) was achieved at 1000 °C and an initial strain rate of $1.0 \times 10^{-4} \text{ s}^{-1}$. The tensile ductility in this material was located in the upper portion of the existing data in HA materials. The post-deformation microstructure of HA indicates that grain-boundary sliding was the predominant mechanism of superplastic flow. The improvement in superplasticity in transparent, nanocrystalline HA arose essentially from the very fine-grain size and fully densified, pore-free microstructure.

AION

Aluminum oxynitride (AION) has a cubic spinel structure with chemical formula of $\text{Al}_{(64+x)/3}\text{O}_{32-x}\text{N}_x$ ($0 \leq x \leq 8$) and is a stable solid solution within the Al_2O_3 -AlN system. AION shows optical transparency over the region from near-ultraviolet to visible and near-IR wavelength. The cubic structure of AION exhibits isotropic optical properties. Furthermore, AION possesses excellent mechanical properties; strength and hardness of AION are known to be superior to conventional sapphire and MgAl_2O_4 spinel. With the combination of good optical and mechanical properties, AION can be used in defense and commercial applications, such as military aircraft missile domes, transparent armors, IR windows, hyper-hemispherical domes, laser windows, military aircraft lenses, semiconductor processing applications, and scanner windows [112]. Unfortunately, AION ceramic is very difficult to sinter because of its high phase formation temperature and low sintering activity or diffusion coefficient. Conventional synthesis of AION ceramics usually needs very high sintering temperature (typically higher than 1850 °C) for a long period (>20 h) [113, 114]. In addition, the high sintering temperature and long sintering time can easily lead to excessive grain growth and coarse microstructure, which in turn seriously lowers the optical properties and mechanical strength of the materials.

Transparent AION bodies have been made by various sintering techniques, such as HP [115], HIP [116, 117], microwave sintering [112], or SPS [118–120]. In SPS, for instance, compacted powder of AION doped with 0.5 wt% Y_2O_3 was first heated to a temperature in a range of 1350–1500 °C at a heating rate of 100 °C/min; then, after holding for 10 min, the heating system was shut down, and the furnace was cooled down to room temperature [120]. The axial pressure was maintained at a level of 40 MPa during the entire sintering process. As a result, the obtained samples sintered at 1350 °C and 1400 °C exhibited high infrared transparency. Figure 12

Fig. 12 The transmittance of AlON ceramics (1.2 mm in thickness) fabricated at 1350 °C and 1400 °C [120]



shows the transmittance of the materials (1.2 mm in thickness) fabricated at 1350 °C and 1400 °C. The maximum infrared transmittance of SPS-processed samples at 1350 °C for 10 min is 77.3% at around 3900 nm. At the same time, the sintered samples have high hardness of 18 GPa. The SPSed materials showed bimodal microstructure comprising the peak grain sizes of 5–10 and 2–3 μm . The high density and small grain size contribute also to the high hardness of the processed transparent ceramics. Similar to other ceramic materials, SPS technique is effective to produce transparent AlON ceramic with excellent mechanical properties.

AlN

Aluminum nitride (AlN) ceramics has attracted greater attentions recently due to their high intrinsic thermal conductivity (320 W/mK), low dielectric constant, thermal expansion coefficient matching with silicon (4.8×10^{-6} 1/K), and good electrical insulation properties. AlN ceramics with a wide band gap of 6.3 eV show great potential as transparent optical and window materials [121–123].

However, AlN is difficult to sinter, because of its strong covalency with wurtzite crystal structure. AlN ceramics with high density have been fabricated by using additives as sintering aids, such as alkaline earth oxides, rare-earth oxides, or mixtures of oxides, fluorides, and carbides. Because of their low sinterability and high impurity levels, the fabrication of transparent AlN bodies has proven to be more difficult than fabrication of oxide ceramics. For example, Kuramoto et al. [122–124] fabricated transparent AlN polycrystals by HP process at 1850–2000 °C for 3–10 h in nitrogen flow with CaO, 3CaO-Al₂O₃ as an additive or even without additive.

Additives have been widely used for sintering high-quality ceramics. For instance, commercial AlN nanopowders doped with 3 wt% amount of CaF₂, Y₃O₂, or MgF₂ were consolidated by HP process at 1800 °C for 3 h under compressive pressure of 30 MPa at a rate of 5 °C/min under a nitrogen atmosphere [125]. As a result, the AlN ceramics prepared from nanopowders exhibited high

transparency. The maximum in-line transmittance is 53.2% at 1910 cm^{-1} for the CaF_2 -doped AlN ceramics, 28.1% at 1817 cm^{-1} for the Y_2O_3 -doped AlN ceramics, and 12.7% at 1820 cm^{-1} for the MgF_2 -doped ceramics, respectively. Among these sintering aids, yttrium oxide is one of the most commonly used oxide additives, because it can react with the low-activity alumina layer on the surface of nitride particles and form liquid-phase yttrium aluminates to promote densification [126–128]. However, the yttrium aluminates formed and distributed along the AlN grain boundaries seriously reduce their transparency. In addition, non-oxide additives including fluorides are also adopted, which promote the densification process by liquid-phase sintering along with clean grain boundaries by evaporation of the secondary phase [129, 130].

SPS has also been used as an effective densification method of AlN ceramics. For example, dense AlN ceramics were prepared by SPS at a sintering temperature of $1700\text{ }^\circ\text{C}$ and a heating rate of $100\text{ }^\circ\text{C}/\text{min}$ under 40 MPa in a nitrogen atmosphere by using 2 wt% of Y_2O_3 , Sm_2O_3 , or Dy_2O_3 as sintering additives [131]. Fine-grained AlN ceramic with grain size of less than $1\text{ }\mu\text{m}$ was synthesized from AlN nanopowder with 1 wt% of $\text{Ca}_3\text{Al}_2\text{O}_6$ by SPS at $1450\text{ }^\circ\text{C}$ for 5 min under 50 MPa of compressive stress [132]. Highly transparent, undoped AlN ceramic was successfully fabricated by SPS technique at the sintering temperature of $1800\text{ }^\circ\text{C}$, compressive pressure of 25 MPa, with different heating rates of $100\text{--}550\text{ }^\circ\text{C}/\text{min}$, and with sintering duration ranging from 4 to 20 min [133]. In another case, undoped AlN and SrF_2 -doped AlN ceramics were consolidated by SPS, and the doped AlN exhibited translucency at the wavelength of longer than 500 nm [134]. SPS technique is an effective method for fabrication of transparent AlN ceramics, as it shortens sintering time and lowers sintering temperature.

Zinc Sulfide (ZnS)

Zinc sulfide (ZnS) has been widely used in many applications, such as optical elements, phosphors, sensors, and photocatalysts. In the wavelength range $8\text{--}14\text{ }\mu\text{m}$, ZnS is a desirable candidate for the IR-transparent ceramics used in military and commercial applications [135, 136]. High-purity ZnS can be used for infrared window and missile dome in defense applications. Dense, IR-transparent ZnS ceramics have been produced by HP [137, 138], chemical vapor deposition (CVD), and CVD followed by HIP [139]. For instance, infrared-transparent ZnS ceramics with transmittance of 77% at wavelengths of 6.74 and $9.29\text{ }\mu\text{m}$ were manufactured by HP at $1000\text{ }^\circ\text{C}$ for 3 h under a uniaxial pressure of 50 MPa at a heating rate of $5\text{ }^\circ\text{C}/\text{min}$ under a vacuum of 10^{-5} mbar [136].

However, high-temperature sintering often causes a decrease in mechanical strength and hardness due to grain growth [140]. In addition, the phase transformation of ZnS ceramics at the relatively low temperature caused deterioration of transparency; the existence of hexagonal phase may pose birefringence that significantly decreases the optical transparency of ZnS ceramics. One of the effective approaches to avoid the drawback is to fabricate ZnS material at lower temperature.

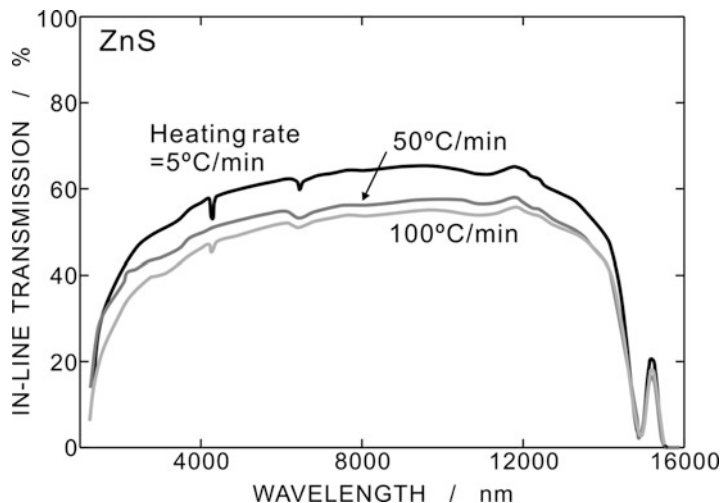


Fig. 13 Transmission of SPSed ZnS bodies with different heating rates from 5 °C/min to 100 °C/min [135]. The thickness of the specimens was 1.5 mm

Therefore, SPS synthesis has been applied to consolidate fully densified ZnS ceramics. Chlique et al. [141] demonstrated ZnS ceramics by SPS sintering with thickness of 0.55 mm, and the transmittance was up to 50% in the range of 8–14 μm .

In another case, the effect of heating rate in SPS processing was extensively investigated to obtain transparent ZnS [135]. The SPS synthesis conditions employed were heating rate in a range of 5–100 °C/min, sintering temperature of 840 °C, sintering time of 5 min, and compressive stress of 80 MPa. As a result, ZnS ceramics with good optical transparency were successfully fabricated at the relatively low SPS sintering temperature with the heating rate of 5 °C/min. The highest in-line transmittance of the SPSed ZnS ceramic body was up to 40% in the wavelength range of 2.0–3.0 μm and 60% in the infrared wavelength range of 5.0–12 μm , as shown in Fig. 13. The content of hexagonal phase of ZnS decreased with the decreasing heating rate.

New Technologies of ECAS/SPS

SPS has five major operating parameters, i.e., field/current waveform, sintering temperature, sintering time, heating rate, and compressive pressure. In order to efficiently manufacture transparent ceramics by SPS, it is important to optimize these parameters, as described above. Recently, more complex schedules of heating and pressurizing as well as energizing electric power have been adopted. Various attempts have also been made to improve the transparency of specimens by changing the material of the die and punches; thermal and electric conductivities directly influence sintering behavior of materials. In addition, new

technologies of ECAS have also been proposed one after another, and several techniques capable of extremely high sintering densification rate have been developed, while transparent body has not yet been produced by such quick and rapid ECAS techniques. Among new ECAS technologies, flash sintering is particularly attracting attention from academic and industrial circles.

Multistep SPS

In conventional sintering, it is well-known that multistep sintering, in which furnace temperature is raised not at uniform heating rate but at more than two steps of heating schedule, is effective for densification and grain size refinement of some ceramics. Most remarkable example was two-step sintering, in which sample was heated to a higher temperature then immediately cooled to a lower temperature for isothermal sintering with a dwelling time of more than several hours [142]; fine-grained and fully densified oxide ceramics, such as Y_2O_3 and $BaTiO_3$, were successfully manufactured. SPS has also attempted to introduce multiple steps into the temperature elevation and pressurization process. Several successful fabrication approaches have been presented.

A two-step pressure method, which enabled a significant improvement in in-line transmittance of high heating rate SPSed alumina was reported by Grasso and co-workers [143]. Commercially available alumina powder could be consolidated at 1150 °C by using SPS at a heating rate of 100 °C/min. The effects of pressure application mode were examined with respect to microstructure, porosity, and transparency. The pressure was applied in two ways. In the first case, a constant pressure of 80 MPa was applied for the entire duration of the sintering process (hereinafter, constant pressure). In the second case, an initial pressure of 35 MPa was applied; subsequently the pressure was increased in 3 min after the beginning of dwelling time (hereinafter, two steps pressure). The application of two-step pressure was found to be very effective to obtain homogeneously densified translucent alumina samples at high heating rate.

Transparent, undoped, and Nd-doped $MgAl_2O_4$ ceramics were produced by SPS with a two-step schedule: fast heating (100 °C/min) with a first dwell of 3 min at 1100 °C without high pressure and then heating at 20 °C/min to 1300 °C for 15 min under progressive uniaxial loading at 130 MPa [144]. Two-step sintering is also effective to densify 8 mol% Y_2O_3 -stabilized cubic ZrO_2 by low-temperature SPS at 1050 °C [145]. In another case, nanocrystalline TiCN ceramics were fabricated by SPS in a multiple-stage regime with sequential increase of pressure from 50 to 70 MPa and simultaneous decrease of heating rate from 100 °C/min to 20 °C/min; the application of multiple-stage regime was beneficial for reduction of grain size and increment of mechanical properties, in comparison to traditional single-stage SPS regime [146]. When using intermediate pressures and standard graphite tools, a two-step pressure schedule might be advantageous to homogenize the microstructure [147].

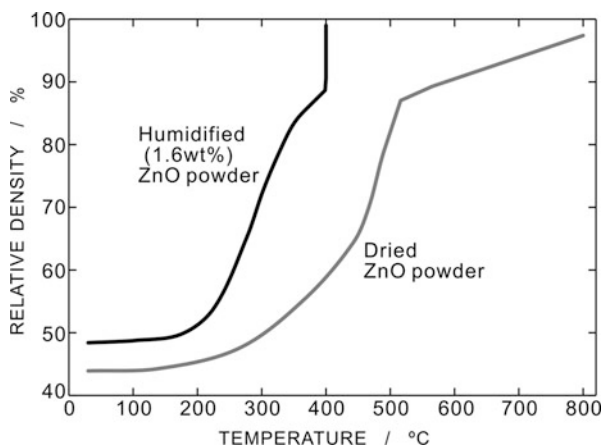
Water-Assisted SPS Process

In recent years, the role of water in sintering densification has attracted attention; enhanced or suppressed sintering rates of various oxide ceramics in the presence of water vapor have been observed. In ECAS, it has been experimentally shown that the presence of water (or water vapor) contributes to the improvement of densification in several ceramics [148–150]. Due to the presence of water, the sintering temperature is drastically reduced. It is therefore expected to manufacture ceramics having microstructures and material properties unprecedented so far.

It has been recently reported that nanocrystalline zinc oxide (ZnO) was processed by SPS to a density above 95% at only 400 °C, which is significantly lower than common sintering temperature even in SPS techniques [149]. Reasons for this unexpected behavior are enhanced particle rearrangement and higher diffusivity, due to the presence of water adsorbed on the surface. Figure 14 shows the densification curves for humidified (1.6 wt %) and dried raw ZnO powder sintered using SPS at a high heating rate of 100 °C/min and maximum temperatures of 400 °C and 800 °C, respectively. The initial green density and the densification behavior of nanocrystalline ZnO are both enhanced by the presence of water in comparison to dry condition. The densification rate is strongly increased by humidification resulting into 99% of the theoretical density for humidified ZnO at 400 °C, whereas dried powder shows a residual porosity of 38% at the same temperature. In addition, full densification is achieved after an isothermal sintering time of only 10 min. Typically the full densification of nanocrystalline zinc oxide by means of HP or SPS requires much longer isothermal durations of more than 1 h and a sintering temperature of at least 800 °C.

According to the authors' analysis, the densification of nanocrystalline ZnO increased with the increasing fraction of surface bound water. Apparent activation energy for sintering densification decreased with the increasing water fraction, indicating a modification in sintering mechanism. The formation of oxygen-hydrogen-related defect complexes was suggested in Kelvin probe force microscopy analysis, and such an interface interaction of surface bound water with the grain

Fig. 14 Densification curves for humidified (1.6 wt%) and dried ZnO powder produced by SPS at a heating rate of 100 °C/min and maximum temperatures of 400 °C and 800 °C, respectively [149]



boundary may result into enhanced densification of ZnO at low temperatures. As mentioned in section “[Role of Microstructure on Optical Properties](#),” it is possible that some defect reactions would trigger enhanced diffusional mass transport and densification process in ECAS. The water-assisted ECAS/SPS will gain theoretical and practical importance in the future.

Flash Sintering

Flash sintering technique has received a lot of international attention in recent years as a drastic, almost instantaneous sintering process, which can be classified into ECAS. Raj and co-workers have demonstrated 3 mol% Y_2O_3 -stabilized tetragonal ZrO_2 polycrystal (3Y-TZP) can be fully densified at 850 °C within 5 s under an electric field of 120 V/cm [151], while the same material can be usually densified by a conventional, pressureless sintering in air at 1400–1500 °C for several hours. The abrupt densification at relatively low sintering temperature is called flash sintering, in distinction from ECAS, in which the enhancement of densification is more gradual. Figure 15a shows typical setup of flash sintering experiment. A strong DC or AC electric field is applied to green compact by electric power supply through platinum wires. The furnace temperature, field strength, specimen current, and densification curve are schematically illustrated in Fig. 15b. The furnace temperature is raised at a constant heating rate. Beyond threshold field strength and furnace temperature, electric conductivity of the green compact abruptly increases, and electric current through the material accordingly increases. The almost instantaneous

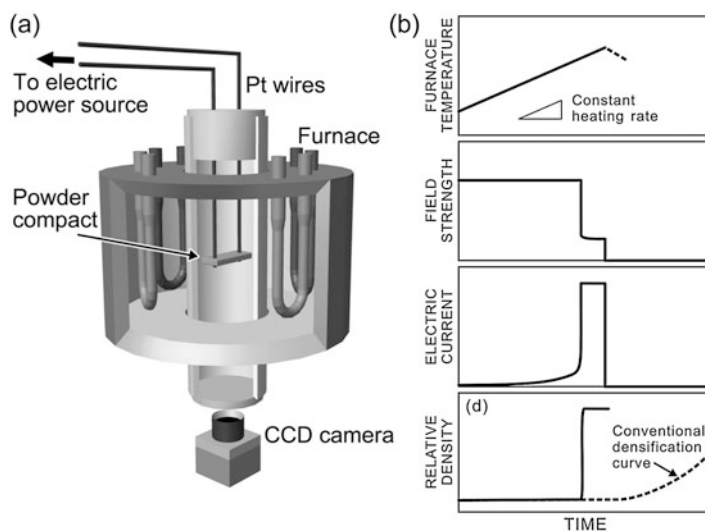


Fig. 15 (a) Typical setup of flash sintering experiment. (b) Schematics of furnace temperature, field strength, specimen current, and densification curve during flash sintering experiment

densification consequently takes place. The densification curves in 3Y-TZP sintered under different DC fields [151] as a function of furnace temperature are depicted in Figure 16. In this figure, the linear shrinkage data presented in ref. [151] were converted to relative density values. As shown in Fig. 16, abrupt densification of TZP occurred under the DC fields of higher than 60 V/cm, and the sintering temperature decreased with the increasing field strength. The flash sintering is characterized by almost immediate densification (typically occurs in just a few seconds) and a nonlinear increase in electric conductivity under a threshold condition of temperature and applied field [151, 152]. The nature of the flash sintering is fundamentally different from FAST, in which fields lead to a gradual enhancement in the sintering without any change in the specimen conductivity. Abrupt densification at low temperature by flash sintering has been demonstrated in various ceramics [153].

Flash sintering technique can be applied to various oxide and non-oxide ceramics, even low-sinterability materials such as Y_2O_3 . For instance, DC fields greater than 300 V/cm can trigger the flash sintering in undoped Y_2O_3 [154]. Conventional sintering requires very high temperatures, typically $> 1600\text{ }^\circ\text{C}$ as noted above, and a vacuum or hydrogen atmosphere. However, by applying an electric field of 1000 V/cm, for instance, a dense Y_2O_3 polycrystal was obtained at $985\text{ }^\circ\text{C}$ in less than 10 s [154].

Nevertheless, full densification is still difficult to be accomplished by flash sintering. Typical example of the suppressed final density was seen in the flash sintering of $BaTiO_3$. Under a strong electric field beyond a critical value, flash sintering posed electric discharge damage in $BaTiO_3$ bodies, resulting in a low density of the sintered body with a number of residual pores and tunnellite

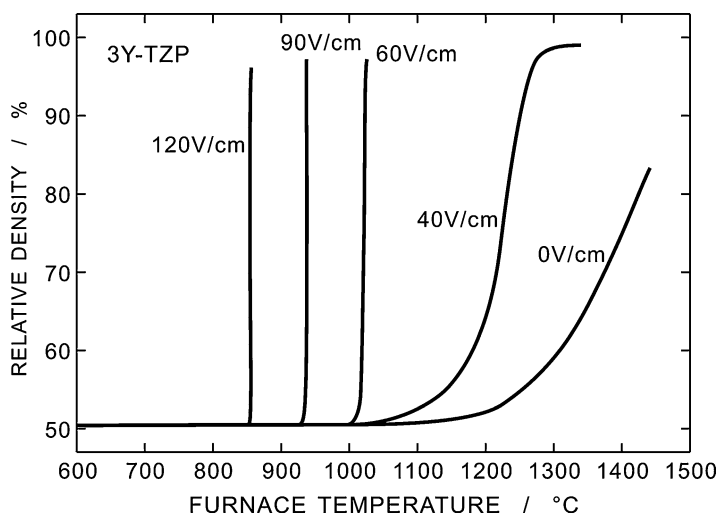


Fig. 16 The densification curves in 3Y-TZP sintered under different DC fields [151] as a function of furnace temperature

physical damages [155, 156]. In addition, crystalline thin layers were generated along BaTiO₃ grain boundaries in the vicinity of the electric discharged damage [157]. The Ba/Ti cation ratio of the secondary crystalline phases was Ti-excess, indicating that Ba cations tended to evaporate because of the excess heat yielded by the discharging.

EELS from grain boundaries and grain interiors in the flash-sintered materials revealed that the increased concentration of electric charge carriers was due to the excess oxygen vacancies generated by the electric fields; the changes in the fine structure of the Ti-L₂₃ and O-K edges energy loss near edge structure (ELNES) were attributed to the excess oxygen vacancies. The excess oxygen vacancies induced by DC electric field was found to retard the sintering rate in the final sintering stage. Therefore, it is necessary to carefully control the specimen current for full densification of BaTiO₃ during flash sintering synthesis. In fact, by controlling current limit and heating schedule, more than 98% of theoretical density was obtained in BaTiO₃ by flash sintering [158]; for the electric current controlled flash sintering synthesis, the electric field of 100 V/cm with limiting current of 72 mA was applied up to 1070 °C, and then the electric field was switched off up to 1300 °C. The material manufactured by the current controlled flash sintering exhibited significantly fine-grained microstructure in comparison to that in conventionally sintered one.

At present, it is still difficult to produce transparent ceramics by flash sintering process. In addition, limited shape and dimensions of material are also disadvantages of flash sintering, as well as SPS so far. In contrast to the several disadvantages, flash sintering is a very attractive method because of the short sintering time and low sintering temperature, and the number of reports on flash sintering and related phenomena highly increases in recent years. It is expected to develop translucent or transparent ceramic bodies by flash sintering with short-time and low-temperature synthesis.

Concluding Remarks

Electric field/current-assisted sintering technology or spark plasma sintering is a versatile processing method for consolidation of various materials. Owing to the direct and rapid heating technology, SPS enables fully densified ceramic bodies consisting of nanoscale grains, which is ideally for achieving transparency of ceramic bodies. Moreover, by controlling the major sintering parameters, i.e., sintering temperature, isothermal sintering time, heating rate, and compressive pressure, transparent ceramics without residual pores can be manufactured by SPS technique, as briefly summarized in this chapter. Manufacturing of dense nanostructured body by SPS is also preferable to improve the mechanical properties of transparent ceramic materials. A number of studies have proven that ECAS/SPS synthesis is feasible for the production of transparent ceramic bodies, at least in the level of laboratory demonstrations.

Nevertheless, much fundamental research and development efforts are still required to use transparent ceramics produced by ECAS/SPS for industrial

applications. Fundamental investigations on the origin of enhanced densification in SPS are needed from atomistic point of view; a significant number of experimental results strongly indicated that some ionic defect reactions are involved during SPS processing. Effects of electrical current/field on mass transport, reactivity, microstructure evolution, and final chemical and physical properties are still remained to be understood. In order to control thermal and electrical conduction and stress distribution as well as mass transportation inside the die during SPS processing, new experimental techniques such as direct measurement of field strength inside a material and theoretical analyses such as FEM calculations must be employed.

On the other hand, for promoting transparent ceramics produced by SPS to industrial use, not only the improvement of physical/chemical properties but also upscaling of products and homogenization of microstructure are key technologies. Use of electro/magnetic fields pioneers new, unexpected technologies of ECAS/SPS. In addition, nanometer-scaled and defect-free microstructures attained by SPS not only improve mechanical strength but also enable superplastic deformation and near-net shape forming of the SPSed transparent ceramics. Scale up of components size and improvement in desirable properties of optically transparent ceramics through development of ECAS/SPS devices and progress in fundamental research on process will advance the industrial applications for the transparent ceramics in the near future.

References

1. Tokita M (2006) *Am Ceram Soc Bull* 85:32
2. Kodaera Y, Hardin CL, Garay JE (2013) *Scr Mater* 69:149
3. Garay JE (2010) *Annu Rev Mater Res* 40:445
4. Grimm N, Scott GE, Sibold JD (1971) *Ceram Bull* 50:962
5. Hayashi K, Kobayashi O, Toyoda S, Morinaga K (1991) *Mater Trans JIM* 32:1024
6. O YT, Koo JB, Hong KJ, Park JS, Shin DC (2004) *Mater Sci Eng A* 374:191
7. Apetz R, van Bruggen PB (2003) *J Am Ceram Soc* 86:480
8. Lallemand L, Fantozzi G, Garnier V, Bonnefont G (2012) *J Eur Ceram Soc* 32:2909
9. Tokita M (1993) *J Soc Powd Tech Jpn* 30:790
10. Tamari N, Tanaka T, Tanaka K, Kondoh I, Kawahara M, Tokita M (1995) *J. Ceram. Soc. Jpn* 103:740
11. Perera DS, Tokita M, Moricca S (1998) *J Eur Ceram Soc* 18:401
12. Misawa T, Shikatani N, Kawakami Y, Enjoji T, Ohtsu Y, Fujita H (2009) *J Mater Sci* 44:1641
13. Orru R, Licheri R, Locci AM, Cincotti A, Cao G (2009) *Mater Sci Eng R* 63:127
14. Chaim R, Marder R, Estournes C (2010) *Scr Mater* 63:211
15. An LQ, Ito A, Goto T (2011) *J Eur Ceram Soc* 31:1597
16. Yang D, Conrad H (2010) *Scr Mater* 63:328
17. Yoshida H, Morita K, Kim B-N, Hiraga K, Yamanaka K, Soga K, Yamamoto T (2011) *J Am Ceram Soc* 94:3301
18. Anselmi-Tamburini U, Gennari S, Garay JE, Munir ZA (2005) *Mater Sci Eng A* 394:139
19. Bernard-Granger G, Guizard C (2007) *Acta Mater* 55:3493
20. Grasso S, Sakka Y, Maizza G (2009) *Sci Technol Adv Mater* 10:053001
21. Tokita M (2014) *Ceram Jpn* 49:91. (in Japanese)
22. Munir ZA, Quach DV, Ohyanagi M (2011) *J Am Ceram Soc* 94:1
23. Krell A, Blank P, Ma H, Hutzler T, Am J (2003) *J Am Ceram Soc* 86:12

24. Wei GC, Rhodes WH (2000) *J Am Ceram Soc* 83:1641
25. Mao XJ, Wang SW, Shimai S, Guo JK (2008) *J Am Ceram Soc* 91:3431
26. Shen ZJ, Johnsson M, Zhao Z, Nygren M (2002) *J Am Ceram Soc* 85:1921
27. Kim B-N, Hiraga K, Morita K, Yoshida H (2007) *Scr Mater* 57:607
28. Kim B-N, Hiraga K, Morita K, Yoshida H (2009) *J Eur Ceram Soc* 29:323
29. Kim B-N, Hiraga K, Morita K, Yoshida H, Miyazaki T, Kagawa Y (2009) *Acta Mater* 57:1319
30. Wang C, Zhao Z (2010) *Mater Res Bull* 45:1127
31. Penilla EH, Kodera Y, Garay JE (2013) *Adv Funct Mater* 23:6036
32. Wang SF, Zhang J, Luo DW, Gu F, Tang DY, Dong ZL, Tan GEB, Que WX, Zhang TS, Li S, Kong LB (2013) *Prog Solid State Chem* 41:20
33. Hou XR, Zhou SM, Jia TT, Lin H, Teng H (2011) *Phys B Condens Matter* 406:3931
34. Micheli AL, Dungan DF, Mantese JV (1992) *J Am Ceram Soc* 75:709
35. Iwasawa J, Nishimizu R, Tokita M, Kiyohara M, Uematsu K (2007) *J Am Ceram Soc* 90:2327
36. Saito N, Matsuda S, Ikegami T (1998) *J Am Ceram Soc* 81:2023
37. Zhang J, Wang S, An L, Liu M, Chen L (2007) *J Lumin* 122–123:8
38. Lefever RA, Matsko J (1967) *Mater Res Bull* 2:865
39. Majima K, Niimi N, Watanabe M, Katsuyama S, Nagai H (1993) *J Alloys Compd* 193:280
40. Ikesue A, Kamata K, Yoshida K (1996) *J Am Ceram Soc* 79:359
41. Serivalsatit K, Kokuoz B, Yazgan-Kokuoz B, Kennedy M, Ballato J (2010) *J Am Ceram Soc* 93:1320
42. Gan L, Park Y-J, Kim H, Kim J-M, Ko J-W, Lee J-W (2015) *Ceram Int* 41:9622
43. Hou XR, Zhou SM, Jia TT, Lin H, Teng H (2011) *J Lumin* 131:1953
44. Podowitz SR, Gaume R, Feigelson RS (2010) *J Am Ceram Soc* 93:82
45. An LQ, Ito A, Goto T (2012) *J Eur Ceram Soc* 32:1035
46. Yoshida H, Morita K, Kim B-N, Hiraga K, Kodo M, Soga K, Yamamoto T (2008) *J Am Ceram Soc* 91:1707
47. Zhang HB, Kim B-N, Morita K, Yoshida H, Hiraga K, Sakka Y (2011) *J Am Ceram Soc* 94:3206
48. Yoshida H, Morita K, Kim B-N, Soga K, Yamamoto T (2018) *J Eur Ceram Soc* 38:1972
49. Garvie RC, Hannink RH, Pascoe RT (1975) *Nature* 258:703
50. Matsui K, Yoshida H, Ikuhara Y (2018) *Int Mater Rev* 63:375
51. Mazdiyasn KS, Lynch CT, Smith JS II (1967) *J Am Ceram Soc* 50:532
52. Tsukuma K, Yamashitaw I, Kusunose T (2008) *J Am Ceram Soc* 91:813
53. Peuchert U, Okano Y, Menke Y, Reichel S, Ikesue A (2009) *J Eur Ceram Soc* 29:283
54. Tsukuma K (1986) *J Mater Sci Lett* 5:1143
55. Casolco SR, Xu J, Garay JE (2008) *Scr Mater* 58:516
56. Anselmi-Tamburini U, Woolman JN, Munir ZA (2007) *Adv Funct Mater* 17:3267
57. Zhang H, Kim B-N, Morita K, Yoshida H, Lim J-H, Hiraga K (2011) *J Am Ceram Soc* 94:2981
58. Klimke J, Trunec M, Krell A (2011) *J Am Ceram Soc* 94:1850
59. Ikegami T, Matsuda SI, Suzuki H (1974) *J Am Ceram Soc* 57:507
60. Chen D, Jordan EH, Gell M (2008) *Scr Mater* 59:757
61. Suzuki M, Ikegami T, Yokoyama M, Komatsu T, Fukahori A (2005) *J Ceram Soc Jpn* 113:149
62. Vasilos T, Spriggs RM (1963) *J Am Ceram Soc* 46:493
63. Vieira JM, Brook RJ (1984) *J Am Ceram Soc* 67:450
64. Ehre D, Gutmanas EY, Chaim R (2005) *J Eur Ceram Soc* 25:3579
65. Itatani K, Tsujimoto T, Kishimoto A (2006) *J Eur Ceram Soc* 26:639
66. Benecke MW, Olson NE, Pask JA (1967) *J Am Ceram Soc* 50:365
67. Fang Y, Agrawal D, Skandan G, Jain M (2004) *Mater Lett* 58:551
68. Kan A, Moriyama T, Takahashi S, Ogawa H (2011) *Jpn J Appl Phys* 50:09NF2
69. Rhodes WH, Sellers DJ (1967) *Am Ceram Soc Bull* 46:469
70. Hart PE, Pask JA (1971) *J Am Ceram Soc* 54:315
71. Chaim R, Shen ZJ, Nygren M (2004) *J Mater Res* 19:2527
72. Tran TB, Hayun S, Navrotsky A, Castro RHR (2012) *J Am Ceram Soc* 95:1185

73. Liu J, Fu ZY, Wang WM, Zhang JY, Wang H, Wang YC, Lee SW, Niihara K (2014) *J Eur Ceram Soc* 34:3095–3102
74. Jiang N, Xie R-J, Liu Q, Li J (2017) *J Eur Ceram Soc* 37:4947
75. Ganesh I (2013) *Int Mater Rev* 58:63
76. Ting C-J, Lu H-Y (2000) *J Am Ceram Soc* 83:1592
77. du Merac MR, Reimanis IE, Kleebe H-J (2015) *J Am Ceram Soc* 98:2130
78. Chiang Y-M, Kingery WD (1989) *J Am Ceram Soc* 72:271
79. Ting CJ, Lu HY (1999) *Acta Mater* 47:817
80. Reimanis IE, Kleebe HJ (2009) *J Am Ceram Soc* 92:1472
81. Wang CT, Lin LS, Yang SJ (1992) *J Am Ceram Soc* 75:2240
82. Bhaduri S, Bhaduri SB (2002) *Ceram Int* 28:153
83. Goldstein A, Goldenberg A, Yeshurun Y, Hefetz M (2008) *J Am Ceram Soc* 91:4141
84. Biswas P, Rajeswari K, Ramavath P, Johnson R, Maiti HS (2013) *J Am Ceram Soc* 96:3042
85. Rodríguez EA, Castillo G-A, Das TK, Puente-Ornelas R, González Y, Arato A-M, Aguilar-Martínez JA (2013) *J Eur Ceram Soc* 33:2767
86. Li J-H, Cai B-Y, Feng W-W, Liu Y-Q, Ma H-W (2013) *Ceram Int* 39:8393
87. Gehre P, Aneziris CG, Berek H, Parr C, Reinmöller M (2015) *J Eur Ceram Soc* 35:1613
88. Frage N, Cohen S, Meir S, Kalabukhov S, Dariel MP (2007) *J Mater Sci* 42:3273
89. Morita K, Kim BN, Hiraga K, Yoshida H (2009) *J Am Ceram Soc* 92:1208
90. Muche DNF, Drazin JW, Mardinly J, Deya S, Castro RHR (2017) *Mater Lett* 186:298
91. Morita K, Kim B-N, Yoshida H, Hiraga K, Sakka Y (2015) *Acta Mater* 84:9
92. Morita K, Kim B-N, Yoshida H, Hiraga K, Sakka Y (2018) *J Eur Ceram Soc* 38:2596
93. Xu GG, Zhang XD, He W, Liu H, Li H (2006) *Mater Lett* 60:962
94. Ikesue A, Furusato I, Kamata K (1995) *J Am Ceram Soc* 78:225
95. Lee HD, Mah TI, Parthasarathy TA (2008) Low-cost processing of fine grained transparent yttrium aluminum garnet. In: 28th international conference on advanced ceramics and composites a: ceramic engineering and science proceedings, vol 25, p 147
96. Zych E, Brecher C (2000) *J Lumin* 90:89
97. Chaim R, Kalina M, Shen JZ (2007) *J Eur Ceram Soc* 27:3331
98. Frage N, Kalabukhov S, Sverdlov N, Ezersky V, Dariel MP (2010) *J Eur Ceram Soc* 30:3331
99. Spina G, Bonnefont G, Palmero P, Fantozzi G, Chevalier J, Montanaro L (2012) *J Eur Ceram Soc* 32:2957
100. Doremus RH (1992) *J Mater Sci* 27:285
101. Dorozhkin SV (2010) *Biomaterials* 31:1465
102. Takikawa K, Akao M (1996) *J Mater Sci Mater Med* 7:439
103. Kotobuki N, Ioku K, Kawagoe D, Fujimore H, Goto S, Ohgushi H (2005) *Biomaterials* 26:779
104. John A, Varma HK, Vijayan S, Bernhardt A, Lode A, Vogel A, Burmeister B, Hanke T, Domaschke H, Gelinsky M (2009) *Biomed Mater* 4:015007. (9pp)
105. Ioku K, Yosimura M, Somiya S (1988) *J. Ceram. Soc. Japan* 96:109
106. Wang J, Shaw LL (2010) *Scr Mater* 63:593
107. Uematsu K, Takagi M, Honda T, Uchida N, Saito K (1989) *J Am Ceram Soc* 72:1476
108. Fang Y, Agrawal DK, Roy DM, Roy R (1995) *Mater Lett* 23:147
109. Eriksson M, Liu Y, Hu J, Gao L, Nygren M, Shen Z (2011) *J Eur Ceram Soc* 31:1533
110. Kim B-N, Prajateljista E, Han Y-H, Son H-W, Sakka Y, Kim S (2013) *Scr Mater* 69:366
111. Yoshida H, Kim B-N, Son H-W, Han Y-H, Kim S (2013) *Scr Mater* 69:155
112. Cheng JP, Agrawal D, Zhang YJ, Roy R (2000) *J Mater Sci Lett* 20:77
113. Yuan XY, Liu XJ, Zhang F, Wang SW (2010) *J Am Ceram Soc* 93:22
114. Yuan XY, Zhang F, Liu XJ, Zhang Z, Wang SW (2011) *J Inorg Mater* 26:499
115. Zientara D, Bucko MM, Lis J (2007) *J Eur Ceram Soc* 27:4051
116. Kumar RS, Rajeswari K, Praveen B, Hareesh UNS, Johnson R (2010) *J Am Ceram Soc* 93:429
117. Chen F, Zhang F, Wang J, Zhang HL, Tian R, Zhang J, Zhang Z, Sun F, Wang SW (2014) *Scr Mater* 81:20
118. Sahin FC, Kanbur HE, Apak B (2012) *J Eur Ceram Soc* 32:925

119. Li X, Luo J, Zhou Y (2015) *J Eur Ceram Soc* 35:2027
120. Shan Y, Wei Z, Sun Z, Xu J, Qin Q, Olevsy EA (2017) *J Mater Res* 32:3279
121. Nakanishi Y (1984) *J Mater Sci Lett* 3:471
122. Kuramoto N, Taniguchi H, Aso I (1986) *IEEE Trans Compon* 9:386
123. Kuramoto N, Taniguchi H, Aso I (1989) *Am Ceram Soc Bull* 68:883
124. Kuramoto N, Taniguchi H (1984) *J Mater Sci Lett* 3:471
125. Xiang M, Zhou Y, Xu W, Li X, Wang K, Pan W (2018) *J Ceram Soc Jpn* 126:241
126. Baranda PS, Knudsen AK, Ruh E (1993) *J Am Ceram Soc* 76:1751
127. Watari K, Hwang HJ, Toriyama M, Kanzaki S (1999) *J Mater Res* 14:1409
128. Panchula ML, Ying JY (2003) *J Am Ceram Soc* 86:1121
129. Jarrige J, Lecompte JP, Mullo J, Müller G (1997) *J Eur Ceram Soc* 17:1891
130. He XL, Ye F, Zhang HJ, Zhou ZQ (2010) *Mater Des* 31:4110
131. He X, Ye F, Liu LM, Zhang HJ (2011) *Mater Sci Technol* 27:513
132. Nishimura T, Sekine K, Yamamoto Y, Hirotsaki N, Ishigaki T (2010) *J Ceram Soc Jpn* 118:1050
133. Fu ZY, Liu JF, Wang H, He DH, Zhang QJ (2004) *Mater Sci Technol* 20:1097
134. Kojima K, Okada G, Fukuda K, Yanagida T (2016) *Radiat Meas* 94:78
135. Chen Y, Zhang L, Zhang J, Liu P, Zhou T, Zhang H, Gong D, Tang D, Shen D (2015) *Opt Mater* 50:36
136. Li Y, Wu Y (2015) *J Am Ceram Soc* 98:2972
137. Chen S, Wu Y (2013) *Am Ceram Soc Bull* 92:32
138. Chlique C, Merdrignac-Conanec O, Hakmeh N, Zhang X, Adam JL (2013) *J Am Ceram Soc* 96:3070
139. McCloy JS, Tustison RW (2013) *Chemical vapor deposited zinc sulfide*. SPIE Press, Bellingham
140. Karaksina EV, Ikonnikov VB, Gavrishchuk EM (2007) *Inorg Mater* 43:452
141. Chlique C, Delaizir G, Merdrignac-Conanec O, Roucau C, Dollé M, Rozier P, Bouquet V, Zhang X (2011) *Opt Mater* 33:706
142. Chen I-W, Wang X-H (2000) *Nature* 404:168
143. Grasso S, Hu CF, Maizza G, Kim B-N, Sakka Y (2011) *J Am Ceram Soc* 94:1405
144. Boulesteix R, Maitre A, Lemanski K, Deren PJ (2017) *J Alloys Compd* 722:358–364
145. Schwarz S, Guillon O (2013) *J Eur Ceram Soc* 33:637
146. Zgalat-Lozynskyy O, Herrmann M, Ragulya A (2011) *J Eur Ceram Soc* 31:809
147. Guillon O, Gonzalez-Julian J, Dargatz B, Kessel T, Schierming G, Räthel J, Herrmann M (2014) *Adv Eng Mater* 16:830
148. Schwarz S, Thron AM, Rufner J, van Benthem K, Guillon O (2012) *J Am Ceram Soc* 95:2451
149. Dargatz B, Gonzalez-Julian J, Bram M, Jakes P, Besmehn A, Schade L, Röder R, Ronning C, Guillon O (2016) *J Eur Ceram Soc* 36:1207
150. Nie J, Zhang Y, Chan JM, Huang R, Luo J (2018) *Scr Mater* 142:79
151. Cologna M, Rashkova B, Raj R (2010) *J Am Ceram Soc* 93:3556
152. Raj R, Cologna M, Francis JSC (2011) *J Am Ceram Soc* 94:1941
153. Dancer CFJ (2016) *Mater Res Express* 3:102001
154. Yoshida H, Sakka Y, Yamamoto T, Lebrun J-M, Raj R (2014) *J Eur Ceram Soc* 34:991
155. M'Peko JC, Francis JSC, Raj R (2014) *J Eur Ceram Soc* 34:3655
156. Uehashi A, Yoshida H, Tokunaga T, Sasaki K, Yamamoto T (2015) *J Ceram Soc Jpn* 123:465
157. Yoshida H, Uehashi A, Tokunaga T, Sasaki K, Yamamoto T (2016) *J Ceram Soc Jpn* 124:388
158. Nakagawa Y, Yoshida H, Uehashi A, Tokunaga T, Sasaki K, Yamamoto T (2017) *J Am Ceram Soc* 100:3843

Part IV

Advanced Ceramics and CMCs for Nuclear Applications



Advanced SiC-SiC Composites for Nuclear Application

17

Tetsuji Noda

Contents

Introduction	642
SiC Fibers	643
Fabrication of SiC Fiber-Reinforced SiC Composites (SiC/SiCs)	644
CVI	644
PIP	649
RS	649
LPS	650
Basic Properties of SiC/SiC Composites Formed by Several Processes	650
Irradiation Responses of SiC/SiC Composites	651
Effects of Neutron Irradiation on the Stability of SiC Fibers	651
Irradiation Effect on SiC/SiC Composites	652
Application of SiC/SiC Composites to Fusion Reactors	656
Design of Blanket Structures for Fusion Reactors	656
Induced Radioactivation and Transmutation of SiC/SiC Composites	657
Helium and Hydrogen Production	659
Chemical Compatibility	660
Manufacturing and Joining	660
Hermeticity	661
Summary and Conclusions	662
References	662

Abstract

The progress of the development of SiC fiber-reinforced SiC (SiC/SiC) composites focusing on applying the composites to nuclear fusion systems is overviewed. The physical and mechanical properties of SiC/SiC composites prepared with chemical vapor infiltration (CVI), polymer impregnation and pyrolysis (PIP), reaction sintering (RS), and liquid-phase sintering (LPS) are presented. Among

T. Noda (✉)

National Institute for Materials Science, Tsukuba, Japan

e-mail: noda.tetsuji@nims.go.jp

various SiC/SiC composites, LPS SiC/SiC composite formed by, so-called nano-powder infiltration and transient eutectoid (NITE) process, with a density close to that of monolithic SiC shows the highest thermal conductivity and mechanical properties. CVI and NITE SiC/SiC composites demonstrate excellent neutron irradiation resistance on thermal conductivity, swelling, flexural strength, and creep properties at up to temperature 1000 °C. The composites also offer low induced activity, favorable chemical compatibility with liquid candidate coolant of Pb-Li and solid breeder materials, and preferable joining characteristics.

Keywords

SiC/SiC composites · CVI · Liquid-phase sintering · Mechanical properties · Neutron irradiation · Compatibility · Joining

Abbreviation

A-SSTR	Advanced steady-state tokamak reactor
BMAS	BaO ₂ -MgO-Al ₂ O ₃ -SiO ₂
BSR	Bend stress relaxation
CMC	Ceramic matrix composite
CVI	Chemical vapor infiltration
D-T	Deuterium-tritium
FCVI	Forced-thermal gradient chemical vapor infiltration
HP	Hot pressing
ITER	International Thermonuclear Experimental Reactor
LPS	Liquid phase sintering
NITE	Nano-powder infiltration and transient eutectoid
PCS	Polycarbosilane
PIP	Polymer impregnation and pyrolysis
PMS	Polymethylsilane
PVS	Polyvinylsilane
RS	Reaction sintering
SEMB	Single-edge notched beam
SiC/SiC	SiC fiber-reinforced SiC
TBM	Test blanket modules

Introduction

SiC has superior heat resistance and excellent thermal conductivity, oxidation resistance, and nuclear characteristics. It is attractive as a structural material in the aerospace and nuclear power industries as well as general commercial materials used for heaters, abrasive and cutting tools, etc. However, since SiC itself is a brittle material, composite material – so-called CMC (ceramic matrix composite) reinforced with particles, whiskers, or long fibers – has been developed so that it can be used as a structural material. Particularly, long-fiber-reinforced CMC is expected to

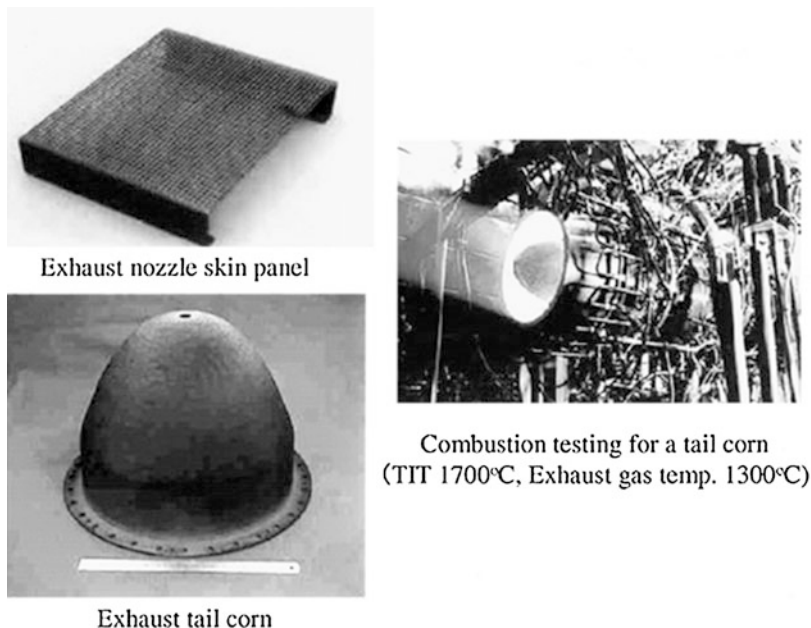


Fig. 1 SiC/SiC components developed under the Super/Hyper-Sonic Transport Propulsion (HYPER) project [1]. (Copyright © 2004 under The Japan Society of Plasma Science and Nuclear Fusion Research)

improve its remarkable mechanical properties. Composites such as carbon fiber/SiC or SiC fiber/SiC are actually applied to spacecraft and aircraft as a composite material of SiC [1].

Figure 1 shows engine components made of SiC/SiC developed under the Super/Hyper-Sonic Transport Propulsion (HYPER) project [1], as an example. In nuclear systems, SiC was used to coat fuel particles for high-temperature gas reactors [2, 3]. Since the invention of continuous SiC fiber [4], SiC composite reinforced by SiC fiber has received noteworthy attention as a practical structural material in nuclear fusion systems [5] and, furthermore, is being examined even as a fuel cladding material in advanced light-water reactors [6].

In the present chapter, we present the progress in developing SiC fiber-reinforced SiC composites (SiC/SiC) including SiC fiber development for nuclear application especially in a fusion reactor.

SiC Fibers

Continuous long SiC fiber with high strength and favorable thermal stability was first produced from oxidation-cured polycarbosilane [4]. Nicalon, a polymer-derived SiC fiber commercialized by Nippon Carbon, is now widely used for CMCs

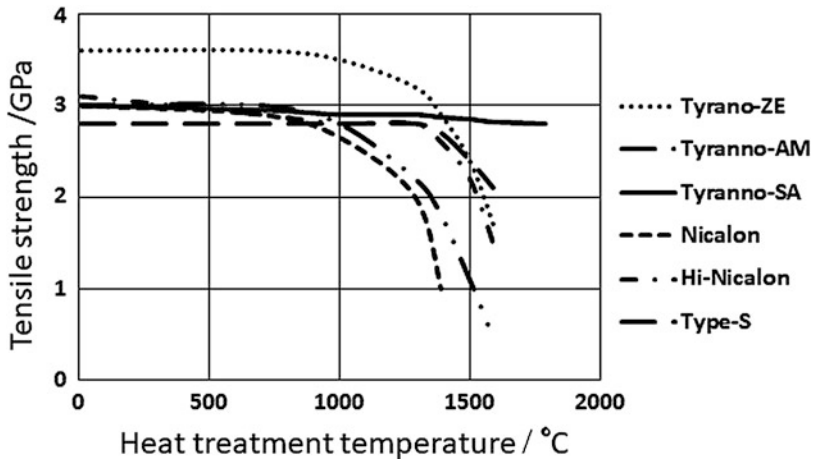


Fig. 2 Thermal stability of SiC fibers

[7]. However, SiC fiber from oxidation-cured polycarbosilane contains a small amount of oxygen which causes the degradation of SiC fiber due to a carbothermal reduction reaction at temperatures above 1300 °C [8]. Hi-Nicalon SiC fiber with low oxygen content was then developed using a curing process with electron-beam irradiation [7]. Hi-Nicalon Type-S high crystalline SiC fiber with near-stoichiometric composition was subsequently produced [8, 9].

Sylramic™ commercialized by Dow Corning is also a crystalline SiC fiber [10]. This fiber contains B₄C and TiB₂ and withstands heat up to about 1400 °C [10]. On the other hand, Tyranno SiC fibers with Ti, Zr, or Al additives were developed by Ube to improve heat resistivity to higher than 1800 °C (Fig. 2) [11, 12]. In Table 1, specifications of several Nicalon and Tyranno fibers developed are summarized. The composition and density of Type-S fiber from Nippon Carbon and Tyranno-SA from Ube are close to the ideal density of SiC crystals. The newly developed Tyranno-SA is especially resistant to temperatures up to 1900 °C [12]. Moreover, it has a higher density and thermal conductivity as compared with those of other SiC fibers.

Fabrication of SiC Fiber-Reinforced SiC Composites (SiC/SiCs)

SiC/SiCs are generally fabricated by methods such as chemical vapor infiltration (CVI), precursor impregnation and pyrolysis (PIP), hot pressing (HP), and reaction sintering (RS). Several processes and properties of SiC/SiC composites are described below:

CVI

CVI is the process of making composites by depositing the matrix material inside the preform through chemical vapor deposition reaction. CVI has

Table 1 Several continuous SiC fibers

	Nicalon™			Tyranno™				Sylramic™
	NL-201	Hi-NL	Type-S	TE	ZE	SA	SA-B	
C/Si	1.34	1.39	1.05	1.37	1.48	1.08	1.08	1.0
Other elements (mass %)	10.1% O	0.5% O	0.2% O	10.2% O 2% Ti	1.7% O 1% Zr	< 0.3% O < 2% Al	< 0.3% O < 2% Al	3%TiB ₂ 1%B ₄ C
Tensile strength (GPa)	2.9	2.8	2.6	3.3	3.5	2.8	2.8	3.2
Tensile modulus (GPa)	205	270	420	190	230	420	280	380
Elongation (%)	1.4	1.0	0.6	1.8	1.5	0.7	1.0	0.8
Mass density (mg/m ³)	2.55	2.74	3.10	2.48	2.55	3.02	3.02	3.0
Crystallite size (nm)	<2	5–10	50	2	2	>200	50–100	100
Thermal conductivity (W/m-K)	1.45	7.9	18.4	1.35	3.78	65	50	40–50

advantages of high purity [13], minimizing damage to fiber preforms because of a relatively low-temperature process compared to others, and making near-net shape products [14, 15]. This process has been widely used as a technique for producing structural SiC composites in transport and energy systems [1, 14, 15]. For SiC/SiCs, the decomposition of chlorosilane gas is generally used to deposit SiC matrix around SiC fibers [14, 15]. There are isothermal, thermal gradient, isothermal-forced flow, and pulsed flow [15] processes for CVI. The subject of CVI is how to fill SiC densely in the preform to create the composite, since pores remained inside the composite cause lowering strength, thermal conductivity, hermeticity (discussed in section “Hermeticity”), etc. Efforts to densify the SiC/SiC by forced-thermal gradient chemical vapor infiltration (FCVI) (Fig. 3) have been made. The high density of the composite can be achieved by minimizing the pore size as much as possible in the preforms and conducting the CVI by optimizing reactant gas pressure and temperature [16–19]. In Fig. 4, the relationship between flexural modulus and density of SiC/SiC produced by the FCVI [18] is shown. The flexural modulus increases with the decrease in the porosity and becomes approximately constant above about 2.7 g/cm³.

Figure 5 shows a typical cross-sectional image of a SiC/SiC composite by FCVI, where the maximum density reached about 2.76 g/cm³ [16].

CMCs are intrinsically brittle materials; however, they show pseudo-deformation behaviors under stress due to fiber de-bonding or pullout from the matrix. Therefore, the interface structure between the fiber and the matrix is important for tolerance against mechanical fracture. Efforts were made to accurately and uniformly control the interface structure to improve the mechanical properties of composites [17]. As a result of examining the coatings of SiC and carbon around SiC fibers along the cross

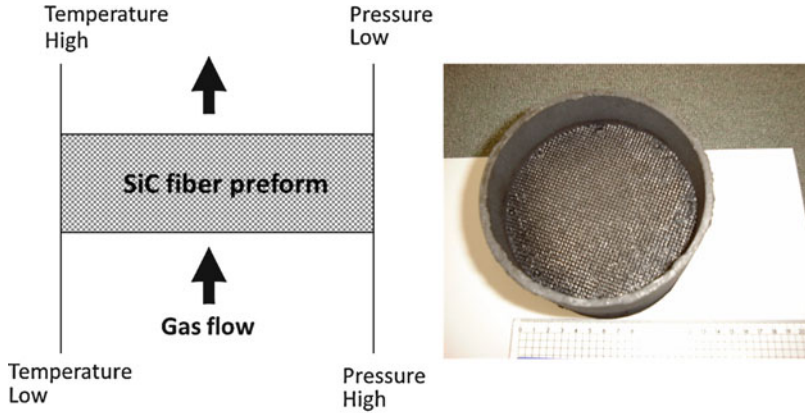


Fig. 3 Schematic drawing of forced CVI (FCVI) and SiC/SiC disk prepared with the FCVI

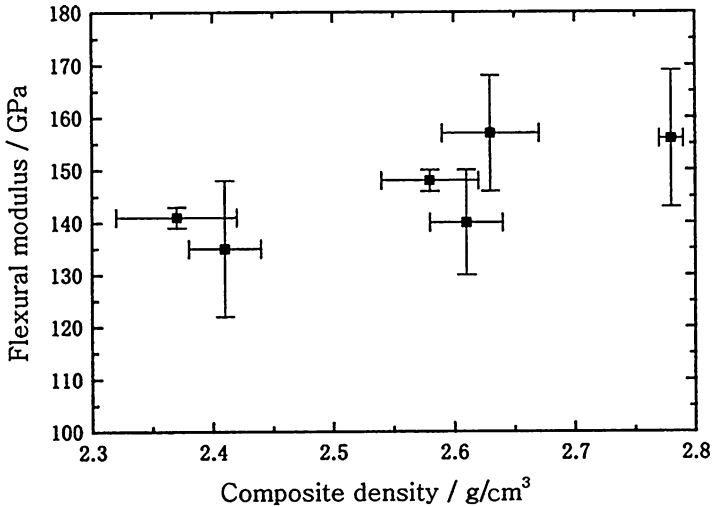


Fig. 4 Density dependence of the flexural modulus of FCVI SiC/SiC composites [18]

section of the preform as it changes temperature, the flow rate and pressure of reactants and the thickness of the SiC and carbon coating layers could be controlled in a range of 0.1–0.8 μm with an error of about 15% throughout the composite. Multiple coatings with a combination of carbon and SiC were conducted several times for the SiC fiber preforms prior to the CVI (Fig. 6). Thin pyrocarbon coatings around SiC fibers effectively improve the mechanical properties of SiC/SiC composites.

Load-displacement curves of CVI SiC/SiC composites with various carbon interlayers between fibers and matrices are shown in Fig. 7. The composites do

Fig. 5 Cross section of SiC/SiC composite prepared by FCVI

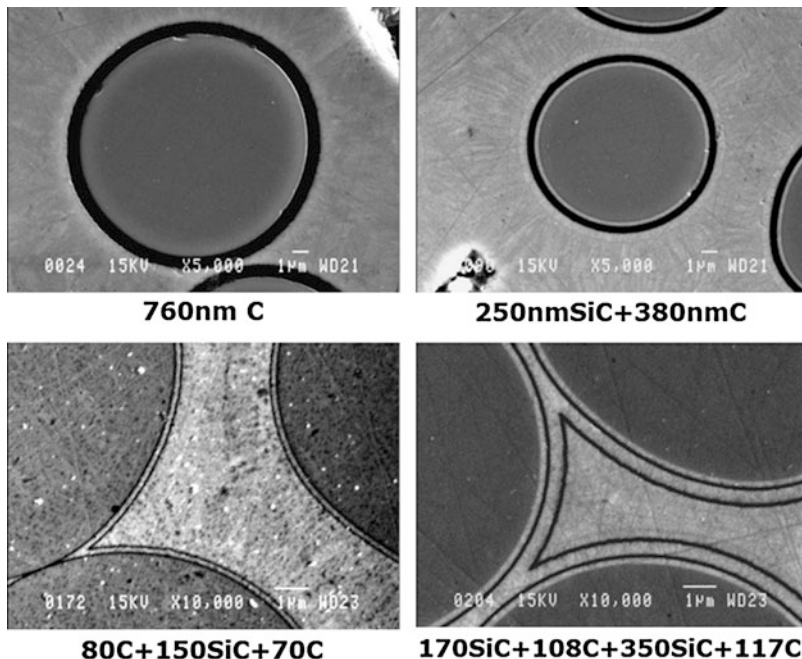
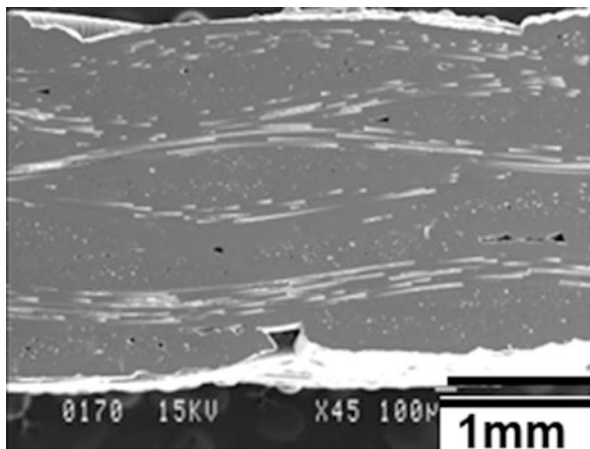


Fig. 6 Multiple coatings of SiC and carbon around SiC fibers of CVI SiC/SiC composites

not show catastrophic fractures. Pseudo-plastic deformation and high fracture strength are observed due to the fiber reinforcement effect.

Figure 8 shows the relation between bending strength and the thickness of the pyrocarbon interlayer. Both the highest strength and proportional limits, respectively, of 723 and 494 MPa were obtained at around 150 nm thickness of the

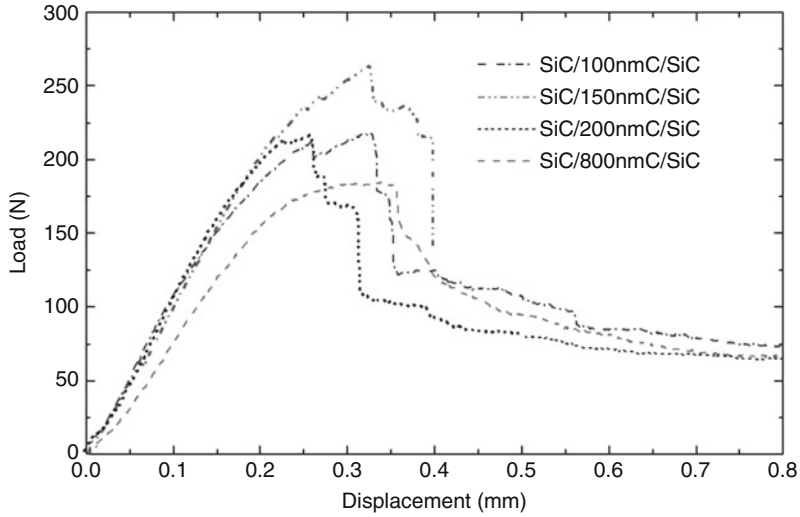


Fig. 7 Load-deflection curves of CVI SiC/SiC composites with different interfacial carbon thickness at room temperature

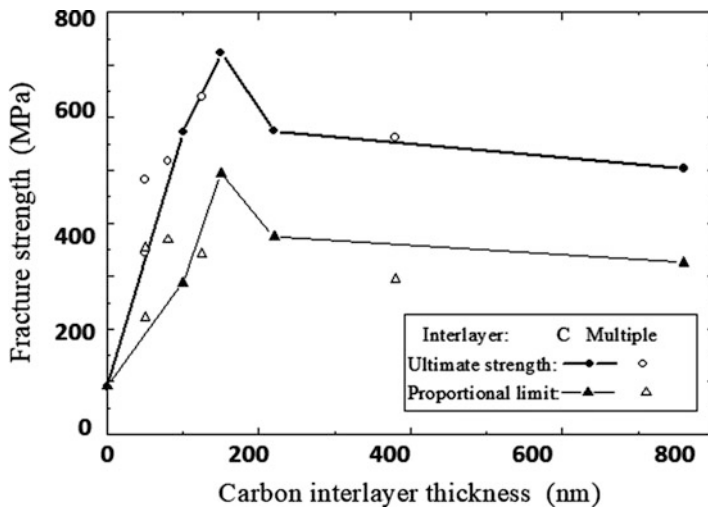


Fig. 8 Effect of carbon interlayer thickness around SiC fibers for CVI SiC/SiC composite on flexural strength

interlayer. The coating of SiC around the fibers also prevents delamination between the fibers and the matrix leading to increased ultimate strength [17].

In the CVI process, nanocrystalline SiC growth was found to further improve the mechanical properties of SiC/SiC composites [20]. SiC nanowires 20–100 nm in

diameter and 100 μm long were successfully grown on SiC fibers. The composite with SiC nanowires showed fracture toughness two times higher than that of the usual SiC/SiC [20].

PIP

The polymer impregnation and pyrolysis (PIP) method has advantages from the perspective of large-scale component fabrication with complicated shapes, microstructural control, and low fabrication cost. In PIP liquid polymer or slurry is impregnated with SiC powder during the preform, forming, and pyrolysis processes. For densification, the impregnation and pyrolysis are repeated [21]. However, it is difficult to achieve high density and fine, uniform fiber distribution due to volume shrinkage and the gas evolution of the polymer precursor during the ceramization process [21]. High density was achieved by adopting polyvinylsilane (PVS) in place of the polycarbosilane (PCS) which is generally used [21]. Low-viscosity liquid forms at ambient temperature, and the thermosetting property of the PVS reduces pores during the pyrolysis process under pressurization. By optimizing the curing temperature, heating rate, and pressure for consolidation, a high density of about 70% was reached [22]. The composite has a strength of 600 MPa and indicated the pullout of fibers in spite of the absence of precoating of the fibers. The other PIP process aiming at the composite with stoichiometric composition of SiC was developed by controlling the mixing ratio of polymethylsilane (PMS) to PCS. The near-stoichiometric composition of SiC was attained at the PMS/(PMS + PCS) weight ratio of 7:10. Furthermore, the high-temperature strength of the PIP was improved by introducing filler materials such as $\text{BaO}_2\text{-MgO-Al}_2\text{O}_3\text{-SiO}_2$ (BMAS) and ZrSiO_4 particles. The tensile strength of the PIP SiC/SiC with ZrSiO_4 filler was two times higher than the composite without the filler at 1400 °C [22]. PIP using microwaves is also being developed as a new technique to improve the polymer-to-ceramic conversion process and shorten the heating time [23].

RS

Reaction sintering (RS) is an effective process for densification [21]. In this process, the slurry of SiC and the graphite powder mixture are impregnated into the preforms under hydraulic pressure of around 6 MPa [21]. The samples formed were reaction sintered by infiltrating molten Si at 1400 °C in a vacuum. By controlling the raw material composition and size of the SiC and carbon powder, the residual silicon phase was minimized. In the case of monolithic RS-SiC, the thermal conductivity exceeded 160 W/m-K independently of the free silicon content [24]. For RS-Hi-Nicalon SiC fiber/SiC, the density and thermal conductivity reached 2.8 g/cm^3 and 49 W/m-K, respectively [21].

LPS

A liquid-phase sintering (LPS) process, called nano-powder infiltration and transient eutectoid (NITE) process, for SiC/SiC composites was developed at Kyoto University [25–27]. This method utilizes the liquid phase of mixed additives of Al₂O₃, Y₂O₃, and SiO₂ to densify the composite. SiC powder slurry with the additives is impregnated into the SiC fiber preform and dried to form prepreg sheets. The stacked prepreg sheets were hot-pressed at temperatures over 1800 °C [27]. In this process, Tyranno-SA fiber, the only SiC fiber with thermal stability above 1800 °C (see Fig. 2), was used. The open porosity was suppressed to 1% or less, and the density of the composite was 3.1 g/cm³ close to ideal value of crystalline SiC of 3.21 g/cm³ [27]. The ultimate tensile strength of around 400 MPa and thermal conductivity of 30 W/m-K were reported [28]. R&D of the NITE SiC/SiC toward industrialization is currently in progress [29].

Basic Properties of SiC/SiC Composites Formed by Several Processes

Table 2 summarizes several properties of SiC/SiC composites as obtained by CVI [18, 30, 31], PIP [21, 32, 33], RS [12, 21, 34], and LPS [27] methods. Properties of CVD SiC [35] are also shown as a reference. The matrix of all SiC and SiC/SiC composites is essentially β -type polycrystalline SiC. Mechanical properties of the composites were evaluated by bending, tensile, and fracture toughness tests. Fracture toughness was measured using single-edge notched beam (SENB) specimens. SiC crystal itself is brittle material. The composites showed strength and toughness almost one order higher than those of SiC crystal. As seen in the load-deflection curves of Fig. 7, catastrophic fracture is not observed for the composite. The pullout of fibers and interfacial de-bonding at the fiber/matrix depress the crack growth rate, leading to increased toughness.

Table 2 Properties of CVD SiC and SiC/SiC composites at room temperature

	CVD SiC [35]	FCVI [16–18, 30, 31]	PTP [21, 32, 33]	RS [12, 21, 34]	LPS [27]
Density (g/cm ³)	3.21	2.6–2.7	~2.5	~2.9	~3.1
Open porosity (%)	0	10–16	13–20	1.9–3.2	0.6–1.0
Flexural strength (MPa)	~470	280–600	270–600	710	~860
Young's modulus (GPa)	~460	140–160	~130	170–220	180–270
Tensile strength (MPa)	–	260–300	~360	400–560	300–400
Fracture toughness (MPa·m ^{1/2})	~2.6	~16	~10	~17	–
Thermal expansion coefficient (10 ^{–6} K ^{–1})	~2.7	~4	–	–	–
Thermal conductivity (W/m-K)	~300	~15	~15	~50	15–40

Among the composites, the LPS SiC/SiC composite showed the lowest porosity, with almost the ideal density of SiC. This composite also indicates flexural and tensile strength as well as thermal conductivity higher than those of composites prepared by CVI, PIP, and RS methods.

Irradiation Responses of SiC/SiC Composites

For the application of SiC/SiC composites to nuclear systems, the stability of various properties of materials against irradiation by neutrons and charged particles is required. In this section, irradiation responses of SiC fibers and SiC/SiC composites are viewed.

Effects of Neutron Irradiation on the Stability of SiC Fibers

The stability of SiC fiber-reinforced SiC composites under irradiation by neutron or charged particles depends on the structure of fibers and SiC crystals.

Silicon carbide fibers with stoichiometry and high crystallinity have been developed to improve mechanical properties (see Table 1).

Figure 9 shows changes in the density of several SiC fibers as a function of neutron fluence [36]. SiC fibers with a composition deviating from 1.0, the ideal value of Si/C, and with fine crystalline size shrink with neutron fluence. Density saturates at around 10^{26} n/m² roughly corresponding to 100 dpa. The shrinkage increases the elastic modulus from 200 to 250 GPa at 15 dpa [37]. In contrast, the density of SiC fibers close to the ideal crystalline SiC slightly decreases since

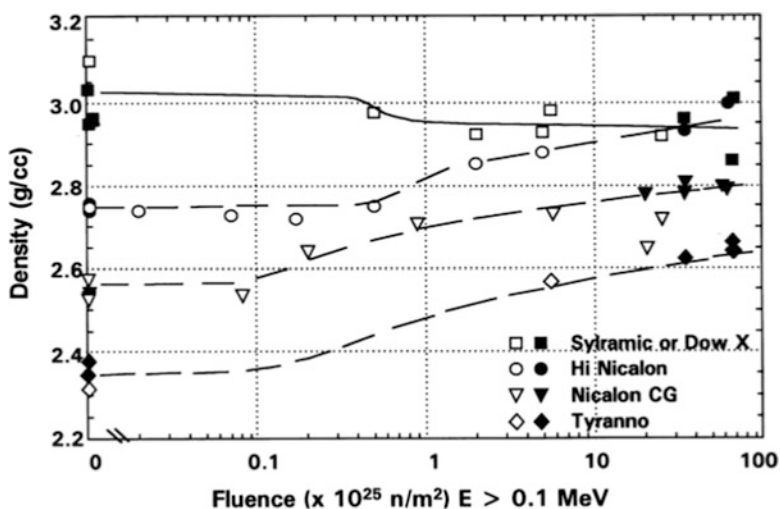


Fig. 9 Effect of neutron irradiation on the density of several SiC fibers [36]

amorphization occurs under neutron irradiation [36]. The threshold dose of amorphization is around 15 dpa at room temperature [37]. Another report [38] explains that irradiation-induced interstitials and vacancies agglomerate into dislocation at around 2×10^{26} n/m² and temperatures higher than 500 °C for β -SiC. The change in defect structure leads to a reduction in the size of the crystal.

Considering the dimensional stability under neutron irradiation, crystalline SiC fibers with a stoichiometric composition are the most suitable for SiC/SiC composites.

Irradiation Effect on SiC/SiC Composites

Physical and mechanical properties of SiC/SiC composites are affected by irradiation of neutron and charged particles.

Thermal Conductivity

The thermal conductivity of SiC/SiC composites tends to decrease with increasing temperature, as with CVD SiC crystals [39, 40]. In Fig. 10, the effects of neutron irradiation on the temperature ranging dependence of the thermal conductivity of SiC/SiC composites are shown [40]. The composites were exposed up to 25 dpa at temperatures ranging from 500 to 1200 °C in a reactor [40]. The thermal conductivity of the composite is reduced by neutron irradiation. However, it indicates an inverse relation to temperature and a slight increase with elevated temperature. Especially after irradiation at 500 and 800 °C, thermal conductivity

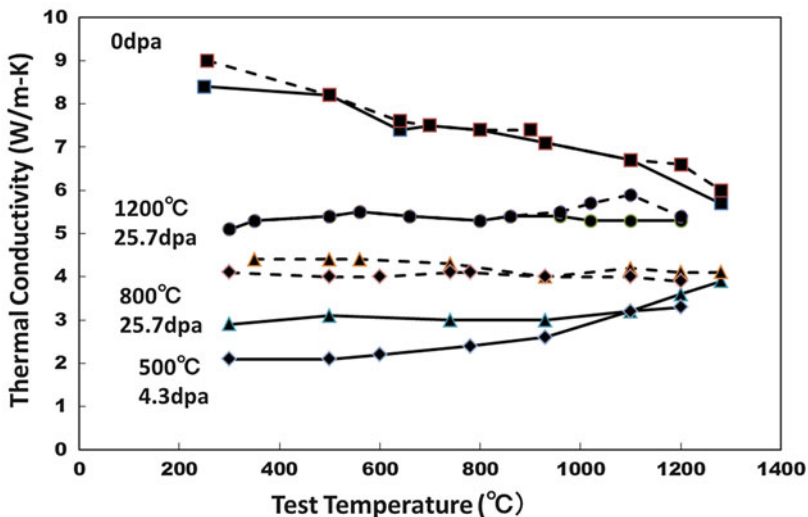


Fig. 10 Thermal conductivity as a function of measured temperature for CVI SiC/SiC composites after irradiated at 500, 800, and 1200 °C in EBR-II reactor. The dashed lines indicate the hysteresis after measuring at high temperatures [39]

increases during cooling from 1200 °C due to an annealing effect [39]. The inverse temperature dependence of thermal conductivity under the irradiation is explained as follows: [39, 40]. The thermal conductivity of ceramic materials such as SiC/SiC is based on phonon transport. The point defects and defect clusters produced by neutron irradiation effectively cause phonon scattering resulting in reduction of thermal conductivity. The mobility of point defects is low in the ceramic composite at low temperatures. However, the recombination of defects is accelerated at elevating temperature; as a result, the concentration of defects is decreased leading to the suppression of thermal conductivity reduction at high temperatures.

Swelling

The dimensional stability of SiC and SiC/SiC composites under neutron irradiation is evaluated as volumetric swelling. Many studies on the swelling of SiC and SiC/SiC composites under neutron and ion irradiation have been conducted. The swelling of SiC and SiC/SiC composites increases with neutron irradiation and tends to saturate at around 1 dpa [41]. In Fig. 11, the relationships between saturated swelling and irradiation temperature for monolithic SiC and SiC/SiC composites are shown. SiC/SiC composites behave by swelling similar to that of monolithic SiC. There seem to be three different radiation-induced swelling regions depending on the temperature [40]. Below 150 °C, the swelling caused by amorphization occurs and saturates at about 10% [40]. Between 150 and 900 °C, point defect swelling dominates [40]. The swelling decreases with increasing temperature due to the recovery of defects and reaches approximately 1% between 600 and 900 °C.

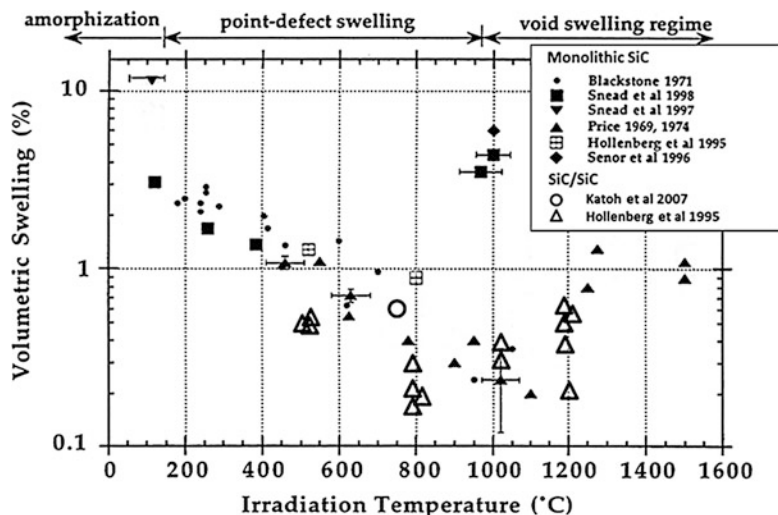


Fig. 11 Radiation-induced swelling of SiC and SiC/SiC composites as a function of irradiation temperature [39–43]

Above 1000 °C, radiation-induced defects aggregate and form voids [40]. The void formation then dominates swelling at temperature above 1000 °C. The void swelling for monolithic SiC is expected to increase with neutron fluence [42]. On SiC/SiC composites, void swelling is approximately 1% at temperatures up to 1600 °C, or 10 dpa lower than that of monolithic SiC [41]. The resistance of the composite against the swelling relates to the interphase structure between the SiC fiber and the SiC matrix [39, 43]. Densification or amorphization occurs under neutron irradiation of SiC fibers (Fig. 9). A multilayer of carbon, SiC, or BN interface as seen in Fig. 6 is considered to improve resistance against neutron damage [43].

Mechanical Properties

Bend, tensile, and indentation tests for SiC/SiC composites with various types of SiC fibers have been made to evaluate the mechanical properties of the composites. In Fig. 12, the flexural strength ratios after and before neutron irradiation are shown as a function of the neutron dose [44]. In earlier works using SiC fibers with nonstoichiometric compositions [39], the strength of the composites was reduced by about 50% by neutron irradiation of about 5 dpa. The decrease in strength saturated for further irradiation exposure up to 100 dpa [39]. As seen in Fig. 12, composites made with stoichiometric SiC fibers such as Hi-Nicalon Type-S and Tyranno-SA showed only a slight increase at initial neutron irradiation of around 1 dpa, and no further degradation in strength occurs at doses up to 25 dpa

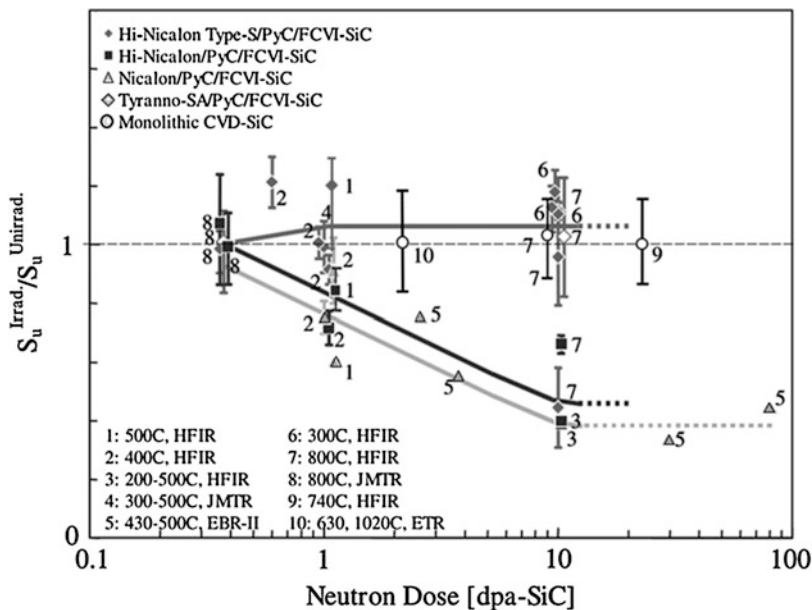


Fig. 12 Ratio of flexural strength for composite irradiated to that for unirradiated, $S_u^{Irrad.}/S_u^{Unirrad.}$, as a function of neutron dose [44]

[44]. Neither was the strength of monolithic CVD SiC affected by neutron irradiation at 25 dpa. The interface structure of pyrocarbon and SiC thin layers between SiC fibers and the SiC matrix is also considered to affect the strength of composites under neutron irradiation. The differential swelling between fibers and the matrix might compensate for the interlayer swelling behavior and retain its strength even at a high dose [37, 44].

The tensile properties for CVI SiC/SiC composites with Hi-Nicalon Type-S and Tyranno-SA fibers were reported by neutron irradiation [45–47]. Katoh et al. examined results of tensile tests for various CVI SiC/SiC composites with interphase structures of pyrocarbon and carbon/SiC multilayers of 5.9 dpa from 200 to 1270 °C [47]. The Young's modulus, ultimate tensile strength, and strain to failure were, respectively, in ranges of 200–280 GPa, 270–310 MPa, and 0.2–0.8% before and after neutron irradiation of 5.9 dpa up to 1270 °C [47]. No significant effect of irradiation on the tensile properties of CVI SiC/SiC composites was observed [47]. A single-fiber push-out test [48] and double-notched shear test [47] to evaluate the interlaminar shear strength between SiC fibers and the SiC matrix under neutron irradiation were conducted. Pyrocarbon interphase was observed to degrade at 0.7–7.7 dpa at temperatures from 380 to 1080 °C, resulting in decreasing interfacial shear strength [48]. However, the tensile properties of the SiC/SiC composites were not apparently changed by neutron irradiation [47–49].

The effects of neutron irradiation on the fracture toughness of polycrystalline β -SiC and CVD SiC using nano-indentation are reported [50, 51]. The fracture toughness changes with the neutron dose and reaches a plateau above 2 dpa [50].

Figure 13 shows the fracture toughness, K_{Ic} , obtained with indentation and plotted against the irradiation temperature for the neutron dose up to 7.7 dpa. Below 400 °C, toughness slightly decreases and increases again with temperatures of up to around 1000 °C independently of the neutron dose [51]. The increase in fracture toughness at high temperatures is explained by crack pinning and deflection [51]. In the case of SiC/SiC composites, similar temperature dependence on fracture toughness is expected [52]. The effect of interphase between SiC fibers and the matrix on the crack growth rate should also be considered under neutron irradiation [52].

Figure 14 shows irradiation creep behaviors of CVD SiC [53] and monofilament CVD SiC [54]. Irradiation creep for CVD SiC with crystalline size of 1–10 μm occurred with bend stress relaxation (BSR) after neutron irradiation of up to 7.7 dpa at temperatures from 780 to 1130 °C [53]. On the other hand, CVD SiC monofilament SCS-6TM [55] was used to examine irradiation creep using the torsion method [54]. A CVD SiC monofilament of 140 μm in diameter that consisted of a multilayer of carbon core and outer CVD SiC was tested using torsion under 12 MeV proton irradiation of up to 0.15 dpa at temperatures from 500 to 1000 °C. The CVD SiC filament with multilayer SiC coatings simulates a SiC/SiC composite [54]. As seen in Fig. 14, irradiation creep is observed due to the mobility of irradiation-induced point defects, such as interstitial atoms and vacancies, below 1000 °C [54]. The creep rate is proportional to the applied stress (Fig. 14) and is almost independent of temperature. Above 1000 °C, irradiation-induced creep decreases, and thermal creep becomes dominant [54].

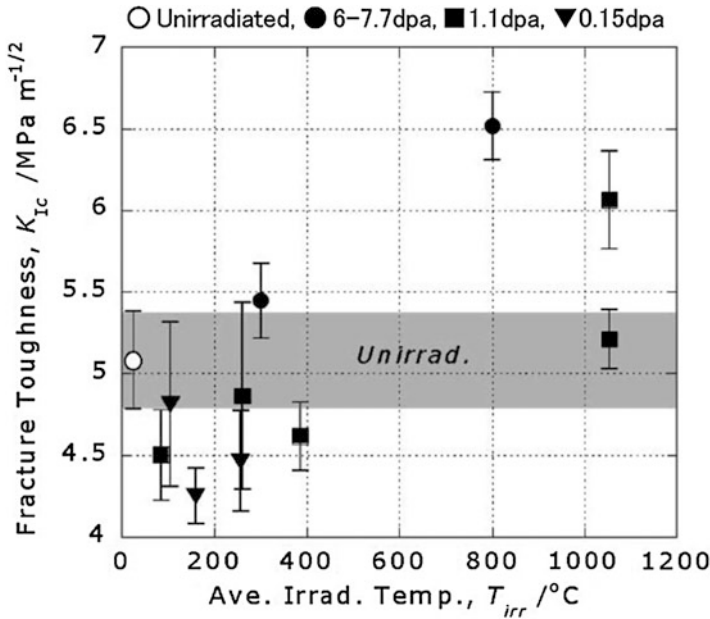


Fig. 13 Fracture toughness of β -SiC measured with indentation as a function of neutron irradiation temperature [51]

Application of SiC/SiC Composites to Fusion Reactors

SiC/SiC composites are attractive as structural materials in a fusion reactor system because of their favorable mechanical and low induced radioactivity properties under high-energy neutron irradiation. Over the past 30 years, research and development on SiC/SiC composites have been conducted in view of their applicability to nuclear fusion reactor materials. In this section, we describe several properties and features of SiC/SiC composites required for fusion reactor systems.

Design of Blanket Structures for Fusion Reactors

Due to their favorable mechanical properties at high temperatures and low activation characteristics, SiC/SiC composites are candidate structural materials for future fusion reactors. Several conceptual designs of tokamak fusion reactor utilizing a deuterium-tritium (D-T) fusion reaction have been proposed [56–60]. Table 3 presents blanket parameters and combinations of candidate materials. The blanket just behind the armor facing the D-T plasma consists of structural material, breeding material that converts lithium to tritium, a neutron multiplier, and coolant that removes heat to generate the electrical output of the reactor. The breeder and coolant for each design are selected in consideration of their compatibility with structural

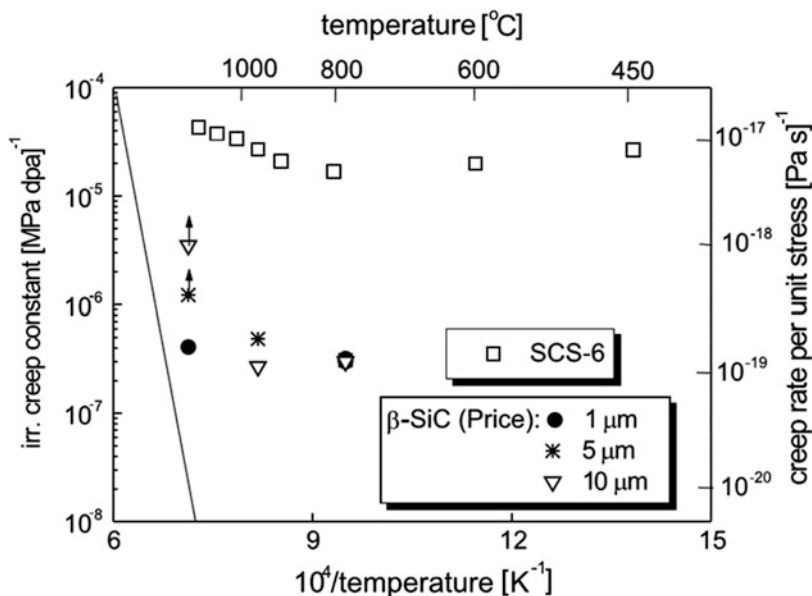


Fig. 14 Irradiation creep rates of monolithic SiC and SiC fiber as a function of temperature [53, 54]. Monolithic SiCs are β -SiC of crystalline size of 1, 5, and 10 μm , irradiated at 7.7 dpa. SCS-6 SiC fiber 140 μm in diameter consists of carbon core and outer β -SiC. The straight line indicates thermal creep rate of monolithic SiC

materials. Thus far, the SiC/SiC composite is proposed as a candidate structural material with ferritic steel and vanadium alloy. In the case of the SiC/SiC composite, the maximum inlet temperature of the coolant is assumed to be around 1000 $^{\circ}\text{C}$ due to its heat resistivity as compared to that of metal alloys. The structural materials are assumed to be replaced after reactor operation of 10–20 $\text{MW}\cdot\text{a}/\text{m}^2$ corresponding to 100–200 dpa irradiation [61].

A tokamak-type of international thermonuclear experimental reactor (ITER) [62] is now being constructed for the realization of a commercial reactor. Although the ITER's purpose is not to generate electricity, a program to install several test blanket modules (TBM) to verify tritium breeding and extract fusion energy through the coolant is progressing [63]. In the TBM designs, material compositions similar to those shown in Table 3 are examined [63].

Induced Radioactivation and Transmutation of SiC/SiC Composites

Low induced radioactivity of materials is one of the key issues in developing structural materials in fusion reactors from the standpoint of reactor maintenance, accident safety, waste disposal, and material recycling [64]. Induced radioactivation and nuclear transmutation on candidate structural materials have been simulated in various conceptual designs of fusion reactors [5, 13, 65].

Table 3 Blanket parameters on several concepts of tokamak-type fusion reactors

Reactor concept	SSTR [56]	ARIES-RS [57]	TAURO [58]	ARIES-AT [59]	A-SSTR2 [60]
Structural material	Fe-8Cr-2 W steel (F82H)	V-4Cr-4Ti	SiC/SiC	SiC/SiC	SiC/SiC
Breeder/multiplier	Li ₂ O/Be (solid)	Li (liq.)	Pb-17Li (liq.)	Pb-17Li (liq.)	Li ₂ TiO ₃ /Be (solid)
Coolant	Water	Li (liq.)	Pb-17Li (liq.)	Pb-17Li (liq.)	He (gas)
Coolant inlet/outlet temp. (°C)	285/325	330/610	800/957	654/1100	600/900
Wall loading (MW/m ²)	3	3.96	2.5	3.2	6.0

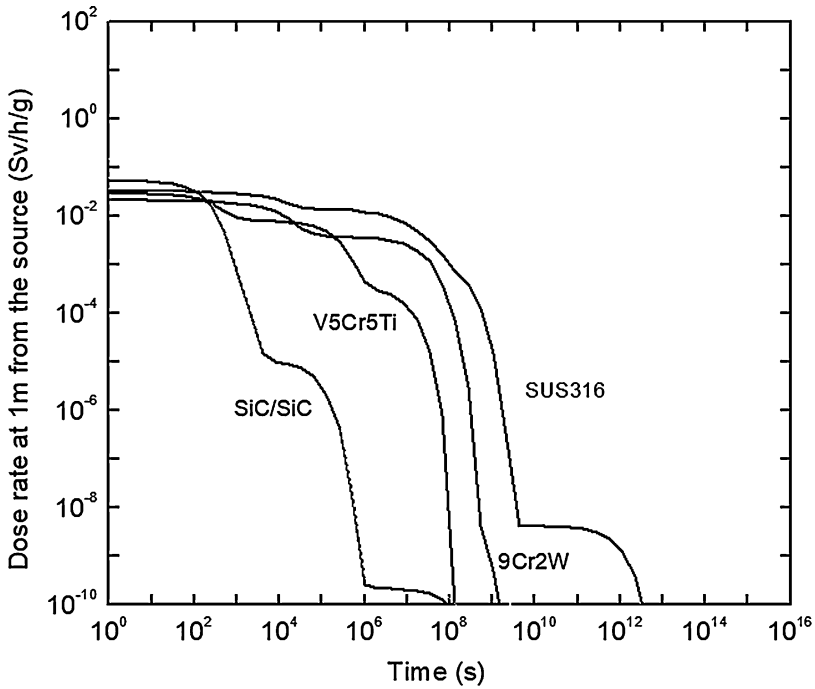
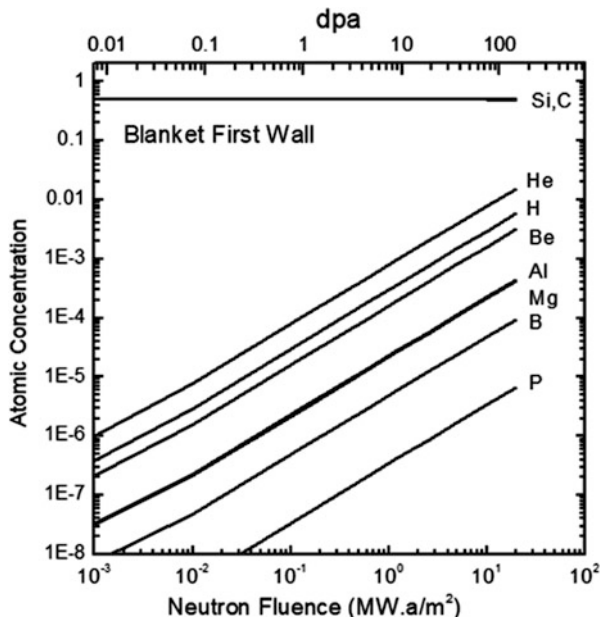
**Fig. 15** γ -Ray dose rate of several candidate blanket structural materials as a function of cooling time after irradiation for 10 MW·a/m²

Figure 15 shows decay behaviors of γ -ray dose rates of several candidate blanket structural materials after irradiation at 10 MW·a/m². The calculation was based on several blanket models [66] similar to those in Table 3. The SiC/SiC composite indicates the very fast decay of the dose rate as compared to other candidate alloys.

Fig. 16 Concentration change of elements in SiC/SiC by transmutation as a function of neutron fluence



The fast decay of γ -ray intensity makes it easier to access to SiC/SiC composites a short time after reactor operation.

Helium and Hydrogen Production

Neutron irradiation produces gaseous species by nuclear transmutation and causes displacement damage of materials. In Fig. 16, the formation of elements from a pure SiC/SiC composite at the position of the blanket first wall is shown as a function of neutron fluence. Among the elements produced, helium and hydrogen gases are accumulated in the composite. The production rates of helium and hydrogen are around 150 and 80 appm/dpa, respectively. In other calculations, 80–170 appm/dpa for helium and 30–70 appm/dpa for hydrogen in various blanket designs are reported [41]. Helium gas of 1000 appm slightly increases swelling but hardly increases the bend strength of SiC under neutron irradiation of 14 dpa at 800 °C [67]. Trace swelling of 0.3% was observed at 1000 °C and 100 dpa under conditions of 60 appm/dpa irradiation for SiC/SiC [68]. The helium diffusion rate becomes remarkable at temperatures higher than 1000 °C [67]. Helium gas production is then concerned with enhancing the swelling of SiC/SiC composites above 1000 °C [52]. The solubility of atomic hydrogen in SiC is negligibly low at around 1000 °C [69]. Hydrogen is also considered to enhance void formation in SiC [52].

Chemical Compatibility

In fusion reactor designs, SiC/SiC composite structural materials are assumed to contact coolant and breeder materials such as liquid Pb-Li, lithium oxide, and He gas at 600–1000 °C (Table 3). The compatibilities of SiC/SiC composites with liquid Pb-17Li and lithium were experimentally and thermodynamically studied [70–72]. SiC is thermodynamically stable at 800 °C in liquid Pb-17Li [70, 72]. No reaction was observed for SiC and SiC/SiC composites in Pb-17Li at temperatures up to 800 °C [70, 71]. The reactivity of SiC with eutectic Pb-Li depends on the concentration of Li [72]. In pure liquid lithium, both SiC and SiC/SiC composites were attacked to form lithium silicide or lithium carbide [70–72].

In a helium gas coolant system, LiAlO₂, Li₂ZrO₃, and Li₄SiO₄ are considered to be solid breeder materials [70, 73, 74]. The results of compatibility tests with SiC and SiC/SiC composites showed that LiAlO₂ and Li₂ZrO₃ are almost stable for 1000 h at 600 and 800 °C, while considerable reaction forming Li₂SiO₃ was observed for Li₄SiO₄ [73, 74]. The relative reactivity with the SiC/SiC composite is reported as Li₄SiO₄ > Li₂ZrO₃ > LiAlO₂ [73]. If silicon oxide is contained in the SiC/SiC composite, Li₂SiO₃ formation reaction should be considered for all of the above solid breeder materials [73].

Helium gas is essentially inert to all materials. However, oxygen or water included in helium gas results in the oxidation of SiC/SiC composites [75, 76]. According to the thermodynamic estimation, SiC will be stable under oxygen pressure of less than 10⁻³ Pa at 900 °C [75]. We should also pay attention to the oxidation of the carbon layer at the interface between SiC fibers and the SiC matrix for the composite [76]. It is reported that oxygen of 100 ppm leads to the weight loss of SiC/SiC composites at 1100 °C due to the formation of carbon oxide [76].

It is necessary to reduce oxygen concentration as low as possible in the helium gas coolant blanket system to avoid the oxidation of SiC/SiC composites and the degradation of solid breeder materials.

Manufacturing and Joining

SiC/SiC composites have already been practically applied in aircraft and aerospace industries, including for use in engines, propulsion components, and heat shields [1, 14, 15, 72]. Studies on manufacturing technology for large-scale SiC/SiC composites for blanket modules of fusion reactors are progressing [76, 77].

In applying SiC/SiC composites to fusion reactor structures, the joining technology is an important issue. For joining between SiC composites, diffusion bonding using a titanium interlayer [76], solid-state displacement reaction joining using Si and TiC [78] or Si-Ti alloy [79], preceramic precursor polymer joining [80], liquid-phase sintering using SiC powder and alumina-yttria additives [81], glass-ceramics joining using CaO-Al₂O₃ [82], etc. have been developed. Bolts and screws for mechanical joining have also been made [76]. The effects of neutron irradiation on

the mechanical strength of these joints have been examined at fluences up to 5 dpa at 500 and 800 °C [83]. The strength of joints prepared with all of the methods above was retained with irradiation [83].

Hermeticity

Tightness against the leakage of helium gas is an important issue for SiC/SiC composites in advanced steady-state tokamak reactor (A-SSTR) blanket structure design [60], where high-pressure helium gas of 10 MPa is assumed as a coolant [44]. The permeation rates of helium for various SiC/SiC composites were measured at 700–1100 °C [84]. The helium gas permeability of the NITE SiC/SiC composite with a dense SiC matrix was in the range of 10^{-13} – 10^{-7} m²/s, while that of the PIP SiC composite with porosity higher than 13% (see Table 2) was relatively low at 10^{-6} – 10^{-4} m²/s [84]. Although an advanced SiC/SiC composite such as NITE has excellent hermetic properties under non-irradiation conditions as seen in Fig. 17, seal coatings on the composite will be necessary, considering the leakage accidentally occurring during the coolant operation [76, 79].

In the designs of ITER and DEMO fusion reactors, tungsten and tungsten alloys are candidate plasma-facing armor and divertor materials [85, 86]. Since blanket structural material on the armor side is exposed to severe high energy neutron irradiation and high heat flux, coatings or platings of tungsten on SiC/SiC composites are considered to be necessary, as well as a gas leak barrier [84]. Tungsten plates were successfully bonded to SiC/SiC composites with diffusion bonding at 1600 °C [87].

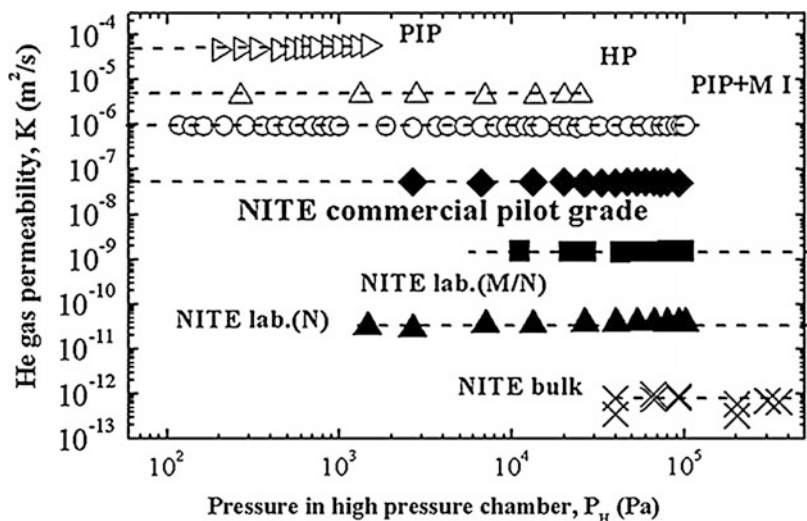


Fig. 17 Helium gas permeability as a function of pressure for various SiC/SiC composites [84]

Summary and Conclusions

In the last 20 years, SiC/SiC composites have been remarkably developed toward their application in structural materials of advanced reactor systems such as fusion reactors. A lot of basic data on processing, fabrication, and the physical, chemical, and mechanical properties of SiC/SiC composites, including properties under neutron irradiation, have been obtained. The research results indicate that SiC/SiC composites have excellent potential as structural materials tolerant to severe high-temperature and irradiation environments. It is necessary to further accumulate material property data on SiC/SiC composites especially under neutron irradiation so that SiC/SiC composites can be used reliably for structural design for advanced nuclear systems.

References

1. Ogasawara T (2004) Recent research activities regarding SiC-based ceramic composites for aerospace applications. *J Plasma Fusion Res* 80:36–41
2. Mizuta N, Ueta S, Aihara J, Shibata T (2017) Confirmation of feasibility of fabrication technology and characterization of high-packing fraction fuel compact for HTGR, JAEA-Technol. 2017-004
3. Price RJ (1973) Neutron irradiation-induced voids in β -silicon carbide. *J Nucl Mater* 48:47–57
4. Yajima S, Hayashi J, Omori M, Okamura K (1976) Development of a silicon carbide fibre with high tensile strength. *Nature* 261:683–685
5. Hopkins G, Cheng ET (1983) Low activation fusion rationale. *Nucl Technol* 4:528–544
6. Deck CP, Jacobsen GM, Sheeder J, Gutierrez O, Zhang J, Stone J, Khalifa HE, Back CA (2015) Characterization of SiC-SiC composites for accident tolerant fuel cladding. *J Nucl Mater* 466:667–681
7. Takeda M, Sakamoto J, Imai Y, Ichikawa H (1999) Thermal stability of the low-oxygen-content silicon carbide fiber, Hi-NicalonTM. *Compos Sci Technol* 59:813–819
8. Ichikawa H, Takeda M, Seguchi T, Okamura K (2000) Development of super heat-resistant silicon carbide fiber. *Materia Japan* 39:190–192
9. Takeda M, Sakamoto J, Saeki A, Ichikawa H (2008) High performance silicon carbide fiber Hi-Nicalon for ceramic matrix composites. *Ceram Eng Sci Proc* 16:37–44
10. Lipowitz J, Rabe JA, Zangvil A, Xu Y (1997) Structure and properties of SylramicTM silicon carbide fiber – a polycrystalline, stoichiometric β – SiC composition. *Ceram Eng Sci Proc* 18:147–157
11. Morishita K, Ochiai S, Okuda H, Ishikawa T, Sato M, Inoue T (2006) Fracture toughness of a crystalline silicon carbide fiber (Tyranno-SA3[®]). *J Am Ceram Soc* 89:2571–2576
12. Ishikawa T, Kaji S, Matsunaga K, Hogami T, Kohtoku Y (1995) Structure and properties of Si-Ti-C-O fibre-bonded ceramic material. *J Mater Sci* 30:6218–6222
13. Noda T, Araki H, Suzuki H (1994) Processing of high-purity SiC composites by chemical vapor infiltration (CVI). *J Nucl Mater* 212-215:823–829
14. Naslain R, Langlais F (1986) CVD-processing of ceramic composite materials. In: Tressler RE et al (eds) Tailoring multiphase and composite ceramics, Materials science research, vol 20. Plenum Press, New York, pp 145–164
15. Besmann TM, Sheldon BW, Lowden RA, Stinton DP (1991) Vapor-phase fabrication and properties of continuous-filament ceramic composites. *Science* 253:1104–1109
16. Noda T, Kohyama A, Katoh Y (2001) Recent progress of SiC-fibers and SiC/SiC-composites for fusion applications. *Phys Scr T91*:124–129

17. Yang W, Kohyama A, Katoh Y, Araki H, Yu J, Noda T (2003) Effect of carbon and silicon carbide/carbide interlayers on the mechanical behavior of Tyranno-SA-fiber-reinforced silicon carbide-matrix composites. *J Am Ceram Soc* 86:851–856
18. Yang W, Noda T, Araki H, Yu J, Kohyama A (2003) Mechanical properties of several advanced Tyranno-SA fiber reinforced CVI-SiC matrix composites. *Mater Sci Eng A345*:28–35
19. Yang W, Araki H, Kohyama A, Busabok C, Hu Q, Suzuki H, Noda T (2003) Flexural strength of plain-woven Tyranno-SA fiber-reinforced SiC matrix composite. *Mater Trans* 44:1797–1801
20. Yang W, Araki H, Tang C, Thaveethavorn S, Kohyama A, Suzuki H, Noda T (2005) Single-crystal SiC nanowires with a thin carbon coating for stronger and tougher ceramic composites. *Adv Mater* 17:1519–1523
21. Suyama S, Kameda T, Itoh Y (2001) Evaluation of microstructure, mechanical and thermal properties of SiC/SiC composites. *J Ceram Soc Japan* 109:619–626
22. Kotani M, Kohyama A, Okamura K, Inoue T (1999) Fabrication of high performance SiC/SiC composite by polymer impregnation and pyrolysis method. *Ceram Eng Sci Proc* 20:309–316
23. Dong SM, Katoh Y, Kohyama A, Schwab ST, Snead LL (2002) Microstructural evolution and mechanical performances of SiC/SiC composites by polymer impregnation/microwave pyrolysis (PIMP) process. *Ceram Int* 28:899–905
24. Lee SP, Katoh Y, Hinoki T, Kotani M, Kohyama A, Suyama S, Itoh Y (2000) Microstructure and bending properties of SiC/SiC composites fabricated by reaction sintering process. *Ceram Eng Sci Proc* 21:339–346
25. Kohyama A, Kishimoto H (2013) SiC/SiC composite materials for nuclear applications. *Nucl Saf Simul* 4:72–79
26. Dong S, Katoh Y, Kohyama A (2003) Preparation of SiC/SiC composites by hot pressing, using Tyranno-SA fiber as reinforcement. *J Am Ceram Soc* 86:26–32
27. Shimoda K, Kohyama A, Hinoki T (2009) High mechanical performance SiC/SiC composites by NITE process with tailoring of appropriate fabrication temperature to fiber fraction. *Compos Sci Technol* 69:1623–1628
28. Katoh Y (2004) Status and properties of SiC-based ceramic composites for fusion and advanced fission applications. *J Plasma Fusion Res* 80:18–23
29. Kohyama A (2012) Industrialization of advanced SiC/SiC composites for environment and energy. *Materia Japan* 51:383–385
30. Yang W, Araki H, Kohyama A, Yu J, Noda T (2002) New Tyranno-Sa fiber reinforced CVI-SiC/SiC compolsite. *J Mater Sci Lett* 21:1411–1413
31. Yang W, Araki H, Thaveethavorn S, Kohyama A, Yu J, Suzuki H, Noda T (2005) Advanced CVI-SiC/SiC composite with in-situ growth of SiC nanowires in the matrix as additional reinforcement. *Mat Sci Forum* 175-479:1009–1012
32. Kotani M, Inoue T, Kohyama A, Katoh Y, Okamura K (2003) Effect of SiC particle dispersion on microstructure and mechanical properties of polymer-derived SiC/SiC composite. *Mater Sci Eng A357*:376–385
33. Kotani M, Ximmer A, Matsuzaki S, Nishiyabu K, Tanaka S (2014) Improvement in matrix microstructure of SiC/SiC composites by incorporation of pore-forming powder. *J Ceram Soc Jpn* 122:863–869
34. Kameda T, Suyama S, Itoh Y, Nishida K (1999) Development of reaction sintered silicon carbide matrix composite and tensile strength properties. *J Ceram Soc Jpn* 107:622–626
35. Graves GA, Iden D (1994) CVD silicon carbide characterization, *RL-TR-94-122*
36. Youngblood GE, Jones RH, Kohyama A, Snead LL (1998) Radiation response of SiC-based fibers. *J Nucl Mater* 258-263:1551–1556
37. Snead LL, ZinkIe SJ, Steiner D (1992) Radiation induced microstructure and mechanical property evolution of SiC/C/SiC composite materials. *J Nucl Mater* 191-194:560–565
38. Yano T, Miyazaki H, Akiyoshi M, Iseki T (1998) X-ray diffractometry and high-resolution electron microscopy of neutron-irradiated SiC to a fluence of 1.9×10^{27} n/m². *J Nucl Mater* 253:78–86
39. Hollenberg GW, Henager CH Jr, Youngblood GE, Trimble DJ, Simonson SA, Newsome GA, Lewis E (1995) The effect of irradiation on the stability and properties of monolithic silicon carbide and SiCf/SiC composites up to 25 dpa. *J Nucl Mater* 219:70–86

40. Zinkle SJ, Snead LL (1998) Thermophysical and mechanical properties of SiC/SiC composites, DOE/ER-0313/24, 93–100
41. Katoh Y, Snead LL, Henager CH Jr, Hasegawa A, Kohyama A, Riccardi B, Hegeman H (2007) Current status and critical issues for development of SiC composites for fusion applications. *J Nucl Mater* 367-370:659–671
42. Price RJ (1973) Neutron irradiation-induced voids in β -silicon carbide. *J Nucl Mater* 48:47–57
43. Snead LL, Osbone MC, Lowden RA, Strizak J, Shinavski RJ, More KL, Eatherly WS, Bailey J, Williams AM (1998) Low dose irradiation performance of SiC interphase SiC/SiC composites. *J Nucl Mater* 253:20–30
44. Jones RH, Giancarli L, Hasegawa A, Katoh Y, Kohyama A, Riccardi B, Snead LL, Weber WJ (2002) Promise and challenges of SiCf/SiC composites for fusion energy applications. *J Nucl Mater* 307-311:1057–1072
45. Ozawa K, Nozawa T, Katoh Y, Hinoki T, Kohyama A (2007) Mechanical properties of advanced SiC/SiC composites after neutron irradiation. *J Nucl Mater* 367-370:713–718
46. Katoh Y, Snead LL, Nozawa T, Kondo S, Busby J (2010) Thermophysical and mechanical properties of near-stoichiometric fiber CVI SiC/SiC composites after neutron irradiation at elevated temperatures. *J Nucl Mater* 403:48–61
47. Katoh Y, Ozawa K, Shih C, Nozawa T, Shinavski RJ, Hasegawa A, Snead LL (2014) Continuous SiC fiber, CVI SiC matrix composites for nuclear applications: properties and irradiation effects. *J Nucl Mater* 448:448–476
48. Nozawa T, Katoh Y, Snead LL (2009) The effect of neutron irradiation on the fiber/matrix interphase of silicon carbide composites. *J Nucl Mater* 384:195–211
49. Nozawa T, Hinoki T, Katoh Y, Kohyama A (2002) Effects of fibers and fabrication processes on mechanical properties of neutron irradiated SiC/SiC composites. *J Nucl Mater* 307-311:1173–1177
50. Hay JC, Snead LL (1999) Mechanical – and physical property changes of neutron-irradiated chemical-vapor-deposited silicon carbide. *J Am Ceram Soc* 82:2490–2496
51. Nogami S, Hasegawa A, Snead LL (2002) Indentation fracture toughness of neutron irradiated silicon carbide. *J Nucl Mater* 207-211:1163–1167
52. Hasegawa A (2004) Neutron irradiation effects in SiC and SiC/SiC composites. *J Plasma Fusion Res* 80:24–30
53. Price RJ (1977) Properties of silicon carbide for nuclear fuel particle coatings. *Nucl Technol* 35:320–336
54. Scholz R, Mueller R, Lesueur D (2002) Light ion irradiation creep of Textron SCS-6™ silicon carbide fibers. *J Nucl Mater* 307-311:1183–1186
55. Specialty Materials, INC., SCS silicon carbide fiber, <http://www.specmaterials.com/siliconcarbidefiber.htm>
56. Seki Y, Kikuchi M, Ando T, Ohara Y, Nishio S, Seki M, Takizuka T, Tani K, Ozeki T, Koizumi K, Matsuda Y, Azumi M, Oikawa A, Madarame H, Mizoguchi T, Iida F, Ozawa Y, Mori S, Yamazaki S, Kobayashi T, Hirata S, Adachi J, Ikeda B, Suzuki Y, Ueda N, Kageyama T, Yamada M, Asahara M, Konishi K, Yokogawa N, Shinya K, Ozaki A, Takase H, Kobayashi S (1990) The steady state Tokamak reactor. In: Proceedings of 13th international conference on plasma physics and controlled fusion research, vol 3. IAEA, pp 473–485
57. Giancarli L, Ferrari M, Fuetterer MA, Malang S (2000) Candidate blanket concepts for a European fusion power plant study. *Fusion Eng Des* 49-50:445–456
58. Giancarli L, Golfier H, Nishio S, Raffray R, Wong C, Yamada R (2002) Progress in blanket designs using SiCf/SiC composites. *Fusion Eng Des* 61-62:307–318
59. Abdou A, Bromberg L, Brown T, Chan VC, Chu MC, Dahigren F, El-Guebaly L, Heitzroeder P, Hendron D, St. John HE, Kessel CE, Lao LL, Longhurst GR, Malang S, Mau TK, Merrill BJ, Miller RL, Mogahed E, Moore RL, Petrie T, Petti DA, Polizer P, Raffray AR, Steiner D, Sviatoslavsky I, Synder P, Syaebler GM, Turnbull AD, Tillack MS, Wagner LM, Wang X, West P, Wilson P (2006) The ARIES-AT advanced tokamak, advanced technology fusion power plant. *Fusion Eng Des* 80:3–23

60. Nishio S, Tobita K, Ushigusa K, Konishi S, Reactor Design Team (2002) Conceptual design of Tokamak high power reactor (A-SSTR2). *J Plasma Fusion Res* 78:1218–1230
61. Raffray AR, Akiba M, Chuyanov V, Giancarli L, Malang S (2002) Breeding blanket concepts for fusion and materials requirements. *J Nucl Mater* 307-311:21–30
62. ITER – the way to new energy <https://www.iter.org/>
63. Konishi T, Enoeda M (2014) The current status of the world ITER test blanket module program. *J Plasma Res* 90:332–337
64. Conn RW, Holdren JP, Sharafat S, Steiner D, Ebst DA, Hogan WJ, Krakowski RA, Miller RL, Najmabadi F, Schultz KR (1990) Economic, safety and environmental prospects of fusion reactors. *Nucl Fusion* 30:1919–1934
65. Seki Y, Tabara T, Aoki I, Ueda S, Nishio S, Kurihara R (1998) Impact of low activation materials on fusion reactor design. *J Nucl Mater* 258-263:1791–1797
66. Noda T, Fujita M (1996) Effect of neutron spectra on the transmutation of first wall materials. *J Nucl Mater* 233-237:1491–1495
67. Snead LL, Scholz R, Hasegawa A, Frias Rebelo A (2002) Experimental simulation of the effect of transmuted helium on the mechanical properties of silicon carbide. *J Nucl Mater* 307-311:1141–1145
68. Kishimoto H, Katoh Y, Kohyama A (2002) Microstructural stability of SiC and SiC/SiC composites under high temperature irradiation environment. *J Nucl Mater* 307-311:1130–1134
69. Causey RA, Wampier WR, Retelle JR, Kaae JL (1993) Tritium migration in vapor-deposited β -silicon carbide. *J Nucl Mater* 203:196–205
70. Fenichi P, Scholz HW (1994) Advanced low-activation materials. Fibre-reinforced ceramic composites. *J Nucl Mater* 212-215:60–68
71. Yoneoka T, Tanaka S, Terai T (2001) Compatibility of SiC/SiC composite materials with molten lithium metal and Li16-Pb84 eutectic alloy. *Mater Trans, JIM* 42:1019–1023
72. Hubberstey P, Sample T (1997) Thermodynamics of the interactions between liquid breeders and ceramic coating materials. *J Nucl Mater* 248:140–146
73. Sample T, Fenici P, Kolbe H, Orecchia L (1994) The compatibility of SiC/SiC composites with ceramic breeder materials. *J Nucl Mater* 212-215:1529–1533
74. Hinoki T, Katoh Y, Snead LL, Jung HC, Ozawa K, Katsui H, Zhong ZH, Kondo S, Park YH, Shih C, Parish CM, Meiner RA, Hasegawa A (2013) Silicon carbide and silicon carbide composites for fusion reactor application. *Mater Trans* 54:472–476
75. Naslain R (2004) Design, preparation and properties of non-oxide CMCs for application in engines and nuclear reactors: an overview. *Compos Sci Technol* 64:155–170
76. Katoh Y, Snead LL, Henager CH Jr, Nozawa T, Hinoki T, Ivekovic A, Novak S, Gonzalez de Vicente SM (2014) Current status and recent research achievements in SiC/SiC composites. *J Nucl Mater* 455:387–397
77. Park JS, Kohyama A, Hinoki T, Shimoda K, Park YH (2007) Efforts on large scale production of NITE-SiC/SiC composites. *J Nucl Mater* 367-370:719–724
78. Henager CH Jr, Kurtz RJ (2011) Low-activation joining of SiC/SiC composites for fusion applications. *J Nucl Mater* 417:375–378
79. Riccardi B, Giancarli L, Hasegawa A, Katoh Y, Kohyama A, Jones RH, Snead LL (2004) Issues and advances in SiC/SiC composites development for fusion reactors. *J Nucl Mater* 329-333:56–65
80. Lewinsohn CA, Singh M, Shibayama T, Hinoki T, Ando M, Katoh Y, Kohyama A (2000) Joining of silicon carbide composites for fusion energy applications. *J Nucl Mater* 283-287:1258–1261
81. Hinoki T, Eiza N, Son SJ, Shimoda K, Lee JK, Kohyama A (2005) Development of joining and coating technique for SiC and SiC/SiC composites utilizing NITE processing. Mechanical properties and performance of engineering ceramics and composites. *Ceram Eng Sci Proc* 26:399–405
82. Ferraris M, Salvo M, Casalegno V, Han S, Katoh Y, Jung HC, Hinoki T, Kohyama A (2011) Joining of SiC-based materials for nuclear energy applications. *J Nucl Mater* 417:379–382

83. Katoh Y, Snead LL, Cheng T, Shih C, Lewis WD, Koyanagi T, Hinoki T, Henager CH Jr, Ferraris M (2014) Radiation-tolerant joining technologies for silicon carbide ceramics and composites. *J Nucl Mater* 448:497–511
84. Hino T, Hayashita E, Kohyama A, Yamauchi Y, Hirohata Y (2007) Helium gas permeability of SiC/SiC composite after heat cycles. *J Nucl Mater* 367-370:736–741
85. Bolt H, Barabash V, Federici G, Linke J, Loarte A, Roth J, Sato K (2002) Plasma facing and high heat flux materials – needs for ITER and beyond. *J Nucl Mater* 307-311:43–52
86. Hasegawa A, Fukuda M, Tanno T, Nogami S (2013) Neutron irradiation behavior of tungsten. *Mater Trans* 54:466–471
87. Kishimoto H, Shibayama T, Shimoda K, Kobayashi T, Kohyama A (2011) Microstructural and mechanical characterization of W/SiC bonding for structural material in fusion. *J Nucl Mater* 417:387–390



Advanced Ceramic Fuels for Sodium-Cooled Fast Reactors **18**

Baldev Raj, P. R. Vasudeva Rao, P. Puthiyavinayagam, and K. Ananthasivan

Contents

Introduction	668
Types of Nuclear Fuels Employed	669
Advanced Fuels	671
Carbide Fuels	671
Phase Diagrams and Physical Properties	671
Carbide Fuel Fabrication	678
Nitride Fuels	681
Phase Diagrams and Physical Properties	681
Fabrication of the Nitride Fuel	683
Irradiation Behavior of Carbide and Nitride Fuels	684
Carbide Fuels	684
Irradiation Behavior of Nitride Fuels	693
Reprocessing of Carbide and Nitride Fuels	697
Conclusion	700
References	700

Baldev Raj: deceased.

B. Raj

National Institute of Advanced Studies (NIAS), Bengaluru, India
e-mail: baldev_dr@nias.iisc.ernet.in; baldev.dr@gmail.com

P. R. Vasudeva Rao (✉)

Homi Bhabha National Institute (HBNI), Mumbai, India
e-mail: prvasudeva.rao@gmail.com

P. Puthiyavinayagam · K. Ananthasivan

Indira Gandhi Centre for Atomic Research [IGCAR], Kalpakkam, India
e-mail: vinayaga@igcar.gov.in; asivan@igcar.gov.in

© Springer Nature Switzerland AG 2020

Y. R. Mahajan, R. Johnson (eds.), *Handbook of Advanced Ceramics and Composites*,
https://doi.org/10.1007/978-3-030-16347-1_21

667

Abstract

Fast-neutron reactors constitute clean energy systems that could provide sustainable nuclear energy for several centuries through efficient utilization of the uranium as well as thorium resources. Ceramic fuels are the current choice for fast reactors. Oxides of uranium and plutonium have been irradiated to levels of burn-up (a measure of energy production per unit mass of fuel) as high as 200,000 MWd/t, and internationally, there has been substantial experience on the fuel cycle of oxides, from fabrication to reprocessing. The irradiation behavior of oxide fuels has been studied extensively and has been well understood. Carbides and nitrides and metallic alloys of uranium and plutonium have been much less studied with respect to power production. However, they possess several advantages such as high thermal conductivity, high metal atom density, and a higher breeding potential, which make them the potential choices for the future fast reactors. At the same time, each fuel form has its challenges and technical issues to be dealt with.

This chapter presents an overview on the advanced ceramic fuels and particularly carbide and nitride fuels for FBRs. Advantages, challenges, and issues of each type of fuel are dealt with relevant details. Basic properties of advanced fuels including the phase diagrams and their behavior under irradiation are highlighted. Further, their irradiation behavior in general and swelling and fission gas release in particular in the context of fuel element design have been brought out. On the fuel cycle aspects, details of different fabrication routes, challenges in each of them, and reprocessing technologies are brought out. Also, a brief section on the international experience is included.

Keywords

SFR · Nuclear fuels · (U-Pu) carbides · (U-Pu) nitrides · Fuel properties · Irradiation behavior · Fuel reprocessing

Introduction

Fast-neutron reactors constitute clean energy systems that could provide sustainable nuclear energy for several centuries through efficient utilization of the uranium as well as thorium resources. As compared to thermal neutron reactors, fast reactors have several advantages. Fast reactor fuels reach much higher levels of burn-up (energy produced per unit mass of fuel) (higher than 100,000 MWd/t) than that reached in thermal reactors, which range from around 7000 MWd/t to around 75,000 MWd/t. Pressurized heavy water reactors (the most common type deployed in India and Canada) reach only around 7000 MWd/t. The high burn-up reached in fast reactors implies high utilization of fuel, less fuel fabrication, and reprocessing capacities per unit energy production. The high temperatures of operation of the fast reactors enable an energy conversion efficiency of around 40%, again an environment-friendly feature. Another

important and unique feature of fast reactors is the possibility of breeding more fissile material than what is consumed for energy production. The breeding process converts fertile (nonfissionable) isotope (e.g., U-238) to fissile isotope (Pu-239), which means effective utilization of the fertile material. Since natural uranium contains only 0.7% of fissile isotope U-235 (balance being fertile isotope U-238), the breeding potential of fast reactors is an important advantage with respect to sustainability. It can, in fact, be argued that fast breeder reactors (FBR) have the energy potential of about 70–100 times that of thermal reactors.

However, fast reactors also represent a complex and challenging technology, mastered by only a few countries in the world. The fuels used in fast reactors operate at high temperatures, face a high flux of fast neutrons, have high linear power ratings (power production per unit length), and reach high burn-up, as mentioned above. The operating conditions are thus hostile to the fuel and structural materials. Ceramic fuels are therefore natural choices for fast reactors.

Oxides of uranium and plutonium have been irradiated to levels of burn-up as high as 200,000 MWd/t [1]. Uranium oxide, with uranium enriched in U-235 to around 30% or a solid solution of uranium, and plutonium oxides have been used as fuels in fast reactors. Internationally, there has been substantial experience on the fuel cycle of oxides, from fabrication to reprocessing. The irradiation behavior of oxide fuels has been studied extensively and has been well understood.

Carbides, nitrides, and metal alloys of U and Pu possess several advantages over oxides, viz., high thermal conductivity, high metal atom density, and a higher breeding capability, which make them the potential choices for the future fast reactors. They are thus termed as “advanced fuels” for fast reactors. At the same time, each fuel form has its challenges and technical issues to be dealt with. There has been very limited experience with the advanced fuels with respect to their fuel cycle as well as deployment for power production. Fast Breeder Test Reactor (FBTR) in India is the only fast reactor that has used uranium, plutonium-mixed carbide as the driver fuel and Experimental Breeder Reactor-II (EBR-II) in the USA is the only fast reactor to have used metallic alloy fuel as the driver fuel. Both these reactors have demonstrated the potential of the advanced fuels.

This chapter presents an overview on the advanced ceramic fuels and particularly carbide and nitride fuels for FBRs. Advantages, challenges and issues of each type of fuel are dealt with relevant details. Starting from the basic properties of advanced fuels, the chapter details the international experience with the fuels and also deals with the fuel cycle.

Types of Nuclear Fuels Employed

The first nuclear reactors that were designed and constructed in the early years had metallic fuel as the preferred choice. They inherently offered the highest breeding ratios and shortest doubling times. Operating experience gained in various reactor development programs throughout the world showed that metal fuel element designs available at that time could not operate reliably to high burn-up levels, due to

dimensional instability in uranium or plutonium metal fuels resulting primarily from anisotropic irradiation growth and swelling. Metal fuels were also not considered to be adequate for high-temperature reactors due to low strength at high temperatures and phase transformations, whereas the ceramics have superior strength at higher temperatures, low thermal expansion, good corrosion resistance, and good radiation stability. The difficulty in the achievement of desirable burn-up levels in metallic fuels led to selection of ceramic fuels as an alternative.

A wide range of ceramic compounds of U and Pu including their oxides, nitrides and carbides could be used as fuels in fast reactors. However, the most preferred choice is the oxide fuel for; i) it is akin to the thermal reactor fuel and hence could be fabricated by a route that is an extension of that used for the former, ii) the other fuels (oxides and nitrides) need development of new infrastructure, iii) the experience on the other fuel forms is rather limited. Therefore, oxide fuel has been the choice for most of the development and demonstration of sodium-cooled fast reactor (SFR) programs worldwide, and thus they have reached industrial maturity. Mixed uranium-plutonium oxide containing up to 30% PuO₂ and UO₂ containing highly enriched uranium ($\geq 85\%$ ²³⁵U) has been successfully used as driver fuels in some fast reactors. Industrial-scale experience on fabrication, irradiation, reprocessing, and re-fabrication of mixed oxide fuels has been established.

Among the less desirable attributes of oxide fuels are their low fissile atom density and the presence of two moderating atoms for each metal atom. Where breeding is desired, these properties are undesirable, so it is not surprising that considerable effort has been given to the study of alternative ceramic fuel forms of the general formula (U, Pu)X, where X = C, N, S, or P. These compounds all have high melting points and higher thermal conductivities. More importantly, they only have one moderating atom per each metal atom and are denser than oxides. The carbides and nitrides have emerged as the more attractive choices on the grounds of their breeding potential and physical properties. Though the main application of advanced fuels would be in sodium-cooled FBRs, the mixed carbide (U,Pu)C has also been considered as promising fuel in gas-cooled FBRs.

Apart from the homogeneous fuels, heterogeneous fuels are also used in nuclear reactors. In the latter, fuel-bearing particles are dispersed in or surrounded by a substantially fuel-free matrix. These are also called as dispersion fuels. They offer certain advantages over conventional fuels. However, only very limited experience exists with these fuel types with reference to fast reactors.

Uranium oxide and (uranium, plutonium) mixed oxide differ in many ways from the metal form; they have a cubic crystal structure and are isotropic as far as their physical properties are concerned. They can exist over a wide range of composition, i.e., they can accommodate both an excess and a deficiency of oxygen atoms. The properties of the oxide fuels vary with the oxygen-to-metal ratio. UO₂ and PuO₂ have similar properties and form solid solution over the entire composition range. Among the advantages that the oxide as fuel offers, its ease of reprocessing is the most important.

Advanced Fuels

Enhanced sustainability, increased safety and economic competitiveness are important goals in the development of nuclear energy. The development and deployment of advanced fuels is one of the elements of this approach. At a fundamental level, advanced fuels should possess superior physical and chemical properties that would enable superior performance. Some of the most important properties include a higher thermal conductivity, higher melting point, higher phase stability and less chemical reactivity toward the clad and coolant materials.

Thus, the advanced fuels as stated earlier possess the following advantages:

- They permit the extraction of higher amount of energy from a given quantity of nuclear fuel, by reaching higher burn-up values; this reduces the quantum of fuel to be fabricated or reprocessed, which would improve economy.
- Their higher thermal conductivity results in lower operating temperatures and in turn offers a higher safety margin.
- They offer a higher breeding ratio which translates to a lower doubling time and thus enable a faster growth of nuclear power by way of generating additional fissile material.

However, for assessing the overall economic competitiveness of nuclear energy, not only the performance of the fuel in the reactor but also the complete nuclear fuel cycle needs to be considered. It should be possible to fabricate as well as reprocess the fuel through safe and economic processes, in order to realize effective utilization of the fuel, towards enhancing sustainability.

Table 1 brings out a comparison between various fuel forms to underscore the advantages of carbide and nitride fuels as “advanced fuels.”

Carbide Fuels

Phase Diagrams and Physical Properties

Phase Diagrams

The thermodynamic properties and the information on the binary as well as multi-component equilibria in the system U-Pu-C-O-N are relevant to advanced fuel fabrication, and in understanding the in-pile behavior of these advanced fuels, including mass transport within the fuel element under steep thermal and chemical potential gradients, chemical compatibility between the fuel, and the cladding and implications of a clad breach in terms of chemistry.

Phase Diagrams of the Pu-C, U-C, and U-Pu-C Systems

The U-C system is characterized by three compounds, viz., UC, U₂C₃, and UC₂. The dicarbide exhibits two allotropic modifications α and β . The monocarbide is

Table 1 General comparison of different types of fuels [2]

Parameter	Oxide	Carbide	Metal	Nitride
	$U_{0.8}Pu_{0.2}O_2$	$U_{0.8}Pu_{0.2}C$	U-19Pu-10Zr (wt%)	$U_{0.8}Pu_{0.2}N$
Density, g/cc	Low (10.97)	Medium (13.6)	High (15.7)	Medium (14.3)
Melting temperature, K	High (3083)	Medium (2750)	Low (1330)	High (3070)
Thermal conductivity, W/m-K (at 2000 K)	Low (2.4)	Medium (21.6)	High (35)	Medium (20)
Thermal expansion coefficient, /K	Low (10×10^{-6})	Low (12×10^{-6})	High (19×10^{-6})	Low (9×10^{-6})
Specific heat, J/kg-K	High (271.5)	Medium (200.7)	Low (108.5)	Medium (204.8)
Crystal structure	Fluorite	NaCl	Multiphase	NaCl
Breeding ratio	Low	Moderate	High	Moderate
Fuel swelling	Moderate	High	High	High
Front-end fuel cycle expertise	Good	Limited	Limited	Very limited
Irradiation data	Good	Limited	Limited	Very limited
Back-end fuel cycle expertise	Good	Moderate	Moderate	Limited

stoichiometric at low temperatures and exists with a significant range of stoichiometry at higher temperatures before congruently melting at 2780 K. The sesquicarbide, even though thermodynamically a stable phase under ambient conditions, is very difficult to synthesize. It transforms into mono- and dicarbides in the temperature range 2096–2110 K.

The system Pu-C is characterized by four compounds, viz., Pu_3C_2 , PuC_{1-x} , Pu_2C_3 , and PuC_{2-x} , and a cascade of peritectics. The dicarbide is a high-temperature phase. Both the mono- and dicarbides of Pu are hypostoichiometric with respect to carbon. The compound Pu_3C_2 decomposes peritectically into the metal Pu and PuC at 848 K [3].

The two binary phase diagrams U-C and Pu-C differ significantly owing to the variation in the stabilities of the mono- and sesquicarbides and the absence of a compound similar to Pu_3C_2 in the system U-C. Both monocarbides are highly dense, metallic compounds, and crystallize in the NaCl-type lattice. In the monocarbides of both U and Pu, the carbon can be replaced by significant amounts of O and N, resulting in a final solid solution $MC_{1-x}O_x$ or $MC_{1-y}N_y$ (where M = U/Pu). The carbides of Pu are vacancy-stabilized compounds, and the monocarbide can accommodate as high as 65 mol% oxygen [4], while its uranium counterpart accommodates about 35 mol% oxygen in its lattice. However, the sesquicarbide phase has very insignificant levels of solubility of oxygen. The dicarbides of both U and Pu are

stabilized by the dissolution of nitrogen. The solubility of nitrogen in the dicarbides is rather low as compared to that in the monocarbide [3]. The non-stoichiometry in the mixed U,Pu carbides decreases with the incorporation of O and N in the lattice. Pu-rich mixed carbides would possess a higher concentration of oxygen and nitrogen impurities.

Some important features of the ternary phase diagram are worth mentioning here. The binary monocarbides and sesquicarbides, being isomorphous, are completely solid soluble and form a complete series of solid solutions. Near the Pu-rich end, these carbides are hypostoichiometric with respect to carbon [4]. The database on fuels (FUELBASE), has the most recently assessed phase diagrams of the systems U-C, Pu-C, U-N, Pu-N and U-Pu-C, U,Pu-N and U-Pu-C-O and U-Pu-C-O-N [5].

The important issue of fuel-clad chemical compatibility can be understood with the help of the thermodynamic analysis of the phase diagrams. Transport of carbon to the clad, from the fuel, known as clad carburization depends on the carbon potential of the fuel. Thus, when the carbon potential of the mixed carbide is more positive than that of the clad, the carburization of the clad is more likely. Figure 1 indicates the temperature dependence of carbon potential of the different mixed carbides as well as that of the AISI 316 clad.

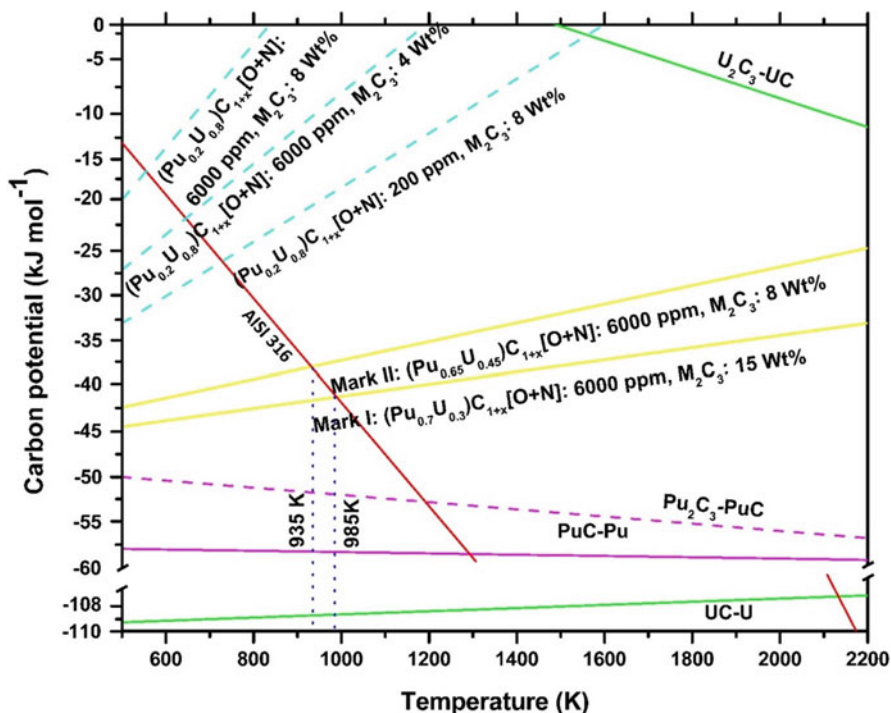


Fig. 1 Temperature dependence of carbon potentials of the mixed carbide fuel and AISI 316 steel. (Reproduced from Ref. [6])

The chemical potential of carbon in the mixed carbide arises from the tendency of carbon to exchange between the mono- and sesquicarbides. This could be represented by Eq. (1).



Factors that stabilize the monocarbide phase shift this equilibrium to the right and cause an increase in the carbon potential. The factors that stabilize the sesquicarbide phase bring about a reduction in the carbon potential by shifting the equilibrium to the left. Thus, dissolution of O and N in the monocarbide fuel increases the carbon potential. The exchange reaction represented by Eq. (2) is thermodynamically favored at 973–1173 K. Hence, an increase in the Pu content brings about preferential segregation of Pu into the sesquicarbide phase. Thus, an increase in the Pu content brings down the carbon potential of the fuel.



The pseudoternary section (UPu)-(UPu)N-C pertaining to the quinary system U-Pu-C-O-N is shown in Fig. 2. It is apparent from this figure that an increase in

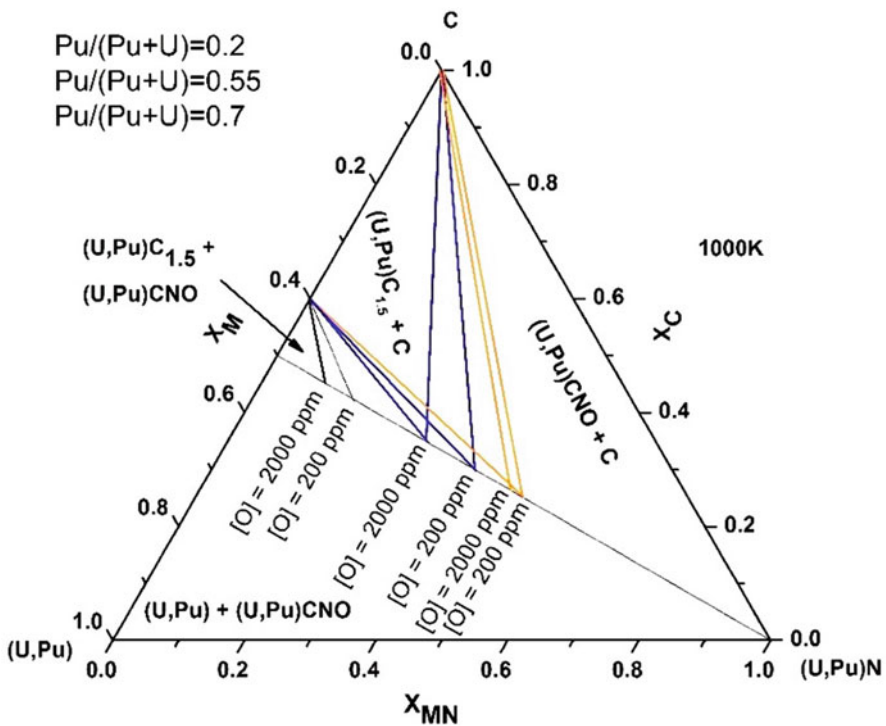


Fig. 2 The pseudoternary equilibrium in the quinary system U-Pu-C-N-O. (Reproduced from Ref. [6])

Table 2 Typical specifications of mixed carbide fuel (both low and high Pu fuels) [3]

	(Pu _{0.7} U _{0.3})C	(Pu _{0.2} U _{0.8})C
Plutonium (wt%)	66 ± 1	21.3 ± 1
Pu/(U + Pu)	0.70	0.225
Oxygen (ppm)	<6000	<360
Oxygen + nitrogen (ppm)	<7500	<400
M ₂ C ₃	5–20	12.5 ± 1.4
Density (%TD)	90 ± 1	80 ± 1
Grain size μm	10–12	12

the O content reduces the composition span of the two-phase region comprising the mono and sesquicarbides. Further, this two-phase region is considerably smaller for those fuels with a lower Pu content. Hence, the restriction on the oxygen and nitrogen impurity levels in the mixed carbide fuels would be more stringent for fuels with lesser Pu content (Table 2).

Thermal Conductivity

Thermal conductivity plays a vital role in the performance of the nuclear fuel. The higher the thermal conductivity, the higher the linear power that can be extracted from the fuel. Figure 3 shows the comparison of thermal conductivities for UC and PuC. The quoted uncertainties are ±10% for UC and ±15% for (U,Pu)C for temperatures above 500 °C. For temperatures below 500 °C, the uncertainties are shown by shaded area in the Fig. 3 [4]. From Figs. 3 and 5, it is evident that the k values of the carbides of PuC are lower than that of UC in the temperature range 500–1500 K. The presence of vacancies in these compounds brings down the thermal conductivity. Stoichiometry is the most important reason for apparent discrepancies. As shown in the same figures, addition of PuC to UC decreases the value of k. Figure 4 shows the thermal conductivities for (U,Pu)C in the hyper- and hypostoichiometric regions. Figure 5 shows the thermal conductivity of the MK-1 carbide fuel used in the FBTR.

Fuel-Clad Compatibility

One of the anticipated problems of carbide fuel is transfer of carbon from hyperstoichiometric (Pu_{0.7}U_{0.3})C fuel containing relatively high oxygen (±0.7 w/o) [3] and high M₂C₃ (10–20%) to SS 316 cladding causing solid- or gas-phase carburization of the latter and subsequent embrittlement. The main factors responsible for clad carburization are the difference in carbon potential (between the clad and the fuel) and CO pressure (p_{CO}) over the carbide fuel which in turn are controlled by M₂C₃ content and residual oxygen. Theoretical calculations have shown that the carbon potential and (p_{CO}) of hyperstoichiometric (Pu_{0.7}U_{0.3})C containing relatively high M₂C₃ (±20%) and high oxygen (±1 w/o) is lower than its uranium-rich counterpart with very low M₂C₃ (±2%) and oxygen (±0.1%) [3].

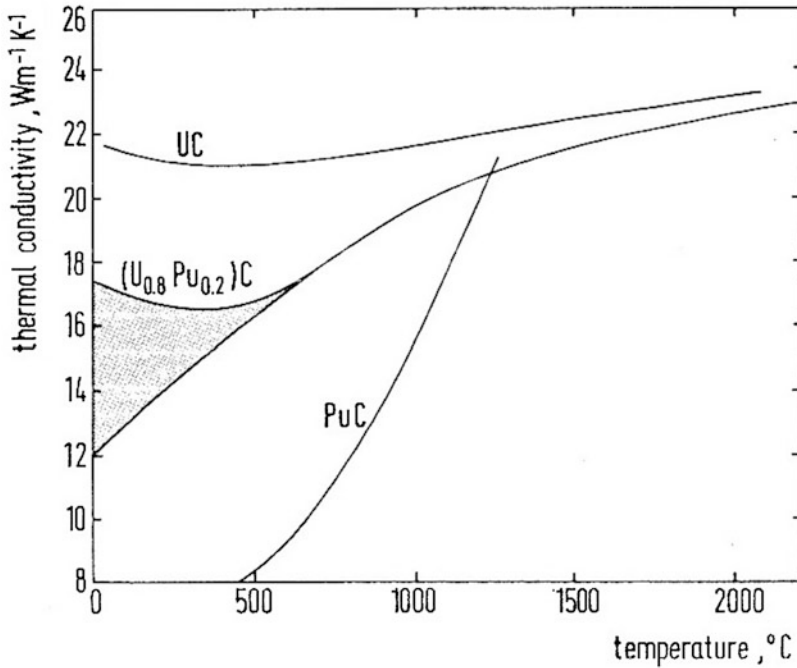


Fig. 3 Comparison of thermal conductivity of UC, PuC, and (U,Pu)C [4]

The pellets containing up to 0.7% oxygen and 20% M_2C_3 caused insignificant carburization of the SS 316 cladding [3]. The depth of carburization was less than $12\mu\text{m}$. However, the pellets containing relatively high oxygen ($\pm 1\%$) and high M_2C_3 (60%) caused carburization of the cladding to depths of up to $90\mu\text{m}$. These values are much lower than the depth of clad carburization reported in case of identical tests carried out with uranium-rich MC containing 15% M_2C_3 and around 0.2% oxygen. Even a carburization depth of $150\mu\text{m}$ was not found to cause any breach in the SS 316 cladding.

Fuel Restructuring

Fuel restructuring plays a vital role in the fuel performance as it affects the temperature distribution and thus all thermally induced phenomena. Sintering, grain growth, gas bubble development and center void formation are initiated at threshold temperatures similar to those observed in oxide pins but at a higher linear heat ratings by a factor of 5 [4]. These observations demonstrate the excellent physical stability of carbide fuel columns and imply a high capacity to endure power transients without melting at the center of the fuel.

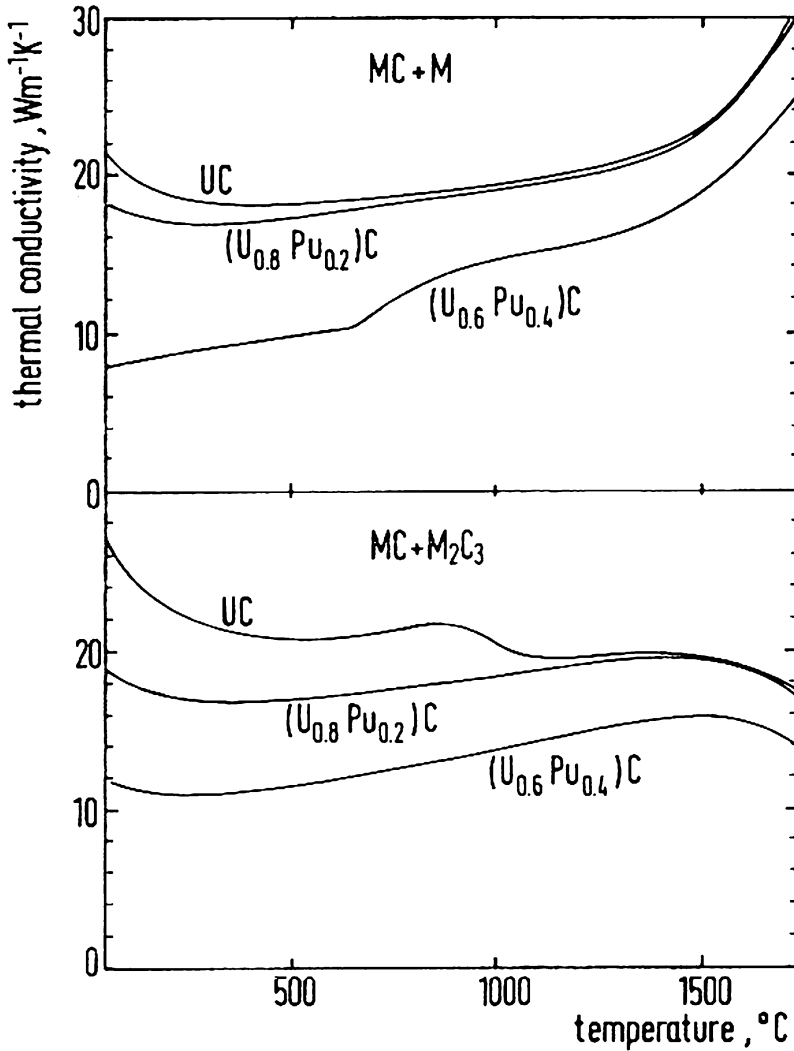


Fig. 4 Thermal conductivity of (U,Pu)C in the hyper- and hypostoichiometric regions [4]

Thermal Creep

The long-time survival of a fuel pin in the fast-neutron environment of a reactor is critically dependent upon the rate of fuel swelling which in turn leads to fuel-clad mechanical interactions. It is generally recognized that fuel swelling is directly related to the plasticity of the fuel which is determined by the deformation, i.e., creep and fracture characteristics of the fuel.

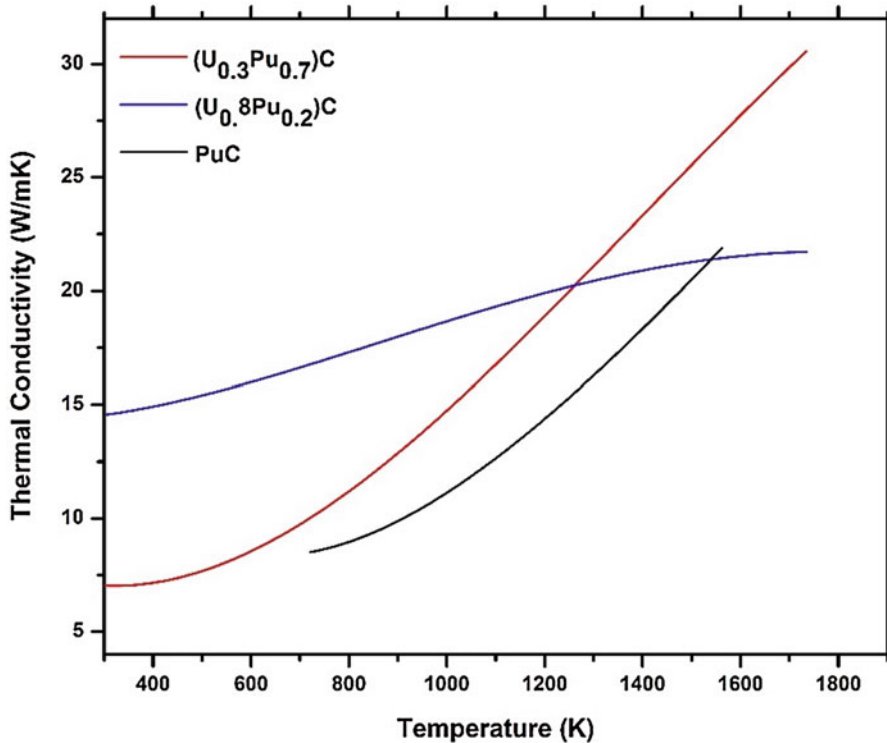


Fig. 5 Thermal conductivity of (U-Pu)C (100% TD) fuels. (Reproduced from Ref. [6])

Figure 6 shows the variation of primary creep rate with time for 20% enriched mixed carbide fuel from the creep tests performed on cylindrical $(U_{0.8}Pu_{0.2})C_{1.0}$ pellets [7].

Carbide Fuel Fabrication

The fabrication of a carbide fuel that meets all the requisite chemical and physical specifications is a challenging task owing to its chemical reactivity. The purity of the inert atmosphere in the dry boxes in the production lines needs to be very high, in order to avoid oxidation of the samples even under ambient conditions. These boxes need to be maintained under a dynamic flow of an inert gas (either N_2 or Ar) with O_2 and H_2O residues less than 50 ppm. Further, during the high-temperature processes used in the preparation and consolidation of both the carbide and nitride fuels, significant loss of Pu could be caused due to vaporization. Such a loss needs to be limited, in order to avoid the variation in the composition of the carbide as well as to avoid condensation of Pu in the colder regions of the furnace, which could cause concerns pertaining to radiological safety [9].

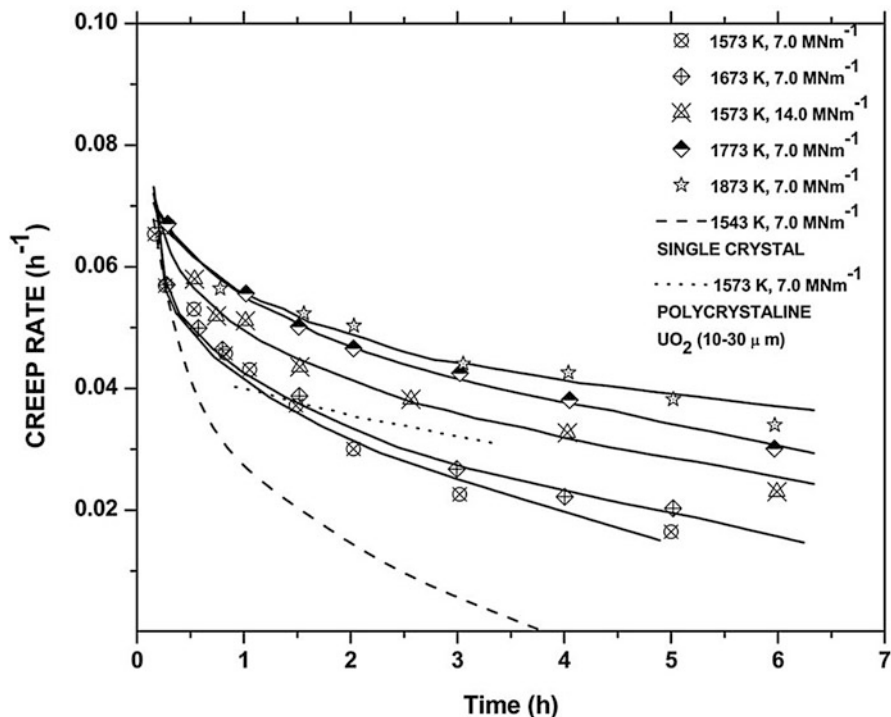


Fig. 6 Variation of primary creep rate with time for $(U_{0.8}Pu_{0.2})C_{1.0}$ [7]

Skull melting with graphite electrodes and arc melting with tungsten electrodes have been employed for the preparation of UC. However, this process results in inhomogeneities or leads to a product with W impurity. Further, these are not easily amenable for industrial-scale production. The hydriding-dehydriding method yields purer carbides. However, handling of pyrophoric finely divided metal powder could lead to oxygen contamination of the product.

The carbothermic route on the contrary is relatively simpler, employs the oxide powders derived from reprocessing, and is amenable for scale up. The carbothermic reduction is usually carried out in a flowing stream of an inert gas. This reaction is made thermodynamically feasible when the CO produced is removed from the reaction site. Removal of CO is accomplished by flowing an inert gas over the reaction mixture. However, the carbothermic process invariably yields a product that is contaminated with significant amounts of oxygen and nitrogen impurities. Nevertheless, the most attractive among the routes for the production of the carbide in large scale is the carbothermic reduction of the oxide. In lieu of UO_2 , PuO_2 , and C, MOX and C could also be mechanically milled and carbothermically reduced to get the carbide fuel. The reduction is usually carried out in a single step. Alternately, the sesquicarbide could be produced first and then reduced to the monocarbide phase. This method, known as the two-step route, is particularly useful when the oxygen impurity in the

monocarbide has to be minimized. However, industrially the single-step method only has been used so far in the large-scale fabrication of the mixed carbide fuel [4, 6, 9]. Richter et al. [10] proposed the direct pressing method for the fabrication of the mixed carbide fuel. In this method, porous carbide pellets produced by carbothermic reduction were directly compacted (without comminution) and sintered. Recently in CEA, France, a one-step reduction process has been studied, in which the oxalates of U (III) and Pu (III) derived from the PUREX process are converted into the carbide [11]. Figure 7 shows the unit processes involved in the preparation of mixed carbide by

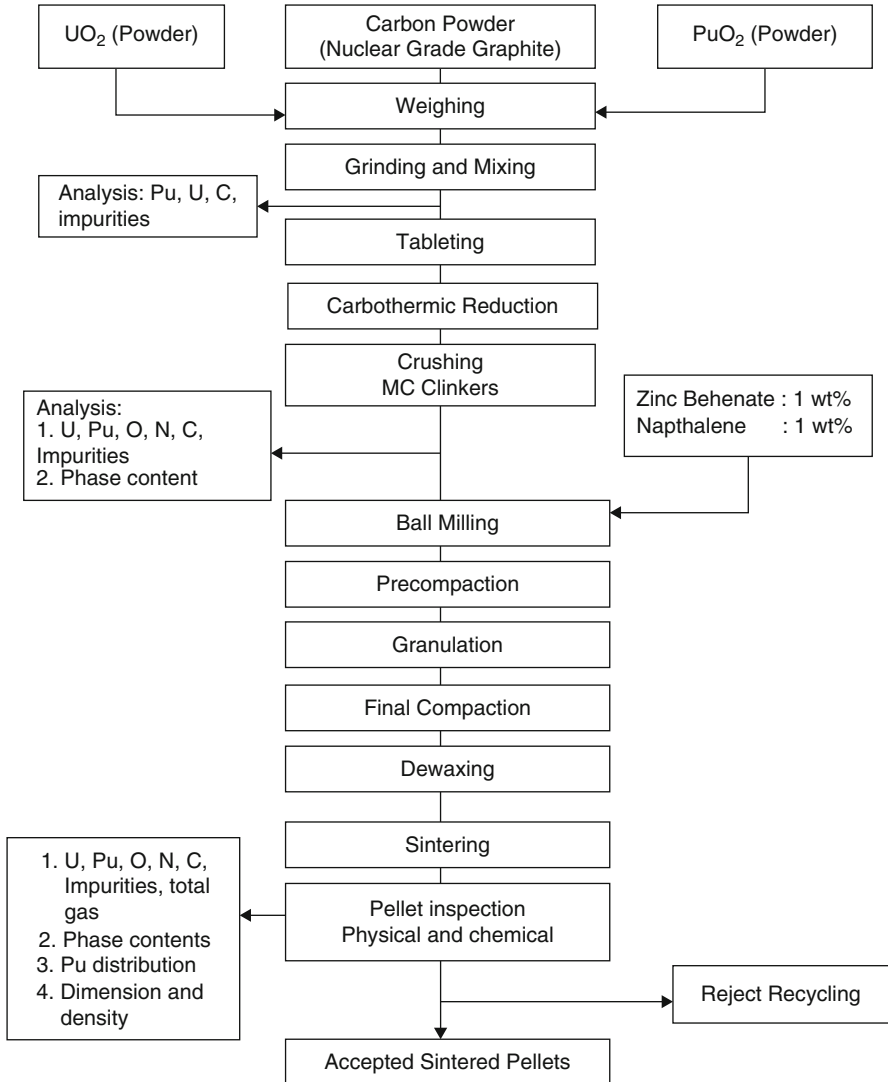


Fig. 7 Fabrication of carbide fuel of Indian fast breeder test reactor [6]

the carbothermic reduction process used in the fabrication of the mixed carbide fuel for FBTR (both Mark I and Mark II) [6].

Nitride Fuels

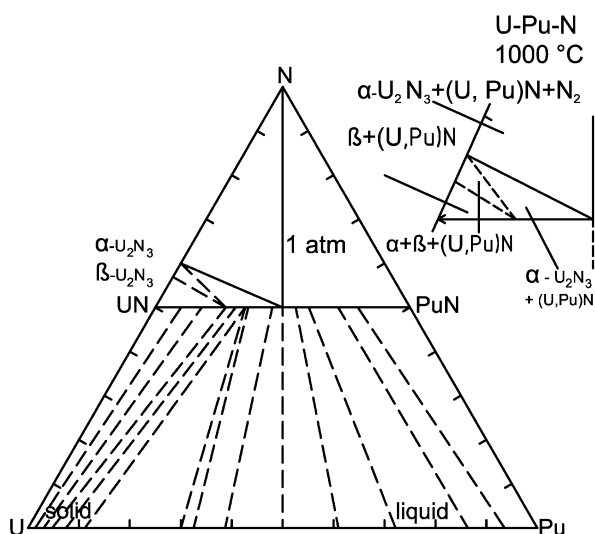
Phase Diagrams and Physical Properties

The U-N, Pu-N, and U-Pu-N Systems

The U-N system is characterized by three compounds, viz., the mono-, sesqui-, and dinitrides. U-N crystallizes in an NaCl-type lattice, while α and β U_2N_3 possess bixbyite-type Mn_2O_3 and A-type La_2O_3 structures, respectively. The dinitride is isotypical with CaF_2 . Both the sesquinitrides and dinitride exhibit substoichiometry with respect to nitrogen, while the mononitride is stoichiometric. The system Pu-N is characterized by a single nitride Pu-N which crystallizes with a NaCl-type structure.

Owing to the existence of only one stable compound, viz., the mononitride in the system Pu-N, the ternary system U-Pu-N is characterized by a complete solid solution of the mononitride alone (Fig. 8). Further, unlike the carbide these nitrides are stoichiometric. It appears that the phase Pu_2N_3 is stabilized in the solid solution M_2N_3 up to a Pu fraction of about 0.15 [12]. Even though nitridation of the clad is less likely, the partial pressure of nitrogen over the higher nitrides is a matter of concern, for there could be in situ generation of nitrogen in the fuel. Hence, hyperstoichiometry is not desirable in the nitride fuels. This is further accentuated by the fact that unlike in the mixed carbide fuel, the N/M ratio increases with the burn-up (much like the oxides). The presence of trace amounts of oxide second phase in the fuel is considered rather advantageous, for it reduces the nitrogen partial

Fig. 8 Isothermal section of the system U-Pu-N at 1273 K [4]



pressures over the fuel [13]. The nitride fuel is less pyrophoric and is easier to handle than the carbide. Comparison of the physical properties of oxides and nitrides can be seen in Table 1.

Thermal Conductivity of Nitride Fuels

The temperature dependence of the thermal conductivity of U-N and (U,Pu)N is depicted in Fig. 9 [4, 14–20]. Similar to the mixed carbide system, the (U,Pu)N has a lower thermal conductivity than U-N. This is due to the introduction of Pu-N in the matrix which has a lower thermal conductivity.

Fuel-Clad Compatibility

Like MC, high-purity stoichiometric MN fuel is not likely to have any chemical interaction with SS 316 cladding. However, uranium-rich MN_{1+x} contains the mixed sesquinitride (M_2N_3) as second phase which has been reported to cause nitriding of SS 316 cladding and consequent loss of its ductility. The clad nitriding occurs according to the following chemical reaction [8]:

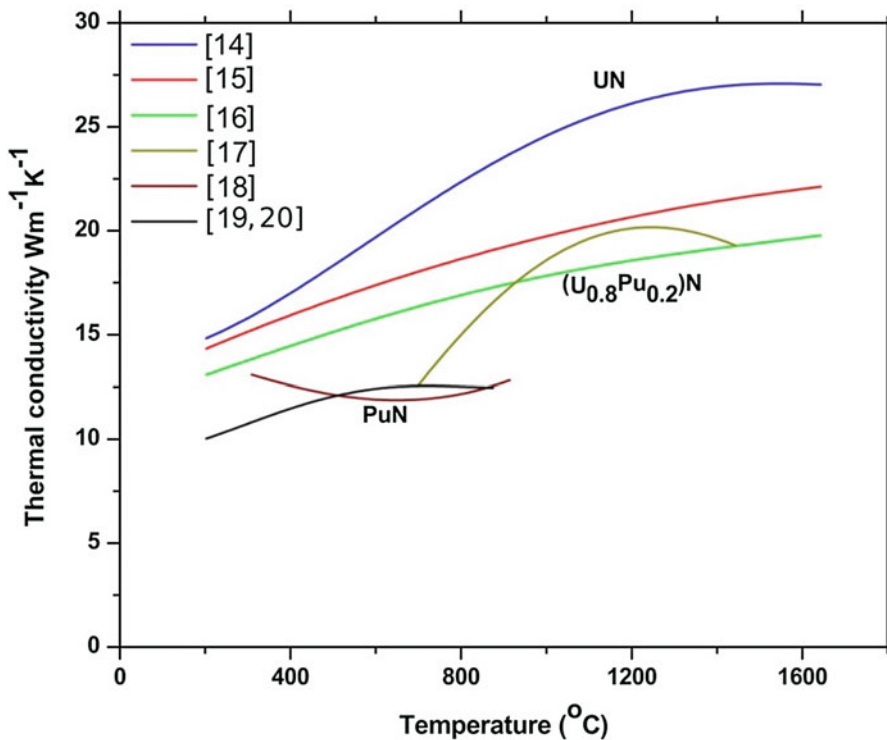
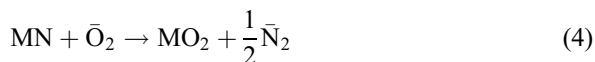


Fig. 9 Comparison of thermal conductivities of nitride fuels [4]

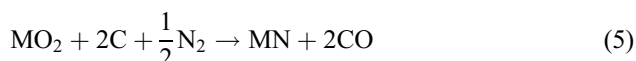
Oxygen impurity in the fuel plays a vital role in controlling nitriding of SS 316 cladding. If the oxygen is present as MO_2 , it stabilizes the M_2N_3 phase and decreases the nitrogen activity, thus reducing clad nitriding. On the other hand, if oxygen is present in MN as solid solution or exists as impurity in the filling gas, it causes oxidation of MN as per the following equation, leading to release nitrogen and nitriding of the clad.



The compatibility test of $(\text{Pu}_{0.7}\text{U}_{0.3})\text{N}$ pellets containing high levels of oxygen (0.5 w/o) with SS 316 cladding tube showed a discontinuous and relatively harder reaction zone of around 35 μm on the SS 316 cladding. Similar observations have also been reported for uranium-rich mixed nitride. The microhardness values at locations in the reaction zone and away from it were 265 VHN and 210 VHN, respectively [8].

Fabrication of the Nitride Fuel

Nitridation of the metal could be gainfully used for the preparation of the nitride. However, control of the stoichiometry especially in the mixed nitrides richer in U is difficult [4]. Nitride is more conveniently prepared through carbothermic reduction. If nitrogen is used instead of the inert gas (argon), and if the quantity of the carbon in the mixture is chosen appropriately, then the product obtained would be a nitride (Eq. 5). This process would be best suited for the large-scale production of the mixed nitride fuels.



Usually temperature in the range of 1773–1973 K is used for the carbothermic reduction (Fig. 8). In order to limit the oxygen pickup in the final product, usually an excess amount of carbon is used in the initial mixture. Subsequently, the excess carbon is removed by reacting it with a mixture of N_2 and H_2 or HCN [21, 22]. In order to avoid the formation of the sesquinitride phase, usually the gas stream is swapped from N_2 to Ar at temperatures below 1673 K. It is to be noted that the sesquinitride is not stable at temperatures above 1673 K. The major impurities present in the nitride are oxygen and carbon. While the monocarbide is completely soluble in the mixed nitride matrix, the solubility of oxygen (MO) is rather limited to 7% and 14% in U-N and Pu-N, respectively [23].

The sintering of nitride is more difficult than the carbide, due to a higher covalency of the MN bond that leads to diminished diffusivities in the lattice. In order to circumvent this difficulty, a higher temperature is to be used for sintering the mixed nitride fuel (1973 K). This increase in the temperature brings about a higher level of oxygen impurity, which in turn decreases the sintered density. Often

choosing the right atmosphere for sintering, viz., H_2 or $Ar + H_2$, helps improve the sintering, for it is surmised that the latter helps enhance the diffusivity of Pu [24]. Typically, mixed mononitrides with a final sintered density of about 85–90% TD have been fabricated by employing the above techniques.

Similar to the carbide fuel, both the direct pressing technique and the sol-gel method can be used for the production of the mixed mononitride [10, 25, 26]. Pressure-assisted techniques that are best suited for sintering covalent compounds could be of great value in the sintering of mixed nitride fuels. Hot isostatic pressing (HIP) [27] and spark plasma sintering [28] have been used in the consolidation of uranium nitride powders. However, these have not been carried out on a production scale suitable for the fabrication of fuels for the fast reactors.

Irradiation Behavior of Carbide and Nitride Fuels

Design of a fuel pin should ensure safe operation of fuel pin under reactor operating conditions and should have adequate safety margins to account for transients and enable effective utilization of fuel to produce cost-effective power. Fuel pin design includes both mechanical design and thermal performance analysis. In the thermal performance analysis, the allowable linear power at which the pin can operate safely is determined by taking into account all the uncertainties as well as off-normal events. The thermal conductivity of the fuel plays a major role in its thermal performance as it determines the temperature drop across the fuel diameter. The thermal conductivity depends upon temperature, porosity and the stoichiometry of the fuel. The fission gas release and fuel swelling have a deterministic role in the mechanical design of the fuel pin. They are interdependent and play an important role in determining the stresses on the clad. The fuel swelling and fission gas release aspects are covered in detail in the following sections with respect to carbide and nitride fuels.

Carbide Fuels

Due to its higher thermal conductivity [2], the thermal gradient across the carbide fuel column is less which in turn leads to reduced migration of pores and restructuring at moderate power, apart from reduced fuel cracking.

One attribute of the U,Pu mixed carbide fuel that renders it markedly different from the mixed oxide fuel is its phase composition. Unlike the U, Pu mixed oxide fuel which is a single-phase material, the carbide fuel used in reactors (as fabricated for irradiation) is biphasic comprising both the mono- (MC) and sesquicarbide (M_2C_3 , where $M = U_{1-x}Pu_x$) phases. The inclusion of the latter is necessitated by the reduction in the C/M ratio with the burn-up since the product of fission such as rare earths tends to “consume” carbon (C/M stoichiometry >1). In other words, if the MC phase alone is used, then during burn-up, a low-melting metallic phase, which forms a low-melting eutectic with the alloying components of the clad, would result.

It is apparent that knowledge on the interrelations between the constituent elements and the impurities and the evolution of C/M ratio of fuel with burn-up, needs to be understood, in order to arrive at fuel specifications.

Even though the carbide fuel is highly reactive towards air and moisture, it is compatible with sodium. Hence, both the concepts of sodium (Na) bonding and helium (He) bonding could be employed in the fabrication of the carbide “fuel pin.” The carbide fuel swells more than the oxide necessitating a fuel pin with a lower smear density. The Na-bonded fuel pins offer some advantage over the He-bonded pins. In the former, owing to the better thermal conductivity of Na, less steeper thermal gradient prevails within the pin, leading to less severe restructuring [3]. However, when Na bonding is used, the smear density has to be reduced further to allow for the volume of the bond sodium, and the density of the fuel pellets has to be higher than that employed in the He-bonded pins. The end of life (EOL) of the Na-bonded pin would be governed by the contact between the pellet and the clad. Further, the Na used in the bond should be of high chemical purity especially with respect to dissolved oxygen. The oxygen concentration in the bond sodium should be restricted to 10 ppm, to avoid reduction in the thermal conductivity of the latter, brought about by the dissolved oxygen [3].

Swelling of Carbide Fuel

One of the most important changes of a fuel under irradiation is its decrease in density, or increase in volume, i.e., swelling. Fission gases formation and retention are the chief causes for the fuel swelling. Fission rare gases (mainly Xe and much less Kr) have a high fission yield and low solubilities. Other volatile fission products (Cs, Rb, I, Br) also contribute to this swelling. Excessive swelling could lead to mechanical interaction between fuel and clad ultimately leading to clad failure. The unrestrained swelling rate per at.% burn-up as a function of temperature is shown in Fig. 10 [29].

Carbide fuels also exhibit higher swelling strains due to their poor release of fission gas. The important factors that affect the fission gas release rate from the carbide fuel are temperature, burn-up, porosity and grain size. Remaining parameters such as stoichiometry, pore size distribution, cracking, etc. also affect the fission gas release to some extent.

Fission Gas Release in Carbide Fuels

Krypton and xenon are the gaseous fission atoms formed during fission reaction. They are completely insoluble in the fuel matrix and precipitate as bubbles. The gaseous fission products are released from the fuel when they reach any space that is connected to free volume. The amount of gases produced depends on the burn-up. In FBRs, due to high burn-ups, large fission gas plenums are provided in the pins. The distribution of different types of bubbles in the fuel matrix is shown schematically in Fig. 11 [30].

Due to the lower operating temperatures, the fission gas release in the carbide fuels is less compared to oxide and metal fuels. Typical fission gas release in a carbide fuel pin as a function of burn-up is shown in Fig. 12. From the available

Fig. 10 Free unrestrained swelling rate of (U,Pu)C in % per at.% burn-up as a function of center temperature [29]

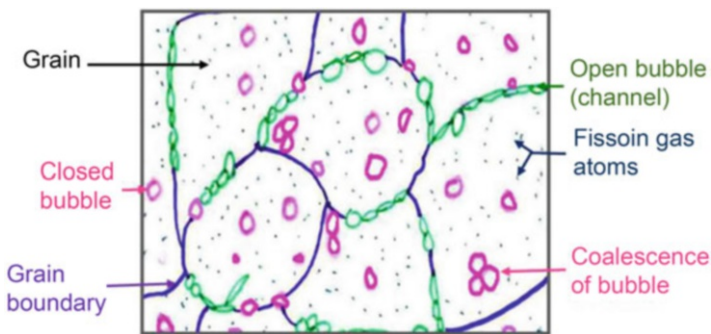
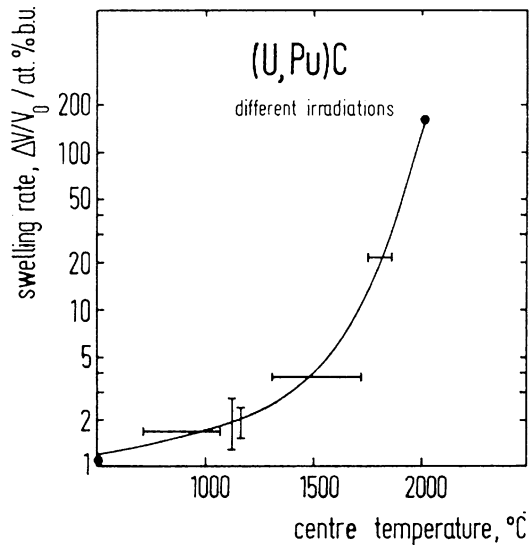


Fig. 11 Fission gas bubbles in fuel matrix [30]

experimental results, it is observed that low- and medium-density fuels release more fission gases than high-density fuel. Un-stoichiometric fuel contains more voids than stoichiometric fuel and hence can contain more gas. Impurities hinder gas diffusion and therefore bubble formation and also bubble motion.

Fission gas release levels in carbide pins are substantially lower compared to oxide fuel pins, reflecting the lower fuel temperatures prevailing in the former. Release rates from carbide are <1% at temperatures below 900 °C but rise to about 5–10% with temperature rising to 1200 °C. At temperatures above 1200 °C, gas release appears to be associated with bubble growth and linkage at grain boundaries and increases almost linearly with temperature to about 70% in pins irradiated at center temperatures >2200 °C (>200 KW/m) [31].

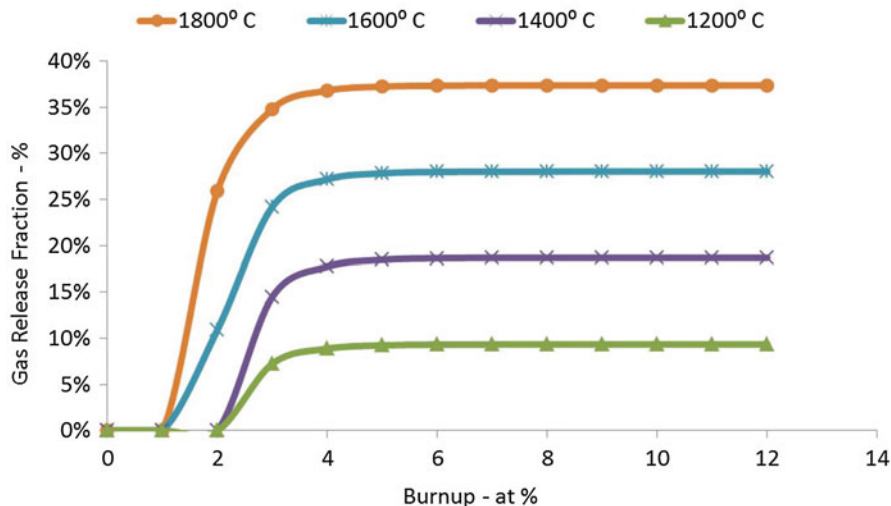


Fig. 12 Fission gas release in carbide fuels as a function of burn-up [30]

International Experience on Carbide Fuels

Mixed carbide fuel chosen as the driver fuel for the Indian Fast Breeder Test Reactor (FBTR) has attained a peak burn-up of 165 GWd/t. Since the fuel used was first of its kind and no information exists regarding the irradiation behavior of this fuel, a conservative burn-up of 50 GWd/t and a linear heat rating of 320 W/cm were initially envisaged for this fuel [32]. Extension of burn-up beyond this design limit required comprehensive performance assessment through postirradiation examination [33].

Even though significant irradiation performance database is available for mixed carbide fuels (Pu content up to 25%), it is much smaller as compared to those pertaining to the metallic and oxide fuels. Through the extensive work carried out in India on the Pu-rich (70%) mixed carbide fuels, irradiation experience has been gained on the same irradiated up to a burn-up of 165 GWd/t.

A schematic of the FBTR fuel pin is shown in Fig. 13 [34]. In this design, 320 mm of mixed carbide fuel pellets are stacked with an insulation pellet at both ends. Solid pellet concept is chosen with a smear density of 82%.

Various nondestructive and destructive examinations were employed for post-irradiation characterization of the mixed carbide fuel. Evaluation of X-radiographs of the fuel pins after 25 GWd/t and 50 GWd/t revealed the presence of pellet-to-pellet gap and pellet-to-clad gap at the end of fuel columns. In the case of fuel pins of 100 GWd/t burn-up, the pellet-to-pellet gap and pellet-to-clad gap appear to have closed at the center of the fuel column. However, pellet-to-pellet gap was still observed in the end of the fuel column. The increase in stack length was found to vary from 1.01% to 2.61%. The radiography of 155 GWd/t fuel pins also indicated the absence of pellet-to-pellet gap and pellet-to-clad gap. Figure 14 shows the trend in the increase in fuel stack length as a function of burn-up [35].

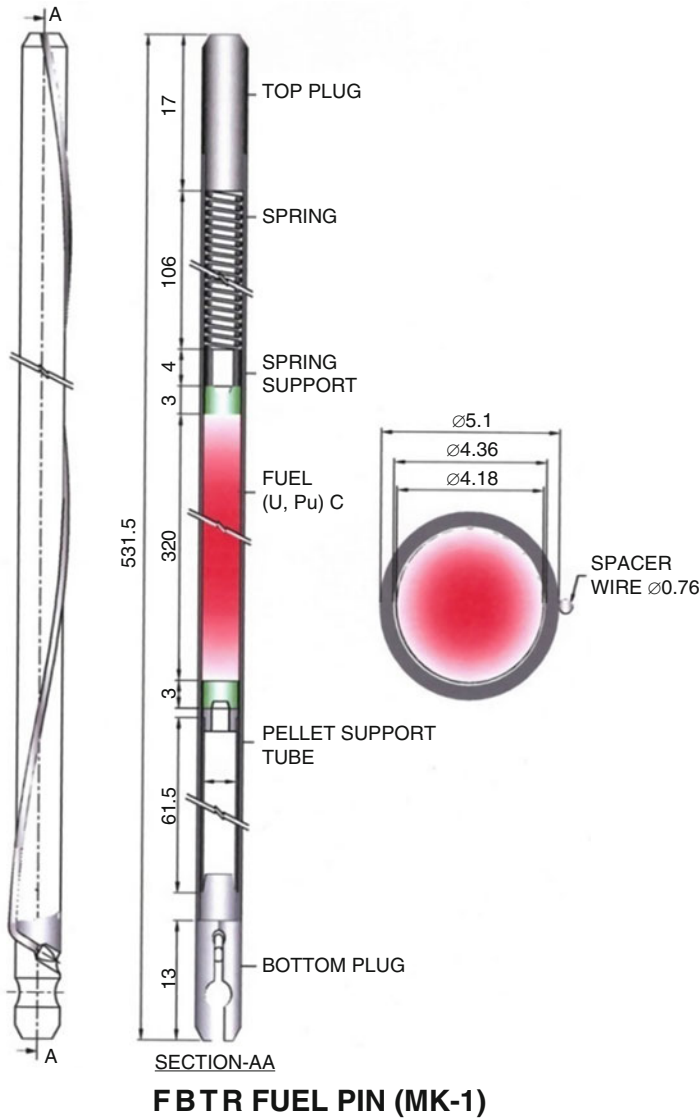


Fig. 13 Schematic showing the details of the He-bonded fuel pin used in FBTR [34]

Fission gas release in fuel pins after 25 GWd/t burn-up was found to be around 1%. In those fuel pins taken up to a burn-up of 50 GWd/t, fission gas release values were found to vary between 8% and 18%. Fission gas release measurements after 100 GWd/t burn-up indicated that the gas release is in the range of 4–14%, and at 155 GWd/t it was 8–16% [36]. The lower fission gas release in 100 GWd/t burn-up fuel pins is attributed to the reduction in fuel operating temperatures due to closure of fuel-clad gap. The estimated value of the fission gas release in the fuel pins that were

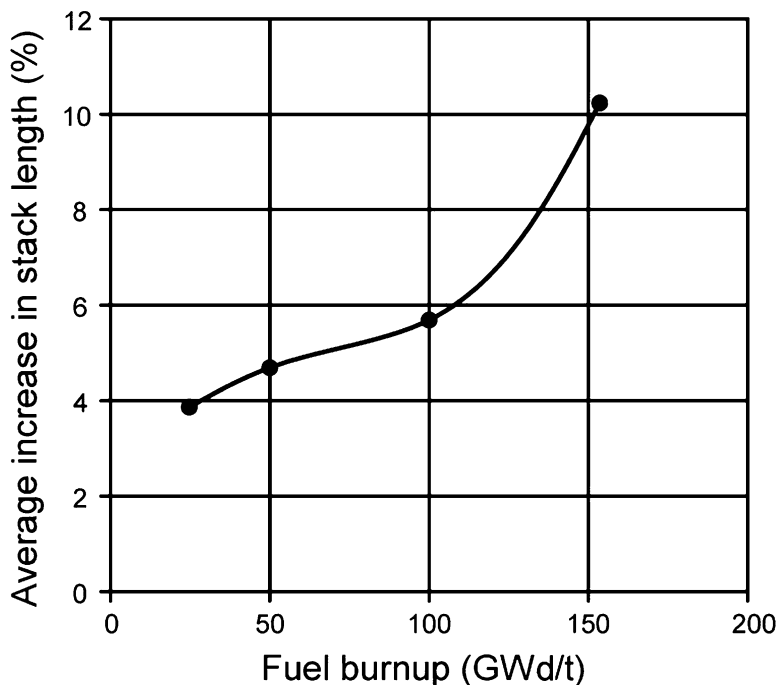


Fig. 14 FBTR MK-1 fuel swelling [35]

Table 3 Fission gas release and plenum pressure

Burn-up (GWd/t)	Fission gas release %	Internal pressure in the fuel pin (MPa)
25	0.16–1	0.12
50	7–8	0.4–0.7
100	3–14	0.5–1.2
155	8.5–15.7	1.15–2.09

taken up to a burn-up of 155 GWd/t was 16%, and the corresponding internal pressure in the fuel pin was measured to be 2.1 MPa. The ratio of xenon to krypton was estimated to be around 13. Table 3 shows the fission gas release values and plenum pressure measured at different levels of burn-up. Typical fission gas release in FBTR Mk-1 fuel irradiated up to 155 GWd/t burn-up is shown in Fig. 15.

The examination of the driver fuel pins at different burn-ups indicated a systematic change in the fuel-clad gap with increasing burn-up. Progressive reduction in the fuel-clad gap and radial cracks were observed in 25 and 50 GWd/t burn-up fuel pins. The fuel-clad cross section of 100 GWd/t burn-up fuel pin revealed the absence of the gap at the center of the fuel column with circumferential cracks, whereas the cross section at the end of the fuel column indicated the presence of minimum fuel-clad gap with radial cracks. At a burn-up of 155 GWd/t, the fuel-clad gap had closed

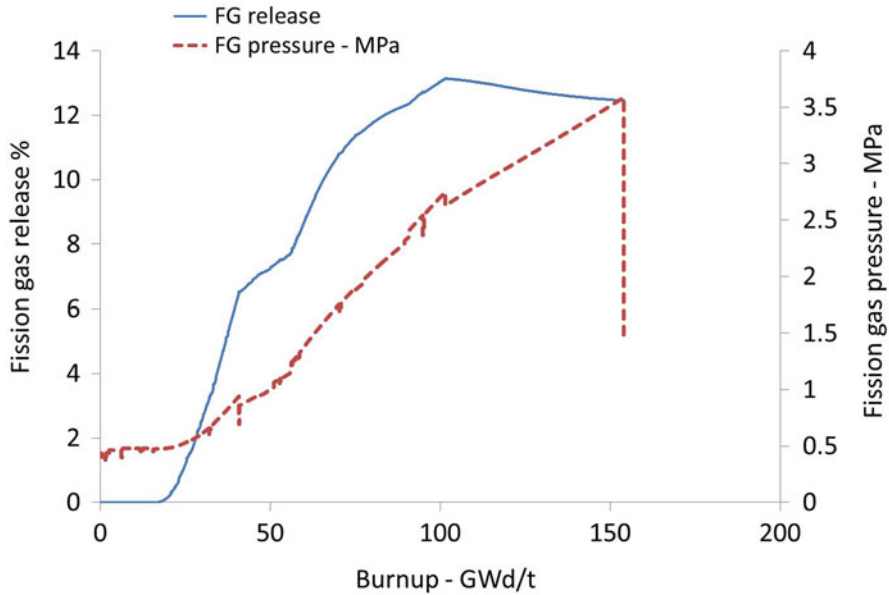


Fig. 15 Typical fission gas release and pin pressure variation in FBTR MK-1 carbide fuel up to 155 GWd/t burn-up [37]

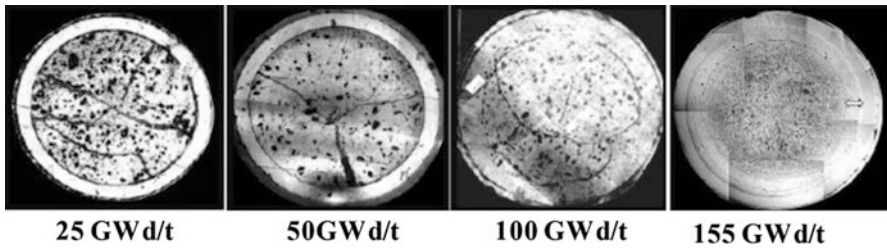


Fig. 16 Photomosaics of fuel pin cross sections at the center of the fuel column of different burn-ups [35, 36]

completely along the entire length of fuel column with circumferential cracks in the center and end of the fuel region indicating initiation of fuel-clad mechanical interaction (FCMI). Figure 16 shows the photomosaics of fuel pin cross sections at the center of the fuel column after 25, 50, 100, and 155 GWd/t burn-up. The above data provide valuable insight about the phenomena under various operating conditions.

In EBR-II, about 470 mixed carbide fuel pins with sodium- and helium-bonded designs were irradiated with various clad materials, viz., SS 316, D9, PE-16, D21, etc. Figure 17 shows the fission gas release in helium- and sodium-bonded mixed carbide fuel irradiated to high burn-ups in EBR-II [4].

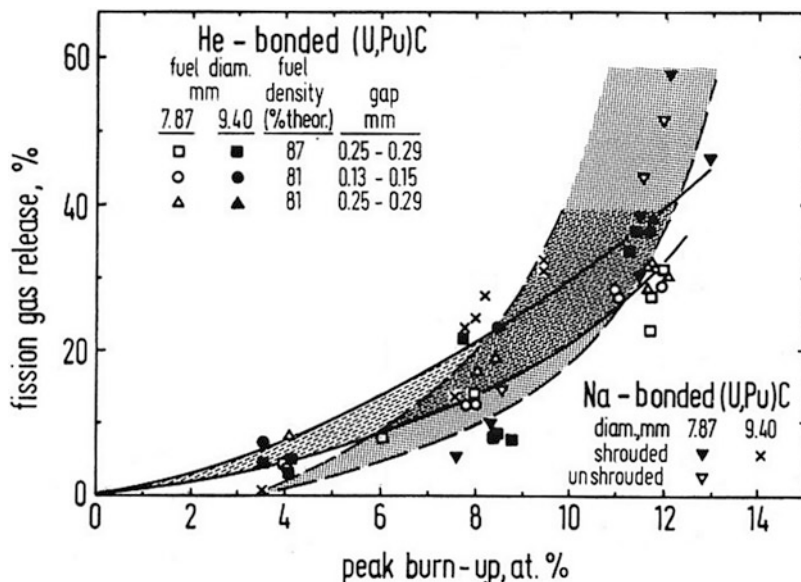


Fig. 17 Fission gas release in helium- and sodium-bonded mixed carbide fuel irradiated to high burn-ups in EBR-II [4]

Helium-bonded and Na-bonded fuel pins with 316 SS cladding have achieved peak burn-ups of 20.7 at.% (192 MWd/kg) and 15.8 at.% (146 MWd/kg), respectively, without any failure which demonstrated the ability of the carbide fuel pins to attain peak burn-ups greater than 12 at.% and peak fluence of 1.4×10^{23} n/cm² ($E > 0.1$ MeV).

MC fuels irradiated in EBR-II (up to 12 at.% burn-up) were subjected to transient over power tests in TREAT to ascertain the margin available for cladding breach. These tests revealed that fuel transient-overpower response would not limit the application of MC fuels to fast reactors. In a “run-beyond-clad-breach” test conducted at EBR-II, it was found that MC fuels have benign response for cladding breach as only a little fuel was released from cladding into the coolant. In summary, the US experience has given the confidence to use MC fuels in SFRs. In particular the He-bonded MC pins with swelling-resistant cladding and with 80% smear density appear to show best performance.

In Germany, several MC fuel pins with sodium and gas bonding were irradiated, and finally, a “reference concept” pin was irradiated in KNK-II (19 pin bundle, 8.5 mm pin, He-bonded, 400 μ m gap, 75% TD smear density, 1.4970 clad, 800 W/cm) up to a target burn-up of 70 GWd/t. Some He-bonded MC pins were irradiated in DFR (UK) and also up to a burn-up of 70 GWd/t.

In the Russian Federation, the carbide core of BR-10 reactor achieved a burn-up of 5 at.%. Some experimental MC fuel pins (both He- and Na-K-bonded pins) were irradiated up to 10 at.% burn-up in BOR-60 reactor without any failure. Also, MC

fuel pins with composition 55% PuC–45% UC and 54.5% PuC–45.5% ZrC were successfully irradiated in BOR-60 reactor at a linear power of 400–450 W/cm up to 8 at.% burn-up without any failure.

In Japan (U, Pu)N and (U, Pu)C fuels were irradiated at Japan Research Reactor-2 and Japan Material Testing Reactor at linear power varying between 420 and 640 W/cm up to a burn-up of 5.5%.

Table 4 gives details about maximum burn-up achieved in various countries. Experimental pins with carbide fuel generally contain 20% PuC, though it is not specifically mentioned for the given burn-up cited in the reference. The maximum burn-up achieved in different reactors (for oxide and metal fuels) along with their fissile enrichment is given in Tables 5 and 6. Some of these pins were power reactor pins, and a few were experimental pins.

Table 4 Carbide fuel

Sl. No.	Reactor (country)	Maximum achieved burn-up (GWd/t of heavy metal)
1	EBR-II experimental pin (USA) [38]	192
2	DFR experimental pin (UK) [39]	70
3	KNK-II experimental pin (Germany) [39]	70
4	FBTR (India)	165
5	BOR-60 (Russia)	10 (at.%)
6	JRR-2, JMTR (Japan)	5.5 (at.%)

Table 5 Oxide fuel [1, 40]

Sl. No.	Reactor (country)	Maximum achieved burn-up (GWd/t of heavy metal)	Fuel enrichment ^a
1	Rapsodie (France)	102	30% PuO ₂ + 70% UO ₂ ^b
2	KNK-II (Germany)	172	88.1–95.1
3	Joyo (Japan)	86.9	34% (max)
4	BOR-60 (Russian Federation)	176	56–90%
5	FFTF (USA)	155	24.6% (max)
6	Phenix (France)	150	23% (max)
7	PFR (UK)	200	28.5% (max)
8	BN-350 (Kazakhstan)	97	26% (max)
9	BN-600 (Russian Federation)	97	26% (max)
10	Superphenix (France)	90	19.7% (max)

^aEnrichment = mass of fissile atoms/mass of fissile and fertile atoms (i.e., ²³⁵U in U-based fuels; ²³⁵U + all Pu isotopes in U/Pu-based fuels)

^bU enriched to 85%

Table 6 Metal fuel [1, 40]

Sl. No.	Reactor (country)	Maximum achieved burn-up (GWd/t of heavy metal)	Fuel composition
1	Fermi (USA)	4	25.6% ^{235}U -10%Mo
2	EBR-II (USA)	80	67% ^{235}U -10%Zr
3	DFR (UK)	3	75% ^{235}U
4	FFTF experimental pin (USA) [41]	141	U-19%Pu-10%Zr
5	EBR-II experimental pin (USA) [42]	200	U-19%Pu-10%Zr

In summary, the Indian and the international experience provide the confidence that MC fuels are indeed advanced fuels with potential for good performance in FBRs.

Irradiation Behavior of Nitride Fuels

The term nitride fuel refers most commonly to uranium mononitride or a solid solution of actinide nitrides, such as (U,Pu)N. The first has been primarily studied due to the potential use of nitrides for space propulsion, whereas the latter is more suitable as a fast breeder reactor fuel. In addition, the so-called uranium-free nitride fuels, typically a solid solution between transuranium actinide (TRU) nitrides and zirconium nitride, have been studied for their potential application in accelerator-driven systems (ADS). Nitride fuel is currently viewed as a potential reference fuel for future fast-neutron commercial power reactors to operate in a fuel self-sufficiency mode, specifically BREST-300 and BN-1200. Besides the power generation reactors, using the nitrides as a fuel for actinides transmutation is currently under consideration in many countries.

Even though the nitride fuel would offer definite advantage over the mixed oxide fuel with respect to density and thermal conductivity, as can be seen in section “Advanced Fuels,” one major problem associated with employment of nitride fuels is dissociation of (U,Pu)N fuel at a temperature of about 1730 °C which is much below the melting point of the fuel. This problem is a critical issue in case of severe accidents, which can be avoided if sufficient over pressure of nitrogen is maintained. Another major cause of concern is the generation of the radiotoxic ^{14}C through ^{14}N (n,p) ^{14}C and He through ^{14}N (n, α) ^{10}B . ^{15}N enrichment is one of the possible solutions, but it is expensive.

Irradiation experience with nitride fuels is inadequate as compared to that on oxide, and as of now the closure of fuel cycle has not been demonstrated. In fact, experience with nitride is much less even as compared to carbide fuels. Typically about 150–200 pins have been irradiated to a burn-up of 9 at.% at a linear heat rate of

45–130 kW/m. However, it is to be noted that the nitrides undergo facile dissolution in nitric acid and are more amenable for aqueous reprocessing [4] than the carbides.

Nitride fuel pins could be operated at a maximum linear power of 700 W/cm and 900 W/cm with helium and sodium as the bonding medium. Also, the helium-bonded fuel pins could be operated even at a power as high as 400–500 W/cm quite safely.

Extensive collation of the data pertaining to the fabrication and irradiation performance of the nitride fuel has been published earlier by Matzke [4] and Blank [43]. Test irradiations had been carried out in the CAPRA project in France in the 1990s to examine the viability of using the mixed nitride for incineration of Pu. Of late, the nitride fuels are being considered for applications related to minor actinide incineration as well. In Japan, considerable work had been carried out in the past on the fabrication of mixed nitride fuels for use in accelerator-driven subcritical systems [44–47].

Swelling of Nitride Fuel

Irradiation performance data suggest that nitrides have low fission gas release and swelling rates ($\sim 1.5\%V/V_0$ per at.% burn-up), in comparison with carbide fuel, thereby favoring high burn-up fuel pin designs. The typical swelling profile of UN fuel as a function of burn-up is given in Fig. 18 [48]. From the recent studies in Russia, the variation of the fuel pellet diameter as a function of local burn-up up to 5.5 at.% is shown in Fig. 19, and the swelling observed corresponding to this burn-up is $7.3 \pm 1.4\%$ [49]. This works out to a maximum swelling rate of 1.6% V/V₀ per at.% burn-up. Not much data are available on the swelling of nitride fuels at higher burn-ups, and it is expected that the swelling rates tend to saturate with burn-up. From the design perspective, assuming a swelling rate of roughly 1.6% per at.% (as against 0.6 per at.% for oxide), with a smear density of 75–78%, approximately 150 GWd/t burn-up could be achieved.

Fig. 18 Swelling rate of UN fuel irradiated in FFTF and EBR-II [48]

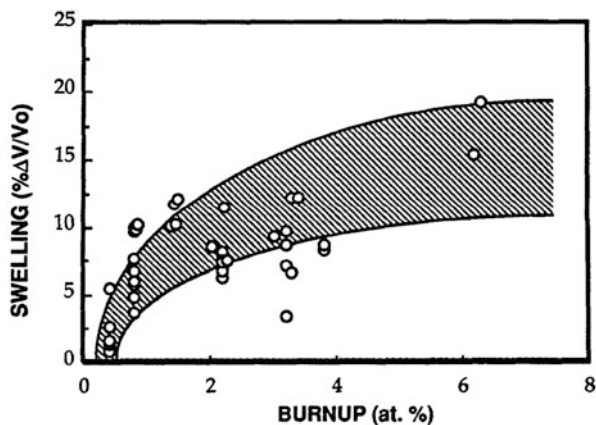
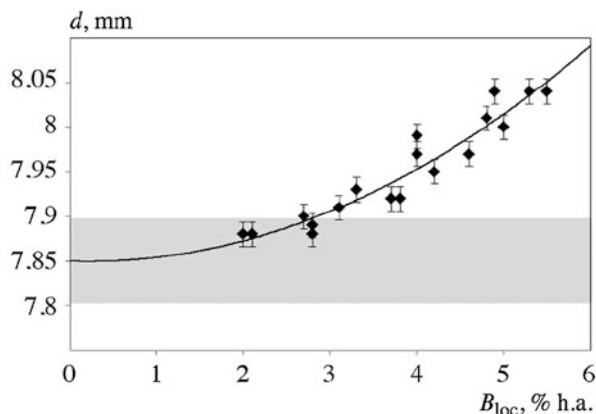


Fig. 19 Diameter of fuel pellets versus local burn-up in a section of a fuel element (shaded area is diameter variance before irradiation) [49]



Fission Gas Release in Nitride Fuels

As mentioned earlier, the number of U-N or mixed nitride pins irradiated is limited when compared to carbide pins. Reference [50] discusses the fission gas release in U-N fuels as a function of temperature, density, and burn-up. The equation is reproduced below (Eq. 6):

$$R = 100 \left[\exp \left(0.0025 \left\{ 90TD^{0.77}B^{0.09} - T \right\} \right) + 1 \right] \quad (6)$$

where, R is fission gas release rate, B is the burn-up, T is temperature, and TD is density of the fuel.

In Joyo, Japan, two mixed nitride pins were irradiated to a burn-up of 4.3 at.% at a LHR of 75 kW/m [51]. The fission gas releases were about 3.3% and 5.2%. In general, it can be stated that the fission gas release in nitride fuels is lower than carbide fuels. Bauer [52] analyzed the fission gas release data as a function of porosity in the mixed nitride fuel. It was observed that at densities greater than about 85% theoretical density, fission gas release can be accounted for recoil from the geometric surface of the pellet. At lower densities, it is expected that the porosities in the pellet are interconnected which would result in the rapid gas release. Figure 20 compares the work carried out by Tanaka et al. [51] with that reported by Bauer et al. [52].

Figure 21 shows the experimental versus predicted fission gas release (FGR) values from model used in the FRAPCON-EP, an empirically based correlation for fission gas release (FGR) in nitride fuel developed by Storms. In FRAPCON-EP, the fission gas release behavior was modeled by fitting the fission gas diffusion coefficient in U-N to FRAPCON's default fission gas release model. The effects of porosity, burn-up, operating temperature, fission rate, and bubble sink strength are addressed by a fitted gas diffusion coefficient [53].

Fig. 20 Gas release in MN fuels [51, 52]

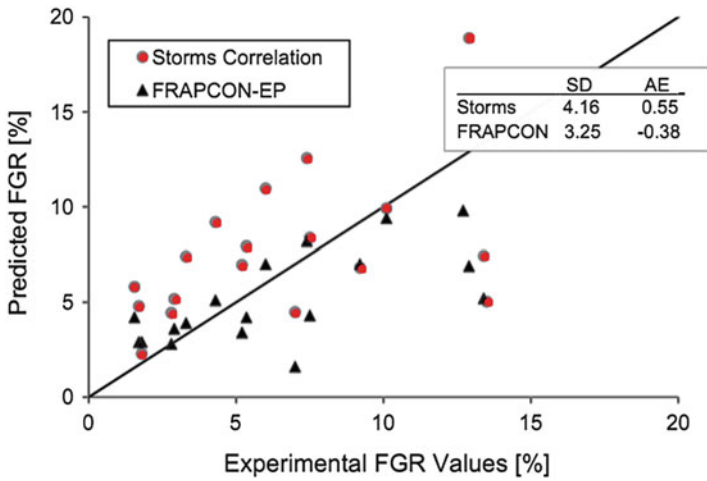
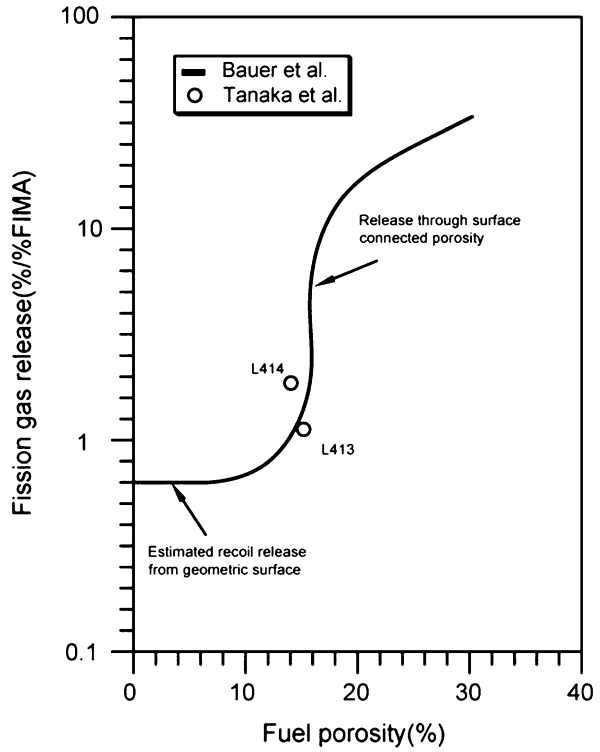


Fig. 21 Predicted fission gas release values from FRAPCON-EP [53]

International Experience of Nitride Fuels

MN fuels, when operated at high temperatures, exhibited extensive cracking and fragmentation during simple start-up and shutdown transients. US irradiation tests have shown that the reason for early fuel failures in MN fuels is the cracking phenomenon. As an engineering solution, a metallic shroud tube was provided around the fuel column which prevented fuel relocation after fragmentation to some extent. However, US specification recommends restricting the peak fuel temperature to less than 1200 °C which will lessen the fragmentation and prevent the usage of shrouds. Another concern in MN fuels is that if the nitrogen overpressure is not maintained, the fuels dissociate at temperatures well below its melting point.

The experimental data on the behavior under irradiation of mixed nitride fuel are given in Table 7.

In Europe, two MN fuel assemblies were irradiated in Phenix reactor; the first assembly consisted of 11 He-bonded MN pins which were irradiated at a maximum linear power of 420 W/cm up to maximum burn-up of 6.9 at.%. The second assembly consisted of 5 He-bonded MN pins which was irradiated at a maximum linear power of 730 W/cm up to maximum burn-up of 5.8 at.% [54].

The Russian nitride program is being pursued with an objective to improve the fabrication method, structure, and composition of fuel, to carry out in-pile tests (in MIR, BOR-60, and commercial BN-1200 reactors) and out-of-pile tests, and to carry out postirradiation examination (PIE) of experimental fuel assemblies. About 500 MN fuel pins had been fabricated for test irradiation in BN 600. Nine of these assemblies are under irradiation, and one assembly had undergone PIE. Also in the BOR-60 reactor, seven fuel assemblies with 7 MN pins each are under irradiation [54].

Among these, the He-bonded MN fuels were irradiated at a high linear power of 1000 W/cm, and in a Russian-French program, high Pu content (45% and 60%) He-bonded MN fuel pins were irradiated [54]. The outcome of these experiments has shown that the operating linear power should be less than 750 W/cm up to a burn-up of 15 at.%, the He-bonded MN fuel density should be less than 85% TD, and the oxygen and carbon content in the fuel should be less than 0.1% [55].

Reprocessing of Carbide and Nitride Fuels

As indicated in the earlier sections, the nuclear fuel is “burnt” only to an extent of around 10% in one cycle of irradiation. For enhancing the utilization of the fissile content, the irradiated fuel has to be reprocessed, once it has reached the target burn-up to recover the fissile material left behind in the fuel pins and refabricate the recovered material in the form of fresh fuel for re-irradiation in the reactor. The concept of recovering and reuse (recycling) of the fuel is called the closure of the fuel cycle. Closed fuel cycle is an important element of sustainability of nuclear

Table 7 Irradiation of nitride fuel in various reactors [54]

Country	Fuel		Reactor	Maximum burn-up, at. %	Maximum linear heat rating (kW/m)	Pellet density, % theoretical
	(U,Pu) N (bonding)	UN (bonding)				
USA	145 fuel elements (He, Na)		EBR-II, ETR, MTR	~9 (Na) 18.7 (He)	78–124	82–97
		>100 fuel elements (He)	FFTF, EBR-II, ETR, MTR	6	>70	87–96
EC	14 fuel elements (He) 1 fuel element (Na)		HFR, SILOE, DFR	5	45–130	81–95
	16 fuel elements (He)		Rapsodie	3.4	130	94
			Phenix	~7	41–73	82–83
Japan	4 fuel elements (He)		JMTR	5.5	65–73	83–86
	2 fuel elements (He)			4.5	80	83–86
Russia		~1300 fuel elements (He)	BR-10	8.8	45	92
	U _{0.8} Pu _{0.2} N, 5 fuel elements (He)		BOR-60	4	104.5	85–86
	U _{0.8} Pu _{0.2} N, 4 fuel elements (He)			8.95	65	85–86
	U _{0.55} Pu _{0.45} N, 2 fuel elements (He)			9.4	41.9	85
	U _{0.35} Pu _{0.65} N, 2 fuel elements (He)			12.1	54.5	85
		91 fuel elements (He)		~11	40	–

energy and has been a core principle in the development of nuclear power in some countries including India and France.

Reprocessing is perhaps the most challenging aspect of nuclear technology, involving as it does complex chemical operations with the irradiated fuel having very high levels of radioactive fission products. It is not therefore surprising that very few countries in the world have mastered this technology, and it is a matter of pride that India is one among these countries.

The options for spent fuel reprocessing, historical background, status of development in different countries, and the national perspectives are covered in detail in Ref. [56].

World over, industrial-scale reprocessing of oxide fuels has been carried out by the PUREX process, which involves dissolution of the fuel in nitric acid and recovery of U and Pu in the dissolver solution through a solvent extraction procedure using tri-n-butyl phosphate dissolved in a normal hydrocarbon diluent as the solvent. A detailed description of various elements of PUREX process can be found in Ref. [57]. The PUREX process has been extensively studied in several countries and also employed on an industrial scale in France and India for reprocessing of oxide fuels from thermal reactors. It has been used for processing metal fuels from thermal reactors as well. In France, the process has also been used for oxide fuels from fast reactors. The vast experience generated across the world has made PUREX process a universal option for reprocessing.

It is important to point out that while there have been studies on the reprocessing of advanced carbide and nitride fuels, both through the aqueous and nonaqueous routes, there has been no plant-scale experience on these processes anywhere in the world, with the exception of India. At IGCAR, Kalpakkam, plutonium-uranium mixed carbide fuel irradiated to a burn-up level as high as 150 GWd/t has been reprocessed on a regular basis in a pilot plant-scale facility called CORAL. The reprocessing process is based on PUREX. The Indian experience on carbide fuel reprocessing is summarized in Ref. [58].

Once the carbide or nitride fuel is dissolved in nitric acid, the solution obtained is amenable to processing by PUREX process, and the process flow sheet can be similar to what is adopted for oxide fuels. There are, however, a few additional aspects that need consideration. The dissolution of carbide fuels in nitric acid causes the formation of a number of organic compounds, only a few of which have been identified (oxalic acid and mellitic acid) [59]. These organic compounds can interfere with the PUREX process, especially with the recovery of Pu. A number of studies have been reported to address this issue. The carbide fuel can be converted to oxide through an oxidation process or pyrohydrolysis process, and this can provide a solution that is free from the organic compounds. However, considering that these are high-temperature processes that are not usually preferred in processing of irradiated fuel, the destruction of the organic compounds after aqueous dissolution is a preferred route. The destruction can be carried out chemically, electrochemically, or photochemically. However, it is not established whether all the organic compounds formed during the dissolution step can be completely destroyed by these processes. Interestingly, the reprocessing of highly irradiated plutonium-rich mixed carbide fuel, discharged from FBTR at Kalpakkam, was carried out without the destruction step.

The dissolution of nitrides in nitric acid is more straightforward and without any additional complications. However, C-14 isotope is formed during the fast reactor irradiation of nitride fuels through reaction of energetic neutrons with N-14 in the nitride fuel. The C-14 isotope, which is beta active, could be released in the form of carbon dioxide in the dissolution step, and this could pose challenges. The use

of nitrogen enriched in N-15 isotope is one route by which the C-14 issue could be avoided, but the economic aspects need a closer look.

Reprocessing of high-plutonium content Pu, U mixed carbide at burn-up levels as high as 150,000 MWd/t has been carried out on a regular basis at IGCAR, Kalpakkam, with good degree of success. It can therefore be expected that reprocessing of nitride fuels may not pose much challenges, except for the C-14 issue mentioned above. However, industrial maturity of the reprocessing of advanced fuels has to await large-scale deployment of these fuels. A techno-economic assessment of the potentials of advanced fuels can be meaningful only at that stage.

Conclusion

Carbide and nitride fuels present a number of desirable features for the accelerated growth of nuclear energy. These include a breeding potential higher than currently used oxide fuels and favorable physical properties. Their chemical reactivity and the lack of adequate industrial-scale experience pose significant challenges. Fabrication of carbide fuels and their subsequent handling needs inert atmosphere, and reprocessing may offer unforeseen challenges when carried out on industrial scale. Economic considerations could, therefore, come in the way of deployment of these advanced fuels in the absence of an emphasis on breeding. However, the long-term sustainability of nuclear power can be achieved only through deployment of fast reactors with closed fuel cycle, and it can be expected that advanced fuels, which are especially suitable for fast reactors, will play a key role in the growth of nuclear energy.

References

1. IAEA TECDOC 1531 (2006) IAEA fast reactor database
2. Konings RJM (2012) *Comprehensive nuclear materials*. Elsevier, Amsterdam
3. Sengupta AK, Agarwal R, Kamath HS (2012) In: Konings RJM (ed) *Comprehensive nuclear materials*. Elsevier, Amsterdam, pp 55–86
4. Matzke HJ (1986) *Science of advanced LMFBR fuels: solid state physics, chemistry, and technology of carbides, nitrides, and carbonitrides of uranium and plutonium*. North-Holland; Amsterdam (Netherlands)
5. Gueneau C, Chatain S, Rado C, Dumas JC, Lechelle J, Defoart F, Dupin N, Sundman R, Noel H, Konings RJM (2006) FUELBASE: a thermodynamic database for advanced nuclear fuels. In: *Proceedings of the HTR2006: third international topical meeting on high temperature reactor technology*, Johannesburg
6. Basak (2009) *Fabrication, properties and irradiation behavior of MOX, carbide and nitride fuels, inert matrix fuels with and without minor actinides*. Joint ICTP/IAEA School on Physics and Technology of Fast Reactors Systems, International Atomic Agency (IAEA), Vienna
7. Singh RN (1977) *Creep behavior of mixed carbide advanced nuclear fuel*. Topical meeting on advanced LMFBR fuels, Tucson 257
8. Ogata T (2012) In: Konings RJM (eds) *Comprehensive nuclear materials*. pp. 55–86
9. Duguay C (2012) *Mastery of (U,Pu)C carbide fuel: from raw materials to final characteristics*. workshop materials innovation for nuclear optimized systems, CEA – INSTN, Saclay, France

10. Richter K, Coquerelle M, Gabolde J, Werner P (1974) Proceedings of symposium on fuel and fuel elements for fast reactors. IAEA, Brussel/Vienna, pp 71–84
11. Handschun A, Dubios S, Vajdez SA, Grandjean SB, leturoq GB, Abraham F (2009) *J Nucl Mater* 385:186–188
12. Lorenzelli R (1968) Contribution a L'Etude du Systeme (U,Pu)C,N, Commissariat a l'Energie Atomique (CEA). France, Fontenay-aux-Roses
13. Sood DD, Aggarwal R, Venugopal V (1997) *J Nucl Mater* 247:293–300
14. Washington ABG (1973) UK Report TRG-2236
15. Alexander CA, Ogden JS, Pardue WM (1970) *Nucl Metall* 17:95
16. Pascard R (1967) *Nucl Metall* 13:345
17. Richter J, Schmidt HE, Tasman HA (1974) Report EUR 5119c
18. Pardue WM, Rough FA, Smith RA (1967) *Nucl Metall* 13:369
19. Dayton RW (1965) US report BMI-1738
20. Keller DL (1968) US Reports BMI-1837 and 1845
21. Muromura T (1982) *J Nucl Sci Technol* 19:638–645
22. Lindemer TB (1972) *J Am Ceram Soc* 55:601–605
23. Greenhaigh OW (1973) *J Am Ceram Soc* 56:553–557
24. Bradbury MH, Matzke H (1978) *J Nucl Mater* 75:68–76
25. Richter K, Guegnon J, Kramer G, Sari C, Wener P (1985) *Nucl Technol* 70:401–407
26. Hedberg M (2014) Nitride production by the internal gelation process. L. Engg. Dissertation, Chalmers University, Gothenburg
27. Speidel EO, Keller DL (1963) Fabrication and property of hot-pressed uranium mononitride. Battelle Memorial Institute, Columbus, BMI-1633
28. Muta H, Kurosaki K, Uno M, Yamanaka S (2009) *J Nucl Mater* 389:186–190
29. Mikailoff H (1974) L'element Combustible Carbure a Joint Helium Pour la Fillerea Neutrons Rapides: Problems Poses par le gonflement du combustible. BIST 196
30. Baldev R et al (2015) Sodium fast reactors with closed fuel cycle. CRC Press, New York
31. Bagley KQ, Bately W, Paris R, Sloss WM, Snape GP (1977) UK irradiation experience relevant to advanced carbide fuel concepts for LMFBRs. In: Proceedings of international meeting on advanced LMFBR fuels, Tucson
32. Govindarajan S, Puthiyavinayagam P, Clement Ravichandar S, Chetal SC, Bhoje SB (1998) Performance of FBTR mixed carbide fuel, influence of high dose irradiation on core structural and fuel materials in advanced reactor. In: Proceedings of IAEA, IAEA-TECDOC-1039:47-56
33. Raj B, Mannan SL, Kasiviswanathan KV, Mathew MD, Karthik V, Venkiteswaran CN, Saibaba M, Puthiyavinayagam P (2006) *Metal Mater Process* 18(1):1–16
34. Naga Sivayya D et al (2015) Development of a fuel modelling code for performance analysis of mixed carbide fuel. In: Characterization and quality control of nuclear fuels, Hyderabad
35. Venkiteswaran CN, Raghu N, Karthik V, Vijayaraghavan A, Anandraj V, Ulaganathan T, Saravanan T, Jayaraj VV, ShajiKurien JP, Johny T, Muralidharan NG, Joseph J, Kasiviswanathan KV (2011) *Energy Procedia* 7:227–233
36. Venkiteswaran CN, Muralidharan NG, Vijayaraghavan A, Joseph J, Venugopal V, Kasiviswanathan KV (2006) *J Nucl Energy Sci Technol* 2(4):352–360
37. IGCAR Internal Report (2016) FBTR/31411/DN/66/RA
38. Harry GR (1983) Status of steady state irradiation testing of mixed carbide fuel designs. US report LA-UR-83-1248
39. Kummerer KR (1984) 15 years of carbide type fast reactor fuel development in Germany: pin irradiation experience. *J Nucl Mater* 124:147–152
40. IAEA TECDOC 1691 (2012) IAEA Status of Fast Reactor Research and Technology Development
41. Baker RB, Bard FE, Leggett RD, Pinter AL (1993) *J Nucl Mater* 204:109–118
42. Paul RG, Porter DL, Crawford DC, Walters LC (1992) Irradiation behavior of metallic fast reactor fuels. *J Nucl Mater* 188:3–9
43. Frost BRT (1994) Materials science and technology, a comprehensive treatment, nuclear materials, vol 10A, Part I. VCH, Weinheim, pp 191–363
44. Suzuki Y, Arai YJ (1998) *J Alloys Compd* 27:271–273

45. Arai Y, Minato KJ (2008) *J Nucl Mater* 344:180–185
46. Minato K, Akabori M, Takano M (2003) *J Nucl Mater* 320:18–24
47. Minato K, Takano M, Otobe H (2009) *J Nucl Mater* 239:23–28
48. Mathews RB (1993) Irradiation performance of nitride fuels. Specialist conference on space nuclear power and propulsion technologies – Materials and fuels. Los Alamos National Laboratory, Podoisk-Moscow, Russia
49. Belyaeva AV (2017) Particulars of uranium-plutonium nitride fuel swelling during low-temperature irradiation in fast reactor to burnup 5.5% h.a. *Atomic Energy* 122(5):319
50. Storms EK (1998) An equation which describes fission gas release from UN reactor fuel. *J Nucl Mater* 158:119–129
51. Tanaka K, Maeda K, Katsuyama K, Inoue M, Iwai T, Arai Y (2004) Fission gas release and swelling in uranium–plutonium mixed nitride fuels. *J Nucl Mater* 327(2–3):77–87
52. Bauer AA, Brown JB, Fromm EO, Storhok VW (1971) Mixed nitride fuel irradiation performance. In: Farmakes R ed. *Fast reactor fuel element technology*, Hinsdale, IL: American Nuclear Society, pp 785–817
53. Feng B (2012) *J Nucl Mater* 427:30–38
54. Troyanov VM, Grachev AF, Zabud'ko LM, Skupov MV (2014) Prospects for using nitride fuel in fast reactors with a closed nuclear fuel cycle. *Atomic Energy* 117(2):85–91
55. IAEA TECDOC – 1374 (2003) Development status of metallic. Dispersion and non-oxide advanced and alternative fuels for power and research reactors. Nuclear Fuel Cycle and Materials Section International Atomic Energy Agency, Vienna, Austria
56. Schultz WW, Berger LL (1990) In: Navratil JD (ed) *Science and technology of TBP*, vol III. CRC Press, Boca Raton
57. Ferris LM, Bradley MJ (1965) *J Am Chem Soc* 87:1710
58. Natarajan R, Raj B (2007) Fast reactor fuel reprocessing technology in India. *J Nucl Sci Technol* 44(3):393–397
59. IAEA-TECDOC-1587 (2008) Spent fuel reprocessing options. Nuclear Fuel Cycle and Materials Section International Atomic Energy Agency, Vienna, Austria



Boron-Based Ceramics and Composites for Nuclear and Space Applications: Synthesis and Consolidation

19

Tammana S. R. C. Murthy , J. K. Sonber, K. Sairam, Sanjib Majumdar, and Vivekanand Kain

Contents

Introduction	704
Refractory/Transition Metal Borides and Its Composites	706
Properties and Applications of Refractory/Transition Metal Borides	706
Synthesis of Refractory/Transition Metal Borides	709
Densification/Consolidation of Refractory/Transition Metal Borides	716
Rare Earth Metal Borides	724
Properties and Applications of Rare Earth Metal Borides	725
Synthesis of Rare Earth Metal Borides	726
Consolidation of Rare Earth Metal Borides	727
Conclusions and Outlook	730
References	731

Abstract

Boron is one of the few elements to possess nuclear properties, which warrant its consideration as neutron absorber material due to its high neutron absorption cross section of 3838 barns (for thermal neutrons, 0.025 eV) for ^{10}B isotope. Boron-based ceramics are used as a control/shutoff rod, neutron shielding for the nuclear reactor as well as spent fuel storage bays, neutron sensors for measuring the neutron flux in a nuclear reactor, and space applications. Refractory and rare earth metal borides possess superior thermophysical properties, which enables to

T. S. R. C. Murthy (✉) · K. Sairam · S. Majumdar · V. Kain
Materials Processing and Corrosion Engineering Division/Department of Atomic Energy, Materials Group, Bhabha Atomic Research Centre, Mumbai, India

Homi Bhabha National Institute, Mumbai, India
e-mail: murthi@barc.gov.in; sairamk@barc.gov.in; sanjib@barc.gov.in; vivkain@barc.gov.in

J. K. Sonber
Materials Processing and Corrosion Engineering Division/Department of Atomic Energy, Materials Group, Bhabha Atomic Research Centre, Mumbai, India
e-mail: jitendra@barc.gov.in

use for high-temperature structural/functional applications. These borides are potential for high-temperature nuclear reactors of Generation IV as neutron absorbers, second-generation solar (receiver materials of concentrated solar power), and space applications such as rocket and hypersonic vehicle components, nozzles, leading edges, and engine components [81, 97, 109, 115]. Refractory metal borides are suitable for space application due to attractive combination of properties such as high melting point (>3000 °C), thermal conductivity, low thermal expansion coefficient, retention of strength at high temperatures, good thermal shock, oxidation, and erosion resistance [61, 81, 105, 118]. Various boron-based ceramics such as B_4C , TiB_2 , ZrB_2 , HfB_2 , NbB_2 , CrB_2 , LaB_6 , CeB_6 , NdB_6 , SmB_6 , YbB_6 , PrB_6 , Gd_2B_4 , and EuB_6 and its composites were synthesized and consolidated by various methods which are cited in the literature. This chapter reviews the work carried out on synthesis, consolidation, properties, and applications of important transition/refractory/rare earth metal borides.

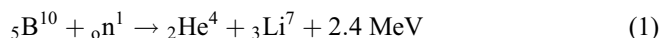
Keywords

Boron · Borides · Nuclear · Space · Synthesis · Consolidation

Introduction

Boron minerals occur mostly as borates which are deposited from volcanic gases or hot springs near volcanic activities. The deposits, predominantly of borax and sassolite, are formed as a result of drying up of shallow saline and alkaline tertiary lakes called “playa” [39]. The principal boron minerals are borax, hydrated sodium borate ($Na_2O \cdot 2B_2O_3 \cdot 10H_2O$), kernite (rasorite), hydrated sodium borate ($Na_2O \cdot 2B_2O_3 \cdot 4H_2O$), colemanite, hydrated calcium borate ($Ca_2B_6O_{11} \cdot 5H_2O$), ulexite, and hydrated sodium calcium borate ($NaCaB_5O_9 \cdot 8H_2O$). The estimated world reserves of boron minerals are about 380 million tons in terms of boric oxide. Countries with sizeable resources of boron minerals are Chile, China, Peru, Russia, Turkey, and the USA. Approximately 61% of the world’s boron reserves are in Turkey. Argentina was the second-leading producer of boron minerals in South America in 2014. China has low-grade boron resources with reserves of 32 million tons [39]. Consumption of borates is mainly by agriculture, ceramic, and glass industries.

Boron has two principal isotopes: B^{10} and B^{11} . The effectiveness of boron as neutron absorber is due to the high absorption cross section of B^{10} isotope. The neutron absorption reaction is given below and is referred as (n, α) reaction 1 [98, 115, 129]:



Naturally occurring boron is having the 19.8% of ^{10}B isotopes and the rest is ^{11}B . The neutron absorption of natural boron is sufficiently high in the low neutron energy range to make it an excellent candidate for use in thermal reactors. At higher

energies, the cross section of most other elements becomes very small, often abruptly low as in the case of cadmium, whereas that of B^{10} decreases monotonically with energy. Absolute neutron absorption cross section values of boron, along the entire energy spectrum, are of sufficient magnitude to make it very effective in the intermediate and fast energy range of neutrons. Boron, europium, and tantalum are recognized as fast neutron absorbers and hence used/tested as a control/shutoff rods in fast neutron nuclear reactors. Among these, B in the form of boron carbide (B_4C) with different enrichment ratios of $^{10}B/^{11}B$ isotope is extensively used the world over in all commercial fast neutron nuclear reactors. In addition to a high absorption cross section, boron has another advantage over other potential neutron absorber materials; the reaction products (helium and lithium) are formed as stable and non-radioactive isotopes. Refractory and rare earth metal borides possess superior thermophysical properties, which enable to use at high-temperature applications. These borides are also potential control/shutoff rods for high-temperature nuclear reactors of Generation IV due to its superior high-temperature properties [81, 97, 109, 113].

Another application of boron is for neutron capture therapy, a form of radiochemotherapy for treatment of certain forms of cancers and arthritis. Four years after the discovery of neutrons in 1932 by J. Chadwick of Cambridge University, a biophysicist, G.L. Locher of the Franklin Institute at Pennsylvania, introduced the concept of neutron capture therapy (NCT). Boron NCT technique is more beneficial due to its nonradioactive, readily available, easily can be introduced into the affected tumour cells. During irradiation of the tumor site by neutrons, the ^{10}B absorbs a low energy neutron and ejects an energetic short-range alpha particle and lithium ion which deposit most of their energy within the cell containing the original ^{10}B atom. Boron NCT is more attractive due to its nonradioactive, readily available, easily can be introduced into affected tumor cells [83].

Refractory/rare earth metal borides are suitable for space application due to attractive combination of properties such as high melting point ($>3000^\circ C$), thermal conductivity, low thermal expansion coefficient, retention of strength at high temperature, good thermal shock resistance, oxidation resistance, and erosion resistance [81, 89, 90, 105, 118]. Among all refractory metal borides, ZrB_2 and HfB_2 are considered as potential candidates for leading edge materials because of their superior oxidation resistance which is attributed to the formation of stable ZrO_2 and HfO_2 oxide scales. ZrO_2 , HfO_2 , and boron oxides are formed due to the oxidation of respective borides when exposed to high temperatures in the presence of oxygen. Boron oxides get evaporated from the system due to its low melting point and high vapor pressure. However, ZrO_2 and HfO_2 are more stable even at high temperatures because of its high melting point ($>2700^\circ C$) and low vapor pressures. Thus ZrB_2 and HfB_2 are superior to other metal borides for ultrahigh-temperature applications. Rare earth metal borides are also potential for ultrahigh-temperature applications.

However, real applications of these materials have been limited due to difficulties associated with their synthesis and consolidation. High melting point, low self-diffusion coefficient, and contamination with oxide layers on the surface of particles

make densification of these compounds extremely difficult. These shortcomings have boosted the research toward the improvement of consolidation/densification. One route employed to improve the sinterability of boride and carbide materials is to add a suitable sinter additive, which lowers the sintering temperature. In certain cases, these sinter additives give the additional benefit with improved fracture toughness and oxidation resistance [7, 81].

Synthesis of refractory/transition/rare earth metal borides was carried out by various methods like direct elemental reaction, carbo-/boro-/metallothermic reductions, and chemical vapor deposition. Consolidation of these materials was carried out by using various powder metallurgy techniques like conventional pressure-less sintering, hot pressing, and advanced sintering techniques like hot isostatic pressing, spark plasma sintering, microwave sintering, flash sintering with or without using the sintering aids, and chemical vapor infiltration. This chapter reviews the work carried out on synthesis, consolidation, properties, and applications of transition/refractory/rare earth metal borides. Some important physical, mechanical, thermal, and nuclear properties of boron and its compounds are given in Table 1.

Refractory/Transition Metal Borides and Its Composites

The development of new high-temperature materials is essential for applications of energy, space, and defense sectors. Refractory/transition metal boride (ZrB_2 , HfB_2 , TiB_2 , etc.)-based composites are potential candidates because they present a good balance of properties required for high-temperature and in aggressive environment applications [1, 81, 116]. Borides are considered better material compared to nitrides and carbides due to superior mechanical and thermal properties as well as having superior oxidation resistance [87, 116]. Some important properties and applications of refractory/transition metal borides and its composites are given in the following section.

Properties and Applications of Refractory/Transition Metal Borides

Important properties of some selected refractory/transition metal borides (TiB_2 , ZrB_2 , HfB_2 , TaB_2 , NbB_2 , CrB_2) are given in Table 1. Apart from nuclear applications as neutron absorbers (as given in Abstract and Introduction), these materials are potential for ultrahigh-temperature applications and so are called ultrahigh-temperature ceramics (UHTC). As with everything in the twentieth century, time was at a premium and no more so than in the aerospace industry during the 1960s [87]. During this period, the interest in UHTCs began; this group of materials was thought to have candidate to withstand the severe aero-thermo-chemical environments of hypersonic flights, reentry space shuttles, etc. Hypersonic speeds are generally associated with flight in the upper stratosphere where gas pressures can be very low, but the presence of oxygen radicals is high [35]. Due to the frictional

Table 1 Physical, mechanical, thermal, and nuclear properties of boron and its compounds [24, 27, 73, 81, 109, 129]

Property	Physical			Mechanical			Thermal			Nuclear	
	Cryst.	Den. g/cc	Elect. res. $\mu\Omega\text{-cm}$	Hard. GPa	Fracture toughness, $\text{MPam}^{1/2}$	FS, MPa	E, GPa	M. Pt. $^{\circ}\text{C}$	TC, W/m/K (50–100 $^{\circ}\text{C}$)		CTE, $10^6/\text{K}$ (500 $^{\circ}\text{C}$)
Boron	Tetra./ Rhom.	2.31–2.46	1.7×10^{12}	49	1.7	–	400	2180	–	8.3	759
B ₄ C	Rhom.	2.52	10^6	28–37	3.0–3.5	300	450–470	2450	30–40	5.0	600
TiB ₂	Hex.	4.52	10–30	25–35	5.0–7.0	700–1000	560	3225	60–120	7.3	502
ZrB ₂	Hex.	6.10	9.2	22–26	4.0–6.0	300	300–350	3245	20–58	6.8	500
HfB ₂	Hex.	11.21	11	21–28	–	350	500	3380	104	6.3	538
NbB ₂	Hex.	6.97	–	18–19	–	–	505	2290	–	–	~500
MoB ₂	Rhom.	7.87	–	24–25	–	–	569	2375	–	–	~500
TaB ₂	Hex.	12.50	–	25	4.5	555	550	3040	–	–	~510
W ₂ B ₅	Hex.	12.79	–	–	–	–	–	2365	–	–	~550
ReB ₂	Hex.	12.7	–	18	–	–	382	2400	–	–	~540
OsB ₂	Ortho.	12.83	–	20	–	–	410	1870	–	–	~510
CrB ₂	Hex.	5.20	30	11–20	3.5	600	211	2200	32	10.5	502
LaB ₆	Cubic	4.72	15	19.7	3.02	126	479	2715	45	6.4	652
EuB ₆	Cubic	4.99	85	18–26	–	183	–	2580	23	6.9	1286
CeB ₆	Cubic	4.80	29	30	4.6	–	379	2550	33.9	7.3	651
GdB ₄	Tetra.	6.47	–	18–21	2.3	–	380	2650	148.5	7	10,408

Rhom., rhombohedral; Hex., hexagonal; Ortho., orthorhombic; Tetra., tetragonal; Cryst., crystal structure; Den., density; Res., resistivity; Hard., hardness; FS, flexural strength; E, Young's modulus; M.Pt., melting point; TC, thermal conductivity; CTE, coefficient of thermal expansion; Σ , thermal neutron absorption cross section; Elect., electrical

heating at the vehicle surface, they generate high-enough thermal loads that alter the properties of the surrounding gases, causing it to vibrate, dissociate, react, excite, and eventually become fully ionizing, all while being surrounded by corrosive plasma layer [124]. UHTCs are used for applications that demand withstanding temperatures above 2000 °C, along with harsh atmospheric conditions as stated above. Such conditions are typically encountered during the reentry of space shuttles into the atmosphere [109, 116]. Hence, a lot of research on UHTCs has been conducted for applications like sharp leading edges, nose cap parts of hypersonic atmospheric reentry vehicles, rocket nozzle inserts, scramjet, and air-augmented propulsion system components, where operating temperatures can exceed 3000 °C [94, 105, 109].

Refractory/transition metal borides and its composites are also used as materials for ball bearings and other structural parts in machines/equipment that are used for high-temperature applications. Research is presently underway to replace refractory metals with advanced ceramics, especially these borides, which possess lower densities and hence higher property-to-weight ratio for fabricating engine components for driving airborne structures [53]. On a different note, apart from the typical applications at the ultrahigh temperatures, the excellent combination of mechanical and tribological properties for the borides, carbides, and nitrides allows them to be extensively used for heavy-duty wear-resistant applications (e.g., cutting tools) [7, 11, 76, 82, 121] and also as armor materials [129]. These materials are candidates for other extreme environments, which encountered in metal processing industries as molten metal crucibles.

Over more than four decades, ballistic performance and dynamic behavior studies have been performed on various ceramics (e.g., AlN, Al₂O₃, B₄C, SiC, TiB₂, WC, ZrO₂). As far as armor applications are concerned, TiB₂ exhibits favorable properties, such as high impact velocity for dwell/penetration transition and deformation-induced hardening. Dandekar et al. [19] assessed the strength properties of TiB₂ under plane shock wave loading in terms of its spall threshold and the shear stress, when a shock compressive stress of 60 GPa was applied. The break, i.e., cusp in the shock wave loading profile of TiB₂ at 4.5–7.0 GPa, is of mechanical nature, and its effect is to decrease the spall threshold values at stresses above the cusp, but below the accepted HEL value of 13–17 GPa. The spall strength of TiB₂ decreases with increasing impact stress and becomes negligible at the HEL. Two-phase ceramics of titanium diboride/alumina with a range of phase assemblage and phase morphologies have been reported for improving the performance. For armor applications, two-phase ceramics exhibit a wide range of fracture toughness values, which are often higher than the constituent ceramic phase, in bulk monolithic form [74].

As far as other applications are concerned, these borides are an attractive material for the aluminum industry, because of its wettability and low solubility in molten aluminum and its good electrical conductivity. Like TiB₂, ZrB₂ is wet by molten metals but is not attacked by them, making it a candidate material for molten metal crucibles, thermowell tubes for steel refining, and in electrical devices as heaters and igniters [60]. The wettability of the TiB₂ + carbon composite material was reported that increases the wettability as the TiB₂ content increases in the composite

[74]. Monolithic hot pressed TiB_2 is completely wetted by aluminum with a contact angle of zero in a cryolite melt at 1253 K (980 °C) [134].

In the present era, where a lot of emphases have been put toward the development of renewable/green energy sources, the refractory/transition metal borides and carbides are important components for structures required for harnessing solar energy as receiver materials for concentrated solar power (CSP) panels. The sole objective of CSP is to increase energy conversion efficiencies by increasing the working temperature [53]. CSP comes under the category of second-generation solar power systems. CSP receiver materials should withstand the high temperatures. The solar receiver is a key element, and a large effort has been devoted to the development of novel receiver architectures enabling raising the plant operating temperature. Carbides and borides of zirconium, hafnium, titanium, and tantalum possess high-temperature properties like high thermal conductivity, hardness, strength, and melting points and are attractive to be used as solar receiver materials. These materials also possess good optical properties like spectral selectivity, low emittance at high temperatures [101]. The main weakness of these carbides is their poor resistance to oxidation. However, it should be emphasized that the introduction of second phases enables it to produce silica-based glass (like SiC , MoSi_2 , TaSi_2 , and all transition-metal silicides) which greatly improves their oxidation resistance [12, 50, 77–79, 92, 114, 119].

Refractory/transition metal borides are extensively used as evaporation boats for vapor coating of aluminum. Fang et al. [25] developed porous TiB_2 electrodes for the alkali metal thermoelectric converter (AMTEC). The electrical performance of these new electrodes was found to be superior to that of the other electrodes, such as TiN or Mo . Because of its chemical inertness, TiB_2 can be expected to show a long-time stable operation. In view of the above-cited potential properties and applications, extensive research and investigations were carried out for the synthesis of these borides by a variety of methods. A brief review on cited literature of synthesis of refractory/transition metal borides is described in the next section.

Synthesis of Refractory/Transition Metal Borides

Refractory/transition metal boride ceramics are having application in forms ranging from coatings/thin films to bulk structures. A variety of synthesis methods were explored by various researchers in the globe based on the end use requirement, properties, commercial viability, and quantity of requirement. For example, carbothermic reduction of metal oxides in the presence of boron carbide is used for producing large quantities of boride powders with a particle size of 1 to 10 microns and purity of 98–99%. On other hand, hard boride coatings for high-speed cutting tools might best be synthesized and deposited by vapor phase methods such as chemical vapor deposition (CVD), physical vapor deposition (PVD), and chemical vapor infiltration (CVI), whereas liquid/gaseous precursors would be preferred to produce ceramic matrices for continuous fiber-reinforced composites. Other high-temperature structural/functional applications demand the fabrication of

dense bulk ceramics with high purity of >99%, which might be best accomplished by processes that combine reactive or chemical synthesis with densification. Hence, a variety of methods are explored based on the requirement of purity and size, some of which will only be capable of producing milligrams of material per day whereas others could produce in kilogram scale [24].

A brief history of the synthesis of refractory/transition metal borides is described here. Synthesis processes for diborides trace back to the late 1800s and early 1900s [24]. Henri Moissan identified a number of boride compounds [66, 68], including mentioning titanium boride in a study of the purification of titanium metal reported in 1895 [67], as part of his pioneering work using the electric arc furnace to produce compounds by fusion processes. In 1901, Tucker and Moody described the synthesis of zirconium boride by reaction of elements, although they assigned the formula Zr_3B_4 to their impure material [130]. Likewise, Wedekind prepared impure borides by vacuum melting [135]. One of the first reports of carbothermal reduction method for making TiB_2 and ZrB_2 (as per reaction 11 of Table 2) was reported by McKenna in 1936 [59]. However, in this era, none of the reported synthesized borides were phase pure. Later on, so many researchers envisaged to produce phase-pure compounds with fine size by a variety of synthesis methods and successfully produced ultrapure compounds with nanoscale-sized particles, whiskers, fibers, etc. [24].

Various synthesis methods of refractory/transition metal borides are listed here and presented in Table 2. Direct elemental reaction (e.g., Zr, Ti, Cr, Hf, and B) [57]; Reduction methods like Carbothermic, borothermic, combined carbo-borothermic, metallothermic; where respective metal oxides (e.g., TiO_2 , HfO_2 , ZrO_2 , Cr_2O_3); [91] are reduced to respective borides [143]. Hydrogen reduction of boron halides in the presence of respective metal or its halides, sol-gel, self-propagating high-temperature synthesis (SHS), mechanical milling of respective oxides and B_2O_3 with metallic magnesium, CVD, molten salt electrolysis, solution-based techniques, and synthesis from polymer precursors are different types of synthesis for borides. Displacement reaction methods are more appropriate for preparing the composite powders, e.g., a mixture of borides with carbides/nitrides as shown in reactions 21 to 24. The powder characteristics such as purity, morphology, surface area, and defect concentration strongly influence the sinterability of powder. All these properties are determined by the synthesis conditions. Thus the selection of the synthesis route and processing parameters is of vital importance for the actual application of the powder. A brief description of each method is explained in the following sections.

Direct Elemental/Solid-State Reaction Method

In this method, respective metallic elements, e.g., Ti, Zr, Hf, and Nb, are directly reacted with elemental boron as per stoichiometric ratio to form the respective boride (TiB_2 , ZrB_2 , HfB_2 , NbB_2) at elevated temperature in vacuum or inert atmosphere as shown in reaction 2 in Table 2. High pure and stoichiometric borides with fine particle/crystal sizes can be prepared by this method. But it is a very expensive method, due to the high cost of starting elemental powders, and also extremely

Table 2 Important chemical reactions involved in the different types of synthesis of refractory/transition metal borides [24, 57, 109, 116, 126]

Type of synthesis reaction	Reaction number
I. Direct elemental/solid-state reaction method	
$M_{(s)} + 2B_{(s)} \rightarrow MB_{2(s)}$	(2)
$MH_{2(s)} + 2B_{(s)} \rightarrow MB_{2(s)} + H_{2(g)}$ (modified elemental reaction)	(3)
$2M_{(s)} + Si_{(s)} + B_4C_{(s)} \rightarrow 2MB_{2(s)} + SiC_{(s)}$ (appropriate for making composite powders)	(4)
$8M_{(s)} + 1.5Si_{(s)} + 2B_4C_{(s)} + 3.5C_{(s)} \rightarrow 4MB_{2(s)} + 1.5SiC_{(s)} + 4MC_{(s)}$ (appropriate for making composite powders)	(5)
$M_{(s)} + 2Si_{(s)} + Mo_{(s)} + 2B_{(s)} \rightarrow MB_{2(s)} + MoSi_{2(s)}$ (appropriate for making composite powders)	(6)
$3M_{(s)} + 2BN_{(s)} \rightarrow MB_{2(s)} + 2MN_{(s)}$ (appropriate for making composite powders)	(7)
$4M_{(s)} + Si_3N_{4(s)} + 3B_4C_{(s)} \rightarrow 4MB_{2(s)} + 3SiC_{(s)} + 4BN_{(s)}$ (appropriate for making composite powders)	(8)
$3M_{(s)} + B_4C_{(s)} \rightarrow 2MB_{2(s)} + MC_{(s)}$ (appropriate for making composite powders)	(9)
$10M_{(s)} + Si_3N_{4(s)} + 3B_4C_{(s)} \rightarrow 6MB_{2(s)} + 3SiC_{(s)} + 4MN_{(s)}$ (appropriate for making composite powders)	(10)
II. Oxide reduction methods	
a. Carbothermic	
$MO_{2(s)} + B_2O_{3(l)} + 5C_{(s)} \rightarrow MB_{2(s)} + 5CO_{(g)}$	(11)
b. Carbothermic in the presence of boron carbide	
$2MO_{2(s)} + B_4C_{(s)} + 3C_{(s)} \rightarrow 2MB_{2(s)} + 4CO_{(g)}$	(12)
c. Borothermic	
$3MO_{2(s)} + 10B_{(s)} \rightarrow 3MB_{2(s)} + 2B_2O_{3(l/g)}$	(13)
d. Carbo and borothermic reduction	
$7MO_{2(s)} + 5B_4C_{(s)} \rightarrow 7MB_{2(s)} + 3B_2O_{3(l/g)} + 5CO_{(g)}$	(14)
e. Metallothermic reduction	
$3MO_{2(s)} + 3B_2O_{3(l)} + 10Al_{(l)} \rightarrow 3MB_{2(s)} + 5Al_2O_{3(s)}$	(15)
$MO_{2(s)} + B_2O_{3(l)} + 5Mg_{(l)} \rightarrow MB_{2(s)} + 5MgO_{(s)}$	(16)
f. Other methods	
$MO_{2(s)} + B_2O_{3(s)} \xrightarrow{*} MB_{2(s)} + 5/2O_{2(g)}$	(17)
III. Chloride reduction/chemical synthesis methods	
$MCl_{4(g)} + 2BCl_{3(g)} + 5H_{2(s)} \rightarrow MB_{2(s)} + 10HCl_{(g)}$	(18)
$2MCl_{4(g)} + 8LiBH_{4(g)} \rightarrow 2MB_{2(s)} + 2B_2H_{6(g)} + 10H_{2(g)} + 8LiCl_{(g)}$	(19)
$MCl_{4(g)} + 2NaBH_{4(g)} \rightarrow MB_{2(s)} + 2NaCl_{(s)} + 4H_{2(g)} + Cl_{2(g)}$	(20)
IV. Displacement reaction method (suitable for making composite powders)	
$MC_{(s)} + 6B_{(s)} \rightarrow MB_{2(s)} + B_4C_{(s)}$	(21)
$2MC_{(s)} + B_4C_{(s)} + 3Si_{(s)} \rightarrow 2MB_{2(s)} + 3SiC_{(s)}$	(22)
$MN_{(s)} + B_{(s)} \rightarrow MB_{2(s)} + BN_{(s)}$	(23)
$4MN_{(s)} + 3B_4C_{(s)} + 3Si_{(s)} \rightarrow 4MB_{2(s)} + 3SiC_{(s)} + 4BN_{(s)}$	(24)

*in the presence of catalyst "CaO + CaF₂"; M, refractory/transition metal; S, solid; l, liquid; g, gas; O, oxygen; C, carbon; N, nitrogen

difficult to handle and store the elemental powders especially due to its pyrophoric nature.

For synthesis from elements, boron and respective metal powders are thoroughly mixed to form a uniform powder mixture, which is then pelletized (making into green compacts) and reacted at high temperatures in the order of 1500 to 2000 °C in the vacuum or inert atmosphere. The partially sintered pellet of boride is then crushed and ground to get fine powders. The purity of the product depends on the purity of starting materials and also contamination during mixing/grinding operations [115]. Some literature cited examples on the preparation of borides by this method are given below.

ZrB₂ ceramic from elemental powders is thermodynamically favorable ($\Delta G_{2000K} - 279.6 \text{ kJ mol}^{-1}$); this route was used to produce ZrB₂ by self-propagating high-temperature synthesis (SHS). Tsuchida et al. (Jitendra Kumar [107]) have prepared ZrB₂-ZrC composite by mechanical activation-assisted SHS using a mixture of Zr, B, and C powders. Submicrometer-sized TiB₂ powder was prepared by mechanical alloying of a mixture of elemental Ti and B powders [37], size of the transition metal and the heat of formation of borides were greatly affected by the mechanical alloying time while producing finer-sized TiB₂. Ultrafine (nanometric) TiB₂ powder was produced through a self-propagating high-temperature synthesis (SHS) process involving the addition of varying amounts of NaCl [44] as diluents. It was reported that 26 nm size TiB₂ powders were obtained by using 20 wt.% NaCl addition [7]. Matsudaira et al. [58] reported that single-phase niobium diboride powder was prepared by direct elemental reaction of niobium (Nb) and amorphous boron (B) powders. Iizumi et al. [38] also prepared NbB₂ powder by the mechanical alloying technique using Nb and B as starting materials. Yeh and Chen [139] have synthesized niobium borides (NbB and NbB₂) by SHS process using elemental powders of Nb and B [97, 131].

Direct elemental reaction methods are very expensive but still preferred for specific applications, where it demands purity, exact stoichiometry, and fine grain size. However, for large-scale commercial production, this method is not viable. Respective metal oxide reduction method is more economical/appropriate for preparing borides due to the abundance of oxide forms.

Oxide Reduction Methods

Carbothermal reduction of the corresponding transition/refractory metal oxides emerged as an economical production route and continues to be the popular method for the synthesis of commercial transition/refractory metal diboride powders [24] as shown in reactions 11 and 12 in Table 2. The resulting powders typically contain oxygen and excess carbon as impurities (up to 1%) along with any metallic impurities present in the starting raw materials. For example, commercial ZrB₂ is produced from naturally occurring zircon ores, which often contain Hf as an impurity [24]. However, certain impurity levels especially carbon and oxygen are possible to reduce to ppm level by vacuum treatment at high temperatures. One has to optimize the temperature, and holding time has to be optimized in order to avoid partial sintering of powders, which leads to difficulties in grinding operations in order to

make into fine size powders. One has to take care while grinding the synthesized powders; many times impurities from grinding media or pickup oxygen from the atmosphere are likely to happen. Although the reduction method is commercially viable, one has to optimize all process parameters in such a way to get the desired phase of pure boride powders with the required particle size. Other metal oxide reduction methods such as borothermic and carbothermic in the presence of boron carbide and metallothermic reduction processes are also attractive for commercial production due to the utilization of inexpensive starting raw materials and ease to minimize the evaporation losses of boron. Few case studies on reduction method used for preparing different borides are summarized here.

Carbothermic reduction of ZrO_2 and B_2O_3 involves cheap raw material but results in the loss of B_2O_3 and the formation of nonstoichiometric powder. The resultant powder also contains some residual carbon [109]. Mishra et al. [63, 64, 109] reported the synthesis of micrometer-sized ZrB_2 powder by carbothermic reduction of ZrO_2 and B_2O_3 at 1800 °C in a vacuum. Khanra et al. [46] have prepared ZrB_2 whiskers by reaction between zirconia, boric acid, and carbon black. Borothermic reduction of ZrO_2 gives pure ZrB_2 at a temperature higher than 1600 °C. This method is not economical for commercial production as it involves the loss of expensive boron in the form of boron oxide. Excess boron is required to get the stoichiometric ZrB_2 [109]. Peshev and Bliznakov [91] reported the preparation of ZrB_2 , TiB_2 , and HfB_2 by reaction between metal dioxides and elemental boron (borothermic reduction) in a vacuum in the temperature range of 1000 °C–1750 °C. It was reported that the boron content in the product is less than the theoretical value due to the loss of boron in the form of suboxides. Millet and Hwang [61] have prepared ZrB_2 by reaction of ZrO_2 and boron (milled for 70 h) at 1100 °C in a vacuum. Mechanical milling enhanced the reactivity of powder, and thus the reaction temperature was brought down considerably. Ran et al. [93] synthesized ZrB_2 powder by using borothermic reduction process in the temperature range of 1000 to 1650 °C with nanometric ZrO_2 starting powder. Residual boron remains in the product when synthesized at a lower temperature of 1000 °C for 2 h in a vacuum, but the removal of residual boron-related species required a temperature of above 1500 °C. Morphology and size of the powders are also strongly influenced by synthesis temperature. Faceted morphology with particle size of 0.15 μm was reported when synthesized at 1000 °C–1200 °C and spherical morphology with a particle size of 0.66 μm at higher temperatures (>1500 °C).

Boron carbide reduction of ZrO_2 is also the most popular method for economical production of ZrB_2 powders, as it involves relatively inexpensive starting raw materials. ZrB_2 powder is synthesized as per reaction –12 at a temperature of >1800 °C in a dynamic vacuum or inert atmosphere. Dynamic vacuum is better than later for fast kinetics of reduction reaction and to achieve the high purities. Usually this process results in some evaporation losses of boron happened in the form of boron suboxides, which leads to end up with some nonstoichiometric boride or unwanted phases (residual carbon) in the product [109, 112]. Usually, excess boron of 15 to 30% is used for getting the stoichiometric ZrB_2 [112]. Guo et al. [29] reported ZrC along with ZrB_2 during the boron carbide reduction method. Single

ZrB₂ phase is obtained by using a 20–25 wt.% excess B₄C. Zhao et al. [143] and Funke and Yudkovskii [28] have produced micrometer-sized ZrB₂ powder by boron carbide reduction method; this is achieved by synthesizing at a lower temperature of 1600 °C and 1700 °C, respectively.

Reactive plasma spraying (RPS) is an alternative route for the synthesis of ZrB₂ when it is desired in the form of a coating. In RPS, a reaction takes place between the precursor particles and the plasma or between powder particles in the presence of plasma. Temperatures involved in plasma spray are very high (about 6000 °C–15000 °C). These high temperatures may significantly reduce the time required for the reaction. In RPS, important parameters, which affect the product quality, are plasma current, voltage, gas flow rate, and spray distance [109]. Karuna Purnapu Rupa et al. [43] have formed ZrB₂ coating using the plasma spray process at a 50 V voltage and 500A current.

Metallothermic reduction of ZrO₂ and B₂O₃ involves cheap raw material and is self-sustainable due to its exothermic nature. This method is mostly adopted for SHS [109]. Mostly magnesium, aluminum, calcium, and silicon are used as reducing agents for metallothermic reductions. Among, magnesium is preferred due to the ease of leach out of its oxide from the product. In this process, one has to ensure the complete consumption of reactants, especially ZrO₂ as it is very difficult to remove from the product by leaching/dissolution due to its refractory nature. However, this could be achieved by using excess Mg and B₂O₃ in the starting mixture [109]. Khanra et al. [45] reported a technique called double SHS (DSHS), in which reaction product of the first SHS is mixed with again Mg and H₃BO₃ powder and subjected to a second SHS in order to avoid any residual ZrO₂ in the final product. Nishiyama et al. [85] synthesized ZrB₂ by magnesiothermic reduction of ZrO₂ and B₂O₃ at a temperature of 800 °C. Setoudeh and Welham [103] have prepared fine ZrB₂ with a crystallite size of ~75 nm by mechanical alloying of ZrO₂, B₂O₃, and Mg for 15 h. Mishra et al. [62, 63] have used the SHS process to produce submicrometer ZrB₂ powder by magnesiothermic reduction. Aluminum was also used as a reducing agent for preparing ZrB₂–Al₂O₃ composite powder [65]. Lee et al. [51] have prepared ZrB₂ cermet by SHS using ZrO₂, B₂O₃, and Al as reactants along with Fe₂O₃ and excess Al.

Synthesis of TiB₂ was also reported by carbothermic reduction with various combination of mixtures, e.g., oxides of boron and titanium; reduction of titanium oxide by boron carbide and carbon; reduction of mixed oxides by metals like aluminum, silicon, and magnesium; mechanical alloying; or self-propagating high-temperature synthesis (SHS) by various authors during past the few decades [57, 74, 126]. Hafnium diboride was also synthesized by borothermic reduction [91], boron carbide reduction [111] [112], metallothermic reduction of HfO₂ in the presence of boron [116], and carbothermic reduction of HfO₂ and B₂O₃ [22, 24]. HfB₂ synthesis is relatively simpler than ZrB₂, in later charge modification (excess boron) required in order to get the single-phase compounds by reduction methods. Peshev et al. [91] reported the formation of NbB₂ by borothermic reduction of Nb₂O₅ in a vacuum. Matsumoto et al. [33] synthesized NbB₂ by melting a mixture of Nb₂O₅ and B in argon plasma arc. CrB₂ also can be synthesized by carbothermic/borothermic/

metallothermic reduction methods [110]. The next section gives a panorama of other methods of synthesis of refractory/transition metal borides like solution-based, molten salt electrolysis, and polymer precursor methods.

Other Methods of Synthesis

Other methods of synthesis include the solution-based, molten salt electrolysis, and polymer precursor methods. These methods will enable to produce ultrafine with very high pure compounds. But the major limitations of these methods are high cost, low productivity, and handling of toxic/explosive gases/solutions.

The solution-based methods are ideal for preparing ultrafine powders due to low-temperature synthesis and intimate contact of the reactants as its starting raw materials are in a liquid state [116]. However, limited studies have been reported on the synthesis of metal borides using these methods. Yan et al. [137] reported ultrafine zirconium diboride (ZrB_2) powders of ~200 nm (specific surface area – 32 m²/g), using inorganic–organic hybrid precursors of zirconium oxychloride ($ZrOCl_2 \cdot 8H_2O$), boric acid, and phenolic resin as sources of zirconia, boron oxide, and carbon, respectively, at a relatively low temperature of 1500 °C. Xie et al. [136] also reported on the synthesis of zirconium diboride by zirconium n-propoxide refluxed with 2,4-pentanedione to form zirconium diketonate. This compound is further hydrolyzed in a controllable fashion to form a zirconia precursor. Boric acid, phenol–formaldehyde, and zirconia precursors were concentrated, dried, pyrolyzed at 800–1100 °C, and exposed to carbothermal reduction heat treatments at 1150–1800 °C, to obtain a spherical particle of 200–600 nm ZrB_2 . Bates and co-workers [7] prepared nanocrystalline (5–100 nm) TiB_2 using a solution-phase reaction of $NaBH_4$ and $TiCl_4$, followed by annealing the amorphous precursor obtained at 900–1100 °C.

Various metal borides are synthesized by molten salt electrolysis method [116]. Frazer et al. [26] deposited ZrB_2 on nickel cathode from ZrO_2 and B_2O_3 dissolved in molten Na_3AlF_6 at 1020 °C (anode graphite). The ZrB_2 deposit was reported to be scaly/dendritic and non-adherent. Devyatkin [21] also reported the deposition of ZrB_2 on nickel cathode from cryolite-alumina melts containing zirconium and boron oxide. Ma et al. [54] have prepared CrB nanorods via reduction–boronation route at 650 °C in molten salt of anhydrous aluminum trichloride using an autoclave.

Polymeric precursor method for synthesis of metal borides is carried out by dispersing a metal oxide in a boron carbide polymeric precursor. On heating, the mixture results in either in situ generation of boron carbide and carbon (precursors for boron and carbon), followed by reaction to produce the metal boride by reduction of metal oxide. The polymer component should be stable, processable and contain both boron and carbon in order to form the boride phase by reduction of metal oxide. Dinitrile polymers have the above-cited characteristics with a good yield to form borides from the condensation polymerization of decaborane with dinitriles [116]. Su et al. [125] prepared the polymer precursor by dispersing ZrO_2 into decaborane dicyanopentane polymer ($-B_{10}H_{12}-NC-(CH_2)_5-CN-$)_x. Crystalline ZrB_2 was obtained by pyrolysis of the abovementioned precursor at 1450 °C.

Displacement reactions are another common method used for the in situ synthesis of borides and composite powders as shown in reactions 21 to 24 [24]. These reactions offer the same advantages as direct synthesis reactions (e.g., low temperatures, high purity, control of particle morphology), but often using less costly or more stable precursors [24]. HfB₂ ceramics containing 22 vol% SiC and 5 vol% ZrC was synthesized below 1200 °C from a mixture of Hf, Si, and B₄C [69].

A variety of synthesis methods were explored and reported for preparing various transition/refractory metal boride powders of different size ranges from few micrometers to nanometers. From the densification/consolidation point of view, emphasis should be placed on obtaining finer size powders with a narrow size distribution, high purity, and single-phase compound with a limited agglomeration [7]. From a classical Herring approach, it can be predicted that a decrease in particle size by one order of magnitude will produce 3–4 orders of magnitude reduction in sintering time, depending on the dominant densification mechanism (lattice diffusion, grain boundary diffusion) [7, 16]. The presence of agglomerates in the starting powders causes a decrease in sinterability and leads to the formation of micro–/macrocracks in the sintered ceramics. Thus, agglomeration is an important issue in the synthesis of nanosized powders [7].

Densification/Consolidation of Refractory/Transition Metal Borides

Densification of refractory/transition metal borides is extremely difficult due to their high melting point, strong covalent bonding, and low intrinsic self-diffusivity. So it demands high temperatures for densification by pressureless sintering techniques. At high temperatures exaggerated grain growth takes place which results in poor mechanical properties due to the formation of microcracks at the grain boundaries [116]. Thus, it is extremely difficult to get uncracked dense borides by pressureless sintering, as no shape accommodation occurs without external pressure and large pores tend to coarsen during high-temperature sintering [7].

In addition, boride powder surfaces are always contaminated with surface oxides such as B₂O₃ and respective metal oxides, which prevent the direct contact between boride particles. Moreover, these oxides promote surface diffusion and evaporation condensation mechanisms. Baik and Becher [6] reported the adverse effect of oxygen contamination, introduced during synthesis and/or subsequent densification of TiB₂. The presence of oxides increases the surface diffusivity, which is accompanied by an increase in grain size and coarsening of pores. In order to achieve higher density and to inhibit abnormal grain growth, it has been suggested that the total oxygen content of the powder must be limited to ≤0.5 wt.% or strong reducing additives need to be used to remove surface oxides [116]. These setbacks have provided the driver for considerable research efforts to improve the sinterability of refractory/transition metal borides in different ways, such as using nanosized starting powders, reactive sintering, pressure-assisted sintering techniques like hot pressing or hot isostatic pressing, and advanced techniques like spark plasma sintering, flash sintering, explosive sintering, microwave sintering, laser sintering, and chemical

vapor infiltration with or without using sintering additives [80]. Benefits of sintering additives to enhance the density with various mechanisms cited in the literature are: (i) it forms a liquid phase at sintering temperature (liquid-phase sintering), (ii) it reduces the surface oxides, and (iii) it increases the defect (structural vacancies) concentration due to chemical reactions (reactive sintering) [96, 109, 116]. Different types of additives have been exploited to improve the sinterability and properties of these borides. Sinter additives can be broadly classified into metallic (e.g., Ni, Fe, Cu, Co, Ti) and nonmetallic (AlN, MoSi₂, CrSi₂, WSi₂, TiSi₂, SiC, Si₃N₄, CrB₂, B₄C, TaC). The selection of sinter additive is also very important as these additives can affect the mechanical, thermal, and oxidation properties of borides. In the following sections, some case studies on densification of different transition/refractory metal borides by various methods are presented. Table 3 compares the densification behavior of borides by different methods.

Pressureless Sintering (PS)

Pressureless sintering is a very simple and economical technique to consolidate near-net shapes of ceramic materials. PS is carried out in two steps: (i) making the green compacts with sufficient handling strength either by uniaxial die compaction or cold isostatic pressing and (ii) heating these green pellets at the set temperatures in a controlled atmosphere at different heating rates. Heating can be done in an induction furnace or resistance heating furnace. Induction furnace heating is suitable for conductive/semiconductive ceramics or else graphite/SiC susceptors have to be used. The major advantage of pressureless sintering technique can fabricate near-finished components which will drastically reduce expensive machining operations. Unfortunately, it is extremely difficult to prepare sound dense shapes of transition/refractory metal borides by pressureless sintering due to low self-diffusivity of these ceramics and other cited reason given in the above section “[Densification/Consolidation of Refractory/Transition Metal Borides](#)” [116].

Farehnholtz et al. [23] reported only 78% densification of monolithic ZrB₂ by sintering at 2050 °C for 2 h. Chamberlain et al. [15] reported a density of ~98%TD of ZrB₂ by pressureless sintering at 2150 °C for 9 hours. ZrB₂-SiC-MoSi₂ composites of 98.7% TD were prepared by pressureless sintering at 2150 °C for 1 h [56]. In the case of HfB₂, a density of 89%TD have been reported by pressureless sintering at 1950 °C [116]. A maximum of 93.1%TD was reported for TiB₂ at 2150 °C in an argon atmosphere, whereas with the addition of 25%MoSi₂ at 1900 °C, 91.3%TD was obtained [75]. A maximum of 93% TD was reported for CrB₂ by pressureless sintering at 1850 °C, 6 h [110].

Hot Pressing (HP)

Pressureless sintering of transition/refractory metal borides without additive is extremely difficult to get the full-dense and sound products as cited above. Hot pressing is the commonly used technique for fabricating dense monolithic borides and its composites. In hot pressing, temperature and pressure are simultaneously applied to the powder compact using die. Heating is usually carried out externally using induction coils or graphite resistors, and the pressure is applied hydraulically/

Table 3 Consolidation of refractory/transition metal borides by different methods

Refractory/transition metal boride	Pressureless sintering			Hot pressing			Spark plasma sintering		
	Processing conditions	Density %TD	Reference	Processing conditions	Density %TD	Reference	Processing conditions	Density %TD	Reference
ZrB ₂	2150 °C, 540 min	98.0	[15]	1900 °C, 32 MPa, 45 min	99.8	[14]	2300 °C, 75 MPa, 3 min	98.0	[102]
HfB ₂	1950 °C, 60 min	89.0	[104]	1850 °C, 35 MPa, 60 min	80.2	[81]	1900 °C, 35 MPa, 15 min	100	[81]
TiB ₂	1900 °C, 120 min	68.5	[81]	1800 °C, 32 MPa, 60 min	97.5	[81]	1400 °C, 40 MPa, 10 min	98.0	[7]
NbB ₂	–	–	–	–	–	–	1900 °C, 50 MPa, 15 min	97.7	[97]
CrB ₂	1800 °C, 3600 min	93.5	[81]	1600 °C, 35 MPa, 120 min	99.8	[81]	1900 °C, 70 MPa, 15 min	98.4	[55]

TD, theoretical density; min, minutes

mechanically. Under the application of pressure, the contact points between particles are at very high stress, and thus diffusion gets increased at those contact points. Particle size influences the density and microstructure of the hot-pressed compacts. Before hot pressing, boride powder is milled by ball/attrition milling or vibratory grinding to obtain a powder of $<2\ \mu\text{m}$ size. The milled powder is filled in the graphite die and then heated to the required temperature in a vacuum or argon atmosphere. When the die temperature is reached to set temperature, uniaxial pressure of around 30–50 MPa is applied. Hot pressing temperature, pressure, heating rate, atmosphere, and holding time affect the properties and microstructure of the densified components. Unfortunately, the hot pressing method is limited to simple shapes, and complex geometry cannot be fabricated by using this technique [109, 116]. Schematic of typical resistant heating-type hot press is presented in Fig. 1.

In general, a temperature around 1800–2000 °C and pressure of 30 MPa are reported for achieving greater than 99% TD in ZrB_2 -based materials. For monolithic ZrB_2 , the hot pressing temperature of 1900 °C and pressure of 32 MPa are reported by Chamberlain et al. [14]. Relatively, HfB_2 is difficult to get full densification at similar conditions of ZrB_2 ; it demands higher temperatures, pressure, and time intervals. Only 80% TD of HfB_2 was reported, when hot pressed at 1850 °C and 35 MPa [81, 116]. Figure 2 presents the hot pressing temperature versus relative density plot of monolithic TiB_2 . From figure 2, it is clear that increasing the

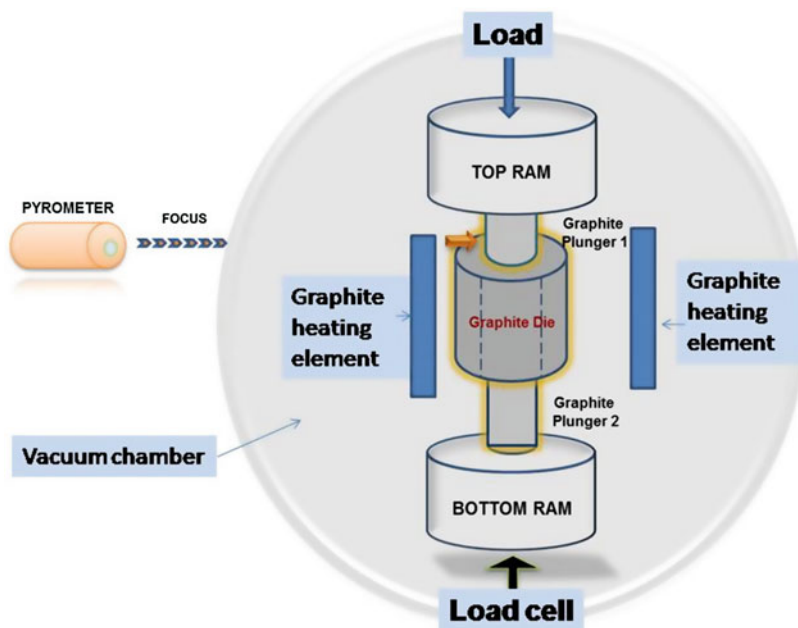


Fig. 1 Schematic of typical hot press used for consolidation of borides in vacuum or inert atmosphere

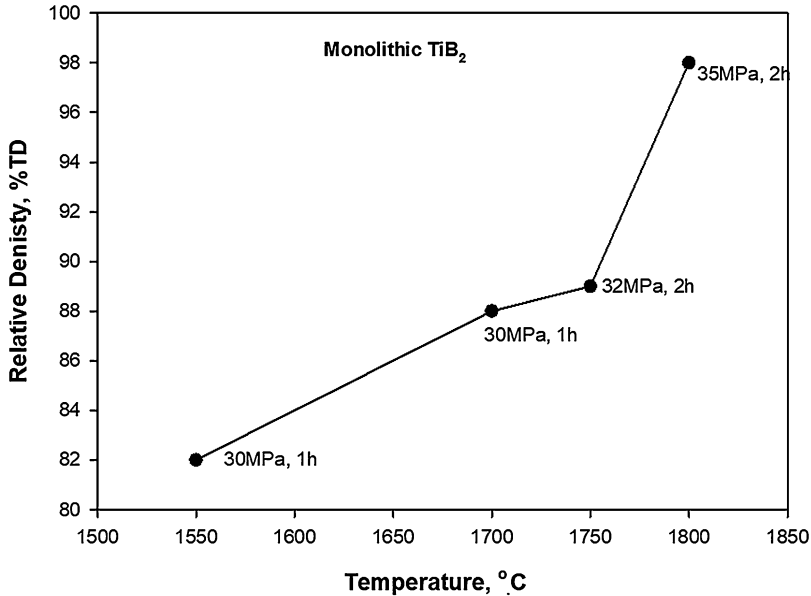


Fig. 2 Relative density versus hot pressing temperature plot of monolithic TiB_2 [81]

temperature and/or pressure helps to enhance the density. The maximum density of 98%TD was reported at 1800 °C, 35 MPa for TiB_2 . Significant improvement in density with a small addition of 2.5% sinter additives (MoSi_2 , TiSi_2 , WSi_2 , ZrSi_2 , CrSi_2) was reported for various transition/refractory metal borides (TiB_2 , ZrB_2 , CrB_2 , HfB_2) [81, 116]. CrB_2 also densified by hot pressing in a temperature range of 1500 °C to 1700 °C at a pressure of 20 to 35 MPa. Further improvement in densification, as well as properties of CrB_2 , was also reported by adding a different type of sinter additive (Nb , EuB_6 , MoSi_2 , etc.) [8, 55, 92, 95]. Further improvement in density without any grain coarsening was achieved relatively at lower temperatures and holding time by advanced sintering technique of spark plasma sintering, and more details are given in the next section.

Spark Plasma Sintering

The materials to be consolidated by using spark plasma sintering (SPS) are placed in a graphite die and punch assembly, similar to hot press. Heating source of SPS is directly passing the pulsed or direct current through die and punch. Schematic of spark plasma sintering (SPS) is presented in Fig. 3 [98]. Temperature is measured on the die surface, which is much lower than the actual sample temperature. The difference in temperature depends on the size of the die and the level of vacuum and insulation. Real densification mechanism in SPS is the debatable topic, and so many hypothetical explanations/models are cited in the literature. Some of the key points are summarized here.

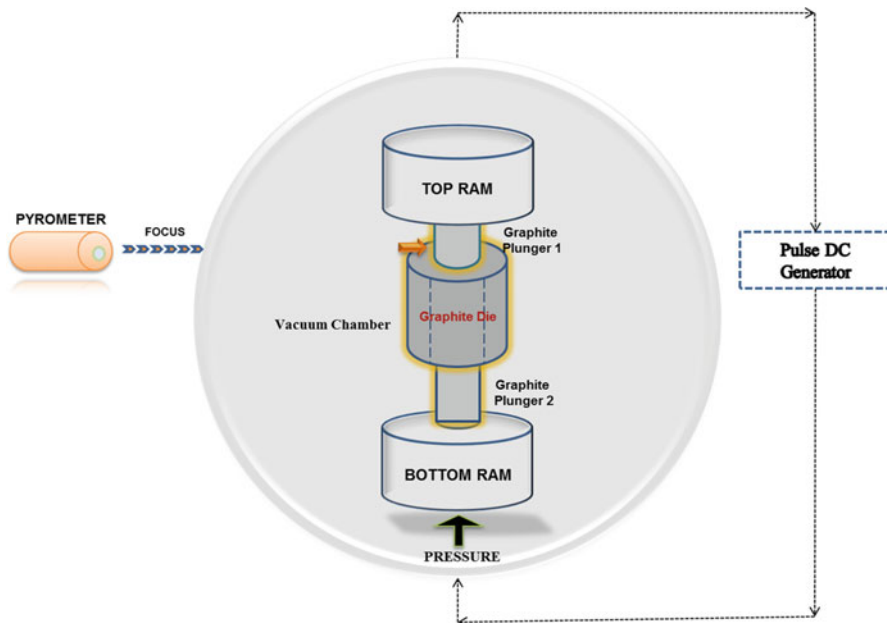


Fig. 3 Schematic of spark plasma sintering (SPS) facility shows the location of temperature measurement by optical pyrometer: reprinted with permission from Elsevier, *Int J Refract Met Hard Mater.*, 2014, 42, Fig. 4 in p. 186 Ref. [98]

The driving force of SPS for densification is provided by passing current directly through the particle material, with simultaneous application of pressure. High shear force in combination with pulsed electric power is initially applied to the particle material to generate electrical discharge that activates the particle surface by evaporation of oxide film, impurities, and moisture (non-oxide ceramic particle surfaces are always contaminated with oxygen) [129]. Subsequently, bonding is accomplished by resistance heating at the contact points between the activated particles in the presence of high pressure. The time and temperature required for consolidation are lowered as high current density is applied in addition to high shear and pressure which leads to localized heating and plastic deformation at interparticle contact points. The rapid sintering, which preferably lasts for less than a few minutes, prevents grain growth and allows the particles to retain their microstructure/size. Grain growth is suppressed by rapid heating and the densification is accelerated at high temperatures [53].

Spark plasma sintering (SPS), plasma-activated sintering (PAS), plasma pressure consolidation (PPC/P2C), and instrumented pulse electro-discharge consolidation are the different names given for the same process [55, 97–99, 129, 142].

It is well known that oxygen contamination, in the form of B_2O_3 and metal oxide, is present on the surface of the boride starting powders, and this limits the densification as explained in section “[Consolidation of Rare Earth Metal Borides.](#)” During

SPS, the use of a pulsed current generates spark discharges, which breaks the surface oxides and possibly enhances densification. The high heating rate increases the current, enhances spark discharge, and further promotes grain boundary diffusion for rapid densification. Grain growth is diffusion-controlled and time-dependent process. In SPS, sufficient time is not allowed to take place the grain growth. So, the grain size of SPS sintered material is always fine, due to a fast rate of heating (few hundred degrees per minute) and very less holding time of few minutes (compared to few hours in hot pressing/pressureless sintering). Few case studies on densification of refractory/transition metal borides by SPS are presented here.

Full-dense ZrB_2 was obtained by SPS at 1900 °C with 3-min holding time and a heating rate of 200–300 °C/min [30]. Akin et al. [4] reported 99% dense bodies of ZrB_2 –20% SiC by SPS at 2000 °C in 5 minutes only. Zhao et al. [144] also reported on SPS of ZrB_2 + SiC composite by reactive sintering of starting powders Zr, Si, and B_4C at 1400 °C and 9 min. Hulbert et al. [36] reported on SPS of HfB_2 –20% SiC composite at 1800 °C and 80 MPa in 8 min. The high-density chromium diboride (98.4% ρ_{th}) was obtained at 1900 °C, 70 MPa, and 15 min by SPS [55]. High-density NbB_2 (~97.7% ρ_{th}) was reported by SPS at 1900 °C for 15-min holding with good mechanical properties of 20 GPa hardness, 4 MPa.m^{1/2} fracture toughness, and 539 GPa elastic modulus [97]. Full-dense TiB_2 and its composites were prepared by SPS and cited in the literature [42, 47, 48, 52, 95]. Manabu et al. reported that addition of TiN to TiB_2 was effective in improving sinterability with fine structure and mechanical properties (bending strength – 373 MPa) [48]. TiB_2 and TiB_2 –SiC composites with carbon nanotube CNTs were prepared by spark plasma sintering. Highest flexural strength and fracture toughens of 925 MPa and 10.4 MPa.m^{1/2} were reported, respectively, for these composites [52]. Titanium diboride–niobium diboride ceramic composites were consolidated by spark plasma sintering (SPS) at 1950 °C with a density > 98% TD with a flexural strength of 330 MPa and 400 MPa at room temperature and 1600 °C, respectively [20]. From Table 3, it is clear that spark plasma sintering allows for getting higher densities at lower temperature and time compared to other sintering techniques (PS or HP). Next section addresses various other consolidation techniques like microwave sintering, hot isostatic pressing, laser sintering, and chemical vapor infiltration.

Other Consolidation Techniques of Transition/Refractory Metal Borides

Catastrophic failures are not tolerated for advanced and sensitive applications such as space, nuclear industry. Hence for specific or sensitive application, defect-free components are very essential. Ceramic materials are always inherently associated with microcracks or defects. Selection of appropriate techniques is very essential to consolidate defect-free ceramic components. Hot isostatic pressing (HIP) is one of the techniques, in which defect-free components can be prepared relatively at lower temperatures (compared to pressureless sintering/hot pressing). The HIP process is also known as gas pressure bonding. HIP is carried out in the combination of elevated temperature and high pressure to form/densify raw materials or preformed components. The application of the pressure is carried out inside a pressure vessel, typically using an inert gas as the pressure-transmitting medium with or without

glass encapsulation of the part. Combination of pressureless sintering followed by HIP is commonly adopted for making dense boride-based components. A resistance-/induction-heated furnace inside the vessel is the temperature source. The high pressure provides a driving force for material transport during sintering which allows the densification to proceed at a considerably lower temperature in comparison to that of traditional sintering. In addition, particularly during the initial stages of the process, the high pressure induces particle rearrangement and high stresses at the particle contact points. A virtually pore/microcrack-free product can be produced at a relatively low temperature by HIPing. The pressure level used in the HIP process is typically in the order of 100–300 MPa, as compared to 30–50 MPa in uniaxial hot pressing, and the isostatic mode of application of pressure is generally more efficient than the uniaxial one [74, 129]. For example, to achieve >95% TD of TiB_2 , it requires 1800 °C by hot pressing (HIP) HIPping at 1500–1600 °C which enables the attainment of similar density with good mechanical properties (hardness ~ 26 GPa and three-point flexural strength ~ 450 MPa) [72].

Microwave sintering is another alternative to conventional densification techniques. In microwave sintering, heating of powder compact is achieved by absorption of microwaves within the material to be sintered. All the materials are not good absorber of microwaves; some materials transmit it and some reflect it. Microwave sintering has the advantages of uniform and rapid heating since the energy is directly coupled into the specimen rather than being conducted into the specimen from an external heat source like conventional resistance heating systems. This results in an effective temperature profile, inverse to the one obtained by conventional heating (i.e., surface hottest, inside coldest). This is one of the big advantages of microwave heating, as it results in much faster heating and drying than conventional methods. The dielectric coefficient of the material determines how good it can be heated by microwaves, and the shape (more correctly, the volume) determines how much microwave energy can be absorbed by the product. Generally, enhanced densification and finer microstructures have been reported for microwave sintered materials. Research shows that high-temperature microwave processes may use 20% of the energy and take less than 20% of the time as compared with conventional gas or electric processes for similar products. High-temperature microwave heating has been widely used by several research groups worldwide in sintering of powdered metals and ceramics. The use of microwaves in ceramic sintering at temperatures ranging up to 1850 °C has been very successfully reported, with excellent results for a wide variety of materials. However, only a few literature reports were cited on microwave sintering of advanced non-oxide ceramics like ZrB_2 and TiB_2 [116, 129].

Titanium diboride (TiB_2) was rapidly sintered to >90%TD at sintering temperatures of 1900–2100 °C with holding time of 30 min or less by microwave heating (2.45 GHz, 6 KW) [34]. A comparison with conventional sintering indicated that microwave sintering of TiB_2 -3 wt.% CrB_2 occurred at a 200 °C lower temperature with significantly improved hardness, grain size, and fracture toughness [7]. Some of the materials do not absorb the microwaves at room temperature, but they absorb it at a higher temperature. The addition of a microwave-absorbing second phase (sintering aids) to ceramics that are microwave transparent can greatly enhance the

interaction of the system with microwaves [116]. For example, Zhu et al. [146] have investigated the microwave sintering of ZrB_2 with 4% B_4C particulate composites. B_4C acted as a microwave absorber for heating of the ZrB_2 matrix and, as a result, achieved >98%TD at a lower temperature of 1720 °C. Similarly, Wang et al. [132] reported $ZrB_2 + SiC$ composite by microwave sintering at 1850 °C, where SiC is a good microwave absorber.

Laser sintering is a rapid prototyping technique that prepares dense shapes by sintering the powder layer by layer. It is a novel technique to fabricate cladding layers as well as freestanding three-dimensional structures of materials. When the powder surface is irradiated by the laser beam, it absorbs energy, and the temperature increases resulting in necking, grain growth, partial melting, and densification. In this technique, contamination is minimal as it is a noncontact process. However, due to the small beam size, this method is suitable only for manufacturing of small objects. Recent research has indicated that laser sintering is very important in processing high-temperature, performance materials into functional components. Laser sintering also plays a vital role in 3-D printing technologies of ceramic materials. Laser power, beam spot size, and scan speed are major processing parameters in laser sintering [116]. Sun et al. [127] reported laser sintering of ZrB_2 with uniform surface morphology. Moreover, the rapid cooling rate of laser sintering results in the formation of needlelike nanostructures at the sintered surface. 3-D nanostructures of ZrB_2 -Zr cermet of >95% TD with 16 GPa hardness were prepared by a combination of laser sintering and induction heating technique [128].

Chemical vapor infiltration (CVI) is a relatively new technique for fabrication of fiber-reinforced ceramic matrix composites (FRCMCs). The main benefit is its ability to produce materials with attractive mechanical properties at relatively low processing temperatures and pressures, which reduce fiber stress and damage. CVI is a near-net-shape process, which aids the production of irregular-shaped components for a wide range of applications. CVI is a processing technique according to which a solid (e.g., a ceramic material) is deposited, within the pore network of a heated substrate, from a chemical reaction taking place between gaseous species which flow (either by diffusion or convection) in the pores (reaction mechanisms are similar to CVD) [40, 123]. Carbon fiber-reinforced ZrB_2 composite was prepared by isothermal CVI using precursors of $ZrCl_4$, BCl_3 , and H_2 [10]. Next section will address the properties, applications, synthesis, and consolidation of rare earth borides and its composites.

Rare Earth Metal Borides

The term “rare earth” denotes the group of 17 chemically similar metallic elements, including scandium, yttrium, and the lanthanides. The lanthanides are the series of elements with atomic numbers 57 to 71, all of which, except promethium, occur in nature. The rare earth elements, being chemically similar to one another, invariably occur together in the minerals and behave as a single chemical entity. The word “rare” in “rare earth” arises more from the historical difficulty in separating and

obtaining them as individual pure elements than from their inherent nonavailability. The close chemical similarity of all the rare earth elements is, first of all, displayed in their occurring together in nature and further by the fact that it took nearly 160 years of efforts by many great names in science to isolate and identify them. It has been borne out by experimental evidence that striking similarities among the chemical properties of the elements and their compounds are the consequence of strikingly similar electronic configurations [31]. Rare earth elements are important constituents of permanent magnets, rechargeable batteries, anticorrosion coatings, and catalysts [13], in addition to its borides. Important properties and applications of rare earth metal borides are discussed in the next section.

Properties and Applications of Rare Earth Metal Borides

Borides of rare earth metals have attracted attention due to their unique combination of physiochemical and thermomechanical properties, especially at elevated temperatures. These borides are characterized by high melting point, hardness, electrical and thermal conductivities, excellent thermal stability, low vapor pressure, and thermal expansion coefficient [70, 122]. Due to high neutron absorption cross section of boron, rare earth borides are candidate materials for neutron absorber applications in nuclear reactors. For example, EuB_6 is one of the candidate materials for control rod application in nuclear reactors. High neutron absorption cross sections of boron (759 barns) and europium (4600 barns) and the ability of EuB_6 (s) structure to accommodate helium atoms (which produced due to neutron absorption reaction) make this compound useful for control rod application in nuclear reactors [41]. They are good thermionic electron emitters due to their low work function, vapor pressure, high brightness, and long service life. Important properties of rare earth metal borides are presented in Table 1. Electronic structure, optical, elastic properties and enthalpies of formation of rare earth metal borides are reported elsewhere [17, 106]. The hexaborides of rare earth are a unique electric resistor material that has near-zero temperature coefficient of resistance, a feature not provided by metals. Formation of glass frits and LaB_6 can be screen printed and fired to provide resistor components required in modern integrated circuitry [31]. Rare earth borides such as LaB_6 , CeB_6 , NdB_6 , GdB_4 , and EuB_6 are excellent control rod materials due to high neutron absorption cross section of B and rare earth elements. CeB_6 and LaB_6 are excellent thermionic electron emitters (used as filaments) due to their low work function of 2.5 eV and 2.6 eV, respectively. LaB_6 is one of the most widely used thermionic emitters which offers better performance (higher emission, current density, higher brightness, higher emission stability, lower energy spread, and longer service life) than tungsten cathodes in a large variety of devices such as high-resolution electron microscopes, electron beam writing units, vacuum electron beam welding machines, electron beam surface reforming and lithography devices, microwave tubes, free electron lasers, and X-ray tubes [2, 32, 138, 145]. Recently, LaB_6 nanoparticles have been found exhibiting a strong absorption of the near-infrared (NIR) and high transmittance of visible light (VL). Therefore,

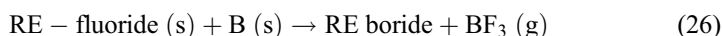
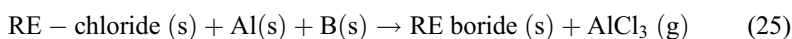
LaB₆ nanoparticles are now considered to be applicable in reduction of solar heat gain fields, such as windows of vehicles and buildings which have a growing demand to filter out the infrared waves of the solar spectrum in modern life [5, 140, 141]. Sani et al reported that “LaB₆ can have a solar absorbance comparable to that of the most advanced solar absorber material in actual plants such as silicon carbide, with a higher spectral selectivity” [100].

CeB₆ also acts as a corrosion inhibitor and prevents stress corrosion cracking of Alloy 600 in a caustic solution [71, 117, 119, 120, 122]. In addition, rare earth borides are potential additives to UHTCs for improving the oxidation resistance for space applications. Presently, the industrial production of the rare earth borides is limited by the difficulty in preparing a product of satisfactory purity by a process that may be extended to an industrial scale [70]. Only limited reports are available on synthesis and consolidation of rare earth borides, which are described in the next two sections, sections “[Synthesis of Rare Earth Metal Borides](#)” and “[Consolidation of Rare Earth Metal Borides](#),” respectively. Table 4 summarized the available data on the synthesis, consolidation, and properties of various rare earth metal borides.

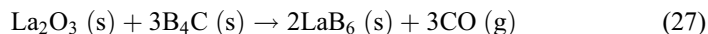
Synthesis of Rare Earth Metal Borides

Synthesis of rare earth (RE) metal borides is also reported by various methods as mentioned in the previous section of refractory/transition metal borides. Hence, the principle and description of each method are not repeated here. Few case studies of various rare earth metal borides by different methods are given here.

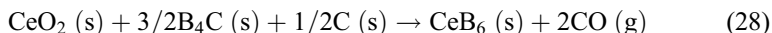
Lanthanum hexaboride films were prepared by direct elemental (lanthanum and boron) reaction at 550 °C for 1 h [88]. Reduction–distillation technique was used to prepare borides of rare earth of lanthanum (as per reaction 25), neodymium (as per reaction 25), and yttrium (as per reaction 26) as per the following chemical reactions [70] at 1200 °C:



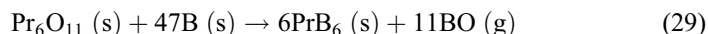
Lanthanum and neodymium borides were prepared without any presence of impurity phases, whereas yttrium hexaboride ended up with impurities of oxygen in the form of YBO₃ due to its tendency to high oxidation [70]. LaB₆ powders were synthesized by mechanochemical reaction of powder blends containing stoichiometric amounts of La₂O₃, B₂O₃, and Mg powders for 5 h with a 10:1 ball to powder ratio. LaB₆ and MgO phases were formed in the product. MgO was leached out using 3.6 M HCl. 75–300 nm size LaB₆ particles were yielded in this process [2]. Nanosized (20 to 350 nm) LaB₆ powders were synthesized from the oxides of La and B via calciothermic reduction by mechanochemistry (mechanical milling) at room temperature with post 6 M HCl leaching [3]. LaB₆ was synthesized by boron carbide reduction of La₂O₃ as per the following reaction (27) at 1500 °C, 2 h in a vacuum, and obtained product is having only 0.3% O as an impurity [119].



Sonber et al. also synthesized EuB_6 , NdB_6 , and GdB_4 by a carbothermic reduction in the presence of boron carbide at 1400 °C (for hexaborides) and 1500 °C (for tetraboride), respectively, for 2 h in 0.001 Pa vacuum [108, 117, 122]. Although this method is economical and feasible to produce in large quantities, end up with oxygen and carbon impurities (~0.5%) each. CeB_6 was synthesized by boron carbide reduction of CeO_2 in the presence of carbon at 1600 °C for 2 h in 0.001 Pa vacuum as per the reaction (28) [120].



YbB_6 synthesized by boron carbide reduction method (Yb_2O_3 and B_4C), which is similar to reaction 27. In situ synthesis combined with sintering at 1750 °C for 2 h in Ar was reported to obtain a porous YbB_6 ceramic, which is having a high compression strength of 21.34 MPa [133]. Synthesis of SmB_6 was reported in the early 1970s by borothermic reduction of samarium oxide at 1650 °C [84]. PrB_6 was also synthesized by borothermic reduction of its oxide by using an electron beam bombardment technique as per the following reaction (29):



Fused salt electrolysis offers an alternative low temperature method and the possibility of obtaining pure stoichiometric compounds due to the selective nature of the process. Pure NdB_6 and SmB_6 have been synthesized by fused salt electrolysis at ~900 °C by using an oxyfluoride bath [86]. LaB_6 nanocubes of 94.7 nm size were synthesized by a molten salt method using LaCl_3 and NaBH_4 as reactants and eutectic mixture of LiCl and KCl as a molten salt medium at 800 °C [141].

Consolidation of Rare Earth Metal Borides

A limited literature data is only available on densification of rare earth metal borides and presented in Table 4. Summary of the available data is described in the following lines. Pressureless sintering, hot pressing, and spark plasma sintering techniques are used for densification. Pressureless sintering of monolithic LaB_6 at 1950 °C resulted in 85.1% density, while hot pressing at the same temperature resulted in near theoretical density (99.9%) [81, 119]. Monolithic CeB_6 was densified to 93% TD by spark plasma sintering at 1900 °C. Addition of 5 wt.% TiSi_2 has increased its density to 97.4% TD at a lower sintering temperature of 1650 °C compared to monolith CeB_6 . The enhanced density is attributed to liquid-phase sintering mechanism assisted by the presence of low melting TiSi_2 phase [81, 120]. In the case of monolithic EuB_6 , only 86% of theoretical density was obtained by hot pressing at 1750 °C and 35 MPa. Addition of 10 wt.% TiSi_2 resulted in a density of 96.2% TD

Table 4 Literature data on synthesis, consolidation, and properties of various rare earth metal borides

Rare earth metal boride	Synthesis method and conditions	Product characteristics	Consolidation method and conditions	Relative density, %TD	Properties	Reference
LaB ₆	Molten salt method; LaCl ₃ and NaBH ₄ as reactants; molten salt medium: eutectic mixture of LiCl and KCl at 800 °C	LaB ₆ nanocubes with mean size of 94.7 nm	–	–	–	[14]
LaB ₆	Direct elemental reaction La + B at 550 °C, 1 h	100–10,000 Å ³ thick LaB ₆ crystalline phase	–	–	–	[88]
LaB ₆	Carbothermic reduction in the presence of B ₄ C at 1500 °C, 2 h, vacuum, as per reaction 27	0.3% O (impurity), single-phase LaB ₆	PS – 1950 °C, 4 h HP – 1950 °C, 35 MPa, 2 h	85.1 100	– Hardness – 20 GPa K _{1c} – 3 MPa.m ^{1/2} Excellent oxidation resistance	[119]
LaB ₆	La ₂ O ₃ -B ₂ O ₃ -Mg Mechanochemical route ball to powder ratio 10:1; 5 h, reducing agent: Mg	75–300 nm size LaB ₆	–	–	–	[2]
LaB ₆	La ₂ O ₃ -B ₂ O ₃ -Ca Mechanochemical route 3 h, reducing agent: Ca; 6 M HCl leaching	20–35 nm size LaB ₆	–	–	–	[3]
LaB ₆	Reduction–distillation; Al-reducing agent; temp. – 1200 °C; as per reaction 25	Single-phase LaB ₆	–	–	–	[70, 71]
NdB ₆	Reduction–distillation; Al-reducing agent; temp. – 1200 °C; as per reaction 25	Single-phase NdB ₆	–	–	–	
YB ₆	Reduction–distillation; temp. – 1200 °C; as per reaction 26	YB ₆ and impurity phases: YBO ₃ , YOF	–	–	–	

EuB ₆	Carbothermic reduction in the presence of B ₄ C at 1400 °C, 2 h, vacuum	0.7% C, 0.3% O (impurity), single-phase EuB ₆	HP – 1750 °C, 35 MPa, 2 h	86.0	Hardness – 18 GPa	[117]
GdB ₄	Carbothermic reduction in the presence of B ₄ C at 1500 °C, 2 h, vacuum	Single-phase GdB ₄	PS – 1800 °C, 2 h HP – 1700 °C, 35 MPa, 2 h	77.1 99.5	Hardness – 21 GPa K _{IC} –2.3 MPa.m ^{1/2} Poor oxidation resistance at 900 °C	[122]
CeB ₆	Carbothermic reduction in the presence of B ₄ C at 1600 °C, 2 h, vacuum, as per reaction 28	0.4% C, 0.2% O (impurity), single-phase CeB ₆	SPS – 1900 °C, 70 MPa, 15 min	93.4	Hardness – 14 GPa K _{IC} –4.6 MPa.m ^{1/2}	[120]
SmB ₆	Borothermic reduction (Sm ₂ O ₃ + B), 1650 °C, 2 h, vacuum	Sm _{0.68} B ₆ to SmB ₆ ; <0.03 wt% O	–	–	–	[84]
SmB ₆	Molten salt electrolysis; Sm ₂ O ₃ , Na ₂ B ₄ O ₇ , and LiF; 900 °C, Ar, current density: 1.0 to 2.3 A/cm ²	Pure crystals SmB ₆ , 72–83 nm	–	–	–	[9]
YbB ₆	Carbothermic reduction in the presence of B ₄ C at 1750 °C, 2 h, Ar	Porous partially sintered YbB ₆	In situ synthesis + PS	41.3%	Compressive strength – 21.34 MPa; suitable for using as a preform for making composites by infiltration methods	[133]
PrB ₆	Borothermic reduction of Pr ₆ O ₁₁ , at vacuum, by electron beam bombardment	Uncontaminated with any other borides phase, PrB ₆	–	–	–	[49]

PS, pressureless sintering; HP, hot pressing; K_{IC}, fracture toughness; SPS, spark plasma sintering

under the same operating conditions. Lower density obtained in monolithic EuB_6 is due to its refractory nature, predominantly covalent bonding, and low intrinsic self-diffusivity [117]. Nanocrystalline and dense LaB_6 of thin films were grown on Si substrates at 500 °C using the pulsed laser deposition (PLD) technique in an inert/vacuum atmosphere. 2.66 eV work function value was reported for the deposited films [18].

Conclusions and Outlook

Important properties, applications, synthesis, and consolidation methods of various transition, refractory, and rare earth metal boride ceramics have been reviewed. Boron-based ceramics are used as a control/shutoff rod, neutron shielding for a nuclear reactor as well as spent fuel storage bays, and neutron sensors for measuring the neutron flux in a nuclear reactor and space applications. Refractory and rare earth metal borides possess superior thermophysical properties, which enables to use for high-temperature structural/functional applications. These borides are potential control/shutoff rods for high-temperature nuclear reactors of Generation IV and second-generation solar and space applications. In spite of these superior properties and applications of these materials, challenges are associated with synthesis and fabrication of components with required purity and densities in commercial scale.

Various synthesis methods of borides are summarized. Among these methods, boron carbide reduction of respective metal oxides is attractive for commercial production point of view, due to its cost consideration of raw materials, reproducibility, feasibility in kg scale, and reliability of phases and purity levels. Laboratory-scale syntheses by chloride reduction, precursor/reactive methods, or chemical routes allow for precise control of particle size and purity for fundamental studies, although these methods are not commercially viable to date. The choice of methods for synthesis can be made based on a balance of cost with the properties of the resulting powders (starting particle size, morphology, purity, stoichiometric phase, etc.). In the future, continued research is indeed to explore various novel synthesis methods to improve the product quality (such as higher purity, smaller particle size for enhanced densification, and control of final microstructure) with energy efficiency. Hence, future research will likely to increase the focus on existing and novel methods that produce ceramic powders with fine particle sizes, very low metallic impurity contents, and very low oxygen/carbon impurity contents.

Due to the high melting point, the presence of an oxide layer on the surface and low self-diffusion and covalent nature and densification of borides are difficult. Pressureless sintering is not enough to get the full density with the desired quality product. Hence, external pressure is a must to densify these materials in the pure form without significant grain growth. Unfortunately, such methods (hot pressing, spark plasma sintering) are limited to simple shapes. New ideas are needed to fabricate dense bodies of borides into various shapes. This can be achieved in the following ways:

- (i) Use of nanosized powders with high specific surface area, so that densification is possible at a lower temperature without using external pressure. For that purpose, the novel synthesis method has to be developed as mentioned above. Some of the techniques are being cited, but they are limited to laboratory scale only.
- (ii) Selection of a suitable sinter additive, which enhances the densification as well as properties without much affecting inherent properties of borides. Significant work has been reported on the use of different sinter additives for refractory/transition metal borides. These results will be extremely useful for the designer for selection of appropriate sintering aids for densification of rare earth metal borides.
- (iii) Explore new densification techniques which can give dense bodies of various shapes. New techniques such as spark plasma sintering and microwave sintering are being used for borides. Advancements are needed to make these techniques capable to produce complex shapes. Moreover, new techniques with better features need to be invented.
- (iv) Joining of the densified components is also critical and important to fabricate the desired shapes and sizes for end user requirement. Research on joining techniques also has to be explored.

References

1. Acharya R, Raja SW, Chhillar S et al (2018) Non-destructive quantification of total boron and its isotopic composition in boron based refractory materials by PIGE and an inter-comparison study using TIMS and titrimetry. *J Anal At Spectrom* 33:33. <https://doi.org/10.1039/c7ja00416h>
2. Ağaogullari D, Duman I, Öveçoğlu ML (2012) Synthesis of LaB₆ powders from La₂O₃, B₂O₃ and Mg blends via a mechanochemical route. *Ceram Int* 38:6203–6214. <https://doi.org/10.1016/j.ceramint.2012.04.073>
3. Ağaogullari D, Balcı Ö, Öveçoğlu ML, Duman İ (2016) Preparation of LaB₆ powders via calciothermic reduction using mechanochemistry and acid leaching. *KONA* 2016:203–218. <https://doi.org/10.14356/kona.2016001>
4. Akin I, Hotta M, Sahin FC et al (2009) Microstructure and densification of ZrB₂-SiC composites prepared by spark plasma sintering. *J Eur Ceram Soc* 29:2379–2385. <https://doi.org/10.1016/j.jeurceramsoc.2009.01.011>
5. Babu MS, Sivanantham A, Chakravarthi BB et al (2017) Enhanced Photoelectrochemical water splitting behaviour of tuned band gap CdSe QDs sensitized LaB₆. *J Nanosci Nanotechnol* 17:437–442. <https://doi.org/10.1166/jnn.2017.12410>
6. Baik S, Becher PF (1987) Effect of oxygen contamination on densification of TiB₂. *J Am Ceram Soc* 70:527–530. <https://doi.org/10.1111/j.1151-2916.1987.tb05699.x>
7. Basu B, Raju GB, Suri AK (2006) Processing and properties of monolithic TiB₂ based materials. *Int Mater Rev* 51:352–374. <https://doi.org/10.1179/174328006X102529>
8. Bedse RD, Sonber JK, Sairam K et al (2015) Processing and characterization of CrB₂-based novel composites. *High Temp Mater Process* 34. <https://doi.org/10.1515/htmp-2014-0084>
9. Berchmans LJ, Visuvasam A, Angappan S et al (2010) Electrosynthesis of samarium hexaboride using tetra borate melt. *Ionics (Kiel)* 16:833–838. <https://doi.org/10.1007/s11581-010-0469-3>

10. Berthon S, Malé G (1997) Infiltration of zirconium diboride by ICVI in porous materials. *Compos Sci Technol* 57:217–227. [https://doi.org/10.1016/S0266-3538\(96\)00131-5](https://doi.org/10.1016/S0266-3538(96)00131-5)
11. Bhatt B, Murthy TSRC, Limaye PK et al (2016) Tribological studies of monolithic chromium diboride against cemented tungsten carbide (WC–Co) under dry condition. *Ceram Int* 42. <https://doi.org/10.1016/j.ceramint.2016.06.208>
12. Carney CM, Parthasarathy TA, Cinibulk MK (2011) Oxidation resistance of hafnium diboride ceramics with additions of silicon carbide and tungsten boride or tungsten carbide. *J Am Ceram Soc* 94:2600–2607. <https://doi.org/10.1111/j.1551-2916.2011.04462.x>
13. Castano CE, Keefe MJO, Fahrenholtz WG (2015) Cerium-based oxide coatings. *Curr Opin Solid State Mater Sci* 19:69–76. <https://doi.org/10.1016/j.cossms.2014.11.005>
14. Chamberlain AL, Fahrenholtz WG, Hilmas GE, Ellerby DT (2004) High-strength zirconium Diboride-based ceramics. *J Am Ceram Soc* 87:1170–1172. <https://doi.org/10.1111/j.1551-2916.2004.01170.x>
15. Chamberlain AL, Fahrenholtz WG, Hilmas GE (2006) Pressureless sintering of zirconium Diboride. *J Am Ceram Soc* 89:450–456. <https://doi.org/10.1111/j.1551-2916.2005.00739.x>
16. Chiang Y, Birnie DP, Kingery WD (1997) *Physical ceramics: principles for ceramic science and engineering*. J. Wiley
17. Colinet C, Tedenac J (2018) Enthalpies of formation of rare-earth borides from first principles. Comparison with experimental values. *Calphad* 62:49–60. <https://doi.org/10.1016/j.calphad.2018.04.004>
18. Craciun V, Cristea D, Socol G et al (2016) Characteristics of LaB₆ thin films grown by pulsed laser deposition. *J Vac Sci Technol A* 34:051509. <https://doi.org/10.1116/1.4960647>
19. Dandekar DP, Benfanti DC (1993) Strength of titanium diboride under shock wave loading. *J Appl Phys* 73:673–679. <https://doi.org/10.1063/1.353350>
20. Demirskyi D, Solodkyi I, Nishimura T, Vasylykiv OO (2019) Fracture and property relationships in the double diboride ceramic composites by spark plasma sintering of TiB₂ and NbB₂. *J Am Ceram Soc* 102:4259. <https://doi.org/10.1111/jace.16276>
21. Devyatkin SV (2001) Electrosynthesis of zirconium boride from Cryolite–alumina melts containing zirconium and boron oxides. *Russ J Electrochem* 37:1308–1311. <https://doi.org/10.1023/A:1013295931573>
22. Fahrenholtz WG, Hilmas GE, Talmy IG, Zaykoski JA (2007) Refractory Diborides of zirconium and hafnium. *J Am Ceram Soc* 90:1347–1364. <https://doi.org/10.1111/j.1551-2916.2007.01583.x>
23. Fahrenholtz WG, Hilmas GE, Zhang SC, Zhu S (2008) Pressureless sintering of zirconium Diboride: particle size and additive effects. *J Am Ceram Soc* 91:1398–1404. <https://doi.org/10.1111/j.1551-2916.2007.02169.x>
24. Fahrenholtz WG, Binner J, Zou J (2016) Synthesis of ultra-refractory transition metal diboride compounds. *J Mater Res* 31:2757–2772. <https://doi.org/10.1557/jmr.2016.210>
25. Fang Q, Knodler R (1992) Porous TiB₂ electrodes for the alkali metal thermoelectric converter. *J Mater Sci* 27:6725–6729. <https://doi.org/10.1007/BF01165960>
26. Frazer EJ, Anthony KE, Welch BJ (1975) Electrodeposition of zirconium diboride from oxides dissolved in molten cryolite. *Electrodepos Surf Treat* 3:169–177. [https://doi.org/10.1016/0300-9416\(75\)90039-5](https://doi.org/10.1016/0300-9416(75)90039-5)
27. Frotscher M, Hölzel M, Albert B (2010) Crystal structures of the metal Diborides ReB₂, RuB₂, and OsB₂ from neutron powder diffraction. *Zeitschrift für Anorg und Allg. Chemie* 636:1783–1786. <https://doi.org/10.1002/zaac.201000101>
28. Funke VF, Yudkovskii SI (1964) Preparation of zirconium boride. *Sov Powder Metall Met Ceram* 2:293–296. <https://doi.org/10.1007/BF00774035>
29. Guo W-M, Zhang G-J (2009) Reaction processes and characterization of ZrB₂ powder prepared by Boro/Carbothermal reduction of ZrO₂ in vacuum. *J Am Ceram Soc* 92:264–267. <https://doi.org/10.1111/j.1551-2916.2008.02836.x>
30. Guo S-Q, Nishimura T, Kagawa Y, Yang J-M (2008) Spark plasma sintering of zirconium Diborides. *J Am Ceram Soc* 91:2848–2855. <https://doi.org/10.1111/j.1551-2916.2008.02587.x>

31. Gupta CKK, Krishnamurthy N (1992) Extractive metallurgy of rare earths. *Int Mater Rev* 37:197–248. <https://doi.org/10.1179/imr.1992.37.1.197>
32. Hang C, Yang L, Liang Y et al (2018) Mesoporous LaB₆ calcium silicate composite: preparation, NIR photothermal conversion and drug delivery properties. *Ceram Int*. 0–1 44:8427. <https://doi.org/10.1016/j.ceramint.2018.02.037>
33. Heller G, Buschbeck K-C, Niedenzu K (1986) Gmelin handbook of inorganic and organometallic chemistry. In: B Boron compounds. 3rd Supplement, Volume 2, Boron and oxygen. Springer, Berlin
34. Holcombe CE, Dykes NL (1991) Microwave sintering of titanium diboride. *J Mater Sci* 26:3730–3738. <https://doi.org/10.1007/BF01184963>
35. Holden M (1986) A review of aerothermal problems associated with hypersonic flight. In: 24th aerospace sciences meeting. American Institute of Aeronautics and Astronautics, Reston
36. Hulbert DM, Jiang D, Dudina DV, Mukherjee AK (2009) The synthesis and consolidation of hard materials by spark plasma sintering. *Int J Refract Met Hard Mater* 27:367–375. <https://doi.org/10.1016/j.ijrmhm.2008.09.011>
37. Hwang Y, Lee JK (2002) Preparation of TiB₂ powders by mechanical alloying. *Mater Lett* 54:1–7. [https://doi.org/10.1016/S0167-577X\(01\)00526-2](https://doi.org/10.1016/S0167-577X(01)00526-2)
38. Iizumi K, Sekiya C, Okada S et al (2006) Mechanochemically assisted preparation of NbB₂ powder. *J Eur Ceram Soc* 26:635–638. <https://doi.org/10.1016/J.JEURCERAMSOC.2005.06.012>
39. Indian Bureau of Mines (2016) Indian minerals yearbook 2015. Indian Miner Yearb 2015 (Part-III Miner Rev 54th edn) 1–9
40. Jaglin D, Binner J, Vaidyanathan B et al (2006) Microwave heated chemical vapor infiltration: densification mechanism of SiC_f/SiC composites. *J Am Ceram Soc* 89:2710–2717. <https://doi.org/10.1111/j.1551-2916.2006.01127.x>
41. Jain A, Kandan R (2017) Determination of the thermodynamic stability of europium boride. *J Therm Anal Calorim* 6:275. <https://doi.org/10.1007/s10973-017-6876-1>
42. Jain D, Reddy KM, Mukhopadhyay A, Basu B (2010) Achieving uniform microstructure and superior mechanical properties in ultrafine grained TiB₂-TiSi₂ composites using innovative multi stage spark plasma sintering. *Mater Sci Eng A* 528:200–207. <https://doi.org/10.1016/j.msea.2010.09.022>
43. Karuna Purnapu Rupa P, Sharma P, Mohanty RM, Balasubramanian K (2010) Microstructure and phase composition of composite coatings formed by plasma spraying of ZrO₂ and B₄C powders. *J Therm Spray Technol* 19:816–823. <https://doi.org/10.1007/s11666-010-9479-y>
44. Khanra AK, Pathak LC, Mishra SK, Godkhindi MM (2004) Effect of NaCl on the synthesis of TiB₂ powder by a self-propagating high-temperature synthesis technique. *Mater Lett* 58:733–738. <https://doi.org/10.1016/j.matlet.2003.06.003>
45. Khanra AK, Pathak LC, Mishra SK, Godkhindi MM (2005) Sintering of ultrafine zirconium diboride powder prepared by modified SHS technique. *Adv Appl Ceram* 104:282–284. <https://doi.org/10.1179/174367605X52077>
46. Khanra AK, Pathak LC, Godkhindi MM (2007) Carbothermal synthesis of zirconium diboride (ZrB₂) whiskers. *Adv Appl Ceram* 106:155–160. <https://doi.org/10.1179/174367607X162019>
47. Kitiwan M, Ito A, Goto T (2014) Spark plasma sintering of TiN-TiB₂ composites. *J Eur Ceram Soc* 34:197–203. <https://doi.org/10.1016/J.JEURCERAMSOC.2013.08.034>
48. Koide M, Jabri K, Saito A et al (2017) Effect of TiN addition on the properties of spark plasma sintered TiB₂. *J Ceram Soc Japan* 125:413–415. <https://doi.org/10.2109/jcersj2.16330>
49. Latini A, Di Pascasio F, Gozzi D (2002) A new synthesis route to light lanthanide borides: borothermic reduction of oxides enhanced by electron beam bombardment. *J Alloys Compd* 346:311–313. [https://doi.org/10.1016/S0925-8388\(02\)00667-9](https://doi.org/10.1016/S0925-8388(02)00667-9)
50. Lee SJ, Kim DK (2008) The oxidation behavior of ZrB₂-based mixed boride. *Key Eng Mater* 403:253–255. Trans Tech Publications, Mie, JAPAN. <https://doi.org/10.4028/www.scientific.net/KEM.403.253>

51. Lee YB, Park HC, Oh KD et al (2000) Self-propagating high-temperature synthesis of ZrB_2 in the system ZrO_2 - B_2O_3 - Fe_2O_3 - Al . *J Mater Sci Lett* 19:469–471
52. Lin J, Yang Y, Zhang H, Gong J (2017) Effects of CNTs content on the microstructure and mechanical properties of spark plasma sintered TiB_2 - SiC ceramics. *Ceram Int* 43:1284–1289. <https://doi.org/10.1016/j.ceramint.2016.10.078>
53. Low I-M, Sakka Y (Yoshio), Hu CF (Chunfeng) (2013) MAX phases and ultra-high temperature ceramics for extreme environments. IGI Global
54. Ma J, Gu Y, Shi L et al (2003) Reduction–boronation route to chromium boride (CrB) nanorods. *Chem Phys Lett* 381:194–198. <https://doi.org/10.1016/j.cplett.2003.09.128>
55. Mahesh B, Sairam K, Sonber JK et al (2015) Sinterability studies of monolithic chromium diboride (CrB_2) by spark plasma sintering. *Int J Refract Met Hard Mater* 52:66. <https://doi.org/10.1016/j.ijrmhm.2015.04.035>
56. Mashhadi M, Shambuli M, Safi S (2016) Effect of $MoSi_2$ addition and particle size of SiC on pressureless sintering behavior and mechanical properties of ZrB_2 - SiC - $MoSi_2$ composites. *J Mater Res Technol* 5:200–205. <https://doi.org/10.1016/J.JMRT.2015.10.003>
57. Matkovich VI (1977) Boron and refractory borides. In: Boron and refractory borides. Springer, Berlin/Heidelberg, pp 1–3
58. Matsudaira T, Itoh H, Naka S, Hamamoto H (1989) Synthesis of niobium boride powder by solid state reaction between niobium and amorphous boron. *J Less Common Met* 155:207–214. [https://doi.org/10.1016/0022-5088\(89\)90229-4](https://doi.org/10.1016/0022-5088(89)90229-4)
59. McKenna PM (1936) Tantalum carbide: its relation to other hard refractory compounds. *Ind Eng Chem* 28:767
60. Meléndez-Martínez JJ, Domínguez-Rodríguez A, Monteverde F et al (2002) Characterisation and high temperature mechanical properties of zirconium boride-based materials. *J Eur Ceram Soc* 22:2543–2549. [https://doi.org/10.1016/S0955-2219\(02\)00114-0](https://doi.org/10.1016/S0955-2219(02)00114-0)
61. Millet P, Hwang T (1996) Preparation of TiB_2 and ZrB_2 . Influence of a mechano-chemical treatment on the borothermic reduction of titania and zirconia. *J Mater Sci* 31:351–355. <https://doi.org/10.1007/BF01139151>
62. Mishra SK, Das SK (2005) Sintering and microstructural behaviour of SHS produced zirconium diboride powder with the addition of C and TiC. *Mater Lett* 59:3467–3470. <https://doi.org/10.1016/j.matlet.2005.06.015>
63. Mishra SK, Pathak LC (2008) Effect of carbon and titanium carbide on sintering behaviour of zirconium diboride. *J Alloys Compd* 465:547–555. <https://doi.org/10.1016/J.JALLCOM.2007.11.004>
64. Mishra SK, Das S, Pathak LC (2004) Defect structures in zirconium diboride powder prepared by self-propagating high-temperature synthesis. *Mater Sci Eng A* 364:249–255. <https://doi.org/10.1016/j.msea.2003.08.021>
65. Mishra SK, Das SK, Sherbacov V (2007) Fabrication of Al_2O_3 - ZrB_2 in situ composite by SHS dynamic compaction: a novel approach. *Compos Sci Technol* 67:2447–2453. <https://doi.org/10.1016/j.compscitech.2006.12.017>
66. Moissan H (1894) Nouvelles Reserches sur le Chrome. *C R Séances* 119:185
67. Moissan H (1895) Préparation et Propriétés du Titane. *C R Séances* 120:290
68. Moissan H (1896) Reserches sur le tungsten. *C R Séances* 123:13
69. Monteverde F (2005) Progress in the fabrication of ultra-high-temperature ceramics: “in situ” synthesis, microstructure and properties of a reactive hot-pressed HfB_2 - SiC composite. *Compos Sci Technol* 65:1869–1879. <https://doi.org/10.1016/j.compscitech.2005.04.003>
70. Mukherjee A, Uttam Jain SK, NK (2013) Rare earth borides synthesis by reduction distillation. *BARC News Letter* 20:155–158
71. Mukherjee A, Gulnar AK, Sahoo DK, Krishnamurthy N (2012) Gas solid techniques for preparation of pure lanthanum hexaboride. *Rare Metals* 31:285–289. <https://doi.org/10.1007/s12598-012-0507-6>

72. Muraoka Y, Yoshinaka M, Hirota K, Yamaguchi O (1996) Hot isostatic pressing of TiB_2 - ZrO_2 (2 Mol% Y_2O_3) composite powders. *Mater Res Bull* 31:787–792. [https://doi.org/10.1016/0025-5408\(96\)00069-4](https://doi.org/10.1016/0025-5408(96)00069-4)
73. Murthy TSRC (2004) Development and Characterization of TiB_2 Based Materials for High Temperature Applications. Indian Institute of Technology Kanpur India (M.Tech. thesis)
74. Murthy TSRC (2014) Effect of Sinter Additives on the Consolidation and Properties of Titanium Diboride Composites. Homi Bhabha National Institute (Ph.D. thesis)
75. Murthy TSRC, Basu B, Balasubramaniam R et al (2006) Processing and properties of TiB_2 with MoSi_2 sinter-additive: a first report. *J Am Ceram Soc* 89:131–138. <https://doi.org/10.1111/j.1551-2916.2005.00652.x>
76. Murthy TSRC, Basu B, Srivastava A et al (2006) Tribological properties of TiB_2 and TiB_2 – MoSi_2 ceramic composites. *J Eur Ceram Soc* 26:1293. <https://doi.org/10.1016/j.jeurceramsoc.2005.01.054>
77. Murthy TSRC, Sonber JK, Subramanian C et al (2009) Effect of CrB_2 addition on densification, properties and oxidation resistance of TiB_2 . *Int J Refract Met Hard Mater* 27:976–984. <https://doi.org/10.1016/j.ijrmhm.2009.06.004>
78. Murthy TSRC, Sonber JK, Subramanian C et al (2012) Densification, characterization and oxidation studies of TiB_2 - WSi_2 composite. *Int J Refract Met Hard Mater* 33:10–21. <https://doi.org/10.1016/j.ijrmhm.2012.02.002>
79. Murthy TSRC, Sonber JK, Subramanian C et al (2013) Densification, characterization and oxidation studies of $(\text{TiCr})\text{B}_2$ +20% MoSi_2 . *Int J Refract Met Hard Mater* 37:12–28. <https://doi.org/10.1016/j.ijrmhm.2012.10.006>
80. Murthy TSRC, Sonber JK, Vishwanadh B et al (2016) Densification, characterization and oxidation studies of novel TiB_2 + EuB_6 compounds. *J Alloys Compd* 670:85–95. <https://doi.org/10.1016/j.jallcom.2016.01.216>
81. Murthy TSRC, Sonber K, Sairam JK et al (2016) Development of refractory and rare earth metal borides & carbides for high temperature applications. *Mater Today Proc* 3:3104–3113. <https://doi.org/10.1016/j.matpr.2016.09.026>
82. Murthy TSRC, Ankata S, Sonber JK et al (2018) Microstructure, thermo-physical, mechanical and wear properties of in-situ formed boron carbide -zirconium diboride composite. *Ceram Silikaty* 62:15–30. <https://doi.org/10.13168/cs.2017.0041>
83. Nedunchezian K, Aswath N, Thiruppathy M, Thirugnanamurthy S (2016) Boron neutron capture therapy – a literature review. *J Clin Diagn Res* 10:ZE01–ZE04. <https://doi.org/10.7860/JCDR/2016/19890.9024>
84. Niihara K (1971) The preparation and nonstoichiometry of samarium hexaboride. *Bull Chem Soc Japan* 44:963–967
85. Nishiyama K, Nakamura T, Utsumi S et al (2009) Preparation of ultrafine boride powders by metallothermic reduction method. *J Phys Conf Ser* 176:012043. <https://doi.org/10.1088/1742-6596/176/1/012043>
86. Ohji T, Singh M, Singh D et al (2010) Advanced processing and manufacturing technologies for structural and multifunctional materials III: a collection of papers presented at the 33rd international conference on advanced ceramics and composites, January 18–23, 2009 Daytona Beach, Florida. Wiley
87. Opeka MM, Talmy IG, Zaykoski JA (2004) Oxidation-based materials selection for 2000°C + hypersonic aerosurfaces: theoretical considerations and historical experience. *J Mater Sci* 39:5887–5904. <https://doi.org/10.1023/B:JMSC.0000041686.21788.77>
88. Paderno YB, Ivanchenko LA, Bessaraba VI, Vereshchak VM (1975) Preparation of lanthanum hexaboride films by synthesis from the elements. *Sov Powder Metall Met Ceram* 14:515–516. <https://doi.org/10.1007/BF00823515>
89. Paul A, Jayaseelan DD, Venugopal S et al (2012) UHTC composites for hypersonic applications. *Am Ceram Soc Bull* 91:22–28

90. Paul A, Binner JGP, Vaidhyanathan B et al (2016) Heat flux mapping of oxyacetylene flames and their use to characterise C₇-HfB₂ composites. *Adv Appl Ceram* 115:158–165
91. Peshev P, Bliznakov G (1968) On the borothermic preparation of titanium, zirconium and hafnium diborides. *J Less Common Met* 14:23–32. [https://doi.org/10.1016/0022-5088\(68\)90199-9](https://doi.org/10.1016/0022-5088(68)90199-9)
92. Raju K, Sonber JK, Murthy TSRC et al (2018) Densification, microstructural evolution, mechanical properties and oxidation study of CrB₂ + EuB₆ composite. *J Mater Eng Perform* 27:2457–2465. <https://doi.org/10.1007/s11665-018-3354-2>
93. Ran S, Van der Biest O, Vleugels J (2010) ZrB₂ powders synthesis by Borothermal reduction. *J Am Ceram Soc* 93:1586–1590. <https://doi.org/10.1111/j.1551-2916.2010.03747.x>
94. Rangaraj L, Divakar C, Jayaram V (2008) Processing of refractory metal borides, carbides and nitrides. *Key Eng Mater* 395:69–88. <https://doi.org/10.4028/www.scientific.net/KEM.395.69>
95. Reddy V, Sonber JK, Sairam K et al (2015) Densification and mechanical properties of CrB₂+MoSi₂ based novel composites. *Ceram Int* 41:7611–7617. <https://doi.org/10.1016/j.ceramint.2015.02.086>
96. Sairam K, Sonber JK, Murthy TSRC et al (2012) Development of B4C–HfB₂ composites by reaction hot pressing. *Int J Refract Met Hard Mater* 35:32–40. <https://doi.org/10.1016/j.ijrmhm.2012.03.004>
97. Sairam K, Sonber JK, Murthy TSRC et al (2014) Reaction spark plasma sintering of niobium diboride. *Int J Refract Met Hard Mater* 43:259. <https://doi.org/10.1016/j.ijrmhm.2013.12.011>
98. Sairam K, Sonber JK, Murthy TSRC et al (2014) Influence of spark plasma sintering parameters on densification and mechanical properties of boron carbide. *Int J Refract Met Hard Mater* 42:185. <https://doi.org/10.1016/j.ijrmhm.2013.09.004>
99. Sairam K, Sonber JK, Murthy TSRC et al (2016) Pressureless sintering of chromium diboride using spark plasma sintering facility. *Int J Refract Met Hard Mater* 58:165. <https://doi.org/10.1016/j.ijrmhm.2016.05.002>
100. Sani E, Mercatelli L, Meucci M et al (2017) Lanthanum hexaboride for solar energy applications. *Sci Rep* 7:1–7. <https://doi.org/10.1038/s41598-017-00749-w>
101. Sani E, Meucci M, Mercatelli L et al (2017) Titanium diboride ceramics for solar thermal absorbers. *Sol Energy Mater Sol Cells* 169:313–319. <https://doi.org/10.1016/j.solmat.2017.05.038>
102. Sciti D, Silvestroni L, Nygren M (2008) Spark plasma sintering of Zr- and Hf-borides with decreasing amounts of MoSi₂ as sintering aid. *J Eur Ceram Soc* 28:1287–1296. <https://doi.org/10.1016/J.JEURCERAMSOC.2007.09.043>
103. Setoudeh N, Welham NJ (2006) Formation of zirconium diboride (ZrB₂) by room temperature mechanochemical reaction between ZrO₂, B₂O₃ and Mg. *J Alloys Compd* 420:225–228. <https://doi.org/10.1016/J.JALLCOM.2005.07.083>
104. Silvestroni L, Sciti D (2007) Effects of MoSi₂ additions on the properties of Hf- and ZrB₂ composites produced by pressureless sintering. *Scr Mater* 57:165–168. <https://doi.org/10.1016/j.scriptamat.2007.02.040>
105. Silvestroni L, Sciti D (2011) Densification of ZrB₂-TaSi₂ and HfB₂-TaSi₂ ultra-high-temperature ceramic composites. *J Am Ceram Soc* 94:1920–1930. <https://doi.org/10.1111/j.1551-2916.2010.04317.x>
106. Singh N, Saini SM, Nautiyal T, Auluck S (2007) Electronic structure and optical properties of rare earth hexaborides RB₆ (R = La, Ce, Pr, Nd, Sm, Eu, Gd). *J Phys Condens Matter* 19:346226. <https://doi.org/10.1088/0953-8984/19/34/346226>
107. Sonber JK (2015) Studies on synthesis, densification and oxidation of zirconium diboride based materials. Homi Bhabha National Institute, PhD Thesis
108. Sonber JK, Murthy Ksajkc TSRC (2016) Effect Of Ndb₆ addition on Densification and Properties of ZrB₂. *Ceram Silikaty* 60:41–47. <https://doi.org/10.13168/cs.2016.0006>
109. Sonber JK, Suri AK (2011) Synthesis and consolidation of zirconium diboride: review. *Adv Appl Ceram* 110:321–334. <https://doi.org/10.1179/1743676111Y.0000000008>

110. Sonber JK, Murthy TSRC, Subramanian C et al (2009) Investigation on synthesis, pressureless sintering and hot pressing of chromium diboride. *Int J Refract Met Hard Mater* 27:912. <https://doi.org/10.1016/j.ijrmhm.2009.05.008>
111. Sonber JK, Murthy TSRC, Subramanian C et al (2010) Investigations on synthesis of HfB₂ and development of a new composite with TiSi₂. *Int J Refract Met Hard Mater* 28:201–210. <https://doi.org/10.1016/j.ijrmhm.2009.09.005>
112. Sonber JK, Murthy TSRC, Subramanian C et al (2011) Investigations on synthesis of ZrB₂ and development of new composites with HfB₂ and TiSi₂. *Int J Refract Met Hard Mater* 29:21. <https://doi.org/10.1016/j.ijrmhm.2010.06.007>
113. Sonber JK, Murthy TSRC, Subramanian C et al (2012) Effect of CrSi₂ and HfB₂ addition on densification and properties of ZrB₂. *Int J Refract Met Hard Mater* 31:125. <https://doi.org/10.1016/j.ijrmhm.2011.10.001>
114. Sonber JK, Murthy TSRC, Subramanian C et al (2012) Effect of EuB₆ addition on densification and properties of ZrB₂. *Int J Refract Met Hard Mater* 35:96–101. <https://doi.org/10.1016/j.ijrmhm.2012.04.012>
115. Sonber JK, Murthy TSRC, Subramanian C et al (2013) Synthesis, Densification and Characterization of Boron Carbide. *Trans Indian Ceram Soc* 72:100. <https://doi.org/10.1080/0371750X.2013.817755>
116. Sonber JK, Murthy TSRC, Subramanian C et al (2013) Processing methods for ultra-high temperature ceramics. In: MAX phases and ultra-high temperature ceramics for extreme environments. IGI Global, Hershey. <https://doi.org/10.4018/978-1-4666-4066-5.ch006>
117. Sonber JK, Murthy TSRC, Subramanian C et al (2013) Synthesis, densification and characterization of EuB₆. *Int J Refract Met Hard Mater* 38:67–72. <https://doi.org/10.1016/j.ijrmhm.2012.12.010>
118. Sonber JK, Murthy TSRC, Subramanian C et al (2014) Effect of WSi₂ addition on densification and properties of ZrB₂. *Adv Appl Ceram* 113:114. <https://doi.org/10.1179/1743676113Y.0000000125>
119. Sonber JK, Sairam K, Murthy TSRC et al (2014) Synthesis, densification and oxidation study of lanthanum hexaboride. *J Eur Ceram Soc* 34:1155. <https://doi.org/10.1016/j.jeurceramsoc.2013.11.023>
120. Sonber JK, Murthy TSRC, Sairam K et al (2016) Effect of TiSi₂ addition on densification of cerium hexaboride. *Ceram Int* 42:891–896. <https://doi.org/10.1016/j.ceramint.2015.09.015>
121. Sonber JK, Murthy TSRC, Sairam K et al (2017) Development and tribological properties of SiC fibre reinforced CrB₂ composite. *J Aust Ceram Soc* 53:309–317. <https://doi.org/10.1007/s41779-017-0039-5>
122. Sonber JK, Murthy TSRC, Sairam K, Kain V (2017) Sintering and oxidation of GdB₄ synthesized by B4C reduction method. *J Korean Ceram Soc* 54:121–127. <https://doi.org/10.4191/kcers.2017.54.2.02>
123. Starr TL, Hablutzl N (2005) Measurement of gas transport through Fiber preforms and densified composites for chemical vapor infiltration. *J Am Ceram Soc* 81:1298–1304. <https://doi.org/10.1111/j.1151-2916.1998.tb02481.x>
124. Stollery JL (1972) Hypersonic flight. *Nature* 240:133. <https://doi.org/10.1038/240133a0>
125. Su K, Sneddon LG (1991) Polymer-precursor routes to metal borides: synthesis of titanium boride (TiB₂) and zirconium boride (ZrB₂). *Chem Mater* 3:10–12. <https://doi.org/10.1021/cm00013a005>
126. Subramanian C, Murthy TSRC, Suri AK (2007) Synthesis and consolidation of titanium diboride. *Int J Refract Met Hard Mater* 25:345. <https://doi.org/10.1016/j.ijrmhm.2006.09.003>
127. Sun C-N, Gupta MC (2008) Laser sintering of ZrB₂. *J Am Ceram Soc* 91:1729–1731. <https://doi.org/10.1111/j.1551-2916.2008.02369.x>
128. Sun C-N, Baldrige T, Gupta MC (2009) Fabrication of ZrB₂-Zr cermet using laser sintering technique. *Mater Lett* 63:2529–2531. <https://doi.org/10.1016/j.matlet.2009.08.059>

129. Suri AK, Subramanian C, Sonber JK, Murthy TSRC (2010) Synthesis and consolidation of boron carbide: a review. *Int Mater Rev* 55:4. <https://doi.org/10.1179/095066009X12506721665211>
130. Tucker SA, Moody HR (1902) The preparation of some new metal borides. *J Chem Soc* 81:14
131. Vishwanadh B, Murthy TSRC, Arya A et al (2016) Synthesis and phase transformation mechanism of Nb₂C carbide phases. *J Alloys Compd* 671:424–434. <https://doi.org/10.1016/j.jallcom.2016.02.092>
132. Wang H-L, Wang C-A, Chen D-L et al (2010) Preparation and characterization of ZrB₂-SiC ultra-high temperature ceramics by microwave sintering. *Front Mater Sci China* 4:276–280. <https://doi.org/10.1007/s11706-010-0091-3>
133. Wang X-F, Xiang H-M, Sun X et al (2015) Porous YbB₆ ceramics prepared by in situ reaction between Yb₂O₃ and B₄C combined with partial sintering. *J Am Ceram Soc* 98:2234–2239. <https://doi.org/10.1111/jace.13606>
134. Watson KD, Toguri JM (1991) The wettability of carbon/TiB₂ composite materials by aluminum in cryolite melts. *Metall Trans B* 22:617–621. <https://doi.org/10.1007/BF02679016>
135. Wedekind E (1913) Synthese von Boriden im elektrischen Vakuumofen. *Berichte der Dtsch Chem Gesellschaft* 46:1198–1207. <https://doi.org/10.1002/cber.191304601155>
136. Xie Y, Sanders TH, Speyer RF (2008) Solution-based synthesis of submicrometer ZrB₂ and ZrB₂-TaB₂. *J Am Ceram Soc* 91:1469–1474. <https://doi.org/10.1111/j.1551-2916.2008.02288.x>
137. Yan Y, Huang Z, Dong S, Jiang D (2006) New route to synthesize ultra-fine zirconium Diboride powders using inorganic/organic hybrid precursors. *J Am Ceram Soc* 89:3585–3588. <https://doi.org/10.1111/j.1551-2916.2006.01269.x>
138. Yang X, Wang P, Wang Z et al (2017) Microstructure, mechanical and thermionic emission properties of a directionally solidified LaB₆-VB₂ eutectic composite. *Mater Des* 133:299–306. <https://doi.org/10.1016/j.matdes.2017.07.069>
139. Yeh CL, Chen WH (2006) Preparation of niobium borides NbB and NbB₂ by self-propagating combustion synthesis. *J Alloys Compd* 420:111–116. <https://doi.org/10.1016/J.JALLCOM.2005.10.031>
140. Yoshio S, Maki K, Adachi K et al (2016) Optical properties of group-3 metal hexaboride nanoparticles by first-principles calculations optical properties of group-3 metal hexaboride nanoparticles by first-principles calculations. *J Chem Phys* 144:234702. <https://doi.org/10.1063/1.4953849>
141. Yu Y, Wang S, Li W, Chen Z (2018) Low temperature synthesis of LaB₆ nanoparticles by a molten salt route. *Powder Technol* 323:203–207. <https://doi.org/10.1016/j.powtec.2017.09.049>
142. Zamora V, Ortiz AL, Guiberteau F, Nygren M (2013) On the enhancement of the spark-plasma sintering kinetics of ZrB₂-SiC powder mixtures subjected to high-energy co-ball-milling. *Ceram Int* 39:4191–4204. <https://doi.org/10.1016/j.ceramint.2012.11.001>
143. Zhao H, He Y, Jin Z (1995) Preparation of zirconium boride powder. *J Am Ceram Soc* 78:2534–2536. <https://doi.org/10.1111/j.1151-2916.1995.tb08696.x>
144. Zhao Y, Wang L-J, Zhang G-J et al (2009) Effect of holding time and pressure on properties of ZrB₂-SiC composite fabricated by the spark plasma sintering reactive synthesis method. *Int J Refract Met Hard Mater* 27:177–180. <https://doi.org/10.1016/j.ijrmhm.2008.02.003>
145. Zhou SL, Zhang JX, Bao LH et al (2014) Enhanced thermionic emission properties in textured two-phase LaB₆-BaB₆ system prepared by spark plasma sintering. *J Alloys Compd* 611:130–134. <https://doi.org/10.1016/j.jallcom.2014.05.067>
146. Zhu S, Fahrenholtz WG, Hilmas GE et al (2008) Microwave sintering of a ZrB₂-B₄C particulate ceramic composite. *Compos Part A Appl Sci Manuf* 39:449–453. <https://doi.org/10.1016/j.compositesa.2008.01.003>



Novel Inorganic Compound Based Sensors for Their Application in Nuclear Energy Programs

20

V. Jayaraman and T. Gnanasekaran

Contents

Introduction	741
Oxides	742
Solid Electrolytes	742
Semiconducting Oxides	749
Hydridehalides	755
Structure and Electrical Conductivity of Alkaline Earth Metal Hydridehalides	755
Need for Measurement of Hydrogen in Liquid Metals and the Choice of Alkaline Earth Hydridehalide Based Solid Electrolyte Materials for Liquid Sodium Systems	758
Experience with Hydridehalides for Monitoring Hydrogen Levels in Liquid Sodium	760
Silver Halides	762
Structure of Silver Halides	762
Effect of Cationic and Anionic Substitution on Conductivity of AgI	762
Silver Halides as Sensors for Halogens	763
Sodium Aluminates	765
Sensor for Sodium Oxide Aerosol	766
Phosphates	767
$\text{Li}_{2-4x}\text{Zr}_{1+x}(\text{PO}_4)_2$ ($x = 0-0.45$): Phase Formation and Electrical Conductivity Studies	768
Sensor for Lithium Activity Measurements	769
Molybdates and Niobates	769
Molybdenum Oxide (MoO_3): Structural Aspects	769
Electrical Conductivity and Gas Sensing Characteristics of Molybdenum Trioxide	771
Typical Analyte Sensing Characteristics of MoO_3	771
Silver Molybdates	772
Niobates	773

V. Jayaraman · T. Gnanasekaran (✉)

Materials Chemistry Division, Materials Chemistry and Metal Fuel Cycle Group, Indira Gandhi Centre for Atomic Research, Kalpakkam, India

e-mail: vjram@igcar.gov.in; gnani.home@gmail.com

© Springer Nature Switzerland AG 2020

Y. R. Mahajan, R. Johnson (eds.), *Handbook of Advanced Ceramics and Composites*, https://doi.org/10.1007/978-3-030-16347-1_23

739

Carbonates and Nitrides	775
Molten Carbonates and Their Use in Galvanic Cells for Measuring Carbon Potentials ...	775
Nitrides for Measurement of Nitrogen Potentials	777
Titanates	779
Conclusions	785
References	785

Abstract

Structure of the inorganic compounds determines their electrical conductivity, dielectric, optical, magnetic properties, etc. These structure and properties together decide the suitability of employing these materials for a given technological application. If electrical conductivity of materials is exploited for application as sensor, the type of conductivity, viz., ionic, electron/hole, and ionic-cum-electronic, exhibited by them needs to be understood. Depending on the type of conduction, they are classified as solid electrolytes, semiconductors, and mixed conductors. Several solid electrolyte systems where conductivity due to cations such as H^+ , Li^+ , Na^+ , Ag^+ , etc. are known, while only a few systems for anions such as H^- , O^{2-} , and F^- are known. The conducting ion present in the solid electrolyte dictates its application as sensor in a chosen process stream, although indirect methods can also be deployed to use a solid electrolyte whose ion of conduction is different from the species to be sensed. The magnitude of ionic conductivity, transport number of the conducting ions, and the stability of the solid electrolyte in the environment of the application need to be evaluated before its selection. Although several semiconducting elements and compounds (oxides, sulfides, nitrides, etc.) are known, the use of elemental semiconductors is generally restricted to electrical and electronic devices. On the other hand, oxide semiconductors find a large application as chemical sensors for process and environmental monitoring. The bandgap, intrinsic and extrinsic conductivity, stability of the compound in the operating environment, temperature, etc. are important parameters that decide their application as sensors. This chapter deals with the selection of solid electrolyte based on oxides, hydridehalides, aluminates, phosphates, and halides their application in various nuclear energy programs. The experience of using semiconducting oxides, niobates, molybdates, etc. for various process monitoring is discussed. A brief mention on the use of titanates for piezoelectric sensor application and molten electrolyte-based sensor systems is made.

Keywords

Solid electrolytes · Semiconducting oxides · Hydridehalides · Silver halides · Sodium aluminates · Phosphates · Molybdates · Niobates · Zirconates · Thorates · Sensors for hydrogen · Oxygen · Ammonia · Chlorine · Iodine · Lithium · Sodium aerosol

List of Abbreviations

ADSS	Accelerator-driven subcritical systems
BCC	Body-centered cubic
BIT	Bismuth titanate
CSZ	Calcia-stabilized zirconia
FBR	Fast breeder reactor
LBE	Lead-bismuth eutectic
MPB	Morphotropic phase boundary
NASICON	Sodium super ionic conductor
PSZ	Partially stabilized zirconia
PZT	Lead zirconate titanate
YDT	Yttria-doped thoria
YSZ	Yttria-stabilized zirconia

Introduction

Structure of the inorganic compounds determines their electrical conductivity, dielectric, optical, magnetic properties, etc. These structure and properties together decide the suitability of employing these materials for a given technological application. If electrical conductivity of materials is exploited for application as sensor, the type of conductivity, viz., ionic, electron/hole, and ionic-electronic, exhibited by them needs to be understood. Depending on the type of conduction, they are classified as solid electrolytes, semiconductors and mixed conductors. Several solid electrolyte systems where conductivity due to cations such as H^+ , Li^+ , Na^+ , Ag^+ , etc. are known while only a few systems for anions such as H^- , O^{2-} , and F^- are known. The conducting ion present in the solid electrolyte dictates its application as sensor in a chosen process stream, although indirect methods can also be deployed to use a solid electrolyte whose ion of conduction is different from the species to be sensed. The magnitude of ionic conductivity, transport number of the conducting ions, and the stability of the solid electrolyte in the environment of the application need to be evaluated before its selection. Although several semiconducting elements and compounds (oxides, sulfides, nitrides, etc.) are known, the use of elemental semiconductors is generally restricted to electrical and electronic devices. On the other hand, oxide semiconductors find a large application as chemical sensors for process and environmental monitoring. The bandgap, intrinsic and extrinsic conductivity, stability of the compound in the operating environment, temperature, etc. are important parameters that decide their application as sensors. This chapter deals with the selection of solid electrolyte based on oxides, hydridehalides, aluminates, phosphates, and halides their application in various nuclear energy programs. The

experience of using semiconducting oxides, niobates, molybdates, etc. for various process monitoring will also be discussed. A brief mention on the use of titanates for piezoelectric sensor application and molten electrolyte-based sensor systems will also be made.

Oxides

Solid Electrolytes

Although several oxides are known to exhibit ionic and mixed conducting (ionic and electronic) properties, the most studied and used oxides with ionic conductivity are zirconia- and thoria-based ones. The room-temperature phase of thoria and the high-temperature phase of zirconia possess fluorite structure, which is essentially a face-centered cubic arrangement of cations with the anions occupying all the tetrahedral sites (shown in Fig. 1) [1]. The fluorite structure has a large number of octahedral voids, which enables ionic diffusion through the structure. In order to enhance oxide ion conductivity of thoria at low temperatures (~ 673 K), aliovalent substitution of thorium ions by either trivalent (normally, Y^{3+}) or divalent (normally, Ca^{2+}) is preferred. In case of zirconia, by similar substitution of aliovalent ions, stabilization of the high-temperature cubic phase at low temperature and enhancement of oxide ion conductivity are achieved. Detailed investigations have been carried out by several research groups to establish the optimum concentration of substitution vis-à-vis enhancement in ionic conductivity at low temperatures [1].

Electrical Properties of Solid Electrolytes

Several research teams have measured and reported the electrical conductivity of zirconia- and thoria-based solid electrolytes. The electrical conductivity of yttria-stabilized zirconia (YSZ) in the temperature range of 1073–1373 K in air is in the range of 0.1 – 0.9 Scm^{-1} [2]. Conductivity of yttria-doped thoria (YDT) ranges from 2.3×10^{-3} to 7.9×10^{-3} Scm^{-1} between 1073 and 1373 K [2]. Conductivity of YSZ and YDT, from the data reported by Nafe [2], is shown in Fig. 2. The Arrhenius plots

Fig. 1 Crystal structure of fluorite

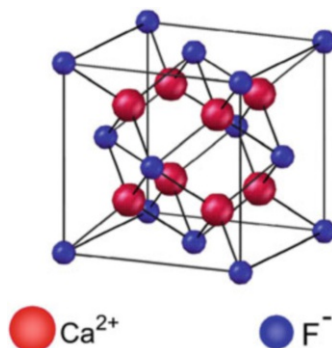
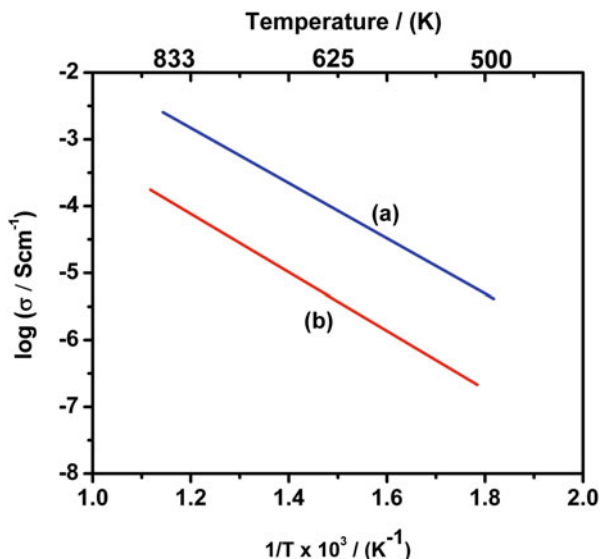


Fig. 2 Electrical conductivity as a function of temperature exhibited by yttria-stabilized zirconia (YSZ) and yttria-doped thoria (YDT) in air [2]

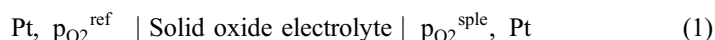


for both the solid electrolytes were found linear up to 573 K. However, a nonlinear behavior was observed for zirconia based electrolytes at lower temperatures (<573 K).

Electrolytic Domain Boundaries of Solid Electrolytes

The electrolytic domain boundaries of a solid oxide electrolyte are defined as the temperature and oxygen pressure ranges over which the contribution from conductivity of oxide ion to its total conductivity is more than 99%. Patterson reported the electrolytic domain boundaries for calcia-stabilized zirconia (CSZ) and yttria-doped thoria as a function of temperature [3] which are shown in Fig. 3. As seen in the figure, at 1273 K the electrolytic domain for CSZ is between 10^5 and 10^{-18} atm of oxygen, while for YDT, it is between 10^{-6} and 10^{-25} atm of oxygen.

A solid oxide electrolyte can be used to measure oxygen partial pressures in a sample by using a potentiometric electrochemical cell of the following configuration:



where $p_{\text{O}_2}^{\text{ref}}$ and $p_{\text{O}_2}^{\text{sple}}$ are partial pressures of oxygen in the reference and sample compartments. When $p_{\text{O}_2}^{\text{ref}}$ and $p_{\text{O}_2}^{\text{sple}}$ are within the electrolytic domain boundaries of the solid electrolyte, emf developed by the cell can be represented by the Nernst equation given below ($p_{\text{O}_2}^{\text{ref}} > p_{\text{O}_2}^{\text{sple}}$):

$$E = (RT/4F) \ln(p_{\text{O}_2}^{\text{ref}}/p_{\text{O}_2}^{\text{sple}}) \quad (2)$$

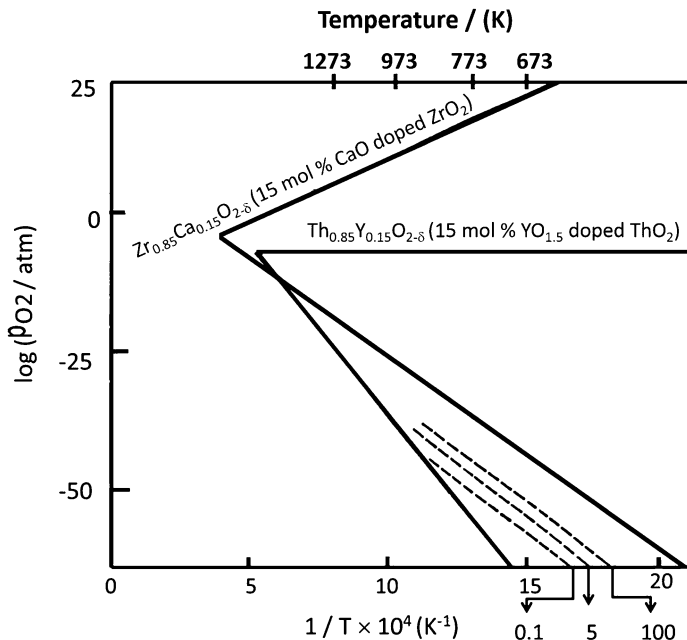


Fig. 3 Electrolytic domain boundaries of calcia-stabilized zirconia (CSZ) and yttria-doped thoria (YDT) (Redrawn and reproduced using the data from References [3] and [4]) Also shown are equilibrium oxygen partial pressures in liquid sodium containing 0.1, 5, and 100 wppm of dissolved oxygen

Use of Oxide Ion-Conducting Solid Electrolytes for Monitoring Oxygen Levels in Sodium

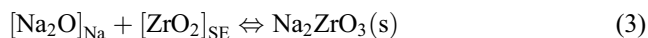
Liquid sodium is the coolant of choice for fast breeder reactor. Liquid sodium is highly compatible with structural steels when the concentration of dissolved oxygen in it is low. However, when the oxygen concentration is above ~ 5 ppm, enhanced corrosion and mass transfer of the alloying components of steels would occur. The threshold concentration levels of oxygen in sodium for the formation of corrosion products are determined by thermochemical stability of various ternary oxides of Na-M-O systems (M = alloying elements in steels), which take part in corrosion and mass transfer processes [5]. Universally accepted method for measuring oxygen activity and concentration in sodium is the use of solid oxide electrolyte-based sensors [6].

Criteria for the Selection of Solid Electrolytes

Chemical Compatibility with Liquid Sodium

Chemical incompatibility of stabilized zirconia electrolytes in sodium at 589 K with an oxygen concentration of ~ 50 ppm was reported by Minushkin and Kolodney [7]. Gibbs energy of formation of the reaction product, namely, sodium zirconate

(Na_2ZrO_3), was reported by Iyer et al. and Maier et al. [8, 9]. Using this data and the following equilibrium, threshold oxygen concentration in sodium above which this attack would occur can be calculated:



At 723 K, this threshold oxygen concentration in sodium corresponds to ~ 0.15 ppm. When sodium oxide reacts with thoria, the ternary compound formed is sodium metathorate, Na_2ThO_3 . Smruti Dash et al. evaluated the Gibbs energy of formation of sodium metathorate [10]. Using this data, the threshold oxygen concentration above which Na_2ThO_3 would be formed can be calculated in a similar manner. At 723 K, this threshold oxygen concentration in liquid sodium is ~ 1250 ppm. Since liquid sodium in coolant circuits contains low levels of oxygen (< 5 ppm), thoria-based electrolytes would be chemically compatible, unlike the zirconia-based electrolytes, as has been observed during their testing. It is to be pointed out that the YDT for sodium service should be very pure and devoid of impurity phases. Impurity phases present in the solid electrolyte can react with sodium and result in the deterioration of the solid electrolyte material. YDT tubes obtained from high purity powders which are isostatically pressed followed by sintering are recommended for construction of the oxygen sensors. Conventional process involving slip casting followed by sintering can introduce undesirable impurities.

Thermomechanical Properties

A liquid metal coolant circuit would experience several thermal cycles and coolant dumping and refill operations during its service. Hence, the sensor using the solid oxide electrolyte would also undergo several thermal excursions during its lifetime in the circuit. The solid electrolyte should possess adequate thermal shock resistance to withstand these thermal excursions. Thermal shock resistance of thoria and zirconia (partially stabilized zirconia – PSZ) are compared with those of the widely used ceramics like alumina and magnesia in Table 1 [11].

Thermal shock resistances of these oxides were calculated using the following relation (11):

$$R_{\text{TS}} = \sigma_f \kappa / (E\alpha) \quad (4)$$

where R_{TS} is the thermal shock resistance, σ_f is the fracture stress (for ceramics, it is often taken as the flexural strength or modulus of rupture (MOR) – defined as the

Table 1 Comparison of thermal shock resistances of certain oxide ceramics

Material	Thermal shock resistance, R_{TS} (W/m)
Al_2O_3 [11]	633
MgO [12]	281
PSZ [11]	575
ThO_2 [12]	143

Table 2 Emf output of YDT-based sensor in sodium at different temperatures studied in authors' laboratory (oxygen content in sodium: 2 ppm) [4]

Temperature (K)	Emf output (V)
663	2.055
683	2.020
703	1.990
723	1.960

stress in a material just before it yields in a flexure test), κ is the thermal conductivity, E is the Young's modulus, and α is the thermal expansion coefficient. This equation shows that ceramics with high fracture stress and thermal conductivity coupled with low Young's modulus and thermal expansion coefficient will exhibit high thermal shock resistance. For comparison, the calculated values for PSZ are assumed to be applicable to stabilized zirconia to a first degree of approximation. It is also assumed that on introduction of yttria into thoria, the listed properties are not affected significantly. As seen in the table, thoria has poor thermal shock resistance, and it is about a factor of four less than that of PSZ. YDT has been chosen as solid electrolyte for oxygen monitoring in liquid sodium circuits because of its favorable electrolytic domain boundaries and chemical compatibility with liquid sodium. However, the design of the sensor and the procedure for operating it in the liquid metal circuit need to be optimized to overcome the poor thermal shock resistance of the solid electrolyte.

In-Sodium Oxygen Sensor Using YDT

One of the constraints for making high-density YDT products from powders prepared by conventional methods has been the requirement of high sintering temperatures (~ 2650 K) [13]. Use of nanocrystalline powders for making the products is shown to reduce the sintering temperature significantly. Towards this end, in the authors' laboratory, conditions for the preparation of nanocrystalline YDT powders by a novel gel combustion method were optimized [14, 15]. Sinterability of the YDT bodies made using these powders at 1923 K in air was established, and the sintered products were found to exhibit a helium leak tightness of less than 10^{-9} S lit/s [15, 16]. Sensors were assembled using Pt/O₂ and Cu/Cu₂O as reference electrodes. These sensors exhibited lifetime of about 1 year and responded to the change in sodium temperature from 623 to 723 K as shown in Table 2 [4].

Sensor for Oxygen Level Monitoring in Lead and Lead-Bismuth Eutectic (LBE)

Lead and lead-bismuth eutectic (LBE) alloy are considered as suitable spallation target cum candidate coolant for the accelerator-driven subcritical systems (ADSS) [17] due to their favorable physical, chemical, and nuclear properties. On the other hand, these coolants are highly corrosive towards the structural steels, and this is due to high solubility of the alloying components of steels in Pb and LBE. However, this corrosion can be minimized significantly by controlling the dissolved oxygen in the

liquid metals whereby a protective oxide layer is formed at the steel-liquid metal interface [18–21]. This protective oxide layer reduces the direct dissolution of the steel components in liquid Pb/LBE owing to the low diffusion coefficients of the alloying components of steels through the oxide film [22]. Hence, continuous control and monitoring of oxygen level in the Pb/LBE are important for ensuring the existence of the passive oxide film at the steel-liquid metal interface.

Sensors based on yttria-stabilized zirconia (YSZ) having high-density ceramic bodies with fine-grained microstructure have been the choice for measuring oxygen in Pb and LBE alloy systems [23, 24]. At the authors' laboratory, partially stabilized zirconia (PSZ: $\text{ZrO}_2 - 5 \text{ mol\% Y}_2\text{O}_3$) has been chosen as solid electrolyte by considering its excellent mechanical strength [4]. Nano powders of PSZ have been synthesized and characterized, and the sinterability of the compacts made from these powders to yield ceramic bodies meeting the required helium leak tightness ($<10^{-9}$ S lit/s) has been established. Towards the fabrication of an oxygen sensor of compact design, sealing of a dense YSZ pellet with 9Cr-1Mo steel has been carried out using a glass solder. The compatibility of the solder glass with the liquid metal was established by equilibrating the samples of the solder with LBE at 723 K for 500 h whereby no change in its mass and appearance were observed. The PSZ to 9Cr-1Mo seal after equilibrating it with LBE at 723 K for 500 h followed by cleaning with glycerin at 423 K also passed the helium leak test ($<10^{-9}$ S lit/s) [25]. Testing of the sensor for oxygen monitoring in liquid lead is under progress.

Use of Oxide Ion-Conducting Solid Electrolytes in Measurements of Thermochemical Properties

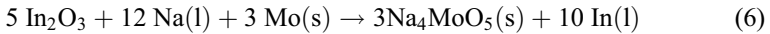
Usefulness of the solid oxide electrolytes for measuring high-temperature thermochemical data was demonstrated by Kiukkola and Wagner about half a century back. In their seminal work published in 1957 [26, 27], Kiukkola and Wagner employed thoria- and zirconia-based solid electrolytes for measuring the Gibbs energies of formation of variety of compounds like oxides, sulfides, halides, selenides, and tellurides at elevated temperatures. Subsequent years have seen the application of this technique for determining the activity of components of metallic alloys and Gibbs energy of formation of various types of compounds. Typical applications are given in References [28–33].

As was mentioned in section “[Use of Oxide Ion-Conducting Solid Electrolytes for Monitoring Oxygen Levels in Sodium](#),” corrosion and mass transfer of structural steels in liquid sodium coolant circuits are enhanced with increase in concentration of dissolved oxygen in the liquid metal. This is due to participation of the ternary compounds of Na-M-O systems (where M = alloying elements in steel, viz., Fe, Cr, Ni, Mo) in the corrosion processes. To determine the threshold oxygen concentration above which these compounds can form in liquid sodium, knowledge on the ternary phase diagrams of the Na-M-O systems and Gibbs energies of formation of compounds that coexist with liquid sodium and the metal M (or its oxide) are required. Phase diagrams of Na-Fe-O, Na-Mo-O, and Na-Ni-O systems have been established at the authors' laboratory and Gibbs energies of formation Na_4FeO_3 , NaCrO_2 , and Na_4MoO_5 which are stable in liquid sodium have also been measured. For example,

Na_4MoO_5 has been established to coexist with liquid sodium and molybdenum metals at temperatures above 681.1 K, while at lower temperatures, only Na_2O coexists with the two metals [34]. Gibbs energy of formation Na_4MoO_5 was determined by constructing the following galvanic cell and measuring the emf as a function of temperature [35].



Mo wire was used as the electrical lead for the sample which was a slurry of $\text{Na}_4\text{MoO}_5(\text{s})$, Mo powder, and liquid sodium contained in an alumina crucible. The cell reaction can be represented as:

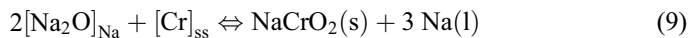


$$\Delta G_{\text{rx}}^0 = -30EF = \Delta G_{\text{f}}^0 \text{Na}_4\text{MoO}_5(\text{s}) - 5\Delta G_{\text{f}}^0 \text{In}_2\text{O}_3(\text{s}) \quad (7)$$

From the measured emf and literature data on Gibbs energy of formation of $\text{In}_2\text{O}_3(\text{s})$, the Gibbs energy of formation of $\text{Na}_4\text{MoO}_5(\text{s})$ could be obtained. In case of Na-Cr-O system, NaCrO_2 is known to coexist with liquid sodium and chromium metals. The presence of the phase field where NaCrO_2 , Cr_2O_3 , and Na_2CrO_4 coexist had also been established [36]. Sreedharan et al. measured the Gibbs energy of formation of NaCrO_2 by constructing the following galvanic cell with YSZ as the solid oxide electrolyte [37].



From the known literature data on Cr_2O_3 and Na_2CrO_4 , Gibbs energy of formation of NaCrO_2 could be obtained. By considering the following equilibrium, threshold oxygen level in liquid sodium for formation of NaCrO_2 could be calculated:



$$\Delta G_{\text{f}}^0 \text{NaCrO}_2(\text{s}) = \Delta G_{\text{f}}^0 \text{Na}_2\text{O}(\text{s}) + 2RT \ln a_{\text{Na}_2\text{O}} + RT \ln a_{\text{Cr}} \quad (10)$$

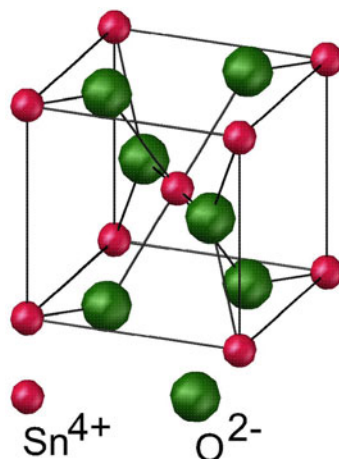
where $\Delta G_{\text{f}}^0 \text{Na}_2\text{O}(\text{s})$, $a_{\text{Na}_2\text{O}}$, and a_{Cr} are standard Gibbs energy of formation of Na_2O , activity of Na_2O in sodium, and activity of chromium in the structural steels. By using the literature data on $\Delta G_{\text{f}}^0 \text{Na}_2\text{O}(\text{s})$ and a_{Cr} , the activity and the threshold concentration of sodium oxide in sodium for the formation of NaCrO_2 could be calculated as ~ 1 ppm at 773 K. By constructing a cell similar to that represented by (5) with the sample electrode consisting of $\text{NaCrO}_2(\text{s})$, $\text{Cr}(\text{s})$, and liquid sodium contained in nickel crucible, Gnanasekaran and Mathews [38] showed the presence of carbon impurity in sodium would result in increase of the threshold oxygen concentrations by the participation of chromium carbides in place of $[\text{Cr}]_{\text{ss}}$ in equilibrium reaction (Eq. 9).

Semiconducting Oxides

Some semiconducting oxides, viz., SnO_2 , ZnO , In_2O_3 , etc., are exploited for sensing of trace levels of various pollutants and flammable gases [39, 40]. These oxides possess different crystal structures, viz., tetragonal (SnO_2), hexagonal (ZnO), and cubic (In_2O_3). Crystal structure of SnO_2 , as a typical example, is shown in Fig. 4. When a metal oxide of typical formula, MO_x , with metal ion valency of M^{n+} has a small fraction of metal ions of lower valency ($\text{M}^{(n-1)+}$) in it, the oxide is known to exhibit n-type conductivity. Examples are SnO_2 , ZnO , etc. When MO_x contains a small fraction of metal ions with higher valency ($\text{M}^{(n+1)+}$), the oxide exhibits p-type conductivity. Examples for this type of oxides are NiO , Cr_2O_3 , etc.

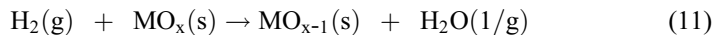
These oxides generally have a narrow non-stoichiometry range, and many of them show chemisorption of oxygen to fill the unsatisfied valence states of metal ions on the surface. When chemisorption of oxygen occurs, several kinds of oxygen adsorbates such as O_2^- , O^- , and O^{2-} are known to form by transferring electrons from the oxide surface [41]. When a thin/thick film of an n-type oxide is exposed to air, its electrical conductivity gets significantly reduced because of the transfer of the electrons from the surface of the oxide to the chemisorbed oxygen species. When a reducing analyte gas is present in ambient air, it reacts with the chemisorbed oxygen species and releases the trapped electrons back to the surface resulting in the increase of the electrical conductivity of the film. On removal of the trace analyte from the ambient, the conductivity of the film gets restored to its original high value. In case of p-type oxides, the changes in conductivity by chemisorption of oxygen and upon reaction of these chemisorbed species with trace reducing gases would be in a direction reverse to what occurs in the case of the n-type oxides. The concentration dependency of conductivity changes has been exploited for measuring the trace levels of the reducing gases present in ambient. Successful functioning of an oxide system in gas sensing application is based on certain general properties which are discussed in the following sections.

Fig. 4 Crystal structure of tin oxide

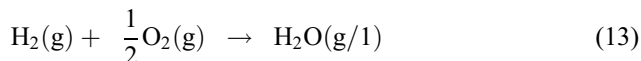


Thermodynamic Characteristics

Seiyama divided the metal oxides into two groups, namely, stable and unstable oxides, by considering the thermodynamic feasibility of their reduction by gases such as hydrogen to the respective metal or to a lower valent oxide [42]. For this purpose, the following two reactions were considered:



where MO_x and MO_{x-1} denote the oxidized and reduced states of the metal oxides, respectively. Sum of these two reactions yields the oxidation reaction of H_2 :



If the standard Gibbs energy change of the reaction (11) is ΔG_1° and that of reaction (12) is ΔG_2° , then the Gibbs energy change ΔG_3° associated with reaction (13) can be expressed as below:

$$\Delta G_3^\circ = \Delta G_1^\circ + \Delta G_2^\circ \quad (14)$$

$$\Delta G_1^\circ = \Delta G_3^\circ - \Delta G_2^\circ \quad (15)$$

A plot of ΔG_1° versus ΔG_2° for various metal oxides would yield a straight line with a slope of -1 . Fig. 5 shows such plot of different metal oxides which are stable in air at 300 K [42, 43]. The figure divides the metal oxides into two groups, namely, oxides for which ΔG_1° is +ve (region A) and those for which ΔG_1° is -ve (region B). Generally, the oxides used for gas sensor application are those which cannot be easily reduced by gases such as hydrogen, and they fall in region A. The oxides which fall in region B are easily converted to lower oxides or to the metallic state by gases such as hydrogen, and they are generally used as redox catalysts. However, it is possible to prepare many mixed oxides based on these binary oxides, and the properties of the resulting oxides can be tailored to suit an application.

Oxygen Chemisorptive Property of Semiconducting Oxides

Chemisorption of oxygen is expected to occur under ambient conditions on all oxides that are stable in air. As mentioned earlier, several kinds of oxygen adsorbates such as O_2^- , O^- , and O^{2-} can form on the surface. Heat of this chemisorption would generally increase with increase in stability of the oxide. A strongly chemisorbed oxygen ion (characterized by high heat of absorption) would not participate in the gas sensing reaction. Therefore, oxides such as MgO and ThO_2 would not be useful as gas sensor material in contrast to systems based on oxides such as SnO_2 and ZnO .

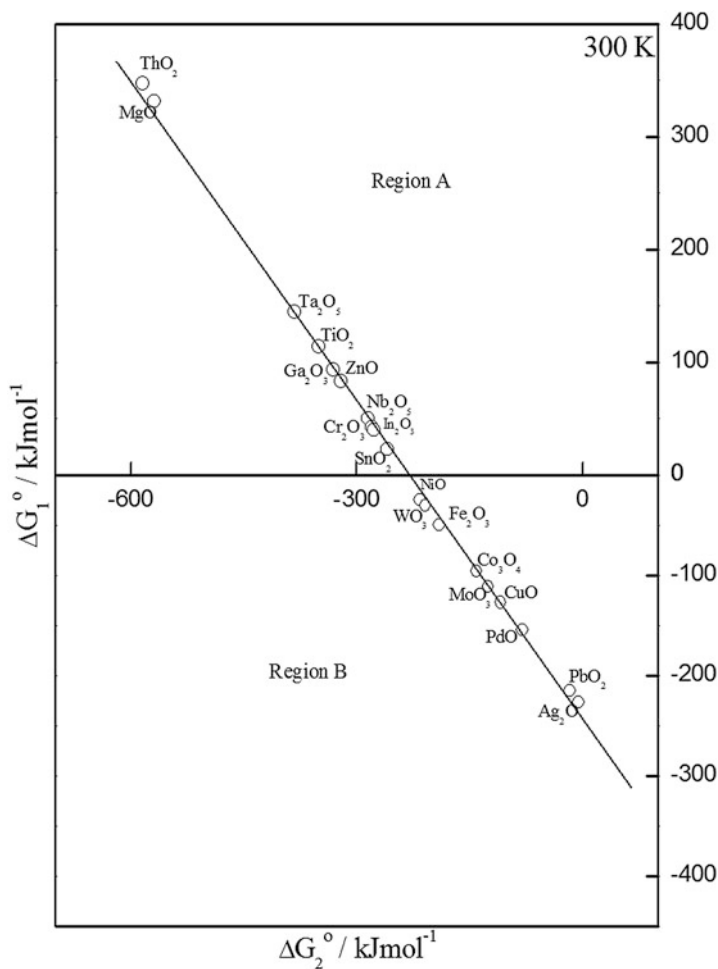


Fig. 5 Gibbs energy changes for reduction by hydrogen (ΔG_1^0) and reoxidation (ΔG_2^0) of metal oxides at 300 K (reactions 11 and 12) [42, 43]

Electrical Properties of Semiconducting Oxides

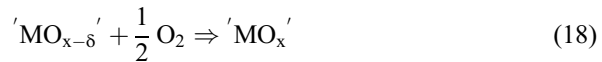
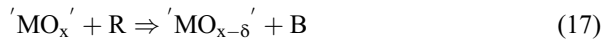
In the case of an n-type oxide, the thickness of the charge depleted zone, i.e., the thickness of the region below the surface from where electrons were transferred to the chemisorbed species, is given by the following expression:

$$L = L_D \sqrt{\frac{2eV_s}{kT}} \quad \text{where} \quad L_D = \left(\frac{kT\epsilon}{q^2n} \right)^{1/2} \quad (16)$$

where L_D , k , T , q , V_s , ϵ , and n are the Debye length of the material, Boltzmann constant, absolute temperature, electron charge, space charge potential, dielectric

constant, and density of charge carriers in the material, respectively. When polycrystalline oxides are involved, each grain would have the space charge region. When the grains are interconnected, as would be the case in a gas sensor, a potential barriers develop at the grain boundaries [40, 41]. Because of the potential barrier, charge flow through the grains is inhibited, and this results in high resistive state of the material in clean air. Debye length of metals and degenerate semiconductors are in the atomic scales, while that of the compounds such as oxides are in nm range. Value of n , i.e., density of the charge carriers, can be modified by incorporating dopants which form solid solutions in the oxide matrix. Since the gas sensors are being operated in ambient air, adsorption of species such as water vapor can also occur, and this can make the situation complex.

The processes that occur on the surface of the oxide material during the gas sensing process can be considered by the following two simultaneous reactions:



where " MO_x " represents the surface sites of an oxide in clean air ambient. In case of metal oxides where oxygen gets chemisorbed on their surfaces, " MO_x " may represent surface site with chemisorbed oxygen species. These species react with the analyte gas to form the oxidation product, B, and convert the surface site to the reduced state " $MO_{x-\delta}$." The electrical conductivity of the metal oxide is significantly altered when the surface characteristics are so altered. The rate at which the reaction occurs (which increases with the concentration of R) would determine the number of reduced states " $MO_{x-\delta}$ " formed and hence the conductivity change. Since the sensor operates in air where oxygen concentration remains large and constant, the rate constant of reaction (17) needs to be higher than that of the reaction (18). When equilibrium is attained, significant number of the reduced " $MO_{x-\delta}$ " states would prevail, and a change in the electrical conductivity of the material can be observed. In addition to the rate of these two reactions, adsorption processes that precede and succeed them also need to be considered.

All the above considerations are valid for oxides which do not exhibit chemisorption of oxygen also. In the case of these oxides, instead of the oxygen adsorbate, a lattice oxide ion of the material present on the surface would take part in the reactions. The analyte gas gets adsorbed on a surface site and reacts with a lattice oxide ion forming the reduced state on the surface " $MO_{x-\delta}$." This leads to the creation of non-stoichiometry in the few atomic layers of the surface of the oxide. When the diffusion coefficient of the oxide ion in the lattice is high, the rate of supply of oxide ions to the surface where the reaction with the analyte gas occurs can be significant. In such cases, non-stoichiometry generated on the surface spreads into the bulk. The extent of non-stoichiometry and the depth to which it extends in the bulk of the material determine the conductivity change observed during the sensing process. Again the rate constant for the reduction of the surface with the analyte gas

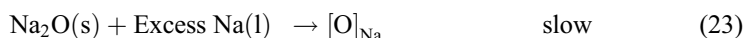
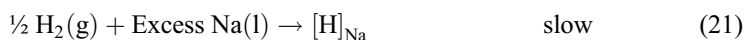
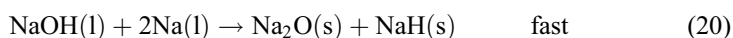
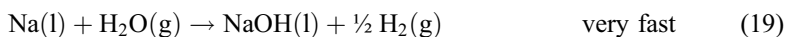
(leading to the creation of the non-stoichiometry) should be higher than that of the reoxidation of the “ $\text{MO}_{x-\delta}$ ” by the oxygen in air to the original state, “ MO_x .” Although the lattice oxygen gets involved in the sensing action, further steps in the mechanism could be different for different oxides. MoO_3 and certain molybdates exhibit this type of mechanism, as would be discussed in section “[Molybdates and Niobates](#).”

Strategies to Improve Selectivity and Sensitivity of the Sensors

The selectivity of a sensor towards a specific analyte in the presence of various other analyte species is determined mainly by the chosen oxide material. In appropriate cases, this can also be achieved by judicious choice of the operating temperature of the sensor, as mentioned earlier. Sensitivity of a sensor can be improved particularly when sensing process involves chemisorbed oxygen species, by choice of the geometry of the sensor either in thin or thick film form. In case of thick film sensors, size of the grains in the sensor film greatly influences the sensitivity. In case of thin films, sensitivity can be modulated by film characteristics such as texturing and connectivity between various grains in addition to the thickness of the film. In case of thick film sensors, it might be possible to achieve the selectivity by varying the thickness of the sensing film. Improved selectivity as well as sensitivity of the sensors can also be achieved by incorporation of appropriate dopants, namely, foreign receptors [44–49].

Three examples are chosen from the experimental results of authors’ laboratory, viz., (a) incorporation of a catalyst in a semiconducting oxide [50], (b) addition of a basic oxide to a semiconducting oxide in order to attract acidic species [51], and (c) addition of a p-type oxide to an n-type semiconductor in order to form p-n junctions [52]. These approaches are adopted to enhance selectivity and sensitivity of particular sensor formulation towards a target analyte.

Liquid sodium coolant of a fast breeder reactor (FBR) transfers the heat energy released by the fission of uranium and plutonium nuclei in the reactor core to water produce steam at the steam generator. For efficient heat transfer at the steam generator and for maintaining integrity, an optimum thickness of the steel tubes which separates liquid sodium from the high-pressure steam is chosen. In spite of rigorous quality control subjected to these steel tubes, a defect developing during the operation of the steam generator can result in steam leak into sodium. Steam that leaks in reacts with liquid sodium to produce NaOH(l) which, in turn, reacts with additional liquid sodium to form $\text{Na}_2\text{O(s)}$, NaH(s) as shown below [53]:



where $[H]_{Na}$ and $[O]_{Na}$ are hydrogen and oxygen dissolved in liquid sodium. Because of the high corrosivity of the molten NaOH towards structural steels, an event of the steam leak needs to be detected at its inception itself which otherwise would result in a large leak due to corrosion/erosion of the steel tubes calling for shutdown of the steam generator.

During a steam leak into liquid sodium, instantaneous formation of NaOH and hydrogen is envisaged (Eq. 19). When the reactor is operating under normal power conditions, temperature of liquid sodium would be ≥ 723 K, and gaseous hydrogen, NaH, and Na_2O will completely dissolve into sodium. In-sodium hydrogen sensors (discussed in section “Hydridehalides”) and oxygen sensors can be used for detecting these leaks. However, when the sodium temperature is about 523 K (during start-up or low-power operation of the reactor), the dissolution kinetics of NaOH and hydrogen (Eqs. 20, 21, 22, and 23) are significantly slow. Thus, the hydrogen evolved, would escape to the argon cover gas over sodium. Monitoring of hydrogen levels in argon plenum is adopted to detect the steam leak at the steam generator under low-power or start-up conditions of the reactor.

Figure 6 shows a typical response of a thin film sensor using palladium added tin oxide towards sensing hydrogen in the argon cover gas of an engineering scale sodium facility at the authors’ institution. In ambients containing oxygen, the palladium introduced in the sensor material will be present as palladium oxide (PdO) in air. Being a p-type oxide, grains of PdO form p-n junctions with the grains of n-type SnO_2 . On interaction with hydrogen gas, PdO gets converted to metallic Pd, and density of p-n junctions gets diminished which results in reduction in the resistance of the film. In this experiment, 40 vppm of hydrogen was introduced into the argon cover gas through liquid sodium (temperature of sodium, 523 K) in the sodium facility, and this was to simulate a steam leak scenario when sodium

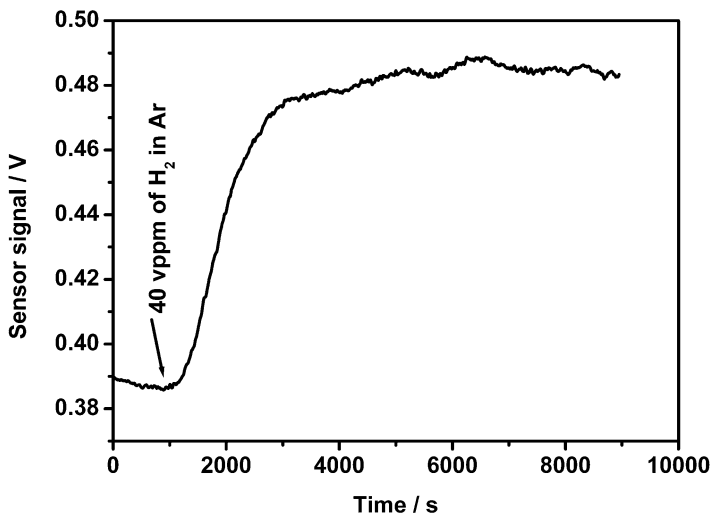


Fig. 6 Response characteristics of Pd-SnO₂ thin film sensor towards 40 vppm of hydrogen injected in argon in an engineering scale sodium facility (hydrogen injected through sodium at 523 K)

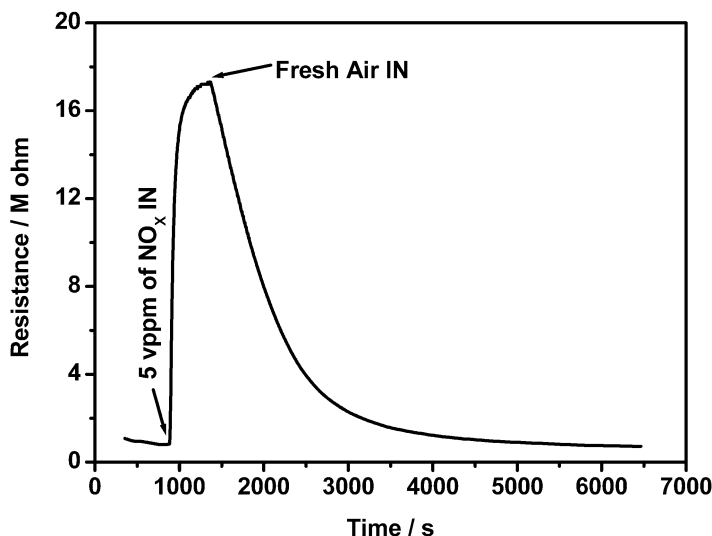


Fig. 7 Typical response of BaO-In₂O₃ thin film sensor towards 5 vppm of NO_x in air at 573 K

temperature is maintained low. Using an in-house developed electronic control and display module, the change in resistance of the sensor film was measured and converted to voltage for presentation. This experiment demonstrated the usefulness of this sensor to sense hydrogen in argon cover gas over sodium systems [50].

Figure 7 shows a typical response of barium oxide (a basic oxide) added indium oxide sensor towards sensing 5 vppm of NO_x in air (an acidic gas – comprising both NO and NO₂). As NO_x exhibits the tendency to withdraw electrons from the n-type semiconducting oxide, the resistance of the film increases on its exposure to the analyte gas [51].

Figure 8 shows a typical response of CuO (p-type semiconductor) incorporated tin oxide for sensing 10 vppm of hydrogen sulfide in air. Initially, due to the formation of p-n junctions, the sample exhibits high resistance. On interaction with H₂S, CuO is converted to CuS, which is a known metallic conductor. Thus, the p-n junctions are transformed to metal-semiconductor junctions, which are better conductors than p-n junctions [52].

Hydridehalides

Structure and Electrical Conductivity of Alkaline Earth Metal Hydridehalides

Alkali and alkaline earth metals and some of the transition and actinide metals (e.g., Ti, Zr, Hf, U, Pu) form stable hydrides. Hydridehalides of the alkali and alkaline earth metals are stoichiometric and ionic (exception being beryllium hydride) and are insulators. Hydridehalides of the other metals exhibit

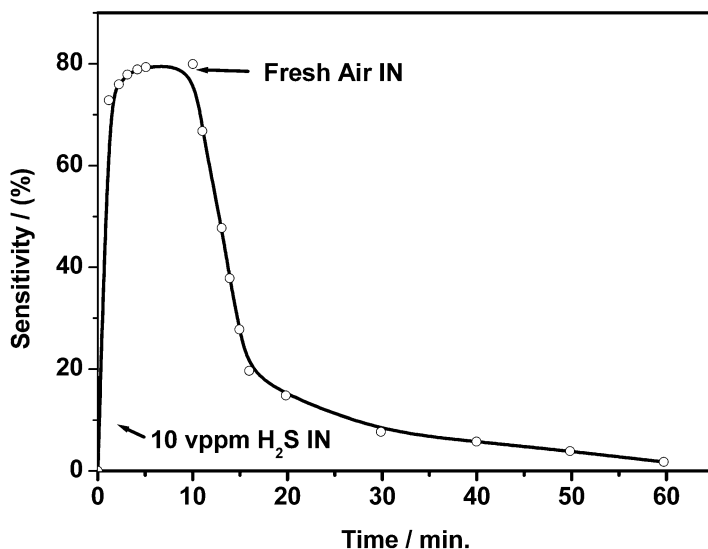
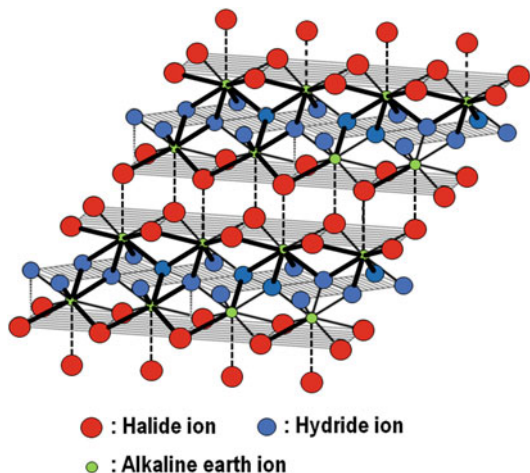


Fig. 8 Typical response of CuO-SnO₂ porous pellet to 10 vppm of H₂S in air

Fig. 9 Crystal structure of alkaline earth hydridehalide



non-stoichiometry and metallic conduction. Thermodynamic stability of the metal hydrides generally follows the order: alkaline earth metal hydrides > alkali metal hydrides > transition and actinide metal hydrides. Alkaline earth metal hydrides combine with their corresponding halides to form the hydridehalides of the general composition MXH (M = Ca, Sr, Ba and X = Cl, Br, I). These hydridehalides adopt the layered PbFCl structure [54], which facilitates hydride ion conductivity in them. The characteristic features of the MXH crystal structure are shown in Fig. 9.

In MHX crystal, the halide ions form a layer with a square pattern. Hydride ions are located above this layer, again in a square pattern but, rotated through 45° . They are situated above the edges of the halide ions. By this arrangement, the distance between $H^- - H^-$ ions are smaller than the distance between two halide ions. The number of ions in the hydride ion layer is twice of those present in the halide ion layer. Each alkaline earth ion is located in antiprism with vertices of four halide and four hydride ions which form square faces of different sizes. Alkaline earth ions are located under one half of the squares of H^- ions. An equal number of the alkaline earth ions are situated above the other half of the squares. These squares in turn form the base faces of further antiprisms which are completed by another layer of X^- ions. In this way total number of alkaline earth ions is equal to the total number of H^- ions. Since there are two layers of X^- ions for every H^- ion layer, the total number of X^- ions is also equal to the total number of alkaline earth ions. Together, these layers form a slab which are limited by X^- ions on either side. In the crystal, these slabs are stacked with staggered adjacent X^- layers. As a consequence, the coordination sphere of each alkaline earth ion is completed by a fifth X^- ion (shown dotted in figure). The layered structure of the hydridehalides enables the high conductivity in these materials. The conductivity arises owing to the presence of point defects, viz., Schottky and anti-Frenkel type defects in the material. Because H^- ion is relatively smaller than the halide ions (ionic radii of H^- , Cl^- , Br^- , and I^- are 110, 180, 195, 215 pm, respectively), its conductivity dominates in these hydridehalides. Since the ionic conductivity depends on the concentration of point defects, the hydride ion conductivity would increase with increase in temperature. It is to be pointed out that the contribution of electronic conductivity also would increase with increase in temperature. At any given temperature, an alkaline earth hydridehalide decomposes leading to release of hydrogen which results in formation of electronic defects in the lattice and hence electronic conductivity. For a given hydridehalide, the concentration of the electronic defects, and hence the electronic conduction, is dependent on its thermodynamic stability, hydrogen partial pressure in the environment, and temperature. Among the different MHX compounds, $MHCl$ and $MHBr$ are thermodynamically more stable than the iodide ion bearing analogues, as evidenced by their standard molar enthalpies of formation given in Table 3 [55].

The hydride ion conductivity of hydridehalides enables them to be used as solid electrolyte for measuring low hydrogen partial pressures in material systems.

Table 3 Standard molar enthalpies of formation of MHX

Alkaline earth metal, M	$\Delta H_f^0 / \text{kJmol}^{-1}$		
	X = Cl	X = Br	X = I
Ca	-504.2 ± 2.1	-446.0 ± 2.1	369.03 ± 2.1
Sr	-525.1 ± 2.1	-463.6 ± 2.1	-386.2 ± 2.1
Ba	-536.0 ± 2.1	-486.2 ± 2.1	-411.3 ± 2.1

Need for Measurement of Hydrogen in Liquid Metals and the Choice of Alkaline Earth Hydridehalide Based Solid Electrolyte Materials for Liquid Sodium Systems

Continuous monitoring of hydrogen in liquid metals is required for efficient operation of the processes and/or from safety point of view. For example, presence of dissolved hydrogen in molten aluminum during its casting results in blisters and pores in the final products, and hence continuous measurement of hydrogen in liquid aluminum is desirable. As discussed in section “[Strategies to Improve Selectivity and Sensitivity of the Sensors](#),” during an event of steam that leak into sodium coolant circuit, steam reacts with liquid metal to produce NaOH(l) which in turn reacts with additional liquid sodium to form Na₂O(s), NaH(s) as shown in Eqs. 19, 20, 21, 22, and 23.

Dissolution of H₂(g), NaH(s), and Na₂O(s) into sodium (reactions 21, 22, and 23) increases the concentrations of dissolved hydrogen and oxygen in the liquid metal, during normal operating conditions of the reactor (sodium temperature > 723 K). Continuous monitoring of dissolved hydrogen in the coolant stream is fast and reliable method to detect the steam leaks at their inception. Although methods exploiting the high thermal conductivity and low atomic mass of hydrogen are available to measure the concentration of hydrogen in liquid metals, they require extraction/separation of hydrogen from the liquid metal prior to its analysis [56, 57]. These methods are generally not sensitive enough at low hydrogen partial pressures (<10⁻⁶ bar).

Electrochemical cells that use either proton- or hydride ion-conducting electrolytes (in liquid or solid state) and built-in suitable configuration are potential candidates for measuring dissolved hydrogen concentration in liquid metals. Cells using proton conducting polymer electrolytes can be used only at low temperatures and in gas streams. They would not be useful for direct and continuous monitoring of low levels of dissolved hydrogen in high-temperature liquid metals. In case of the liquid electrolytes, it is necessary to contain them in thin metallic thimbles that are permeable to hydrogen and compatible with liquid metals. Owing to long-term corrosion by molten salts and use of thin components, cells using liquid electrolytes are generally not preferred for long-term operations. High-temperature proton conductors such as indium oxide-doped calcium zirconate have been used for measuring hydrogen levels in molten aluminum [58]. This involved equilibrating an inert gas such as argon with the molten aluminum followed by measuring the equilibrium hydrogen partial pressure in the inert gas using the emf cell with indium oxide-doped calcium zirconate at relatively low temperatures. These cells are characterized by their large response time. In addition, the method requires long equilibration times with an inert gas which makes it not suitable for application in liquid sodium circuit of a FBR. Indium oxide-doped calcium zirconate ceramic electrolyte is chemically incompatible with liquid sodium (indium sesquioxide is thermodynamically less stable than monoxides of alkali metals), and this precludes the operation of the cell by directly immersing the electrolyte in liquid sodium. Also, because of its very high

melting point, melt casting the electrolyte without contamination in a suitable shape within a hydrogen permeable and sodium compatible thin metallic thimble and use as hydrogen sensor is not easy. (A solid filled thin metallic thimble is mechanically sound and can withstand freezing-melting cycles of the surrounding liquid metal system. However, chemical compatibilities with the electrolyte during the melt casting and long-term corrosion by the liquid metal need to be considered for choosing the metallic membrane.)

Thermal properties of the alkaline earth hydridehalides show that they also melt at relatively high temperatures (>973 K), either congruently or incongruently [59–61]. High melting temperatures, their decomposition behavior, and high sensitivity to air and moisture pose problems while melt casting the electrolyte in thin-walled iron thimbles. Iron, which is permeable to hydrogen and compatible with liquid sodium as well as the electrolyte, is the suitable material for the thimble. Choosing a composite electrolyte in which the alkaline earth hydridehalide is one of the phases and possesses lower melting temperature could make the melt casting simpler. Phase diagram of CaCl_2 - CaHCl system (Fig. 10) shows that a composition containing 40 mol% CaHCl -60 mol% CaCl_2 forms a eutectic, and the eutectic temperature is 901 K [56]. CaBr_2 - CaHBr system has a eutectic at a composition of ~ 65 mol% CaBr_2 and ~ 35 mol% CaHBr (Fig. 11), and the eutectic temperature is lower at 853 K [57].

By choosing a composition close to that of the eutectic, melt casting of the electrolytes can be carried out at relatively lower temperatures. Smith constructed galvanic cells using the CaHCl - CaCl_2 composite and melt cast of the electrolyte with Li-LiH reference electrode and tested them in liquid sodium system [61–64]. Detailed studies conducted later indicated satisfactory performance of these sensors in liquid sodium only when dissolved hydrogen levels were high [59, 60]. Owing to low conductivity of this electrolyte system, extrinsic electronic impurities present in the electrolyte significantly affect the performance of the cell at low levels of hydrogen in sodium. It is to be pointed out that the structures of CaCl_2 and CaBr_2 (*oP6*) are identical as in the case of CaHCl and CaHBr (*tP6*).

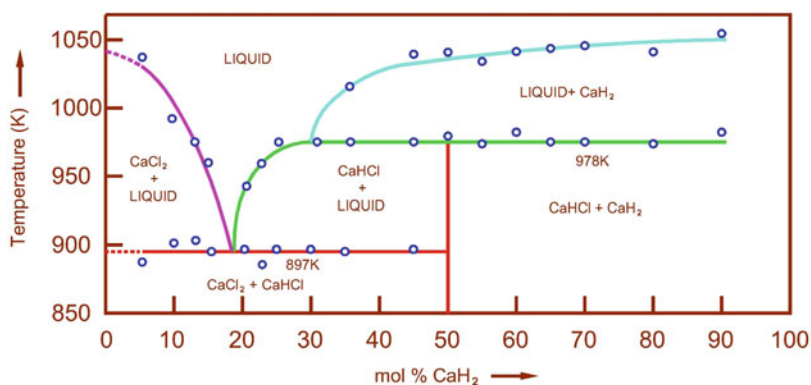
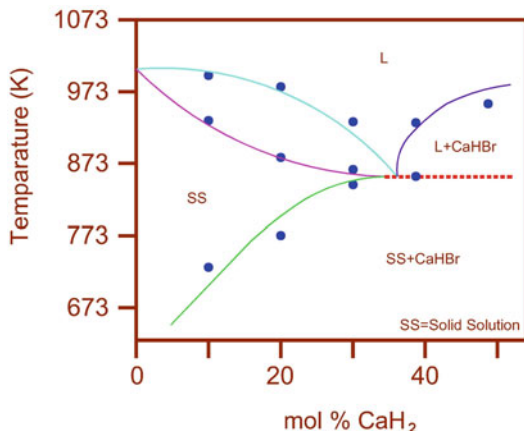


Fig. 10 Phase diagram of CaCl_2 - CaH_2 system

Fig. 11 Partial phase diagram of $\text{CaBr}_2\text{-CaH}_2$ system



Hydride ion conductivity in CaHBr-CaBr_2 composite electrolyte is higher than that in CaHCl-CaCl_2 electrolyte because of the following:

- (1) H^- ion conductivity in CaHBr is expected to be higher than in CaHCl because of the larger size of Br^- compared to Cl^- .
- (2) H^- ion conductivity in the accompanying CaBr_2 phase is higher than in the CaCl_2 phase because of (i) higher solubility of CaHBr in CaBr_2 than that of CaHCl in CaCl_2 at all temperatures, (ii) lower solidus temperature in CaHBr-CaBr_2 system than in CaHCl-CaCl_2 system.

Experience with Hydridehalides for Monitoring Hydrogen Levels in Liquid Sodium

A galvanic cell based on CaHBr-CaBr_2 composite electrolyte using $\text{Mg}_2\text{Ca-Mg-CaH}_2$ reference electrode has been found to operate satisfactorily down to low hydrogen concentrations in sodium. The schematics of the construction of the galvanic cell is shown in Fig. 12. The emf of the cell is given by Nernst equation given below:

$$E = (RT/2F) \ln (p_{\text{H}_2})^{\text{ref}} / (p_{\text{H}_2})^{\text{sple}} \quad (24)$$

$(p_{\text{H}_2})^{\text{sple}}$ can be related to the dissolved hydrogen concentration in sodium by Eq. (25)

$$C_{\text{H}}^{\text{Na}} = K_{\text{S}} (P_{\text{H}_2}^{\text{sple}})^{1/2} \quad (25)$$

where C_{H}^{Na} is dissolved hydrogen concentration in sodium and K_{S} is the Sievert's constant for Na-H system.

Fig. 12 Schematics of the galvanic cell using calcium hydride bromide electrolyte for measuring hydrogen concentrations in liquid sodium metal

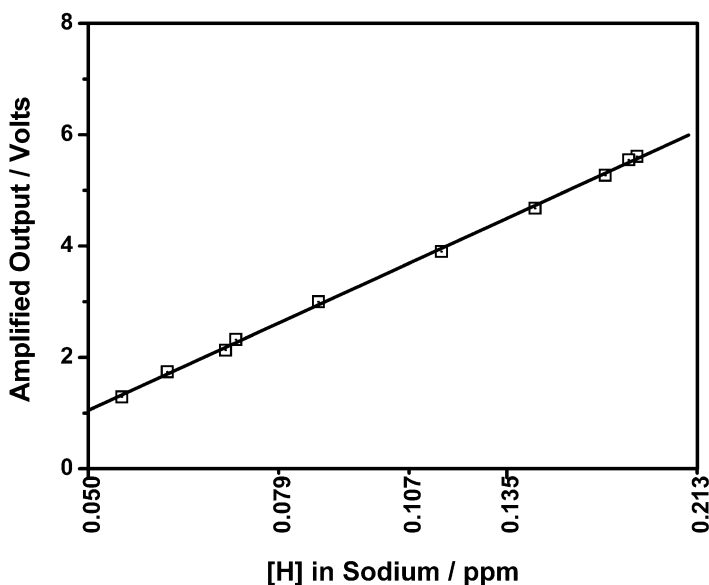
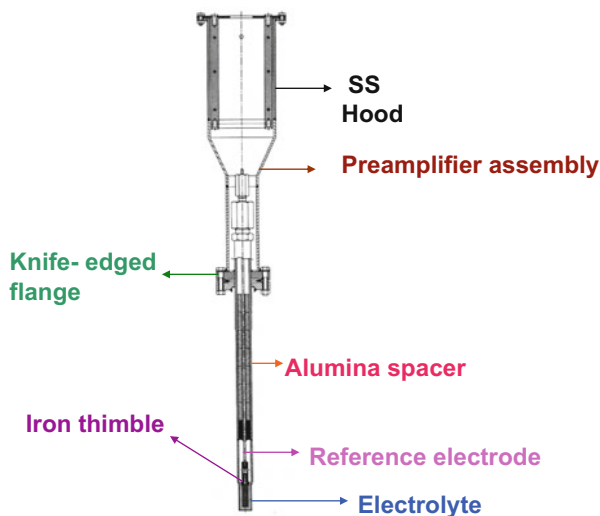


Fig. 13 Semilog plot showing the typical variation of the output of the galvanic cell with dissolved hydrogen concentration (cell operating temperature = 723 K)

The electrolyte was melt cast in the thin-walled iron thimble after in situ formation of CaHBr from Ca metal in presence of CaBr₂. The cells could be constructed with reproducible characteristics. A typical calibration graph, given in Fig. 13, shows the expected variation of cell output as a function of hydrogen concentration in liquid sodium. It is seen that these galvanic cells could be used to measure down

to about 60 ppb of dissolved hydrogen in sodium at 723 K. The response times of these sensors are in the order of a few seconds which are adequate for their use in the coolant circuit of a FBR.

Silver Halides

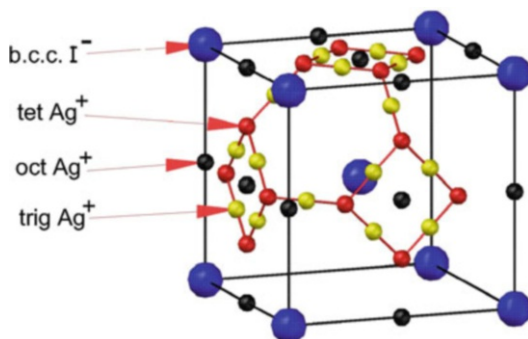
Structure of Silver Halides

Silver iodide exists in three allotropic modifications in the temperature range of 298–673 K. The β - and γ -phase are poorly conducting phases [65], whereas the α -phase is a highly conducting phase above ~ 420 K until it melts at ~ 831 K [66]. γ -Phase exhibits BCC structure with anion close packing, whereas β -phase exhibits hexagonal structure at room temperature. Above the β to α transition temperature, the wurtzite structure of α -AgI is stable until it melts. The conductivity arises due to the 42 interstitial voids which are present in the wurtzite structure of α -AgI. The scheme representing the void networks of α -AgI is shown in Fig. 14. There are 6 octahedral, 12 tetrahedral, and 24 trigonal sites in a unit cell for α -AgI. The movement of two Ag^+ ions in all these interstitial voids gives the high conductivity for AgI in α -phase. This phase is reported to have conductivity of about 0.5 Scm^{-1} .

Effect of Cationic and Anionic Substitution on Conductivity of AgI

With an objective of achieving high ionic conductivity in AgI at low temperatures, at least two different methodologies were adopted: (a) by mixing AgI with other halides like RbI, CsI, Hg_2I_2 , etc. to prepare new phases and (b) substitution of cation or anion in AgI. RbAg_4I_5 exhibits conductivity at room temperature [68]. An admixture of AgI and Ag_2CsI_3 was also reported to show better conductivity compared to AgI [69]. The significance of adding a cation like Cu^+ (ionic radius: 77 pm) in AgI [70, 71] was with the intention of substituting a second mobile ion

Fig. 14 Crystal structure of α -AgI representing the 42 interstitial voids. tet represents tetragonal, oct represents octahedral void, and trig represents trigonal void [67]

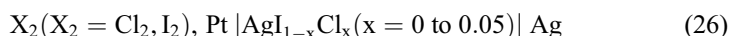


(Cu^+ ion) in AgI. Both Cu^+ and Ag^+ possess good ionic mobilities in solids [72]. Introduction of ions like Cs^+ (ionic radius: 167 pm [68]) which are larger than Ag^+ ion (ionic radius: 115 pm) causes the lattice loosening [73–75] resulting in increased bulk conductivity and reduction in the temperature of β to α phase transition. In case of Cd substituted AgI, the transition temperature was lowered to 397 K [76]. The substitutions of anions in AgI and the solubility limit of the corresponding silver compounds in AgI have been reported [77, 78]. Substitution of Cl^- in place of I^- was reported by Ihara et al. [79]. These authors also observed the reduction in β to α phase transition temperature in AgI with AgCl incorporation [79].

Clinsha et al. investigated the influence on the substitution of chloride in place of iodide in AgI matrix towards the solid solution formation, beta to alpha transition temperature, electrical conductivity, etc. [80, 81]. These studies showed that the solubility limit of AgCl in AgI matrix lies between 4 and 5 mol.% at 300 K [80, 81]. Different compositions, viz., $\text{AgI}_{1-x}\text{Cl}_x$ ($x = 0$ to 0.05), were evaluated for iodine vapor and chlorine gas sensing properties.

Silver Halides as Sensors for Halogens

Electrochemical cells of following configuration were assembled, and experiments were carried out at 428 K towards sensing of iodine vapor and chlorine gas in argon and air ambient, respectively [81]:



In this configuration, silver acts as the reference electrode, and platinum is used as the working electrode. EMF output of an electrochemical cell with the fixed activity at the reference electrode can be represented by the Nernst equation given below:

$$E = \frac{RT}{F} \ln \frac{a_i'}{a_i''} \quad (27)$$

where a_i' and a_i'' are the activities of the species of interest in the reference and sample electrodes, respectively. If the activity of the reference electrode is fixed as unity, then the emf of the cell reduces to:

$$E = \frac{RT}{F} \ln \frac{1}{a_i''} \quad (28)$$

Iodine sensing behavior of the cell was evaluated for concentrations varying between 6 and 200 vppm of iodine in argon. Figure 15 shows a typical iodine sensing response of the cell using AgI as the solid electrolyte for 6 vppm of iodine vapor in argon at 428 K.

Similarly, $\text{AgI}_{0.95}\text{Cl}_{0.05}$ was found to sense chlorine down to 17 vppb. Figure 16 shows typical sensing characteristics of this electrolyte towards 17 vppb of

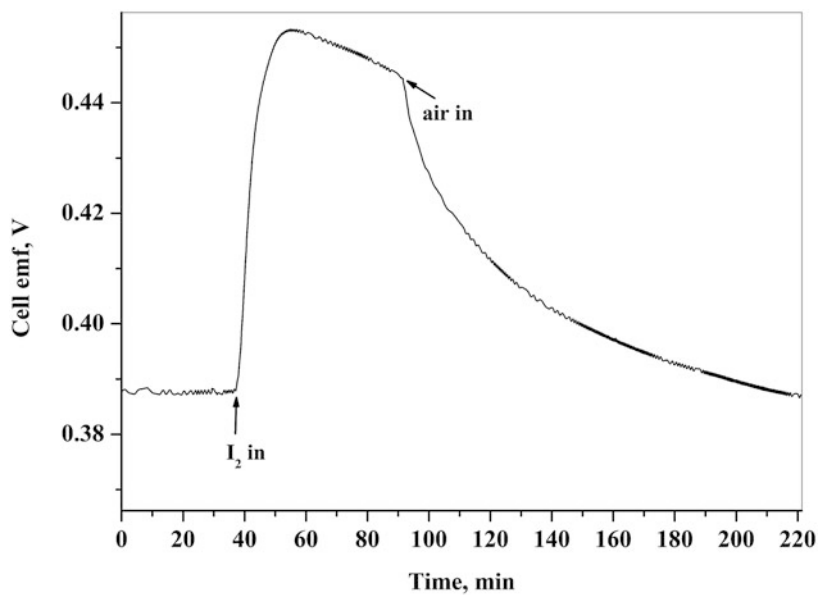


Fig. 15 Sensing characteristics of AgI (disc form) towards 6 vppm of iodine vapor in argon at 428 K [81]

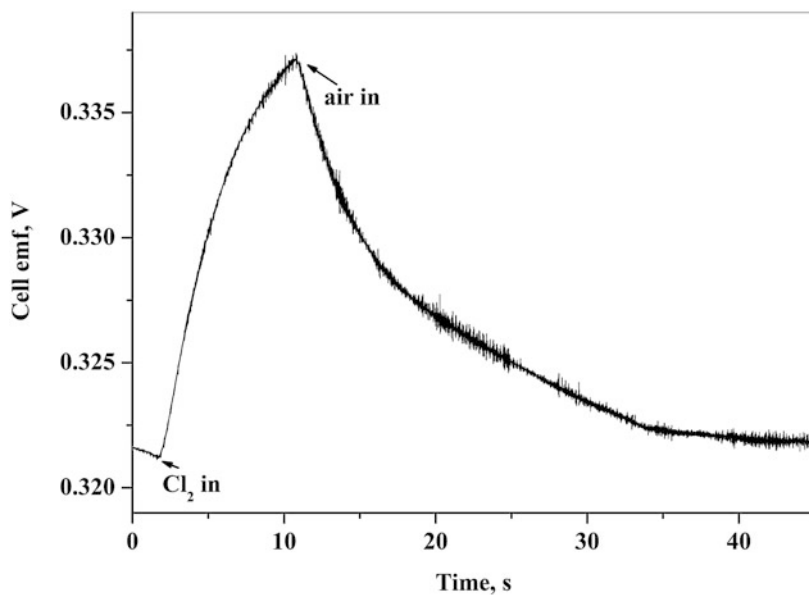


Fig. 16 Typical response of AgI_{0.95}Cl_{0.05} (disc form) towards 17 vppb of chlorine in air at 428 K [81]

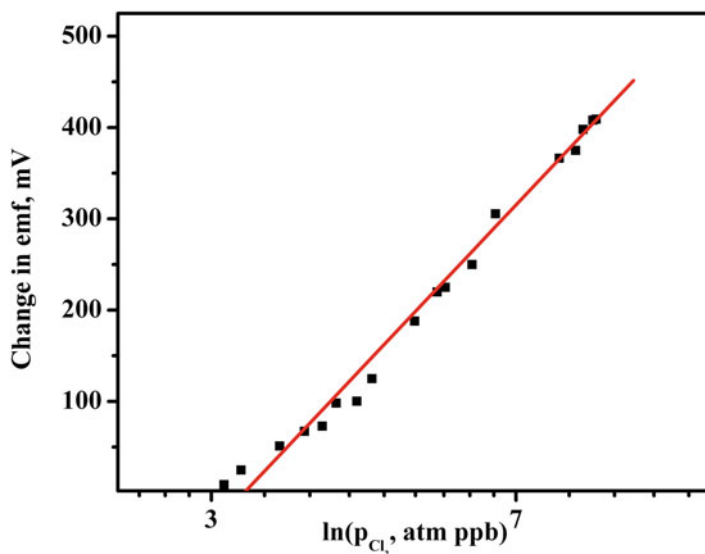


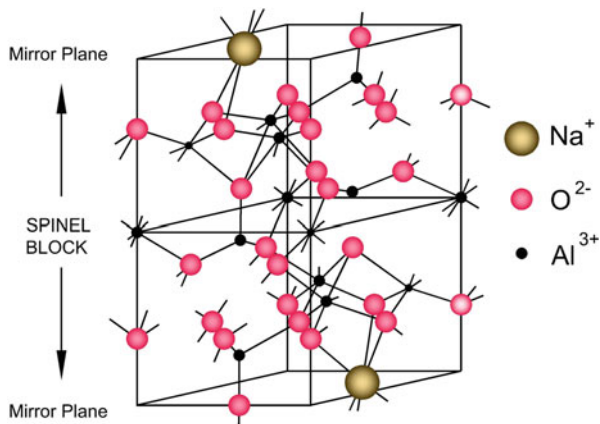
Fig. 17 Semilog plot showing the typical calibration graph for measuring trace levels of chlorine with $AgI_{0.95}Cl_{0.05}$ electrolyte in disc form in air at 428 K [81]

chlorine at 428 K. It was also found that it is capable of sensing chlorine up to 15 vppm (Fig. 17), thus possessing a dynamic range of three orders for measuring trace levels of chlorine in air.

Sodium Aluminates

Beta-alumina is a class of compounds with general formula, $M_2O \cdot xAl_2O_3$, where M is typically Na, K, Li, etc. and where x varies from 5 to 11. When the value of x ranges from 5 to 7, the phase is designated by β'' , and when x falls between 8 and 11, the phase is called as β [82]. These compounds possess a characteristic layered structure [83, 84], with alkali ions present in the loosely packed layer and aluminum and oxygen constitute the spinel block. The layer containing the alkali ions has a low atomic density. The spinel blocks are comprised of four layers of oxygen ions in a cubic close-packed arrangement with small Al^{3+} ions accommodated in both octahedral and tetrahedral interstices, but not in the same proportion as in spinel, $MgAl_2O_4$. Due to this type of structure, they exhibit high conductivity towards the species present in the layer, namely, Na, K, Li, etc. Figure 18 shows a schematic crystal structure of sodium-beta-alumina [85]. This class of compounds is known to exhibit conductivity of about 0.1 Scm^{-1} at 623 K [85]. They find applications in sodium secondary batteries, thermoelectric converters, fuel cells, sensors, etc. Takikawa et al. reported the use of sodium-beta-alumina towards the measurement of sodium vapor pressure [86].

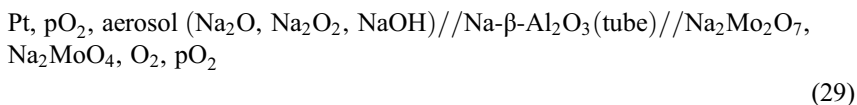
Fig. 18 Crystal structure of Na- β -Al₂O₃



Sensor for Sodium Oxide Aerosol

In the event of an accidental leak of the high-temperature liquid sodium coolant (from fast reactor, engineering scale facility, etc.) to air ambient, the liquid metal reacts with oxygen and moisture leading to sodium fires. These fires produce aerosol containing oxides of sodium (Na₂O and Na₂O₂), NaOH, Na₂CO₃, etc. At the authors' laboratory, two EMF cells of the following configurations were constructed using Na- β -Al₂O₃, one in tubular form and the other in wafer form, for detecting the sodium fires by continuous monitoring of sodium oxide aerosols in air [87]:

Tubular Sensor



Wafer Sensor



Tubular form of sensor was constructed from Na- β -Al₂O₃ tubes. Ternary oxide-based system, viz., Na₂MoO₄(s)–Na₂Mo₂O₇(s)–O₂(g), was used as the reference electrode in the cell. In the wafer sensor, a thin disc of Na- β -Al₂O₃ was used with Au/Au₂Na as reference electrode.

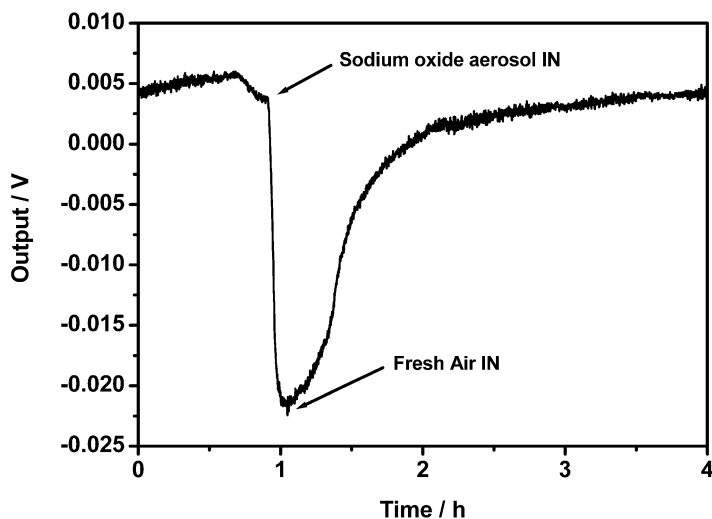


Fig. 19 Typical response exhibited by wafer sensor for sodium oxide aerosol (sensor operating temperature: 623 K)

Figure 19 shows the typical response shown by the wafer sensor, operated at 623 K towards sodium oxide aerosol. Figure 20 depicts the response of this sensor to sodium oxide aerosol generated in an engineering scale sodium facility.

Phosphates

Phosphates generally exhibit tendency to accommodate metal ions of different oxidation state in their structure. The famous examples are monazite, apatite, chlorapatite, etc. [88, 89]. This ability of accommodating different metal ions helps in realizing unusual electrical conductivity and other physical properties. An example to cite is NASICON (sodium super ionic conductor), $\text{Na}_{1+x}\text{Zr}_2\text{Si}_x\text{P}_{3-x}\text{O}_{12}$, ($0 < x < 3$), which is a three-dimensional sodium ion conductor [90, 91]. Chavez et al. reported the conducting properties of different lithium zirconium phosphates, viz., $\text{LiZr}_2(\text{PO}_4)_3$, $\text{Li}_2\text{Zr}(\text{PO}_4)_2$ and $\text{Li}_{0.6}\text{Zr}_{1.35}(\text{PO}_4)_2$ [92]. Sree Rama Murthy et al. prepared a series of compositions with nominal formula, $\text{Li}_{2-4x}\text{Zr}_{1+x}(\text{PO}_4)_2$ ($x = 0-0.45$), and carried out detailed investigations on the solid solution formation range, presence of different classes of compounds, their lithium ion transport number, lithium ion conductivity, and compatibility with lead-lithium alloys [93].

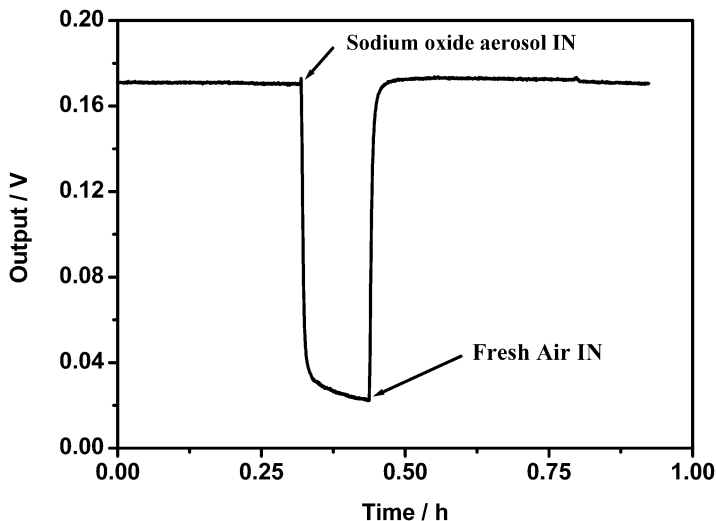


Fig. 20 Response characteristics of wafer sensor on exposure to sodium oxide aerosol generated in engineering scale sodium facility (operating temperature of sensor: 623 K)

$\text{Li}_{2-4x}\text{Zr}_{1+x}(\text{PO}_4)_2$ ($x = 0-0.45$): Phase Formation and Electrical Conductivity Studies

X-ray diffraction studies on the compositions with nominal formula, $\text{Li}_{2-4x}\text{Zr}_{1+x}(\text{PO}_4)_2$ ($x = 0 - 0.45$), provided the following information: the lithium-rich compositions ($x = 0.10$ and 0.25) showed identical pattern corresponding to $\text{Li}_2\text{Zr}(\text{PO}_4)_2$. For the composition with $x = 0.45$ (lithium deficient), the pattern matched with $\text{Zr}_{1.5}(\text{PO}_4)_2$. But, the composition $\text{Li}_{0.6}\text{Zr}_{1.35}(\text{PO}_4)_2$ ($x = 0.35$) possessed a combined pattern of $\text{Li}_2\text{Zr}(\text{PO}_4)_2$ and $\text{Zr}_{1.5}(\text{PO}_4)_2$ [93].

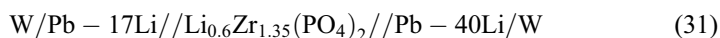
The typical conductivity values of the compositions with $x = 0$ to 0.35 ($\text{Li}_2\text{Zr}(\text{PO}_4)_2$, $\text{Li}_{1.5}\text{Zr}_{1.125}(\text{PO}_4)_2$, $\text{Li}_{1.0}\text{Zr}_{1.25}(\text{PO}_4)_2$, and $\text{Li}_{0.6}\text{Zr}_{1.35}(\text{PO}_4)_2$) were about 10^{-5}Scm^{-1} , while the composition $\text{Li}_{0.2}\text{Zr}_{1.45}(\text{PO}_4)_2$ ($x = 0.45$) was $\sim 10^{-7} \text{Scm}^{-1}$ at 500 K. These values indicate the following features: (a) when the structure is with fully occupied lithium ions, the conductivity is low, (b) the conductivity is marginally higher in the middle range of lithium concentration, and (c) the conductivity becomes the lowest for the composition with the lowest concentration of lithium ions. This behavior could be due to the substitution of zirconium ion by lithium ions, which leads to creation of more vacancies as a result of the charge difference between these two ions (in the structure with nominal composition, $\text{Li}_{2-4x}\text{Zr}_{1+x}(\text{PO}_4)_2$). This observation was further corroborated with the lithium ion transport numbers exhibited by $\text{Li}_2\text{Zr}(\text{PO}_4)_2$, $\text{Li}_{1.5}\text{Zr}_{1.125}(\text{PO}_4)_2$, and $\text{Li}_{0.6}\text{Zr}_{1.35}(\text{PO}_4)_2$ in the temperature range of 498–673 K. The transport numbers of lithium ion in $\text{Li}_2\text{Zr}(\text{PO}_4)_2$, $\text{Li}_{0.6}\text{Zr}_{1.35}(\text{PO}_4)_2$, and $\text{Li}_{1.5}\text{Zr}_{1.125}(\text{PO}_4)_2$ were found to be 0.94, 0.99, and 0.98, respectively, in the temperature range of 498–673 K.

In a nutshell, lithium-deficient phase, $\text{Li}_{0.2}\text{Zr}_{1.45}(\text{PO}_4)_2$, had the least conductivity because of limited conducting lithium ions. Lithium-rich phase, for example, stoichiometric $\text{Li}_2\text{Zr}(\text{PO}_4)_2$, also exhibited relatively less conductivity, possibly due to limited vacancies for hopping. Intermediate-range lithium-deficient compositions of $\text{Li}_{2-4x}\text{Zr}_{1+x}(\text{PO}_4)_2$ ($x = 0.125, 0.25$) showed the highest conductivity because of the availability of more ion-conducting species and lithium ion vacancies for hopping. The trend was also supported by the transport number of lithium ion in the respective phases.

Sensor for Lithium Activity Measurements

Lead-lithium (17 at %) alloy is considered as one of the candidate materials for use as both coolant and breeder in fusion reactors [94, 95]. Depletion of lithium from this alloy is expected owing to the nuclear reactions and possible chemical interactions with structural materials [96–99]. Thus, the alloy composition varies continuously and leads to the modification of the physical properties, like eutectic temperature, viscosity, flow characteristics, etc. Periodic replenishment of lithium is required to avoid the change in the aforementioned physical properties, which is possible by continuously monitoring the lithium activity in the alloy.

As the compound $\text{Li}_{0.6}\text{Zr}_{1.35}(\text{PO}_4)_2$ exhibited the highest conductivity among the compositions, its compatibility study with Pb-17Li and Pb-40Li alloys was performed at 723 K up to 2000 h. These studies showed that this compound was stable in these alloys, and hence this compound $\text{Li}_{0.6}\text{Zr}_{1.35}(\text{PO}_4)_2$ was employed for assembling a sensor for measuring lithium activity. EMF cell of the following configuration using the electrolyte in a crucible form was constructed:



Pb-40Li (biphasic composition) was used as the reference electrode in the cell, which was placed inside the $\text{Li}_{0.6}\text{Zr}_{1.35}(\text{PO}_4)_2$ crucible with tungsten wire as electrical lead. Theoretical emf of the cell as a function of temperature was calculated and plotted in (Fig. 21). As shown in the figure, the emf increases with temperature up to ~ 723 K and decreases above 723 K. The measured open circuit voltage was found to be about -55 mV, which closely matched with the theoretical value of 64 mV [93].

Molybdates and Niobates

Molybdenum Oxide (MoO_3): Structural Aspects

The structure of MoO_3 is based on a series of bilayers that are oriented perpendicular to the [010] y-axis as shown in Fig. 22a. Each bilayer consists of two sublayers of distorted MoO_6 octahedra to give three crystallographically inequivalent oxygen

Fig. 21 Theoretically computed variation of the open circuit voltage of W/Pb – 17Li//Li_{0.6}Zr_{1.35}(PO₄)₂//Pb – 40Li/W with temperature (*refers to experimental value obtained) [93]

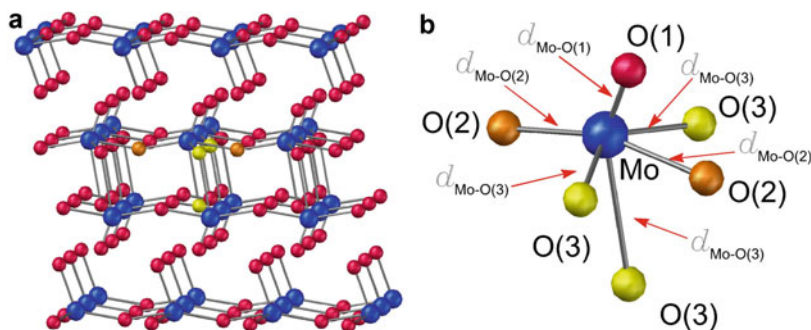
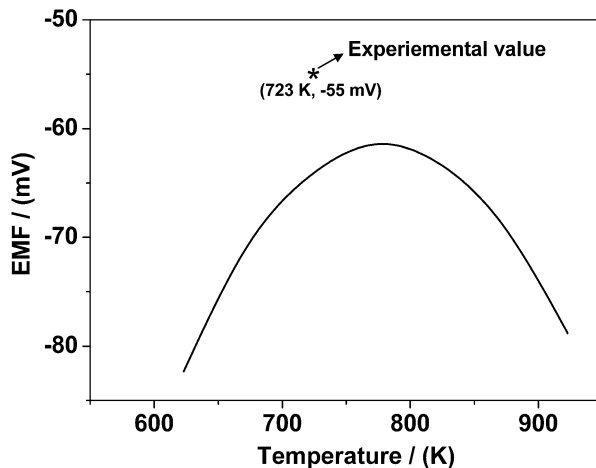


Fig. 22 (a) Crystal structure of orthorhombic MoO₃ showing the layered structure along the (010) direction and (b) structure of MoO₆ distorted octahedra [40] – Mo-O(1), Mo-O(2), Mo-O(3) have different bond angles

sites as shown in Fig. 22b. Each bilayer interacts with the adjacent bilayer in the [010] direction through a weak non-covalent van der Waals interaction. There are no dangling bonds on the [010] surface. Oxygen positioned in these shear structures are in labile state [100, 40, 45].

In the MoO system, MoO₃ and MoO₂ are the oxides with 6+ and 4+ oxidation states of molybdenum metal. In addition to these two oxides, several suboxides with well-defined stoichiometry and having average valences between 6.0 and 4 (e.g., Mo₁₈O₅₂, Mo₁₇O₄₇, Mo₉O₂₆, Mo₈O₂₃, Mo₅O₁₄, Mo₄O₁₁) also exist in this system. The deviation from stoichiometry of O/Mo = 3 is stabilized by the elimination of complete rows of anion point defects in specific crystallographic planes by simultaneous shear displacement and crystal structural collapse of the planes, by crystallographic shear (CS) mechanism (Fig. 23). The lower O/Mo in a suboxide is incorporated by the formation of CS planes of edge-sharing octahedra in a specific crystallographic orientation. When an oxide is reduced, the driving force

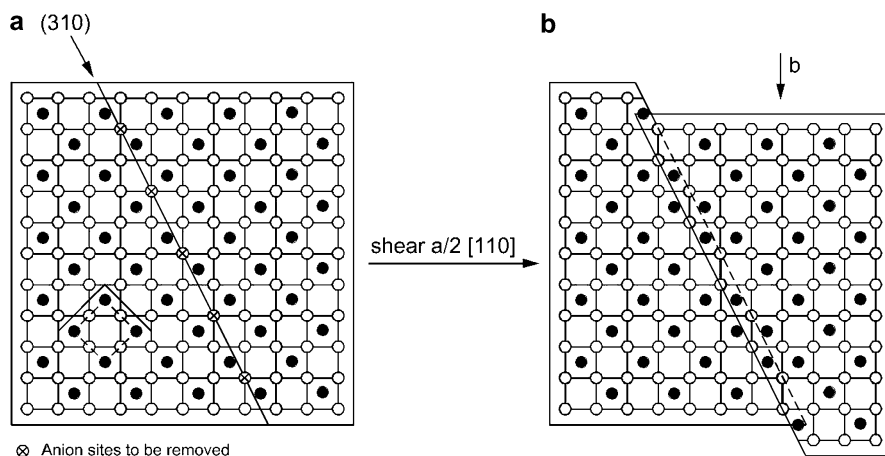


Fig. 23 Principles of crystallographic shear (CS) in MoO_3 : (a) formation of anion vacancies and (b) elimination of the vacancies by crystal shear and collapse [102]

for the formation of CS planes is to lower the Gibbs energy of the system and preservation of the cation octahedral coordination (Fig. 23) [42, 101, 102].

Electrical Conductivity and Gas Sensing Characteristics of Molybdenum Trioxide

Sunu et al. identified the existence of non-stoichiometry in MoO_3 by the presence of some fraction of molybdenum in +5 state, confirmed by EPR studies [103, 43, 104]. The electrical conductivity of MoO_3 was found to be about 10^{-6} Scm^{-1} at 773 K in air [43, 104]. It was also found out from the electrical conductivity of MoO_3 in various atmospheres that it did not chemisorb oxygen [102].

Usefulness of MoO_3 as a catalyst for oxidizing organic compounds has been reported [105]. Lattice oxygen gets involved in this catalysis [106, 107]. The mechanism of this catalytic action was studied in detail by Mars et al. [108]. Section “[Electrical Properties of Semiconducting Oxides](#)” provided the analyte sensing properties mediated by chemisorbed oxide ions on the surface of semiconducting oxides and also by lattice oxygens by certain semiconducting oxides, which do not chemisorb oxide ions due to certain special crystal structures. In molybdenum trioxide, participation of lattice oxygen in the sensing process of analytes is envisaged. However, the general steps of absorption of analytes, diffusion process, and desorption of product species remain the same.

Typical Analyte Sensing Characteristics of MoO_3

Molybdenum trioxide was found to exhibit significant change in its conductivity on exposure to ammonia of a few hundred ppm levels in air. Further, it was also

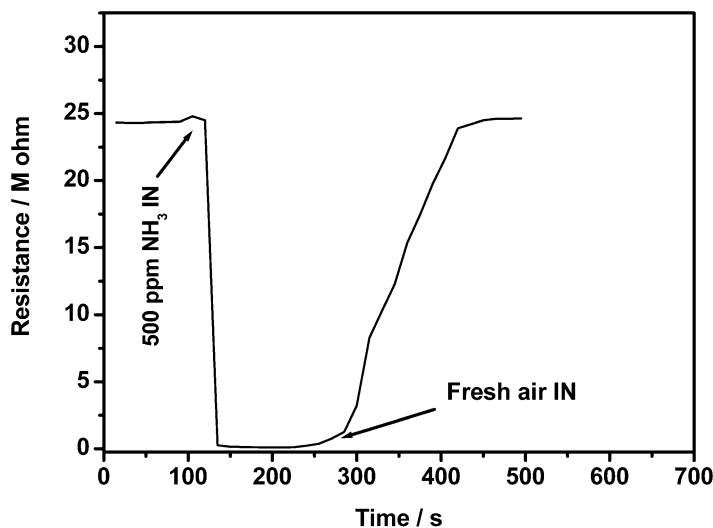


Fig. 24 Typical response and retrace characteristics of porous pellet sensors of MoO_3 towards 500 ppm of ammonia in air at 673 K

observed that selective sensing of ammonia over hydrogen in the temperature range of 493–623 K. Detailed investigations revealed the formation of lower oxides, viz., MoO_2 , Mo_4O_{11} , and molybdenum nitride (Mo_2N), on exposure of ammonia to molybdenum trioxide. These compounds are known to exhibit higher conductivity when compared to MoO_3 , and hence the sensing action was explained [43]. The chemical reaction is shown in the following equation:

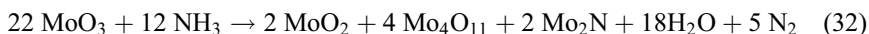


Figure 24 shows the typical response characteristics MoO_3 in porous pellet form for 500 ppm of ammonia in air at 673 K.

Silver Molybdates

Silver oxide (Ag_2O) and molybdenum trioxide (MoO_3) are known to form several ternary compounds, viz., Ag_2MoO_4 , $\text{Ag}_2\text{Mo}_2\text{O}_7$, $\text{Ag}_2\text{Mo}_4\text{O}_{13}$, and $\text{Ag}_6\text{Mo}_{10}\text{O}_{33}$ [43]. Among these compounds, $\text{Ag}_6\text{Mo}_{10}\text{O}_{33}$ is known to conduct by silver ions significantly, with a minor contribution from electrons [109, 43]. The structure of this compound is shown in Fig. 25: this essentially has MoO_6 octahedra flanking silver ions arranged in a layered fashion, from both the sides, and, thus, enabling the conduction by silver ions. Sunu et al. measured the electrical conductivity and silver ion transport number of this compound at different temperatures [109, 43]. The conductivity value was reported to be 10^{-3}Scm^{-1} at 773 K in air. Silver ion transport number was reported to be 0.9 and 0.5 at 533 and 683 K, respectively.

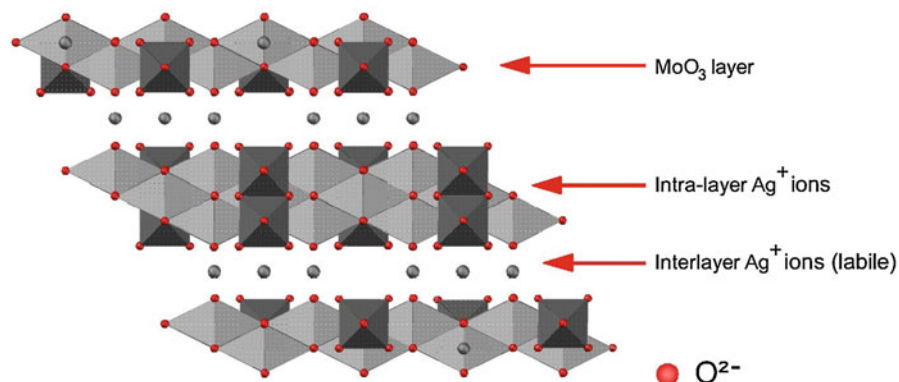
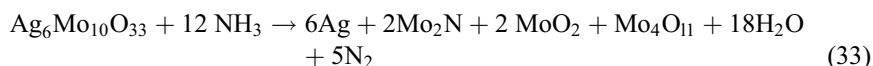


Fig. 25 Structure of silver decamolybdate

Like molybdenum trioxide, silver decamolybdate was also found to react with ammonia and exhibited two to three orders of change in electrical conductivity. The resultant products formed in situ were elucidated by different physicochemical techniques and were found to be Ag, MoO₂, Mo₄O₁₁, and Mo₂N. These intermediates are known to possess higher electrical conductivity than silver decamolybdate. The following equation depicts the sensing process:



On re-exposure to air, the products formed react in situ to provide the starting compound and hence retrace to the background electrical conductivity. Due to this enhanced affinity for such reaction between Ag₆Mo₁₀O₃₃ and ammonia, a thick film sensor of silver decamolybdate was found to sense down to 2 vppm of ammonia in air at 578 K [110]. Figure 26 shows the typical response of this compound towards 4 vppm of ammonia at 578 K.

Niobates

Niobium pentoxide (Nb₂O₅) has been explored for monitoring of oxygen in the internal combustion engines to ensure complete burning of the fuel [111]. Nb₂O₅ has also been shown to sense trace level gases [112, 113]. By suitably doping, it can be tuned to sense hydrogen and methane at low temperatures [114, 115]. Use of chromium niobate (CrNbO₄) towards gas sensing applications is reported in literature [116–118]. Chromium niobate is a rutile structured compound (Fig. 27i and ii). The ionic sizes of Cr³⁺ (61.5 pm) and Nb⁵⁺ (64 pm) with octahedral coordination are similar [119], and this is responsible for random distribution of metal ions at 2a position of the rutile structure (Fig. 27i) [120].

Fig. 26 Typical response characteristics of $\text{Ag}_6\text{Mo}_{10}\text{O}_{33}$ thick film towards 4 vppm of ammonia at 578 K

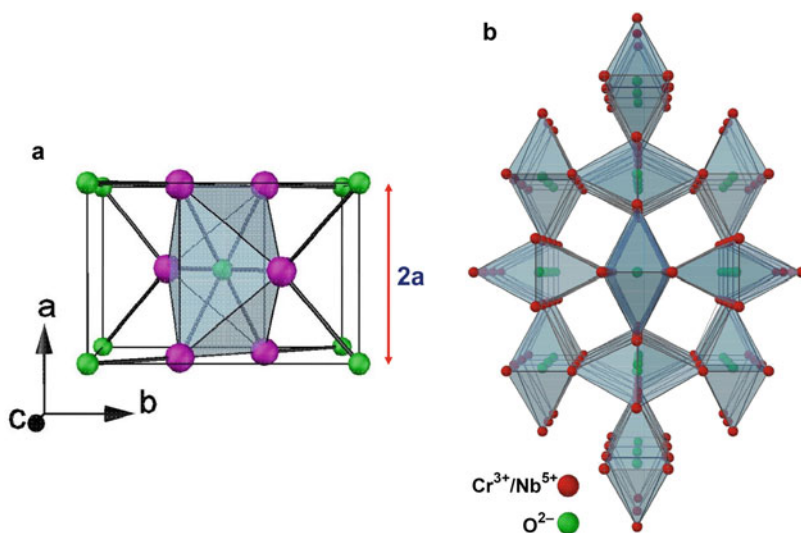
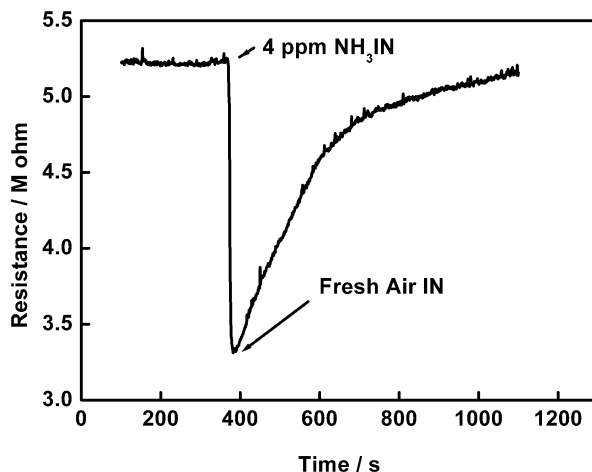


Fig. 27 (i) Unit cell of CrNbO_4 and (ii) lattice of CrNbO_4 showing oxygen polyhedra

CrNbO_4 was reported to be a p-type semiconductor, due to metal vacancies [121]. Due to this property and also because of its open structure (Fig. 27ii), several teams explored its gas sensing properties [114–116]. The typical analytes studied were CO , H_2 , NH_3 , C_3H_8 , ethanol, petroleum gas (PG), etc. [116–118]. Electrical conductivity studies in different atmospheres (oxygen, air, and argon) showed nearly same conductivity value in the temperature range of 370–710 K. Further, the activation energies for the conduction process in these atmospheres were nearly same [122]. Thus, these data provided the clue that chromium niobate may not

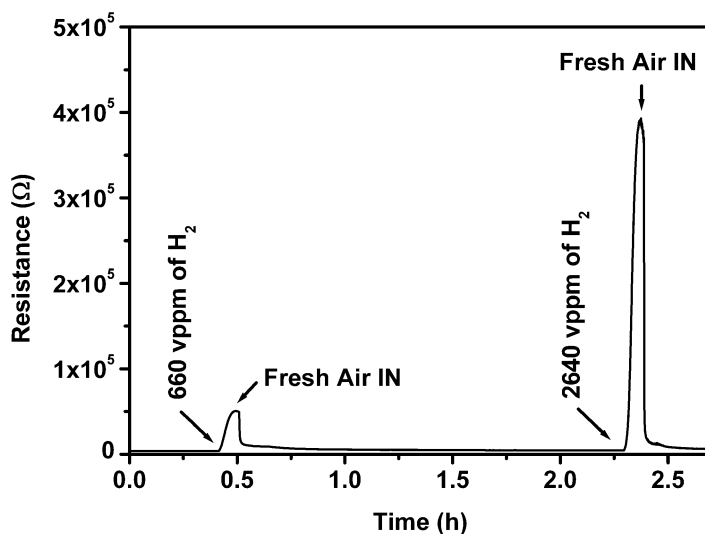


Fig. 28 Typical response patterns of CrNbO_4 towards 660 and 2640 of vppm of H_2 in air at 613 K

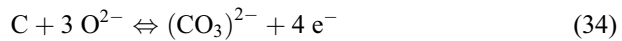
chemisorb oxygen on its surface. Further, the gas sensing of analyte may be mediated by lattice oxygen. Sree Rama Murthy et al. carried out detailed investigations on the hydrogen sensing properties of this compound [122]. These studies demonstrated its usefulness to sense hydrogen from 50 to 4000 vppm at 613 K. The typical sensing behavior of this compound towards 660 and 2640 vppm of hydrogen in air is shown in Fig. 28. Participation of lattice oxygen in the sensing process was also elucidated by Sree Rama Murthy et al. The well-known semiconducting oxides like SnO_2 and ZnO are known to exhibit sensitivity towards different analytes in a limited range only, viz., a few tens of vppm or about 100 vppm. The reason for the limited range of sensing is attributed to the participation of chemisorbed oxygen ions in the gas sensing process, whereas the rutile structure of chromium niobate, with the participation of labile lattice oxygen, enabled the sensing of a wide range of hydrogen concentration. Additionally this compound did not exhibit cross sensitivity towards species like ammonia, petroleum gas, and NO_x , even in 1000s of vppm level.

Carbonates and Nitrides

Molten Carbonates and Their Use in Galvanic Cells for Measuring Carbon Potentials

Molten carbonates find application as electrolyte in high-temperature molten carbonate fuel cells. Hobdell and co-workers [123–125] showed that a molten eutectic of Li_2CO_3 and Na_2CO_3 (52 mol % Li_2CO_3 and 48% Na_2CO_3 with eutectic

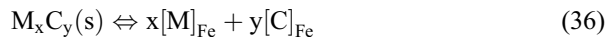
temperature of 774 K) can be used as electrolyte in galvanic cells for measuring carbon activity in gaseous and liquid metal media. Carbon, being an interstitial alloying element in structural steels, has a strong bearing on their mechanical strength. Its concentration in steels should be maintained within a specified limit. In liquid sodium coolant circuits of fast breeder reactors with austenitic and/or ferritic steels as structural material, measurement of carbon activity in liquid sodium is desirable to identify the carburizing/decarburizing potential of the coolant. Hobdell and co-workers showed that molten $\text{Li}_2\text{CO}_3\text{-Na}_2\text{CO}_3$ electrolyte-based galvanic cell can meet this application. The electrode reaction in this cell involving four electrons can be represented as [125]:



In these cells, the carbonate electrolyte was contained in thin-walled iron thimble which has relatively high diffusion coefficient for carbon. Graphite or carburized iron was used as reference electrode, and the cell was operated at temperatures above 923 K. After immersion in liquid sodium, carbon activity in iron thimble and sodium becomes equal, and the galvanic cell establishes an emf across the molten carbonate electrolyte as dictated by Nernst equation:

$$E = (RT/4F) \ln(a_c)^{\text{ref}} / (a_c)^{\text{sple}} \quad (35)$$

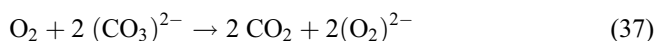
Experiments have shown that the cells could be used for measuring the carbon activity in liquid sodium in the range above 10^{-2} . The low measurable limit of carbon activity is set by the carbide forming metallic impurities present in the iron thimble. The impurities originate from the initial starting iron stock material. They also get slowly deposited on the outer wall of the iron thimble by corrosion and mass transport of Cr, Mn, and Mo from stainless steel structural materials used. The carbides formed by these impurities dictate the carbon activity on the iron thimble side of the galvanic cell by the following equilibrium:



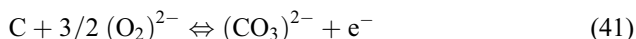
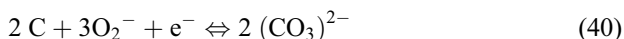
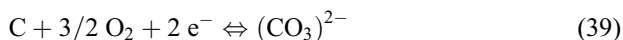
where $\text{M}_x\text{C}_y(\text{s})$ is the composition of the carbide formed by the impurity metal M, and $[\text{M}]_{\text{Fe}}$ and $[\text{C}]_{\text{Fe}}$ are the concentrations of M and C present in solid solution in iron thimble, respectively.

One of the problems observed with these galvanic cells was the mass transport of iron from the inside wall of the iron thimble to the reference electrode. The deposited iron grows as whiskers extending radially from the reference electrode leading ultimately to the shorting of the cell. It has also been observed that many of the cells generate emf values lower than those predicted by Nernst equation (35). Decarburization of the carburized iron reference electrode was also observed on prolonged operation [126]. The electrochemical origin of the abovementioned processes has been analyzed by Rajan Babu et al. [127]. Experimental data on molten carbonate fuel cells, which use a eutectic mixture of either Li_2CO_3 and

K_2CO_3 (62 mol% Li_2CO_3 and 38 mol% K_2CO_3 with eutectic temperature of 771 K) or Li_2CO_3 and Na_2CO_3 (52 mol % Li_2CO_3 and 48% Na_2CO_3 with eutectic temperature of 774 K) and operate at 873 K to 923 K, show that oxygen has significant solubility in these molten salts. Ionic species such as the superoxide (O_2^-), the peroxide (O_2^{2-}), etc. can be stabilized in the molten carbonate by the following chemical interactions (37, 38) [128–130]:



These electrochemical reactions at the electrodes where the molecular oxygen and superoxide and peroxide species take part can be represented by Eqs. (39, 40, and 41) given below:



It can be seen that the electrode reactions involve less number of electrons than that represented by Eq. 31 and can produce emf of opposite polarity (compare Eqs. 36 and 37 with Eq. 31). These reactions could also be used to explain the decarburization behavior of the carburized iron reference electrode. These effects are dependent on the oxygen partial pressure in the gas plenum over the molten carbonate since it determines the concentration of molecular oxygen, superoxide and peroxide species in the melt. Rajan Babu et al. calculated the maximum permissible oxygen partial pressures that could be tolerated over the molten salt [127]. By introducing a getter made of calcium metal granules in the gas plenum, the authors could reduce the oxygen to very low levels and showed that cells exhibited theoretical behavior. Schematics of electrochemical carbon meter for measuring carbon activity in sodium is shown in Fig. 29. Temperature dependence of one such meter during its operation in a static sodium system is shown in Fig. 30.

Nitrides for Measurement of Nitrogen Potentials

Nitrogen forms a very stable compound with lithium metal, namely, Li_3N . Li_3N has high solubility in lithium metal, and at 463 K (M.pt. of Li = 453.5 K) the solubility is about 1500 wppm. Corrosion of structural materials by liquid lithium is enhanced by the presence dissolved nitrogen. This enhancement of corrosion in case of structural steels is due to the formation of ternary nitrides such as Li_9CrN_5 and Li_3FeN_2 [131]. Hence, monitoring the dissolved nitrogen levels in lithium circuits is essential. Although off-line methods to determine the concentration of dissolved nitrogen in

Fig. 29 Schematics of electrochemical carbon meter for measuring carbon activity in sodium

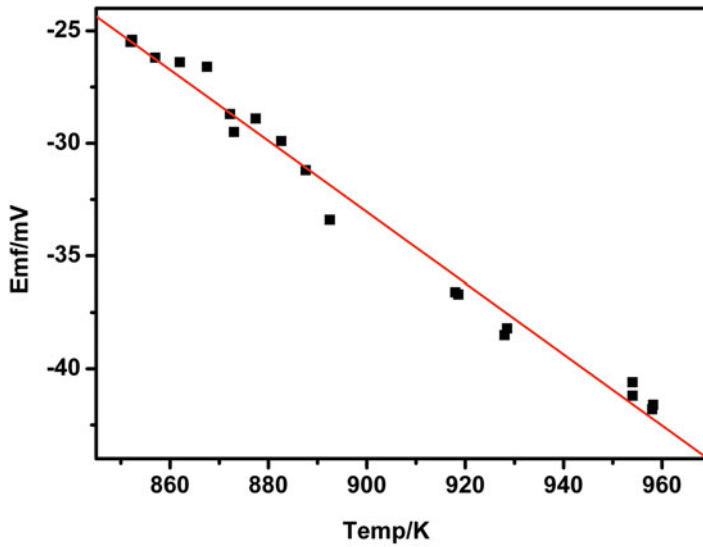
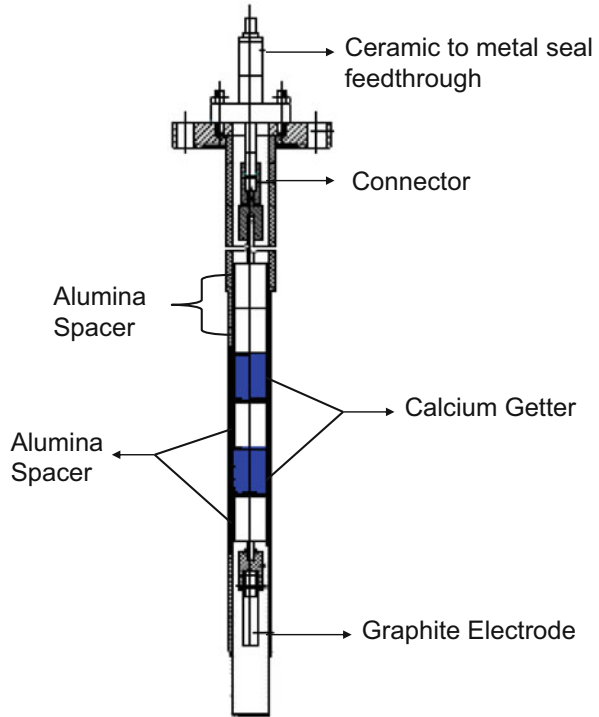


Fig. 30 Temperature dependence of the output of electrochemical carbon meter

lithium by dissolving a lithium sample in water and analyzing the evolved ammonia exists, it would be advantageous to have an online analytical method to identify a sudden increase in nitrogen concentration owing to an air leak into the liquid metal circuit and taking remedial actions. Adams et al. [132] proposed a resistivity meter which involved measuring the resistivity of liquid lithium flowing through a small tube of uniform cross section whose temperature was precisely controlled and relating it to the dissolved impurity concentration. The resistivity meters are not specific and are sensitive only at high concentrations of the impurity in liquid lithium. At low concentrations they would not be useful for reliable analysis. Barker et al. [133] proposed a molten salt-based electrochemical nitrogen meter of the following configuration for measurement of nitrogen activity in liquid lithium systems:



The electrolyte uses a eutectic mixture of LiF-LiCl (which was pre-purified by passing chlorine gas through the molten salt) saturated with Li_3N . The electrolyte was contained in a thin thimble made of pure iron. A mixture of powders of Ti and TiN contained in a 0.55 mm thick closed iron tube was used as reference electrode. The authors tested the meter at 873 K using metal-metal nitride couples as samples. Data on use of this meter in operating lithium systems is not available. It is to be pointed out that carbon is also an impurity of importance in lithium systems and carbon forms lithium acetylide, Li_2C_2 , on interaction with lithium metal. In view of the relatively higher diffusion coefficient of carbon than that of nitrogen through iron, the performance of the nitrogen sensor is expected to be influenced by the presence of carbon in lithium particularly at high carbon levels.

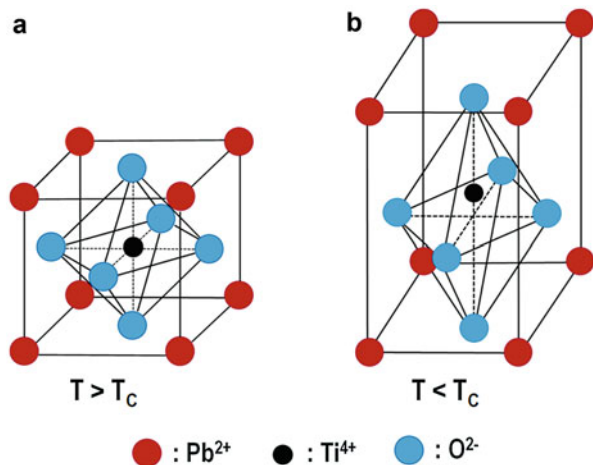
Titanates

Oxide-based electroceramic materials are being explored for a wide variety of electrical, optical, and magnetic applications. Among them, titanate-based piezoelectric materials form a special class and are under investigation for more than 70 years. Piezoelectricity, which is a subset of ferroelectricity, is the interplay between electrical and mechanical energies and refers to the ability to generate an electric potential in response to applied mechanical stress (direct piezoelectric effect). A material exhibiting the direct piezoelectric effect exhibits the converse piezoelectric effect also, that is, the production of stress when an electric field is applied. Piezoelectricity is exhibited only by those crystalline materials which have no center of symmetry. Among them, titanates of lead, lanthanum, and barium (RTiO_3 where $\text{R} = \text{Pb, La, and Ba}$) having perovskite structure and bismuth titanate ($\text{Bi}_3\text{Ti}_4\text{O}_{12}$) which belongs to Aurivillius family are important piezoelectric ceramic materials. These piezoelectric perovskite oxides undergo first-order phase transition on cooling from high to low temperatures which is characterized by transformation of the high-symmetry cubic perovskite to slightly disordered ferroelectric structures

with tetragonal, orthorhombic, and rhombohedral symmetry. The transformation temperature below which the material has the structure with no center of symmetry is called Curie temperature.

Figure 31a shows the structure of perovskite PbTiO_3 above its Curie temperature ($T_c = 763$ K). In the perovskite structure, lead and oxide ions together make up face-centered cubic array. Titanium ions occupy the center of the unit cell, and they are octahedrally coordinated by the oxide ions. Below 763 K, the phase assumes the disordered tetragonal structure as shown in Fig. 31b. It is seen that the oxygen octahedron is shifted off the center of the cuboid box formed by Pb^{2+} ions. The Ti^{4+} ions are also shifted from the center of the unit cell. In this distorted tetragonal structure, the center of positive and negative charges does not coincide in the unit cell which generates an electric dipole in it. In a polycrystalline piezoelectric ceramic, each grain possesses regions with uniform polarization called ferroelectric domains. Within a domain, all the electric dipoles associated with unit cells are aligned in the same direction. Each grain may have many domains, which are separated by boundaries called domain walls. Adjacent domains may have their polarization vectors at right angles to one another or in antiparallel directions. The boundaries between these domains are, correspondingly, known as 180° or 90° domain walls. Because of the random orientations of these domains, a piezoelectric ceramic would not exhibit any piezoelectric properties after its chemical synthesis. By applying a sufficiently high electric field (which is called poling), the domains can be made aligned with the field. When the electric field is removed, a remnant polarization and remnant strain are retained in the sample, and the sample exhibits piezoelectricity. It is to be pointed out that domains in a polycrystalline material cannot be perfectly aligned with the applied electric field, except when the grain is coincidentally oriented with its c- or a-axis in the direction of the field. However, their polarization vectors can be aligned so as to maximize the component resolved in the direction of the field, i.e., the polar axis. On the other hand, it is possible in principle to orient all domains in a single

Fig. 31 (a) Crystal structure of lead titanate (symmetric) above Curie temperature, T_c , and (b) disordered tetragonal structure of lead titanate below Curie temperature, T_c



crystal material in one direction by applying the electric field in an appropriate direction. It is to be pointed out that the orientation of the polarization vectors of the domains in a single direction can progressively become disordered again when the piezoelectric material is held at high temperatures (though below Curie temperature).

To identify the directions in a piezoceramic element, three axes are used. These axes, termed as 1, 2, and 3, are analogous to the classical three-dimensional orthogonal set of x -, y -, and z -axes. The polar axis is labelled as 3. The piezoelectric constants relating the mechanical strain produced by an applied electric field are termed as the strain constants, or the “d” coefficients. Depending on the directions in which the electric field is applied and the mechanical strains are generated with respect to the polar axis, these constants are labelled. For example, the first subscript in d_{31} denotes that the electric field is applied parallel to the polar axis (i.e., direction 3) and the mechanical strain is produced in direction 1 (i.e., perpendicular to the polar axis). The coefficient d_{33} denotes that the applied electric field and the mechanical strain produced are parallel to polar axis. The units of d coefficients are expressed as meters per meter and per volts per meter (meters per volt). Similarly, the piezoelectric constants relating to the electric field produced by a mechanical stress are termed as the voltage constants, or the “g” coefficients. The electromechanical coupling coefficient (also simply referred to as the coupling coefficient) is defined as the ratio of the mechanical energy accumulated in response to an electrical input or vice versa. Piezoelectric materials find applications in several fields – inkjet and fuel injection actuators, shock sensors, resonators, ultrasonic motors, energy harvesters, sonar services, etc. In addition to the values of d_{ij} and g_{ij} , and electromechanical coupling coefficients, properties such as dielectric constant, electrical conductivity, and aging characteristics are deciding factors for these applications, though the importance of an individual property for every other application can be different.

Piezoelectric properties of lead zirconate titanate (PZT), a solid solution of PbTiO_3 with PbZrO_3 , are much higher than those of PbTiO_3 . PbZrO_3 exhibits antiferroelectricity which can be considered as a crystalline substance having two sublattices that are polarized in antiparallel direction and which can be made ferroelectric by application of an electric field. PZT has perovskite structure with Zr randomly substituting for Ti positions in the unit cell shown in Fig. 31. Phase diagram of PbTiO_3 - PbZrO_3 (Fig. 32) shows that the Curie temperature varies monotonously from 503 K at pure PbZrO_3 to 763 K at pure PbTiO_3 [134]. At temperatures below the line showing the variation of Curie temperature with composition, the material exhibits ferroelectricity at nearly all compositions. In the composition region where the Zr/Ti ratio varies between 100/0 and 94/6, the solid solution is an antiferroelectric orthorhombic phase exhibiting no observable piezoelectric effect. The rest of the region below the T_C versus composition line is divided into two parts by a morphotropic phase boundary (MPB): (1) a tetragonal phase region on the Ti-rich side and (2) a rhombohedral phase region on the Zr-rich side. At room temperature, this boundary is at the point where $\text{Zr/Ti} = 52/48$. PZT solid solutions of this composition exhibit superior piezoelectric properties. The

Fig. 32 Phase diagram of PbZrO_3 - PbTiO_3 system adapted from Ref. [134]

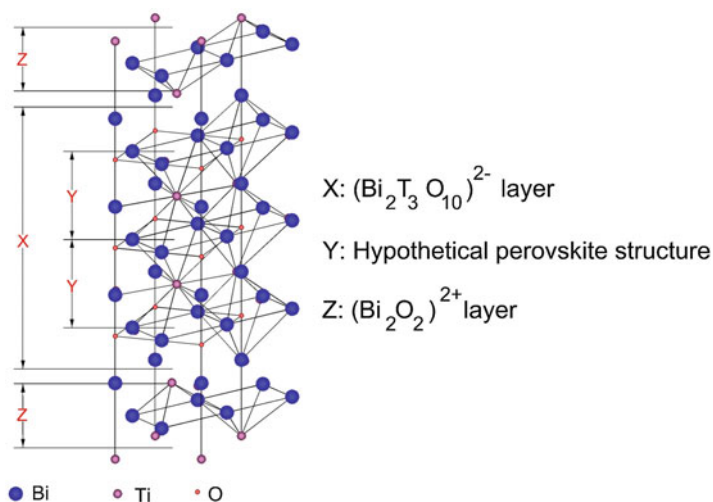
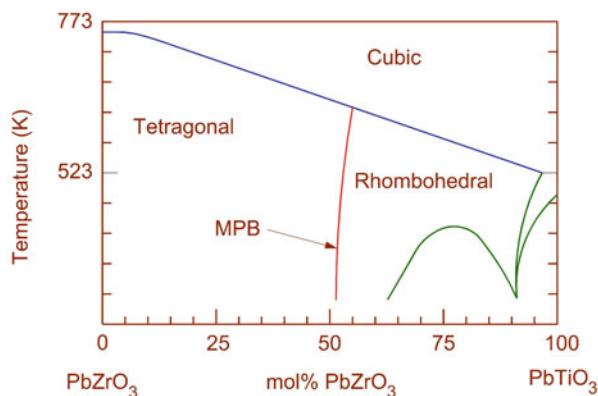


Fig. 33 Layered structure of $\text{Bi}_4\text{Ti}_3\text{O}_{12}$

values of d_{ij} and g_{ij} and dielectric constant reach very high values at and around this composition.

Bismuth titanate (BIT), $\text{Bi}_4\text{Ti}_3\text{O}_{12}$, is a layered ferroelectric oxide belonging to the Aurivillius family. It has high Curie temperature (948 K) and high dielectric constant. The structure of bismuth titanate is characterized by the perovskite-like $(\text{Bi}_2\text{Ti}_3\text{O}_{10})^{2-}$ layers sandwiched between $(\text{Bi}_2\text{O}_2)^{2+}$ layers along its crystallographic c-axis. An idealized structure of bismuth titanate showing the bismuth oxide layers and pseudo perovskite units is shown in Fig. 33. Important piezoelectric properties of PZT and bismuth titanate ($\text{Bi}_4\text{Ti}_3\text{O}_{12}$) are given in Table 4.

Polycrystalline bismuth titanate ceramics exhibit ionic and p-type mixed conduction and the ionic conduction dominates at high temperatures. Studies on electrical conductivity of single crystals had showed the anisotropic electrical conductivity

Table 4 Characteristics of piezoelectric materials

Material	Structure	Curie temperature (°C)	Piezoelectric coefficient (pC/N)	Relative dielectric constant
PZT (soft)	Perovskite	365	~ 600	3400
PZT (hard)	Perovskite	350	~200	1700
Bi ₄ Ti ₃ O ₁₂ (BIT)	(Bi ₂ O ₂) ²⁺ layered	650	~20	–
LiNbO ₃	Corundum	1150	6	~30

along the a- and c-axes with the maximum value along the c-axis. While p-type conduction is dominant along the c-axis, ionic conduction is dominant along the a-axis of the crystal. It was also shown that the defects responsible for the electrical conduction preferentially existed in the perovskite layer. As the electrical conductivity of pure bismuth titanate is relatively high, poling a polycrystalline sample prepared by conventional methods is difficult. This limitation is minimized by restricting the growth of the crystal along the c-axis and allowing its growth along the a-b plane. The electrical conductivity can also be reduced by use of dopants with higher valency such as Nb⁵⁺, W⁶⁺, and Ta⁵⁺ which substitute at the Ti⁴⁺ positions [135–138]. It has been possible to synthesize the pristine and doped (Bi₄Ti₃O₁₂) with grains in plate-like structure, i.e., with growth enhanced in a-b plane, by employing hot forging methods or by molten salt-based synthesis [139–143].

In a liquid metal cooled nuclear reactor, there is a need to monitor various components that are immersed in the coolant for the plant safety and operational convenience. Conventional techniques employed in aqueous systems cannot be employed in liquid metal systems because of the high temperatures involved and because of the opacity of the metals. Piezoelectric-based ultrasonic transducers, which function both as signal transmitters and receivers, are being developed for this purpose in different laboratories. Desirable properties of the piezoelectric material to be used in these transducers are high d_{33} and g_{33} values, a high value of ratio of d_{33}/d_{31} and g_{33}/g_{31} , high Curie temperatures, and low aging characteristics. PZT and BIT are generally chosen for these applications, the former for prolonged operation up to 523 K, while the latter is intended for use up to 723 K. The schematic of a typical ultrasonic transducer developed for use in liquid metal systems is shown in Fig. 34. Occasionally, ultrasonic transducers which are used for time-of-flight ranging and for liquid level measurement systems incorporate a damping element. The damping element is bonded to the back of the piezoelectric element to limit the duration of vibration and reduce the ringing effect.

In an ultrasonic transducer, a piezoelectric disc of appropriate thickness, which determines the frequency of operation of the transducer, is acoustically bonded to the metal wear plate (also called as diaphragm) by one of the techniques: (1) placing a thin metal foil under compressive load, (2) using high-temperature epoxies, (3) using glass or alloy solders, and (4) diffusion bonding. Choice of the method depends on

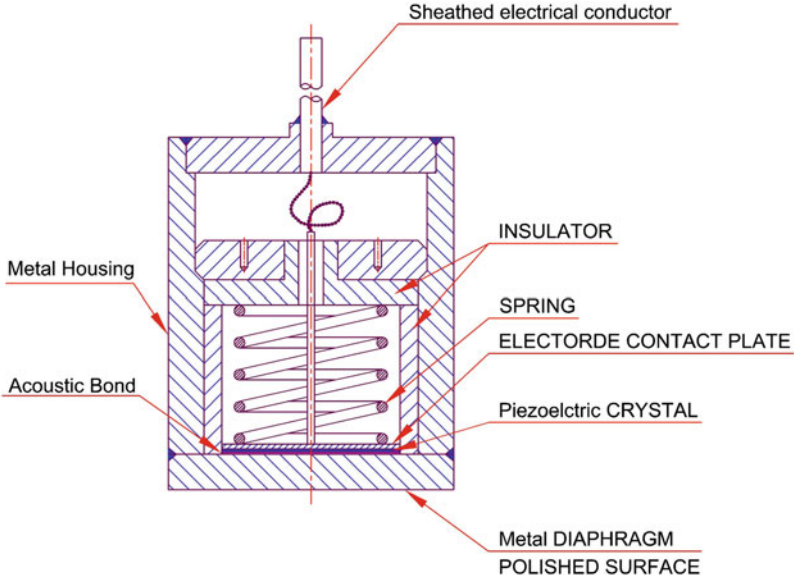


Fig. 34 Schematic ultrasonic transducer for use in liquid sodium system

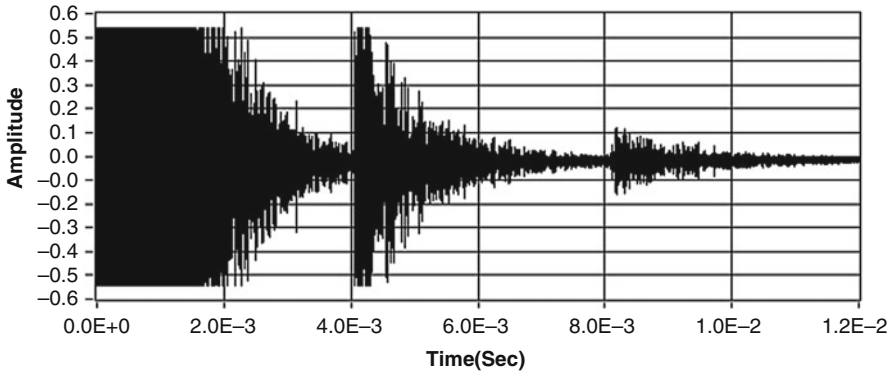


Fig. 35 A-scan waveform with echo from a target kept at a distance of 5 m distance in liquid sodium from the transducer

the maximum operating temperature, relative differences in coefficients of thermal expansion of materials at the bonded area, and the total intended period of operation of the transducer. The material for the wear plate depends on the desired wetting characteristics, and its thickness is chosen to match the acoustic impedances. For use up to 493 K in liquid sodium systems, a PZT disc was acoustically bonded to nickel diaphragm using an alloy solder. A-scan waveform with echo

from a target kept at a distance of 5 m from a 1 MHz transducer in liquid sodium at 453 K is shown in Fig. 35 [144].

Conclusions

Crystal structure of certain inorganic compounds, viz., oxides, hydridehalides, aluminates, phosphates, and halides, was considered. Electrical conductivity of these compounds was considered for possible application as sensors. The ionic conductivity could be correlated to certain special crystal structures, aliovalent substitution of cations, temperature induced phase transitions, etc. On the other hand, semiconducting property was found to originate from presence of metal ion in valence state different considering the matrix, and/or anion deficiency, aliovalent substitution, etc. Usefulness of these compounds in sensing applications in nuclear energy programs was discussed. Applications, both in liquid sodium and gaseous process streams/ambience, were dealt. Materials compatibility in liquid sodium, necessary design features of some of the sensors, and performance in actual conditions were deliberated. A brief mention on the use of molten electrolytes in sensing application was also made.

References

1. Geller S (ed) (1977) Solid electrolytes. Springer, Berlin
2. Nafe H (1984) Ionic conductivity of ThO_2 - and ZrO_2 -based electrolytes between 300 and 2000 K. *Solid State Ionics* 13:255–263
3. Patterson JW (1971) Conduction domains for solid electrolytes. *J Electrochem Soc* 118:1033–1039
4. Jayaraman V, Gnanasekaran T (2016) Review – evolution of the development of in-sodium oxygen sensor and its present status. *J Electrochem Soc* 163:B395–B402
5. Borgstedt HU, Mathews CK (1987) Applied chemistry of alkali metals, chapter 5. Plenum Press, New York
6. Hobdell MR, Smith CA (1982) Electrochemical techniques for monitoring dissolved carbon, hydrogen and oxygen in liquid sodium. *J Nucl Mater* 110:125–139
7. Minushkin B, Kolodney M (1967) United Nuclear Corporation, United States Atomic Energy Commission (USAEC) Report UNC-5131
8. Iyer VS, Venugopal V, Mohapatra S, Singh Z, Roy KN, Prasad R, Sood DD (1988) Standard molar Gibbs free energy of formation of NaZrO_3 . *J. Chem Thermodyn* 20:781–784
9. Maier J, Warhus U (1986) Thermodynamic investigations of Na_2ZrO_3 by electrochemical means. *J Chem Thermodyn* 18:309–316
10. Dash S, Singh Z, Parida SC, Venugopal V (2005) Thermodynamic studies on $\text{Rb}_2\text{ThO}_3(\text{S})$. *J Alloys Compd* 398:219–227
11. Carter CB, Norton MG (2007) Ceramics materials – science and engineering, chapter 34. Springer, New York
12. Kingery WD, Bowen HK, Uhlmann DR (2004) Introduction to ceramics, 2nd edn. Wiley, New York
13. Greskovich C, O'Clair CR, Curran MJ (1972) Preparation of Y_2O_3 doped ThO_2 . *J Am Ceram Soc* 55:324–325

14. Ganesan R, Vivekanandhan S, Gnanasekaran T, Periaswami G, Srinivasa RS (2004) Novel approach for the bulk synthesis of nanocrystalline yttria doped thoria powders via polymeric precursor routes. *J Nucl Mater* 325:134–140
15. Jayaraman V, Krishnamurthy D, Ganesan R, Thiruvengadasami A, Sudha R, Prasad MVR, Gnanasekaran T (2007) Development of yttria-doped thoria solid electrolyte for use in liquid sodium systems. *Ionics* 13:299–303
16. Ganesan R, Jayaraman V, Rajan Babu S, Sridharan R, Gnanasekaran T (2011) Development of sensors for on-line monitoring of nonmetallic impurities in liquid sodium. *J Nucl Sci Technol* 48:483–489
17. Takizuka T, Tsujimoto K, Sasa T, Kenji NK, Takano H (2002) Design study of lead-bismuth cooled ADS dedicated to nuclear waste transmutation. *Prog Nucl Energy* 40:505–512
18. Gorynin IV, Korzov GP, Markov VC, Lavrukhin VS, Yakovlev VA (1998) Structural materials for power plants with heavy liquid metals as coolants. In: Proceedings of the conference on heavy metal liquid coolants in nuclear technology (HLMC-98), Obninsk, vol 1, pp 120–132
19. Gromov BF, Orlov YI, Martynov PN, Gulevsky VA (1998) The problems of technology of the heavy liquid metal coolants (Lead-Bismuth, Lead), In: Proceedings of the conference on heavy metal liquid coolants in nuclear technology (HLMC-98), Obninsk, Russia, Vol 1, pp 87–91
20. Martynov PN, Orlov YI (1998) Slagging process in lead-bismuth loop- prevention and elimination of critical situations, In: Proceedings of the conference on heavy metal liquid coolants in nuclear technology (HLMC-98), Obninsk, Russia, Vol 2, pp 565–576
21. Li N (2002) Active control of oxygen in molten lead–bismuth eutectic systems to prevent steel corrosion and coolant contamination. *J Nucl Mater* 300:73–81
22. Zhang J, Li N (2008) Review of the studies on fundamental issues in LBE corrosion. *J Nucl Mater* 373:351–377
23. Blokhin VA, Budylov EG, Velikanovich RI, Gorelov IN, Deryugin AN, Ivleva JI, Kozina MI, Musikhin YA, Ponimash ID, Sorokin AD, Shimkevich AL, Shmatko AB, Sherbakov EG (1998) Experience gained in creating and operating solid electrolyte meters of oxygen activity in lead-bismuth coolant. In: Proceedings of the conference on heavy metal liquid coolants in nuclear technology (HLMC-98), Obninsk, vol 2, pp 631–635
24. Konys J, Schroer C, Wedemeyer O (2009) Electrochemical oxygen sensors for corrosion control in lead-cooled nuclear reactors. *Corros Sci* 65:798–808
25. Sahu SK, Ganesan R, Jayaraman V, Gnanasekaran T (2012) Development of zirconia based oxygen sensor for lead and lead-bismuth eutectic. *Mat Sci Forum* 710:751–756
26. Kiukkola K, Wagner C (1957) Galvanic cells for the determination of the standard molar free energy of formation of metal halides, oxides, and sulfides at elevated temperatures. *J Electrochem Soc* 104:308–316
27. Kiukkola K, Wagner C (1957) Measurements on galvanic cells involving solid electrolytes, *J Electrochem Soc* 104:379–387
28. Jacob KT, Alcock CB (1973) Activity of indium in α -solid solutions of Cu + In, Au + In and Cu + Au + In alloys. *Acta Metall* 21:1011–1016
29. Katayama I, Shimazawa K, Zivkovic D, Manasijevic D, Zivkovic Z, Yamashita H (2005) Experimental study on gallium activity in the Ga-In-Tl alloys by EMF method with zirconia solid electrolyte. *Thermochim Acta* 431:138–143
30. Jendrzeczyk-Handzli D (2018) Thermodynamic properties of liquid silver-gold-gallium alloys determined from EMF measurements with solid YSZ electrolyte. *Thermochim Acta* 662:126–134
31. Jacob KT, Gupta P (2015) Oxygen potentials and phase equilibria in the system Ca–Co–O and thermodynamic properties of $\text{Ca}_3\text{Co}_2\text{O}_6$ and $\text{Ca}_3\text{Co}_4\text{O}_9$. *J Solid State Chem* 221:57–65
32. Jacob KT, Gupta P, Han D, Uda T (2013) Thermodynamics of NdRhO_3 and phase relations in the system Nd–Rh–O. *Calphad* 43:71–79

33. Aiswarya PM, Ganesan R, Gnanasekaran T (2017) Partial phase diagrams of Pb-Mo-O system and the standard molar Gibbs energy of formation of PbMoO_4 and Pb_2MoO_5 . *J Nucl Mater* 493:310–321
34. Gnanasekaran T, Mahendran KH, Kutty KVG, Mathews CK (1989) Phase diagram studies on the Na-Mo-O system. *J Nucl Mater* 165:210–216
35. Gnanasekaran T, Mahendran KH, Periaswami G, Mathews CK, Borgstedt HU (1987) Stability of ternary oxygen compounds of molybdenum in liquid sodium. *J Nucl Mater* 150:113–127
36. Knights CF, Phillips BA (1977) Phase diagrams and thermodynamic studies of the Cs-Cr-O, Na-Cr-O and Na-Fe-O systems and their relationships to the corrosion of steels by caesium and sodium. In: Glasser FP, Potter PE (eds) High temperature chemistry of inorganic and ceramic materials, Special publication no. 30. Chemical Society, London, pp 134–145
37. Sreedharan OM, Madan BS, Gnanamoorthy JB (1983) Threshold oxygen levels in Na (l) for the formation of NaCrO_2 (s) on 18-8 stainless steels from accurate thermodynamic measurements. *J Nucl Mater* 119:296–300
38. Gnanasekaran T, Mathews CK (1986) Threshold oxygen levels in sodium necessary for the formation of NaCrO_2 in sodium-steel systems. *J Nucl Mater* 140:202–213
39. Moseley PT, Toefield BC (eds) (1987) Solid state gas sensors. Adam Hilger, Bristol
40. Yamazoe N, Miura N (1991) Some basic aspects of semiconductor gas sensors. In: Yamaguchi S (ed) Chemical sensor technology, vol 3. Kodansha Ltd., Tokyo. (1992), pp 19–42
41. Morrison SR (1978) Adsorption and desorption. In: The chemical physics of surfaces. Plenum Press, New York, pp 251–295
42. Seiyama T (1988) Surface reactivity of oxide materials in oxidation-reduction environment. In: Nowotny J, Dufour LC (eds) Materials science monographs, vol 47. Elsevier, New York, pp 189–217
43. Sunu S (2004) Investigations on electrical and gas sensing properties of pure and doped MoO_3 and WO_3 , PhD Thesis, University of Madras
44. Yamazoe N (1991) New approaches for improving semiconductor gas sensors. *Sensors Actuators B* 5:7–19
45. Mitsudo H (1980) Ceramics for gas and humidity sensors (part 1) – gas sensor. *Ceramics* 15:339–345
46. Kanefusa S, Nitta M, Haradome M (1980) Thick film gas leak detector for town gas. *J Chem Soc Jpn* 75:1591–1595
47. Yamazoe N, Kurokawa Y, Seiyama T (1983) Effects of additives on semiconductor gas sensors. *Sensors Actuators* 4:283–289
48. Suzuki T, Yamazaki T, Yoshioka H, Hikichi K (1988) Influence of thickness on H_2 gas sensor properties in polycrystalline SnO_x films prepared by ion-beam sputtering. *J Mater Sci* 23:1106–1111
49. McAleer JF, Moseley PT, Norris JOW, Williams DE, Toefield BC (1988) Tin dioxide gas sensors. Part 2 – the role of surface additives. *J Chem Soc Faraday Trans 1* 84:441–457
50. Sree Rama Murthy A, Ashok Kumar A, Prabhu E, Clinsha PC, Lakshmigandhan I, Chandramouli S, Mahendran KH, Gnanasekar KI, Jayaraman V, Nashine BK, Rajan KK, Gnanasekaran T (2014) Performance of semiconducting oxide based hydrogen sensor for argon cover gas in engineering scale sodium facility. *Nucl Engg Design* 273:555–559
51. Shekhar C, Gnanasekar KI, Prabhu E, Jayaraman V, Gnanasekaran T (2011) $\text{In}_2\text{O}_3 + x \text{BaO}$ ($x = 0.5 - 5$ at.%) – a novel material for trace level detection of NO_x in the Ambient. *Sensors Actuators B Chem* 155:19–27
52. Mangamma G, Jayaraman V, Gnanasekaran T, Periaswami G (1998) Effect of Silica addition on H_2S sensing properties of CuO-SnO_2 sensors. *Sensors Actuators B* 53:133–139
53. Gnanasekaran T (1999) Thermochemistry of binary Na-NaH and ternary Na-O-H systems and the kinetics of reaction of hydrogen/water with liquid sodium – a review. *J Nucl Mater* 274:252–272
54. Müller U (2006) Inorganic structural chemistry, 2nd edn. Wiley, West Sussex

55. Ehrlich P, Peik K, Koch E (1963) Thermochemische Messungen an den Hydridhalogeniden der Erdalkalimetalle. *Z fuer Anorganische und Allegemeine Chemie* 324:113–224
56. Ramanathan V, Babu B, Rajendran B, Sahu HK (2001) Nickel diffuser based instrumentation for real time detection of hydrogen concentration in liquid sodium in fast breeder test reactor. In: Proceedings eighth national seminar on physics and technology of sensors, Kalpakkam, 27 Feb –1 Mar 2001, C-11.1-3
57. Funada T, Nihei I, Yuhara S, Nakasuji T (1979) Measurements of hydrogen concentration in liquid sodium by using an inert gas carrier method. *Nucl Technol* 45:158–165
58. Hills MP, Thompson C, Henson MA, Moores A, Schwandt C, Kumar RV (2009) Accurate measurement of hydrogen in molten aluminium using current reversal mode. In: Bearne G (ed) Proceedings of the technical sessions presented by the TMS aluminum committee at the TMS 2009 annual meeting & exhibition, San Francisco, 15–19 Feb 2009. Minerals, Metals and Materials Society, Warrendale, pp 707–712
59. Sridharan R, Mahendran KH, Gnanasekaran T, Periaswami G, Varadaraju UV, Mathews CK (1995) On the phase relationships and electrical properties in the $\text{CaCl}_2 - \text{CaH}_2$ system. *J Nucl Mater* 223:72–79
60. Joseph K, Sujatha K, Nagaraj S, Mahendran KH, Sridharan R, Periaswami G, Gnanasekaran T (2000) Investigations on the phase equilibria of some hydride ion conducting electrolyte systems and their application for hydrogen monitoring in sodium coolant. *J Nucl Mater* 344:285–290
61. Smith CA (1972) An electrochemical hydrogen concentration cell – with application to sodium systems, British Nuclear Laboratories, CEBG Report, RD/B/N-2331
62. Bouchacourt M, Debergh P, Oberlin C and Saint Paul P (1984), EdF experience on analysis of non-metallic impurities in sodium. In: Proceedings of the 3rd international conference on liquid metal engineering and technology, Oxford, 9–13 Apr 1984, vol 1, pp 45–52
63. Mason L, Morrison NS, Robertson CM, Trevillion A (1984) The monitoring of oxygen, hydrogen and carbon in the sodium circuits of PFR. In: Proceedings of the 3rd international conference on liquid metal engineering and technology, Oxford, 9–13 Apr 1984, vol 1, pp 53–60
64. Smith CA, Simm PA (1984) Calibration and performance of galvanic cell hydrogen and oxygen meters in sodium. In: Proceedings of the 3rd international conference on liquid metal engineering and technology, Oxford, 9–13 Apr 1984, vol 3, pp 111–116
65. Pankratz LB (1984) Thermodynamic properties of halides, Bulletin 874, US Department of the Interior, Bureau of Mines, 830 pp
66. Makiura R, Yonemura T, Yamada T, Yamauchi M, Ikeda R, Kitagawa H, Takata M (2009) Size-controlled stabilisation of the superionic phase to room temperature in polymer-coated AgI nanoparticles. *Nat Mater* 8:476–480
67. Hull S (2004) Superionics: crystal structures and conduction processes. *Rep Prog Phys* 67:1233–1314
68. West AR (1989) Solid state chemistry and its applications. Wiley, New York
69. Rodriguez LA, Zapata J, Vargas RA, Pena Lara D, Diosa JE (2016) Superionic behaviour in the $x\text{AgI} - (1-x)\text{CsAg}_2\text{I}_3$ polycrystalline system. *J Phys Chem Solids* 93:126–130
70. Shannon RD (1976) Revised effective ionic radii and systematic studies of interatomic distances in halides and chalcogenides. *Acta Crystallogr Sect A* A32:751–767
71. Bazan JC, Schmidt JA (1976) A Cu(I) ion conductor obtained by replacement of Ag(I) in $\alpha\text{-AgI}$. *J Appl Electrochem* 6:411–415
72. Armstrong RD, Bulmer RS, Dickinson T (1973) Some factors responsible for high ionic conductivity in simple solid compounds. In: van Gool W (ed) Fast ion transport in solids. North Holland Publishing Company, Amsterdam, pp 269–284
73. Shahi K, Wagner JB Jr (1980) Anomalous ionic conduction in AgBr-AgI mixed crystals and multiphase systems. *Phys Rev B* 23:6417–6421

74. Bazan JC, Pettigrosso RS (1994) A DSC and conductivity study of the influence of cesium ion on the beta to alpha transition in silver iodide. In: Chowdari BVR, Yahaya M, Talib IB, Salleh MM (eds) Solid state ionics materials. World Scientific, Singapore, pp 205–210
75. Rifuiddin MH (2007) Superionic conducting phase in Cd-substituted CsAgI_3 . Solid State Commn 144:293–295
76. El Kettai M, Malugani JP, Mercier R, Tachez M (1986) Phase transitions and conductivity in superionic $\text{Ag}_3\text{SI}_{1-x}\text{Br}_x$ solid solutions. Solid State Ionics 20:87–92
77. Beeken RB, Wright TJ, Sakuma T (1999) Effect of chloride substitution in the fast ion conductor Ag_3SBr . J Appl Phys 85:7635–7638
78. West AR (2007) Solid state chemistry and its applications. Wiley, New York
79. Ihara S, Warita Y, Suzuki K (1984) Ionic conductivity in $\text{Ag}_{1-x}\text{Cl}_x$. Phys Status Solidi A 86:729–734
80. Clinsha PC, Gnanasekar KI, Jayaraman V, Gnanasekaran T (2015) $\text{AgI}_{1-x}\text{Cl}_x$ ($x = 0-0.05$) electrolytes for trace level sensing of chlorine. In: Proceedings 2nd international symposium of physics and technology of sensors, IEEE Xplore, pp 94–96
81. Clinsha PC (2017) Studies on synthesis, characterization of $\text{AgI}_{1-x}\text{Cl}_x$ solid solutions for I_2 and Cl_2 sensing properties, PhD Thesis, Homi Bhabha National Institute (University)
82. Kummer JT (1992) β -Alumina electrolytes. Prog Solid State Chem 7:141–175
83. DeVries RC, Roth WI (1969) Critical evaluation of the literature data on beta alumina and related phases: I-phase equilibria and characterization of beta alumina phases. Am Ceram Soc 52:364–369
84. Bragg WL, Gottfried C, West J (1931) The structure of β alumina. Z Krist 77:255–274
85. Sudworth JL, Tilley AR (1985) The sodium sulphur battery. Chapman & Hall, London
86. Takikawa O, Imai A, Harata M (1982) Characteristics of the Na/beta-alumina/Na cell as a sodium vapor pressure sensor. Solid State Ionics 7:101–107
87. Jayaraman V, Prabhu E, Sree Rama Murthy A, Clinsha PC, Gnanasekar KI, Gnanasekaran T (2014) Na – β – Al_2O_3 based sensor for sodium aerosol. Sensors Actuators B 202:9–13
88. Asumathraman R, Gnanasekar KI, Clinsha PC, Ravindran TR, Govindan Kutty KV (2015) Investigations on the charge compensation on Ca and U substitution in CePO_4 by using XPS, XRD and Raman spectroscopy. Ceram Int 41:3731–3739
89. Jena H, Maji BK, Asumathraman R, Govindan Kutty KV (2012) Synthesis and thermal characterization of glass bonded Ca-chloroapatite matrices for pyrochemical chloride waste immobilization. J Non-Crystalline Solids 358:1681–1686
90. Hong HYP (1976) Crystal structures and crystal chemistry in the system $\text{Na}_{1+x}\text{Zr}_2\text{Si}_x\text{P}_{3-x}\text{O}_{12}$. Mater Res Bull 11:173–182
91. Goodenough JB, Hong HYP, Kafalas JA (1976) Fast Na^+ ion transport in skeleton structures. Mater Res Bull 11:203–220
92. Chavez ML, Quintana P, West AR (1986) New Li^+ ion conductors, $\text{Li}_{2-4x}\text{Zr}_{1+x}(\text{PO}_4)_2$. Mat Res Bull 21:1411–1416
93. Sree Rama Murthy A, Jayaraman V, Gnanasekaran T (2017) Preparation and characterization of some lithium – ion conductors. Solid State Ionics 303:138–143
94. Vella G, Aiello G, Fuetterer MA, Giancarli L, Oliveri E, Tavassoli F (1998) Water-cooled Pb–17Li test blanket module for ITER: impact of the structural material grade on the neutronic responses. J Nucl Mater 258–263:357–361
95. Tas H, Malang S, Reiter F, Sannier J (1988) Liquid breeder materials. J Nucl Mater 155–157:178–187
96. Hubberstey P (1997) Pb-17Li and lithium: a thermodynamic rationalisation of their radically different chemistry. J Nucl Mater 247:208–214
97. Hubberstey P, Sample T, Barker MG (1991) Continuous monitoring of the composition of liquid Pb-17Li eutectic using electrical resistivity methods. J Nucl Mater 179–181:886–890
98. Conrad R (1991) Irradiation experiments on liquid tritium breeding material Pb-17Li in the HFR Petten. Fusion Eng Des 14:289–297

99. Conrad R, Debarberis L, Coen V, Flament T (1991) Irradiation of liquid breeder material Pb-17Li with in-situ tritium release measurements in the LIBRETTO 2 experiment. *J Nucl Mater* 179–181:875–878
100. Yamazoe N, Fuchigami J, Kishikawa M, Seiyama T (1979) Interactions of tin oxide surface with O₂, H₂O and H₂. *Suf Sci* 86:335–344
101. Watson J, Ihokura K (1999) Gas sensing materials. *MRS Bull* 24:14–17
102. Bielanski A, Haber J (1979) Oxygen in catalysis on transition metal oxides. *Catal Rev – Sci Eng* 19:1–41
103. Kadam RM, Sastry MD, Iyer RM, Gopalakrishnan IK, Yakhmi JV (1997) Electron paramagnetic resonance studies in HgMo₆S₈ doped with Cu²⁺: evidence for cationic mobility. *J Phys Condens Matter* 9:551–556
104. Sunu SS, Prabhu E, Jayaraman V, Gnanasekar KI, Gnanasekaran T (2004) Electrical conductivity and gas sensing properties of MoO₃. *Sensors Actuators B Chem* 101:161–174
105. Huffman DE (1987) Studies in molybdenum catalysts – I. Metal vapor reactions of molybdenum trioxide with various alkoxy silanes, II. Investigations of oxide supported molybdenum catalysts prepared from molybdenum (VI) dioxodiethoxide, PhD Thesis, Oregon State University
106. Brazdol JF, Suresh DD, Grasselli RK (1980) Redox kinetics of bismuth molybdate ammoxidation catalysts. *J Catalysis* 66:347–367
107. Zhai Z, Getsoian AB, Bell AT (2013) The kinetics of selective oxidation of propene on bismuth vanadium molybdenum oxide catalysts. *J Catalysis* 308:25–36
108. Mars P, van Krevelen DW (1954) Oxidations carried out by means of vanadium oxides catalysts. *Chem Eng Sci* 3:41–59
109. Sunu SS, Jayaraman V, Prabhu E, Gnanasekar KI, Gnanasekaran T (2004) Ag₆Mo₁₀O₃₃ – a new silver ion conducting ammonia sensor material. *Ionics* 10:244253
110. Prabhu E, Muthuraja S, Gnanasekar KI, Jayaraman V, Sivabalan S, Gnanasekaran T (2008) Ammonia sensing properties of thick and thin films of Ag₆Mo₁₀O₃₃ and Cr_{1.8}Ti_{0.2}O_{3+δ}. *Surf Engg* 24:170–175
111. Kohli A, Wang CC, Akbar SA (1999) Niobium pentoxide as a lean-range oxygen sensor. *Sensors Actuators B* 56:121–128
112. Kukli K, Ritala M, Leskela M (2001) Development of dielectric properties of niobium oxide, tantalum oxide and aluminium oxide based nanolayered materials. *J Electrochem Soc* 148: F35–F41
113. Wang Z, Hu Y, Wang W, Zhang X, Wang B, Tian H et al (2012) Fast and highly-sensitive hydrogen sensing of Nb₂O₅ nanowires at room temperature. *Int J Hydrog Energy* 37:4526–4532
114. Yu J, Yuan L, Wen H, Shafiei M, Field MR, Liang J et al (2013) Hydrothermally formed functional niobium oxide doped tungsten nanorods. *Nanotechnology* 24:495–501
115. Yu J, Wen H, Shafiei M, Field MR, Liu ZF, Wlodarski W et al (2013) A hydrogen/methane sensor based on niobium tungsten oxide nanorods synthesized by hydrothermal method. *Sensors Actuators B* 184:118–129
116. Meixner H, Lampe U (1996) Metal oxide sensors. *Sensors Actuators B* 33:198–202
117. Henshaw GS, Dusastre V, Williams DE (1996) Selectivity and composition dependence of gas sensitive resistors. Part 3 – properties of the solid solution series (CrNbO₄)_x(Sn_{1-y}SbO₂)_{1-x} (0 ≤ x ≤ 1, y = 0, 0.01, 0.5). *J Mater Chem* 6:1351–1354
118. Henshaw GS, Morris L, Gellman LJ, Williams DE (1996) Selectivity and composition dependence of gas sensitive resistors. Part 4 – properties of some rutile solid solution compounds. *J Mater Chem* 6:1883–1887
119. Greenwood NN, Earnshaw A (2012) Chemistry of the elements. Elsevier Science, Amsterdam
120. Christensen AN, Johansson A, Lebech B (1976) Magnetic properties and structure of chromium niobium oxide and iron tantalum oxide. *J Phys C Solid State Phys* 9:2601–2610
121. Sree Rama Murthy A (2016) PhD thesis, Indian Institute of Science, Bangalore

122. Sree Rama Murthy A, Gnanasekar KI, Jayaraman V, Umarji AM, Gnanasekaran T (2015) Conductometric sensing of H_2 by chromium niobate. *IEEE Sensors J* 15:7054–7460
123. Salzano FJ, Newman L, Hobbell MR (1971) An electrochemical carbon meter for use in sodium. *Nucl Technol* 10:335–347
124. Hobbell MR, Gwyther JR (1975) The use of alkali carbonates in carbon concentration cells. *J Appl Electrochem* 5:263–269
125. Hobbell MR, Trevillion EA, Gwyther JR, Tyfield SP (1982) Calibration tests of an electrochemical carbon meter. *J Electrochem Soc* 129:2746–2748
126. Hobbell MR, Gwyther JR (1973) Development and use of electrochemical techniques for studying carbon behavior in liquid alkali metal systems, in: Proc. of the international conference on liquid alkali metals, Nottingham University, England, 4–6 Apr 1973, British Nuclear Energy Society, London, pp 127–132
127. Rajan Babu S, Reshmi PR, Gnanasekaran T (2012) An electrochemical meter for measuring carbon potential in molten sodium. *Electrochim Acta* 59:522–530
128. Cassir M, Moutiers G, Daynck J (1993) Stability and characterization of oxygen species in alkali molten carbonate: a thermodynamic and electrochemical approach. *J Electrochem Soc* 140:3114–3123
129. Appleby AJ, Nicholson S (1977) Reduction of oxygen in alkali carbonate melts. *J Electroanal Chem* 83:309–328
130. Appleby AJ, Nicholson S (1980) Reduction of oxygen in lithium-potassium carbonate melt. *J Electroanal Chem* 112:71–76
131. Barker MG, Hubberstey P, Dadd AT, Frankham SA (1983) The interaction of chromium with nitrogen dissolved in liquid lithium. *J Nucl Mater* 114:143–149
132. Adams PF, Down MG, Hubberstey P, Pulham RJ (1975) Solubilities, and solution and solvation enthalpies, for nitrogen and hydrogen in liquid lithium. *J Less-Common Met* 42:325–334
133. Barker MG, Chamberlain DK, Frankham SA, Moon NJ, Smith SE (1988) Electrochemical measurements in liquid alkali metals. In: Proceedings of the 4th international conference on liquid metal engineering and technology, Avignon, 7–21 Oct 1988, vol 3, pp 606–1–606-10
134. Jaffe B, Cook WR Jr, Jaffe H (1971) Piezoelectric ceramics. Academic Press, London, p 131
135. Hong SH, McKinstry ST, Messing GL (2000) Dielectric and electromechanical properties of textured niobium-doped bismuth titanate ceramics. *J Am Ceram Soc* 83:113–118
136. Sakai T, Watanabe T, Osada M, Kakihana M, Noguchui Y, Miyayama M, Funakubo H (2003) Crystal structure and ferroelectric property of tungsten-substituted $Bi_4Ti_3O_{12}$ thin films prepared by metal-organic chemical vapor deposition. *J Appl Phys* 42:2850–2852
137. Kim JK, Song TK, Kim SS, Kim J (2002) Ferroelectric properties of tungsten-doped bismuth titanate thin film prepared by sol–gel route. *Mater Letter* 57:964–968
138. Ng SH, Xue J, Wang J (2002) Bismuth titanate from mechanical activation of a chemically coprecipitated precursor. *J Am Ceram Soc* 85:2660–2665
139. Takenaka T, Sakata K (1980) Grain orientation and electrical properties of hot forged $Bi_4Ti_3O_{12}$ ceramics. *Jpn J Appl Phys* 19:31–39
140. Fuierer PA, Nichtawitz A (1994) Electric field assisted hot forging of bismuth titanate. In: Proceedings of 1994 IEEE symposium on applications of ferroelectrics, University Park, 7–10 Aug 1994, pp 126–129
141. Zaremba T (2009) Anisotropic grain growth of bismuth titanate in molten salt fluxes. *Z Kristallogr Suppl* 30:477–482
142. Chen Jie G, Song ZC (2011) Molten salt synthesis of anisotropic $Bi_4Ti_3O_{12}$ particles. *Adv Mater Res* 284:1452–1455
143. Kimura T, Yamaguchi Y (1983) Fused salt synthesis of $Bi_4Ti_3O_{12}$. *Ceram Int* 9:13–17
144. Asokane C et al Indira Gandhi Centre for Atomic Research, Kalpakkam (unpublished results)



Processing of Barium Zinc Tantalate (BZT) Microwave Dielectric Ceramics for RF Window Application in Fusion Reactor

21

Swathi Manivannan and Dibakar Das

Contents

Introduction	795
RF Window	795
Material Requirements	795
Overview of Ceramics for RF Window Application	797
BZT Ceramics	799
Effect of Processing Conditions on Densification and Dielectric Properties	800
Microwave Sintering of BZT	807
Change in Ordering and Sinterability of BZT by Specific Site Doping	816
Fabrication of RF Window	824
Conclusions	825
References	826

Abstract

The ever-increasing energy demand by the human civilization and rapid depletion of conventional fossil fuel has triggered the scientists and engineers to look for alternative source of energy. Fusion energy, where four hydrogen nuclei combine to produce one helium nucleus with subsequent release of enormous amount of energy, could very well meet the future energy demand. Radio-frequency (RF) power is used as one of the noninductive methods to maintain the fusion plasma current under steady-state condition. RF window, used in the transmission line, acts as a vacuum barrier and transmits the microwave (MW) power to the plasma and hence a very critical component in the transmission line. Microwave dielectric ceramics, with high-quality factor/low loss, high dielectric constant, good temperature stability, high dielectric strength, high thermal conductivity, high mechanical strength, and ability to braze to the base metal, are most preferred materials for RF window application. High-purity dense alumina

S. Manivannan · D. Das (✉)

School of Engineering Sciences and Technology (SEST), University of Hyderabad,
Hyderabad, India

e-mail: swathicr@yahoo.com; ddse@uohyd.ernet.in

© Springer Nature Switzerland AG 2020

Y. R. Mahajan, R. Johnson (eds.), *Handbook of Advanced Ceramics and Composites*,
https://doi.org/10.1007/978-3-030-16347-1_24

793

ceramics is the most common material for such application as of now. But the lower dielectric constant of Al_2O_3 ceramic poses a serious problem in thermal management of the window sections, and hence an alternate material is preferred. Barium zinc tantalate $\text{Ba}(\text{Zn}_{1/3}\text{Ta}_{2/3})\text{O}_3$ (BZT) is a well-known microwave dielectric ceramics with excellent properties such as high dielectric constant (ϵ_r), low loss ($\tan\delta$), very low temperature coefficient of resonance frequency (τ_f), and high-quality factor in the microwave frequency range and hence could be a potential candidate for MW window application. But, the major drawback in processing BZT ceramics at high temperatures is the volatilization of low-melting Zn from the BZT composition rendering the final product containing lot of defects including the presence of other phases. This chapter deals with the processing of BZT ceramics with properties suitable for RF window application. The effect of processing conditions and sintering techniques on development of mechanically robust BZT ceramics with highest density (close to the theoretical density), high dielectric constant, low loss (high-quality factor, Q), very low and stable temperature coefficient of resonance frequency, and high thermal conductivity has been discussed in detail.

Keywords

RF window · Dielectric ceramics · BZT · Microwave sintering · Brazing

List of Abbreviations

BKZT	$\text{Ba}_{1-x}\text{K}_x(\text{Zn}_{(1-x)/3}\text{Ta}_{(2+x)/3})\text{O}_3$
BLZT	$\text{Ba}_{1-x}\text{La}_x(\text{Zn}_{(1+x)/3}\text{Ta}_{(2-x)/3})\text{O}_3$
BLZTG	$\text{Ba}_{1-x}\text{La}_x(\text{Zn}_{(1+x-2y)/3}\text{Ta}_{(2-x-y)/3}\text{Ga}_y)\text{O}_3$
BMN	$\text{Ba}(\text{Mg}_{1/3}\text{Nb}_{2/3})\text{O}_3$
BMT	$\text{Ba}(\text{Mg}_{1/3}\text{Ta}_{2/3})\text{O}_3$
BZN	$\text{Ba}(\text{Zn}_{1/3}\text{Nb}_{2/3})\text{O}_3$
BZT	Barium zinc tantalate ($\text{Ba}(\text{Zn}_{1/3}\text{Ta}_{2/3})\text{O}_3$)
BZT-SGT	$0.95\text{BaZn}_{1/3}\text{Ta}_{2/3}\text{O}_3-0.05\text{SrGa}_{1/2}\text{Ta}_{1/2}\text{O}_3$
DRs	Dielectric resonators
EM	Electromagnetic
FWHM	Full width at half maxima
LHCD	Lower hybrid current drive
MLCC	Multilayer ceramic capacitors
MW	Microwave
POP	Plaster of paris
RF	Radio-frequency
SEE	Secondary electron emission
SEM	Scanning electron microscope
TD	Theoretical density
UHV	Ultrahigh vacuum
XRD	X-ray diffraction

Introduction

Fusion power has been considered as one of the promising new and clean alternates to meet the increasing demand of energy in the future. The isotopes of hydrogen (deuterium and tritium) are heated to 100 million degree celsius to yield helium and enormous amount of energy. Since the energy from fusion reaction is free from carbon and the reaction is highly energy efficient, research is pioneering in the field to develop technologies in order to generate and utilize the fusion power effectively. Efforts have been made in realizing the confinement of fusion power in pilot plant scale, and international fusion research has developed few programs to address the challenges involved in generation of commercial fusion power plants. Small amount of fuel is injected in the reactor, and it is heated to create plasma. Tokamak-based fusion reactor is considered as one of the successful systems to magnetically confine the plasma against the reactor walls [1].

There are several heating mechanisms in the reactor to drive steady-state currents in plasma [2]. Plasma acts as a secondary of an inductive transformer, and the toroid magnet at the center acts as primary winding, thereby inducing plasma current. Such inductive ohmic heating is intrinsically pulsed in nature and provides one third of energy required for maintaining plasma in steady state. In neutral-beam injection heating, neutral hydrogen atoms are injected in the reactor wherein they impart the energy to plasma particles, thereby heating it. Radio-frequency (RF) heating is one of the most widely used noninductive heating mechanisms where RF power is used to heat plasma at low hybrid frequencies.

RF Window

In RF heating, lower hybrid current drive (LHCD) system based on a grill-type antenna has in-vessel system comprising of antenna, RF window, and transmission line. RF window, used in the transmission line, acts as a vacuum barrier and transmits the microwave power. Hence it is one of the critical components that limit the power that is coupled to plasma. RF window consists of a single titanium frame with 2×32 slots in which ceramic components are inserted. The ceramic samples should be brazed to the Ti frame to provide leakproof joints. The in-vessel system is supposed to give good RF performance and UHV compatibility [3].

Material Requirements

The desirable properties of dielectric ceramic used in RF window application are as follows:

Low dielectric loss/high-quality factor

Energy dissipation due to intrinsic and extrinsic factors contributes to dielectric loss in a system. Density, microstructural defects, grain boundaries,

vacancies, dopants, etc. contribute to the extrinsic parameters. Intrinsic losses depend on the crystal structure and its symmetry. Hence, for application as RF window, dielectric ceramics should have lower dielectric loss to enable least power dissipation. The power loss in microwave frequencies could be quantified by quality factor of the system. For perfect crystals, quality factor (Q) is an inverse of dielectric loss ($\tan \delta$).

$$Q = 2\pi \frac{\text{maximum energy stored per cycle}}{\text{average energy dissipated per cycle}} \quad (1)$$

The dielectric loss is mainly attributed to the interaction of phonons with the applied field. Losses due to coupling ($1/Q_{\text{ext}}$), dielectric ($1/Q_d$), conduction of metallic plates ($1/Q_c$), and radiation ($1/Q_r$) together contribute to the total dielectric loss of the system. Since Q value determines the selectivity of a resonator to a given frequency, higher Q values are required for enhanced performance of the RF window section.

High dielectric constant

The interaction of AC field with the crystal lattice modifies the equilibrium of phonon system. Thermal stresses will be generated due to dielectric relaxation. Hence, the dimensions of the window section and proper designing of cooling channels play a vital role in preventing the failure of the RF window. The wavelength inside the dielectric is inversely proportional to the square root of its permittivity. Hence for a fixed resonant frequency, dimension of high ϵ_r ceramic dielectric required will be less in comparison with low ϵ_r dielectric. Since thicker sections of RF ceramic window are prone to cracks due to slow dissipation of heat leading to ultimate failure of the window, high dielectric constant ceramic material is required [4].

Good temperature stability and high dielectric strength

The measure of drift in resonant frequency with variations in temperature is quantified using the term temperature coefficient of resonant frequency (τ_f). Since energy dissipation in the form of heat occurs during operation, drift in resonant frequency with increase in temperature is not favorable. For efficient heating of plasma, τ_f should be close to zero. High dielectric strength is also a prerequisite to prevent breakdown of ceramic.

High thermal conductivity

In the fusion reactor, since the in-vessel line lies inside the reactor vessel, continuous bombardment of electrons on the ceramic surface leads to thermal heating of the window sections. The heat generated during operation (due to interaction of RF with the dielectric and multipacting) needs to be dissipated at a faster rate, and high thermal conductivity is required to prevent crack generation due to localized heat spots [5].

High mechanical strength

Structural loads lead to fracture in ceramics, and hence high mechanical strength is required for dielectric material used as RF window

Ability to braze to the frame material

Several designs have been proposed to ensure better RF performance during noninductive heating using RF power. In all these cases, the ceramic window sections have to be brazed to the metal flange. The window sections were to be inserted in the slot of frame material. In order to ensure UHV compatible leakproof assembly, the sections are to be brazed to frame material. Hence feasibility to braze multiple ceramic sections to the frame is also an important property [6].

Overview of Ceramics for RF Window Application

High-purity dense alumina ceramics is the most common material for RF window application. The properties of alumina ceramics were investigated in detail by varying the process parameters and its effect on densification. The effect of various sintering additives on densification and RF performance of aluminum oxide window sections has been reported already [4]. Luminescence due to multipacting has been observed in RF window with alumina ceramic sections. Various coatings were given on the ceramic surface to decrease the secondary electron emission (SEE) and thereby reducing the effects of multipacting. Various parameters like porosity, purity of raw material used, microstructure, SEE, dielectric loss, etc. contribute to dielectric breakdown leading to ultimate failure of the RF window.

Feasibility of using beryllium oxide in planar waveguide has been tested, and it has been seen that the sample exhibited good RF performance (return loss better than 32 dB and insertion loss less than 0.05 dB) for low power operations. The central region of the ceramic had higher temperature than that is predicted from the thermal modeling analysis when subjected to high power operations. The loss was five times higher in comparison with the anticipated values from modeling analysis. Use of BeO ceramics for high-power CW operations was restricted due to issues with heat dissipation and increase in dielectric loss of the material during operation. It is not commonly preferred as a window material due to its toxicity [7].

Feasibility of using boron nitride as window material has also been explored. The rate at which the temperature at the center of the ceramic was increasing during operation is quite high for samples with higher thickness. It has been seen that the thermal loads due to the interaction of RF with ceramic was really high which prevented this material for use in high-power fusion reactor. Boron nitride had better thermal conductivity but low dielectric loss in comparison with sapphire. The rate of increase in temperature with increasing thickness of the window was quite moderate for sapphire window sections showed luminescence and were able to transfer only one fourth of the power transmitted by alumina [8]. The loss tangent for aluminum nitride is higher when compared with alumina. But the material had better thermal conductivity compared to alumina. When AlN window sections were

subjected to operation at RF frequencies, it suffered from serious drawbacks (poor RF performance, low resistivity, and multipacting) which will led to failure of RF window [9].

Since RF performance plays a vital role in deciding the successful functioning of RF window, a detailed review on various electro-ceramics revealed that superior dielectric properties were seen in many of the ABO_3 perovskite class of ceramics. The perovskite structure has the ability to accommodate broad range of substitutions so that robust series of properties can be tailored to meet specific requirements. For ideal perovskite, the value of tolerance factor (τ) is equal to one, but structures with lower symmetry can also exist as perovskites. The perovskite structure can accommodate alio-valent substitution in A site and B site, and the general formula is given as $A(B'_x B''_y)O_3$ or $(A'_x A''_y)BO_3$. The complex perovskite structure $A^{2+}(B^{2+}_{1/3} B^{5+}_{2/3})O_3$ in which higher valence B^{5+} ions occur twice than that of lower valence B^{2+} ions has gained ample attention as the dielectric properties were relatively better in comparison with other complex perovskites. Copious studies were carried out on tailoring different properties by various atomic substitutions.

$Ba(Mg_{1/3}Ta_{2/3})O_3$ (BMT), $Ba(Zn_{1/3}Ta_{2/3})O_3$ (BZT), and $Ba(Zn_{1/3}Nb_{2/3})O_3$ (BZN) systems have been extensively studied due to their attractive dielectric properties that are ideal for microwave applications. B-site ordering in these perovskite structures dictates the dielectric behavior of the system, and hence a huge importance is given in establishing this ordering. The stability of B-site ordering differs for niobate and tantalate systems in spite of having similar ordered structures. This behavior is attributed to the difference in covalency of the two systems.

Matsumoto et al. [10] reported $Ba(Mg_{1/3}Ta_{2/3})O_3$ (BMT) with good dielectric properties ($Q \times f - 430,000$ GHz, $\epsilon_r - 24$, $\tau_f - 8$ ppm/ $^\circ$ C). But the disadvantage involved in preparing BMT is that it requires high sintering temperature (1650 $^\circ$ C) due to poor sinterability followed by long hours of annealing to establish B-site ordering. The dielectric properties ($Q \times f - 96,000$ GHz, $\epsilon_r - 42$, $\tau_f - 30$ ppm/ $^\circ$ C) of $Ba(Zn_{1/3}Nb_{2/3})O_3$ synthesized by solid-state reaction were not that superior to BMT. Several authors tailored the dielectric properties of BZN by doping with Co, Ga, Ce, etc. Also the effect of glassy additives on sinterability and dielectric properties has been studied. Thermal stability of the system is improved by formulating solid solution with SZN but at the compromise of quality factor of the system [11].

The dielectric constant of $Ba(Mn_{1/3}Ta_{2/3})O_3$ is higher than BMT ceramics, and the system possess low loss ($Q \times f - 104,000$ GHz). But the system requires special atmosphere during sintering which hampered the commercial exploitation of the material [12]. A number of studies on preparation of $Ba(Mg_{1/3}Nb_{2/3})O_3$ (BMN) by chemical and solid-state routes were reported. BMN samples with small Mg deficiency showed better properties ($Q \times f - 96,000$ GHz, $\epsilon_r - 32$, $\tau_f - 30$ ppm/ $^\circ$ C). The relatively high τ_f of this system prevents it from practical applications [13].

$Ba(Zn_{1/3}Ta_{2/3})O_3$ (BZT) is a well-known dielectric ceramics with excellent microwave dielectric properties and having high dielectric constant ($\epsilon_r - 28$), low loss ($QXf - 168,000$ GHz), and very low τ_f (~ 0.5) in the microwave frequency range. Since BZT system has got better quality factor in spite of having high dielectric constant, this system has been extensively studied for dielectric resonator

applications [14]. BZT also possesses small τ_f values (close to zero) in comparison with other complex perovskites making it a better choice for RF window application.

BZT Ceramics

BZT ceramics, with such excellent microwave dielectric properties, are suitable for different microwave and millimeter wave device applications including filters in base station of mobile and satellite application, dielectric resonators, multilayer ceramic capacitors (MLCC), etc. [15]. One of the main disadvantages in processing BZT ceramics is that the thermal treatments required to achieve maximum density and preferred crystal structure are quite high temperatures for longer duration. It has been seen in literatures that the final dielectric properties are greatly influenced by the thermal history and purity of the raw materials used.

Volatilization of zinc during sintering and annealing of the sample is one of the primary constraints that prevents consistent dielectric behavior of this material due to various zinc-deficient secondary phase formation. Several approaches were undertaken to suppress the secondary phase formation and to improve densification. Doping BZT with oxides which contain cations having ionic radii similar to that of zinc was carried out to compensate for Zn loss during high-temperature treatments. CeO_2 , Al_2O_3 , Ga_2O_3 , ZrO_2 , and TiO_2 were some of the few oxide additives that have been added to BZT to improve the dielectric performance of the system [16–20]. Even though the addition of other oxides and salts helps in reducing the sintering temperature and Zn loss from the system (thereby increasing the density and hence reducing the porosity), the presence of other cations (such as Ni, Zr, Ti, Ga, etc.) alters the ionic environment of the native ions (such as Ba, Zn, Ta, O_2 , etc.) and hence influences the dielectric behavior of the system.

The effect of adding low-melting sintering additives (B_2O_3 , Li salt, and CuO) to the system to decrease the sintering temperature on the dielectric properties has already reported in the literature [18, 21]. It has been seen that the glassy phase due to the addition of flux improves densification but the dielectric properties of pure BZT were far superior to the sample containing flux. Also, the mechanical strength of the sample will be greatly influenced by the addition of flux to the system as it will be inherently weak due to the presence of glassy phase. Several efforts have also been made to use dopant consisting of similar ions as that of BZT in order to suppress the extended defects arising from other oxides and salts doping in BZT matrix. Doping with barium tungstate (BaWO_4) under zinc oxide (ZnO) muffling (covering the BZT pellet with ZnO powder) conditions results in improved structural and dielectric properties [22]. Nanosized BZT powder, synthesized by wet chemical route, was doped with Ga_2O_3 and sintered by muffling with calcined BZT powder. But, only 90% of the theoretical density has been achieved [23]. Quite a lot of efforts have been made to suppress the Zn loss from BZT ceramics, thereby improving the structural and dielectric properties.

It has been already seen that the processing history and hence the extrinsic parameters play a vital role in determining the performance of the RF window.

Hence, the main challenges involved in fabrication of BZT as window section includes sintering the material to high density (close to theoretical density), suppression of secondary phase formation due to zinc volatilization, efficient processing route to produce samples with larger dimensions, tuning dielectric properties to obtain good RF performance, and also study on the feasibility of brazing the ceramic with the metal frame.

Effect of Processing Conditions on Densification and Dielectric Properties

Synthesis by solid-state reaction is one of the widely preferred synthesis methods as it can yield large quantity of powders cost-effectively. Stoichiometric quantities of constituent high-purity oxides and carbonates were taken and mixed to get a homogenous mixture. The mix is then heat-treated to obtain the desired phase. Wet chemical synthesis of BZT did not help in better densification, and the powders so obtained could not be sintered to higher density without the formation of secondary phases. The properties of BZT powders obtained by hydrothermal synthesis were not superior to the powders synthesized by solid-state method. Solid-state synthesis method was considered to be the best option so as to cost-effectively produce large quantity of powders for preparation of BZT samples with large dimensions. Density and dielectric properties of this BZT ceramics depend upon the way it is processed, and hence the steps for processing and sintering conditions must be carefully monitored and controlled for the best results. Therefore various processing conditions and techniques have to be employed, and careful attention has to be paid for the preparation of the BZT samples. The flowchart (in Fig. 1) shows the

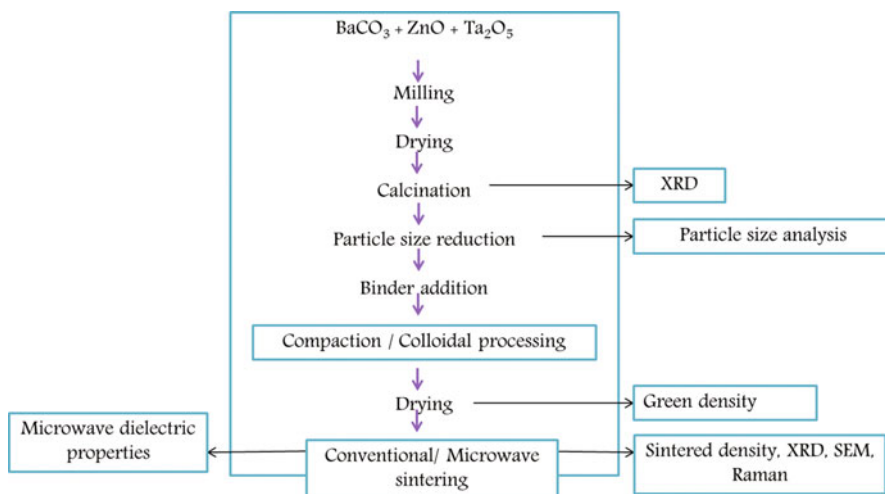


Fig. 1 Process flowchart illustrating preparation and characterization of pure BZT

preparation, processing, and characterization of BZT. The obviousness of correct combination of different processing parameters will lead to the desired properties, and this has been elaborated in subsequent topics.

Effect of Starting Particle Size

Green density of the ceramic samples plays a vital role in deciding the sintering kinetics of the samples. The main factors which determine the packing efficiency in green sample are particle size, distribution, and particle morphology. Calcination temperature and time also play a vital role in determining the density and dielectric behavior of the samples. Since low volatilizing zinc is present in the composition, any occurrence of residual unreacted phase after calcination in the system leads to secondary phase formation. Hence, calcination time and temperature were optimized to get maximum densification and better RF performance. The calcined powders were milled prior to consolidation to enhance the sintering behavior. It has been seen that with increase in milling time, the mean particle size decreases, and the distribution becomes narrow (Fig. 2a). Decrease in density with increasing milling time duration (beyond 8 h) could be attributed to narrow particle size distribution as it is associated with low packing efficiency in the green sample. Since the dielectric loss has close dependence on sintered density, the quality factor of samples follows almost the same trend as that of density. The influence of particle size and its distribution on densification and dielectric properties are represented in Fig. 2b.

Effect of Peak Sintering Temperature and Dwell Time

The process of sintering progresses by several diffusion mechanisms which occur simultaneously with increase in temperature. Hence peak sintering temperature and dwell time at the peak sintering temperature play a vital role in determining the final properties of the ceramics. The samples after consolidation by compaction process were subjected to different sintering temperature and dwell time. Densification behavior of BZT ceramics sintered at different temperatures and soaking time is shown in Fig. 3a. The sintered density increases with increase in sintering temperature and dwell time at peak temperature. At lower sintering temperature of 1400 °C, the samples were densified only to 88%TD. Increasing the dwell time from 2 h to 4 h did not improve the densification predominantly. Maximum sintered density (96.3%TD) was obtained for sample sintered at 1600 °C for 2 h. Increase in dwell time at this temperature led to decrease in density. The possible reasons for decrease in density could be due to the exaggerated grain growth or due to formation of zinc-deficient secondary phases. X-ray diffraction pattern of the samples sintered at different temperatures (shown in Fig. 3b) showed the presence of zinc-deficient secondary phases (BaTa_2O_6 and $\text{Ba}_8\text{ZnTa}_6\text{O}_{24}$). The occurrence of these phases becomes more predominant in sample sintered at 1600 °C. Elemental distribution of the sample sintered at 1600 °C indicates that the sample sintered at higher temperatures shows nonuniformity in the distribution of zinc. Sample sintered at higher temperatures had a skin layer (white color) which corresponds to the

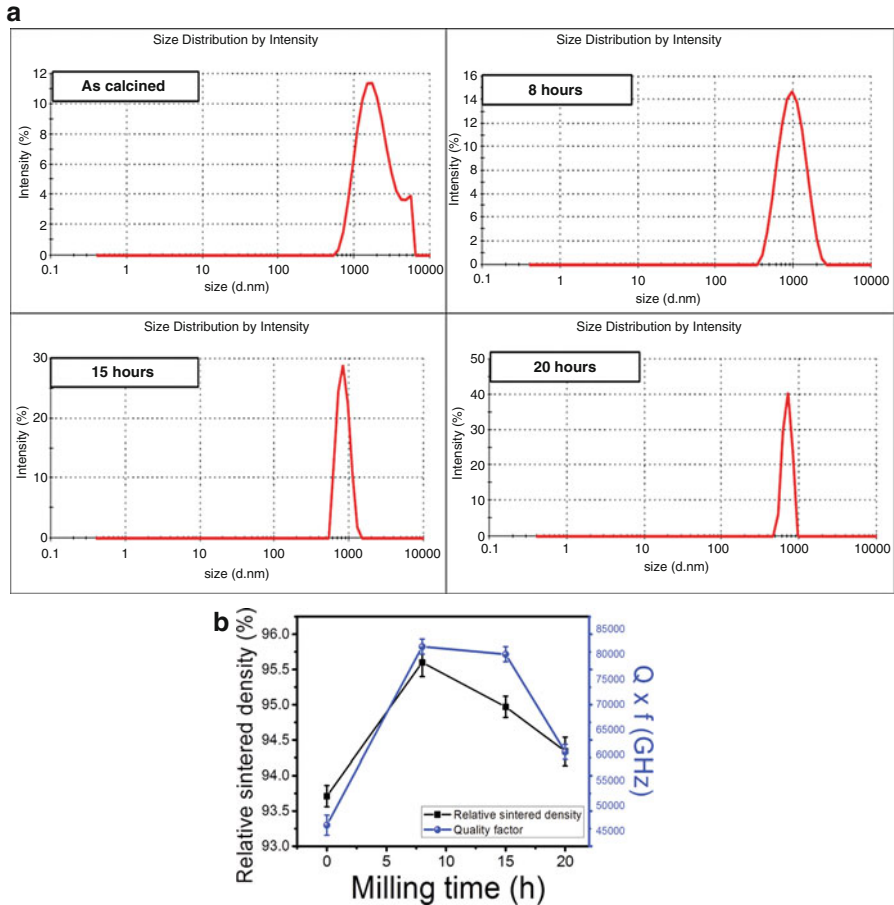
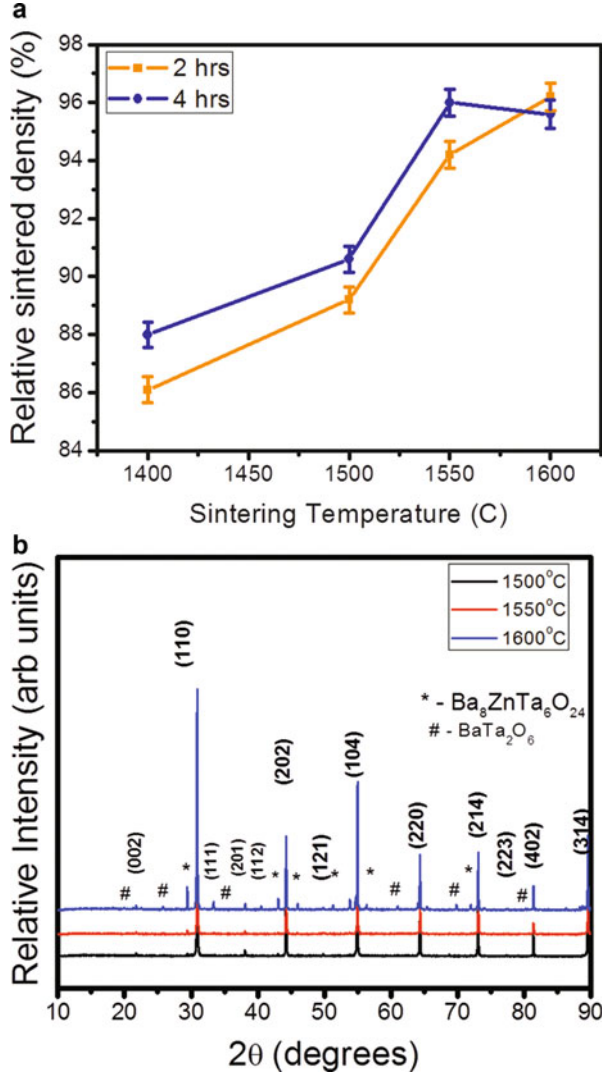


Fig. 2 Effect of milling time on (a) particle size and its distribution and (b) sintered density and quality factor

formation of zinc-deficient secondary phase as seen in XRD and SEM results. Though increase in temperature led to increase in sintered density of the sample, higher sintering temperatures led to zinc volatilization which is known to be detrimental for dielectric and mechanical properties of the sample.

Heating rates have a significant role to play in densification of ceramics. Samples were sintered at 1600 °C for 2 h with a faster heating ramp (10 °C / min) to suppress zinc volatilization. The sintered density of the sample with fast heating rate led to 94% of TD. When a slow heating rate was followed, -1 °C/min up to 500 °C followed by a soak of 1 h at 500 °C/800 °C and 3 °C up to the peak temperature led to a maximum density of 97% of TD. Also, high rate of heating leads to the formation of elastic strains which can adversely affect the dielectric properties.

Fig. 3 Effect of sintering temperature and dwell time on (a) densification (b) XRD pattern indicating secondary phase formation



Effect of Flux Addition

Since volatilization of Zn is a critical issue in processing of BZT, several approaches were identified to suppress the same. The details of work done in prior arts have been elucidated in section “BZT Ceramics.” One of the approaches was to add low-melting additives, thereby enhancing the densification behavior of BZT ceramics. It has been seen that addition of small quantity of B_2O_3 to BZT enhanced the density and dielectric properties of the system [21]. Since metallization followed by brazing/direct brazing is one of the critical steps in fabrication of RF window, the samples containing the flux were polished to give a smooth surface finish. These samples did not

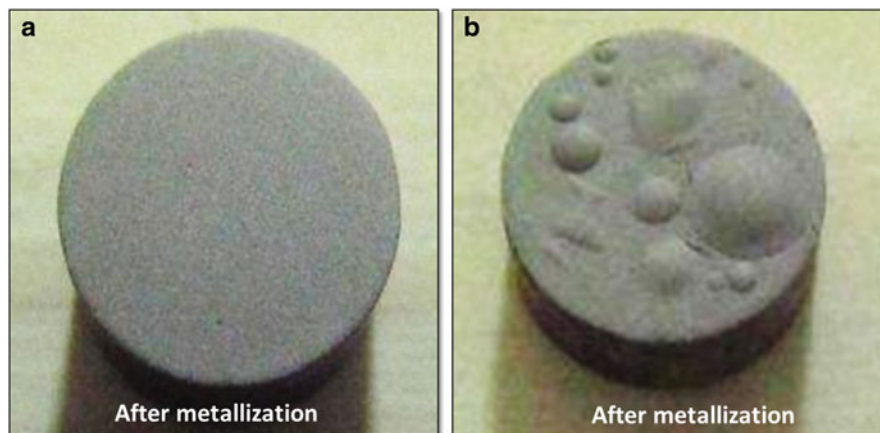


Fig. 4 Surface of metallized ceramic samples: (a) pure BZT and (b) BZT with B_2O_3

have sufficient mechanical strength and hence could not give smooth surface. Pure BZT samples and samples with flux were subjected to metallization. Typical appearance of surface of the sample after metallization process is shown in Fig. 4. Irregular surface finish in samples with flux led to poor metallized layer containing irregularities in the surface and hence cannot be brazed to create UHV compatibility.

Effect of Sintering Atmospheres

BZT ceramics are quite sensitive to the structure and property for small changes in the bulk chemistry and stoichiometry. Sintering environment has a great effect on the properties of BZT because of the presence of low volatilizing zinc in the formulation. Different sintering environments were created by muffling the green BZT pellets with different powder compositions. Heating rates and other processing parameters were kept constant to evaluate the effect of different sintering atmospheres on the final properties of BZT pellet.

In order to reduce the zinc volatilization, the pellet was sintered with ZnO powder at 1550 °C for 2 h. Sintering with ZnO powder did not suppress zinc volatilization. Sintering at 1550 °C for 2 h in the presence of Zn pellets also did not suppress zinc volatilization, and the intensity of the zinc-deficient phase is quite high in X-ray diffraction analysis.

Sintering in positive oxygen partial pressure was tried at three different sintering temperatures (1100 °C, 1200 °C, and 1300 °C). Maximum density of 75% of TD was obtained for the sample sintered at 1300 °C. Reaction bed sintering with calcined BZT powder at 1600 °C for 2 h resulted in uniform microstructure with good microwave dielectric properties (Fig. 5a). Volatilization of zinc is minimized, and suppression in formation of zinc-deficient secondary phase led to marginal improvement in densification. Dense and uniform microstructure with clear grain boundary is revealed in the fracture surface of sample sintered at 1600 °C for 2 h. Elemental mapping of the sample reveals that the distribution of zinc is more uniform leading to

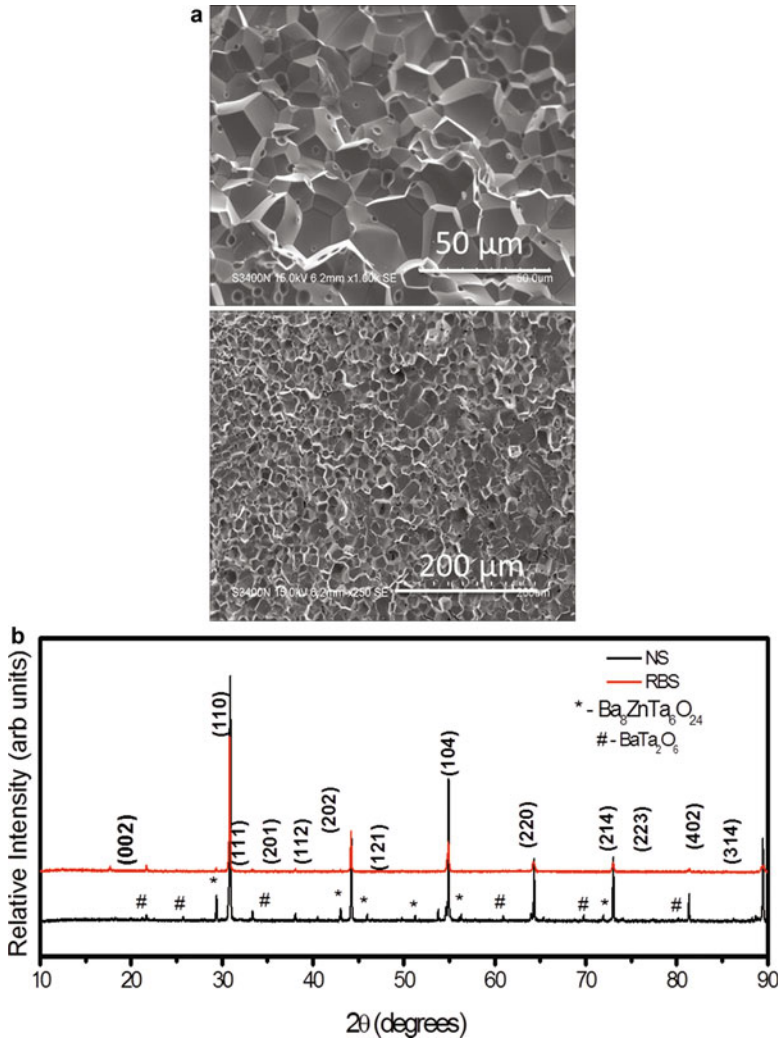


Fig. 5 Reaction bed sintering of BZT. (a) Microstructure, (b) XRD pattern of samples conventionally sintered (NS), and reaction bed sintered (RBS) at 1600 °C

better densification and good microwave dielectric properties. XRD of samples conventionally sintered and reaction bed sintered at 1600 °C are shown in Fig. 5b. It can be seen that zinc-deficient secondary phases dominated in normal sintered samples in comparison with the reaction bed sintered samples.

Effect of Consolidation Technique

Processing parameters optimized for preparing smaller ceramic samples were used to scale up to larger dimensions for fabricating window sections. The main issues

realized during the fabrication of large window sections were warpage, density gradients along the window section, and nonuniform zinc distribution. In spite of using binder to improve the green strength of the sample and lubricant during compaction to suppress the die-wall friction, conventional compaction processing of large rectangular slabs leads to density gradients which in turn cause crack like voids in the sintered body. The density variation in the sample is in between 96% and 98% of the theoretical density. Microstructural analysis of the rectangular slabs has revealed that the distribution of zinc is not uniform in the sample. Elemental distribution of zinc at various regions on the sample is not uniform, and there are regions deficient of zinc in spite of muffling with calcined BZT powder. Also, reaction bed sintering of large rectangular bars required large quantity of BZT powder to suppress zinc volatilization. The change in color after sintering is also not uniform throughout the sample. X-ray diffraction analysis of the sintered samples at different depths of the sample from the surface has shown extra peaks corresponding to the zinc-deficient phases and intensity of those peaks change with respect to the sintering environment (Fig. 6). The intensity of these peaks varies with the zinc content in the sample, and it is greatly influenced by the sintering environment.

BZT ceramics find application widely in the field of dielectric resonators (DRs) and filters for which smaller ceramics pucks are required. Hence, not much importance was given to the consolidation method other than compaction. Works pertaining to the effect of shaping on densification and RF performance were limited. Shaping by colloidal processing technique has an advantage of producing green body with uniform particle packing. Stability of suspension and the solid loading determines the microstructure of the green body. It has been observed that slip casting of BZT suspension containing optimum quantity of dispersant and maximum solid loading led to a maximum sintered density of 96%TD.

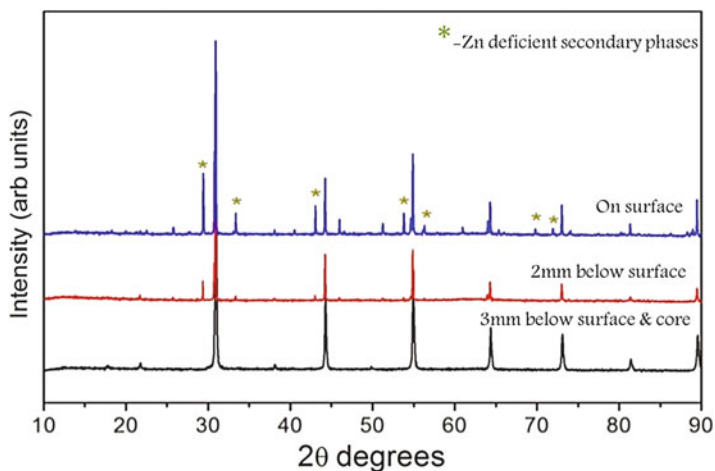


Fig. 6 XRD pattern taken from different depths of the sample from the surface

Also, the dielectric properties of the samples were not better than the compacted samples. This could be attributed to the presence of impurities in the sample from POP mold. Egg white has been identified as one of the efficient eco-friendly gelling agents suitable for gel casting of ceramics. Hence, the effect of egg white concentration in the premix solution of BZT suspension has been studied, and it has been seen that there is a marginal difference in densification behavior in comparison with the samples processed by slip casting. Higher percentages of egg white in premix did not permit the increase in solid loading due to the viscous nature of egg white, thereby adversely affecting the improvement in green density. The decrease in green density was well reflected in the sintered density, which in turn decreased the quality factor of the samples. In order to compare the influence of gelling agents on densification behavior of BZT, conventional gel casting was carried out. Samples prepared from suspensions containing optimized concentrations of monomer and cross-linker showed a maximum sintered density of 98%TD and better dielectric properties when compared with other colloidal processing techniques. The effect of shaping process on densification and shrinkage behavior of BZT ceramics are summarized in Fig. 7. It can be seen that maximum shrinkage was seen in samples processed by slip casting technique. The values remain least for conventional gel casting techniques indicating the efficiency of the process for near-net shaping of BZT ceramics for various applications. Also, the dielectric properties of the samples were better than the samples prepared by other processing techniques even without annealing [24].

Microwave Sintering of BZT

It has already been seen that the issues pertaining to sintering of large rectangular sections include warpage, density differences, and occurrence of zinc-deficient phases. In order to address these issues, one of the possible solutions could be to use microwave energy for sintering. Molecular-level interaction of the material with EM field leads to volumetric heating of the samples, thereby suppressing thermal gradients in the sample. In conventional sintering thermal energy is delivered to the sample by conduction. Since ceramics are poor conductors of heat, there will be a temperature gradient in the sample leading to difference in temperature. This gradient could possibly be attributed to variation in zinc distribution. There are several zinc-deficient secondary phases identified during sintering. In general, many low loss dielectric ceramics have poor microwave-absorbing capacities, and hence the main challenge involved in microwave sintering of BZT is to ensure good coupling with microwaves during heating. As anticipated, the coupling efficiency of BZT with microwaves was really poor. Maximum densification that could be achieved was only 84%TD even at 1500 °C. In order to have some reactivity during sintering, the constituent oxides were mixed and compacted. They were heat-treated at 1300 °C in conventional furnace, and the sample was crushed and pelletized again. The sample so obtained showed only 77% TD when microwave sintered at 1500 °C.

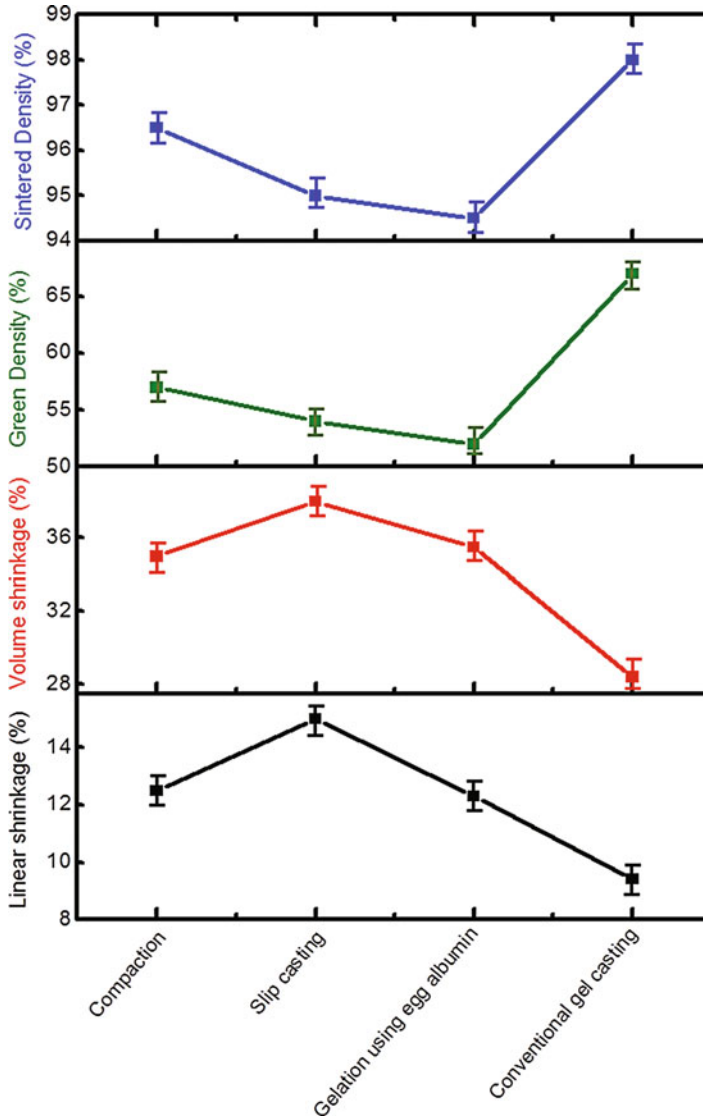


Fig. 7 Effect of consolidation technique on densification and shrinkage behavior of BZT

Densification of BZT by Microwave Sintering

In order to ensure efficient interaction of BZT with microwaves, hybrid heating with the help of susceptors is done to increase the temperature to critical temperature beyond which BZT starts coupling with microwaves. Also few additives which are known to couple effectively with microwaves have been added to BZT before compaction, and the densification behavior has been studied. Oxides (Cr_2O_3 , Fe_2O_3 , Al_2O_3 , MgO , ZrO_2) were added to pure BZT after calcination. The oxides were

intimately mixed and compacted. BZT containing Cr_2O_3 , Fe_2O_3 and ZrO_2 showed better densification in comparison with other oxide additives. It has been seen that the processing time required for achieving maximum density by conventional sintering is too long (~30 h) when compared to microwave sintering (~3 h). Temperature and concentration of dopants played a vital role in determining the density of the final compact. In BZT with Cr_2O_3 , Fe_2O_3 as additives, it has been seen that increase in sintering temperature beyond 1450 °C led to decrease in density. Densification behavior of samples containing Cr_2O_3 and Fe_2O_3 showed similar trend. The density of the samples containing these oxide additives microwave sintered at 1400 °C is presented in Fig. 8a. In case of sample with ZrO_2 addition, higher concentrations of dopants (≥ 1 mol%) were required for better densification by microwave sintering in comparison with the conventional sintering of the system. It has been already observed by Yang et al. [25] that BZT samples conventionally sintered with ZrO_2 as additive have improved the densification behavior and dielectric properties of BZT. Influence of ZrO_2 content on the sintered densities of BZT – $x\text{ZrO}_2$ ($x = 0$ to 3 mol%) samples 1400 °C microwave and 1550 °C conventionally sintered is presented in Fig. 8b. 98% TD was obtained for sample containing 2 mol% of ZrO_2 in microwave sintering. All samples, which are conventionally sintered with ZrO_2 as additive, had density > 95% TD.

Microstructural Analysis

From the density data, it has been seen that the densification behavior is being governed by the temperature and concentration of dopants. Efforts to understand the effect of these factors on microstructure have shown that increase in peak sintering temperature (≥ 1450 °C) led to the development of anisotropic grains which in turn decreased the density. Fig. 9a shows the microstructure of BZT – $x\text{Fe}_2\text{O}_3$ ($x = 2$ mol%) samples sintered at 1300 °C–1500 °C in microwave sintering furnace. Pure BZT, which was in an intermediate stage of sintering even at a temperature of 1450 °C, showed drastic increase in density with addition of Fe_2O_3 . Even at a lower sintering temperature (1300 °C), there was a drastic decrease in the continuous pore phase area compared to pure BZT, and small irregular grains were observed. Increase in temperature led to increase in grain growth of the sample, and dense microstructure with small irregular grains was seen in sample sintered at 1400 °C. Anisotropic elongated grains were observed in the dense matrix of irregular grains in samples sintered at 1400 °C. Growth of anisotropic grains predominated with increase in temperature leading to decrease in density. Though not much literatures are available on the effect of additives during microwave sintering on microstructures, there are quite a few to compare the effect of various additives on conventional sintering of BZT. BaWO_4 and Ga_2O_3 addition to BZT led to growth of longer anisotropic grains in uncommon fashion [18, 22]. Many possible explanations have been given for the formation of anisotropic grain growth. Many a times, the growth of such structures is related to the formation of zinc-deficient phases. Since in microwave sintering the growth of such structures was seen with increase in sintering temperature, this could be attributed to presence of some secondary phases.

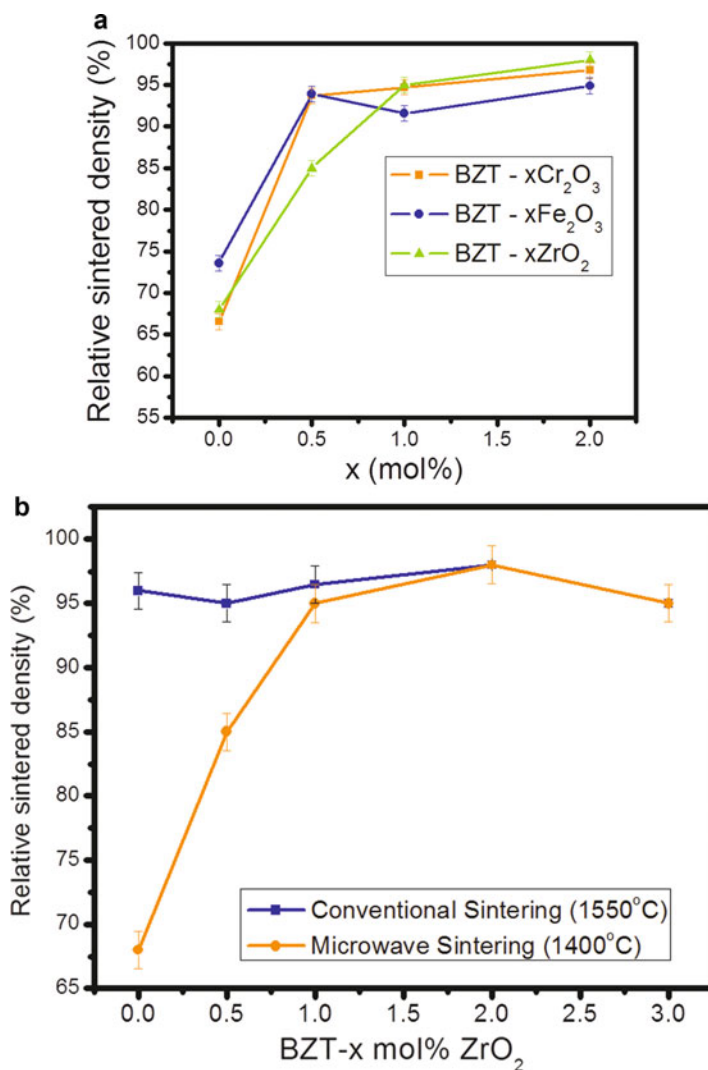


Fig. 8 (a) Role of additives on densification of BZT by microwave sintering (1400 °C). (b) Effect of ZrO₂ on conventional and microwave sintering of BZT

Figure 9b shows the microstructures of BZT – xZrO₂(x = 0.5 to 3 mol%) samples sintered at 1400 °C in microwave sintering furnace. Even for small addition of ZrO₂ to BZT (0.5 mol%), small grains as well as anisotropic grains were observed in the microstructure. As the concentration of ZrO₂ is increased, bar-shaped grains tend to evolve in the matrix containing small grains. Grain growth is improved for BZT – 2 mol %ZrO₂ samples leading to dense microstructure formed from acicular grains with

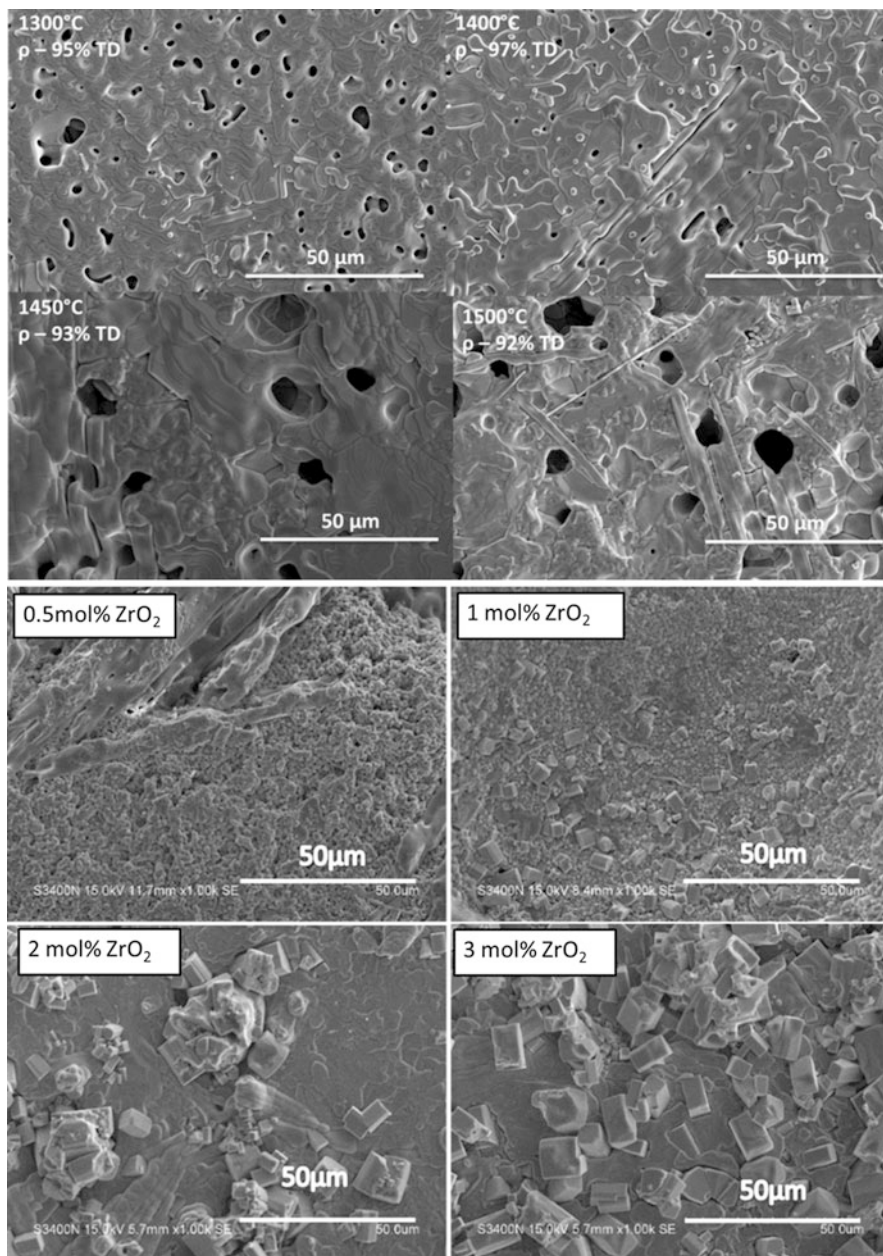


Fig. 9 (a) Microstructure of BZT – $x\text{Fe}_2\text{O}_3$ ($x = 2$ mol%) samples sintered at 1300 °C–1500 °C in microwave sintering furnace. (b) Microstructures of BZT – $x\text{ZrO}_2$ ($x = 0.5$ to 3 mol%) samples sintered at 1400 °C in microwave sintering furnace

diffused grain boundary. Clusters of bar-shaped grains were seen in the sample with 2 mol% ZrO_2 . Growth of bar-shaped grains was found to be predominant as concentration of ZrO_2 is increased to 3 mol%. A comparison with the conventional sintering of BZT- ZrO_2 showed that similar bar-shaped grains were seen and it was attributed to the presence of Ta-rich phase ($\text{Ba}_{0.5}\text{TaO}_3$). Several literatures have reported that addition of dopants in which the cations have similar ionic radii as that of Zn has led to better dielectric properties. Hence, in selecting the dopants for improving the coupling of BZT with microwaves, due attention was taken to ensure that the ionic radii of the cations match to the radius of B-site ions of perovskite structure. Presence of abnormal grains at higher sintering temperature suggests that Zn vacancies were created even in microwave sintering in spite of short processing time at higher temperatures.

Microwave Dielectric Properties

As discussed in section “[Material Requirements](#),” the dielectric loss of the ceramic depends on various factors including density, microstructural defects, and grain boundaries. Apart from these factors, the dielectric properties of pure BZT, especially quality factor, mainly depend on crystallographic orientation of Zn and Ta ions in the lattice. It has been observed that the densities of the samples were found to increase up to 1450 °C beyond which there was a decrease in density due to abnormal grain growth. Since the loss of the samples was governed by density, similar trend was followed even in the quality factor measurement. Smaller grains were present in the samples sintered at 1300 °C and 1400 °C. With increase in temperature, the grain growth of the sample increased, which led to decrease in grain boundary area. This led to better properties for sample sintered at 1450 °C. Marginal decrease in density for samples sintered at 1500 °C led to poor dielectric properties. Since microwave sintering of samples is done at relatively faster heating rates, the samples are prone to have stresses, and this in turn could affect the dielectric properties. Hence, the samples were annealed for a shorter duration at lower temperatures to relieve the stresses. The dielectric properties for the samples containing Cr_2O_3 , Fe_2O_3 as dopants are summarized in Table 1. The quality factor of BZT-x

Table 1 Summary of dielectric properties of BZT-x ($\text{Cr}_2\text{O}_3/\text{Fe}_2\text{O}_3/\text{ZrO}_2$)

BZT	Microwave sintering			
	Order parameter	Qxf	ϵ_r	τ_f
0.5 Cr_2O_3	0.74	55,000	28.5	-1.89
1 Cr_2O_3	0.68	56,500	28.2	-2.7
2 Cr_2O_3	0.67	38,000	27.9	-3.2
0.5 Fe_2O_3	0.79	53,500	29.3	-1.1
1 Fe_2O_3	0.76	42,000	29.1	-1.5
2 Fe_2O_3	-	22,000	29.7	-2.3
0.5 ZrO_2	0.76	45,300	29.5	1.3
1 ZrO_2	0.69	86,450	29.8	2.7
2 ZrO_2	-	98,450	29.7	3.5
3 ZrO_2	-	81,680	29.1	4.7

Cr_2O_3 samples ($x = 0.5$ and 1 mol%) was higher compared to samples with $x = 2$ mol%. In case of samples containing Fe_2O_3 , the quality factor values were found to decrease with increasing concentration of dopants. BZT-xZrO_2 had superior dielectric properties in comparison with samples with other oxide dopants. BZT-BaZrO_3 is one of the extensively studied systems due to its attractive dielectric properties. It has been seen that the zirconium ions are capable of stabilizing the grain boundaries against dielectric loss and hence has been considered as one of the best choices of dopants. The crystal structure and space group of BaZrO_3 are similar to that of BZT, thereby reducing the chance for decrease in quality factor due to the presence of secondary phase. There is a marginal decrease in the dielectric constant value with increasing concentration of Cr_2O_3 , and this could be attributed to low dielectric polarizability of Cr_2O_3 (1.45). τ_f values increase in the negative side with increasing concentration of Cr_2O_3 . Dielectric constant value decreases with increasing concentration of Fe_2O_3 . But the values are marginally higher than that of samples containing Cr_2O_3 , and this can be attributed to higher ionic polarizability of Fe^{3+} ions. The temperature coefficient of resonant frequency (τ_f) values increases in the negative side with increasing concentration of Fe_2O_3 , and the trend is the same as that of samples containing Cr_2O_3 . The dielectric constant values tend to increase with increase in concentration of ZrO_2 up to 2 mol% concentration of additive. Zirconium ions have higher ionic polarizability in comparison with Fe^{3+} and Cr^{3+} ions. It is generally seen that the value of the dielectric constant increases only when the polarizability of the ions in the additive oxide is higher than the average ionic polarizability. Also the presence of extra phases influences the value of dielectric constant. The temperature coefficient of resonant frequency increases with increasing concentration of ZrO_2 .

Crystal Structure and Ordering

There are several reports on crystal structure and ordering of BZT system from XRD pattern. In BZT, Zn and Ta ions adopt 1:2 ordering along [111] direction of the cubic unit cell. Such an ordering leads to superlattice reflections, and the intensity of such reflection to the intensity of fundamental reflection is used to quantify the degree of ordering in the system.

The degree of ordering in the system is estimated by the order parameter which is defined as below,

$$S = \sqrt{\frac{[I_{100}/I_{110,012}]_{obs}}{[I_{100}/I_{110,012}]_{cal}}} \quad (2)$$

where $[I_{100}/I_{110,012}]_{obs}$ is the ratio of observed intensity of the superlattice reflection to that of the fundamental reflection. $[I_{100}/I_{110,012}]_{cal}$ is the calculated intensity ratio for completely ordered ideal sample, and the value is 0.037 [26].

There are numerous factors that determine the ordering of the system. Some of them include thermal treatment, difference in valency of B-site ions involved in the system, valency of A-site ions, presence of fluxing agents, domain size, etc. Presence

of large number of secondary phases after sintering led to difficulty in correlating the structure to property of the system. XRD analysis shows that in BZT containing different dopants, the secondary phase $\text{Ba}_8\text{ZnTa}_6\text{O}_{24}$ is present due to volatilization of zinc from the system. Though the peak sintering temperature required to achieve maximum sintered density is decreased during microwave processing and shorter processing times have been used, zinc-deficient secondary phases were seen in the sample. In all samples, the order parameter values increase with increasing sintering temperature. The XRD pattern of BZT-0.5 Fe_2O_3 sintered at 1300°C – 1500°C in microwave sintering furnace is presented in Fig. 10. The inset of the figure shows the typical values of S parameter with increase in sintering temperature. It can be seen that the S parameter value increases with increase in sintering temperature. The variation in order parameter values of the system containing different dopants did not follow a uniform trend with increasing concentration of dopants. It has been seen in the literatures that dopants in many cases were found to be detrimental to ordering. In some cases, the dielectric properties of the system were indifferent to the ordering in system. The ordering in the system as a function of dopant concentration is indicated in Table 1 as order parameter values. In case of Cr_2O_3 , ordering existed in all concentrations up to 2 mol%, but the value of S parameter decreased indicating that presence of Cr^{3+} ions in lattice disrupts the ordering. S values were found to decrease with increasing concentrations of Fe_2O_3 , and the peak corresponding to ordering was completely absent in BZT-2 Fe_2O_3 samples. Ordering in ZrO_2 containing BZT samples also decreased with increasing concentration of the dopant, and it is completely lost for concentrations >2 mol%. It has been seen that conventional sintering of ZrO_2 containing BZT samples showed better properties despite loss in ordering of the system, which is attributed to the

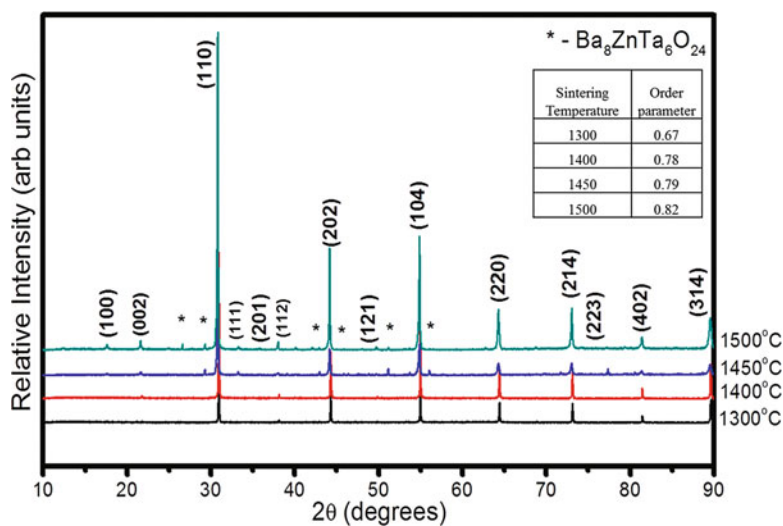


Fig. 10 XRD pattern of BZT-0.5 Fe_2O_3 sintered at 1300°C – 1500°C in microwave sintering furnace. Inset: Variation of S parameter with increasing sintering temperature

Table 2 Crystallite size of BZT-0.5Fe₂O₃ for various sintering temperatures and FWHM of A_{1g}(O) mode in Raman spectra

Sintering temperature	Order parameter	FWHM
1300 °C	0.67	38.7
1400 °C	0.78	36.7
1450 °C	0.79	35.6
1500 °C	0.82	34.5

stabilization of ordered-disordered domain boundaries with Zr ions. Similar behavior of the system has been seen when subjected to microwave sintering.

The lattice parameter values from XRD also gave an indication of the ordering in the system. The “c” axes of the hexagonal unit cell tend to increase in magnitude with increase in ordering. The lattice parameter values calculated for BZT with different additives indicated that the c/a values decreased with increasing concentration of dopants, which is in accordance with the order parameter values. Another shortcoming of microwave sintering of BZT is that the dielectric properties were not that superior to the samples sintered in conventional sintering furnace. Crystallite size calculation of various systems sintered using microwave power revealed that the samples had comparatively lower value than the conventionally sintered samples. Typical values of crystallite size of the BZT-0.5Fe₂O₃ samples sintered at different sintering temperatures are shown in Table 2. The inferior values in quality factor of microwave sintered samples could also be attributed to smaller crystallite size.

Raman Spectroscopic Studies

The change in structure from disordered to ordered one is accompanied by a change in symmetry of the system. The modes of vibration in the system hence change, and so, Raman spectroscopic studies can be one of the tools to examine the ordering in the system. The space group of disordered structure exists is pm3 m, while in ordered structure, it exists in P $\bar{3}$ m1 symmetry. This change in symmetry is reflected by the appearance of three extra reflections corresponding to the wavenumbers 158, 212, and 262 cm⁻¹. The stretching mode of oxygen octahedra (A_{1g}(O) mode) occurs at 806 cm⁻¹, and FWHM of the peak is generally taken into account to correlate with the dielectric loss of the samples. The Raman spectroscopic analysis of samples sintered using microwaves was in good correlation with the order parameter values obtained from X-ray diffraction pattern. In BZT-xFe₂O₃ system, from the XRD data, it has been seen that ordering of the system decreased with increasing concentration of the Fe₂O₃, and when x = 2 mol%, ordering is completely lost in the system. The Raman spectra of BZT samples containing 0 to 2 mol% Fe₂O₃ sintered at 1450 °C in microwave furnace is given in Fig. 11. The modes of vibrations corresponding to ordering (E_g(O), E_g(Ta), A_{1g}(Ta)) were absent for x = 2 mol% which is in accordance with the XRD data. Improvement in ordering with increasing sintering temperature is also reflected in FWHM of A_{1g}(O) mode. Thus, Raman spectroscopy is a useful tool to study the lattice vibrational modes and ordering in the system, and the results were correlated with order parameter values calculated from XRD.

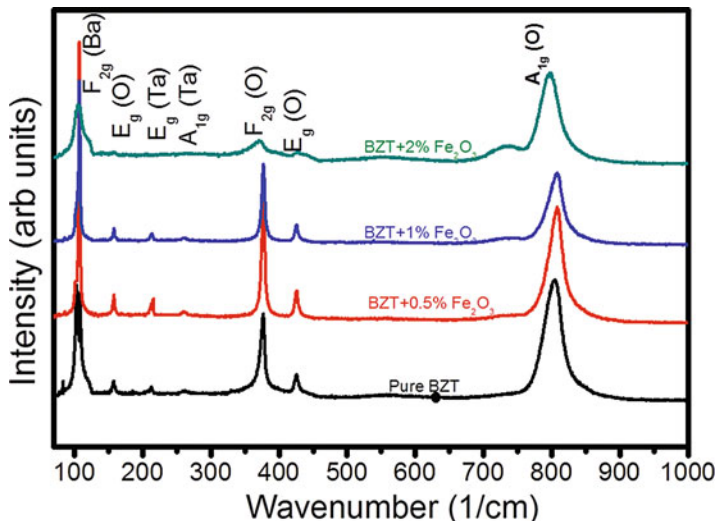


Fig. 11 Raman spectra of BZT samples containing 0 to 2 mol% Fe_2O_3 sintered at 1450°C in microwave furnace

Change in Ordering and Sinterability of BZT by Specific Site Doping

The flexibility to design the composition of the ceramic materials to tailor their dielectric properties is always interesting to meet the ever-increasing demand of these materials in various applications. The dielectric properties are generally tuned by different approaches including additive/dopant addition [27], altering the stoichiometry [28], formation of solid solution [17], texturing [29], mechanical compensation technique [30], and surface coating [31]. Several advanced sintering techniques including liquid phase sintering and addition of different dopants have been researched to tailor the dielectric properties of BZT ceramics. Efforts have been made to tune the microwave dielectric properties of BZT by doping with suitable oxides at low sintering temperatures. Change in ordering and its influence on the microwave dielectric properties have been observed in La-/K-substituted BZT ceramics [32]. An increasing transformation from 1:2 to 1:1 ordering has been observed in $\text{Ba}_{1-x}\text{La}_x(\text{Zn}_{(1+x)/3}\text{Ta}_{(2-x)/3})\text{O}_3$ (BLZT) ceramics with increasing La content in the BZT lattice. In $\text{Ba}_{1-x}\text{K}_x(\text{Zn}_{(1-x)/3}\text{Ta}_{(2+x)/3})\text{O}_3$ (BKZT) ceramics, on the other hand, a monotonous decrease in 1:2 ordering has been observed with increasing K content. The 1:2 ordered domains of BLZT ceramics first shrink in size with increasing La content and then transform into 1:1 ordered domain, and the sizes of these new domains increase with increase in La content. The quality factor, subsequently, decreases at lower La content for BLZT ceramics due to reduced 1:2 ordering, but a subsequent increase-then-decrease behavior in Q has been attributed to factors other than long-range ordering. A lattice super structure caused by hexagonal ordering and its influence on the quality factor was observed

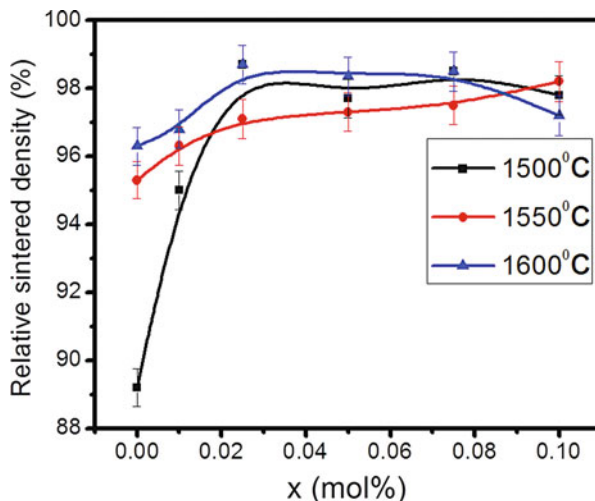
in $\text{Ba}(\text{Zn}_{1/3}\text{Ta}_{2/3})\text{O}_3$ - $(\text{Sr},\text{Ba})(\text{Ga}_{1/2}\text{Ta}_{1/2})\text{O}_3$ ceramics [33]. A significant enhancement in the Q value has been observed in $\text{Ba}(\text{Zn}_{1/3}\text{Ta}_{2/3})\text{O}_3$ - $\text{Sr}(\text{Ga}_{1/2}\text{Ta}_{1/2})\text{O}_3$ ceramics containing 5 mol% $\text{Sr}(\text{Ga}_{1/2}\text{Ta}_{1/2})\text{O}_3$. A further increase in Q has been achieved when 75% of the Sr in $\text{Sr}(\text{Ga}_{1/2}\text{Ta}_{1/2})\text{O}_3$ is replaced by Ba in $\text{Ba}(\text{Zn}_{1/3}\text{Ta}_{2/3})\text{O}_3$ - $\text{Sr}(\text{Ga}_{1/2}\text{Ta}_{1/2})\text{O}_3$ ceramics. Ordering of the B-site cations in $0.95\text{BaZn}_{1/3}\text{Ta}_{2/3}\text{O}_3$ - $0.05\text{SrGa}_{1/2}\text{Ta}_{1/2}\text{O}_3$ (BZT-SGT) ceramics has been investigated [34]. XRD patterns from samples sintered at $1550^\circ\text{C}/2\text{ h}$ with a subsequent annealing and quenching in between 1400°C and 1600°C revealed an order-disorder phase transition $\sim 1500^\circ\text{C}$. Samples heat-treated at temperature $\geq 1500^\circ\text{C}$ (including as sintered samples, $1525^\circ\text{C}/2\text{ h}$) exhibited short-range 1:2 ordering along all $\langle 111 \rangle$ directions resulting in an average short-range face-centered cubic structure. Samples annealed and quenched from temperature below 1500°C showed 1:2 ordering. TEM data revealed a microstructure consisting of 1:2 small ordered domains in the center of all grains. With every second grain exhibited a concentric shell composed of an ordered single domain, containing elongated translational but not orientational domains [34]. A significant enhancement in unloaded quality factors $Q = 54,000$ to $78,000$ at 2 GHz was reported after annealing the samples for 24 h.

In this section, the structure-property correlations of BZT will be elaborated on the results of substitution of donor ions, La^{3+} in the A site and Ga^{3+} in the B site of BZT lattice. Alio-valent substitution in A site is expected to compensate for the local charges and hence influence the degree of ordering in the system. Ga ions in the B site of BZT lattice is known to improve the sinterability and quality factor of BZT [18]. Modifications in the degree of ordering and sinterability of the system are known to be related to high Q . Substitution of smaller ions (La in A site and Ga in B site) may lead to nonlinear changes in the dielectric constant and τ_f . Summary on the effect of specific site doping in $\text{Ba}_{1-x}\text{La}_x(\text{Zn}_{(1-x-2y)/3}\text{Ta}_{(2-x-y)/3}\text{Ga}_y)\text{O}_3$ (BLZTG) ceramics ($x, y = 0, 0.01, 0.025, 0.05, 0.075, 0.1$) will be discussed in this section.

Densification Behavior

Rate of densification of BZT is improved in the presence of La and Ga ions even at a lower temperature of 1500°C . Fig. 12 shows the effect of La and Ga ions in the lattice on the densification behavior of BZT for different sintering temperatures. At lower sintering temperature (1500°C), pure BZT gets densified up to 89% of TD. When $x = 0.01$, densification rapidly increases, and a maximum of 95% of TD has been achieved. Ninety-eight percent of TD has been achieved when $x = 0.025$, and thereafter it remains almost constant with further addition of La and Ga. The variation in density is marginal with increase in sintering temperature. Addition of Ga_2O_3 to BZT has enhanced the relative density, and a maximum density of 96% of TD has been achieved after sintering at 1600°C by J.-I. Yang et al. [18]. Improved densification in $\text{BZT}+x\text{Ga}_2\text{O}_3$ has been attributed to the grain growth due to presence of Ga ions. Higher rate of densification at lower temperature (1500°C) in BLZTG could be attributed to the increased ionic mobility due to the presence of La ions in the "A" site of perovskite lattice and enhanced grain growth due to Ga ions in the B site.

Fig. 12 Variation of relative sintered density as a function of composition in $\text{Ba}_{1-x}\text{La}_x(\text{Zn}_{(1+x-2y)/3}\text{Ta}_{(2-x-y)/3}\text{Ga}_y)\text{O}_3$



Microstructural Analysis

Dielectric loss properties depend on several factors including density, microstructure, secondary phase, and cation ordering. Hence microstructure of BLZTG ceramics has been studied to investigate the variation in density with increasing concentration of La and Ga ions. Fig. 13 shows the microstructure of $\text{Ba}_{1-x}\text{La}_x(\text{Zn}_{(1+x-2y)/3}\text{Ta}_{(2-x-y)/3}\text{Ga}_y)\text{O}_3$ ($x, y = 0, 0.01, 0.025, 0.05, 0.075, 0.1$) sintered at 1550 °C. In pure BZT, elongated grains with an average grain size of 4.5 μm have been seen. When $x, y = 0.01$, elongated grains (average grain size of 13 μm) and small equiaxed grains (average grain size of 2 μm) coexisted. With further increase in concentration, morphology of the grains gradually changes, and cuboidal grains with an average grain size of 11 μm have been observed for $x, y = 0.075$. Grain morphology and size remain almost the same for $x, y = 0.1$. It can be clearly seen from the microstructures that grain growth is enhanced, which is in accordance with the increase in density with La and Ga addition. Grain growth phenomenon has also been observed by J.-I. Yang et al. [18] in BZT with Ga_2O_3 as additive, and a maximum average grain size of 10 μm has been seen in samples with 1 mol% addition of Ga_2O_3 . Pure BZT without any hexagonal superstructure is reported to have a homogenous microstructure [35]. High-temperature sintering and annealing of BZT led to the formation of zinc-deficient secondary phases which is reflected by the presence of anisotropic grains in pure BZT. This is in accordance with the microstructure obtained by Tolmer and Desgardin in which the presence of hexagonal zinc-deficient phase led to the formation of anisotropic grains [36]. The changes in the grain morphology with increasing concentration of dopants could be attributed either to the presence of secondary phases or change in the crystal structure. Since the changes in grain morphology in pure BZT and in BLZTG systems were found to be closely related to the presence of secondary phase and the crystal structure, the samples were characterized by XRD. Substitution of La

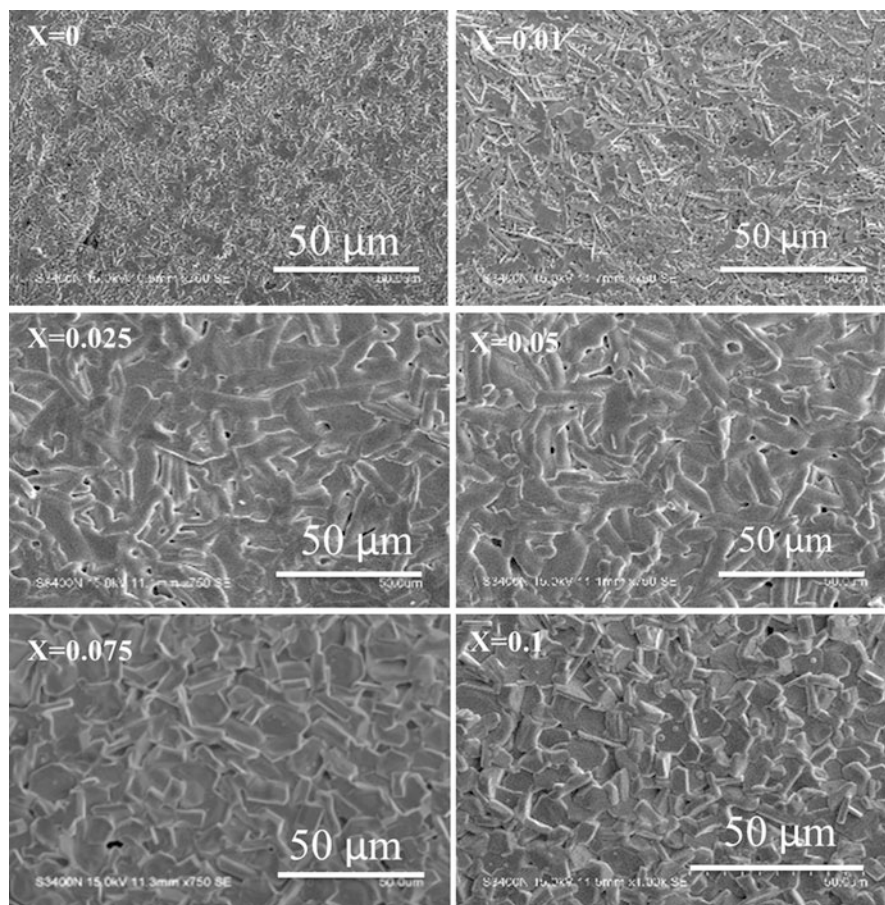


Fig. 13 Microstructure of $\text{Ba}_{1-x}\text{La}_x (\text{Zn}_{(1+x-2y)/3} \text{Ta}_{(2-x-y)/3} \text{Ga}_y)\text{O}_3$ ($x/y = 0$ to 0.1 mol%) samples sintered at 1550 °C

ion in the A site of ABO_3 lattice is known to create changes in the ordering of B-site ions [37].

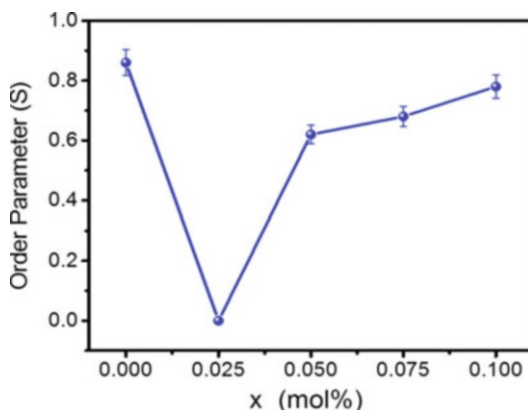
Investigation of Crystal Structure and Ordering by XRD and Raman Spectroscopy

Crystal structure and changes in ordering, as examined by X-ray diffraction pattern, reveal that the intensities and peak positions of fundamental reflections in BZT and BLZTG systems remain identical, whereas there is a change in the superlattice reflections. The variation in lattice parameter and order parameter with increasing concentrations of La and Ga is shown in Table 3 and Fig. 14, respectively. The lattice parameter values of pure BZT were well in agreement with the values reported in literature [38]. Increasing concentration of La and Ga in BLZTG system leads to

Table 3 Summary of the lattice parameters of $\text{Ba}_{1-x}\text{La}_x(\text{Zn}_{(1+x-2y)/3}\text{Ta}_{(2-x-y)/3}\text{Ga}_y)\text{O}_3$

x/y (mol%)	a (Å)	c (Å)
0	5.7805	7.0783
0.01	5.7821	7.0751
0.025	5.7754	7.0694
0.05	4.7269	–
0.075	4.6784	–
0.1	4.6452	–

Fig. 14 Variation of order parameter in BLZTG ceramics as a function of composition (x)



change in crystal structure from hexagonal to cubic, and hence for $x > 0.025$, the lattice parameters were given for cubic system. The expansion of c-axis in hexagonal structure of BZT is associated with ordering of B-site ions. Pure BZT and BLZTG ($x, y = 0.01, 0.025$) were indexed based on hexagonal unit cell. Presence of Ga ions in B site did not permit the expansion in c-axis thus hindering the ordering of Zn-Ta-Ta ions in BLZTG system. Superlattice reflections corresponding to B-site ordering in pure BZT ($(100)_h$ and $(101)_h$) begin to disappear with the addition of La and Ga ions. When $x = 0.05$, a new set of superlattice reflections corresponding to 1:1 ordering begins to evolve, and the unit cell is indexed based on cubic system. The ordering parameter corresponding to 1:1 ordering is calculated based on the integrated intensity ratio of I_{111}/I_{220} [37]. The 1:1 ordering gets evolved at $x = 0.05$, but there is a marginal increase in the order parameter value for higher concentrations of La and Ga. It has been observed that 1:2 ordering in BLZT is gradually replaced by 1:1 ordering and a maximum order parameter (corresponding to 1:1 ordering) value of 0.84 has been observed. In a certain composition range of BLZT, there is a coexistence of 1:1 and 1:2 ordering, and order parameter tends to increase with increasing concentration of La in BLZT ceramics [37]. But in case of BLZTG ceramics, the marginal increase in order parameter value with increasing concentrations of La and Ga could be attributed to the presence of Ga ions in the B site. Ordering is favored in compound with higher valency difference in B-site

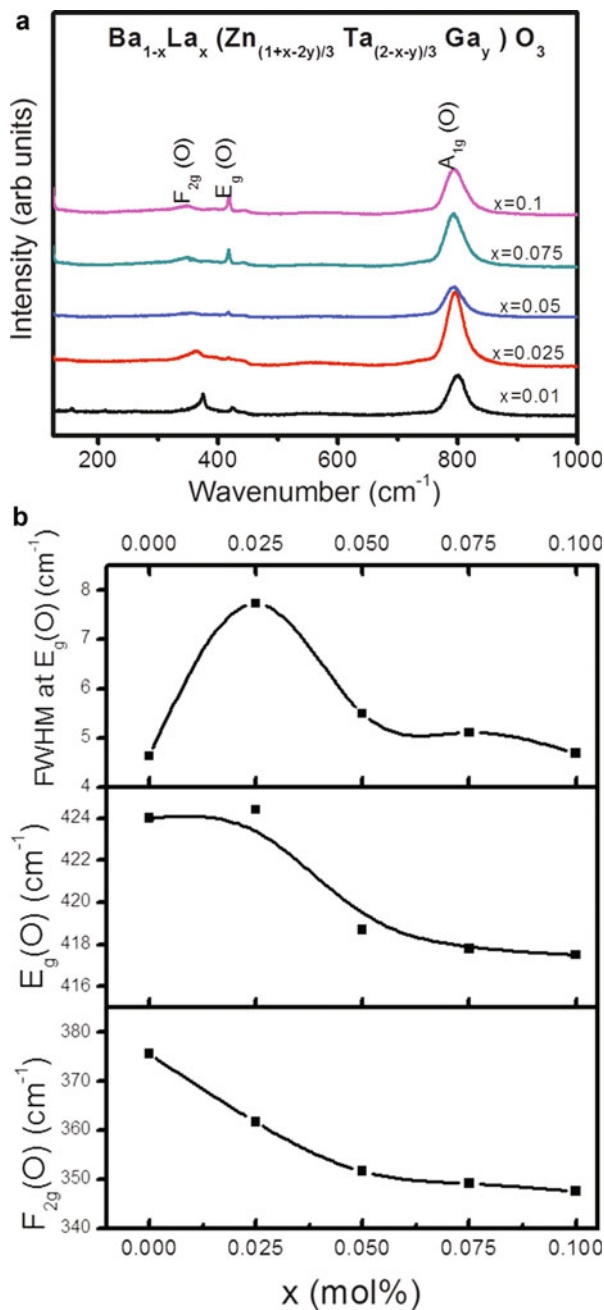
ions involved. Ga^{3+} ions in B site prevents the growth of 1:1 ordered domains formed due to the presence of La^{3+} in A site.

The influence of La and Ga ions in the local structure of BZT is studied using Raman spectroscopy (Fig. 15). The peaks were indexed based on ref. [39]. The peaks corresponding to the torsional modes of vibration of B-site atoms (375 cm^{-1} and 424 cm^{-1}) broaden and shift with increasing concentration of La and Ga. Peak at 375 cm^{-1} tends to broaden and gradually shifts to 347.5 cm^{-1} for $x = 0.1$. Peak at 424 cm^{-1} mode tends to broaden till $x = 0.025$, and for $x \geq 0.05$, the peak shifts to 418 cm^{-1} and then sharpens again. FWHM of peak at 424 cm^{-1} remains minimum for pure BZT due to the presence of 1:2 ordering. The broadening of peak (as reflected by increase in FWHM) for $x = 0.025$ could be attributed to the loss in B-site ordering which is in accordance with the X-ray diffraction pattern. FWHM tends to decrease for $x = 0.05$, which could be due to the onset of 1:1 ordering. There is a marginal variation in FWHM with further increase in La and Ga concentration. The results are in agreement with the order parameter calculated from X-ray diffraction pattern. The broadening and peak shifting behavior of BLZTG ceramics are in accordance with the results obtained by Cheng-Chang Lee et al. [37]. La substitution in A site also influences the local structure leading to changes in the torsional modes of vibration of B-site atoms. E_g (O) mode in BLZT originally broadens for the composition range wherein the B-site ordering is completely lost. With increasing concentration (as 1:1 ordering evolves), the peak shifts from 424 cm^{-1} to 414 cm^{-1} .

Dielectric Properties

The dielectric properties of BLZTG system were evaluated to study its influence on changes in ordering of the system. Quality factor values of the samples are presented in Fig. 16a. It can be seen that samples sintered at $1500\text{ }^\circ\text{C}$ and $1550\text{ }^\circ\text{C}$ tend to increase with increasing x up to a concentration of $x = 0.025$. The values decrease with increasing concentration of La and Ga. For samples sintered at $1600\text{ }^\circ\text{C}$, pure BZT samples tend to show maximum value. $Q \times f$ values decrease for $x = 0.01$ and then increase for $x = 0.025$. With further increase in concentration (up to $x = 0.1$), quality factor value decreases. Relative density of pure BZT samples sintered at $1500\text{ }^\circ\text{C}$ and $1550\text{ }^\circ\text{C}$ for 2 h was poor in comparison with sample containing La and Ga. Hence low $Q \times f$ values of pure BZT could be attributed to poor densification. The increase in values (for $x = 0.01$ and 0.025) of $Q \times f$ in spite of decrease in ordering in the system could be attributed to better densification and grain growth in comparison with pure BZT. Pure BZT sample shows a maximum $Q \times f$ value of $\sim 75000\text{GHz}$ when sintered at $1600\text{ }^\circ\text{C}$. The $Q \times f$ values of pure BZT reported here were less due to the fact that no precautions were taken to minimize zinc volatilization during sintering. Zinc volatilization tends to increase with increasing sintering temperature [26]. The value suddenly drops to $\sim 35000\text{GHz}$ for $x = 0.01$, which could be due to the disruption of ordering in the system. The $Q \times f$ value for $x = 0.025$ increases in spite of disruption in ordering. The reason could be attributed to increase in concentration of Ga ions in the B site. For $x \geq 0.05$,

Fig. 15 (a) Raman spectrum of BLZTG ($x = 0$ to 0.1 mol %) samples sintered at 1550 °C. (b) Variation of Raman modes of BLZTG ($x = 0$ to 0.1 mol%) as a function of composition



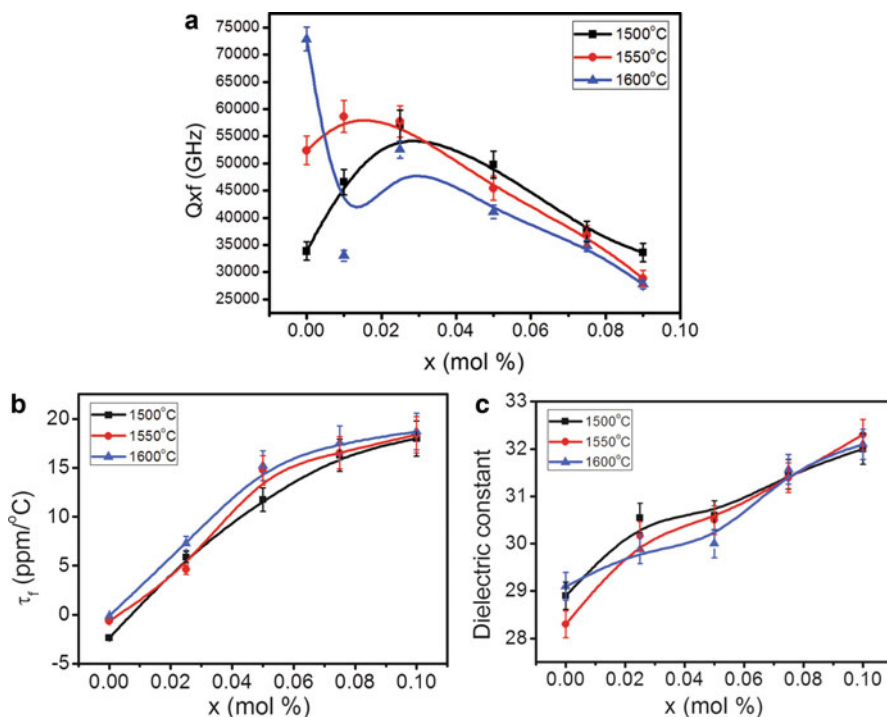


Fig. 16 (a) Variation of quality factor ($Q \times f$) as a function of composition in BLZTG samples for different sintering temperatures. (b) Variation of τ_f as a function of composition of BLZTG ($x = 0$ to 0.1 mol%) samples for different sintering temperatures. (c) Variation of dielectric constant as a function of composition of BLZTG ($x = 0$ to 0.1 mol%) samples for different sintering temperatures

$Q \times f$ values decrease for samples sintered at all temperatures. The reason for decrease in the values could be ascribed to the presence of 1:1 ordering.

Temperature coefficient of resonance frequency (τ_f) of dielectric mainly depends on temperature coefficient of relative permittivity (τ_ϵ), which is influenced by ordering, octahedral tilting, and ionic polarizability. Since there is a change in ordering as well as the dielectric permittivity, τ_f of BLZTG increases with increasing concentration of dopants (as shown in Fig. 16b). The dielectric constant value of BLZTG system tends to increase with increasing concentration of dopants (as shown in Fig. 16c). Nonlinear change of ϵ_r versus composition was observed for the BLZTG complex perovskites. Increase in the dielectric constant could be attributed to higher ionic polarizability of La cation. ϵ_r of $A(B'B'')O_3 - A'(B_1'B_1'')O_3$ shows a linear change with changes in composition when the A-site ions are the same ($A = A'$). Since the A-site ions are different ($A = Ba, A' = La$), ϵ_r change nonlinearly with composition [40].

It can be seen from the investigation of specific site doping to BZT that combination of densification and good dielectric properties of BZT system is quite a challenging task. Also, there are quite a few numbers of dopants which are capable of yielding good density without the formation of secondary phases. The importance of symmetry on dielectric performance has been elaborated for many important electro-ceramic systems. BZT can be recognized as one of the complex systems that is quite sensitive to the processing conditions to achieve good density and dielectric properties.

Fabrication of RF Window

It has been stated in section “[Material Requirements](#)” that the ability to braze the ceramic to metal frame is one of the important requirements in fabrication of RF window. The factors that impose challenges in preparing a leakproof joint between the metal and ceramics include poor wetting capability of ceramics, dissimilarities in the physical properties of metal and ceramic, enhanced thermal stability of ceramics compared to metals, etc. Brazing is one of the effective processes for joining of metal and ceramics [41]. It is usually done after metallization of the ceramic surfaces. There are numerous studies on metallization of the most common RF window ceramic (Al_2O_3) followed by brazing. Metallization is done usually by moly-manganese process in which the ceramic surface is layered by thin metallizing coating followed by sintering at suitable temperature to ensure a strong and adhered metal layer to facilitate joining of the ceramic to large metal assemblies [42]. Liquid phase is formed at the interphase during high-temperature heat treatment which fills the pores to ensure a sound joint between the metal and ceramic. The adhesion of ceramic and metal in moly-manganese process is brought about by the subsequent progression of the following processes: reduction and dissolution process in reducing sintering atmosphere, liquid phase formation, and crystallization from the melt [43]. The metallized ceramic is then brazed with the metal piece.

Among various methods active alloy brazing is considered to be the most economical and efficient technique in joining metal and ceramic [44]. In case of RF window, fabrication of metal-ceramic joint is the most critical process as the window is expected to act as a vacuum barrier and hence has to be UHV compatible. In this brazing procedure, the active metal in the filler gets migrated to the surface of ceramic and forms intermetallic compounds to establish metal-ceramic interface. The feasibility of active alloy brazing BZT with Ti6Al4V alloy using different filler materials has been investigated, and primary leak test results of brazed joints have been reported in this section. The details of the tests carried out are described below.

Ag-Cu alloy with a few percent of Ti (Cusil-ABA) is one of the widely used fillers due to its ability to impart good wettability at appropriate temperature with degrading Ti6Al4V alloy. The filler material is placed in the form of foil between the ceramic and Ti6Al4V frame. A gap of 50 μm is maintained during brazing, and the entire assembly is placed in vacuum furnace and heat-treated at various

Table 4 Leak test results of brazing using (a) Cusil-ABA filler alloy and (b) Palladium based filler alloy

Filler	Sample dimensions	Characterization	Remarks
(a)			
Cusil-ABA	Circular disc (25 mm dia) – 1	Visible leak test using IPA	Pass
	Circular disc (10 mm dia) – 1		Fail
	Square (15 mm × 15 mm) – 1	Leak test using He (1 bar gauge pressure)	Fail
(b)			
Ag-58.5%, Cu 31.5%, Pd-10% in wire form (T – 850 °C)	Circular disc (25 mm dia) – 1	Visible leak test using IPA	Fail
	Circular disc (10 mm dia) – 1		Fail
	Square (15 mm × 15 mm) – 1	Leak test using He (1 bar gauge pressure)	Fail

temperatures based on the melting point of the filler alloys. Careful attention was paid to the heating schedule during brazing with Cusil-ABA.

The brazed samples were then subjected to visible leak test using isopropyl alcohol and leak tested under pressure using He (1 bar gauge pressure) to check the integrity of the joint. The results of the leak test are summarized in Table 4. Palladium-based filler alloy is taken in the form of wire, and an allowance of 50 μm is maintained during brazing. The alloy had a melting temperature of 850 °C. The samples upon brazing at 890 °C showed small cracks at the peripheries, and so samples failed during leak test under pressure even at less than 1 bar pressure range. TiCuNi filler alloy in the form of foil (50 μm thick) is used for brazing BZT with Ti6Al4V frame. The samples could not pass the leak test under pressure of 1 bar. In order to improve the integrity of the joints, the samples were re-brazed using Cusil-ABA alloy. The samples before and after re-brazing are shown in Fig. 17a–d, respectively. Components were pressurized at 1 bar pressure using helium gas. Main leakage was found at edges and also on broad side where clearance was large around 0.2 mm approximately (before re-brazing). Re-brazing the samples improved the integrity at the ceramic-joint interface. Leak at the edges could be addressed by fabricating ceramic and frame slots with rounded corners. This also enables easy placing of the braze filler alloy at the joints. Studies on brazing using other filler alloys and metallization followed by brazing can be done to improve the quality of the brazed joint.

Conclusions

One of the factors that constrains the effective use of RF power to heat up the plasma in fusion reactor is the performance of RF window. The critical demands for the window from materials perspective have been summarized, and an overview of properties that is required for satisfactory functioning of the RF window assembly

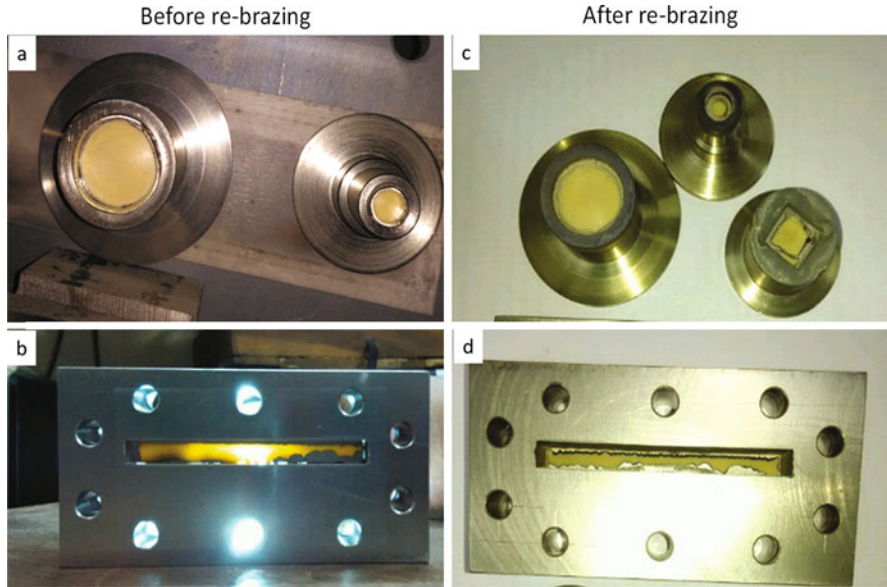


Fig. 17 BZT samples (a, b) before re-brazing and (c, d) after re-brazing

has been discussed briefly. Based on the requirements for the application, the advantages and disadvantages of the candidate materials for the window application are discussed. Due to the attractive dielectric properties of BZT, feasibility studies on using this material for RF window application have been carried out. The effect of various processing parameters such as particle size and distribution, sintering temperature, dwell time at peak sintering temperature, flux addition and its impact on surface finish, and colloidal processing on densification of BZT had been described. Investigation on microwave sintering and the effect of additives added to improve the microwave coupling on densification and RF characteristics has been reported. Specific site doping and its effect on the ordering in the system have been explained using BLZTG system. Efforts to braze the BZT window sections to the metal frame and some preliminary studies on the active alloy brazing have been presented.

References

1. Wootton AJ, Wiley JC, Edmonds PH, Ross DW (1997) Compact tokamak reactors. *Nucl Fusion* 37(7):927
2. Goldston RJ (1984) Energy confinement scaling in Tokamaks: some implications of recent experiments with Ohmic and strong auxiliary heating. *Plasma Phys Control Fusion* 26(1A):87–103
3. Sharma PK, Rao SL, Ramella KK, Bora D (2008) Design, fabrication and testing of UHV compatible high power RF devices for lower hybrid current drive system on SST-1 tokamak. *Fusion Eng Des* 83(4):601–605
4. Cummings KA, Risbud SH (2000) Dielectric materials for window applications. *J Phys Chem Solids* 61(4):551–560

5. Saito Y, Michizono S, Anami S, Kobayashi S (1993) Surface flashover on alumina rf windows for high-power use. *IEEE Trans Electr Insul* 28(4):566–573
6. Pimenta JS, Buschinelli AJA, do Nascimento RM, Martinelli AE, Rimmel J (2013) Brazing of zirconia to titanium using Ag-Cu and Au-Ni filler alloys. *Soldag Insp (Sao Paulo)* 18(4):349–357
7. Pisharody M, Barnes P, Chojnacki E, Durand R, Hays T, Kaplan R, Kirchgessner J, Reilly J et al (1996) High power window tests on a 500 MHz planar waveguide window for the CESR upgrade. *Proc Part Accel Conf* 3:1720–1722
8. Kesari V, Singh A, Seshadri R, Kamath S (2016) Boron Nitride and Sapphire windows for 95-GHz Gaussian RF beam. *IEEE Trans Electron Devices* 63(8):1–5
9. Neubauer M, Rimmer RA (1991) High power co-axial srf coupler. WE5PFP044. Proceedings of PAC09, Vancouver, BC, Canada, pp 2095–2097
10. Matsumoto H, Tamura H, Wakino K (1991) Ba(Mg,Ta)O₃-BaSnO₃ high-Q dielectric resonator. *Jpn J Appl Phys* 30(9B):2347–2349
11. Nomura S, Toyama K, Kaneta K (1982) Ba(Mg_{1/3} Ta_{2/3})O₃ ceramics with temperature-stable high dielectric constant and low microwave loss. *Jpn J Appl Phys* 21(10):624–626
12. Nomura S, Kaneta K (1984) Ba(Mn_{1/3} Ta_{2/3})O₃ ceramic with ultra-low loss at microwave frequency. *Jpn J Appl Phys* 23(4R):507–508
13. Chen MY, Chia CT, Lin IN, Lin LJ, Ahn CW, Nahm S (2006) Microwave properties of Ba(Mg_{1/3}Ta_{2/3})O₃, Ba(Mg_{1/3}Nb_{2/3})O₃ and Ba(Co_{1/3}Nb_{2/3})O₃ ceramics revealed by Raman scattering. *J Eur Ceram Soc* 26(10–11):1965–1968
14. Desu SB, O'Bryan HM (1985) Microwave loss quality of BaZn_{1/3}Ta_{2/3}O₃ ceramics. *J Solid State Chem* 68(10):546–551
15. Moulson AJ, Herbert JM (1990) Dielectrics and insulators. In: *Electroceramics*. Chapman and Hall, London, pp 300–310
16. Tamura H, Konoike T, Sakabe Y, Wakino K (2006) Improved high-Q dielectric resonator with complex perovskite structure. *J Am Ceram Soc* 67(4):59–61
17. Roulland F, Allainmat G, Pollet M, Marinel S (2005) Low temperature sintering of the binary complex perovskite oxides xBa(Zn_{1/3}Ta_{2/3})O₃+(1-x)Ba (Mg_{1/3}Ta_{2/3})O₃. *J Eur Ceram Soc* 25(12):2763–2768
18. Yang J-I, Nahm S, Choi C-H, Lee H-J, Kim J-C, Park H-M (2002) Effect of Ga₂O₃ on microstructure and microwave dielectric properties of Ba(Zn_{1/3}Ta_{2/3})O₃ ceramics. *Jpn J Appl Phys* 41(Part 1, No. 2A):702–706
19. Jeong Y-H, Kim M-H, Nahm S, Lee W-S, Yoo M-J, Kang N-K, Lee H-J (2005) Effect of Ta₂O₅ on microstructure and microwave dielectric properties of Ba(Zn_{1/3}Ta_{2/3})O₃ ceramic. *Jpn J Appl Phys* 44(2):956–960
20. Varma MR, Kataria ND (2007) Effect of dopants on the low temperature microwave dielectric properties of Ba(Zn_{1/3}Ta_{2/3})O₃ ceramics. *J Mater Sci Mater Electron* 18(4):441–446
21. Lee CJ, Pezzotti G, Kang SH, Kim DJ, Hong KS (2006) Quantitative analysis of lattice distortion in Ba(Zn_{1/3}Ta_{2/3})O₃ microwave dielectric ceramics with added B₂O₃ using Raman spectroscopy. *J Eur Ceram Soc* 26(8):1385–1391
22. Kim JS, Kim JW, Cheon CI, Kim YS, Nahm S, Byun JD (2001) Effect of chemical element doping and sintering atmosphere on the microwave dielectric properties of barium zinc tantalates. *J Eur Ceram Soc* 21(15):2599–2604
23. Varma MR, Biju S, Sebastian MT (2006) Preparation of phase pure Ba(Zn_{1/3}Ta_{2/3})O₃ nanopowders for microwave dielectric resonator applications. *J Eur Ceram Soc* 26(10–11):1903–1907
24. Manivannan S, Joseph A, Sharma PK, Raju KCJ, Das D (2017) Effect of colloidal processing on densification and dielectric properties of Ba(Zn_{1/3}Ta_{2/3})O₃ ceramics. *Ceram Int* 43(15):12658–12666
25. Yang J-I, Nahm S, Yoon S-J, Park H-M, Lee H-J (2004) Structural variation and microwave dielectric properties of ZrO₂ added Ba(Zn_{1/3}Ta_{2/3})O₃ ceramics. *Jpn J Appl Phys* 43(1):211–214
26. Bieringer M, Moussa SM, Noailles LD, Burrows A, Kiely CJ, Rosseinsky MJ, Ibberson RM (2003) Cation ordering, domain growth, and zinc loss in the microwave dielectric oxide Ba₃ZnTa₂O₉. *Chem Mater* 15(2):586–597

27. Tamura H, Sagala DA, Wakino K (1986) Lattice vibrations of $\text{Ba}(\text{Zn}_{1/3}\text{Ta}_{2/3})\text{O}_3$ crystal with ordered perovskite structure. *Jpn J Appl Phys* 25(Part 1, No. 6):787–791
28. Surendran KP, Sebastian MT, Mohanan P, Moreira RL, Dias A (2005) Effect of non-stoichiometry on the structure and microwave dielectric properties of $\text{Ba}(\text{Mg}_{0.33}\text{Ta}_{0.67})\text{O}_3$. *Chem Mater* 17(1):142–151
29. Wada K, Kakimoto K, Ohsato H (2004) Anisotropic microwave dielectric properties of textured $\text{Ba}_4\text{Sm}_{9.33}\text{Ti}_{18}\text{O}_{54}$ ceramics. *Key Eng Mater* 269:207–210
30. Dick GJ, Santiago DG, Wang RT (1994) Temperature compensated sapphire resonator for ultra-stable oscillator capability at temperatures above 77 kelvin. *Proc IEEE 48th Annu Symp Freq Control* 42:421–432
31. Alford NM, Breeze J, Penn SJ, Poole M (2000) Layered Al_2O_3 - TiO_2 composite dielectric resonators with tuneable temperature coefficient for microwave applications. *IEE Proc Sci Meas Technol* 147(6):269–273
32. Lee C-C, Chou C-C, Tsai D-S (1997) Effect of La/K A-site substitutions on the ordering of $\text{Ba}(\text{Zn}_{1/3}\text{Ta}_{2/3})\text{O}_3$. *J Am Ceram Soc* 80(11):2885–2890
33. Kageyama K (1992) Crystal structure and microwave dielectric properties of $\text{Ba}(\text{Zn}_{1/3}\text{Ta}_{2/3})_{0.3}$ - $(\text{Sr},\text{Ba})(\text{Ga}_{1/2}\text{Ta}_{1/2})_{0.3}$ ceramics. *J Am Ceram Soc* 75(7):1767–1771
34. Reaney IM, Wise PL, Qazi I, Miller CA, Price TJ, Cannell DS, Iddles DM, Rosseinsky MJ, Moussa SM, Bieringer M, Noailles LD, Ibberson RM (2003) Ordering and quality factor in $0.95\text{BaZn}_{1/3}\text{Ta}_{2/3}\text{O}_3$ - $0.05\text{SrGa}_{1/2}\text{Ta}_{1/2}\text{O}_3$ production resonators. *J Eur Ceram Soc* 23:3021–3034
35. Koga E, Yamagishi Y, Moriwake H, Kakimoto K, Ohsato H (2006) Large Q factor variation within dense, highly ordered $\text{Ba}(\text{Zn}_{1/3}\text{Ta}_{2/3})\text{O}_3$ system. *J Eur Ceram Soc* 26(10–11):1961–1964
36. Tolmer V, Desgardin G (1997) Low-temperature sintering and influence of the process on the dielectric properties of $\text{Ba}(\text{Zn}_{1/3}\text{Ta}_{2/3})\text{O}_3$. *J Am Ceram Soc* 80(8):1981–1991
37. Lee C-C, Chou C-C, Tsai D-S (1998) Variation in the ordering of $\text{Ba}(\text{Zn}_{1/3}\text{Ta}_{2/3})\text{O}_3$ with A-site substitutions. *Ferroelectrics* 206(1):293–305
38. Galasso F, Pyle J (1963) Ordering in compounds of the $\text{A}(\text{B}'_{0.33}\text{Ta}_{0.67})\text{O}_3$ type. *Inorg Chem* 2(3):482–484
39. Marinel S, Roulland F, d'Astorg S, Chaouchi A (2007) Effects of the sintering atmosphere on the $\text{BaZn}_{1/3}\text{Ta}_{2/3}\text{O}_3$ based Cu multilayer ceramic capacitors. *J Eur Ceram Soc* 27(13–15):3605–3608
40. Nomura S, Uchino K (1983) Recent applications of PMN-based electrostrictors. *Ferroelectrics* 50(1):197–202
41. John AF (1999) Ceramic brazing. *Mater World* 7(11):686–688
42. Pimenta JS, Buschinelli AJA, do Nascimento RM, Martinelli AE, Rimmel J (2010) Joining of zirconia mechanically metallized with titanium. *Cerâmica* 56:212–221
43. Twentyman ME, Popper P (1975) High-temperature metallizing. *J Mater Sci* 10(5):791–798
44. Jacobson DM, Humpston G (2005) Principles of brazing. ASM International, Materials Park

Part V

Ceramics, CMCs, and PMCs for Aeronautics and Space Applications



SiC-Based Composites Through Liquid Infiltration Routes

22

Suresh Kumar, Ashok Ranjan, L. M. Manocha, and N. Eswara Prasad

Contents

Introduction	832
Reinforcements	834
Carbon Fiber	834
Carbon Fabric	835
Woven Preform	836
Needle-Punch Preform	836
Interface and Interphase	837
General Properties of C/SiC Composites	839
PIP-Based C/SiC Composite Fabrication	839
Important Process Parameters	842
Mechanical Characterization	843
Properties of the PIP-Based C/SiC Composites	844
Properties of M40 J Fiber-Based UD C/SiC Composites	848
PIP-Based 2D C/SiC Composites	850
Thermal Shock Properties of 2D C/SiC Composites	852
LSI-Based C/SiC Composite Fabrication	853
LSI Process	853
Properties of LSI-Based C/SiC Composites	859
Mechanical Properties of LSI-Based C/SiC Composite	860
Thermal Properties of LSI-Based C/SiC Composites	863
Oxidative and Erosive Behavior of LSI-Based C/SiC Composites	867
Typical Applications of the C/SiC Composites	872
Summary and Conclusions	872
References	873

S. Kumar (✉) · A. Ranjan · L. M. Manocha · N. E. Prasad
Defence Materials and Stores Research and Development Establishment, DRDO, Kanpur, India
e-mail: skumar@dmsrde.drdo.in; drashokranjan25@gmail.com; manocha52@rediffmail.com

Abstract

Carbon fiber-reinforced silicon carbide matrix composites (called C/SiC or C/C-SiC) represent a relatively new class of structural materials. These composites have emerged as one of the most promising materials for high-temperature applications in defense and aerospace sectors. They are fabricated via chemical vapor infiltration (CVI), polymer impregnation and pyrolysis (PIP), and liquid silicon infiltration (LSI) processing routes. Several new manufacturing processes have been developed during the last few years based on short fiber reinforcements and inexpensive precursor polymer, respectively. These composites possess high mass-specific properties, structural and dimensional stability at high temperature, low coefficient of thermal expansion, high thermal conductivity, and desirable oxidation resistance. These properties have gained increasing importance of the C/SiC composites and thus make them as most preferred materials for the aerospace, defense, and civil/industrial applications like thrust vectoring control vanes, nozzles, brake disks and pads, clutches, furnace charging devices, etc. This chapter presents the processing and characterization of the C/SiC composite fabricated by liquid infiltration routes, viz., PIP and LSI. Typical properties of the C/SiC composites like mechanical, thermal, and ablative are presented. Few established and potential application of these composites are discussed briefly.

Keywords

Ceramics · Composites · C/SiC composites · PIP · LSI · Mechanical properties

Introduction

Since the 1970s, carbon fiber reinforcement-based ceramic composites have been developed as lightweight structures for aerospace applications. These composites are generally termed as ceramic matrix composites (CMCs). Carbon fiber-reinforced composites had been designed for limited life due to limitation of carbonaceous material under oxidizing environmental conditions which prevail in aerospace and defense products. The most recognized applications of these materials were rocket nozzles, throat inserts, jet-vanes, engine flaps, leading edges of the spacecraft, and brake disks of an aircraft [1–5]. Service duration of these components varies from few seconds (jet-vanes) to several hours (brake disks) under the specified and stringent conditions which call for the stability of the C/SiC composites at the highest thermomechanical loads [1–5]. Considering the oxidation resistance and service time requirement of these composites for the above mentioned applications, several studies were carried out at different leading research laboratories across the world on replacing the carbon matrix by ceramic matrix, by oxidation protection coating on the carbon composite, and by modifying the matrix composition by

adding refractory metals and ceramics [1–5]. Silicon carbide has been considered as an appropriate matrix material for the carbon fiber-reinforced composites due to its high-temperature stability, high oxidation resistance and thermal shock stability, etc. [1–7]. The manufacturing techniques of the carbon composites can be used for the liquid process route-based C/SiC composites without much modification [1–5]. Broadly, the C/SiC composites combine the advantageous properties of the monolithic SiC and high damage tolerance properties of the carbon-carbon composite. However, the mechanisms which cause high damage tolerance are completely different from the polymer-based composites. In the case of the polymer-based composites, the polymer matrices are reinforced with the strong and stiff fibers, whereas in case of the C/SiC composites, the matrix is weak and of low strength and stiffness, but its thermal stability is higher. Fiber loading in the polymer matrix-based composites is much higher and is able to stop the matrix crack without much damage [1–3]. It is also a fact that the bonding between the matrix and fibers is high in case of the polymer matrix-based composites. The stiffness of the polymer matrices and the reinforcing fibers are very different, and the matrix get stressed only slightly; thus energy release rate of a matrix crack is low because of the modest matrix strength.

In case of the ceramic matrix composites, the stiffness of the reinforcing fibers and matrix are in the same order of magnitude [8, 9]. Adequate fiber/matrix bonding results into similar stresses in the matrix as well as in the fibers. The fractured matrix in the CMCs does not sustain against high stress; therefore, the damage tolerance is relatively lower than the monolithic ceramics as the crack of the matrix propagates into the fibers without much energy consumption. While in the case of low fiber/matrix bonding, the matrix is nearly stress-free, and crack of the matrix passes parallel to the fiber axis and thus leads to high fracture toughness. But, very low fiber/matrix bonding leads to shear failure mostly dominated by the de-bonding, and such kind of composites is usually not suitable for structural applications in aerospace or defense sectors where reliability of the composites has to be of the highest order. Instead, the damage-tolerant CMCs are being fabricated by tailored interface [1–3]. The interphase material should be compatible with the fiber as well as matrix and should not react with the fibers.

Similar to the polymer and metal matrix composites, fracture behavior and the structural properties of the CMCs are dominated by their reinforcing fibers. Also, the fibers should have high stiffness and must not degrade at the temperatures where processing is carried out. Carbon fibers are known for their high stiffness and thermal stability under an inert atmosphere. Carbon fibers are commercially available in various forms like tow, fabric, and preforms.

LSI-based C/SiC composites have been developed by various agencies like DLR, NASA, SNECMA, and DRDO for various advanced applications [1–3]. PIP-based C/SiC composites are also being developed by several agencies including those who have developed LSI-based C/SiC composites [1–3, 10–13]. In this chapter, a summary of the work done at different leading agencies would be presented, whereas the work carried out by the authors in India would be covered in details.

Reinforcements

Selection of the reinforcement is very important for fabricating the C/SiC composites for a specific application. There are several grades of the carbon fibers available with the leading manufacturers. Depending on the ultimate structural requirements, the grade of the fiber should be chosen. Processing method of the composite also dictates the requirement of a particular grade of fiber. The following factors should be considered for selecting a specific grade carbon fiber reinforcement for a given application.

- (1) Requirement of thermal and structural properties in the final product
- (2) Processing method
- (3) Ultimate processing temperature
- (4) Shape and size of the final product

Though the basic reinforcement is carbon fiber, for practical use, it can be used in the form of fiber tow, fabric, woven preform needle punch, etc.

Carbon Fiber

Processing temperature of the C/SiC composite varies between 1000 and 1800 °C [1–3, 10, 11]; therefore, the reinforcing fibers must not degrade during the process. The fibers are chosen considering the processing temperature of the composite and the properties required in the final product. Carbon fiber properties vary with the starting precursor of the fiber, the processing method, and the heat treatment temperature. Carbon fiber is commercially available in the form of tows like 1 k (1000 carbon filaments), 3 k (3000 carbon filaments), 6 k (6000 carbon filaments), and 12 k (12,000 carbon filaments). Based on the starting precursor material, the carbon fibers are classified into the following category [3, 14].

- Rayon-based carbon fibers
- PAN-based carbon fibers
- Pitch-based carbon fibers
 - Mesophase pitch-based
 - Isotropic pitch-based
- Gas-phase-grown carbon fibers

Typical properties of the commercially available carbon fibers are listed in Table 1 [3, 14].

For most of the practical use, the carbon fiber is woven into the two directional carbon fabrics or woven to fabricate preforms of 2D, 3D, and 4D. Here “D” means the number of directions of carbon fiber in the preform. From Table 1, it is evident that the T700, T800, and T1000 grade fiber should be used for the products

Table 1 Typical properties of the carbon fibers

Trade name	Density (g/cm ³)	Tensile modulus (GPa)	Elongation (%)	Tensile strength (MPa)	Thermal conductivity Cal/cm s°C	CTE m/m°C
T300	1.76	230	1.5	3530	0.0250	-0.41×10^{-6}
T700S	1.80	230	2.1	4900	0.0224	-0.30×10^{-6}
T800S	1.80	294	2.0	5880	0.0839	-0.56×10^{-6}
T1000G	1.80	294	2.2	6370	0.0765	-0.55×10^{-6}
M40 J	1.77	377	1.2	4410	0.1640	-0.83×10^{-6}
M50J	1.88	475	0.8	4120	0.3720	-1.10×10^{-6}
M60J	1.93	588	0.7	3920	—	—

Table 2 Specifications of the T300-fiber based 8H satin carbon cloth

S. No	Property	8H satin
1	Ends/inch	24 ± 1
2	Picks/inch	24 ± 1
3	Arial density (g/m ²)	380 ± 40
4	Width (nominal)	1 meter
5	Thickness (mm)	0.45 ± 0.05
6	Breaking load for warp (kg/inch)	180 (min)
7	Breaking load for, weft (kg/inch)	180 (min)

experiencing high structural loads, whereas the T300 grade fibers can be used for all other moderately loaded products. M40J, M50J, and M60J fibers have higher thermal conductivity; therefore they should be used where rapid heat dissipation from the composite is a prime requirement. Rayon-based fibers are used for the ablative components, and their thermal conductivity is considered to be the lowest. Fiber tows are recommended to be used for the processing like filament winding and extrusion and also for the preform making greater than 2D.

Carbon Fabric

Carbon fabric cloth is most widely used reinforcement for making bi-directional C/SiC composites due to its ease in processing. The carbon fabric is woven by using an appropriate fiber tow (1K, 3K, etc.) in different patterns like plain weave, twill weave, and satin weave. However, for the C/SiC composite fabrication, satin weave carbon fabric is preferred due to its wrapping ability to any shape. Some typical properties of 3 k, T300 carbon fiber-based 8H satin weave patterned carbon fabric are shown in Table 2. Similarly, properties of the other weave pattern may be obtained from the fabric manufactures.

Woven Preform

Woven preforms are the other common means of using carbon fiber as reinforcement. Carbon fibers are anisotropic where their mechanical and thermal properties are greatly different along their axis and radially [15–18]. Depending on the structural load requirements, a definite fiber volume fraction needs to be maintained in different directions of the composite structure. Bi-directional fiber-reinforced composites are the most basic composites and widely used for the cases where adequate fiber-matrix bonding can be assured. In case of the C/SiC composites, the fiber/matrix bonding is tailored by using an interface in order to make these composites damage-tolerant. In presence of the lower fiber-matrix bonding forces, these composites tend to fail under shear. In order to improve the shear properties of these composites, third direction carbon fibers are introduced. The reinforcing fibers are arranged in required number of directions to develop a multiple directional fibrous object called preform, and the process of their fabrication is called the preforming process. Fiber direction in a preform provides the required strength and modulus in the specified directions. Therefore, the preforms provide near-net shape composite product that meets the directional thermomechanical property requirements in the ultimate structure. Also, they help the composite structure to absorb all the thermal stresses, those that get generated during the processing and often result in a delamination in bi-directional composite structure.

Different shaped preforms are developed depending on the requirement of the product, e.g., in the form of simple cubical blocks for a typical regular shape product, hollow cylinders for fabricating tubes and casings, conical contours for fabricating the typical aerodynamic shapes, surfaces of revolution and near-net shape complex geometries and I-beam product shapes, etc. Their fabrication can be manual, semi-automated, or fully automatic using the multi-axis weaving machines. Triaxial weaving is also well developed where fabrics have multiple layers and delamination can be prevented due to the presence of the Z-direction fibers [19, 20]. There are several other types of preform like 4D, 5D, and 7D. Simple geometries of the commonly used preforms are shown in Fig. 1. However, details of their fabrication can be found elsewhere [19–21].

Needle-Punch Preform

Needle-punched preforms are more homogeneous with respect to the pore cavity size. In case of the 3D, 4D, and 5D preforms, the size of the pore cavities at the crossover point of the carbon fiber tows is much larger. In the case of the needle-punch preforms, such large-sized cavities do not exist. Also, these types of preform are of low cost and have unique features. The preforms are made using the needle-punching technique. Multiple needles are employed with protruded barbs on the lateral sides. The needles move up and down and penetrate the layered materials repeatedly. The barbs on the needles hook some fibers in the layered materials and insert them vertically in descending motion. These third direction fibers provide a

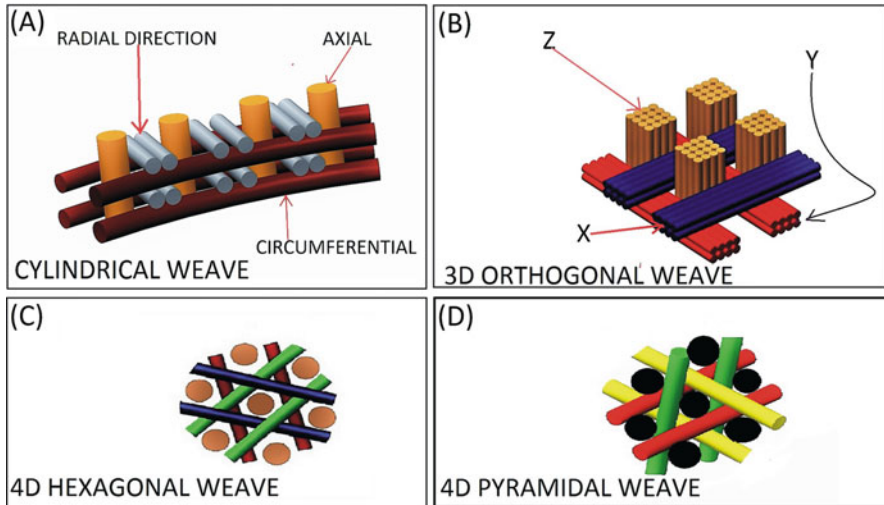


Fig. 1 Typical patterns for multidirectional carbon fiber preforms [3]

reinforcing effect between the layers and improve the delaminating behavior of the bi-directional composites [22–24]. These preforms are suitable for producing small and complex composite parts.

Interface and Interphase

The interface and interphase play a major role in load transfer from the matrix to the reinforcing fiber and vice versa. It also introduces damage tolerance and enhances the toughness in the ceramic matrix composites. In one way, the mechanical properties and lifetime of the CMCs depend largely on the fiber/matrix interface or interphase. There are two vital requirements in the C/SiC composites, viz., (i) higher strength translation of the reinforcement and (ii) high toughness. Concept of weak interfaces has been commonly used to increase the fracture toughness of the composite. When the matrix has a lower failure strain than the fibers, the interface is likely to debond in the presence of matrix micro-cracks. The weak interface imparts the toughness, but at the same time, it may be detrimental to the composite strength. Requirement of high strength in the structure requires (higher strength translation) a strong interface or strong adhesive fiber/matrix bond for efficient load transfer from the reinforcing fiber to the matrix. Thus, the requirements of a damage-tolerant tough composite and strong composite are opposite in nature. Therefore, a balance has to be maintained between the strong fiber/matrix bond vs. damage tolerance/strength of the composite. In general, the interface is a thin film (< 500 nm) of a material having features like low shear strength, survivability at the composite fabrication

temperature, chemical inertness to the fiber and matrix, etc. [3, 25]. Most of the liquid infiltration processes of fabrication of the C/SiC composites lead to strong bonds between the matrix and the fibers. The strong bonds are formed due to possible chemical interaction between the reinforcing fiber and matrix which diffuse into each other and thus provide stronger bonding. This diffusion led bonding may be prevented by applying a suitable nonreactive interface.

The interface is coated onto the reinforcing fiber surface before composite processing, followed by the matrix building either through the gaseous deposition route or by infiltration of the source materials in liquid form. Different concepts for the interphase have been suggested for the CMCs, specifically for the C/SiC and SiC/SiC composites [26, 27]. Typical schemes of the interfaces are shown in Fig. 2 [3]. The most common interfaces are SiC, boron nitride (BN), and pyrocarbon (PyC) or their combinations.

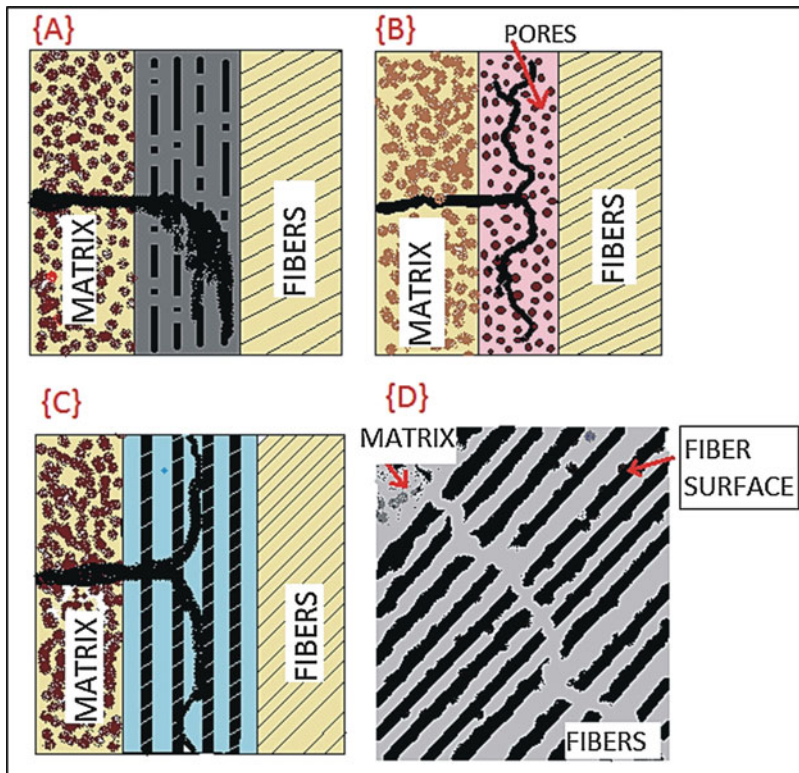


Fig. 2 Typical schemes of the interfaces [3]. (With permission from Springer Nature, C/C and C/SiC Composites for Aerospace Applications, Suresh Kumar, K. Chandra Shekar, B. Jana et al. 2017)

General Properties of C/SiC Composites

The key characteristics of monolithic SiC are high thermal and chemical stability, hardness, abrasive and wear resistance, brittle in nature, and low damage tolerance. During the loading, some cracks get initiated by local overloads which cannot be stopped or deviated; rather, they propagate in the bulk ceramic. The propagation of the cracks without much deviation leads to catastrophic failure of the monolithic ceramics. In general, such cracks would start from some preexisting pores, micro-cracks, and surface flaws. Therefore, the strength of the monolithic SiC is determined by the distribution of these imperfections and their quantity and size which are governed by Weibull statistics. Due to this reason, large structures are required to be designed of high wall thicknesses to control the stress levels at much lower levels than the material capability which ensures high survivability and reliability of large components. However, the reliability and fracture behavior of the monolithic ceramics can be improved by incorporation of the high strength continuous reinforcing fibers. CMCs thus combine the outstanding properties of the monolithic ceramics with other desired qualities like quasi-ductile fracture features, high fracture toughness, low Young's modulus, low CTE, high thermal shock resistance, and low density which improves their specific strength.

Integration of the carbon fibers does not really increase the strength of the monolithic SiC and often results in a reduction of the stiffness, compared to the bulk SiC. But, the carbon fiber integration into the SiC increases the toughness and reliability of the C/SiC composites significantly due to enhanced energy dissipating mechanisms such as crack deflection, crack branching, and their stoppage at the fiber-matrix interfaces [28, 29]. To realize the various modes of fracture such as the crack deflection, crack branching, and crack bridging, the fibers should be embedded in the weak fiber/matrix interface or weak matrix system. A typical scheme of crack deflection and crack arresting is shown in Fig. 3.

Crack bridging is difficult to be realized in a strong fiber/matrix system due to a very low effective fiber length because of their limited elongation property which results in brittle fracture behavior. However, if the fiber/matrix bonding is weak, the fiber is able to disbond from the matrix which increases the effective length of the fiber and decreases the strain rate. This mechanism helps in bridging the advancing cracks and allows to fabricate a less brittle and damage-tolerant material. Due to this reason, fiber content and fiber orientation are the two main parameters which determine the strength values of the C/SiC structures. Therefore, thin-walled and lightweight structures of the C/SiC composites can be fabricated in similar way as in the case of the polymer based composites.

PIP-Based C/SiC Composite Fabrication

PIP process is one of the most preferred processes to fabricate the C/SiC composites of complex geometries of low thickness and large size [2, 10, 11]. It comprises preform fabrication and infiltration of a low viscosity silicon containing

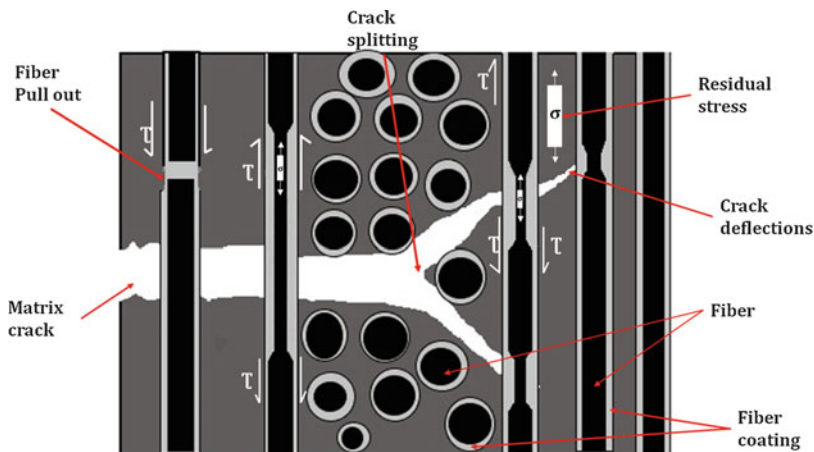


Fig. 3 A typical scheme of crack arrest and deflection in ceramic composite

polymer-like polycarbosilane into the preform. The infiltration process is driven by the capillary forces which in turn depends on the pore diameter and physical properties of the polymer like viscosity, density, surface tension, and angle of contact between the reinforcement and impregnating polymer solution/resin. Due to its dependency on the capillary forces, infiltration process is commonly conducted at normal pressure. But, if the thickness of the component is large, then it may also be vacuum- or pressure-assisted. The preform may be fabricated by laying up multiple carbon fabric layers or by weaving of the carbon fiber tows. The polymer impregnated preform to be pyrolyzed, i.e., heating in the absence of oxygen at a controlled rate. During pyrolysis, the polymer decomposes and converts into a SiC-based ceramic. Thus, the carbon fiber-reinforced SiC matrix composites are fabricated. The preceramic polymers (polymer precursors) like polycarbosilane (PCS) composed of carbon (C) and silicon (Si). Silicon-based preceramic polymers have been developed since the 1960s and are used for the formation of bulk ceramics, ceramic matrices, and fibers, as well as for coatings [30]. SiC matrix is derived from the PCS at relatively low temperatures at about 850–1050 °C [31–34]. In order to increase matrix density and temperature stability, the matrix can be transformed to crystalline β -SiC by a subsequent heat treatment at temperatures of 1500–1600 °C under an inert atmosphere. The weight fraction of ceramic to the initial polymer is reported of the order of 65% by mass. While other similar preceramic polymers may also contain nitrogen (N), oxygen (O), boron (B), aluminum (Al), and titanium (Ti) apart from the carbon and silicon. The polysilazane may be converted into SiCN or Si₃N₄ with ceramic yield up to 90% by mass. During pyrolysis, the volatiles such as CO, hydrogen (H₂), CO₂, CH₂, and H₂O are released, and the ceramic matrix like SiC or SiCN is obtained.

DMSRDE has taken lead in developing PIP-based C/SiC composite using polycarbosilane as Si-C matrix source [10, 11, 13, 35–37]. Polycarbosilanes (PCSs) have

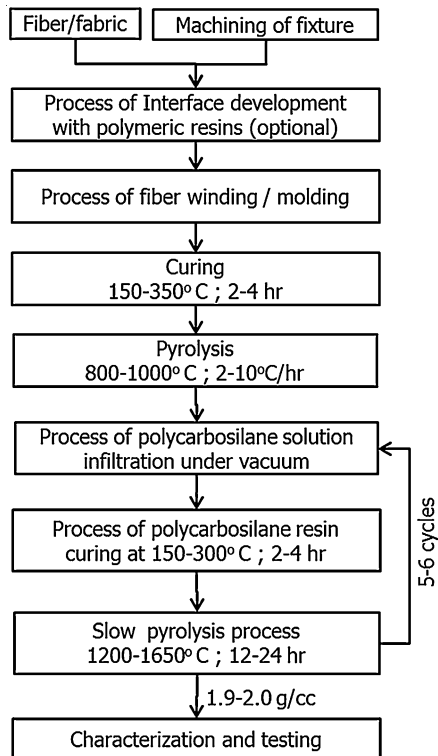
been used to fabricate C/SiC composites. A typical process for fabricating C/SiC composites is shown in Fig. 4.

Due to high shrinkage of the matrix during the pyrolysis, a large volume of the pores get generates. In order to fill the pyrolysis led porosity, multiple re-infiltration by the polymer resin/solution followed by pyrolysis is required. The infiltration-pyrolysis cycle is repeated 4–10 times in order to decrease the residual porosity of the ceramic matrix. However, the number of infiltration cycles depends on the ceramic content of the preceramic polymer and component thickness.

PIP process has several advantages like (i) relatively low process temperature, which prevents fiber damage; (ii) better control of the ceramic matrix microstructure and composition; (iii) near-net shape fabrication of the complex geometries of the composite; (iv) possibility of using different grades of fiber reinforcements along with the secondary reinforcement like particulates, short fibers, and nano-fillers; (v) using the process, graded matrix may be obtained by impregnating the different composition preceramic polymers in sequence; and (vi) the matrix is free from the residual silicon.

There are few disadvantages associated with the PIP process which are given as follows: (i) the process time is large due to multiple infiltration-pyrolysis cycles; (ii) cost of the products fabricated using PIP is higher compared to LSI-based C/SiC

Fig. 4 Schematic of the processing of PIP-based C/SiC composites



composite due to long process cycles and costly raw materials; (iii) residual porosity and the microstructure affect the mechanical properties of the resulting C/SiC composites.

There are different process parameters which are believed to have significant impact on the final properties of the composite. Using the design of experiment procedure, relative effect of the main process parameters is studied by Suresh Kumar et al. [10, 11, 13, 36, 37]; the process is summarized below.

Important Process Parameters

Design of experiments (DOE) can be used to identify the relative importance of the individual process parameters and also to study their interaction effects [38]. Importance of the process parameters can be determined by carrying out the screening experiments. DOE has been used to analyze relative importance of the process parameter for the UD C/SiC composites fabricated via PIP process. Critical process parameters are identified using the response table, normal probability curve, analysis of variance (ANOVA), and regression analysis. Apart from the processing parameters like pyrolysis temperature, rate of heating and ceramic yield of the PCS precursor, etc., physical properties of the C/SiC composites like fiber properties, preform type, fiber volume fraction (V_f), density, and test specimen size play vital role to obtain mechanical and thermal properties from a given composite [12, 39–41]. Two-level full fractional design of experiments was employed to develop the experimental matrix and to carry out the desired experiments [12], through the factorial design, the most influential parameters are identified.

Scheme of Investigation

The following steps were used [12]:

- a) Identifying the important and influential process parameters which can be controlled independently as factors
- b) Fixing of the upper and lower limits of the identified factors
- c) Developing the experimental design matrix using factorial design of experiments
- d) Conducting the experiments as per the design matrix
- e) Assessing the real or chance effect of the factors by constructing response table and normal probability plot
- f) Analyzing the results using analysis of variance (ANOVA)
- g) Developing linear expression to estimate flexural strength of UD C/SiC composite as a function of the factors

Identifying the Important Factors

The following factors are considered to be important which can be controlled independently and have significant influence on the mechanical properties of the C/SiC composite [12, 39–41]. Softening point of polycarbosilane-ceramic yield depends on the softening point of PCS, and also it controls the extent of the matrix

shrinkage which in turn affects the micro-crack pattern and residual porosity in the composite.

PCS resin of various softening points (110–250°C) results into C/SiC composites having different mechanical properties [12, 39–41].

Pyrolysis temperature – ultimate temperature at which the composite is pyrolyzed decides the type of the crystalline phases and also dictates the possibility of fiber/matrix reaction if any. The C/SiC composites using the PIP process are fabricated at temperatures between 1400 °C and 1600 °C [12, 39–41].

Fiber volume fraction (V_f) – fiber volume fraction and fiber orientation affect the shrinking nature of the matrix and ultimately control the mechanical properties thereof. Beyond a certain V_f , the reinforcement becomes ineffective due to nonuniform load transfer in association with the fragmented matrix obtained in PIP-based C/SiC composites. V_f has been studied between 40% and 60% [12, 39–41].

Composite density – density of the composite and residual porosity are interrelated. The higher is the density, the lower would be the residual porosity. With increasing number of infiltration and pyrolysis cycles, density tends to increase, while the residual porosity decreases. The porosity acts as defect and influences the load-bearing capability of the C/SiC composites. It is very important for the PIP-based C/SiC composites, as the maximum attainable density of these composites depends on the size of the composite. Smaller and thinner C/SiC composites can be densified to the higher densities, e.g., even up to 1.9 g/cm³, while the thicker and larger C/SiC composite components cannot be densified to this extent with similar number of infiltration cycles. Sometime fabricator has to make a balance between the required number of infiltration cycles and density. Normally, C/SiC composite having a minimum density of 1.7 g/cm³ offers a reasonably good strength [12, 39–41].

Mechanical Characterization

CMC with a low matrix content (down to zero) would have tensile strength close to the tensile strength of the fiber, but bending strength will be low, whereas the CMC with a low fiber content (down to zero) would have high bending strength (close to the strength of the monolithic ceramic), but elongation under tensile load would be $\leq 0.05\%$ [2, 42–44]. Therefore, incorporation of fibers in different directions/orientation leads to anisotropy, but elongation and damage tolerance get improve compared to the monolithics. The resulting material is anisotropic. In-plane tensile strength of the 2D C/SiC composite would be much higher than its through-thickness strength. Also, in this case the crack between the layers is not bridged by fibers. Therefore, the interlaminar shear strength (ILSS) and the strength perpendicular to the 2D fiber orientation are low for these materials.

The C/SiC composites are intended to be used for the applications where components experience different types of structural loading like, bending, tensile, compressive and impact. These loads might act simultaneously or in an independent manner. Therefore, compressive, flexural, tensile, and ILS strength are used widely for designing of the C/SiC composites structures. Though there are several test

standards like BIS, ASTM, DIN, IS, etc., ASTM standards are used most commonly. Sometime nonstandard techniques are also used for the samples which do not conform to the dimensions as suggested in these standards.

Flexural strength: Flexural tests provide information on the strength and deformation behavior of the materials under complex bending load. It is also used to measure the ultimate strength of a specified material under bending load. Under the bending load, the stress distribution in the material is nonuniform. The nonuniform stress distribution in the specimen and different mechanical behaviors of the continuous fiber-reinforced ceramic matrix composites (CFCC) in tension or compression lead to ambiguity of strength interpretation. Therefore, for design purpose, flexural strength data are not recommended. However this property of the material is widely used for comparison of the different materials/processes. The flexural behavior and strength of a CFCC depend on its inherent resistance to fracture, the presence of the fracture sources or accumulative damage process or their combination. Detailed testing procedure for different geometry specimens is given in ASTM C-1341 (2006).

Tensile strength: Uniaxial loaded tensile tests provide mechanical behavior information of the uniformly stressed material. Uniform stress state is required to evaluate nonlinear stress-strain behavior which may develop as the result of cumulative damage processes, e.g., matrix cracking, matrix/fiber de-bonding, fiber fracture, delamination, etc. This property is widely used for designing of the C/SiC composite components. By measuring extension of the material under tensile load, elastic modulus can also be measured. For accurate measurement of the elastic modulus, strain gauges need to be attached with the specimen. Detailed testing procedure for measuring tensile stress is given in ASTM C-1275 (2000).

Interlaminar shear strength: Interlaminar shear strength characteristic describes the shear strength between the laminate planes. It is determined using a short beam shear (SBS) test. It makes use of the fact that shear stresses always occur in a flexure test. If the span is small in comparison to the specimen thickness, the shear stresses are very large in comparison to the normal stresses get generated by the bending moment. In this way, shear stress can be generated in brittle matrix materials, which enable measurement of the shear strength. The shear strength of the matrix material or the quality of the fiber-matrix bonding can be characterized depending on the break type. This test method is relatively simple to employ and requires a simple tool that has good alignment options and precise centring of the die. For this reason, the method is often used in quality control and is suitable for comparing different materials processed at different condition. However, the method determines only in-plane shear properties. Detailed procedure for ILSS measurement is given in ASTM D-2344.

Properties of the PIP-Based C/SiC Composites

There are several reports on the mechanical properties of the C/SiC composites fabricated via PIP process [10, 11, 13, 36–38]. The properties are not uniform due to the following reasons:

- Type of precursor used as source for the SiC matrix
- Pyrolysis temperature
- Density of the composites
- Type of carbon fiber
- Fiber volume fraction
- Fiber orientation and
- Testing parameters

Therefore, it becomes very difficult for the designers to accept any reported property for designing the C/SiC composite structure. Extensive studies are carried out by the authors of this chapter to study the effect of composite processing parameters, fiber direction, and fiber type on the mechanical properties of the PIP-based C/SiC composites [10, 11, 13, 35–37] using the in-house developed polycarbosilane precursor. The properties are summarized in the following sections.

Flexural Strength of UD C/SiC Composites Using T300 Fibers

As mentioned earlier, there are several grades of carbon fibers which are used for fabricating high-temperature composites. T300 grade carbon fibers are the most widely used for fabricating CMCs. Typical stress-extension curve of the PIP-based UD C/SiC fabricated at different temperatures and fiber volume fractions of T300 fibers and having different densities are shown in Fig. 5 [12].

The stress-strain curves greatly vary with the density of the composite. The composite having 60% V_f and 1.9 g/cm³ density has the highest slope, while the samples having 40% V_f and 1.5 g/cm³ density have the least slope [12]. The stress-strain curves indicate the phenomena of crack arresting, branching, and/or deflection for almost all combination of the process parameters. It is evident from the figure that the failure is non-brittle for the composites processed at 1400 °C, while the composites fabricated at 1600 °C are somewhat brittle [12]. Typical microstructure images of the UD C/SiC composite fabricated at 1400 and 1600 °C are shown in Fig. 6 (a–b), while the composites fabricated at 1600 °C are shown in Fig. 6 (c–d).

It is evident from Fig. 6 that the fabrication temperature greatly influences the microstructure of the matrix. Therefore, the properties at 1400 and 1600 °C are found to be different [12, 36]. It may also be concluded that the brittle failure of the composites at 1600 °C might be due to degradation of the fibers at higher temperature when they come in contact with the SiC matrix built from the PCS. Surface reaction at higher temperature can take place between carbon fibers and SiC matrix as CO(g) evolve from the pyrolyzed PCS between 1400 and 1600 °C. This reaction damages the fiber surface, and the fiber-matrix bonding becomes stronger which result into brittle failure [12, 36].

Tensile Strength of UD C/SiC Composites Using T300 Fibers

Typical stress-extension curve of the PIP-based UD C/SiC fabricated at 1600 °C without any interface is shown in Fig. 7 [12, 36, 37]. It is evident from Fig. 7 that the tensile strength trend is similar to the flexural strength.

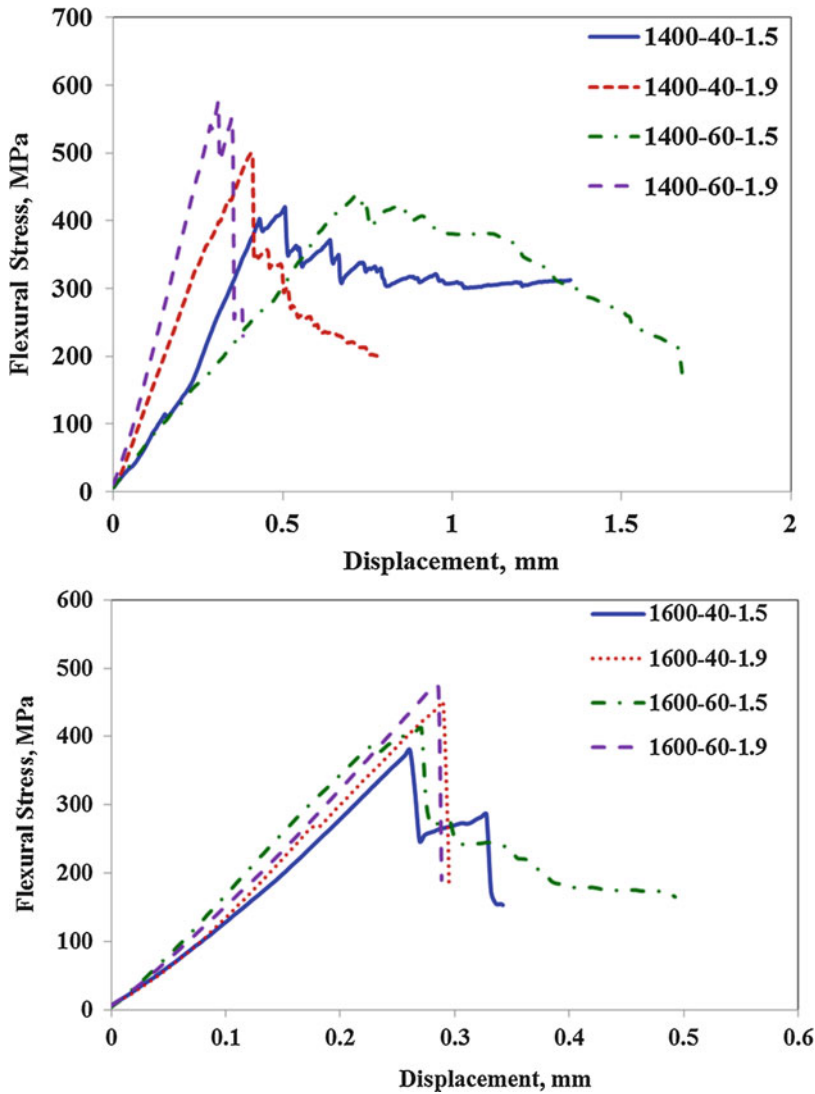


Fig. 5 Typical stress-extension curve of the PIP-based UD C/SiC fabricated at different temperature and fiber volume fractions of T300 fibers [12]

With increasing pyrolysis temperature, the strength is found to be decreased. Also, the composite becomes highly brittle with the increasing pyrolysis temperature. Mechanism of brittleness might be similar to the mechanism proposed for flexural strength. Some typical microstructure of the tensile-tested specimens is shown in Fig. 8.

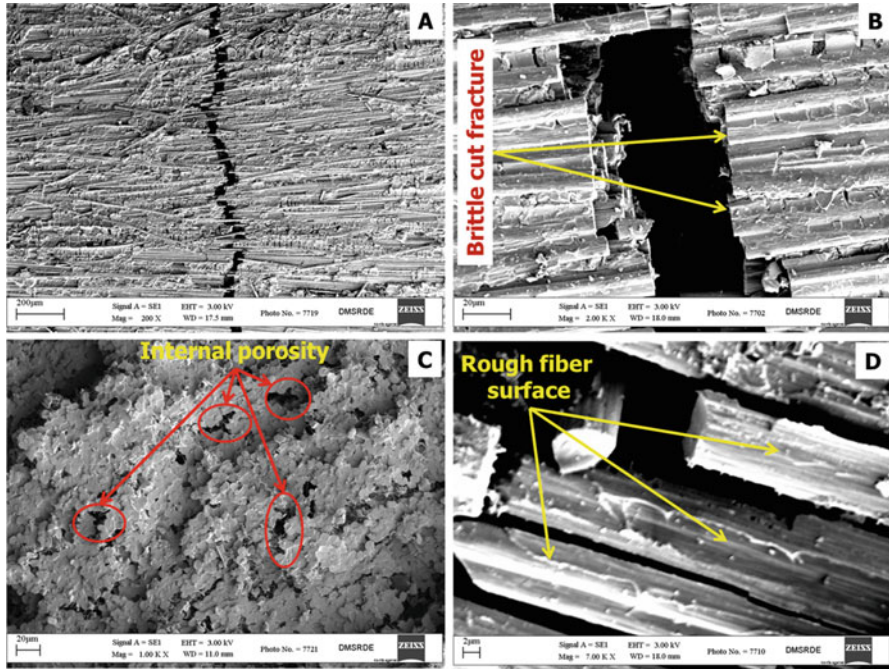
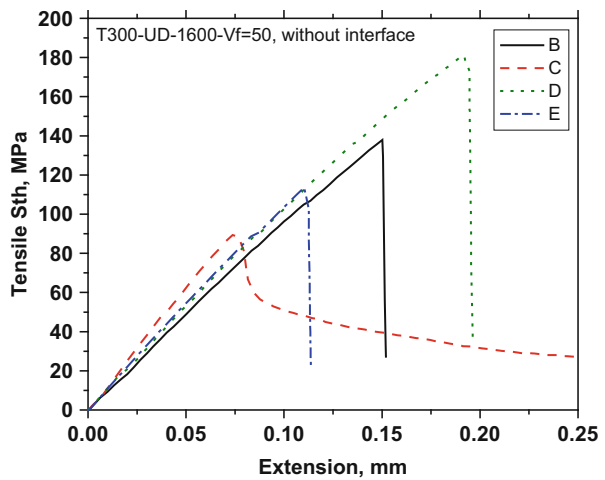


Fig. 6 Typical microstructure images of the UD C/SiC composite fabricated at 1400 °C and 1600 °C [12]

Fig. 7 Typical stress-extension curve of the PIP-based UD C/SiC fabricated at 1600 °C without any interface



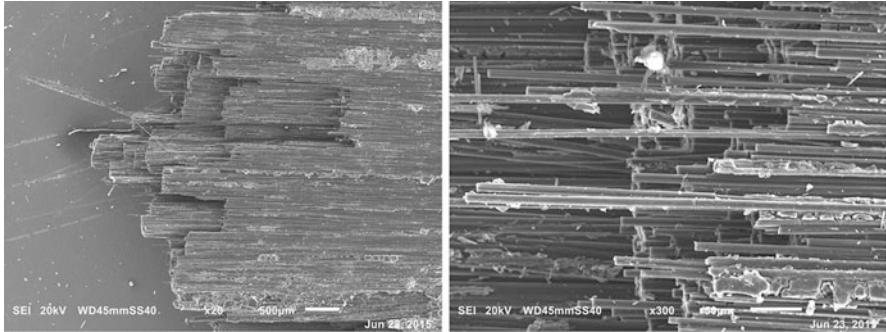


Fig. 8 Typical microstructure of the tensile-tested specimens fabricated at 1600 °C without any interface

Properties of M40 J Fiber-Based UD C/SiC Composites

Recently studies have been conducted using M40J fiber where effect of pyrolysis temperature on flexural strength is studied [13]. M40J fiber-based C/SiC composites were fabricated at 1400, 1500, and 1600 °C and were characterized for flexural strength. Average flexural strength was reported to be 691 ± 23 MPa, 654.6 ± 24 MPa, and 504 ± 31 MPa at the pyrolysis temperatures of 1400, 1500, and 1600 °C, respectively. Typical flexural stress-strain curves of the composites specimens pyrolyzed at 1400, 1500, and 1600 °C temperatures are shown in Fig. 9.

Flexural strength of the M40J fiber-based UD C/SiC composite strength is reported to be higher than the composites fabricated using T300 fibers. It may be understood from the tensile strength of these two different types of fibers as shown in Table 1. Tensile strength and modulus of the M40J carbon fibers are higher than the T300 carbon fibers. Also, the M40J fibers are processed at higher temperature than the T300 carbon fibers. Higher process temperature alters the surface groups on the fibers. The prevailing surface groups control the fiber-matrix bonding in the PIP-based C/SiC composites. Therefore, improved properties are expected with M40J grade carbon fibers. Perhaps this is one of the main reasons that the M40J fiber-based composites are stronger than the composites fabricated using T300 fibers [12, 13].

Strength varies at different processing conditions due to the fact that at different process conditions, morphological features such as micro-cracks and fiber/matrix local delaminations are different. These differences are unavoidable due to the different CTEs of the constituents of the composite, nonuniformity in the shrinkage of the composite during the pyrolysis, and different thermal stresses due to different V_f and pyrolysis temperature. The deformation sequenced is reported as (i) matrix cracking, (ii) fiber de-bonding from the matrix, and (iii) fiber tow failure. With increase of the load, the sample exhibits a linear deformation stage and then a deviation occurs due to micro-cracking in the matrix. After reaching the ultimate load, the stress drops gradually, demonstrating a pseudo-ductile fracture behavior associated with fiber pullout, bridging, and sliding. The characteristic morphological features of fracture in M40J fiber-based C/SiC composite is shown in Fig. 10. The EDS mapping shown in Fig. 10 E(E1-E3)

Fig. 9 Typical flexural stress-strain curves of the composites specimens pyrolyzed at 1400, 1500, and 1600 °C

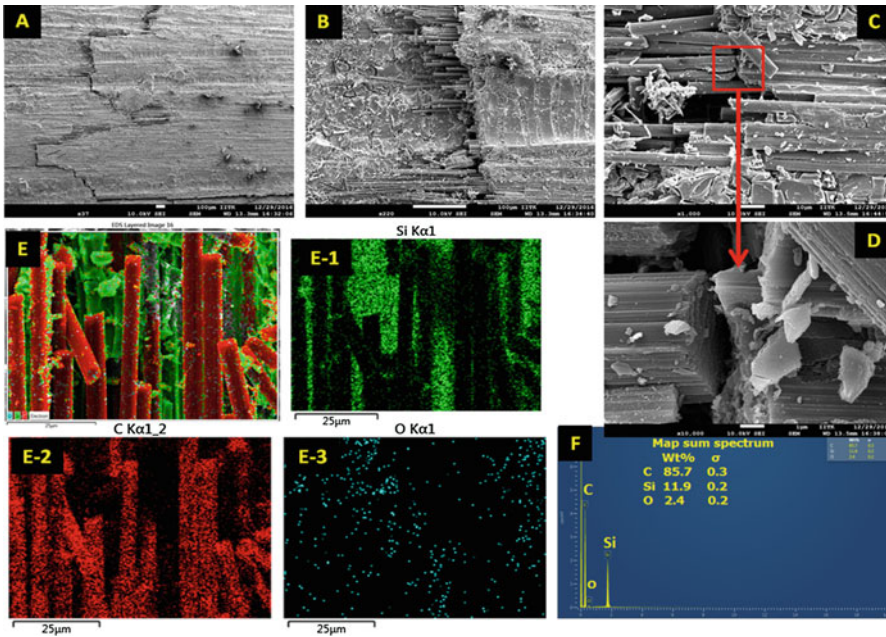
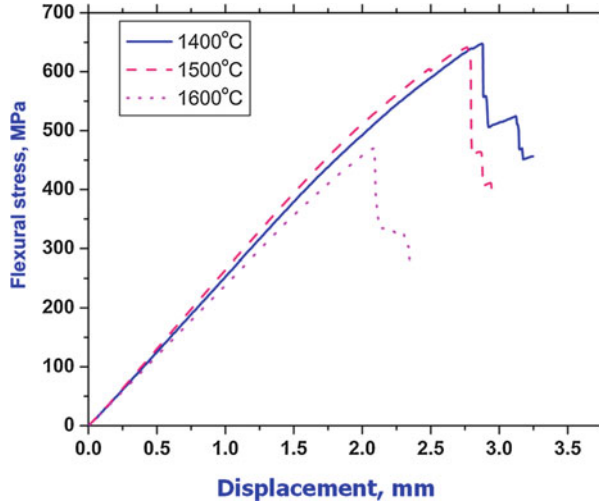


Fig. 10 Microstructure and EDS analysis of the C/SiC composites-based M40J fibers and those pyrolyzed at 1400 °C [13]. (With permission from Elsevier, Ceramics International, Fabrication and characterization of PIP based C/SiC composites having improved mechanical properties using high modulus M40J carbon fiber as reinforcement, Suresh Kumar, Bablu M, Manoj K. Mishra, Ashok Ranjan, N. Eswara Prasad 2017)

where carbon is represented by red color, silicon by green color, and oxygen by blue color shows uniform distribution and non-reacted surface of the carbon fiber. EDX analysis of the surface is shown in Fig. 10 F.

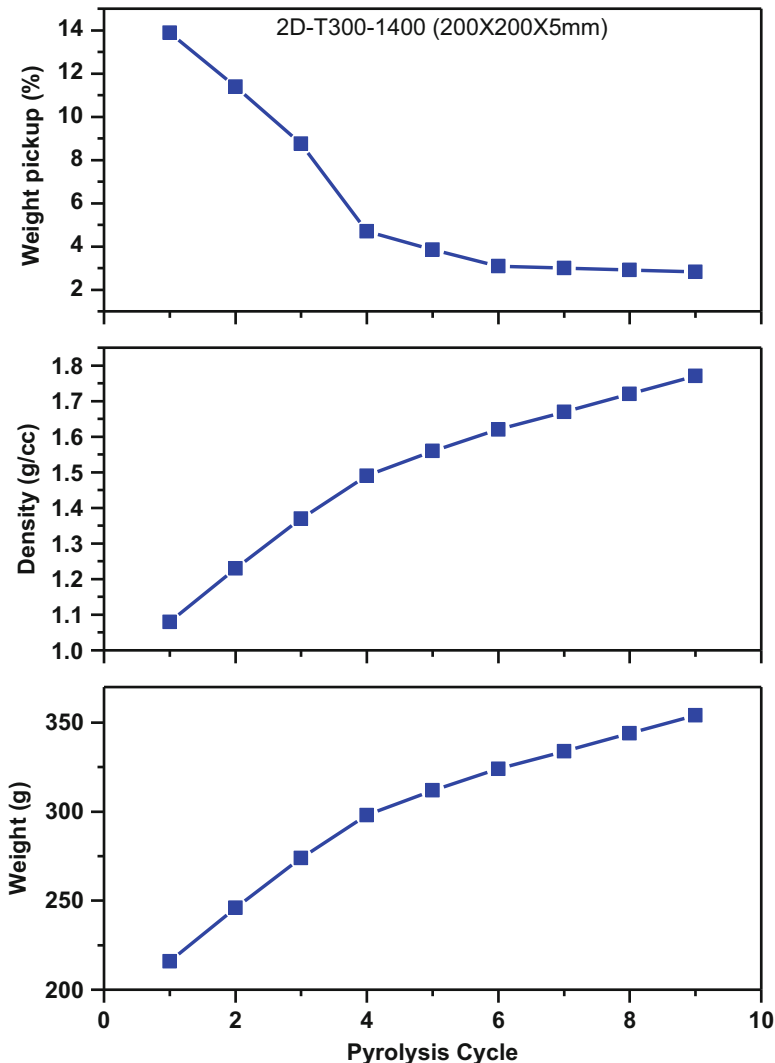


Fig. 11 Typical weight pickup trend for a 5 mm thick 2D C/SiC composite

PIP-Based 2D C/SiC Composites

2D C-SiC composite laminates of size 200x200x5mm to 200x200x40mm were fabricated using PIP method following the process as shown in Fig. 4. Typical weight pickup trend for a 5-mm-thick and 40-mm-thick (data extracted from the laboratory data, yet to be published) composite during subsequent densification cycles is shown in Figs. 11 and 12, respectively.

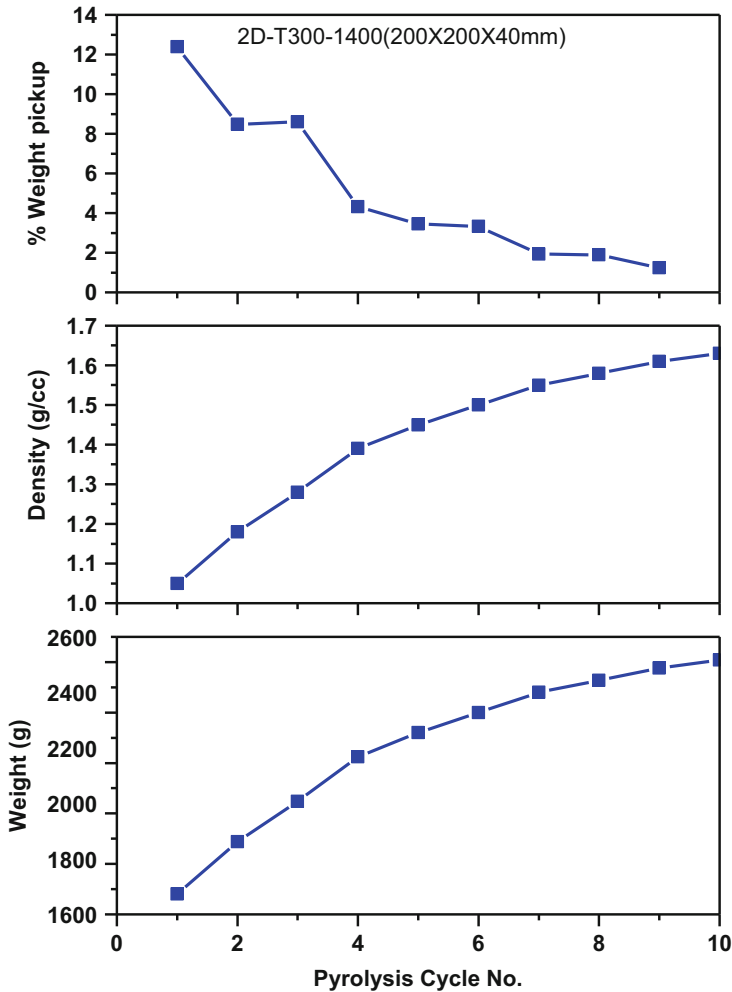


Fig. 12 Typical weight pickup trends for a 40 mm thick 2D C/SiC composite

The composites have been characterized for flexural and ILSS properties. The composite samples were cut using water-jet cutting technique to obtain flexural test specimens. Microstructure of the as fabricated composite and the surface of the water-jet cut C/SiC composite are shown in Fig. 13. The microstructure shows that there are few minor pores in the composite. Also, it is evident from the water-jet cut sample that the surface is not uniform at microscopic level. However, the samples were tested in as received condition after water-jet cutting. Flexural strengths of 2D C/SiC composites fabricated using T300 fibers are shown in Fig. 14. It is evident from Fig. 14 that the flexural strengths of all the specimens from a composite are very near and the failure trend shows a pseudo-ductile failure.

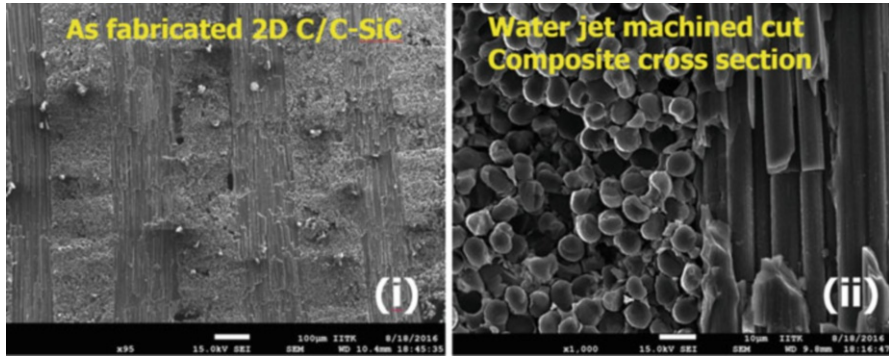


Fig. 13 Microstructure of the as fabricated composite and the surface of the water-jet cut C/SiC composite

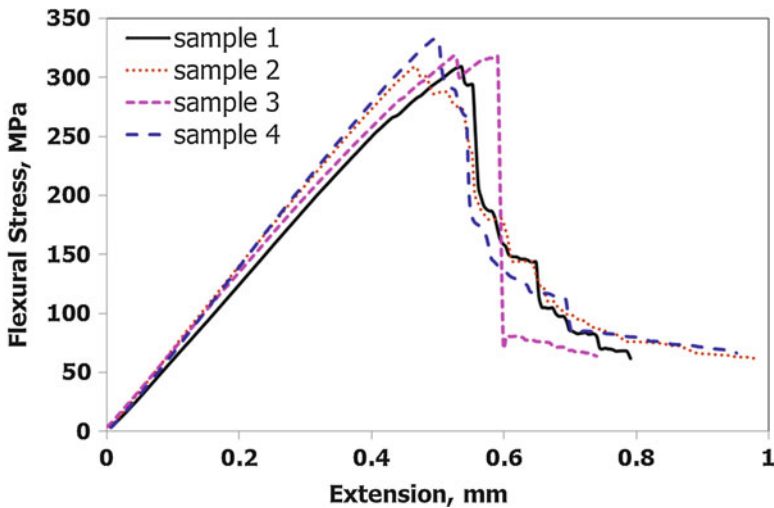
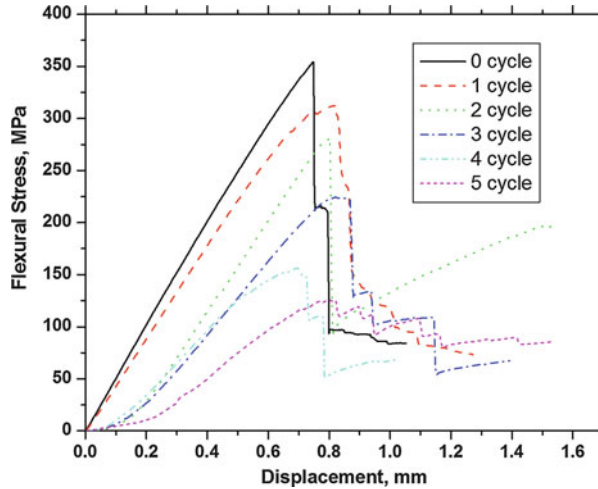


Fig. 14 Flexural strength of 2D C/SiC composites fabricated using T300 fibers

Thermal Shock Properties of 2D C/SiC Composites

On several occasions, the C/SiC composites have to perform under thermal shock environment 2D C/SiC composite test specimens are exposed to sudden heating under oxyacetylene flame to study their thermal shock cum oxidative properties [11, 37]. The specimens were heated up to five times where exposure time was maintained for 20s. The C/SiC composite found to be intact with no apparent damage due to thermal shock test under oxyacetylene flame [11, 37]. However, the surface of the samples gets oxidized, and a net weight loss is reported. The weight loss reported to be increased with increasing heating cycles. Average flexural and shear strength of the as fabricated composites are reported to be about 330 MPa and 14.5 MPa,

Fig. 15 Typical flexural stress vs. extension curves of the randomly selected specimens showing effect of heating cycles [11]. (With permission from Elsevier, Ceramics International, Fabrication of 2D C/C-SiC composites using PIP based hybrid process and investigation of mechanical properties degradation under cyclic heating, Suresh Kumar, M. Bablu, Ashok Ranjan, L. M. Manocha, N. Eswara Prasad 2017)



respectively. After five heating and cooling cycles, average flexural and shear strength were about 120 MPa and 5.5 MPa, respectively.

Mechanical properties are reduced with the heating cycles Fig. 15. Typical flexural stress vs. extension curves of the randomly selected specimens (after different exposure cycle) are shown in Fig. 15.

Slope of the stress-strain curves changes greatly with the increasing heating cycles, and flexural strength is decreased with the increasing heating cycles. After first heating cycle, the mean average strength is reduced to about 94.5% of the flexural strength of the as fabricated composite. After second, third, fourth, and fifth cycles, the average strength is reduced to about 85%, 68%, 49%, and 37%, respectively, of the flexural strength of the as fabricated composite [11, 37].

LSI-Based C/SiC Composite Fabrication

LSI Process

Liquid silicon infiltration (LSI) process is based on the reaction of molten silicon with the carbon matrix where molten silicon raises into the pores of the C/C composite by capillary action at a temperature exceeding its melting point (1420 °C). During the capillary infiltration of molten silicon, reaction between carbon and silicon takes place simultaneously. Therefore, it is a type of reactive melt infiltration (RMI) technique. The liquid silicon wets the approachable surface of the C/C composite. The silicon molten mass soaks into the pores out of which some material reacts and some remains unreacted. The melt reacts with carbon forming silicon carbide according to the reaction shown in Fig. 16.

SiC produced during the reaction gets deposited inside the pores of the C/C composite and thus fills the preform pores and forms the carbon fiber-reinforced SiC

Fig. 16 Reaction scheme of molten silicon and carbon

	1450-1650°C		
Elements	C	+ Si	→ SiC
Mol. wt.	12	28	40
Density g/cm³	2.2	2.32	3.2
Volume, cm³	5.45	12.0	12.5
Material and volume balance for LSI process			

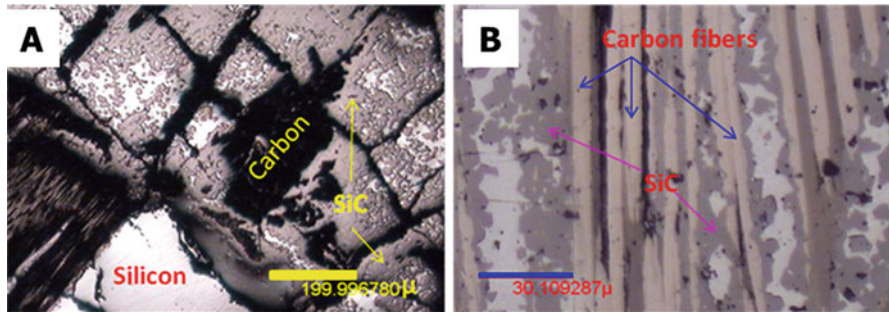


Fig. 17 Typical optical image of a siliconized C/C composite

matrix composite. The volume of one mole SiC is less than the sum of the volumes of one mole of silicon and one mole of carbon by about 25%; therefore liquid silicon keeps infiltrating into the pores of the composite, and net volume uptake of molten silicon is higher than the initial volume occupied by the pores. The initial pore volume fraction providing complete conversion of carbon into silicon carbide is about 0.56. Therefore, a specific porosity value of the composite can only result into the 100% conversion of carbon and infiltrated silicon to SiC. If the initial pore volume fraction is lower than 0.562, the infiltration results in entrapping residual-free silicon or vice versa. A typical optical image of a siliconized C/C composite is shown in Fig. 17.

Reaction between silicon and carbon is instantaneous and requires very short time. But the time requirement for the molten silicon infiltration is much larger compared to the reaction time. In general, all the three phases, viz., carbon, silicon, and SiC, would be there at any given time of silicon infiltration. The phases at two different temperatures and times are shown in the XRD spectra given in Fig. 18.

In general, 8–10% residual silicon is reported in the LSI-based C/SiC composites. LSI-based manufacturing process consists the following three steps:

1. Layup and fixation of the fibers, shaped as the desired component
2. Infiltration of the matrix material

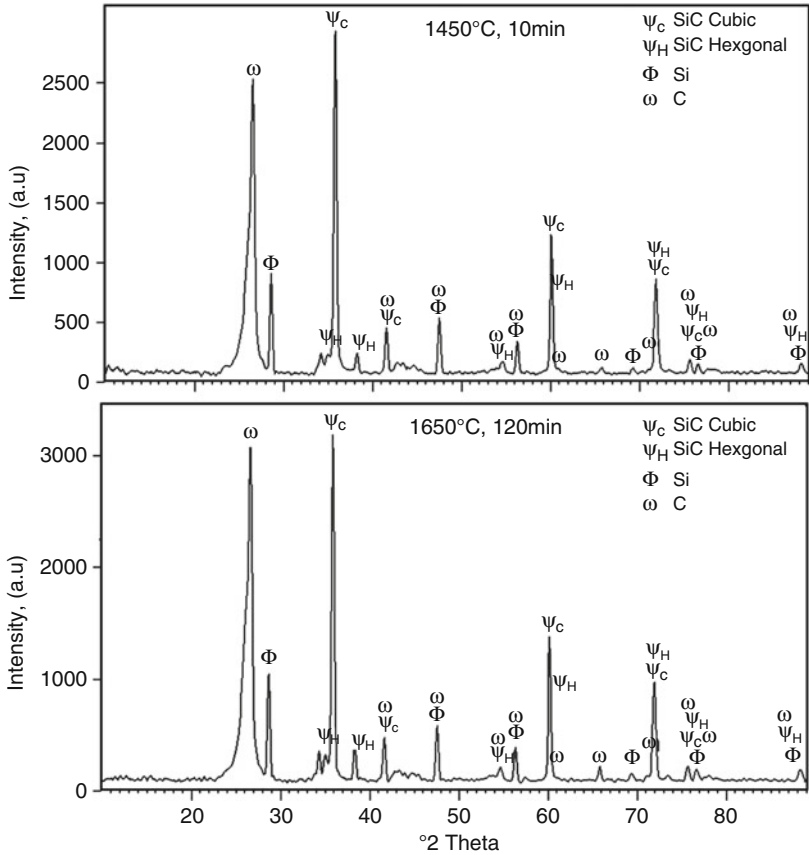


Fig. 18 Typical XRD spectra of LSI-based C/SiC composites siliconized at 1450 and 1650 °C

3. Final machining and, if required, further treatments like coating or impregnation of the intrinsic porosity

The C/C composite preform can be fabricated by the following three methods:

1. Using phenolic resins as carbon source [2]
2. Using coal-tar pitch as carbon source [45]
3. Using gaseous route to deposit carbon on the fibrous preform [2]

In either case, the pore network and microstructure are important for its complete infiltration by silicon and the reaction of carbon matrix to the infiltrated silicon. In general, moderate size pores having good interconnectivity can only allow complete infiltration. Smaller pores tend to choke very fast due to SiC formation, and very large pores do not provide sufficient capillary forces so that molten silicon gets suck into the pores. A typical pore size distribution in C/C composite fabricated by

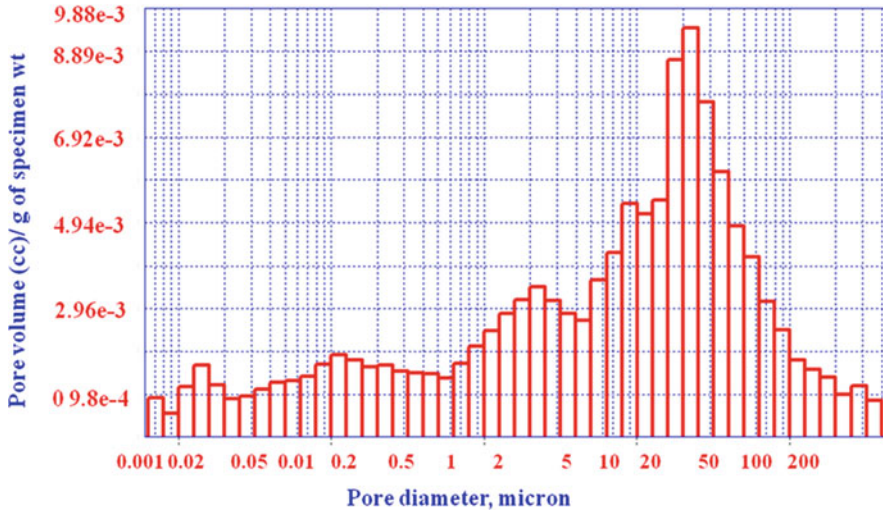


Fig. 19 A typical pore size distribution in C/C composite fabricated by coal-tar pitch as carbon source and having density between 1.5 and 1.6 g/cc

coal-tar pitch as carbon source and having density between 1.5 and 1.6 g/cc is shown in Fig. 19. It shows that the pores in C/C vary from submicron diameter to over 200 microns diameter. The larger pores are reported to be helpful in infiltrating the longer components [15, 45–47].

The infiltrated silicon is chemically active and can also react with the carbon fibers in the event those are not protected. A protective barrier coating of SiC, C, or Si₃N₄ may prevent the possibility of reaction between silicon and fibers. The general process scheme for LSI is shown in Fig. 20, and each process step is explained in the subsequent paragraphs.

LSI Process Steps

The very first step of composite fabrication is fabrication of C/C composite having adequate porosity and pore interconnectivity. Using the fibrous preforms, the C/C composites can be fabricated by using the thermoset resins like phenolics, polyimides or similar resins [2]. Coal-tar/petroleum pitch has also been used for fabricating C/C composites [15, 45–47]. CVD process to deposit carbon directly from the gaseous precursors like CH₄ and acetylene, and other low boiling hydrocarbons has also been used for fabricating C/C composite. Selection of the process purely depends on the availability of the infrastructure and the composite properties. CVD-based C/C composites have slightly better properties compared to the other two processes. Thermosetting resin-based fabrication is better for fabricating symmetrical components like nozzles using the filament winding procedure [2]. Coal-tar pitch-based C/C composites have several advantages like fabricating very large size composites which are difficult to be fabricated using the thermosetting resins and CVD process. The brief description of the process of LSI stages is given in the subsequent paragraphs.

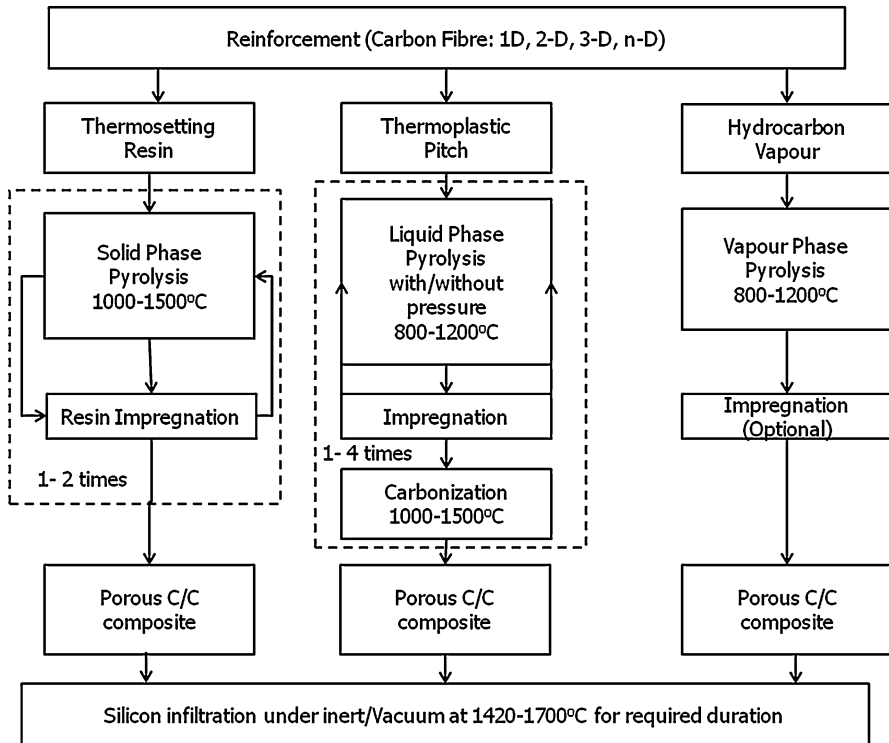


Fig. 20 The general process scheme for LSI-based C/SiC composite fabrication

Stage-1: Fabrication of Porous C/C Composite

Thermosetting resin based: The reinforcing fibrous preforms made out of tow, tape, integral woven, or needle punching are impregnated with a carbon source like phenolic resins using the standard techniques like hand brush, preparation machine, or RTM. The prepregs are laid up in a mold cavity followed by application of temperature and pressure. The applied temperature and pressure thus give shape to the prepregs. Other molding methods may also be used like vacuum bag molding or compression molding. The shaped composites are subjected to pyrolysis where the composite is heated in absence of air between 1000 and 1600 °C. During pyrolysis, the composite decomposes into some low molecular gases like H₂, H₂O, and CO and a solid mass of carbon. The resulting low molecular gases thus leaves behind pores or channels while they escape from the bulk material. The porous C/C composite may be machined to the near-net shape article shape before molten silicon is infiltrated into it.

Coal-tar pitch-based C/C preform fabrication: High strength carbon fiber reinforcement in the form of woven fabric and tows is used to fabricate fibrous carbon preforms. Low quinoline-soluble coal-tar pitch is used for densification of fibrous preforms, and high purity silicon metal is used for siliconization.

The carbon fibrous preforms were prepared by appropriate methods to fabricate 3D stitched, 3D woven, and 4D woven preform [3]. The carbon fibrous configurations were rigidified by vacuum infiltration with coal-tar pitch at 200–300 °C followed by carbonization at 900–1000 °C and graphitization at 2500–2600 °C and hot isostatic pressure impregnation carbonization (HIPIC) at 1000 bar, 800 °C in inert atmosphere to obtain the C/C composite preforms of densities 1.55–1.60 g/cm³.

CVD-based C/C composite fabrication [2, 3]: CVD process is widely used for fabricating C/C composite. It is accepted that the CVI process is the most appropriate process for fabricating high-performance C/C composites. CVI process is carried out at relatively lower temperature, and the matrix composition and microstructure is controlled quite effectively without any organic by-products. It leads to PyC with different microstructures and textures. General process parameters are deposition temperatures (1000–1300 °C), pressure (2–100 mbar), gas flow rates (depending on the reactor size), and methane/hydrogen (0.2–0.5). High-density C/C composites with high mechanical properties: an optimum value of residence time and methane to hydrogen ratio should be used at the given temperature range.

Stage-2: Silicon Infiltration

In this process step, molten silicon is allowed to infiltrate in the porous C/C preform at temperatures 1450–1650 °C, above the melting point of silicon which melts at around 1420 °C. Silicon is available in the form of powder of various size and also in the form of granules ranging from few millimeters to few centimeters. Though very high purity electronic grade silicon is available, but for composite fabrication, metallurgical grade silicon can also be used. The porous C/C composite and silicon are to be kept into a graphite crucible. The crucible along with the job to be placed into a furnace (inert/vacuum) and temperature of the furnace should be raised above the melting point of silicon. Si-infiltration in the C/C composite having adequate porosity takes place by capillary forces where no additional pressure is applied. However, siliconization is performed under vacuum up to 1 mm Hg which results into better silicon infiltration where almost all the open porosity can be filled with molten silicon. Siliconization step has been described in detail elsewhere [2, 3].

Advantages and Limitations of LSI

LSI has several advantages like low cost, short production time, low residual porosity, high thermal conductivity due to low porosity, and high electrical conductivity due to carbon fiber reinforcement, and using this process, very complex and near-net shapes may be fabricated as there is no change in the dimensions of the composite. The process is having some demerits as well, e.g., high temperature of the molten silicon damages the unprotected reinforcement; residual silicon deteriorates the mechanical properties and thermal stability at high temperature and relatively lower mechanical properties compared to the PIP- and CVI-based C/SiC composites.

Properties of LSI-Based C/SiC Composites

Properties of the LSI-based C/SiC composite are largely dependent on the completion of the silicon infiltration process and carbon matrix and silicon reaction. Molten silicon infiltration process has been described using the Darcy's Law and Washburn equation [15, 46–48]. As per the Washburn equation, the infiltration kinetics is governed by the pore diameter, height of the component, and the physical properties of silicon at the process temperature [15, 46–48]. Comparative mechanical and thermal properties reported for 2D C/SiC composites fabricated by different process routes are given in Table 3.

In India, significant work has been done by Suresh Kumar et al. using coal-tar pitch as carbon source which is summarized in the subsequent sections.

Similar to the PIP process, the properties of the LSI-based C/SiC composites are affected by the following main parameters:

- Type of precursor used for the carbon matrix source
- Interface material and its thickness
- Pyrolysis temperature
- Siliconization temperature
- Porosity before and after silicon infiltration
- Residual silicon
- Density of the composites
- Type of carbon fiber
- Fiber volume fraction
- Fiber orientation or preform type and
- Testing parameters, etc.

Table 3 Typical properties of the 2D C/SiC composites [2, 3, 6, 14, 30, 33]

Property	Units	2D composites fabricated by different routes		
		CVD	PIP	LSI
Fiber content (V_f)	Vol.%	42–44	50–55	
Density	g/cm^3	1.7–1.8	1.7–1.75	2.4
Flexural strength	MPa	250–330	300–350	180–200
Tensile strength	MPa	200–250	185–230	80–190
Strain to failure	%	0.3–1.1	0.2–0.35	0.15–0.35
Thermal conductivity	W/m K	11.53 (100 °C)	35–7	30 – 35
Specific heat	J/kg K	900 (100 °C)		800 (RT)
CTE ($\times 10^{-6}$)	$\text{m/m}^\circ\text{C}$ (\parallel)	2–3	–0.5–2.5	1.0–1.5
	$\text{m/m}^\circ\text{C}$ (\perp)	4–7		5.5–6.0

Mechanical Properties of LSI-Based C/SiC Composite

Using the coal-tar pitch as carbon source, three different types of preforms were used for fabricating C/C composites which were siliconized at three different temperatures, viz., 1450, 1550, and 1650 °C, for different time durations ranging from 10 to 120 min. The C/C porous composites were having initial porosity in the range 17–20% and fiber volume fraction in the range 40–45%. The summary of the mechanical properties reported for different types of C/SiC composites fabricated using coal-tar pitch a carbon source is given in Table 4 [4, 15, 45–47, 52].

Scattering is reported in the properties of CMCs and also in the C/SiC composites [2, 3, 6, 47]. In 3D stitched C/SiC composites, the scattering was mostly interpreted due to the natural pores generated during the fabrication of C/C composite and do not get completely filled during silicon infiltration. A typical optical cross-sectional view of a 3D stitched C/SiC composite having internal unfilled pores is shown in Fig. 21. The unfilled pores which exist in the bulk of the composite act as stress concentration points, and specimen fails at the point where stress in the composite exceeds the strength of the material. The distribution of such pores in the composite is not uniform, and thus the strength values vary greatly from specimen to specimen.

Second reason is reported due to variation of V_f from specimen to specimen. In practical cases, the thickness of the test specimen is maintained close to the value recommended in the test standards. If the material is homogeneous, then the load at which samples would fail should be constant. But, in C/SiC composites, the strength of the reinforcing fibers and the matrix vary greatly. Practically, it is the reinforcement which bears entire load. Though the V_f is maintained on the bulk level, at specimen level, keeping the V_f same for all the test specimens is difficult. Many a times, thickness of the test specimen varies between 3 and 4 mm. Theoretically, in 3-mm-thick 3D stitched C/SiC composites, five layers of fabric and four layers of matrix having equal thickness should exist. But, during machining samples may be fabricated where four layers of fabric and five layers of matrix might be there in 3-mm-thick sample. In both cases effective V_f is about 60 and 48%, respectively. Such variation in the specimens would be reflected in their load-bearing capability. Thus scattering is unavoidable in C/SiC composites. However, it can be minimized by proper processing parameters and by good selection of specimens.

Position of the third direction fiber in the test specimen is another major reason reported for the variation in the strength values of the 3D stitched C/SiC composite. Typical image of the two different flexural test specimens is shown in Fig. 22. In sample 22(a), there is no third direction fiber in the center of the span length, while in 22(b) two numbers of third direction fibers are located exactly in the middle of the span length. The specimens where third direction fibers fall in the center of the span length would fail at slightly lower load compared to the other [47, 48]. The third direction fiber helps in keeping the fabric layers together, but it weakens the structure locally. In fact third direction fiber acts as a defect and may cause variation in the strength values of the specimen depending on their numbers and location within the span length.

Table 4 Typical mechanical properties of the LSI-based C/SiC composites fabricated using coal-tar pitch as carbon source [4, 15, 45–47, 52]

	3D stitched C/SiC												3D woven C/SiC			4D woven
	1450 °C				1550 °C				1650 °C				1650 °C			1650 °C
	10	30	120		10	30	120		10	30	120		X	Y	Z	U
Silicization temperature																
Silicization time, min																
Direction	In-plane															
Flexural strength, MPa	Max	164	177	194.2	167	178	184	169	179	203	222	213	205	150	145	
	Min	109	129	138.5	123	141	141	120	127	147.2	162	162	169	162	169	
	Avg	139.3	153	165.9	146.6	157.6	158	146.5	147.2	176.9	190	188	184	188	184	
	s.d	19.8	17.2	16.1	14.7	13.5	12.1	14.8	18.2	17.8	NA	NA	NA	NA	NA	
Tensile strength, MPa	Max	NA	78	81	NA	77	97	NA	89	102	NA	NA	NA	NA		
	Min	NA	52	51	NA	52	75	NA	64	68	NA	NA	NA	NA		
	Avg	NA	62	68.1	NA	67.8	84.7	NA	73.7	90	NA	NA	NA	NA		
Compressive strength, MPa	NA	NA	NA	NA	NA	NA	NA	NA	NA	NA	NA	NA	NA	NA		
	NA	NA	NA	NA	NA	NA	NA	NA	NA	NA	NA	NA	NA	NA		
														188	170	

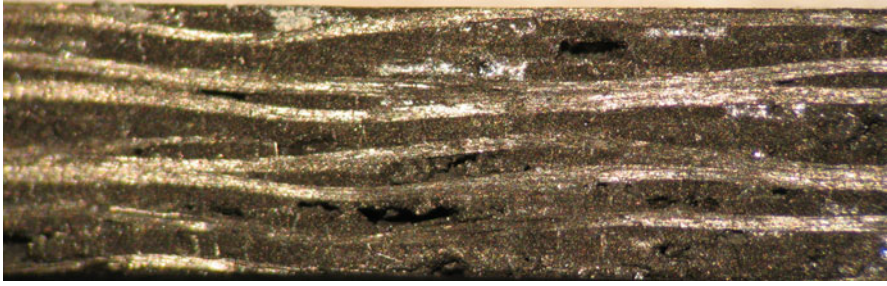


Fig. 21 A typical optical cross-sectional view of as fabricated 3D stitched C/SiC composite

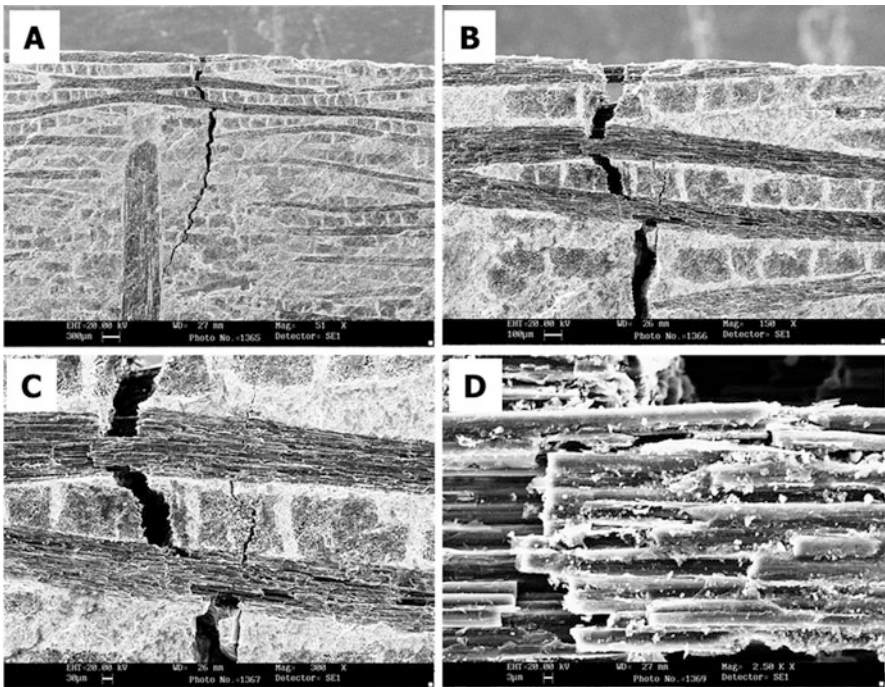


Fig. 22 Typical crack propagation in 3D stitched C/SiC composites under bending load

Typical crack propagation in 3D stitched C/SiC composites under bending and tensile loading are shown in Figs. 22 and 23, respectively.

3D stitched C/SiC composites have shown excellent fracture toughness [47]. Good fracture toughness even without any interface is achieved due to a large number of fiber pull-out as seen in Fig. 24.

Crack propagation in 3D woven C/SiC composites is found to be a bit different than the 3D stitched C/SiC composites. The crack follows the axis of tow in case of 3D woven C/SiC composites, and the tows fail when critical load exceeds for the

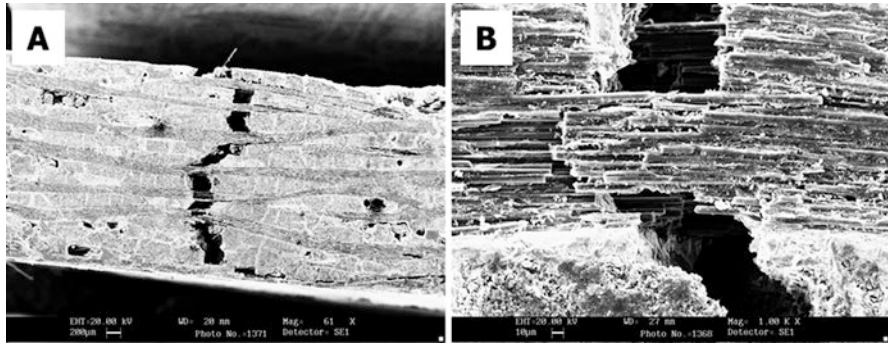


Fig. 23 Typical crack propagation in 3D stitched C/SiC composites under tensile load

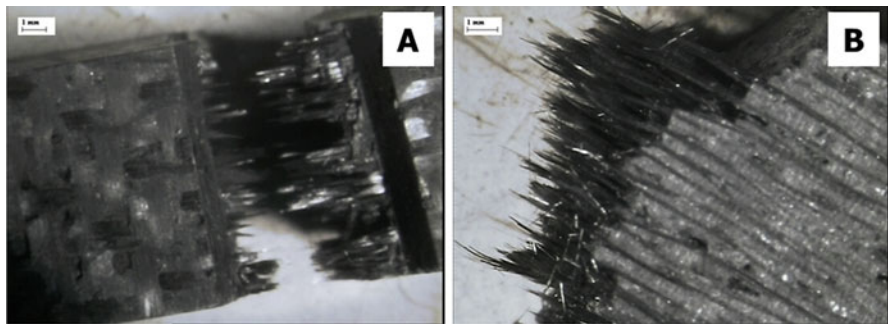


Fig. 24 Typical fractured 3D stitched C/SiC composite

tow. A typical crack propagation in 3D woven C/SiC composite specimen under bending load is shown in Fig. 25.

Thermal Properties of LSI-Based C/SiC Composites

High-temperature capabilities of the C/SiC composites are a key performance benefit for aerospace and other discussed applications. The material has to perform across a broad temperature range. Thermal diffusivity/conductivity, specific heat, and coefficient-of-thermal-expansion (CTE) are the key thermal properties which are required as an input while designing a C/SiC composite components for these applications [2, 3, 49–51].

Thermal Diffusivity

Suresh Kumar et al. has studied the effect of siliconization condition on thermal diffusivity and CTE of the 3D stitched C/SiC composites. Also the values of thermal

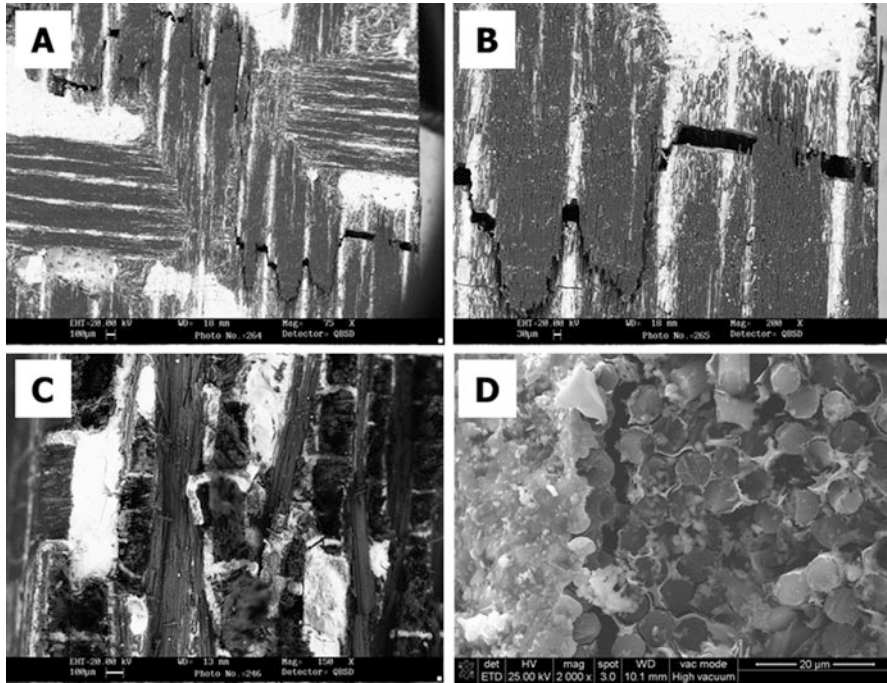


Fig. 25 Typical crack propagation in 3D woven C/SiC composites under bending load

diffusivities and CTE have been determined for different preform-based C/SiC composites [49, 50]. Summary of the thermal diffusivity of 3D stitched and 3D and 4D woven C/SiC composites which were siliconized at 1650 °C for 120 min is given in Table 5 for their different directions [18].

For all the types of composites, thermal diffusivity values decrease with the temperature. For 3D stitched C/SiC, the in-plane thermal-diffusivities values are two to three times higher than those in the through-thickness direction. Thermal diffusivity of 3D and 4D woven in different directions is found to be in similar magnitude of through-thickness value of 3D stitched C/SiC composites. The reasons and mechanism of thermal transport in the C/SiC composites are given elsewhere [4, 15, 18, 52].

CTE of C/SiC Composites

Similar to thermal diffusivity, CTE of different types of C/SiC composites was determined and reported [4, 15, 16, 52]. Summary of CTE of the 3D stitched and 3D, 4D woven C/SiC composites which were siliconized at 1650 °C for 120 min is given in Table 6 for their different directions.

For 3D stitched C/SiC composites, the in-plane CTE varies in the range of 1.0×10^{-3} to $9.55 \times 10^{-5}/^{\circ}\text{C}$, while CTE in its through-thickness direction varies in the range of 1.46×10^{-4} to $3.22 \times 10^{-3}/^{\circ}\text{C}$. The through-thickness direction

Table 5 Thermal diffusivity of the LSi-based C/SiC composites fabricated using coal-tar pitch as carbon source [3, 4, 15, 18, 52]

Preform/composite type	3D stitched, 1650 °C, 120 min			3D woven C/SiC composite, 1650 °C, 120 min			4D woven C/SiC composite, 1650 °C, 120 min			
	Thermal diffusivity, mm ² /s	Through thickness		X	Y	Z	Thermal diffusivity, mm ² /s	U	Z	Specific heat, J/g °C
Direction	In-plane						Temperature, K			U/Z
Temperature, K										
302	74.086	35.328		34.78	33.508	37.688	313	38.94	34.162	0.75
372	58.742	27.497		26.521	25.483	28.84	373	30.12	26.564	0.912
473	36.455	16.889		21.671	20.701	23.351	573	16.38	14.21	1.326
573	NA	NA		16.32	15.919	17.861	773	11.408	9.976	1.59
873	24.49	11.062		11.012	10.789	12.193	973	9.176	7.83	1.751
1173	19.43	8.667		8.762	8.51	9.209	1172	8.37	7.344	1.855
1273	17.081	7.032		7.98	8.127	8.796	1372	7.874	6.588	1.917
1473	15.944	6.115		7.571	7.364	7.969	1572	6.696	5.94	1.959

Table 6 CTE of the LSI-based C/SiC composites fabricated using coal-tar pitch as carbon source [2–4, 15, 16, 52]

Preform/ composite type	3D stitched, 1650 °C, 120 min		3D woven C/SiC composite, 1650 °C, 120 min			4D woven C/SiC composite, 1650 °C, 120 min	
Direction	In- plane	Through thickness	X	Y	Z	U	Z
Temperature, °C	CTE/°C						
25	6.45E-05	1.46E-04	1.13E-06	1E-06	1.54E-06	3.29E-05	3.40E-05
100	9.21E-05	3.08E-04	-1.5E-08	-5.5E-08	2.26E-07	-5.44E-05	-5.35E-05
200	9.55E-05	5.48E-04	-4.6E-07	-4.9E-07	-3.2E-07	-2.45E-04	-2.40E-04
300	1.47E-04	8.38E-04	-4.7E-07	-4.1E-07	-3.3E-07	3.14E-04	2.90E-04
400	2.30E-04	1.14E-03	-2.9E-07	-2.6E-07	-2E-07	-2.83E-04	-2.76E-04
500	3.24E-04	1.42E-03	-1.3E-07	-1.4E-07	2.55E-08	-2.20E-04	-1.80E-04
600	4.51E-04	1.69E-03	4.4E-08	-1E-08	2.43E-07	-1.50E-04	-1.40E-04
700	6.30E-04	2.05E-03	2.8E-07	1.76E-07	3.95E-07	3.40E-05	3.20E-05
800	8.11E-04	2.43E-03	4.74E-07	3.72E-07	5.47E-07	1.62E-04	1.58E-04
900	1.00E-03	2.81E-03	6.93E-07	5.66E-07	7.31E-07	2.74E-04	2.65E-04
1000	1.25E-03	3.22E-03	9.23E-07	6.99E-07	8.71E-07	3.42E-04	3.20E-04

CTEs were found to be three to four times that of in-plane at same siliconization conditions. In-plane CTE is controlled by SiC/silicon matrix at low temperatures and weft carbon fibers and interfacial thermal stress at high temperatures [16]. CTE of all the C/SiC composites in in-plane is much lower than the CTE's of silicon and SiC. Through-thickness direction CTE was found to be the highest for the composites which are having the highest residual silicon and least for the composites which have the least residual silicon and the highest SiC and porosity. CTE is the least for 3D woven C/SiC composites for any direction due to the low CTE of carbon fibers. In case of 3D woven C/SiC composites, the samples are cut in such a way that the one-third fibers are in parallel to the specimen length. Since, CTE of the carbon fibers along the axis is least among the constituents of C/SiC composites the effective CTE of the 3D woven C/SiC composite is closer to the CTE of the carbon fiber. In case of 4D C/SiC composites, the fibers oriented in transverse direction to the CTE measuring length contribute significantly to the sample expansion [2–4]. It

is well known that the radial CTE of carbon fibers is almost 10 times higher than the CTE of carbon fiber along its axis [2–4].

Oxidative and Erosive Behavior of LSI-Based C/SiC Composites

C/SiC composite components have to perform under oxidative environment of the following nature:

- i) Clean and stagnant gas with high concentration of oxygen. e.g. High temperature use of C/SiC composites under stagnant air.
- ii) Another condition like thermodynamic heating of TPS where the oxidation and erosion due to high flow of clean gases take place.
- iii) These composites are used for the liquid propulsion systems where thermal shock and the oxidation due to high flow of the plume gases contain H₂O, CO, and some underreacted O₂.
- iv) Extreme erosion takes place in the solid propellant-based systems like thrust vectoring control (jet-vanes), throat insert, and nozzles. These components would face severe erosion due to alumina particles and chemical erosion due to temperature and oxidation.

Many researchers have studied the ablation characteristics of C/SiC composite under the oxyacetylene torch environment [53–55]. However, oxyacetylene flame does not simulate the propulsion conditions of a rocket motor with respect to the chemical composition of the plume, thermal energy, and shear forces responsible for mechanical erosion [53–55]. The oxidation behavior of CVD/CVI processed, LSI processed, and hybrid (CVI + LSI) processed C/SiC's has been reported for the temperature range 500–1400 °C [56]. The hybrid C/SiC was fabricated by developing a carbon matrix using the standard CVI process, followed by molten silicon infiltration [56]. Below 900 °C the oxidation rate was lowest for the CVD/CVI-based composite, followed by the (CVI + LSI)-based and LSI-based C/SiC's. Above 1000 °C the oxidation of the CVD/CVI-based C/SiC was faster than that of the LSI-based and (CVI + LSI)-based composites. Also important is the initial oxidation temperature, which was 526, 552, and 710 °C for the LSI-based, (CVI + LSI)-based, and CVD/CVI-based composites, respectively [56].

Typical test environment and the results of erosion and oxidation of LSI-based C/SiC composites are briefly described below.

Oxidation Under Quartz Lamp Heating

To observe thermal shock resistance, it is desirable to expose the composites to sudden heating through quartz heating lamps (infrared heaters, IR). Different sets of the 3D woven C/SiC composite samples of dimension 100x10x5mm were exposed to the heating lamps as shown in Fig. 26.

The heating through quartz lamps could raise the temperature of the samples within few seconds. The sudden rise in temperature results into thermal shock and

Fig. 26 Kinetic heating testing of C/SiC composites



might have created some micro-cracks on the surface. The surrounding oxidative conditions thus oxidize the material specially the carbonaceous matter like carbon fiber and unreacted carbon. The oxidation of the carbon fibers thus reduces its load-carrying capacity. Residual strength after different thermal shock cycles were investigated by Suresh Kumar et al. [15]. The composite becomes porous and weak after repeated thermal shock cum oxidation cycles. A typical microstructure of the as fabricated, 3D woven C/SiC composite, composite after single time exposure to kinetic heating lamps and four times exposure, is shown in Fig 27a–d.

Erosion Under Plume of Solid Propellant

3D stitched C/SiC composite fabricated using LSI is used successfully for thrust vector control for aluminum-based solid propellant fed rocket motor. As mentioned earlier, these jet-vanes face severe erosion due to combined action of mechanical and chemical loads and are tested to study erosion resistance. The jet-vanes showed excellent resistance to thermo-oxidative erosion; average linear and mass erosion rates were 1 mm/s and 5 g/s, respectively [5]. Morphology of the eroded surfaces of the jet-vanes is shown in Fig. 28. The morphology suggests that alumina particles in the plume hit the leading edge of the jet-vane, damage it, and some material is eroded away. Once carbon fibers get exposed directly to the plume, these may be both eroded and oxidized. The residual silicon melts and reacts with oxygen to form silica which in turn reacts with SiC matrix. The matrix of SiC, silicon, and unreacted carbon is loosened and erode by high shear forces [5].

Erosion Under Plume of Liquid Propellant

In case of propulsion conditions, it is the ablation of the composite material which is prevailing rather than the simple oxidation. Ablation is a multi-scale and multi-physics process which includes thermochemical erosion along with thermophysical and thermomechanical denudation. There are several variables which affect the ablation like temperature, pressure, velocity, and the nature of the combustion gas composition [57–62].

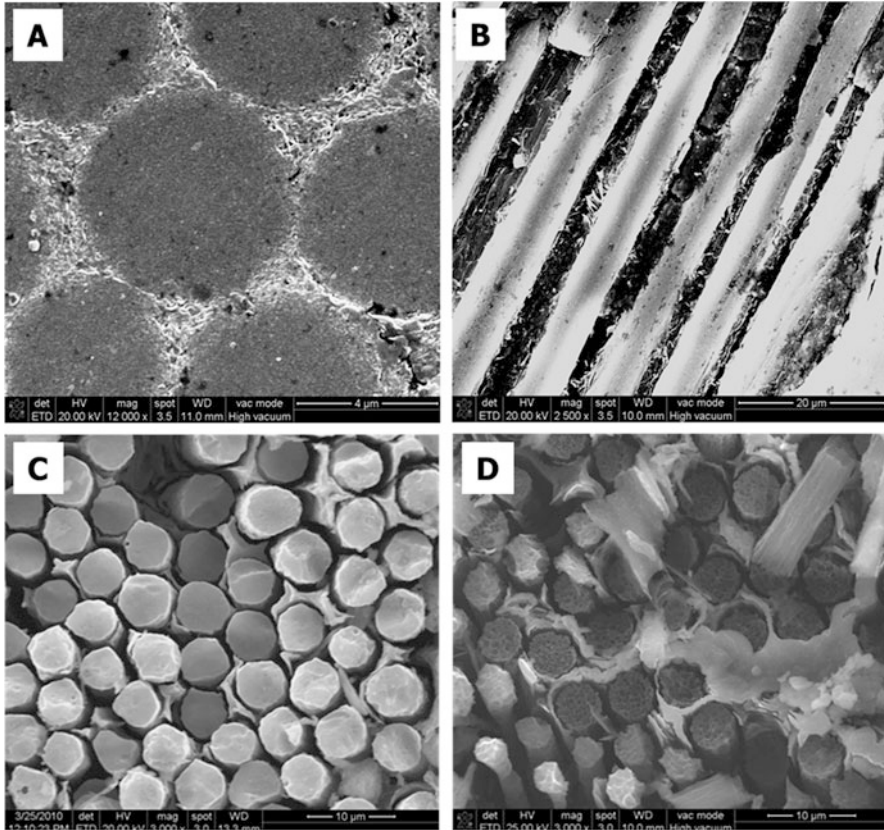


Fig. 27 Microstructure of 3D woven C/SiC composite after thermal shocks under quartz heating lamps [11]. (With permission from Elsevier, Ceramics International, Fabrication of 2D C/C-SiC composites using PIP based hybrid process and investigation of mechanical properties degradation under cyclic heating, Suresh Kumar, M. Bablu, Ashok Ranjan, L.M. Manocha, N. Eswara Prasad 2017)

Due to its proprietary nature, the ablation information of the C/SiC composite material is scarce as the data generation involves high cost of rocket-motor testing and material. The materials developed by different researchers are somewhat different; therefore the data available in the open literature cannot be used as such. However, the literature survey provides a range and approximate data. Most of the times, the material is evaluated for the key properties before its actual use as a rocket motor nozzle of any system. Uniform thermomechanical properties and high ceramic contents are the two major requirements for a structure to be used in nozzles or in throat inserts of the rocket motor. High ceramic content and improved thermo-mechanical properties would improve the ablation resistance and overall nozzle performance. Uniform properties and high ceramic content in a composite may be obtained by selecting appropriate fiber architecture and the process parameters [15, 16, 18, 53–55]. Ablation properties of the C/SiC composite nozzle fabricated

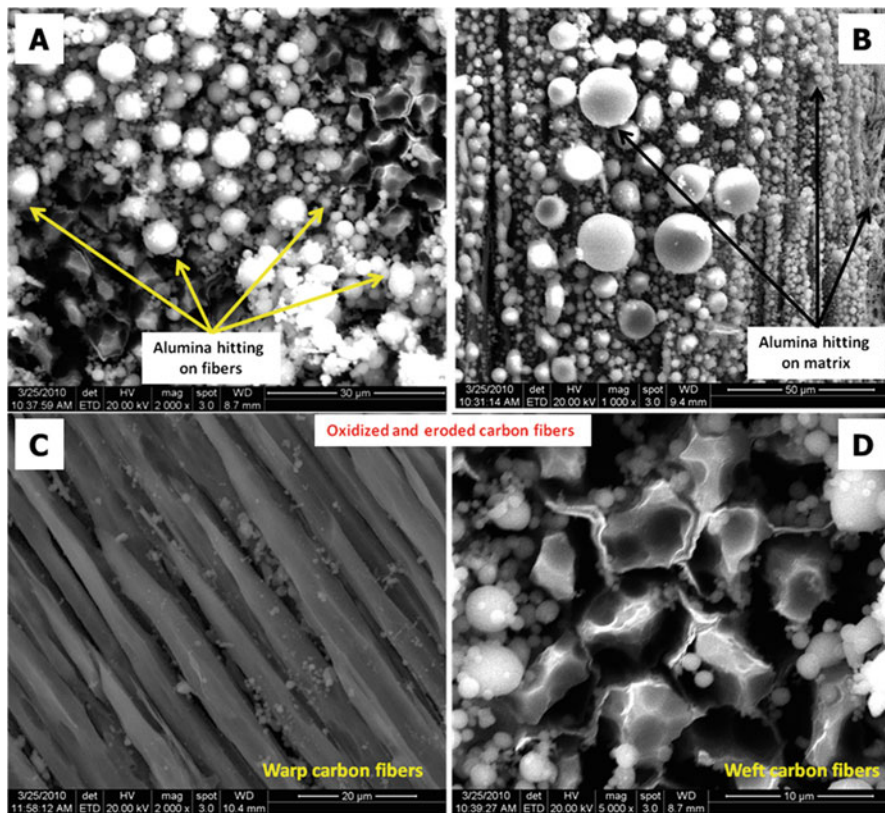


Fig. 28 Typical morphology of the eroded surfaces of the 3D stitched LSI-based C/SiC composite jet-vanes tested under aluminized solid propellant [5]. (With permission from Elsevier, Journal of the European Ceramic Society, Fabrication and erosion studies of C–SiC composite Jet Vanes in solid rocket motor exhaust, Suresh Kumar, Anil Kumar, K. Sampath, V.V. Bhanu Prasad, J.C. Chaudhary, A.K. Gupta, G. Rohini Devi 2011)

using CVI process are also reported for ethanol/oxygen propulsion system [53]. 4D C/SiC composite nozzle fabricated following the LSI process is evaluated under UH25/N₂O₄ propulsion system for 30 s. The overall mass erosion rate and the linear ablation rate of the nozzle were found to be 0.119 kg/m²s and 0.05 mm/s, respectively [4]. The C/SiC composite nozzle has shown excellent thermal shock and ablation resistance against the liquid propulsion exhaust gases consisting of very high concentration of the oxidizing species like OH, O₂, H₂O, CO₂, etc. at high temperature [4]. Linear ablation is found to be symmetrical in a plane perpendicular to the nozzle axis due to the uniform thermal and mechanical properties, but it varies along the nozzle length. The average ablation rate at the throat is the highest; it is found to be 0.05 mm/s [4]. Similar to the jet-vanes erosion under solid propellant plume, in liquid propellant plume also, the residual silicon melts and reacts with

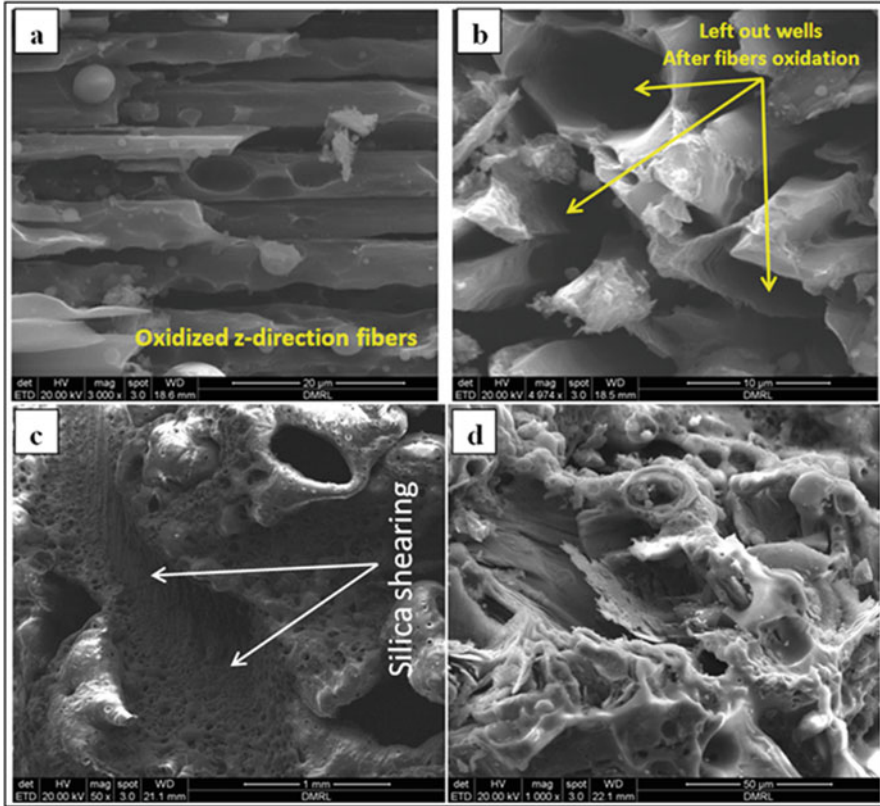


Fig. 29 Typical morphology of the eroded surfaces of the 4D woven LSI-based C/SiC composite nozzle tested under liquid propellant [4]. (With permission from John Wiley and Sons, International Journal of Applied Ceramic Technology, Fabrication and Ablation Studies of 4D C/SiC Composite Nozzle Under Liquid Propulsion, Raghvendra Rao Mokhasunavisu, Ramesh Babu Mala, Anil Kumar, et al. 2015)

oxygen of the combustion gases to form SiO_2 which in turn reacts with the SiC matrix. During oxidation of the C/SiC composite, there is a net loss of mass in spite of the gain due to passive oxidation of silicon. Thus, the loose nozzle structure erodes at higher rate due to high shear forces in the convergent and throat portion. However, the SiO_2 layer protects the carbon fibers against the possible oxidation in the divergent portion where temperature is lower and its layer covers its entire surface. A typical morphology of the ablated surface of the 4D C/SiC composite nozzle is presented in Fig. 29. The morphology of the ablated surfaces revealed that the material removal is due to both chemical and mechanical phenomenon. Chemical ablation is higher in the convergent section due to the high temperature while it is lower in the mechanical erosion which dominates at the throat due to the higher shear stresses [4].

Typical Applications of the C/SiC Composites

Due to their unique combination of density, thermal and mechanical properties, carbon-fiber-reinforced SiC composites are used in numerous application of aerospace and defense. Also there are some important applications in high-temperature industries. These composites are used at extreme temperatures up to 2500 °C for short durations like thrust vectoring controls and rocket propulsion systems. However, PIP-based C/SiC composite development was initiated mainly for space applications, like TPSs of the reusable spacecraft. Their excellent stability under high temperature and thermal shock absorption capability are the main reasons for their preference for hot gas liners in aeroengines and in rocket propulsion. Apart from the high-temperature applications, these composites are also used for satellite structures requiring high precision and dimensional stability. PIP-based C/SiC composites are used for structural applications, whereas LSI-processed C/C-SiC composites are mostly used for industrial applications and brake disks applications. Details of different applications are beyond the scope of this chapter but can be obtained from our earlier publications and other reputed sources [2, 3, 6, 14, 30, 33].

Summary and Conclusions

C-C/SiC and C/SiC composites have been under investigation for a long time. Several leading agencies around the world have developed state-of-the-art facilities for the reinforcements, preforming, processing, and characterization of these composites. Though the processing of C/SiC composites has been established for CVD, LSI, and PIP methods, still industrial use of the C/SiC material is limited. Mostly, the focus is there on the high-end applications pertaining to rocket propulsion, TPS, and aircraft brakes. Use of this material for high-end applications became possible only due to continuous improvement in the manufacturing processes. The improved process methodologies not only have increased the performance of the material, in terms of strength and oxidation resistance capability, but also improved its reliability. Several C/SiC composite products have been realized under the aegis of NASA, Russia, and the European Union for defense and aerospace applications. A significant amount of work has been done in the last two decades in India also. PIP technology has been developed for fabricating UD, 2D, and 3D stitched C/SiC composites including the realization of shaped articles. 3D stitched C/SiC composite jet-vanes and 4D woven C/SiC nozzles have been made using the LSI process where coal-tar pitch has been used as carbon source. Also, the state-of-the-art process equipments with new technologies have been investigated successfully which have precise control to tailor the morphologies by varying the rate of heating and overall to reduce the process time. The main challenges in contemplating to use the C/SiC for different applications are their large scattering and variability of properties. The properties are different from different sources of manufacturing and also differ from lab to lab. The other challenges are their heterogeneity and inhomogeneities with localized imperfections and defects, which cannot be controlled as per need, however, with strict control they can be minimized. For estimating their real performance

under the specific condition and load scenario, the defects of the components should be detected by some reliable Non-Destructive Testing (NDT) along with simulation models. Realistic simulation tools should be developed in order to provide a reliable lifetime prediction so that C/SiC composite products can be deployed into the mission critical modules with full assurance. Research continues to develop a reliable design methodology, automation of the preforming process, NDT, life estimations, and the joining of C/C and C/SiC composites with other materials. Last but not the least, cost-efficient tools and strategies should be evolved in the country for the machining of the C/SiC components having multiple curvatures and high ceramic contents.

References

1. Beyer S, Schmid S, Mair F et al (2006) Advanced composite materials for current and future propulsion and industrial applications. *Adv Sci Technol* 50:178–171
2. Heidenreich B (2015) C/SiC and C/C-SiC composites, ceramic matrix composites: materials, modeling and technology. In: Bansal NP, Lamon J (eds) *Ceramic Matrix Composites: Materials, Modeling and Technology*, 1st edn. The American Ceramic Society, Wiley, p 147–216
3. Kumar S, Shekar KC, Jana B, Manocha LM, Eswara Prasad N (2017) C/C and C/SiC composites for aerospace applications. In: Prasad N, Wanhill R (eds) *Aerospace materials and material technologies*. Indian Institute of Metals Series. Springer, Singapore, pp 343–369
4. Kumar S, Kumar A, Ramesh Babu M, Raghvendra Rao M (2015) Fabrication and ablation studies of 4D C/SiC composite nozzle under liquid propulsion. *Int J Appl Ceram Tech* 12(S3): E176–E190
5. Kumar S, Kumar A, Sampath K, Bhanu Prasad VV, Chaudhary JC, Gupta AK, Rohini Devi G (2011) Fabrication and erosion studies of C–SiC composite jet vanes in solid rocket motor exhaust. *J Eur Ceram Soc* 31(13):2425–2431
6. Weiß R (2001) Carbon fibre reinforced CMCs: manufacture, properties, oxidation protection. In: Krenkel W, Naslain R, Schneider H (eds) *High temperature ceramic matrix composites*. Wiley-VCH, Weinheim, pp 440–456
7. Meinhardt J, Woyke T, Raether F, Kienzle A (2006) Measurement and simulation of the oxidation of carbon fibers and C/SiC ceramic. *Adv Sci Technol* 45:1489–1494
8. Naslain R (2004) Design, preparation and properties of non-oxide CMCs for application in engines and nuclear reactors: an overview. *Compos Sci Technol* 64:155–170
9. Berdoyes M (2006) Snecma propulsion solide advanced technology SRM nozzles. In: *History and future*, AIAA 2006–4596. California. <https://doi.org/10.2514/6.2006-4596>
10. Kumar S, Misra MK, Mondal S, Gupta RK, Mishra R, Ranjan A, Saxena AK (2015) Polycarbosilane based UD C/SiC composites: effect of in-situ grown SiC nano-pins on mechanical properties. *Ceram Int* 41(10):12849–12860
11. Kumar S, Bablu M, Ranjan A, Manocha LM, Eswara PN (2017) Fabrication of 2D C/C-SiC composites using PIP based hybrid process and investigation of mechanical properties degradation under cyclic heating. *Ceram Int* 43(3):3414–3423
12. Kumar S, Bablu M, Janghela S, Misra MK, Mishra R, Ranjan A, Eswara PN (2018) Factorial design, processing, characterization and microstructure analysis of PIP-based C/SiC composites. *Bull Mater Sci* 41(17). <https://doi.org/10.1007/s12034-017-1535-5>
13. Kumar S, Bablu M, Misra MK, Ranjan A, Eswara PN (2017) Fabrication and characterization of PIP based C/SiC composites having improved mechanical properties using high modulus M40J carbon fibre as reinforcement. *Ceram Int* 43(11):8153–8162
14. Savage G (1993) Carbon-carbon composites. SPRINGER-SCIENCE+BUSINESS MEDIA, B. V.; pp 1–385. Springer Netherlands. <https://doi.org/10.1007/978-94-011-1586-5>

15. Kumar S, Kumar A, Rohini DG, Gupta AK (2011) Preparation of 3D orthogonal woven C-SiC composite and its characterization for thermo-mechanical properties. *Mater Sci Eng A* 528:6210–6216
16. Kumar S, Kumar A, Shukla A, Rohini DG, Gupta AK (2009) Investigation of thermal expansion of 3D-stitched C-SiC composites. *J Eur Ceram Soc* 29(13):2849–2855
17. Pradere C, Sauder C (2008) Transverse and longitudinal coefficient of thermal expansion of carbon fibers at high temperatures (300–2500 K). *Carbon* 46:1874–1884
18. Kumar S, Kumar A, Shukla A, Rohini DG, Gupta AK (2009) Thermal-diffusivity measurement of 3D-stitched C-SiC composites. *J Eur Ceram Soc* 29(3):489–495
19. Kamiya R, Cheeseman BA, Popper P et al (2000) Some recent advances in the fabrication and design of three dimensional textile preforms: a review. *Compos Sci Technol* 60:33–47
20. Mouritz AP, Bannister MK, Falzon PJ et al (1999) Review of applications for advanced three dimensional fiber textile composites. *Composites A* 30:1445–1461
21. Kadir B et al (2012) Multiaxis three-dimensional weaving for composites: a review. *Text Res J* 82(7):725–743
22. Lee JY, Kang TJ (2005) Thermal conductivity of needle punched preforms made of carbon and OxiPAN fibres. *Polym Polym Compos* 13(1):83–92
23. Evans MJ, Williams KA, Fisher R (1997) Manufacture of carbon fibre preform. US Patent 5599603, 1997
24. Evans MJ, Williams KA, Fisher R (1996) Ultra-high performance carbon composites. US Patent 5503893, 1996
25. Naslain R (1998) The design of the fibre-matrix interfacial zone in ceramic matrix composites. *Compos* 29A:1145–1155
26. Kerans RJ, Hay RS, Parthasarathy TA, Cinibulk MK (2002) Interface design for oxidation-resistant ceramic composites. *J Am Ceram Soc* 85(11):2599–2632
27. Naslain R, Dugne O, Guette A, Se'vely J, Robin-Brosse C, Rocher JP (1991) Boron nitride interphase in ceramic matrix composites. *J Am Ceram Soc* 74:2482–2488
28. Hutchinson JW, Jensen HM (1990) Models of fiber debonding and pullout in brittle composites with friction. *Mech Mater*, Elsevier 9:139–163
29. Evans AG, Zok FW, Mackin TJ (1995) High temperature mechanical behavior of ceramic composites. Butterworth-Heinemann, Boston, pp 3–84
30. Motz G, Schmidt S, Beyer S (2008) The PIP-process: precursor properties and applications in ceramic matrix composites, In: Krenkel W (ed) *Ceramic Matrix Composites: Fiber Reinforced Ceramics and their Applications*. Wiley-VCH Verlag, Weinheim, p 357–359
31. Whitmarsh CW, Interrante LV (1992) Carbosilane polymer precursors to silicon carbide ceramics. US Patent 5153295, 1992
32. Jian K, Chen ZH, Ma QS, Zheng WW (2005) Effects of pyrolysis processes on the microstructures and mechanical properties of C_f/SiC composites using polycarbosilane. *Mater Sci Eng A* 390:154–158
33. Ly H, Taylor R, Day RJ, Heatley F (2001) Conversion of Polycarbosilane (PCS) to SiC-Based Ceramic Part 1. Characterisation of PCS and Curing Products. *J Mater Sci* 36:4037–4043. <https://doi.org/10.1023/A:1017942826657>
34. Sherwood WJ (2003) CMCs come down to earth. *Am Ceram Soc Bull* 82(8):25–27
35. Rak ZS (2001) A process for C_f/SiC composites using liquid polymer infiltration. *J Am Ceram Soc* 84:2235–2239
36. Mishra MK, Barua SK, Kumar S (2018) Development of PIP based C/SiC UD composites. DRDO-DMSR-IPH-TCR-545-2018
37. Bablu SK (2018) Development of 2D C/SiC composites through PIP route. DRDO-DMSR-IPH-TCR-546-2018
38. Njoya D, Hajjaji M (2015) Quantification of the effects of manufacturing factors on ceramic properties using full factorial design. *J Asian Ceramic Soc* 3(1):32–37
39. Ma C, Guo L, Li H, Tan W, Duan T, Liu N, Zhang M (2016) Effects of high-temperature annealing on the microstructures and mechanical properties of C/C-ZrC-SiC composites prepared by precursor infiltration and pyrolysis. *Mater Des* 90:373–378

40. Zhao S, Zhou X, Yu J (2014) Effect of heat treatment on the mechanical properties of PIP–SiC/SiC composites fabricated with a consolidation process. *Ceram Int* 40(3):3879–3885
41. Sreeja R, Swaminathan B, Painuly A, Sebastian TV, Packirisamy S (2010) Allylhydridopoly-carbosilane (AHPCS) as matrix resin for C/SiC ceramic matrix composites. *Mater Sci Eng B* 168(1–3):204–220
42. Lamouroux F, Bertrand S, Pailler R, Naslain R, Cataldi M (1999) Oxidation-resistant carbon-fiber-reinforced ceramic-matrix composites. *Compos Sci Technol* 59(7):1073–1085
43. Langlais F (2000) In: Kelly A, Zweben C, Warren R (Eds) *Comprehensive composite materials, carbon/carbon. Cement and ceramic matrix composites*, vol 4. Elsevier, Amsterdam, p 611
44. Chawla KK (2003) *Ceramic matrix composites*, 2nd edn. Kluwer Academic Publishers, Boston
45. Kumar S, Chandra R, Kumar A, Eswara PN, Manocha LM (2015) C/SiC composites for propulsion application. *Compos Nanostruct* 7:225–230
46. Kumar S, Kumar A, Rohini DG, Shukla A, Gupta AK (2009) Capillary infiltration studies of liquids into 3D-stitched C–C preforms: part B: kinetics of silicon infiltration. *J Eur Ceram Soc* 29(12):2651–2657
47. Kumar S, Kumari S, Kumar A, Shukla A, Rohini DG, Gupta AK (2011) Investigation of effect of siliconization conditions on mechanical properties of 3D-stitched C–SiC composites. *Mater Sci Eng A* 528(3):1016–1022
48. Srikanth I, Daniel A, Kumar S, Padmavathi N, Singh V, Ghosal P, Kumar A, Rohini DG (2010) Nano silica modified carbon–phenolic composites for enhanced ablation resistance. *Scr Mater* 63(2):200–203
49. Krenkel W, Heidenreich B, Renz R (2002) C/C–SiC composites for advanced friction systems. *Adv Eng Mater* 4(7):427–436
50. Krenkel W (2004) Carbon fiber reinforced CMC for high performance structures. *Int J Appl Ceram Tech* 1(2):188–200
51. *Handbook of Ceramic Composites* (2005) In: Bansal NP (Eds) (2005)
52. Kumar S, Kushwaha J, Mondal S, Kumar A, Jain RK, Rohini DG (2013) Fabrication and ablation testing of 4D C/C composite at 10 MW/m² heat flux under a plasma arc heater. *Mater Sci Eng A* 566:102–111
53. Chen B, Litong Z, Laifei C, Xingang L (2009) Ablation behavior of a three-dimensional carbon/silicon carbide composite nozzle in an ethanol/oxygen combustion gas generator. *Int J Appl Ceram Technol* 6(2):182–189
54. Fang D, Chen Z, Song Y, Sun Z (2009) Morphology and microstructure of 2.5 dimension C/SiC composites ablated by oxyacetylene torch. *Ceram Int* 35(3):1249–1253
55. Opila EJ, Nguyen QGN (1998) Oxidation of chemically-vapor-deposited silicon carbide in carbon dioxide. *J Am Ceram Soc* 81(7):1949–1952
56. Zhi-Qiao Y, Feng C, Xiang X, Peng X, Hong-Bo Z, Bai-Yun H (2010) Oxidation behavior of CVI, MSI and CVI+MSI C/SiC composites. *Trans Nonferrous Met Soc China* 20(4):590–596
57. Geisler RL (1978) The relationship between solid-propellant formulation variables and nozzle recession rates. JANNAF Rocket Nozzle Technology Subcommittee Meeting, Lancaster, July, 1978
58. Swope LW, Berard MF (1964) Effects of solid-rocket propellant formulations and exhaust-gas chemistries on the erosion of graphite nozzles. In: AIAA solid propellant rocket conference, Palo Alto
59. Acharya R, Kuo KK (2006) Effect of chamber pressure & propellant composition on erosion rate of graphite rocket nozzle. In: Proceedings of 44th, AIAA aerospace sciences meeting and exhibit, Reno, NV, paper no. AIAA 2006–363, American Institute of Aeronautics and Astronautics, Reston, 1–15, 2006
60. Chen B, Zhang LT, Cheng LF, Luan XG (2009) Erosion resistance of needled carbon/carbon composites exposed to solid rocket motor plumes. *Carbon* 47(6):1474–1479
61. Kuo KK, Keswani ST (1985) A comprehensive theoretical model for carbon–carbon composite nozzle recession. *Compos Sci Technol* 42(3–4):145–164
62. Maisonneuve Y (1997) Ablation of solid–fuel booster nozzle materials. *Aerosp Sci Technol* 1(4):277–289



Carbon Fiber Reinforced Silicon Carbide Ceramic Matrix Composites

23

Processing and Characterization When Fabricated by CVI and Hybrid Technique

Andi Udayakumar, M. Rizvan Basha, Sarabjit Singh, Sweety Kumari, and V. V. Bhanu Prasad

Contents

Introduction	878
Methods of Preparations of C_f/SiC and C_f-C/SiC Composites	880
Liquid Phase Route	881
Gas Phase Route	882
Behavior of C_f/SiC and C_f-C/SiC Composites	889
General Remarks	889
Mechanical Behavior	890
Thermal Behavior	896
Tribological Behavior	898
Oxidation Behavior	901
Applications	903
Space Vehicle Components	904
Friction Systems	905
Components of Rocket Motors and Jet Engines	905
Calibration Standards and Components in the Telescope	906
Components for Energy Systems	907
Conclusion	908
References	908

Abstract

Carbon fiber reinforced silicon carbide matrix composites (C_f/SiC & $C_f/C-SiC$) have been extensively studied as a new class of thermo-structural materials as an alternate candidate for C_f/C composites for increased oxidation resistance and for applications in the oxidizing environment for the past one to two decades. In

A. Udayakumar (✉) · M. R. Basha
Materials Science Division, CSIR-National Aerospace Laboratories, Bengaluru, India
e-mail: audayk@yahoo.com

S. Singh · S. Kumari · V. V. B. Prasad
Ceramics and Composites, Defence Metallurgical Research Laboratory, Hyderabad, India
e-mail: sarabdrdo@gmail.com; bhanuprasad2002@yahoo.com

recent years, many new processing techniques have been developed to process these composites. However, chemical vapor infiltration (CVI) and hybrid process [CVI + Molten silicon infiltration (MSI) and CVI+polymer impregnation and pyrolysis (CVI+PIP)] are more promising to develop the C_f/SiC composites with better properties. These composites possess superior properties such as high specific strength, specific modulus at high temperature, high-temperature chemical properties, and good tribological properties. Hence, they are being thoroughly studied for application in a hypersonic vehicle, some components in military engines and reusable space vehicle, brake disc for aircraft, jet vanes, emergency brakes in cranes, calibration plates, fuel tube in a nuclear fission reactor, furnace charges devices, etc. This chapter describes the general introduction about C_f/SiC and $C_f/C-SiC$ composites, their various processing routes, properties, key results, and the prominent application areas.

Keywords

Ceramic Matrix Composites · C_f/SiC & $C_f/C-SiC$ composites · C/C composites · Chemical Vapor Infiltration (CVI) · Molten silicon infiltration (MSI) · Polymer impregnation and pyrolysis (PIP) · Hybrid process · Multi-layer interface · Tribological properties · Jet vanes

Introduction

The nonoxide ceramic matrix composites (CMC), such as carbon fiber/carbon (C_f/C), were developed in the 1970s as lightweight structures for aerospace applications. Because of the limited life of these composites in the aggressive environmental conditions and availability of little information about their long-term behavior, they had to be designed for limited life structures. In order to improve the oxidation resistance and hence the application lifetime of these composites, the carbon matrix was replaced by ceramics in particular silicon carbide (SiC) due to its high oxidation resistance, superior temperature capability, and thermal shock stability along with high creep resistance. The composite obtained is so-called carbon fiber reinforced silicon carbide (C_f/SiC) ceramic matrix composite.

This effort has gained attention since the similar manufacturing techniques could be used for the fabrication of C_f/SiC composites as in the case of C_f/C composite preparation. C_f/SiC composites are used in many applications which include rocket nozzles, gas turbine engine flaps, leading edges of spacecraft, and aircraft brake discs [1–3]. Continuous fiber reinforced ceramic matrix composites (CFCC) where carbon fiber reinforcements embedded in silicon carbide matrix (C_f/SiC) are a relatively new class of high-temperature structural materials.

Generally, CFCC has been developed to combine the advantageous properties of monolithic ceramics with a high damage tolerance. These materials are characterized by the fact that the stiffness of both fibers and the matrix are of the same order of magnitude. Strong fiber/matrix interfacial bond develops high tensile stresses in the matrix resulting in low damage tolerance of the C_f/SiC composites. On the other

hand, poor fiber/matrix bonding leads to a nearly stress-free matrix and high fracture toughness. However, as the de-bonding and shear properties mainly depend on frictional effects, such type of composites are usually not suitable as the structural materials. Damage tolerant CFCC, therefore, require moderate fiber/matrix bond strength (10–20 MPa) with an adapted interface. The interface microstructure can be of different types namely: sharp thin interface, noninteractive interface, in situ reacted interface, porous interface, and multilayered interface, and it is responsible for crack arresting and deflecting microcracks. It is observed from the literature that pyrolytic carbon (PyC), boron nitride (BN), and multilayered interfaces [(PyC/SiC)_n or (BN/SiC)_n; n is the number of alternating layers] are generally applied through CVI technique to the reinforcing fiber before SiC matrix infiltration. SiC matrix is obtained through CVI and other processes such as polymer impregnation and pyrolysis (PIP) and molten silicon infiltration (MSI).

Carbon fibers have to be embedded in a SiC matrix to produce C_f/SiC and C_f/C-SiC composites. In general, SiC can be added either by gaseous or liquid route. The gaseous route involves the deposition of SiC from the high-temperature chemical reaction of gaseous precursors such as Methyltrichlorosilane (CH₃SiCl₃), Dimethyldichlorosilane ((CH₃)₂SiCl₂), etc. A liquid route is further subdivided into two categories namely: with and without in-situ reaction. The liquid route without in situ reaction deals with pyrolysis of polymeric ceramic precursors (Organometallic materials) such as polycarbosilane (PCS), polysilazine (PS), polycarbosiloxane, etc. liquid phase route with in situ reaction deals with the direct chemical reaction between molten liquid silicon and carbon and lead to the formation of SiC matrix.

In general, three processing methods are involved in manufacturing C_f/SiC and C_f/C-SiC classes of ceramic matrix composites, namely:

1. Chemical vapor infiltration (CVI) process
2. Polymer impregnation and pyrolysis (PIP) combined with CVI (Hybrid route - CVI+PIP) and
3. Molten silicon infiltration (MSI) combined with CVI (Hybrid route – CVI+MSI).

Details of these processes are described in the following section. In general, all the above processing methods involve the following steps:

- Carbon fiber preform preparation
- Application of tailored fiber/matrix interface coating to the fibers
- Building up of SiC matrix (or) self-healing matrix
- Seal coating and environmental barrier coating (EBC)

C_f/SiC materials are basically fiber-dominant materials. Hence, improved material properties can be obtained by using intermediate modulus (e.g., Toroyca T800) and high modulus (e.g., Toroyca M40) fibers results in enhanced tensile strength and young's modulus. Ultra high modulus fibers are not generally used due to the cost consideration. Carbon fiber tow with fiber counts ranging from 1000 to 6000 (1-6K) is normally preferred to obtain the final composite with a homogeneous distribution

of fiber and matrix while taking advantage of the fiber properties as much as possible along with process friendliness (infiltration or impregnation of friendly precursors).

Carbon fiber tows are first made in to a preform, which is usually done by various techniques such as lay-up involving the stacking of cut bi-directionally woven (2D) fabric layers and or with unidirectional fabric (UD) layers with the orientation ($0^\circ/90^\circ$) (orthotropic) or ($0^\circ/90^\circ, \pm 45^\circ$) orientation (quasi-isotropic), other approaches involve lay-up with stitching (2.5D fiber architecture), noobing (3D noninterlaced fiber architecture), 3D weaving (angle interlocked), and filament winding and braiding combined with stitching and needling (resulting 2.5D.3D). Generally, 2.5D and 3D/4D fiber architectures have advantages to form free-standing near-net shaped preforms, which are ideal for gas phase infiltration. Multifiber architecture is even more suitable to obtain the composites with high inter-laminar shear stress and quasi-isotropic thermal and mechanical properties for better load and thermal management application.

Methods of Preparations of C_f/SiC and $C_f/C/SiC$ Composites

In general, CVI and hybrid processes like CVI+PIP and CVI+MSI are used to manufacture C_f/SiC and $C_f/C-SiC$ ceramic matrix composites. The flow diagram of various processes available to produce CFCC is given in Fig. 1. Since ceramic

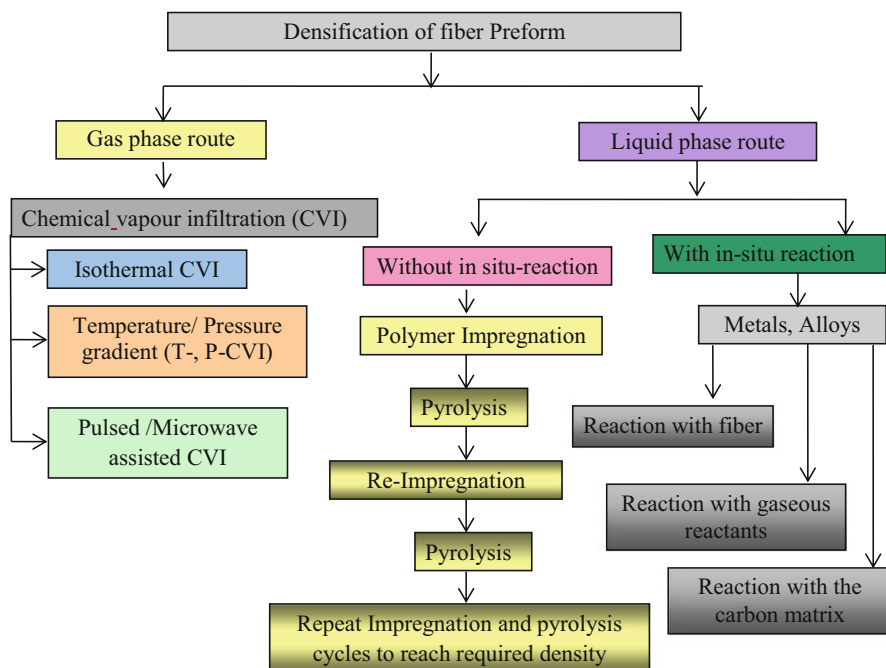


Fig. 1 A flow diagram showing the various routes available for the processing of CMCs

fiber is brittle and often is of limited high temperature stability, all these steps require moderate temperature/pressure. There are three processing routes for making CMCs: namely, liquid phase, gas phase, and hybrid routes. Under the liquid phase route, the techniques can be classified into two classes: without in situ reaction and with in-situ reaction.

Liquid Phase Route

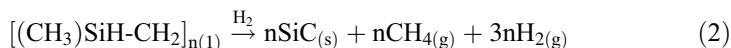
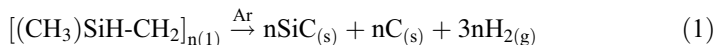
In the liquid phase route, the matrix is formed from a liquid precursor into the fiber preform. The precursor is first impregnated into the reinforcement, then the solvent (if any) is evaporated and the residue is decomposed and finally sintered at moderate temperature. The precursor can be a polymer (pitch or phenolic resin for carbon matrix, polysilazane or polycarbosilane for SiC matrix) or slurry (prepared with appropriate ceramic powder). Slurry infiltration process is perhaps the most important technique used to produce carbon fiber reinforced CMCs. This process involves two stages:

1. Incorporation of the liquid precursor matrix phase into the preform (reinforcement phase)
2. Matrix consolidation by sintering (pressureless sintering, hot pressing, hot isostatic pressing)

In polymer impregnation and pyrolysis (PIP) technique, the matrix precursor is a polymer, such as a pitch or phenolic resin for C matrix and a polycarbosilane (PCS) resin for the SiC matrix. Typically, the PIP process involves four steps namely:

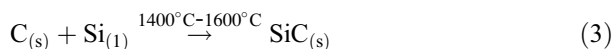
- (i) The impregnation of the liquid precursor (molten polymer or solution) in the preform, for example, by a technique similar to resin transfer molding (RTM). Pressure is applied to the liquid to infiltrate into the preform already arranged in a mold, and maintained under vacuum.
- (ii) The in situ curing of the polymer.
- (iii) The pyrolysis of the polymer at about 1000 °C in an inert atmosphere.
- (iv) The sintering or crystallization treatment of the residue to obtain the required phase.

One of the advantages of the PIP process is that it relies upon industrially proven and well-known technologies. Moreover, the pyrolysis residue is amorphous or nanocrystalline phase and can be sintered or crystallized at a relatively low temperature. Finally, the process is well suited to form a matrix of complex composition (e.g., Si-B-C system). Conversely, the PIP process has also several drawbacks. Firstly, the gaseous species formed during the pyrolysis step lower the ceramic yield and lead to a porous pyrolytic residue, according to the following overall reactions for the conversion of a PCS precursor into the ceramic phase [2].



The corresponding ceramic yield from these reactions is ~90% and 69%, respectively. Hence, several PIP cycles (typically 6–10) are required to achieve a fairly high densification. The yield of pyrolysis can be improved by loading the liquid precursor with a ceramic powder, but this addition increases the precursor viscosity rendering more difficulty for the impregnation step. Designing a low cost polymer with high ceramic yield remains a challenge and overcoming the problem of residual pores in the composites fabricated by PIP is another challenge.

In the liquid phase technique with in situ reaction, the precursor can be an element in the molten state (Si for SiC). Reactive melt infiltration (RMI)/MSI is a liquid phase route with in-situ reaction. In the RMI/MSI process, a fiber preform is infiltrated with an element in the molten state, the later reacting with the preform, a porous carbon matrix in a controlled atmosphere to form the in situ ceramic matrix. This process is well suited for elements with relatively low melting points, such as aluminum for the growth of alumina or silicon for the growth of the SiC matrix. The process of getting SiC matrix composites through RMI/MSI involves two main steps: firstly, a preform coated with a suitable interfacial thin film having a thickness in the range of few hundred nanometers is consolidated with reactive carbon resulting from the pyrolysis of the liquid organic precursor. In a second step, it is infiltrated with liquid silicon at a high temperature (1550 °C), which reacts with carbon to form SiC (Eq. 3).



Molten silicon is rising up in the preform under the effect of capillary forces. When the amount of carbon deposited in the first step and the liquid silicon flow are properly adjusted, the preform porosity can be almost totally filled with the in-situ formed ceramic matrix [3, 4]. RMI [3] is a fast process, which yields near-net shaped composites with very low residual porosity (<5%) and hence high thermal conductivity. Conversely, it is a high temperature process requiring the use of fibers with high thermal stability, such as high modulus (HM)-carbon fibers. Since liquid silicon is very reactive, the interface (thin monolayer) should be protected. One possibility is to use a dual interface, such as PyC-SiC or BN-SiC fiber coating.

The SiC based matrix often contains significant amounts of free silicon. One way to solve this problem is to replace silicon by a suitable alloy, such as Si-Mo alloy in which Mo reacting with excess silicon to form the refractory MoSi₂ (silicide).

Gas Phase Route

In the gas phase route or chemical vapor infiltration (CVI) process, the interface, matrix, and even the environmental barrier coating (EBC) are successively deposited

from appropriate gaseous precursors under reduced pressure and at moderate temperature (typically 900–1400 °C). The growth rate mechanisms are the same in CVI and chemical vapor deposition (CVD) processes, but unlike CVD, the convection and diffusion in CVI are taking place not only along the substrate surface (i.e., external mass transport), but it also occurs through as well (i.e., internal mass transport). Furthermore, the surface area available for deposition (of the porous preform) is much larger as compared to dense CVD substrates. Therefore, the reactant depletion effects are more severe in the CVI process.

Chemical Vapor Infiltration

CVI is the variant of the CVD process used to manufacture various refractory matrix materials (e.g., SiC, C, Si₃N₄, B₄C, BN) of reinforced ceramic composites. The CVI process was developed in 1962 to densify porous graphite by infiltration with carbon matrix [5]. It is a reactive process that differs from the physical vapor deposition (PVD) technique, that involves physical evaporation, sputtering and sublimation [6]. During CVI process, the gaseous precursors are allowed to infiltrate into the fibrous preform via chemical diffusion reaction at high temperature and atmospheric or low pressure to deposit a solid refractory material on the surface of the fibers present in the preform. The by-products and unreacted reactants are driven out of the preform, unlike in the CVD process. Though CVI and CVD are governed by the same thermodynamics and chemistry, their kinetics is different. In the CVI process, the processing conditions are tailored in such a way that the deposition process occurs at slow reaction kinetics in a low temperature regime to obtain maximum uniform infiltration and densification of the composites [7]. CVI is a special case of CVD and it is a complex additive type of process technique carried out at high temperature and low pressure. The schematic diagram of typical CVI reactor generally used for the deposition and infiltration of SiC, C, and BN is shown in Fig. 2.

Any CVI system will have the four subsystems: namely, gas handling system (to monitor the reactant gases and allow the flow to the reactor), the high temperature reaction chamber for the reaction to occur, exhaust system to create the process pressure and to pump out the reaction by-products/unreacted reactants, and control system to control the process parameters (temperature, pressure, and flow, etc.). CVI has unique characteristics such as good throwing power, the ability to deposit refractory materials at temperatures far below the normal ceramic processing (e.g., hot pressing, hot isostatic pressing and shaping followed by sintering) temperatures, and the capability of producing materials of exceptionally high purity with improved mechanical properties. Since the temperature and pressure involved in the CVI process are not very high, very little thermal, chemical, and mechanical damages to the reinforcement are observed as compared to the conventional densification and the hot pressing methods.

There are various types of CVI processes (shown in Fig. 3), namely, isothermal-isobaric CVI (ICVI), isothermal forced flow CVI (FCVI), thermal gradient CVI (TGCVI), thermal gradient forced flow CVI (TGFCVI), pulsed CVI (PCVI), and microwave assisted CVI (MWCVI). In ICVI, the gaseous reactants are transported into the porous preform (heated to constant temperature) via diffusion and deposit

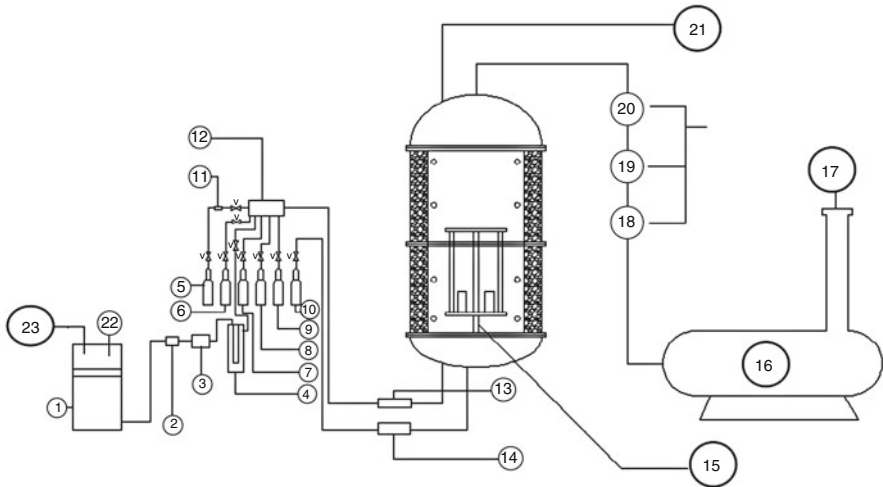


Fig. 2 Schematic diagram of a typical CVD/CVI reactor: (1) MTS Tank, (2) Filter, (3) Liquid mass flow controller, (4) Evaporator, (5) Argon (6) H₂, (7) N₂, (8) CH₄, (9) NH₃, (10) BCl₃, (11) Mass flow controller, (12) Gas mixer, (13) and (14) Non return valve. (15) Turn table, (16) Scrubber, (17) Exhaust, (18) Liquid ring pump, (19) Booster pump 1, (20) Booster pump 2, (21) Reactor, (22) Gauge, and (23) Argon

the solid matrix after the decomposition/chemical reaction. In this process, the deposition rate is intentionally made slow with less efficiency to minimize the overlay coating and to have the uniform and optimum densification. The process is interrupted at regular intervals for surface machining to open up the closed surface pores for increasing the infiltration rate and uniformity. Longer densification time (>400 h) is required to achieve the required density.

In the FCVI process, the reactants are forced through the preform to increase the infiltration rate [8]. The temperature gradient is created in the preform and gaseous reactants are transported into the preform via chemical diffusion in TGCVI process to increase the infiltration rate. The infiltration process starts off from the hotter region of the preform and proceeds toward its colder region, and thereby, increase the uniformity and minimize the occurrence of clogging (the phenomenon of premature closure of pores). This method is very effective for small products having regular cross sectional geometry. In TGFCVI process, in addition to thermal gradient across the preform, the gaseous reactants are forced through the preform to have the uniform and increased infiltration rate. In the microwave assisted CVI, the preform is heated using microwave energy. If the preform is not microwave absorbent in nature, it is seeded with the susceptor to heat the preform. Since the microwave heating is volumetric heating and heat transfer is inside-out, uniform and enhanced infiltration is achieved.

In the Pulsed CVI, the reactor is evacuated; reactant gases are sent into the reactor and allowed to react. After the reaction, the by-products are pumped out. This procedure is repeated until the required density is obtained. The above said CVI

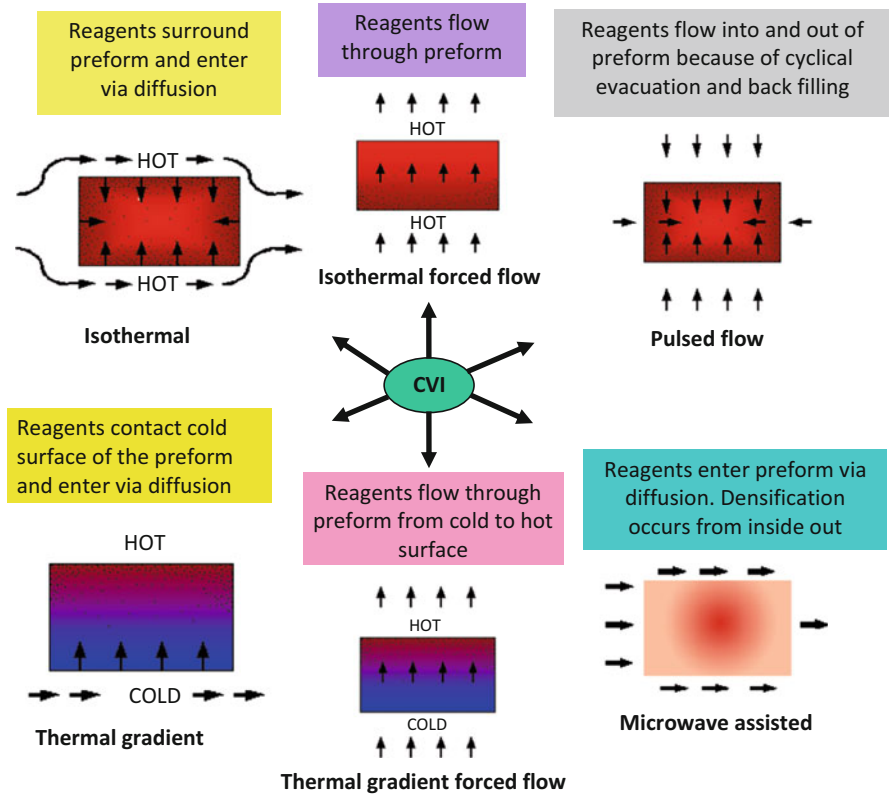


Fig. 3 A schematic showing the various types of CVI processes

processes have their own advantages and disadvantages. Various precursor systems like Methane-Silicon tetrachloride, Methyl trichlorosilane (MTS)-Hydrogen, and Dimethyldichlorosilane-Hydrogen are used to compose CVD/CVI-SiC [9]. The advantage of MTS over other precursors is that carbon and silicon are present in the ratio of 1:1 to form stoichiometric SiC. It also exists in liquid form at room temperature with high vapor pressure and it can be evaporated and transported to the reactor using hydrogen as a carrier gas. The ICVI is the one, which is commercially preferred since it could be used to make large, complex, and irregular geometries.

Advantages of CVI:

- The process utilizes low temperature and the stresses generated are much smaller and this minimizes damage to fibers in the preform.
- Precoating can be done in the same equipment to form fiber-matrix interface for obtaining higher toughness.
- The process can be used to densify the product obtained through other processes.
- The fabrication of complex shaped components is possible.
- The matrix materials of very high purity can be produced.

Disadvantages:

- Very slow process and precursors are expensive.
- Precursors are hazardous to health and need environmental safety precautions.

Hybrid Route

Since CVI, PIP, and MSI techniques to produce respective C_f/SiC composites have their own advantages and drawbacks, it would be appropriate to combine the two (or even more) of them in order to shorten the overall densification time or/and to lower the residual porosity or to design a matrix with a specific microstructure. There is a variety of such integrated (or hybrid) processing routes. Generally, CVI is the method of choice for the deposition of an interface on the fibers of a preform, whatever may be the method used to infiltrate the matrix. Both CVI and PIP yield composites with a significant residual porosity. Although this porosity can be sealed with an over-coating by CVD/CVI, such a coating often undergoes microcracking. Hence, it would be more appropriate to add one MSI-step: liquid silicon (or any other suitable liquid alloys) filling the residual porosity and hermetically sealing the composite. Even more complex processing strategies have been envisaged [10–12]. Interestingly, combined processing routes can also be used to design matrices with a diverse microstructures. CVI+PIP and CVI+MSI are the most preferred hybrid routes being followed to develop C_f/SiC and $C_f/C-SiC$ composites. Techniques such as slurry infiltration followed by sintering and sol-gel infiltration followed by sintering are not discussed here.

CVI+PIP

In this approach, the carbon fiber preforms are first coated with required interphase materials via CVI process and the interface is protected with SiC prime coating via the CVI. The interface and SiC prime coating protect the fiber from the aggressive environment created during the pyrolysis reaction of organic polymer (e.g., Phenolic) used for obtaining the carbon matrix. The interface coated C-fiber preforms are then impregnated with the pre-ceramic polymer (e.g., polycarbosilane) either in melt form or solution form and subsequently cured and pyrolyzed at high temperature (e.g., 1000 °C under Ar atmosphere). During the pyrolysis process, SiC matrix build-up takes place via thermal decomposition of preceramic polymers. Subsequently, heat treatment at a temperature greater than 1200 °C is carried out to improve the crystallinity of SiC matrix formed [13]. Polymer impregnation and pyrolysis cycles are repeated few times (4–7 cycles) to achieve the required density of C_f/SiC composites. PIP route is one of the most advanced methods for the preparation of complex and large shaped C_f/SiC components in the aerospace industries [14].

The companies such as Astrium ST/EADSIW (Germany), Herakles (France), COI ceramics Inc. (COIC, USA) MS Production (Slovenia), and others are manufacturing C_f/SiC materials via PIP+CVI. This hybrid technique is very interesting because of less production time compared to C_f/SiC composite through CVI alone. To speed up the densification, the SiC nano-powders can also be added to the

PCS solution. The flow charts showing the preparation of C_f/SiC and $C_f/C-SiC$ composites via CVI+PIP and CVI+LSI are shown in Figs. 4 and 5.

CVI+MSI

In this approach, the carbon fiber preforms are first coated with required interphase materials via CVI process and the interface is protected with SiC prime coating via the CVI. The interface and SiC prime coating protects the fiber from the aggressive environment created during the pyrolysis reaction of organic polymer (e.g., Phenolic resin) used for obtaining the C matrix.

The interface and SiC coated C-fiber preforms are impregnated with phenolic resin via wet lay-up or resin transfer/infusion molding technique or vacuum impregnation methods. The phenolic resin solution can be prepared by mixing phenolic resin powder and ethanol using mechanical stirrer at a temperature of about

Fig. 4 Flow chart showing the preparation of C_f/SiC composites via CVI+PIP

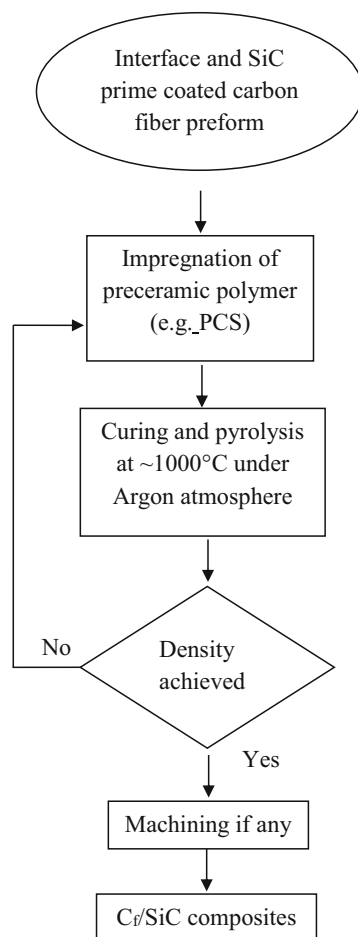
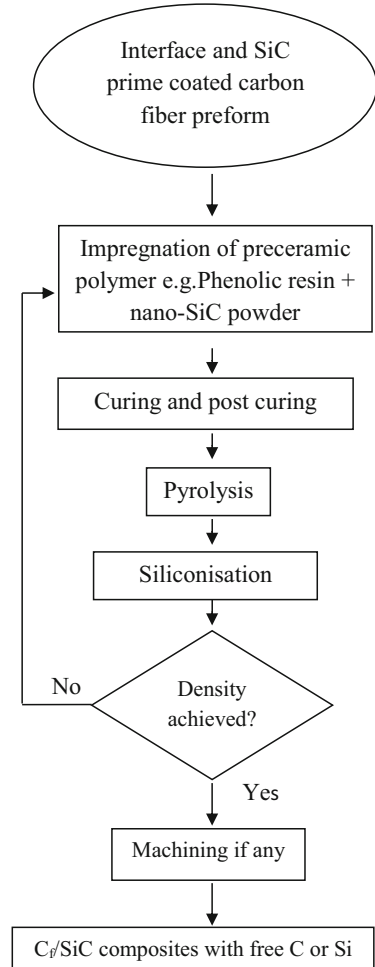


Fig. 5 Flow chart showing the preparation of C_f/C -SiC composites via CVI+MSI



40–50 °C. Liquid phenolic resin can also be used for impregnation. After curing and postcuring, the pyrolysis is carried out at 1000 °C with argon flowing to obtain porous C_f/C composites.

A porous C_f/C composite having a network of pores and cracks is then infiltrated by molten Si mostly using capillary pressure. The melt infiltration rate can also be enhanced by the application of external pressure and processing in the vacuum. Porous C_f/C preform is also subjected to high temperature treatment (e.g., >2000 °C) in order to graphitize the carbon constituents to have an additional contraction of carbon matrix, which resulted in an increased porosity of C_f/C preform and a higher Si uptake during siliconization. Increased content of Si/SiC matrix in the composites leads to higher thermal conductivity.

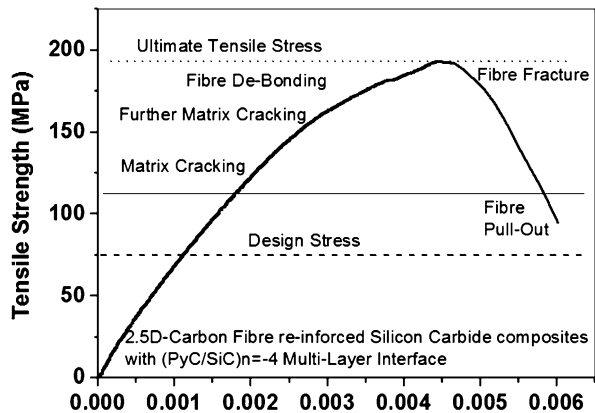
Behavior of C_f/SiC and C_f-C/SiC Composites

General Remarks

C_f/SiC and $C_f/C-SiC$ composites are light weight advanced ceramic matrix composites having the density in the range of 1.9–2.4 g cm⁻³ depending on the fiber architecture and the manufacturing method used. The density of these materials is little higher than that of carbon fiber reinforced plastics-CFRP ($\rho = 1500$ kg/m³) and that of magnesium ($\rho = 1740$ kg/m³), but lower than that of aluminum ($\rho = 2700$ kg/m³). Open porosity of these composites is typically in the range of 5–15% depending on the processing routes adopted. CVI-generated C_f/SiC composites will have open porosity in the range of 8–15% as a result of the competition between the premature pore closure (canning) and in-depth growth mechanisms. In the case of PIP-derived C_f/SiC composites, the residual open porosity is in the range of 6–10%. C_f/SiC and $C_f/C-SiC$ composites with significantly high density and low porosity (1–4%) are obtained in the case of melt infiltration technique (MSI).

Volume fractions of different phases (C, SiC, Si, etc.,) in these composites may vary with respect to the processing methods and the type of reinforcements (short fiber or long fiber, braided, stitched, angle interlocked, etc.,) used. These composites with tailored fiber-matrix interface become flaw insensitive (damage tolerant and forgiving in nature) compared to monolithic ceramics. C_f/SiC , $C_f/C-SiC$ composites will exhibit a nonlinear stress-strain behavior due to various energy dissipation mechanisms such as matrix cracking, fiber de-bonding, fiber sliding, crack bridging, fiber pull-out, etc., operating in the material (Fig. 6). Fiber reinforced ceramic matrix composites (in particular C_f/SiC , and $C_f/C-SiC$) offer high specific strength and stiffness at temperatures greater than 900 °C among the available engineering materials today [26]. Hence, these composites are the most preferred candidate materials for lightweight components subjected to high mechanical and thermal stresses.

Fig. 6 Typical tensile behavior of CVI-generated C/SiC composites



These composite becomes damage tolerant, if the fiber-matrix interface (PyC, BN, $(\text{PyC/SiC})_n = 4$, $(\text{PyC/BN})_n = 4$, etc.) is tailored (type of interface, nature of interface (thin interface, porous interface, multilayer interface, etc.), fiber-matrix interface bond strength (strong enough to transfer the load from matrix to fiber and weak enough to facilitate the de-bonding), the thermodynamic stability of an interface, and thickness of the interface).

Mechanical Behavior

Carbon fiber reinforced silicon carbide matrix (C_f/SiC) composites offer outstanding mechanical properties compared to conventional materials, which mainly depend on properties of constituents, volume fractions of phases (reinforcement, interface, matrix, etc.), composite's microstructure, and external protective coatings (e.g., seal coating, environmental barrier coating). Anisotropic to nearly isotropic behavior is observed in these composites depending on the fiber architecture (nD-fiber architecture; $n = 1, 2, 2.5, 3, 4$, etc., the braided structure, filament winding, nonwoven, etc.). Mechanical properties of C_f/SiC composites are strongly influenced by the carbon fiber and hence the type of the fiber, fiber orientation, and method of integration of the fibers in the composites. Mechanical properties of CVI-generated C_f/SiC composites at room temperature and elevated (1000 °C and 1400 °C) temperatures have been well studied by A. Lacombe, et al. [15]. Tensile strength and modulus are quite stable up to 1400 °C while flexural strength of these composites is found to increase with increasing temperature.

Tensile fatigue behavior of 2D- C_f/SiC composites at ambient temperature and 1100 °C (under tensile/tensile loads under an inert atmosphere at 100 Hz) has been studied [15] and reported that property retention (nearly identical to the initially measured values; rupture strength of 370 MPa and elongation of 0.9%) is excellent after 10^6 cycles. It is also reported that residual strengths are the same as the values measured initially at any fatigue stress level (75% of initial tensile fracture strength).

Behavior of C_f/SiC composites with pyrocarbon (PyC) interface prepared through CVI under flexural loading (3-point bending test) at room temperature and elevated temperatures (1200 °C and 1300 °C) is shown in Fig. 7 [16]. PyC is obtained by cracking methane (at a pressure of 1–2 mbar and temperature of 960 °C). The fiber volume fraction (V_f) of 0.35 is used. It is observed that composites exhibited a “nonlinear failure behavior” as required. PyC interface thickness is in the range of 0.3–0.35 μm (Fig. 8) [16].

It is also found that SiC seal coating as a final manufacturing step improves the mechanical behavior and offers the protection to the carbon species of the composites from the oxidizing environment. Flexural strength data of these composites is summarized in Table 1 [16]. Mechanical properties of 3-D noninterlaced C_f/SiC composites prepared through hybrid process (i.e., combining ICVI with PIP process) is listed in Table 2 [17].

Tensile and flexural plots obtained for the 3-D $C_f/\text{C-SiC}$ composites are shown in Fig. 9a–c [17]. From these results, it is evident that the nonlinear behavior is present and it is attributed to tailored interface thickness (Fig. 9d) [17] and various fracture

Fig. 7 Flexural behavior of the uncoated and seal coated samples, curves I and II-uncoated samples tested at room temperature and 1200 °C, III-SiC seal coated sample tested at 1300 °C

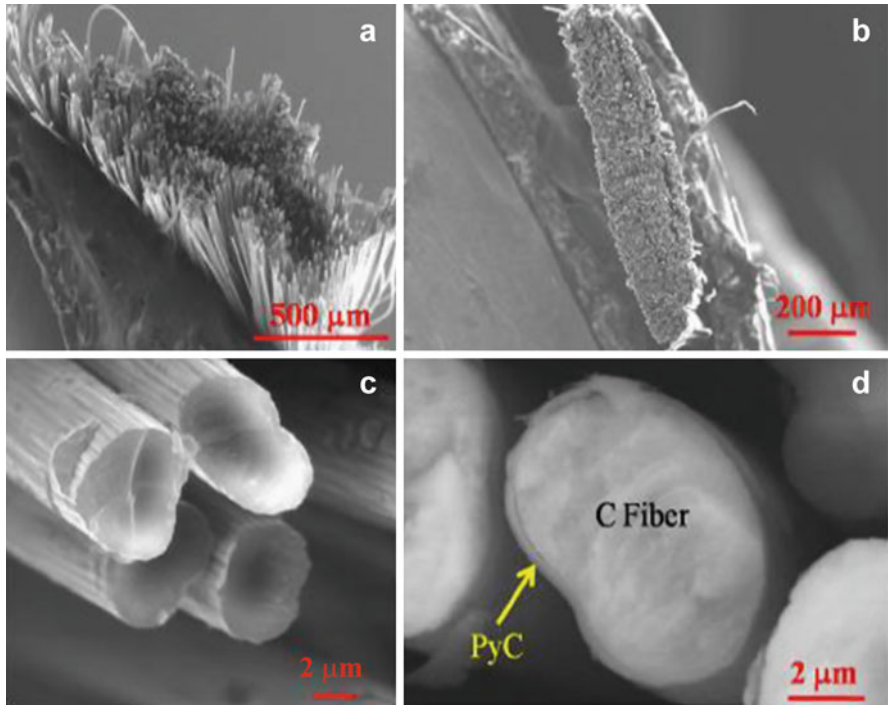
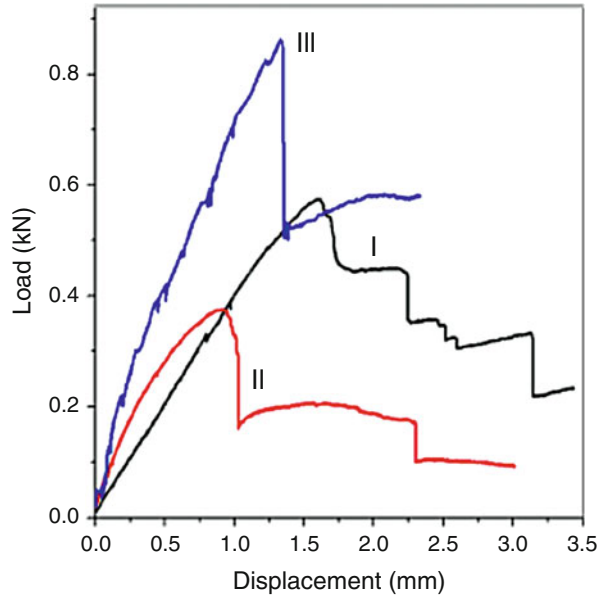


Fig. 8 SEM images of (a) uncoated and (b) the PyC coated carbon fibers (c) and (d) shows their respective SEM images at higher magnifications

Table 1 Properties of ICVI-generated C_f/SiC composites [16]

Property	Value
Fiber reinforcement	T 300 3 K, 8-Harness satin woven
Fiber volume fraction	0.35
Fiber architecture	Cloth lay-up with stitching (2.5-D)
Density	2.1–2.2 g cm ⁻³
Porosity	10–14%
Flexural strength (3 point) at RT (not SiC seal coated)	315 MPa
Flexural strength (3 _{pt}) at 1200 °C (not SiC seal coated)	200 MPa
Flexural strength (3 _{pt}) at 1200 °C (SiC seal coated)	370 MPa
Flexural strength (3 _{pt}) at 1300 °C (SiC seal coated)	380 MPa

Table 2 Mechanical properties of 3-D noninterlaced C_f/SiC composites prepared through hybrid process [17]

Property	Value
Fiber	T300 12 K Carbon fiber
Preform and fiber architecture	3-D noninterlaced, noobed
Process used	ICVI and PIP using polysilazane precursor
Density	1.94 g cm ⁻³
Flexural strength (3 _{pt}) at 28 °C	280 MPa
Fracture toughness (K _{IC}) at 28 °C	39 ± 1.9 MPa m ^{1/2}
Young's modulus	35 ± 1.7 GPa
Tensile strength at 28 °C	178 ± 25.7 MPa
Tensile strength at 500 °C	194 ± 15 MPa
Strain to failure	0.75 ± 0.1
Work of fracture	2.8 kJ/m ²
Dynamic fracture toughness through Charpy impact test	44.8 kJ/m ²
Interlaminar shear stress	93.0 MPa

processes operative in these materials (Fig. 10) [17]. The very low strength obtained for these composites tested at 1000 °C in air atmosphere is due to the oxidation of PyC interface and the carbon fiber reinforcement. It confirms that the CVD SiC seal coating is not enough to protect these composites from the oxidative environment. These composites exhibited superior shear strength and fracture toughness. The low room temperature strength is due to the bigger inter-bundle porosity present in the composites.

2.5-D C_f/SiC composites using T300-3 K carbon fiber, 8-Harness satin woven cloth reinforcement, with different fiber-matrix interfaces (e.g., PyC, BN, (PyC/SiC)_{n = 4} multilayer interface) and different V_f are developed by CSIR-NAL, through ICVI process. The key results obtained are presented herewith. The density of all the cases of composites is in the range of 2.0–2.3 g cm⁻³. Flexural fatigue

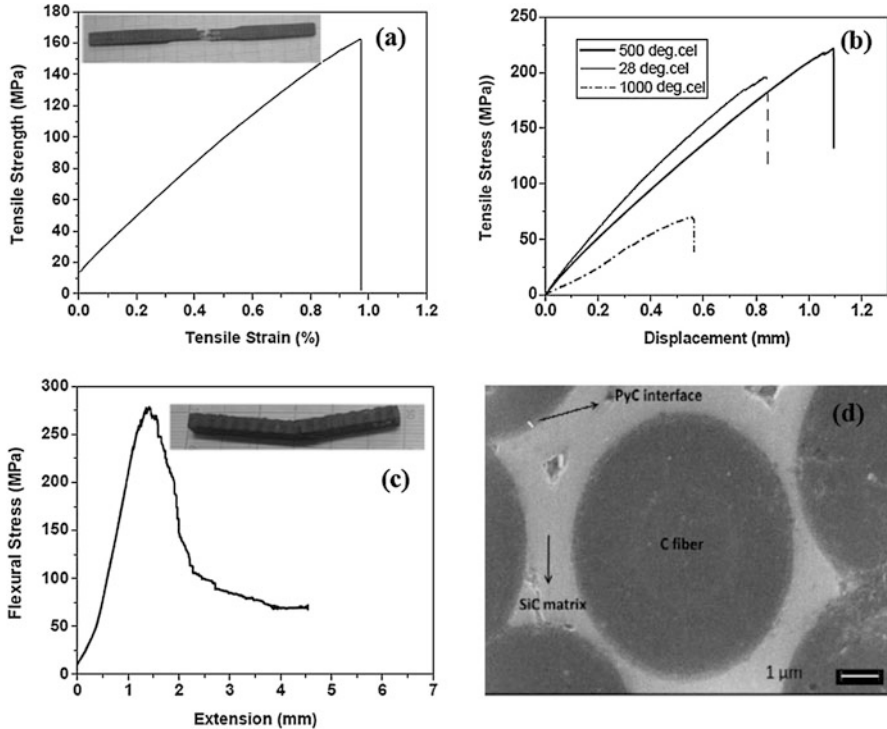


Fig. 9 Tensile and flexural plots for the 3-D C_f/C -SiC composites (a) Tensile versus Strain curve at RT (b) Tensile versus Displacement curve at RT, 500 °C and 1000 °C (c) Stress versus extension trend obtained for 3-D C_f/C -SiC composites under flexural loading and (d) SEM microstructure showing PyC interface [17]

behavior of 2.5-D C_f/SiC composites (as-cut and not CVD-SiC seal coated) with V_f of 0.35 under flexural loading (3 point bend) in air atmosphere at room temperature and elevated temperatures (800 °C, 1000 °C, and 1200 °C) is shown in Fig. 11. Flexural stress versus displacement plots obtained for 2.5-D C_f/SiC composites (with CVD-SiC seal coated) with V_f of 0.35 under flexural loading at 1200 °C and 1300 °C, respectively, are shown in Fig. 12.

It is observed from Fig. 11 that the strength decreases with increasing temperature. It can be attributed to the oxidation of PyC interface and carbon fiber reinforcement. This is because the as-cut composite will have de-laminations present at the cut surfaces and therefore, carbon fiber and PyC interfaces are exposed directly to the oxidizing environment. Oxygen ingress through the de-laminations and openings of as-cut surfaces and some matrix cracks will lead to active oxidation and subsequently would result in strength reduction. It is also clear from Fig. 12 that the CVD-SiC seal coating has enhanced the high temperature flexural strength of up to 450 MPa at 1300 °C, which is significantly high compared to room temperature flexural strength (307 MPa). This increase in strength is also due to the structural ordering occurring in the carbon fiber at higher temperatures.

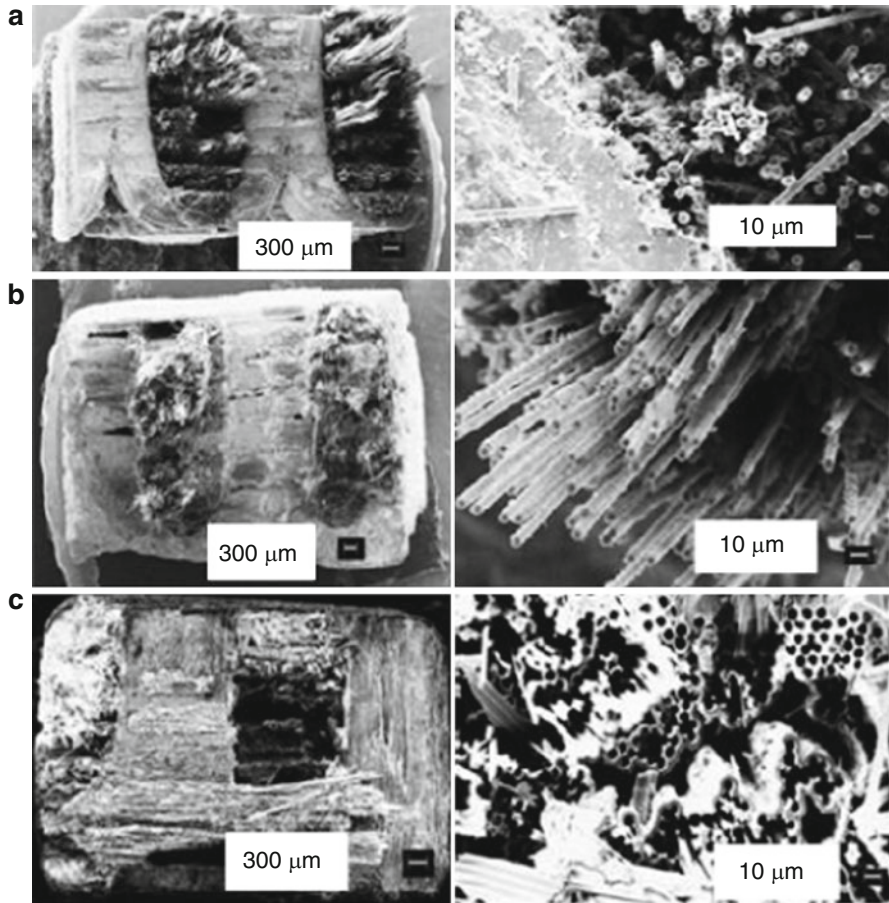


Fig. 10 SEM micrographs of tensile fractured surfaces of 3-D C_f/SiC composites tested at (a) RT, (b) tested at 500 °C, and (c) tested at 1000 °C [17]

The composites having PyC interface showed higher values of flexural as well as tensile strength in comparison to the BN interface. At 1400 °C, the flexural strength of the samples having PyC interface was observed to be 350–400 MPa in comparison to 170–200 MPa for the samples having BN interface. In addition, CVD seal coating showed higher values of tensile as well as flexural strength as compared to the uncoated ones. The lowest values obtained for the composites with BN interface is due to thermodynamically unstable BN interface. Due to the moisture absorption and subsequent reaction with trapped unreacted BCl₃ and NH₃ gases forming an intermediate compound and its reaction with the matrix causing the high interfacial bond strength and leads to poor mechanical properties.

The CVD seal coated composites having PyC interface showed the tensile strength of 180–200 MPa at 1500 °C (Fig. 13). Lower tensile strength obtained for

Fig. 11 Flexural behavior of 2.5-D C_f/SiC composites at room temperature and elevated temperatures (800 °C, 1000 °C, 1200 °C)

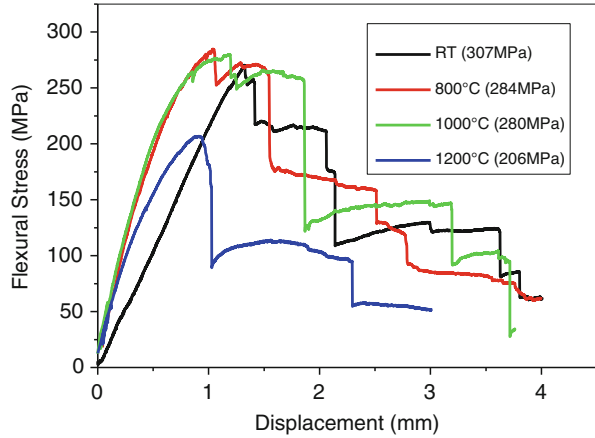
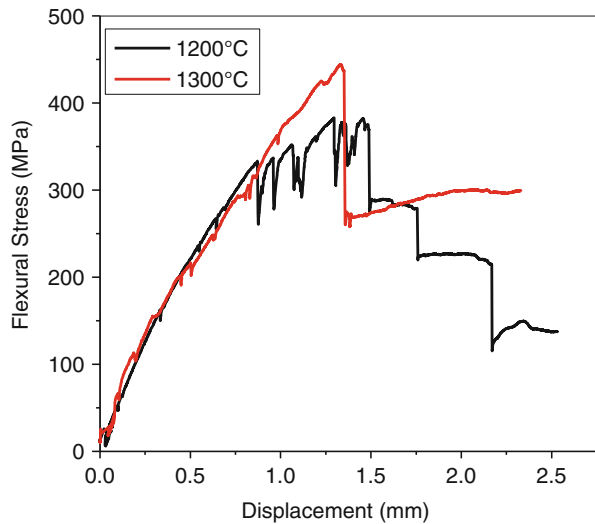


Fig. 12 Flexural stress versus displacement plots obtained for 2.5-D C_f/SiC composites (CVD-SiC seal coated) at 1200 °C and 1300 °C



the composites (having no SiC seal coating) at 1200 °C in the oxidizing atmosphere is attributed to oxidation (Fig. 13).

Tensile behavior of C_f/SiC composites having two different multilayer interface thicknesses (different deposition timings: 25 min. (thin interface-ML1) and 45 min. (thick interface-ML2)) at 1200 °C is shown in Fig. 14. It is observed that the composites with thicker interface showed a higher value of the tensile strength at the test temperature of 1300 °C and this may be attributed to high enough interfacial bond strength between fiber and matrix. The properties of C_f/SiC and $C_f/C-SiC$ composites, developed through various techniques (CVI, PIP, MSI, and hybrid (CVI + PIP/CVI+MSI)) are different [18]. Fiber reinforcement type, fiber architecture,

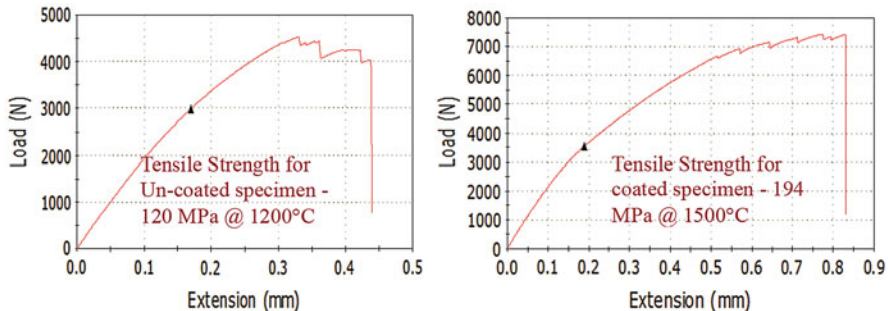
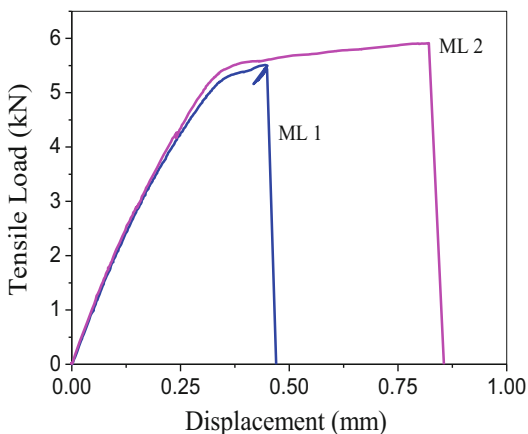


Fig. 13 High temperature tensile behavior of uncoated and SiC seal coated C_f/SiC composites at 1200 °C and 1300 °C

Fig. 14 Tensile behavior of 2.5-D C_f/SiC composites having two different multi-layer interface thicknesses (different deposition timings: 25 min. (thin interface-ML1) and 45 min. (thick interface-ML2)) at 1300 °C in dry air



fiber surface treatment, and the manufacturing technique used for the fabrication decide the final mechanical and thermal properties of these composites.

A homogeneous and crystalline SiC matrix, the weak interface between the fiber and matrix, nil fiber damage during the processing (e.g., CVI) can lead to high mechanical properties. Superior strength values and damage tolerance can be obtained for the CVI generated composites [18]. It is noted that CVI generated C_f/SiC composite materials show high tensile strength and strain values (340 MPa and strain of 0.7%) for composites based on 2-D fiber architecture. These superior properties are mainly due to the homogeneous PyC interface coating, highly crystalline SiC matrix, and low pressure/medium temperature involved during CVI process.

Thermal Behavior

The unique property of carbon fiber-reinforced SiC composites (C_f/SiC) is the outstanding high-temperature stability comparable to C_f/C composites. C_f/SiC

composites show strength increasing trend with respect to temperature [19–22]. Hence, C_f/SiC-based hot structures are generally designed based on room temperature properties. In this way some safety margin is naturally built-in, when these structures are used at high temperatures. The coefficient of thermal expansion of the carbon fiber in fiber direction is generally negative in the temperature range up to 200 °C and hence they offer the opportunity to generate the composites which are tailored to specific expansion behavior by combining SiC matrix having positive thermal expansion co-efficient with the varied orientation of fibers. The thermal expansion co-efficient of 2-D-C_f/C-SiC is generally low over a wide temperature range. By modifying the C_f/C and SiC proportions in the C_f/C-SiC composites, the negative expansion behavior of the embedded carbon fibers may be compensated by an increase of the ceramic content, thereby rendering an expansion-neutral behavior.

In-plane thermal properties of C_f/SiC composites are primarily determined by carbon fiber (offering a very low co-efficient of thermal expansion (CTE)) ($\alpha_{f\parallel}, RT = -0.83 \text{ to } 0.1 \times 10^{-6} K^{-1}$) compared to the SiC matrix ($\alpha_{SiC}, RT = 4.0 - 5.0 \times 10^{-6} K^{-1}$). Hence, the CTE of C_f/SiC composites is generally low ($\alpha_{Cf/SiC\parallel} RT = -1 \text{ to } 3.5 \times 10^{-6} K^{-1}$). The In-plane-CTE of C_f/SiC (α_{\parallel}, RT) can be obtained in the range of ($\alpha = -0.5 \text{ to } 0.8 \times 10^{-6} K^{-1}$) by varying the volume fractions of fiber and matrix and fiber architecture. Dimensionally stable C_f/C-SiC composite structure with CTE ($\alpha_{\parallel}, = 0 \pm 0.1 \times 10^{-6} K^{-1}$) in a temperature range of -30 °C to +50 °C could be tailored [24, 25]. SiC and C matrix controls the properties in the transverse direction (\perp) and leading to CTE in the range of $\alpha_{\perp}, RT = 2.0-5.5 \times 10^{-6} K^{-1}$. Anisotropy is observed in CTE of short fiber based C_f/SiC composite (both in \parallel and \perp direction) and this is attributed to the characteristic fiber orientation. Density and fiber volume fraction in the composite have a strong effect on the transverse (\perp) thermal conductivity [26]. Lower values correspond to bi-directionally woven fabric reinforcement, whereas higher densities refer to short fiber reinforcement. As the fiber volume fraction increases, the SiC content decreases and the thermal conductivity also decreases. Thermal conductivity (\perp) of C_f/C-SiC composite decreases with increasing of temperature like other materials and the same relationship between thermal conductivity (\perp) and the temperature is followed by different C_f/C-SiC composites prepared by varying the fiber architecture and the processing parameters [27]. The average decrease in thermal conductivity (\perp) between 30 °C and 900 °C is approximately 30%.

Longitudinal CTE of ICVI-generated 2.5-D C_f/SiC composites (developed at CSIR-NAL) with (PyC/SiC)_{n = 4} multilayer interface as a function of temperature is shown in Fig. 15a. Expansion/contraction behavior is smooth and uniform. The mean CTE of $3.15 \times 10^{-6}/^{\circ}C$ and $2.96 \times 10^{-6}/^{\circ}C$ is obtained during the heating (temperature range of 100–1300 °C) and cooling (1300 °C–300 °C), respectively. This value is in good agreement with the literature values [15]. The lower CTE obtained during cooling may be due to the compressive thermal stress (causing changes in PyC/SiC interfaces) acting over the reinforcing fibers by the matrix due to thermal mismatch. The specific heat capacity of CVI generated 2.5-D C_f/SiC composites and CVD SiC (developed at NAL) obtained (ASTM 1269) as a function of temperature is shown in Fig. 15b.

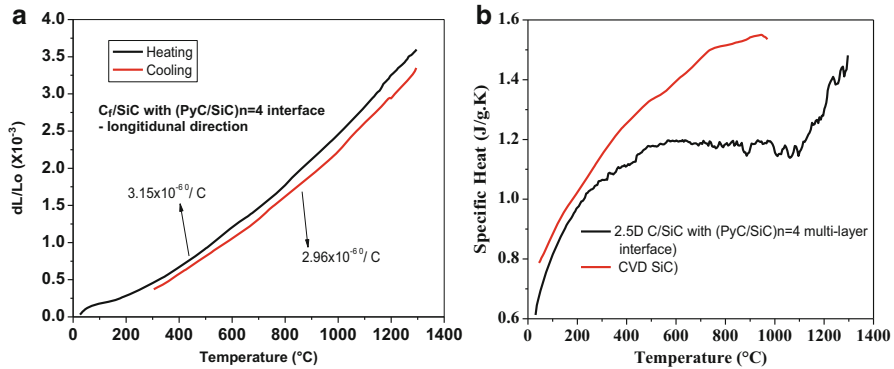


Fig. 15 Thermal behavior of 2.5D-CVI generated C_f/SiC composites with $(PyC/SiC)_n = 4$ multi-layer interface: (a) CTE and (b) Specific heat capacity

It is observed that the specific heat values of both composite and CVD SiC are more or less same up to about $300\text{ }^\circ\text{C}$ and the specific heat capacity of CVD β -SiC is higher at high temperatures compared to that of composites. It is also found that specific heat capacity values and its trend with respect to temperature are similar to the published literature [15, 28].

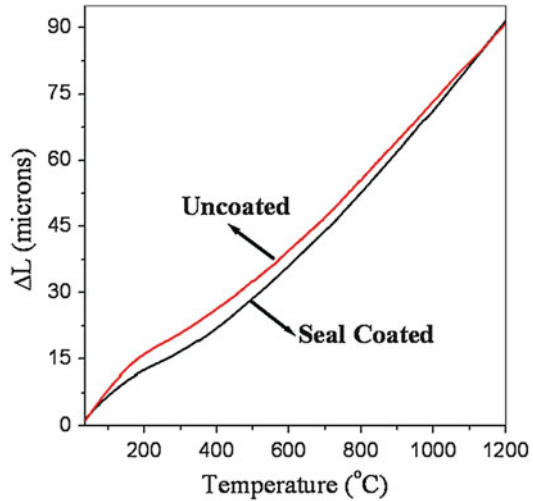
The thermal expansion curves for the uncoated and SiC seal coated C_f/SiC composite samples with PyC interphase obtained by dilatometer study (heating the samples up to $1200\text{ }^\circ\text{C}$) are shown in Fig. 16 [16].

On measuring the weights of the samples before and after the test, it was noticed that the samples with SiC seal coating showed a much lower weight loss with respect to the uncoated sample. CTE values of seal-coated and uncoated samples at $1200\text{ }^\circ\text{C}$ are nearly the same. CTE values of uncoated and coated samples in the temperature range of $500\text{ }^\circ\text{C}$ – $1200\text{ }^\circ\text{C}$ are in the range of $3\text{--}4 \times 10^{-6}/^\circ\text{K}$ and $2.5\text{--}3.5 \times 10^{-6}/^\circ\text{K}$, respectively [16]. The transverse-thermal conductivity values of above composites are in the ranges from 7 to 12 W/m K corresponding to the temperature range of RT– $1000\text{ }^\circ\text{C}$.

Tribological Behavior

Aircraft brakes are an important component for aircraft landing and take-off safety, which must work as friction parts to produce required stopping torque under various service environmental conditions, as heat sinks to dissipate the kinetic energy of the aircraft and keep lower temperature, and as structural elements to transfer torque to the tyres. Due to advancements of science and technology in the aeronautical field, aircraft with an increase in size and weight became reality. These special aircraft demand shorter and shorter landing/take-off distance, which results in significantly increased landing and take-off energy. Therefore, the trend in development is focused on brake materials, which always desire for higher energy adsorption.

Fig. 16 Thermal expansion of 2.5 D C_f/SiC composites with PyC interface (seal coated and uncoated samples) [16]



C_f/SiC and $C_f/C-SiC$ are better candidates for brake applications, since they retain the advantages of C_f/C composites and overcoming the disadvantages of C_f/C composite and show some excellent properties such as high and stable friction coefficient, long life, low wear rate, and lower sensitivity to environment and oxidation. Composites of these classes made via CVI and hybrid routes (CVI+PIP or CVI+MSI) offers superior tribological properties in terms of high wear resistance and high coefficient of friction. Improved damage tolerance comes from carbon fiber embedded in these composites in comparison to monolithic SiC and improved wear resistance comes from SiC matrix compared to C_f/C composites. SiC is suitable as matrix material due to its superior temperature and thermal shock resistance as well as the high creep and wear resistance.

Higher refractoriness and thermal shock resistance, higher wear resistance, and co-efficient of friction (COF) and their tailor-ability over a wider range make C_f/SiC and $C_f/C-SiC$ composite materials for successful applications in brakes and other systems. Transfer of heat energy generated from the outer friction surface while braking to the center of the brake component is the key requirement to avoid/minimize the overheating of friction surface, that is, the composite should have high transverse (\perp) thermal conductivity to achieve stable high COF and low wear rates. Modification in microstructure of the 2D- $C_f/C-SiC$ composite leads to improvement in required properties (high \perp thermal conductivity and high and stable COF) [33].

As the high SiC content is a mandate in outer friction surface, the following approaches are being pursued for the better brake performance [28]:

- $C_f/C-SiC$ composites with a gradual increase of SiC content from the center to the outer surface of the composite
- $C_f/C-SiC$ composite with CVD-SiC seal coating

Zhuan Li et al. [29] reported that 3D-C_f/C-SiC composites with carbon nano fiber (CNF) grown on the carbon fiber reinforcement exhibited excellent behavior with high static friction co-efficient (0.38) and dynamic coefficient of friction (0.29) and 50 °C decrease in the temperature of friction surface.

Because of the existence of CNF, crack bridging mechanisms is operative for cracking to occur perpendicular to the interface and arrest the crack propagation more efficiently. It is also possible for good bonding between the fiber and the matrix. Hence, matrix and fiber cannot easily be peeled off during the braking process and a lower linear wear rate of C_f/C-SiC composites with CNFs modification is achieved. Typical brake curves of C_f/C-SiC with CNF modification show [29–30] three stages, namely: (i) the early brake, (ii) middle brake, and (iii) later brake. A slight “prepeak” at the early brake stage is observed, which is corresponding to the grain abrasive mechanism similar to unmodified C_f/C-SiC composites. It is reported that during early brake stage, many brittle asperities on the friction surface including PyC, SiC, and Si phases break off because of the shearing and compressive force, and plough on the friction surface and the material removal by microcutting. Grain abrasion, fatigue wear, adhesive wear, and oxidation abrasion and the interaction between the above four types of wears are the main wear mechanisms of the friction pair of C_f/C-SiC with CNF modification and metallic counterpart.

3D needled C_f/SiC composites are modified with graphite to decrease and disperse the free silicon [31]. It is reported that average friction coefficient under the dry condition of C_f/SiC modified with graphite was lower than that of unmodified C_f/SiC composites. It is also seen that linear wear rate of C_f/SiC modified with graphite is lower compared to C_f/SiC unmodified and it is due to lower amount of free silicon and uniform distribution. C_f/SiC composites with dual matrices prepared via CVI and MSI showed superior tribological properties such as high COF, good abrasion resistance, and steady COF under braking [29]. It was also reported that the COF fluctuates between 0.41 and 0.54 with the increase of braking speed, and the wear rate is insensitive to the brake speed and maintained about 0.02 cm³/MJ.

The wear performance is generally studied based on the volume wear, which can be calculated from the following equation:

$$W = [(m_1 - m_2) / \rho A] \quad (4)$$

where W is volume wear (cm³/MJ), m₁ and m₂ – the weight of the specimen before and after braking tests, respectively, (g), ρ-density of the composites (g cm⁻³) and A- braking work (MJ).

A typical relationship between friction coefficient and wear rates with brake speeds and braking cycles of C_f/C-SiC composites is reported by Li Zhaun et al [30]. It was observed that the friction coefficient reduces first and then increases to ≈0.50 at 16 m s⁻¹ and thereafter decreases with the increase of braking speed and wear rates are insensitive to brake speed and steady state is reached after 200 cycles. Wear mechanism changes as a function of braking speed from abrasion at the low braking speed of 8 m/s (microconvex bodies break off by shearing and compressive force. The ruptured asperities generated through rupture are pulverized and hence the

friction film forming capability is low. New asperities in the friction surface increase with the increase of brake distance). The debris generated due to deformation, shearing, and breaking of asperities plough on the friction surface to adhesion at 12 m s^{-1} and 16 m s^{-1} (a large number of asperities are sheared and pulverized and more debris are formed, covered and formed the frictional film. This lowers the contact area of friction surface and reduces the friction resistance and the friction coefficient and the adhesive mechanism dominates) to fatigue and oxidation at 20 m s^{-1} and 24 m s^{-1} respectively (temperature increase up to $1000 \text{ }^\circ\text{C}$ can cause the oxidation and leads to oxidation wear. The pressure and friction heat can cause unstable temperature and pressure held on the surface of the C_f/C -SiC composites. Because of the differences in thermal expansion of constituents in C_f/C -SiC composites, the differences in thermal expansion of frictional surface and subsurface, thermal stresses are generated. Microcracks on the friction surface rub repeatedly with the mating hard steel disc causing fatigue wear).

C_f/SiC composites brakes exhibit a high static friction coefficient, low wear rate, and lower sensitivity to wet condition compared to 3D needled C_f/C aircraft brake materials [32]. The braking curve of 3D needled C_f/SiC materials under normal condition is matching the landing response of aircraft with an antiskid braking system, which would impart higher brake efficiency [33]. Grain-abrasion, oxidation-abrasion, fatigue wear, and adhesive wear are the main wear mechanisms of the 3D-needled C_f/SiC brake materials generated via CVI combined with MSI. Grain abrasion is beneficial to improve the frictional properties. However, it would increase the wear. Therefore, SiC content and grain size of the C_f/SiC should be controlled. Free silicon content in C_f/SiC is a significant factor in the adhesive wear. When Si content reached some point, rotor and stator could stick together after braking, disaster would happen during landing. Adhesive wear would cause a serious wear rate, a huge unstable friction coefficient and even disaster. Hence, Si content in the C_f/SiC brake materials must be controlled.

C_f/SiC brake materials having the sandwich structure are also developed to have the improved distribution of phases. These sandwiched C_f/SiC composites have two functional layers for friction and an inner mechanical functional layer (less Si content) denser and high Si content to offer better mechanical strengths. It is reported that frictional properties under the wet condition of the C_f/SiC with sandwich structure were superior to that of the 3D needled C_f/SiC composites. The static coefficient of friction of C_f/SiC with sandwich structure [32] is also higher than that of the 3D needled C_f/SiC composites. It has also been shown that the braking was smoother for C_f/SiC with sandwich structure than that of 3D needled C_f/SiC composites. High wear stability of C_f/SiC materials is demonstrated through disk-on-disk tests (disks of identical materials) and pairs of carbon/ceramic materials show a lower wear rate compared to carbon/carbon [34, 35].

Oxidation Behavior

Due to thermal expansion mismatch between the fiber and matrix (for C = -0.1 to $1.1 \times 10^{-6} / ^\circ\text{C}$ and $7 \times 10^{-6} / ^\circ\text{C}$ (longitudinal/radial CTE), for SiC = $4.8 \times 10^{-6} / ^\circ\text{C}$),

C_f/SiC composites are prone to microcracks and pores when cooled from processing temperature (≈ 1000 °C). These defects are the reason for the decrease in mechanical properties of composites and serve as a passage for intake of oxygen which results in oxidation of C_f/SiC composites under high-temperature oxidizing atmosphere. In order to enhance the oxidation resistance of C_f/SiC composites, multilayer interfaces, self-healing matrix, dual matrices, environmental barrier coating, and self-healing coatings such as glass forming agent (e.g., B-bearing SiC) are necessary.

Lamouroux et al. (1994a, 1994b) [37] proposed and described the model for oxidation behavior of a SiC coated 2-D C_f/SiC composites. Various processes occurring during the oxidation of C_f/SiC composites [38] are mentioned below:

- Step 1: Oxygen ingress through microcracks
- Step 2: At the bottom of the microcracks, diffusion of oxygen through internal pores of the composites to the carbon surfaces
- Step 3: At the bottom of the microcracks, diffusion of oxygen through internal pores of the composites to the carbon fiber or interfacial surfaces
- Step 4: Diffusion of gaseous species such as CO/CO₂, formed as a result of the reaction between C and O₂ in the opposite direction towards the external environment
- Step 5: Reaction of O₂ with SiC on the crack wall

SiO₂ formation due to the passive oxidation of SiC alters the width of the microcracks and facilitates the sealing process. The significant contribution of the model for the composites with 2-D fiber architecture towards an understanding of oxidation behavior of real fiber reinforced ceramic matrix composites is that it takes into account of microcracks evolution, microcracks size, and microcracks distribution with respect to SiC external coating damage under mechanical loading. SiC having decomposition temperature more than 2300 °C exhibits high temperature stability and oxidation resistance in the dry air atmosphere. SiO₂ layer formed due to passive oxidation at temperatures above 600–800 °C is very effective in stopping the further ingress of oxygen. In reducing atmosphere (low partial pressure of O₂), gaseous SiO with high vapor pressure is formed at temperatures higher than 1000 °C due to active oxidation, causing the decomposition of SiC. The major drawback of SiC is its poor corrosion resistance at high partial pressures of O₂ in an atmosphere containing water vapor leads to SiO₂ and Si(OH)₄ formation and causing severe thermal degradation at temperatures higher than 1000 °C at high gas velocity in alkali containing atmosphere. The residual silicon present in the MSI-derived C_f/SiC and C_f/C-SiC composites oxidize at high temperature (passive oxidation condition) and forming SiO₂ to protect the composites. At service temperature (more than 1400 °C), the residual silicon melts and leaves the composites leading to higher porosity and poor mechanical properties.

Mullite/Yttrium silicate multilayer coating is applied over PIP-derived C_f/SiC composites as the oxidation protective coating via plasma spray technique [39]. The effectiveness of the coating against oxidation was studied by means of heat treatment of the C_f/SiC composites at 1500 °C in static air for 1 h. The results showed that the

weight loss of the coated composites was only 3.4% and exhibited high flexural strength retention (95.3% of the original strength).

ZrB₂-SiC coating is also considered for C_f/SiC composites to improve oxidation and thermal shock resistance. ZrB₂-SiC coating (about 200 μm thick) applied through the slurry method over 3-D C_f/SiC composites developed via PIP played a significant role in improving the resistance to the thermal shock [40]. In the case of uncoated specimens, the higher weight loss of about 57.5% is observed, compared to the weight loss of the coated specimen (37.6%). The mass loss is mainly caused by the oxidation of carbon fibers.

ZrO₂ and B₂O₃ oxides are formed when ZrB₂ oxidize at elevated temperature [41]. The volatilization of B₂O₃ happens at 1200 °C leaving ZrO₂ on the coating [42]. The oxidation paths are sealed by the oxides (ZrO₂ and SiO₂) and eventually protect the SiC matrix and C fiber leading to less oxidation and the coating exhibits the self-sealing and antidiffusion capabilities. It is also confirmed that coated C_f/SiC composites showed higher strength compared to uncoated composites under thermal shock conditions.

An efficient oxidation protection coatings such as CVD-SiC monolayer coating and (C_f/SiC)_n multilayer coatings are also developed through CVD technique (ICVI and Iso-pressure/pulsed CVD) for the C_f/SiC composites prepared through PIP technique [43]. It is reported that the monolayer SiC coating is quite dense and adherent to the C_f/SiC substrate and few microcracks are observed in the case of multilayer coatings. It is also reported that the oxidation resistance of C_f/SiC composites coated with two different types (SiC monolayer/(C_f/SiC)_n multilayer) coatings is significantly improved.

Applications

The development of CMC is primarily driven by aerospace sector since development started in the 1970s. Peak temperature (as high as 1800 °C), extremely high thermal gradient, and high heating rates (in the order of several hundred kelvin per second) are attained in the thermal protection systems (TPS) of spacecraft during the re-entry phase. C_f/C materials with oxidation protection coating are used in the extremely hot regions of TPS of the space shuttle (e.g., nose tip, wing leading edge) since the conventional materials failed under the extreme mechanical and thermal loads. To improve the robustness of the CMC in an oxidizing atmosphere, the carbon matrix is replaced by SiC matrix. The oxidation preventing interface coating, self-healing matrices, and environmental barrier coating (EBC) have been adopted to obtain robust CMCs such as C_f/SiC and C_f/C-SiC [23, 36].

As radiative heat transfer is an important mode (since convective heat transfer is low at higher altitude) of cooling the hot structures of hypersonic vehicles, the knowledge of emissivity of the material is required to understand and design the structure for better thermal management. An emissivity of a sample is the ratio of energy emitted by the sample to energy emitted by an ideal emitter or blackbody. Emissivity is expressed as follows:

$$\varepsilon_s(\lambda, \theta, \varphi, T) = i_s(\lambda, \theta, \varphi, T)/i_b(\lambda, T) \quad (5)$$

where ε_s is the emissivity of the sample, $i_s(\lambda, \theta, \varphi, T)$ is the energy emitted by the sample per unit time, per solid angle per wavelength, at temperature T , and $i_b(\lambda, T)$ is the energy emitted by an ideal emitter (by Planck's law). Total emissivity of C_f/SiC composites (developed through CVI) is 0.8 [15]. Catalycity is another important property, which is defined as the catalytic efficiency shown by a material with respect to the recombination occurring on the surface of atomic species due to the chemical reactivity of unsaturated valences of surface atoms. Re-entry condition of the vehicle in hypersonic speed creates a shock wave, leading to extremely high temperature. The created excited species such as ions, atoms, molecules, electrons enter into the boundary layer via diffusion and react with materials of the vehicle. Atomic oxygen and nitrogen present can strike the surface of the vehicle and recombine to form molecular species (O_2 , N_2 , NO) by exothermic reactions, which will subsequently increase the surface temperatures and damage the integrity of the materials. Hence, the knowledge about catalycity is needed for the better design of TPS. The low catalycity and high emissivity exhibited by C_f/SiC composites make this material suitable for hot structures of re-entry vehicles [44–45].

Space Vehicle Components

Due to low co-efficient of thermal expansion and high modulus, $C_f/C-SiC$ materials show excellent thermal shock stability. During the ascent and re-entry phases of flight, the vehicle is subjected to thermal shocks and cyclic mechanical loading under ablative or passive oxidizing atmosphere for few tens of hours. Such conditions are satisfied with modern composites such as C_f/SiC and $C_f/C-SiC$. Liquid phase infiltration (LPI) derived $C_f/C-SiC$ composites are used for the first time in the TPS system of the Buran (Fig. 17) in the former Soviet Union. Figure 18: X-38 Body flaps made of CVI and LPI-generated C_f/SiC Composites [26].

Fig. 17 LPI-generated C_f/SiC nose caps in Buran (with permission from publisher) [26]



Fig. 18 X-38 Body flaps made of CVI and LPI-generated C_f/SiC Composites (with permission from publisher) [26]



C_f/SiC composite materials are used in various parts (C-SiC antenna, C-SiC TPS, nose cap and leading edges, flexible external insulation, C-SiC elevons and body flaps, C-SiC box) of spacecraft [46].

Friction Systems

C_f/SiC and $C_f/C-SiC$ friction materials are being used as brake materials in aircraft, high-end automobile and emergency brakes in crane, because of their superior properties, such as low density, high temperature strength, high refractoriness, high abrasive wear resistance, excellent thermal shock resistance, good dimensional stability at high temperature, high corrosion resistance compared to their metallic counterparts (e.g., grey cast iron). Though C_f/SiC and $C_f/C-SiC$ materials are of slightly higher density compared to C_f/C composites (used as brake discs in aircraft and racing cars), they offer significantly low wear. More interestingly, tribological properties of C_f/SiC and $C_f/C-SiC$ composites are independent of temperature and humidity. Hence, COF is high and stable at all operating conditions (including low temperatures). Thus, major drawbacks of C_f/C composites friction systems such as low COF at ambient temperature and in a humid environment (“early morning disease”) are overcome. MSI-generated C_f/SiC -based automobile brake discs are introduced into serial production by Porsche in 2001 [47]. CMC brakes are available as standard or optional in Porsche, Audi, as well as in several sports car from Ferrari and DaimlerChrysler. CMC brake discs offer a weight saving up to 50% compared to cast iron brake disc for automotive application. C_f/SiC brake discs are lifetime disks having a service life of 3,00,000 km.

Components of Rocket Motors and Jet Engines

Properties such as thermal conductivity and hermeticity are to be considered in terms of thermal shock resistance and leakage considerations for the materials to be used in

the hot section of Jet engines. Because of the superior high-temperature mechanical properties of C_f/SiC composites, Nickel-based superalloys (e.g., Inconel 718) is replaced by C_f/SiC and increased efficiency, safety, and reduced weight as noise/pollution level are achieved. C_f/SiC outer flaps (Fig. 19) are successfully developed through CVI by Snecma Propulsion Solide and used in military aircraft (M-88-2 jet engine) [48, 49]. C_f/SiC composite materials have proven their performance and suitability for short term applications at extreme mechanical, thermal and environmental loads (e.g., Military rocket motors).

C_f/SiC and $C_f/C-SiC$ composite jet vanes are now used in thrust vector control of missiles with solid fuel propulsion. Since the operation time is very short, the oxidation of C_f/SiC or $C_f/C-SiC$ composites is not critical. MSI-generated $C_f/C-SiC$ composite jet vanes developed by DLR is shown in Fig. 20. At the end of nozzle extension, the rotatable jet vanes are positioned in the exhaust stream to provide high steering forces soon after takeoff, when the outer aerodynamic steering devices are yet to become effective and the rocket velocity is low [49]. In this scenario, high stresses in the shaft and temperature as high as 3000 K in the leading edges are occurring. Furthermore, this leads to a high heating rate (several thousands of kelvin per second) and local thermal gradient of 200 K min^{-1} in the blade area. In addition to the above severe thermal conditions, the exhaust stream is very abrasive due to the presence of ceramic particles (e.g., Alumina). High abrasive resistance of C_f/SiC and $C_f/C-SiC$ composites is achieved by having higher ceramic content and CVD SiC coating. C_f/SiC and $C_f/C-SiC$ composites offer a weight saving up to 90% compared to metallic jet vanes.

Calibration Standards and Components in the Telescope

Low expansion structures are realized by using C_f/SiC composites having low thermal expansion co-efficient in combination with high elastic constant and stability (i.e., material properties are not influenced by ambient conditions (e.g., humidity)

Fig. 19 C_f/SiC outer flaps developed through CVI by Snecma propulsion (with permission from publisher) [26]

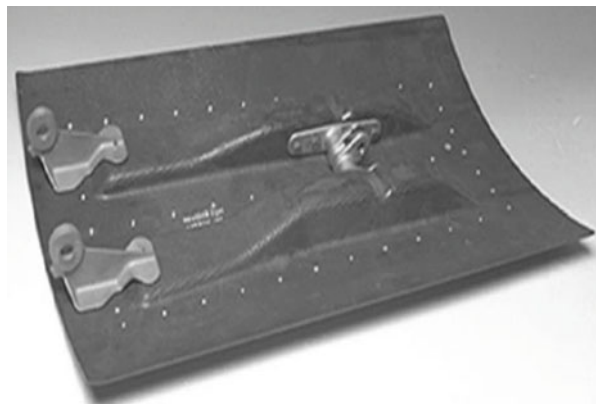


Fig. 20 LSI-generated $C_f/C-SiC$ composites jet vanes developed by DLR (with permission from publisher) [26]



[50, 51]. Calibrating bodies (standards) made using $C_f/C-SiC$ composites are used in industrial measurement technology (e.g., CMM-coordination measuring machine) to check the accuracy in measuring lengths and angular displacements. These precision components should have a very low and constant thermal expansion coefficient in the temperature range of $-30\text{ }^{\circ}\text{C}$ to $+50\text{ }^{\circ}\text{C}$. Lightweight and robustness makes these composites easy to handle. Optical systems based satellite communications offer high data rates with low energy consumption compared to the systems based on radio waves. However, optical systems demand high precision and stability on components. In this application, the thermal and dimensional stability is very important and it is met by novel $C_f/C-SiC$ composites [27].

Components for Energy Systems

Besides all the applications of C_f/SiC composites, the most economical and attractive field is primary structures in the energy industry. To improve manufacture processes and surface coatings for the long-term usage of C_f/SiC composites under corrosive environments, several types of research studies are being continued despite their limitations of oxidation resistance.

The development of a double-pipe heat exchanger in bayonet-pipe technique, which is planned to use for hybrid processes with indirectly fired gas turbines using coal [27], is the first step taken for the fabrication of ceramics in energy and power station engineering. The indirect firing of a gas turbine is accomplished by high-temperature heat exchanger. The coaxially arranged fiber ceramic pipes allow the flow of air to be heated. In cross-counter direction, the flue gas flows around the pipe rows laid out in a staggered arrangement. The tensile stresses caused by longitudinal expansion are reduced by mounting the coated $C_f/C-SiC$ pipes separately in

corresponding pipe floors. To overcome the microporosity in C_f/C -SiC composites, the multilayered coatings for corrosion protection are important for this application. These protective coatings act as a sealing agent for pressurized pipes and also provide protection to the matrix and the carbon fibers from oxidation and corrosion [52, 53].

The thermal incinerator chamber components need very high mechanical, thermal, and corrosive resistance, especially if the problematic waste is incinerated. In incineration installations, moving firing grates made of C_f/SiC with a high ceramic content accompanying a forward feed of the material to be burned is already in operation [54]. To achieve an optimization of the incineration, these C_f/SiC components are made as hollow bodies; thus, additional air could be introduced via holes.

Conclusion

Carbon fiber reinforced silicon carbide (C_f/SiC and $Cf-C/SiC$) composites are superior class of materials for high temperature structural applications in strategic sectors such as defense, space, and nuclear energy compared to conventional Cf/C composites. Depending on the reinforcing fiber type, fiber architecture, fiber pre-treatment, interface coating (interface type, interface coating thickness, etc.), matrix type (single matrix or laminated type of matrix, etc.), process adapted for obtaining the matrices, seal coating, environmental barrier coating, etc., Cf/SiC and $Cf-C/SiC$ composites offer varied microstructure and properties. Hence, each aspect of manufacturing is to be carefully controlled to obtain the quality products for intended applications. Recent times, CMC manufacturers are putting efforts to integrate artificial intelligence (AI) into the manufacturing line for better process control and obtain composites with more reliable properties accompanied by minimal rejections. Chemical vapor infiltration (CVI) process is generally used to manufacture Cf/SiC composites with outstanding properties. However, PIP and MSI processes are becoming more popular for manufacturing these composites while cost per component is concern. Successful application of these composites in various fields, which includes automobile, power sectors, etc., will demand for hybrid process approach to manufacture these advanced composites. There is an urgent need to have more field trials in every possible fields of applications, which can increase the demand and eventually decrease the cost per component. Studies such as life prediction and modeling are also becoming more important so that we can have better theoretical understanding of these developing composites.

References

1. Krenkel W (2005) Hand book of ceramic matrix composites. Wiley, Milton, Australia
2. Yajima S, Hasegawa Y, Okamura K, Matsuzawa I (1978) Development of high tensile strength silicon carbide fiber using an organosilicon polymer precursor. *Nature* 273:525–527
3. Luthra KL, Singh RN, Brun MK (1993) Toughened silicon composites and preliminary properties. *Bull Am Ceram Soc* 72(7):79–85

4. Corman GS, Brun MK, Luthra KL (2000) SiC fiber reinforced SiC-Si matrix composites prepared by melt infiltration(MI) for gas turbine engine applications. In: International gas turbine and aeroengine congress and exhibition. Indianapolis, New York, 7–10, June 1999
5. Bickardike RL, Brown AR, Hughes G, Ranson H (1962) The deposition of pyrolytic carbon in the pores of the bonded and unbonded carbon powders. In: Mrosowski S, Studebaker MC, Walker PL (eds) Proceedings of fifth conference on carbon, vol I. New York, pp 575–583
6. Hitchman ML, Jensen KF (1993) Chemical vapor deposition: principles and applications. Academic, London
7. Starr TL (1988) Deposition kinetics in forced flow/thermal gradient CVI. *Ceram Eng Sci Proc* 9:803–811
8. Roman YG, Stinton DP, Besmann TM (1991) Development of high density fiber reinforced silicon carbide FCVI composites. *J Phys IV C2*:689–695
9. Stinton DP, Besmann TM, Lowden RA (1988) Advanced ceramics by chemical vapor deposition techniques. *Bull Am Ceram Soc* 67:350–355
10. Katoh Y, Dong SM, Kohyama A (2002) A novel processing technique of silicon carbide-based ceramic composites for high temperature applications. *Ceram Trans* 144:77–86
11. Nakano K, Suzuki K, Drissi-Habti M, Kanno Y (1998) Processing and characterization of 3D carbon fiber reinforced silicon carbide and silicon nitride matrix composites. *Ceram Trans* 99:157–166
12. Suzuki K, Kume S, Nakano K, Chou TW (1998) Fabrication and characterization of 3D-C/SiC composites via slurry and PCVI joint process. *Key Eng Mater* 164–165:113–116
13. Motz G, Schmidt S, Beyer S (2008) The PIP-process: precursor properties and applications. In: Krenkel W (ed) *Ceramic matrix composites*. Wiley-VCH Verlag, Weinheim, pp 357–359
14. Schmidt S, Beyer S, Knabe H, Immich H, Meistring R, Gessler A (2005) Ceramic matrix composites: a challenge in space propulsion technology applications. *J Appl Ceram Technol* 2(2):85–96
15. Lacombe A, Rouges JM (1990) Ceramic matrix composites, Societe Europeene de Propulsion, AIAA-90-3837
16. Singh S et al (2015) Microstructural-property correlation of CVI processed C_f/SiC composites and property enhancement as a function of CVD SiC seal coating. *Ceram Int* 41:14896–14907
17. Udayakumar A et al (2014) Mechanical properties of 3D noninterlaced C_f/SiC composites prepared through hybrid process (CVI+PIP). *Int J Mater Metall Eng* 8:9
18. Diefendorf RJ, Boisvert RP (1988) Siliciumcarbid-Composites durch polymere Ausgangswerkstoffe. In: Proceedings of Verbundwerk. Demat Exposition Managing, Frankfurt, pp 13.01–13.37
19. Krenkel W (2003) Designing with C/C-SiC composites. In: Bansal NP et al (eds) *Advances in ceramic matrix composites IX*, vol 153, pp 103–123. *Ceram Trans*
20. SGL Carbon Group (2005) SIGRASIC 6010 GNJ, Faserverstärkte Keramik für Bremsscheiben
21. Weiss R (2001) Carbon fiber reinforced CMCs: manufacture, properties, oxidation protection. In: Krenkel W, Naslain R, Schneider H (eds) *High temperature ceramic matrix composites*. Wiley-VCH, Weinheim, pp 440–456
22. Schafer W, Vogel WD (2003) Faserverstärkte Keramiken hergestellt durch Polymerinfiltration. In: Krenkel W (ed) *Keramische Verbundwerkstoffe*. Wiley-VCH, Weinheim, pp 76–94
23. Muhltrater A, Leuchs M (2001) Applications of non-oxide CMC. In: Krenkel W, Naslain R, Schneider H (eds) *High temperature ceramic matrix composites*. Wiley-VCH, Weinheim, pp 288–289
24. Schoppachet A et al (2000) Use of ceramic matrix composites in high precision laser communication optics. In: European conference on spacecraft structures, materials and mechanical testing. ESTEC, Noordwijk
25. Heidenreichet B et al (2010) C/C -SiC telescope structure for the laser communication terminal in TerraSAR-X. In: Krenkel W, Lamon J (eds) *High temperature ceramic matrix composites*. Aviso Verlagsges, Berlin, pp 505–512
26. Klaus Drechsler et al (2009) Carbon fiber reinforced composites. Wiley-VCH Verlag GmbH. https://doi.org/10.1002/14356007.m05_m02

27. Bansal NP (2005) Handbook of ceramic composites. Springer, Kluwer Academic Publishers New York, Boston, Dordrecht, London, Moscow
28. Krenkel W (2003) C/C-SiC composites for hot structures and advanced friction systems. *Ceram Eng Sci Proc* 24(4):583–592
29. Li Z et al (2015) Preparation and tribological properties of C/C-SiC brake composites modified by in situ grown carbon nanofibers. *Ceram Int* 41:11733–11740
30. Zhaun L et al (2010) Manufacture and properties of carbon fiber-reinforced C/SiC dual matrix composites. *Carbon* 25(3):225–231
31. Jian-Xin Z et al (2010) Microstructure and frictional properties of 3D needled C/SiC brake materials modified with graphite. *Trans Nonfer Met Soc China* 20:2289–2293
32. Fan S et al (2016) Progress of ceramic matrix composites brake materials for aircraft application. *Rev Adv Mater Sci* 44:313–325
33. Fan S et al (2008) Microstructure and Tribological properties of advanced carbon/silicon carbide aircraft brake materials. *Compos Sci Technol* 68:3002–3009
34. Fohl J, Wiedemeyer J (2000) Forschungsberichte der. DKG 15(I)
35. Fohl J, Wiedemeyer J (2001) Kap. 8.3.1.3: Qualifikation Von Faserverbundkeramik für friktion-sanwendunge. In: Kriegesmann J (ed) DKG-Handbuch. Deutscher Wirtschaftsdienst, Köln
36. Bansal NP, Lamon J Ceramic matrix composites materials, modelling and technology. The American Ceramic Society, Wiley, Hoboken
37. Lamouroux F, Camus G (1994) Oxidation effects on the mechanical properties of 2D woven C/SiC composites. *J Eur Ceram Soc* 14:177–188
38. Kelly A, Zweban C (2000) Comprehensive composite materials, vol 4. Elsevier, Pergamon, Cambridge University Press, UK
39. Zhao S, Zhou X, Wang H (2014) Oxidation resistant behaviour of Mullite/Yttrium silicate multilayer coating for C/SiC composites at 1500°C. *Key Eng Mater* 602–603:430–433
40. Yang X et al (2016) ZrB₂-SiC as a protective coating for C/SiC composites: effect of high temperature oxidation on thermal shock property and protection mechanism. *J Asian Ceram Soc* 4:159–163
41. Chamberlain AL, Fahrenholtz WG, Hilmas GE, Ellerby D (2009) Reactive processing of zirconium diboride. *J Eur Ceram Soc* 29(16):3401–3408
42. Fahrenholtz W (2005) The ZrB₂ volatility diagram. *J Am Ceram Soc* 88(12):3509–3512
43. Donga S, Wena H, Zhoua Q, Dinga Y (2009) Preparation of oxidation-protective SiC coatings for C/SiC composites by pulsed chemical vapor deposition. *J Ceram Process Res* 10(3):278–285
44. Alfano D (2011) Spectroscopic properties of carbon fiber reinforced silicon carbide composites for aerospace applications, Italian Aerospace Research Centre
45. Weihs H, Reimer T, Laux T (2004) Mechanical architecture and status of the flight unit of the Sharp Edge Flight Experiment SHEFEX. IAF Congress, Vancouver
46. Roger R (2005) Naslain, SiC-matrix composites: nonbrittle ceramics for thermo-structural application. *Int J Appl Ceram Technol* 2(2):75–84
47. Koehler RJ (2001) Manuscript of the presentation at the shareholders' meeting of the SGL Carbon Group 2001, Germany
48. Fitzer E, Gadow R (1986) Fiber-reinforced silicon carbide. *Am Ceram Soc Bull* 65:368–372
49. Frieß M et al (2005) Keramische Verbundstrukturen für hochagile Flugkörper. In: Proceedings des Deutschen Luft- und Raumfahrtkongress 2005. Friedrichshafen
50. Kochendörfer R, Lützenburger N (2001) Applications of CMCs made via the Liquid Silicon Infiltration (LSI) technique, high temperature ceramic matrix composites (eds: Krenkel W, Naslain R, Schneider H). Wiley-VCH, Weinheim, pp 277–287
51. Renz R, Heidenreich B, Krenkel W, Schöppach A, Richter F (2001) CMC materials for lightweight and low CTE applications, high temperature ceramic matrix composites (eds: Krenkel W, Naslain R, Schneider H). Wiley-VCH, Weinheim, pp 839–845

-
52. Schmidt J, Scheiffle M, Krenkel W (2001) Engineering of CMC tubular components, high temperature ceramic matrix composites (eds: Krenkel W, Naslain R, Schneider R). Wiley-VCH, Weinheim, pp 826–831
 53. Labanti M, Martignani G, Mingazzini C, Minocari GL, Pilotti L, Ricci A, Weiss R (2001) Evaluation of damage by oxidation corrosion at high temperatures of coated C/C-SiC ceramic composite, high temperature ceramic matrix composites (eds: Krenkel W, Naslain R, Schneider H). Wiley-VCH, Weinheim, pp 218–223
 54. ECM, Cestic[®] Kohlefaserverstrktes Siliciumcarbid, Produktinformation



Development of Polycarbosilane (PCS) Polymer and PCS-Derived SiC Fibers and Their Composites

24

Rakesh Kumar Gupta, Raghvesh Mishra, Suresh Kumar,
Ashok Ranjan, L. M. Manocha, and N. Eswara Prasad

Contents

Introduction	914
Silicon Polymers	916
Organosilicon Polymers as Preceramic Polymers for the Synthesis of Si-Based Ceramics ...	917
Polysilanes	919
Polycarbosilanes	920
Yajima Strategy	921
Ring-Opening Polymerization (ROP) Reactions	922
Polycondensation of Chloromethylchlorosilane	922
PCSs from Reaction of Chlorosilanes with Methylene Halides	922
PCSs from Chlorosilanes and Acetylides	923
PCS Using Hydrosilylation Reactions	923
Processing of PCSs	923
Outlook for Silicon-Based Preceramic Polymers	924
Conclusion	925
References	926

Abstract

Ceramics, in general, are high temperature materials that have low density, low coefficient thermal expansion, excellent mechanical properties (strength, hardness), high thermo-oxidative stability, and excellent chemical resistance. There-

R. K. Gupta (✉) · R. Mishra

Defence Materials and Stores Research and Development Establishment, Kanpur, India

e-mail: rk Gupta180@gmail.com; raghwesh_drdo@rediffmail.com

S. Kumar · A. Ranjan · L. M. Manocha · N. E. Prasad

Defence Materials and Stores Research and Development Establishment, DRDO, Kanpur, India

e-mail: skumar@dmsrde.drdo.in; drashokranjan25@gmail.com; manocha52@rediffmail.com; neswarap@gmail.com

© Springer Nature Switzerland AG 2020

Y. R. Mahajan, R. Johnson (eds.), *Handbook of Advanced Ceramics and Composites*,

https://doi.org/10.1007/978-3-030-16347-1_29

913

fore, these have been extensively explored for high temperature structural applications. Among many ceramics, silicon carbide (SiC) is one of the most promising non-oxide ceramics for applications in extreme environmental conditions. It has excellent combination of thermomechanical, chemical, and oxidation resistance properties that qualifies it to be highly suited for aerospace, defense, and nuclear applications. Processing of complicated structures through conventional powder processing route is difficult which led to the development of precursor-based route for processing of complicated shapes of ceramics. Silicon-based polymeric precursors have been intensively researched as source of SiC ceramics. This chapter broadly covers the development of various polymeric materials as precursors for different ceramics. Various chemical synthetic methods have been included and a brief account of the processing of ceramics has been given. Main focus is on the organo-silicon precursor materials, particularly polysilanes and polycarbosilanes (PCSs), these are potential sources of SiC-based ceramics. Chapter ends with a brief outlook of precursors' route for ceramics.

Keywords

Precursor Polymer · Polysilane · Polycarbosilane · Silicon Carbide · SiC Fibers · CMC · SiC Composites

Introduction

Ceramics, in general, are high-temperature materials having low density, low thermal expansion coefficient, high strength, high elastic modulus, high hardness, high thermo-oxidative thermal stability, and excellent chemical resistance. Therefore, these have been extensively explored for high-temperature structural applications. Ceramics are traditionally manufactured using powder compaction or filler binder route followed by sintering or thermal evaporation deposition techniques. But most of the ceramic raw materials are intractable in nature and, if the sintering is not done in a controlled way, may lead to distortions and variation in properties [1]. Therefore it is not easy to make complicated structures using conventional ceramic processing techniques, thus restricting the applications of ceramics. In addition, the processing temperatures are also high. To overcome these problems, alternative processing techniques based on solution processing methods needed to be investigated. During the last few decades, with the advancements of ceramic fibers, the ceramic matrix composites (CMCs), particularly continuous fiber ceramic matrix composites (CFCMC), have gained much attraction as high-temperature structural materials since by using these fibers, many desirable high-temperature properties including high strength and modulus may be achieved [2-4]. Future energy-efficient heat engines and high-subsonic, supersonic airplanes and spacecrafts will utilize high-performance structural materials in selected elevated temperature areas. Therefore, the CMC field becomes increasingly important. The conventional ceramic processing technologies pose many limitations in processing of CFCMCs. Therefore, it becomes all the more important to look for alternative routes

for processing of fibrous composites wherein it is essential to maintain the lay-up of the fibers as well as efficiently translate the fiber properties to the composites. The progress in polymer synthetic chemistry and ease of manipulating the polymer structures incorporating desired elements in the polymer chain, which on high-temperature processing lead to polymer-derived ceramics, emerging as a novel ceramic processing technology through liquid processing route. Such polymers, known as ceramic polymer precursor, after processing, yield ceramics with retention of shape, size, and engineering dimensions as well as the desired elements in the products with desired functional properties. The ceramic polymeric precursors have attracted great deal of attention due to its advantage over the powder-based ceramic processing such as fabricating unconventional structures and producing ceramics at comparatively lower temperatures.

SiC is a promising non-oxide ceramic having exceptional thermal stability, semi-conducting properties, chemical inertness, high resistance to oxidation, superior mechanical properties, extreme hardness, etc. [5, 6]. SiC in solid form is generally processed using powder compaction and reaction sintering route. The tendency to resist deformation at very high temperature presented a challenge for the fabrication of different shapes like films and fibers from powders, thus restricting their applications. Therefore, SiC fibers were first produced using CVD technique, but this needed a substrate like tungsten or carbon which posed peculiar crack problems due to difference in coefficient of thermal expansion of the two materials. Moreover, this technique results in high-diameter fibers of 100 μ or more. The stiffness also presented problems when using these fibers for making composites using filament winding techniques or woven structures. This required development of small diameter ceramic fibers with desired stiffness and having excellent mechanical and thermal properties. This was to be achieved using polymer pyrolysis technology similar to that of carbon fibers. This necessitated the development of a suitable polymer that could be processed into desired shape using conventional polymer forming methods and whose subsequent pyrolysis gives the needed ceramic. For such polymers, which could serve as useful precursors, through their pyrolysis, to ceramics, the term “preceramic polymers” was adopted [7].

Dunogues et al. [8] have pointed out in their review that an idealized preceramic polymer should possess a combination of the following properties: (1) sufficiently high molecular weight of the precursor polymers to prevent any volatilization of oligomers; (2) polymeric structures containing cages or rings to decrease the elimination of volatile fragments resulting from backbone cleavage and the latent reactivity in the polymers to obtain thermally induced cross-linking; (3) viscoelastic properties such as fusibility, and solubility to ensure easy processing; and (4) low organic group content to increase ceramic yield and avoid the production of excess free carbon. Moreover, through this route, different elemental substituents and variations in the polymer microstructure can be processed which dramatically affect the final ceramic properties.

These precursor polymers have attracted great deal of attention because ceramic forms, such as fibers and films and complex forms, which are difficult to be obtained, using conventional powder processing methods, can be fabricated with ease at comparatively lower temperatures [9–11].

After their discovery and first successful experiment, the growing interest for this new methodology led to further significant improvements of their chemistry,

synthesis, processing, and properties. Many different classes of preceramic polymers have been synthesized in the last decades, the most important being polysiloxanes, polysilazanes, and polycarbosilanes [12]. With this methodology it was possible to obtain not only binary ceramics such as Si_3N_4 or SiC , but also more complex compositions such as SiOC and SiCN systems could be processed. Increasing the sophistication of the starting precursors could lead to further improvements of the properties of the final ceramics: the introduction of boron atoms inside the starting polymers could produce ceramics in the quaternary SiBCN system. Furthermore, the chemical modification of the starting polymers with precursors of metallic elements like Al, Zr, and Ti could provide a further increase of the complexity of the system, for the realization of ceramic components with a wider variety of compositions with outstanding thermal properties [13–17].

The relatively low cost of the precursors, the wide variety of compositions achievable, the characteristic microstructure (which is, in most cases, impossible to be achieved by conventional methods), the unique and exceptional thermomechanical and chemical properties of the final ceramics, and the possibility of shaping the precursors using well-established, conventional polymer forming methods such as polymer infiltration pyrolysis (PIP), injection molding, coating, extrusion, resin transfer molding (RTM), fiber drawing, and many others make this route an extremely promising route for a relatively simple realization of ceramic components.

Polycarbosilane (PCS) is the most prevalent polymeric precursor for SiC ceramic and has been widely used for making SiC fibers and composites since the pioneering work done by Yajima and co-workers [18, 19].

In order to get SiC fibers and matrices of required properties and composition, it is essential to have suitable PCS. Several reports are available in which PCS has been modified by incorporating metal, organic moieties, or other groups into the main chain. The most widely used process for functionalization is reaction of Si–H groups of PCSs with metal salts and unsaturated organic moieties. For example, Ti-incorporated PCS (Ti-PCS) has been prepared by the reaction of Si-H group containing PCS with titanium alkoxides to give better spinnability to fibers [20]. Similarly iron-containing PCS (Fe-PCS) has also been synthesized by the reaction of PCS with iron acetylacetonate [21]. Fe-PCS upon pyrolysis gives magnetic SiC having EMI absorbing properties [22]. Monolithic SiC structures were obtained by pyrolysis of epoxy modified PCS [23].

Silicon Polymers

Silicon, among the elements, is the most unique in its ability to homo-catenate and form stable long chains in a manner similar to carbon. Silicon polymers include polysiloxanes, PSs, PCSs, polysilazanes, etc. In addition to polymers that contain only carbon or other “organic” atoms in the chain, polymers containing “inorganic” atoms can also be formed. These compounds are of interest because they offer the opportunity to develop new technological applications due to their reactivity, structure, and physical properties. Many are now known. The most widely developed,

containing silicon as inorganic atom, are polysiloxanes, PSs, and PCSs [24]. Another common class is the polyphosphazenes [25]. PSs and PCSs are important preceramic polymers [26–28].

Organosilicon Polymers as Preceramic Polymers for the Synthesis of Si-Based Ceramics

Preceramic polymer could generally be referred as a class of hybrid materials, consisting of Si-based polymeric chains and side chain functionalities. A simple and schematic representation of a silicon-based polymer monomeric unit is shown in Fig. 1. The main backbone is constituted by silicon atoms bonded to a generic X group, with X=Si, O, NH, CH₂ or N=C=N. The nature of X is the most important variable, since it determines the class of the final polymer: Si–Si backbone defines the PS class, while Si–O, Si–NH, Si–BR, Si–CH₂, and Si–N=C=N define the polysiloxanes, polysilazanes, polyborosilanes, PCSs, and polysilylcarbodiimides, respectively (Table 1).

R₁ and R₂, the side chain functional groups, are generally carbon-based (e.g., H, alkyl, aryl, etc.). The nature of these side groups determines the properties and characteristics of the polymers. By modifying R groups, properties like solubility, thermal stability, and viscosity as a function of the temperature can be tailored easily [26].

In principle, since more than one X group could be present at the same time inside the polymer backbone, a wider range of possible polymer compositions must be considered [29]. For example, polyborosiloxanes are a class of hybrid polymers where both X=B and X=O are present in the main chain. A more comprehensive

Fig. 1 General structure of silicon-based preceramic polymers

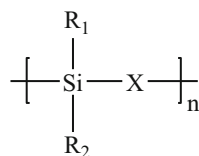


Table 1 Main types of silicon-based preceramic polymers, depending on the group “X” of polymer backbone

Group “X”	Type of polymer
O	Polysiloxanes, polysilsesquioxanes
Si	PSs
C	Polycarbosilanes
N	Polysilazanes, polysilsesquiazanes
B	Polyborosilanes

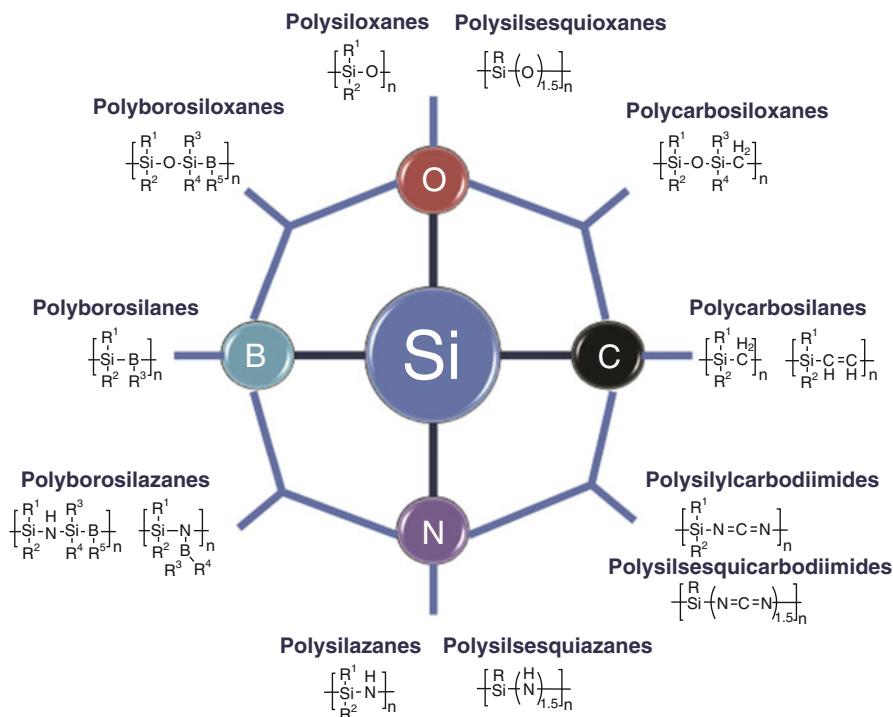


Fig. 2 Main types of silicon-based preceramic polymers in the Si–O–C–N–B system [26]

description and graphical representation of silicon-based preceramic polymers are thus presented in Fig. 2, as schematized by Colombo et al. [26].

Although, in principle, it is possible to achieve a wide variety of preceramic polymers, all the classes of preceramic polymers have not become equally “popular” and widespread in the recent past. Apart from the properties and performance of the final ceramics, other factors must be considered during the selection of a preceramic polymer. The cost-effectiveness of the precursors is one of the most important parameters of a material or a component, especially from industrial point of view. Another important factor is specific handling that every precursor requires, which could be influenced by its chemical durability, thermal stability, toxicity, and reactivity toward the atmosphere or other substances, which inevitably influence all the aspects of its processing.

Among all, polysiloxanes definitely represent the most studied class of preceramic polymers [30]; their low price and high thermochemical stability make them the preferred choice for the easy realization of silicon oxycarbide glasses with very interesting thermomechanical properties up to nearly 1200 °C.

When there is requirement of higher thermal stability, other classes of preceramic polymers should be considered, for example, PCS (for ~1400 °C) or polyborosilazanes (for ~1600 °C). The higher performance of polymers (such as

polysilazane, PCS, etc.) are accompanied by higher costs of the precursors, more complex synthesis routes, often higher reactivity toward other substances (like moisture and oxygen), and higher toxicity. These factors, generally, increase processing complexity and pose hindrance in their applicability on an industrial scale.

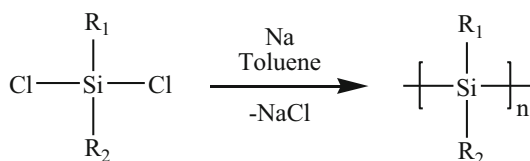
The most important synthesis routes for the production of silicon-based precursor polymers are based on chlorosilanes as main starting compounds [26, 31]. Many synthesis methods have been proposed during the last decades (e.g., sol-gel), but the chlorosilane route is the most preferred choice because, in most cases, chlorosilanes are by-products of silicone industry and offer the advantages of low cost, availability, and easily achievable high purity by distillation [32]. The general formula of chlorosilanes is R_xSiCl_{4-x} , where $0 \leq x \leq 3$ and R are a generic side group. Nowadays, the chemistry of organochlorosilanes is very well known, and the reactivity of this class of compounds has been extensively exploited for the synthesis of many different organosilicon polymers such as PSs, PCSs, polysilsesquioxanes, polyborosilazanes, polysilylcarbodiimides, polyorganosilazanes, etc.

Polysilanes

PSs are a class of Si-based polymers in which one-dimensional backbone is composed of Si atoms only with organic side chain groups [33]. The first PS derivatives were reported by Kipping [34] in 1921 by reacting dichlorodiphenylsilane with sodium, and even today, his method of sodium-mediated dechlorination (Wurtz-type coupling) remains one of the most common methods for PS synthesis [35]. The Wurtz-type coupling is shown in Fig. 3. Burkhard described the preparation of the simple dialkyl derivatives, polydimethylsilane, using Wurtz coupling [36]. It is highly crystalline and practically insoluble in any organic solvent and on heating decomposes beyond 250 °C. Burkhard's description led that polydimethylsilane (PDMS) is quite intractable, and perhaps it was the reason no one touched upon PSs and area was nearly dead for the next three decades until classical work of Yajima on PCSs in 1975, when he found that permethyl polymer $(Me_2Si)_n$ or its cyclic oligomers $(Me_2Si)_6$ can be converted into PCS which give rise to SiC on pyrolysis. Soon after that polydimethyl-co-polymethylphenylsilane was synthesized. It was soluble and meltable.

Silicon polymers resulting from monomers by Wurtz-type coupling were insoluble and possessing highly cross-linked and complicated structures [37]. The synthesis of linear and soluble PS involves the condensation of monomer by Grignard reaction [8]

Fig. 3 Synthesis of PSs by Wurtz-type coupling



as shown in Fig. 4. Usually, functionalization of PSs after polymerization process was employed to introduce the required functional groups [38].

Polycarbosilanes

Polymers that contain both Si and C in their backbone structure are called PCSs. A simplified general structure is shown in Fig. 5, but, in reality, PCSs show a much more complex structure. Besides Si–C bonds, Si–Si bonds may be present. The structure may also contain rings, cages, and complex hyperbranching, thus modifying overall Si:C ratio and final ceramic yield.

PCSs represent one of the most interesting and technologically important classes of preceramic polymers. The main interest that has led to the synthesis and continued improvement of PCSs was focused on the preparation of precursor polymers for SiC ceramic, and this class of organosilicon polymers was first to be used successfully in precursor route of ceramics, i.e., high-performance SiC fibers (Nicalon™ by Nippon Carbon Co. and Tyranno™ by UBE Industries), pioneered by Verbeek and of Yajima [14, 39]. Besides the use of PCSs as SiC precursor, they can also find applications as functional materials, such as photoresist and semiconductors. Because of their good electrical conductivity, unsaturated PCSs could be used in electronic applications such as compact capacitors, electromagnetic shielding of computers, piezoelectric sensors, smart windows (with tunable color and transparency), antistatic coatings, transistors, LEDs, lasers, and solar cells [40]. Other important applications that are opening up for these potential polymers are, in areas such as nanotechnology [41, 42], surface science, biomedicine, catalysis, electrochemistry, liquid crystals, organo-inorganic hybrids, nanocomposites, etc.

Several synthetic routes have been developed by researchers for PCSs; few important ones are discussed below.

Fig. 4 Synthesis of PSs by Grignard reaction

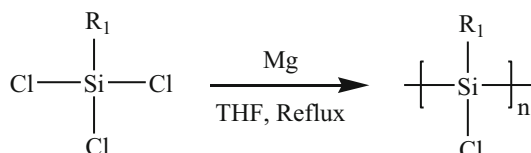


Fig. 5 Simplified general structure of PCSs

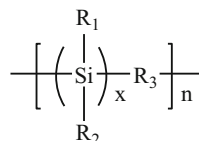
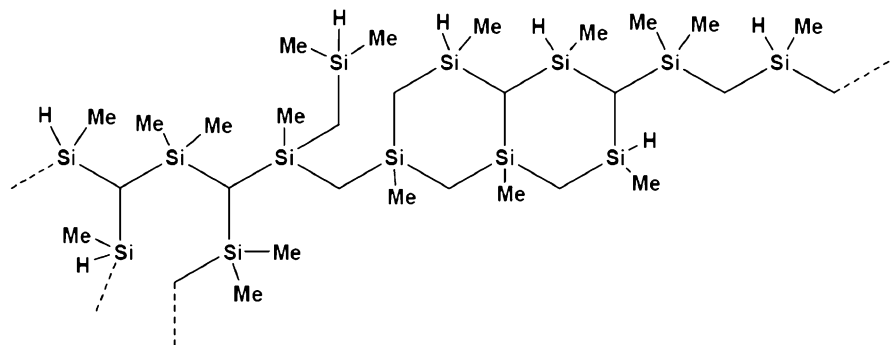
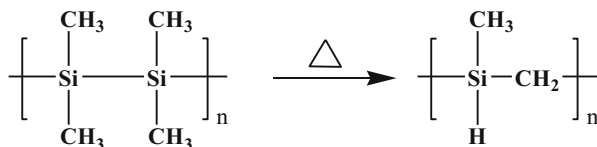


Fig. 6 Kumada rearrangement of PDMS**Fig. 7** Model structure of Yajima PCS

Yajima Strategy

The very first and most famous approach for synthesis of PCSs was proposed by Yajima [13, 14]. Dichlorosilanes were used to get PSs which were subjected to thermal backbone rearrangement, i.e., Kumada rearrangement [43], to get PCSs. Kumada rearrangement involves cleavage of Si–Si bonds of PSs and formation of Si–C bonds as shown in Fig. 6 for PDMS.

The actual structure of the Yajima PCS (as obtained by Kumada rearrangement) has complicated structure which is reflected in its largely insoluble character and easy cross-linking in air. The Yajima strategy for processing of SiC fibers typically involved melt spinning of PCS followed by thermal treatment in air to get fiber structure. The most acknowledged structure of the Yajima PCS is shown in Fig. 7.

The PCS prepared by this method, under pressure in autoclave, from PDMS (obtained in 50–60% yield) was referred to as Mark I. Mark II PCS was obtained by adding small amounts of $(\text{Ph}_2\text{Si})_n$ in PDMS or Ph_2SiCl_2 in Me_2SiCl_2 and processed in a manner similar to Mark I. Mark II was found to possess better spinnability than Mark I [8]. Continued use of autoclave play a crucial role in the synthesis of Mark I and its variant Mark II polymer.

Mark III PCS was obtained, in an alternative way, under atmospheric pressure conditions and circumvented the use of expensive autoclave. PDMS was heated at 350–400 °C under atmospheric pressure with “catalyst” polyborodiphenylsiloxane (PBDPSO) to give high ceramic yielding PCS [8, 24].

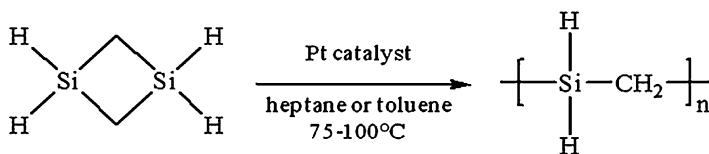


Fig. 8 Synthesis of PCS from 1,3-disilacyclobutane

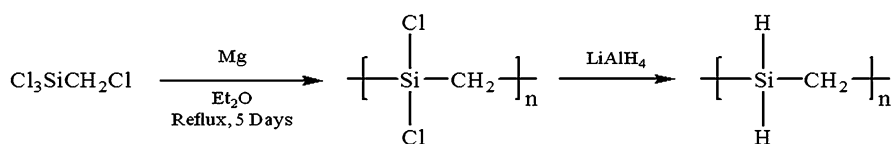


Fig. 9 Synthesis of PCS by polycondensation of chloromethylchlorosilane

Ring-Opening Polymerization (ROP) Reactions

The PCS can be prepared by the ring-opening polymerization of 1,3-disilacyclobutane using Pt-group metal derivatives as catalyst (Fig. 8). Smith claimed the preparation of poly(silylmethylene) by ring-opening polymerization of small amounts of 1,3-disilacyclobutane in heptane, using Pt-group metal derivatives as catalyst [44]. This polymer gave a SiC ceramic with 85% yield at 900 °C in argon when heated for 1 h.

Polycondensation of Chloromethylchlorosilane

Polycondensation of chloromethylchlorosilanes, chlorosilanes with methylene halides, chlorosilanes with acetylides, and chlorosilanes with unsaturated hydrocarbons give rise to PCSs. Whitmarsh and Interrante [45] have prepared a highly branched PCS by Grignard coupling of (chloromethyl)trichlorosilane with Mg in diethyl ether, followed by reduction with LiAlH₄ as shown in Fig. 9.

PCSs from Reaction of Chlorosilanes with Methylene Halides

Habel et al. [46] have prepared a series of PCSs by condensation of dichlorosilanes and methylene bromide with sodium in xylene and studied their transformation into ceramics as shown in Fig. 10. They also investigated the halogenation of poly(diphenylsilylmethylene) or poly(methylphenylsilylmethylene) with hydrogen halides and aluminum halide as a catalyst.

Generally, PCS prepared from dihalomethanes is obtained in good yields but with moderate molecular weight. In particular, the use of the inexpensive methylene chloride seems to be an alternative to the Yajima PCS if fibers can be easily obtained from polymers with Si-H bonds.

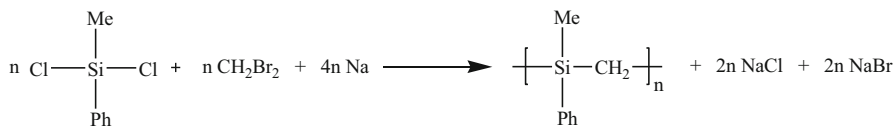


Fig. 10 Synthesis of PCS by polycondensation of chlorosilane with methylene bromide

PCSs from Chlorosilanes and Acetylides

Barton's and Corriu's groups have almost simultaneously investigated the use of poly(silylacetylene)s as precursors to SiC fibers. These soluble polymers are easily prepared by co-condensation of dichlorosilanes with dilithioacetylides. Maghsoodi and Meyer [47, 48] have obtained polymers with average molecular weight range 20–30,000 and 20–80% TGA residues at 1100 °C. They could make SiC fibers from these PCS after spinning and curing thermally or photochemically followed by pyrolysis. The authors have also synthesized poly(silyldiacetylene)s or poly(disilyldiacetylene)s with hexachlorobutadiene as starting material, in good yields.

PCS Using Hydrosilylation Reactions

Corriu [49] used the hydrosilylation of vinylhydrogenosilanes, first described by Curry [50], for the preparation of linear poly(silethylene)s. They used Pt- or Rh-based catalysts for this reaction. Spectral data (NMR) revealed that product of β -hydrosilylation predominantly forming linear $-\text{Si}-\text{CH}_2-\text{CH}_2-\text{Si}-$ (70–85%) rather than branched $-\text{SiCHMe}-$ units.

Processing of PCSs

Shaping

Easy shaping of preceramic polymer is one of the most advantageous aspects of the precursor polymer route. If compared with common powder processing routes, polymeric system has the potential advantage of an easy fabrication of green compacts with no need for additional binders. Moreover, the possibility of obtaining a machinable component prior to the polymer-to-ceramic conversion is a remarkable advantage, since it permits a more precise shape control without confronting all the problems related to ceramic brittleness and tool wear. The common polymer shaping methods such as pressing [51, 52], extrusion, injection molding [53], coating by spraying, dip coating, spin coating, and chemical vapor deposition (CVD) [54] can, in principle, be used for processing of preceramic polymers. Special polymer forming methods, using preceramic polymers enables it to realize some special shapes and components – generally very difficult to produce with powder processing route. Some typical examples are fiber drawing [55], infiltration of preformed

scaffolds to get CMCs [56], ceramic joining [57], preparation of highly porous ceramic components by direct foaming, or other techniques such as sacrificial templates [58].

Cross-Linking

After getting the required shape using some shaping process, the cross-linking of preceramic polymer is important to induce non-meltability which is essential during pyrolysis step, when polymer transforms into ceramic.

If suitable functional groups are available in polymer structure, such as $-OH$, $-H$, or $-vinyl$ groups that could undergo condensation or addition reactions, then polymer can, in general, be cured thermally by heating up to 150 – 250 °C. Other cross-linking methods could involve the use of UV radiation, γ -rays, electron beams and the use of reactive substances, gases, or plasma [59–62]. Precursor polymer cross-linking is also of fundamental importance in order to obtain high ceramic yields upon pyrolysis [63]. Effective cross-linking process results in highly branched network of polymeric molecules, thus a lower content of oligomers and low molecular weight chains that could volatilize during pyrolysis, thus increasing the final ceramic yield.

Conversion of Polymer into Ceramic (Ceramization)

The polymer-to-ceramic conversion (ceramization) represents probably the most important step in the whole preceramic polymer processing route of ceramics and is the result of a thermal decomposition process above ~ 400 °C where a totally inorganic, nonvolatile residue is formed.

The mechanism involved in the pyrolysis process is generally quite complex. This involves structural rearrangements and radical reactions that result in the cleavage of chemical bonds (e.g., $Si-H$, $Si-C$, and $C-H$), the release of organic functional groups (e.g., CH_4 , C_6H_6), and the formation of an inorganic network [26]. The whole ceramization process comprises a sequence of distinct rearrangement reactions, each occurring in its specific temperature range. In the case of PCSs, for example, it has been shown that in the 550 – 750 °C range, methane is the main volatile specie released while at higher temperature (700 – 1100 °C), the release of hydrogen is observed [64]. At temperatures of 400 – 600 °C, a porous network with open channels is formed which, upon further heating at temperatures >800 °C, can diminish (transient porosity). A simplified representation of the weight loss (TG curve) and structural rearrangements of a PCS preceramic polymer during heat treatment in inert (Ar) atmosphere, as reported by Greil [29], is shown in Fig. 11.

Outlook for Silicon-Based Preceramic Polymers

As stated above, developments in preceramic polymers, specially silicon-based preceramic polymers, have opened a new field for ceramics and their applicability in different products; a lot can still be done through incorporation of small amounts

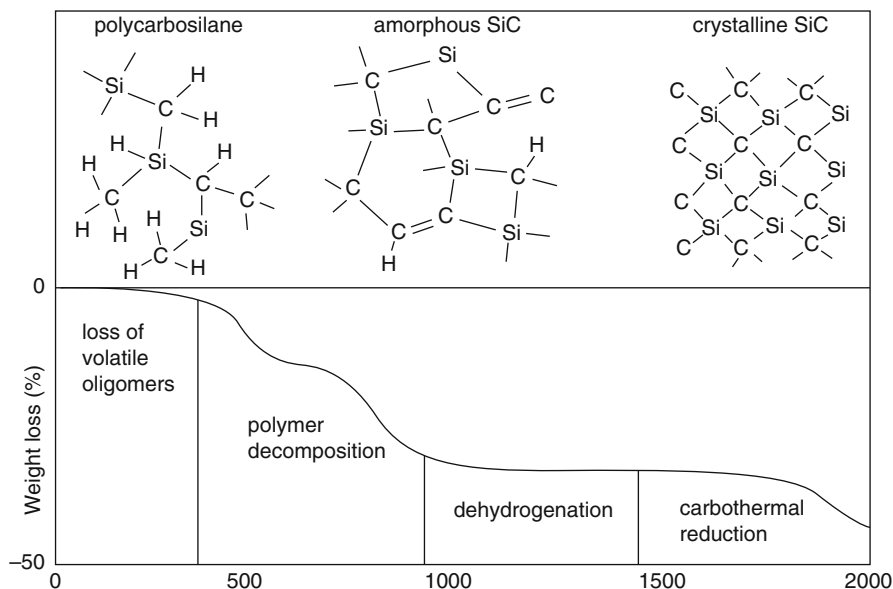


Fig. 11 Typical structural transformations during inert atmosphere pyrolysis process of preceramic polymers (PCSs) [26]

of Al, Z, B, etc. Incorporation of these elements not only influences the processing of preceramic precursors but also influences their further processing steps to ultimate ceramics such as cross-linking, stabilization, heat treatment, and microstructure of the final ceramic products and their properties. It is through these incorporations that SiC fibers and SiC-SiC composites with high temperature stability and application in the temperature range up to 1800 °C have been successfully developed.

Conclusion

Precursor-based processing of ceramics has attracted great deal of attention, particularly in last few decades, for a range of simple to complex ceramic systems, and the area of PCS synthesis and its various applications is one of them. Efforts are continuously being put to improve the properties of PCSs to process it easily into SiC products with highest ceramic yield, C/Si ratio closer to 1 with retention of shape of the product. The most important applications of PCS that have emerged are SiC-based fibers and composites among other applications such as foams, films, and coatings. In spite of tremendous research, further improvements in the properties of PCSs and their synthetic methods and studies of process parameters are need of the hour to further enhance the performance of resulting SiC ceramic products, such as fibers, foams, films, coatings, and composites.

References

1. Hench LL, Ulrich DR (1984) *Ultrastructure processing of ceramics, glasses and composites*. Wiley, New York
2. Krenkel W (2005) Carbon fibre reinforced silicon carbide composites (C/SiC, C/C-SiC). In: Bansal NP (ed) *Handbook of ceramic composites*. Springer, Boston, pp 117–148
3. Kumar S, Kumar A, Sampath V, Prasad VVB, Chaudhary JC, Gupta AK, Devi GR (2011) Fabrication and erosion studies of C-SiC composite jet vanes in solid rocket motor exhaust. *J Eur Ceram Soc* 31:2425–2431
4. Kohyama A, Kotani M, Katoh Y, Nakayasu T, Sato M, Yamamura T, Okamura K (2000) High-performance SiC/SiC composites by improved PIP processing with new precursor polymers. *J Nucl Mater* 283:565–569
5. Choyke WJ, Matsunami H, Pensl G (eds) (2004) *Silicon carbide: recent major advances*, 2 vol. Springer, Berlin
6. Kimoto T, Cooper JA (2014) *Fundamentals of silicon carbide technology: growth, characterization, devices and applications*. Wiley-IEEE Press, Hoboken
7. Wynne KJ, Rice RW (1984) Ceramics via polymer pyrolysis. *Annu Rev Mater Sci* 14:297–334
8. Birot M, Pillot J, Dunogues J (1995) *Comprehensive chemistry of polycarbosilanes, polysilazanes, and polycarbosilazanes as precursors of ceramics*. *Chem Rev* 95:1443–1477
9. Loh PP, Bao X, Nangrejo MR, Edirisinghe MJ (2000) Preparation of silicon carbide foams using polymeric precursor solutions. *J Mater Sci Lett* 35:4365–4372
10. Ainger FW, Herbert JM (1960) The preparation of phosphorus-nitrogen compounds as non-porous solids. In: Popper P (ed) *Special ceramics*. Academic, New York, pp 168–182
11. Chantrell PG, Popper P (1965) *Inorganic polymers and ceramics*. In: Popper P (ed) *Special ceramics*. Academic, New York, pp 87–103
12. Mera G, Riedel R (2009) Organosilicon-based polymers as precursors for ceramics. In: Colombo P, Riedel R, Soraru GD, Kleebe H-J (eds) *Polymer derived ceramics: from nanostructure to applications*. DEStech Publications, Lancaster, p 51
13. Yajima S, Hayashi J, Omori M (1975) Continuous silicon carbide fiber of high tensile strength. *Chem Lett* 4(9):931–934
14. Yajima S, Hasegawa Y, Okamura K, Matsuzawa I (1978) Development of high tensile strength silicon carbide fibre using an organosilicon polymer precursor. *Nature* 273:525–527
15. Yu Y, Tai J, Tang X, Guo Y, Tang M, Li X (2008) Continuous Si–C–O–Al fiber derived from aluminum-containing polycarbosilane precursor. *Composites A* 39:1101–1105
16. Babonneau F, Soraru GD (1991) Synthesis and characterization of Si-Zr-C-O ceramics from polymer precursors. *J Eur Ceram Soc* 8:29–34
17. Yang HS, Kwon OH, Lee JD, Kang PH (1996) Preparation and characteristics of titanium-modified silicon carbide fiber. *J Ind Eng Chem* 2(2):106–115
18. Yajima S, Okamura K, Hayashi J (1975) Structural analysis in continuous silicon carbide fibre of high tensile strength. *Chem Lett* 4(12):1209–1212
19. Yajima S, Okamura K, Hasegawa Y (1981) Method of producing silicon carbide fibers. US Patent 4,283,376
20. Okamura K, Sato M, Matsuzawa T, Seguchi T, Kawanishi S (1988) Silicon based ceramic fibers. *Ceram Eng Sci Proc* 9:909–918
21. Mishra R, Tiwari RK, Saxena AK (2009) Synthesis of Fe–SiC nanowires via precursor route. *J Inorg Organomet Polym* 19:223–227
22. Ginzburg M, MacLachlan MJ, Yang SM, Coombs N, Coyle TW, Raju NP, Greedan JE, Herber RH, Ozin GA, Manners I (2002) Genesis of nanostructured, magnetically tunable ceramics from the pyrolysis of cross-linked polyferrocenylsilane networks and formation of shaped macroscopic objects and micron scale patterns by micro molding inside silicon wafers. *J Am Chem Soc* 124(11):2625–2639
23. Kawasaki S, Murase H, Fujiki T, Nishida R, Sakai S, Zaima H (2000) Epoxy resin composition and moldings. European Patent Applications EP0970981A1

24. Allcock HR, Mark JE, West R (1992) Inorganic polymers. Prentice Hall, Englewood Cliffs
25. Allcock HR (2002) Chemistry and applications of polyphosphazenes. Wiley, Hoboken
26. Colombo P, Mera G, Riedel R, Soraru GD (2010) Polymer-derived ceramics: 40 years of research and innovation in advanced ceramics. *J Am Ceram Soc* 93(7):1805–1837
27. Pawlenko S (1986) Organosilicon chemistry. Walter de Gruyter, New York
28. Brook MA (2000) Silicon in organic, organometallic, and polymer chemistry. Wiley, New York
29. Greil P (2000) Polymer derived engineering ceramics. *Adv Eng Mater* 2(6):339–348
30. Abe Y, Gunji T (2004) Oligo- and polysiloxanes. *Prog Polym Sci* 29(3):149–182
31. Seyferth D (1988) Polycarbosilanes: an overview. In: Inorganic and organometallic polymers. ACS symposium series 360. American Chemical Society, Washington, DC, pp 21–42
32. Stark FO, Falender JR, Wright AP (1982) Silicones. In: Wilkinson G (ed) Comprehensive organometallic chemistry, vol 2. Pergamon Press, Oxford
33. Koe J (2009) Contemporary polysilane synthesis and functionalization. *Polym Int* 58:255–260
34. Kipping FS, Sands JE (1921) Organic derivatives of silicon. Part XXV. Saturated and unsaturated silicohydrocarbons, Si₄Ph₈. *J Chem Soc* 119:830–847
35. Miller RD, Michl J (1989) Polysilane high polymers. *Chem Rev* 89:1359–1410
36. Burkhard C (1949) Polydimethylsilanes. *J Am Chem Soc* 71:963–964
37. West R, David LD, Djurovich PI, Stearley KL, Srinivasan KSV, Yu H (1981) Phenylmethylpolysilanes: formable silane copolymers with potential semiconducting properties. *J Am Chem Soc* 103:7352–7354
38. Horiguchi R, Onishi Y, Hayase S (1988) High molecular weight polysilanes with phenol moieties. *Macromolecules* 21:304–309
39. Verbeek V (1973) Ger. Offen. 2218960 (Bayer AG); US Patent 3853567
40. Zeldin M, Wynne KJ, Allcock HR (1988) Inorganic and organometallic polymers. ACS symposium series 360. American Chemical Society, Washington, DC
41. Tsirlin AM, Shcherbakova GI, Florina EK, Popova NA, Gubin SP, Moroz EM, Riedel R, Kroke E, Steen M (2002) Nano-structured metal containing polymer precursors for high temperature non-oxide ceramics and ceramic fibers- syntheses, pyrolyses and properties. *J Eur Ceram Soc* 22:2577–2585
42. Gupta RK, Mishra R, Mukhopadhyay K, Tiwari RK, Ranjan A, Saxena AK (2009) A new technique for coating silicon carbide onto carbon nanotubes using a polycarbosilane precursor. *Silicon* 1(2):125–129
43. Shiina K, Kumada M (1958) Thermal rearrangement of hexamethyldisilane to trimethyl (dimethylsilylmethyl)silane. *J Org Chem* 23:139–139
44. Smith TL Jr (1986) US Patent 4,631,179
45. Whitmarsh CK, Interrante LV (1991) Synthesis and structure of a highly branched polycarbosilane derived from (chloromethyl)trichlorosilane. *Organometallics* 10:1336–1344
46. Habel W, Haeusler W, Oelschläger A, Sartori P (2008) Chapter 89, New modified polycarbosilanes. In: Auner N, Weis J (eds) Organosilicon chemistry II: from molecules to materials. Wiley-VCH, Weinheim
47. Maghsoodi SI, Pang Y, Barton TJ (1990) Efficient, “one-pot” synthesis of silylene-acetylene and disilylene-acetylene preceramic polymers from trichloroethylene. *J Polym Sci A Polym Chem* 28:955–965
48. Meyer MK, Akinc M, Maghsoodi SI, Zhang X, Barton TJ (1991) Silylene-acetylene polymers as precursors to SiC fibers. *Ceram Eng Sci Proc* 12:1019–1031
49. Boury B, Corriu R, Leclercq D, Mutin P, Planeix JM, Vioux A (1991) A poly(vinylsilane): a precursor to silicon carbide. 1. Preparation and characterization. *Organometallics* 10:1457–1461
50. Curry JW (1956) The synthesis and polymerization of organosilanes containing vinyl and hydrogen joined to the same silicon atom. *J Am Chem Soc* 78:1686–1689
51. Rocha RMD, Greil P, Bressiani JC, Bressiani AHDA (2005) Complex- shaped ceramic composites obtained by machining compact polymer- filler mixtures. *Mater Res* 8(2):191–196
52. Galusek D, Sedlacek J, Riedel R (2007) Al₂O₃-SiC composites by warm pressing and sintering of an organosilicon polymer-coated alumina powder. *J Eur Ceram Soc* 27:2385–2392

53. Zhang T, Evans JRG, Woodthorpe J (1995) Injection moulding of silicon carbide using an organic vehicle based on a preceramic polymer. *J Eur Ceram Soc* 15:729–734
54. Colombo P, Paulson TE, Pantano CG (1997) Synthesis of silicon carbide thin films with polycarbosilane (PCS). *J Am Ceram Soc* 80:2333–2340
55. Bunsell AR, Piant A (2006) A review of the development of three generations of small diameter silicon carbide fibers. *J Mater Sci* 41:823–839
56. Erdal M, Guceri SI, Danforth SC (1999) Impregnation molding of particle-filled preceramic polymers: process modeling. *J Am Ceram Soc* 82:2017–2028
57. Colombo P, Sglavo V, Pippel E, Woltersdorf J (1988) Joining of reaction-bonded silicon carbide using a preceramic polymer. *J Mater Sci* 33:2409–2416
58. Vakifahmetoglu C, Menapace I, Hirsch A, Biasetto L, Hauser R, Riedel R, Colombo P (2009) Highly porous macro- and micro-cellular ceramics from a polysilazane precursor. *Ceram Int* 35(8):3281–3290
59. Janakiraman N, Aldinger F (2009) Fabrication and characterization of fully dense Si-C-N ceramics from a poly(ureamethylvinyl)silazane precursor. *J Eur Ceram Soc* 29:163–173
60. Liew LA, Liu Y, Luo R, Cross T, An L, Bright VM, Dunn M, Daily JW, Raj R (2002) Fabrication of SiCN MEMS by photopolymerization of pre-ceramic polymer. *Sens Actuators A* 95:143–151
61. Idesaki A, Sugimoto M, Tanaka S, Narisawa M, Okamura K, Itoh M (2004) Synthesis of a minute SiC product from polyvinylsilane with radiation curing Part I Radiation curing of polyvinylsilane. *J Mater Sci* 39:5689–5694
62. Idesaki A, Narisawa M, Okamura K, Sugimoto M, Morita Y, Seguchi T, Itoh M (2001) Application of electron beam curing for silicon carbide fiber synthesis from blend polymer of polycarbosilane and polyvinylsilane. *Radiat Phys Chem* 60:483–487
63. Schulz M, Borner M, Gottert J, Hanemann T, Hausselt J, Motz G (2004) Cross linking behavior of preceramic polymers effected by UV- and synchrotron radiation. *Adv Eng Mater* 6:676–680
64. Yu Z, Yang L, Min H, Zhang P, Liu A, Riedel R (2015) High-ceramic-yield precursor to SiC-based ceramic: a hyperbranched polytitaniumcarbosilane bearing self-catalyzing units. *J Eur Ceram Soc* 35(2):851–858



Development of Carbon Nanotube-Reinforced Ceramic Matrix Nanocomposites for Advanced Structural Applications

25

Luv Gurnani and Amartya Mukhopadhyay

Contents

Introduction	930
Key Issues and Challenges in Development of CNT-Reinforced CMCs	933
CNT Dispersion Within Bulk Ceramic Matrix and Sintering of CNT-Reinforced CMCs	933
Degree of Interfacial Bonding Between CNT and Ceramic Matrix	934
CNT-Reinforced Bulk Ceramic Matrix Composites: Processing and Microstructure Evolution	934
Dispersion of Carbon Nanotubes Using Surface Modification or Chemical Functionalization Techniques	935
Overview of Processing Routes for Development of Bulk Ceramic-CNT Composites ...	936
Mechanical Properties of CNT-Reinforced Ceramic Matrix Composites	945
Tribological Properties of CNT-Reinforced Ceramic Matrix Composites	953
Possible Toughening Mechanisms in Carbon Nanotube-Reinforced Ceramic Nanocomposites	958
Potential Applications of Carbon Nanotube-Reinforced Ceramic Matrix Composites	966
Summary and Outlook	967
References	969

Abstract

Ceramic matrix composites containing fiber reinforcements possess superior mechanical and tribological properties, as compared to their monolithic counterparts, that render them better suited for engineering applications demanding high strength, wear resistance, and resistance to thermal shock. Among the wide range of reinforcements used for toughening the otherwise intrinsically brittle bulk ceramic materials, carbon nanotubes (CNTs), owing to their excellent physical,

L. Gurnani · A. Mukhopadhyay (✉)

High Temperature and Energy Materials Laboratory, Department of Metallurgical Engineering and Materials Science, IIT Bombay, Powai, Mumbai, India

e-mail: luvgurnani@gmail.com; amartya_mukhopadhyay@iitb.ac.in

© Springer Nature Switzerland AG 2020

929

Y. R. Mahajan, R. Johnson (eds.), *Handbook of Advanced Ceramics and Composites*,
https://doi.org/10.1007/978-3-030-16347-1_30

mechanical, and thermal properties, are considered to be one of the most promising reinforcement types. The exceptional mechanical properties of CNTs offer excellent opportunities toward the development of considerably stronger and tougher ceramic nanocomposite systems for potential applications in aircraft and aerospace industries. However, there are many challenges with respect to the processing of CNT-reinforced bulk ceramic materials that limit their commercial applications to a considerable extent. Additionally, dispersion of the CNTs, optimization of the CNT volume fractions, development of suitable CNT/matrix interfaces, and distribution within the sintered polycrystalline ceramic microstructures are some of the aspects that need particular attention. Continuing research efforts have been directed toward addressing issues related to such aspects, in a bid to attain best possible combination of mechanical and tribological properties. With regard to microstructure development, achieving uniform distribution of well-dispersed CNTs within the sintered polycrystalline ceramic matrix (i.e., reinforcing the grain interiors and not just the grain boundaries with CNTs) has been found to be particularly difficult, until very recently. In these contexts, after discussing some of the basic aspects of carbon nanotubes and ceramic-CNT composites, the present chapter provides a comprehensive review of the overall status of research and development in CNT-reinforced ceramic matrix composites, with particular emphasis on a variety of processing techniques investigated to date in a bid to optimize the quality of CNT dispersion, character of the CNT-matrix interfaces, eventual densification of the composites, and also cost-effectiveness. The influences of CNT reinforcements on the properties of some of the important ceramic systems for advanced structural applications are discussed, with an emphasis towards fracture behavior and the possible toughening mechanisms. This review also highlights the more recent research efforts that have been conducted to address the issues concerning inhomogeneous dispersion and distribution of CNTs within the ceramic matrix, thus aiming toward the realization of the full potential of CNTs as reinforcing fibers. Lastly, the various potential applications for ceramic-CNT composites as structural materials have been highlighted, with an outlook toward the scope for future developments and issues that need to be further addressed.

Keywords

Ceramic nanocomposites · Carbon nanotubes · Processing · Mechanical properties · Tribological properties

Introduction

Ceramic materials, owing to their superior thermal stability, corrosion resistance, chemical inertness, resistance to thermal shock, high strength, and stiffness, in addition to their light weight characteristics, are better suited for engineering applications concerned with exposure to high temperature and harsh environmental conditions and as part of airborne structures, as compared to the metallic materials. These wide range of applications for ceramic materials range from the more

conventional applications, as in process metallurgical and/or chemical industries where exposure to molten metals and slags demands high refractoriness, good oxidation, and corrosion resistance, to the more advanced structural applications such as components/parts of air- or spaceborne vehicles which demand high property-to-weight ratios. However, despite possessing such superior properties, as best suited for the aforementioned applications, the inherent brittleness (i.e., low fracture toughness) of ceramics, especially in the monolithic (or unreinforced) form, tends to limit their usage in the form of bulk structural components. Such a high level of mechanical unreliability and tendency to fail catastrophically in service conditions owing to the poor resistance to crack propagation of (monolithic) ceramics have been, over decades, a matter of grave concern for the scientific and engineering community. Against this backdrop, the development of ceramic matrix composites (CMCs) brought some remedial measures for this Achilles' heel of the bulk monolithic ceramics. The incorporation of a wide variety of reinforcements in the form of particulates and fibers [1–13] into the bulk inorganic glasses, glass-ceramics, and polycrystalline ceramic matrices has been explored over the past three to four decades. There have been extensive reports on the improvement in fracture toughness of the glass matrix and ceramic matrix composites reinforced with fibers like carbon, SiC, and alumina [1–8], as compared to their monolithic counterparts, which render CMCs as attractive materials for structural applications.

Ever since the very discovery of carbon nanotubes (CNTs) by Sumio Iijima in 1991 [14], the interest toward the use of this material (then considered as “wonder” material) as a potential reinforcement in CMCs has skyrocketed over the years. The remarkable physical (densities as low as 1.5–2.0 g/cc) and mechanical (with axial Young's modulus or E up to ~ 1 TPa [15] and tensile strength ~ 60 GPa [16] for individual perfect nanotube) properties of CNTs offer a wide range of possibilities for the development of extremely strong, tough, and damage-tolerant bulk ceramic matrix composites reinforced with carbon nanotubes. Moreover, in light of the toughening mechanisms (to be detailed in the subsequent sections), the exceptionally high aspect (length to diameter) ratio of CNTs (usually >1000) potentially offer advantage over their micron-scale counterparts (viz., carbon fibers) in terms of the efficient load transfer with the matrix. Structurally, the diameter of a carbon nanotube can range from around 1 nm [17] to an upper limit of ~ 100 nm with lengths in the order of microns (even centimeters as reported in [18]). A typical carbon nanotube may consist of one or more coaxial/concentric graphitic cylinders, resulting in single or multiwalled nanotubes (SWCNTs/MWCNTs), respectively. On the contrary, the diameters of the commercially available carbon (pitch and PAN) fibers are of the order of 7–20 μm , while the vapor-grown carbon fibers (VGCFs) exhibit a wider range of intermediate diameters [19].

Over the last 10–15 years, extensive research efforts have been directed toward the application of CNTs as potential toughening agents in the ceramic matrices. The prospects of developing advanced engineering material based on CNT-reinforced CMCs that would manifest, to some extent, the remarkable and extraordinary properties of CNTs are largely dependent upon how the key issues and challenges associated with the processing of ceramic-CNT nanocomposites are addressed. These include obtaining CNTs with good structural integrity (free from defects

and impurity contents) and intrinsically good mechanical properties at a reasonable cost, optimizing the volume fractions of CNT reinforcements, achieving homogeneous dispersion and distribution of CNTs within the bulk inorganic glass/glass-ceramic/polycrystalline ceramic matrices, developing an appropriate degree of CNT-matrix interfacial bonding, and obtaining highest possible densification (% of theoretical density) of the ceramic matrices without inducing structural damage to the reinforced CNTs. Unfortunately, the appealing properties of CNTs and their potential role in toughening the inherently brittle ceramic matrices have yet not lived up to the expected potential of CNTs being the “ultimate next-generation fiber” till date primarily due to the aforementioned bottlenecks. A survey of the open literature database reveals a huge scatter and inconsistency in the quantitative improvements in fracture toughness of the CNT-reinforced CMCs, with % improvements ranging from significantly low (3%) [20] to exceptionally high (200%) [21] reported till date. The role and extent of toughening mechanisms like debonding, fiber pull-out, crack bridging, and crack deflection and the associated mechanistic models [8] prevalent in conventional micron-scale fiber-reinforced composites have not been clearly extrapolated and established to such nanoscale reinforcements (CNTs) with high aspect ratios. The possibility of other deformation and toughening mechanisms at such lower dimensional scales and subsequent formulation of some postulates need to be explored to explain the extent of toughening in CNT-reinforced CMCs.

In light of this, the present chapter (comprised of eight sections) encompasses a broad understanding of the overall aspects of processing-microstructure-property relationships in carbon nanotube-reinforced ceramic matrix composites which would eventually determine the anticipated potential of CNTs in strengthening and toughening of the otherwise inherently brittle structural ceramic materials. This chapter will thus commence with the major challenges involved in the development of CNT-reinforced CMCs, particularly in terms of uniform dispersion of CNTs within the bulk ceramic matrices, which have till date hindered harnessing the full potential of CNT reinforcements in bulk ceramics. The later sections will present an overview of different processing routes investigated till date for incorporation of CNTs into some of the commercially important ceramic or glass matrices in light of effectively mitigating the challenges associated with dispersion of CNTs and obtaining optimum CNT/matrix interfacial strength within these ceramic-/glass-based materials. The influence of these processing techniques on the microstructural evolution in as-consolidated ceramic-CNT nanocomposites and its correlation to the bulk mechanical (especially the fracture toughness) and tribological properties of these composites will be extensively discussed. A critical assessment of the characterization techniques used for estimating the fracture toughness of CNT-reinforced will also be presented in the later sections. An overview of literature database on mechanical and tribological properties of some of the widely investigated ceramic-CNT nanocomposites would be followed by the important discussion on the dominant toughening mechanisms operative in CNT-reinforced ceramic, with a primary motive to gain deeper insights into the toughening mechanisms peculiar and unique to composites containing such nanoscale reinforcements (CNTs), thereby establishing the fundamental difference relative to the conventional micron-scale fiber-reinforced ceramic composites. Lastly, the various potential applications envisaged for such composite materials have been

presented, with the final section giving an outlook toward the scope for future developments in such CNT-reinforced CMCs.

Key Issues and Challenges in Development of CNT-Reinforced CMCs

CNT Dispersion Within Bulk Ceramic Matrix and Sintering of CNT-Reinforced CMCs

One of the biggest bottlenecks in developing tough and strong CNT-reinforced ceramic nanocomposites has been achieving a good dispersion of CNTs within the polycrystalline ceramic or glass/glass-ceramic matrix. It is of paramount importance that the individual carbon nanotubes are uniformly/homogeneously dispersed and separated from each other within the matrix in order to avoid the extremely deleterious effects of agglomeration/entanglement of CNTs on the properties of composite. CNTs, owing to their very high aspect ratios and surface areas, combined with the surface van der Waals forces, have natural tendency to agglomerate and entangle into ropes or bundles. In the case of ceramic and glass matrices, agglomeration tendency increases particularly for high loading fractions of CNT, wherein the matrix continuity is lost since there occurs the shortage of matrix material to fully penetrate or “wet” the large surface area of the reinforcement. Such agglomerates act as defect sites leading to stress concentrations that can promote crack formation and hence premature failure. On a different perspective, such entanglements also introduce void spaces or porosities within the bulk ceramic material. Overall, the above two effects have the potential to lead to degradation of the properties even with respect to the monolithic counterpart. On the contrary, in an ideal dispersion, each CNT is loaded individually, stress transfer is fully exploited over maximum interfacial area, and toughening offered would be higher. Therefore, in such nanocomposite systems, the higher volume fractions (typically above 2–3 vol%) of CNTs tend to deteriorate the properties which otherwise can be improved at lower loading fractions of CNTs, thus being one of the bottlenecks toward achieving the full potential/promise of CNT reinforcements. In order to attain good dispersion of the nanotubes, it is primarily important to adopt a suitable processing route for incorporation of CNTs into the ceramic matrix. The first and foremost step usually involves dispersion of CNTs in a suitable solvent by methods primarily based on application of shear forces, using high-shear mixers or ultrasonic probes [22]. Here, caution needs to be exercised because too high shear forces may in turn lead to excess agglomeration, while excess ultrasonication may lead to breakage of the CNTs [23, 24], thus introducing defects, shortening their lengths (or aspect ratios), and concomitantly rendering them inferior with respect to their desired properties. Sometimes centrifuging is also tried. However, again, too high a centrifugal force may bring the CNTs too close to each other, leading to entanglement/aggregation of the CNTs. Quite often, the surface of the CNT is modified, either by direct functionalization chemistry or by the use of surfactants [22], in order to render them more stable in a given dispersing media or to improve compatibility with a given matrix powder and/or matrix precursor. However, again, excess functionalization may

lead to creation of structural defects [25], thus rendering the CNTs inferior in terms of their stiffness and strength.

The other challenge is obtaining near-theoretical density upon sintering of CNT-reinforced ceramics due to the strong hindrance toward densification, as provided by the CNTs. This renders the conventional pressureless sintering technique almost unsuited for sintering of CNT-reinforced ceramic composites. Hence, the more advanced sintering techniques, such as hot pressing (HP), hot isostatic pressing (HIP), and spark plasma sintering (SPS), are usually used for the densification of CNT-reinforced CMCs. Furthermore, the sintering needs to be performed either in inert atmosphere or vacuum due to the possibility of the CNTs getting oxidized in air atmosphere at above 600 °C [26]. Lastly, for a high-quality CNT-reinforced CMC, it must be ensured that the combination of dispersion, mixing, and sintering techniques should not induce structural damage to the nanotubes. The above are some of the factors that have hindered the development of CNT-reinforced ceramic composites regularly at the commercial level.

Degree of Interfacial Bonding Between CNT and Ceramic Matrix

Based on knowledge gained from the more conventional micron-scale fiber-reinforced composites [5, 8], it is extremely important to achieve an appropriate degree of interfacial bonding between the ceramic matrix and the CNTs in the as-fabricated nanocomposite [19, 22, 27]. It is likely that the CNT-bound interfaces might follow the interfacial mechanisms of their conventional fiber-reinforced ceramic counterparts, wherein the desired interfacial strength is neither too strong nor too weak (viz., preferably, of intermediate strength). This is for maximizing the energy consumed for debonding at the fiber/CNT interface (as needed for enhancing fracture toughness) while at the same time allowing effective transfer of load across the interface. An interface of similar character is likely to promote the familiar energy dissipation mechanisms of fiber (CNT)/matrix debonding, crack bridging by reinforcing fiber, and fiber pull-out. Too weak a bonding between the “reinforcing” CNT and the ceramic matrix is not only expected to lead to inefficient reinforcement but is likely to also result in local stress concentration, crack initiation, and ultimately failure. By contrast, too strong interfaces would not significantly improve the fracture toughness due to suppressed fiber/matrix debonding. However, it needs to be acknowledged here that the consequences of the reduction of diameter of the reinforcing fiber by several orders of magnitude (say, from micron scale to nanoscale; as in the case of CNTs) on the mechanics at the interface are still uncertain.

CNT-Reinforced Bulk Ceramic Matrix Composites: Processing and Microstructure Evolution

As discussed in the previous section, the choice of a suitable processing route for successful development of CNT-reinforced ceramic nanocomposites is mainly governed by the extent to which the following major challenges are overcome,

viz., (a) homogeneous dispersion of CNTs within the bulk ceramic matrix, avoiding the natural propensity of CNTs to agglomerate/entangle into bundles, (b) prevention of degradation of CNTs during different stages of processing (viz., ultrasonication, surface modification/chemical treatment of CNTs, and during sintering/densification of the ceramic nanocomposite at high temperatures, usually >1200 °C), (c) achieving near-theoretical densities upon sintering of CNT-reinforced CMCs, and (d) obtaining an optimum interfacial bonding between the CNT and the matrix in order to achieve an effective load transfer across the interface.

The development of bulk ceramic nanocomposites containing CNT reinforcements broadly includes three stages of processing: (a) obtaining stable agglomerate-free dispersion of purified (devoid of metal catalyst particles and amorphous carbon) CNTs in a suitable solvent (such as water or other polar solvents), (b) mixing/incorporation of well-dispersed CNTs in the parent ceramic matrix powder or matrix precursor, and (c) consolidation/sintering of ceramic-CNT mixture to near-theoretical density leading to formation of CNT-reinforced bulk ceramic nanocomposites. Each of these steps impact the success/failure with respect to the aforementioned aspects and also considerably influence the microstructure development, as further detailed below.

Dispersion of Carbon Nanotubes Using Surface Modification or Chemical Functionalization Techniques

Perfect CNTs, like graphite, are inherently inert possessing almost negligible surface charges. In practice, commercially available CNTs, particularly nanotubes grown via chemical vapor deposition (CVD), do possess a degree of surface functionalization [19] but are generally available in agglomerated or entangled state and also contain impurities of metal catalyst particles or amorphous carbon. The surface modification of carbon nanotubes has been a subject of intensive research since the 1990s, primarily motivated toward purification and stabilizing dispersion (in an appropriate solvent) of CNTs prior to incorporation in polymer, metal, glass, or ceramic matrices [19, 22, 27, 28]. The basic strategies used for dispersion of CNTs involve (a) using π - π -induced interactions via physical adsorption of π -aromatic compounds in solvents [29]; (b) making other noncovalent (van der Waals, physical adsorption) bonding-induced barriers to agglomeration, for instance, wrapping the CNTs with surfactants and polymers [29, 30] or by using charged nanoparticles (such as ZrO_2) [31]; and (c) inducing covalently bonded sidewall functionalization of CNTs. Such chemical modification of the CNT sidewalls by forming covalent bonds between the CNTs and different functional groups, such as aliphatic amines, carboxylates, esters, etc. [32–34], can greatly improve the dispersion.

Figure 1 presents an overall schematic representation of different methodologies of surface modification or functionalization of CNTs, namely, noncovalent/covalent functionalization and defect functionalization [35]. Noncovalent functionalization modifies the outer surface of CNTs without affecting the sp^2 network of graphitic carbon by absorption or wrapping around of polymer molecules or charged nanoparticles around CNT. Covalent functionalization involves functional entities

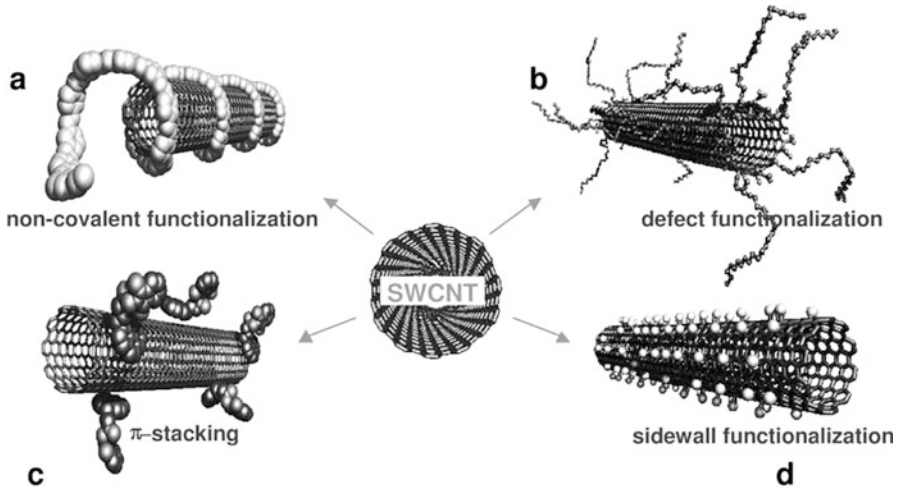


Fig. 1 Different methodologies for functionalization of SWCNTs: (a) noncovalent functionalization involving wrapping of CNTs with polymers; (b) functionalization on structural defects; (c) noncovalent functionalization with molecules π -stacking; (d) sidewall functionalization. (Images reused from [35] with permission from John Wiley and Sons)

covalently bonded to the nanotube's carbon scaffold either at the terminals or at the sidewalls of the tubes. Sidewall functionalization induces a change in hybridization of covalently bonded carbon atoms from sp^2 to sp^3 , while defect functionalization occurs at oxygenated sites and structural defects such as irregularities associated with the presence of pentagons and heptagons in the hexagonal framework of graphene.

Overview of Processing Routes for Development of Bulk Ceramic-CNT Composites

In terms of the final (post-sintering) microstructural evolution, the ceramic-CNT nanocomposites can be fabricated using either directionally oriented or randomly oriented CNTs. Figure 2a, b [36] presents schematic representations of such directionally oriented CNT-reinforced ceramic nanocomposites. In the bulk nanocomposites containing randomly oriented CNTs, the microstructure development differs with respect to the ceramic matrix, whether polycrystalline or glass. For polycrystalline matrices, it is more frequently observed that the nanotubes exist as bundles along the grain boundaries [20, 21, 37] (Fig. 2c; [36]), although a few microstructural developments characterized by CNTs penetrating the matrix grains (Fig. 2d; [36]) have also been achieved [38–41]. For glasses or glass-ceramics, which are devoid of grains/grain boundaries, it is possible to develop glass-CNT nanocomposites with CNTs dispersed homogeneously (Fig. 2e; [36]) throughout the

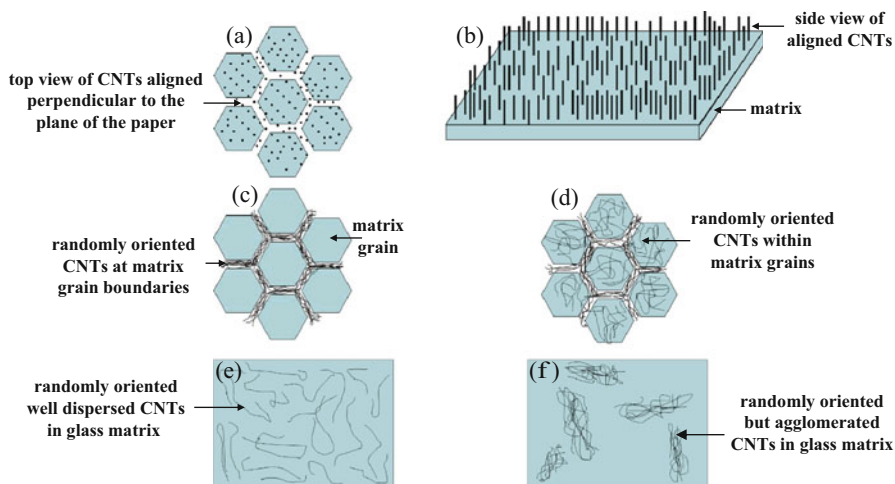


Fig. 2 Schematic representation of the different microstructural developments possible for CNT-reinforced ceramic nanocomposites via (a) top view and (b) side view of directionally oriented (aligned) CNT-ceramic nanocomposites; randomly oriented CNT-polycrystalline ceramic nanocomposites containing (c) CNTs at matrix grain boundaries only and (d) CNTs also within matrix grains; and randomly oriented glass-CNT nanocomposites containing (e) well-dispersed nanotubes and (f) nanotube agglomerates. (Images reused from [36])

bulk [42, 43]. However, it is observed that CNTs tend to form agglomerates (Fig. 2f; [36]) even in such nanocomposites [44, 45].

The dispersed (and most likely functionalized) CNTs are mixed either directly with the concerned ceramic matrix powder via currently available techniques such as conventional powder processing and colloidal processing or mixed with the matrix precursor in the form of a clear sol followed by conversion to gel (sol-gel processing) for glass [42, 43], as well as polycrystalline ceramic matrix (as per a route very recently proposed by our group [39]). Alternately, the CNTs can be synthesized/grown by catalytic growth on the surface of ceramic powder particles and also within the purposefully engineered pores of the ceramic matrix itself (viz., via in-situ growth of CNTs by CVD).

Conventional Powder Processing Route

The early stages of development of bulk ceramic-CNT nanocomposites mostly involved the use of conventional powder metallurgical routes, owing to the reduced costs, lesser processing times, and higher yields prevalent in such processing techniques. The CNTs are mixed with the powders of the concerned ceramic or glass matrix, usually under wet conditions, using ultrasonication and/or wet ball milling and subsequently followed by sintering [21, 44–46]. Generally, the CNTs are dispersed separately in a suitable solvent using ultrasonication, and the resultant dispersion is added to the slurry of ceramic powder (dispersed in either similar or compatible solvent), followed by ball milling of the slurry mixture under controlled

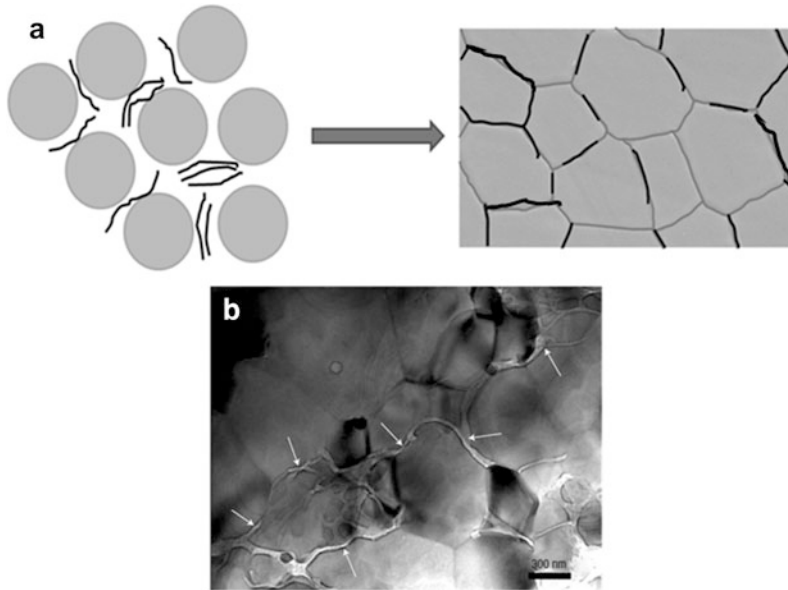


Fig. 3 (a) Schematic illustration of clustering of CNTs during physical mixing with ceramic powder particles and subsequent aggregation of CNTs at the matrix grain boundaries during densification, which is evident from (b) the consolidated microstructure of Al_2O_3 -5.7 vol% SWCNT, with white arrows indicating the CNTs present along the grain boundaries while the grain interiors being completely devoid of CNT reinforcement. (Image (b) reused from [21] with permission from Springer Nature)

conditions to minimize damage to the CNTs. The ball-milled slurry is then dried, crushed, and sieved, followed by densification using mostly hot pressing or spark plasma sintering.

The conventional powder processing technique, though cost-effective, has failed to be an effective means to achieve homogeneous dispersion of CNTs in polycrystalline ceramic or glass matrices. As shown schematically in Fig. 3a and is evident from the TEM micrograph of ball-milled Al_2O_3 -5.7 vol% SWCNTs in Fig. 3b [21], the CNTs, owing to their high aspect ratios, have natural geometrical tendency, to cluster into the voids between the larger ceramic powder particles during physical mixing/ball milling, and thus the absence of any driving force for the CNTs to penetrate into the bulk from the powder particle surface leads to segregation of CNTs at the grain boundaries of the polycrystalline ceramic matrix [19, 21, 22, 39, 42], with the grain interiors being almost completely devoid of any reinforcing CNT. From the viewpoint of mechanical properties, such microstructure, as characterized by nonuniform distribution of CNTs, is expected to considerably reduce the participation of the reinforcing CNTs toward arresting the propagation of transgranular cracks.

The problem is often exacerbated upon physical mixing of higher volume fractions (usually more than 5%) of CNTs with the ceramic/glass powders, leading

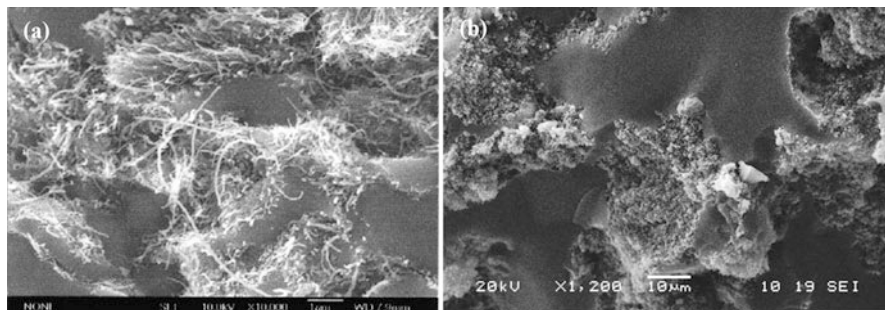


Fig. 4 SEM images of fractured surface showing the presence of agglomerated carbon nanotubes in hot-pressed (a) SiO₂-10 vol% MWCNT nanocomposite and (b) borosilicate glass-10 wt% MWCNT nanocomposite. (Images reused from (a) [47] and (b) [44] with permission from Elsevier)

to poor densification/sinterability and consequent deterioration of mechanical properties in both the polycrystalline ceramic [21] and glass matrices [44] due to the excessive agglomeration of such rigid, non-densifying inclusions inhibiting diffusion processes or giving rise to increased viscosity of the overall system at the sintering temperature. Zhan et al. [21] have reported inadequate densification (only 86–95% of theoretical density) despite the use of activated sintering techniques like SPS for physically mixed Al₂O₃-10 vol% SWCNTs. Similar observations (as shown in Fig. 4) regarding highly inhomogeneous dispersion of MWCNTs have been reported for SiO₂ [47] and borosilicate [44, 45] glass-based matrices as well while adopting conventional powder processing routes for development of such glass-MWCNT nanocomposites.

In-Situ Growth of Carbon Nanotubes in Ceramic Matrix by Chemical Vapor Deposition (CVD)

In order to facilitate incorporation of larger volume fractions of CNTs and simultaneously obviate the pre-consolidation processing routes necessary to debundle or monodisperse the as-received agglomerated carbon nanotubes, attempts were directed toward direct synthesis of ceramic (mostly oxides)-CNT composite powders (which would eventually be sintered to yield the bulk ceramic-CNT nanocomposites) via in-situ catalytic growth of CNTs over the active metal nanoparticles (such as Fe or Co) impregnated within the oxide ceramic powder. In this regard, the pioneering works conducted by Peigney and co-workers [48–54] demonstrated that selective reduction of oxide (such as α -Al₂O₃, MgO, and MgAl₂O₄) solid solutions containing homogeneously dissolved transition metal (Fe, Co or Fe/Co alloy) cations as dopants using CH₄:H₂ gas mixture could lead to in-situ formation of pristine metallic nanoparticles (particle sizes close to 10 nm) which are active sites for the catalytic growth of CNTs. The resulting CNT-metal-oxide composite powders contained a large volume fraction of both single- and multiwalled CNTs with diameters ranging from 1.5 to 15 nm, which were subsequently hot pressed to form the nanocomposites. Peigney et al. also reported, perhaps for the first time, that the

long bundles of CNTs could be aligned in the bulk ceramic matrices (Al_2O_3 , MgO , MgAl_2O_4) using high-temperature extrusion technique [53], exploiting the fact that, when the average grain size is sufficiently decreased (less than about $1\ \mu\text{m}$), many polycrystalline ceramics exhibit superplasticity, enabling the use of thermo-mechanical processing for such materials. Nanotubes were incorporated in-situ, as described above, into the metal catalyst containing oxide powders (with mean particle sizes, $100\ \text{nm}$) with the composite powders subsequently being extruded at high temperatures ($1500\text{--}1600\ \text{°C}$) in a graphite die under vacuum. The alignment of the CNTs was clearly observed in the oxide matrices as shown in fractured surface SEM images (Fig. 5). Moreover, the presence of CNTs facilitated the superplastic forming by inhibiting the matrix grain growth and acting as lubricating agents.

However, the in-situ incorporation of the long bundles of CNTs has not yielded the expected improvement in mechanical properties, with the fracture toughness of the hot-pressed CNT-containing ceramic composites being lower than those of the unreinforced metal catalyst-containing oxide ceramics possibly because of the lower sinter densities (87–93% of theoretical) of the CNT-metal-oxide composites [50–53]. The in-situ growth of CNTs in bulk ceramic matrices appears to be an attractive processing route, in terms of scalability and reasonably uniform distribution of CNTs over the surface of the oxide particles, but the CNT dispersion through the bulk of the composite is quite inhibited. The network of CNTs over the surface of oxide particles also creates a barrier to efficient sintering of the composite. This approach based on in-situ catalytic growth of CNTs provides no scope for manipulation of the interface properties to improve the mechanical properties. Additionally, the hot pressing at high temperatures ($1500\text{--}1600\ \text{°C}$) induces significant damage to the nanotubes (more pronounced in MgO -based nanocomposites) [50–53] resulting in formation of disordered graphene layers at the matrix grain boundaries. The presence of other deleterious species such as amorphous carbon, metal carbides, and thick and short nanotubes in both the as-synthesized CNT-containing metal-oxide powders and the resultant composites further adds to the drawbacks of these in-situ processing techniques. In short, such processing techniques may hold

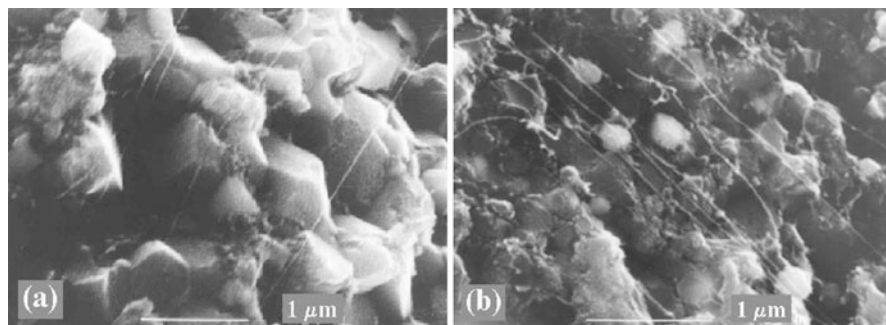


Fig. 5 Scanning electron micrographs revealing the alignment of CNTs in fractured surfaces of (a) CNT-Fe- Al_2O_3 and (b) CNT-Fe/Co- MgAl_2O_4 composites developed via high-temperature extrusion process (at $1500\ \text{°C}$). (Images reused from [53] with permission from Elsevier)

significance for certain functional applications but tend to be less appealing for manifesting the anticipated macroscopic reinforcement effects of CNTs in structural ceramics.

On a different note, the fundamentals of in-situ catalytic growth of carbon nanotubes in ceramic matrices using chemical vapor deposition (CVD) have been efficiently utilized by introducing carefully controlled and innovative design of certain microstructural aspects in the ceramic matrices, in order to directly elucidate the reinforcement or toughening mechanisms operative in CNT-reinforced ceramic matrix composites. Xia et al. [55–57] have reported the formation of highly ordered, vertically aligned arrays of nearly parallel MWCNTs in amorphous nanoporous alumina matrix. A hexagonal array of straight pores (of sizes 30–40 nm) was generated in this amorphous oxide support, having a thickness of 20 μm . Ni or Co metal catalyst particles were deposited within these pores in order to facilitate catalytic growth (using CVD) of highly ordered unidirectional MWCNTs up the pore walls. Such novel microstructural characteristics containing vertically aligned MWCNTs have been reported for amorphous Si_3N_4 -MWCNT composites (the architecture being thin film instead of nanoporous) using a combination of chemical vapor deposition (CVD) and chemical vapor infiltration (CVI) techniques [58–60].

Even though the aforementioned composites containing highly oriented CNTs may not hold significance for structural applications as the corresponding architectures do not represent the bulk materials, these microstructural designs, indeed, give deeper insights and more concrete evidences of toughening and deformation mechanisms (based on detailed SEM observations and relevant numerical models [55, 56, 58–60]) as well as the frictional properties [57] prevalent in CNT-reinforced ceramic composites (will be discussed in detail in the later sections). Moreover, these highly ordered unidirectional CNT-reinforced ceramics, unlike the randomly oriented composites, are amenable to well-defined mechanistic models which would provide a basis for comparison and/or differentiation of the toughening/reinforcement mechanisms between the micron-scale continuous fiber-reinforced ceramics and their CNT-reinforced counterparts.

Colloidal Processing

The intimate mixing and/or dispersion of CNTs with the ceramic or glass matrix can be achieved by allowing the ceramic particles (of similar diameters to the CNTs) to uniformly coat the surface of the CNTs. The formation of stable colloidal suspensions of CNTs and ceramic nanoparticles by adjusting the surface chemistry of these two concerned species and exercising stringent control over the processing conditions (such as pH, temperature, etc.) is a primary requirement for achieving such intimate dispersions. The colloidal processing routes, involving coating of ceramic nanoparticles over the surface of CNTs, are primarily based on the phenomenon of heterocoagulation or heteroaggregation of oppositely charged nanoparticles. Heterocoagulation takes place when two electrostatically stabilized colloidal suspensions (one of ceramic matrix particles and the other of CNTs in the present context) are intermixed such that the two sets of species have opposite surface charges which promote the coating process. The nanoparticle coatings effectively

shield the undesirable attractive van der Waals interactions between the CNTs, thus preventing their agglomeration.

As discussed earlier, the covalent C–C bonding in pristine CNTs does not allow the CNTs to readily disperse in polar solvents such as water. Hence, the surfaces of as-synthesized CNTs are usually modified by oxidative chemical treatments which simultaneously purify (remove impurities such as amorphous carbon and metal catalyst particles) and functionalize the CNTs. The CNTs are, most frequently, purified and oxidized in a solution of concentrated nitric acid (HNO_3) or a mixture of concentrated HNO_3 and concentrated sulfuric acid (H_2SO_4) [19, 37, 61, 62] developing a negative surface charge over the CNTs by decorating their surface with oxygenated functional groups, viz., carboxyl and hydroxyl groups. These acidic groups promote electrostatic repulsion amongst the CNTs and thus stabilize the CNT dispersion in polar solvents.

The use of certain organic surfactants may also prove effective in tailoring the surface properties of both the CNTs and ceramic matrix particles during the heterocoagulation process. The entangled CNTs and ceramic particles are usually dispersed in surfactant solutions using ultrasonication [63]. Typical cationic surfactants (which induce positive charge) include cetyltrimethylammonium bromide (CTAB) and polyethylene amine (PEI), while common anionic surfactants (which induce negative charge) include polyacrylic acid (PAA), sodium dodecyl sulfate (SDS), and sodium dodecyl benzyl sulfonate (SDBS) [19]. The surface charges on the CNTs, as well as on any given ceramic particle, can be generally manipulated as desired by the use of different organic surfactants or dispersants. Though the surfactants get burnt out during sintering, they sometimes have a tendency to introduce undesirable impurities.

Colloidal processing, based on heterocoagulation, has been explored for different polycrystalline ceramic matrices such as Al_2O_3 [40, 41, 61, 63, 64], TiO_2 [65], and Si_3N_4 [66]. It must be noted here that intimate mixing of CNTs with the ceramic particles is established by adjusting the surface chemistry of both the phases during low-temperature colloidal processing. However, the retention of such homogenous dispersion of CNTs in the bulk ceramic matrix after sintering has not been successful to a considerable extent, with only few reports [40, 41, 67] revealing good quality dispersion involving minor fraction of CNTs present within the matrix grains as well. This is primarily because of the re-agglomeration tendency of CNTs upon solvent removal [62, 67, 68]. Even if the as-received agglomerated/entangled CNTs are uniformly dispersed using the aforementioned surface functionalization techniques coupled with sonication in a suitable solvent, any small change (say in temperature, pH, solvent volume, ionic strength) during the solvent removal process or while mixing with ceramic matrix powders would eventually promote re-agglomeration or segregation (more pronounced at higher volume fractions) of CNTs.

Sol-Gel-Based Processing Routes

Sol-gel-based processing techniques provide an attractive and alternate approach for achieving a homogenous dispersion of CNTs in polycrystalline ceramics or glass matrices. CNTs are usually dispersed (using ultrasonication) in a clear solution

(known as sol) of a molecular precursor (not the powders) of the desired ceramic matrix. The sol containing dispersed CNTs undergoes a condensation reaction resulting in formation of a thick and highly viscous gel network which entraps the CNTs [19, 69]. This gel network is then dried or calcined, crushed, and sieved followed by consolidation of the dried gel powders. The glass (such as SiO_2 , borosilicate) [70–74] and glass-ceramic (such as borosilicate) [42, 43] based materials have been the most widely investigated systems for incorporation of CNTs using the sol-gel techniques, with limited reports on polycrystalline ceramics (such as Al_2O_3) [39, 75] as well.

In principle, the sol-gel-based processing routes ought to provide an effective means to obtain uniform dispersions of CNTs. However, re-agglomeration of CNTs (more severe for higher volume fractions) in the precursor solutions has been a matter of serious concern, owing to the longer times for sol to gel conversion process which mostly involves boiling or evaporation of the precursor solution. Mo et al. [75] have reported fairly uniform dispersion of 1.5 vol% CNTs but high degree of agglomeration (as shown in Fig. 6) for 3.3 vol% CNTs in alumina-CNT nanocomposite developed by sol-gel process followed by spark plasma sintering.

In order to mitigate the re-agglomeration tendency of CNTs in the sol-gel process, Thomas et al. [72] have demonstrated that the surface modification of MWCNTs with the help of organosilanes, stabilizes the dispersion in the sol, resulting in uniform distribution (Fig. 7) of CNTs in borosilicate glass matrix after consolidation, for maximum up to 3 wt% of MWCNTs.

The research efforts, introducing innovative, yet facile variations to the sol-gel process, by Chu et al. [42] and Mukhopadhyay et al. [43], have been quite significant in achieving an excellent degree of dispersion with almost negligible agglomeration of MWCNTs having concentrations as high as 10 wt% in alumino-borosilicate (ABS) glass-ceramic matrices. The researchers employed ultrasonication-assisted sol-gel processing technique to uniformly disperse up to 15 wt% MWCNTs in ABS matrix. The MWCNTs were functionalized or rather esterified using chemical treatments [42], and the chemistry of the sol was chosen so as to be mutually

Fig. 6 Agglomeration of CNTs at triple junctions, as illustrated by the SEM image of fractured surface of Al_2O_3 -3.3 vol% CNT nanocomposite developed via sol-gel route followed by SPS. (Image reused from [75] with permission from Elsevier)

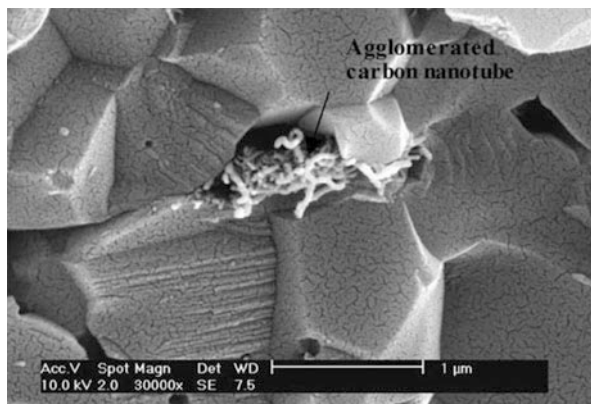
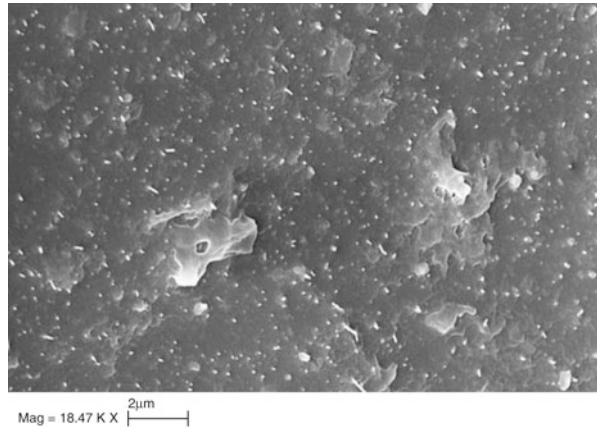


Fig. 7 FEG-SEM image of fractured surface of borosilicate glass-2 wt% MWCNT composite showing highly uniform dispersion of CNTs. (Image reused from [72] with permission from Elsevier)



compatible to the esterified MWCNTs, thereby maintaining good quality of MWCNT dispersion with the matrix precursor. The ultrasound-assisted in-situ sol-gel processing used here effectively controls the degree of dispersion of the CNTs during the gelation period when the volatile constituents of the sol get removed such that the increase in viscosity slows down the diffusion of dispersed CNTs and hence prevent their re-bundling. On the contrary, in traditional sol-gel routes, heating for removal of volatile matter accelerates the re-agglomeration of the CNTs. The ultrasonic waves propagating through a solution also accelerate chemical reactions and thus the gelation time, which otherwise ranges from several hours to a few days in conventional sol-gel processing. The representative SEM micrographs (Fig. 8) of the fractured surfaces of ABS glass-ceramic-MWCNT nanocomposites reveal highly uniform and intimate dispersion of MWCNTs (up to 10 wt%) in the glass-ceramic matrix, while the onset of agglomeration of MWCNTs in ABS-15 wt% MWCNT composites [43].

Achieving Intragranular CNT Reinforcement

Recently, similar principles of ultrasonication-assisted sol-gel processing have been successfully used in our group, by Satam et al. [39], for achieving very uniform and homogeneous distribution (perhaps the best till date) of multiwalled carbon nanotubes (up to 5 vol%) in bulk polycrystalline alumina matrix, thus leading to the development of near-ideal sintered ceramic composite microstructure, characterized by the presence of both intergranular and intragranular MWCNT reinforcements. The innovative processing route adopted here has been schematically depicted in Fig. 9a. The pre-dispersed (in ethanol) functionalized MWCNTs were added in the clear sol of alumina precursor (aluminum-tri-sec-butoxide dissolved in ethanol) under ultrasonication followed by rapid (within a few seconds) gelation to “entrap/freeze” the MWCNTs in dispersed state. The dried and ground gels were calcined at 750 °C in Ar atmosphere. Unlike the case where MWCNTs tend to occupy the voids between the crystalline ceramic (e.g., α -Al₂O₃) powder particles during physical mixing/ball milling and eventually segregate at the matrix grain boundaries

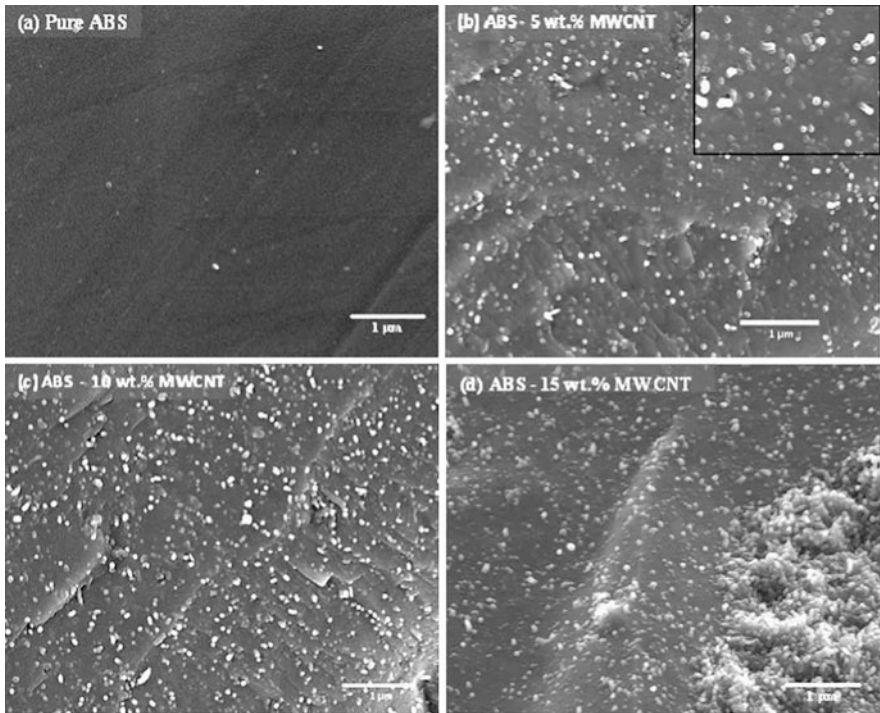


Fig. 8 SEM images of fractured surfaces of (a) ABS glass ceramic not having any MWCNT; (b) ABS-5 wt% MWCNT nanocomposite; (c) ABS-10 wt% MWCNT nanocomposite; and (d) ABS-15 wt% MWCNT nanocomposite. It is of importance that the MWCNTs could be homogeneously dispersed in the nanocomposite containing even up to 10 wt% MWCNT (b, c). (Images reused from [57] with permission from Elsevier)

post-sintering (Fig. 9b), this uniquely designed sol-gel-based route allows the in-situ crystallization of the ceramic ($\alpha\text{-Al}_2\text{O}_3$) matrix around the uniformly dispersed network of CNTs during the sintering (SPS) of calcined gel powders and thus leads to the formation of idealized polycrystalline ceramic-MWCNT nanocomposite microstructures (Fig. 9c, d) having intragranular MWCNT reinforcements.

Mechanical Properties of CNT-Reinforced Ceramic Matrix Composites

By virtue of their remarkable physical and mechanical properties accompanied with very high aspect ratios (>1000), CNTs have been anticipated to be one of the most promising reinforcements for improving the mechanical properties, particularly the fracture toughness, of the otherwise brittle structural ceramic materials. In this context, extensive research investigations have been carried out to explore the effects of CNT reinforcements on the mechanical properties of some of the commercially

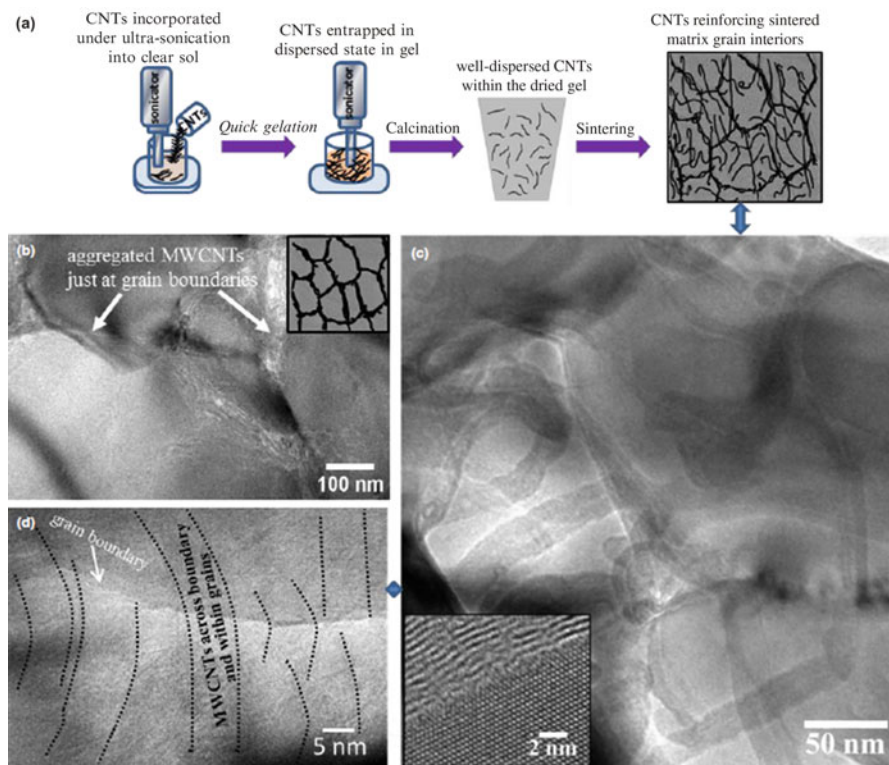


Fig. 9 (a) Schematic representations for the processing route used and the idealized microstructure type having both inter- and intragranular MWCNTs. Representative TEM images obtained with as-sintered (b) “ball-milled” (inset schematically illustrating the non-ideal microstructure type) and (c, d) “sol-gelled” Al_2O_3 -5 vol% MWCNT. Presence of MWCNTs within the matrix grains can be seen in c, d (similar inset in (c) presents high-resolution image across the interface between an intragranular MWCNT and Al_2O_3 grain). (Images reused from [39] with permission from John Wiley and Sons)

important engineering ceramic materials, such as Al_2O_3 (being the most widely investigated system) [20, 21, 37–41, 61, 76, 77], ZrO_2 [46, 78, 79], SiC [80–83], Si_3N_4 [66, 84, 85], and hydroxyapatite (HAp) [86–89], and glass-based matrices such as SiO_2 [47, 71, 90], borosilicate [44, 45, 72], and alumino-borosilicate (ABS) [42, 43]. The effects of CNT reinforcements on the mechanical properties of different polycrystalline ceramics, glasses, and glass-ceramics are summarized in Table 1. It must be noted that the following discussion is concerned mainly with ceramic nanocomposites reinforced with randomly oriented CNTs.

Though a number of studies have reported significant improvements (as high as ~200%) in the mechanical properties of CNT-reinforced ceramic or glass matrix composites with respect to their monolithic counterparts, there have been several reports which exemplify almost negligible or quite modest (as low as ~3%) improvement in the mechanical properties, more specifically the fracture toughness, of

Table 1 Effects of CNT reinforcements on the mechanical properties of various nanocomposites based on polycrystalline ceramics, glasses, and glass-ceramics. (Sintering techniques are abbreviated as SPS, spark plasma sintering; HP, hot pressing; PS, pressureless sintering. Methods of fracture toughness measurements are abbreviated as VI, measurement of crack lengths around Vickers indentation; SEVNB, single-edge V-notched beam; SENB, single-edged notched beam)

Polycrystalline ceramic/ glass matrix	% CNT reinforcements	Sintering technique	Improvement in mechanical properties (%) with respect to matrix		Method used for fracture toughness measurement	References
			Fracture toughness	Flexural strength		
Al ₂ O ₃	5.7 vol% SWCNT	SPS	140%	–	VI	Zhan et al. [21]
	10 vol% SWCNT		194%	–		
	10 vol% SWCNT	SPS	Negligible	–	SEVNB	Wang et al. [20]
	3 vol% MWCNT	HP	79%	13%	SENB	Wei et al. [38]
	1 vol% MWCNT	SPS	40%	–	VI	Cha et al. [76]
	0.9 vol% MWCNT	SPS	25%	27%	SENB	Yamamoto et al. [77]
	5 vol% MWCNT	SPS	33%	–	VI	Satam et al. [39]
	10 vol% MWCNT	SPS	67%	–	SEVNB	Liu et al. [64]

(continued)

Table 1 (continued)

Polycrystalline ceramic/ glass matrix	% CNT reinforcements	Sintering technique	Improvement in mechanical properties (%) with respect to matrix			Method used for fracture toughness measurement	References
			Fracture toughness	Flexural strength			
SiC	10 vol% MWCNT	HP	10%	10%	SENB	Ma et al. [80]	
HAp	3 wt% MWCNT	PS	200%	150%	SENB	Li et al. [86]	
BSG glass	10 wt% MWCNT	HP	11%	-40% (decrease)	SENB	Boccacini et al. [45]	
SiO ₂ glass	5 vol% MWCNT	HP	100%	65%	VI	Ning et al. [47]	
	10 vol% MWCNT		30%				
ABS glass-ceramic	10 wt% MWCNT	HP	150%	100%	SEVNB	Mukhopadhyay et al. [43]	

ceramic nanocomposites containing CNT reinforcements. In fact, a few studies on CNT-reinforced glass matrices such as borosilicate (BSG) indicate that the incorporation of MWCNTs (10 wt%) degrade the mechanical properties of the composites as compared to the unreinforced BSG [45]. Such inconsistencies across various investigations emphasize the fact that, till date, there is no unified consensus on the improvements achieved in the fracture toughness and strength of CNT-reinforced ceramic nanocomposites and the role of CNTs as potential reinforcing/toughening elements in inherently brittle ceramic matrices has not been fully realized as expected. This scatter in the mechanical properties of CNT-reinforced CMCs may be primarily attributed to significant differences in the processing routes adopted for development of such composites, the quality of CNTs used (in terms of purity, defect density, and structural integrity), the relative sinter densities of the composites, degree of dispersion of CNTs in both the powder precursors and the consolidated/as-sintered microstructures, the CNT-matrix interfacial properties, and, more importantly, the test specimen preparation and characterization techniques used for quantitative estimation of the mechanical properties, especially the fracture toughness of these nanocomposites.

The characterization techniques used for estimating the fracture toughness of the CNT-reinforced CMC mainly involve Vickers indentation (VI), single-edged notched beam (SENB) bend tests, and single-edged V-notched beam (SEVNB) bend tests [69]. Majority of the research investigations [19, 21, 47, 75, 76, 91], owing to the small volume of test specimens, involve the usage of Vickers indentation technique for measuring the fracture toughness of these nanocomposites. The VI method basically uses a conventional Vickers hardness testing equipment to make an indent on a polished specimen surface, creating a plastically deformed region underneath the indent with cracks emanating radially outward and downward from the indent. The crack length at a given load is an indication of the fracture toughness of the tested material (the tougher the material, the shorter the crack lengths), which is estimated using the following equation [92]:

$$K_{IC} = \alpha \cdot \left(\frac{E}{H}\right)^{\frac{1}{2}} \cdot \left(\frac{P}{c^{3/2}}\right) \quad (1)$$

where E and H are, respectively, the elastic modulus and hardness of the material, P is the applied load, c is the radial crack length, and α is an empirical constant which depends on the geometry of the indenter [92].

Based on the measurement of indentation crack lengths, Zhan et al. [21] reported that nearly threefold improvement in fracture toughness ($9.7 \text{ MPa m}^{1/2}$) over that of monolithic Al_2O_3 ($3.3 \text{ MPa m}^{1/2}$) is possible via incorporation of 10 vol% SWCNT in Al_2O_3 nanocomposites processed via conventional physical mixing route followed by consolidation using SPS. However, these results were later claimed to be perhaps invalid for such SWCNT-reinforced nanocomposites by Wang and co-workers [20], who demonstrated nearly complete suppression of cracking around the indentations in SPS-processed Al_2O_3 -10 vol% SWCNT, but not the true fracture toughness.

They also reported that incorporation of similar volume fraction of graphite particles in place of SWCNTs suppressed the indentation cracking to the same extent, thereby discrediting the unique role of SWCNTs in improving the fracture toughness of the Al_2O_3 -based nanocomposites. Moreover, negligible increment in fracture toughness for similarly processed Al_2O_3 -SWCNT nanocomposites ($3.32 \text{ MPa m}^{1/2}$), with respect to pure Al_2O_3 ($3.22 \text{ MPa m}^{1/2}$), could be observed when the more standard and reliable single-edged V-notched beam (SEVNB) technique was used for measuring the fracture toughness of the same. Nevertheless, based on the observations of suppression of indentation-induced cracking, it was claimed that the nanocomposites possess improved contact damage resistance with respect to monolithic Al_2O_3 .

A critical review by Quinn and Bradt [93] (recommended for further reading) on the Vickers indentation method for measurement of fracture toughness highlights the discrepancies in this technique and further validates the claims of Wang et al. [20]. The authors have recommended [93] that the VI technique should not be employed for determination of absolute values of K_{IC} in ceramics/ceramic composites but it can still be applied for relative comparison of materials in terms of their resistance to locally induced damage. In fact, there has been a long, though interesting, discussion through a series of research articles [94–96], debating over the reliability of different fracture toughness measurement techniques (both Vickers indentation and SEVNB tests) particularly for CNT-reinforced ceramic matrix composites. The effective use of the SENB or SEVNB tests requires precise control over specimen preparation and pre-notch root radius. The uniform standards are sometimes omitted or ignored, primarily due to material constraints, as larger specimens (for, e.g., test beams of dimensions $3 \times 4 \times 50 \text{ mm}^3$) would be ideally required for statistically reliable results [19]. The limitations on obtaining large quantities of ceramic-CNT composite powders and subsequently maintaining the homogenous dispersion of CNTs in such large-sized specimens of as-sintered nanocomposites sometimes render Vickers indentation method advantageous (though not reliable for estimating absolute values of K_{IC}) over SEVNB, as it can be conducted on smaller-sized specimens without requiring any complex sample preparation procedures. Moreover, given the small specimen volume, a well-dispersed ceramic-CNT composite system most likely would give a uniform and reproducible set of data despite the micron-scale of the indentation. Nonetheless, both the techniques (VI and SEVNB) have been frequently employed either for determination of relative resistances to crack propagation (indentation toughness) under contact loading or for more reliable quantitative estimation of macroscopic/bulk fracture toughness (K_{IC}) of ceramic nanocomposites incorporated with CNTs.

Wei et al. [38] have reported an increase (w.r.t. hot-pressed monolithic Al_2O_3) in fracture toughness by $\sim 79\%$ (measured using single-edged notched beam (SENB) technique) and bend strength by $\sim 13\%$ for the hot-pressed Al_2O_3 -3 vol% MWCNT nanocomposites having fairly homogeneous microstructures containing MWCNTs along the matrix grains boundaries, as well as within the grains obtained as a result of careful purification and dispersion of MWCNTs in colloidal suspensions. In another investigation [77], which again focused on achieving homogeneous

dispersion of MWCNTs in Al_2O_3 via proper functionalization of MWCNTs, considerably improved fracture toughness (by $\sim 25\%$; SENB) and bend strength (by $\sim 27\%$; three-point bending) with respect to monolithic Al_2O_3 were reported for SPS-processed Al_2O_3 -0.9 vol% MWCNT nanocomposites. Recent investigations by our research group [39] have highlighted the significance of an innovative processing route based on rapid sol-gel technique (as discussed in the previous section) in tailoring the idealized microstructures characterized by highly homogeneous dispersion of up to 5 vol% of randomly oriented multiwalled carbon nanotubes present within the polycrystalline Al_2O_3 matrix grains as well as along the grain boundaries. Al_2O_3 -5 vol% MWCNT nanocomposites processed via sol-gel route followed by SPS exhibited an increment in indentation toughness by $\sim 33\%$ with respect to monolithic Al_2O_3 . In contrast, Al_2O_3 -5 vol% MWCNT nanocomposites processed via conventional physical mixing/ball milling of MWCNTs with α - Al_2O_3 powders followed by SPS under similar conditions exhibited $\sim 22\%$ improvement in indentation toughness as compared to pure Al_2O_3 , the lesser improvement being possibly because of the absence of intragranular CNT reinforcement in these “ball-milled” composites, unlike the case of “sol-gelled” composites.

The reports concerning investigations of mechanical properties of other polycrystalline ceramics (particularly the non-oxide based ceramics such as SiC [80–83], TaC [97, 98], and Si_3N_4 [66, 84, 85]) incorporating carbon nanotubes are relatively sparse. Corral et al. have reported the development of Si_3N_4 -SWCNT (up to 6 vol%) nanocomposites, using colloidal processing, followed by SPS [85]. Though the composites possessed improved grindability as compared to monolithic Si_3N_4 , no systematic trend in densification and thereby hardness and fracture toughness of the composites could be obtained despite a number of sintering trials (at different temperatures and holding durations) conducted to optimize the densification and mechanical properties of the composites. Ma et al. [80] have reported modest improvements in bend strength ($\sim 10\%$) and fracture toughness ($\sim 10\%$; measured using SENB) for hot-pressed SiC-10 vol% CNT composites as compared to monolithic SiC. Such insignificant increments were attributed to the poor dispersion quality of CNTs in the composites as well as weaker SiC-CNT interface since the processing route involved direct wet mixing (without any purification and functionalization treatments) of SiC powders and CNT, using ultrasonication. In another work, SiC-coated MWCNTs were incorporated as reinforcing elements in SiC matrix in order to achieve good interfacial adhesion between MWCNTs and SiC [81]. The SPS-processed SiC-5 vol% SiC-coated MWCNT composites exhibited improved indentation toughness (by $\sim 77\%$) w.r.t. monolithic SiC at 9.8 N test load. However, the improvement in indentation toughness of the composites was merely $\sim 12\%$ (w.r.t. monolithic SiC) when the test load was increased to 19.6 N. This inconsistency in the estimated values of indentation toughness was not explained in this work.

A few notable research efforts, over the past decade, have demonstrated the role of CNTs as potential toughening elements in bio-ceramic materials, such as those based on hydroxyapatite (HAp) [86–89]. In a significant development, Li et al. [86] developed hydroxyapatite (HAp)-3 wt% MWCNT nano-biocomposites via

pressureless sintering in vacuum. The nanocomposites sintered in vacuum possessed significantly improved fracture toughness (by ~200%) and bend strength (by ~150%) with respect to pure HAp.

As can be seen from above discussion, extensive research investigations have been carried out on CNT-reinforced polycrystalline ceramics. In contrast, comparatively little work has been done on the development and characterization of glass-CNT nanocomposites. Ning et al. [47] developed SiO₂-MWCNT nanocomposites by physical mixing of SiO₂ powders and as-received nanotubes in ethanol using ultrasonication, followed by hot pressing. Considerable improvements in the bend strength (by ~65%) and indentation toughness (by ~100%) with respect to unreinforced SiO₂ glass were reported for the SiO₂-5 vol% MWCNT nanocomposites. However, further increase in nanotube content led to deterioration in the mechanical properties, which was attributed to excessive agglomeration of the MWCNTs in the SiO₂ matrix (see Fig. 4a).

Borosilicate glass (BSG) is considered to be one of the most important glasses with respect to technological applications. Boccaccini and co-workers [44, 45] tried to develop dense BSG-10 wt% MWCNT nanocomposites via conventional powder processing route followed by hot pressing. However, extremely poor densification (maximum of 85%) was achieved, and observation of fractured surfaces of the hot-pressed nanocomposites revealed that the MWCNTs were severely agglomerated (see Fig. 4b). Such low densities, along with defects induced by excessive agglomeration of the MWCNTs, resulted in the nanocomposites possessing poorer mechanical properties even with respect to the unreinforced borosilicate glass [45]. In another investigation, the same research group were able to develop dense BSG-MWCNT nanocomposites via sol-gel-based processing route followed by hot pressing [72]. Good dispersion of the nanotubes was obtained for the nanocomposites containing up to 2 wt% MWCNTs, resulting in considerable improvement in the hardness (by ~15%) and compressive strength (by ~75%) with respect to unreinforced borosilicate glass.

Bryan and co-workers [42, 43] developed a novel processing technique (refer to section “[Sol-Gel-Based Processing Routes](#)”), comprising careful purification and functionalization of multiwalled carbon nanotubes, followed by ultrasonication-assisted sol-gel processing and subsequent hot pressing of alumino-borosilicate (ABS) glass-ceramic-MWCNT nanocomposites. This processing route allowed the development of dense nanocomposites, containing uniformly dispersed CNTs with contents up to 10 wt% in ABS glass-ceramic matrix. The ABS-10 wt% MWCNT nanocomposite exhibited remarkable improvement in mechanical properties as compared to unreinforced ABS [43], possessing almost twofold increment in strength and ~150% improvement in fracture toughness (estimated by using SEVNB 4-point bend tests) with respect to monolithic ABS glass-ceramic.

The research investigations discussed so far were mainly concerned with room temperature mechanical properties of the CNT-reinforced ceramic matrix composites. Ceramic materials, by virtue of their high melting points and good thermal stability, are ideally suited for high-temperature structural applications. In the context of CNT-reinforced CMCs, only a few research works [53, 99–103] have been

based on investigation of high-temperature mechanical properties, owing to the technical difficulties associated with oxidation of CNTs (at temperatures >600 °C in air atmosphere) and the requirement of vacuum or inert atmosphere in mechanical testing equipments. Nevertheless, it is quite noteworthy that the bulk ceramic nanocomposites containing carbon nanotubes possess superior high-temperature mechanical properties as compared to their monolithic counterparts. Peigney et al. [53] reported that CNT-reinforced Al_2O_3 possessed relative ease of superplastic forming as compared to unreinforced Al_2O_3 , during high-temperature extrusion in vacuum, possibly because of the ability of CNTs to withstand extreme shear stresses that arise during extrusion. In another significant study, Solvas et al. [99] reported that Al_2O_3 -10 vol% SWCNT nanocomposites developed via colloidal processing followed by SPS exhibited enhanced creep resistance by two orders of magnitude as compared to monolithic Al_2O_3 . This is attributed to the unique grain boundary structure of these nanocomposites, where the SWCNTs segregated along the Al_2O_3 grain boundaries partially obstruct the grain boundary sliding in the composites. Schaller and co-workers [101–103] have reported significant reduction in high-temperature mechanical loss ($\tan \varphi$) and steady-state creep rate for yttria-stabilized zirconia (3Y-TZP) ceramics reinforced with CNTs as compared to pure 3Y-TZP, as a result of partial blocking of grain boundary sliding due to incorporation of CNTs.

Tribological Properties of CNT-Reinforced Ceramic Matrix Composites

Since the current demands and/or need for energy-efficient systems, cost-effectiveness, and longer life spans of the mechanical components/parts rely heavily on the tribological (wear and friction) properties, in addition to the mechanical properties of the materials in concern, the potential of bulk ceramics/ceramic composites for advanced structural applications not only depends on their strength and fracture toughness but is also governed by their resistance to wear damage. Hence, critical microstructural design/engineering with a viewpoint of optimizing and improving tribological properties, such as controlling friction and wear, is reckoned to be one of the key strategies for enhancing the performance of structural ceramic materials in macroscaled as well as micro-/nanoscaled assemblies. In this context, considerable research efforts have demonstrated the feasibility of developing CNT-reinforced bulk ceramic nanocomposites (mostly Al_2O_3 -based) exhibiting superior wear resistance and lower frictional coefficient as compared to the monolithic ceramics [57, 104–106]. As discussed earlier, the ceramic nanocomposites containing CNTs possess high resistance to crack growth under contact damage conditions [20], which provides a strong ground for applications of these materials in bearings, wear-resistant machine parts, seals, and prostheses, where contact loading conditions are prevalent. Furthermore, the excellent lubricating properties of CNTs (owing to their graphitic structure), high endurance against compressive and tensile forces prior to failure, and great flexibility in response to shear stresses

[107, 108] play a pivotal role in improving the wear and friction behavior of CNT-reinforced CMCs.

In a significant development, An and co-workers [104] reported that incorporation of up to 4 wt% of MWCNTs via in-situ catalytic growth (using CVD) in Al_2O_3 matrix, followed by hot pressing, resulted in significant reduction in wear loss and coefficient of friction in the Al_2O_3 -MWCNT composites as compared to unreinforced Al_2O_3 . The enhancement in wear resistance of the composites (containing up to 4 wt% MWCNTs) was attributed to the higher microhardness (as a consequence of finer grain size) of the same with respect to unreinforced Al_2O_3 , while the lowering of frictional coefficient was possibly because of the lubricating properties of the CNTs and the rolling motion of CNTs at the interface between the counter body (sliding ball) and surface of the specimen. However, as shown in Fig. 10, increase in MWCNT contents beyond 4 wt% led to deterioration of both hardness and tribological properties because of the onset of agglomeration of MWCNTs and poor interfacial adhesion between the MWCNT and Al_2O_3 matrix. A weaker interfacial bonding between the matrix and carbon nanotubes would possibly lead to CNTs being dragged out of the surface of the specimen under wear damage, thereby losing their lubrication characteristics [105].

Xia et al. [57] have performed systematic studies to elucidate the effects of careful microstructural engineering (in terms of the dimensions and orientation/alignment of CNTs) on the tribological properties of nanoporous amorphous alumina-CNT composites, with the tribological tests conducted at different length scales, viz., pin-on-disk (macroscale wear), microscratch (micron-scale wear), and AFM (nanoscale wear). The composites containing highly ordered vertically aligned array of parallel CNTs within the pre-defined pores in the amorphous alumina matrix were developed

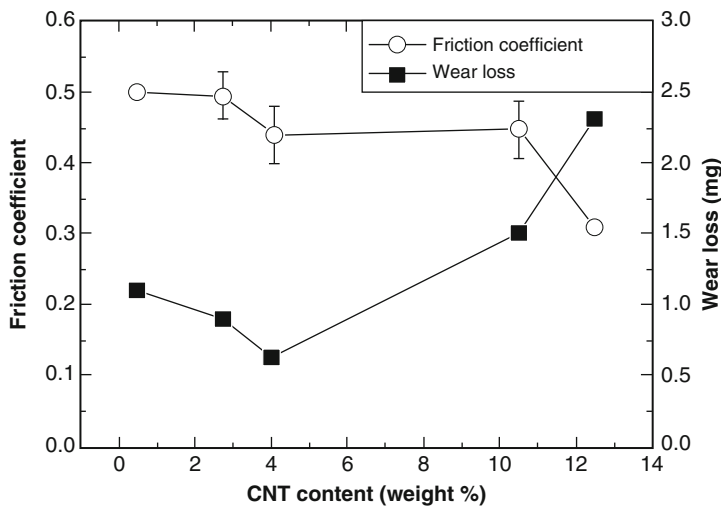


Fig. 10 Effects of CNT concentrations on the wear and friction properties of Al_2O_3 -MWCNT nanocomposites. (Image reused from [104] with permission from Elsevier)

by the in-situ processing route as reported by the same research group [55] (refer to section “[In-Situ Growth of Carbon Nanotubes in Ceramic Matrix by Chemical Vapor Deposition \(CVD\)](#)”). Since the CNTs, sticking out of the matrix surface by approximately 0.5 nm (calculated using finite element models), made direct contact with the sliding tip/ball at the sliding interface, in each of the tribological test setup, the composites containing thicker-walled CNTs possessed lower frictional coefficients and better wear resistance as compared to both the monolithic Al_2O_3 and composites containing thin-walled CNTs. This is because of the higher stiffness and buckling resistance of thick-walled CNTs which prevent the direct contact of the weaker matrix with the sliding tip and thereby results in clean surfaces with less wear debris (as shown in Fig. 11c, d). In contrast, the thin-walled CNTs tend to buckle at the same applied load resulting in direct sliding contact with the matrix and thus higher amount of wear debris on the frictional surface (Fig. 11a, b). Hence, the composites containing thin-walled CNTs exhibited nearly the same frictional behavior as unreinforced Al_2O_3 [57]. However, at higher normal loads, the COF values for all the three materials reach the similar levels since the thick-walled CNTs also tend to buckle at such applied loads. Such observations demonstrate that critical

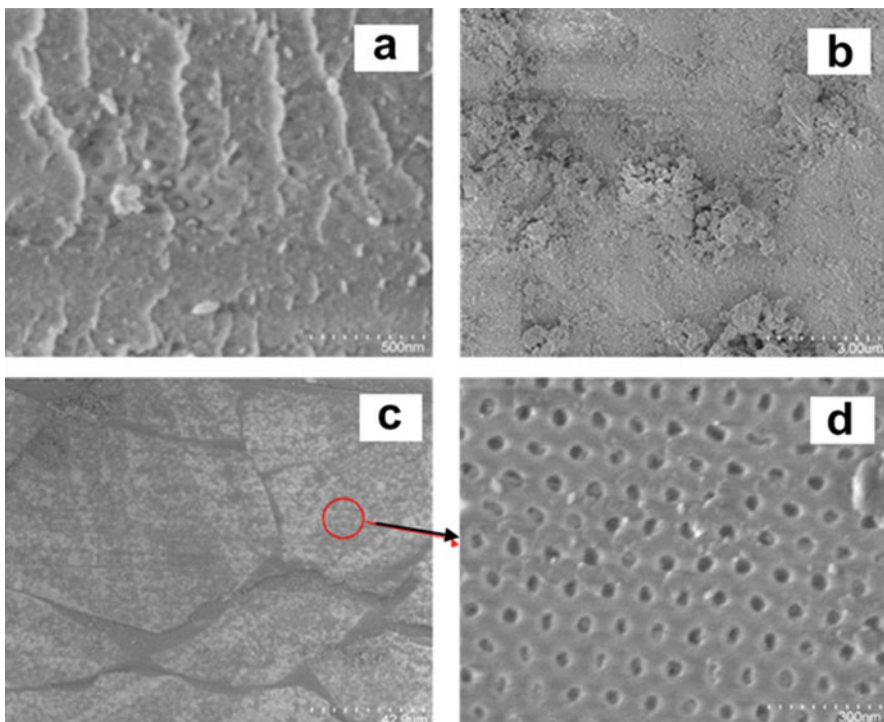


Fig. 11 Pin-on-disk tested surfaces of (a) nanoporous Al_2O_3 , (b) thin-walled Al_2O_3 -CNT composite, and (c) thick-walled Al_2O_3 -CNT composite and (d) magnified region of (c) showing a relatively cleaner surface. (Images reused from [57] with permission from Elsevier)

microstructural engineering (by tailoring the thickness and orientation of CNTs in this case) forms a key strategy for enhancement of mechanical and tribological performance of CNT-reinforced CMCs.

The recently published research work by our group [39] (refer to section “Achieving Intragranular CNT Reinforcemen” for processing related details) further demonstrates the significance of carefully tailoring the microstructural evolution (here, in terms of homogenous dispersion of randomly oriented MWCNTs in polycrystalline Al_2O_3 matrix) to enhance the mechanical and tribological properties of the CMCs. In fact, one of the most prominent features of this research work was the achievement of extremely high wear resistance in Al_2O_3 -MWCNT nanocomposites (with $\sim 95\%$ reduction in abrasive wear rates with respect to pure Al_2O_3) containing both intergranular and intragranular CNT reinforcements (see Fig. 9) obtained using ultrasonication-assisted rapid sol-gel technique followed by SPS. As shown in Fig. 12a, Al_2O_3 -2.5 vol% MWCNT “sol-gelled” composites possessed improved wear resistance as compared to both monolithic Al_2O_3 and the conventional Al_2O_3 -2.5 vol% MWCNT “ball-milled” composites. The worn surfaces of “sol-gelled” Al_2O_3 -2.5 vol% MWCNT appeared relatively smooth and undamaged, with almost complete absence of grain pull-out (Fig. 12d). In contrast, the worn surfaces for monolithic Al_2O_3 revealed severe wear damage by brittle fracture-

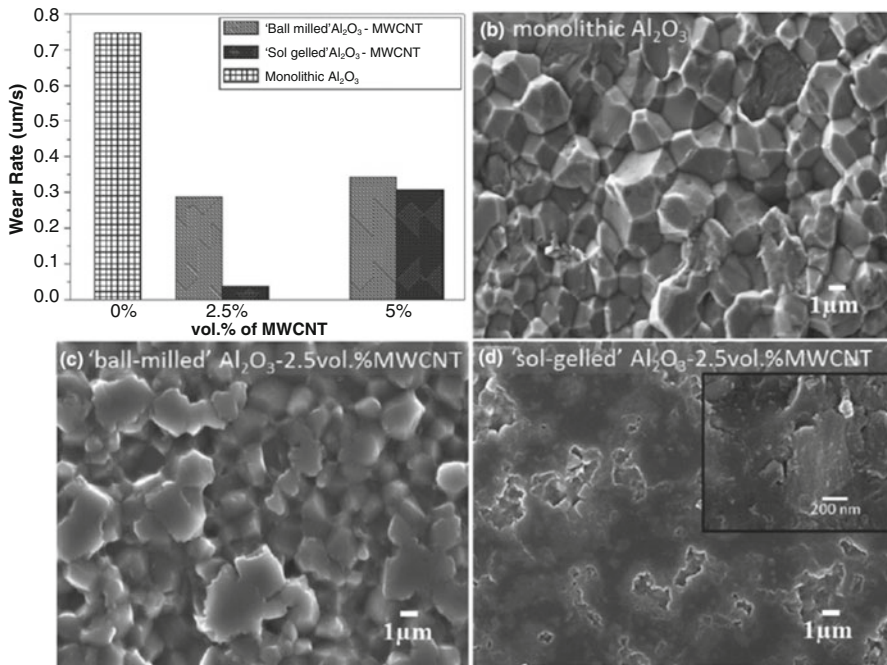


Fig. 12 Effects of the quality of dispersion of MWCNT reinforcements on the (a) abrasive wear rates and (b–d) SEM micrographs of the worn surfaces under depicting wear mechanisms in Al_2O_3 -MWCNT nanocomposites. (Images reused from [39] with permission from John Wiley and Sons)

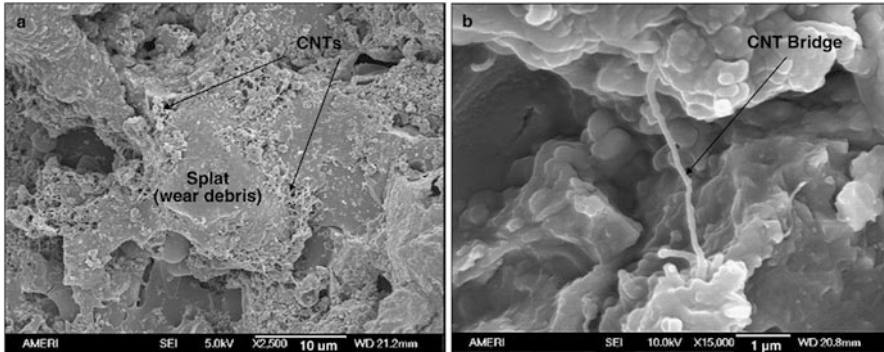


Fig. 13 (a) Worn surface of CNT-reinforced plasma-sprayed HAP coating revealing splat anchoring by carbon nanotubes and (b) higher-magnification SEM image showing splat bridging by CNTs. (Images reused from [109] with permission from Elsevier)

induced grain pull-outs (Fig. 12b), which got marginally suppressed for the “ball-milled” Al_2O_3 -2.5 vol% MWCNT composite (Fig. 12c). The change of fracture mode from predominantly intergranular (in monolithic Al_2O_3 and “ball-milled” Al_2O_3 -MWCNT composites) to almost completely transgranular in “sol-gelled” Al_2O_3 -MWCNT composites possibly suppressed the material removal by brittle fracture-induced pull-outs in the latter during wear damage.

In more significant research investigations, the promising role of CNTs in improving the wear resistance has also been demonstrated for hydroxyapatite (HAP)-based bio-ceramics [88, 109], the potential materials for load-bearing biomedical (prostheses) applications, which otherwise are extremely brittle ($K_{IC} \sim 1 \text{ MPa m}^{-1/2}$) [88] and poor wear resistant restricting their clinical trials. Lahiri et al. [88] reported $\sim 66\%$ reduction in wear rates and $\sim 60\%$ reduction in frictional coefficient for HAP-4 wt% MWCNT bio-nanocomposite as compared to the unreinforced HAP. Enhancement in wear resistance was attributed to the improvement (with respect to pure HAP) in mechanical properties (modulus, hardness, and indentation toughness) along with the reduction in coefficient of friction (COF) for the HAP-MWCNT composites. It was proposed that the high lateral shear stress present in macroscale sliding wear exfoliates/peels off the graphene layers from the surface of multiwalled carbon nanotube, which get incorporated into the wear debris and act as a lubricant film at the sliding interface, thereby reducing the COF in the HAP-MWCNT composites. Such mechanisms, based on exfoliation of CNTs due to high shear stresses, have also been proposed in CNT-reinforced yttria-stabilized zirconia composites possessing nearly 3.8-fold decrease in COF with respect to unreinforced zirconia [79].

Balani et al. [109] have also investigated the tribological behavior of CNT-reinforced hydroxyapatite coatings under simulated body fluid (SBF) conditions using pin-on-disk wear test setup. CNT-reinforced plasma-sprayed HAP coatings possessed superior wear resistance as compared to that of unreinforced HAP

coating. In addition to providing lubrication properties, reinforced CNTs effectively suppressed microcracking during abrasive wear. The carbon nanotubes also provided anchoring/bridging action between the adjacent splats (see Fig. 13), thereby locking the splats in place and preventing their separation resulting in reduced wear losses in the composites.

Possible Toughening Mechanisms in Carbon Nanotube-Reinforced Ceramic Nanocomposites

Despite considerable debate over the influence of CNT reinforcements on the mechanical properties of bulk polycrystalline ceramic and glass matrices, it has now been realized that incorporation of CNTs can improve (though the extent of improvement may vary depending upon several factors as discussed earlier) the fracture toughness of the otherwise brittle ceramic matrices. At the same time, it has also been demonstrated that careful engineering of the processing routes for achieving good dispersion of the nanotubes in the ceramic matrix, along with optimum CNT/matrix interfacial strength, is critical for retrieving the maximum possible benefits of CNT reinforcements in ceramic-CNT nanocomposites.

In order to directly elucidate the toughening mechanisms operative in CNT-reinforced ceramic matrix composites, Xia et al. [55] carefully observed the nanoindentation-induced controlled cracking at different orientations with respect to highly ordered arrays of parallel MWCNTs in an alumina matrix. Such nanocomposites were produced by growing MWCNTs via CVD (using Ni and Co as catalyst) inside arrays of well-oriented open nanopores (~30–40 nm in diameter) present in amorphous alumina developed by anodizing high-purity aluminum. Critical analysis revealed that all the toughening mechanisms typical of conventional fiber-reinforced composites are operative in CNT-reinforced ceramics as well, bridging of matrix cracks by reinforcing CNTs (Fig. 14b), pull-out of the broken CNTs on the fractured surfaces (Fig. 14c), and crack deflection at CNT/matrix interface (Fig. 14a). Such bridging by the nanotubes restrains the crack from opening and reduces the driving force for crack propagation in the matrix [5, 55, 110, 111]. Energy is consumed as elastic strain energy stored in the bridging fibers getting stretched with increase in the crack opening [5, 55, 110, 111]. Additionally, energy is dissipated in the form of the work required to pull the embedded broken fibers out against any residual frictional stresses at the fiber/matrix interface.

In the study by Xia et al. [55], it was also observed that deformation around indentations can be accommodated by lateral buckling or collapse of the nanotubes in shear bands. Such nanotube collapse in shear bands virtually prevents propagation of cracks emanating from indentation corners (refer to [55] for more details). It must be recalled here that other groups have also reported suppression of cracking around Vickers indentations for Al₂O₃-CNT [20] nanocomposites as compared to the unreinforced Al₂O₃ matrix. Such observations suggest that that ceramic-CNT nanocomposites can possess multiaxial damage tolerance against contact loading, providing direct evidences of a new deformation and/or toughening mechanism for

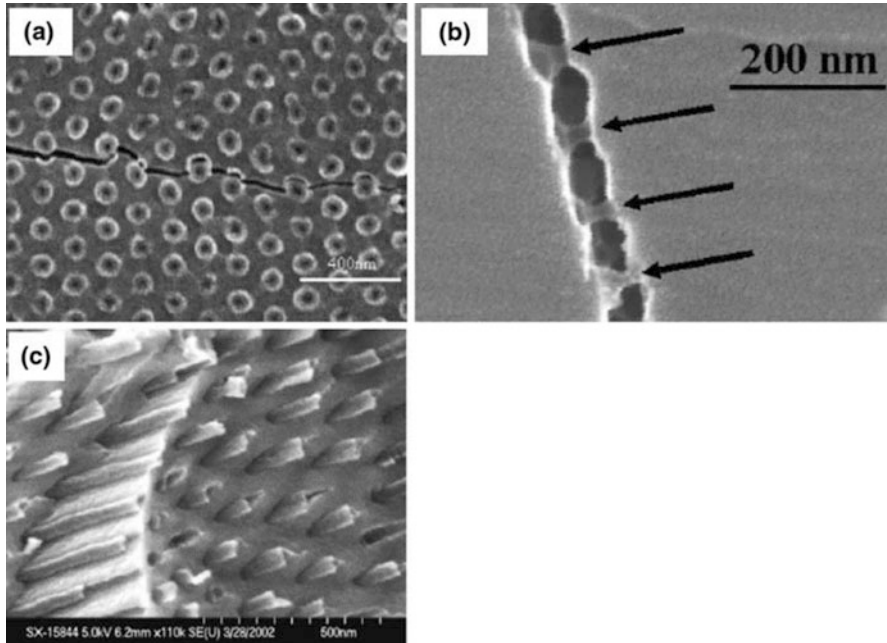


Fig. 14 SEM images providing direct evidences for toughening mechanisms operative in ceramic-CNT nanocomposites via (a) crack deflection at matrix/CNT interface in ordered Al_2O_3 -MWCNT nanocomposites; (b) crack bridging by nanotubes; (c) pulled-out nanotubes, along with residual holes, on the fractured surface of ordered Al_2O_3 -MWCNT nanocomposites. (Images reused from [19] with permission from Springer Nature)

these nanoscale reinforcements which is not encountered for the conventional micron-scale fiber reinforcement.

However, in the case of bulk polycrystalline ceramics reinforced with randomly oriented CNTs (unlike the highly ordered CNTs in thin nanoporous ceramic as discussed above), there have been very few systematic studies [37, 64, 68, 112–115] which incisively corroborate the quantitative estimates of the fracture toughness of such composites with the qualitative investigations of toughening mechanisms and actual reinforcing ability of such nanoscale reinforcements in ceramic materials. The relatively sparse nature of such studies is owed to significant variation in microstructural evolution (more specifically in terms of CNT dispersion and interfacial bonding between CNT/matrix) across a wide range of processing routes adopted for development of CNT-reinforced CMCs. Most of the investigations, based on SEM observations of indentation cracks and fractured surfaces, have proposed only the classical toughening mechanisms (viz., crack bridging by CNTs, crack deflection at nanotube/matrix interface, and CNT pull-out) [19, 41, 69, 77, 116], the hallmarks of conventional micron-scale fiber, or whisker-reinforced CMCs, in ceramic nanocomposites containing randomly oriented CNTs. However, such investigations do not provide any concrete evidences

of load-bearing ability of CNTs and about the possibility of other deformation mechanisms in such nanoscale, highly flexible (unlike rigid and micrometer-sized fibers/whiskers) reinforcements. Moreover, SEM observations of the fractured surfaces do not provide a complete assessment of the toughening mechanisms involved, since the presence of CNTs on the fractured surfaces may not necessarily indicate the energy-dissipating frictional pull-out of CNTs. This presence may as well be related to relaxation of nanotubes, which entirely or partially lied on the propagating crack plane and just tend to deflect the crack without being loaded [68].

In his commentary article [115], Padture has argued that the energy-dissipating frictional pull-out mechanisms would be quite unlikely in Al_2O_3 -SWCNT nanocomposites (developed using colloidal processing followed by SPS) owing to their unique grain boundary structure [37], which is markedly different than that of the conventional fiber-reinforced ceramics. The microstructures (Fig. 15) of conventional fiber-reinforced ceramic composites are usually characterized by rigid fibers (having diameter around μm to tens of μm and length around several μm to hundreds of μm) embedded within a fine-grained ceramic matrix [69, 115]. The fiber/matrix interface in such composites is critically designed to debond on encountering a crack. The crack-wake gets bridged (see Fig. 15b) by the fiber with ultimate pull-out of the fiber as the crack advances. However, larger-sized fibers introduce larger flaws, resulting in loss of strength of the ceramic composites (a typical trade-off between strength and toughness in composites).

In contrast, the nanoscale SWCNTs having great flexibility do not embed within the ceramic matrix (Fig. 16) and thus are unlikely to pull out. Here, the SWCNT bundles present at the grain boundaries in these composites appear to unfurl (or uncoil) in the wake of the crack as the crack propagates intergranularly (intergranular fracture because of the weaker grain boundary due to the presence of the SWCNTs at the grain boundaries). The uncoiled nanotubes tend to stretch as

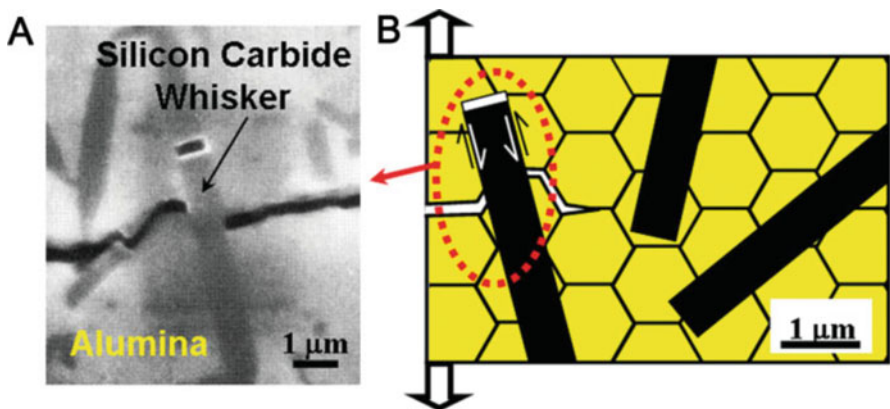


Fig. 15 (a) Scanning electron micrograph and (b) schematic representation of frictional pull-out and crack-wake bridging by SiC whisker in Al_2O_3 -based ceramic composite. (Images reused from [115] with permission from John Wiley and Sons)

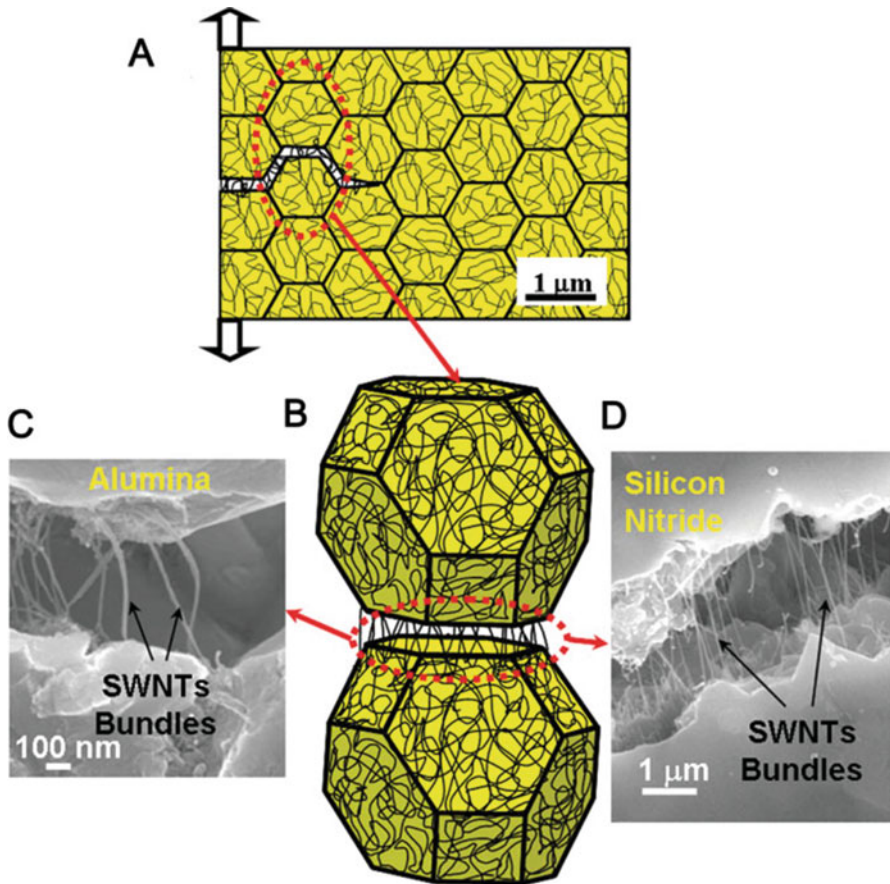


Fig. 16 (a) Schematic representation of an intergranular crack in ceramic-SWCNT composite; (b) detailed 3D view of the separated grains of polycrystalline ceramic and crack bridging by the taut single-walled nanotube; SEM observations of bridged cracks in (c) Al_2O_3 -SWCNT composites and (d) Si_3N_4 -SWCNT composites. (Images reused from [115] with permission from John Wiley and Sons)

the crack advances further, until both the ends of SWCNTs are anchored in the grain boundary. These stretched SWCNTs impede crack propagation by bridging the grains [115, 117] (as shown schematically in Fig. 16a, b and evident from SEM images in Fig. 16c, d) instead of crack bridging followed by conventional frictional pull-out. As the crack propagates further, the anchored SWCNTs at the far end of the crack opening will eventually pull out or fracture or get detached from the grain boundaries. Such unfurling and stretching mechanisms proposed in ceramic-SWCNT nanocomposites render tempting possibilities of developing ceramic composites with high strength as well as high toughness which is quite rare combination in composites.

The mechanisms proposed above mainly pertain to polycrystalline ceramic nanocomposites containing entangled network of single-walled carbon nanotubes along the grain boundaries. However, a fair amount of progress has been made in terms of careful engineering of processing routes (mainly based on colloidal processing [40, 41, 67, 68] and sol-gel [39]-based techniques) for developing ceramic nanocomposites containing uniformly and individually dispersed multiwalled carbon nanotubes well embedded within and having an intimate contact with the parent ceramic matrix grains [40, 41, 67, 68]. It, therefore, becomes interesting to look into the peculiar toughening mechanisms and reinforcing ability of such nanoscale and flexible MWCNTs (in terms of effective load transfer to the CNTs) in these nanocomposites, apart from the classical mechanisms prevalent in conventional micron-scale fiber-reinforced ceramic composites. In this context, the recent development in in-situ characterization techniques (using electron microscopes equipped with in-situ mechanical testing fixtures) has provided significant insights into the deformation, damage, and/or toughening mechanisms of MWCNTs incorporated into a polycrystalline ceramic matrix (such as Al_2O_3) [64, 68, 112, 113].

In a significant research investigation, Estili and co-workers [113] directly investigated the load-bearing ability (LBA) of an individual multiwalled carbon nanotube embedded in a ceramic ($\alpha\text{-Al}_2\text{O}_3$) environment, with the help of a unique in-situ technique, in which an electron microscope equipped with a nano-manipulation system was employed. The fully dense $\alpha\text{-Al}_2\text{O}_3$ nanocomposites containing intimately dispersed MWCNTs were developed using colloidal powder processing routes followed by SPS [40, 41]. Since the MWCNTs embedded within the ceramic (here $\alpha\text{-Al}_2\text{O}_3$) matrix are bound to experience both bending and tensile loads during bridging of the cracks propagating in the ceramic matrix, these in-situ mechanical tests were performed under tensile-bending conditions. The unloaded (partially detached from the Al_2O_3 matrix without any frictional pull-out) MWCNTs lying on the fractured surface of Al_2O_3 were carefully selected for these in-situ pull-out experiments. The test results showed absolutely no carbon nanotube pull-out from the ceramic matrix surface. Instead, the failure of multiwalled CNTs via the characteristic “sword-in-sheath” failure mechanism (breakage of outermost graphene layers followed by eventual collapse of the inner core) [16, 114] was reported (see Fig. 17a), which is generally considered to be potential energy-dissipating mechanism during matrix crack growth. Moreover, as can be seen in Fig. 17a, the dimensions of the two broken nanotube parts were quite different indicating the simultaneous failure of many graphenic walls at different locations along the length of MWCNT (rather than common one-layer failures) [68]. These unprecedented observations revealed the presence of very high MWCNT/matrix interfacial shear resistance [68, 112, 113] which exceeded even the breaking resistance of an individual near-perfect MWCNT (not embedded in a ceramic environment), thereby indicating ultimate load transfer from the ceramic matrix to MWCNTs. Such strong interfacial shear resistance is attributed to the intimate contact of MWCNT with the Al_2O_3 matrix formed as a result of complete filling of the nanoscale inhomogeneity/surface defect in MWCNT (arising due to functionalization) by the alumina matrix (see Fig. 17b) in such Al_2O_3 -MWCNT composites developed by an unique colloidal

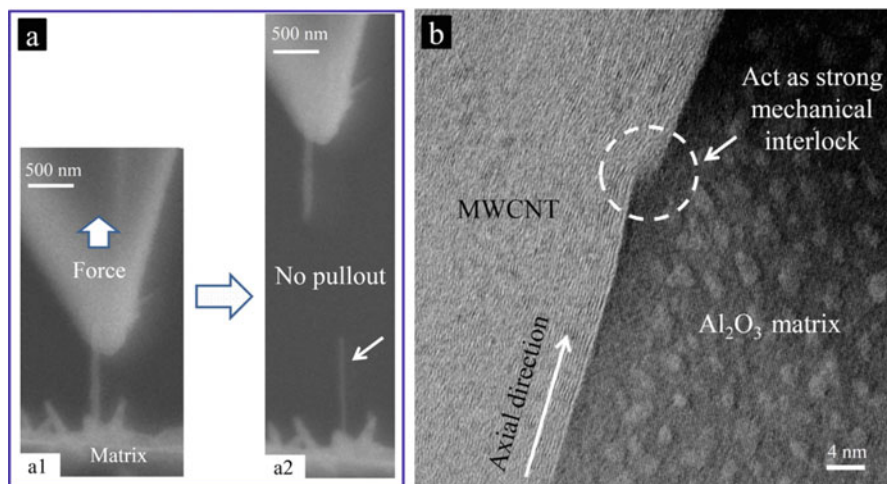


Fig. 17 (a) In-situ SEM images depicting failure of an embedded MWCNT under tensile loading, which confirms no CNT pull-out; (b) high-resolution transmission electron micrograph showing a MWCNT/ Al_2O_3 interface, where the surface defect of MWCNT is completely wetted by the Al_2O_3 matrix. (Images reused from [68], under the terms of Creative Commons Attribution 3.0)

processing route followed by SPS [40, 41]. Such an intimate contact induces high radial compressive stresses [68, 112, 113] on the MWCNT by the surrounding ceramic matrix which tend to clamp the MWCNT resulting in strong MWCNT/matrix interfacial shear resistance.

In one of the most recent research works, Liu et al. [64] have critically investigated the modes of toughening by both ex-situ (SEM observations of crack growth prior to failure and post failure fractured surfaces) and in-situ (simultaneous and direct SEM observations with increase in applied load on pre-cracked specimens) characterizations of crack propagation in pre-cracked (a sharp “V” notch) test specimens of isotropic Al_2O_3 -10 vol% MWCNTs developed using the similar colloidal processing route [40, 41] followed by SPS. In some cases, to make specimens more electrically conductive (to avoid charging effect in SEM) for better in-situ SEM observations, TiN powder was added to Al_2O_3 nanopowder before mixing with colloidal suspension of MWCNTs. Ex-situ SEM observations of the matrix crack revealed crack-wake bridging by MWCNTs along with tapered appearance of pulled-out MWCNTs (Fig. 18a). Interestingly, the density of the MWCNT bridges along the wake of the crack was quite high, with each MWCNT bridge in a given crack plane separated approximately by 500 nm. Since the diameter and content of MWCNT are, respectively, ~ 50 nm and 10 vol%, it appears from the above observation that almost every nanotube in the composite, irrespective of its orientation w.r.t. crack plane, takes part in crack bridging. The fractured surface of the nanocomposite (Fig. 18b) also revealed the tapered (owing to the “sword-in-sheath” failure mechanism) MWCNTs pull-outs. It was proposed that the “frictional” pull-out of MWCNT at the Al_2O_3 /MWCNT interface is quite unlikely because of the

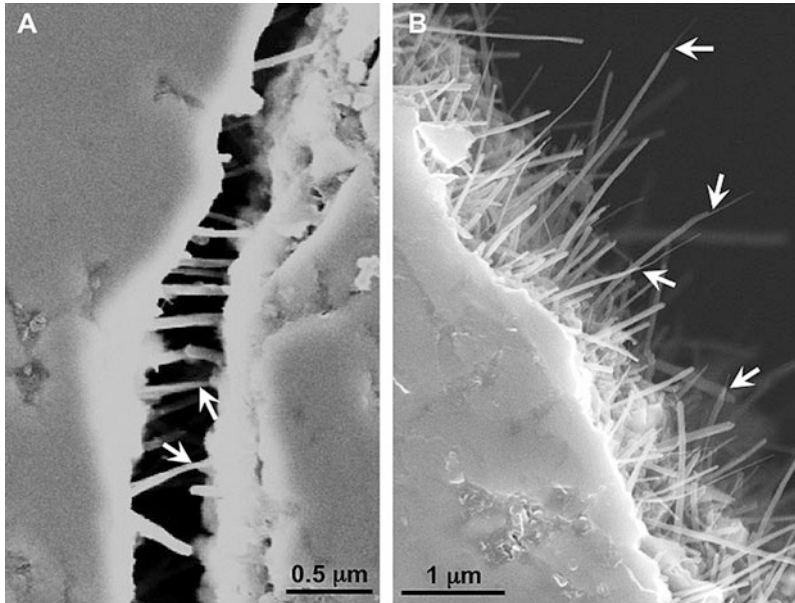


Fig. 18 SEM micrographs of Al_2O_3 -10 vol% MWCNT nanocomposite showing (a) crack bridging by MWCNTs and tapered MWCNTs (white arrows) prior to specimen failure, (b) fractured surface showing “sword-in-sheath” (tapered) failure in MWCNT pull-outs (white arrows). (Images reused from [64] with permission from Elsevier)

clamping of MWCNTs embedded inside Al_2O_3 matrix by very high compressive residual stresses (roughly -3.7 GPa [64]). Instead, the pull-out of crack-bridging MWCNT occurs primarily by “sword-in-sheath” failure of weakly bonded layers of MWCNT at different locations along the length of MWCNT.

The in-situ SEM observations of crack propagation in Al_2O_3 -MWCNT nanocomposites (containing 15 vol% TiN to minimize charging of specimen during SEM) revealed some unique and interesting toughening mechanisms. Figure 19a–e represents a sequence of SEM micrographs obtained from a fixed crack-wake location away from the crack tip, with simultaneous increase in applied load and stable propagation (downward) of the crack tip. Similar to the ex-situ observations, the in-situ SEM observations revealed crack bridging by MWCNTs and “sword-in-sheath” failure-induced MWCNT pull-outs (with increase in crack opening as seen in Fig. 19d, e). Perhaps, the most intriguing observation from in-situ characterization of crack propagation (Fig. 19) was the dramatic increase in the density of aligned MWCNT bridges as the separation between the crack walls increases with increase in applied load (the regions just behind the crack tip containing nonaligned MWCNTs as shown in inset of Fig. 19b). The crack bridging by extensively aligned MWCNTs is well expected in ceramic nanocomposites containing highly ordered/

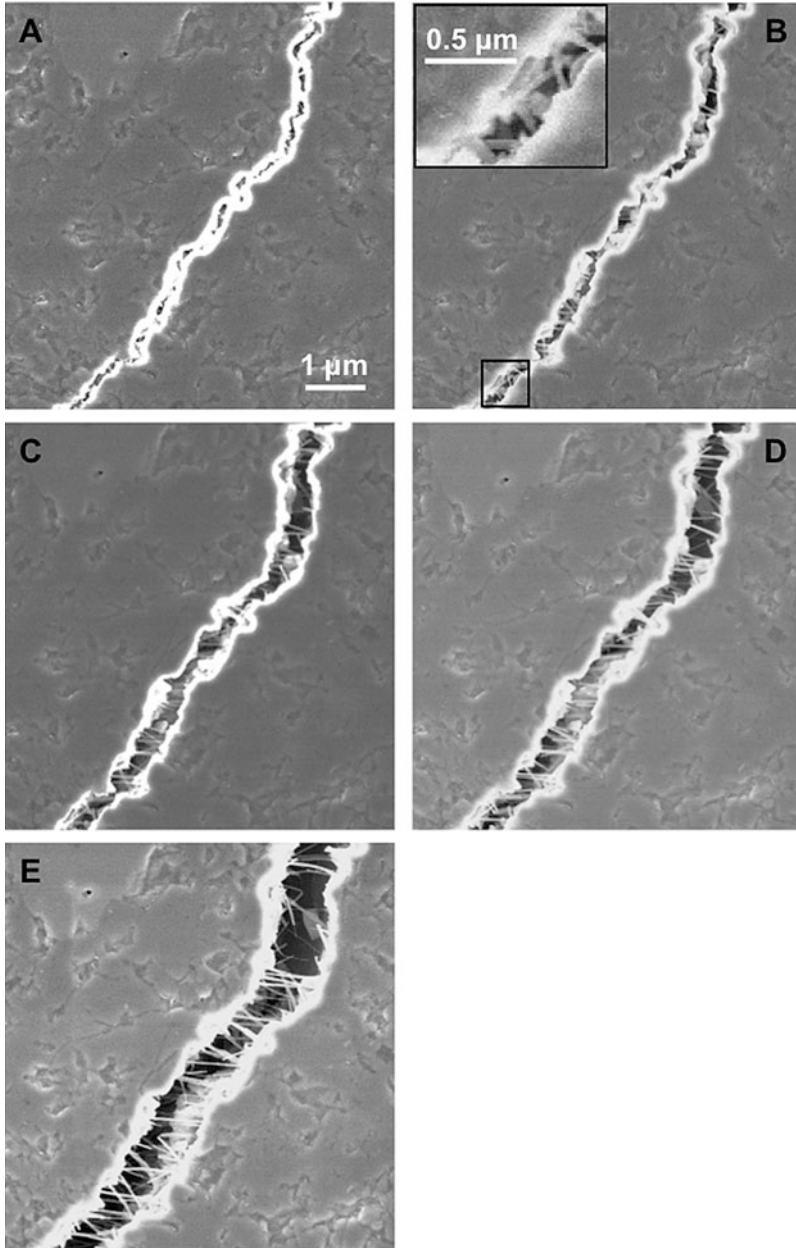


Fig. 19 In-situ SEM images obtained from a fixed location of crack opening behind the crack tip in Al_2O_3 -15vol%TiN-10 vol% MWCNT nanocomposite, as the crack advances downward. (Images reused from [64] with permission from Elsevier)

oriented array of MWCNTs [55]. However, the materials in concern here are isotropic polycrystalline nanocomposites containing randomly oriented MWCNTs. These in-situ observations therefore suggest that during stable crack growth in such polycrystalline ceramic nanocomposites, the randomly oriented MWCNTs bridging the cracks have a tendency to disentangle or unfurl and eventually get aligned as the crack-wall separation increases. This unfurling behavior is possibly attributed to the excellent flexibility of the MWCNTs (by virtue of their nanoscale dimensions and high aspect ratios) as compared to the conventional micron-scale fiber reinforcements. The aforementioned unprecedented toughening mechanisms based on the alignment (by “unfurling”) of the otherwise randomly oriented MWCNT crack-wake bridges and non-frictional pull-out of the multiwalled carbon nanotubes are unique to these polycrystalline ceramic nanocomposites containing such flexible nanoscale reinforcements.

Potential Applications of Carbon Nanotube-Reinforced Ceramic Matrix Composites

Despite a multitude of research efforts extending over a decade or two, directed toward the development of CNT-reinforced ceramic nanocomposites possessing improved fracture toughness as compared to the monolithic ceramics, the commercial market penetration of these nanocomposites for advanced structural applications has been severely limited owing to high capital costs involved in large-scale production or fabrication of these otherwise fascinating composites. Such capital intensive production stems from the high costs of synthesis of CNTs (relative to other widely used particulate or fiber reinforcements), non-scalable processing routes for efficient and uniform dispersion of CNTs within the ceramic matrix, and the widespread use of highly expensive sintering techniques (like SPS) to fully densify the CNT-reinforced CMCs. Moreover, the near-net shape forming of such composites for their application in structural components/parts is severely restricted since the pressureless sintering techniques have been rendered ineffective for their fabrication [19, 69]. The following discussion presents an overview of potential structural applications as envisioned for CNT-reinforced ceramic nanocomposites, the commercial realization of which can be possible once the methods of fabrication and production of such composites become scalable, competitive, and cost-effective.

CNT-reinforced CMCs can be potential materials of choice for more traditional cutting tool applications demanding high strength and wear/abrasion resistance. The performance of the cutting tool directly affects the surface finish of the material being machined as well as the processing accuracy, cost, and efficiency of machining. Al_2O_3 - and Si_3N_4 -based ceramics/ceramic composites are some of the widely used materials for high-speed cutting tools required higher productivity [118]. CNT-reinforced Al_2O_3 nanocomposites, in particular, have been demonstrated to possess high strength [77], fracture toughness [77, 117], and very high wear resistance [39, 104] and can thereby prevent or minimize chipping of the cutting tool

during machining. Moreover, the lubricating properties of CNTs would aid in minimizing the heat losses due to friction and thus improve the processing efficiency.

CNT-reinforced CMCs may prove to be potential structural materials for modern and advanced engineering applications in defense sector. For instance, body armors demand materials having high strength, fracture toughness, impact resistance, and more importantly lightweight for best ballistic performance. Boron carbide (B_4C) has been deemed to be one of the most suitable materials of choice for such applications owing to its exceptionally high hardness and low density (2.5 g/cm^3) [119]. However, its extreme brittleness and difficulty to form dense material have severely limited its practical applications such as those in body armors. The development of exceptionally tough and dense B_4C -CNT composites has been successfully demonstrated by chemical vapor filtration (CVI) of B_4C into an aligned network of MWCNTs [119]. This may open up the possibilities of the usage of such ultralightweight (with density of CNTs being lesser than B_4C itself), hard, and tough CNT-reinforced composites for ballistic applications.

One of the most important and potential applications of CNT-reinforced CMCs which has gained unprecedented research interests over the years is in the field of prostheses, with such tough and damage-tolerant composites being promising materials for arthroplastic implants. One such bioactive ceramic material which has been extensively studied is hydroxyapatite [HAp; $Ca_{10}(PO_4)_6(OH)_2$]. This bio-ceramic basically mimics the bone structure as its chemical composition and crystal structure are close to that of natural bone [88, 89, 109] and hence is an attractive material for substitution and reconstruction of damaged bone in the human body. However, extremely brittle nature, poor strength, and wear resistance impede the clinical/orthopedic applications of such biologically active ceramics. The reinforcement of carbon nanotubes in HAp-based ceramics has resulted in significant improvement in strength, fracture toughness, and wear resistance of HAp-CNT biocomposites (w.r.t. unreinforced HAp) [88, 89, 109]. Such enhanced mechanical and tribological properties coupled with biocompatibility [89, 109] render the CNT-reinforced HAp bio-nanocomposite excellent materials for applications as load-bearing bio-implants.

Summary and Outlook

The unique closed shell elongated tube-like structure of carbon nanotubes (CNTs), as derived from planar graphenic/graphitic sheets, imparts excellent strength, stiffness, and flexibility in such nanotubes, also having very high aspect ratios, thus rendering them promising reinforcement materials for improving the mechanical (in particular, fracture toughness) and tribological properties of the otherwise intrinsically brittle ceramic materials. The key toward achieving potentially strong, tough, and damage-tolerant CNT-reinforced CMCs lies in the development of carefully engineered and optimized processing routes which promote homogenous dispersion/distribution of undamaged CNTs (which otherwise have natural propensity for agglomeration), along with the required CNT/matrix interfacial strength in the fully dense ceramic matrix composites. Attempts and some very recent progress

have been made toward achieving uniform dispersion/distribution of reinforcing CNTs (with CNTs present inside polycrystalline ceramic matrix grains, rather than segregating only at grain boundaries) in bulk ceramic matrix (Al_2O_3) by adopting wet-chemical synthesis-based processing routes (colloidal processing [40, 41] and sol-gel route [39]). The development of these carefully tailored homogeneous ceramic-CNT nanocomposite microstructures has facilitated unravelling improved and new [64, 112, 113] toughening mechanisms, such as alignment of randomly oriented MWCNT crack bridges by unfurling of MWCNTs and non-frictional pull-out of “sword-in-sheath” failed MWCNTs that are typical of CNT-reinforced CMCs and fundamentally different to the classical toughening mechanisms in conventional fiber-reinforced ceramics. However, the quantitative estimates of fracture toughness (measured using more standard SEVNB tests rather than VI tests) have still been fairly inconsistent, revealing only modest improvements in some cases [64], despite the development of such homogenous microstructures and existence of unique toughening mechanisms. Thus, more research efforts need to be directed toward further validation of the quantitative estimates of K_{IC} by developing suitable models (in light of the unique toughness mechanisms proposed) and correlating the measured values with microstructural variations in such composites. The reproducibility of such microstructures demanding stringent control over the processing conditions also needs further investigation. Furthermore, most of these research investigations have been confined to Al_2O_3 -based composites. The possibilities of such microstructure evolution, characterized by well-dispersed/distributed CNTs with high degree of CNT/matrix interfacial bonding, are widely unexplored in other commercially important non-oxide (carbides, nitrides, borides)-based ceramics, where the manifestations of the remarkable properties of CNTs have still been insignificant, till date.

Even though the use of activated sintering techniques (in particular, spark plasma sintering) has been beneficial toward achieving near-theoretical densification in CNT-reinforced CMCs with minimum damage to the CNTs, the large-scale commercial use of such techniques is quite improbable because of high costs and confinement to production of simpler shapes. More research efforts are needed to develop processing techniques (in terms of improving sinterability of CNT-ceramic powder mixtures), rendering effective use of more cost-effective pressureless sintering techniques for near-net shape forming of CNT-reinforced CMCs, thereby facilitating their widespread commercial applications. The high-temperature mechanical properties (creep resistance) of CNT-reinforced ceramic composites are quite fascinating and particularly important because the ceramics/ceramic composites are ideal choice (over metals and polymers) of materials for high-temperature applications. Such properties would ensure longer life spans of CMCs under service. However, the oxidation of CNTs in air or oxidizing atmosphere is a matter of concern for high-temperature applications of CNT-reinforced CMCs. The development of oxidation-resistant coatings over the surface of CNTs and reinforcement of such coated CNTs into the ceramic matrix without damaging the CNT/matrix interfacial strength are interesting research areas which need to be explored in order to render the highly creep-resistant CNT-reinforced CMCs suitable for applications

under high-temperature and harsh conditions. Lastly, the scalability of carefully engineered processing techniques needs to be looked into with consistent efforts toward the overall cost reduction for large-scale production of CNT-reinforced CMCs in order to commercially realize their envisaged advanced structural applications in manufacturing, aerospace, defense, etc. and load-bearing applications in biomedical implants (prostheses).

References

1. Crivelli-Visconti I, Cooper GA (1969) Mechanical properties of a new carbon fibre material. *Nature* 221:754–755
2. Marshall DB, Evans AG (1985) Failure mechanisms in ceramic-fiber/ceramic-matrix composites. *J Am Ceram Soc* 68:225–231
3. Sternitzke M (1997) Structural ceramic nanocomposites. *J Eur Ceram Soc* 17:1061–1082
4. Mukhopadhyay A, Basu B (2007) Consolidation–microstructure–property relationships in bulk nanoceramics and ceramic nanocomposites: a review. *Int Mater Rev* 52:257–288
5. Awaji H, Choi SM, Yagi E (2002) Mechanisms of toughening and strengthening in ceramic-based nanocomposites. *Mech Mater* 34:411–422
6. Brennan JJ, Prewo KM (1982) Silicon carbide fibre reinforced glass-ceramic matrix composites exhibiting high strength and toughness. *J Mater Sci* 17:2371–2383
7. Levi CG, Yang JY, Dagleish BJ, Zok FW, Evans AG (1998) Processing and performance of an all-oxide ceramic composite. *J Am Ceram Soc* 81:2077–2086
8. Dassios KG (2007) A review of the pull-out mechanism in the fracture of brittle-matrix fibre-reinforced composites. *Adv Compos Lett* 16:17–24
9. Klug T, Bruckner R (1994) Preparation of C-fibre borosilicate glass composites: influence of the fibre type on mechanical properties. *J Mater Sci* 29:4013–4021
10. Beyerle DS, Spearing SM, Zok FW, Evans AG (1992) Damage and failure in unidirectional ceramic-matrix composites. *J Am Ceram Soc* 75:2719–2725
11. Evans AG, Zok FW (1994) The physics and mechanics of fibre-reinforced brittle matrix composites. *J Mater Sci* 29:3857–3896
12. Davidge RW, Green TJ (1968) The strength of two-phase ceramic/glass materials. *J Mater Sci* 3:629–634
13. Niihara K (1991) New design concept of structural ceramics. *J Ceram Soc Jpn* 99:974–982
14. Iijima S (1991) Helical microtubules of graphitic carbon. *Nature* 354:56–58
15. Treacy MMJ, Ebbesen TW, Gibson JM (1996) Exceptionally high Young's modulus observed for individual carbon nanotubes. *Nature* 381:678–680
16. Yu MF, Lourie O, Dyer MJ, Moloni K, Kelly TF, Ruoff RS (2000) Strength and breaking mechanism of multiwalled carbon nanotubes under tensile load. *Science* 287:637–640
17. Iijima S, Ichihashi T (1993) Single-shell carbon nanotubes of 1-nm diameter. *Nature* 363:603–605
18. Zheng LX, O'Connell MJ, Doorn SK, Liao XZ, Zhao YH, Akhadov EA, Hoffbauer MA, Roop BJ, Jia QX, Dye RC, Peterson DE, Huang SM, Liu J, Zhu YT (2004) Ultralong single-wall carbon nanotubes. *Nat Mater* 3:673–676
19. Cho J, Boccaccini AR, Shaffer MSP (2009) Ceramic matrix composites containing carbon nanotubes. *J Mater Sci* 44:1934–1951
20. Wang X, Padture NP, Tanaka H (2004) Contact-damage-resistant ceramic/single-wall carbon nanotubes and ceramic/graphite composites. *Nat Mater* 3:539–544
21. Zhan GD, Kuntz JD, Wan J, Mukherjee AK (2003) Single-wall carbon nanotubes as attractive toughening agents in alumina-based nanocomposites. *Nat Mater* 2:38–42
22. Harris PJF (2004) Carbon nanotube composites. *Int Mater Rev* 49:31–43

23. Lu KL, Lago RM, Chen YK, Green MLH, Harris PJF, Tsang SC (1996) Mechanical damage of carbon nanotubes by ultrasound. *Carbon* 34:814–816
24. Niyogi S, Hamon MA, Perea DE, Kang CB, Zhao B, Pal SK, Wyant AE, Itkis ME, Haddon RC (2003) Ultrasonic dispersions of single-walled carbon nanotubes. *J Phys Chem B* 107: 8799–8804
25. Monthieux M, Smith BW, Burtiaux B, Claye A, Fischer JE, Luzzi DE (2001) Sensitivity of single-wall carbon nanotubes to chemical processing: an electron microscopy investigation. *Carbon* 39:1251–1272
26. Galaveen SC, Satam MK, Gurnani L, Venkateswaran T, Mukhopadhyay A (2016) Facile-low temperature route towards development of SiC-based coating on carbon nanotubes for improved oxidation resistance. *J Mater Sci* 51:8543–8549
27. Curtin WA, Sheldon BW (2004) CNT-reinforced ceramics and metals. *Mater Today* 7:44–49
28. Thostenson ET, Ren Z, Chou TW (2001) Advances in the science and technology of carbon nanotubes and their composites: a review. *Compos Sci Technol* 61:1899–1912
29. Shigeta M, Komatsu M, Nakashima N (2006) Individual solubilization of single-walled carbon nanotubes using totally aromatic polyimide. *Chem Phys Lett* 418:115–118
30. Star A, Stoddart JF (2002) Dispersion and solubilization of single-walled carbon nanotubes with a hyperbranched polymer. *Macromolecules* 35:7516–7520
31. Zhu J, Yudasaka M, Zhang M, Iijima S (2004) Dispersing carbon nanotubes in water: a noncovalent and nonorganic way. *J Phys Chem B* 108:11317–11320
32. Paredes JI, Burghard M (2004) Dispersions of individual single-walled carbon nanotubes of high length. *Langmuir* 20:5149–5152
33. Shaffer MSP, Fan X, Windle AH (1998) Dispersion and packing of carbon nanotubes. *Carbon* 36:1603–1612
34. Perepichka DF, Wudl F, Wilson SR, Schuster DI (2004) The dissolution of carbon nanotubes in aniline, revisited. *J Mater Chem* 14:2749–2752
35. Muller TJJ, Bunz UHF (2007) Functional organic materials: syntheses, strategies and applications. Wiley-VCH Verlag GmbH & Co. KGaA, Weinheim
36. Mukhopadhyay A (2009) Fabrication and properties of oxide nanocomposites containing uniformly dispersed second phases. PhD thesis, University of Oxford, Oxford, UK
37. Vasiliev AL, Poyato R, Pature NP (2007) Single-wall carbon nanotubes at ceramic grain boundaries. *Scr Mater* 56:461–463
38. Wei T, Fan Z, Luo G, Wei F (2008) A new structure for multi-walled carbon nanotubes reinforced alumina nanocomposite with high strength and toughness. *Mater Lett* 62:641–644
39. Satam MK, Gurnani L, Vishwanathe S, Mukhopadhyay A (2016) Development of carbon nanotube reinforced bulk polycrystalline ceramics with intragranular carbon nanotube reinforcement. *J Am Ceram Soc* 99:2905–2908
40. Estili M, Kawasaki A (2008) An approach to mass-producing individually alumina-decorated multi-walled carbon nanotubes with optimized and controlled compositions. *Scr Mater* 58: 906–909
41. Estili M, Kawasaki A, Sakamoto H, Mekuchi Y, Kuno M, Tsukada T (2008) The homogeneous dispersion of surfactantless, slightly disordered, crystalline, multiwalled carbon nanotubes in α -alumina ceramics for structural reinforcement. *Acta Mater* 56:4070–4079
42. Chu BTT, Tobias G, Salzmann CG, Ballesteros B, Grobert N, Todd RI, Green ML (2008) Fabrication of carbon-nanotube-reinforced glass–ceramic nanocomposites by ultrasonic in situ sol–gel processing. *J Mater Chem* 18:5344
43. Mukhopadhyay A, Chu BTT, Green MLH, Todd RI (2010) Understanding the mechanical reinforcement of uniformly dispersed multiwalled carbon nanotubes in aluminoborosilicate glass ceramic. *Acta Mater* 58:2685–2697
44. Boccaccini AR, Acevedo DR, Brusatin G, Colombo P (2005) Borosilicate glass matrix composites containing multi-wall carbon nanotubes. *J Eur Ceram Soc* 25:1515–1523
45. Boccaccini AR, Thomas BJC, Brusatin G, Colombo P (2007) Mechanical and electrical properties of hot-pressed borosilicate glass matrix composites containing multi-wall carbon nanotubes. *J Mater Sci* 42:2030–2036

46. Chintapalli RK, Marro FG, Milsom B, Reece M, Anglada M (2012) Processing and characterization of high-density zirconia-carbon nanotube composites. *Mater Sci Eng A* 549:50–59
47. Ning J, Zhang J, Pan Y, Guo J (2003) Fabrication and mechanical properties of SiO₂ matrix composites reinforced by carbon nanotube. *Mater Sci Eng A* 357:392–396
48. Peigney A, Laurent C, Dobigeon F, Rousset A (1997) Carbon nanotubes grown in situ by a novel catalytic method. *J Mater Res* 12:613–615
49. Peigney A, Laurent C, Dumortier O, Rousset A (1998) Carbon nanotubes–Fe–alumina nanocomposites. Part I: influence of the Fe content on the synthesis of powders. *J Eur Ceram Soc* 18:1995–2004
50. Laurent C, Peigney A, Dumortier O, Rousset A (1998) Carbon nanotubes–Fe–alumina nanocomposites. Part II: microstructure and mechanical properties of the hot-pressed composites. *J Eur Ceram Soc* 18:2005–2013
51. Flahaut E, Peigney A, Laurent C, Marlière C, Chastel F, Rousset A (2000) Carbon nanotube-metal-oxide nanocomposites: microstructure, electrical conductivity and mechanical properties. *Acta Mater* 48:3803–3812
52. Peigney A, Laurent C, Flahaut E, Rousset A (2000) Carbon nanotubes in novel ceramic matrix nanocomposites. *Ceram Int* 26:677–683
53. Peigney A, Flahaut E, Laurent C, Chastel F, Rousset A (2002) Aligned carbon nanotubes in ceramic-matrix nanocomposites prepared by high-temperature extrusion. *Chem Phys Lett* 352:20–25
54. Peigney A (2003) Composite materials: tougher ceramics with nanotubes. *Nat Mater* 2:15–16
55. Xia Z, Riester L, Curtin WA, Li H, Sheldon BW, Liang J, Chang B, Xu JM (2004) Direct observation of toughening mechanisms in carbon nanotube ceramic matrix composites. *Acta Mater* 52:931–944
56. Xia Z, Curtin WA, Sheldon BW (2004) Fracture toughness of highly ordered carbon nanotube/alumina nanocomposites. *J Eng Mater Technol* 126:238
57. Xia ZH, Lou J, Curtin WA (2008) A multiscale experiment on the tribological behavior of aligned carbon nanotube/ceramic composites. *Scr Mater* 58:223–226
58. Kothari AK, Jian K, Rankin J, Sheldon BW (2008) Comparison between carbon nanotube and carbon nanofiber reinforcements in amorphous silicon nitride coatings. *J Am Ceram Soc* 91:2743–2746
59. Kothari AK, Hu S, Xia Z, Konca E, Sheldon BW (2012) Enhanced fracture toughness in carbon-nanotube-reinforced amorphous silicon nitride nanocomposite coatings. *Acta Mater* 60:3333–3339
60. Vasudevan S, Kothari A, Sheldon BW (2016) Direct observation of toughening and R-curve behavior in carbon nanotube reinforced silicon nitride. *Scr Mater* 124:112–116
61. Poyato R, Vasiliev AL, Pature NP, Tanaka H, Nishimura T (2006) Aqueous colloidal processing of single-wall carbon nanotubes and their composites with ceramics. *Nanotechnology* 17:1770–1777
62. Zhang SC, Fahrenholtz WG, Hilmis GE, Yadlowsky EJ (2010) Pressureless sintering of carbon nanotube–Al₂O₃ composites. *J Eur Ceram Soc* 30:1373–1380
63. Fan J, Zhao D, Wu M, Xu Z, Song J (2006) Preparation and microstructure of multi-wall carbon nanotubes-toughened Al₂O₃ composite. *J Am Ceram Soc* 89:750–753
64. Liu Y, Ramirez C, Zhang L, Wu W, Pature NP (2017) In situ direct observation of toughening in isotropic nanocomposites of alumina ceramic and multiwall carbon nanotubes. *Acta Mater* 127:203–210
65. Sun J, Iwasa M, Gao L, Zhang Q (2004) Single-walled carbon nanotubes coated with titania nanoparticles. *Carbon* 42:895–899
66. Balázs C, Fényi B, Hegman N, Kövér Z, Wéber F, Vértsey Z, Kónya Z, Kiricsi I, Biró LP, Arató P (2006) Development of CNT/Si₃N₄ composites with improved mechanical and electrical properties. *Compos Part B Eng* 37:418–424
67. Estili M, Kawasaki A, Sakka Y (2012) Highly concentrated 3D macrostructure of individual carbon nanotubes in a ceramic environment. *Adv Mater* 24:4322–4326

68. Estili M, Sakka Y (2014) Recent advances in understanding the reinforcing ability and mechanism of carbon nanotubes in ceramic matrix composites. *Sci Technol Adv Mater* 15:64902
69. Zapata-Solvas E, Gómez-García D, Domínguez-Rodríguez A (2012) Towards physical properties tailoring of carbon nanotubes-reinforced ceramic matrix composites. *J Eur Ceram Soc* 32:3001–3020
70. Berguiga L, Bellessa J, Vocanson F, Bernstein E, Plenet JC (2006) Carbon nanotube silica glass composites in thin films by the sol-gel technique. *Opt Mater* 28:167–171
71. Zhang Y, Shen Y, Han D, Wang Z, Song J, Niu L (2006) Reinforcement of silica with single-walled carbon nanotubes through covalent functionalization. *J Mater Chem* 16:4592–4597
72. Thomas BJC, Shaffer MSP, Boccaccini AR (2009) Sol-gel route to carbon nanotube borosilicate glass composites. *Compos Part A Appl Sci Manuf* 40:837–845
73. López AJ, Rico A, Rodríguez J, Rams J (2010) Tough ceramic coatings: carbon nanotube reinforced silica sol-gel. *Appl Surf Sci* 256:6375–6384
74. López AJ, Ureña A, Rams J (2011) Wear resistant coatings: silica sol-gel reinforced with carbon nanotubes. *Thin Solid Films* 519:7904–7910
75. Mo CB, Cha SI, Kim KT, Lee KH, Hong SH (2005) Fabrication of carbon nanotube reinforced alumina matrix nanocomposite by sol-gel process. *Mater Sci Eng A* 395:124–128
76. Cha SI, Kim KT, Lee KH, Mo CB, Hong SH (2005) Strengthening and toughening of carbon nanotube reinforced alumina nanocomposite fabricated by molecular level mixing process. *Scr Mater* 53:793–797
77. Yamamoto G, Omori M, Hashida T, Kimura H (2008) A novel structure for carbon nanotube reinforced alumina composites with improved mechanical properties. *Nanotechnology* 19:315708
78. Echeberria J, Rodríguez N, Vleugels J, Vanmeensel K, Reyes-Rojas A, Garcia-Reyes A, Domínguez-Rios C, Aguilar-Elguezabal A, Bocanegra-Bernal MH (2012) Hard and tough carbon nanotube-reinforced zirconia-toughened alumina composites prepared by spark plasma sintering. *Carbon* 50:706–717
79. Kasperski A, Weibel A, Alkattan D, Estournès C, Turq V, Laurent C, Peigney A (2013) Microhardness and friction coefficient of multi-walled carbon nanotube-yttria-stabilized ZrO₂ composites prepared by spark plasma sintering. *Scr Mater* 69:338–341
80. Ma RZ, Wu J, Wei BQ, Liang J, Wu DH (1998) Processing and properties of carbon nanotubes-nano-SiC ceramic. *J Mater Sci* 33:5243–5246
81. Morisada Y, Miyamoto Y, Takaura Y, Hirota K, Tamari N (2007) Mechanical properties of SiC composites incorporating SiC-coated multi-walled carbon nanotubes. *Int J Refract Met Hard Mater* 25:322–327
82. Sarkar K, Sarkar S, Das PK (2016) Spark plasma sintered multiwalled carbon nanotube/silicon carbide composites: densification, microstructure, and tribo-mechanical characterization. *J Mater Sci* 51:6697–6710
83. Gu Z, Yang Y, Li K, Tao X, Eres G, Howe JY, Zhang L, Li X, Pan Z (2011) Aligned carbon nanotube-reinforced silicon carbide composites produced by chemical vapor infiltration. *Carbon* 49:2475–2482
84. Balázs C, Shen Z, Kónya Z, Kasztovszky Z, Wéber F, Vertesy Z, Biro LP, Kiricsi I, Arato P (2005) Processing of carbon nanotube reinforced silicon nitride composites by spark plasma sintering. *Compos Sci Technol* 65:727–733
85. Corral EL, Cesarano J, Shyam A, Lara-Curzio E, Bell N, Stuecker J, Perry N, Di Prima M, Munir Z, Garay J, Barrera EV (2008) Engineered nanostructures for multifunctional single-walled carbon nanotube reinforced silicon nitride nanocomposites. *J Am Ceram Soc* 91: 3129–3137
86. Li A, Sun K, Dong W, Zhao D (2007) Mechanical properties, microstructure and histocompatibility of MWCNTs/HAp biocomposites. *Mater Lett* 61:1839–1844
87. Meng YH, Tang CY, Tsui CP, Chen DZ (2008) Fabrication and characterization of needle-like nano-HA and HA/MWNT composites. *J Mater Sci Mater Med* 19:75–81

88. Lahiri D, Singh V, Keshri AK, Seal S, Agarwal A (2010) Carbon nanotube toughened hydroxyapatite by spark plasma sintering: microstructural evolution and multiscale tribological properties. *Carbon* 48:3103–3120
89. Lei T, Wang L, Ouyang C, Li NF, Zhou LS (2011) In situ preparation and enhanced mechanical properties of carbon nanotube/hydroxyapatite composites. *Int J Appl Ceram Technol* 8:532–539
90. Guo S, Sivakumar R, Kagawa Y (2007) Multiwall carbon nanotube-SiO₂ nanocomposites: sintering, elastic properties, and fracture toughness. *Adv Eng Mater* 9:84–87
91. Sun J, Gao L, Li W (2002) Colloidal processing of carbon nanotube/alumina composites. *Chem Mater* 14:5169–5172
92. Anstis GR, Chantikul P, Lawn BR, Marshall DB (1981) A critical evaluation of indentation techniques for measuring fracture toughness: I, direct crack measurements. *J Am Ceram Soc* 64:533–538
93. Quinn GD, Bradt RC (2007) On the vickers indentation fracture toughness test. *J Am Ceram Soc* 90:673–680
94. Jiang D, Thomson K, Kuntz JD, Ager JW, Mukherjee AK (2007) Effect of sintering temperature on a single-wall carbon nanotube-toughened alumina-based nanocomposite. *Scr Mater* 56:959–962
95. Pature NP, Curtin WA (2008) Comment on “Effect of sintering temperature on a single-wall carbon nanotube-toughened alumina-based composite”. *Scr Mater* 58:989–990
96. Jiang D, Mukherjee AK (2008) Response to comment on “Effect of sintering temperature on single-wall carbon nanotube toughened alumina-based nanocomposite”. *Scr Mater* 58: 991–993
97. Bakshi SR, Musaramthota V, Virzi DA, Keshri AK, Lahiri D, Singh V, Seal S, Agarwal A (2011) Spark plasma sintered tantalum carbide-carbon nanotube composite: effect of pressure, carbon nanotube length and dispersion technique on microstructure and mechanical properties. *Mater Sci Eng A* 528:2538–2547
98. Nisar A, Ariharan S, Balani K (2016) Synergistic reinforcement of carbon nanotubes and silicon carbide for toughening tantalum carbide based ultrahigh temperature ceramic. *J Mater Res* 31:682–692
99. Zapata-Solvas E, Poyato R, Gómez-García D, Domínguez-Rodríguez A, Radmilovic V, Pature NP (2008) Creep-resistant composites of alumina and single-wall carbon nanotubes. *Appl Phys Lett* 92:111912
100. Zapata-Solvas E, Gómez-García D, Poyato R, Lee Z, Castillo-Rodríguez M, Domínguez-Rodríguez A, Radmilovic V, Pature NP (2010) Microstructural effects on the creep deformation of alumina/single-wall carbon nanotubes composites. *J Am Ceram Soc* 93:2042–2047
101. Daraktchiev M, Van de Moortèle B, Schaller R, Couteau E, Forró L (2005) Effects of carbon nanotubes on grain boundary sliding in zirconia polycrystals. *Adv Mater* 17:88–91
102. Ionascu C, Schaller R (2006) Influence of carbon nanotubes and silicon carbide whiskers on the mechanical loss due to grain boundary sliding in 3-mol% yttria-stabilized tetragonal zirconia polycrystals. *Mater Sci Eng A* 442:175–178
103. Mazaheri M, Mari D, Hesabi ZR, Schaller R, Fantozzi G (2011) Multi-walled carbon nanotube/nanostructured zirconia composites: outstanding mechanical properties in a wide range of temperature. *Compos Sci Technol* 71:939–945
104. An JW, You DH, Lim DS (2003) Tribological properties of hot-pressed alumina-CNT composites. *Wear* 255:677–681
105. Ahmad I, Kennedy A, Zhu YQ (2010) Wear resistant properties of multi-walled carbon nanotubes reinforced Al₂O₃ nanocomposites. *Wear* 269:71–78
106. Lim DS, You DH, Choi HJ, Lim SH, Jang H (2005) Effect of CNT distribution on tribological behavior of alumina-CNT composites. *Wear* 259:539–544
107. Zhai W, Srikanth N, Kong LB, Zhou K (2017) Carbon nanomaterials in tribology. *Carbon* 119:150–171
108. Ni B, Sinnott SB (2001) Tribological properties of carbon nanotube bundles predicted from atomistic simulations. *Surf Sci* 487:87–96

109. Balani K, Chen Y, Harimkar SP, Dahotre NB, Agarwal A (2007) Tribological behavior of plasma-sprayed carbon nanotube-reinforced hydroxyapatite coating in physiological solution. *Acta Biomater* 3:944–951
110. Wells JK, Beaumont PWR (1985) Debonding and pull-out processes in fibrous composites. *J Mater Sci* 20:1275–1284
111. Suzuki T, Sato M, Sakai M (2011) Fiber pullout processes and mechanisms of a carbon fiber reinforced silicon nitride ceramic composite. *J Mater Res* 7:2869–2875
112. Estili M, Kawasaki A (2010) Engineering strong intergraphene shear resistance in multi-walled carbon nanotubes and dramatic tensile improvements. *Adv Mater* 22:607–610
113. Estili M, Kawasaki A, Pittini-Yamada Y, Utke I, Michler J (2011) In situ characterization of tensile-bending load bearing ability of multi-walled carbon nanotubes in alumina-based nanocomposites. *J Mater Chem* 21:4272–4278
114. Yamamoto G, Shirasu K, Hashida T, Takagi T, Suk JW, An J, Piner RD, Ruoff RS (2011) Nanotube fracture during the failure of carbon nanotube/alumina composites. *Carbon* 49:3709–3716
115. Padtare NP (2009) Multifunctional composites of ceramics and single-walled carbon nanotubes. *Adv Mater* 21:1767–1770
116. Ahmad I, Unwin M, Cao H, Chen H, Zhao H, Kennedy A, Zhu YQ (2010) Multi-walled carbon nanotubes reinforced Al_2O_3 nanocomposites: mechanical properties and interfacial investigations. *Compos Sci Technol* 70:1199–1206
117. Fan JP, Zhuang DM, Zhao DQ, Zhang G, Wu MS, Wei F, Fan ZJ (2006) Toughening and reinforcing alumina matrix composite with single-wall carbon nanotubes. *Appl Phys Lett* 89:1–4
118. Li L, Li Y (2017) Development and trend of ceramic cutting tools from the perspective of mechanical processing. *IOP Conf Ser Earth Environ Sci* 94:012062
119. Li K, Yang Y, Gu Z, Howe JY, Eres G, Zhang L, Li X, Pan Z (2014) Approaching carbon nanotube reinforcing limit in B_4C matrix composites produced by chemical vapor infiltration. *Adv Eng Mater* 16:161–166



Polymer-Derived Ceramics and Their Space Applications **26**

S. Packirisamy, K. J. Sreejith, Deepa Devapal, and B. Swaminathan

Contents

Introduction	978
Synthesis, Characterization, and Ceramic Conversion of Pre ceramic Polymers	980
Silicon Containing Polymers	980
Ceramics from Carbonaceous Polymers	1007
Active Filler Controlled Pyrolysis (AFCOP)	1009
Polymer-Derived Ceramics for Space Applications	1010
Ceramic Matrix Composites	1012
Protective Coatings	1023
Ceramic Adhesives	1045
Lightweight Ceramics	1051
Concluding Remarks and Perspectives	1063
References	1065

S. Packirisamy (✉)

Ceramic Matrix Products Division, Analytical Spectroscopy and Ceramics Group, PCM Entity, Vikram Sarabhai Space Centre, Indian Space Research Organization, Thiruvananthapuram, India

Advanced Polymeric Materials Research Laboratory, Department of Chemistry and Biochemistry, School of Basic Sciences and Research, Sharda University, Greater Noida, India

e-mail: spackirisamy@yahoo.com; s.packirisamy@sharda.ac.in

K. J. Sreejith · D. Devapal

Ceramic Matrix Products Division, Analytical Spectroscopy and Ceramics Group, PCM Entity, Vikram Sarabhai Space Centre, Indian Space Research Organization, Thiruvananthapuram, India

e-mail: kjsreejith@gmail.com; kj_sreejith@vssc.gov.in; ddevapal2000@yahoo.com

B. Swaminathan

Ceramic Matrix Products Division, Analytical Spectroscopy and Ceramics Group, PCM Entity, Vikram Sarabhai Space Centre, Indian Space Research Organization, Thiruvananthapuram, India

Morgan Advanced Materials, Murugappa Mogan Thermal Ceramics Ltd., Ranipet, Vellore District, Tamil Nadu, India

e-mail: swami1423@gmail.com

Abstract

Inorganic and organometallic polymers capable of giving high ceramic residue (more than 50 wt%) on heat treatment in an inert atmosphere are called “pre-ceramic polymers.” As they are polymeric in nature, processing techniques used for conventional polymer processing can be easily adopted. They can be applied as coating, cast into film and drawn into fiber and then converted into corresponding ceramic material. Amorphous materials that are thermally stable to very high temperatures with compositions not obtainable with common synthetic methods can be obtained from preceramic polymers. Kinetic stabilization of less stable phases, adaptability of various fabrication capabilities of polymer process engineering, formation of nanoceramics of desired composition, pressureless sintering, and machinability are the main advantages of obtaining ceramics from polymeric precursors.

Polymer-derived ceramics find applications as oxidation resistant high temperature ceramic materials in the form of fiber, coatings and adhesives, and matrix of ceramic matrix composites for use by aerospace, nuclear, and defense establishments. In addition, they are also being investigated for end-use in biomedical devices, drug delivery systems, water remediation, energy storage devices, micro-electronics, and nanosensors.

The present chapter deals with synthesis, characterization, and ceramic conversion of silicon-based preceramic polymers, and ceramics from carbonaceous polymers, and their possible space applications. In view of the voluminous literature, equal emphasis could not be given to many of the developments in the area of preceramic polymers and the discussion is confined to relevant systems which have the scope for space applications.

Keywords

Polymer-derived ceramics · Preceramic polymers · Space applications · Thermal protection systems · Ceramic matrix composites · Oxidation resistant coatings · Thermal barrier coatings · Atomic oxygen resistant coatings · Ceramic adhesives · Lightweight ceramics

Abbreviations

3-APTES	3-Aminopropyltriethoxysilane
ABSE	Amino-bis(silylethane)
AFCOP	Active Filler Controlled Polymer Pyrolysis
AO	Atomic Oxygen
APMDEOS	3-Aminopropylmethyldiethoxysilane
BCTS	Boron-Modified CTS
BLS	Boundary Layer Splitter
BMG	Methyl and Glycidoxy Group Containing Poly(borosiloxane)
BMV	Methyl and Vinyl Group Containing Poly(borosiloxane)
BN	Boron Nitride

BP	Poly(phenylborosiloxane)
BPV	Phenyl and Vinyl Group Containing Poly(borosiloxane)
BSAS	Barium-Strontium-Aluminosilicate
CMC	Ceramics Matrix Composite
CNT	Carbon Nano Tube
CTE	Coefficient of Thermal Expansion
CTS	1,3,5-Trimethyl-1',3',5'-trivinylcyclotrisilazane
CVD	Chemical Vapor Deposition
CVI	Chemical Vapor Infiltration
DMDCS	Dimethyldichlorosilane
DPDCS	Diphenyldichlorosilane
EBC	Environmental Barrier Coating
EC	Eddy Current
FESEM	Field Emission Scanning Electron Microscopy
FM	Fiber to Matrix
GPTMOS	Glycidoxypropyltrimethoxysilane
HDA	High Density Ablative
HFH	Heat Flux History
HRTEM	High Resolution Transition Electron Microscopy
ILSS	Interlaminar Shear Strength
IMI	Internal Multiscreen Insulation
KHS	Kinetic Heat Simulation
LAM	Liquid Apogee Motor
LEO	Low Earth Orbit
LSI	Liquid Silicon Infiltration
MAS-NMR	Magic Angle Spinning-Nuclear Magnetic Resonance
MAX Phase	In MAX phase M is an early transition metal, A is an A-group element, and X is either carbon and/or nitrogen
MEMS	Micro-Electromechanical Systems
MTEOS	Methyltriethoxysilane
MTMOS	Methyltrimethoxysilane
MVDCS	Methylvinylchlorosilane
MWCNT	Multi Wall Carbon Nano Tube
NMR	Nuclear Magnetic Resonance
PBDPS	Polyborodiphenylsiloxane
PBS	Polyborosiloxane
PCS	Polycarbosilane
PDC	Polymer-Derived Ceramic
PHPS	Perhydridopolysilazane
PIP	Polymer Infiltration and Pyrolysis
PSH	Polysilanehydrocarbon
PTEOS	Phenyltriethoxysilane
PTMOS	Phenyltrimethoxysilane
PVD	Physical Vapor Deposition
RLV-TD	Reusable Launch Vehicle-Technology Demonstrator

RMI	Reactive Melt Infiltration
SEM	Scanning Electron Microscopy
SWLE	Side Wall Leading Edge
TBC	Thermal Barrier Coating
TEM	Transmitting Electron Microscopy
TEOS	Tetraethoxysilane
THF	Tetrahydrofuran
TMOS	Tetramethoxysilane
TPhBS	Titanophenylborosiloxane
TPS	Thermal Protection System
UHTC	Ultra High Temperature Ceramic
VTEOS	Vinyltriethoxysilane
VTMEOS	Vinyltris(2-methoxyethoxy)silane
WLE	Wing Leading Edge
XRD	X-Ray Diffraction
ZBS	Zirconoborosiloxane
ZPhBS	Zirconophenylborosiloxane
ZTBS	Zirconotitanoborosiloxane

Introduction

The ever-increasing demand for more efficient and powerful aircraft and spacecraft engines which have to operate in extreme operating conditions such as high temperatures, fast speeds, high stresses and hostile environment has fueled the demand for developing and qualifying newer engineered ceramics/advanced ceramic materials [1, 2]. The feasibility of combining many metallic and nonmetallic atoms to form ceramics in several atomic structural arrangements provides enormous scope to material scientists to invent new ceramic materials to meet the requirements of aerospace industry [1].

Among the various routes available for obtaining advanced ceramics, polymer-derived ceramic (PDC) route offers the most convenient and easily adoptable method for obtaining advanced ceramics in desired composition and shape. The advancement of PDCs owes its origin to the pyrolysis of polymers to obtain solid materials such as graphite, glassy carbon, carbon fibers, and carbon-carbon composites. Extension of this concept to inorganic and organometallic polymers led to the development of PDCs as fibers, composites, coatings, adhesives, and cellular materials. The journey of PDCs began with Chantrell and Popper [3], when they demonstrated for the first time that monolithic silicon nitride could be prepared by molding polysilazane to the desired shape followed by pyrolysis. However, this fast emerging field got impetus only by mid-1970s when Verbeek et al. [4] in Germany reported the preparation of non-oxide ceramic fiber comprising of silicon carbide and silicon nitride by pyrolyzing polysilazane and polycarbosilazane, and Yajima and coworkers [5] in Japan prepared polycarbosilane (PCS) from polydimethylsilane and evaluated it as precursor for silicon carbide fiber.

The production of ceramics by pyrolysis of polymeric precursors presents many advantages over the conventional methods of ceramic preparation [6]. The advantages include low temperature processability, high purity of the ceramics, the ability to control the composition of the ceramics, easiness in the preparation of shaped objects, and the ability to generate products in a variety of forms such as coatings, films, joints, monolithic bodies, foams, and fibers (Fig. 1). Over the years, PDCs have gained importance, as evidenced by the number of research publications, reviews, patents, international conferences and workshops conducted and books published relating to this topic [7–13]. From the commercial point of view, the global market of PDCs in 2017 is only USD 437.16 million [14], very much less compared to that of a well-known polymer, polyethylene (USD 163 billion). At present, the market of PDCs is primarily due to the demand for exploring high-end applications in aerospace, defense, energy, and semiconductor sectors, and the market survey predicts a compounded annual growth rate of 10.2% during the period 2017–2022 [14]. Once the enabling technologies based on PDCs are inducted into actual applications in the above sectors, the demand for PDCs is expected to grow at a much faster rate.

The present review highlights the developments on PDCs with a special focus on the following space applications: (i) matrix resins for CMCs required for thermostructural applications, (ii) protective coatings for nonmetallic and metallic substrates, and atomic oxygen resistant coatings, (iii) ceramic adhesives for joining different substrates, and (iv) lightweight ceramics for advanced thermal protection systems. This review is not an attempt to present a detailed account of the developments in PDCs, and in view of the voluminous research work in this area, readers attention is drawn to excellent reviews, book chapters, and books on this topic.

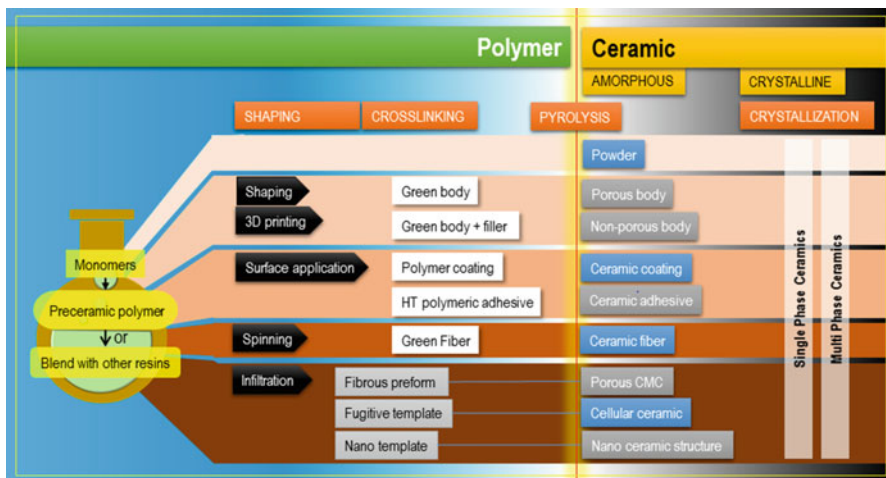


Fig. 1 Polymer-derived ceramic (PDC) route to ceramic products. (Adopted from Ref. [6])

Synthesis, Characterization, and Ceramic Conversion of Preceramic Polymers

The composition, number of phases, phase distribution, and the microstructure of the final ceramic obtained are largely influenced by the type and the molecular structure of preceramic polymer. In view of this, research efforts toward synthesizing novel preceramic polymers with the desired physicochemical properties, optimizing the thermolysis conditions to maximize the ceramic yield, and improving the high temperature capability and environmental stability of ceramics obtained therefrom continue to be unabated.

The transformation of preceramic polymer to ceramics involves mainly the following three steps (Fig. 2): (i) shaping and cross-linking of these precursors to form two- or three-dimensional preceramic networks, (ii) transformation of the networks into amorphous covalent ceramics (organic/inorganic transition) by heat treatment, and (iii) crystallization of the amorphous solids into thermodynamically stable phases via different metastable intermediates [6, 7].

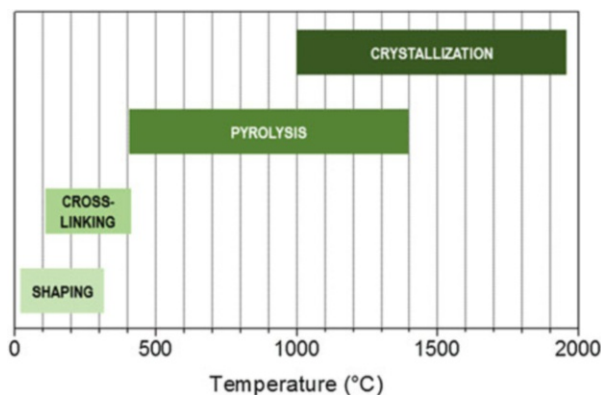
Silicon Containing Polymers

This class of polymers is the most widely studied precursors for ceramics, and this is attributed to easy availability of variety of organosilicon monomers in large quantities at an affordable cost. Different Si-containing polymers having the general formula, $-(RR_1Si-X)-$ can be synthesized by suitable choice of monomers and synthetic routes as precursors for SiC, SiBC, SiOC, SiOBC, MOSiOC (where M stands for metallic element), Si_3N_4 , SiCN, and SiBCN ceramics (Fig. 3).

Polysilanes and Polycarbosilanes

Following the pioneering work of Yajima et al. [5] on the conversion of intractable polydimethylsilane to PCS (Scheme 1), the initial efforts were focused toward

Fig. 2 Conversion of preceramic polymer to ceramic. (Adopted from Ref. [7])



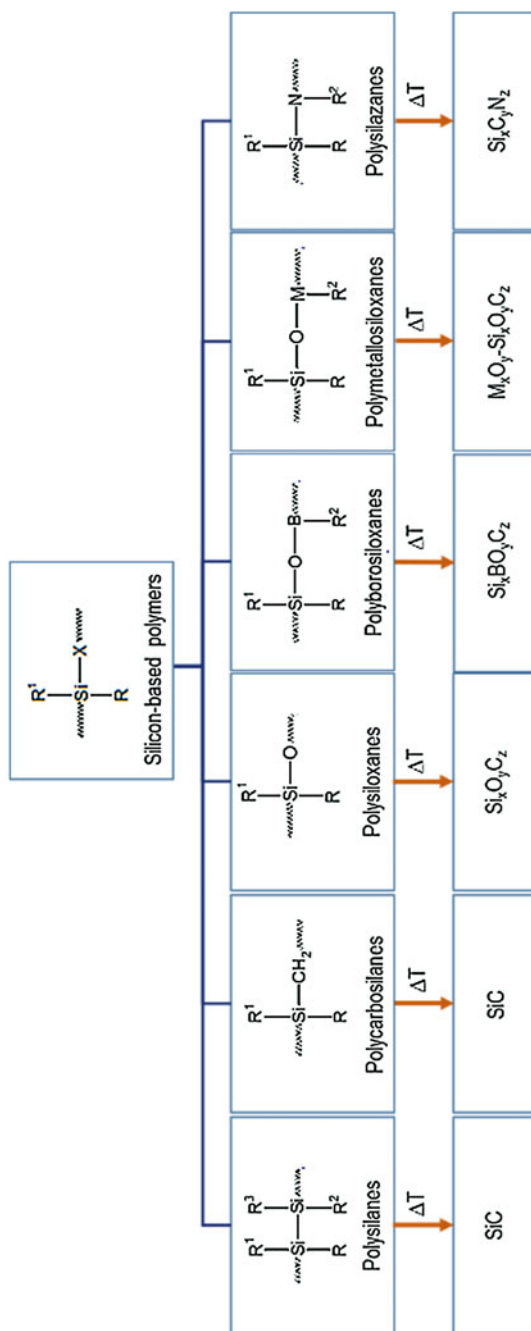
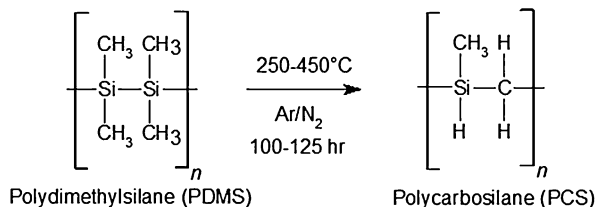


Fig. 3 Ceramic conversion of silicon containing polymers. (Adapted from [7])

Scheme 1 Yajima's process for the synthesis of polycarbosilane from polydimethylsilane [5]



obtaining SiC fibers and modifying PCS to incorporate metallic elements such Al, Ti, and Zr to improve the high temperature capability of SiC fibers [15, 16].

In 1980s, PCS gained its significance not only as precursors for SiC fibers or metal modified SiC fibers but also for many other applications including that of matrix resins for CMCs. The research work on PCS has been carried out over the years with the aim of achieving one or more of the following objectives: (i) obtaining PCS with near stoichiometric composition [17], (ii) cross-linking/modification/curing to improve the ceramic residue [18], (iii) minimizing oxygen incorporation during curing [19], (iv) catalyst systems for pressureless synthesis of PCS [20], and (v) chemical modification of PCS to obtain new ceramic systems [21, 22]. Though the synthesis of PCS from intractable polydimethylsilane was reported in 1975, the interest on this precursor is not diminishing as indicated by the number of patents and papers published in recent years.

Extensive studies on the ceramic conversion of PCS [23, 24] and metal modified PCS have been reported [25, 26]. PCS on heat treatment in an inert atmosphere gives amorphous SiC at around 800 °C which on further heat treatment at temperatures above 1200 °C gets converted to β -SiC (Fig. 4) with crystallite size of 3–10 nm [22]. If the starting PCS is rich in carbon, the PDC obtained is β -SiC with nanodomains of carbon dispersed in the ceramic matrix. In the case of metal (M) modified PCS, the PDC obtained is usually a mixed non-oxide ceramic comprising of metal carbide and β -SiC or SiMCO [Fig. 5].

The research work on polysilastylene, a soluble polysilane (Scheme 2), by West et al. [27] and soluble vinyl-functionalized polysilanes and branched polysilanes/polycarbosilane (Scheme 3) by Schilling et al. [28] has motivated many researchers to synthesize soluble precursors directly without the need for converting polysilane to polycarbosilane. Many such precursors gave poor ceramic yield, and cross-linking by UV irradiation or by chemical means was required to improve the ceramic yield [29]. Schilling et al. [28] observed that branching at silicon improved the ceramic yield and reported the synthesis of branched or vinyl-functionalized silanes, polycarbosilanes, and polysilahydrocarbons (PSH) through the reaction of organochlorosilane monomers with vinylic monomers or through the reaction of vinyl-functionalized chlorosilanes with organochlorosilane monomers under dechlorination conditions (Scheme 3).

Packirisamy et al. [30–33] synthesized PSHs through the dechlorination of diorganodichlorosilane using sodium in the presence of styrene (Scheme 4). In general, PSHs gave poor ceramic residue (5–25%), and some of them containing polysilyl blocks and methylphenylsilyl units were converted to tractable

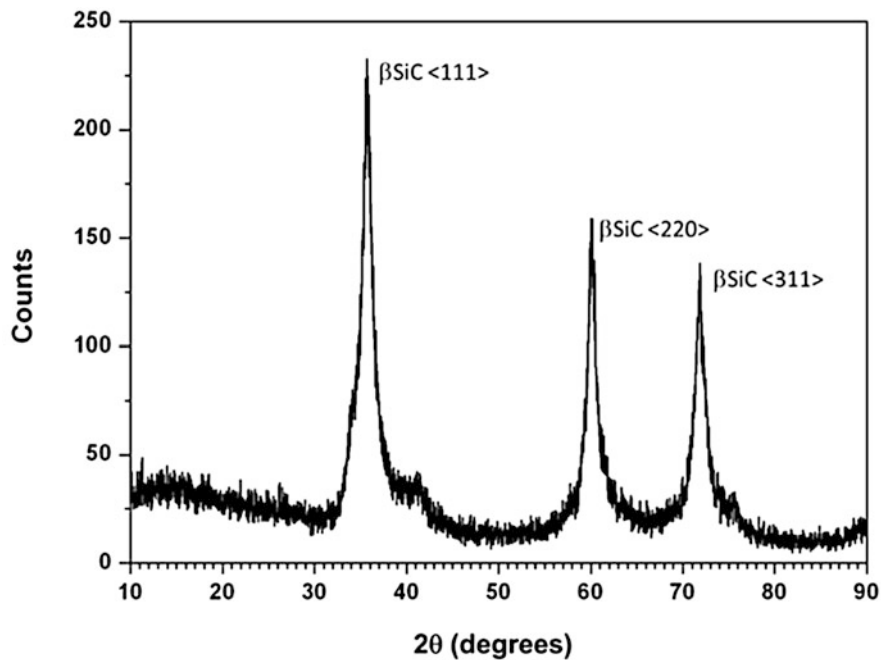


Fig. 4 XRD pattern of ceramics obtained from PCS at 1500 °C [22]

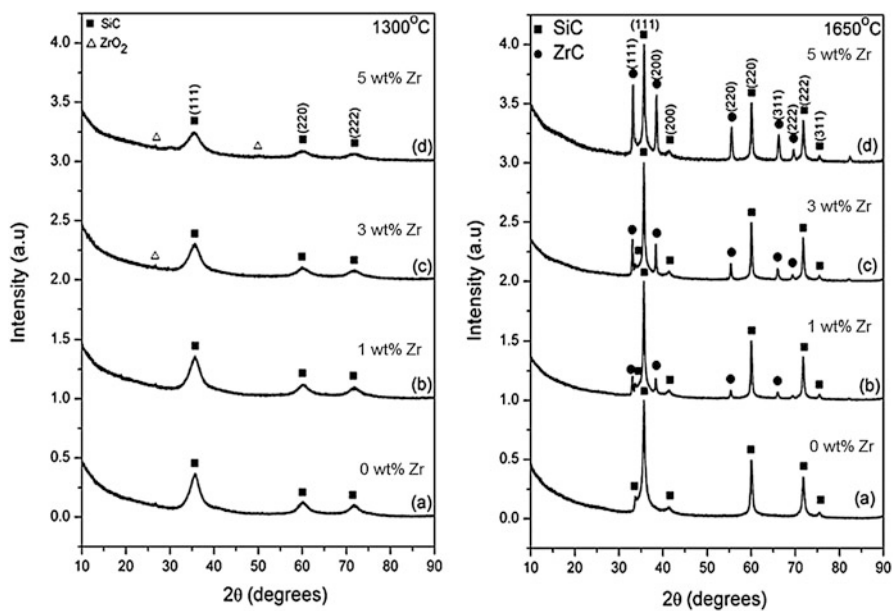
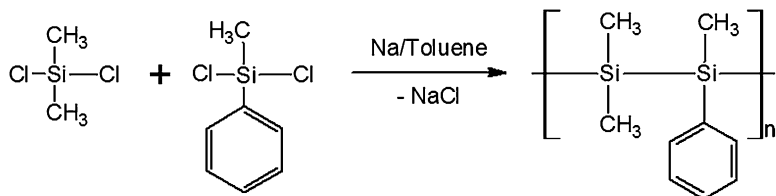
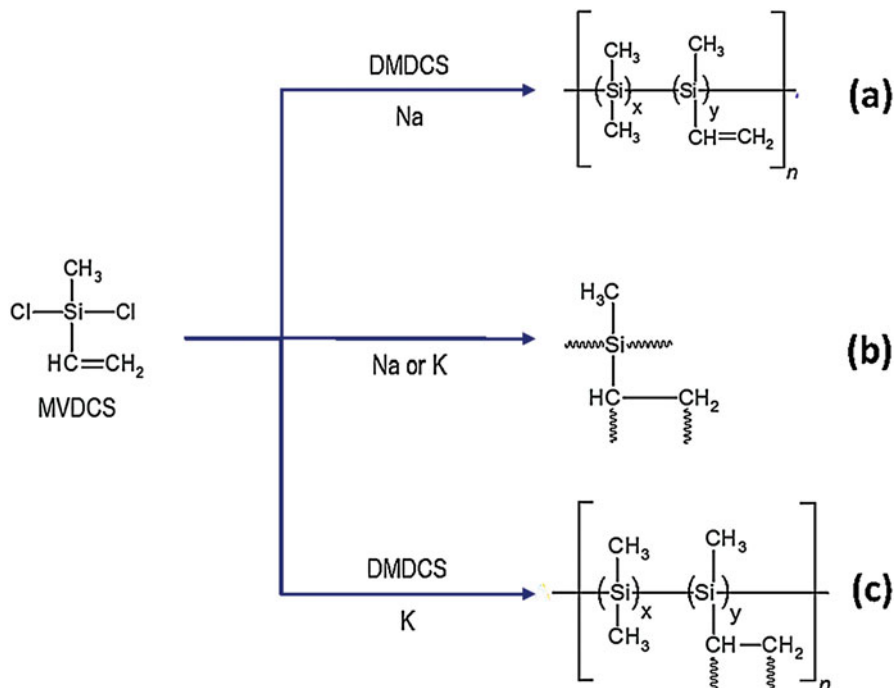


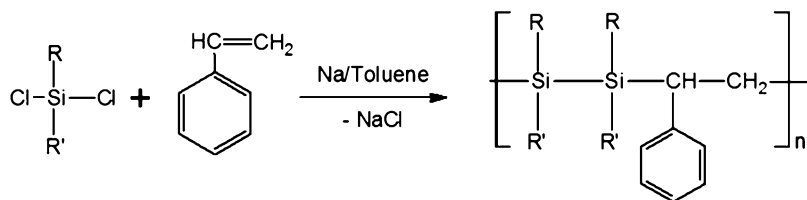
Fig. 5 XRD of PCS modified with $\text{Zr}(\text{acac})_4$. (Reproduced from Ref. [21] with permission from Springer Nature)



Scheme 2 Synthesis of poly(dimethylsilylene-co-methylphenylsilylene) [polysilastylene] [27]



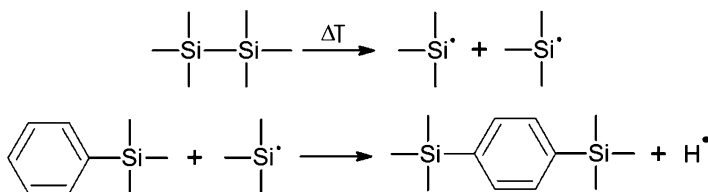
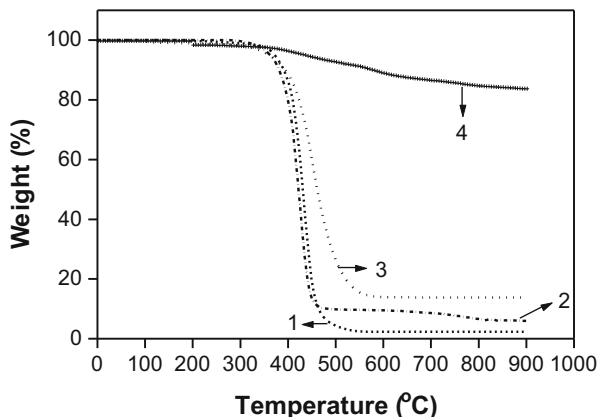
Scheme 3 Synthesis of (a) vinyl-functionalized polysilane, (b) polycarbosilane, and (c) branched polysilane [28]



Where, R = CH₃
R' = CH₃ or Ph

Scheme 4 Synthesis of polydisilahydrocarbon from diorganodichlorosilane and styrene [30, 34]

Fig. 6 Thermogravimetric curves of: 1. PSH containing dimethyldisilyl units (PSH-1), 2. PSH containing dimethyldisilyl and phenylmethyldisilyl units (PSH-2), 3. PSH-1 heat treated at 420 °C, and 4. PSH-2 heat treated at 420 °C [34]



Scheme 5 Phenylene insertion taking place in PSH containing dimethyldisilyl and phenylmethyldisilyl units (PSH-2) during heat treatment [34]

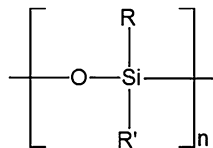
polycarbosilanes through heat treatment at 420 °C in a partially confined environment and these polymers gave ceramic residue of 40–85% at 900 °C (Fig. 6) [34]. The high ceramic residue (85%) of PCS from PSH containing methylphenylsilylene is attributed to phenylene insertion reaction (Scheme 5).

Polysiloxanes and Polysilsesquioxanes

Polysiloxanes (Fig. 7) are the most studied ones among inorganic polymers [35]. Hydrolysis of diorganodichlorosilanes (R_2SiCl_2) is widely used for the synthesis of polysiloxanes. Synthesis of polysiloxanes by ring opening polymerization of cyclic trimers and tetramers has largely replaced the hydrolysis approach [36]. Depending on the functionality of the side chains, polysiloxanes can be linear or cross-linked networks.

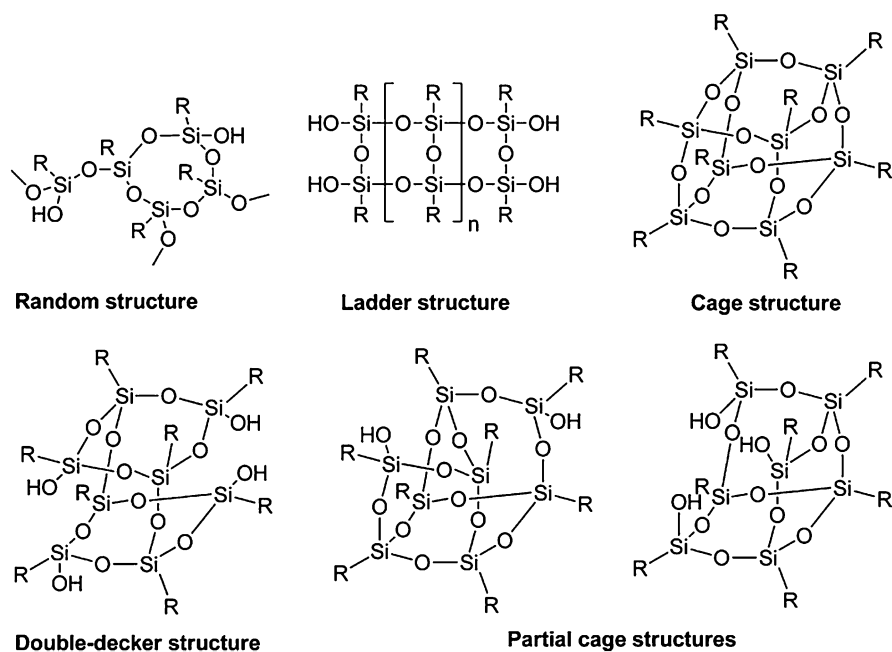
Cross-linked polysiloxanes [36] and polysilsesquioxanes (Fig. 8) have been prepared by the sol-gel process through hydrolysis and condensation reactions of organically modified silicon alkoxides [36, 37].

Polysiloxanes and polysilsesquioxanes on pyrolysis give siliconoxycarbide (SiOC) glasses [38]. Compared to fused SiO_2 , carbon-rich SiOC glasses have superior mechanical properties at elevated temperatures, in particular, improved creep resistance [39]. By the addition of ceramic or metallic particles, the mechanical and physical properties of SiOC matrix can be modified [40].

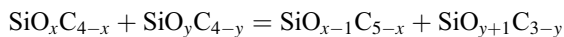
Fig. 7 Polysiloxane structure

Where,

R & R' = H, Me, Ph, OEt, OH, etc.

**Fig. 8** General types of poly(organosilsesquioxane)s. (Reproduced from Ref. [37] with permission from American Chemical Society)

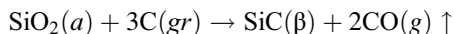
The microstructural evolution of SiOC glasses from polysiloxanes and polysilsesquioxanes has been studied in detail by many researchers [41–46]. During heat treatment at temperatures above 900 °C, redistribution reactions take place between Si-O and Si-C bonds as given in the general equation below [46]:



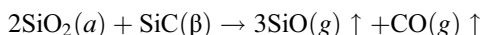
where x and y are integers, $0 < x \leq 4$, and $0 \leq y < 4$.

The free carbon phase formed at 600 °C remains unchanged up to 1350 °C as evidenced by ^{29}Si -NMR spectra and chemical analysis. Investigation by Saha and

Raj [44] suggests that the temperature regimes at which SiCO crystallizes into β -SiC overlaps with the conditions where a carbothermal reaction between silica and carbon as shown below takes place:

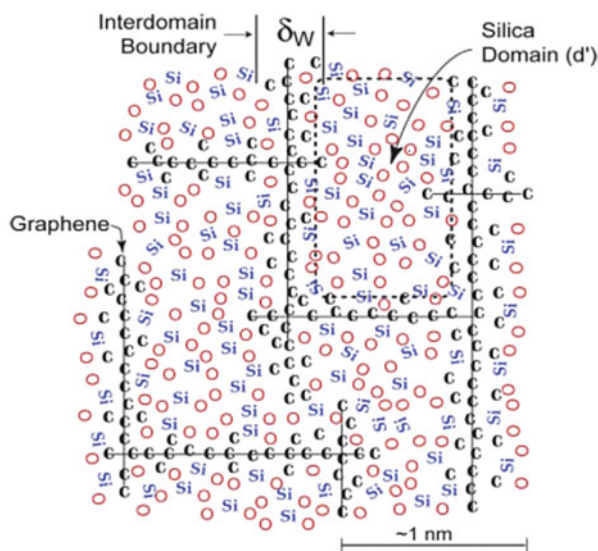


Thus, SiOC may crystallize in two ways: (i) the amorphous structure may phase separate into stoichiometric compositions of SiO₂, SiC, and C and then crystallize; and (ii) a second pathway is the growth of β -SiC accompanying the carbothermal reduction of silica, as given above. Crystallization may occur by a combination of decomposition as well as phase separation. At temperatures above 1400 °C, the silica phase can react with SiC to volatilize into SiO and CO as shown below:



Saha et al. [43] proposed a simple geometrical model based on surface-to-volume ratio of the domains which was moderately successful in predicting the domain size in SiOC (Fig. 9). The principal assumptions in this model are based on the framework of the amorphous structure justified on the basis of NMR data and on the creep and viscoelastic behavior of the SiOC ceramic at temperatures beyond 1000 °C. Subsequent to proposing this model, it was shown that amorphous SiOC ceramics can be etched with hydrofluoric acid leaving behind a porous structure with a median pore diameter of approximately 3 nm. The change in the composition after etching shows that only silica is removed.

Fig. 9 Proposed model for the nanodomain structures in polymer-derived SiCO. (Reproduced from Ref. [43] with permission from John Wiley and Sons)

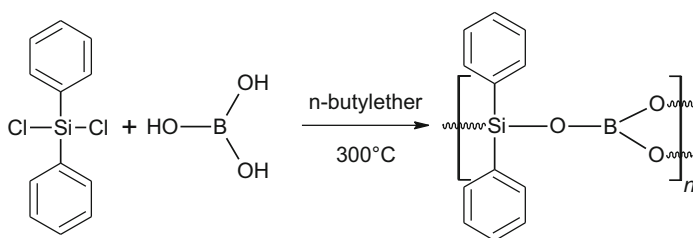


Polyborosiloxanes

Polyborosiloxanes have been an exploration target because of their thermodynamically stable backbone linkage. Though polyborosiloxanes could not be used as high temperature polymers due to poor hydrolytic stability, they serve as cost-effective precursors for siliconboronoxycarbide (SiBOC) ceramics. They have also been investigated in sol-gel chemistry as precursors for borosilicate glasses. Several methods have been described for the synthesis of polymers containing -Si-O-B-O-linkages using di- and tri-functional silicon compounds as the source of silicon, and boric acid, borontrioxide, borontrichloride, boron tribromide, borate esters, and phenylboronic acid as the source of boron [47–50].

Yajima et al. [48] synthesized poly(borodiphenylsiloxane) (PBDPS) by reacting boric acid with diphenyldichlorosilane (DPDCS) (Scheme 6). PBDPS was obtained in 92% yield and found to be far more moisture resistant than its analog prepared from boric acid and dimethyldichlorosilane [48]. PBDPS was used as a catalyst for the conversion of intractable polydimethylsilane to polycarbosilane [51]. It was also evaluated as a binder for making SiC and Si₃N₄ sintered bodies [52]. Synthesis of PBDPS through the reaction of boric acid with diphenylsilanol in dibutylether or N-methyl-2-pyrrolidone has also been reported [53].

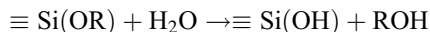
Sol-gel process was extensively used with the aim of preparing, via cocondensation reactions between TEOS and triethylborate or boric acid, a more homogeneous SiO₂-B₂O₃ gel as precursor for borosilicate glass and fibers [49, 50, 54]. It is found that the boron atoms are present in the silica matrix as a separate B₂O₃ and/or B(OH)₃ phase [55]. This is attributed to the well-known reactivity of the B-O-Si bonds toward hydrolysis. The borosiloxane linkages that might form in the early stages of the sol-gel process are consumed at the end when increasing amount of water is produced via condensation [54]. Soraru et al. [56] demonstrated that if a modified silicon alkoxide, such as RSi(OEt)₃, where R=Me, Et, or Vi is cohydrolyzed with tetraethylborate, then a large amount of trigonal BO₃ units are incorporated in the hybrid siloxane-network via B-O-Si bridges, leading to borosiloxane gels. The resulting gels appear homogeneous, clear, and no evidence of the formation of a crystalline B(OH)₃ can be detected. The retention of B-O-Si bonds in the hybrid borosilicate gels is partly due to: (i) the low hydrolysis ratio used in the sol-gel synthesis (H₂O/Si = 1.5), (ii) the in situ protection that the hydrophobic organic groups bonded to silicon provide against water attack, and (iii) the



Scheme 6 Synthesis of poly(borodiphenylsiloxane) [48]

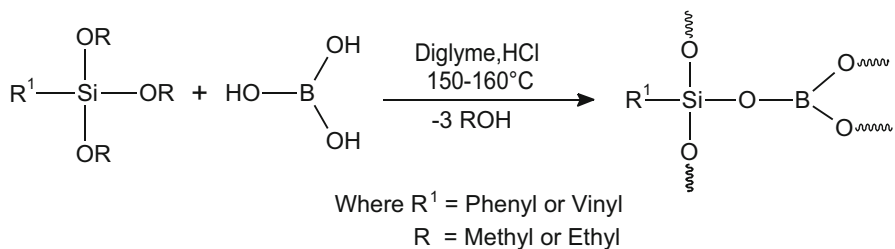
higher electron density at the silicon atoms in the organically substituted gels which strengthen the Si-O bonds.

Hydrolysis and condensation reactions in an anhydrous sol-gel system comprising TEOS, boric acid, and ethanol were studied by Zha et al. [57]. Boric acid is able to hydrolyze TEOS directly, and subsequent condensation reactions form borosiloxane and siloxane linkages. Since water is absent from the initial mixture, the usual first step (as shown below) in a silica-based sol-gel reaction, hydrolysis of the silicon alkoxide, cannot occur.



Zha et al. [57] prepared borosiloxane sol by reacting boric acid and TEOS in ethanol in multiple steps in order to achieve uniformity of the sol. The anhydrous mixture is indefinitely stable against gelation, but can be readily gelled by addition of NaOH in ethanol, and this system is useful for preparing borosilicate glasses at lower temperatures with good homogeneity. In a similar approach, Soraru et al. [58] prepared borosilicate gel by dissolving boric acid in organoalkoxysilane under stirring at 78 °C without any external addition of water and then leaving the solution left open for gelation. ¹¹B-MAS NMR spectroscopic studies of dried gels confirmed the incorporation of boron atoms into the siloxane network via B-O-Si bridges. On the other hand, when a conventional tetrafunctional silicon alkoxide such as tetramethoxysilane (TMOS) or TEOS is reacted with boric acid, the expected borosilicate gels are not formed.

In a modification of the above approach, Ambadas et al. [34, 59] synthesized borosiloxane oligomers through the condensation of boric acid with phenyltrimethoxysilane (PTMOS) and vinyltriethoxysilane (VTEOS) in diglyme (Scheme 7). The extent of reaction was controlled by the removal of alkyl alcohol formed as the by-product and the oligomers were soluble in diglyme. The advantage of this approach is that resinous borosiloxane oligomers are obtained in 3–5 h without waiting for days for gelation. The oligomers, poly(vinylborosiloxane) (BSiO-I) and poly(phenylborosiloxane) (BSiO-II), were soluble in common organic solvents such as tetrahydrofuran, 1,4-dioxane, toluene, and diglyme. BOSi-I and BOSi-II gave ceramic residue of 85% and 65%, respectively, at 900 °C (Fig. 10).



Scheme 7 Synthesis of poly(borosiloxane)s from boric acid and organotrialkoxysilane [59]

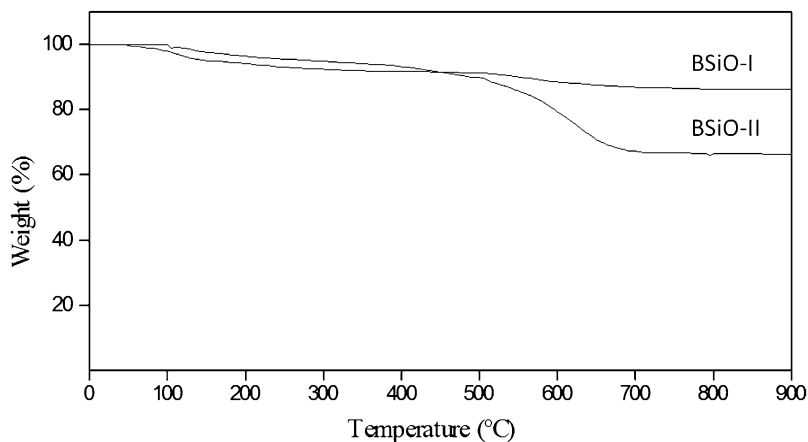


Fig. 10 TG curves of poly(vinylborosiloxane) [BSiO-I] and poly(phenylborosiloxane) [BSiO-II]. (Reproduced from Ref. [59] with permission from Springer Nature)

Following the above work, synthesis of several poly(borosiloxane)s by reacting boric acid with different organotrialkoxysilanes and their mixtures was investigated [60–66] with a view to understand the effect of organic substituent on silicon on the processability, molecular weight, microstructure, thermal stability, ceramic residue, and the stability of ceramic phase at high temperatures. Devapal et al. [63] observed that T_3 structures are formed more when boric acid is reacted with phenyltrimethoxysilane than with phenyltriethoxysilane (Fig. 11). The ratio of peak intensities of T_3 to T_2 (Fig. 11) is 1:0.34 for BSiPh-1 and 1:0.68 for BSiPh-2. This shows that T_3 structures are formed more when PTMOS is used which is attributed to the higher reactivity of PTMOS compared to that of PTEOS.

When the synthesis of borosiloxane oligomers is carried out in the absence of hydrochloric acid, hydrolysis of Si–OR to Si–OH and the subsequent reaction of Si–OH with B–OH forming Si–O–B bond or its self-condensation forming Si–O–Si bond are ruled out, and the most predominant reaction would be the reaction of Si–OR with B–OH forming Si–O–B bond with the elimination of ROH. This process has been successfully used for the synthesis of epoxy-, vinyl-, and epoxy- and vinyl- (in the same backbone) functionalized borosiloxane oligomers eliminating premature gelation [60].

The purpose of incorporating epoxy and vinyl group in borosiloxane oligomers is to provide additional cross-linking sites which can be made use of during processing of these oligomers as matrix resins for composites and infiltrating resins. However, while attempting to remove the solvent, dioxane/diglyme, premature gelation was observed. In order to overcome this problem, the nonaqueous sol-gel process was further modified by eliminating the use of solvent [66] and this process is termed as “solventless non-aqueous sol-gel process.” Molecular weight and ceramic residue of some of the poly(borosiloxane)s synthesized by reacting boric acid with organoalkoxysilane or mixtures of organoalkoxysilanes are given in Table 1. It is obvious that

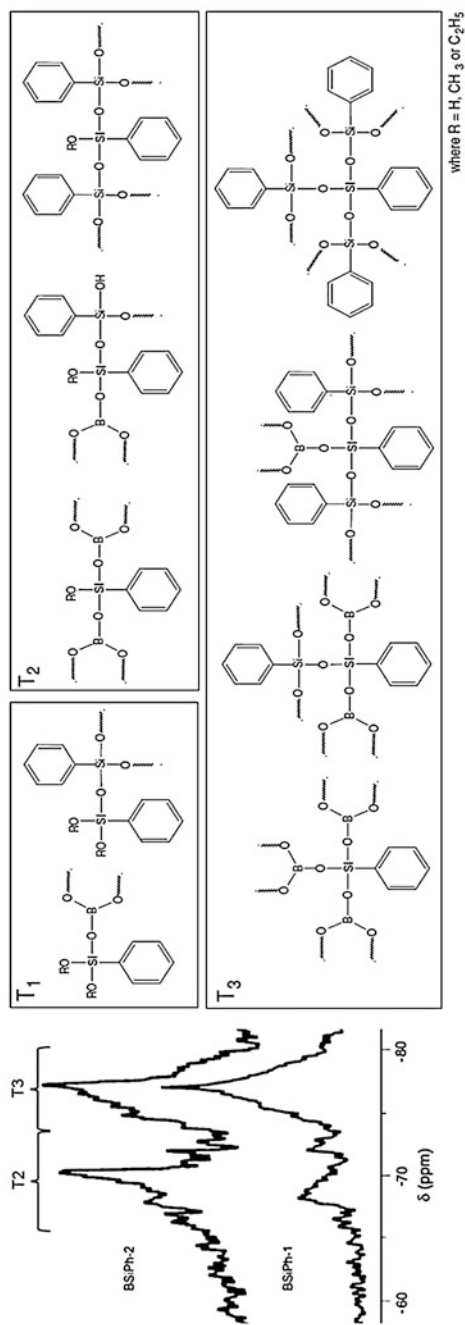


Fig. 11 ²⁹Si NMR spectra and structural units present in poly(phenylborosiloxane)s synthesized from boric acid and PTMOS/PTEOS. (Reproduced from Ref. [63] with permission from Springer Nature)

Table 1 Molecular weight data and ceramic residue of poly(borosiloxane)s synthesized from boric acid and organoalkoxysilanes (1:2 mole ratio)

Alkoxysilane(s)	\bar{M}_w	\bar{M}_{peak}	\bar{M}_n	PDI	Ceramic residue (wt %) at 900 °C	Reference
MTEOS	2160	1460	1760	1.48	84.0	61
PTEOS	1950	1320	1440	1.35	69.0	60
VTEOS	3010	1000	1130	3.01	86.2	60
VTEMOS	2160	1360	1430	1.6	83.7	61,64
GPTMOS	4070	2020	1600	2.54	42.0	60
VTEOS + PTEOS (1:1 mole ratio)	1560	1260	1040	1.24	81.0	62
VTEOS + MTEOS (1:1 mole ratio)	9840	2360	2420	4.07	87.0	62
VTEOS + GPTEOS (1:1 mole ratio)	1810	2840	1760	1.61	56.0	62

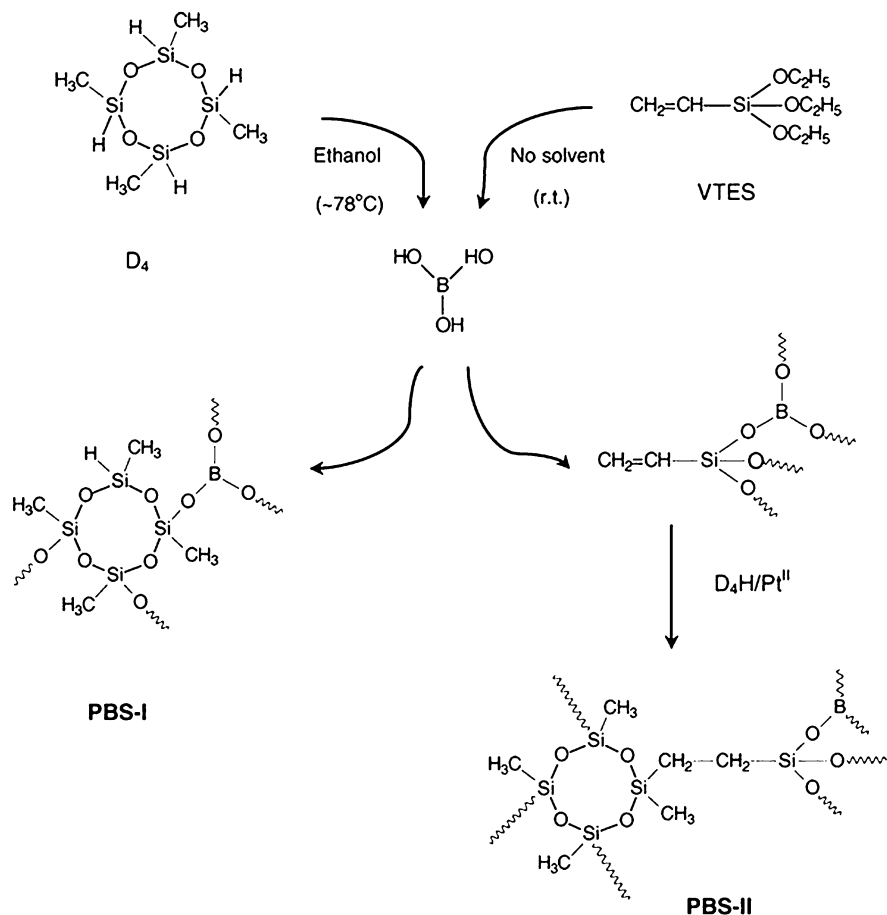
using a mixture of VTEOS and MTEOS is advantageous as it gives borosiloxane oligomer having both higher ceramic residue and molecular weight.

Schiavon et al. [67] synthesized novel poly(borosiloxanes), with a B/Si molar ratio of 0.2 through a dehydrogen coupling reaction of 1,3,5,7-tetramethyl-1,3,5,7-tetracyclo-tetrasiloxane (D_4H) and boric acid, and by hydrolysis/condensation reactions of VTEOS and boric acid, followed by a hydrosilylation reaction with D_4H (Scheme 8). The ceramic yields for PBS-I and PBS-II at 1000 °C were 90.8 wt% and 89.8 wt%, respectively.

Rubinsztajn reported [68] a new synthetic procedure, viz., dehydrocarbon condensation for the preparation of poly(borosiloxane). Trimethyl borate is reacted with diphenylsilane in the presence of tris(pentafluorophenyl)borane in heptane leading to the formation of Si–O–B linkages with the release of methane (Scheme 9). This polymer gave ceramic residue of 54% (at 800 °C in nitrogen atmosphere).

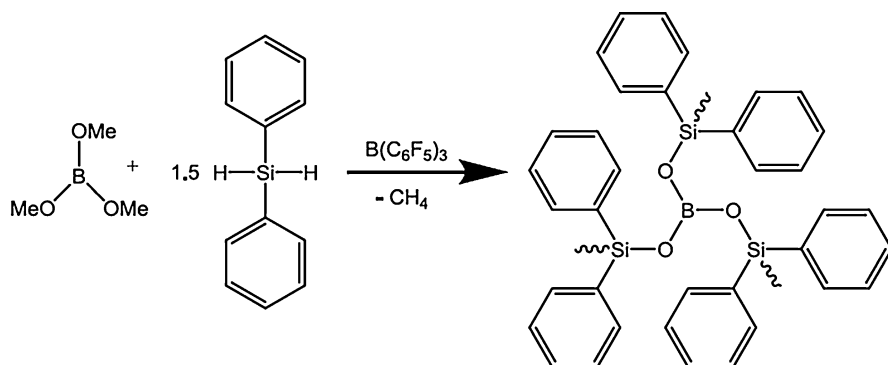
Polyborosiloxanes synthesized from boric acid or its derivatives have boron content of maximum 6–7 wt%. Attempts to incorporate higher boron content by increasing the boric acid to alkoxysilane ratio beyond a certain limit have not been successful as boric acid precipitates from the reaction mixture on standing. One way of improving boron content is by incorporating boron-hydride cage structures in the borosiloxane network. This has been achieved by reacting decaborane (14) [$B_{10}H_{14}$] with 3-aminopropylmethyldiethoxysilane (APMDEOS) in diglyme to obtain ethoxysilyl-functionalized adduct and then reacting it with boric acid [60] in tetrahydrofuran (THF) at 65 °C. It is noticed that the adduct obtained by reacting decaborane and APMDEOS is soluble in THF, whereas the product obtained after the reaction with boric acid is insoluble in organic solvents. This oligomer has boron content of 17.5% and gives a ceramic residue of 86% (boron content of 16.7%) at 900 °C in inert atmosphere.

Ceramic conversion studies of poly(borosiloxane)s: Schiavon et al. [69] investigated the evolution of ceramics from SiBOC glasses and compared them with SiOC glasses using XRD, and ^{29}Si -MAS-NMR and ^{11}B -MAS-NMR spectroscopic



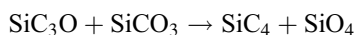
Scheme 8 Synthesis of polyborosiloxanes from cyclic hydrosiloxane (D₄H) and boric acid. (Reproduced from Ref. [67] with permission from Elsevier)

techniques. SiBOC glass was obtained by pyrolysis of borosiloxane gel prepared by sol-gel process from MTEOS and boric acid, and SiOC glass was obtained by pyrolysis of siloxane gel prepared by sol-gel process of MTEOS. Based on the ceramic yield and the chemical analysis it is concluded that SiOC and SiBOC glasses are thermally stable in the temperature range from 1000 °C to 1500 °C. The weight loss is very much limited up to 1500 °C, and the elemental composition is constant, suggesting that the carbothermal reduction between the SiO₂-rich and carbon-rich domains is not active. Thus, the progressive formation of β-SiC nanocrystals, which has been revealed by the XRD study (Figs. 12 and 13) for the SiOC and SiBOC glasses, cannot be ascribed to a decomposition process. It has to be related to a nucleation and crystallization phenomenon that occurs without compositional changes similar to the type of evolution well-known for ternary SiOC glasses.



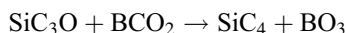
Scheme 9 Synthesis of polyborosiloxane by dehydrocarbon condensation. (Reproduced from Ref. [68] with permission from Springer Nature)

The phase separation into SiC_4 and SiO_4 domains occurs through redistribution reactions of Si–C and Si–O bonds as shown below:



This mechanism is quite local with respect to the silicon atoms and can easily account for the nucleation of very small β -SiC crystals (18 Å at 1500 °C), such as those observed for the ternary SiOC glass. The growth rate of SiC in SiOC glasses is very low because of the extremely high viscosity of the SiOC glass which can be up to 2 or 3 orders of magnitude higher than pure SiO_2 glass. Such a high viscosity suggests an extremely low mobility of silicon and carbon atoms in the SiOC network. The XRD study shows that the addition of boron atoms to the SiOC network increases the crystallization kinetics of β -SiC (Figs. 12 and 13).

Based on ^{29}Si - and ^{11}B -MAS NMR spectral studies, Schiavon et al. [69] suggested that the SiBOC glasses produced at 1200 °C are formed by a homogeneous amorphous network based on mixed siliconoxycarbide and boronoxycarbide units. From 1200 °C to 1400 °C, that is, during the crystallization of β -SiC, the mixed BC_2O and BCO_2 units are consumed and $\text{B}(\text{OSi})_3$ units are formed. This evolution is more pronounced for the SiBOC glass with the highest amount of boron ($\text{B}/\text{Si} = 0.3$). The formation of SiC nuclei occurs through redistribution reactions of Si–C, B–C, Si–O, and B–O bonds that involve, at the same time, mixed silicon oxycarbide ($\text{SiC}_x\text{O}_{4-x}$, $0 \leq x \leq 4$) and boron oxycarbide ($\text{BC}_y\text{O}_{3-y}$, $0 \leq y \leq 2$) units as shown below:



At the end of this process, boron atoms are present in trigonal borosilicate sites, $\text{B}(\text{OSi})_3$, and the amorphous matrix, in which the SiC nanocrystals are dispersed, is regarded as a borosilicate-based matrix [69].

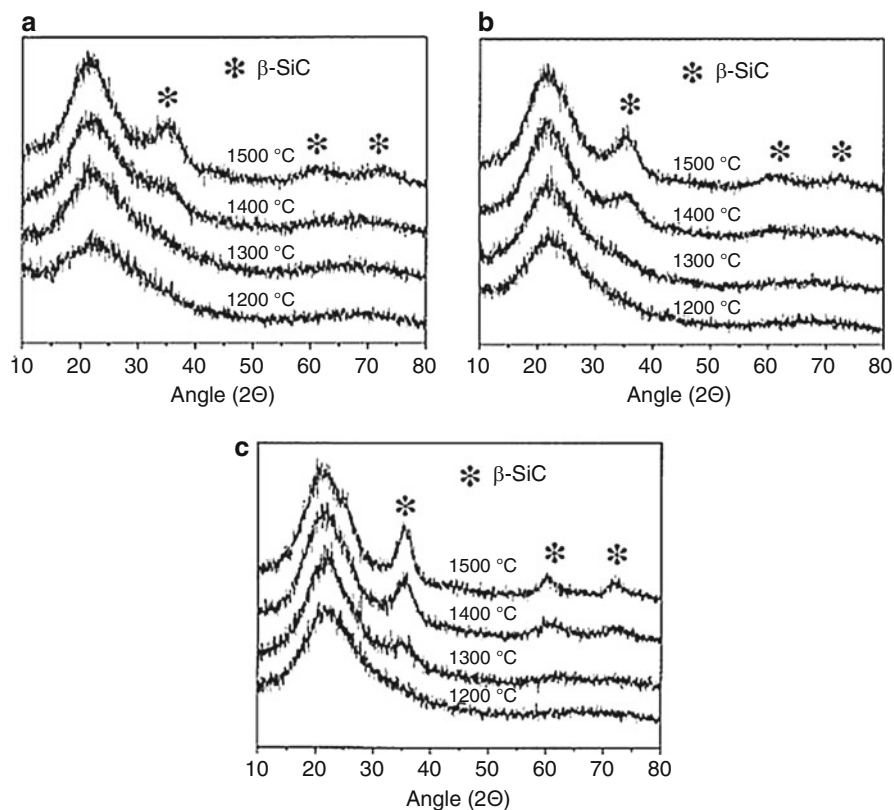


Fig. 12 Evolution of XRD spectra with pyrolysis temperature for (a) pure SiOC glass, (b) SiBOC, B/Si ratio 0.1, and (c) SiBOC, B/Si ratio 0.3. (Reproduced from Ref. [69] with permission from John Wiley and Sons)

Researchers at the Vikram Sarabhai Space Centre [61–65, 70, 71] investigated the ceramic conversion at 900 °C, 1500 °C, and 1650 °C of borosiloxane oligomers synthesized by nonaqueous sol-gel process and by solventless nonaqueous sol-gel process for different monomer feed ratios (described earlier). Varying the monomer feed ratio is expected to influence B/Si ratio in the oligomer which in turn would influence the concentration and distribution of silicon oxycarbide units, boron oxycarbide units, and nanodomains of carbon. The formation of β -SiC nanocrystallite in these systems is explained in line with the exchange reactions proposed by Schiavon et al. [69]. The basic difference between the polyborosiloxane prepared by sol-gel process and the nonaqueous sol-gel process is that in the latter case B-O-Si linkages are formed in the initial (sol) stage itself which could influence the crystallization kinetics.

XRD patterns of ceramics obtained at 900 °C, 1500 °C, and 1650 °C from polyphenylborosiloxane and polyvinylborosiloxane are given in Fig. 14.

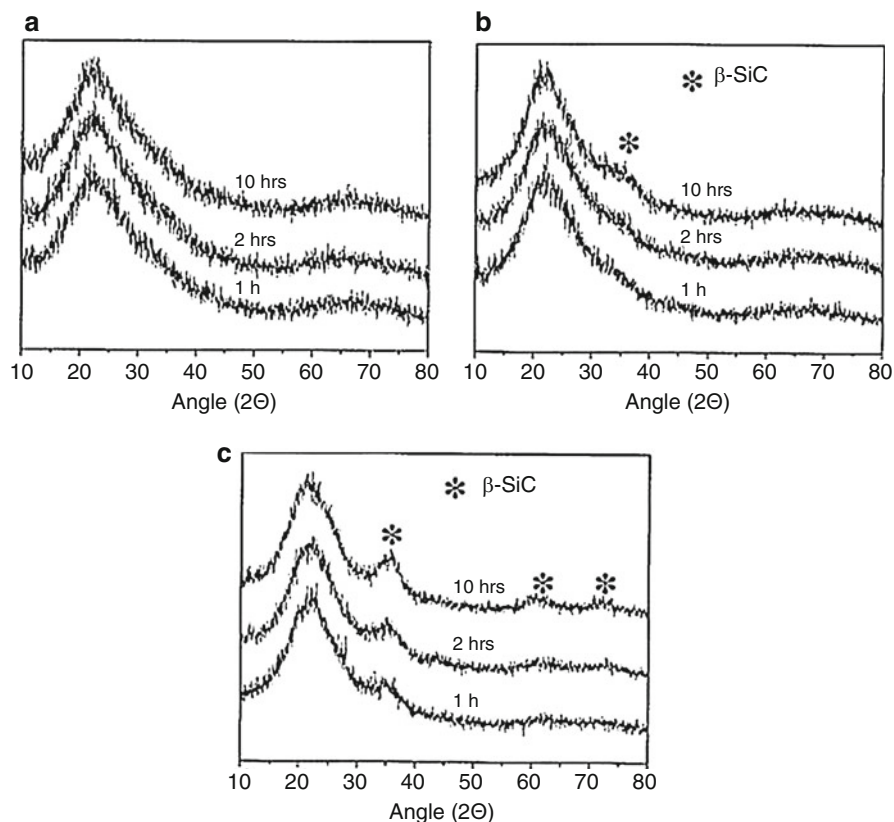
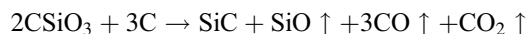


Fig. 13 Evolution of XRD spectra with time during isothermal annealing at 1300 °C for (a) pure SiOC glass, (b) SiBOC, B/Si ratio 0.1, and (c) SiBOC, B/Si ratio 0.3. (Reproduced from Ref. [69] with permission from John Wiley and Sons)

It is seen that up to 1500 °C, the ceramic residue remains amorphous and forms β -SiC at 1650 °C. When the temperature is increased from 1500 °C to 1650 °C, the carbothermal reduction between SiO_2 -rich and carbon-rich domains of the oxycarbide glass is more predominant resulting in the formation of crystalline SiC and volatile species (SiO , CO , and CO_2) [72] as given below:



In variance with the reported observation [63] that poly(phenylborosiloxane) synthesized from PTEOS and boric acid by nonaqueous sol-gel process (in diglyme using HCl as catalyst) does not form β -SiC at 1500 °C, Sreejith [62] observed that SiBOC obtained from poly(phenylborosiloxane) synthesized by solventless nonaqueous sol-gel process undergoes exchange reactions and carbothermic reduction at 1500 °C resulting in the formation of β -SiC under similar

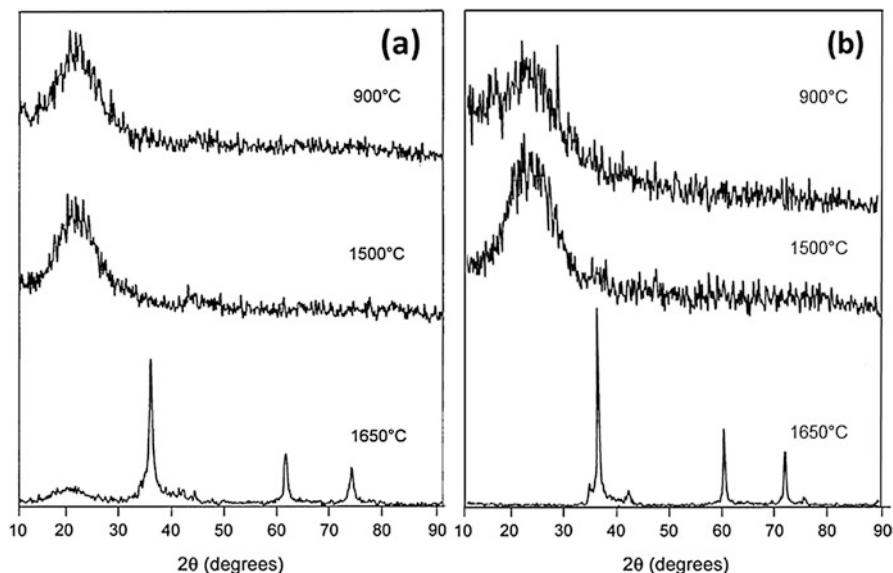


Fig. 14 Evolution of XRD spectra with temperature for ceramic obtained from (a) poly(phenylborosiloxane) and (b) poly(vinylborosiloxane) [60]

heat treatment conditions. It is also observed that boric acid:PTEOS ratio in the monomer feed influences the crystallization characteristics at 1500 °C.

Sreejith [62] also studied the ceramic conversion of borosiloxane oligomers obtained from boric acid and mixtures of organoalkoxysilanes [(PTEOS+VTEOS) (BPV); MTEOS+VTEOS (BMV) and MTEOS+GPTMOS (BMG)] for varying monomer feed ratios synthesized by solventless nonaqueous sol-gel process. It is observed that the crystallization characteristics of borosiloxane oligomers obtained from mixtures of organoalkoxysilane appear to be different from that of borosiloxane oligomers from the corresponding organoalkoxysilanes particularly at 1500 °C. Unlike polyphenylborosiloxane, poly-vinylborosiloxane, and BPV systems, for BMV and BMG systems, SiBOC ceramic obtained by pyrolysis at 900 °C was quite stable at 1500 °C and even at 1650 °C considerable amount of SiBOC glassy phase was observed suggesting that reducing the carbon content in the SiBOC ceramic has a profound effect on the crystallization characteristics. Zhang et al. [73] claimed that sol-gel derived SiBOC ceramic from methyltrimethoxysilane (MTMOS) and MTEOS mixture and boric acid on heat treatment at 1600 °C resulted in the formation of β -SiC nanocrystals and free carbon. Structural analysis by TEM and Raman spectral analysis suggests the presence of highly graphitized free carbon at 1600 °C. Turbostratic graphite with 10–20 layers of graphene is clearly observed in TEM, confirming the significant promoting effect of B on the graphitization of free carbon (Fig. 15).

Devapal [60] studied the ceramic conversion of $B_{10}H_{12}$ -cage containing borosiloxane oligomer (BSiDB-1) having high boron content (17.5%). It gives

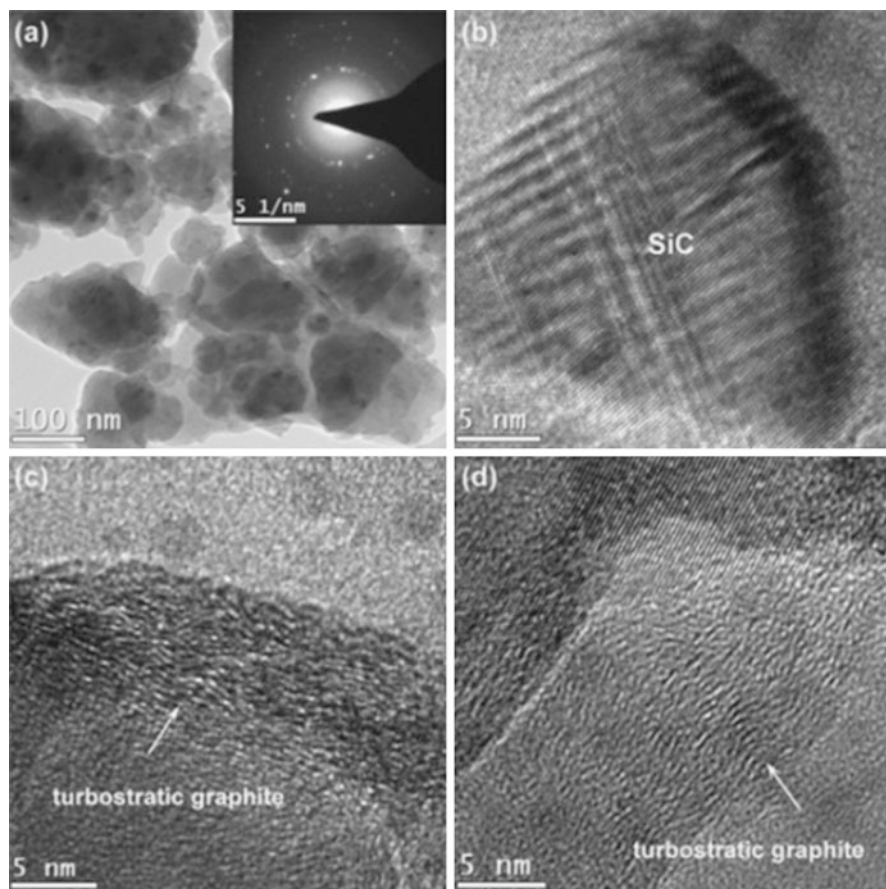


Fig. 15 HRTEM images of ceramic from sol-gel derived borosiloxane prepared from MTMOS and MTEOS mixture and boric acid. (Reproduced from Ref. [73] with permission from Elsevier)

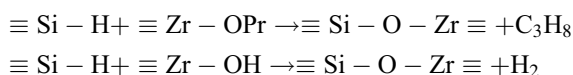
mixed non-oxide ceramics containing nanocrystallites of β -SiC (53.9 nm) and h-BN (25.7 nm). It is interesting to note that BSiDB-1 on heat treatment at 1650 °C does not give B_4C . This is attributed to the absence of direct B-C bond in the oligomer where boron atom of decaborane is directly attached to the nitrogen atom of the Lewis base.

Devapal [60] synthesized glass forming borosiloxane oligomers by nonaqueous sol-gel process. The advantage of this approach is that there is molecular level distribution of Si-O and B-O units and, hence, would give a glass with uniform composition compared to the one obtained by melting of SiO_2 - B_2O_3 mixture. The oligomers give ceramic residue in the range of 73–80% at 900 °C in argon atmosphere. XRD studies suggest that the glass formed from this type of oligomer is quite stable, and formation of crystalline SiO_2 (cristoballite) is not noticed even after annealing at 1650 °C for 2 h in argon atmosphere.

Polymetallosiloxanes

Inorganic polymers closely related to the polyorganosiloxanes are the polymetallosiloxane polymers. Initial interest on polymetallosiloxane is to improve the thermal stability of siloxane backbone through the incorporation of metal. As the metallosiloxane bond in the main chain is easily converted to oxide ceramic materials, polymetallosiloxanes are used as precursors for $\text{SiO}_2\text{-M}_x\text{O}_y$ ceramics in the form of fibers, thin films, bulk bodies, and fine powders [74]. Polymetallosiloxanes were synthesized by the reaction of silicic acid or partially hydrolyzed tetraethoxysilane with a metal chelate compound, metal alkoxide, or metal chloride [54, 75]. The polymetallosiloxanes are, however, random copolymers of siloxane domain and metallosiloxane domain, because it is difficult to control their microstructure by conventional synthetic techniques. Over the years, with the advancements in the field of polymer-derived siliconoxycarbide ceramics, polymetallosiloxanes are considered more as precursors for metal modified SiOC ceramics rather than as precursors for $\text{SiO}_2\text{-M}_x\text{O}_y$ oxide ceramics. The thermal alteration of hybrid polydimethylsiloxane–titania nanometer sized composites (nanocomposites) has been studied up to 1600 °C to determine the changes of SiOC phase as a function of temperature and titania content. The samples were prepared by the sol-gel method starting from molecular precursors, diethoxydimethylsilane, and titanium isopropoxide. Between 500 °C and 800 °C, the polymer-to-ceramic conversion takes place for all samples with the formation of different oxycarbide phases and the structure of SiOC and titanium oxycarbide phases has been influenced by the titania content in the gel [76].

Liu et al. [77] obtained SiOC and SiZrOC ceramics starting from the hydrosilane system without and with zirconium-n-propoxide $[\text{Zr}(\text{OPr})_4]$ by sol-gel route. The precursor structure indicated that the presence of Si-H bonds led to a different cross-linking mechanism of SiZrOC precursor, where the Si-H bonds were involved in the formation of Si-O-Zr bonds as shown below:



The presence of Zr caused a lower content of sp^3 carbon in SiZrOC ceramics. At above 1400 °C, the sp^3 carbon to silicon ratio in both ceramics increased due to carbothermal reduction, especially rapidly for SiOC ceramics, suggesting the carbothermal reduction in SiZrOC ceramics has been strongly suppressed by the presence of ZrO_2 .

Ionescu et al. [78] prepared polymer-derived SiOC/ ZrO_2 ceramic nanocomposites by modification of polysilsesquioxanes with zirconium alkoxide to incorporate Zr in the siloxane network structures. Umicevic et al. [79] studied the evolution of the environment of Hf sites in a hafnium-alkoxide-modified polysilsesquioxane upon polymer-to-ceramic transformation via the perturbed angular correlation (PAC) method. The results of the PAC measurements on samples thermally treated at temperatures from 400 °C to 1300 °C indicate that Hf is surrounded only by oxygen at all studied temperatures. This finding is in agreement with the

evolution pathway of polymer-derived SiHfOC ceramics, which were reported to be generated as single-phase amorphous materials upon pyrolysis of alkoxide-modified polysiloxanes and subsequently to phase separate and crystallize toward HfO₂/SiOC nanocomposites.

SiZrOC fibers were prepared from polyzirconosiloxane gels by using polyvinylpyrrolidone as spinning agent [80]. Yan et al. [81] prepared polyhafnosiloxane (PHfSO) by a sol-gel process of a mixture of TEOS, HfCl₄, and dimethyldiethoxysilane. Pyrolysis of PHfSO gel fibers yields dense SiOC/HfO₂ fibers with high ceramic yield of 81 wt%. The SiOC/HfO₂ fibers have tensile strength of 930 MPa and exhibit good thermal stability up to 1500 °C.

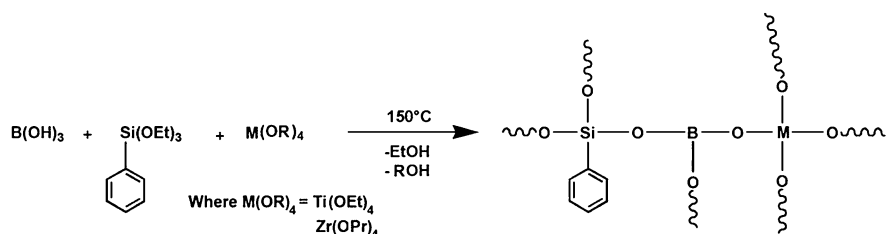
Polymetalborosiloxanes

A new class of precursors, viz., polymetalborosiloxanes, was synthesized by Swaminathan [22] from boric acid, alkoxysilane, and metal alkoxides which were evaluated as precursors for metal-modified SiBOC ceramics. Titanoborosiloxanes and zirconoborosiloxane oligomers were synthesized by reacting titanium tetrathoxide and zirconium tetrapropoxide, respectively, with boric acid and phenyltriethoxysilane by solvent less process (Scheme 10).

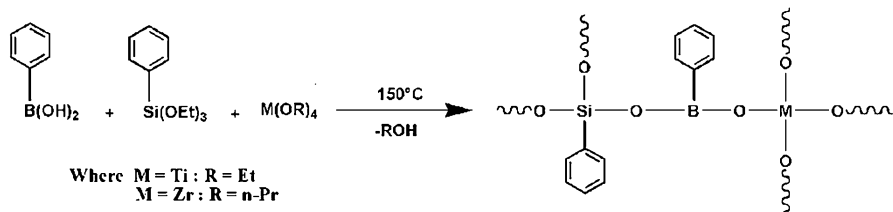
Heat treatment of titanoborosiloxane oligomers in argon atmosphere at 900 °C, results in the formation of TiO₂ (Anatase) and TiO₂ (Rutile). When the heat-treatment temperature is increased to 1500 °C and 1650 °C, formation of titanium sub-oxides is observed which is attributed to the reaction of TiO₂ (Rutile) with free carbon formed from the oligomer. Mixed non-oxide ceramics, viz., SiC-TiB₂ and SiC-B₄C-TiB₂, are formed when titanoborosiloxane mixed with graphite powder and elemental boron, respectively, are heat treated at 1500 °C [22]. Zirconoborosiloxane oligomer was completely converted into mixed non-oxide ultra-high temperature ceramic, viz., ZrB₂-SiC-ZrC ceramics, by carbothermic reduction at 1500 °C using phenolic resin as the source of carbon.

In an attempt to increase the carbon content of the ceramics, titanoborosiloxane (TPhBS) and zirconoborosiloxane (ZPhBS) oligomers were synthesized by reacting phenyl boronic acid (in place of boric acid), PTEOS and Ti(OEt)₄/Zr(OPr)₄ in 1:1:1 mole ratio by solventless nonaqueous sol-gel process (Scheme 11) [22].

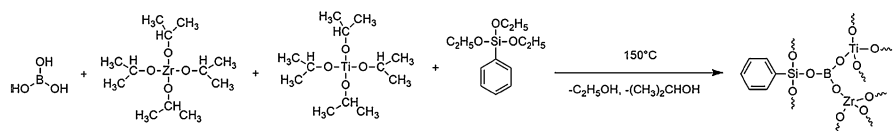
Unlike ZBS synthesized from boric acid, ZPhBS was soluble in common organic solvents even after the removal of the by-products ethanol and propanol. The



Scheme 10 Synthesis of polymetalborosiloxanes [22]



Scheme 11 Synthesis of metalloborosiloxanes from phenyl boronic acid [22]



Scheme 12 Synthesis of zirconotitanaborosiloxane oligomer. (Reproduced from Ref. [82] with permission from Springer Nature)

improved solubility of ZPhBS compared to that of ZBS is attributed to the presence of phenyl group in the former. TPhBS and ZPhBS give ceramic residue of 72% and 68%, respectively, at 900 °C. Ceramic conversion studies of TPhBS and ZPhBS at 1500 °C suggest that the ceramic from TPhBS consists of Ti_3O_5 and TiC in the wt. ratio of 93:7, whereas the ceramic from ZPhBS consists of m-ZrO₂, t-ZrO₂, and ZrSiO₄ (Zircon) in the wt. ratio of 59:20:21. This suggests that under the chosen experimental conditions, titanium oxide ceramics undergo carbothermic reduction more readily than the zirconium oxide ceramics. Raman spectral studies suggest that amorphous carbon present in TPhBS-derived ceramic is consumed during the heat treatment for carbothermic reduction whereas it remains unreacted in ZPhBS-derived ceramic.

In a recent study, Anurag et al. [82] reported the synthesis of zirconotitanaborosiloxane (ZTBS) which gave a ceramic residue of ~58% at 900 °C in argon atmosphere. On borothermal reduction at 1500 °C of ZTBS, oxide free mixed UHTC was obtained (Scheme 12).

Zhang et al. [83] recently reported the synthesis of a precursor for SiZrBOC ceramic. The precursor was synthesized by reacting boric acid with methyltriethoxysilane and zirconylchloride octahydrate by sol-gel process followed by solvothermal process at 130 °C. SiZrBOC ceramic is obtained in 84% yield at 1400 °C and is quite stable in air up to 1400 °C.

Polysilazanes and Polycarbosilazanes

Polysilazanes and polycarbosilazanes are characterized by having a -Si-N- backbone or a -R-Si-N- backbone, respectively [84]. They are generally prepared either by ammonolysis or aminolysis of organochlorosilanes. Ammonolysis of MeHSiCl_2 resulted in a cyclic silazane $(\text{MeSiHNH})_{3-4}$ and a linear polymer (Scheme 13).



Scheme 13 Synthesis of polysilazane [84]

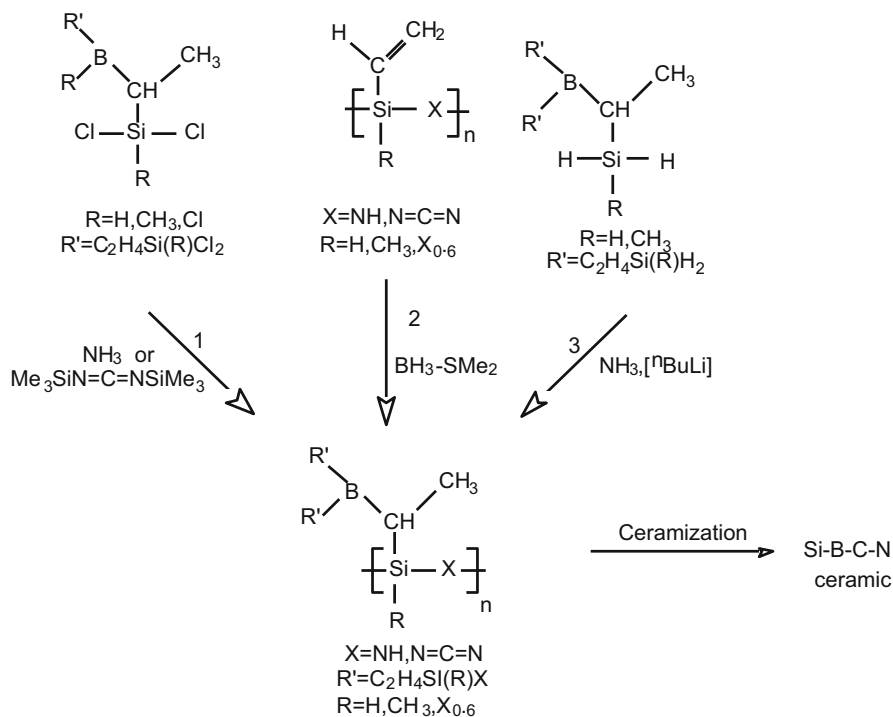
Synthesis of polysilazanes and polycarbosilazanes and their conversion to Si-N and Si-C-N ceramics have been extensively reviewed [85–87], and hence, a detailed account of the chronological development has not been included in the present chapter. However, some of the recent research work has been included in this chapter.

Wang et al. [88] reported the synthesis of ethynyl-terminated silazane precursors which gave ceramic residue of 84% at 900 °C. This precursor on heat treatment at 1450 °C gave mixed non-oxide ceramics (SiC and Si₃N₄ and free C). Jun et al. [89] reported laser pyrolysis of polysilazane precursor using Nd:YAG laser to SiC, and the complete transformation from organic to inorganic had taken place when the laser scanning power was 600 W. This procedure was useful for obtaining SiC coating on steel substrate. Sun et al. [90] studied the ceramic conversion of polyvinylsilazane with ZrB₂ filler. SiCN matrix formed from polyvinylsilazane remained amorphous up to 1400 °C in argon, and XRD studies indicated the presence of ZrO₂ at 1100 °C, ZrC/ZrN at 1200 °C, and Zr₂CN at 1500 °C which account for the improved high temperature stability of the ceramic.

Polymeric Precursors for SiBCN Ceramics

In order to enhance the properties of SiCN ceramics, boron atoms were added at molecular level to obtain boron-modified silicon carbonitride ceramics. SiBCN ceramics retain their amorphous nature even above 1440 °C due to the formation of B(C)N layers which prevented carbothermic reduction of SiCN ceramic phases by surrounding them. A review by Viard et al. [91] highlights the preparation of PDC fibers with a special focus on amorphous SiCN and SiBCN networks using melt-spinning and electrospinning processes. Niebylski [92] synthesized organoborosilazane polymers by reacting polysilazane with trialkoxy, triaryloxy, or tri(aryloxy)boroxine. Chemical modification of hydridopolysilazane was performed by reacting it with liquid borazine at low temperatures to obtain boron-modified polysilazane [93]. Chemical modification of hydridopolysilazanes with monofunctional boranes such as pinacolborane (Me₂CO)₂BH, 1,3-dimethyl-1,3-diaza-2-borocyclopentane (CH₂NMe)₂BH, and 2,4-diethylborazine (Et₂B₃N₃H₄) has also been reported [94].

The synthesis and thermal behavior of boron-modified polysilazanes {B[C₂H₄Si(R)NH]₃}_n and polysilylcarbodiimides {B[C₂H₄Si(R)NCN]₃}_n were reported by Aldinger and Weinmann (Scheme 14) [95]. These SiBCN ceramic precursors were obtained by treating vinyl-substituted polysilylcarbodiimides [(H₂C=CH)(R)-SiNCN]_n with borane-dimethyl-sulfide BH₃·S(CH₃)₂. The polysilylcarbodiimides themselves were synthesized via treatment of vinyl-substituted chlorosilanes (H₂C=CH)(R)SiCl₂ with cyanamide, H₂N-C≡N, in presence of pyridine, or via



Scheme 14 Synthesis of boron-modified silazanes. (Adopted from Ref. [95])

the reaction of the vinyl-substituted chlorosilanes with bis(trimethylsilyl) carbodiimide. The synthesis by a novel reaction pathway and the polymer-to-ceramic conversion of boron-containing polysilylcarbodiimides were reported by Weinmann et al. [96]. Reaction of tris(hydridosilylethyl)boranes with different amounts of cyanamide in THF followed by thermolysis of such compounds in an argon atmosphere affords SiBCN ceramics in 65–85% yield.

Sarkar et al. [97] synthesized SiBCN ceramic precursor through a simple dehydrocoupling and hydroboration reaction of an oligosilazane containing amine and vinyl groups with $(\text{BH}_3)\text{Me}_2\text{S}$. This modified precursor was pyrolyzed to obtain SiBCN ceramics. Solid-state NMR studies indicated that ceramics formed were a mixture of hexagonal boron nitride along with turbostratic boron nitride and BN_2C ceramics. Increasing pyrolysis temperature leads to the transformation of BN_2C groups into BN_3 and “free” carbon. Gao et al. [98] studied the significance of the processing route on the nanostructure evaluation of carbon-rich SiCN and SiBCN ceramics. Bulk carbon-rich SiCN and SiBCN ceramics were successfully produced by hot pressing of polyphenylvinyl and polyborophenyl-silylcarbodiimide.

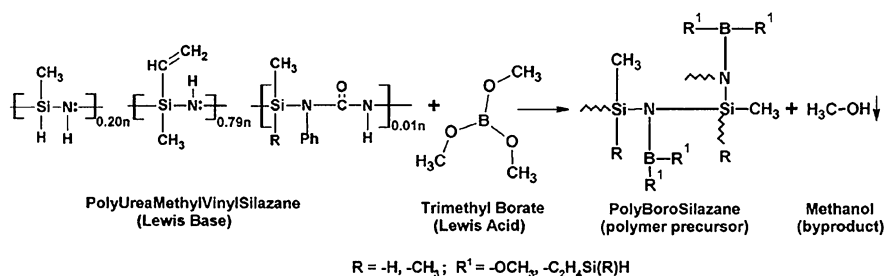
Five different SiBCN polymeric precursors with B/N atomic ratios ranging from 1:3 to 1:0.5 were synthesized by Muller et al. [99] and converted to ceramics by thermolysis at 1400 °C in 70–75% yield. Yu et al. [100] prepared polyborosilazane

precursors for SiBCN ceramics by using 9-borabicyclo-[1,3,3] nonane and copolysilazanes as starting materials, involving the hydroboration reaction between vinyl groups of polysilazane and B–H groups of 9-BBN under mild conditions and converted to ceramics. The crystallization behavior and microstructures of PBSZ-derived SiBCN ceramics reveal that the crystallization begins at 1600 °C. Further heating at 1800 °C gave XRD patterns for mixed SiC, Si₃N₄, and BN(C). It is observed that the introduction of boron improves the thermal stability and ceramic density while inhibiting the SiC crystallization. Singh et al. [101] reported boron-modified silazane liquid precursor by reacting polyureamethylvinylsilazane with ethylborate (Scheme 15), and this precursor was used for preparing SiBCN-coated MWCNT.

Using this precursor, nanocomposites with CNTs were also prepared which can be applied as hard, lightweight coatings on turbine blades, or on clothing. Dispersion of CNTs, fullerenes, and other nanofillers within the ceramic matrix results in nanocomposites with tunable semiconductor properties [102]. The introduction of CNTs in nanocomposites resulted in increased heat resistance to 15,000 W/cm²-about 10 times greater than heat experienced by rocket nozzles.

A new kind of polyborosilazane was synthesized by Zeng et al. [103] from hexamethylcyclotrisilazane by exposure to borontrichloride. Heat treatment of the polymer at 1800 °C resulted in BN crystals. Schiavon et al. [104] synthesized polyborosilazanes with varying Si/B molar ratios, via hydroboration, of vinyl-substituted cyclotrisilazane, [CH₂=CH(CH₃)SiNH]₃, with BH₃.N(CH₃)₃. The polyborosilazanes were pyrolyzed up to 1000 °C under argon atmosphere, which resulted in amorphous SiBCN glasses. The SiBCN glass with B/Si = 3 was amorphous up to 1700 °C, and at this temperature, β-SiC and β-Si₃N₄ were formed. At 2000 °C, β-SiC and BN were formed.

Ganesh and Renjith [105] reported a simple and low cost route for preparing SiBCN precursors by reacting boric acid with 1,3,5-trimethyl-1',3',5'-trivinylcyclotrisilazane (CTS) in the molar ratio of 1:1, 1:3, and 1:5. The changes in CTS concentration have affected the ceramic phases, morphology, and elemental composition of ceramics obtained from boron-modified CTS (BCTS). The results revealed the formation of β-SiC, β-Si₃N₄, and oxide ceramic phases with BCTS for the molar ratios of 1:1 and 1:3, whereas turbostratic BN(C) ceramic phase was formed in addition to other phases with BCTS in the molar ratio of 1:5.



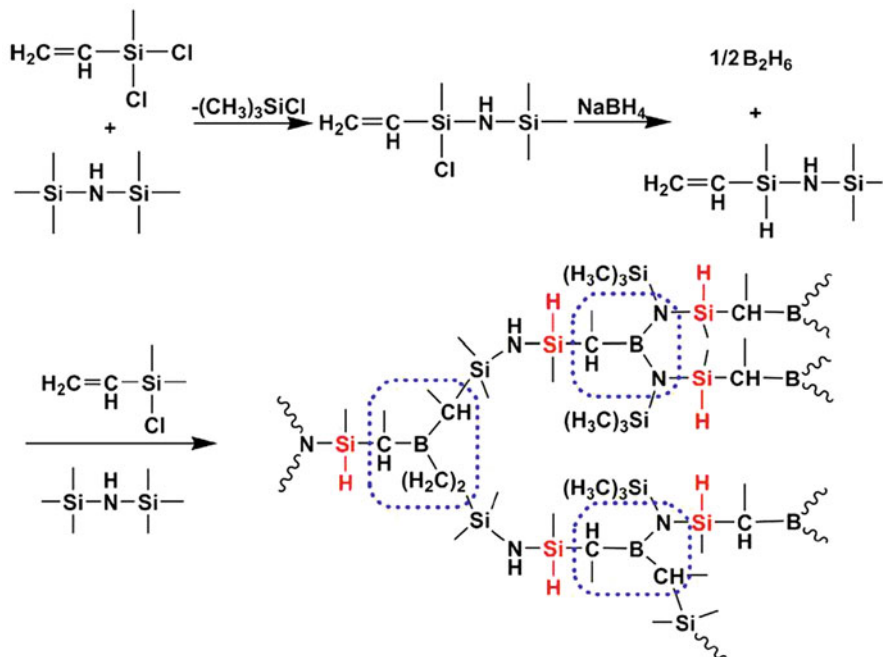
Scheme 15 Synthesis of boron-modified polysilazane [101]

Polyorganoborosilazane was synthesized via monomer route from a single-source precursor and thermolyzed at 1300 °C in argon atmosphere by Kousaalya et al. [106]. The crystallite size was found to increase from 2 nm to 8 nm with increase in dwelling time. A liquid polymeric precursor to SiBCN ceramics was synthesized via dehydrogenation of polymethylsilane and borazine by Wang et al. [107]. Si-H bonds in polymethylsilane react with N-H or B-H bonds in borazine to form cross-linked polymer with viscosity of 850 mPa.s which gave β -SiC and Si₃N₄ crystals on heat treatment at 1600 °C. Si/C/N/H polymers with Si:C atomic ratios ≥ 1 were synthesized by Gerstel et al. [108] through Wurtz-type coupling and subsequent ammonolysis of ClSiH(Me)NHSiH(Me)Cl and MeSiHCl₂ or H₂SiCl₂. These polymers were subsequently reacted with a borane to obtain three different precursors which were transformed into SiBCN ceramic materials by thermolysis at 1400 °C. The high-temperature behavior up to 2150 °C was investigated by thermogravimetric analysis and XRD.

Liu et al. [109] reported the self-healing mechanism of SiBCN ceramics derived from hyperbranched polyborosilazanes. The self-healing ability of cracks was enhanced at 1000 °C in air with the increase of oxidation time. The ceramics with high content of boron show much more obvious self-healing performance due to the formation of SiO₂, B₂O₃, and B₂O₃·SiO₂ which fill the crack and prevent the damage of substrates. Bechelany et al. [110] investigated spark plasma sintering in the temperature range of 1500–1900 °C at 100 MPa to obtain SiBCN monoliths from SiBCN powders prepared from boron-modified polycarbosilazane in nitrogen or ammonia atmosphere. Lee et al. [111] reported an easy and cost-effective precursor for SiBCN by reacting trichlorosilane, borotrichloride, and hexamethyldisilazane at a mole ratio of 1:1:4.

Zhao et al. [112] synthesized liquid polyborosilazane through a novel method which used sodiumborohydride as boron source. The reaction sequence is given in Scheme 16. Vinylmethylchlorosilane was reacted with hexamethyldisilazane and the resultant product was reacted with sodium borohydride to obtain polyvinylsilazane with Si-H groups. This product was further reacted with dimethylvinylsilane and hexamethylenedisilazane. Vinyl groups present in the precursor underwent hydroboration reaction with diborane formed from sodium borate in the earlier step. The SiBCN ceramic formed at 1400 °C contained B-N, Si-N, and Si-C bonds with smooth and dense surface and still retained principally amorphous structure up to 1600 °C. In addition, the viscosity of the polyborosilazane was 65 mPa.s, and hence, found application as precursor for PIP process for the fabrication of CMCs.

In a simplified reaction process, SiBCN precursors were synthesized by one step co-condensation of propylamine, BCl₃, and SiCl₄/SiHCl₃ [113]. These polymers gave ceramic residue of about 65% at 900 °C in nitrogen atmosphere. Type of ceramics formed from polyborosilazane precursor depends on the atmosphere used for pyrolysis. Ceramics formed under nitrogen undergoes carbothermal reduction with Si-N bonds and free carbon at above 1650 °C to form SiC, whereas the same precursor sintered in ammonia atmosphere did not undergo carbothermal reduction and remained as Si₃N₄ and BN at 1650 °C [110]. Ceramic conversion of polyborosilazane in air resulted in SiBCNO ceramics along with nano quartz and



Scheme 16 Synthetic route for poly(borosilazane) containing active Si-H group. (Reproduced from Ref. [112] with permission from Elsevier)

amorphous B_2O_3 [114]. Tamayo et al. [115] converted sol-gels prepared by reacting TEOS, 3-APTES, triethylborate, and hydroxyl-terminated polydimethylsiloxane with SiBCNO ceramics by carrying out pyrolysis under nitrogen followed by ammonolysis using NH_3/N_2 gas mixture. During pyrolysis nitrogen atom was effectively incorporated in the ceramics without replacing carbon. Less graphitized structure was observed due to the reduced mobility of carbon atoms in the mixed (B)CN bonds [115]. SiBN ceramic fibers with less than 0.1 wt% carbon were obtained from polyborosilazane precursor synthesized from hexamethyldisilazane, HSiCl_3 , BCl_3 , and CH_3NH_2 using a multistep polymerization process [116] and a single step polymerization process [117].

Metal Modified Precursors for SiCN Ceramics

Similar to the modification of polysilazane to boron-modified polysilazane, polysilazanes can be easily modified with aluminum and transition metal alkoxides/metal amido complexes to form $\text{Si}(\text{M})\text{CN}$ ceramics where M is Al, Ti, Zr, Hf, etc. Different synthetic approaches for metal modified polysilazane or polysilacarodiimides were reviewed by Mera et al. [12] and Ionescu et al. [118]. The ceramic formed from these precursors depends on the chemical composition of precursor and the atmosphere in which ceramic conversion was carried out. Aluminum-modified polysilazanes referred to as polyaluminosilazanes were synthesized by reacting polysilazane with

aluminum-containing monomers such as $\text{Al}(\text{CH}_3)_3$, AlH_3 , $(\text{CH}_3\text{CH}_2)_3\text{Al}$, $(\text{CH}_3)_2\text{AlNH}_2$, and aluminum trialkoxide, and these precursors on thermal conversion gave SiAlCN ceramics in high yield [119]. Polymer-derived SiAlCN exhibited much better oxidation and hot-corrosion resistance than other silicon-based ceramics at temperatures up to 1400 °C [120], which makes this material suitable for making micro-sensors and MEMS devices for harsh environments. Oxidation studies revealed that SiAlCN possesses a lower oxidation rate than SiCN. The better oxidation resistance of SiAlCN is attributed to the oxide layer containing Al, which slowed down oxygen diffusion relative to that with pure SiO_2 .

Ceramics from Carbonaceous Polymers

Phenolic resins are extensively used in the production of composite materials especially for phenolic resin-carbon fabric composites. In line with the developments in the area of high temperature materials, phenolic resins were also evaluated as precursors for carbide ceramics, especially SiC. The thermosetting property of phenolic resins can be effectively made use of in the preparation of complex ceramic components. For preparing SiC, phenolic resin is first mixed with silicon or silicon compounds and cured, and then the cured material is heat treated at 1500 °C or above.

SiC ceramic powders were synthesized by reacting/mixing phenolic resins with any of the silicon sources such as elemental silicon [121], silica formed by sol-gel process [122], fumed silica [123], and rice husk silica [124] followed by reaction sintering. Phenol-furfuraldehyde resin was also used as carbonaceous polymer in place of phenol-formaldehyde resin for obtaining SiC [125]. SiC powders were synthesized by the coat-mix process, with phenolic resin and silicon powders as starting materials [121]. The results show that higher sintering temperature and close to stoichiometric equivalence of carbon and silicon are required for producing high purity SiC powders. As the sintering temperature is raised to 1500 °C, the formation of SiC occurs which is based on the liquid-solid reaction. High purity SiC (99.8 wt%) powders can be easily obtained by this method. Tetraethoxysilane and phenolic resin were used for preparing a homogeneous binary carbonaceous silica xerogel, and nickel nitrate was employed as a pore-adjusting reagent.

From phenolic resin, SiC porous structures [122, 123], SiC coating [126], SiC ceramic wires [124, 125], SiC hollow spheres [127], SiC fibers [128], and SiC/SiC composites [129] were prepared. Porous SiC ceramics with hybrid pore structure, which is a combination of tubular pores and network SiC struts in the tubular pores, were fabricated via sol-gel conversion of carbonized pine wood with phenolic resin/ SiO_2 sol followed by carbonization and carbothermal reduction reaction at elevated temperatures in argon atmosphere [122]. Phenol-furfuraldehyde resin-elemental Si mix on sintering at 1500 °C gave nano β -SiC powder along with SiC wires/fibers having diameter in nano to submicron range [125]. Prabhakaran et al. [125] observed that in the XRD pattern of SiC wires/fibers the diffraction line corresponding to $\langle 220 \rangle$ plane at $2\theta = 59.95$ has the highest relative intensity (Fig. 16), and it differs

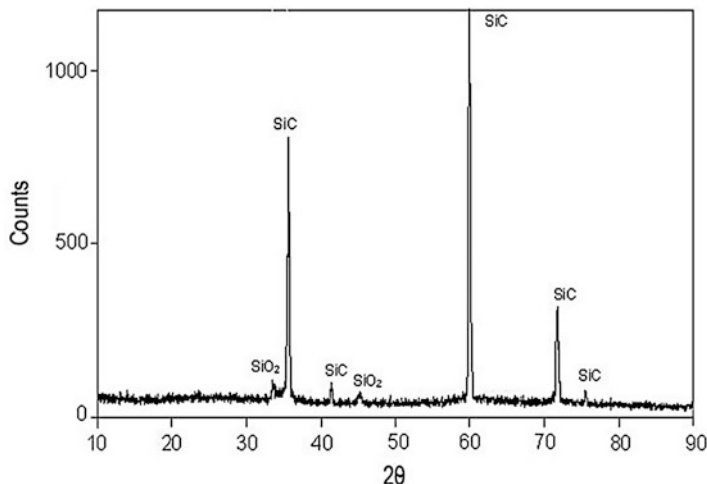


Fig. 16 XRD pattern of SiC ceramic wires from phenol-furfuraldehyde and elemental silicon. (Reproduced from Ref. [125] with permission from Springer Nature)

from the standard powder diffraction pattern of β -SiC where multi-oriented random crystals with $\langle 111 \rangle$ plane at $2\theta = 35.96$ showed the highest intensity. This is attributed to formation of single crystalline SiC formed with orientation along $\langle 111 \rangle$ plane.

Hollow spheres of phenolic resin/silica composite were synthesized by macroscopic phase separation during aerosol-assisted spraying [127]. The spheres were converted into carbon-silica hollow spheres by pyrolyzing at $900\text{ }^\circ\text{C}$, which on further heat treatment at $1450\text{ }^\circ\text{C}$ were converted into SiC hollow spheres.

SiC fibers are particularly desirable reinforcement materials for a variety of composites because of their thermal and oxidation resistance as well as high tensile strength and Young's modulus. However, SiC fibers are expensive both because of the costly precursors and the number of steps involved in this process. A cost-effective route is reported for SiC fibers, requiring only two steps: synthesis of silicon dioxide-organic hybrid fibers by sol-gel processing and the carbothermal reduction of the hybrid fibers in an argon atmosphere [128]. Advantages of this process include the relative low-cost of the starting materials, the two-step process, and the high purity of the SiC fibers produced.

Phenolic resins were also used for preparing multicomponent ceramics and ultra-high temperature ceramics [130–139]. Phenolic resin was used as an effective source that could provide free carbon for fabrication of the SiC nanoparticles by in situ reaction with Si_3N_4 and SiO_2 [130]. Sizes of the formed SiC particles were in the range of 50–300 nm. Limited quantity addition of polymer resulted in high porosity whereas excessive additions caused agglomeration of residual carbon and SiC, creating fatal flaws in the final material.

Hybrid gels were synthesized from liquid mixtures composed of TEOS, titanium tetraisopropoxide/titanium tetrakis(2,4-pentadionate), and phenolic resin [131, 132],

and these gels on pyrolysis at 1500 °C yielded SiC-TiC ceramics. Si-B-C ceramic composites were prepared using SiB₆, B₄C, and phenolic resin as a carbon source by pressure-less sintering in argon atmosphere to determine their potential for applications as high hardness and high temperature composites [133]. XRD patterns of the sintered bodies show the presence of B₄C and SiC. Aluminum-containing carbide, Al₄SiC₄, was successfully synthesized using a mixture of Al(OH)₃, SiO₂, and phenolic resin by a carbothermal reduction process [134]. Phenolic resin-TaCl₅ precursor was recently used for preparing nanocrystalline TaC powder [135]. Porous Si₃N₄ ceramics with gradient distributions of SiC and pores were fabricated by directional nitridation sintering of diatomite preforms with phenolic resin as a carbon source and pore forming agent [136]. Ganesh Babu and Devasia [137, 138] modified phenolic resin with boric acid and the modified resin was reacted with Si to obtain self-healing ceramic matrix comprising of SiC, B₄C, and SiB₆. On oxidation, borosilicate glass is formed which heals the cracks thereby preventing the inward diffusion of oxygen.

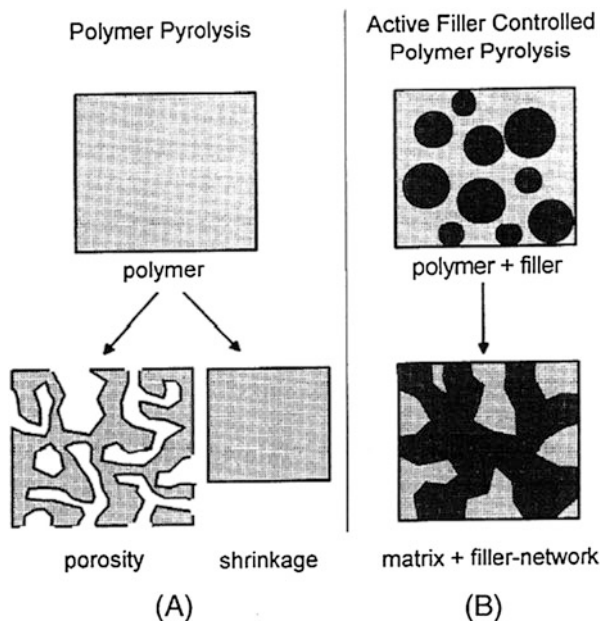
In a recent study, ZrB₂-SiC ceramic powder was synthesized by mixing zircon (ZrSiO₄) and B₄C powders with phenolic resin in 6.6:1:3.6 wt. ratio followed by heat treatment at 1500 °C and 1650 °C [140]. XRD patterns of the ceramic indicate that the ceramic conversion was incomplete at 1500 °C and contains unreacted zircon along with SiO₂ and ZrB₂. When the temperature was increased to 1650 °C, the oxide impurities were converted into ZrB₂-SiC. It is worth noting that zirconoborosiloxane oligomers mixed with phenolic resin was converted completely into ZrB₂-SiC ceramics at 1500 °C [22].

Active Filler Controlled Pyrolysis (AFCOP)

Production of bulk ceramics from preceramic polymers suffers from the disadvantages that extraordinary volume shrinkage and pronounced increase in density occur during polymer to ceramic conversion due to which extensive cracking and pore formation take place. Shrinkage and porosity formation could be overcome partly by filling the polymer matrix with inert fillers such as SiC, B₄C, Si₃N₄, and BN. However, when reactive filler particles are used in place of inert fillers, near net shape bulk ceramic can be obtained due to the compensation of shrinkage of the polymer by appropriate filler expansion resulting from the reaction of the filler particles with decomposition products of the polymer phase or reaction atmosphere. This approach is known as Active Filler Controlled Polymer Pyrolysis (AFCOP) [141–143]. The concept of AFCOP is depicted in Fig. 17 [143].

Dispersion of Ti, Cr, V, Mo, Si, B, CrSi₂, MoSi₂, etc. was used as active fillers for poly(silsesquioxane) [142]. The concept introduced by Greil [141, 143] has been extensively used to obtain dense bulk ceramic bodies, crack free coatings, CMCs with reduced porosity, and for obtaining a variety of novel composite ceramic systems including UHTCs. A detailed discussion on density calculations and percentage of active filler to be used in polymer pyrolysis is beyond the scope of this chapter, and readers' attention is drawn to related research publications [141–144].

Fig. 17 Microstructural changes during polymer-ceramic conversion: (a) filler-free polymer pyrolysis involving extended porosity or shrinkage and (b) active-filler-controlled polymer pyrolysis with near-net-shape precursor-ceramic conversion. (Reproduced from Ref. [143] with permission from John Wiley and Sons)



Vipin et al. [145] applied AFCOP concept for obtaining “shrinkage-free ceramic” from vinyl-group containing poly(borosiloxane) (BMV) using titanium silicide [TiSi_2] as active filler. The optimum concentration of TiSi_2 active filler was found to be 15.6 wt% for heat treatment of BMV at 1500°C (Fig. 18a). Addition of excess TiSi_2 beyond the optimum concentration resulted in a volume expansion. The BMV system exhibited the evolution of SiC phase without any stacking faults but the BMV+ TiSi_2 systems exhibited the evolution of SiC phase with stacking faults (Fig. 18b). It is evident from Fig. 18b that the TiSi_2 filler-incorporated polymer system at 1500°C provides a mixture of non-oxide ceramic phases (TiB_2 , TiB, and TiC), as a major constituent, and oxide phases (SiO_2 , TiOC, and $\text{B}_2\text{O}_3\text{-SiO}_2$) as minor constituents.

At still higher heat treatment temperatures of 1800°C and 2000°C , the evolution of $\alpha\text{-SiC}$, TiB_2 , $\beta\text{-SiC}$, TiB, TiC ceramic phases, and Ti_3SiC_2 MAX phase is observed (Fig. 19) [146]. Ti_3SiC_2 MAX phase is normally produced by expensive and complicated hot isostatic pressing technique. Hence, the evolution of MAX phase from preceramic polymer route offers a very promising approach for the production of this advanced engineering material.

Polymer-Derived Ceramics for Space Applications

Space applications require materials, which are capable of withstanding extreme service conditions, for example, nose-cone, leading edges, and rocket nozzles made of ceramic composites and oxidation-protected C/C composites which should

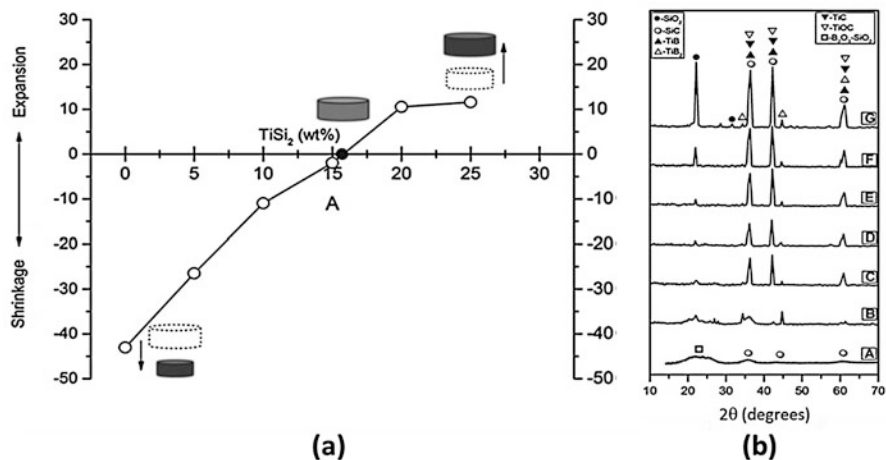


Fig. 18 Effect of TiSi₂ filler addition on the ceramic conversion of poly(methylvinylborosiloxane): (a) Volume expansion vs. wt% of TiSi₂ and (b) XRD patterns: (A) 0 wt%TiSi₂, (B) 5 wt% TiSi₂, (C) 10 wt% TiSi₂, (D) 15 wt% TiSi₂, (E) 20 wt% TiSi₂, (F) 25 wt% TiSi₂, (G) 30 wt% TiSi₂. (Reproduced from Ref. [145] with permission from authors)

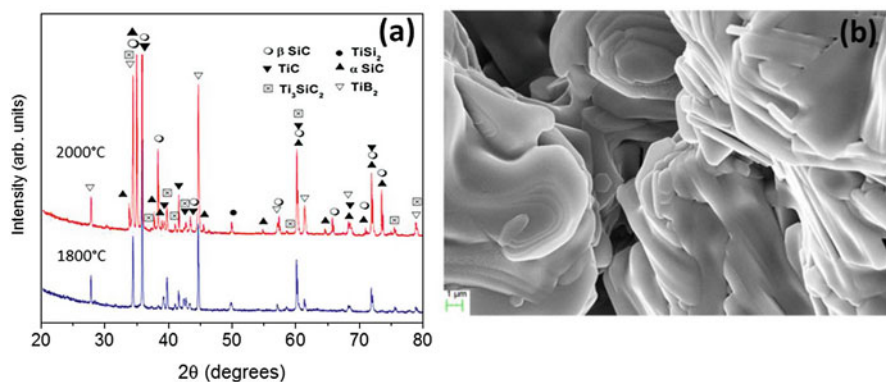


Fig. 19 (a) XRD patterns and (b) SEM images of the ceramic obtained from TiSi₂ filler added poly(methylvinylborosiloxane), showing the formation of MAX phase. (Reproduced from Ref. [146] with permission from Elsevier)

withstand high temperatures in an oxidizing environment. Likewise, materials used in the construction of spacecraft and space station placed in Low Earth orbit (LEO) should be capable of withstanding attack by atomic oxygen. Lightweight ceramic materials, as advanced thermal protection systems and ceramic adhesives for joining of ceramic components are also required for various space applications. This section focuses on the use of preceramic polymers and carbonaceous polymers in the fabrication of CMCs and lightweight ceramics, preparation of ceramic coatings and ceramic adhesives.

Ceramic Matrix Composites

CMCs are a subgroup of composite materials as well as a subgroup of technical ceramics. They consist of ceramic fibers embedded in a ceramic matrix, thus forming a ceramic fiber reinforced ceramic material. Among CMCs, carbon fiber and silicon carbide fiber reinforced composites with SiC matrix have gained importance as high temperature CMCs. SiC, a non-oxide covalent ceramic, exhibits high creep resistance and, hence, retains high strength up to 1650 °C. In an oxidizing atmosphere at these temperatures, SiC undergoes passive oxidation to silica (SiO₂) which prevents further oxidation of the remaining SiC. This property of SiC makes it superior to C and eventually, C/SiC composite superior to C/C composite. Carbon, in any form – graphite matrix or fiber – starts oxidizing above 450 °C giving gaseous CO₂, which erodes the entire material and, thus, needs to be protected from oxidizing environment above 450 °C. A suitable oxidation resistant coating (generally SiC coating) is used to protect the C/C composite, particularly, when used in space reentry vehicles. However, due to difference in coefficient of thermal expansion (CTE) of C and SiC, the SiC coating spalled-off leading to the failure of the mission. Thus, fiber reinforced CMCs are considered more reliable for reentry missions. Besides the excellent oxidation resistance, higher specific mechanical properties of CMCs at higher temperatures, compared to that of metal alloys, qualify them as high temperature structural materials for aerospace applications [147, 148].

Among the well-known CMCs, viz., C/SiC, SiC/SiC, and C/C-SiC composites, C/SiC and C/C-SiC composites, are extensively used as hot structures. SiC/SiC composites, though has the best oxidation resistance, has limitation in strength retention beyond 1400 °C. A wide variety of thermal protection systems and hot structures has emerged (Fig. 20) as the sustainable approach, as the space industry has moved from rocket launchers to shuttle orbiters to scramjet-based hypersonic vehicles [149].

The application areas of CMCs include aero-engine combustor liners, ducts, nozzle flaps, acoustic liners, turbine vanes, turbine blades, and turbine disks [150, 151], re-entry vehicles [152–154], as substrate for SiC mirrors [155], brakes for military and commercial aircrafts [156], as high temperature ceramic fasteners [157], and in radiation-cooled nozzle extensions and combustion chambers for small thrusters [158]. The major end-use of C/SiC composites is as thermal protection systems (TPS) [159–162]. CMCs also showed good performance in rocket motor parts reaching temperatures of 2700 °C, withstanding the chemical and physical erosion [163].

The potential use of SiC-matrix composites as hot structures of spacecraft was demonstrated at the prototype level some years ago with the “Hermes” (European space shuttle project). Here, the temperature envisaged was from 800 °C to 1600 °C, during the ascent and reentry phases of the flight, and the structures withstood thermal shocks and cyclic mechanical loading under ablative or passive oxidizing atmospheres [164].

C/SiC was proposed as a suitable candidate for the nose-cap of X-38 reentry vehicle by NASA which was designed to be a technology demonstrator for the Crew

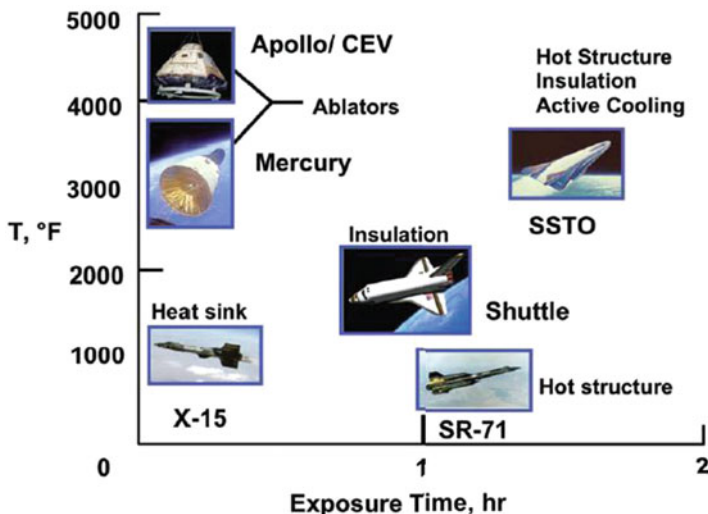


Fig. 20 Thermal structures for aerospace applications. (Reproduced from Ref. [149])

Return Vehicle (CRV) from the International Space Station (ISS) (Fig. 21) [165]. During the reentry phase the nose cap of X-38 experiences surface temperatures of up to 1750 °C. C/C-SiC nose-cap was envisaged in the EXPERT program of ESA. ESA has developed the intermediate experimental vehicle (IXV) project for addressing the basic European needs for reentry from LEO, which uses C/SiC TPS components [166] (Fig. 22).

Existing satellite thrusters and liquid apogee motor (LAM) engines use high temperature alloys where the permissible operating temperature is 1300 °C. The use of C/SiC composite as combustion chamber and nozzle material can increase the maximum combustion temperature above 1650 °C without any oxidation protection coating [167]. With suitable functionally gradient coating the operating temperature can be further increased which will result in enhancing the specific impulse of the thruster. In view of the advantages of C/SiC composites, they are being evaluated as satellite thrusters (Fig. 23), nozzles, nozzle extensions (Fig. 24), and combustion chambers [167, 168].

C/SiC composite is also used for the fabrication of lightweight mirrors and as face sheets in the construction of internal multiscreen insulation (IMI) [149] and ceramic sandwich structures (Fig. 25) [169, 170].

Fiber reinforced CMCs are fabricated by producing a dense ceramic matrix around carbon or silicon carbide fibers. The build-up of the dense matrix is mainly done by three techniques using: (i) gaseous reactants by chemical vapor infiltration (CVI), (ii) polymeric reactants by polymer infiltration and pyrolysis (PIP) process, and (iii) molten elements reacting with the preforms (by reactive melt infiltration (RMI)/liquid silicon infiltration (LSI)), each having their own advantages and limitations.

In general, the matrix should be homogeneously distributed in the preform with limited residual porosity. Another important aspect is the fiber to matrix

Fig. 21 Nose-cap of X-38 (NASA). (Reproduced from Ref. [165] with permission from John Wiley and Sons)

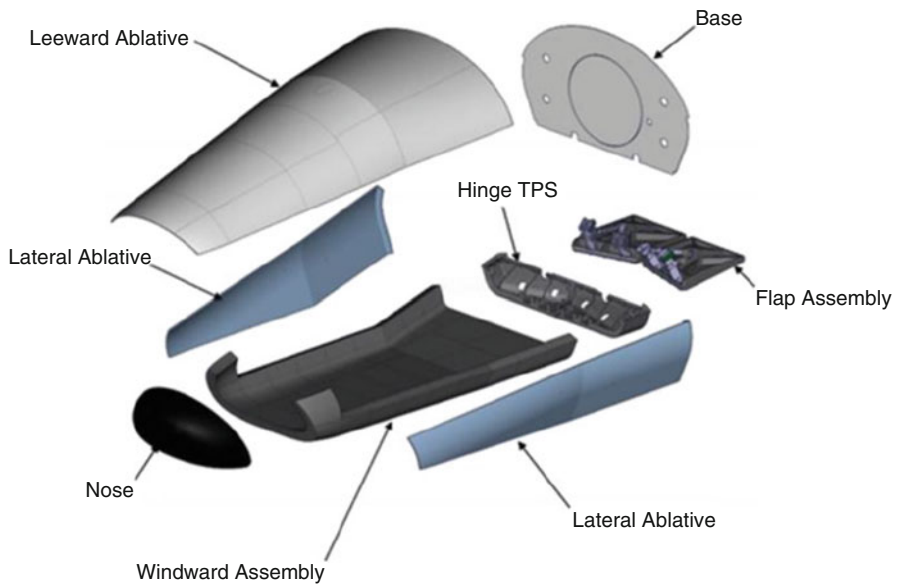


Fig. 22 C/SiC Components for IXV (ESA): (a) Nose assembly, (b) shingles-based windward assembly, and (c) flap assembly. (Reproduced from Ref. [166] with permission from Elsevier)

(FM) bonding. In conventional composites (like Kevlar/epoxy or carbon/epoxy), the matrix (like epoxy) is ductile enough to pass on the stress to the fibers. However, in CMCs, the matrix is as stiff as the fibers, which makes it impossible for the matrix to pass on the load to the fibers. The fiber reinforcements can enhance the toughness of the CMC, only if the FM bonding is weak. The concept of weak FM bonding helping

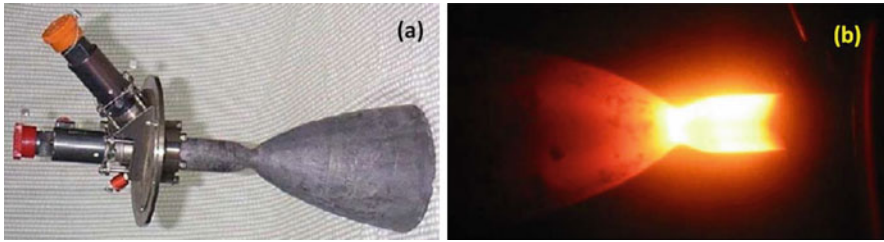


Fig. 23 (a) 150 N bipropellant C/SiC rocket engine, (b) hot fire of 150 N bipropellant C/SiC rocket engine. (Reproduced from Ref. [167] with permission from Elsevier)

Fig. 24 C/SiC nozzle extensions developed for Vulcan cryogenic engine (ULA). (Reproduced from Ref. [168] with permission from John Wiley and Sons)



in crack deflection is explained in Fig. 26. The weak FM bonding is mainly established by providing a thin layer (less than 1 μm) of another material on the carbon fibers by the CVI process [171].

In the case of C/SiC composite without interphase coating fiber-matrix adhesion is strong and hence, the fracture propagates through the fiber, and the composite behaves like a monolithic material. When an interphase coating such as BN or pyro carbon is given onto the fiber reinforcement matrix, cracks get diverted around the fibers as shown in Fig. 26 and the composite exhibits good fiber-pullout contributing to improved fracture toughness of the composite.

The design of CMCs calls for selection of a suitable reinforcement and a compatible matrix, appropriate fiber-matrix (FM) interphase, the combination capable of exhibiting high mechanical and thermal properties, and high chemical compatibility with the high service temperature. Carbon fiber or SiC fiber woven as fabric or in multiple dimensions is the most preferred reinforcement. Carbon and SiC are the mostly preferred material for matrix. As FM interphase, hexagonal boron

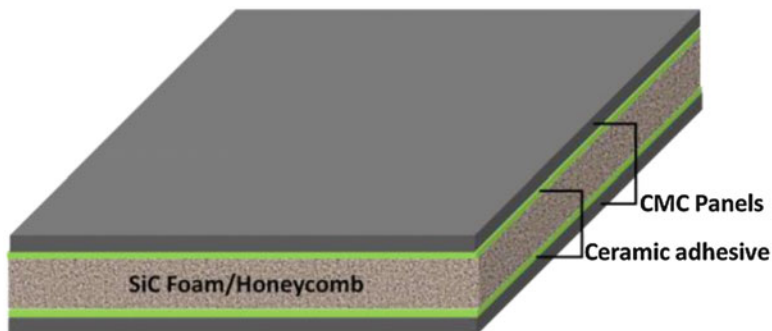
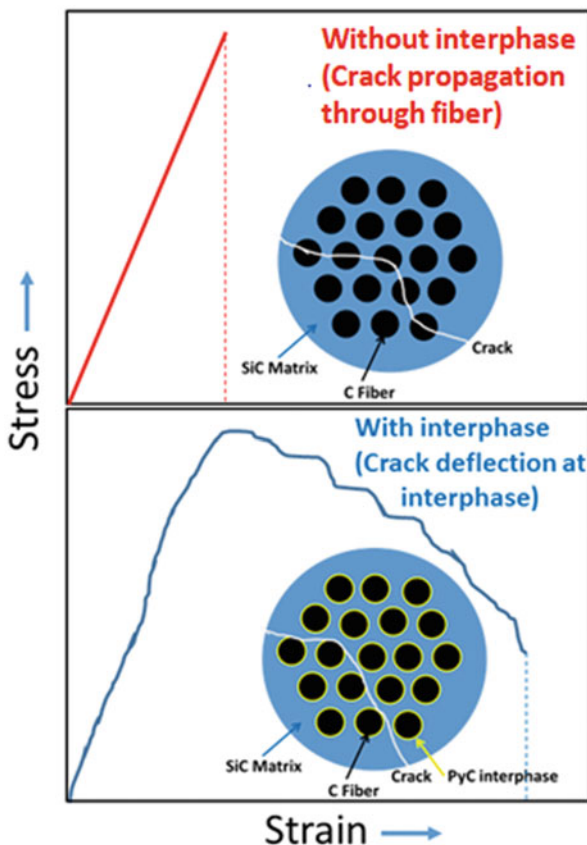


Fig. 25 Schematic of a ceramic sandwich structure

Fig. 26 Schematic representation of the role of interphase in crack deflection



nitride (BN) and pyrolytic carbon are mainly used [172–175]. Multilayer interphase coatings have also been attempted to improve the thermomechanical properties of CMCs [171, 176].

The matrix phase in CMC can be single or multiple phases with compositional variations. C/SiC composites are the simplest in terms of the composition of the matrix. C/SiC composites are usually fabricated by the well-established CVI process and by this process both the interphase coating of the reinforcement fiber/fabric and SiC matrix are obtained. Though CVI process is useful in fabricating C/SiC composites with required mechanical properties, the fabrication of composites by this process suffers from the following disadvantages: (i) quite high initial investment in establishing CVI furnace and its high maintenance cost, (ii) use of corrosive chemicals such as boron trichloride and methylchlorosilanes, (iii) requirement of specially designed graphite molds for uniform deposition of interphase coating and uniform densification of matrix, (iv) difficulty in fabricating components having complicated shape and larger size, (v) blockage of the surface pores due to matrix deposition preventing the penetration of gas into the interior of the components which limits the thickness of the components that could be fabricated by this process, (vi) low efficiency of the process, for example, the conversion of gaseous precursors to SiC is less than 15%, and (vii) environmental/pollution-related issues relating to neutralizing the unreacted gaseous monomers. Though the basic CVI process has undergone several modifications/improvements to overcome the above problems, fabrication of CMCs by CVI process remains to be costly and time consuming.

Polymer-derived ceramics route offers solution to most of the problems associated with CVI process. As discussed earlier, preceramic polymer can be used as the precursor matrix for the desired ceramics and any one of the polymer matrix composite preparation methods such as hand-lay-up, autoclave molding, resin transfer molding, and filament winding can be used to form the green composite. This method takes the full advantage of the low temperature processability of preceramic polymers. After pyrolysis, the porous composite is subjected to infiltration and pyrolysis cycles to obtain a dense CMC, and this procedure is known as polymer-infiltration-pyrolysis (PIP) process (Fig. 27) [177].

Even for the fabrication of CMCs by PIP process, it may be required to use CVI/CVD furnace for interphase coating onto fiber reinforcement. Though PIP process is relatively simple and cost effective, care must be taken in each processing step, particularly the pyrolysis step. During pyrolysis, evolution of gases due to the decomposition of precursor matrix takes place leaving behind the amorphous ceramic matrix which results in shrinkage of the matrix and formation of pores, voids, and micro-cracks. Sudden evolution of gases may lead to delamination of the green composite, and to overcome this problem, the first pyrolysis step is to be carried out at a slow heating rate. Repeated PIP process may also deteriorate the strength of fiber reinforcement due to the possible reaction of matrix with the interphase coating/fiber. Pyrolysis temperature should be carefully chosen such that the reinforcing fiber of choice does not lose its strength [177].

Efforts to visualize and to assess the distribution of voids created in the matrix during polymer to ceramic conversion, by using X-ray computed tomography is promising [178]. These approaches can help in formulating physics-based models in composite fabrication processes (Fig. 28).

Silicon carbide matrix: Various preceramic polymers such as polysilane [179], polymethylsilane [180], polyvinylsilane [181], polycarbosilane [182–184],

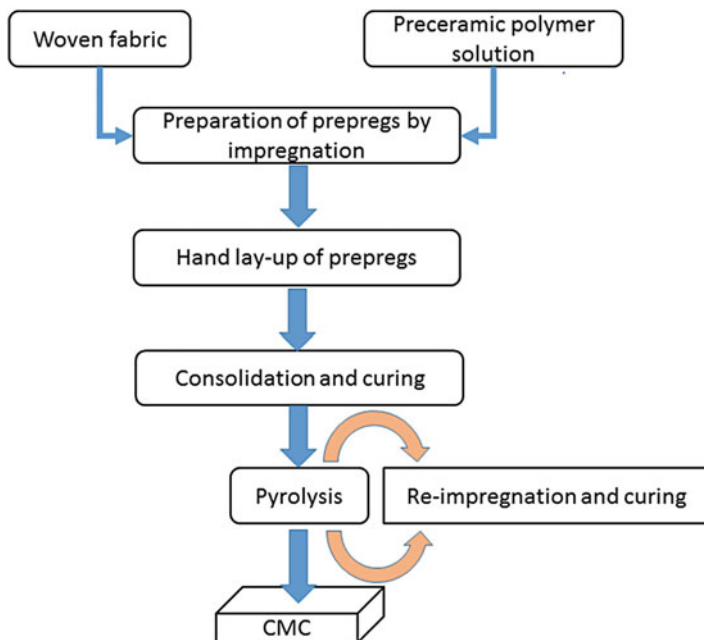


Fig. 27 Flow chart for fabrication of composite by PIP. (Reproduced from Ref. [177] with permission from Elsevier)

polycarbosilane with $\text{AlN-Y}_2\text{O}_3$ as sintering additive [185], co-polymer of polycarbosilane and polymethylsilane [186], polytitanocarbosilane [187], polyzirconocarbosilane [188], and allylhydrido-polycarbosilane [189, 190] were used to prepare SiC matrix. Starfire SMP-10 was one of the initial commercially available polycarbosilane precursors to stoichiometric SiC. High cost of these resins has impeded the commercial applications of polymer-derived CMCs as in the case of automobile brake discs [191].

SiC matrix has also been obtained by carbothermal reaction of Si or SiO_2 . Prabhakaran [61] and Ajith [192] have investigated the fabrication of C/SiC composites from carbonaceous polymer such as phenol-formaldehyde and phenol-furfural resins [61], as a cost-effective approach. As no interphase coating was used to protect the carbon fiber, the reaction of Si with carbon fiber could not be eliminated. However, the composite fabricated by this process retained the mechanical property at 1500 °C (Table 2).

Infiltrating C/SiC composite with polycarbosilane and borosiloxane oligomer followed by pyrolysis at 1500 °C [192] considerably improved the oxidation resistance. 2D C/SiC composites with and without pyrocarbon interphase were fabricated using boron modified phenol-formaldehyde resin as matrix precursor and these composites exhibited flexural strength of 102 MPa and 38 MPa, respectively [138].

SiOC matrix: The search for a low-cost resin ended up in a range of SiOC precursors. Among the commercially available resins for SiOC, Starfire system's

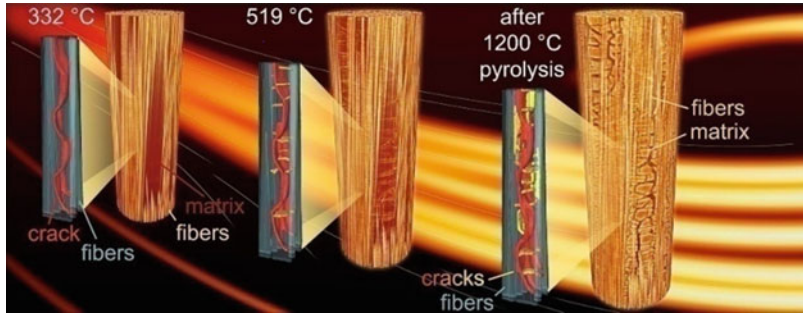


Fig. 28 In situ 3D visualization of composite microstructure during polymer-to-ceramic conversion. (Reproduced from Ref. [178] with permission from Elsevier)

Table 2 Flexural strength of C/SiC composite from phenol-formaldehyde resins (Reinforcement: Toray 3 K carbon fabric without interphase coating) [192]

Test temperature (°C)	Flexural strength (MPa)	
	Mean	SD
RT	72.79	10.92
1000	76.14	1.47
1300	79.20	10.35
1500	79.40	5.15

Polyamic range of resins were the widely used ones. Comparing the oxidation resistance of these resins, Polyamic RD-212a and RD-036a resulted in 100% mass retention after oxidation while RD-688a, RD-642, and RD-684 polymers, which yield progressively higher carbon content ceramics, resulted in progressively lower mass retention and therefore lower oxidation resistance [191]. Considerable amount of work is carried out by researchers on SiOC matrix composites from siloxane resins [193–196]. Polysiloxane with titanium [197] and silicon [198] and polysilsesquioxane with boron [199] as filler were reported to address the problem of voids and shrinkage to certain extent. Srinivasan and Tiwari [199] noted that despite its high temperature property, polysilsesquioxane has several limitations which prevent its use as matrix resins for CMCs and advocated the use of alternate resins such as borosiloxanes, carborane-siloxanes, and other boron-nitrogen containing polymers. For the fabrication of C/SiOC CMCs, “Fast Sol-Gel Process” is also reported [200]. In this method, green composites were fabricated by coating fast-sol-gel derived resins onto fabric preforms followed by hot press and pyrolysis. Carbon content in the matrix influenced the flexural strength. In C/SiOC composites, the matrix contains nano-crystallites of SiC embedded in an amorphous SiOC matrix. The SiOC matrix has good oxidation resistance but has poor creep resistance at higher temperatures due to the presence of silica nano domains. Use of SiBOC matrix in place of SiOC improves the oxidation resistance further, as SiBOC matrix on oxidation forms stable borosilicate glass and also influences the crystallization kinetics as discussed earlier. The ability of borosiloxane oligomers to give SiBOC ceramic in good yield on pyrolysis is an advantage to use them as matrix resin for CMCs [201, 202].

CMC was fabricated by impregnating pitch-based carbon fiber strand (high tensile strength type) with poly(diphenylborosiloxane) solution containing β -SiC powder, followed by molding in a metallic mold, heat treating in air at 500 °C and then at 1000 °C in nitrogen atmosphere [53]. The mechanical property increases with the increase in Si/B ratio in the precursor. The composite prepared from the precursor having Si/B ratio of 3:1 exhibited maximum bending strength of 320 MPa and Young's modulus of 55 GPa. CMCs were also fabricated from 2.5-dimensionally woven carbon fabric using polyborosiloxane as matrix precursor [203]. This composite having density of 1.62 g/cm³ gave a bending strength of 83 MPa and exhibited more toughness and higher fracture energy compared to CMC fabricated from satin weave carbon fabric.

Schiavon et al. [204] evaluated poly(methylborosiloxane) prepared from boric acid and methyltriethoxysilane as matrix resin for preparing C/SiBOC unidirectional composite. SEM studies indicate good adhesion between carbon fiber and ceramic phase. This composite has improved oxidation resistance compared to C/SiOC composite.

Borosiloxane oligomers synthesized by nonaqueous sol-gel process have been evaluated by researchers at the Vikram Sarabhai Space Centre as matrix resin for carbon fiber and SiC fiber reinforced composites and arrived at a propriety composition which gives maximum flexural strength at room temperature and at elevated temperatures. To begin with poly(phenylborosiloxane) [BP], BP with pyrolyzed BP and BP with elemental silicon were evaluated as matrix precursors to obtain CMCs designated as CMC-1, CMC-2, and CMC-3, respectively [201]. A number of PIP and heat treatment cycles are required to get a densified composite (Fig. 28). CMC-1 requires maximum number of processing cycles to achieve the saturation density. On the other hand, CMC-2 prepared using pyrolyzed PBS as filler requires lesser processing cycles compared to CMC-1. CMC-3 prepared using elemental silicon as filler requires the least number of densification cycles (Fig. 29a). SEM images of cross section of CMC-1 are shown in Fig. 29b, c. Figure 29b shows the presence of both densified matrix and carbon fiber reinforcement. In spite of many PIP cycles voids are seen in the composite (Fig. 29c) which is attributed to the flaws in the green composite.

Flexural strength values of the composites are given in Table 3. Among the three composites, CMC-3 has the lowest flexural strength and this is attributed to the reaction of elemental silicon with carbon fiber. Use of pyrolyzed BP as filler has contributed toward increasing the flexural strength and reducing the number of infiltration cycles. The higher flexural strength of CMC-2 is attributed to proper sintering of the matrix which helps in improving the inherent load bearing capacity of the matrix, thereby increasing the bending strength [205]. Yet another reason for improved flexural strength of CMC-2 is less number of infiltration and heat treatment cycles, which helps in minimizing the microcracks and differential shrinkage of the matrix [206]. CMC-1, CMC-2, and CMC-3 on oxidation in air at 1000 °C in air undergo weight loss of 23.2–26.2% as against 82.9% for C/C composite.

Devasia et al. [207, 208] explored the possibility of obtaining pyrocarbon inter-phase coating onto carbon fiber through polymer pyrolysis route. Carbon fiber was

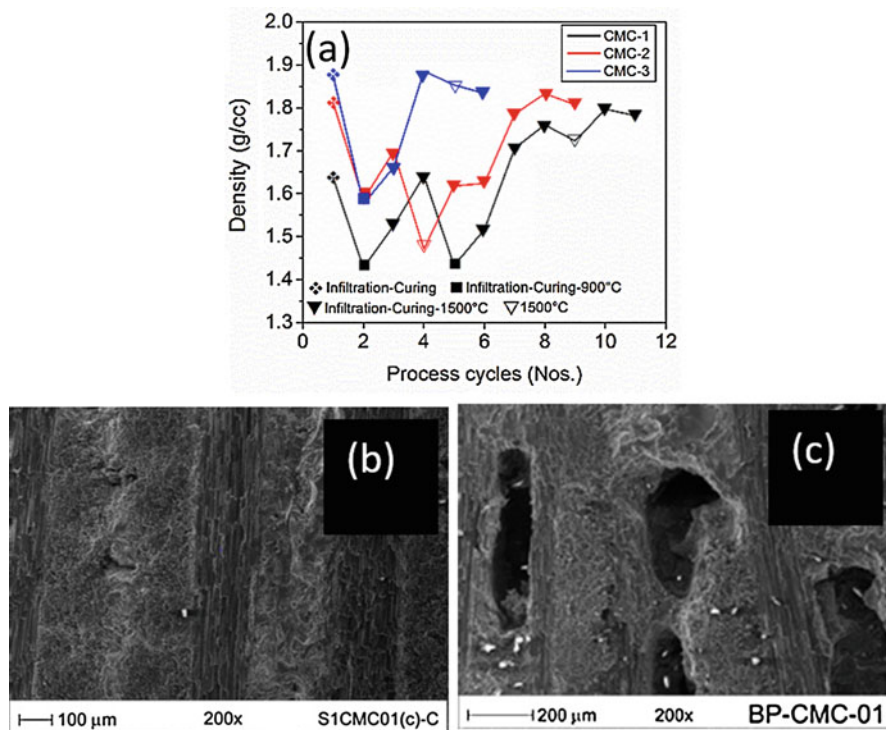


Fig. 29 (a) PIP Densification of phenyl borosiloxane derived CMC, (b) SEM of cross section of CMC-1, and (c) SEM of cross section of CMC-1 showing voids [201]

Table 3 Flexural strength values of CMCs [201]

Sample	Density (g/cc)	Flexural strength (MPa)
CMC-1	1.78	145
CMC-2	1.81	173
CMC-3	1.83	110

coated with poly(acrylonitrile-co-itaconic acid) by dip coating process and then pyrolyzed in the temperature range of 1000–1500 °C to obtain the PyC coating. The advantage of this approach is that it eliminates the need to use CVI furnace for obtaining interphase coating. Maximum improvement in flexural strength is observed for C/SiBOC composite prepared from PyC coated carbon fabric and poly(phenylborosiloxane) for the interphase coating thickness of 0.5 μm. SEM studies indicate that PyC coating of 0.5 μm improves the fiber-pullout which is responsible for the improvement in flexural strength (Fig. 30).

A detailed evaluation of different borosiloxane oligomers as precursor matrix suggests that mechanical properties of C/SiBOC composite are influenced by the organoalkoxysilane used for the synthesis of borosiloxane oligomers, nature of

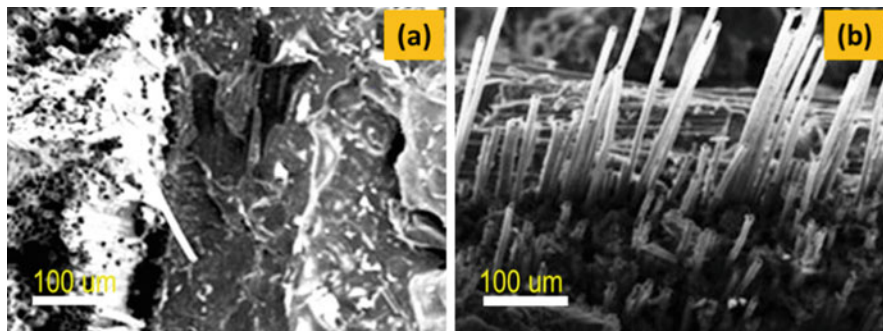


Fig. 30 SEM of fractured surface of C/SiBOC composite from polyphenylborosiloxane: (a) without and (b) with PyC coating (0.5 μm). (Reproduced from Ref. [208] with permission from Elsevier)]

Table 4 Comparison of flexural strength of C/SiBOC composite prepared from different borosiloxane oligomers

Sl No.	Alkoxysilane(s) ^a	System code	Flexural strength (MPa)	Reference
1	PTEOS	PBS	145	[62, 208]
2	PTEOS	PBS (PyC ^b coated C fiber)	163	[207, 208]
3	PTEOS	PBS+Si	110	[62, 201]
4	PTEOS	PBS+PyBPS	173	[62, 201]
5	VTEOS	VBS	124	[210]
6	VTEOS	VBS+MWCNT (3%)	171	[210]
7	VTEOS + MTEOS	BMV	265	[62, 209]
8	VTEOS + MTEOS	BMV (BN coated carbon fiber)	285	[62, 209]

^aBoric acid: Alkoxysilane ratio = 1:2 except in Sl. No. 7

^bPyrocarbon interphase coating obtained from polyacrylonitrile

additives, and interphase coatings. The flexural strength of different C/SiBOC composite systems from borosiloxane oligomers is compared in Table 4.

It is observed that C/SiBOC composite from BMV resin gives the maximum flexural strength. SiBOC ceramics obtained from BMV oligomers are less prone to SiC crystallization as discussed earlier. The increased stability of SiBOC phase from BMV is responsible for improving the load bearing capacity of the composite [209].

As C/SiBOC composite prepared from BMV resin gives the maximum flexural strength of 265 MPa, attempts have been made to make use of this resin for fabricating C/SiBOC composite for space applications. Initial trials have been focused on fabricating shaped composites, avoiding delamination and warping of composites by using suitable molds, and adjusting the heat treatment process. After standardizing the process, BMV has been successfully used for fabricating pylon leading edge and prototype air-breathing engine combustion chamber and wing



Fig. 31 Shaped CMC components from borosiloxane [209]

leading edge trial segment for reusable launch vehicle (Fig. 31) by vacuum assisted resin transfer molding.

In order to qualify BMV-based composites for inducting into the space program, it is necessary to study the high temperature characteristics and oxidation resistance. The composite retains mechanical properties up to 1000 °C (Table 5).

Long duration oxidation resistance test of BMV-based CMC was carried out at 1000 °C. The CMC samples were exposed to 1000 °C in a muffle furnace. The composite shows a cumulative mass loss of 39% after 60 min (Fig. 32a).

Mass loss of the C/C composite is observed to be four times as compared to that of C/SiBOC composite. The higher oxidation resistance of C/SiBOC is attributed to the oxidation stable matrix and protection of carbon fiber bundles by SiBOC. The mass loss of 39% for C/SiBOC is mainly due to the burnout of carbon fibers getting exposed on machining as evident from SEM. If proper oxidation protection is provided, this mass loss can be considerably minimized.

Protective Coatings

Oxidation Resistant and Environmental Barrier Coatings for Carbon/Carbon and Ceramic Matrix Composites

Advanced C/C composites have attractive properties such as high strength up to 2200 °C in inert atmosphere, low density, low coefficient of thermal expansion and thermal shock resistance [211]. For these reasons, they are considered as the most

Table 5 Comparison of Mechanical properties of C/SiBOC composite at room temperature and at 1000 °C [209]

Temperature	Flexural strength (MPa)	Tensile strength (MPa)	ILSS
RT	236	153	10
1000 °C	264	142	13

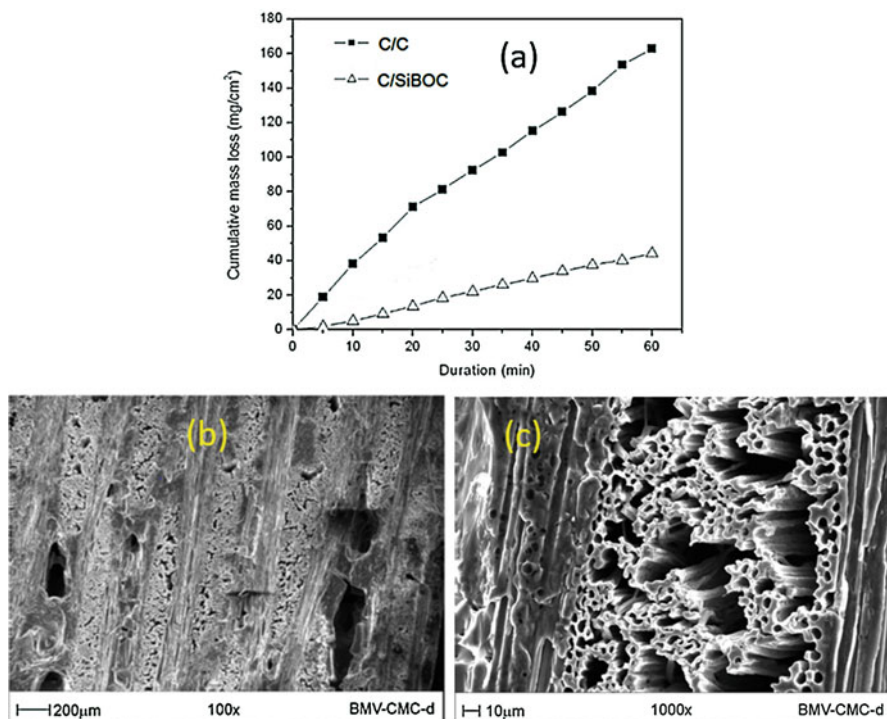


Fig. 32 Evaluation of oxidation resistance of BMV-based C/SiBOC at 1000 °C in air: (a) comparison of C/SiBOC with C/C composite, (b) matrix after oxidation, and (c) burnout of carbon fiber bundles [62]

suitable candidate for hot structures such as nosecone and leading edges of reentry vehicles and reusable space shuttles [212]. However, in an oxidizing environment, they undergo degradation above 500 °C, which drastically brings down their properties. Hence, they need protection against oxidation if they are to be used for the above applications.

Multilayered oxidation resistant coating is the popular choice for the protection of C/C composites against oxidation [211]. A typical multilayer coating consists of three parts. An initial sealant layer is applied to the substrate by either slurry painting, spraying, or CVD. A primary oxidation barrier is then applied by CVD, consisting of near stoichiometric SiC or siliconized SiC. Because of the thermal expansion mismatch between the fiber-reinforced substrate and the primary

oxidation barrier, a network of cracks develop within the coating upon cooling down from the deposition temperature of CVD coating. Higher the deposition temperature, wider the cracks that are developed and these cracks provide paths for the diffusion of oxidizing species to the substrate. In order to seal the cracks on SiC coating, in the last step of the coating process borosilicate/silicate glass coating is applied by painting, spraying, or impregnation using B_2O_3 - SiO_2 mixture, tetraethoxysilane, or by sol-gel process. Cracks also develop in the SiC coating when SiC-coated C/C composites are subjected to high temperatures during reentry, due to thermal expansion mismatch between SiC coating and C/C composite. The glass coating that is applied over SiC coating should be capable of sealing the cracks which are formed during the processing of the coating and also the cracks which are formed during the flight. Thus, it is necessary that the glass coating should melt at a slightly lower temperature than the service temperature, in order to ensure its melting and flowing into the cracks. In addition to sealing the cracks, the glass coating offers yet another advantage, viz., protection against moisture absorption by SiC coating and by the component [213]. If glass coating is not applied over SiC coating, it would absorb moisture and the moisture absorbed at the interface between the SiC coating and the substrate would form water vapor/steam when heat load is applied onto the substrate [214]. This would result in the development of internal pressure at the interface causing rupture of the coating from the substrate when the SiC coated composite experiences higher temperatures.

Several variants of the oxidation protection methodology have been reported in patent literature [215–217] and in research publications [218–222] to improve the performance of the coating with respect to the following aspects: (i) to eliminate/reduce the cracks on the oxidation protection coating by way of minimizing the thermal expansion mismatch between the composite substrate and the coating, (ii) to improve the adhesion of the coating with the substrate, (iii) to increase the high temperature capability of the coating, (iv) to improve the service life and reusability, and (v) to modify the coating to incorporate environmental barrier capability, particularly, resistance to degradation of the ceramic coating to water vapor.

Though ceramic matrix composites such as C/SiC and C/C-SiC and UHTC composites are more resistant to oxidation compared to C/C composites, they also require oxidation protection in order to extend their service life. The oxidation protection methods of C/C composites are adopted as such or suitably modified to meet the requirements of other composite systems. It is likely that the protective coatings may be damaged during installation or operation process. The destruction of these coatings may cause oxidation of C/C composites leading to serious accident [223], and hence, suitable repair systems are to be developed. Unlike the high temperature coating process, the in situ repair process has to be a low temperature process and should be easily adoptable. Polymeric precursors would be the best choice for the repair work as they can be cured into a cross-linked network by UV light [224] or by slight heating [225].

The shrinkage of the films during pyrolysis at high temperatures and the resultant cracks could be avoided by adding inert or active fillers [226]. It is reported that polymer-derived ceramics show excellent oxidation resistance [120, 227] and water

vapor corrosion resistance [228, 229]. In view of the obvious advantages of polymer-derived ceramics, preceramic polymers such as PCS [230], polysilazanes [231], polysiloxanes [227], boron containing polymers [232, 233], and boron and silicon containing polymers [92, 234, 235] have emerged as promising alternatives for the protection of C/C composites, CMCs, carbon fibers, ceramic fibers, and metals against oxidation.

Oxidation resistant coating for C/C-SiC composite was reported by Bill and Heimann [231] using liquid polysilazane with silicon powder as filler. The composite was coated by dip coating process and then subjected to pyrolysis at 1100 °C at a slow heating rate (0.7–1.2 °C/min). Ceramic coating thickness of ~5 μm was achieved in each dip coating and pyrolysis cycle. The adherence of the ceramic layer on the C/C-SiC material depends on the pretreatment of the substrate as well as on the pyrolysis conditions. Adhesion of the ceramic layer on the C/C-SiC substrate was determined by the direct pull method and the adhesive strength was in the range of 6–14 MPa. The adhesion of the ceramic layers could be increased by 30% by additional annealing of the samples in nitrogen atmosphere at 1350 °C. The observed improvement was probably due to nitridation of the silicon filler.

The oxidation behavior of the coating and the ability to protect the C/C-SiC substrate against oxidation were investigated using thermogravimetric analysis [231]. Both samples were heated in air up to 1000 °C at a rate of 1 °C/min and then cooled down at a rate of 8 °C/min. The reference sample exhibited a weight loss of more than 50% whereas the sample coated with 10 μm thick ceramic layer lost about 30% of its original weight. Oxidation resistance test conducted at 1160 °C and 1260 °C suggested that all the carbon fiber reinforcement was burned off both in the coated and uncoated samples though it took more time for the coated sample. The reason for the weight loss in the case of coated sample is attributed to the porosity and micro-cracks in the coating.

Wang et al. [236] formulated a single layer and multilayer repair coating based on polysilazane. Single layer coating slurry was prepared by mixing of polysilazane solution in ethanol and ZrC powder followed by ball milling. The slurry was brushed on the damaged areas of C/C composites followed by curing using an infrared lamp. For the multilayer coating structure, silicon powder, mullite powder, and borosilicate glass powder were used as the raw materials for different layers. The fabrication process for each layer is similar to the single-layer process. Oxidation resistance test indicated that single layer coating was not able to effectively protect the coating-damaged C/C composites. On the other hand, the multilayer coatings could protect the C/C composites from static oxidation at 1300 °C and 1500 °C. The plasma wind tunnel test was carried out with heat flux 4.0 MW/m², stagnation pressure 3.5 kPa, and air velocity of 2 Mach. The multilayer coating withstood this test condition for 1000 s.

Manocha and Manocha [237] investigated the oxidation resistance of methylsilsesquioxane-based SiOC coating on C/C composites. Methylsilsesquioxane resin was dissolved in a mixture of toluene and isopropylalcohol, and the cross-linking agent 3-aminopropyltriethoxysilane (2%) was mixed with the solution. C/C composite coupons were coated with the resin solution and cured at room temperature

followed by post curing at 150 °C. The samples were heat treated at 1000 °C in nitrogen atmosphere. The composites were further coated with the resin to fill cracks, if any, developed during the first heat treatment. The coated samples were heat treated to 1250 °C in nitrogen. Oxidation behavior of the coated and uncoated samples was studied thermo-gravimetrically, by heating the samples to 1200 °C at a heating rate of 10 °C/min under the flow (100 mL/min) of compressed air and recording the weight loss at different temperatures. Uncoated C/C composite had experienced complete weight loss at 950 °C whereas the SiOC coated composite had exhibited less than 1% weight loss in the temperature region 800–1200 °C. The results suggest that SiOC coating offers very good protection to C/C composite against oxidation.

Niu et al. [238] fabricated $\text{MoSi}_2\text{-SiOC-Si}_3\text{N}_4$ coating over SiC coated C/C composite by slurry method. The slurry was prepared by dispersing MoSi_2 and Si_3N_4 powders in a high hydrogen silicone oil (H-PSO) and using tetramethyl tetra vinylcyclotetrasiloxane (Vi-D₄) as cross-linker and platinum chloride as catalyst. The coating was heat treated at 1000 °C for 2 h in nitrogen atmosphere to obtain $\text{MoSi}_2\text{-SiOC-Si}_3\text{N}_4$. The average coating thickness was 140 μm. For comparison, $\text{MoSi}_2\text{-SiOC}$ outer coating was prepared by the same slurry method. The isothermal oxidation curves of the C/C composites with different outer coatings at 1500 °C in air are shown in Fig. 33. It is observed that $\text{MoSi}_2\text{-SiOC-Si}_3\text{N}_4$ exhibits superior oxidative protective abilities compared to $\text{MoSi}_2\text{-SiOC}$. The antioxidation properties of $\text{MoSi}_2\text{-SiOC-Si}_3\text{N}_4$ multiphase coatings are influenced by Si_3N_4 content. From Fig. 33a it is evident that the $\text{MoSi}_2\text{-SiOC/SiC}$ coated C/C specimen exhibits an excellent oxidation resistance in the first 20 h with a negligible weight loss of 0.5%. However, as seen from Fig. 35b the weight loss rate increases gradually until the weight loss reaches up to 5.52% for 80 h. The above data infers that $\text{MoSi}_2\text{-SiOC}$ coating offers limited protection. The reason for this observation is that the CTE of MoSi_2 is $8.1 \times 10^{-6} \text{ K}^{-1}$ is much higher than that of the inner SiC ($4.45 \times 10^{-6} \text{ K}^{-1}$), and hence, stress-induced micro-cracks are formed with the

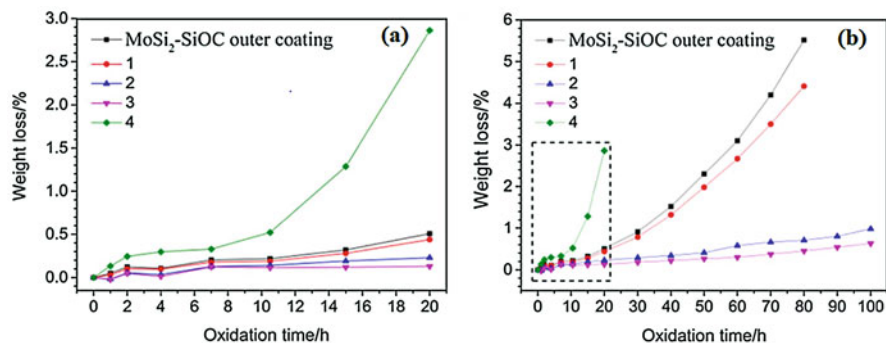
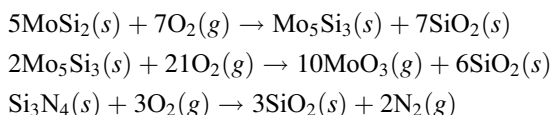


Fig. 33 Weight loss curves of different coated samples at 1773 K in air: (a) 20 h and (b) 80 h (1: $\text{MoSi}_2\text{-SiOC-(15\%)\text{Si}_3\text{N}_4$; 2: $\text{MoSi}_2\text{-SiOC-(30\%)\text{Si}_3\text{N}_4$; 3: $\text{MoSi}_2\text{-SiOC-(45\%)\text{Si}_3\text{N}_4$; 4: $\text{MoSi}_2\text{-SiOC-(60\%)\text{Si}_3\text{N}_4$). (Reproduced from Ref. [238] with permission from Elsevier)

increase in temperature. These cracks provide the diffusion pathways for oxygen to get access to the matrix, leading to the increase in rate of oxidation at the later stage. The mismatch of CTE between the outer and inner coating is minimized by introduction of Si_3N_4 with a lower CTE ($2.7 \times 10^{-6} \text{ K}^{-1}$). It is seen that MoSi_2 -SiOC- Si_3N_4 /SiC coating with Si_3N_4 content of 30% or 45% could protect C/C matrix from oxidation at 1500 °C for 100 h. However, the coating with 60% Si_3N_4 could give the oxidation protection to C/C composites just for a short period of time.

XRD studies of the coating after exposure to 1500 °C suggest that MoSi_2 -SiOC and MoSi_2 -SiOC-(45%) Si_3N_4 coatings consist of SiO_2 , Mo_5Si_3 , and MoSi_2 phases. Based on this inference, the following reaction scheme was proposed [238]:



The above reactions generate SiO_2 . Especially, the oxidation of MoSi_2 is characterized by the selective oxidation of Si. SiO_2 formed in sufficient quantity forms a dense film, which effectively serves as a barrier against oxygen attacking the matrix. This is evident from SEM studies of the samples subjected to oxidation at 1500 °C. At medium temperature of 800 °C, MoSi_2 -SiOC/SiC coated sample has a significant weight loss of 6.76% after oxidation for 10 h whereas MoSi_2 -SiOC-(45%) Si_3N_4 /SiC coated C/C sample has a better oxidation resistance with weight loss of 2.11% after oxidation for the same time. The oxidation resistance of both the coatings at 1500 °C is better than that observed at 800 °C mainly because SiO_2 formed at this temperature has a poor self-healing ability.

C/SiC composites exhibit excellent oxidation resistance in dry air, due to the formation of a dense silica layer on their surface [239, 240]. However, the water vapor containing in combustion environment removes the formed silica quickly, resulting in the mass loss and failure of the C/SiC composites [241, 242]. Hence, environmental barrier coatings (EBCs) are applied in order to protect the C/SiC composites from corrosion in combustion gas [243]. Liu et al. [225] investigated two-component polysiloxane-derived SiOC-barium-strontium-aluminosilicate (SiOC-BSAS) coating as environmental barrier coating for C/SiC composites. Polysiloxane-BSAS (40 wt%) slurry was uniformly brushed on C/SiC composite. After curing at 100 °C, the coating was subjected to pyrolysis at 900 °C followed by heat treatment at 1350 °C under the flow of argon to obtain SiOC-BSAS coated C/SiC composite. The oxidation behavior of SiOC-BSAS coated C/SiC composite was studied at 1250 °C in dry air for 100 h. The weight loss and the residual flexural strength of coated and uncoated C/SiC composites are compared in Fig. 34.

The weight loss for C/SiC composites without SiOC-BSAS coatings increases with the increase in exposure time. The weight loss is 8.5% after the composites are oxidized for 100 h whereas the weight loss for the composite coated with SiOC-BSAS is only about 3 wt% for the same duration. In the case of residual flexural strength, the composites with SiOC-BSAS coatings retain 72% of their original

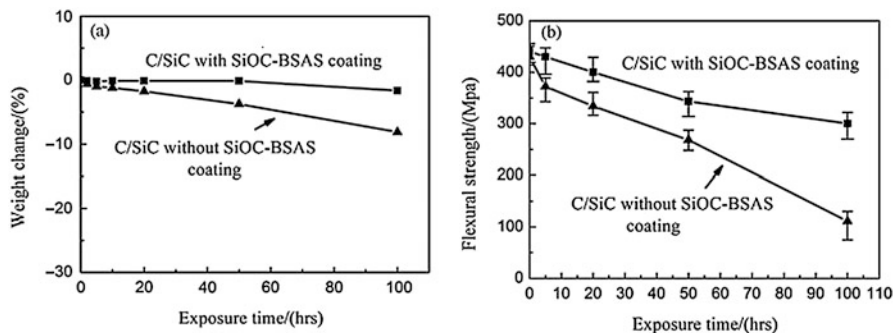


Fig. 34 The oxidation behavior of C/SiC composites with and without SiOC–BSAS coatings in dry air at 1250 °C as a function of oxidation time: (a) weight change, (b) residual flexural strength. (Reproduced from Ref. [225] with permission from John Wiley and Sons)

strength after oxidized for 100 h, while the composites without coating retain only 25% of their original strength.

The water vapor corrosion behavior of uncoated and SiOC–BSAS-coated C/SiC composites was carried out at the temperature of 1250 °C in an atmosphere of 50% O₂–50% H₂O with a flowing rate of $8.5 \times 10^{-4} \text{ m s}^{-1}$ (Fig. 35).

C/SiC composites without SiOC–BSAS coating undergo a considerable weight loss, while the ones with SiOC–BSAS coatings show little weight loss during corrosion in water vapor [225]. The results indicate that the polymer-derived SiOC–BSAS coatings can effectively block oxygen and the water vapor attack. In the case of uncoated composite, SiC matrix reacts with oxygen and water vapor to form SiO₂ scale on the surface of the composite at the very beginning of water vapor corrosion. Though this process results in weight gain, the silica formed reacts with water vapor resulting in the formation of gaseous Si(OH)₄ which causes weight loss. This recession process leads to the formation of cracks in the composite through which oxygen and water vapor diffuse into the composite. As far as the residual flexural strength is concerned, C/SiC composite with SiOC-BSAS coating retains 80% of the original flexural strength even after exposure to water vapor at 1250 °C for 200 h.

Liu et al. [244] have studied SiCN–Sc₂Si₂O₇ as environmental barrier coatings for C/SiC composite using polysilazane as binder and Li₂CO₃ as sintering aid. The dense SiCN–Sc₂Si₂O₇ coatings were obtained after heat treatment at 1250 °C for 2 h under argon. Addition of Li₂CO₃ as sintering aid lowered the sintering temperature by about 200 °C. Water vapor corrosion of the C/SiC composites with and without SiCN–Sc₂Si₂O₇ coatings were carried out at 1250 °C for 200 h. The results showed that the SiCN–Sc₂Si₂O₇ coatings could effectively block the water vapor attack at high temperatures, and the sintering additive did not deteriorate the corrosion resistance of the SiCN–Sc₂Si₂O₇ coatings.

Boron and silicon containing polymers are ideally suited for protection of C/C composites as they would form mixed non-oxide ceramics on heat treatment, having better thermo oxidative stability than simple non-oxide ceramics [245]. On

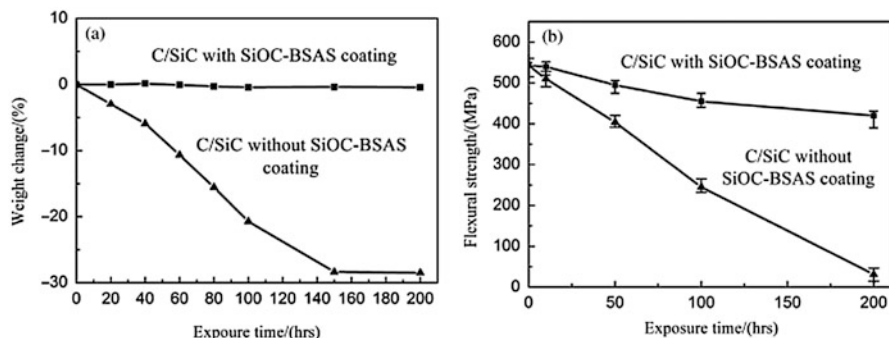


Fig. 35 Corrosion behavior of C/SiC composites (a) weight change and (b) residual flexural strength as a function of corrosion time with and without SiOC-BSAS coating. (Reproduced from Ref. [225] with permission from John Wiley and Sons)

oxidation, the mixed non-oxide ceramics would form borosilicate glass which can melt and flow into the cracks thereby sealing the pathways for oxygen entry [246]. Devapal [60] evaluated poly(phenylborosiloxane)-based SiC coating for the protection of C/C composites. Initial attempts to prepare SiC coating by heat treatment of poly(phenylborosiloxane) with SiC inert filler has not been successful due to the poor adhesion of the coating onto C/C composite. In order to overcome this problem, poly(phenylborosiloxane) was blended with addition-curable phenolic resin. Addition-curable phenolic resin was chosen in place of conventional phenolic resin as the former gives higher carbon residue. Elemental silicon and SiC were used as fillers. The amount of silicon was chosen in such a way that there is no free carbon left in the sintered coating. The precursor coating was applied onto C/C composite coupons by spray coating, cured at 150 °C, pyrolyzed at 900 °C, and then heat treated at 1450 °C. The coating process was repeated to get a crack free coating of required thickness (150–200 μm). SiC coated and uncoated C/C composite coupons were subjected to oxidation test in a muffle furnace maintained at 1000 °C. The samples were removed at 5 min interval and allowed to cool to room temperature and weighed. The samples were exposed to the oxidizing environment for a total period of 50 min. This exposure is a severe test as the sample is taken to high temperature rapidly and brought back to room temperature suddenly which would cause thermal shock. Scanning electron micrographs of uncoated C-C composite and SiC coated C-C composite before and after exposure to oxidizing environment are shown in Fig. 36. The mass loss of uncoated C/C composite is about four times higher than that of SiC coated C-C composite. After 50 min of exposure to the oxidizing environment, SiC coated C/C composite loses 45.77 mg/cm² whereas uncoated C/C composite loses 197.05 mg/cm². It is noticed that while the dimension of the sample remained the same in the case of SiC coated C/C composite, for uncoated C/C composite the dimension of the sample decrease continuously on exposure to oxidizing environment. The mass loss of 45.77 mg/cm² after 50 min of exposure for

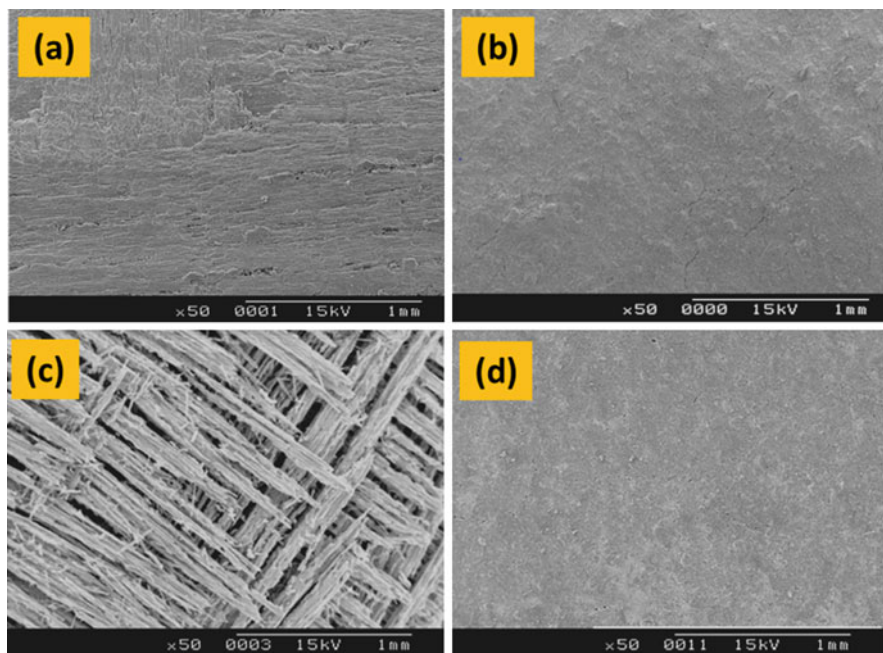


Fig. 36 SEM of (a) C/C composite, (b) SiC coated C/C before, (c) C/C composite, and (d) SiC coated C/C composite after oxidation [60]

SiC coated C/C composite suggests that there are certain defects in the SiC coating through which oxygen gets entry to C/C composite causing erosion.

From the micrographs it is quite evident that the uncoated C/C composite undergoes extensive surface erosion leading to degradation of both the matrix and the reinforcement. No such surface erosion is noticed on the SiC coated C/C composite. As discussed earlier, about 9.71% mass loss is noticed for the coated composite on exposure to oxidizing environment. A closer look at the SEM of SiC coated C/C composite before exposure to oxidizing environment reveals the presence of micro-cracks (Fig. 37).

These cracks were probably formed when the sample was allowed to cool after sintering. Though the cooling rate was slow (3 °C/min), the formation of cracks could not be eliminated probably due to the thermal expansion mismatch of C-C composite and SiC coating and also due to the shrinkage caused by the evolution of volatiles from borosiloxane oligomer and addition-curable phenolic resin. The cracks on SiC coating formed during sintering and in actual service can be sealed by providing an overlay glass coating. For this purpose, a borosiloxane oligomer devoid of carbon was prepared by reacting boric acid with tetraethoxysilane by nonaqueous sol-gel process. At temperatures above 1400 °C, it melts and forms a smooth glass coating (Fig. 38).

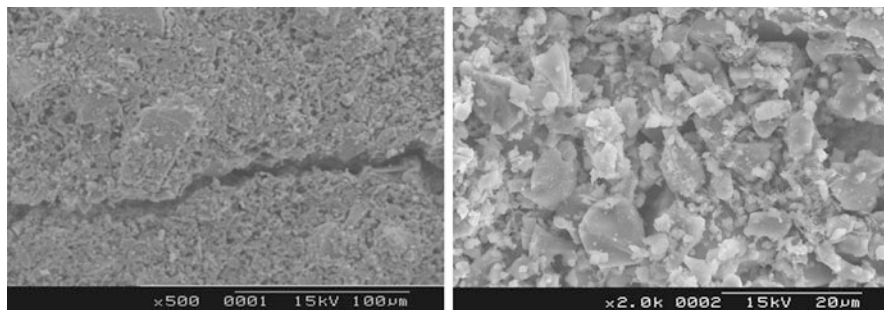


Fig. 37 SEM images of SiC coated C/C composite exposed to oxidizing environment [60]

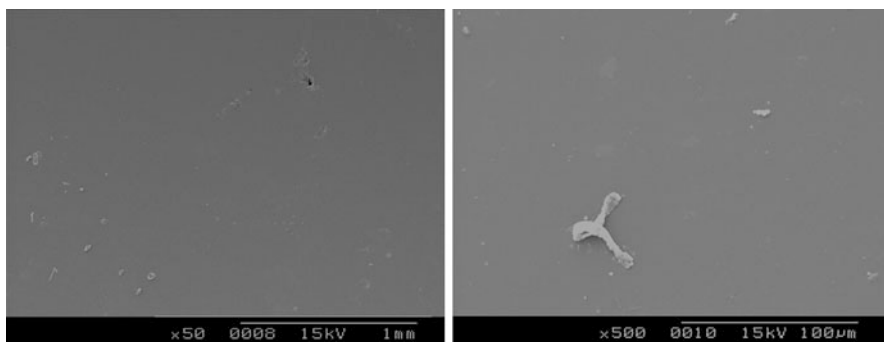


Fig. 38 SEM of glass coating from boric acid and tetraethoxysilane [60]

Possibility of using phenolic resin-based SiC coating for protecting C/C composites as thermal protection system/thermostructural material for reusable launch vehicle, pylon leading edges, and splitter for air-breathing engines and reentry missions have been explored by researchers at the Vikram Sarabhai Space Centre [247, 248]. Phenolic resins such as phenol-formaldehyde and phenol-furfuraldehyde or addition-curable phenolic resins with elemental silicon and glass forming additives were used as the precursor for oxidation resistant coatings. In a multilayer coating process, the composition of each layer is suitably adjusted to achieve a final coating of desired thickness with good adhesion to the substrate. Glass forming additives in the top most layer ensure that the coating is free from cracks. Eddy current (EC) methodology was used for nondestructive assessment of thickness of SiC coating on C/C composite [249]. Unlike in other techniques, where approximate coating thickness is determined by weight gain method, this technique can be used for evaluation of the coating thickness with error less than $\pm 5 \mu\text{m}$. The methodology could identify undercoated (thickness $< 20 \mu\text{m}$) specimens. Thus, it is possible to assess the efficacy of coating process and to readily identify thin coatings using Eddy current imaging. Based on this input, rework on the coating can be carried out to achieve uniform/desired thickness.

For qualifying the multilayer SiC coated C/C composite for use in reusable launch vehicle demonstrator, C/C composite coupons with multilayer SiC coating (thickness: coating of $\sim 200\text{--}250\ \mu\text{m}$) were subjected to kinetic heat simulation (KHS) and arc-jet tests. The actual temperature encountered by the coating was $\sim 1600\ ^\circ\text{C}$. SEM images of the SiC coated samples before and after kinetic heating simulation test are shown in Fig. 39. Practically no mass loss was observed after KHS test.

In order to improve the capability of SiC coating, after two layers of SiC coating silicide-based glass coating is given as the outermost layer. C/C composites with this multilayer coating were subjected to the required heat flux in the plasma wind tunnel facility. The coating withstood the test without undergoing erosion.

C/C composite nose cap was coated with multilayer SiC coating of thickness $\sim 250\ \mu\text{m}$ [247] and was successfully flown in the India's first Reusable Launch Vehicle Demonstrator (RLV-TD) (Fig. 40) [248, 250].

Yet another area of application for SiC coated C/C composites is in air breathing engines (scramjet engines). They are being developed as an advanced alternative for conventional jet engines, for improving the long-term performance and reusability. Conventional jet engines use a compressor to squeeze air into the engine, then spray fuel into the compressed air and ignite it to produce thrust by funneling it through the back. On the other hand, a scramjet engine uses the speed of the aircraft to compress the air into the engine and, hence, requires very few moving parts for its operation. A scramjet engine consists of a constricted tube through which inlet air is compressed by the high speed of the vehicle, a combustion chamber where fuel is combusted, and a nozzle through which the exhaust jet leaves at higher speed than the inlet air.

Air breathing engines should have significantly higher specific impulse within the atmosphere than rocket engines. To achieve this, the incoming air should be directed into the combustion chamber to attain supersonic compression. This is accomplished by using leading edge structures as the tip portion of the inlet body. Its main function is to direct the incoming air into the combustion chamber. One of the key issues in developing an air breathing engine is the oxidation protection of these leading edges

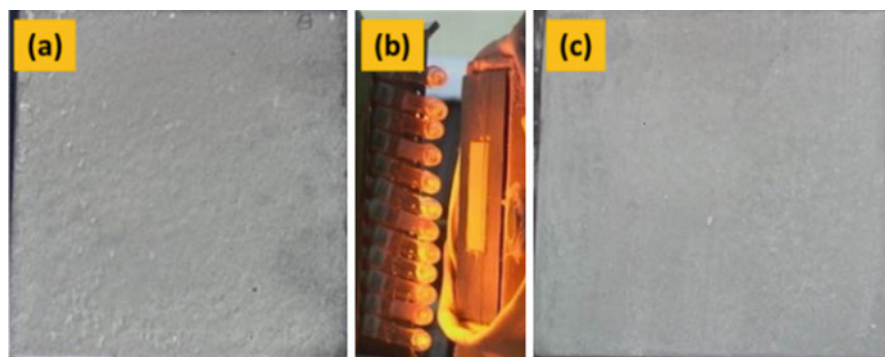


Fig. 39 SiC coated C/C sample (a) before, (b) during, and (c) after KHS test



Fig. 40 (a) RLV-TD with SiC coated C/C composite nose cap (inset), (b) RLV-TD in launch pad [248, 250]

as the engine is operated at high temperatures. Predictions for the top speed of a scramjet engine vary between Mach 12 and Mach 24 (orbital velocity) [251]. Studies often plan on “active cooling,” where coolant circulating throughout the vehicle skin prevents it from disintegration. Often the coolant is the fuel itself, in much the same way that modern rockets use their own fuel and oxidizer as coolant for their engines. All cooling systems add weight and complexity to a launch system and reduce its efficiency. The increased cooling requirements of scramjet engines result in lower efficiency. In place of such a complex system, a single material can be used which can withstand the following: (i) very high temperatures, (ii) steady-state and transient localized heating from shock waves, (iii) high aerodynamic loads, (iv) high fluctuating pressure loads, (v) severe flutter, vibration, fluctuating, and thermally induced pressures, and (vi) erosion from airflow over the vehicle and through the engine.

SiC coated C/C composite is one of the primary candidate materials for use in air-breathing engine as combustion chamber, pylon leading edges, and sidewall leading edges. As the leading edge would face a severe thermooxidative environment compared to the rest of the components, the focus has been to develop a suitable process for SiC coating of C/C composite leading edges. SiC coating process similar to the one used for reusable launch vehicle using phenolic resin as carbonaceous binder was used for obtaining SiC coated C/C composites. Both brush coating and spray coating techniques were used to achieve a coating thickness (for three layers) of $\sim 200 \mu\text{m}$. The SiC coated C/C leading edge (Fig. 41) obtained after buffing was subjected to arc-jet test, simulating the operational environment of an air breathing engine. During the test, the leading edge was exposed to a heat flux of 250 W/cm^2 using a jet of argon plasma containing 25% O_2 for duration of 14.5 s. The leading edge was allowed to cool in the test stand. The coating was free from cracks. The test was repeated for a duration of 20 s and then for 40 s. The surface temperature profile of the leading edge during the third test (40 s duration) is shown in Fig. 42.

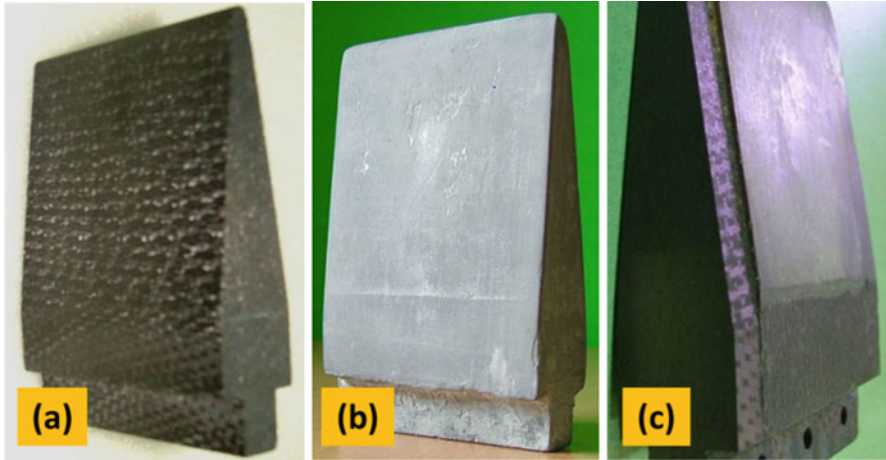


Fig. 41 SiC coated C/C composite pylon leading edge: (a) uncoated C/C composite, (b) SiC coated C/C composite, (c) SiC coating after buffing

Even after three exposures, the coating was intact without any erosion. Thus, the sample was able to withstand the arc-jet test for the required flight conditions. As the SiC coated leading edge withstood the above test, another leading edge with SiC coating was subjected to heat flux corresponding to air breathing propulsion and the coating withstood the test without any erosion. During the actual use, the full length of the leading edge would experience the severity of the environment. In an attempt, to simulate this condition, the width of the leading edge was reduced from 67 mm to 15 mm so that the full length of the leading edge gets exposed to arc-jet. No erosion is observed, and the color change observed at tip is attributed to the loss of excess carbon during arc-jet test (Fig. 43).

After successful testing of SiC coated C/C pylon leading edges, they were further subjected to ground level test under pressure. SiC coated pylon leading edges (width 67 mm and radius of curvature 1 mm) were subjected to hot test under the following test conditions for a duration of 16 s as against the actual requirement of 7 s: temperature 1527 °C, air pressure 12 bar, oxygen pressure 2.5 bar (20.8%) by volume, and Mach No. 2.5. The coating was intact without any erosion. Boundary layer splitter (BLS) and Side Wall Leading Edge (SWLE) with two layers of SiC coating and one top layer silicide coating were tested in arc-jet facility for qualifying these components in scramjet engine test. SiC coated pylon leading edges, BLS and SWLE were successfully tested in the scramjet engine technology demonstrator at Mach 6 using Advanced Technology Vehicle in August 2016 [252].

Depending on the mission, the oxidation protection coating thickness and composition required are to be fine-tuned to meet the mission objectives. The SiC coating procedure described for reusable launch vehicle and air-breathing engine dual mode ramjet engine module could not meet the requirements of ballistic reentry. In a ballistic reentry, TPS experiences stagnation temperature well above 2000 °C.

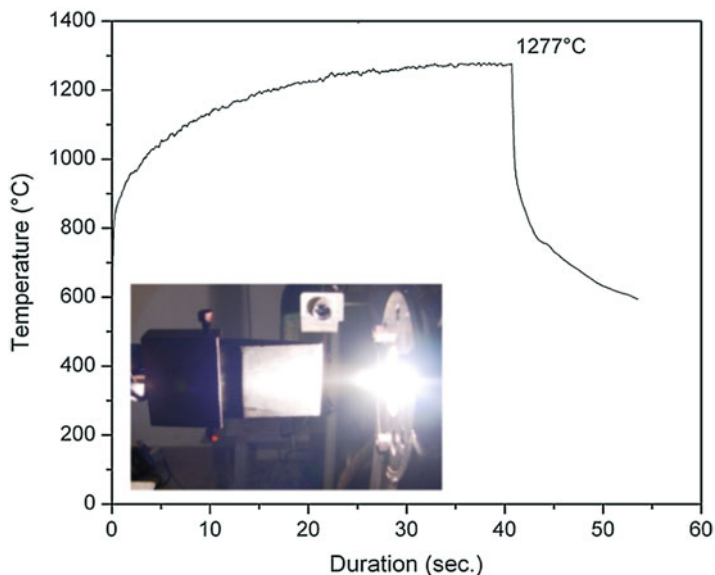


Fig. 42 Arc-jet testing (third test) of SiC coated pylon leading edge



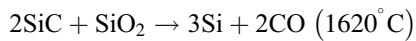
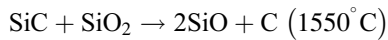
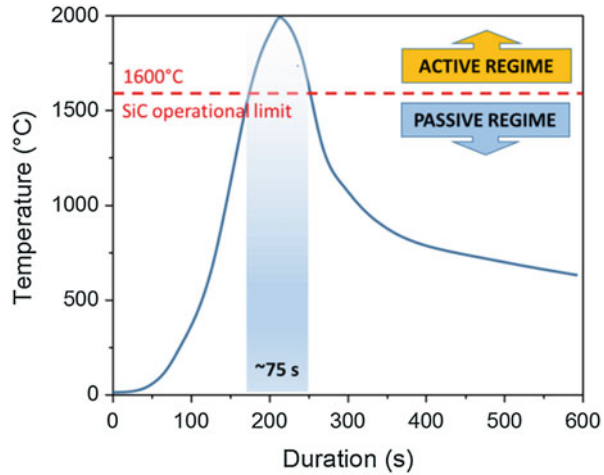
Fig. 43 SiC coated leading edge (width 15 mm; radius of curvature 1 mm): (a) before and (b) after exposure to arc-jet

A typical temperature history of SiC coated C/C composite during ballistic reentry mission is given in Fig. 44 [253].

SiC coating is suited for use at temperatures below 1620 °C and above this temperature under low partial pressures of oxygen, considerable erosion takes place. When the temperature increases above 1620 °C the oxidation completely shifts from passive to active oxidation, causing sudden increase in temperature which is known as “Temperature Jump Effect” [254]. The reactions involving SiC which take place at different temperature regimes are given below:



Fig. 44 Temperature history of SiC coated C/C composite during ballistic reentry [253]



Below 1420 °C passive oxidation of SiC takes place forming SiO₂ which prevents further oxidation of SiC. Transition from active oxidation to passive oxidation takes place forming gaseous SiO in the temperature range of 1420–1620 °C, and above 1620 °C, active oxidation only occurs resulting in considerable erosion of the coating. Increasing the coating thickness from 250 μm to 500 μm could not protect C/C composite thermal protection system. Sreeja et al. [255] investigated the possibility of giving an unsintered coating over SiC coating which will take away the initial heat by way of pyrolysis of carbonaceous polymer used as a binder and bring down the temperature below 1620 °C. This concept was tested using graphite substrate (Fig. 45).

It is observed that the unsintered sealant coating is able to bring down the stagnation temperature by about 600 °C [255]. Hence, this sealant coating was given over SiC coating to shift the active oxidation to passive oxidation. Yet another advantage of giving a sealant coating is that it would seal the cracks in SiC coating formed during processing. This approach has been successfully adopted for oxidation protection of C/C composite noseshell (Fig. 46).

Carbonaceous polymer-based coating process which was used successfully for protecting C/C composites was not adhering well to C/SiBOC composites and a multilayer coating process was developed in which pyrolyzed borosiloxane oligomer was used as a filler in addition to glass forming additives. The coating withstood the heat flux history of reentry vehicle [256].

Fig. 45 Temperature profile of (a) uncoated and (b) sealant coated sample [255]

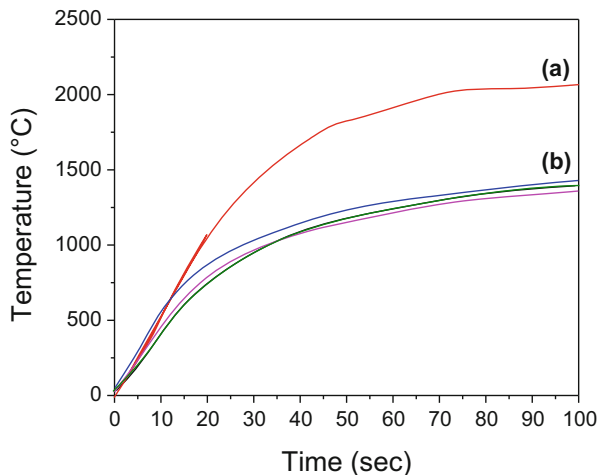


Fig. 46 SiC coated C/C noseshell (dia. 960 mm) with sealant coating [255]



Oxidation Resistant/Environmental Barrier Coatings on Metals

High temperature metals and alloys are extensively used as hot structural components in aerospace industry as turbine blades, exhaust nozzles, actively cooled combustion chambers, etc. [257]. These metal surfaces are to be protected at high temperatures in order to prevent oxidation by corrosive gases and the catalytic activity of the metal surface which enhances the surface temperature. Hence, it is required to design a suitable protection system comprising of inhibitors, sealants, and coatings for these metallic hot structures at high temperature [258]. Different precursors such as polymethylsilsesquioxane [259], poly(hydridomethylsiloxane) [260], polysiloxane [261, 262], polymethoxymethylsiloxane [262], and hydroxy-terminated linear polysiloxane [262] were investigated on substrates such as steel, stainless steel, titanium, aluminum, magnesium, and zinc using various coating methods such as spray coating, dip coating, spin coating, and PE-CVD. Polymer-derived ceramic coatings for oxidation protection of metal substrates have been

described in recent reviews [13, 263], and hence, the discussion is confined to a few of the important developments in this area.

Günthner et al. [264] prepared PHPS by the ammonolysis of dichlorosilane and ABSE polycarbosilazane by ammonolysis of bis(dichloromethyl)silylethane, and evaluated them as protective coatings for SS. PHPS and ABSE, on heat treatment at 800 °C, form ceramic-like gradient coatings, which successfully protected stainless steel sheets from oxidation up to 1000 °C. The gradient Si(N)CrO layers act as a diffusion barrier against oxygen and reduce the weight gain and the oxidation kinetic constant up to two orders in magnitude (Fig. 47).

Pyrolysis of precursor to ceramics results in porosity and residual stress caused by the shrinkage. These problems can be overcome by the use of passive fillers like BN, ZrO₂, or Al₂O₃ and active fillers like ZrSi₂ and TiSi₂ [264]. Günthner et al. [265] formulated a high performance environmental barrier coating system consisting of a perhydridopolysilazane (PHPS) bond coat and a polysilazane-based glass/ceramic composite top coat for mild steel substrates. The thermal treatment of the coating was performed in air at 800 °C. The critical coating thickness of the coating systems was increased up to 100 μm by optimizing the volume fraction of the fillers and the processing parameters. Cyclic oxidation tests showed that the coating system protects mild steel against oxidation up to 700 °C. Wang et al. [266] studied PDC matrix composite coatings for oxidation protection of Inconel 617, a superalloy, using a simple dip coating method. Three coating systems, viz., SiON coating, particle filled SiOC coating, and their combined coating system, were evaluated by conducting long time

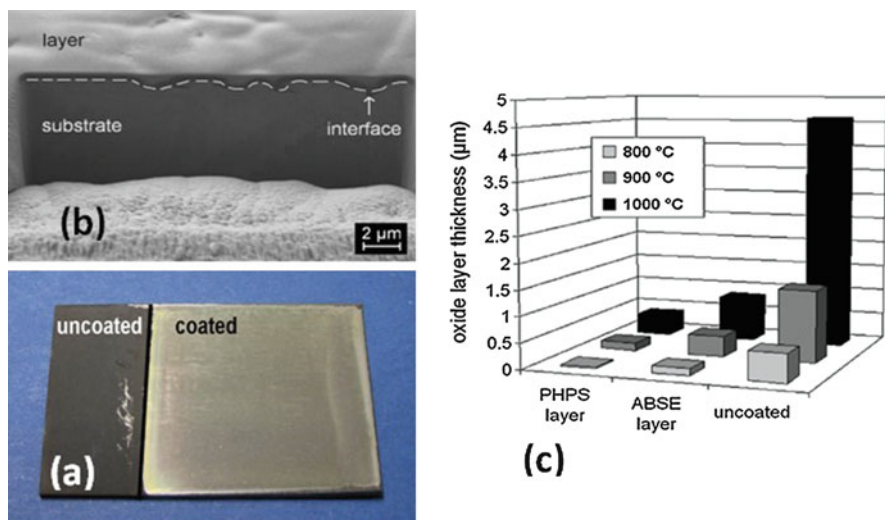


Fig. 47 (a) PHPS coated steel substrate oxidized at 1000 °C for 1 h in air, (b) SEM of the coated substrate oxidized at 500 °C for 1 h in air, and (c) Oxide layer thickness after oxidation at 1000 °C for 10 h in air. (Reproduced from Ref. [264] with permission from Elsevier)

static oxidation test at 800 °C for 100–200 h. The double layer coating system comprising of SiON bond coat and particle filled SiOC top coat was found to be the most effect one in maintaining the integrity of the substrate subjected oxidation test for 200 h.

Parchoviansky et al. [267] also investigated a double layer coating system with a PDC bond coat and a glass/ceramic filled PDC top coat as an effective solution for overcoming the disadvantages of PDC-based coatings. The bond coat has multiple roles in the coating system: it protects the metallic surface, increases the adhesion between the surface and the top coat, and reduces the CTE mismatch between the metal and the top coat. A double layer coating consisting of polysilazane based bond-coat was prepared from both PHPS and Durazane1800[®] (prepared by the co-ammonolysis of dichloromethylvinylsilane and dichloromethylsilane), and tested for its high temperature oxidation resistance. The top coat contained high melting SiO₂-Al₂O₃-ZrO₂ glass microspheres. At 900 °C, the TBC has reduced the mass gain due to oxidation to about one-half of that in uncoated steel oxidized under the same conditions.

Riffard et al. [268] evaluated commercially available polysilazane resin (without any filler) for protecting AISI 304 Stainless Steel from oxidation. The coating was applied either by dip or spray coating process. During pyrolysis of the coating at 800 °C for 1 h in air, the initial PHPS-based coating reacted with oxygen leading to the formation of an amorphous silica layer at the steel surface which acts as a diffusion barrier for the chemical diffusing species. This amorphous silica layer acts as a protective glass which provides complete separation of the AISI 304 steel surface from the oxidizing environment.

Polysiloxane-based EBC system for steel in oxidizing environments was developed by Nguyen et al. [269]. Different fillers such as alumina, Al flakes, Cr, Si, W, Zn, and glass frits were used to get a coating thickness of ~36.7 μm. The coating showed good adhesion with the substrate, owing to the lower shrinkage of the ceramic due to the presence of fillers. The presence of glass frits improved the adhesion because of the dissolution of the oxide layer already present on the metal at the interface into glass.

Molybdenum alloys containing boron and silicon are replacing nickel-based super alloys, due to their high physical-mechanical characteristics at high temperatures [270]. On exposure to air, Mo alloys form MoO₃, which evaporates in the temperature range between 400 °C to 800 °C resulting in poor oxidation resistance of these alloys. Mo₅SiB₂ filled PHPS was used as coating for protecting Mo-Si-B alloy [270]. This coating was effective in reducing the oxidation rate by 50% at 1100 °C. The improvement in oxidation resistance is attributed to the presence of amorphous SiO_xN_y phase and silica phase formed from free Si present in the PHPS-derived ceramic.

Thermal Barrier Coatings for Metals

Oxidant resistant coatings and environmental barrier coatings for metals described in the preceding section may not bring down the surface temperature of metallic substrate. In order to induce a temperature drop on the metal surface, it is essential

to develop thermal barrier coatings (TBCs) [271, 272] the concept of which is given in Fig. 48.

The earliest TBCs were frit enamels based on alumina/zirconia which were applied to aircraft engine components in the 1950s [273]. The effectiveness of these coatings was limited by the relatively high thermal conductivity of alumina and low phase stability of zirconia-based materials. The use of TBCs has resulted in a significant improvement in the efficiency of aircraft gas turbines [274] and the same is achievable in land-based gas turbines. By using TBCs temperature differentials across the coating of as much as ~ 300 °C can be achieved. This temperature drop reduces the thermally activated oxidation rate of the bond coat applied to metal components and hence, delays failure by oxidation. It also retards the onset of thermally induced failure mechanisms that contribute to component durability and life.

One of the important developments was the introduction of NiCrAlY bond coats and yttria-stabilized zirconia (YSZ) topcoats in the mid-1970s. YSZ has become the preferred TBC layer material because of its low thermal conductivity, relatively high coefficient of thermal expansion (CTE), and good erosion resistance [275]. While the low thermal conductivity facilitates in bringing down the surface temperature, the high CTE helps to increase the thermal stress capability. In practice, yttria concentration is kept in the range of 6–8 wt%, since this composition results in the formation of a metastable tetragonal phase, which resists the monoclinic transformation of the composition upon cooling. This maximizes spallation life of coatings by inhibiting crack propagation and volume change upon cooling.

By attaching an adherent layer of a low thermal conductivity material to the metal surface, a temperature drop can be induced across the thickness of the layer. This results in a reduction in the metal temperature of the component to which it is applied. Using this approach, temperature drops up to 170 °C at the metal surface have been estimated for 300–400 μm thick yttria-stabilized zirconia coatings. This temperature drop reduces the (thermally activated) oxidation rate of the bond coat

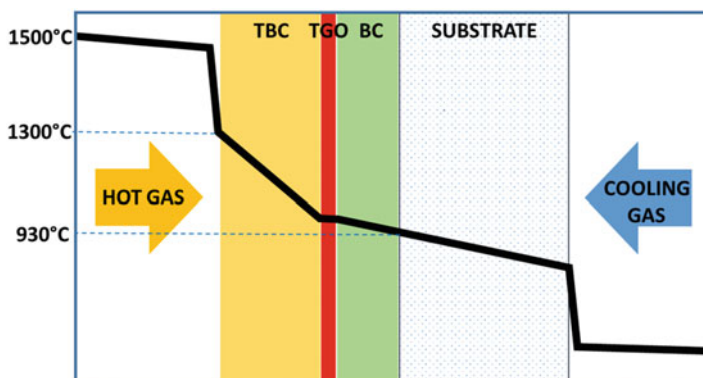


Fig. 48 Schematic of a typical TBC showing distribution of temperature (BC: bond coat; TGO: thermally grown oxide). (Reproduced from Ref. [272] with permission from Elsevier)

applied to metal components, and so delays failure by oxidation. It also retards the onset of thermally induced failure mechanisms that contribute to component durability and life.

In launch vehicles for regions where the flight-induced heating is substantial, thermal protection system (TPS) is used on structural members so that the surface temperature is brought below the temperature where the structural strength degradation is substantial. On the other hand, a hot structural material is that which functionally sustains both the thermal loads as well as the structural loads. The hot structural members in reentry/reusable vehicles are its nose-cap, wing leading edges (WE), elevons, and rudders of which the nose-cap is made of C/C and WLE and vertical tail edges are made of 15CDV6/Inconel metallic alloy. These alloys are also candidate materials in the construction of air-breathing engines. The protective TBC coating required for enabling the application of these alloys must have high emissivity and be thermally and structurally stable during heating and cooling phase.

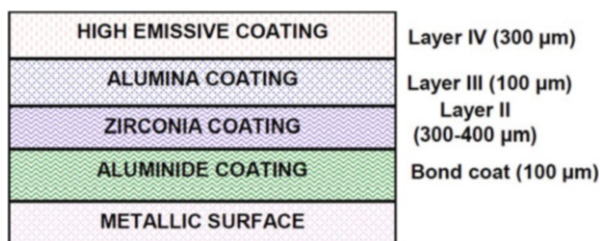
Different techniques are used for deposition of TBCs [275–278]: (i) physical vapor deposition (PVD), (ii) electron beam physical vapor deposition (EB-PVD), (iii) chemical vapor deposition (CVD), (iv) plasma spraying, and (v) polymer-derived ceramic (PDC) route. Of the methods used for TBCs, PDC route is the most recent one which takes advantage of high ceramic yield of the precursors, high purity of starting materials, lower capital investments, lower processing temperatures, variation of micro porosity to tailor the microstructure, and optimization of erosion resistance.

Specifically, for space application, a four-layered coating system (Fig. 49) consisting of bond coat, thermal insulative layer, alumina layer, and final high emissive layer using siloxane as binder has been developed [279] for 15CDV6 steel substrate and the coating performance was evaluated using IR lamp heating simulations at a heat flux of 8.5 W/cm^2 for 1035 s. The tests showed good results for the ceramic coating system with a back wall temperature of $299 \text{ }^\circ\text{C}$. But the coating peeled off during cooling process. This problem has been overcome by using polysilsesquioxane as binder and by modifying the coating process [280]. The modified TBC was tested successfully at 8.5 W/cm^2 for 1035 s (Fig. 50).

Atomic Oxygen Resistant Coatings

The LEO space is a complex, energetic environment, which ranges from an altitude of 200–700 km and from an inclination of $0\text{--}60^\circ$ above the equatorial plane

Fig. 49 Schematic of TBC on metallic substrate using siloxane as binder [279]



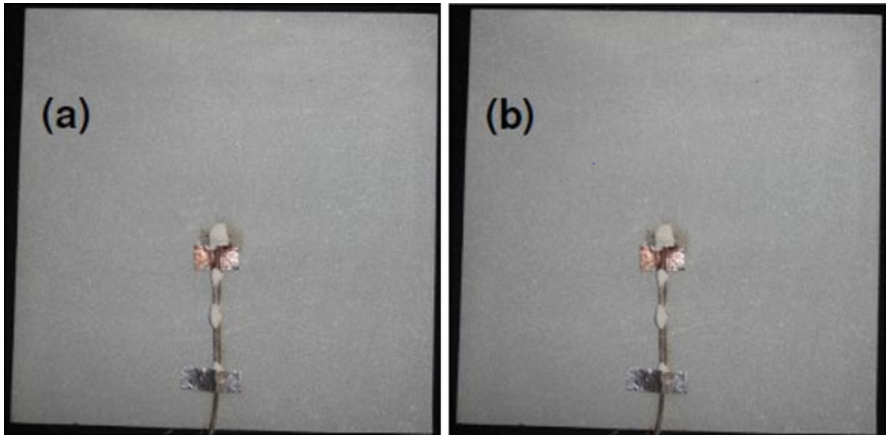
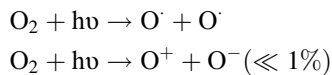


Fig. 50 TBC coating developed via spray coating technique (a) before and (b) after IR lamp heating test [280]

[281]. Effects of different constituents of the space environment on spacecraft materials play a crucial role in determining the system function, reliability, and lifetime. Direct entry to the low earth space environment causes profound alterations of thermal, mechanical, and optical properties of polymeric materials [282]. These effects typically depend on interactions between the spacecraft and the diverse elements of the space environment itself such as: (i) atomic oxygen (AO) on spacecraft materials, (ii) micrometeroid and debris impact, (iii) ultra-high vacuum, (iv) far ultraviolet hard radiation and particles generally, (v) charged particles bombardment, and (vi) space craft charging. In particular, one of the most important factors that gives serious damage to many polymeric materials is AO which is a dominant neutral species in LEO, formed by the photo-dissociation of molecular oxygen as shown below:



AO formed by photodissociation has a very high probability of long-term survival in the low earth altitudes because there is an appropriate O_2 density here to facilitate reasonable AO production and low probability of interaction with neighboring atoms or molecules. The number density of AO at about 300 km altitude is $\sim 2 \times 10^9$ (minimum) to 8×10^9 atoms/cm³ (maximum) during solar activity [281]. At LEO altitudes, the neutral atmosphere consists primarily of AO (80%) and nitrogen molecules (20%).

Though the average thermal velocity of the gas molecules at low earth altitudes is very low, the spacecraft orbiting in the LEO rams into the AO environment at a velocity of 8 km/s producing collision energy in the range of 4.5–5 eV which is adequate enough to cause bond scission in spacecraft materials. Thus, the interaction

of AO with materials used in the construction of spacecrafts and space stations may result in surface erosion, changes in chemical composition and surface morphology, changes in optical properties and formation of particulate and molecular contamination of the spacecraft/space station surfaces [282–284]. To overcome this problem, it is necessary to develop materials that are resistant to AO attack or protect the materials susceptible to AO attack with AO resistant coatings. Metal oxide coatings that have negligible rates can serve as AO resistant coatings. Lack of flexibility, requirement of elaborate sputtering techniques, and pinhole defects of metal oxide coatings are of major concern. Inorganic and inorganic-organic hybrid polymers such as polysiloxanes [285, 286], polysilsesquioxanes [287], polysilahydrocarbons [288], polyphosphazenes [289], phosphorus containing polyimides [290–292], siloxane-imides [293], polyhedral oligomeric silsesquioxane (POSS)-polyimides [294], siloxane-epoxy [295], siloxane-imide-epoxy [296], carborane-siloxanes [297], decaborane-based polymers [298], and polysilazanes [299–301] are capable of overcoming these problems. These polymers on exposure to AO form a thin oxide layer, preventing further reaction of the coating with AO. Even if, AO penetrates into the next layer due to surface defects, the unoxidized virgin polymer underneath the oxide layer would provide self-healing. The thermal expansion coefficients of the virgin polymer and the polymeric substrate are usually close to each other due to which the crack formation on the surface of the coating would be prevented. In this section, the discussion is limited to a few representative precursor systems to exemplify the use of virgin preceramic polymers for yet another space application and a detailed account on AO resistant materials/coating is beyond the scope of this section.

Devapal et al. [288] evaluated the AO resistance of a polydisilahydrocarbon, viz., poly(tetramethyldisilylene-co-styrene) [PTMDSS], whose structure is shown in Fig. 51. PTMDSS offered good protection to polyimide film and carbon composite against AO attack which is clearly seen from the SEM images (Fig. 51). However, this coating was somewhat tacky in nature and this problem was overcome by partly replacing dimethylsilyl units with phenylmethyl silyl units [60].

Chang et al. [301] synthesized a polysilazane by aminolysis of dichloromethylvinylsilane, and the polymer was evaluated for its AO erosion on Kapton film in a ground-based simulator. The mass loss, optical properties, and SEM surface morphology of the samples before and after AO exposure indicate that the polysilazane coating protects Kapton from AO erosion effectively (Fig. 52).

AO resistant coatings have also been obtained by sol-gel process. Arjun et al. [285] synthesized a polysiloxane by acid catalyzed hydrolysis reaction of methyltriethoxysilane and 1,1,3,3-diethoxytetramethyldisiloxane and used this resin for protecting aluminized Kapton, carbon polyimide (C-PI) composite, and glass polyimide composite from AO attack. The mass loss data (Table 6) and FESEM of uncoated and polysiloxane coated samples exposed to AO suggest that polysiloxane obtained by sol-gel process offers excellent protection against AO attack.

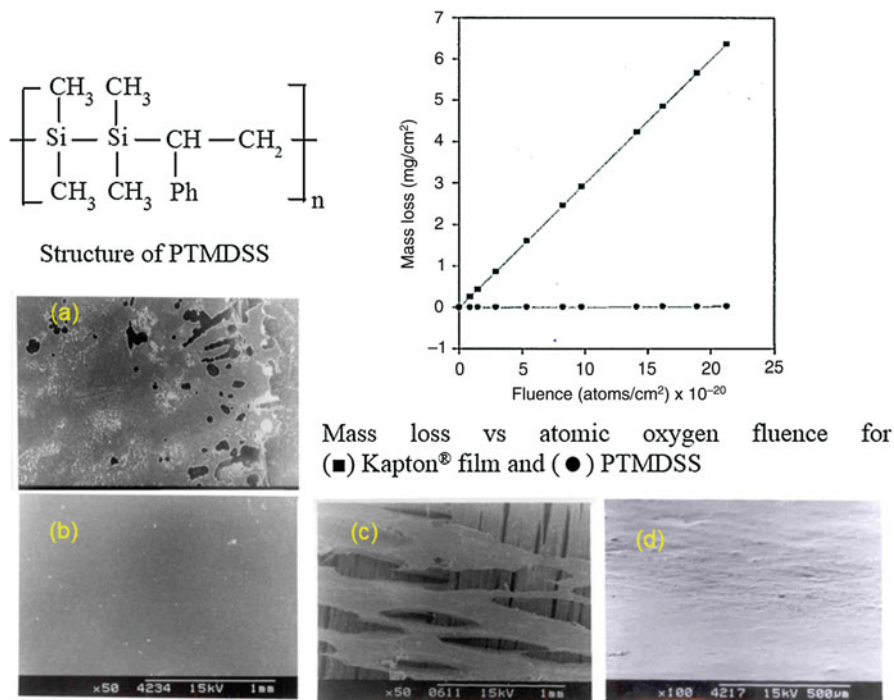


Fig. 51 Evaluation of PTMDSS as atomic oxygen resistant material: SEM of (a) uncoated aluminized Kapton[®] film, (b) PTMDSS coated aluminized Kapton[®] film, (c) uncoated C-polyimide composite, and (d) PTMDSS coated C-polyimide composite exposed to atomic oxygen. (Reproduced from Ref. [288] with permission from John Wiley and Sons)

Ceramic Adhesives

The engineering designs of ceramics and composite components in aeronautics, space transportation, energy, and nuclear industries require fabrication and manufacturing of large and complex shaped parts of various thicknesses. In many instances, it is more economical to build up complex shapes by joining simple geometrical shapes. Thus, joining and attachment have been recognized as enabling technologies for successful utilization of ceramic components in various demanding applications [302–304]. In space applications, C/C-, CMC-, and UHTC-based materials are being evaluated in structural parts such as leading edges, nosecone, and nozzles for hypersonic vehicles, which require proper joining technologies. Requirement also exists for non-space applications such as joining of C/C to Cu alloys and SiC/SiC to SiC/SiC for nuclear components and to join radiator sub elements for heat rejection systems. Different types of joining techniques, viz., brazing, diffusion bonding, riveting, bolting, and adhesive bonding, are currently under usage/progress for ceramic components. Advanced technologies such as

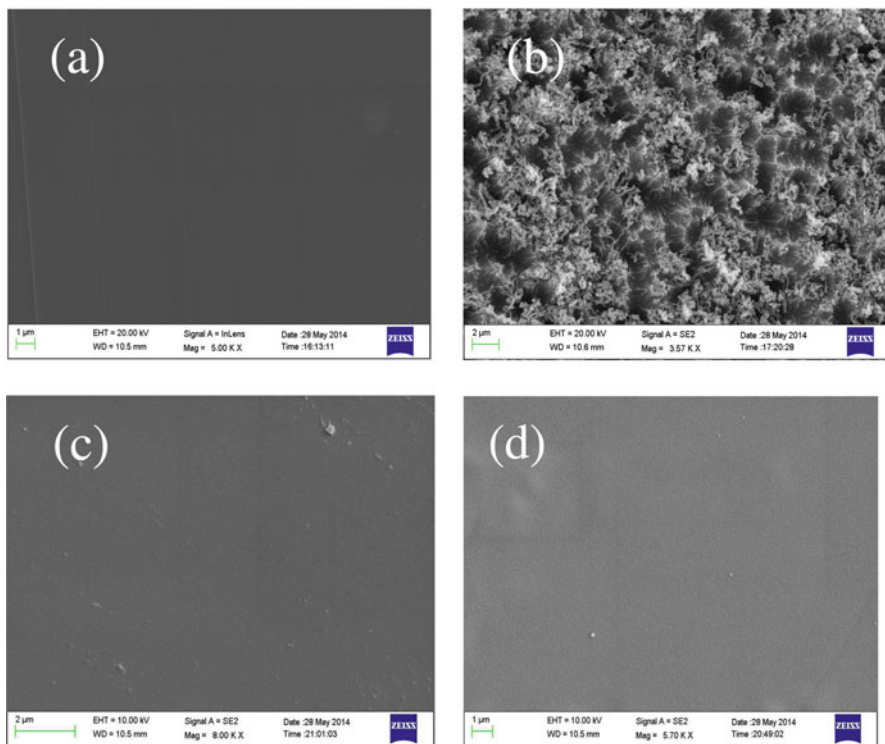
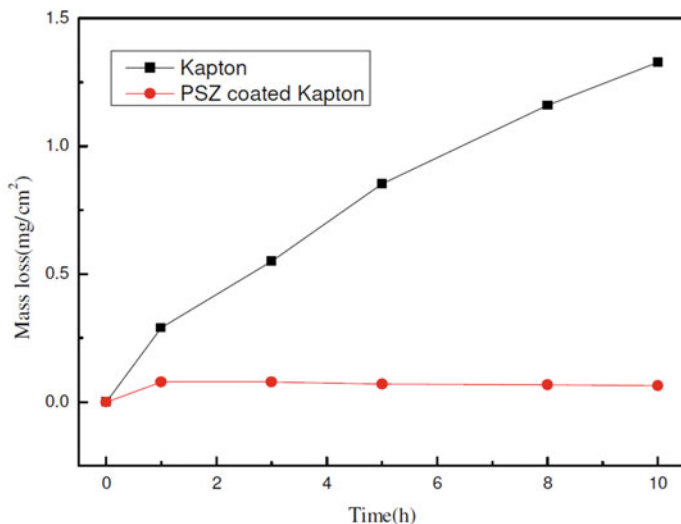


Fig. 52 AO erosion kinetics for Kapton and Silazane coated Kapton and SEM of (a) Kapton film, (b) exposed Kapton, (c) coated Kapton, and (d) exposed coated Kapton. (Reproduced from Ref. [301] with permission from John Wiley and Sons)

Table 6 Mass loss data of aluminized Kapton, C-polyimide composite, and Glass-polyimide composite without and with polysiloxane coating exposed to AO fluence of 1.5×10^{20} atoms/cm². (Adopted from Ref. [285])

Substrates	Mass loss (mg/cm ²) of uncoated samples	Mass loss (mg/cm ²) of polysiloxane coated
Aluminized Kapton	0.48	0.08
C-polyimide composite	4.02	0.09
Glass-polyimide composite	1.77	0.16

ceramic joining using affordable robust ceramic joining (ARCJ) technology, bonding of ceramics to metal by brazing, microwave assisted joining, transient liquid phase bonding, and spark plasma joining have also been developed. The major disadvantage of these techniques lies in huge energy wastage to attain high temperatures, high facility cost of the process, and severe damage to the substrates.

The main technical and performance requirements of a ceramic adhesive joint are: (i) use temperature > 1200 °C, (ii) good strength and oxidation resistance properties, (iii) low CTE mismatch to minimize residual stresses and good thermal shock resistance, (iv) leak tight joints, (v) reliable and affordable technique adaptable to in-field installation, and (vi) service and repair [304]. The other technical challenges involved are in the design and selection of joints, materials related issues, thermo-mechanical properties of the joints, and environmental effects on joint properties. In general, on comparing with other joining techniques, adhesives contribute highly to structural integrity, ease of manufacturing, enhanced performance, improved safety, and cost and time savings. The continuity of the adhesive bond plays a vital role as the loading is borne by the whole bonding plane, not by one or several points. However, the main problem with the application of adhesive for spacecraft is high temperatures. The high temperature adhesive should possess good bonding properties with the various substrates and should withstand the high temperature and various stresses that the system may encounter during reentry. A class of material with such high temperature resistance is ceramic adhesives. Like any other adhesive bonding, the uniform stress area is maintained with a low strain rate during mechanical tests. Further, due to the thin layer of the adhesive, it essentially behaves like a thin film and this would limit the generation of triaxial state of stress within the bonded area leading to overcoming the brittle behavior of ceramics, resulting in its usefulness for structural applications in aerospace industry. The polymeric adhesives (modified epoxies, polyimides, etc.) would undergo cross-linking or chain scission within the polymeric matrix on exposure to high energy radiations, and there is a considerable influence on the mechanical strength of the polymer, while the ceramic adhesives after processing are capable of withstanding high energy radiation and there is no deterioration observed in joint strength. The normal high temperature ceramic adhesives comprise of inorganic materials based on fluorides, sulfides, and oxides of transition and non-transition metals of nearly eutectic composition dispersed within the ceramic matrix. However, if the strain rates are high, there would be limitations in applying this adhesive although the other performances are good.

Thus, a series of heat resistant and high structural adhesive for space applications for frequent usage in heat resistant environments has to be developed.

As moved by the tragedy of failure of Columbia in February 2003, worldwide extensive research has been initiated for developing ultra-high temperature ceramic adhesives to repair cracks and holes on the shuttle wings and nose during voyage of manned mission. NASA has developed an adhesive called Non-Oxide Adhesive eXperimental (NOAX), a high-tech formulation of preceramic sealant (hydridopolycarbosilane) mixed with silicon carbide powder and other fillers designed to meet NASA's stringent specifications for space flight. The adhesive was used to fill cracks or losses in protective coatings up to 0.5 mm wide and 100 mm long, and it was designed to get semirigid after exposure to several hundred degrees of heat, but would not harden completely until it experienced the extreme temperature of reentry into earth's atmosphere [305–307]. Another ceramic adhesive, viz., Glenn Refractory Adhesive for Bonding and Exterior Repair (GRABER), was developed at the NASA Glenn Research Centre for the repair of reinforced carbon/carbon (RCC) composite thermal protection systems structures [308]. The GRABER material has shown multiuse capability for the in-space repair of small cracks and as an adhesive and sealant for RCC-leading edge material. It is a refractory adhesive paste with desired ceramic fillers in polymer/phenolic resin matrix with appropriate additives such as surfactants. The paste was applied to the damaged or cracked area of the RCC composite components with a caulking gun, and cured at 100–120 °C which transformed into a high temperature ceramic during reentry conditions. The repaired samples were successfully tested (Fig. 53) under the arc-jet facility at the NASA Johnson Space Centre.

Sreeja et al. [255] formulated a ceramic adhesive useful for joining different substrates for space applications. Phenol-formaldehyde/phenol-furfuraldehyde resins were mixed with elemental silicon and glass forming additives to formulate adhesives which cured at temperatures below 200 °C. The adhesive underwent in situ polymer to ceramic conversion at high temperatures/re-entry conditions with the simultaneous formation of SiC and silica-based glass which sealed the cracks formed during the conversion process. This was proved by carrying out arc jet testing of

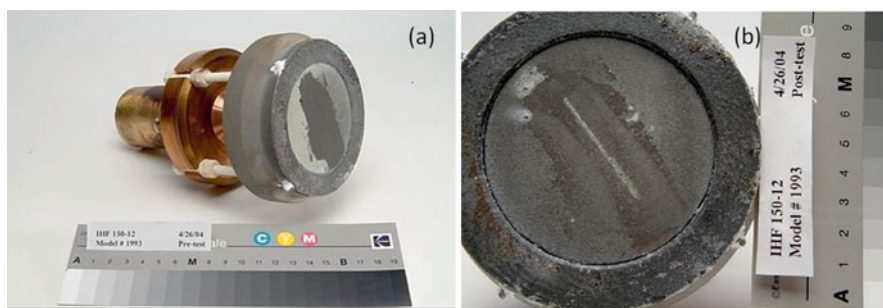


Fig. 53 RCC specimen with crack (width: 0.89 mm) repaired: (a) pre-arc jet test and (b) post-arc jet test. (Adopted from Ref. [308])

graphite specimens joined together using phenolic resin at reentry conditions. The high temperature ceramic adhesive was also evaluated for crack repair of C/C composites and CMCs. A cavity of dimension 20 mm × 2 mm × 1 mm was made in SiC coated C/C coupon and sealed with the high temperature adhesive, cured and tested under arc-jet (Heat flux of 300 W/cm² for 50 s; 20% O₂) (Fig. 54). The repaired part remained intact (Fig. 55). There was negligible mass loss observed and the joint was intact.

Besides, carbonaceous polymers and hydridopolycarbosilane, other preceramic polymers have also been evaluated for applications as high temperature adhesives [309–317]. The development of ceramic adhesives from preceramic polymer route is noted for its easy application and significantly lower processing temperature. Also, there is no problem of residual reactant products, which may adversely affect the joining as in the case of reaction based approach. However, large volume shrinkage associated with the conversion of preceramic precursors to covalently bonded network structures leads to formation of cracks during processing. The use of inert fillers such as SiC, B₄C, Al₂O₃, and silica and active fillers such as Al, Si, Si-Al, Ti, MoSi₂, CrSi₂, and TiSi₂ improves the strength and quality of joints [309]. The final properties of joints such as maximum temperature of use, chemical compatibility with substrates or fillers, thermal expansion, gas evolution, yield, wetting behavior, processing procedure, joint density, presence of cracks, joint thickness, shrinkage stresses, joint microstructure, and composition are found to be affected by several parameters. These parameters are the following: polymer composition, polymer ceramic yield, rheology of joining mixture, heat treatment (maximum temperature, dwell time, heating rate, atmosphere), type and amount of fillers, and type of substrate (composition, surface morphology) [309].

A new class of material, inorganic geopolymer, has been intensively studied as a viable economical alternative to organic polymers and inorganic cements in developing refractory adhesives for military and aircraft applications [318]. Geopolymer-based adhesives have exceptionally high thermal and chemical stability, compressive

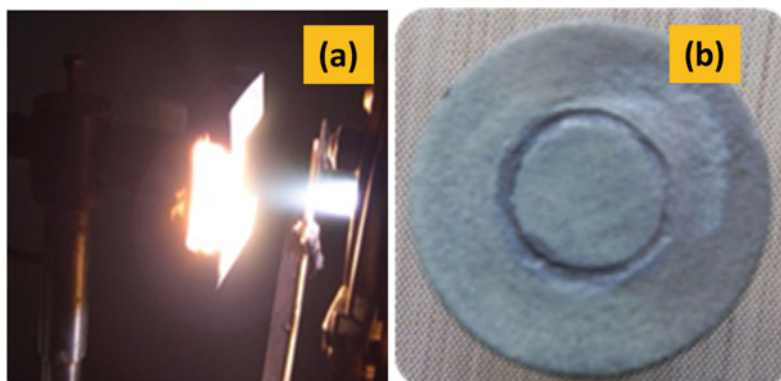


Fig. 54 Graphite test specimen assembled together using high temperature adhesive: (a) arc jet testing and (b) tested specimen [255]

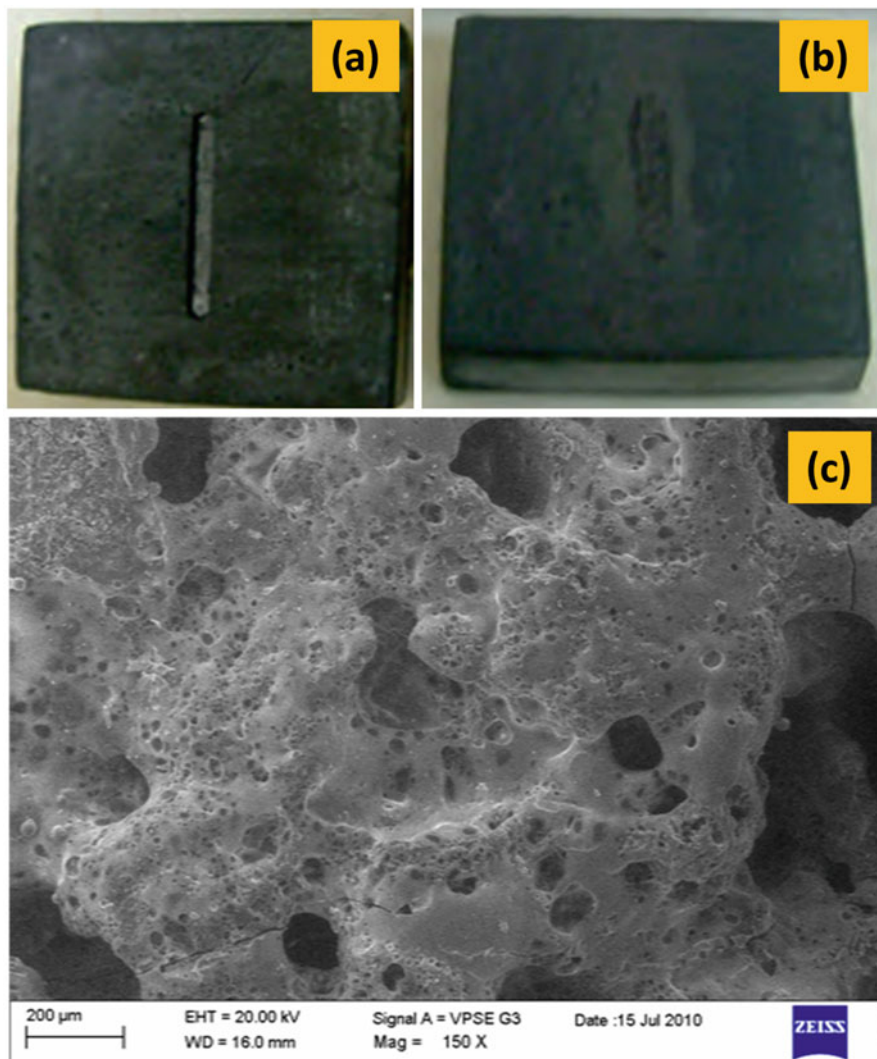


Fig. 55 (a) Cavity in SiC coated C/C composite, (b) cavity filled with high-temperature adhesive, and (c) SEM of repaired part after test [255]

strength, and adhesive behavior. Geopolymers are inorganic aluminosilicates formed by polycondensing tetrahedral silica (SiO_4) and alumina at ambient or low temperatures ($<150^\circ\text{C}$) into polymeric structures. Lower ratios of $\text{SiO}_2:\text{K}_2\text{O} = 1\text{--}3$ result in three-dimensional cross-linked rigid networks with brittle properties, whereas higher ratios of $\text{SiO}_2:\text{K}_2\text{O} = 3\text{--}15$ give rise to two-dimensional/linearly linked structures with adhesive and rubbery properties. Compared to silicate-based adhesive compositions, aluminosilicate-based adhesive compositions (geopolymers)

have excellent physicochemical and mechanical properties, which include low density, micro-porosity or nano-porosity, negligible shrinkage, high strength, thermal stability, high surface hardness, and fire and chemical resistance. They have high melting points but can undergo structural transformations at lower temperatures without causing the materials to change dimension and porosity. These desirable properties render these materials as ceramic adhesives. The alkali silicate solid or liquid solution is used for dissolution of raw materials to form reactive precursors required for geopolymerization.

Sreeja et al. [319] developed an alkali activated aluminosilicate geopolymer for bonding metals to ceramics and metal to metal, for high temperature applications. The bonding was achieved at 175 °C by solid state reaction of alkaline solution of alkalisilicate precursor with the refractory filler, contributing to the bulk aluminosilicate matrix. This adhesive was used for bonding silica tile to Inconel (Fig. 56). The bonding remains intact even after heating to 500 °C in a muffle furnace.

Lightweight Ceramics

Lightweight ceramics include ceramic foam, ceramic honeycomb, ceramic sandwich structures, and shingles. These materials have been evaluated for space applications as lightweight thermal protection systems, micrometeoroid and debris protection systems, and space mirrors.

Cellular Ceramics/Ceramic Foam

Cellular ceramics are ceramic materials with good level of porosity, where the porosity is present as repeating or non-repeating hollow cells. The cells can be regular in size and shape as in a honeycomb structure or irregular as in a foam structure. Other architectures also exist such as interconnected structures [320]. Cellular materials are characterized by low density, high specific area, high tortuosity of flow paths, and low thermal conductivity [321].

Fig. 56 Inconel/silica tile bonded specimen after heated to 500 °C in a muffle furnace [319]



The characteristics of cellular ceramic depend on the morphology of the cells which is strongly influenced by the processing methodology. Each fabrication method is best suited for producing a specific range of cell sizes, cell size distribution, and overall amount of porosity [322]. Wide range of processing routes such as replication technique or polymeric sponge method, direct foaming method, and burn-out technique were developed to produce ceramic foams. The basic principles of these methods are schematically presented in Fig. 57 [323].

CVD/CVI method is also used for the preparation of ceramic foam [324]. The preparation of ceramic foams adopting these techniques has been extensively reviewed by several authors [320–326], and hence, a detailed account of these techniques has been avoided in this review.

The use of preceramic polymers for the fabrication of cellular ceramics offers various advantages over the conventional route using ceramic powders in a slurry containing stabilizers, binders, and sintering aids. Some of the problems faced in the conventional route are: difficulty in maintaining good suspension of the solid particles, achieving good infiltration into porous templates, controlling the viscosity,

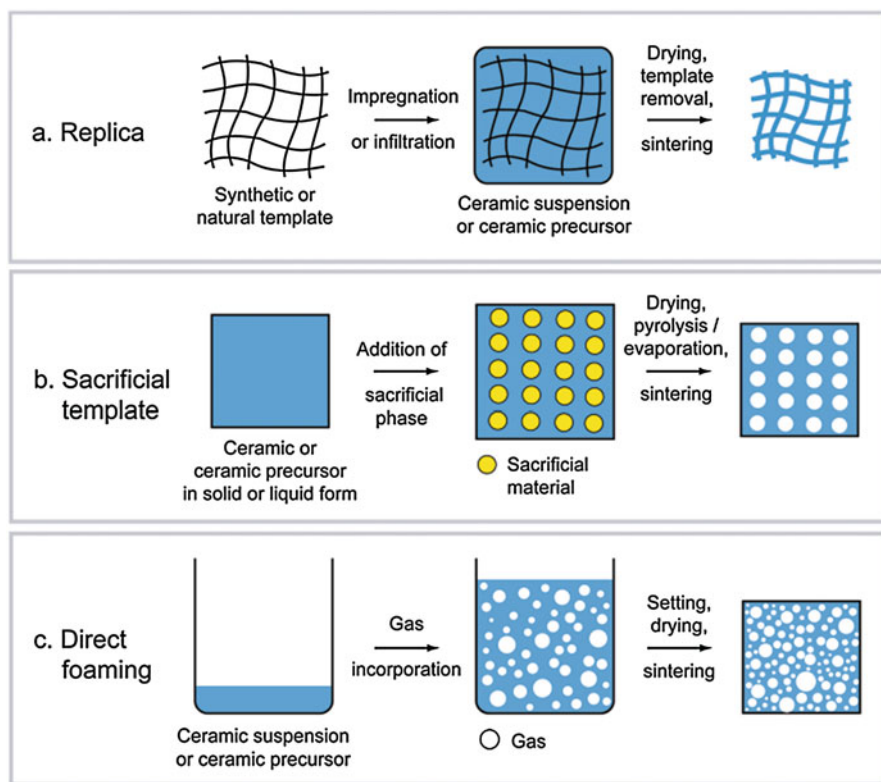


Fig. 57 Schematic representation of fabrication process of ceramic foam. (Reproduced from Ref. [323] with permission from John Wiley and Sons)

structure collapse due to binder burnout, and high temperatures required for sintering. Use of preceramic polymers successfully addresses these issues and provides additional benefits such as control over the nano-level ceramic composition, ability to adapt to novel processing methods, and the option to easily machine the precursor foam after curing.

Fabrication of ceramic foams using preceramic polymers is done via three different routes: (i) using replica, (ii) using porogens, and (iii) direct foaming [327, 328]. The replica method and the use of porogens result in open cell foams, and direct foaming method can result in both closed and open celled foams [329]. Though replica method is widely used industrially for the fabrication of open cell ceramic foams, mechanical properties are lower due to the presence of hollow strut left behind by the fugitive replica. In this context, the other two methods offer great potential for improving the properties.

Among the preceramic polymers, polycarbosilane [330–332] and polysiloxane [333–335] are highly utilized for the fabrication of cellular ceramic materials. Polysiloxanes have the advantage over PCS in terms of lower cost, availability of multitude of variants in bulk, and the ability to self-foam. The self-foaming nature of polysiloxane results from the presence of $-OH$ and $-R$ groups in the polymer structure, which on heating cross-links and generates alcohols and water which escape during the curing, forming the porosity [336].

In general, it is observed that the compressive strength of SiOC foams decrease with increase in pyrolysis temperature from 1000 °C to 1400 °C [334]. This may be attributed to the carbothermal reaction, resulting in SiO evolution, which in turn weakens the struts. Various attempts have been made to improve compressive strength by nano-casting approach [337], by compressive molding followed by sintering at 1750 °C [338] or by using sintering aid [339] or SiC filler [340]. An interesting point to note here is that whereas SiOC foams lose strength on heat treatment at higher temperature due to carbothermal reaction, causing damage to the load bearing struts, SiC foam can retain the strength due to the absence of carbothermal reaction. In fact, it is reported that SiC foams from polycarbosilane show a decrease in pore size [341], which can enhance its load bearing characteristics, with increased strut density. PIP process also provides an option to densify the struts as the polymers can infiltrate the polyurethane template resulting in dense struts [342].

Silicon-boron-oxycarbide (SiBOC) foam was prepared from polymethylborosiloxane resin [343]. The foam showed good mechanical integrity and shape retention with shrinkage. The real density of the struts was measured to be 1.93 g/cc. Geometrical density showed a change from 0.15 g/cc for the polymeric foam to 0.18 g/cc for the ceramic foam. SEM images of the cross-section of strut are shown in Fig. 58. The images clearly depict the evolution of SiBOC hollow strut from the triangular polyurethane strut.

Kim et al. [344] converted polysiloxane-phenolic resin mixture into microcellular SiC ceramics with cell density greater than 10^9 cells/cm³ and cells smaller than 20 μm. This involved the following steps: (i) fabricating a formed body from a mixture of polysiloxane, phenolic resin (used as a carbon source), polymer

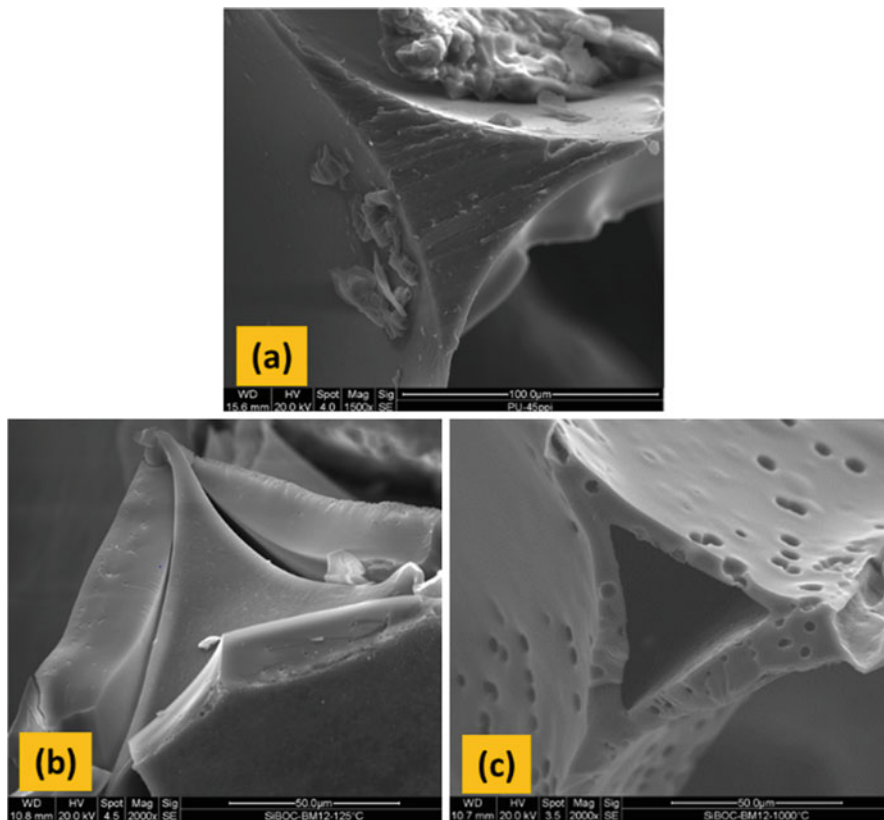


Fig. 58 SEM images of the strut cross-section of the foam obtained at different stages of its preparation: (a) of the template PU foam, (b) of the template after first cycle of coating with methylborosiloxane and cross-linking, and (c) of the final SiBOC foam. (Reproduced from Ref. [343] with permission from John Wiley and Sons)

microbeads (used as sacrificial templates), and $\text{Al}_2\text{O}_3\text{-Y}_2\text{O}_3$ (an optional sintering additive), (ii) cross-linking the polysiloxane in the formed body, (iii) transforming the polysiloxane and phenolic resin by pyrolysis into silicon oxycarbide and C, respectively; and (iv) synthesizing SiC by carbothermal reduction. By controlling the microbead and additive contents, it was possible to adjust the porosity so that it ranged from 60% to 95%.

Novel routes for the fabrication of cellular materials are also emerging. A method for sizing and aligning pores via freeze casting is reported [345]. The pores align in the freezing direction of the polymer and the pores become narrower with freezing temperature [346]. Macro/mesoporous SiOC ceramic monoliths of anisotropic structure were prepared by freeze casting, using methylphenyl polysiloxane or methylpolysiloxane and (3-aminopropyl)triethoxysilane as precursors. The very low thermal conductivities and relatively high compressive strength are very promising for use in

cryogenic engineering [347]. Porous SiC ceramics with low oxygen content were prepared by freeze casting using divinylbenzene (DVB) as a cross-linker for PCS. A clear improvement in compressive strength with increasing PCS content is seen, with the highest compressive strength of 18.7 MPa found for samples with 20 wt% [348].

Recently, ceramic aerogels were prepared by PDC route [349, 350]. A combination of ultra-low density and low thermal conductivity makes aerogel a sought after TPS material for space applications. Radiative conduction in foam core TPS materials can be reduced by infiltrating aerogels into the pores of the foam, which in turn adds to the strength of the foam structure also.

In addition to conventional preceramic polymers, phenolic resin has also been investigated as precursor for SiC foam [192]. Phenolic resin was blended with SiC and elemental silicon, and acetone was used as solvent to adjust the viscosity of the slurry. Polyurethane foam was infiltrated with this slurry, cured, pyrolyzed and then heat treated at 1500 °C to obtain SiC foam having density of 0.15 g/cc and average pore diameter of 350 μm. SiC foam specimens having density varying from 0.15 to 0.75 g/cm³ were prepared by controlling the number of densification cycles using the same slurry.

Porous SiC bodies were prepared by powder compaction method [192]. The polyurethane foam infiltrated with precursor slurry and cured at 75 °C was crushed to a fine powder. It was mixed with phenolic resin-based precursor slurry and molded under pressure to form the desired shape and cured at a temperature of 175 °C. This green body was then removed from the mold and pyrolyzed at 900 °C followed by sintering at 1500 °C under inert atmosphere for allowing the formation and densification of SiC. Further densification was done by repeated infiltration with preceramic slurry followed by pyrolysis and sintering. By this process, porous SiC bodies having density in the range 0.9 g/cc to 1.75 g/cc were prepared.

Porous SiC bodies prepared by densification of SiC foam and powder compaction method described above were machined to get leading edges and subjected to arc-jet test at 250 W/cm² in air for 15 s (Figs. 59 and 60). Leading edge prepared by densification of SiC foam withstood the test without any erosion or mass loss whereas slight erosion was observed for the leading edge prepared by powder compaction method.

Ajith [192] explored the possibility of using SiC foam tile as a hot structure in an oxidizing environment. SiC foam tile of density 0.75 g/cm³ (size: 150 mm × 150 mm × 20 mm), prepared by densifying SiC foam of density 0.2 g/cm³ by polymer-infiltration-pyrolysis (PIP) process using phenolic precursor slurry, was subjected to kinetic heat simulation (KHS) test.

KHS tests were conducted at two different heat flux history (HFH) for the windward region of a typical reentry vehicle with a maximum heat flux of 4.1 W/cm² and 17.5 W/cm², corresponding to two different trajectories. Maximum temperature of 426 K and 742 K was experienced at the backwall of SiC tile upon exposure after ~500 s and ~600 s, respectively, when the tile was subjected to two different heat flux history. Inspection of the tile after these two tests indicates that the tile retains its integrity without any weight loss (Fig. 61).

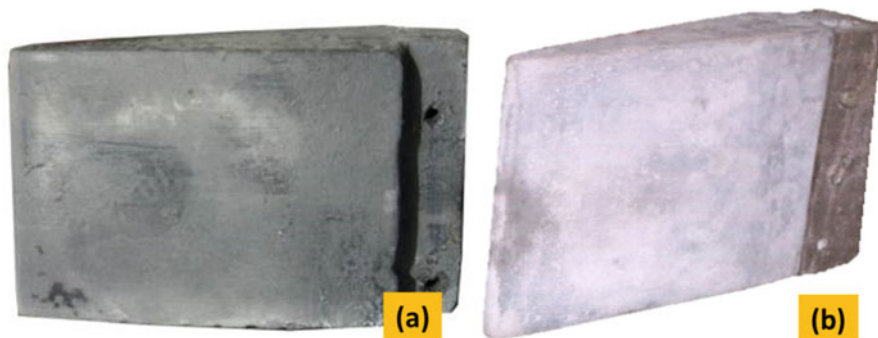


Fig. 59 Leading edge after arc-jet test: (a) densification method and (b) powder compaction method [192]

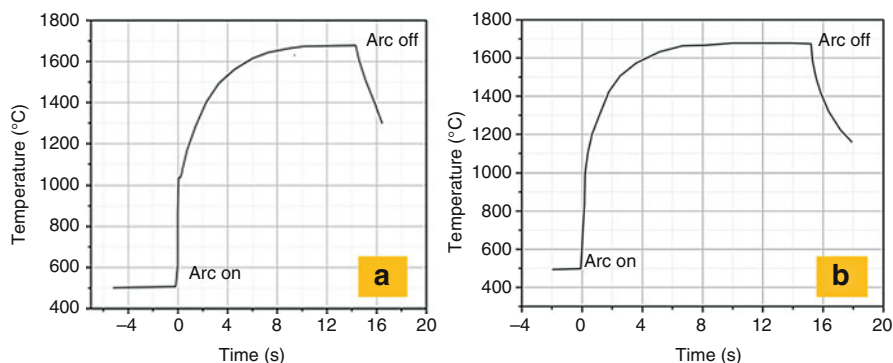


Fig. 60 Temperature profile of the leading edge during arc-jet test: (a) for leading edge prepared by densification method and (b) for leading edge prepared by compaction method [192]

Refractory foams also find application in transpiration cooling in hypersonic vehicles [351]. Ultramet's transpiration-cooled combustion chambers with ceramic foam (or metallic foam) increase performance and reduce cost. By allowing a small portion of the fuel to flow directly through the wall, wall temperatures are kept low, and oxidation of the chamber wall is virtually eliminated. A foam core transpiration-cooled engine offers all the advantages of a foam core regeneratively cooled engine with certain additional benefits. Increased coolant flow can be easily directed at areas subjected to the greatest heat flux. The inner wall of the entire chamber is maintained under nonoxidizing conditions, thus eliminating concern about oxidation. The need for fuel-film cooling is eliminated, which simplifies the injector design. Because only 2–5% of the total fuel flow is needed for transpiration and since no fuel-film cooling is needed, most of the fuel can be used for combustion and burned efficiently. The lower coolant volume reduces cost and weight associated with turbo-machinery. In transpiration cooling, open-cell structural foam is combined with a fine porosity liner at the inner surface with tailorable permeability. Only 2% of the total fuel flow is required for cooling.

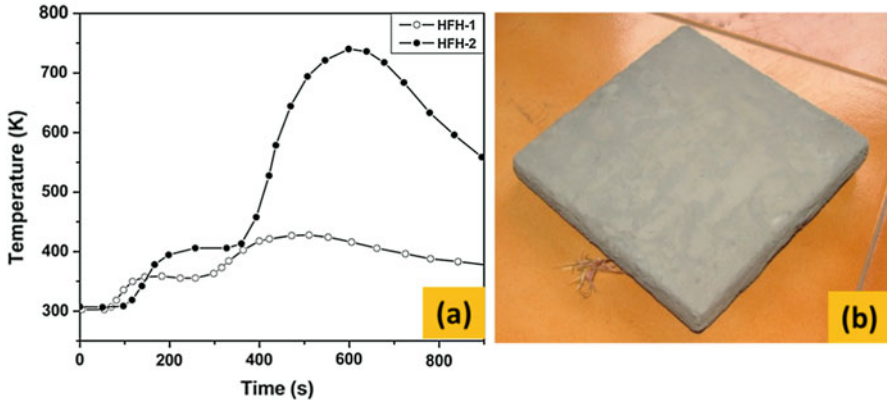


Fig. 61 (a) Backwall temperature of SiC foam tile subjected to KHS, (b) SiC foam tile after two KHS tests [192]

SiC foam has also been used for preparing lightweight space mirrors [352]. In these applications closed cell SiC foam is coated with SiC and then coated with silicon. The ceramic closed-cell foam possesses as little as 5% of the density of its solid counterpart, which gives it attractive thermal and inertial properties. The foam-core optic's low mass can dramatically improve closed loop performance for active beam steering. The advantage of the foam core is that it is physically incapable of producing print-through which is a concern in geometrical light weighting of SiC mirrors.

Ceramic Honeycomb

Ceramic honeycomb structures are conventionally produced by the process of extrusion. The material to be extruded is usually a mixture of ceramic powders which has been plasticized to give favorable extrusion performance [353]. Ceramic honeycomb was also prepared by embedding ceramic fiber tape in a ceramic matrix [354, 355]. A fabric tape or sheet formed of fibers of high-temperature material is impregnated with the liquid ceramic precursor, which contains either a preceramic polymer dissolved in a liquid vehicle, a colloidal suspension of a preceramic material, or any other suitable liquid form of a precursor. The impregnated tape or sheet is then heated to evaporate the vehicle, the tapes or sheets are formed into the corrugated shape in accordance with the desired dimensions of a honeycomb structure and cured to retain the corrugated shape. A high temperature ceramic-based adhesive or preceramic adhesive/binder is applied to the nodes of the corrugations where the strips will be joined to form the honeycomb, and the sheets are stacked in the honeycomb arrangement. The adhesive is then cured at 100–300 °C, followed by pyrolysis at 1100–1200 °C. The resulting honeycomb is then dipped again in the same slurry used initially, and pyrolyzed is once again.

In another approach, aluminum and paper honeycomb were dipped in a precursor slurry comprising of phenolic resin, SiC powder, and elemental silicon powder and

cured at 150–200 °C, pyrolyzed at 900 °C, and then heat treated at 1500 °C to obtain SiC honeycomb [62].

Ceramic Sandwich Structures

The concept of the construction of sandwich structures using polymeric foam and honeycomb can be extended to the construction of ceramic sandwich structures for high temperature applications. Light weight ceramics such as ceramic foam and ceramic honeycomb can be made use of as core materials since they have significant weight advantage (low density) and high thermal insulation characteristics [356, 357]. In addition to the core materials, the fabrication of ceramic sandwich structures requires high temperature resistant face sheets, ceramic adhesives, and/or ceramic fasteners. A ceramic sandwich structure constructed using C/SiC composite as face sheets and SiC foam as the core material was evaluated as an internal multiscreen thermal insulation in place of silica tile in reentry vehicles [358].

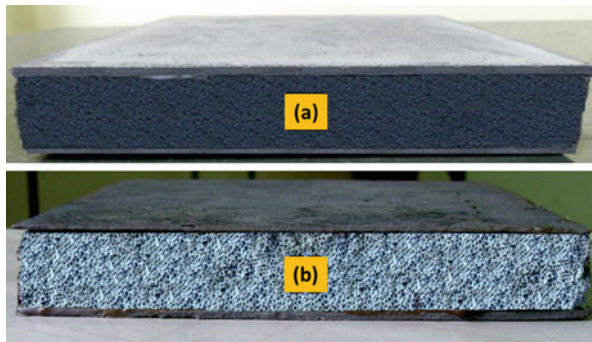
Sreejith [62] evaluated three ceramic sandwich structures with C/SiC composite as face sheets and SiC foam (FCS-01), SiC honeycomb prepared from paper honeycomb (HCS-01) and SiC honeycomb prepared from aluminum honeycomb (HCS-02) as core material as thermal protection system for the windward region of reusable launch vehicle. For the construction of the sandwich panels, phenolic resin-based ceramic adhesive was used for bonding C/SiC face sheets with the core. These sandwich structures having thickness of 20–30 mm and density of 0.48–0.52 g/cc were subjected to KHS test, and the results are summarized in Table 7. All the three sandwich structures withstood the test maintaining the structural integrity. From the results presented in Table 7, it is evident that FCS-01 with the lowest thickness of 20 mm shows the least backwall temperature of 412 °C, though it has been subjected to higher heat flux compared to the other two structures. Compared to honeycomb sandwiches (HCS-01 and HCS-02), in the foam sandwich (FCS-01), the open channel across the core is minimized to a greater extent or totally avoided.

Ajith [192] prepared two sandwich structures of dimension 150 mm × 150 mm × 25 mm with C/SiC face sheets using SiC foam prepared from phenolic resin-based precursor slurry and SiC Durofoam[®] (Fig. 62). These sandwich structures were subjected to KHS test with the maximum heat flux of 4.1 W/cm². Backwall temperature of 139 °C and 173 °C was observed for IMI-1 and IMI-2, respectively. As the backwall temperature was lower for IMI-2, it was subjected to second test with maximum heat flux of 24 W/cm² and the backwall temperature observed was

Table 7 KHS test results of ceramic sandwich structures [62]

Sample	Height (mm)	Emissivity	Density (g/cc)	Maximum front wall heat flux, H_{\max} (W/cm ²)	Maximum backwall temperature, T_{\max} (°C)	Time lag between H_{\max} and T_{\max} (s)
HCS-01	25	0.87	0.52	16	495	100
HCS-02	30	0.82	0.48	20	420	125
FCS-01	20	0.89	0.50	24	412	180

Fig. 62 Sandwich structures with SiC foam core and C/SiC face sheets: (a) IMI-1 with Durofoam[®] and (b) IMI-II with SiC foam prepared by template method using phenolic slurry



412 °C. It is worth noting that IMI-1 experienced a higher backwall temperature of 601 °C even when tested at a maximum heat flux of 17.5 W/cm². Less temperature experienced at the back-wall of IMI-2 may be due to the less contact area as the pore size of SiC foam in IMI-2 is more than that of Durofoam[®], and hence, heat transfer by conduction from the facesheet to the foam will be less than that of Durofoam[®]. In addition, the discontinuity of the damaged struts of SiC foam of IMI-2, as evidenced by SEM, also probably contributes in reducing the heat conduction through the core.

Ajith [192] investigated ceramic sandwich-ablative hybrid system for high heat flux conditions. A hybrid TPS (Fig. 63) (Density: 0.54 g/cm³) was fabricated by bonding a high density ablative (HDA) composite onto ceramic sandwich structure with C/SiC face sheets and Durofoam[®] core which was subjected to sandwich of size 150 mm × 150 mm × 25 mm using the high temperature ceramic adhesive.

The HDA composite of 5 mm thickness (Density: 1.38 g/cm³) was made using 90 wt% chopped silica fiber and 10 wt% phenolic resin. The total thickness of the hybrid system was 30 mm with an overall density of 0.54 g/cm³.

Maximum backwall temperature of 320 °C was observed for the hybrid system when subjected to KHS test with maximum heat flux of 90 W/cm². It is worth noting that the sandwich structure without ablative has exhibited a back wall temperature of 601 °C at the maximum heat flux of 17.5 W/cm² as discussed earlier. Thus, it is evident that the ablative layer takes away part of the heat load resulting in the reduction of the backwall temperature. The hybrid system withstood the test without delamination of the sandwich structure. However, the ablative composite underwent charring resulting in the development of surface cracks and loosening of silica fibers (Fig. 64).

Ortona et al. [170] described an integrated assembly method for preparing ceramic sandwich structures with CMC face sheets and structural grade ceramic foam, having density of 0.36–0.38 g/cm³ and porosity of 86–87%. SiC_f preforms were obtained by laying up fabric plies, pre-impregnated with a small amount of phenolic resin, cured in an autoclave, and pyrolyzed in argon atmosphere. Ceramic foam was bonded to pyrolyzed preform face sheets using SiC-filled polysilazane adhesive and cured in an autoclave. After pyrolysis, assembled sandwiches were

Fig. 63 Ceramic-Ablative hybrid TPS

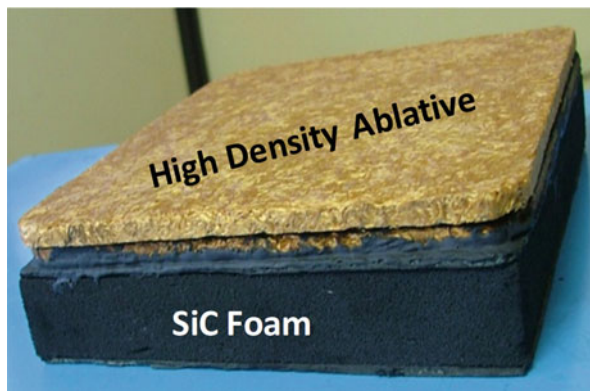


Fig. 64 Ceramic-ablative hybrid TPS after KHS test (two views)

then impregnated on both sides of the sandwich skins with polysilazane using a brush. PIP was repeated five times to get the required strength for the CMC face sheets. Joining skins to ceramic core before their actual densification allows a strong grip of the bonding layer both to the CMC laminates and to the foam. Both CMC and foam are embedded into the polymer-derived ceramic layer and, thus, mechanically fastened to it.

Wang et al. [359] described a procedure for the fabrication of ceramic sandwich structures in which the SiC core foam was modified with SiO₂ to reduce the thermal conductivity. The advantage of modifying SiC foam core with SiO₂ is explained in the heat transfer model (Fig. 65). From Fig. 65a it is obvious that the radiation can pass through the large pores between SiC skeletons easily and directly. On the other hand, it is noticed from Fig. 68b that the radiation is blocked by SiO₂ powder. SiO₂ particles have high extinction coefficient and can absorb the radiation energy significantly after radiation through multiple reflection. Thus, most of the heat transferred through solid SiO₂ powders is by heat conduction. As the SiO₂ particles

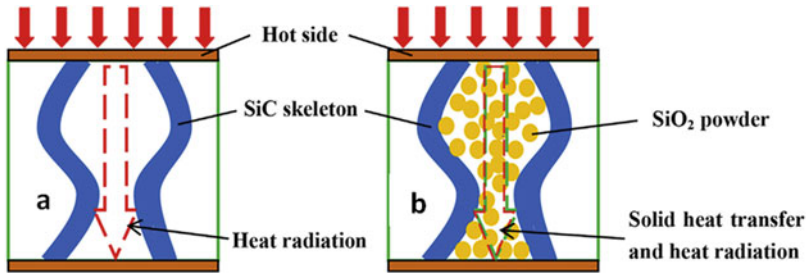


Fig. 65 The heat transfer models for SiC foam core and compound core. (Reproduced from Ref. [359] with permission from Elsevier)

are not completely fused, solid heat conduction efficiency is much lower than heat radiation, and therefore the compound core exhibits a better performance in the sandwich structure.

Ceramic foam core sandwich structures are also considered for application as space mirrors [360]. Foam-core sandwich panels offer exceptional stiffness-to-weight ratios, and Ultramet has used this architecture for advanced mirror systems. Foam-core mirrors employ an optical faceplate that is attached to the surface of a foam billet, and, if stiffness requirements demand, a second face plate can be added to the rear surface.

CMC Shingles

Pichon et al. [162] proposed a new concept for the construction of lightweight CMC structures, viz., CMC shingles as advanced thermal protection system for the windward region of reusable launch vehicles. This concept is explained in Fig. 66. The shingle concept is divided into two sets of elements: (i) the ones with mechanical functions (mechanical shell, fasteners, and stand-offs) and (ii) the ones with thermal functions (inner insulation layers, seals, and insulating washers). The material needed for the mechanical shell has to be mechanically very efficient and resistant to highly constrained thermal environments, but its thermal conductivity characteristics are not important. The internal insulation and seals that do not require high mechanical properties can be composed of low weight, flexible, and higher performance insulating materials. The attachment system of the panel to the airframe structure must resist relatively high temperatures to enable the thermal expansion of the panel and transmit out-of-plane mechanical loads between the panel and the cold structure.

Pichon et al. [162] constructed the shingles using carbon fiber reinforced preform. This preform was based on one ply multilayer woven fabric which was assembled by weaving to result in a self-stiffened panel (Fig. 67). The molding of these panels was performed on a carbon/epoxy composite material mold which was capable of withstanding at least the temperature needed for hardening the process. Then the preform was hardened by a liquid route. The SiC matrix was added by CVI densification on a simple graphite frame holding the part. After grinding, deburring,

Fig. 66 The shingle concept. (Reproduced from Ref. [162] with permission from Elsevier)

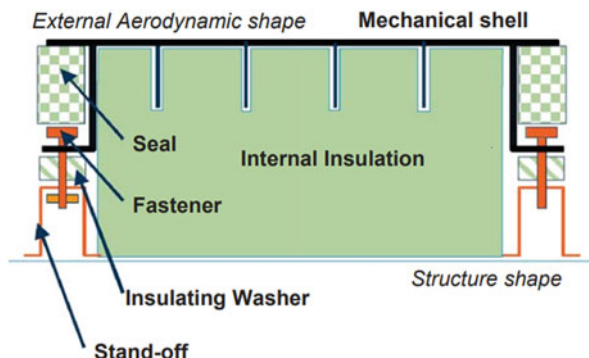
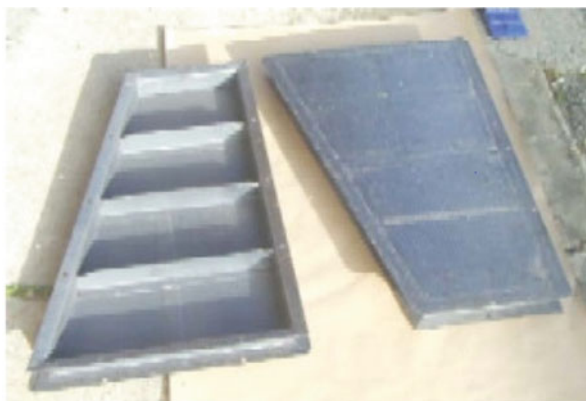


Fig. 67 Shingles manufactured from C/SiC composite. (Reproduced from Ref. [162] with permission from Elsevier)



and drilling of the holes, the SiC densification process by CVI was performed once again and oxidation protection coating was added, if necessary. The shingle was subjected to mechanical testing, dynamic vibrational testing, acoustic testing, thermal, and thermomechanical tests. The shingles withstood the tests without noticeable damage.

In a variation of the above shingles approach, Ajith [192] prepared C/SiC paneled lightweight ceramic structures by using prefabricated C/SiC composite panels, ceramic adhesive, and zirconia felt (Fig. 68). This shingle specimen was subjected to two KHS tests with maximum heat flux of 4 W/cm^2 and 17.5 W/cm^2 and backwall temperatures of $150 \text{ }^\circ\text{C}$ and $445 \text{ }^\circ\text{C}$. It is noticed that the backwall temperature is slightly higher than that of IMI-2 prepared using SiC foam from phenolic resin slurry. This may be due to following reasons: (i) higher insulating characteristics of SiC foam than that of zirconia felt and (ii) C/SiC partition walls may conduct heat from the front wall to the back-wall.

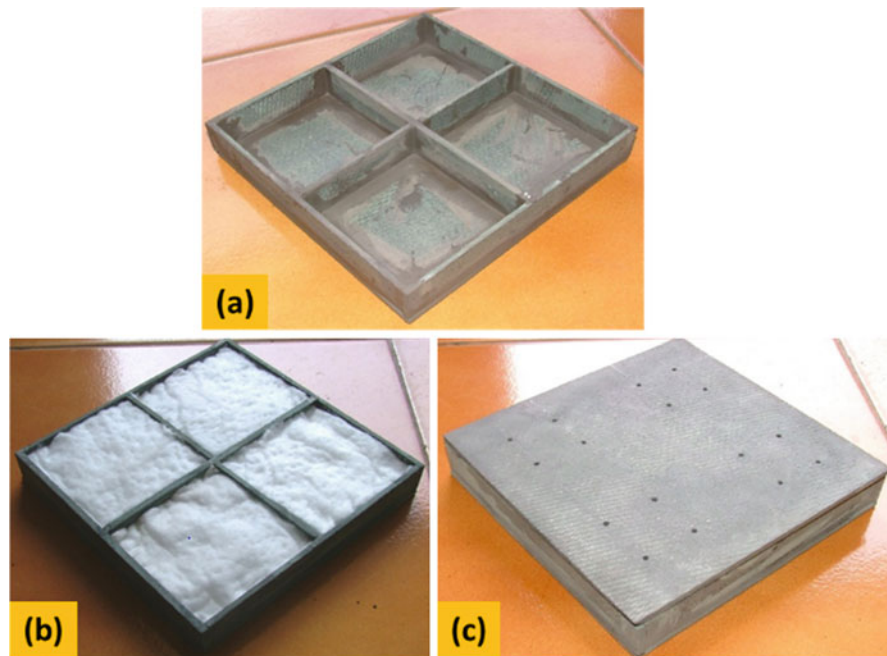


Fig. 68 Construction of C/SiC shingles (150 mm × 150 mm × 25 mm) [192]

Concluding Remarks and Perspectives

The field of polymer-derived ceramics has witnessed tremendous growth over the last 50 years resulting in the creation of vast knowledge base with voluminous data which provide valuable inputs for taking forward this fascinating area of interdisciplinary research to the next level. In the initial years, the focus was to synthesize silicon-based processable precursors for non-oxide ceramic fibers for high temperature applications. Gradually, the emphasis got shifted toward synthesizing speciality monomers or synthesizing newer precursors, understanding the transformation of polymeric phase to ceramic phase and the effect of heat treatment conditions on the microstructure and phase stability of the ceramic formed. In an attempt to increase the phase stability and high temperature capability of ceramics, precursors were designed to give multicomponent ceramics/mixed non-oxide ceramic systems. Over the years, considerable progress is made in this direction, and a large number of UHTC precursors have been synthesized with the main purpose of obtaining ceramic systems which can go well beyond the capability of SiC in terms of thermooxidative stability and retention of properties at temperatures above 1600 °C.

Though the initial efforts in the area of PDCs were focused on synthesizing preceramic polymers devoid of oxygen, in the last three decades, polysiloxanes have gained importance for obtaining siliconoxycarbide (SiCO) ceramics. The

relative ease of synthesis of such polymers coupled with the fact that SiCO ceramics can be obtained only through PDC route has motivated researchers to explore the realm of polysiloxanes and related materials. The surge in research activities in this area led to exploring other polymeric systems such as polysilsesquioxanes, polyborosiloxanes, polymetallosiloxanes, and polymetalloborosiloxanes as potential precursors for SiOC, SiBOC, and Si(M)BOC. A great deal of work on polysiloxanes and related materials is concerned with the phase stability of SiOC glasses and the role played by boron, metallic constituent, and nanodomains of carbon present in these systems.

With the advancements in the field of nanotechnology, PDCs have attained much more significance in terms of both scientific understanding and their utilization in various fields. Though the initial interest on PDCs was to obtain high temperature materials such as ceramic fibers, coatings, and matrix for CMCs, in recent years, PDCs have been explored for various applications which include biomedical applications, drug delivery systems, water remediation, energy storage devices, microelectronics, and nanosensors.

The main objective of this chapter was to focus on preceramic polymers which find applications in space research. While discussing this aspect, ceramics obtained from carbonaceous polymers were also included in the discussion, as they offer cost-effective approach for obtaining high temperature materials. In spite of concerted efforts for developing high temperature materials such as CMCs and UHTCs, C/C composites with oxidation protective coatings, obtained through conventional process, are preferred for most of the high temperature materials requirement for space applications. This is mainly due to the pedigree of C/C composites and the availability of carbon fibers of different grades to meet the specific requirements. Despite the fact that ceramic matrix composites, ceramic coatings, and lightweight ceramics from PDCs have caught the attention of researchers in the area of materials science and technology, the acceptance of PDC-based components for space applications as replacement for oxidation protected C/C composites and silica tiles, a lightweight ceramic material, is still evasive though they have been flown as candidate materials in experimental space vehicles. The scenario is expected to change in the coming years with the advancement in manufacturing processes such as additive manufacturing/3-D printing, hybrid CVI+PIP process, and joining techniques.

In order to penetrate into the domain of high temperature materials, the cost of precursors for PDCs should be brought down drastically. Yet another major concern is the porosity of PDC-based components particularly for applications as exit cones and satellite thrusters. Though the porosity aspect is partly addressed through AFCOP approach, this method could not be effectively utilized as the active fillers tend to react with reinforcement/interphase coating adversely affecting the mechanical properties of CMCs. To take advantage of AFCOP approach, it is imperative to develop suitable protective coatings onto carbon fiber so that the number of infiltration steps can be reduced. Another concern that requires attention is eliminating/reducing the deterioration of reinforcement due to reaction with pyrolysis products. This problem can be minimized by using flash pyrolysis technique. However, this

technique is to be adopted from making miniature components to large-sized components required for space applications.

In the domain of PDC coatings, there is considerable scope particularly for providing interphase coating onto fiber reinforcement and this approach can reduce the cost of production of CMCs by eliminating the need for CVI/CVD furnace for interphase coating. With the advancements on UHTC precursors, new functionally graded coatings for protection of composite structures and metal substrates can be envisaged. As far as the thermal barrier coatings are concerned, there is a need to develop precursors for top coat capable of withstanding higher temperatures. There is considerable scope for fine tuning the microstructure of the coating to increase the temperature gradient between the front wall and back wall. Yet another area of interest is use of preceramic polymers-based atomic oxygen resistant coatings and composites for the construction of spacecrafts and low earth orbit space structures/space stations.

In the area of ceramic adhesives, researchers should take advantage of the availability of new precursors for UHTCs. Suitable adhesive formulations based on UHTC precursors are to be developed for joining of CMCs and ultra-high temperature CMCs with super alloys and other substrates. As it becomes increasingly difficult to prepare large components, joining of ceramic components becomes inevitable. Reliability of such joints is to be addressed through health monitoring procedures involving nondestructive testing techniques.

The advancements in the field of additive manufacturing are expected to boost the development and production of lightweight ceramics as advanced thermal protection systems. Production of near net shaped lightweight ceramic materials with improved high temperature capability are expected to replace silica tile in the near future. Scope exists on realizing hybrid advanced thermal protection systems combining ablative systems with CMCs resulting in mass saving with improved reliability for future manned missions and interplanetary missions.

In conclusion, interdisciplinary approach with active participation of researchers in the field of chemistry, materials science, and engineering is the way forward to realize the vision of using PDC-based materials for space applications and outer space exploration.

References

1. Rosso M (2006) Ceramic and metal matrix composites: routes and properties. *J Mater Process Technol* 175:364–375
2. Guire ED (2013) Ceramic engineering in aerospace. *J Am Ceram Soc.* <http://ceramics.org/learn-about-ceramics/ceramic-engineering-in-aerospace>. Accessed 30 June 2018
3. Chantrell PG, Popper P (1965) Inorganic polymers and ceramics. In: Popper P (ed) *Special ceramics 1964*. Academic, New York, pp 87–103
4. Verbeek W (1973) Production of shaped articles of homogeneous mixtures of silicon carbide and nitride. US Patent 3,853,567
5. Yajima S, Hayashi J, Omori M et al (1976) Development of a silicon carbide fibre with high tensile strength. *Nature* 261:683–685

6. Bill J, Aldinger F (1999) Polymer-derived covalent ceramics. In: Bill J, Wakai F, Aldinger F (eds) Precursor-derived ceramics. Wiley-VCH, Weinheim, pp 33–51
7. Colombo P, Mera G, Riedel R et al (2010) Polymer-derived ceramics: 40 years of research and innovation in advanced ceramics. *J Am Ceram Soc* 93:1805–1837
8. Colombo P, Riedel R, Soraru GD et al (2010) Polymer derived ceramics: from nano-structure to applications. Destech Publications, Lancaster
9. Emanuel I, Mera G, Riedel R (2014) Polymer-derived ceramics (PDCs): materials design towards applications at ultrahigh-temperatures and in extreme environments. In: Nanotechnology: concepts, methodologies, tools, and applications. IGI Global, pp 1108–1139
10. Konegger T, Torrey J, Flores O et al (2014) Ceramics for sustainable energy technologies with a focus on polymer-derived ceramics. In: Novel combustion concepts for sustainable energy development. Springer India, New Delhi, pp 501–533
11. Low I-M, Sakka Y, Hu CF (2013) MAX phases and ultra-high temperature ceramics for extreme environments. In: Johnston (ed) Polymer derived ceramics. Engineering Science Reference, Hershey, pp 203–245
12. Mera G, Gallei M, Bernard S et al (2015) Ceramic nanocomposites from tailor-made pre-ceramic polymers. *Nanomaterials* 5:468–540
13. Lu K, Erb D (2018) Polymer derived silicon oxycarbide-based coatings. *Int Mater Rev* 63:139–161
14. BCC Research Staff (2018) Polymer-derived ceramics: global markets through 2022. In: Staff Rep. AVM161A, BCC Res. <https://www.bccresearch.com/market-research/advanced-materials/polymer-derived-ceramics-market-report-avm161a.html>. Accessed 30 June 2018
15. Yamamura T, Ishikawa T, Shibuya M et al (1988) Development of a new continuous Si-Ti-C-O fibre using an organometallic polymer precursor. *J Mater Sci* 23:2589–2594
16. Suzuki K, Kumagawa K, Kamiyama T et al (2002) Characterization of the medium-range structure of Si-Al-C-O, Si-Zr-C-O and Si-Al-C tyrannofibers by small angle X-ray scattering. *J Mater Sci* 37:949–953
17. Qian X, Zhou Q, Ni LZ (2015) Preceramic polymer as precursor for near-stoichiometric silicon carbon with high ceramic yield. *J Appl Polym Sci* 132(4):7–13
18. Zhong X, Pei X, Miao Y et al (2017) Accelerating the crosslinking process of hyper branched polycarbosilane by UV irradiation. *J Eur Ceram Soc* 37(10):3263–3270
19. Hong J, Cho KY, Shin DG et al (2015) Room temperature reaction of polycarbosilane with iodine under different atmospheres for polymer-derived silicon carbide fibres. *RSC Adv* 5(102):83847–83856
20. Tian Y, Ge M, Zhang W et al (2015) Metallocene catalytic insertion polymerization of 1-silene to polycarbosilanes. *Sci Rep* 5(1):16274
21. Vijay VV, Nair SG, Sreejith KJ et al (2016) Synthesis, ceramic conversion and microstructure analysis of zirconium modified polycarbosilane. *J Inorg Organomet Polym* 26:302–311
22. Swaminathan B (2012) Studies on silicon containing inorganic and organometallic polymers. PhD thesis, University of Kerala, Thiruvananthapuram
23. Ly HQ, Taylor R, Day RJ et al (2001) Conversion of polycarbosilane (PCS) to SiC-based ceramic. Part 1. Characterisation of PCS and curing products. *J Mater Sci* 36(16):4037–4043
24. Ly HQ, Taylor R, Day RJ et al (2001) Conversion of polycarbosilane (PCS) to SiC-based ceramic. Part 2. Pyrolysis. *J Mater Sci* 36(16):4045–4057
25. Lu Y, Chen F, An P et al (2016) Polymer precursor synthesis of TaC–SiC ultra high temperature ceramic nanocomposites. *RSC Adv* 6(91):88770–88776
26. Amoros P, Beltran D, Guillem C et al (2002) Synthesis and characterization of SiC/MC/C ceramics (M = Ti, Zr, Hf) starting from totally non-oxidic precursors. *Chem Mater* 14:1585–1590
27. West R, David LD, Djurovich PI et al (1981) Phenylmethylpolysilane: formable silane copolymers with potential semiconducting properties. *J Am Chem Soc* 103:7352–7355
28. Schilling CL Jr (1986) Polymeric routes to silicon carbide. *Brit Polym J* 18:355–358
29. West R (1986) The polysilane high polymers. *J Organomet Chem* 300:327–346

30. Rama Rao M, Packirisamy S, Ravindran PV et al (1992) Synthesis and characterization of poly (tetramethyldisilylene-co-styrene). *Macromolecules* 25:5165–5170
31. Packirisamy S, Ambadas G, Rama Rao M et al (2003) ^{29}Si -NMR spectral studies of poly-disilalahydrocarbons. *Eur Polym J* 39:1077
32. Ambadas G, Packirisamy S, Radhakrishnan TS et al (2004) Synthesis, characterization and thermal properties of poly(methylvinylsilylene-co-styrene). *J Appl Polym Sci* 91:3774
33. Devapal D, Packirisamy S, Ambadas G et al (2004) Thermal degradation kinetics of poly (methylvinylsilylene-co-styrene). *Thermochim Acta* 409:151
34. Ambadas G (2000) Studies on polysilalahydrocarbons and boron and silicon containing pre-ceramic polymers. PhD thesis, University of Kerala, Thiruvananthapuram
35. Mark JE, Allcock HR, West R (2005) *Inorganic polymers*, 2nd edn. Oxford University Press, New York
36. Abe Y, Gunji T (2004) Oligo- and polysiloxanes. *Prog Polym Sci* 29:149–182
37. Baney RH, Itoh M, Sakakibara A et al (1995) Silsesquioxanes. *Chem Rev* 95:1409–1430
38. Stabler C, Ionescu E, Graczyk-Zajac M et al (2018) Silicon oxycarbide glasses and glass-ceramics: “all-rounder” materials for advanced structural and functional applications. *J Am Ceram Soc* 101:4817–4856
39. Soraru GD, Dallapiccola E, Dandrea G (1996) Mechanical Characterization of sol–gel-derived silicon oxycarbide glasses. *J Am Ceram Soc* 79:2074–2080
40. Melcher R, Cromme P, Scheffler M et al (2003) Centrifugal casting of thin-walled ceramic tubes from preceramic polymers. *J Am Ceram Soc* 86:1211–1213
41. Brequel H, Parmentier J, Walter S et al (2004) Systematic structural characterization of the high-temperature behavior of nearly stoichiometric silicon oxycarbide glasses. *Chem Mater* 16:2585–2598
42. Kleebe HJ, Blum JD (2008) SiOC ceramic with high excess free carbon. *J Eur Ceram Soc* 28:1037–1042
43. Saha A, Raj R (2006) A model for nano domains in polymer-derived SiCO. *J Am Ceram Soc* 89(7):2188–2195
44. Saha A, Raj R (2007) Crystallization maps for SiCO amorphous ceramics. *J Am Ceram Soc* 90(2):578–583
45. Papendorf B, Ionescu E, Kleebe HJ et al (2012) High-temperature creep behavior of dense SiOC-based ceramic nanocomposites: microstructural and phase composition effects. *J Am Ceram Soc* 96(1):272–280
46. Wang F, Apple T, Gill W (2001) Thermal redistribution reactions of Blackglas ceramic. *J Appl Polym Sci* 81:143–152
47. Noll W (2012) Chapter 7. In: *Chemistry and technology of silicones*. Elsevier, New York, pp 332–339
48. Yajima S, Okamura K, Hayashi J et al (1977) Pyrolysis of a polyborodiphenylsiloxane. *Nature* 266:521–522
49. Kasgoz A, Misono T, Abe Y (1994) Preparation and properties of polyborosiloxanes as precursors for borosilicate formation of $\text{SiO}_2\text{--B}_2\text{O}_3$ gel fibers and oxides by the sol-gel method using tetraacetoxysilane and boron tri-n-butoxide. *J Polym Sci A Polym Chem* 32(6):1049–1056
50. Kasgoz A, Kuramata M, Abe Y (1999) Preparation and properties of borosilicate gels by the reaction of tetraacetoxysilane with boron tri-n-butoxide. *J Mater Sci* 34(24):6137–6141
51. Yajima S, Okamura K, Hayashi J et al (1978) Development of high tensile strength silicon carbide fibre using an organosilicon polymer precursor. *Nature* 273:525–527
52. Yajima S, Shishido T, Hamano M (1977) SiC and Si_3N_4 sintered bodies with new borodiphenylsiloxane polymers as binder. *Nature* 266:522–524
53. Hoshii S, Kojima A, Otani S (1996) Mechanical properties and oxidation resistivity of carbon fiber/ceramic composites prepared from borosiloxane. *J Mater Res* 11(10):2536–2540
54. Abe Y, Gunji T, Kimata Y et al (1990) Preparation of polymetalloxanes as a precursor for oxide ceramics. *J Non-Cryst Solids* 121(1–3):21–25

55. Irwin AD, Holmgren JS, Jonas J (1988) Solid state ^{29}Si and ^{11}B NMR studies of sol-gel derived borosilicates. *J Non-Cryst Solids* 101(2–3):249–254
56. Soraru GD, Dallabona N, Gervais C et al (1999) Organically modified $\text{SiO}_2\text{--B}_2\text{O}_3$ gels displaying a high content of borosiloxane (B–O–Si) bonds. *Chem Mater* 11(4):910–919
57. Zha C, Atkins GR, Masters AF (1998) Preparation and spectroscopy of anhydrous borosilicate sols and their application to thin films. *J Non-Cryst Solids* 242(1):63–67
58. Soraru GD, Babonneau F, Gervais C et al (2000) Hybrid $\text{RSiO}_{1.5}/\text{B}_2\text{O}_3$ gels from modified silicon alkoxides and boric acid. *J Sol-Gel Sci Technol* 18(1):11–19
59. Ambadas G, Packirisamy S, Ninan KN (2002) Synthesis, characterization and thermal properties of boron and silicon containing preceramic oligomers. *J Mater Sci Lett* 21:1003–1005
60. Devapal D (2007) Studies on inorganic and organometallic polymers. PhD thesis, Mahatma Gandhi University, Kottayam
61. Prabhakaran PV (2008) Studies on non-oxide ceramics derived from polymers and their applications. PhD thesis, University of Kerala, Thiruvananthapuram
62. Sreejith KJ (2010) Polymer derived ceramics and their high temperature applications. PhD thesis, University of Kerala, Thiruvananthapuram
63. Devapal D, Packirisamy S, Sreejith KJ et al (2010) Synthesis, characterization and ceramic conversion studies of borosiloxane oligomers from phenyltrialkoxysilanes. *J Inorg Organomet Polym* 20:666–674
64. Sreejith KJ, Prabhakaran PV, Laly KP et al (2016) Vinyl-functionalized poly(borosiloxane) as precursor for SiC/SiBOC nanocomposite. *Ceram Int* 42:15285–15293
65. Devapal D, Sreejith KJ, Swaminathan B et al (2020) Influence of heat treatment temperature on the microstructure evolution of poly(vinylborosiloxane) derived ceramics. *J Inorg Organomet Polym*. <https://doi.org/10.1007/s10904-020-01457-1>
66. Devapal D, Packirisamy S, Prabhakaran PV et al (2016) Process for solventless synthesis of resinous borosiloxane oligomer precursors for ceramics. Indian Patent 277874
67. Schiavon MA, Armelin NA, Yoshida I (2008) Novel poly(borosiloxane) precursors to amorphous SiBCO ceramics. *Mater Chem Phys* 112:1047–1054
68. Rubinsztajn S (2014) New facile process for synthesis of borosiloxane resins. *J Inorg Organomet Polym Mater* 24(6):1092–1095
69. Schiavon MA, Gervais C, Babonneau F et al (2004) Crystallization behavior of novel silicon boron oxycarbide glasses. *J Am Ceram Soc* 87(2):203–208
70. Sasikala TS, Thomas D, Devapal D (2016) Studies on evolution of nano SiC ceramics from allylborosiloxane. *Ceram Int* 41(1):1618–1626
71. Sasikala TS, Devapal D (2015) Studies on high temperature evolution of polymer derived nano SiC ceramics. *Mater Sci Forum* 830–831:493–497
72. Parmentier J, Soraru GD, Babonneau F (2001) Influence of the microstructure on the high temperature behavior of gel-derived SiOC glasses. *J Eur Ceram Soc* 21:101–108
73. Zhang X, Liu C, Hong C et al (2015) Sol-gel-derived SiBOC ceramics with highly graphitized free carbon. *Ceram Int* 41:15292–15296
74. Struchkov YT, Lindeman SV (1995) Structures of Polymetalloorganosiloxanates – a novel class of organosilicon metal complexes. *J Organomet Chem* 488:9–14
75. Gunji T, Sopyan IIS, Abe Y (1994) Synthesis of polytitanosiloxanes and their transformation to $\text{SiO}_2\text{--TiO}_2$ ceramic fibers. *J Polym Sci A Polym Chem* 32:3133–3139
76. Dire S, Ceccato R, Babonneau F (2005) Structural and microstructural evolution during pyrolysis of hybrid polydimethylsiloxane-titania nanocomposites. *J Sol-Gel Sci Technol* 34:53–62
77. Liu C, Pan R, Hong C et al (2016) Effects of Zr on the precursor architecture and high-temperature nanostructure evolution of SiOC polymer derived ceramics. *J Eur Ceram Soc* 36:395–402
78. Ionescu E, Linck C, Fasel C et al (2010) Polymer derived SiOC/ZrO₂ ceramic nanocomposites with excellent high-temperature stability. *J Am Ceram Soc* 93:241–250

79. Umicevic AB, Cekic BD, Cavor JNB et al (2015) Evolution of the local structure at Hf sites in SiHfOC upon ceramization of a hafnium-alkoxide-modified polyselsesqui-oxane: a perturbed angular correlation study. *J Eur Ceram Soc* 35:29–35
80. Su D, Yan X, Liu N et al (2016) Preparation and characterization of continuous SiZrOC fibers by polyvinyl pyrrolidone-assisted sol-gel process. *J Mater Sci* 51:1418–1427
81. Yan X, Su D, Duan H et al (2015) Preparation of SiOC/HfO₂ fibers from silicon alkoxides and tetrachloride hafnium by a sol-gel process. *Mater Lett* 148:196–199
82. Kamal A, Rajasekhar BV, Painuly A et al (2019) A novel precursor for the synthesis of mixed non-oxide ultra high temperature ceramics. *J Inorg Organomet Polym* 30:1578–1588
83. Zhang Z, Xu S, Huang J et al (2020) Straight forward synthesis and molecular structure optimization of novel SiZrBOC ceramic precursor via sol-gel and solvothermal approach. *Ceram Int*:46:3866–46:3874
84. Seyferth D, Wiseman GH, Prud'homme C (1983) A liquid silazane precursor to silicon nitride. *J Am Ceram Soc* 66(1):C-13–C-14
85. Birot M, Pilot J-P, Dunogues J (1995) Comprehensive chemistry of polycarbosilanes, polysilazanes, and polycarbosilazanes as precursors of ceramics. *Chem Rev* 95:1443–1477
86. Lukacs A III (2007) Polysilazane precursors to advanced ceramics. *Am Ceram Soc Bull* 86:9301–9306
87. Weinmann M, Ionescu E, Riedel R et al (2013) Precursor-derived ceramics. In: *Handbook of advanced ceramics: materials, applications, processing, and properties*. Academic/Elsevier, pp 1025–1101
88. Wang C, Song N, Ni L et al (2016) Synthesis, thermal properties, and ceramization of a novel ethynylaniline-terminated polysilazane. *High Perform Polym* 28:359–367
89. Jun L, YuLin Q, Ping Z et al (2017) Synthesis of SiC ceramics from polysilazane by laser pyrolysis. *Surf Coat Technol* 321:491–495
90. Sun Y, Li Y, Su D et al (2015) Preparation and characterization of high temperature SiCN/ZrB₂ ceramic composite. *Ceram Int* 41(3):3947–3951
91. Viard A, Miele P, Bernard S (2016) Review on polymer-derived ceramics route toward SiCN and SiBCN fibers: from chemistry of polycarbosilazanes to the design and characterization of ceramic fibers. *J Ceram Soc Jpn* 124(10):967–980
92. Niebyski LM (1990) Pre ceramic compositions and ceramic products. US Patent 4,910,173
93. Su K, Remsen EE, Zank GA et al (1993) Synthesis, characterization, and ceramic conversion reactions of borazine-modified hydridopolysilazanes: new polymeric precursors to silicon nitride carbide boride (SiNCB) ceramic composites. *Chem Mater* 5:547–556
94. Wideman T, Cortz E, Remsen EE et al (1998) Reactions of monofunctional boranes with hydridopolysilazane: synthesis, characterization, and ceramic conversion reactions of new processible precursors to SiNCB ceramic materials. *Chem Mater* 10:2218–2230
95. Weinmann M (1999) High temperature stable ceramics from inorganic polymers. In: Bill J, Wakai F, Aldinger F (eds) *Precursor-derived ceramics*. Wiley-VCH, Weinheim, pp 83–92
96. Weinmann M, Horz M, Berger F et al (2002) Dehydrocoupling of tris(hydridosilyl)ethyl boranes and cyanamide: a novel access to boron-containing polysilylcarbodiimides. *J Organomet Chem* 659:29–42
97. Sarkar S, Gan Z, An L et al (2011) Structural evolution of polymer-derived amorphous SiBCN ceramics at high temperature. *J Phys Chem C* 115:24993–25000
98. Gao Y, Mera G, Nguyen H et al (2012) Processing route dramatically influencing the nanostructure of carbon-rich SiCN and SiBCN polymer-derived ceramics. Part I: low temperature thermal transformation. *J Euro Ceram Soc* 32:1857–1866
99. Muller A, Peng J, Seifert HS et al (2002) Si-B-C-N ceramic precursors derived from dichlorodivinylsilane and chlorotrivinylsilane. 2. Ceramization of polymers and high-temperature behavior of ceramic materials. *Chem Mater* 14:3406–3412
100. Yu Z, Zhou C, Li R et al (2012) Synthesis and ceramic conversion of a novel processible polyboronsilazane precursor to SiBCN ceramic. *Ceram Int* 38:4635–4643

101. Singh G, Bhandavat R (2016) Boron-modified silazanes for synthesis of SiBCN ceramics. US Patent 9,453,111
102. Bhandavat R (2013) Molecular precursor derived SiBCN/CNT and SiOC/CNT composite nanowires for energy based applications. PhD thesis, Kansas State University, Manhattan, Kansas
103. Zeng YC, Chun XF, Yong CS et al (2004) Synthesis of polyborosilazane and its utilization as a precursor to boron nitride. *J Appl Polym Sci* 94:105109
104. Schiavon MA, Soraru GD, Valeria I et al (2004) Poly(borosilazanes) as precursors of SiBCN glasses: synthesis and high temperature properties. *J Non-Cryst Solids* 348:156–161
105. Ganesh Babu T, Devasia R (2019) Simple and low cost synthetic route for SiBCN ceramic powder from a boron modified cyclotrisilazane. *J Am Ceram Soc* 102:476–489
106. Koussaalya AB, Kumar R, Packirisamy S (2013) Characterization of free carbon in the as-thermolyzed Si–B–C–N ceramic from a polyorganoborosilazane precursor. *J Adv Ceram* 2(4):325–332
107. Wang X, Wang H, Wang JS et al (2018) Synthesis, characterization and ceramic conversion of a liquid polymeric precursor to SiBCN ceramic via borazine-modified polymethylsilane. *J Mater Sci* 53:11242–11252
108. Gerstel P, Muller A, Bill J et al (2003) Synthesis and high-temperature behavior of Si/B/C/N precursor-derived ceramics without “free carbon”. *Chem Mater* 15:4980–4986
109. Liu F, Kong J, Luo C et al (2015) High temperature self-healing SiBCN ceramics derived from hyperbranched polyborosilazanes. *Adv Compos Hybrid Mater* 1:506–517
110. Bechelany MC, Salameh C, Viard A et al (2015) Preparation of polymer-derived Si-B-C-N monoliths by spark plasma sintering technique. *J Eur Ceram Soc* 35:1361–1374
111. Lee J, Butt DP, Baney RH et al (2005) Synthesis and pyrolysis of novel polysilazane to SiBCN ceramic. *J Non-Cryst Solids* 351:2995–3005
112. Zhao H, Chen L, Luan X et al (2016) Synthesis, pyrolysis of a novel liquid SiBCN ceramic precursor and its application in ceramic matrix composites. *J Eur Ceram Soc* 37:1321–1329
113. Zhang C, Liu Y, Han K et al (2018) Effect of boron content on structure and high thermal stability of Polyborosilazane precursor. *Adv Funct Mater* 87:795–803
114. Luan X, Zhang Q, Yu R et al (2019) Polyborosilazane-derived high temperature resistant SiBCNO. *Adv Eng Mater* 1801295:1–7
115. Tamayo A, Alonso R, Maza M et al (2016) Combined pyrolysis-ammonolysis treatment to retain C during nitridation of SiBOCN ceramics. *J Ceram Soc Jpn* 124(10):996–1002
116. Liu Y, Peng S, Cui Y et al (2017) Fabrication and properties of precursor-derived SiBN ternary ceramic fibers. *Mater Design* 128:150–156
117. Liu Y, Chen K, Peng S et al (2019) Synthesis and pyrolysis mechanism of a novel polymeric precursor for SiBN ternary ceramic fibers. *Ceram Int* 45:20172–20177
118. Ionescu E, Bernard S, Lucas R et al (2019) Polymer-derived ultra-high temperature ceramics (UHTCs) and related materials. *Adv Eng Mater* 21:1900269
119. Dhamne A, Xu W, Fookes BG et al (2005) Polymer–ceramic conversion of liquid polyaluminasilazanes for SiAlCN ceramics. *J Am Ceram Soc* 88:2415–2419
120. Wang Y, Fan Y, Zhang L et al (2006) Polymer-derived SiAlCN ceramics resist oxidation at 1400°C. *Scr Mater* 55:295–297
121. Shi L, Zhao H, Tang C (2009) Purity of SiC powders fabricated by coat-mix. *Int J Miner Metall Mater* 16:230–235
122. Qian JM, Jin ZH (2006) Preparation and characterization of porous, biomorphic SiC ceramic with hybrid pore structure. *J Eur Ceram Soc* 26:1311–1316
123. Jung YS, Kwon OJ, Oh SM (2002) Formation of silica-coated carbon powder and conversion to spherical β -silicon carbide by carbothermal reduction. *J Am Ceram Soc* 85:2134–2136
124. Li W, Huang Q, Guo H et al (2018) Green synthesis and photoluminescence property of β -SiC nanowires from rice husk silica and phenolic resin. *Ceram Int* 44:4500–4503
125. Prabhakaran PV, Sreejith KJ, Swaminathan B et al (2009) Silicon carbide wires of nano to sub-micron size from phenol-furfuraldehyde resin. *J Mater Sci* 44:528–533

126. Ma CCM, Tai NH, Chang WC et al (1996) Microstructure and oxidation resistance of SiC coated carbon-carbon composites via pressure less reaction sintering. *J Mater Sci* 31:649–654
127. Yu X, Ding S, Meng Z (2008) Aerosol assisted synthesis of silica/phenolic resin composite mesoporous hollow spheres. *Colloid Polym Sci* 286:1361–1368
128. Hasegawa I (1996) New potentially economic process for fabricating nonoxide ceramic fibers. *Mater Tech* 11:14–15
129. Song N, Zhang H, Liu H et al (2017) Effects of SiC whiskers on the mechanical properties and microstructure of SiC ceramics by reactive sintering. *Ceram Int* 43:6786–6790
130. Zhang W, Wang H, Jin Z (2005) Gel casting and properties of porous silicon carbide/silicon nitride composite ceramics. *Mater Lett* 59:250–256
131. Nishimura T, Ishihara S, Yoshioka Y et al (2009) Synthesis of non-oxide ceramic fine-powders from organic precursors. *Key Eng Mater* 403:269–272
132. Hasegawa I, Nakamura T, Kajiwara M (1996) Synthesis of continuous silicon carbide-titanium carbide hybrid fibers through sol-gel processing. *Mater Res Bull* 31:869–875
133. Hwang GC, Matsushita J (2008) Fabrication and properties of SiB6-B4C with phenolic resin as a carbon source. *J Mater Sci Technol* 24:102–104
134. Lee JS, Lee SH, Nishimura T et al (2009) Hexagonal plate-like ternary carbide particulates synthesized by a carbothermal reduction process: processing parameters and synthesis mechanism. *J Am Ceram Soc* 92:1030–1035
135. Cheng Z, Foroughi P, Behrens A (2017) Synthesis of nanocrystalline TaC powders via single-step high temperature spray pyrolysis from solution precursors. *Ceram Int* 43:3431–3434
136. Li X, Yuan G, Zhou Y et al (2018) Electromagnetic properties of porous Si₃N₄ ceramics with gradient distributions of SiC and pores fabricated by directional in-situ nitridation reaction. *Ceram Int* 44:1176–1181
137. Ganesh Babu T, Devasia R (2016) Boron-modified phenol formaldehyde resin-based self-healing matrix for Cf/SiBOC composites. *Adv Appl Ceram* 115(8):457–469
138. Ganesh Babu T, Devasia R (2016) Boron modified phenol formaldehyde derived Cf/SiBOC composites with improved mechanical strength for high temperature applications. *J Inorg Organomet Polym Mater* 26(4):764–772
139. Li F, Huang X, Zhang G (2017) Chapter 3. Preparation of ultra-high temperature ceramics-based materials by sol-gel routes. In: Usha C (ed) *Recent applications in sol-gel synthesis*. InTech Publisher, Croatia
140. Nitin C, Devapal D, Prabhakaran PV (2019) Synthesis of zirconium diboride based ultra high temperature ceramics via preceramic route. *Ceram Int* 45:25092–25096
141. Greil P, Seibold M (1991) Modelling of dimensional changes during polymer-ceramic conversion for bulk component fabrication. *J Mater Sci* 27:1053–1060
142. Emy T, Seibold M, Jarchow O et al (1993) Microstructure development of oxycarbide composites during active-filler-controlled polymer pyrolysis. *J Am Ceram Soc* 76:206–213
143. Greil P (1995) Active-filler-controlled pyrolysis of preceramic polymers. *J Am Ceram Soc* 78:835–848
144. Greil P (2012) Advancements in polymer-filler derived ceramics. *J Korean Ceram Soc* 49:279–286
145. Vijay V, Bhuvaneshwari S, Biju VM et al (2016) Influence of titanium silicide active filler on the microstructure evolution of borosiloxane-derived Si-B-O-C ceramics. *J Ceram Sci Technol* 07(01):97–106
146. Vijay V, Biju VM, Devasia R (2016) Active filler controlled polymer pyrolysis – a promising route for the fabrication of advanced ceramics. *Ceram Int* 42(14):15592–15596
147. Chawla KK (2003) *Ceramic matrix composites*, 2nd edn. Kluwer Academic Publishers, Norwell
148. Marshall DB, Cox BN (2008) Integral textile ceramic structures. *Annu Rev Mater Sci* 38:425–443
149. Glass D (2008) Ceramic matrix composite (CMC) thermal protection systems (TPS) and hot structures for hypersonic vehicles. In: 15th AIAA international space planes and hypersonic systems and technologies conference, p 2682

150. Ohnabe H, Masaki S, Onozuka M et al (1999) Potential application of ceramic matrix composites to aero-engine components. *Compos Part A Appl Sci Manuf* 30:489–496
151. Zhang QM (2011) Research on ceramic matrix composites (CMC) for aerospace applications. *Adv Mater Res* 284–286:324–329
152. Scigliano R, Belardo M, De Stefano FM et al (2016) Thermo-mechanical numerical model set-up and validation approach for a CMC control surface for re-entry vehicles. *AIAA*. <https://doi.org/10.2514/6.2016-5626>
153. Belardo M, De M, Fumo S et al (2017) Development of an Italian technology for CMC control surface for re-entry applications. In: 7th European conference for aeronautics and space sciences. <https://doi.org/10.13009/EUCASS2017-428>
154. Zuber C, Reimer T, Stubicar K et al (2010) Manufacturing of the CMC nose cap for the EXPERT spacecraft. *Ceram Eng Sci Proc* 31(8):59–72
155. Harnisch B, Kunkel B, Deyerler M et al (1998) Ultra-lightweight C/SiC mirrors and structures. *ESA Bull* 95(8):148–152
156. Vaidyaraman S, Purdy M, Walker T et al (2006) C/SiC material evaluation for aircraft brake applications. In: *High temperature ceramic matrix composites*. Wiley-VCH, Weinheim, pp 802–808
157. Li G, Zhang C, Hu H et al (2012) Preparation and mechanical properties of C/SiC nuts and bolts. *Mater Sci Eng A* 547:1–5
158. Schmidt S, Beyer S, Knabe H et al (2004) Advanced ceramic matrix composite materials for current and future propulsion technology applications. *Acta Astronaut* 55:409–420
159. Balat-Pichelin M, Charpentier L, Panerai F et al (2015) Passive/active oxidation transition for CMC structural materials designed for the IXV vehicle re-entry phase. *J Eur Ceram Soc* 35:487–502
160. Franklin KM, Weinberg DJ, Tran TT (2003) Large thermal protection system panel. US Patent 6,505,794
161. Scotti S, Clay C, Rezin M (2003) Structures and materials technologies for extreme environments applied to reusable launch vehicles. In: *AIAA international air and space symposium and exposition: the next 100 years*. <https://doi.org/10.2514/6.2003-2697>
162. Pichon T, Barreateau R, Soyris P et al (2009) CMC thermal protection system for future reusable launch vehicles: generic shingle technological maturation and tests. *Acta Astronaut* 65:165–176
163. Olufsen F, Orbekk E (2017) Application of CMC materials in rocket propulsion. In: M Singh, T Ohji, S Dong, D Koch, et al (eds) *Advances in high temperature ceramic matrix composites and materials for sustainable development*. Wiley, Hoboken, pp 367–374
164. Christin F (2002) Design, fabrication, and application of thermostructural composites (TSC) like C/C, C/SiC, and SiC/SiC composites. *Adv Eng Mater* 4(12):903–912
165. Krenkel W (2004) Carbon fiber reinforced CMC for high-performance structures. *Int J Appl Ceram Technol* 1(2):188–200
166. Buffenoir F, Zeppa C, Pichon T et al (2016) Development and flight qualification of the C–SiC thermal protection systems for the IXV. *Acta Astronaut* 124:85–89
167. Liu C, Chen J, Han H et al (2004) A long duration and high reliability liquid apogee engine for satellites. *Acta Astronaut* 55:401–408
168. Schmidt S, Beyer S, Immich H et al (2005) Ceramic matrix composites: a challenge in space-propulsion technology applications. *Int J Appl Ceram Technol* 2(2):85–96
169. Keller K, Pfeiffer E, Handrick K et al (2006) Advanced high temperature insulations. In: *5th European workshop on thermal protection systems and hot structures*, Noordwijk
170. Ortona A, Pusterla S, Gianella S (2011) An integrated assembly method of sandwich structured ceramic matrix composites. *J Eur Ceram Soc* 31:1821–1826
171. Naslain R (1998) The design of the fibre-matrix interfacial zone in ceramic matrix composites. *Compos Part A Appl Sci Manuf* 29(9–10):1145–1155
172. Yin J, Lee SH, Feng L et al (2015) The effects of SiC precursors on the microstructures and mechanical properties of SiCf/SiC composites prepared via polymer impregnation and pyrolysis process. *Ceram Int* 41:4145–4153

173. Lii DF, Huang JL, Tsui LJ et al (2002) Formation of BN films on carbon fibers by dip-coating. *Surf Coat Technol* 150:269–276
174. Einset EO, Patibandla NB, Luthra KL (1994) Processing conditions for boron nitride coatings in fiber bundles via chemical vapor deposition. *J Am Ceram Soc* 77:3081–3086
175. Hackl G, Gerhard H, Popovska N (2006) Coating of carbon short fibers with thin ceramic layers by chemical vapor deposition. *Thin Solid Films* 513:217–222
176. Naslain R (2004) Design, preparation and properties of non-oxide CMCs for application in engines and nuclear reactors: an overview. *Compos Sci Technol* 64(2):155–170
177. Kopeliovich D (2014) Advances in the manufacture of ceramic matrix composites using infiltration techniques (Chapter 5). In: Low IM (ed) *Advances in ceramic matrix composites*. Woodhead Publishing, Cambridge, UK, pp 79–108
178. Larson NM, Zok FW (2018) In-situ 3D visualization of composite microstructure during polymer-to-ceramic conversion. *Acta Mater* 144:579–589
179. Streckert HH, Sheehan JE, Mazdiyasn K (1991) Method for providing a silicon carbide matrix in carbon-fiber reinforced composites. US Patent 5,067,999
180. Liu L, Li X, Xing X et al (2008) A modified polymethylsilane as the precursor for ceramic matrix composites. *J Organomet Chem* 693:917–922
181. Kotani M, Kohyama A, Katoh Y (2001) Development of SiC/SiC composites by PIP in combination with RS. *J Nucl Mater* 289:37–41
182. Ly HQ, Taylor R, Day RJ (2001) Carbon fibre-reinforced CMCs by PCS infiltration. *J Mater Sci* 36:4027–4035
183. Suo J, Chen Z, Xiao J et al (2005) Influence of an initial hot-press processing step on the mechanical properties of 3D-C/SiC composites fabricated via PIP. *Ceram Int* 31:447–452
184. Swaminathan B, Painuly A, Manwatkar SK et al (2010) Polymer derived C/C-SiC and C/C-SIBOC ceramics for space applications. In: Krenkel W, Lamon J (eds) *High temperature ceramic materials and composites*. AVISO VerlagsgesellschaftmbH, Berlin, pp 719–723
185. He X, Zhang X, Zhang C et al (2001) Microstructures of a carbon fiber-reinforced silicon-carbide composite produced by precursor pyrolysis and hot pressing. *Compos Sci Technol* 61:117–123
186. Kohyama A, Kotani M, Katoh Y et al (2000) High-performance SiC/SiC composites by improved PIP processing with new precursor polymers. *J Nucl Mater* 283–287:565–569
187. Wang QK, Hu HF, Zheng WW et al (2007) Preparation and property study of 3D Cf/Si-Ti-C-O composites fabricated with polytitanocarbosilane by PIP process. *Key Eng Mater* 336–338:1242–1244
188. Ochiai S, Kimura S, Tanaka H et al (2004) Residual strength of PIP-processed SiC/SiC single-tow minicomposite exposed at high temperatures in air as a function of exposure temperature and time. *Compos Part A Appl Sci Manuf* 35:41–50
189. Sreeja R, Swaminathan B, Painuly A et al (2010) Allylhydridopolycarbosilane (AHPCS) as matrix resin for C/SiC ceramic matrix composites. *Mater Sci Eng B* 168:204–207
190. King D, Apostolov Z, Key T et al (2018) Novel processing approach to polymer-derived ceramic matrix composites. *Int J Appl Ceram Technol* 15:399–408
191. Bongio EV, Lewis SL, Welson DR et al (2009) Polymer derived ceramic matrix composites for friction applications. *Adv Appl Ceram* 108:483–487
192. Ajith R (2012) Studies on lightweight ceramics and ceramic matrix composites from polymeric precursors. PhD thesis, University of Kerala
193. Gadow R, Kern F, Ulutas H (2005) Mechanical properties of ceramic matrix composites with siloxane matrix and liquid phase coated carbon fiber reinforcement. *J Eur Ceram Soc* 25:221–225
194. Suttor D, Erny T, Greil P (1997) Fiber-reinforced ceramic-matrix composites with a Polysiloxane/boron-derived matrix. *J Am Ceram Soc* 80:1831–1840
195. Pina SRO, Pardini LC, Yoshida IVP (2007) Carbon fiber/ceramic matrix composites: processing, oxidation and mechanical properties. *J Mater Sci* 42:4245–4253
196. Liedtke V, Olivares IH, Langer M et al (2007) Sol-gel-based carbon/silicon carbide. *J Eur Ceram Soc* 27:1267–1272

197. Akkas HD, Ovecoglu ML, Tanoglu M (2006) Silicon oxycarbide-based composites produced from pyrolysis of polysiloxanes with active Ti filler. *J Eur Ceram Soc* 26:3441–3449
198. Rocha RM, Cairo C, Graca ML (2006) Formation of carbon fiber-reinforced ceramic matrix composites with polysiloxane/silicon derived matrix. *Mater Sci Eng A* 437:268–273
199. Srinivasan K, Tiwari SN (1990) Development of polysilsesquioxane composites. NASA-CR-180263
200. Yair H, Liedtke V (2003) Sol-gel derived C-SiC composites and protective coatings for sustained durability in the space environment. *Int Mater Space Environ* 540:67–74
201. Sreejith KJ, Packirisamy S (2010) Phenyl borosiloxane derived ceramic matrix composites. In: Krenkel W, Lamon J (eds) *High temperature ceramic materials and composites*. AVISO Verlagsgesellschaft mbH, Berlin, pp 712–718
202. Vijay V, Siva S, Sreejith KJ et al (2018) Effect of boron inclusion in SiOC polymer derived matrix on the mechanical and oxidation resistance properties of fiber reinforced composites. *Mater Chem Phys* 205:269–277
203. Hoshii S, Kojima A, Ooi H et al (1996) Preparation of CF/ceramic composite using 2.5-dimensionally (quintuple) wove CF cloth. *Carbon* 34:283–284
204. Siqueira RL, Yoshida IVP, Pardini LC et al (2007) Poly(borosiloxanes) as precursors for carbon fiber ceramic matrix composites. *Mater Res* 10:147–151
205. Thünemann M, Herzog A, Vogt U et al (2004) Porous SiC-preforms by Intergranular binding with preceramic polymers. *Adv Eng Mater* 6:167–172
206. Herzog A, Thünemann M, Vogt U et al (2005) Novel application of ceramic precursors for the fabrication of composites. *J Eur Ceram Soc* 25:187–192
207. Devasia R, Nair SG, Sreejith KJ et al (2018) Fiber-reinforced ceramic matrix composite material with polymer derived interphase coating. Indian Patent 299956
208. Nair SG, Sreejith KJ, Packirisamy S et al (2018) Polymer derived PyC interphase coating for C/SiBOC composites. *Mater Chem Phys* 204:179–186
209. Sreejith KJ, Rajasekhar BV, Vijay V et al (2018) Polymer-derived C_f/SiBOC ceramic matrix composites and a method of production thereof. Indian Patent Appl. No. 201841020417
210. Devapal D, Gopakumar MP, Painuly A et al (2014) Development of C/SiBOC ceramic matrix composite from vinylborosiloxane as matrix resin. In: ISAMPE national conference on composites (INCCOM-13), Thiruvananthapuram
211. Fitzer E, Manocha LM (1998) Applications of carbon/carbon composites. In: *Carbon reinforcements and carbon/carbon composites*. Springer, Berlin/Heidelberg, pp 310–336
212. Sheehan JE, Buesking KW, Sullivan BJ (1994) Carbon-carbon composites. *Annu Rev Mater Sci* 24(1):19–44
213. Isola C, Appendino P, Bosco F et al (1998) Protective glass coating for carbon-carbon composites. *Carbon* 36(7–8):1213–1218
214. Fu QG, Li HJ, Shi XH et al (2005) Silicon carbide coating to protect carbon/carbon composites against oxidation. *Scr Mater* 52(9):923–927
215. Carter JA (1996) Oxidation protection for carbon/carbon composites. US Patent 5,536,574
216. Gray PE (1990) Oxidation protection for carbon/carbon composites. US Patent 4,894,286
217. Weir RL, Pearsall JA (1990) Glass ceramic precursor compositions containing titanium diboride. US Patent 4,931,413
218. Chu Y, Li H, Fu Q et al (2012) Oxidation protection of C/C composites with a multilayer coating of SiC and Si⁺ SiC+ SiC nanowires. *Carbon* 50(3):1280–1288
219. Li J, Luo R, Lin C et al (2007) Oxidation resistance of a gradient self-healing coating for carbon/carbon composites. *Carbon* 45(13):2471–2478
220. Li HJ, Xue H, Wang YJ et al (2007) A MoSi₂-SiC-Si oxidation protective coating for carbon/carbon composites. *Surf Coat Technol* 201(24):9444–9447
221. Fu QG, Li HJ, Li KZ et al (2007) A SiC/glass oxidation protective coating for carbon/carbon composites for application at 1173K. *Carbon* 4(45):892–894
222. Morimoto T, Ogura Y, Kondo M et al (1995) Multilayer coating for carbon-carbon composites. *Carbon* 33(4):351–357

223. Maclean JP (2004) Analysis of the Columbia shuttle disaster – anatomy of a flawed investigation in a pathological organization. *J Sci Explor* 18(2):187–215
224. Li H, Zhang L, Cheng L et al (2009) UV curing behavior of a highly branched polycarbosilane. *J Mater Sci* 44(4):970–975
225. Liu J, Zhang L, Liu Q et al (2010) Polymer-derived SiOC–barium–strontium aluminosilicate coatings as an environmental barrier for C/SiC composites. *J Am Ceram Soc* 93(12):4148–4152
226. Lee KN, Fox DS, Eldridge JI et al (2003) Upper temperature limit of environmental barrier coatings based on mullite and BSAS. *J Am Ceram Soc* 86(8):1299–1306
227. Wang Y, Li H, Zhang L et al (2009) Oxidation behavior of polymer derived SiCO powders. *Ceram Int* 35(3):1129–1132
228. Wang Y, Fei W, An L (2006) Oxidation/corrosion of polymer-derived SiAlCN ceramics in water vapor. *J Am Ceram Soc* 89(3):1079–1082
229. An LN, Wang YG, Bharadwaj L et al (2004) Silicoaluminum carbonitride with anomalously high resistance to oxidation and hot corrosion. *Adv Eng Mater* 6(5):337–340
230. Mucalo MR, Milestone NB, Vickridge IC et al (1994) Preparation of ceramic coatings from pre-ceramic precursors. *J Mater Sci* 29(17):4487–4499
231. Bill J, Heimann D (1996) Polymer-derived ceramic coatings on C/C–SiC composites. *J Eur Ceram Soc* 16(10):1115–1120
232. Bonnetot B, Guilhon F, Viala JC et al (1995) Boron nitride matrixes and coatings obtained from tris (methylamino) borane. Application to the protection of graphite against oxidation. *Chem Mater* 7(2):299–303
233. Paciorek KJ, Masuda SR, Kratzer RH et al (1991) Processable precursor for boron nitride coatings and matrixes. *Chem Mater* 3(1):88–91
234. Niebyski LM (1990) Organoborosilazane. US Patent 4,921,925
235. Baldus HP, Jansen M, Wagner O (1994) New materials in the system Si-(N, C)-B and their characterization. *Key Eng Mater* 89:75–80
236. Wang K, Luo L, Lu Y et al (2015) In-field repair of the damaged coatings for C/C composites. *Ceram Int* 41(6):7549–7555
237. Manocha LM, Manocha SM (1995) Studies on solution-derived ceramic coatings for oxidation protection of carbon-carbon composites. *Carbon* 33(4):435–440
238. Niu F, Wang Y, Abbas I et al (2017) A MoSi₂-SiOC-Si₃N₄/SiC anti-oxidation coating for C/C composites prepared at relatively low temperature. *Ceram Int* 43(3):3238–3245
239. Schiroky GH (1987) Oxidation behavior of chemically vapor-deposited silicon carbide. *Adv Ceram Mater* 2(2):137–141
240. Jacobson NS, Opila EJ, Lee KN (2001) Oxidation and corrosion of ceramics and ceramic matrix composites. *Curr Opin Solid State Mater Sci* 5(4):301–309
241. Jacobson NS (1993) Corrosion of silicon-based ceramics in combustion environments. *J Am Ceram Soc* 76(1):3–28
242. More KL, Tortorelli PF, Ferber MK et al (2000) Observations of accelerated silicon carbide recession by oxidation at high water-vapor pressures. *J Am Ceram Soc* 83(1):211–213
243. Eaton HE, Linsey GD (2002) Accelerated oxidation of SiC CMCs by water vapor and protection via environmental barrier coating approach. *J Eur Ceram Soc* 22(14–15):2741–2747
244. Liu J, Zhang L, Yang J et al (2012) Fabrication of SiCN–Sc₂Si₂O₇ coatings on C/SiC composites at low temperatures. *J Eur Ceram Soc* 32(3):705–710
245. Riedel R, Bill J, Kienzle A (1996) Boron-modified inorganic polymers – precursors for the synthesis of multicomponent ceramics. *Appl Organomet Chem* 10(3–4):241–256
246. Kobayashi K, Maeda K, Sano H et al (1995) Formation and oxidation resistance of the coating formed on carbon material composed of B₄C–SiC powders. *Carbon* 33(4):397–403
247. Devapal D, Gopakumar MP, Prabhakaran PV et al (2018) An oxidation resistance coating composition and a method of preparation thereof. Indian Patent Appl No. 201841020187, 30 May 2018

248. Packirisamy S (2018) Polymer-derived ceramics for space applications. Feature article in souvenir of international conference on recent trends in materials science and technology, October 2018, India
249. Thirunavukkarasu S, Rao BPC, Jayakumar T et al (2011) Eddy current methodology for nondestructive assessment of thickness of silicon carbide coating on carbon-carbon composites. *Aerosp Sci Technol* 63(3):223–229
250. <https://www.newscientist.com/article/2089757-indias-reusable-space-plane-takes-its-first-test-flight/>. Accessed 27 Aug 2018
251. Kors D (1990) Design considerations for combined air breathing-rocket propulsion systems. In 2nd International aerospace planes conference, Orlando, 1990-5216
252. <https://www.isro.gov.in/launchers/isro%E2%80%99s-scramjet-engine-technology-demonstrator-successfully-flight-tested>. Accessed 2 Sept 2018
253. Vijay V, Devasia R (2013) Process document on silicon carbide based oxidation protection coating on C/C composite for SRE-II Project Technical Report, PCM/ASCG/CMPD/QC/01/2013
254. Hald H (2003) Operational limits for reusable space transportation systems due to physical boundaries of C/SiC materials. *Aerosp Sci Technol* 7(7):551–559
255. Sreeja R, Sebastain TV, Prabhakaran PV et al (2018) Precursor based ceramic coating and adhesive compositions for high temperature applications. Indian Patent 304496
256. Vanitha R (2014) Thermal response evaluation of SiC coated C/C composite for RLV nose cap and ceramic matrix composite for RLV wing leading edge. Technical Report No. AHTD/PN/38/2014. Vikram Sarabhai Space Centre, Thiruvananthapuram
257. Swadyba L, Moskal G, Mendala B et al (2007) Characterisation of APS TBC system during isothermal oxidation at 1100°C. *Arch Mater Sci Eng* 758:758
258. Mercier D, Gauntt BD, Brochu M (2011) Thermal stability and oxidation behavior of nanostructured NiCoCrAlY coatings. *Surf Coat Technol* 205(17–18):4162–4168
259. Simendinger III WH (2005) Thermal barrier composition. US Patent Appl No. US2005/0106381 A1
260. Torrey JD, Bordia RK, Henager CH et al (2006) Composite polymer derived ceramic system for oxidizing environments. *J Mater Sci* 41(14):4617–4622
261. Torrey JD, Bordia RK (2008) Mechanical properties of polymer-derived ceramic composite coatings on steel. *J Eur Ceram Soc* 28(1):253–257
262. Kappa M, Kebianyor A, Scheffler M (2010) A two-component preceramic polymer system for structured coatings on metals. *Thin Solid Films* 519(1):301–305
263. Barroso G, Li Q, Bordia RK et al (2019) Polymeric and ceramic silicon-based coatings – a review. *J Mater Chem A* 7:1936–1963
264. Günthner M, Kraus T, Dierdorf A et al (2009) Advanced coatings on the basis of Si(C)N precursors for protection of steel against oxidation. *J Eur Ceram Soc* 29(10):2061–2068
265. Günthner M, Schütz A, Glatzel U et al (2011) High performance environmental barrier coatings, part I: passive filler loaded SiCN system for steel. *J Eur Ceram Soc* 31(15):3003–3010
266. Wang K, Günthner M, Motz G et al (2011) High performance environmental barrier coatings, part II: active filler loaded SiOC system for superalloys. *J Eur Ceram Soc* 31(15):3011–3020
267. Parchoviansky M, Petrikova I, Barroso GS et al (2018) Corrosion and oxidation behavior of polymer derived ceramic coatings with passive Glass fillers on AISI 441 stainless steel. *Ceramics-Silikáty* 62(2):146–157
268. Riffard F, Joannet E, Buscail H et al (2017) Beneficial effect of a pre-ceramic polymer coating on the protection at 900°C of a commercial AISI 304 stainless steel. *Oxid Met* 88(1–2):211–220
269. Nguyen MD, Bang JW, Bin AS et al (2017) Novel polymer-derived ceramic environmental barrier coating system for carbon steel in oxidizing environments. *J Eur Ceram Soc* 37(5):2001–2010

270. Smokovych I, Hasemann G, Krüger M et al (2017) Polymer derived oxidation barrier coatings for Mo-Si-B alloys. *J Eur Ceram Soc* 37(15):4559–4565
271. Soechting FO (1995) A design perspective on thermal barrier coatings. In: Thermal barrier coating workshop, NASA Conference Publication 3312, Cleveland, pp 1–15
272. Ranjbar-Far M, Absi J, Shahidi S et al (2011) Impact of the non-homogenous temperature distribution and the coatings process modeling on the thermal barrier coatings system. *Mater Des* 32(2):728–735
273. Miller RA (1995) Thermal barrier coatings for aircraft engines – history and directions. In: Thermal barrier coating workshop, NASA CP 3312, p 17
274. Stiger MJ, Yanar NM, Topping MG et al (1999) Thermal barrier coatings for the 21st century. *Z Met* 90(12):1069–1078
275. Klemens PG (1993) Thermal conductivity of zirconia. In: Wills KE, Dinwiddie RB, Graves RS (eds) Thermal conductivity, vol 23. Technomics, Lancaster, p 209
276. Bose S (2017) High temperature coatings. Butterworth-Heinemann, Elsevier Publishers, Oxford, UK, p 199
277. Padtare NP, Gell M, Jordan EH (2002) Thermal barrier coatings for gas-turbine engine applications. *Science* 296(5566):280–284
278. Xu H, Guo H (eds) (2011) Thermal barrier coatings. Elsevier, Oxford, UK
279. Devapal D, Sebastain TV, Prabhakaran PV et al (2012) Thermal barrier coating on metallic substrates by preceramic route. Paper presented in the international symposium on metals and materials, Thiruvananthapuram
280. Devapal D, Sebastian TV, Kirubaharan K et al (2019) Process for multilayer thermal barrier coating for protection of metallic substrates from extreme temperature conditions. Indian Patent 322018
281. Teichman A, Stein BA (1988) NASA/SDIO space environmental effects on materials workshop, Hampton, Part 2, NASA-L-16575-PT-2
282. De Groh KK, Banks BA, Sharon KR et al (2018) Chapter 28, Degradation of spacecraft materials. In: Kutz M (ed) Handbook of environmental degradation of materials, 3rd edn. Elsevier, Cambridge, MA, pp 601–645
283. Reddy MR (1995) Effect of low earth orbit atomic oxygen on spacecraft materials. *J Mater Sci* 30:281–307
284. Packirisamy S, Schwam D, Litt MH (1995) Atomic oxygen resistant coatings for low earth orbit space structures. *J Mater Sci* 30:308–320
285. Arjun GN, Lincy TL, Sajitha TS et al (2015) Atomic oxygen resistant polysiloxane coatings for low earth orbit space structures. *Mater Sci Forum* 830:699–702
286. Xu M, Zhao Y, Zhang X et al (2019) Highly homogeneous polysiloxane flexible coating for low earth orbital spacecraft with ultra-efficient atomic oxygen resistance and self-healing behaviour. *ACS Appl Polym Mater*. <https://doi.org/10.1021/acsapm.9b00671>
287. Wang X, Li Y, Qian Y et al (2018) Mechanically robust atomic oxygen-resistant coatings capable of autonomously healing damage in low earth orbit space environment. *Adv Mater* 1803854:1–7
288. Devapal D, Packirisamy S, Korulla RM (2004) Atomic oxygen resistant coating from poly (tetramethyldisilylene-co-styrene). *J Appl Polym Sci* 94(6):2368–2375
289. Devapal D, Packirisamy S, Nair CPR (2006) Phosphazene-based polymers as atomic oxygen resistant materials. *J Mater Sci* 41:5764–5766
290. Wu B, Zhang Y, Yang D et al (2019) Self-healing anti-atomic-oxygen phosphorus-containing polyimide film via molecular level incorporation of nanocage trisilanolphenyl POSS: preparation and characterization. *Polymers* 11(1013):1–19
291. Maldar NN, Medhi M, Packirisamy S (2017) Aromatic bisetherimides having pendant diphenyl phosphine oxide and a process for preparing the same. Indian Patent 279815
292. Maldar NN, Medhi M, Packirisamy S (2016) Aromatic diamines with pendant styryl phosphine oxide group and a process for preparing the same. Indian Patent 274744

293. Chunbo W, Haifu J, Dongbo T et al (2019) Atomic oxygen effects on polymers containing silicon or phosphorus: mass loss, erosion yield, and surface morphology. *High Perform Polym* 31(8):969–976
294. Song G, Li X, Jiang Q et al (2015) A novel structural polyimide material with synergistic phosphorus and POSS for atomic oxygen resistance. *RSC Adv* 5(16):11980–11988
295. Packirisamy S, Abraham G, Ramaswamy R et al (2008) A process for producing siloxane polymers having atomic oxygen resistance and a method of producing articles coated therewith. Indian Patent 216622
296. Packirisamy S, Abraham G, Ramaswamy R et al (2008) A process for the synthesis of siloxane-imide-epoxy resins. Indian Patent 216620
297. Schwam D, Litt MH (1996) Evaluation of atomic oxygen resistant coatings for space structures. *Adv Perform Mater* 3(2):153–169
298. Packirisamy S (1996) Decaborane(14)-based polymers. *Prog Polym Sci* 21(4):707–773
299. Hu L, Li M, Xu C et al (2009) A polysilazane coating protecting polyimide from atomic oxygen and vacuum ultraviolet radiation erosion. *Surf Coat Technol* 203(22):3338–3343
300. Hu L, Li M, Xu C et al (2011) Perhydropolysilazane derived silica coating protecting Kapton from atomic oxygen attack. *Thin Solid Films* 520:1063
301. Chang YC, Liu TZ, Zhang H et al (2014) Protection of kapton from atomic oxygen erosion using a polysilazane coating. *Appl Mech Mater* 651:65–68
302. Hanson W, Fernie J (1998) Ceramic joining – an overview. *Mater World* 6(9):524–536
303. Singh M (2011) Ceramic integration technologies for aerospace and energy systems: technical challenges and opportunities. NASA Technical Report No. 20110012028
304. Kim JJ, Park JW, Eagar TW (2003) Interfacial microstructure of partial transient liquid phase bonded Si_3N_4 -to-Inco_ne₁ 718 joints. *Mater Sci Eng A* 344(1–2):240–244
305. Morrissey SR (2005) New materials for aging space shuttle. *Chem Eng News* 83(44):26–29
306. Riedell JA, Easler TE (2009) Ceramic material suitable for repair of a space vehicle component in a microgravity and vacuum environment, method of making same, and method of repairing a space vehicle component. US Patent 7,628,878 B2
307. Lyndon B (2013) Ceramic adhesive and methods for on-orbit repair of re-entry vehicles. NASA Technical Briefs, 20130013565, May 2013, p 15
308. Singh M (2007) In space repair and refurbishment of thermal protection systems structures of reusable launch vehicles. NASA Technical Report No. 20070031665
309. Lewinsohn CA, Colombo P, Reimanis I et al (2001) Stresses occurring during joining of ceramics using preceramic polymers. *J Am Ceram Soc* 84(10):2240–2244
310. Colombo P, Donato A, Riccardi B et al (2002) Joining SiC-based ceramics and composites with pre-ceramic polymers. *Ceram Trans* 144:323–334
311. Bernardo E, Parcianello G, Colombo P et al (2012) SiAlON ceramics from preceramic polymers and nano-sized fillers: application in ceramic joining. *J Eur Ceram Soc* 32:1329–1335
312. Luan X, Chang S, Riedel R et al (2018) An air stable high temperature adhesive from modified SiBCN precursor synthesized via polymer-derived-ceramic route. *Ceram Int* 44(7):8476–8483
313. Luan X, Chang S, Yu R et al (2019) Effect of PSO and TiB₂ content on the high temperature adhesion strength of SiBCNO ceramic. *Ceram Int* 45(7):9515–9521
314. Wang X, Wang J, Wang H (2019) Preparation, structural evolution, and performance of heat-resistant organosilicon polymer adhesives for joining SiC ceramics. *J Adhes* 95:85–102
315. Zhong Z, Xu H, Zhang X et al (2018) Bonding ZrB₂-SiC-G ceramics using modified organic adhesive for engineering applications at ultra high temperatures in air. *Ceram Int* 44(4):3810–3815
316. Wang X, Wang J, Wang H (2015) Joining of SiC ceramics via a novel liquid preceramic polymer (V-PMS). *Ceram Int* 41:7283–7288
317. Wang X, Shi J, Wang H (2019) Preparation, properties, and structural evolution of a novel polyborosilazane adhesive, temperature-resistant to 1600°C for joining SiC ceramics. *J Alloys Compd* 772:912–919
318. Davidovits J (1991) Geopolymers: inorganic polymeric new materials. *J Therm Anal Calorim* 37(8):1633–1656

319. Sreeja R, Prabhakaran PV, Manwatkar SK et al (2012) Adhesive joining of metal to metal and metal to ceramic by precursor route. Paper presented in the international symposium on metals and materials, Thiruvananthapuram
320. Scheffler M, Colombo P (eds) (2005) Cellular ceramics: structure, manufacturing, properties and applications. Wiley-VCH, Weinheim
321. Colombo P, Bernardo E (2008) Cellular structures (Chapter 10). In: Riedel R, Chen I-W (eds) Ceramics science and technology. Structures, vol 1. Wiley-VCH, Weinheim, pp 407–441
322. Ohji T, Fukushima M (2012) Macro-porous ceramics: processing and properties. *Int Mater Rev* 57(2):115–131
323. André R, Studart W, Urs T (2006) Processing routes to macroporous ceramics: a review. *J Am Ceram Soc* 89(6):1771–1789
324. Arpin KA, Hill C, Justin W et al (2007) Ceramic foam processing by the chemical vapor infiltration of a graphite felt with SiC for ceramic composite applications. In: Tandon R (ed) Mechanical properties and performance of engineering ceramics and composites II. Wiley, Hoboken, pp 415–422
325. Borchardt L, Hoffmann C, Oschatz M et al (2012) Preparation and application of cellular and nanoporous carbides. *Chem Soc Rev* 41:5053–5067
326. Vakifahmetoglu C, Zeydanli D, Colombo P (2016) Porous polymer-derived ceramics. *Mater Sci Eng* 106:1–30
327. Colombo P, Bernardo E (2003) Macro- and micro-cellular porous ceramics from preceramic polymers. *Compos Sci Technol* 63:2353–2359
328. Zhang H, D'Angelo Nunes P, Wilhelm M et al (2016) Hierarchically ordered micro/meso/macroporous polymer-derived ceramic monoliths fabricated by freeze-casting. *J Eur Ceram Soc* 36:51–58
329. Colombo P (2006) Conventional and novel processing methods for cellular ceramics. *Philos Trans A Math Phys Eng Sci* 364:109–124
330. Jana P, Zera E, Sorarù GD (2017) Processing of preceramic polymer to low density silicon carbide foam. *Mater Des* 116:278–286
331. Mishra MK, Kumar S, Ranjan A et al (2018) Processing, properties and microstructure of SiC foam derived from epoxy-modified polycarbosilane. *Ceram Int* 44:1859–1867
332. Fukushima M, Colombo P (2012) Silicon carbide-based foams from direct blowing of polycarbosilane. *J Eur Ceram Soc* 32:503–510
333. Strachota A, Černý M, Chlup Z et al (2015) Preparation of finely macroporous SiOC foams with high mechanical properties and with hierarchical porosity via pyrolysis of a siloxane/epoxide composite. *Ceram Int* 41:8402–8410
334. Wolff F, Ceron NB, Fey T et al (2012) Extrusion foaming of a preceramic silicone resin with a variety of profiles and morphologies. *Adv Eng Mater* 14:1110–1115
335. Chen H, Parthasarathy TA, Cinibulk MK et al (2014) Processing, characterization, and modeling of room-temperature-vulcanized silicone-derived ceramic foams. *J Am Ceram Soc* 97:733–741
336. Zeschky J, Höfner T, Arnold C et al (2005) Polysilsesquioxane derived ceramic foams with gradient porosity. *Acta Mater* 53:927–937
337. Yuan X, Lü J, Yan X et al (2011) Preparation of ordered mesoporous silicon carbide monoliths via preceramic polymer nanocasting. *Microporous Mesoporous Mater* 142:754–758
338. Eom J-H, Kim Y-W, Park CB et al (2012) Effect of forming methods on porosity and compressive strength of polysiloxane-derived porous silicon carbide ceramics. *J Ceram Soc Japan* 120:199–203
339. Manoj KBV, Zhai W, Eom J-H et al (2011) Processing highly porous SiC ceramics using poly(ether-co-octene) and hollow microsphere templates. *J Mater Sci* 46:3664–3667
340. Reschke V, Laskowsky A, Kappa M (2011) Polymer derived ceramic foams with additional strut porosity. *Mater Sci* 3–4:57–61
341. Wang J, Oschatz M, Biemelt T et al (2013) Preparation of cubic ordered mesoporous silicon carbide monoliths by pressure assisted preceramic polymer nanocasting. *Microporous Mesoporous Mater* 168:142–147

342. Nangrejo MR, Bao X, Edirisinghe MJ (2000) The structure of ceramic foams produced using polymeric precursors. *J Mater Sci Lett* 19:787–789
343. Sreejith KJ, Fey T, Greil P (2014) Siliconboronoxycarbide (SiBOC) foam from methyl borosiloxane. *Ceram Trans* 243:47–60
344. Kim Y-W, Kim S-H, Song I-H et al (2005) Fabrication of open-cell, microcellular silicon carbide ceramics by carbothermal reduction. *J Am Ceram Soc* 88(10):2949–2951
345. Naviroj M, Miller SM, Colombo P et al (2015) Directionally aligned macroporous SiOC via freeze casting of preceramic polymers. *J Eur Ceram Soc* 35:2225–2232
346. Yoon B-H, Lee E-J, Kim H-E et al (2007) Highly aligned porous silicon carbide ceramics by freezing polycarbosilane/camphene solution. *J Am Ceram Soc* 90:1753–1759
347. Zhang H, Lana C, Wilhelm M et al (2017) Macro/mesoporous SiOC ceramics of anisotropic structure for cryogenic engineering. *Mater Des* 134:207–217
348. Xue F, Zhou K, Wu N et al (2018) Porous SiC ceramics with dendritic pore structures by freeze casting from chemical cross-linked polycarbosilane. *Ceram Int* 44:6293–6299
349. Assefa D, Zera E, Campostrini R et al (2016) Polymer-derived SiOC aerogel with hierarchical porosity through HF etching. *Ceram Int* 42:11805–11809
350. Pradeep VS, Ayana DG, Graczyk-Zajac M et al (2015) High rate capability of SiOC ceramic aerogels with tailored porosity as anode materials for Li-ion batteries. *Electrochim Acta* 157:41–45
351. <https://ultramet.com/propulsion-system-components/liquid-rocket-engines/>. Accessed 18 Mar 2019
352. Kelso S, Goodman B (2006) Foam core enables stiff lightweight mirrors. *SPIE News*. <https://doi.org/10.1117/2.1200607.0258>
353. Williams JL, Lachman IM, Patil MD et al (1994) Cellular ceramic substrates. *MRS Proc* 368:283–292
354. Han JH, Hegedus AG, (1992) Method for producing a fiber-reinforced ceramic honeycomb panel. US Patent 5,078,818
355. Petrisko RA, Stark GL, Petrark DR et al (1998) US Patent 5,851,403
356. Cagliostro DE, Riccitiello SR (1989) Ceramic honeycomb structures and method thereof. US Patent 4,824,711
357. Pearson WR, Daws DE (2000) Method of adhering ceramic foams. US Patent 6,099,671
358. Daryabeigi K, Miller SD, Cunningham GR (2007) NASA Langley Research Center Document ID: 2008001356
359. Wang Y, Chen Z, Yu S et al (2017) Improved sandwich structured ceramic matrix composites with excellent thermal insulation. *Compos Part B* 129:180–186
360. <https://ultramet.com/refractory-open-cell-foams/mirrors/>. Accessed 13 Apr 2019



PZT and Lead-Free Piezo Ceramics for Aerospace and Energy Applications

27

P. K. Panda and B. Sahoo

Contents

Introduction	1082
Structure of Lead Zirconate Titanate (PZT)	1083
Morphotropic Phase Boundary of PZT	1083
Effect of Various Dopants on Properties of PZT	1084
Development of Piezoelectric Materials	1086
Lead Zirconate Titanate (PZT)	1086
Lead-Free Piezo Materials	1087
Barium Zirconate Titanate (BZT)-Based Lead-Free Piezo Materials	1088
Fabrication of PZT Unimorphs, Bimorphs, and Multilayered Devices	1090
Preparation of PZT Tapes	1090
Fabrication of PZT Bimorphs and Unimorphs	1090
Fabrication of PZT Multilayered (ML) Stacks	1091
Fabrication of Lead-Free ML Stack and Characterization	1092
Energy Harvesting Study Using PZT Devices	1093
Measurement of Output Voltage at Different Span Length and Resonance Frequencies ...	1095
Measurement of Output Voltage from PZT Sample with Different Force Levels	1096
Applications of Piezoelectric Materials and Devices	1096
Aerospace Applications of PZT Ceramics/Devices	1096
Health Monitoring of Aircraft Structures	1097
Noise, Vibration, and Shape Control of Aircraft Structures	1098
Fuel Level Sensors	1098
PZT Energy Harvester in MAVs	1098
Conclusions	1099
References	1099

P. K. Panda (✉) · B. Sahoo

Materials Science Division, CSIR-National Aerospace Laboratories, Bangalore, India

e-mail: pkpanda@nal.res.in

© Springer Nature Switzerland AG 2020

Y. R. Mahajan, R. Johnson (eds.), *Handbook of Advanced Ceramics and Composites*,
https://doi.org/10.1007/978-3-030-16347-1_32

1081

Abstract

Lead zirconate titanate (PZT)-based piezoelectric materials are well known for their superb piezoelectric properties, which makes them ideally suited for various applications ranging from household gas lighter to sensors and actuators in high-end aerospace applications such as vibration control of airplane wings, flutter control, structural health monitoring of airplane structures, vibration energy harvesting etc. Recently, R&D on lead-free piezoelectric materials are gaining attention due to toxic effect of lead-based PZTs. Lead-free materials of comparable piezoelectric properties to PZT have been developed; however, performance of these materials in multilayered device form is yet to be established. In recent years, research on renewable energy/clean energy is in great demand to control pollution level. Piezoelectric material-based energy harvesters are quite promising due to use of unused vibration energy. Power harvested from such systems in micro- to milliwatt level is very much suitable for charging mobile phone, functioning of TV remote, working of low-wattage sensors, etc. In this chapter, preparation of PZT- and BZT-based lead-free piezo materials; fabrication of multilayered devices (bimorphs, multilayered stacks, etc.) using tape casting technique; characterization of ferroelectric, piezoelectric, and dielectric properties; applications such as vibration control and energy harvesting especially aimed at aerospace sector have been described.

Keywords

PZT · Lead-free piezo · Energy harvesting · Multilayer device · Aerospace applications

Introduction

Lead zirconate titanate $\text{Pb}(\text{Zr},\text{Ti})\text{O}_3$ (PZT) is a multicomponent synthetic piezoelectric material with very good piezoelectric properties [1, 2]. It consists of lead titanate (PT) and lead zirconate (PZ) as the basic constituents. Its piezoelectric, dielectric, and ferroelectric properties generally varied by changing the PT and PZ ratio. Further, the properties of PZT can be enhanced using various donor and acceptor type dopants in place of lead and Zr/Ti substituted in the perovskite structure of PZT [3–8]. The main advantages of PZT over other smart materials (PVDF, Nitinol) are (i) fast response time, (ii) response over wide range of frequency, (iii) non-interference to the surrounding magnetic field, (iv) high block force, (v) inert/resistance to the environment, (vi) formation of solid solutions with large number of dopants; therefore, the properties can be tailor-made according to the requirement.

Generation of electric charges with application of mechanical stress is the characteristic of piezoelectric materials known as direct piezoelectric effect suitable for sensor application. These materials also change dimensions/generate strain on application of an electric field known as converse piezoelectric effect, suitable for actuator application. Therefore, these materials are widely used for fabrication of

sensors, actuators, transducers, etc. for various applications such as aerospace vibration control, energy harvesting, medical diagnostics, defense, and industrial/consumer products [9–12].

Piezoelectric effect was discovered by Jacques and Pierre Curie in 1880 [1]. They found that some of the natural occurring crystals such as Quartz, Rochelle salts, potassium dihydrogen phosphate and its isomorphs are piezoelectric. The actual use of piezoelectric material came into existence during World War I, i.e., use of quartz as a resonator material in SONAR for detection of submarines. In reality, serious studies gather momentum on piezoelectric materials after the discovery of high dielectric constant in barium titanate during 1941. There were three basic steps in the discovery and understanding of piezoelectricity in polycrystalline ceramics like barium titanate. The first was the discovery of high dielectric constant. The second step was the realization that the cause of the high dielectric constant was due to ferroelectricity (the presence of a spontaneous electric moment in a crystal which can be changed in its orientation between two or more distinct crystallographic directions by applying an external field). The third significant step was the discovery of poling process. During that time it was not clear how the direct or the converse piezoelectric effect could occur in a polycrystalline material. The decisive step was the poling process, i.e., application of a high DC voltage sufficient to reverse electric moments of spontaneously polarized regions in the polycrystalline ceramics. The first publication on poled piezoelectric barium titanate was made by S. Roberts during 1947 [1]. The first commercial piezoelectric barium titanate devices were phonographic pickups marketed by Sonotone Corporation in 1947. Rapid development on improvement of piezoelectric and other dielectric properties of barium titanate was followed by compositional modifications. The advancement of great practical importance was realized after the discovery of very strong and stable piezoelectric effect in lead zirconate titanate (PZT) and its solid solutions during 1952 [1, 3]. Subsequently, many scientific discoveries had taken place both in improvement of properties and application front.

Structure of Lead Zirconate Titanate (PZT)

Lead zirconate titanate (PZT) is a polycrystalline material and crystallizes in ABO_3 perovskite structure. The structure can be described as a simple cubic unit cell where “A” is the large cation on the corners, “B” the smaller cation in body center, and “O” oxygens in the face-centered position of the cube. The structure is a network of corner-linked oxygen octahedral, with smaller cations (Zr^{4+} or Ti^{4+}) filling the octahedral holes and the large cations (Pb^{2+}) filling the dodecahedral holes [1]. There are many empty spaces available in the octahedral hole; therefore, the Zr^{4+} or Ti^{4+} ions freely moved to a new position on application of electric field (poling).

Morphotropic Phase Boundary of PZT

Generally, the crystal structure of a material changes with change in temperature. It is also observed that an abrupt structural change occurs in the ceramic solid solutions

with change in the composition almost independent of temperature. This is called a morphotropic phase boundary (MPB). Typically, it occurs at a critical composition where two phases of the material are energetically very similar but structurally different [13]. Thus, in the case of solid solutions of ferroelectric compositions, many physical and electrical parameters change noticeably at the MPB. In case of PZT, MPB composition falls in the range of 48–56 mole % of zirconia [14, 15]. However, the exact range varies with different precursors, processing conditions, etc.

Effect of Various Dopants on Properties of PZT

Dopants have remarkable effect on properties of piezoelectric materials. These are cations of similar ionic radii which replace the parent ion in the crystal structure, and the basic structure can be modified with a wide range of properties suitable for various applications. From literature, it is observed that three types of additives are used for compositional modification of PZTs. These are (i) isovalent additives, (ii) soft additives, and (iii) hard additives. Isovalent additives generally reduce the Curie point and simultaneously increase the permittivity of the samples. Soft additives create lead vacancy in the PZT structure, thereby increasing the domain wall mobility and consequently increasing the piezoelectric, dielectric, and ferroelectric properties. Use of “hard” additives creates oxygen vacancies in the structure, thereby constraining the domain wall motion which decreases the above properties.

Isovalent additives are of similar valence and ionic radii of the replaced ions, for example, Ba^{2+} or Sr^{2+} replaces Pb^{2+} and Sn^{4+} replaces Zr^{4+} . These additives lower the Curie point, enhance the permittivity, lower the loss factor, lower the compliance, and enhance the aging rate. F. Kulcsar et al. [16] studied the effect of Sr^{2+} and Ca^{2+} substitution in Pb^{2+} site of PZT. It was observed that strontium decreases the Curie point of undoped PZT by 9.5°C for every atom % substitution and raised the dielectric constant at room temperature. The d_{33} value of the composition is increased since the coupling factor and elastic modulus are not greatly influenced. M. Cerqueira et al. [17] and J. Bernard et al. [18] observed that both P_r and k_p values were found to increase with increase in Ca^{2+} concentration. H. Kanai et al. [19] studied the substitution of alkaline earth ions such as Ca^{2+} , Sr^{2+} , and Ba^{2+} in Pb^{2+} site and observed that the dielectric constant increases while the loss factor decreases. Isovalent substitution on Zr^{4+} , Ti^{4+} site by Sn^{4+} was reported by K. Markowski et al. [20] on PLZT ceramics. They observed that with increase in Sn^{4+} content the room temperature dielectric constant decreases, and the dielectric maxima peaks become more diffuse.

Donor additives or soft doping ions have higher valence than the replaced ions. These include mostly rare earth and transition metal ions such as La^{3+} , Nd^{3+} , Nb^{5+} , Ta^{5+} , Sb^{5+} , W^{6+} , etc. Some exceptional changes that occur by the soft doping are increase in piezoelectric charge constant, dielectric constant, and increase in resistivity [3, 4, 21]. These changes are mostly due to formation of lead vacancies in the PZT structure to maintain the charge neutrality which enhance the domain wall

mobility. Generally, when the ions with larger ionic radii, such as La^{3+} , Nd^{3+} , etc. occupy the A-sites replacing the Pb^{2+} ions, extra positive charges are introduced into the lattice. So a Pb vacancy is created in the lattice to maintain electrical neutrality. Similar situation happened in the B-site also. These lattice vacancies helped in the transfer of atoms from one point to another easily with application of even smaller electric field, thereby increasing the domain wall mobility. A number of researchers [7, 22–28] studied the effect of this type of additives and reported the observed properties. La^{3+} is a familiar donor ion on Pb^{2+} site, and its effect on the properties of PZT has been studied by many authors [7, 22–25]. G. H. Haertling [2] in his paper reported that PZT modified with La^{3+} has shown an increase in squareness of the hysteresis loop, decrease in the coercive field (E_c), improvement in the dielectric constant, higher electromechanical coupling coefficient, increase in the mechanical compliance (S), and enhancement in the optical transparency. P.H. Xiang et al. [22] in their study reported that increase in lanthanum substitution increases the level of diffuseness of the phase transition and 7.6 mol% lanthanum-modified PZT exhibits relaxor behavior. They also reported the tetragonality of the PZT which decreases with increase in La^{3+} concentration. Nb^{5+} is a donor dopant for B-site substitution in PZT materials. Its effect on properties of PZT was studied by many researchers [29, 30]. It enhances the domain wall motion, thereby increasing the properties significantly. M. Pereira et al. [29] reported that Nb^{5+} doping reduces the diffusion coefficient due to creation of lead vacancies at A-site, which are responsible to inhibit the ion mass transportation. In addition, niobium oxide (Nb_2O_5) also acts as a good sintering aid for PZT-based materials which decreases the Curie temperature and is helpful in enhancing the polarization switching. S. Y. Chu et al. [30] reported that niobium oxide enhances the density of PZT material and effectively improves the dielectric and piezoelectric properties. The Nb^{5+} -doped PZTs have high electromechanical coupling coefficient that makes them suitable for piezoelectric transformers, actuators, transducers, and broadband SAW device applications.

The third additives are **acceptor**-type substitutions, known as hard dopants. These include K^+ and Na^+ , which occupy the A-sites, and Fe^{3+} , Co^{2+} , Co^{3+} , Mn^{2+} , Mn^{3+} , Ni^{2+} , Al^{3+} , Ga^{3+} , In^{3+} , Cr^{3+} , Sc^{3+} , etc. which occupy the B-sites in the perovskite structure. Hard doping generally decreases the domain wall movement; therefore, it is difficult or hard to pole the PZT. These dopants lower the piezoelectric constant, dielectric constant, dielectric loss, coupling factor, and bulk resistivity and increase the coercive field, mechanical quality factor, etc. Hard dopants are lower valence ions replaced with a higher valence ion, therefore creating oxygen vacancies in the lattice to maintain the necessary electrical neutrality. Effects of hard dopants on dielectric, piezoelectric, and ferroelectric properties of PZT have been studied by a number of authors [31–35]. T. B. Weston et al. [32] studied the effect of iron oxide (up to 8 mole %) on morphotropic phase boundary composition of PZT. According to them, the dielectric constant and dissipation factor decrease by addition of iron oxide, whereas the mechanical quality factor increases. They further observed that the presence of iron oxide inhibits the grain growth and reduces the limiting grain size below which the electromechanical properties change rapidly with grain size.

D.C. Lee [33] in his thesis reported that PZT behaves as anti-ferroelectric with addition of scandium.

Apart from the abovementioned additives, there are some other dopants such as Cr and U possessing variable valence which play the role of both as softener and as hardener. While Cr-doped PZT has a high Q_m , its dielectric loss is more, and k_p is less with increase in dopant [1]. Similarly, U-doped samples have low aging rate, high mechanical Q_m for rhombohedral composition, high dissipation factor, and normal coupling factor. Multiple ion doping is also often used for better piezoelectric properties. The effects of such combined dopant were studied by many authors [36–40]. V. Singh et al. [38] studied the effect of La^{3+} substitution on ferroelectric properties of Nb^{5+} -doped PZT and reported that La^{3+} substitution increases the dielectric and piezoelectric constants and reduces dielectric loss. J. H. Park et al. [40] studied that MnO_2 - Nb_2O_5 -co-doped PZT ceramic is better than the PZTs doped with only Nb^{5+} or Mn^{4+} .

At CSIR-National Aerospace Laboratories (NAL), development of PZT powder of high piezo properties ($d_{33} > 550$ pC/N) and fabrication of unimorph, bimorph, and multilayered (ML) devices by tape casting have been carried out [41–48]. Similarly, R&D on lead-free piezo materials and energy harvesting using PZTs have been carried out [49–54]. This chapter presents a comprehensive study on R&D of PZT and lead-free piezo materials, fabrication of different types of devices for aerospace, and energy harvesting application.

Development of Piezoelectric Materials

Lead Zirconate Titanate (PZT)

PZT is a solid solution of ferroelectric PbTiO_3 (PT) ($T_c = 490$ °C) and antiferroelectric PbZrO_3 (PZ) ($T_c = 230$ °C) phases. Excellent piezoelectric, dielectric, and ferroelectric properties were observed near morphotropic phase boundary (MPB) having Zr:Ti ratio of 53:47. Further, the properties of PZT are enhanced by addition of various dopants and have been explored by many researchers [3–8]. A number of methods are used for preparation of PZT powders such as mixed oxide, co-precipitation, sol-gel, spray pyrolysis, hydrothermal synthesis, molten salt synthesis, etc. [55–60]. The conventional method of its preparation is by mixed oxide route. In this process, the individual oxide powders are mixed thoroughly in a ball mill to produce a homogeneous powder mixture. This process is very simple and cost-effective; however, it is not free from certain drawbacks such as (i) the powders are inhomogeneous at micro-level, therefore difficult to maintain the stoichiometry, (ii) the reaction temperature is relatively high leading to high lead loss, (iii) slow reaction rate because of low diffusion process, etc. The above drawbacks degrade the piezo and ferroelectric properties.

Coprecipitation from solution is one of the best wet chemical techniques for the preparation of PZT materials. Several parameters, such as pH of the solution, mixing rates, temperature, concentration, etc., have to be controlled for producing

Table 1 Properties of PZT powders

Properties	150 g/batch	1 kg/batch	10 kg/batch
Density (% Th)	99.0	98.8	98.7
Piezoelectric charge constant (d_{33}) pC/N	598	584	555
Relative dielectric constant (K)	3875	3651	3120
Dissipation factor ($\tan \delta$) at 100 Hz	0.025	0.028	0.023

satisfactory results. The composition control, purity, and morphology of the resulting products are good. However, different rates of precipitation of each individual compound may lead to microscopic inhomogeneity, and agglomerates are generally formed during calcination, as with other solution techniques. By controlling the synthesis conditions, this method can produce stoichiometric PZT powders of high purity with fine particle size at a relatively moderate cost and is applied widely to synthesize electroceramic powder in industry.

In the process, analytical grade lead nitrate, zirconyl nitrate solution, and titanyl nitrate were used as precursors for the preparation of PZT powders [5, 8]. The powders were coprecipitated from the combined salt solutions using dilute ammonium hydroxide, filtered, dried, and calcined to form PZT phase. Calcined powders were shaped into circular pellets, sintered in the temperature range 1200–1300 °C, and poled, and various electrical properties were measured. Using the above chemical route, PZT-5H grade powders were prepared at lab scale (150 g/batch) and upscaled to 1 kg and also relatively high scale (10 kg/batch) without scarifying much of the piezoelectric charge constant (d_{33}). The room temperature properties of in-house prepared PZT powders are presented in Table 1.

Lead-Free Piezo Materials

In recent years, lead-free piezo materials are encouraged due to toxicity of PbO present in PZT [49, 61, 62]. A considerable amount of lead oxide is released into the air and water during the fabrication and disposal process of lead-bearing material which severely threatens the surroundings and human health. Therefore, the European Union and USA already imposed ban on lead-bearing materials for betterment of human life [63]. This ban has triggered researchers, to develop safer lead-free piezo materials of similar electrical properties in place of lead oxide-based PZTs. In the last 10–12 years, a number of lead-free piezo ceramic materials have been developed with encouraging electrical properties such as modified barium titanates, barium zirconate titanate, sodium potassium niobate (KNN), and bismuth sodium titanate to mention a few. In spite of the widespread efforts worldwide, the properties and performances of lead-free materials have yet to reach the stage of PZT ceramics. Drawbacks of lead-free ceramics are e.g., the KNN system shows high piezoelectric response and broad working temperature range but requires special fabrication processes to minimize porosity level [62, 64]. BNT-based ceramics prepared by the conventional solid state reaction method result in dense samples,

but their properties are not as good as KNN-based ceramics [65]. Further, these compositions are corrosive and volatile due to presence of alkalis and damages the furnace lining, heating elements, etc.; therefore, special care should be taken during the heat treatment process. Processing of barium titanate-based materials requires very high sintering temperature >1400 °C. In spite of various disadvantages, one of the most advantageous points of lead-free piezo materials is low density compared to PZT ($<2/3$ of PZT). This is an important positive factor for fabrication of devices used for underwater application. Suitable lead-free materials and devices are yet to be developed for practical use. While many research labs are engaged in development of new materials, few labs are working on development of usable devices/actuators and sensors for various applications. At CSIR-NAL development of lead-free piezo materials and also fabrication of piezo multilayered stacks/actuators are under progress.

Barium Zirconate Titanate (BZT)-Based Lead-Free Piezo Materials

A number of lead-free piezo systems are discovered in the last two decades [66–68]. Although BaTiO_3 was developed long back, researchers are still working on this system, as it is lead-free in nature. Also, there is no corrosive ingredient at high temperature like KNN, BNT, BKT, etc. systems. Barium titanate has been modified further as barium zirconium titanate (BZT) by addition of Zr^{4+} , which affects the crystal structure and electrical properties. A number of dopants have been tried by researchers to improve the properties of BZT lead-free ceramics [69–74]. In this section, effect of alkaline earth metal ions such as Mg^{2+} , Ca^{2+} , and Sr^{2+} on microstructure and electrical properties of BZT is described.

$(\text{Ba}_{1-x}\text{A}_x)(\text{Ti}_{0.98}\text{Zr}_{0.02})\text{O}_3$ piezoelectric ceramics doped with MgO, CaO, and SrO in the range 0–0.03 mol were prepared by the mixed oxide route. Calculated amount of the constituents were weighed accurately and mixed thoroughly. The powders were put in a container along with required amount of ethanol and zirconia balls and milled for 24 h. After milling the powders were dried, calcined at 1000 °C for 4 h, de-agglomerated, granulated using polyvinyl alcohol (2 wt%), and pressed into circular pellet. The pressed pellets were sintered at 1150 °C for 3 h. The sintered pellets were polished, electroded with silver paste, and poled under a DC voltage of 3–4 kV/mm in a silicone oil bath for 40 min.

Characterization of BZT-Based Lead-Free Piezo Ceramics

The poled pellets of MgO-, CaO-, and SrO-doped BZT lead-free piezo materials were characterized for piezoelectric properties. The samples of 0.01 mol MgO-, 0.015 mol CaO-, and 0.015 mol SrO-doped BZT shows better properties. The details of these four samples are presented in Table 2.

Dielectric Properties

Dielectric constant and loss factor of BZT and BCZT samples were measured at different frequencies and varying temperature, and the resultant graphs are presented in Figs. 1 and 2, respectively. In the case of pure BZT, there is sharp

Table 2 Details of lead-free piezo pellets [53]

Sl. No.	Dia. (mm)	Thickness (mm)	Amount of dopant (mol)	d_{33} (pC/N)
Barium zirconate titanate (BZT)	12.2	1.4	0.0	104
BMZT	11.38	0.98	0.01	164
BCZT	11.23	1.6	0.015	248
BSZT	11.03	1.68	0.015	330

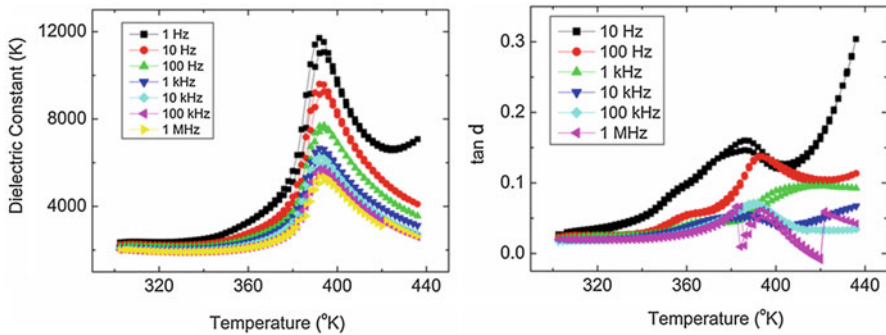


Fig. 1 Dielectric constant and loss factor of BZT with change in temperature

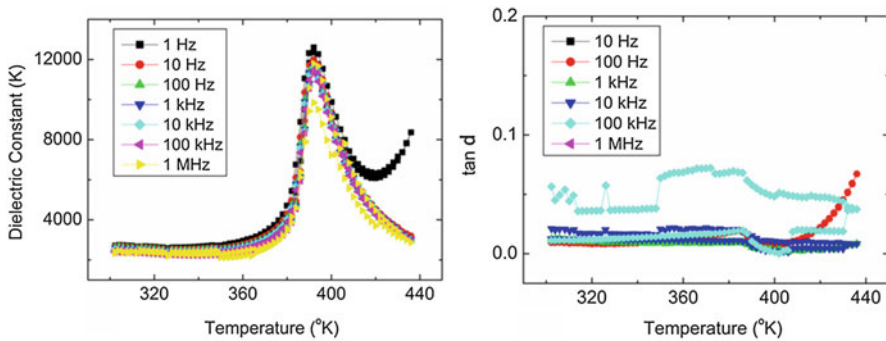


Fig. 2 Dielectric constant and loss factor of BCZT with change in temperature

increase of dielectric constant after 380 °K and reached maximum at 395 °K and then decreased further with the increase in temperature. With the increase in frequency, the maxima of the dielectric constant and loss factor were found decreased (Fig. 1). In the case of pure BCZT, the trend in dielectric constant with temperature is similar to pure BZT, but there is not much variation in dielectric constant with change in frequency (Fig. 2).

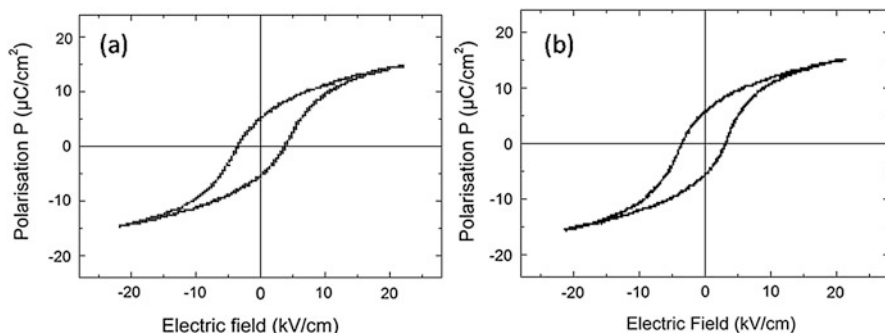


Fig. 3 Typical hysteresis loop of (a) BZT and (b) BCZT pellets

Polarization Measurements

Hysteresis loop of pure BZT and Ca^{2+} -doped BZT at room temperature and their plots are presented in Fig. 3. The remnant polarization (P_r) and coercive field of pure BZT are $5 \mu\text{C}/\text{cm}^2$ and $5 \text{ kV}/\text{cm}$ and for Ca^{2+} -doped BZT are $6.5 \mu\text{C}/\text{cm}^2$ and $4 \text{ kV}/\text{cm}$, respectively.

Fabrication of PZT Unimorphs, Bimorphs, and Multilayered Devices

PZT devices in the form of unimorph (single layer), bimorphs (two layers), and multilayered stacks were fabricated by tape casting technique.

Preparation of PZT Tapes

PZT powder slurry was prepared in two stages using required amount of PZT powder, organic solvents, dispersant, binder, and plasticizers described elsewhere [46, 47]. The well-optimized slurry of proper viscosity was tape casted on a silicone-coated Mylar sheet, and tape thickness of $100\text{--}300 \mu\text{m}$ was prepared by a laboratory tape caster (Fig. 4). The density of green tape measured is $4.7 \text{ g}/\text{cc}$ (60.25% theoretical).

Fabrication of PZT Bimorphs and Unimorphs

PZT tapes of thickness $300 \mu\text{m}$ were used for fabrication of bimorphs. The tape was cut into rectangular shapes and was sintered at $1250^\circ\text{C}/2 \text{ h}$. The sintered tapes were leveled, electroded, and poled at $2 \text{ kV}/\text{mm}$ in a silicone oil bath for 30 min. Parallel bimorph was prepared using two such sintered and poled pieces with an

Fig. 4 Photograph of PZT tape

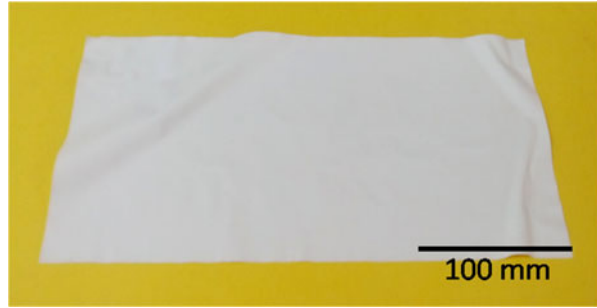
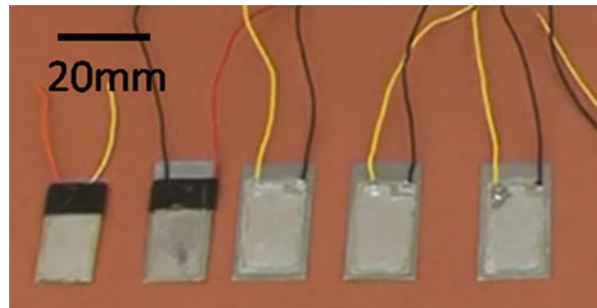


Fig. 5 Photograph of fabricated PZT bimorphs and unimorphs



aluminum foil in the middle. PZT unimorphs were also fabricated using one PZT plate glued on an aluminum sheet. The photograph of fabricated PZT bimorphs and unimorphs is presented in Fig. 5. These devices were used for energy harvesting study.

Fabrication of PZT Multilayered (ML) Stacks

PZT tape of thickness $\sim 100 \mu\text{m}$ was used for fabrication PZT ML stack. After preparation of tape, it was dried, cut into required dimensions, screen printed with platinum electrode paste, and dried. The individual layers were then stacked, laminated using uniaxial stacking machine, and iso-pressed. Binder burnout of the stacks was carried out at 620°C for 2 h. Co-firing of the stacks was done very carefully with slow heating rate in the temperature range $1150\text{--}1250^\circ\text{C}$ to obtain high-density and crack- and delamination-free ML stack. The stacks were leveled to have parallel surface and electroded, and two terminals were drawn by soldering the wires. The photograph of PZT ML stacks is presented in Fig. 6, and the details are tabulated in Table 3. The stacks were then poled at 2 kV/mm for 45 min and characterized for displacement and block force.

Fig. 6 Photograph of fabricated PZT ML stacks

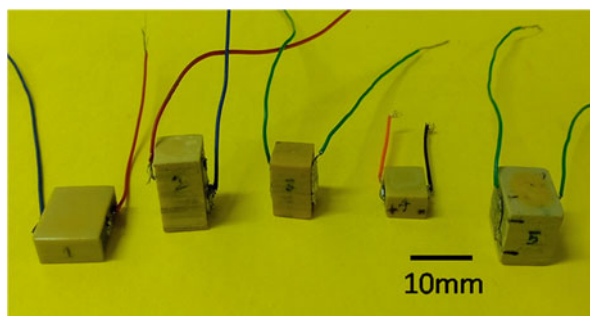


Table 3 Properties of PZT ML stacks

Sl. no.	Height (cm)	Length (cm)	Width (cm)	Displacement (μm)	Block force (N)	Voltage applied (V)
PZT-MLS-1	0.489	1.24	1.171	4.0	4500	175
PZT-MLS-2	1.26	0.835	0.75	9.0	1550	175
PZT-MLS-3	0.994	0.75	0.65	6.0	1450	175
PZT-MLS-4	0.45	0.804	0.785	3.0	1870	175
PZT-MLS-5	0.952	1.18	0.94	6.0	3100	175

Fabrication of Lead-Free ML Stack and Characterization

Lead-free BCZT multilayered stacks were fabricated by following the fabrication procedure same as PZT multilayered stacks. The green lead-free BCZT tapes of thickness $\sim 135 \mu\text{m}$ were dried and precisely cut into required dimensions. The layers were screen printed using Ag-Pd (75:25) electrode paste and dried thoroughly. The individual layers are stacked and laminated using a stacking machine. The green stacks have been vacuum sealed and iso-pressed uniaxially at 35 MPa for 20 min.

Binder burnout and sintering are crucial steps to get desired properties of multilayered stacks. Binder burnout is a vital step for the removal of organics present in the green stage of the actuator. To avoid delamination of layers, heat treatment was done with slow rate to expel all organic binders and other volatile matters. The binder burnout was carried out at $620^\circ\text{C}/2 \text{ h}$ with very slow heating rate ($15^\circ\text{C}/1 \text{ h}$) and sintering at 1120°C for 2 h ($20^\circ\text{C}/1 \text{ h}$). The sintered BCZT stacks were leveled, finished, electroded (Ag-paste) on both the sides, and then cured at $620^\circ\text{C}/1 \text{ h}$. The photograph of in-house fabricated lead-free piezo multilayer stacks is presented in Fig. 7. The ML stacks were poled under hot silicone oil bath for 45 min with application of 2–3 kV/mm DC electric field at room temperature. The displacement and block force of the ML stacks were measured and tabulated in Table 4.

Fig. 7 Typical photograph of fabricated lead-free piezo ML stacks

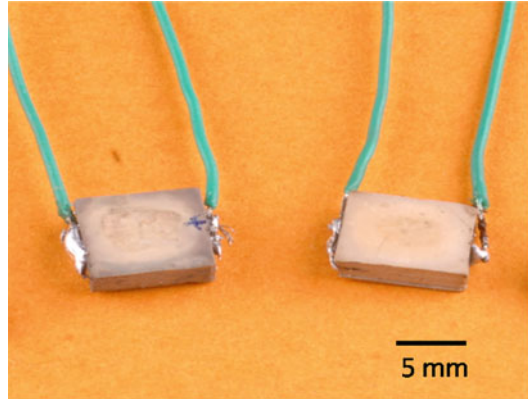


Table 4 Properties of BCZT multilayer stacks fabricated by tape casting method

Sl. no.	Height (mm)	Length (mm)	Width (mm)	Applied voltage (V)	Displacement (μm)	Block force (N)
LF-MLS-1	6.3	9.78	6.38	175	2–3	426
LF-MLS-2	6.0	9.74	6.66	175	2	418

It is observed that the properties (displacement and block force) of lead-free ML stacks are less compared to the properties of PZT ML stack.

Energy Harvesting Study Using PZT Devices

Energy harvesting (EH), particularly EH, of clean energy is an important topic of research. There are various sources of renewable energy available such as solar energy, geothermal energy, wind mills, water flow, mechanical vibration, etc. [75, 76]. Among these, vibration energy harvesting using piezoelectric (PZT) materials is getting more attention wherein a piezoelectric material (PZT bimorph, unimorph, etc.) is used for generation of electrical energy when mechanically stressed/vibrated. The quantum of harvested energy is very low (micro- to milliwatts), but the energy is very useful for low-powered electronic equipment such as powering TV remote, mobile phones, electric flashlight torch, small portable FM radio, self-powering wireless sensor network, mobile platforms, etc. [77, 78]. Moreover, PZT-based energy harvesting systems can be embedded on the vibrating bodies, and the generated energy is useful to drive the electronics by removing/minimizing the option of using an external power source, use of external connecting wires, and periodic replacement of external batteries [79]. The energy-generating mechanism in vibration energy harvester is quite simple without any turbine or

engine (the prime mover). A simple PZT unimorph/bimorph generally fulfills the purpose [80].

The research on vibration energy harvesting using piezoelectric devices started during the 1980s, but comprehensive studies on vibration energy harvesting really started late 1990s with development of devices using three different PZT devices by Media Lab at MIT [81]. Thereafter energy harvesting study using PZT unimorphs, bimorphs, multilayered stacks, etc. were studied by a number of authors. Kim et al. studied the energy harvesting performance of soft and hard PZT as a function of temperature and observed a slightly higher output power from hard PZT-based device compared to soft PZT-based device with increase in temperature up to 100 °C [82]. M. Okayasu et al. studied the electric power generation from PZT with different loading conditions and reported that more power is generated with increase of applied load and generated power was found more under compressive loading than during tensile loading [83]. Roundy et al. investigated the piezoelectric energy harvester performance using PZT bimorph on a cantilever beam and reported the generator has a power output of 250 μ W at 120 Hz [84]. White et al. designed and developed a piezoelectric energy harvester using piezoelectric thin films. The device can generate 3 μ W at 80.1 Hz under 0.8 mm vibration amplitude, while the other similar generator can generate 2 μ W under 09 mm amplitude at the same frequency [85].

Energy harvesting study of the PZT unimorphs was carried out using an assembled test setup. The system consists of (i) a vibrator with power amplifier, (ii) function generator, (iii) data accusation system, (iv) force sensor, (v) accelerometer and (vi) cantilever assembly, and (vii) output recording device. Photographs of energy harvesting setup are presented in Fig. 8.

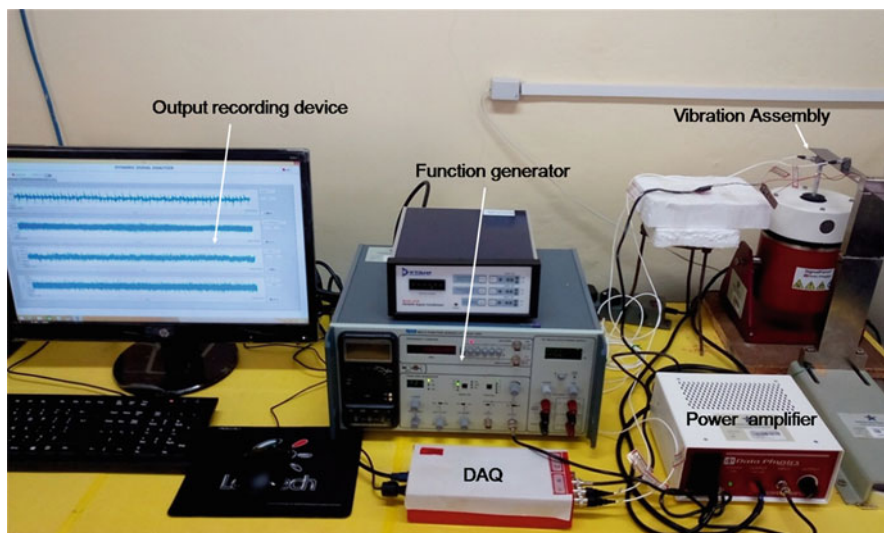


Fig. 8 Photograph of energy harvesting setup

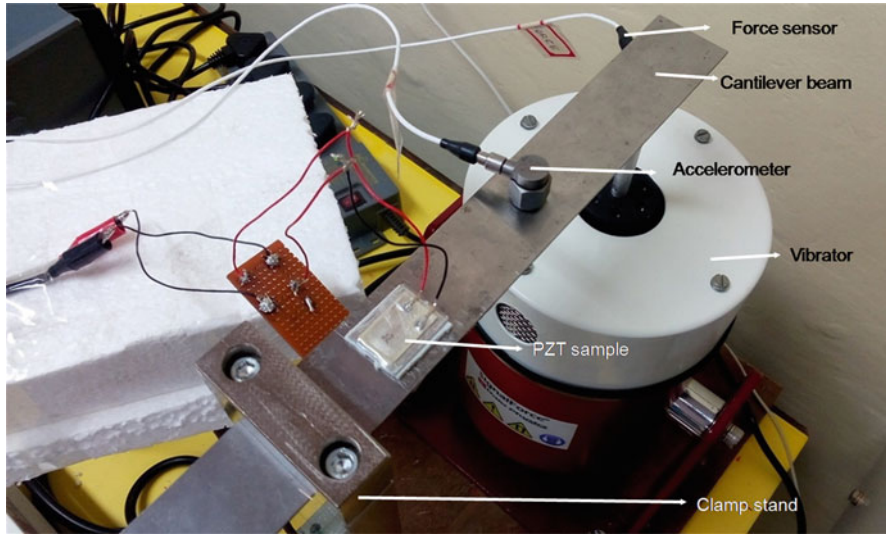


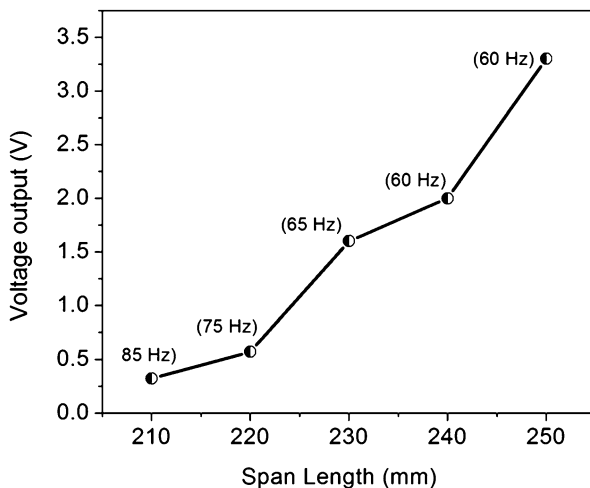
Fig. 9 Cantilever arrangement and vibration setup assembly

PZT test sample was fixed on a SS cantilever beam and the beam was vibrated using the vibrator. The force sensor was fixed on top of the plunger of the vibrator to measure the applied force on the beam. In the beginning of the experiment, the vibrator was powered suitably by the power amplifier to generate a proper sine wave signal from the force sensor both in free and loading condition. In loading condition, one end of a cantilever beam is fixed on top of the force sensor, and the other end of the beam was clamped on a stand. The PZT sample was placed suitably on the cantilever beam to generate maximum energy during vibration (Fig. 9). In general, PZT device was connected parallel with a capacitor and resistor and excited by a vibrator at a particular frequency. Random charge generated by the PZT device was converted into a stable rectified DC voltage using a rectifier circuit. The rectified DC voltage accumulated across the capacitor was measured.

Measurement of Output Voltage at Different Span Length and Resonance Frequencies

PZT sample was placed on the cantilever beam near the clamp where bending effect is maximum and the beam was vibrated at a constant force of 0.75 N at resonance frequencies (60 Hz, 65 Hz, 75 Hz, and 85 Hz) corresponding to the span length (250 mm, 240 mm, 230 mm, 220 mm, and 210 mm), respectively. The output voltage generated from the PZT sample was recorded and plotted in Fig. 10. It is observed that the output voltage is increased with increase in span length.

Fig. 10 Output voltage with different span length and corresponding resonance frequencies



Measurement of Output Voltage from PZT Sample with Different Force Levels

In this case the sample was vibrated at 60 Hz with varying force levels from 0–4.5 N, and the generated output voltage was recorded and plotted in Fig. 11. It is observed that the output voltage is increased with the increase in force level.

Applications of Piezoelectric Materials and Devices

Soft PZTs have very good piezoelectric, dielectric, and ferroelectric properties and, therefore, are widely used for various applications such as actuators and sensors for aerospace vibration control [86–89], ultrasonic motor [90, 91], sonar transducers [92], accelerometers [93], in drug delivery systems, in smart toilets, in gas igniters, in inkjet printers, etc.

Aerospace Applications of PZT Ceramics/Devices

In recent days there is an intense competition among the aircraft makers to reduce the cost of aircrafts while maintaining very good safety standards and their performances. Therefore, the industries always need new type of materials which are reliable and robust for the use. Smart materials are quite often used for these purposes. Among the smart material group, the piezoelectric (PZT) materials and devices have the advantages of (i) high modulus of elasticity (10^5N/m^2) similar to metals, (ii) fast response time (in micro seconds), (iii) noninterference (insensitive to electromagnetic fields and radiations), (iv) formation of solid solutions with large number of dopants, (v) manipulation of crystal structure to produce large number

Fig. 11 Output voltage with different input force levels

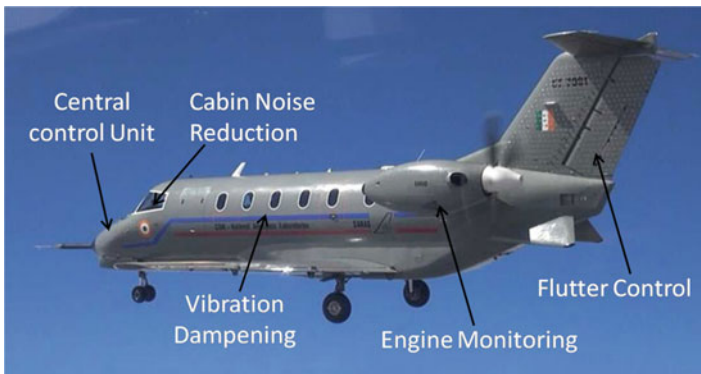
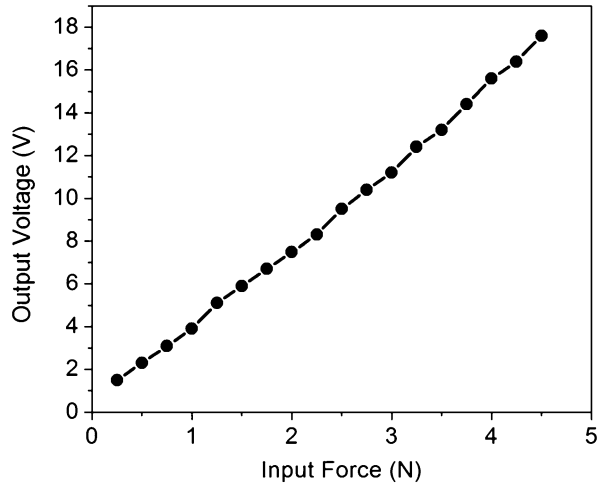


Fig. 12 PZT devices at different parts of aircraft structure

of different materials with varied properties, and (vi) high block force, low power consumption, resistance to several environments, etc. Therefore, PZT devices are vastly used for a number of applications in aerospace structure such as vibration control/vibration dampening, cabin noise reduction, flutter control, flap positioning, impact reduction, engine condition monitoring, fuel tank level sensors, etc. (Fig. 12).

Health Monitoring of Aircraft Structures

Integrity of aircraft structures is monitored by periodical checking of defects/cracks in various points of aircraft. Monitoring the structural health of aircraft is very much necessary from safety and reliability point of view. PZT

unimorphs/patches are frequently used for detection of cracks, delamination, etc. by embedding them on the aircraft structures [48, 94]. Generally, the natural frequency of vibration of a defect structure is quite different from a defect-free structure of same materials. PZT patch sensors are prompt enough to distinguish these frequencies of vibration and can detect the defects in the aerospace structures in the very early stage, thereby saving a lot of money for the aerospace industry.

Noise, Vibration, and Shape Control of Aircraft Structures

Noise in the cabin of aircraft is produced due to irregular vibration of various parts which may cause discomfort to the pilot for smooth operation. PZT sensors and actuators along with a control unit (generally called a smart system) are used for reduction of noise/control of the vibration of structures [95]. Similarly, shape control of aircraft is very much important for smooth aerodynamic lifting and reduction of drag on components. PZT linear actuators are frequently used for this purpose. These actuators operate linearly, using only tensile and compressive forces to correct the structural deformations produced by air pressure.

Fuel Level Sensors

PZT transducers are used for measuring the level of fuel in the fuel tank of aircraft. The devices are placed at different parts of fuel tank. With application of electric field, the PZT material in the transducer vibrates/oscillates. The sound waves generated from the PZT are reflected from the surface of the fuel and received by another transducer. The signal generally processed by a control unit provides the real-time fuel present in the tank.

PZT Energy Harvester in MAVs

MAVs are miniature UAVs used for remote observations in defense and research purpose. A key challenge in the development of MAVs is to accommodate long-life power source in a limited weight and volume. Addition of a piezoelectric energy harvesting facility on MAV increases the flight endurance from few minutes to few hours (or continuous) by recharging the batteries/super capacitors for extending the endurance of MAV flights. The main reasons or advantages for selection of a piezoelectric material for energy-harvesting are (i) noninterference, (ii) high energy density (three times more than the electromagnetic), and (iii) continuous availability of power (unlike solar energy). A typical photograph of MAV with PZT embedded on its wings is presented in Fig. 13.

Fig. 13 PZT devices on wings of MAV for energy harvesting



Conclusions

In this chapter, preparation and properties of PZT powder in lab scale as well as relatively large scale and fabrication of ML stacks by tape casting technique and their characterization are very well elaborated. Lead-free piezo materials in the BZT system doped with alkaline earth metal oxide as dopant were prepared. Among all dopants, SrO-doped BZT showed better piezoelectric properties. BSZT powder was prepared in large quantity (100 g), its ML stack was fabricated, and the properties were measured. The displacement and block force of BSZT ML stacks were found to be less as compared to PZT ML stacks. Energy harvesting study using PZT devices (unimorphs, bimorphs, and ML stacks) was carried out. Maximum output voltage 17.6 V was measured from PZT unimorph at cantilever span length of 250 mm and at resonance frequency of 60 Hz when applied with 4.5 N input forces.

PZT is an interesting, versatile material with many engineering applications. Alternate to PZT materials is going to be a reality in the near future. Both PZT and lead-free piezo materials offer a lot of opportunities for researchers to explore synthesis of high-performance piezo materials and also for novel applications.

Acknowledgments The authors sincerely thank NPSM, NPMAS, CSIR FYPs, NRB, and DeitY for the financial support.

References

1. Jaffe B, Jaffe H, Cook WR (1971) Piezoelectric ceramics. Academic, London
2. Haertling GH (1999) Ferroelectric ceramics: history and technology. *J Am Ceram Soc* 82:797–818
3. Singh DJ, Ghita M, Fornari M, Halilov SV (2006) Role of A-site and B-site ions in perovskite ferroelectricity. *Ferroelectrics* 338:73–79
4. Kinase W, Harada K (2006) Ferroelectricity of perovskite type crystal ABO_3 for the various A ions. *Ferroelectrics* 333:21–26

5. Sahoo B, Jaleel VA, Panda PK (2006) Development of PZT powders by wet chemical method and fabrication of multilayered stacks/actuators. *Mater Sci Eng B* 126:80–85
6. Qiu W, Hng HH (2002) Effects of dopants on the microstructure and properties of PZT ceramics. *Mater Chem Phys* 75:151–156
7. Garg A, Agrawal DC (2001) Effect of rare earth (Er, Gd, Eu, Nd, and La) and bismuth additives on the mechanical and piezoelectric properties of lead zirconate titanate ceramics. *Mater Sci Eng B* 86:134–143
8. Sahoo B, Panda PK (2013) Effect of lanthanum, neodymium on piezoelectric, dielectric and ferroelectric properties of PZT. *J Adv Ceram* 2:37–41
9. Chandrashekhara K, Agarwal AN (1993) Active vibration control of laminated composite plates using piezoelectric devices: a finite element approach. *J Intell Mater Syst Struct* 4:496–508
10. Cattafesta LN, Garg S, Shukla D (2001) Development of piezoelectric actuators for active flow control. *AIAA J* 39:1562–1568
11. Panda PK, Sahoo B, Chandraiah M et al (2015) Piezoelectric energy harvesting using PZT bimorphs and multilayered stacks. *J Electron Mater* 44:4349–4353
12. Howells CA (2009) Piezoelectric energy harvesting. *Energy Convers Manage* 50:1847–1850
13. Bhalla AS, Guo R, Alberta EF (2002) Some comments on the morphotropic phase boundary and property diagrams in ferroelectric relaxor systems. *Mater Lett* 54:264–268
14. Isupov VA (1980) Reasons for discrepancies relating to the range of coexistence of phases in lead zirconate–titanate solid solutions. *Sov Phys Solid State* 22:98–101
15. Kala T (1983) Contribution to the study of tetragonal and rhombohedral phase coexistence in the $\text{PbZrO}_3\text{--PbTiO}_3$ system. *Phys Status Solidi* 78:277–282
16. Kulcsar F (1959) Electromechanical properties of lead titanate zirconate ceramics with lead partially replaced by calcium or strontium. *J Am Ceram Soc* 42:49–51
17. Cerqueira M, Nasar RS, Longo E et al (1997) Piezoelectric behavior of PZT doped with calcium: a combined experimental and theoretical study. *J Mater Sci* 32:2381–2386
18. Bernard J (1971) *Piezoelectric ceramics*, 1st edn. Academic, London
19. Kanai H, Furukawa O, Abe H, Yamashita Y (1994) Dielectric properties of $(\text{Pb}_{1-x}\text{X}_x)(\text{Zr}_{0.7}\text{Ti}_{0.3})\text{O}_3$ (X= Ca, Sr, Ba) ceramics. *J Am Ceram Soc* 77:2620–2624
20. Markowski K, Park SE, Yoshikawa S, Cross LE (1996) Effect of compositional variations in the lead lanthanum zirconate stannate titanate system on electrical properties. *J Am Ceram Soc* 79:3297–3304
21. Hng QW, Hoon H (2002) Effects of dopants on the microstructure and properties of PZT ceramics. *Mater Chem Phys* 75:151–156
22. Xiang PH, Zhong N, Dong XL, Liang RH, Yang H, Feng CD (2004) Fabrication and dielectric properties of lanthanum-modified lead zirconate titanate using co-precipitation powder coating. *Mater Lett* 58:2675–2678
23. Dai X, Digiovanni A, Viehland D (1993) Dielectric properties of tetragonal lanthanum modified lead zirconate titanate ceramics. *J Appl Phys* 74:3399–3405
24. Stashans A, Maldonado F (2007) A quantum mechanical study of La-doped $\text{Pb}(\text{Zr,Ti})\text{O}_3$. *Phys B Condens Matter* 392:237–241
25. Sharma S, Singh R, Goel TC, Chandra S (2006) Synthesis, structural and electrical properties of La modified PZT system. *Comput Mater Sci* 37:86–89
26. Mohidden MA, Kumar A, Yadav KL (2007) Effect of Nd doping on structural, dielectric and thermodynamic properties of PZT (65/35) ceramics. *Phys B Condens Matter* 395:1–9
27. Juneja JK, Prakash C, Thakur OP, Sharma TP (2002) Dielectric and piezoelectric properties of PZT substituted with samarium. *Ferroelectr Lett* 29:11–16
28. Khazanchi R, Sharma S, Goel TC (2005) Effect of rare earth europium substitution on the microstructure, dielectric, ferroelectric and pyroelectric properties of PZT ceramics. *J Electroceram* 14:113–118
29. Pereira M, Peixoto AG, Gomes MJM (2001) Effect of Nb doping on microstructural and electrical properties of the PZT ceramics. *J Eur Ceram Soc* 21:1353–1356

30. Chu SY, Chen TY, Tsai IT (2003) Effects of sintering temperature on the dielectric and piezoelectric properties of Nb-Doped PZT ceramics and their applications. *Integr Ferroelectr* 58:1293–1303
31. Yadav KL, Choudhary RNP (2005) Piezoelectric properties of modified PZT ceramics. *Ferroelectrics* 325:87–94
32. Weston TB, Webster AH, Nanara VMM (1969) Lead zirconate-Lead titanate piezoelectric ceramic with Iron oxide additions. *J Am Ceram Soc* 52:253–257
33. Lee DC (1970) Sintering Sc and Nb modified Lead zirconate titanate. M.S. thesis, University of California, Berkeley, p 35
34. Tan Q, Xu Z, Li JF, Viehland D (1996) Influence of lower valent A-site modifications on the structure property relations of lead zirconate titanate. *J Appl Phys* 80:5866–5874
35. Choudhary RNP, Mal J (2002) Diffuse phase transition in Cs-modified PLZT ferroelectrics. *Mater Sci Eng B* 90:1–6
36. Boucher E, Guiffard B, Lebrun L, Guyomar D (2006) Effects of Zr/Ti ratio on structural, dielectric and piezoelectric properties of Mn and (Mn, F) doped lead zirconate titanate ceramics. *Ceram Int* 32:479–485
37. Abdessalerm N, Boutarfaia A (2007) Effect of composition on the electromechanical properties of $\text{Pb}_{0.9}[(\text{Zr}_x \text{Ti}_{0.9-x})(\text{Cr}_{1/5}, \text{Zn}_{1/5}, \text{Sb}_{1/5})_{0.1}]\text{O}_3$ ceramics. *Ceram Int* 33:293–296
38. Singh V, Kumar HH, Kharat DK, Hait S, Kulkarni MP (2006) Effect of lanthanum substitution on ferroelectric properties of niobium doped PZT ceramics. *Mater Lett* 60:2964–2968
39. Banerjee A, Bandyopadhyay A, Bose S (2006) Influence of La_2O_3 , SrO, and ZnO addition on PZT. *J Am Ceram Soc* 89:1594–1600
40. Park JH, Kim BK, Song KH, Park SJ (1995) Piezoelectric properties of Nb_2O_5 doped and MnO_2 - Nb_2O_5 co-doped $\text{Pb}(\text{Zr}_{0.53}\text{Ti}_{0.47})\text{O}_3$ ceramics. *J Mater Sci* 6:95–101
41. Panda PK, Sahoo B (2005) Preparation of pyrochlore-free PMN powder by semi-wet chemical route. *Mater Chem Phys* 93:231–236
42. Sahoo B, Panda PK (2007) Dielectric, ferroelectric and piezoelectric properties of $(1-x)[\text{Pb}_{0.9}\text{La}_{0.09}(\text{Zr}_{0.60}\text{Ti}_{0.40})\text{O}_3] - x[\text{Pb}(\text{Mg}_{1/3}\text{Nb}_{2/3})\text{O}_3]$, $0 \leq x \leq 1$. *J Mater Sci* 42:4270–4275
43. Sahoo B, Panda PK (2007) Effect of CeO_2 on dielectric, ferroelectric and piezoelectric properties of PMN–PT (67/33) compositions. *J Mater Sci* 42:4745–4752
44. Sahoo B, Panda PK (2007) Ferroelectric, dielectric and piezoelectric properties of $\text{Pb}_{1-x}\text{Cex}(\text{Zr}_{0.60}\text{Ti}_{0.40})\text{O}_3$, $0 \leq x \leq 0.08$. *J Mater Sci* 42:9684–9688
45. Sahoo B, Panda PK (2012) Fabrication of simple and ring-type piezo actuators and their characterization. *Smart Mater Res* 2012:821847
46. Panda PK, Sahoo B, Raja S et al (2012) Electromechanical and dynamic characterization of in-house-fabricated amplified piezo actuator. *Smart Mater Res* 2012:203625 (8 pages)
47. Panda PK, Sahoo B (2014) Development and characterization of PZT multilayered stacks for vibration control. In: Vinoy KJ, Ananthasuresh GK, Pratap R, Krupanidhi SB (eds) *Micro and smart device and systems*. Springer, India, pp 143–154
48. Panda PK (2017) Piezoceramic materials and devices for aerospace applications. In: Eswara Prasad N, Wanhill RJH (eds) *Aerospace materials and materials technology*, vol 1. Springer Science + Business Media, Singapore, pp 501–518
49. Panda PK (2009) Review: environmental friendly lead-free piezoelectric materials. *J Mater Sci* 44:5049–5062
50. Chandraiah M, Sahoo B, Panda PK (2016) Synthesis and electrical properties of CaO doped BZT lead free piezo ceramics. *Ferroelectrics* 494:192–199
51. Chandraiah M, Sahoo B, Panda PK (2015) Effect of MgO on piezoelectric, dielectric and ferroelectric properties of $(\text{Ba}_{1-x}\text{Mg}_x)(\text{Ti}_{0.98}\text{Zr}_{0.02})\text{O}_3$ lead-free piezoceramics. *J Mater Sci Mater Electron* 26:6801–6806
52. Chandraiah M, Panda PK (2015) Effect of SrO on piezoelectric, dielectric and ferroelectric properties of $(\text{Ba}_{1-x}\text{Sr}_x)(\text{Ti}_{0.98}\text{Zr}_{0.02})\text{O}_3$ lead free piezoceramics. *J Mater Sci Mater Electron* 26:3143–3147

53. Chandraiah M, Panda PK (2015) Effect of dopants ($A=Mg^{2+}$, Ca^{2+} and Sr^{2+}) on ferroelectric, dielectric and piezoelectric properties of $(Ba_{1-x}A_x)(Ti_{0.98}Zr_{0.02})O_3$ lead-free piezo ceramics. *Ceram Int* 41:8040–8045
54. Panda PK, Sahoo B (2015) PZT to Lead free piezo ceramics: a review. *Ferroelectrics* 474:128–143
55. Kong LB, Ma J (2001) PZT ceramics formed directly from oxides via reactive sintering. *Mater Lett* 51:95–100
56. Lee BW (2004) Synthesis and characterization of compositionally modified PZT by wet chemical preparation from aqueous solution. *J Eur Ceram Soc* 24:925–929
57. Bezzi F, Costa AL, Piazza D et al (2005) PZT prepared by spray drying: from powder synthesis to electromechanical properties. *J Eur Ceram Soc* 25:3323–3334
58. Linardos S, Zhang Q, Alcock JR (2006) Preparation of sub-micron PZT particles with the sol-gel technique. *J Eur Ceram Soc* 26:117–123
59. Maher GH, Hutchins CE, Ross SD (1993) Preparation and characterization of ceramic fine powders produced by the emulsion process. *Am Ceram Soc Bull* 75:72–76
60. Deng Y, Liu L, Cheng Y et al (2003) Hydrothermal synthesis and characterization of nanocrystalline PZT powders. *Mater Lett* 57:1675–1678
61. Rodel J, Jo W, Seifert KTP et al (2009) Perspective on the development of lead-free piezoceramics. *J Am Ceram Soc* 92:1153–1177
62. Shrout TR, Zhang SJ (2007) Lead-free piezoceramics: alternatives for PZT? *J Electroceram* 19:111–124
63. Ringgaard E, Wurlitzer T (2005) Lead-free piezoceramics based on alkali niobates. *J Eur Ceram Soc* 25:2701–2706
64. Guo H, Zhang S, Beckman S, Tan X (2013) Microstructural origin for the piezoelectricity evolution in $(K_{0.5}Na_{0.5})NbO_3$ -based lead-free ceramics. *J Appl Phys* 114:154102
65. Ma C, Tan X (2010) Phase diagram of unpoled lead-free $(1-x)(Bi_{1/2}Na_{1/2})TiO_3-xBaTiO_3$ ceramics. *Solid State Commun* 150:1497–1500
66. Ringgaard E, Wurlitzer T, Wolny WW (2005) Properties of lead-free piezoceramics based on alkali niobates. *Ferroelectrics* 319:323–333
67. Takenaka T, Nagata H (2005) Current status and prospects of lead-free piezoelectric ceramics. *J Eur Ceram Soc* 25:2693–2700
68. Liu W, Ren X (2009) Large piezoelectric effect in Pb-free ceramics. *Phys Rev Lett* 103:257602
69. Chen ZH, Ding JN, Xu JJ et al (2014) Dy_2O_3 doped $(Ba_{0.85}Ca_{0.15})(Ti_{0.90}Zr_{0.10})O_3$ ceramics. *Ferroelectrics* 460:49–56
70. Cui Y, Liu X, Jiang M et al (2012) Lead-free $(Ba_{0.85}Ca_{0.15})(Ti_{0.9}Zr_{0.1})O_3-CeO_2$ ceramics with high piezoelectric coefficient obtained by low sintering temperature. *Ceram Int* 38:4761–4764
71. Li W, Hao J, Bai W, Xu R et al (2012) Enhancement of the temperature stabilities in yttrium doped $(Ba_{0.99}Ca_{0.01})(Ti_{0.98}Zr_{0.02})O_3$ ceramics. *J Alloys Compd* 531:46–49
72. Li W, Xu Z, Chu R, Fu P (2012) Effect of Ho doping on piezoelectric properties of BCZT ceramics. *Ceram Int* 38:4353–4355
73. Cai W, Fu CL, Gao JC, Zhao CX (2011) Dielectric properties and microstructure of Mg doped barium titanate ceramics. *Adv Appl Ceram* 110:181–185
74. Bera J, Rout SK (2007) Synthesis of $(Ba_{1-x}Sr_x)(Ti_{0.5}Zr_{0.5})O_3$ ceramics and effect of Sr content on room temperature dielectric properties. *J Electroceram* 18:33–37
75. Lallart M, Guyomar D, Jayet Y, Petit L et al (2008) Synchronized switch harvesting applied to self-powered smart systems: piezoactive microgenerators for autonomous wireless receivers. *Sensors Actuators A* 147:263–272
76. Harb A (2011) Energy harvesting: state-of-the-art. *Renew Energy* 36:2641–2654
77. Meninger S, Mur-Miranda JO, Amirtharajah R, Chandrakasan AP (2001) Vibration-to-electric energy conversion. *IEEE Trans VLSI Syst* 9:64–76
78. Kim HW, Priya S, Uchino K, Newnham RE (2005) Piezoelectric energy harvesting under high pre-stressed cyclic vibrations. *J Electroceram* 15:27–34

79. Shen D, Park JH, Noh JH et al (2009) Micro machined PZT cantilever based on SOI structure for low frequency vibration energy harvesting. *Sensors Actuators A* 154:103–108
80. Siddique ARM, Mahmud S, Heyst SV (2015) A comprehensive review on vibration based micro power generators using electromagnetic and piezoelectric transducer mechanisms. *Energy Convers Manag* 106:728–747
81. Shenck NS (1999) A demonstration of useful electric energy generation from piezoceramics in a shoe. M.S. thesis. MIT, Cambridge, MA
82. Kim SB, Park JH, Ahn H, Liu D, Kim DJ (2011) Temperature effects on output power of piezoelectric vibration energy harvesters. *Microelectron J* 42:988–991
83. Okayasu M, Sato D, Sato Y, Konno M, Shiraishi T (2012) A study of the effects of vibration on the electric power generation properties of lead zirconate titanate piezoelectric ceramic. *Ceram Int* 38:4445–4451
84. Roundy S, Wright PK, Rabaey J (2003) A study of low level vibrations as a power source for wireless sensor nodes. *Comput Commun* 26:1131–1144
85. White NM, Jones PG, Beeby SP (2001) A novel thick-film piezoelectric micro-generator. *Smart Mater Struct* 10:850–852
86. Haertling GH (1994) Rainbow ceramics-a new type of ultra-high-displacement actuator. *Am Ceram Soc Bull* 73:93–96
87. Kanayama K, Mase H, Saigoh H (1991) Gap structure multilayer piezoelectric actuator. *J Appl Phys* 30:2281–2284
88. Uchino K (1993) Ceramic actuators: principles and applications. *Mater Res Bull* 18:42–48
89. Newnham RE (1998) Functional composites for sensors and actuators: smart materials. The Pennsylvania Academy of Science, Harrisburg
90. Wallaschek J (1995) Piezoelectric ultrasonic motors. *J Intell Mater Syst Struct* 6:71–73
91. Uchino K (1994) Piezoelectric actuators/ultrasonic motors. In: *Proceedings of the Ninth IEEE International Symposium on Applications of Ferro-electrics*. Institute of Electrical and Electronics Engineers, New York, pp 319–324
92. Newnham RE, Bowen LJ, Klicker KA, Cross LE (1980) Composite piezoelectric transducers. *Mater Eng* 2:93–97
93. Chang SH, Wang HC (1990) A high speed impact actuator using multilayer piezoelectric ceramics. *Sens Actuators A* 24:239–244
94. Prasad SE, Waechter DF, Blacow RG, King HW, Yaman Y (2005) Application of piezoelectrics to smart structures. *Proceedings of II conference on smart structures and materials*, Portugal, Eccomas, Barcelona, pp 1–16
95. Elliot SJ, Nelson PA (1993) Active noise control. *IEEE Signal Process Mag* 10:12–35



Processing of Ceramic Foams for Thermal Protection

28

Sujith Vijayan, Praveen Wilson, and Kuttan Prabhakaran

Contents

Introduction	1106
Thermal Conductivity of Ceramic Foams	1107
Mechanical Strength	1108
Thermal Shock Resistance of Ceramic Foams	1110
Processing of Ceramic Foams	1110
Polymer Foam Template Method	1112
Sacrificial Template Method	1113
Ceramic Foams by Freeze Casting	1114
Emulsion Templating	1116
Direct Foaming	1119
Gelcasting	1120
Particle-Stabilized Foams	1123
Thermo-foaming	1124
Ceramic Foams from Pre-ceramic Polymers	1127
Thermal Conductivity of Ceramic Foams Prepared by Various Methods	1128
Summary	1129
References	1131

Abstract

The rapid industrialization and increased space exploration activities necessitate the development of materials of low thermal conductivity capable of withstanding very high temperatures. These materials are called thermal protection materials. They are used either to protect the nearby persons from the heat flux of

S. Vijayan · P. Wilson · K. Prabhakaran (✉)
Department of Chemistry, The Indian Institute of Space Science and Technology (IIST),
Thiruvananthapuram, Kerala, India
e-mail: kp2952002@gmail.com

high-temperature heat treatments in industries or to protect the instruments and astronauts within the crew cabin of a space vehicle from the intense heat flux generated during its reentry into the atmosphere. The high-temperature ceramics such as alumina, silica, zirconia, mullite, SiC, silicon nitride, and silicon oxycarbide are capable of withstanding high temperatures. The materials of choice at extremely high temperatures (above 2000 °C) are either carbon or ultrahigh-temperature ceramics. They include borides and nitrides such as TiB₂, ZrB₂, HfB₂, TiN, ZrN, etc. These materials in their dense state though withstand high temperatures they also exhibit relatively high thermal conductivity. In addition to the high-temperature capability, the thermal protection materials should be light in weight and have low thermal conductivity. The aspect of low density is of utmost importance in thermal protection materials used for space applications as an increase in weight increases the amount of fuel required for takeoff and subsequent reentry. The way to achieve lightweight and low thermal conductivity in ceramic materials is by making them porous. The porous ceramics with porosity greater than 70 vol% are called ceramic foams.

Keywords

Ceramic foams · Processing · Microstructure · Porosity · Thermal conductivity · Compressive strength

Introduction

A ceramic foam can be defined as a continuous ceramic matrix consisting of a three-dimensional array of pores (called cells) interconnected to each other via struts with an inherent porosity of >70 vol%. In addition to low thermal conductivity and density, the ceramic foams have low gas absorption, low thermal capacity, high thermal stability, high thermal cycling capacity, and very good shock resistance. Another important aspect is their easy production of different sizes and shapes. Ceramic foams can be divided into three categories based on their cell morphology and cell interconnectivity. They are open-cellular, closed-cellular, and reticulated ceramics. In the case of open-cellular ceramics, the neighboring cells are interconnected through one or more cell windows which facilitate the transport of materials between them. In the case of closed-cellular ceramic foams, the cells are isolated from each other preventing the transport of matter. Reticulated ceramics can be considered as an extension of open-cellular ceramics, where the entire foam is an interconnected network of pore struts. Typically, reticulated ceramics have a very high porosity (>95 vol%) and low mechanical strength. In addition to these three types, there are foams with a combination of open and closed pores. Typical microstructures of closed-cellular, open-cellular, and reticulated ceramic foams are given in Fig. 1.

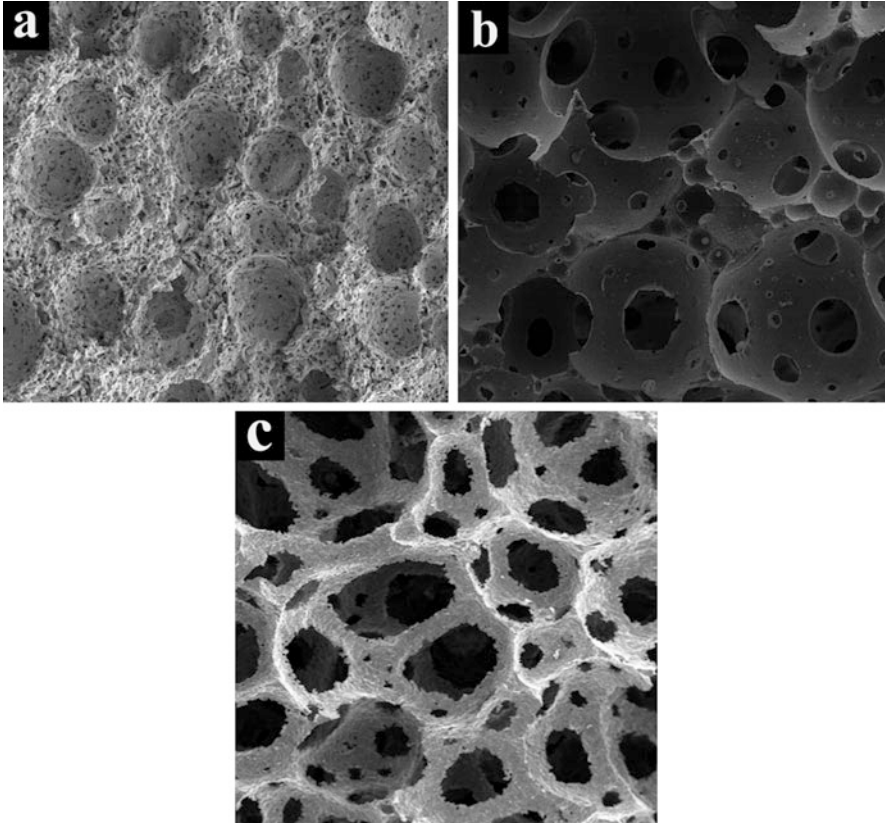


Fig. 1 Microstructure of typical (a) closed-cellular, (b) open-cellular, and (c) reticulated ceramic foams

Thermal Conductivity of Ceramic Foams

Thermal conductivity k ($\text{Wm}^{-1}\text{K}^{-1}$) of a material is the measure of its ability to conduct heat. It can be defined as the amount of heat transferred by conduction through a unit cross-sectional area of the material, with the temperature gradient perpendicular to the area. The thermal conductivity can be expressed in terms of Fourier's law as shown in Eq. (1) below:

$$q' = -k\partial T/\partial x \quad (1)$$

where q' is heat flux and $\partial T/\partial x$ is temperature gradient along one direction.

Ceramic foams are composite materials, in which one phase is a gas, usually air. The heat transfer through gas must also be considered in addition to the thermal conduction through solids. Gases are capable of conduction, convection, and radiative transfer of heat. Therefore, the thermal conductivity of ceramic foam has four contributions: conduction through the solid (k_s), conduction through the gas (k_g), convection within the cell walls (k_c), and radiation through the cell walls and across the cell voids (k_r). The total thermal conductivity, k , can be now defined as

$$k = k_s + k_g + k_c + k_r \quad (2)$$

The convection contribution to thermal conductivity is suppressed in cellular solids due to their smaller cells. The heat conduction through the foams is mainly attributed to the conduction through the solid and through the gas filled in the cells. Ashby proposed an equation which is completely dependent on the relative density as shown below [1]:

$$k = \frac{1}{3} \left[\left(\frac{\rho}{\rho_0} \right) + 2 \left(\frac{\rho}{\rho_0} \right)^{3/2} \right] k_s + \left[1 - \left(\frac{\rho}{\rho_0} \right) \right] k_g \quad (3)$$

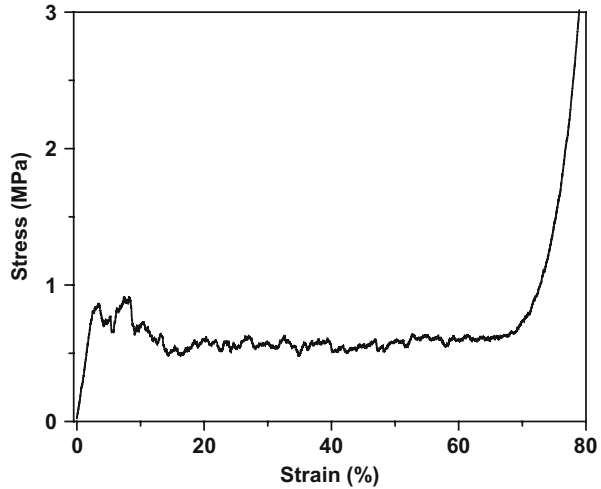
Where ρ_0 is the theoretical density of the dense ceramic and ρ is the bulk density of the foam. The term associated with the gas, often negligible, becomes important in foams intended for thermal insulation since these have a low relative density and a conductivity approaching that of a gas.

Mechanical Strength

The mechanical strength of brittle foam materials like ceramic foam is generally measured in terms of its compressive strength or crushing strength. Figure 2 shows a typical compressive stress-strain graph of the elastic-brittle solid foam. The stress-strain graph generally contains an initial linear elastic region followed by a plateau stress region and a region of densification. The initial linear elastic region depends on the cell size, relative density, and nature of the solid. After the elastic region, the cells start collapsing, and the cell collapse continues throughout the plateau region. The debris formed by the cell collapse fill the cells in the remaining foam that resulted in an increase of foam density which is responsible for the increase of stress in the densification region. The stress corresponding to the plateau region is taken as the compressive strength, and the slope of the initial elastic region in the stress-strain graph is taken as Young's modulus. Generally, the increase in relative density of the foam increases Young's modulus and compressive strength and decreases the strain at which densification starts.

The compressive strength of ceramic foams depends on the porosity, cell size, and microstructure of the struts. In general, the compressive strength of brittle foam

Fig. 2 Typical compressive stress-strain graph of a ceramic foam



increases with the decrease of porosity and pore size. The presence of pores in the struts of the foam decreases its compressive strength. Due to the porous struts, the reticulated ceramics exhibit very low compressive strength. The closed-cell foams show better mechanical properties than their open-cell counterparts at similar porosity. The compressive strength of ceramic foams is in the order of closed cellular > open cellular >> reticulated. In order to understand the mechanical behavior of ceramic foams, it is necessary to understand the relationship between mechanical properties and porosity or relative density. Many models have been proposed that contain expressions which describe these relationships. The Young's modulus of brittle open-cellular solids is best modeled using the Eq. (1) proposed by Gibson and Ashby [1].

$$\frac{E}{E_0} = C \left(\frac{\rho}{\rho_0} \right)^n \quad (4)$$

Verma et al. [2] used a similar Eq. (2) to model the compressive strength of open-cellular ceramics.

$$\frac{\sigma}{\sigma_0} = C \left(\frac{\rho}{\rho_0} \right)^n \quad (5)$$

where E and E_0 are Young's modulus, while σ and σ_0 are the compressive strength of the ceramic foam and fully dense ceramic, respectively. ρ and ρ_0 are the densities of the foam and fully dense ceramic, respectively. The values of C and n for the relation between E/E_0 and ρ/ρ_0 are expected to be ~ 1 and ~ 2 , respectively, for brittle open-cellular foams with a cubic array of cells. However, in the majority of the reported ceramic foam materials, the C and n values deviate from the theoretical ones due to their deviation from the cubic morphology and broad distribution of cell sizes.

Thermal Shock Resistance of Ceramic Foams

Thermal stresses arise in a body when its surface experiences a sudden change in temperature resulting in the formation of cracks within the body. The thermal stress arising due to the rapid cooling of a body can be expressed as Eq. (6) [1, 3, 4]

$$\sigma_t = \frac{E \alpha \Delta T}{1 - \nu} \quad (6)$$

where E is Young's modulus, α is the coefficient of thermal expansion, ν is the Poisson's ratio, and ΔT is the temperature difference. When the thermal stress exceeds the fracture strength, a crack develops and propagates leading to the failure [1]. The thermal shock resistance of a ceramic solid can be expressed in the terms of temperature and fracture stress as Eq. (7)

$$R_s = \frac{\sigma_f(1 - \nu)}{E \alpha} \quad (7)$$

where R_s is thermal shock resistance of solid and σ_f is fracture or flexural strength.

Open-cellular ceramic foams find applications in molten metal filtration, burners, solid oxide fuel cells, and catalytic converters due to low weight, high-temperature stability and high permeability [5, 6]. In all these applications, foams are subjected to elevated temperatures (>800 °C), fast heating and cooling rates, and temperature gradients which results in the formation of thermal stresses in the body over a time period. Hence, the thermal shock resistance is an important factor determining the use of ceramic foams for high-temperature applications.

By substituting the value of Young's modulus [$E = C_1 E_s (\rho/\rho_s)^2$] and fracture strength [$\sigma_f = C_2 \sigma_{fs} (\rho/\rho_s)^{1.5}$] [7] of foams in Eq. (7), the thermal shock resistance of an isotropic foam material is obtained as

$$R_b = R_s (C_2/C_1) (\rho/\rho_s)^{-0.5} \quad (8)$$

That is the thermal shock resistance of a foam which increases with an increase in thermal shock resistance of the solid and increase in porosity.

Processing of Ceramic Foams

The ceramic foams are prepared from respective ceramic fine powders or pre-ceramic polymers. The conversion of ceramic powder to ceramic foams is achieved through either dry powder pressing or colloidal processing. In the dry pressing method, a mixture of ceramic powder and pore-forming agent is consolidated by pressing. Removal of the pore template by burnout followed by sintering results in the formation of ceramic foam. The powder pressing method is mostly limited to ceramic foams of lower porosity. On the other hand, the

colloidal processing route uses a well-dispersed suspension of the ceramic powder in an aqueous or nonaqueous medium. The colloidal processing produces ceramic foams of higher porosity compared to the powder pressing using pore templates. Moreover, the ceramic foams produced from colloidal suspensions have dense cell walls and struts that result in better mechanical strength. Therefore, the majority of the foam production methods in the literature are through the colloidal route. The processing of ceramic foams from powder suspension requires a thorough understanding of ceramic powder dispersion in a liquid medium.

Ceramic powder dispersion in a liquid involves the manipulation and control of the interparticle interactions such as van der Waals attraction and electrostatic and polymer-induced steric repulsions. The well-dispersed powder suspension is achieved when the electrostatic or polymer-induced steric repulsion between the particles in the liquid medium overcomes the van der Waals attractive forces naturally existing between them. The understanding of the interaction between the solvent molecules and the powder surface is also very important. In the case of oxide ceramics, due to the more ionic nature of the bonds, the particle surface is easily charged when coming in contact with protic solvent molecules. Due to the interaction of ionic species in solution with its surface, an oxide ceramic particle acquires negative or positive surface charge. Water is the most preferred solvent for the dispersion of the oxide ceramics with H^+ and OH^- as the ionic species. In such case, the amount of positive or negative site on the particle surface is determined by the pH of the aqueous solution. By adjusting the pH, a net positive or negative charge can be obtained on the particle surface. The counterions from the solution are attracted to the interface from a diffused ion cloud adjacent to the particle surface. This is called as an electrical double layer. The thickness of this double layer is determined by the concentration and valency of the ions in the solution. When the concentration of the ions in the solution is high, it results in a thin double layer leading to poor stability of the dispersions. The thickness of the double layer can be defined in the terms of Debye length ($1/\kappa$) which is given by Eq. (9) [8].

$$\frac{1}{\kappa} = \left(\frac{\epsilon \epsilon_0 k T}{e^2 \sum_i n_i z_i^2} \right) \quad (9)$$

where e is the electronic charge, k is the Boltzmann constant, T is the temperature, n_i is the concentration of ions with charge z_i , ϵ is the dielectric constant of the liquid, and ϵ_0 is the permittivity of vacuum. The energy due to the repulsion of spherical particles due to the double layer can be given by Eq. (10) [8]

$$V_{\text{elect}} = 2\pi\epsilon_r\epsilon_0a\Psi_0^2e^{-\kappa h} \quad (10)$$

where a is particle radius, h is minimum separation distance between particle surfaces, and Ψ_0 is surface potential.

In the case of nonaqueous solvents, controlling the pH does not yield stable dispersions. In such cases, suitable polymeric dispersants are added to prepare stable colloidal suspensions. The polymeric molecules adsorb on the surface of the particles. Upon the close approach of two particles covered with adsorbed polymer layers, the interpenetration of the polymer layers gives rise to a repulsive force known as steric stabilization. To be effective, the adsorbed polymer layers must be of sufficient thickness and density in order to overcome the van der Waals attraction between particles. The steric stabilization can be explained in terms of osmotic effect. When two ceramic particles with the adsorbed polymer layer come together, it creates an area of low solvent concentration between them. Due to the osmotic pressure, the solvent molecules are forced into this area separating the ceramic particles. A combination of electrostatic and steric stabilization is used for the preparation of ceramic powder suspensions of high solid loadings in an aqueous medium. The dispersion mechanism in these cases is termed electrosteric. In this, polyelectrolytes are widely used as dispersants. Polyelectrolytes are molecules which contain one or more ionizable groups, either a carboxylic or sulfonic group, and have structures ranging from homopolymers to block copolymers. Polyelectrolyte adsorption is strongly influenced by the chemical and physical properties of the solid surfaces and solvent medium. The adsorption behavior and conformation of polyelectrolyte species can be modulated by tailoring the pH and temperature. The various methods for the preparation of ceramic foams from the colloidal dispersion of powders are discussed in the subsequent sections. More detailed discussion on powder dispersions in the aqueous and nonaqueous medium is found elsewhere.

Polymer Foam Template Method

In the polymer foam template method, the structure of polymer foam is replicated in ceramic. The cell size of the ceramic foams is decided by the cell size of the polymer foam template. The method uses flexible polyurethane foams of desired pore size as the template. In this, the polymer foam is impregnated with the aqueous ceramic powder suspension containing a suitable binder. The excess ceramic powder suspension filled in the pores is removed by squeezing the slurry impregnated polymer foam by rolling. Thus obtained polymer foam coated with the ceramic powder on the cell walls and webs is dried, binder removed and sintered to produce the ceramic foam. A pictorial representation of the polymer foam replication method is shown in Fig. 3. Multiple impregnations are used to increase the cell wall and strut thicknesses. The reticulated ceramic foams are generally prepared by the polymer foam template method. The main drawback of this method is that the ceramic foams produced have porous struts. The reticulated ceramic foams produced by the polymer foam template method have low crushing strength due to their porous struts. Impregnation of the reticulated ceramic foams with the ceramic powder suspension is used to increase their crushing strength [9, 10].

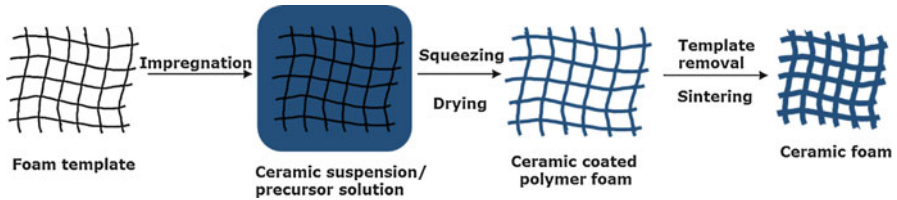


Fig. 3 Pictorial representation of polymer foam template method

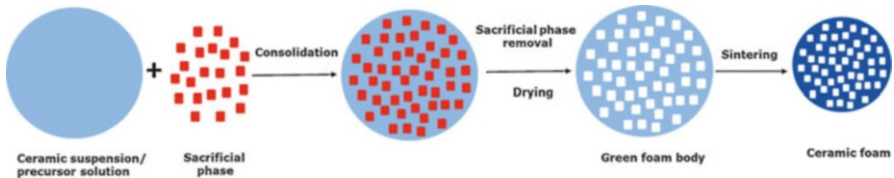


Fig. 4 Schematic of the sacrificial template-based process

Sacrificial Template Method

The sacrificial template method involves the use of fugitive particles which act as the pore-forming agents. These fugitives are either mixed with the ceramic powder or dispersed within the ceramic slurry or precursor solution to ensure homogenous mixing. The dry ceramic powder-fugitive mixture is conformed to shape by compaction in a mold. On the other hand, fugitive particle-dispersed ceramic powder suspensions and precursor solutions are consolidated by casting in a mold followed by setting and drying. The fugitives are removed either by evaporation, pyrolysis, or leaching out using a suitable solvent. The green body obtained is then sintered to get the ceramic foam. A schematic of the fugitive template-based process for the preparation of ceramic foams is shown in Fig. 4.

The porosity can be controlled by adjusting the amount of the sacrificial phase. The size and shape of the fugitives affect the pore size and pore morphology of the porous ceramic. The pore-forming agents can be generally classified into organic, inorganic, and metallic. Synthetic and natural organics used as pore templates are often extracted through pyrolysis by applying long thermal treatments at temperatures between 200 °C and 600 °C. On the other hand, salts used as pore template are removed by leaching with hot water. The typical microstructure of ceramic foam prepared using NaCl as pore template is shown in Fig. 5. The long periods required for complete pyrolysis of the organic component and the extensive amount of gaseous by-products generated during this process are the main disadvantages of using organic materials as the sacrificial phase. In addition, fugitive template-based process produces ceramic foams with relatively low porosity. The porosity of ceramic achieved by various sacrificial templates is given in Table. 1.

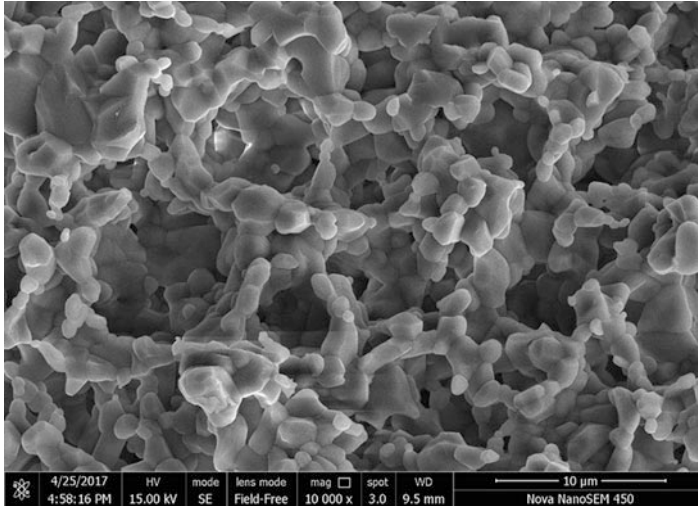


Fig. 5 Microstructure of ceramic foam prepared using NaCl as pore template

Table 1 The maximum porosity achieved in ceramics with various sacrificial pore templates

Sl. no	Sacrificial phase	Ceramic system	Porosity (%)
1.	Polymethyl methacrylate (PMMA)	Yttria-stabilized zirconia (YSZ)	51.6
2.	PMMA	Silicon carbide (SiC)	77
3.	PMMA	β -Tricalcium phosphate	80
4.	PMMA	Alumina	77.2
5.	Graphite powder	Mullite-SiC	43.4
6.	Starch	Silicon nitride (Si_3N_4)	23.8
7.	Starch	Mullite	60
8.	Phosphoric acid	Si_3N_4	63
9.	Poppy seed	Alumina	37.6
10.	Potato starch, almond crust	Hydroxyapatite	59.2
11.	Wax spheres	Hydroxyapatite	42.5
12.	Cotton thread	Alumina	35
13.	Wheat particles	Alumina	76.7
14.	Rayon fibers	Mullite	59.3
15.	Carbon fibers	Alumina	38

Ceramic Foams by Freeze Casting

Freeze casting is a versatile method widely studied for the preparation of ceramic foams with a wide range of porosity and pore structure [11]. In this, the frozen solvent crystals function as pore template. In the freeze casting process, the ceramic

powder suspension cast in a mold is set by freezing the dispersion medium. The ceramic particles in the suspension are expelled to the boundaries of crystallized solvent. The frozen dispersion medium is subsequently removed by sublimation, and then the resulting green body is sintered to produce the ceramic foam. The space created by the removal of the crystallized dispersion medium remained as the pores in the sintered ceramics. The anisotropic growth of the solidifying dispersing medium to produce unidirectional aligned pores is favored by creating a temperature gradient. This is achieved by extracting heat from the suspension from one direction using specially designed molds having well-insulated surfaces except one. The thermally conducting surface of the mold containing the ceramic powder suspension is placed on a platform cooled by liquid nitrogen to achieve the directional cooling. During solidification of the ceramic powder suspension by extracting heat from one side, the ceramic particles expelled that are arranged in a specific way result in well-defined directional (lamellar) microstructures. Extraction of heat from the opposite directions is also attempted to control the lamellar microstructure [12]. On the other hand, the freezing conditions can be controlled to achieve uniform temperature and freezing rate throughout the sample to inhibit the directional growth of the solidified dispersion medium [13, 14]. This results in the homogeneous cellular microstructure of the ceramic foams with open-pore structure. Figure 6 shows the schematic of the freeze casting technique. There are four major steps in the freeze casting process: preparation of the slurry, controlled solidification of the dispersion medium, sublimation of the frozen dispersion medium, and finally sintering of the green body. The dispersion medium is the most important factor in the freeze casting process as it affects both the process and the microstructure of the final product. Other parameters controlling the pore structure are substrate temperature, cooling rate, and an additive which control the crystal growth [15, 16]. Nevertheless, the porosity of the ceramic foam is decided by the slurry concentration. That is, the porosity increases with a decrease in ceramic powder concentration in the slurry. Water, camphene, naphthalene, t-butyl alcohol, etc. are the commonly used dispersion medium [17–22].

Water is the most commonly used dispersion medium for freeze casting due to its environmentally friendly and abundant nature. Ceramic foams with lamellar

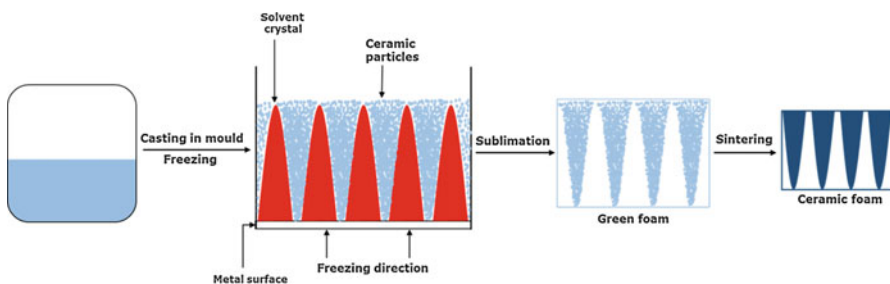
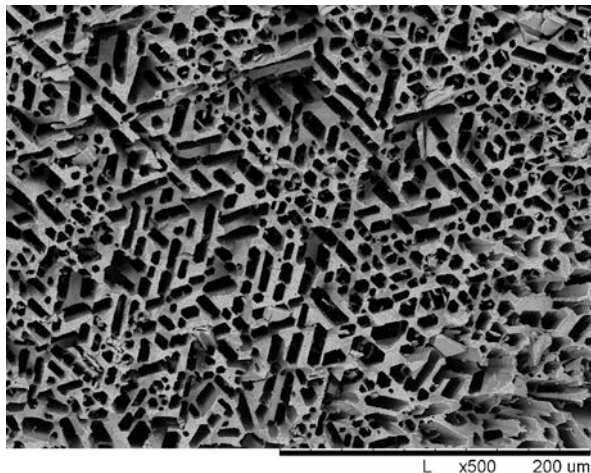


Fig. 6 Schematic of freeze casting technique

Fig. 7 Typical microstructure of freeze-cast ceramic foams showing unidirectional aligned pores



pore structure and open-cellular morphology are produced from aqueous powder suspensions by freeze casting. The additives such as glycerol, PVA, and gelatin are used to control the growth of ice crystals and thereby control the foam microstructure [16, 23, 24]. The use of camphene instead of water gives advantages in terms of higher ($60\text{ }^{\circ}\text{C}$) freezing temperature and easy removal of the frozen medium by sublimation at room temperature. However, the preparation of the slurry for freeze casting needs to be done above the melting point of camphene. The aqueous- and camphene-based freeze casting is attempted for various ceramic systems such as alumina, mullite, zirconia, hydroxyapatite, silicon nitride, and silicon carbide. Porosity as high as 89 and 95 vol% is achieved with the aqueous- and camphene-based freeze casting, respectively. The typical microstructure (along the freezing direction) of ceramic foam produced by freeze casting showing the unidirectional alignment of pores is shown in Fig. 7.

Emulsion Templating

The ceramic foams prepared using fugitive particles as pore template are limited to lower porosity. Just like the fugitive particles, the immiscible solvent droplets dispersed in a ceramic powder suspension can function as a template for pores. The principle of this method is adopted from the preparation of polymer foams using high internal phase emulsion. In this, an organic liquid (oil) immiscible with water is dispersed in an aqueous ceramic powder suspension using the principle of emulsions. That is, a suitable emulsifying agent is used for the dispersion of the oil phase in the aqueous ceramic powder suspension. Subsequently, the oil droplets are removed after gelation and drying of the emulsion. The oil-removed emulsion bodies are sintered to produce the ceramic foams. The emulsion templating method is originally reported for the preparation of macroporous ceramics with ordered

pores through sol-gel route [25, 26]. In this, nonaqueous emulsion fractionated into a narrow droplet size was mixed with sols prepared by the hydrolysis and condensation of the metal alkoxides. Subsequent gelation by further condensation of the prepolymer sol followed by removal of the emulsion droplets and sintering resulted in ceramic foams with ordered pores. However, the gels undergo large shrinkage during drying and sintering. Moreover, the preparation starting from ceramic powders is more economically viable than the sol-gel route.

Recently, a method based on a high alkane phase emulsified suspensions (HAPES) using decane as the oil phase [26–28] has been studied for the preparation of ceramic foams with interconnected spherical cell structure. In this, the emulsions cast in an open mold could be removed from the mold only after partial or complete drying which hampers the production rate. This problem was resolved by using an oil phase which becomes solid on cooling. Vitorino et al. [29] reported the preparation of alumina foams by emulsion templating method using liquid paraffin as the oil phase. In this, the aqueous ceramic powder suspension is emulsified by dispersing molten wax at a temperature above its melting point. The emulsion cast in a mold undergoes setting during cooling due to the solidification of wax and gelation of the aqueous ceramic powder suspension. Gelling agents such as gelatin, agar, and carrageenan which dissolve in hot water and form a strong gel on cooling due to physical cross-linking are used for the setting of the aqueous powder suspension in the emulsion. The molten naphthalene is also used as an oil phase which is a solid at room temperature. The advantage of naphthalene over wax is the ability of the former to expel from the body by sublimation. However, the toxic nature of naphthalene prevents its use for the production of ceramic foams. Moreover, the foams prepared from naphthalene-based emulsions have highly distorted pore structure against the interconnected spherical cellular structure obtained for other emulsion-based processes. The typical microstructure of alumina foams prepared using naphthalene as an oil phase is shown in Fig. 8.

The hydrogenated vegetable oil (HVO) is used as an eco-friendly oil phase for the preparation of ceramic foams by emulsion templating. In this, the molten hydrogenated vegetable oil is dispersed in an aqueous ceramic powder suspension containing carrageenan gelling agent using sodium dodecyl sulfate emulsifying agent at a temperature of ~ 85 °C to form medium and high internal phase emulsions. The thus obtained stable emulsions with low viscosities are cast in suitable molds and subsequently set by cooling. The gelled bodies are strong enough to remove from the mold without any deformation. The gelled bodies dried at ambient temperature are extracted with either toluene or petroleum ether to remove the HVO. The HVO-removed bodies are sintered to produce ceramic foams. The flowchart of the HVO-based emulsion templating method is shown in Fig. 9.

The porosity of the ceramic foams is decided by the volume fraction of aqueous alumina slurry and HVO to alumina slurry volume ratio. On the other hand, the cell size depends on the concentration of the emulsifying agent and stirring speed used for emulsion preparation. The porosity of alumina foams could be modulated in the

Fig. 8 Microstructure of alumina foams prepared using naphthalene as an oil phase

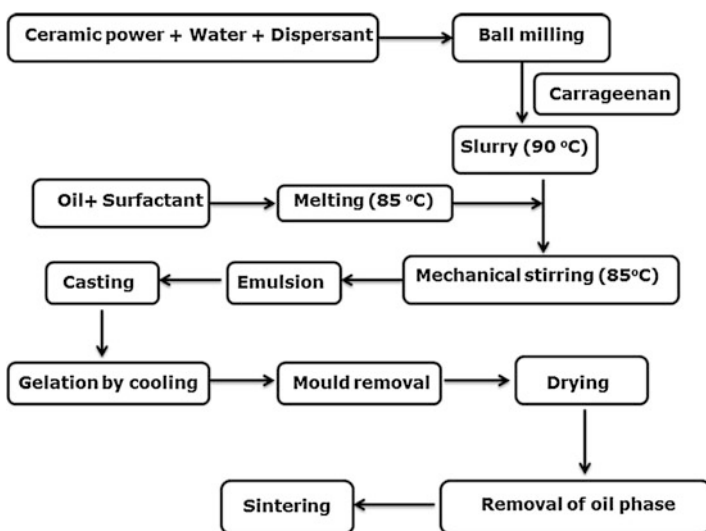
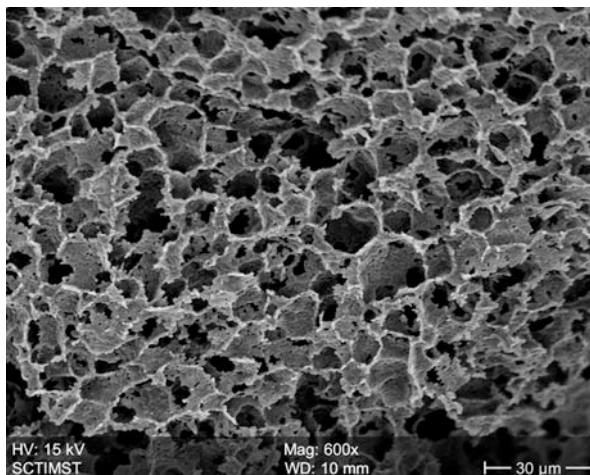
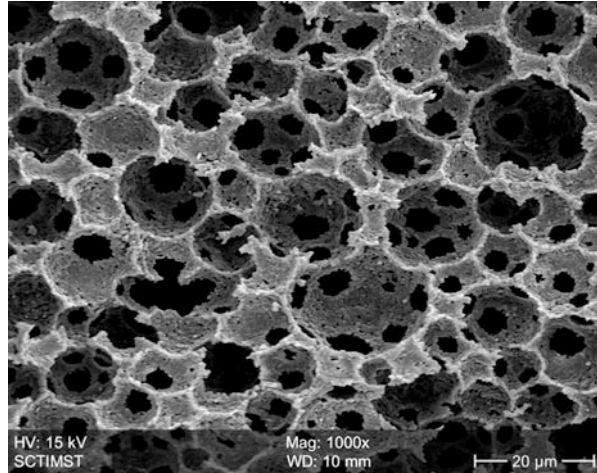


Fig. 9 Flowchart of HVO-based emulsion templating method

range of 70.7–92.5 vol% by changing the hydrogenated vegetable oil to aqueous alumina slurry volume ratios in the range of 1.3–2.7 and using aqueous slurries of alumina concentrations in the range of 10–30 vol%. The foams produced have an interconnected cellular structure. The HVO-based emulsion route produces ceramic foams with relatively lower cell size. The cell sizes obtained are in the range of 5–27 μm . The compressive strength and Young’s modulus of the alumina ceramic foams are in the ranges 2.74–39.6 and 64.5–2350 MPa, respectively, at porosity in

Fig. 10 Microstructure of alumina foam prepared by HVO-based emulsion templating method



the range of 70.7–92.5 vol% [30, 31]. The photograph of an alumina foam body and its microstructure is shown in Fig. 10.

Direct Foaming

In the direct foaming method, wet foams are produced by incorporating air into ceramic powder suspensions by mechanical frothing or by the injection of gases. The wet foam cast in a mold is subsequently set, dried, and then sintered at elevated temperatures to get the ceramic foam. The total porosity of the ceramic foam depends on the number of air bubbles incorporated in the ceramic suspension. The pore morphology and pore size of the foams depend on the stabilization of the air bubbles in the wet foams. Several transformations in the bubble structure, which destabilize the foams, occur within the interval between foam generation and foam setting [32]:

1. Ostwald ripening, i.e., smaller bubbles shrink, while bigger ones grow in size.
2. Creaming of bubbles, i.e., a foam layer forms on top of bulk liquid.
3. Deformation of bubbles.
4. Drainage of liquid from foam to bulk.
5. Coalescence due to rupture of bubbles.

The liquid foams are thermodynamically unstable, due to their high interfacial free energy. Here, the interfacial free energy is the minimum amount of work required to create the air-liquid interface in the bubbles. The driving force for the above transformations occurring in foamed suspensions is to reduce the interfacial free energy. The above transformations can be minimized by the addition of suitable surface-acting agents or surfactants to the suspensions before foaming. A surfactant is a substance that alters the surface or interfacial free energy by adsorbing

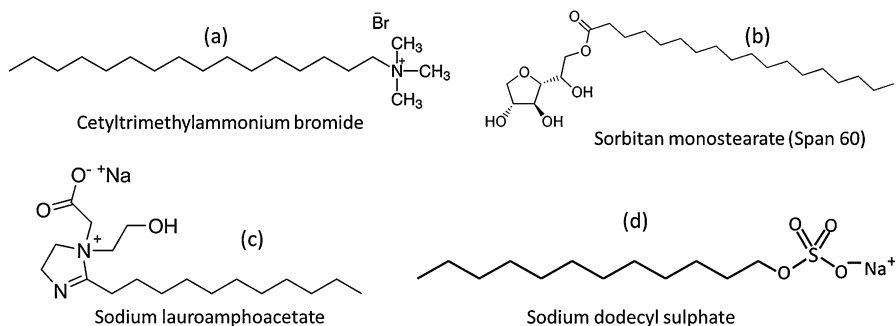


Fig. 11 Surfactants used for foaming (a) cationic, (b) neutral, (c) zwitterionic, and (d) anionic

onto the surfaces or interfaces [33]. Amphiphilic molecules with a nonpolar hydrophobic portion, called a tail attached to a hydrophilic group termed head, are used as surfactants. The hydrophobic part is mostly hydrocarbon chain consisting of 8–18 carbon atoms. The surfactants are classified into four categories based on their head. They are cationic, anionic, nonionic, and amphoteric or zwitterionic [33, 34]. The cationic and anionic surfactants have positively and negatively charged head groups, whereas the nonionic surfactants have a neutral head group. The zwitterionic surfactant possesses both positive and negative groups in their structure. The commonly used surfactants for the preparation of ceramic foams are given in Fig. 11. In addition to the above class of surfactants, proteins such as collagen, egg white, and whey protein are also used to stabilize bubbles generated in ceramic powder suspensions for the preparation of ceramic foams. The selection of surfactant is very important as the stability of the wet foam depends on the nature of surfactants. Therefore, the porosity and foam microstructure are directly dependent on the nature of the surfactant used. In many cases, a mixture of surfactant is proved to produce foams with better porosity and microstructure.

The surfactant-stabilized wet foams have only interim stability. They tend to collapse during drying. Therefore, an additional stabilization by setting the foamed ceramic powder suspension is essential. The in situ polymerization of organic monomers and the cross-linking agent is one of the ways to set the surfactant-stabilized wet foams. The alternative methods include gelation by coagulation of proteins and physical cross-linking of certain carbohydrate polymers. The process utilizing in situ polymerization of organic monomers is called gelcasting.

Gelcasting

Gelcasting, a colloidal processing method originally developed for the fabrication of high-quality, complex-shaped dense ceramic bodies by means of in situ polymerization, is extended for the preparation of ceramic foams. In this, the ceramic powder suspension containing the organic monomer and cross-linking agent is foamed using

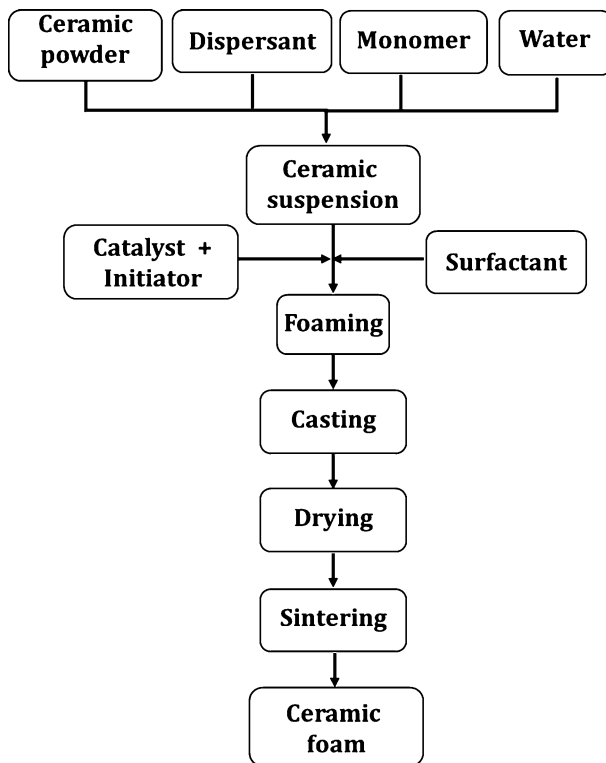


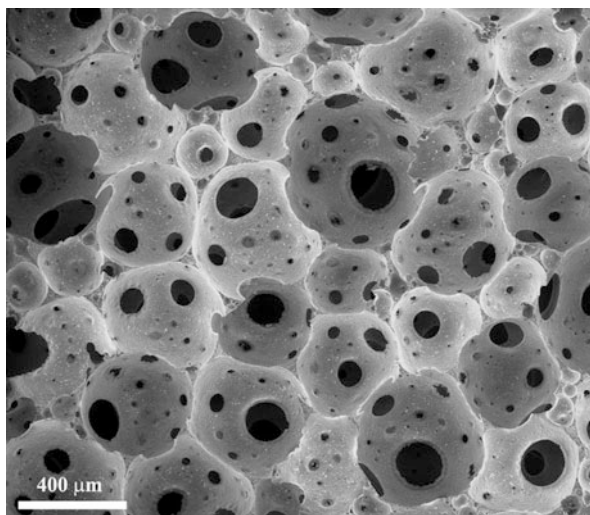
Fig. 12 Flowchart of the gelcasting process for the preparation ceramic foams

a suitable surfactant by incorporating a gas. The foamed suspension cast in a mold is set by in situ polymerization. The gelled foam is removed from the mold, dried, binder removed, and sintered to produce the ceramic foams. The flowchart of the gelcasting process for the preparation of ceramic foams is shown in Fig. 12. A range of monomer and cross-linker systems are studied for the preparation of a large number of ceramic foam materials (Table 2).

Gelcasting produces foams with interconnected cellular structure with high porosity. The ceramic foams produced by gelcasting exhibit nonporous struts resulting in superior crushing strength. The typical microstructure of alumina foam produced by gelcasting is given in Fig. 13. Gelcasting techniques utilizing environmentally friendly biopolymers as gel formers for the manufacturing of ceramic foams are intensively studied. Different biopolymers such as gelatin, proteins like ovalbumin and bovine serum albumin, agar, and starch have recently been applied as nontoxic components for the fabrication of porous ceramics [35–39]. In this, the setting of the foamed suspensions is not due to in situ polymerization but due to physical cross-linking through hydrogen-bonding interactions. The various gelcasting systems and achieved porosity of the foams are presented in Table 2. A continuous process for gelcasting fabrication of ceramic foams has been

Table 2 Various gelcasting systems and achieved porosity of the foams

Sl. no	Gel system	Ceramic system	Porosity (%)
1.	2-Hydroxyethyl methacrylate and poly(ethylene glycol 1000) dimethacrylate	Mg _{0.9} Co _{0.1} Al ₂ O ₄	98
2.	Acrylamide (AM), N,N'-methylenebisacrylamide (MBAM), and ammonium persulfate (APS)	Alumina	82
3.	AM and MBAM	Alumina	88
4.	N,N,N',N'-tetramethylethylene diamine and APS	Hydroxyapatite	90
5.	AM and MBAM	Mullite	73.5
6.	Starch	Alumina	73
7.	Starch	Hydroxyapatite	70
8.	Starch	Silica	82
9.	Agar	SiC	88
10.	Agar	Alumina and mullite	83
11.	Agarose	Hydroxyapatite	90
12.	Agarose	Alumina	90
13.	Egg white protein	Hydroxyapatite	75
14.	Ovalbumin	Alumina	96
15.	Bovine serum albumin	Alumina	92.3
16.	Gelatin and polyvinyl alcohol	Alumina	95

Fig. 13 Microstructure of alumina foam prepared by gelcasting

reported [40]. In this, preformed N₂ bubbles from a separate canister are mixed with the gelcasting slurry instead of bubbling nitrogen gas in conventional method to produce the wet foam. Compared to conventional methods using N₂ gas to generate

bubbles, porous ceramic produced using the new method displayed lower density, higher open and total porosities, and broad pore size distribution.

Particle-Stabilized Foams

The aqueous foams produced using a surfactant are thermodynamically unstable. Therefore, the foamed ceramic powder suspensions undergo either coalescence or Ostwald ripening unless timely set by gelation. This leads to either foam collapse or the formation of large cells within the final foam microstructure. Colloidal particles have been used instead of surfactants for the stabilization of liquid-liquid and gas-liquid interfaces to produce emulsions and foams [41–43]. The foams produced by stabilization of liquid-air interface by colloidal particles are called particle-stabilized foams. In this, the particles adsorb on the liquid-gas interface and thereby reduce the interfacial free energy. The critical parameter deciding the adsorption of colloidal particles on the liquid-gas interface is the wetting behavior (contact angle) of the particle with the liquid. The ideal contact angle for producing particle-stabilized foams is in the range of 60–80° [42]. That is, the particles are only partially wetted by the fluid. The contact angle of colloidal particles at fluid interfaces depends on the surface chemistry, roughness, impurities, and particle size. The advantage of particle-stabilized foams over the surfactant-stabilized ones is their superior thermodynamic stability [43]. Therefore, aqueous ceramic powder suspensions foamed using colloidal particles can be dried without coalescence or Ostwald ripening even in the absence of an additional setting mechanism such as in situ polymerization or coagulation.

The preparation of particle-stabilized foams is rather simple. The process involves agitation of aqueous ceramic powder suspension containing short-chain amphiphilic (<8 carbon atoms) molecules to form foamed ceramic powder suspension [44]. The amphiphilic molecules convert the hydrophilic oxide ceramic particles to partially hydrophobic by adsorbing on their surface. That is, the ceramic particles are partially hydrophobized in situ by the amphiphilic molecules. The amphiphilic molecules such as propionic, valeric, butyric, and enanthic acid are used for partial hydrophobization [45]. The air bubbles incorporated in the powder suspension by agitation are stabilized by the adsorption of partially hydrophobized particles on the air-liquid interface. The foamed ceramic powder suspensions are subsequently dried and sintered to produce the ceramic foam. The schematic representation of particle-stabilized foam is shown in Fig. 14. A combination of particle stabilization and gelcasting using calcium aluminate as a setting agent is also used for the preparation of ceramic foams [46]. Alumina, silica, zirconia, zirconia toughened alumina, and silicon nitride foams are prepared through the particle-stabilized foaming method. The advantages of this method are that it produces ceramic foams with high porosity, relatively low cell size, uniform pore size distribution, and superior crushing strength. Ceramic foams with porosity as high as 95 vol% are produced by the particle-stabilized foam route [45].

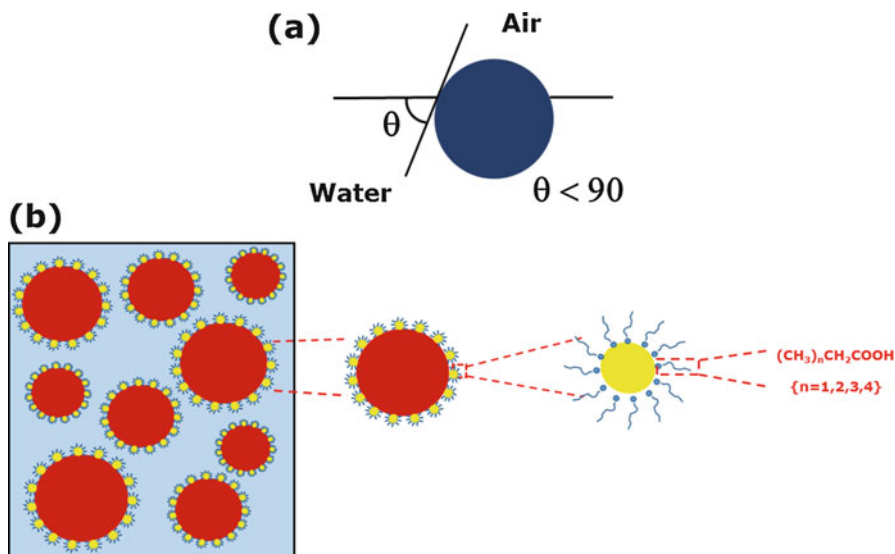


Fig. 14 Schematic representation of (a) particles at the air-liquid interface and (b) particle stabilization of wet foams

Thermo-foaming

The principle of preparation of polymer foams involves foaming by generating gas bubbles in the polymer medium or polymerizable organic material using a blowing agent. The foamed polymer is subsequently stabilized by setting by further polymerization and cross-linking reactions. The blowing agent can be a liquid which evaporates at the foaming temperature or a solid which decomposes and generates the gas at the foaming temperature. The principle of polymer foam preparation is adapted for the preparation of ceramic foams. In this, a sufficient amount of the ceramic powder is incorporated into the polymer or polymerizable organic material before foaming and setting. The solid foam is subsequently heated to remove the organic matter and sintered to produce the ceramic foam.

Sucrose is studied as an organic medium for the preparation of ceramic foams by thermo-foaming. The oxide ceramic powders such as alumina, silica, etc. disperse in molten sucrose due to the hydrophilic interaction between the powder surface and sucrose hydroxyl groups. The ceramic powder dispersed molten sucrose undergoes foaming when heated at temperatures in the range of 120–150 °C due to the water vapor generated by the hydroxyl condensation between glucose and fructose anhydride formed from the sucrose. The bubbles created by the water vapor are stabilized by an increase in viscosity due to polymerization and ceramic particles adsorbed on the molten sucrose-air interface by the particle stabilization mechanism. The setting of the foamed dispersions into solid bodies is by the continued polymerization



Fig. 15 Flowchart of thermo-foaming process and photograph of alumina foam

(caramelization) through the hydroxyl condensation. The foaming time, foam setting time, and foam rise depend on the alumina powder to sucrose weight ratio and foaming temperature. Sucrose polymer burnout and sintering produces alumina foam bodies of smaller sizes without any cracks. On the other hand, an intermediate carbonization step is inevitable to prevent the cracking of larger bodies. A considerable shrinkage of the body occurs during carbonization, and the carbon produced from the sucrose polymer binds the alumina particles that prevent cracking. The process flowchart and photograph of an alumina foam body produced by thermo-foaming are shown in Fig. 15.

The porosity of alumina and mullite ceramic foams produced using thermo-foaming depends on the ceramic powder to sucrose weight ratio and foaming temperature. The alumina and mullite foams produced by the thermo-foaming process have interconnected cellular structure with cell sizes in the ranges of 0.4–1.6 and 0.49–1.58 mm, respectively. The foaming time and foam setting time in thermo-foaming of powder dispersions in molten sucrose can be considerably decreased by using magnesium nitrate as a blowing agent. The faster foaming and foam setting is by the faster $-OH$ condensation due to the catalytic effect of nitric acid produced by the hydrolysis of magnesium nitrate. The magnesium nitrate not only modulates the porosity and cell size but also changes the foam microstructure from cellular- to reticulate-like. Figure 16 shows the typical foam microstructure produced with and without magnesium nitrate blowing agent.

Low-density silicon carbide foams are also prepared by the thermo-foaming of silicon powder dispersions in molten sucrose. In this, the carbon required for reaction with silicon to form silicon carbide is derived from the sucrose. The thermo-foaming of silicon powder dispersions in molten sucrose at appropriate silicon to sucrose weight ratio followed by carbonization at 900 °C in inert

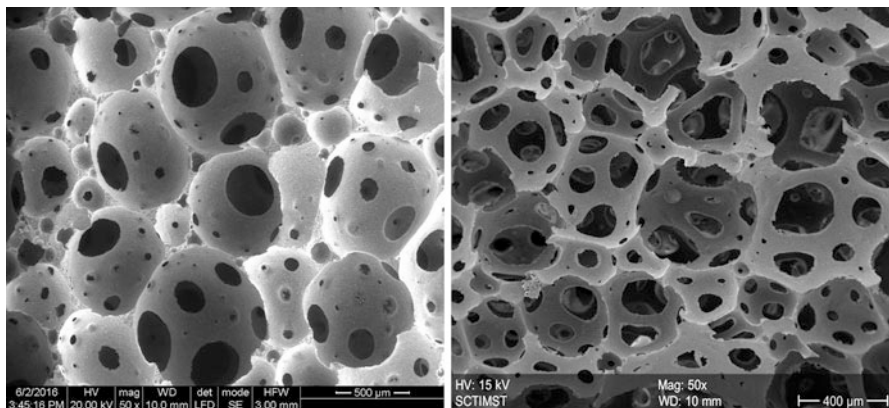


Fig. 16 Foam microstructure of alumina foam produced (a) with and (b) without magnesium nitrate blowing agent

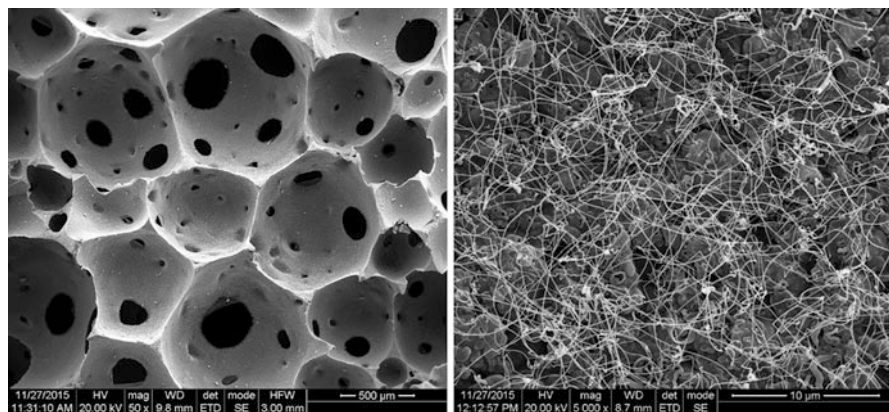


Fig. 17 SEM showing (a) cellular structure and (b) nanowire growth on cell walls of thermofoamed SiC foam

atmosphere produces stoichiometric carbon-silicon composite foams. Subsequent high-temperature (~ 1500 °C) heat treatment in inert atmosphere results in the reaction between carbon and silicon to form SiC foams. The density of the SiC foams is controlled in the range of 0.08–0.168 by controlling the foaming temperature and magnesium nitrate concentration. The SiC foams have interconnected cellular structure with cell sizes in the range of 0.55–1.12 mm. Cell walls of the SiC foams are decorated with SiC nanowires grown by vapor-liquid-solid and vapor-solid mechanisms. The SEM photograph showing the cellular structure and SiC nanowires on the cell wall surface is shown in Fig. 17.

Ceramic Foams from Pre-ceramic Polymers

A pre-ceramic polymer is a polymer which on pyrolysis yields a ceramic. The ceramic materials prepared from pre-ceramic polymers are known as polymer-derived ceramics (PDC). They include silicon carbide (SiC), silicon oxycarbide (SiOC), silicon nitride (Si₃N₄), SiO₂, SiNC, etc. The earliest known pre-ceramic polymers are organosilicon compounds. They were used for the preparation of silicon-based ceramics such as SiC and SiOC. The pre-ceramic polymers are widely studied for the preparation of SiC and SiOC ceramic foams. The general structure of some of the pre-ceramic polymers used for the preparation of ceramic foams is given in Fig. 18.

The methods for the preparation of foams from pre-ceramic polymer include direct foaming, polymer foam replication, and sacrificial template. The direct foaming involves two techniques, the melt foaming of the precursor and foaming of the precursor solution using blowing agents. The melt foaming method employs the use of a powder precursor. In this, the pre-ceramic polymer powder is melted and then transferred to a preheated mold at temperatures in the range of 250–270 °C. The molten polymer starts to cross-link; the gases evolved during this process foam the molten polymer which is then set by the completion of the cross-linking, forming a thermoset foam. The green foam is then pyrolyzed in inert conditions or air atmosphere to get the ceramic foam. In some of the cases, the foaming is due to blowing agents mixed with the precursor prior to the melt foaming stage. In the second case, the pre-ceramic precursor solution is foamed at room temperatures using blowing agents and set by the cross-linking of the polymer precursor. The green foam is dried and then pyrolyzed or sintered to get the final product.

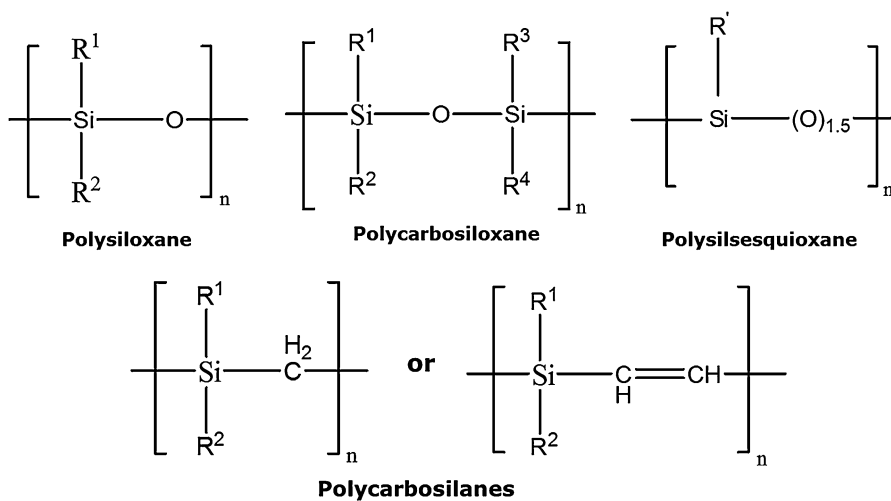
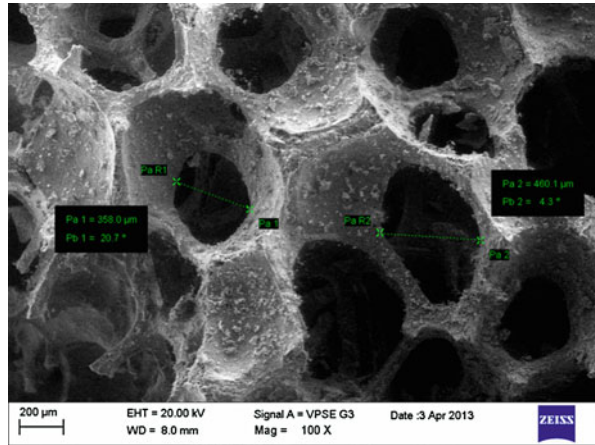


Fig. 18 Structures of pre-ceramic polymers used for the preparation of SiC and SiOC ceramic foams (R¹, R², R³, and R⁴ stand for alkyl or aryl groups)

Fig. 19 Microstructure of SiC foam prepared by polymer foam replication using polycarbosilane



The polymer foam replication method uses polyurethane foam template. The pre-ceramic polymer solution is impregnated into the polyurethane foam till maximum coverage is ensured. The excess solution is then drained, the impregnated foam is dried, and the template is removed by pyrolysis at 600 °C to get the green. The sintering of the green foam in inert atmosphere results in the ceramic foam. In the sacrificial template method, pore templates such as polymer beads, expanded microspheres, microbeads, etc. are dispersed within the pre-ceramic polymer and then cross-linked by heating at temperatures between 180 °C and 250 °C. The green body is then dried, pyrolyzed to remove the template, and sintered in an inert atmosphere to get the ceramic foam. The SEM micrograph of SiC foam prepared from a polycarbosilane by polymer foam replication method is shown in Fig. 19.

The freeze casting and emulsion templating methods are also studied for the preparation of ceramic foams from pre-ceramic polymers. In the former, a pre-ceramic polymer solution is frozen to crystallize the solvent, and then the solvent crystals are removed by sublimation to form pre-ceramic polymer foams with aligned pores. Subsequent pyrolysis and sintering produce ceramic foams. The emulsion route uses emulsification of pre-ceramic polymer solution in a nonaqueous solvent using a suitable emulsifying agent followed by drying, cross-linking of the pre-ceramic polymer, and pyrolyzing to produce ceramic foams with interconnected cellular structure. The maximum porosity of SiC and SiOC foams achieved by various processing methods from different pre-ceramic polymers is summarized in Table 3.

Thermal Conductivity of Ceramic Foams Prepared by Various Methods

Thermal insulation helps to reduce power consumption during thermal processing of materials and also protects the surrounding space from thermal hazard. Generally, ceramic foam materials possess high-temperature stability, low thermal conductivity, and thermal shock resistance, and these are key requirements for thermal

Table 3 Maximum porosity of ceramic foams prepared from pre-ceramic polymers by various processing methods

Sl. no	Pre-ceramic polymer	Process	Foam	Porosity (%)
1.	Methylhydroxylsiloxane	Direct foaming	SiOC	94
2.	Methylhydroxylsiloxane	Replication	SiOC	90
3.	Methylpolysiloxane	Replication	SiC	92
4.	Methylpolysiloxane/PMMA	Sacrificial template	SiC	85
5.	YR3370 polysiloxane/PMMA	Sacrificial template	SiOC	80
6.	Methylpolysiloxane/rice bran	Sacrificial template	SiOC	46
7.	Polymethylsiloxane/PMMA	Sacrificial template	SiC	76
8.	Polyallylhydridocarbosilane	Emulsion templating	SiC	35
9.	Poly(methylsilsesquioxane)	Emulsion templating	Si/C/ O	40
10.	Poly(methylsilsesquioxane)	Emulsion templating	SiOC	80
11.	Polycarbosilane/HIPE	Emulsion templating	SiC	92
12.	PCS Nippon type S	Direct foaming	SiC	45
13.	Methyl phenyl poly(silsesquioxane)	Melt foaming	SiOC	87
14.	Silres(polysiloxane)/TBA-camphene	Freeze casting	SiOC	94.8
15.	Polymethylsiloxane	Freeze casting	SiOC	74

insulators [6, 47]. Both open-cellular and closed-cellular foams with high porosity are excellent candidates for thermal insulation. However, closed-cell ceramic foams have lower thermal conductivity values compared to open-cell foams due to their isolated pore structure and hence are more suitable for thermal insulation. The foams needed for thermal insulation must have near identical pore size distribution and high porosity. Normally, gelcasting and direct foaming techniques are used for the preparation of such foams. Table 4 lists the thermal conductivity of ceramic foams prepared by various processing routes. The ceramic foams prepared by various routes exhibited thermal conductivity in the range of 0.027–0.37 W/mK. The thermal conductivity of ceramic foams is further decreased by filling their pores with aerogels [48, 49]. The ceramic foam skeleton provides adequate strength for the aerogels which are otherwise known to be highly fragile. On the other hand, the aerogel filled in the cells of ceramic foam materials provides very high thermal insulation.

Summary

Ceramic foams are ideal candidates for thermal protection materials due to their low thermal conductivity, high-temperature stability, excellent thermal shock resistance, and low density. The ceramic foams are prepared from the respective ceramic powders or pre-ceramic polymers. A wide range of processing methods starting from powder pressing using fugitive pore-forming additives to freeze casting of powder suspensions is used for the development of ceramic foams. The colloidal processing methods

Table 4 Thermal conductivity of ceramic foams prepared by various processing routes

Sl. no.	Ceramic foam	Processing route	Porosity (vol%)	Thermal conductivity (W/mK)	Reference
1.	Mullite	Gelcasting	86	0.09	[50]
2.	Alumina	Foam gelcasting	97.5	0.12	[51]
3.	Anorthite	Foam gelcasting	91	0.018	[52]
4.	Y ₂ SiO ₅	Foam gelcasting	92	0.054	[53]
5.	Alumina	Direct foaming	91	0.05	[54]
6.	Anorthite	Direct foaming	94	0.042	[55]
7.	Zirconia	Particle-stabilized foaming	97.9	0.027	[56]
8.	Mullite-Corundum	Direct foaming	73.7	0.287	[57]
9.	Silicon carbide	Thermo-foaming	97.5	0.076	[58]
10.	Kaolin	Direct foaming	95	0.23	[59]
11.	Mullite	Foam gelcasting	81	0.14	[60]
12.	Glass ceramic	Direct foaming	80	0.37	[61]
13.	Diatomite	Foam gelcasting	84.5	0.097	[62]
14.	Kaolin	Direct foaming	90	0.054	[63]
15.	MgAl ₂ O ₄	Foam gelcasting	75.1	0.24	[64]
16.	γ-Y ₂ Si ₂ O ₇	Foam gelcasting	84.9	0.23	[65]
17.	Mullite	Direct foaming	77.3	0.37	[66]
18.	YSZ	Freeze casting	39.25	0.045	[48]
19.	Y ₂ SiO ₅	Freeze casting	86.4	0.069	[49]
20.	Mullite	Sacrificial template	79	0.114	[67]
21.	Mullite	Freeze casting	91	0.23	[68]

provide better control over the porosity, pore size, pore morphology, and pore interconnectivity. Direct foaming, freeze casting, and emulsion templating are the major colloidal processing routes for ceramic foam production. The wet foams produced by particle stabilization mechanism have more thermodynamic stability which enables their drying without foam collapse even without setting. On the other hand, the surfactant-stabilized foams require an additional setting mechanism by in situ polymerization or coagulation to avoid the foam collapse. The emulsion-based methods use immiscible liquid droplets dispersed in ceramic powder suspension, whereas in freeze casting, the crystals of dispersion medium produced on freezing act as pore templates. The freeze casting produces ceramic foams with homogenous pore structure as well as aligned lamellar pore structure depending on the freezing condition and additives used to control solvent crystallization. The thermo-foaming using powder dispersions in molten sucrose enables the production of alumina, mullite, and SiC foam bodies with interconnected cellular structure. SiC and SiOC foams are prepared from pre-ceramic polymers using most of the abovementioned processing routes.

References

1. Gibson LJ, Ashby MF (1997) Cellular solids. Structure and properties. Cambridge University Press, Cambridge. <https://doi.org/10.1017/CBO9781139878326>
2. Verma J, Mitra R, Vijayakumar M (2013) Processing of silica foam using steam heating and its characterization. *J Eur Ceram Soc* 33:943–951. <https://doi.org/10.1016/j.jeurceramsoc.2012.11.010>
3. Orenstein RM, Green DJ (1992) Thermal shock behavior of open-cell ceramic foams. *J Am Ceram Soc* 75:1899–1905. <https://doi.org/10.1111/j.1151-2916.1992.tb07214.x>
4. Vedula VR, Green DJ, Hellman JR (1999) Thermal shock resistance of ceramic foams. *J Am Ceram Soc* 82:649–656. <https://doi.org/10.1111/j.1151-2916.1999.tb01813.x>
5. Ohji T, Fukushima M (2012) Macro-porous ceramics: processing and properties. *Int Mater Rev* 57:115–131. <https://doi.org/10.1179/1743280411Y.0000000006>
6. Studart AR, Gonzenbach UT, Tervoort E, Gauckler LJ (2006) Processing routes to macroporous ceramics: a review. *J Am Ceram Soc* 89:1771–1789. <https://doi.org/10.1111/j.1551-2916.2006.01044.x>
7. Zhang J, Ashby MF (1989) Theoretical studies on isotropic foams. University of Cambridge Department of Engineering, Cambridge
8. Lewis JA (2004) Colloidal processing of ceramics. *J Am Ceram Soc* 83:2341–2359. <https://doi.org/10.1111/j.1151-2916.2000.tb01560.x>
9. Zhu X, Jiang D, Tan S, Zhang Z (2004) Improvement in the strut thickness of reticulated porous ceramics. *J Am Ceram Soc* 84:1654–1656. <https://doi.org/10.1111/j.1151-2916.2001.tb00895.x>
10. Vogt UF, Gorbar M, Dimopoulos-Eggenschwiler P, Broenstrup A, Wagner G, Colombo P (2010) Improving the properties of ceramic foams by a vacuum infiltration process. *J Eur Ceram Soc* 30:3005–3011. <https://doi.org/10.1016/j.jeurceramsoc.2010.06.003>
11. Deville S (2008) Freeze-casting of porous ceramics: a review of current achievements and issues. *Adv Eng Mater* 10:155–169
12. Waschkies T, Oberacker R, Hoffmann MJ (2009) Control of lamellae spacing during freeze casting of ceramics using double-side cooling as a novel processing route. *J Am Ceram Soc* 92: S79–S84. <https://doi.org/10.1111/j.1551-2916.2008.02673.x>
13. Hu L, Wang C-A, Huang Y, Sun C, Lu S, Hu Z (2010) Control of pore channel size during freeze casting of porous YSZ ceramics with unidirectionally aligned channels using different freezing temperatures. *J Eur Ceram Soc* 30:3389–3396. <https://doi.org/10.1016/j.jeurceramsoc.2010.07.032>
14. Xia Y, Zeng Y-P, Jiang D (2012) Microstructure and mechanical properties of porous Si₃N₄ ceramics prepared by freeze-casting. *Mater Des* 33:98–103. <https://doi.org/10.1016/J.MATDES.2011.06.023>
15. Zuo KH, Zeng Y, Jiang D (2010) Effect of cooling rate and polyvinyl alcohol on the morphology of porous hydroxyapatite ceramics. *Mater Des* 31:3090–3094. <https://doi.org/10.1016/J.MATDES.2009.12.044>
16. Zuo KH, Zeng Y-P, Jiang D (2010) Effect of polyvinyl alcohol additive on the pore structure and morphology of the freeze-cast hydroxyapatite ceramics. *Mater Sci Eng C* 30:283–287. <https://doi.org/10.1016/j.msec.2009.11.003>
17. Deville S, Saiz E, Tomsia AP (2006) Freeze casting of hydroxyapatite scaffolds for bone tissue engineering. *Biomaterials* 27:5480–5489. <https://doi.org/10.1016/j.biomaterials.2006.06.028>
18. Fu Q, Rahaman MN, Dogan F, Bal BS (2008) Freeze casting of porous hydroxyapatite scaffolds. I. Processing and general microstructure. *J Biomed Mater Res Part B Appl Biomater* 86:125–135. <https://doi.org/10.1002/jbm.b.30997>
19. Araki K, Halloran JW (2005) Porous ceramic bodies with interconnected pore channels by a novel freeze casting technique. *J Am Ceram Soc* 88:1108–1114. <https://doi.org/10.1111/j.1551-2916.2005.00176.x>
20. Araki K, Halloran JW (2004) Room-temperature freeze casting for ceramics with nonaqueous sublimable vehicles in the naphthalene-camphor eutectic system. *J Am Ceram Soc* 87:2014–2019. <https://doi.org/10.1111/j.1151-2916.2004.tb06353.x>

21. Chen R, Wang C-A, Huang Y, Ma L, Lin W (2007) Ceramics with special porous structures fabricated by freeze-gelcasting: using tert-butyl alcohol as a template. *J Am Ceram Soc* 90:3478–3484. <https://doi.org/10.1111/j.1551-2916.2007.01957.x>
22. Yang TY, Lee JM, Yoon SY, Park HC (2010) Hydroxyapatite scaffolds processed using a TBA-based freeze-gel casting/polymer sponge technique. *J Mater Sci Mater Med* 21:1495–1502. <https://doi.org/10.1007/s10856-010-4000-1>
23. Sofie SW, Dogan F (2004) Freeze casting of aqueous alumina slurries with glycerol. *J Am Ceram Soc* 84:1459–1464. <https://doi.org/10.1111/j.1151-2916.2001.tb00860.x>
24. Zhang Y, Zuo K, Zeng Y-P (2009) Effects of gelatin addition on the microstructure of freeze-cast porous hydroxyapatite ceramics. *Ceram Int* 35:2151–2154. <https://doi.org/10.1016/j.ceramint.2008.11.022>
25. Imhof A, Pine DJ (1997) Ordered macroporous materials by emulsion templating. *Nature* 389:948–951. <https://doi.org/10.1038/40105>
26. Ewais EMM, Barg S, Grathwohl G, Garamoon AA, Morgan NN (2011) Processing of open porous zirconia via alkane-phase emulsified suspensions for plasma applications. *Int J Appl Ceram Technol* 8:85–93. <https://doi.org/10.1111/j.1744-7402.2010.02521.x>
27. Barg S, de Moraes EG, Koch D, Grathwohl G (2009) New cellular ceramics from high alkane phase emulsified suspensions (HAPES). *J Eur Ceram Soc* 29:2439–2446. <https://doi.org/10.1016/j.jeurceramsoc.2009.02.003>
28. Barg S, Soltmann C, Andrade M, Koch D, Grathwohl G (2008) Cellular ceramics by direct foaming of emulsified ceramic powder suspensions. *J Am Ceram Soc* 91:2823–2829. <https://doi.org/10.1111/j.1551-2916.2008.02553.x>
29. Vitorino N, Abrantes JCC, Frade JR (2013) Cellular ceramics processed by paraffin emulsified suspensions with collagen consolidation. *Mater Lett* 98:120–123. <https://doi.org/10.1016/J.MATLET.2013.02.020>
30. Vijayan S, Narasimman R, Prabhakaran K (2014) Freeze gelcasting of hydrogenated vegetable oil-in-aqueous alumina slurry emulsions for the preparation of macroporous ceramics. *J Eur Ceram Soc* 34:4347–4354. <https://doi.org/10.1016/j.jeurceramsoc.2014.07.014>
31. Vijayan S, Narasimman R, Prabhakaran K (2015) Effect of emulsion composition on gel strength and porosity in the preparation of macroporous alumina ceramics by freeze gelcasting. *J Asian Ceram Soc* 3:279–286. <https://doi.org/10.1016/j.jascer.2015.05.007>
32. Wilson AJ (1989) *Foams: physics, chemistry and structure*. Springer Science & Business Media, London
33. Rosen MJ, Kunjappu JT (2012) *Surfactants and interfacial phenomena*. Wiley, Hoboken
34. Tadros TF (2006) *Applied surfactants: principles and applications*. Wiley, Weinheim
35. Ortega FS, Valenzuela FAO, Scuracchio CH, Pandolfelli VC (2003) Alternative gelling agents for the gelcasting of ceramic foams. *J Eur Ceram Soc* 23:75–80. [https://doi.org/10.1016/S0955-2219\(02\)00075-4](https://doi.org/10.1016/S0955-2219(02)00075-4)
36. Lyckfeldt O, Brandt J, Lesca S (2000) Protein forming – a novel shaping technique for ceramics. *J Eur Ceram Soc* 20:2551–2559. [https://doi.org/10.1016/S0955-2219\(00\)00136-9](https://doi.org/10.1016/S0955-2219(00)00136-9)
37. Dhara S, Bhargava P (2004) Egg white as an environmentally friendly low-cost binder for gelcasting of ceramics. *J Am Ceram Soc* 84:3048–3050. <https://doi.org/10.1111/j.1151-2916.2001.tb01137.x>
38. Potoczek M (2008) Gelcasting of alumina foams using agarose solutions. *Ceram Int* 34:661–667. <https://doi.org/10.1016/j.ceramint.2007.02.001>
39. Lyckfeldt O, Ferreira JMF (1998) Processing of porous ceramics by ‘starch consolidation’. *J Eur Ceram Soc* 18:131–140. [https://doi.org/10.1016/S0955-2219\(97\)00101-5](https://doi.org/10.1016/S0955-2219(97)00101-5)
40. Zhang F-Z, Kato T, Fuji M, Takahashi M (2006) Gelcasting fabrication of porous ceramics using a continuous process. *J Eur Ceram Soc* 26:667–671. <https://doi.org/10.1016/j.jeurceramsoc.2005.07.021>
41. Aveyard R, Binks BP, Clint JH (2003) Emulsions stabilised solely by colloidal particles. *Adv Colloid Interf Sci* 100:503–546. [https://doi.org/10.1016/S0001-8686\(02\)00069-6](https://doi.org/10.1016/S0001-8686(02)00069-6)

42. Binks BP (2002) Particles as surfactants – similarities and differences. *Curr Opin Colloid Interface Sci* 7:21–41. [https://doi.org/10.1016/S1359-0294\(02\)00008-0](https://doi.org/10.1016/S1359-0294(02)00008-0)
43. Du Z, Bilbao-Montoya MP, Binks BP, Dickinson E, Ettelaie R, Murray BS (2003) Outstanding stability of particle-stabilized bubbles. *Langmuir* 19:3106–3108. <https://doi.org/10.1021/la034042n>
44. Gonzenbach UT, Studart AR, Tervoort E, Gauckler LJ (2006) Ultrastable particle-stabilized foams. *Angew Chem Int Ed Eng* 45:3526–3530. <https://doi.org/10.1002/anie.200503676>
45. Gonzenbach UT, Studart AR, Tervoort E, Gauckler LJ (2007) Macroporous ceramics from particle-stabilized wet foams. *J Am Ceram Soc* 90:16–22. <https://doi.org/10.1111/j.1551-2916.2006.01328.x>
46. Chuanuwatanakul C, Tallon C, Dunstan DE, Franks GV (2011) Controlling the microstructure of ceramic particle stabilized foams: influence of contact angle and particle aggregation. *Soft Matter* 7:11464–11474. <https://doi.org/10.1039/C1SM06477K>
47. Liu P, Chen G-F (2014) *Porous materials: processing and applications*, First edit. Elsevier, Oxford
48. Hu L, Wang C-A, Huang Y (2011) Porous YSZ ceramics with unidirectionally aligned pore channel structure: lowering thermal conductivity by silica aerogels impregnation. *J Eur Ceram Soc* 31:2915–2922. <https://doi.org/10.1016/J.JEURCERAMSOC.2011.07.014>
49. Zhang R, Qu Q, Han B, Wang B (2016) A novel silica aerogel/porous Y_2SiO_5 ceramics with low thermal conductivity and enhanced mechanical properties prepared by freeze casting and impregnation. *Mater Lett* 175:219–222. <https://doi.org/10.1016/J.MATLET.2016.04.051>
50. Gong L, Wang Y, Cheng X, Zhang R, Zhang H (2014) Porous mullite ceramics with low thermal conductivity prepared by foaming and starch consolidation. *J Porous Mater* 21:15–21. <https://doi.org/10.1007/s10934-013-9741-z>
51. Shimizu T, Matsuura K, Furue H, Matsuzak K (2013) Thermal conductivity of high porosity alumina refractory bricks made by a slurry gelation and foaming method. *J Eur Ceram Soc* 33:3429–3435. <https://doi.org/10.1016/J.JEURCERAMSOC.2013.07.001>
52. Han Y, Li C, Bian C, Li S, Wang C-A (2013) Porous anorthite ceramics with ultra-low thermal conductivity. *J Eur Ceram Soc* 33:2573–2578. <https://doi.org/10.1016/J.JEURCERAMSOC.2013.04.006>
53. Wu Z, Sun L, Pan J, Wang J (2018) Highly porous Y_2SiO_5 ceramic with extremely low thermal conductivity prepared by foam-gelcasting-freeze drying method. *J Am Ceram Soc* 101:1042–1047
54. Lo YW, Wei WCJ, Hsueh CH (2011) Low thermal conductivity of porous Al_2O_3 foams for SOFC insulation. *Mater Chem Phys* 129:326–330. <https://doi.org/10.1016/J.MATCHEMPHYS.2011.04.023>
55. Li Y, Cheng X, Gong L, Feng J, Cao W, Zhang R, Zhang H (2015) Fabrication and characterization of anorthite foam ceramics having low thermal conductivity. *J Eur Ceram Soc* 35:267–275. <https://doi.org/10.1016/J.JEURCERAMSOC.2014.08.045>
56. Huo W-L, Zhang X-Y, Chen Y-G, Lu Y-J, Liu W-T, Xi X-Q, Wang Y-L, Xu J, Yang J-L (2016) Highly porous zirconia ceramic foams with low thermal conductivity from particle-stabilized foams. *J Am Ceram Soc* 99:3512–3515. <https://doi.org/10.1111/jace.14555>
57. Zhou W, Yan W, Li N, Li Y, Dai Y, Zhang Z, Ma S (2019) Fabrication of mullite-corundum foamed ceramics for thermal insulation and effect of micro-pore-foaming agent on their properties. *J Alloys Compd* 785:1030–1037. <https://doi.org/10.1016/J.JALLCOM.2019.01.212>
58. Vijayan S, Wilson P, Sreeja R, Prabhakaran K (2017) Ultralight SiC foams with improved strength from sucrose and silicon powder using magnesium nitrate blowing agent. *Mater Lett* 194:126–129. <https://doi.org/10.1016/J.MATLET.2017.02.032>
59. Bourret J, Tessier-Doyen N, Naït-Ali B, Pennec F, Alzina A, Peyratout CS, Smith DS (2013) Effect of the pore volume fraction on the thermal conductivity and mechanical properties of kaolin-based foams. *J Eur Ceram Soc* 33:1487–1495. <https://doi.org/10.1016/J.JEURCERAMSOC.2012.10.022>

60. Yang F, Li C, Lin Y, Wang C-A (2012) Effects of sintering temperature on properties of porous mullite/corundum ceramics. *Mater Lett* 73:36–39. <https://doi.org/10.1016/J.MATLET.2011.12.087>
61. Zhu M, Ji R, Li Z, Wang H, Liu L, Zhang Z (2016) Preparation of glass ceramic foams for thermal insulation applications from coal fly ash and waste glass. *Constr Build Mater* 112:398–405. <https://doi.org/10.1016/J.CONBUILDMAT.2016.02.183>
62. Han L, Li F, Deng X, Wang J, Zhang H, Zhang S (2017) Foam-gelcasting preparation, microstructure and thermal insulation performance of porous diatomite ceramics with hierarchical pore structures. *J Eur Ceram Soc* 37:2717–2725. <https://doi.org/10.1016/J.JEURCERAMSOC.2017.02.032>
63. Bourret J, Michot A, Tessier-Doyen N, Naït-Ali B, Pennec F, Alzina A, Vicente J, Peyratout CS, Smith DS (2014) Thermal conductivity of very porous kaolin-based ceramics. *J Am Ceram Soc* 97:938–944
64. Deng X, Wang J, Liu J, Zhang H, Han L, Zhang S (2016) Low cost foam-gelcasting preparation and characterization of porous magnesium aluminate spinel ($MgAl_2O_4$) ceramics. *Ceram Int* 42:18215–18222. <https://doi.org/10.1016/J.CERAMINT.2016.08.145>
65. Wu Z, Sun L, Wan P, Li J, Hu Z, Wang J (2015) In situ foam-gelcasting fabrication and properties of highly porous γ - $Y_2Si_2O_7$ ceramic with multiple pore structures. *Scr Mater* 103:6–9. <https://doi.org/10.1016/J.SCRIPTAMAT.2015.02.024>
66. Guo H, Ye F, Li W, Song X, Xie G (2015) Preparation and characterization of foamed microporous mullite ceramics based on kyanite. *Ceram Int* 41:14645–14651. <https://doi.org/10.1016/J.CERAMINT.2015.07.186>
67. Ge S, Lin L, Zhang H, Bi Y, Zheng Y, Li J, Deng X, Zhang S (2018) Synthesis of hierarchically porous mullite ceramics with improved thermal insulation via foam-gelcasting combined with pore former addition. *Adv Appl Ceram* 117:493–499. <https://doi.org/10.1080/17436753.2018.1502065>
68. Fukushima M, Yoshizawa Y (2016) Fabrication and morphology control of highly porous mullite thermal insulators prepared by gelation freezing route. *J Eur Ceram Soc* 36:2947–2953. <https://doi.org/10.1016/J.JEURCERAMSOC.2015.09.041>



Silicon Carbide-Based Lightweight Mirror Blanks for Space Optics Applications

29

Dulal Chandra Jana and Bhaskar Prasad Saha

Contents

Introduction	1136
Design Considerations	1137
Mechanical Properties	1137
Thermal Properties	1138
General Requirements	1138
Candidate Materials	1139
Metallic Mirrors	1140
Monolithic Glass and Glass-Ceramic Mirrors	1141
Silicon Carbide Mirrors	1141
Foam-Based Mirrors	1142
Carbon Fiber-Reinforced Polymers (CFRPs)	1142
Flow Sheet Diagram for Processing of SiC Mirror Blanks	1143
Processing of Lightweight SiC Substrates	1144
Raw Materials and Green Forming	1144
Low-Temperature Heat Treatment	1146
Green Machining	1147
Sintering	1148
Aspheric Profile on S-SiC Substrates	1149
Properties of S-SiC Substrates	1150
Weibull Statistics and Reliability of S-SiC	1151
CVD-SiC Coating	1154
CVD Parameters	1155
Properties of CVD-SiC Coating	1157
Conclusions	1159
References	1161

D. C. Jana · B. P. Saha (✉)

Centre for Non-Oxide Ceramics, International Advanced Research Centre for Powder Metallurgy and New Materials (ARCI), Hyderabad, India

e-mail: janad@arci.res.in; bpsaha@arci.res.in

© Springer Nature Switzerland AG 2020

Y. R. Mahajan, R. Johnson (eds.), *Handbook of Advanced Ceramics and Composites*,
https://doi.org/10.1007/978-3-030-16347-1_37

1135

Abstract

The advantages of the reflective optics over the refractive one for optical imaging in the spaceborne telescopes have been demonstrated over the years. The performance of such optical systems is continually increasing through the use of lightweight and larger mirrors. The use of several materials including ultra-low expansion (ULE) glass, Zerodur glass-ceramics, monolithic aluminum, optical grade beryllium, etc. as the mirrors for space optics is known for decades. Nowadays, silicon carbide (SiC)-based space mirrors have become the most attractive choice because of their excellent mechanical and thermal figure of merits. The superior mechanical and thermal properties of SiC allow in accommodating the complex designs and higher lightweighting over the conventional materials. In addition, a very high surface figure precision ($< \lambda/20$) and very low surface roughness (~ 0.1 nm) can be achieved in SiC. This chapter discusses the superiority of SiC as mirrors over the existing materials for application in space optics. Subsequently, the detailed processing of SiC-based lightweight mirror blanks involving the production of sintered SiC (S-SiC) substrates followed by cladding with a fully dense SiC coating by chemical vapor deposition (CVD) technique is discussed.

Keywords

Silicon carbide (SiC) · Mirror blanks · Figure of merit · Athermal optics
lightweighting · Sintering · CVD · Surface roughness

Introduction

The requirement of large aperture, lightweight, and high-precision optics is continually increasing in the new-generation telescopes for enhanced surveillance, faster communication, and large astronomical observatory systems [1, 2]. The primary mirror is the heart of a reflective telescope that collects and focuses the light on a secondary mirror. The function of the rest of the components including secondary mirror is to support the primary mirror for signal detection. The major constraints for manufacturing of these mirrors are size, mass, natural frequency, dimensional stability, launching cost, reliability in service, etc. [1]. Therefore, design and analysis of the mirrors play the crucial role in the weight minimization and performance optimization of the payload. It appears that the currently used mirror materials including low expansion glass and beryllium have reached the limit of lightweighting. The requirement of further light mass mirrors can only be achieved by the development of newer materials [3, 4]. To meet the much-anticipated demand for geometrical and operational constraints, a great deal of effort is being made to produce the mirrors based on several advanced engineered materials, viz., SiC and its composites and foam structures, polymer-based hybrid materials, microsphere arrays, etc. [1, 3]. The development of mirrors out of these materials is not only the current interest of scientific research but also the scaling up of the cost-effective manufacturing process.

This chapter discusses the various factors to design the high-performance mirrors from the material's standpoint. Subsequently, the chapter highlights different class of materials that are being currently used in space optics followed by a brief discussion on a few selective futuristic mirror materials. Further, the chapter focuses on the various steps for processing of lightweight SiC mirrors blanks. The effect of important parameters in producing defect-free mirror blanks and issues involved in scaling up the SiC-based mirror technology are also discussed.

Design Considerations

The stringent operational and functional requirements of the space telescopes demand for light mass mirrors, and the extent of lightweighting in a large mirror is crucial for several reasons [3, 5]: (a) to reduce the payload and simplify the design of the support and handling systems, (b) weight of a mirror along with its support structure have a cascading effect on the launching cost, and (c) the reduction of the thermal mass that decreases the time required to attain the temperature equilibrium with the surroundings. However, weight reduction is encountered by the stiffness degradation which in turn affects the mechanical stability and deterioration of the mirror figure of merit and performance. Therefore, a great deal of efforts are being made over a period of time for the development of new materials as well as efficient design for weight reduction of spaceborne mirrors without compromising their stiffness.

Mechanical Properties

The significant structural consideration in the design of the large mirrors is the deflection under self-load that is to be restricted within a specified limit to avoid the changes in focal length of the mirrors. Different combinations of Young's modulus (E) and density (ρ), often called them as figure of merits, are used for comparing the structural efficiency of various candidate materials [5–7]. The comparison of the ratio between E and ρ , specific stiffness, usually indicates that the material with the highest stiffness will be the lightest or exhibit the lowest deflection under self-load. However, other proportionality factors between E and ρ are used for accurate comparison. As, for example, the minimum self-deflection for a system with a specified mass can be obtained through the maximization of $\frac{E}{\rho^3}$. Similarly, $\left(\frac{E}{\rho^2}\right)^{1/2}$ is to be maximized for optimization of the mirror geometry for the mass-critical applications with a specified limit of self-deflection [6]. Another important design consideration is the natural frequency (first order) which is to be higher than a minimum in order to withstand the severe loads encountered during launch and also to meet the operational requirement in the orbit. It may be noted that the natural (or fundamental) frequency is proportional to the square root of specific stiffness (E/ρ). Therefore, the materials with higher E/ρ not only lower the self-deflection but also increase the natural frequency. The other important mechanical properties for

the design considerations are the strength, fracture behavior, and the reliability of the components in service for a long duration.

Thermal Properties

The dimensional instability caused by thermal fluctuations of mirror materials is the paramount design consideration from thermal properties viewpoint [8]. The sources of such fluctuations in the space observatory systems could be due to the periodic eclipsing of the sun by rotation of the earth and/or changes of its orientation with reference to the sun by the ground control command. The changes in bulk temperature across an isotropic and homogeneous material will affect the focal length but not the figure of the mirrors. On the contrary, the temperature gradient across the mirrors (diameter and/or thickness) is more detrimental because that can change both the focal length and figure.

The significant thermal properties that determine the magnitude of fluctuations are coefficient of linear thermal expansion (CTE or α), thermal conductivity (k), and specific heat (C_p) [6, 8]. A low CTE material possesses better dimensional stability and thereby reduces the thermal effects, i.e., changes in the focal length and figure of the mirrors, whereas higher thermal conductivity reduces the temperature gradient in the mirrors. The requirement of low CTE and high thermal conductivity is often cast into a single-parameter k/α that is to be maximized in the selection of mirror material. The ratio of k/α is known as the steady-state thermal figure of merit which indicates the overall thermal displacement of a body under a specified steady-state thermal input. The specific heat (C_p) is a measure of heat to change per unit temperature of a body with unit mass. Therefore, the materials with high heat capacity resist the changes in temperature that can induce a distortion.

Thermal diffusivity is another important parameter derived from thermal conductivity (k), specific heat (C_p), and density (ρ). The thermal diffusivity (D) is expressed as $\frac{k}{\rho C_p}$ and indicates how fast a material with nonuniform temperature distribution can achieve the thermal equilibrium. The ratio D/α is another figure of merit which is known as the transient distortion coefficient [6]. This ratio represents the time for dissipation of a thermal distortion under a unit temperature gradient.

General Requirements

In addition to the requirement of lightweight, mechanical, and thermal properties, a few of the general requirements of a candidate material for space mirrors are listed below [8]:

- Dimensional stability over a period of time even for decades
- Very low or no internal stress as the stress relaxation during long service would result in the changes in dimensions and thereby degrade the figure
- Stable phase and microstructure with the changes in ambient temperature especially for the mirrors in cryogenic environments

- Adaptable to fine polishing to generate a surface with very low roughness and also for coating with a thin layer of reflecting metals through vacuum deposition techniques
- Sufficient mechanical rigidity and strength for handling and integration with the support structure
- Resistance to atomic oxygen degradation and stability under cryogenic environment
- Cost-effective process technology for manufacturing of larger mirrors

Candidate Materials

As discussed above, a group of properties, e.g., physical, mechanical, thermal, optical, and ease of fabrication, must be taken into account for the selection of a material that suits best for a given application of the mirror. A variety of materials have been used as the mirrors in different fields over the past several decades. Nowadays, the choices come down to the monolithic aluminum, optical grade beryllium, ultra-low expansion (ULE) glass, Zerodur glass, and silicon carbide (SiC) based on the combination of properties and cost-effective processing. The comparison of properties of these candidate materials is listed in Table 1 [5–9].

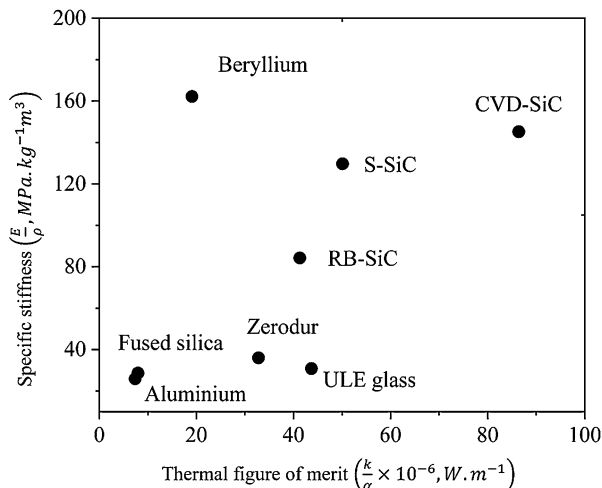
Excluding SiC, the materials shown in Table 1 can be grouped into two categories: metals and glass or glass-ceramics. The metals exhibit higher thermal conductivity compared to the glasses and glass-ceramics [5]. The second category of materials has much lower coefficient of thermal expansion (CTE) and higher Young's modulus (E). In comparison, SiC scores over the other candidate materials

Table 1 Properties of commonly used mirror materials [5–9]

Property	Unit	Desired	ULE glass	Zerodur	Aluminum	Beryllium	SiC ^a
Density (ρ)	$\text{g}\cdot\text{cm}^{-3}$	Small	2.21	2.53	2.70	1.85	3.21
Young's modulus (E)	GPa	Large	68	91	70	300	466
Poisson's ratio (ν)	–	Small	0.18	0.24	0.33	0.08	0.21
Strength (σ_{\max})	MPa	Large	50	57	310	240	440
CTE $\times 10^{-6}$ at 273 K (α_{273})	K^{-1}	Small	0.03	0.05	23	11	2.2
CTE $\times 10^{-6}$ at 40 K (α_{40})	K^{-1}	Small	–0.90	0.70	2.5	0.05	0.05
Thermal conductivity (k)	$\text{W}\cdot\text{m}^{-1}\cdot\text{K}^{-1}$	Large	1.31	1.64	170	210	190
Specific heat (C_p)	$\text{J}\cdot\text{kg}^{-1}\cdot\text{K}^{-1}$	Large	760	820	890	1900	730
Thermal diffusivity ($D \times 10^{-6}$)	$\text{m}^2\cdot\text{s}^{-1}$	Large	0.78	0.77	69	57.2	80.0
Specific stiffness ($\frac{E}{\rho}$)	$\frac{\text{MPa}}{\text{Kg}^{-1}\cdot\text{m}^3}$	Large	30.8	36.0	25.9	162.2	145.2
Thermal figure of merit ($\frac{k}{\alpha} \times 10^{-6}$)	$\text{W}\cdot\text{m}^{-1}$	Large	43.7	32.8	7.39	19.1	86.4

^aProperties of SiC grown by chemical vapor deposition (CVD) technique is shown for comparison

Fig. 1 The specific stiffness (E/ρ) versus thermal figure of merit (k/α) map of candidate mirror materials [8]



because of its high specific stiffness (E/ρ), superior thermal stability (low CTE and high thermal conductivity), excellent polishability (low surface roughness and figure), and chemical inertness. As observed from Table 1, aluminum as mirror material exhibits the lowest structural as well as the thermal figure of merit. The specific stiffness of SiC is comparable to beryllium, and it is about five and four times higher to that of ultra-low expansion (ULE) glass and Zerodur glass-ceramics, respectively. The thermal figure of merit of SiC is found to be much higher than any other candidate materials that makes it attractive to use as mirrors especially in athermal optics. The structural figure of merit (E/ρ or specific stiffness) and thermal figure of merit (k/α) maps of commonly used mirror materials are also shown in Fig. 1 [8]. The salient features of different class of mirror materials including their advantages, limitations, and technological aspects for processing are briefly discussed below.

Metallic Mirrors

The metallic mirrors such as aluminum, nickel, molybdenum, etc. are common as they can be formed, machined, polished, and handled easily in addition to the ease of availability and relatively inexpensive [3]. Also, most of the metals exhibit high reflectivity; therefore, they do not require any reflective coatings. However, the performance of metallic mirrors is limited by the high CTE and creep properties [10]. Among other metallic mirrors materials, the low CTE of beryllium at cryogenic temperature (almost 0 below -203 °C) makes it an attractive mirror material [11]. Beryllium mirrors are known for infrared imaging at cryogenic temperatures also because of its other superior properties including low density, high stiffness, and thermal conductivity. The widespread use of beryllium is limited by its high cost,

toxicity, low material removal rate, and anisotropic behavior because of its hexagonal crystal structure [3].

Monolithic Glass and Glass-Ceramic Mirrors

The extensive use of silica (SiO_2)-based glasses for the mirror blank applications are known for hundreds of years. Glasses exhibit relatively low softening point, and they can be formed easily into large and complex shapes. Subsequently, they are machined, ground, polished, and coated with metals of high reflective characteristics. Glass-based mirrors are good optical materials [3, 11, 12] because of the absence of grain structure (amorphous) and low hardness that allows precise figuring ($\sim \lambda/20$, where λ is the optical wavelength for measuring surface figure, e.g., 560 nm) and extremely smooth surfaces (root mean square or RMS surface roughness as low as 3 Å). The amorphous structure of glass has the advantage to vary the glass compositions over a wide range for the control of CTE. Corning glass [3] produces ultra-low expansion (ULE) glass employing fused silica and 7-wt.% titania (TiO_2), and the resultant material has the CTE of the order of magnitude less than the commonly used soda-lime-silica glass (Table 1). Also, the CTE of glass-based mirrors is tailored through homogeneous precipitation of negative CTE phases in the glass matrix. For example, Schott-manufactured Zerodur glass is a glass-ceramic system that contains Li_2O , Al_2O_3 , and SiO_2 (LAS) along with a small amount of TiO_2 [6].

One of the disadvantages of glass mirrors is the poor mechanical properties including low stiffness that restricts the extent of lightweighting beyond a certain limit in order to maintain the mechanical stability, i.e., self-weight deflection. Also, the glass-based mirrors are not suitable for athermal optics because of the low thermal conductivity [3].

Silicon Carbide Mirrors

Silicon carbide (SiC) has been recognized as an attractive material for a long time for application in optics because of its several outstanding properties such as its reasonably low density, superior mechanical, excellent thermal properties, and high resistance toward oxidation, corrosion, and environmental degradation [1, 13–17]. Although the high hardness of SiC leads to the longer polishing time, the surfaces can be polished down to the very low RMS surface roughness, and the polished surfaces are extremely durable and resistant to cracks. Additionally, SiC is a wide bandgap (2.20–2.86 eV) material; therefore, SiC mirrors can be used in a wider range of the spectrum [16].

There are various types of SiC-based materials, and the properties of each type vary considerably depending on its processing history [3, 16]. A few of the commonly used SiC materials are sintered, hot pressed, siliconized or reaction bonded, single crystal, chemical vapor deposited (CVD), etc. As far as the SiC-based mirror blanks are concerned, they should not be mistaken as single material. An assembly

of SiC mirror blank consists of lightweight SiC substrates (α -SiC) coated with the dense SiC coating (β -SiC) by CVD process. The substrates can be produced from SiC powders by (a) reaction bonding (RB) technique through infiltration of Si melt or vapor into a SiC/C preform or (b) hot pressing/pressureless sintering in the presence of additives. Although the SiC substrates meet all the structural and thermal requirements, the parts made through powder consolidation techniques limits their polishability to a very smooth surface due to the presence of residual porosity and non-homogenous microstructure [1]. Therefore, SiC substrates are coated with a theoretically dense CVD-SiC coating that can be polished to generate extremely smooth optical surfaces (RMS surface roughness of about 0.1 nm). The various aspects for manufacturing of sintered SiC substrates followed by CVD-SiC coating are discussed in the following sections.

Foam-Based Mirrors

In the advancement of lightweighting, the futuristic materials for mirror applications are considered to be the foams, fibrous composites, and hybrid materials [2, 9]. The foams with tailored porosity and pore interconnectivity can provide structural support to the dense facesheet preventing deformation under self-load and also allow a substantial decrease of the mirror weight. The foams produced from a variety of materials including aluminum, silicon, carbon, and SiC have been reported [3].

The advantages of excellent intrinsic properties of SiC can be combined with the foams to manufacture a very lightweight and stiff mirror for space optics. The structural design of such substrates is based on a foamed SiC core sandwiched between two SiC facesheets [18]. The processing of foamed core involves the use of polyurethane foam as the template which is impregnated with an aqueous slurry of SiC and C. Subsequently, the foams are dried and converted to RB-SiC foams through liquid Si infiltration at about 1700 °C. Then the RB-SiC facesheets are deposited on either side of the foamed core. Such a sandwich structure is analogous to the human bone structure that optimizes between the lightweighting and stiffness. The effectiveness of the foamed core sandwich structure is governed by the optimum thickness of the skin and the foamed core [19]. Finally, a fully dense CVD-SiC layer is applied on the skin for generation of a polishable optical surface.

Carbon Fiber-Reinforced Polymers (CFRPs)

Recently, a new class of carbon fiber-reinforced polymers (CFRPs) are gaining momentum in the field of space science to meet the structural and thermal requirements [2, 20, 21]. CFRP-based materials produced by optical surface transformation (OST) process have the excellent mechanical and thermal properties, e.g., high stiffness, high modulus, high thermal conductivity, and ultra-low CTE, along with the ability to tailor the CTE values to near zero over a broad temperature range. Therefore, CFRPs are being considered to be an attractive mirror material for low-cost, high-performance telescopes.

Although CFRPs are not traditionally considered for optical applications, several of the carbon fiber properties including high elastic modulus (200 to 600 GPa) and high strength (2.7 GPa to 6.3 GPa) are quite interesting to the mirror community as the fibers can be coupled with the polymer matrix to achieve the high mechanical and thermal figure of merits. The high specific stiffness, low CTE, and isotropic characteristics can be met in the processed CFRPs by the specially laid fibers in the resin matrix. The RMS surface roughness of 0.8 nm has been reported in the replicated CFRP-based mirrors [22]. Also, the mirrors built from these materials through a highly cost-effective technique have been used in the seeking of faintest objects in the universe or to discern the earth-like planets hidden in the larger collecting areas in the space.

One of the known disadvantages of CFRP-based mirrors is the microscale deformation on substrate surface, known as the resin print-through. Therefore, the ability to fabricate CFRP mirrors in the past has been limited by the surface roughness of the replicated mirrors. The thermal expansion mismatch between the reinforced fibers and polymer matrix is believed to be the dominant cause for print-through defects in CFRP mirrors. However, the fiber print-through defects can be mitigated by the use of a thicker resin layer [20]. Another disadvantage is the moisture absorption by the resin with prolonged use that could be minimized by applying a layer of an aluminum coating.

Flow Sheet Diagram for Processing of SiC Mirror Blanks

A typical flow diagram for processing of SiC mirrors blanks is shown in Fig. 2 [23]. As shown in Fig. 2, the manufacturing of SiC mirror blanks involves the processing of lightweight and sintered SiC support structure, i.e., S-SiC substrates, followed by the deposition of dense SiC coating by chemical vapor deposition (CVD) technique. SiC powder (by Acheson method) mixed with phenolic resin as the binder and B₄C as the sintering additives are used for manufacturing of S-SiC substrates. Green substrates are fabricated by uniaxial dry pressing of raw SiC powder in a steel die or combination of uniaxial and cold isostatic pressing in order to minimize the density variation across the large substrates. Following the green forming, the substrates are heat treated for de-binding between 400 °C and 500 °C to increase the strength for the increase of strength. The substrates are then subjected to lightweighting and profile generation in a five-axis computer numeric control (CNC) machine. The machined parts are sintered above 2100 °C for 1–2 h in a vacuum-sintering furnace with a continuous flow of argon.

Prior to CVD-SiC coating of S-SiC substrates are subjected to precise dimensional control including front face profile, rear surface flatness, diameter, thickness, circularity, etc. by surface grinding technique using diamond-coated tools. Then the front face of the substrates is coated with a dense SiC coating by CVD technique through decomposition of methyltrichlorosilane [(CH₃)₃SiCl₃ or MTS] in the presence of excess hydrogen above 1300 °C. The deposition of theoretically dense SiC coating by CVD technique is achieved through optimization of various parameters including temperature, reactants ratio, partial pressure, and flow rates and

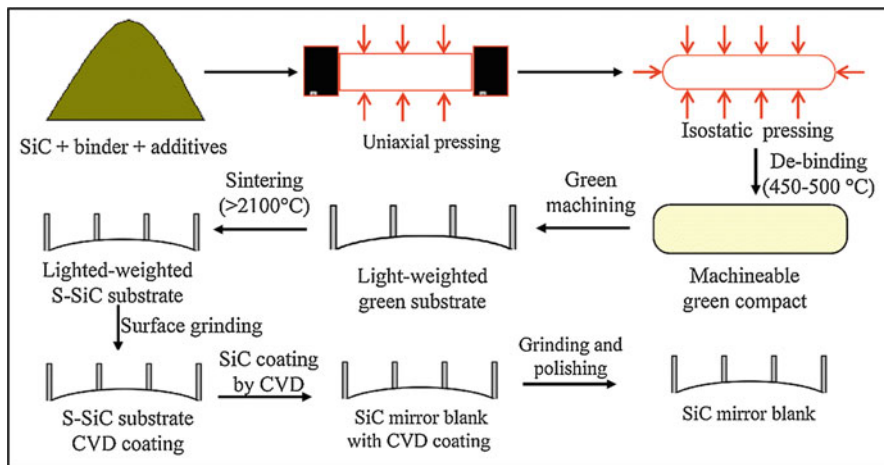


Fig. 2 Flow sheet diagram for processing of SiC-based mirror blanks [23]

also the substrate orientation with reference to the gas flow direction. Subsequent to the CVD-SiC coating, the blanks are subjected to profile generation and polishing for the generation of an optical surface having the RMS surface roughness of about 0.1 nm. The steps involved for the generation of optical surface are the grinding of CVD-coated surface for the removal of nonuniform coating followed by profile generation and diamond grit polishing. The generation of final surface might involve ion beam polishing depending on the final surface roughness to be achieved on the mirror blanks.

Processing of Lightweight SiC Substrates

Raw Materials and Green Forming

The raw SiC powder, containing sintering additives used for green forming of the substrates should have characteristics of easy formability. Typically, the raw powder consists of spherical-shaped granules formed through spray-drying of an aqueous slurry of submicron-size SiC powder mixed with binder and additives. The comparison between the spray-dried granules and the primary particles in a raw SiC powder with reference to the size and morphology is shown in Fig. 3. The size of spherical-shaped granules as shown in Fig. 3a is found to be in the range of 10–80 μm that consists of about 0.7 μm size (average) angular shape primary particles (Fig. 3b). The larger-size spray-dried spherical granules exhibit improved flowability over the irregular-shape submicron-size primary particles and therefore capable of filling the die cavities with intricate geometries. Therefore, an additive-mixed granulated form of SiC powder is preferred to that of the primary particles for the production of green bodies with uniform density distribution.

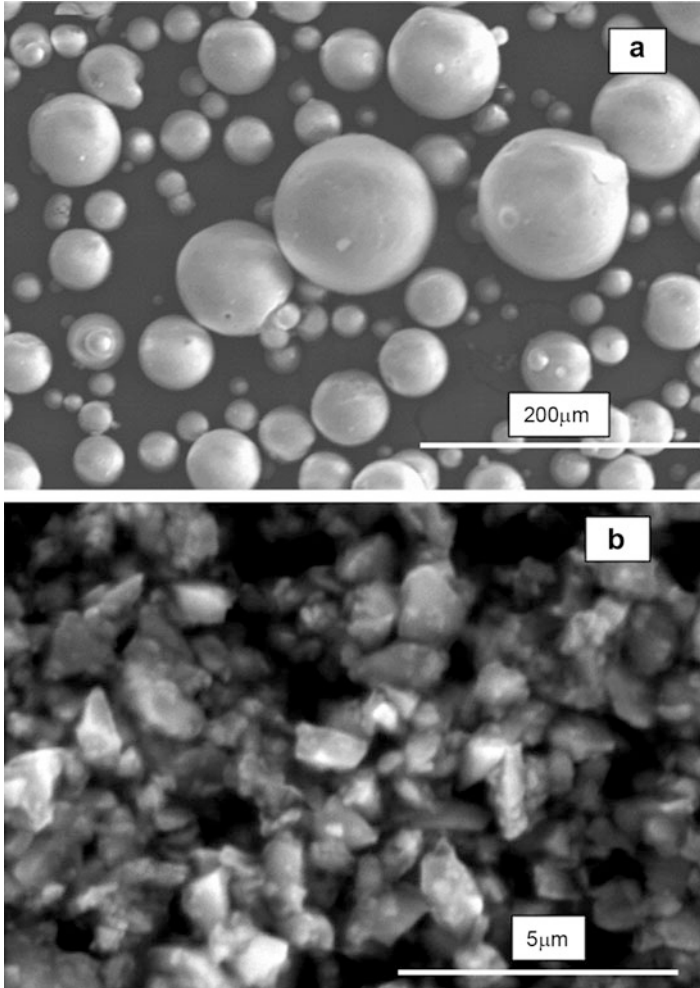
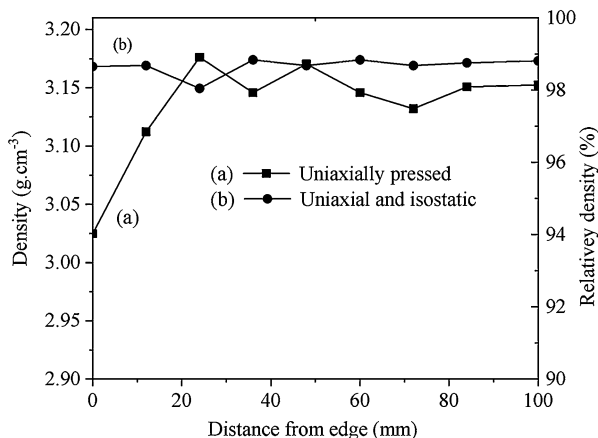


Fig. 3 The shape and morphology of (a) spray-dried granules and (b) primary particles of SiC powder [27]

The formulation of spray-dried powder contains phenolic resin as the binder that serves the dual purpose for the processing of S-SiC substrates. The phenolic resin-based binder adds strength to the bodies which helps in green machining of SiC substrates for lightweighting and profile generation. In addition, the decomposition of the resin in an inert atmosphere yields carbon residue which acts as one of the additives for the sintering of SiC. The other additive present in the raw powder could be B or B₄C.

The first step of substrate fabrication involves the dry pressing of raw SiC powder into the green compacts of simple shapes, e.g., circular discs, using a steel die through uniaxial pressing. The green bodies with large aspect ratio formed through

Fig. 4 The variation of bulk density (BD) across the diameter of a 200 mm (diameter) \times 20 mm (thick) S-SiC substrates fabricated by (a) uniaxial pressing and (b) combination of uniaxial and isostatic pressing



uniaxial pressing exhibit density variation from edges to center due to the pressure difference created by the die wall friction. In order to minimize the density variation in the large substrates, pre-shaped green components (by uniaxial pressing) are subjected to cold isostatic pressing at higher pressure. Alternately, the green substrates with uniform density could be produced directly through isostatic pressing of the powder in a flexible rubber mold. However, warpages are unavoidable in the green bodies formed through direct isostatic pressing that calls for additional machining of the substrates. Such type of additional machining could be eliminated through isostatic pressing of pre-shaped substrates.

The improvement of density variation in a 200 mm (diameter) \times 20 mm (thickness) sintered SiC substrate produced through uniaxial pressing followed by isostatic pressing compared to a substrate produced directly by uniaxial pressing is shown in Fig. 4. It can be observed from the figure that the density variation across the substrates formed through the combination of uniaxial and isostatic pressing is limited within 0.6% theoretical density of SiC to that of 4.6% in the uniaxially pressed substrate. The presence of density variation across the body could be one of the primary sources of defects, e.g., dimensional instability, porosity, and non-homogenous microstructure, resulting in failure under thermomechanical loads especially for the brittle materials like SiC. Therefore, the improvement of density variation through two-stage pressing enhances the reliability of SiC mirrors in service.

Low-Temperature Heat Treatment

Following the compaction of SiC powder into simple shapes, green substrates are heat treated at low temperature (400–500 °C) for the removal of organic binders through temperature-assisted decomposition. The heat treatment of green SiC bodies requires an inert atmosphere in order to prevent its oxidation. Also, the decomposition of phenolic resin in the inert atmosphere results in carbon residue that acts as an

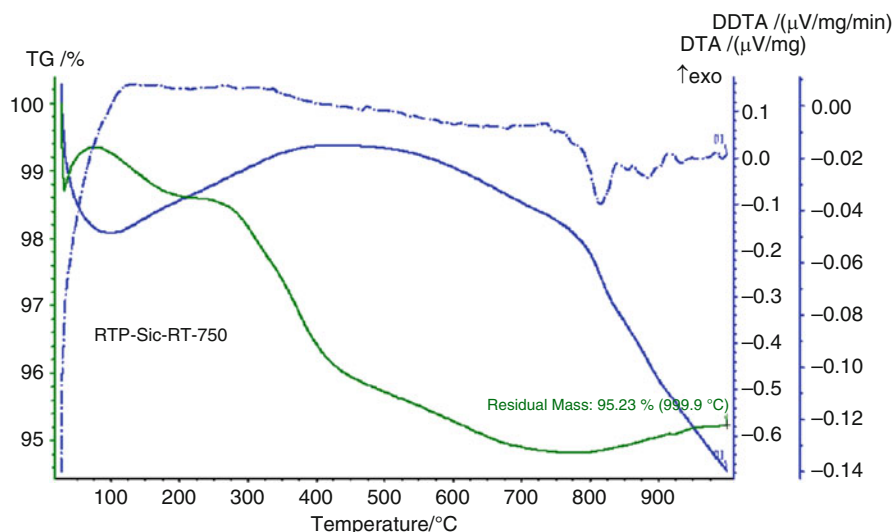


Fig. 5 TG-DSC profile of binder-containing spray-dried SiC powder in argon atmosphere

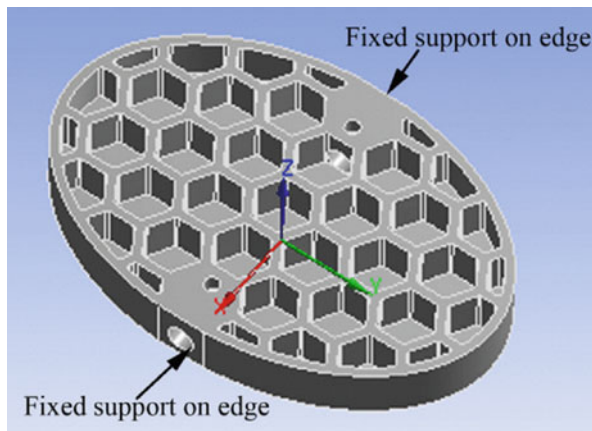
additive for sintering SiC at the higher temperature. Thermogravimetric-differential scanning calorimetry (TG-DSC) analysis of phenolic resin-containing SiC powder (Fig. 5) shows the decomposition behavior of resin with the increase of temperature. It could be observed from the TG profile that the decomposition begins at about 250 °C. Although the major weight loss is observed in the range of 300–500 °C, gradual weight loss continues up to 750 °C. Therefore, the thermal decomposition of resin is incomplete in the temperature range of 400–500 °C. However, the partially decomposed resin network significantly improves the strength of the green bodies and helps in machining of the substrates.

The decomposition of organic binders is associated with the evolution of gaseous products and, therefore, requires control on the gas evolution reactions to prevent cracks in the bodies during de-binding. Faster heating has twofold deleterious effects especially for the substrates with the larger thickness that are (a) rapid generation and entrapment of gaseous products and (b) nonuniform temperature distribution across the body due to the low thermal conductivity of green parts. As a result of that, green substrates are prone to crack formation during de-binding at rapid heating rates. Therefore, slower heating and allowing thermal equilibrium at intermittent temperature can prevent crack formation in the larger substrates. The preferred rate of heating could be as low as <0.5 °C/min for de-binding of 1000 mm (diameter) \times 100 mm (thickness) green SiC substrates.

Green Machining

Subsequent to the low-temperature heat treatment, the manufacturing of the lightweight SiC mirrors demands extensive machining of the substrates (solid blocks)

Fig. 6 Lightweighting pattern and support structure in a 3D model 150-mm-diameter SiC mirror prototype [5]



fabricated through dry pressing. Lightweighting is achieved through material removal from the rear side of the substrates. The design of an efficient lightweighting pattern is nothing but the optimization between the bending stiffness and the extent of material removal [5, 24, 25]. Computer-aided simulation such as finite element method (FEM) packages [24] are commonly used for the designing of the lightweighting patterns. Also, machining is carried out for fabrication of various support structures and generation of the curved profile (convex or concave with a specified radius of curvature) on the front face of the substrates. A typical lightweighting pattern in a 150-mm-diameter prototype including supports on its edge is shown in Fig. 6 [5]. However, SiC is known as one of the hardest materials next to diamond, the cubic form of BN and B₄C. Therefore, major machining of sintered SiC parts is not commercially viable from the point of long duration and huge investment required for the equipment with diamond tooling.

In view of the difficulty in machining of sintered SiC, major material removal operations, e.g., rear side lightweighting, fabrication of support structure, and front face profile generation, are carried in the green stage of the substrates. Subsequent to the powder pressing and binder removal, the solid blocks are subjected to machining in a computer-programmable five-axis CNC machine to a predesigned lightweighting pattern. The increase of green strength of the substrates through heat treatment in the temperature range of 400–500 °C is beneficial for green machining and handling. The extent of lightweighting in the SiC-based mirrors could be as high as about 80%.

Sintering

SiC is difficult to sinter in the absence of sintering additives and external pressure [26]. The lack of inherent sinterability of SiC is attributed to the presence of covalent chemical bonds in it. The kinetic and thermodynamic phenomena associated with the poor sinterability are also explained based on its strong and

directional covalent bonding. The activation energy (AE) for Si and C diffusion in pure SiC is very high due to the high energy involved in the formation and movement of structural defects.

In the manufacturing of S-SiC substrates, the densification under pressureless sintering conditions is achieved by the use of B and C additives that contained in the raw powder in the form of B₄C and phenolic resin, respectively. The sintering temperature of SiC is as high as 2100 °C or higher with a continuous flow of argon. The substrates undergo about 20% linear shrinkage during sintering, and the shrinkage is isotropic. However, the substrates display a measurable change in dimensions only above 1600 °C [27]. Therefore, slower heating rate (~1 °C/min) is adopted above 1600 °C to prevent cracks and warpages during the sintering of lightweight substrates.

The sintering of SiC using B and C additives was discovered by Prochazka [28] of General Electric in 1975. The author demonstrated the sintering of SiC in the absence of a substantial amount of liquid-phase. Hence, the sintering of SiC in the presence of B and C additives is commonly known as the solid-state sintering. The role of B and C in influencing mass transport mechanism for the densification of SiC is not yet fully understood, although SiC densification occurs due to the reduction of grain boundary energy [28], the transient liquid-phase sintering [29], and the activation of grain boundary diffusion [30] as reported in the literature. Recent studies [27] on the measurement of Activation Energy (AE) through constant heating rate (CHR) experiments suggest lattice diffusion is the predominant mechanism for solid-state sintering of SiC. The properties of S-SiC sintered at 2150 °C are discussed in the following subsections.

Aspheric Profile on S-SiC Substrates

The fabrication of SiC mirrors should include two important aspects from the viewpoint of the functional requirements of the mirrors. First one is the generation of an aspheric profile on the mirror surface for the elimination of spherical aberrations in reflected rays. The other is the maintenance of uniform thickness of CVD-SiC coating as the differential expansion between the substrate and coating would limit the application of SiC mirrors in athermal optics. The reflecting surface of SC mirrors is produced through aspheric surface grinding of CVD-SiC coating followed by polishing. Therefore, uniform CVD-SiC coating thickness in the mirror could be maintained through the generation of an identical profile on the S-SiC substrates to that of the final mirror. The aspheric profile on S-SiC substrates is generated by lapping using a reference tool with a negative profile of the targeted mirror blank.

Also, the fabrication of mirrors demands precise control of the overall dimensions of mirrors including rear surface flatness, diameter, thickness, circularity, and the dimensions of the support structure. As, for example, in a mirror of 500 mm (diameter) × 50 mm (thickness), the final dimensions are to be controlled within the limit of few tens of micrometers. Therefore, machining of sintered substrates is

unavoidable in order to eliminate the warpages and nonuniform shrinkage during sintering of large-size components in spite of the high hardness and slow material removal rates in SiC. The S-SiC substrates are machined to the final dimension through surface grinding techniques using diamond tools.

Properties of S-SiC Substrates

In the manufacturing of S-SiC substrates, the coupons processed along with the substrates could be used for batch qualification through measurement of various target properties, whereas each substrates is tested nondestructively (die penetration, radiography, etc.) to ensure that the substrates are free from any surface cracks or internal defects. Typical properties of S-SiC coupons are shown in Table 2.

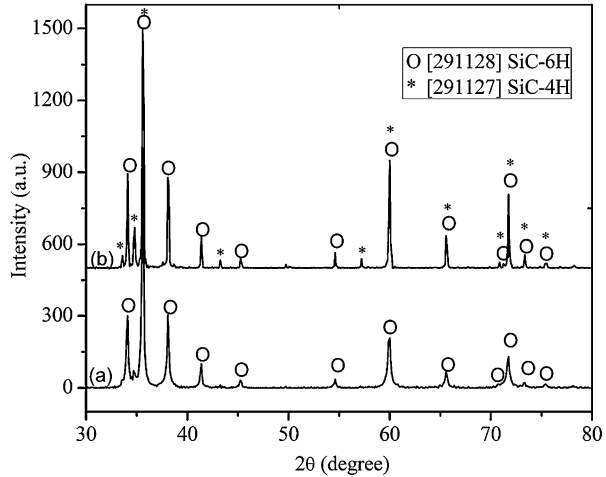
The bulk density (BD) of 2150 °C sintered S-SiC observed to be 3.16 g/cm³ (98.4% relative density, RD) as compared to 1.75 g.cm⁻³ (54.5% RD) in the green specimens. X-ray diffraction (XRD) studies show that the sintered body consists of polycrystalline hexagonal (α) phase of SiC. Also, it is observed that the α -phase in S-SiC-sintered specimen consists of 6H and 4H polytypes compared to the starting powder consisting of only 6H polytype as shown in Fig. 7. This could be attributed to the existence of a large number of polytypic modifications of SiC based on the hexagonal unit cell with the same basal plane but only differing in the stacking of unit layers along the c-axis. SEM micrographs of polished surfaces and etched microstructure of S-SiC are shown in Fig. 8. The presence of residual porosity on the polished surface (Fig. 8a) indicates that the S-SiC produced through pressureless

Table 2 Properties of S-SiC sintered at 2150 °C

Property	Measurement technique	Value
Green density (g.cm ⁻³)	Weight and dimension	1.75 + 0.015
Bulk density (BD, g.cm ⁻³) ^a	Archimedes principle	3.16 + 0.005
Phase	X-ray diffraction (XRD)	α (hexagonal) SiC (6H and 4H polytypes)
Vickers hardness (HV, kg.mm ⁻²)	500 g load	2530 + 80
Flexural strength (MPa)	Four-point flexural test on 4 × 3 × 50 mm ³ specimens	219 + 22
Fracture toughness (MPa.√m)	Single-edge notch beam (SENB)	3.43 + 0.2
Young's modulus (GPa)	Impulse excitation technique (IET)	422 + 20
Weibull modulus	Four-point flexural strength on minimum of 40 specimen	11.2
Thermal conductivity (W.m ⁻¹ .K ⁻¹)	Laser flash	142.7 + 6.5
Coefficient of thermal expansion (CTE × 10 ⁻⁶)	Dilatometer	2.52 (from -125 to RT) 4.49 (from RT to 1000 °C)

^aBD measurements were carried out on sintered S-SiC

Fig. 7 X-ray diffraction (XRD) pattern of (a) raw SiC powder and (b) S-SiC sintered at 2150 °C [31]



sintering could not be sintered to full density. Hence, the S-SiC substrates are required to be coated with fully dense SiC coating on the reflective surface by CVD technique for mirror application. The thermally etched SEM micrograph of S-SiC (Fig. 8b) reveals that the microstructure consists of interconnected duplex grains (equiaxed and elongated).

Vickers hardness (HV) of S-SiC is observed to be more than 2500 kg mm⁻² at 500 g load. S-SiC shows the decreases of HV with an increase in indentation load, i.e., indentation size effect (ISE) in the range of 50–500 g load [31]. Young's modulus of S-SiC by impulse excitation technique (IET) method is found to be more than 420 GPa, whereas the fracture toughness (K_{IC}) of S-SiC is found to be 3.43 MPa√m. Although S-SiC exhibits moderate toughness compared to other ceramics [32], it is also brittle and fails catastrophically. SEM micrograph on the fracture surface of S-SiC (Fig. 9) shows the transgranular fracture without any sign of plastic deformation [31].

The thermal conductivity of SiC at room temperature (RT) measured by laser flash technique is observed to be 142 W.m⁻¹.k⁻¹ compared to 60 W.m⁻¹.k⁻¹ at 600 °C (Fig. 10). The heat conduction by phonons contributes to the relatively high value of thermal conductivity in covalently bonded SiC. The decrease of thermal conductivity of S-SiC with the increase of temperature depicted in Fig. 10 is attributed to the inverse relationship between phonon mean free path and absolute temperature [33]. The coefficient of thermal expansion (CTE) observed to be 2.52 and 4.49×10^{-6} K⁻¹ in the temperature range of -125 °C to RT and RT to 1000 °C, respectively.

Weibull Statistics and Reliability of S-SiC

SiC shows strength variability, i.e., failure strength varies from one sample to another because of its inherent defect structure being processed through powder

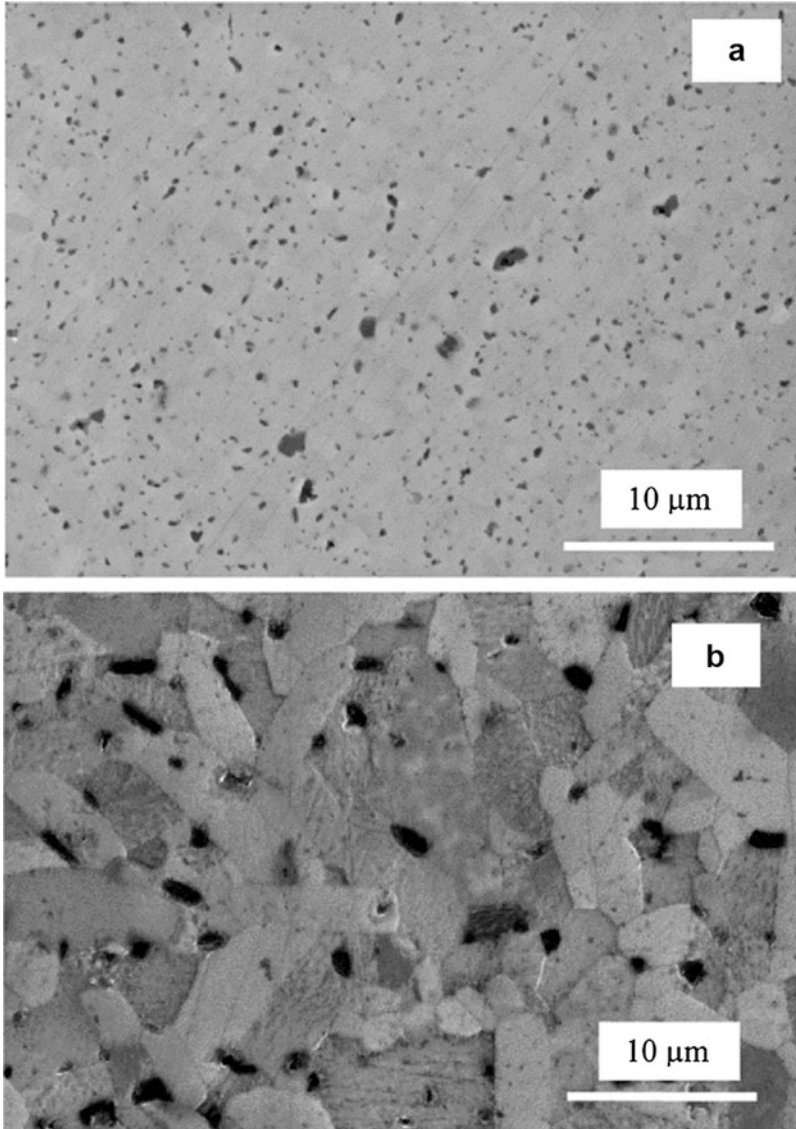


Fig. 8 SEM micrographs on (a) polished and (b) thermally etched surfaces of S-SiC [31]

processing technique. The variation of strength in brittle materials is addressed with the help of statistical approaches including generalized exponential relationship, log-normal, and Weibull and gamma distribution to predict the probability of failure [34]. The reliability of S-SiC substrates is analyzed with the help of two-parameter Weibull statistic from the variation of four-point bending strength of S-SiC specimens. The expression for two-parameter Weibull distribution [35] is as follows:

Fig. 9 SEM micrograph on the fracture surface of S-SiC [31]

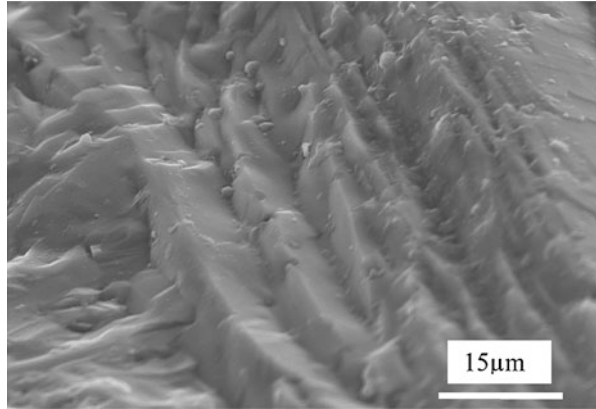
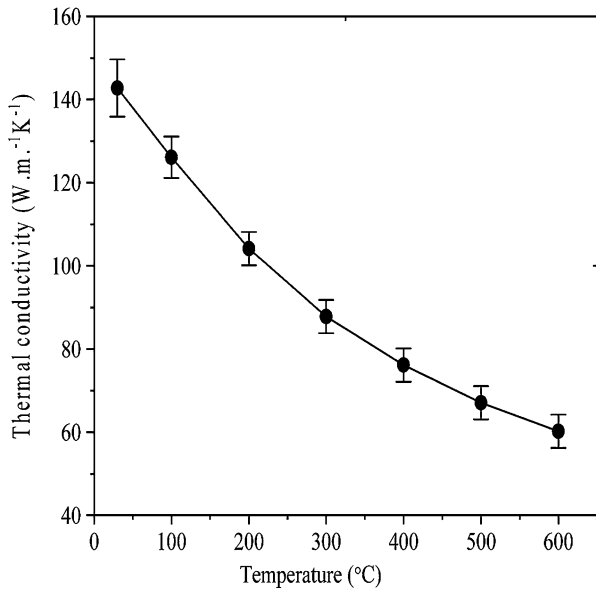


Fig. 10 The changes in thermal conductivity of S-SiC with the increase of temperature



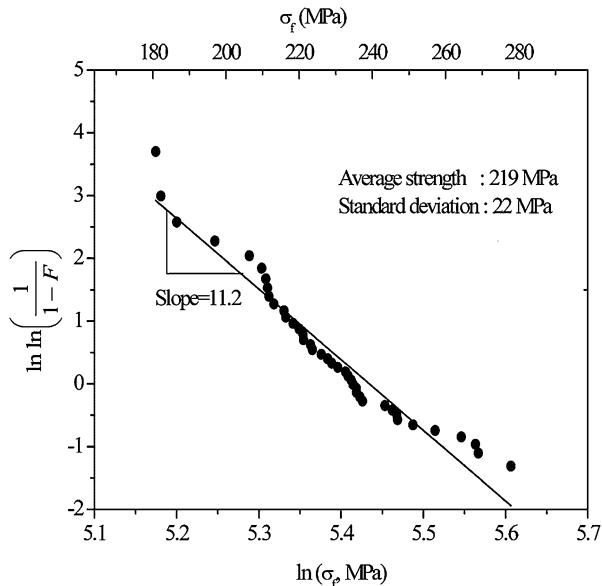
$$\ln\ln\left(\frac{1}{1-F}\right) = m\ln\sigma_f - m\ln\sigma_0^* \tag{1}$$

where F is the probability of failure, σ_f is the fracture strength, σ_0^* is the scaling parameter, and m is the Weibull modulus. The probability of failure F is estimated as per the following equation:

$$F = \frac{j}{N + 1} \tag{2}$$

where j is the j^{th} specimen in a group of N specimens ranked in the order of increasing fracture strength. The plot of a double logarithmic left-hand side of

Fig. 11 Double logarithmic Weibull function versus logarithm of four-point bending strength of S-SiC sintered at 2150 °C [31]



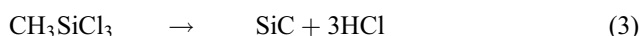
Eq. (1) versus $\ln \sigma_f$, Weibull plot is shown in Fig. 11 and m is determined from the slope of the best fit straight line. A high m value is an indicator of the uniform distribution of critical flaws with the high degree of reliability of parts in service and vice versa. Based on the varied strength between 177 and 272 MPa on a minimum of 40 specimens (average strength and standard deviation 219 MPa and 22 MPa, respectively), the estimated value of Weibull modulus is found to be 11.2. Also, the estimated size of critical flaws (32–110 μm) based on flexural strength and fracture toughness indicates that machining defects are one of the primary reasons for failure in S-SiC ceramics [31, 36].

CVD-SiC Coating

It has been mentioned that the SiC substrates produced either by reaction bonding (through molten metal Si infiltration into a C/SiC preform) or pressureless sintering (in the presence C and B additives) have the limitations in achieving the full density. Also, the non-homogeneity in a substrate due to the presence of sintering aids and porosity restrict to achieve the minimum surface roughness and optical properties requirements upon polishing [16, 37]. Fully dense SiC cladding layer can be grown on the SiC substrates by CVD method through the decomposition of Si- and C-containing precursor chemical(s). The synthesis of CVD-SiC involves the formation of the solid phase SiC directly from vapor at a temperature much lower compared to the sintering of SiC. Also, the formation of CVD-SiC avoids powder forming and sintering processes and the incorporation of sintering aids. Therefore,

CVD-grown polycrystalline SiC could be theoretically dense, thereby exhibiting superior mechanical, thermal, and optical properties and excellent polishability [38–40].

The precursors used for the synthesis of CVD-SiC could be a single material containing both Si and C or two different chemicals as the sources for Si and C [16, 41, 42]. Carbosilanes, e.g., CH_3SiCl_3 , $(\text{CH}_3)_2\text{SiCl}_2$, etc., are of typical single-source chemical that contributes both Si and C. In the other category, different silanes, e.g., SiCl_4 and SiHCl_3 , and hydrocarbons, e.g., CH_4 , C_3H_8 , C_5H_{10} , etc., are used for Si and C, respectively. The widely used starting material for CVD-SiC is methyltrichlorosilane [CH_3SiCl_3 , MTS] because of its ability to produce stoichiometric SiC and easy availability in large quantities and it is relatively inexpensive. Studies on the pyrolysis of MTS in the presence of H_2 for the synthesis of SiC are well reported [41–44]. The chemical reaction for the synthesis of CVD-SiC through decomposition of MTS is as follows.



The reaction is carried out in the presence of H_2 which helps in the stepwise decomposition of MTS, i.e., kinetics of SiC formation [45–47]. The commonly used other source gases and synthesis temperature are reported elsewhere [16, 43].

CVD Parameters

The schematic of CVD-SiC synthesis is shown in Fig. 12. The basic elements of a CVD setup consist of a gas feeding system, a reactor, heaters assembly, and a pumping system for removal of waste gas followed by a scrubber for waste gas treatment. In addition, the system should be equipped with the controllers and measuring devices for monitoring the various process parameters [16, 41] including temperature, pressure, input flow rate, pumping speed, etc. Since MTS is a liquid (boiling point: 66 °C) at ambient temperature, a carrier gas (H_2 or Ar) is passed through the liquid precursor for its transportation into the reactor in the vapor form. The rate of MTS feeding is maintained through the control of MTS bath temperature and carrier gas flow rate. Additional Ar and H_2 gas can be mixed with the MTS flow to control the partial pressure and stoichiometry of the reactants. While H_2 controls the decomposition kinetics of MTS, Ar is used as the diluent gas. The MTS decomposes within a hot wall reactor furnace chamber heated directly by electrical resistance. Hot wall reactors are suitable for CVD-SiC coating of large substrates with complicated shapes. The deposition temperature of MTS varies in the range of 1300–1500 °C. Subsequent to the formation of SiC deposits within the reactor, the exhaust gases are pumped into the scrubber system for neutralization of chlorine compounds, and finally, Ar and H_2 gases are released into the atmosphere.

The pyrolysis of MTS in excess H_2 is widely reported [16, 41, 45] for production of CVD-SiC. The formation of stoichiometric SiC is influenced by the various conditions including deposition temperature, pressure, and H_2/MTS ratio. The

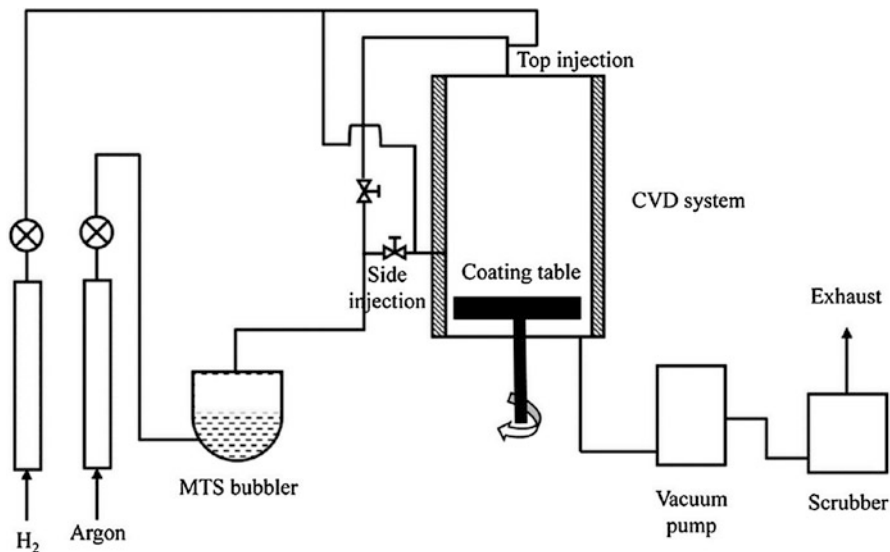


Fig. 12 Schematic diagram of CVD setup for SiC coating along with the gas handling and scrubber assembly [16]

relationship among the solid composition and controlling parameters for the synthesis of CVD-SiC is shown in Fig. 13 [43, 48, 49]. As seen from the figure, there is a range of several process conditions, e.g., temperature, pressure, and H₂/MTS, for obtaining the stoichiometric SiC. The CVD-SiC deposits are rich with the excess of Si at high pressure, low temperature, and high H₂/MTS ratio compared to C-rich deposits which are formed at low chamber pressure, higher temperature, and a low ratio of H₂/MTS. Between these extremes, stoichiometric SiC is produced.

In addition to the stoichiometry, the process variables also influence the phase, morphology, and properties of the SiC deposits. The formation of pure β -SiC (cubic, FCC) is favored in the temperature range of 1300–1500 °C with a low H₂/MTS ratio. The proportion of α -SiC (hexagonal) in the CVD deposit increases with the increase of temperature. The morphology of CVD-grown material such as amorphous, polycrystalline, grain size, texture, etc. is also a function of the process parameters. The effect of various conditions on the structure of CVD-SiC deposit is shown in Fig. 14 [49]. The figure demonstrates that the amorphous smooth deposits are formed relatively at low temperature (< 1200 °C) compared to the large faceted crystal obtained at high temperatures, whereas CVD-SiC grown at intermediate temperatures, low pressure, and high H₂/MTS ratio exhibits columnar morphology. The optical grade CVD-SiC for mirrors should be a fully dense, polycrystalline, and fine-grained structure. Additionally, it should be capable to withstand the manufacturing processes including surface grinding and polishing in order to produce the extremely smooth optical surfaces. Typical process conditions for the formation of CVD-SiC for space-based SiC mirrors are shown in Table 3 [16].

Fig. 13 Effect of process parameters (temperature, pressure, and H_2/MTS ratio) on the solid composition for the synthesis of CVD-SiC [48, 49]

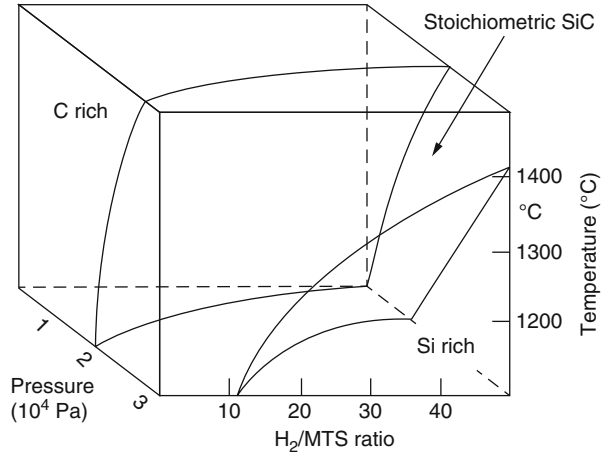
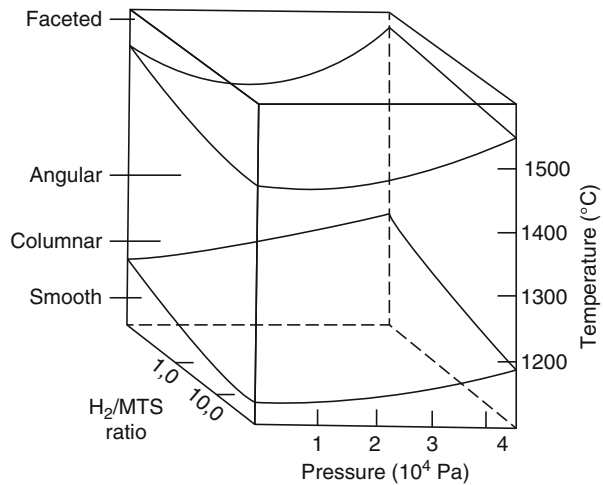


Fig. 14 Morphology of CVD-grown SiC with respect to the various process conditions (temperature, pressure, and H_2/MTS ratio) [48, 49]



Properties of CVD-SiC Coating

The important properties of thus formed CVD-SiC are summarized in Table 4 [16, 38]. As seen from the table, the material is theoretically dense phase pure β (cubic) SiC with an average grain size of between 5 and 10 μm . The mechanical properties of CVD-SiC including hardness, flexural strength, and Young's modulus are found to be higher than S-SiC (Table 2) or reaction-bonded SiC. The reported CTE values of CVD-SiC are as low as $2.6 \times 10^{-6} \text{ K}^{-1}$ and $0.44 \times 10^{-6} \text{ K}^{-1}$ at room temperature (RT) and -160°C , respectively. The relatively low CTE of this material, as well as its compatibility with SiC-based substrates, makes it suitable for spaceborne mirrors. The higher thermal conductivity of CVD-SiC than S-SiC substrates is obvious as the former is free from defects like impurities or voids. The

Table 3 Typical parameters for CVD-SiC coating for mirror applications [16]

Pressure	200 torr
Temperature	1350 °C
Gas partial pressure:	
H ₂	53 torr
Ar	136 torr
MTS	10.6 torr
H ₂ /MTS feed ratio	5.0
Deposition rate	~ 1.5 μm/min

Table 4 Properties of CVD-SiC coating [16, 38]

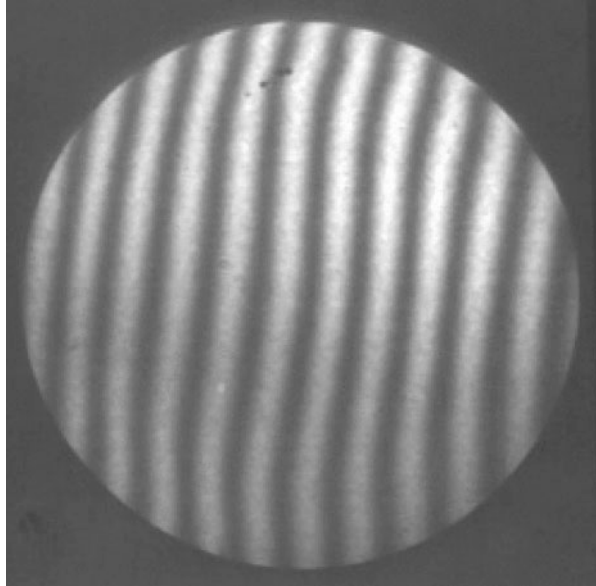
Property	Measurement technique	Value
Crystal structure	X-ray diffraction (XRD)	β (cubic)
Grain size		5–10 μm
Density (g.cm ⁻³)	Archimedes principle	3.21
Chemical purity		99.999%
Vickers hardness (HV, kg.mm ⁻²)	500 g load	2597 + 120
Flexural strength (MPa)	Four-point flexural test	595
Fracture toughness (MPa.√m)	Micro-indentation	3.3
Young's modulus (GPa)	Acoustic	466
Poisson's ratio		0.21
CTE × 10 ⁻⁶ (K ⁻¹)		
at -160 °C		0.44
at 40 °C		2.57
at 300 °C		4.10
Thermal conductivity (W.m ⁻¹ .K ⁻¹)		193
Polishability (nm)		< 0.1

presence of any minute defects like voids, cracks, etc. would lead to the rejection of the mirror blank as the scattering from such defect centers would hamper the mirror reflectivity, thereby degrading the image quality.

The polishability of CVD-SiC has the great scientific and technological significance. CVD-grown SiC exhibits excellent polishability as the material is fully dense, homogenous, free of impurities, and isotropic in nature. The generation of the optical surface on the CVD-SiC coating of the mirror blanks involves removal of the nonuniform coating through surface grinding followed by figuring of the mirror surface. The fringe pattern on a 100-mm-diameter flat CVD-SiC-coated mirror blank during the progress of surface figuring is shown in Fig. 15. The surface figure measured by laser phase-shifting interferometry technique through measurement of the fringe interspacing corresponds to $\lambda/4$ (where λ is 560 nm).

Subsequent to the figuring, the optical surface of the mirror blank is polished using the suspension of diamond particles down to 1 μm. An optical micrograph on a polished surface of CVD-SiC is shown in Fig. 16a. As seen from the figure, the

Fig. 15 Fringe pattern on a 100-mm-diameter polished CVD-SiC-coated mirror blank by laser phase-shift interferometer method



surface is free from any second phase, voids and impurities compared to the polished surfaces of S-SiC (Fig. 16b). The final polishing of CVD-SiC by ion beam technique can achieve the root mean square (RMS) surface roughness of about 0.1 nm [50]. A photograph of 100-mm-diameter CVD-SiC-coated and polished mirror blank is shown in Fig. 17. The reflectivity of polished CVD-SiC is limited within about 20% in the visible-infrared region of the spectrum. Therefore, the final use of the material for mirror application requires coating with a highly reflective material such as gold, silver, or aluminum by physical vapor deposition (PVD) techniques.

Conclusions

SiC is considered to be the next-generation mirror materials for athermal optics application over the currently used glass and beryllium-based mirrors because of its superior mechanical and thermal figure of merits in combination with the superior polishability and high chemical inertness. The SiC-based mirror blanks consist of a lightweight SiC substrate coated with theoretically dense SiC (β -SiC) by CVD process. Although SiC-based substrates meet the structural and thermal requirements of the mirrors, they cannot be polished to the optically smooth surfaces as the substrates are formed through powder metallurgy routes exhibiting non-homogenous microstructure and residual porosity. Hence, the SiC substrates are coated with a fully dense CVD-SiC coating which is polished to the smooth optical surfaces (RMS roughness \sim 0.1 nm).

Although SiC appears to be an ideal material for mirror applications, the time involved in the various stages of processing could be of several months which

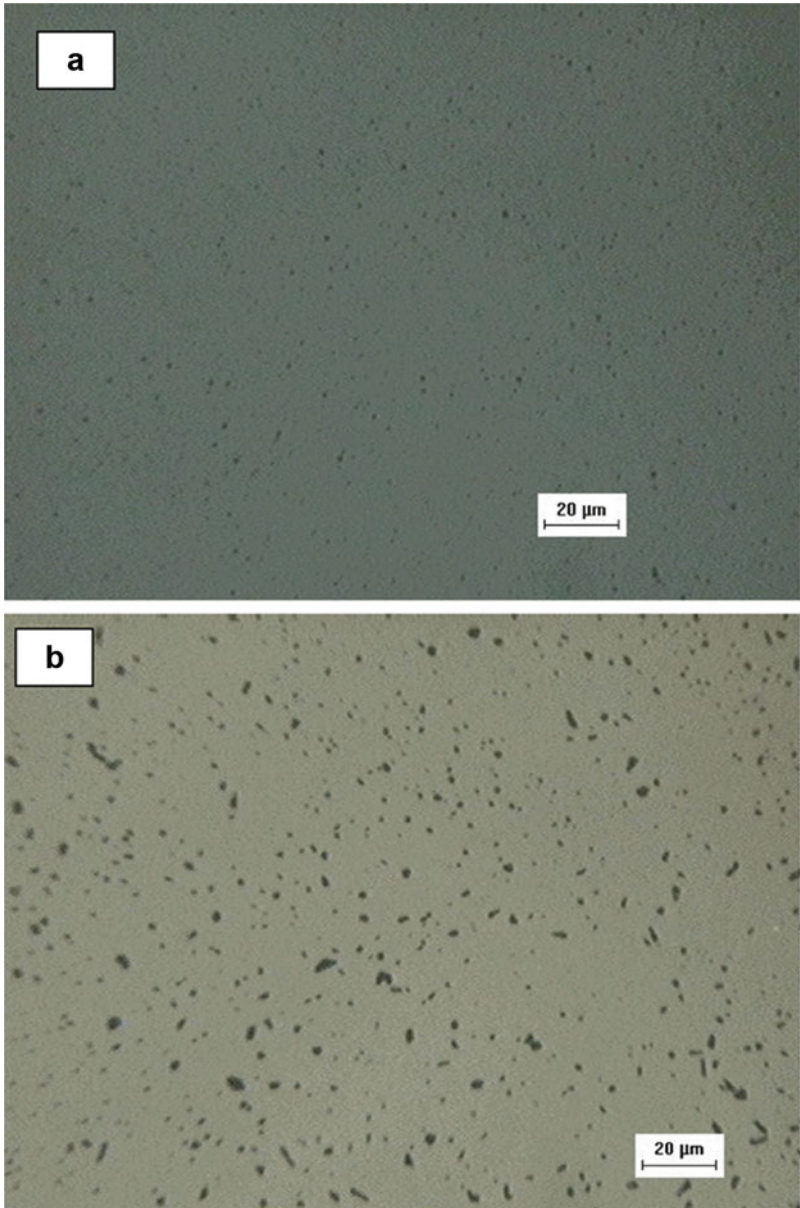
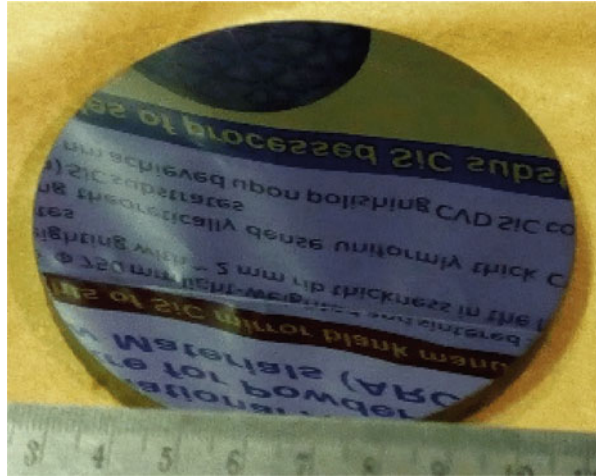


Fig. 16 Polished surface optical micrograph of (a) CVD-SiC and (b) S-SiC

increases the manufacturing cost of the mirrors. Therefore, the use of SiC mirrors has been limited to the niche applications for high-performance optical components for extreme environments rather than the widespread use of SiC as mirrors and other optical components.

Fig. 17 100-mm-diameter CVD-SiC-coated and polished mirror blank



References

1. Matson LE, Chen MY, deBlonk D, Palusinski IA (2008) Silicon carbide technologies for lightweighted aerospace mirrors. Paper presented at the advanced Maui optical and space surveillance technologies conference, Maui, HI 16–19 September 2008
2. Chen PC, Saha TT, Smith AM, Romeo R (1998) Progress in very lightweight optics using graphite fiber composite materials. *Opt Eng* 37:666–676
3. Matson LE, Mollenhauer DH (2004) Advanced materials and processes for large, lightweight, space-based mirrors. *AMPTIAC Q* 8:67–74
4. Enya K, Nakagawa T, Kaneda H, Onaka T, Ozaki T, Kume M (2007) Microscopic surface structure of C/SiC composite mirrors for space cryogenic telescopes. *Appl Opt* 46:2049–2056
5. Gou S, Zhang G, Li L, Wang W, Zhao X (2009) Effect of materials and modelling on the design of the space based lightweight mirrors. *Mater Des* 30:9–14
6. Paquin RA (1999) Materials for optical systems. In: Ahmad A (ed) *Optomechanical engineering handbook*. CRC Press LLC, Boca Raton, pp 1–20
7. Vukobratovich D (1999) Lightweight mirror design. In: Ahmad A (ed) *Optomechanical engineering handbook*. CRC Press LLC, Boca Raton, pp 1–40
8. Bely PY (2003) *The design and construction of large optical telescopes*. Springer, New York
9. Ealey MA, Wellman JA (1996) Ultralightweight silicon carbide mirror design. In: *Advanced materials for optical and precision structures*. Denver, 11 November 1996, *Proc SPIE* vol 2857: 73–77
10. Rozelot JP, Bingham R, Walker DD (1992) Aluminium mirrors versus glass mirrors. In: Ulrich MH (ed) *Progress in telescope and instrumentation technologies*, ESO conference and workshop proceedings, Garching, 27–30 April 1992, pp 71–74
11. Hashiguchi DH, Heberling J, Campbell J, Morales A, Sayer A (2015) New decade of shaped beryllium blanks. In: *Material technologies and applications to optics, structures, components, and sub-systems II*, San Diego, 2 September 2015, *Proc. SPIE* vol 9574: 957403-1
12. Westerhoff T, Werner T (2017) Zerodur expanding capabilities and capacity for future spaceborne and ground-based telescopes. In: *Astronomical Optics: Design, Manufacture, and Test of Space and Ground Systems*, San Diego, 08–11 August, 2017, *Proc SPIE* 10401: 104010R

13. Yamada K, Mohri M (1991) Properties and applications of silicon carbide ceramics. In: Somiya S, Inomata Y (eds) *Silicon carbide ceramics-1: fundamentals and solid reaction*. New York, Elsevier Applied Science, pp 13–44
14. Tanaka H (2011) Silicon carbide powder and sintered materials. *J Ceram Soc Jap* 119:218–233
15. Chen Y, Wang H, Tang J, Liu H, Chen S, Fan Q (2007) Fabrication of lightweight SiC space mirror. *Key Eng Mater* 336–338:1151–1154
16. Goela JS, Pickering MA, Taylor RL (1994) Chemical vapour deposited β -SiC for optics applications. In: *Chemical vapor deposition of refractory metals and ceramics III*, Boston, 28–30 November, 1994, *Mat Res Soc Symp Proc* 363, pp 71–87
17. Zang Y, Zhang J, Han J, He X, Yao W (2004) Large-scale fabrication of lightweight Si/SiC composite for optical mirror. *Mater Lett* 58:1204–1208
18. Novi A, Basile G, Citterio O, Ghigo M, Caso A, Cattaneo G, Svelto GF (2001) Lightweight SiC foamed mirrors for space applications. In: *Optomechanical design and engineering*, San Diego, 5 November 2001, *Proc SPIE* 4444: 59–65
19. Gibson LJ, Ashby MF (1997) *Cellular solids: structure and properties*, 2nd edn. Cambridge University Press, Cambridge
20. Utsunomiya S, Kamiya T, Shimizu R (2013) Development of CFRP mirrors for space telescopes. In: *Material technologies and applications to optics, structures, components, and sub-systems*, San Diego, 30 September 2013, *Proc SPIE* 8837: 88370P
21. Wilcox CC, Santiago F, Jungwirth ME, Martinez T, Restaino SR, Bagwell B, Romeo R (2014) First light with a carbon fiber reinforced polymer 0.4-meter telescope. In: *MEMS Adaptive Optics VIII*, San Francisco, 02 February 2014, *Proc SPIE* 8978: 897805
22. Steeves J, Laslandesa M, Pellegrino S, Reddingb D, Bradfordb CS, Wallaceb JK, Barbeec T (2014) Design, fabrication and testing of active carbon shell mirrors for space telescope applications. In: *Advances in optical and mechanical technologies for telescopes and instrumentation*, Montréal, 28 July 2014, *Proc SPIE* 9151: 915105
23. Safa F, Levallois F, Bougoïn M, Castel D (1997) Silicon carbide technology for submillimetre space based telescopes. In: *48th international astronomical congress*, Turin, 6–10 October 1997, pp 1–10
24. Lee HB, Suk JY, Bae JI (2015) Trade study of all lightweight primary mirror and metering structure for spaceborne telescopes. In: Krodel M, Robichaud JL, Goodman WA (eds) *Material technologies and applications to optics, structures, components, and sub-systems II*, San Diego, 10–13 August, 2015, *Proc SPIE* 9574: 95740D
25. Guo SW, Zhang GY, Wang WY, Zhao XZ (2006) Design and analysis of lightweight pointing mirror used in space camera. *J Phys Conf Ser* 48:620–624
26. Greskovich C, Rosolowski JH (1976) Sintering of covalent solids. *J Am Ceram Soc* 59:336–343
27. Jana DC, Sundararajan G, Chattopadhyay K (2018) Effective activation energy for the solid-state sintering of silicon carbide ceramics. *Metal Mater Trans A (Accepted)* 49:5599
28. Prochazka S (1975) The role of boron and carbon in the sintering of silicon carbide. In: Popper P (ed) *Special ceramics*, 6th edn. British Ceramic Research Association, Stoke-on Trent, pp 171–182
29. Gubernat A, Stobierski L (2003) Sintering of silicon carbide I. Effect of carbon. *Ceram Int* 29:287–292
30. Malinge A, Coupe A, Petitcorps Y, Pailler R (2012) Pressureless sintering of beta-silicon carbide nanoparticles. *J Eur Ceram Soc* 32:4393–4400
31. Jana DC, Barick P, Saha BP (2018) Effect of sintering temperature on density and mechanical properties of solid-state sintered silicon carbide ceramics and evaluation of failure origin. *J Mater Eng Perform* 27:2960–2966
32. Nesmelov DD, Perevislov SN (2015) Reaction sintered materials based on boron carbide and silicon carbide. *Glas Ceram* 71:313–319
33. Kingery WD, Bowen HK, Uhlmann RD (1976) *Introduction to ceramics*, 2nd edn. Wiley, New York

34. Basu B, Tiwari D, Kundu D, Prasad R (2009) Is weibull distribution the most appropriate statistical strength distribution for brittle materials? *Ceram Int* 35:237–246
35. Green D (1998) *An introduction to mechanical properties of ceramics*, 1st edn. Cambridge University press, New York
36. Wereszczak AA, Kirkland TP, Strong KT Jr (2010) Size-scaling of tensile failure stress in a hot-pressed silicon carbide. *Int J Appl Ceram Technol* 7:635–642
37. Pickering MA, Taylor RL, Keeley JT, Graves GA (1990) Chemically vapour deposited silicon carbide (SiC) for optical applications. *Nucl Instrum Methods Phys Res Sect A* 291:95–100
38. Goela JS, Pickering MA, Taylor RL, Murry BW, Lompadro A (1991) Properties of chemical-vapour-deposited silicon carbide for optics applications in severe environments. *Appl Opt* 30:3166–3175
39. Haigis B, Pickering M (1993) CVD scaled up for commercial production of bulk SiC. *Am Ceram Soc Bull* 72:74–78
40. Rehn V, Choyke WJ (1980) SiC mirrors for synchrotron radiation. *Nucl Inst Methods* 177:173–178
41. Goela JS, Taylor RL (1991) Fabrication of lightweight ceramic mirrors by means of a chemical vapour deposition process. US patent 5,071,596, 10 Dec 1991
42. Hirai T, Sasaki M (1991) Silicon carbide prepared by chemical vapour deposition. In: Somiya S, Inomata Y (eds) *Silicon carbide ceramics-1: fundamentals and solid reaction*. New York, Elsevier Applied Science, pp 77–97
43. Schlichting J (1980) Chemical vapor deposition of silicon carbide. *Powder Metall Int* 12:141–147
44. Wang H, Singh RN, Goela JS (1995) Effects of postdeposition treatments of the mechanical properties of a chemical-vapor-deposited silicon carbide. *J Am Ceram Soc* 78:2437–2442
45. Motojima S, Hasegawa M (1990) Chemical vapor deposition of SiC layers from a gas mixture of $\text{CH}_3\text{SiCl}_3 + \text{H}_2$ (+ Ar), and effects of the linear velocity and Ar addition. *J Vac Sci Technol A* 8:3763–3768
46. Huo Y, Chen Y (2008) Effect of deposition temperature on the growth characteristics of CVD SiC coatings. *Key Eng Mater* 368–372:846–848
47. Lu C, Cheng L, Zhao C, Zhang L, Xu Y (2009) Kinetics of chemical vapor deposition of SiC from methyltrichlorosilane and hydrogen. *Appl Surf Sci* 255:7495–7499
48. Schlichting J (1980) Chemical vapor deposition of silicon carbide. *Powder Metall Int* 12:196–200
49. Chin J, Gantzel K, Hudson G (1977) The structure of chemical vapour deposited silicon carbide. *Thin Solid Films* 40:57–72
50. Pickering MA, Goela JS, Burns LE (1994) Highly polishable highly thermally conductive silicon carbide. US Patent 5,374,412, 20 Dec 1994

Part VI

**Intermediate and Very High Temperature
Ceramics**



Silicides and Silicide Matrix Composites for High-Temperature Structural Applications **30**

R. Mitra

Contents

Introduction	1168
Phase Equilibria and Crystal Structures of Selected Silicide-Based Alloy Systems	1169
Molybdenum Silicides	1169
Tungsten Silicides	1170
Titanium Silicides	1170
Niobium Silicides	1173
Processing	1174
Mechanical Behavior	1176
Deformation Behavior of C11 _b Structured Silicides	1177
Deformation Behavior C40 Structured Silicides	1181
Deformation Behavior of Mo-Si-B Based Multiphase Alloys	1183
Deformation Behavior of Titanium Silicides	1184
Niobium Silicide-Based Multiphase Alloys	1186
Flexural Strength and Fracture Behavior	1186
Oxidation Behavior	1196
Molybdenum Silicides	1198
Titanium Silicides	1206
Niobium Silicides	1209
Applications	1210
Conclusions	1212
References	1213

Abstract

There is a strong push in recent years for development of high-performance materials to be used in the hot-end components of aero-engines at temperatures beyond the operating range for nickel-based superalloys. The interest in silicides

R. Mitra (✉)

Department of Metallurgical and Materials Engineering, Indian Institute of Technology, Kharagpur, West Bengal, India

e-mail: rahul@metal.iitkgp.ac.in

and silicide-matrix composites arises from their high melting points, ability of strength retention, along with impressive oxidation resistance at elevated temperatures, which are considered as desirable. Among the silicides, the molybdenum-, titanium-, and niobium-based multiphase alloys and composites have been found to be the most promising. Whereas MoSi_2 has the best high-temperature oxidation resistance among the silicides, its ambient temperature fracture toughness as well as high-temperature strength retention are poor, and then, there are serious difficulties in near-net shaping of components. Therefore, starting from MoSi_2 based composites with ceramic reinforcements, a significant attention has been paid during the last two decades to the development of multiphase Mo-Si-B based ternary alloys with bcc- Mo_{ss} , Mo_3Si , and Mo_5SiB_2 . While crack-arrest and plastic deformation of the ductile bcc- Mo_{ss} contributes to toughening, the presence of Mo_3Si and Mo_5SiB_2 assists in retention of high-temperature strength, as well as formation of a borosilicate scale to protect against oxidation. In the multi-component Nb-Si-X alloys, the presence of ductile Nb_{ss} is responsible for toughness enhancement, whereas the intermetallic silicides or Laves phases contribute to strength retention. This chapter will provide an overview of the crystal structures and phase equilibria in Mo-Si, Ti-Si, and Nb-Si based systems, processing methodologies, evolution of microstructure, mechanical properties, oxidation behavior, and potential applications.

Keywords

Molybdenum silicides · Niobium silicides · Titanium silicides · Oxidation · Oxide scale · Oxidation kinetics · Diffusion · Reactions

Introduction

The structural intermetallics and their multiphase alloys with high melting points are of interest for applications in specific load-bearing components for aero-engine and automotive systems, as well as in selected nuclear and power generation equipment requiring strength retention at elevated temperatures. In the binary phase diagrams, the intermetallics appear as high-melting line compounds with either fixed stoichiometric ratios between the constituent metals or as phases having a range of compositions or solubility, which may vary with temperature. Formation of the intermetallic phases is preferred, provided the Hume-Rothery rules for solid-solution alloying are not satisfied. Typically, the ordered solid solutions tend to form in a binary alloy system, if the bonding between a pair of unlike partner atoms is stronger than that between the like atoms, and therefore, each atom in the alloy tries to have a maximum number of unlike nearest neighbors. The ordered intermetallic phase can be considered as an example of regular solution with large negative enthalpy of mixing [1]:

$$H_0 = H_{AB} - (H_{AA} + H_{BB})/2 \ll 0 \quad (1)$$

where H_{AB} , H_{AA} , and H_{BB} are the heats of formation of A-B, A-A, and B-B bonds, respectively. For stoichiometric intermetallic compositions, strictly periodic arrangements of atoms are attained. As expected, the formation and evolution of intermetallic phases in the microstructure depends on their thermodynamic stability. However, metastable phases with inhomogeneous compositions are often formed during solidification, and therefore, equilibrium phases are obtained in the microstructure only after a suitable heat-treatment.

Significant research has been carried out for development of intermetallics for various types of structural and functional applications. The properties of interest for high-temperature aerospace applications are high melting point, ductility, and toughness at ambient temperature, as well as strength retention and resistance to environmental degradation at elevated temperatures. Overviews containing information on basic fundamentals regarding phase equilibria, processing, structure, and properties of intermetallics as well as development of selected intermetallic-types have been published in the form of books, chapters, and papers [2–5]. In this chapter, an effort has been made to provide a concise overview of structural silicides, which have received maximum attention over past three decades due to their promise for use at elevated temperatures.

Phase Equilibria and Crystal Structures of Selected Silicide-Based Alloy Systems

Molybdenum Silicides

The binary Mo-Si phase diagram shows the presence of stoichiometric line compounds with compositions of Mo_3Si and MoSi_2 , as shown in Fig. 1 [6]. On the other hand, the Mo_5Si_3 has a homogeneity range of 3 at.% Si. MoSi_2 has a body-centered tetragonal (bct) structure ($C11_b$, $tI8$) with 8 atoms in the unit cell, as illustrated schematically in Fig. 2a. However, it possesses a typical hexagonal structure ($C40$, $hP9$) (Fig. 2b) at high temperature (1900 °C). The $\text{Mo}(\text{Si},\text{Al})_2$ formed on alloying with Al in excess of 3 at.% also possesses $C40$ structure [7–9]. Interestingly, the c/a ratio for the perfect hexagonal arrangement is $6^{1/2} = 0.2449$ nm [9], which is very close to that of the $C11_b$ structure ($c/a = 0.2452$ nm). The Mo_5Si_3 also possesses tetragonal structure with its unit cell containing 32 atoms (20 Mo atoms and 12 atoms of Si, $D8_m$, $tI32$), as depicted schematically in Fig. 2c [10]. On the other hand, Mo_3Si has a cubic structure ($A15$, $cP8$) comprising 8 atoms in the unit cell, with 6 atoms of Mo and 2 atoms of Si, as shown schematically in Fig. 2d.

A significant attention has been drawn by the Mo-Si-B alloys for high temperature aerospace applications. The Mo-rich section of the ternary isothermal phase diagram of the Mo-Si-B system corresponding to 1600 °C is shown in Fig. 3a [11]. The Mo-Si-B ternary alloys can be designed to have the optimum volume fractions of Mo_{ss} (Mo-rich solid solution also known as α -Mo), Mo_3Si , and Mo_5SiB_2 phases. All the three-phases have nearly fixed compositions with quite limited solid solubility for other elements, and hence provide microstructural stability at high temperatures. The Mo_{ss} phase has bcc structure with solubility for Si and B atoms as 3 at.% and < 1 at.%,

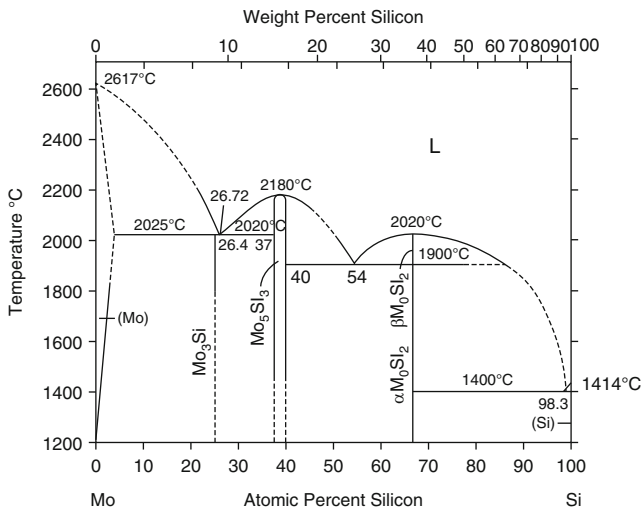


Fig. 1 Binary Mo-Si phase equilibrium diagram, showing the presence of intermetallics, MoSi₂, Mo₅Si₃, and Mo₃Si [6]

respectively, while the Mo₃Si possesses single-phase composition close to 76Mo-24Si (at.%) [12]. On the other hand, Mo₅SiB₂ possesses body-centered tetragonal structure (*D*8₇, *tI*32) with 32 atoms in the unit cell, comprising 20 atoms of Mo, 4 atoms of Si, and 8 atoms of B, as illustrated schematically in Fig. 3b. In the unit cell of Mo₅SiB₂, three layers can be identified, the first comprising only Mo atoms, the second having only Si atoms, and the third having a mixture of Mo and Si atoms.

Tungsten Silicides

WSi₂ is known to have a crystal structure, lattice constants, as well as electronic structure similar to that of MoSi₂ [13]. Hence, WSi₂ is reported to form an isomorphous solid solution with MoSi₂. Interestingly, both the melting temperatures and coefficients of thermal expansion of MoSi₂ and WSi₂ are also similar. Therefore, W has been widely preferred as an alloying element for solid solution strengthening of MoSi₂ [14]. However, both deformation behavior and brittle-to-ductile transition temperature (BDTT) of MoSi₂ and WSi₂ single crystals are significantly different, in spite of their crystal structures being same [15–17]. Such a difference in mechanical behavior may be ascribed to the more directional nature of bonds in WSi₂ to that of MoSi₂ [18].

Titanium Silicides

A typical illustration of the binary equilibrium phase diagram of the Ti-Si system is shown in Fig. 4 and shows the existence of the intermetallics, Ti₃Si, Ti₅Si₄, Ti₅Si₃,

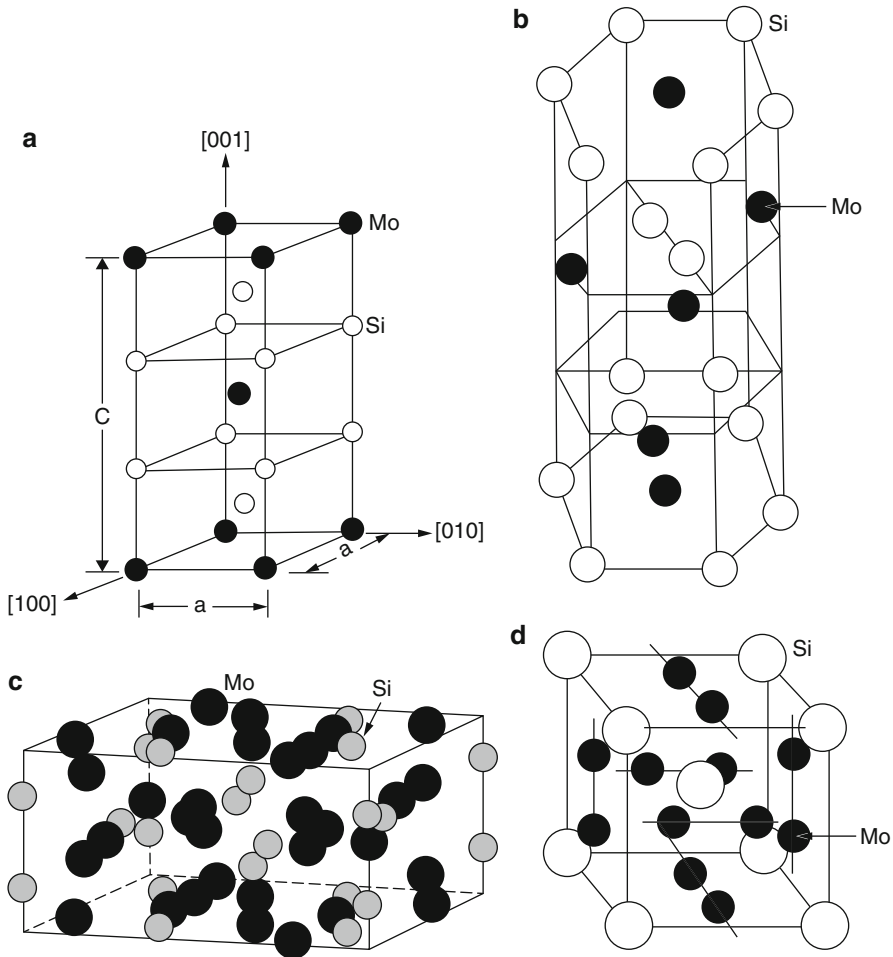


Fig. 2 Schematic illustrations of the unit cells of (a) MoSi₂ (C11b, tI8), (b) MoSi₂ (C40, hP9), (c) Mo₅Si₃ (D8_m, tI32), and (d) Mo₃Si (A15, cP8) [7]

TiSi, and TiSi₂ [6]. The phase diagram indicates that the Ti₅Si₃ has a homogeneity range of 4 at.%, whereas all other intermetallics (Ti₃Si, Ti₅Si₄, TiSi, and TiSi₂) in this phase diagram are typically line compounds with fixed composition. A few earlier investigations have reported that Ti₅Si₃ has high solubility for C, N, and O, indicating that these elements play a very important role in stabilizing the hexagonal structure [19, 20]. The Ti₅Si₃ is known to possess a hexagonal Mn₅Si₃-type structure (D8₈, hP16) having 16 atoms, which include 10 atoms of Ti and 6 atoms of Si (Fig. 5) [7]. A typical unit cell of Ti₅Si₃ is reported to contain two sublattices of Ti and one of Si. The Ti sublattice (1) contains atoms at $(1/3, 2/3, 0)$, $(2/3, 1/3, 0)$, $(2/3, 1/3, 1/2)$, and $(1/3, 2/3, 1/2)$. In this unit cell, the atoms of the Ti sublattice (2) are located at $(0, 0.2358, 1/4)$, $(0.7642, 0.7642, 1/4)$, $(0.2358, 0, 1/4)$, $(0.2358, 0.2358, 3/4)$,

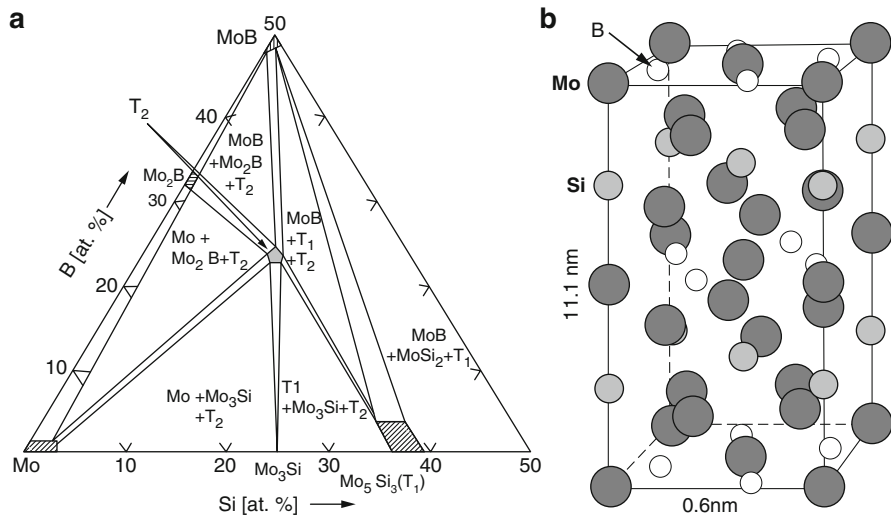


Fig. 3 Schematic illustrations of (a) Isothermal section at 1600 °C from the Mo-Si-B ternary phase diagram [11], and (b) unit cell of $\text{Mo}_5\text{Si}_3\text{B}_2$ (D8₁, tI32)

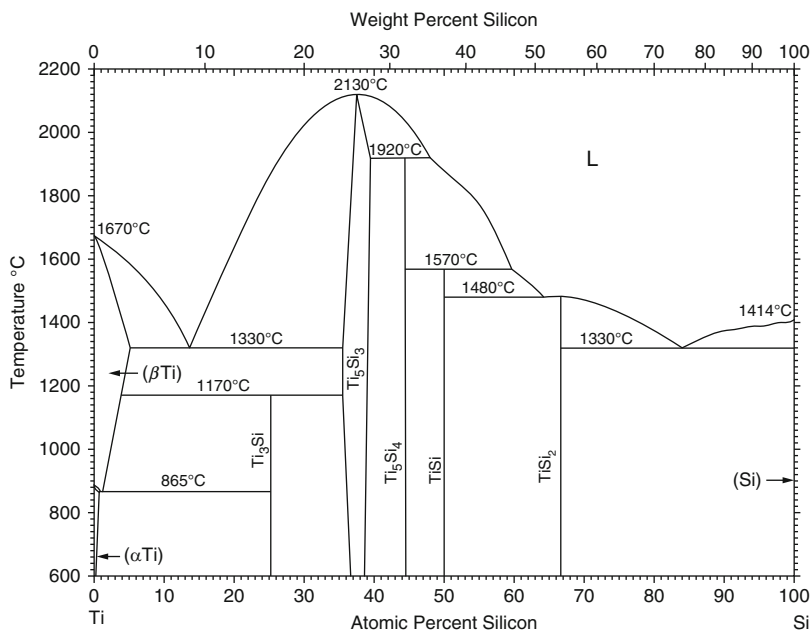
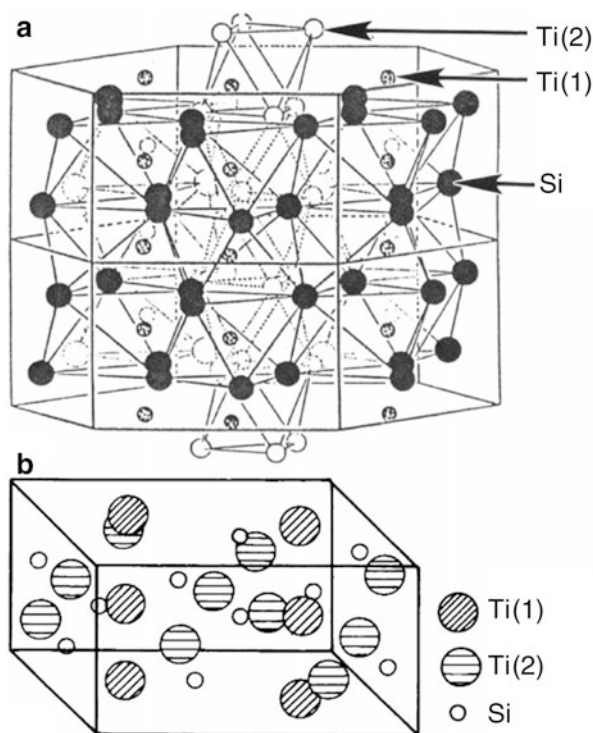


Fig. 4 Binary equilibrium phase diagram of the Ti-Si system, showing the compositions of Ti_3Si , Ti_5Si_4 , Ti_5Si_3 , TiSi , and TiSi_2 [6]

Fig. 5 Schematic illustration of Ti_5Si_3 unit cell (D_{8h} , hP9) showing (a) hexagonal structure, and (b) position of atoms in Cartesian coordinates [5]



(0.7642, 0, $\frac{3}{4}$), and (0, 0.7642, $\frac{3}{4}$), whereas the atomic locations of Si are (0, 0.5992, $\frac{1}{4}$), (0.4008, 0.4008, $\frac{1}{4}$), (0.5992, 0, $\frac{1}{4}$), (0.5992, 0.5992, $\frac{3}{4}$), (0.4008, 0, $\frac{3}{4}$), and (0, 0.4008, $\frac{3}{4}$). The c-direction ([0001]) contains the chains of Ti and Si atoms [21]. The observed brittleness of Ti_5Si_3 is ascribed to low crystal symmetry and highly covalent bonding in this intermetallic, which increases the magnitude of Peierls stress required for dislocation motion. Therefore, the dislocation density in Ti_5Si_3 is found to be very low [22, 23].

Niobium Silicides

The intermetallic phases in the binary equilibrium Nb-Si phase diagram are NbSi_2 , Nb_5Si_3 , and Nb_3Si , as shown in Fig. 6 [24–26]. The Nb-Si binary phase diagram shows a eutectic reaction point at 1880 °C for the composition of 18.2 at.% Si, where the reaction taking place is $L \rightarrow \text{bcc-Nb solid solution} + \text{Nb}_3\text{Si}$. A eutectoid reaction at around 1700 °C leads to the decomposition of the Nb_3Si phase into Nb-rich solid solution (Nb_{ss}) and Nb_5Si_3 . While Nb_{ss} has a bcc structure, the Nb_5Si_3 has a tetragonal structure. Based on the initial composition, the Nb_{ss} or Nb_5Si_3 present could be primary or secondary phases, the latter being the product of eutectoid reaction. NbSi_2 is a stoichiometric compound having hexagonal, C40 crystal structure (Fig. 2b), similar to that of the $\text{Mo}(\text{Si},\text{Al})_2$.

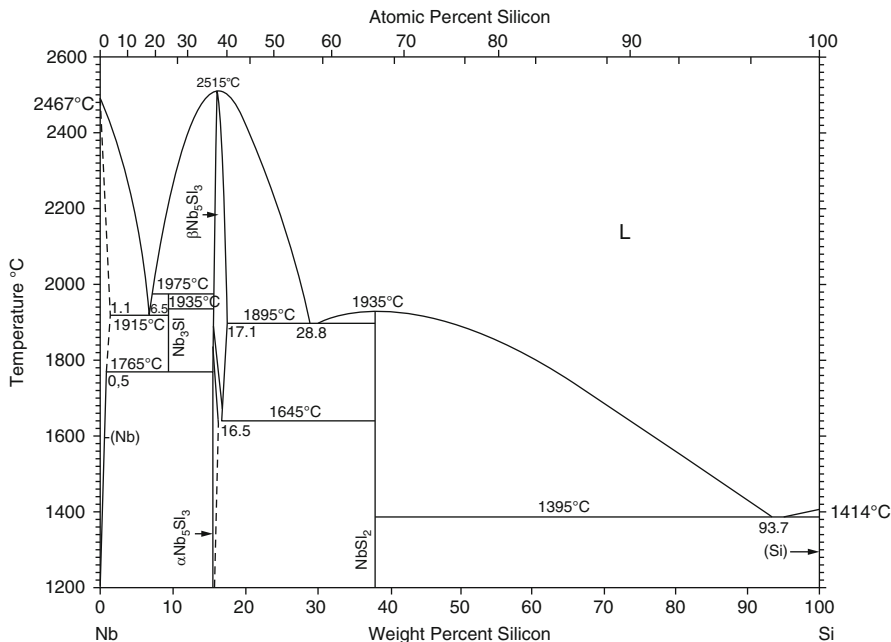


Fig. 6 Binary equilibrium phase diagram of the Nb-Si system, showing the compositions of Nb_3Si , Nb_5Si_3 , and NbSi_2

Table 1 Melting points and densities of selected silicides of Mo, W, Ti, and Nb

Silicide	MoSi_2	Mo_5Si_3	Mo_3Si	Mo_5SiB_2	WSi_2	Ti_5Si_3	NbSi_2	Nb_5Si_3
Melting point (°C)	2020	2180	2025	2160–2200	2160	2130	1920	2484
Density (g/cc)	6.24	8.24	8.9	8.8	9.86	4.32	5.62	7.16

The aforementioned silicides have evoked interest within the scientific community because of their high melting point along with moderate density, as is evident from the data in Table 1. The highest melting point alone is not the criteria for pursuing research on a material, as the ease of processing as well as mechanical properties along with high-temperature oxidation resistance need to be considered.

Processing

Bulk silicides and silicide matrix composites can be processed by both ingot (or liquid) and powder metallurgy routes, whereas coatings of suitable compositions are usually prepared by various thin or thick film deposition methods. The purity of raw materials used along with the adopted methods of process not only have a strong influence on the impurity content but also affects the evolution of microstructure, which in turn influence the mechanical properties. Special methods of processing

have been widely developed to tailor the level of purity, and control the matrix grain size or sizes of dispersed phases, all of which are known to have a strong impact on the mechanical properties.

The ingot metallurgy processing methods used to fabricate the silicides and silicide-matrix composites include arc-melting [26, 27], induction skull melting [28], XD processing [29–31], directional solidification [32], single crystal growth [33], investment casting [34], etc. Conventional methods of single crystal growth such as Bridgman or Czochralski techniques cannot be used, because of the high melting point (≥ 2000 °C) of the silicides. Hence, alternative processes involving electron beam float zone, inductively coupled plasma pedestal growth, and induction float zone in atmospheric and pressurized chambers have been developed for producing single crystals of the high melting silicides [34, 35]. Vacuum induction melting is one of the most common techniques for melting of intermetallic alloys in ceramic crucibles. In this process, the crucible or mold material is chosen, so as to avoid any kind of chemical reaction with the melt. Liquid metallurgy route also includes nonequilibrium solidification processing such as rapid solidification, which involves rapid heat-extraction to form products in the form of powders and ribbons. Rapid solidification processing of powders is carried out with the help of high-pressure gas atomization, or rotating electrode process [36, 37]. In the high-pressure gas atomization process, convective cooling with the help of inert gas such as argon is used to split the molten metal stream and to quench the droplets. On the other hand, the rotating electrode process uses a plasma arc to melt the end of a rotating electrode, so that small droplets are ejected and cooled by convective heat transfer to solidify into powders, which are collected in an inert gas chamber. The powder particle size obtained through gas atomization is finer than that obtained by the rotating electrode process.

Nonequilibrium processing also includes thermal spray processing, in which the melt is sprayed by acceleration to high velocity on to a substrate [38]. This process termed as “splat” is usually carried out in the form of flame spraying, arc-wire spraying, or plasma spraying, which leads to the formation of a stream of molten particles accelerated in a high-velocity gas stream towards a substrate. The substrate for thermal spraying can be either at ambient temperature, or more likely preheated to facilitate bonding between the splats. Some of the commercialized thermal spray processes are “Osprey” process and low-pressure plasma spraying (LPPS). In the Osprey process, melting is carried out in a bottom-pour crucible, from where it is atomized by a high-velocity gas stream and accelerated towards a substrate. The plasma spraying carried out in a low-pressure inert/reducing environment, is useful for thermal spraying of intermetallic alloys, which are sensitive to interstitial contamination by pick up of oxygen or nitrogen.

The popular methods of producing single crystals of intermetallics are Czochralski pulling, Bridgman method, zone refining, or floating zone method [39]. The alloys are usually melted in a water-cooled hearth in vacuum or argon atmosphere. In the Czochralski technique, a seed crystal is slowly raised from a molten bath to grow single crystal of a given intermetallic alloy in a chosen crystallographic direction. In the Bridgman method, the entire specimen is in liquid state, and the process of solidification is initiated at one end of the melt by moving

the specimen and heat source relative to one another. It is possible to grow single crystals in a specific orientation by introducing a constriction in the crucible, or by introducing a seed crystal with a desired orientation.

The powder metallurgy processing techniques involve consolidation of the powders to form densified intermetallic alloys of a specified composition as the end product. The powders could either have the specified composition of the intermetallic alloy, or synthesized reactively from elemental precursors. For some of the intermetallic alloys, reactive synthesis from the blend of elemental powders is deliberately combined with application of pressure using either uniaxial hot pressing or hot isostatic pressing. Here, the reactions taking place during synthesis are exothermic and release sufficient heat to drive the reaction forward towards completion. The self-propagating high-temperature synthesis process is one such process, where the reaction is ignited by applying heat in the form of either laser pulse or electric discharge to one of the surfaces of the elemental powder compact [40]. The initial heating rate is fast enough to trigger a rapid reaction between the elemental raw materials, which in turn leads to adiabatic heating with rise in temperature to the ignition temperature. As the reaction becomes self-sustaining due to its own enthalpy, the external heating source is no more required. If the reaction initiation temperature is higher than the melting point of one of the reactant elements, then the presence of transient liquid phase aides in enhancing the reaction kinetics and the process of densification, as observed in case of the molybdenum silicides.

Mechanical Behavior

The mechanical behavior of silicides includes deformation and fracture mechanisms at both ambient and elevated temperatures, and these are strongly dependent on their crystal structures and microstructures. As expected, both strength and fracture toughness of silicides are functions of the complexity of their crystal structures, as well as degree of order and crystallographic anisotropy, which in turn influence the nature of defects formed in these materials. On the other hand, the mechanical properties of multiphase silicide-based alloys are influenced to a large extent by the presence of ductile and brittle microstructural constituents. Both stability of dislocations and their mobility depend on the structure and planarity of the dislocation cores in these alloys. Like other intermetallics, the polycrystalline silicides also exhibit brittle behavior, because less than 5 independent slip systems are operative. However, additional slip systems become operative or dislocation climb becomes possible with increase in temperature, which in turn contributes to brittle-to-ductile transition in these materials. Of course, in the multiphase silicide-based intermetallic alloys, the volume fraction of different phases also has a strong role to play in their deformation and fracture behavior. Strength retention at elevated temperature is an issue, which is addressed through either suitable alloying or addition of reinforcement. The deformation behavior of various refractory metal silicides depends on their crystal structures and compositions, which in turn govern the amount of Peierls stress required for dislocation motion in these materials.

Deformation Behavior of C11_b Structured Silicides

The shortest lattice translation vectors in a unit cell with C11_b structure are $\langle 100 \rangle$, $\frac{1}{2} \langle 111 \rangle$, and $\langle 110 \rangle$ and therefore these are also the preferred Burgers vectors, because such dislocations have lower self-energies. The slip systems operative in the C11_b structured MoSi₂ are shown schematically in Fig. 7. The single crystals of MoSi₂ exhibit plastic deformation, when tested in compression even at room temperature [41], while the polycrystalline specimens show ductile behavior only at 1100 °C or above and in some cases at 1300 °C [42]. Such sharp difference in the deformation behaviors of single and polycrystalline MoSi₂ is attributed to the absence of 5 independent slip systems in the latter type of material. In case of anisotropic single crystals, the deformation behavior and the types of operating slip systems depend very much on the crystal orientation.

On the basis of an exhaustive study carried out on the deformation behavior of MoSi₂ single crystals between -196 °C and 1500 °C, Ito et al. have reported that [001]-oriented crystals involving the activation of $\{0\bar{1}3\} \langle 331 \rangle$ slip system deform only above 1300 °C, while deformation could be observed at room temperatures in

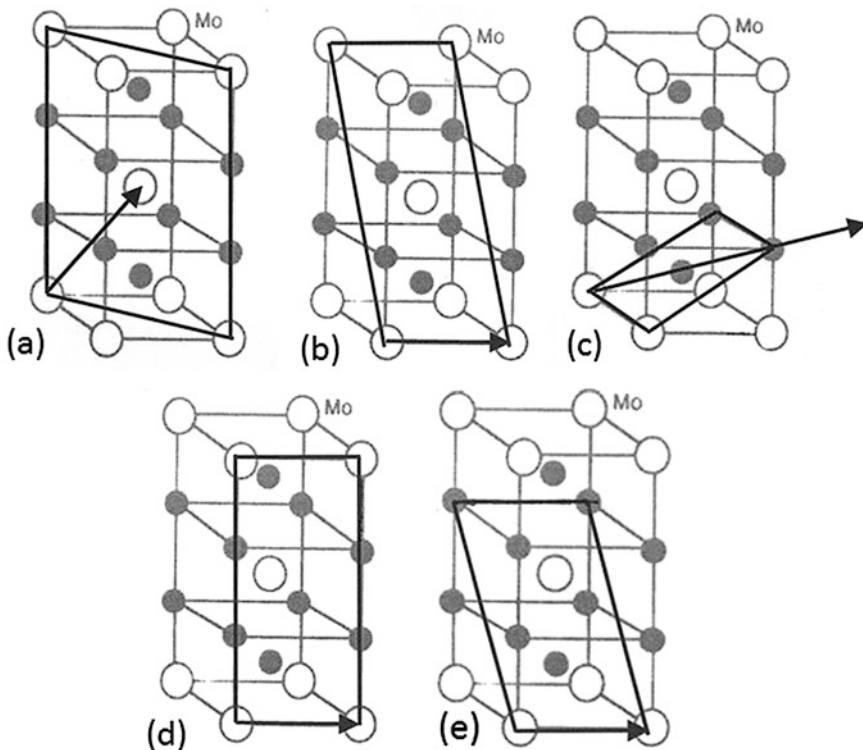


Fig. 7 Schematic illustration of slip systems in C11_b structured MoSi₂: $\{1\bar{1}0\} \langle 111 \rangle$, $\{011\} \langle 100 \rangle$, $\{010\} \langle 100 \rangle$, $\{023\} \langle 100 \rangle$, and $\{0\bar{1}3\} \langle 331 \rangle$ [5, 7, 41]

the crystals with other orientations [41]. It should be noted that the unit cell of MoSi₂ contains Mo-Si-Si-Mo covalent bonds along the [001] direction, which makes it harder to deform compared to that for stress axis in other directions. The five slip systems are $\{1\bar{1}0\} \langle 111 \rangle$, $\{011\} \langle 100 \rangle$, $\{010\} \langle 100 \rangle$, $\{023\} \langle 100 \rangle$, and $\{0\bar{1}3\} \langle 331 \rangle$, and their operation depends on the crystal orientation during loading. At temperatures ≥ 1200 °C, $\langle 100 \rangle$ or $\frac{1}{2}\langle 111 \rangle$ dislocations have been found to predominate. At temperatures of ≥ 1300 °C, edge dislocations with Burgers vector along $\langle 100 \rangle$, $\langle 110 \rangle$, and $\langle 111 \rangle$ have been observed in planes different from the regular slip planes, which is suggestive of the predominance of climb [43].

Apparently, the BDTT of the polycrystalline MoSi₂ has also been found to depend on the silica (SiO₂) content of the specimens, which in turn depends on the purity of raw materials and method of processing [44, 45]. Patankar and Lewandowski [45] have reported the BDTT of MoSi₂ processed by mechanical alloying and hot pressing to be ≈ 1100 °C. On the other hand, Aikin [42] as well as Srinivasan, Schwarz and co-workers [43, 46] have reported a reduced BDTT of 1000 °C in high oxygen containing MoSi₂ and 1300 °C in case of high purity MoSi₂. The variation in the BDTT with oxygen content as well as grain size is attributed to premature softening of the SiO₂ particles at the grain boundaries during high-temperature deformation. The elevated temperature yield strengths of polycrystalline MoSi₂ depend on microstructural parameters such as grain size [47, 48], SiO₂ content [45, 47, 49, 50], type of alloying elements [51–53], and presence of reinforcements [49, 54–57], as well as specific test conditions [47] including both temperature and strain rates. At lower temperatures or higher strain rates, the MoSi₂ has been found to follow typical Hall-Petch type behavior, because the grain boundaries act as barriers to dislocation motion, and as a result, the finer grain size leads to higher strength. On the other hand, at higher temperatures or reduced strain rates, the effect of thermally activated diffusion process is more predominant in the fine-grained specimens, probably because the grain boundaries act as sources and sinks for vacancies and dislocations. This type of behavior is illustrated in Fig. 8. The SiO₂ particles are globular to begin with, and do not wet the grain boundaries (Fig. 9a). At higher temperatures, the SiO₂ particles at the grain boundaries undergo softening and visco-plastic flow by shear and thereafter undergo cracking, as shown in Fig. 9b. Alloying of commercially available (from H.C. Starck, Germany) MoSi₂ with Al has led to in-situ reduction of SiO₂ impurity to form α -Al₂O₃ [59]. The microstructure of the MoSi₂-5.5 at.% Al alloy has been found to contain C11_b structured Mo(Si,Al)₂ (2.5 at.% Al in solid solution) alloy as the matrix along with dispersion of in-situ formed α -Al₂O₃ particles. In contrast, the microstructure of the MoSi₂-9 at.% Al alloy has shown the presence of both C11_b structured Mo(Si,Al)₂ with 3.1 at.% Al in solid solution, C40 Mo(Si,Al)₂, as well as α -Al₂O₃ particles. Minor alloying additions of Al to polycrystalline MoSi₂ have been found to increase the elevated temperature yield strength up to 1300 °C, as the SiO₂ present in the raw materials is converted to Al₂O₃ by an in-situ reaction during processing [58, 59]. Addition of 2–4 wt.% C, which leads to the formation of a high volume fraction of SiC by displacement reaction with SiO₂, enhances the high-temperature hardness as well as the yield strength [60].

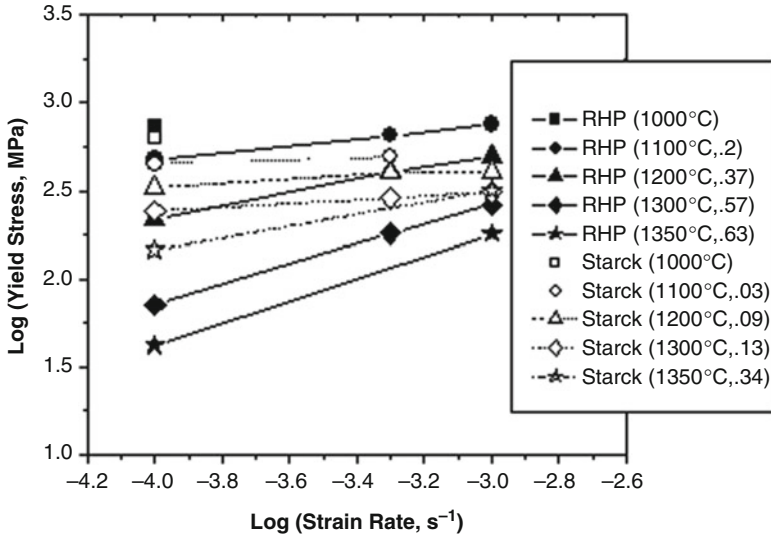


Fig. 8 Log-log plots showing variation of yield strength of coarse-grained ($\approx 27 \mu\text{m}$ grain size) obtained by hot-pressing Starck MoSi_2 and fine-grained ($\approx 5 \mu\text{m}$) MoSi_2 (obtained by reactive hot pressing of Mo and Si powders) with strain rate for various test temperatures [5, 58]. (Reprinted with permission from Elsevier)

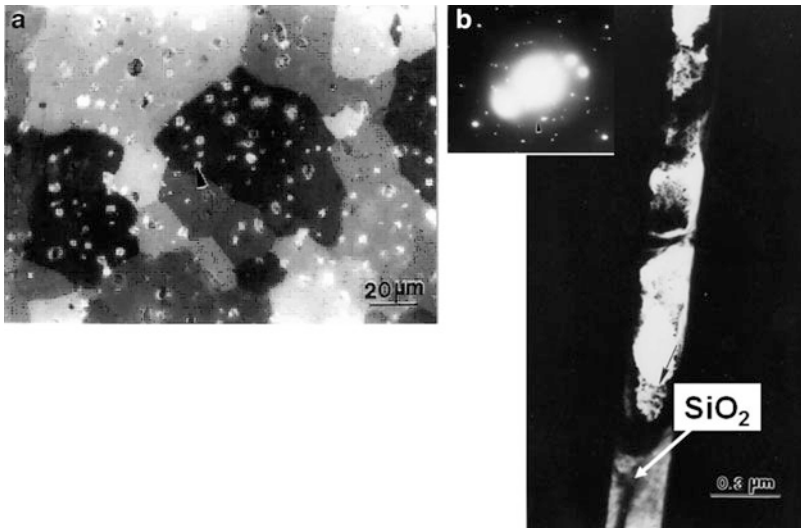


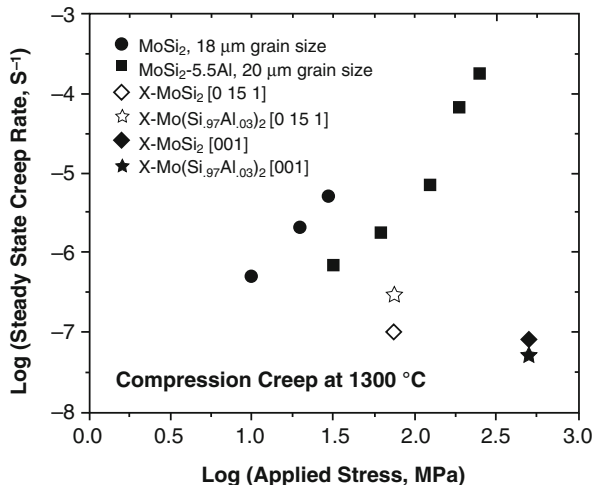
Fig. 9 (a) Polarized light optical micrograph showing SiO_2 particles at grain boundaries of hot-pressed MoSi_2 , and (b) TEM image showing an interfacial SiO_2 film with crack in MoSi_2 deformed at 1200°C [47]. (Reprinted by permission from Springer Nature)

The results of creep behavior of different silicides of Mo, Ti, and Nb as reported in the literature are summarized in Table 2 [22, 58, 61–68]. Studies on creep behavior of MoSi₂ single crystals have shown a strong dependence on crystallographic orientations, as well as involvement of both dislocation glide and climb [5, 7, 62]. The <001> direction of stress-axis has been found to be the hardest orientation for creep. Similar to the observations for the tests carried out at constant strain rates, TEM examination of the creep tested specimens have shown evidence for presence of <100> dislocations as well as decomposition of the <331> dislocations into

Table 2 Results of creep tests on selected Mo-, Ti-, and Nb-Silicide based composites

Mo-Silicide	Temperature (°C)	Stress exponent	Activation energy (kJ/mole)	Proposed mechanism	Ref
MoSi ₂ Single Crystal [210] [0 15 1] [001]	1200	3	251	Dislocation mechanism	[61]
	1200–1400	2.19	372		[62]
		2.43	327		
Polycrystalline MoSi ₂	1200	1 4–5	160 430	Diffusion creep Dislocation creep	[63]
MoSi ₂ -Al + Al ₂ O ₃	1200	1.9 = 3.7	271–415	Diffusion creep Dislocation creep	[63]
MoSi ₂ -SiC composite	1200	4.2		Dislocation creep	[58]
Mo ₅ Si ₃ single crystal [314]	1200–1400	6	510	Dislocation creep	[64]
Mo ₅ SiB ₂ single crystal [021] [001]	1500–1600	6.8	740	Dislocation creep	[65]
		4.3	400		
Mo-12Si-8.5B	1300	3.2	295	Dislocation creep	[66]
Ti ₅ Si ₃ (20–50 μm grain size)	1000–1200	3.0	350	Dislocation creep	[22]
Ti ₅ Si ₃ (6 μm grain size)	1200–1400	3.0	620–640	Dislocation creep	[63]
Ti ₅ Si ₃ -20 vol.% TiB ₂	1200–1400	2.0	NA		[63]
Ti ₅ Si ₃ -8 wt% Al	1200–1400	2.0	NA		[63]
Nb ₅ Si ₃	1373–1673	0.9	NA	Diffusion creep	[67]
Nb-10Si	1473	2.7	NA	Dislocation creep	[67]
Nb-16Si	1473	3.1	NA	Dislocation creep	[68]

Fig. 10 Comparison of steady state creep rates of polycrystalline MoSi_2 and MoSi_2 -5.5 at.% Al alloy, as well as single crystals of MoSi_2 and $\text{Mo}(\text{Si}_{0.97}\text{Al}_{0.03})_2$ tested with [0 15 1] and [001] orientations at 1300 °C [58]. Single crystals are marked as “X.” (Reprinted with permission from Elsevier)



$\langle 110 \rangle$ and $\langle 111 \rangle$ type perfect dislocations. However, the creep strengths of MoSi_2 single crystals have been found to be significantly higher than that of their polycrystalline samples, as shown in Fig. 10 [7, 62]. It has been observed that alloying of MoSi_2 with W or addition of SiC reinforcements leads to increase in creep resistance. However, grain size of MoSi_2 has been found to have a strong effect on its creep resistance [63]. Reduction in grain size on SiC addition combined with the presence of SiO_2 at grain boundaries has been found to lower the creep resistance. Alloying with C or Al has been found to help in enhancing the creep resistance by reducing the SiO_2 through in-situ displacement reaction, as shown in Figs. 11 and 12. Creep-strengthening is observed with Al-addition as long as the C11_b structure of MoSi_2 is stable, whereas formation of the C40 structured $\text{Mo}(\text{Si},\text{Al})_2$ leads to lower creep resistance. The best results are obtained in creep, if the matrix grain size can be kept coarse with addition of SiC as reinforcement, by keeping the SiO_2 content low. The stress exponents of MoSi_2 range between 1 and 5 depending on either temperature or stress used for the test, grain size, SiO_2 content, or alloying additions [58, 62, 63]. Interestingly, a strong effect of grain size has been observed even in dislocation creep regime, probably because five independent slip systems are not available till almost 1300 °C, and therefore strain incompatibility is accommodated by grain-boundary sliding. In a review on the creep behavior of intermetallics and composites, Sadananda and Feng have shown that at 1100 °C, the creep resistance of the MoSi_2 -based composites is superior to that of either TiAl- or NiAl-based composites and also that of the MAR-M 240 superalloy [69].

Deformation Behavior C40 Structured Silicides

Plastic deformation behavior of the C40 structured $\text{Mo}(\text{Si},\text{Al})_2$ single crystals has been studied by Inui et al. [70]. The $\text{Mo}(\text{Si},\text{Al})_2$ single crystals have shown plastic

Fig. 11 Steady state creep rates of MoSi₂ with varying SiO₂ content and SiC reinforcements added externally or formed by in-situ reaction with C [58]. (Reprinted with permission from Elsevier)

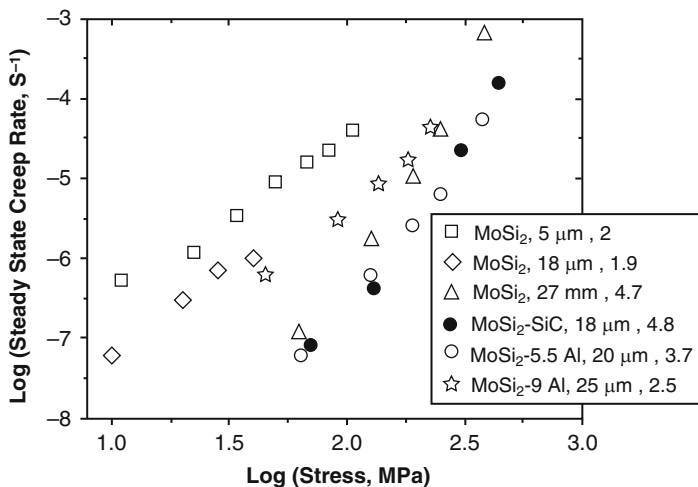
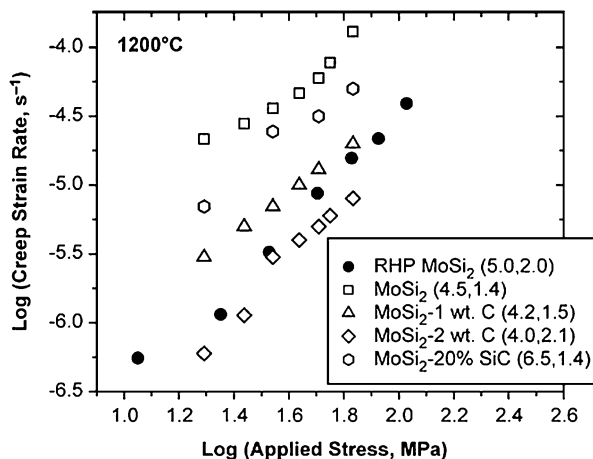


Fig. 12 Comparison of steady state creep rates of polycrystalline MoSi₂ with grain sizes of 5 μm, 18 μm, and 27 μm; MoSi₂-20 vol.% SiC composite with matrix grain size of 18 μm; and MoSi₂-5.5 and 9 at.% Al alloys with matrix grain sizes of 20 μm and 25 μm, respectively [58]. The stress exponents are shown next to grain size. (Reprinted with permission from Elsevier)

flow at temperatures ≥ 1100 °C for orientations involving the operation of (0001) $\langle 11\bar{2}0 \rangle$ basal slip with dislocations having $b = 1/3 \langle 11\bar{2}0 \rangle$. However, if the Al concentration is higher as in case of the Mo(Si_{0.85},Al_{0.20})₂ crystals, plastic deformation is initiated only at 1200 °C instead of 1100 °C, which is followed by decrease in the yield strength with increasing temperature, as usually expected due to thermal activation of dislocation motion. It has been proposed that the basal slip occurs through “synchroshear” mechanism, involving the dissociation of the perfect

dislocations into partials with Burgers vector of $1/6 \langle 11\bar{2}0 \rangle$, separated by stacking fault. In this mechanism, spreading of the core of the perfect dislocation in the basal planes makes their cross-slip into the prismatic planes difficult. The “synchroshear” mechanism of deformation as observed also in the CrSi_2 has been attributed to a greater fraction of directional bonding and lower stability of the C40 phase compared to the C11_b phase [8, 70]. The C40 silicides deforming by “synchroshear” mechanism shows higher values of CRSS, compared to those deforming by more regular dislocation mechanism. Therefore, the yield stress has been found to decrease very sharply as the test temperature is raised from 1100 °C to 1200 °C.

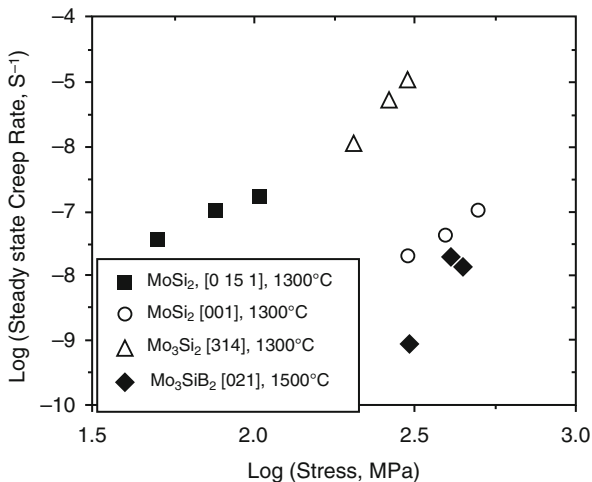
The only slip system observed in the C40-structured NbSi_2 is $(0001) \langle 1\bar{2}10 \rangle$, and plastic deformation has been observed at temperatures ≥ 500 °C [8, 71, 72]. Furthermore, the single crystals of NbSi_2 pre-deformed at 1400 °C have shown plastic deformation at temperatures as low as 200 °C. It is intuitive that prior plastic deformation at 1400 °C creates a reasonable density of potentially mobile dislocations, which enhances the ductility or reduces the BDTT and yield stress at lower temperatures.

Deformation Behavior of Mo-Si-B Based Multiphase Alloys

The ternary Mo-Si-B alloys are designed to contain mixtures of Mo_{ss} , Mo_3Si , and Mo_5SiB_2 , in which the presence of ductile Mo_{ss} phase enhances the toughness, whereas the mixture of Mo_3Si and Mo_5SiB_2 contributes to strength as well as formation of the protective borosilicate scale in oxidizing environments at elevated temperatures [73]. The yield strength of Mo_3Si has been found to depend strongly on its stoichiometry, and decreases as the Si concentration is increased from 22 to 25 at.%. Studies using the TEM have shown the operative slip system to be $(001) \langle 100 \rangle$, with dislocations of mixed character. Studies on high-temperature deformation behavior of Mo_5SiB_2 have shown its creep resistance to be three times superior to that of MoSi_2 [74]. Studies on high-temperature deformation of single crystals have shown the existence of a large amount of anisotropy in yield strength. Creep studies of Mo_5SiB_2 in the temperature range of 1220–1320 °C, has shown $\{001\} \langle 010 \rangle$ and $\{001\} \langle 110 \rangle$ slip systems to be operative [74]. This observation can be justified on the basis of the fact that $\langle 010 \rangle$ is the shortest lattice vector (measuring 0.6 nm) in the Mo_5SiB_2 phase, followed by $\langle 110 \rangle$, while the $\{001\}$ plane is ranked as second in the density of packing. The steady state creep rates of the single crystals of MoSi_2 , Mo_3Si , Mo_5Si_3 , and Mo_5SiB_2 have been compared in Fig. 13, which shows that Mo_5SiB_2 is more resistant to creep compared to the other Mo-silicides.

In recent years, a break-through has been achieved through development of superplastic Mo-Si-B alloys [75, 76]. An ultrafine (submicrometer phase size) three-phase Mo-2.7Nb-8.9Si-7.7B alloy, processed in steps involving mechanical alloying of the elemental powders in hydrogen environment, followed by cold isostatic pressing of these powders at 200 MPa, sintering at 1450 °C in hydrogen atmosphere, and hot isostatic pressing at 1500 °C, has shown superplastic behavior with 200–400% tensile strain to failure in the tests carried out using strain rate of

Fig. 13 Plots depicting the variation of steady-state creep rates of single crystals of MoSi_2 , Mo_3Si , Mo_5Si_3 , and Mo_5SiB_2 [5]



10^{-3} s^{-1} at 1300°C . Analysis of the results of these tests has shown the values of stress exponent and activation energy for creep to be 2.3 and 470 kJ/mol, respectively. The value of activation energy has been found to be reasonably close to that of Mo self-diffusion (≈ 405 kJ/mol), which indicates that diffusion of Mo plays an important role in accommodating strains caused by sliding of grain boundaries or interfaces. Superplasticity has been reported by Li et al. for the powder metallurgy processed fine-grained ($3 \mu\text{m}$) Mo-9Si-8B-3Hf alloy, when subjected to tests at strain rate of $3 \times 10^{-4} \text{ s}^{-1}$ in the temperature range of 1400 – 1560°C , and additionally at $1 \times 10^{-3} \text{ s}^{-1}$ at 1530°C or 1560°C [76]. The tensile strain to failure is reported to vary in the range of 156–410%, with the maximum elongation being observed for the test carried out with a strain rate of $3 \times 10^{-4} \text{ s}^{-1}$ at 1560°C .

Deformation Behavior of Titanium Silicides

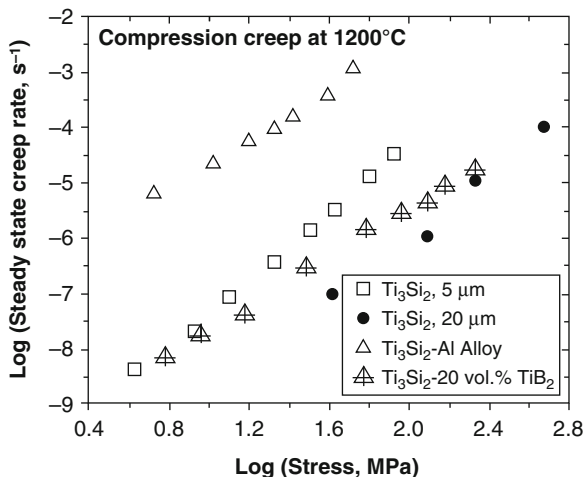
Compression tests carried out on the single crystals of Ti_5Si_3 by Umakoshi and Nakashima at strain rate of $2 \times 10^{-4} \text{ s}^{-1}$ in the temperature range of 1300 – 1500°C have shown decrease in yield strength, accompanied by a sharp increase in ductility with increasing temperature [77]. The yield strengths of Ti_5Si_3 single crystals at a particular temperature strongly depend on the crystal orientation, similar to the observations reported for Mo-silicides. Moreover, TEM studies of the post-deformed microstructures have shown the presence of dislocations and a large number of deformation twins, based on which twinning in the $\{10\bar{1}2\} \langle 10\bar{1}\bar{1} \rangle$ system has been proposed as the major mode of deformation.

Polycrystalline Ti_5Si_3 with coarse grain size ranging between 20 and $50 \mu\text{m}$ has been tested in compression between 1000°C and 1500°C by Rosenkranz et al. at strain rate of 10^{-4} s^{-1} [22]. In another study, Ti_5Si_3 with an average grain size of $5 \mu\text{m}$ has been tested in the temperature range of 1100 – 1200°C at the strain rate of

10^{-3} s^{-1} by Mitra [23]. Serrated plastic flow has been observed in case of polycrystalline Ti_5Si_3 as well. Serrated plastic flow has also been observed during the compressive deformation of Ti_5Si_3 , probably due to the pinning of dislocations by the interstitial elements such as C, N, and O. Similar to the behavior of MoSi_2 , the yield strength of fine-grained Ti_5Si_3 is greater than that of the coarse-grained samples at higher strain rate and lower temperature, while the trend is reversed at lower strain rates and higher temperatures. The dependence of yield strength on grain size, temperature, and strain rates suggest that there is indeed a very strong role of grain boundaries in the process of deformation. Similar to the earlier reported behavior of single crystals, the flow curves show a sharp drop in the yield strength with increasing temperature [23].

Some of the results of creep experiments carried out on the Ti_5Si_3 -based materials are shown in Table 2. The investigation by Rosenkranz et al. has shown the stress exponent to be ≈ 3 in the temperature range of 1000–1200 °C [22], which is the same as that reported by Sadananda et al. in the temperature range of 1200–1400 °C [23]. A similar stress exponent of 3.0 for both coarse and fine grain size specimens suggests that power-law type behavior with dislocation-glide controlled creep is operative in both types of materials. However, the steady-state creep rates of the fine-grained Ti_5Si_3 have been found to be greater than those of the coarse-grained specimens (Fig. 14), indicating grain size dependence even in the dislocation creep regime, and this behavior is somewhat similar to that observed in case of the MoSi_2 [63]. In case of the Ti_5Si_3 , the apparent activation energy in the temperature regime of 1200–1400 °C has been found to be higher compared to that in the range of 1000–1200 °C. This observation may be ascribed to the predominance of grain boundary diffusion at lower temperatures and that of lattice diffusion at higher temperatures, by considering that the former process has much lower activation energy.

Fig. 14 Plots depicting the variation of steady-state creep rates obtained by testing Ti_5Si_3 with 5 and 20 μm grain size, Ti_5Si_3 -20 vol.% TiB_2 composite, and Ti_5Si_3 -Al alloy at 1200 °C



Niobium Silicide-Based Multiphase Alloys

High temperature yielding and creep behavior of the Nb_{ss}-Nb₅Si₃ two-phase alloys have been extensively investigated and reported in the literature [29, 78–87]. Moreover, the flexural strength at room temperature has been found to be between 500 and 700 MPa, and a drastic fall in strength could be observed only above a temperature range of 1100–1450 °C, depending on the composition of these composites. The stress exponent of Nb or Nb_{ss} [85–87] and Nb₅Si₃ [67] has been reported as 5.8 and 1, respectively, while that of the in-situ Nb_{ss}-Nb₅Si₃ composite has been found to be between 2 and 3 [67]. Some of the results have been shown in Table 2. Furthermore, the creep rates of the binary Nb_{ss}-Nb₅Si₃ dual phase alloys have been found to be similar to those of the Ni-based superalloys. Through analyses of the experimental results, it has been shown that creep behavior of the monolithic Nb₅Si₃ is controlled by the diffusion of Nb atoms in Nb₅Si₃ [78].

Solid solution strengthening plays a significant role in the high temperature deformation of multicomponent Nb-silicides. Studies on the mechanical behavior of the Nb-Si-Mo alloys have shown direct evidence for significant solid solution strengthening of the Nb_{ss} phase [88, 89]. Studies have also shown impressive strength retention by the multicomponent Nb-Si based alloys at temperatures exceeding 1200 °C. For example, high temperature tensile deformation of in-situ processed multiphase Nb-silicides with the composition of Nb-18Si-5Mo-5Hf-2C, which are constituted by Nb_{ss} and (Nb,X)₅Si₃ (X = Mo or Hf) phases, have shown maximum yield strength of about 320 MPa at 1300 °C [90]. The amount of elongation is increased from as low as 0.8% at 1200 °C to 37% at 1300 °C with further increase to 72% at 1400 °C, suggesting that the BDTT of this alloy lies between 1200 °C and 1300 °C. The Nb-8Hf-25Ti-18Si alloys have shown 0.1% creep strain at a stress of 140 MPa and 1200 °C, which can be considered as superiority with respect to the second generation Ni-base superalloys (2GSX).

Flexural Strength and Fracture Behavior

The silicides of Mo, W, Ti and Nb in their polycrystalline form are brittle at ambient temperatures, and show limited ductility at elevated temperatures. High melting points and partial covalent bonding between metal and Si atoms lead to high Young's modulus in the silicides of Mo, W, Ti, and Nb. The fracture behavior of silicides is of interest due to the inherent brittle character of these materials. The Young's modulus, BDTT, and fracture toughness of various Mo, W, Ti, and Nb-based silicides are presented in Table 3.

At ambient temperature, coarse-grained MoSi₂ have exhibited failure by transgranular cleavage as shown in Fig. 15a [49], which may be ascribed to the presence of well-defined cleavage planes requiring fewer bonds to break during failure, and having lower surface energies [100]. In contrast, the samples with much finer grain size have shown mostly intergranular fracture (Fig. 15b) [49], as has been observed in ceramics with anisotropic properties [101]. The cause of anisotropic properties in

Table 3 Young's modulus, BDTT, fracture toughness, and coefficient of thermal expansion of selected silicides of Mo, W, Ti, and Nb. "S" and "P" stand for single and polycrystalline silicides, respectively. α and "AR" stand for CTE and anisotropy (of CTE) ratio, respectively. Subscript "a" and "c" are used for directions in tetragonal or hexagonal unit cell

Silicide	MoSi ₂	Mo ₅ Si ₃	Mo ₃ Si	Mo ₅ SiB ₂	WSi ₂	Ti ₅ Si ₃	NbSi ₂	Nb ₅ Si ₃
Young's modulus (GPa)	440	323	295	383	468	156	363	188
Ref.	[5, 7]							
BDTT (°C)	RT (S) [15] 1100-1300 (P) [42]	1250 (S) [Yoshimi] [91]	1400 (P) [12]	1500 (S) [92]	1100 (S) [16, 17]	1200 (S) [82]	400 (S) [72]	
Fracture toughness (MPa√m)	1.9-4 (S) [17] 2.5-4 (P) [55, 93]	2-2.5 (S) [10] 2.9 (P) [21]	3.0 (P) [12]	2.0 (S) [94]	3.7 (S) [95]	2.1-3.2 (P) [22, 23]	NA	1-3 (P) [96]
CTE (α) at 27 °C ($\times 10^6$ K)	S: $\alpha_a = 8.2$ $\alpha_c = 9.4$ AR = 1.15 [10] P: 7-10 [97]	S: $\alpha_a = 5.2$ $\alpha_c = 11.5$ AR = 2.2 [10, 64]	P: 3 [12]	S: $\alpha_a = 7.1$ $\alpha_c = 8.6$ AR = 1.2 (27 °C) - 1.6 (1000 °C) P: 6 [98]		S: $\alpha_a = 5.1$ $\alpha_c = 22.2$ AR = 4.1 [99]		S: $\alpha_a = 8.7$ $\alpha_c = 20.4$ AR = 2.5 [99]

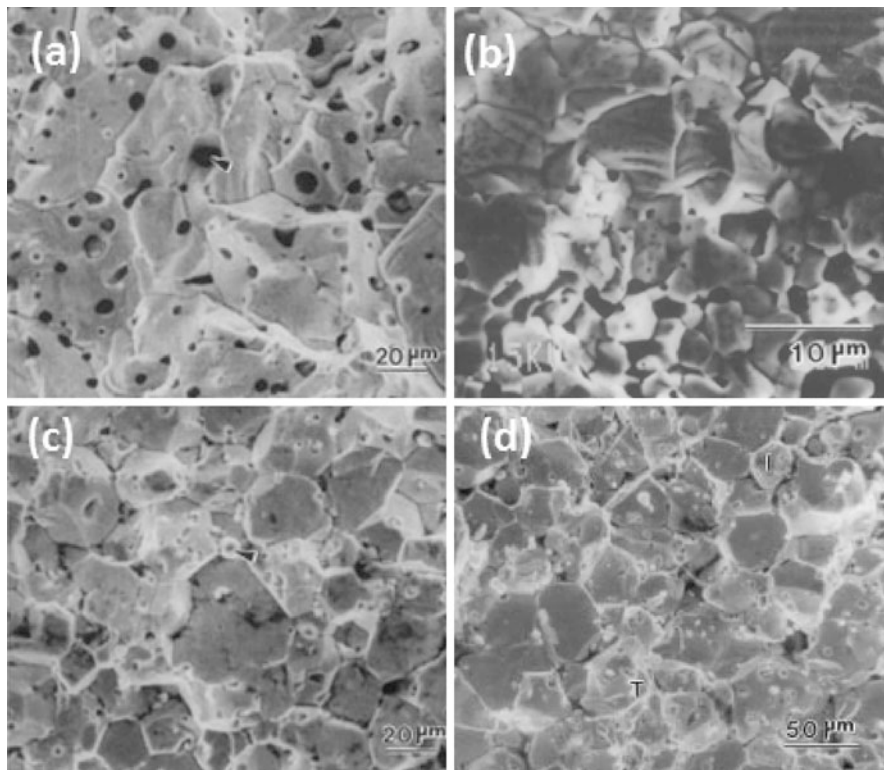


Fig. 15 SEM (SE) images of the fracture surfaces depicting (a) transgranular and (b) intergranular morphologies in MoSi₂ with fine (5 μm) and coarse (25 μm) grain sizes, respectively, as well as mostly intergranular morphology in (c) MoSi₂-5.5 at.% Al and (d) MoSi₂-9 at.% Al alloys with coarse (25 μm) grain size [49, 59]. (Reprinted with permission from Elsevier)

MoSi₂ may be ascribed to its directional bonding [18]. Interestingly, the MoSi₂ alloyed with 5.5 at.% Al has shown typically intergranular fracture surface morphology, as shown in Fig. 15c.

The ways being commonly followed to improve the fracture toughness of the binary Mo and Ti silicides are alloying or addition of ductile or brittle reinforcements. Alloying with suitable elements have been tried to either alter the nature of interatomic bonding with increase in metallic character [5, 7, 23, 52, 93]. Addition of brittle ceramic reinforcements in discontinuous form such as particles or whiskers of SiC, or particles of Si₃N₄, TiC, and TiB₂ to MoSi₂ have led to toughening by crack deflection and crack bridging, whereas reinforcing with tetragonal ZrO₂ has also caused transformation toughening [55, 92, 93, 102, 103]. The cracks at corners of Vickers indentations formed in MoSi₂ and MoSi₂-9 at% Al alloy under a load of 20 kgf are transgranular in MoSi₂ and intergranular in MoSi₂-9 at% Al alloy, as shown in Fig. 16(a) and (b), respectively, which is consistent with the results shown in Fig. 15. In the MoSi₂-5.5 at.% Al alloy, deflection of cracks by in-situ formed

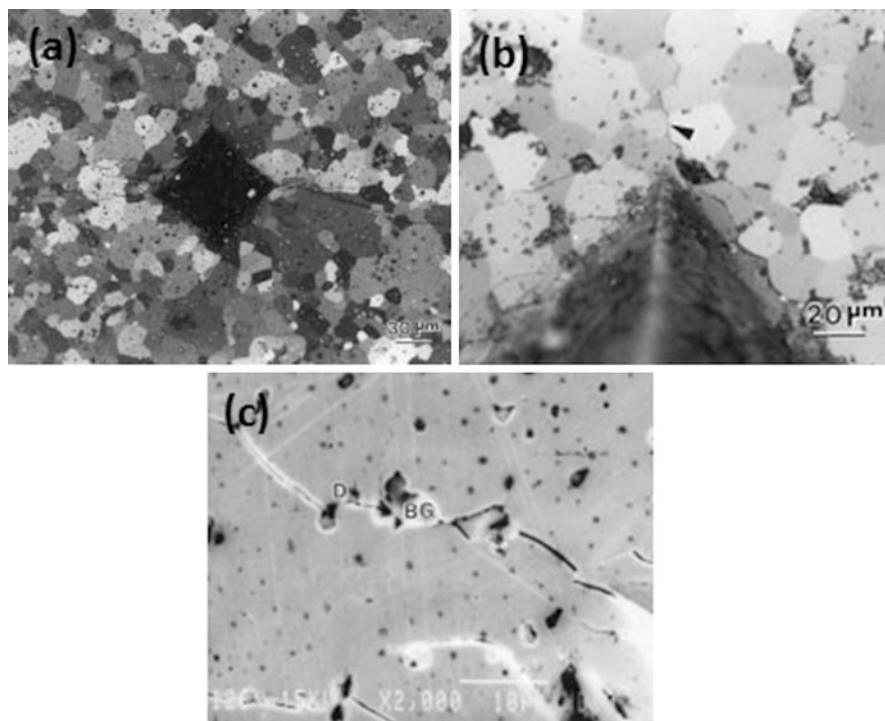


Fig. 16 SEM (SE) images showing cracks at the corners of indentations following (a) transgranular path in the MoSi_2 , (b) intergranular path in the MoSi_2 -9 at.% Al alloy, and (c) crack path in the MoSi_2 -5.5 at.% Al alloy showing evidence of deflection (D) and bridging (BG) by in-situ formed $\alpha\text{-Al}_2\text{O}_3$ particles [59]. (Reprinted with permission from Elsevier)

$\alpha\text{-Al}_2\text{O}_3$ particles has also contributed to toughening as shown in Fig. 16c [59]. Furthermore, the intergranular crack propagation leads to crack branching and deflection, which in turn enhances the crack path tortuosity and helps in increasing fracture toughness. The fracture toughness of MoSi_2 -5.5 at.% Al and MoSi_2 -9 at.% Al alloys have been found by three point bend tests on single edge notch bend tests as $4.67 \pm 0.15 \text{ MPa}\sqrt{\text{m}}$ and $6.4 \pm 0.1 \text{ MP}\sqrt{\text{m}}$, respectively, whereas that of unalloyed MoSi_2 has been reported as $4.3 \pm 0.1 \text{ MP}\sqrt{\text{m}}$.

A major limitation of the approach of brittle ceramic reinforcement addition is just a modest increase in fracture toughness, with slightly higher toughening being achieved through crack deflection or crack-bridging by the use of SiC or Si_3N_4 whiskers or through transformation toughening in ZrO_2 [102]. Selected results from a few earlier studies on fracture toughness and flexural tests on Mo-silicides having brittle phase reinforcements are shown in Table 4. The tetragonal to monoclinic phase transformation of ZrO_2 leads to compressive stresses, which not only aid in closure of cracks but also lead to microcracking in the brittle matrix. Whereas the formation of microcracks contributes to toughening by crack branching, their presence lowers the flexural strength. The compressive stresses accompanying the

Table 4 Results of selected studies to evaluate fracture toughness and flexural strengths of brittle phase reinforced MoSi₂ matrix composites

Material	Processing	Fracture toughness (MPa√m)	Fracture toughness test	Flexural strength (MPa)	Reference
MoSi ₂ MoSi ₂ -20SiC _w	Hot pressed (at 1625 °C)	5.3 8.20	Chevron-notched	140–160 310	[93]
MoSi ₂ MoSi ₂ -20TiC MoSi ₂ -20SiC _w	Hot Pressed (at 1700 °C)	4.8 5.0 6.4	3-pt. single edge notch bend	263	[104]
MoSi ₂ MoSi ₂ -30PSZ MoSi ₂ -20ZrO ₂ (unstable-YSZ)	Hot pressed (1700 °C) Hot Isostatic Pressed	2.6 6.6 7.9	Indentation		[102]
MoSi ₂ - 10ZrO ₂ -10SiC	(1700 °C)	3.8–6.8		250–600	
MoSi ₂ -30-50 Si ₃ N ₄ MoSi ₂ -30 Si ₃ N ₄ -30SCS-6	Hot pressed and HIPed	5.2 35 65	CNB (RT) 1400 °C/Ar 1400 °C/Ar		[103]

tetragonal to monoclinic phase transformation of ZrO₂ has been found to cause the plastic deformation of MoSi₂ with formation of dislocations, which also has promoted toughening. A higher density of dislocations aids in reducing the BDTT. Typical R-curve behavior could be obtained in the hybrid MoSi₂-SiC-ZrO₂ composites, and the fracture toughness has been found to be ~3 times that of MoSi₂ [92, 102]. Similar result has been observed on reinforcing Ti₅Si₃ with brittle ceramic reinforcements [5, 7, 23]. Much greater increase in fracture toughness has been observed in the hybrid composite of MoSi₂ reinforced with Si₃N₄ whiskers and continuous SiC fibers. At high temperatures (1400 °C in argon atmosphere), the fracture toughness of MoSi₂-30 vol.% Si₃N₄ and MoSi₂-30 SiC_f-30 Si₃N_{4p} hybrid composites has been found to be 35 MPa√m. and 65 MPa√m, respectively [103]. The weak interfacial bond between MoSi₂ matrix and SiC fibers leads to fiber-matrix debonding, followed by delamination and increase in crack path tortuosity. In tune with this type of failure mechanism, the plots of load against displacement have been found to be nonlinear, indicating the occurrence of noncatastrophic failure, with absorption of higher energy. Besides the fracture toughness, the flexural strength of the MoSi₂-based composites has been reported to increase significantly on reinforcement addition [100, 102].

The ductile reinforcements, which have been tried are discontinuously distributed particles, or random short fibers of Nb or Ta or continuous fibers, wires, or filaments of Nb, Mo, W, and W-1%ThO₂ [5, 7, 105–107]. The addition of discontinuous ductile reinforcements has not led to a significant increase in fracture toughness as deformation of the dispersed ductile phase is known to be constrained by the strong interfaces, particularly if chemical reaction products are formed. An example is the formation of Mo₅Si₃ at the interface between MoSi₂ and Mo, or Nb₅Si₃ in MoSi₂-Nb interfaces. Therefore, Nb foils with ceramic coating have led to formation of weak

interfaces and damage tolerant behavior with interfacial debonding followed by plastic deformation and work hardening of the ductile Nb foil. Although the increase in fracture toughness was insignificant for the MoSi_2 -Nb foil composite, the amount of energy absorbed for fracture has been found to be quite significant.

The ductile phase formed in-situ in the ternary or multicomponent intermetallic alloys formed by the use of Mo-Si-B or Nb-Si-X systems has contributed to significant increase in fracture toughness, depending on its size and volume fraction by arresting and blunting propagating cracks. Examples of crack arrest, blunting, and bridging by the ductile Mo_{ss} phase in Mo-Si-B alloy system is shown in Fig. 17a [73]. Selected results from a few earlier studies on fracture toughness and flexural tests on Mo-silicides having ductile phase contributing to toughness are shown in Table 5. In general, a range of fracture toughness of ≈ 7 – $15 \text{ MPa}\sqrt{\text{m}}$ has been observed at room temperature in the Mo-Si-B alloys [108–114].

Presence of a significant volume fraction ($\geq 30\%$) of the Mo_{ss} phase leads to toughening by crack arrest and bridging, because the plastic deformation and work hardening of the ductile phase consumes a significant amount of energy. Particularly, the Mo-Si-B alloys with coarse Mo_{ss} phase forming a more or less continuous network have shown a considerable improvement in fracture toughness to a range of 15 – $21 \text{ MPa}\sqrt{\text{m}}$. In this material, a typical R-curve behavior with crack extension is found to be more prominent [109, 110, 114] as crack-arrest by the presence of the ductile Mo_{ss} phase leads to enhanced damage tolerance [73, 110]. The load-displacement plots obtained from fracture toughness tests on three point bend specimens of these alloys, as shown in Fig. 17b, have been found to be nonlinear with distinct evidence of work-hardening of the ductile Mo_{ss} phase, which in turn increases the total energy absorbed during failure [73]. Interestingly, it has been reported that the alloy with 30 vol.% of coarse Mo_{ss} phase shows much higher fracture toughness, compared to that with about 50 vol.% fine Mo_{ss} , suggesting the importance of the size of the dispersed ductile phase for trapping or bridging a propagating crack. Kruzic et al. have shown a significantly high fracture toughness ($\sim 21 \text{ MPa}\sqrt{\text{m}}$) in case of the hot isostatically pressed Mo20Si10B alloy having a

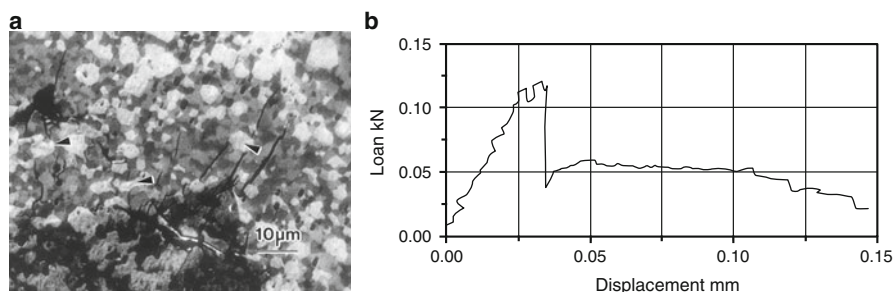


Fig. 17 (a) SEM image depicting an indentation crack being blunted by the dispersed ductile α -Mo phase in 76Mo-14Si-10B alloy; and (b) a typical load-displacement plot showing nonlinearity after peak load is reached, indicating the occurrence of non-catastrophic failure [73]. (Reprinted with permission from Elsevier)

Table 5 Results of a few studies on fracture toughness and flexural strength evaluation of Mo-silicides containing ductile phase

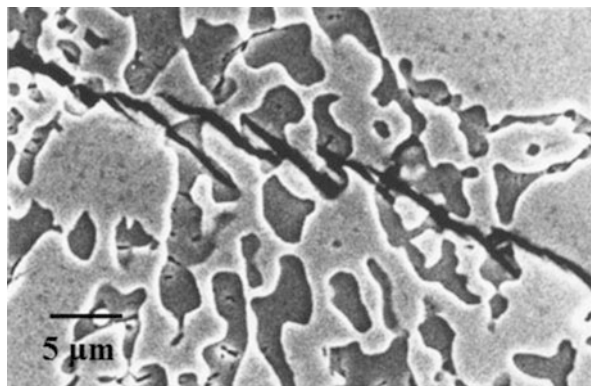
Material	Processing	Fracture toughness (MPa√m)	Fracture toughness test	Flexural strength (MPa)	Reference
MoSi ₂ -Nb (laminated) Uncoated Nb Al ₂ O ₃ coated ZrO ₂ coated	Hot Pressed (1400 °C)	15.2 ± 1.3 14.0 ± 1.5 12.8 ± 1.5	4 pt. bend Chevron notched		Xiao and Abbaschian [106]
MoSi ₂ and MoSi ₂ -20wt% Ta	Low pressure plasma spray	4.5 ± 0.173 9.97 ± 0.35	Chevron notched 4 pt. bend		Castro et al. [107]
Mo12Si8.5B Mo12Si8.5B	Powder metallurgy Ingot metallurgy, annealed At 1600 °C.	14.0–15.6 9.1–9.8	Chevron notched	376–412 484–539	Schneibel et al. [108]
Mo20Si10B	Arc-melted, HIPed At 1600 °C	13.5–15.1	Chevron notched		Schneibel et al. [109]
Mo20Si10B With coarse Mo _{ss}	HIPed At 1600 °C	21	Disc shaped CT		Kruzic et al. [110]
Mo14Si10B	Hot pressed At 1600 °C	5.0 ± 0.8	SENB	404 ± 10	Mitra et al. [73]

dispersion of coarse α -Mo phase [110]. Recently, a study by Schneibel et al. has shown that improvement in ductility of the Mo_{ss} phase by the addition of either Zr or MgAl₂O₄ particles lowers the minimum amount of the ductile phase required to achieve a noticeable increase in fracture toughness [113]. The fracture toughness shows a marked improvement with increasing temperature by ~50% at 1300 °C, because the ductility of the Mo_{ss} phase is significantly increased, and its flow stress decreases rapidly due to the enhanced thermally activated dislocation movement.

The fracture toughness values of monolithic Nb₅Si₃ is very low, and lie in the range of ≈ 1.0 – 3.0 MPa√m [96]. However, the presence of ductile Nb_{ss} in the composite microstructure of the Nb-Si based alloys along with Nb₅Si₃ has been found to enhance the fracture toughness in a significant manner. The presence of ductile Nb_{ss} phase in the niobium-silicide based multiphase composites aides in toughening of these materials by bridging or arresting of advancing cracks. In the Nb-Si-Mo alloys, the presence of coarse eutectic has been found to be more effective in bridging or blunting of cracks in comparison to fine eutectic or hypo-eutectic Nb_{ss} phase (Fig. 18) [88].

It has been reported in the literature that the fracture toughness of the Nb-Si alloys depends to a large extent on the processing conditions, which is obvious from the

Fig. 18 SEM image showing bridging or blunting of cracks by the coarse Nb_{5Si_3} lamellar constituent in the Nb-Si-Mo alloy [88]. (Reprinted with permission from Elsevier)



selected results of a few earlier studies on fracture toughness of the Nb-silicides having ductile phase, as shown in Table 6. For example, the fracture toughness of the Nb-10 Si (at.%) alloy has been found as $\approx 9.6 \text{ MPa}\sqrt{\text{m}}$ in arc-melted condition, and this is significantly enhanced to the range of $\approx 14\text{--}22 \text{ MPa}\sqrt{\text{m}}$ on being processed by directional solidification followed by extrusion and heat treatment at 1500°C for 100 h [25]. Furthermore, a study by Rigney and Lewandowski has shown typical R-curve behavior for the Nb-Si alloys, which is characterized by rise in stress intensity factors from 8 to $36 \text{ MPa}\sqrt{\text{m}}$ with increasing crack length [78]. The fracture toughness of the as-cast Nb-Si alloy is lowered to $\approx 5.4 \text{ MPa}\sqrt{\text{m}}$ on increasing the Si content to about 16 at.%, as the volume fraction of Nb_5Si_3 is raised. However, on annealing at 1500°C for 100 h, the fracture toughness of this alloy has been found to exhibit a modest increase to $\approx 7.5 \text{ MPa}\sqrt{\text{m}}$ [5], and this value increased to $9 \text{ MPa}\sqrt{\text{m}}$ on alloying with W and B [28, 104], whereas a more significant increase to $13\text{--}16 \text{ MPa}\sqrt{\text{m}}$ has been observed on addition of Ti, Cr, and Al [84]. Further improvement in the fracture toughness to the range of $18.2\text{--}23.3 \text{ MPa}\sqrt{\text{m}}$ has been reported for the alloys containing Hf [28]. Besides, the results in Table 6 also show that there is a remarkable increase in flexural strength either on alloying or on secondary processing like hot extrusion. Therefore, multicomponent Nb-Si based alloys with composite microstructure are considered to be promising for engineering applications.

The fracture toughness values of monolithic WSi_2 [95], Ti_5Si_3 [22, 23], and Nb_5Si_3 [96] are very poor and lie in the range of $\approx 1.5\text{--}4.0 \text{ MPa}\sqrt{\text{m}}$. The single crystals of WSi_2 tested with [001] direction parallel or perpendicular to the notch during 4-point bend tests have shown fracture toughness of ≈ 3.1 or $3.7 \text{ MPa}\sqrt{\text{m}}$, respectively [95]. Similar fracture toughness values could be estimated from the tests on the single crystals of the (Mo,W) Si_2 alloys as well. Fracture toughness does not increase much on alloying of the aforementioned intermetallics, because the metal-silicon covalent bond-directionality is hardly altered.

The major problem with Ti_5Si_3 is its high coefficient of thermal expansion (CTE) anisotropy (~ 4.1) along c and a axes [99], which results in significantly large internal stresses being experienced during cooling from the temperature of processing, and

Table 6 Selected results of fracture toughness and flexural tests carried out on variously processed Nb-silicide based alloys

Material	Processing	Fracture toughness (MPa√m)	Mechanical tests	Flexural strength (MPa)	Reference
Nb-10 Si Nb-16 Si	As-cast As-cast, 1500 °C: 100 h Extruded Extruded, 1500 °C: 100 h As-cast As-cast 1500 °C: 100 h	8.9–9.5 9.6–9.7 16.4–16.5 20.3–21.1 5.4 6.4–8.1	SENB 3 pt. bend Tests	480 500	[71]
Nb-Ti-Hf-Cr-Al-Si	As-cast	18.2–23.3	SENB, tensile	820	[33]
Nb-10 Si	As-cast, hot extruded	24.1 ± 2.2	SENB	638 ± 104	[78]
Nb(10–22)Si Nb(5–22)Si5Mo Nb(10–22) Si15Mo	Arc melted or directionally solidified	4–12 10–15 6–8	SENB		[115]
Nb19.1Si5.2Mo Nb17.9Si26.3Mo Nb12.8Si4.1Mo Nb12.3Si14.8Mo	Arc-melted	8.8 ± 0.8 5.5 ± 0.2 6.6 ± 0.3 5.6 ± 0.5	SENB		[88]
Nb10W10Si6B	Arc-melted, 1597 °C, 100 h	8–9	SENB, tensile σ_{YS} σ_{UTS}	840–935 1300–1450	[104]
Layered: Nb-Nb ₅ Si ₃	Field activated reaction and densification	21–30	Micro- indentation		[115]

therefore, microcrack formation is caused inside the grains [21, 23, 116]. It has been conclusively shown that grain size reduction in Ti₅Si₃ significantly lowers the adverse impact of CTE anisotropy, because the possibility of microcrack formation due to thermal stresses is reduced, and as a result, increase in both hardness and fracture toughness has been reported [21]. Therefore, the room temperature fracture toughness of Ti₅Si₃ has been found to increase from 2.1 MPa√m [22] for the coarse-grained (20–50 μm size) microstructure to 2.7 MPa√m [117] or 3.2 MPa√m [23] for relatively fine-grained (5–6 μm size) samples. Furthermore, typical R-curve type behavior has been also observed suggesting improvement in fracture resistance with reduction in the grain size. While the fracture toughness of the coarse-grained (20–50 μm) has been reported to increase to 7.5 MPa√m at 800 °C, it increases to about 12 MPa√m for grain size in the range of 5–6 μm [118]. Therefore, it can be inferred that the reduction in grain size is more helpful for increase in fracture toughness at elevated temperatures than that at the ambient temperature.

Moreover, both hardness and fracture toughness of the polycrystalline Ti_5Si_3 could be noticeably improved either by alloying or by adding reinforcements [23, 118, 119]. The positive effect of alloying on reduction of both directionality of interatomic bonding and CTE anisotropy has been demonstrated. For example, alloying of Ti_5Si_3 with Nb has resulted in a significant reduction in the CTE anisotropy, along with the reduced propensity for microcrack formation [99, 120]. Furthermore, the presence of ceramic reinforcements leads to R-curve behavior through crack deflection and bridging [23]. Figure 19a and b compare the indentation cracking pattern observed in Ti_5Si_3 and Ti_5Si_3 -TiC composite. The composite material has shown much greater frequency of crack deflection at higher angles due to the presence of TiC reinforcement, and therefore, the crack path appears to be highly tortuous (Fig. 19c). Further improvement in fracture toughness can be achieved in this material by suitable design of microstructure, processing, and addition of ductile phase. For example, a unidirectionally solidified Ti- Ti_5Si_3 composite produced by electron beam zone melting has exhibited a much higher fracture toughness of $\approx 11 \text{ MP}\sqrt{\text{m}}$ at the ambient temperature [118].

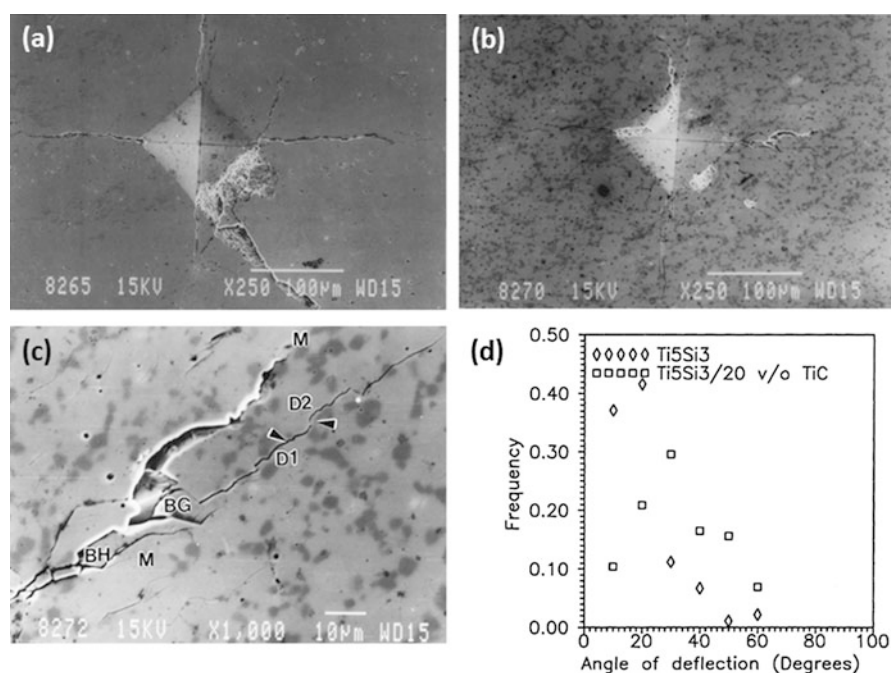


Fig. 19 SEM (SE) image depicting Vickers indentation with cracks at corners in (a) Ti_5Si_3 and (b) Ti_5Si_3 -TiC composite; (c) magnified view of the indentation crack in Ti_5Si_3 -TiC composite showing clear evidence of crack branching (BH), bridging (BG), and deflection (D2), as well as (d) the plots of frequency against crack deflection angles [23]. (Reprinted by permission from Springer Nature)

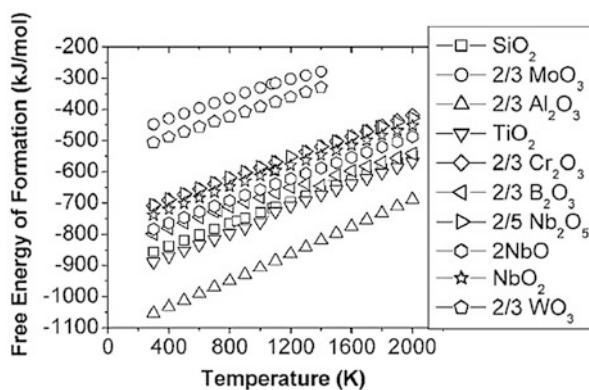
Oxidation Behavior

Resistance against environmental degradation by oxidation is one of the key properties of interest for the silicide-based materials to be used at elevated temperatures. Basic information on oxidation behavior of structural silicides can be found in some of the earlier reviews [121, 122]. Silicides and silicon-based ceramics derive their resistance to oxidation from a continuous and adherent film of amorphous SiO_2 . The silicides used at elevated temperatures should be of optimum composition, so as to form a protective passive silica-rich scale to restrict environmental damage. Even if a protective scale is able to form at elevated temperatures, its growth rate at intermediate temperatures is too sluggish to ensure protection against oxidation. Absence of a stable and protective scale along with defects in the silicides of Mo, Nb, or Ti can lead to accelerated or catastrophic oxidation under. The possible mechanisms of oxidation at different temperatures need to be well-understood for devising ways of restricting the amount of environmental degradation. Suitable silicide-based coatings with an acceptable level of oxidation resistance have been also developed for the intermetallic alloys, where formation of a passive scale is not possible. In this section, the oxidation behavior is being discussed along with the mechanisms involved in formation of stable and protective scale, which should also be strongly adherent to the underneath alloy substrate.

The silicides being considered for application at elevated temperatures are protected against environmental degradation by formation of a passivating silica-based scale, which restricts further oxidation of the underlying substrate. For the oxide scale to be fully protective, the following requirements should be met [122]:

- (i) The oxide in the outer scale should have higher thermodynamic stability compared to that of the oxides of other alloying elements (Fig. 20).
- (ii) The rate of growth should be slow to ensure it is continuous, dense, and pore-free.
- (iii) The oxide scale should have a strong adherence with the underneath substrate, along with its resistance to spallation.

Fig. 20 Plots depicting the variation of free energy per mole of oxygen with absolute temperature for formation of selected oxides [123]



(iv) Ability to heal itself on spallation or damage.

Oxidation reactions causing the formation of protective oxide scales generally follow a parabolic rate law as follows:

$$(\Delta w)^2 = k_p \cdot t \quad (2)$$

where Δw is the mass gain due to oxidation, k_p is the parabolic rate constant, and t is the duration of exposure. This reaction can also be written as:

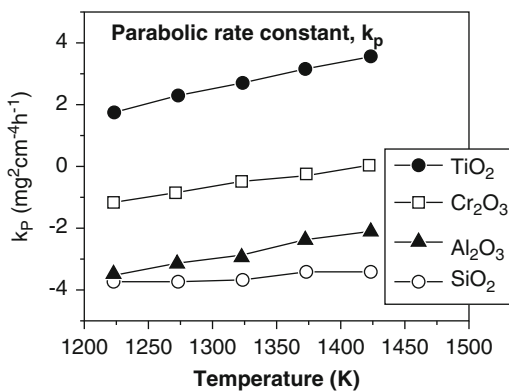
$$x^2 = k_p \cdot t \quad (3)$$

where x is the thickness of the oxide scale. Experimental results often show minor deviations from the parabolic rate law. A more general form of the above-mentioned rate equation is:

$$(\Delta w)^n = k \cdot t \quad (4)$$

where n is oxidation exponent, and k is rate constant. The kinetics can be considered as linear, parabolic or slower than parabolic if $n \approx 1, 2,$ or > 2 , respectively. The rate of oxide scale growth is controlled by diffusion of either oxygen anions or oxidizing species comprising the metallic atoms in the intermetallic alloy. The process of diffusion is driven by electrochemical potential gradient across the oxide scale. Therefore, diffusion of the slowest species through the oxide scale can be considered as the rate controlling step in formation of the oxide scales. The diffusion kinetics of a given species through any oxide scale is dependent on the latter's crystallographic and defect structure as well as electronic characteristics (n-type or p-type). Plots depicting the variation of parabolic rate constants of selected oxide scales with temperature are shown in Fig. 21 [5, 124]. The low diffusivities of anions and cations manifest in low parabolic rate constants for the growth of SiO_2 and Al_2O_3 ,

Fig. 21 Plots depicting the variation of parabolic rate constants for growth of selected oxide scales with temperature [5, 124]

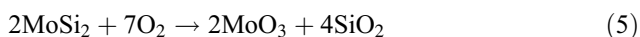


when compared to other oxides (Fig. 21). Therefore, it is appropriate to infer that the scales of Al_2O_3 and SiO_2 are the most protective, because of their high thermodynamic stability and low diffusivities for both cations and anions. At temperatures ≥ 900 °C, the growth rate of SiO_2 is less than that of Al_2O_3 , whereas the opposite is observed at lower temperatures. Therefore, at temperatures ≥ 900 °C, the SiO_2 scale formed on the silicides offers much better oxidation resistance compared to the Al_2O_3 films formed on the aluminide-based intermetallics.

The scale of SiO_2 is protective at temperatures up to 1700 °C, beyond which increase in its defect density enhances the penetration of oxygen anions through the scale [125]. Among the silicides, the best oxidation resistance is demonstrated by MoSi_2 , which also shows increase in resistivity with increasing temperature. Therefore, this material is used as heating element in oxidizing atmospheres and is also of interest for developing as a structural material. However, formation of a protective scale is not possible, if simultaneous oxidation of the constituent metallic alloying elements occurs along with formation of SiO_2 and the oxides of alloying elements remain in the scale.

Molybdenum Silicides

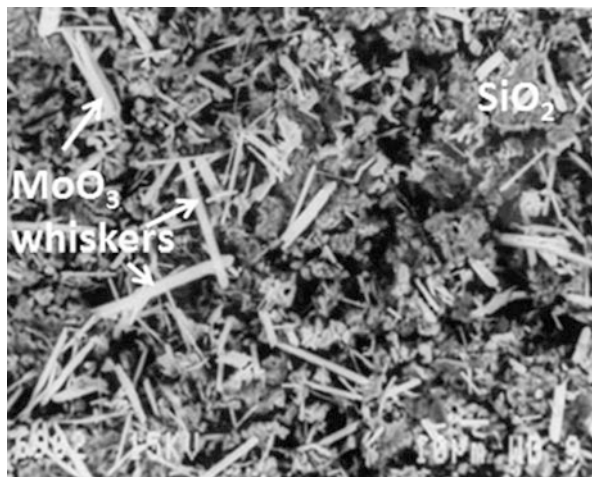
The oxidation behavior of MoSi_2 is found to vary based on the temperature range of study, which are as follows 400–600 °C, 600–1000 °C, 1000–1700 °C, and that above 1700 °C. These temperature regimes may be considered as a modification of the subdivisions discussed in an earlier publication by Bertiss et al. [126]. In the temperature range of 400–600 °C, MoSi_2 undergoes accelerated oxidation ending with disintegration into lumps of powders, which has been termed as pesting in the literature [127–131]. It has been proposed that the oxidation of MoSi_2 proceeds according to the reaction:



The SiO_2 scale is not continuous and protective, because of the competitive growth with that of Mo-oxides, particularly MoO_3 , which does not volatilize much at 500 °C. The slow diffusion of Si at lower temperatures also explains the cause for lower parabolic rate constant for the growth of SiO_2 than that of MoO_3 [127]. It has been reported that the diffusivity of Si increases above 800 °C, particularly due to the high concentration of Si vacancies in MoSi_2 [132].

Whiskers, rod, or plate-shaped crystals of MoO_3 have been found in the oxide scale after an incubation period during exposure of MoSi_2 and MoSi_2 -SiC composite at 500 °C (Fig. 22) [133]. Pesting of MoSi_2 is known to be most severe at 500 °C. Embrittlement of the grain boundaries, which provides the short circuit paths of diffusion of oxygen, was proposed as the mechanism by Westbrook et al. [131]. Preferential oxidation has been observed at cracks and porosities, with the chances of pest-disintegration increasing with increasing amount of porosities [130]. Yanagihara et al. have demonstrated that the initial cracks left by processing have a bigger role in

Fig. 22 Top surface of the oxide scale formed on MoSi₂-20 vol.% SiC composite exposed at 500 °C for 250 h [133]



pest disintegration as compared to the grain boundaries, because the formation of the initial oxide of Mo-Si-O formed at crack tips involves 200% volume expansion, accompanied by increased stress concentration [134]. Alloying of MoSi₂ with elements, such as Al, Ti, Zr, and Y, having affinity for oxidation stronger than that of Si, is reported to be suppressing pesting because these elements oxidize selectively, arresting the internal oxidation of Si [135]. A typical oxidation reaction can be written as:



Meschter has proposed that the transition from pesting to non-pesting type, that is non-protective to partially protective oxidation, takes place in MoSi₂ in the range of 500–550 °C [128]. Further observations have suggested that the oxide scales formed in the temperature range of 600–1000 °C are non-protective, although pesting does not occur [125, 126]. The continuous formation and volatilization of MoO₃ leaves behind pores and does not allow a continuous film of SiO₂ to form below 1000 °C. At temperatures in the range of 1000–1700 °C, a stable oxide scale of SiO₂ is able to form, as shown in Fig. 23. This oxide scale is protective, and the kinetics is found to follow a parabolic rate law. The MoO₃ forms during heating and then volatilizes. Thereafter, an adherent, continuous, viscous, and self-healing SiO₂ scale is created as a barrier layer between oxygen and the underlying alloy.

In the oxidation studies at temperatures up to 1775 °C, Yanagihara et al. have reported a higher rate of oxidation in the Mo(Si_{1-x}Al_x)₂ intermetallic alloy, compared to that in MoSi₂ [137]. However, in case of cyclic oxidation up to 1750 °C, the spallation of the Mo(Si_{1-x}Al_x)₂ has been found to be lower in comparison to that of MoSi₂, because amorphous SiO₂ to β-crystoballite phase transformation accompanied by volume expansion and internal stresses is inhibited in case of the former alloy due to kinetic reasons. The suppression of crystallization of SiO₂ in Mo(Si_{1-x}Al_x)₂

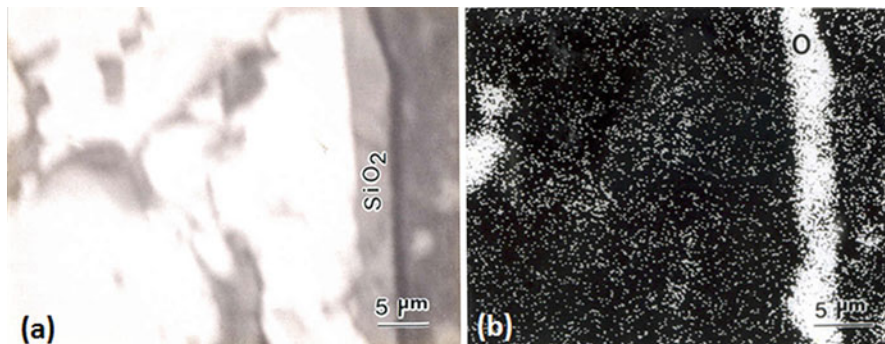


Fig. 23 Oxide scale of MoSi_2 after exposure in air at $1200\text{ }^\circ\text{C}$: (a) EPMA (BSE) image and (b) wavelength-dispersive x-ray map of O [136]. (Reprinted with permission from Elsevier)

explains why better adherence of this oxide scale is observed at higher temperatures. For minor alloying with 2.8, 5.5, and 9 at.% Al, the isothermal oxidation rates at $1200\text{ }^\circ\text{C}$ in air have been found to be higher compared to that of MoSi_2 [136]. The oxide scale in the MoSi_2 -Al alloys has been reported to be constituted by a mixture of $\alpha\text{-Al}_2\text{O}_3$ and SiO_2 in case of the MoSi_2 -2.8 at.% Al alloy, and by $\alpha\text{-Al}_2\text{O}_3$ in case of the MoSi_2 -5.5 and 9 at.% Al alloys. The presence of Al_2O_3 in place of SiO_2 may be justified by lower free energy of formation of the former oxide than that of latter, and reasonably higher activity of Al in these MoSi_2 -5.5 and 9 at.% Al alloys.

It has been proposed that B_2O_3 forms in the scale of MoSi_2 - TiB_2 composite and protects against pesting in the temperature range of $400\text{--}600\text{ }^\circ\text{C}$ [138]. Here too, SiO_2 has a lower free energy of formation per mole of oxygen, but B_2O_3 forms due to kinetic reasons. While MoSi_2 - SiC_f (SCS-6) composites have been disintegrated to powder on subjecting to 24 cycles between ambient temperature and $500\text{ }^\circ\text{C}$, MoSi_2 -30 vol.% Si_3N_4 - SiC_f (SCS-6) hybrid composite is found to maintain its integrity after even 200 cycles, as reported by Kowalik and Hebsur [139].

The mechanisms involved in improvement of oxidation resistance of Mo_5Si_3 through boron additions and Mo-Si-B alloys have been well-investigated. It has been observed that alloying of Mo_5Si_3 with about 2 wt.% B leads to a decrease in the rate of oxidation by five orders of magnitude at $1200\text{ }^\circ\text{C}$ and also arrests catastrophic pest disintegration at $800\text{ }^\circ\text{C}$ [140]. Normally, the entire time-span of oxidation is classified into a period of rapid mass loss, followed by that of steady state or a reduced rate of oxidation. It has been proposed that the formation of B_2O_3 with reasonably high fluidity at $800\text{ }^\circ\text{C}$ enables viscous sintering of the oxide scale to close the pores, which forms during the transient oxidation period due to volatilization of MoO_3 [140]. The oxidation behavior of the Mo-Si-B alloys containing $\alpha\text{-Mo}$, Mo_3Si , and Mo_5SiB_2 as constituent phases is quite different from that of alloys having a phase mixture of Mo_3Si , Mo_5Si_3 , and Mo_5SiB_2 . It is intuitive that the Si/B ratio plays a very critical role in the oxidation behavior of the Mo-Si-B alloys. Studies on the oxidation behavior of near-eutectic Mo-Si-B alloys with Si/B ratios of 0.5, 0.71, and 1.0 by Supatarawanich et al., have shown that the oxidation resistance

at 800 °C is greater in an alloy with Si/B ratio of 0.5, because of having higher volume fraction of Mo_5SiB_2 phase [141]. On the other hand, the alloy with Si/B ratio of 1.0, having a higher volume fraction of Mo_3Si , has shown the best oxidation resistance at 1300 °C.

Studies on oxidation behavior of the 76Mo14Si10B alloy have shown relatively minor mass gain in the range of 400–600 °C and unabated mass loss between 700 °C and 800 °C due to formation and subsequent vaporization of MoO_3 (Fig. 24) [142]. On the other hand, on exposure of this alloy in the range of 800–1300 °C, mass loss has been observed in the initial stages, which is followed by a stable regime of no change in mass (Fig. 24) [143]. The exposure at 1150 °C leads to the formation of a more or less stable and protective scale of $\text{B}_2\text{O}_3\text{-SiO}_2$ after noticeable amount of mass loss during the initial transient stage. Formation of this protective scale on prior exposure of 76Mo14Si10B alloy at 1150 °C has been found to resist the damage due to thermal shock caused by air cooling and also significantly reduce the oxidation rate at the intermediate critical temperature range of 700–900 °C [144]. A recent study has shown the transient stage at 1150 °C to last for 8 min, when mass loss occurs due to preferential oxidation of the Mo_{ss} phase to form volatile MoO_3 , as illustrated in Fig. 25 [145]. It has been noticed that oxidation of Mo_{ss} phase occurs first, and this is followed by the formation of silica and borosilicate glass by oxidation of Mo_3Si and Mo_5SiB_2 , respectively. The oxidation of Mo_{ss} leads to the formation and vaporization of MoO_3 , which in turn causes the formation of cavities. These cavities are then covered by viscoplastic flow of borosilicate glass, which protects the underneath substrate from further oxidation. The SEM images depicting the various stages of oxide scale formation are shown in Figs. 26 and 27.

Based on a study on the formation mechanism of protective borosilicate scale in case of the Mo-3 wt.% Si-1 wt.% B alloy containing a mixture of Mo_{ss} , Mo_3Si , and

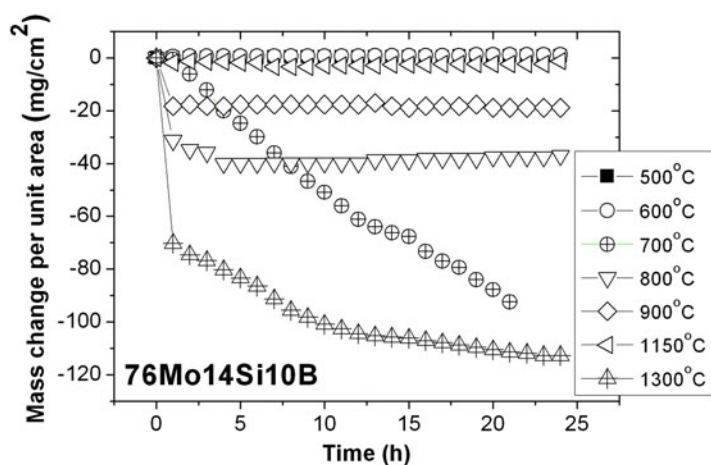


Fig. 24 Plots showing the change in mass of 76Mo-14Si-10B alloy isothermally exposed for 24 h in the temperature range of 500–1300 °C [142, 143]

Fig. 25 Plots depicting the variation of mass loss with time of exposure up to 10 min and 24 h. It shows that a stable regime of no observable mass change is observed after exposure for 8 h. The results of test up to 24 h show that the stable regime reached after 8 min is continued up to 24 h [145]. (Reprinted with permission from Elsevier)

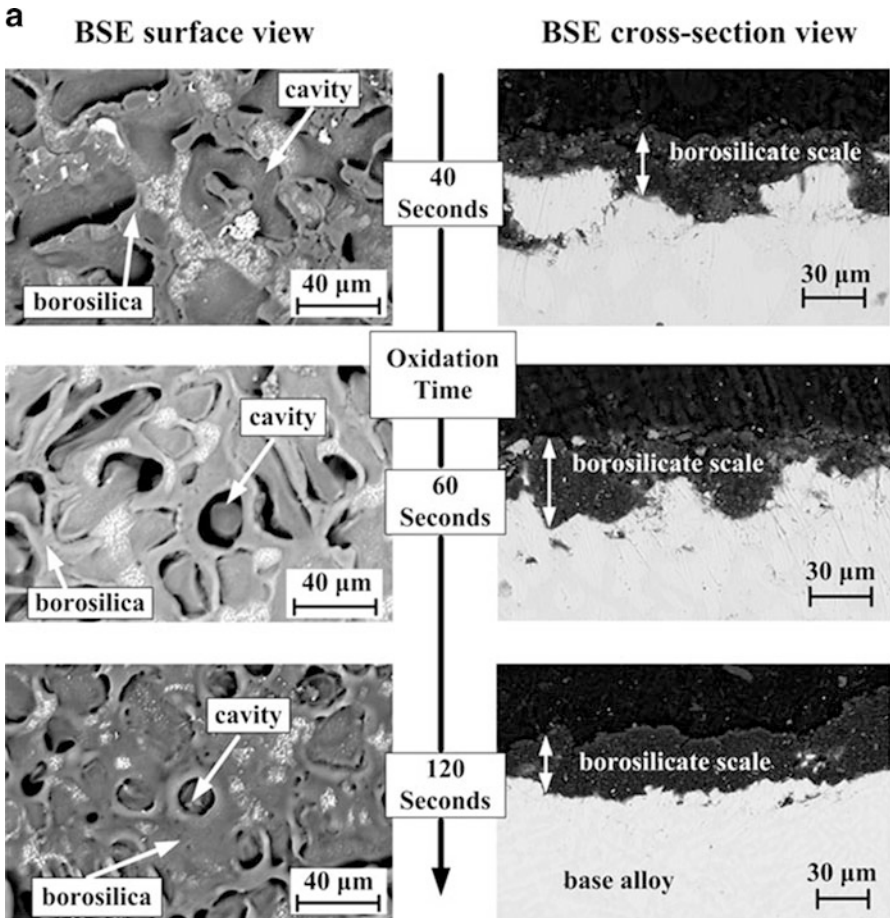
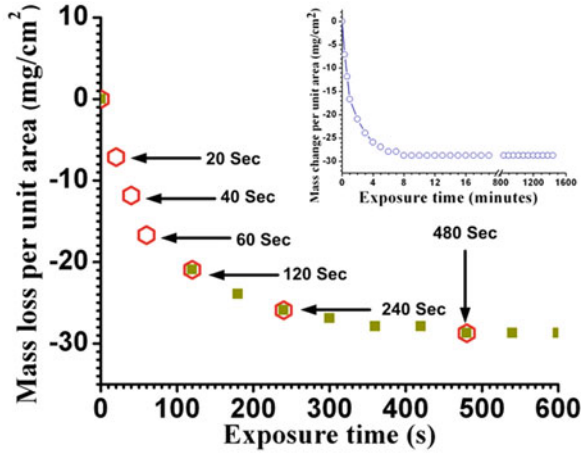


Fig. 26 (continued)

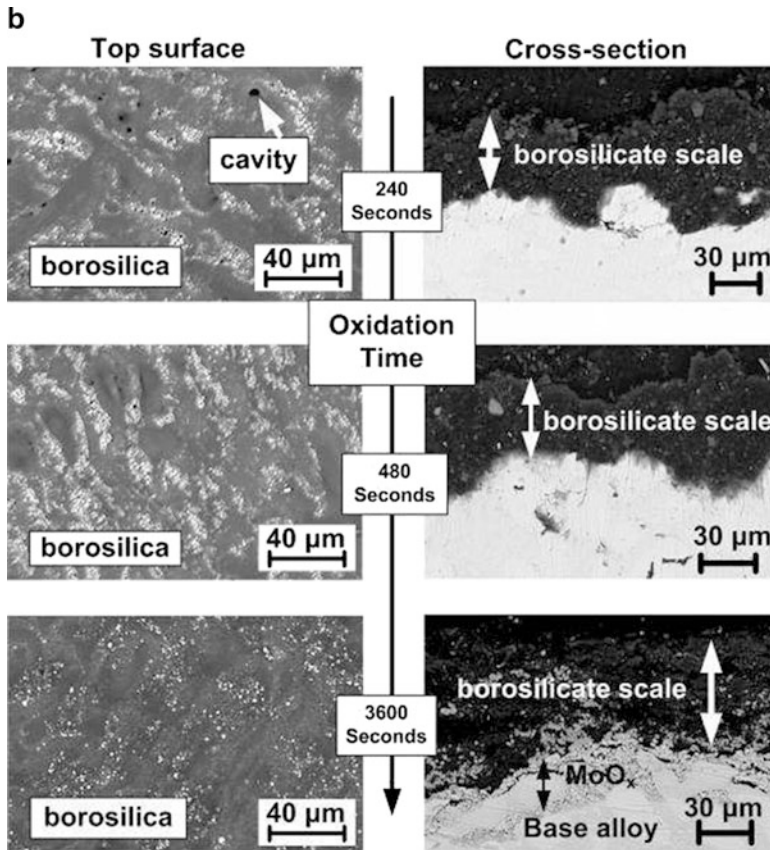
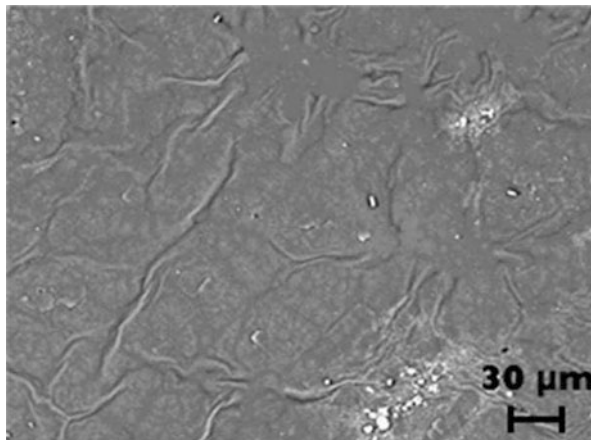


Fig. 26 SEM (BSE) images depicting the morphology of the top surface of the oxide scale formed on the 76Mo-14Si-10B alloy after: (a) 40 s, 60 s, 120 s of exposure (left) and BSE images of the oxide-alloy cross-section (right); and (b) after 240 s, 480 s, 3600 s of exposure (left) and BSE images of the oxide-alloy cross-section (right) [145]. (Reprinted with permission from Elsevier)

Mo₅SiB₂ phases, Helmick et al. have proposed the following stages: (i) the borosilicate scale develops channels at locations corresponding to interphase boundaries within the alloy microstructure in the initial stages of development; and (ii) vaporization of MoO₃ through these channels facilitates the accumulation of B₂O₃-SiO₂ on the underneath MoO₂ surface [146]. It is intuitive that the viscosity plays a major role as it controls the ability of B₂O₃-SiO₂ scale to flow and fill up the pores and channels left by vaporization of MoO₃. The viscosity of this scale is controlled by temperature and the amounts of B₂O₃ and MoO₃ dissolved in it. The presence of Mo or MoO₂ in preference to the MoO₃ in the oxide scale proves that the borosilicate or SiO₂ layer acts as an effective barrier limiting the oxygen flux to oxide-alloy interface. It has been shown by Das et al. that formation of impervious B₂O₃-SiO₂ scale at the surface at the end of transient stage of oxidation leads to

Fig. 27 SEM image depicting evidence for viscoplastic flow of B_2O_3 - SiO_2 scale on the surface of 76Mo-14Si-10B alloy [145]. (Reprinted with permission from Elsevier)



reduction of partial pressure of oxygen at the alloy-oxide interface, which leads to reduction of Mo-oxides to Mo following the sequence, $MoO_3 \rightarrow MoO_2 \rightarrow Mo$ [147]. It has been also reported that addition of Ce to the Mo-Si-B alloys reduces the duration of transient stage in the temperature range of 900–1300 °C and makes the subsequent steady state regime more well-defined. On the other hand, Al addition has not been found to have a deleterious effect on the stability of the borosilicate scale due to dissolution of Al_2O_3 followed by precipitation of Al-borate and mullite. This observation has been found to be consistent with the results reported earlier by Paswan et al. [142–144].

Yoshimi et al. have shown that the incorporation of SiO_2 in the microstructure of the Mo-Si-B alloys causes a significant rise in oxidation resistance [148]. A study by Rioult et al. to examine the effect of microstructural size scale on oxidation behavior of Mo-14.2Si-9.6 (at.%) B alloys containing $Mo_{ss} + Mo_3Si + Mo_5SiB_2$ has shown that the samples having refined microstructures with finer phase size and larger interfacial area exhibit a reduced transient stage of oxidation required to form a protective oxide scale, which in turn is responsible for superior oxidation resistance [149]. It has been shown that a more uniform distribution of the Mo_5SiB_2 phase in the microstructure of the Mo-Si-B alloys enhances the diffusivity of B into the porous SiO_2 -rich glass formed above the Mo_3Si , which in turn enhances its self-healing capacity to form a continuous and protective glassy scale on the surface. Another study has shown that addition of 1 at.% Zr to Mo-9Si-8B alloy has also shown reduced transient period of oxidation, which in turn has lowered the net mass till 1100 °C [150]. The reduction of transient stage has been attributed to enhanced kinetics of formation of the protective oxide-scale promoted by enhanced diffusivity of Si and B in the refined microstructure with larger interfacial area. On the other hand, formation of ZrO_2 and its phase transformation in the oxide scale has led to formation of cracks and accelerated oxidation at temperatures ≥ 1200 °C [150]. However, a recent study by Kumar et al. on the oxidation behavior of arc-melted or spark-plasma sintered Mo-14Si-10B-2Zr (Zr added to Mo-14Si-10B at the expense of Mo

keeping Si:B = 1.4:1) and 77.5Mo12Si8.5B2Zr (Zr added to Mo-12Si-8.5B at the expense of Mo keeping Si:B = 1.4:1) has exhibited superior oxidation resistance compared to the base alloys in the investigated temperature range of 800–1300 °C [151]. This observation has been ascribed to the consumption of volatile MoO₃ to form Mo(ZrO₄)₂, as well as the microstructural refinement to enhance the kinetics of formation of protective borosilicate scale. Formation of ZrSiO₄ has been observed in case of the arc-melted alloy samples exposed at 1300 °C and in case of the spark-plasma sintered alloys at temperatures ≥1000 °C. As most of the ZrO₂ has been consumed in formation of Mo(ZrO₄)₂ or ZrSiO₄, the damage caused by the stresses introduced by its phase transformation could be avoided in these alloys. Moreover, ZrO₂ is known to dissolve in B₂O₃–SiO₂ glass, and stabilize it with increase in its density and viscosity, by increasing the strength of SiO⁴⁺ tetrahedral network, and reducing the tendency of glass to crystallize. These observations are different from those reported in case of the study on oxidation behavior of the Mo-9Si-8B, probably due to higher Si content and Si/B ratio in the alloys examined by Kumar et al.

A study by Kumar et al. has shown that 0.5 or 1 at.% Fe in addition to Mo-14Si-10B alloy leads to refinement of Mo_{ss} dendrites as well as Mo₃Si + Mo₅SiB₂ eutectic, which in turn have enhanced the kinetics of borosilicate scale formation, thereby causing a significant reduction of net mass loss at temperatures in the range of 800–1300 °C, as shown in Fig. 28 [152]. Addition of Fe as alloying element at the expense of Mo has also led the reduction of Mo_{ss} volume fraction by 9 vol.%, which has reduced the amount of MoO₃ formed in the initial or transient stage of oxidation. Furthermore, the presence of Fe²⁺ and Fe³⁺ as network former and network modifier,

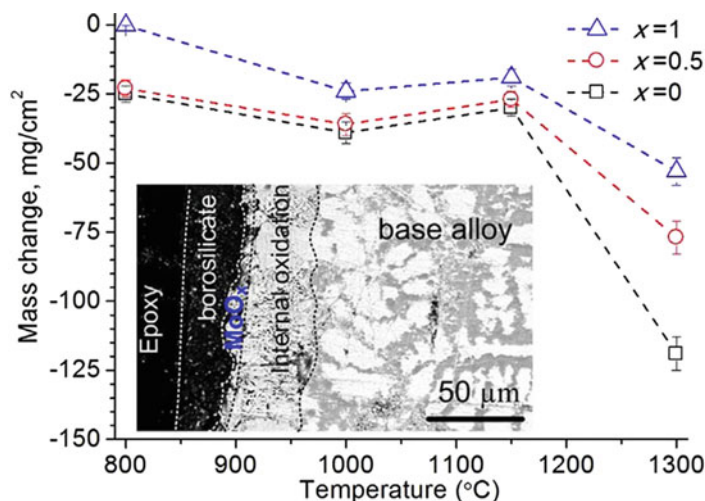


Fig. 28 Plots depicting the variation of net mass change in Mo-Si-B-Fe (0, 0.5, 1 at.%) alloy after exposure for 24 h with temperature, along with an SEM (BSE) micrograph depicting the oxide scale [152]. (Reprinted with permission from Elsevier)

respectively, is known to enhance its fluidity of the borosilicate scale, which in turn has aided in its sintering with closure of porosities. The hardness measured after removal of the oxide scale has shown a decrease of ~4–7%, indicating that damage in the subsurface region is limited as ingress of oxygen is inhibited by formation of protective oxide scale. Experiments on oxidation of the Mo-14Si-10B alloy as well as those having 0.5 or 1 at% Fe have also less mass, when exposed in moist air at temperatures in the range of 700–1300 °C [153, 154].

It may be noted that although refinement of microstructure promotes the oxidation resistance by enhancing the kinetics of oxide scale formation, presence of coarse and interconnected Mo_{ss} is reported to be desirable for high-fracture toughness. Therefore, optimization of microstructure is required. Additionally, surface treatments or coatings are being developed for protection against oxidation. Sakidja et al. have developed a process for pack-cementation coating of Al on the Mo-rich Mo-Si-B alloys in order to form a coating of Mo₃Al₈ rich layer, which leads to the formation of protective Al₂O₃ scale on the surface [155]. This scale has been found to be protective in a wide temperature range of 732–1372 °C. Further, it has been also shown that Si pack-cementation of Mo-Si-B alloy leads to the formation of an outer layer of MoSi₂ [156]. It may be noted that during high temperature exposure, this MoSi₂ layer is further converted by inter-diffusion of constituent elements to B-containing Mo₅Si₃ in contact with the Mo₅SiB₂ layer, and therefore, the oxidation resistance is significantly enhanced.

In a study by Majumdar, pack siliconization of the Mo–9Si–8B–0.75Y (at.%) alloy has been carried out with the objective of forming MoSi₂ coating at the surface [157]. A continuous layer of MoB has been reported to develop at the MoSi₂ coating-alloy substrate interface on isothermal and cyclic exposure (4 cycles) at 750 °C and 900 °C, respectively, whereas an additional interlayer of Mo₅SiB₂ between MoB and alloy has been found after cyclic exposure (4 cycles) at 1400 °C. Presence of an inner layer of MoB or MoB+Mo₅SiB₂ between outer MoSi₂ coating and the investigated alloy is reported to have acted as an effective diffusion barrier, restricting the depletion of Si from MoSi₂ and formation of Mo₅Si₃ with inferior oxidation resistance during exposure at 750 °C and 900 °C. However, on cyclic exposure for 4 cycles at 1400 °C, a layer of B doped Mo₅Si₃ has been found to form at the MoSi₂-MoB interface. A continuous and self-healing film of SiO₂ has been found to form after isothermal or cyclic exposures at 750 °C, 900 °C, and 1400 °C. The cracks developed during thermal cycles are reported to be healed by flow of SiO₂, and therefore, oxidation resistance could be significantly improved.

Titanium Silicides

Ti₅Si₃ processed by hot-isostatic pressing of powders obtained by pulverizing of arc-melted buttons has shown catastrophic degradation on exposure at 1000 °C [158]. In contrast, a study by Rosenkranz et al. has shown that the

oxidation kinetics of Ti_5Si_3 at 1000 °C typically follows a parabolic rate law [22], where the oxide scale is constituted by TiO_2 and SiO_2 . This observation may be attributed to slightly lower or comparable free energy of formation of TiO_2 compared to that of SiO_2 at a given temperature, as shown in Fig. 20. Studies by Thom et al. in the temperature range of 700–1000 °C has shown that decrease in grain size leads to increase in oxidation rates [158]. This observation has indicated that grain boundary diffusion has a major role to play in the formation of oxide scale, comprising predominantly TiO_2 (rutile) with a relatively less amount of SiO_2 , which has been found to grow in thickness with increasing temperature.

A study on Ti_5Si_3 samples containing 5% TiSi in the microstructure and processed by hot-pressing of $\text{TiH}_2 + \text{Si}$ powders has shown excellent resistance to oxidation at temperatures up to 1200 °C [159]. As observed in this study, the values of “ n ” [in $(\Delta W)^n = kt$] have been found to be 3.819 at 1200 °C and 0.732 at 1300 °C. In other words, the oxidation kinetics follows a rate slower than that predicted by parabolic rate law at 1200 °C, whereas it is significantly larger at 1300 °C (Fig. 2b). Further, the oxidation rates are found to be much larger at 1400 °C. In a similar manner, Ti_5Si_3 processed by electron beam melting and containing small amounts of Ti_5Si_4 and TiSi in its microstructure has shown excellent oxidation resistance with parabolic rate law being followed at 1200 °C [160]. Furthermore, the oxidation resistance of the Ti_5Si_3 samples containing excess Si (such as $\text{Ti}_5\text{Si}_{3.2}$) or $\text{Ti}_5\text{Si}_3\text{C}_{0.5}$ has been found to be impressive at 1000 °C [161], quite unlike that reported in Ref. [158]. This observation suggests a strong influence of the density and composition of Ti_5Si_3 on its oxidation behavior.

The oxide scale formed at 1200 °C has shown an outer layer constituted by TiO_2 and inner layer containing SiO_2 (Fig. 29) [159]. Considering the fact that TiO_2 has a slightly lower free energy of formation and a higher parabolic rate constant compared to that of SiO_2 , and the partial pressure of oxygen required for Ti/ TiO_2 thermodynamic equilibrium is less than that of Si/ SiO_2 , it is possible that formation of TiO_2 precedes that of SiO_2 [159, 162]. Furthermore, the presence of TiO_2 as the outer layer (Fig. 29) suggests that the rate of oxidation is controlled by outward diffusion of Ti^{4+} through the oxide scale from the oxide-alloy interface to oxide-air interface. Even the Ti^{4+} ions at the oxide-metal interface have to diffuse through the intermediate SiO_2 layer, resulting in a growth rate slower than that predicted by the parabolic rate law at 1200 °C. Therefore, the key to achieving oxidation resistance in Ti_5Si_3 would be the formation of a stable, impervious, and adherent SiO_2 layer at the Ti_5Si_3 -oxide interface, which would not only inhibit further ingress of oxygen anions but also restrict outward diffusion of Ti^{4+} cations. The activation energy for oxidation of Ti_5Si_3 in the temperature range of 1000–1300 °C has been found to be 46.09 kcal/mol [159], which is only 0.57 times that measured for MoSi_2 in a similar temperature regime [163]. Figure 30 shows the plots comparing the oxidation rates of MoSi_2 and Ti_5Si_3 at 1200 °C. From the results in these plots, it is obvious that MoSi_2 is much more oxidation resistant compared to Ti_5Si_3 .

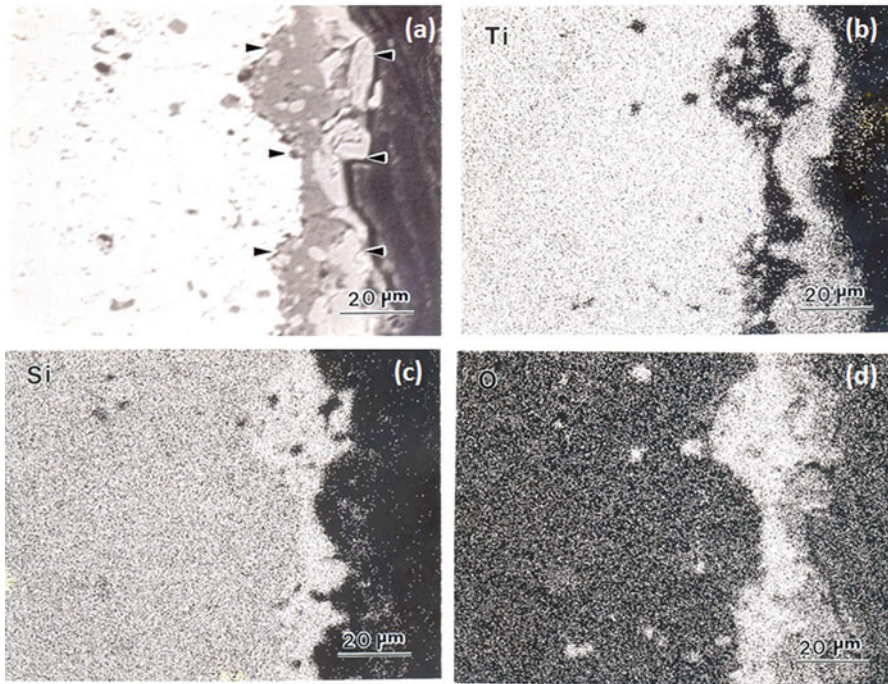
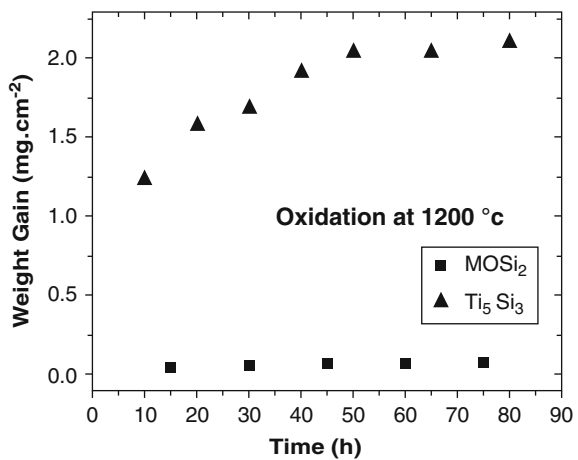


Fig. 29 Cross-sectional microstructure of the oxide scale formed on isothermal exposure of Ti_5Si_3 at 1200 °C for 24 h: (a) EPMA (BSE) image, and WDS X-ray maps of (b) Ti, (c) Si, and (d) O [159]. (Reprinted by permission from Springer Nature)

Fig. 30 Plots depicting the change in mass observed in $MoSi_2$ and Ti_5Si_3 with duration of exposure at 1200 °C [142, 143, 159]



Niobium Silicides

NbSi_2 shows pest disintegration between 500 °C and 850 °C [164]. Arc-melted NbSi_2 has been found to disintegrate on exposure in air at 500 °C and 750 °C for 160 h and 3 h, respectively [165]. On the other hand, defect-free single crystals of NbSi_2 have not shown any evidence of pesting, indicating that grain boundaries and porosities have a significant role in promoting accelerated oxidation in cast alloys. Pesting of NbSi_2 has shown three regimes, which are associated with formation of various Nb-oxide forms, NbO_2 , $\alpha\text{-Nb}_2\text{O}_5$, and $\beta\text{-Nb}_2\text{O}_5$ [164]. It is interesting to note that although the free energies of formation of all the Nb-oxides are higher in comparison to that of SiO_2 , yet the Nb-oxides are formed at reactively lower temperatures. Their formation can be attributed to slow diffusivity of Si at lower temperatures and lower parabolic rate constant of SiO_2 .

Nb_5Si_3 undergoes accelerated pest oxidation in the temperature regime of 750–1000 °C forming Nb_2O_5 , and complete disintegration has been observed within 1–3 h of exposure at 1000 °C [165, 166]. The susceptibility for pest disintegration of Nb-silicides is owing to the mismatch between the CTEs of the oxidation products. It may be noted that the CTE of Nb_2O_5 is just 1/4th of that of Nb_5Si_3 [167]. The lower CTE of the oxide scale, coupled with volume expansion accompanying its formation leads to compressive residual stresses inside the scale and its spallation during cooling. Again, the diffusion coefficient of oxygen in Nb_2O_5 is greater than that in SiO_2 at 1000 °C by nearly three orders of magnitude.

Efforts involving the use of Ti, Al, and Hf as alloying elements, the oxides of which have a lower free energy of formation compared to SiO_2 , have shown significant success for improving the pest oxidation resistance of the Nb-silicide based alloys [168, 169]. Alloying with Al and Hf has been found to restrict the damage due to pesting in the Nb-Si alloys. However, the best results for eliminating damage in the temperature regime of 750–950 °C has been observed on alloying with Sn [25]. Furthermore, the diffusivity of oxygen through Nb_{ss} is reduced by solid solution alloying with Ta, Cr, and Al [170]. Presence of Al also reduces the susceptibility to pesting at 800 °C. Optimum oxidation resistance, coupled with high creep strength has been achieved for compositions with Nb:(Ti + Hf) ratios of 1.8 to 2.1 and Si levels of 17 to 19%. Alloying with Cr and Al has been found to be the most beneficial for oxidation resistance [35, 84]. Increasing the concentration of Cr to 5 at.% stabilizes the Cr-rich Laves phases. For Ge addition, the best properties are observed at 6 at.% concentration, while B addition is found to be beneficial in the range of 2–6 at.%, beyond which it is detrimental. Furthermore, addition of Fe to replace Cr as alloying element has been found to be beneficial too.

Alloying of Nb-Si based alloys with Mo has been found to improve high-temperature oxidation resistance of these alloys, which is obvious from the isothermal oxidation kinetics of alloys with varying Mo concentrations, as shown in Fig. 31 [171]. Presence of Mo reduces the activity of Nb, thereby promoting the formation of a continuous and impervious layer of SiO_2 at the alloy-oxide interface (Fig. 31). The free energy of formation of MoO_2 is the closest to that of Nb_2O_5 among the oxides of Mo

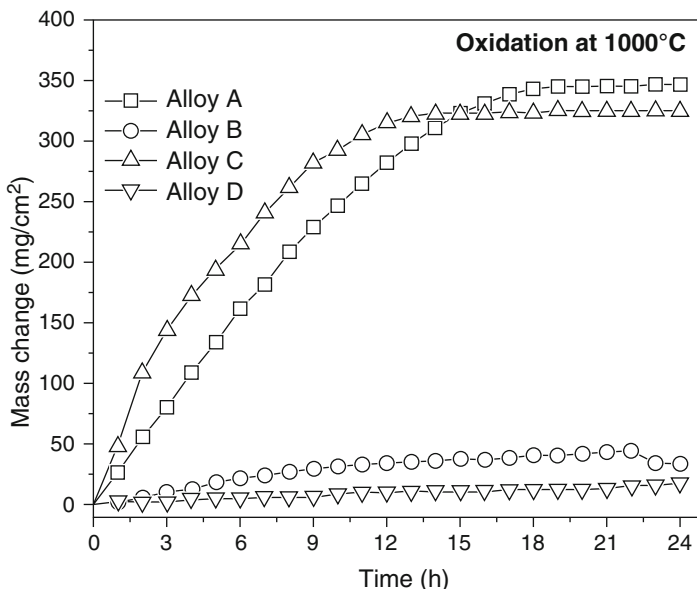


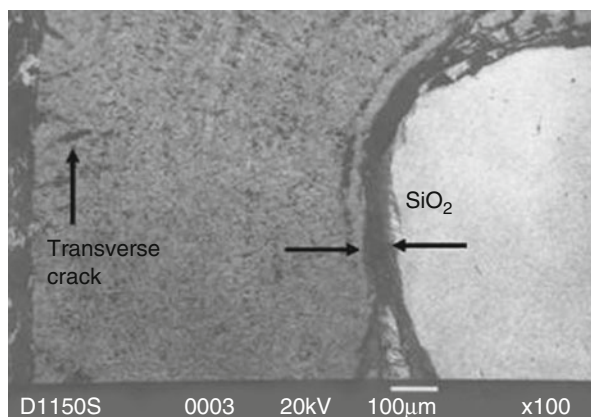
Fig. 31 Plots depicting the kinetics of isothermal oxidation during exposure for 24 h at 1000 °C for alloys with compositions: Nb-19Si-5Mo (Alloy A), (b) Nb-18Si-26Mo (Alloy B), (c) Nb-13Si-4Mo (Alloy C), and (d) Nb-12Si-15Mo (Alloy D) [171]. (Reprinted by permission from Springer Nature)

[123]. Moreover, the radii of Mo^{4+} and Nb^{5+} ions are 0.70 and 0.69 Å, respectively, whereas the Mo^{6+} ion has a radius of 0.62 Å. Hence, it is intuitive that the Mo ion would dissolve in the Nb_2O_5 in the form of Mo^{4+} , thereby substituting the Nb^{5+} sites. It should be also noted that in contrast to the n-type character of Nb_2O_5 and SiO_2 , MoO_2 is an amphoteric conductor. As the Mo^{4+} cations have a lower valence compared to that of Nb^{5+} , substitution of the former type of cation in the Nb_2O_5 is expected to lower the concentration of anion vacancies and thereby reduce the rate of oxygen anion diffusion through the oxide scale. Furthermore, the oxides of Mo have lower melting points compared to that of Nb_2O_5 , and therefore, the sinterability of the oxide scale is improved significantly. The reduction of void surface area through sintering of the oxide scale is expected to reduce the rate of oxygen penetration through surface diffusion significantly. The contribution of Mo addition to oxide-scale densification has been confirmed by the observation of higher smoothness and less porosity on the top surfaces of the oxide scale formed on the Nb-Si-Mo alloys with higher Mo content (Fig. 32).

Applications

On the basis of the data compiled from engines over a period of 70 years, Dimiduk and Perepezko have shown that the overall efficiency actually decreases with increasing turbine rotor inlet temperatures [111]. The decrease in efficiency is

Fig. 32 SEM (BSE) image of the cross section of the oxide scale formed on the Nb-12Si-15Mo alloy due to the exposure at 1150 °C for 24 h. The SiO₂ layer at the metal oxide interface is shown with a pair of arrows. Transverse cracks (single arrow) are visible in the oxide scale [171]. (Reprinted by permission from Springer Nature)



attributed to the requirement for advanced air-cooling schemes of the hot-end components, which are exposed to temperatures close to their melting points. The efficiency of the engine can only be improved, keeping the power of the engine same, or pushing it higher by switching to materials suitable for temperatures beyond those of the third generation Ni-based superalloys, so that cooling is not required. The new generation of gas turbine engines requires higher inlet temperatures in order to ensure larger extent of fuel combustion, which is necessary for improvement of efficiency. As a result, the gas turbine materials are exposed to increased service temperatures, because of which enhanced degree of high-temperature oxidation and hot-corrosion attack are expected. For sea-based aircrafts and marine gas turbines, the problem of degradation is more serious due to the exposure to an aggressive environment comprising sulfur, vanadium, and sodium from the fuel and various halides from the seawater. Moreover, the conventional MCrAlY (M = Ni, Co or Ni + Co) type of coatings are known to be protective only at temperatures ≤ 1150 °C [172]. Therefore, certain new types of intermetallic alloys based protective coatings are being developed for applications at even higher temperatures.

For use in a variety of engineering components, the key hurdle lies in processing of near net shapes with desirable microstructures and mechanical properties. Whereas certain types of brittle intermetallic ingots exhibit cracking due to thermal stresses during cooling, now it is possible to melt and cast ingots weighing 500 kg or more using advanced techniques. Casting is the preferred technique for fabricating engine-related products. The mold needs to be suitably designed for reducing the stresses by eliminating sharp thickness gradients as well as corners and notches. One of the problems during solidification is segregation of solute elements, which is minimized by homogenization heat treatments and hot working. The as-cast ingots are either hot extruded or isothermally forged. For extrusion, canning is carried out to avoid surface cracking. Extrusion of the in-situ Nb_{ss}-Nb₅Si₃ based multi-component composites has been carried out by encapsulating homogenized cast ingots in Mo cans at 1350 °C or 1400 °C with a ratio of 6:1 [173].

For several decades, MoSi₂-based heating elements, popularly known as superkanthal are in use for temperatures up to 1700 °C. Superkanthal contains fine grains of MoSi₂, bonded together with a network of alumino-silicate (xAl₂O₃.ySiO₂) glass phase [174, 175]. In recent years, Kanthal Super 1900 heating elements, containing solid solution alloy of MoSi₂ and WSi₂ have come into use. The life of the heating elements would probably increase with the use of composites and alloys with better creep resistance and fracture toughness [5, 7, 176].

Molybdenum silicides-based hybrid composites (MoSi₂-Si₃N_{4(p)}-SiC_f) are candidate materials for the blade outer air seal (BOAS), which is designed to maintain a small gap between itself and the blade, and is exposed to high turbine gas temperatures and thermal stresses [177]. The turbine efficiency is adversely affected, if the gap between the blade and the seal is increased. The high fracture toughness, impact energy, and resistance to peening and high temperature isothermal as well as cyclic oxidation of the MoSi₂-based hybrid composites, which are comparable to that of superalloys, contribute to the promise for applications in aircraft engine components [177]. Gas burner testing at Pratt and Whitney has proved that the MoSi₂-Si₃N₄ and MoSi₂-SiC composites have significant thermal shock resistance in the simulated jet fuel combustion environment. Other potential applications of molybdenum silicide-based composites include diesel engine glow plugs, molten-metal lances, protective sheaths for high temperature sensors, and industrial gas burners.

Niobium silicides based composites are also being developed for applications in airfoils. A prototype of the investment cast Nb-silicide based airfoil has been fabricated [35]. Although investment casting offers a method of producing near-net shaped aerospace components including blades and vanes, further research is required for process development.

Conclusions

The Mo-, Ti-, and Nb- silicides belong to a class of high-temperature materials, which have been studied extensively, keeping in mind a variety of structural applications in aerospace and automotive applications as well as power generation equipment requiring exposure at elevated temperatures or corrosive environments. The ability to retain strength at elevated temperatures depends on their melting points and complexities of crystal structures, which in turn govern their deformation and fracture behavior. The oxidation resistance of these materials at various temperatures depends on the type of oxide scale (silica, borosilicate, or mixed with other oxides) formed along its continuity and stability, which in turn controls its ability to be protective of the underneath alloy against further degradation. One of the major hurdles is the inherent brittleness of these materials at ambient temperatures, which is either due to high Peierls barrier to dislocation motion caused by directional bonding or complex low symmetry crystal structures. Efforts to make these materials relatively tougher by alloying with suitable elements or by designing multiphase composites with interconnected ductile phase have been successful to a large extent, but this is achieved often at the expense of high temperature strength. The advantage

of multiphase and multicomponent Mo-Si-B-X alloys is their ability to retain strength at elevated temperatures, as well as oxidation resistance being promoted by the formation of borosilicate scale. However, it is necessary to optimize the microstructure of these multicomponent multiphase silicide based alloys to achieve the desirable combination of high fracture toughness at ambient temperature along with high-temperature strength retention and oxidation resistance.

References

1. Gottstein G (2006) Physical foundations of materials science. Springer, Noida, Chapter 4, p 107
2. Westbrook JH, Fleischer RL (1994) Intermetallic compounds: principles and practice. Vol. 1 and Vol. 2. Wiley, Chichester
3. Sauthoff G (1995) Intermetallics. Wiley VCH, Weinheim
4. Stoloff NS, Sikka VK (1996) Physical metallurgy and processing of intermetallic compounds. Springer, New York
5. Mitra R (2015) Structural intermetallics and intermetallic matrix composites. IIT Kharagpur Research Monograph Series. CRC Press/Taylor and Francis Group/Springer, Boca Raton, Florida, USA
6. Murray JL (1987) Binary alloy phase diagrams. In: Massalski TB, Okamoto H, Subramanian PR, Kacprzak L (eds) The Mo-Si (Molybdenum-silicon) system. ASM, Materials Park
7. Mitra R (2006) Mechanical behavior and oxidation resistance of structural silicides. *Inter Mater Rev* 51(1):13–64
8. Inui H, Yamaguchi M (2001) Deformation mechanisms of transition-metal disilicides with the hexagonal C40 structure. *Intermetallics* 9:857–862
9. Inui H, Moriwaki M, Ito K, Yamaguchi M (1998) Plastic deformation of single crystals of Mo(Si, Al)₂ with the C40 structure. *Philos Mag A* 77(2):375–394
10. Chu F, Thom DJ, McClellan K, Peralta P, He Y (1999) Synthesis and properties of Mo₅Si₃ single crystals. *Intermetallics* 7:611–620
11. Nowotny H, Dimakopoulou E, Kudielka H (1957) Investigations in the ternary systems: molybdenum-silicon-boron, tungsten-silicon-boron and system: VSi₂-TaSi₂ (in German). *Monatsh Chem* 88:180–192
12. Rosales I, Schneibel JH (2000) Stoichiometry and mechanical properties of Mo₃Si. *Intermetallics* 8(8):885–889
13. Bhattacharyya BK, Bylander DM, Kleinman L (1985) Comparison of fully relativistic energy-bands and cohesive energies of MoSi₂ and WSi₂. *Phys Rev B* 32(12):7973–7978
14. Petrovic JJ, Honnell RE (1990) SiC reinforced-MoSi₂/WSi₂ alloy matrix composites. *Ceram Eng Sci Proc* 11:734–744
15. Ito K, Inui H, Shirai Y, Yamaguchi M (1995) Plastic deformation of MoSi₂ single crystals. *Philos Mag* 72(4):1075–1097
16. Ito K, Yano T, Nakamoto T, Inui H, Yamaguchi M (1999) Plastic deformation of WSi₂ single crystals with the C11b structure. *Acta Mater* 47(3):937–949
17. Ito K, Yano T, Nakamoto T, Inui H, Yamaguchi M (1996) Plastic deformation of MoSi₂ and WSi₂ single crystals and directionally solidified MoSi₂-based alloys. *Intermetallics* 4:S119–S131
18. Tanaka K, Inui H, Yamaguchi M, Koiwa M (1999) Directional atomic bonds in MoSi₂ and other transition-metal disilicides with the C11_b, C40 and C54 structures. *Mater Sci Eng A* 261:158–164
19. Nowotny H (1963) Alloy chemistry of transition element borides. In: Beck PA (ed) Electronic structure and alloy chemistry of the transition elements. Interscience, New York, pp 179–220

20. Sambasivan S, Petuskey WT (1994) Phase chemistry in the Ti–Si–N system: thermochemical review with phase stability diagrams. *J Mater Res* 9(9):2362–2369
21. Thom AJ, Meyer MK, Kim Y, Akinc M (1994) Evaluation of $A_5Si_3Z_x$ intermetallics for use as high temperature structural materials. In: Ravi VA, Srivatsan TS, Moore JJ (eds) Processing and fabrication of advanced materials III. TMS, Warrendale, pp 413–438
22. Rosenkranz R, Frommeyer G, Smarsly W (1992) Microstructures and properties of high melting point intermetallic Ti_5Si_3 and $TiSi_2$ compounds. *Mater Sci Eng A* 152(1–2):288–294
23. Mitra R (1998) Microstructure and mechanical behavior of reaction hot-pressed titanium silicide and titanium silicide-based alloys and composites. *Metall Mater Trans A* 29(6):1629–1641
24. Schlesinger ME, Okamoto H, Gokhale AB, Abbaschian R (1993) The Nb–Si (Niobium–Silicon) system. *J Phase Equil* 14(4):502–509
25. Bewlay BP, Jackson MR, Zhao J-C, Subramanian PR (2003) A review of very-high-temperature Nb-silicide-based composites. *Metall Mater Trans A* 34(10):2043–2052
26. Zhao J-C, Bewlay BP, Jackson MR, Peluso LA (2001) Alloying and phase stability in niobium silicide in-situ composites. GE research and development report no. 2001CRD090
27. Schneibel JH, Liu CT, Heatherly L, Kramer MJ (1998) Assessment of processing routes and strength of a 3-phase molybdenum boron silicide (Mo_5Si_3 – Mo_5SiB_2 – Mo_3Si). *Scripta Mater* 38:1169–1176
28. Mendiratta MG, Dimiduk DM (1991) Phase relations and transformation kinetics in the high Nb region of the Nb–Si system. *Scripta Metall Mater* 25:237–242
29. Bewlay BP, Jackson MR, Subramanian PR (1999) Processing high-temperature refractory-metal silicide in-situ composites. *JOM* 51:32–36
30. Brupbacher JM, Christodoulou L, Nagale DC (1987) Process for forming composites having an intermetallic containing matrix. U.S. Patent 4,710,348
31. Christodoulou L, Nagale DC, Brupbacher JM (1988) Composites having an intermetallic containing matrix. U.S. Patent 4,774,052
32. Brupbacher JM, Christodoulou L, Nagale DC (1990) Process for forming composites having an intermetallic containing matrix. U.S. Patent 4,916,029
33. Bewlay BP, Jackson MR, Lipsitt HA (1996) The balance of mechanical and environmental properties of a multielement niobium-niobium silicide-based in situ composite. *Metall Mater Trans A* 27:3801–3808
34. Hirano T, Nakamura M, Hirano K, Umakoshi Y (1991) Single crystal growth and mechanical properties of $MoSi_2$ and WSi_2 . *Ceram Eng Sci Proc* 12:1619–1632
35. Bewlay BP, Jackson MR, Zhao JC, Subramanian PR, Mendiratta MG, Lewandowski JJ (2003) Ultrahigh-temperature Nb-silicide-based composites. *MRS Bull* 28:646–653
36. Breig PG, Scott SW (1989) Induction skull melting of titanium aluminides. *Mater Manuf Proc* 4:73–83
37. McCullough C, Valencia JJ, Levi CG, Mehrabian R (1990) Microstructural analysis of rapidly solidified Ti_3Al -X powders. *Mater Sci Eng A* 124:83–101
38. Shih DS, Scarr GK, Chestnut JC On microstructural evolution of gas atomized Ti-50 at.% Al-2 at.% Nb powder. In: Koch CC, Liu CT, Stoloff NS, Taub AI (eds) High temperature ordered intermetallic alloys III, *Mater Res Soc Symp Proc*, vol 133. MRS, Pittsburgh, pp 167–174
39. Goodman CHL (1974) *Crystal growth theory and techniques*. Plenum, New York
40. Morsi K (2001) Review: reaction synthesis processing of Ni–Al intermetallic materials. *Mater Sci Eng A* 299:1–15
41. Ito K, Inui H, Shirai Y, Yamaguchi M (1995) Plastic deformation of $MoSi_2$ single crystals. *Phil Mag A* 72:1075–1097
42. Aikin RM Jr (1992) On the ductile-to-brittle transition temperature in $MoSi_2$. *Scripta Metall Mater* 26:1025–1030
43. Nakano T, Azuma M, Umakoshi Y (2002) Tensile deformation and fracture behaviour in $NbSi_2$ and $MoSi_2$ single crystals. *Acta Mater* 50:3731–3742

44. Srinivasan SR, Schwarz RB, Embury JD (1993) Ductile-to-brittle transition in MoSi₂. In: Baker I, Whittenberger JD, Darolia R, Yoo MH (eds) High temperature ordered intermetallics V, Mater Res Soc Symp Proc vol 288. MRS, Pittsburgh, p 1099
45. Patankar SN, Lewandowski JJ (1993) Effect of processing on the high temperature mechanical properties of MoSi₂. In: Baker I, Darolia R, Whittenberger JD, Yoo MH (eds) High-temperature ordered intermetallic alloys V, Mater Res Soc Symp Proc, vol 288. MRS, Warrendale, p 829
46. Schwarz RB, Srinivasan SR, Petrovic JJ, Maggiore CJ (1992) Synthesis of molybdenum disilicide by mechanical alloying. Mater Sci Eng A 155:75–83
47. Mitra R, Prasad NE, Kumari S, Rao AV (2003) High-temperature deformation behavior of coarse- and fine-grained MoSi₂ with different silica contents. Metall Mater Trans A 34:1069–1088
48. Hardwick DA, Martin PL, Patankar SN, Lewandowski JJ (1993) Processing-microstructure-property relationships in polycrystalline MoSi₂. In: Darolia R, Lewandowski JJ, Liu CT, Martin PL, Miracle DB, Nathal MV (eds) Structural intermetallics. TMS, Warrendale, p 665
49. Mitra R, Mahajan YR, Prasad NE, Chiou WA (1997) Processing—microstructure—property relationships in reaction hot-pressed MoSi₂ and MoSi₂/SiC_p composites. Mater Sci Eng A 225:105–117
50. Jayashankar JS, Ross EN, Eason PD, Kaufman MJ (1997) Processing of MoSi₂-based intermetallics. Mater Sci Eng A 239–240:485–492
51. Stergiou A, Tsakirooulos P (1995) Study of the effects of Al, Ta, W additions on the microstructure and properties of MoSi₂ base alloys. In: Baker I, Hanada S, Horton J, Noebe RD, Schwartz DS (eds) High temperature ordered intermetallics VI, Mater Res Soc Symp Proc, vol 364. MRS, Warrendale, pp 911–916
52. Harada Y, Murata Y, Morinaga M (1998) Solid solution softening and hardening in alloyed MoSi₂. Intermetallics 6:529–535
53. Sharif AA, Misra A, Petrovic JJ, Mitchell TE (2001) Solid solution hardening and softening in MoSi₂ alloys. Scripta Mater 44:879–884
54. Carter DH, Petrovic JJ, Honnell RE, Gibbs WS (1989) SiC-MoSi₂ composites. Ceram Eng Sci Proc 10:1121–1129
55. Suryanarayanan R, Sastry SML, Jerina KL (1994) Mechanical-properties of molybdenum disilicide based materials consolidated by hot isostatic pressing (HIP). Acta Metall Mater 42:3751–3757
56. Aikin RM Jr (1991) Structure and properties of in-situ reinforced MoSi₂. Ceram Eng Sci Proc 12(9–10):1643–1655
57. Aikin RM Jr (1992) Strengthening of discontinuously reinforced MoSi₂ composites at high temperatures. Mater Sci Eng A 155:121–133
58. Mitra R, Sadananda K, Feng CR (2004) Effect of microstructural parameters and Al alloying on creep behavior, threshold stress and activation volumes of molybdenum disilicides. Intermetallics 12:827–836
59. Mitra R, Rao VVR, Rao AV (1999) Effect of small aluminum additions on microstructure and mechanical properties of molybdenum di-silicide. Intermetallics 7:213–232
60. Maloy SA, Heuer AH, Lewandowski JJ, Petrovic JJ (1991) Carbon additions to molybdenum disilicide: improved high-temperature mechanical properties. J Am Ceram Soc 74:2704–2706
61. Bose S (1992) Engineering aspect of creep deformation of molybdenum disilicide. Mater Sci Eng A 155:217–225
62. Inui H, Ishikawa K, Yamaguchi M (2000) Creep deformation of single crystals of binary and some ternary MoSi₂ with the C11_b structure. Intermetallics 8:1159–1168
63. Sadananda K, Feng CR, Mitra R, Deevi SC (1999) Creep and fatigue properties of high temperature silicides and their composites. Mater Sci Eng A 261:223–238
64. Mason DP, Vanaken DC (1995) On the creep of directionally solidified MoSi₂-Mo₅Si₃ eutectics. Acta Metall Mater 43:1201–1210

65. Hayashi T, Ito K, Ihara K, Fujikura M, Yamaguchi M (2004) Creep of single crystalline and polycrystalline T-2 phase in the Mo–Si–B system. *Intermetallics* 12:699–704
66. Schneibel JH (2003) High temperature strength of Mo–Mo₃Si–Mo₅SiB₂ molybdenum silicides. *Intermetallics* 11:625–632
67. Subramanian PR, Parthasarathy TA, Mendiratta MG, Dimiduk DM (1995) Compressive creep-behavior of Nb₅Si₃. *Scripta Metall Mater* 32:1227–1232
68. Subramanian PR, Mendiratta MG, Dimiduk DM (1994) Microstructures and mechanical behavior of Nb–Ti based beta+silicide alloys. In: Briant CL, Petrovic JJ, Bewlay B, BP VAK, Lipsitt HA (eds) High temperature silicides and refractory alloys, *Mater Res Soc Symp Proc*, vol 322. MRS, Warrendale, p 491
69. Sadananda K, Feng CR (1993) The creep of intermetallics and their composites. *JOM* 45(5):45–48
70. Inui H, Moriwaki M, Ito K, Yamaguchi M (1998) Plastic deformation of single crystals of Mo(Si,Al)₂ with the C40 structure. *Phil Mag A* 77:375–394
71. Mendiratta MG, Lewandowski JJ, Dimiduk DM (1991) Strength and ductile-phase toughening in the 2-phase Nb/Nb₅Si₃ alloys. *Metall Trans A* 22:1573–1583
72. Moriwaki M, Ito K, Inui H, Yamaguchi M (1997) Plastic deformation of single crystals of NbSi₂ with the C40 structure. *Mater Sci Eng A* 239–240:69–74
73. Mitra R, Srivastava AK, Prasad NE, Kumari S (2006) Microstructure and mechanical behavior of reaction hot pressed multiphase Mo–Si–B and Mo–Si–B–Al intermetallic alloys. *Intermetallics* 14:1461–1471
74. Meyer MK, Kramer MJ, Akinc M (1996) Compressive creep behavior of Mo₅Si₃ with the addition of boron. *Intermetallics* 4:273–281
75. Jehanno P, Heilmaier M, Saage H, Heyse H, Boning M, Kestler H, Schneibel JH (2006) Superplasticity of a multiphase refractory Mo–Si–B alloy. *Scripta Mater* 55:525–528
76. Li ZK, Yu JL, Zheng X, Zhang JJ, Liu H, Bai R, Wang H, Wang DH, Wang WS (2011) Superplasticity of a multiphase fine-grained Mo–Si–B alloy. *Powder Technol* 214:54–56
77. Umakoshi Y, Nakashima T (1994) High temperature deformation of Ti₅Si₃ single crystals with D8₈ structure. *Scripta Metall Mater* 30(11):1431–1436
78. Rigney JD, Singh PM, Lewandowski JJ (1992) Environmental effects on ductile-phase toughening in Nb₅Si₃–Nb composites. *JOM* 44:36–41
79. Subramanian PR, Mendiratta MG, Dimiduk DM (1996) The development of Nb-based advanced intermetallic alloys for structural applications. *JOM* 48:33–38
80. Subramanian PR, Mendiratta MG, Dimiduk DM, Stucke MA (1997) Advanced intermetallic alloys-beyond gamma titanium aluminides. *Mater Sci Eng A* 239-240:1–13
81. Zhao J-C, Bewlay BP, Jackson MR, Peluso LA (2001) Alloying and phase stability in Niobium silicide in-situ composites. In: Hemker KJ, Dimiduk DM, Clemens H, Darolia R, Inui H, Larsen JM, Sikka VK, Thomas M, Whittenberger JD (eds) *Proceeding of the 2001 intermetallics symposium on structural intermetallics*. TMS, Warrendale, p 483
82. Balsone SJ, Bewlay BP, Jackson MR et al (2001) Materials beyond superalloys: exploiting high-temperature composites. GE research and development report no 2001CRD098
83. Balsone SJ, Bewlay BP, Jackson MR et al (2001) Materials beyond superalloys: Exploiting high temperature composites. In: Hemker KJ, Dimiduk DM, Clemens H, Darolia R, Inui H, Larsen JM, Sikka VK, Thomas M, Whittenberger JD (eds) *Proceedings of 2001 intermetallics symposium on structural intermetallics*. TMS, Warrendale, p 99
84. Bewlay BP, Jackson MR, Zhao JC, Subramanian PR (2002) A review of very high-temperature Nb-silicide based composites. GE research and development report no. 2002GRC172
85. Henshall GA, Strum MJ (1995) Simulations of creep in ductile-phase toughened Nb₅Si₃/Nb in situ composites. In: Baker I, Hanada S, Horton J, Noebe RD, Schwartz DS (eds) *High temperature ordered intermetallics VI*, *Mater Res Soc Symp Proc*, vol 364. MRS, Warrendale, pp 937–942
86. Henshall GA, Strum MJ (1994) Simulations of deformation in composites with two steady-state creeping phases. *Scripta Metall Mater* 30:845–850

87. Henshall GA, Subramanian PR, Strum MJ, Mendiratta MG (1997) Continuum predictions of deformation in composites with two creeping phases in Nb₅Si₃/Nb composites. *Acta Mater* 45:3135–3142
88. Chattopadhyay K, Balachandran G, Mitra R, Ray KK (2006) Effect of Mo on microstructure and mechanical behaviour of as-cast Nb₅Si₃-Nb₅Si₃ in situ composites. *Intermetallics* 14:1452–1460
89. Mitra R, Chattopadhyay K, Srivastava AK, Ray KK, Eswara Prasad N (2009) Effect of ductile and brittle phases on deformation and fracture behaviour of molybdenum and niobium silicide based composites. *Key Eng Mater* 395:179–192
90. Kim JH, Tabaru T, Hirai H, Kitahara A, Hanada S (2003) Tensile properties of a refractory metal base in situ composite consisting of an Nb solid solution and hexagonal Nb₅Si₃. *Scr Mater* 48:1439–1444
91. Yoshimi K, Yoo MH, Wereszczak AA, Borowicz SM, George EP, Zee RH (2001) Yielding and flow behavior of Mo₅Si₃ single crystals. *Scr Mater* 45:1321–1326
92. Petrovic JJ (2000) Toughening strategies for MoSi₂-based high temperature structural silicides. *Intermetallics* 8:1175–1182
93. Gac FD, Petrovic JJ (1985) Feasibility of a composite of SiC whiskers in an MoSi₂ matrix. *J Am Ceram Soc* 68:C200–C201
94. Ihara K, Ito K, Tanaka K, Yamaguchi M (2002) Mechanical properties of Mo₅SiB₂ single crystals. *Mater Sci Eng A* 329–331:222–227
95. Inui H, Ito K, Nakamoto T, Ishikawa K, Yamaguchi M (2001) Stacking faults on (001) and their influence on the deformation and fracture behavior of single crystals of MoSi₂-WSi₂ solid-solutions with the C11_b structure. *Mater Sci Eng A* 314:31–38
96. Nekkanti RK, Dimiduk DM (1990) Ductile-phase toughening in niobium-niobium silicide powder processed composite. In: Anton DL, McMeeking R, Miracle D, Martin PL (eds) *Intermetallic matrix composites I*, Mater Res Soc Symp Proc, vol 194. MRS, Warrendale, pp 175–182
97. Vasudevan AK, Petrovic JJ (1992) A comparative overview of molybdenum disilicide composites. *Mater Sci Eng A* 155:1–17
98. Ito K, Ihara K, Tanaka K, Fujikura M, Yamaguchi M (2001) Physical and mechanical properties of single crystals of the T-2 phase in the Mo-Si-B system. *Intermetallics* 9:591–602
99. Zhang L, Wu J (1997) Thermal expansion and elastic moduli of the silicide based intermetallic alloys Ti₅Si₃(X) and Nb₅Si₃. *Scr Mater* 38:307–313
100. Waghmare UV, Bulatov V, Kaxiras E, Duesbery MS (1999) Microalloying for ductility in molybdenum disilicide. *Mater Sci Eng A* 261:147–157
101. Rice RW, Freiman SW (1981) Grain-size dependence of fracture energy in ceramics: 11, a model for noncubic materials. *J Am Ceram Soc* 64(6):350
102. Petrovic JJ, Bhattacharya AK, Honnell RE, Mitchell TE, Wade RK, McClellan KJ (1992) ZrO₂ and ZrO₂-SiC particle reinforced MoSi₂ matrix composites. *Mater Sci Eng A* 155:259–266
103. Hebsur MG (1999) Development and characterization of SiC(f)/ MoSi₂ -Si₃N₄(p) hybrid composites. *Mater Sci Eng A* 261:24–37
104. Sha J, Hirai H, Tabaru T, Kitahara A, Ueno H, Hanada S (2004) High-temperature strength and room-temperature toughness of Nb-W-Si-B alloys prepared by arc-melting. *Mater Sci Eng A* 364:151–158
105. Maloney MJ, Hecht RJ (1992) Development of continuous-fiber-reinforced MoSi₂-base composites. *Mater Sci Eng A* 155:19–31
106. Xiao L, Kim YS, Abbaschian R, Hecht RJ (1991) Processing and mechanical properties of niobium-reinforced MoSi₂ composites. *Mater Sci Eng A* 144:277–285
107. Castro RG, Smith RW, Rollett AD, Stanek PW (1992) Toughness of dense MoSi₂ and MoSi₂-tantalum composites produced by low pressure plasma deposition. *Scr Metall Mater* 26:207–212

108. Seneibel JH, Kramer MJ, Unal O, Wright RN (2001) Processing and mechanical properties of molybdenum silicide with the composition Mo-12Si-8.5B (at.%). *Intermetallics* 9:25–31
109. Schneibel JH, Kramer MJ, Easton DS (2002) A Mo-Si-B intermetallic alloy with a continuous alpha-Mo matrix. *Scripta Mater* 46:217–221
110. Kruzic JJ, Schneibel JH, Ritchie RO (2004) Fracture and fatigue resistance of Mo-Si-B alloys for ultrahigh-temperature structural applications. *Scripta Mater* 50:459–464
111. Dimiduk DM, Perepezko JH (2003) Mo-Si-B alloys: developing a revolutionary turbine-engine material. *MRS Bull* 28:639–645
112. Choe H, Schneibel JH, Ritchie RO (2003) On the fracture and fatigue properties of Mo-Mo₃Si-Mo₅SiB₂ refractory intermetallic alloys at ambient to elevated temperatures (25 degrees C to 1300 degrees C). *Metall Mater Trans A* 34:225–239
113. Schneibel JH, Ritchie RO, Kruzic JJ, Tortorelli PF (2005) Optimizaton of Mo-Si-B intermetallic alloys. *Metall Mater Trans A* 36:525–531
114. Choe H, Chen D, Schneibel JH, Ritchie RO (2001) Ambient to high temperature fracture toughness and fatigue-crack propagation behavior in a Mo-12Si-8.5B (at.%) intermetallic. *Intermetallics* 9:319–329
115. Kim WY, Tanaka H, Hanada S (2002) High temperature strength at 1773 K and room temperature fracture toughness of Nbss/Nb₅Si₃ in situ composites alloyed with Mo. *J Mater Sci* 37:2885–2891
116. Shah DM, Berczik D, Anton DL, Hecht R (1992) Appraisal of other silicides as structural materials. *Mater Sci Eng A* 155:45–57
117. Min KS, Ardell AJ, Eck SJ, Chen FC (1995) A small-specimen investigation of the fracture-toughness of Ti₅Si₃. *J Mater Sci* 30:5479–5483
118. Ruess S, Vehoff H (1990) Temperature dependence of the fracture toughness of single phase and two phase intermetallics. *Scripta Mater* 24:1021–1026
119. Bhattacharya AK (1991) Effect of silicon-carbide reinforcement on the properties of combustion-synthesized titanium silicide. *J Am Ceram Soc* 74:2707–2710
120. Zhang L, Wu J (1998) Ti₅Si₃ and Ti₃Si₃-based alloys: alloying behavior, microstructure and mechanical property evaluation. *Acta Mater* 46:3535–3546
121. Doychak J (1995) Oxidation behavior of high temperature intermetallics. In: Westbrook JH, Fleischer RL (eds) *Intermetallic compounds and practice, vol 1, principles*. Wiley, Chichester, pp 977–1015
122. Meier GH, Pettit FS (1992) The oxidation behavior of intermetallic compounds. *Mater Sci Eng A* 153:548–560
123. Barin I (1989) *Thermochemical data of pure substances, vol 1 and 2*. VCH, Weinheim
124. Raj SV (1995) An evaluation of the properties of Cr₃Si alloyed with Mo. *Mater Sci Eng A* 201:229–241
125. Schlichting J (1978) Molybdenum disilicide as a component in modern high-temperature solid solutions. *High Temp High Press* 10:241–269
126. Bertziss DA, Cerchiara RR, Gulbransen EA, Pettit FS, Meier GH (1992) Oxidation of MoSi₂ and comparison with other silicide materials. *Mater Sci Eng A* 155:165–181
127. Meier GH (1996) Research on oxidation and embrittlement of intermetallic compounds in the U.S. *Mater Corros* 47:595–618
128. Meschter PJ (1992) Low-temperature oxidation of molybdenum disilicide. *Metall Trans A* 23:1763–1772
129. Chou TC, Nieh TG (1992) New observations of MoSi₂ pest at 500 °C. *Scripta Metall Mater* 26:1637–1642
130. Chou TC, Nieh TG (1993) Pesting of the high-temperature intermetallic MoSi₂. *JOM* 45:15–21
131. Westbrook JH, Wood DL (1964) “PEST” degradation in beryllides, silicides, aluminides, and related compounds. *J Nucl Mater* 12:208–215
132. Guder S, Bartsch M, Yamaguchi M, Messerschmidt U (1999) Dislocation processes during the deformation of MoSi₂ single crystals in a soft orientation. *Mater Sci Eng A* 261:139–146

133. Mitra R, Rama Rao VV, Mahajan YR (1997) Oxidation behaviour of reaction hot pressed MoSi₂-SiC composites at 500 °C. *Mater Sci Technol* 13:415–419
134. Yanagihara K, Przybylski K, Maruyama T (1997) The role of microstructure on pesting during oxidation of MoSi₂ and Mo(Si,Al)₂ at 773 K. *Oxid Metall* 47(3–4):277–293
135. Yanagihara K, Maruyama T, Nagata K (1996) Effect of third elements on the pesting suppression of Mo-Si-X intermetallics (X=Al, Ta, Ti, Zr and Y). *Intermetallics* 4:S133–S139
136. Mitra R, Rama Rao VV (1999) Effect of minor alloying with Al on oxidation behaviour of MoSi₂ at 1200 °C. *Mater Sci Eng A* 260:146–160
137. Yanagihara K, Maruyama T, Nagata K (1993) Isothermal and cyclic oxidation of Mo(Si_{1-x}, Al_x)₂ up to 2048 K. *Mater Trans JIM* 34:1200–1206
138. Cook J, Khan A, Lee E, Mahapatra R (1992) Oxidation of MoSi₂-based composites. *Mater Sci Eng A* 155:183–198
139. Kowalik RW, Hebsur MG (1999) Cyclic oxidation study of MoSi₂-Si₃N₄ base composites. *Mater Sci Eng A* 261:300–303
140. Meyer MK, Akinc M (1996) Oxidation behavior of boron-modified Mo₅Si₃ at 800 -1300°C. *J Am Ceram Soc* 79:938–944
141. Supatarawanich V, Johnson DR, Liu CT (2003) Effects of microstructure on the oxidation behavior of multiphase Mo-Si-B alloys. *Mater Sci Eng A* 344:328–339
142. Paswan S, Mitra R, Roy SK (2006) Isothermal oxidation behaviour of Mo-Si-B and Mo-Si-B-Al alloys in the temperature range of 400–800 °C. *Mater Sci Eng A* 424:251–265
143. Paswan S, Mitra R, Roy SK (2007) Oxidation behaviour of the Mo-Si-B and Mo-Si-B-Al alloys in the temperature range of 700–1300 °C. *Intermetallics* 15:1217–1227
144. Paswan S, Mitra R, Roy SK (2009) Nonisothermal and cyclic oxidation behavior of Mo-Si-B and Mo-Si-B-Al alloys. *Metall Mater Trans A* 40:2644–2658
145. Roy B, Das J, Mitra R (2013) Transient stage oxidation behavior of Mo₇₆Si₁₄B₁₀ alloy at 1150 °C. *Corros Sci* 68:231–237
146. Helmick DA, Meier GH, Pettit FS (2005) The development of protective borosilicate layers on a Mo-3Si-1B (wt%) alloy. *Metall Mater Trans A* 36A:3371–3383
147. Das J, Roy B, Kumar NK, Mitra R (2017) High temperature oxidation response of Al/Ce doped Mo-Si-B composites. *Intermetallics* 83(2017):101–109
148. Yoshimi K, Nakatani S, Hanada S, Ko S-H, Park Y-H (2002) Synthesis and high temperature oxidation of Mo-Si-B-O pseudo in-situ composites. *Sci Technol Adv Mater* 3:181–192
149. Rioult FA, Imhoff SD, Sakidja R, Perepezko JH (2009) Transient oxidation of Mo-Si-B alloys: effect of the microstructure size scale. *Acta Mater* 57:4600–4613
150. Burk S, Gorr B, Trindade VB, Christ H-J (2010) Transient oxidation of Mo-Si-B alloys: effect of the microstructure size scale. *Oxid Met* 73:163–181
151. Kumar NK, Das J, Mitra R (2019) Effect of Zr addition on microstructure, hardness and oxidation behavior of arc-melted and spark plasma sintered multiphase Mo-Si-B alloys. *Metall Mater Trans A* 50:2041–2060
152. Kumar NK, Roy B, Mitra R, Das J (2017) Improvement of oxidation resistance of arc-melted Mo₇₆Si₁₄B₁₀ by microstructure control upon minor Fe addition. *Intermetallics* 88:28–30
153. Kumar NK, Mitra R, Das J (2019) Effect of moist environment on the oxidation behaviour of Mo_{76-x}Si₁₄B₁₀Fe_x (x = 0, 0.5, 1 at.%) ultrafine composites in the range of 700–800 °C. *Corr Sci* 155:86–96
154. Kumar NK, Mitra R, Das J (2019) Effect of Fe addition and moist environment on the high temperature oxidation behavior of Mo_{76-x}Si₁₄B₁₀Fe_x (x = 0, 0.5, 1 at.%) composites. *Intermetallics* 111:106498. <https://doi.org/10.1016/j.intermet.2019.106498>
155. Sakidja R, Rioult F, Werner J, Perepezko JH (2006) Aluminum pack cementation of Mo-Si-B alloys. *Scripta Mater* 55(10):903–906
156. Sakidja R, Park JS, Hamann J, Perepezko JH (2005) Synthesis of oxidation resistant silicide coatings on Mo-Si-B alloys. *Scripta Mater* 53(6):723–728
157. Majumdar S (2017) Isothermal and cyclic oxidation resistance of pack siliconized Mo-Si-B alloy. *Appl Surf Sci* 414:18–24

158. Thom AJ, Kim Y, Akinc M (1993) Effect of processing on oxidation of Ti_5Si_3 . In: Baker I, Whittenberger JD, Darolia R, Yoo MH (eds) High-temperature ordered intermetallic alloys V, Mater Res Soc Symp Proc, vol 288. MRS, Warrendale, pp 1037–1042
159. Mitra R, Rama Rao VV (1988) Elevated-temperature oxidation behavior of titanium silicide and titanium silicide based alloy and composite. Metall Mater Trans A 29:1665–1675
160. Taniguchi S, Minamida T, Shibata T (1997) Oxidation behavior of Ti_5Si_3 at temperatures between 1400 and 1700 K. Mater Sci Forum 251-254:227–234
161. Williams JJ, Akinc M (2002) Oxidation resistance of Ti_5Si_3 and $Ti_5Si_3Z_x$ at 1000 °C (Z = C, N, or O). Oxid Met 58:57–71
162. Rahmel A, Spencer PJ (1991) Thermodynamic aspects of TiAl and $TiSi_2$ oxidation: the Al–Ti–O and Si–Ti–O phase diagrams. Oxid Met 35(1–2):53–68
163. Wirkus CD, Wilder DR (1996) High-temperature oxidation of molybdenum disilicide. J Am Ceram Soc 49:173–177
164. Pitman SH, Tsakiroopoulos P (1995) Study of the microstructure and oxidation of NbSi₂ base alloys. In: Horton J, Baker I, Hanada S, Noebe RD, Schwartz DS (eds) High-temperature ordered intermetallic alloys VI, Mater Res Soc Symp Proc 364:1321–1326
165. Liu Y, Thom AJ, Kramer MJ, Akinc M (2003) Processing and oxidation of Nb–Si–B intermetallics. In: Srivatsan TS, Ravi VA (eds) Processing and fabrication of advanced materials for high temperature applications. TMS, Warrendale, pp 413–420
166. Jackson MR, Rowe RG, Skelly DW (1995) Oxidation of some intermetallic compounds and intermetallic matrix composites. In: Horton J, Baker I, Hanada S, Noebe RD, Schwartz DS (eds) High-temperature ordered intermetallic alloys VI, Mater Res Soc Symp Proc 364:1339–44
167. Douglass DL (1963) The thermal expansion of niobium pentoxide and its effect on the spaling of niobium oxidation films. J Less-Common Met 5(2):151–157
168. Bewlay BP, Jackson MR, Gigliotti MFX (2001) Niobium silicide high temperature in-situ composites. In: Fleischer RL, Westbrook JH (eds) Intermetallic compounds – principles and practice, vol 3. Wiley, Chichester, pp 541–560
169. Menon ESK, Mendiratta MG, Dimiduk DM (2001) High temperature oxidation mechanisms in Nb-silicide bearing multicomponent alloys. In: Hemker KJ, Dimiduk DM, Clemens H, Darolia R, Inui H, Larsen JM, Sikka VK, Thomas M, Whittenberger JD (eds) Structural intermetallics 2001. TMS, Warrendale, pp 591–600
170. Zelenitsas K, Tsakiroopoulos P (2006) Effect of Al, Cr and Ta additions on the oxidation behaviour of Nb–Ti–Si in situ composites at 800°C. Mater Sci Eng A 416:269–280
171. Chattopadhyay K, Mitra R, Ray KK (2008) Non-isothermal and isothermal oxidation behaviour of the Nb–Si–Mo alloys. Metall Mater Trans A 39:577–592
172. Swadźba R, Hetmańczyk M, Soźanska M, Witala B, Swadźba L (2011) Structure and cyclic oxidation resistance of Pt, Pt/Pd-modified and simple aluminide coatings on CMSX-4 superalloy. Surf Coat Technol 206:1538–1544
173. Bewlay BP, Jackson MR, Lipsitt HA (1996) The balance of mechanical and environmental properties of a multi-element niobium-niobium silicide-based *in-situ* composite. Metall Mater Trans A 27:3801–3808
174. Keiffer R, Konopicky K, Benesovsky F (1951) Austrian Patent 179,100
175. Kanthal (1953) Swedish Patent 155,836
176. Yao Z, Stiglich J, Sudarshan TS (1999) Molybdenum silicide based materials and their properties. J Mater Eng Perform 8:291–304
177. Petrovic JJ (1997) High temperature structural silicides. In: Wood RK (ed) Papers presented at the 98th annual meeting and the ceramic manufacturing council's workshop and exposition, April 14–17, 1996 Indianapolis, Indiana and September 22–15, 1996 Charlotte, Ceram Eng Sci Proc, vol 18. The American Ceramic Society, Westerville, pp 3–17



High-Temperature Environmental Degradation Behavior of Ultrahigh-Temperature Ceramic Composites

31

Case Examples of Zirconium and Hafnium Diboride

R. Mitra, M. Mallik, and Sunil Kashyap

Contents

Introduction	1222
Design of Materials for Protection Against Degradation	1223
Thermodynamics and Kinetics of Environmental Degradation by Oxidation of ZrB ₂ - and HfB ₂ -Based Composites	1224
Oxidation Behavior of ZrB ₂ - and HfB ₂ -Based Composites Under Standard Test Conditions in Laboratory Air	1226
Non-isothermal Oxidation Behavior	1226
Isothermal Oxidation Behavior for Short and Long Durations of Exposure	1229
Cyclic Oxidation	1239
Oxidation Behavior During Creep	1241
Oxidation in Extreme Environments with High Heat Flux	1244
Oxidation During Arc Jet Test	1244
Oxidation During Ablation Tests	1245
Oxidation Under Water Steam	1252
Summary	1252
References	1253

R. Mitra (✉)

Department of Metallurgical and Materials Engineering, Indian Institute of Technology, Kharagpur, West Bengal, India

e-mail: rahul@metal.iitkgp.ac.in

M. Mallik

Department of Metallurgical and Materials Engineering, National Institute of Technology Durgapur, Durgapur, West Bengal, India

e-mail: manabmallik@gmail.com

S. Kashyap

Department of Metallurgical and Materials Engineering, Indian Institute of Technology Kharagpur, Kharagpur, West Bengal, India

e-mail: sunil.kashyap90@gmail.com

Abstract

In recent years, there is a very strong interest for the development of zirconium and hafnium diboride-based ultrahigh-temperature composites (UHTCs) for use in nose cones and leading edges of hypersonic vehicles, which are subjected to high temperatures and ablative environment during reentry into the earth atmosphere. An overview of the literature on high-temperature environmental degradation behavior of zirconium and hafnium diboride-based UHTCs has been presented, with emphasis on their resistance to oxidation under non-isothermal, isothermal, and cyclic conditions, as well as under ablative conditions during reentry at ~ 2000 °C. It has been observed that using SiC and Si-bearing reinforcements such as Si_3N_4 and MoSi_2 aids in the formation of a borosilicate scale on the surfaces, which is capable of protecting partially or fully against further damage under extreme environments, depending on the temperature. Formation of oxidation products at grain boundaries and interfaces during creep contributes to damage by grain boundary sliding and intergranular cracking. Both nature of oxidation products and mechanisms of their formation leading to degradation are found to vary significantly with the temperature regimes of exposure. On subjecting to ablative exposure at temperatures close to 2000 °C, active oxidation of SiC along with vaporization of B_2O_3 influences the kinetics and mechanisms of degradation. Formation of ZrO_2 -rich oxide scale at such temperatures is believed to play the role of an in situ formed thermal barrier coating, which protects the composite underneath from damage. The effects of reinforcements and their volume fractions on oxidation and ablative behavior have been discussed.

Keywords

Zirconium Diboride · Hafnium Diboride · Composite · Oxidation behavior · Non-isothermal oxidation · Isothermal Oxidation · Cyclic oxidation · Borosilicate scale · Ablation · Creep

Introduction

In recent years, there is a very strong interest in the scientific community related to the aerospace sector for the development of materials with desirable properties for applications in the leading edges of wings and nose cones of next-generation hypersonic and reentry vehicles. The hypersonic leading edge applications involve exposure to oxidizing and aerothermal heating. Sharp leading edges and nose tips are designed to withstand exposure to high temperatures (>2200 °C) and severe thermal gradients in both neutral and oxidizing environments. High melting temperatures, as well as resistance to both oxidation and ablation, are the primary required properties for the aforementioned applications [1–3]. Zirconium diboride (ZrB_2) and hafnium diboride (HfB_2) belong to a class of ultrahigh-temperature ceramics (UHTCs), which not only have melting temperature in excess of 3000 °C [4] but also possess

chemical and physical stability at both high temperatures and reactive atmospheres. The applications of ZrB_2 and HfB_2 involve oxidizing conditions at elevated temperatures. Other reactive environments such as propellants from rocket motors and erosive conditions are also encountered. Due to the inadequate oxidation resistance of monolithic ZrB_2 at high temperatures, its widespread structural application is severely restricted [5, 6]. It is known that the ZrB_2 forms an oxide scale comprising ZrO_2 and B_2O_3 . The B_2O_3 melts at temperatures exceeding $450\text{ }^\circ\text{C}$ and vaporizes at temperatures $\geq 1100\text{ }^\circ\text{C}$. The ZrO_2 scale is not found to be protective due to its porous character, and therefore the presence of viscous B_2O_3 aids in forming a protective scale up to $1000\text{ }^\circ\text{C}$. The oxidation resistance of ZrB_2 deteriorates sharply above $1000\text{ }^\circ\text{C}$, as the viscosity of B_2O_3 (l) decreases and its vapor pressure increases. Moreover, possibility of phase transformations of ZrO_2 on heating or cooling across the monoclinic to tetragonal transformation temperature ($\sim 1170\text{ }^\circ\text{C}$) leads to change in volume which in turn introduces residual stresses and cracking. In a similar manner, oxidation of HfB_2 leads to the formation of HfO_2 and B_2O_3 . Although HfO_2 does not undergo phase transformations, it is not found to be protective after the B_2O_3 vaporizes at temperatures $\geq 1100\text{ }^\circ\text{C}$, because of its porous character. Moreover, the intercrystalline boundaries in polycrystalline ZrO_2 or HfO_2 provide short circuit paths for diffusion of oxygen anions.

A survey of the existing literature indicates that reinforcement of ZrB_2 with Si-rich ceramic phases such as SiC [5, 7] or $MoSi_2$ [8] or Si_3N_4 [7, 9] leads to significant improvement in both oxidation resistance and mechanical properties. These Si-rich ceramics when exposed in air at high temperature form a protective scale of SiO_2 , which effectively restricts further ingress of oxygen. In the case of the ZrB_2 -based composites with Si-rich ceramic phase as reinforcement, improvement of oxidation resistance is observed due to the formation of borosilicate (B_2O_3 - SiO_2)-rich scale [3, 5–8]. The presence of B_2O_3 in the borosilicate scale enhances its plasticity and therefore enables it to undergo viscoplastic flow to cover up cracks and porosities. In other words, the borosilicate scale exhibits self-healing character as its viscoplastic flow makes it possible to close porosities and heal cracks formed in the oxide scale. In this manner, both further growth of the oxide scale and its spallation can be restricted. It may be noted that the improvement of oxidation resistance by addition of SiC in ZrB_2 -based composites is also associated with increase in strength and fracture toughness of the monolithic ZrB_2 [5, 7–10].

Design of Materials for Protection Against Degradation

The following requirements should be met for the oxide scale to be fully protective [11]:

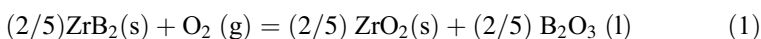
- (i) The oxide in the outer scale should have relatively higher thermodynamic stability compared to that of the oxides of other alloying elements.

- (ii) The rate of growth should be slow enough to ensure that it is continuous, dense, and pore-free.
- (iii) The oxide scale should have sufficient adherence with the underneath alloy, so as to resist spallation due to internal stresses arising during growth.
- (iv) Ability for self-healing on localized spallation or damage.

Based on the aforementioned conditions, it is necessary to examine the conditions leading to the formation of protective oxide scale on ZrB₂- and HfB₂-based composites during exposure at elevated temperatures.

Thermodynamics and Kinetics of Environmental Degradation by Oxidation of ZrB₂- and HfB₂-Based Composites

It is well-accepted that the thermodynamic stability of oxidation products scales with their negative free energy of formation and is inversely proportional to their vapor pressure. When exposed to atmosphere at elevated temperatures, ZrB₂ and HfB₂ ceramics undergo oxidation according to the following reactions:



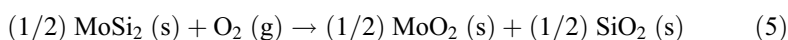
Further B₂O₃ vaporizes above ~1100 °C as there is a sharp increase in its vapor pressure.



Earlier studies on isothermal oxidation of ZrB₂/HfB₂ between 800 and 1100 °C have shown formation of ZrO₂/HfO₂ and an outer protective layer of B₂O₃ (l), which restricts the diffusion of oxygen anions [12–14]. However, at temperatures ≥1100 °C, the vapor pressure of B₂O₃ is increased sharply, leading to its vaporization and acceleration in oxidation rate of ZrB₂ and HfB₂ [12, 15]. But mass gain of HfB₂ is significantly lower than the ZrB₂ at all temperatures. Mass change of these diborides is associated with mass loss of B₂O₃ evaporation and mass gain due to the formation of condensed phases. Continued mass gain is observed due to the mass of oxide (ZrO₂ or HfO₂) formed being greater than the sum of the masses of reacted diboride and vaporized B₂O₃.

As both ZrO₂ and HfO₂ are typically anion-deficient semiconductors with oxygen vacancies, the diffusion of oxygen anions is significant in these oxides. Hence, ZrB₂ and HfB₂ in monolithic form are not suitable for ultrahigh-temperature applications in aero-propulsion systems due to their poor oxidation resistance [5, 16]. Reinforcement of these UHTCs with either SiC or MoSi₂ improves both oxidation resistance and mechanical properties significantly, as has been reported in some of the earlier studies [8, 17]. In fact, Loehman has proposed that the most promising material for

use in sharp leading edges on hypersonic vehicles is the composites of these ceramics with SiC reinforcements [18]. The oxidation resistance of ZrB_2 and HfB_2 was improved by the addition of SiC, which reduces the oxidation rate by a remarkable amount due to the formation of a silica-rich protective scale [5, 14, 19–21]. Rezaie et al. have reported that the ZrB_2 -30% SiC composite exhibits passive oxidation behavior in which the diffusion of oxygen anions (O^{2-}) through protective molten layers containing B_2O_3 and/or SiO_2 controls the rate of oxidation [20]. The oxidation reactions involving SiC and $MoSi_2$ are as follows:



At elevated temperatures, the borosilicate glass is known to undergo viscoplastic flow and thereby aids in covering porosities and cracks in the oxide scale to protect from further oxidation. In other words, the formation of borosilicate scale and its ability for viscoplastic flow are responsible for its self-healing character, which is desirable for stable behavior during exposure for long duration at elevated temperature. The Gibbs free energy change per mole of oxygen for Reactions (1), (2), and (3) has been calculated for different temperature ranges (ZrB_2 , 298–2500 K, and

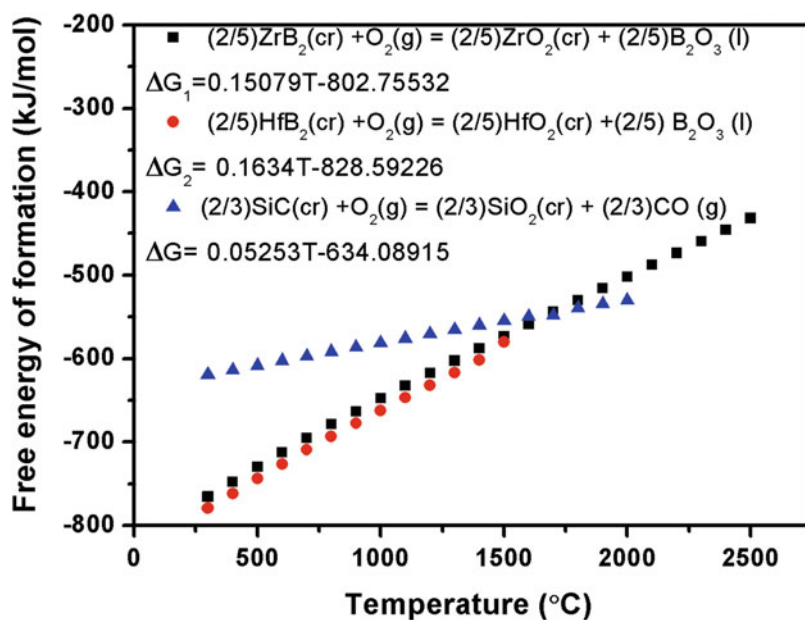


Fig. 1 Plots depicting the variation of free energy change per mole of oxygen with absolute temperature for Reactions (1–3). (Thermodynamic data have been taken from references [22, 23])

HfB₂, 298–1500 K) using the available thermodynamic data [22, 23], and the results are plotted in Fig. 1. From the plots in this figure, it is observed that the free energy changes per mole of oxygen for the Reactions (1) and (2) are almost similar, indicating that the corresponding oxidation products such as B₂O₃ and ZrO₂/HfO₂ are thermodynamically stable at elevated temperatures. As the free energy of the reaction to form ZrO₂ or HfO₂ is more negative compared to that for oxidation of SiC, formation of the former type of oxide is preferred till 1705 °C. As the diffusivity of oxygen anion in amorphous SiO₂ is low, the kinetics of its growth is also reported to be slow [24, 25]. Therefore, formation of SiO₂ is possible only by simultaneous oxidation of SiC with ZrB₂ or HfB₂, provided the volume fraction of the former constituent in the composite is sufficiently high. As the B₂O₃-SiO₂ phase diagram has a eutectic at a temperature as low as ~450 °C [26], and provided the amount of B₂O₃ formed by oxidation of ZrB₂ or HfB₂ is significantly large, the borosilicate (B₂O₃-SiO₂) glass is expected to have high fluidity and undergo viscoplastic flow. However, reduction in viscosity of the oxide scale due to the presence of excess amount of B₂O₃ would enhance the kinetics of mass transfer of O²⁻ through it. Therefore, it is intuitive to propose that an optimum amount of SiC should be present in these composites, so that a desirable ratio of SiO₂ to B₂O₃ is maintained at a given temperature.

Oxidation Behavior of ZrB₂- and HfB₂-Based Composites Under Standard Test Conditions in Laboratory Air

The oxidation behavior of ZrB₂- and HfB₂-based composites has been studied by carrying out experiments under non-isothermal, isothermal, or cyclic conditions. The isothermal oxidation behavior of the composite depends on the nature of the oxide scale formed both during heating and in the initial stages of isothermal exposure at a given temperature. Traditional isothermal oxidation studies also do not take into account the mass changes or the fraction of the composite oxidized during heating or cooling. These arguments can be considered to be relevant for explaining the significance of non-isothermal and cyclic oxidation behavior along with the isothermal oxidation tests.

Non-isothermal Oxidation Behavior

The non-isothermal oxidation behavior of the composites is studied using thermal gravimetric analysis (TGA). For such tests, a small specimen having mass < 10 mg is subjected to heating from ambient temperature to 1400 °C inside the TGA, and the mass change is measured in air at elevated temperature. Dry alumina (Al₂O₃) powder is used as reference during thermal analysis. The results of the non-isothermal oxidation experiments provide an idea of the critical temperatures for the initiation of oxidation and the progress of oxidation reactions involving the different constituent phases, which may induce either mass gain or mass loss during heating.

The oxidation behavior of monolithic ZrB_2 and its composites has been examined as a function of temperature by Chamberlain et al. [21]. Oxidation mechanism of ZrB_2 is known to involve the formation of ZrO_2 and B_2O_3 , which is the dominant chemical process between 800 and 1200 °C. The mass gain is started just below 800 °C and is continued at a constant rate up to ~1200 °C due to the formation of molten B_2O_3 . The rate of mass gain has been found to be similar for all compositions (ZrB_2 , ZrB_2 -10% SiC, ZrB_2 -20% SiC, and ZrB_2 -30% SiC) up to ~1200 °C, and the oxidation rate of ZrB_2 has been found to increase drastically compared to the composites at temperatures above 1200 °C, as the B_2O_3 vaporizes rapidly leaving behind a porous and non-protective ZrO_2 scale. In the case of the ZrB_2 -SiC composites, the oxidation of SiC is started at 1200 °C and is continued up to 1500 °C. For the ZrB_2 -SiC composites heated from 1200 to 1400 °C, the vaporization of B_2O_3 and oxidation of SiC are the dominant chemical processes. The mass gain expressed as a fraction of the original mass has been found to be significantly lower due to addition of SiC as reinforcement till 1500 °C. The TGA results of this study have shown the mass gain to decrease from ~0.05 mg/mm² for pure ZrB_2 to ~0.01 mg/mm² for ZrB_2 containing 30 vol% SiC [21]. The results of the study by Chamberlain can be considered to be in tune with the report on formation of a protective oxide scale comprising the borosilicate glass on addition of SiC as reinforcement in the ZrB_2 -SiC composites as reported by Monteverde and Bellosi [27].

Plots depicting the variation of mass change normalized by initial mass with temperature for ZS (ZrB_2 -20 vol.% SiC), ZSS (ZrB_2 -20 vol.% SiC-5 vol.% Si_3N_4), ZZSS (ZrB_2 -20 vol.% ZrC -20 vol.% SiC-5 vol.% Si_3N_4), and HS (HfB_2 -20 vol.% SiC), obtained from studies using TGA, are shown in Fig. 2 [28, 29]. The results in

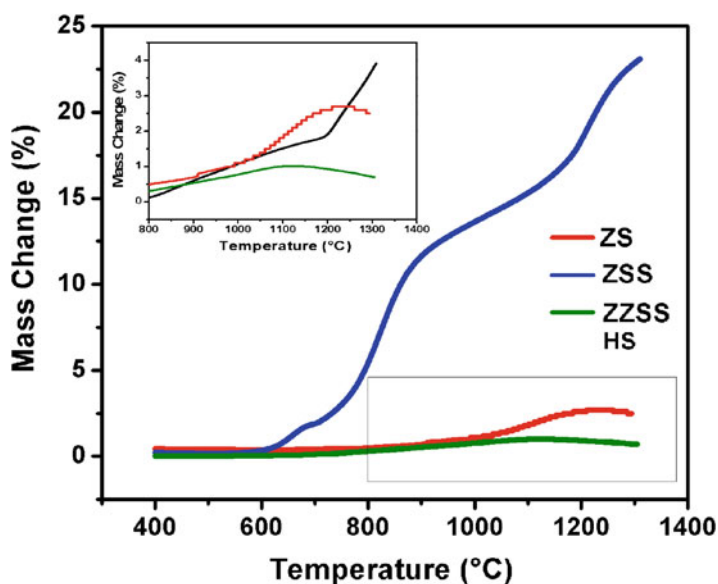


Fig. 2 Plots depicting the variation of mass change as fraction of initial mass with temperature [29]

this figure indicate that mass gain starts at 740 °C for the ZS composite and continues at an approximately constant rate up to 1200 °C, above which a relatively sharp increase in mass gain is observed. The mass gain for the ZSS composites is initiated just below ~800 °C, followed by an approximately constant rate up to 1200 °C, above which a small amount of mass loss is observed. The TGA plot corresponding to the ZZSS composite shows initiation of mass gain at ~600 °C, which is lower than the temperatures for detectable mass gain for either ZS or ZSS composite, and mass gain increases rapidly with increasing temperature up to 1300 °C. On the other hand, the mass gain is initiated in the HS composite at around ~500 °C and is relatively small till 700 °C, and then it increases almost linearly with temperature in the range of ~700–1100 °C. This gain is followed by mass loss at temperatures ≥ 1100 °C causing an apparent decrease in total mass increase. It should also be noted that the mass gain observed at a given temperature in the HS composite is lower than that for ZS, ZSS, or ZZSS composites.

The results in Fig. 2 have confirmed that the rate of formation of HfO_2 is relatively slower compared to that of ZrO_2 , and mass loss caused by accelerated vaporization of B_2O_3 beyond 1100 °C may be the reason for the observed net mass loss [29]. Oxidation of SiC in the ZrB_2 -SiC composite has been reported to occur at temperatures > 1100 °C, although its rate is known to be less than that of ZrB_2 till about 1200 °C [30]. Therefore, net mass gain is observed in the case of the ZrB_2 -based composites. On the other hand, as the rate of formation of HfO_2 is slow, rapid oxidation of SiC with formation and escape of CO may have resulted in mass loss observed in the HS during heating.

Pure ZrC is reported to be completely oxidized at 700 °C during continuous heating, but ZrB_2 does not oxidize significantly at this temperature [5, 12]. The initial mass gain could also be due to the dissolution of oxygen in ZrC, leading to the formation of an intermediate phase such as oxycarbide (ZrC_xO_y). The ZrC can accommodate oxygen into the lattice positions, probably along the grain boundaries [31]. The formation of oxycarbide is rapid in the initial stages and is controlled by diffusion process. The ZrO_2 forms a fine-grained porous scale, which allows ingress of oxygen through the pores to the ZrC particles, and therefore provides low oxidation resistance [5].

Plots depicting the variation of mass change normalized by the initial mass of HSS (HfB_2 -19 vol.% SiC-5.8 vol.% Si_3N_4), HSH (HfB_2 -19.5 vol. % β -SiC-3 vol.% HfN), ZHSH (ZrB_2 -37.5 vol.% HfB_2 -19.5 vol.% β -SiC-3 vol.% HfN), HT (HfB_2 -15 vol.% TaSi_2), ZM (ZrB_2 -2.3 vol.% MoSi_2), and ZMS (ZrB_2 -15 vol.% SiC-2 vol.% MoSi_2) with temperature, obtained from studies using TGA, are shown in Fig. 3 [10, 17, 32, 33]. Interestingly, the TGA plot corresponding to the HSS composite shows the start of mass gain at ~700 °C followed by mild slowdown above 800 °C. The TGA plot shows a noticeable decrease in mass at temperatures above ~1100 °C due to the vaporization of B_2O_3 (l). Mass gain is observed as the oxidation of SiC starts above 1200 °C, leading to formation of the nonvolatile SiO_2 , which further arrests the mass loss by forming an outer layer comprising typically viscous borosilicate glass, which is protective in nature. The wavy pattern of the TGA plots of HSH and ZHSH suggests the instability of

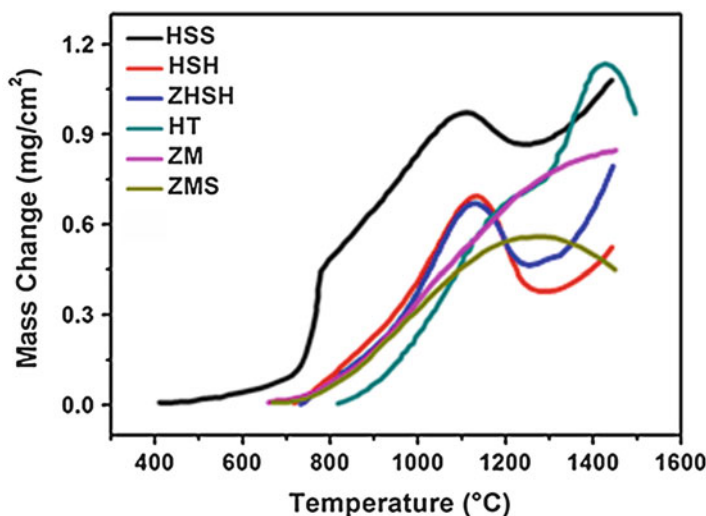


Fig. 3 Plots depicting the variation of mass change with temperature for various ZrB_2 - and HfB_2 -based composites using data from the literature [10, 17, 32, 33]

oxide scale formed over the outer surface of the composites. The TGA plot of the HT shows that oxidation involving mass gain starts at around 800 °C and continues up to 1400 °C, which is followed by mass loss. Furthermore, the TGA plots of ZM and ZMS show that the SiC addition decreases their oxidation rates quite significantly. Results of selected additional non-isothermal oxidation tests are shown in Table 1.

Isothermal Oxidation Behavior for Short and Long Durations of Exposure

Results of selected recent studies on the isothermal oxidation behavior of ZrB_2 , HfB_2 , and their composites, along with the processing method and exposure conditions, are shown in Table 1. Examination of the results in this table shows that oxidation resistance of the ZrB_2 -SiC composites is improved with increasing SiC content at temperatures up to 1500 °C.

The isothermal oxidation behavior of ZrB_2 -based ultrahigh-temperature ceramic composites containing either 20 or 30 vol.% SiC as the reinforcement has been investigated by Han et al. at 1800 °C under different oxygen partial pressures [40]. At this temperature, high SiC content is reported to be beneficial for oxidation resistance of the ZrB_2 -SiC composite at high-oxygen partial pressure, whereas it is detrimental at low-oxygen partial pressure due to rapid active oxidation of SiC. The SiC tends to form a partially interconnected network in three dimensions, and the degree of such interconnectivity in the matrix is found to increase with increasing SiC content. In this context, optimization of the composition and microstructure for

Table 1 Results of selected studies on oxidation of ZrB₂, HfB₂, and their composites

Material	Heating rate (°C/min)/ exposure time (min)	Type of oxidation test	Temperature (°C)	Observation related to kinetics	Oxidation products	Reference
ZrB ₂	HP, 2200	Isothermal	1200–1400	Mass gain	ZrO ₂ and B ₂ O ₃	[5]
ZrC	HP, 2300	Non-isothermal	25–700	Completely oxidized	ZrO ₂ and CO	[5]
ZrB ₂ /SiC		Isothermal	1200–1400	Low rate of oxidation	Below 1200 °C – ZrO ₂ and liquid B ₂ O ₃ Above 1200 °C – borosilicate glass	[5]
ZrB ₂	10 °C/min	Non-isothermal	25–1500	13 mg/cm ²	—	[19]
ZrB ₂ -10 SiC			25–1500	4.3 mg/cm ²	SiO ₂ -rich layer	
ZrB ₂ -20 SiC			25–1500	3.1 mg/cm ²	SiO ₂ -rich layer	
ZrB ₂ -30 SiC			25–1500	1.8 mg/cm ²	SiO ₂ -rich layer	
ZrB ₂ -10 SiC	600 min	Isothermal	1500	~17.2 mg/cm ²	ZrO ₂ , amorphous SiO ₂	[34]
ZrB ₂ -20 SiC	100 min	Isothermal	1627	4.42 mg/cm ²	ZrO ₂ (m), ZrO ₂ (c)	[35]
ZrB ₂ -20 SiC	50 min	Isothermal	1800	12.89 mg/cm ²	ZrO ₂ , amorphous SiO ₂	[36]
ZrB ₂ -30 SiC	600 min	Isothermal	1500	~6.3 mg/cm ²	ZrO ₂ , amorphous SiO ₂	[34]
ZrB ₂ -33 SiC	100 min	Isothermal	1627	5.3 mg/cm ²	ZrO ₂ (m), ZrO ₂ (c)	[35]
ZrB ₂ -20 MoSi ₂	6000 min	Isothermal	1400		ZrSiO ₄ , ZrO ₂ (m)	[8]
ZrB ₂ -20 SiC-20 TaSi ₂	100 min	Isothermal	1627	0.7 mg/cm ²	ZrO ₂ (m), ZrO ₂ (c)	[35]
ZrB ₂ -20 SiC-20 TaC	100 min	Isothermal	1627	20.61 mg/cm ²	ZrO ₂ (t), ZrO ₂ (m)	[35]
HfB ₂ -20 SiC	100 min	Isothermal	1627	2.12 mg/cm ²	HfO ₂ (m)	[35]

(continued)

Table 1 (continued)

Material	Heating rate (°C/min)/ exposure time (min)	Type of oxidation test	Temperature (°C)	Observation related to kinetics	Oxidation products	Reference
HfB ₂ -20 SiC	60 min	Isothermal	1400 or 1600 or 1800 or 1900 or 2000	1.57 or 3.06 or 3.31 or 7.68 or 22.05 mg/cm ²	HfO ₂ , SiO ₂ and Si-O-C inclusions	[37]
HfB ₂ -20 MoSi ₂	1700 min	Isothermal	1400	1.3 mg/cm ²	HfO ₂ (m), HfSiO ₄	[38]
HfB ₂ -20 SiC-20 TaSi ₂	100 min	Isothermal	1627	3.18 mg/cm ²	HfO ₂ (m), HfO ₂ (c), HfSiO ₄	[35]
HfB ₂ -22.1 SiC-5.9 HfC	20 min	Isothermal	1700	1.85 mg/cm ²	Amorphous SiO ₂ , HfO ₂	[39]
HfB ₂ -19 SiC-5.8 Si ₃ N ₄	60 min	Isothermal	1250	0.50 mg/cm ²	Amorphous SiO ₂	[10]
HfB ₂ -19 SiC-5.8 Si ₃ N ₄	60 min	Isothermal	1350	0.65 mg/cm ²	Amorphous SiO ₂	[10]

improved oxidation resistance should reduce the degree of the SiC interconnectivity in the matrix. The SiC content in the ZrB₂ matrix has been optimized for maximizing the oxidation resistance at 1900 °C by Han et al. by carrying out isothermal oxidation tests on composites having 10, 20, or 30 vol% SiC at 1900 °C for 1 h in air [41]. The results have shown that the SiC-depleted layer and the ZrO₂-rich layer in the ZrB₂-20 vol% SiC composite are less likely to spall and remain more adherent than that in ZrB₂-10 vol% SiC or ZrB₂-30 vol% SiC composites. The ZrB₂-20 vol% SiC composites have exhibited excellent oxidation resistance at 2200 °C, where the SiC is no longer responsible for the improvement in oxidation resistance of the composites at 2200 °C. At this temperature, the ZrO₂ is recrystallized into a dense coherent subscale, which protects the underlying ceramic from catastrophic oxidation [42].

Besides the SiC, addition of MoSi₂ [8] or TiSi₂ [19] is also reported to significantly improve the oxidation resistance of diborides. It should be noted that Sciti et al. have reported that the addition of 20 vol.% MoSi₂ is not enough to protect the ZrB₂-based composites at temperatures above 1200 °C, as significant degradation is observed between 1200 and 1400 °C, where the subsurface oxidation is accelerated by formation of cracks and the presence of fast-oxidizing species like Mo in the near-surface region.

The effect of various additives such as TiB₂, HfB₂, CrB₂, TaB, TaSi₂, LaB₆, La₂O₃, and AlN on the oxidation behavior of ZrB₂-based ultrahigh-temperature

ceramics (UHTCs) at 1800 °C was investigated by Hu et al. [43]. The additions of CrB₂ and HfB₂ to the ZrB₂-SiC composites have exhibited minor effect on the structural evolution of the oxide scale and oxidation resistance. A study by Peng et al. has shown that TaSi₂ is more effective than TaB₂ for improving the oxidation resistance of ZrB₂ [44]. The addition of 4 mol% WC to ZrB₂ has reduced the mass gain due to exposure at 1600 °C for 3 h by ~63% [45]. It has been noticed that WO₃ forms a low melting eutectic mixture with ZrO₂, which promotes the densification of a typical ZrO₂-rich outer scale with equiaxed grain structure.

The oxidation behavior of three-phase ceramic composites (ZrB₂/ZrC/SiC) has been compared with that of pure ZrB₂ and ZrC by Opeka et al. [5] and with ZrB₂-SiC composites by Mitra et al. [28, 46]. Whereas the presence of SiC is found to be beneficial for facilitating the formation of protective borosilicate glass in the oxide scale, the ZrC reduces the oxidation resistance by formation of carbon monoxide which escapes by leaving a scale of porous ZrO₂. In contrast, the addition of 5 vol.% Si₃N₄ to the ZrB₂-20 vol.% SiC composite has been found to promote the formation of protective borosilicate scale and thereby enhance the oxidation resistance [47].

The presence of SiC particles as reinforcement substantially enhances the oxidation resistance of HfB₂ [35, 48]. The addition of Si₃N₄ or TaSi₂ is reported to improve the oxidation resistance of the HfB₂-SiC composite further. The oxidation resistance of a hot-pressed HfB₂-SiC-Si₃N₄ composite exposed at temperatures up to 1600 °C in air has been studied by Monteverde et al. [10, 39]. An isothermal thermogravimetric test at 1450 °C for a duration exceeding 20 h has shown that the oxidation kinetics fits a para-linear law until 10 h, when a partial rupture of external oxide scale occurs (i.e., a breakaway reaction). Afterward, the mass gain data fits a linear relationship with time of exposure. The main oxidation products have been reported as HfO₂ and a borosilicate glass. The release of volatile oxidation products is found to have an appreciable impact for exposure below 1350 °C. It has been further shown that at temperatures higher than about 1400 °C, the presence of SiC particles markedly improves the oxidation resistance due to the formation of a protective borosilicate glassy coating on the exposed surfaces, which plugs the pores and effectively seals the grain boundaries, which may allow short-circuit diffusion of oxygen anions [10].

Variation of Mass Change with Time

The oxidation kinetics of ZrB₂- and HfB₂-based composites depends on the formation of a protective borosilicate scale, which usually depends on temperature and duration of exposure. It has been noticed that during the initial stages of exposure, a stable oxide scale is not formed due to the competitive oxidation of multiple elements. In fact, no definite trend emerges, because of simultaneous mass gain due to formation of ZrO₂ and SiO₂ along with vaporization of B₂O₃ as well as formation and escape of CO. For example, during exposure of ZrB₂-SiC and HfB₂-SiC composites for the first 1 h, both gain and loss in mass have been observed in these composites after various intervals, as shown in Fig. 4 [29, 47, 49]. The results depicted in this figure show net mass loss in the HS composite at the 10th minute of exposure at 1200 °C as well as at both 20th and 30th minute of exposure at 1300 °C.

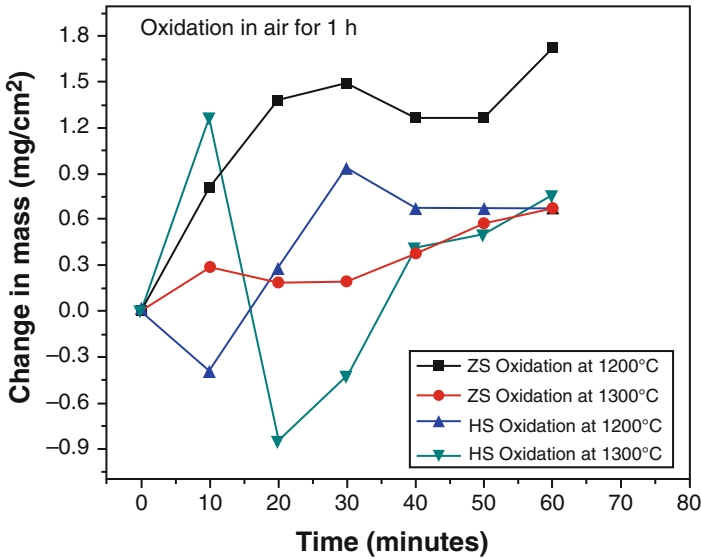


Fig. 4 Plots depicting the variation of mass change as fraction of initial mass with duration of exposure up to 1 h [29, 47]. (Reprinted with permission from Elsevier)

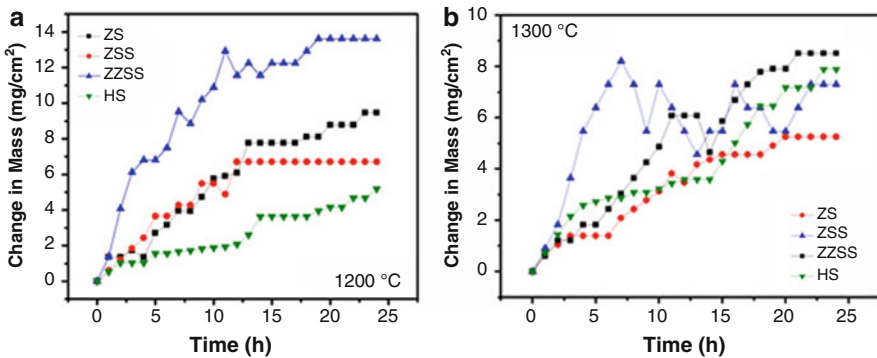


Fig. 5 Plots depicting the variation of mass change with duration of exposure up to 24 h at (a) 1200 °C and (b) 1300 °C [29, 46, 47]

In contrast, net mass gain has been observed on exposure of the ZS composite at both 1200 °C and 1300 °C, which may be attributed to dominance of the formation of ZrO_2 and SiO_2 . The results in Fig. 4 also demonstrate that the variation of mass gain with duration of exposure does not appear to follow a definite trend in the first hour of exposure.

The results of isothermal oxidation tests for 24 h at 1200 and 1300 °C, as depicted in Fig. 5, have shown a stable regime with negligible mass change only in the case of the ZSS being exposed at the former temperature [47]. The stable regime could be

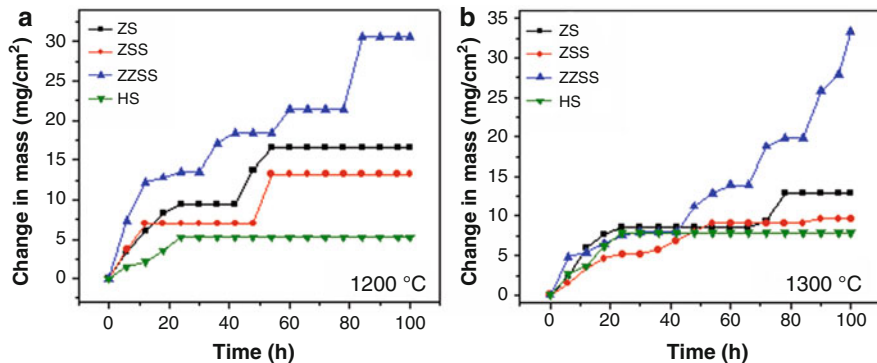


Fig. 6 Plots depicting the variation of mass change with duration of exposure up to 100 h at (a) 1200 °C and (b) 1300 °C [29, 46, 47]

either due to the formation of a continuous and protective B_2O_3 - SiO_2 scale or due to a dynamic equilibrium between mass gain and loss. For all other samples being tested at 1200 or 1300 °C, the stable regime is punctuated with distinct intervals of mass gain or loss. This observation suggests that a stable and protective scale of B_2O_3 - SiO_2 is formed after a certain minimum duration of exposure at 1200 or 1300 °C, but it is not stable beyond a certain period and is probably punctured due to internal stresses generated by formation of CO or vaporization of B_2O_3 , which are expected to escape by forming pores.

The results of isothermal exposure for 100 h at 1200 °C and 1300 °C as depicted in Fig. 6 have shown a stable regime being achieved in the case of the HS after about 24 h, whereas similar observation was recorded for ZS and ZSS after 54 h at 1200 °C but earlier at 1300 °C [29, 46, 47]. This study has also shown that under isothermal conditions, the HS has superior oxidation resistance compared to the investigated ZrB_2 -based composites, considering that its mass change is found to be the least at both 1200 °C and 1300 °C.

Evolution of Oxidation Scale

Phase identification by XRD analyses has shown the presence of tetragonal (t) and monoclinic (m) ZrO_2 in the oxide scales of the ZrB_2 -based composites [29, 46, 47]. In addition, $ZrSiO_4$ has been also found in the oxide scales of all the ZrB_2 -based composites with the exception of ZS exposed at 1200 °C. The peaks of Si_2N_2O have been also detected in the XRD pattern of the oxide scale formed on the ZSS composites. Furthermore, on comparison of XRD patterns from oxide scales formed after 24 h exposure with those from the scales by exposing for 100 h, the t- ZrO_2 peaks in the latter pattern have been found to be relatively higher. In a manner similar to the ZS, the XRD pattern obtained from the oxide scale of the HS composite has shown the peaks of HfO_2 (monoclinic) and $HfSiO_4$.

Observation of cross-sectional microstructures of the oxide scales formed on either ZS on isothermal exposure at 1200 °C and 1300 °C for 24 h has shown the

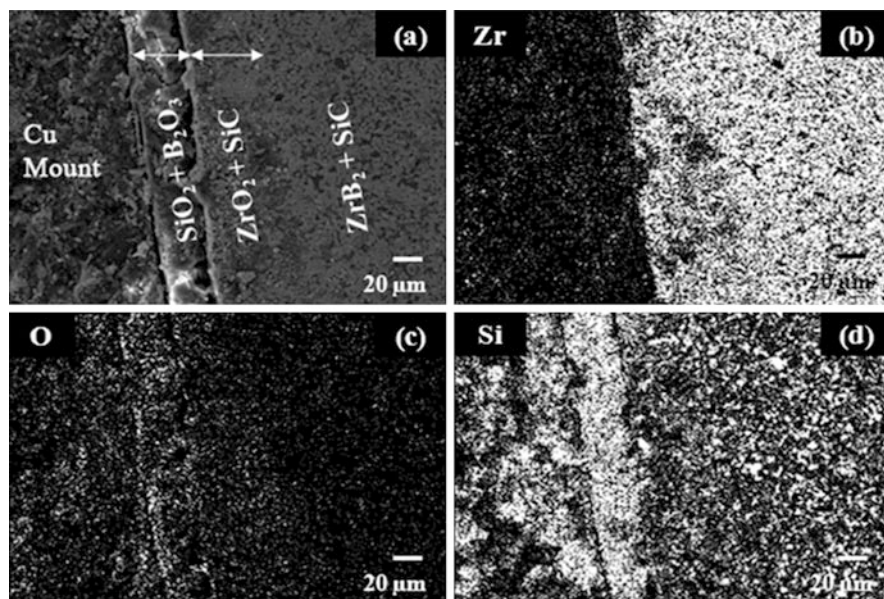


Fig. 7 Cross-sectional microstructure of the oxide scale in ZS exposed at 1200 °C for 24 h: (a) SEM (BSE) image depicting the presence of various constituent layers, as well as EDS X-ray maps of (b) Zr, (c) O, and (d) Si [29]. (Reprinted with permission from Elsevier)

formation of B_2O_3 - SiO_2 as the outer layer, followed by a layer containing $ZrO_2 + SiC$ or $HfO_2 + SiC$ at the interface with underlying composite substrate (Fig. 7) [29]. The cross-sectional microstructures of the oxide scales formed on ZS and HS after 100 h are shown in Figs. 8 and 9, respectively. On comparison of the oxide scales formed at 1200 and 1300 °C, it has been found that thickness of the oxide scales formed on the HS as a fraction of the original sample dimension is consistently less than that on the ZS and the difference is higher by an order of magnitude after 100 h (Table 2). This observation suggests that the protective B_2O_3 - SiO_2 layer is more stable in case of the HS compared to that in the ZS. It is intuitive that the growth of oxide scale is controlled by diffusion of oxygen anions through the outer B_2O_3 - SiO_2 layer. Moreover, the thickness of oxide scales formed on the ZSS isothermally exposed at 1300 °C for both 24 h and 100 h are significantly less than that observed on the ZS subjected to similar exposure, and this observation is consistent with less mass gain observed in the case of the former composite, as shown in Figs. 5 and 6.

In tune with the XRD results, typical SEM images depicting top surfaces of the oxide scales formed on the ZS composite after exposure for 1 h at 1200 °C and 1300 °C (Fig. 10) have exhibited formation of B_2O_3 - SiO_2 scale with dispersion of ZrO_2 particles and cavities having clusters of ZrO_2 particles. SEM investigations have also revealed that the top surfaces of oxide scales formed after exposure at 1200 °C or 1300 °C for 1 h are significantly rough and porous. However, after exposure for 24 h, the oxide scale formed on the ZS at 1200 °C appears smooth and

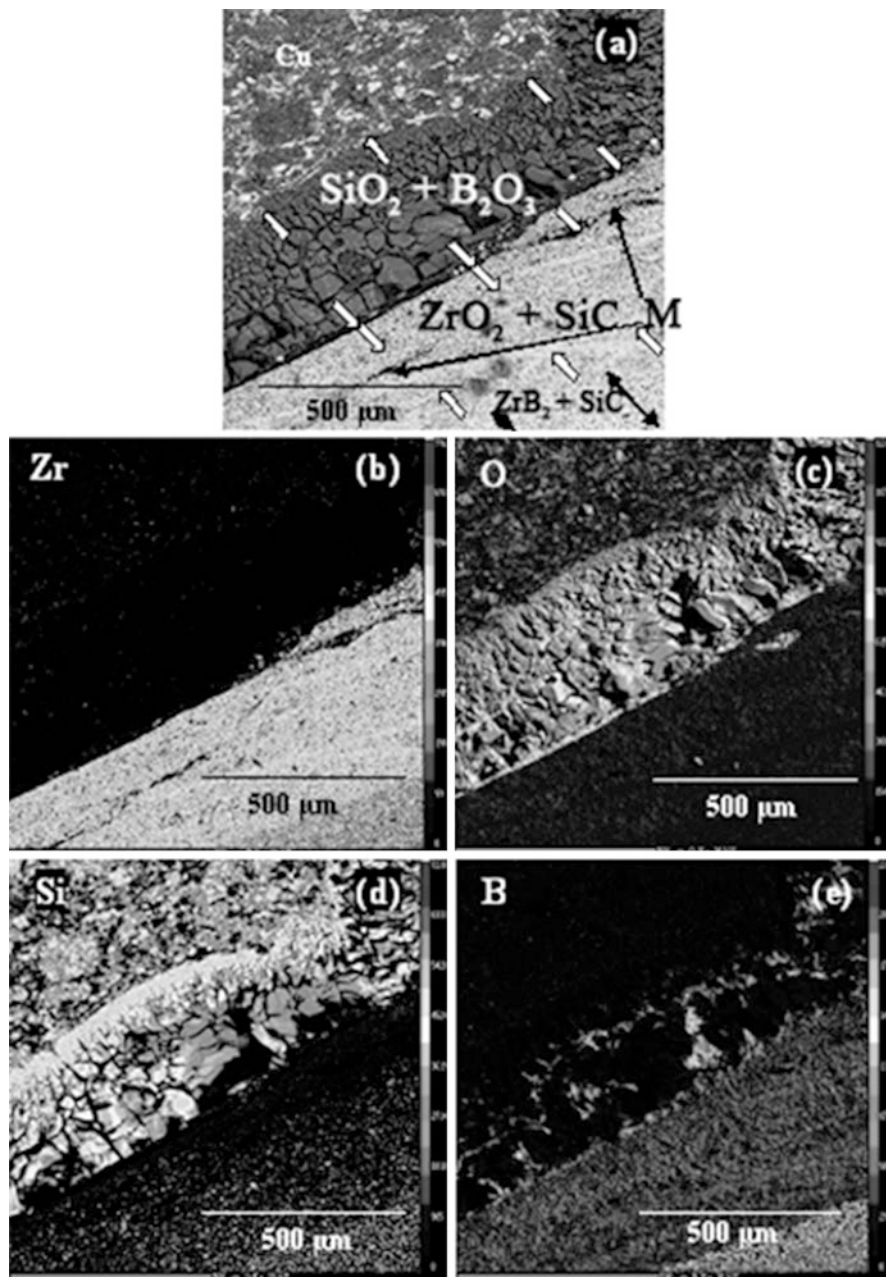


Fig. 8 Cross-sectional microstructure of the oxide scale in ZS exposed at 1300 °C for 100 h: (a) SEM (BSE) image depicting the presence of various constituent layers, as well as EDS X-ray maps of (b) Zr, (c) O, (d) Si, (e) B [29]. (Reprinted with permission from Elsevier)

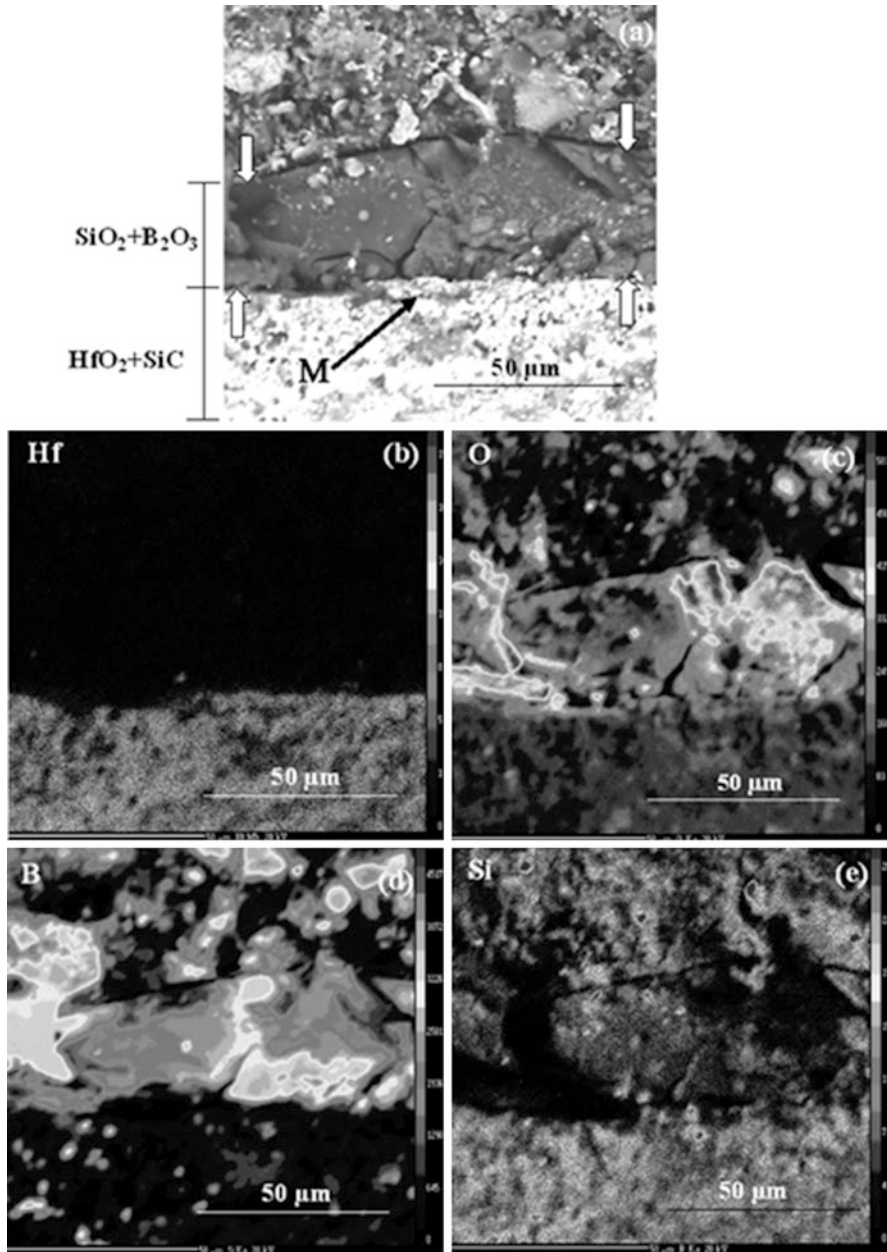


Fig. 9 Cross-sectional microstructure of the oxide scale in HS exposed at 1300 °C for 100 h: (a) SEM (BSE) image depicting the presence of various constituent layers, as well as EDS X-ray maps of (b) Zr, (c) O, (d) Si, (e) B [29]

Table 2 Thicknesses of preoxidized specimens, unoxidized part of specimens, and the layers within the oxide scales formed on ZS, ZSS, ZZSS, and HS composites, subjected to isothermal exposure at 1200 or 1300 °C for 24 and 100 h with data from Ref. [29, 47, 49]

Composite	Conditions of exposures: temperature-time	Thickness of			
		Preoxidized sample (μm)	Unoxidized material (% of material thickness)	$\text{SiO}_2 + \text{B}_2\text{O}_3$ layer (μm)	$\text{ZrO}_2 + \text{SiC}$ layer (μm)
ZS	1200 °C–24 h	4000	95.5	34 ± 4	56 ± 1
ZS	1200 °C–100 h	3200	69.2	233 ± 11	259 ± 9
ZS	1300 °C–24 h	4000	91.2	36 ± 2	139 ± 1
ZS	1300 °C–100 h	4100	62.7	375 ± 40	389 ± 30
ZSS	1200 °C–24 h	4000	94.7	25 ± 6	70 ± 6
ZSS	1200 °C–100 h	4000	89.6	100 ± 14	109 ± 7
ZSS	1300 °C–24 h	3900	93.6	30 ± 5	64 ± 5
ZSS	1300 °C–100 h	4000	76.5	189 ± 43	282 ± 89
ZZSS	1200 °C–24 h	4000	81.25	145 ± 50	230 ± 19
ZZSS	1200 °C–100 h	3700	60	196.5 ± 67 ($\text{ZrO}_2 + \text{SiO}_2$)	564 ± 55 $\text{ZrO}_2 + \text{ZrC}$
ZZSS	1300 °C–24 h	3900	78.56	164 ± 13	254 ± 38
ZZSS	1300 °C–100 h	4100	61	334 ± 83	475 ± 52
HS	1200 °C–24 h	4000	97.9	15 ± 5	26 ± 1
HS	1200 °C–100 h	3940	96.9	27 ± 5	33 ± 7
HS	1300 °C–24 h	3900	96.9	25 ± 4	34 ± 1
HS	1300 °C–100 h	3800	96.6	29 ± 3	35 ± 1.5

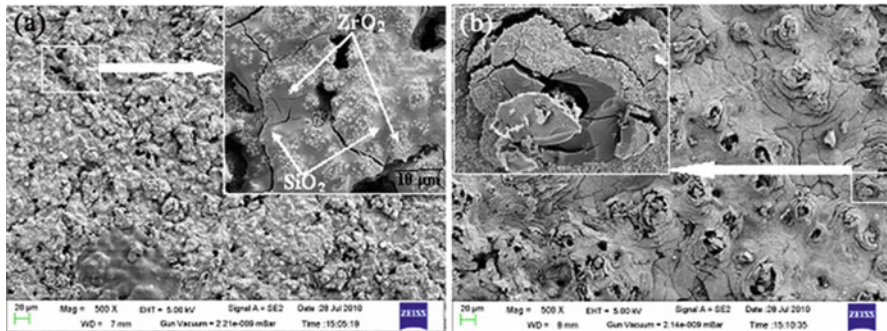


Fig. 10 SEM images depicting the top surface microstructures of the oxide scales formed on the ZS exposed for 1 h at (a) 1200 °C and (b) 1300 °C [29]. (Reprinted with permission from Elsevier)

sintered with fewer pores, whereas that formed at 1300 °C is rough and porous, as shown in Fig. 11. This observation may be ascribed to greater mass loss through vaporization of B_2O_3 and more rapid oxidation of SiC to form CO at 1300 °C.

Investigations of the oxide scale top surfaces of the $\text{ZrB}_2\text{-SiC}$ composites have shown typical flower petal-type formations [29, 49, 50]. However, interestingly this morphology has been found to be less predominant at 1200 °C than that at 1300 °C.

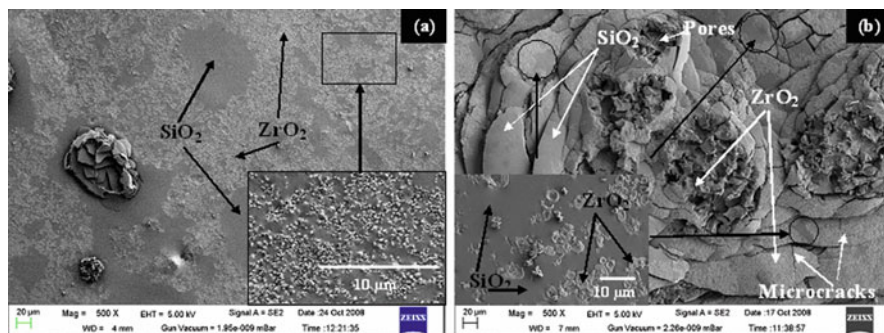


Fig. 11 SEM images depicting the top surface microstructures of the oxide scales formed on the ZS exposed for 24 h at (a) 1200 °C and (b) 1300 °C [29]. (Reprinted with permission from Elsevier)

Development of this morphology can be explained by considering the mechanisms of early stages of oxidation of this composite. Obviously, the growth rate of SiO_2 is greater at 1300 °C than that at 1200 °C. However, the susceptibility of ZrB_2 to oxidation as well as the rates of formation and escape of B_2O_3 (g) + CO (g) is also greater at the higher temperature. Therefore, the bubbles formed in the viscous B_2O_3 - SiO_2 scale tend to swell and are subsequently ruptured with escape of volatile products. Vaporization of B_2O_3 at temperatures ≥ 1100 °C [10, 21] and its escape along with CO (g) are therefore considered to be the primary causes for the formation of porosities. Furthermore, based on a model proposed by Parthasarathy et al. [51], it may be also suggested that monoclinic to tetragonal transformation of ZrO_2 above 1170 °C involving volume shrinkage of ~ 3 –6% would lead to the creation of porosities. Creation of porosities makes it easier for the atmospheric oxygen to reach the interface (between the oxide layer and substrate), and further oxidation of both SiC and ZrB_2 is promoted, until a protective SiO_2 -rich scale (Fig. 11b) is formed after exposure for a period of ~ 24 h. Subsequently, this scale is healed either by formation of fresh SiO_2 or by viscoplastic flow, and therefore mass loss is arrested. The process of repeated rupturing and healing by formation of SiO_2 as described above is expected to give rise to the flower petal-type appearance of the oxide scale surface on the ZrB_2 -SiC composite [50]. It is intuitive that the amount of volatilization of B_2O_3 (l) followed by its escape in gaseous form is greater at 1300 °C than that at 1200 °C, and therefore the oxide scale formed at the higher temperature appears to be more porous. The cracks present in the SiO_2 -rich smooth locations of oxide scales of the investigated composites are believed to be generated by stresses associated with ionic diffusion [52], growth of ZrO_2 or HfO_2 , pressure exerted by CO (g) and volatile B_2O_3 (g) formed in subsurface locations, as well as volume changes associated with the formation of oxidation products [53].

Cyclic Oxidation

Cyclic oxidation experiments at 1300 °C have exhibited quite contrasting results (Fig. 12) compared to those obtained from isothermal tests, with the HS showing higher mass gain compared to both ZS and ZSS for cyclic exposure between 6 and

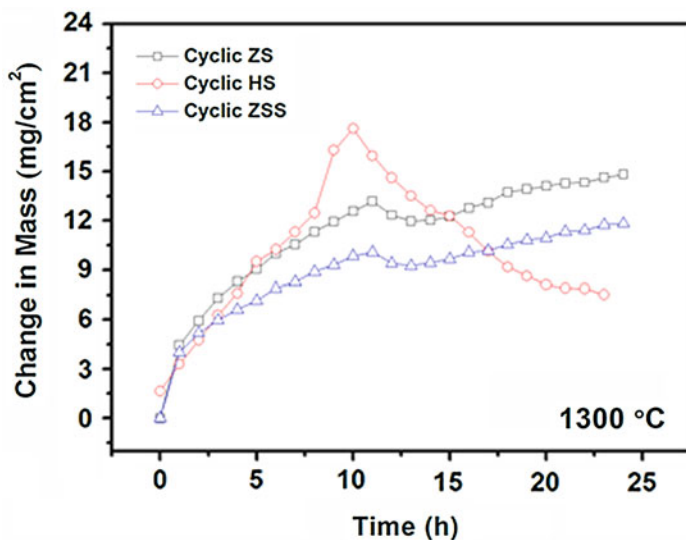


Fig. 12 Plots depicting the variation of mass change observed in ZS, ZSS, and HS composites with duration of cyclic exposure for 24 h at 1300 °C [29, 49]

12 h, which is followed by a sharp decrease in mass, which is suggestive of cracking and spallation of the oxide scale [29]. The cyclic oxidation tests have also shown less mass gain being observed for the ZSS compared to that of ZS or HS, confirming the former material's superior oxidation resistance. Furthermore, it is noticed that the mass gain through cyclic oxidation as observed for a given composite exceeds that by isothermal oxidation for a similar duration. Comparison of the oxide scales formed by cyclic exposure with those formed by isothermal oxidation at the same temperature has shown much greater amount of damage in the former type of scale. For example, the oxide scale formed by cyclic exposure of HS has shown greater amount of HfO_2 compared to that under isothermal condition, as well as formation of crater by spallation (Fig. 13). Examination of the SEM images as depicted in Fig. 13 also indicates that the oxide scale formed on the HS by cyclic exposure at 1300 °C for 24 h is more severely damaged compared to the oxide scale formed on the ZS. The lower stability of the oxide scale under cyclic exposure has been attributed to the damage caused due to residual strains caused by thermal expansion mismatch between the oxide scale and underneath substrate, and this has been confirmed by measurements using X-ray diffraction [29]. It may be noted that the coefficients of thermal expansion (CTE) of ZrB_2 and HfB_2 are $5.9 \times 10^{-6} \text{ }^\circ\text{C}^{-1}$ and $7.6 \times 10^{-6} \text{ }^\circ\text{C}^{-1}$, respectively. On the other hand, the CTEs of monoclinic ZrO_2 and HfO_2 are $7 \times 10^{-6} \text{ }^\circ\text{C}^{-1}$ and $4.4 \times 10^{-6} \text{ }^\circ\text{C}^{-1}$, respectively, indicating that the thermal mismatch observed in case of the HfB_2 -SiC composite is greater than that in ZrB_2 -SiC composite. Furthermore, the thermal expansion coefficient of SiO_2 is reported as $\sim 0.5 \times 10^{-6} \text{ }^\circ\text{C}^{-1}$. This suggests that the SiO_2 layer would expand or contract less compared to the underneath layer rich in ZrO_2 or HfO_2 during heating

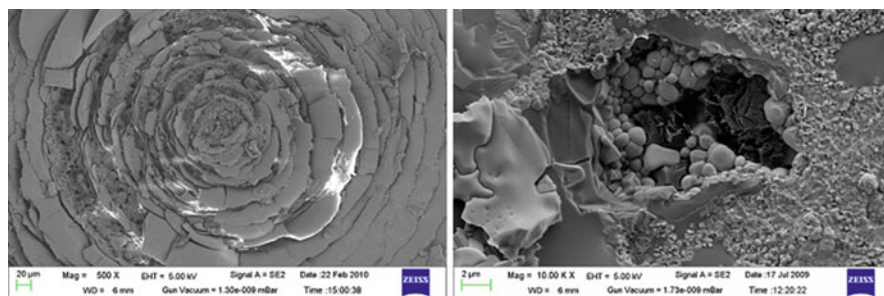


Fig. 13 SEM images depicting the top surfaces of the oxide scales formed after cyclic exposure for 24 h at 1300 °C on (a) ZS and (b) HS [29]. (Reprinted with permission from Elsevier)

or cooling cycles, respectively, and the stresses generated as a result are responsible for formation of cracks. In the case of $\text{ZrB}_2\text{-SiC}$ composite, volume expansion is observed owing to tetragonal-to-monoclinic transformation of ZrO_2 , which leads to compressive strain. However, the resulting strain mismatch is partly neutralized by higher contraction of ZrO_2 compared to SiO_2 due to greater CTE of the former oxide phase.

Oxidation Behavior During Creep

The formation of oxide scale on $\text{ZrB}_2\text{-SiC}$ -based composites during isothermal exposure under compressive creep condition at temperatures in the range of 1300–1425 °C in laboratory air has been examined [54]. During the exposure duration up to 30 h under compressive load, the growth of oxide scale has been found to be limited and has only a limited influence on creep damage. Even if the ZSS composite has exhibited superior oxidation resistance compared to the ZS, the creep rate of the former composite has been found to be greater due to the formation of glassy phase at matrix grain boundaries or $\text{ZrB}_2\text{-SiC}$ interfaces, which undergoes softening and promotes grain boundary sliding. Interestingly, the thickness of oxide scales formed on the ZSS during creep at 1300 and 1400 °C under compressive stresses in the range of 109–141 MPa has been found to be thicker compared to those formed on the ZS subjected to creep exposure for longer durations (Table 3). The net oxide scale thickness has been found to comprise ~6–13% of the cross-sectional volume after the completion of creep test. Although the oxide scale may not have a direct role in creep behavior for shorter durations of exposure, diffusion kinetics of oxygen anions through this scale is expected to have a strong influence on creep behavior for longer durations of exposure. In fact, a greater density of interfacial cracks has been observed closer to the oxide scale formed in these composites, suggesting ingress of oxygen to form the intergranular glassy film, whose presence promote inter-grain sliding followed by formation of such cracks (Fig. 14). It is interesting to note that contrary to the trend being followed by the thickness of the oxide scales formed on the samples isothermally exposed at 1300 °C (as shown in

Table 3 Thickness of the oxide scales formed during creep tests [49, 54]

Sample	Temperature (°C)	Experimental conditions	Oxide scale thickness	Exposure time	% oxide scale thickness $\{(2t_{ox}/t_s) \times 100\}$
ZS	1300	109.375 MPa, 125 MPa 140.625 MPa	$136 \pm 54 \mu\text{m}$	36 h	6.8
	1400	109.375 MPa, 125 MPa 140.625 MPa	$157 \pm 38 \mu\text{m}$	42 h	8
ZSS	1300	109.375 MPa, 125 MPa 140.625 MPa	$159 \pm 36 \mu\text{m}$	26 h	8
	1400	109.375 MPa, 125 MPa 140.625 MPa	$266 \pm 56 \mu\text{m}$	21 h	13

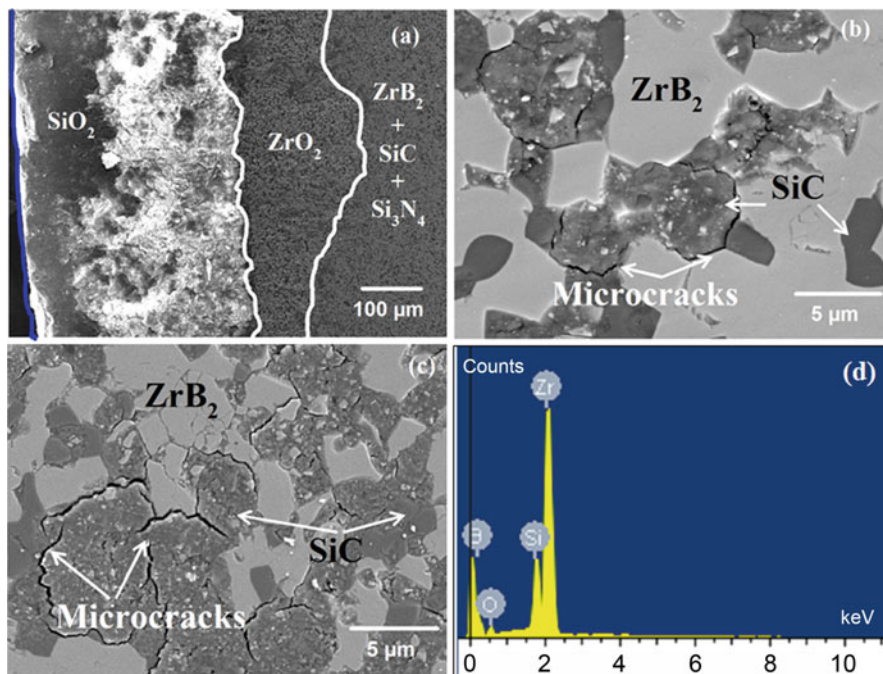


Fig. 14 SEM images depicting the post-creep microstructures of samples tested at 1400 °C under 140.6 MPa: (a) cross-section of the oxide scale on the ZSS composite and damage at ZrB₂ grain boundary or ZrB₂-SiC interface in (b) ZS and (c) ZSS composites, as well as (d) EDS spectrum from the interface confirming presence of oxides [54]. (Reprinted with permission from John Wiley and Sons)

Table 3), the post-creep oxide scale thickness of the ZSS is greater than that of the ZS (Table 2). This observation clearly suggests that the oxide scale growth rate is faster in the case of the ZSS than that in ZS, when subjected to creep. Considering that the extent of damage through formation of interfacial cracks is greater near the oxide-composite interface, the observation of higher oxide scale growth rate in case of the ZSS can be considered to be in tune with its creep resistance being inferior to that of the ZS. It is intuitive that the oxide scale in the ZSS showing higher strain rate during creep would crack by a greater amount on being subjected to compressive stress, which in turn would lead to further ingress of oxygen and therefore faster kinetics of oxide scale growth.

A more recent study carried out on creep behavior of ZrB_2 -20 vol.% SiC -14 vol.% LaB_6 composites containing B_4C and C as additives has shown the formation of an outer continuous layer comprising a mixture of $\text{La}_2\text{Zr}_2\text{O}_7$ and $\text{La}_2\text{Si}_2\text{O}_7$, followed by ZrSiO_4 , $\text{ZrO}_2 + \text{SiO}_2 + \text{SiC}$, and then an inner layer of SiO_2 at the oxide-composite interface (Fig. 15) [55]. A similar layered oxide scale has been also observed in the case of the creep-tested ZrB_2 - SiC composite containing 10 vol.% LaB_6 , with the outermost La-rich layer being discontinuous. As La is more reactive than other elemental constituents in the composite, it has been proposed that the LaB_6 is preferentially oxidized during the initial stages of exposure, and thereafter the inner layers comprising ZrSiO_4 and $\text{ZrO}_2 + \text{SiC}$ grow at the oxide-composite interface, with ingress of oxygen through the La-rich top layer in the oxide scale. Comparison of the oxide scales formed on the creep-tested samples with those formed during isothermal exposure without the application of load show the former type of oxide scales to be thicker in comparison (Table 4). This observation has been attributed to greater damage of the oxide scale under compressive stress being applied during creep. On the basis of thickness of oxide scale and net penetration depth of oxygen, it has been inferred that the oxidation resistance of ZrB_2 -20 vol.% SiC composites with 10 and 14 vol.% LaB_6 is similar during isothermal exposure at 1300°C , whereas it is superior for the latter composite when subjected to compressive creep at the same temperature.

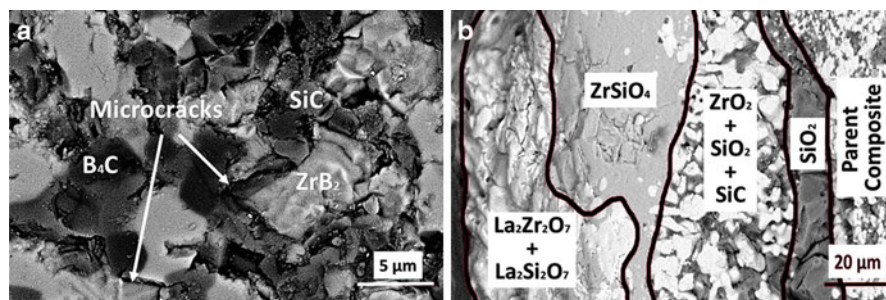


Fig. 15 SEM (BSE) images depicting the microstructures of the ZrB_2 -20 SiC -14 LaB_6 composite samples creep-tested at 1300°C under 78 MPa, showing (a) microcracks at the grain boundaries and (b) constituents of various layers within the oxide scale [55]. (Reprinted with permission from Elsevier)

Table 4 The thickness of the oxide scales formed during creep tests under 47 MPa stress or isothermally exposure for same duration without stress at 1300 °C [55]

Composites	Creep/ oxidation duration (h)	Oxide scale thickness t_{oxide} (μm) and O_2 penetration				Percentage of oxide scale thickness 2. $t_{\text{oxide}}/t_{\text{specimen}}$ (%)	
		Creep		Oxidation		Creep	Oxidation
		Oxide	Oxygen penetration	Oxide	Oxygen penetration		
ZSBCL-7	6	67 \pm 11	93 \pm 15	60 \pm 16	77 \pm 11	3.4	3.0
ZSBCL-10	8	141 \pm 21	80 \pm 14	89 \pm 31	51 \pm 23	7.1	4.5
ZSBCL-14	12	175 \pm 18	75 \pm 8	145 \pm 25	34 \pm 9	8.7	7.2

However, the creep resistance of the composite with 10 vol.% LaB_6 composite has been found to be superior due to its grain size being coarser and its greater ability to resist plastic deformation.

Oxidation in Extreme Environments with High Heat Flux

Oxidation During Arc Jet Test

In sharp contrast with non-isothermal thermogravimetric or isothermal oxidation studies, the arc heater testing is widely used as typically more closely simulating the environment that is expected to be encountered during the course of a typical hypersonic flight or atmospheric reentry because of the high heat fluxes, low pressure ionic atmosphere (i.e., O instead of O_2), and high gas velocities [21, 35, 56, 57]. In this type of test, the sample and holder are attached to a water-cooled sting arm, which serves to move the sample in and out of the flow. The surface temperature of the specimen is monitored by a two-color optical pyrometer as it increases very rapidly depending upon the applied heat flux. Analysis of the sample cross-section after arc jet testing at a heat flux of 350 W/cm^2 has revealed the presence of three distinct layers in the oxide scale. The outer layer of the oxide scale formed on the HfB_2 -SiC composite is mainly composed of HfO_2 , whereas the layer beneath has been found to be depleted in SiC. Here, the SiC has been depleted by oxidation, leaving behind a porous HfB_2 matrix. Below the SiC-depleted zone, the base composite has been found to be present [35]. However, in a study by Chamberlain et al. on arc jet testing of ZrB_2 -SiC composites using similar heat flux condition as above, the existence of four distinct layers comprising a surface layer of ZrO_2 , a mixed oxide layer, a SiC-depleted layer, as well as the unaltered ZrB_2 -SiC composite lying underneath has been reported [21]. Further, arc jet testing has confirmed that the oxide forming samples (ZrB_2 -SiC or HfB_2 -SiC composites) experience much lower conversion depths and lower SiC depletion depths compared to the samples subjected to isothermal exposure [56].

In an earlier study, the surface temperature of the specimen has been monitored by a two-color optical pyrometer during rise in temperature from the ambient to ~ 1700 °C within ~ 30 s [56]. Interestingly, the surface temperature has been found to increase slowly thereafter till 1800 °C after 600 s. Examination of the cross-sectional microstructures of the arc jet tested specimens using SEM and EDS analyses has revealed the presence of three distinct layers, with the outermost layer comprising primarily HfO_2 , a SiC-depleted region with porous HfB_2 matrix created by the active oxidation of SiC involving the formation and escape of CO, and then the unaffected base composite [53].

Oxidation During Ablation Tests

Ablation is defined as the vaporization or melting of part of the outer surface of a spacecraft on heating to temperatures exceeding 1800 °C by friction with atmosphere. When a space vehicle enters the earth's atmosphere, it has a large amount of kinetic energy, which must be dissipated in a controlled manner for the vehicle to survive. A large fraction of this energy is transferred to the atmosphere as heat energy; and the remainder manifests as the aerodynamic heat input to the vehicle body. The limited capability of metals to absorb or radiate this heat has led to the use of ablation-resistant ceramic material. Such materials are designed to play an important role in the protection of vehicles returning from space. The primary requirement of ablation shield is that the material should have adequate ability to dispose of a large amount of heat for a small amount of material loss.

High-temperature ablation-resistant ceramic composites examined by Bull et al. include mixed diborides and/or carbides of zirconium and hafnium along with SiC, such as ZrB_2 and ZrC with SiC, as well as HfB_2 and HfC with SiC [58]. The ablation resistance has been measured through arc jet tests using 0.75 inch diameter and 0.25 inch thick sample coupons mounted in a 1.25 inch graphite block. Each sample has been exposed at 400 W/cm^2 heat flux for 5 min. It has been observed and documented that formation of a coherent and passivating oxide scale on the surface is responsible for ablation resistance. Table 5 shows the thermal ablation properties of a few selected ZrB_2 - and HfB_2 -based composites, as reported in the literature. The effective conversion rates and peak surface temperatures indicate the amount of resistance to ablation. A negative conversion rate implies growth of oxide scale on the heated surface, while a positive value suggests spallation or conversion of the surface layers [58].

Table 5 Thermal ablation properties of the ZrB_2 - and HfB_2 -based composites [58]

Composite	Peak surface temperature (°C)	Effective conversion rate ($\mu\text{m}/\text{min}$)
$\text{ZrB}_2/20 \text{ ZrC}/16 \text{ SiC}$	2020	-0.98 (excellent)
$\text{ZrC}/20 \text{ ZrB}_2/16 \text{ SiC}$	2100	-6.83
$\text{ZrB}_2/20 \text{ SiC}$	2200	-17.78
$\text{HfB}_2/20 \text{ SiC}$	1810	+3.47

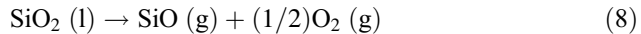
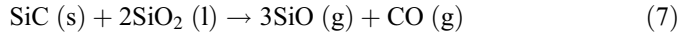
The ablation behavior of the ZrB₂-20 vol% SiC UHTC has been determined using ground simulated atmospheric reentry conditions with different heat fluxes by Zhang et al. [59]. They have reported little change in either mass or configuration after ablation at ~1660 °C but severe oxidation and ablation at 2300 °C. These results suggest that the ZrB₂-SiC composite is unable to offer adequate resistance to the applied aerothermal load [59]. Therefore, the effect of different additives (AlN/C/BN/ZrO₂, etc.) on ablation properties of ZrB₂/HfB₂-SiC composites has been examined by a number of researchers [60–66].

Li et al. have reported that AlN has a negative effect on the ablation resistance of ZrB₂-SiC composites at or above 2600 °C [62]. On the other hand, Weng et al. have reported that the HfB₂-SiC-AlN composite has superior ablation resistance compared to that of the HfB₂-SiC composite [63]. However, the surface temperatures observed for these composites are not the same. Higher surface temperature observed in the case of the HfB₂-SiC composite has been used to explain its higher erosion rates [63]. Some of the thermal ablation properties of the ZrB₂/HfB₂-SiC-based composites as listed in Table 6 show that ZrO₂ addition leads to better resistance to ablation than other additives. The ZrB₂- and HfB₂-based UHTCs have also exhibited an excellent thermal-oxidative and configurational stability under supersonic conditions, which suggests that these materials can be considered as the potential candidates for use in leading edges.

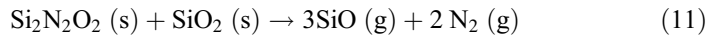
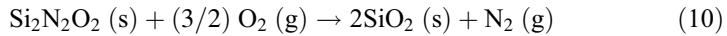
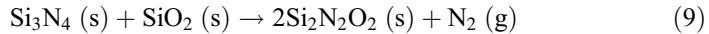
During ablative exposure at temperatures close to 2000 °C, mass loss of the UHTCs containing SiC as reinforcement is ascribed to active oxidation of SiC through the following reactions [49, 67]:

Table 6 Thermal ablation properties of the ZrB₂-SiC- and HfB₂-SiC-based composites

Composition (Vol.%)	Test conditions	Maximum surface temperature (°C)	Mass change (mg/cm ²)	Exposure time (Sec)	Reference
ZrB ₂ -10 vol.% SiC-10 vol.% ZrO ₂	Oxyacetylene flame	2000	-0.0120	600	[65]
ZrB ₂ -10 vol.% SiC-20 vol.% ZrO ₂	Oxyacetylene flame	2000	-0.02065	600	[65]
ZrB ₂ -20 vol.% SiC	Arc jet	1660	0.000	600	[59]
ZrB ₂ -20 vol.% SiC	Arc jet	2330	-319.53 (15.75%)	600	[59]
HfB ₂ -20 vol.% SiC	Oxyacetylene flame	2300	-971.79	300	[63]
HfB ₂ -20 SiC-10AlN	Oxyacetylene flame	2200	-537.58	300	[63]



Furthermore, the mass loss in Si_3N_4 containing composites may be attributed to its instability at high temperature. The possible reactions are as follows:

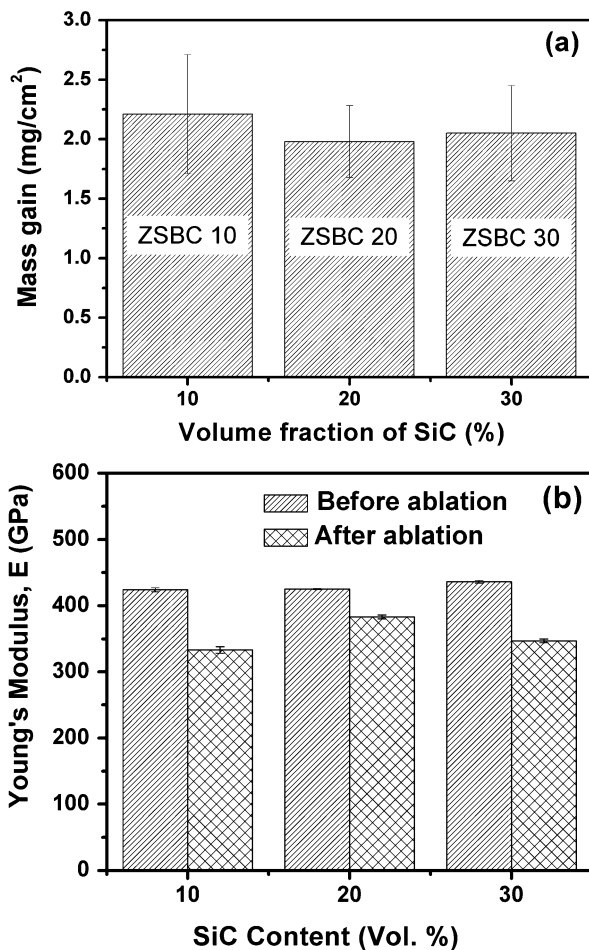


Other possible reactions during ablation test are Reactions (1–3). In the oxide scale of $\text{ZrB}_2\text{-SiC}$ composites subjected to ablation tests, ZrSiO_4 has been also found, which is expected to be formed by reactions between ZrO_2 and SiO_2 .

The surface temperatures of the $\text{ZrB}_2\text{-SiC}$ composites reach $\sim 2200^\circ\text{C}$ during the ablation tests. At such temperatures, the equilibrium partial pressures of oxygen for oxidation of ZrB_2 and SiC at 2200°C have been reported as 10^{-10} and 10^{-9} atm, respectively [42], which suggests that the latter phase is more prone to oxidation. At this temperature, the presence of SiC can be considered as detrimental to some extent due to its active oxidation according to Reactions (7) and (8), followed by formation and escape of SiO (g) and CO (g) [27, 42, 67, 68]. The stability of the oxide scale depends on volatilization and decomposition of the oxidation products with high vapor pressures. The vapor pressures of B_2O_3 , SiO_2 , and ZrO_2 at 2200°C are reported as 2.76 atm, 1.77×10^{-4} atm, and 2.47×10^{-7} atm, respectively [42], which indicates a decreasing order of volatility for these oxidation products. At high temperatures, the $\text{SiO}_2 \text{ (l)}$ either decomposes to form SiO (g) or reacts with CO (g) formed by oxidation of SiC to form SiO (g) . Moreover, B_2O_3 is also known to vaporize rapidly on heating beyond 1100°C . The escape of volatile gaseous products severely degrades the initially formed protective glassy scale by leading to its rupture and allowing further ingress of oxygen from the oxide-air interface to the composite substrate underneath, which in turn leads to significantly enhanced oxidation kinetics.

Based on the aforementioned discussion, it is obvious that among the oxidation products, ZrO_2 has the lowest vapor pressure, and therefore it is stable. However, the ZrO_2 scale is reported to be porous and develops cracks due to phase transformations during heating and cooling cycles, as shown in Fig. 16 [67]. Among these $\text{ZrB}_2\text{-SiC}$ composites with SiC volume fractions in the range of 10–30%, the composite with 20 vol.% SiC has been found to be most resistant to ablation. The pressureless sintered and $> 98\%$ dense $\text{ZrB}_2\text{-(10–30) vol.\% SiC}$ composites with 5.6 vol.% B_4C and 4.8 vol.% C as additives have been exposed to neutral oxyacetylene flame leading to surface temperatures in the range of $2180\text{--}2250^\circ\text{C}$ for 10 min, and the resulting damage has been estimated from the changes in mass and Young's modulus. These studies have shown the amount of damage to be minimum in the case of the composite with 20 vol.% SiC (Fig. 16). Study of the top surfaces of the oxide

Fig. 16 Bar charts showing changes in (a) mass and (b) Young's modulus in the composites with varying SiC content after ablation test at 2200 °C for 10 min [67]. (Reprinted with permission from Elsevier)



scales formed on the investigated composites as depicted in Fig. 17 has exhibited the presence of porosities in case of all the composites. A qualitative comparison shows the average size of pores to be the finest in the case of the oxide scale formed on the composite with 20 vol.% SiC particles and the coarsest in the oxide scale of the composite with 30 vol.% SiC. The oxide scale on the composite with 30 vol.% SiC particles has also exhibited the widest cracks and discontinuities. The oxide scale cross-sections as shown in Fig. 18 exhibit a layered structure with the outermost layer comprising Zr-Si-O, whereas the XRD patterns from these scales have shown the presence of peaks representing monoclinic ZrO_2 and $ZrSiO_4$ (Fig. 19). Based on the analysis of XRD results, it has been found that maximum amount of $ZrSiO_4$ formed in the oxide scale is formed in the ZSBC-20 composite during the ablation test. On examination of ZrO_2 - SiO_2 phase diagram as shown in Fig. 20, it is observed that a liquid phase coexists with tetragonal ZrO_2 at 2200 °C toward the

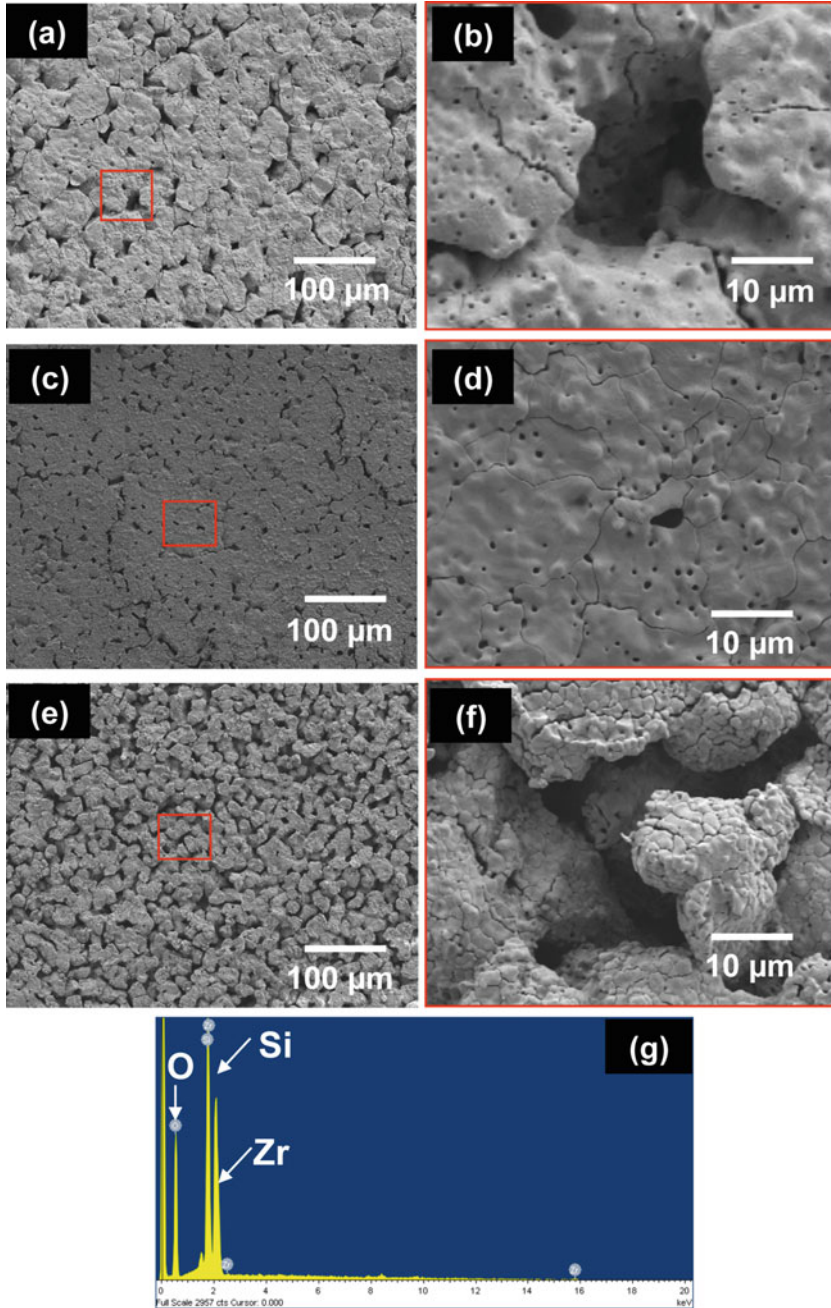


Fig. 17 SEM (SE) images of the top surfaces of the oxide scales formed on ablation-tested pressureless-sintered ZrB_2 -based composites with (a) 10, (b) 20, and (c) 30 vol.% SiC reinforcement [67]. (Reprinted with permission from Elsevier)

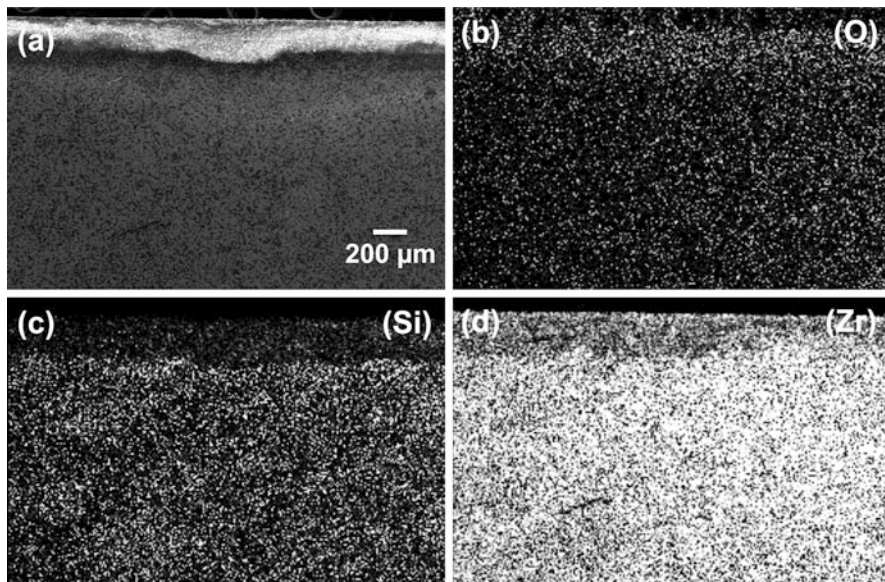
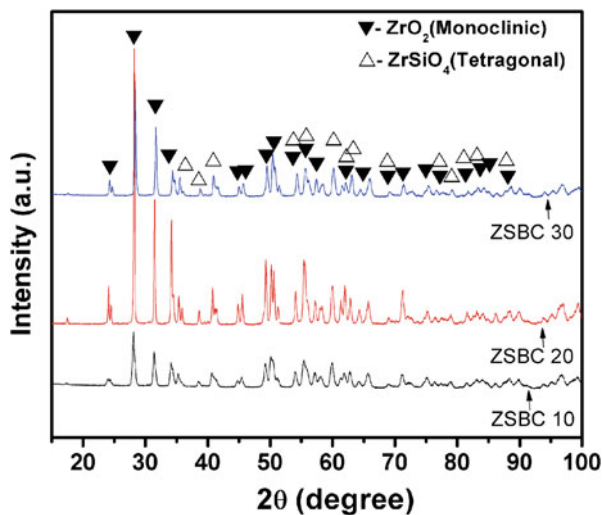


Fig. 18 Cross-section of the oxide scale formed on the pressureless-sintered ZrB_2 -20 vol.% SiC composite by exposure for 10 min during ablation test: (a) SEM (SE) image, as well as EDS X-Ray maps of (b) Zr, (c) Si, and (d) O [67]. (Reprinted with permission from Elsevier)

Fig. 19 XRD patterns from the oxide scales formed by ablation test on the pressureless-sintered ZrB_2 -based composites with 10, 20, and 30 vol.% SiC particles [67]. (Reprinted with permission from Elsevier)



ZrO_2 -rich side, and the amount of liquid increases with increasing SiO_2 content [69]. During cooling, this liquid solidifies into tetragonal ZrO_2 + cristobalite at 1960 °C, which is converted at 1949 °C to mixtures of $ZrSiO_4$ + tetragonal ZrO_2 or $ZrSiO_4$ + SiO_2 , depending on the SiO_2 content of the oxide scale. It is intuitive that

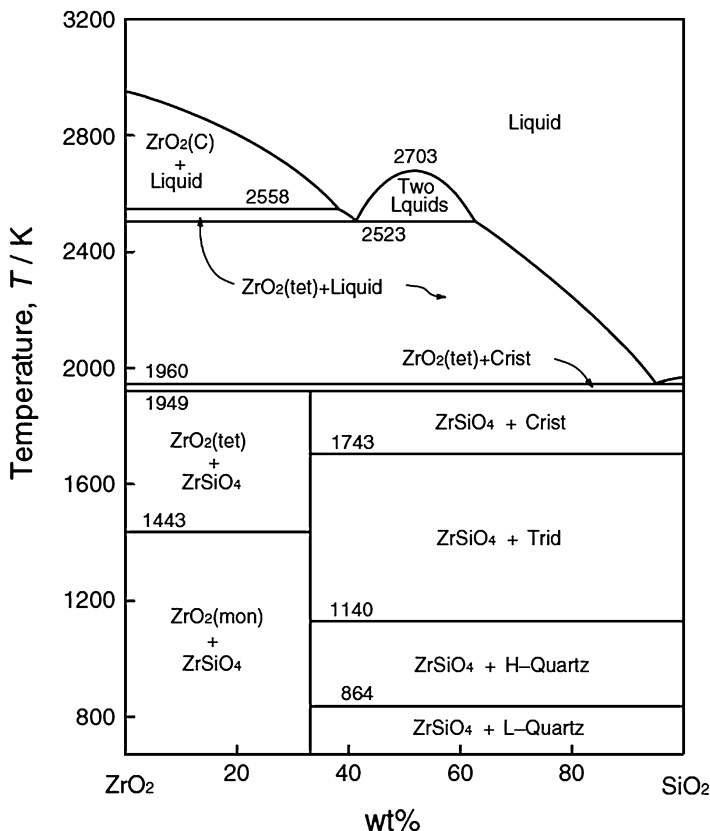


Fig. 20 ZrO₂-SiO₂ phase equilibria [69]

formation of ZrSiO₄ occurs during heating by reaction between ZrO₂ and SiO₂, which are already present in the oxide scale. However, ZrSiO₄ is expected to decompose into ZrO₂ and cristobalite with increase in temperature beyond 1949 °C, and this is followed by formation of liquid phase along with tetragonal ZrO₂ on further heating. Formation of this liquid is expected to aide in closure of porosities along with sintering of the oxide scale and in this manner creates a barrier for retarding the diffusion of oxygen anions. The ZrB₂-10 vol.% SiC composite having the lowest SiC content is expected to form a relatively lower amount of SiO₂ in its oxide scale, and therefore the amount of liquid phase formed at the high temperature of ablative exposure is expected to be less. On the other hand, the pressureless-sintered ZrB₂-30 vol.% SiC composite with higher SiC has shown a higher degree of active oxidation. Therefore, the ZrB₂-20 vol.% SiC composite can be considered to have nearly optimum ratio of ZrO₂ to SiO₂ in its oxide scale, such that the latter oxide at the surface is consumed to a larger extent for formation of ZrSiO₄, such that a sufficiently large amount of liquid forms during high-temperature exposure. This mechanism could explain the reason for

higher smoothness as well as relatively smaller size of pores found in the oxide scale of the pressureless-sintered ZrB₂-20 vol.% SiC composite compared to those having 10 or 30 vol.% SiC reinforcement (Fig. 17). The porous ZrO₂-rich scale has relatively poor thermal conductivity and therefore acts as a thermal barrier coating during exposure at 2200 °C. Formation of thermally insulating ZrO₂-rich layer may also contribute to protection of the underneath substrate from damage.

Oxidation Under Water Steam

The effect of environmental conditions on oxidation behavior of ZrB₂-20 vol.% SiC (ZS), HfB₂-20 vol.% SiC (HS), and ZrB₂-30 vol.% C-14 vol.% SiC (ZCS) composites has been investigated by Nguyen et al. [70]. The isothermal oxidation test was conducted in an environment containing 90% vapor and 10% air at 1200, 1300, and 1400 °C for 10 h. These oxidation results obtained in typically low-velocity water vapor when compared with those obtained from the tests conducted in a stagnant air furnace and with high-pressure burner rig have been found to be relatively insignificant. Volatility, spallation, and accelerated recession of these composites are strongly dependent on the gas velocity.

The moist air oxidation mechanism behavior of ZrB₂-20 vol% SiC (ZS), HfB₂-20 vol % SiC (HS), and HfB₂-20 vol% SiC-3 vol% Y₂O₃ (HSY) composites have been evaluated at temperatures up to 2400 °C by Guérineau and Jankowiak [71]. All these materials have shown limited oxidation at temperatures below 1550 °C. Significant cracks and spallation have been observed on the oxide surfaces of ZrB₂-SiC and HfB₂-SiC composites at 1990 °C and 2200 °C. The introduction of 3 vol.% Y₂O₃ in the HfB₂-20 SiC composite has been found to stabilize the cubic HfO₂ phase and form Y₂Si₂O₇ phase that reduces the damage due to thermal stresses.

Summary

For the ZrB₂- and HfB₂-based composites, SiC is the preferred reinforcement to achieve adequate oxidation resistance through the formation of a viscoplastic B₂O₃-SiO₂ scale. It has been noticed that HfB₂-SiC composites possess superior oxidation resistance compared to ZrB₂-SiC composites under isothermal conditions up to 1300 °C due to the internal stresses caused by tetragonal to monoclinic phase transformation of ZrO₂. However, the oxidation resistance of the HfB₂-SiC composites is found to be inferior on cyclic exposure due to greater thermal expansion mismatch between the HfO₂ and underneath substrate. For exposure at temperatures above 1800 °C, the presence of SiC beyond 20 vol.% is not helpful due to active oxidation of SiC. In the case of the ZrB₂-SiC composite, formation of ZrSiO₄ in the oxide scale is considered to be desirable to inhibit phase transformation of ZrO₂, as

well as formation of volatile SiO. Under ablative conditions with high heat flux and low-oxygen partial pressure, formation of ZrO₂- or HfO₂-rich scale is desirable due to its role in thermal protection of the underneath substrate as well as protection against oxidation, whereas greater than 20 vol.% SiC is detrimental.

References

1. Jackson TA, Eklund DR, Fink AJ (2004) High speed propulsion: performance advantage of advanced materials. *J Mater Sci* 39:5905–5913
2. Vanwie DM, Drewary DG Jr, King DE, Hudson CM (2004) The hypersonic environment: required operating conditions and design challenges. *J Mater Sci* 39:5915–5924
3. Kolodziej P (1997) Aerothermal performance constraints for hypervelocity small radius unswept leading edges and nose-tips, vol 112204. Ames Research Centre, Moffett Field, California, USA: NASA Technical Memorandum
4. Cutler RA (1992) Engineering properties of borides. In: Schneider SJ (ed) *Ceramics and glasses, Engineered materials handbook*, vol 4. ASM International, Materials Park, pp 787–803
5. Opeka MM, Talmy IG, Wuchina EJ, Zaykoski JA, Causey SJ (1999) Mechanical, thermal, and oxidation properties of refractory hafnium and zirconium compounds. *J Eur Ceram Soc* 19:2405–2414
6. Levine SR, Opila EJ, Halbig MC, Kiser JD, Singh M, Salem JA (2002) Evaluation of ultra high temperature ceramics for aeropropulsion use. *J Eur Ceram Soc* 22:2757–3276
7. Talmy IG, Zaykoski JA, Opeka MM (2008) High-temperature chemistry and oxidation of ZrB₂ ceramics containing SiC, Si₃N₄, Ta₅Si₃ and TaSi₂. *J Am Ceram Soc* 91:2250–2257
8. Sciti D, Brach M, Bellosi A (2005) Long-term oxidation behavior and mechanical strength degradation of a pressurelessly sintered ZrB₂-MoSi₂ ceramic. *Scr Mater* 53:1297–1302
9. Bellosi A, Montevede F (2003) Ultra-refractory ceramics: the use of sintering aids to obtain microstructural control and properties improvement. *Key Eng Mater* 264–268:787–792
10. Montevede F, Bellosi A (2005) The resistance to oxidation of an HfB₂-SiC composite. *J Eur Ceram Soc* 25:1025–1031
11. Meier GH, Pettit FS (1992) The oxidation behavior of intermetallic compounds. *Mater Sci Eng A* 153:548–560
12. Kuriakose AK, Margrave JL (1964) The oxidation kinetics of zirconium diboride and zirconium carbide at high temperatures. *J Electrochem Soc* 111:827–831
13. Berkowitz-Mattuck JB (1966) High-temperature oxidation III. Zirconium and hafnium Diboride. *J Electrochem Soc* 113(9):908–994
14. Tripp WC, Graham HC (1971) Thermogravimetric study of the oxidation of ZrB₂ in the temperature range of 800–1500 °C. *J Electrochem Soc* 118:1195–1199
15. Fahrenheitz WG (2005) The ZrB₂ volatility diagram. *J Am Ceram Soc* 88(12):3509–3512
16. Levine SR, Opila EJ, Halbig MC, Kiser JD, Singh M, Salem JA (2002) Evaluation of ultra-high temperature ceramics for aeropropulsion use. *J Eur Ceram Soc* 22:2757–2767
17. Montevede F (2005) The thermal stability in air of hot-pressed diboride matrix composites for uses at ultra-high temperatures. *Corr Sci* 47:2020–2033
18. Loehman RE (2004) Ultrahigh-temperature ceramics for hypersonic vehicle applications. *Indus Heating Pittsburgh and Troy* 71:36–38
19. Fahrenheitz WG, Hilmas GE, Chamberlain AL, Zimmermann JW (2004) Processing and characterization of ZrB₂-based ultra-high temperature monolithic and fibrous monolithic ceramics. *J Mater Sci* 39:5951–5957
20. Rezaie A, Fahrenheitz WG, Hilmas GE (2007) Effect of hot pressing time and temperature on the microstructure and mechanical properties of ZrB₂-SiC. *J Mater Sci* 42:2735–2744

21. Chemberlain A, Fahrenholtz W, Hilmas G, Ellerby D (2005) Oxidation of ZrB₂-SiC ceramics under atmospheric and re-entry conditions. *Refract Appl Trans* 1(2):1–8
22. Chase MW Jr (1998) NIST-JANAF thermochemical tables, 4th edn. American Chemical Society and the American Institute of Physics, Woodbury
23. Barin I (1995) Thermochemical data of pure substances, 3rd edn. VCH Publishers, Inc., New York
24. Raj SV (1995) An evaluation of the properties of Cr₃Si alloyed with Mo. *Mater Sci Eng A* 201:229–241
25. Nesbitt JM, Lowell CE (1993) High temperature oxidation of intermetallics. In: High temperature ordered intermetallic alloys V. MRS Symposium Proceedings, vol 288, pp 107–118
26. Rockett TJ, Foster WR (1965) Phase relations in the system boron oxide-silica. *J Am Ceram Soc* 48(2):75–80
27. Monteverde F, Bellosi A (2003) Oxidation of ZrB₂-based ceramics in dry air. *J Electrochem Soc* 150:B552–B559
28. Mitra R, Upender S, Mallik M, Chakraborty S, Ray KK (2009) Mechanical, thermal, and oxidation behaviour of zirconium diboride based ultra-high temperature ceramic composites. *Key Eng Mater* 395:55–68
29. Mallik M, Ray KK, Mitra R (2011) Oxidation behavior of hot pressed ZrB₂-SiC and HfB₂-SiC composites. *J Eur Ceram Soc* 31(1–2):199–215
30. Tripp WC, Davis HH, Graham HC (1973) Effect of an SiC addition on the oxidation of ZrB₂. *Am Ceram Soc Bull* 52:612–616
31. Shimada S, Ishil T (1990) Oxidation kinetics of zirconium carbide at relatively low temperatures. *J Am Ceram Soc* 73(10):2804–2808
32. Sciti D, Medri V, Silvestroni L (2010) Oxidation behaviour of HfB₂-15 vol.% TaSi₂ at low, intermediate and high temperatures. *Scr Mater* 63:601–604
33. Monteverde F (2009) The addition of SiC particles into a MoSi₂-doped ZrB₂ matrix: effects on densification, microstructure and thermo-physical properties. *Mater Chem Phys* 113:626–633
34. Guo WM, Zhang GJ (2010) Oxidation resistance and strength retention of ZrB₂-SiC ceramics. *J Eur Ceram Soc* 30:2387–2395
35. Opila E, Levine S, Lorincz J (2004) Oxidation of ZrB₂- and HfB₂-based ultra-high temperature ceramics: effect of Ta additions. *J Mater Sci* 39:5969–5977
36. Li X, Zhang X, Han J, Hong C, Han W (2008) A technique for ultrahigh temperature oxidation studies of ZrB₂-SiC. *Mater Lett* 62(17–18):2848–2850
37. Carney CM (2009) Oxidation resistance of hafnium diboride-silicon carbide from 1400 to 2000 °C. *J Mater Sci* 44:5673–5681
38. Sciti D, Balbo A, Bellosi A (2009) Oxidation behaviour of a pressureless sintered HfB₂-MoSi₂ composite. *J Eur Ceram Soc* 29(9):1809–1815
39. Monteverde F (2005) Progress in the fabrication of ultra-high-temperature ceramics, “in situ” synthesis, microstructure and properties of a reactive hot-pressed HfB₂-SiC composite. *Comp Sci Tech* 65:1869–1879
40. Han J, Hu P, Zhang X, Meng S (2007) Oxidation behavior of zirconium diboride-silicon carbide at 1800 °C. *Scr Mater* 57:825–828
41. Han W, Hu P, Zhang X, Han J, Meng S (2008) High-temperature oxidation at 1900 °C of ZrB₂-xSiC ultrahigh-temperature ceramic composites. *J Am Ceram Soc* 91(10):3328–3334
42. Han J, Hu P, Zhang X, Meng S, Han W (2008b) Oxidation-resistant ZrB₂-SiC composites at 2200 °C. *Comp Sci Tech* 68:799–806
43. Hu P, Zhang X, Han J, Luo DS (2010) Effect of various additives on the oxidation behavior of ZrB₂-based ultra-high-temperature ceramics at 1800 °C. *J Am Ceram Soc* 93(2):345–349
44. Peng F, Speyer RF (2008) Oxidation resistance of fully dense ZrB₂ with SiC, TaB₂, and TaSi₂ additives. *J Am Ceram Soc* 91(5):1489–1494
45. Zhang SC, Hilmas GE, Fahrenholtz WG (2008) Improved oxidation resistance of zirconium diboride by tungsten carbide additions. *J Am Ceram Soc* 91(11):3530–3535

46. Mallik M, Mitra R, Ray KK (2009) Oxidation behavior of three ZrB₂ based ultra-high temperature ceramic composites. In: Sampe Europe 30th international jubilee conference and forum session, vol 7B, pp 467–474
47. Mallik M, Ray KK, Mitra R (2017) Effect of Si₃N₄ addition on oxidation resistance of ZrB₂-SiC composites. *Coatings* 7:92. <https://doi.org/10.3390/coatings707092>
48. Opeka MM, Talmy IG, Zaykoski JA (2004) Oxidation-based materials selection for 2000 °C + hypersonic aerosurfaces: theoretical considerations and historical experience. *J Mater Sci* 39:5887–5904
49. Mallik M (2014) Structure-property relations in zirconium and hafnium diboride based ultra high temperature ceramic composites. Ph.D dissertation, Indian Institute of Technology Kharagpur, Kharagpur 721302, West Bengal
50. Talmy IG, Zaykoski JA, Opeka MM, Dallek S (2001) Oxidation of ZrB₂ ceramics modified with SiC and group IV-VI transition metal borides. In: McNallan M, Opila E (eds) High temperature corrosion and materials chemistry III. The Electrochemical Society, Inc., Pennington, pp 144–158
51. Parthasarathy TA, Rapp RA, Opeka M, Kerans RJ (2009) Effects of phase change and oxygen permeability in oxide scales on oxidation kinetics of ZrB₂ and HfB₂. *J Am Ceram Soc* 92(5):1079–1086
52. Krishnamurty R, Srolovitz DJ (2003) Stress distributions in growing oxide films. *Acta Mater* 51(8):2171–2190
53. Chatterjee UK, Bose SK, Roy SK (2001) Environmental degradation of metals. Marcel Dekker Inc., New York
54. Mallik M, Ray KK, Mitra R (2014) Effect of Si₃N₄ addition on compressive creep behavior of hot pressed ZrB₂-SiC composites. *J Am Ceram Soc* 97(9):2957–2964
55. Kashyap SK, Mitra R (2019) Effect of LaB₆ additions on densification, microstructure, and creep with oxide scale formation in ZrB₂-SiC composites sintered by spark plasma sintering. *J Eur Ceram Soc* 39:2782–2793
56. Gasch M, Ellerby D, Irby E, Beckman S, Gusman M, Johnson S (2004) Processing, properties and arc jet oxidation of hafnium diboride/silicon carbide ultra-high temperature ceramics. *J Mater Sci* 39(19):5925–5937
57. Savino R, Fumo MDS, Silvestroni L, Sciti D (2008) Arc-jet testing on HfB₂ and HfC-based ultra-high temperature ceramic materials. *J Eur Ceram Soc* 28:1899–1907
58. Bull J, White MJ, Kaufman L (1998) Ablation resistant zirconium and hafnium ceramics. US Patent No 5 750 450
59. Zhang X, Hu P, Han J, Meng S (2008) Ablation behavior of ZrB₂-SiC ultra-high temperature ceramics under simulated atmospheric re-entry conditions. *Comp Sci Tech* 68:1718–1726
60. Wang C, Wang H, Huang Y, Fang D (2007) Preparation and flame ablation/oxidation behavior of ZrB₂/SiC ultra-high temperature ceramic composites. *Key Eng Mater* 351:142–146
61. Cheng Z, Zhou C, Tian T, Sun C, Shi Z, Fan J (2008) Pressureless sintering of ultra-high temperature ZrB₂-SiC ceramics. *Key Eng Mater* 368-372:1746–1749
62. Li G, Han W, Zhang X, Han J, Meng S (2009) Ablation resistance of ZrB₂-SiC-AlN ceramic composites. *J Alloys Comp* 479:299–302
63. Weng L, Zhang X, Han W, Han J (2009) Fabrication and evaluation on thermal stability of hafnium diboride matrix composite at severe oxidation condition. *Int J Ref Met Hard Mater* 27:711–717
64. Wu H, Zhang W (2009) Mechanical properties and ablation behavior of machinable ZrB₂-SiC-BN ceramics. *Adv Mater Res* 79-82:2011–2014
65. Zhou S, Li W, Hu P, Hong C, Weng L (2009) Ablation behavior of ZrB₂-SiC-ZrO₂ ceramic composites by means of the oxyacetylene torch. *Corr Sci* 51:2071–2079
66. Zhou C, Wang Y, Cheng Z, Wang C, Sun JC, Feng B (2010) Ablation resistance of pressureless sintered ZrB₂-based ceramics. *Adv Mater Res* 105-106:199–202
67. Mallik M, Kailath AJ, Ray KK, Mitra R (2017) Effect of SiC content on electrical, thermal, and ablative properties of pressureless sintered ZrB₂-based ultrahigh temperature ceramic composites. *J Eur Ceram Soc* 37(2):559–572

68. Rezaie A, Fahrenholtz WG, Hilmas GE (2007) Evolution of structure during the oxidation of zirconium diboride-silicon carbide in air up to 1500 °C. *J Eur Ceram Soc* 27:2495–2501
69. Suzuki M, Sodeoka S, Inoue T (2005) Structure control of plasma sprayed zircon coating by substrate preheating and post heat treatment. *Mater Trans JIM* 46:669–674
70. Nguyen QGN, Opila EJ, Robinson RC (2004) Oxidation of ultrahigh temperature ceramics in water vapor. *J Electrochem Soc* 151(8):B558–B562
71. Guérineau V, Julian-Jankowiak A (2018) Oxidation mechanisms under water vapour conditions of ZrB₂-SiC and HfB₂-SiC based materials up to 2400 °C. *J Eur Ceram Soc* 38:421–432

Part VII

Materials for Sustainable Energy Applications



Hybrid Supercapacitor-Battery Energy Storage

32

Mainul Akhtar and S. B. Majumder

Contents

Introduction	1260
Definitions	1263
Supercapacitor and Li-Ion Battery	1264
Supercapacitor	1264
Lithium-Ion Battery	1269
Hybridization Approach: Toward High Energy and Power System	1272
Internal Serial Hybrid (ISH)	1274
Internal Parallel Hybrid (IPH)	1286
Future Direction of the Research on Hybrid Supercapacitor-Battery	1292
Conclusion	1293
References	1294

Abstract

Hybrid supercapacitor-battery is one of the most attractive material candidates for high energy as well as high power density rechargeable lithium (Li) as well as sodium ion (Na) batteries. Mostly two types of hybrids are being actively studied for electric vehicles and storage of renewable energies. Internal serial hybrid is an asymmetric electrochemical capacitor with one electric double-layer capacitor and another battery-type electrode. On the other hand, in internal parallel hybrids, supercapacitor and battery materials are mixed together to form bi-material-type electrode. A brief literature review provides the state of the art of various asymmetric electrochemical capacitors reported in recent times. Subsequently we have described the role of current densities and electrode potential window in designing the internal serial hybrid electrodes. Mass ratio between the two

M. Akhtar · S. B. Majumder (✉)

Materials Science Centre, Indian Institute of Technology, Kharagpur, India

e-mail: akhtarrock08@gmail.com; subhasish@matsc.iitkgp.ac.in

© Springer Nature Switzerland AG 2020

Y. R. Mahajan, R. Johnson (eds.), *Handbook of Advanced Ceramics and Composites*,

https://doi.org/10.1007/978-3-030-16347-1_43

1259

electrodes grossly influences the electrochemical performance of internal serial hybrids. Theoretical basis of the calculation of voltage, specific capacitance, energy, and power densities of internal serial hybrid has been described in detail. The theoretically estimated parameters match quite well with the experimentally obtained values for activated carbon (AC)//lithium nickel manganese oxide (LNMO) asymmetric electrochemical capacitor made in our laboratory. As compared to serial hybrid, limited reports are available on internal parallel hybrid for Li- and/or Na-ion batteries. A brief literature review on this type of hybrids is made to illustrate the outstanding research issues of this type of hybrids. We have reported excellent electrochemical performance of sodium vanadium phosphate ($\text{Na}_3\text{V}_2(\text{PO}_4)_3$)-activated carbon (AC) bi-material electrodes for lithium-ion rechargeable batteries.

Keywords

Li-ion battery · Supercapacitor · Internal serial hybrid · Internal parallel hybrid · Energy storage

Introduction

Underwater vehicles for the use of naval defense require high power as well as high energy rechargeable batteries in order to travel long distances at high speed. Due to both weight and space limitations, we need novel rechargeable batteries to replace bulky zinc-silver oxide (Zn-AgO) batteries currently used by navy for their underwater vehicles. In addition to its weight and size, imported Zn-AgO batteries are expensive and have limited wet life (maximum of 9 months since alkali electrolytes are filled), higher self-discharge rate, and long charging time (15–20 h). Also formation of Zn dendrite and evolution of hydrogen gas during operation pose serious safety issue, and more importantly these batteries fail to deliver adequate energy and power densities demanded by modern underwater vehicles [1].

Li-ion rechargeable batteries with higher energy densities, longer life, maintenance-free operation, and lower self-discharge rate could be an effective alternate to Zn-AgO battery. Performance of Li-ion batteries desirable for underwater vehicle applications is mostly dependent on characteristics of electrode materials such as capacities, higher potential for cathode/lower potential for anode, reversible Li^+ intercalation, reasonably good electronic conductivity, stability, and lower cost. To the best of our knowledge, none of the commercially available cathode and/or anode materials (used in Li-ion batteries for consumer electronic applications) are able to provide both higher energy and power densities required for applications relevant for security and defense.

In addition to develop custom-made battery modules for defense-related applications, the need of sustainable energy storage devices is increasing day by day. Traditionally natural resources (mainly coal, gasoline, petroleum, etc.) are being used as energy sources for high-scale energy applications. These energy resources are nonrenewable, and their use pollutes the ambient. To attain cleaner ambient,

extensive research is now being pursued to replace fossil fuels with various renewable energy resources. Solar power and wind energy have emerged as popular clean efficient energy resources. But the implementation of these renewable energies deal with some serious concerns – capital cost and intermittent nature of energy production as sun does not shine or wind does not blow always [2, 3]. Adequate research and development is needed to make renewable energy resources as reliable and primary sources of energy. In such case energy storage plays a crucial role for the growth of these technologies to make them commercially viable. Various technologies are used to store renewable energies [4]. Electrochemical energy storage is considered one of the most viable technologies for its integration with renewable energies. In electrochemical energy storage, electrical energy from renewable sources is stored in the form of chemical energy. Rechargeable Li-ion battery and supercapacitor are considered most useful for electrochemical energy storage [5].

Li-ion batteries store electrical energy in the form of chemical energy, and energy conversion occurs by redox reactions at the anode and cathode. A discharging battery has two terminals – positive terminal or cathode (where redox reaction occurs at higher voltage) and negative terminal or anode (where redox reaction occurs at lower voltage). Cathode and anode are relative terms, the more positive electrode is called cathode, and the more negative electrode is called anode. Li-ion batteries can store high energy ($\sim 200 \text{ Whkg}^{-1}$) as the whole volume of the active mass participates in the redox reactions. But Li-ion battery takes hours to charge and discharge. The rate of charge and discharge process is limited by the solid-state diffusion of Li ions in the bulk of the electrode materials. Since Li^+ diffusion is a slow process, it requires several hours to charge a battery. High rate discharge also deteriorates the capacity of Li-ion cells. Li-ion batteries are considered as high energy but low power density storage device. Li-ion batteries are heavily used in portable electronic market for powering mobile phones, computers, laptops, digital cameras, mp3 players, watches, etc. Recently they are also being used in large-scale applications like electric cars (HEV, PHEV, etc.), power backup for buildings with rooftop solar or windmill installations, to support power grid, etc.

Conventional supercapacitors (termed as electrochemical double-layer capacitor (EDLC)) store electrical energy by electrostatic adsorption and desorption processes, and no redox reaction is involved in energy conversion. On the basis of cell structure, these capacitors may be symmetric (same electrodes on both sides) or asymmetric (two different type electrodes) in nature. On the basis of the nature of electrodes (positive or negative), the electrolyte ions are attracted toward the electrodes; hence electric double layers are formed at the electrode/electrolyte interfaces. Supercapacitors can be charged or discharged very fast, as charged is stored due to the electrostatic attraction and no chemical reaction is involved. Supercapacitors cannot store high energy as the electric charges are accumulated only on the surface of the electrodes. The full volume of the electrodes cannot be used in this process. Hence, supercapacitors are considered as a high power ($\sim 3 \text{ KWkg}^{-1}$) and low energy density ($\sim 5 \text{ Whkg}^{-1}$) storage device. If high power is repeatedly needed for short period of time, supercapacitor is considered to be the best choice. For example, one of the interesting uses of supercapacitor is for regenerative braking (i.e., temporary storage of energy when a vehicle comes to stop and then reused when it starts to

move again) in automobiles. They are also used in consumer electronics such as in photographic flashes, portable media players and speakers, etc. Recently, they are also used in hybrid electric vehicles, electric buses and backup power for wind turbines, etc. Supercapacitors can also offer the possibility of designing power systems more efficiently for soldiers. A soldier relies heavily on batteries for electrical power in the battlefield. Use of a variety of versatile electronic equipment in the battlefield demands ever-increasing power of the battery carried by the soldiers. Soldiers nowadays are carrying numerous types of batteries to power these electronic equipments [6]. As a viable solution, one should design a rational power distribution system for soldiers utilizing a smarter battery management system (BMS). Such BMS would use supercapacitors in conjunction with high energy density rechargeable batteries to reduce the dead load of existing batteries.

The electrochemical properties of Li-ion cell and supercapacitor are complementary to each other. According to the specific needs of various consumer electronic devices, electric vehicles, and storage of renewable energies, Li-ion cells should yield appropriate energy and power density values. Like in hybrid electric vehicles, the high energy of battery aids the vehicle to cover long distance, and high power drives it at high speed. Li-ion battery and supercapacitor cannot singly fulfil the requirement of high energy and power as Li-ion battery suffers from high power and supercapacitor from storing high energy. Hence from the last decade, research has been initiated, and various approaches have been persuaded to improve the energy and power in a single device. One of them is the combination of high energy density Li-ion batteries and high power density supercapacitors in a single device called hybrid supercapacitor-battery, a novel energy storage system, which is expected to share the advantageous features of each individual component [7]. Figure 1 shows the Ragone plots of the energy-storing devices, the X-axis represents how much energy system contains, and Y-axis shows how fast that energy can be delivered. The hybrid battery-supercapacitor system stands in between the energy spectrum of supercapacitor and battery and acts as a bridge between them. The energy density of the hybrid system is greater than supercapacitor and less than battery, and power density is greater than battery and less than supercapacitor. Our chapter is devoted to

Fig. 1 Ragone plot for supercapacitor, battery, and supercapacitor-battery hybrid devices

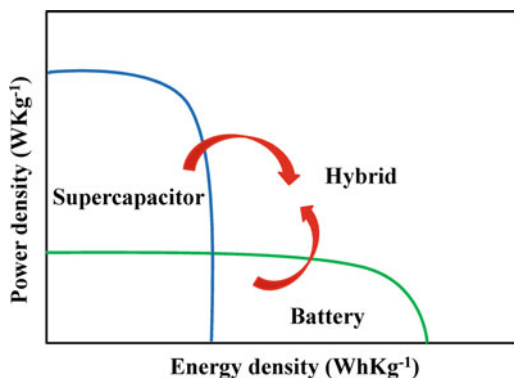


Table 1 Advantages and disadvantages of Li-ion battery and supercapacitor

Advantages	Disadvantage
Li-ion battery 1. High energy density (100–250 Whkg ⁻¹) 2. Nominal cell voltage 3.2–3.3 V 3. Flat voltage discharge plateau 4. Rate of self-discharge very low (<5% per month) 5. Less costlier than supercapacitor (\$ 0.25 to 1/Wh)	1. Low power density (250–340 Wkg ⁻¹) 2. Limited cycle life (<1000 cycles) 3. Long charging time (>1 h) 4. Need protection circuitry from being overcharged or overheated 5. More temperature sensitive than capacitors
Supercapacitor 1. High power density (1000–3000 Wkg ⁻¹) 2. Long cycle life (500 and higher) 3. Very short charging time (within few minutes) 4. Excellent temperature performance, due to low internal resistance does not heat as much as batteries	1. Low energy density (~5 Whkg ⁻¹) 2. Low cell voltage (2.5 to 2.7 V) 3. Linear discharge voltage 4. High self-discharge (40 to 50% per month) 5. High cost (~ \$ 10 /Wh)

describe the state of the art of such supercapacitor – battery hybrids and its allied varieties. As and where it is appropriate, we have also described our laboratory results on these types of hybrid energy storage systems (Table 1).

Definitions

The following are the list of battery definitions and terminologies [8]:

Battery: An electrochemical device that produces electrical energy from stored chemical energy. It consists of two or more electrically connected cells. Cell is the basic building block of battery. The main components of a cell are anode, cathode, and an electrolyte in between them.

Supercapacitor: The electrochemical capacitors are referred as supercapacitor or ultracapacitor. They are of two types – electrochemical double-layer capacitor (EDLC) and pseudocapacitors. The EDLCs store energy electrostatically in an electric field. The pseudocapacitors store energy by faradaic electron charge transfer reactions.

Capacity: The amount of energy can be withdrawn at a certain discharge current from a fully charged state of a battery. It is denoted by Ah or mAh or Wh.

Capacitance: It is the ability to store electrical charge of a capacitor. SI unit is farad (F). Capacity can be converted to capacitance by the following equation if the charge-discharge curve is linear.

$$C_s(\text{F/g}) = \text{Specific capacity}(\text{mAhg}^{-1}) \times \frac{3600}{dV(\text{mV})}$$

C-Rate: The measure of the rate at which the battery is charged and discharged. 10C, 1C, and 0.1C rate means the battery will discharge fully in 1/10 h, 1 h, and 10 h.

Specific Energy/Energy Density: The amount of energy battery stored per unit mass, expressed in watt-hours/kilogram (Whkg^{-1}).

Specific Power/Power Density: It is the energy delivery rate of battery, expressed in Watts per kilogram (Wkg^{-1}).

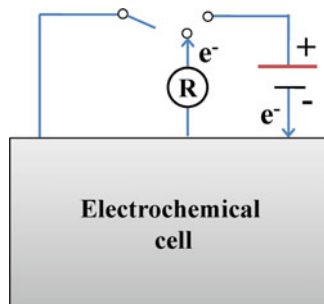
Supercapacitor and Li-Ion Battery

Electrochemical energy storage devices (viz., fuel cell, battery, supercapacitor, etc.) convert the stored chemical energy or electric potential energy into electrical energy and vice versa. The energy conversion reaction takes place at the interface of electrodes and electrolyte. All types of the electrochemical cell comprise of mainly three components – a negative electrode, a positive electrode, and an electrolyte. The ions and electrons transfer between the negative and positive electrode in an electrochemical cell; ions transfer through the electrolyte and electron through the external circuit [5]. The basic schematic has been shown in Fig. 2. When an electrochemical cell is connected with the charging circuit, some finite charge is stored in the cell. During discharge of the cell, stored charge is released by providing current through the load (R). On the basis of mechanism of energy storage and energy conversion inside an electrochemical cell, the electrochemical energy storage devices may be of different types. The energy storage and energy conversion process in supercapacitor and Li-ion battery will be discussed details in the following section.

Supercapacitor

The electrochemical capacitor sometimes referred to as *supercapacitor* or *ultra-capacitor* is a unique energy storage device which bridges the gap between *conventional capacitor* and the *batteries* in terms of their working mechanism and properties. The electrochemical capacitors are constructed in a same fashion like batteries in which two electrodes are immersed in an electrolyte and physically separated by a separator [9]. Based upon the energy storage and energy conversion mechanism and current R&D trends, electrochemical capacitors can be divided into three general classes – *electrochemical double-layer capacitor (EDLC)*,

Fig. 2 Schematic of a typical electrochemical energy storage system



pseudocapacitor, and *hybrid capacitor*. The EDLCs store charge by non-faradaic process (no oxidation-reduction reaction takes place), the pseudocapacitors use faradaic process (involves the charge transfer chemical reaction between electrode and electrolyte), and the hybrid capacitors use a combination of both faradaic and non-faradaic processes.

Electrochemical Double-Layer Capacitor (EDLC)

Like conventional supercapacitor, EDLCs also store charge electrostatically or non-faradaic process, but they do not possess any dielectric. Figure 3 schematically shows the formation of various electrochemical double layers following Helmholtz, Gouy-Chapman and Stern-Grahame model. The electrochemical double-layer models are described in the following section [2, 10].

The simplest and first *Helmholtz theory* was given by Hermann von Helmholtz. It postulates that the surface charge is neutralized by an array of opposite sign counterions. The thickness of the counterions (which forms the compact layer) is limited by the size of the solvent molecule. Essentially the double layer is formed by two layers of opposite charges separated by distance d . The electrode surface potential is linearly dissipated from the surface to the outer Helmholtz plane. The second model, *the diffuse layer model* or *Gouy-Chapman model*, was proposed by Louis George Gouy and David Leonard Chapman. It was suggested that counterions are not rigidly held with the charged surface; rather they diffuse into the electrolyte due to their thermal motion. The concentration variation of the counterions near the

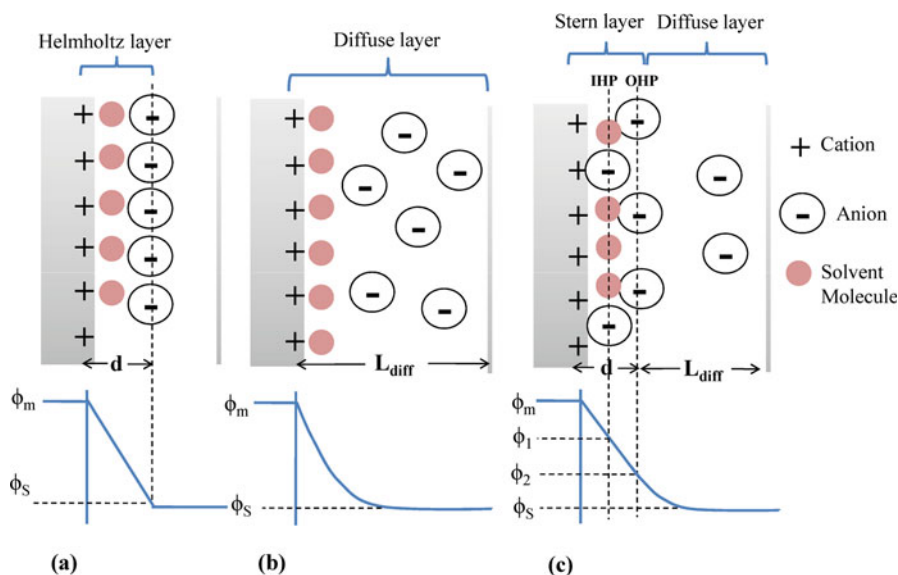


Fig. 3 Schematic representation of electrochemical double-layer models – (a) Helmholtz model, (b) Gouy-Chapman model, and (c) Stern-Grahame model in which IHP and OHP represent the inner and outer Helmholtz plane

charged surface follows the Boltzmann distribution, and hence the electric potential exponentially decreases away from the charged surface of the electrolyte (Fig. 3). The third and more reliable model, known as *Stern-Grahame model*, basically combines the *Helmholtz* and *Gouy-Chapman model* in series. In this model, some ions are especially adsorbed by the surface as suggested by Helmholtz and form the *Stern layer*, while the others diffuse through the bulk of the electrolyte and form the *Gouy-Chapman diffuse layer*. The potential drops linearly up to the Stern layer. Thereafter exponential potential drop extends to the bulk of the electrolyte.

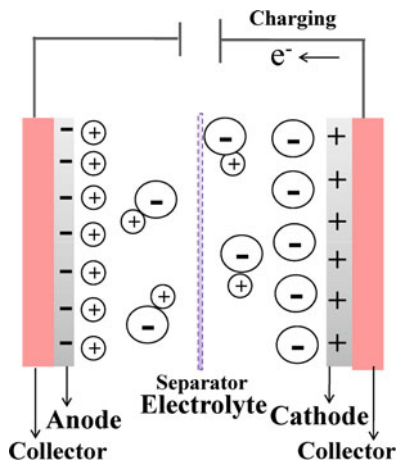
Figure 4 shows a typical double-layer capacitor in charged condition. When an external voltage is applied, the surface of electrodes in EDLC are become charged. The positive charged electrode attracts equal number of negative charges which are diffused across the separator and form anion double layer at positive electrode-electrolyte interface. The same process takes place at the negative electrode to maintain the charge neutrality of the system, as it attracts the positive ions from the system and forms cation double layer in the opposite side of the cell. So a complete electrochemical double-layer capacitor possesses two electric double layers on the interface of positive and negative electrodes. As the complete capacitor is formed by two capacitors in series, the total capacitance (C_T) is calculated as follows:

$$\frac{1}{C_T} = \frac{1}{C_+} + \frac{1}{C_-} \quad (1)$$

In Eq. 1, C_+ and C_- are the capacitance value of positive and negative electrodes. The double-layer capacitance can be calculated as follows [11].

$$C_{dl} = \frac{Q}{V} = \varepsilon_0 \varepsilon_r \frac{A}{d} \quad (2)$$

Fig. 4 Schematics of the working principle of electrochemical supercapacitor



where C is the capacitance of a single electrode, Q is the stored charge at voltage window V , ϵ_0 and ϵ_r are dielectric constants of electrolyte and vacuum, A is the exposed surface area of electrode, and d is the charge separation distance. The capacitance of capacitor is independent of voltage. Capacitance value depends on the characteristics of the electrode materials (surface area and pore size distribution). When C_{dl} is constant for EDLCs, then response current (I) can be derived as follows [11, 12].

$$I = \frac{dQ}{dt} = \frac{d(C_{dl}V)}{dt} = C_{dl} \frac{dV}{dt} = C_{dl}v \quad (3)$$

For an ideal capacitor, if the voltage scan rate (dV/dt) is kept constant, the response current (I) will also be constant, which results a perfect rectangular-shaped I - V curve (Fig. 5a). Any deviation from the rectangular shape denotes non-ideal capacitor behavior (i.e., some contribution of pseudocapacitance) as shown in Fig. 5b. If a double-layer capacitor is charged and discharged at constant current rate (i.e., I is constant over the charge-discharge period), then according to Eq. 3, dV/dt will be constant (Fig. 6a). This results in a triangular-shaped charge-discharge behavior for ideal capacitor. For non-ideal capacitor (introduces pseudocapacitive nature), the nonlinearity is introduced in the charge-discharge behavior (Fig. 6b). Carbonaceous materials (viz., activated carbon, carbon nanotube, carbon aerogels, carbon nanofibers, graphene, etc.) are generally used for making electrode of electrochemical double-layer capacitors for their high surface area and porous structure [13].

Pseudocapacitor

The other type of electrochemical capacitor is termed as pseudocapacitor (also named as redox capacitor) which stores the energy by faradaic processes but still behaves like a EDLC. In this type of capacitor, charge transfer reactions occur between the electrode and electrolyte at the surface or near-surface region of the electrode. The charge transfer reactions include electro-sorption/electro-desorption,

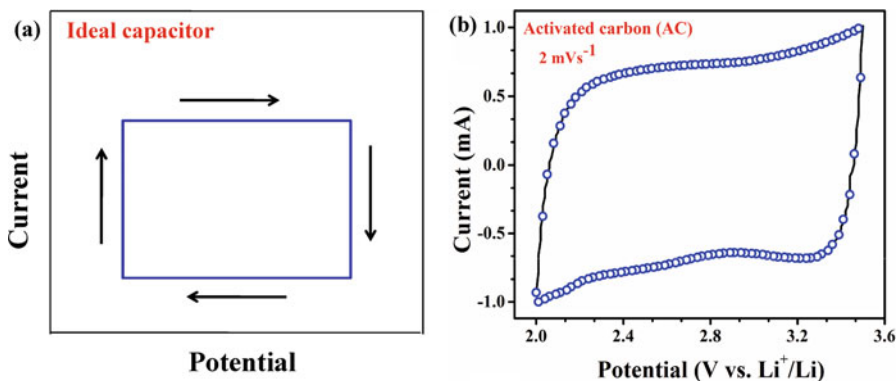


Fig. 5 Cyclic voltammograms of (a) ideal capacitor (schematic) and (b) activated carbon (AC) (measured at 2 mVs^{-1})

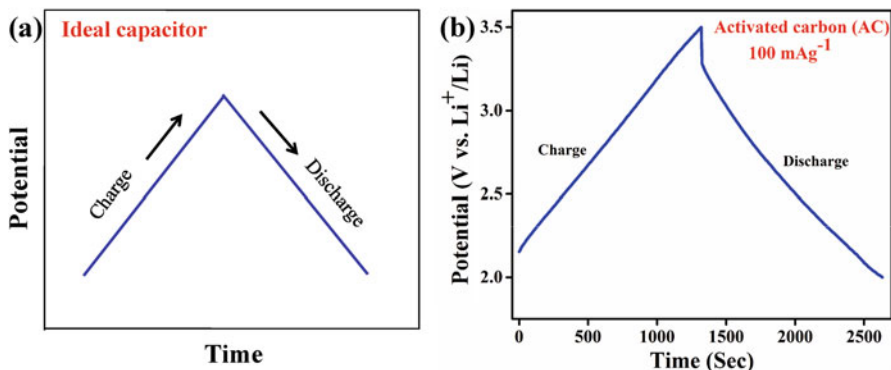


Fig. 6 Charge-discharge curves for (a) ideal capacitor (schematic) and (b) activated carbon (AC) (measured at 50 mA g^{-1})

oxidation/reduction, and also doping/de-doping, especially in active polymer electrodes. Like EDLCs, the accumulation of charge in pseudocapacitor is potential dependent. But the reactions in pseudocapacitor are faradaic in nature unlike electrostatic in EDLCs. In pseudocapacitor, the faradaic reaction occurs over a wide range of potential, unlike battery where the redox reaction occurs at constant potential results in a flat charge-discharge profile [9, 14]. The electrode materials use pseudocapacitive energy storage including transition metal oxides (RuO_2 , MnO_2 , etc.) and conducting polymers (polyaniline, polythiophene, polypyrrole, etc.) [15].

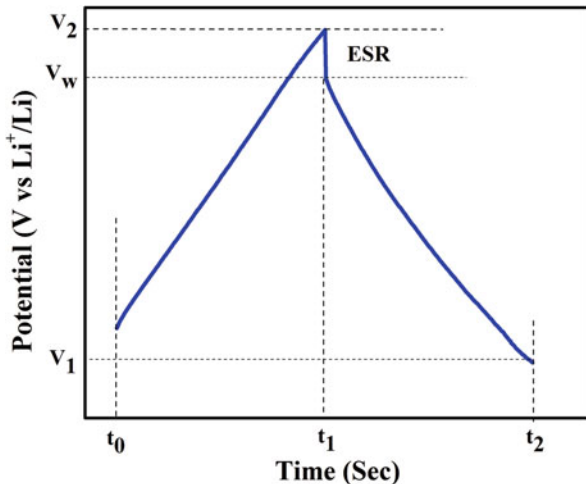
Pseudocapacitive materials behave more like a capacitor in its electrochemical signature (i.e., stored charge varies almost linearly with the voltage in the selected potential window), but charge storage involves faradaic process typically exhibited in battery materials. Oxides such as RuO_2 and MnO_2 show pseudocapacitive behavior. The battery materials on the other hand mostly yield flat charge-discharge plateau, and the oxidation and reduction peaks (during charging and discharging, respectively) are clearly identified in cyclic voltammetry curves. However, in smaller dimensions (viz., as reported in 6-nm-thick LiCoO_2 thin film), the battery materials might behave like a pseudocapacitor as most of the reactant sites of the electrode are exposed to the surface in contact with electrolyte [16, 17].

Electrochemical Measurement

Figure 7 shows a typical charge-discharge profile (measured at 50 mA g^{-1}) of an electrochemical capacitor. The capacitor is charged at t_1 seconds and then discharged at t_2 seconds in the voltage window of V_2 to V_1 . The initial direct fall of voltage (from V_2 to V_w) during discharge is due to the internal resistance acting like a resistor in series with the capacitor called *equivalent series resistance (ESR)*. The specific capacity, specific capacitance, energy density, and power density can be calculated from the V - t graph as follows:

The *specific capacity* of the capacitor can be expressed as follows:

Fig. 7 Typical charge-discharge profile of an electrochemical capacitor (measured at 50 mA g^{-1})



$$C(\text{mAhg}^{-1}) = \frac{i \times \Delta t}{3600 \times m} \tag{4}$$

where i is the constant current in mA, Δt ($= t_2 - t_1$) is the discharge time in second, and m is the total active mass of electrodes (in mg). Capacity can be directly converted to capacitance, as the charge-discharge curve is linear in nature. The *specific capacitance* of the capacitor is calculated using V-t graph as follows:

$$C_S(\text{Fg}^{-1}) = \frac{i(t_2 - t_1)}{m(V_1 - V_2)} \text{ or specific capacity (mAhg}^{-1}) \times \frac{3600}{dV(\text{mV})} \tag{5}$$

The *energy density* is calculated from the area under the V-t graph and expressed as

$$E(\text{WhKg}^{-1}) = \frac{1}{2} C_S(\text{Fg}^{-1})(V_1^2 - V_2^2)(V^2) \times \frac{1000}{3600} \tag{6}$$

$$E(\text{WhKg}^{-1}) = \frac{1}{7.2} C_S(\text{Fg}^{-1})(V_1^2 - V_2^2)(V^2)$$

The time rate of energy delivery is the power density and calculated as

$$P(\text{WKg}^{-1}) = \frac{E}{\Delta t/3600} \tag{7}$$

Lithium-Ion Battery

The primary functional components of a lithium-ion battery are anode, cathode, and electrolyte. The materials used as an electrode in battery are capable of intercalating or reversibly accommodate lithium ions. The most commercially popular negative

electrode materials are carbon (graphite), $\text{Li}_4\text{Ti}_5\text{O}_{12}$, etc. Generally, three types of materials such as layered oxide (viz., lithium cobalt oxide), polyanion (viz., lithium iron phosphate), and spinel (viz., lithium manganese oxide) are used as cathode material in lithium-ion battery. The selection of the electrolyte depends on the potential window of the cell. The electrolyte solution commonly comprises a lithium salt (such as LiPF_6 , LiBF_4 , or LiClO_4) dissolved in a mixture of organic solvents (such as EC, DMC, and DEC). The combination of LiCoO_2 as cathode and graphite as anode is the most common electrode system for lithium-ion battery.

Working Principle of Li-Ion Battery

The electrodes in lithium-ion battery act as host of lithium ions and provide lithium ions to move in or out of the structure called intercalation (insertion of lithium ions) or de-intercalation (extraction of lithium ions) process. The electrolyte provides the pathway for shuttling of lithium ion ions between the anode and cathode across the separator. The electron flow is blocked by the separator through the electrolyte. The electrons are released from one current collector through the external circuit to another current collector.

The schematic of the charge-discharge process exemplified by LiCoO_2 (cathode) and graphite (anode) systems is shown in Fig. 8. The operative electrochemical reactions are shown as follows [18].

Anode reaction:

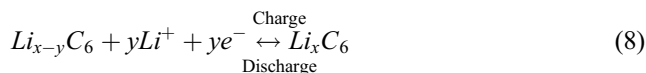
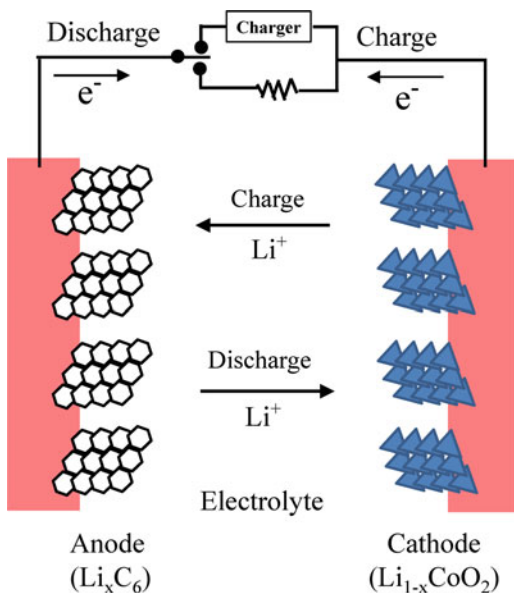
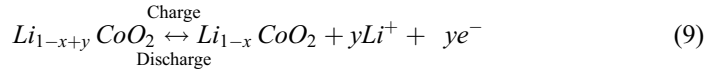


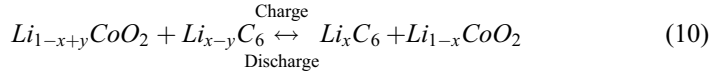
Fig. 8 Schematic of the charge-discharge process of lithium-ion cell



Cathode reaction:



Overall reaction:



During charging, lithium ions are extracted from the cathode and conducted through the electrolyte to the anode. To compensate the charge in cathode, Co^{3+} gives up an electron to the outer circuit and converts into Co^{4+} . The lithium ion from the electrolyte incorporates into the structure of graphite layer, and hence it accepts an electron from the outer circuit to pi-electron cloud for charge neutrality. During discharge, the entire process occurs in reverse direction.

The voltage and capacity of an electrochemical cell are dependent on the electrode materials used. The voltage is calculated from the chemical potential of the electrodes. The chemical potential is the thermodynamic quantity describing the change in Gibbs free energy as a function of change in lithium concentration in the host matrix. If G is the Gibbs free energy and (x) is the total number of inserted lithium atoms, then chemical potential (μ) of that electrode will be:

$$\begin{aligned} \mu &= [\mu_C^{Li}(x) - \mu_A^{Li}] \\ \mu &= \int_{x_1}^{x_2} [\mu_C^{Li}(x) - \mu_A^{Li}] dx_{Li|x_2 \rightarrow x_1=x} / (x_2 - x_1) \\ \mu &= [G_{C(Li=x_2)} - G_{C(Li=x_1)} - (x_2 - x_1)G_{A(Li)}]_{Li|x_2 \rightarrow x_1=x} / (x_2 - x_1) \\ \mu &= \frac{\partial G(x)}{\partial x} \end{aligned} \quad (11)$$

The change in Gibbs free energy (dG) is the maximum amount of work obtained from an electrochemical cell of open circuit voltage E and can be expressed as

$$dG = -nFE \quad (12)$$

where n is the total no of electrons participated in electrode reaction ($n = 1$ for Li^+/Li pair), F is the Faraday constant, and E is the potential difference between the electrodes. The electric potential (E) of the cell can be obtained from the combination of Eqs. (11 and 12):

$$\begin{aligned} -nFE &= (\mu_C - \mu_A) \\ E &= \frac{-(\mu_c - \mu_a)}{F} \end{aligned} \quad (13)$$

where μ_c and μ_a are the chemical potentials of cathode and anode. The electric potential of a cell plays a vital role on selecting an electrolyte. To avoid unwanted reduction or oxidation reactions of electrolyte during charge-discharge process, the bandgap energy (E) of the electrolyte should have the higher value than the redox energies of cathode (E_c) and/or anode (E_a). So higher bandgap organic electrolytes are the best choice for lithium-ion battery [19, 20].

Hybridization Approach: Toward High Energy and Power System

As mentioned earlier, the EDLCs can deliver high power, but it lacks high energy. The low energy density of EDLCs limits its use in several high energy applications. The low energy density of EDLCs can be explained as follows [21].

- (i) It can't store large amount of energy, as the charge is stored only at the surface of the electrode due to the formation of electrochemical double layer at the electrode-electrolyte interface. The charge density is very low as compared to the large ion participation in the bulk of the electrode due to redox reaction in the pseudocapacitors and Li-ion batteries.
- (ii) The charge transfer reactions in EDLCs are voltage dependent, i.e., with the progression of charge transfer, the potential of the EDLCs changes linearly. The voltage decreases progressively during the discharge for EDLCs. So the cell voltage is low as compared to the Li-ion battery where the voltage is pinned at certain value during charge and discharge.
- (iii) For EDLCs, the energy density also depends on the ion concentration of the electrolyte. In EDLCs, the opposite ions in the electrolytes are consumed at the electrodes during charging. In Li-ion battery, at one end lithium ions are collected from one electrode into electrolyte and depleted to the opposite electrode at the other end.

In order to increase the energy density of the EDLCs and simultaneously to maintain the high power density and long cycleability of the system, pseudocapacitor or battery-type materials are introduced with EDLCs. Various types of possible hybridization approaches for the integration of pseudocapacitors and batteries with EDLCs have been shown in Fig. 9. These approaches are summarized as follows [22, 23].

The readily available supercapacitor and battery devices can be connected externally by wire either in serial or parallel combination resulting in (external) serial and parallel hybrid devices, respectively. Among the two types of external hybridization, the parallel external hybridization is very common in internal combustion engine cracking, hybrid electric vehicles, and pulsed applications. The hybrid device yields more power density as compared to the battery (faradaic type) and more energy density as compared to the supercapacitor (EDLC type). For pulsed application, this type of combination is very useful, as it outperforms both the battery and EDLCs. In

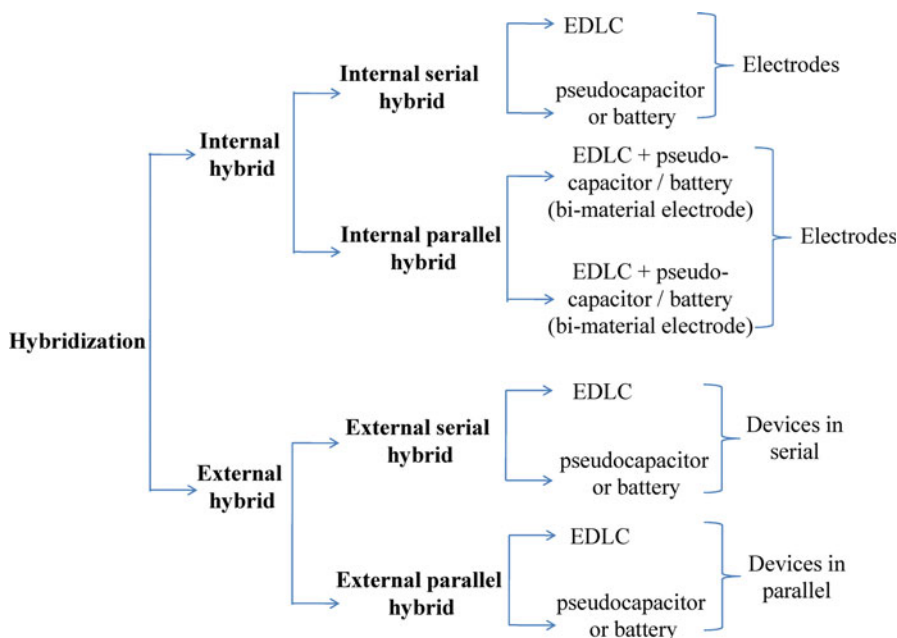


Fig. 9 Schematic representation of plausible approaches of hybridization using EDLC battery and pseudocapacitors

this case, the EDLCs provide the power during the pulse, and at rest period the battery energizes EDLCs.

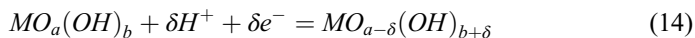
The same approach of hybridization can be made internally at electrode level inside an electrochemical cell. Thus, in an electrochemical cell, if one of the electrodes is of EDLC type and the other one is of faradaic type (viz., pseudocapacitor or battery), the combination is termed as *internal serial hybrid (ISH)*. These types of systems are also named as *hybrid electrochemical capacitor (HEC)* or *hybrid capacitor*. When lithium ions are intercalating species, then such electrochemical cells are usually termed as *lithium-ion hybrid electrochemical capacitor (Li-HEC)* or *lithium-ion capacitor* or *lithium capacitor*. Alternatively, if an electrode of an electrochemical cell consists of faradaic and EDLC types of materials, they are termed as *bi-material electrodes*. The cells consist of such bi-material electrodes are named as *internal parallel hybrid*. The *internal serial* and *parallel hybrids* are the two extreme cases of electrode combinations. Apart from these, other intermediate combinations are also possible. For example, one electrode may be of *bi-material types*, and the other one is of *faradaic* or *EDLC* types. Since a wide spectrum of electrode materials (EDLC, pseudocapacitor, and battery types) and their combinations can be proposed, further classification of internal hybrid system remains quite complex in nature. The state of the art of the internal serial hybrids and internal parallel hybrids is reviewed as follows.

Internal Serial Hybrid (ISH)

As mentioned earlier, internal serial hybrids combine pseudocapacitors or battery materials with non-faradaic-type EDLCs. Two different types of electrodes with different electrochemically active materials in ISHs exhibit different voltage profiles during charging and discharging (linear for EDLC type and usually plateau type in battery-type electrodes). Proper selection of electrodes in ISHs can offer wide working voltage window, larger capacity, as well as energy density values [24]. Depending upon the working voltage window, the faradaic electrodes can be used as either positive or negative electrodes. The EDLC-type electrodes are mostly activated carbon and derivatives of carbons such as graphene, carbon nanotube, reduced graphene oxide, carbon nanofoam, etc. [25]. As outlined in the following section, for ISHs, various types of faradaic electrodes have been explored using aqueous and nonaqueous electrolyte [23].

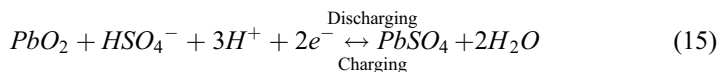
Faradaic Materials Used in ISH with Aqueous Electrolyte

Transition metal oxides: Metal oxides are the most common faradaic electrodes used for internal serial hybrids. It includes manganese oxide, nickel oxide, ruthenium oxide, cobalt oxide, etc. Sometimes hydroxides of these elements are also used for making the electrodes for such asymmetric combination (with EDLC-type activated carbon (AC)). They are used with AC using mostly aqueous electrolyte. The pseudocapacitance from these types of compounds in aqueous media originates due to the change of oxidation state of the transition metals. The transition metal oxides form interfacial oxycation species [e.g., $MO_a(OH)_b$] at different oxidation state and exchange protons and/or alkali cations (viz., K^+ , Na^+ , etc.) with the electrolyte medium. The associated reactions are as follows:



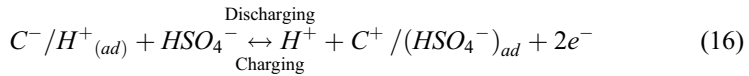
where $MO_a(OH)_b$ and $MO_{a-\delta}(OH)_{b+\delta}$ are interfacial species for $MO_x \cdot nH_2O$ at higher and lower oxidation state [26, 27].

Lead compounds: Using the technology of lead-acid battery and replacing the lead with AC, the internal serial hybrid system $PbO_2//AC$ has been conceptualized. Several research outputs have been found based on the activated carbon as negative and mixture of lead oxide and lead sulfate as positive electrode in aqueous sulfuric acid media [28]. The positive side of the asymmetric cell exactly follows the reaction as in lead-acid battery. The following reversible reaction occurs in this type of electrochemical cell during charging and discharging process.



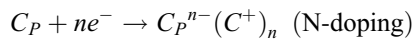
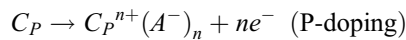
The faradaic reaction at positive side involves the sulfation of the PbO_2 electrode with the change of Pb(IV)/Pb(II) oxidation states. Simultaneously the recharging of

electric double-layer-type AC occurs on the other side of the cell. The double-layer formation at AC anode can be described as follows:

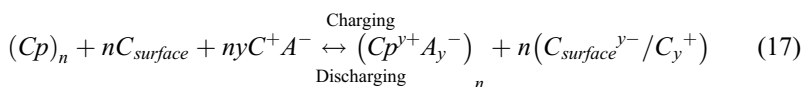


At the charged state of the capacitor, positively charged proton (H^+) forms double layer with negatively charged carbon electrode surface. During discharging, protons flow to the electrolyte, and bi-sulfate (HSO_4^-) anions adsorb onto the positively charged carbon cathode [29, 30].

Conducting polymers: The π -conjugated conducting polymers have received a great importance for the use in electrochemical capacitors. The conducting polymers most commonly used for supercapacitor applications are polypyrrole, polyaniline, and derivatives of polythiophene [31]. The conducting polymers can be positively or negatively charged by ion insertion in the polymer matrix. It can be p-doped or n-doped according to the insertion of anions or cations, respectively, into it. The charging processes of the conducting polymers are as follows:



The p-dopable polymers are used as positive electrodes and n-dopable as negative electrodes. However, n-doped polymer supercapacitors are very rare due to the requirement of very high negative voltage for n-doping. Numerous literature reviews reported p-doped conducting polymers as positive electrode with double-layer-type activated carbon as negative electrode for ISH capacitor [32, 33]. In this type of hybrid combination, reactions follow the following equations:



At charged state, the conducting polymer become fully p-doped (or intercalated) state and AC become polarized state forming cation double layer. During discharge, the anions are de-doped (or de-intercalated) from the conducting polymer, and simultaneously the activated carbon is depolarized.

Li⁺-/Na⁺-ion insertion (battery) type: The Li⁺ insertion compounds are combined with activated carbon to form asymmetric ISHs. The literature reviews reported for hybrid Li insertion system using aqueous electrolyte are mainly based on manganese oxide [34, 35]. The Li⁺-ion insertion compound (like LiMn₂O₄) is used as a positive electrode in combination with AC as a negative electrode in Li⁺ ion aqueous electrolyte (like Li₂SO₄). In this hybrid capacitor system, during charging, Li⁺ ions are de-intercalated from the insertion cathode and are migrated through the electrolyte to the negative double-layer-type AC electrode. Simultaneously, Li⁺ ions are

electrostatically attracted by the negatively charged AC surface and adsorbed onto it to form the electrochemical cation double layer. The electrolyte mainly functions like an ionic conductor as similar to the electrolyte in battery system; it is not consumed through the process of charging and discharging. So, this type of system overcomes the electrolyte depletion problem, as it is found for EDLCs or hybrid system using metal oxide or hydroxide, Li-based anode ($\text{Li}_4\text{Ti}_5\text{O}_{12}$), etc. [36].

Faradaic Materials Used in ISH Electrodes with Organic Electrolyte

The internal serial hybrid (ISH) consisting of lithium-ion insertion (i.e., battery/faradaic-type) and activated carbon- or other carbon based material (i.e., EDLC-type) electrodes in organic media has been widely discussed by several research groups. This type of system is also called *lithium hybrid electrochemical capacitor (Li-HEC)* or *lithium-ion capacitor* or simply *lithium capacitor*. The lithium batteries are intrinsically low power device with limited cycle life, where the EDLCs are low energy devices with excellent cycleability. To mitigate the relative disadvantages of lithium-ion battery and supercapacitor, they are combined in a single cell in non-aqueous (organic) electrolyte medium. The battery-type faradaic electrode may be used as a positive or a negative electrode (see Table 2). Table 2 summarizes the prominent results related to the ISHs using battery- and EDLC-type electrodes in nonaqueous (or organic) electrolyte medium. For positive electrode, the intercalation compound should have high oxidation potential (>3 V vs. Li^+/Li) and high specific capacity. Various types of layered oxides ($\text{LiNi}_{1/3}\text{Mn}_{1/3}\text{Co}_{1/3}\text{O}_2$), spinel oxides (LiMn_2O_4 , $\text{LiNi}_{0.5}\text{Mn}_{1.5}\text{O}_4$, etc.), phosphates [LiCoPO_4 , $\text{Li}_3\text{V}_2(\text{PO}_4)_3$, etc.], and fluorophosphates (LiVPO_4F) have been employed as positive electrode for Li-HECs. For negative electrode, the insertion electrodes should have low reduction potential (<2 V vs. Li^+/Li) with high specific capacity. Numerous insertion compounds have been found which intercalates Li ions at potential below 2 V vs. Li^+/Li . A wide variety of materials including transition metal oxides [$\text{TiO}_2(\text{B})$, $\alpha\text{-MnO}_2$,

Table 2 Characteristics of ISH system using battery- and EDLC-type electrodes in organic electrolyte

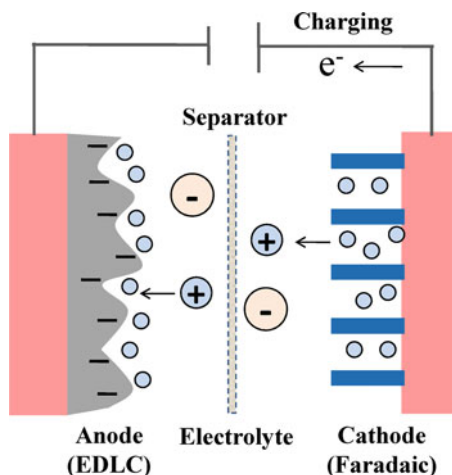
Negative electrode	Positive electrode	Potential window (V)	Specific energy (WhKg^{-1})	Specific power (WKg^{-1})	Year	References
$\text{Li}_4\text{Ti}_5\text{O}_{12}$	AC	1.0–3.0	25	–	2001	37
AC	$\text{LiNi}_{0.5}\text{Mn}_{1.5}\text{O}_4$	1.5–2.8	55	–	2005	38
AC	LiMn_2O_4	1–3	45	1200	2011	22
$\text{Li}_4\text{Ti}_5\text{O}_{12}$	AC	1–3	30	1300		
$\text{Li}_4\text{Ti}_5\text{O}_{12}$	AC	0–3	69	–	2013	39
$\text{Li}_2\text{CoPO}_4\text{F}$	AC	0–3	24	–	2013	40
$\text{LiNi}_{0.5}\text{Mn}_{1.5}\text{O}_4$	AC	1.5–3.25	19	–	2015	41
$\text{Li}_3\text{V}_2(\text{PO}_4)_3\text{-C}$	AC	0.5–2.75	25	325	2015	42
AC	$\text{Li}_3\text{V}_2(\text{PO}_4)_3\text{-C}$	0.5–2.75	27	255		
$\text{H}_2\text{T}_{12}\text{O}_{25}$	AC	1.5–2.8	35–4	179–5383	2015	43
AC	LiVPO_4F	1–3	30	–	2016	44

$\text{Li}_4\text{Ti}_5\text{O}_{12}$, LiCrTiO_4 , $\text{H}_2\text{T}_{12}\text{O}_{25}$, etc.], carbonaceous materials (graphite, graphene, Li-doped carbon, etc.), hydroxides (FeOOH), polyanions [TiP_2O_7 , $\text{LiTi}_2(\text{PO}_4)_3$, $\text{Li}_2\text{CoPO}_4\text{F}$, $\text{Li}_3\text{V}_2(\text{PO}_4)$, etc.], silicates ($\text{Li}_2\text{FeSiO}_4$, $\text{Li}_2\text{MnSiO}_4$, etc.), and borates (LiMnBO_3 , etc.) have been classified for use of negative electrodes for *Li-HECs*. The faradaic insertion electrodes utilized for Li-HECs should have excellent cycleability and rate capability to adjust with the performance attributed by the high surface area EDLC-type carbonaceous materials. This type of hybridization has first reported in the battery field in 2001 by Amatucci's group [37]. They used nanostructured $\text{Li}_4\text{Ti}_5\text{O}_{12}$ as negative electrode with activated carbon as positive electrode, designed a $\text{Li}_4\text{Ti}_5\text{O}_{12}/\text{AC}$ hybrid system which exhibits a sloping voltage of 3 to 1.5 V with energy density of 20 Whkg^{-1} . Subsequently, several research works have been reported on various combinations of insertion-type battery materials with EDLC-type carbonaceous electrodes.

As tabulated in Table 2, in ISHs, mostly battery materials are used as negative electrode, whereas EDLC type carbonaceous materials are used as positive electrodes. The working principle in Li-HECs (where positive electrode is battery and negative electrode is EDLC) is different from the Li-HECs (where positive electrode is EDLC and negative electrode is battery). The role of positive and negative electrodes and electrolyte in these two types of Li-HECs has been discussed below.

Li-HECs as battery-type positive electrode: Various types of positive insertion electrodes including but not limited to $\text{LiNi}_{0.5}\text{Mn}_{1.5}\text{O}_4$, LiMn_2O_4 , $\text{Li}_3\text{V}_2(\text{PO}_4)$, LiVPO_4F , etc. have been used with high surface area AC as negative electrode in Li-HEC. The charge storage mechanism in this type of ISHs is schematically shown in Fig. 10. During charging, Li^+ ions are extracted out (de-intercalate) from the Li-containing insertion-type battery electrode, and simultaneously, to balance the charge, Li^+ ions present in the electrolyte are attracted by the negatively charged carbon surface and adsorbed onto the electrode surface forming cation double layer. During discharge, the Li^+ ions present in the electrolyte intercalate back into

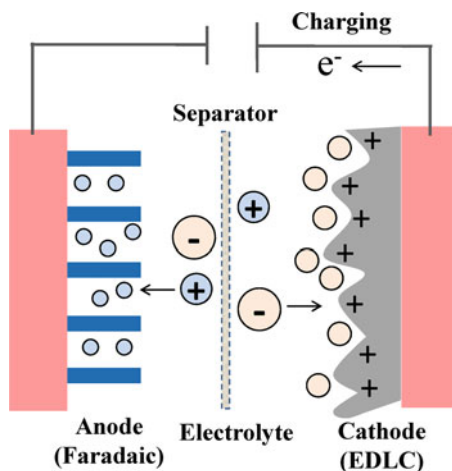
Fig. 10 Schematic of charging process in Li-HEC (battery as positive electrode)



insertion-type crystal lattice and are simultaneously desorbed from the surface of carbon and suspended back into the electrolyte solution [44]. The high surface area carbon electrode realized cation double-layer formation during the process. To prevent electrolyte reduction, the carbon in a half-cell configuration, i.e., (Li//AC), should be tested from open circuit potential to the decomposition (reduction) potential of the electrolyte. The operating mechanism of electrolyte in this type of ISH is similar to Li-ion battery chemistry. The electrolyte works simply as an ionic carrier for lithium ions. In this system, Li^+ ions are introduced to electrolyte solution from one end one electrode and are depleted at other end other electrode. The molarity of the electrolyte solution remains constant during charge and discharge process. So, at high current charge-discharge, salt concentration polarization is a limiting factor to the rate capability of the electrolyte [45].

Li-HECs as battery-type negative electrode: The ISHs using battery-type electrodes as anode with EDLCs as cathodes have been proposed and extensively investigated by several authors in the last decades. It was initiated in 2001 by Amatucci's group utilizing the asymmetric combination $\text{Li}_4\text{Ti}_5\text{O}_{12}$ //AC and WO_2 //AC, etc. [37]. The mechanism of charge storage in such Li-HECs is explained schematically in Fig. 11. During charging of the cell, Li^+ ions (from the electrolyte solution) are inserted (or intercalated) into the crystal lattice of insertion electrode. Simultaneously, the anions (PF_6^- , BF_4^- , etc.) (from the electrolyte solution) are attracted by the positively charged carbon surface and adsorbed onto the electrode surface forming anion double layer. During discharging, the Li^+ ion is extracted out (or de-intercalated) from the crystal lattice of the battery electrode, and simultaneously the adsorbed anions (PF_6^- , BF_4^-) are desorbed from the negatively charged counter EDLC electrode to the electrolyte solution. Here, anion double layer forms on the positive EDLC electrode. When the EDLC-type electrodes (with high surface area) are exposed to high voltage (>4.5 V), the oxidation of nonaqueous electrolyte cannot be avoided. In view to

Fig. 11 Schematic of charging process in Li-HEC (battery as negative electrode)



this, charge-discharge profile of Li//AC needs to be tested in different voltage windows to identify the appropriate potential window without any oxidation of the electrolyte [45].

It is to be noted that the electrolyte (in Li-HECs where battery acts as negative electrode) behaves differently as compared to conventional lithium-ion batteries and/or Li-HEC (where insertion-type electrode is cathode). In Li-HECs (when battery-type electrode acts as anode), opposite ions present in the electrolytes (viz., Li^+ , PF_6^-) are depleted during the charging process. Consequently, during discharge anions and cations come back into the electrolyte. Through this process, the molarity of the electrolyte solution experiences a wide swing during each charge and discharge. Hence, one needs to optimize the salt concentration of the electrolyte so that the ionic conductivity of organic electrolyte does not get affected during charge-discharge. In general salt concentration polarization is a limiting factor for Li-ion battery and/or Li-HECs (with battery as cathode). During fast discharge in Li-ion batteries, Li^+ ions are extracted out (or de-intercalated) from the anodes and simultaneously inserted (or intercalated) into the cathodes. This results in local excess of positive ions (Li^+) and negative ions (PF_6^- , BF_4^- , etc.) near anode and near cathode, respectively. To equilibrate the charge difference, the anions (PF_6^- , BF_4^- , etc.) are diffused through the electrolyte to the anode side. Hence, the electrolyte salt is depleted at cathode and becomes excess at anode side. The process is reversed during fast charging in Li-ion battery. As opposed to this, in Li-HECs (with battery as anode and EDLCs as cathode), during fast discharge, a symmetric driving force attracts the Li^+ ions and PF_6^- (or BF_4^- , etc.) ions toward electrolyte, and none of them (Li^+ and $\text{PF}_6^-/\text{BF}_4^-$) are depleted at one electrode like conventional Li-ion batteries or Li-HEC (with battery as cathode). Therefore, in Li-HEC (with battery as anode), the rate capability is found to be improved due to reduced concentration gradient of constituent ions in the electrolyte [37, 45].

Requirement of Electrode Matching in Li-HEC

In order to optimize the electrochemical performance of the faradaic- and EDLC-type hybrid electrochemical cell, appropriate matching of the active mass, potential window, and current is required. Matching of the aforesaid parameters is very important to design these asymmetric hybrid cells. For ideal electrode matching, the current passing through anode and/or the capacity of anode should be equal to the current passing through cathode and/or the capacity of cathode. Two dissimilar (faradaic and EDLCs) electrodes of different specific capacities are used together to design asymmetric hybrid capacitors. The capacity is balanced by varying the mass of the individual electrodes to take the full advantage of the performance of both materials in their optimal potential range. To maintain equal capacity (of anode and cathode) or equal current flowing (through anode and cathode), the mass ratio (x) can be defined by the following equations.

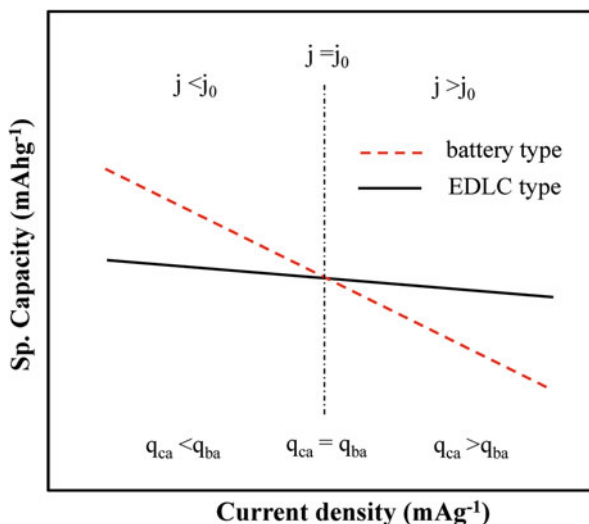
$$Q = m_{ca}q_{ca} = m_{ba}q_{ba}; x = \frac{m_{ba}}{m_{ca}} = \frac{q_{ca}}{q_{ba}} \quad (18)$$

$$J = m_{ba}j_{ba} = m_{ca}j_{ca}; x = \frac{m_{ba}}{m_{ca}} = \frac{j_{ca}}{j_{ba}} \quad (19)$$

where Q and J are the total charge and total current passing through the positive and negative electrodes, respectively. m_{ba} , q_{ba} , and j_{ba} are the active mass, specific capacity, and current density for battery-type electrode, whereas m_{ca} , q_{ca} , and j_{ca} are the active mass, specific capacity, and current density of EDLC-type electrode. The mass ratio depends on the current density at which the individual electrodes are charged and discharged. Again, the mass ratio value influences the voltage window of the asymmetric hybrid capacitor [46, 47].

Current matching: Ideally at a particular specific current, the specific capacities of the electrodes should be taken into account to fix the mass ratio. However, it is inconvenient to follow, when the rate performance of the hybrid capacitor is measured. The schematic in Fig. 12 shows the variation of specific capacities with current density for battery- and EDLC-type electrodes. In battery-type electrode, the charge-discharge kinetics is typically limited by the solid-state diffusion of lithium ions into the electrodes. The diffusion of lithium ions into the bulk of active materials is a slow process. Here during fast charge-discharge, Li^+ ions cannot diffuse fast resulting in sharp capacity loss for battery-type materials (see Fig. 12). In contrast to battery, EDLCs realize charge adsorption/desorption on the surface of the electrode. It is a comparatively fast process. Specific capacity is marginally reduced with the increase in current density in EDLCs. As in Fig. 12, when $x = 1$, then $q_{ca} = q_{ba}$ at certain current density ($j = j_0$). If $j > j_0$, then $q_{ca} > q_{ba}$; therefore, to match the current density between the electrodes, mass of the battery material must be reduced proportionately. Similarly, when $q_{ca} < q_{ba}$ (at $j < j_0$), for current matching, mass of the battery material must be increased proportionately.

Fig. 12 Schematic of specific capacity vs. current density curves for battery- and EDLC-type electrodes



Potential matching: EDLCs accumulate charge on the electrode/electrolyte interface by coulombic attraction force resulting in linear charge-discharge characteristics. Li rechargeable batteries store charge by redox reaction throughout the volume of the electrode. Li-ion batteries usually exhibit flat discharge plateau. During the asymmetric combination between battery and EDLCs, first appropriate EDLC voltage window is fixed. Accordingly, the mass ratio is adjusted. This has been better explained in the next section. If the battery content is further increased, the potential window for EDLC electrode accords with its electrochemical safe window (ESW) (selected based on half-cell measurement), and the increased battery mass does not affect much the ESW for battery electrode. This yields same voltage window of the asymmetric capacitor, as it was observed for mass balanced asymmetric capacitor. In contrast, the voltage window of EDLC differs significantly from its ESW when the mass content of EDLC exceeds. This alters the voltage window of asymmetric device as compared to mass balanced asymmetric capacitor.

Electrochemical Performance of ISH-Type AC//LiNi_{0.5}Mn_{1.5}O₄ Hybrid Capacitor Made in Our Laboratory

Typical charge-discharge profiles (in the form of V vs. t) of battery-type (viz., LiNi_{0.5}Mn_{1.5}O₄) cathode and EDLC-type activated carbon (AC) anode, measured in our laboratory, are shown in Fig. 13a and b, respectively. The electrochemical signature of LiNi_{0.5}Mn_{1.5}O₄ shows a flat charge-discharge plateau at around 4.7 V, which can be attributed to the valence change of nickel (Ni³⁺/Ni⁴⁺). The Li//LiNi_{0.5}Mn_{1.5}O₄ half-cell is cycled in the voltage window of 3.5 to 4.8 V (@50mA g⁻¹). The LiNi_{0.5}Mn_{1.5}O₄ delivered a specific capacity of 125 mAhg⁻¹. In the voltage window of 2.0 to 3.5 V, the charge-discharge profile of AC shows linear-type double-layer capacitance behavior. The electric double-layer forms in AC due to the electrostatic adsorbing-desorbing of PF₆⁻¹ anions at electrode-electrolyte interface. The AC delivered a reversible specific capacity of ~ 37 mAhg⁻¹ (@50mA g⁻¹). An internal serial hybrid (ISH) capacitor has been constructed

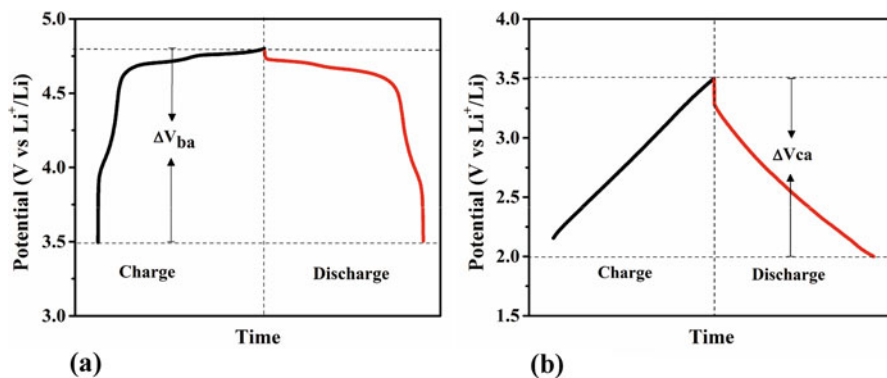


Fig. 13 Electrochemical charge-discharge profile of (a) LiNi_{0.5}Mn_{1.5}O₄ (in the potential window 3.5 and 4.8 V vs. Li⁺/Li) and (b) AC (in the potential window 2.0 and 3.5 V vs. Li⁺/Li)

using $\text{LiNi}_{0.5}\text{Mn}_{1.5}\text{O}_4$ as cathode and AC as anode. A schematic of charge-discharge profile of the hybrid electrochemical capacitor (lower panel) along with the charge-discharge profile of battery- and EDLC-type electrode in half-cell configuration (upper panel) has been shown in Fig. 14.

The symbols in Fig. 14 represent:

ΔV_{ba} = Potential window of $\text{LiNi}_{0.5}\text{Mn}_{1.5}\text{O}_4$ cathode

ΔV_{ca} = Potential window of AC anode

$V_{ba,ds}$ = Potential at discharging start for $\text{LiNi}_{0.5}\text{Mn}_{1.5}\text{O}_4$ cathode

$V_{ba,de}$ = Potential at discharging end for $\text{LiNi}_{0.5}\text{Mn}_{1.5}\text{O}_4$ cathode

$V_{ca,ds}$ = Potential at discharging start for AC anode

$V_{ca,de}$ = Potential at discharging end for AC anode

$V_{hyb,ds}$ = Potential at discharging start for HEC

$V_{hyb,de}$ = Potential at discharging end for HEC

In line with the analyses made by Li et al., the theoretical basis of the calculation of voltage, specific capacitance, and energy and power densities of internal serial hybrid using $\text{LiNi}_{0.5}\text{Mn}_{1.5}\text{O}_4$ as cathode and AC as anode has been described in details as follows [47].

Estimation of Li-HEC voltage:

The charging voltage ($V_{hyb,ds}$) of the hybrid capacitor can be expressed as

$$V_{hyb,ds} = (\Delta V_{ca} + \Delta V_{ba}) + V_{hyb,de} \quad (20)$$

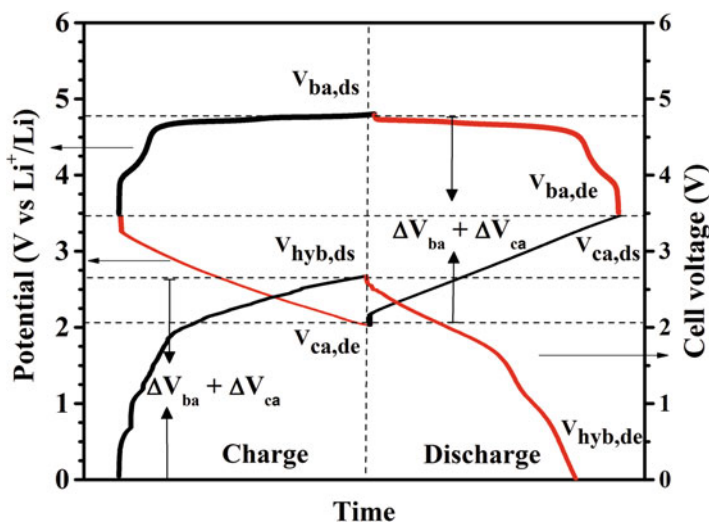


Fig. 14 Schematic of the electrochemical charge-discharge profile (V vs. t) of Li-HEC between 0 and 2.7 V, $\text{LiNi}_{0.5}\text{Mn}_{1.5}\text{O}_4$ between 3.5 and 4.8 V vs. Li^+/Li , and AC between 2.0 and 3.5 V vs. Li^+/Li

$$V_{hyb,de} = |V_{ba,de} - V_{ca,ds}| \quad (21)$$

As the battery-type material (voltage vs. capacity) curve shows a flat plateau, it is better to select the battery-type electrode potential at a platform to avoid overcharge or overdischarge of the hybrid capacitor.

- (i) If ($m_{ba} > m_{ca}$), i.e., active mass of battery-type material is excessive.

During charging of the HEC, the battery material will not be fully charged; at the mean time EDLC will be over discharged. For EDLC material, ΔV_{ca} will be maximum. For battery material, ΔV_{ba} will not be changed appreciably as the potential curve is flat.

$$\text{So, } V_{hyb,ds} \simeq (\Delta V_{ca} + \Delta V_{ba}) + V_{hyb,de}$$

- (ii) If ($m_{ba} < m_{ca}$), i.e., EDLC-type material is excessive.

During charging of the HEC, the battery material will be fully charged, but EDLC will not be fully discharged. The full voltage window of the EDLC will not be utilized. So,

$$V_{hyb,ds} = (\Delta V_{ca,mod} + \Delta V_{ba}) + V_{hyb,de}$$

$\Delta V_{ca,mod}$ can be calculated from sp. capacity vs. sp. capacitance relationship for linear charge-discharge profile of EDLC:

$$\begin{aligned} \Delta V_{ca,mod} &= q_{cap} \times \frac{3.6}{C_{ca}} \\ \Delta V_{ca,mod} &= \frac{m_{ba}}{m_{ca}} q_{ba} \times \frac{3.6}{C_{ca}} \\ \Delta V_{ca,mod} &= \frac{3.6 q_{ba}}{C_{ca}} x \end{aligned}$$

So, total charged voltage of the hybrid capacitor will be

$$V_{hyb,ds} = \left(\frac{3.6 q_{ba}}{C_{ca}} x + \Delta V_{ba} \right) + V_{hyb,de} \quad (22)$$

Capacitance of Li-HEC:

As the battery and EDLC are in series in ISH type of hybrid HEC, the total capacitance of the asymmetric device can be obtained by the following relationship:

$$\frac{1}{C_{hyb}} = \frac{1}{m_{ca} C_{ca}} + \frac{1}{m_{ba} C_{ba}}$$

The specific capacitance ($C_{hyb,av}$) can be expressed as follows:

$$\begin{aligned}
C_{hyb,av} &= \frac{C_{hyb}}{m_{ba} + m_{ca}} \\
\frac{1}{C_{hyb,av}} &= (m_{ba} + m_{ca}) \left(\frac{1}{m_{ca}C_{ca}} + \frac{1}{m_{ba}C_{ba}} \right) \\
\frac{1}{C_{hyb,av}} &= (m_{ba} + m_{ca}) \left(\frac{1}{m_{ca}C_{ca}} + \frac{\Delta V_{ba}}{m_{ca}C_{ca}\Delta V_{ca}} \right) \\
&\quad \times \left[m_{ba}C_{ba} = m_{ba} \frac{q_{ba}}{\Delta V_{ba}} = m_{ca} \frac{q_{ca}}{\Delta V_{ba}} = m_{ca} \frac{C_{ca}\Delta V_{ca}}{\Delta V_{ba}} \right] \quad (23) \\
\frac{1}{C_{hyb,av}} &= \left(1 + \frac{m_{ba}}{m_{ca}} \right) \left(1 + \frac{\Delta V_{ba}}{\Delta V_{ca}} \right) \frac{1}{C_{ca}} \\
C_{hyb,av} &= \frac{1}{\left(1 + \frac{\Delta V_{ba}}{\Delta V_{ca}} \right) \left(1 + \frac{m_{ba}}{m_{ca}} \right)} C_{ca}
\end{aligned}$$

Energy density of Li-HEC:

The energy density can be calculated from the area under the V-t graph and can be expressed as

$$\begin{aligned}
E_{hyb,av} (WhKg^{-1}) &= \frac{1}{7.2} C_{hyb,av} (Fg^{-1}) (V_{hyb,ds}^2 - V_{hyb,de}^2) (V^2) \\
E_{hyb,max} &= \frac{1}{7.2} C_{hyb,av} (V_{hyb,ds}^2) \left[\text{when, } V_{hyb,de} = 0 \right] \quad (24)
\end{aligned}$$

Power density of Li-HEC:

Power is the energy delivery rate and expressed as

$$P_{hyb,av} (WKg^{-1}) = \frac{E_{hyb,av} (WhKg^{-1})}{\Delta t_{hyb} (s) / 3600} \quad (25)$$

The discharge time t_{hyb} (s) of the hybrid capacitor can be obtained from the following relationship:

$$\begin{aligned}
C_{hyb,av} &= 1000 \frac{J_{hyb} (t_{hyb,de} - t_{hyb,ds})}{(m_{ba} + m_{ca}) (V_{hyb,ds} - V_{hyb,de})} \\
\Delta t_{hyb} &= 1000 C_{hyb,av} \Delta V_{hyb,ds} \times \frac{(m_{ba} + m_{ca})}{J_{hyb}} \\
\Delta t_{hyb} &= 1000 C_{hyb,av} \Delta V_{hyb,ds} \times \frac{(m_{ba} + m_{ca})}{m_{ba}j_{ba}} [J_{hyb} = m_{ba}j_{ba} = m_{ca}j_{ca}] \quad (26) \\
\Delta t_{hyb} &= 1000 C_{hyb,av} \Delta V_{hyb,ds} \times \left(\frac{1}{j_{ba}} + \frac{m_{ca}}{m_{ba}j_{ba}} \right) \left[j_{ca} = \frac{m_{ba}j_{ba}}{m_{ca}} \right] \\
\Delta t_{hyb} (s) &= 1000 C_{hyb,av} (Fg^{-1}) \Delta V_{hyb,ds} (V) \times \left(\frac{1}{j_{ba} (mAg^{-1})} + \frac{1}{j_{ca} (mAg^{-1})} \right)
\end{aligned}$$

The value of energy density ($E_{hyb,av}$) and discharge time (Δt_{hyb}) of hybrid capacitor is replaced in Eq. 23.

$$\begin{aligned}
 P_{hyb,av}(WKg^{-1}) &= 3600 \frac{\frac{1}{7.2} C_{hyb,av}(Fg^{-1}) (V_{hyb,ds}^2 - V_{hyb,de}^2) (V^2)}{1000 C_{hyb,av}(Fg^{-1}) \Delta V_{hyb,ds}(V) \times \left(\frac{1}{j_{ba}(mA g^{-1})} + \frac{1}{j_{ca}(mA g^{-1})} \right)} \\
 P_{hyb,av} &= \frac{1}{2} \frac{(V_{hyb,ds} - V_{hyb,de})(V_{hyb,ds} + V_{hyb,de})}{(V_{hyb,ds} - V_{hyb,de})} \times \frac{j_{ba}}{\left(1 + \frac{j_{ba}}{j_{ca}}\right)} \left[m_{ba} j_{ba} = m_{ca} j_{ca}; x = \frac{m_{ba}}{m_{ca}} = \frac{j_{ca}}{j_{ba}} \right] \\
 P_{hyb,av}(WKg^{-1}) &= \frac{1}{2} \frac{(V_{hyb,ds} + V_{hyb,de})(V)}{\left(1 + \frac{1}{x}\right)} j_{ba}(mA g^{-1})
 \end{aligned} \tag{27}$$

Using the above equations, the performances of hybrid electrochemical capacitor AC//LiNi_{0.5}Mn_{1.5}O₄ have been evaluated. The mass ratio was calculated 1:3, considering 105 mAhg⁻¹ (~87% of 120 mAhg⁻¹) of specific capacity of LNMO and 35 mAhg⁻¹ of specific capacities for AC electrode at 50 mAh⁻¹ current rates. The hybrid cell shows slightly sloping discharge curve in the voltage range from 2.5 to 1 V, and most of the capacity is obtained in this voltage range. The hybrid cell delivered the reversible discharge capacity of 25 mAhg⁻¹. The maximum energy and power density for the hybrid cell have been estimated as 26.5 Whkg⁻¹ and 34 Wkg⁻¹, respectively.

Salient Features Need to Be Addressed for Optimal Performance of Li-HECs

The salient features decide the electrochemical behavior of Li-HEC (ISH-type) devices may be categorized as follows [48].

- (i) The overall capacitance of the hybrid device is more influenced by the electrode of smaller capacitance. The net overall capacitance of the hybrid electrochemical capacitor with respect to the capacitance of the individual electrodes is given by the following relationship:

$$\frac{1}{C_{hyb}} = \frac{1}{C_{bat}} + \frac{1}{C_{cap}}$$

It is very important that the entire potential window of electrode of smaller capacitance should be used; otherwise the capacitance of the hybrid device falls significantly.

- (ii) The current rate performance of the hybrid device is limited by the battery-type electrodes. The tuning of structural and morphological property of battery electrode is necessary to make it compatible with the current rate performance of capacitive electrode. The rate performance of battery material can be improved by using advanced synthesized techniques (like electrospinning), surface coating by conducting CNT/graphene, etc.
- (iii) The hybrid cell should be operated at capacitive electrode-limited condition to protect the battery electrode from deep discharge. Thus it yields longer cycle

life. To achieve this, the effective equivalent active mass of the battery electrode should be excess in respect to the active mass of capacitive electrode.

Internal Parallel Hybrid (IPH)

In recent time ISH type electrochemical capacitors have extensively been studied, however, they are still plagued with capacity fading, poor energy as well as power densities. The insertion-type battery electrode determines the current rate performance in Li-HEC. As mentioned earlier, battery-type electrodes have slower charge transfer kinetics compared to electric double-layer capacitors. The charge transfer kinetics of battery electrode must be improved to achieve the maximum performance from such asymmetric system [49]. In Li-HEC, lithium pre-doping of negative electrode (e.g., graphite) leads to poor reliability. Li pre-doping is also inconvenient for mass production [50]. The safe potential window of nonaqueous electrolyte is 1 to 4.5 V vs. Li^+/Li . This suggests charging of Li-HECs beyond 4.5 V, or deep discharging below 1 V might cause electrolyte decomposition.

To circumvent these problems, novel electrode systems must be designed to yield safer hybrid capacitor with higher energy and power densities. Like conducting material is used in conjunction with battery to make bi-material electrode. Various approaches have been adopted to design such novel electrodes which can be grouped into the following categories. Bi-material-type electrodes consist of electrochemically active materials with different charge storage mechanisms; faradaic (e.g., battery-type) materials use redox reaction, and EDLC (e.g., conducting carbonaceous type)-type materials use electrostatic double-layer formation to store electrical charge. Such asymmetric capacitors (using positive as well as negative bi-material electrodes) are termed as internal parallel hybrid (IPH) capacitors (see Table 3). Table 3 summarizes few recently reported results of internal parallel hybrid capacitor in nonaqueous electrolyte medium. The charge storage mechanism of IPH capacitors is illustrated in the following subsection. Till date, hand count reports are available which used only bi-material electrodes both as positive and negative electrodes [22, 60]. In most of the literature reports, people have used one bi-material-type electrode (positive or negative side) in conjunction with other electrodes (mostly EDLC type) in hybrid asymmetric configuration. We have reviewed some of the popular bi-material electrodes as described below.

Nanostructured composite or nano-hybrid capacitor (NHC): Nanostructured ultrafast bi-material electrodes are composed of nanostructured intercalation battery (mainly $\text{Li}_4\text{Ti}_5\text{O}_{12}$) [61] or pseudocapacitive materials (such as transition metal oxide or conducting polymers), highly dispersed and entangled in a matrix of nano-carbon. Several research groups have recently reported the electrochemical performance of NHCs, where nanostructured battery-type materials are dispersed in carbonaceous matrices [62]. The combination of nanostructured transition metal oxides (MnO_2 , RuO_2 , other oxides, etc.) and carbonaceous nano-materials (viz., activated carbon, CNTs, carbon nanofibers, graphene, etc.) was actively explored as nanostructured hybrid composite electrodes for Li-HECs (IPH type). The conducting

Table 3 Characteristics of ISH system using battery- and EDLC-type electrodes in organic electrolyte

Negative electrode	Positive electrode	Potential window (V)	Electrochemical performance	Year	References
Li ₄ Ti ₅ O ₁₂	LiCoO ₂ + AC	1.6–3.2	Sp. energy 40 WhKg ⁻¹	2004	51
Li ₄ Ti ₅ O ₁₂	LiFePO ₄ + AC	1–2.6	Sp. capacity 40.08 mAg ⁻¹	2007	52
Li ₄ Ti ₅ O ₁₂	LiMn ₂ O ₄ + AC	1.0–2.8	Sp. energy 16.47 WhKg ⁻¹	2009	53
Li ₄ Ti ₅ O ₁₂	LiMn ₂ O ₄ + AC	1.0–3.0	Sp. energy 71 Whkg ⁻¹ Sp. power 12 KWkg ⁻¹	2011	22
Li	LiMn ₂ O ₄ + AC	3.3–4.3	Sp. capacity 67 mAg ⁻¹	2011	54
Li	LiMn ₂ O ₄ + AC	3.3–4.3	Sp. capacity 72 mAg ⁻¹	2011	55
Li ₄ Ti ₅ O ₁₂ + AC	AC	0.5–3.5	Sp. energy 32 WhKg ¹ Sp. power 6000 WKg ⁻¹	2012	56
MCMB	LiFePO ₄ + AC	2.0–3.8	Sp. energy 69.02 WhKg ⁻¹ Sp. capacity 23.80 mAg ⁻¹	2012	57
Li	LiFePO ₄ + AC	2.7–4.3	Sp. capacity 37 mAg ⁻¹	2012	58
Li	Li ₃ V _{1.95} Ni _{0.05} (PO ₄) ₃ + AC	3.0–4.3 1.5–3.0	Sp. capacity 61 mAg ⁻¹ Sp. capacity 24 mAg ⁻¹	2016	59
Li ₄ Ti ₅ O ₁₂ + AC	LiMn ₂ O ₄ + AC	1–3	Sp. capacity 56.4 mAg ⁻¹	2017	60

polymers like polyaniline (PAni), polypyrrole (PPy), polythiophene, etc. hybridized with carbon nanostructured materials (AC, CNFs, carbon cloth, CNTs, graphene, etc.) show synergistic effect, as the carbon matrix acts as a framework that prevents the strain due to the volume changes associated with the polymers during charging and discharging. Ternary hybrid nanostructured electrodes based on metal oxide, conducting polymers, and conducting carbons have been recently explored for next-generation IPH electrodes.

Segmented arrangement of battery and EDLC materials: The bi-material electrodes can be fabricated in a segmented configuration in which one part is made up of battery-type materials and the other is of EDLC-type materials. The setup is made up in such a way that current passing through each individual material can be monitored by current sensors (see Fig. 15). Individual current contribution can in turn be

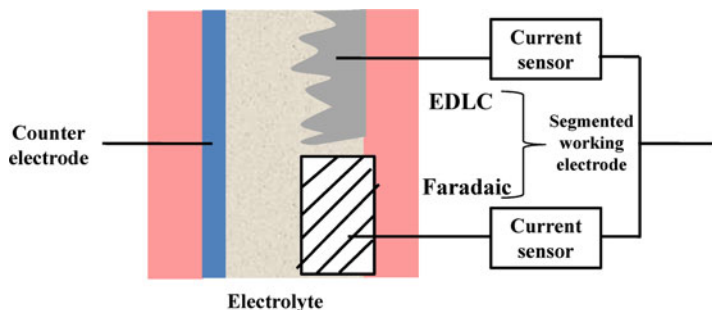


Fig. 15 Schematic of the segmented bi-material electrode (with current sensor) used in an electrochemical cell

monitored as a function of total current as well as the weight ratio of these two components. It has been reported that at high current rate, the electrode exhibits EDLC-like behavior, whereas at low current rate, it is faradaic in nature. The current rate shows very little effect on the EDLC part of the electrode. When the segmented electrode is pulsed discharged, it was observed that the current is mostly passed through the EDLC part (during pulsing) and at rest period faradaic part recharges the EDLC segment. This kind of IPH device has been demonstrated by Lam et al. [63] in 2006, and he has patented it naming “UltraBattery™.” In such ultrabattery, activated carbon and lead were used in segmented configuration as negative electrode, whereas lead dioxide (PbO_2) plate was used as positive electrode. This configuration exhibited better rate performance and pulse charge-discharge capability as compared to the regular lead-acid battery. Cericola et al. [55] fabricated segmented electrode based on faradaic type (LiMn_2O_4) with EDLC type (AC) and demonstrated that mass ratio and C-rate have dominant influence on current sharing between the two constituents of segmented cathode.

Simple mixing of faradaic- and EDLC-type materials: In this type of internal parallel hybrid, the faradaic- and EDLC-type materials are thoroughly mixed together (in different weight ratios) to yield bi-material electrodes. Due to synergistic effect between the faradaic and carbonaceous components, hybrid capacitors yield improved electrochemical characteristics as compared to its individual constituents. For example, Cericola et al. [54] reported the individual electrochemical behavior of faradaic-type LiMn_2O_4 and EDLC-type AC and compared with the bi-material electrode made up of LiMn_2O_4 and AC. As a synergistic effect, the bi-material electrode outperformed AC at low current and LiMn_2O_4 at high current rates. The beneficial effect of AC in bi-material electrode of AC and LiFePO_4 has been reported by Bockenfeld et al. [58]. The presence of AC in such hybrid electrode increases the conductivity of the composite by entangling the LFP particles in the electrode and modifies the porosity around the LFP particles. Due to the porous nature of the bi-material electrodes, the charge-discharge characteristics are reported to be improved because of better insertion of liquid electrolyte into the electrode.

Charge Storage Process in Bi-Material Electrode

The charge storage process in bi-material electrodes are controlled by redox reactions (due to the presence of battery) and electrostatic adsorption-desorption process (due to the presence of EDLCs). The active electrochemical potential range of faradaic and EDLC materials should overlap to the entire working potential window of the bi-material electrode, i.e., the working potential window of EDLC should span the redox potential window of the faradaic material [64]. The charge storage process in hybrid bi-material electrode can be illustrated in the line of Dubal et al. [49]. The charge storage in bi-material electrode can be divided into three distinct parts as schematically shown in Fig. 16. The EDLC component is first charged due to the formation of electrochemical double layer by electrostatic ions from electrolyte solution. This process continues until q_1 charge is stored and the system reached to the oxidation reaction potential (ΔV_b) of faradaic component. The potential profile shows a typical EDLC-type linear curve in this initial charging process. Now the faradaic component is charged through electrochemical redox reaction maintaining flat voltage plateau until the system stores Q_b amount of charge. At the end of the charging process, the EDLC component is again charged from potential ΔV_b , and it continues until q_2 is stored and system reached to the maximum potential (ΔV_{bc}) of the hybrid electrode. The potential profile again shows a typical EDLC-type linear curve at the final state of the charging process. Thus total charge (Q) is stored by the bi-material electrode due to the contribution of faradaic component (Q_b), and the EDLC component ($Q_c = q_1 + q_2$) is as follows:

$$Q = Q_b + Q_c = Q_b + (q_1 + q_2)$$

The plausible working principle of bi-material-type IPH capacitors is illustrated in the following subsection.

Plausible Working Principle of IPH Capacitor with Bi-Material Electrodes

The schematic of a typical internal parallel hybrid electrochemical capacitor is shown in Fig. 17. The hybrid capacitor consists of two bi-material electrodes of different electrode combination. The role of the individual constituents of bi-material electrodes are as follows: faradaic materials enhances its energy density for having higher nominal voltage and capacity. The EDLC type material increases its power

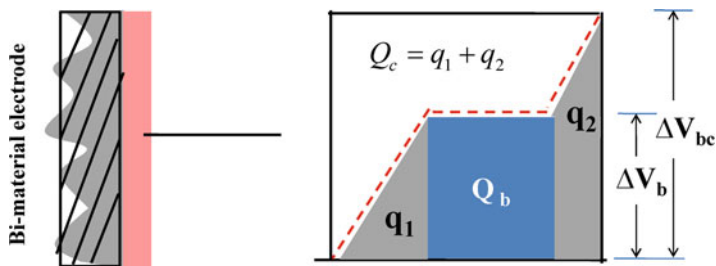
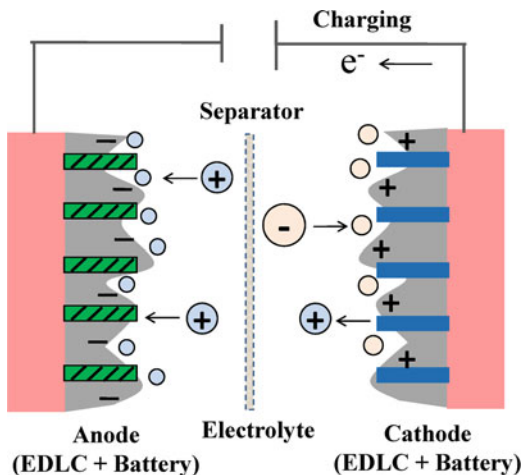


Fig. 16 Schematic of charge storage in hybrid bi-material electrode

Fig. 17 Schematic of charging process in internal parallel hybrid capacitor



density due to their fast electrostatic adsorption-desorption process, which results in superior electronic conductivity. During charging, Li^+ ions are de-intercalated from the insertion-type battery (cathode), and simultaneously Li^+ ions in the electrolyte are intercalated within the negative insertion-type battery (anode). Additionally, anions (viz., PF_6^- , BF_4^- , etc. present in the electrolytes) are attracted by the positively charged carbon surface and form anion double layer. Similarly the cations (i.e., Li^+ ions present in the electrolyte solution) are attracted by the negatively charged carbon surface and form cation double layer. During discharge, the Li^+ ions are migrated to the opposite direction, i.e., de-intercalated from the insertion-type battery (anode) and intercalated into the insertion-type battery (cathode). The cation double layer forms now on positive electrode and anion double layer on the negative electrode. It is observed that the electrode at which Li^+ ions intercalated forms the cation double layer with Li^+ ions during charging and discharging. Affluence of Li^+ ions in close proximity of insertion-type material eventually enhances the intercalation of Li^+ ions in insertion-type materials [65]. As a result it is expected that both energy and power density of these bi-material-type IPH capacitors will be grossly improved by circumventing the problem of Li^+ ion depletion especially during high-rate charging and discharging.

Half-Cell Electrochemical Performance of Bi-Material-Type $\text{Na}_3\text{V}_2(\text{PO}_4)_3@\text{C}/\text{AC}$ Hybrid Capacitor Made in Our Laboratory

The faradaic-type $\text{Na}_3\text{V}_2(\text{PO}_4)_3@\text{C}$ (carbon-coated NVP) and EDLC-type AC were mixed (40:60 weight ratio), and a bi-material electrode ($\text{NVC}@\text{C}/\text{AC}$) was made in our laboratory. The electrochemical performance of these individual components ($\text{Na}_3\text{V}_2(\text{PO}_4)_3@\text{C}$ and AC) and bi-material electrode were investigated in half-cell configuration using lithium metal foil as counter and reference electrode. Figure 18 shows the voltage vs. capacity profiles (in the potential window of 2.5–4.1 V) of the galvanostatic charge-discharge for battery-type NVP@C, bi-material NVP@C/AC,

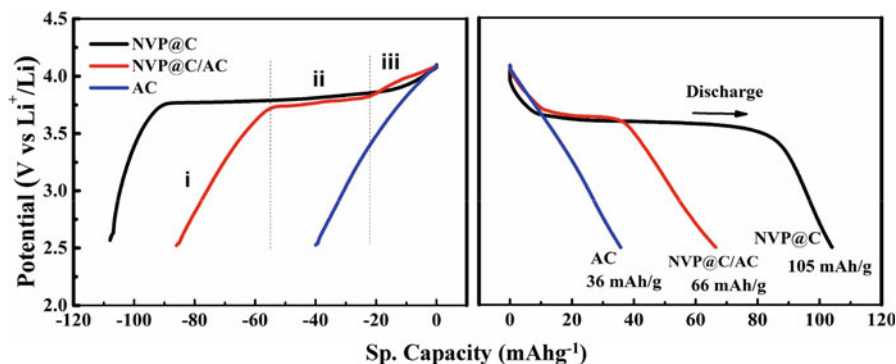


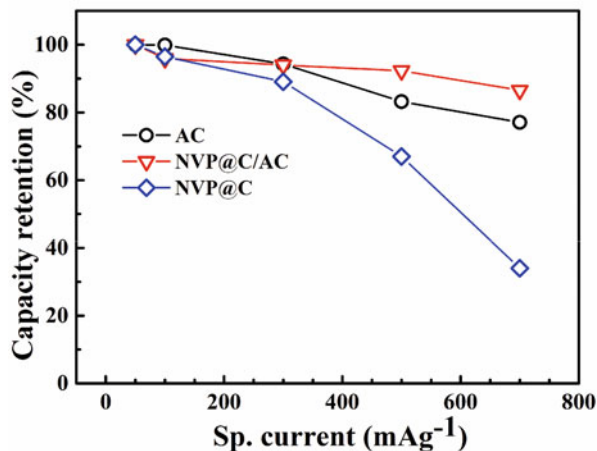
Fig. 18 Galvanostatic charge-discharge profiles of NVP@C, NVP@C/AC, and AC at 50 mA g^{-1}

and double-layer-type AC electrodes at 50 mA g^{-1} . The potential profile for the AC electrode is found to be linear in the working potential window suggesting typical characteristic of electrochemical double-layer capacitance behavior. The AC delivered a reversible capacity 36 mAhg^{-1} , which corresponds to a specific capacitance value of 81 Fg^{-1} . In case of Li//AC half-cell, during charging, Li^+ ions are reduced at Li metal-negative electrode, and simultaneously PF_6^- ions adsorbed onto the activated carbon-positive electrode forming anion double layer. The charge stored in Li//AC is due to the coulombic attraction force without any redox reaction. The NVP@C electrode is characterized by typical battery-type potential profile with a flat plateau near $\sim 3.7 \text{ V vs. Li}^+/\text{Li}$. The reversible discharge capacity for NVP@C was estimated to be $\sim 105 \text{ mAh/g}$. For the first charging in Li//NVP@C, two Na^+ ions de-intercalate from the crystal lattice forming a flat voltage plateau around $\sim 3.8 \text{ V}$.

The potential profile of bi-material NVP@C/AC electrode exhibits the characteristic features of constituent materials. During the charge-discharge cycling, a very small deviation in voltage plateaus is observed in bi-material NVP@C/AC electrode as compared to NVP@C. As shown in Fig. 17, the charge profile of bi-material NVP@C/AC electrode can be divided into three distinct parts [54]. In region (i) below 3.6 V , the potential profile shows a typical capacitor like linear behavior, and capacity in this region is mostly contributed by the AC. In the middle, the plateau (region ii) in the voltage (3.6 to 3.8 V) shows a typical battery feature. The faradaic reaction of battery-type NVP@C material is mainly contributing the capacity to the bi-material electrode in this region. At the end of the charging process (region iii, above 3.8 V), the linear voltage confirms the battery-type NVP@C is fully oxidized and the capacity is obtained mainly from the electrostatic adsorption of PF_6^- to the AC electrolyte/electrode interface. In a reverse way, the discharge follows the same reaction mechanism as charging.

The discharge capacities with different current rates (from 50 to 700 mA g^{-1}) of NVP@C, NVP@C/AC, and AC are shown in Fig. 19. The charging current was kept constant at 50 mA g^{-1} during the rate capability measurements. The NVP@C and AC delivered discharge capacities of 104 mAhg^{-1} and 35 mAhg^{-1} , respectively, at lower current rate of 50 mA g^{-1} . The bi-material NVP@C/AC electrode provides

Fig. 19 The capacity retention characteristics of NVP@C, NVP@C/AC, and AC at different current rates



specific capacity of 67 mAhg^{-1} . The specific capacity of bi-material electrode is in between the specific capacities of NVP@C and AC, which is nearly equal to the predicted value obtained from mixed rule. At high current rate (700 mA g^{-1}), the specific capacity of NVP@C falls drastically and retains only 34% of its initial capacity. Though carbon coating is done on NVP@C particles, slow Li^+ ion kinetics mainly hinders the capacity of NVP@C at higher rate. The NVP@C/AC and AC electrodes show exceptional capacity retention at higher currents and retain 86% and 77% of its initial capacity at 700 mA g^{-1} . Interestingly at higher current rate of 700 mA g^{-1} , the NVP@C/AC delivers specific capacity of 58 mAhg^{-1} which exceeds the specific capacities of 35 mAhg^{-1} and 27 mAhg^{-1} estimated for NVP@C/AC and AC, respectively. These results indicate that bi-material NVP@C/AC electrode can be used as a potential cathode material for Li-ion battery. The improved electrochemical performance of bi-material electrode can be attributed to the synergistic effect between NVP@C and AC materials.

Future Direction of the Research on Hybrid Supercapacitor-Battery

- As mentioned earlier, as compared to ISH type, research on IPH-type capacitor is at its infancy. For this type of hybrids, good understanding of the interfacial chemistry between faradaic and capacitive components (in bi-material electrodes) needs to be developed.
- Achieving higher energy density together with power density still remains a major drawback of this kind of capacitors. In view to this, we feel that various combinations of faradaic and capacitive components need to be used. In other words, unlike presently explored bi-material electrodes, the constituent components should not be limited to two only.

- Nanostructured electrodes need to be explored to provide open structure, maintaining connectivity between faradaic and capacitive components might be a major issue, and to circumvent it, encapsulation with graphene or making composite with carbon nanotube might be a fruitful approach.
- As demonstrated in the present work, we have undertaken a novel approach to use sodium vanadium phosphate (NVP, a cathode material used for Na-ion battery) for Li-ion intercalation. In half-cell configuration (using Li as negative electrode and lithium salt-based electrolyte), after the first charge, Na-ions de-intercalate and come into the electrolyte. During discharge Li^+ intercalates into NVP. Since the ionic radius of Na^+ is larger than Li^+ , Li^+ intercalation is easier in NVP as compared to any lithium-based electrode. Such approach was found to yield superior power density of the bi-material electrodes. This kind of bi-material electrodes needs to be further characterized in full-cell configuration.
- For commercial adaptation of ISH and IPH capacitors, extensive research should be undertaken to develop suitable current collectors, separator, and electrolyte materials.

Conclusion

The chapter describes the state of the art of novel rechargeable hybrid battery-supercapacitor-type electrochemical storage device useful for security and defense, electric vehicles, and renewable energy storage. These hybrids are demonstrated to be most attractive material candidates for high energy as well as high power density rechargeable lithium (Li) batteries. We have described two types of hybrids for the aforesaid applications. Internal serial hybrid is an asymmetric electrochemical capacitor with one electric double-layer capacitor and another battery-type electrode. On the other hand, in internal parallel hybrids, supercapacitor and battery materials are mixed together to form bi-material-type electrode. We have reviewed the state of the art of various asymmetric electrochemical capacitors reported in recent times. Subsequently, deriving relevant numerical equations, we have illustrated the role of current densities and electrode potential window in designing the internal serial hybrid electrodes. It was highlighted that the mass ratio between the two electrodes grossly influences the electrochemical performance of internal serial hybrids. Using the derived equations, we have estimated the potential window, capacity, capacitance, and energy/power densities for activated carbon (AC)-lithium nickel manganese oxide ($\text{LiMn}_{1.5}\text{Ni}_{0.5}\text{O}_4$ (LMNO)) asymmetric electrochemical capacitor fabricated in our laboratory in coin-cell configuration. We have reported that the lithium hybrid electrochemical capacitor (ISH configuration) delivered reversible discharge capacity of 25 mAhg^{-1} . The maximum energy and power density have been estimated to be 26.5 Whkg^{-1} and 34 Wkg^{-1} , respectively. As compared to serial hybrids, limited reports are available on internal parallel hybrid for Li-ion batteries. A brief literature review is made to illustrate the outstanding research issues of this type of hybrids. Finally, we have reported excellent electrochemical performance of sodium vanadium phosphate ($\text{Na}_3\text{V}_2(\text{PO}_4)_3$ (NVP))-activated carbon

(AC) bi-material electrodes for lithium-ion rechargeable batteries. The bi-material NVP@C/AC electrode outperforms the other electrodes at high specific currents and shows better capacity retention than the pure battery NVP@C and capacitor-type AC electrodes. At higher current rate of 700 mA g^{-1} , the NVP@C/AC delivers a specific capacity of 58 mAh g^{-1} which exceeds the specific capacities of 35 mAh g^{-1} and 27 mAh g^{-1} estimated for NVP@C/AC and AC, respectively.

Acknowledgments The work was supported financially by project grants vide sanction letter F. No.: 3-18/2015-T.S-I (Vol. IV) dated 17-05-2017 (IMPRINT, supported by MHRD and DRDO) and sanction EMR/2016/007537, dated 16-03-2018 (supported by SERB, DST). Mr. Mainul Akhtar wishes to thank Mr. Kirtan Sahoo (Materials Science Centre) for fruitful discussion.

References

1. Skelton J, Serenyi R (1997) Improved silver/zinc secondary cells for underwater applications. *J Power Sources* 65:39–45
2. Conway BE (1999) *Electrochemical capacitors: scientific fundamentals and technological applications*. Kluwer-Plenum, New York
3. Kousksou T, Bruel P, Jamil A, El Rhafiki T, Zeraoui Y (2014) Energy storage: applications and challenges. *Sol Energy Mater Sol Cells* 120:59–80
4. Evans A, Strezov V, Evans TJ (2012) Assessment of utility energy storage options for increased renewable energy penetration. *Renew Sustain Energy Rev* 16:4141–4147
5. Winter M, Brodd RJ (2004) What are batteries, fuel cells, and supercapacitors? *Chem Rev* 104:4245–4269
6. Cameron CG (2006) Supercapacitor materials for soldier systems. Defence Research and Development Canada – Atlantic, Technical Memorandum, DRDO Atlantic TM 2006-142
7. Kepros MA, Van Schalkwijk WA (2002) Back to the future? Return of the hybrid. *Electrochem Soc Interface* 11:34–37
8. MIT Electric Vehicle Team (2008) A guide to understanding battery specification. http://web.mit.edu/evt/summary_battery_specifications
9. Burke A (2000) Ultracapacitors: why, how, and where is the technology. *J Power Sources* 91:37–50
10. Schougaard SB, Bélanger D (2014) Electrochemical energy storage systems. In: *Functional materials: for energy, sustainable development and biomedical sciences*. Walter de Gruyter GmbH, Berlin/Boston
11. Liu J, Wang J, Xu C, Jiang H, Li C, Zhang L, Lin J, Shen ZX (2018) Advanced energy storage devices: basic principles, analytical methods, and rational materials design. *Adv Sci*. <https://doi.org/10.1002/advs.201700322>
12. Trasatti S, Kurzweil P (1994) Electrochemical supercapacitors as versatile energy stores. *Platin Met Rev* 38:46–56
13. Saleem AM, Desmaris V, Enoksson P (2016) Performance enhancement of carbon nano-materials for supercapacitors. *J Nanomater*. <https://doi.org/10.1155/2016/1537269>
14. Agrawal R, Hao Y, Song Y, Chen C, Wang C (2015) Hybridization of lithium-ion batteries and electrochemical capacitors: fabrication and challenges. *Energy Harvest Storage Mater Devices Appl* VI 9493:94930B
15. Halper MS, Ellenbogen JC (2006) *Supercapacitors: a brief overview*. MITRE Corporation, McLean
16. Brousse T, Bélanger D, Long JW (2015) To be or not to be pseudocapacitive? *J Electrochem Soc* 162:A5185–A5189

17. Simon P, Gogotsi Y, Dunn B (2014) Where do batteries end and supercapacitors begin? *Science* 343(80):1210–1211
18. Krivik P, Baca P (2013) Electrochemical energy storage. In: Zoba AF (ed) *Energy-storage-technologies-and-applications*. InTech, Rijeca
19. Gao J, Shi SQ, Li H (2015) Brief overview of electrochemical potential in lithium ion batteries. *Chin Phys B*. <https://doi.org/10.1088/1674-1056/25/1/018210>
20. Liu C, Neale ZG, Cao G (2016) Understanding electrochemical potentials of cathode materials in rechargeable batteries. *Mater Today* 19:109–123
21. Zheng JP (2003) The limitations of energy density of battery/double-layer capacitor asymmetric cells. *J Electrochem Soc* 150:484–492
22. Cericola D, Novák P, Wokaun A, Kötz R (2011) Hybridization of electrochemical capacitors and rechargeable batteries: an experimental analysis of the different possible approaches utilizing activated carbon, $\text{Li}_4\text{Ti}_5\text{O}_{12}$ and LiMn_2O_4 . *J Power Sources* 196:10305–10313
23. Cericola D, Kötz R (2012) Hybridization of rechargeable batteries and electrochemical capacitors: principles and limits. *Electrochim Acta* 72:1–17
24. Aida T, Yamada K, Morita M (2006) An advanced hybrid electrochemical capacitor that uses a wide potential range at the positive electrode. *Electrochem Solid-State Lett* 9:534–536
25. Béguin F, Presser V, Balducci A, Frackowiak E (2014) Carbons and electrolytes for advanced supercapacitors. *Adv Mater* 26:2219–2251
26. Hu CC, Tsou TW (2002) Ideal capacitive behaviour of hydrous manganese oxide prepared by anodic deposition. *Electrochem Commun* 4:105–109
27. Hu CC, Huang YH (1999) Cyclic voltammetric deposition of hydrous ruthenium oxide for electrochemical supercapacitors. *J Electrochem Soc* 146(7):2465–2471
28. Yu N, Gao L, Zhao S, Wang Z (2009) Electrodeposited PbO_2 thin film as positive electrode in PbO_2/AC hybrid capacitor. *Electrochim Acta* 54:3835–3841
29. Perret P, Khani Z, Brousse T, Bélanger D, Guay D (2011) Carbon/ PbO_2 asymmetric electrochemical capacitor based on methanesulfonic acid electrolyte. *Electrochim Acta* 56:8122–8128
30. Volfkovich YM, Shmatko PA (2003) Electric double layer capacitor? N CX 2: US Patent 6,628,504 B2, 30 Sept 2003
31. Snook GA, Kao P, Best AS (2011) Conducting-polymer-based supercapacitor devices and electrodes. *J Power Sources* 196:1–12
32. Park JH, Park OO (2002) Hybrid electrochemical supercapacitors based on polyaniline and activated carbon electrodes. *J Power Sources* 111:185–190
33. Arbizzani C, Mastragostino M, Soavi F (2001) New trends in electrochemical supercapacitors. *J Power Sources* 100:164–170
34. Wang YG, Xia YY (2005) A new concept hybrid electrochemical supercapacitor: Carbon/ LiMn_2O_4 aqueous system. *Electrochem Commun* 7:1138–1142
35. Hanna O, Luski S, Brousse T, Aurbach D (2017) Aqueous energy-storage cells based on activated carbon and LiMn_2O_4 electrodes. *J Power Sources* 354:148–156
36. Wang YG, Xia YY (2006) Hybrid aqueous energy storage cells using activated carbon and lithium-intercalated compounds I. The C/ LiMn_2O_4 system. *J Electrochem Soc* 153:450–454
37. Amatucci GG, Badway F, Du Pasquier A, Zheng T (2001) An asymmetric hybrid nonaqueous energy storage cell. *J Electrochem Soc* 148:930–939
38. Li H, Cheng L, Xia Y (2005) A hybrid electrochemical supercapacitor based on a 5 V Li-ion battery cathode and active carbon. *Electrochem Solid-State Lett* 8:433–436
39. Jain A, Aravindan V, Jayaraman S, Kumar PS, Balasubramanian R, Ramakrishna S, Madhavi S, Srinivasan MP (2013) Activated carbons derived from coconut shells as high energy density cathode material for Li-ion capacitors. *Sci Rep* 3:1–6
40. Karthikeyan K, Amaresh S, Kim KJ, Kim SH, Chung KY, Cho BW, Lee YS (2013) A high performance hybrid capacitor with $\text{Li}_2\text{CoPO}_4\text{F}$ cathode and activated carbon anode. *Nanoscale* 5:5958–5964
41. Arun N, Jain A, Aravindan V, Jayaraman S, Chui Ling W, Srinivasan MP, Madhavi S (2015) Nanostructured spinel $\text{LiNi}_{0.5}\text{Mn}_{1.5}\text{O}_4$ as new insertion anode for advanced Li-ion capacitors with high power capability. *Nano Energy* 12:69–75

42. Satish R, Aravindan V, Ling WC, Madhavi S (2015) Carbon-coated $\text{Li}_3\text{V}_2(\text{PO}_4)_3$ as insertion type electrode for lithium-ion hybrid electrochemical capacitors: an evaluation of anode and cathodic performance. *J Power Sources* 281:310–317
43. Lee SH, Kim HK, Lee JH, Lee SG, Lee YH (2015) Fabrication and electrochemical properties of cylindrical hybrid supercapacitor using $\text{H}_2\text{Ti}_{12}\text{O}_{25}$ as anode material. *Mater Lett* 143:101–104
44. Satish R, Aravindan V, Ling WC, Madhavi S (2016) LiVPO_4F : a new cathode for high-energy lithium ion capacitors. *ChemistrySelect* 1:3316–3322
45. Aravindan V, Gnanaraj J, Lee YS, Madhavi S (2014) Insertion-type electrodes for nonaqueous Li-ion capacitors. *Chem Rev* 114:11619–11635
46. Dsoke S, Fuchs B, Gucciardi E, Wohlfahrt-Mehrens M (2015) The importance of the electrode mass ratio in a Li-ion capacitor based on activated carbon and $\text{Li}_4\text{Ti}_5\text{O}_{12}$. *J Power Sources* 282:385–393
47. Li J, Gao F (2009) Analysis of electrodes matching for asymmetric electrochemical capacitor. *J Power Sources* 194:1184–1193
48. Pell WG, Conway BE (2004) Peculiarities and requirements of asymmetric capacitor devices based on combination of capacitor and battery-type electrodes. *J Power Sources* 136:334–345
49. Dubal DP, Ayyad O, Ruiz V, Gómez-Romero P (2015) Hybrid energy storage: the merging of battery and supercapacitor chemistries. *Chem Soc Rev* 44:1777–1790
50. Naoi K (2010) “Nanohybrid capacitor”: the next generation electrochemical capacitors. *Fuel Cells* 10:825–833
51. Pasquier A Du, Plitz I, Gural J, Badway F, Amatucci GG (2004) Power-ion battery: bridging the gap between Li-ion and supercapacitor chemistries. *J Power Sources* 136:160–170
52. Hu X, Huai Y, Lin Z, Suo J, Deng Z (2007) A $(\text{LiFePO}_4\text{-AC})/\text{Li}_4\text{Ti}_5\text{O}_{12}$ hybrid battery capacitor. *J Electrochem Soc* 154:1026–1030
53. Hu X, Deng Z, Suo J, Pan Z (2009) A high rate, high capacity and long life $(\text{LiMn}_2\text{O}_4 + \text{AC})/\text{Li}_4\text{Ti}_5\text{O}_{12}$ hybrid battery-supercapacitor. *J Power Sources* 187:635–639
54. Cericola D, Novák P, Wokaun A, Kötz R (2011) Mixed bi-material electrodes based on LiMn_2O_4 and activated carbon for hybrid electrochemical energy storage devices. *Electrochim Acta* 56:8403–8411
55. Cericola D, Novák P, Wokaun A, Kötz R (2011) Segmented bi-material electrodes of activated carbon and LiMn_2O_4 for electrochemical hybrid storage devices: effect of mass ratio and C-rate on current sharing. *Electrochim Acta* 56:1288–1293
56. Choi HS, Im JH, Kim T, Park JH, Park CR (2012) Advanced energy storage device: a hybrid BatCap system consisting of battery-supercapacitor hybrid electrodes based on $\text{Li}_4\text{Ti}_5\text{O}_{12}$ -activated-carbon hybrid nanotubes. *J Mater Chem* 22:16986–16993
57. Ping LN, Zheng JM, Shi ZQ, Qi J, Wang CY (2013) Electrochemical performance of MCMB/ $(\text{AC}+\text{LiFePO}_4)$ lithium-ion capacitors. *Chin Sci Bull* 58:689–695
58. Böckenfeld N, Placke T, Winter M, Passerini S, Balducci A (2012) The influence of activated carbon on the performance of lithium iron phosphate based electrodes. *Electrochim Acta* 76:130–136
59. Secchiaroli M, Marassi R, Wohlfahrt-Mehrens M, Dsoke S (2016) The synergic effect of activated carbon and $\text{Li}_3\text{V}_{1.95}\text{Ni}_{0.05}(\text{PO}_4)_3/\text{C}$ for the development of high energy and power electrodes. *Electrochim Acta* 219:425–434
60. Ruan D, Huang Y, Li L, Yuan J, Qiao Z (2017) A $\text{Li}_4\text{Ti}_5\text{O}_{12}+\text{AC}/\text{LiMn}_2\text{O}_4+\text{AC}$ hybrid battery capacitor with good cycle performance. *J Alloys Compd* 695:1685–1690
61. Naoi K, Ishimoto S, Miyamoto JI, Naoi W (2012) Second generation “nanohybrid supercapacitor”: evolution of capacitive energy storage devices. *Energy Environ Sci* 5:9363–9373
62. Yu G, Xie X, Pan L, Bao Z, Cui Y (2013) Hybrid nanostructured materials for high-performance electrochemical capacitors. *Nano Energy* 2:213–234
63. Lam LT, Louey R (2006) Development of ultra-battery for hybrid-electric vehicle applications. *J Power Sources* 158:1140–1148
64. Bai L, Li C, Anani AA; Thomas G, Wu H, Lian KK, Denton FR, Howard JN (1998) High power, high energy, hybrid electrode and electrical energy storage device made therefrom. US Patent 5,744,258, 28 Apr 1998
65. Plitz I, Dupasquier A, Badway F, Gural J, Pereira N, Gmitter A, Amatucci GG (2006) The design of alternative nonaqueous high power chemistries. *Appl Phys A Mater Sci Process* 82:615–626



Recent Developments in Electrode Materials for Lithium-Ion Batteries for Energy Storage Application

33

Moodakare B. Sahana and Raghavan Gopalan

Contents

Introduction	1298
Lithium-Ion Cell Characteristics	1299
Lithium-Ion Cell Processing Steps	1304
Lithium-Ion Battery Material Cost Breakdown	1305
Properties of Electrode Materials Used in Commercial Lithium-Ion Battery	1306
Recent Development in Traditional Cathode Materials	1307
Lithium Layered Oxide	1307
Spinel LiMn_2O_4	1317
Phospho-olivine	1319
Recent Development in Traditional Anode Materials	1321
Soft Carbon	1324
Hard Carbon	1325
Lithium Titanium Oxide	1325
Recent Development in New Electrode Materials	1327
Conversion Reaction Materials	1327
Summary and Outlook	1328
References	1330

Abstract

Lithium-ion battery is a promising energy storage solution for effective use of renewable energy sources due to higher volumetric and gravimetric energy density. The advancement of lithium-ion battery technology in terms of energy, power density, cost, safety, operating temperature, and charging/discharging cycle life depends on performance of electrode materials: cathode, anode, and electrolyte. While graphite or hard carbon is mainly used as anode, three types of

M. B. Sahana (✉) · R. Gopalan

Centre for Automotive Energy Materials, International Advanced Research Centre for Powder Metallurgy and New Materials, IITM Research Park, Chennai, India

e-mail: sahanamb@arci.res.in; sahanamb@gmail.com; gopy@arci.res.in

© Springer Nature Switzerland AG 2020

1297

Y. R. Mahajan, R. Johnson (eds.), *Handbook of Advanced Ceramics and Composites*,
https://doi.org/10.1007/978-3-030-16347-1_44

cathode chemistry, (i) lithium transition metal layered oxide, (ii) derivatives of spinel LiMn_2O_4 , and (iii) phospho-olivine, are used in the commercial lithium-ion batteries. Modifications such as composition, protective coating, doping, and morphological tailoring had continuously led into the enhanced performance of the active materials and are further expected to improve. Continuous efforts in development of new class of materials such as conversion and alloying electrode materials are being carried out in order to improve energy and power density of lithium-ion batteries. In this chapter we will be discussing the recent development of traditional cathode and anode materials like graphite, hard carbon, lithium transition metal layered oxide, and derivatives of spinel LiMn_2O_4 , LiFePO_4 , and new class of active materials.

Keywords

Lithium-ion battery · Cathode and anode materials · Fabrication · Cost · Lithium transition metal layered oxide · Lithium transition metal spinel · Phospho-olivines · Conversion reaction electrodes

Introduction

Energy storage systems are an integral part of vast majority of the modern technology and are mainly classified into five different categories: (i) chemical, (ii) electrical, (iii) electrochemical, (iv) mechanical, and (v) thermal. There is no single system that will suffice various applications. Energy storage systems are selected by considering various facts such as investment costs, capacity, energy density, power ratings, cycle life, and efficiency. Further depending whether the application is stationary or portable and required duration of the storage, energy storage system is chosen. For the portable applications, electrochemical energy storage systems are the best choice given their higher energy density and easy conversion from the electrochemical energy to electrical energy. Most commonly known electrochemical storage systems are super-capacitors and batteries. While super-capacitors are used where very high power density is needed, batteries dominate portable technologies, where high energy density is required.

Though there are many battery chemistries that are being considered for portable applications, only a few are commercially produced like NiMH, Li-ion, ZEBRA, and improved lead acid batteries. Battery technologies, such as Li-metal polymer, lithium sulfur, and NaS, have undergone field demonstration trials. Many of the battery chemistries such as Li-air, Na-ion battery, Al-air, Zn-air, zinc-chlorine, Fe-air, silicon-air, conversion batteries, organic lithium batteries, Mg-ion, Na-ion, nickel-lithium, and lithium copper are still at an infancy stage with a laboratory scale R&D being seriously pursued. Figure 1 provides energy and power density of various electrochemical storage systems that are currently used and are under development for portable systems both for electronic and traction technology [1]. Currently lithium-ion battery (LIB) and nickel metal hydride (NiMH) batteries

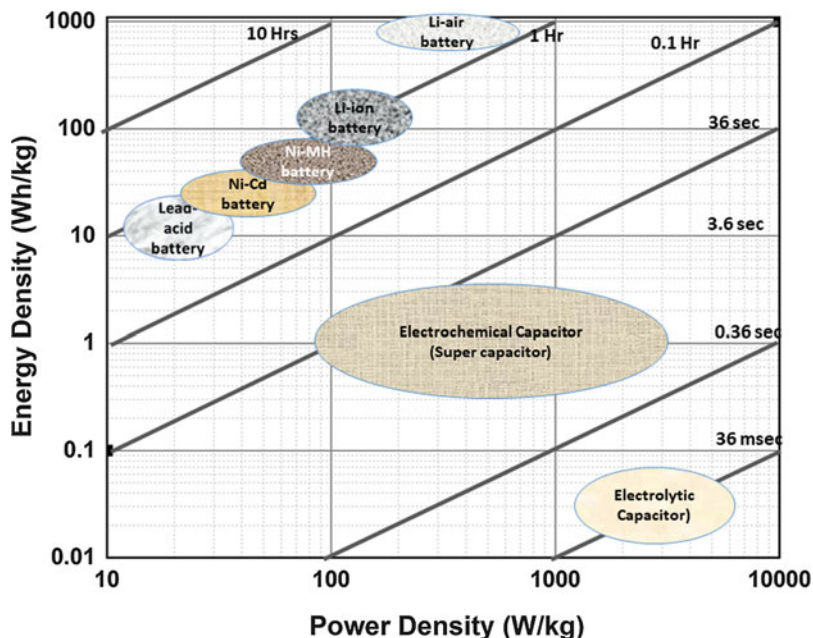


Fig. 1 Energy and power density of various electrochemical systems that are currently under consideration for traction applications

are two main battery types that are used in hybrid and full electric vehicles. While NiMH batteries are dominating HEV industry by increasing fuel efficiency, Li-ion batteries are the only candidates that meet HEV and EV demands. Because of the limited specific energy of ~ 100 Wh/kg, fully charged NiMH works for about 30 km. This restricts its application only to HEVs and prevents its usage in complete EV applications. However, LIB when fully charged can go up to 150 km, making it most promising candidate for electric transportation. Lithium-ion batteries consist of battery management system and number of battery modulus, comprised of Li-ion cells connected in parallel and series. The quality of the battery is decided by its (i) gravimetric specific energy (Whg^{-1}), (ii) volumetric capacity (Ahcm^{-3}), (iii) power capability, (iv) durability, (v) safety (vi) thermal stability, and (vii) cost. The characteristics of the batteries depend on the intrinsic electrochemical characteristics of the active materials and on the design engineering of the cells, batteries, and modules.

Lithium-Ion Cell Characteristics

The active constituents of lithium-ion cell are positive and negative electrodes and separator soaked in electrolyte. The schematic representation of lithium-ion cell functioning is given in Fig. 2. During charging, the lithium-ion deintercalates from

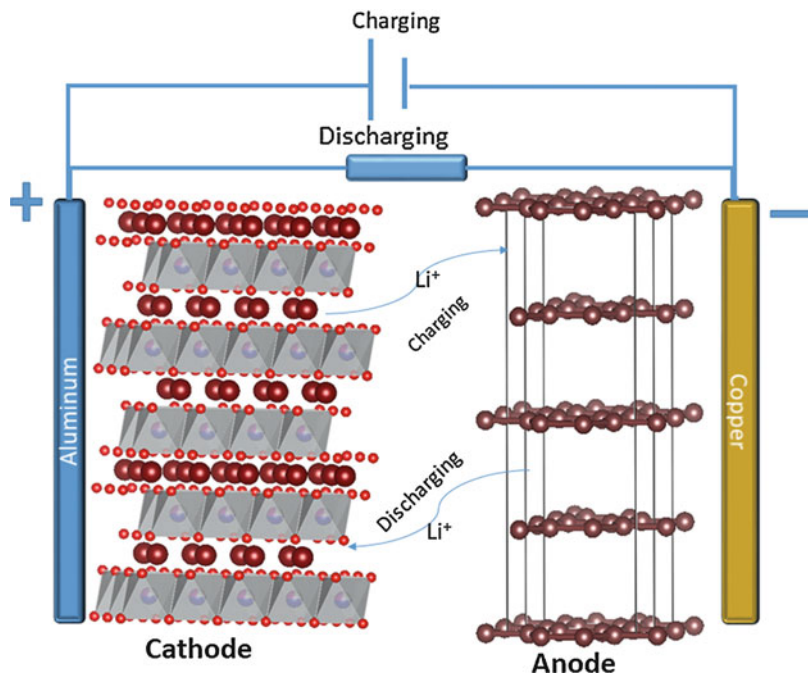


Fig. 2 The schematic representation of lithium-ion cell functioning

the cathode, travels through the electrolyte, and intercalates at the anode. The intercalation/deintercalation of the Li^+ is facilitated at the electrode by the redox reaction. While during charging the positive electrode undergoes oxidation and releases the electron to the outer circuit, and negative electrode undergoes the reduction reaction by gaining the electron. During discharging the oxidation and reduction takes place at negative and positive electrodes, respectively, and the electron and lithium-ion moves from negative electrode to positive electrode. Conventionally positive electrodes are called cathode, and negative electrodes are called anode in LIB, though the electrodes perform alternatively the cathode/anode function during charge/discharging. The energy storage density (E) of the cell depends on the electrochemical potential difference of anode and cathode (V_{oc}) and their lithium intercalation ability (Q) and is given by $E = QV_{oc}$. While lithium insertion capacity depends on how much of lithium can be inserted/extracted from lithium insertion compound ($\text{Li}_x\text{M}_y\text{X}_z$) per unit volume or weight (Ah/cm^3 or Ah/kg), the cell potential depends on the lithium electrochemical potential for positive and negative electrode. The availability of multiple valences for metal, M , and the number of Li sites available in $\text{Li}_x\text{M}_y\text{X}_z$ host for reversible lithium insertion/extraction determine cell's capacity. The open circuit potential of lithium-ion is given by

$$V_{oc} = \frac{\mu_{\text{Li}(c)} - \mu_{\text{Li}(a)}}{F} \quad (1)$$

where F is Faradic constant, and μ_A and μ_C are the lithium electrochemical potential for the anode and cathode, respectively [2]. The choice of electrode depends upon the values of μ_A and μ_C and their positions relative to the highest occupied molecular orbit and lowest unoccupied molecular orbit (HOMO-LUMO) of the electrolyte. For the electrolyte stability, it is required that μ_A and μ_C to have lower and higher energy than that of the LUMO and HOMO of the electrolyte, respectively, while the higher μ_A than LUMO will reduce the electrolyte and lower μ_C than HOMO will oxidize the electrolyte, as shown in Fig. 3a. In order to maximize the cell voltage, insertion

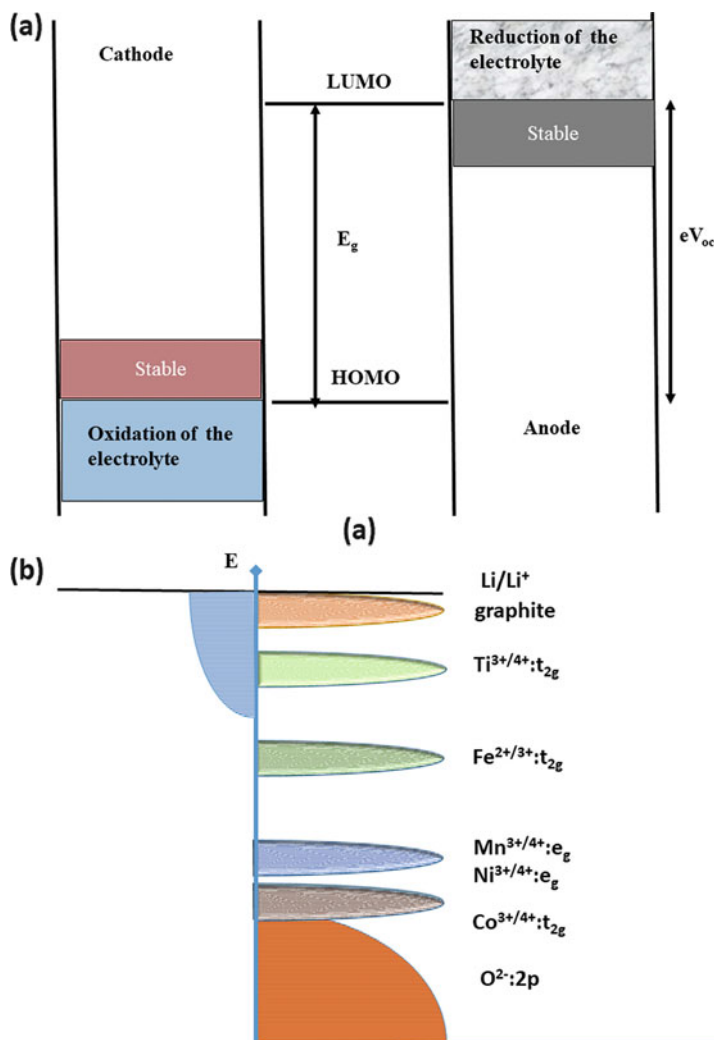


Fig. 3 (a) Schematic of relative position of lithium electrochemical potential for the anode and cathode relative to HOMO and LUMO of the electrolyte. (b) The relative redox potentials of various transition metals at different oxidation state w.r.t Li/Li^+ . (Adopted from Ref. [11])

materials with a low μ_C are considered as cathode, and the ones having high μ_a are suitable for anode materials. The relative redox potentials of various transition metals at different oxidation state w.r.t Li/Li^+ are given in Fig. 3b. This means that the lithium insertion compound with transition metal ion in higher oxidation state is a good candidate as cathode and the one with low oxidation state as an anode [3]. The M_y in $\text{Li}_x\text{M}_y\text{X}_z$ should exist in different oxidation states to accommodate lithium-ion insertion/deinsertion and should be of low atomic weight. This makes 3D transition metal ions preferable candidate for M^{n+} . The various electrode materials currently under consideration along with the specific capacity and potential range are given in Fig. 4. Further, electronic and ionic conductivity of lithium insertion compounds decides the charge/discharging rate capabilities [3]. In addition to the reversible energy and rate capability, the life cycle of the cell plays a crucial role, in practical applications. For better cyclic stability of the cell, the electrodes should not react adversely with the electrolyte, and there should be minimum or no structural changes involved during the entire region of lithium insertion/deinsertion. Unless the redox energies of the insertion electrodes are within the HOMO-LUMO bandgap of the electrolyte, throughout charging/discharging process, there will be undesirable electrolyte oxidation/reduction. Another aspect that is crucial for commercialization is the cost and environmental friendliness. In addition to the conditions defined earlier for the electrode materials, the electrolyte should also satisfy numerous benchmarks. While the good ionic conductivity of the electrolyte minimizes the IR drop and ohmic polarization,

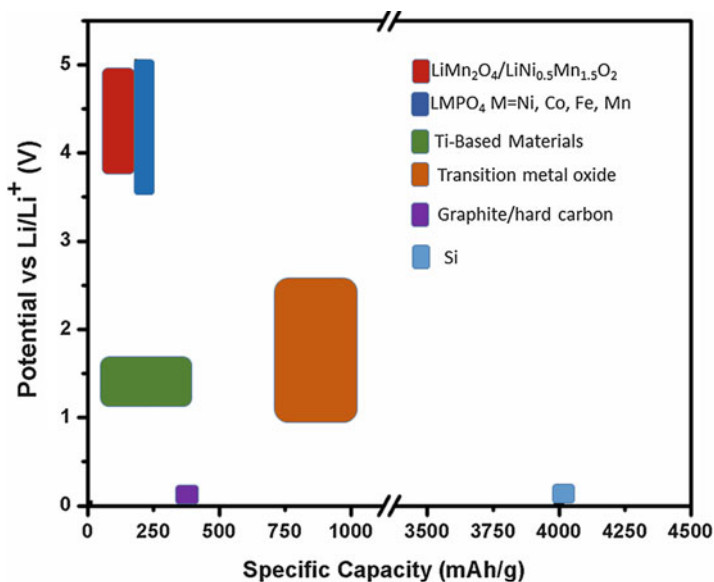


Fig. 4 The various electrode materials currently under consideration along with the specific capacity potential range

the electronic insulating behavior prevents the internal short-circuiting. The low ohmic polarization is very essential for achieving high energy at fast charging/discharging (high rate or power capability). Furthermore to the intrinsic properties of the active materials detailed above, the cell performance significantly depends on the electrode architectures. The transportation of Li-ion and electron during cell charging can be recognized in the following steps [4]:

- (i) The Li-ion and the electron dissociate from the cathode concurrently and move toward electrolyte and the current collector, respectively, via solid-state diffusion.
- (ii) The Li^+ passes through the interface between electrode and electrolyte and then to the electrolyte.
- (iii) The electron, driven by the applied voltage difference between positive and negative electrode, passes through cathode particles, conductive additive, and their interfaces toward the current collector and migrates to the external circuit.
- (iv) While the electron passes through the current collector electrode interface, the Li-ion passes through the SEI layer and the SEI/anode interface.
- (v) The electron and the Li-ion enter the anode materials simultaneously via solid-state diffusion.

During the discharging process, the direction of lithium-ion and electron movement occurs in the opposite direction. Power density (P), the rate at which energy is released, is expressed as

$$P = \frac{QV_{op}}{t} = \frac{V_{op}^2}{R} \quad (2)$$

where “ t ” is the time and R is the internal resistance, which is the sum of electronic, ionic, and interfacial resistance [4]. The battery capacity is normalized by expressing charging/discharging currents in C-rate. One C (nC) rate means that full capacity of the battery will be charged/discharged in $1(1/n)$ hour. The open circuit and the operating voltage difference ($V_{oc} - V_{op}$) is termed as overpotential (Z) and is mainly caused by (1) ohmic polarization arising from the resistance of cell components and their interface; (2) charge transfer activation polarization of the redox reaction at anode and cathode; and (3) concentration polarization related to the mass transport constraints [2]. Therefore in addition to intrinsic properties of the electrode materials, extrinsic properties of the electrodes too play a decisive role in determining the lithium cell characteristics such as energy, rate capability, and cycle life. The initial material performance needs to be transferred to the cell, through proper engineering of the electrode coating process and cell assembly. In-depth understanding of the manufacturing process steps are necessary to minimize the production-related losses of the primary material characteristics. However, there is only a few investigations on the effect of electrode or cell production processes on the subsequent physical and electrochemical properties.

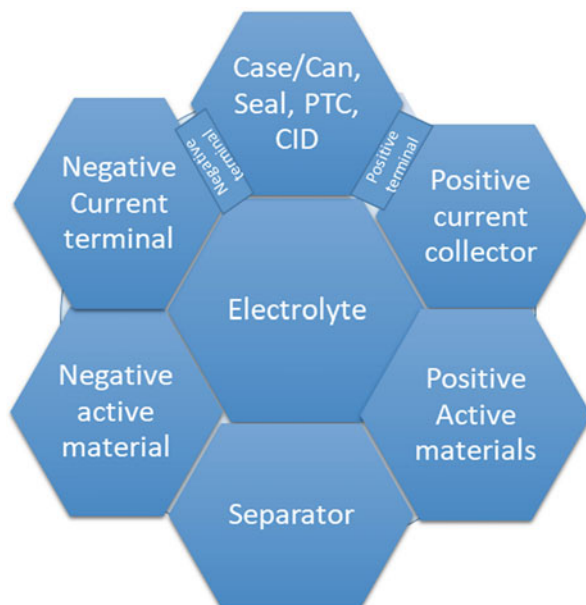
Lithium-Ion Cell Processing Steps

Figure 5 illustrates the various parts found in a commercial cell. The boundary between hexagonal-hexagonal and hexagonal-rectangle in the schematic signifies the various interfaces between the components. For the better electrochemical characteristics such as energy stored and released, cyclability, and rate capability, the engineering of components of the battery and its interface are very crucial [5]. The main requirement is to have uniform current distribution through the current collector, electrode coating, and the interface between the two. Current distribution across the electrode coating is determined both by the conductivity of the active mass and the electrode structure. Current distribution within the electrode structure is decided by (i) electrode microstructure including porosity and distribution of conductive additive, (ii) thickness of the electrode, (iii) the binding properties of the electrode material to the current collector, and (iv) ratio of conductive additive and binder to active powder. Further the balance of cathode to anode capacity and the electrolyte conductivity plays a decisive part in optimizing the electrochemical characteristic of the cell. Incorporating safety devices such as positive temperature coefficient (PTC) resistor, current interrupt device (CID), and shutdown separator ensures the safety of the cell.

The Li-ion battery is manufactured by the following processes:

- (i) Preparation of electrode slurry consisting of active material, binder, and conductive additive using a compatible solvent
- (ii) Coating of positive and negative electrode slurry on thin aluminum and copper foil, respectively

Fig. 5 Various parts found in a commercial cell with the boundary between the hexagonal and the rectangles signifies the various interfaces between the components. (Adopted from Ref. [12])



- (iii) Drying cathode and anode electrode
- (iv) Calendaring the electrodes to control the electrode porosity
- (v) Slitting the electrodes for desired dimension and winding cathode with a separator between them
- (vi) Tab fixing to the electrodes
- (vii) Inserting the wound electrodes into a battery case
- (viii) Filling with electrolyte under vacuum, and sealing the battery case
- (ix) Carrying out the SEI formation cycle

After the SEI layer is formed, they are stored (aged) for a given period of time [6, 7].

Lithium-Ion Battery Material Cost Breakdown

In addition to the electrochemical characteristics such as energy density, rate capability, cyclic life, and safety, the cost of the battery is an important issue, in the manufacturing and commercialization of the battery pack. Around 70% of the battery pack is attributed to the active and supporting material of the battery, and more than 50% of the material cost comes from cathode, anode [8], and separator [9] (Figs. 6 and 7). The cost of the lithium-ion packs depends on various factors, such as

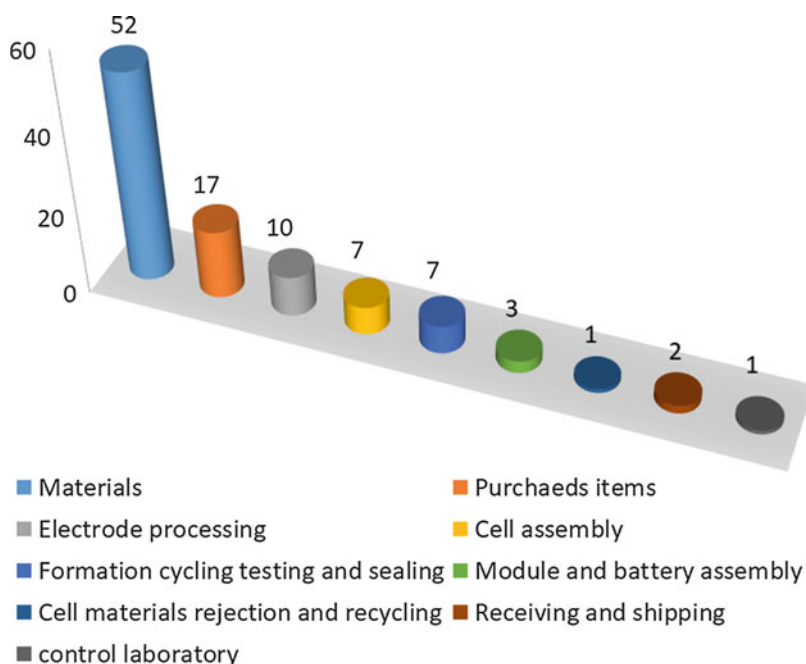
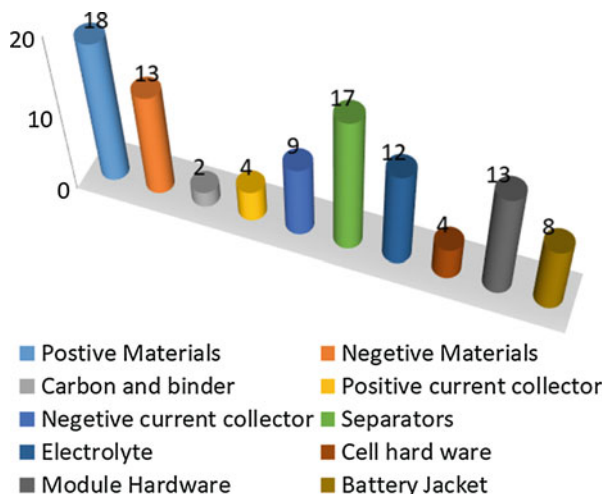


Fig. 6 Overall cost breakdown of lithium-ion battery pack

Fig. 7 Cost breakdown of lithium-ion battery pack of the materials used



design of cell, pack, and material chemistry used. There is constant effort in modeling the cost prediction of the lithium-ion battery packs considering battery design and the production quantity. The details of the material cost as of 2015 are given by Gaëtan et al. [9]. Because of the variation in the energy density of different positive materials, the cost per kg for the positive active materials doesn't essentially translate into the cost of the lithium-ion pack. For example, though the cost of NMC is higher than LMO, the LIB packs with either of the chemistry have similar prices, due to NMC's higher energy density [9].

Properties of Electrode Materials Used in Commercial Lithium-Ion Battery

In a commercial cell in general, graphite and lithium transition metal oxide or phosphate are used as an anode and cathode, respectively, and the details of the materials that are used from various manufactures are given in Ref [10]. While the lithium transition metal oxides, $\text{LiNi}_x\text{Mn}_y\text{Co}_{1-x-y}\text{O}_2$ (NMC) and $\text{LiNi}_x\text{Co}_y\text{Al}_{1-x-y}\text{O}_2$ (NCA), are derived from original LiCoO_2 , $\text{LiNi}_{0.5}\text{Mn}_{1.5}\text{O}_2$ (LNMO) is the derivative of spinel LiMn_2O_4 (LMO). Various versions of NMC such as NMC532, NMC442, NMC811, and NMC 333 (NMC 111), where the numbers at the end of the name represent the atomic ration of Ni, Co, and Mn, are commercially used. There is no single cathode material that is advantageous over the other, and all of them have certain pros and cons and have been used at different technologies. Spider net chart given in Fig. 8 compares the safety, cost, energy, power, and performance of the electrode materials that are considered [10, 11]. From spider net chart, it is evident that if an electrode material has an edge in one of the characteristic, there is always a compromise in another. For example, LFP is best suited for applications requiring high safety but with limited energy and power. NCA is best suited for high-energy and high-power applications with limited safety and calendar life.

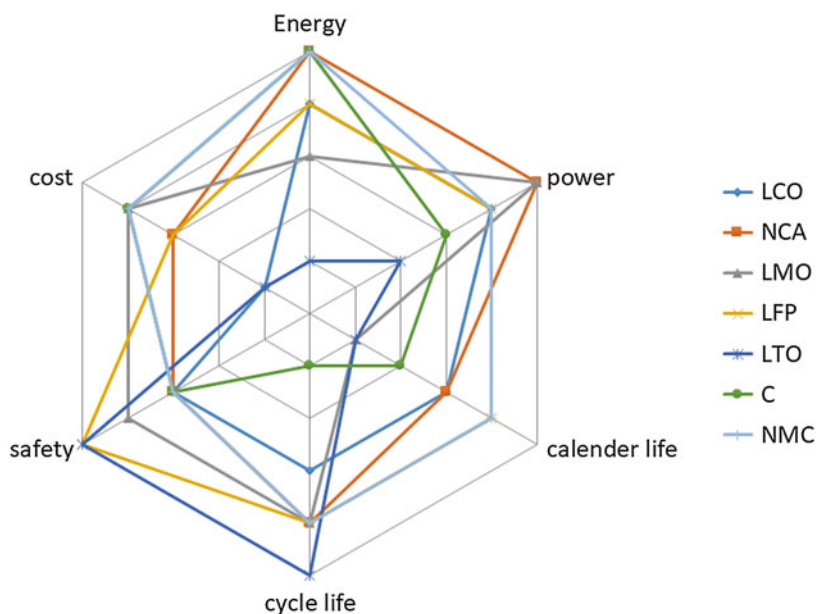


Fig. 8 The comparison of various properties of the electrode materials that are being used in LIB technology

The energy density W of lithium-ion battery depends on both the cathode and anode material and is given by

$$W = \frac{V}{K_+ + K_-} \times 0.5 \text{ Whkg}^{-1} \quad (3)$$

$$K_{\pm} = \frac{M}{n_e \times 26.8 \times 10^3} \quad (4)$$

where V is the working voltage, M is the active material molar mass (g/mol), n_e is the number of electron involved in the redox reaction, and 26.8 corresponds to Faraday constant in Ah. The energy density calculated [12] using Eq. 3, the working voltage and the specific capacity for LIB cells with various cathode materials and graphite as anode are given in Fig. 9.

Recent Development in Traditional Cathode Materials

Lithium Layered Oxide

LiMO_2 ($M = \text{Co}, \text{Mn}$ or Ni) has layered rock salt structure and belongs to $R\bar{3}m$ space group as presented in Fig. 10. The layered transition metal oxide comprises of a cubic close-packed (ccp) array of oxygen with three MO_2 sheets per unit cell, and the

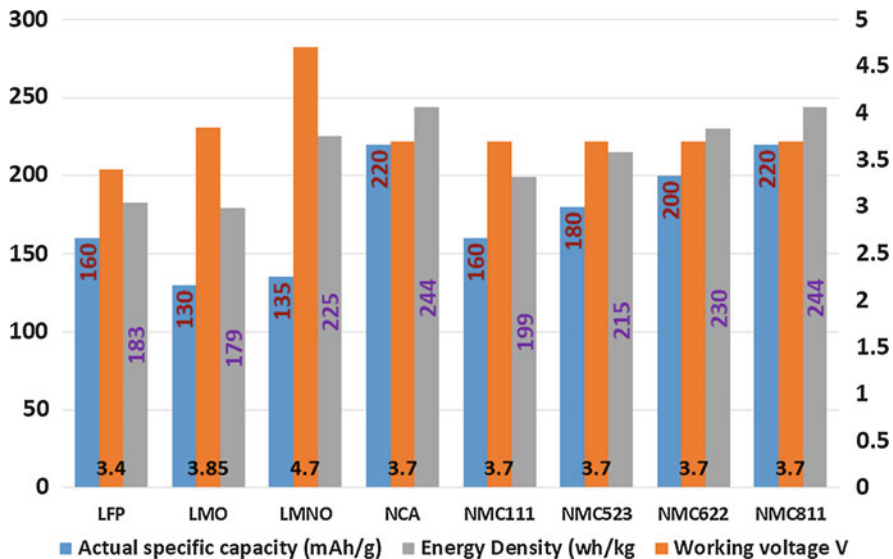


Fig. 9 The energy density calculated using Eq. 3, the working voltage, and the specific capacity for LIB cells with various cathode materials and graphite as anode

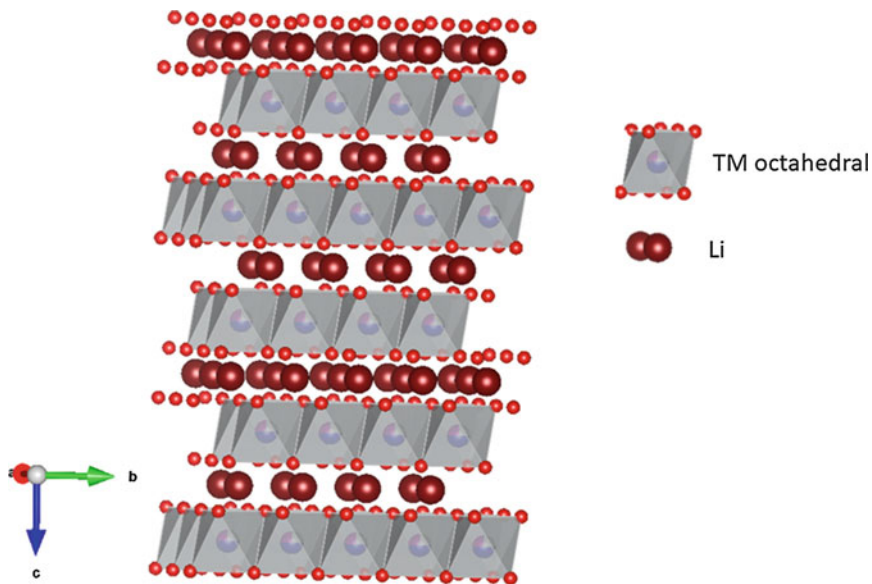


Fig. 10 The crystal structure of LiMO_2

Li^+ ions occupy the octahedral interstitial sites and therefore is called as O3 (O = octahedral, 3 = number of MO_2 sheets) layer structure. The detailed crystal structure of the transition layer oxide is given in [13]. In LiMO_2 , interconnected lithium-lithium ions and M-M interaction in the LiO_6 and MO_6 octahedral arrangements provide better ionic and electronic conductivity, respectively. The review article by Park et al. [14] provides a detailed comparison of electronic and diffusivity of Li-ion in commercially important electrode materials. Fully charged and discharge cathodes have MO_2 and LiMO_2 composition respectively. The oxidation state of M is equal to $4+$ in MO_2 and $3+$ in LiMO_2 .

LiCoO_2 (LCO)

LiCoO_2 is mainly used only in batteries for small-scale application and has not been considered for electric vehicles and hybrid vehicle application since cobalt is not cost-effective [13]. Because of the poor chemical stability after Li^+ extraction of more than 50%, LiCoO_2 can deliver a reversible practical capacity of only 140 mAh/g, though its theoretical capacity is 274 mAhg^{-1} . Lithium deintercalation over 0.5 per molecule in LiCoO_2 oxidizes O^{2-} due to the overlapping of the $\text{Co}^{3+/4+} : t_{2g}$ and $\text{O}^{2-} : 2p$ band [15]. The oxygen evolution from LiCoO_2 when overcharged increases with increase in temperature giving rise to safety concerns. In situ aberration-corrected transmission electron microscopy and electron energy loss spectroscopy at high temperatures confirm the evolution of oxygen from the surface of LiCoO_2 [16]. When the charge cutoff voltage is increased beyond 4.2 V versus Li/Li^+ , hexagonal to monoclinic phase transition and Co dissolution in the electrolyte are observed. The phase transition develops the elastic strains and micro-cracks in LiCoO_2 particles and increases the active material/current collector interface resistance. The chemical degradation, increase in the internal resistance, and dissolution of Co in the electrolyte have prevented the use of LiCoO_2 in electric vehicle applications. Various strategies, such as doping with elements like Mg and Mn in low concentration [17], surface coatings, and additives in electrolytes, have been employed. The metal oxide coatings that have been employed are MgO , SnO_2 , SiO_2 , ZnO , CuO , etc. However, no significant improvement in the electrochemical properties at higher cutoff voltage could be achieved. A recent review article by Sujith Kalluri et al. details surface engineering strategies used to develop high-energy LiCoO_2 [18]. Park et al. used ALD technique to grow Al_2O_3 and Al-W-F on LiCoO_2 powders and electrode coating and thereby increasing the cyclic stability at higher cutoff voltage [19]. Glassy boron oxide coating over LiCoO_2 had improved the cyclic stability even with the cut of voltage of 4.5 V versus Li/Li^+ . David et al. had investigated over 55 combinations of electrolyte additives in LiCoO_2 -graphite cells and suggest that combination of electrolyte additives has better impact on the electrochemical properties than the single electrolyte additive. The combination of additives needs to be selected depending on the applications, for example, of 2 wt.% vinylene carbonate, 2 wt.% vinyl ethylene carbonate, and 2 wt.% fluoroethylene carbonate will be a better choice for low rate, long lifetime applications [20]. Besides

the continuous effort in increasing the achievable practical capacity, the focus is to recycle and re-functionalize the electrochemical properties of the used LiCoO_2 , given the high cost of cobalt. Environmental concerns and sustainability of the resources are the driving force for the effort of recycling lithium-ion batteries. Though the high discharge voltage of LiCoO_2 is attractive, it suffers from high price, reduced thermal stability, and poor cyclic permanence at higher C-rate and with deep cycling. Thermal stability of LiCoO_2 is the lowest among the entire commercial electrode.

$\text{LiNi}_{1-x-y}\text{Co}_x\text{Mn}_y\text{O}_2$ (NMC)

LiNiO_2 and LiMnO_2 could in principle drastically lower the cost of the cathode material, compared to LiCoO_2 . Nonetheless, it is very challenging to synthesize defect-free electrochemically active LiNiO_2 and LiMnO_2 and therefore not attractive cathode material. LiMnO_2 converts to spinel upon cycling, resulting in irreversible capacity. In LiNiO_2 , because of the similarity in the radius of Ni^{2+} and Li^+ , there is a strong tendency for Ni^{2+} to occupy Li^+ site, reducing the overall concentration of Li [21]. Typical electron configurations of the transition metal in the layered oxides LiMO_2 are given in Fig. 11. While Co^{3+} has all the outer most electrons in t_{2g} state, Mn^{3+} and Ni^{3+} have a lone electron in e_g level. Therefore, Mn^{3+} and Ni^{3+} are vulnerable to a Jahn-Teller (J-T) distortion where degeneracy between the two e_g orbitals is broken owing to the elongation of the bonds along the octahedral axes. The splitting of the e_g reduces the overall energy of the solid. In Ni^{3+} and Mn^{3+} , the electrons singly occupy lower-energy e_g orbitals. The major problems of Jahn-Teller distortion in LiNiO_2 and LiMnO_2 can be overcome by using mixed transition metal

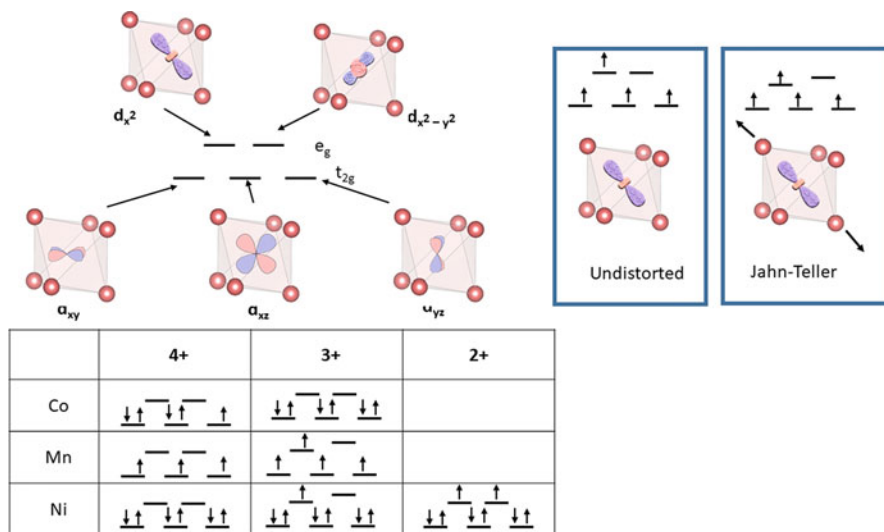
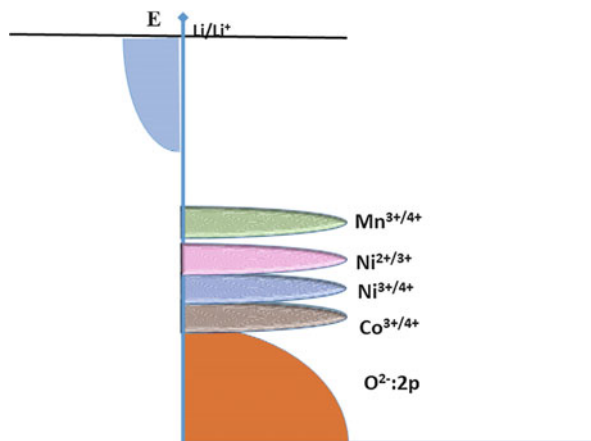


Fig. 11 Typical electron configuration of transition metals in different oxidation states in layered oxide. (Adopted from Ref. [13])

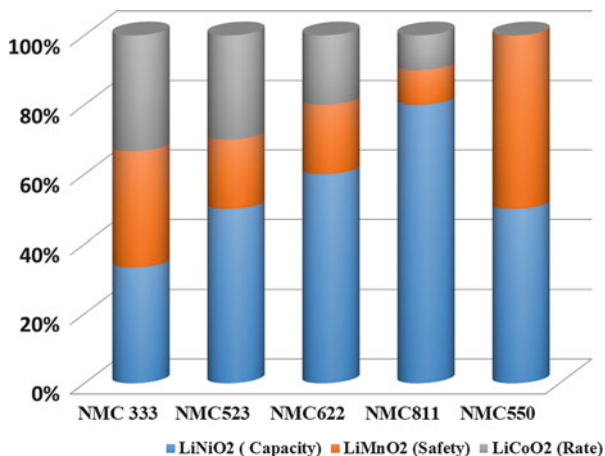
layered oxide, $\text{LiNi}_{1-x}\text{Co}_x\text{Mn}_y\text{O}_2$ [22]. The energy level of the redox pair increases in the order of $\text{Co}^{3+}/\text{Co}^{4+}$, $\text{Ni}^{3+}/\text{Ni}^{4+}$, $\text{Ni}^{2+}/\text{Ni}^{3+}$, and $\text{Mn}^{3+}/\text{Mn}^{4+}$ in $\text{LiNi}_{1-x}\text{Co}_x\text{Mn}_y\text{O}_2$, and their relative position with respect to oxygen 2p band is given in Fig. 12. In NMC, Mn^{3+} will spontaneously donate electrons to Ni^{3+} to become Mn^{4+} , because of the lower energy of $\text{Ni}^{2+}/\text{Ni}^{3+}$ couple compared to $\text{Mn}^{3+}/\text{Mn}^{4+}$ [13]. Therefore in NMC where Ni concentration is more than that of Mn content, oxidation state of Mn is 4+, and it remains electrochemically inactive during the intercalation process. The deintercalation of Li^+ from NMC initially takes place through the oxidation of Ni^{2+} to Ni^{3+} , followed by Ni^{3+} to Ni^{4+} , and then finally by Co^{3+} to Co^{4+} . By having mixed transition metal in LiMO_2 , the relative position of the redox energy levels of the transition metals can be tailored. The electron transfer from Mn to Ni, which results in the oxidation of Mn to Mn^{4+} , and Ni to Ni^{2+} is believed to diminish the failure mode characteristic to layered oxides containing Ni^{3+} and spinel oxides containing Mn^{3+} . Since Mn^{4+} cannot be readily reduced to Mn^{2+} , it is unlikely to migrate to tetrahedral sites preventing the conversion to spinel structure. This also reduces the dissolution of Mn in the electrolyte, since Mn^{4+} is less susceptible to dissolution than Mn^{3+} . For example, Manthiram et al. found that the level of Mn dissolution is negligible in NMC 333 compared to LiMn_2O_4 . Further, the prevention of Jahn-Teller distortions in NMC due to 4+ oxidation state of Mn precludes mechanical stresses. While NMCs still include Co, the required quantity is far less than that in LiCoO_2 . Since the energy levels of Co and Ni are overlapping as shown in Fig. 12, the oxidation of Co^{3+} begins, before the complete oxidation of Ni^{3+} , resulting in a smooth increase in the voltage in charging/discharging curves. Further, due to the reduced electrostatic repulsion, it has been thought that Li^+ diffusion at low x in $\text{Li}_{1-x}\text{MO}_2$ will experience less electrostatic repulsion [23]. The reduced oxidation state of Ni also helps in preventing the surface reaction associated with Ni. In the mixed transition metal layered oxide, most initial work was dedicated on NMC with equal concentration of Ni, Mn, and Co (NMC 333 or NMC 111), which is considered as the solid solutions of LiCoO_2 and $\text{LiNi}_{0.5}\text{Mn}_{0.5}\text{O}_2$. Addition of Co to

Fig. 12 The potential of various redox couples with respect to Li/Li^+ of commercially used electrode materials, layered LiMO_2 (M = Mn, Co, and Ni)



$\text{LiNi}_{0.5}\text{Mn}_{0.5}\text{O}_2$ reduced the ion mixing about 2–3% from 10% resulting in better rate performance [24]. The various lithium mixed metal layered oxides that are considered as the cathode material in lithium-ion battery are provided in Fig. 13. Recently, there is strong drive to increase the Ni content in NMC to reduce the price due to cobalt; however, this results in increased ion mixing and reduced rate capability. In NMC 442, NMC 992, with slight increase in the Ni and Mn concentration, the discharge capacity increases marginally, and the rate capability is not affected much by the reduction on the cobalt concentration [25]. With further increase in the Ni content, NMC behaves more like LiNiO_2 and is accompanied by its underlying challenges. When Ni content is more than Mn, the excess Ni will be in the 3+, and degeneracy of the e_g band will be broken and will become chemically instable. Figure 14 shows the predicted increase in the capacity of two scenarios with increase in the nickel content in NMC. The blue bars correspond to values that are currently achieved, and the red bars correspond to achievable capacity with modified improved use of the electrolyte [26–28] for two cuts of voltages 4.2 V and 4.4 V. The capacity can be improved both by increasing the nickel content and by increasing the cut of voltage. Typically, with increase in the Ni content, the practical specific capacities increase, rising to about 190–200 mAh/g for NMC-811, compared to 160 mAh/g for NMC-442, with the upper cutoff voltage of 4.3 V versus Li/Li^+ . The increase in the charging cut of voltage from 4.2 to 4.7 V versus Li increases specific capacity for NMC 333 from 140 to 170 mAh and for NMC 955 from 185 to 195 mAh/g. This makes the Ni-rich NMCs specifically attractive for vehicle applications. According to the prediction from Myung et al. [26], the combination of Ni-rich NMC cathode and graphite-Si blend anode is the only hope to achieve 300 Wh/kg requirement of the EV applications. However, the drawbacks such as reduced cyclic stability, poor rate capability, and thermal stability, coming from increased nickel content or increased charging cut of voltage, need to be tackled before these materials can be effectively employed for these applications. In both the Ni-rich NMC and NMC with lower concentration of Ni but high charging cut of

Fig. 13 The various lithium mixed metal layered oxide that is considered as the cathode material in lithium-ion battery



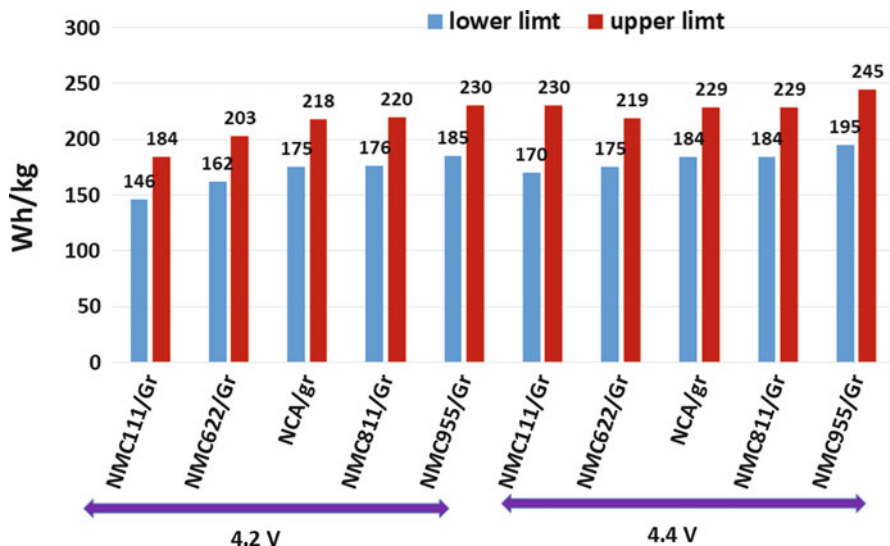


Fig. 14 The predicted increase in the capacity of two scenarios with increase in the nickel content in NMC

voltage, at the end of the charge, the cathode material will predominantly comprise of highly reactive Ni^{4+} . Gas evolution and capacity fading are a common scenario in both cases, since Ni^{4+} reduces to stabilize Ni^{2+} by releasing oxygen giving rise to unwanted side reactions with the electrolyte. This ultimately leads poor stability at room and high temperatures giving rise to serious safety issues. Noh et al. observed decrease in the onset temperature with increase in Ni concentration in NMC, for example, the thermal decomposition onset temperature of NCM433 and NCM811 is 250 °C and 150 °C, respectively [28]. Similarly, even in NMC 333, when the charging cut of voltage increased from 4.2 to 4.4 V, the thermal stability dropped from 210 °C to 180 °C.

$\text{LiNi}_{1-x-y}\text{Co}_x\text{Al}_y\text{O}_2$ (NCA)

As an improvement to the LCO, NCA was developed in the early 2000s. NCA is the cathode material that has been employed in many of the commercially available LIB. For example, Tesla Model S (BEV), BMW Active Hybrid 7 (HEV), and the Daimler S Class Hybrid (HEV) employed LIB having NCA as cathode material. Only difference between $\text{Li}(\text{Ni}_{1-x-y}\text{Co}_x\text{Al}_y)\text{O}_2$ (NCA) and Ni-rich NMC in the electrochemically inactive element. The inactive elements Mn and Al help in stabilizing the structure of NMC and NCA respectively. However, a large concentration of Al^{3+} decreases the reversible capacity due to inactiveness of the aluminum. Very similar to Ni-rich NMC, the cyclic and thermal stability becomes an issue, when operated at high current, cut of charging voltage and temperature [26]. The capacity and power fading of NCA is mainly attribute the microstructural changes such as the crack at the surface and conversion of NCA to NiO phase at the surface and cationic disorder.

The low electronic and ionic conductivity of NiO increases the charge transfer resistance during cycling. Various techniques such as spectroscopy, TEM, and STEM were used to determine the location and thickness of NiO formation during cycling. Numerous investigations suggest the formation ~ 5 nm thick NiO- or $\text{Li}_x\text{Ni}_{1-x}\text{O}$ -like phase at grain surface and the boundaries during the first cycle, and there is an interface structure of 20 nm between NiO and layered structure. Another cause for energy and power fading in NCA is the development of Li_2CO_3 and LiOH coating at the surface. During the synthesis of NCA, slightly higher concentration of lithium with respect to Ni, Co, and aluminum is used to overcome the formation of lithium-deficient NCA. Unreacted excess lithium resides on the surface of NCA most probably as Li_2O and reacts with the moisture and CO_2 to form LiOH or Li_2CO_3 . When Ni content is more than 60%, the residual Li concentration is around 6000–25,000 ppm. The residual lithium causes the gelation during the slurry preparation leading to substandard electrode coatings. The acceptable residue level of lithium in NCA and Ni-rich NMC is 3000 ppm or lower. In addition even the lithium from the surface of NCA reacts with CO_2 from the atmosphere. The prolonged exposure of NCA to open atmosphere leads to the formation of Li_2CO_3 at the surface [29], which increases the interparticle and charge transfer resistance giving rise poor cyclability and rate capability. Further the morphological changes that arise after cycling NCA are also responsible for the degradation of the cell comprising of NCA. The particle cracking is one of the main morphological changes that are observed in the cycled NCA. The crack in the particle reduces the interparticle electrical contact and leads to increased surface area exposure to the electrolyte, leading to parasitic reactions with the moisture present in the electrolyte. Ni-rich layered oxides, $\text{LiNi}_{1-x-y}\text{Co}_x\text{Al}_y\text{O}_2$ and $\text{LiNi}_{1-x-y}\text{Co}_x\text{Mn}_y\text{O}_2$, will be the dominating cathode materials for electric vehicle application in the near future. While NCM523 is the most studied Ni-rich NMC in recent years, NCM811 will be a better candidate provided that safety issues and thermal stability issues are taken care. Various strategies have been employed in the literature to increase the stability of Ni-rich NMC and NCA.

Modification to NMC and NCA

Surface modification for the electrode materials are carried out to decrease the direct interaction with the electrolyte solvents and to prevent the parasitic reactions [30]. The surface coating prevents the dissolution of transition metal and the development of cathode SEI layers [31]. It is reported that SiO_2 , TiO_2 , and Li_2ZrO_3 coatings have improved the thermal stability of NMC. The Effects of Surface Coating on Gas Evolution and Impedance Growth was investigated by Xiong et al. using the pouch cell [32]. Maxwell et al. have reviewed the most widely used surface modification in lithium layered transition metal oxide [13]. The materials considered are ZrO_2 , CeO_2 , Al_2O_3 , ZnO , CuO , and Sb_2O_3 ; fluorides such as AlF_3 , LaF_3 , and ZrF_x ; phosphates FePO_4 and AlPO_4 ; reduced graphene oxide; $\text{Al}(\text{OH})_3$, TiO_2 , and V_2O_5 ; surface fluorination; and Li_2SiO_3 , Li_3PO_4 , and Li_2ZrO_3 . The ionic conductors that are considered for coating are lithium lanthanum titanium oxides (LLTO), LiFePO_4 , Li_3PO_4 , and Li_3VO_4 . According to the survey by Maxwell et al., the best improvement in cycling stability of NMC at high voltages are

observed with FePO_4 , LLTO, and AlF_3 coatings. Not all the materials that are considered for coating are good electronic conductors as well as ionic conductors. Therefore to overcome this issue, successive coatings of electronic and ionic conductive layers are coated. Chen et al. [33] coated dual-conductive coating layers of Li_3PO_4 and PPy on NMC811, where PPy was used to reduce the resistivity and Li_3PO_4 to increase ionic conductivity. In addition to protect the surface of particles during cycling, surface coating are also used to suppress the intergranular cracking caused by the microstrain during repetitive delithiation/lithiation processes. However, achieving uniform optimum thickness coating over the active materials requires large number of process parameter optimization. The higher the coating thickness, the higher the charge polarization, and when the thickness is very small and not uniform, the scavengers in the electrolytes still find a way to reach the active material. The coating can be classified into three types: (i) conventional coating, (ii) core-shell thick coating, and (iii) nano-coating. In the conventional coating, wet chemistry techniques are generally employed to coat protective layers on electrode powder [34]. Nevertheless, getting uniform protective layer is very challenging, and the coating parameters need to be optimized for every coating and the active material. To achieve uniformity in the coating and better control over the thickness, CVD and ALD techniques are also employed in some of the investigations. However, both CVD and ALD techniques are not versatile techniques to be used in large-scale production of the active materials. Core-shell structure architecture, with high capacity inner core and higher stability less prone to electrolyte attack shell, was introduced to increase the cyclic stability. However, because of difference in the volume expansion between the two layers during charging/discharging, the voids are formed between the core and the shell leading to poor cyclic stability. Percolation of the ion and electrons is hindered due to the void at the core-shell interface. Concentration gradient is another new concept that has been introduced to overcome the formation of void at the core-shell interface [35]. In the concentration gradient active material, while the concentration of the stable transition metal gradually rises from center to the surface, the transition metal that is responsible for higher capacity gradually decreases [35]. The review by Peiyu Hou et al. has detailed about the advantages of the core-shell and concentration gradient NMC in increasing the electrochemical properties. Another approach to increase the cyclic stability of Ni-rich layer oxides is bulk substitution with different elements at cation, anion, or both cation and anion sites. The elements that are considered for cation substitution are Mg, Fe, Al, Mo, V, Ti, Cr, and Cu. Though a large number of transition metals are considered for cation substitution, fluorine is the most investigated anion substitution. The various elements that are explored as bulk dopants in NMC and NCA are reviewed recently by Maxwell et al. [13]. The effect of doping in Ni-rich NMC and NCA is not well understood and is mostly trial and error way. Theoretical investigation on substitution effect in Ni-rich layered oxide by Chaoping Liang et al. shows that a single dopant will not solve all the issues related to Ni-rich layered oxide, since a given dopant mitigates some drawback while deteriorating others [36]. Therefore the new strategy of multicomponent doping needs to be considered for further improvement of the Ni-rich NMC and NCA.

Lithium-Rich Layered Oxide

Li- and Mn-rich layered oxide is another promising candidate as its practical achievable specific capacity is 250 mAhg^{-1} well beyond the classical layered oxide when cycled in a potential from 2.0 to 4.8 V versus Li/Li^+ . The large number of review articles [13, 37] on various aspect of LLO published recently depicts the importance and potential this material has. There are two proposed structural models for LLO, single-phase solid solution with the formula $\text{Li}_{1+x}(\text{Mn, Ni, Co})_{1-x}\text{O}_2$ and a composite of two phases with formula $x\text{Li}_2\text{MnO}_3 \cdot (1-x)\text{Li}(\text{Mn, Ni, Co})\text{O}_2$ [37], and the crystal structure is provided in Fig. 15. Though composite model is mostly accepted configuration of the LLO, whether the structure is two-phase nano-composite or monophasic solid solution depends on the detailed composition and synthesis parameters of the material. During the first cycle of galvanostatic charging of LLO, the voltage gradually increases from the V_{oc} to $\sim 4.4 \text{ V}$ due to the deintercalation of Li^+ from LiMO_2 . The extraction of Li and O_2 evolution from the Li_2MnO_3 take place above 4.4 V and give rise to the formation of spinel-like phase [38]. This region of the voltage capacity curves is characterized by long plateau. Therefore the activation Li_2MnO_3 at the high voltages in the first charging is very crucial for achieving very high capacity [38]. During subsequent discharging/charging of Li^+ , the intercalation/deintercalation takes place into and out of both Li_xMO_2 and spinel-like phase formed during charging in the first cycle. The anomalous capacity of LLOs was hypothesized to come from the reversible redox activity of the oxygen [37]. Though the high irreversible capacity of LLO is very attractive, its practical application is hindered due to unsolved fundamental material problems. The huge first cycle irreversibility, low power capability, gradual voltage, and capacity fading in each charging/discharging cycle need to be addressed before LLO to be seriously considered for commercialization. The first cycle irreversibility is thought to be due to (i) oxygen loss from the Li_2MnO_3 , (ii) transition metal occupying Li sites in TM and Li layers, and (iii) electrolyte solution decomposition

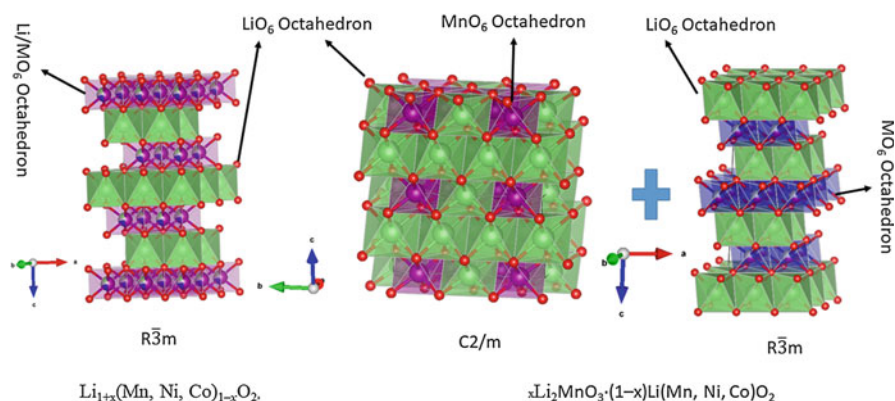


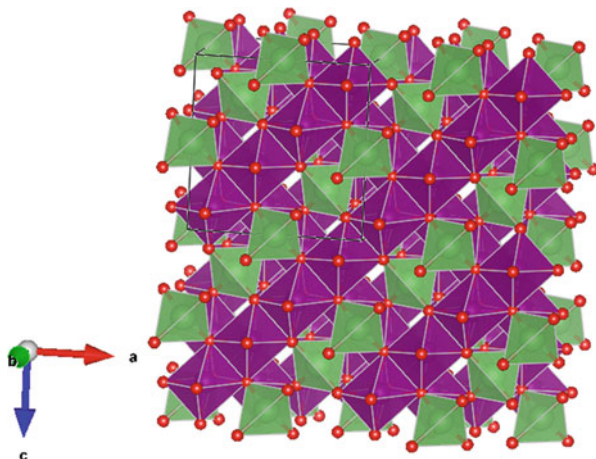
Fig. 15 The two proposed structural models for LLO, (i) single-phase solid solution with the formula $\text{Li}_{1+x}(\text{Mn, Ni, Co})_{1-x}\text{O}_2$ and (ii) composite of two phases with formula $x\text{Li}_2\text{MnO}_3 \cdot (1-x)\text{Li}(\text{Mn, Ni, Co})\text{O}_2$

at voltages higher than 4.5 V. Various types of surface coatings are employed to reduce the first cycle irreversibly. The surface coating that are tried in recent years are Al_2O_3 , V_2O_5 , nanogold, AlPO_4 , AlF_3 , CoPO_4 , $\text{Li}_x\text{Mn}_{1.5}\text{Ni}_{0.5}\text{O}_4$ Li_2MnO_3 nanoscale surface coating, and surfacenetritation. Another approach is to blend the electrochemically active materials such as LiFePO_4 , spinel $\text{Li}_4\text{Mn}_5\text{O}_{12}$ or LiV_3O_8 , and $\text{VO}_2(\text{B})$ with lithium-rich layered oxides. Though these techniques have reduced the loss in the capacity during first cycle, none of them are successful in completely removing the irreversibility. Transition metal migration and trapping at tetrahedral sites are responsible for voltage decay in each cycle. Surface localized defect spinel phase $(\text{Li})\text{Mn}_{2-x}\text{Ni}_x\text{O}_4$ that is formed when charged above 4.5 V in the first cycle grows into the bulk during subsequent cycling is also responsible for the slow voltage decay found in LLO. Various frequently employed techniques in improving the properties of the electrode materials such as surface modification, doping, concentration gradient, and engineering the electrolyte have been used in reducing the voltage decay and cyclic capacity of LLO. In a new approach developed recently, controlled creation of oxygen vacancies up to 20 nm at the surface has appreciably inhibited the gas release from the surface. The oxygen vacancies created by gas-solid interface reaction also favors the ionic diffusion environment in the bulk. Further investigation of the chemically treated LLO suggests that besides the creation of oxygen vacancies, the NH_3 treatment leads to bulk reduction of Mn and Co, creation of Li_2CO_3 , Li_2O , and LiOH , and nitridation of the surface. There are constant efforts to overcome the first cycle irreversibility and poor cyclic stability by optimization of the composition of LLO. The cycling voltage window of LLO is another parameter that crucially decides the cyclic stability of LLO. Though higher cutoff voltages give better capacity, limiting the cutoff voltage below 4.4 V after the initial activation cycle helps in improving the cyclic stability. The cyclic stability, voltage decay, and reversible capacity of LLO depend on the first cycle charging, and hence the temperature at which activation has been carried out crucially decides the electrochemical characteristics of LLO [37].

Spinel LiMn_2O_4

The spinel LiMn_2O_4 is used in the batteries by many of the electric vehicle manufactures, mainly as the blend with NMC or NCA. While high operating voltage, lower cost, environmentally friendliness, abundance of Mn, and higher rate capability are attractive features, poor cyclic and thermal stability and low specific capacity are the drawbacks of LMO [39]. It has a three-dimensional structure with Li occupying tetrahedral 8a sites and Mn in octahedral 16d sites (Fig. 16) in a cubic close-packed oxygen anion array. Three-dimensional intercalation of Li^+ takes place through its diffusion across vacant tetrahedral and octahedral interstitial sites. Recent review by Bhandari et al. details the various reasons for the dissolution of Mn in the electrolyte [40]. Mn dissolution into the electrolyte ($\text{Mn}^{3+} \rightarrow \text{Mn}^{2+} + \text{Mn}^{4+}$) and irreversible crystal phase transition due to Jahn-Teller distortion of Mn^{3+} with high spin are few of the reasons for the poor cyclability of LMO [39]. The

Fig. 16 The crystal structure of LiMn_2O_4 . The LiO_6 and MnO_6 are represented by the green and purple octahedron, respectively



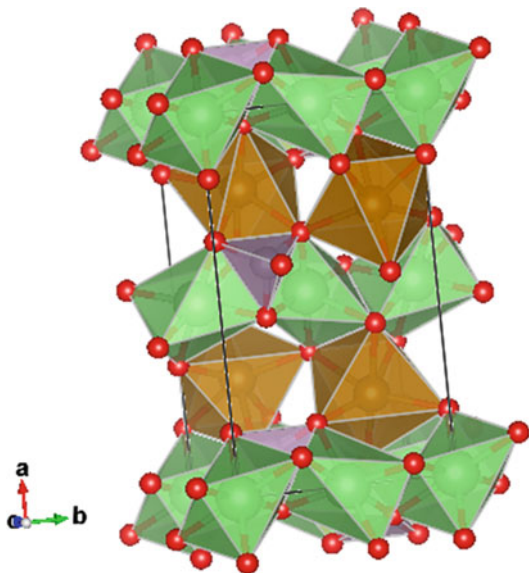
dissolution of Mn adversely affects the anode SEI layer formation and reduces the overall stability of the cell. In addition to the parasitic side reaction with the electrolyte, the oxygen loss under charged state of LMO reduces the cyclability further. Daichun Tang et al. used XPS, EELS, STEM, and DFT calculations to investigate the Mn dissolution and oxygen release under the charged state [41]. The surface structural conversion from delithiated LiMn_2O_4 to Mn_3O_4 is the main reason for the dissolution of manganese and oxygen loss. Introducing various types of additives to the electrolyte reduces the degradation of the electrode due to electrolyte interaction. The functional additives such as tris(trimethylsilyl) borate, heptamethyl disilazane, and ethanolamine diethyl phenylphosphonite are used for stabilization of the LiPF_6 salt. Electrolyte additives such as N,N_0 -diethyl-amino trimethylsilane, hexamethyldisilazane, and heptamethyldisilazane were investigated to remove HF and H_2O from the electrolyte and thereby preventing the acid attack on the surface of LiMn_2O_4 . The electrolyte additives tailor the characteristics of the SEI layer both on positive and negative electrode. To modify the anode SEI passivation layers, additives with a lower LUMO energy than that of the traditional solvents were used and to modify the protective layers on the cathodes additives with higher HOMO energy are used. Various new salts, such as LiBOB , LiDFOB , $\text{Li}_2\text{B}_{12}\text{F}_{12}$, and LiBETI , have been investigated for LiMn_2O_4 -based batteries. Elemental doping is a commonly used strategy to modify the band diagram of the material and thereby to increase the stability of the electrode. Cation, anion, and dual and multiple ion-doping methodologies have been used to increase the electrochemical characteristics of LiMn_2O_4 . The effects of various doping elements are reviewed recently by Goajie et al. [42]. In LiMn_2O_4 , the average oxidation state of manganese is $3.5+$, and it can be increased by the substitution of Mn with elements having oxidation state that is less than $3.5+$. The higher oxidation state of Mn than $3.5+$, in spinel, increases the cyclic stability, by suppressing Jahn-Teller distortions, phase transitions, and Mn dissolution. However, substituting Mn in LMO with lower oxidation state elements reduces the capacity and the voltage and therefore always has

trade-off between the capacity and cyclic stability. Further the charge-discharge curve of $\text{Li}_x\text{M}_y\text{Mn}_{2-y}\text{O}_4$ ($\text{M} = \text{Fe}, \text{Co}, \text{Cr}, \text{Al}, \text{etc.}$) [43] involves two steps: the first voltage step is related to the redox of Mn ions, and the second voltage step is related redox reaction of the dopant in the spinel. However, $\text{LiNi}_{0.5}\text{Mn}_{1.5}\text{O}_4$, depending upon the preparation method, is known to have a one-step discharge curve [44]. Gao et al. have investigated the changes in the band diagram and ultraviolet photoelectron spectroscopy of $\text{LiNi}_x\text{Mn}_{2-x}\text{O}_4$ with nickel concentration and its implication on the voltage plateau at 4.7 V w.r.t Li/Li^+ [45]. $\text{LiMn}_{1.5}\text{Ni}_{0.5}\text{O}_4$ exists in two different crystal structures with characteristic arrangements of Ni^{2+} and Mn^{4+} in the lattice, which are generally referred as ordered and disordered spinel [46]. The detailed crystal structures of both phases are provided in a recent review article on spinel cathode by Kim et al. [47]. The disordered $\text{LiMn}_{1.5}\text{Ni}_{0.5}\text{O}_4$ spinel has superior rate capability due to higher electrical conductivity and lithium diffusion coefficient than that of the ordered spinel. To improve the rate capability and cyclic stability especially at high temperature, diverse methodologies such as surface coating, crystal facets control, electrolyte stabilization, and nanodomain engineering have been perceived as detailed in the review article by Jia Lu et al. [48]. The surface coating that is used to stabilize the LiMn_2O_4 /electrolyte interface has been summarized by Ting-Feng et al. [49]. The microstructure and the orientation of the surface that is interacting with the electrolyte crucially determine the rate capabilities and cyclic stability. While scaling down the particle size increased rate capability, the increased surface area associated with it increases Mn dissolution and unwanted reaction with the electrolyte. Therefore, various microstructures such as large porous structure and radial interior channels, nano/micro-hierarchical structures, and porous LiMn_2O_4 hollow nanofibers have been considered for improving the power capability and cyclic stability. Using the truncated octahedral crystal structure, the cyclability and rate capabilities are optimized. In this structure, the crystal orientation experiencing minimum Mn dissolution is exposed to electrolyte, and the direction, which supports the Li diffusion but has high Mn dissolution is truncated to small surface area [50].

Phospho-olivine

The layered lithium oxides and the spinel lithium oxides are prone for oxygen release during charging due to substantial overlap of the 3d bands of the transition metal with the upper part of the O^{2-}_{2p} band. This problem can be overcome by using compound with lower-valent redox couple $\text{Fe}^{2+/3+}$, where 3d bands are far above the 2p band of the oxygen. Nonetheless, this increase in the redox energy decreases the overall cell voltage in iron oxide. However, due to the inductive effect, the redox energy of $\text{Fe}^{2+}/\text{Fe}^{3+}$ can be reduced drastically in polyanion compounds compared to that of the oxides. The relative redox energy positions of the $\text{Fe}^{2+}/\text{Fe}^{3+}$ w.r.t Li/Li^+ in different lithium insertion hosts containing Fe and resulting cell voltages are schematically given in Fig. 17 [51]. The feature of tailoring the redox potential of the lithium insertion material has been established by Goodenough et al. [52]. The use of

Fig. 17 The relative redox energy positions of the $\text{Fe}^{2+}/\text{Fe}^{3+}$ w.r.t Li/Li^+ in different lithium insertion hosts containing Fe and resulting cell voltages



polyanions such as $(\text{SO}_4)^{2-}$, $(\text{PO}_4)^{3-}$, and $(\text{MO}_4)^{3-}$ lowers the $\text{Fe}^{2+}/\text{Fe}^{3+}$ energy relative to the Fermi level of the Li/Li^+ . Therefore cell voltage reductions because of the $\text{Fe}^{2+}/\text{Fe}^{3+}$ lower oxidation state, in comparison with that of transition metal in layered oxide, are compensated by the Fe-O-P inductive effects. The higher thermal stability and prevention of release oxygen of the phospho-olivines come from the strong covalence band between phosphor and oxygen and the rigidity of the $(\text{PO}_4)^{3-}$ units, which makes it the safest cathode material.

LiFePO₄

LiFePO₄ is the maximum investigated phospho-olivine cathode material for LIB applications which deliver higher capacity (170 mAhg⁻¹) at reasonable power capabilities. Though the LiFePO₄ is very stable, cost-effective, and environmental friendly, its electronic and ionic conductivities are relatively low compared to other lithium insertion electrodes [51]. At room temperature, the electronic conductivity (σ) of LiCoO₂, LiMn₂O₄, and LiFePO₄ is 10^{-3} Scm⁻¹, 2×10^{-5} to 5×10^{-5} Scm⁻¹, and 10^{-9} to 10^{-10} Scm⁻¹, respectively. The lithium ionic diffusion coefficients are 5×10^{-9} cm²s⁻¹, 10^{-13} cm²s⁻¹, and 10^{-16} cm²s⁻¹ for LiCoO₂, LiFePO₄, and FePO₄, respectively. The ionic and electronic conductivities of LiFePO₄ are the lowest among all the cathode materials that are considered for lithium-ion battery. Exact value of diffusion coefficient of LiFePO₄ depends on the ratio of LiFePO₄ and FePO₄ and the x value in Li_{1-x}FePO₄ during the charging and discharging. The LiFePO₄ comprised of distorted hexagonal close-packed oxygen array, where P⁵⁺ occupies the tetrahedral site and Li⁺ and Fe²⁺ ions occupy edge and corner sharing octahedron, respectively (Fig. 17). Unlike the layered and spinel structures, in LiFePO₄ charging/discharging takes place through a two-phase FePO₄/LiFePO₄

reaction, which has the similar structure. However, at the beginning, charging of LiFePO_4 is known to be present as $\text{Li}_{1-x}\text{FePO}_4$ and x value depends on the particle size. The miscibility gap of LiFePO_4 entirely disappears when the particle size reaches critical value [53]. The intercalation/deintercalation of the lithium ion takes place along the tunnels parallel to the [010] direction, as reported by Ceder's group [54] and Islam's group [55], restricting the rate capability. Most commonly employed method to improve the Li^+ and e^- conductivity of LiFePO_4 is either to reduce the [56] particles size or to coat the material with conductive materials [57]. Though various materials are investigated as the coating material for LiFePO_4 , carbon-based materials are found to be more suitable, given that it increases the electronic conductivity and it is inert to HF attack. However, the thickness of the carbon coating needs to be controlled, to prevent the reduction in the gravimetric capacity of the materials. In addition to carbon coating and particle size reduction, various types of doping such as Li-site, Fe-site, and O-site and multi-element doping are considered for increasing the electronic and ionic conductivity of LiFePO_4 . A recent review article from Zhengrui et al. elaborates the effects of various types of doping and controversies involved [57].

LiMnPO_4

LiMnPO_4 (LMP) has higher discharge potential of 4.13 V compared with the 3.43 V of LiFePO_4 [51]. However, the practical achievable specific capacity is even as moderate current densities are low, due to extremely low ionic and electrical conductivities. Further, due to extreme J-T distortion, there is large kinetic impediment at the boundary between MnPO_4 and LiMnPO_4 . The electrical conductivity of LiMnPO_4 is five orders lower than already insulating LiFePO_4 [3]. Therefore, adopting the methodologies used to improve LiFePO_4 electronic and ionic conductivities are not effective as far as LiMnPO_4 is concerned. As an alternative the solid solution $\text{LiMn}_y\text{Fe}_{1-y}\text{PO}_4$ (LMFP) is investigated by various groups, as it operates at voltage window of 3.4–4.1 V, higher than LiFePO_4 and within the band gap of HOMO and LUMO of the electrolyte [58].

LiCoPO_4

Lithium cobalt phosphate, LiCoPO_4 (LCP), is not a potential candidate as a cathode material for practical application, though it has high operating potential of (4.8 V vs Li^0/Li^+), possess good theoretical capacity (167 mAgh^{-1}) and undergoes minute volume changes during charging/discharging. Similar to LiMnPO_4 , the LiCoPO_4 is an insulator with very poor electronic and ionic conductivities [59].

Recent Development in Traditional Anode Materials

Though using Li metal, as an anode will deliver highest voltage and energy density for a cell, Li is explosion hazardous material. To circumvent the safety concerns, metallic Li is replaced by Li insertion material in LIB. The use of Li^+ rather than Li metal solves the dendrite growth concerns and the safety issues related to the

Li-metal cells. However, the redox potential with respect to Li^0/Li^+ of the insertion material should be as small as possible to be used as an anode. Similar to cathode material, it should be lightweight, should have decent electronic and ionic conductivities, and should be environmentally friendly and cost-effective (Fig. 18). The anode materials that are considered for LIB are graphite, LTO, Si, Ge, and Sn, and their reported lithiation/delithiation potential, volume changes, and ionic conductivity are given in Ref [60, 61]. The carbonaceous anode is the negative electrode of choice and facilitates the Li-ion battery to be used as commercially viable storage technique. Graphite is a layered material that comprises of hexagonal graphene sheets of sp^2 hybridized carbon atoms, which are stacked along the c -axis by weak van der Waals forces into an ABAB... stacking sequence (Fig. 19) [5]. The anisotropic structure of graphite with basal and edge plane that are normal and parallel to the c -axis, respectively, is a principal feature that establishes the properties of lithium intercalation within graphite. During charging, Li^+ intercalates into carbon and forms lithiated carbon Li_xC_n , with maximum of one lithium per six carbon host in highly crystalline graphite. In graphite, intercalation of Li^+ takes place through the edge surface in a stepwise process, accompanied by the shift in the stacking order to AA from ABAB. The intercalation of Li leads to the formation of periodic layers of Li-occupied and Li-unoccupied graphitic layers, which is called as stage formation and is designated by stage index "s." The stage index corresponds to the number of graphene layers in-between lithium layers. In the first cycling during charging, the potential drops rapidly at ~ 0.8 V w.r.t to Li. The main intercalation/deintercalation of Li^+ takes place at potentials lower than 0.25 V versus lithium which is characterized by four potential plateaus (Fig. 20). The details of the stages ($s = \text{I, II, III,}$

Fig. 18 The crystal structure of LiFePO_4 . The LiO_6 and FeO_6 are represented by the gray and green octahedron, respectively. PO_4 is represented by purple tetrahedron

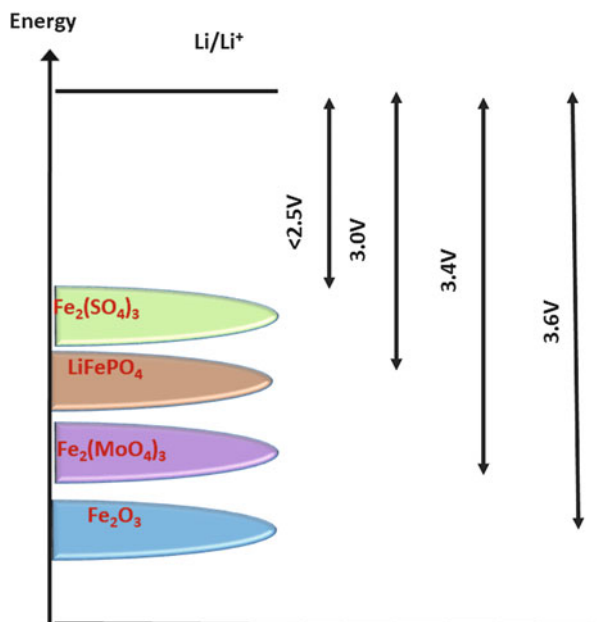


Fig. 19 Hexagonal graphene sheets of sp^2 hybridized carbon atoms, which are stacked along the c-axis by weak van der Waals forces into an ABAB... stacking sequence

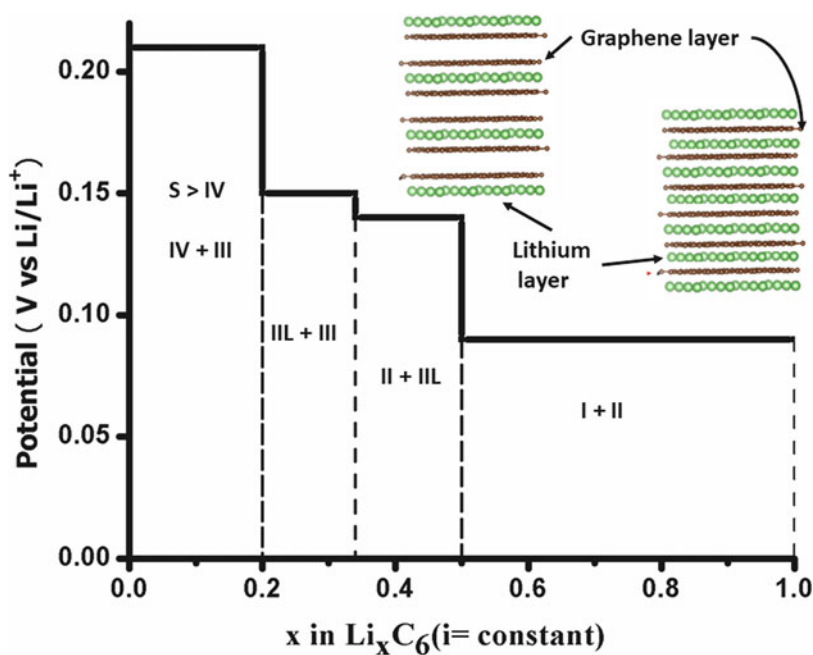
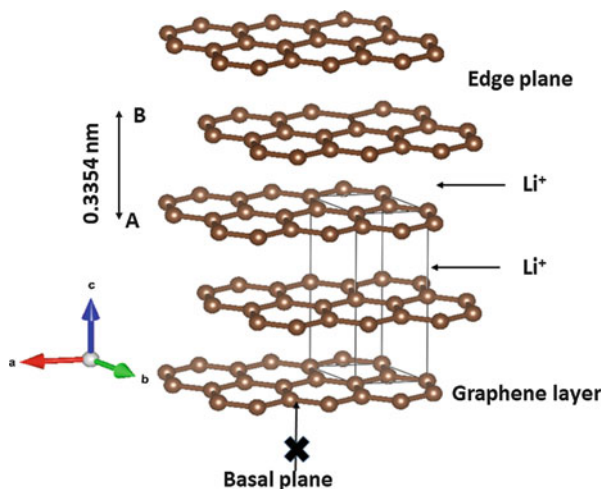


Fig. 20 Stage formation during the intercalation/deintercalation in graphite

III, and IV) formed during the intercalation/deintercalation are reviewed by Winter et al. [61]. The theoretical capacity of graphite cycled between Li and I stage intercalated LiC_6 is 372 mAhg^{-1} . The irreversible capacity of graphite during the first cycle ranges from 20 to 40 mAh/g, and the subsequent cycles have ~100%

capacity reversibility. Furthermore, the electronic and ionic conductivities of graphite are more than 10^{-3} Scm^{-1} and 10^{-8} to $10^{-10} \text{ cm}^2\text{s}^{-1}$, respectively. The lithium electrochemical potential for graphite is higher than the LUMO of the electrolyte; therefore the electrolyte decomposition takes place during the first cycle, which leads to the formation of SEI layer at the anode surface. The SEI passivation film subdues subsequent decomposition of the solvent and helps in improving the safety and the durability of the cell [62]. The amount of SEI layer formed depends on the nature of the carbonaceous material that is used in the cell. Soft carbon (graphitizable) and hard carbon (non-graphitizable) are two types of carbonaceous anodes that are used in commercial lithium-ion cells. While both types of carbons are comprised of graphitic hexagonal layers, the arrangements of the crystallites differ in soft and hard carbon. The misalignment of the crystallites, in soft carbon, is minimum therefore by the heat treatment can easily be graphitized. On the other hand, crystallites in the hard carbon are completely misaligned and hence cannot be graphitized even at temperatures $>2000 \text{ }^\circ\text{C}$. Soft and hard carbons' proposed structural models [61] are given Fig. 21.

Soft Carbon

The soft carbons that are used in most of the commercialized LIB are mesocarbon microbead, massive artificial graphite, mesophase pitch-based carbon fiber, and vapor-grown carbon fiber, which have good cyclability and coulombic efficiency greater than 90% [61]. There is continuous further effort to increase its practical achievable capacity by tailoring the microstructure. Because of ability to modify the electronic structure and physical and chemical characteristics by quantum confinements of the electron states, nanostructured carbon under diverse forms (nanotubes, nanorings, graphene, mesoporous) is extensively investigated. The nanostructured materials have delivered the capacity in excess of the theoretical capacity of crystalline graphite, due to electronic modifications and increase in the number of Li-ion storage sites in small closed spaces [63]. Along the edge planes, single crystalline

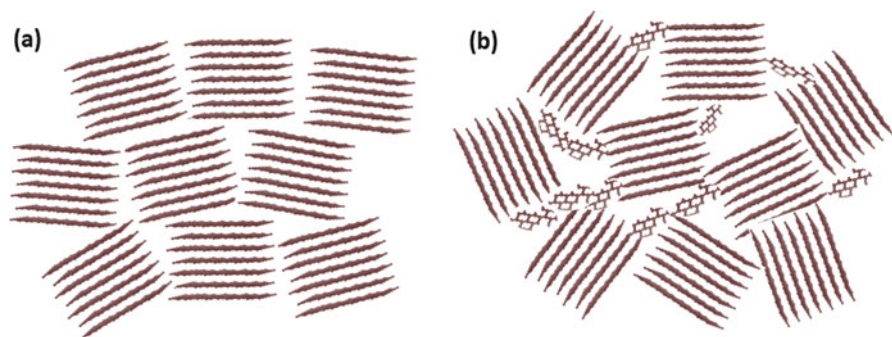


Fig. 21 The structure model of (a) soft carbon and (b) hard carbon

graphitic particles suffer 10% strain through Li intercalation, which damages the SEI layer and reduces the cyclability. Thin layer of amorphous carbon is coated to prevent exposure of the edge plane to electrolyte [64].

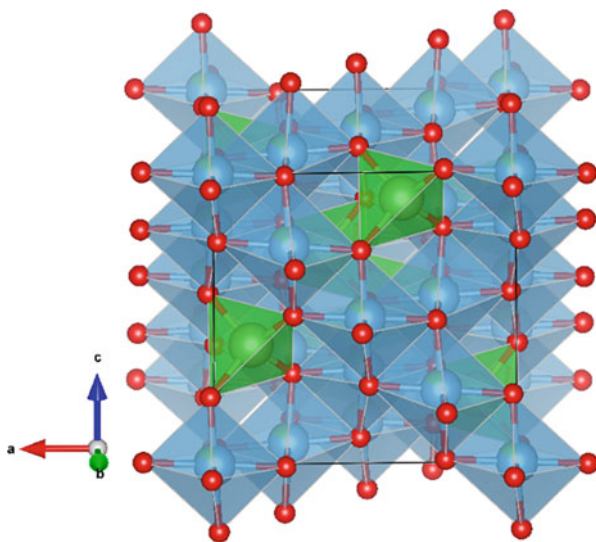
Hard Carbon

Though hard carbon can deliver very high capacity ranging from 200 to 600 mAhg^{-1} , its rate capability is very poor due to sluggish diffusion of Li through the voids and the defects. Unlike soft carbon, the volume expansion in hard carbon is isotropic; therefore the strain involved during lithium intercalation is not pronounced. However, the reversibility in the initial cycles is lower in the hard carbon, due to the high fraction of edge planes that are in contact with the electrolyte giving rise to increased quantity of SEI formation. The huge loss of lithium during the initial cycles in SEI formation prevents the complete utilization of lithium for further charging and discharging and thus reduces the achievable capacity in full lithium-ion cells. Further the volumetric capacity of the cell fabricated using hard carbon is low due to intrinsic voids [65, 66].

Lithium Titanium Oxide

$\text{Li}_4\text{Ti}_5\text{O}_{12}$ has a spinel structure ($\text{Fd}\bar{3}m$), with lithium occupying 8a tetrahedral sites and titanium in the octahedral 16d sites in the cubic oxygen array as shown in Fig. 22. During the intercalation, in addition to the intercalated Li-ion, three lithium-ions at 8a site migrate into the empty 16c sites.

Fig. 22 The crystal structure $\text{Li}_4\text{Ti}_5\text{O}_{12}$



Thus during the lithium intercalation, $[\text{Li}_3]_{8a}[\text{Ti}_5\text{Li}]_{16d}[\text{O}_{12}]_{32e}$ transfers into a rock salt $\text{Li}_7\text{Ti}_5\text{O}_{12}([\text{Li}_6]_{16c}[\text{Ti}_5\text{Li}]_{16d}[\text{O}_{12}]_{32e})$ at a potential of 1.55 V w.r.t to Li^0/Li^+ . Further intercalation of Li at potential below 1.0 V, the intercalated Li occupies 8a and 8b sites and yields $\text{Li}_9\text{Ti}_5\text{O}_{12}$, which can be represented by $[\text{Li}_x]_{8a}[\text{Li}_y]_{8b}[\text{Li}_6]_{16c}[\text{Li}_{2-x-y}]_{48f}[\text{Ti}_5\text{Li}]_{16d}[\text{O}_{12}]_{32e}$. The charging/discharging in the potential window of 0 to 2 V, with respect to Li/Li^+ , leads to very minimum volume change of less than 0.2% in the structure. Consequently, voltage hysteresis in its charge-discharge profile of LTO is very small and has been termed as zero strain material. Furthermore, there is no loss of Li^+ due to SEI formation, since LTO is charged/discharged in a potential above 1 V, which is within the E_g of the electrolyte. The operating voltage of lithium-ion cell with various cathode and LTO as the anode is given in Fig. 23 [67]. In addition, it has relatively high volumetric capacity, cycle life, and thermal stability. Therefore, despite the reduced cell voltage and higher cost of Ti, LTO has been commercialized [68, 69]. The various aspects that need to be considered in the full cell with LTO as anode are reviewed recently by Xu et al. [67]. Though LTO has many benefits, the poor electronic conductivity of $10^{-13} \text{ Scm}^{-1}$ and poor Li^+ diffusion coefficient in the order of 10^{-9} to $10^{-16} \text{ cm}^2\text{s}^{-1}$ of its pristine form adversely affect its specific capacity and rate capability. Another issue with pristine LTO is gassing during cycling and regular storage. There are extensive efforts to overcome the intrinsic low electronic and ionic conductivity and the gas release during charging/discharging of LTO by tailoring the morphology, controlling size and defect chemistry, modifying the surface, and doping [70].

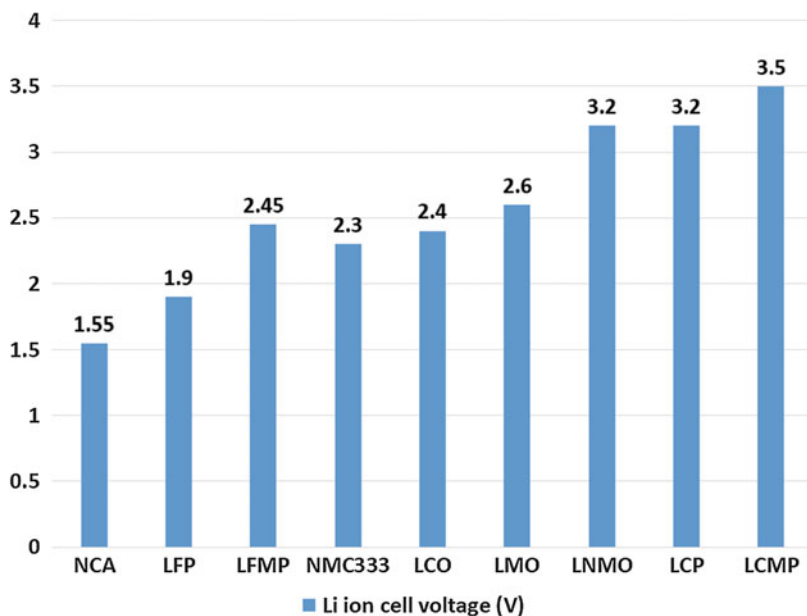


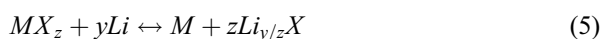
Fig. 23 The operating voltage of lithium-ion cell with various cathode and LTO as the anode

Recent Development in New Electrode Materials

Lithium insertion conventional electrodes are limited by the capacity [71]. In layered oxide charging/discharging of the cell is accompanied by change in the oxidation state of the TM only by one. This restricts the availability of only one electron per molecule of the layered oxide-giving rise to limited capacity. With the insertion electrodes, even after sophisticated engineering, it is not possible to cater the demands of EV and HEV [72]. Therefore, new electrode materials that react with lithium, with alternative mechanisms, are explored recently [73]. Though these materials open the possibility of increasing the capacity significantly, the associated structural changes are not within the acceptable limits of the commercial lithium-ion batteries. Unfortunately, even with incorporation of the complex functional binders or additives in the electrodes, the inherent volume and structural changes of these materials cannot be buffered. Therefore, accompanied voltage hysteresis and short cycle life make these materials less attractive for commercial applications.

Conversion Reaction Materials

The reaction of the conversion materials with lithium produces entirely new product having completely different structural and chemical properties. There are two types of conversion reaction materials named Type A and Type B with similar concept [74]. Oxides, sulfides, phosphides, nitrides, and fluorides of transition metal are the promising Type A conversion reaction materials and have potential to deliver high capacity with theoretical value ranging from 500 to 1500 mAhg⁻¹. While oxides and sulfides of transition metal are investigated as anode, fluorides are candidates for cathode electrode. The charging/discharging of Type A and Type B conversion materials can be expressed by the chemical reactions 5 and 6, respectively.



where M = single or mixed transition metal; X = single or mixed anion such as sulfides, fluorides, phosphides, and nitrides; and y = oxidation state of X. Above reactions are the representation of the overall process, which comprise of many intermittent stages. During the transformation through various stages, the material undergoes complex sequence of structural and chemical changes, the details of which are material specific. During the first cycle, the chemical reaction with Li is accompanied with the reduction in particle size to 1–10 nanometers. After the first lithiation, the electrode is comprised of nanoparticles of transition metal embedded in Li_{y/z}X in lithiated state. The schematic illustration of the process [73] is given in Fig. 24. The conversion materials are known to deliver practical capacity higher than the theoretical capacity accompanied with large hysteresis in voltage during charging and discharging. The contributing factors for practical capacity higher than theoretical

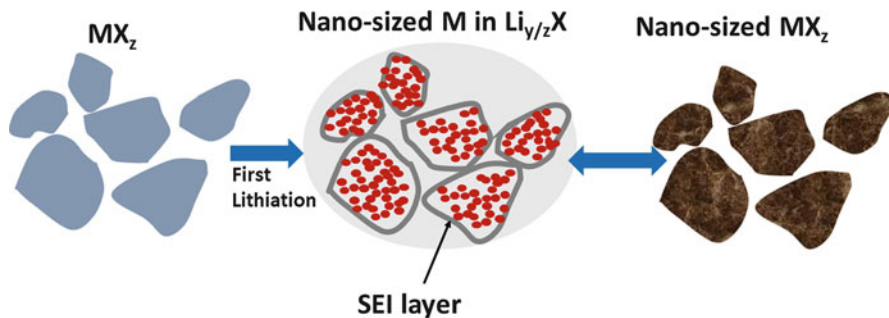


Fig. 24 Schematic illustration of first cycle charging and subsequent lithiation and delithiation in conversion electrodes. (Adopted from Ref [76])

are (i) reversible surface lithium storage at the interfaces of the nanoparticles and (ii) electrolyte decomposition to electrochemically active products, which contributes up to 40% of the total practical capacity delivered by the material. However, some amount of the electrolyte decomposes into irreversible products during the first lithiation, giving rise to irretrievable capacity in the first cycle. Nonetheless, the capacities are considerably larger than what conventional electrode materials deliver. The abundance and cost-effectiveness have made it very attractive, leading to significant interest in the field of conversion materials. The large number reviews that addressing various issues of conversion materials that has appeared recently reveals the interest in this field [73, 75]. The major bottlenecks that prevent the commercialization of conversion material are (i) poor rate performance due to low electronic conductivity, (ii) deterioration of the electrode with charging/discharging cycle due to large volume expansion, (iii) substantial battery heating due to huge hysteresis of charging/discharging voltages, and (iv) solubility of $Li_{y/z}X$ compounds in the electrolyte [76]. Various approaches have been employed to confront each of the issues. Scaffolding the active material with suitable conductive additive like graphene and metals [75–80] and engineering the grain size with special interest in reducing the size are considered to improve the electronic and ionic conductivity. In an effort to reduce the volume change during the lithiation and delithiation, appropriate combination of active material [81], particle size, shape, electrolyte composition, and binder is extensively investigated. In addition the electrode engineering plays a decisive role in accommodating the stress involved due to volume change. Electrolyte design and/or a selection of appropriate choice of electrolyte had helped in improving the reduction of the irreversible capacity loss and voltage hysteresis.

Summary and Outlook

Lithium-ion (Li-ion) batteries are used as energy storage system in various technologies ranging from portable electronic system, storage system for power supply from photovoltaic and wind energy, and electric and hybrid electric vehicles. LIB is

considered for wide scope of application demanding batteries to operate under large spectrum of operating conditions. Especially for military application, battery needs to be safely operating in a wide temperature range. These batteries need to be robust to overcome the abuse it undergoes. The battery has to be designed depending on the targeted application, and the electrode material and electrolyte need to be chosen wisely. Despite the limited capacity due to the number of crystallographic sites accessible for lithium intercalation and associated structural and chemical deterioration at deep charge, insertion electrodes will dominate the battery technology. The strategies that are commonly employed to overcome the structural and chemical instabilities are surface coating, doping and concentration gradient, engineering the particles morphology, and proper choice of electrolyte additives.

- (i) Coating: Surface coating on active materials are used to minimize the direct contact with the electrolyte, so that unwanted parasitic reactions can be minimized. The coatings, if selected properly, can be used to increase the cyclability, safety, and the power rate. Coating material, method, thickness, and the electrode/coating interface play a crucial role in determining to what extent the instability in the electrode materials can be tackled. The strategy of coating has been employed for many years, with the focus on the investigating consequences of coating materials and methods on the electrochemical characteristics of the electrode materials. Conversely, the theoretical comprehensive investigation on the impact of different factors arising from surface coating is scarce.
- (ii) Doping and concentration gradient: The approaches of various types of doping such as anion, cation, and multiple ion have been extensively investigated with the intention to modify the band diagram of the materials. By engineering the chemical potential of the redox couple, it is expected to increase safety and rate capability. Further to exploit the advantages of different redox couples, a concentration gradient approach has been recently explored.
- (iii) Engineering the particles morphology: The electrode material microstructure has decisive role in tailoring the lithium-ion conductivity, electron conductivity, and the electrolyte-electrode interface. While the smaller particle size increases both the electron and ionic conductivity, the stability of the material reduces.
- (iv) Electrolyte additives: The morphology and the chemical composition of SEI layered are partially controlled by the electrolyte solvents. Since SEI is very crucial in determining cyclability and the reversible capacity, the chemical composition of the electrolyte and the solvents determines the characteristic of the SEI layer. There is an enormous scope to improve the cyclic stability and reversible capacity by suitably engineering the electrolyte band diagram of the electrolyte.

In addition to research interest to improve structural and chemical stability of the insertion electrode materials, there is renewed attention on Li-metal anode use. However, the near term approach would be to improve the electrochemical characteristics of the insertion electrode. Alongside with improving the properties of

electrode materials, because of limited supply of the active material and the use of expensive metal electrodes, the research on recycling the lithium-ion batteries is emerging.

References

1. Yoo HD, Markevich E, Salitra G, Sharon D, Aurbach D (2014) On the challenge of developing advanced technologies for electrochemical energy storage and conversion. *Mater Today* 17(3):110–121
2. Goodenough JB, Park KS (2013) The Li-Ion Rechargeable Battery: a Perspective. *J Am Chem Soc* 135(4):1167–1176
3. Liu C, Neale ZG, Cao G (2016) Understanding electrochemical potentials of cathode materials in rechargeable batteries. *Mater Today* 19(2):109–123
4. Tang Y, Zhang Y, Li W, Ma B, Chen X (2015) Rational material design for ultrafast rechargeable lithium-ion batteries. *Chem Soc Rev* 44(17):5926–5940
5. Tagawa K, Brodd RJ (2009) Production processes for fabrication of lithium-ion batteries. In: Yoshio M, Brodd RJ, Kozawa A (eds) *Lithium-ion batteries: science and technologies*. Springer, New York, pp 181–194
6. Bockholt H, Indrikova M, Netz A, Golks F, Kwade A (2016) The interaction of consecutive process steps in the manufacturing of lithium-ion battery electrodes with regard to structural and electrochemical properties. *J Power Sources* 325:140–151
7. An SJ, Li J, Du Z, Daniel C, Wood DL III (2017) Fast formation cycling for lithium ion batteries. *J Power Sources* 342:846–852
8. Nelson PA, Gallagher KG, Bloom ID, Dees DW (2012) Modeling the performance and cost of lithium-ion batteries for electric-drive vehicles, 2nd edn. Argonne National Lab (ANL), Argonne. Medium: ED; Size: 140p
9. Gaëtan P, Alex R, Sébastien M, Daniel F (2015) Cost modeling of lithium-ion battery cells for automotive applications. *Energy Sci Eng* 3(1):71–82
10. Blomgren GE (2017) The development and future of lithium ion batteries. *J Electrochem Soc* 164(1):A5019–A5025
11. Manthiram A (2017) An outlook on lithium ion battery technology. *ACS Cent Sci* 3(10):1063–1069
12. Ding Y, Mu D, Wu B, Wang R, Zhao Z, Wu F (2017) Recent progresses on nickel-rich layered oxide positive electrode materials used in lithium-ion batteries for electric vehicles. *Appl Energy* 195:586–599
13. Radin MD, Hy S, Sina M, Fang C, Liu H, Vinkeviciute J, Zhang M, Whittingham MS, Meng YS, Van der Ven A (2017) Narrowing the gap between theoretical and practical capacities in Li-ion layered oxide cathode materials. *Adv Energy Mater* 7(20):1602888
14. Park M, Zhang X, Chung M, Less GB, Sastry AM (2010) A review of conduction phenomena in Li-ion batteries. *J Power Sources* 195(24):7904–7929
15. Venkatraman S, Shin Y, Manthiram A (2003) Phase relationships and structural and chemical stabilities of charged $\text{Li}_{1-x}\text{CoO}_{2-\delta}$ and $\text{Li}_{1-x}\text{Ni}_{0.85}\text{Co}_{0.15}\text{O}_{2-\delta}$ cathodes. *Electrochem Solid-State Lett* 6(1):A9–A12
16. Sharifi-Asl S, Soto FA, Nie AM, Yuan YF, Asayesh-Ardakani H, Foroozan T, Yurkiv V, Song B, Mashayek F, Klie RF, Amine K, Lu J, Balbuena PB, Shahbazian-Yassar R (2017) Facet-dependent thermal instability in LiCoO_2 . *Nano Lett* 17(4):2165–2171
17. Liu A, Li J, Shunmugasundaram R, Dahn JR (2017) Synthesis of Mg and Mn doped LiCoO_2 and effects on high voltage cycling. *J Electrochem Soc* 164(7):A1655–A1664
18. Kalluri S, Yoon M, Jo M, Park S, Myeong S, Kim J, Dou SX, Guo ZP, Cho J (2017) Surface engineering strategies of layered LiCoO_2 cathode material to realize high-energy and high-voltage Li-ion cells. *Adv Energy Mater* 7(1):21

19. Park JS, Mane AU, Elam JW, Croy JR (2017) Atomic layer deposition of Al–W–fluoride on LiCoO₂ cathodes: comparison of particle- and electrode-level coatings. *ACS Omega* 2(7): 3724–3729
20. Wang DY, Sinha NN, Petibon R, Burns JC, Dahn JR (2014) A systematic study of well-known electrolyte additives in LiCoO₂/graphite pouch cells. *J Power Sources* 251:311–318
21. Orendorff CJ, Doughty DH (2012) Lithium ion battery safety. *Electrochem Soc Interface* 21(2):35
22. Delmas C, Menetrier M, Croguennec L, Saadoune I, Rougier A, Poullier C, Prado G, Grune M, Fournes L (1999) An overview of the Li(Ni,M)O₂ systems: syntheses, structures and properties. *Electrochim Acta* 45(1–2):243–253
23. Choi W, Manthiram A (2006) Comparison of metal ion dissolutions from lithium ion battery cathodes. *J Electrochem Soc* 153(9):A1760–A1764
24. Kang K, Ceder G (2006) Factors that affect Li mobility in layered lithium transition metal oxides. *Phys Rev B* 74(9):094105
25. Tian CX, Lin F, Doeff MM (2018) Electrochemical characteristics of layered transition metal oxide cathode materials for lithium ion batteries: surface, bulk behavior, and thermal properties. *Acc Chem Res* 51(1):89–96
26. Myung S-T, Maglia F, Park K-J, Yoon CS, Lamp P, Kim S-J, Sun Y-K (2017) Nickel-rich layered cathode materials for automotive lithium-ion batteries: achievements and perspectives. *ACS Energy Lett* 2(1):196–223
27. Xu J, Lin F, Doeff MM, Tong W (2017) A review of Ni-based layered oxides for rechargeable Li-ion batteries. *J Mater Chem A* 5(3):874–901
28. Noh HJ, Youn S, Yoon CS, Sun YK (2013) Comparison of the structural and electrochemical properties of layered Li[Ni_xCo_yMn_z]O₂ (x=1/3, 0.5, 0.6, 0.7, 0.8 and 0.85) cathode material for lithium-ion batteries. *J Power Sources* 233:121–130
29. Sasaki T, Nonaka T, Oka H, Okuda C, Ito Y, Kondo Y, Takeuchi Y, Ukyo Y, Tatsumi K, Muto S (2009) Capacity-fading mechanisms of LiNiO₂-based lithium-ion batteries. *J Electrochem Soc* 156(4):A289–A293
30. Vasu S, Sahana MB, Sudakar C, Gopalan R, Sundararajan G (2017) In-situ carbon encapsulation of LiNi_{1/3}Co_{1/3}Mn_{1/3}O₂ using pillared ethylene glycol trapped in the metal hydroxide interlayers for enhanced cyclic stability. *Electrochim Acta* 251:363–377
31. Zuo DX, Tian GL, Li X, Chen D, Shu KY (2017) Recent progress in surface coating of cathode materials for lithium ion secondary batteries. *J Alloys Compd* 706:24–40
32. Xiong DJ, Hynes T, Ellis LD, Dahn JR (2017) Effects of surface coating on gas evolution and impedance growth at Li[Ni_xMn_yCo_{1-x-y}]O₂ positive electrodes in Li-ion cells. *J Electrochem Soc* 164(13):A3174–A3181
33. Chen S, He T, Su Y, Lu Y, Ban L, Chen L, Zhang Q, Wang J, Chen R, Wu F (2017) Ni-rich LiNi_{0.8}Co_{0.1}Mn_{0.1}O₂ oxide coated by dual-conductive layers as high performance cathode for lithium-ion batteries. *ACS Appl Mater Interfaces* 9(35):29732–29743
34. Xia Y, Zheng J, Wang C, Gu M (2018) Designing principle for Ni-rich cathode materials with high energy density for practical applications. *Nano Energy* 49:434–452
35. Hou PY, Zhang HZ, Zi ZY, Zhang LQ, Xu XJ (2017) Core-shell and concentration-gradient cathodes prepared via co-precipitation reaction for advanced lithium-ion batteries. *J Mater Chem A* 5(9):4254–4279
36. Liang C, Kong F, Longo RC, Kc S, Kim J-S, Jeon S, Choi S, Cho K (2016) Unraveling the origin of instability in Ni-rich LiNi_{1-2x}Co_xMn_xO₂ (NCM) cathode materials. *J Phys Chem C* 120(12):6383–6393
37. Erickson EM, Schipper F, Penki TR, Shin JY, Erk C, Chesneau FF, Markovsky B, Aurbach D (2017) Review-recent advances and remaining challenges for lithium ion battery cathodes II: lithium-rich, xLi₂MnO₃ (1-x)LiNi_aCo_bMn_cO₂. *J Electrochem Soc* 164(1):A6341–A6348
38. Kumar NP, Erickson EM, Florian S, Rao PT, Nookala M, Philipp A, Hadar S, Francis A, Boris M, Doron A (2018) Review on challenges and recent advances in the electrochemical performance of high capacity Li- and Mn-rich cathode materials for Li-Ion batteries. *Adv Energy Mater* 8(8):1702397

39. Thackeray MM, Croy JR, Lee E, Gutierrez A, He M, Park JS, Yonemoto BT, Long BR, Blauwkamp JD, Johnson CS, Shin Y, David WIF (2018) The quest for manganese-rich electrodes for lithium batteries: strategic design and electrochemical behavior. *Sustain Energy Fuel* 2(7):1375–1397
40. Bhandari A, Bhattacharya J (2017) Review-manganese dissolution from spinel cathode: few unanswered questions. *J Electrochem Soc* 164(2):A106–A127
41. Tang DC, Sun Y, Yang ZZ, Ben LB, Gu L, Huang XJ (2014) Surface structure evolution of LiMn_2O_4 cathode material upon charge/discharge. *Chem Mater* 26(11):3535–3543
42. Xu GJ, Liu ZH, Zhang CJ, Cui GL, Chen LQ (2015) Strategies for improving the cyclability and thermo-stability of LiMn_2O_4 -based batteries at elevated temperatures. *J Mater Chem A* 3(8):4092–4123
43. Lee JH, Hong JK, Jang DH, Sun YK, Oh SM (2000) Degradation mechanisms in doped spinels of $\text{LiM}_{0.05}\text{Mn}_{1.95}\text{O}_4$ (M=Li, B, Al, Co, and Ni) for Li secondary batteries. *J Power Sources* 89(1):7–14
44. Bellitto C, Bauer EM, Righini G, Green MA, Branford WR, Antonini A, Pasquali M (2004) The effect of doping LiMn_2O_4 spinel on its use as a cathode in Li-ion batteries: neutron diffraction and electrochemical studies. *J Phys Chem Solids* 65(1):29–37
45. Gao Y, Myrtle K, Zhang MJ, Reimers JN, Dahn JR (1996) Valence band of $\text{LiNi}_x\text{Mn}_{2-x}\text{O}_4$ and its effects on the voltage profiles of $\text{LiNi}_x\text{Mn}_{2-x}\text{O}_4/\text{Li}$ electrochemical cells. *Phys Rev B* 54(23):16670–16675
46. Santhanam R, Rambabu B (2010) Research progress in high voltage spinel $\text{LiNi}_{0.5}\text{Mn}_{1.5}\text{O}_4$ material. *J Power Sources* 195(17):5442–5451
47. Kim JH, Myung ST, Yoon CS, Kang SG, Sun YK (2004) Comparative study of $\text{LiNi}_{0.5}\text{Mn}_{1.5}\text{O}_{4-\delta}$ and $\text{LiNi}_{0.5}\text{Mn}_{1.5}\text{O}_4$ cathodes having two crystallographic structures: $Fd\bar{3}m$ and $P4_332$. *Chem Mat* 16(5):906–914
48. Lu J, Lee KS (2016) Spinel cathodes for advanced lithium ion batteries: a review of challenges and recent progress. *Mater Technol* 31(11):628–641
49. Yi TF, Zhu YR, Zhu XD, Shu J, Yue CB, Zhou AN (2009) A review of recent developments in the surface modification of LiMn_2O_4 as cathode material of power lithium-ion battery. *Ionics* 15(6):779–784
50. Kim JS, Kim K, Cho W, Shin WH, Kanno R, Choi JW (2012) A truncated manganese spinel cathode for excellent power and lifetime in lithium-ion batteries. *Nano Lett* 12(12):6358–6365
51. Padhi AK, Nanjundaswamy KS, Goodenough JB (1997) Phospho-olivines as positive-electrode materials for rechargeable lithium batteries. *J Electrochem Soc* 144(4):1188–1194
52. Padhi AK, Nanjundaswamy KS, Masquelier C, Okada S, Goodenough JB (1997) Effect of structure on the $\text{Fe}^{3+}/\text{Fe}^{2+}$ redox couple in iron phosphates. *J Electrochem Soc* 144(5):1609–1613
53. Meethong N, Huang H-YS, Carter WC, Chiang Y-M (2007) Size-dependent lithium miscibility gap in nanoscale $\text{Li}_{1-x}\text{FePO}_4$. *Electrochem Solid-State Lett* 10(5):A134–A138
54. Morgan D, Van der Ven A, Ceder G (2004) Li conductivity in Li_xMPO_4 (M = Mn, Fe, Co, Ni) olivine materials. *Electrochem Solid-State Lett* 7(2):A30–A32
55. Islam MS, Driscoll DJ, Fisher CAJ, Slater PR (2005) Atomic-scale investigation of defects, dopants, and lithium transport in the LiFePO_4 olivine-type battery material. *Chem Mat* 17(20):5085–5092
56. Yiyang L, Sophie M, Jongwoo L, Chul LS, Gent WE, Stefano M, Harinarayan K, Tolek T, David S, David KAL, Chueh CW (2015) Effects of particle size, electronic connectivity, and incoherent nanoscale domains on the sequence of lithiation in LiFePO_4 porous electrodes. *Adv Mater* 27(42):6591–6597
57. Li L, Wu L, Wu F, Song S, Zhang X, Fu C, Yuan D, Xiang Y (2017) Review – recent research progress in surface modification of LiFePO_4 cathode materials. *J Electrochem Soc* 164(9):A2138–A2150
58. Sahana MB, Vasu S, Sasikala N, Anandan S, Sepehri-Amin H, Sudakar C, Gopalan R (2014) Raman spectral signature of Mn-rich nanoscale phase segregations in carbon free $\text{LiFe}_{1-x}\text{Mn}_x\text{PO}_4$ prepared by hydrothermal technique. *RSC Adv* 4(110):64429–64437

59. Zaghbi K, Mauger A, Julien CM (2015) Olivine-based cathode materials. In: Zhang Z, Zhang SS (eds) Rechargeable batteries: materials, technologies and new trends. Springer, Cham, pp 25–65
60. Nitta N, Wu F, Lee JT, Yushin G (2015) Li-ion battery materials: present and future. *Mater Today* 18(5):252–264
61. Winter M, Moeller K-C, Besenhard JO (2003) Carbonaceous and graphitic anodes. In: Nazri G-A, Pistoia G (eds) Lithium batteries: science and technology. Springer, Boston, pp 145–194
62. Peled E, Menkin S (2017) Review-SEI: past, present and future. *J Electrochem Soc* 164(7): A1703–A1719
63. Qi W, Shapter JG, Wu Q, Yin T, Gao G, Cui D (2017) Nanostructured anode materials for lithium-ion batteries: principle, recent progress and future perspectives. *J Mater Chem A* 5(37):19521–19540
64. Nozaki H, Nagaoka K, Hoshi K, Ohta N, Inagaki M (2009) Carbon-coated graphite for anode of lithium ion rechargeable batteries: carbon coating conditions and precursors. *J Power Sources* 194(1):486–493
65. Zheng H, Qu Q, Zhang L, Liu G, Battaglia VS (2012) Hard carbon: a promising lithium-ion battery anode for high temperature applications with ionic electrolyte. *RSC Adv* 2(11): 4904–4912
66. Liu YH, Xue JS, Zheng T, Dahn JR (1996) Mechanism of lithium insertion in hard carbons prepared by pyrolysis of epoxy resins. *Carbon* 34(2):193–200
67. Xu GJ, Han PX, Dong SM, Liu HS, Cui GL, Chen LQ (2017) $\text{Li}_4\text{Ti}_5\text{O}_{12}$ -based energy conversion and storage systems: status and prospects. *Coord Chem Rev* 343:139–184
68. Jung HG, Jang MW, Hassoun J, Sun YK, Scrosati B (2011) A high-rate long-life $\text{Li}_4\text{Ti}_5\text{O}_{12}/\text{Li}[\text{Ni}_{0.45}\text{Co}_{0.1}\text{Mn}_{1.45}]\text{O}_4$ lithium-ion battery. *Nat Commun* 2:516
69. Lv W, Gu J, Niu Y, Wen K, He W (2017) Review-gassing mechanism and suppressing solutions in $\text{Li}_4\text{Ti}_5\text{O}_{12}$ -based lithium-ion batteries. *J Electrochem Soc* 164(9):A2213–A2224
70. Sha YJ, Xu XM, Li L, Cai R, Shao ZP (2016) Hierarchical carbon-coated acanthosphere-like $\text{Li}_4\text{Ti}_5\text{O}_{12}$ microspheres for high-power lithium-ion batteries. *J Power Sources* 314:18–27
71. Etacheri V, Marom R, Elazari R, Salitra G, Aurbach D (2011) Challenges in the development of advanced Li-ion batteries: a review. *Energy Environ Sci* 4(9):3243–3262
72. Wu HB, Chen JS, Hng HH, Lou XW (2012) Nanostructured metal oxide-based materials as advanced anodes for lithium-ion batteries. *Nanoscale* 4(8):2526–2542
73. Rosa Palacin M (2009) Recent advances in rechargeable battery materials: a chemist's perspective. *Chem Soc Rev* 38(9):2565–2575
74. Gao X-P, Yang H-X (2010) Multi-electron reaction materials for high energy density batteries. *Energy Environ Sci* 3(2):174–189
75. Yu SH, Feng XR, Zhang N, Seok J, Abruna HD (2018) Understanding conversion-type electrodes for lithium rechargeable batteries. *Acc Chem Res* 51(2):273–281
76. Kraysberg A, Ein-Eli Y (2017) A critical review-promises and barriers of conversion electrodes for Li-ion batteries. *J Solid State Electrochem* 21(7):1907–1923
77. Li H, Balaya P, Maier J (2004) Li-storage via heterogeneous reaction in selected binary metal fluorides and oxides. *J Electrochem Soc* 151(11):A1878–A1885
78. Croguennec L, Palacin MR (2015) Recent achievements on inorganic electrode materials for lithium-ion batteries. *J Am Chem Soc* 137(9):3140–3156
79. Zhang Y, Zhou Q, Zhu J, Yan Q, Dou SX, Sun W (2017) Nanostructured metal chalcogenides for energy storage and electrocatalysis. *Adv Funct Mater* 27(35):1702317
80. Mahmood N, Tang T, Hou Y (2016) Nanostructured anode materials for lithium ion batteries: progress, challenge and perspective. *Adv Energy Mater* 6(17):1600374
81. Huang T, Yang YX, Pu KC, Zhang JX, Gao MX, Pan HG, Liu YF (2017) Linking particle size to improved electrochemical performance of SiO anodes for Li-ion batteries. *RSC Adv* 7(4):2273–2280



Nano-configured Opto-electric Ceramic Systems for Photo-electrochemical Hydrogen Energy

34

Pramod H. Borse

Contents

Introduction	1336
Metal Titanates	1340
TiO ₂ and SrTiO ₃	1340
A New Member: Visible Light Active – Black TiO ₂	1341
Metal Ferrites	1345
Metal Tungstates	1348
Metal Vanadates	1349
Metal Sulfides	1352
Other New Systems (Nitrides, Phosphides)	1353
Nitrides	1353
Black Phosphorous	1356
Efficient Nano-Configured Ceramics for Hydrogen Energy Application	1358
Conclusion	1361
References	1361

Abstract

Functional materials such as electro-optic or opto-electric ceramics are of fundamental as well as of technological interest in the context to energy application. Since, natural resources those include sunlight, wind, water, are available in abundance on our planet earth, ever-growing human energy requirements necessitates and demands a way to make their use for generation of renewable energy. Ceramics are excellent candidates in view of their exciting optical, mechanical, thermal, electrical, and corrosion-resistant properties. Photocatalytic material systems have fascinating ability to split water molecules under the presence of photon and electrical energy, by virtue of their suitable band energetics with

P. H. Borse (✉)

International Advanced Research Centre for Powder Metallurgy and New Materials, (ARCI),
Balapur, Hyderabad, India

e-mail: phborse@arci.res.in; pborse@physics.org

© Springer Nature Switzerland AG 2020

Y. R. Mahajan, R. Johnson (eds.), *Handbook of Advanced Ceramics and Composites*,
https://doi.org/10.1007/978-3-030-16347-1_52

1335

respect to water redox levels. The water splitting phenomenon is important *wrt* hydrogen energy technology which demands energy production via renewable energy sources. Photo-/electrocatalysts which are capable of efficiently splitting water molecule with a sustainable performance are highly desirable. The physicochemical study of materials to identify best suited photocatalyst has been a topic of prime interest. The present chapter discusses *nano*-configured photocatalysts reported till date and compares their performance and scope with respect to their commercialization for hydrogen-producing technologies.

Keywords

Photoelectrochemical · Hydrogen energy · Nano photocatalyst · Opto- Electric ceramics · Metal oxides · Sulfides · Ferrites · Nitrides · Phosphides · Photo assisted energy · Functional · Energy

Introduction

Opto-electric or electro-optic ceramics are the special class of functional materials which find a rewarding place in photo-associated energy applications [1, 2]. Especially their functionality is of utmost importance in case of energy-related applications such as wet photovoltaics and dry photovoltaics [3–5]. Here the material system is expected to be optically and electronically active so that whenever the material is under the influence of photons/electrons, it produces useful energy due to photoexcited electrons across the valence and conduction band. Particularly, in wet photovoltaics, the photocatalysis/photoelectrochemical mechanism necessitates the utilization of photoactive ceramic system *as* TiO₂ [6], Fe₂O₃ [7], WO₃ [8], BiVO₄ [9], CdS [10], BP [11], TiON [12], etc. As shown in Scheme 1, there are several ceramic oxide systems *as* titanates, ferrites, tungstates, and non-oxide *as* sulfides, nitrides, carbides, etc., which display exciting opto-electric properties desirable for photocatalytic hydrogen energy production.

Photocatalytic (PC) and photoelectrocatalytic (PEC) hydrogen production via water splitting (WS) is one of the most attractive routes to generate renewable fuel. Such PC and PEC technology is expected to dominate the energy sector in the decades to come unless other cheaper energy technologies become inaccessible or hydrogen technology become economical [13]. This technology demands discovery of an efficient and stable hydrogen-producing material. This new PC/PEC material should exhibit well-suited electronic and optical properties which thermodynamically should favor the reduction and oxidation of water to yield stoichiometric hydrogen and oxygen during complete splitting of water molecule [14, 15]. Figure 1 schematically shows band energetics of known photocatalysts (*ceramic materials*) indicating how their valence band (VB) and conduction band (CB) are placed with respect to redox level of water. In brief it shows how water reduction level (H^+/H_2) and water oxidation level (O_2/H_2O), respectively, display their energy with respect to their VB and CB edges. The straddling VB and CB edges across the redox levels of H₂O molecule facilitate the reduction or oxidation of H₂O.

Scheme 1 Schematic showing categorization of known opto-electric ceramic photocatalysts

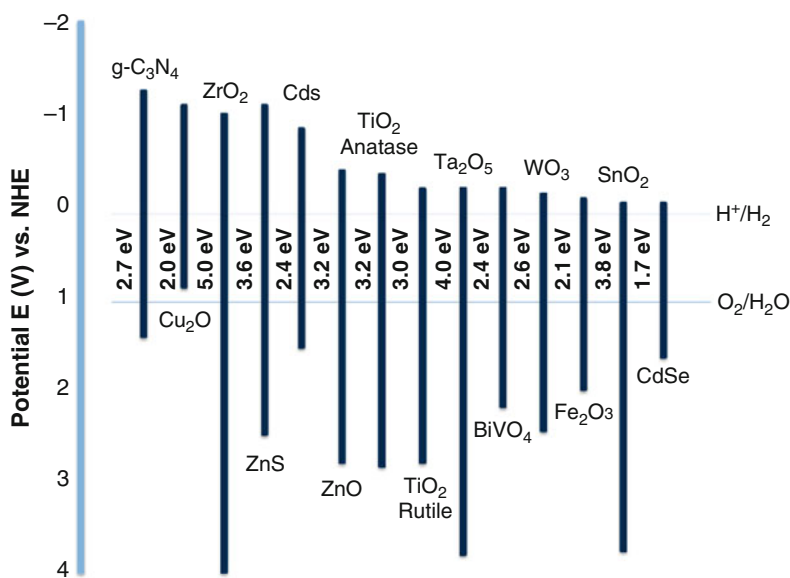
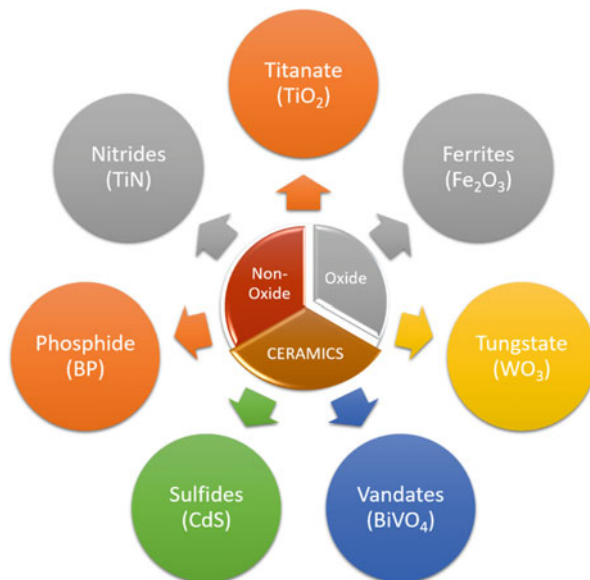


Fig. 1 Band energetics of some of the typical opto-electric ceramic photocatalysts

Let us understand the mechanism of PEC water splitting that generates useful hydrogen/oxygen via photoreduction or photooxidation. The schematic depicted in Fig. 2 clearly shows that a typical PEC setup consists of an electrically biased photoanode (*for water oxidation*) and photocathode (*for water*

reduction) immersed in an electrolyte. For simplicity, we discuss the specific case of a set of electrode consisting of photoanode and counter electrode, where photons illuminating the photoanode (*made of opto-electric ceramic*) facilitate production of exciton (*electron-hole pair*). This yields hole (h^+) at valence band and electron (e^-) at conduction band of the light-active photoanode. Such exciton facilitates photo-oxidation of water molecule by virtue of h^+ at anode and via e^- flowing to the cathode that reacts at the cathode/electrolyte interface to yield hydrogen gas molecule. It may be noted that the electronic structure of the electrode material plays a vital role as seen in Figs. 1 and 2, to enable the material to facilitate redox reaction over it. In addition, the band energetics also controls undesirable $e-h$ recombination reaction, a suited synergy yields the stability of the electrode material in electrolyte which is highly desirable to obtain sustainable hydrogen production. Thus electronic and optical structure is a key to identify best suited photocatalytic material. It may be added that during the redox reaction-related charge transports in electrode-electrolyte system, the type of “material electrical conductivity” of photocatalyst either *p-type* or *n-type*, decides its applicability for the water reduction reaction or water oxidation reactions, respectively, in line with Fig. 1.

We discuss here various opto-electric ceramics that constitute a special class of photocatalyst as indicated in Scheme 1, viz., different metal oxides as titanate, ferrite, tungstates, vanadates, etc. As a general observation, in these ceramic oxides (except *titanate*, *niobates*, *tantalates*), the *d*-orbitals play an important role in rendering appropriate band energetics for the photo- and photoelectro-induced water splitting reaction.

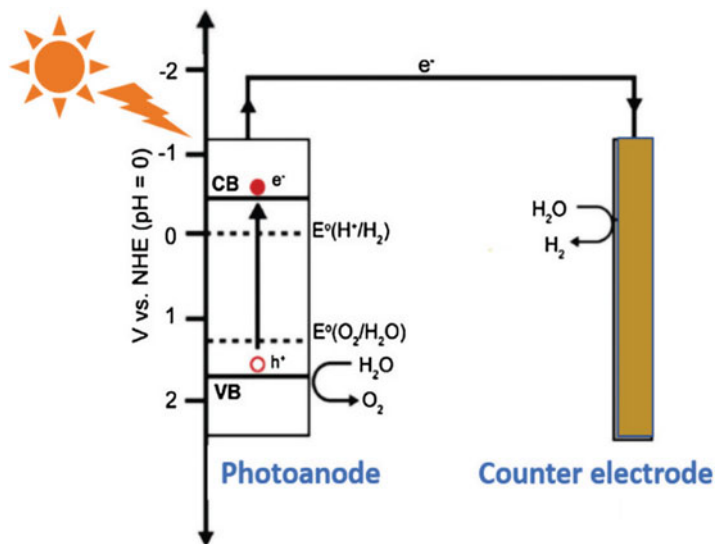


Fig. 2 Schematic explaining mechanism of working of photoelectrochemical cell for water splitting

Tables 1 and 2 show various physicochemical properties of the known photocatalysts reported in literature [8]. It mostly does imply that none of the material system possesses all the properties which are desirable for a good photocatalyst. Say, for instance, titanates are electrochemically very stable and nontoxic by nature, but they exhibit a very large band gap (3.2 eV), which makes them unsuitable for solar light absorption. On the contrary, ferrite, vanadates, and sulfides, though well suited for the visible light absorption (exhibit low band gap), show pH selective stability or overall a very poor stability (as in sulfides). So the material ranging from TiO₂ to CdS exhibits wide differences in their properties; thus, they cannot be treated as *an ideal material* for the visible light photocatalysis.

At this point, it may be added that computational simulations of electronic and optical properties of a lattice are known to guide the experimentalist for understanding the suitability of the material for solar photocatalysis. Such properties can be simulated by using density functional theory (DFT), a quantum mechanical-based modeling [12, 13]. Thus, the DFT results and their correlation for improving understanding of photocatalyst have been appropriately mentioned at various instances in the review below.

There is an exhaustive list of the materials that can be found in different review papers in literature. Here we aim to describe in detail the important candidate in

Table 1 Comparison of important physico-chemical properties of titanates, ferrites, tungstates as known opto-electric ceramic photocatalysts

	Property	TiO ₂	Fe ₂ O ₃	WO ₃
Crystal structure details	Crystal phases	Anatase, rutile, brookite	Hematite, maghemite	Tungstite, meymacite, hydrotungstite
	Lattice symmetry	Tetragonal	Rhombohedral	Monoclinic
	Lattice parameters (nm)	a = 0.378 b = 0.951	a = 0.5035 c = 1.374	A = 0.73, b = 0.753, c = 0.768, b = 90.54
Opto-electronic details	Optical band gap (eV)	3.2	2.2	2.8
	Absorption	UV region	Visible region	Visible region
	Mobility (cm ² V ⁻¹ S ⁻¹)	4	<0.01	6.5 cm ² /vs
	Dielectric constant	60	32	50
	Stability	Stable in aqueous media and under illumination	Stable in aqueous media for pH > 3 and under illumination	Photo and chemical stability in acidic and semi acidic over pH less than 8
	Toxicity	Nontoxic	Nontoxic	Nontoxic
	Density (g/cm ³)	3.89	5.25	7.16

Table 2 Comparison of important physico-chemical properties of vanadates, sulphides, phosphides and nitrides as know opto-electric ceramic photocatalysts

	Property	BiVO ₄	CdS	BP	TiN
Crystal structure details	Crystal phases	Pucherite, clinobisvanite, dreyerite	Greenockite, hawleyite	Phosphorous	Osbornite
	Lattice symmetry	Monoclinic	Hexagonal, cubic	Orthorhombic	Cubic
	Lattice parameters (nm)	A = 0.309, b = 0.308, c = 0.312, b = 90.34	a = 0.413, c = 0.674	A1 = 0.36, a2 = 0.45	A = 0.424
Optoelectronic details	Optical band gap (eV)	2.6	2.4	0.3,1.5 (monolayer)	3.4
	Absorption	Visible region	Visible region	Visible and near infrared region	Visible region
	Mobility (cm ² V ⁻¹ . S ⁻¹)	0.2	340	1000	—
	Dielectric constant	0.02	8.9	12.5	
	Stability	Near neutral aqueous environment	Corrosive both chemically and under illumination	Easily degrades in oxides atmosphere.	Chemically stable in almost acids except nitric acid
	Toxicity	Nontoxic	Toxic	Nontoxic	Nontoxic
	Density (gm/cm ³)	6.1	4.8	2.6	5.2

mentioned category as well as to provide a futuristic view on the opto-electric ceramic with respect to its application in visible light-induced water splitting. Accordingly, the following section briefly and explicitly reviews the past and recent work for the respective systems.

Metal Titanates

TiO₂ and SrTiO₃

Extensive work has been carried out on titanates, viz., TiO₂, SrTiO₃, and BaTiO₃, and a number of ternary phase metal oxides though they were proved to be very stable; however, their optical response in UV range hindered their suitability for the solar hydrogen generation.

TiO₂ is an earliest example known to be useful for photoelectrowater splitting after the work of Fujishima and Honda in 1972 [3]. It [16] is known to exist in different crystalline phases, viz., anatase, rutile [17], and brookite [18], among which the anatase is known to be a better photocatalyst [19]. It exhibits tetragonal crystal structure with band gap of 3.2 eV; it is environment-friendly and shows good stability in aqueous solution under the photo-illumination. There were several efforts to engineer its band gap by method of anionic and cationic doping to enable it to absorb visible light radiation [12]. Asahi et al. doped different dopants as C, N, S, etc. at the substitutional sites of oxygen that led to induce the defect state in the band structure of TiO₂, thus making it suitable to absorb visible light photons [12, 20]. However such materials did not yield very high efficiency for visible light water splitting in view of their *low coefficient of absorption* [21, 22]. Table 3 lists various TiO₂-based opto-electric ceramics reported in literature [4, 5] for water splitting under UV light radiation. It may be noted that due to the suitable band energetics of TiO₂ (see Fig. 1), it can photooxidize or photoreduce water molecule in the presence of some scavenger or co-catalyst. The anatase form of TiO₂ has been studied exhaustively and is known to be better as well as efficient compared to the other structural phases of TiO₂ [28]. It may be noted that the efficiencies reported in various reports are dependent on various parameters with respect to power of light source, electrolyte used, scavengers, co-catalysts, etc. Thus it becomes difficult to compare the efficiencies, though they are presented in Table 3. Essentially, it may be noted from Table 3 that mesoporous TiO₂ modified with Pt shows 6925 μmol/hr. (which is the highest) of hydrogen evolution under 300 W Hg arc lamp, whereas nanostructure configuration of TiO₂ yields 0.9 mA/cm² of photocurrent generation. Due to variation in such parameters, it may not be an easy task to compare the performance of photocatalysts.

Among other titanates, SrTiO₃ (STO)-based perovskite system has been of tremendous interest, and there are several reports on utilization of STO as photocatalysts [38–40]. Unfortunately, analogous to TiO₂, STO also exhibits wide band gap (3.2 eV) and thus responds poorly to the visible light photons. Nonetheless, there does exist some reports on the band gap engineering of STO via method of *metal-ion* doping at Ti site [38–40]. Table 4 lists various perovskite, ternary titanate (SrTiO₃, BaTiO₃, La₂TiO₅) related opto-electric ceramics reported for water splitting under UV light radiation.

It can be noted from Table 4 that though STO show capability of photooxidation and photoreduction of water, LaTiO₅ and La₂Ti₂O₇ layered structures show the highest evolution of hydrogen.

A New Member: Visible Light Active – Black TiO₂

It is worth mentioning that, as the band gap of TiO₂ has posed a major limitation to its usage for solar water splitting, to overcome this limitation, several researchers have attempted band gap narrowing of TiO₂ via doping, composite formation, etc. However, the reports on black TiO₂ have everyone in race of using TiO₂ system

Table 3 Hydrogen evolution performance of various types of titanates (TiO₂ based) during photoelectrocatalytic water splitting

S. no	Electrode type	Details of the experimental parameters and photocurrent density	Synthesis/ deposition method	Co-catal./H ₂ (μmol/h)	Co-catal./O ₂ (μmol/h)	QY %
1	TiO ₂ (anatase) [28]	Light source, 500 W hg; electrolyte, water vapor	MCB TiO ₂	Rh/1497		29 (340 nm)
2	TiO ₂ (anatase) [23]	Light source, 450 W hg; electrolyte, NaOH	MCB TiO ₂	NiO _x /32	NiO _x /14	–
3	TiO ₂ (anatase, 78%) [24]	Light source, 400 W hg; electrolyte, Na ₂ CO ₃	P25 TiO ₂	Pt/1893	Pt/957	–
4	TiO ₂ (anatase, 78%) [25]	Light source, 250 W hg; electrolyte, pure water	P25 TiO ₂	Pt/353	Pt/177	1.4 (300–400 nm)
5	TiO ₂ [26]	Light source, 300 W Xe; electrolyte, CH ₃ OH	Hydrolysis, calcination	Pt/3300	–	–
6	TiO ₂ (rutile/ anatase) [27]	Light source, 300 W Xe; electrolyte, CH ₃ OH	Impregnation, calcination	Pt/6700	–	–
7	Colloid TiO ₂ [28, 29]	Light source, 450 W Hg; electrolyte HCl	Hydrolysis	Pt – RuO ₂ / 4000	–	30 (310 nm)
8	Mesoporous TiO ₂ [36]	Light source, 300 W Hg; electrolyte, CH ₃ OH	Solgel method	Pt/6925	–	–
9	TiO ₂ nanowires [30]	Light source, 450 W Hg; electrolyte, CH ₃ OH	Electrospinning and solgel	54	–	–
10	TiO ₂ nanotubes [31]	Light source, 300 W Hg; electrolyte, CH ₃ OH	Hydrothermal	285	–	–

(continued)

Table 3 (continued)

S. no	Electrode type	Details of the experimental parameters and photocurrent density	Synthesis/ deposition method	Co-catal./H ₂ (μmol/h)	Co-catal./O ₂ (μmol/h)	QY %
11	TiO ₂ nanosheets [32]	Light source, 300 W Hg; electrolyte, CH ₃ OH	Hydrothermal	117.6	–	–
12	SrTiO ₃ [33]	Light source, 400 W Hg; electrolyte, NaOH	Alfa-Ventron	NiO _x /70	NiO _x /32	–
13	SrTiO ₃ /TiO ₂ [34]	Light source, 150 W Hg; electrolyte, HCOOH	Solid-state reaction	560	–	–
14	TiO ₂ [35]	Sensitizer Ru (bpy) ₃ ²⁺ ; sacrificial reagent, water, MeOH vapor; light source, 500 W Xe	Dye sensitized	–	0.9	–
15	TiO ₂ (anatase) [36]	Light source, Hg-Q; reactant solution, water vapor	–	Rh/449	–	29
16	TiO ₂ [23]	Light source, Hg-P; reactant solution, 3 M NaOH	–	NiO _x /6	NiO _x /2	–
17	TiO ₂ [24]	Light source, Hg-Q; reactant solution, 2.2 M Na ₂ CO ₃	–	Pt/568	Pt/287	–
18	TiO ₂ [25]	Light source, Hg-Q; reactant solution, pure water	–	Pt/106	Pt/53	–
19	TiO ₂ (nanotubes) [37]	0.90 mA/cm ² at 1.23 V vs. RHE; electrolyte, 1 M KOH	Anodization	–	–	–

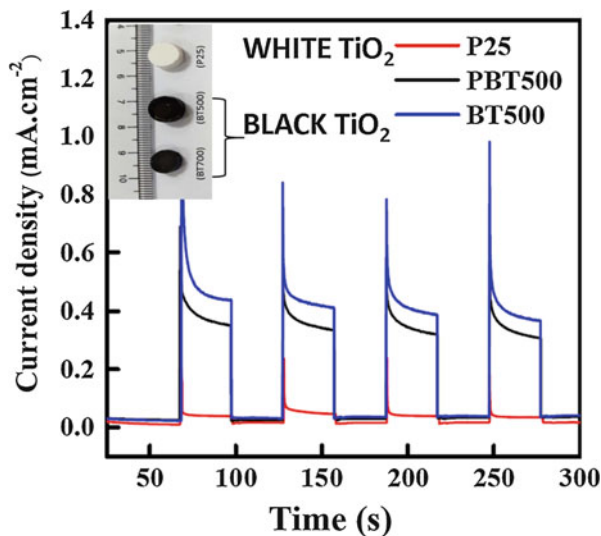
QY quantum yield

Table 4 Hydrogen and oxygen evolution performance of various types of titanates (SrTiO₃ based) during photo-/electrocatalytic water splitting

S. no	Electrode type	Details of the experimental parameters and photocurrent density	Synthesis/ deposition method	Co-catal. /H ₂	Co-catal. /O ₂	QY %
20	TiO ₂ (nanowalls) [41]	2.6 mA/cm ² at 1.23 V vs. RHE; electrolyte, 1 M NaOH	Hydrothermal	–	–	–
21	SrTiO ₃ (perovskite) [33]	Light source, Hg-Xe-P; reactant solution, pure water	Reduction	Rh/27	Rh/14	–
22	SrTiO ₃ (perovskite) [33]	Light source, Hg-P; reactant solution, 5 M NaOH	Impregnation	NiO _x /40	NiO _x /19	–
23	LaTiO ₅ [42]	Light source, Hg-Q; reactant solution, pure water	Solid-state reaction	NiO _x /442	–	–
24	La ₂ Ti ₃ O ₉ (layered perovskite) [42–45]	Light source, Hg-Q; reactant solution, pure water	Solid-state reaction	NiO _x /386	–	–
25	La ₂ Ti ₂ O ₇ (layered perovskite) [46]	Light source, Hg-Q; reactant solution, pure water	Solid-state reaction (polymerized complex)	NiO _x /441	–	12 (<360 nm)
26	KTiNbO ₅ (layered structure) [46]	Light source, Hg-Q; reactant solution, pure water	Polymerizable complex technique	NiO _x /30	NiO _x /10	–
27	Na ₂ Ti ₆ O ₁₃ (tunnel structure) [47]	Light source, Xe-Q; reactant solution, pure water	Calcination	RuO ₂ /7.3	RuO ₂ /3.5	–

for solar water splitting [48, 49]. In one of such attempts, it was found that *hydrogenation of TiO₂ lattice leads to a disordered crystal structure* that yields mid-gap states in TiO₂ electronic structure and uplifts the TiO₂ valence band edge [69]. Effectively, this yields an optical structure suitable to absorb visible and infrared light photons thereby making black TiO₂ suitable for visible light photocatalysis. Figure 3 shows the large photocurrent generated by black TiO₂ under solar light illumination. The color is indicative of the low band gap of black TiO₂ as compared to white TiO₂.

Fig. 3 Comparison of photocurrent of *white* TiO_2 (P25) and *black* TiO_2 generated under solar light radiation. Inset clearly shows the difference in the color of black TiO_2 indicating its low band gap characteristics. (Permission-Ref. [49])



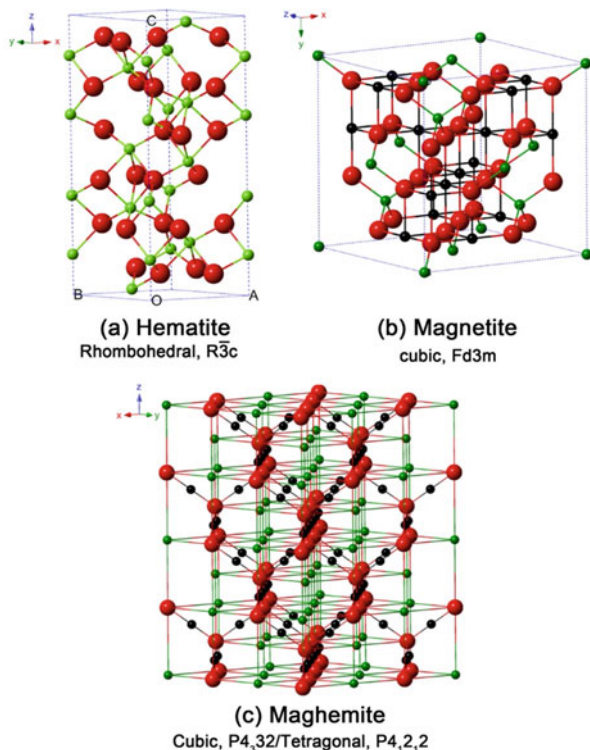
Metal Ferrites

Among various Fe-containing oxides (hematite, magnetite, maghemite ferrites (Fe_2O_3 $\alpha/\beta/\gamma$)), as shown in Fig. 4, hematite phase is the best known and most extensively studied photocatalyst system since it displays a band gap (~ 2.2 eV) in the visible light range. Iron oxide is an earth-abundant material that is the fourth most common material found in the earth's crust [50, 51]. Iron-containing oxides display various interesting physicochemical properties based on the oxidation state of Fe (+2, +3) and structural phase iron oxide as indicated in Table 1.

Most commonly they are known to exhibit band gap value in the range of ~ 2 eV. Alpha phase iron oxide (α Fe_2O_3) has been an important photocatalyst; consequently, there are several reports on its application for photoelectrochemical hydrogen generation [52–59]. It has the most suitable optical property which is desirable for photooxidizing water; however, it inherently exhibits poor electrical property like electrical mobility or low hole diffusion length. *Incidentally*, in the past, it failed to display expected performance as photoanode [51, 58, 59], but with the advent of new processing technologies and nanoprocessing methodologies, there are several reports on fabrication of efficient hematite photoanodes [52, 53]. It may be noted that in spite of suitable optical properties and valence band edge, *low hole diffusion length* (~ 5 nm) of the hematite [60] was a major hurdle for its utilization as photoanode. Nonetheless, impurity [61]- or nanostructuring [52]-based electrical property tuning was thus shown to yield very high photocurrents and solar-to-hydrogen (STH) conversion rates over hematite photoanodes as given in Table 5.

Table 5 shows comparison of PEC performance of various types of nanostructured Fe_2O_3 indicating that nanostructuring of Fe_2O_3 has yielded an improved

Fig. 4 Schematic of different crystal structures exhibited by bulk iron oxide. Hematite phase of Fe_2O_3 is a suitable system useful in PEC cell photoanode



performance as photoanode in PEC cell [61]. In a typical case, Fig. 5 clearly exhibits that in contrast to past reports on poor performance of bulk-based ferrite electrodes, a doped and nanostructured Fe_2O_3 photoanode indicates large photocurrent generation upon (Sn, Zr) co-doping in $\text{Fe}_2\text{O}_3/\text{NiOOH}$ system of electrode. Stability also seems to improve to a large value, under solar-simulated radiation [74]. The electrical and optical property tuning is thus exploited for fabrication of iron-based photoanodes.

Apart from this known system, there are various other perovskite (BiFeO_3) or ternary ($\text{Sr}_2\text{FeNbO}_6$, CaFe_2O_4 , MgFe_2O_4 , ZnFe_2O_4) ferrite systems that are known to be reported in literature [51, 53–58, 61]. Such opto-electric ceramic systems have also been found to be useful in photoanode applications in PEC cell. Dom et al. [61] have given a detailed perspective on such ferrites with respect to their PEC applications. Among the ternary ferrites, ZnFe_2O_4 has been the most reported in various combinations of doped system, nanostructured system, and composite system [75]. Table 6 shows the comparison of some of the water photooxidation efficiencies of reported ZnFe_2O_4 spinel ferrites.

Table 5 Comparison of PEC results of some doped and nanostructured hematite films indicating superior performance in contrast to known poor behavior of bulk Fe₂O₃ photoanode

S. no	Electrode type	Synthesis/ deposition method	Details of the experimental parameters and photocurrent density	Photo conversion efficiency STH/PCE/ APCE/ IPCE ^a (%)
1	Nanoclusters [62]	Relative ballistic deposition on FTO	Electrolyte, 1MKOH; applied bias, 0.5 V; light source, AM1.5; photocurrent density, 0.55 mA/ cm ²	IPCE, 10% at 420 nm
2	Cauliflower-type nanostructures [63]	CVD	3 mA/cm ² at 1.23 V vs. RHE	NR ^b
3	Nanocrystalline film [64]	Spray pyrolysis	Applied bias, 0.2 V vs. SCE; light source irradiance, 50 mW/ cm ² ; electrolyte, 1MNaOH	1.84% PCE
4	Modified nanostructured electrodes [65]	Spray pyrolysis	Light source, 150 W Xe; electrolyte, 1MNaOH	NR
5	Self-oriented nanorod array electrodes [66]	RF sputtering	Photocurrent density, 0.72 mA/ cm ² ; irradiance, W xenon; applied bias, 0.5 V vs. ag/AgCl	NR
6	Spin-coated nanostructured electrodes [67]	Spin coating deposition solution	Photocurrent density, 15 mA/ cm ² ; applied bias, 1.6 V vs. RHE; light source, AM1.5G	IPCE, 37% at 300 nm
7	Nanowire arrays [68]	Plasma oxidation of iron foils	Photocurrent density, 0.38 mA/ cm ² ; electrolyte, 1 M NaOH; applied bias, 1.5 V vs. RHE, 1–5 microns thick	NR
8	Nanonet-based heteronanostructure [69]	Atomic layer deposition	Photocurrent density, 2.7 mA/ cm ² ; applied bias, 1.53 V vs. RHE	46% at 400 nm
9	Nanostructured Fe ₂ O ₃ [70]	AACVD	Photocurrent density, 540 μA/ cm ² ; electrolyte, 1 M NaOH; ref. electrode, ag/AgCl; light source, AM1.5, class A solar simulator	NR
10	Nanostructured Fe ₂ O ₃ [71]	APCVD	Photocurrent density, 600 μA/ cm ² ; applied bias, 1.23 V vs. RHE; electrolyte, 1 M NaOH; light source, AM1.5; irradiance, 100 mW/cm ²	NR
11	Nanostructured Fe ₂ O ₃ [72]	Spray pyrolysis	Photocurrent density, 14 μA/cm ² ; applied bias, 1.23 V vs. RHE; electrolyte, 1 M NaOH; light source, AM1.5; irradiance, 100 mW/cm ²	NR

(continued)

Table 5 (continued)

S. no	Electrode type	Synthesis/ deposition method	Details of the experimental parameters and photocurrent density	Photo conversion efficiency STH/PCE/ APCE/ IPCE ^a (%)
12	Nanostructured Fe ₂ O ₃ [72]	USP	Photocurrent density, 1070 $\mu\text{A}/\text{cm}^2$; applied bias, 1.23 V vs. RHE; electrolyte, 1MNaOH	NR
13	Nanostructured Fe ₂ O ₃ [73]	Spray pyrolysis	Photocurrent density, 200 $\mu\text{A}/\text{cm}^2$; applied bias, 0.2 V vs. SHE; electrolyte, 1 M NaOH; light source, 50 mW Xe lamp	NR
14	Nanostructured Fe ₂ O ₃ [72]	Spray pyrolysis	Photocurrent density, 700 $\mu\text{A}/\text{cm}^2$; 0.7 V vs. NHE; electrolyte, 1MNaOH + Na ₂ SO ₄ ; AM1.5, 200 W Xe lamp	NR

References [100] and references therein

STH solar to hydrogen conversion efficiency, PCE power conversion efficiency, IPCE incident photon current conversion efficiency, APCE applied potential conversion efficiency. IPCE ~EQE and ABPE ~STH

^aPhoto-conversion efficiency is reported in different forms, viz., STH, PCE, IPCE, and APCE Ref. [17]

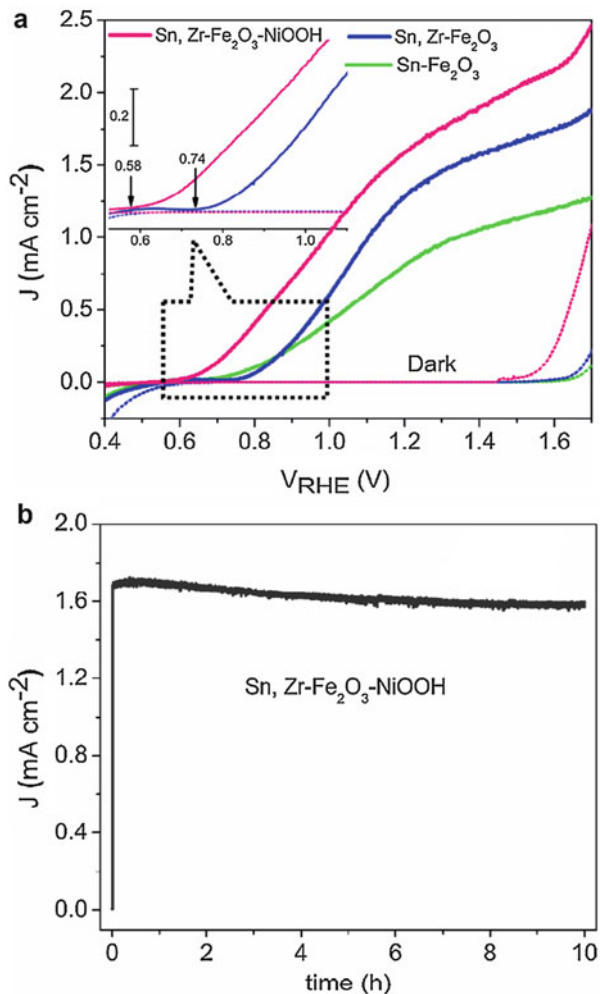
^bNR, not reported

Metal Tungstates

The next opto-electrically active ceramic candidate that has tremendous potential with respect to solar hydrogen production is W-based oxide ranging from tungsten trioxide to its ternary oxide. It is another suitable photocatalyst (*n-type*) preferred after Fe₂O₃, due to its low cost, eco-friendliness, and narrow band gap (2.2–2.8 eV) [83–93]. It is known to be highly stable in acidic condition. It is also known to have long hole diffusion length of 150 nm in contrast to 4–5 nm of Fe₂O₃; however, similar to Fe₂O₃, WO₃ also has high (0.4 V) potential for water oxidation. In spite of its several advantages, it is not a very efficient photoanode in individual form due to its thermodynamic stability with respect to anodic photocorrosion. In view of the importance of WO₃ with respect to its well-suited physicochemical properties, it was studied to achieve a photoanode with best PEC performance [85–88]. Its PEC properties were tailored based on nanostructuring, doping, or composite formation [86, 88–92]. Accordingly, there are several opto-electric ceramic systems, viz., NiWO₄ [93], Bi₂WO₆, BiFeWO₆, and MWO₄ (M = Ni, Cu, Co, Ni).

It is worth mentioning that in spite of tremendous work being carried in using tungstate systems, they have not been shown (Table 7) to demonstrate very high performances.

Fig. 5 (a) Photocurrent density as a function of applied potential in dark and illumination; (b) photocurrent density – time lot measured at 1.23 V. All measurements were performed under 1 sun simulated light illumination (AM 1.5G, 100 mW cm⁻²). (Permission Ref. [74])



Metal Vanadates

Vanadates such as BiVO₄ (BVO), BiCu₂VO₆, etc. are the recent material systems [96–100] that have been explored as photocatalytic active candidates especially due to their narrow band gap characteristics. Especially, BiVO₄ [97] has been shown to perform efficiently in 2015, which led to an exponential rise in its publications. It is known to exist in three polymorphs as pucherite, dreyerite, and clinobisvanate, the last clinobisvanate with monoclinic crystal structure being the most photoactive phase. It is known to exhibit band gap of 2.4–2.5 eV, whereas monoclinic scheelite phase shows low band gap due to V 3d–O 2p π levels. However it too poses a serious limitation of very slow transfer rate of photogenerated holes from BVO to the electrolyte. Figure 6

Table 6 Comparison of solar water oxidation performances of ZnFe₂O₄ photoanodes where ZnFe₂O₄ was used as a single photon absorber. (Permission Ref. [114])

Electrode	Preparation method	Onset (V _{RHE})	J at 1.23 V _{RHE} (mA cm ⁻²)	Electrolyte	IPCE at 400 nm and 1.23 V _{RHE}	Stability
ZnFe ₂ O ₄ [56]	Aerogel-assisted chemical vapor deposition	0.88	0.35	pH 14 NaOH	10%	–
ZnFe ₂ O ₄ [76]	Drop-casting a Zn solution on FeOOH followed by annealing and microwave treatment	0.64	0.24	pH 14 NaOH	7%	3 h stable
ZnFe ₂ O ₄ [77]	Drop-casting a Zn solution on FeOOH followed by annealing and H ₂ treatment	0.75	0.32	pH 14 NaOH	–	3 h stable
ZnFe ₂ O ₄ /NiFeO _x [78]	Drop-casting a Zn solution on FeOOH followed by annealing and H ₂ treatment	0.53	0.35	pH 14 NaOH	8% at 1.1 V _{RHE}	24 h stable
TiO ₂ /ZnFe ₂ O ₄ /NiFeO _x [79]	Drop-casting a Zn solution on FeOOH followed by microwave treatment and H ₂ treatment	0.62	0.92	pH 14 NaOH	8%	11 h stable
ZnFe ₂ O ₄ /NiFeO _x [80]	Drop-casting a Zn solution on FeOOH followed by annealing and H ₂ heat treatment	0.85	1.00	pH 14 NaOH	6%	–
ZnFe ₂ O ₄ [81]	Atomic layer deposition on an inverse opal-structured substrate	0.90	0.26	pH 13 NaOH	2%	3 h stable
ZnFe ₂ O ₄ [82]	Spray pyrolysis, Ti doping	0.95	0.35	pH 14 NaOH	3%	–

Table 7 Comparison of solar water splitting performances of *metal tungstate* photoanodes/ photocatalyst

S. no	Electrode type	Synthesis/ deposition method	Details of the experimental parameters and photocurrent density	Co-catal. /H ₂ (μmol/h)	Co-catal. /O ₂ (μmol/h)
1	WO ₃ [93, 94]	As received	Light source, Xe-L42	–	65
2	PbWO ₄ (scheelite) [95]	Solid-state reaction	Light source, hg-Xe-Q; reactant solution, pure water	RuO ₂ /24	RuO ₂ /12
3	Bi ₂ WO ₆ [96]	Calcination	Light source, Xe-L42	–	3

Ref. [4] and references are therein

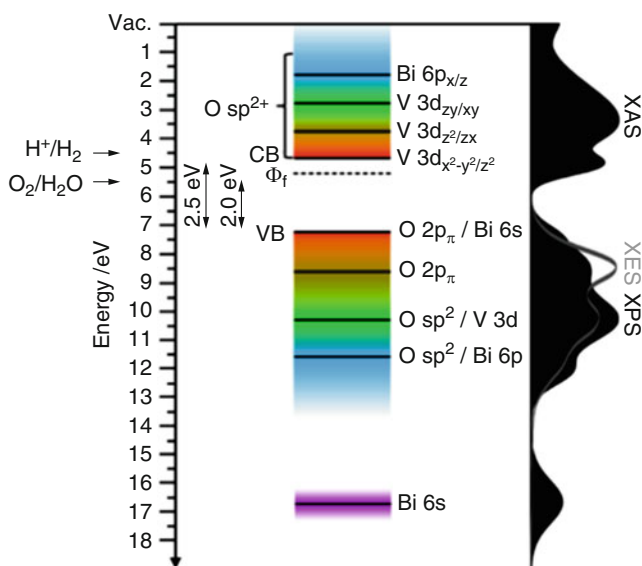


Fig. 6 Energy-level diagram summarizing the findings of this work for the electronic structure of monoclinic scheelite BiVO₄. The dominant orbital character in each region is represented with respect to the vacuum level. Experimental spectra of X-ray absorption to the empty states of the conduction band and X-ray and photoelectron emission from filled states of the valence band are presented on the right. The energy positions of the relevant water splitting redox reactions H⁺/H₂ and O₂/H₂O are indicated on the energy axis at 4.44 and 5.67 eV below the vacuum level. The Fermi energy position at the surface of the material, determined by photoelectron spectroscopy, is specific to the analyzed thin film because it is a function of doping and surface band bending (Permission Ref. [101])

shows that V 3d and O 2p π levels straddle the redox level of water. It was expected that theoretically BVO can yield good stability and STH of 9.2%. Experimentally, however BVO still exhibits problem of poor charge transport and low absorption coefficient. To enhance the charge transfer rate, it is thus necessary to dope V⁺⁵ in BVO by metal ions as W⁺⁶ or Mo⁺⁶ as well as nanostructuring the electrode to attain high photocurrents [103, 104].

Table 8 shows that BVO shows maximum oxygen evolution. There have been exhaustive studies, but no expected high performance has been achieved; thus, there is a lot of scope for further research. We have not included exhaustive list as the main objective here is to project the possible opto-electric ceramic family that finds applications as visible light photocatalyst.

Metal Sulfides

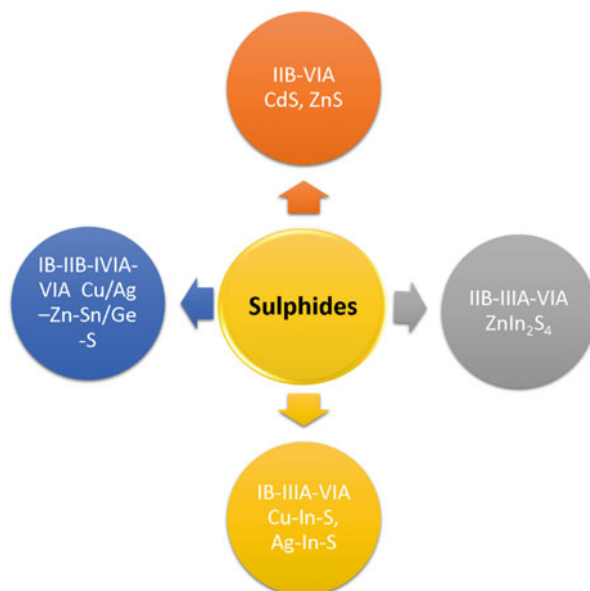
Most of the sulfides such as CdS exhibit high conduction band position with respect to the reduction level of water. They also show very suitable optical properties that are useful in solar light absorption. They display an electronic structure where metal cation exhibits d¹⁰ *electronic* configuration. Accordingly, conduction band of metal sulfides is composed of d and sp. orbitals, whereas valence band is made of s 3p levels. These valence band edges are thus more negative in contrast to O 2p orbitals. In essence the conduction band in sulfides is negative enough to reduce water and shows a narrow band gap desirable for solar light absorption. As shown in Scheme 2, the genealogy of various sulfide photocatalysts is categorized as IIB–VIA, IIB–IIIA–VIA, IA–IIIA–VIA, and IB–IIB–IVA–VIA sulfides based on elemental stoichiometry [107].

There is an in-depth study on sulfides that demonstrated their roles as photocatalyst or photoanode for water splitting [107–114]. Cadmium sulfide is the most efficient and cost effective single system photocatalyst known among all the existing materials [108]. Bulk CdS has a band gap of 2.4 eV; it exhibits hexagonal and cubic crystal phases. It has shown best efficiencies in most of the reports; however, the sulfides suffer because of photocorrosive instability

Table 8 Comparison of solar water oxidation performances of BiVO₄ photoanodes and other vanadate photoanodes

S. no	Electrode type	Details of the experimental parameters and photocurrent density	Co-catal. / O ₂
1	BiVO ₄ [101, 102]	Light source, Xe-L42	421
2	BiVO ₄ (n-type) [155, 156]	Mobility (μ) \sim 0.02 cm ² V ⁻¹ s ⁻¹ ; band gap, 2.4–2.5, 6.7 mA/cm ² at 1.23 volts vs. RHE	Not reported
3	BiCu ₂ VO ₆ [105]	Light source, Xe-L42	2.3
4	BiZn ₂ VO ₆ [106]	Light source, Xe-L42	6

Scheme 2 Type of opto-electric sulfides based on their position in the periodic table. They exhibit suitable properties for PEC water splitting. Ref. [107]



[109–111]. Specifically, its low water oxidation kinetics gives rise to accumulation of photogenerated holes, thereby leading to photocorrosion. There are several attempts to arrest this photocorrosion. Still, there is compelling need to address this challenge of instability of sulfide, which would thus yield a sustainable performance from sulfides. It has been found that CdS in conjunction with ZnS leads to improved performance. Nonetheless, ZnS also yields very high hydrogen generation under UV radiation as shown in Table 10; however, it is necessary to produce hydrogen under solar radiation. Nanostructuring of CdS [120] yielded very large hydrogen production of 27,333 $\mu\text{mole/h-g}$ as shown in Table 9. There are several reports on various types of sulfides, viz., CdS-ZnS [114], ZnInS₄ [115], CdIn₂S₄ [116], AgGa₂In₃S₈ [132], and AgInZn₇S₉ [117], but their performance, in individual form, was not found to be better than CdS, so they have not been discussed. However, the later section does show finer discussion of modified sulfides with respect to hydrogen evolution performance.

Other New Systems (Nitrides, Phosphides)

Nitrides

Nitrides are the structurally diverse class of important opto-electric ceramic material system that can be categorized in the following way. Accordingly, **group IVA**, C₃N₄, Si₃N₄, Ge₃N₄, and Ta₃N₅, are useful for photocatalytic and catalytic applications; **group IV B**, TiN, Zr₃N₄, and Hf₃N₄, are useful for hard coating and biomedical

Table 9 Comparison of solar water reduction performances of cadmium sulfide-related systems

S. no	Electrode type	Synthesis/ deposition method	Details of the experimental parameters and photocurrent density	Co-catal. / H ₂ (μmol/h)	QY %
1	Pt/CdS [117]	Mixing and grinding	Light source, 500 W Hg; reactant solution, Na ₂ SO ₃	40	35 (at 436 nm)
2	CdS [111]	Spray pyrolysis deposition	Solar simulator AM 1.5G; IPCE	–	5
3	ZnS [118]	Single jet	Light source, 200 W Hg; reactant solution, Na ₂ SO ₃ + H ₃ PO ₂ + NaOH	13,000	90 (at 313 nm)
4	CdS-ZnS [119]	Stirring and precipitation	Light source, 300 W Hg; reactant solution, Na ₂ SO ₃ + Na ₂ S	250	0.60
5	Nanosheet CdS [120]	Hydrothermal	Visible light via filter λ ⁻ 420 nm	27,333	60 (420 nm)
6	CdS [121]	Precipitation	Light source, 300 W Xe (>420 nm); reactant solution, lactic acid	MoS ₂ / 5400 ^a	93 (420 nm)
7	CdS [122]	Precipitation and hydrothermal method	Light source, 300 W Xe (>420 nm); reactant solution, Na ₂ S + Na ₂ SO ₃	Pt-PdS/ 29233 ^a	
8	CdS [123]	Precipitation	Light source, 500 W Hg (>420 nm); reactant solution, Na ₂ S + Na ₂ SO ₃	WC/ 1350 ^a	
9	CdS-ZnS [124]	H ₂ S thermal sulfurization	Light source, 350 W Xe (>430 nm); reactant solution, Na ₂ S + Na ₂ SO ₃	900 ^a	10.2 (420 nm)

^a Unit of H₂ evolution micro mol/h/g

applications; and **group IIIA**, AlN, InN, and GaN are useful for solid-state lighting and high-power electronics applications [136].

Among the nitrides, as shown in Table 11, Ta₃N₄, GaN, and graphitic C₃N₄ have been reported as potential photocatalyst or photoanode systems for water splitting [137]. In general, the valence band of nitrides is composed of N 2*p* levels, and the conduction band is composed of metal-based orbitals, like Ta 5*d* in Ta₃N₄. Among the reported ones, Liu et al. have cited highest photocurrent of 12.1 mA/cm² at 1.23 V vs. RHE over a Ta₃N₄ electrode modified by Co cubane/Ir complex/Ni(OH)_x/ferrihydrite/TiO_x under 1 sun AM 1.5 G radiation. Similarly, GaN and C₃N₄ also showed very efficient performance for water splitting in GaN and hydrogen generation in C₃N₄ nitride. It may be noted at this point that nitrides and related systems show poor stability.

Table 10 Comparison of solar water reduction performances of different sulfide systems

S. no	Electrode type	Synthesis/ deposition method	Details of the experimental parameters and photocurrent density	Co-catal. /H ₂	QY %
10	AgInZn ₇ S ₉ [125]	Precipitation and calcination	Light source, 300 W Xe (>420 nm); reactant solution, Na ₂ S + Na ₂ SO ₃	Pt/ 3164.7 ^a	20 (420 nm)
11	ZnIn ₂ S ₄ [126]	Hydrothermal method	Light source, 300 W Xe (>420 nm); reactant solution, Na ₂ S + Na ₂ SO ₃	Pt/231 ^a	–
12	ZnIn ₂ S ₄ [127]	Surfactant- assisted hydrothermal method	Light source, 300 W Xe (>430 nm); reactant solution, Na ₂ S + Na ₂ SO ₃	Pt/562 ^a	18.4 (420 nm)
13	AgGa _{0.9} In _{0.1} S ₂ [128]	Solid-state reaction	Light source, 300 W Xe (>420 nm); reactant solution, Na ₂ S + Na ₂ SO ₃	Pt/3500 ^a	–
14	CdIn ₂ S ₄ [129]	Hydrothermal method	Light source, 450 W Xe (>420 nm); reactant solution, H ₂ S + KOH	6960 ^a	17.1 (500 nm)
15	CdIn ₂ S ₄ [130]	Surfactant- assisted hydrothermal method	Reactant solution, KOH (photodecomposition of H ₂ S); incident light >420 nm	6476	–
16	Cd _{0.1} Zn _{0.9} S [131]	Hydrothermal method	Reactant solution, Na ₂ SO ₃ and Na ₂ S; incident radiation, visible light	21,850	–
17	CdS. ZnS [132]	Coprecipitation method	Reactant solution, Na ₂ SO ₃ and Na ₂ S; incident radiation, sunlight	2283.9	–
18	ZnIn ₂ S ₄ [133]	Hydrothermal method	Reactant solution, Na ₂ SO ₃ and Na ₂ S; incident light >420 nm	Pt/8420	34.3 (at 420 nm)
19	AgGa ₂ In ₃ S ₈ [134]	Heat-treated solid-state reaction method	Reactant solution, K ₂ SO ₃ and Na ₂ S; incident light >420 nm	Rh/ 3433.3	15 (at 460 nm)
20	CuGa ₂ In ₃ S ₈ [135]	Heat-treated solid-state reaction method	Reactant solution, K ₂ SO ₃ and Na ₂ S; incident light >420 nm	Rh/ 10666.7	15 (at 560 nm)
21	AgInZn ₇ S ₉ [135]			Pt/3133	35 (at 420 nm)

(continued)

Table 10 (continued)

S. no	Electrode type	Synthesis/ deposition method	Details of the experimental parameters and photocurrent density	Co-catal. /H ₂	QY %
		Coprecipitation and heat-treated method	Reactant solution, Na ₂ SO ₃ and Na ₂ S; incident light >420 nm		
22	(CuIn) _x Cd ₂ (1-x)S ₂ [134]	Low- temperature hydrothermal method	Reactant solution, Na ₂ SO ₃ and Na ₂ S; incident light >420 nm	649.9, Pt/2456	Pt/ 26.5 (at 420 nm)
23	ZnS- CuInS ₂ - AgInS ₂ [135]	Coprecipitation and heat-treated method	Reactant solution, K ₂ SO ₃ and Na ₂ S; incident light >420 nm	Ru/ 7733.3	–

^a Unit of H₂ evolution micro mol/h/g

Table 11 Comparison of solar water splitting performances of nitride systems

S. no	Electrode type	Synthesis/ deposition method	Details of the experimental parameters and photocurrent density	Co- catal. / H ₂ (μmol/ h)	Co- catal. / O ₂ (μmol/ h)	QY %
1	Ta ₃ N ₅ [138]	Nitridation	Band gap, 2.1 eV	Pt/10	420	0.1 (H ₂), 10 (O ₂), (at 420–600 nm)
2	Ta ₃ N ₅ [137]	Anodization/ nitridation	Co(OH) _x decoration, 5.3 mA cm ⁻² at 1.2 VRHE in 1 M KOH under simulated AM 1.5G	–	–	–
3	GaN [139]	MBE	Methanol/ AgNO ₃ 300 W Xe lamp	Rh/ Cr ₂ O ₃ /5	/50	0.5 AQE
4	C ₃ N ₄ [140]	Heat treatment	Solar simulated light; triethanolamine	Pt/5261	–	29.2% at 400 nm

Black Phosphorous

Black phosphorous [141] is another new class of two-dimensional (2D) materials that has joined the 2D family of graphene and transition metal chalcogenides (TMC) and emerged as a promising nanomaterial. It has shown exotic electronic and optical

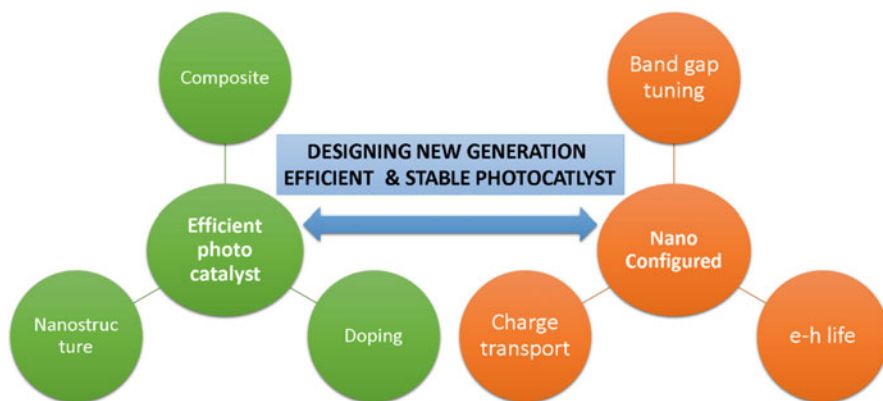
Table 12 Comparison of photo-induced water splitting performances of black phosphorous system

S. no	Electrode type	Synthesis/ deposition method	Details of the experimental parameters and photocurrent density	Co-catal. /H ₂ ($\mu\text{mol/h}$)	QY %
1	BP (nanosheets) [143]	Solvothermal	300 W Xe lamp coupled with a UV cutoff filter ($\lambda > 420$ nm); electrolyte, pure water	Pt/447 g^{-1}	4 (at 420 nm)
2	BP/CN (heterostructured) [144]	Ball milling	A blue LED lamp (440–445 nm); electrolyte, water + IPA	786 g^{-1}	–
4	BP (nanoflakes) [142]	Solvent exfoliation method	Light source, solar simulator 100 mWcm^{-2} ; ethylenediaminetetraacetic acid (EDTA)	RGO – Pt/3.4 g^{-1} (>420 nm), 0.84 g^{-1} (>780 nm)	8.7 (at 420 nm), 1.58 5 (at 780 nm)
5	BP (quantum dots) [145]	Facile solution- based method	Under visible light irradiation (>420 nm)	–	–
6	BP (nanosheets) [146]	Solvothermal	Xe lamp irradiation ($\lambda \geq 420$ nm); electrolyte, pure water	CoP/131.6 g^{-1}	AQE 42.55 (at 430 nm)

properties as shown in Table 2. Accordingly, it has shown tremendous potential for photovoltaic, opto-electronic, and biological applications. This V group element of the periodic table is known to exist in three main allotropes: white, red, and black types. Among these allotropes, black phosphorous is thermodynamically known to be the most stable, practically non-inflammable, chemically less reactive, and insoluble in most solvents. It exhibits three crystal structures, viz., simple cubic, orthorhombic, and rhombohedral. Recent reports have shown that black phosphorous (BP) can be a promising candidate for photo-induced water splitting [142], owing to its exotic optical and electronic properties of its layered structure. Importantly it exhibits a layer-dependent band gap of 0.3–1.5 eV as one looks at the bulk BP to a few layered nanosheets of BP. Table 12 compares the performance of BP-based photocatalyst and PEC systems [142–146]. It can be seen that unlike graphene layers or MoS₂ nanosheets, BP nanosheets can be directly used as photocatalyst/electrode for water splitting application; in one such work, Tian et al. [146] showed how modification of BP sheets with CoP nanoparticles yielded very high apparent quantum efficiency of 42.55% under 430 nm photons.

Efficient Nano-Configured Ceramics for Hydrogen Energy Application

Earlier sections have clearly revealed that till date there is no individual material system that can, in its single form, facilitate water splitting. This can be correlated to the inefficacy of the materials to yield ideal physicochemical properties and thus enable an ideal photo-splitting of water molecule. To state further, as shown in Scheme 3, it is thus necessary to tune the band gap, control *electron-hole recombination kinetics*, and *charge transport dynamics* in any PEC system. The tunability of the properties can be achieved by making use of (1) composite approach, (2) anionic/cationic doping, or (3) nanostructuring. Scheme 3 clearly indicates that interplay



Scheme 3 Art of designing and fabrication of efficient and stable new generation photocatalyst

Table 13 Comparison of solar water splitting performances of nano-configured photocatalyst/ photoelectrodes fabricated using various opto-electric ceramic systems

S. no	Electrode type	Details of the experimental parameters	Performance
1	TiO ₂ nanotubes [31]	Light source, 300 W Hg; electrolyte, CH ₃ OH	H ₂ generation, 285 μmolh ⁻¹ g ⁻¹
2	TiO ₂ (nanotubes) [147]	Light source, 95 mWcm ⁻² UV lamp; electrolyte, 1 M KOH	Photocurrent density (J), 26 mA/cm ² ; efficiency (η) = 16.5%
3	TiO ₂ (nanowalls) [41]	Electrolyte, 1 M NaOH; applied potential, 1.23 V vs. RHE	Photocurrent density (J), 2.6 mA/cm ²
4	CdS (flower-like microsphere) [148]	Co-catalyst, 0.5% wt. Pt; sacrificial agent, 10 vol% lactic acid	H ₂ generation, 9374 μmolh ⁻¹ g ⁻¹ ; QE, 24.7% (at 420 nm)
5	ZnInS ₄ (flower-like microsphere) [115]	Co-catalyst, 1.0% wt. Pt; sacrificial agent, 0.25 M Na ₂ SO ₃ + 0.35 M Na ₂ S	H ₂ generation, 8420 μmolh ⁻¹ g ⁻¹ ; QE, 34.3% (at 420 nm)
6	TiO ₂ /ZnO (hedgehogs and fan blades) [149]	Photodegradation	Target pollutant, MO; activity (K _{app} , 10 ⁻³ min ⁻¹), 30 min/97% (0.117)
7	Bi ₂ S ₃ [150]	Photodegradation	Target pollutant, MO; activity (K _{app} , 10 ⁻³ min ⁻¹), 97%/97% (77.6)
8	γ-Fe ₂ O ₃ /ZnO [151]	Photodegradation	Target pollutant, MB; activity (K _{app} , 10 ⁻³ min ⁻¹), 50 min/95.2%
9	CdTe-ZnO-N [152]	Light source, 100 mW UV lamp; electrolyte, 0.5 M Na ₂ SO ₄	Photocurrent density (J), 0.46 mA/cm ² ; photo conversion (η) = 1% at 0.5 V vs Ag/AgCl
10	RGO-Fe ₂ O ₃ [153]	Light source, 500 mWcm ⁻² UV lamp; electrolyte, 1 M NaOH	Photocurrent density (J), 6.7 mA/cm ² ; efficiency (η) = 0.76%
11	BiVO ₄ + Fe ₂ O ₃ (dual photoanode) + 2 - Si (PV)-Pt (dark cathode) [154]	Dual photoanode and Si cathode	Water splitting application; solar to energy conversion efficiency, 7.70%
12	SnO ₂ /graphene [155]	Electrolyte, 0.1 M NaHCO ₃ ; applied potential, -1.8 V vs. RHE	FE, 93.6%
13	MoS ₂ /Mo - Terminated edges [156]	Electrolyte, EMIM-BF ₄ ^{**} ; applied potential, -0.77 V vs. RHE	FE, 98%; CO production
14	InP NWs/MOS _x [157]	-	Open circuit potential, +0.55 V vs. RHE; J ₀ vs. RHE = 22.0 mA/cm ⁻² ; J _{sc} = 22.0 mA/cm ⁻² ; STH, 17.0%; robustness, 7% current loss after 1 h at 0 V _{RHE}

(continued)

Table 13 (continued)

S. no	Electrode type	Details of the experimental parameters	Performance
15	Pt/ITO/(n ⁺ -ia-Si)/n-Si/(i-pa-Si)?ITO [158]	–	HER*** application; solar to energy conversion efficiency, 13.26%
16	Pn ⁺ -Si/au mesh (nano porous) [159]	Electrolyte, 0.2 M KHCO ₃ ; applied potential, –0.03 V vs. RHE	FE, 91%; CO production
17	pn ⁺ -Si/F/SnO ₂ /TiO ₂ /Ir [160]	–	HER*** application; solar to energy conversion efficiency, 10.90%
18	GaAS/InGaP/TiO ₂ /Ni (photoanode)-Pd-C (dark cathode) [161]	–	CO ₂ reduction; solar to energy conversion efficiency, 10.00%
19	P – Si/SrTiO ₃ /Ti/Pt [162]	–	Open circuit potential, +0.45 V vs. RHE; J ₀ vs. RHE = 25 mA/cm ⁻² ; J _{sc} = 35 mA/cm ⁻² ; STH, 4.9%; robustness, over 35 h at –0.2 V _{RHE}
20	GaAS/AuGe/Ni/Au/Pt [163]	–	Open circuit potential, +1.022 V vs. RHE; J ₀ vs. RHE = 22.5 mA/cm ⁻² ; J _{sc} = 22.5 mA/cm ⁻² ; STH, 6.4%; robustness, 11% current loss after 8 day at 0 V _{RHE}
21	Cu (In, Ga)Se ₂ /CdS/Ti/Pt [164]	–	Open circuit potential, +0.65 V vs. RHE; J ₀ vs. RHE = 25.0 mA/cm ⁻² ; STH, 5.4% at +0.3 V _{RHE} ; robustness, 3 h at +0.3 V _{RHE} ; lost 20% activity
22	Si/n ⁺⁺ – GaN/InGaN/p ⁺ – GaN [165]	–	Open circuit potential, +0.5 V vs. RHE; J ₀ vs. RHE = 40.6 mA/cm ⁻² ; J _{sc} = 40.6 mA/cm ⁻² ; STH, 8.7% at +0.33 V _{RHE} ; robustness, stable for 3 h at 0.06 V _{RHE}
23	P – Cu ₂ O/AZO/TiO ₂ /MoS _{2+x} [166]	–	Open circuit potential, +0.48 V vs. RHE; J ₀ vs. RHE = 6.3 mA/cm ⁻² ; STH, 7.7% at +0V _{RHE} ; robustness, degraded gradually over 10 h

FE Faradic efficiency, EMIM–BF₄ 1-ethyl-3-methylimidazolium tetrafluoroborate, HER hydrogen evolution reaction, J₀ dark saturation current density, J_{sc} photocurrent density at short circuit, W-H tungsten-halogen lamp, STH solar to hydrogen conversion efficiency

of material property tuning and nanostructuring can be used to attain an ideal type of photocatalyst/photoelectrocatalyst. This section clearly shows how material property tuning yields improved performance toward water splitting under

radiation. Table 13 shows various aspects of property tuning that yields near to ideal performance desirable for cost effective, sustainable, and efficient hydrogen generation under sunlight.

Conclusion

Opto-electric ceramics showing suitable low band gap (~ 2.2 eV), desirable band energetics, electrochemical properties, and catalytic sites can be used as visible light photocatalysts/photoelectrocatalysts for splitting water under solar light radiation. Till date there is no effective water splitting system that has been found to exist, but nano-configured photocatalysts/photoelectrocatalysts can be suitably fabricated for making the ideally suited material for sustainable generation of hydrogen energy under solar light.

Acknowledgments The authors thank the support of the Director, ARCI, DST Lab, India.

References

1. Patra KK et al (2017) Possibly scalable solar hydrogen generation with quasi-artificial leaf approach. *Sci Rep* 7:6515
2. Reece SY et al (2011) Wireless solar water splitting using silicon-based semiconductors and earth-abundant catalysts. *Science* 334:645–648
3. Chen X et al (2010) Semiconductor-based photocatalytic hydrogen generation. *Chem Rev* 110:6503–6570
4. Kamat PV et al (2010) Beyond photovoltaics: semiconductor nanoarchitectures for liquid-junction solar cells. *Chem Rev* 110:6664–6688
5. Kudo A et al (2009) Heterogeneous photocatalyst materials for water splitting. *Chem Soc Rev* 38:253–278
6. Fujishima A, Honda K (1972) Electrochemical photolysis of water at a semiconductor electrode. *Nature* 238:37–38
7. Kment S (2017) Photoanodes based on TiO_2 and $\alpha\text{-Fe}_2\text{O}_3$ for solar water splitting – superior role of 1D nanoarchitectures and of combined heterostructures. *Chem Soc Rev* 46:3716–3769
8. Zou Z (2001) Direct splitting of water under visible light irradiation with an oxide semiconductor photocatalyst. *Nature* 414:625–627
9. Scaife DE (1980) Oxide semiconductors in photoelectrochemical conversion of solar energy. *Sol Energy* 25:41
10. Cheng L et al (2018) CdS-based photocatalysts. *Energy Environ Sci* 11:1362–1391
11. Tian B et al (2018) Supported black phosphorus nanosheets as hydrogen-evolving photocatalyst achieving 5.4% energy conversion efficiency at 353 K. *Nature Commun* 9:1397. Zhu M et al (2017) Black phosphorus: a promising two dimensional visible and near-infrared-activated photocatalyst for hydrogen evolution. *Appl Catal B Environ* 217:285–292
12. Asahi R et al (2001) Visible-light photocatalysis in nitrogen-doped titanium oxides. *Science* 293:269–271
13. Borse PH (2017) Hydrogen from water. In: Mondal/Dalai (eds) Sustainable utilization of natural resources. Taylor & Francis group, Boca Raton, CRC Press. pp 441–457
14. Gratzel M et al (2001) Photoelectrochemical cells. *Nature* 414:338–344
15. Murphy AB et al (2006) Efficiency of solar water splitting using semiconductor electrodes. *Int J Hydrog Energy* 31:1999–2017

16. Fujishima A, Rao TN, Tryk DA (2000) Titanium dioxide photocatalysis. *J Photochem Photobiol C* 1(1):1–21
17. Borse PH et al (2002) Synthesis and investigations of rutile phase nanoparticles of TiO₂. *J Mater Sci Mater Electron* 13(9):553–559
18. Ranade MR et al (2002) Energetics of nanocrystalline TiO₂. *Proc Natl Acad Sci* 99(2):6476–6481
19. Luttrell T et al (2014) Why is anatase a better photocatalyst than rutile? – Model studies on epitaxial TiO₂ films. *Sci Rep* 4:4043
20. Asahi R et al (2014) Nitrogen-doped titanium dioxide as visible-light-sensitive photocatalyst: designs, developments, and prospects. *Chem Rev* 114:9824–9852
21. Serpone N (2006) Is the band gap of pristine TiO₂ narrowed by anion- and cation-doping of titanium dioxide in second-generation photocatalysts? *J Phys Chem B* 110(48): 24287–24299
22. Yamaguti K et al (1985) Photolysis of water over metallized powdered titanium dioxide. *J Chem Soc Faraday Trans I* 81:1237–1246
23. Kudo A et al (1987) Photocatalytic activities of TiO₂ loaded with NiO. *Chem Phys Lett* 133:517–519
24. Sayama K et al (1997) Effect of carbonate salt addition on the photocatalytic decomposition of liquid water over catalyst. *J Chem Soc Faraday Trans* 93:1647–1654
25. Tabata S et al (1995) Stoichiometric photocatalytic decomposition of pure water in Pt/TiO₂ aqueous suspension system. *Catal Lett* 34:245–249
26. Shi J et al (2007) Photoluminescence characteristics of TiO₂ and their relationship to the photoassisted reaction of water/methanol mixture. *J Phys Chem C* 111:693–669
27. Zhang J et al (2008) Importance of the relationship between surface phases and photocatalytic activity of TiO₂. *Angew Chem Int Ed* 47:1766–1769
28. Duonghong D et al (1981) Dynamics of light-induced water cleavage in colloidal systems. *J Am Chem Soc* 103:4685–4690
29. Sreethawong T et al (2007) Quantifying influence of operational parameters on photocatalytic H₂ evolution over Pt-loaded nanocrystalline mesoporous TiO₂ prepared by single-step sol–gel process with surfactant template. *J Power Sources* 165:861–869
30. Jitputti J et al (2008) Synthesis of TiO₂ nanowires and their photocatalytic activity for hydrogen evolution. *Catal Commun* 9:1265–1271
31. Jitputti J et al (2008) Synthesis of TiO₂ nanotubes and its photocatalytic activity for H₂ evolution. *Jpn J Appl Phys* 47:751–756
32. Jitputti J et al (2009) Low temperature hydrothermal synthesis of monodispersed flower-like titanate nanosheets. *Catal Commun* 10:378–382
33. Domen K et al (1980) Photocatalytic decomposition of water vapour on an NiO–SrTiO₃ catalyst. *J Chem Soc Chem Commun* 12:543–544
34. Zielinska B et al (2008) Photocatalytic hydrogen generation over alkaline-earth titanates in the presence of electron donors. *Int J Hydrog Energy* 33:1797–1180
35. Kajiwara T et al (1982) Dynamics of luminescence from Ru(bpy)₃Cl₂ adsorbed on semiconductor surfaces. *J Phys Chem* 86:4516–4452
36. Yamaguti K et al (1985) Photolysis of water over metallized powdered titanium dioxide. *J Chem Soc Faraday Trans I* (81):1237–1246
37. Zhang Z et al (2010) Photoelectrochemical water splitting on highly smooth and ordered TiO₂ nanotube arrays for hydrogen generation. *Int J Hydrog Energy* 35:8528–8535
38. Konta R et al (2004) Photocatalytic activities of noble metal ion doped SrTiO₃ under visible light irradiation. *J Phys Chem B* 108(26):8992–8995
39. Bae SW et al (2008) Dopant dependent band gap tailoring of hydrothermally prepared cubic SrTi_xM_{1-x}O₃ (M=Ru,Rh,Ir,Pt,Pd) nanoparticles as visible light photocatalyst. *Appl Phys Lett* 92(10):104107–104110
40. Iwashina K et al (2011) Rh-doped SrTiO₃ photocatalyst electrode showing cathodic photocurrent for water splitting under visible-light irradiation. *J Amer Chem Soc* 133(34):13272–13275
41. Liu M et al (2011) Water photolysis with a cross-linked titanium dioxide nanowire anode. *Chem Sci* 2:80–87

42. Kim J et al (2005) Highly efficient overall water splitting through optimization of preparation and operation conditions of layered perovskite photocatalysts. *Top Catal* 35:295–230
43. Kim HG et al (1999) Highly donor-doped (110) layered perovskite materials as novel photocatalysts for overall water splitting. *Chem Commun* 1077–107
44. Song H et al (2007) Hydrothermal synthesis of flaky crystallized $\text{La}_2\text{Ti}_2\text{O}_7$ for producing hydrogen from photocatalytic water splitting. *Catal Lett* 113:54–58
45. Ji SM et al (2007) Photocatalytic hydrogen production from natural seawater. *J Photochem Photobiol* 189:141–144
46. Takahashi H et al (1999) Synthesis of NiO-loaded KTiNbO_5 photocatalysts by a novel polymerizable complex method. *J Alloys Compd* 285:77–78
47. Inoue Y, et al (1990) Photocatalytic activity of sodium hexatitanate, $\text{Na}_2\text{Ti}_6\text{O}_{13}$, with a tunnel structure for decomposition of water. *J Chem Soc Chem Commun* 1298–129
48. Chen X et al (2011) Increasing solar absorption for photocatalysis with black hydrogenated titanium dioxide nanocrystals. *Science* 331(6018):746–750
49. Katal R, Salehi M, Davood Abadi Farahani MH, Masudy-Panah S, Ong SL, Hu J (2018) Preparation of a new type of black TiO_2 under vacuum atmosphere for sunlight photocatalysis. *ACS Appl Mater Interfaces* 10(41):35316–35326E
50. Jeong D, Borse PH, Jang JS, Lee JS, Cho CR, Bae JS, Park S, Jung OS, Ryu SM, Won MS, Kim HG (2009) Physical and optical properties of nanocrystalline calcium ferrite synthesized by the polymerized complex method. *J Nanosci Nanotech* 9:3568
51. McDonald KJ et al (2011) Synthesis and photoelectrochemical properties of $\text{Fe}_2\text{O}_3/\text{ZnFe}_2\text{O}_4$ composite photoanodes for use in solar water oxidation. *Chem Mater* 23(21):4863–4869
52. Borse et al (2008) Phase and photoelectrochemical behavior of solution-processed Fe_2O_3 nanocrystals for oxidation of water under solar light. *Appl Phys Lett* 93:173103
53. Joshi UA et al (2008) Microwave synthesis of single-crystalline perovskite BiFeO_3 nanocubes for photoelectrode and photocatalytic applications. *Appl Phys Lett* 92(24):242106–242108
54. Kim HG et al (2009) Fabrication of $\text{CaFe}_2\text{O}_4/\text{MgFe}_2\text{O}_4$ bulk heterojunction for enhanced visible light photocatalysis 5889–5891
55. Jang JS et al (2009) Synthesis of zinc ferrite and its photocatalytic application under visible light. *J Korean Phys Soc* 54(1):204–208
56. Tahir AA et al (2010) Photoelectrochemical water splitting at nanostructured ZnFe_2O_4 electrodes. *J Photochem Photobiol A-Chem* 216:119–125
57. Dom R et al (2011) Synthesis of a hydrogen producing nanocrystalline ZnFe_2O_4 visible light photocatalyst using a rapid microwave irradiation method. *RSC Adv* 2(33):12782–12791
58. Dom R et al (2011) Synthesis of solar active nanocrystalline ferrite, MFe_2O_4 (M: Ca, Zn, Mg) photocatalyst by microwave irradiation. *Sol Stat Commun* 151:470–473
59. Mayer MT, Lin Y, Yuan G, Wang D (2013) Forming heterojunctions at the nanoscale for improved photoelectrochemical water splitting by semiconductor materials: case studies on hematite. *Acc Chem Res* 46:1558–1566
60. Kennedy H, Frese KW (1978) Photooxidation of water at $\alpha\text{-Fe}_2\text{O}_3$ electrodes. *J Electrochem Soc* 125:709
61. Dom R et al (2013) Investigation of solar photoelectrochemical hydrogen generation ability of ferrites for energy production. *Mater Sci Forum* 764:97–115
62. Nathan T et al (2010) Reactive ballistic deposition of $\alpha\text{-Fe}_2\text{O}_3$ thin films for photoelectrochemical water oxidation. *ACS Nano* 4:1977–1986
63. Tilley SD et al (2010) Light-induced water splitting with hematite: improved nanostructure and iridium oxide. *Int Ed* 49:6405–6408
64. Khan SUM et al (1999) Photoelectrochemical splitting of water at nanocrystalline n- Fe_2O_3 thin-film electrodes. *J Phys Chem B* 103:7184–7189
65. Satsangi VR et al (2008) Nanostructured hematite for photoelectrochemical generation of hydrogen. *Int J Hydrog Energy* 33:312–318
66. Chang CY et al (2012) Self-oriented iron oxide nanorod array thin film for photoelectrochemical hydrogen production. *Int J Hydrogen Energy* 37:13616–13622
67. Souza FL et al (2009) Nanostructured hematite thin films produced by spin-coating deposition solution: application in water splitting. *Sol Energy Mat Sol Cells* 93:362–368

68. Boris DC et al (2012) Photoelectrochemical activity of as-grown, α - Fe_2O_3 nanowire array electrodes for water splitting. *Nanotechnology* 23:194009–194017
69. Lin Y et al (2011) Nanonet-based hematite hetero nanostructures for efficient solar water splitting. *J Am Chem Soc* 133:2398–2401
70. Yarahmadi SS et al (2009) Fabrication of nanostructured α - Fe_2O_3 electrodes using ferrocene for solar hydrogen generation. *Mater Lett* 63:523–526
71. Tahir AA et al (2009) Nanostructured α - Fe_2O_3 thin films for photoelectrochemical hydrogen generation. *Chem Mater* 21:3763–3772
72. Majumder SA et al (1994) Photo electrolysis of water at bare and electrocatalyst covered thin film iron oxide electrode. *Int J Hydrog Energy* 19:881–888
73. Ingler WB et al (2004) Photo response of spray pyrolytically synthesized magnesium doped iron (III) oxide (p - Fe_2O_3) thin films under solar simulated light illumination. *Thin Sol Films* 461:301–308
74. Tamirat AG et al (2015) Photoelectrochemical water splitting at low applied potential using a NiOOH coated codoped (Sn, Zr) α - Fe_2O_3 photoanode. *J Mat Chem A* 3:5949–5961
75. Lee DK et al. (2019) Progress on ternary oxide-based photoanodes for use in photoelectrochemical cells for solar water splitting, *Chem Soc Rev* 1–32. <https://doi.org/10.1039/C8CS00761F>
76. Kim JH et al (2015) Awakening solar water-splitting activity of ZnFe_2O_4 nanorods by hybrid microwave annealing. *Adv Energy Mater* 5(6):1401933
77. Kim JH et al (2015) Defective ZnFe_2O_4 nanorods with oxygen vacancy for photoelectrochemical water splitting. *Nanoscale* 7(45):19144–19151
78. Guijarro N et al (2018) Evaluating spinel ferrites MFe_2O_4 ($M = \text{Cu, Mg, Zn}$) as photoanodes for solar water oxidation: prospects and limitations. *Sustain Energy Fuels* 2:103–117
79. Kim JH (2018) A multitude of modifications strategy of ZnFe_2O_4 nanorod photoanodes for enhanced photoelectrochemical water splitting activity. *J Mater Chem A* 6:12693–12700
80. Zhu X (2018) Spinel structural disorder influences solar-water-splitting performance of ZnFe_2O_4 nanorod photoanodes. *Adv Mater* 30:1801612
81. Hufnagel AG (2016) Zinc ferrite photoanode nanomorphologies with favorable kinetics for water-splitting. *Adv Funct Mater* 26:4435–4443
82. Guo Y (2017) A facile spray pyrolysis method to prepare Ti-doped ZnFe_2O_4 for boosting photoelectrochemical water splitting. *J Mater Chem A* 2017(5):7571–7577
83. Bignozzi CA et al (2013) Nanostructured photoelectrodes based on WO_3 : applications to photooxidation of aqueous electrolytes. *Chem Soc Rev* 42:2228–2246
84. Hong SJ et al (2009) Size effects of WO_3 nanocrystals for photooxidation of water in particulate suspension and photoelectrochemical film systems. *Int J Hydrog Energy* 34:3234–3242
85. Zheng JY et al (2015) Tuning of the crystal engineering and photoelectrochemical properties of crystalline tungsten oxide for optoelectronic device applications. *CrystEngComm* 17(32):6070–6093
86. Arutanit O et al (2016) Tailored synthesis of macroporous Pt/WO_3 photocatalyst with nano-aggregates via flame assisted spray pyrolysis. *AIChE J* 62(11):3864–3873
87. Tahir MB et al (2018) WO_3 nanostructures-based photocatalyst approach towards degradation of RhB dye. *J Inorg Organomet Polym Mater* 28(3):1107–1113
88. Wu K et al (2018) One-step synthesis of sulfur and tungstate co-doped porous $g\text{-C}_3\text{N}_4$ microrods with remarkably enhanced visible-light photocatalytic performances. *Appl Surf Sci* 462:991–1001
89. Do TH et al (2016) Superior photoelectrochemical activity of self-assembled NiWO_4 - WO_3 heteroepitaxy. *Nano Energy* 23:153–160
90. Priya A et al (2018) A low-cost visible light active $\text{BiFeWO}_6/\text{TiO}_2$ nanocomposite with an efficient photocatalytic and photoelectrochemical performance. *Opt Mater* 81:84–92. 269
91. Lopez XA et al (2016) Synthesis, characterization and photocatalytic evaluation of MWO_4 ($M = \text{Ni, Co, Cu}$ and Mn) tungstates. *Int J Hydrog Energy* 41(48):23312–23317
92. Hu T et al (2018) Iron-doped bismuth tungstate with an excellent photocatalytic performance. *ChemCatChem* 10(14):3040–3048. Nakajima T et al (2016) WO_3 nanosponge photoanodes

- with high applied bias photon-to-current efficiency for solar hydrogen and peroxydisulfate production. *J Mater Chem A* 4:17809–1781
93. Prévot MS, Sivula K (2013) Photoelectrochemical tandem cells for solar water splitting. *J Phys Chem C* 117:17879–17893. Gratzel M et al (1983) Energy resources through photochemistry and catalysis. Academic Press, New York
 94. Saito N et al (2004) A new photocatalyst of RuO₂-loaded PbWO₄ for overall splitting of water. *Chem Lett* 33:1452–1453
 95. Kudo A et al (1999) H₂ or O₂ evolution from aqueous solutions on layered oxide photocatalysts consisting of Bi³⁺ with 6s² configuration and d⁰ transition metal ions. *Chem Lett* 28:1103–1104
 96. Kudo A et al (1998) Photocatalytic O₂ evolution under visible light irradiation on BiVO₄ in aqueous AgNO₃ solution. *Catal Lett* 53:229–230
 97. Kim TW, Choi K-S (2014) Nanoporous BiVO₄ photoanodes with dual-layer oxygen evolution catalysts for solar water splitting. *Science* 343:990–994
 98. Yoon H et al (2015) Nanotextured pillars of electro sprayed bismuth vanadate for efficient photoelectrochemical water splitting. *Langmuir* 31(12):3727–3737
 99. Nasiri A et al (2017) Manganese vanadate nanostructure: facile precipitation preparation, characterization, and investigation of their photocatalyst activity. *J Mater Sci Mater Electron* 28(12):9096–9101
 100. Yao X et al (2018) Scale-up of BiVO₄ photoanode for water splitting in photoelectrochemical cell: issues and challenges. *Energy Technol* 6(1):100–110
 101. Cooper JK et al (2014) Electronic structure of monoclinic BiVO₄. *Chem Mater* 26(18):5365–5365
 102. Cooper JK et al (2015) Indirect bandgap and optical properties of monoclinic bismuth vanadate. *J Phys Chem C* 119:2969–2974
 103. Abdi FF et al (2013) The origin of slow carrier transport in BiVO₄ thin film photoanodes: a time-resolved microwave conductivity study. *J Phys Chem Lett* 4:2752–2757
 104. Pihosh Y et al (2015) Photocatalytic generation of hydrogen by core-shell WO₃/BiVO₄ nanorods with ultimate water splitting efficiency. *Sci Rep* 5:11141
 105. Liu H et al (2005) Bismuth-copper vanadate BiCu₂VO₆ as a novel photocatalyst for efficient visible-light-driven oxygen evolution. *ChemPhysChem* 6:2499–2250
 106. Liu H et al (2006) A visible – light responsive photocatalyst, BiZn₂VO₆ for efficient O₂ – photoevolution from aqueous particulate suspension. *Electrochem Solid-State Lett* 9:G187. Abdi FF et al (2017) Recent developments in complex metal oxide photoelectrodes. *J Phys D Appl Phys* 50:193002–19302
 107. Zhang K et al (2013) Metal sulphide semiconductors for photocatalytic hydrogen production. *Catal Sci Technol* 1–19. <https://doi.org/10.1039/c3cy00018d>
 108. Pareek A et al (2013) Fabrication of large area nanorod like structured CdS photoanode for solar H₂ generation using spray pyrolysis technique. *Int J Hydrog Energy* 38:36–44
 109. Pareek A et al (2014) Stabilizing effect in nano-titania functionalized CdS photoanode for sustained hydrogen generation. *Int J Hydrog Energy* 39:4170–4180
 110. Pareek A et al (2014) Nano-niobia modification of CdS photoanode for efficient and stable photoelectrochemical cell. *Langmuir* 30:15540
 111. Pareek A et al (2013) Fabrication of a highly efficient and stable nano-modified photoanode for solar H₂ generation. *RSC Adv* 3:19905–19908
 112. Pareek A et al (2017) Nano-architecture based photoelectrochemical water oxidation efficiency enhancement by CdS photoanodes. *Mater Res Express* 4:026203
 113. Pareek A et al (2017) Ultrathin MoS₂-MoO₃ nanosheets functionalized CdS photoanodes for effective charge transfer in photoelectrochemical (PEC) cells. *J Mater Chem A* 5:1541–1547
 114. Kimi M et al (2012) Preparation of Cu-doped Cd_{0.1}Zn_{0.9}S solid solution by hydrothermal method and its enhanced activity for hydrogen production under visible light irradiation. *J Photochem Photobiol A* 230:15–22
 115. Chai B et al (2011) Template-free hydrothermal synthesis of ZnIn₂S₄ floriated microsphere as an efficient photocatalyst for H₂ production under visible-light irradiation. *J Phys Chem C* 115:6149–6155

116. Bhirud A et al (2011) Surfactant tunable hierarchical nanostructures of CdIn₂S₄ and their photohydrogen production under solar light. *Int J Hydrog Energy* 36:11628–11639
117. Matsumura M et al (1983) Photocatalytic hydrogen production from solutions of sulfite using platinumized cadmium sulfide powder. *J Phys Chem* 87:3807–3808
118. Reber JF et al (1984) Photochemical production of hydrogen with zinc sulfide suspensions. *J Phys Chem* 88:5903–5913
119. Xing C et al (2006) Band structure-controlled solid solution of Cd_{1-x}Zn_xS photocatalyst for hydrogen production by water splitting. *Int J Hydrog Energy* 31:2018–2024
120. Jang JS et al (2007) Solvothermal synthesis of CdS nanowires for photocatalytic hydrogen and electricity production. *J Phys Chem C* 111:13280–13287
121. Zong X et al (2008) Enhancement of photocatalytic H₂ evolution on CdS by loading MoS₂ as cocatalyst under visible light irradiation. *J Am Chem Soc* 130:7176–7177
122. Yan H et al (2009) Visible-light-driven hydrogen production with extremely high quantum efficiency on Pt-PdS/CdS photocatalyst. *J Catal* 266:165–168
123. Jang JS et al (2008) Role of platinum-like tungsten carbide as cocatalyst of CdS photocatalyst for hydrogen production under visible light irradiation. *Appl Catal A* 346:149–154
124. Zhang K et al (2007) Significantly improved photocatalytic hydrogen production activity over Cd_{1-x}Zn_xS photocatalysts prepared by a novel thermal sulfuration method. *Int J Hydrog Energy* 32:4685–4691
125. Tsuji I et al (2004) Photocatalytic H₂ evolution reaction from aqueous solutions over band structure-controlled (AgIn)_xZn_{2(1-x)}S₂ solid solution photocatalysts with visible-light response and their surface nanostructures. *J Am Chem Soc* 126:13406–13413
126. Lei Z et al (2003) Photocatalytic water reduction under visible light on a novel ZnIn₂S₄ catalyst synthesized by hydrothermal method. *Chem Commun* 17:2142–2143
127. Shen S et al (2009) Optical and photocatalytic properties of visible-light-driven ZnIn₂S₄ photocatalysts synthesized via a surfactant-assisted hydrothermal method. *Mater Res Bull* 44:100–105
128. Jang JS et al (2008) Indium induced band gap tailoring in Ag Ga_{1-x}In_xS₂ chalcopyrite structure for visible light photocatalysis. *J Chem Phys* 128:1–6
129. Kale BB et al (2006) CdIn₂S₄ nanotubes and “marigold” nanostructures: a visible-light photocatalyst. *Adv Funct Mater* 16:1349–1354
130. Bhirud A et al (2011) Surfactant tunable hierarchical nanostructures of CdIn₂S₄ and their photohydrogen production under solar light. *Int J Hydrog Energy* 36:11628–11639
131. Pareek A et al (2017) Nanostructure Zn–Cu co-doped CdS chalcogenide electrodes for optoelectric-power and H₂ generation. *Int J Hydrog Energy* 42(1):125–132
132. Roy AM et al (2003) Immobilization of CdS, ZnS and mixed ZnS–CdS on filter paper. Effect of hydrogen production from alkaline Na₂S/Na₂S₂O₃ solution. *J Photochem Photobiol A* 157:87–92
133. Chai B et al (2011) Template-free hydrothermal synthesis of ZnIn₂S₄ floriated microsphere as an efficient photocatalyst for H₂ production under visible-light irradiation. *J Phys Chem C* 115:6149–6155
134. Kaga H et al (2010) Solar hydrogen production over novel metal sulfide photocatalysts of AGa₂In₃S₈ (A = Cu or Ag) with layered structures. *Chem Commun* 46:3779–3781
135. Kudo A et al (2002) AgInZn₇S₉ solid solution photocatalyst for H₂ evolution from aqueous solutions under visible light irradiation. *Chem Commun* 2(17):1958–1959
136. Gregory DH et al (1999) Structural families in nitride chemistry. *J Chem Soc Dalton Trans* 3:259–270
137. Su J et al (2017) Stability and performance of sulfide-, nitride-, and phosphide-based. *J Phys Chem Letts* 8:5228–5238
138. Liu G et al (2016) Enabling an integrated tantalum nitride photoanode to approach the theoretical photocurrent limit for solar water splitting. *Energy Environ Sci* 9:1327–1334
139. Wang D et al (2011) Wafer-level photocatalytic water splitting on GaN nanowire arrays grown by molecular beam epitaxy. *Nano Lett* 11:2353–2357

140. Gholipour MR et al (2017) Post-calcined carbon nitride nanosheets as an efficient photocatalyst for hydrogen production under visible light irradiation. *ACS Sustain Chem Eng* 5:213–220
141. Island JO et al (2015) Environmental instability of few-layer black phosphorus. *2D Mater* 2:011002
142. Zhu M et al (2017) Black phosphorus: a promising two dimensional visible and near-infrared-activated photocatalyst for hydrogen evolution. *Appl Catal* 217:285–229
143. Tian B et al (2018) Facile bottom-up synthesis of partially oxidized black phosphorus nanosheets as metal-free photocatalyst for hydrogen evolution. *Proc Natl Acad Sci* 1–6. <https://doi.org/10.1073/pnas.1800069115>
144. Wen M et al (2018) A low-cost metal-free photocatalyst based on black phosphorus. *Adv Sci* 1801321:1–7
145. Yuan Y-J et al (2018) Bandgap-tunable black phosphorus quantum dots: visible-light-active photocatalysts. *Chem Commun* 54:960–963
146. Tian B et al (2018) Supported black phosphorus nanosheets as hydrogen-evolving photocatalyst achieving 5.4% energy conversion efficiency at 353 K. *Nat Commun* 9:1397. -1-11
147. Paulose M et al (2006) Anodic growth of highly ordered TiO₂ nanotube arrays to 134 μm in length. *J Phys Chem B* 110:16179–16184
148. Xiang Q (2013) Hierarchical porous CdS nanosheet-assembled flowers with enhanced visible-light photocatalytic H₂-production performance. *Appl Cat B* 138:299–303
149. Zha R (2015) Ultraviolet photocatalytic degradation of methyl orange by nanostructured TiO₂/ZnO heterojunctions. *J Mater Chem A* 3:6565–6657
150. Chen F (2013) Facile synthesis of Bi₂S₃ hierarchical nanostructure with enhanced photocatalytic activity. *J Colloid Interface Sci* 404:110–116
151. Liu Y (2012) A magnetically separable photocatalyst based on nest – like γ-Fe₂O₃/ZnO double – shelled hollow structures with enhanced photocatalytic activity. *Nanoscale* 4:183–187
152. Chen CK et al (2014) Quantum-dot-sensitized nitrogen-doped ZnO for efficient photoelectrochemical water splitting. *Eur J Inorg Chem* 2014:773–779
153. Chandrasekaran S et al (2015) Highly – ordered maghemite/reduced graphene oxide nanocomposites for high performance photoelectrochemical water splitting. *RSC Adv* 5:29159–29166
154. Kim JH et al (2016) Hetero – type dual photoanodes for unbiased solar water splitting with extended light harvesting. *Nat Commun* 7:1–9
155. Zhang S et al (2014) Nanostructured tin catalysts for selective electrochemical reduction of carbon dioxide to formate. *J Am Chem Soc* 136:1734–1173
156. Asadi M et al (2014) Robust carbon dioxide reduction on molybdenum disulphide edges. *Nat Commun* 5:1–8
157. Gao L et al (2014) Photoelectrochemical hydrogen production on InP nanowire arrays with molybdenum sulfide electrocatalysts. *Nano Lett* 14:3715–3719
158. Wang H-P et al (2015) High-performance a-Si/c-Si heterojunction photoelectrodes for photoelectrochemical oxygen and hydrogen evolution. *Nano Lett* 15:2817–2282
159. Song JT et al (2017) Bimetallic cobalt-based phosphide zeolitic imidazolate framework: CoP_x phase-dependent electrical conductivity and hydrogen atom adsorption energy for efficient overall water splitting. *Adv Energy Mater* 7:16011003
160. Kast MG et al (2014) Solution-deposited F:SnO₂/TiO₂ as a base-stable protective layer and antireflective coating for microtextured buried-junction H₂-evolving Si photocathode. *ACS Appl Mater Interfaces* 6:22830–22837
161. Zhou X et al (2016) Solar driven reduction of 1 atm of CO₂ to formate at 10% energy – conversion efficiency by use of a TiO₂ protected III – V tandem Photoanode in conjunction with a bipolar membrane and a Pd/C cathode. *ACS Energy Lett* 1:764–777
162. Ji L et al (2014) A silicon based photocathode for water reduction with an epitaxial SrTiO₃ protection layer and a nanostructured catalyst. *Nat Nanotechnol* 10:84

163. Kang D et al (2017) Printed assemblies of GaAs photoelectrodes with decoupled optical and reactive interfaces for unassisted water splitting. *Nat Energy* 2:17043
164. Kumagai H et al (2015) Efficient solar hydrogen production from neutral electrolytes using surface modified Cu(In, Ga)Se₂ photocathodes. *J Mater Chem A* 3:8300–8307
165. Fan S et al (2015) High efficiency solar to hydrogen conversion on monolithically integrated InGaN/GaN/Si adaptive tunnel junction photocathode. *Nano Lett* 15:2721–2722
166. Morales-Guio CG et al (2015) Photoelectrochemical hydrogen production in alkaline solutions using Cu₂O coated with earth – abundant hydrogen evolution catalysts. *Angew Chem Int Ed Engl* 54:664

Part VIII

**Ceramic Coatings and Their Processes for
Critical Applications**



New-Generation Ceramic Coatings for High-Temperature Applications by Liquid Feedstock Plasma Spraying

35

S. Joshi, N. Markocsan, P. Nylén, and G. Sivakumar

Contents

Introduction	1372
Thermal Spraying Using Liquid Feedstock	1373
Suspension Plasma Spraying	1375
Processing	1376
Microstructure	1379
Versatility: Materials and Functionality	1381
Solution Precursor Plasma Spraying	1389
Processing	1390
Microstructure	1393
Versatility: Materials and Functionality	1397
Hybrid Powder-Liquid Feedstock Processing	1398
Processing	1400
Possible Coating Architectures	1401
Microstructures	1402
Versatility: Materials and Functionality	1403
Conclusions	1404
References	1406

Abstract

Plasma spraying with liquid feedstock offers an exciting opportunity to obtain coatings with characteristics that are vastly different from those produced using conventional spray-grade powders. The two extensively investigated variants of

S. Joshi (✉) · N. Markocsan · P. Nylén
University West, Trollhättan, Sweden
e-mail: shrikant.joshi@hv.se; nicolaie.markocsan@hv.se; per.nylen@hv.se

G. Sivakumar
International Advanced Research Centre for Powder Metallurgy and New Materials (ARCI),
Hyderabad, India
e-mail: gsivakumar@arci.res.in

this technique are suspension plasma spraying (SPS), which utilizes a suspension of fine powders in an appropriate medium, and solution precursor plasma spraying (SPPS), which involves use of a suitable solution precursor that can form the desired particles in situ. The advent of axial injection plasma spray systems in recent times has also eliminated concerns regarding low deposition rates/efficiencies associated with liquid feedstock. The 10–100 μm size particles that constitute conventional spray powders lead to individual splats that are more than an order of magnitude larger compared to those resulting from the fine (approximately 100 nm–2 μm in size) particles already present in suspensions in SPS or formed in situ in SPPS. The distinct characteristics of the resulting coatings are directly attributable to the above very dissimilar splats (“building blocks” for coatings) responsible for their formation. This chapter discusses the salient features associated with SPS and SPPS processing, highlights their versatility for depositing a vast range of ceramic coatings with diverse functional attributes, and discusses their utility, particularly for high-temperature applications through some illustrative examples. A further extension of liquid feedstock plasma processing to enable use of hybrid powder-liquid combinations for plasma spraying is also discussed. This presents a novel approach to explore new material combinations, create various function-dependent coating architectures with multi-scale features, and enable convenient realization of layered, composite, and graded coatings as demonstrated through specific examples.

Keywords

Liquid feedstock · Plasma spray · Suspension · Solution precursor · Coatings · Layered · Composite · Functionally graded

Introduction

Thermal spraying has gained widespread industrial acceptance over the years for depositing coatings to meet diverse functional requirements. The availability of numerous variants of the thermal spray technique, the diversity of available spray materials, and the continuing advances in spray equipment and associated control systems have together created new opportunities for various industrial stakeholders. The wide portfolio of thermal spray variants, such as flame spray, arc spray, atmospheric plasma spray (APS), high-velocity oxy-fuel (HVOF) spray, detonation spray, cold spray, etc., provides distinct gas temperature-gas velocity windows for particle heat-up and acceleration, offering a range of quality and cost [1]. The versatility of the thermal spray process is also unmatched by any other surface modification technology by virtue of an overwhelming choice of feedstock available in the form of powders, wire, or rods [1, 2], enabling tailoring of surface properties for any given coating application. Although the typically low deposition efficiencies (usually <60%) associated with thermal spraying have been a concern for long, the recent availability of high-power, axial-feed plasma spray systems reflects the advancements in thermal spray equipment aimed at addressing the above issue [3].

In recent times, there has been increasing interest in spraying nano- or submicron-sized powders to obtain refined microstructures that can translate into superior properties [4]. However, thermal spraying of fine-sized feedstock poses numerous challenges, the most dominant being the difficulty in injecting nano- and submicron-sized particles into the core of a thermal spray plume/flame [5]. Powders comprising fine particles do not possess good flowability, and their low momentum also seriously limits their ability to penetrate the high-velocity gas streams associated with most popular thermal spray techniques, making it difficult to achieve controlled powder feeding [6]. Spraying fine powder particles in a conventional manner can also be an environmental issue and cause health problem for thermal spray operators. Although attempts to agglomerate the nano-/submicron-sized particles have been made, inhomogeneous melting characteristics of the agglomerated particles in the plume have often been noted [7, 8]. In view of the above, alternative approaches involving use of a liquid medium, either in the form of a suspension of fine particles or as a solution precursor containing dissolved salts which can lead to particle generation in situ, have been conceived [3, 6, 9–12]. These suspension and solution precursor-based thermal spray processes constitute the central theme of this chapter.

Thermal Spraying Using Liquid Feedstock

As briefly mentioned above, liquid feedstock employed for thermal spraying can be broadly classified into two types: (a) suspensions and (b) solution precursors. The former utilizes fine powders (comprising particles approximately 100 nm–2 μm in size) suspended in a suitable solvent, typically water or alcohol, to obviate the problems associated with their feeding without the need for an additional agglomeration step [4, 12, 13]. The injection of a suspension through a dedicated feeding device into a plasma/HVOF plume to deposit coatings has been the subject of growing research in recent times. The process requires a stable suspension of the desired powder, prepared in an aqueous or organic solvent. The mechanism leading to coating formation is discussed in a subsequent section. It is pertinent to note that plasma spraying has been the method of choice for a vast majority of suspension-based coating efforts, by virtue of the availability of a high-energy flux that is needed to eliminate the solvent [14]. Thus, this chapter will particularly focus on suspension plasma spraying (SPS), rather than using suspensions with other thermal spray variants. The relatively recent development enabling axial injection of feedstock, and thereby permitting far more effective utilization of the energy available in the plasma plume, has been found to afford even greater versatility and is a potential game changer for liquid feedstock plasma spraying. Apart from eliminating concerns regarding low deposition rates/efficiencies associated with liquid feedstock, axial SPS has also been demonstrated to enable considerable microstructure control through proper selection of processing conditions [15]. Relatively few but growing number of reports on suspension spraying employing HVOF torches (termed s-HVOF) also represents additional possibilities of generating fine-structured coatings with interesting deposition characteristics using suspensions [16].

Although considerably more challenging, the utilization of solution precursors rather than suspensions potentially stands to provide further added benefits. For example, the latter relies on pre-synthesis of nano- or submicron particles, which is more expensive compared to conventional powder feedstock. Hence, a process involving single-step consolidation of in situ formed nanoparticles is more advantageous. Accordingly, solution precursor spraying is another variant of liquid feedstock-based thermal spraying that is deemed interesting. In contrast to the growing academic and industrial interest in SPS, attention to use of solution precursors as feedstock for thermal spraying has been rather subdued. This can be attributed to the even higher energy demands imposed by the solution precursors compared to suspensions [12]. By and large, the higher energy demand results from the additional steps leading to pyrolysis and in situ powder formation that are needed when precursor salts are used [9, 12, 17, 18]. This correspondingly compounds the challenges in achieving commercially interesting throughputs (e.g., coating thickness per pass) using conventional radial feed systems. Consequently, a majority of prior efforts exploring the solution precursor approach have relied on plasma spraying due to energy considerations [6, 12, 13, 19–28]. Thus, apart from SPS, solution precursor plasma spraying (SPPS) is the other area of focus in this chapter. In the context of SPPS, too, the newer axial plasma spray systems appear a much more promising alternative due to the improved thermal energy utilization that it enables.

In case of both SPS and SPPS, the process setup is nearly identical to that employed in a conventional APS process, wherein the powder feeder is replaced with a liquid injection device comprising a pressurized precursor tank and an atomizer. A typical arrangement is schematically illustrated in Fig. 1 [9]. Although the figure depicts radial injection of feedstock, it can also be readily adapted for axial-feed plasma spray systems mentioned above. The fact that a suitable feeder to deliver the liquid feedstock is the only hardware that is additionally required apart from a routine APS setup makes induction of the SPS/SPPS into a regular plasma spray line quite straightforward. Notwithstanding the fact that availability of significantly higher thermal energy is conducive for coating formation using precursor salts, some studies on HVOF spraying of solution precursors have also been reported [29].

An extension of liquid feedstock thermal spraying, by combining it with conventional powder processing, has also been demonstrated to present a novel method for depositing coatings with unusual microstructures. The above hybrid approach involves either sequential or simultaneous feeding of powder feedstock and a suspension/precursor solution with independent control of their feed rates, to conveniently realize diverse coating architectures [30, 31]. Depending upon the strategy adopted for feeding powder and liquid feedstocks, layered (sequential feeding), composite (simultaneous feeding with constant feed rates), as well as functionally graded coatings (simultaneous feeding with progressively varying relative feed rates) can be achieved, opening up exciting avenues for realizing function-specific architectures [21].

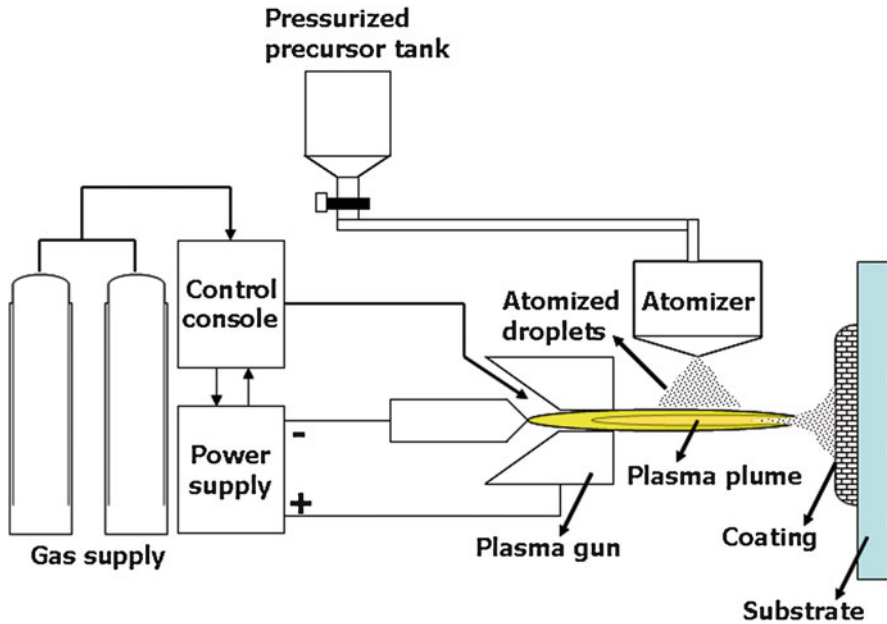


Fig. 1 Schematic illustration of a typical liquid feedstock delivery arrangement that can be utilized for SPS and SPPS [9]

The application potential of the above liquid feedstock and powder-liquid hybrid feedstock approaches is immense. Accordingly, the following sections discuss the salient features of the SPS, SPPS, and hybrid techniques, highlighting their versatility for depositing a vast range of ceramic coatings with diverse functional attributes. Their utility, particularly for high-temperature applications, is also discussed through some illustrative examples.

Suspension Plasma Spraying

Among all the liquid feedstock thermal spray approaches, the SPS technique has been the most widely investigated. Although most early efforts were motivated by the desire to seek pathways to address issues associated with utilizing fine powder feedstock (20 nm–5 μm) for coating deposition [6], the versatility of the approach and its inherent ability to yield unique microstructures was soon realized. For example, thermal barrier coatings (TBCs) produced by conventional APS have been widely used in the gas turbine industry for several decades, and, more recently, coatings deposited by electron beam physical vapor deposition (EBPVD) have emerged as an alternative due to their inherent strain-tolerant columnar structure. The SPS technique has been shown to be capable of cost-effectively yielding such columnar microstructures. Thus, the attractive TBC applications have predominantly

fueled the widespread initial interest in SPS deposition of yttria-stabilized zirconia (YSZ), which has now gradually begun to be extended to other functional applications also.

Processing

In SPS, fine powder particles (solute) are mixed with a liquid (solvent) to form a suspension, which is injected into the plasma plume as the feedstock material [32–34]. The most commonly used solvents are water, alcohol (typically ethanol), or their suitable mixtures. While both water and alcohol have distinct advantages and shortcomings, it is acknowledged that the type of solvent plays a key role in determining the coating microstructure. The heat required to vaporize ethanol is one-third of that necessary for water, which leads to higher power being needed for spraying aqueous suspensions [35].

Consequently, the deposition efficiency is also typically higher in case of the former with, for example, the efficiency being nearly doubled when switching from a water-based YSZ suspension to an ethanol-based YSZ suspension, all other parameters being identical [36]. The solute is usually a ceramic powder, with particle size ranging from nano-metric to a few microns. In practice, 25 wt.% solid loading (powder quantity) in the suspension is commonly used, although there is a constant desire to increase the solids content in a suspension in an effort to enhance throughput. The solid loading is also occasionally dictated by the type of solute and solvent as well as by the type of the microstructure being targeted, since it influences the viscosity and surface tension of the suspension which crucially govern SPS coating formation.

An illustration of the various stages involved in coating formation in case of SPS, from the time the suspension is injected to the eventual deposition of the corresponding coating on the substrate, is depicted in Fig. 2 [37]. Powders of different sizes/morphology used in the suspension, and their state just prior to impact with the substrate, are also shown; these significantly influence the microstructure of the resulting coating. It is important to have a good understanding of each of the represented stages in order to develop an ability to control the process and influence the resulting coating microstructure.

The first stage corresponds to injection of the suspension. The suspension can be injected into the plasma plume either radially or axially, as illustrated in Fig. 3 [37]. In case of radial injection, the size and velocity of the suspension droplets at injection play a particularly crucial role since the momentum of droplets can significantly influence their trajectories in-flight as they traverse through the plasma plume. For example, very small droplets may not be able to penetrate the plasma at all and “bounce off,” whereas large droplets may completely pass through the plasma plume as illustrated in Fig. 3a, reaching the substrate in unmolten condition in both cases due to their inability to fully utilize the energy available in the plasma plume. Moreover, suspension droplets of varying size entering different zones of the plasma plume experience different dwell times (the total time a droplet spends in the

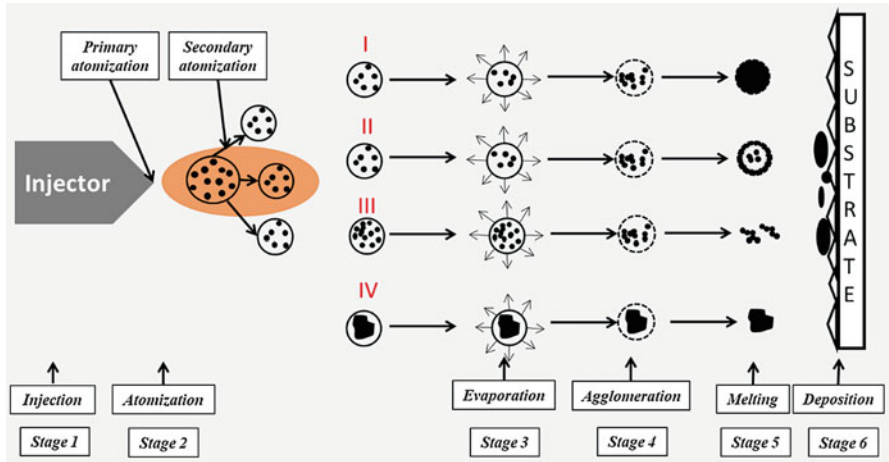


Fig. 2 Schematic of various stages of a suspension droplet having varied constituent particle sizes, i.e., medium (I and II), very fine (III), and coarse (IV), in-flight during plasma spraying, from injection of the suspension to the final deposition on the substrate [37]

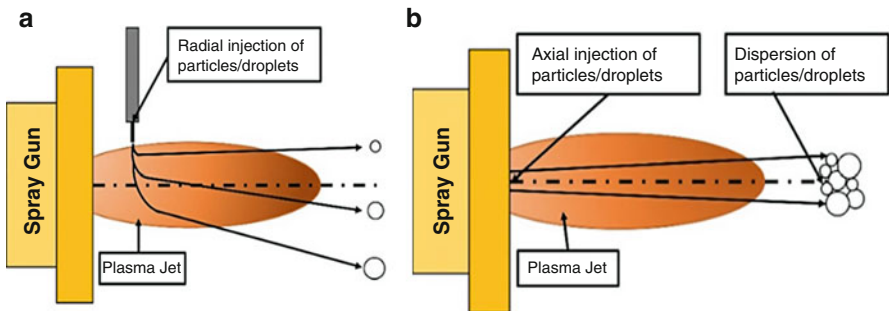


Fig. 3 Schematic of radial injection (a) versus axial injection (b) of liquid feedstock [37]

plasma plume), and this leads to a variable heat-up and acceleration of the droplets. The net outcome is often a heterogeneous microstructure and/or overspray. The above problems are significantly mitigated when axial injection is resorted to, as the trajectory of all particles is predominantly coaxial with the plasma plume and variations in particle heat-up and acceleration are minimized. Additionally, introduction of the suspension in such a manner permits more intimate droplet-plasma contact for effective utilization of the plasma energy, thereby also enabling higher throughputs. Thus, the relatively recent advent of high-energy axial-feed plasma systems is a game changer for energy-intensive liquid feedstock spraying.

In the second stage, the injected suspension undergoes atomization to form fine droplets that follow the plasma stream. Atomization is driven by a balance between two competing driving forces: while the drag from the plasma generates a shear force on the droplet that tends to disintegrate the droplet further, the surface tension resists

its further breakup. Fazilleau et al. [38] modelled droplet breakup during SPS processing and derived a relation between the various suspension parameters and the atomized suspension droplet size, as shown in Eq. 1 [39]:

$$D = \frac{8 \sigma}{C_D \rho u^2} \quad (1)$$

In the above expression, D (m) is the droplet diameter following atomization, σ (N/m) is the surface tension of the suspension, C_D is the dimensionless drag coefficient, ρ (kg/m³) is the density, and u (m/s) is the plasma stream velocity. From the above equation, it can be seen that formation of a smaller droplet is facilitated by a lower surface tension and a higher plasma drag force, which depends on plasma density and velocity. The viscosity of the suspension, which is not discussed in the above equation, also influences atomization with a lower viscosity favoring greater atomization of the suspension [35].

After the suspension droplets are formed, they are rapidly heated up by the plasma stream having temperatures in excess of 15,000 K in the core, resulting in evaporation of the solvent. The vaporization step consumes a significant amount of thermal energy from the plasma. Since a “colder” plasma may result in insufficient melting of the remnant solid particles following vaporization of the solvent, more powerful plasma guns capable of providing higher thermal energy are needed for suspension plasma spraying as compared to conventional powder spraying. The droplets are also concurrently accelerated during the vaporization stage. After the solvent evaporates, the fine remaining particles also tend to undergo agglomeration. The extent of agglomeration is governed by the size of the particles as has been attempted to be illustrated in Fig. 2. For example, in case IV where there are coarse powder particles constituting the original suspension, the agglomeration stage is not valid; however, when the constituent powder particle size is extremely fine as in case III, the agglomeration can be notable. The particles may also often be sintered or fused into larger particles, and all of the above can potentially alter the initial characteristics (such as mean particle size) of the solute particles originally suspended in the solvent.

Complete vaporization of the solvent brings the fine solid powder particles, agglomerated or otherwise, in direct contact with the plasma whereupon they are expected to undergo melting. The extent of melting of the particles is governed by the particle size as well as by the operating parameters such as power employed during the process, composition of plasma gases (and thereby enthalpy), dwell time, and feed rate of the suspension [39–41].

In the final stages of coating formation, the molten or semi-molten particles are accelerated toward the substrate where they form fine “splats” on impact. Each incoming molten particle solidifies on a previously formed splat leading to coating deposition. Overlapping of the splats as a consequence of relative gun-substrate traverse leads to desired area coverage, while stacking up of the solidified splats leads to the desired coating thickness. These “splats” are essentially the building blocks for coating formation, and their shape, as well as other microstructural

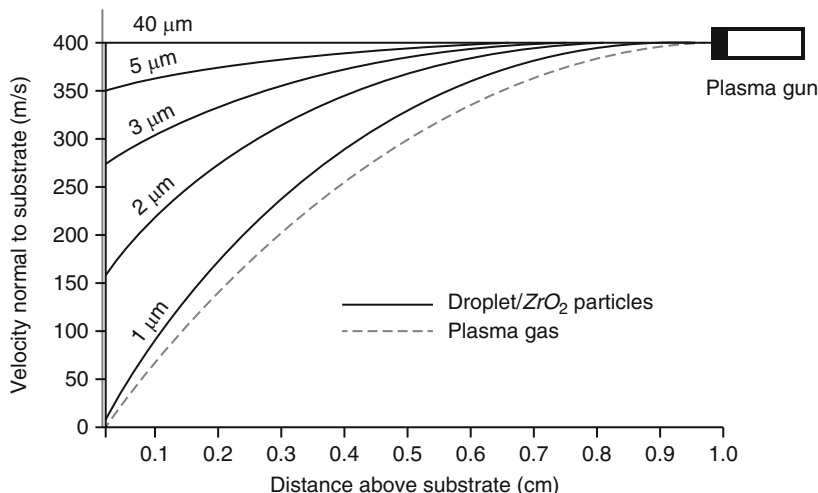


Fig. 5 Schematic showing the effect of plasma flow on trajectory of droplets of varying momentum prior to final impact with the substrate [37]

coating formation mechanism in SPS is complex. However, the considerable influence of particle momentum on its trajectory in SPS as discussed above, combined with the comparable magnitude of particle size and surface asperities, provides the possibility of tailoring different types of microstructures. This, in turn, leads to different properties of the coatings. As the very fine particles follow the trajectory of the plasma stream, in close proximity to the substrate, they travel in a nearly tangential direction to the substrate and impact the substrate's asperities at shallow angles. When they "stick" on the asperities at such shallow angles as depicted in Fig. 4, both lateral and vertical growths are enabled during subsequent successive impact of the molten particles, which leads to formation of columns and their growth during the entire spraying process. A typical columnar microstructure of a SPS TBC is presented in Fig. 6 [43].

Based on the above concepts, VanEvery et al. [44] have proposed three distinct types of coating microstructures in SPS. If the droplet size after the fragmentation is extremely small ($<1 \mu\text{m}$), the shadowing effect is larger, which can generate a columnar-type structure. Droplets having a relatively higher momentum ($>1 \mu\text{m}$) but still small enough to be affected by the plasma flow ($<5 \mu\text{m}$) can form a structure with some porosity bands within the columns, which can be termed as a feathery columnar structure. Evolution of such columns is illustrated in Fig. 7 [37] where it can be clearly seen how columns build up after 1, 2, 3, and 60 layers deposition (passes) on a bond coat asperity due to the shadowing effect. After only 2–3 passes, it can be clearly seen that columns and intercolumnar gaps start developing contours on the substrate's rough surface. Further larger droplets ($>5 \mu\text{m}$) have an even higher momentum and impact the substrate almost perpendicularly. This can result in a dense coating (with no columnar structure) or a vertically cracked coating. The above three types of coatings are exemplified in Fig. 8 which illustrates the

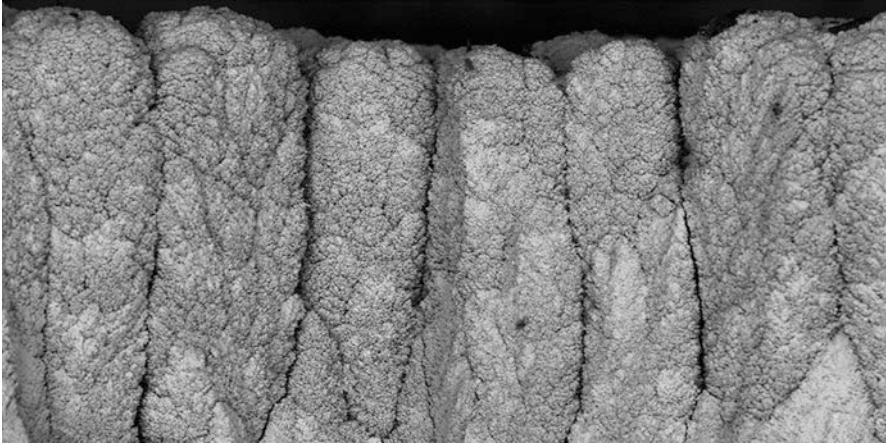


Fig. 6 Typical columnar microstructure of a SPS TBC [43]

microstructural tailoring that is possible in case SPS [45]. Depending on a specific combination of numerous factors such as feedstock material, spray technique, spray parameters, etc., any of a wide range of structures similar to these can be obtained.

Apart from the typical microstructural features present in standard APS TBCs, the SPS coatings are characterized by some additional ones such as spacing between columns (intercolumnar spacing) or very fine (sub-micrometric or nano-metric) pores, which may be either interconnected or isolated. All these different features are marked in Figs. 9 and 10, which show a typical cross section and top view, respectively, of a SPS TBC.

Versatility: Materials and Functionality

All microstructural features shown in Figs. 8, 9, and 10 can significantly affect both the thermally insulating nature as well as the lifetime of the SPS TBCs. Vertical cracks or intercolumnar spacing are through the thickness of the TBC, and they confer strain tolerance to coatings [46, 47]. Branching cracks and inter-pass porosity bands are perpendicular to the direction of heat flow within the coating and, hence, can act as significant thermal barriers within the coating [46, 48]. Other fine features such as cracks and pores also help in decreasing the overall thermal conductivity of the coating.

Since the microstructure of an SPS TBC can vary significantly as presented in Fig. 8 and also plays a central role in determining the functional performance of the coatings, it is important to have a good understanding of factors governing coating formation. For example, Ganvir et al. have revealed the close correlation between spray conditions and the in-flight characteristics of the particles which, in turn, influence coating formation and the resulting microstructures [49]. Using an axial suspension feeding capable plasma spray gun (Mettech III) and a feedstock

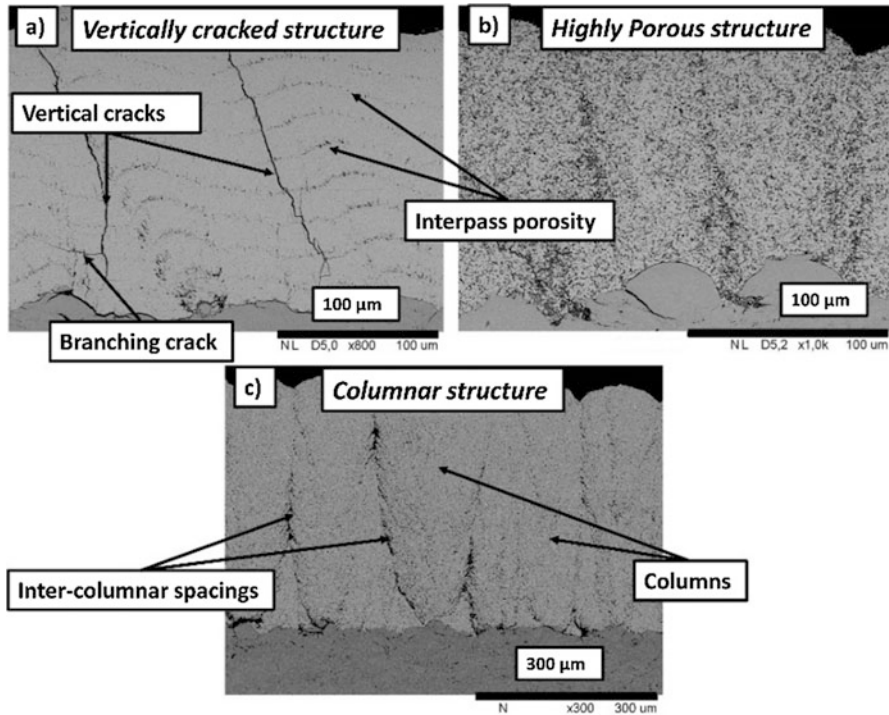


Fig. 8 SEM micrographs of cross sections of SPS-derived coatings, showing the variety of microstructures of TBCs which can be produced by suspension plasma spraying. (Vertically cracked (a), highly porous (b), and columnar (c)) [45]

consisting of ethanol and 25 wt.% 8YSZ powder ($D_{50} = 492$ nm), five different sets of process parameters (Table 1) were employed to produce top coats on identical substrate specimens [49]. As can be observed in Fig. 11a, b, the total porosity in the top coat as well as the content of both fine pores ($<1 \mu\text{m}^2$) and coarse pores ($>1 \mu\text{m}^2$) can vary significantly with spray conditions [49]. Microstructural features can also undergo changes when the coatings are exposed to cyclic thermal loads, as reflected in considerable variation in the coarse-fine porosity distribution in as-sprayed and heat-treated conditions (Fig. 11). Upon long time exposure to elevated temperatures, sintering can occur in coatings. A commonly observed effect of sintering on the exposed coatings is that the smaller microstructural features (fine pores and cracks) tend to coalesce depending on their size and shape, as well as upon the time and temperature of exposure. Healing of the small pores/cracks leads to reduction in fine porosity content after heat treatment (Fig. 11b) but is also accompanied by a volume contraction of the columns that results in increasing the intercolumnar spacing and globally to increasing coarse porosity content (Fig. 11a). This mechanism seems to be valid for most of the investigated coatings presented in Fig. 11, excepting sample Exp4 that shows an inverse trend. As the

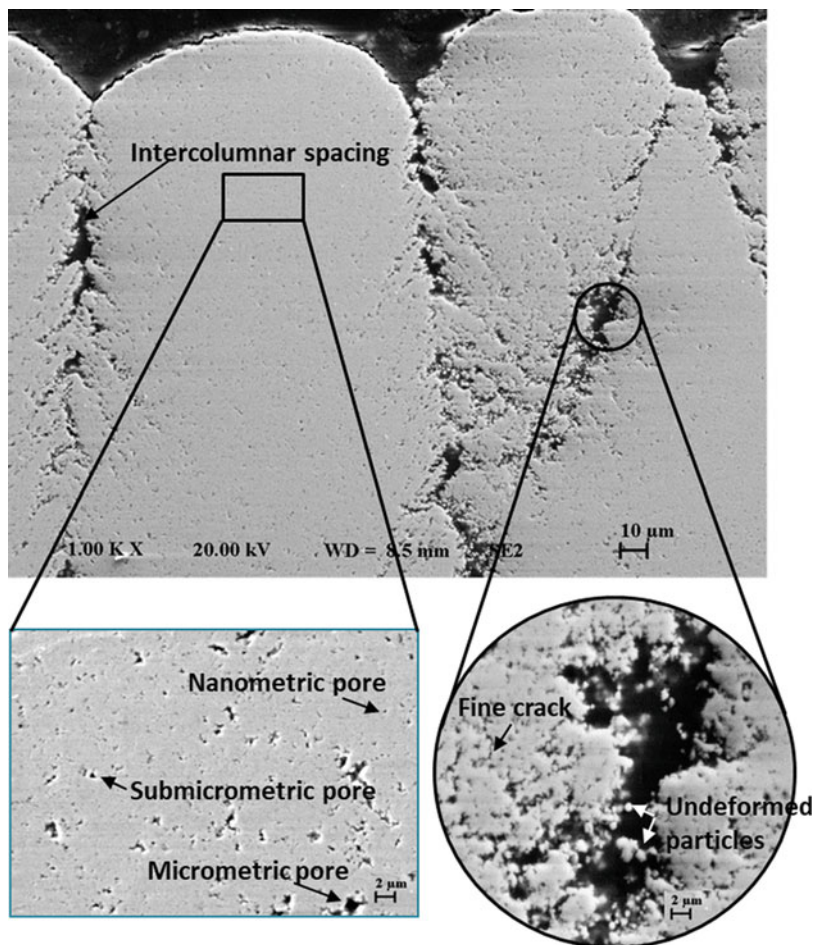


Fig. 9 SEM micrographs of a cross section of a SPS TBC showing various characteristic microstructural features

authors of the study observed, this particular sample had a relatively high total porosity content with a mean pore size higher than in the rest of the coatings. Thus, the sintering effect manifested more in the form of partial healing of the fine and coarse pores within the columns, while the intercolumnar spacing did not change significantly. Thus, both the fine and coarse porosities were found to decrease upon high-temperature exposure.

The thermal properties of the coatings are also affected by the above microstructural variations in terms of pore volume content as well as size and shape of pores. Figure 12 presents the thermal conductivity of the samples presented in Fig. 11, measured by laser flash techniques [49]. As expected, the lower thermal conductivity values are observed in coatings with higher porosity. It was also found that the

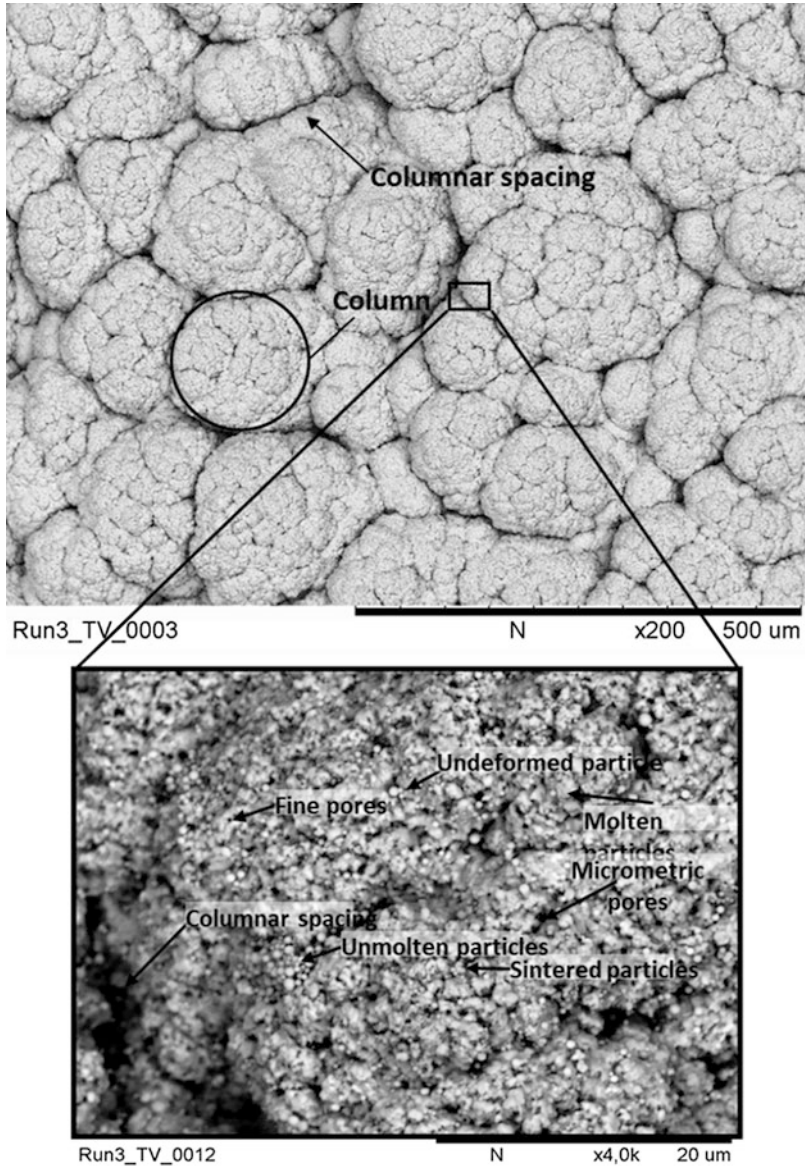
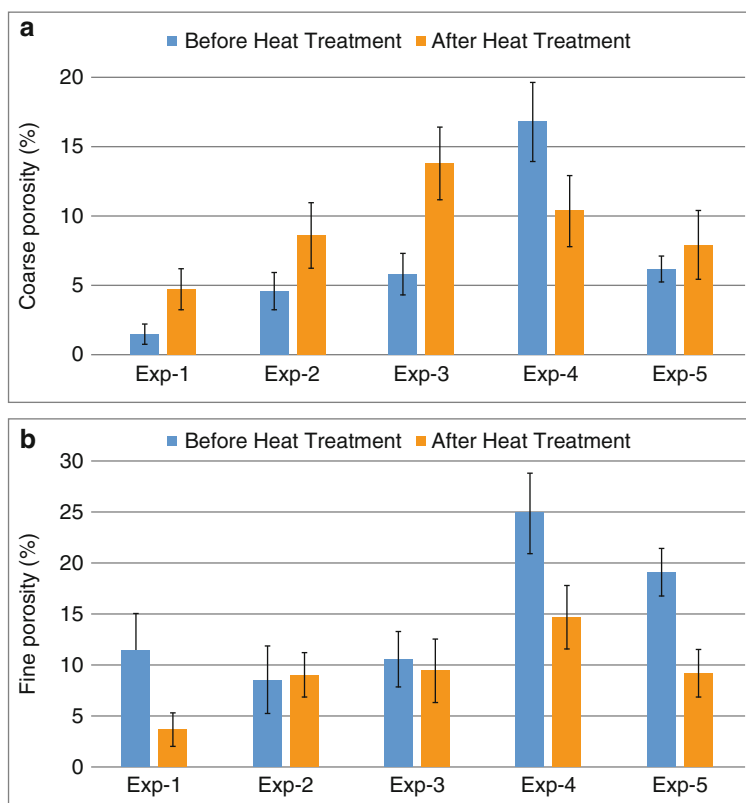


Fig. 10 SEM micrographs of a top view of a SPS TBCs showing various characteristic microstructural features

coatings respond differently to heat treatment, in terms of variations in thermal conductivity (Fig. 12). No specific trend in thermal conductivity with heat treatment was discerned: the heat treatment was found to either increase or decrease the thermal conductivity, and, in some samples, it even remained nearly unchanged.

Table 1 Process conditions employed for depositing coatings presented in Figs. 10 and 11 [49]

Process parameter	Specimen nomenclature				
	Exp1	Exp2	Exp3	Exp4	Exp5
Spray distance (mm)	75	50	100	100	100
Surface speed (cm/s)	145.5	75	75	216	216
Suspension feed rate (mL/min)	70	45	45	100	45
Total gas flow rate (L/min)	250	200	300	300	200
Total power during spray (kW)	125	101	124	124	116
Total enthalpy during spray (kJ)	13	11.2	12.5	12.5	11.2

**Fig. 11** (a) Coarse porosity and (b) fine porosity values before and after isothermal heat treatment (argon at 1150 °C for 200 h) determined by image analysis technique [49]

Among the samples with significant variation in thermal conductivity after heat treatment was Exp3. Although the exact reason for the significant reduction of thermal conductivity in this particular case is not well understood, the authors of the study [49] have explained this based on a combination of three types of microstructural changes observed after heat treatment, namely, sintering, pore

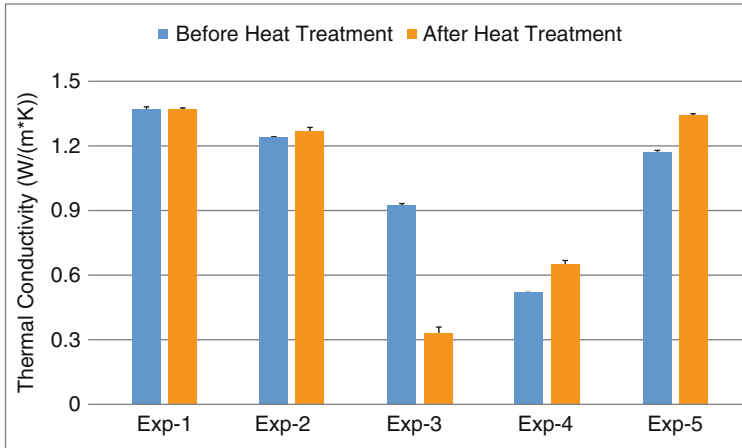


Fig. 12 Thermal conductivity of various SPS TBCs before and after heat treatment as determined by laser flash technique [49]

coarsening, and crystallite size growth. It is known that the scattering interfaces in TBCs affect the thermal conductivity of the coatings due to phonon scattering. Sintering decreases the porosity by healing the pores/cracks (reducing the scattering interfaces) leading to a thermal conductivity increase. Pore coarsening, on the other hand, increases the overall porosity, thus causing thermal conductivity decrease. Growth in crystallite size decreases the grain boundary interfaces and can increase the thermal conductivity, similar to sintering.

As in case of conventional powder-derived TBCs, 8 wt.% partial stabilized zirconia (8YSZ) is the most widely used material for suspension plasma spraying of TBCs. With its continuous deployment in the gas turbine industry for more than three decades, 8YSZ has been one of the materials with highest longevity in thermal spraying [50]. A unique combination of low thermal conductivity, high thermal expansion, and good mechanical properties make 8YSZ the material of choice for demanding high-temperature insulating applications. The main drawback of 8YSZ, however, is that its working temperature is limited to 1200 °C. Beyond this temperature, apart from significant sintering, irreversible phase transformations occur which can contribute to premature coating failure. With increasing demand for improved efficiency of gas turbine engines, higher inlet temperature of the engine is one of the envisaged approaches. Therefore, intensive work has been dedicated to exploring new TBC materials capable of performing at higher operating temperatures without compromising important requirements such as sintering resistance, phase stability, thermal conductivity, oxidation resistance, and resistance to CMAS -(calcium-magnesium-aluminosilicate).

In response to the above, new ceramic materials such as pyrochlores, perovskites, hexaaluminates, etc. have been proposed as alternatives to YSZ for high-temperature applications [51–53]. As far as powder plasma spraying is concerned, significant improvement in the functional performance (thermal conductivity, thermal cyclic life) of the TBCs has been reported using perovskite, pyrochlore, and garnet

compositions compared to YSZ [54–57]. However, these new TBC materials have so far been mostly studied as coatings deposited by APS or EB-PVD, and relatively few SPS efforts focusing on these materials have been reported. In one such study, the family of pyrochlores of rare earth zirconates has been shown to be very promising as they offer the lowest thermal conductivity over many other ceramic materials including YSZ as well as a high thermal expansion coefficient (CTE) almost similar to YSZ [58]. Two of the most studied pyrochlores are gadolinium zirconate ($\text{Gd}_2\text{Zr}_2\text{O}_7$, henceforth referred to as GZ) and lanthanum zirconate ($\text{La}_2\text{Zr}_2\text{O}_7$, henceforth referred to as LZ). The main drawback of LZ is the difficulty in preserving the desired stoichiometry of the coating material due to the propensity of La_2O_3 to evaporate during spraying [59–61]. On the other hand, GZ shows good stability at temperatures over 1200 °C [62], besides exhibiting very good resistance to sintering and CMAS attack [63, 64]. Yet, a significant limitation of GZ is its lower fracture toughness compared to YSZ [65, 66], which seriously restricts its resistance to thermal shock. It also has a tendency to react with the alumina from the thermally grown oxide (TGO) layer that develops at the top coat/bond coat interface, thus limiting the capacity of the TBC to withstand long thermal exposure [53].

A possible solution to overcome the abovementioned limitations while preserving the outstanding high-temperature properties of GZ is to spray it as a multilayered coating system [67, 68]. The thermal properties and functional performance of double-layered GZ/YSZ and triple-layered GZ/GZ/YSZ systems have been compared to standard single layer YSZ by Mahade et al. [39, 62, 69–72]. The reason for adding the third GZ layer was to improve the erosion resistance and CMAS penetration by adding a dense and thin (approx. 30 μm) layer on the top. The microstructural SEM images of the above double- and triple-layered GZ-YSZ coating systems, along with a conventional YSZ-based TBC, sprayed on identical substrates and bond coats, are shown in Fig. 13 [71].

Thermal conductivity measurements by laser flash technique have revealed superior properties of GZ-based top coats as compared to a YSZ TBC. Thermal conductivity of the GZ TBCs was reported to be lower at both room temperature and over the entire temperature range of interest between RT and 1000 °C [62, 69]. The GZ-based multilayered TBCs also exhibited superior performance during lifetime assessment tests, i.e., thermal cyclic fatigue at 1100 °C and 1200 °C and cyclic thermal shock at 1300 °C. Given the inferior mechanical properties of bulk GZ, the double-layered GZ TBC had the lowest erosion resistance followed by the triple-layered GZ, while the single-layer YSZ had the best erosion performance [72]. Due to the columnar structure of the SPS TBCs, the erosion performance of the YSZ coatings is better than that of corresponding APS (dry powder) TBCs and comparable to EB-PVD TBCs [71]. It is pertinent to mention that the erosion results of GZ-based multilayered TBC are not very dissimilar to those of the YSZ TBC sprayed by APS [71].

Although the main focus of SPS research has hitherto been on TBCs, there is now a growing emphasis on its use for realizing other functional coatings too. By virtue of the possibility of spraying nano- and submicron-sized particles suspended in different solvents, the SPS coatings can be tailored to produce a variety of microstructures such as porous columnar, dense vertically cracked, etc. [73–75]. The possibility to realize

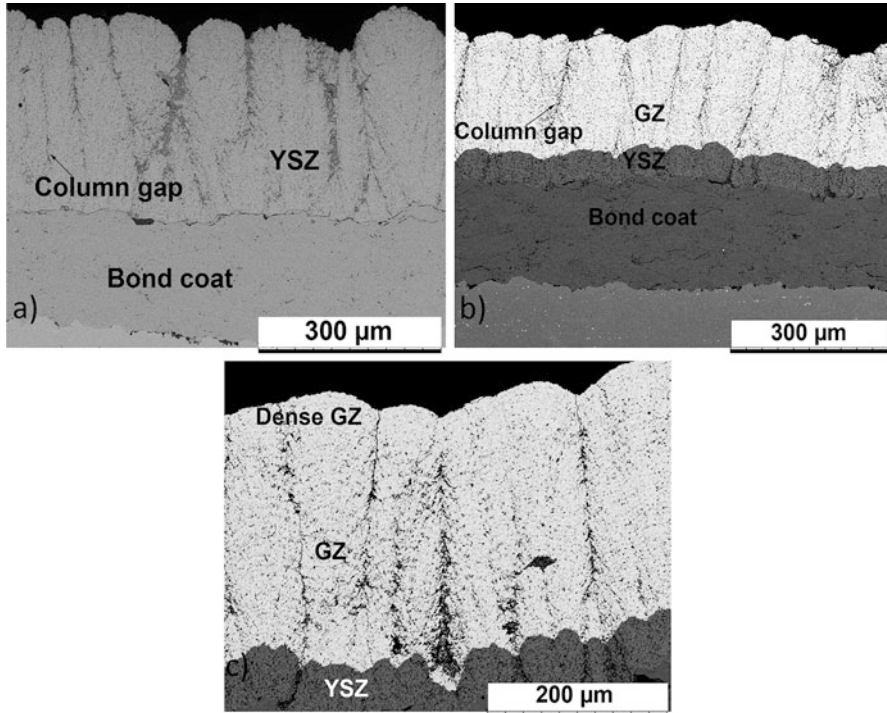


Fig. 13 SEM micrographs of cross sections of different TBC systems: (a) single layer YSZ; (b) double layer GZ/YSZ; (c) triple layer GZ/GZ/YSZ TBC [71]

refined Al_2O_3 microstructures more appropriate for wear resistance applications than APS coatings has also been demonstrated by Goel et al. [76]. Preliminary work in the authors' group exploring the potential of SPS Cr_2O_3 , Cr_3C_2 , and TiC coatings has also shown promise of exploiting SPS for developing a new generation of wear resistance coatings [10, 77]. A typically dense SPS-derived layer of Cr_2O_3 with fine porosity is shown in Fig. 14 [77]. Mubarak et al. have reported SPS processing of SiC coatings [78], while Berghaus et al. have shown the capability of SPS to minimize in-flight oxidation of WC-Co feedstock [79]. In recent times, an increasing number of other functional applications employing the SPS route have also been reported. These include coatings for superhydrophobic and icephobic [80], photocatalytic [81], and biomedical [82] applications.

Solution Precursor Plasma Spraying

SPPS is an exciting method to produce a wide variety of functional oxide ceramic coatings, starting with appropriate precursor salts dissolved in a suitable solvent, in contrast to either a conventional "coarse" powder feedstock or a suspension

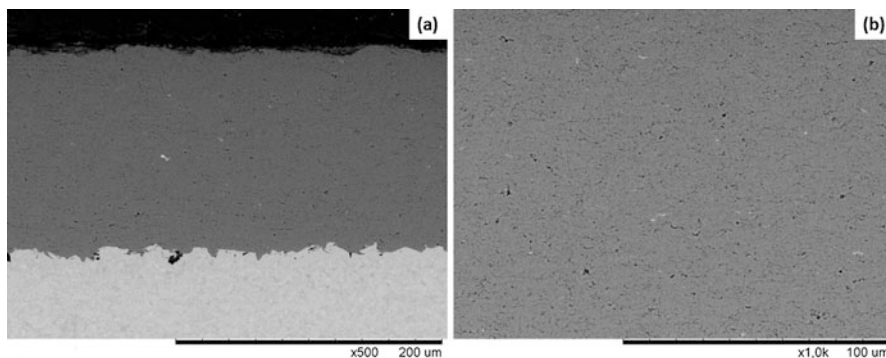


Fig. 14 SEM image of cross section of SPS Cr₂O₃ showing (a) low-magnification cross-sectional overview and (b) high-magnification microstructure with fine distributed porosity [77]

involving already formed “fine” powders suspended in a solvent. The technique utilizes aqueous/organic chemical precursor solutions fed into the high-temperature plasma plume employing a dedicated delivery device as shown previously in Fig. 1. The SPPS process opens up new avenues for developing compositionally complex functional oxide coatings. Some of the main potential benefits are as follows:

- Ability to create nanosized microstructures without any feeding problems normally associated with powder-based systems
- Flexible, rapid exploration of novel precursor compositions and their combinations
- Circumvention of expensive powder feedstock
- Better control over chemistry of the deposit

Processing

The idea of utilizing solution precursors for synthesizing ultrafine particles using a combustion flame dates well back to the 1960s. Such salts were decomposed in the presence of natural gas and air for producing metal oxide (TiO₂, SiO₂, etc.) powders from corresponding metal chlorides in hydrocarbon flames [83]. Subsequently, many variants of this process have emerged for synthesizing powders as well as films through spray pyrolysis-based routes, and SPPS is one such attractive variant. To develop thick ceramic oxide films/coatings, solutions of metal salt precursors like nitrates, acetates, isopropoxides, butoxides, etc., dissolved in a suitable solvent like water, methanol, isopropanol, etc., have been employed [18, 23–25]. A number of steps, including droplet breakup, solvent evaporation, solute precipitation, gelation, pyrolysis, sintering, and melting, have been proposed to be involved during the transformation of an injected precursor droplet into a coating [20, 84–87]. A plausible sequence of event proposed in the literature is schematically shown in Fig. 15 [85]. Moreover, all these steps need to occur in a relatively short time scale that is

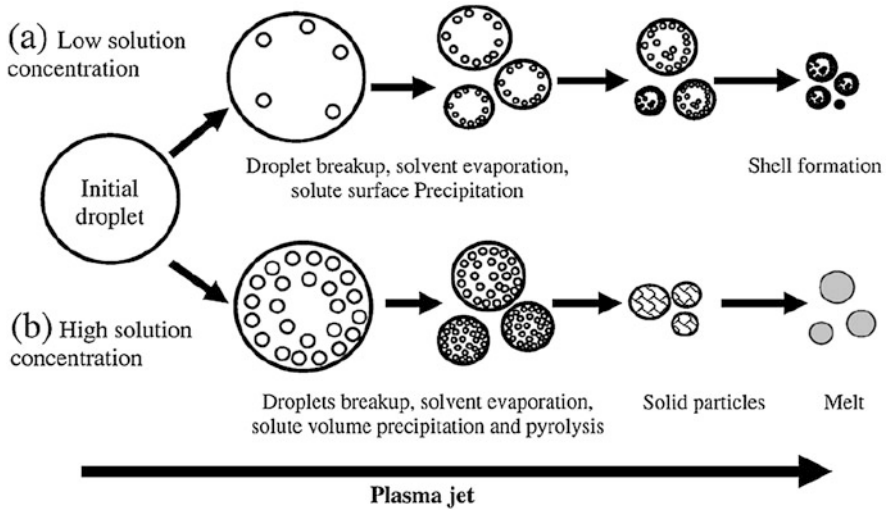


Fig. 15 Schematic illustration of steps typically associated with coating formation by the SPPS route [85]

typical of plasma spraying, usually of the order of milliseconds. Thus, a high-energy source is preferred, and this is the reason why high-energy plasma spray is widely used for precursor-based deposition than any of the other thermal spray variants [18–28, 51, 88–94]. A prominent feature of SPPS is the possibility of single-step consolidation, which avoids the need for any secondary treatment processes that are typically adopted in spray pyrolysis routes [95–97].

In case of SPPS, the high-intensity plasma source can also be used to preheat the substrate which, in turn, not only enhances the bonding of the impacting splats but also leads to enhanced diffusion and surface mobility of the adsorbed atoms on the substrate surface during deposition [84]. Among the various precursor-based deposition processes, the rapid reaction rates and high deposition rates are specific advantages of the SPPS process. As may be expected, the process parameters play a crucial role and need to be optimized to achieve the desired coating characteristics. These parameters include both the spray process variables (like plasma power, gas flow rates, nozzle type, standoff distance, substrate temperature, etc.) and the precursor-related variables (such as chemistry, concentration, and flow rate).

A vast majority of early SPPS studies were primarily focused on YSZ coatings, due to the immediate industrial applications of TBCs in land-based and aero gas turbines, SOFCs, etc. The first step in deposition of SPPS YSZ coatings involves the formulation of appropriate precursors to achieve coatings with desired characteristics. It is pertinent to point out that the choice of zirconia-forming precursors usually includes zirconium alkoxides, zirconium oxychloride, or zirconium acetate. In general, alkoxides of yttrium and zirconium are highly moisture sensitive and readily form precipitates upon exposure to environment, while chlorides are known to

produce harmful fumes, and, thus, their use is avoidable [98]. Zirconium acetate has the ability to dissolve in water to form an aqueous solution, and the exothermic reaction resulting from the carbonaceous species can be an added benefit during spraying of energy-intensive solution precursors. Similarly, yttrium acetate, yttrium isopropoxide, and yttrium nitrate have been used as yttria-forming precursors in prior studies [99]. Apart from the relatively lower cost of yttrium nitrate compared to yttrium acetate, one additional factor that makes the former an attractive choice is the fact that Y_2O_3 forms at a relatively lower temperature of 450 °C when yttrium nitrate is used, whereas complete transformation from yttrium acetate to Y_2O_3 occurs only at 650 °C [99]. Such considerations usually dictate the selection of an appropriate precursor for deposition of a targeted chemistry by SPPS.

Notwithstanding a reasonably large number of studies involving SPPS, one of the reasons why the mechanism of coating formation during SPPS processing was not well understood for long was because the in-flight diagnostic tools successfully used with various conventional thermal spray processes involving coarser powder particles could not be used with SPPS. The typically fine size ($\sim 1 \mu\text{m}$) of droplets/particles associated with SPPS was a major hurdle, and, hence, development of a good process understanding has relied on investigation of particles collected in-flight and a study of the splat morphologies [4, 85, 100]. The latter approach has been found to be extremely useful in gaining valuable insights into in-flight particle generation and splat formation leading to coating deposition [9].

Figure 16 reveals an illustrative example of how different processing conditions can lead to vastly varying particle morphologies during SPPS of an aluminum nitrate precursor for deposition of alumina coatings [101]. For example, use of a lower plasma power results in an irregularly shaped particle which corresponds to the presence of a mainly unpyrolyzed precursor. On the other hand, the hollow particles seen in the figure are an outcome of precursor droplets experiencing high surface evaporation rates when exposed to high plasma power. The precursor concentration and the droplet trajectory within the plasma plume also significantly influence the pyrolysis action and, if appropriate conditions exist, lead to formation of solid particles as desired.

Similar to studies on in-flight particle generation, investigation of splat morphologies can also be extremely revealing, as clearly illustrated in Fig. 17 [101]. The remnant gel-like unpyrolyzed mass at low plasma power levels does not lead to formation of well-defined splats. Significant amount of fine spherical particles can result from secondary pyrolysis of such unpyrolyzed mass upon impacting the preheated substrate. At higher plasma power levels, molten splats can be observed. The precursor chemistry, too, plays a crucial role. For example, splats observed with use of a modified aluminum acetate precursor yielded splats with greater degree of melting even at low plasma power levels compared to an aluminum nitrate precursor during alumina coating deposition. Use of organic solvents increases specific enthalpy, and their lower surface tension presumably also assists defragmentation of droplets and facilitates transformation and/or melting of particles prior to impact with the substrate [101].

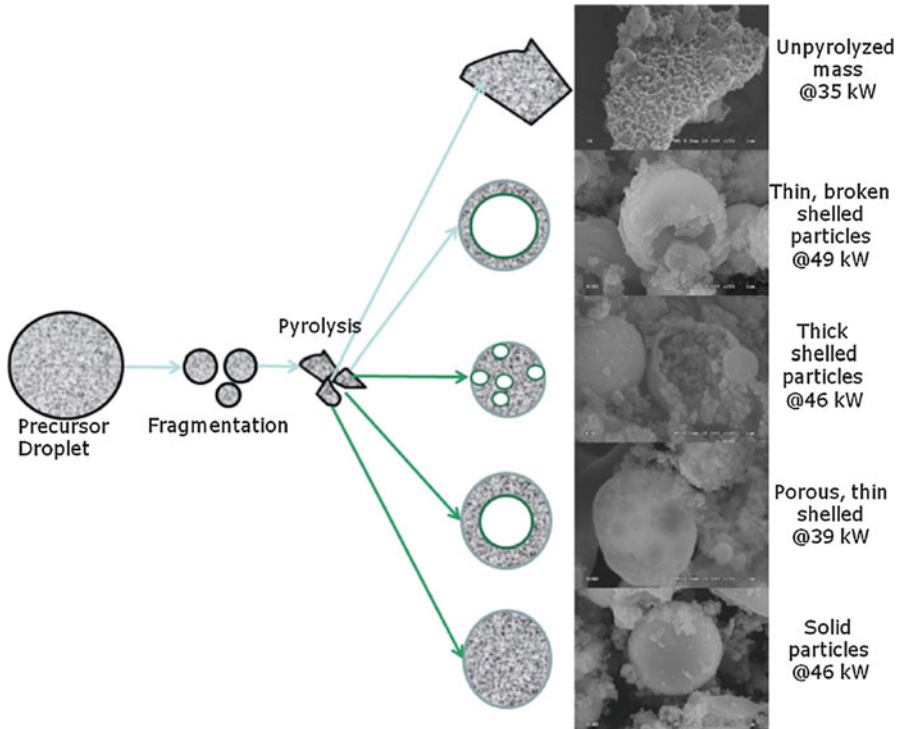


Fig. 16 Summary of different in-flight-formed particle morphologies during SPPS deposition of alumina coatings at varied processing conditions [101]

Microstructure

A primary reason, aside from the considerable application potential, why development of TBCs employing SPPS technique had greatly attracted the spray community initially is the inherent advantages that this route offers over conventional powder-based atmospheric plasma-sprayed coatings [18, 23–25]. In terms of coating characteristics, SPPS-deposited YSZ coatings have been shown to possess interesting intrinsic features like fine grains, vertical cracks, fine-distributed porosity, reduced inter-splat boundary sizes between the lamellae, etc. The superior reported durability of SPPS TBCs over conventional APS TBCs is attributed to the unique microstructure in case of the former, which provides better strain tolerance and toughness [23–25].

Based on the improved understanding of coating formation through studies on in-flight particle generation and subsequent splat formation on impacting the substrate as discussed above, the role of process parameters like plasma current, standoff distance, primary/secondary gas flow rates, substrate preheat temperature, precursor feed rate, etc. is now better appreciated. Of course, the splat formation also has a direct bearing on the resulting microstructure. The microstructures of SPPS YSZ coatings generated at varied plasma powers and substrate preheat temperatures are

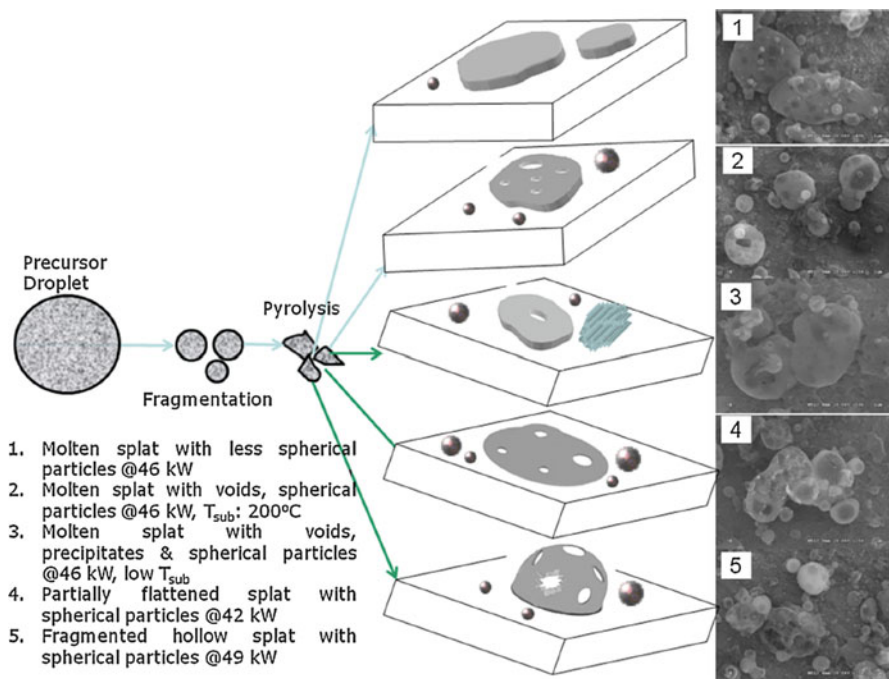


Fig. 17 Summary of splat formation during SPPS deposition of alumina coatings at varied processing conditions [101]

shown in Fig. 18, and these clearly correlate with the in-flight particle formation and splatting characteristics [9]. The importance of thermal energy input in promoting precursor pyrolysis and subsequent melting of particles formed in situ, and additionally of the substrate temperature in subsequently forming disk-shaped splats, can be discerned from the coating microstructures shown in Fig. 18 [9]. Both the combinations, low plasma power with substrate preheat and high plasma power with no preheat, lead to relatively higher porosity and inferior deposition rates thereby correlating well with earlier findings of incomplete YSZ particle formation under these conditions. On the other hand, higher plasma powers with substrate preheat yielded relatively denser coatings because of complete pyrolysis due to enhanced thermal energy. Very higher plasma power leads to substantially dense regions in the microstructure with accompanying cracks and pores, the latter being plausibly due to significant splashing or disintegration of splats shown previously.

Although the SPPS YSZ coatings meet some of the key guidelines on microstructure and characteristics for TBCs [102] in terms of finer splats, smaller pores, absence of horizontal cracks, etc., the superior thermal cycling performance of these coatings is derived from the presence of vertical cracks. It has been shown that the SPPS YSZ microstructures can be engineered to make the coatings more strain tolerant and contribute to thermal cycling life enhancement. Following the approach of investigating in-flight particle generation and splat formation as previously

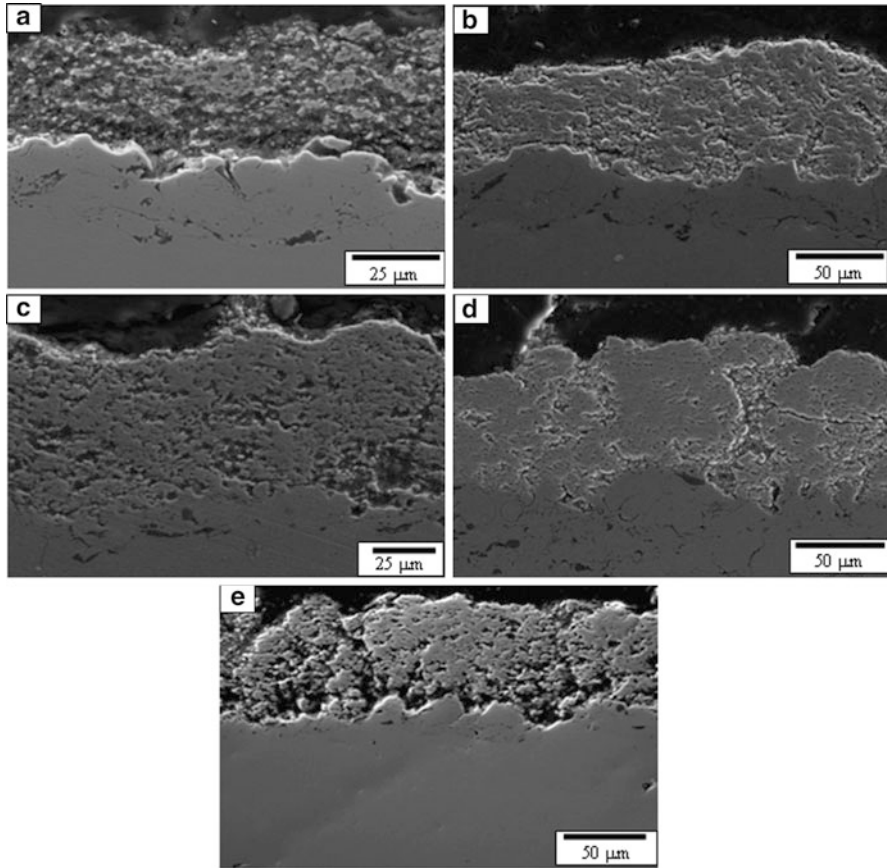


Fig. 18 Cross-sectional microstructure of SPPS YSZ coatings generated employing different deposition conditions, (a) plasma power-35 kW with $T_{\text{sub}}=500\text{ }^{\circ}\text{C}$, (b) plasma power-42 kW with $T_{\text{sub}}=500\text{ }^{\circ}\text{C}$, (c) plasma power-46 kW with $T_{\text{sub}}=500\text{ }^{\circ}\text{C}$, (d) plasma power-49 kW with $T_{\text{sub}}=500\text{ }^{\circ}\text{C}$, (e) plasma power-46 kW with no preheat [9]

discussed at different precursor flow rates, it was observed that varied amounts of unpyrolyzed mass, secondary particles resulting from pyrolysis on the preheated substrate surface or on previously deposited splats, pores/voids, etc., can get incorporated during coating buildup. YSZ coatings generated at constant plasma spray and liquid injection parameters, but with varying precursor flow rates, have been found to result in distinct microstructures [103]. Depending on the employed process conditions, fully molten regions, unmelted particles, pores, and even incorporated unpyrolyzed precursor present in varying extent constitute the coating microstructure during early stages of coating formation. The unpyrolyzed mass is reported to be responsible for producing pyrolytic stress, attributable to volumetric changes associated with release of acetates, nitrates, and water molecules that constitute the solution precursors. Beyond a certain unpyrolyzed precursor content incorporated

during coating buildup, this stress can even exceed the tensile strength of YSZ coatings and manifest in the form of vertical cracks in the microstructure [86]. The mechanism of vertical crack formation has been discussed in considerable detail elsewhere [103] and schematically illustrated in Fig. 19. Such an understanding of

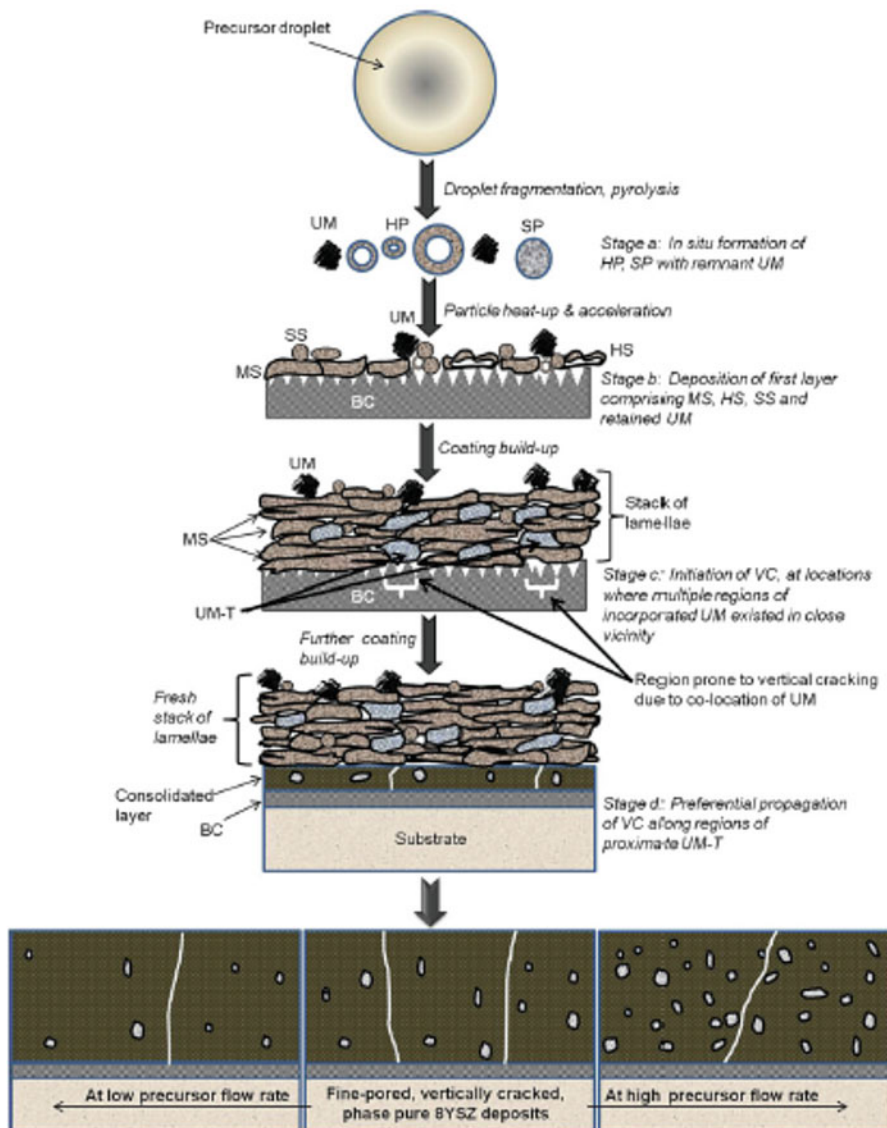


Fig. 19 Schematic representation of vertical formation mechanism in solution precursor plasma-sprayed YSZ coatings. (Nomenclature: *UM* unpyrolyzed mass, *HP* hollow particles, *SS* spherical particles from secondary pyrolysis, *HS* hollow splats, *MS* molten splats, *VC* vertical cracks, *UM-T* unpyrolyzed mass after transformation, *BC* bond coat) [103]

vertical crack formation in a TBC microstructure can potentially enable designing TBCs with alternate promising chemistries such as GZ, LZ, CeO₂-ZrO₂-Y₂O₃, etc.

It is pertinent to note that the approximate stress reduction through introduction of vertical cracks in brittle ceramics can be more than 50%, thereby bearing promise to substantially delay onset of spallation as compared to conventional APS TBCs without vertical cracks [104]. Although the crack density in SPPS YSZ microstructures is significantly lower than in case of electron beam physical vapor deposition (EBPVD) YSZ, it is comparable with reported values for the segmented dense vertically cracked YSZ microstructures realized by APS [103].

Thermal shock resistance is an important performance requirement for any TBC. Prior work has shown the thermal cycling behavior of SPPS YSZ to be significantly better than the APS YSZ coatings [30]. Some reports have also indicated that its durability could be even better than that of the dense vertically cracked (DVC) and EB-PVD YSZ. The superior durability of SPPS TBCs over that of other coatings is attributed to the improved strain tolerance and toughness of the SPPS TBCs [18, 23–25].

As previously discussed, development of coatings resistant to CMAS attack is yet another growing requirement. Due to the versatility of SPPS, the process can be conveniently adapted to deposit multilayered coatings or to even modify the chemical composition of the top layer. A typical two-layered architecture having, for example, a Gd₂O₃-doped La₂Ce₂O₇ over a conventional YSZ/MCrAlY can provide multiple functionalities in terms of low thermal conductivity, hot corrosion resistance, and the ability to crystallize into the Ca₂(La_xCe_{1-x})₈(SiO₄)₆O_{6-x} apatite phase to arrest infiltration of CMAS [105, 106]. An alternative formulation incorporating Al₂O₃ and TiO₂ formers into a YSZ-forming precursor also has potential to create the necessary coating chemistry that can mitigate CMAS attack [51]. The SPPS route provides a very convenient pathway to modify the TBC chemistry as determined by the end applications.

Versatility: Materials and Functionality

Over the years, plasma spraying of solution precursors has been demonstrated to be an exciting method to produce a wide variety of functional oxide ceramic coatings, starting with appropriate precursor chemistries, and provides a convenient pathway to deposit nanostructured coatings. The earlier limitations in understanding the SPPS process mainly due to lack of relevant particle diagnostic tools have been addressed by various meticulously designed studies [9, 12] including investigation of in-flight-formed particles and subsequent splat formation as discussed above. These studies have been educative and can form the basis for design and development of novel coating systems. Research efforts by various groups on SPPS coatings have demonstrated that the process is versatile and allows convenient deposition of many diverse oxides to yield exciting properties [12, 19, 24, 26–28, 88, 93].

One promising class of SPPS coatings is the TiO₂-based photocatalytic coatings known for their attractive semiconductor characteristics like large bandgap, chemical

stability, nontoxicity, and low cost. However, its relative inactivity under visible-light illumination is a limitation which can be overcome by Cu^{2+} -modified Ti^{3+} self-doping. The SPPS technique has been shown to be well-suited to achieve coatings with such complex chemistries via a one-step process [107]. SPPS-deposited TiO_2 -based coatings have also been found to exhibit good antibacterial activity for inactivation of *Escherichia coli* pathogens under blue LED illumination [107]. ZnFe_2O_4 [26, 108], CdS [88], and ZnO coatings [109, 110] for photocatalytic applications by SPPS have been reported. The SPPS technique has also been used to deposit a catalytic $\text{CuO}/\text{ZnO}/\text{Al}_2\text{O}_3$ layer on micro-channelized surfaces of proton exchange membrane fuel cells (PEMFCs) [111]. Compared to other conventional multistep deposition cum-sintering approaches, the possibility of achieving high surface area and fine pores with a single-step SPPS method has great implications for industrialization. Apart from the above, anode and cathode coatings of Ni-YSZ [19] and LaSrMnO_3 [93] for SOFC applications have been successfully demonstrated using SPPS. Coatings of LiFePO_4 , LiCoO_2 , Co_3O_4 [112], V_2O_5 [113], etc. have also been studied for Li-ion battery applications and exhibited good charge-discharge characteristics. Nanostructured ceria coatings deposited for high-temperature corrosion and oxidation resistance [90], $\text{Eu:Y}_2\text{O}_3$ phosphor coating for photoluminescence [114], and orthorhombic $\alpha\text{-MoO}_3$ for super capacitor electrode applications [115] also reflect the wide-ranging potential of SPPS. Yttrium iron garnet ($\text{Y}_3\text{Fe}_5\text{O}_{12}$), $\text{Ni}_{0.5}\text{Zn}_{0.5}\text{Fe}_2\text{O}_4$, and $\text{Ni}_{0.5}\text{Zn}_{0.5}\text{Fe}_2\text{O}_4/\text{SiO}_2$ coatings [28, 116] produced by SPPS have shown single phase of spinel ferrite with nanocrystalline features and are a good example of how coatings with extremely complex chemistries can be realized by virtue of the atomic-level mixing possible in SPPS. A partial list of coatings already reported using plasma spraying or flame spraying of solution precursors is provided in Table 2.

Although the concept of solution precursor-based spraying was first introduced in the 1990s and its versatility as well as benefits has since been demonstrated through several studies, no significant headway has been made as far as its commercialization is concerned [117]. A primary reason can be attributed to the low deposition rates reported in case of solution precursor spraying processes that demand high-energy consumption [118], especially with radial feed plasma torches that have typically been employed in such studies. Therefore, augmentation of deposition rates of solution-based thermal spray approaches to levels acceptable for their industrial acceptance is desirable, as indeed is identification and validation of niche applications. Prior work has already shown that the role of plasma power on deposition rate is immense [119] and, therefore, the recent advent of high-power axial-feed plasma spray systems could be potential game changers for SPPS.

Hybrid Powder-Liquid Feedstock Processing

As discussed above, both SPS and SPPS are already two extensively investigated variants of liquid feedstock-based thermal spray processing with demonstrated ability to deposit varied coatings with refined microstructural features. The

Table 2 Partial list of coatings thermal sprayed using solution precursors

Coating	Starting precursors	Reference
ZrO ₂ -Y ₂ O ₃	Zirconium acetate + yttrium nitrate Zirconium acetate + yttrium acetate	[9, 17, 20, 23, 24, 86, 103, 104, 125]
TiO ₂	Titanium isopropoxide in ethanol	[100]
CeO ₂	Cerium nitrate hexahydrate in water	[90]
ZnFe ₂ O ₄	Zinc nitrate + iron nitrate in water	[108]
Ce-doped Ba(Zr _{0.2} Ti _{0.8})O ₃	Dehydrated Ba(II)-acetate, Zr(IV)-nitrate, Ce(IV)-nitrate, and Ti(IV)-isopropoxide	[27]
NiO-YSZ	Nickel nitrate + yttrium nitrate + zirconium nitrate + Et OH	[92]
LaSrMnO ₃	Lanthanum nitrate + strontium nitrate + manganese nitrate + water Lanthanum nitrate + strontium nitrate + manganese acetate + water	[93, 126]
Dy:YAG	Aluminum nitrate + yttrium nitrate + dysprosium nitrate + water	[94]
Hydroxyapatite	Calcium nitrate + diammonium phosphate + ammonium hydroxide + water	[127]
La ₂ Zr ₂ O ₇	Lanthanum nitrate mixed with zirconium oxynitrate or zirconium oxychloride or zirconium acetate hydroxide	[128]
Eu:Y ₂ O ₃	Yttrium nitrate hexahydrate + europium nitrate pentahydrate in ethanol	[114]
Yttrium aluminum garnet (YAG)	Yttrium nitrate hexahydrate + aluminum nitrate octahydrate + citric acid monohydrate + water + ethanol	[89]
Yttrium iron garnet (YIG)	Yttrium nitrate + ferric nitrate + water	[116]
Ni _{0.5} Zn _{0.5} Fe ₂ O ₄	Ni, Zn, and Fe salts dissolved in water	[28]
LiFePO ₄	Iron oxalate + lithium hydroxide + ammonium phosphate + sucrose + water	[112]
LiCoO ₂	Lithium hydroxide + cobalt nitrate + sucrose + water	[112]
Li(Ni _x Co _{1-x} Mn _x)O ₂	Lithium hydroxide + nickel nitrate + cobalt nitrate + Manganese nitrate + sucrose + water	[112]
Li _{1+x} Al _x Ti _{2-x} (PO ₄) ₃	Lithium hydroxide + aluminum nitrate + titanium isopropoxides + ammonium phosphate + water	[112]
CdS	Cadmium chloride + thiourea + water	[88]
V ₂ O ₅	Ammonium vanadium oxide dissolved in oxalic acid	[113]
Al ₂ O ₃	Aluminum isopropoxide + isopropanol Aluminum acetate + acetic acid + water	[129]
ZnO	Zinc acetate dehydrate	[109, 110]
Co ₃ O ₄	Cobalt acetate tetrahydrate + water	[112]
Indium oxide	Indium (III) chloride + water	[129]
Orthorhombic α-MoO ₃	Ammonium molybdate tetrahydrate + water	[115]
CoFe ₂ O ₄	Cobalt nitrate hexahydrate + iron nitrate nonahydrate + water	[130]
CuO-ZnO-Al ₂ O ₃	Copper nitrate + zinc nitrate + aluminum nitrate + water	[111]

present-day availability of spray systems that permits improved thermal exchange between the energy-demanding liquid feedstock and the plasma plume by enabling axial injection also makes this an opportune time to further explore possibilities with suspensions and solution precursors. In this context, hybrid powder-liquid feedstock spraying provides an opportunity to conveniently combine constituents at vastly different relative length scales, by using them in the form of conventional “coarse” spray-grade powders (usually 10–100 μm in size) or as fine particles (approximately 100 nm–2 μm) already suspended in a suitable medium or generated in situ from a solution precursor [120, 121]. The resulting splats of constituent molten particles, which are the building blocks for thermal-sprayed coatings, also differ by more than an order of magnitude, and the consequent combination of coarse-fine features can potentially yield unique coating microstructures.

Processing

A key aspect of realizing the powder-liquid hybrid coatings is the independently controllable introduction of conventional micron-sized powder feedstock and liquid feedstock in the form of solution or suspension into the plasma plume to form the desired coatings [120, 121]. One such experimental arrangement is shown in Fig. 20 and utilizes the “standard” coaxial liquid feedstock injector tube, with the suspension fed into the inner tube as usual but with the atomizing gas being replaced by a powder-entrained carrier gas [121]. The carrier gas also serves to atomize the liquid

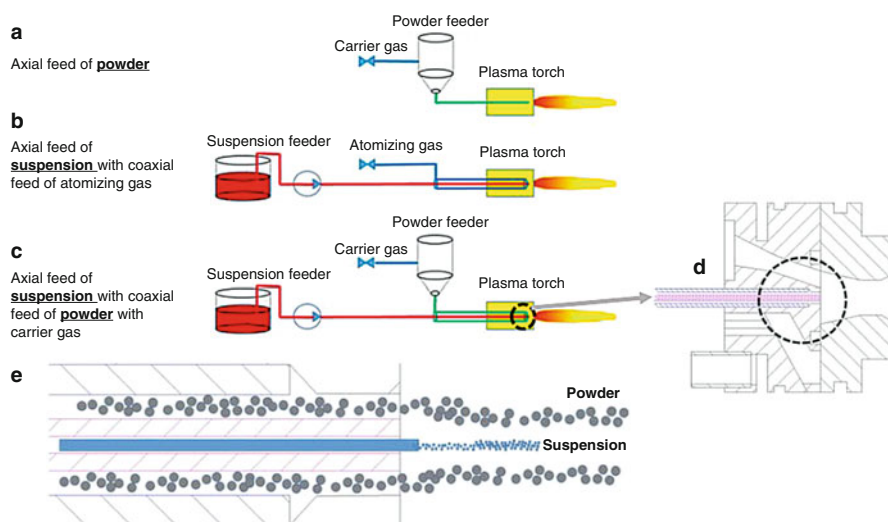


Fig. 20 Schematic illustration of an axial-feed plasma spray system depicting (a) usual powder delivery mechanism, (b) usual suspension delivery mechanism, and (c) proposed arrangement for hybrid powder-suspension delivery, with blowups (d), and (e) showing the coaxial feedstock injector tube and its effective utilization [121]

droplets at the end of the coaxial tube, as depicted in Fig. 5. Individual control of the amounts of powder, liquid, and atomizing/carrier gas fed is a salient feature of this arrangement, with ability to completely turn off either of the feedlines. As is apparent from the figure, different variations of the feeding arrangement to allow both constituents to be fed radially or one radially and the other axially are conveniently possible.

Possible Coating Architectures

The above arrangement can be readily utilized to yield different unique coating architectures that are function-specific and could be relevant for varied applications [21, 30, 31, 120–124]. For example, sequential injection of powder and liquid feedstock can yield a layered coating comprising powder-derived and solution precursor-/suspension-derived layers in either order, with each involving features of very distinct length scales. Similarly, simultaneous powder-liquid feeding can yield composite coatings with a distributed fine second phase in a coarser matrix or vice versa. As a specific case of the simultaneous feeding, the relative feed rates of the two constituents can also be continuously varied to achieve functionally graded coatings. Such on-demand architectures, schematically illustrated in Fig. 21 [121], are not convenient to realize by conventional thermal spray methods.

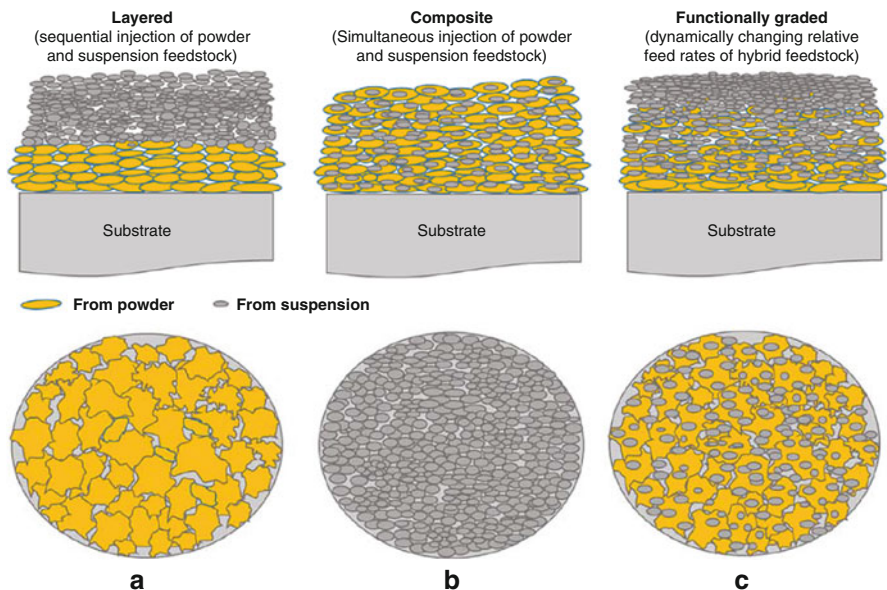


Fig. 21 Schematic illustration of (top) different coating architectures achievable using hybrid powder-liquid plasma spraying and (bottom) surface morphologies depicting (a) “coarse” powder-derived splats, (b) “fine” splats originating from suspension/solution precursor, and (c) the mixed coarse-fine splats formed in case of a composite coating [121]

Microstructures

The authors have demonstrated realization of each of the above architectures utilizing both solution precursors and suspensions in tandem with powder feedstock, employing different material systems in separate studies [21, 30, 31, 120–123]. The choice of the materials was dictated by relevant practical applications and illustrated the generic applicability of the powder-liquid hybrid approach, with virtually no constraints imposed by the choice of powder and/or liquid feedstock. For example, Fig. 22 [121] depicts the surface micrographs of different powder-suspension composite coatings, clearly showing the very different sizes of splats ensuing from the powder and suspension constituents. Similarly, Fig. 23 [120] shows examples of typical layered, composite, and graded coating architectures developed using three different combinations of powder and solution precursor feedstocks.

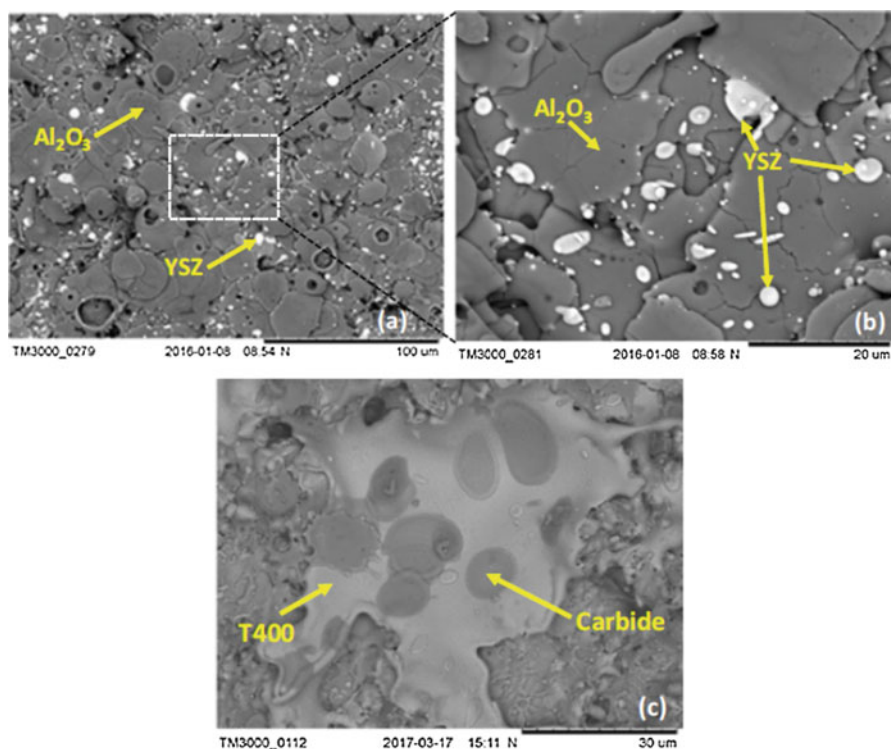


Fig. 22 Surface morphology of composite coatings deposited by simultaneous spraying of a powder and a suspension showing multi-scale splat structure: (a) Al_2O_3 powder-YSZ suspension, low magnification; (b) Al_2O_3 powder-YSZ suspension, high magnification; and (c) T400 powder- Cr_3C_2 suspension, high magnification [121]

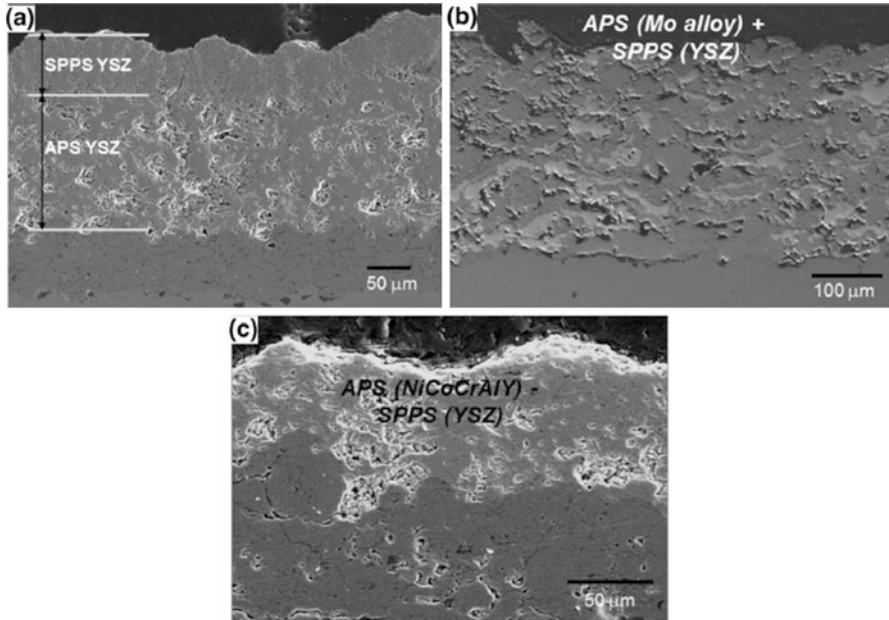


Fig. 23 Illustrative examples of typical coating architectures developed through hybrid processing: (a) layered coatings by sequential feeding of YSZ powder (APS) and YSZ-forming precursor (SPPS), (b) composite coating by simultaneous feeding of a Mo alloy powder (APS) and YSZ-forming precursor (SPPS), (c) graded microstructure by simultaneous feeding of NiCoCrAlY powder (APS) and YSZ-forming precursor (SPPS) with controlled variation in their relative feed rates [120]

Versatility: Materials and Functionality

The versatility of the powder-liquid hybrid spraying approach is already amply evident from the discussion in the preceding section. It is apparent that the method can be harnessed to spray virtually any material combination, permitting great flexibility in deposition of complex coating systems. The wide range of suspensions and solution precursors that have been employed to deposit coatings already, combined with the overwhelmingly large portfolio of spray-grade powders that are commercially available, opens new vistas for producing superior coatings with unique combinations of materials. The abundant choice of materials is further complemented by the ability to realize tailored architectures leading to numerous possibilities. Only a couple of examples are illustrated herein based on the authors' prior work to highlight the performance benefits of the composite hybrid coatings. For example, the unique properties achieved through hybrid processing of "composite" YSZ (powder) – YSZ (solution precursor) coatings were found to exhibit enhanced erosion resistance compared to the stand-alone SPPS and APS YSZ coatings as shown in Fig. 24 [120]. The role of in situ formed submicron-sized splats within the large-sized powder-based splats plausibly improves toughness,

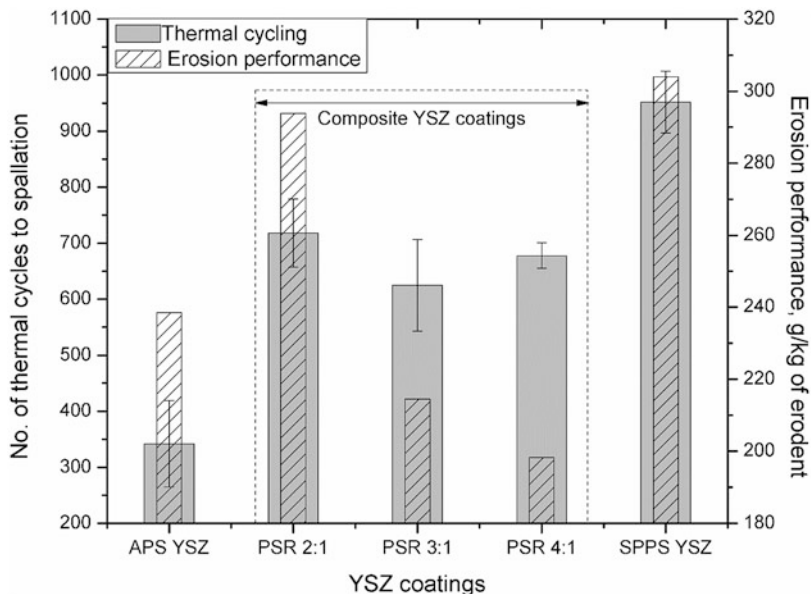


Fig. 24 Thermal cycling and erosive wear performance of composite APS-SPPS YSZ coatings in comparison with stand-alone SPPS and APS YSZ coatings [120]

leading to better erosion resistance as well as better thermal cyclic life. This can find relevance in TBCs deployed in dust-laden environments. In yet another study involving such composite YSZ coatings deposited by the powder-solution precursor hybrid plasma spraying technique, the hybrid YSZ TBCs were found to perform better than the APS and SPPS YSZ coatings under hot corrosion conditions at 900 °C in both chloride and vanadate salt environments [123].

In another example of nanocomposite coatings deposited using hybrid powder-solution precursor plasma spraying, a molybdenum-based alloy powder (Mo + NiCrBSiFe+NiAlMo) and a YSZ-forming precursor were simultaneously sprayed to achieve enhanced scuffing wear resistance [21] for potential piston ring applications. The incorporation of fine-sized YSZ was observed to enhance wear behavior under dry as well as lubricated sliding conditions as depicted in Fig. 25 [21].

Conclusions

Liquid feedstock thermal spraying represents an exciting approach to obtain coatings with vastly different properties compared to the conventional powder-derived coatings. Since use of a liquid feedstock in the form of either a suspension or a solution precursor demands more energy because of the need to evaporate the solvent, SPS and SPPS have been the two more widely investigated variants of the

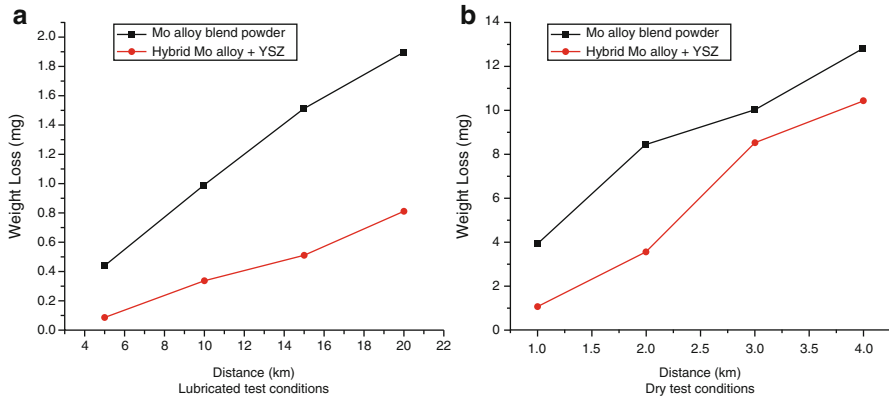


Fig. 25 Wear test results for powder-based APS and hybrid APS + SPPS powder + solution precursor-based coatings tested under (a) lubricated conditions and (b) dry conditions [21]

above approach by virtue of the high thermal energy offered by a plasma plume. Both of the above have matured considerably in recent years, as a result of numerous research efforts that have contributed handsomely to enhancing the knowledge base by providing crucial insights into mechanisms responsible for coating formation. The recent availability of axial feed capable plasma spray systems has also addressed concerns regarding low deposition rates/efficiencies previously associated with use of liquid feedstock by virtue of the considerably improved thermal exchange between the plasma plume and the injected feedstock compared to conventional radial feeding. The process parameter impact on characteristics as well as performance of resulting coatings is also now well understood and has laid the foundation for increasing versatility of the above techniques, leading to a remarkable widening of the portfolio of coating materials that can be deposited.

The above versatility has led to realization of diverse functionalities that can be harnessed for a wide range of industrially relevant applications, e.g., advanced thermal barriers, wear resistance, corrosion-oxidation protection, etc. The ability of SPS and SPPS routes to uniformly deposit coatings much thinner than conventional APS coatings also opens possibilities for some niche applications to be explored in the future. Extension of SPS and SPPS to enable use of hybrid powder-liquid feedstock for plasma spraying presents a novel approach that promises to further expand the horizon. The potential of hybrid processing to explore new material combinations and create tailored function-dependent coating architectures, such as layered, composite, and graded coatings with multi-scale features, has already been demonstrated and appears to be an exciting pathway to achieve superior properties. This method enables spraying of virtually any material combination, allowing tremendous flexibility in fabrication of complex coating systems.

References

1. Pawlowski L (1995) *The science and engineering of thermal spray coatings*. Wiley, Chichester/New York
2. Schneider KE, Belashchenko V, Dratwinski M, Siegmann S, Zagorski A (2006) *Thermal spraying for power generation components*. Wiley-VCH Verlag GmbH & Co. KGaA, Weinheim
3. Markocsan N, Gupta M, Joshi S, Nylén P, Li XH, Wigren J (2017) Liquid feedstock plasma spraying: an emerging process for advanced thermal barrier coatings. *J Therm Spray Technol* 26(6):1104–1114. Springer New York LLC
4. Fauchais P, Etchart-Salas R, Rat V, Coudert JF, Caron N, Wittmann-Ténéze K (2008) Parameters controlling liquid plasma spraying: solutions, sols, or suspensions. *J Therm Spray Technol* 17(1):31–59
5. Karthikeyan J, Berndt CC, Reddy S, Wang J-Y, King AH, Herman H (2005) Nanomaterial deposits formed by DC plasma spraying of liquid feedstocks. *J Am Ceram Soc* 81(1):121–128
6. Pawlowski L (2009) Suspension and solution thermal spray coatings. *Surf Coat Technol* 203(19):2807–2829
7. Lima RS, Marple BR (2007) Thermal spray coatings engineered from nanostructured ceramic agglomerated powders for structural, thermal barrier and biomedical applications: a review. *J Therm Spray Technol* 16(1):40–63
8. Qiao Y, Fischer TE, Dent A (2003) The effects of fuel chemistry and feedstock powder structure on the mechanical and tribological properties of HVOF thermal-sprayed WC-Co coatings with very fine structures. *Surf Coat Technol* 172(1):24–41
9. Govindarajan S, Dusane RO, Joshi SV (2011) In situ particle generation and splat formation during solution precursor plasma spraying of Yttria-stabilized zirconia coatings. *J Am Ceram Soc* 94(12):4191–4199
10. Mahade S, Narayan K, Govindarajan S, Björklund S, Curry N, Joshi S (2019) Exploiting suspension plasma spraying to deposit wear-resistant carbide coatings. *Materials* 12(15):2344
11. Fauchais P et al (2013) Suspension and solution plasma spraying. *J Phys D Appl Phys* 46(22)
12. Fauchais P, Montavon G, Lima RS, Marple BR (2011) Engineering a new class of thermal spray nano-based microstructures from agglomerated nanostructured particles, suspensions and solutions: an invited review. *J Phys D Appl Phys* 44(9):093001
13. Fauchais P, Montavon G (2010) Latest developments in suspension and liquid precursor thermal spraying. *J Therm Spray Technol* 19(1–2):226–239
14. Tesar T, Musalek R, Medricky J, Cizek J (2019) On growth of suspension plasma-sprayed coatings deposited by high-enthalpy plasma torch. *Surf Coat Technol* 371:333–343
15. Zhou D, Guillon O, Vaßen R (2017) Development of YSZ thermal barrier coatings using axial suspension plasma spraying. *Coatings* 7(8):120
16. Bai M, Maher H, Pala Z, Hussain T (2018) Microstructure and phase stability of suspension high velocity oxy-fuel sprayed yttria stabilised zirconia coatings from aqueous and ethanol based suspensions. *J Eur Ceram Soc* 38(4):1878–1887
17. Karthikeyan J, Berndt CC, Tikkanen J, Wang JY, King AH, Herman H (1997) Nanomaterial powders and deposits prepared by flame spray processing of liquid precursors. *Nanostructured Mater* 8(1):61–74
18. Gell M et al (2008) Thermal barrier coatings made by the solution precursor plasma spray process. *J Therm Spray Technol* 17(1):124–135
19. Coyle TW, Wang Y (2007) Solution precursor plasma spray (SPPS) of Ni-YSZ SOFC anode coatings. In: *Thermal spray 2007: global coating solutions*, pp 699–704
20. Jordan EH, Gell M, Jiang C, Wang J, Nair B (2014) High temperature thermal barrier coating made by the solution precursor plasma spray process. In: *Volume 6: ceramics; controls, diagnostics and instrumentation; education; manufacturing materials and metallurgy*
21. Lohia A, Sivakumar G, Ramakrishna M, Joshi SV (2014) Deposition of nanocomposite coatings employing a hybrid APS + SPPS technique. *J Therm Spray Technol* 23:1054–1064

22. Karthikeyan J, Berndt CC, Tikkanen J, Reddy S, Herman H (1997) Plasma spray synthesis of nanomaterial powders and deposits. *Mater Sci Eng A* 238(2):275–286
23. Padture NP et al (2001) Towards durable thermal barrier coatings with novel microstructures deposited by solution-precursor plasma spray. *Acta Mater* 49(12):2251–2257
24. Jordan EH et al (2004) Superior thermal barrier coatings using solution precursor plasma spray. *J Therm Spray Technol* 13(1):57–65
25. Gell M, Xie L, Ma X, Jordan EH, Padture NP (2004) Highly durable thermal barrier coatings made by the solution precursor plasma spray process. *Surf Coat Technol* 177–178:97–102
26. Dom R, Sivakumar G, Hebalkar NY, Joshi SV, Borse PH (2012) Deposition of nanostructured photocatalytic zinc ferrite films using solution precursor plasma spraying. *Mater Res Bull* 47(3):562–570
27. Garcia E, Zhang ZB, Coyle TW, Hao SE, Mu SL (2007) Liquid precursors plasma spraying of TiO₂ and Ce-doped Ba(Zr_{0.2}Ti_{0.8})O₃ coatings. In: *Thermal spray 2007: global coating solutions*, pp 650–654
28. Ma TD, Ge XQ, Zhang SH, Roth YD, Xiao J (2004) Solution plasma spray synthesis of NiZnFe₂O₄ magnetic nanocomposite thick films. In: *International thermal spray conference 2004*
29. Ma XQ, Roth J, Gandy DW, Frederick GJ (2006) A new high-velocity oxygen fuel process for making finely structured and highly bonded Inconel alloy layers from liquid feedstock. In: *Proceedings of the international thermal spray conference, 2006*, pp 670–675
30. Joshi SV, Sivakumar G, Raghuvver T, Dusane RO (2014) Hybrid plasma-sprayed thermal barrier coatings using powder and solution precursor feedstock. *J Therm Spray Technol* 23(4):616–624
31. Gopal V, Goel S, Manivasagam G, Joshi S (2019) Performance of hybrid powder-suspension axial plasma sprayed Al₂O₃-YSZ coatings in bovine serum solution. *Materials* 12(12):1922
32. Kassner H, Siegert R, Hathiramani D, Vassen R, Stoeber D (2008) Application of suspension plasma spraying (SPS) for manufacture of ceramic coatings. *J Therm Spray Technol* 17(1):115–123
33. Toma FL, Potthoff A, Berger LM, Leyens C (2015) Demands, potentials, and economic aspects of thermal spraying with suspensions: a critical review. *J Therm Spray Technol* 24(7):1143–1152
34. Vaen R, Kaner H, Mauer G, Stöver D (2010) Suspension plasma spraying: process characteristics and applications. *J Therm Spray Technol* 19(1–2):219–225
35. Rampon R, Marchand O, Filiatré C, Bertrand G (2008) Influence of suspension characteristics on coatings microstructure obtained by suspension plasma spraying. *Surf Coat Technol* 202(18):4337–4342
36. Pateyron B, Calve N, Pawłowski L (2013) Influence of water and ethanol on transport properties of the jets used in suspension plasma spraying. *Surf Coat Technol* 220:257–260
37. Ganvir A (2018) Design of suspension plasma sprayed thermal barrier coatings. Ph.D. thesis, University West, ISBN 978-91-87531-92-7, Trollhättan
38. Fazilleau J, Delbos C, Rat V, Coudert JF, Fauchais P, Pateyron B (2006) Phenomena involved in suspension plasma spraying part 1: suspension injection and behavior. *Plasma Chem Plasma Process* 26(4):371–391
39. Mahade S (2018) Functional performance of gadolinium Zirconate/Yttria stabilized zirconia multi-layered thermal barrier coatings. Ph.D. thesis, ISBN 978-91-87531-86-6, Trollhättan
40. Fauchais P, Rat V, Coudert JF, Etchart-Salas R, Montavon G (2008) Operating parameters for suspension and solution plasma-spray coatings. *Surf Coat Technol* 202(18):4309–4317
41. Kaßner H, Vaßen R, Stöver D (2008) Study on instant droplet and particle stages during suspension plasma spraying (SPS). *Surf Coat Technol* 202(18):4355–4361
42. Oberste-Berghaus J, Bouaricha S, Legoux J-G, Moreau C (2005) Injection conditions and in-flight particles states in suspension plasma spraying of alumina and zirconia nano-ceramics. In: *Thermal spray 2005: proceedings of the international thermal spray conference*, pp 512–518

43. Aranke O (2018) Effect of spray parameters on micro-structure and lifetime of suspension plasma sprayed thermal barrier coatings. Master Thesis, University West, URN: urn:nbn:se:hv:diva-12986, Trollhättan
44. Vanevery K et al (2011) Column formation in suspension plasma-sprayed coatings and resultant thermal properties. *J Therm Spray Technol* 20(4):817–828
45. Ganvir A, Curry N, Björklund S, Markocsan N, Nylén P (2015) Characterization of micro-structure and thermal properties of YSZ coatings obtained by axial suspension plasma spraying (ASPS). *J Therm Spray Technol* 24(7):1195–1204
46. Guo H, Kuroda S, Murakami H (2006) Microstructures and properties of plasma-sprayed segmented thermal barrier coatings. *J Am Ceram Soc* 89(4):1432–1439
47. Carpio P et al (2013) Correlation of thermal conductivity of suspension plasma sprayed yttria stabilized zirconia coatings with some microstructural effects. *Mater Lett* 107:370–373
48. Schwingel D, Taylor R, Haubold T, Wigren J, Gualco C (1998) Mechanical and thermo-physical properties of thick PYSZ thermal barrier coatings: correlation with microstructure and spraying parameters. *Surf Coat Technol* 108–109(1–3):99–106
49. Ganvir A, Markocsan N, Joshi S (2016) Influence of isothermal heat treatment on porosity and crystallite size in axial suspension plasma sprayed thermal barrier coatings for gas turbine applications. *Coatings* 7(1):4
50. Stecura S (1979) Effects of compositional changes on the performance of a thermal barrier coating system for aircraft gas turbine engines. In: Presented at the American ceramic society, annual conference on composites and advanced materials, Merritt Island
51. Aygun A, Vasiliev AL, Padtare NP, Ma X (2007) Novel thermal barrier coatings that are resistant to high-temperature attack by glassy deposits. *Acta Mater* 55(20):6734–6745
52. Stöver D, Pracht G, Lehmann H, Dietrich M, Döring J-E, Vaßen R (2004) New material concepts for the next generation of plasma-sprayed thermal barrier coatings. *J Therm Spray Technol* 13(1):76–83
53. Leckie RM, Krämer S, Rühle M, Levi CG (2005) Thermochemical compatibility between alumina and ZrO_2 - $GdO_{3/2}$ thermal barrier coatings. *Acta Mater* 53(11):3281–3292
54. Jarligo MO, Mack DE, Vassen R, Stöver D (2009) Application of plasma-sprayed complex perovskites as thermal barrier coatings. *J Therm Spray Technol* 18(2):187–193
55. Ma W, Mack D, Malzbender J, Vaßen R, Stöver D (2008) Yb_2O_3 and Gd_2O_3 doped strontium zirconate for thermal barrier coatings. *J Eur Ceram Soc* 28(16):3071–3081
56. Padtare NP, Klemens PG (2005) Low thermal conductivity in garnets. *J Am Ceram Soc* 80(4):1018–1020
57. Guo X, Lu Z, Jung Y-G, Li L, Knapp J, Zhang J (2016) Thermal properties, thermal shock, and thermal cycling behavior of Lanthanum Zirconate-based thermal barrier coatings. *Metall Mater Trans E* 3(2):64–70
58. Vaßen R, Jarligo MO, Steinke T, Mack DE, Stöver D (2010) Overview on advanced thermal barrier coatings. *Surf Coat Technol* 205(4):938–942
59. Clarke DR, Phillpot SR (2005) Thermal barrier coating materials. *Mater Today* 8(6):22–29
60. Vassen R, Cao X, Tietz F, Basu D, Stöver D (2000) Zirconates as new materials for thermal barrier coatings. *J Am Ceram Soc* 83(8):2023–2028
61. Wu J et al (2004) Low-thermal-conductivity rare-earth zirconates for potential thermal-barrier-coating applications. *J Am Ceram Soc* 85(12):3031–3035
62. Mahade S, Curry N, Björklund S, Markocsan N, Nylén P, Vaßen R (2017) Functional performance of $Gd_2Zr_2O_7/YSZ$ multi-layered thermal barrier coatings deposited by suspension plasma spray. *Surf Coat Technol* 318:208–216
63. Drexler JM, Ortiz AL, Padtare NP (2012) Composition effects of thermal barrier coating ceramics on their interaction with molten Ca-Mg-Al-silicate (CMAS) glass. *Acta Mater* 60(15):5437–5447
64. Gledhill AD, Reddy KM, Drexler JM, Shinoda K, Sampath S, Padtare NP (2011) Mitigation of damage from molten fly ash to air-plasma-sprayed thermal barrier coatings. *Mater Sci Eng A* 528(24):7214–7221

65. Bakan E, Mack DE, Mauer G, Vaßen R (2014) Gadolinium Zirconate/YSZ thermal barrier coatings: plasma spraying, microstructure, and thermal cycling behavior. *J Am Ceram Soc* 97 (12):4045–4051
66. Zhong X et al (2014) Thermal shock behavior of toughened gadolinium zirconate/YSZ double-ceramic-layered thermal barrier coating. *J Alloys Compd* 593:50–55
67. Lee KS, Lee DH, Kim TW (2014) Microstructure controls in Gadolinium Zirconate/YSZ double layers and their properties. *J Ceram Soc Japan* 122(1428):668–673
68. Bakan E, Mack DE, Mauer G, Mücke R, Vaßen R (2015) Porosity–property relationships of plasma-sprayed $Gd_2Zr_2O_7$ /YSZ thermal barrier coatings. *J Am Ceram Soc* 98(8):2647–2654
69. Mahade S, Curry N, Björklund S, Markocsan N, Nylén P (2015) Thermal conductivity and thermal cyclic fatigue of multilayered $Gd_2Zr_2O_7$ /YSZ thermal barrier coatings processed by suspension plasma spray. *Surf Coat Technol* 283:329–336
70. Mahade S, Li R, Curry N, Björklund S, Markocsan N, Nylén P (2016) Isothermal oxidation behavior of $Gd_2Zr_2O_7$ /YSZ multilayered thermal barrier coatings. *Int J Appl Ceram Technol* 13(3):443–450
71. Mahade S, Curry N, Björklund S, Markocsan N, Nylén P, Vaßen R (2017) Erosion performance of gadolinium Zirconate-based thermal barrier coatings processed by suspension plasma spray. *J Therm Spray Technol* 26(1–2):108–115
72. Mahade S, Zhou D, Curry N, Markocsan N, Nylén P, Vaßen R (2019) Tailored microstructures of gadolinium zirconate/YSZ multi-layered thermal barrier coatings produced by suspension plasma spray: durability and erosion testing. *J Mater Process Technol* 264:283–294
73. Algenaid W, Ganvir A, Filomena Calinas R, Varghese J, Rajulapati K, Joshi S (2019) Influence of microstructure on the erosion behaviour of suspension plasma sprayed thermal barrier coatings. *Surf Coat Technol* 375:86–99
74. Ganvir A, Joshi S, Markocsan N, Vassen R (2018) Tailoring columnar microstructure of axial suspension plasma sprayed TBCs for superior thermal shock performance. *Mater Des* 144:192–208
75. Ganvir A, Filomena R, Markocsan N, Curry N, Joshi S (2019) Experimental visualization of microstructure evolution during suspension plasma spraying of thermal barrier coatings. *J Eur Ceram Soc* 39(2–3):470–481
76. Goel S, Björklund S, Curry N, Wiklund U, Joshi SV (2017) Axial suspension plasma spraying of Al_2O_3 coatings for superior tribological properties. *Surf Coat Technol* 315:80–87
77. Aranke O, Algenaid W, Awe S, Joshi S (2019) Coatings for automotive gray cast iron brake discs: a review. *Coatings* 9:552
78. Mubarak F, Espallargas N (2015) Suspension plasma spraying of sub-micron silicon carbide composite coatings. *J Therm Spray Technol* 24(5):817–825
79. Berghaus JO, Marple B, Moreau C (2006) Suspension plasma spraying of nanostructured WC-12Co coatings. *J Therm Spray Technol* 15:676–681
80. Tejero-Martin D, Rezvani Rad M, McDonald A, Hussain T (2019) Beyond traditional coatings: a review on thermal-sprayed functional and smart coatings. *J Therm Spray Technol* 28(4):598–644. Springer New York LLC
81. Robinson BW et al (2015) Suspension plasma sprayed coatings using dilute hydrothermally produced titania feedstocks for photocatalytic applications. *J Mater Chem A* 3(24):12680–12689
82. Jian Zhou S, Bai Y, Ma W, dong Chen W (2019) Suspension plasma-sprayed fluoridated hydroxyapatite/calcium silicate composite coatings for biomedical applications. *J Therm Spray Technol* 28(5):1025–1038
83. Nielsen ML, Hamilton PM, Walsh RJ (1963) Ultrafine metal oxides by decomposition of salts in a flame. In: Kuhn WE, Lamprey H, Sheer C (eds) *Ultrafine particles*. Wiley, New York, p 181
84. Bhatia T et al (2002) Mechanisms of ceramic coating deposition in solution-precursor plasma spray. *J Mater Res* 17(9):2363–2372

85. Chen D, Jordan EH, Gell M (2008) Effect of solution concentration on splat formation and coating microstructure using the solution precursor plasma spray process. *Surf Coat Technol* 202(10):2132–2138
86. Xie L et al (2006) Formation of vertical cracks in solution-precursor plasma-sprayed thermal barrier coatings. *Surf Coat Technol* 201(3–4):1058–1064
87. Jiang C, Jordan EH, Harris AB, Gell M, Roth J (2015) Double-layer gadolinium zirconate/yttria-stabilized zirconia thermal barrier coatings deposited by the solution precursor plasma spray process. *J Therm Spray Technol* 24(6):895–906
88. Tummala R, Guduru RK, Mohanty PS (2012) Solution precursor plasma deposition of nanostructured CdS thin films. *Mater Res Bull* 47(3):700–707
89. Gell M, Wang J, Kumar R, Roth J, Jiang C, Jordan EH (2018) Higher temperature thermal barrier coatings with the combined use of yttrium aluminum garnet and the solution precursor plasma spray process. *J Therm Spray Technol* 27(4):543–555
90. Viswanathan V, Filmlalter R, Patil S, Deshpande S, Seal S (2007) High-temperature oxidation behavior of solution precursor plasma sprayed Nanoceria coating on martensitic steels. *J Am Ceram Soc* 90(3):870–877
91. Singh V, Karakoti A, Kumar A, Saha A, Basu S, Seal S (2010) Precursor dependent microstructure evolution and nonstoichiometry in nanostructured cerium oxide coatings using the solution precursor plasma spray technique. *J Am Ceram Soc* 93(11):3700–3708
92. Michaux P, Montavon G, Grimaud A, Denoirjean A, Fauchais P (2010) Elaboration of porous NiO/8YSZ layers by several SPS and SPPS routes. *J Therm Spray Technol* 19(1–2):317–327
93. Wang Y, Coyle TW (2011) Solution precursor plasma spray of porous $\text{La}_{1-x}\text{Sr}_x\text{MnO}_3$ perovskite coatings for SOFC cathode application. *J Fuel Cell Sci Technol* 8(2)
94. Chen D, Jordan EH, Renfro MW, Gell M (2009) Dy: YAG phosphor coating using the solution precursor plasma spray process. *J Am Ceram Soc* 92(1):268–271
95. Laine RM, Marchal JC, Sun HP, Pan XQ (2006) Nano- $\alpha\text{-Al}_2\text{O}_3$ by liquid-feed flame spray pyrolysis. *Nat Mater* 5(9):710–712
96. Jun BS, Lee SJ, Messing GL (2006) Synthesis of Nano-scaled $\alpha\text{-Al}_2\text{O}_3$ particles by combustion spray pyrolysis. *Key Eng Mater* 317–318:207–210
97. Hinklin T et al (2004) Liquid-feed flame spray pyrolysis of metalloorganic and inorganic alumina sources in the production of nanoalumina powders. *Chem Mater* 16(1):21–30
98. Smith RM, Zhou XD, Huebner W, Anderson HU (2004) Novel yttrium-stabilized zirconia polymeric precursor for the fabrication of thin films. *J Mater Res* 19(9):2708–2713
99. Ismail HM, Hussein GAM (1996) Texture properties of yttrium oxides generated from different inorganic precursors. *Powder Technol* 87(1):87–92
100. Chen D, Jordan EH, Gell M, Ma X (2008) Dense TiO_2 coating using the solution precursor plasma spray process. *J Am Ceram Soc* 91(3):865–872
101. Sivakumar G, Ramakrishna M, Dusane RO, Joshi SV (2015) Effect of SPPS process parameters on in-flight particle generation and splat formation to achieve pure $\alpha\text{-Al}_2\text{O}_3$ coatings. *J Therm Spray Technol* 24(7):1221–1234
102. Schlichting KW, Padture NP, Jordan EH, Gell M (2003) Failure modes in plasma-sprayed thermal barrier coatings. *Mater Sci Eng A* 342(1–2):120–130
103. Govindarajan S, Dusane RO, Joshi SV (2014) Understanding the formation of vertical cracks in solution precursor plasma sprayed yttria-stabilized zirconia coatings. *J Am Ceram Soc* 97(11):3396–3406
104. Gell M, Xie L, Jordan EH, Padture NP (2004) Mechanisms of spallation of solution precursor plasma spray thermal barrier coatings. *Surf Coat Technol* 188–189(1-3. SPEC.ISS.):101–106
105. Praveen K, Sravani N, Alroy RJ, Shanmugavelayutham G, Sivakumar G (2019) Hot corrosion behaviour of atmospheric and solution precursor plasma sprayed $(\text{La}_{0.9}\text{Gd}_{0.1})_2\text{Ce}_2\text{O}_7$ coatings in sulfate and vanadate environments. *J Eur Ceram Soc* 39(14):4233–4244
106. Gao L, Guo H, Gong S, Xu H (2014) Plasma-sprayed $\text{La}_2\text{Ce}_2\text{O}_7$ thermal barrier coatings against calcium-magnesium-alumina-silicate penetration. *J Eur Ceram Soc* 34(10):2553–2561

107. Kumar R, Govindarajan S, Janardhana RKSK, Rao TN, Joshi SV, Anandan S (2016) Facile one-step route for the development of in situ Cocatalyst-modified Ti³⁺ self-doped TiO₂ for improved visible-light photocatalytic activity. *ACS Appl Mater Interfaces* 8(41):27642–27653
108. Dom R, Kumar GS, Hebalkar NY, Joshi SV, Borse PH (2013) Eco-friendly ferrite nanocomposite photoelectrode for improved solar hydrogen generation. *RSC Adv* 3(35):15217–15224
109. Tummala R, Guduru RK, Mohanty PS (2011) Solution precursor plasma deposition of nanostructured ZnO coatings. *Mater Res Bull* 46(8):1276–1282
110. Yu Z, Moussa H, Liu M, Schneider R, Moliere M, Liao H (2018) Solution precursor plasma spray process as an alternative rapid one-step route for the development of hierarchical ZnO films for improved photocatalytic degradation. *Ceram Int* 44(2):2085–2092
111. Nehe P, Sivakumar G, Kumar S (2015) Solution precursor plasma spray (SPPS) technique of catalyst coating for hydrogen production in a single channel with cavities plate type methanol based microreformer. *Chem Eng J* 277:168–175
112. Mohanty PS, Anton SBCM, Guduru KR (2010) Direct thermal spray synthesis of Li ion battery components, US patent No. US20100323118A1
113. Varadaraajan V, Satishkumar BC, Nanda J, Mohanty P (2011) Direct synthesis of nanostructured V₂O₅ films using solution plasma spray approach for lithium battery applications. *J Power Sources* 196(24):10704–10711
114. Chen D, Jordan EH, Renfro MW, Gell M (2012) Solution precursor plasma spray Eu: Y₂O₃ phosphor coating. *Int J Appl Ceram Technol* 9(3):636–641
115. Golozar M, Chien K, Coyle TW (2012) Orthorhombic α -MoO₃ coatings with lath-shaped morphology developed by SPPS: applications to super-capacitors. *J Therm Spray Technol* 21(3–4):469–479
116. Guo XZ et al (2005) Synthesis of yttrium iron garnet (YIG) by citrate-nitrate gel combustion and precursor plasma spray processes. *J Magn Magn Mater* 295(2):145–154
117. Killinger A, Gadow R, Mauer G, Guignard A, Vaen R, Stöver D (2011) Review of new developments in suspension and solution precursor thermal spray processes. *J Therm Spray Technol* 20(4):677–695
118. Moign A, Vardelle A, Themelis NJ, Legoux JG (2010) Life cycle assessment of using powder and liquid precursors in plasma spraying: the case of yttria-stabilized zirconia. *Surf Coat Technol* 205(2):668–673
119. Marr M, Kuhn J, Metcalfe C, Harris J, Kesler O (2014) Electrochemical performance of solid oxide fuel cells having electrolytes made by suspension and solution precursor plasma spraying. *J Power Sources* 245:398–405
120. Joshi SV, Sivakumar G (2015) Hybrid processing with powders and solutions: a novel approach to deposit composite coatings. *J Therm Spray Technol* 24(7):1166–1186
121. Björklund S, Goel S, Joshi S (2018) Function-dependent coating architectures by hybrid powder-suspension plasma spraying: injector design, processing and concept validation. *Mater Des* 142:56–65
122. Sivakumar G, Banerjee S, Raja VS, Joshi SV (2018) Hot corrosion behavior of plasma sprayed powder-solution precursor hybrid thermal barrier coatings. *Surf Coat Technol* 349:452–461
123. Ajay A, Raja VS, Sivakumar G, Joshi SV (2015) Hot corrosion behavior of solution precursor and atmospheric plasma sprayed thermal barrier coatings. *Corros Sci* 98:271–279
124. Tesar T, Musalek R, Lukac F, Medricky J, Cizeka J, Rimal V, Joshi S, Chraska T (2019) Increasing α -phase content of alumina-chromia coatings deposited by suspension plasma spraying using hybrid and intermixed concepts. *Surf Coat Technol* 371:298–311
125. Chen D, Gell M, Jordan EH, Cao E, Ma X (2007) Thermal stability of air plasma spray and solution precursor plasma spray thermal barrier coatings. *J Am Ceram Soc* 90(10):3160–3166
126. Duarte W, Rossignol S, Vardelle M (2014) La₂Zr₂O₇(LZ) coatings by liquid feedstock plasma spraying: the role of precursors. *J Therm Spray Technol* 23(8):1425–1435

127. Candidato RT, Sokołowski Pawełand L, Pawłowski G, Lecomte-Nana CC, Denoirjean A (2017) Development of hydroxyapatite coatings by solution precursor plasma spray process and their microstructural characterization. *Surf Coat Technol* 318:39–49
128. Wang WZ, Coyle T, Zhao D (2014) Preparation of lanthanum zirconate coatings by the solution precursor plasma spray. *J Therm Spray Technol* 23(5):827–832
129. Sivakumar G, Dusane RO, Joshi SV (2013) A novel approach to process phase pure α -Al₂O₃ coatings by solution precursor plasma spraying. *J Eur Ceram Soc* 33(13–14):2823–2829
130. Sanpo N, Siao A, Ang M, Hasan F, Wang J, Berndt CC (2012) Phases and microstructures of solution precursor plasma sprayed cobalt ferrite splats. In: *Proceedings of 5th Asian thermal spray conference*, pp 145–146



Multifunctional Sol-Gel Nanocomposite Coatings for Aerospace, Energy, and Strategic Applications: Challenges and Perspectives

36

R. Subasri and K. R. C. Soma Raju

Contents

Introduction to Sol-Gel-Derived Nanocomposite Coatings and Their Key Features	1415
Applications of Sol-Gel Coatings for Aerospace Sector	1417
Chrome-Free Conversion Coatings on Aluminum Alloys	1417
Ultrahydrophobic/Superhydrophobic/Icephobic Coatings	1418
Scratch-Resistant Coatings on Transparent Plastics	1420
Antibacterial Coatings	1422
Applications for Energy Sector with Focus on Solar-Selective Coatings for Use in Heat ...	1424
Collection Element of Solar Thermal Power Plants	1424
About Concentrated Solar Power Plant (CSPP) and Parabolic Trough Collector (PTC)	1424
Heat Collection Element (HCE) and Role of Solar-Selective Coatings (SSC)	1425
Sol-Gel-Derived SSC	1428
Applications for Defense and Strategic Sectors	1431
Sensors for Detecting Chemical/Biological Agents and Radiation	1431
Radiation Sensors	1435
Functional Coatings for Ceramic Radomes/IR Windows	1435
Concluding Remarks	1437
References	1438

Abstract

Sol-gel technique is a wet chemical synthesis procedure involving the hydrolysis of either a fully hydrolyzable metal/silicon alkoxide or an organically modified silane followed by condensation and polymerization reactions. Through this method, ceramics, glasses, and hybrid nanocomposite materials of high purity and homogeneity can be produced than when obtained through conventional processes that involve high-temperature treatment conditions. Sol-gel-derived hybrid nanocomposite coatings combine the interesting properties such as

R. Subasri (✉) · K. R. C. S. Raju
Centre for Sol-Gel Coatings, International Advanced Research Centre for Powder Metallurgy and New Materials (ARCI), Hyderabad, India
e-mail: subasri@arci.res.in; somarajuk@arci.res.in

flexibility, hardness, etc. drawn from an organic polymer and an inorganic glass and hence are of great interest for aerospace, energy, and defense applications, due to their distinct advantages. Varied functionalities like corrosion protection, antireflection, scratch resistance, antibacterial, water/oil repellent, erosion resistant, and antistatic are possible to be obtained using this technique. Sol-gel nanocomposite films on appropriate substrates are also capable of being used as sensors for detecting chemical/biological warfare agents as well as for sensing ionizing radiation in the environment. Despite many advantages of this technique, there are still certain challenges that need to be circumvented in order to fully harness the potential of the coatings derived from this process. This chapter mainly focuses on the potential applications of sol-gel nanocomposite coatings for aerospace, energy, and strategic sectors, where challenges in using them for applications and future perspectives on how they can be mitigated are discussed.

Keywords

Sol-gel nanocomposite coatings · Chrome-free · Corrosion resistant · Nanocontainers · Self-healing · Solar selective · Antimicrobial, scratch resistant · (Ultra)hydrophobic · Chemical/biological sensor

List of Abbreviations

γ -MAPTS	γ -trimethoxysilylpropylmethacrylate
APTMS	3-trimethoxysilylpropylamine
AR	Antireflective
ATMOS	bis[3-(trimethoxysilyl)-propyl]amine
CEST	Carboxyethylsilanetriol sodium salt
CFU	Colony formation units
CNT	Carbon nanotube
CSP	Concentrated solar power
CSPP	Concentrated Solar Power Plant
DienTMOS	(3-trimethoxysilylpropyl)diethylenetriamine
DNA	Deoxyribonucleic acid
DNI	Direct normal irradiance
enTMOS	Bis [3-(trimethoxysilyl)-propyl]ethylenediamine
FIB	Focused ion beam
HCE	Heat Collection Element
HMVF	High metal volume fraction
IR	Infrared
LMVF	Low metal volume fraction
MPTES	3-mercapto-propyltriethoxysilane
MTES	Triethoxymethylsilane
MTMS	Trimethoxymethylsilane
NO	Nitrogen monoxide
OD	Optical density

PC	Polycarbonate
PDA	polydiacetylene
PDMS	Poly-dimethylsiloxane
PMPS	Polymethylphenylsiloxane
PTC	Parabolic Trough Collector
PV	Photovoltaic
PVDF	Polyvinylidene fluoride
PVP	Poly-vinylpyrrolidone
RH	Relative humidity
ROS	Reactive oxygen species
RT	Room temperature
SNR	Signal-to-noise ratio
SSC	Solar-Selective Coatings
TEOS	Tetraethoxysilane
TMOS	Tetramethoxysilane
UV	Ultraviolet
VTES	Vinyltriethoxysilane

Introduction to Sol-Gel-Derived Nanocomposite Coatings and Their Key Features

Sol-gel process is defined by its characteristic hydrolysis and condensation reactions of metal/silicon alkoxides to form metal/silicon oxide network colloidal particles dispersed in a continuous liquid phase called sol, which is followed by gelation of the sol as a result of further progress of hydrolysis and condensation reactions, leading to the growth of the particles and evaporation of liquid phase and leaving solid as a major phase [1]. Sol-gel process can lead to different products, namely, powders, coatings, fibers, and aerogels, depending on how the liquid phase is removed from the sol. When fully hydrolyzable alkoxides are used as starting materials, pure inorganic sols are obtained from which pure inorganic coatings can be derived. Pure inorganic sol-gel coatings have one major drawback regarding coating thickness, wherein thickness higher than 1 micrometer cannot be obtained in a single coating deposition step. Organic-inorganic hybrid coatings can be obtained by two methods: (1) hydrolysis and condensation of organically modified silanes in conjunction with silicon/metal alkoxides or (2) through introduction of polymers into the metal/silicon oxide network. In case of the former, the organic moieties in the organically modified silanes could either be polymerizable or non-polymerizable. In this case, the organic and inorganic networks are bonded either through covalent or ionocovalent bonding. In the case of the organic-inorganic hybrid coatings, the inorganic moiety gives good mechanical properties, and the organic moiety provides flexibility, compatibility with organic primers/paints [2], and possibility of achieving higher coating thickness at a lower curing temperature (<100 °C), as compared to 400–800 °C for curing the pure inorganic coatings.

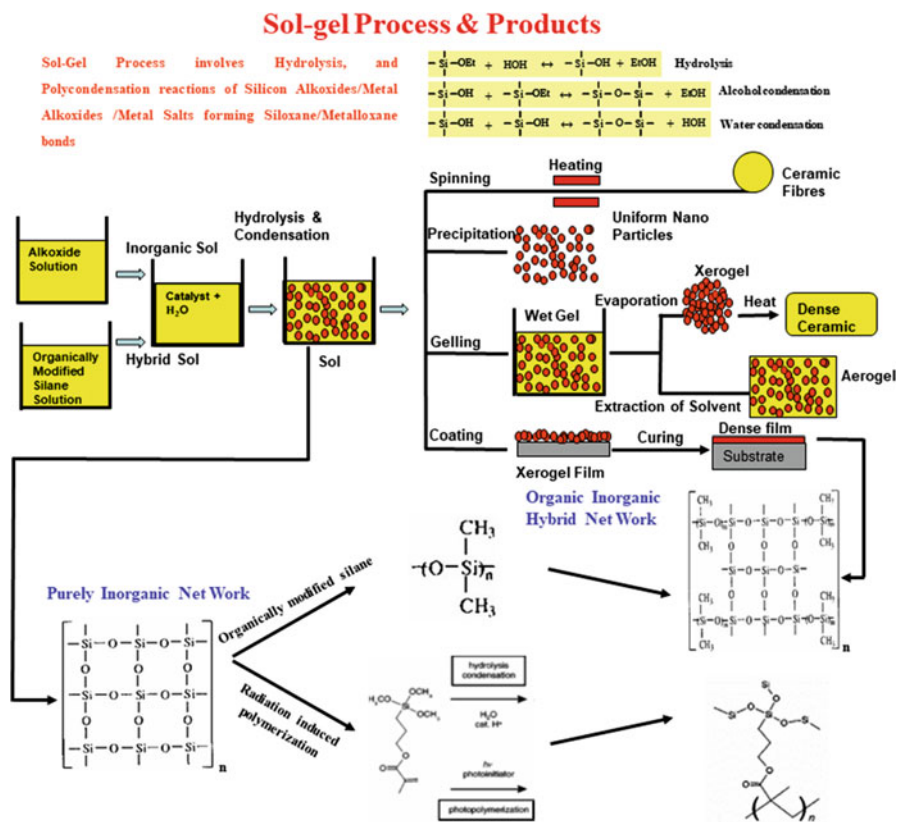


Fig. 1 Schematic showing different products of a sol-gel reaction

Organic-inorganic hybrid sol-gel coatings also are compatible with various kinds of corrosion inhibitors, pigments, etc. [3, 4]. Figure 1 shows a schematic of the different products that a sol-gel processing can lead to. The most commonly used organically modified precursors are methyltriethoxysilane, methyltrimethoxysilane, vinyltriethoxysilane, phenyltrimethoxysilane, 3-aminopropyltrimethoxysilane, 3-methacryloxypropyltrimethoxysilane, 3-glycidoxypropyltrimethoxysilane, etc. Hybrid nanocomposite coatings can be obtained by physical dispersion of nanoparticles into the hybrid sol-gel matrix or by synthesizing the sol with suitable precursors so as to generate required metal oxide network nanoparticles in situ in the hybrid sol-gel matrix. Sol-gel-derived pure inorganic and organic-inorganic hybrid nanocomposite coatings have been explored for various applications, like corrosion mitigation (barrier and self-healing type), antireflective, solar selective, solar control, antibacterial, self-cleaning/photocatalytic, easy-to-clean, and scratch and abrasion resistances, which have potential applications in aerospace, energy, and strategic sectors.

Applications of Sol-Gel Coatings for Aerospace Sector

Chrome-Free Conversion Coatings on Aluminum Alloys

Aluminum alloys are economical, one of the few selected from the family of lightweight materials with high strength-to-weight ratio and hence are predominantly used in aerospace applications as structural materials [5]. Their resistance to uniform corrosion is well-known due to the thin passivating oxide layer formed on the surface. However, the passive layer is deteriorated in chloride- or sulfate-containing electrolytes, which results in pitting corrosion. Prevention of corrosion through deposition of paints is the most convenient method. The barrier protection depends on the dense structure and thickness of the coating system. Since direct application of paints on metal substrates does not yield good adhesion, conversion coatings along with primers are commonly used prior to application of paints. Conversion coatings have two roles to play, namely, (a) improving the adhesion of primer with the substrate and (b) rendering a self-healing (or self-repairing) effect when there is damage in the paint and primer layer that extends down to the substrate. Hexavalent chromium-based conversion coating is known to be the best self-healing coating with unmatched performance. However, chromate conversion coatings have been globally banned due to their carcinogenic effect [6, 7]. Consequently, worldwide researchers are seriously investigating various materials to identify an effective self-healing alternative to replace hexavalent chrome [8–10]. Pure inorganic and organic-inorganic hybrid coatings derived from the sol-gel route have mainly been investigated for this purpose. In order to enhance the corrosion resistance, corrosion inhibitors are added into the sol-gel coating matrix or paint. Direct addition of corrosion inhibitors to the sol-gel matrix for prolonged corrosion protection was reported to be deleterious to the barrier properties of the coating [11, 12]. More recent methods of achieving long-lasting corrosion protection are (a) by incorporation of corrosion inhibitors packaged inside “smart” nanocontainers which are dispersed in a sol-gel matrix to obtain self-healing coatings and (b) by employing barrier coatings as top coat, which are also capable of rendering superhydrophobic effect [13].

Certain coatings are called self-healing coatings as they have the ability of automatically repairing any damage such as scratch caused by the external force, thereby preventing corrosion of the underlying substrate without human intervention. These are particularly interesting from an application point of view [14]. The concept of using self-healing coatings for corrosion protection of metals originated from self-healing polymers, where any defect/scratch in the polymer could be autonomically healed by incorporating containers with monomers and catalysts into the polymer [15]. Whenever there is a scratch/crack in the polymer material, the monomer and catalyst are released from their respective containers and polymerized to heal the crack. However, a majority of these materials have serious chemical and mechanical limitations, hindering their use as coatings for practical applications. Appropriate modifications to the chemistry of the self-healing materials make them amenable to be incorporated as a part of the coating matrix to

yield self-healing coatings, which are highly stable to species present in the environment. The encapsulation provides a means to contain other chemical agents also that can provide multi-functionalities like corrosion inhibition, antimicrobial activity, self-cleaning property, etc. in addition to self-healing effect. Recent focus has been on using inorganic systems as encapsulation materials. Carbon nanotubes (CNTs), clay nanotubes, mesoporous silica, and layered clays have been used as nanocontainers to encapsulate the corrosion inhibitors [16–27].

Ultrahydrophobic/Superhydrophobic/Icephobic Coatings

A surface is called “superhydrophobic” if it exhibits nearly zero wetting. Superhydrophobic surface can be obtained by creating an appropriate optimum roughness that has micro- and nanostructural hierarchical features and simultaneously passivating with a coating that has low-surface energy. Superhydrophobic surfaces possess self-cleaning property since dust does not adhere to them. There have been several reports on development of superhydrophobic coatings for self-cleaning applications [28–31]. Figures 2 and 3 depict the wetting behavior of a hydrophobic and superhydrophobic surface, respectively, as per models proposed by Young, Wenzel, and Cassie-Baxter. Superhydrophobic surfaces have been reported to be generated by top-down techniques like lithography, template-based

Fig. 2 A schematic representation of water drop on a surface in equilibrium state, as presented by Young [36]. (Reproduced with permission from Taylor and Francis)

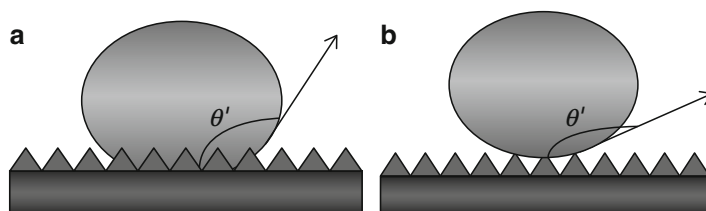
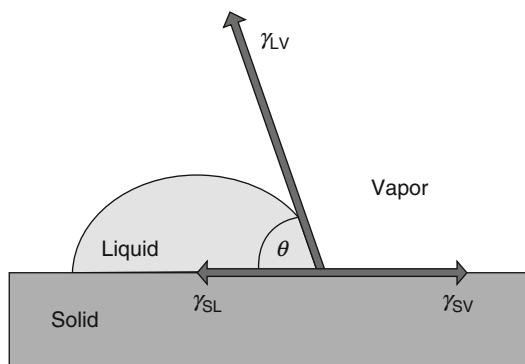
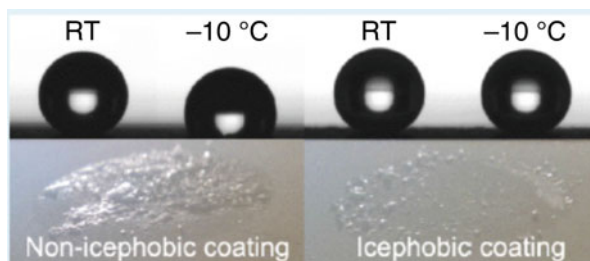


Fig. 3 (a) Wenzel model and (b) Cassie-Baxter model [36]. (Reproduced with permission from Taylor and Francis)

synthesis, and atmospheric RF plasma deposition of surfaces with CF_x nanoparticles without the use of any roughness generation and vacuum systems. Bottom-up approaches like self-assembly/self-organization where nanostructures can be manipulated into ordered arrays to impart a functionality to the material, chemical vapor deposition, electrochemical deposition, and chemical bath deposition have also been reported to yield superhydrophobic surfaces. A combination of both these approaches can also be employed. Wet chemical technique like sol-gel deposition is known to be versatile and cost-effective in creating a superhydrophobic surface. Superhydrophobic surfaces also can be potential candidates for exhibiting icephobic properties. Icing on critical structures such as hydroelectric power lines, high-tension insulators, wind turbines, aircrafts, ship hulls, highways, and automobile windshields is a serious problem that calls for immediate mitigation, since it poses system operational issues and safety concerns. Commonly employed strategies to mitigate ice buildup are based on chemical, mechanical, or thermal deicing methods, and they have several shortcomings. Normally, freezing point depressants such as NaCl, KCl, $CaCl_2$, and $MgCl_2$ are used as deicing agents for highways, and ethylene glycol and propylene glycol, alone or in combination with sodium formate, calcium magnesium acetate, sodium acetate, and urea, are used as deicing fluids for aircraft wings and runways. Both systems are time-consuming and expensive. Moreover, the deicing fluids are toxic and not eco-friendly. Alternatively, ice on the wing surface can be removed by mechanical means such as simple scraping or by introducing vigorous vibration to the body. But such methods may likely to cause damage to the surfaces, thereby reducing their service life. Though heating the affected surface is found to be an effective method to melt ice, it is not efficient and economical as large quantity of energy is required. It can be seen that none of the aforementioned techniques prevent formation of ice and its accumulation over a period of time. These methods are used only after accumulation of ice over the affected parts. Therefore, the best practice would be a preventive method, i.e., to make a surface to which ice would not adhere to at all. Such a surface is termed as an “icephobic” surface [32–34]. It has been reported that there is an electrostatic interaction between ice and surface of material on which ice forms, the resulting energy is substantially higher than the intermolecular chemical bond energy and van der Waals forces of attraction. Use of coating materials with a very low dielectric constant on the ice-forming surface would help in reducing the electrostatic interactions at the ice-dielectric interface, thereby aiding in considerably reducing the adhesion strength of ice [35]. Ice may not adhere to an engineered superhydrophobic surface as water droplet does not wet it. Hence, superhydrophobic surfaces are also expected to be icephobic. Although there are several studies reported on sol-gel-derived hydrophobic surfaces, there are only few reports on superhydrophobic coatings as icephobic coatings [36–40]. Few reports have investigated on the use of metal oxide nanoparticles such as ZnO, TiO_2 , etc. and polymers such as Teflon on etched metal surfaces for producing icephobic surfaces [36, 37]. It was shown that coatings that exhibited superhydrophobicity also exhibited reduced ice adhesion.

However, recent studies show that the icephobic property is greatly influenced by both surface morphology and its intrinsic surface free energy [38, 39] which is

Fig. 4 Wetting behaviors of non-icephobic and icephobic coatings at room temperature and at -10°C . (Reprinted (adapted) with permission from [39]. Copyright (2014) American Chemical Society)



evident from Fig. 4. Though both superhydrophobic coatings exhibited higher water contact angle at room temperature, they could not exhibit similar behavior at sub-zero temperatures. It has also been shown that as compared to a non-icephobic coating, the icing temperature of icephobic coatings can be lowered by up to 6.9° [39]. Nucleation temperature lowering is influenced by three favorable conditions, namely, the surface roughness, Cassie wetting mode, and low-surface free energy.

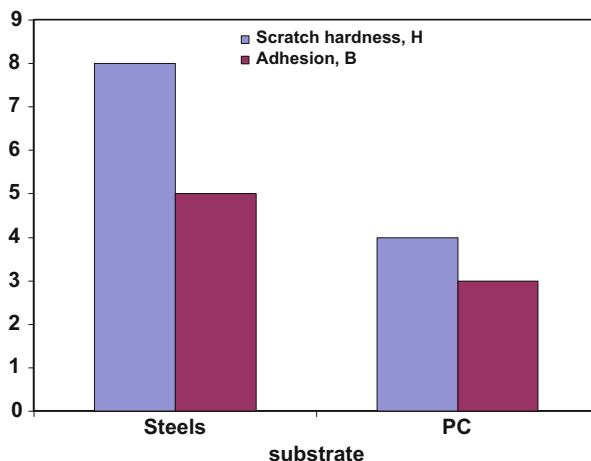
It needs to be mentioned here that though there are few studies on the applicability of superhydrophobic coatings as icephobic coatings, there are not many studies on standardization of the test procedures. Hence, immediate priority would be to formulate a standard test procedure. This is one of the challenges that need to be addressed before commercialization of such coatings could take place.

Scratch-Resistant Coatings on Transparent Plastics

Sol-gel compositions are synthesized based on coating property requirement and composition of the substrate on which the coatings are to be applied. Coatings on metals and other inorganic materials like glass can be heat treated at higher temperatures, but plastics have to be heat treated at lower than their glass transition temperatures. Sol-gel science has evolved over the years from pure inorganic coatings to successful development of present day organic-inorganic hybrid coatings. Curing temperature range between 50°C to a maximum of 500°C are reported. Organically modified silanes are used for the synthesis of sols for hybrid coatings [41–57]. Organic groups of such silanes could be non-polymerizable, such as aryl or alkyl groups which do not participate in cross-linking, or they could be polymerizable like the vinyl, epoxy, or acryl groups that participate in cross-linking of precursors. Even in hybrid coatings, though the same sol is coated on metals and plastics, the coating properties largely differ based on the curing conditions. As can be seen from the following Fig. 5, present authors have observed that a silica-zirconia coating has exhibited a pencil scratch hardness of more than 8H and an adhesion strength of 5B on steel substrates, while the same composition results in a pencil scratch hardness of 4H with an adhesion strength of 3B on polycarbonate (PC).

Adhesion of the coating to the substrate also depends on the precursors used for the sol synthesis. Even organic catalysts are used for the sol synthesis if coatings are

Fig. 5 Effect of curing conditions on the mechanical properties of silica-zirconia coating. (unpublished work)



meant for plastic substrates. It was reported that an adhesion-promoting zirconium propoxide was used for sol synthesis [58], which promoted zirconia-type bonds and acted as a catalyst to open 3-glycidoxypropyltrimethoxysilane epoxy rings resulting in more polymerized organic domains. This has reportedly increased plasticity of the coating and hence resistance to scratch loads. Recent investigations show that even with low-temperature heat treatment at 110 °C for 3 h, zirconia nanofluids provide excellent adhesion and a scratch hardness of 5H on PC while maintaining an optical transmission of 96%. Furthermore, an optimum amount of hydrolyzing agent, i.e., water [59], can promote silica network formation resulting in high hardness and significant scratch resistance.

Many practical applications require multifunctional properties which a single precursor cannot meet, and hence, composite coatings are explored. Combination of two or more metal alkoxide precursors results in highly cross-linked network materials from Al_2O_3 , TiO_2 , SiO_2 , ZrO_2 , etc. blending best properties of each of the constituent of the total composition. In situ prepared nanoparticulate oxide networks of such nanocomposite hard coatings will exhibit improved scratch and abrasion resistance which is beyond the typical values exhibited by coatings obtained through single precursor coatings. Alternatively, composite coatings can also be obtained from a sol that is prepared from hydrolysis and condensation of organically modified alkoxysilane which results in simple silica network, and additionally one or two components can be chosen from pre-prepared nanoparticles of ZnO , SiC , Al_2O_3 , AlOOH , TiO_2 , SiO_2 , Y_2O_3 , ZrO_2 , CeO_2 , and SnO_2 , iron oxides, and Ta_2O_5 as per the functional requirement of the coating. However, SiO_2 particles and/or precursors that can result in SiO_2 network with suitable organic ligands are particularly preferred for many applications. Alkoxysilanes such as tetramethoxysilane (TMOS), tetraethoxysilane (TEOS), trimethoxymethylsilane (MTMS), triethoxymethylsilane (MTES), 3-trimethoxysilylpropylamine (APTMS), and γ -trimethoxysilylpropylmethacrylate (γ -MAPTS) are some of precursors prominently used for the synthesis of sols used to deposit hard coatings on plastics [60, 61].

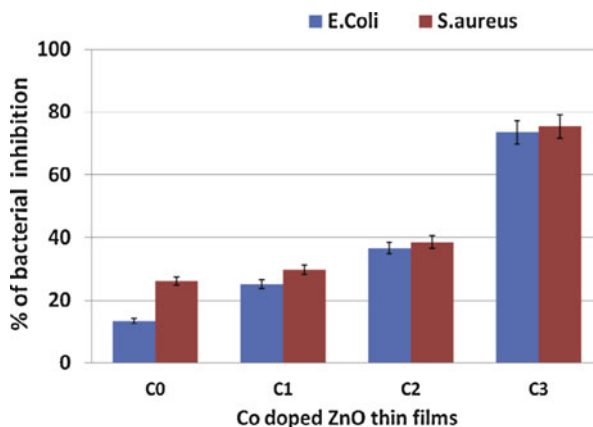
Hard poly(methylsiloxane)s and colloidal silica coating formulations introduced by industrial majors like General Electric Co., Dupont Co., and Lucite have been in use for several decades now in Europe and the USA to improve scratch and abrasion resistance of polycarbonate head lamps and side windows of automobiles. Excellent scratch and abrasion resistance while maintaining high transparency at low processing temperature are the main features responsible for successful industrialization of the above products. As per 1997 industrial statistics, 64% of ophthalmic lenses used in the USA are made of CR39 monomer, and 47% of them are coated with hard sol-gel materials. Vinyltriethoxysilane (VTES)- and 3-mercaptopropyltriethoxysilane (MPTES)-derived UV curable compositions were used for the above applications. A joint venture company with a name Exatec[®] was floated by General Electric Plastics and Bayer AG with a sole aim of replacing automotive glass with coated polycarbonate sheet [62]. PC is transparent to microwave, and hence microwave heating was also evaluated as a rapid curing method to selectively cure only the coating applied on PC while maintaining excellent hardness [63, 64].

Antibacterial Coatings

Bacteria are one of the first and most widely available families of microorganisms on earth. While some of them are useful, some of them are harmful for the survival of human life. Even today, health and life expectancy of human being is largely dependent on controlling breeding and spreading of these bacteria. Microorganisms are found everywhere right from simple office desk, computer keyboard, mobile, money purse, pen, spectacles, hearing aids, dress material, socks, railings of buildings, vehicle doors, handles, steering wheels and passenger seats, food packaging to toilet seats, and much more. Such a long list implies how easily a person can be affected while using any one of them. Moreover, keeping surgical devices, operation theaters, and labs in sterile condition is one of the toughest tasks as they are breeding grounds for some of the strains of bacteria and a greatest threat to the patients with poor immune system. Some of the naturally available materials such as silver, copper, titanium oxide, ZnO, natamycin, quaternary amine compounds, phosphonium salts, and natural substances like tea tree oil and chitosan [65–67] have excellent antibacterial property. As presented in Fig. 6, one of such studies shows that cobalt doping reduces the band gap energy of ZnO and hence exhibits a better photocatalytic activity under visible light irradiation.

Escherichia coli and *Staphylococcus aureus* bacteria were used to assess the bactericidal efficiency of the ZnO films doped with different concentrations of Co. The improvement in antibacterial activity of Co-doped ZnO films was attributed to the high charge separation efficiency and reactive oxygen species (ROS) generation ability of the films which in turn enhanced their photocatalytic degradation property. C0 to C3 in the figure refer to the concentration of Co from 0 to 15 wt% in steps of 5 wt%. Among other materials, silver is highly toxic to bacteria but do not pose any serious trouble to human life. Hence it has been a highly sought after material for antibacterial effect. Nanopowder, rods, and tubes are the most efficient

Fig. 6 Bacterial inhibition of Co-doped ZnO thin films tested against *E. coli* and *S. aureus* bacteria while monitoring the optical density (OD) at 600 nm [67]



forms of silver due to large surface to volume ratio and, hence, are easy to release silver ions for antibacterial functionality. Silver ions destruct bacterial cell wall, cause degradation of its plasma membrane, and prevent bacterial reproduction through binding to its DNA base. A low concentration (2.5 wt%) of silver is shown to be sufficient for the required antibacterial activity [68]. Organic-inorganic hybrid sol-gel coatings are flexible, hard, solvent resistant, long-lasting, and economical, possess high toughness, and easy to formulate, apply, and cure. Hybrid sol-gel coatings such as SiO_2 , Al_2O_3 , TiO_2 , and ZrO_2 and their combinations are being extensively used as a host material for nanosilver particles to apply as coating on surfaces of interest. However, the sol composition is designed based on the substrate to be coated, as some of the substrates such as metals and inorganic materials can be heat treated at higher temperatures ($\approx 500^\circ\text{C}$), while some of the materials like paper, leather, and plastics have to be heat treated at lower temperatures ($\approx 50^\circ\text{C}$). Radiation curing is used quite often for the substrates that are temperature sensitive. Mechanical properties such as hardness and scratch and abrasion resistance of the coatings are strongly influenced by the above factors and can be tailor-made to meet the end requirements. Coatings can be applied by spin, dip, spray, pour, brush, and sponge techniques. Coatings are tested in *Staphylococcus aureus*, *Escherichia coli*, and *Pseudomonas aeruginosa* cultures. The presence of *Staphylococcus aureus* is found in human respiratory tract and the skin and is responsible for skin infections, respiratory diseases, and food poisoning. *Escherichia coli* is commonly found in the lower intestine of humans and other animals. They are responsible for food contamination and poisoning. *Pseudomonas aeruginosa* is found in soil, water, skin flora, and man-made environments. It is said to be the toughest strain that can survive in any harsh environment. It is considered to be inactive for healthy people but can be dangerous to the people with compromised immune system.

Coated samples are tested in incubators with 90% RH and 37°C for 24 h. Colony formation units (CFU/ml) are first counted on the control as well as test sample over which bacterial growth has been initiated. Subsequently, cell reduction can be

computed using this formula: $\text{Cell reduction\%} = \{1 - \text{test sample CFU per ml} / \text{control sample CFU per ml}\} \times 100$. Test specimen is judged to be antibacterial if the estimated cell reduction is found to be more than 99%. Treatment of textile fibers with nanosilver-containing sol-gel hybrid coatings opens new possibilities for the improvement of additional functionalities such as antimicrobial property for odor-free dress material. These coatings can also be used for drug delivery devices, implants, water purification, human tissue, and antifouling applications. A recent study shows that zinc-encapsulated silica nanoparticles produced through sol-gel process exhibit efficient antimicrobial activity and lower toxicity than other aforementioned materials paving its potential for the development of effective antimicrobial nanoparticle agents [69].

Applications for Energy Sector with Focus on Solar-Selective Coatings for Use in Heat

Collection Element of Solar Thermal Power Plants

The increasing need for energy around the globe has motivated the scientists to develop technologies that helped in the utilization of renewable energy resources such as geothermal, wind, and solar radiation for generation of power. Out of the three sources, solar energy is copious and is available in all regions of the globe and, hence, has attracted as a major alternative energy resource. Direct normal irradiance (DNI) is a parameter used to assess whether a particular region is suitable for solar power generation or not. DNI is defined as the flux of radiant energy, i.e., power received by a surface of unit area which is always kept perpendicular to the sun rays that are coming in a straight line from the direction of sun at its current position in the sky [70]. A worldwide mapping of global estimate of long-term yearly DNI is depicted in Fig. 7. Regions starting from yellow color shade moving toward brown and pink indicate the areas well suited for concentrated solar power (CSP) technology, since such areas experience more than 1500 kWh/m² of long-term average DNI per year.

About Concentrated Solar Power Plant (CSPP) and Parabolic Trough Collector (PTC)

Semiconducting materials absorb photons from light and emit electrons. An electric current results when such free electrons are collected and transferred through wires. A photovoltaic (PV) device is made based on this principle, which converts sunlight directly into electricity through quantum conversion, whereas thermal conversion helps in solar thermal device to convert solar radiation into heat and subsequently converts it into electricity using a typical thermal power plant or engine. Conversion efficiency of solar thermal energy units that use conventional molten salt as heat transfer fluid is reported to be 39.9%, and more recent results show that the

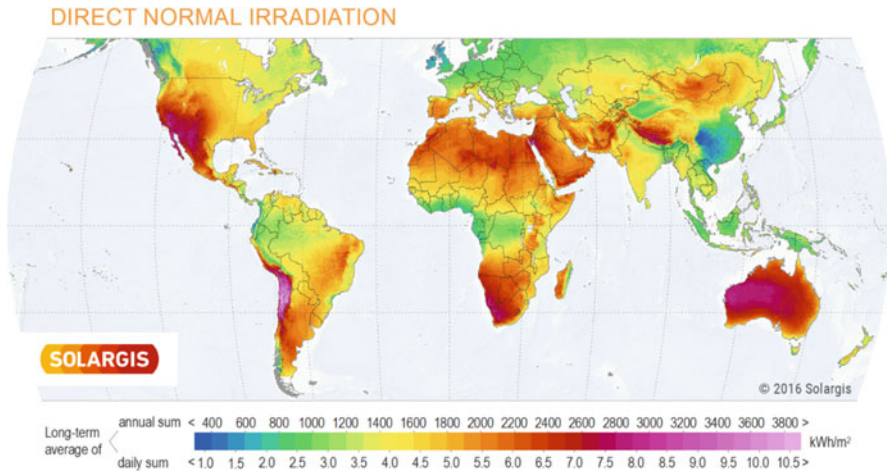


Fig. 7 Global long-term average estimate of DNI. (Source: public domain DNI Solar Map © 2016 Solargis)

efficiency can be further enhanced to 45.4% with new heat transfer fluid and a super critical Rankine cycle used with a heliostat-based design. As against, a typical photovoltaic unit has a conversion efficiency of 20–27% only [71–73]. Concentrated solar power plant (CSPP) systems use multiples of mirrors to reflect a large amount of solar radiation and concentrate onto a small area as in a heliostat design. Parabolic trough collector (PTC) is one of the most commonly used devices for CSPP. PTC uses a parabolic trough mirror to reflect the light as a concentrated beam onto a metallic-selective absorber tube placed at its focal point. A thermic fluid running through the tube then gets heated up to the operating temperature, which depends on PTC design. As shown in Fig. 8, heat from the thermic fluid is then transferred to water through a separate heat exchanger to generate steam and is subsequently used to run a turbine for power generation. Solar thermal collectors are categorized into low-, intermediate-, and high-temperature collectors based on type of concentration such as no concentration flat plate, medium-concentration, and high-concentration designs with operating temperatures reported to be < 200 °C, 150–500 °C, and >500 °C, respectively, for different applications.

Heat Collection Element (HCE) and Role of Solar-Selective Coatings (SSC)

In order to utilize solar radiation effectively, there should be an absorber material that can absorb this radiation and transmit the same to convert the radiation to do useful work. However, the material that absorbs such energy also gets heated and starts radiating the energy back at wavelengths of 1500 nm or more. Hence, for effective utilization of energy, the absorbed energy should not be radiated back, which means

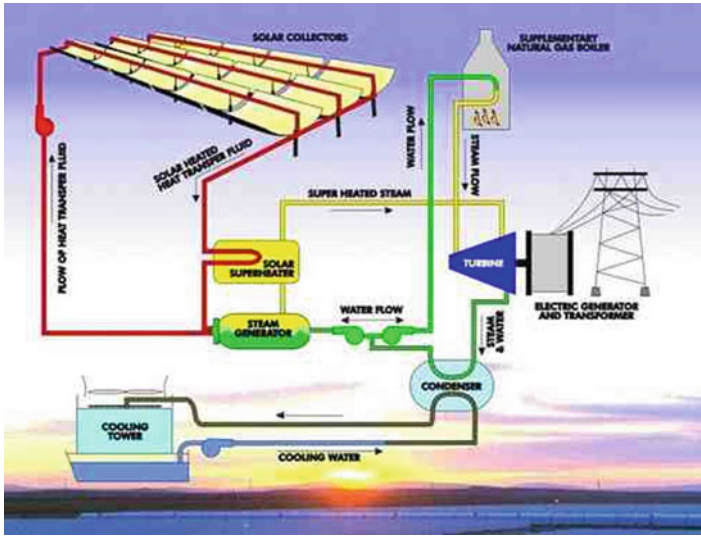


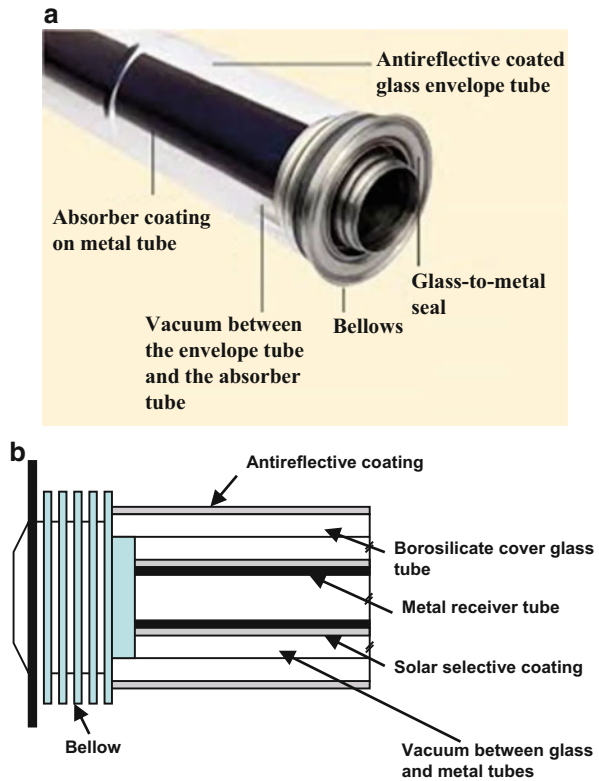
Fig. 8 Schematic representation of the CSP-based PTC design. (Source: public domain)

the same material, while absorbing the solar radiation over the wavelength range 300–1500 nm, should also simultaneously act as a mirror for the infrared radiation. This property is termed as low emittance. No naturally available material has such contrasting properties, and hence, surface engineering is the only solution for obtaining high-absorbing and low-emitting surface, which is termed as solar-selective property or spectral selectivity. This implies that ideally, the absorption over the active solar wavelength range should be 100%, while the IR emission should be zero.

Figure 9 shows a heat collector element (HCE) which is a tubular radiation absorber device that contains a metallic tube encased in a borosilicate cover glass tube. HCE is the most essential element of PTC responsible for the efficient conversion of flux of radiant energy to thermal energy. The annular space of the absorber tube and borosilicate glass tube is most commonly evacuated to minimize heat loss due to convection [74]. The absorber tube is deposited with a solar-selective coating (SSC) for enhanced efficiency in converting solar radiation to thermal energy. There are six types of SSCs, namely:

- (a) Intrinsic: modified transition metals and semiconductors such as metallic W, HfC, and V_2O_5 .
- (b) Semiconductor-metal tandems: semiconductors such as Si, Ge, and PbS with a band gap of 0.5 eV to 1.26 eV absorb short wavelength radiation with underlying metal substrate providing necessary low emittance.
- (c) Multilayer absorbers: multilayer interference stacks where metals such as Mo, Ag, Cu, etc. are used as absorber materials, while Al_2O_3 , SiO_2 , and CeO_2 were used as dielectric layers stable up to 400 °C.

Fig. 9 (a) Heat collection element. (Source: public domain) and (b) its schematic representation



- (d) Metal-dielectric composite coatings: a highly absorbing cermet material where metal nanoparticles such as Ni, Cu, Ag, V, Cr, or Mo dispersed in a SiO_2 or Al_2O_3 dielectric composite are used as absorber material on a polished highly reflective metal surface.
- (e) Textured surfaces: optical trapping of solar radiation is possible with the use of textured oxide coating on a highly reflective polished mirror like substrate surface by multiple reflections among the pores and dendrite-like structures.
- (f) Selective solar-transmitting coatings on a black body absorber: doped semiconductor such as $\text{SnO}_2:\text{F}$, $\text{SnO}_2:\text{Sb}$, or $\text{ZnO}:\text{Al}$ which when deposited on an absorber shall result in selectively solar-transmitting coating [75].

Hexavalent chrome-based electrolytic coating was one of the earliest successful candidate materials for SSC. But it is no longer being considered as such, due to its toxic and carcinogenic nature. Vacuum-based vapor deposition techniques were used to develop various compositions that could be used as semiconductor-metal tandems, multilayer absorbers, and metal-dielectric composites as next-generation SSC. Most efficient vapor-deposited SSCs are multilayered coatings. One of the metal

coatings such as Ni, Cr, Cu, or Ag is used as first layer on substrate to reflect back infrared (IR) radiation. A nanocermet-based absorber layer is applied as a second layer, and an antireflective (AR) top coat is applied as a third layer [76].

Surface plasmon resonance effect is described as the collective oscillation of the conduction band electrons of the metal nanoparticles manifested due to the interaction of their conduction electrons with incident photons. These nanoparticles are distributed in dielectric matrix of nanocermet coatings and are said to be responsible for exhibiting high absorbance in the visible wavelength range of solar spectrum. One of the nanoscale metal particles of Ni, Cu, Co, Mo, W, Pt, etc. dispersed in NiO, Cr₂O₃, or Al₂O₃ matrix and deposited routinely by vapor-based processes is being used as cermet absorbers. Multilayered composites such as TiN_xO_y, TiC/TiN_xO_y/AlN, etc. are also proven to be successful candidate materials for SSC applications. SiO₂ nanocoatings are applied as antireflective coatings over the absorber multilayers. In a new high-temperature tandem absorber, non-oxide multilayered TiAlN/TiAlON/Si₃N₄ coating stack was also proposed, where first and second layers were used as absorber layers, while the third Si₃N₄ was used as an antireflective layer [77, 78]. The absorbance values of such multilayer solar-selective stacks ranged between 90% and 97% with emittances in the range 0.04–0.14. Though these coatings exhibit very good solar-selective properties, vacuum-based coating lines need to be set up for their production and, hence, are quite expensive.

Sol-Gel-Derived SSC

Nanocomposite sol-gel-derived SSCs are eco-friendly; adherent to many substrate materials such as metals, glass, and plastics; and amenable to large-scale automation and, hence, seem to be promising candidates for use as SSCs [79]. In such a case, instead of deposition of the metal IR reflective coating, ground and polished substrates themselves were used in conjunction with sol-gel compositions to generate the SSCs. Carbon nanoparticles in ZnO and NiO matrix [80] and CuCoMnO_x and CuFeMnO₄ spinels [81] are some of the novel compositions proposed in the recent years.

Graded metal-dielectric composites that meet the dual purpose of acting as radiation absorbers and IR reflective layers are some of the successful candidates for SSCs. Some of the published literature further used double cermet layer films, where the first layer on substrate was a cermet layer with high metal volume fraction (HMF) in a dielectric matrix followed by a second cermet layer with low metal volume fraction (LMVF) in a dielectric matrix [82–84]. Metals such Cu, Ni, Ag, and Au incorporated in sol-gel dielectric matrix of TiO₂, Al₂O₃, etc. have also been shown to be promising for solar thermal applications. A cross section of sol-gel-derived five-layered Ag-TiO₂/TiO₂/SiO₂/TiO₂/SiO₂ coating [85] when prepared using focused ion beam (FIB) and observed through a high-resolution microscope is shown in Fig. 10. Figure 10a shows the cross section of the as-cut sample using FIB, and Fig. 10b depicts the cross section with the same coating stack observed under an SEM where sample was prepared using a conventional technique.

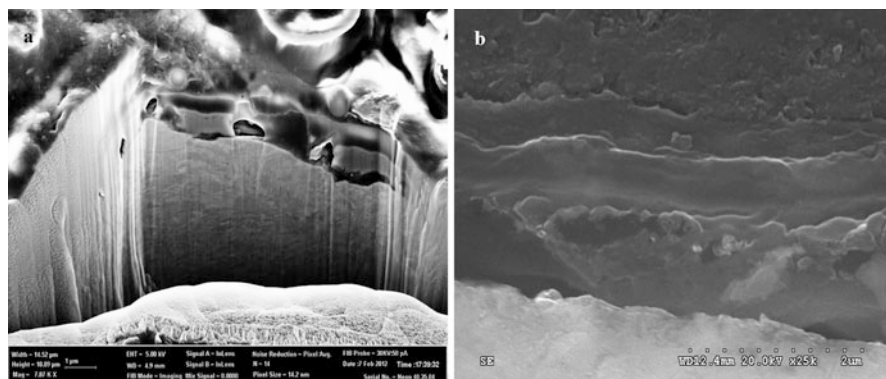


Fig. 10 (a) Micro image of a five-layered Ag-TiO₂/TiO₂/SiO₂/TiO₂/SiO₂ coating absorber stack (a) as cut using FIB and (b) cross-sectional image after preparing the sample using a conventional technique. (Unpublished work)

Fig 11 SEM image of the surface of a five-layered Ag-TiO₂/TiO₂/SiO₂/TiO₂/SiO₂ coating. (Unpublished work)

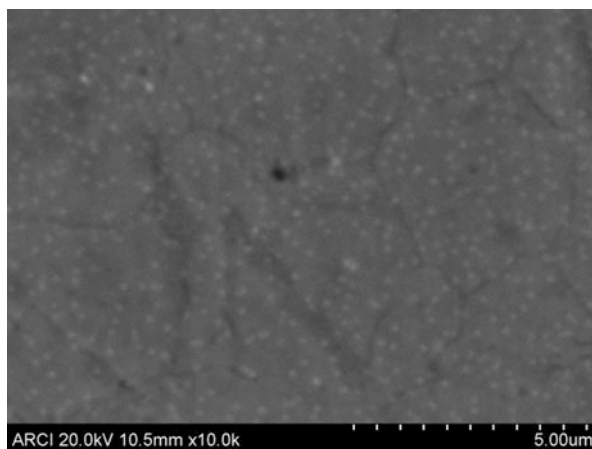
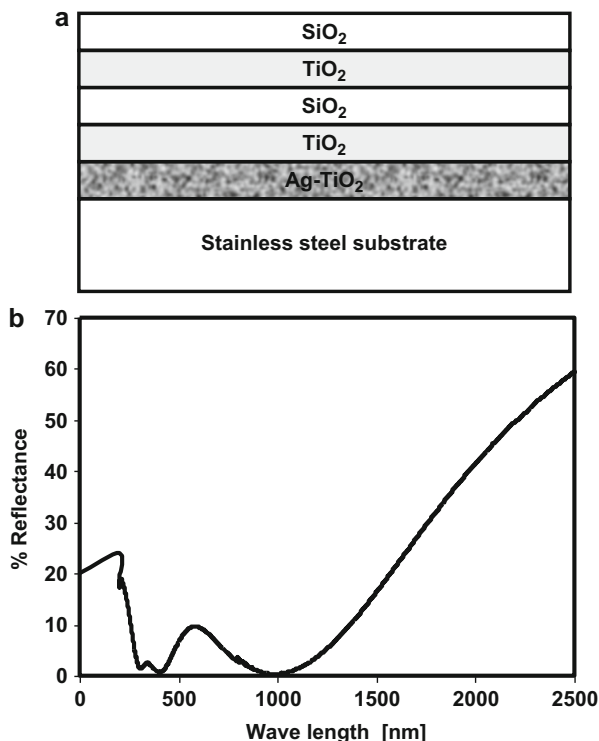


Figure 11 depicts the SEM image of the surface of a five-layered Ag-TiO₂/TiO₂/SiO₂/TiO₂/SiO₂ coating, showing the presence of Ag nanoparticles dispersed in the amorphous sol-gel matrix.

Figure 12 shows the schematic and UV-Vis-NIR spectrum of one of the most successful sol-gel-derived solar-selective coating stacks where nanometer-thick alternating high- and low-refractive index TiO₂ and SiO₂ coatings were used to enhance the visible light absorbance while maintaining lower reflectance [85]. In another recent study, a high-absorbance solar-selective coating with a Cu-Co-Mn-O as first layer on substrate followed by Cu-Co-Mn-Si-O as second layer and finally Si-O as a third antireflecting three-layered stack was proposed [81]. Single layer Ni-Al₂O₃ nanocomposite coatings on aluminum substrates were also reported to have exhibited an absorbance of 85% and emissivity

Fig. 12 (a) Schematic representation of the coating stack adopted for multilayered solar-selective coatings on SS321 substrate and (b) the corresponding UV-Vis-NIR spectrum where $\alpha = 95 \pm 1\%$, $\varepsilon = 0.14$ [85]



of 0.05. However, when two layers of Ni-Al₂O₃ with a top antireflective layer of SiO₂ were deposited, the optical properties were found to improve the absorbance values of 93% and emissivity of 0.05 and were also stable in air up to 300 °C. Recently, there has been an increased interest in SSCs based on Cu-Co-Mn-O. It was shown that the absorbance of a single layer Cu-Co-Mn-O was 0.86, which could be enhanced to 0.94 when a Si-O layer was applied as a second layer. The absorption was further enhanced to 0.96 when the coating stack was designed as Cu-Co-Mn-O first layer, Cu-Co-Mn-Si-O second layer, and Si-O third layer [81]. It was also clearly stated that the thickness of Cu-Co-Mn-Si layer was 110 nm comprising agglomerates of nanocrystalline grains that are 5–20 nm in diameter. Table 1 summarizes the properties of some of the most successful sol-gel nanocomposite coating stacks as SSCs.

Sol-gel-derived solar-selective nanocomposite coatings can be quite promising for scale-up and for use in heat collection elements of solar thermal power plants. They have an immense potential to replace the toxic hexavalent chrome-based coatings as well as coatings generated using the cost-intensive vapor-based deposition technology. However, ample care must be taken to control the thickness and metal volume fraction of the respective layers in order to obtain optimum optical properties. Accelerated testing and extensive field trials may be required to evaluate their durability under service conditions.

Table 1 Most successful sol-gel solar-selective compositions

Sl. No	Composition	Substrate	Absorptance (%)	Emissivity	Reference
1	Al ₂ O ₃ :Ni	Aluminium	97	0.05	82
2	Cu-Mn-Si oxides	Aluminium	95	0.035	81
3	Ag-TiO ₂ /TiO ₂ /SiO ₂	Stainless steel	95	0.15	85
4	Cu-Co-Mn-Si-O	Stainless steel	96	0.12	81
5	Ni-Al ₂ O ₃	Aluminum	93	0.05	84

Applications for Defense and Strategic Sectors

Sensors for Detecting Chemical/Biological Agents and Radiation

Optical sensors are beginning to be applied for sensing, which offers higher resolution, high signal-to-noise ratio (SNR), and thus large dynamic range for the parameters under investigation. Fluorescence-based chemical sensors and biosensors are being routinely used in chemical and biochemical analysis due to their high selectivity, sensitivity, simplicity, and fastness. Bio-organically doped sol-gel compositions result in diverse properties leading to their potential use in many wide-ranging areas of material science such as optical materials, biocatalysts, electrochemistry, immunochemistry, chemical sensors, biosensors, etc. Physiological changes of armed forces in the battlefield can be monitored with the help of sol-gel-derived biosensors. Sol-gel matrices are capable of being used as a very good host matrix to immobilize analyte-sensitive reagents. Analyte-sensitive reagents can be added during sol synthesis such that the reagent molecules can be encapsulated in the porous sol-gel coating structure and still permeate through the pores to sense the environment surrounding it. The composition of the sol-gel coating layer depends on the metal alkoxides selected for required functionality during sol synthesis. The advantage of producing the matrix through sol-gel technique is the possibility to obtain homogeneous, pure matrices that can densify at low temperatures. Sol-gel coatings can be used as optical transducer materials for monitoring chemical/biological warfare agents such as radioactive material use or toxic gases. Here, the change in color triggered by the reaction of the immobilized sensing material molecule in the sol-gel coating matrix strip with that of the surrounding atmosphere can be handy for the user in the affected area. A schematic of capsule-based pH sensor where a fluorescent dye is encapsulated in a polyelectrolyte membrane made by layer-by-layer assembly and the response of the capsule-based pH sensor to local environment is depicted in Fig. 13 [86]. A similar concept has also been used for clinical diagnosis, food and drinking water quality assessment (pH and dissolved oxygen monitoring), pollution monitoring, and its control for military applications [86].

Sol-gel aerogel glasses have been successfully used for sensing wide-ranging analytes such as color test for cations, pH indication, anions, and organic molecules if a suitable analytical reagent is trapped in highly porous network and is exposed to

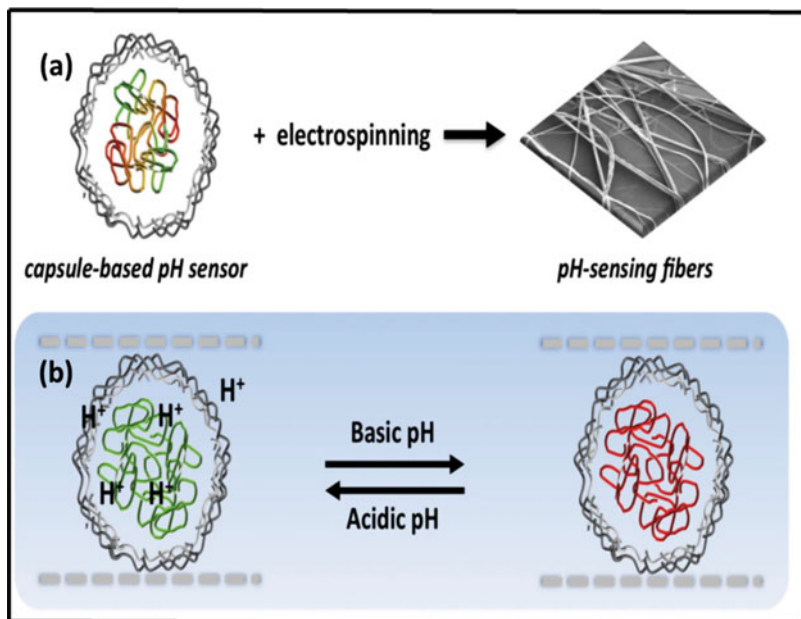


Fig. 13 Schematic of (a) capsule-based pH sensor with the fluorescent dye encapsulated in a polyelectrolyte membrane made by layer-by-layer assembly along with SEM image showing the wires obtained via electrospinning and (b) response of the capsule-based pH sensor to local environment [86]

pore volume. For example, the use of dimethylglyoxime reagent helps in detecting Ni^{+2} cation by turning a colorless glass into a red color. A red brownish glass prepared by co-trapping sodium rhodizonate and BaF_2 turns colorless due to bleaching effect of SO_4^{2-} inorganic anion. Phenolphthalein and thymolphthalein doped glass can be used to detect protons for the use of pH indication. Even an inorganic ferrous salt can be trapped in sol-gel glass and used to detect organic analyte such as orthophenanthroline in a solution by changing a white glass to a characteristic red color. Sensor reaction times are as low as 1 s to as high as 30 min. Major advantages of such sensors include stable and inert glass substrate and simple preparation technique and can be easily prepared in various shapes as well as thin films [87]. Detection of toxic metal ions like cadmium, lead, or cyanide anions in potable groundwater being supplied for military personnel employed in remote locations is very essential. This is because the presence of cadmium and lead in a very low concentration <1 mg/l will have deleterious effect on animals and environment. They have potential to damage kidneys and reproductive systems. Anthryl tetra acid for cadmium detection and acetonitrile based for lead detection sol-gel composition coatings can be used as selective sensors. Iron (III) porphyrin encompassed titanium carboxylate based sol-gel coating was proposed as a cyanide sensor. Oxalate oxidase encompassed sol-gel coating for oxalate sensing; porphyrin-bound dextran in sol-gel coatings was also developed for mercury sensors [88].

Cobalt tetrakis porphyrin-doped sol-gel synthesized silica glass was proposed to be used for nitrogen monoxide (NO) sensing; other biomolecules such as myoglobin, cytochrome, and hemoproteins were demonstrated for sensing O₂, NO, and CO. Here, the organically modified silica sol-gels are capable of showing changes in volume with respect to the interactions with solvents.

Thus, sol-gel technology has a great potential to be used as gas sensors for both toxic and nontoxic analytes. Sensors for Cl₂ gas are useful for use during wartime. The sol-gel technology makes it possible to make sensors for Cl₂ gas. The weight (or swelling) of silicate matrices prepared using sol-gel method varies with chlorine content like NaCl/CaCl₂ [89]. The enhanced swelling of these silicate matrices in high ionic strength can be explained by the development of significant osmotic pressure in the sol-gels. The movement of these ions along with their respective hydration spheres results in the swelling of the sol-gels. This effect creates a critical osmotic pressure within the framework that leads to swelling of the gel. The volume change during swelling is proportional to the Cl₂ gas content. Various silanes like bis[3-(trimethoxysilyl)-propyl]ethylenediamine (enTMOS), carboxyethylsilanetriol, sodium salt (CEST), (3-trimethoxysilylpropyl)diethylenetriamine (DienTMOS), and bis[3-(trimethoxysilyl)-propyl]amine (ATMOS) were investigated as silicate matrices for use in Cl₂, pH, and salt sensors [89]. Figure 14 compares the response of ATMOS and enTMOS sol-gels to NaCl and MgSO₄. The response of these hybrid sol-gels with respect to pH is shown in Table 2 [89].

Also, the organosilica sol-gels containing ionizable functional groups such as NH or COOH exhibited responses to variations in pH of the surrounding medium. The ionizable groups present in the materials lead to protonation/deprotonation as a consequence of change in pH due to changes in the electrostatic interactions, which leads to volume changes that can be detected. In general, it is found that the

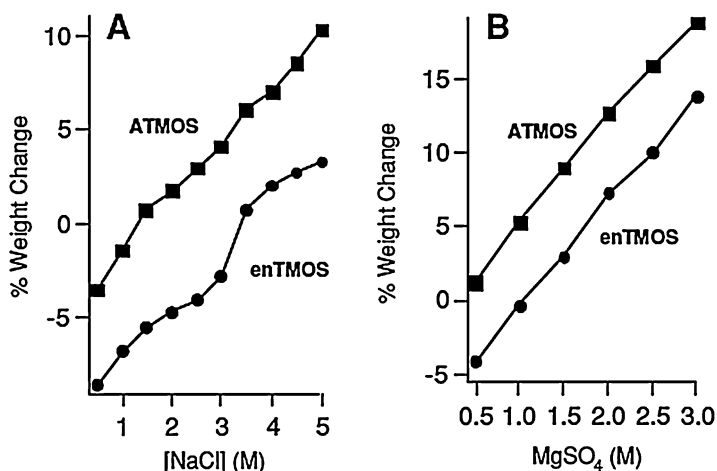


Fig. 14 Response of ATMOS and enTMOS sol-gels to salt. (a) shows the response to NaCl, and (b) shows the response to MgSO₄ [89]

Table 2 Response of hybrid sol-gels with respect to pH. (Ref [89])

pH	enTMOS+CEST, % mole fraction CEST			enTMOS+DienTMOS	enTMOS	ATMOS
	32.0	26.0	22.0			
Hydrophobic estimate						
	3.20	3.35	3.45	3.11	4.0	6.0
% Weight change of hybrid sol-gels						
1.22	+19.8	+12.1	+18.6	+24.7	-0.14	+35.0
2.44	+18.0	+5.2	+10.45	+1.5	-4.5	+31.0
2.78	+8.6	-3.9	+5.5	-5.3	-6.0	+28.0
4.15	-7.0	-8.4	+0.03	-4.0	-6.6	+9.2
5.92	-19.0	-4.7	+3.6	-6.2	-6.5	+7.5
7.00	-3.5	-10.0	-0.25	-12.5	-7.6	+2.1
8.08	-37.0	-9.3	-5.7	-13.4	-8.5	-3.2
9.33	-34.0	-10.0	-2.8	-15.0	-9.0	-4.7
10.83	-14.4	-10.0	-1.4	-15.2	-9.1	-4.5
11.71	-45.4	-5.6	-0.63	-15.0	-8.2	-3.0
12.27	-37.4	-3.9	-0.55	-10.0	-5.7	-2.2

enTMOS, Bis[3-(trimethoxysilyl)propyl]ethylenediamine; CEST, carboxyethylsilanetriol; sodium salt; DienTMOS, (3-trimethoxysilylpropyl)diethylenetriamine; ATMOS, bis[3-(trimethoxysilyl)propyl]amine

organosilica sol-gels containing amino groups undergo shrinkage at high pH, while at low pH they exhibit swelling. Sol-gel coatings were also successfully used as fiber-optic oxygen sensors with tunable oxygen sensitivity. Electro-spun fibers synthesized through sol-gel process were used for pH sensing [90]. When doped with fluorescent molecules such as Rhodamine 6G and fluorescein, they can be used as laser dye. Customized sol-gel compositions can also be used for sound detection [91]. Mesoporous silica films with an excellent heat-insulating property and the relatively low dielectric value play an important role in electronic and magnetic devices; those with pore sizes of 5–50 nm are also of interest for applications in photonics, optoelectronics, lightweight structural material, thermal insulation, and optical coating [91–94]. All such sensors may be useful to the armed forces during wartime and for rescue teams during natural calamities.

Sol-gel coating is the most suitable technology to generate sensors that mimic natural biological system as many exotic material combinations can be synthesized in near-theoretical purity and used in managing bioterrorism. Electronic nose that works based on sol-gel coatings can smell biochemical/poisonous warfare agents such as anthrax, sarin, and mustard gas in the real-time battlefield applications. Such sensors are fabricated using functionally tunable nanoporous thin films deposited by sol-gel compositions and were subsequently chemically grafted with sulfonation and esterification (amino acid) reactions. Sensing material swells due to the analyte based on diffusion into nanostructure of sol-gel coatings and extent of interaction between polymeric sol-gel coating and analyte. It is said that such grafting techniques impart hydrophobicity and bioactivity, thereby behaving quite similar to

biological nose [95, 96]. People living in remote areas especially armed forces and allied services posted at the frontiers/borders are forced to stock food items for longer periods which quite often exceed or come close to the expiry of shelf life by the time the item is consumed. One of the current reviews shows that a microencapsulation technology can be used for the development of functional coatings such as thermochromic materials for packaging. Food storage and its packaging can be one of the prominent fields where encapsulated thermochromic materials can be deposited in a nanostructured sol-gel matrix for food quality testing and as a shelf life indicator. VO_2 -doped SiO_2 , VO_2 - and W-doped VO_2 , and $\text{V}_{1-x-y}\text{W}_x\text{Si}_y\text{O}_2$ were reported to be some of the successful coating compositions experimented using sol-gel process. Another interesting application for VO_2 coatings is that it can be used as energy efficient thermochromic smart windows that have potential to save 9.4% electricity consumption for the shelters used to house defense personnel working in extreme temperature conditions. Color transition properties of polydiacetylene (PDA), polyvinylpyrrolidone (PVP), and ZnO nanocomposites exhibit controlled reversible thermochromic properties and hence have also been in use for chemical and biosensors applications [97].

Radiation Sensors

Luminescence spectra of rare earth ions are quite informative, and in particular excited states of Eu^{3+} have a strong dependence on dosage levels of gamma radiation. It was shown that the magnetic dipole transition ${}^5\text{D}_0\text{-}{}^7\text{F}_1$ of the europium ion presents a 900% enhancement for irradiation doses up to 400 Gy. Based on this character, Eu^{3+} -doped sol-gel synthesized silica glass was successfully developed as a detector for detecting gamma radiation that can be used as economic radiation dosimeter for nuclear installations, in nuclear warfare, and during natural disasters. Such behavior was shown to be due to the high local symmetry of europium ion-doped glass as against low symmetry found in glasses produced through conventional melting process [98]. The absorption spectra of irradiated Nd_2O_3 -doped silicate glass magnetic dipole transition ${}^5\text{D}_0\text{-}{}^7\text{F}_1$ of Nd^{3+} ions were found to present huge defects for irradiation doses up to 18 kGy. This shows that Nd^{3+} ions also have huge potential for use as a radiation detector due to the reason that these ions exhibit enhanced absorption of gamma radiation, which reflects in color change due to irradiation that lasts for as high as 7 days [99].

Functional Coatings for Ceramic Radomes/IR Windows

A structure that is meant for protecting the radar equipment such as its antenna and related hardware from aggressive weather, wind, rain, sand, and ice etc., during its flight is referred as radome. It is made of a material which is transparent to electromagnetic signal that emanates or is received by the antenna. High-density polyethylene, polyurethane foam, PTFE-coated fabric, aramid, quartz, alumina,

pyroceram, silica, silicon nitride, polyimide laminate, and fiber glass are some of the commonly used materials for radome fabrication. Radome performance is affected due to many factors such as aerodynamic heating, static charge build-up, erosion due to rain, etc.; during projectile flight, absorption of water, and formation of water film on radome surface; and during its storage and throughout its service. With the advent of modern designs, the structural integrity of radome is necessary over and above 350 °C.

The present practice to overcome aforementioned problems and to prolong the life of radomes is to apply protective coatings. Aerodynamic heating is the heat which builds up on the surface of the body that is moving at very high speeds due to air friction. Hence, even optimally designed radome of hypersonic and reentry vehicles requires proper heat shield that is electrically transparent during operation. Hence, low dielectric constant materials are conventionally used as ablative coatings which sacrifice themselves by absorbing the energy and expending the mass to achieve heat absorption either by blocking or dissipation of heat, thereby protecting the hardware underneath the radome. Silicon resins such as polydimethylsiloxane (PDMS) and polymethylphenylsiloxane (PMPS) have Si-O bonds with high bond energy (443.7 kJ/mol) and about 51% high ionic character resulting in excellent thermal and thermal oxidative stability and hence has become an attractive candidate for use as ablative coatings [100]. When the projectile is moving at very high speed, static electricity builds up on the surface of radome due to friction with high-velocity air and particles within air. The build-up is so high that it causes discharge resulting in interference with the electronic hardware of the radome and damages it by generating pin holes on its surface. Conductive coatings are applied on the outer surface of radome to impart antistatic property. Usually such coatings are very thin such that the transmission losses are negligible and maintain low resistance to allow the static charge to discharge softly and minimize electrical interference.

Highly reflective layers wherein TiO₂-, ZnO-, and ZnS-loaded resins are applied as thin coating on outer surface of radome are required to protect against high-energy band radiation inputs. SiO₂-based coatings have also been suggested to be used as antireflective and antiflash coatings wherever necessary [101].

High-speed projectile radomes that are moving at speeds over 400 km/h face severe erosion wear due to rain, dust, ice, and sand particles. during flight. Erosion induces pitting, and its intensity varies based on the radome geometry, material, and its velocity leading to catastrophic failure of radome. Radome materials such as Alumina and Pyroceram (trademark material) have excellent erosion resistance and hence do not require any protective coating. However, materials such as glass fabric-resin laminates, neoprene-coated glass fabric polyester, silicon nitride, and steatite require protective coatings. There are different types of erosion-resistant coatings such as neoprene, polyurethane, fluoroelastomer, and ceramic. Recently, there has been considerable effort by a group of researchers for the development of sol-gel coating recipes for protecting the surface against liquid impact erosion due to the fact that the hybrid sol-gel coatings have the advantage of combined properties of both polymeric materials such as flexibility and low-temperature curability

and that of ceramic materials such as good hardness and abrasion resistance. Hybrid coatings are said to have flexibility to absorb kinetic energy and avoid cracking due to the impact of the raindrop and, hence, found to be quite promising. In a recent study, it was found that a simple silica sol was able to enhance rain erosion resistance provided the sol composition could be managed in such a way that the final coating contains more inorganic cross-linking. Moreover, the statistical experimental design shows that hydrolysis water content is the most important factor in enhancing the erosion resistance of the silica sol recipe that was optimized at 3/7 as the molar ratio of GPTMS/TEOS precursors with higher water content and 130 °C curing temperature for 90 min resulting in coatings that have 6H pencil scratch hardness [102]. The above detailed investigative results substantiated the conclusions of a previous similar study with same set of precursors for sol preparation. It was found that externally added ZrO₂ nanoparticles to SiO₂ sol-gel coatings reinforced the coating and exhibited enhanced rain erosion resistance, when more inorganic cross-linking could be obtained. The rain erosion resistance of such coatings was comparable to that obtained for commercially available erosion protection coatings [103].

Water has a high dielectric constant and very high loss tangent for microwave/millimeter wave frequency. Hence, its ingress due to absorption of water or moisture by the porous or hygroscopic radome material fitted on a projectile during its storage period can degrade the critical sensor and guidance hardware housed in it causing reflection transmission and phase delay variations. This in turn will produce attenuation and aberration. Silicone-based resins are suitable candidates for coating application as they have good high-temperature capability. A recent investigation shows that CaO-B₂O₃-SiO₂ sol composition coated on silicon nitride radome material exhibited increase in the temperature coefficient of dielectric constant with the coating at 9.2 GHz frequency and found that the temperature stability of dielectric loss has improved due to coating [104]. Super hydrophobic sol-gel coating composition based on polyvinylidene fluoride (PVDF) and SiO₂ micro-sized particles could effectively protect radomes from absorbing the moisture by physical sealing and due to water repelling behavior of the coating, thereby eliminating formation of water film on the radome surface. The average static water contact angle of the coating was measured to be 157.5°, while its rolling angle was 9°. The coating exhibited high thermal stability and mechanical durability [105].

As a summary, it can be proposed that a judiciously selected multifunctional hybrid sol-gel coating composition could be a single layer solution that meets the requirement of being a good sealant to prevent water absorption, provide rain water erosion resistance and capable of efficiently protecting the radomes from severe environments during the flight of projectile.

Concluding Remarks

It can be seen from the above discussion that sol-gel coatings for corrosion protection applications seem to be the most potential end use for aerospace applications. Introduction of superhydrophobicity/icephobicity or self-healing property in such

corrosion protection coatings prolongs the corrosion resistance and adds substantial value to the protective coatings. Hard coatings are also equally promising for use on various substrates like transparent plastics, metals, and glass. The use of sol-gel coatings for sensing applications also seem to be promising. Though successful commercialization of these coatings has been possible to a certain extent, the sol-gel technology is still in the growth stage, and the high cost of raw materials will continue to be a determining factor for the widespread use of this coating technology. To sum up, there is a vast potential for use of sol-gel-derived/wet chemical-derived coatings for aerospace, energy, and strategic applications. Commercialization of appropriate technologies calls for strong synergy between the know-how provider like R&D institutes and the user industries.

References

1. Brinker CJ, Scherer GW (1990) Sol-Gel science: the physics and chemistry of Sol-Gel processing. Academic, San Diego
2. Zheludkevich ML, Salvado IM, Ferreira SMG (2005) Sol-gel coatings for corrosion protection of metals. *J Mater Chem* 15:5099–5111
3. Romero PG, Sanchez C (2004) Functional hybrid materials. Wiley-VCH Verlag GmbH & Co. KGaA, Weinheim
4. Kickelbick G (2007) Hybrid materials: synthesis, characterization and applications. Wiley-VCH Verlag GmbH & Co. KGaA, Weinheim
5. Boyer R (2006) Aircraft materials. In: Mortensen A (ed) Concise encyclopedia of composite materials, 2nd edn. Elsevier Science, Amsterdam
6. Ghali E (2000) Aluminium and aluminium alloys. In: Revie RW (ed) Uhlig's corrosion handbook, 2nd edn. The Electrochemical Society Inc. & John Wiley and Sons Inc, New York, pp 677–715
7. Markley TA, Mardel JI, Hughes AE, Hinton BRW, Glenn AM, Forsyth M (2011) Chromate replacement in coatings for corrosion protection of aerospace aluminium alloys. *Mater Corros* 62(9):836
8. Subasri R (2015) Improving corrosion resistance of metals/alloys using hybrid nanocomposite coatings synthesized through sol-gel processing. In: Aliofkhaezrai M (ed) Comprehensive guide for nanocoatings technology, volume 3: properties and development. Nova Science Publishers Inc, New York, pp 123–142
9. Kulinich SA, Akhtar AS (2012) On conversion coating treatments to replace chromating for Al alloy: recent developments and possible future directions. *Russ J Non-Ferrous Met* 53:176–203
10. Droniou P, Fristad WE, Liang JL (2005) Nanoceramic-based conversion coating: ecological and economic benefits position process as a viable alternative to phosphating systems. *Met Finish* 103:41–43
11. Wang D, Bierwagen GP (2008) Review: sol-gel coatings on metals for corrosion protection. *Prog Org Coat* 64:327–338
12. Shchukin DG, Zheludkevich ML, Yasakau K, Lamaka S, Ferreira MGS, Mohwald H (2006) Layer-by-layer assembled nanocontainers for self-healing corrosion protection. *Adv Mater* 18:1672–1678
13. Zhang D, Wang L, Qian H, Li X (2016) Superhydrophobic surfaces for corrosion protection: a review of recent progresses and future directions. *J Coat Technol Res* 13:11–29
14. Tedim J, Poznyak SK, Kuznetsova A, Raps D, Hack T, Zheludkevich ML, Ferreira MGS (2010) Enhancement of active corrosion protection via combination of inhibitor-loaded nanocontainers. *ACS Appl Mater Interfaces* 2:1528–1535

15. Jud K, Kausch HH, Williams JG (1981) Fracture mechanics studies of crack healing and welding of polymers. *J Mater Sci* 16:204–210
16. Kumar N, Subasri R (2012) Self-healing coatings by sol-gel process: a review of recent patent literature. *Recent Pat Corros Sci* 2:148–163
17. Skorb EV, Fix D, Andreeva DV, Mohwald H, Shchukin DG (2009) Surface-modified mesoporous SiO₂ containers for corrosion protection. *Adv Funct Mater* 19:2373–2379
18. Mishra T, Mohanty AK, Tiwari SK (2013) Recent development in clay based functional coating for corrosion protection. *Key Eng Mater* 571:93–109
19. Lanzara G, Yoon Y, Liu H, Peng S, Lee WI (2009) Carbon nanotube reservoirs for self-healing materials. *Nanotechnology* 20:335704–335711
20. Jung IK, Gurav JL, Bangi UKH, Baek S, Ho Park H (2012) Silica xerogel films hybridized with carbon nanotubes by single step sol-gel processing. *J Non-Cryst Solids* 358:550–556
21. Zheludkevich ML, Poznyak SK, Rodrigues LM, Raps D, Hack T, Dick LF, Nunes T, Ferreira MGS (2010) Active protection coatings with layered double hydroxide nanocontainers of corrosion inhibitor. *Corros Sci* 52:602–611
22. Tedim J, Zheludkevich ML, Salak AN, Lisenkov A, Ferreira MGS (2011) Nanostructured LDH-container layer with active protection functionality. *J Mater Chem* 21:2115464–2115470
23. Stimpfling T, Leroux F, Hintze-Bruening H (2014) Organo-modified layered double hydroxide in coating formulation to protect AA 2024 from corrosion. *Colloids Surf A: Physicochem Eng Asp* 458:147–154
24. Lvov YM, Shchukin DG, Mohwald H, Price RR (2008) Halloysite clay nanotubes for controlled release of protective agents. *ACS Nano* 2:814–820
25. Abdullayev E, Lvov Y (2011) Clay nanotubes for controlled release of protective agents- a review. *J Nanosci Nanotechnol* 11:10007–10026
26. Abdullayev E, Lvov Y (2010) Clay nanotubes for corrosion inhibitor encapsulation: release control with end stoppers. *J Mater Chem* 20:6681–6687
27. Fix D, Andreeva DV, Lvov YM, Shchukin DG, Mohwald H (2009) Application of inhibitor-loaded halloysite nanotubes in active anti-corrosive coatings. *Adv Funct Mater* 19:1720–1727
28. Darmanin T, Guittard F (2014) Recent advances in the potential applications of bioinspired superhydrophobic materials. *J Mater Chem A* 2:16319–16359
29. Parkin IP (2005) Palgrave RG, Self-cleaning coatings. *J Mater Chem* 1:1689–1695
30. Ganesh VA, Raut HK, Nair AS, Ramakrishna S (2011) A review on self-cleaning coatings. *J Mater Chem* 21:16304–16322
31. Ragesh P, Ganesh VA, Nair SV, Nair AS (2014) A review on self-cleaning and multifunctional materials. *J Mater Chem A* 2:14773–14797
32. Parent O, Ilinca A (2011) Anti-icing and de-icing techniques for wind turbines: Critical review. *Cold Reg Sci Technol* 65:88–96
33. Fillion RM, Riahi AR, Edrissy A (2014) A review of icing prevention in photovoltaic devices by surface engineering. *Renew Sust Energ Rev* 32:797–809
34. Yingdi Y, Nengzhen L, Xiangao X, Yiming X, Qinghua Z, Xiaoli Z (2014) Fabricating mechanism and preparation of anti-icing & icephobic coating. *Prog Chem* 26:214–222
35. Ryzhkin IA, Petrenko VF (1997) Physical mechanisms responsible for ice adhesion. *J Phys Chem B* 101:6267–6270
36. Sarkar DK, Farzaneh M (2009) Superhydrophobic coatings with reduced ice adhesion. *J Adhes Sci Technol* 23:1215–1237
37. Saleema N, Farzaneh M, Paynter RW, Sarkar DK (2011) Prevention of ice accretion on aluminum surfaces by enhancing their hydrophobic properties. *J Adhes Sci Technol* 25:27–40
38. Huang Y, Hu M, Yi S, Liu X, Li H, Huang C, Luo Y, Li Y (2012) Preparation and characterization of silica/fluorinated acrylate copolymers hybrid films and the investigation of their icephobicity. *Thin Solid Films* 520:5644–5651
39. Fu Q, Wu X, Kumar D, Ho JWC, Kanhere PD, Srikanth N, Liu E, Wilson P, Chen Z (2014) Development of sol-gel icephobic coatings: effect of surface roughness and surface energy. *ACS Appl Mater Interfaces* 6:20685–20692

40. Fu QT, Liu EJ, Wilson P, Chen Z (2015) Ice nucleation behaviour on sol–gel coatings with different surface energy and roughness. *Phys Chem Chem Phys* 17:21492–21500
41. Medda SK, De G (2009) Inorganic-organic nanocomposite-based hard coatings on plastics using in-situ generated nano-SiO₂ bonded with ≡Si-O-Si-PEO hybrid network. *Ind Eng Chem Res* 48:4326–4333
42. Medda SK, Kundu D, De G (2003) Inorganic-organic hybrid coatings on polycarbonate, spectroscopic studies on the simultaneous polymerizations of methacrylate and silica networks. *J Non-Cryst Solids* 318:149–156
43. Hwang DK, Moon JH, Shul YG, Jung KT, Kim DH, Lee DW (2003) Scratch resistant and transparent UV- protective coating on polycarbonate. *J Sol-Gel Sci Technol* 26:783–787
44. Lee MS, Jo NJ (2002) Coating of methyltriethoxysilane-modified colloidal silica on polymer substrates for abrasion resistance. *J Sol-Gel Sci Technol* 24:175–180
45. Wouters MEL, Wolfs DP, van der Linde MC, Hovens JHP, Tinnemans AHA (2004) Transparent UV curable antistatic hybrid coatings on polycarbonate prepared by the sol-gel method. *Prog Org Coat* 51:312–320
46. Sangermano M, Messori M (2010) Scratch resistance enhancement of polymer coatings. *Macromol Mater Eng* 295:603–612
47. Jeon SJ, Lee JJ, Kim W, Chang TS, Koo SM (2008) Hard coating films based on organosilane-modified boehmite nanoparticles under UV/thermal dual curing. *Thin Solid Films* 516:3904–3909
48. Kasemann R, Schmidt HK, Wintrich E (1994) A new type of a sol-gel-derived inorganic-organic nanocomposite. *Proc Mater Res Soc* 346:915–921
49. Chen Q, Tan JGH, Shen SC, Liu YC, Ng WK, Zeng XT (2007) Effect of boehmite nanorods on the properties of glycidoxypropyl-trimethoxysilane (GPTS) hybrid coatings. *J Sol-Gel Sci Technol* 44:125–131
50. Amerio E, Fabbri P, Malucelli G, Messori M, Sangermano M, Taurino R (2008) Scratch resistance of nano-silica reinforced acrylic coatings. *Prog Org Coat* 62:129–133
51. Sowntharya L, Gundakaram RC, Soma Raju KRC, Subasri R (2013) Effect of addition of surface modified nanosilica into silica-zirconia hybrid sol-gel matrix. *Ceram Int* 39:4245–4252
52. Sowntharya L, Lavanya S, Ravi Chandra G, Hebalkar NY, Subasri R (2012) Investigations on the mechanical properties of hybrid nanocomposite hard coatings on polycarbonate. *Ceram Int* 38:4221–4228
53. Gururaj T, Soma Raju KRC, Subasri R, Padmanabham G (2018) Indian patent no. 295221 entitled “Improved scratch and abrasion resistant compositions for coating plastic surfaces, A process for their preparation and a process for coating using the compositions”
54. Hozumi A, Kato Y, Takai O (1996) Two-layer hard coatings on transparent resin substrates for improvement of abrasion resistance. *Surf Coat Technol* 82:16–22
55. Shin YJ, Oh MH, Yoon YS, Shin JS (2008) Hard coatings on polycarbonate plate by sol-gel reactions of melamine derivative PHEMA and silicates. *Polym Eng Sci* 48:1289–1295
56. Gururaj T, Subasri R, Soma Raju KRC, Padmanabham G (2011) Effect of plasma pre-treatment on adhesion and mechanical properties of UV-curable coatings on plastics. *Appl Surf Sci* 257:4360–4364
57. Soma Raju KRC, Sowntharya L, Lavanya S, Subasri R (2012) Effect of plasma pre-treatment on adhesion and mechanical properties of sol-gel nanocomposite coatings on polycarbonate. *Compos Interfaces* 19:259–270
58. Le Bail N, Lioni K, Benayoun S, Pavan S, Thompson L, Gervais C, Dubois G, Toury T (2015) Scratch-resistant sol–gel coatings on pristine polycarbonate. *New J Chem* 39:8302–8310
59. Yavas H, Öztürk Selçuk CD, Özhan AES, Durucan C (2014) A parametric study on processing of scratch resistant hybrid sol–gel silica coatings on polycarbonate. *Thin Solid Films* 556:112–119
60. Raju KRCS, Subasri R (2015) Sol-gel nanocomposite hard coatings. In: Aliofkhazraei M (ed) *Anti-abrasive nanocoatings: current and future applications*. Woodhead Publishing (an imprint of Elsevier), Sawston, pp 105–132

61. Subasri R (2013) Properties of nanocomposite hard coatings on polycarbonate. In: Mittal V (ed) Polymer nanocomposite coatings. CRC Press (Taylor & Francis Group), Boca Raton, pp 167–184
62. Schottner G (2001) Hybrid sol-gel-derived polymers: applications of multifunctional materials. *Chem Mater* 13:3422–3435
63. Dinelli M, Fabbri E, Bondioli F (2011) TiO₂–SiO₂ hard coating on polycarbonate substrate by microwave assisted sol–gel technique. *J Sol-Gel Sci Technol* 58:463–469
64. Sowntharya L, Subasri R (2013) A comparative study of different curing techniques for SiO₂-TiO₂ hybrid coatings on polycarbonate. *Ceram Int* 39:4689–4693
65. Berendjchi A, Khajavi R, Yazdanshenas ME (2011) Fabrication of superhydrophobic and antibacterial surface on cotton fabric by doped silica-based sols with nanoparticles of copper. *Nanoscale Res Lett* 6:594
66. Lantano C, Alfieri I, Cavazza A, Corradini C, Lorenzi A, Zucchetto A, Montenero A (2014) Natamycin based sol–gel antimicrobial coatings on polylactic acid films for food packaging. *Food Chem* 165:342–347
67. Poongodi G, Anandan P, Mohan Kumar R, Jayavel R (2015) Studies on visible light photocatalytic and antibacterial activities of nanostructured cobalt doped ZnO thin films prepared by sol–gel spin coating method. *Spectrochim Acta A Mol Biomol Spectrosc* 148:237–243
68. Ismail WA, Ali ZA, Puteh R (2013) Transparent nanocrystallite silver for antibacterial coating. *J Nanomater* 2013. Article ID 901452
69. Halevas E, Nday CM, Kaprara E, Psycharis V, Raptopoulou CP, Jackson GE, Litsardakis G, Salifoglou A (2015) Sol–gel encapsulation of binary Zn(II) compounds in silica nanoparticles: structure–activity correlations in hybrid materials targeting Zn(II) antibacterial use. *J Inorg Biochem* 151:150–163
70. Zhang Y, Smith SJ, Kyle GP, Stackhouse PW Jr (2010) Modeling the potential for thermal concentrating solar power technologies. *Energy Policy* 38:7884–7897
71. Granqvist CG (1991) Solar energy materials. *Appl Phys A Mater Sci Process* 52:83–93
72. Stine WB, Greyer M (2001) Power from the Sun (e-book). Power from the sun, WorldCat.org. <http://www.powerfromthesun.net>
73. Mills D (2004) Advances in solar thermal electricity technology. *Sol Energy* 76:19–31
74. Behar O, Khellaf A, Mohammedi K (2013) A review of studies on central receiver solar thermal power plants. *Renew Sust Energ Rev* 23:12–39
75. Kennedy CE (2002) Review of mid-to high temperature solar selective absorber materials, technical report July 2002, NREL/TP-520-31267, National Renewable Energy Laboratory, Golden, USA. Contract no: DE-AC36-99-GO10337
76. Shuxi Z, Ewa W (2006) Optimization of solar absorbing three-layered coatings. *Sol Energy Mater Sol Cells* 90:243–261
77. Selvakumar N, Barshilia HC (2012) Review of physical vapor deposited (PVD) spectrally selective coatings for mid- and high- temperature solar thermal applications. *Sol Energy Mater Sol Cells* 98:1–23
78. Barshilia HC, Prashant Kumar KS, Rajam BA (2011) Structure and optical properties of Ag–Al₂O₃ nanocermet solar selective coatings prepared using unbalanced magnetron sputtering. *Sol Energy Mater Sol Cells* 95:1707–1715
79. Mathews PA, Kalidindi SRRC, Bhardwaj S, Subasri R (2013) Sol–gel functional coatings for solar thermal applications: a review of recent patent literature. *Recent Pat Mater Sci* 6:195–213
80. Joly M, Antonetti Y, Python M, Gonzalez Lazo MA, Gascou T, Hessler-Wyser A, Scartezzini JL, Schüler A (2014) A selective solar absorber coating on receiver tubes for CSP –energy-efficient production process by sol-gel dip-coating and subsequent induction heating. *Energy Procedia* 57:487–496
81. Katumba G, Olumekor L, Forbes A, Makiwa G, Mwakikunga B, Lu J, Wäckelgard E (2008) Optical, thermal and structural characteristics of carbon nano particles embedded in ZnO and NiO as selective absorbers. *Sol Energy Mater Sol Cells* 92:1285–1292
82. Bostrom T, Westin G, Wackelgard E (2007) Optimization of solution-chemically derived solar absorber spectrally selective surface. *Sol Energy Mater Sol Cells* 91:38–43

83. Bostrom T, Jensen J, Valizadeh S, Westin G, Wackelgard E (2008) ERDA of Ni-Al₂O₃/SiO₂ solar thermal selective absorbers. *Sol Energy Mater Sol Cells* 92:1177–1182
84. Li Z, Zhao J, Ren L (2012) Aqueous solution-chemical derived Ni-Al₂O₃ solar selective absorbing coatings. *Sol Energy Mater Sol Cells* 105:90–95
85. Subasri R, Soma Raju KRC, Reddy DS, Hebalkar NY, Padmanabham G (2016) Sol-gel derived solar selective coatings on SS 321 substrates for solar thermal applications. *Thin Solid Films* 598:46–53
86. del Mercato LL, Moffa M, Rinaldi R, Pisignano D (2015) Ratiometric organic fibers for localized and reversible ion sensing with micrometer-scale spatial resolution. *Small* 11:6417–6424
87. Zusman R, Rottman C, Ottolenghi M, Avnir D (1990) Doped sol-gel glasses as chemical sensors. *J Non-Cryst Solids* 122:107–109
88. Chaudhury NK, Gupta R, Gulia S (2007) Sol-gel technology for sensor applications. *Def Sci J* 57:241–253
89. Rao MS, Gray J, Dave BC (2003) Smart glasses: molecular programming of dynamic responses in organosilica sol-gels. *J Sol-Gel Sci Technol* 26:553–560
90. MacCraith BD, Ruddy V, Potter C, O’Kelly B, McGlip JF (1991) Optical waveguide sensor using evanescent wave excitation of fluorescent, dye in sol-gel glass. *Electron Lett* 27:1247–1248
91. Husing N, Schubert U (1998) Aerogel airy material: Structure, chemistry, structure and properties. *Angew Chem Int Ed* 37:22–29
92. Horowitz E, Dawnay EJC, Fardad MA, Green M, Yeatman EM (1997) Towards better control of sol-gel film processing for optical device applications. *J Non Linear Opt Phys Mater* 6:1–18
93. Moon HJ, Hyung HP, Dong JK, Sang HH, Choi SY, Paik JT (1997) SiO₂ aerogel film as a novel intermetal dielectric. *J Appl Phys* 82:1299–1305
94. Davis ME (2002) Ordered porous materials for emerging applications. *Nature* 417:813–816
95. Raman VI, Palmese GR (2005) Nanoporous thermosetting polymers. *Langmuir* 21:1539–1546
96. Mougnot P, Koch M, Dupont I, Schneider YJ, Marchand-Brynaert J (1996) Surface functionalisation of polyethylene terephthalate film and membranes by controlled wet chemistry: II reactivity assays of hydroxyl chain ends. *J Colloid Interface Sci* 177:162–170
97. Cheng Y, Zhang X, Fang C, Chen J, Wang Z (2018) Discoloration mechanism, structures and recent applications of thermochromic materials via different methods: A review. *J Mater Sci Technol*. <https://doi.org/10.1016/j.jmst.2018.05.016>
98. Pedroza G, de Azevedo WM, Khoury HJ, de Silva EF Jr (2002) Gamma radiation detection using sol-gel doped with lanthanides ions. *Appl Radiat Isot* 56:563–566
99. Hanaa HM (2011) Effect of gamma-irradiation on the optical properties of silicate glass doped Nd₂O₃ prepared by sol-gel technique. *J Radiat Res Appl Sci* 4:1107–1120
100. Sun JT, Huang YD, Cao HL, Gong GF (2004) Effects of ambient-temperature curing agents on the thermal stability of poly(methylphenylsiloxane). *Polym Degrad Stab* 85:725–731
101. Wouters MEL, Wolfs DP, van der Linde MC, Hovens JHP, Tinnemans AHA (2004) Transparent UV curable antistatic hybrid coatings on polycarbonate prepared by the sol-gel method. *Prog Org Coat* 51:312–320
102. Najafabadi AH, Razavi RS, M R, Rahim H (2014) A new approach of improving rain erosion resistance of nanocomposite sol-gel coatings by optimization process factors. *Met Mater Trans A* 45:2522–2531
103. Grundwurm M, Nuyken O, Meyer M, Wehr J, Schupp N (2007) Sol-gel derived erosion protection coatings against damage caused by liquid impact. *Wear* 263:318–329
104. Yu-wei S, Shu-bin W, Jian ZHANG (2011) Effects of CBS coating on dielectric properties of porous Si₃N₄ ceramic at high temperature and high frequency. *J Mater Eng* 1:42–45
105. Yonglin L, Qiuru W, Jichuan H (2014) Fabrication of durable superhydrophobic coatings with hierarchical structure on inorganic radome materials. *Ceram Int* 40:10907–10914



Materials Aspects of Thermal Barrier Coatings

37

Ashutosh S. Gandhi

Contents

Introduction	1444
Bond Coats	1446
Thermal Barrier Coatings	1447
Yttria-Stabilized Zirconia TBCs	1447
Testing and Characterization of TBCs	1448
Factors Affecting the Durability of YSZ Thermal Barrier Coatings	1450
New Materials for TBCs	1455
Guidelines for Obtaining Low Thermal Conductivity	1456
Summary	1460
References	1460

Abstract

Thermal barrier coatings (TBCs) are being used for the past few decades for providing thermal insulation to metallic components of hot parts of gas turbine engines. The low thermal conductivity ceramic coatings contribute toward maintaining a large temperature difference between the hot gases in the gas turbine and the superalloy components. High engine efficiency as well as prolonged component lifetime can be achieved by integrating TBCs with gas turbine components at the design stage itself. While yttria-stabilized zirconia emerged as the work-horse TBC material, a few other advanced compositions are also being used by some of the engine manufacturers. Prominent among these are zirconia-based compositions with rare-earth oxide additions, either with tetragonal or pyrochlore structure. A lot of research activity has focused on durability issues relevant to the TBC technology, for enhancing reliability as well as performance. Phase transformations, oxidation-induced residual stress, changes in fracture

A. S. Gandhi (✉)
Metallurgical Engineering and Materials Science, Indian Institute of Technology Bombay, Mumbai, India
e-mail: agandhi@iitb.ac.in

toughness, and thermochemical attack by contaminants ingested by the engine are some of the important degradation mechanisms governing durability.

Keywords

Thermal barrier coatings · Bond coat · Yttria stabilised zirconia · Thermal conductivity · EBPVD · Plasma spray · CMAS · Pyrochlore · Hot corrosion · Multilayer

Introduction

Gas turbines are energy conversion devices with unmatched power to weight ratio. They play a crucial role in aviation and stationary power generation. Currently, there is a major shift toward renewable energy sources worldwide for mitigating the environmental impact of fossil fuel usage. Land-based power generation using gas turbines running on fossil fuels is facing a stiff challenge from solar power generation technologies. In aviation propulsion, however, fossil fuel-based gas turbine engines are the only practical option for the foreseeable future, even if efforts are underway to develop aircraft propelled by alternative energy sources like solar power or hydrogen. It is therefore very important to decrease the emission of greenhouse gases by aviation gas turbine engines. Even stationary power generation by gas turbines can benefit from technologies that decrease the greenhouse gas emissions per unit of electricity generated, since a complete shift toward renewable energy sources is not feasible, given the ever-increasing demand for energy. Even so, in this chapter, the focus is on aviation gas turbine engines. Employing high-temperature protective coatings enhances the overall efficiency of gas turbines. A perspective is provided on the materials used for such coatings. Let us first consider the motivation behind the development of such coatings.

There are various strategies that can be adopted to enhance the fuel efficiency of an aircraft. The most important among these is lightweighting. This is achieved by using materials with high specific strength, as well as improved designs of various components. The other strategy is to enhance the thermodynamic efficiency of gas turbine engines. It is well-known that the thermodynamic efficiency η of gas turbines, which operate according to the Brayton cycle, is given by the ratio of two temperatures:

$$\eta = 1 - (T_{\text{atmospheric}}/T_{\text{compressor exit}}) \quad (1)$$

The compressor exit temperature also determines the turbine inlet temperature after the combustor. The higher the turbine inlet temperature, the greater is the efficiency of the Brayton cycle. Let us now consider the approaches that can increase the turbine inlet temperature. The first approach is to use materials that have as high a temperature capability as possible. The second is to incorporate cooling technology that keeps the hot section materials within their temperature limit while allowing

increased gas temperatures. Both these approaches are adopted in tandem in developing modern gas turbine engines. As far as materials selection is concerned, protective coatings have become an integral part of this strategy for enhancing the operating temperature.

The high-temperature materials used in gas turbines have been developed with primary focus on creep resistance. Oxidation and hot corrosion, however, are also important considerations. It is well-known that creep resistance of an alloy can be enhanced by incorporating second phase particles in the form of precipitates to impede dislocation activity. Diffusion creep can be minimized by decreasing the amount of grain boundaries in an alloy. These pointers have led to the development of some of the most advanced alloys, in the form of single crystal nickel base superalloys with γ' -Ni₃Al precipitates in the γ matrix of nickel-rich solid solution. A large number of alloying additions are present in the superalloys, making them perhaps the most complex of engineering alloys [1]. Since these alloys have been developed to maximize creep resistance, their oxidation and corrosion resistance is not the best. Hence, special alloys have been developed with excellent resistance to oxidation and corrosion [2]. These are deposited as coatings on the advanced superalloys and are now known as bond coats (BCs). The term bond coat is used because these oxidation protection alloy coatings enhance the adhesion of thermal barrier coatings deposited on them. Protection against environmental degradation is achieved in the bond coats by forming an impervious oxide scale, preferably of aluminum oxide (α -Al₂O₃) on the bond coat. As this scale is formed by thermally activated oxidation under exposure to atmospheric oxygen, it is termed as thermally grown oxide (TGO).

Further enhancement in the operating temperature of superalloys can be achieved by employing a thermal insulating coating called “thermal barrier coating” (TBC) deposited on the bond coat described above. This is a coating made of an oxide ceramic material with low thermal conductivity and sufficiently high melting point. Such a coating, also referred to as the top coat, in conjunction with active cooling, is able to keep the underlying metallic part cooler by more than 100 °C in the absence of TBC [3]. A TBC enhances the durability of the metallic hot section parts by restricting their temperatures to values significantly below their rated capacity and can potentially facilitate operating the gas turbine with surface temperature exceeding the alloy temperature rating. It is clear that thermal barrier coatings improve the overall efficiency of gas turbines. Modern gas turbines typically consist of various superalloy components coated with metallic bond coats and ceramic thermal barrier coatings, starting from the combustor going all the way to the last stage turbine, including shrouds and vanes.

With superalloys approaching the limits of their temperature capability, considerable research efforts have been expended in developing the next generation of high-temperature materials. Ceramic fiber reinforced ceramic matrix composites (CMCs) have emerged as the most promising class of materials for this purpose [3]. These composites offer many benefits in gas turbine applications. The CMCs, however, require coatings for protecting them against the harsh environment of a gas turbine. These coatings are termed as environmental barrier coatings (EBCs).

TBCs are ever-growing field of knowledge. Technological and scientific advances are being made constantly. The goal of this chapter, however, is to elucidate the well-established features of these topics, rather than review cutting-edge research. Some directions of current research are mentioned sporadically all the same.

Bond Coats

Before elaborating on the materials used for TBCs, a brief description of the bond coat materials and their deposition processes will be useful [2, 4]. The main class of bond coat alloys are of the MCrAlY type where M = Fe, Co, or Ni. Many commercial alloys are available, in the form of powders suitable for deposition by thermal spray techniques. The NiCoCrAlY-type bond coats offer the best performance. These typically consist of a γ solid solution and β -NiAl phase. A good bond coat should favor the formation of stable α -Al₂O₃ TGO scale as early as possible during thermal exposure. Transition oxides may form at the beginning, consisting of θ -Al₂O₃ or spinels containing Ni and Cr. The α -Al₂O₃ oxide scale should have good adhesion with the alloy, and also with the TBC. The thickening of TGO induces stresses in the coating system, which often is the origin of TBC failure, as discussed later. The presence of yttrium in the bond coat slows down the growth rate of the TGO, which is beneficial for TBC durability. The MCrAlY-type bond coats are deposited by thermal spray techniques such as plasma spray, high-velocity oxy-fuel (HVOF), high-velocity air fuel (HVOF), or cold spray. A few variants of plasma spray have been used over the years. Low-pressure plasma spray (LPPS) which is done in a large vacuum chamber gives good results by preventing significant oxidation of the bond coat during deposition. Air plasma spray (APS), while cheaper than LPPS, produces bond coats with extensive oxidation during deposition. A work around for this issue is argon-shrouded plasma spray technique. Electron beam physical vapor deposition (EBPVD) is also used for bond coat deposition as it has the ability to deposit dense, clean coatings with reactive elements, though it is an expensive process. Surface roughness of the bond coats is an important aspect that influences the TBC adhesion, as well as early transition to the stable α -Al₂O₃. Modern development in MCrAlY bond coats consists of incorporating various reactive elements, such as Hf and Si into the alloys, as well as improvements in processing of commercially available alloys.

The other type of bond coats is platinum-modified nickel aluminide (Ni-Pt)Al. These coatings are processed by electroplating 5–10 μm of platinum onto the superalloy followed by aluminizing. Aluminum deposition is done by one of the following processes: pack cementation, vapor phase aluminizing, or chemical vapor deposition. An interdiffusion treatment is carried out after both Pt and Al are deposited. Nickel from the superalloy reacts with the deposited metals to form β -NiAl phase with partial substitution of Ni with Pt. An interdiffusion zone (IDZ) is formed below the bond coat, which is undesirable as it is a region of lower creep resistance than the main alloy. Over the last few years, research efforts have focussed

on minimizing the IDZ by adjusting the processing conditions or by incorporating diffusion barrier layer.

Thermal Barrier Coatings

The primary function of a thermal barrier coating is to provide thermal insulation to superalloy components in gas turbine hot sections. According to Miller [5], the idea of using ceramic coatings on gas turbine engine components dates back to the mid-1940s. These coatings have been used since the 1970s, starting with stationary gas turbines and implemented in aircraft engines soon after. The materials of early TBCs were zirconia stabilized with either magnesia or calcia, which gave way to yttria-stabilized zirconia. Initially, TBCs were deposited using air plasma spray. In the late 1980s, EBPVD technique was developed for TBC deposition. Successful implementation of TBCs requires a material not only with sufficiently low thermal conductivity but also a clutch of other attributes. It should have high enough melting temperature to retain its mechanical integrity at the operating temperature. Since the operation of a gas turbine engine involves thermal cycling, the superalloy component expands and contracts. The thermal barrier coating should have coefficient of thermal expansion (CTE) close to that of the superalloy ($\sim 1.5 \times 10^{-5} \text{ K}^{-1}$) so that the thermal stress does not cause early failure of the coating. These basic considerations make zirconia ceramics a good choice as TBCs, as the material thermal conductivity can be as low as $\sim 2 \text{ W m}^{-1} \text{ K}^{-1}$, and the CTE $\sim 1 \times 10^{-5} \text{ K}^{-1}$ [6]. The successful development of TBC technology, however, is founded on deeper understanding of materials science and engineering aspects of these materials. Some of these aspects of TBC materials are dealt with here.

Yttria-Stabilized Zirconia TBCs

The conventional thermal barrier coating material is yttria-stabilized zirconia (YSZ) with 6–8 wt. % Y_2O_3 . The coating thickness is in the range of ~ 150 to $500 \mu\text{m}$, depending on the component coated. There are two techniques of coating deposition that are well established, APS and EBPVD [7]. The latter technique, being more expensive than APS, is used for depositing TBCs on the more critical components such as high-pressure turbine blades in aircraft engines. The coatings are porous, which is a desirable feature because pores decrease the thermal conductivity and the effective elastic modulus of the coating. The lower elastic modulus mitigates the thermal stresses developed due to the CTE mismatch among the layers of the TBC system. Measurement of porosity in actual TBCs is not trivial, and it is believed that the values can range from 5% to 25%, depending on the processing conditions and subsequent thermal exposure in service. The typical cross sections of TBCs deposited by either APS or EBPVD are shown in Fig. 1 [8, 9].

The APS coatings have a lamellar structure and contain crack-like voids roughly parallel to the substrate, as well as round voids. These features are a result of high

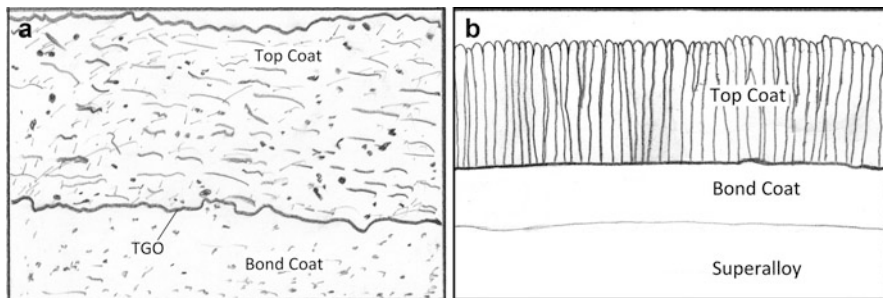


Fig. 1 Typical cross sections of TBCs. (a) APS and (b) EBPVD

velocity impact of molten droplets of YSZ which spread out before rapidly solidifying. Each individual deposit is known as a splat. The coating thickness is built splat by splat, leading to inter-splat voids as shown in Fig. 1. The orientation of the inter-splat voids parallel to the superalloy substrate is responsible for significantly lower thermal conductivity of $\sim 1 \text{ W m}^{-1} \text{ K}^{-1}$ in APS coatings, than that of the dense YSZ. In contrast to APS coatings, EBPVD coatings have a characteristic columnar structure due to preferential growth along certain crystallographic directions during deposition. There is a consensus in the TBC community that the columnar structure imparts lower in-plane elastic modulus to EBPVD coatings, in comparison with APS coatings of the same material, although precise measurement of elastic modulus is not straightforward. Overall for TBCs, the in-plane elastic modulus is in the range of $\sim 50\text{--}150 \text{ GPa}$. The thermal conductivity of EBPVD YSZ coatings, $\sim 1.1\text{--}1.5 \text{ W m}^{-1} \text{ K}^{-1}$, is marginally higher than that of APS coatings of the same composition.

Testing and Characterization of TBCs

Assessing the durability of TBCs is essential for their successful deployment in service. Durability depends on many factors, like composition (yttria content of YSZ), processing parameters, substrate surface condition, as well as service conditions. While data from the service life of the coatings should provide the best insight into their durability, the coatings need to be evaluated in a satisfactory manner prior to deployment in service to ensure adequate confidence in their ability to serve without catastrophic failure. There are two main testing methods for assessing durability, furnace thermal cycling and burner rig testing. A vast array of characterization and testing techniques are used for evaluating thermal barrier coatings in the laboratory [10, 11]. Salient such techniques are presented here.

A furnace cycling test (FCT) consists of a chamber maintained at the temperature of testing and an actuator attached to a refractory stage on which coating specimens are kept. The actuator is programmed to rapidly insert the specimen stage into the

furnace using a hydraulic or pneumatic mechanism, keep it there for the required period, and rapidly remove it right after. The actuator is also programmed to carry out specified number of such cycles. The rapid insertion of the specimens into the furnace and removal from it simulate the rapid temperature excursions in the operation of a gas turbine engine. The holding time of each cycle typically is in the range of ~15–120 min. The specimens used in FCT are in the form of discs of ~25 mm with substrate thickness of ~3–5 mm. The coating thickness obviously is the same as in the application of the coating. The number of cycles accumulated before failure of the TBC is reported. Thermal cycling may be interrupted before coating failure for investigating the changes occurring in the coating system leading to ultimate failure.

A burner rig simulates the combustion environment of a gas turbine more closely than furnace thermal cycling. It is, however, the more expensive testing method as the rig needs adequate design features for achieving realistic combustion conditions. A burner rig typically consists of a horizontal cylindrical refractory chamber with a specimen holder installed inside. A fuel burning nozzle directs the flame at the specimen. The burner rig chamber can also be pressurized to simulate service conditions. Specimens are in the form of rods of superalloy coated with BC and TBC. A specimen carousel is used sometimes, on which a few specimens are mounted. The carousel rotates to bring each specimen in the path of the flame for fixed time interval. Some burner rigs incorporate cooling of the metallic substrate with an air jet so that the TBC is under a temperature gradient mimicking the application conditions. The specimens need to be prepared suitably to allow air-jet cooling.

Apart from FCT and burner rig, which are relatively widely available for research, high heat flux testing with temperature gradient is also used, notably by NASA. This is an expensive testing facility wherein a high-power laser is used for heating the TBC while the metallic substrate is cooled by a controlled airflow. A suite of instrumentation is used for monitoring the specimen during high heat flux testing.

Other important types of characterization for TBCs are:

- Thermal conductivity measurement, e.g., by laser flash technique
- Elastic modulus (in-plane and out-of-plane) by indentation, bend tests, other mechanical tests
- Porosity and surface area by Archimedes technique, mercury porosimetry, neutron scattering, small-angle X-ray scattering, and BET nitrogen adsorption
- Residual stress measurements by mechanical methods
- X-Ray diffraction for phase identification and texture and residual stress measurements
- Raman spectroscopy for phase identification
- Photostimulated luminescence piezospectroscopy for stress measurements on the TGO
- Electron microscopy, including analytical electron microscopy

Factors Affecting the Durability of YSZ Thermal Barrier Coatings

It is important to first understand what constitutes the failure of a TBC. If a small piece of the top coat chips off (i.e., spalls off), it may not be considered as failure since only a small fraction of the total coated surface of a component is exposed to the engine environment. Top coat spallation from a certain fraction of the coated surface area of a component is termed as TBC failure, requiring recoating of the component (after removing the remaining original coating). It is clear that prior to TBC spallation, the coating system experiences distress leading to buildup of stresses and damage up to some critical level. As the TBC is exposed to high temperatures and rapid temperature excursions for hundreds, or even thousands, of hours, many processes occur in the system, giving rise to distress. The TBC system has two metallic layers (superalloy and bond coat) and two ceramic layers (TGO and the top coat). Changes occur within each layer during thermal exposure, and the layers interact with each other. The changes are thermochemical or thermo-mechanical and are explained below.

Growth of TGO, Residual Stresses, and Intrinsic Failures of TBCs

It should be noted that oxygen ion diffusion in yttria-stabilized zirconia is extremely fast, exemplified by the high values of ionic conductivity it exhibits. As a result, in spite of the presence of the YSZ top coat, the oxygen partial pressure at the top coat/TGO interface is approximately the same as it would be in the absence of the top coat. The availability of oxygen leads to steady growth of the TGO during TBC service. This would be the case even if the top coat had no porosity. Growth of the TGO induces growth stresses in the TBC system, and these stresses are the main cause of intrinsic failure of the TBC. The TGO not only thickens but also grows laterally, though much less than in the thickness direction. Since it is constrained by the bond coat and the top coat, the lateral growth of the TGO leads to increased waviness in its profile. This process is called ratcheting or rumpling. It is believed that interdiffusion processes between the bond coat and the superalloy, as well as aluminum loss to the TGO, also exacerbate rumpling of the TGO. Rumpling and ratcheting are necessarily accompanied by deformation of the bond coat [12]. This feature is typical of the (Ni, Pt)Al bond coats. The MCrAlY bond coats exhibit other features, especially formation of spinels and yttrium aluminum garnet “pegs.” At ambient temperature, thermal expansion mismatch adds to the growth stresses in the TGO, which can be in the range of ~3–6 GPa [13]. Such residual stress can cause crack initiation and propagation in the interfacial region of the TBC system. The typical intrinsic failure modes are summarized in Fig. 2. While failures due to rumpling/ratcheting and edge delamination are caused by stresses built up during TGO growth and thermal cycling, void formation in the bond coat is due to extensive loss of aluminum. Prolonging TBC life against intrinsic failures requires a deceleration of TGO growth and enhanced strength and toughness of the various layers of the TBC system.

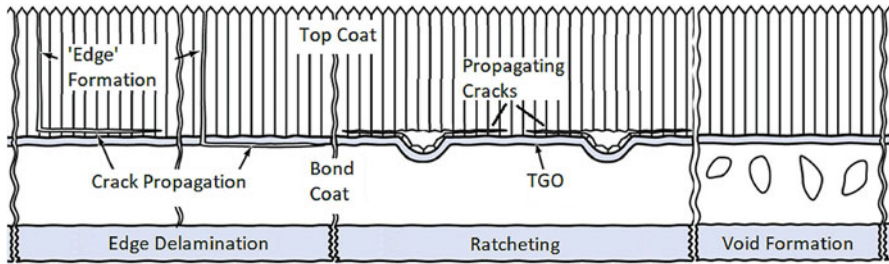


Fig. 2 Schematic diagram of intrinsic failure of EBPVD thermal barrier coatings [14]

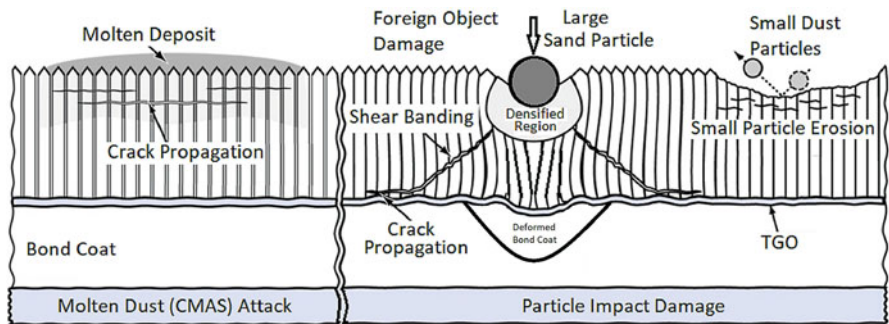


Fig. 3 Extrinsic failure modes of TBCs. Here, FOD means foreign object damage, and CMAS means calcium-magnesium-alumino-silicates [14]

Extrinsic Failures of TBCs

The intrinsic failures are due to processes happening within the TBC system. Failure of TBCs may also be caused by their interaction with the engine environment [15]. Such extrinsic failures are summarized in Fig. 3. Erosion is caused by small dust particles with size much smaller than the TBC thickness, entering the gas stream of the gas turbine with melting point higher than the gas temperature [16]. The loss of material in erosion is caused by stress waves traversing through the TBC thickness and reflecting back at the TBC/TGO interface [17]. Foreign object damage (FOD) is caused by large particles, with size comparable to the TBC thickness. At the service temperature, the top coat deforms plastically upon impact by the large particle to form a densification zone. A shear band forms in a conical fashion right down to the TBC/TGO interface. The shear band consists of some plastic deformation followed by cracking. This is a large-scale damage to the TBC and a major concern for gas turbines operating in sandy environment, such as aircraft plying in desert landscapes or in areas with active volcanos with skies filled with volcanic ash. Another important extrinsic failure mechanism due to ingestion of particles is known as CMAS attack. Calcium-magnesium-alumino-silicates are minerals which can melt at

temperatures encountered in gas turbines. The molten CMAS infiltrates the porous top coat down to the depth at which the temperature is high enough. During cooling after engine shutoff, the CMAS solidifies (or goes through glass transition) and becomes rigid, leading to thermal stresses in the TBC which may be sufficient for it to crack. The top coat may also dissolve in the molten CMAS to some extent at engine operating temperatures. Strategies to mitigate CMAS attack involve deploying alternative materials in the top coat, mostly as an additional external layer, that prevents CMAS infiltration by reacting with it and raising the melting temperature [15, 18]. Examples of CMAS-resistant materials are alumina and rare-earth zirconates with pyrochlore structure, especially $\text{Gd}_2\text{Zr}_2\text{O}_7$.

Another extrinsic failure mechanism of TBCs is hot corrosion, or molten salt attack. This mechanism is relevant to the gas turbines operating under conditions leading to the ingestion of sulfur, vanadium, and alkali metal salts like chlorides. Fuels contaminated with sulfur and vanadium may have to be used in land-based, power generation gas turbines. Engines operating in marine environments may ingest salts from seawater. Such contamination leads molten salts to deposit on hot section components, causing degradation reactions [19, 20]. This degradation is called hot corrosion. Hot corrosion of superalloys without TBCs has been studied extensively and will not be described here. The low melting salt deposits cause destabilization of t' YSZ by thermochemical reactions at temperatures of ~ 700 – 1000 °C. Destabilization consists of formation of m - ZrO_2 and yttrium compounds. This is undesirable as appearance of m is detrimental to TBC durability. While the reaction kinetics and products of hot corrosion vary with the composition of the molten salts, the mechanism of hot corrosion of TBCs consists of dissolution of YSZ during high temperature exposure and reprecipitation in the form of m - ZrO_2 and yttrium compounds [21]. The mechanism of TBC hot corrosion has been loosely described as leaching of yttria from YSZ, leading to destabilization of t' YSZ to form monoclinic zirconia. However, the diffusion rates of yttrium in YSZ are not high enough at temperatures of hot corrosion for it to leach out of the TBC [22]. On the other hand, dissolution of YSZ into the molten salt deposit up to saturation can occur during gas turbine operation, followed by separate precipitation of zirconia and yttria compounds. Depending on the salt composition, the various compounds formed in hot corrosion of YSZ top coats are m - ZrO_2 , ZrOS , YVO_4 , Y_2O_3 , NaYV_2O_7 , etc. Prevention of hot corrosion can be achieved by preventing contamination, for instance, by using clean fuels. This, however, may not always be possible. Certain inhibitors of hot corrosion may be used. Alternatively, similar to CMAS attack mitigation, a hot-corrosion-resistant outer layer may be added to the TBC system. It should be noted that hot corrosion is limited to intermediate temperatures, typically below 950 °C since the salts evaporate away at higher temperatures. On the other hand, CMAS attack occurs at high temperatures, ~ 1200 – 1250 °C. As a result, hot corrosion is not an important problem for aviation gas turbines since only clean fuel is used in aircraft. Power generation gas turbines are more susceptible to hot corrosion, especially components without TBCs, as they are exposed to temperatures at which hot corrosion is an issue. Degradation by CMAS attack, however, is an increasingly important problem with increasing gas turbine operating temperatures.

New materials resistant to CMAS attack are being developed so that the potential of TBCs can be fully realized in future gas turbines.

Phase Transformations

Both APS and EBPVD deposition processes produce the YSZ top coat (with 6–8 wt. % Y_2O_3) in the form of a metastable extended solid solution of yttria in zirconia represented by the symbol t' . The prime indicates that the tetragonal zirconia cannot transform to monoclinic zirconia (m), and hence t' is described as “non-transformable.” The composition and the temperature ranges in which the t' phase is favored over other metastable phases are shown in Fig. 2 as the triangular blue-colored region. See [23] for a treatment of thermodynamics of metastability. Note that the label “m + c” applies to the *equilibrium* state from pure zirconia up to the cubic fluorite phase (c) solvus. At TBC operating temperatures, precipitation of c occurs, leading to a t + c two-phase state. The t matrix is depleted in yttria because of Y-rich c phase formation. This Y-depleted tetragonal phase becomes “transformable,” i.e., can convert to m during cooling. Upon prolonged thermal exposure, large volume fraction of m may form in the TBC during the cooling cycle. It is well-known that the t to m transformation is martensitic and, more importantly, is associated with volume expansion that can induce sufficient stresses to cause cracking. These phase transformations represent the ultimate limiting processes for durability of t' YSZ TBCs (Fig. 4).

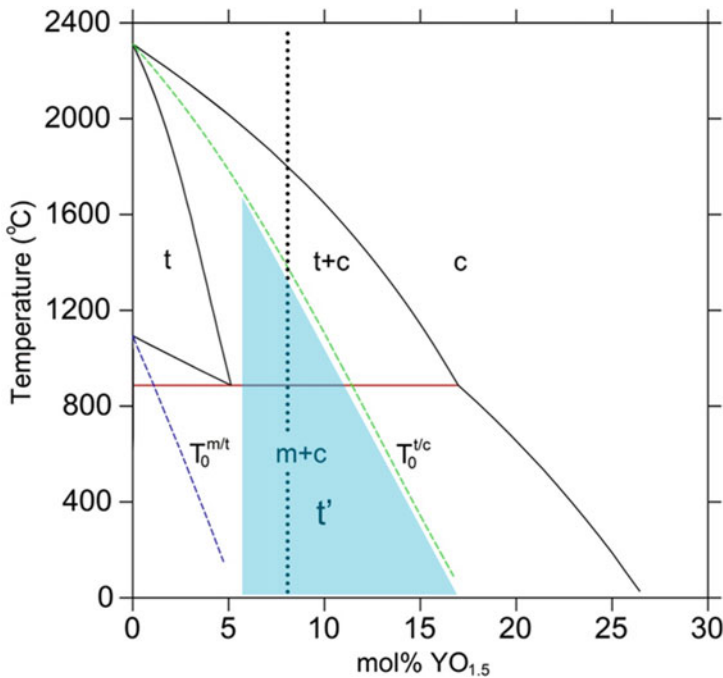


Fig. 4 Zirconia-rich part of the ZrO_2 - Y_2O_3 phase diagram showing metastable phase hierarchy. (Courtesy: K.C. Harikumar)

Precipitation is broadly the mechanism of high-temperature phase transformation of t' . While cubic fluorite precipitates form at the high temperature, room temperature phase assembly can be complicated. In the absence of t to m transformation during cooling, the room temperature phase assembly should ideally be $t + c$. However, many different phase combinations have been observed in different coatings and also laboratory specimens consisting of powders and sintered compacts. The most widely used technique of phase identification is X-ray diffraction, supported by synchrotron XRD, electron microscopy, and Raman spectroscopy. Miller [24] first reported the presence of two tetragonal phases and one cubic phase in aged air plasma-sprayed YSZ coatings. The two tetragonal phases were thought to be the original t' and a newly formed tetragonal phase (t) with lower yttria content. Others have observed only $t + c$ phase assembly, whether APS coatings, EBPVD coatings, or sintered compacts [25–28]. On the other hand, there are reports of formation of three tetragonal phases, differing in their c/a ratios, denoted as t , t' , and t'' , apart from c , and sometimes monoclinic (m) as well. The mechanisms of formation of such wide variety of phase assemblies are not understood and are topic of current research. It is postulated that apart from precipitation, stress-induced spinodal decomposition may be active in these materials, under different conditions of processing and temperature [27, 29, 30].

The phase transformation of t' TBC is not relevant only in terms of the formation of monoclinic zirconia in a disruptive manner. The mechanical properties of the initially t' TBC change significantly during aging, which must be taken into account in design of the coating or in developing models to predict durability. The fracture toughness of sintered YSZ with 8 mol%YO_{1.5} decreased drastically upon short thermal exposure at 1150 and 1250 °C but recovered during prolonged aging up to 192 h [28]. Similar observations were made on t' zirconia stabilized with YbO_{1.5} or GdO_{1.5}, as well as co-doped zirconia [31–34]. Changes in fracture toughness of YSZ coatings upon aging have also been reported [35, 36]. Correlations of changes in the properties of the TBC with phase transformations are being studied.

Sintering

The porous nature of the top coat has already been described as a desirable feature. Any porous object has relatively large surface area, which is associated with higher Gibbs energy than the bulk material. Hence, there is a thermodynamic driving force for decreasing the total surface area, i.e., decrease in porosity. This process is nothing but sintering. Since the TBC system is exposed to high temperatures for thousands of hours, diffusion rates are significant, bringing about considerable sintering. The two important properties affected adversely by sintering are thermal conductivity and elastic modulus of the top coat [37–44]. Sintering in APS coatings consists of interlamellar pore closure and crack healing, as well as reduction and shape evolution of closed porosity. In the EBPVD coatings, the feathery morphology smoothens out. Closed pores inside the columns may also shrink. The TBC columns fuse with each other at a few points. It is important to develop an understanding of the sintering kinetics of the particular top coat, and the rate of increase in thermal conductivity and

elastic modulus under the service conditions. Since surface area and curvature effects drive sintering, TBC sintering kinetics may be studied by measuring the internal surface area as a function of thermal exposure. Adsorption isotherm technique, for example, can be used for recording the surface area changes in EBPVD coatings; they have significant amount of open porosity in the forms of intercolumnar gaps and feathery morphology. The main drawback of using surface area as a measure of TBC sintering is that there are no straightforward correlations with thermal conductivity or elastic modulus. Hence, it is more useful to track the changes in these properties of interest directly.

Life Prediction and Prime Reliance

Since YSZ is the most widely used material of TBCs, a large amount of data exists with various engine manufacturers as well as in the open literature. Empirical as well as deterministic models have been developed for predicting TBC lifetime [10, 45–48]. Despite the advances made in TBC technology, however, the TBC surface temperature is not allowed to exceed the capability of the underlying superalloy. In case of TBC spallation, the superalloy is exposed to the hot gases and needs to survive till the next inspection and repair. Realization of the promise of TBC technology, to facilitate further enhancement in engine efficiency by allowing TBC surface temperatures higher than superalloy capability, requires the TBCs to be prime reliant. The top coat should not fail in an unpredictable fashion. Prime reliance can only be achieved by developing nonempirical models rooted in the understanding of mechanics and materials science of TBCs. These models need to adequately address extrinsic as well as intrinsic failures. Continuous condition monitoring of the coating is required by developing sensors to collect important parameters during service, such as temperature and residual stresses. Moreover, new TBC materials are needed as alternatives to YSZ, and as layers for specific purposes such as resisting CMAS attack or generating signal for a sensor.

New Materials for TBCs

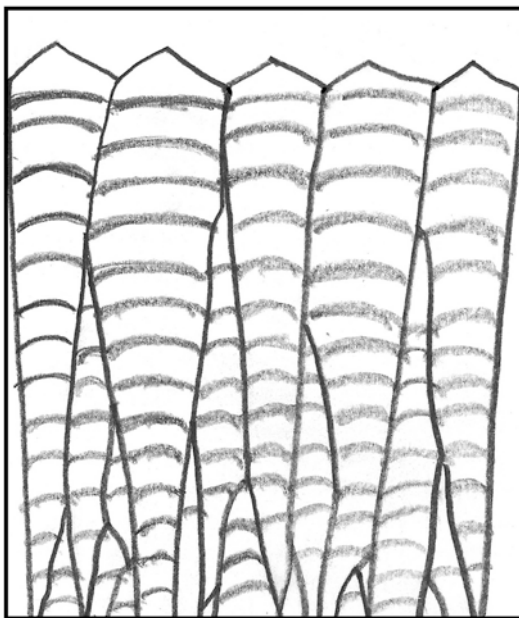
Alternatives to t' YSZ are required primarily to decrease the thermal conductivity and increase the temperature capability of the top coat. Metastable nature of the t' phase of YSZ limits its temperature of application since transformation to the $t + c$ state may be too rapid at high temperature, leading to spontaneous formation of monoclinic zirconia phase (m) very early in thermal cycling. This may lead to cracking of the coating due to volume expansion associated with m formation. Decrease in thermal conductivity of YSZ with 6–8 wt. % Y_2O_3 can be achieved by modifying the coating microstructure. Alternatively, new materials with thermal conductivity much lower than YSZ have been developed. Apart from low thermal conductivity, research efforts have also been directed at improving the fracture toughness of top coat materials. Resistance to extrinsic failure, i.e., erosion, foreign object damage, hot corrosion, and CMAS attack, has also been the focus of the search for alternative TBC materials.

Guidelines for Obtaining Low Thermal Conductivity

Microstructural Features for Lower Thermal Conductivity

Given the success of YSZ as TBC, a lot of research work focussed on obtaining low thermal conductivity in YSZ coatings by incorporating various microstructural features, both by APS and EBPVD. Heat conduction through the TBC is by phonon transport. Radiative heat transfer is almost equal to conduction at TBC service temperatures. Therefore microstructural features which impede both radiation and conduction have been incorporated into TBCs in various research studies [13, 49]. Porosity in the top coat decreases thermal conductivity. However, too much of porosity would make the coating fragile. The shape of the pore also determines its effectiveness in conductivity reduction [50]. As the crack-like voids in APS coatings are normal to the direction of heat transfer, they are more effective than the intercolumnar gaps in EBPVD which are parallel to heat flux. Some of the special features introduced in EBPVD coatings for decreasing heat transfer are shown in Fig. 5. Greater photon scattering can be achieved if dense and porous layers are introduced in the coating with periodicity designed to act as a quarter wavelength filter of the relevant radiation. Such coatings do possess lower thermal conductivity than typical EBPVD coatings by a factor of about 0.55 [49]. Such layers of alternating high and low porosity can be introduced by plasma-assisted PVD, which makes processing slower and expensive. The longevity of such coating architectures has not been adequately investigated, especially in terms of sintering, and hence such techniques are not widely used in industrial practice.

Fig. 5 Illustrating the concept of layering in a TBC for greater phonon scattering



Materials Features for Low k

Processing considerations and coarsening phenomena during service make it difficult to implement some of the engineered microstructural features discussed above. Lower coating conductivity can be achieved by using materials with inherently lower thermal conductivity than YSZ. A simple model proposed by Clarke [51] provides an insight into the factors governing thermal conductivity. At a temperature above Debye temperature, the minimum thermal conductivity (neglecting radiative heat transfer) is approximately given by the following equation [52]:

$$\kappa_{\min} = 0.87k_B\bar{\Omega}_a^{2/3}(E/\rho)^{1/2} \quad (2)$$

Here $\bar{\Omega}_a = [M/(m\rho N_{Av})]$ is the average volume per atom, E is the elastic modulus, ρ is the density, M is the molar mass, m is the number of atoms per formula unit, and N_{Av} is Avogadro's number. Based on considerations leading to Eq. (2), low thermal conductivity may be achieved if a material has a large molecular (molar) mass, a complex crystal structure, nondirectional bonding, and a large number of different atoms per molecule or unit cell. Additionally, large number of point defects and grain boundaries would further decrease the thermal conductivity.

Over the last couple of decades, a lot of different oxide ceramic materials with thermal conductivity less than $\sim 1 \text{ W m}^{-1} \text{ K}^{-1}$ have been identified [52–54]. Many compositions are based on addition of multiple rare-earth (lanthanoid) oxides to zirconia [55, 56]. The idea is to retain the t' phase while decreasing the thermal conductivity due to the presence of heavy stabilizer cations. A few such compositions have found favor with engine manufacturers since the properties other than thermal conductivity, as well as processing, are similar to the standard YSZ TBCs. The second family of materials to succeed in reaching real gas turbine application is pyrochlore structure zirconates [57, 58]. Lanthanum zirconate and gadolinium zirconate ($\text{La}_2\text{Zr}_2\text{O}_7$ and $\text{Gd}_2\text{Zr}_2\text{O}_7$) are the two materials studied the most. Gadolinium zirconate has found favor with engine manufacturers because of its processability as well as low thermal conductivity and high thermal expansion coefficient. The other materials with low thermal conductivity are based on ceria, hafnia, garnets, magnetoplumbites, rare-earth phosphates, yttrium tantalate, tungstates, molybdates, etc. Some of the roadblocks in the successful application of alternatives to YSZ include thermal instability, lack of chemical compatibility with the TGO, high vapor pressures, fast sintering kinetics, poor thermal shock resistance, and difficulties in coating deposition.

A Note on Nanocrystalline TBCs

It was predicted theoretically that nanocrystalline YSZ would have significantly lower thermal conductivity than microcrystalline YSZ [59]. It must be noted, however, that the benefit of nanocrystallinity would not be significant at high temperatures relevant to TBCs. Experimental investigation has shown that the grain size effect down to 50 nm grain size is insignificant [60]. Grain sizes of 10 nm or even smaller may impart significantly low thermal conductivity to the

coating. Processing difficulties in obtaining such truly nanometric crystallites in TBCs would make such coatings considerably more expensive than conventional TBCs. Moreover, materials tend to undergo coarsening processes at elevated temperatures. The nanocrystalline TBC is therefore likely to coarsen during service to an extent that would negate all the efforts put into developing the nanocrystallinity.

A Note on Gradient TBCs

Functionally graded materials are those in which the proportions of two or more phases are varied systematically along one direction to achieve gradual change in the property of interest, instead of a sharp change in the said property that could lead to undesirable system behavior. Since a TBC system consists of two metallic and two ceramic layers (including the TGO), and the properties such as thermal expansion coefficient, elastic constants, and fracture toughness change drastically across each interface (more so at the metal-ceramic interface), the gradient approach is appealing. Significant research efforts have been expended in developing gradient TBCs, e.g., by mixing bond coat powders with YSZ powders during plasma spraying, and varying their proportions, to obtain a decreasing volume fraction of the bond coat material across the thickness of the coating, going from the interface toward the surface of the coating. The thermal expansion coefficient of the gradient coatings would vary gradually along the thickness direction, presumably mitigating thermal stresses. Such gradient coatings, however, have not been successfully put into service *especially in gas turbines*. Many problems are faced in implementing the gradient concept in TBCs for gas turbines, apart from processing challenges and cost. The overall thermal conductivity of the gradient coatings would be significantly higher than single-material conventional ceramic top coats. Hence, the thickness of the gradient coating would be much larger than the conventional TBC. Since the TBC mass is considered as parasitic loading, its thickness should be as small as possible. The disparity in the thermal expansion behavior of the two materials in the gradient coating would generate large local thermal stresses. The metallic phase in the gradient coating would experience severe oxidation, with attendant volume changes and stress buildup, leading to coating failure faster than conventional TBCs. Some of the gradient concepts may be based on mixing alumina particles with YSZ. Although oxidation is not an issue in such a case, the other problems outlined here are applicable.

A Note on Multilayered TBCs

The multilayer concept is different from the gradient concept. The conventional TBC system is itself a multilayered one, with two metallic (superalloy and bond coat) and two ceramic (TGO and top coat) layers. In advanced TBC systems, additional layers may be introduced to serve specific functions. For instance, many of the new low- k TBC materials are not thermochemically compatible with the TGO. Hence, a thin layer of conventional YSZ is deposited on the bond coat before depositing the low- k material. The low- k material may also not possess adequate fracture toughness or thermal expansion coefficient. The YSZ interlayer not only prevents chemical reaction between the TGO and the low- k top coat but also mitigates failure because

of its higher fracture toughness and thermal expansion coefficient. Such a multilayer configuration exploits the desirable properties of each material in the coating system. Additional layers of different materials may also be used for introducing new functionalities in the TBC system. For instance, an outer layer of materials resistant to attack by molten salts (hot corrosion) or, perhaps more importantly, CMAS attack may be deposited [15]. The multilayer concept is also useful in incorporating sensing capability in the TBC system. Layers of materials that may be spectroscopically active may be deposited inside the top coat at various levels along the thickness. These layers would emit their signature radiation, either due to the high service temperature or excited by an incident laser incorporated in the external sensing instrumentation. The signal emitted by the active layer would be useful for monitoring temperature or the structural health of the coating [61–64]. Typical strategy for sensing layer is to dope with rare-earth cations. Sometimes, the multilayer concept may involve different microstructures of the same material [36]. For example, using the conventional YSZ material, it is possible to deposit an inner layer of high fracture toughness (due to low porosity) in contact with the TGO, followed by a low thermal conductivity layer with higher porosity than the first layer. An outer high fracture toughness layer may be deposited for resisting erosion.

Enhancing the Fracture Toughness of TBCs

The reason behind the success of 7YSZ with initial t' phase as a thermal barrier coating was investigated for many years [65]. The thermal conductivity of YSZ decreases with increasing yttria content, so that cubic (fully stabilized) zirconia has lower thermal conductivity than the t' YSZ. However, the thermal cyclic life of cubic zirconia TBCs is significantly poorer than t' YSZ. Comparison of the intrinsic fracture toughness of various stabilized zirconia materials shows that the t' YSZ fracture toughness is higher than that of fully stabilized (cubic) zirconia. Hence, fracture toughness emerges as one of the most important properties for TBCs. Since transformation toughening in t' is not possible, the relatively high fracture toughness was ascribed to ferroelastic toughening [66].

The ferroelastic toughening mechanism [67, 68], when ferroelastic domains have already formed, consists of switching of those domains which are oriented favorably in relation to the stress near the crack tip. The contribution to toughness [66] is given by:

$$\Delta\Gamma = 2f_s h \tau_c \gamma \quad (3)$$

where f_s is the volume fraction of the material experiencing ferroelastic domain switching in the process zone of width h . The critical stress τ_c is called the coercive stress for ferroelastic domain switching. The associated strain is γ , given by:

$$\gamma = (2/3)[(c/a) - 1] \quad (4)$$

Here c and a are the tetragonal phase lattice parameters. The higher the c/a ratio, the higher is the toughness. If ferroelastic domains are not already present, they must

first be nucleated. The critical stress in such cases would be the stress required to nucleate domains. In view of these considerations, it is believed that tetragonal phases with higher c/a ratio would possess high fracture toughness. Based on this consideration, a few compositions with tetragonal structure have been studied [33, 34, 46, 69–73]. It should be noted, however, that the c/a ratio is not the dominant parameter influencing ferroelastic toughening. The critical stress for domain switching is an important factor. Moreover, it has been shown that microstructural parameters such as domain or crystallite size also influence the toughness [28, 31, 32].

Summary

In this chapter, the materials aspects of thermal barrier coatings have been discussed. As remarked at the beginning, the aim is to present the well-established concepts and understanding of this important field, rather than the most current research review. Thermal barrier coatings are integral part of modern gas turbines. Yttria-stabilized zirconia with around 7 wt. % yttria, with the non-transformable t' structure, is still the material of choice as a TBC. The durability and reliability of 7YSZ coatings is determined by processing, and the intrinsic and extrinsic failure mechanisms. Phase transformations and fracture toughness are important materials aspects of t' YSZ coatings. Resistance to CMAS (molten dust) attack has become the most important extrinsic failure mechanism as the operating temperatures increase further. New materials for TBCs that have been successfully deployed in service are of two types. One is gadolinium zirconate with the pyrochlore structure, and the other is zirconia with multiple rare-earth oxides as stabilizers. Both these types of materials have significantly lower thermal conductivity than YSZ. However, these materials are not thermochemically compatible with the TGO. Hence, a YSZ interlayer is used prior to deposition of these new TBC materials. Search for new compositions continues, not only in search of lower thermal conductivity but also high fracture toughness, resistance to CMAS, and incorporating a sensor property in the coating. As the materials aspects of TBCs are understood, the reliability of the coatings will improve. The ultimate goal of making TBCs prime reliant cannot be realized without profound understanding of TBC materials aspects.

References

1. Pollock TM (2016) Alloy design for aircraft engines. *Nat Mater* 15:809–815
2. Naumenko D, Pillai R, Chyrkin A, Quadackers WJ (2017) Overview on recent developments of bondcoats for plasma-sprayed thermal barrier coatings. *J Therm Spray Technol* 26:1743–1757
3. Padture NP (2016) Advanced structural ceramics in aerospace propulsion. *Nat Mater* 15:804–809
4. Pollock TM, Lipkin DM, Hemker KJ (2012) Multifunctional coating interlayers for thermal-barrier systems. *MRS Bull* 37:923–931
5. Miller RA (1987) Current status of thermal barrier coatings – an overview. *Surf Coat Technol* 30:1–11

6. Evans AG, Mumm DR, Hutchinson JW, Meier GH, Pettit FS (2001) Mechanisms controlling the durability of thermal barrier coatings. *Prog Mater Sci* 46:505–553
7. Mattox DM (2018) Chapter 5 – Thermal evaporation and deposition in vacuum. In: Mattox DM (ed) *The foundations of vacuum coating technology*, 2nd edn. William Andrew Publishing, Oxford, pp 151–184. <https://doi.org/10.1016/B978-0-12-813084-1.00005-4>
8. Pature NP, Gell M, Jordan EH (2002) Thermal barrier coatings for gas-turbine engine applications. *Science* 296:280–284
9. Wright PK (1998) Influence of cyclic strain on life of a PVD TBC. *Mater Sci Eng A* 245:191–200
10. Vaßen R, Kagawa Y, Subramanian R, Zombo P, Zhu D (2012) Testing and evaluation of thermal-barrier coatings. *MRS Bull* 37:911–916
11. Ang ASM, Berndt CC (2014) A review of testing methods for thermal spray coatings. *Int Mater Rev* 59:179–223
12. Clarke DR, Levi CG (2003) Materials design for the next generation thermal barrier coatings. *Annu Rev Mater Res* 33:383–417
13. Darolia R (2013) Thermal barrier coatings technology: critical review, progress update, remaining challenges and prospects. *Int Mater Rev* 58:315–348
14. Evans AG, Clarke DR, Levi CG (2008) The influence of oxides on the performance of advanced gas turbines. *J Eur Ceram Soc* 28:1405–1419
15. Levi CG, Hutchinson JW, Vidal-Sétif MH, Johnson CA (2012) Environmental degradation of thermal-barrier coatings by molten deposits. *MRS Bull* 37:932–941
16. Wellman RG, Nicholls JR (2000) Some observations on erosion mechanisms of EB PVD TBCS. *Wear* 242:89–96
17. Chen X et al (2004) Mechanisms governing the high temperature erosion of thermal barrier coatings. *Wear* 256:735–746
18. Viswanathan V, Dwivedi G, Sampath S (2015) Multilayer, multimaterial thermal barrier coating systems: design, synthesis, and performance assessment. *J Am Ceram Soc* 98:1769–1777
19. Luthra KL, Spacil HS (1982) Impurity deposits in gas turbines from fuels containing sodium and vanadium. *J Electrochem Soc* 129:649–656
20. Nagelberg AS (1985) Destabilization of yttria-stabilized zirconia induced by molten sodium vanadate-sodium sulfate melts. *J Electrochem Soc* 132:2502–2507
21. Reddy N, Gandhi AS (2013) Molten salt attack on t' yttria-stabilised zirconia by dissolution and precipitation. *J Eur Ceram Soc* 33:1867–1874
22. Kilo M et al (2003) Cation self-diffusion of 44 Ca, 88 Y, and 96 Zr in single-crystalline calcia- and yttria-doped zirconia. *J Appl Phys* 94:7547–7552
23. Levi CG (1998) Metastability and microstructure evolution in the synthesis of precursors. *Acta Mater* 46:787–800
24. Miller RA, Smialek JL, Garlick RG (1981) Phase stability in plasma-sprayed, partially stabilized zirconia-yttria. In: *Advances in ceramics*, vol 3. Am Ceram Soc, Columbus, pp 241–253
25. Lugh V, Clarke DR (2005) Transformation of electron-beam physical vapor-deposited 8 wt% yttria-stabilized zirconia thermal barrier coatings. *J Am Ceram Soc* 88:2552–2558
26. Lugh V, Clarke DR (2005) High temperature aging of YSZ coatings and subsequent transformation at low temperature. *Surf Coat Technol* 200:1287–1291
27. Lipkin DM et al (2013) Phase evolution upon aging of air-plasma sprayed t' -zirconia coatings: I – synchrotron X-ray diffraction. *J Am Ceram Soc* 96:290–298
28. Loganathan A, Gandhi AS (2012) Effect of phase transformations on the fracture toughness of t' yttria stabilized zirconia. *Mater Sci Eng A* 556:927–935
29. Krogstad JA et al (2013) Phase evolution upon aging of air plasma sprayed t' -zirconia coatings: II-microstructure evolution. *J Am Ceram Soc* 96:299–307
30. Krogstad JA et al (2015) In situ diffraction study of the high-temperature decomposition of t' -zirconia. *J Am Ceram Soc* 98:247–254
31. Loganathan A, Gandhi AS (2012) Effect of high-temperature aging on the fracture toughness of ytterbia-stabilized t' zirconia. *Ser Mater* 67:285–288
32. Loganathan A, Gandhi AS (2017) Toughness evolution in Gd- and Y-stabilized zirconia thermal barrier materials upon high-temperature exposure. *J Mater Sci* 52:7199–7206

33. Loganathan A, Gandhi AS (2011) Fracture toughness of t' ZrO₂ stabilised with MO1.5 (M = Y, Yb & Gd) for thermal barrier application. *Trans Indian Inst Metals* 64:71–74
34. Ponnuchamy MB, Gandhi AS (2015) Phase and fracture toughness evolution during isothermal annealing of spark plasma sintered zirconia co-doped with Yb, Gd and Nd oxides. *J Eur Ceram Soc* 35:1879–1887
35. Ren X, Pan W (2014) Mechanical properties of high-temperature-degraded yttria-stabilized zirconia. *Acta Mater* 69:397–406
36. Dwivedi G, Viswanathan V, Sampath S, Shyam A, Lara-Curzio E (2014) Fracture toughness of plasma-sprayed thermal barrier ceramics: influence of processing, microstructure, and thermal aging. *J Am Ceram Soc* 97:2736–2744
37. Renteria AF, Saruhan B, Schulz U, Raetzer-scheibe H (2006) Effect of morphology on thermal conductivity of EB-PVD PYSZ TBCs. *Surf Coat Technol* 201:2611–2620
38. Zhu D, Miller RA (2000) Thermal conductivity and elastic modulus evolution of thermal barrier coatings under high heat flux conditions. *J Therm Spray Technol* 9:175–180
39. Cernuschi F, Lorenzoni L, Ahmaniemi S, Vuoristo P, Mäntylä T (2005) Studies of the sintering kinetics of thick thermal barrier coatings by thermal diffusivity measurements. *J Eur Ceram Soc* 25:393–400
40. Matsumoto M, Yamaguchi N, Matsubara H (2004) Low thermal conductivity and high temperature stability of ZrO₂-Y₂O₃-La₂O₃ coatings produced by electron beam PVD. *Scr Mater* 50:867–871
41. Guo S, Kagawa Y (2006) Effect of thermal exposure on hardness and Young's modulus of EB-PVD yttria-partially-stabilized zirconia thermal barrier coatings. *Ceram Int* 32:263–270
42. Rätzer-Scheibe HJ, Schulz U (2007) The effects of heat treatment and gas atmosphere on the thermal conductivity of APS and EB-PVD PYSZ thermal barrier coatings. *Surf Coat Technol* 201:7880–7888
43. Lugh V, Tolpygo VK, Clarke DR (2004) Microstructural aspects of the sintering of thermal barrier coatings. *Mater Sci Eng A* 368:212–221
44. Leyens C, Schulz U, Pint BA, Wright IG (1999) Influence of electron beam physical vapor deposited thermal barrier coating microstructure on thermal barrier coating system performance under cyclic oxidation conditions. *Surf Coat Technol* 120–121:68–76
45. Evans AG, He MY, Hutchinson JW (2001) Mechanics-based scaling laws for the durability of thermal barrier coatings. *Prog Mater Sci*. [https://doi.org/10.1016/S0079-6425\(00\)00007-4](https://doi.org/10.1016/S0079-6425(00)00007-4)
46. Clarke DR, Oechsner M, Padture NP (2012) Thermal-barrier coatings for more efficient gas-turbine engines. *MRS Bull* 37:891–898
47. Lin CK, Berndt CC (1995) Statistical analysis of microhardness variations in thermal spray coatings. *J Mater Sci* 30:111–117
48. Burns AJ, Subramanian R, Kempshall BW, Sohn YH (2004) Microstructure of as-coated thermal barrier coatings with varying lifetimes. *Surf Coat Technol* 177–178:89–96
49. Nicholls JR, Lawson KJ, Johnstone A, Rickerby DS (2002) Methods to reduce the thermal conductivity of EB-PVD TBCs. *Surf Coat Technol* 152:383–391
50. Lu TJ, Levi CG, Wadley HNG, Evans AG (2001) Distributed porosity as a control parameter for oxide thermal barriers made by physical vapor deposition. *J Am Ceram Soc* 84:2937–2946
51. Clarke DR (2003) Materials selection guidelines for low thermal conductivity thermal barrier coatings. *Surf Coat Technol* 163:67–74
52. Levi CG (2004) Emerging materials and processes for thermal barrier systems. *Curr Opin Solid State Mater Sci* 8:77–91
53. Pan W, Phillpot SR, Wan C, Chernatynskiy A, Qu Z (2012) Low thermal conductivity oxides. *MRS Bull* 37:917–922
54. Winter MR, Clarke DR (2007) Oxide materials with low thermal conductivity. *J Am Ceram Soc*. <https://doi.org/10.1111/j.1551-2916.2006.01410.x>
55. Zhu D, Chen YL, Miller RA (2003) Defect clustering and nano phase structure characterization of Multi-component rare earth oxide doped Zirconia-yttria thermal barrier coatings, 27th

- International Cocoa Beach Conference on Advanced Ceramics and Composites: A Editors Waltraud M. Kriven and Hau-Tay Lin. *Amn Ceram Soc ISSN 0 196-62 19*
56. Zhu D, Miller RA (2005) Development of advanced low conductivity thermal barrier coatings. *Int J Appl Ceram Technol* 1:86–94
 57. Vassen R, Cao X, Tietz F, Basu D, Sto D (2000) Zirconates as new materials for thermal barrier coating. *J Am Ceram Soc* 28:2023–2028
 58. Bakan E, Vaßen R (2017) Ceramic top coats of plasma-sprayed thermal barrier coatings: materials, processes, and properties. *J Therm Spray Technol* 26:992–1010
 59. Klemens PG (1997) Theory of thermal conductivity of nanophase materials. In: TMS annual meeting, pp 97–104
 60. Raghavan S, Wang H, Dinwiddie RB, Porter WD, Mayo MJ (1998) The effect of grain size, porosity and yttria content on the thermal conductivity of nanocrystalline zirconia. *Scr Mater* 39:1119–1125
 61. Gentleman MM, Clarke DR (2004) Concepts for luminescence sensing of thermal barrier coatings. *Surf Coat Technol* 188–189:93–100
 62. Chambers MD, Clarke DR (2009) Doped oxides for high-temperature luminescence and lifetime thermometry. *Annu Rev Mater Res* 39:325–359
 63. Wang X, Lee G, Atkinson A (2009) Investigation of TBCs on turbine blades by photoluminescence piezospectroscopy. *Acta Mater* 57:182–195
 64. Clarke DR, Christensen RJ, Tolpygo V (1997) The evolution of oxidation stresses in zirconia thermal barrier coated superalloy leading to spalling failure. *Surf Coat Technol* 94–95:89–93
 65. Stecura S (1985) Optimization of the NiCrAl-Y/ZrO₂-Y₂O₃ thermal barrier system. NASA-TM-86905; NASA Lewis Research Center: Cleveland
 66. Mercer C, Williams JR, Clarke DR, Evans AG (2007) On a ferroelastic mechanism governing the toughness of metastable tetragonal-prime (t') yttria-stabilized zirconia. <https://doi.org/10.1098/rspa.2007.1829>
 67. Virkar AV (1998) Role of ferroelasticity in toughening of zirconia ceramics. *Key Eng Mater* 153-154:183–210
 68. Baither D et al (2001) Ferroelastic and plastic deformation of t' -zirconia single crystals. *J Am Ceram Soc* 84:1755–1762
 69. Schaedler TA, Leckie RM, Kraemer S, Evans AG, Levi CG (2007) Toughening of non-transformable t' -YSZ by addition of Titania. *J Am Ceram Soc* 3901:3896–3901
 70. Krogstad JA, Lepple M, Levi CG (2013) Opportunities for improved TBC durability in the CeO₂-TiO₂-ZrO₂ system. *Surf Coat Technol* 221:44–52
 71. Bolon AM, Gentleman MM (2011) Raman spectroscopic observations of ferroelastic switching in ceria-stabilized zirconia. *J Am Ceram Soc* 94:4478–4482
 72. Pitek FM, Levi CG (2007) Opportunities for TBCs in the ZrO₂ - YO_{1.5} - TaO_{2.5} system. *Surf Coat Technol* 201:6044–6050
 73. Shian S et al (2014) The tetragonal-monoclinic, ferroelastic transformation in yttrium tantalate and effect of zirconia alloying. *Acta Mater* 69:196–202



Processing of Ceramic and Cermet Composite Coatings for Strategic and Aerospace Applications

38

L. Rama Krishna, P. Suresh Babu, Manish Tak, D. Srinivasa Rao, G. Padmanabham, and G. Sundararajan

Contents

Introduction and Brief Scope	1466
Thermal Spray	1467
Atmospheric Plasma Spray (APS)	1467
High-Velocity Oxygen Fuel (HVOF) Spray	1468
Detonation Spray Coating (DSC)	1468
Influence of Process Parameters on Microstructure of Thermal Spray Coatings	1469
Oxide Ceramic Coatings	1471
Cermet Coatings	1476
Applications of Thermal Spray Coatings	1481
Ceramic Composite Coatings Through Micro-arc Oxidation Coating Technology on Al Alloys	1484
The MAO Process and Technological Elements	1486
Mechanism of MAO Coating Formation	1488
Tribological Performance	1492
Corrosion Performance	1496
Fatigue Performance	1498
Applications of MAO Coatings	1502
Laser Cladding on Titanium Alloys for Aerospace Applications	1502
Summary and Concluding Remarks	1517
References	1520

L. R. Krishna (✉)

International Advanced Research Centre for Powder Metallurgy and New Materials, (ARCI),
Balapur, Hyderabad, India
e-mail: lrama@arci.res.in

P. S. Babu · M. Tak · D. S. Rao · G. Padmanabham · G. Sundararajan
International Advanced Research Centre for Powder Metallurgy and New Materials,
Balapur, Hyderabad, India
e-mail: pitchuka@arci.res.in; manish@arci.res.in; dsraoarci@yahoo.co.in; gp@arci.res.in;
gsundar@arci.res.in

© Springer Nature Switzerland AG 2020

Y. R. Mahajan, R. Johnson (eds.), *Handbook of Advanced Ceramics and Composites*,
https://doi.org/10.1007/978-3-030-16347-1_51

1465

Abstract

This chapter deals with a variety of ceramic and cermet composite coatings capable of protecting the industrial components including strategic and aerospace sectors from various damage mechanisms such as wear, corrosion, oxidation, thermal, fatigue, and combinations thereof. To enable such coating deposition, a spectrum of processing techniques such as plasma spray, high-velocity oxy-fuel spray, detonation spray, micro-arc oxidation, and laser cladding techniques were utilized and considered for detailed discussion. Under each of the aforementioned techniques, the processing fundamentals, influence of process variables, typical microstructures, properties, and performance of the resulting coatings were briefly presented. However, only the coatings that are functionally relevant in the working temperature up to 800 °C were considered in this chapter. A special emphasis has been placed to provide the understanding of structure-property-performance aspects of different coatings such that the information can be correlated with the typical industrial requirements. Further, both the demonstrated and potential applications specifically pertaining to strategic and aerospace sectors were exemplified.

Keywords

Thermal spray · Plasma spray · HVOF · Detonation spray · Micro-arc oxidation · Plasma electrolytic oxidation · Laser cladding · Wear · Corrosion · Oxidation

Introduction and Brief Scope

Among various thermal spray technological options, the conventional air plasma spraying (APS) has been the workhorse for depositing the ceramic coatings for a large variety of applications. With the advent of relatively advanced technologies such as high-velocity oxy-fuel spray (HVOF) and the detonation spray coating (DSC), primarily relying more on the kinetic energy of the in-flight spray particle than the excessive combustion zone temperatures, depositing the denser, harder coatings with preferred phase retention capabilities, the ceramic and cermet composite coatings deposited by HVOF and DSC techniques are being applied for a variety of strategic and aerospace applications. Furthermore, the recent advancements in design and development of a variety of feedstock powders that differ not only in terms of particle morphology but also in terms of closely controlled chemistries have further widened the window of industrial applications.

The chapter discusses the brief influence of process parameters leading to the formation of critical microstructural features; resulting mechanical, tribological, and electrochemical properties of coatings pertaining to Al_2O_3 , $\text{Al}_2\text{O}_3\text{-TiO}_2$, Cr_2O_3 , $\text{Cr}_2\text{O}_3\text{-Al}_2\text{O}_3$, WC-Co , WC-Co-Ni , WC-Co-Cr , WC-Ni , and $\text{Cr}_3\text{C}_2\text{-NiCr}$ as deposited through APS, DSC, and HVOF processes; and their application to cater the demands of various strategic and aerospace applications. In addition, the

micro-arc oxidation (MAO) which is a recent advancement in depositing ultrahard Al_2O_3 -based composite coatings on different Al alloys for critical applications demanding high wear, corrosion, and fatigue resistances is also presented. Moreover, the efficacy of TiC- and TaC-based laser clad coatings was also briefly presented and discussed in the context of aerospace application development. In the above backdrop, this chapter presents various applications whose operational temperature is in between the room temperature and 800 °C, while the thermal barrier coatings (TBCs) based on APS and electron beam physical vapor deposition (EB-PVD) are purposefully left out of the scope of this chapter, which have been dealt as a separate chapter in this book.

Thermal Spray

The thermal spray processes have been extensively employed onto the surface of the components which need to be protected from various damage mechanisms and their combinations such as wear, corrosion, high-temperature oxidation, and fatigue. The coated components enable their usage in automotive, aerospace, strategic, power generation, and marine applications [1, 2]. In general, thermal spray process involving molten or semi-molten feedstock in the form of powder, wire, or rod is accelerated toward the targeted substrate where it impacts thus facilitates forming a dense coating [2]. Further, several thermal spray techniques were developed by means of varying the source of feedstock heating and in-flight particle acceleration levels [1–5]. The general temperature and velocity ranges involved in various thermal spray processes are shown in Fig. 1. Brief details about the process fundamentals of selected spray systems mostly used for deposition of ceramic and cermet coatings such as air plasma spray (APS), high-velocity oxy-fuel (HVOF) spray, and detonation spray coating (DSC) system techniques are discussed below to centrally provide basic information on a single platform of this chapter.

Atmospheric Plasma Spray (APS)

Plasma spraying is one of the thermal spray variants extensively used for deposition of most nonreactive materials which can melt owing to its characteristic of high temperatures in the plasma plume [1, 4]. Plasma is generated by the breakdown of gas due to high voltage electrical discharge. The typical plasma generator consists of water-cooled copper anode and tungsten cathode, wherein the neutral/inert gas is passed around the cathode and subsequently led to the concentric anode such that the gas gets ionized by the DC power supplied in between anode and cathode. The high temperature produced as a result of ionization is utilized as plasma stream and is useful for concurrent melting and subsequent particle acceleration in the plume with the help of carrier gas to form a coating on the component.

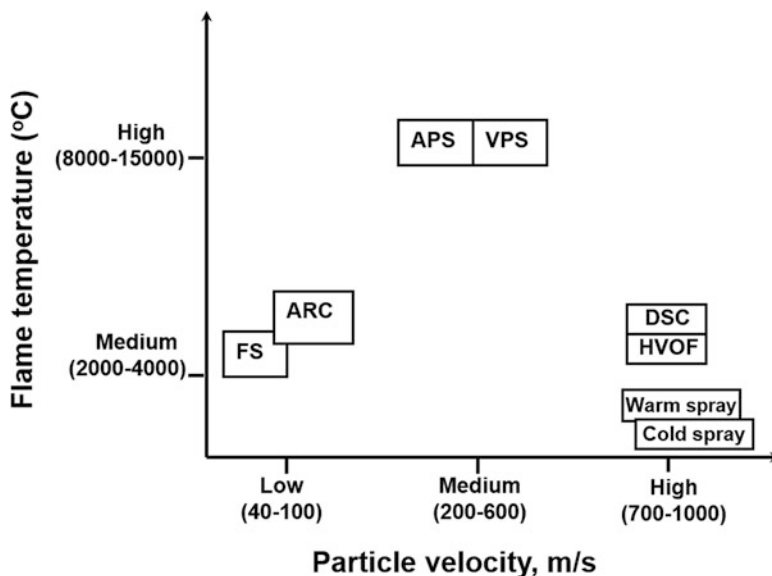


Fig. 1 Temperature and velocity ranges involved among the family of thermal spray processes

High-Velocity Oxygen Fuel (HVOF) Spray

Ever since the invention of HVOF spray in the early 1980s, it has been widely used to deposit carbide-, metal-, and alloy-based coatings on various industrial components [1, 6]. The HVOF thermal spray technique involves a combustion chamber where the fuel (methane, propane, kerosene) reacts with oxygen or air and produces the heat which is utilized for heating the feedstock powders and then the high-pressure gas allows the heated powders to accelerate through a nozzle and eventually sprayed onto substrate with supersonic speed causing the generation of dense coatings.

Detonation Spray Coating (DSC)

Unlike the other thermal spray techniques, detonation spray coating technique (DSC) is a “pulsed” spray deposition technique. The first detonation spray gun (D-Gun™) was developed by Union Carbide, USA, in 1954 and later at IMPR (I), Ukraine, in 1965 [5, 7, 8]. In the detonation spray process, pre-measured quantities of fuel (methane, propane, acetylene) and oxygen in the combustion chamber are ignited using a spark plug so that the controlled explosion is created. The feedstock material is introduced into the chamber; explosion-driven temperature is utilized to

heat up the powder particles to moderate temperatures and then accelerated by detonation wave front through the long barrel toward the open end through the detonation wave medium to form thick, dense coatings with exceptionally good bond strength between the substrate and the coating.

Influence of Process Parameters on Microstructure of Thermal Spray Coatings

In thermal spray, the coating microstructure is layer by layer due to deposition of individual particles one over the other and therefore leaves a room always for porosity, splat boundaries, oxide inclusions, unmelted particles, and cracks [1]. Hence, the coating performance, as strongly dependent on its microstructure, is dependent on the spray process parameters employed and also on the characteristics of the starting powder (feedstock) from which the coating is realized [9–11]. Similarly, the degree of phase transformations depends on the quantum of heat transferred to the particles in the respective spray system, which in turn depends on the flame temperature of the fuel used and on the characteristics of the spray powder. Due to the relatively low particle velocities attained in the air plasma spray (APS), the porosity in the coatings generally ranges from 5% to 15%, and more oxidation of feedstock powder takes place due to higher temperatures involved. Therefore, the APS technique is predominantly used for deposition of oxides and to a significantly lesser extent for depositing cermet and composite coatings [1, 2]. In view of the above, it is imperative that the power input (40–200 kW), gas type (Ar, He, H₂, and N₂), and gas flow rates (100–200 sLm) will be optimized in case of plasma spray coating based on the material to be coated. High-velocity techniques like HVOF and DSC are widely used for deposition of cermets, composites, and alloy coatings due to low temperature and high velocities involved in these processes as compared to the plasma spray technique [3, 4]. In addition, it is noteworthy that the DSC can be employed for deposition of oxide, nitride, and fly ash coatings as well [12–14]. The electric power (in the case of APS) or oxygen-to-fuel ratio (in the case of HVOF, DSC) needs to be optimized based on the type of material being deposited. For example, in case of DSC system, more oxygen-to-fuel ratios (2:2.5) with higher gas volumes are used to deposit oxide coatings [11, 12]. In contrast, while depositing cermet and alloy coatings, lower oxygen-to-fuel ratios are preferred (1.16:1.50) to achieve dense coatings with minimum thermally induced phase transformation [11, 15]. Similarly, in the case of HVOF, the gun design, fuel type, and fuel ratio are optimized for depositing cermet coatings [1].

Once a suitable spray process for deposition of required coating is identified, the other important process parameter to obtain dense coating with good interfacial bonding is the standoff distance (distance from the gun edge to the surface of component being coated). The velocity and temperature of particle change

abruptly when it comes out from the gun exit and travels in the air medium along with the combustion gases. Therefore, an optimum distance should be maintained between the gun exit and coated component to deposit the dense coatings [8]. Further, the influence of powder manufacturing route as well as the particle's size range also needs to be paid due attention [11, 16, 17]. The dense powders are heated to a lower degree during spraying and therefore reduce the risk of phase transformation during the coating deposition. Accordingly, the HVOF-sprayed WC-Co-Cr coatings deposited using spherical and porous powder (agglomerated and sintered) exhibited notably lower erosion resistance than the coatings obtained by angular and coarse powder (sintered and crushed) as feedstock [16]. This behavior is attributed to the higher amount of dissolved carbides and the presence of Cr-rich phases in the coatings obtained through spherical and porous powder. However, it is to be noted that the order of merit for the manufacturing route to obtain dense coatings changes with feedstock composition. Further, some compositions cannot be obtained through sintered and crushed route due to process limitations. In such a situation, the overall goal of optimization of process parameters is strongly related to its morphology and size distribution itself. In the above context, one can also expect that the powder manufacturing route also influences the eventual coating microstructure.

Accordingly, the influence of powder size distribution on the coating structure, phase composition, and performance was investigated for metallic, ceramic, and cermet coatings [11]. It was reported that the particles of finer size range exhibit a high degree of phase transformation rather than the coarser size range particles emphasizing a separate process parameter window needs to be employed for spraying particles with different size ranges although the other conditions such as manufacturing route and chemical composition are identical. It is to be noted that in general, the relatively coarser range (50–100 μm) feedstock is used for plasma spraying, while it is significantly finer (5–45 μm) in the case of HVOF and DSC techniques. Such a selection is primarily based on the thermal and kinetic energy combination involved in each of the aforementioned processes. In the absence of adequate flowability, the powders may get clogged either in the feeder or gun and produce inhomogeneous coatings. Therefore, careful selection of feedstock is vital for maximizing the beneficial properties of thermal spray coatings. In the above context, it is clear that the ability to select proper feedstock material and employ the right spray technique and optimum processing parameters is the key ingredient for achieving the best set of microstructure, properties, and performance of any industrial component.

Further, the melting point, ductility, hardness, and thermal conductivity of the particle and the substrate material influence the coating microstructure. The relative hardness of the particle and substrate material affects the relative deformation behavior of the impacting particle on the substrate, whereas the thermal conductivity of the particle and substrate material affects the kinetics of heat dissipation once the splat is formed. Among most thermal spray coatings, bonding is mainly due to mechanical interlocking and to a lesser extent the metallurgical bonding between coating and substrate. Therefore, as a pre-coating operation, the component surface

to be grit blasted before the actual coating deposition to remove the oil, dirt, etc. from the substrate surface to achieve good interface bonding. Sometimes an intermediate layer will be deposited on the substrate to reduce the coefficient of thermal expansion difference between the actual coating and substrate and hence better coating properties.

Oxide Ceramic Coatings

The oxide ceramic coatings are principally used to combat abrasive wear and corrosion and to enhance electrical and thermal insulation. These coatings are popularly being used in the fields of paper industry for roll coatings, textile industry for guides and pulleys, and marine applications such as propeller shaft-bearing sleeves, pump seals, and others. Among this class of materials, Al_2O_3 , TiO_2 , Cr_2O_3 , and their combinations are the widely investigated coatings [18–20]. Accordingly, the addition of TiO_2 to a larger extent in Al_2O_3 and to a lesser extent in Cr_2O_3 coatings has been popularly employed to obtain soft binder phase. Studies also considered investigating the influence of other oxides like SiO_2 , ZrO_2 , and CeO_2 in varying proportions added either separately or along with TiO_2 - to Al_2O_3 - or Cr_2O_3 -based coatings for different applications [18, 19]. The microstructure and properties of oxide coatings deposited by APS and DSC are discussed in detail in the following part of this section.

Among the available options of thermal spraying, owing to its high plume temperatures, the air plasma spraying (APS) has been extensively used to deposit oxide coatings. The typical cross section of alumina coating deposited by APS exhibits a lamellar splat structure with dispersed pores ranging from 1 to 10 μm size as illustrated in Fig. 2a [21]. Further, the plasma-sprayed alumina coating derived out of 5–30 μm size feedstock typically exhibits the splats, dense network of minute thermally induced micro-cracks, thus dividing each splat into a conglomerate of loosely held pieces. Interestingly, the size of individual splats is found to be principally dependent on the feedstock size and to a lesser extent on the processing conditions. In most cases, a bond coat of Ni-based alloy is applied on the component surface over which Al_2O_3 coating is deposited. The coatings are found to exhibit 6–10% porosity, the shape of the pore being spherical as a composite contribution of unmolten particles, splat boundaries, and gas entrapment. However, the coatings were found to exhibit superior interlamellar cohesion. The $\gamma\text{-Al}_2\text{O}_3$ phase is the major phase present in plasma-sprayed alumina coatings which is otherwise 100% $\alpha\text{-Al}_2\text{O}_3$ phase in the initial feedstock. Such a phase change from $\alpha \rightarrow \gamma$ is promoted by rapid cooling of the molten splats [22]. Depending upon the feedstock size employed, the hardness of plasma-sprayed alumina coating varies between 650 and 1070 HV.

Although, the atmospheric plasma spraying (APS) is the most versatile thermal spray method for depositing oxide coatings, the detonation spraying (D-Gun) has emerged as another promising thermal spray technique capable of depositing dense coatings with retained $\alpha\text{-Al}_2\text{O}_3$ phase proportion in the final coating with

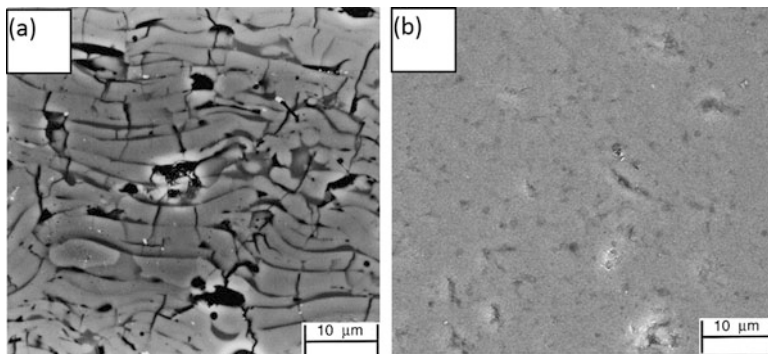


Fig. 2 Cross section SEM images of (a) plasma and (b) detonation sprayed alumina coating [21]

significantly improved hardness and tribological performance [11, 12]. The γ - Al_2O_3 phase has mechanical properties that are known to be inferior to the stable α - Al_2O_3 phase [23]. In addition, in the case of detonation-sprayed coatings, lower thermal energy and higher particle velocity during spraying provide several characteristic advantages such as lower porosity and higher bond strength. Also, it is to be noted that the typical micro-crack network is absent in the case of detonation-sprayed alumina coatings as can be seen from the cross-sectional SEM image of DSC- Al_2O_3 coating shown in Fig. 2b [11]. Together with poor bonding between splats and imperfections in the form of pores and thermally induced micro-cracks, it is well established that the properties of plasma-sprayed coatings are considerably inferior to that of detonation-sprayed coatings.

The use of composite in preference to pure aluminum oxide has certain advantages. Titanium oxide has lower melting point, and its compatibility effectively binds alumina grains leading to further increased density, machinability, and corrosion resistance [24, 25]. In addition, an increase in adhesion strength with increasing TiO_2 proportion in the Al_2O_3 - TiO_2 composite coating is also to be noted. In this connection, the coatings with varying degrees of TiO_2 content added to Al_2O_3 were designed for meeting specific application demands. Accordingly, the Al_2O_3 - TiO_2 coatings provide the combination of high electric resistance and fracture toughness. Whereas, the coatings with higher TiO_2 content up to 40 wt. % possess good electrical conductivity due to oxygen loss in TiO_2 phase leading to the formation of nonstoichiometric suboxides and oxygen-deficient lattice in rutile TiO_2 . The microstructure of Al_2O_3 -40 TiO_2 coating exhibits a typical lamellar structure as shown in Fig. 3 indicating small- and large-size pores formed in the second phase (TiO_2) [26]. It is interesting to note that, though the hardness of Al_2O_3 decreases with increasing addition of TiO_2 , the abrasive wear performance is not impaired. But the corrosion resistance of Al_2O_3 with 13 wt. % TiO_2 is slightly inferior to Al_2O_3 coating in 1 N H_2SO_4 solution due to more defects present with increasing of coating thickness (Fig. 4) [27]. However, the corrosion-resistant oxide coatings are superior than plasma-sprayed Cr3C2-NiCr coatings tested under identical conditions. A detailed discussion on thermally sprayed cermet coatings will be found in the next

Fig. 3 Typical lamellar structure of plasma sprayed Al_2O_3 -40 wt.% TiO_2 coating [26]

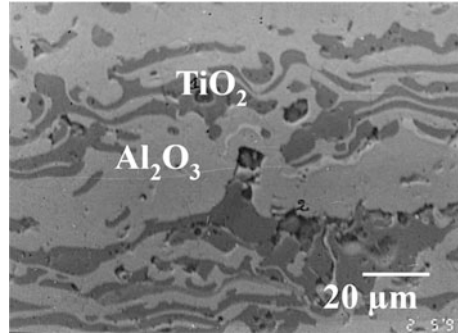
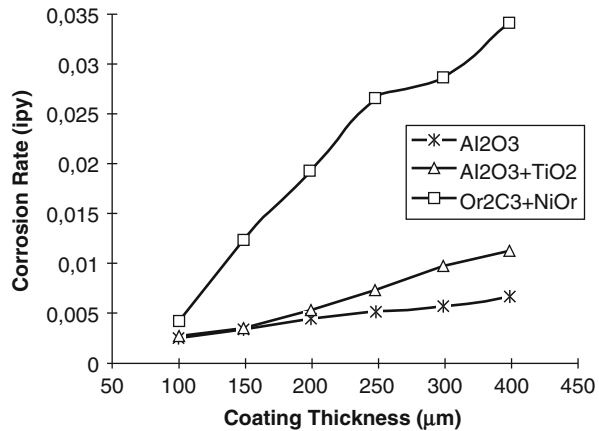


Fig. 4 Corrosion rate of plasma sprayed ceramic and cermet coatings in 1N H_2SO_4 solution as a function of coating thickness [27]



section. Yet, another alumina-based composite coating although less studied was Al_2O_3 - ZrO_2 system [18]. The microhardness of these coatings deposited through HVOF spraying using hydrogen as a fuel gas is found to be around 718 HV, and the abrasion wear rate is found to be significantly superior to other composite coatings such as Cr_2O_3 -5 SiO_2 -3 TiO_2 and Cr_2O_3 -25 TiO_2 and pure TiO_2 coatings. In spite of the above interesting results obtained with Al_2O_3 - ZrO_2 system, not many studies were conducted yet in this direction, and therefore, the fundamental role of ZrO_2 when added to Al_2O_3 is not yet clearly understood.

The properties and performance of pure TiO_2 -based coatings were also of specific interest and investigated in detail [18, 19, 28]. From the processing point of view, titania is a very interesting material owing to its moderately lower melting point of 1855 °C. The TiO_2 coatings were employed for many years in anti-wear applications, namely, propeller shaft-bearing sleeve of boats and pump seals, where abrasive action of contacting surfaces is intense. Furthermore, since titania is known to be a bio-inert material, it is often mixed with hydroxyapatite in order to produce biomedical coatings with enhanced surface characteristics [28]. In addition, titania being a known material for its photocatalytic properties, thermally sprayed TiO_2 coatings were also employed for photocatalytic applications [29]. The TiO_2 -based coatings

are popularly deposited using APS, HVOF, and DSC techniques [18, 19, 29, 30]. The coatings typically exhibit a distinct lamellar structure and bimodal distribution of porosity, with coarse pores (3–10 μm) and finer (0.1 μm) interlamellar pores. As one can expect, the high particle velocities attained in HVOF and DSC processes tend to decrease the amount of coarse and interlamellar pores in the coating; the improved cohesive strength is paramount for producing abrasion-resistant ceramic coatings. The porosity content of plasma-sprayed TiO_2 coating is around 2%, and the microhardness is in the range of 720–850 HV, while the porosity and microhardness values of HVOF-deposited TiO_2 coatings are <1% and 780–830 HV, respectively.

In addition to the aforementioned oxide ceramics, chromium oxide (Cr_2O_3) is also one of the popularly used coating materials [20, 31, 32]. It is to be noted that the plasma spraying is more popularly employed for depositing chromia (Cr_2O_3) coatings. These coatings, being the hardest among the thermally sprayed ceramics, do not exhibit any visible lamellar structure, and in general, the porosity content is <2% as shown in Fig. 5a. A relatively larger feedstock size in the range of 20–45 μm results in higher coating microhardness (1760 HV), while a 5–20 μm size feedstock results in lower microhardness (1570) [31]. At the same time, the microhardness in excess of 1930 HV was also reported [33]. Due to such high hardness, these coatings do not exhibit any signs of plastic deformation-associated wear mechanisms such as microcutting and microplothing but undergo brittle fracture and inter-splat-assisted cracking during the wear tests. The overall abrasive wear performance of chromia coatings is much superior to all oxide ceramic coatings discussed so far and is in good comparison with that of sintered bulk alumina. However, the Cr_2O_3 coatings are exclusively deposited by atmospheric plasma spray (APS), whereas the Al_2O_3 , TiO_2 , and the composite of these two coatings are produced by APS and DSC techniques. The cross-sectional Cr_2O_3 -25 wt.% Al_2O_3 coating deposited by detonation spray technique is shown in Fig. 5b with alternative layer of Cr_2O_3 and Al_2O_3 with good inter-splat bonding and dense coating with better wear and corrosion properties compared to plasma-sprayed Cr_2O_3 coating showing inter-splat regions

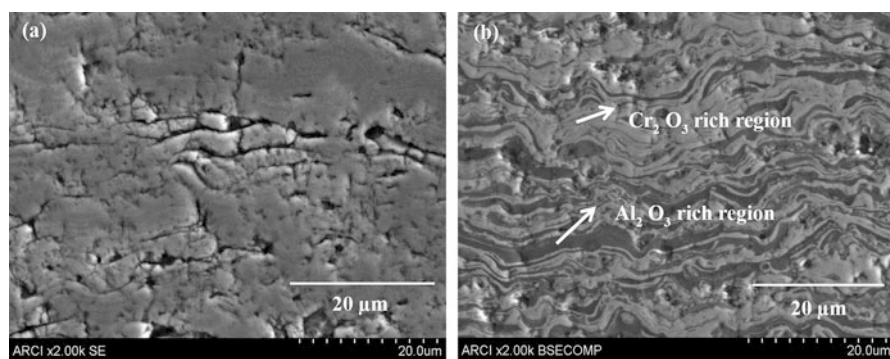


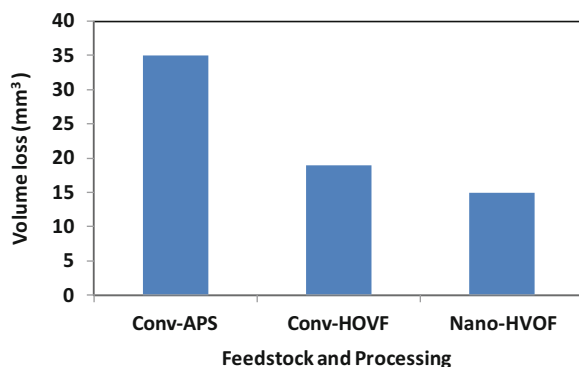
Fig. 5 Cross-sectional SEM images of (a) plasma sprayed Cr_2O_3 coating and (b) detonation sprayed Cr_2O_3 - Al_2O_3 coating [34]

and cracks [34]. In the view of the above, the Cr_2O_3 and plasma spray are generally treated as synonymous to each other.

As the industrial applicability and acceptance of thermal spray coatings gained popularity, a great deal of attention has been paid subsequently toward the development of oxide coatings using nanostructured feedstock and comparative evaluation of the conventional and nanostructured oxide coatings [19, 28, 35, 36]. The microstructure of HVOF-sprayed nanostructured coating illustrates the absence of typical lamellar structure and unmolten or semi-molten particles thus enhances the overall integrity of the coating. Further, HVOF-sprayed TiO_2 deposited from nanostructured feedstock exhibited superior abrasion resistance and crack propagation resistance when compared to coating deposited by APS using conventional feedstock [36]. The better crack resistance property in the nanostructured ceramic coatings is due to randomly dispersed nano-zones embedded well within the coating microstructure [36]. Due to the presence of such nano-zones, the residual stresses turnout to be more compressive than the conventional titania coatings. Upon indentation on the coating cross section, the plasma-sprayed conventional titania coatings exhibit a completely different behavior as compared to the HVOF-deposited nanostructured titania coatings. In the former case, two dominant cracks parallel to the substrate surface emanate from the corners of the indentation, while in the latter case, besides being shorter, four cracks of approximately the same length emanating from the four corners of the indentation demonstrate that the HVOF-sprayed nanostructured titania coating is more isotropic and therefore offers superior crack propagation resistance than the conventional plasma-sprayed titania coatings. As a result of this, the nanostructured titania coatings deposited by HVOF technique exhibits significantly lower volume loss than the conventional titania powder deposited by HVOF as depicted in Fig. 6 [36].

Similarly, the nanostructured TiO_2 coatings deposited by HVOF were compared with that of plasma-sprayed conventional Al_2O_3 -13 TiO_2 coatings [35]. The outcome suggests that the plasma-sprayed conventional alumina-titania coating is 33% harder than the HVOF-sprayed nanostructured titania. However, such a higher hardness does not translate into better tribological performance. Therefore, the general argument that the nanostructured materials are harder than the conventional ones cannot

Fig. 6 Abrasive wear loss of coatings obtained from conventional and nanostructured TiO_2 coating by HVOF and APS [36]



be rationalized to explain the less hardness but higher abrasion resistance as demonstrated by the HVOF-sprayed nano-TiO₂ coatings. The HVOF-sprayed nanostructured titania exhibits higher toughness due to twice the crack propagation resistance than that of the air plasma-sprayed conventional alumina-titania coating. The nano-zones in the nanostructured coating act as crack arresters and enhance the toughness and wear resistance. Accordingly, the wear scar of the HVOF-sprayed nanostructured titania is very smooth, indicating plastic deformation-assisted features, whereas the rough and fractured wear scar of the air plasma-sprayed alumina-titania coating indicates the brittle failure as the predominant wear mechanism rationalized the hardness-toughness-wear resistance relationships in the conventional and nanostructured coatings. The machinability can be improved by depositing ceramic coatings with nanostructured feedstock.

Cermet Coatings

As mentioned before, the thermally sprayed cermet coatings have emerged as a viable solution for a wide range of wear resistance applications to improve the service life of various industrial components. Tungsten carbide- and chromium carbide-based coatings are frequently used for many of the applications in gas turbine, steam turbine, and aeroengine to improve the resistance to sliding and abrasive and erosive wear mostly up to 450 °C and 750 °C, respectively [37]. Also, for the tribological performance under the aforementioned wear modes, the carbide coatings are considered to be a viable alternative to hard chrome plating due to the strict environmental regulations and associated cost concerns with regard to the electroplating process [38–40]. Although the cermet coatings are deposited by many variants of thermal spray processes, the high-velocity oxy-fuel (HVOF) and detonation gun spray (DSC) are most commonly employed for depositing these coatings to avoid the reduction of carbides to brittle carbides and oxy-carbides [15, 41]. Such undesired decomposition is controlled by employing much lower temperature of the powder particles in the exhaust gas stream and less in-flight time as compared to that in APS. Therefore, the higher particle velocities in the high-velocity processes (HVOF, DSC) contributes to the improved bond strength, density, and reduced oxide content in the coatings.

The WC phase decomposes when the WC-Co particles are exposed to higher thermal energy in the deposition process. The microstructure of initial feedstock and detonation-sprayed WC-Co coatings as a function of oxy-fuel (OF) ratio clearly illustrate that the WC decomposition increases with increasing of OF ratio as shown in Fig. 7. Accordingly, the coating deposited at 1.16 microstructure is very similar to the initial feedstock with less than 3% decarburization. In contrast, the decarburization increases up to 30% when the OF ratio is increased to 2.0. Further, the presence of other carbon-deficient phases such as W₂C, W, Co₆W₆C, and quantum of amorphous matrix also increased with increasing in OF ratio. Such phase changes in the WC-Co coating appear to have a direct influence on the coating properties. Interestingly, the mixed Co matrix phases significantly reduce the wear resistance

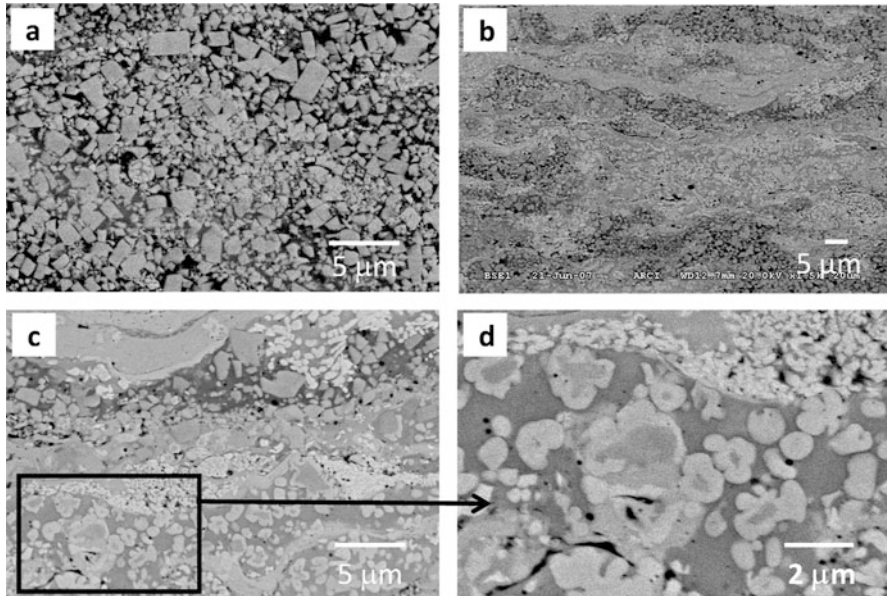


Fig. 7 SEM images in BSE mode of WC-12Co coating cross-sections deposited at (a) 1.16 oxy/fuel ratio, (b) 2.0 oxy/fuel ratio, and (c, d) are higher magnification images of (b) depicting W_2C rim and W dendrites [15]

however improve the corrosion resistance of WC-Co coatings. In view of such a contrasting observation, the process conditions need to be chosen wisely to produce the coatings with moderate particle melting and good inter-splat bonding for achieving better combination of wear and corrosion resistances [42, 43].

There exists a large variety of coatings belonging to the family of cermets, namely, WC-Co, WC-Co-Cr, WC-VC-Co, Cr_3C_2 -NiCr, TiC, TiC-Ni, TiB_2 , Ni(Cr)- TiB_2 , and FeCr-TiC. Among the aforementioned coatings, the WC- and Cr_3C_2 -based coatings containing different binder phases such as Co, Cr in WC-based, and NiCr in Cr_3C_2 -based coatings occupy the lion's share of research interest due to their well-established applications in a large variety of industrial applications demanding higher wear resistance and thermal stability at moderately higher temperature regimes. The WC-Co coatings without the addition of any other elements/compounds itself is of major interest for a long time. As mentioned before, although the high-velocity processes are preferably employed for depositing these coatings, there exist few earlier studies (1998–2000) utilizing the plasma spray processes as well [44, 45]. It is important to mention that the interlamellar cohesion is the most critical parameter for achieving the best possible abrasion resistance.

It was a well-established fact that most WC-based coatings employ either Co, Cr, or Ni as the binder phases because of their good wettability with WC grains. Therefore, yet another subclass of WC-based coatings investigated so far is the addition of element like Cr or hard compounds like VC to the WC-Co system.

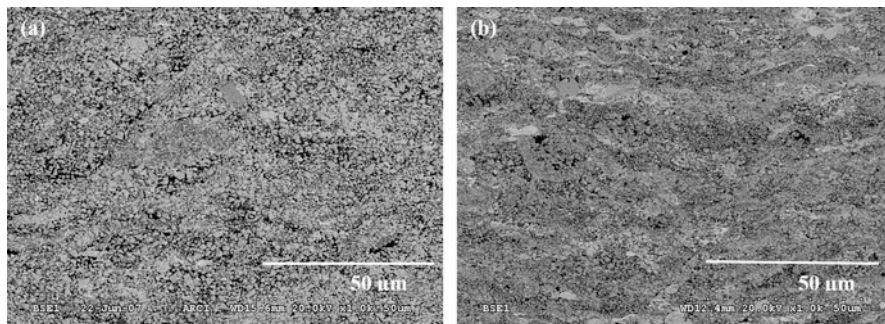


Fig. 8 SEM images of (a) conventional and (b) nano-WC-Co coating cross-sections deposited at 1.30 oxy/fuel ratio by detonation spray technique

In general, in applications where abrasive wear is of primary importance, the WC-Co powder with 12 or 17 wt. % Co is popularly used, whereas WC-(6-10)Co-(4-8)Cr powder is preferred when the combination of corrosion resistance is also demanded. Accordingly, the detailed investigations pertaining to the influence of spray parameters on temperature and velocity of particle-in-flight, resulting from coating properties [46] and the wear performance of WC-Co-Cr coatings in comparison with the WC-Co coatings [17, 47], illustrate that the overall hardness, wear resistance, and microstructure of WC-Co-Cr coatings are comparable to WC-Co coatings, while the corrosion resistance of WC-Co-Cr is considerably higher. A complete replacement of Co with other matrix metals like Ni- and Fe-based matrix as well as addition of CrC, Cr, and Ni to WC cermets exhibits better combination of wear and corrosion resistances [48, 49]. There has been emphasis to replace Co not only because it is expensive but also because of its limited availability.

Similar to the case of oxide coatings, the nanostructured WC-Co-based coatings deposited by HVOF and DSC were evaluated for comparative properties and performance against conventional WC-Co coatings [41, 50]. The greater degree of decomposition experienced by the nanocomposite powder particles during spraying thus results in a larger elemental tungsten concentration in the amorphous binder phase than the case of conventional coatings. This difference can be qualitatively observed from Fig. 8 wherein the bright binder phase is much more evident in the nanocomposite. However, it can be expected that proper optimization of spray parameters could reduce nanocomposite degradation, increased coating hardness, and wear resistance than the conventional coatings [50]. The excessive particle temperatures causing extensive decarburization forms brittle phases, reduces the ductility, and increases wear rate due to localized microfractures which needs to be paid special attention during optimization of spray parameters to leverage the basic advantages of very fine microstructures produced by nanostructured WC-Co cermet coatings [51].

Another important class of cermet coatings that have been well studied and employed for a variety of industrial applications after WC-Co coatings are the $\text{Cr}_x\text{C}_y\text{-NiCr}$ cermet coatings generally employed for imparting wear resistance in

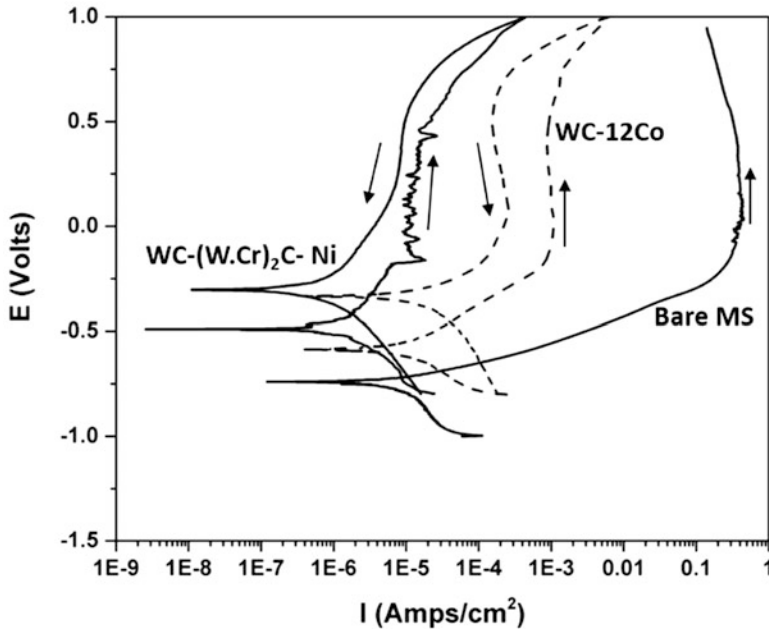


Fig. 9 Potentiodynamic polarization curves of detonation sprayed WC-Co and WC-(W,Cr)₂C-Ni coatings in 3.5 wt.% NaCl solution [52]

high-temperature environments. Excellent corrosion and oxidation resistance of nickel chromium alloy coupled with moderately good wear resistance of chromium carbide at temperatures up to 750 °C drive this class of cermet coatings for high-temperature applications. Nevertheless, Cr_xC_y-NiCr cermet coatings are also being employed for low-temperature corrosive service conditions. Similar to the WC decomposition during WC-Co coating deposition, CrC also decomposes during the coating deposition as well. Further, the combination of WC-(W, Cr)₂C-Ni coating showed better corrosion properties without change in wear properties (Fig. 9) [52].

The traditional coating such as hard chrome plating is popular and being used over the past few decades for wear and corrosion resistance applications. Owing to its eco-friendly nature and capability of depositing diverse feedstock including metals, alloys, ceramics, and cermets, thermally sprayed coatings are now being extensively used in various applications as a safe and viable replacement to hard chrome plating. In the aerospace sector, the coatings deposited on landing gear components undergo diverse damage mechanisms such as wear, corrosion and fatigue (cyclic loading), or the combination [53–55]. In general, hard chrome plating clearly demonstrates notable debit in fatigue life. However, the fatigue performance further degrades with the accelerated hard chrome plating process due to increased crack density and irregularities within the coating. Furthermore, the fatigue life drastically decreases with the increasing coating thicknesses due to the fact that

the crack propagation within the coating and across the coating-substrate interface is quick enough to impart such a debit in overall fatigue life.

The WC- and Cr_3C_2 -based cermet coatings were widely deposited on ferrous and nonferrous alloys through HVOF and DSC techniques. Accordingly, the fatigue behavior of WC-based cermet coatings was extensively studied under different cyclic loading modes such as rotating bending and axial and uniaxial tension-compression loads [54–65]. In order to realize the WC-based cermet coatings superiority, fatigue property was compared with the conventional hard chrome coatings along with wear and corrosion performances. Accordingly, the WC-Co coating demonstrates a fatigue debit of $\sim 13.6\%$ under rotating bending load ($R = -1$) and 11.7% under axial load ($R = 0.1$) when compared with the uncoated substrate. The amount of fatigue debit for hard chrome coatings (having $160\ \mu\text{m}$ thickness) is $\sim 48\%$ under rotating bending load and $\sim 53\%$ under axial load which clearly exhibits the advantage of thermal spray coatings [54]. In addition to this, a $20\text{-}\mu\text{m}$ -thick hard chrome coating also evidenced a fatigue debit of $9\text{--}14\%$ to its corresponding bare (uncoated) substrate indicating that the rate of fatigue life degradation accelerates with the increasing coating thickness itself [59]. Further, the WC-Ni, WC-CoCr, WC-CoCr/NiWCrSiFeB, and WC-CrC-Ni coatings having thickness in the range of $100\text{--}200\ \mu\text{m}$ as deposited on AISI 4340 steel substrate through HVOF technique also evidenced inferior fatigue life [55–57, 61]. However, the extent of fatigue life degradation is very less compared to the hard chrome coatings. The thermally sprayed WC-Co coatings typically experienced the delamination of the coating under the fatigue or cyclic loading.

Although, most of the thermal spray coatings demonstrated clear fatigue debit, while few other studies have reported enhancement in the fatigue life of coated substrate. The WC-Ni, WC-CoCr, and Cr_3C_2 -NiCr coatings as deposited on structural steels exhibited enhanced fatigue life, and the detailed residual stress measurements are in clear support of the reported fatigue life [58, 60, 62]. The substrate's surface condition, coating defects and irregularities, residual stress profiles within the coating and around the coating-substrate interface, and the underlying substrate are expected to play a significant role in overall fatigue performance.

The thermal and kinetic energies associated in the individual thermal spray processing technique are crucial in attaining the best combination of microstructural phases and process-induced residual stresses in the coating. The compositional changes, phase formation, decarburization, and oxidation of feedstock primarily depend up on the thermal energy of the process. The particle's kinetic energy is responsible for work hardening or peening effect which results in inducing compressive residual stresses. Generally, the compressive residual stresses are responsible in enhancing the fatigue life of the aerospace components by retarding the crack propagation. However, the magnitude of these compressive residual stresses is also important in accomplishing such a beneficial effect which in turn depends on the feedstock, substrate condition, temperature of the particle-in-flight, and coating deposition parameters. In the case of cermet coatings, higher binder matrix would be advantageous in imparting high compressive residual stresses. Sometimes, the oxidation or decarburization phenomenon while depositing the coating may result in

complex phase formation which is unfavorable as it can induce undesirable residual stresses. The induced compressive residual stresses as a result of impact of feedstock particles with high kinetic energy can be measured/quantified by in situ beam curvature during layer-by-layer coating deposition. Further, these residual stresses can be tailored to a desired magnitude by analyzing in situ beam curvature and altering the depositing conditions accordingly [60, 63]. Furthermore, WC-Co-Cr coatings deposited on 6XXX and 7XXX Al alloys also evidenced moderate enhancement in fatigue life as compared to corresponding bare substrate. However, higher fatigue life about 3–10 times was noticed for as coated condition in 3 wt. % NaCl corrosion medium indicates widespread usage of coated components in diverse application sectors [64, 65].

To conclude, although the efforts laid so far toward investigating the efficacy of thermal spray cermet coatings are marginally significant, a systematic, well-focused research aimed at understanding the comprehensive tribological performance of a handful set of coatings is still absent, and it is essential if the replacement of hard chrome coatings through thermal spray techniques is to be realized in a full-fledged manner. The research in this direction is also useful to not only the technical standpoint but also assists in safeguarding the environment by putting hold on some conventional non-eco-friendly electrolytic techniques. Further, the development of Ni-, Co-, and Fe-based matrix for WC-based cermets is very essential to replace the Co as well as to use these coating for better wear as well as corrosion resistance application up to moderate temperatures.

Applications of Thermal Spray Coatings

Thermally sprayed ceramic and cermet coatings are often used to resist severe wear in diverse industrial applications like aerospace, strategic, and power generation. In fact, aerospace industry is the first industry to completely accept the thermal spray coatings [66]. Several components in aerospace engine like turbine blades, flame tube seals, and liners are coated with different materials by thermal spray techniques to enhance the part life and their performance.

Oxide coatings are most widely used for corrosion and wear resistance required in marine components. The Al_2O_3 , $\text{Al}_2\text{O}_3\text{-TiO}_2$, and TiO_2 coatings are deposited on vanes and roller in turbines, main shafts, and ball valves in ships. Accordingly, Al_2O_3 coatings deposited on various parts in turbine are shown in Fig. 10. Submarine seals are coated with Cr_2O_3 coatings to increase corrosion resistance and reduce the friction between moving and stationary parts. A $\text{Cr}_2\text{O}_3\text{-Al}_2\text{O}_3$ coating deposited on submarine seal by detonation spray technique is shown in Fig. 11 (b). Further, the nanostructured $\text{Al}_2\text{O}_3\text{-13 wt. % TiO}_2$ coatings deposited by plasma spray techniques exhibit superior properties like two times wear resistance and improved bond strength. Toward capitalizing such properties, the marine counter ship's main shafts are coated with $\text{Al}_2\text{O}_3\text{-13% TiO}_2$, while the worn-out main shaft coated with nano- $\text{Al}_2\text{O}_3\text{-13 wt. % TiO}_2$ is shown in Fig. 12. The shiny surface with no wear marks was noticed on the main shaft coated with nano- $\text{Al}_2\text{O}_3\text{-13 wt. % TiO}_2$ and after 7 years of



Fig. 10 Various turbine engine parts coated with Al_2O_3 coating

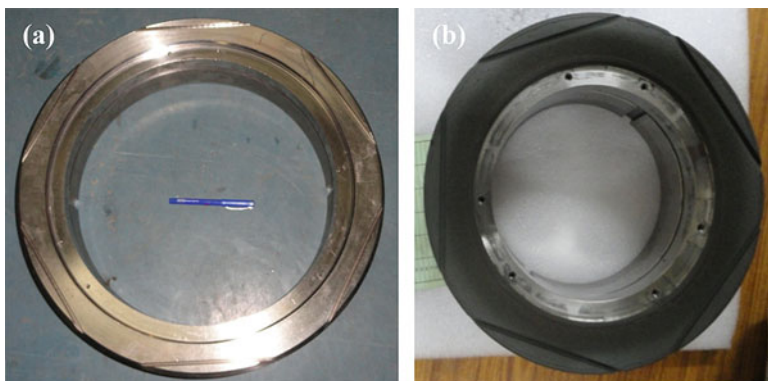


Fig. 11 Submarine shaft seal (a) uncoated and (b) coated with Cr_2O_3 -20% Al_2O_3 by detonation spray technique

its service (Fig. 12b). At present, all US counter marine ships have its shafts coated with nano- Al_2O_3 -13 wt. % TiO_2 [54]. Ball valves used in harsh corrosion environment are being coated with conventional Cr_2O_3 coating. Figure 13a shows a large part of the coating removed. However, the nano- TiO_2 -coated ball valve (Fig. 13b) performed better than Cr_2O_3 -coated ball valve when exposed to the same service conditions [67].

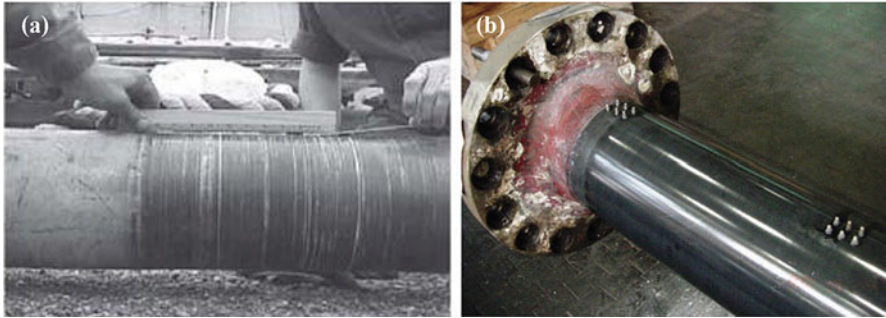


Fig. 12 Marine ship main shaft (a) worn out and (b) coated with nano- Al_2O_3 -13% TiO_2 by plasma after 7 year of service life [66]



Fig. 13 Ball valve (a) coated with Cr_2O_3 and (b) coated with nano- TiO_2 after exposure to identical service life [67]

Carbide coatings are used in a wide array of application ranging from aerospace and land-based turbine components, power plants, hydraulic valves, pump housings, boiler tubes, and also as substitutes for hard chrome coatings. Two families of carbides are commonly used in thermal spraying, namely, the chromium carbides and tungsten carbides. Cr_3C_2 -NiCr materials have good erosion wear properties up to 750°C in corrosive conditions. In comparison to Cr_3C_2 -NiCr coatings, WC-Co coatings have excellent wear and erosion resistance but are limited to a maximum service temperature of 450°C and preferably non-corrosive atmospheres. Addition of chromium is found to improve corrosion resistance of WC-based cermets. WC-Co coatings are well-accepted solution for airplane landing gear shaft for enhancing the wear resistance as a replacement to hard chrome plating (Fig. 14). As mentioned in the case of oxide coatings, cermet coatings are being deposited on several components of turbine for better erosion wear resistance. It is also to be noted that the thermal spray techniques are often used as a refurbishment tool for enhancing the service life in a cost-effective

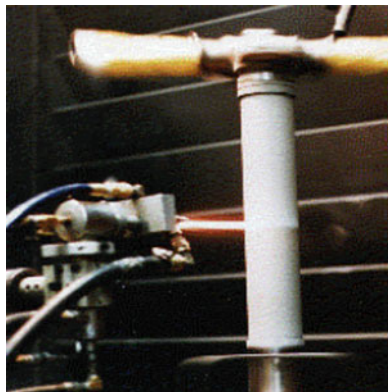


Fig. 14 Bruce D. Sartwell et al. NRL, DC, Aircraft landing gear (Boeing 737) during deposition of WC-Co coating by HVOF technique (<https://pdfs.semanticscholar.org/0b94/84e5171db79a84d22917deb464ce278449c1.pdf>)

manner. Accordingly, the worn region of LP III blade (snubber abutment face) refurbished with WC-Co coating by detonation spray technique is shown in Fig. 15. Further, Cr_3C_2 -NiCr coatings that have been used in many aero and marine components where wear and corrosion resistance are very important. In this direction, the naval submarine pump part coated with Cr_3C_2 -NiCr coating by DSC is shown in Fig. 16. It is to be noted that the applications exemplified in this section are only the part of marine and aerospace applications in line with the theme of this book and the applications in other sectors such as automotive, power, and pulp and paper have not been considered within the scope of this chapter.

Ceramic Composite Coatings Through Micro-arc Oxidation Coating Technology on Al Alloys

Micro-arc oxidation (MAO), also popularly known as plasma electrolytic oxidation (PEO), is a process of converting the surface of valve metals such as Al, Ti, Mg, Ta, Zr, and their alloys into their respective oxide coatings [68–71]. The process has recently gained global R&D momentum in recognition as it employs eco-friendly alkaline electrolyte medium and provides ceramic composite coatings that are significantly thicker, harder, stronger, and wear and corrosion resistant than the conventional processes such as anodizing, hard anodizing, and hard chrome plating [72–75]. The base electrolyte in the MAO process is generally selected from the group of silicates, hydroxides, aluminates, and phosphates of different metals added to the deionized water. In addition, the flexibility to employ either soluble or insoluble additives to the base electrolyte provides an additional advantage of tailoring the coating composition which enables creation of a spectrum of composite

Fig. 15 Refurbished helicopter's LP III blade at snubber abutment part by WC-Co coating using detonation spray technique



Fig. 16 Naval submarine pump shaft coated with wear and corrosion resistance Cr_3C_2 -25NiCr by detonation spray technique

coatings for diverse industrial applications including the aerospace sector, attracting a great deal of attention in the recent times. Although many metals and their alloys as listed before are amenable for MAO processing, only surface-modified Al alloys through MAO process were only considered within the scope of this chapter. However, since the MAO process is relatively new in the context of surface engineering of nonferrous materials, the basic description of the process, associated equipment, advantages and limitations, and mechanism of coating formation that are mostly common for MAO treatment of any amenable material have been included in

this chapter. In addition, the phase formation and associated mechanisms, mechanical properties, and performance of the coatings under diverse damage mechanisms such as wear, friction, corrosion, and fatigue as specific to MAO-treated Al alloys along with the opportunities, challenges, and future R&D directions have been included within the scope of this chapter so as to provide a comprehensive understanding that paves the path for realizing potential applications in aerospace industry.

The MAO Process and Technological Elements

The three basic elements of MAO processing equipment are (a) electrical power control system, (b) reaction chamber, and (c) heat exchanger. Out of the aforementioned three systems, the key for the entire technology is the power control system which is responsible for maintaining the current-voltage (I-V) characteristics suitable for coating formation as shown in Fig. 17. The power controllers are designed to function with simple direct current (DC), pulsed DC, simple alternating current (AC), or bipolar AC power [76–79]. Of all these power modes, owing to their ability to deposit dense and adherent coatings, the bipolar AC power controllers have gained significant interest. The manner in which the conventional sinusoidal AC

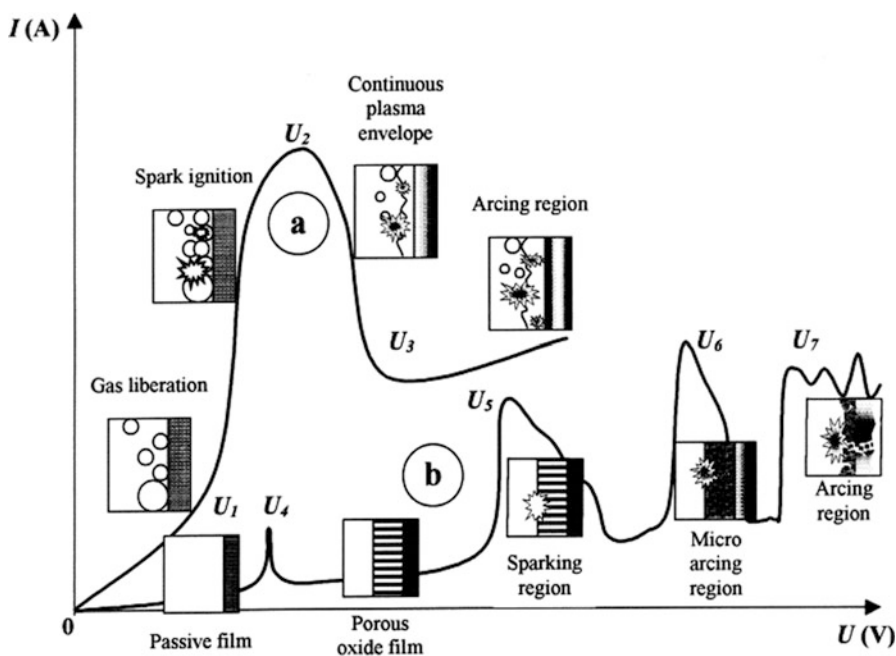


Fig. 17 Current-voltage (I-V) characteristics for the plasma electrolysis processes [68]

wave forms are managed leading to the sharp pulses that result in uniform, hard, and adherent coatings with impressive portfolio of mechanical, tribological, and corrosion-resistant properties is discussed elsewhere [79].

Since the MAO process employs higher voltages and current densities than the traditional electrolytic processes, the reaction chamber in which the surface gets oxidized during the process is typically designed with non-conductive materials such as acrylic or polypropylene (PP). However, in the case of large reaction chambers, owing to the limited mechanical load-bearing capacity of acrylic and PP, the steel chambers insulated with fiber-reinforced plastic (FRP) are utilized. The components to be coated are immersed in the electrolyte medium through specially designed jigs and fixtures. Owing to the plasma-driven oxidation reactions as discussed in the mechanism of coating formation in this chapter, the thermal energy released from the components being coated into the surrounding electrolyte is significantly high and therefore needs a heat exchanging system.

In the small-scale MAO processing equipment, the heat exchanger is designed in the form of a water jacket around the heat exchanger wherein the ice is constantly added into the water jacket to avoid overheating of electrolyte. The overheating of electrolyte is unwanted as it adversely affects the coating formation rate and increases the isothermal evaporation rates of the electrolyte. To some extent, the localized heating and bubble formation on the coating surface are avoided by means of providing a mechanical stirrer or a magnetic stirrer in the electrolytic medium. However, as is the case with the design of moderate (20–75 kW) to large-scale (75–500 kW) MAO processing equipment, the best method to maintain a uniform electrolyte temperature all through the oxidation process is to have a continuous circulation of electrolyte through an external heat exchanger (shell and tube). The hot electrolyte from the reaction chamber is passed through the heat exchanger, and the cooled electrolyte is fed into a separate reservoir which in turn keeps feeding the electrolyte medium into the reaction chamber at a fixed temperature and flow rate through the aid of a pump. Unlike the conventional anodizing process, the MAO process does not require the electrolyte temperature to be maintained at sub-zero limits. Instead, the electrolyte temperature is in general maintained at room temperature (25 °C) throughout the MAO process. The electrolyte flow rate is controlled through a variable flow drive connected to the pump such that the flow rate can be increased with increasing surface area of the components being coated in the reaction chamber for effective heat transfer. Such an equipment architecture ensures maintaining the constant electrolyte temperature irrespective of the size and surface area of the component. Further, the continuous circulation of electrolyte helps preventing any gaseous envelope formation around the components being coated and also helps maintaining uniform temperature and chemistry of the electrolyte. The typical schematic of MAO process and the corresponding equipment in operation are shown in Figs. 18 and 19, respectively.

Fig. 18 Schematic of micro arc oxidation process with Al being coated through specially regulated AC power supply and an external heat exchanger to maintain the electrolyte temperature constant throughout the coating deposition

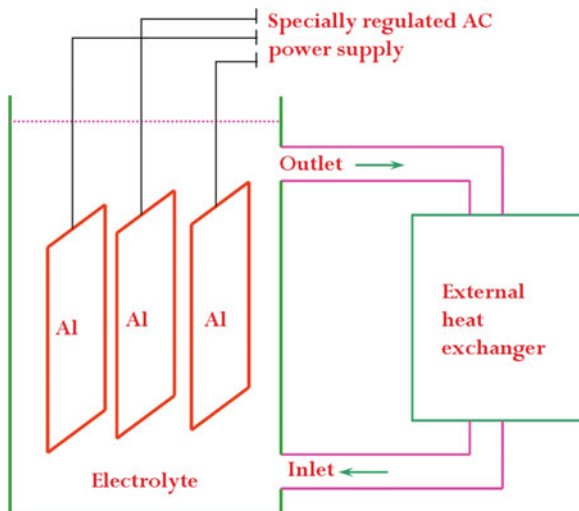


Fig. 19 Micro Arc Oxidation (MAO) lab scale equipment in operation illustrating control panel and reaction chamber (inset image) in which the component being treated exhibit illumination due to plasma discharges



Mechanism of MAO Coating Formation

The formation of MAO coating on Al alloys is quite unique and very interesting owing to the fact that the coatings formed are crystalline unlike the amorphous

phase formation in anodizing process. It is very clear from the vast literature available that the mechanism of coating formation in anodizing process is largely controlled by diffusion of Al^{3+} ions from the substrate through the barrier layer leading to the formation of alumina at the substrate-coating interface itself, and therefore the coating grows from beneath [80]. Accordingly, the typical hexagonal array of pores that are formed during the initial stages continues to be the source of electrolyte reservoir and supplies oxygen ions throughout the process to form alumina. This is the reason why if once the pores become inactive due to either the intermittent power failure or if the component is taken out of the bath, the coating formation cannot continue further. The only way to increase the coating thickness further is by means of stripping the entire preexisting coating and allowing the fresh anodic coating formation. It is to be noted that the anodic oxide layer formed is by way of concurrent consumption of substrate material, and therefore the repeated stripping and re-coating would eventually change the component dimensions.

On the contrary, MAO coating formation is driven by electrothermal and electrochemical reactions driven by the intense electrical discharges throughout the process [81–83]. The thin insulating layer formed during the initial anodic oxidation acts as building block for the subsequent coating formation. Owing to the electrical insulation offered by the initial oxide layer, the controlled electrical discharges drive the formation of plasma column into which Al ions from the substrate and anionic components including oxygen ions are drawn and promote the formation of alumina. The plasma generated in the breakdown channel is of high temperature, and the high-pressure column which melts the aluminum oxide and ejects the molten product out of the channel resembles a miniaturized volcanic eruption as schematically illustrated in Fig. 20. The pulsed power supply creates the strong electric fields around the component being coated, and therefore the molten aluminum oxide is spread on the coating surface in the form of typical pancakes. The ejected molten oxide undergoes rapid solidification on the coating surface by the quenching action of surrounding electrolyte medium. The thinner pancakes with relatively large spread as shown in Fig. 21 are the key phenomenon behind the formation of denser coatings

Fig. 20 Schematic of MAO coating formation mechanism representing miniaturized volcanic eruption with molten reaction product flows out of the channel and solidifies on the top surface of the previously formed coating

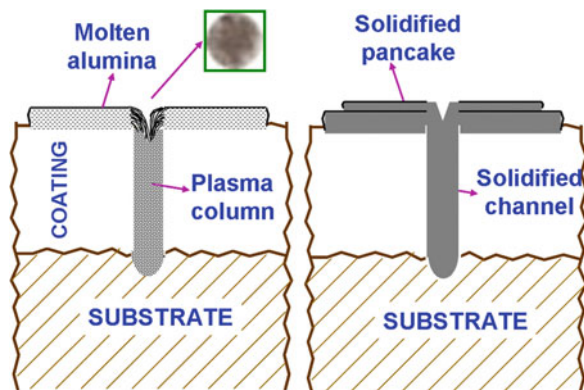
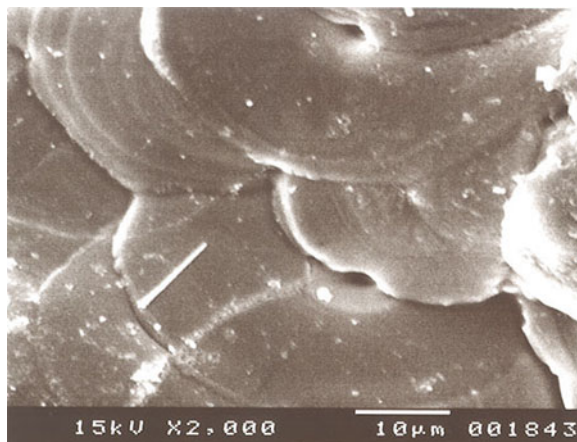


Fig. 21 Typical surface morphology of MAO coating demonstrating overlapping pancake like structures formed out of rapidly solidified alumina leading to the formation of thicker coatings [83]



[83]. On contrary, the parabolic pancakes lead to the formation of porous coatings. Depending upon the frequency of power supply, the typical life of discharge events is of the order of few milliseconds; toward the end of its life, the channel gets cooled; and the alumina also gets formed on the channel walls eventually leading to the closure of the channel. However, due to rapid quenching, the shrinkage cavities can be seen at the apex of the channel as it is the lastly solidified portion as shown in Fig. 21. In a nutshell, the overlapping pancakes of solidified alumina on the coating surface contribute to the overall increase in coating thickness. However, it shall be noted that the individual pancake boundaries will not sustain its identity as the subsequent breakdown channel formation in its vicinity causing melting, resolidification, refining, and phase transformations as the subsequent coating built up continues. In view of this mechanism, it is now clear that the new coating deposition is always on the top of the previously formed coating unlike the coating formation mechanism of anodizing discussed before.

What is even more interesting is the phase formation under the action of plasma discharges in the case of MAO treatment of Al alloys. The rapid solidification of pancakes promotes the formation of $\gamma\text{-Al}_2\text{O}_3$ phase due to the favorable thermodynamic conditions. The large portion of the thermal energy generated within the plasma discharge although gets dissipated through the molten reaction products being ejected out of it, the higher energy density is adequate for simultaneous heating of the surrounding coating and drives the $\gamma\text{-Al}_2\text{O}_3 \rightarrow \alpha\text{-Al}_2\text{O}_3$ phase transformation [83]. Accordingly, each discharge channel not only contributes to the increased coating thickness but also contributes to the $\gamma \rightarrow \alpha$ phase transformation around its vicinity; therefore the thicker coatings are expected to have more $\alpha\text{-Al}_2\text{O}_3$ phase proportion within the bulk of the coating than a thinner coating. The cubic $\gamma\text{-Al}_2\text{O}_3$ phase is relatively less harder (800–900 HV), while the $\alpha\text{-Al}_2\text{O}_3$ phase is the hardest (2100–2200 HV) and imparts the load-bearing capacity under tribological situations [23]. The typical distribution of $\gamma\text{-Al}_2\text{O}_3$ and $\alpha\text{-Al}_2\text{O}_3$ phases within the coating wherein

Fig. 22 Continuously decreasing microhardness with increasing distance from the substrate-coating interface (towards the surface) confirms the functional gradient nature of the coating [83]

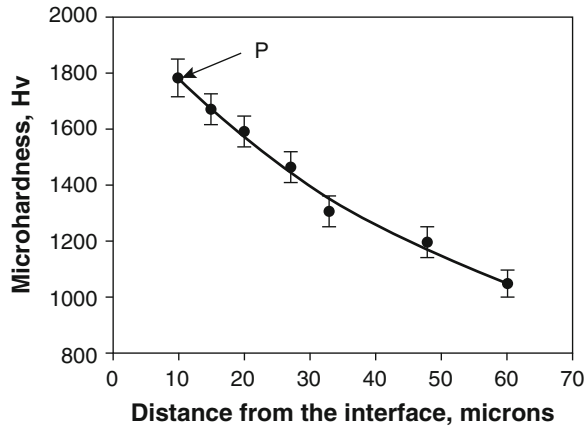
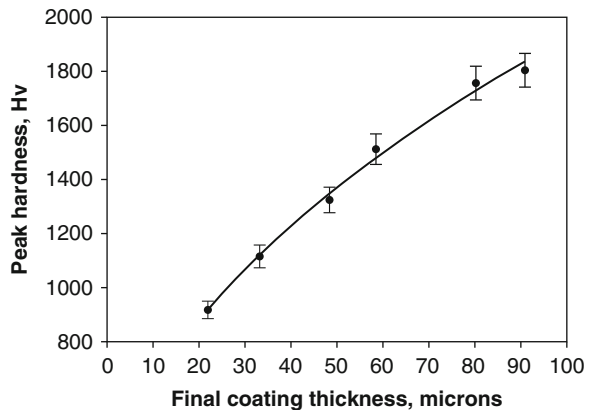


Fig. 23 Peak hardness (hardness at a distance of 10 μm from the substrate-coating interface) of MAO coating as a function of final coating thickness [83]



the relative proportion of cubic $\gamma\text{-Al}_2\text{O}_3$ phase is dominant on the coating surface and the hexagonal (or rhombohedral) $\alpha\text{-Al}_2\text{O}_3$ phase proportion is dominant at the substrate-coating interface offers a hardness gradient across its coating thickness as shown in Fig. 22. As a logical extension to this phenomenon, it is now understandable that the peak hardness, defined as the hardness close to the substrate-coating interface, changes with the final coating thickness as shown in Fig. 23 [83].

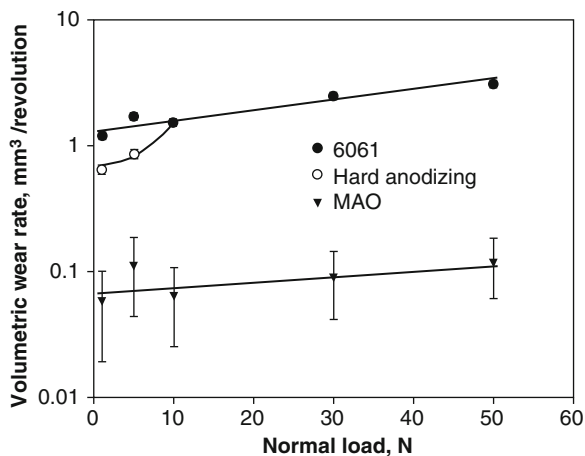
In view of the aforementioned radically different mechanism of MAO coating formation, the resultant coating sets a perfect example for a gradient composite coating with varying mechanical properties across its thickness. Therefore, the MAO process can be readily visualized as an elegant tool in the hands of a materials design scientist wherein the surfaces with different properties can be created by simply altering the coating thickness itself. Furthermore, as mentioned before, soluble and non-soluble additives can be added to the base electrolyte such that the additives would become the part of coating and therefore new functional features can also be

added to the coatings [84–90]. In view of these radical combination of coating formation mechanism, accompanied dense microstructure, and mechanical properties, these coatings offer enhanced protection against numerous material degradation mechanisms such as wear, friction, corrosion, thermal, electrical, and fatigue damages. Such portfolio of properties has led to the demonstration of numerous industrial applications encompassing textile, automotive, petrochemical, wire-drawing, energy, electronics, mobile communications, pharmaceuticals, and aerospace sectors. In addition, the industrial components usually made of steel, for combating severe wear, corrosion, and fatigue damage, are now being replaced with the MAO-coated Al alloys for capitalizing the potential weight saving especially in automotive and aerospace sectors as separately discussed in the following sections.

Tribological Performance

For any new technology to evolve and become industrially relevant, the technological output needs to be critically compared with the competing materials and processes that were already used by the industry. Accordingly, the MAO coatings were compared with the well-established hard anodized (HA) coatings. The MAO and hard anodized coatings of identical thickness ($50 \mu\text{m} \pm 2 \mu\text{m}$) and surface roughness were deposited on 6061-T6 Al alloy used for a variety of structural applications including aerospace sector [72, 75, 91]. The coatings were subjected to abrasive wear tests as a function of normal load and erosive wear tests as a function of erodent velocity and angle of impingement. The results clearly indicate that the MAO coatings being 3–4 times harder than HA offer increased abrasive wear resistance by a factor of 12 at severe wear conditions as compared to HA and 30 times lower wear rate than the uncoated substrate. As clearly seen from Fig. 24, at higher normal loads, the rate of material removal is very high in the case of HA coatings leading to complete coating removal,

Fig. 24 Three-body abrasive wear performance of MAO coated 6061-T6 Al alloy as a function of applied load in comparison with hard anodizing coating and corresponding bare substrate [72]



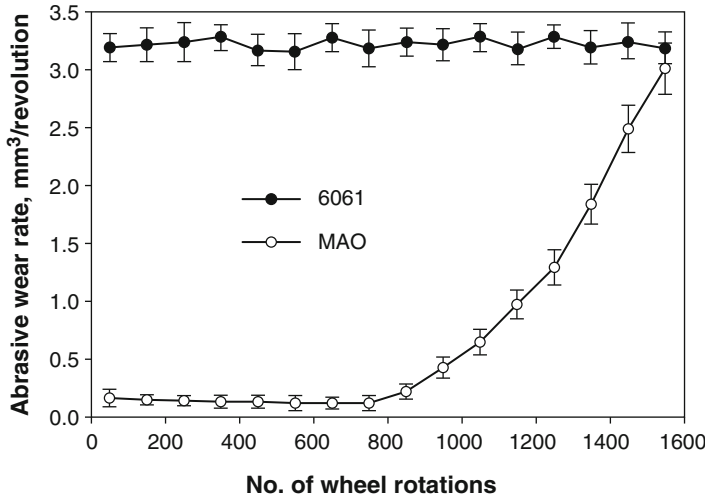
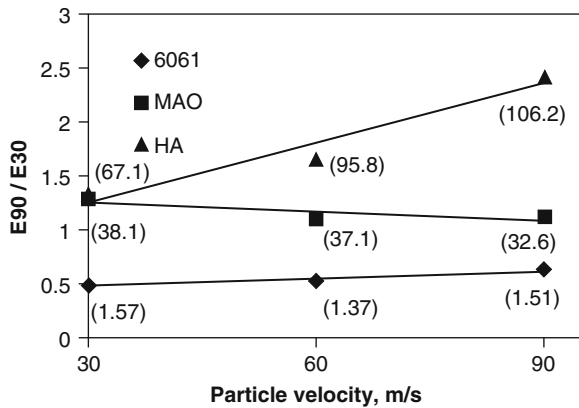


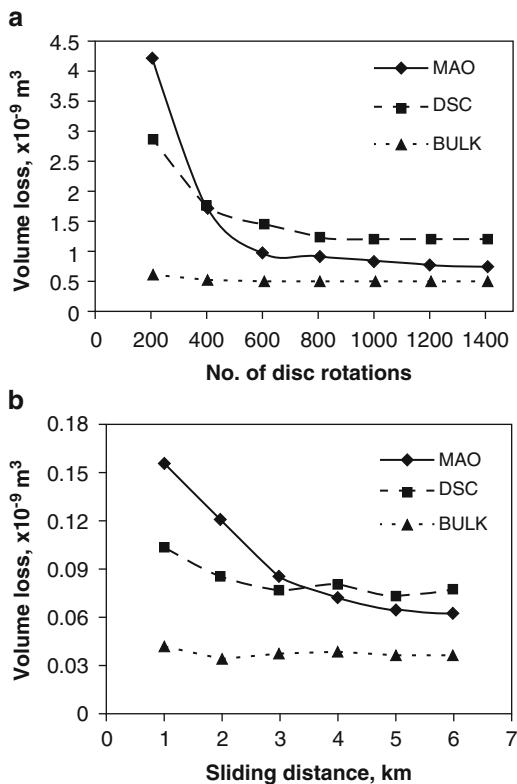
Fig. 25 Abrasive wear behavior of MAO coated 6061-T6 Al alloy as a function of abrasive wheel rotation at 50 N normal load [72]

Fig. 26 Erosive wear performance of MAO, hard anodized coatings in comparison with 6061-T6 Al alloy. The values provided in braces corresponds to the respective erosion efficiency at the given particle velocity for each material [72]



and thereafter the wear rate is equal to that of the parent substrate, while the MAO coating continues to exhibit identically lower material removal rate as the wear progresses. It is also clear from Fig. 25 that the MAO coating has superior load-bearing capacity as it exhibits the first substrate appearance only after 800 abrasive wheel rotations, while coating removal is gradual thereafter and becomes equal to the parent substrate only after another 800 wheel rotations (complete coating removal after a total of 1600 rotations), indicating that the coating is not only abrasion resistant but also the substrate-coating adhesion is extremely good. Furthermore, the ratio of erosion rate at normal and oblique impact angles (E_{90}/E_{30}) is close to unity for the MAO coating than the HA coating with more than unity with increasing erodent particle velocities as shown in Fig. 26 clearly indicating the better erosion performance of former coating than the latter [72].

Fig. 27 Wear behavior of MAO, DSC coatings and bulk Al_2O_3 under (a) three-body abrasion and (b) sliding wear modes [75]



Among the thermally sprayed coatings that are popular to deposit high-performance alumina coatings, the detonation spray coating (DSC) has been very popular. Therefore, the DSC alumina coatings were also comparatively evaluated against the MAO coatings deposited on 6061 Al alloy substrate. The abrasive, erosion, and sliding wear rates of MAO coatings tested under ASTM G65, ASTM G76-83, and ASTM G99, respectively, clearly highlight the fact that the tribological performance of MAO coatings is better than the detonation-sprayed alumina coatings and close to that of bulk alumina as shown in Fig. 27 [75, 91–93]. This particular behavior is attributed to the higher proportion of $\alpha\text{-Al}_2\text{O}_3$ phase in the MAO coatings than the detonation-sprayed coatings and also to the fact that the MAO coatings are metallurgically (strongly) bonded with the substrate whereas the thermally sprayed coatings are mechanically bonded. The phase gradient nature of the MAO coatings was found to be responsible for increasing hardness and modulus and concurrently decreasing wear rate by a factor of 10 as the probing volume moves from the surface to the near-interface regions across the coating thickness. Such an exceptionally better tribological performance under diverse wear modes has paved the path for realizing many industrial applications in aerospace and other sectors.

Yet another interesting feature of MAO process is its ability to treat almost all varieties of Al alloys including those difficult-to-anodize class Al-Si cast alloys. The

Fig. 28 Variation in MAO coating deposition rates with respect to different substrate (Al alloy) materials [94]

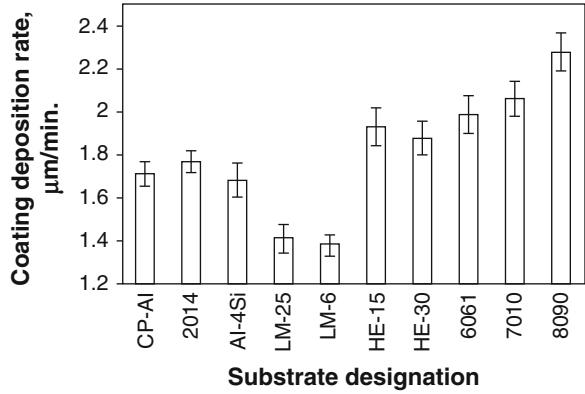
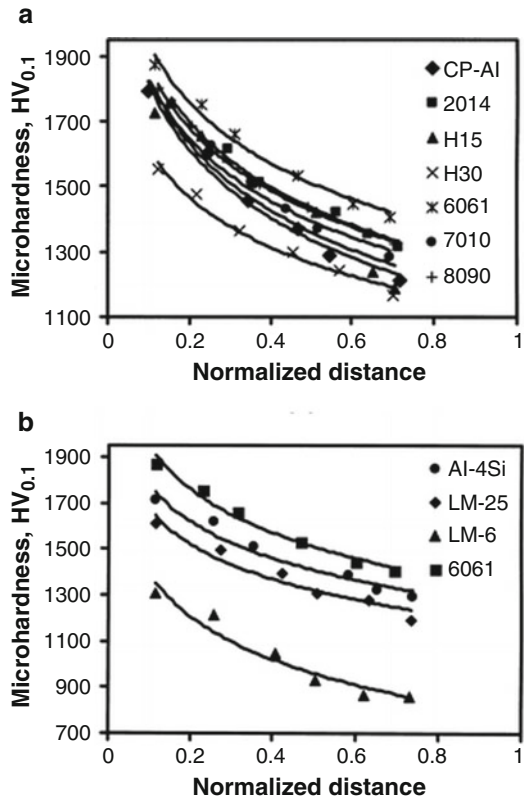
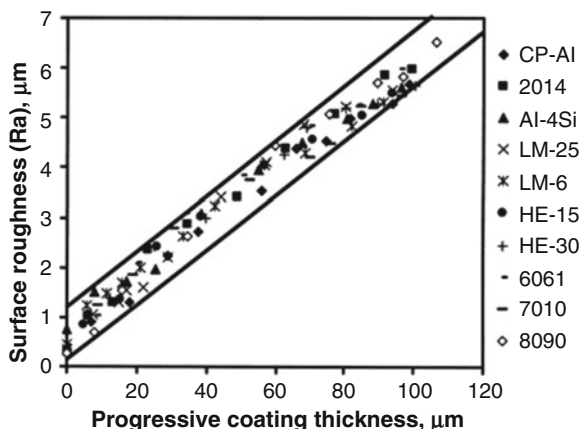


Fig. 29 Variation in microhardness of MAO coatings as a function of normalized distance from the substrate-coating interface for (a) Non-Si containing and (b) Si containing Al alloys [94]



coating deposition kinetics are a bit sluggish on high-silicon-containing Al alloys as shown in Fig. 28; microhardness decreases with increasing silicon content in the substrate alloy as shown in Fig. 29 as the increasing silicon promotes the formation of relatively softer aluminosilicate (mullite) phase [94]. However, mullite phase

Fig. 30 Surface roughness (R_a , μm) of MAO coating deposited on different aluminum alloy substrates as a function of progressive coating thickness [94]



formed on Al-Si alloys is found to be glossy and therefore reduces the coefficient of friction and concurrently reduces wear rate under sliding wear mode [94]. This observation can be utilized to design the low-friction (more mullite phase) coatings by adding more of silicate-bearing chemical constituent such as sodium metasilicate to the base electrolyte even in the case of non-silicon-containing Al alloys. While doing so, the increasing microscopic porosity in the coating with increasing mullite phase needs to be accounted properly.

Owing to the typical mechanism of coating formation as explained before, the surface roughness of deposited MAO coatings is always higher than the hard anodized and hard-chrome-plated substrates. One interesting feature that can be noticed is that the surface roughness of MAO coatings is a function of final coating thickness alone and is independent of alloy chemistry as can be readily seen from Fig. 30 [94]. Therefore, for the industrial applications needing smooth-surface finish, the MAO coatings are generally subjected to mechanical grinding or polishing so that the surface roughness can be brought down to a level as low as $0.1 \mu\text{m Ra}$.

Corrosion Performance

Apart from the wear resistance, many industrial components demand concurrent corrosion protection. Therefore, many researchers across the globe have reported numerous studies on the corrosion behavior of MAO coatings deposited on a wide variety of Al, Mg, Ti, Ta, and Zr metals and their alloys. The basic philosophy boils down to the fact that the MAO coatings offer substantially improved corrosion protection due to their barrier nature restricting the ingress of corrosion species [95–99]. Since the MAO coatings are dense and can be grown to a wide window of thicknesses ranging from 100 to 200 μm as compared to the usual coating thickness range of 10–50 μm with anodizing and hard anodizing, these coatings offer a substantial window of flexibility in terms of designing sufficiently thick coatings

for a given industrially specific component scenario. Accordingly, $50 \pm 5 \mu\text{m}$ MAO coatings deposited at two different current densities under constant voltage mode illustrate negligible weight loss as compared to bare substrate even after prolonged immersion in 3.5 wt. % NaCl solution as shown in Fig. 31, and the potentiodynamic polarization results demonstrate (Fig. 32) that the MAO coatings offer the corrosion rate (a) one order lower than the hard anodized coatings and (b) two orders lower corrosion rate than the SS-316 austenitic stainless steel and bare 6061 Al alloy [95]. It is noteworthy that even after 600 h of exposure to 3.5 wt. % NaCl solution both in the immersion tests and salt spray tests, the MAO coatings did not exhibit any visual evidence of pits on the coating surface demonstrating the potential utility of these coatings in the corrosion-prone environments [95].

Fig. 31 Corrosion behavior of Bare and MAO coated 6061-T6 alloy as estimated through weight loss measurements as a function of duration of immersion in 3.5 wt.% NaCl solution [95]

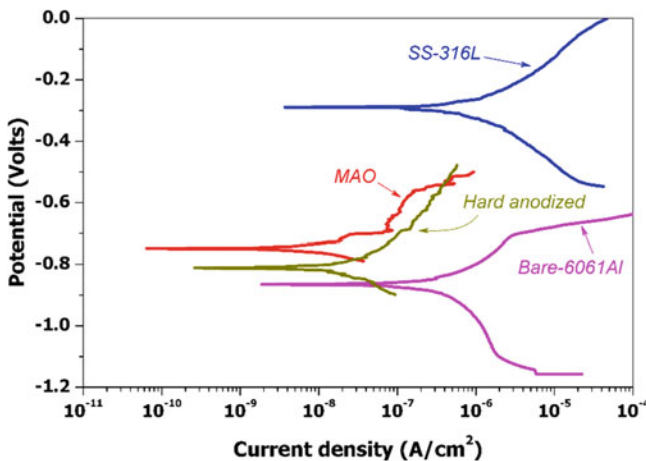
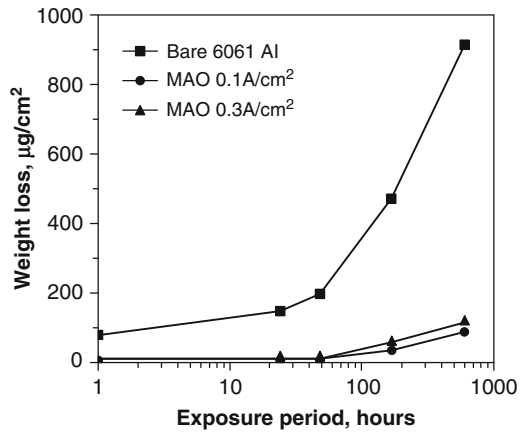
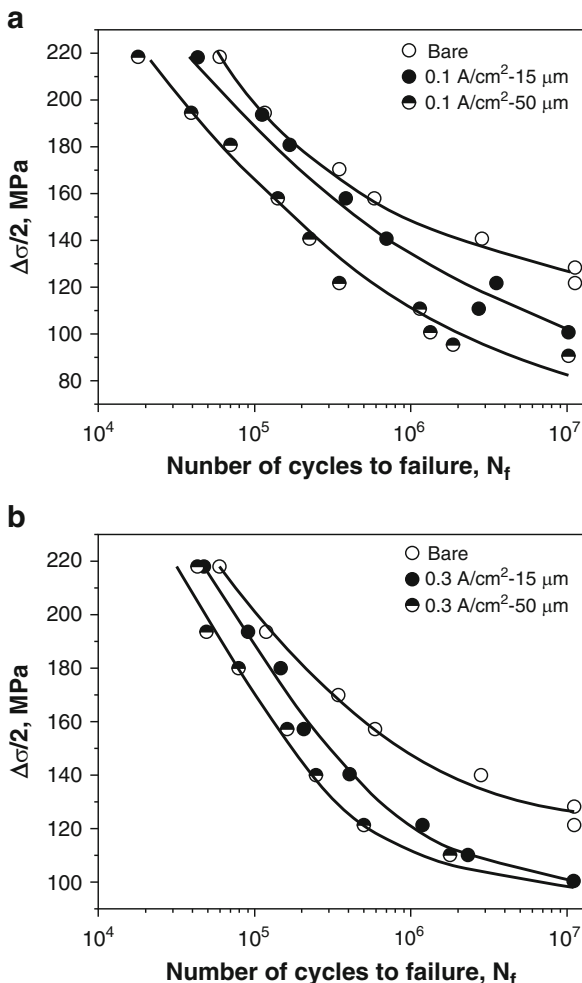


Fig. 32 Potentiodynamic polarization behavior of MAO and HA coatings deposited on 6061-T6 aluminum alloy in comparison with SS 316L stainless steel evaluated in 3.5 wt.% NaCl solution [95]

Fig. 33 Fatigue behavior of MAO coatings corresponds to two different thicknesses deposited at a current density of (a) 0.1 A/cm² and (b) 0.3 A/cm² in comparison with untreated 6061-T6 Al alloy [100]



Fatigue Performance

One of the specific requirements of aerospace structural members such as landing gear components requires a combination of properties such as wear, corrosion, and fatigue simultaneously. Many materials and processes have been designed to meet one or two of these properties but not many options are available to cater all three properties in a single material. On the prima facie, the similar situation is true even for MAO and hard anodized coatings as they meet the wear and corrosion performance needed but not the fatigue performance. Accordingly, a significant fatigue debit in the case of 15-μm- and 50-μm-thick MAO coatings deposited at different current densities can be seen from Fig. 33a and b [100]. The following are the

important phenomena that can be inferred from the data presented in Fig. 33a and b in conjunction with other studies reported:

- (a) Despite of debit in fatigue performance with respect to uncoated substrate, the thinner MAO coating performs better than the thicker coating. However, the thinner coatings are not adequate for wear and corrosion protection due to the minimized α -Al₂O₃ content in the coating.
- (b) In general, the lower current density appears to be better fatigue performer among the thicker coatings deposited at any given current density, while the opposite is true in the case of thinner coatings. This particular observation is attributed to the inevitable influence of localized defects within the coating whose origin is associated with the discharge channels formed during the coating formation.
- (c) In the case of thicker MAO coatings which are of specific interest as they provide adequate wear and corrosion protection, the crack nucleation is the rate controlling step as the favorably oriented and grown crack readily cuts across the metallurgically bonded substrate-coating interface easily, thereby explaining the fatigue debit than the corresponding substrate.
- (d) On the other hand, thicker coatings with increased surface roughness and other defects offer ready crack nucleation sites, and therefore crack nucleation and propagation happen rather easily and cause ~30–40% reduction in fatigue life of corresponding bare substrate. One way to address this issue is by means of reducing the current density gradually during the period of last minute(s) of coating deposition such that the discharge channel-originated coating surface defects can be minimized as shown in Fig. 34 [23].
- (e) Due to the presence of pores extended all the way till the substrate-coating interface in the case of hard anodized coatings due to the reasons interconnected with the typical coating formation mechanism explained before, the fatigue debit to an order of 50% as compared to the uncoated (bare) Al alloy substrate is noticed.

Although both MAO and hard anodized coatings exhibit fatigue debit than the corresponding bare substrate, it can be noticed that the extent of fatigue debit is more in the case of the latter than the former [100–102]. However, the aerospace industry typically looks for the material – coating solution – wherein the fatigue performance of coated component is at least identical to that of uncoated substrate, while the corrosion and wear protection is significantly enhanced.

Toward the aforementioned goal of increasing the fatigue life, the traditional approach of shot peening prior to the MAO coating has been investigated. Different shot peening mediums such as cast steel, alumina, and glass beads of three different size ranges starting from 210 μm to 850 μm were employed for shot peening [103]. The prior shot peening was found to be effective in introducing compressive residual stresses in the surface and subsurface regions of the Al alloy in such a way that the compressive stresses are retained beneath the substrate-coating interface even after the coating deposition. The combined process of shot peening followed by

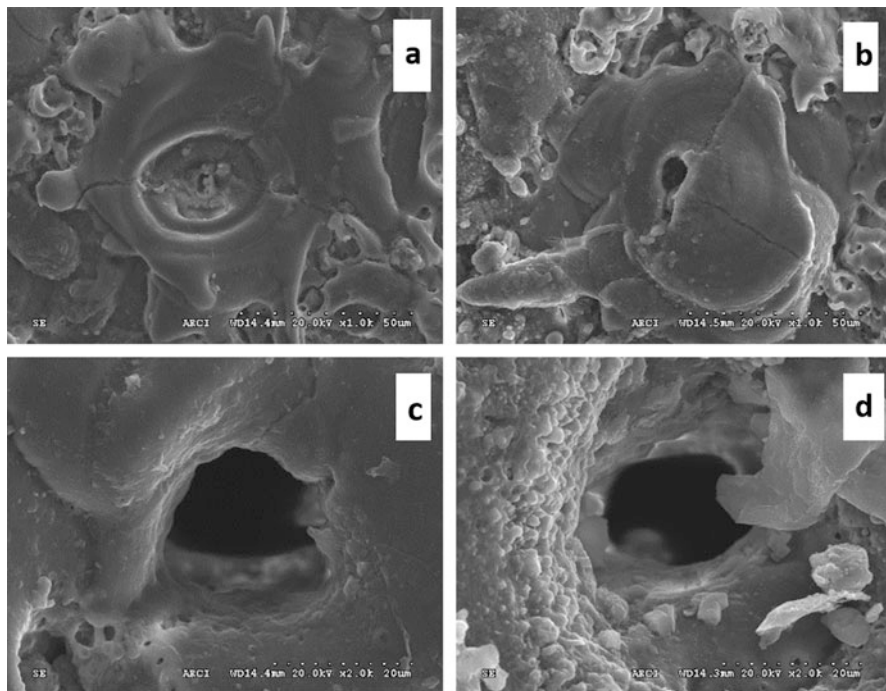


Fig. 34 Surface morphology of MAO coatings deposited on Al alloy when (a, b) current density is gradually decreased and (c, d) power supply is abruptly terminated [23]

MAO coating (SP + MAO) has indeed yielded 10–15 times improvement in fatigue life as compared to the corresponding bare substrate as shown in Fig. 35 which is a significant breakthrough in this direction for realizing the application of MAO coatings for simultaneous protection of aerospace components from wear, corrosion, and fatigue [103]. On contrary, the most important point to be noted is that the simple shot peening does not always guarantee the improvement in fatigue life as such benefit is related to (a) the magnitude of subsurface residual stresses generated together with (b) the depth of peened region prior to the MAO coating deposition which in turn depends upon shot peening variables such as peening material, size, shape, density, blast pressure, and shot velocity. In order to simplify the understanding and to incorporate all such variables, the shot velocity measured just before its impact on the substrate surface was utilized to calculate the kinetic energy. The average kinetic energy is then utilized to correlate the same with the benchmark ratio (ratio of fatigue life of coated substrate with the uncoated substrate) as shown in Fig. 36 [103]. Accordingly, the least critical kinetic energy that is required for obtaining fatigue life of SP + MAO coating equal to that of bare substrate is ~ 0.2 millijoule (mJ), while the average kinetic energy more than 1.0 mJ guarantees the fatigue performance of an order magnitude higher than the corresponding bare substrate as can be noticed from Fig. 36 [103]. It may be noted that the

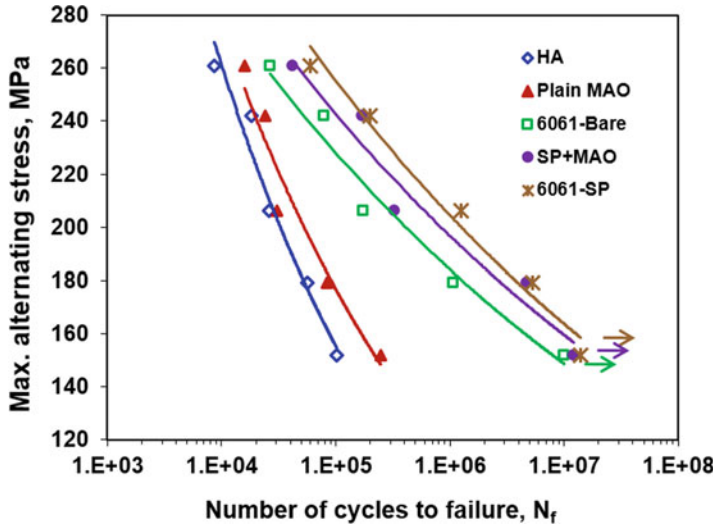


Fig. 35 High cycle fatigue behavior of 6061-T6 aluminum alloy with and without different surface treatments indicating phenomenal enhancement in fatigue performance with prior shot peened MAO coatings [103]

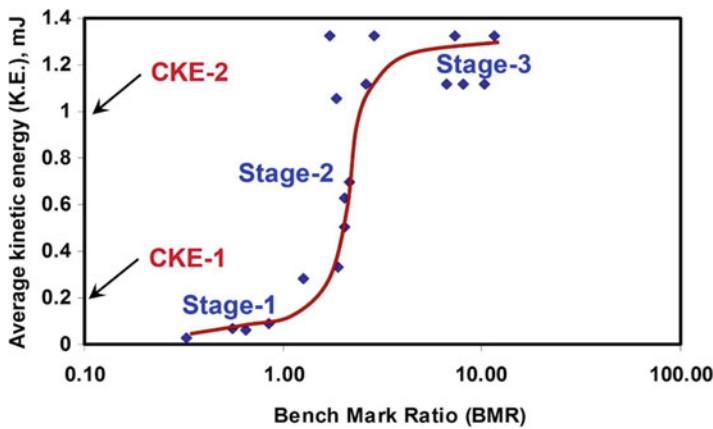


Fig. 36 Interrelationship between the ratio of fatigue life of prior shot peened + MAO coated and uncoated substrate (defined as bench mark ratio, BMR) with the average kinetic energy of shot medium illustrating two critical kinetic energy levels (CKE-1, CKE-2) needed for increasing BMR $\gg 1$ [103]

aforementioned methodology enables the quicker design of a combination of shot peening process variables such that the benefits of fatigue life extension are fruitfully realized for aerospace and other structural application of Al alloys needing simultaneous protection from wear, corrosion, and fatigue.

Applications of MAO Coatings

Taking the advantage of the eco-friendly nature of the MAO process coupled with excellent tribological performance and wear resistance offered, many industrial applications of textile, automotive, petrochemical, biomedical, wire-drawing, mobile communications, and pharmaceutical sectors have already been demonstrated by the large number of research and industry groups working around the globe. Enthused by the outcome, the research groups have already been engaged in demonstrating the MAO coatings for the aerospace industry as well. The following are few examples in this direction wherein the aerospace industry is expected to reap the potential benefits of this exciting technology.

In the place of conventional oil-filled core transformers, aluminum foil transformers (AFTs) are becoming popular devices due to their inherent characteristic properties such as maintenance free, light weight, compact, and high energy density transfer capacities. The general design of AFTs includes aluminum foils of 30–50 μm thickness sandwiched by a polymer film of 50–60 μm thickness. The primary advantage of lightweighting the transformer with AFTs is further propelled if the polymer film can be replaced with a thin yet dense insulating oxide layer of 0.5–1.0 μm thickness with sufficient dielectric insulation. However, the conventional MAO coating deposition systems work on batch coating operations than the continuous mode. Depending upon the transformer capacity being designed, several tens of meter- to few kilometer-long foils need to be provided with thin coating on either side of the foil such that the new-generation AFTs can be made. To realize such goal, a continuous coating deposition system was designed, built, and demonstrated as shown in Fig. 37 whose technical details are provided elsewhere [104, 105]. The compact AFT prepared using the MAO-coated foils as shown in Fig. 38a and b is expected to be potentially explored by the aerospace industry.

Many of the landing gear components need to be fatigue resistant in addition to the simultaneous wear and corrosion protection. The interesting portfolio of fatigue properties of an order magnitude improved over the performance of bare Al alloys (as against a 30–50% debit offered by conventionally coated substrates) in conjunction with excellent wear, friction, and corrosion performance of new-generation MAO coatings as illustrated in this chapter is also expected to drive its utilization by the aerospace industry.

Further, taking the advantage of very low thermal and electrical conductivity, MAO coatings offer substantial promise in providing an effective solution for design and development of next-generation thermal management systems and the high power bus bars in aircrafts and satellites.

Laser Cladding on Titanium Alloys for Aerospace Applications

Titanium alloys are popularly being used as important structural and dynamic components in aerospace applications due to its interesting portfolio of properties such as low density, high specific strength, and exceptional corrosion resistance

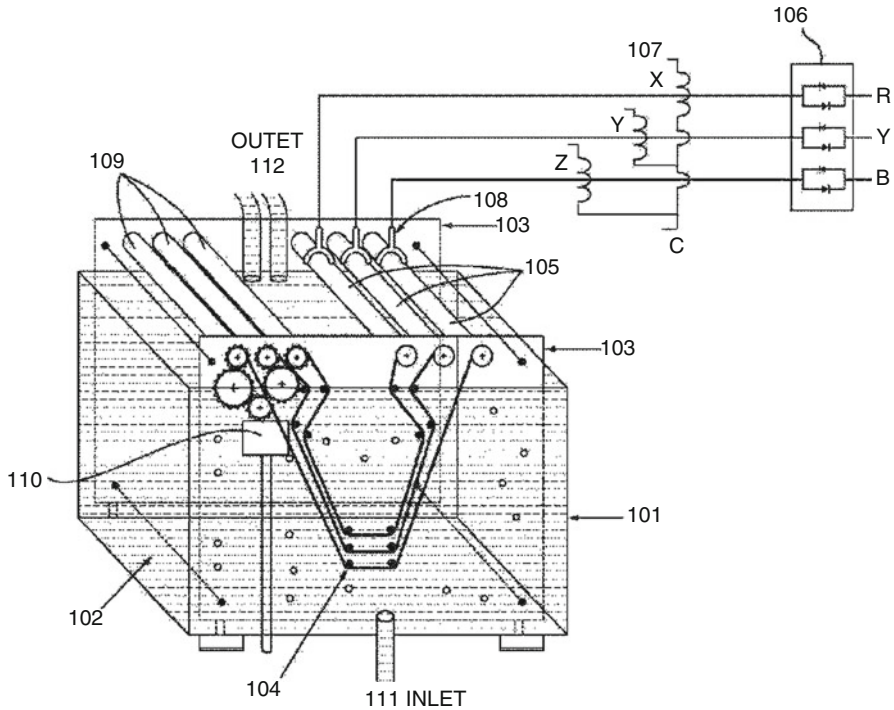


Fig. 37 Design of continuous coating deposition system based on MAO process for treating long foils and wires. The details of the individual design elements, their material of construction and working principle were available elsewhere [104, 105]

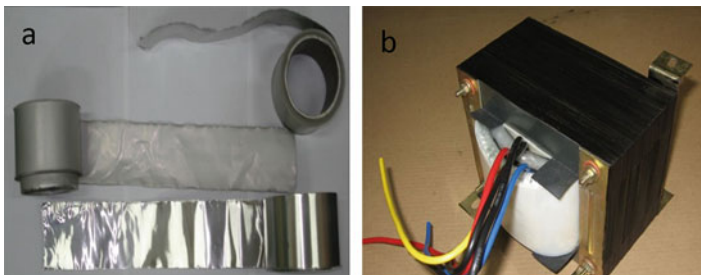


Fig. 38 Thin, long foils deposited with continuous MAO coater (dull foils are coated, bright is as received), aluminum foil transformer designed with MAO treated foils

[106–108]. However, low surface hardness (approx. 350 HV) and poor wear resistance restrict the use of Ti alloys as moving contact surfaces [108, 109]. Lower high-temperature oxidation resistance is another limitation toward their use in high-temperature environments above 500 °C [110]. Therefore, there is a thrust in research interest towards development of suitable cermet coatings for titanium and its alloys to enhance its hardness and wear resistance. Since many of the aero engine

applications demand high-temperature wear and oxidation protection, it is an area of interest for development of suitable cermet coatings. Accordingly, toward the above objective, laser cladding of Ti alloys with TiC- and TiCN-based cermet coatings being studied worldwide has been dealt in this part of the chapter.

Laser cladding is a powder-based deposition process where a stream of powder is fed in the path of laser which eventually melts and deposits onto the substrate. Laser cladding process which is also known as direct metal deposition (DMD) is being widely accepted in all engineering sectors such as aerospace, automobile, power, strategic, and others due to its unique benefits such as highly localized process, minimal and controlled heat input, metallurgical bond with negligible dilution, minimal distortion, highly repeatable, and ease of automation [111, 112]. Laser cladding or DMD is gaining popularity in mainly two broad classifications, namely, for protection and refurbishment. The component-specific protection includes deposition of selected materials on the substrate to enhance its required functionality and overall life expectancy. The basic objective behind such surface modification includes the protection against wear, corrosion, and thermal degradation, whereas the refurbishment includes localized deposition without disturbing the base component either metallurgically or geometrically. Yet another interesting feature of laser cladding-based repair in aerospace industry has been to deal with the manufacturing defects.

Often, it is too much to expect any bulk material to provide all the combinations of material properties specifically suitable for working under harsh working environments; a suitable protective coating with the required properties is deemed to be an effective solution for enhancing components' overall life and in-service performance. A suitable metal matrix composite (MMC) cermet coating can improve the functionality of base material by combating premature component failure in wear and corrosive environments at elevated temperatures. In metal matrix composite or cermet coatings, ceramic particles are distributed in the metal matrix. The metal matrix not only acts as a binder for accommodating the ceramic particles to enhance the overall toughness of the coating but also reduces the accumulation of interfacial stresses at the coating-substrate interface. Laser clad MMC coatings exhibit uniform ceramic particle distribution, metallurgical bond with the substrate, and stronger particle-matrix interface, thus attaining high hardness and toughness. In laser cladding process, the energy input is controlled effectively such that the adverse melting of ceramic particles and undesirable formation of secondary carbides or other deteriorating phases are minimized [112, 113]. As mentioned before, in laser cladding, a thermal process wherein melting of the clad and substrate material takes place together to generate a metallurgical bond at the interface, the melt pool experiences high cooling rate resulting in simultaneous accumulation of higher magnitude residual stresses at the interface. Besides, the mismatch in coefficient of thermal expansion between the substrate and the clad material also contributes to the increased interfacial stresses that may eventually result in cracking. Therefore, the selection of the matrix material is of great importance to minimize interfacial stresses and maximize the particle-matrix interfacial bonding. Yet another interesting feature

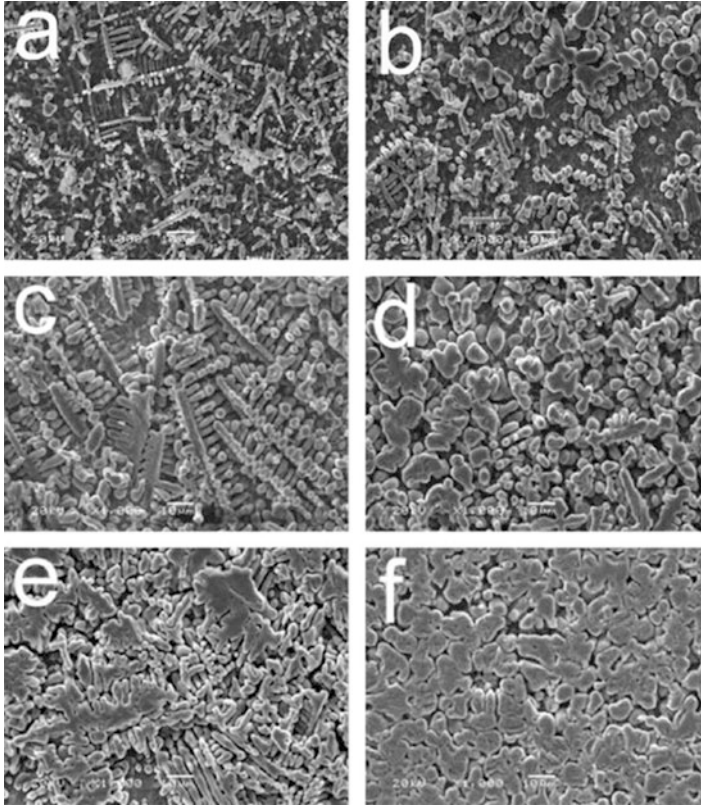


Fig. 39 Typical SEM morphologies of the TiC/Ti₃Al coating with (a) 10 vol.% TiC, (b) 20 vol.% TiC, (c, d) 30 vol.% TiC, and (e, f) 40 vol.% TiC powder [116]

of laser cladding has been its flexibility to in situ vary the composition of the cermet coating and alter the ceramic to matrix ratio.

Toward capitalizing the aforementioned advantages, the TiC-reinforced cermet coatings with a potential to enhance the surface hardness up to 4 times that of the substrate [114] and concurrently improved wear resistance to the tune of 1–2 orders of magnitude were examined [115]. The TiC-based cermet coatings are usually generated by mixing of Ti-, Ni-, or Co-based matrix with other powders. For instance, TiC-reinforced Ti₃Al coating on pure Ti substrate by laser cladding of Ti-40 at. %Al powder with TiC powder in different ratios is shown in Fig. 39 [116]. Dendritic and granular TiC phases are distributed in the Ti-Al intermetallic matrix. Addition of TiC reinforcement also enhances wear resistance of the coating significantly, as shown in Fig. 40. 40% TiC-reinforced Ti₃Al coating showed excellent wear resistance. Similarly, TiC-reinforced coatings using different ratios of Ti and TiC powders on Ti-6Al-4 V substrate showed improvement in the abrasive wear resistance with increase in TiC content as shown in Fig. 41 [117].

Fig. 40 Wear volume of the Ti_3Al coating and the TiC/Ti_3Al IMC coatings with different volume fraction of TiC powder sliding against AISI52100 steel ball under 5 N normal load [116]

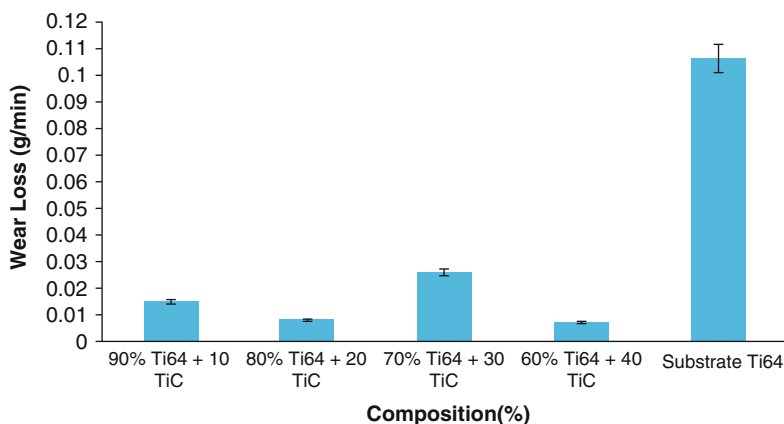
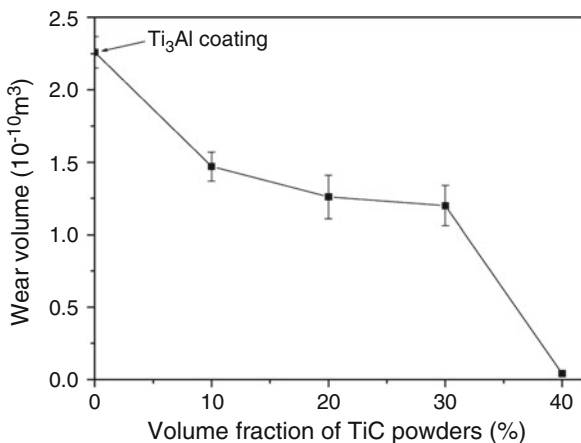


Fig. 41 Abrasive wear performance of the MMCs with different Ti–TiC compositions [117]

Laser cladding using a pre-placed powder mixture containing $Ni_5Al + hBN + B_4C + SiC$ on Ti-6Al-4 V forms the eventual phases such as TiC , TiB_2 , $NiTi_2$, B_4C , and SiC in the coating and thereby enhances the tribological performance [118]. Similarly, microstructure of $Ti_3Al/TiAl + TiC$ composite deposited on Ti-6Al-4 V alloy by laser cladding of $Al + 30\%TiC$ consists of dendritic morphology of TiC phases in the matrix mainly composed of $Ti_3Al/TiAl$ intermetallic compounds as shown in Fig. 42. The coating demonstrates the wear resistance twice as that of the substrate material as shown in Fig. 43 [115].

It is also noteworthy that the surface hardness and tribological performance can also be concurrently improved by incorporating additional elements that contribute to the improved toughness of the coating. Accordingly, $Ti(C,N)$ -reinforced Ni-based cermet coatings generated by laser cladding of $Ni60 + C + TiN$ powder exhibit improvement in wear resistance up to 26 times that of the Ti-6Al-4 V

Fig. 42 SEM micrograph of the dendrite and the $Ti_3Al/TiAl$ matrix in the Al + 30 wt. % TiC laser cladding layer [115]

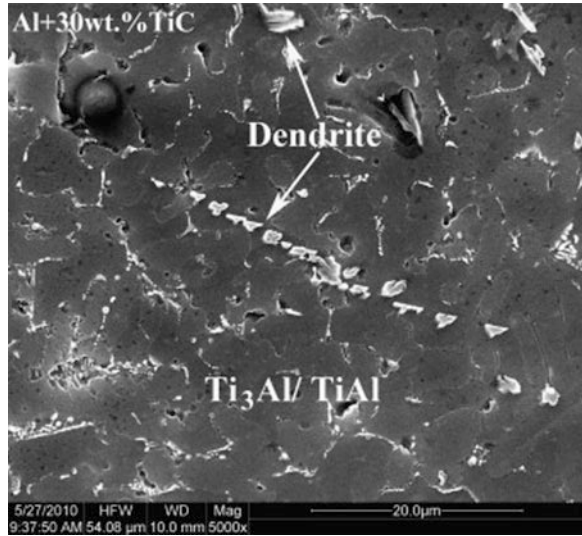
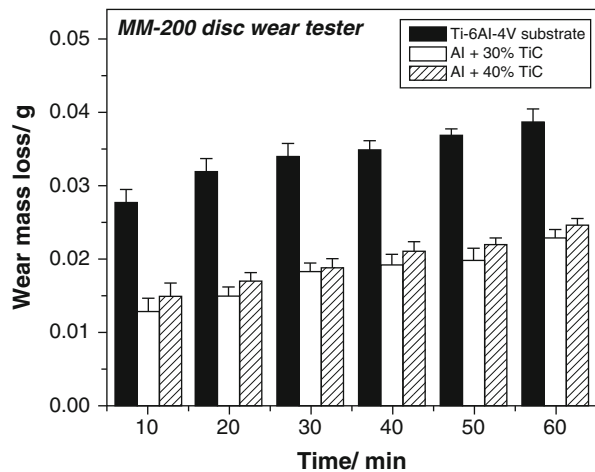


Fig. 43 Wear mass loss of the $Ti_3Al/TiAl + TiC$ ceramic layers and the Ti-6Al-4V alloy [115]



substrate simply by incorporating 8% Mo into the coating [119]. Addition of Mo reduces the solid solubility of TiN or Ti(C,N) in the Ni matrix and therefore generates tiny undissolved TiN particles that act as the nucleation sites for the subsequent grain formation leading to the microstructure with refined grains as shown in Fig. 44. Element analysis indicates black core as a TiN phase as it is rich in Ti and N, whereas the gray rim phase is rich in Mo. Figure 45 shows the schematic illustration of the microstructural evolution and grain growth. The addition of Mo creates uniformly dispersed core-rim structure with improved wettability of precipitates with the matrix phase resulting in significantly improved hardness-toughness combination that imparts excellent wear resistance

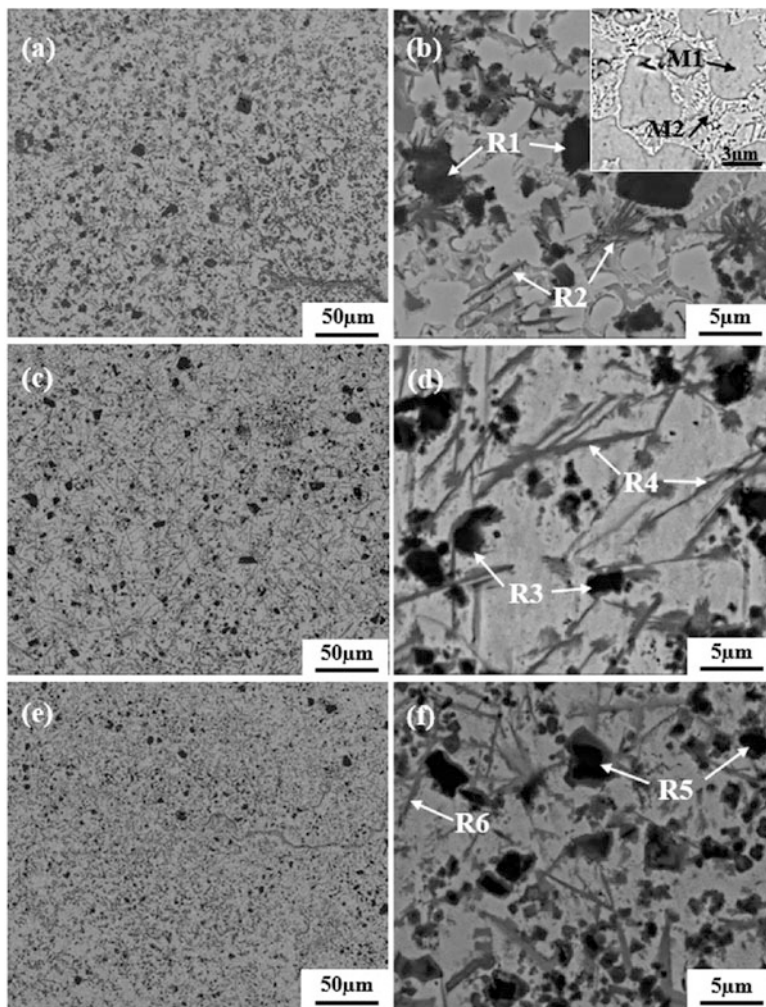


Fig. 44 Microstructure morphologies of the middle section typically for: (a, b) 0Mo coating; (c, d) 4Mo coating; (e, f) 8Mo coating. [119]

as shown in Fig. 46. It is evident that addition of Mo in coating can significantly improve wear performance.

The Ti_5Si_3 -/TiC-reinforced Co-based cermet coatings also exhibit improved wear resistance with the increasing addition of SiC particles [120]. However, such an improvement is not simply because of harder SiC particles in the coating, but the decomposed SiC phase into elemental Si and C and promotes the formation of TiC phases and Ti_5Si_3 phases in the form of coralline-like eutectics as shown in Fig. 47. At the same time, increase in SiC content in the coating leads to smaller and irregular TiC phases uniformly distributed in the coating. By virtue of the aforementioned two

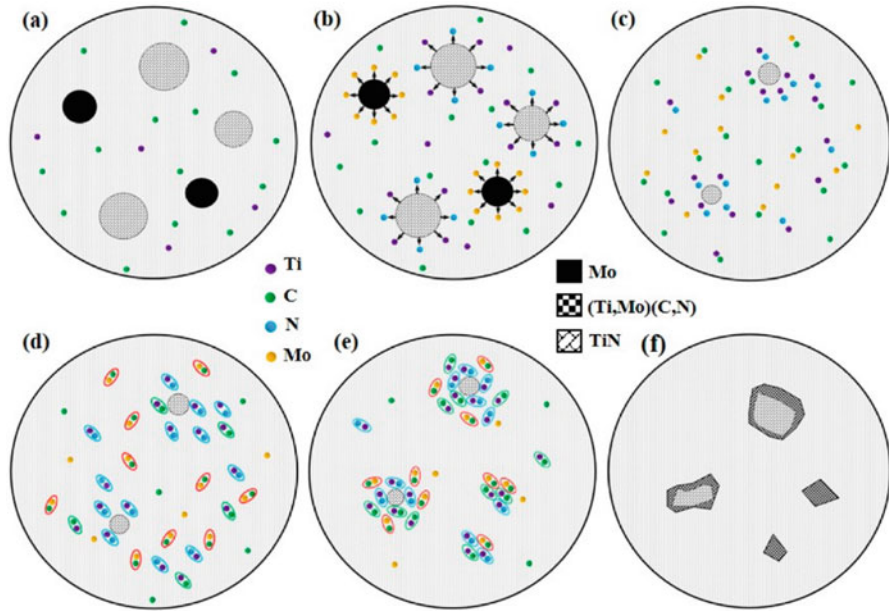


Fig. 45 The diagram illustration for the formation mechanism of Ti(C,N) and the action mechanism of Mo: (a) the formation of initial molten pool; (b) dissolution of TiN and Mo; (c) partially melted large TiN particles; (d) the formation of TiN, TiC and MoC; (e) the formation and growth of Ti(C,N); (f) the effect of Mo on the Ti(C,N). [119]

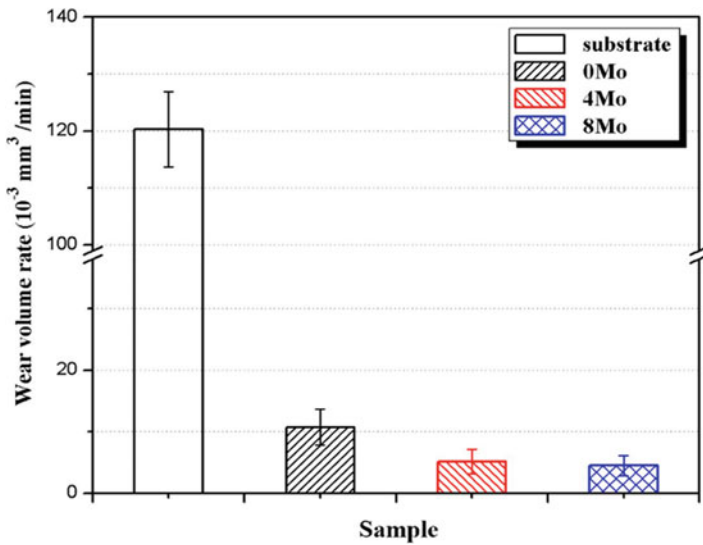


Fig. 46 Wear volume rate for substrate and coatings [119]

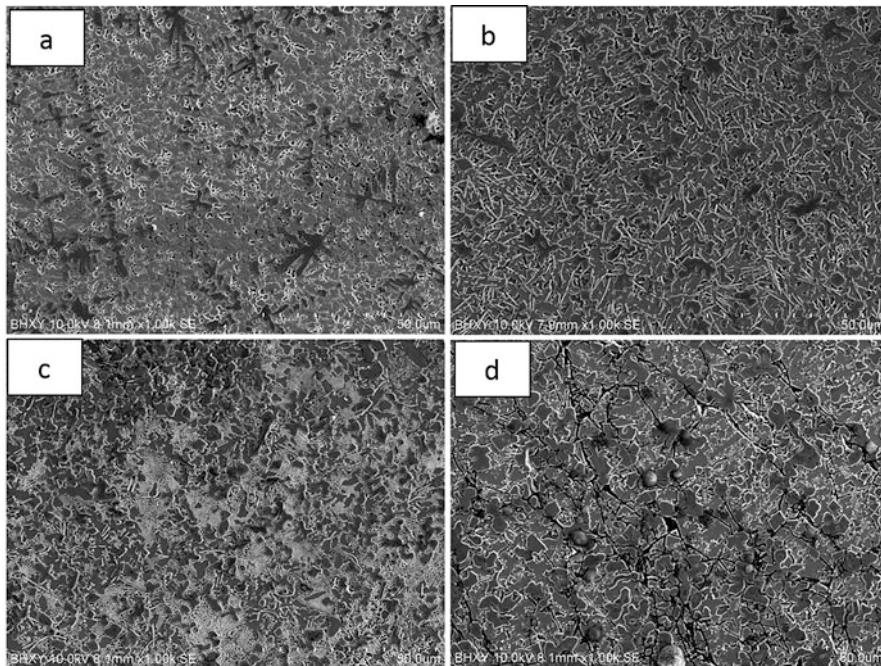


Fig. 47 SEM micrographs at top layer of the composite coating with (a) Co42-5SiC powder, (b) Co42-10SiC powder, (c) Co42-15SiC powder, and (d) Co42-20SiC powder [120]

distinct mechanisms, the addition of SiC enhanced the microhardness of the cermet coating by 3 times and the wear resistance up to 60 times as shown in Fig. 48. However, although the increase in SiC content of the coating up to 15 wt. % led to improved wear resistance as discussed, further increase beyond the above threshold resulted in cracking as can be noticed in Fig. 47. These results clearly illustrate the need for thorough understanding of the microstructure and phase combination such that property-performance maximization can be achieved without any adverse effects.

Reduction in the friction coefficient to enhance the component and its counterpart's life is important especially for the high-temperature, high-contact stress and dry wear conditions. It can be achieved by adding additional self-lubricating elements such as CaF_2 and WS_2 which provide a self-lubricating medium or form a protective lubricant layer during friction loading. Accordingly, the $\gamma\text{-NiCrAlTi/TiC} + \text{TiWC}_2/\text{CrS} + \text{Ti}_2\text{CS}$ composite coating formed by laser cladding of $\text{NiCr/Cr}_3\text{C}_2\text{-WS}_2$ powder exhibited excellent wear resistance both at room temperature and elevated temperature up to 600 °C due to combined effect of (i) hard TiC and TiWC_2 carbides and (ii) relatively softer CrS, Ti_2CS self-lubricating sulfide phases [109]. The friction coefficient of the cermet coatings is reduced from 0.47 to 0.30, whereas the wear rates were reduced by 90% as compared to that of Ti-6Al-4 V substrate as shown in Fig. 49a, b.

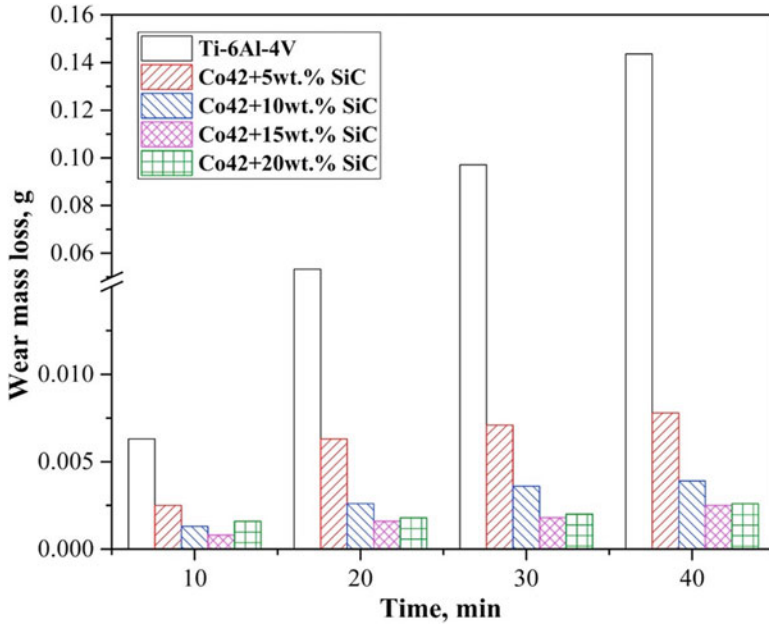


Fig. 48 Wear mass loss of the specimens as a function of sliding time [120]

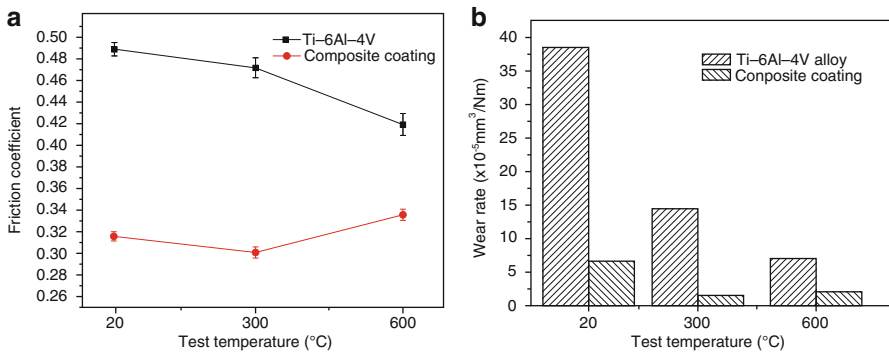


Fig. 49 (a) Friction coefficient and (b) wear rate of Ti-6Al-4V substrate and laser clad coating as functions of temperature [109]

Titanium alloys can oxidize easily which restricts their uses in high-temperature applications. High-temperature oxidation-resistant cermet coatings can widen their applications. NiCr-Cr₃C₂ cermet coatings are widely used for high-temperature wear and oxidation resistance. Laser cladding of NiCr-Cr₃C₂ coatings on Ti-48Al-2Cr-2Nb substrate forms Cr₇C₃- and TiC-reinforced coatings where Cr₇C₃ carbides present in the form of blocky hypereutectic and fine lamellar and TiC in particulate and dendritic phase [121]. NiCr-Cr₃C₂ cermet coatings can give 2 times

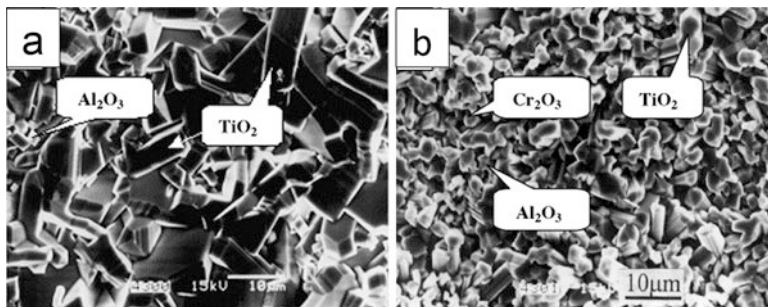


Fig. 50 SEM micrograph of the (a) TiAl alloys substrate and (b) laser clad coating with NiCr–50% Cr₃C₂ powder after exposure at 1000 °C for 50 h [121]

improvement in wear resistance and high-temperature oxidation resistance at 1000 °C. Formation of TiO₂ is a preferred reaction compared to Al₂O₃ which results in TiO₂ layer on the entire surface when heated at high temperature, whereas in laser clad coatings, presence of Cr₇C₃ carbides disturbs the spread of TiO₂ formation resulting in comparatively higher amount of Al₂O₃ with Cr₂O₃ oxides as shown in Fig. 50.

Similarly, laser cladding of NiCr and Cr₃C₂ powder on Ti-6Al-4 V substrate promotes the formation of γ -NiCrAlTi + TiC phases in the resulting cermet coating [108]. It is interesting to note that the formation of TiC phase is driven by the reaction between carbon (sourced from the decomposed Cr₃C₂ phase) and Ti (sourced either from the clad material or through substrate dilution) as it has lower Gibbs standard free energy formation (–221.75 kJ/mol) and due to higher carbide-forming capability of titanium [108]. Owing to the high melting point of TiC (3140 °C), its primary precipitation as TiC phase in the melt pool is understandable. Further, the addition of CaF₂ to the γ -NiCrAlTi matrix also improves the high-temperature wear resistance of the coating as CaF₂ acts as a self-solid lubricant due to its hexagonal structure with low shear strength and lower friction coefficient in the temperature range of 250–700 °C [108]. Figure 51 a and b shows the SEM micrograph of the γ -NiCrAlTi/TiC and γ -NiCrAlTi/TiC/CaF₂ coatings, respectively, where TiC particles are marked as A, the NiCrAlTi solid solution is marked as B, and fine particles of CaF₂ dispersed in the matrix are marked as C. In this regard, the CaF₂ particulates, due to its lower melting point and lower density, tend to float on the surface and therefore create a self-lubricating layer resulting in improved wear resistance at elevated temperatures (as shown in Fig. 52) which is an important phenomenon to be considered.

Similarly, the TaC-reinforced TiNi cermet coatings enhance the high-temperature oxidation and wear resistances of Ti-6Al-4 V material. Laser cladding of NiCrBSi powder with varied concentration of TaC revealed the formation of Ti₂Ni, TiNi, and TiB₂ phases along with TiC intermetallic compound and additional Ta₂O₅ and TaC phases [122]. Further, the addition of TaC in cermet coating results in microstructural refinement by way of increased Ta in the solid solution and eventually improves the

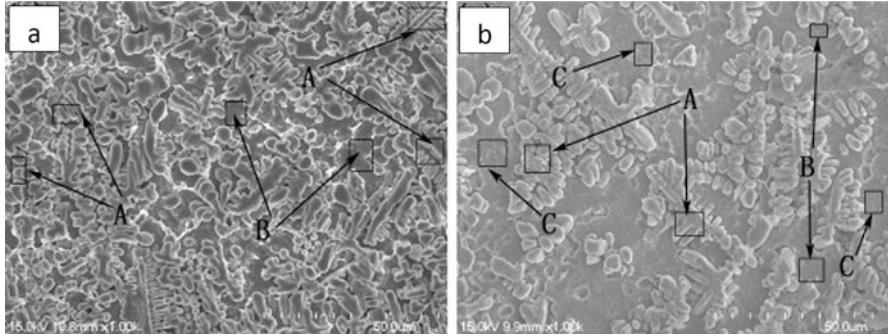


Fig. 51 SEM micrographs of (a) \sqrt{r} -NiCrAlTi/TiC coating and (b) \sqrt{r} -NiCrAlTi/TiC/CaF₂ coating at intermediate region [108]

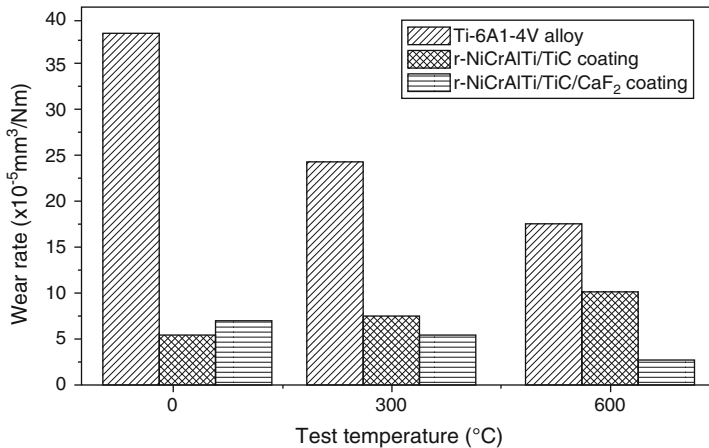


Fig. 52 Wear rates of the Ti6Al4V substrate and composite coatings versus temperature under the dry sliding wear test [108]

coating hardness. Significant improvement in high-temperature wear (Fig. 53) and oxidation resistances (Fig. 54) was also noticed due to the formation of Ta₂O₅ oxide layer that exhibits lower coefficient of friction than TiO₂.

Laser clad coating is a thermal process with highly localized heat input which includes melting and rapid solidifications resulting in metastable phases. The in-service structural stability of the clad coating is adversely affected by its subsequent transformation of these metastable phases to equilibrium phases upon exposure to high temperature. Furthermore, ceramic particles having different coefficient of thermal expansion than the metal may result in higher residual stresses during rapid solidification that may eventually result in cracking. A lot more attention is required in the development of suitable post-clad heat treatment (PCHT) that can minimize the residual stresses at interface and readjust the microstructure to a more

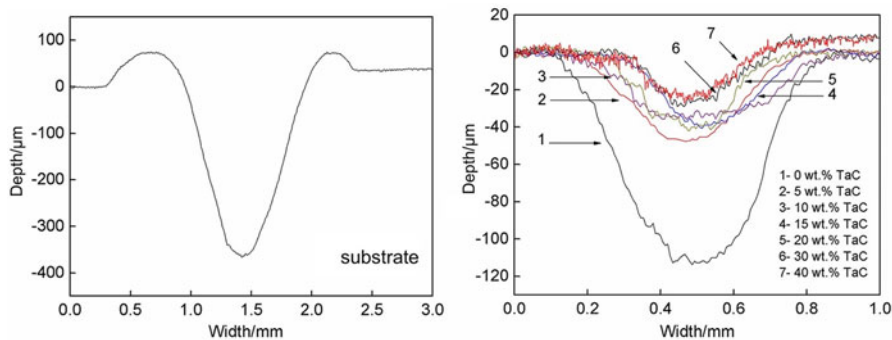


Fig. 53 The wear profiles of the substrate and coatings with different contents of TaC addition after wear tests at 600 °C for 30 min [122]

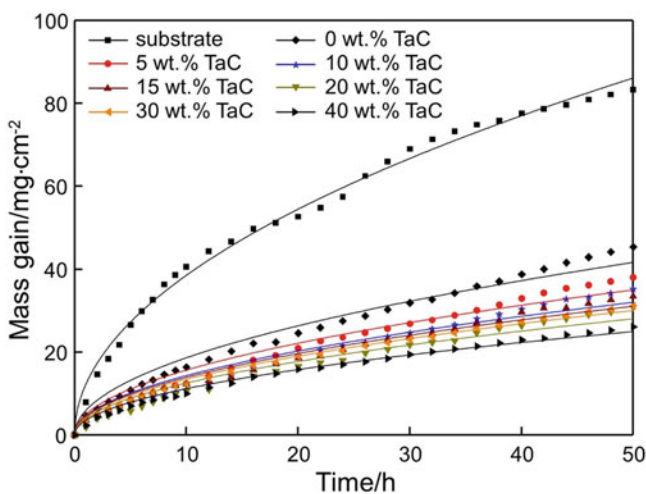


Fig. 54 The mass gain of the substrate and coatings in an oxidation test at 1000 °C in air for 50 h [122]

stable one. For instance, laser clad cermet coating using NiCrBSi +30%WC on Ti-6Al-4 V substrate was evaluated for improvement in microstructural and tribological properties when post-clad heat treated at different temperatures such as 700 °C, 800 °C, and 900 °C for 1 h [123]. SEM micrographs as shown in Fig. 55 reveal the clad microstructure of the coating which mainly consists of cellular dendrites of TiC and fine particles of WC distributed in the matrix of Ni-Ti. Equiaxed/lath-shaped solid solution of (W,Ti)C was also observed. With increase in the PCHT temperature, a thin granular layer of Ni-Ti-rich nano-sized precipitates is observed in Ni₃Ti phase and almost entirely covers the Ni₃Ti at PCHT 900 °C. At PCHT 900 °C, precipitation of Cr₃C₂ was also observed. The increase in PCHT not only altered the microstructure but also enhanced its hardness due to fine

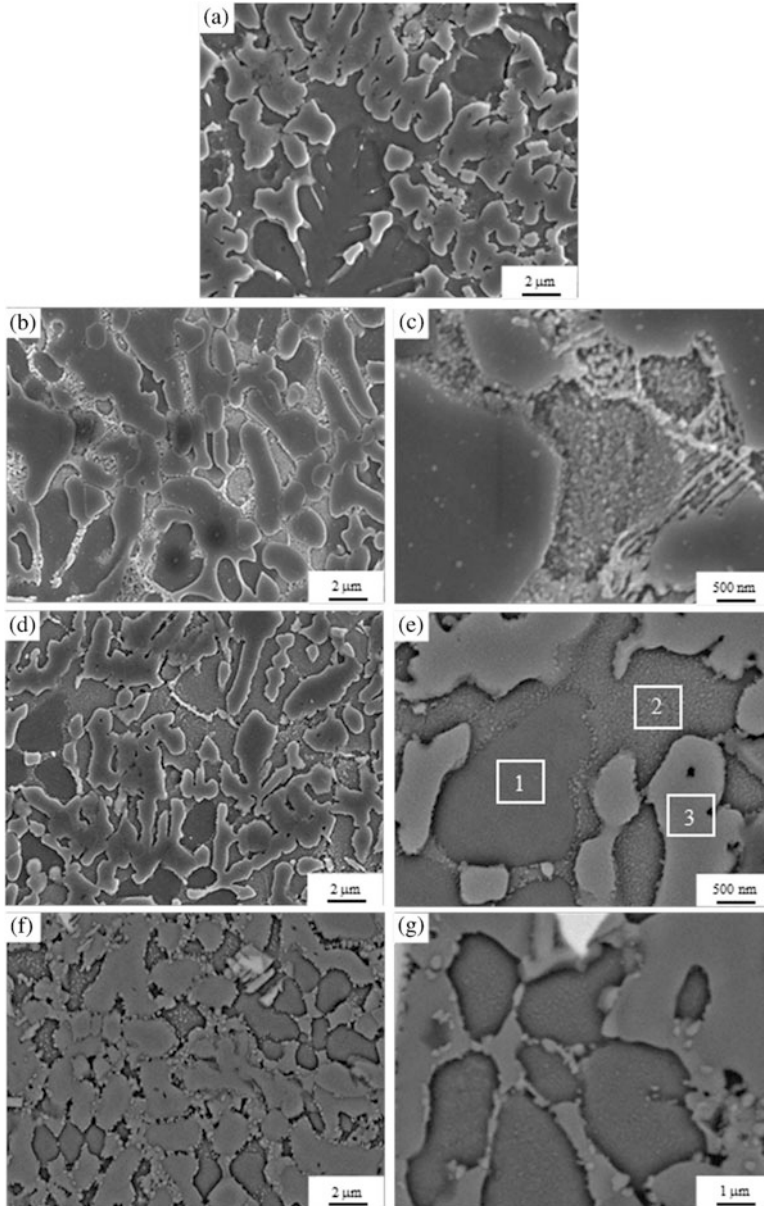


Fig. 55 SEM micrographs of coating (a) as-clad; (b, c) 700 °C; (d, e) 800 °C; (f, g) 900 °C [123]

precipitation in the matrix as shown in Fig. 56. PCHT also enhanced its wear properties and reduced its cracking susceptibility during wear as shown in Fig. 57. It is evident that PCHT can play an important role in improving the coating performance during service.

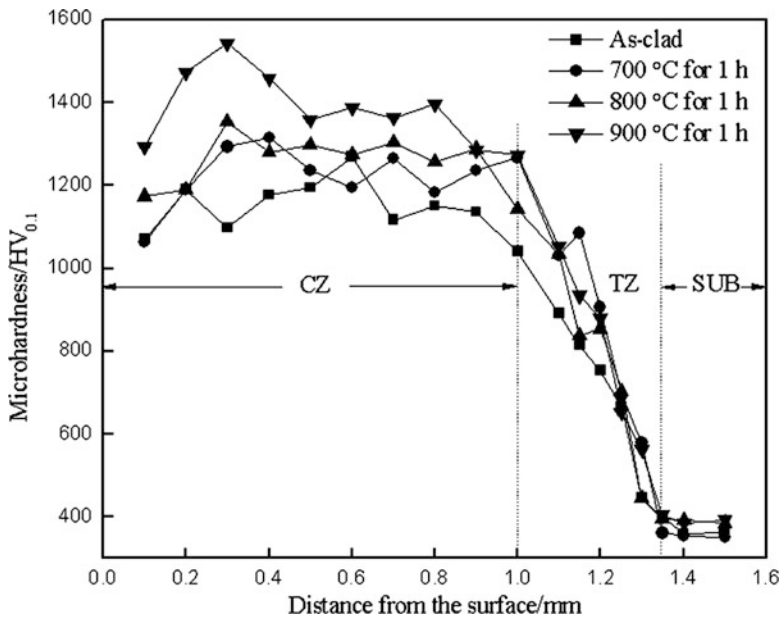


Fig. 56 Cross-sectional micro-hardness profiles of the coatings treated at various PCHT for 1 h [123]

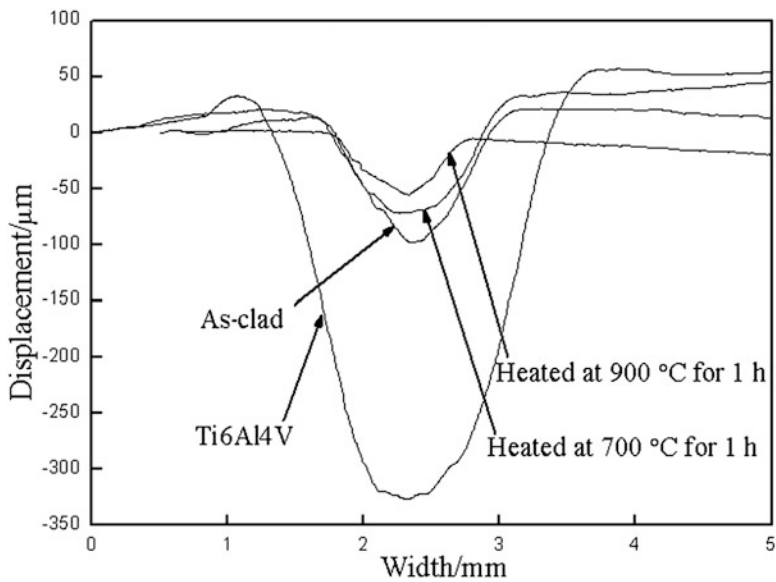


Fig. 57 Wear depth profiles of the substrate and the coatings [123]

Yet another material of specific interest has been the titanium diboride (TiB_2) due to its exceptional hardness, high-temperature oxidation, and wear resistances. These interesting portfolio of properties paves the path for realizing TiB_2 -reinforced cermet coatings as a potential candidate for wear resistance and oxidation resistance applications. During laser processing, the TiB_2 partially dissolves in the Ti metal matrix and forms finer needlelike TiB phases. Apart from enhancing the mechanical properties and fatigue performance, the TiB phase has an added advantage that its density and coefficient of thermal expansion are almost identical to that of titanium and therefore minimizes stress accumulation at the matrix-boride interface [124].

Summary and Concluding Remarks

Strategic sector and aerospace industry often demand the components made out of high-performance materials to meet the required performance. This can be achieved either by development of components from advanced alloy composition or by altering the existing component surface with suitable coating material. A majority of the applications demand better resistance against wear, corrosion, thermal oxidation, and fatigue. The aerospace components such as critical parts of turbine, landing gear, and other structural parts are being coated with thermally sprayed oxides and cermets to enhance their protection capabilities. A wide range of oxide compositions deposited by various thermal spray techniques have been used in aerospace sector, namely, Al_2O_3 , TiO_2 , and Cr_2O_3 , with addition of SiO_2 , ZrO_2 , and CeO_2 for wear, corrosion, and dielectric applications. Similarly, various WC- and Cr_3C_2 -based cermet coatings with different matrix compositions are being coated on the components for wear and corrosion protection with the functional temperatures up to 750°C . It is well established that the WC-Co coatings perform excellent at room temperature wear conditions. The addition of small amount of Cr to WC-Co improves the corrosion resistance significantly which has opened a new window to replace hard chrome plating. Moreover, the addition of Cr to WC-Ni coating significantly enhances the corrosion protection without deteriorating the wear properties while being effective up to 750°C temperature. Further, the Cr_3C_2 -NiCr coatings are being deposited on various components for better wear and corrosion properties at varied temperatures. Therefore, the oxide and cermet coatings as mentioned above are also being deposited on ship shafts, submarine seals, shafts, and valves for wear, friction, and corrosion protection, and therefore the overall objective of life cycle enhancement was achieved.

Besides, the thermal spray techniques are also being used to refurbish and repair the damaged components to extend the service life in a cost-effective manner. The development of gradient coatings and advanced alloy coatings by thermal spray to cater the typical demands of aerospace and strategic sectors needing high erosion and oxidation resistances at elevated temperature and other harsh working conditions is currently in progress. Further, the research to simultaneously improve the strength and toughness of Al_2O_3 thermal spray coatings by addition of carbon nanotubes (CNT) / graphene nanoplatelets (GNP) exhibited encouraging results and may find

newer application. The increased bend strength and fracture toughness of Al_2O_3 by the addition CNTs/GNPs by 10% and 100%, respectively, are a notable progress in this direction [125, 126]. In view of the prevailing ambiguity in the reported literature on the fatigue performance of thermally sprayed coatings, comprehensive studies are yet to be conducted for understanding the fatigue behavior so as to identify the coating type and its processing conditions for realizing the full potential. Despite interesting characteristic properties of Al_2O_3 - ZrO_2 coatings, not many studies were reported so far to unravel the fundamental role of ZrO_2 when added to Al_2O_3 in thermally sprayed coatings for potential nuclear industry applications. The recently emerged family member of thermal spray technique, namely, the cold gas dynamic spray (CGDS), has been of specific interest as it employs the far lower thermal energy than any other counterpart, and therefore 100% phase retention is its special characteristic advantage. Although the CGDS technology has been initially portrayed to be best suited for spraying low-melting metals and alloys, the recent developments in terms of design of special nozzle geometries to spray refractory hard metals and alloys of Ta, Nb, and age-hardenable Al alloys are expected to pave path for the futuristic applications in the aerospace and strategic sectors.

The primary advantage of MAO process has been its ability to work under alkaline electrolytic medium, therefore demonstrating its eco-friendly nature as against many acid-based conventional technologies, namely, anodizing, hard anodizing, and hard chrome plating. However, such an advantage is retained only if the chemical constituents added to the base electrolyte are chosen carefully. Yet another exciting feature of the MAO technology is the direct utilization of AC power received from industrial electrical mains meaning that the components to be coated themselves would become the electrodes in the bath and all the components get coated simultaneously without any redundancy of using insoluble cathodes as is the case with conventional anodizing; therefore, high throughput is achieved. In addition, the higher coating deposition rates to the tune of 1.5–2.0 $\mu\text{m}/\text{min}$ (5–8 times higher deposition rate than anodizing) also contribute to the high throughput and less coating turnaround period in the industrial scenario. Further, even more exciting is the fact that the MAO process doesn't need any special pretreatment procedures such as alkaline etching, degreasing, desmutting, and intermittent rinsing like other conventional processes but only needs simple surface cleaning to remove dust, dirt, and oils. However, the high voltages and relatively higher current densities employed in the MAO process as compared to the conventional anodizing process demands the design of special jigs and fixtures for component holding in the bath as well as to achieve selective area oxidation. The ability of depositing uniform, thin, electrically insulating oxide coating on Al foils through the MAO technology forms the basis for the manufacturing of energy-efficient aluminum foil transformers (AFTs) for its application in the aircraft. Further, MAO-coated Al alloys are being used in the place of steel parts which is very relevant to aerospace industry where weight management is of specific interest. Further, studies are initiated to develop oxide coating on nuclear reactor materials to increase the neutron absorption

capability of reactor components made of active metals and alloys. The methods to simultaneously enhance the wear, corrosion, and fatigue performances of components subjected to static, dynamic, cyclic stresses and sliding contacts working in the corrosion-prone environment are also of specific interest to the aerospace and marine industry.

Yet another greatest advantage of MAO process over the competing conventional processes has been its ability to include both soluble and insoluble additives into its bath and therefore tailor the coating chemistry suitable for a variety of functional applications. However, the rate at which the additives are consumed in the bath needs proper replenishment such that the coatings with identical composition can be produced on large number of parts using the same bath in a cost-effective manner. Another important aspect that needs attention has been the settling tendency of insoluble additives which shall require special treatments such as charge functionalization or mechanical stirring or continuous electrolyte circulation with enough vigor or even reducing the particle size to nanometer levels such that the particle settling is minimized. The above aspects merit more focused R&D investigations such that the lab-scale ideas can be successfully transformed onto the industrial scale. It is strongly believed that the aforementioned challenges need to be simultaneously addressed by the global R&D community such that the MAO technology and its potential benefits in terms of exciting levels of enhanced properties on metals and alloys of Al, Mg, Ta, Ti, and Zr can be judiciously utilized for the long-run benefits of aerospace and strategic sectors.

Laser cladding is another deposition technique where coating is generated by melting the powder of required composition on substrate resulting in stronger metallurgical bond at the clad-substrate interface. Ti and its alloys have been widely used in the aerospace industry owing to their strength and better corrosion properties, and there have been focused efforts to improve the surface hardness and wear and high-temperature oxidation resistances. Laser clad metal matrix cermet composite coatings on Ti alloys are widely being studied in order to extend its uses in high-temperature and wear applications. TiC- and Ti(C, N)-reinforced cermet coatings are showing promising results in increasing hardness and wear resistance. Further, addition of self-lubricating elements such as CaF_2 and WS_2 has enhanced wear performance of Ti alloys to manifolds. However, TaC- and Cr_3C_2 -reinforced MMC coatings demonstrated promising results in improving oxidation and wear resistance at elevated temperature. TiB- and TiB_2 -reinforced coatings are also gaining research attention for enhancing hardness and wear resistance of Ti alloys as TiB_2 has high-temperature oxidation and wear resistance and it is one of the hardest materials, which makes TiB_2 -reinforced cermet coatings a potential candidate for wear resistance and oxidation resistance applications. TiB_2 partially dissolves in the Ti metal matrix and forms very fine needlelike TiB phases. TiB has an added advantage that their density and coefficient of thermal expansion are not very different from titanium which minimizes stress accumulation at the matrix and boride interface; moreover, TiB and Ti MMC can enhance mechanical properties and

fatigue performance. It is to be noted that laser clad cermet coatings are promising in enhancing respective properties; however, issues related to the residual stresses generated due to the mismatch in coefficient of thermal expansion between the coating and substrate materials may eventually result in cracking and need to be studied in much detail. Various other aspects such as (a) microstructural and structural stability during the operation at elevated temperatures, (b) development of suitable post-clad heat treatment for respective coatings for improved microstructural and structural stability, and (c) effect on interfacial strength, fatigue, and creep performances needs to be examined with a holistic approach and therefore becomes the potential direction for the future research in this field.

References

1. Davis JR (ed) (2004) Handbook of thermal spray technology. ASM International, Materials Park
2. Pawlowski L (2008) The science and engineering of thermal spray coatings. Wiley, Chichester
3. Fauchais PL, Heberlein JVR, Boulos M (2014) Thermal spray fundamentals: from powder to part. Springer, New York
4. Heimann RB (1994) Plasma-spray coatings. VCH publishers, Weinheim
5. Sundararajan G, Rao DS, Kumar GS, Joshi SV (2013) Detonation spray coatings. In: Wang J, Chung W (eds) Encyclopedia of tribology. Springer, Boston, MA, pp 736–742
6. Wood RJK (2010) Tribology of thermal sprayed WC-Co coatings. *Int J Refract Met Hard Mater* 28:82–94
7. Kadyrov E (1996) Gas-particle interaction in detonation spraying systems. *J Therm Spray Technol* 5:185–195
8. Smurov I, Ulianitsky V (2011) Computer controlled detonation spraying: a spraying process upgraded to advanced applications. *WIT Trans Eng Sci* 71:265–276
9. Qiao Y, Fischer TE, Dent A (2003) The effects of fuel chemistry and feedstock powder on the mechanical and tribological properties of HVOF thermal-sprayed WC-Co coatings with very fine structures. *Surf Coat Technol* 172:24–41
10. Raju KRCS, Rao DS, Kumar GS, Sen D, Sundararajan G (2000) The influence of powder characteristics on the properties of detonation sprayed Cr_3C_2 -25NiCr coatings. In: Proceedings of the ITSC 2000, Canada, pp 309–316
11. Babu PS, Rao DS, Rao GVN, Sundararajan G (2007) Effect of feedstock size and its distribution on the properties of detonation sprayed coatings. *J Therm Spray Technol* 16:281–290
12. Sundararajan G, Kumar GS, Rao DS (2001) The interrelationship between particle temperature and velocity, splat formation and deposition efficiency in detonation sprayed Al_2O_3 coatings. In: Proceedings of the ITSC 2001, Singapore, pp 849–858
13. Krishna LR, Rao DS, Sundararajan G (2003) Coatability and characterization of fly ash deposited on mild steel by detonation spraying. *J Therm Spray Technol* 12:77–79
14. Krishna LR, Sen D, Rao YS, Rao GVN, Sundararajan G (2002) Thermal spray coating of aluminum nitride utilizing detonation spray technique. *J Mater Res* 17:2514–2523
15. Babu PS, Basu B, Sundararajan G (2008) Processing-structure-property correlation and decarburization phenomenon in detonation sprayed WC-12Co coatings. *Acta Mater* 56:5012–5026
16. Legoux JG, Arsenault B, Hawthorne H, Immarigeon JP (2003) Erosion behavior of WC-10Co-4Cr HVOF coatings. In: Thermal spray 2003: advancing the science & applying the technology. ASM International, Materials Park, pp 405–410

17. Lovelock HLDV, Vanwyk P (1998) Effect of powder type and composition on the erosion and abrasion of HP/HVOF deposited WC-Co coatings. In: Proceedings of the ITSC, 25–29 May, Nice, France, pp 193–198
18. Niemi K, Rekola S, Vuoristo P, Laurila J, Vippola M, Mantyla T (2003) Advanced oxide ceramic coatings for applications demanding high wear resistance. In: Thermal spray 2003: advancing the science & applying the technology. ASM International, Materials Park, pp 233–236
19. Leblanc L (2003) Abrasion and sliding wear of nanostructured ceramic coatings. In: Thermal spray 2003: advancing the science & applying the technology. ASM International, Materials Park, pp 291–299
20. Bolelli G, Cannillo V, Lusvarghi L, Manfredini T (2006) Wear behavior of thermally sprayed ceramic oxide coatings. *Wear* 261:1298–1315
21. Westergard R, Erickson LC, Axen N, Hawthorne HM, Hogmark S (1998) The erosion and characteristics of alumina coatings by plasma sprayed under different spraying conditions. *Tribol Int* 31:271–279
22. McPherson R (1980) On the formation of thermally sprayed alumina coatings. *J Mater Sci* 15:3141–3149
23. Krishna LR, Gupta PSVNB, Sundararajan G (2015) The influence of phase gradient within the micro arc oxidation (MAO) coatings on mechanical and tribological behaviors. *Surf Coat Technol* 269:54–63
24. Yilmaz R, Kurt AO, Demir A, Tatli Z (2007) Effects of TiO₂ on the mechanical properties of the Al₂O₃-TiO₂ plasma sprayed coating. *J Eur Ceram Soc* 27:1319–1323
25. Jia SK, Zou Y, Xu J-Y, Wang J, Yu L (2015) Effect of TiO₂ content on properties of Al₂O₃ thermal barrier coatings by plasma spraying. *Trans Nonferrous Metals Soc China* 25:175–183
26. Ramachandran K, Selvarajan V, Ananthapadmanabhan PV, Sreekumar KP (1998) Microstructure, adhesion, microhardness, abrasive wear resistance and electrical resistivity of the plasma sprayed alumina and alumina–titania coatings. *Thin Solid Films* 315:144–152
27. Celik E, Sengil IA, Avci E (1997) Effect of some parameters on corrosion behavior of plasma-sprayed coatings. *Surf Coat Technol* 97:355–360
28. Lima RS, Leblanc L, Marple BR (2004) Abrasion behavior of nano-structured and conventional titania coatings thermally sprayed via APS, VPS and HVOF. In: Proceedings of the ITSC2004, Osaka, Japan, ASM International, pp 1034–1039
29. Lima RS, Marple BR (2007) Thermal spray coatings engineered from nanostructured ceramic agglomerated powders for structural, thermal barrier and biomedical applications: a review. *J Therm Spray Technol* 16:40–63
30. Dosta S, Robotti M, Garcia Segura S, Brillas E, Cano IG, Guilemany JM (2016) Influence of atmospheric plasma spraying on the solar photoelectron-catalytic properties of TiO₂ coatings. *Appl Catal B Environ* 189:151–159
31. Westergard R, Axen N, Wiklund U, Hogmark S (2000) An evaluation of plasma sprayed ceramic coatings by erosion, abrasion and bend testing. *Wear* 246:12–19
32. Zamani P, Valefi Z (2017) Microstructure, phase composition and mechanical properties of plasma sprayed Al₂O₃, Cr₂O₃ and Cr₂O₃-Al₂O₃ composite coatings. *Surf Coat Technol* 316:138–145
33. Erickson LC, Westergard R, Wiklund U, Axen N, Hawthorne M, Hogmark S (1998) Cohesion in plasma sprayed coatings-A comparison between evaluation methods. *Wear* 214:30–37
34. Babu PS, Sen D, Jyothirmayi A, Krishana LR, Rao DS (2018) Influence of microstructure on the wear and corrosion behavior of detonation sprayed Cr₂O₃-Al₂O₃ and plasma sprayed Cr₂O₃ coatings. *Ceram Int* 44:2351–2357
35. Lima RS, Marple BR (2005) Superior performance of high-velocity oxyfuel-sprayed nanostructured TiO₂ in comparison to air plasma-sprayed conventional Al₂O₃-TiO₂. *J Therm Spray Technol* 14:397–404
36. Lima RS, Marple BR (2006) From APS to HVOF spraying of conventional and nanostructured titania feedstock powders: a study on the enhancement of the mechanical properties. *Suf Coat Technol* 200:3428–3437

37. Rodrigues M, Klisans J, Bavaresco L, Scagni A, Arenas F (2001) Wear resistance of HVOF sprayed carbide coatings. In: Thermal spray 2001. ASM International, Materials Park
38. Berger LM, Saaro S, Naumann T, Kasparova M, Zahalka F (2010) Influence of feedstock powder characteristics and spray processes on microstructure and properties of WC-(W, Cr) 2C-Ni hardmetal coatings. *Surf Coat Technol* 205:1080–1087
39. Magnani M, Suegama PH, Espallargas N, Dosta S, Fugivara CS, Guilemany JM, Benedetti AV (2008) Influence of HVOF parameters on the corrosion and wear resistance of WC-Co coatings sprayed on AA7050 T7. *Surf Coat Technol* 202:4746–4757
40. Bozzi AC, de Mello JDB (1999) Wear resistance and wear mechanism of WC-12%Co thermal sprayed coatings in three-body abrasion. *Wear* 233–235:575–587
41. Stewart DA, Shipway PH, McCartney DG (1999) Abrasive wear behavior of conventional and nanocomposite HVOF-sprayed WC-Co coatings. *Wear* 225–229:789–798
42. Babu PS, Basu B, Sundararajan G (2010) Abrasive wear behavior of detonation sprayed WC-12Co coatings: influence of decarburization and abrasive characteristics. *Wear* 268:1387–1399
43. Babu PS, Basu B, Sundararajan G (2011) The influence of erodent hardness on the erosion behavior of detonation sprayed WC-12Co coatings. *Wear* 270:903–913
44. Chen H, Hutchings IM (1998) Abrasive wear resistance of plasma sprayed tungsten carbide cobalt coatings. *Surf Coat Technol* 107:106–114
45. Liao H, Normand B, Coddet C (2000) Influence of coating microstructure on the abrasive wear resistance of WC/Co cermet coatings. *Surf Coat Technol* 124:235–242
46. Zhao LD, Maurer M, Fischer F, Dicks R, Lugscheider E (2004) Influence of spray parameters on the particles in-flight properties and properties of HVOF coating of WC-CoCr. *Wear* 257:41–46
47. Schwetke R, Kreye H (1999) Microstructure and properties of tungsten carbide coatings sprayed with various high velocity oxygen fuel spray systems. *J Therm Spray Technol* 8:433–439
48. Sobolev VV, Guilemany JM, Miguel JR, Calero JA (1996) Investigation of the development of coating structure during high velocity oxy-fuel (HVOF) spraying of WC-Ni powder particles. *Surf Coat Technol* 82:114–120
49. Wijewardane S (2015) Thermal spray coatings in renewable energy applications. In: Future development of thermal spray coatings: Types, Designs, Manufacture & Applications, Ed: Nuria Esparallargas, Woodhead Publishing, Cambridge, UK pp 241–257
50. Babu PS, Basu B, Sundararajan G (2013) A comparison of mechanical and tribological behavior of nanostructured and conventional WC-12Co detonation-sprayed coatings. *J Therm Spray Technol* 22:479–490
51. Liu YR, Qiao YF, He JH, Lavernia EJ, Fischer TE (2002) Near-nanostructured WC-18 pct Co coatings with low amounts of non-WC carbide phase: Part II. Hardness and resistance to sliding and abrasive wear. *Metal Mater Trans A* 33:159–164
52. Babu PS, Rao PC, Jyothirmayi A, Phani PS, Krishna LR, Rao DS (2018) Evaluation of microstructure, property and performance of detonation sprayed WC-(W,Cr)2C-Ni coatings. *Surf Coat Technol* 335:345–354
53. Savarimuthu AC, Taber HF, Megat I, Shadley JR, Rybicki EF, Cornell WC, Emery WA, Somerville DA, Nuse JD (2001) Sliding wear behavior of tungsten carbide thermal spray coatings for replacement of chromium electroplate in aircraft applications. *J Therm Spray Technol* 10:502–510
54. Nascimento MP, Souza RC, Miguel IM, Pigatin WL, Voorwald HJC (2001) Effects of tungsten carbide thermal spray coating by HP/HVOF and hard chromium electroplating on AISI 4340 high strength steel. *Surf Coat Technol* 138:113–124
55. Agüero A, Camon F, de Blas JG, del Hoyo JC, Muelas R, Santaballa A, Ulargui S, Valles P (2011) HVOF-deposited WCCoCr as replacement for hard Cr in landing gear actuators. *J Therm Spray Technol* 20(6):1292–1309

56. Junior GS, Voorwald HJC, Vieira LFS, Cioffi MOH, Bonora RG (2010) Evaluation of WC-10Ni thermal spray coating with shot peening on the fatigue strength of AISI 4340 steel. *Procedia Eng* 2:649–656
57. Bonora RG, Voorwald HJC, Cioffi MOH, Junior GS, Santos LFV (2010) Fatigue in AISI 4340 steel thermal spray coating by HVOF for aeronautic application. *Procedia Eng* 2:1617–1623
58. Souza RC, Voorwald HJC, Cioffi MOH (2008) Fatigue strength of HVOF sprayed Cr₃C₂-25NiCr and WC-10Ni on AISI 4340 steel. *Surf Coat Technol* 203:191–198
59. Hermosilla WAG, Chicot D, Lesage J, Sosa JGLB, Gruescu IC, Staia MH, Cabrera ESP (2010) Effect of substrate roughness on the fatigue behavior of a SAE 1045 steel coated with a WC-10Co-4Cr cermet, deposited by HVOF thermal spray. *Mater Sci Eng A* 527:6551–6561
60. Vackel A, Sampath S (2017) Fatigue behavior of thermal sprayed WC-CoCr- steel systems: role of process and deposition parameters. *Surf Coat Technol* 315:408–416
61. Sosa JGLB, Santana YY, Gutierrez CJV, Chicot D, Lesage J, Decoopman X, Lost A, Staia MH, Cabrera ESP (2013) Fatigue behavior of a structural steel coated with a WC-10Co-4Cr/ Colmonoy 88 deposit by HVOF thermal spraying. *Surf Coat Technol* 220:248–256
62. Varis T, Suhonen T, Calonius O, Cuban J, Pietola M (2016) Optimization of HVOF Cr₃C₂-NiCr coating for increased fatigue performance. *Surf Coat Technol* 305:123–131
63. Vackel A, Dwivedi G, Sampath S (2015) Structurally integrated, damage-tolerant, thermal spray coatings. *JOM* 67:1540–1553
64. Gutierrez CJV, Chacon GEG, Sosa JGLB, Pineiro A, Staia MH, Lesage J, Chicot D, Mesmacque G, Cabrera ESP (2008) Fatigue and corrosion fatigue behavior of an AA6063-T6 aluminum alloy coated with a WC-10Co-4Cr alloy deposited by HVOF thermal spraying. *Surf Coat Technol* 202:4572–4577
65. Cabrera ESP, Staia MH, Santana YY, Zorrilla EJM, Lesage J, Chicot D, Sosa JGLB, Perez EO, Gutierrez CJV (2013) Fatigue behavior of AA7075-T6 aluminum alloy coated with a WC-10Co-4Cr cermet by HVOF thermal spray. *Surf Coat Technol* 220:122–130
66. https://titanium.org/resource/resmgr/2010_2014.../Kim&Punga_2010_Industrial_20.pdf
67. Kim GE, Walker J (2007) Successful application of nanostructured Titanium Dioxide coating for high-pressure acid-leach application. *J Therm Spray Technol* 16:34–39
68. Yerokhin AL, Nie X, Leyland A, Matthews A, Doney SJ (1999) Plasma electrolysis for surface engineering. *Surf Coat Technol* 122(2–3):73–93
69. Coquillat AS, Campos EM, Mohedano M, Corria RM, Ramos V, Arrabal R, Matykina E (2018) In vitro and in vivo evaluation of PEO modified titanium for bone implant applications. *Surf Coat Technol* 347:358–368
70. Sowa M, Simka W (2018) Electrochemical impedance and polarization corrosion studies of tantalum surface modified by DC plasma electrolytic oxidation. *Materials* 11(4):545. <https://doi.org/10.3390/ma11040545>
71. Farrakhov RG, Mukaeva VR, Fatkullin AR, Gorbakov MV, Tarasov PV, Lazarev DM, Ramesh Babu N, Parfenov EV (2018) Plasma electrolytic oxidation treatment mode influence on corrosion properties of coatings obtained on Zr-1Nb alloy in silicate-phosphate electrolyte. *Mater Sci Eng* 291(1):012006
72. Krishna LR, Purnima AS, Sundararajan G (2006) A comparative study of tribological behavior of micro arc oxidation and hard-anodized coatings. *Wear* 261:1095–1101
73. Kumar SA, Pradhan S, Raman SGS, Gnanamoorthy R (2014) Performance of alumina coatings prepared by hard anodizing, micro arc oxidation and detonation spray processes on Al-Mg-Si alloy under fretting wear loading. *Proc Inst Mech Eng Part J J Eng Tribol* 228(4):454–462
74. Venugopal A, Srinath J, Narayanan PR, Sharma SC, George KM (2014) Corrosion and multi-scale mechanical behavior of plasma electrolytic oxidation (PEO) and hard anodized (HA) coatings on AA 2219 aluminum alloy. *Mater Sci Forum* 830–831:627–630

75. Krishna LR, Somaraju KRC, Sundararajan G (2003) The tribological performance of ultra-hard ceramic composite coatings obtained through microarc oxidation. *Surf Coat Technol* 163–164:484–490
76. Dehnavi V, Luan BL, Liu XY, Shoosmith DW, Rohani S (2015) Correlation between plasma electrolytic oxidation treatment stages and coating microstructure on aluminum under unipolar pulsed DC mode. *Surf Coat Technol* 269:91–99
77. Gowtham S, Arunnellaiappan T, Babu NR (2016) An investigation on pulsed DC plasma electrolytic oxidation of cp-Ti and its corrosion behavior in simulated body fluid. *Surf Coat Technol* 301:63–73
78. Yerokhin AL, Shatrov A, Samsonov V, Shashkov P, Pilkington A, Leyland A, Matthews A (2005) Oxide ceramic coatings on aluminum alloys produced by pulsed bipolar plasma electrolytic oxidation process. *Surf Coat Technol* 199:150–157
79. Krishna LR, Rybalko AV, Sundararajan G (2005) Process for forming coatings on metallic bodies and an apparatus for carrying out the process. US Patent 6,893,551
80. Lerner LM (2010) Hard anodizing of aerospace aluminum alloys. *Trans Inst Met Finish* 88:21–24
81. Dujardin L, Viola A, Henrion G (2005) Diagnostics of an electrolytic micro arc process for aluminium alloy oxidation. *Surf Coat Technol* 2000:804–808
82. Curran JA, Clyne TW (2006) Porosity in plasma electrolytic oxide coatings. *Acta Mater* 54:1985–1993
83. Sundararajan G, Krishna LR (2003) Mechanisms underlying the formation of thick alumina coatings through the MAO coating technology. *Surf Coat Technol* 167:269–277
84. Arunnellaiappan T, Ashfaq M, Rama Krishna L, Rameshbabu N (2016) Fabrication of corrosion-resistant Al_2O_3 - CeO_2 composite coatings on AA7075 via plasma electrolytic oxidation coupled with electrophoretic deposition. *Ceram Int* 42:5897–5905
85. Sandhyarani M, Rameshbabu N, Venkateswarlu K, Krishna LR (2014) Fabrication, characterization and in-vitro evaluation of nanostructured zirconia/hydroxyapatite composite film on zirconium. *Surf Coat Technol* 238:58–67
86. Arunnellaiappan T, Arun S, Hariprasad S, Gowtham S, Krishna LR, Rameshbabu N (2018) Fabrication of corrosion resistant hydrophobic ceramic nanocomposite coatings on PEO treated AA7075. *Ceram Int* 44(1):874–884
87. Arunnellaiappan T, Krishna LR, Anoop S, Uma Rani R, Rameshbabu N (2016) Fabrication of multifunctional black PEO coatings on AA7075 for spacecraft applications. *Surf Coat Technol* 307:735–746
88. Ma KJ, Al Bosta MMS, Wu WT (2014) Preparation of self-lubricating composite coatings through a micro arc oxidation with graphite in electrolyte solution. *Surf Coat Technol* 259:318–324
89. Li HX, Song RG, Ji ZG (2012) Effect of nano-additive TiO_2 on performance of micro arc oxidation coatings formed on 6063 aluminum alloy. *Trans Nonferrous Metals Soc China* 23:406–411
90. Huang D, Zhang X, Wu D, Zhou X (2014) Effects of rare earth (RE) additives on performances of micro arc oxidation coatings formed on aluminum alloy. *Adv Mater Res* 850–851:140–143
91. Nie X, Meletis EI, Jiang JC, Leyland A, Yerokhin AL, Matthews A (2002) Abrasive wear/corrosion properties and TEM analysis of Al_2O_3 coatings fabricated using plasma electrolysis. *Surf Coat Technol* 149(2–3):245–251
92. Xie HJ, Cheng YL, Li SX, Cao JH, Cao L (2017) Wear and corrosion resistant coatings on surface of cast A356 aluminum alloy by plasma electrolytic oxidation in moderately concentrated aluminate electrolytes. *Trans Nonferrous Metals Soc China* 27:336–351
93. Yin B, Peng Z, Liang J, Jin K, Zhu S, Yang J, Qiao Z (2016) Tribological behavior and mechanism of self-lubricating wear-resistant composite coatings fabricated by one-step plasma electrolytic oxidation. *Tribol Int* 97:97–107

94. Krishna LR, Purnima AS, Wasekar NP, Sundararajan G (2007) Kinetics and properties of micro arc oxidation coatings deposited on commercial Al alloys. *Metall Mater Trans A* 38A:370–378
95. Wasekar NP, Jyothirmayi A, Krishna LR, Sundararajan G (2008) Effect of micro arc oxidation coatings on corrosion resistance of 6061 Al alloy. *J Mater Eng Perform* 17(5):708–713
96. Krishna LR, Poshal G, Sundararajan G (2010) Influence of electrolyte chemistry on morphology and corrosion resistance of micro arc oxidation coatings deposited on magnesium. *Mater Metall Trans A* 41(13):3499–3508
97. Krishna LR, Sundararajan G (2014) Aqueous corrosion behaviour of micro arc oxidation (MAO) coated magnesium alloys – a critical review. *JOM* 66(6):1045–1060
98. Venugopal A, Srinath J, Krishna LR, Narayanan PR, Sharma SC, Venkitakrishnan PV (2016) Corrosion and nanomechanical behaviors of plasma electrolytic oxidation coated AA7020-T6 aluminum alloy. *Mater Sci Eng A* 660:39–46
99. Venugopal A, Panda R, Manwatkar S, Sreekumar K, Krishna LR, Sundararajan G (2012) Effect of microstructure on the localized corrosion and stress corrosion behaviours of plasma-electrolytic-oxidation-treated AA7075 aluminum alloy forging in 3.5wt.%NaCl solution. *Int J Corros*:823967. <https://doi.org/10.1155/2012/823967>
100. Wasekar NP, Ravi N, Babu PS, Rama Krishna L, Sundararajan G (2010) High-cycle fatigue behavior of microarc oxidation coatings deposited on a 6061-T6 Al alloy. *Metall Mater Trans A* 41(1):255–265
101. Sundararajan G, Wasekar NP, Ravi N (2010) The influence of the coating technique on the high cycle fatigue life of alumina coated Al 6061 alloy. *Trans Indian Inst Metals* 62:203–208
102. Camargo A, Voorwald H (2007) Influence of anodization on the fatigue strength of 7050-T7451 aluminum alloy. *Fatigue Fract Eng Mater Struct* 30:993–1007
103. Krishna LR, Madhavi Y, Sahithi T, Wasekar NP, Chavan NM, Rao DS (2018) Influence of prior shot peening variables on the fatigue life of micro arc oxidation coated 6061-T6 Al alloy. *Int J Fatigue* 106:165–174
104. Krishna LR, Wasekar NP, Sundararajan G (2013) A process for continuous coating deposition and an apparatus for carrying out the process. US Patent 8,486,237
105. Krishna LR, Wasekar NP, Sundararajan G (2016) Process for continuous coating deposition and an apparatus for carrying out the process. US Patent 9,365,945
106. Lin Y, Yao J, Lei Y, Fu H, Wang L (2016) Microstructure and properties of TiB₂-TiB reinforced titanium matrix composite coating by laser cladding. *Opt Lasers Eng* 86:216–227
107. Sun RL, Lei YW, Niu W (2009) Laser clad TiC reinforced NiCrBSi composite coatings on Ti-6Al-4V alloy using a CW CO₂ laser. *Surf Coat Technol* 203:1395–1399
108. Xiang Z-F, Liu X-B, Ren J, Luo J, Shi S-H, Chen Y, Shi G-L, Wu S-H (2014) Investigation of laser cladding high temperature anti-wear composite coatings on Ti6Al4V alloy with the addition of self-lubricant CaF₂. *Appl Surf Sci* 313:243–250
109. Liu X-B, Meng X-J, Liu H-Q, Shi G-L, Wu S-H, Sun C-F, Wang M-D, Qi L-H (2014) Development and characterization of laser clad high temperature self-lubricating wear resistant composite coatings on Ti-6Al-4V alloy. *Mater Des* 55:404–409
110. Yang Y, Zhang D, Yan W, Zheng Y (2010) Microstructure and wear properties of TiCN/Ti coatings on titanium alloy by laser cladding. *Opt Lasers Eng* 48:119–124
111. Shariff SM, Tak M, Ojha H, Padmanabham G (2009) Characteristics and erosive wear performance of Ni-Cr based coatings on SS-310 steel by diode-laser cladding and weld-overlay processes. In: Proceedings of international conference on surface modification technologies (SMT-23), Chennai
112. Tak M, Shariff SM, Sake V, Padmanabham G (2012) A novel method of pulsed laser-cladding or effective control of melting of WC particulates in NiCr-WC composite coatings. In: Proceedings of 31st international congress on applications of lasers & electro-optics (ICALEO 2012), pp 515–523

113. Venkatesh L, Samajdar I, Tak M, Doherty RD, Gundakaram RC, Prasad KS, Joshi SV (2015) Microstructure and phase evolution in laser clad chromium carbide-NiCrMoNb. *Appl Surf Sci* 357:2391–2401
114. Yang Y, Guo N, Li J (2013) Synthesizing, microstructure and microhardness distribution of Ti–Si–C–N/TiCN composite coating on Ti–6Al–4V by laser cladding. *Surf Coat Technol* 219:1–7
115. Li J, Chen C, Squartini T, He Q (2010) A study on wear resistance and microcrack of the Ti3Al/TiAl+TiC ceramic layer deposited by laser cladding on Ti–6Al–4V alloy. *Appl Surf Sci* 257:1550–1555
116. Yuping P, Guo B, Zhou J, Zhang S, Zhou H, Chen J (2008) Microstructure and tribological properties of in situ synthesized TiC, TiN, and SiC reinforced Ti3Al intermetallic matrix composite coatings on pure Ti by laser cladding. *Appl Surf Sci* 255:2697–2703
117. Ochonogor OF, Meacock C, Abdulwahab M, Pityana S, Popoola API (2012) Effects of Ti and TiC ceramic powder on laser-cladded Ti–6Al–4V in situ intermetallic composite. *Appl Surf Sci* 263:591–596
118. Dhanda M, Haldar B, Saha P (2014) Development and characterization of hard and wear resistant MMC coating on Ti-6Al-4V substrate by laser cladding. *Procedia Mater Sci* 6:1226–1232
119. Wu F, Chen T, Wang H, Liu D (2017) Effect of Mo on microstructures and wear properties of in situ synthesized Ti(C,N)/Ni-based composite coatings by laser cladding. *Materials* 10:1047–1059
120. Weng F, Yu H, Liu J, Chen C, Dai J, Zhao Z (2017) Microstructure and wear property of the Ti₅Si₃/TiC reinforced Co-based coatings fabricated by laser cladding on Ti-6Al-4V. *Opt Laser Technol* 92:156–162
121. Liu X-B, Wang H-M (2006) Modification of tribology and high-temperature behaviour of Ti–48Al–2Cr–2Nb intermetallic alloy by laser cladding. *Appl Surf Sci* 252:5735–5744
122. Lv YH, Li J, Tao YF, Hu LF (2017) High-temperature wear and oxidation behaviours of TiNi/Ti₂Ni matrix composite coatings with TaC addition prepared on Ti6Al4V by laser cladding. *Appl Surf Sci* 402:478–494
123. Li GJ, Li J, Luo X (2014) Effects of high temperature treatment on microstructure and mechanical properties of laser-clad NiCrBSi/WC coatings on titanium alloy substrate. *Mater Charact* 98:83–92
124. Lin Y, Lei Y, Li X, Zhi X, Fu H (2016) A study of TiB₂/TiB gradient coating by laser cladding on titanium alloy. *Opt Lasers Eng* 82:48–55
125. Nieto A, Bisht A, Lahiri D, Zhang C, Agarwal A (2017) Graphene reinforced metal and ceramic matrix composites: a review. *Int Mater Rev* 62:241–302
126. Balani K, Rao SB, Yao Chen, Tapas L, Agarwal A (2007) Role of powder treatment and carbon nanotube dispersion in the fracture toughening of plasma-sprayed aluminum oxide-carbon nanotube nanocomposites. *J Nanosci Nanotechnol* 7:3553–3562

Index

A

- Ablation, 1245
- Abrasive slurry jet micro-machining (ASJM), 587
- Accelerator driven sub-critical systems (ADSS), 746
- Acetylides, 923
- Activated carbon (AC), 1281–1285
- Active filler controlled pyrolysis (AFCOP), 1009–1011
- Additive manufacturing (AM)
 - classification, 321–324
 - technology, 320
 - See also* Ceramics
- Advanced electronics, 6
- Advanced fuels, 671, 672
- Advanced steady state tokamak reactor (A-SSTR) blanket structure design, 661
- Aerospace applications, 1096
 - titanium alloys, laser cladding on, 1502–1517
- Aerospace sector, sol-gel nanocomposite coatings
 - aluminum alloys, chrome-free conversion coatings on, 1417–1418
 - anti-bacterial coatings, 1422–1424
 - transparent plastics, scratch resistant coatings on, 1420–1422
 - ultrahydrophobic/superhydrophobic/icephobic coatings, 1418–1420
- Aesthetics, 344
- Aircraft structures, 1097, 1098
- Airplanes and missile carriers, 254
- Air plasma spray/spraying (APS), 1446, 1447, 1453, 1456, 1466, 1467, 1469, 1471, 1474, 1476
- Air-to-air missiles, 253
- Air-to-surface missiles, 253
- Alkaline earth hydridehalide
 - crystal structure of, 756
 - thermal properties of, 759
- Al₂O₃, 611–615
- Alternating current (AC), 1486
- Alumina, 271, 361
 - foams, 1117
 - rich spinel, 498
- Alumina-zirconia composite material, 335
- Aluminium oxynitride (AlON) transparent polycrystalline armour, 450–452
- Alumino-borosilicate (ABS), 943, 945, 946, 952
- Aluminum alloys, chrome-free conversion coatings on, 1417–1418
- Aluminum foil transformers (AFTs), 1502
- Aluminum nitride (AlN) ceramics, 627–628
- Aluminum oxynitride, 626–627
- Alzheimer disease, 112
- Analysis of variance (ANOVA), 842
- Anisotropy, 897
- Anomalous scattering, 480
- Antennas
 - dielectric resonator, 199–200
 - low-temperature cofired ceramics, 202–204
 - metamaterial based, 200–202
 - microstrip, 197–198
- Anthryl tetra acid, 1432
- Anti-aircraft missile complex, 253, 270
- Antibacterial coatings, 1422–1424
- Antibacterial property, 336
- Antimicrobial activity, 1424
- Applicant country, 328
- Application based records, 336
- Aramid fibers, 368–370
- Arc-jet test, 1033, 1036, 1056, 1244
- Artificial bone manufacturing, 342

- Athermal optics, 1140, 1141, 1149, 1159
 Atmospheric plasma spray (APS), 1372, 1374, 1375, 1379, 1388, 1397, 1404, 1405
 Atomic oxygen resistant coatings, 979, 1042–1044
 Atomization, 1377
 Autoclave process, 375
- B**
- Ballistic impact studies, 376, 407
 Ballistic limit tests, 390–392
 Barium zinc tantalate (BZT) ceramics, 799–800
 consolidation technique, 805–807
 densification behavior, 817
 dielectric properties, 821–824
 flux addition, 803–804
 microstructural analysis, 818–819
 microwave sintering, 807–815
 particle size, 801
 peak sintering temperature and dwell time, 801–802
 sintering atmospheres, 804–805
 XRD and Raman spectroscopy, crystal structure and ordering, 819–821
 Barium zirconium titanate (BZT), 1088–1090
 Basket weave, 417
 BaTiO₃ aerogels, 133
 Battery
 definition, 1263
 lithium-ion (*see* Lithium-ion battery)
 Battery management system (BMS), 1262
 Beam bending, 12
 Bend stress relaxation (BSR), 655
 Beryllium mirrors, 1140
 Beryllium oxide, 271, 277, 797
 Beta-alumina, 765
 Bioceramics, 334, 336
 Birefringent crystals, 438
 Bismuth titanate (Bi₄Ti₃O₁₂), 782, 783
 Black phosphorous (BP), 1354–1358
 Black TiO₂, 1341–1345
 Blade outer air seal (BOAS), 1212
 Bond coats (BCs), 1445–1447
 Bore-sight error (BSE), 258–262
 Boron
 carbide, 335, 363
 isotopes, 704
 minerals, 704
 neutron capture therapy, 705
 nitride, 271, 277
 physical, mechanical, thermal and nuclear properties, 707–708
 Borosilicate glass, 1225
 Boundary layer splitter (BLS), 1035
 Bowl-feed polishing, 575
 Brayton cycle, 1444
 Brazing, 800, 803, 824, 826
 Bridgman method, 1175
 Brittle-to-ductile transition temperature (BDTT), 1170, 1178, 1183, 1186, 1187, 1190
 Bruceton test method, 391
 Brunauer, Emmett, and Teller (BET) method, 127
 Business intelligence, 330
 B33Y, 327
 BZT lead-free piezo materials
 characterization, 1088
 dielectric constant and loss factor, 1088, 1089
 polarization measurements, 1090
 BZT microwave dielectric ceramics,
 see Barium zinc tantalate (BZT) ceramics
- C**
- CaBr₂-CaH₂ system, 760
 CaCl₂-CaH₂ system, 759
 Calcium hydride bromide electrolyte, 761
 Calcium-magnesium-alumino-silicate (CMAS), 1387, 1388, 1397, 1451, 1455, 1459, 1460
 Capacitance, 1263, 1266, 1267
 Carbide fuel, 684–685, 692
 fabrication, 678–681
 fission gas release, 685–687
 fuel processing, 697–700
 international experience, 687–693
 phase diagrams, 671–675
 swelling, 685, 686
 thermal conductivity, 675–678
 thermal creep, 678, 679
 Carbonaceous polymers, 1007–1009
 Carbonates, molten, 775–777
 Carbon-based nanomaterials, 14, 15
 Carbon fiber reinforced polymers, 1142
 Carbon fiber reinforced silicon carbide ceramic matrix composites (C/SiC), 889
 applications, 872
 calibration standards and components, telescope, 906–907
 carbon fabric, 835
 energy systems, components for, 907–908
 friction systems, 905

- gas phase route, 882–888
- general properties, 839
- liquid phase route, 881–882
- LSI based, 853–871
- mechanical behavior, 890–896
- oxidation behavior, 901–903
- PIP based, 839–853
- rocket motors and jet engines, components, 905–907
- space vehicle components, 904–905
- strong bonds, 838
- thermal behavior, 896–898
- tribological behavior, 898–901
- Carbon fiber reinforcement, 834–835
 - needle punch preform, 836–837
 - woven preforms, 836
- Carbon nanotube (CNT), 931, 1517
 - aerogels, 137
- Carbon nanotube reinforced ceramic matrix nanocomposites
 - applications, 966–967
 - bulk ceramic matrix and sintering, 933–934
 - colloidal processing, 941–942
 - conventional powder processing route, 937–939
 - CVD, *in-situ* growth, 939–941
 - interfacial bonding, 934
 - intragranular CNT reinforcement, 944–946
 - mechanical properties, 945–953
 - microstructural developments, 937
 - sol-gel based processing routes, 942–945
 - surface modification/chemical functionalization techniques, 935–936
 - toughening mechanisms, 958–965
 - tribological properties, 953–957
- Carbothermic reduction, 679
- Cellulose aerogels, 135
- Ceramic adhesives, 979, 1011, 1045–1051, 1058, 1059, 1062, 1065
- Ceramic and cermet composite coatings
 - MAO coating technology, on Al alloys, 1484–1502
 - thermal spray (*see* Thermal spray)
- Ceramic based composite materials, 345, 346
- Ceramic based radomes, 189–190
- Ceramic composite armour, 405
 - alumina, 361
 - approaches for energy dissipation improvement, 425–428
 - aramid fibers, 368–370
 - ballistic impact, 407
 - ballistic limit tests, 390–392
 - ballistic test methodologies, 380–394
 - boron carbide, 363
 - ceramics, 413–415
 - ceramic tile configuration, 423
 - classification of materials, 361
 - composite laminates, 367
 - confinement and wrapping, 425
 - cross-section, 406
 - depth of penetration, 409
 - depth of penetration test, 383–388
 - design issues, 421–425
 - effects of projectile parameters, 412–413
 - energy dissipating mechanism, 409–411
 - fabrics, 417–418
 - fibers, 416–417
 - future research, 431
 - futuristic materials, 398–399
 - manufacturing process, 407
 - material choices, 413–421
 - matrix, 372–373, 418–419
 - modules, 394–399
 - multilayered, 405
 - multiple hit resistance, 429–430
 - penetration in ceramics, 375–377
 - penetration in composite laminates, 377–379
 - penetration, perforation and ballistic limit, 408
 - performance comparison, 419
 - pressing, 364–365
 - pressure sintering, 365
 - protective areal density method, 393–394
 - reaction bonding, 366
 - reinforcement, 367–372
 - relative thickness of components, 421–425
 - residual velocity test, 389–390
 - semi-infinite backing test method, 388–389
 - silicon carbide, 362
 - sintering, 365
 - threat levels and standards, 382–383
 - titanium diboride, 363–364
 - ultra high molecular weight polyethylene fibers, 370–371
 - wave propagation, 408
- Ceramic foams
 - categories, 1106
 - compressive stress-strain graph, 1108
 - definition, 1106
 - direct foaming method, 1119–1120
 - emulsion templating, 1116–1119
 - freeze casting, 1113–1116
 - gelcasting, 1120–1122
 - mechanical strength, 1108–1109

- Ceramic foams (*cont.*)
 particle stabilized foams, 1123
 polymer foam template method, 1112
 pre-ceramic polymer, 1127–1128
 processing, 1110–1112
 sacrificial template method, 1113
 thermal conductivity, 1107–1108, 1128–1130
 thermal shock resistance, 1110
 thermo-foaming, 1124–1126
 Young's modulus, 1109
- Ceramic matrix composites (CMCs), 642, 643, 645, 832, 833, 837, 839, 843, 845, 860, 878, 881, 903, 905, 914, 979, 1005, 1009, 1012, 1013, 1017, 1020, 1026, 1045, 1049, 1059, 1445
 application areas, 1012
 borosiloxane, 1023
 design, 1015
 flexural strength values, 1021
 matrix phase in, 1017
 PIP process, 1017
 shingles, 1061–1062
 silicon carbide matrix, 1017
 SiOC matrix, 1018
- Ceramic on-demand extrusion (CODE), 323
- Ceramic polymer precursor, 915
- Ceramics, 914
 aerospace and strategic applications, 345–347
 components, 321
 extrusion process, 323
 focus fields, 331–344
 fused deposition printing, 322
 patenting trends, 325–331
 photopolymer material, 324
See also Three dimensional printing (3D printing)
- Ce:YAG based glass-ceramic phosphor, 484
- Chemical/biological sensor, 1431–1435
- Chemical and biological warfare (CBW) diagnostics, 17–24
- Chemical vapor deposition (CVD), 883, 894, 903, 923, 935, 939–941, 958
- Chemical vapor infiltration (CVI), 644–650, 652, 655, 883, 941, 967, 1013, 1017, 1021, 1052, 1061
 advantages, 885
 disadvantages, 886
 FCVI, 884
 ICVI, 883, 885
 MSI, 887–888
 MWCVI, 883
- PIP, 886–887
 pulsed CVI, 884
 TGCVI, 884
- Chemo-mechanical polishing (CMP), 574–575
- Chemoresistive gas sensors, 103
- Chloromethylchlorosilanes, 922
- Chlorosilanes, 919
 acetylides, 923
 methylene halides, 922
- Chrome-free conversion coatings, 1417–1418
- Chromium niobate (CrNbO₄), 773, 774
- Chromium oxide, 1474
- Civilian market, 6
- Closed cellular ceramic foams
 compressive strength, 1109
 microstructure, 1107
 thermal conductivity, 1129
- Coarse porosity, 1383, 1386
- Coatings, 1372, 1376, 1378, 1380, 1383, 1386, 1388, 1391, 1399, 1401, 1405
- Coefficient of friction (COF), 899, 955, 957
- Coefficient of linear thermal expansion, 1138
- Coefficient of thermal expansion (CTE), 476, 864–867, 897, 1012, 1027, 1040, 1041, 1047, 1187, 1193, 1195, 1209, 1447
- Coherence correlation interferometry (CCI), 593–594
- Cold gas dynamic spray (CGDS), 1518
- Cold isostatic pressing (CIP) method, 220, 221, 506
- Cold pressing, 365
- Cold spray, 1372
- Colloidal processing, 941–942
- Colloidal processing route, 1111
- Colony formation units (CFU), 1423
- Colour filter glasses, 571
- Comminution, 410
- Compatibility, SiC/SiC composites, 659–660
- Complementary split ring resonator (CSRR), 19, 20
- Composite(s)
 alumina-zirconia, 335
 ceramic-metal, 335
 ceramics, 331
 coatings, 1401, 1403
 gypsum, 337
 metal-glass, 336
 oxide/non-oxide materials, 334
 polyetheretherketone/nano-hydroxyapatite, 336
- Compression moulding process, 407

- Compressive stress waves, 408
Computer aided design (CAD), 320
Concentrated solar power (CSP) panels, 709
Concentrated solar power plant (CSPP), 1425
Conduction band (CB), 1336
Continuous direct light processing (CDLP), 324
Continuous fiber ceramic matrix composites (CFCMC), 914
Continuous fiber reinforced ceramic matrix composites, 844
Continuous liquid interphase printing (CLIP), 324
Conventional powder processing route, 937–939
Converse piezoelectric effect, 1082
Conversion reaction materials, 1327–1328
Co-precipitation, 1086
Co-precursor method, 126
CORAL, 699
Corrosion, 1467, 1471, 1472, 1474, 1477, 1479, 1481, 1482, 1484, 1487, 1492, 1501, 1502, 1504, 1517, 1519
 performance, 1496–1498
 resistance, 1417, 1438
Corundum, 361, 611
Crack
 arresting, 839
 branching, 839
 bridging, 839
 deflection, 839, 840
 propagation, 848, 862, 864
Cracking phenomenon, 697
C-rate, 1263
Crystallization of glass, 465–467
Crystallographic shear (CS), 770, 771
CSIR-National Aerospace Laboratories (NAL), 1086
Curie temperature, 780, 783
CVD-SiC coating, 1154
 parameters for mirror applications, 1155–1156, 1158
 and polished mirror blank, 1161
 properties, 1157–1159
 schematic diagram, 1156
Chemical vapor infiltration (CVI)
Czochevski technique, 1175
- D**
Darcy's law, 859
2D C/SiC composites, 850
 flexural strength, 852
 microstructure, 852
 thermal shock properties, 852–853
 typical weight pickup trend, 850, 851
 water jet cut, 852
Defense sector, PLZT ceramics
 energy harvesting applications, 242–243
 non-destructive testing, 244
 ring and stack actuators, 243
Deformation behavior
 C11b structured silicides, 1176–1181
 C40 structured silicides, 1181–1183
 Mo-Si-B based multiphase alloys, 1183–1184
 titanium silicides, 1184–1185
Delithiation process, 1315, 1328
Dense vertically cracked (DVC), 1397
Densification, 605, 608–610
 3Y-TZP, 633
 ZnO, 631
Density functional theory (DFT), 1339
Dental restoration, 340, 341
Dentistry, 345
Deposition efficiency, 1376
Depth of penetration (DOP) test, 383–388
Design of experiments (DOE), 842
Detonation spray, 1372
Detonation spray coating (DSC), 1466–1469, 1471, 1474, 1478, 1480, 1484, 1494
D Gun™, 1468
DICOR®, 488
Dielectric ceramics, BZT, *see* Barium zinc tantalate (BZT) ceramics
Dielectric resonator (DR), 806
 antenna, 199–202
 characteristics, 168–173
 filters, 204
 oscillators, 205
Die pressing, 365
Differential efficiency factor, 384
Differential thermal analysis (DTA), 41
Diffusion-controlled densification, 610
Diffusion creep, 1445
Digital light processing (DLP), 324
Dilatometric curve, ZnS, 544
Dinitrile polymers, 715
Diphenyldichlorosilane (DPDCS), 988
Direct current (DC), 1486
Direct foaming method, 1119–1120
Direct ink writing (DIW), 322, 335, 338
Direct laser microfusion (DLM), 323
Direct metal deposition (DMD), 1504
Direct normal irradiance (DNI), 1424
Direct piezoelectric effect, 1082
Direct write assembly, 322

- Dispersion fuels, 670
Donor additives/soft doping ions, 1084
3D Printing of Ceramics, 325, 328
Dry alumina (Al₂O₃) powder, 1226
Dry-powder pressing, 290
Differential thermal analysis (DTA)
Ductile backing laminate, 360
Ductile grinding, 573
Durofoam[®], 1059
3D workbench/printer table model, 343
Dyneema[®], 371
- E**
Eddy current (EC) methodology, 1032
E-glass, 416
Eglass-epoxy performance, 419
Elastic emission machining (EEM), 575–577
Electrical conductivity
 YDT, 742, 743
 YSZ, 742, 743
Electrical permittivity, 14
Electric current, 609, 632, 634
Electric double layer transistor (EDLT)
 device, 91
Electric field, 609, 613, 634
Electric field/current assisted sintering, 603
 flash sintering, 632–634 (*see also* Spark
 plasma sintering)
 water-assisted process, 631–632
Electrochemical double layer capacitor
 (EDLC), 1261, 1265, 1281
 charge transfer reactions in, 1272
 diffuse layer model/Gouy Chapman
 model, 1265
 energy density, 1272
 faradaic, 1288
 Helmholtz theory, 1265
 segmented arrangement of battery,
 1287–1288
 Stern-Grahame model, 1266
 total capacitance, 1266
 voltage scan rate, 1267
Electrochemical energy storage, 1261, 1264
Electrochemical exfoliation, 93
Electrochemical safe window (ESW), 1281
Electrochemical storage systems, 1298, 1299
Electrolyte additives, 1318
Electromagnetic (EM) radiation, 18
Electromagnetic interference (EMI) waves, 151
Electromagnetic radiation, 338
Electromagnetic shielding (EMS), 13, 16
Electron beam physical vapor deposition
 (EB-PVD), 1397, 1446, 1448, 1451,
 1453, 1456, 1467
Electronic sensors, 10
Electrophoresis, 297–299
Elemental doping, 1318
Emulsion templating, 1116–1119
Energy absorption, 143
Energy density, 1262, 1264, 1268, 1269, 1272,
 1274, 1277, 1284, 1290, 1292
Energy dissipation mechanisms, 409–411
Energy harvesting (EH)
 external power source, 1093
 force level, 1096
 PZT unimorphs, 1094
 quantum, 1093
 renewable energy, 1093
 set up, 1094
 span length and resonance
 frequencies, 1095
 vibration energy, 1094
 vibrator, 1095
Energy storage, hybrid supercapacitor-battery,
 see Supercapacitor
Engineering manufacturing industry, 340
Environmental barrier coatings (EBCs),
 903, 1445
 for carbon/carbon and ceramic matrix
 composites, 1023–1037
 on metals, 1037–1040
Epoxies, 266
Equipment based records, 336
Equivalent series resistance (ESR), 1268
Erosion
 liquid propellant, 868–871
 solid propellant, 868–870
Extrusion based printing method, 337, 339
Extrusion element, 343
Extrusion free forming (EFF), 323
Eye safe laser, 483
- F**
Faradaic materials, ISH
 aqueous electrolyte, 1274–1276
 organic electrolyte, 1276–1279
Fast breeder reactor (FBR), 753, 758, 762
Fast ceramics production (FCP), 324
Fast neutron reactors
 advanced fuels, 669
 advantages, 668
 features, 669

- Feeders, 344
 Ferrites, 1345–1346
 Ferroelectric polarization vs. electric field (*P-E*)
 hysteresis loops, 228–229
 Fiber/matrix bonding, 833, 836, 837, 839, 844,
 845, 848
 Fiber-reinforced plastic (FRP), 266–267, 1487
 Fibrous composites, 915
 Field assisted sintering technique (FAST), 514
 Field effect phototransistors, 102
 Figure of merit, 1137, 1138, 1140
 Filament winding techniques, 915
 Fine porosity, 1383, 1386, 1389
 Finite element modeling (FEM), 608
 Fire blocking blanket (FBB), 144
 Fission gas release, 696
 in helium and sodium bonded mixed carbide
 fuel, 690, 691
 and plenum pressure, 689
 Flame spray pyrolysis, 499
 Flash sintering, 518–523, 632–634
 Flash X-ray (FXR) systems, 389
 Flexural strength, 844
 UD C/SiC composites, T300 fibers, 845
 Flow CVI (FCVI), 883, 884
 Fluorescence based chemical sensors, 1431
 Fluorite, crystal structure, 742
 Fluoro-phlogopite, 485
 Foams based mirrors, 1142
 Focused ion beam (FIB), 1428
 Forced CVI (FCVI), 645, 646
 Foreign object damage (FOD), 1451
 Fourier's law, 1107
 Freeze casting, 1113–1116
 Fresh feed polishing, 573–574
 Friction systems, 905
 Fuel level sensors, 1098
 Fuel reprocessing, 697–700
 Functionally graded coatings, 1374, 1401
 Furnace cycling test (FCT), 1448, 1449
 Fused deposition modelling, 343
 Fused deposition of ceramics (FDC), 323
 Fused feedstock deposition (FFD), 323
 Fused filament fabrication, 335
 Fused silica ceramics and composites, 252–303
 Fusion reactors, SiC/SiC composites
 blanket structures, design, 656–657
 chemical compatibility, 660
 helium and hydrogen production, 659
 hermeticity, 661
 induced radioactivation and transmutation,
 657–659
 manufacturing and joining, 660–661
- G**
 Galvanic cell
 calcium hydride bromide electrolyte, 761
 with dissolved hydrogen concentration, 761
 Galvanostatic charging, 1316
 Gaseous heat conduction, 127
 Gelcasting, 1120–1123
 Gelcasting of fused silica radomes, 299
 Gibbs energy, 744, 745, 747, 748, 750, 751, 771
 Gibbs free energy, 539, 1225, 1271
 Glass-based mirrors, 1141
 Glass ceramics, 463
 armour systems, 448–449
 coefficient of thermal expansion, 476
 features, 463–464
 formation, 465–467
 machinable (*see* Machinable glass-
 ceramics)
 systems, 473–474
 transparent, 477–484
 Glass fibers, 367–368, 416
 Glass transition, 464–465
 Glenn Refractory Adhesive for Bonding and
 Exterior repair (GRABER), 1048
 Gouy Chapman model, 1265
 Grain size, 604, 605, 611–615, 618–621
 Graphene aerogel, 137
 Grignard reaction, 920
- H**
 Handgun bullets, 412
 Hard anodized (HA) coatings, 1492
 Hard carbon, 1324, 1325
 Hard dopants, 1085
 Healthcare segment, 341
 Heat collection element (HCE), 1426, 1430
 Helmholtz theory, 1265
 Heterocoagulation, 941, 942
 Heterogeneous nucleation, 469–470
 Hexavalent chromium-based conversion
 coating, 1417
 HfB₂–SiC–AlN composites, 1246
 High alkane phase emulsions (HAPES), 1117
 High energy mechano-chemical ball
 milling, 221
 High metal volume fraction (HMFV), 1428
 High-velocity oxy-fuel (HVOF) spray,
 1372, 1374
 High-velocity oxygen fuel (HVOF) spray,
 1466, 1468, 1470, 1473, 1475
 Hollow-core photonic bandgap fiber
 (HC-PBF), 10

- Homogenous nucleation, 467–469
- Hot corrosion, 1445
- Hot isostatic pressing (HIP), 512–514
refractory/transition metal boride ceramics, 722
- Hot-isostatic-pressure-impregnation-carbonization (HIPIC), 858
- High velocity oxygen fuel (HVOF) spray
- Hybrid powder-liquid feedstock processing
coating architectures, 1401
materials and functionality, 1403–1404
microstructure, 1402
- Hydridehalides
alkaline earth metal hydrides, structure and electrical conductivity, 755–757
hydrogen in liquid metals and alkaline earth hydridehalide, 758–761
hydrogen levels, in liquid sodium, 760–761
- Hydriding–dehydriding method, 679
- Hydrogenated vegetable oil, 1117
- Hydrolysis induced aqueous gelcasting, 299
- Hydrosilylation, 923
- Hydroxyapatite, 342, 625–626
- I**
- Infiltration-pyrolysis cycle, 841
- In-line transmission, 613
in Al_2O_3 , 614
AlON ceramics, 627
 MgAl_2O_4 , 623
 Y_2O_3 , 617
 Y_2O_3 -stabilized cubic ZrO_2 , 619
ZnS, 629
 ZrO_2 , 620
- Innovations, 342, 343
- In situ* polymerization, 1120
- Integral armour, 406
- Interdiffusion zone (IDZ), 1446
- Interface defeat, 376
- Inter laminar shear strength (ILSS), 379, 843
- Internal parallel hybrid (IPH), 1286, 1292
bi-material electrode, charge storage process in, 1289
bi-material electrodes, capacitor with, 1289–1290
bi-material type $\text{Na}_3\text{V}_2(\text{PO}_4)_3@C/AC$ hybrid capacitor, half cell electrochemical performance, 1290–1292
faradaic and EDLC type materials, 1288
nano-structured composite/nano-hybrid capacitor, 1286–1287
segmented arrangement of battery and EDLC materials, 1287–1288
- Internal serial hybrid (ISH), 1274, 1292
 $AC/LiNi_{0.5}Mn_{1.5}O_4$ hybrid capacitor, 1281–1285
conducting polymers, 1275
electrode matching, in Li-HEC, 1279–1281
lead compounds, 1274–1275
 Li^+/Na^+ ion insertion (battery) type, 1275–1276
organic electrolyte, 1276–1279
salient features, Li-HECs, 1285–1286
transition metal oxides, 1274
- International Patent Classification (IPC), 326
- International thermonuclear experimental reactor (ITER), 657, 661
- Inter-splat voids, 1448
- Inverse spinel, 498
- Ion beam polishing, 586
- Ionic conductivity of spinel, 519
- Iron containing PCS (Fe-PCS), 916
- Iron oxide, 134
- Irradiation behavior
carbide fuels, 684–693
nitride fuels, 693–698
- Irradiation responses, of SiC/SiC composites, *see* SiC fiber-reinforced SiC (SiC/SiC) composites
- Isostatic pressing, 365
- Isothermal-isobaric CVI (ICVI), 883
- Isothermal oxidation behavior, 1229–1232
mass variation with time, 1232–1234
oxidation scale, 1234–1239
- Isothermal thermogravimetric test, 1232
- Isovalent additives, 1084
- J**
- Jahn-Teller distortion, 1310, 1317
- Jetting/material jetting technology, 323
- Joining, SiC/SiC composites, 660–661
- K**
- Kevlar fibers, 416
- Kinetic energy threats, 382
- Kinetic heat simulation (KHS) test, 1033, 1055, 1058, 1059
- Kinetics of crystallization, 470–473
- Knoop hardness, zinc sulphide ceramics, 550

L

- Laminate fabrication process, 374
- La-PNS-PZT powder processing
 - binder addition and granulation, 47
 - electroding, 49
 - forming, 48
 - lapping, 49
 - microstructural analysis, 49
 - poling, 50
 - sintering, 48
- Large area maskless photopolymerization (LAMP), 324
- Laser cladding, on titanium alloys, 1502–1517
- Laser flash technique, 1384, 1387, 1388
- Laser glasses, 571
- Laser polishing, 585–586
- Laser sintering based AM process, 339
- Layered coatings, 1403
- Lead-bismuth eutectic (LBE) alloy, 746–747
- Lead free piezo materials, 1087, 1088
- Lead titanate (PT), 1082
- Lead zirconate (PZ), 1082
- Lead zirconate titanate (PZT), 37
 - advantages, 1082
 - aerospace, 1096
 - aircraft structures, 1097
 - bimorphs and unimorphs, 1090
 - ceramics, 10
 - crystals, 1083
 - donor and acceptor type dopants, 1082
 - dopants properties, 1084–1086
 - EH, 1093–1096
 - fuel level sensors, 1098
 - MAVs, 1098, 1099
 - ML stacks, 1091, 1093
 - MPB, 1083
 - piezoelectricity, 1083, 1086, 1087
 - preparation, 1090
 - structure, 1083
- $\text{Li}_4\text{Ti}_5\text{O}_{12}$, 1325
- LiCoO_2 , 1309–1310
- LiFePO_4 , 1320–1321
- Light scattering, 478–479
- Lightweight ceramics, 979, 1011
 - cellular ceramics/ceramic foam, 1051–1057
 - ceramic honeycomb, 1057–1058
 - ceramic sandwich structures, 1058–1061
 - CMC shingles, 1061–1062
- Lightweighting, 1137, 1142, 1147–1148
- Light weight mirror, 154
- Li-intercalation assisted exfoliation, 93
- Li-ion batteries, 106
- LiMnPO_4 , 1321
- LiMO_2 , 1308
- $\text{Li}(\text{Ni}_{1-x-y}\text{Co}_x\text{Al}_y)\text{O}_2$, 1313–1314
- $\text{LiNi}_{1-x-y}\text{Co}_x\text{Mn}_y\text{O}_2$, 1310–1313
- Liquid/solvent exfoliation, 92
- Liquid feedstock plasma spraying
 - hybrid powder-liquid feedstock processing, 1398–1404
 - SPPS, 1389–1398
 - SPS, 1375–1389
- Liquid phase sintering (LPS), 365, 650, 651
- Liquid silicon infiltration (LSI) based C/SiC composite fabrication, 859, 867
 - advantages and limitations, 858
 - coal tar pitch, 857
 - CTE, 864–867
 - CVD process, 858
 - general process scheme, 857
 - liquid propellant, erosion, 868–871
 - manufacturing process, 854
 - mechanical properties, 860–864
 - oxidation, quartz lamp heating, 867–869
 - silicon infiltration, 858
 - solid propellant, erosion, 868–870
 - thermal diffusivity, 863–864
- thermosetting resin based, 857
 - typical pore size distribution, 855, 856
 - XRD spectra, 854, 855
- Lithiation process, 1315, 1328
- Lithium hybrid electrochemical capacitor (Li-HEC), 1276
 - as battery type negative electrode, 1278–1279
 - as battery type positive electrode, 1277–1278
 - capacitance, 1283
 - current matching, 1280
 - energy density, 1284
 - estimation, 1282
 - potential matching, 1281
 - power density, 1284
 - salient features, 1285–1286
- Lithium ion battery, 1269, 1298
 - anode materials, 1321–1326
 - anode reaction, 1270
 - cathode materials, 1307–1321
 - cathode reaction, 1271
 - cell characteristics, 1299–1303
 - conversion reaction materials, 1327–1328
 - cost break down, 1305
 - energy density, 1308
 - Gibbs free energy, 1271
 - layered transition metal oxide, 1307–1317
 - materials cost break down, 1305–1306

- Lithium ion battery (*cont.*)
 overall reaction, 1271
 phospho-olivine, 1319–1321
 processing steps, 1303–1305
 spinel, 1317–1319
- Lithium titanium oxide, 1325–1326
- Lithium transition metal layered oxide, 1307
 LiCoO_2 , 1309–1310
 $\text{Li}(\text{Ni}_{1-x-y}\text{Co}_x\text{Al}_y)\text{O}_2$, 1313–1314
 $\text{LiNi}_{1-x-y}\text{Co}_x\text{Mn}_y\text{O}_2$, 1310–1313
 lithium rich layered oxide, 1316–1317
 properties of electrode materials, 1306
- Lithography based ceramic manufacturing, 324
- Low Earth orbit (LEO), 1011, 1013, 1042, 1043
- Lower hybrid current drive (LHCD), 795
- Lower thermal conductivity, TBC, 1456–1460
- Low expansion glasses, 572
- Low metal volume fraction (LMVF), 1428
- Low pressure plasma spray (LPPS), 1175, 1446
- M**
- M40J fiber based UD C/SiC composites,
 846–849
- Machinable glass-ceramics, 485
 BIOVERIT[®], 490
 DICOR[®], 488
 MACOR[®], 487–489
 preparation method, 490
 with alkaline phlogopite phase, 485–486
 with non-alkaline phlogopite phases, 489
- Mach-Zehnder interferometer, 11, 12
- MACOR[®], 487–489
- Magnesia rich spinel, 498
- Magnesium aluminate, 622–624
- Magnesium aluminate (MgAl_2O_4) spinel, 496
 armour, 452–454
 characterisation, 523–525
 crystallography, 498
 flash sintering, 518–523
 phase diagram, 498–499
 powder for transparent ceramic applications,
 502–504
 powder production, 499–502
 properties, 497
 shaping and densification, 503–509
 slip casting, 509–514
 spark plasma sintering, 514–518
- Magnetic ferrite nanoparticles, 142
- Magnetic permeability, 14, 15
- Magnetorheological finishing (MRF), 577–585
- Mechanical activation (MA)
 Man-portable air defense system
 (MANPADS), 151
 Mass gain, 1228
 Materials science, 6
 Mechanical activation (MA), 43, 221
 crystal structure, 52
 electrical output, 62
 electromechanical properties, 54–56
 high energy ball milling, 44
 microstructure, 53
 particle morphology, 46
 Mechanical behavior, 1176
 C11b structured silicides, 1177–1181
 C40 structured silicides, 1181–1183
 flexural strength and fracture behavior,
 1186–1195
 Mo-Si-B based multiphase alloys,
 1183–1184
 niobium silicide based multiphase alloys,
 1185–1186
 titanium silicides, 1184–1185
 Mechanical exfoliation, 92
 Mechanical properties, of SiC/SiC composites,
 646, 648, 652, 654–655, 662
 Mechanical strength, 606, 618, 622, 628
 Medical industry, 340
 Melt foaming method, 1127
 3-Mercaptopropyltriethoxysilane
 (MPTES), 1422
 Mescall zone, 376
 Mesocarbon microbead massive artificial
 graphite, 1324
 Metal
 ferrites, 1345–1346
 sulphides, 1352–1353
 titanates, 1340–1341
 tungstates, 1348
 vanadates, 1348–1352
 Metal-dielectric composite coatings, 1427
 Metal fuels, 670, 693
 Metal-glass based composites, 336
 Metal matrix composite (MMC) cermet
 coating, 1504
 Metal oxide aerogels, 132–134
 Metamaterial based antennas, 200–202
 Metamaterials, 7
 MgO , 620–621
 Mica, 485
 Micro arc oxidation (MAO) coating,
 1484–1486
 applications, 1502
 corrosion performance, 1496–1497
 fatigue performance, 1498–1501

- formation, 1488–1492
 - technological elements, 1486–1487
 - tribological performance, 1492–1496
 - Microbotic deposition, 322
 - Microstrip antennas, 197
 - Microstructure
 - hybrid powder-liquid feedstock processing, 1401–1402
 - of polycrystalline ceramics, 604, 605
 - solution precursor plasma spraying, 1392–1397
 - suspension plasma spraying, 1379–1381, 1383
 - Microwave sintering of BZT, 807
 - crystal structure and ordering, 813–815
 - densification, 808–809
 - microstructural analysis, 809–812
 - microwave dielectric properties, 812–813
 - Raman spectroscopic studies, 815
 - Microwave sintering, 723
 - Mie theory, 620
 - Military and aerospace applications
 - dielectric inks/paints, 177–178
 - EMI shielding materials, 191–197
 - HTCC and LTCC substrate packages, 173–176
 - ultra-low temperature co-fired ceramic packages, 177
 - Mirror blanks, space optics
 - carbon fiber reinforced polymers, 1142
 - foams based mirrors, 1142
 - mechanical properties, 1137–1138
 - metallic mirrors, 1140
 - monolithic glass and glass-ceramic mirrors, 1141
 - requirements, 1138–1139
 - silicon carbide mirrors, 1141–1142
 - thermal properties, 1138
 - Modulus of rupture (MOR), 745
 - Molten carbonates, carbon potentials, galvanic cells, 775–777
 - Molten salt electrolysis method, 715
 - Molten silicon, 853, 854, 858
 - Molten silicon infiltration (MSI), 879, 882, 887–888
 - Molybdenum disulfide
 - biomedical applications, 112
 - catalysis and energy storage, 92–94
 - chemical exfoliation, 92–94
 - crystal structure, 80
 - electronic band structure, 81–82
 - electronic devices, 97
 - environmental applications, 110
 - hydrothermal routes, 96
 - lubrication, 106–108
 - magnetic properties, 89–90
 - mechanical behavior, 85
 - mechanical exfoliation, 92
 - memory devices, 102
 - microstructure, 83
 - optical properties, 88
 - optoelectronic devices, 97
 - oxidation behavior, 87
 - phase stability, 84–85
 - piezoelectric coefficient, 88
 - sensors, 102–104
 - sulfurization, 95–96
 - superconductivity, 90
 - thermoelectric behavior, 87
 - thermolysis, 96
 - tribological properties, 86
 - vapor deposition, 94
 - Molybdenum nitride (Mo_2N), 772
 - Molybdenum silicides, 1169–1172
 - oxidation behavior, 1198–1206
 - Molybdenum trioxide (MoO_3)
 - crystallographic shear, 770, 771
 - crystal structure, 770
 - electrical conductivity and gas sensing characteristics, 771
 - sensing characteristics, 771–772
 - Monolithic aerogels, 139
 - Monolithic SiC, 833, 839
 - Morphotropic phase boundary (MPB), 781, 1084, 1086
 - Mullite/Yttrium silicate multilayer coating, 902
 - Multi-jet fusion (MJF), 323, 338
 - Multilayer absorbers, 1426
 - Multilayer ceramic capacitors (MLCC), 799
 - Multilayered coating system, 1388
 - Multiphase jet solidification (MJS), 323
 - Multiple hit resistance, 429–430
 - Multi-step spark plasma sintering, 630
 - Multi-walled nanotubes (MWCNTs), 939, 941, 943, 946, 949, 952, 954, 956, 958, 962, 968
- N**
- Nanocomposite(s), 14, 17, 21, 28
 - coatings, 1404
 - Nanocontainers, 1417, 1418
 - Nanofilled composites, 427
 - Nano-hybrid capacitor (NHC), 1286–1287

- Nano-La-PNS-PZT-synthesis
 HRTEM, 46
 mechanical activation, 43
 NiSb₂O₆ and TG-DT analysis, 40–43
 process flow chart, 41
 progressive phase formation, 44–46
- Nanomaterials, advanced sensor development,
 defence applications, *see* Sensor
 development, defence applications
- Nanoporous aerogels
 as adsorbent and purifier for toxic gases, 148
 artificial muscles for robots, 153
 carbon aerogels, 137–139
 composites, 140
 core-shell aerogels, 134
 dielectric materials, 154
 as energy absorber, 142–143
 energy storage devices, 152–153
 for environmental remediation, 149–150
 granules, 139
 infrasound detection, 152
 metallic aerogels, 134
 metal oxide aerogels, 132–134
 microelectromechanical systems, 152
 mirror substrate, 154
 monolithic aerogels, 139
 organic aerogel, 135–137
 radar antennas, 154–155
 self-cleaning surfaces, 152
 sensors, 151
 silica aerogel, 125
 for storage, 148
 synthesis, 125
 thermal insulation, 143–147
- Nano-powder infiltration and transient
 eutectoid (NITE), 650, 661
- Negative permittivity, 17
- Nernst equation, 743, 760, 763, 776
- Neutron capture therapy, 705
- Neutron irradiation, 651–653, 656, 659, 662
- Niobates, 773–775
- Niobia aerogels, 133
- Niobium pentoxide (Nb₂O₅), 773
- Niobium silicides, 1173–1174, 1212
 mechanical behavior, 1185–1186
 oxidation behavior, 1207–1211
- Nitride(s), 1353–1354
 nitrogen potentials, measurement of,
 777–779
- Nitride fuel
 fission gas release, 695
 fuel processing, 697–700
 international experience, 697
 phase diagram, 681
 swelling, 694
 thermal conductivity, 682
- Nitroxyceram, 302–310
- Non destructive test (NDT), 244
- Non-isothermal oxidation behavior, 1226–1229
- Non-Oxide Adhesive eXperimental
 (NOAX), 1048
- Non-oxide ceramics, 345, 347
- Nontransparent fused silica glass, 289
- Non-woven fabrics, 372, 417
- Normalized differential efficiency, 385
- Normal spinel, 498
- Nucleation
 heterogeneous, 469–471
 homogenous, 467–469
- O**
- Ogive shape, 262–266, 299, 300, 311
- Open cellular ceramic foams
 applications, 1110
 compressive strength, 1109
 microstructure, 1107
- Optical fibers, 10, 12, 20, 21, 25, 28
- Optical glasses and glass ceramics, nano
 finishing
 abrasive slurry jet machining, 587–588
 atomic force microscope, 591
 chemical polishing, 574–575
 coherence correlation interferometry,
 593–594
 ductile grinding, 573
 EEM, 576–577
 float polishing, 575, 597–598
 fresh feed polishing, 573–574
 ion beam polishing, 586
 laser polishing, 585–586
 magnetorheological finishing, 577–585
 phase shift interferometry, 593
 plasma-assisted etching, 588
 scanning electron microscope, 591–592
 stylus profiler technique, 591
 test plate technique, 589–591
 white light interferometry, 592
- Optical path difference (OPD), 589, 590
- Optical spectral analyser (OSA), 11
- Opto-electric ceramic systems, for photo-
 electrochemical hydrogen energy
 black phosphorous, 1354–1358
 black TiO₂, 1341–1345
 ferrites, 1345–1346
 nitrides, 1353–1354

- sulphides, 1352–1353
 - titanates, 1340–1341
 - tungstates, 1346–1348
 - vanadates, 1348–1352
 - Organic-inorganic hybrid coatings, 1415
 - Original equipment manufacturer (OEMs), 345
 - Orthopaedics, 345
 - Orthopedic applications, 341
 - Osprey process, 1175
 - Oxidation, 1445
 - Micro arc oxidation (MAO)
 - quartz lamp heating, 867–869
 - Oxidation behavior, 1196–1198
 - molybdenum silicides, 1198–1206
 - niobium silicides, 1209–1211
 - titanium silicides, 1206–1208
 - Oxidation resistant coating
 - for carbon/carbon and ceramic matrix composites, 1023–1037
 - on metals, 1037–1040
 - Oxide(s)
 - based ceramic printing materials, 334
 - ceramic coatings, 1471–1476
 - fuel, 670, 692
 - non-oxide materials, 334
 - semiconducting, 749–755
 - solid electrolytes, 742–748
 - Oxide based ceramic printing materials, 334
 - Oxide ceramics, 345, 346
 - Al_2O_3 , 611–615
 - MgAl_2O_4 , 622–624
 - MgO , 620–621
 - Y_2O_3 , 615–617
 - YAG, 624–625
 - ZrO_2 , 617–620
 - Oxy-fluoride glass-ceramic system, 483
 - Oxy-fuel (OF) ratio, 1476
 - Oxygen vacancies, 1224, 1317
- P**
- Parabolic trough collector (PTC), 1425, 1426
 - Paraboloidal antenna, 253
 - Particle cracking, 1314
 - Particle stabilized foams, 1123–1124
 - Patenting trends
 - country/organization wise patents, 327–330
 - focus field-wise patents, 330–331
 - year-wise patents, 325–327
 - Patent landscaping, 331
 - Patinformatics, 330
 - Perhydropolysilazane (PHPS), 1039, 1040
 - Phase analysis and micro-structural characterization, 222–225
 - Phase change material, 146
 - Phase shift interferometry (PSI), 593
 - Phase transition behavior, 60
 - Phenol direct binding (PDB), 324
 - Phenomenological analysis of densification, 609
 - Phonon scattering, 1456
 - Phosphates, 767
 - $\text{Li}_{2-4x}\text{Zr}_{1+x}(\text{PO}_4)_2$ ($x = 0-0.45$), phase formation and electrical conductivity studies, 768–769
 - lithium activity measurements, sensor for, 769–770
 - Phospho-olivines, 1319
 - LiCoPO_4 , 1321
 - LiFePO_4 , 1320–1321
 - LiMnPO_4 , 1321
 - Photocatalytic (PC), 1336
 - Photo curing, 339
 - Photo electrocatalytic (PEC), 1336, 1337
 - Photomosaics of fuel pin cross sections, 690
 - Photonic crystal fibers (PCFs), 10, 25
 - Photopolymerization, 339, 344
 - Photo-voltaic (PV) device, 1424
 - Piezoelectric applications, 343
 - Piezoelectric barium titanate, 1083
 - Piezoelectric effect, 62
 - Piezoelectricity, 779
 - Piezoelectric materials, 10, 783–785
 - BZT, 1088–1090
 - lead free piezo materials, 1087, 1088
 - PZT powders, 1086, 1087
 - Piezoelectric strain, vs. electric field hysteresis loops, 236–238
 - Pitch lap, 575, 597–598
 - Plane strain fracture toughness studies, 553–554
 - Plasma-assisted etching, 588
 - Plasma cleaning mechanism, 344
 - Plasma electrolytic oxidation (PEO), *see* Micro arc oxidation (MAO) coating
 - Plasma spray, 1467, 1469, 1472, 1474, 1475, 1477, 1481
 - Plasma spraying, liquid feedstock, *see* Liquid feedstock plasma spraying
 - PLZT ceramics
 - in defense sector
 - energy harvesting applications, 242–243
 - non-destructive testing, 244
 - ring and stack actuators, 243
 - definition, 217

- PLZT ceramics (*cont.*)
 dielectric constant, 225–228
 for materials processing, 221–222
 temperature dependent electromechanical coupling factor, 241–242
- Polarization maintaining photonic-crystal-fiber (PM-PCF), 11, 13, 25, 26
- Poling, 49, 780
- Poling conditions
 constant, 231
 optimization, 220, 234
 of PLZT ceramics, 222
 for ultra-high piezoelectric properties, 229–236
- Poly(borodiphenylsiloxane) (PBDPS), 988
- Polyborosiloxanes, 917, 988–998
- Polycarbosilane (PCS), 840, 842, 845
 ceramization, 924
 chloromethylchlorosilanes, 922
 chlorosilanes, 922, 923
 cross-linking, 924
 electronic applications, 920
 hydrosilylation, 923
 organosilicon polymers, 917–919
 PSs, 919, 920
 ROP, 922
 shaping, 923
 SiC ceramics, 916
 silicon based preceramic polymers, 924
 silicon polymers, 916
 structural transformations, 925
 structure, 920
 Yajima strategy, 921
- Polycarbosilanes, 980–985
- Polydiacetylene, 149
- Polydimethylsilane (PDMS), 919
- Polyelectrolyte adsorption, 1112
- Polymer-ceramic composites, microwave substrate applications, 178–183
- Polymer-derived ceramics (PDCs), for space applications
 atomic oxygen resistant coatings, 1042–1047
 ceramic adhesives, 1045–1051
 CMCs, 1012–1023
 lightweight ceramics, 1051–1062
 oxidation resistant/environmental barrier coatings, for carbon/carbon and ceramic matrix composites, 1023–1037
 oxidation resistant/environmental barrier coatings, on metals, 1038–1040
 thermal barrier coatings, for metals, 1040–1043
- Polymer foam template method, 1112–1113
- Polymer impregnation and pyrolysis (PIP), 649, 651, 661, 879, 881, 886–887
- Polymer impregnation and pyrolysis (PIP) based C/SiC composite fabrication
 advantages, 841
 composite density, 843
 2D C/SiC composites, 850–853
 disadvantages, 841
 DMSRDE, 840
 fiber volume fraction, 843
 flexural strength of UD C/SiC composites, T300 fibers, 845
 interlaminar shear strength, 844
 M40J fiber based UD C/SiC composites, 848–849
 mechanical characterization, 843–844
 polycarbosilane, softening point, 842
 pyrolysis temperature, 843
 scheme of investigation, 842
 tensile strength of UD C/SiC composites, T300 fibers, 845–848
- Polymer infiltration and pyrolysis (PIP), 916, 1005, 1013, 1017, 1018, 1020, 1021, 1053, 1055, 1060
- Polymerization, 324
- Polymer pyrolysis technology, 915
- Polymer-to-ceramic conversion (ceramization), 924
- Polymetalborosiloxanes, 1000–1001
- Polymetallosiloxanes, 998–1000
- Poly-methyl-metha-acrylate (PMMA), 21, 22
- Polymethylsilane (PMS), 649
- Poly(methylsiloxane)s, 1422
- Poly para phenylene terephthalamide polymer, 369
- Poly propylene (PP), 1487
- Polysilanes (PSs), 919, 920, 980–985
- Polysilazanes, 1001, 1002, 1004, 1006, 1026, 1029, 1040, 1044, 1059
- Polysiloxanes, 918, 985, 986, 1000, 1019, 1026, 1038, 1040, 1044, 1053, 1054, 1063
- Polysilsesquioxanes, 985, 986, 999, 1019, 1042, 1044, 1064
- Poly(tetramethyldisilylene-co-styrene) (PTMDSS), 1044, 1045
- Polytypism, 362
- Poly(vinylidene fluoride) (PVDF), 14, 17, 1437
- Polyvinylsilane (PVS), 649
- Post clad heat treatment (PCHT), 1513
- Powder bed fusion, 323, 338
- Power density, 1262, 1264, 1268, 1269, 1272, 1284, 1285, 1290, 1292, 1293, 1303

- Power harvesting, 61
 evaluation, 62
 module, 65–66
- Pre ceramic polymers, 915–919, 980
 AFCOP, 1009–1011
 carbonaceous polymers, 1007–1009
 silicon containing polymers, 980–1007
- Precipitation, 1454
- Preforming process, 836, 837
- Pressing, 364–365
- Pressureless sintering, 717
- Pressure transducer, 5
- Projectile penetration efficiency, 388
- Protective areal density method, 393–394
- Pseudocapacitor, 1267–1268
- Pulsed CVI (PCVI), 883
- Pulsed electric current-assisted sintering (PECS), *see* Electric field/current assisted sintering
- Pulsed electric current sintering (PECS), 514
- Pulverisation, 410
- Pure cellulose nanocrystal (CNC)
 synthesis, 135
- PUREX process, 699
- Purple sand mud material, 334
- Lead zirconate titanate (PZT)
- Q**
- Quantum confinement effect, 82
- Quarter-wave regarding antireflection coating application, 559
- Quasi elastic neutron scattering (QENS), 509
- Quasi-static damage, 376
- R**
- Radar frequency (RF) seeker, 253
- Radar-guided missiles, 255
- Radar waves, 13
- Radial confinements, 385
- Radiation sensors, 1435
- Radio frequency (RF) window, 797
 application, 797–799
 fabrication, 824–825
 high dielectric constant, 796
 high mechanical strength, 797
 high thermal conductivity, 796
 low dielectric loss/high quality factor, 795–796
 temperature stability and high dielectric strength, 796
- Radomes
 advantages and disadvantages, 272
 alumina, 271
 beryllium oxide and boron nitride, 277
 bore-sight error, 258–262
 ceramics for hypervelocity applications, 267–277
 comparative properties of ceramic materials, 268, 279
 construction material, 256
 description, 253
 glass and fiber-reinforced plastics, 266–267
 materials for high performance aircraft and missiles, 266
 monolithic half-wave radome wall thickness, 264, 265
 nose shapes, 260
 prerequisite properties of material used, 256, 257
 silicon nitride and silicon aluminum oxynitride, 277
- Sitall, 273
- slip-cast fused-silica ceramics, 274–277
 (*see also* Slip-cast fused-silica (SCFS) radomes)
 surface temperature, 283, 284
 tangent Ogive shape derivation, 262–266
 thermal stress, 283–285
 wall structure, 264
- Ragone plots, 1262
- Raman spectroscopic studies, 815
- Rare earth metal borides, 724
 consolidation, 727
 properties and applications, 725–726
 synthesis, 726–727
- Ratcheting, 1450
- Rate-controlling mechanism, 610
- Rayleigh scattering, 478, 480
- Rayon based fibers, 835
- Reaction bonded boron carbide, 363
- Reaction bonded silicon carbide, 362
- Reaction bonding, 366
- Reaction sintering (RS), 649
- Reactive melt infiltration (RMI), 853, 882
- Reactive oxygen species (ROS), 1422
- Reactive plasma spraying (RPS), 714
- Reactive sintering temperature
 crystal structure, 55
 electromechanical properties, 58–59
 microstructure, 57–58
- Reflection, 437
- Refractory/transition metal boride ceramics
 chemical reactions involved in synthesis, 710–711
 chemical vapour infiltration, 724
 densification/consolidation, 716–724

- Refractory/transition metal boride ceramics
(*cont.*)
 displacement reactions, 716
 hot isostatic pressing, 722
 hot pressing, 717–720
 laser sintering, 724
 microwave sintering, 723
 molten salt electrolysis method, 715
 oxide reduction method, 712–715
 polymeric precursor method, 715
 pressureless sintering, 717
 properties and applications, 706–709
 solid state reaction method, 710–712
 solution based methods, 715
 spark plasma sintering, 720–722
- Reinforced carbon/carbon (RCC)
 composite, 1048
- Residual strength, 428
- Residual velocity test, 389–390
- Resin transfer molding (RTM), 881, 916
- Reticulated ceramic foams
 compressive strength, 1109
 microstructure, 1107
 preparation, 1112
- Ring opening polymerization (ROP), 922
- Robocasting (RC), 322
- Rolled homogeneous armour, 409
- Rolled homogeneous armour, 360, 394, 397
- Rotating electrode process, 1175
- Rubber-ceramic composites, flexible and stretchable applications, 185–189
- Russian nitride programme, 697
- S**
- Sacrificial template method, 1113
- Sagnac interferometer, 11
- Sapphire (single crystal alumina) transparent polycrystalline armour, 449–450
- Satellite test of equivalence principle (STEP), 148
- Scanning electron microscopy (SEM), 49, 225
- Scratch resistant coatings, on transparent plastics, 1420–1422
- Secondary electron emission (SEE), 797
- Selective laser melting (SLM), 323, 338
- Selective laser sintering (SLS), 323, 338, 339
- Self-healing coatings, 1417, 1418
- Semiconducting oxides, 749
 electrical properties, 751–753
 oxygen chemisorptive property of, 750
 sensors, selectivity and sensitivity, 753–755
 thermodynamic characteristics, 750–751
- Semi-infinite backing test method, 388–389
- Scanning electron microscopy (SEM)
- Sensor development, defence applications
 challenges, 27
 high frequency detections, 13–17
 low electric and magnetic field detections, 25
 low frequency detections, 9–12
 low (ppm/ppb) concentration detections, for CBW diagnostics, 17–24
 strategic requirements, 7–9
- Shear waves, 408
- Short beam shear (SBS) test, 844
- SiC fiber-reinforced SiC (SiC/SiC) composites
 basic properties, 650–651
 CVI, 644–649
 fusion reactors, 656–661
 LPS, 650
 mechanical properties, 654–655
 PIP, 649
 RS, 649
 swelling, 653–654
 thermal conductivity, 652–653
- SiC fibers, 915
- SiCO based photosensitive, 336
- Side wall leading edge (SWLE), 1035
- Signal-to-noise ratio (SNR), 1431
- Silica aerogel, 125
 nanoporous structure, 127
 organic precursors, 126
 refractive index, 130
 SEM, 127
 sol-gel technique, 126
 insulating materials, 129
- Silicides and silicide matrix composites
 applications, 1210–1212
 C11b structure, 1177–1181
 C40 structure, 1181–1183
 flexural strength and fracture behavior, 1186–1195
 ingot metallurgy processing methods, 1175
 molybdenum, 1169–1172, 1198–1206
 Mo-Si-B based multiphase alloys, 1183–1184
 niobium, 1173–1174, 1186, 1207–1211
 non-equilibrium processing, 1175
 titanium, 1170–1173, 1184–1185, 1206–1208
 tungsten, 1170
- Silicon aluminum oxynitride, 277
- Silicon-based preceramic polymers, 840, 917, 918, 924
- Silicon carbide, 338, 346, 362

- Silicon carbide mirror blanks, 1141–1142
flow sheet diagram for processing, 1143–1144
- Silicon containing polymers, 980–981
polyborosiloxanes, 988–998
polymetalborosiloxanes, 1000–1001
polymetallosiloxanes, 999–1000
polysilanes and polycarbosilanes, 980–985
polysilazanes and polycarbosilazanes, 1001–1002
polysiloxanes and polysilsesquioxanes, 985–987
SiBCN ceramics, 1002–1006
SiCN ceramics, 1006–1007
- Silicone resins, 266
- Silicon nitride (Si_3N_4), 277, 338, 346
- Silicon polymers, 916
- Silver halides
conductivity of AgI, cationic and anionic substitution on, 762–763
as sensors for halogens, 763–765
structure, 762
- Silver molybdates, 772–774
- Single-edged notched beam (SENB), 949, 951
- Single-edged V-notched beam (SEVNB), 950, 952, 968
- Single mode fiber (SMF), 10, 13
- Single-wall carbon nanotubes (SWCNTs), 936, 938, 939, 949, 951, 953, 960, 961
- Sintered SiC substrates
aspheric profile, 1149–1150
double logarithmic Weibull function vs. logarithm of four-point bending strength, 1154
fracture surface, 1153
green machining, 1147–1148
low temperature heat treatment, 1146–1147
properties, 1150
raw materials and green forming, 1144–1146
sintering, 1148–1149
thermal conductivity, 1153
Weibull statistics and reliability, 1151–1154
X-ray diffraction, 1151
- Sintering, 48, 365, 510–512, 1148–1149, 1454–1455
thermal evaporation deposition techniques, 914
- $\text{SiO}_2/\text{Si}_3\text{N}_4$ -BN composites
ablation test, 309
SEM microstructure, 309, 310
- Sitall ceramics, 271, 273
- Slip-cast fused-silica (SCFS) radomes, 274–277
advantages, 289
characteristics, 277–287
coefficient of linear thermal expansion, 281
composites, 301–302
damage dependence vs. drop load, 283
dielectric constant vs. temperature, 278
electrophoresis, 297–299
fabrication, 290
gelcasting, 299
hydrolysis induced aqueous gelcasting, 299
loss tangent vs. temperature, 278, 279
precursor powders, slips and plaster molds, 293
pressure casting effect on wall thickness, 295–297
pressure slip-casting, 291, 292
properties, 252–294
properties of precursor slips and cast preforms, 293, 294
rain erosion property, 280
raw material resources, 287–290
resistivity vs. temperature, 292
sintering regime parameters, 293, 294
spectroscopic analysis of fused silica grains, 291, 293
surface passivation to seal porous structure, 300–301
tan δ variation with porosity and moisture absorption capacity, 282, 283
thermal conductivity, 291
thermal shock-properties, 279
viscosity change with temperature, 288, 289
molten-cast fused-silica, 291
- Slip casting, spinel powder
densification, 510–514
with higher solid loading, 509–510
- Smart sensors, 5, 8, 17
- Soda-lime glass (SLG), 442
- Sodium aluminates, 765–767
- Sodium cooled fast reactor (SFR), 670
- Sodium oxide aerosol, sensor, 766–767
- Soft armour, 405
- Soft carbon, 1324
- Solar selective coatings (SSC), 1426, 1428, 1430
- Solar-to-hydrogen (STH) conversion rates, 1345
- Sol-gel based processing, 942–945
- Sol-gel nanocomposite coatings
aerospace sector, 1417–1424
ceramic radomes/IR windows, functional coatings, 1435–1437

- Sol-gel nanocomposite coatings (*cont.*)
 chemical/biological agent, sensors for
 detecting, 1431–1435
 energy sector, 1424–1430
 radiation sensors, 1435
- Sol-gel process, 985, 988, 990, 993, 995, 998,
 1000, 1001, 1007, 1020, 1025, 1031,
 1044
- Sol-gel reaction, 125, 126
- Solid heat conduction, 129
- Solid oxide electrolyte, 742
 chemical compatibility with liquid sodium,
 744–745
 electrical properties, 742–743
 electrolytic domain boundaries, 743–744
 in-sodium oxygen sensor, YDT, 746
 lead and LBE, 746–747
 sodium, oxygen levels, 744
 thermochemical properties, 747–748
 thermomechanical properties, 745–746
- Solid rocket motor casing, 144
- Solid-state sintering, 365
- Solution precursor plasma spraying (SPPS),
 1374, 1375, 1391, 1393, 1394
 benefits, 1390
 materials and functionality, 1397–1398
 microstructure, 1393–1397
 processing, 1390–1392
 YSZ coatings, 1391, 1394, 1396
- Sonar waves, 10
- Spark plasma sintering, 514–518
 advantages, 604
 Al_2O_3 , 611–615
 aluminum nitride ceramics, 627–628
 aluminum oxynitride, 626–627
 apparatus, 606–608
 flash sintering, 632–634
 historical background, 610–611
 hydroxyapatite, 625–626
 magnesium aluminate spinel, 622–624
 mechanism of densification, 608–610
 MgO ceramics, 620–621
 multi-step, 630
 operating parameters, 629
 refractory/transition metal boride ceramics,
 720–722
 water-assisted process, 631–632
 Y_2O_3 , 615–617
 YAG, 624–625
 zinc sulfide, 628–629
 zirconia ceramics, 617–620
- Specific capacitance, 1269, 1282, 1283, 1291
- Specific capacity, 1268
- Specific energy/energy density, 1264
- Specific power/power density, 1264
- Spectra[®], 371
- Sphalerite, 535
- Spinel, 1317–1319
- STANAG 4569 test standard, 398
- Standard Tessellation Language (STL), 321
- Steady-state thermal figure of merit, 1138
- Steel confinement, 384
- Stereolithography (SL), 324, 335
- Steric stabilization, 1112
- Stern-Grahame model, 1266
- Stress-extension curve, 845, 847
- Stress-strain curve, 845
- Sucrose, 1124
- Sulphides, 1352–1353
- Super/Hyper-Sonic Transport Propulsion
 (HYPER) project, 643
- Supercapacitor, 106
 definition, 1263
 EDLC, 1265–1267
 electrochemical measurement, 1268–1269
 pseudocapacitor, 1267–1268
- Superhydrophobic coatings, 1418, 1420
- Superhydrophobic silica aerogels, 149
- Superhydrophobic surfaces, 152
- Surface engineering strategies, 1309
- Surface passivation of spinel powder, 503
- Surface plasmon resonance (SPR), 17
 effect, 1428
- Surface roughness, 1141, 1143, 1154
- Surface-to-air missiles, 253
- Surfactant, 1119
- Suspension plasma spraying (SPS), 1373,
 1375–1376, 1379
 materials and functionality, 1381–1389
 microstructure, 1379–1381, 1383
 processing, 1376–1379
- ## T
- Tactical-technical characteristics
 airplanes and potential missile carriers, 254
 radar-guided missiles, 255
- Tapecasting technique, 1090
- Temperature-pressure-controlled reactor
 systems, 95
- Tensile strength, 844
 UD C/SiC composites, T300 fibers,
 845–848
- Test blanket modules (TBM), 657
- Tetraethoxysilane, 126
- Tetrasilic mica, 488

- Thermo gravimetric analysis (TGA)
- Thermal barrier coating (TBC), 1445, 1467
fracture toughness, 1459–1460
gradient TBCs, 1458
materials features for low k , 1457
for metals, 1040–1043
microstructural features for lower thermal conductivity, 1456
multilayered TBCs, 1458–1459
nanocrystalline TBCs, 1457–1458
primary function, 1447
SPPS, 1393
SPS, 1381, 1384, 1385, 1387
YSZ, 1447–1455
- Thermal conductivity, 897, 1381, 1384, 1387, 1388, 1397
of SiC/SiC composites, 652–653
- Thermal diffusivity, 863–864, 1138
- Thermal expansion coefficient, 1388
- Thermal gradient forced flow CVI (TGFCVI), 883, 884
- Thermally grown oxide (TGO), 1388, 1445, 1446, 1450, 1459
- Thermal meteoroid garment (TMG), 146
- Thermal protection systems (TPS), 979, 1011, 1013, 1032, 1035, 1037, 1042, 1048, 1051, 1055, 1058, 1061, 1065
- Thermal spray, 1467
applications, 1481–1484
APS, 1467
cermet coatings, 1476–1481
coating microstructure, 1469–1471
DSC, 1468–1469
HVOF spray, 1468
oxide ceramic coatings, 1471–1476
processing, 1175
- Thermo-foaming, 1124–1126
- Thermo gravimetric analysis (TGA), 41
- Thermolysis, 96
- Thermoplastic matrix, 373
- Thermoplastic polymer, 369
- Thermoset matrixes, 373
- Thermosetting resin, 857
- Three dimensional printing (3D printing)
aircrafts, 345
antibacterial property, 336
ceramics, 324, 331, 332, 334, 340, 341
clay material, 334
extrusion, 335, 337
fabrication, 347
low shrinkage, 336
MJF, 338
powder bed fusion, 338
principle, 320
ultralow temperature, 339
versatility, 341
- Ti incorporated PCS (Ti-PCS), 916
- Tin oxide, crystal structure, 749
- TiO₂-based photocatalytic coatings, 1397
- Tissue engineering, 341, 342
- Titanates, 779–785
SrTiO₃, 1341
TiO₂, 1341
- Titania, 133
- Titanium alloys, laser cladding, 1502–1517
- Titanium diboride, 363–364, 723
- Titanium silicides, 1170–1173
deformation behavior, 1184–1185
oxidation behavior, 1206–1208
- Transition metal chalcogenides (TMD), 1356
- Transmission-wavelength curves approach, 614
- Transparent armour
aluminium oxynitride (AlON) transparent polycrystalline armour, 450–452
characteristics, 436
commercial applications, 437
emerging transparent ceramic materials, 443–447
glass ceramics armour systems, 448–449
magnesium aluminate spinel armour, 452–454
mechanical properties, 439–441
sapphire (single crystal alumina) transparent polycrystalline armour, 449–450
traditional (soda-lime glass based) transparent armour and limitations, 442–448
typical system, 441
- Transparent glass-ceramics, 478
anomalous scattering, 480
in photonics, 483–484
theories of light scattering, 478–479
zero expansion, 481–482
- Transportable shelters, 145
- Triaxial weaving, 836
- Tribological properties, 932
of CNT-reinforced ceramic matrix composites, 953–957
- Tubular sensor, 766
- Tungstates, 1348
- Tungsten carbide, 346
- Tungsten disulfide
bio-medical applications, 112
chemical exfoliation, 92–94
crystal structure, 80
electronic band structure, 81–82

- Tungsten disulfide (*cont.*)
 electronic devices, 97
 environmental applications, 110
 lubrication, 106–108
 magnetic properties, 88–90
 mechanical behavior, 85
 mechanical exfoliation, 92
 memory devices, 102
 microstructure, 83
 optical properties, 88
 optoelectronic devices, 97
 oxidation behavior, 87
 phase stability, 84–85
 sensors, 102–104
 superconductivity, 90
 thermoelectric behavior, 87
 thermolysis, 96
 tribological properties, 86
 vapor deposition, 94
- Tungsten silicides, 1170
- U**
 UD C/SiC composites, M40J fiber, 846–849
 UD C/SiC composites, T300 fibers
 flexural strength, 845
 tensile strength, 845–848
- Ultra high molecular weight polyethylene
 fibers, 370–371
- Ultra-high temperature ceramics (UHTC), 706
- Ultrahydrophobic/superhydrophobic/icephobic
 coatings, 1418–1420
- Ultra-low temperature co-fired ceramic
 (ULTCC) technology, 177
- Ultra-wide band (UWB) technology, 198
- Uni-axial loaded tensile tests, 844
- Unidirectional (UD) fabrics, 372
- (U-Pu) carbides, 678
- (U-Pu) nitrides, 681
- Urania aerogels, 134
- Uranium free nitride fuels, 693
- URLIM software, 285
- V**
 Vacuum assisted resin transfer mould
 (VARTM), 375, 407
- Vacuum induction melting, 1175
- Valence band (VB), 1336
- Vanadates, 1348–1352
- Vanadium oxide aerogel, 133
- Vapor deposition techniques, 1427
- Vaporization, 1378
- Vapor-grown carbon fibers (VGCFs), 931
- Vat polymerization, 324
- Vickers hardness, 623
- Vickers indentation (VI), 949, 950, 958
- Vinyltriethoxysilane (VTES), 1422
- Viscous sintering, 365
- W**
 Wafer sensor, 766, 768
- Washburn equation, 859
- Water-assisted spark plasma sintering, 631–632
- Water-splitting (WS), 1336, 1338
- Weak interfaces, 837
- Wear, 1467, 1471, 1474, 1476, 1478, 1479,
 1481, 1483, 1484, 1492, 1494, 1496,
 1498, 1499, 1501, 1506, 1510, 1512,
 1517, 1519
- Weibull statistics, 839
- White light emitting diodes (WLEDs), 484
- Woven fabrics, 372, 417
- Woven preforms, 836
- Wurtz type coupling, 919
- X**
 X-aerogels, 137
- X-ray diffraction (XRD), 44–46, 802, 805, 814,
 815, 817, 819–821
- Y**
 Y₂O₃, 615–617
- Y₃Al₅O₁₂ (YAG), 624–625
- Yajima strategy, 921
- Young's modulus, 746
- Yttria doped thoria (YDT), 742, 745, 746
- Yttria stabilised zirconia (YSZ) TBCs
 extrinsic failures, 1451–1453
 growth of TGO, residual stresses and
 intrinsic failures, 1450–1451
 life prediction and prime reliance, 1455
 phase transformation, 1453–1454
 sintering, 1454–1455
 testing and characterisation, 1448–1449
- Yttria-stabilized-zirconia (YSZ), 742, 743, 747,
 748, 1376, 1387, 1389, 1391, 1393,
 1397, 1403

Z

- Z-direction fibers, 836
- Zerodur[®], 476, 481
- Ziegler-Natta polymerization method, 371
- Zinc sulfide (ZnS), 628–629
- Zinc sulphide ceramics, 533
 - anti-reflection coating, 559–562
 - compression strength, 551
 - CVDHT-ZS, 543–545
 - CVD processing, 539–543
 - density measurement, 547
 - erosion protective coating, 562
 - fabrication process, 536
 - flexural strength, 550
 - fractography, 557
 - hot isostatic pressing, 545–546
 - IR transmission measurements, 558–559
 - Knoop hardness, 550
 - microstructure analysis, 549–550
 - PHIP-ZS, 545–547
 - plane strain fracture toughness studies, 553–554
 - R-curves, 556–557
 - total fracture energy release rate, 554–556
 - transmission curves and the optical properties, 535
 - X-ray diffraction, 548
- Zirconia based dental implants, 342
- Zirconia ceramics, 617–620
- Zirconia-toughened alumina, 362
- Zirconium and hafnium diboride based ultra-high temperature composites, 1222
 - ablation properties, 1245–1251
 - arc jet test, 1244
 - creep, 1241–1244
 - cyclic oxidation, 1239–1241
 - isothermal oxidation behavior, 1229–1239
 - material design for protection against degradation, 1223
 - non-isothermal oxidation behavior, 1226–1229
 - oxidation under water steam, 1252
 - thermodynamics and kinetics of environmental degradation, 1224–1225
- Zwitterionic surfactant, 1120
- Zylon fibers, 416